Edited by
Michel Che and Jacques C. Védrine

Characterization of Solid Materials and Heterogeneous Catalysts

Related Titles

Mittemeijer, E. J. / Welzel, U. (eds.)

Modern Diffraction Methods

2012

ISBN: 978-3-527-32279-4

Deutschmann, Olaf (ed.)

Modeling and Simulation of Heterogeneous Catalytic Reactions

2011

ISBN: 978-3-527-32120-9

Schlücker, Sebastian (ed.)

Surface Enhanced Raman Spectroscopy

Analytical, Biophysical and Life Science Applications

2010

ISBN: 978-3-527-32567-2

de Jong, K. P. (ed.)

Synthesis of Solid Catalysts

2009

ISBN: 978-3-527-32040-0

Mizuno, N. (ed.)

Modern Heterogeneous Oxidation Catalysis

Design, Reactions and Characterization

2009

ISBN: 978-3-527-31859-9

Ozkan, U. S. (ed.)

Design of Heterogeneous Catalysts

New Approaches based on Synthesis, Characterization and Modeling

2009

ISBN: 978-3-527-32079-0

Leng, Y.

Materials Characterization

Introduction to Microscopic and Spectroscopic Methods

2008

ISBN: 978-0-470-82298-2

Ertl, G., Knözinger, H., Schüth, F., Weitkamp, J. (eds.)

Handbook of Heterogeneous Catalysis

8 Volumes

2008

ISBN: 978-3-527-31241-2

Reimers, W., Pyzalla, A. R., Schreyer, A., Clemens, H. (eds.)

Neutrons and Synchrotron Radiation in Engineering Materials Science

From Fundamentals to Material and Component Characterization

2008

ISBN: 978-3-527-31533-8

Niemantsverdriet, J. W.

Spectroscopy in Catalysis

An Introduction

2007

ISBN: 978-3-527-31651-9

Edited by Michel Che and Jacques C. Védrine

Characterization of Solid Materials and Heterogeneous Catalysts

From Structure to Surface Reactivity

Volume 1



WILEY-VCH Verlag GmbH & Co. KGaA

The Editors

Prof. Dr. Ing. Michel Che
Institut Universitaire de France and
Université Pierre et Marie Curie
Laboratoire de Réactivité de Surface
4, Place Jussieu
75252 Paris Cedex 05
France

Prof. Dr. Ing. Jacques C. Védrine
Université Pierre et Marie Curie
Laboratoire de Réactivité de Surface
4, Place Jussieu
75252 Paris Cedex 05
France

Please cite this document as follows:
M. Che, J. C. Védrine: Characterization of Solid Materials and Heterogeneous Catalysts - From Structure to Surface Reactivity, Page(s). 2012.
Copyright Wiley-VCH Verlag GmbH & Co. KGaA.
Reproduced with permission.

All books published by **Wiley-VCH** are carefully produced. Nevertheless, authors, editors, and publisher do not warrant the information contained in these books, including this book, to be free of errors. Readers are advised to keep in mind that statements, data, illustrations, procedural details or other items may inadvertently be inaccurate.

Library of Congress Card No.: applied for

British Library Cataloguing-in-Publication Data
A catalogue record for this book is available from the British Library.

Bibliographic information published by the Deutsche Nationalbibliothek
The Deutsche Nationalbibliothek lists this publication in the Deutsche Nationalbibliografie; detailed bibliographic data are available on the Internet at http://dnb.d-nb.de.

© 2012 Wiley-VCH Verlag & Co. KGaA,
Boschstr. 12, 69469 Weinheim, Germany

All rights reserved (including those of translation into other languages). No part of this book may be reproduced in any form – by photoprinting, microfilm, or any other means – nor transmitted or translated into a machine language without written permission from the publishers. Registered names, trademarks, etc. used in this book, even when not specifically marked as such, are not to be considered unprotected by law.

Composition Thomson Digital, Noida, India
Printing and Binding Strauss GmbH, Mörlenbach
Cover Design Design Formgeber, Eppelheim

Printed in the Federal Republic of Germany
Printed on acid-free paper

Print ISBN: 978-3-527-32687-7
ePub ISBN: 978-3-527-64533-6
ePdf ISBN: 978-3-527-64534-3
mobi ISBN: 978-3-527-64535-0
oBook ISBN: 978-3-527-64532-9

For our mentor Dr. Boris Imelik, and our Families

Contents

About the Editors *XIX*
List of Contributors *XXI*

Preface *XXVII*
Michel Che and Jacques C. Védrine
General Introduction *XXXI*
Michel Che and Jacques C. Védrine

Overview on Physical Techniques for Investigating Model Solid Catalysts *XLV*
Gerhard Ertl
Overview on Physical Techniques for Investigating Porous Catalysts *LV*
John Meurig Thomas

Volume 1

Part One Molecular/Local Spectroscopies *1*

1 Infrared Spectroscopy *3*
Frédéric Thibault-Starzyk and Françoise Maugé
1.1 Introduction *3*
1.2 Principles of IR Spectroscopy and Basic Knowledge for Its Use *3*
1.2.1 IR Light *3*
1.2.2 Matter–Radiation Interaction *4*
1.2.3 Spectrometry, Interferometry *4*
1.2.4 Limitations of and Problems with the Fourier Transform *6*
1.3 Experimental Considerations *7*
1.3.1 Technical Aspects of the Fourier Transform *7*
1.3.2 Practical Implementation *8*
1.3.2.1 Transmission Experiments, Quantitative Aspects *8*
1.3.2.2 Diffuse Reflection *9*
1.4 Use of IR Spectroscopy to Characterize Solids *11*
1.4.1 IR Spectrum and Structure of a Solid *11*

1.4.1.1 The Example of Zeolites *11*
1.4.1.2 Substitution of Metals in the Structure of Zeolites *13*
1.4.2 Activation: Cleaning the Sample to Observe Surface Sites *13*
1.4.2.1 Experimental Aspects *13*
1.4.2.2 Activation – Cleaning the Sample to Observe Surface Sites *14*
1.4.3 The Spectrum of OH Groups *17*
1.4.3.1 OH Groups on Alumina *18*
1.4.3.2 OH Groups in Zeolites *18*
1.4.4 Characterization of Acidity with Probe Molecules *20*
1.4.4.1 Brønsted Sites: Hydrogen Bonding and IR Spectroscopy *21*
1.4.4.2 Molecular Probes for Lewis Acidity *24*
1.4.4.3 Common Probe Molecules for Acidity *24*
1.4.5 Characterization of Basicity with Probe Molecules *32*
1.4.5.1 CO_2 as a Probe for Basic Sites *32*
1.4.5.2 Protic Molecules *33*
1.4.5.3 Methanol *33*
1.4.6 Probes for Supported Metal Catalysts *34*
1.4.7 Probes for Sulfide Catalysts *36*
1.4.8 Quantitative Analysis by Coupling IR Spectroscopy with Gravimetry *38*
1.5 Application to Surface Reactivity: *Operando* Spectroscopy *39*
1.5.1 Experimental Setup for *Operando* IR Spectroscopy and Reactions Conditions *40*
1.5.2 Examples of *Operando* IR Measurements *40*
1.6 Conclusion *45*
References *45*

2 Raman and UV-Raman Spectroscopies *49*
Fengtao Fan, Zhaochi Feng, and Can Li
2.1 Introduction *49*
2.1.1 Raman Spectroscopy *49*
2.1.2 FT-Raman Spectroscopy *51*
2.1.3 UV Raman Spectroscopy *53*
2.1.4 Resonance Raman Spectroscopy *53*
2.2 Characterization of Active Sites and Phase Structure of Metal Oxides *55*
2.2.1 Identification of the Active Species on Metal Oxides *55*
2.2.2 Phase Transformation in the Surface Region of Metal Oxides *56*
2.3 Characterization of Surface Metal Oxide Species on Supported Metal Oxides *59*
2.4 Electron–Phonon Coupling in Nanostructured Materials *63*
2.5 Characterization of sp^2 Carbon Materials *64*
2.6 Characterization of Transition Metal-Containing Microporous and Mesoporous Materials *67*
2.6.1 Identification of the Isolated Quadrivalent Transition Metal Sites in Microporous and Mesoporous Materials *67*
2.6.2 Identification of the Isolated Trivalent Transition Metal Sites in Microporous and Mesoporous Materials *69*

2.6.3 Identification of Extra-Framework Active Sites in Microporous and Mesoporous Materials *71*
2.7 Synthesis Mechanisms of Molecular Sieves *73*
2.7.1 Assembling Zeolites from Prefabricated Units *73*
2.7.2 Assembling Fe-ZSM-5 from Active Centers and Silicate Building Units *74*
2.7.3 A Real-Time Probing for the Crystallization Process: *In Situ* Raman Spectroscopy *76*
2.8 Conclusions *80*
References *81*

3 Electronic Spectroscopy: Ultra Violet-visible and Near IR Spectroscopies *89*
Friederike C. Jentoft
3.1 Introduction and Overview *89*
3.1.1 Scope *89*
3.1.2 History *89*
3.1.3 Overview *91*
3.2 UV–vis–NIR Spectra *93*
3.2.1 Spectra Representation *93*
3.2.1.1 Spectral Position of Absorption Features *93*
3.2.1.2 Intensity of Absorption Features *93*
3.2.2 Spectra Processing *98*
3.2.3 Transitions in Molecular Species *99*
3.2.3.1 Selection Rules *99*
3.2.3.2 Individual Molecules *99*
3.2.3.3 Composite Species: Metal Complexes *101*
3.2.4 Transitions in Extended Solid Structures *104*
3.2.4.1 Bandgaps *104*
3.2.4.2 Metallic Colloids: Localized Surface Plasmon Resonance *106*
3.2.5 Quantitative Analysis *107*
3.3 Experimental Considerations *108*
3.3.1 Instrumentation: Spectrometers, Sources, and Detectors *108*
3.3.1.1 Overview of Essential Instrument Components *108*
3.3.1.2 Instrument Selection Criteria for Measurements of Solids *110*
3.3.2 Optical Configuration and Cells for Controlled Environments *110*
3.3.2.1 Transmission Mode *111*
3.3.2.2 Cells for Use in Transmission Mode *111*
3.3.2.3 Diffuse Reflection Mode: Integrating Spheres *112*
3.3.2.4 Cells for Use with Integrating Spheres *113*
3.3.2.5 Diffuse Reflection Mode: Mirror Optics *115*
3.3.2.6 Cells for Use with Mirror Optics Attachment *116*
3.3.2.7 Diffuse Reflection Mode: Fiber-Optic Probes *117*
3.3.2.8 Cells for Use with Fiber-Optic Probes *118*
3.3.2.9 Combination of UV–vis–NIR with Other Techniques *119*
3.4 Formation and Alteration of Solids *120*

3.4.1 Precursor Analysis *120*
3.4.2 Solid Formation *121*
3.4.3 Characterization of Solids *122*
3.4.3.1 Isomorphous Substitution of Framework Cations in Zeolites *123*
3.4.3.2 Ion Exchange in Zeolites *124*
3.4.3.3 Dispersion of Supported Metal Oxide Species *125*
3.4.3.4 Bandgap Determination in Semiconductors *125*
3.4.3.5 Spatially Resolved Spectroscopy of Specimens with Compositional Variation on the Millimeter Scale *127*
3.4.3.6 Spatially Resolved Spectroscopy of Specimens with Compositional Variation on the Micrometer Scale *127*
3.4.4 Probing of Surface Properties *129*
3.4.5 Dynamic Experiments *129*
3.4.5.1 Dehydration *129*
3.5 Surface Reactivity and Catalysis *130*
3.5.1 Oxidation State and Coordination Changes *130*
3.5.1.1 Oxidation State of Transition Metals in Supported MO_x Moieties or Solid Solutions *130*
3.5.1.2 Supported Metals: Oxidation State and Particle Size and Shape *131*
3.5.2 Hydrocarbon Species on Surfaces *133*
3.5.2.1 Reference Spectra *133*
3.5.2.2 Surface Hydrocarbon Pool Under Reaction Conditions *137*
3.5.2.3 Deactivation and Regeneration *138*
3.6 Conclusions *139*
References *140*

4 Photoluminescence Spectroscopy *149*
Masaya Matsuoka, Masakazu Saito, and Masakazu Anpo
4.1 Introduction *149*
4.2 Basic Principles of Photoluminescence *150*
4.3 General Aspects of Photoluminescence Measurements *153*
4.3.1 Steady-State Photoluminescence Measurements *153*
4.3.2 Time-Resolved Photoluminescence Measurements *154*
4.4 Characterization of Catalysts by Photoluminescence and Time-Resolved Photoluminescence Spectroscopy *156*
4.4.1 *In Situ* Photoluminescence of Microcrystalline MgO *156*
4.4.2 *In Situ* Photoluminescence of Bulk TiO_2 Photocatalysts *159*
4.4.3 *In Situ* Photoluminescence of Highly Dispersed Transition Metal Ions and Oxides *163*
4.4.3.1 V-Containing BEA Zeolite Catalysts *163*
4.4.3.2 Ag^+/MFI Catalysts *165*
4.5 Investigations of the Dynamics of Photocatalysis by Time-Resolved Photoluminescence Spectroscopy *165*

4.5.1 Dynamics of Photocatalytic Reactions on TiO_2 Photocatalysts *166*
4.5.2 Dynamics of Photocatalytic Reactions on Highly Dispersed Transition Metal Ion and Oxide Catalysts *169*
4.5.2.1 Cu^+/Zeolite Catalysts *169*
4.5.2.2 Ti Oxide/Zeolite Catalysts *175*
4.5.2.3 Mo Oxide/SiO_2 Catalysts *177*
4.6 Conclusion *182*
References *182*

5 Neutron Scattering *185*
Hervé Jobic
5.1 Introduction *185*
5.2 Introduction to the Theory *186*
5.2.1 Properties of Neutrons *186*
5.2.2 Scattering Cross-Sections *187*
5.2.3 Coherent and Incoherent Scattering *188*
5.3 Experimental *190*
5.4 Structure *192*
5.5 Dynamics *194*
5.5.1 Vibrational Spectroscopy *195*
5.5.2 Diffusive Motions *197*
5.5.2.1 Neutron Spin-Echo Technique *198*
5.5.2.2 Rotational Motion *201*
5.5.2.3 Translational Motion *202*
5.6 Conclusion *208*
References *208*

6 Sum Frequency Generation and Infrared Reflection Absorption Spectroscopy *211*
Karin Föttinger, Christian Weilach, and Günther Rupprechter
6.1 Introduction *211*
6.2 Theoretical Background of SFG *213*
6.2.1 SFG Signal Intensity and Selection Rules *215*
6.2.2 Surface Concentration (Coverage) and SFG Signal Intensity *216*
6.3 Spectrometer Setup *217*
6.3.1 Modes of Operation *218*
6.4 Case Studies *221*
6.4.1 Metal Single-Crystal Surfaces *221*
6.4.2 Bimetallic Surfaces *228*
6.4.3 Oxide Surfaces *233*
6.4.4 Metal Nanoparticles on Oxide Surfaces *240*
6.5 Conclusion *245*
References *245*

7 Infra Red Reflection Absorption Spectroscopy and Polarisation Modulation-IRRAS *255*
Christophe Méthivier and Claire-Marie Pradier
7.1 Introduction *255*
7.1.1 Some History *256*
7.2 Principle of IRAS *258*
7.3 Principle of PM-IRAS *261*
7.4 Applications of IRAS and PM-IRAS *263*
7.4.1 Formation of Self-Assembled Monolayers *263*
7.4.2 Adsorption of Organic Small Molecules and Chirality *266*
7.4.3 Monitoring Surface Reactivity and Catalysis *268*
7.4.3.1 Oxidation of CO on Ru *268*
7.4.3.2 CO hydrogenation on Ru *270*
7.4.3.3 Vinyl Acetate Synthesis Reaction on Pd *270*
7.4.3.4 Oxidation of NH_3 and reduction of N_2O by NH_3 on Cu *272*
7.4.3.5 Decomposition of Methanol on Pd *275*
7.4.3.6 Dissociation of NO on Rh *275*
7.4.3.7 Reactivity/Storage of NO on Metal and Oxide Surfaces *277*
7.4.4 Surface Functionalization and Elaboration of Sensors *281*
7.4.5 PM-IRAS in the Liquid Phase *282*
7.5 Conclusion *285*
References *286*

8 Nuclear Magnetic Resonance Spectroscopy *289*
Lynn F. Gladden, Michal Lutecki, and James McGregor
8.1 Introduction and Historical Perspective *289*
8.2 Theory *291*
8.2.1 Basic Principles of NMR *291*
8.2.1.1 Zeeman Interaction *292*
8.2.1.2 Dipolar Interaction *292*
8.2.1.3 Chemical Shift Interaction *293*
8.2.1.4 Quadrupolar Interaction *293*
8.2.1.5 Indirect Electron Coupled Interaction *294*
8.2.2 Relaxation Times *294*
8.2.3 Application of Magnetic Field Gradients *295*
8.2.3.1 Magnetic Resonance Imaging *295*
8.2.3.2 Measuring Flow and Diffusion *296*
8.3 Popular NMR Techniques for Studying Solids *297*
8.3.1 General Techniques for Bulk and Surface Characterization *298*
8.3.2 Studying Quadrupolar Systems with $I > {}^1/_2$ *299*
8.3.3 Techniques for Measuring Heteronuclear Dipolar Couplings *300*
8.4 Characterization of Heterogeneous Catalysts *302*
8.4.1 Silica- and Alumina-Containing Materials *303*
8.4.1.1 Pure Silicas and Aluminas *303*
8.4.1.2 Zeolites and Aluminosilicates *304*

8.4.2 Vanadium-Containing Materials *305*
8.4.3 Surface Acidity and Basicity *306*
8.5 Porosity, Adsorption, and Transport Processes *308*
8.5.1 Porosity *308*
8.5.1.1 ^{129}Xe NMR *308*
8.5.1.2 T_1 and T_2 Relaxometry *309*
8.5.1.3 Magnetic Resonance Imaging *310*
8.5.2 Adsorption *311*
8.5.3 Diffusion *312*
8.6 "*In Situ*" NMR *313*
8.6.1 Experimental Apparatus *314*
8.6.1.1 Batch Conditions *314*
8.6.1.2 Flow Conditions *315*
8.6.2 Applications *317*
8.6.2.1 Batch Conditions *317*
8.6.2.2 Flow Conditions *322*
8.6.2.3 Coupling with a Second Technique *325*
8.7 Towards "*Operando*" Studies *329*
8.8 Conclusion and Outlook *331*
References *332*

9 Electron Paramagnetic Resonance Spectroscopy *343*
Piotr Pietrzyk, Zbigniew Sojka, and Elio Giamello
9.1 Introduction *343*
9.1.1 Interaction of Matter with a Magnetic Field *343*
9.1.2 Experimental Approaches in EPR *344*
9.2 Principles of EPR *345*
9.2.1 The Zeeman Effect and the Resonance Phenomenon *346*
9.2.2 Spin Resonance and Spin Relaxation *348*
9.3 Electron–Nucleus Hyperfine Interaction *350*
9.3.1 The Hydrogen Atom ($S = 1/2$ and $I = 1/2$) *353*
9.3.2 Hyperfine Interaction in Polynuclear Systems *355*
9.4 Experimental Background *356*
9.5 Anisotropy of Magnetic Interactions in EPR: the *g*, *A*, and *D* Tensors *359*
9.5.1 The *g* Tensor *361*
9.5.2 The *A* Tensor *362*
9.5.3 The Electron–Electron Interactions in $S > 1/2$ Systems: The *D* Tensor *363*
9.5.4 The Spin-Hamiltonian *366*
9.6 EPR Spectra and the Solid State: Single Crystal Versus Powders *366*
9.6.1 Powder EPR Spectra *367*
9.7 Guidelines to Interpretation of EPR Spectra *368*
9.7.1 Classification of EPR Spectra and Determination of Spectral Parameters *368*

9.7.2 Unusual Spectral Features and Puzzling Lineshapes *372*
9.7.3 Dynamic Lineshape Effects and Partially Averaged Signals *376*
9.8 Computer Simulation of Powder Spectra *378*
9.9 Molecular Interpretation of Parameters *380*
9.9.1 *g*-Tensor *380*
9.9.2 Hyperfine Tensor *383*
9.10 Quantum Chemical Calculations of Magnetic Parameters *386*
9.11 Advanced EPR Techniques *388*
9.11.1 Electron Spin Echo-Based Techniques *388*
9.12 Characteristics of EPR Techniques in Application to Catalysis and Surfaces *389*
9.12.1 Distinction Between Surface and Bulk Species *390*
9.12.2 Poorly Resolved Spectra – Multifrequency Approach *392*
9.12.3 Overlapping Signals *394*
9.12.4 Strain Broadening and Smearing of Features with High Angular Anisotropy *395*
9.12.5 Use of Probe Molecules and Spin Labels *396*
9.13 Interfacial and Surface Charge-Transfer Processes *398*
9.14 *In Situ* and *Operando* EPR Techniques *399*
9.15 Conclusions and Prospects *403*
References *403*

10 Mössbauer Spectroscopy *407*
Lorenzo Stievano and Friedrich E. Wagner
10.1 Introduction *407*
10.2 The Mössbauer Effect *409*
10.3 Radiation Source *411*
10.4 Mössbauer Absorbers *414*
10.5 Hyperfine Interactions *414*
10.5.1 Electric Monopole Interaction *415*
10.5.2 Magnetic Dipole Interaction *417*
10.5.3 Electric Quadrupole Interaction *419*
10.6 Experimental Setups *421*
10.6.1 Transmission Mössbauer Spectroscopy *421*
10.6.2 Surface-Sensitive Mössbauer Spectroscopy *422*
10.6.3 Emission Mössbauer Spectroscopy *423*
10.7 Evaluation of Experimental Data *424*
10.7.1 Spectra Folding *424*
10.7.2 Spectra Fitting *424*
10.8 Theoretical Calculation of Mössbauer Parameters *426*
10.9 Common Mössbauer-Active Transitions *427*
10.9.1 The 14.4keV Mössbauer Transition of ^{57}Fe *427*
10.9.2 The 89.4 keV Mössbauer Transition of ^{99}Ru *429*
10.9.3 The 23.9 keV Mössbauer Transition of ^{119}Sn *430*

10.9.4 The 37.1 keV Mössbauer Transition of ^{121}Sb *432*
10.9.5 The 73.0 keV Mössbauer Transition of ^{193}Ir *432*
10.9.6 The 77.3 keV Mössbauer Transition of ^{197}Au *433*
10.10 Survey of Applications of the Mössbauer Effect in the Study of Catalytic Materials *434*
10.10.1 ^{197}Au Mössbauer Spectroscopy in the Study of Gold Catalysts *435*
10.10.1.1 Electronic Properties: Au/Al_2O_3 Oxidation Catalysts *435*
10.10.1.2 Determination of Chemical Composition: Supported AuPd Alloys *436*
10.10.1.3 Determination of Lamb–Mössbauer *f*-Factors for Quantitative Analyses: Au/Activated Carbon Catalysts for the Hydrochlorination of Acetylene *437*
10.10.1.4 Identification of Surface Species: Gold Nanoparticles Embedded in Mylar *438*
10.10.2 ^{57}Fe Mössbauer Spectroscopic Study of Iron-Containing Catalysts *439*
10.10.2.1 Superparamagnetism and the Determination of Particle Sizes: Fe/C Catalysts for CO Hydrogenation *440*
10.10.2.2 *In Situ* Measurements: Iron-Based Fischer–Tropsch Catalysts *443*
10.10.2.3 Emission Mössbauer Spectroscopy: Cobalt-Based Fischer–Tropsch Catalysts *444*
10.10.3 ^{119}Sn Mössbauer Study of Bimetallic Tin-Containing Catalysts *446*
10.11 Conclusion *447*
References *448*

11 Low Energy Ion Scattering and Secondary Ion Mass Spectrometry *453*
Norbert Kruse and Sergey Chenakin
11.1 Introduction *453*
11.2 Secondary Ion Mass Spectrometry *457*
11.2.1 Basic Principles *457*
11.2.2 Potential of SIMS *459*
11.3 Low-Energy Ion Scattering (Ion Scattering Spectroscopy) *461*
11.3.1 Main Concepts *461*
11.3.2 Potentialities of LEIS *463*
11.4 Single-Crystal and Polycrystalline Metal Surfaces *465*
11.4.1 Surface Defects and Adsorption of Simple Molecules *465*
11.4.2 Adsorption of Organic Molecules *469*
11.4.3 Oxidation and Corrosion *470*
11.5 Amorphous Metallic Alloys *472*
11.6 From Model to Real Catalysts *474*
11.6.1 Structural Effects *474*
11.6.2 Dispersion Effects *477*
11.6.3 Preparation and Activation Effects *480*
11.6.4 Compositional Effects in Various Catalytic Reactions *484*
11.6.4.1 CO Hydrogenation *484*

11.6.4.2 Hydrocarbon Oxidation *486*
11.6.4.3 Hydrogenation and Oxidative Dehydrogenation *489*
11.6.5 Promotion and Poisoning Effects *489*
11.6.5.1 CO Hydrogenation to Methanol *490*
11.6.5.2 CO Oxidation *490*
11.6.5.3 Hydrocarbon Partial and Total Oxidation *492*
11.6.5.4 Cracking *494*
11.6.5.5 Beckmann Rearrangement *494*
11.6.5.6 Aldose Oxidation *495*
11.6.5.7 Nitrite and Nitrate Reduction *495*
11.6.5.8 Cl-Related Effects in Various Reactions *496*
11.6.6 Active Sites *497*
11.7 Conclusion *501*
References *502*

12 X-ray Absorption Spectroscopy *511*
Christophe Geantet and Christophe Pichon
12.1 Introduction *511*
12.2 History of X-Ray Absorption Spectroscopy *511*
12.3 Principle of X-Ray Absorption Spectroscopy: XANES, EXAFS *512*
12.4 Experimentation and Data Processing *515*
12.5 Application to Oxide Materials *521*
12.6 Applications to the Study of Sulfide Catalysts *524*
12.6.1 Structure of the Active Phase *524*
12.6.2 Activation of Sulfide Catalysts *525*
12.7 Application to Metal Catalysts *527*
12.7.1 Structure and Size of (Bi-)Metallic Particles *528*
12.7.2 Evolution of the Bimetallic Structure Under Reaction or Poisoning Conditions *530*
12.8 Conclusion and Perspectives *533*
References *534*

13 Auger Electron, X ray and UV Photoelectron Spectroscopies *537*
Wolfgang Grünert
13.1 Introduction *537*
13.1.1 The Relation Between XPS, UPS, and AES *537*
13.1.2 A Glimpse at History *539*
13.2 Sources of Analytical Information *540*
13.2.1 XPS Binding Energies *540*
13.2.1.1 Parameters Affecting XPS Binding Energies *540*
13.2.1.2 Theoretical Prediction of XPS Binding Energies *545*
13.2.1.3 Practical Aspects *547*
13.2.2 The Analytical Potential of XPS Lineshapes *548*
13.2.2.1 Spin–Orbit Splitting *548*
13.2.2.2 Charge Transfer Satellites *549*

13.2.2.3 Other Shake-Up Type Satellites *550*
13.2.2.4 Multiplet Splitting *551*
13.2.3 Surface Sensitivity: Working with XPS Intensities *553*
13.2.3.1 Homogeneous and Inhomogeneous Sampling Region *553*
13.2.3.2 Increasing the Surface Sensitivity of XPS *557*
13.2.3.3 Determining XPS Intensities – Lineshapes and Signal Backgrounds *560*
13.2.4 XAES and XPS – Structural Sensitivity via the Auger Parameter *562*
13.2.5 Ultraviolet Photoelectron Spectroscopy *565*
13.2.6 XPS and Other Methods *566*
13.3 Instrumentation *567*
13.3.1 Conventional XPS *567*
13.3.2 Lateral Resolution, Imaging *569*
13.3.3 Ambient-Pressure Photoelectron Spectroscopy (APPES) *570*
13.4 Case Studies *571*
13.4.1 Combination of Methods: Strong Metal–Support Interaction in a Ag/TiO_2 Catalyst *571*
13.4.2 Depth Resolution: the Surface Composition of Stoichiometric Bulk Mixed Vanadates and Molybdates *573*
13.4.3 APPES: on the Doorstep of a New Age of XPS *574*
13.5 Outlook *578*
References *579*

14 Single Molecule Spectroscopy *585*
Timo Lebold, Jens Michaelis, Thomas Bein, and Christoph Bräuchle
14.1 Introduction *585*
14.2 Description of the Method *586*
14.3 Experimental Considerations and Constraints *591*
14.4 Mesoporous Silica Materials *592*
14.5 Selected Studies *593*
14.5.1 Correlating Dynamic and Structural Information by Combining Single-Molecule Microscopy and High-Resolution Transmission Electron Microscopy *593*
14.5.2 Analyzing the Diffusion Dynamics Within a Silica Mesopore with One-Channel Accuracy Using Single-Molecule Microscopy and Single-Particle Tracking *595*
14.5.3 Analyzing Orientational and Spectral Dynamics at Adsorption Sites Inside a CTAB Templated Thin Mesoporous Silica Film *598*
14.5.4 Visualization of the Mechanisms Governing the Structure Formation of Mesoporous Silica Nanochannels *601*
14.6 Conclusion *605*
References *605*

Volume 2

Part Two Macroscopic Techniques *609*

15 X-Ray Diffraction and Small Angle X-Ray Scattering *611*
Malte Behrens and Robert Schlögl

16 Transmission Electron Microscopy *655*
John Meurig Thomas and Caterina Ducati

17 Scanning Probe Microscopy and Spectroscopy *703*
Tomoaki Nishino

18 Thermal Methods *747*
Adrien Mekki-Berrada and Aline Auroux

19 Surface Area/Porosity, Adsorption, Diffusion *853*
Philip L. Llewellyn, Emily Bloch, and Sandrine Bourrelly

Part Three Characterization of the Fluid Phase (Gas and/or Liquid) *881*

20 Mass Spectrometry *883*
Sandra Alves and Jean-Claude Tabet

21 Chromatographic Methods *953*
Fabrice Bertoncini, Didier Thiebaut, Marion Courtiade, and Thomas Dutriez

22 Transient Techniques: Temporal Analysis of Products and Steady State Isotopic Transient Kinetic Analysis *1013*
Angelos M. Efstathiou, John T. Gleaves, and Gregory S. Yablonsky

Part Four Advanced Characterization *1075*

23 Techniques Coupling for Catalyst Characterisation *1077*
Andrew M. Beale, Matthew G. O'Brien, and Bert M. Weckhuysen

24 Quantum Chemistry Methods *1119*
Philippe Sautet

Conclusions *1147*
Michel Che and Jacques C. Védrine

Index *1153*

About the Editors

Michel Che

After a chemical engineering degree from Ecole Supérieure de Chimie Industrielle (Lyon, F), M. Che joined the Institut de Recherches sur la Catalyse (Lyon) as member of CNRS (National Center of Scientific Research). After a Doctorat ès Sciences in 1968 (Université de Lyon), he was postdoctoral fellow (1969-1971) at Princeton University. Between 1972 and 1982, he frequently worked as visiting scientist at the Atomic Energy Research Establishment at Harwell (UK). He became Professor at Université Pierre & Marie Curie-Paris 6 in 1975, and Senior Member of Institut Universitaire de France in 1995.

His research concerns the reactivity of solid surfaces investigated from a molecular standpoint based on the combined use of transition metal complexes, specific isotopes and physical techniques. His work, which led to 450 publications and 5 patents, has contributed to improve our understanding of the elementary processes developing at solid/liquid (gas) interfaces and to bridge the gap between homo- and heterogeneous catalysis.

Michel Che was President-Founder of EFCATS, the European Federation of Catalysis Societies (creating the biennial EuropaCat congresses), and later President of the International Association of Catalysis Societies. He received awards in France (A. Joannides and P. Sue), Netherlands (J. H. Van't Hoff), Poland (M. Sklodowska-Curie & P. Curie lectureship), Germany (Von Humboldt - Gay-Lussac Award, and GDCh Grignard-Wittig lectureship), UK (RSC Centenary lectureship), USA (Frontiers in Chemical Research lectureship, Texas), Japan (Japanese Society for the Promotion of Science lectureship), China (Gold Medal of Chinese Academy of Sciences, Friendship Award and International Science and Technology Cooperation Award) and Europe (François Gault EFCATS lectureship). His work earned him several honorary doctorates and fellowships (German Academy of Sciences-Leopoldina, Academia Europaea, Hungarian Academy of Sciences, Polish Academy of Arts and Sciences).

Jacques C. Védrine

After a chemical engineering degree from Ecole Supérieure de Chimie Industrielle (Lyon, F), J.C. Védrine joined the Institut de Recherches sur la Catalyse (IRC) in Lyon as member of CNRS. After a Docteur ès Sciences degree in 1968 (Université de Lyon), he was post-doc in USA at Varian Ass., Palo Alto (1969-1970) and Princeton University (1970-1971). He then returned to IRC and became deputy director in 1988. In 1998, he moved to the University of Liverpool, UK as Chair Professor and Deputy Director of the Leverhulme Centre for Innovative Catalysis. In 2003, he returned to France and was chargé de mission at the Ministry of National Education and Research. In 2006, he joined the Laboratory of Surface Reactivity at Université Pierre & Marie Curie, Paris.

His scientific interests cover heterogeneous catalysis, especially selective oxidation on mixed metal oxides, acid catalysis on oxide-based systems and acidity strength and nature determination. He worked on combinatorial catalysis (high throughput technique) and contributed in the 1990s to the EUROCAT group activities in standardizing heterogeneous catalyst characterization. He co-authored over 350 publications and a few patents, and co-edited 7 books. He is one of the Editors of Appl. Catal. A: General.

One of his major contributions was to organize in the 1980s regular training sessions to help researchers use complementary physical techniques to improve the characterization of solid catalysts, including under working conditions. This led to two books on Physical Characterization of Solid Catalysts (Technip, Paris, 1988 and Plenum Press, New York, 1994).

He was awarded the Grand Prix Pierre Sue of the French Chemical Society (SCF) in 2001. He was elected President of Catalysis Division of SCF (1994-1997), President of EFCATS (1997-1999) and President of the Acid-Base World Organization (2005-2009). He holds honorary doctorate from the University of Lisbon.

List of Contributors

Sandra Alves
Université Pierre et Marie Curie, CNRS
Institut Parisien de Chimie
Moléculaire
Laboratoire de Chimie Biologique
Organique et Structurale
4 place Jussieu
75252 Paris
France

Masakazu Anpo
Osaka Prefecture University
Graduate School of Engineering
Department of Applied Chemistry
1-1 Gakuen-cho, Naka-Ku
Sakai-City
Osaka 599-8531
Japan

Aline Auroux
Université Lyon 1, CNRS
Institut de Recherches sur la Catalyse et
l'Environnement de Lyon
2 avenue Albert Einstein
69626 Villeurbanne
France

Andrew M. Beale
Utrecht University
Debye Institute for
NanoMaterials Science
Inorganic Chemistry and
Catalysis Group
Sorbonnelaan 16
3584 CA Utrecht
The Netherlands

Malte Behrens
Fritz-Haber-Institut der
Max-Planck-Gesellschaft
Faradayweg 4–6
14195 Berlin
Germany

Thomas Bein
Ludwig-Maximilians University of
Munich
Department of Chemistry
Center for Nanoscience and Center for
Integrated Protein Science
Butenandtstraße 11
81377 Munich
Germany

Fabrice Bertoncini
IFP Energies Nouvelles
Établissement de LYON
Catalysis and Separation Division
Rond-Point de l'Échangeur de Solaize
69360 Solaize
France

Emily Bloch
Université Aix-Marseille, CNRS
Centre de St. Jérôme
Laboratoire Chimie Provence
avenue Normandie-Niemen
13397 Marseille
France

Sandrine Bourrelly
Université Aix-Marseille, CNRS
Centre de St. Jérôme
Laboratoire Chimie Provence
avenue Normandie-Niemen
13397 Marseille
France

Christoph Bräuchle
Ludwig-Maximilians University of Munich
Department of Chemistry
Center for Nanoscience and Center for Integrated Protein Science
Butenandtstraße 11
81377 Munich
Germany

Michel Che
Institut Universitaire de France
Université Pierre et Marie Curie, CNRS
Laboratoire de Réactivité de Surface
4 place Jussieu
75252 Paris
France

Sergey Chenakin
Université Libre de Bruxelles (ULB)
Chimie-Physique des Matériaux
CP 243 Campus Plaine
1050 Brussels
Belgium

Marion Courtiade
IFP Energies Nouvelles
Établissement de LYON
Physics and Analysis Division
Rond-Point de l'Échangeur de Solaize
69360 Solaize
France

Caterina Ducati
University of Cambridge
Department of Materials Science and Metallurgy
Pembroke Street
Cambridge CB2 3QZ
UK

Thomas Dutriez
IFP Energies Nouvelles
Établissement de LYON
Physics and Analysis Division
Rond-Point de l'Échangeur de Solaize
69360 Solaize
France

Angelos M. Efstathiou
University of Cyprus
Chemistry Department
Heterogeneous Catalysis Laboratory
University Campus
1678 Nicosia
Cyprus

Gerhard Ertl
Fritz-Haber-Institut der Max-Planck-Gesellschaft
Faradayweg 4–6
14195 Berlin
Germany

Fengtao Fan
Chinese Academy of Sciences
Dalian Institute of Chemical Physics
State Key Laboratory of Catalysis
457 Zhongshan Road
Dalian 116023
China

Zhaochi Feng
Chinese Academy of Sciences
Dalian Institute of Chemical Physics
State Key Laboratory of Catalysis
457 Zhongshan Road
Dalian 116023
China

Karin Föttinger
Vienna University of Technology
Institute of Materials Chemistry
Getreidemarkt 9 BC
1060 Vienna
Austria

Christophe Geantet
Université Lyon 1, CNRS
Institut de Recherches sur la Catalyse et l'Environnement de Lyon
2 avenue Albert Einstein
69626 Villeurbanne
France

Elio Giamello
Università di Torino
Dipartimento di Chimica IFM and NIS Centre of Excellence
via P. Giuria 7
10125 Turin
Italy

Lynn F. Gladden
University of Cambridge
Department of Chemical Engineering and Biotechnology
Pembroke Street
Cambridge CB2 3RA
UK

John T. Gleaves
Washington University in St. Louis
Department of Energy, Environmental and Chemical Engineering
1 Brookings Drive
St. Louis, MO 63130
USA

Wolfgang Grünert
Ruhr-Universität Bochum
Lehrstuhl Technische Chemie
Universitätsstraße 150
44801 Bochum
Germany

Friederike C. Jentoft
University of Oklahoma
School of Chemical, Biological and Materials Engineering
Sarkeys Energy Center T-335
100 East Boyd Street
Norman, OK 73019
USA

Hervé Jobic
Université Lyon 1, CNRS
Institut de Recherches sur la Catalyse et l'Environnement de Lyon
2 avenue Albert Einstein
69626 Villeurbanne
France

Norbert Kruse
Université Libre de Bruxelles (ULB)
Chimie-Physique des Matériaux
CP 243 Campus Plaine
1050 Brussels
Belgium

Timo Lebold
Ludwig-Maximilians University of Munich
Department of Chemistry
Center for Nanoscience and Center for Integrated Protein Science
Butenandtstraße 11
81377 Munich
Germany

Can Li
Chinese Academy of Sciences
Dalian Institute of Chemical Physics
State Key Laboratory of Catalysis
457 Zhongshan Road
Dalian 116023
China

Philip L. Llewellyn
Université Aix-Marseille, CNRS
Centre de St. Jérôme
Laboratoire Chimie Provence
avenue Normandie-Niemen
13397 Marseille
France

Michal Lutecki
University of Cambridge
Department of Chemical Engineering
and Biotechnology
Pembroke Street
Cambridge CB2 3RA
UK

Masaya Matsuoka
Osaka Prefecture University
Graduate School of Engineering
Department of Applied Chemistry
1-1 Gakuen-cho, Naka-Ku
Sakai-City
Osaka 599-8531
Japan

Françoise Maugé
ENSICAEN–Université de Caen, CNRS
Laboratoire Catalyse et Spectrochimie
6 boulevard Maréchal Juin
14050 Caen
France

James McGregor
University of Cambridge
Department of Chemical Engineering
and Biotechnology
Pembroke Street
Cambridge CB2 3RA
UK

Adrien Mekki-Berrada
Université Lyon 1, CNRS
Institut de Recherches sur la Catalyse et
l'Environnement de Lyon
2 avenue Albert Einstein
69626 Villeurbanne
France

Christophe Méthivier
Université Pierre et Marie Curie, CNRS
Laboratoire de Réactivité de Surface
4 place Jussieu
75252 Paris
France

Jens Michaelis
Ludwig-Maximilians University of
Munich
Department of Chemistry
Center for Nanoscience and Center for
Integrated Protein Science
Butenandtstraße 11
81377 Munich
Germany

Tomoaki Nishino
Osaka Prefecture University
Research Organization for the
21st century
Nanoscience and Nanotechnology
Research Center
Sakai
Osaka 599-8570
Japan

Matthew G. O'Brien
Utrecht University
Debye Institute for
NanoMaterials Science
Inorganic Chemistry and
Catalysis Group
Sorbonnelaan 16
3584 CA Utrecht
The Netherlands

Christophe Pichon
IFP Energies Nouvelles
Établissement de LYON
Physics and Analysis Division
Rond-Point de l'Échangeur de Solaize
69360 Solaize
France

Piotr Pietrzyk
Jagiellonian University
Faculty of Chemistry
ul. Ingardena 3
30-060 Krakow
Poland

Claire-Marie Pradier
Université Pierre et Marie Curie, CNRS
Laboratoire de Réactivité de Surface
4 place Jussieu
75252 Paris
France

Günther Rupprechter
Vienna University of Technology
Institute of Materials Chemistry
Getreidemarkt 9 BC
1060 Vienna
Austria

Masakazu Saito
Osaka Prefecture University
Graduate School of Engineering
Department of Applied Chemistry
1-1 Gakuen-cho, Naka-Ku
Sakai-City
Osaka 599-8531
Japan

Philippe Sautet
Université Lyon 1, CNRS
Ecole Normale Supérieure de Lyon
Institut de Chimie
15 parvis Descartes
69342 Lyon
France

Robert Schlögl
Fritz-Haber-Institut der
Max-Planck-Gesellschaft
Faradayweg 4–6
14195 Berlin
Germany

Zbigniew Sojka
Jagiellonian University
Faculty of Chemistry
ul. Ingardena 3
30-060 Krakow
Poland

Lorenzo Stievano
Université Montpellier 2
Institut Charles Gerhardt, CNRS
place Eugène Bataillon
34095 Montpellier
France

Jean-Claude Tabet
Université Pierre et Marie Curie, CNRS
Institut Parisien de Chimie
Moléculaire
Laboratoire de Chimie Biologique
Organique et Structurale
4 place Jussieu
75252 Paris
France

Frédéric Thibault-Starzyk
ENSICAEN–Université de Caen, CNRS
Laboratoire Catalyse et Spectrochimie
6 boulevard Maréchal Juin
14050 Caen
France

Didier Thiebaut
CNRS
Laboratoire Physicochimie des
Electrolytes Colloïdes et Sciences
Analytiques
ESPCI ParisTech
10 rue Vauquelin
75231 Paris
France

John Meurig Thomas
University of Cambridge
Department of Materials Science and Metallurgy
Pembroke Street
Cambridge CB2 3QZ
UK

Jacques C. Védrine
Université Pierre et Marie Curie, CNRS
Laboratoire de Réactivité de Surface
4 place Jussieu
75252 Paris
France

Friedrich E. Wagner
Technische Universität München
Physik-Department E15
James-Franck-Strasse 1
85748 Garching
Germany

Bert M. Weckhuysen
Utrecht University
Debye Institute for NanoMaterials Science
Inorganic Chemistry and Catalysis Group
Sorbonnelaan 16
3584 CA Utrecht
The Netherlands

Christian Weilach
Vienna University of Technology
Institute of Materials Chemistry
Getreidemarkt 9 BC
1060 Vienna
Austria

Gregory S. Yablonsky
Saint Louis University
Parks College of Engineering
Department of Chemistry
3450 Lindell Boulevard
St. Louis, MO 63130
USA

Preface

Michel Che and Jacques C. Védrine

The spectacular progress achieved in chemistry is largely due to the use of physical techniques implemented at the level of the element, molecule, or phase with reliability and accuracy unattainable a few decades ago. Moreover, microscopic (molecular) and macroscopic (molar) information can be obtained by small-scale and often non-destructive experiments. Many of these techniques are now in routine use, essentially because of the progress of technology and availability of always more powerful and user-friendly computers.

We therefore thought that it was timely to provide a survey of the major techniques used to characterize solid materials and investigate their surface reactivity, a domain of chemistry, relevant to a variety of fields including adsorption, geochemistry, coatings, electrochemistry, corrosion, formation of biofilms, toxicity and catalysis. Those fields however do not require the same surface reactivity: for corrosion, the latter has to be inhibited, or even suppressed, because of its dramatic consequences on metals, while for catalysis not only it has to be enhanced but also selectively oriented to obtain the desired product.

From all the fields related to surface reactivity, catalysis appears to be unique because i) it has a large industrial impact, ii) it lies at the core of chemistry, i.e., starting with chemistry to prepare the catalytic system and ending with chemistry to promote a specific reaction, and iii) it involves physical and chemical processes developing mostly at liquid-solid, solid-solid, and/or gas-solid interfaces present at the successive steps of catalyst life, from its preparation to its use in the catalytic reaction. For those reasons, catalysis will be used as the directing thread of this book.

Investigations on solid materials have shown that their surfaces may change with the chemical environment to which they are exposed and that the more divided the solid, the more reactive it becomes. This book title illustrates this paradigm, with its dual aspects, the structure of the material on one hand and its surface reactivity on the other. For instance, for metals, it is known that metal-metal bond distances at the surface often contract under vacuum with respect to the bulk, while they relax in the presence of gaseous molecules reaching values close to those characteristic of the bulk. For alloys or mixed oxides, surface enrichment in one component is often

observed under reaction conditions. For some reactions, e.g. selective oxidation of olefins on metal oxide catalysts, the surface atoms of the solid catalyst may react, and even be incorporated into reactant molecules. For such redox-type reactions, surface atoms have to be mobile enough to allow the redox process to occur.

This book is intended to consider all those aspects with the objective to offer a general survey on the "Characterization of Solid Materials: From Structure to Surface Reactivity", useful to junior and senior research scientists, engineers and industrialists. We deemed it essential to present a portofolio of the techniques most frequently used and to dwell on those which appear to be most promising. For this reason, the space allocated to each chapter is different. Although still used, some techniques are not discussed in this book, because little improvement has been achieved since the publication of earlier books in 1988 [1] and 1994 [2].

Because of the large number of chapters/authors, consistency and homogeneity were felt to be essential. Therefore, the following format was suggested to authors:

1) Introduction covering the discovery and development of the technique,
2) Description of the basic phenomenon with a theoretical background including, where appropriate, its dimension/time/energy scales, energy states, terminology, units (those conventionally used in the field but also SI units), the strategy used and the essential parameters necessary to interpret experimental data,
3) Experimental considerations/constraints, relative to the characterization technique and to the surface reactivity,
4) Uses of the technique for the characterization of both model and real solid materials at different stages of their life (i.e., during preparation, functionalization, chemical or thermal activation, surface reactivity) with emphasis on the coupling with other techniques with its advantages and disadvantages,
5) Key examples of application of the technique to surface reactivity. For the field of catalysis, the reaction, deactivation, ageing, and regeneration steps had to be considered with emphasis on the identification and implication of intermediates in reaction mechanisms,
6) Conclusions including information gained with the technique, its advantages, limitations, and latest developments,
7) References.

We have tried to offer a book presenting a unique set of features:

- it deals with an ensemble of physical techniques commonly used at present to i) characterize solid materials and ii) investigate their surface reactivity,
- it provides overviews written by two outstanding scholars who have largely contributed to the development of physical techniques to investigate solid materials (single crystals and porous catalysts),
- each chapter aims at being both general and concise enough for the readers to understand the technique, and the meaning of the essential key parameters,
- it gives general data for each technique, with its historical background, domains of energy involved, spatial and time resolution, experimental constraints

(vacuum or presence of gaseous phase, temperature,...), atomic/molecular or macroscopic aspects,
- it emphasises the characterization of the solid material throughout its life: from its preparation to its application in surface reactivity-related domains,
- it includes the use of both experimental and theoretical approaches as a guide in designing experiments and interpreting results,
- it deals with both model and real solid materials,
- it aims at being a toolbox from which any researcher should be able to find the appropriate technique(s) for solving a specific problem.

To conclude, this book aims at being pedagogical, illustrative and practical, hoping that after having read the book, the reader be in a position to identify the most appropriate technique(s) able to answer his questions.

References

1 Imelik, B. and Védrine, J.C. (Eds.) (1988) *Les Techniques Physiques de Caractérisation des Catalyseurs*, Technip, Paris.
2 Imelik, B. and Védrine, J.C. (Eds.) (1994) *Catalyst Characterization: Physical Techniques for Solid Materials*, Plenum Press, New York.

General Introduction

Michel Che and Jacques C. Védrine

The two main goals of the book are to show how physical techniques can be used to characterize solid materials and to investigate their surface reactivity. The first goal corresponds to establishing the "identity card" of the material, including its structure, morphology, porosity, and chemical composition, and the second to obtaining characteristics of the surface related to its reactivity (nature and number of surface sites, subsequent modification upon functionalization, nature and number of adsorbed species and possible intermediates in surface-promoted phenomenon/reaction).

1
Basic Phenomenon and Classification of Physical Techniques

All techniques are based on the same phenomenon, often referred to as the Propst diagram (Figure 1): an incident beam hits the sample, giving rise to an emitted beam which is detected and analyzed because of the information it contains, leading to the "fingerprint" of the solid and/or of species or reaction intermediates adsorbed on it. The incident beam can be composed of photons, electrons, ions, neutrals, or magnetic, electric, acoustic, or thermal fields, and also the emitted beam.

Table 1 presents the main acronyms of the physical techniques presented or mentioned in this book and Table 2 gives the classification of typical techniques as a function of the nature of the incident and emitted beams. In Table 2, one distinguishes the diagonal techniques, for which incident and emitted beams are identical in nature and the information comes from the analysis of the modifications in intensity, energy, or frequency of the incident beam, from the off-diagonal techniques (shaded areas) for which those two beams are different in nature [2].

Table 3 lists the main spectroscopic techniques and associated events as a function of the characteristics of the incident beam (energy, domain of the electromagnetic spectrum, wavelength, and frequency).

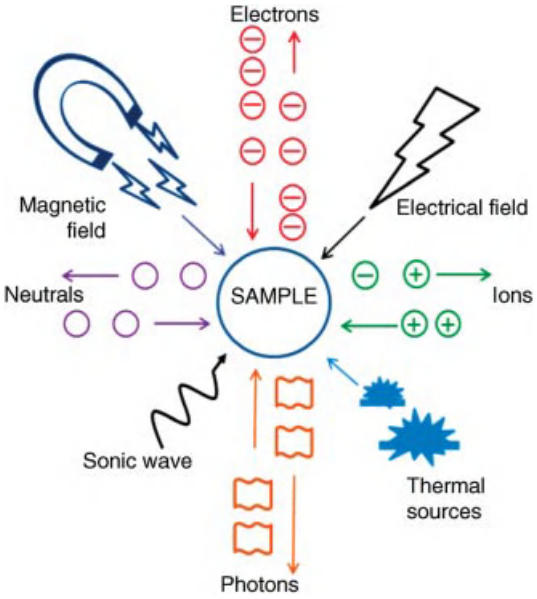


Figure 1 Basic phenomenon of physical techniques. The incident beams are defined by arrows oriented towards the sample while the emitted beams are defined by arrows oriented away from the sample. Adapted from [1].

Table 1 Acronyms and names of the techniques presented or mentioned in this book.

Acronym	Technique
AA	atomic absorption
AC-EM	aberration-corrected-electron microscopy
ADF	annular dark field
AES	Auger electron spectroscopy
AFM	atomic force microscopy
AIUP	angle-integrated ultraviolet spectroscopy
APS	appearance potential spectroscopy
ATR	attenuated total reflection
CEMS	conversion electron Mössbauer spectroscopy
CL	cathodoluminescence
CTEM	conventional transmission electron microscopy
CV	cyclic voltammetry
DFT	density functional theory
DRIFTS	diffuse reflectance infrared Fourier transform spectroscopy
DRUV-vis	diffuse reflectance UV-vis
DSC	differential scanning calorimetry
DTA	differential thermal analysis
DTG	differential thermogravimetry
ED	electron diffraction
EDS	energy-dispersive spectroscopy
EDX	energy-dispersive X-ray
EELS	electron energy loss spectroscopy

Table 1 (*Continued*)

Acronym	Technique
EF-TEM	energy-filtered-transmission electron microscopy
EI-MS	electron ionization-mass spectrometry
EL	electroluminescence
ELDOR	electron-electron double resonance
ENDOR	electron-nuclear double resonance
EPR/ESR	electron paramagnetic (spin) resonance
ESCA	electron spectroscopy for chemical analysis
ESD	electron-stimulated desorption
ESI-MS	electrospray ionization-mass spectrometry
ETEM	environmental transmission electron microscopy
EXAFS	extended X-ray absorption fine structure
EXELFS	extended X-ray electron loss fine structure
FABMS	fast atom bombardment mass spectrometry
FEM/FIM	field emission microscopy/field ion microscopy
FMR	ferromagnetic resonance
FTIR	Fourier transform infrared
GC	gas chromatography
GC-MS	gas chromatography-mass spectrometry
HAADF	high-angle annular dark field
HREELS	high-resolution electron energy loss spectroscopy
HRSTEM	high-resolution scanning transmission electron microscopy
HRTEM	high-resolution transmission electron microscopy
IMM	ion microprobe microanalysis
INS	inelastic neutron scattering
IR	infrared
IRAS or IRRAS	infrared reflection/absorption spectroscopy
IS	impedance spectroscopy
ISS	ion scattering spectroscopy
LASER	light amplification by stimulated emission of radiation
LEED	low-energy electron diffraction
LEIS	low-energy ion scattering
LMMS	laser microprobe mass spectrometry
LRS	laser Raman spectroscopy
MASER	microwave amplification by stimulated emission of radiation
MAS-NMR	magic angle spinning-nuclear magnetic resonance
MRI	magnetic resonance imaging
MS	mass spectrometry
ND	neutron diffraction
NEXAFS	near-edge X-ray absorption fine structure
NMR	nuclear magnetic resonance
PAS	photoacoustic spectroscopy
PD-MS	plasma desorption-mass spectrometry
PFG-NMR	pulsed field gradient-nuclear magnetic resonance
PIXE	proton-induced X-ray emission
PLS	photoluminescence spectroscopy
PM-IRAS	polarization modulation-infrared reflection/absorption spectroscopy

(*Continued*)

Table 1 (*Continued*)

Acronym	Technique
QCM	quartz crystal microbalance
QENS	quasi-elastic neutron scattering
QMS	quadrupole mass spectrometry
RAIRS	reflection/absorption infrared spectroscopy
RBS	Rutherford backscattering spectroscopy
REAPDOR	rotational echo adiabatic passage double resonance
REDOR	rotational echo double resonance
RS	Raman spectroscopy
RRS	resonance Raman spectroscopy
SANS	small-angle neutron scattering
SAXS	small-angle X-ray scattering
SEDOR	spin-echo double resonance
SEM	scanning electron microscopy
SEM-NMR	spin-echo mapping-nuclear magnetic resonance
SERS	surface-enhanced Raman spectroscopy
SEXAFS	surface-extended X-ray absorption fine structure
SFG	sum frequency generation
SHG	second harmonic generation
SIMS	secondary ion mass spectrometry
SPR	surface plasmon resonance
SSITKA	steady-state isotopic transient kinetics analysis
STEM	scanning transmission electron microscopy
STM	scanning tunneling microscopy
TAP	temporal analysis of products
TDS	thermal desorption spectroscopy
TE	thermionic emission
TEDOR	transferred echo double resonance
TEM	transmission electron microscopy
TG	thermogravimetry
TGA	thermogravimetric analysis
TPD/TPO/TPR	temperature-programmed desorption/oxidation/reduction
TR-PLS	time-resolved-photoluminescence spectroscopy
TRAPDOR	transfer of population in double resonance
UPS	ultraviolet photoelectron spectroscopy
UV-vis	ultraviolet-visible
UV-RS	UV-Raman spectroscopy
UV-RRS	UV-resonance Raman spectroscopy
WAXS	wide-angle X-ray scattering
XANES	X-ray absorption near-edge spectroscopy
XAS	X-ray absorption spectroscopy
XPS	X-ray photoelectron spectroscopy
XRD	X-ray diffraction
XRE	X-ray emission
XRF	X-ray fluorescence

Table 2 Classification of typical techniques as a function of the nature of the incident and emitted beams. Adapted from [2].

Beam	Incident					
Emitted	**Neutrals**	**Ions**	**Electrons**	**Photons**	**Electric/ magnetic field**	**Thermal/ acoustic field**
Neutrals	INS, ND		ESD, EI-MS			TPD, DTG, TG
Ions	FABMS, MS, QMS	SIMS, ISS, RBS, IMM, LEIS		LMMS	FIM	TE
Electrons			AES, EELS, LEED, SEM, TEM	UPS, XPS	FEM, STM	
Photons		PIXE	CL, EDX, XRE	ATR, IR, EPR, EXAFS, LRS, NMR, PLS, RRS, RS, SAXS, SERS, UV-vis, XANES, XRD, XRF		
Electric/magnetic field					CV, IS	
Thermal/ acoustic field	Calorimetry			PAS		DSC, DTA

Table 3 Main spectroscopic techniques and associated events as a function of the characteristics of the incident beam[a]. Adapted from [2].

Technique	Event	E (kJ mol^{-1})	Domain	λ (m)	ν (s^{-1})
NMR	Nuclear spin flip	10^{-5}	Radio	10^{1}	10^{7}
EPR	Electron spin flip	10^{-3}	Microwave	10^{-1}	10^{9}
IR, Raman	Molecular rotation Molecular vibration	10^{-1}	IR	10^{-3}	10^{11}
			NIR	10^{-5}	10^{13}
UV-vis	Valence electron transition	10^{3}	Visible	10^{-7}	10^{15}
			UV		
UPS	Valence electron excitation	10^{5}	Vacuum UV	10^{-9}	10^{17}
XPS XAS	Core electron excitation	10^{7}	X-rays	10^{-11}	10^{19}
Mössbauer	Nuclear transition	10^{9}	γ-rays	10^{-13}	10^{21}

a) The figures, not to scale, are provided to give an idea of the domain of energy, wavelength, and frequency.

2
Coupling of Physical Techniques

The coupling of physical techniques has been a major advance in physical chemistry in the past decades and has become increasingly popular in chemical, environmental, biochemical, biological, and forensic laboratories, successfully solving most difficult problems such as speciation and trace analysis, which any single technique cannot solve.

Tandem GC–MS is one of the earliest and best examples – combining the separation power of gas chromatography with the identification ability of modern mass spectrometry is a powerful means to analyze complex mixtures. Calorimetry is another example: while it easily leads to the adsorption heat versus coverage, its coupling with laser Raman spectroscopy can simultaneously provide structural and thermal information. The quartz balance, which easily provides quantitative data, is a powerful addition to more qualitative techniques such as IR and IRAS. Coupling AFM and tunable lasers has also been developed for investigating living cell modifications upon incorporation of a foreign element. Thus, coupling AFM with IR spectroscopy can provide a chemical mapping of different structures absorbing in the IR domain at the sub-cell scale (AFM resolution ~ 10 nm) [3]. Many other couplings have been developed and are described in this book.

3
The Latest Challenge: Characterization of the Surface Reactivity of Solid Materials Under Working/Catalytic Reaction Conditions

The latest challenge in surface-related fields is to characterize the solid materials under working conditions, that is, in the real conditions of their applications (such as adsorption, geochemistry, coatings, electrochemistry, corrosion, formation of biofilms, and toxicity) involving most often the presence of gas–solid and/or liquid–solid interfaces. This implies a single cell where characterization and application concern the same sample with simultaneous control of the experimental parameters (e.g., temperature, pressure, concentration, flow, reactivity cell characteristics) which influence surface reactivity.

For the outstanding case of catalysis, the challenge is more involved because the application consists of a molecular reaction taking place at the catalyst surface. Hence characterization and reaction have to be performed in the same cell, under reaction conditions (reactants, flow, temperature, pressure, concentration, and reactor characteristics) and with simultaneous online analysis of reactants and products allowing the determination of the catalyst activity and selectivity. The cell also acts as a catalysis reactor.

In the past, the terms "*in situ*" [4] and "*operando*" [5, 6], although originally precisely defined, have unfortunately often been misused, as discussed elsewhere [7–10], because characterization and catalytic reaction were not performed in the same cell and with simultaneous online analysis of reactants and products. To obtain truly meaningful catalytic data, it is worth recalling that the "characterization–catalytic reaction" cell has to be designed so as to avoid any diffusion problems.

4
Book Content and Chapter Order

The solid material sees its properties change as one moves from the bulk to its surface. These changes are dramatically dependent on its morphology (particle size, specific surface area, porosity) and on the external conditions to which it is subjected (presence of a gas or liquid phase, with their associated parameters, for example, nature, composition, pressure, concentration, presence of ions, notably transition metal ions, etc.). In general terms, the more divided the solid is, the more reactive it becomes. The book title illustrates this paradigm, with its dual aspects, the material on the one hand and its surface reactivity on the other.

Between the solid material (Chapters 1–14) and the fluid phase (gas and/or liquid) (Chapters 20–22), inherent to most applications, lies the solid–fluid interface, the nature of which has been much investigated over the past decades. The intricacy of this interface is illustrated by Figure 2, in the case of transition metal complexes interacting with an oxide surface [11]. Depending on the experimental conditions, various types of interaction can be identified, resulting in a variety of species (with different ligands, symmetries, and nuclearities) referred to as speciation defined [12] as "the distribution of an element (M in Figure 2) amongst defined chemical species in a given system." Speciation, which concerns both the aqueous solution and the oxide support [13], constitutes one of the most challenging problems in analytical chemistry: how to determine the nature and concentration of each species.

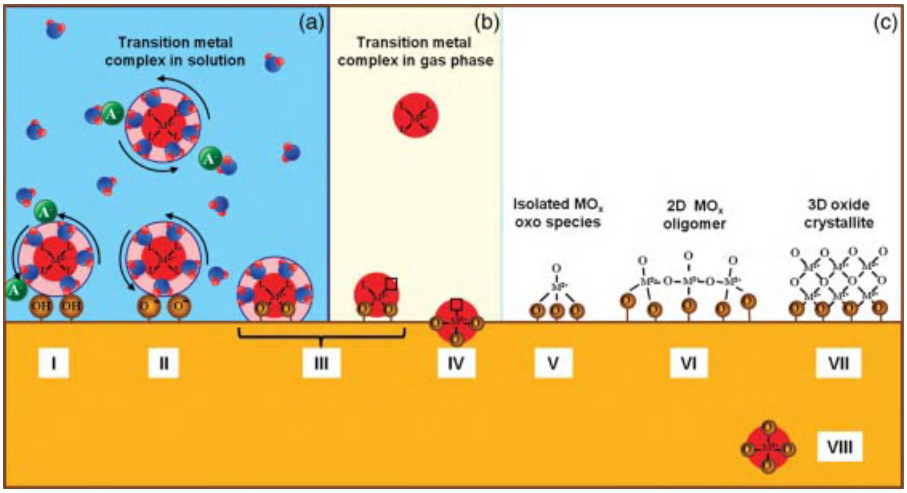


Figure 2 Transition metal complex $[ML_n]^{q+/q-}$ (M = transition metal, L = ligand, n = number of ligands, and q = charge of the complex) interacting with an oxide surface after deposition [from the liquid (a) or gas phase (b)] and further thermal treatment (c). In models I–VIII, the oxide support acts as surface solvent (I), counter ion (II), surface bidentate ligand (III), framework ligand (IV), surface ligand (V–VII), and solid solvent (VIII). Note that the nuclearity of the final complex may differ from that of the starting complex. Designed from [11].

Figure 2 also shows that the coordination sphere of the transition metal ion can be very different from that of the original complex in the liquid or gas phase and that the oxide is a very versatile entity (e.g., solvent, counter ion, ligand, framework and solid solution).

The chapters in this book are arranged in four parts. Part one is devoted to molecular/local spectroscopies (Chapters 1–14). Part two is devoted to macroscopic techniques (Chapters 15–19). Part three is devoted to the characterization of the fluid phase (gas and/or liquid) (Chapters 20–22) in relation to the surface reactivity of solid materials. Part four (Chapters 23 and 24) is concerned with advanced characterization: Chapter 23 deals with techniques used in reaction conditions whereas Chapter 24 describes theoretical calculations and modeling to describe solid materials and their reactivity.

5
SI Units and Conversions

We have seen (Table 3) that, depending on the technique, the incident and emitted beams do not have the same nature and that their characteristics (energy, frequency, and wavelength) vary over wide ranges. From the various effects induced, valuable information on the solid material can be obtained.

In all chapters, the units used are those of the "Système International d'Unités" (SI). However, for historical reasons, the practitioners of each technique have adopted certain habits, which have persisted, even after the IUPAC recommendations. Thus, it is common practice to see units such as wavenumber (cm^{-1}) in IR and Raman wavelength (nm) in UV–visible and energy (eV) in XPS and EXAFS. To help the reader to move from one system to the other, tables are provided which list the base units of the SI system (Table 4), the units derived from the latter (Table 5), the interconversion of energy and pressure units (Tables 6 and 7), and the fundamental physical constants (Table 8) based on the Bureau International des Poids et Mesures [14] and IUPAC [15] recommendations.

Table 4 Base SI units. Adapted from [14, 15].

Base quantity			SI base unit	
Name	**Symbol**	**Dimension**	**Name**	**Symbol**
Length	l	L	metre	m
Mass	m	M	kilogram	kg
Time	t	T	second	s
Electric current	I	I	ampere	A
Thermodynamic temperature	T	Θ	kelvin	K
Amount of substance	n	N	mole	mol
Luminous intensity	I_V	J	candela	cd

Table 5 Units derived from the base SI units. Adapted from [15].

Derived quantity	Name	Symbol	Expression in terms of SI units
Frequency	hertz	Hz	s^{-1}
Force	newton	N	$m\,kg\,s^{-2}$
Pressure, stress	pascal	Pa	$N\,m^{-2} = m^{-1}\,kg\,s^{-2}$
Energy, work, heat	joule	J	$N\,m = m^2\,kg\,s^{-2}$
Power, radiant flux	watt	W	$J\,s^{-1} = m^2\,kg\,s^{-3}$
Electric charge	coulomb	C	A s
Electric potential	volt	V	$J\,C^{-1} = m^2\,kg\,s^{-3}\,A^{-1}$
Electric resistance	ohm	Ω	$V\,A^{-1} = m^2\,kg\,s^{-3}\,A^{-2}$
Electric conductance	siemens	S	$\Omega^{-1} = m^{-2}\,kg^{-1}\,s^3\,A^2$
Electric capacitance	farad	F	$C\,V^{-1} = m^{-2}\,kg^{-1}\,s^4\,A^2$
Magnetic flux	weber	Wb	$V\,s = m^2\,kg\,s^{-2}\,A^{-1}$
Magnetic flux density	tesla	T	$Wb\,m^{-2} = kg\,s^{-2}\,A^{-1}$
Inductance	henry	H	$V A^{-1}\,s = m^2\,kg\,s^{-2}\,A^{-2}$
Celsius temperature	degree Celsius	°C	
Luminous flux	lumen	lm	$cd\,sr = cd$
Illuminance	lux	lx	$lm\,m^{-2} = cd\,m^{-2}$
Radioactivity	becquerel	Bq	s^{-1}
Radioactivity dose	sievert	Sv	$J\,kg^{-1} = m^2\,s^{-2}$
Plane angle	radian	rad	
Solid angle	steradian	sr	

Table 6 Interconversion of energy units. Adapted from [15].

	joule	erg	eV	cm^{-1}
1 J	1	10^7	$6.241\,510 \times 10^{18}$	$5.034\,117 \times 10^{22}$
1 erg	10^{-7}	1	$6.241\,510 \times 10^{11}$	$5.034\,117 \times 10^{15}$
1 eV	$1.602\,176 \times 10^{-19}$	$1.602\,176 \times 10^{-12}$	1	8065.545
$1\,cm^{-1}$	$1.986\,446 \times 10^{-23}$	$1.986\,446 \times 10^{-16}$	$1.239\,842 \times 10^{-4}$	1

Table 7 Interconversion of pressure units. Adapted from [15].

	Pa	bar	atm	Torr (mmHg)	psi
1 Pa	= 1	$= 10^{-5}$	$\approx 9.869\,23 \times 10^{-6}$	$\approx 7.500\,62 \times 10^{-3}$	$\approx 1.450\,38 \times 10^{-4}$
1 bar	$= 10^5$	= 1	≈ 0.986 923	≈ 750.062	≈ 14.5038
1 atm	= 101 325	= 1.013 25	= 1	= 760	≈ 14.6959
1 Torr	≈ 133.322	$\approx 1.333\,22 \times 10^{-3}$	$\approx 1.315\,79 \times 10^{-3}$	= 1	$\approx 1.933\,68 \times 10^{-2}$
1 psi	≈ 6894.76	$\approx 6.894\,76 \times 10^{-2}$	$\approx 6.804\,60 \times 10^{-2}$	≈ 51.714 94	= 1

Table 8 Fundamental physical constants[a]. Adapted from [15].

Quantity	Symbol	Value[a]
Speed of light in vacuum	c_0, c	299 792 458 m s^{-1} (defined)
Planck's constant	h	$6.626\,068\,96(33) \times 10^{-34}$ J s
	$\hbar = h/2\pi$	$1.054\,571\,628(53) \times 10^{-34}$ J s
Elementary charge	e	$1.602\,176\,487(40) \times 10^{-19}$ C
Electron mass	m_e	$9.109\,382\,15(45) \times 10^{-31}$ kg
Proton mass	m_p	$1.672\,621\,637(83) \times 10^{-27}$ kg
Atomic mass constant	$m_u = 1$ u	$1.660\,538\,782(83) \times 10^{-27}$ kg
Avogadro's constant	N_A	$6.022\,141\,79(30) \times 10^{23}$ mol^{-1}
Boltzmann constant	k, k_B	$1.380\,650\,4(24) \times 10^{-23}$ J K^{-1}
Faraday constant	$F = N_A e$	$9.648\,533\,99(24) \times 10^{4}$ C mol^{-1}
Molar gas constant	$R = N_A k$	8.314 472(15) J K^{-1} mol^{-1}
Zero of the Celsius scale		273.15 K (defined)
Standard atmosphere		101 325 Pa (defined)
Bohr radius	$a_0 = 4\pi\varepsilon_0\hbar^2/m_e e^2$	$5.291\,772\,085\,9(36) \times 10^{-11}$ m
Rydberg constant	$R_\infty = E_h/2hc_0$	$1.097\,373\,156\,852\,7(73) \times 10^{7}$ m^{-1}
Bohr magneton	$\mu_B = e\hbar/2m_e$	$9.274\,009\,15(23) \times 10^{-24}$ J T^{-1}
Electron magnetic moment	μ_e	$-9.284\,763\,77(23) \times 10^{-24}$ J T^{-1}
Landé g factor (free electron)	g_e	$-2.002\,319\,304\,362\,2(15)$
Nuclear magneton	$\mu_N = e\hbar/2m_p$	$5.050\,783\,24(13) \times 10^{-27}$ J T^{-1}
Proton magnetic moment	μ_p	$1.410\,606\,662(37) \times 10^{-26}$ J T^{-1}
Proton gyromagnetic ratio	$\gamma_p = 4\pi\mu_p/h$	$2.675\,222\,099(70) \times 10^{8}$ s^{-1} T^{-1}
Newtonian gravitation constant	G	$6.674\,28(67) \times 10^{-11}$ m^3 kg^{-1} s^{-2}
Gravity standard acceleration	g_n	9.806 65 m s^{-2} (defined)

a) The standard deviation uncertainty in the least significant digits is given in parentheses.

Table 9, giving the prefixes used to denote decimal multiples and submultiples of SI units, is provided to remain in phase with the progress of the nanoworld (Submultiple column) and the huge progress made in computer memories (Multiple column). Finally, Table 10 gives a summary of the parameters related to the samples analyzed by physical techniques.

Table 9 SI prefixes and prefixes for binary multiples. From [15].

Submultiple	Name	Symbol	Multiple	Prefix	Symbol
10^{-1}	deci	d	10	deca	da
10^{-2}	centi	c	10^{2}	hecto	h
10^{-3}	milli	m	10^{3}	kilo	k
10^{-6}	micro	μ	10^{6}	mega	M
10^{-9}	nano	n	10^{9}	giga	G
10^{-12}	pico	p	10^{12}	tera	T
10^{-15}	femto	f	10^{15}	peta	P
10^{-18}	atto	a	10^{18}	exa	E
10^{-21}	zepto	z	10^{21}	zeta	Z
10^{-24}	yocto	y	10^{24}	yotta	Y

Table 10 Parameters relevant to selected physical techniques[a]. Adapted from [16].

Parameter	Molecular spectroscopy			Resonance			Neutrons	Thermal techniques
	IR, PAS	Raman	UV-vis	EPR, FMR	NMR	Mössbauer		
Sample preparation	Easy	Easy	Easy	Easy	Easy	Easy	Difficult	Easy
Area analyzed[b]	cm^2	μm^2	cm^2	cm^2	cm^2	cm^2	mm^2	mm^2
Thickness analyzed[b]	mm	mm	mm	mm	mm	100 µm	0.1 mm	mm
Sample degradation	Weak	Possible	No	No	No	No	Possible	Possible
Quantitative analysis	Possible	Possible	Possible	Yes	Yes	Yes	Yes	Yes
Gaseous atmosphere	Yes	Yes	Yes	Yes	Yes	Yes	Yes	Possible
Temperature range (°C)[b),c)]	LT/300	LT/300	LT/300	LT/1000	LT/200	LT/400	LT/800	No limit
Information	functional groups, species nature	functional groups, species nature	oxidation state, ion symmetry, species nature	species nature, oxidation state, environment symmetry	functional groups	oxidation state, environment symmetry	species nature, atomic structure	adsorption/ formation energy

(*Continued*)

Table 10 (*Continued*)

Parameter	Surface				X ray			Magnetism	Electrical conductivity
	EELS	XPS	AES	SIMS	XRD	EXAFS	Radial distribution		
Sample preparation	Difficult	Easy	Easy	Easy	Easy	Easy	Easy	Easy	Easy
Area analyzed[b)]	cm^2	cm^2	cm^2	cm^2	mm^2	mm^2	mm^2	cm^2	cm^2
Thickness analyzed[b)]	μm	2–5 nm	1–2 nm	0.2–0.3 nm	mm	mm	mm	mm	mm
Sample degradation	Very slight	Possible	Possible	No	No	No	No	No	No
Quantitative analysis	–	Yes	Possible	Possible	Yes	Yes	Yes	Yes	Yes
Gaseous atmosphere	No	Difficult	Difficult	No	Yes	Yes	Yes	Possible	Possible
Temperature range (°C)[b),c)]	Ambient	LT/600	LT/600	Ambient	LT/1000	LT/1000	LT/1000	LT/500	LT/800
Information	metal–ligand bonding	oxidation state, surface composition	surface composition	surface composition	crystallite structure/size	element environment, number of ligands	element environment	magnetization degree, crystallite size	conduction type, species nature

a) The techniques mentioned in this table but not presented in this book are discussed in [16].
b) The data are approximate and meant to give an order of magnitude.
c) LT means either liquid helium or nitrogen temperature.

With all the techniques presented in this book, it now becomes possible to analyze samples of a great variety of solid materials related to surface reactivity at large, showing the immense potential of physical chemistry, even in unexpected domains such as music [17], painting [18], sparkling beverages [19], and gastronomy [20].

Acknowledgments

The authors are most grateful to Mrs. F. Sarrazin and Dr. F. Averseng (Université Pierre et Marie Curie – Paris 6) and Prof. L. Bonneviot (ENS Lyon) for their most valuable help in preparing some of the tables and figures.

References

1 Cover of the series *Studies in Surface Science and Catalysis*, Elsevier, Amsterdam.
2 Sojka, Z. and Che, M. (2008) *J. Chem. Educ.*, **85**, 934.
3 Dazzi, A. and Policar, C. (2011) in *Biointerface Characterization by Advanced IR Spectroscopy* (Eds. C-M. Pradier and Y.J. Chabal), Elsevier, Amsterdam, Chapter IX, p. 245.
4 Haw, J. (Ed.) (2002) *In-Situ Spectroscopy in Heterogeneous Catalysis*, Wiley-VCH Verlag GmbH, Weinheim.
5 Bañares, M. (Ed.) (2009) *In situ to operando spectroscopy: from proof of concept to industrial application. Top. Catal.*, **52**, 1301.
6 Weckhuysen, B.M. (2003) *Phys. Chem. Chem. Phys.*, **5**, 4351.
7 Ertl, G., Knözinger, H., and Weitkamp, J. (Eds.) (1997) *Handbook of Heterogeneous Catalysis*, vol. 2, Wiley-VCH Verlag GmbH, Weinheim.
8 Ertl, G., Knözinger, H., Schüth, F., and Weitkamp, J. (Eds.) (2008) *Handbook of Heterogeneous Catalysis*, 2nd edn., vol. 2, Wiley-VCH Verlag GmbH, Weinheim.
9 Gates, B.C. and Knözinger, H. (Eds.) (2006) *Physical characterization of solid catalysts in the functioning state. Adv. Catal.*, **50**, 1–283; Gates, B.C. and Knözinger, H. (Eds.) (2007) *Physical characterization of solid catalysts in the functioning state. Adv. Catal.*, **51**, 1–382.
10 Gates, B.C., Knözinger, H., and Jentoft, F.C. (Eds.) (2009) *Physical characterization of solid catalysts in the functioning state. Adv. Catal.*, **52**, 1–465.
11 Che, M. and Bonneviot, L. (1988) *Pure Appl. Chem.*, **60**, 1369.
12 Templeton, D.M., Ariese, F., Cornelis, R., Danielsson, L.G., Muntau, H., van Leeuwen, H.P., and Lobinski, R. (2000) *Pure Appl. Chem.*, **72**, 1453.
13 Dzwigaj, S. and Che, M. (2011) *Catal. Today*, **169**, 232.
14 Bureau International des Poids et Mesures (2006) *The International System of Units (SI)*, 8th edn., Stedi Media, Paris, pp. 94 and 111.
15 Cohen, E.R., Cvitas, T., Frey, J.G., Holmström, B., Kuchitsu, K., Marquardt, R., Mills, I., Pavese, F., Quack, M., Stohner, J., Strauss, H.L., Takami, M., and Thor, A.J. (2008) *Quantities, Units and Symbols in Physical Chemistry, IUPAC Green Book*, 3rd edn, 2nd Printing, IUPAC and RSC Publishing, Cambridge, pp. 4, 89, 234, 233, 111 and 91 for Tables 4, 5, 6, 7, 8 and 9, respectively.
16 Imelik, B. and Védrine, J.C. (Eds.) (1994) *Catalyst Characterization: Physical Techniques for Solid Materials*, Plenum Press, New York, p. 7.
17 Echard, J.P., Bertrand, L., von Bohlen, A., Le Hô, A.-S., Paris, C., Bellot-Gurlet, L., Soulier, B., Lattuati-Dorieux, A., Thao, S., Robinet, L., Lavédrine, B., and Vaiedlich, S. (2010) *Angew. Chem. Int. Ed.*, **49**, 197.
18 de Viguerie, L., Walter, P., Laval, E., Martin, B., and Solé, S.A. (2010) *Angew. Chem. Int. Ed.*, **49**, 1.
19 Liger-Belair, G., Polidori, G., and Jeandet, P. (2008) *Chem. Soc. Rev.*, **37**, 2490.
20 This, H. (2002) *Angew. Chem. Int. Ed.*, **41**, 83; (2009) *Acc. Chem. Res.*, **42**, 575.

Overview on Physical Techniques for Investigating Model Solid Catalysts

Gerhard Ertl

1 Why Model Systems?

A "real" catalyst consists usually of nanoparticles exposing different crystal planes and various structural defects with complex chemical composition. All these factors have their effect on the chemical reactivity. A possible strategy to solve this problem had been suggested by I. Langmuir already many years ago [1]. "*Most finely divided catalysts must have structures of great complexity. In order to simplify our theoretical consideration of reactions at surfaces, let us confine our attentions to reactions on plane surfaces. If the principles in this case are well understood, it should then be possible to extend the theory to the case of porous bodies. In general, we should look upon the surface as consisting of a checkerboard. . .*"

This "surface science" approach that Langmuir had in mind was not yet accessible in his days, but was beginning to become available only in the 1960s with the development of novel physical methods which enable chemical analysis as well as investigation of the structural, electronic, vibrational, and dynamic properties of solid surfaces [2–7]. In fact, low energy electron diffraction (LEED) was the first of these techniques which was used to follow the kinetics of chemical reactions on well-defined single crystal surfaces [52, 53]. In recent years, scanning probe techniques, in particular scanning tunneling microscopy (STM) proved to be most powerful for direct observation of processes on atomic scale [8–12]. Since many of these techniques involve the interaction of particles (e.g., electrons) with matter, the pressure in the apparatus has to be in the ultrahigh vacuum (UHV). The pressures have also to be low enough for keeping the clean surface free from adsorbing species for long enough time. This effect causes the so-called "pressure gap" between the conditions of "real" catalysis and surface science studies.

There exist various possibilities to overcome this pressure gap. First one should keep in mind that the surface concentration of a certain species *in equilibrium* depends not only on pressure but also on temperature, so that lowering the temperature may compensate the difference in pressure. Second, special high pressure enclosure cells permit the reaction to be performed at elevated pressure,

Characterization of Solid Materials and Heterogeneous Catalysts: From Structure to Surface Reactivity, First Edition. Edited by Michel Che and Jacques C. Védrine.
© 2012 Wiley-VCH Verlag GmbH & Co. KGaA. Published 2012 by Wiley-VCH Verlag GmbH & Co. KGaA.

while the sample may afterwards be transferred into the UHV region [13, 14], and finally, apart from probing the surface with electromagnetic radiation, investigations at elevated pressures may also be performed with devices in which the sample-probe distance is below the mean free path of gaseous species. For example, at 1 mbar an electron with 400 eV kinetic energy will travel about 4 mm before undergoing an inelastic collision [35]. Such *in situ* measurements can be achieved by scanning tunneling microscopy, electron microscopy and photoelectron spectroscopy.

Apart from the "pressure gap" there exists also a "materials gap" between well-defined single crystal surfaces and "real" catalysts. Attempts to approach to the latter systems are made by controlled introduction of surface defects or foreign atoms, as well as by the use of bimetallic surfaces, well-defined oxide films or small particles with controlled size.

Despite these apparent shortcomings, the "surface science" approach has been successfully applied to elucidate the molecular mechanisms of important catalytic reactions even under industrial conditions, among which ammonia synthesis on promoted iron catalysts is most notable [15]. These results would not have been attained otherwise and justify the investigations with model systems. In the following short overview the main physical techniques applied in this context will be presented.

2
Interactions of Molecules with Surfaces; Kinetics and Dynamics

Catalysis at surfaces is concerned with the rates of chemical reactions. Therefore investigation of the kinetic properties of molecules interacting with surfaces is mandatory for understanding the underlying mechanisms. An advantage of model systems consists in the fact that due to the large mean free path of gaseous particles transport processes can usually be neglected, and because of the low reaction rates the processes are essentially isothermal.

Energies of adsorption may be determined by sophisticated calorimetric methods [16, 17] or, less elaborate, through measurements during adsorption-desorption equilibrium. If in this case, the coverage θ is determined as a function of temperature T and partial pressure p of the gaseous species, the isosteric heat of adsorption E_{ad} is derived through application of the Clausius-Clapeyron equation

$$\left.\frac{d(\ln p)}{d(1/T)}\right|_{v=\text{const}} = -\frac{E_{ad}}{R}$$

from plots of lnp over 1/T at the respective coverage. This technique requires accurate determination of the coverage under conditions of adsorption-desorption equilibrium.

More convenient, but less accurate data about adsorption energetics can be obtained from studies of the desorption kinetics through thermal desorption spectroscopy (TDS) or temperature programmed desorption (TPD) [6, 18]. The principle of this technique is rather simple and straightforward: After dosing an

adsorbate to surface by gas adsorption, the sample temperature is continuously increased and the flux of desorbing particles is monitored by a quadrupole mass spectrometer (QMS) as a function of time. Detailed analysis yields the kinetics of desorption (including reaction order, as well as activation energy and preexponential) as a function of coverage. Since adsorption is frequently non-activated, in this way also the adsorption energy is derived. Instead of monitoring the desorbing species, in catalytic reactions also the kinetics of product release into the gas phase can be recorded in this way (temperature programmed reaction spectroscopy = TPRS). Investigation of more "real" surfaces is also frequently performed along these strategies.

Data on the kinetics of adsorption (= sticking coefficient) can again be derived from TPD data by monitoring the desorbed amount as a function of the preceding gas exposure. A convenient technique for the determination of fairly high sticking coefficients was developed by King and Wells [19] by measuring pressure changes in conjunction with molecular beam dosing.

More details and accurate results on the kinetics of adsorption and desorption may be obtained by the use of molecular beam techniques. Two types of molecular beams may be applied: Knudsen (or thermal) and supersonic beams. The former mimick the interaction with molecules carrying the normal thermal energy, while the latter may be used to study the influence of the translational energy of the impinging particles on the dynamics. By periodically modulating the flux of the incident molecules and recording the phase lag of the species coming off the surface the mean residence time before desorption or reaction, respectively, can be determined. In this way it was for example for the first time possible to unequivocally establish the operation of the Langmuir-Hinshelwood (LH) mechanism in CO oxidation on a Pd (111) surface by measuring the delay time between adsorption and product formation down to about 10^{-4} s, leading also to the activation energy of the LH step [20].

Full insight into the distribution of energy among the various degrees of freedom of the particles coming off the surface may be obtained in state resolved experiments combining molecular beam and laser spectroscopic techniques [21]. Time resolution down to the femtosecond region can eventually be reached by two-pulse correlation methods [22].

3
The Structure of Surfaces

The application of optical and electron microscopies is possible not only with model surfaces but also with real systems, whereby the second group, however, again is restricted to high vacuum conditions. Microscopy with atomic resolution, on the other hand, was achieved for the first time by field ion microscopy (FIM) [23] invented by E. W. Müller in 1951 [24]. This technique requires sharp (radius <50 nm) metal tips at low temperature in an atmosphere of an imaging gas (mostly He) as well as the application of a strong electric field of a few V/Å. These factors cause severe restrictions of the applicability of this technique and hence it is no longer widely in use.

It took several decades to reach a real breakthrough in this field by the development of the scanning tunneling microscope (STM) [25] which technique found already many applications in surface studies [8–10]. In this way it was for example possible to directly image atomic steps as "active sites" in dissociation [26] or to analyze surface diffusion of adsorbates on atomic scale [27]. The application of STM requires flat and conducting surfaces, but may operate also at high pressures [12, 28, 29] and even in liquids, for example, in electrochemical studies.

The restriction to conducting surfaces is no longer existent if instead of the STM the atomic force microscope (AFM) is applied [30]. With this technique, an atomically sharp tip is scanned across a surface and the force between the tip and the sample is determined by recording the deflection of a micromechanical cantilever spring. Thereby the surface topography can be studied even down to atomic resolution [31]. A recently developed technique thus enabled even visualization of the 3d distribution of water molecules at a mica-water interface [32]. However, routine applications under ambient conditions reduces the lateral resolution usually to a few nm.

The actual atomic coordinates at the surfaces of single crystals are accessible by the use of diffraction techniques. While x-rays penetrate deeply into the bulk of solids this probe is only applicable with special geometric arrangements, for example, with grazing-incidence configuration [3]. Most powerful in this respect, however, is the technique of low energy electron diffraction (LEED). The mean free path of electrons in the kinetic energy range between about 20 and 500 eV is of the order of less than 1 nm, so that the elastically scattered electrons of this kind carry information only from the few topmost atomic layers [2–6]. While the position of the diffraction spots provide the geometry of the unit cell of the surface lattice, the determination of the actual atomic positions requires analysis of the intensity/voltage data (I/V-curves) by application of an elaborate dynamical multiple scattering theory [33]. In the case of more disordered surfaces more local diffraction techniques such as photoelectron diffraction (PED) or surface extended X-ray absorption fine structure (SEXAFS) can be used to derive information about the local geometry of surface atoms. As a consequence of the complexity of analysis the number of quantitatively solved structures is still rather small if compared with the large amount of data for bulk structures. The NIST (NIST = National Institute of Standards and Technology) Surface Structure Data base listed only about 1400 quantitatively solved surface structures, mostly of elemental metals and derived from LEED [33].

Low energy electrons may also be used for imaging surface structures in the sophisticated low energy emission microscope (LEEM) [38].

4
Electron Spectroscopies

Various techniques based on analysis of electrons emitted from a surface serve mainly as sources for elemental analysis and for probing the valence state of the topmost layers. The small mean free paths of electrons with energies $\leq$500 eV as

mentioned before render these techniques surface sensitive, while their application is again restricted to low pressure conditions.

Among these, Auger electron spectroscopy (AES) is the oldest and most versatile, because it can be readily incorporated into a LEED apparatus [2–7]. Typically electron bombardment of a sample with energies around a few keV creates a hole in the inner shells of a hit atom which is subsequently filled by transition of an electron from a higher level, whereby the energy is transferred to another (bound) electron which is then ejected. Measurement of the kinetic energies of these Auger electrons then provides information about the elemental nature of the emitting atoms, while quantitative analysis can be derived from the intensities. AES is in principle able to detect any element except H and He. However, with increasing atomic number, the competition by radiative relaxation of the core hole through x-ray fluorescence increases. The exact energies and lineshapes of Auger transitions are usually not taken into account since signals from different elements are mostly widely separated from each other, while, however, also overlaps may occur which render quantitative analysis more problematic. The composition of the probed surface near region can be derived with fair accuracy by use of the relative sensitive factors as tabulated in the Handbook of Auger Electron Spectroscopy [34].

Direct emission of an electron can be achieved by absorption of a photon whose energy hν exceeds the binding energy of the bond electron E_B, whereby the kinetic energy of the emitted electron $E_k = h\nu - E_B$ is measured and provides E_B. Core electrons are excited by absorption of X-rays either from laboratory sources or from a synchrotron, and this method is then denoted as X-ray photoelectron spectroscopy (XPS). The advantage of synchrotron radiation sources is the much higher photon flux and the possibility of continuously varying the photon energy. In addition, the high photon intensity permits focusing to small spots of few ten nanometers in diameter. Since the energies of core electrons are to a first approximation independent of the atomic environment, XPS is particularly useful for elemental (qualitative as well as quantitative) analysis. Typical variations of the binding energies are denoted as chemical shifts and are dependent on the bonding of the analyzed atom, in particular its oxidation state. This technique is not restricted to flat or even single crystal surfaces and is therefore frequently applied also to "real" surfaces. The still existing restriction to low pressures can to some extent be overcome by novel designs with differential pumping and additional electrostatic lens focussing of the emitted electrons so that the sample can be operated at ambient (i.e., up to the mbar) pressure region [35].

By scanning the photon energy with the use of synchrotron radiation a core level is resonantly excited when the photon energy matches the difference in energy between this level and the first unoccupied state. By recording the spectral region near the threshold in XANES (X-ray absorption near edge structure) or NEXAFS (near edge X-ray absorption fine structure) one can probe the electronic structure of unoccupied levels [36], while variations of the absorption cross section with photon energy over a wider range causes characteristic oscillations due to interference phenomena between outgoing electrons and those scattered by neighboring atoms. This is the basis of the powerful EXAFS technique which can be applied to any kind of samples even at higher pressures. If instead of fluorescence the electrons emitted by the

sample are recorded the technique becomes again surface sensitive for flat model surfaces.

If instead of X-ray photons near ultraviolet radiation is used the emitted electrons originate from the valence levels of the sample: ultraviolet photoelectron spectroscopy (UPS). This technique is particularly well suited to study the bonding at surfaces. Usually a He lamp with photon energies of 21.2 or 40.8 eV is used to investigate the band structure of the topmost atomic layers of the solid as well as the levels of an adsorbate, whereby the full information on energy and momentum of the emitted electrons is derived from angle resolved measurements (ARUPS). Of course, again a synchrotron with variable photon energy may be used as light source.

By the application of very short laser pulses, multiphoton photoelectron spectroscopy may be performed which allows investigation of the dynamics of electronic excitations down to the femtosecond time domain [37].

In photoelectron spectroscopy the photon energy usually exceeds the work function of the sample significantly. If the photon energy is close to the work function the local intensity of photoemitted electrons will be affected by the dipole moments of adsorbed species. If this intensity distribution is probed by a laterally resolving technique in a photoemission electron microscope (PEEM) [39] the lateral distribution of adsorbed species can be imaged with a spatial resolution of better than 100 nm. In this way the formation and propagation of spatio-temporal concentration patterns of adsorbates during a catalytic reaction on mesoscopic length scale may directly be followed [40].

The ultimate step consists in combining electron microscopy with electron spectroscopy, where the energy distributions of electrons from individual small areas are recorded. An example of such a microspectrometer is presented by the SMART project installed at the Berlin BESSY synchrotron with an ultimate lateral resolution of 2 nm at an energy resolution of 100 meV [41].

Finally, a completely different electron spectroscopic technique will be mentioned which has been frequently applied with large area samples for identification of surface radicals: electron paramagnetic resonance (EPR), also known as electron spin resonance spectroscopy (ESR). Due to advanced experimental design features the sensitivity of this technique could recently be improved substantially so that now also low area single crystal surfaces become accessible for investigation [42].

5
Vibrational Spectroscopies

Vibrational spectroscopies are probably the most widely used techniques in chemistry to identify the molecular nature of a species and of its modification by bonding. This is also the case for surfaces and adsorbates including model systems [43].

Most common for "real" systems is infrared absorption spectroscopy which can also be adopted to small area single crystal surfaces by reflection of the primary beam at the surface near grazing incidence, a technique denoted as reflection absorption infrared spectroscopy (RAIRS) or infrared reflection absorption spectroscopy (IRAS).

Apart from identifying characteristic bands, their relative intensities may also serve to derive the coverage of adsorbates. IR spectroscopy is, of course, only applicable if the radiation is not strongly absorbed by the substrate, and low frequency vibrations $\leq 1000\,cm^{-1}$ are hence not accessible. On the other hand, the high spectral resolution allows also to monitor subtle effects on the vibrational spectra of adsorbates, such as the influence of temperature as a consequence of coupling to other modes [44]. No restriction with respect to pressure exist with this purely optical method.

This is no longer the case with a technique which has been widely in use with UHV single crystal studies: high resolution electron energy loss spectroscopy (HREELS) [45]. Here a collimated monochromatic beam of electrons is scattered at a surface whose energy distribution is analyzed afterwards. The impinging electrons may loose part of their energy by excitations of molecular vibrations either by dipole scattering like in IR spectroscopy or by impact scattering which mechanism is not governed by dipole selection rules so that also infrared inactive modes may be probed. An advantage of this technique is that it can also probe the low frequency range $<1000\,cm^{-1}$, whereby also the adsorbate-substrate bond and even phonons become accessible. On the other hand, it is only applicable in UHV, and the resolution is rather poor ($\sim 10\,cm^{-1}$).

Another purely optical technique for probing vibrational spectra without any pressure restrictions is sum frequency generation (SFG) spectroscopy [46]. Typically a laser beam with constant frequency in the visible and another one tunable in the infrared range are directed onto the surface and the output beam is analyzed. By tuning the IR radiation over a resonance for excitation the vibration spectrum is obtained. As a second-order nonlinear optical process, no signal is obtained from centrosymmetric media such as gases, liquids or most solids, so that this technique becomes highly surface sensitive. This method has for example been successfully applied to detect surface intermediates on single crystal surfaces at high pressures [47]. Since for intensity reasons short laser pulses are used instead of cw radiation, by means of pulse delay techniques even time resolved processes can be probed by this method down to a temporal resolution <1 ps [22].

Ordinary Raman spectroscopy is not sensitive enough for flat model surfaces, but the situation may be improved by many orders of magnitude with surface enhanced Raman spectroscopy (SERS) whereby even single molecules may be detected [48]. The underlying mechanism involves most likely the excitation of localized surface plasmons, and as a consequence the technique is essentially restricted to rough silver surfaces. A recent modification transfers this requirement to a Ag tip, which is approached to an arbitrary surface (tip enhanced Raman spectroscopy = TERS) [49]. By thus combining Raman spectroscopy with STM [50] even single molecule detection with a lateral resolution of 15 nm could recently be reached [51].

6 Conclusions

One can safely conclude that the introduction of surface physical methods into the investigation of model surfaces has revolutionized our knowledge about the

molecular mechanisms underlying heterogeneous catalysis. The most recent milestone in the development of these methods is represented by 4D electron microscopy [54] in which ultrafast laser techniques are combined with electron microscopy to follow the motion of individual atoms on a timescale of femtoseconds. Further progress of this field is to be expected during the coming years by which still more complex (and even biological) systems undergoing reactions at surfaces will become accessible for detailed investigation.

References

1 Langmuir, I. (1922) *Trans. Faraday Soc.*, **17**, 607.
2 Ertl, G. and Küppers, J. (1985) *Low Energy Electrons and Surface Chemistry*, 2nd edn, VCH Weinheim.
3 Woodruff, D.P. and Delchar, T.A. (1994) *Modern Techniques of Surface Science*, Cambridge Univ. Press, Cambridge.
4 Somorjai, G.A. (1994) *Introduction to Surface Chemistry and Catalysis*, John Wiley & Sons, New York.
5 Vickermann, J.C. (1997) *Surface Analysis: The Principal Techniques*, John Wiley & Sons, New York.
6 Kolasinski, K.W. (2008) *Surface Science*, 2nd edn, John Wiley & Sons, New York.
7 Somorjai, G.A. and Li, Y. (2010) *Introduction to Surface Chemistry and Catalysis*, 2nd edn, John Wiley & Sons, New York.
8 Besenbacher, F. (1996) *Rep. Progr. Phys.*, **59**.
9 Besenbacher, F., Lauritsen, J.V., and Wang, R.T. (2008) *Handbook of Heterogeneous Catalysis*, vol. 2 (eds G. Ertl, H. Knözinger, F. Schüth, and J. Weitkamp), John Wiley & Sons, p. 833.
10 Wintterlin, J. (2000) *Adv. Catal.*, **45**, 131.
11 Lauritsen, J.V. and Besenbacher, F. (2006) *Adv. Catal.*, **50**, 97.
12 Tao, F. and Salmeron, M. (2011) *Science*, **331**, 171.
13 Cabrera, A.L., Spencer, N.D., Kozak, E., Davies, T.W., and Somorjai, G.A. (1982) *Rev. Sci. Instr.*, **53**, 1893.
14 Campbell, C.T. (1989) *Adv. Catal.*, **36**, 1.
15 Ertl, G. (2009) *Reactions at Solid Surfaces*, John Wiley & Sons, p. 123.
16 Ge, Q., Kose, R., and King, D.A. (2000) *Adv. Catal.*, **45**, 207.
17 Stuckless, J.I., Frei, N.A., and Campbell, C.T. (1998) *Rev. Sci. Instr.*, **62**, 2427.
18 Yates, J.T. (1985) *Solid State Physics: Surfaces. Methods of Experimental Physics*, vol. 22 (eds R.L. Park and M.G. Lagally), Academic Press, New York, p. 425.
19 King, D.A. and Wells, M.G. (1972) *Surf. Sci.*, **29**, 454.
20 Engel, T. and Ertl, G. (1978) *J. Chem. Phys.*, **69**, 1267.
21 Barker, J.A. and Auerbach, D.J. (1985) *Surf. Sci. Rep.*, **4**, 1.
22 Bonn, M., Hess, C., Funk, S., Miners, J.H., Persson, B.N.N., Wolf, M., and Ertl, G. (2000) *Phys. Rev. Lett.*, **84**, 4653.
23 Müller, E.W. and Tsong, T.T. (1969) *Field Ion Microscopy*, Elsevier, Amsterdam.
24 Müller, E.W. (1951) *Z. Phys.*, **131**, 136.
25 Binnig, G., Rohrer, H., Gerber, C., and Weibel, E. (1982) *Phys. Rev. Lett.*, **49**, 57.
26 Zambelli, T., Wintterlin, J., Trost, J., and Ertl, G. (1996) *Science*, **273**, 1688.
27 Zambelli, T., Trost, J., Wintterlin, J., and Ertl, G. (1996) *Phys. Rev. Lett.*, **76**, 795.
28 Rössler, M., Geng, P., and Wintterlin, J. (2005) *Rev. Sci. Instr.*, **76**, 023705.
29 Tao, F., Tang, D., Salmeron, M., and Somorjai, G.A. (2008) *Rev. Sci. Instr.*, **19**, 084101.
30 Binnig, G., Quate, C.F., and Gerber, C. (1986) *Phys. Rev. Lett.*, **56**, 930.
31 Gross, L., Mohl, F., Moll, N., Liljeroth, P., and Meyer, G. (2009) *Science*, **325**, 1110.
32 Fukuma, T., Ueda, Y., Yoshioka, S., and Asakawa, H. (2010) *Phys. Rev. Lett.*, **104**, 016101.
33 Hermann, K. (2011) *Crystallography and surface structure*, Wiley-VCH.
34 Childs, K.D., Carlson, B.A., La Vanier, L.A., Moulder, J.F., Paul, D.F., Stickle,

W.F., and Watson, G.D. (1995) *Handbook of Auger Electron Spectroscopy*, 3rd edn, Physical Electronics, Eden Prairier, Mn.
35 Salmeron, M. and Schlögl, R. (2008) *Surf. Sci. Rep.*, **63**, 169.
36 Stöhr, J. (1992) *NEXAFS Spectroscopy*, Springer, Berlin.
37 Gudde, J., Berthold, W., and Hofer, U. (2006) *Chem. Rev.*, **106**, 4261.
38 Bauer, E. (1994) *Surf. Sci.*, **299/300**, 102.
39 Engel, W., Kordesch, M.E., Rotermund, H.H., Kubala, S., and von Oertzen, A. (1991) *Ultramicroscopy*, **36**, 148.
40 Imbihl, R. and Ertl, G. (1995) *Chem. Rev.*, **95**, 697.
41 Schmidt, Th. *et al.* (2002) *Surf. Rev. Lett.*, **9**, 223.
42 Freund, H.J., Nilius, N., Risse, Th., Schauermann, S., and Schmidt, Th. (2011) *Chem. Phys. Chem.*, **12**, 79.
43 Yates, J.T. and Madey, T.E. (eds) (1987) *Vibrational Spectroscopy of Molecules on Surfaces*, Plenum Press, New York.
44 Jakob, P. and Persson, B.N.J. (1997) *Phys. Rev.*, **B56**, 10644.
45 Ibach, H. and Mills, D.L. (1982) *Electron Energy Loss Specgtroscopy and Surface Vibrations*, Academic Press, New York.
46 Shen, Y.R. (1989) *Nature*, **337**, 519.
47 Cremer, P.S., Su, X.C., Somorjai, G.A., and Shen, Y.R. (1998) *J. Mol. Cat. A*, **131**, 225.
48 Blackie, J., Le Ru, E.C., and Etchegoin, P.G. (2009) *J. Am. Chem. Soc.*, **131**, 14466.
49 Stöckle, R.M., Suh, Y.D., Deckert, V., and Zenobi, R. (2000) *Chem. Phys. Lett.*, **318**, 131.
50 Pettinger, B., Ren, B., Picardi, G., Schuster, R., and Ertl, G. (2004) *Phys. Rev. Lett.*, **92**, 09601.
51 Steidtner, J. and Pettinger, B. (2008) *Phys. Rev. Lett.*, **100**, 236101.
52 Ertl, G. (1967) *Surf. Sci.*, **7**, 309.
53 Ertl, G. and Rau, P. (1969) *Surf. Sci.*, **15**, 443.
54 Zewail, A.H. and Thomas, J.M. (2010) *4D Electron Microscopy, Imaging in Space and Time*, Imperial College Press, London.

Overview on Physical Techniques for Investigating Porous Catalysts

John Meurig Thomas

1 Why Porous and Nanoporous Systems?

Although model systems using single crystals, as described [1] in the preceeding chapter, have enormously enlarged our knowledge of the individual processes known to occur during the course of catalysis by polycrystalline solids composed of complex chemical systems, the great advantage that most porous, and *all* nanoporous (i.e., open structure) catalysts, possess is that they are amenable to *in situ* characterization under the most severe of ambient conditions. Because such solids have, in effect, three-dimensional surfaces and have high pore volumes, all the techniques of X-ray spectroscopy, and all the variants of infra red and Raman spectroscopy, Mössbauer spectroscopy, as well as all the techniques of nuclear magnetic, and electron paramagnetic resonance may be deployed to characterize such solid catalysts [2, 3] – see Figure 1. Moreover, as Llewellyn *et al.* [4] in this volume show, it is readily possible, especially by gas adsorption and cognate techniques (summarized earlier in the Handbook edited by Sing, Schüth and Weitkamp [5], to retrieve the precise surface area, porosity and pore-size distributions, as well as the diffusivity of fluids in porous catalysts.

Adsorption and conversion of reacting species at the (inner) surfaces of these nanoporous catalysts may therefore be traced using one or more of the techniques mentioned above, as well as some others to be outlined below. Typically, with access to synchrotron radiation, the nature of the catalytically active site, its change during the course of catalytic turnover, its "expired" and "re-activated" (regenerated) states may be identified in atomic detail, as was done by Maschmeyer *et al.* [6] in their study of the epoxdiation of cyclohexene at a Ti^{iv} –centered active site located at the inner-surface of a Ti-mesoporous silica catalyst.

Llewellyn *et al.* [4], as well as others [5] have illustrated how readily one may determine the micro- and meso-porosity of a nanoporous solid. (To be sure, the IUPAC convention stipulates that micropores are those that have diameter less than

Characterization of Solid Materials and Heterogeneous Catalysts: From Structure to Surface Reactivity, First Edition. Edited by Michel Che and Jacques C. Védrine.
© 2012 Wiley-VCH Verlag GmbH & Co. KGaA. Published 2012 by Wiley-VCH Verlag GmbH & Co. KGaA.

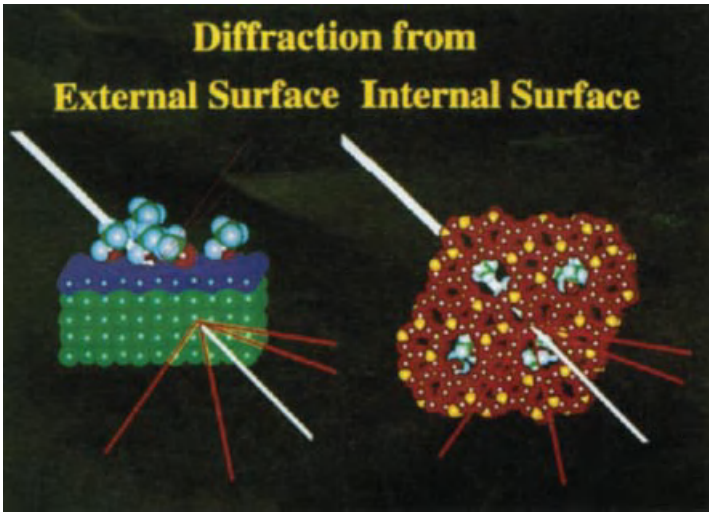


Figure 1 Illustration of the relative ease of probing experimentally the nature and properties of species at the internal surfaces of regular porous solids (right) compared with those of the exterior surface of a non-porous solid [2].

or equal to 20 Å; and mesoporous those that range from 20 to 500 Å or so). These days, increasing use is being made of so-called meso-cellular foam – see, *for example*, ref. [7], where dynamic kinetic resolution of esters is carried out using such a porous solid as a support for nanoparticles of Pd and immobilized *Candida antartica* lipase A. This trend is likely to increase.

In addition to the well-known, thermally stable, high-area, microporous solids, typified by zeotypes (i.e., naturally occurring and synthetic zeolites, aluminophosphates, silicoalumino phosphates and the like) that exhibit good catalytic properties [8, 9]) and the ever-increasing range of mesoporous oxides (based on silica and, nowadays, many metal oxides in mesoporous forms), there are also available several other types of porous solids that may be readily functionalised to behave as selective and/or active heterogeneous catalysts [10].

2
New Families of Nanoporous Catalysts

During the past decade there has been a burgeoning of new types of nanoporous solids, and many of the individual types are of considerable potential – in some cases already proven – as heterogeneous catalysts. It is instructive to tabulate the rich variety of nanoporous types that are of relevance catalytically. This is done in Table 1, with accompanying brief comments on the quintessential features of each type.

Table 1 New Families of Nanoporous Catalysts and Adsorbents (The entries in this Table are not comprehensive and are given in rough chronological order of publication).

Title of Work	Senior Author	Refs.
Systemic Design of Pore Size and Functionality in Isoreticular MOFs and their Application to Methane Storage	Yaghi	[11]
Amorphous Metal Fluorides with Extraordinary High Surface Areas	Kemmitz	[12]
Exploiting the Synergy Between Co-ordination Chemistry and Molecular Imprinting in the Quest for New Catalysts	Gagné	[13]
Nanoporous Metal-Containing Nickel Phosphates: A Class of Shape-Selective Catalyst	Chang, Park and Cheetham	[14]
A Microporous Scandium Terephthalate with High Thermal Stability	Wright and Ferey	[15]
Ordered Mesoporous Materials in Catalysis	Schüth	[16]
Chiral Three-Dimensional Microporous Nickel Aspatate with Extended Ni-O-Ni Bonding	Jacobson	[17]
A Family of Nanoporous Materials Based on An Amino Acid Backbone	Rosseinsky	[18]
Insight into the Construction of Open-framework Aluminophosphates	Yu and Xu	[19]
A Shape-selective Catalyst for Epoxidation of Cyclic Olefines: The Nanoporous Nieckel Phosphate VSB-5	Chang	[20]
Design of Open-Framework Germanates by Combining Different Building Units	Zou	[21]
Amphiphilic Organosilane-directed Synthesis of Crystalline Zeolite with Tunable Mesoporosity	Ryoo	[22]
How Hydration Drastically Improves Adsorption Selectivity for CO_2 over CH_4 in the Flexible Cr Terephthalate MIL-53	Llewellyn	[23]
Metal-organic Frameworks – Prospective Industrial Applications	Müller	[24]
Porous Solids Get Organized	Van Santen	[25]
High H_2 Adsorption by Co-ordination- Framework Materials	Schröder, Champness and Hubberstey	[26]
The Flexibility Window in Zeolites	Thorpe	[27]
High-temperature-stable Catalysts by Hollow Sphere Encapsulation	Schüth	[28]
Heterogeneous Asymmetric Catalysis with Homochiral Metal-organic Frameworks: Network-structure-dependent Catalytic Activity	Lin	[29]
Zeolite A Imidazolate Frameworks	Hayashi and Yaghi	[30]
The Next Generation of Shape- persistent Zeolite Analogues: Covalent Organic Frameworks	Masterlerz	[31]
Designer Pores Made Easy	Zaworotko	[32]
Kinetic Gate-opening Process in a Flexible Porous Co-ordination Polymer	Kitagawa	[33]
A Biporous Co-ordination Framework with High H_2 Storage Density	Habberstey, Champness and Schröder	[34]

(*continued*)

Table 1 (*Continued*)

Title of Work	Senior Author	Refs.
Generation of a Solid Brønsted Acid Site in a Chiral Framework	Rosseinsky	[35]
A Zeolite Family with Chiral and Achiral Structures Built from the Same Building Layer	Zou	[36]
Formation Mechanism of Porous Anodic Al and Ti Oxides	Zhou	[37]
Chiral Zeolitic Materials: Structural Insights and Synthetic Challenges	Zou	[38]
Enantioselective Catalysts with Homochiral Metal Organic Frameworks	Lin	[39]
Bridging the Materials Gap in Catalysis: Entrapment of Molecular Catalysts in Functional Support and Beyond	Thomas and Driess	[40]
A Crystalline Imine-Linked 3D Porous Covalent Organic Framework	O'Keeffe and Yaghi	[41]
Formation, Microstructures and Crystallization of Anodic TiO_2 Tubular Arrays	Zhou	[42]
Oxidation of Organic Compounds by Sulfonated Porous Carbon and H_2O_2	Shokrolaki	[43]
Enlightened Pores	Rosseinsky	[44]
Regioselectively Controlled Synthesis of Colloidial Mushroom Nanostructures and their Hollow Derivatives	Lu	[45]
Designing Heterogeneous Catalysts by Incorporating Enzyme-like Functionalities into MOFs	Lillerud and Olsbye	[46]
Photoactivation of Nanoporous Crystal for On-demand Guest Trapping and Conversion	Kitagawa	[47]
Depart-Siting Selectivity in Nanoporous Catalysts: Rational Use of Templates	Gomez-Hortigüela	[48]
Catalysis by MOFs	Van Bokhoven	[49]
Manganese-containing Porous Silicates: Synthesis, Structural Properties and Catalytic Applications	Tusar	[50]
Role of Hydrocarbons in Pore Expansion and Contraction of a Flexible MOF	Thallapally	[51]
Vitalising Porous Inorganic Silica Networks with Organic Functions: Periodic Organosilicas and Related Hybrid Materials	Fröba	[52]
A Salicylbisiniene Cage Compound with High Surface Area and Selective CO_2 CH_4 Adsorption	Mastalerz	[53]
Targeted Synthesis of Single Site Vanadyl Species on the Surface and in Framework of Silicate Building Block Materials	Barnes	[54]
Nanoporous Organics Enter the Cage Age	Cooper	[55]
Modular and Predictable Assembly of Porous Organic Molecular Crystals	Jones, Cora and Day	[56]

Notes(a). Two early comprehensive accounts of Open-Structure Heterogeneous Catalysts are given in references [57, 58].(b). Hypothetical Zeolitic Frameworks and the Systemic Enumeration of Microporous Solids with the aim of achieving Designer Heterogeneous catalysts are given in references [59, 60].(c). An extensive collection of informative papers, published in 2004, on numerous kinds of nanoporous materials is given in reference [61].(d). Regular meetings of COPS (Characterization of Porous Soilds) take place *ca* every three years. Proceedings of this meetings are worthy of consultation.

3
Which Physical Techniques are Preferred for the Characterization of Nanoporous and Powdered Catalysts?

Elsewhere in this text essentially all techniques currently deployed for the characterization of catalysts have been fully described. Here we summarize those that are likely to be much used for porous solids in the future; but we initially recall those that, notwithstanding their extreme importance for investigating model solid catalysts, are unlikely ever to play a significant role, for obvious practical reasons, in characterizing nanoporous materials. These include STM, AFM, polarization-modulation IR spectroscopy and LEED. However, much useful information pertaining to the crystal growth of nanoporous materials may be garnered by combining, as was done by Anderson *et al*. [62] high-resolution scanning electron microscopy with atomic force microscopy.

The central importance of transmission electron microscopy in the characterization of all the major kinds of solid catalysts is described in this publication in the chapter by Thomas and Ducati [63], as well as in even more recent reports by Su [64], by Thomas and Midgley [65] and by Zewail and co-workers [66], who have adapted conventional scanning electron microscopy so as to investigate the spatio-temporal visualization of surface dynamics following the initiation of change effected by femtosecond heating or excitation pulses [67].

Among the techniques required to characterize nanoporous catalysts described in this text, arguably the single most important one is that of gas adsorption for retrieving the surface area, porosity, pore-size distribution of, as well as adsorption in and diffusion of guest species within nanoporous catalysts. The reader is referred to Chapter by Llewellyn *et al*. [4], and earlier publications by protagonists in this field – see references [68–72].

The elemental composition of nanoporous catalysts is derived from a range of the traditional analytic techniques of atomic emission (or absorption) spectroscopy, supplemented by other techniques such as photoelectron spectroscopy [73, 74]. And the 3D distributions of elements can be readily retrieved from energy-filtered electron tomography [67]. Infrared spectroscopy [75] Raman Spectroscopy [76] as well as UV-visible spectroscopy [77] are invaluable for identifying both the composition of the nanoporous hosts and adsorbed guest species. Variants of solid-state NMR, such as the *in situ* method devised by Harris [78–80], are also invaluable.

4
The Special Merits of New Techniques and Recent Advances in Older Ones

Here we briefly discuss the continuing advances and promises associated primarily with electron microscopy (EM) on the one hand and synchrotron radiation (SR) on the other. (An earlier discussion of their relative strengths is contained in Chapter 7 of reference [67]. Dramatic technical advances are still being made with both in EM and in the deployment of SR; and their impact in the study of dynamic processes

involving nanoporous catalysts are likely to be profound chemical significance, especially for *in situ* characterization.

Given that, in the hands of Zewail and co-workers – see references [65–67] for recent summaries – femtosecond pulses of thermal or electronic excitation can be delivered to a specific, highly localized region of a specimen under investigation, and that spatial resolutions to less than a nanometer can be consequentially monitored, it will soon become feasible to probe the free energy landscape [79a] of both guest and host in a nanoporous catalyst. But it is not only on the dynamic side of structural characterization by EM that we may expect further advances. The long and successful paths taken by workers such as Klug, Henderson, Unwin, Crowther and others in the Laboratory of Molecular Biology, Cambridge, in retrieving the structure of viruses and other macromolecules from electron micrographs – see Chapter 7 of reference [67] for a summary – have led to yet further important advances. Thus Glaser *et al.* [79b] have succeeded to minimize beam-induced (radiation) damage of an organic specimen to such a degree that they can image, with perfect contrast, materials like paraffin monolayer crystals. In addition the pioneering work of Baumeister and colleagues in Martinsried on *electron cryomicroscopy*, especially cryo electron tomography, is likely to be applicable for future specialized investigations of organic-inorganic composite porous materials, where beam-sensitivity is a troublesome problem.

For new zeolitic (microporous) and highly ordered mesoporous solids the *combined use of X-ray powder diffractometry and electron microscopy* is likely to prove useful, as it was in the solution of the structure of the zeolitic catalyst IM-5 [80]. This is one of the most complex of known zeolites: it has an unusually large unit cell (C-centered orthorhombic with $a = 14.299\,\text{Å}$, $b = 57.413\,\text{Å}$ and $c = 20.143\,\text{Å}$) with a unit cell volume that is almost triple that of ZSM-5. Baerlocher *et al.* [80] solved this structure using the so-called charge-flipping structure–solution algorithm of Oszlanyi and Sütö [81], extended to facilitate the combined use of powder diffraction and EM.

For non-ordered porous catalysts, or those in which individual crystallites of a powdered specimen exhibit structural and compositional heterogeneity, EM will remain the supreme technique because of its highly local (in a spatial sense) nature. And the utility of XPS as a preliminary procedure must not be under-estimated. Where co-crystal formation is pronounced, *tetrahertz* (i.e., far infra red) time-domain *spectroscopy* will prove very useful, as recent work has already shown [82]. One very powerful recent technique involving chiral crystals – and many nanoporous catalysts of this kind are now to hand [29, 83] – is that of *vibrational optical activity*, pioneered and recently reviewed by Barron and Buckingham [84].

Molecular simulation of guest species inside nanoporous hosts is also very well-developed, and much has been gained by a combined use of molecular dynamics simulation and dynamically corrected transition-state theory in understanding the diffusion of H_2 through metal-organic-frameworks (MOFs) [85].

In Silico investigations are already playing an important role in the characterization and design of new microporous catalysts. By adopting the so-called *configurational-bias Monte Carlo approach* [86], Smit *et al.* [87] can now simulate the behavior of large molecules (typically *n*-decane) inside micropores. As well as computing sorption

isotherms that coincide with experimentally determined ones, they can now predict (and indeed have already patented) the comparatively new zeolite framework structure known as GON and SFE as prime candidates for future industrial catalytic use. Such work harmonizes with the drive, experimentally, to visualize single-molecule diffusion in nanoporous materials, described elsewhere in this book [88] and in other work [89].

Although photoelectron spectroscopy cannot be used for *in situ* studies of porous solids, for the characterization of such materials in vacuo the *combined use of electron spectroscopy and electron microscopy* constitutes a powerful pair of techniques. As mentioned earlier, XPS is an invaluable preliminary aid in identifying the surface composition of polycrystalline and porous catalysts. In Ertl's article above [1] we are reminded of the potential of microspectrometers such as that involved in the SMART project installed at the Berlin BESSY synchrotron.

We end this overview by briefly recalling the *importance of synchrotron radiation* is characterizing nanoporous catalysts.

As a result of impressive methodological advances in recent years, thanks to the work of Harris *et al.* [90], David and others [91], the *determination of crystal structure from powder (X-ray) diffraction data* has now become a common place. Harris's pioneering work entailed the use of Monte Carlo methods, but other approaches are equally powerful.

Determinations of crystal structures in this way is greatly facilitated by the high degree of monochromaticity of synchrotron radiation. In addition, because of its extremely high intensity, ultra minute single-crystals of host-guest nanoporous solids, such as DAF-5 (a microcrystalline Co ALPO) containing its organic template, are readily amenable to single-crystal structural determination [92].

Synchrotron radiation also readily permits of the *study of the crystallization of templated microporous catalysts* (like Co ALPO-5) [93]; and a specially designed cell for *in situ*, solid-liquid interactions involving nanoporous solids has proved invaluable in such studies [57, 94]. Early on, at the Davy Faraday Laboratory of the Royal Institution of Great Britain, this author with GN Greaves devized a method of *recording in parallel X-ray diffraction patterns* and *X-ray absorption spectra* [95, 96]. The particular merit of recording XR diffraction and XR absorption data in parallel is that both short-range and long-range crystallographic order of a nanoporous solid may be probed *in situ*. Such an approach was used by Roberts *et al.* [97] to follow the course of crystallization of a titanosillicate which was expected to be a microporous solid. It transpired from the Ti EXAFS study [97] that the produced solid catalyst was a rather open layered structure containing 5-co-ordinated Ti^{iv} ions, a rather unusual state of co-ordination for this ion.

Numerous other studies of great relevance to the characterization of nanoporous catalysts may be effected by using synchrotron radiation. Not only can the actual course of catalytic turnover be directly probed by steady-state or time-resolved XAFS measurements – as in the Ti^{iv} centered epoxidation of alkenes [6] – but the precise oxidation state of the active site in a framework-substituted transition-metal ion (such as Co^{III} or Mn^{III} in MAPO catalysts [98–100], can be determined as well as other wide-ranging possibilities. These include combined small-angle and wide-angle X-ray

scattering (SAXS and WAXS), and the whole gamut of X-ray tomography of the kind pursued by Larabell and Le Gros and others at Berkeley, USA - see references [101–103] for further details.

5
The Potential and Promise of Neutron Scattering

In general terms, few techniques rival neutron scattering as a means of generating structural information especially of those materials that consist predominantly of light atoms. The ^{1}H and ^{2}H locations on the framework a solid microporous acids, for example, and the precise disposition of an organic molecule (such as pyridine within zeolite L [105] (in which, for experimental convenience, Al^{3+} ions are replaced by Ga^{3+}) are but two examples. The fact that neutrons readily penetrate even stainless steel reactors is another great advantage for their use in *in situ* studies. As well as the strictly structural aspects derivable from neutron powder diffraction coupled to Rietveld profile analysis there is also the scope for retrieval of spectroscopic information such as low-frequency vibrations associated with light atoms bonded to metal ions. An early example of the potential of neutron scattering studies conducted at low temperatures (*ca* 4 K) is illustrated in Figure 2, where the "free" protons that are responsible for catalytic cracking of hydrocarbons, and which are generated by the cation hydrolysis affected by the highly polarizing La^{3+} cations in ultra-stable La^{3+}-exchanged zeolite Y, are readily identified [106, 107].

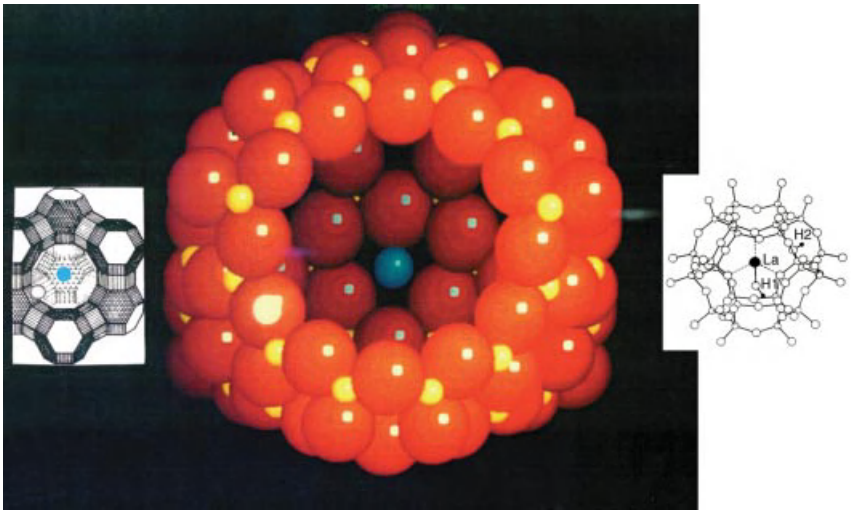


Figure 2 La^{3+} ion-exchanged zeolite Y, a typical commercial cracking catalyst, has La $(OH)^{2+}$ ions and H^{+} ions attached loosely to framework oxygens. The latter initiate cracking of hydrocarbons via carbenium and carbonium ions (see also JM Thomas and WJ Thomas: "*Principles and Practice of Heterogeneous Catalysis*" (1997), page 223, Wiley VCH).

With the availability of spallation sources of high-flux neutrons, as now exists in the Rutherford-Appleton Laboratory in the UK and elsewhere, much valuable information pertaining to nanoporous catalysts of an ordered kind should be retrievable under both static and dynamic (*in situ*) conditions.

References

1 Ertl, G. (2012) this book.
2 Thomas, J.M. (1996) *Faraday Disc.*, **105**, 1.
3 Thomas, J.M., Hernadez-Garrido, J.C., Raja, R., and Bell, R.G. (2008) *Phys. Chem. Chem. Phys.*, **11**, 2799.
4 Llewellyn, P.L., Bloch, E., and Bounelly, S. (2012) this book.
5 Sing, K.S.W., Schüth, F. and Weitkamp, T. (eds) (2000) *Handbook of Porous Solids*, Wiley- VCH.
6 Maschmeyer, T., Rey, F., Sarkar, G., and Thomas, J.M. (1995) *Nature*, **378**, 159.
7 Engström, K., Shakeri, M., and Backvall, J.E. (2011) *Eur. J. Org. Chem.*, **1827**.
8 Branto, P.J., Hall, P.G., and Sing, K.S.W. (1993) *Chem. Commun.*, **1257**.
9 Rouquerol, F., Rouquerol, J., and Sing, K. (1999) *Adsorption by Powders and Porous Solids: Principles, Methodology and Applications*, Academic Press.
10 Schwickhardt, M., Johasan, T., Schmidt, W., and Schüth, F. (2002) *Chem. Mater.*, **14**, 3913.
11 Eddaoudi, M., Kim, J., Rosi, N., Vodak, D., Wachter, J., O'Keefe, M., and Yaghi, O.M. (2002) *Science*, **295**, 469.
12 Kermmitz, E., Gross, U., Rüdingersand, S., and Shekar, C.S. (2003) *Angew. Chemie. Intl. Ed.*, **42**, 4251.
13 Becker, J.J. and Gagné, M.R. (2004) *Acc. Chem. Res.*, **37**, 798.
14 Chang, J.S., Hwang, J.-S., Jhung, S.W., Park, S.-E., Férey, G., and Cheetham, A.K. (2004) *Angew. Chemie. Intl. Ed.*, **43**, 2819.
15 Miller, S.R., Wright, P.A., Serre, C., Loiseau, T., Marrat, J., and Férey, G. (2005) *Chem. Commun.*, 3850.
16 Taguchi, A. and Schüth, F. (2005) *Micropor. and Mesopor. Mater.*, **77**, 1.
17 Anokhina, E.V., Go, Y.B., Lee, Y., Vogt, T., and Jacobson, A.J. (2006) *J. Amer. Chem. Soc.*, **128**, 9957.
18 Vaidhyanathan, R., Bradshaw, D., Rebitty, J.-N., Barrio, J.P., Gould, J.A., Berry, N.G., and Rosseinsky, M.J. (2006) *Angew. Chemie. Intl. Ed.*, **45**, 6495.
19 Yu, J. and Xu, R. (2006) *Chem. Soc. Rev.*, **35**, 593.
20 Jhung, S.H., Lee, J.-H., Cheetham, A.K., Férey, G., and Chang, J.-S. (2006) *J. Catal.*, **239**, 97.
21 Christensen, K.E., Shi, L., Cownadson, T., Ren, T., Dadachov, M.S., and Zou, X. (2006) *J. Amer. Chem. Soc.*, **128**, 14238.
22 Choi, M., Cho, H.S., Srivastava, R., Verkatesan, C., Choi, D.-H., and Ryoo, R. (2006) *Nature Mater.*, **5**, 718.
23 Llewellyn, P.L., Bourelly, S., Serre, C., Filinchuk, Y., and Férey, G. (2006) *Angew. Chemie. Intl. Ed.*, **45**, 7751.
24 Müller, U., Schubert, M., Teich, F., Puetter, H., Schierle-Arndt, K., and Pastre, J. (2006) *J. Mater. Chem.*, **16**, 626.
25 van Santen, R.A. (2006) *Nature*, **444**, 46.
26 Lin, X., Jia, J., Zhao, X., Thomas, K.M., Blake, A.J., Walker, G.S., Champness, N.R., Habberstey, P., and Schröder, M. (2006) *Angew. Chemie. Intl. Ed.*, **45**, 7358.
27 Santbaeva, A., Wells, S.A., Treacy, M.M.J., and Thorpe, M.F. (2006) *Nature Mater.*, **5**, 962.
28 Arnal, P.M., Comothi, M., and Schüth, F. (2006) *Angew. Chemie. Intl. Ed.*, **45**, 8224.
29 Wu, C.-D. and Lin, D. (2007) *ibid*, **46**, 1075.
30 Hayashi, H., Cote, A.P., Furukawa, H., O'Keoffe, M., and Yaghi, O.M. (2007) *Nature Mater.*, **6**, 501.
31 Mastalerz, M. (2008) *Angew. Chemie. Intl. Ed.*, **47**, 445.
32 Zaworotko, M.J. (2008) *Nature*, **451**, 410.
33 Tanaka, D., Nakagawa, K., Higuchi, M., Hosike, S., Kubota, Y., Kobayashi, T.C., Takata, M., and Kitagawa, S. (2008) *Angew. Chemie. Intl. Ed.*, **47**, 3914.

34 Yang, W., Lin, X., Jia, J., Blake, A.J., Wilson, C., Hubberstey, P., Champness, N.R., and Schröder, M. (2008) *Chem. Commun.*, 359.

35 Ingelson, M.J., Barrio, J.P., Basca, J., Dickinson, C., Park, H., and Rosseinsky, M.J. (2008) *ibid*, 1287.

36 Tang, L., Shi, L., Borneau, C., Sin, J., Yue, H., Ojiva, A., Lee, B.L., Kritiskos, M., Bell, R.G., Bacsih, Z., Mink, J., and Zou, X. (2008) *Nature Mater.*, **7**, 381.

37 Su, Z. and Zhou, W. (2008) *Adv. Mater.*, **20**, 3663.

38 Yu, J. and Xu, R. (2008) *J. Mater. Chem.*, **18**, 4021.

39 Ma, L., Abrey, C., and Lin, W. (2009) *Chem. Soc. Rev.*, **38**, 1248.

40 Thomas, A. and Driess, M. (2009) *Angew. Chemie. Intl. Ed.*, **48**, 1890.

41 Uribe-Romo, F.J., Hunt, J.R., Furukawo, H., Klöck, Cl., O'Keeffe, M., and Yaghi, O.M. (2009) *J. Amer. Chem. Soc.*, **131**, 4570;See also Yaghi, D.M. *et al.* (2011) *J. Amer. Chem. Soc.*, **133**, 759.

42 Su, Z. and Zhou, W. (2009) *J. Mater. Chem.*, **19**, 2301.

43 Shokrolahi, A., Zali, A., and Keshavarz, M.H. (2010) *Chin. J. Catal.*, **31**, 1427.

44 Rosseinsky, M.J. (2010) *Nature Mater.*, **9**, 609.

45 Feyen, M., Weldenhaler, C., Schüth, F., and Lu, A.-H. (2010) *J. Amer. Chem. Soc.*, **132**, 6791.

46 Lullerud, K.P., Olsbye, U., and Tilset, M. (2010) *Topics Catal.*, **53**, 859.

47 Sato, H., Matsuda, R., Sugimoto, K., Takota, M., and Kitagawa, S. (2010) *Nature Mater.*, **9**, 661.

48 Gomez-Hortiguela, L., Pinar, A.B., Cora, F., and Perez-Pariente, J. (2010) *Chem.Commun.*, **46**, 2073.

49 Ronocchiani, M. and van Bokhoven, J.A. (2011) *Phys. Chem. Chem. Phys.*, **13**, 6388.

50 Tusar, N.N., Jank, S., and Gläser, R. (2011) *Chem. Cat. Chem.*, **3**, 254.

51 Matkuri, A.K., Thallapally, P.K., Nune, S.K., Fernandez, C.A., McGrail, P., and Attwood, J.L. (2011) *Chem. Commun.*, **47**, 7077.

52 Hoffmann, F. and Fröba, M. (2011) *Chem. Soc. Rev.*, **40**, 608.

53 Mastalerz, M., Schnieder, M.W., Oppel, I.M., and Presly, O. (2011) *Angew. Chem. Intl. Ed.*, **50**, 1046.

54 Lee, M.-Y., Jiao, J., Mayes, R., Hagmanard, E., and Barnes, C.E. (2011) *Catal. Today*, **160**, 153.

55 Cooper, A.I. (2011) *Angew. Chemie. Intl. Ed.*, **50**, 996.

56 Jones, J.T.A., Hasall, T. *et al.* (2011) *Nature*, **474**, 367.

57 Thomas, J.M. (1999) *Angew. Chemie. Intl. Ed.*, **38**, 3588.

58 Cheetham, A.K., Férey, G., and Louiseau, T. (1999) *Angew. Chemie. Intl. Ed.*, **38**, 3268.

59 Thomas, J.M. and Klinowski, J. (2007) *Angew. Chemie. Intl. Ed.*, **46**, 7160.

60 Majda, D., Almeida Paz, F.A., Friedrichs, O.D., Foster, M.D., Simplerer, A., Bell, R.G., and Klinowski, J. (2008) *J. Phys. Chem. C.*, **112**, 1040.

61 Lu, G.Q. and Zhao, X.S. (eds) (2004) *Nanoporous Materials: Science and Engineering*, Imperial College Press.

62 Stevens, S.M., Cubillas, P., Janssen, K., Teraski, O., Anderson, M.W., Wright, P.A., and Castro, M. (2008) *Chem. Commun.*, 3894.

63 Thomas, J.M. and Ducati, C., this book.

64 Su, D.S. (2010) *Angew. Chemie. Intl. Ed.* doi: 10.1002/anie 201004614

65 Thomas, J.M. and Midgley, P.A. (2011) *Chem. Phys.* doi: 10.1016/j.chemphys 2011.04.023

66 Mohammed, D.F., Yang, D.-S., Pal, S.K., and Zewail, A.H. (2011) *J. Amer. Chem. Soc.* doi: 101.1021/ja2031322

67 Zewail, A.H. and Thomas, J.M. (2010) *4D Electron Microscopy: Imaging in Space and Time*, Imperial College Press, London.

68 Gregg, S.J. and Sing, K.S.W. (1982) *Adsorption, Surface Area and Porosity*, 2nd edn, Academic Press, New York.

69 Ruthven, D.M. (1984) *Principles of Adsorption and Adsorption Processes*, Wiley Interscience, Wenheim.

70 Lastokie, C., Gubbins, K.E., and Quirke, N. (1993) *J. Phys. Chem.*, **97**, 4786.

71 Karge, H.G. and Weitkamp, J. (2008) *Adsorption and Diffusion*, Wiley-VCH.

72 Neimark, A.V., Lin, Y., Ravikovitch, P.I., and Thomas, M. (2009) *Carbon*, **47**, 1612.

73 Evans, S., Adams, J.M., Reid, P.I., Thomas, J.M., and Walters, M.J. (1979) *Anal. Chem.*, **49**, 2001.

74 Grünert, W. (2012) this book.

75 Thibault-Starzyck, F. and Maugé, F. (2012) this book.

76 Fan, F., Feng, Z., and Li, C. (2012) this book.

77 Jentoft, F. (2012) this book.

78 Xu, M., Harris, K.D.M., and Thomas, J.M. (2009) *Solid Stat Nucl. Magn. Reson.*, **131**, 223.

79 (a) See example, figure 6 of reference [65] and Kwon, O.H., Ortalan, V., and Zewail, A.H. (2011) *Ultramicroscopy*, **111**, 90;(b) Gläser, R.M., McMullan, G., Faruqi, A.R., and Henderson, R. (2011) *Ultramicroscopy*, **111**, 90.

80 Baerlocher, C., Gramm, F., Massüger, L., McCusker, L.B., He, Z., Hovmöller, S., and Zou, X. (2007) *Science*, **315**, 1113.

81 Oslanyi, G. and Süto, A. (2005) *Acta Crystallogr.*, **A61**, 147.

82 Nguyen, K.L., Friscic, T., Day, G.M., Gladden, L.F., and Jones, W. (2007) *Nature Mater.*, **6**, 206.

83 Yue, Q., Yang, J., Li, G.H., Li, G.-D., and Chen, J.S. (2000) *Inorg. Chem.*, **45**, 443.

84 Barron, L.D. and Buckingham, A.D. (2010) *Chem. Phys. Lett.*, **492**, 199.

85 Lu, B., Yangm, Q., Xu, C., Zhong, C., and Smit, B. (2008) *Phys. Chem. Chem. Phys.*, **10**, 3244.

86 Siepmann, J.I. and Frenkel, D. (1998) *Mol. Phys.*, **75**, 59.

87 Smit, B. and Maesen, T.L.M. (2008) *Nature*, **457**, 671.

88 Bräuchle, C., Lebold, T., and Bein, T. (2012) this book.

89 Zürner, A., Kirrstein, J., Döblinger, M., Bräuchle, C., and Bein, T. (2007) *Nature*, **450**, 705.

90 Harris, K.D.M., Fremayne, M., Lightfoot, P., and Bruce, P.G. (1994) *J. Amer. Chem. Soc.*, **116**, 3543.

91 David, W.I.F., Sharkland, K., McCuscker, L.B., and Baerlocher, C.H. (eds) (2012) *Structure Determination from Powder Diffraction Data*, OUP.

92 Sankar, G., Wyles, J.K., Jones, R.H., Thomas, J.M., Catlow, C.R.A., Lewis, D.W., Clegg, W., Coles, S.J., and Seat, S.J. (1998) *Chem. Commun.*, **117**.

93 Rey, F., Sarkar, G., Thomas, J.M., Barrett, P.A., Lewis, D.W., and Catlow, C.R.A. (1995) *Chem. of Materials*, **7**, 1435.

94 Shannon, I.J., Maschmeyer, T., Sankar, G., Thomas, J.M., Jones, R.H., and Madill, D. (1997) *Catal. Lett.*, **44**, 23.

95 Couves, J.W., Thomas, J.M., Greaves, G.N., Waller, D., Jones, R.H., Dent, A.J., and Derbyshire, G.E. (1991) *Nature*, **354**, 465;See also Bokhoven, J.A. *et al.* (2004) in *In Situ Spectroscopy of Catalysts* (ed. B.M. Weckhuysen), American Scientific Publishers and BS Clausenand Topsøe, H. (1993) *Catal. Lett.*, **20**, 2.

96 Sankar, G., Thomas, J.M., Rey, F., and Greaves, G.N. (1995) *Chem. Commun.*, 2549.

97 Roberts, M.A., Sankar, G., Thomas, J.M., Jones, R.H., Du, H., Chen, J., Pang, W., and Xu, R. (1996) *Nature*, **381**, 401.

98 Thomas, J.M. and Raja, R. (1998) *Chem. Commun.*, 1841.

99 Thomas, J.M., Greaves, G.N., Sankar, G., Wright, P.A., Chen, J., Dent, A.J., and Marchese, L. (1994) *Angew. Chemie. Intl. Ed.*, **33**, 1871.

100 Gomez-Hortiguela, L., Cora, F., and Catlow, C.R.A. (2011) *ACS Catalysis*, **1**, 18.

101 Larabell, C.A. and Le Gros, M.A. (2004) *Mol. Biol. Cell*, **15**, 957.

102 Le Gros, M.A., McDermott, G., and Larabell, C.A. (2005) *Curr. Opin. Struct. Biol.*, **15**, 593.

103 Midgley, P.A., Ward, E.P.W., Hungria, A.B., and Thomas, J.M. (2007) *Chem. Soc. Rev.*, **136**, 1477.

104 Chao, W., Harteneck, B.D., Liddle, A., Anderson, E.H., and Atwood, D.T. (2005) *Nature*, **435**, 1210.

105 Wright, P.A., Thomas, J.M., Cheetham, A.K., and Nowak, A.K. (1985) *Nature*, **318**, 611.

106 Cheetham, A.K., Eddy, M.K., and Thomas, J.M. (1984) *Chem. Commun.*, 1238.

107 Thomas, J.M. (2011) *Micropo. Mesopor. Mater.*, **146**, 3.

Part One
Molecular/Local Spectroscopies

Characterization of Solid Materials and Heterogeneous Catalysts: From Structure to Surface Reactivity, First Edition.
Edited by Michel Che and Jacques C. Védrine.
© 2012 Wiley-VCH Verlag GmbH & Co. KGaA. Published 2012 by Wiley-VCH Verlag GmbH & Co. KGaA.

1
Infrared Spectroscopy

Frédéric Thibault-Starzyk and Françoise Maugé

1.1
Introduction

Infrared (IR) light was discovered by Herschel in 1800 [1, 2] and the first commercial IR spectrometers appeared during World War II. IR spectroscopy has been used to study powdered heterogeneous catalysts since the 1960s, and *in situ* studies of working catalysts were first published in the 1970s [3]. IR spectroscopy underwent a complete renaissance when Fourier transform (FT) instruments became available in the 1980s, greatly improving the sensitivity of the technique and the quality of the spectra. Routine FTIR spectrometers appeared in chemistry laboratories around 1980. Their price has decreased steadily over time, and also that of the necessary hardware for mathematical treatment. Most heterogeneous catalysis laboratories now have an IR spectrometer, and it is now one of the basic techniques for the characterization of heterogeneous catalysts [4, 5]. Commercial cells are available for *in situ* IR studies during reactivity tests, leading to a steady increase in the number of publications in *in situ* IR spectroscopy. More than 15% of papers published in the field of heterogeneous catalysis present IR results. Our aim here is to give the beginner the necessary background and basic knowledge to start an IR study of their material. Experimental aspects will be presented, with the important points that should not be overlooked in order to obtain valid results. The complex spectra obtained by IR spectroscopy on the surface of a catalyst contain a true wealth of information. We have attempted to cover all of the main points, and give directions for further exploration.

1.2
Principles of IR Spectroscopy and Basic Knowledge for Its Use

1.2.1
IR Light

The mid-IR region, in which we are interested here, covers the range of the electromagnetic spectrum from 25 to 2.5 μm, that is, in wavenumber terms, from

Characterization of Solid Materials and Heterogeneous Catalysts: From Structure to Surface Reactivity, First Edition. Edited by Michel Che and Jacques C. Védrine.
© 2012 Wiley-VCH Verlag GmbH & Co. KGaA. Published 2012 by Wiley-VCH Verlag GmbH & Co. KGaA.

400 to 4000 cm^{-1}. The frequency of the radiation is denoted by ν, and the wavelength is $\lambda = c/\nu$.

The unit used in IR spectroscopy is the wavenumber, $\overline{\nu} = 1/\lambda = \nu/c$. It is the number of periods (number of waves) observed per centimeter, hence the wavenumber unit is cm^{-1}.

The energy of the quanta associated to the radiation is proportional to ν (and to $\overline{\nu}$): $E = h\nu$.

1.2.2 Matter–Radiation Interaction

Depending on the frequency and on the type of interaction with matter, various spectroscopic techniques can be developed. Radiation with a given frequency ν can change the energy of a system from the level E_i to the level E_f (and this radiation can thus be absorbed) only if that frequency is

$$\nu = \frac{E_f - E_i}{h}$$

Only the vibrations corresponding to a variation in the dipole moment in the molecule will lead to an absorption band in IR spectroscopy (the others will be active in Raman). In the mid-IR region, the radiation energy corresponds to changes in molecular vibration and rotation energies. The IR radiation will therefore be capable of changing the speed of rotations and vibrations in molecules each time it is tuned to the corresponding energies. The rotation energy is much lower than the vibration energy, and they will be observed in the lower region of the spectrum (lower $\overline{\nu}$). With lighter atoms, and with greater bond strengths, faster vibrations are observed in the higher wavenumber region. IR bands at lower wavenumbers will be observed with heavier atoms and with weaker bonds. Heavy and large atoms and molecules will rotate more slowly and will lead to rotation levels with IR bands in the low $\overline{\nu}$ region, towards the far-IR and microwave regions.

1.2.3 Spectrometry, Interferometry

Older spectrometers analyzed light with the aid of a monochromator. Wavelengths were analyzed in sequence, by dispersing light using a prism or a grid. Modern spectrometers are based on an interferometer. All wavenumbers are analyzed simultaneously and are digitally distinguished by Fourier analysis. The gain in energy is huge, since the whole of the light beam is collected.

In an interferometer (Figure 1.1), the light beam is divided into two on a beamsplitter before it reaches the sample. The two beams are recombined by two mirrors and sent to the sample, but one of the mirrors is mobile and can create a longer or shorter path on the way to the sample. The two beams will interfere depending on the path difference δ. During the measurement, the moving mirror scans so that the intensity (V) of the light collected on the detector depends on the

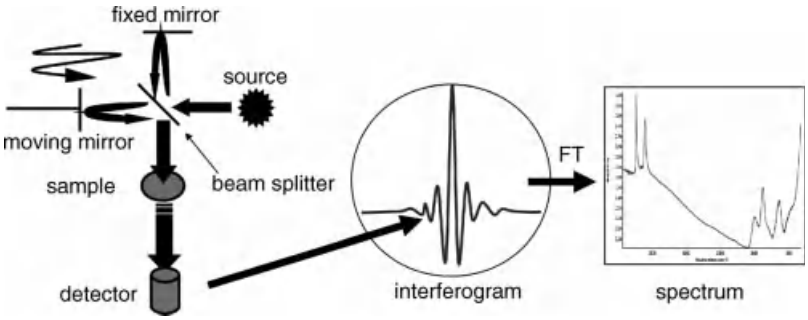


Figure 1.1 Design of an interferometric spectrometer.

intensity of the light from the source (I), on the frequency (ν_0) of the light, and on the position of the mirror (constructive or destructive interference depending on δ):

$$V(\delta) = I[1 + \cos(2\pi\nu_0\delta)]$$

The interferogram (intensity as a function of the path difference) is a sine function (more exactly, a cosine function) (Figure 1.2). The Fourier transform will lead back to the value of ν_0:

$$I(\nu) = \int V(\delta)\cos(2\pi\nu\delta)\,\mathrm{d}\delta$$

With polychromatic light, the interferogram will be the sum of several cosine functions with various periods: they all co-add in the middle ($\delta = 0$), and add more and more destructively with increasing δ, eventually summing to zero at infinite path difference (Figure 1.3). With increasing number of cosine functions, the results resemble more and more the typical interferogram observed on an interferometer for polychromatic light.

Fourier's theory states that any complex function can be analyzed as the sum of sine functions. The Fourier transform allows these functions to be re-found, and will yield the frequencies of the bands present in the interferogram. A continuous source is considered as the sum of an infinite number of bands. From the difference between

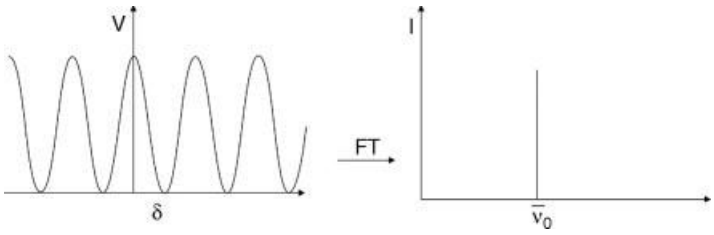


Figure 1.2 Interferogram of a monochromatic light and its Fourier transform (only the positive part of the Fourier transform is shown).

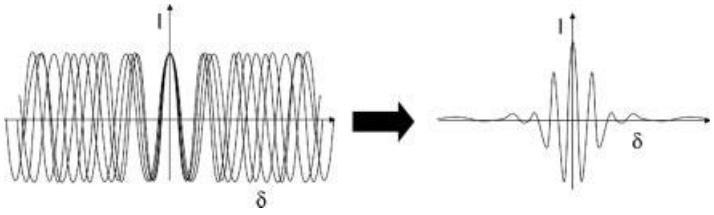


Figure 1.3 Sum of cosine functions with various periods, forming the interferogram of a polychromatic light.

the spectrum of the instrument (so-called background spectrum) and the spectrum of the instrument plus sample, the spectrum of the sample can be obtained.

1.2.4
Limitations of and Problems with the Fourier Transform

This method can only be applied rigorously when the integration is done between $-\infty$ and $+\infty$, but the measurement is (usually) only done between the limits of the movement of the mirror with a path difference between $-l$ and $+l$. The interferogram is thus actually the convolution product between the "infinite" interferogram and a rectangular function. The Fourier transform of a rectangular function is a sinc function (cardinal sine) (Figure 1.4).

Each spectral line will therefore be convoluted with this sinc function. It will be deformed, and shaped similarly to the sinc function. Each line, if assumed initially to be infinitely narrow, will be enlarged and will have side bands. These lobes can be removed by decreasing the relative contribution of the sides of the interferogram, by convoluting it with another function such as triangular, Happ–Genzel, and so on. This method is called apodization (removal of band feet). The main drawback is band broadening. The minimum width of the lines obtained is therefore linked to the integration limits $-l$ and $+l$ and to the path of the mirror. The larger the rectangular function (the greater the move of the mirror), the better is the spectral resolution.

To improve the graphical aspect of the spectrum, by a method very close to an interpolation, the size of the interferogram can by artificially increased by adding

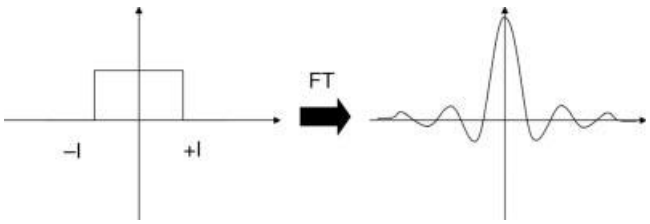


Figure 1.4 Rectangular function (path difference between $-l$ and $+l$) and its Fourier transform, the sinc function.

zeros on its sides, where the values will anyway be very close to zero. This is called zero filling. A doubling of the size of the interferogram corresponds to a zero filling factor of 2, and so on. The spectrum is in this way smoothed in agreement with the interferogram. Despite the possible observation of new lobes on some lines, this computing trick does not improve the spectral resolution, in contrast to a greater path difference with the moving mirror. No new information is added to the interferogram, but better advantage is taken of it. On solids (and for adsorbed phases) the intrinsic width of the bands is large, and there is no need to work at a resolution better than 2 cm^{-1}, but in order to obtain the best accuracy on the position of the band, one or two levels of zero filling are needed. By decreasing the "optical" resolution, the displacement of the moving mirror is limited, and so is the time needed for the complete scan. This is useful for improving time resolution for *in situ* or *operando* experiments.

1.3
Experimental Considerations

1.3.1
Technical Aspects of the Fourier Transform

The IR signal is digitalized to obtain the numerical data for the Fourier transform. The analog to digital converter must be very precisely synchronized with the movement of the moving mirror, and the position of this mirror must be known continuously with great accuracy. A second light, perfectly monochromatic (an He–Ne laser at 15 798 cm^{-1}), is used to form a secondary interferogram that will be used just for that purpose. This second interferogram is a sine function of the optical retardation (path difference). One point of the main interferogram will be collected each time the second interferogram is at its maximum (when the sine function is 1), that is, every 0.3164 μm during the course of the mirror. The stability of the laser and of the electric zero for the instrument will therefore be of paramount importance for the reliability of the spectrometer. This will provide the interval for the sampling, and the next step will be to determine the origin of the interferogram: the point where the path difference with the moving mirror is zero (zero path difference, ZPD). This is usually taken as the maximum value for the IR interferogram.

The IR source is usually a globar (glowing bar): a rod of silicon carbide heated by an electric current, at temperatures between 800 K (4500–300 cm^{-1}) and 1200 K (8000–50 cm^{-1}).

Two main types of detectors are used, thermal (measuring heat on a target) and quantum detectors (counting photons) with different sensitivity, response speed, and spectral range. Thermal detectors are also called DTGS (deuterated triglycine sulfate), and quantum detectors MCT (mercury–cadmium–tellurium), type A or B, cooled with liquid nitrogen. Much more sensitive and faster, MCT detectors are also much more expensive. They are needed for operando studies, or for working in diffuse reflection mode. DTGS detectors quickly lose sensitivity with increasing ambient

temperature, but their response is more linear with increasing absorbance (at low signal).

The nature of the beamsplitter will influence the available spectral range of the spectrometer. It is KBr for the mid-infrared region, and extended KBr beamsplitters allow working from 400 to 7000 or 8000 cm^{-1}, which is clearly a strong advantage for studying OH groups (these beamsplitters provide more energy between 3500 and 4000 cm^{-1}) or for harmonics and combination bands. For the near- or far-IR regions (not very commonly used in catalysis), specific beamsplitters are employed (quartz or CaF_2, and CsI or Mylar, respectively).

1.3.2 Practical Implementation

We present here some general experimental considerations for IR spectroscopy. The experimental setup for each type of experiment will be presented in the corresponding sections: *in situ* and static conditions in Section 1.4.2.1, and operando and flow conditions in Section 1.5.1.

1.3.2.1 Transmission Experiments, Quantitative Aspects

Most often, IR experiments are performed in the transmission mode (Figure 1.5). The light passes through the sample, which is simply placed in the IR beam, between the source (incident intensity $I_{0\nu}$ at frequency ν) and the detector (measured intensity I_ν). $I_{R\nu}$ is the intensity reflected by the sample; it does not reach the detector. For quantitative modeling, the sample is assumed to behave like a parallel-faced plate (thickness e).

Kirchhoff's law is

$$T + \rho + A = 1$$

where T is the transmittance (I/I_0), ρ is the reflectance (I_R/I_0), and A is the absorption, energy absorbed by the sample (and diffused away from the detector). In transmission experiments, reflected and diffused energies are kept as low as possible, and are actually neglected. The measured value is T, which can be transformed in absorbance, or optical density: $d = \log(1/T)$ (a decimal logarithm is used here, but

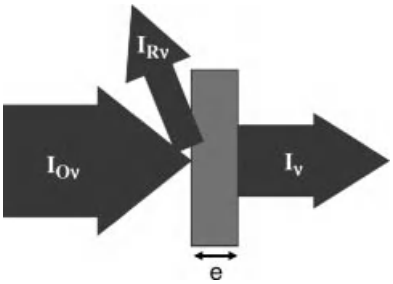


Figure 1.5 The transmission experiment.

some spectroscopists, especially in Russia, use the natural logarithm, which can completely modify the values and the molar absorbance coefficients).

Light attenuation follows the Beer–Lambert law:

$$T = I/I_0 = \exp(-\kappa_\nu ce)$$

where e is the sample thickness, c is the concentration of absorbing species, and κ_ν is the molar absorption coefficient (in $mol^{-1}\,dm^3\,m^{-1}$) at frequency ν. This law can also be written in terms of the optical density:

$$d = \varepsilon_\nu ce$$

where ε_ν is then the molar absorption coefficient (also in $mol^{-1}\,dm^3\,cm^{-1}$) and $\varepsilon = \kappa/2.3$. It is noteworthy that in powders, the particle size influences ε, which slightly increases with decreasing particle size. In the commonly used pellets, ε is not directly accessible. The amount of species interacting with the light beam is ce, and the following expression is used:

$$ce = n/S$$

where n is the number of adsorbing species in the pellet and S is the area of the pellet. It follows that

$$d = \varepsilon_\nu \left(\frac{n \times 10^{-3}}{S}\right)$$

with n in μmol. Depending on authors, and in order to simplify the equations, the units used for ε are commonly $mol^{-1}\,dm^3\,cm^{-1}$, or $mol^{-1}\,cm^2$ (1000 times difference). The maximum absorbance or integrated area can be used for measuring a band. The latter is much more sensitive to baseline perturbations, but much less to differences in temperature or resolution. The integrated area is expressed in cm^{-1}, and the molar absorption coefficient will then be expressed in $mol^{-1}\,cm$, or more commonly in $\mu mol^{-1}\,cm$. On solids, calibration curves are necessary, and the Beer–Lambert law is not always valid (especially with hydrogen bonds [6]).

1.3.2.2 **Diffuse Reflection**

Diffuse reflection is another technique for measuring the IR spectrum. It became popular with the increased sensitivity of detectors and of FT spectrometers, and with available commercial cells. The light is no longer observed through a wafer, but reflected in all directions by the powder. The tedious and difficult task of making the wafer is avoided, and the powder is simply placed in a cup.

The light that hits the powder can be reflected as on the surface of a mirror, and this is specular reflection. Light can also penetrate the sample and be partly absorbed or transmitted further. The penetrating light can also be partially absorbed, reflected, and refracted inside the sample, and diffused back towards the surface of the sample; this is diffuse reflection (Figure 1.6).

If the sample is thick enough (a few millimeters), the intensity passing through the sample will be zero. If the specular reflection is weak enough (matt surface, fine

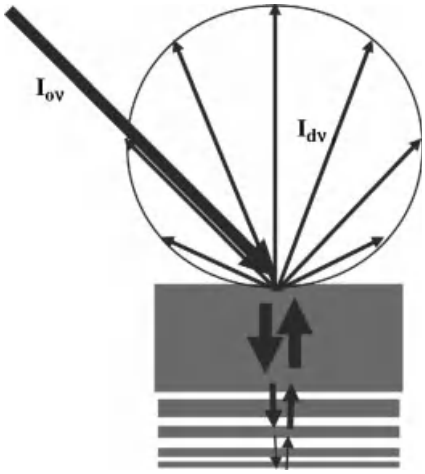


Figure 1.6 The diffuse reflection experiment.

powder), then the intensity of diffused light I_d will provide information about absorbed light in the sample. For a sample dispersed in a nonabsorbing matrix (such as KBr), the resulting spectrum is very similar to a spectrum recorded in transmission mode. However, the quantitative laws are not the same. The Kubelka–Munk function can be used to convert data so that band intensities are (to a first approximation) proportional to the amount of species observed. Optical density (absorbance units) can still be used for very weak bands, since the Kubelka–Munk function tends to be proportional to concentration at low absorbed intensity. It is, however, a misuse (absorbance is defined together with transmittance; it should be defined here with reflectance) and this approximation ceases to be correct as soon as the intensity increases.

The signal obtained depends on the light diffusion coefficient in the material. This coefficient is strongly linked to particle size, and depends directly on the ratio between particle size and wavelength. When the particle size is of the same order of magnitude as the wavelength, band intensities are linearly proportional to the wavelength. With smaller particles, bands are narrower, but their intensity is even more dependent on the wavelength. With larger particles, the intensity is more constant (but bands are broader). However, using the same molar absorption coefficient as in transmission is not possible.

Band intensities in diffuse reflection are also very much influenced by the temperature, which influences the diffusion coefficient in solids. Specular reflection can also be (relatively) important in spectral regions close to strong absorptions, and "false transparency" regions can appear in the spectrum (especially around structure vibrations in oxides). Checking the transmission spectrum is therefore an important aid before spending much time on the interpretation of the diffuse reflection spectra of solids.

1.4
Use of IR Spectroscopy to Characterize Solids

1.4.1
IR Spectrum and Structure of a Solid

The easiest way to measure the IR spectrum of a solid is to place the powder as a suspension in a neutral oil (Nujol) or, more generally, to disperse it (0.5–1%) in potassium bromide (KBr). The resulting powder is pressed (5–8 ton cm^{-2}, 5–8 $\times$ 10^8 Pa) to form a pellet placed directly in the IR beam. Such a method cannot be used for characterizing the surface properties of catalysts (e.g., with probe molecule adsorption studies), but can provide interesting information about the structure of the materials.

1.4.1.1 The Example of Zeolites

The KBr matrix method is used as a very general approach for the initial characterization of zeolites. The main bands observed are due to structure vibrations between 400 and 1300 cm^{-1} (Figure 1.7). These bands have been assigned to ν(T–O) vibrations:

- symmetrical: 700–850 cm^{-1}
- asymmetric: 1000–1200 cm^{-1}

Some of these were assigned to vibrations internal or external to the TO_4 tetrahedra. Modeling of framework vibrations in zeolites showed that these bands could not be assigned to the vibration of any particular interatomic bond, but rather that they are all produced by the vibrations of the network as a whole.

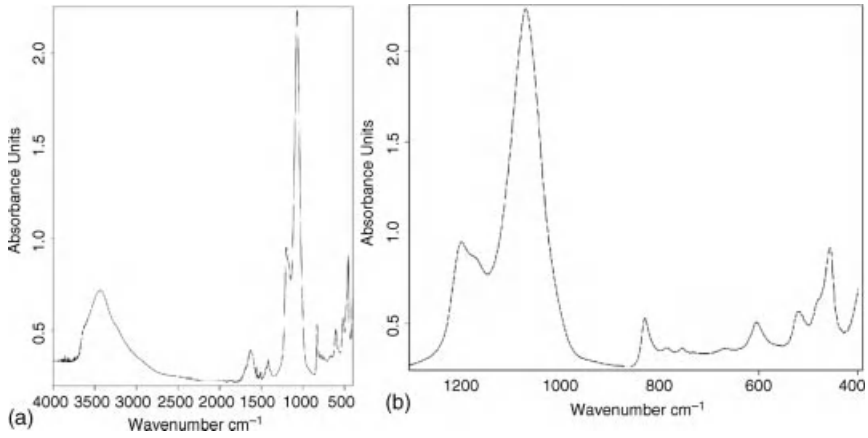


Figure 1.7 (a) Spectrum of a steamed Y zeolite, as KBr matrix pellet. (b) Zoom on the range of the structure vibrations.

The intensity of some of these structure vibration bands changes linearly with the amount of aluminum in the framework, and they are therefore assumed to be mostly due to Al–O vibrations. They can sometimes be used to measure the Al content [number of framework Al atoms per unit cell $N_{Al(F)}$]. Empirical relationships have been established between their frequency and the framework Si/Al ratio, as determined by other techniques such as NMR spectroscopy. The faujasite (FAU) structure is probably the one that has attracted the most attention in this area, especially in the pioneering work of Flanigen [7] and Lunsford [8]. For the bands at 1050 (ν_1) and 810 cm^{-1} (ν_2), the following relations were determined:

$$N_{Al(F)} = 0.766(1066.7 - \nu_1)$$
$$N_{Al(F)} = 1.007(832.8 - \nu_2)$$

The frequency of these bands decrease with decreasing Si/Al ratio, but they are also influenced by any extra-framework phase present, and a vibration more specific to hexagonal prisms at 600 cm^{-1} (and thus to the framework itself) is sometimes preferred. Chevreau and co-workers [9] showed that the frequency of this ν_3 band is linked to the aluminum concentration, and its intensity to the crystallinity of the sample (Figure 1.8):

$$N_{Al(F)} = -1.401\nu_3 + 856$$

It should be noted that cation exchange also influences the frequency of structure vibration bands in zeolites. Other structures are also well known: beta-zeolite [10] and mordenite [11]. In mordenite, the amount of Al per unit cell ($Al_{s/UC}$) has been linked to the frequency of a ν(Al–O) vibration band at about 650 cm^{-1}:

$\nu(Al–O) = 654 - 4.6Al_{s/UC}$ in the absence of sodium
$\nu(Al–O) = 651 - 3.8Al_{s/UC}$ when sodium is present in the zeolite.

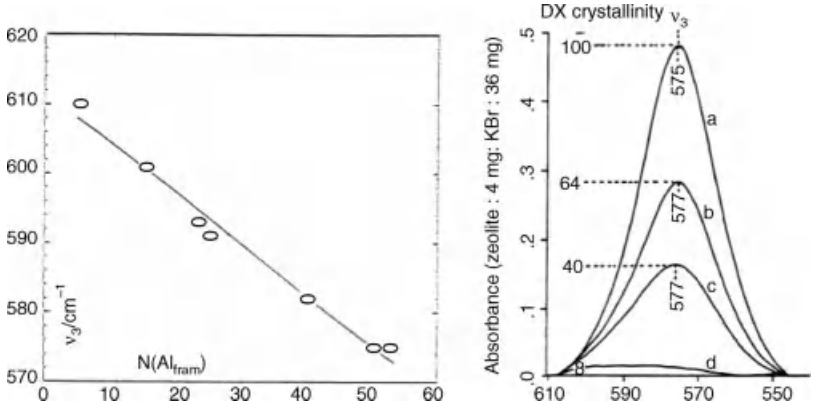


Figure 1.8 Monitoring framework aluminum content and crystallinity using structure vibration bands [9].

1.4.1.2 Substitution of Metals in the Structure of Zeolites

IR spectroscopy has been used for studying atom substitution in the framework of zeolites by looking at framework vibrations. In substitution by boron, for example, new bands can be detected at 1380, 920, 700 and 620 cm^{-1} [ν(B–O) and ν(B–O–Si) vibration bands]. New Brønsted acid sites were also detected on introducing heteroelements in AlPOs, and a new ν(OH) band appearing in the 3500–4000 cm^{-1} region can be another indication for the introduction of heteroelements.

1.4.2
Activation: Cleaning the Sample to Observe Surface Sites

The surface properties of solid powders (acid sites or adsorption of reactants on catalysts, for example) can only be studied on the pure sample after removal of unwanted surface species (physisorbed species, water, etc.) by the so-called activation treatment. Valuable information on surface sites can be obtained from analysis of the OH groups (Section 1.4.3), from identification of residual impurities (Section 1.4.2.2.2), or by using adsorbed probe molecules (Section 1.4.4).

1.4.2.1 Experimental Aspects

Most characterization work on surface properties is performed in the transmission mode. This should only be done with a self-supporting wafer of the pure solid, that is, without any KBr matrix that would contaminate the surface and introduce external ions. This wafer must be very thin (generally 10–20 mg for 2 cm^2) so that it remains IR transparent, and must only be pressed very gently ($<$500 kg cm^{-2}, 5×10^7 Pa) so that neither gas diffusion nor the structure of the solid are perturbed. This point must be strongly emphasized, since it is much easier to make a wafer by using higher pressure, but the quality of the results can be greatly affected, by damaging delicate crystal structures or by hindering gas diffusion and adsorption of probe molecules.

When the wafer is not thin enough, the energy collected by the detector will be too low: the spectrum will be noisy and (worse) the detector will not operate within its linearity range, leading to non-quantitative results. In order to avoid losing a linear response, the spectrum baseline must be low enough that bands do not reach intensities higher than 2 (or at very worst 3) in the range where no structure bands are present. This is especially true for liquid nitrogen-cooled MCT detectors, which are much more sensitive than the less expensive DTGS detectors, but for which this important drawback must be kept in mind.

Conversely, care must be taken to have very strong absorption of light by structure bands. If the optical density is not at least 4 (often 6) for the intense structure vibrations bands (typically below 1200 cm^{-1}), then energy reaches the detector where it should not. The wafer might be damaged (fractured) or wrongly aligned in the IR beam. Here again, no good quantitative results can be obtained.

1.4.2.1.1 Infrared Cell for *In Situ* Studies The wafer is placed in an IR cell allowing heating of the sample under vacuum and also adsorption of controlled doses (or a

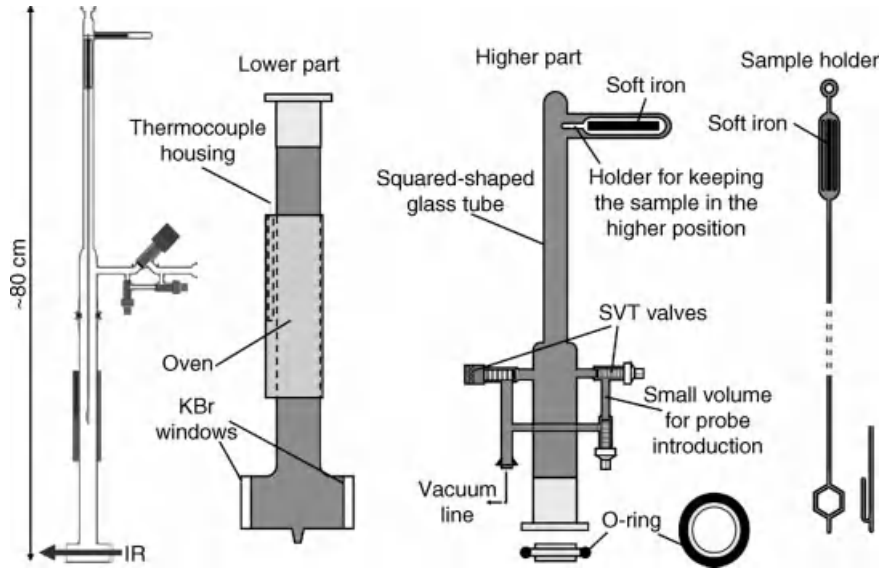


Figure 1.9 IR cell for transmission studies of solid catalysts under a controlled atmosphere (*in situ* studies). The sample holder can be moved from the lower (IR beam) to the higher position (oven) without opening or moving the cell by using magnets as handles. (Drawing by P. Bazin).

flow) of gas (Figure 1.9). Heating is commonly applied outside the IR beam, and the sample holder can move between the heating position and the position for recording the IR spectrum in the beam. Some studies must be performed at low temperatures and this is done by cooling the bottom of the cell with liquid nitrogen (or another cooling agent).

Depending on the measurement, various experimental conditions can be needed, for example, heating to 750–950 K for activation, cooling to 100 K for some probe molecule adsorption, or heating under a gas flow and under high pressure for catalyst activation under the reaction conditions. Many different cells have been designed by various laboratories working in the field in order to obtain these conditions. Special cells were designed for studying the surface *in situ* in a dynamic mode, so that the catalyst can be under working conditions (*operando*). These are presented later (Section 1.5.1).

1.4.2.2 **Activation – Cleaning the Sample to Observe Surface Sites**

Much useful information on a catalyst can be obtained during and after the activation process concerning the decomposition of organic precursors and formation of active sites.

1.4.2.2.1 **The Example of Zeolites** During activation of a zeolite, adsorbed water and any organic molecule such as the synthesis template are removed. The decrease in the amount of water can be monitored by the decrease in the intensities of the bands of

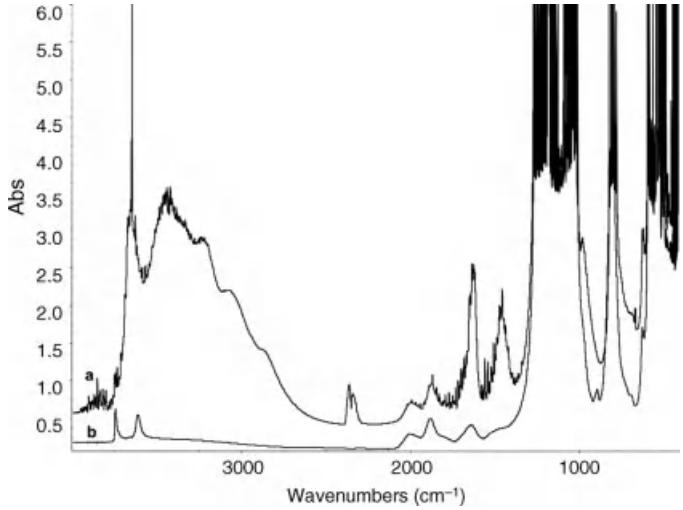


Figure 1.10 Spectrum of an MFI-type zeolite, (a) before (NH_4-MFI) and (b) after (H-MFI) activation treatment. The intense structure bands are visible below 1100 cm^{-1}, in addition to bands for water and ammonium before activation.

molecular water: the ν(OH) and the δ(OH) vibration bands (a very broad band around 3500 cm^{-1} and a broad band at ~1630 cm^{-1} respectively) (Figure 1.10). For a zeolite in the NH_4^+ form, the leaving ammonium group is visible as a band around 1460 cm^{-1} and controlling the activation is easy.

Some very sensitive zeolites, such as mordenite and aluminum-rich zeolites can easily be damaged during activation, and a self-steaming process can take place when the thermal treatment is too fast, thus leading to an extra-framework phase in the solid. This can be checked after the activation by verifying the absence of any vibration bands for AlOH groups [ν(OH) bands around 3660 cm^{-1}] and by measuring the number of Lewis sites by pyridine adsorption at the end of the experiment (a defect-free zeolite should contain no Lewis sites) (Figure 1.11).

If the activation is aimed at removing the templating agent in a zeolite, the corresponding IR bands must first be identified, and their progressive disappearance can be directly monitored *in situ* during the calcination treatment (Figure 1.12). These organic species cannot be removed by heating the solid under vacuum, but rather under air or a few torr of ozone.

1.4.2.2.2 **Residual Impurities** After metal oxide activation, even at high temperatures (>773 K), some bands below 1600 cm^{-1} could remain. They characterize the presence of remaining impurities, which are related to the history of the material (including the nature of the precursors or the solvent used for metal oxide preparation). The identification of the nature, structure, and amount of residual impurities such as carbonate, nitrate, and sulfate species, is important since they can modify the properties of the pure metal oxides, by blocking the accessibility of reactant to surface

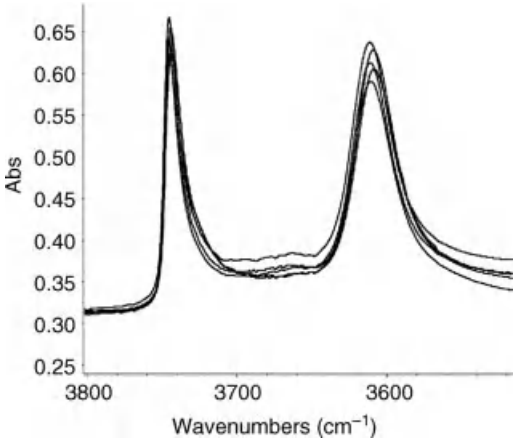


Figure 1.11 ν(OH) bands in MFI-type zeolites after various calcination procedures. Weak bands are visible around 3660 cm^{-1} showing the presence of an extra-framework aluminic phase in some of the samples.

sites, or by generating Brønsted and Lewis acidity (basicity) at the expense of the intrinsic basicity (acidity).

Carbonates The contact of the CO_2 present in air with metal oxide basic sites, such as oxygen or OH anions, leads to the formation of carbonate or hydrogencarbonate

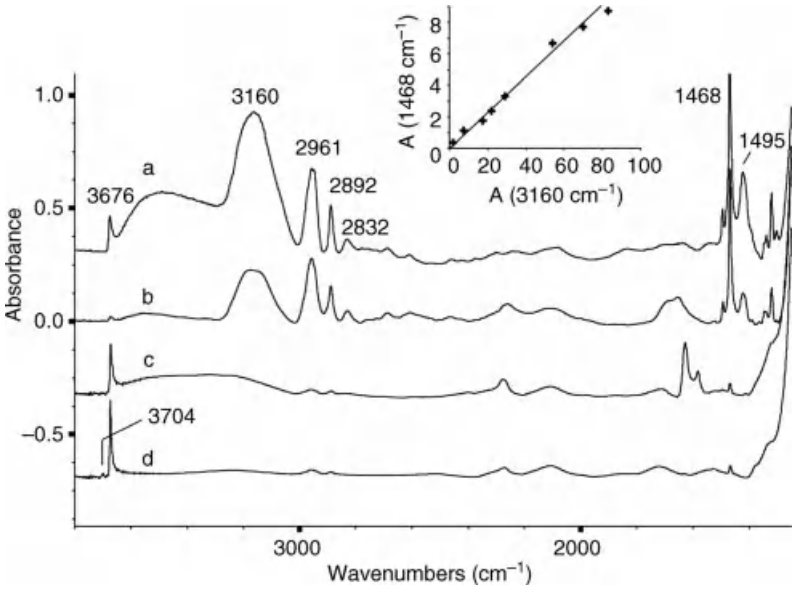


Figure 1.12 *In situ* calcination (from a to d) of cloverite under ozone in the IR cell [12]. The bands at 1468 and 3160 cm^{-1} are assigned to the template, and their progressive disappearance shows the corresponding increase in free OH groups on the surface (after evacuation, spectrum d).

groups, respectively. The free carbonate ion (D_{3h} symmetry) presents one asymmetric ν(CO) vibration at 1415 cm^{-1}. In the adsorbed state, its symmetry is lowered and two ν_3(CO) bands appear as a result of the splitting of the degenerate asymmetric ν(CO) vibration. The $\Delta\nu_3$ splitting is thought to characterize the structure of the species formed. Hence different structures of carbonate species can be identified as unidentate, bidentate, and bridging carbonates with a $\Delta\nu_3$ of about 100, 300, and 400 cm^{-1}, respectively. Thermal stability can also be a way to differentiate these species since unidentate are less stable than bidentate carbonates. Carbonate species with a strong resistance to thermal decomposition and a fairly low $\Delta\nu_3$ splitting can correspond to a polydentate structure, that is, a bulk-like or subsurface species.

Nitrates Similarly to carbonates, the free nitrate anion has D_{3h} symmetry. Two ν_3(NO) bands appear with adsorbed nitrates (instead of only one at 1380 cm^{-1} for the free anion) and the ν(NO) at ~1050 cm^{-1} becomes IR active (instead of being only Raman active). Similarly to carbonate ions, the splitting of the ν_3(NO) vibration and its thermal stability are greater for bidentate than for monodentate species. The similarity between NO_3^- and CO_3^{2-} spectra can lead to difficult band assignments when both species are present.

Sulfates Surface sulfate species on activated oxides are characterized by a band at ~1340 cm^{-1} together with several bands below 1260 cm^{-1}. They are specific to the single S = O group with the sulfur atom anchored to the oxide surface through three S–O–M linkages. Stable bulk surface species can also be formed on oxide presenting strong basic properties.

Note that other contaminants, such as chloride or sodium ions, could also be present but they do not lead to any characteristic IR band. However, it should be kept in mind that their presence could strongly modify oxide surface properties.

1.4.3
The Spectrum of OH Groups

The surfaces of metal oxides are preferentially terminated by hydroxyl groups, leading to important patterns in the mid-IR spectrum. The IR bands for OH groups can be ν(OH), δ(OH), or γ(OH). Elongation vibrations in OH groups are denoted ν(OH). They produce absorption bands in the IR spectrum between 3500 and 3800 cm^{-1}. The δ(OH) vibration is a deformation of the OH bond parallel to the plane of the two bonds on the oxygen atom (in-plane deformation). It leads to a band in the middle part of the mid-IR spectrum, between 1200 and 2000 cm^{-1}. The γ(OH) vibration is a deformation of the OH group out of the plane of the bonds on the O atom, leading to an IR band in the low-frequency region, usually below 1500 cm^{-1}.

The free hydroxyl groups gives a unique fingerprint of the acid sites (Brønsted acidity in oxides is brought about by the presence of OH groups), but also give indications on the structure of the subsurface oxide.

Theoretical studies helped in understanding the various parameters influencing the frequency of the ν(OH) band: the coordination number of the oxygen atom, the

coordination number of the neighboring cation (M), the location on defective crystal configurations (edge, corner or kink), the presence of cationic vacancies in the direct vicinity of the OH group, the electronegativity of the cation, and the oxidation state of the cation. DFT calculations indicate the presence of H-bonded OH groups even after oxide activation. Such bonds, of course, also strongly influence the frequency of the ν(OH) vibration.

Experiments and *ab initio* calculations both show that the ν(OH) frequency decreases when the number of associated cations M increases. This is in good agreement with the empirical basis assuming that cations have an electron-withdrawing effect on the electronic density of the OH group, then increasing the polarization of the OH bond. The frequency of these bands can be used as a first indication of the strength of the corresponding Brønsted sites: the stronger the acidity of the OH group, the lower is the electronic density between the oxygen and the hydrogen atoms (the bond strength decreases) and the lower the ν(OH) band frequency. This is not, however, a direct measurement of acidity, and this rule is often not valid. The ν(OH) frequency has a similar value, $3745 \pm 3\,cm^{-1}$, for a basic oxide such as MgO, for a weakly acidic amorphous silica, and for a strongly Brønsted acid such as amorphous silica–alumina [13]. The frequency of the ν(OH) band is strongly influenced by the local environment of the site, by the presence of neighboring OH groups or oxygen atoms (linked to the size of the pores and to the presence of the extra-framework phase in zeolites). The frequency of the ν(OH) vibration bands therefore cannot be used for the comparison of acid strengths in different solids, and not even for various sites located differently on the same solid.

1.4.3.1 OH Groups on Alumina

On alumina, at least five ν(OH) bands can be detected (at about 3790, 3770, 3755, 3730, and $3680\,cm^{-1}$). In the 1970s, several empirical models were proposed to account for these various OH groups. Considering the coordination number of bulk alumina oxygen atoms (4), only three types of surface OH groups are expected (referred to as type I, II, and III) [14]. Taking into account the different coordination numbers of aluminum cations (IV and VI), and the structure of the preferentially exposed planes of γ-alumina, Knözinger and Ratnasamy identified five different OH groups [15]. In more recent work using DFT calculations, Digne *et al.* proposed some differences in the assignments of the ν(OH) bands, but the general trends are similar [16].

1.4.3.2 OH Groups in Zeolites

Several different types of OH groups can be distinguished in zeolites. The two main types of sites are easily observed in MFI-type zeolites (Figures 1.10 and 1.11):

- $3745\,cm^{-1}$: vibration of isolated silanol groups, similar to those observed in silica, very weakly acidic
- $3610\,cm^{-1}$: bridged hydroxyl groups (SiOHAl), Brønsted acid sites.

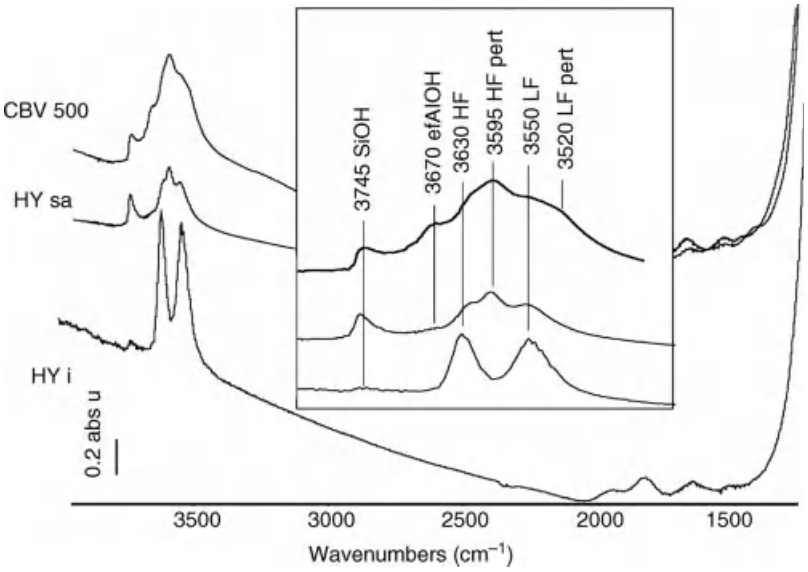


Figure 1.13 Spectra of activated HY zeolites: modified by isomorphic substitution (HYi), steamed and acid washed (HYsa), and industrially steam treated (CBV500). The inset shows a detail of the ν(OH), with silanols at 3740 cm^{-1}, OH groups in large cavities (HF at 3615 cm^{-1}) and in hexagonal prisms and sodalite cavities (LF at 3555 cm^{-1}). OH groups perturbed by extra-framework phase HF_{pert} and BF_{pert} are visible on steamed samples. The OH corresponding to the HF_{pert} is sometimes described as superacidic. The band at 3660 cm^{-1} comes from the ν(AlO–H) vibration in the extra-framework aluminic phase.

In the H-MFI zeolite, these bridged OH groups only lead to one ν(OH) vibration band, but in more complex structures such as mordenites or faujasites, the number of different ν(OH) bands increases. In the example of Y zeolite (Figure 1.13), we also observe:

- 3630 cm^{-1}: high-frequency (HF) band for OH in the supercages
- 3550 cm^{-1}: low-frequency (LF) band for OH groups in the sodalite units or hexagonal prisms of the structure.

When an extra-framework phase is also present in the sample, it will perturb the OH groups and produce additional bands:

- 3600 cm^{-1}: perturbed HF band bearing the strongest acidity (so-called enhanced acidity)
- 3520 cm^{-1}: perturbed LF band, probably also enhanced acidity, but out of reach for most molecules, and therefore without any direct role in acidity or catalysis.

Other nonacidic OH groups are also visible with lower intensity:

- 3660–3680 cm^{-1}: aluminic OH (extra-framework phase)
- 3775–3785 cm^{-1}: aluminic OH groups, often described as basic.

ν(OH) bands are slightly shifted to lower wavenumbers with increasing temperature, and can be observed 15–20 cm^{-1} lower at 450 °C than at ambient temperature. Upon heating, these bands also broaden. Conversely, on cooling (e.g., with liquid nitrogen for some adsorption studies), the ν(OH) bands become narrower and shift to higher wavenumbers.

ν(OH) bands with very similar frequencies can correspond to Brønsted sites with very different acid strengths, and they can only be distinguished by the use of probe molecules.

1.4.4 Characterization of Acidity with Probe Molecules

Acidity is in many cases the key point for catalytic activity. IR spectroscopy has long been used for the characterization of acidity since Brønsted acid sites are directly visible in the IR spectrum, and OH groups lead to very typical vibration bands. Lewis sites are most often not directly detected, and probe molecules must be employed.

IR spectroscopy is adapted to follow probe molecule adsorption on the catalyst surface, and thus to obtain information on the nature, strength, local arrangement, and amount of surface sites: acidic, basic, metal, or sulfide sites. On the choice of the probe molecule depends the type of information investigated [17].

A lot of information can be obtained by studying molecular interactions between a basic probe molecule and the surface of an acidic solid. Modifications in the spectrum of the probe molecule will indicate the type, strength, and density of sites on the surface. When an H-bond appears, its strength can be measured by IR spectroscopy, and corresponds to the acid strength of the site. Band intensities indicate the number of sites. The type of information obtained will be selected by carefully choosing the probe molecule for the study. Some probe molecules can even be used during the reaction for spectroscopic studies of the catalyst under working conditions (so-called *operando* studies, see the definition in Section 1.5). The ideal properties of IR probe molecules depending on the type of catalyst under study were given about 15 years ago by Lercher *et al.* [18] and Knoezinger *et al.* [19]. The basic strength, the size of the molecule, and its spectral response to a perturbation (band intensities and sensitivity of the frequency to the perturbation) are all important points. The molecule must be stable on the surface, and not be hydrolyzed or oxidized. It needs to be easily adsorbed on the solid (only vapors are introduced in the cell containing the solid sample). Several probe molecules can be used simultaneously or more commonly in sequence.

Acid sites can be Lewis or Brønsted sites. Coordinatively unsaturated sites (cations) are electron acceptors, and thus Lewis acids. OH groups can give their proton away and are Brønsted sites. Lewis sites will bind to nucleophilic molecules. Brønsted sites will form with the basic probe molecule various types of complexes. Depending on the strength of the site (and of the probe), a weak or strong H-bond can be formed, or even a more or less dissociated ion pair. When the size of the molecule is comparable to that of the oxide cavity, electron densities in the basic molecule are modified, the basicity of the probe can be enhanced, and the proton transfer can occur more easily.

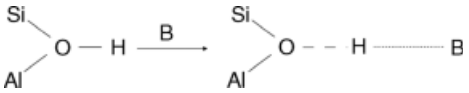


Figure 1.14 Interaction of a base with a Brønsted site and creation of an H-bond.

All of these parameters show that the basicity of the probe molecule cannot be considered without the solid, and that it is always a pair at work.

1.4.4.1 Brønsted Sites: Hydrogen Bonding and IR Spectroscopy

When a H-bond is created between the probe molecule and a hydroxyl group on the surface (Figure 1.14), the electron density between the oxygen and hydrogen atoms decreases, the distance between them increases, and the OH bonding is weakened. The elongation vibration ν(OH) becomes slower, and the corresponding ν(OH) band is shifted to lower wavenumbers (red or bathochromic shift). Other modifications are induced by the elongation of the OH bond: the variation of the dipolar moment during the vibration also increases, and the integrated intensity of the ν(OH) vibration band increases. For reasons that we will explain later, the ν(OH) band also broadens when the proton is engaged in H-bonding, and the maximum intensity decreases (the band "flattens").

1.4.4.1.1 Quantification of the ν(OH) Shift [20] The size of the bathochromic shift of the ν(OH) band, denoted $\Delta\nu$(OH), is a good measurement for the formation enthalpy for H-bonding (bond strength, ΔH). There is no simple relationship between ΔH and $\Delta\nu$(OH), but similarly to the case of cyclohexanol in various solvent, ΔH is considered to be proportional to $\sqrt{\Delta\nu(\mathrm{OH})}$. A series of bases can be used to build a scale with which acids can be compared. This is the so-called BHW method (Bellamy–Hallam–Williams) (Figure 1.15). In that case, the ratio of $\Delta\nu$(OH) to the frequency ν_0 for the free OH group is preferred. For two acids 1 and 2, the points obtained for the series of bases will fit a straight line:

$$\left(\frac{\Delta\nu}{\nu_0}\right)_1 = A + B\left(\frac{\Delta\nu}{\nu_0}\right)_2$$

where B is the relative strength of 1 compared with 2. B can be linked to parameters describing the Brønsted acid strength, such as pK_a.

1.4.4.1.2 Distortion of ν(OH) When an H-bond is created, the width at half-maximum increases considerably for the ν(OH) vibration band [22]. This can be explained partly by the deformation of the OH vibrator, because of the interaction between the proton and a second nucleophilic center.

In the extreme case of protonation, the curve of the energy as a function of the O–H interatomic distance (Morse curve) presents two separate minima: one with the proton on the oxygen atom, and the other (deeper) one for the proton transferred on the nucleophilic probe molecule (Figure 1.16). In the case of a moderate interaction, the Morse curve is already far from that of a harmonic oscillator.

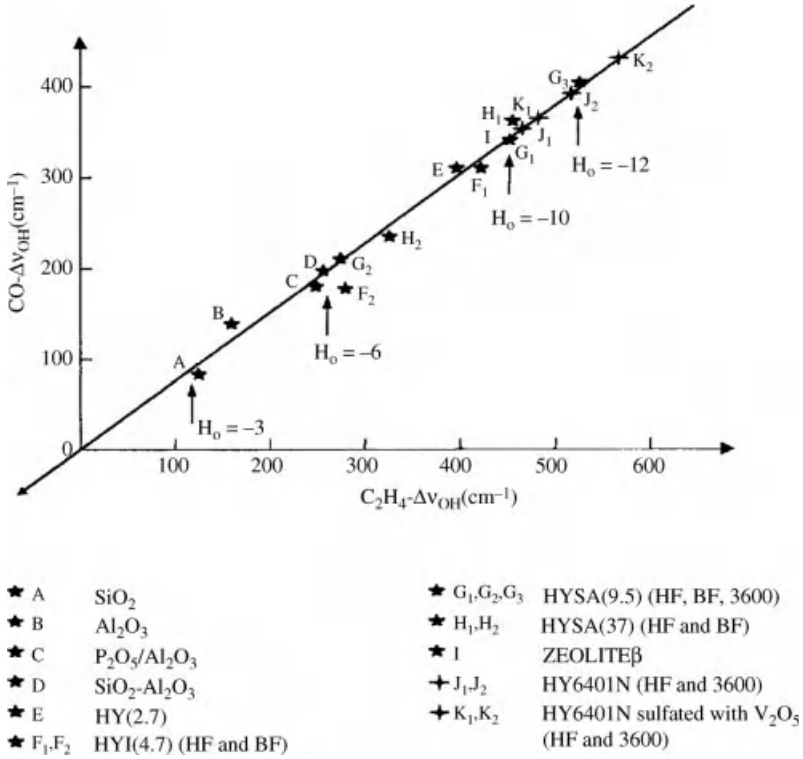


Figure 1.15 BHW curve on acid catalysts – acidity scale obtained by comparison of $\Delta\nu$(OH) between CO and ethylene. After [21]

A second possible reason for the broadening of the ν(OH) band can be the presence of many different acidic hydroxyl groups, in a heterogeneous distribution. In solid acids with a complex structure, a seemingly simple ν(OH) band can in fact represent the overlap of many bands due to sites differing slightly in environment and acidity.

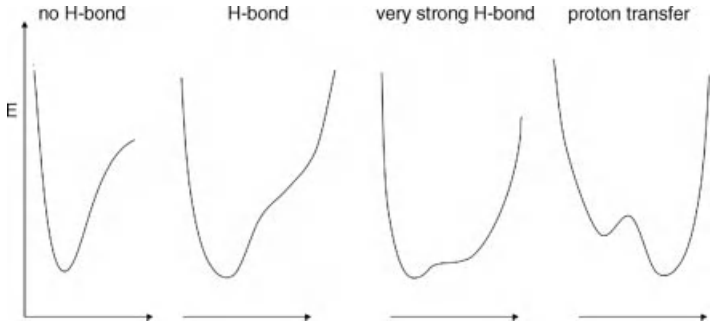


Figure 1.16 Energy as a function of OH distance in an acidic hydroxy group, in the presence of a probe molecule (Morse function).

Since band shifts can be very different from one to another, $\nu(OH)_{assoc}$ for associated OH groups will be a more or less resolved band group whereas $\nu(OH)_{free}$ for free OH groups seems like a unique band.

1.4.4.1.3 **Evans' Windows** Fermi resonances can also increase the complex aspect of the spectrum for $\nu(OH)_{assoc}$. Fermi resonances generally arise when the fundamental vibration comes very close to a combination band with the same symmetry. The overlap will not be simple, and both bands seem to reject one another. Both bands will be shifted and the spacing between them will be larger than it should have been without the resonance. When one of the bands is very large [as expected for $\nu(OH)_{assoc}$] and the other one is narrow, the narrow band will in fact appear like a transmission window in the broad band. The first harmonic of the δ(OH) vibration (in-plane deformation of the OH group) coming very close to the $\nu(OH)_{ass}$ creates a so-called Evans' window [23–26] (Figure 1.17). This is very typical and indicative of very strong H-bonding. The ν(OH) band broadens and shifts to lower wavenumbers, eventually overlapping the two δ(OH) and two γ(OH) harmonics, themselves shifted to higher wavenumbers by the H-bonding. The band structure observed is often referred to as an A, B, C system. H-bond strengths for OH bands in A, B, C systems

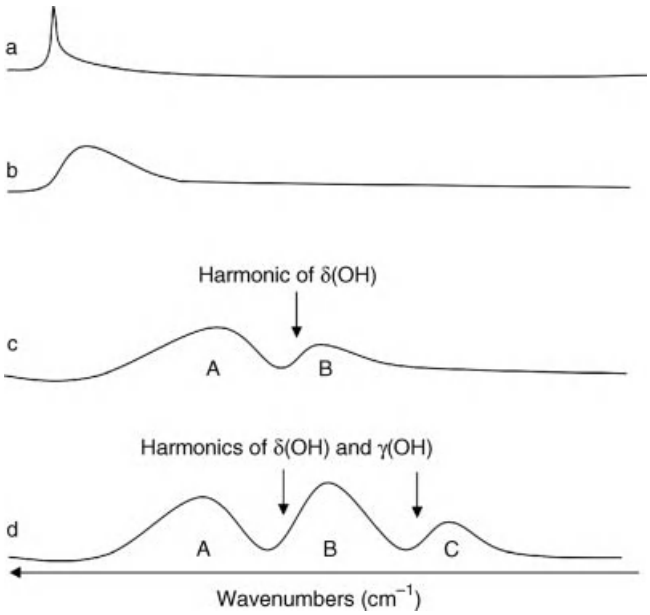


Figure 1.17 Evans' window on a ν(OH) vibration in the case of a strong H-bond: (a) free ν(OH), no H-bond; (b) ν(OH) perturbed by a H-bond; (c) strong H-bond, overlap with the first harmonic of the δ(OH) deformation vibration, the AB band system appears (the harmonics themselves are too weak to be observed directly); (d) very strong H-bond, overlap with both the harmonics of δ(OH) and γ(OH), the C band appears.

can be compared by using the wavenumber values of the center of gravity of each band system.

1.4.4.2 Molecular Probes for Lewis Acidity

Lewis acidity is characterized by the absence of any proton at play. No direct observation of any vibration band for the acidic site is possible. It is only by the influence of the site on a probe molecule that IR observation will give information on the Lewis site. Some probe molecules are particularly sensitive to interaction with Lewis sites, and their IR bands can be clearly modified differently by Brønsted and by Lewis sites. These are mostly pyridines, carbon monoxide, nitriles, and ammonia. These probe molecules are described below.

Transformation of a Lewis into a Brønsted site is possible when water or H_2S is adsorbed on the surface [27–29]. Lewis acidity can be masked, and the acidity is transferred to the proton on the adsorbed molecule, thus showing Brønsted acidity. The reverse is also possible, and a Brønsted site can be transformed into a Lewis site, for example, when alkenes are present on the surface. Alkenes can be protonated by Brønsted sites and form carbenium ions that can be detected with a probe molecule (acetonitrile, for example) while the OH group disappears [30, 31].

1.4.4.3 Common Probe Molecules for Acidity

The most common probes for the characterization of acidity in solids are amines (pyridines, NH_3), carbon monoxide, nitriles, nitrogen, and oxygen. Any nucleophilic molecule is a base, and the above list is, of course, not exclusive. Many molecules correspond to the criteria for good probe molecules, and benzene, ozone, ketones, alcohols, halogenated alkanes, dioxane, tetrahydrofuran (THF), and dimethyl sulfoxide (DMSO), for example, have been used.

1.4.4.3.1 **Pyridines** Pyridine is one of the most commonly used probes for the study of solid acids [32–35]. It is easy to use and gives information on the type and amount of sites on the surface. It is a very strong base, protonated on strong Brønsted acid sites (BASs) and coordinated strongly on Lewis acid sites (LASs). With weak BASs such as the silanol group of silica, it can form H-bonds. Three types of complexes can thus be observed on the surface of an oxide: PyH^+, PyL, and Py–HO (together with physisorbed pseudo-liquid pyridine). All three can be identified by the frequency of the bands from the vibration of the heteroaromatic cycle between 1400 and 1700 cm^{-1}. The bands due to the 19b and 8a vibration modes (Table 1.1) are very sensitive to coordination on the nitrogen atom and are used to identify and quantify the sites. The shift of the 8a mode is used to measure the strength of LASs. The spectral region of the νCH(D) vibration is not often used, but it contains interesting information. Both νCH(D) frequency and intensity are sensitive to the adsorption mode and allow one to distinguish between H-bonded, protonated, and coordinated species (Figure 1.18). It was found that the study of ν(CH) modes is more reliable than that of the 8a and 19b modes to distinguish H-bonded from weakly coordinated species. An example of such an application was given for the cases of CeO_2, MgO, and CaO [36].

Table 1.1 Typical frequencies (cm^{-1}) for adsorption of pyridine on a solid acid[a].

	ν_{8a} ν(CC)	ν_{8b} ν(CC)	ν_{19a} ν(CN)	ν_{19b} ν(CN)
Gas	1584	1580	1483	1440
H-bond	1595	1580	1490 ww	1445
Lewis	1630–1600	1580 ww	1490 ww	1450
Brønsted	1640	1610	1490	1545

a) Data for the gas are given as a reference. ww: very weak band.

Adsorption of pyridine is most easily performed by saturation of the sample and evacuation at increasing temperature. The adsorption is done, after thermal activation of the solid under vacuum, by putting the sample under 1 Torr of pyridine vapor in the cell (the gas line must be isolated and evacuated quickly to avoid pollution of all gaskets and unheated surfaces). On micro- or mesoporous materials, closing the cell and heating the sample at 473 K for a few minutes with the pyridine vapor improves diffusion of the probe inside the solid cavities and insures a correct interaction with the adsorption sites. The cell is then evacuated at the same temperature (before cooling) in order to remove all physisorbed pyridine. On strongly adsorbing solids, such as zeolites, a high temperature (473 K) is needed to obtain clear and unambiguous spectra. It should be noted that at high pyridine coverage, protonated pyridine dimers can sometimes be formed. For weakly acidic solids, a progressive thermodesorption can be tried instead of direct evacuation at 473 K, but the measure of real (strong) BASs is only valid after desorption under vacuum at high temperature.

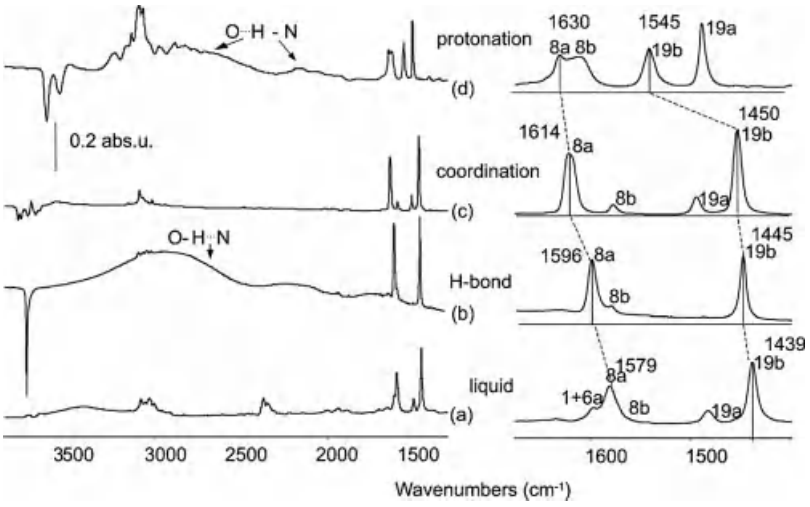


Figure 1.18 Spectra for pyridine in the 1400–4000 cm^{-1} region: (a) in the liquid phase; (b) after adsorption on silica and evacuation at room temperature; (c) on alumina, with evacuation at 100 °C; (d) on HY at 200 °C. Spectra by A. Vimont.

Molar absorption coefficients given in the literature can be used for quantitative measurements. The bands of interest must be integrated and the area multiplied by the value of the coefficient to determine the amount of pyridine on the surface, and thus the number of sites (to be divided by the sample weight and by the surface of the water to calculate the number of sites per gram). Typical values are $\varepsilon_{1545}(\text{pyH}^+) = 1.3\ \mu\text{mol}^{-1}\ \text{cm}$ for Brønsted sites and $\varepsilon_{1450}(\text{pyL}) = 1.5\text{–}2\ \mu\text{mol}^{-1}\ \text{cm}$ for Lewis sites. The values measured for ε by various authors can be very different. The temperature of the desorption of physisorbed pyridine or the adsorption of a significant amount of the probe on the cell walls might be the reason for this. In a combined IR–gravimetric experiment, the need for a temperature as high as 473 K was shown, and the value of $\varepsilon_{1545}(\text{pyH}^+) = 1.36 \pm 0.03\ \mu\text{mol}^{-1}\ \text{cm}$ was confirmed on an H–Y zeolite. These absorption coefficients are considered to be valid for one given solid only, however, and results obtained in that way must be considered as a first approximation.

1.4.4.3.2 **Substituted Pyridines** 2,6-Dimethylpyridine (DMP or lutidine) can be more convenient than pyridine to detect weak Brønsted acidity due to its higher basicity ($pK_a = 6.7$ compared with 5.2 for pyridine) [37–39]. As an example, no Brønsted acid sites were detected by pyridine adsorption on TiO_2–ZrO_2 mixed oxides whereas, under the same conditions, the formation of protonated species was observed by adsorption of DMP [40]. Spectral features in the 1660–1550 cm^{-1} range (ν_{8a} and ν_{8b} vibrations) account for the different adsorption modes of DMP with the solid surface (Table 1.2) [41]. Another advantage of this probe compared with pyridine is its ability to give information on Brønsted acid strength (Figure 1.19). The positions of ν_{8a} and ν^*(NH) bands in the spectrum of protonated DMP vary with the strength of Brønsted acidity: the higher the ν^*(NH) wavenumber and the lower the ν_{8a} wavenumber, the stronger is the acidity. On a series of zeolites, it was shown that the ranking obtained with DMP adsorption is correlated with that obtained by CO adsorption. On tungsten oxide or niobium oxide supported on titania, the determination of molar absorption coefficient of protonated DMP [$\varepsilon(\nu_{8a} + \nu_{8b}) \approx 6.8\ \mu\text{mol}^{-1}$ cm] allowed the quantification of both strong and medium Brønsted acid sites [42].

Substituted pyridines are also used as Brønsted-specific probes, especially in zeolites. Access of the nitrogen atom to the acid site is hindered by the neighboring substituents. Since the proton in Brønsted sites protrudes from the surface of the solid (in contrast to electronic vacancies on Lewis sites), DMP and collidine interact

Table 1.2 Typical frequencies (cm^{-1}) for 2,6-dimethylpyridine according to its adsorption modes.

	ν_{8a} ν(CC)	ν_{8b} ν(CC)	ν_{19a} ν(CN)	ν_{19b} ν(CN)
Gas	1584	1580	1480	1410
H-bond	~1602	1580	1480	1410
Lewis	1595–1620	1580	1477	1410
Brønsted	1640–1655	1630	1473	1415

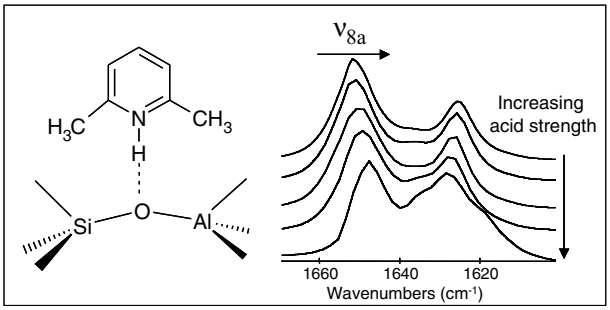


Figure 1.19 Spectra in the 1600–1700 cm^{-1} region for DMP protonated on different zeolites [from top to bottom: LiHNaY, KHNaY, HY(2.9), HNaX, HYSA]. From [41]

more easily with Brønsted than with Lewis sites, and some selectivity can be observed. Steric hindrance around Brønsted sites can also decrease the interaction with the basic probe, and the H-bond can be weaker than with an unsubstituted pyridine. Great care must be taken in the use of these probes.

1.4.4.3.3 **Accessibility of Sites** To be active in a catalytic reaction, a surface site must be accessible to reactants and products. An accessibility index (ACI) was derived from IR spectroscopy of substituted alkylpyridines with different sizes (pyridine 0.57, DMP 0.67, and collidine 0.74 nm) over hierarchical ZSM-5 crystals. The samples were prepared by selective silicon extraction of a parent commercial sample in alkaline medium (desilication) and contained different degrees of intracrystalline mesoporosity. The enhanced accessibility of acid sites in the hierarchical zeolites was shown. A relatively bulky molecule such as collidine, which probes practically no acid site in the parent medium-pore MFI structure, can access up to 40% of the Brønsted sites in the mesoporous sample. The ACI is a powerful tool to standardize acid site accessibility in zeolites and can be used to rank the effectiveness of synthetic strategies towards hierarchical zeolites (mesoporous crystals, nanocrystals, and composites) [43].

1.4.4.3.4 **Carbon Monoxide** Carbon monoxide is also very important a probe molecule [44–47]. It is a weak base, which is not protonated but can perturb the proton by interaction with the carbon atom in the molecule. Since the interaction is often weak with acid sites, the adsorption must be performed at low temperature (100 K in a liquid nitrogen-cooled cell) (Figure 1.20). The frequency of the ν(CO) vibration band is very sensitive to coordination and can shift from 2138 cm^{-1} (starting position, pseudo-liquid CO at 100 K on the surface) up to 2170 cm^{-1} on Brønsted sites and 2240 cm^{-1} for strong Lewis sites (Table 1.3). At the same time, on Brønsted sites, H-bonding between CO and the proton induces a large red shift of the ν(OH) vibration band. A clear relationship has been shown between the $\Delta\nu$(OH) shift and the position of the ν(CO) frequency, showing the quality of the scale obtained for ranking solid acids with this probe molecule (Figure 1.21). It should be noted that the frequency of the ν(CO) band is influenced by the coverage level, and that the value must be extrapolated to zero coverage by performing a progressive adsorption [48].

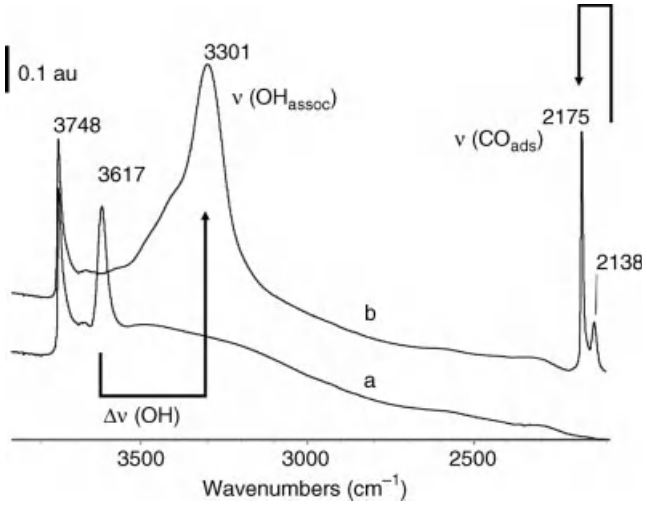


Figure 1.20 Spectrum of an H-ZSM5 zeolite (a) before and (b) after adsorption of CO at 100 K.

Carbon monoxide can be used quantitatively for measuring the number of sites. By progressive introduction of known amounts of the probe molecule (a few milliliters under a few millibars pressure, all accurately measured) inside the cell, the amount of CO introduced when saturation is reached and the molar absorbance coefficient can be determined accurately (Figure 1.22). A typical value for the molar absorbance coefficient on Brønsted sites is $\varepsilon\nu(\mathrm{CO}) = 2.7\ \mathrm{cm\ \mu mol^{-1}}$.

Carbon monoxide is also an excellent probe molecule for metals and sulfides, and this is detailed in the relevant sections.

1.4.4.3.5 **Pyridine–CO Coadsorption** Successive coadsorption of pyridine(s) and CO allows the measurement of acidity in various environments on the same catalyst. This is especially true for zeolites. Mordenite, for example, if activated with great care, contains Brønsted sites which are not accessible to pyridine in the side pockets of the structure. Sites located in the large channels can therefore be perturbed by the initial introduction of pyridine in the pore system. Adsorption of CO in a second step will only reach OH acid sites which are out of reach of pyridine, in the small side pockets. The response measured after CO adsorption will give a measurement of the amount

Table 1.3 Typical frequencies ($\mathrm{cm^{-1}}$) for bands after CO adsorption.

	Silanol groups	Brønsted sites	Lewis sites
ν(CO)	~2150	2155–2180	2190–2240
$\Delta\nu$(CO)	~15	20–45	50–100
$\Delta\nu$(OH)	~90	100–400	

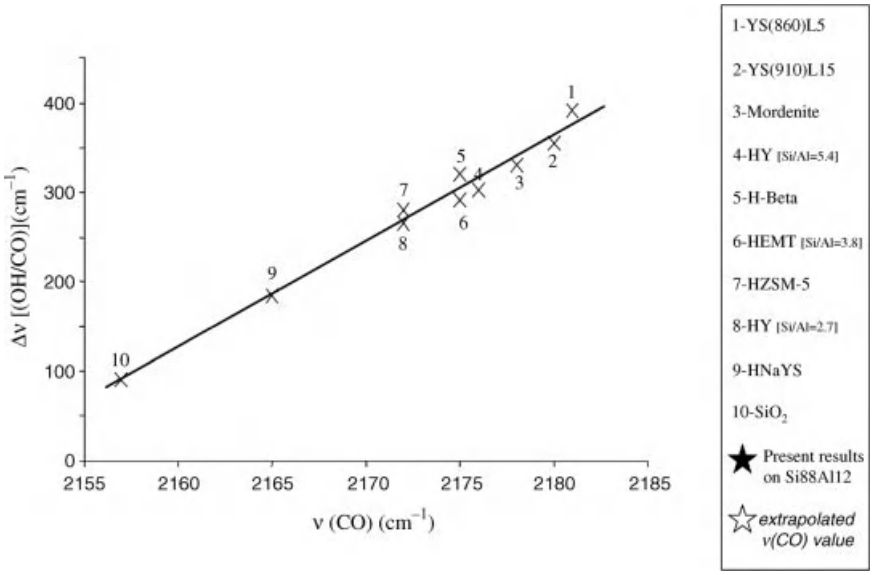


Figure 1.21 $\Delta\nu$(OH) and the corresponding ν(CO) for various acidic solids and zeolites. . From [13]

and strength of sites in the side pockets, which can be compared with the situation in the absence of pyridine, when all sites are probed by CO. The sites in the side-pockets were measured as slightly weaker than in the main channels, and represented one-third of the total amount [11, 49]. The same was done in dealuminated mordenites, and pyridines with increasing size were used to show the increase in accessibility in the pores of mordenite after dealumination. Even di-*tert*-butylpyridine was able to probe Brønsted sites in the dealuminated mordenite, thus showing that the pore structure was largely modified [50, 51].

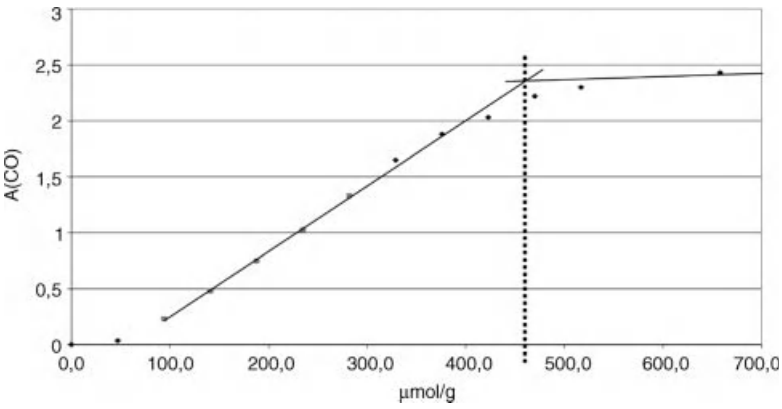


Figure 1.22 Determination of the amount of surface sites on a solid by progressive introduction of CO in controlled amounts inside the cell.

1.4.4.3.6 **Acetonitrile** Acetonitrile is a stronger base than CO [52–54]. It can be adsorbed at room temperature on Lewis and Brønsted sites in oxides. It is a small molecule, and it can access most of the acid sites (Table 1.4). Its fairly strong basicity makes it very interesting, since it is the probe that forms the strongest possible H-bond with Brønsted sites before the proton is actually transferred: it is with acetonitrile that the strongest H-bond is formed, and the largest $\Delta\nu$(OH) is observed. Acetonitrile can be protonated, but only by acids at the limit of superacidity [55], or by very strong acid sites upon heating. Protonation of acetonitrile can also be produced by strong confinement by acidic sites in some zeolite pores. The protonation temperature of acetonitrile has been used to build a scale for acidity, producing a ranking of acidic catalysts in agreement with results in saturated hydrocarbon conversion at high temperature. The transfer of the proton from the zeolite to acetonitrile occurs only at high temperature, and that temperature is a good indication of the difficulty of the catalytic proton transfer from the solid acid to the hydrocarbon, which is the initial step of the conversion of saturated hydrocarbons on acidic zeolites. This measurement takes into account the influence of confinement on the proton transfer. It is in fact the only probe molecule acidity scale agreeing with catalysis results for demanding reactions [56].

One of the main difficulties with acetonitrile is the presence of many Fermi resonances in the spectrum. The ν(CN) vibration in adsorbed CH_3CN is split into a doublet because of interaction between the vibrations of the CH and CN groups. This is avoided by using CD_3CN instead of CH_3CN. The $\nu(C\equiv N)$ is fairly sensitive to molecular interactions, and shifts up to 2330 cm^{-1} on strong Lewis sites (Table 1.4).

The very strong H-bond formed on Brønsted sites also produces a very typical shift of the ν(OH) band, with Evan's windows as described earlier (Figure 1.23). The value of $\Delta\nu$(OH) can be estimated by the position of the center of gravity of the A, B (C) system, allowing a close comparison of Brønsted sites in various solids. This is a very strong point for using deuterated acetonitrile rather than pyridine for measuring the strength of Brønsted acid sites.

1.4.4.3.7 **Ammonia** Simple and aliphatic amines are strong bases, and can be (rather complex) probe molecules. They can form many different adsorbed species, interacting with both Lewis and Brønsted sites, by autoassociation and protonation, and they can also interact with basic sites [57]. The autoassociation of the base can lead to the formation of new complexes with hydroxy groups and to the broadening of the $\nu(OH)_{assoc}$ band, which can sometimes disappear completely. Ammonia itself is a

Table 1.4 Typical frequencies (cm^{-1}) for the various states of adsorbed acetonitrile.

	Physisorption	Silanol groups	Brønsted sites	Protonation	Lewis sites
$\nu(C\equiv N)$	2245	~2285	2295–2300	2310–2320	2325–2330
$\Delta\nu(C\equiv N)$	0	~40	50–55	~70	~85
$\Delta\nu$(OH)	0	~300	500–1000	—	—

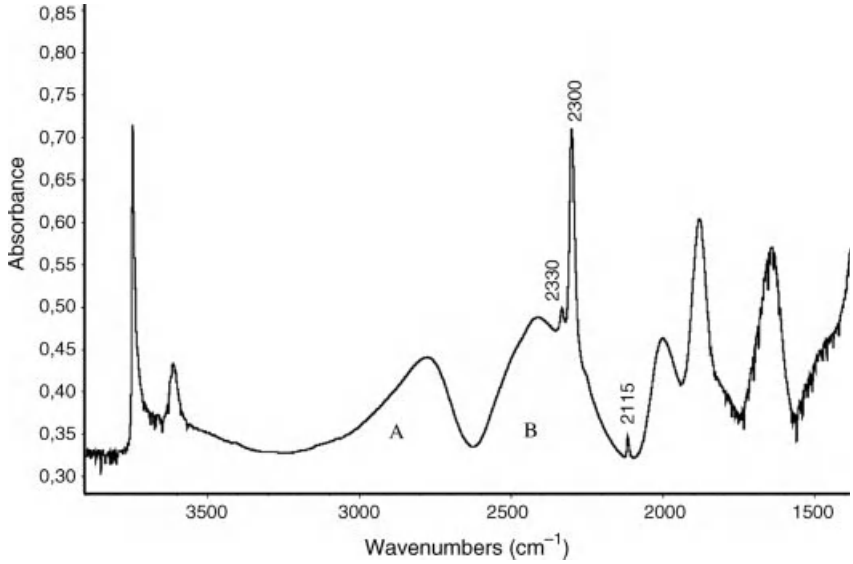


Figure 1.23 Spectrum of H-ZSM5 after adsorption of CD_3CN at room temperature, in such an amount as not to saturate all acidic sites. The A, B system and the Evans' window are clearly visible, and also the $\nu(C\equiv N)$ band due to adsorption on Lewis sites at 2330 cm^{-1} and on Brønsted sites at 2300 cm^{-1}. The band at 2115 cm^{-1} is due to the vibration of the CD_3 group.

particularly strong base, with a very small size, and it will reach all acid sites on a solid. The various types of adsorbed ammonia, protonated or not, can be distinguished in the IR spectrum (Figure 1.24, Table 1.5).

Dissociative adsorption of ammonia has also been observed (NH_3/NH_2^- pK_a = 38), and the strong basicity of the probe makes it not very specific. Many IR studies have shown that ammonia adsorption is a very complex phenomenon, and it use is not recommended.

Aliphatic amine are also not much used because of their even stronger basicity and lower specificity. They are reactive molecules and can also give a proton away. Quantitative measurements are difficult because the amount of adsorbed amine depends more on the "area" of the molecule itself than on its interaction with the acid site.

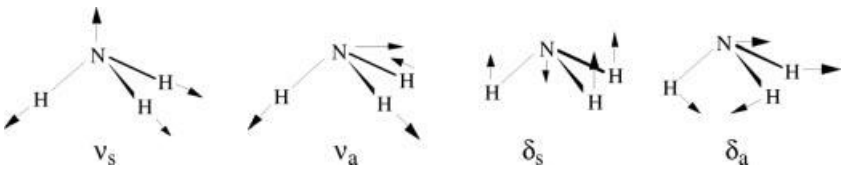


Figure 1.24 Vibrations in the ammonia molecule.

Table 1.5 Typical frequencies (cm^{-1}) observed upon adsorption of NH_3 on a solid acid[a].

	νa	νs	δa	δs
Gas	3444	3336	1628	950
H-bond	3408	3309	1625	1036
Lewis:				
ZrO_2	3380	3280	1610	1230–1190
ZnO	3420–3350		1630	1220
Al_2O_3	3400	3270	1620	1280–1240
NH_3-BF_3	3343	3279	1599	1438
Strong Brønsted: NH_4^-	3145 (ν_3)	3040 (ν_1) (R)	1680 (ν_2) (R)	1400 (ν_4)

a) Data for the gas are reported as a reference. (R) indicates a band active only in Raman spectroscopy.

1.4.4.3.8 **Other Main Probe Molecules for Acid Sites** Homonuclear diatomic molecules, such as hydrogen, nitrogen, and oxygen, are normally not detected in IR spectroscopy. They can, however, be adsorbed on the surface of catalysts at low temperature, and are deformed (polarized) by such adsorption. These molecules then lose their symmetry and become IR active. The local electric field (adsorbing cation) influences the frequency of the vibration band of the molecule, and nitrogen has been used, for example, for characterizing cations and acidic protons in mordenite. One of the main advantages of these diatomic probes is the invisibility of the gas phase, which does not interfere with the quality of the spectra. Nitrogen is a very weak base; it interacts weakly with the sites and allows a very fine differentiation of acid strengths.

Benzene is another weak base interacting with the protons via its π-electron cloud. It allows a fine scaling of acid sites differing only slightly in strength, but the assignment of the various possible types of interactions can be difficult. Benzene can suffer from important steric restraints, and it has been reported not to reach many hindered sites.

1.4.5 Characterization of Basicity with Probe Molecules

Acidic probe molecules can be used for the characterization of basic catalysts. This is very similar to the characterization of acidic sites by basic probe molecules, but the interaction is often much more complex and the acidic probe molecule more reactive. The literature on the topic is not as rich as for acidity, although a few review papers have been published [58, 59].

1.4.5.1 CO_2 as a Probe for Basic Sites

Carbon dioxide is the most commonly used probe molecule for characterizing basic sites. As described earlier, CO_2 either reacts with basic hydroxy groups and forms surface hydrogencarbonates or it reacts with oxygen anions and forms carbonates. Various structures of carbonate species can be formed depending on the various environments of basic sites. The formation of hydrogencarbonates reveals the basic

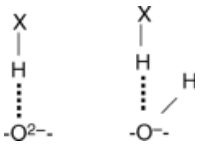


Figure 1.25 Interaction modes of an acidic protic molecule (XH) with basic centers.

properties of very high-frequency OH groups with bands around 3780 cm^{-1} on beta-zeolites that correspond to basic OH groups attached to Lewis acidic Al atoms [60]. Comparing the intensity of bands specific to hydrogencarbonate species on various oxides is a way to rank their basic properties and to predict their activity toward COS hydrolysis [61]. However, CO_2 is not a good probe for assessing the basic strength and quantification of the basic sites is not direct with CO_2.

1.4.5.2 **Protic Molecules**

Adsorption of acidic protic molecules such as acetylene, propyne (methylacetylene), butyne (ethylacetylene), pyrrole (C_4H_5N), and chloroform ($CHCl_3$) is an interesting way to probe the basic strength of surface sites. Indeed, the ν(X–H) shift (X = C or N) that is observed after H-bonding of the probe with the surface is a good indicator of the basic strength of the sites (Figure 1.25). However, determining the nature of the basic sites is not easy with this method. These probes tend to decompose and to modify the catalyst surface properties. Hence weakly reactive molecules will be preferred.

Pyrrole, containing an NH moiety, can form H-bonds with basic oxygen atoms on oxides and zeolites. The ν(NH) vibration band is shifted, and the value of the shift, $\Delta\nu$(NH), accounts for the strength of the H-bond. If formation of pyrrolate ions occurs, it prevents the assessment of basicity.

Similarly, the extent of the ν(CH) band shift of H-bonded chloroform accounts for the strength of the basic sites. However, dissociation of chloroform on acid–base sites contaminates the surface with chlorine ions.

Propyne and acetylene are interesting probes forming H-bonds between the acidic ≡CH groups and the basic sites. On strongly basic oxides such as MgO, a shift of the ν(≡CH) vibration of propyne from 3334 cm^{-1} in the gas phase down to ∼3255 cm^{-1} can be observed. Note that propyne can also interact with acidic sites, and forms complexes via its C≡C bond with the weakly acidic silanol groups on silica. Propyne is generally preferred over butyne, which polymerizes more easily.

1.4.5.3 **Methanol**

Methanol, the simplest alcohol molecule, is widely used to characterize basic oxides such as MgO, ThO_2, CeO_2, and ZrO_2 [62–67]. The adsorption modes of methanol, that is, the dissociative adsorption that leads to the formation of hydroxyl and methoxy groups and molecular adsorption, can be discriminated by IR spectroscopy (Figure 1.26). On MgO, the three ν(OC) bands observed at about 1115, 1090, and 1065 cm^{-1} are assigned to the two types of dissociated methanol corresponding to

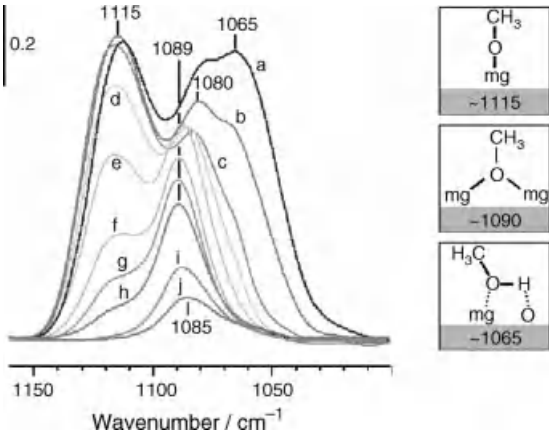


Figure 1.26 IR spectra of methanol introduced at room temperature on MgO activated at 1023 K, followed by evacuation at (a) room temperature, (b) 348, (c) 398, (d) 448, (e) 498, (f) 548, (g) 598, (h) 648, (i) 698, and (j) 723 K from [66].

linear and bridged methoxy species and to undissociated methanol, respectively. According to DFT calculations, dissociation occurs on surface defects and the formation of these two types of methoxy species can be related to the surface topology, that is, convex and concaves zones of the surface leading to linear and bridged methoxy group formation, respectively [67–69].

By coupling IR spectroscopy with volumetric or thermogravimetric measurements, the molar absorption coefficients of ν(OC) vibration of the various forms of adsorbed methanol could be accurately determined (for MgO, $\varepsilon_{\text{undissociated}} = 2.5$ $\mu\text{mol}^{-1}\,\text{cm}$; $\varepsilon_{\text{I}} = \varepsilon_{\text{II}} = 6.1\,\mu\text{mol}^{-1}\,\text{cm}$) (Figure 1.27). Thanks to these results, IR spectroscopy becomes the only method that allows one both to discriminate and to quantify the defects on complex surfaces such as that of MgO, in terms of concentrations of convex and concave defective zones.

1.4.6
Probes for Supported Metal Catalysts

IR spectroscopy is a powerful technique to study the adsorption of molecules on well-defined metal surfaces and also on metals supported on oxides. For metal characterization, NO can be used as a probe molecule [70], but CO is the most frequently used probe, and a number of reviews on CO adsorption on metals are available [46, 71–73]. The advantage of CO is the high absorption coefficient of the ν(CO) mode and the high sensitivity of its frequency to the oxidation state of the site, to its geometry and to its coordinative unsaturation degree. The (strong) chemical bond between CO and the metal involves electron donation from the 5σ orbital of CO to the metal and back-donation from metal d orbitals into the empty $2\pi^*$ antibonding orbital of CO. Since the 5σ orbital is weakly anti bonding and the $2\pi^*$ orbital is strongly antibonding,

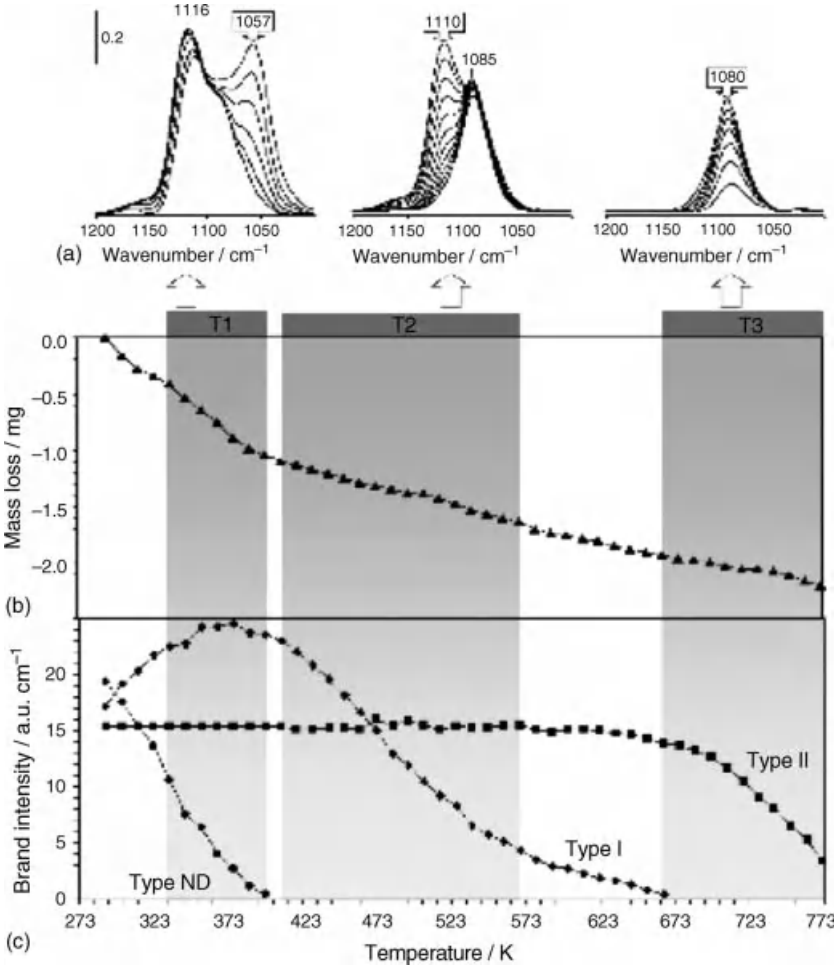


Figure 1.27 (a) Infrared spectral changes, (b) mass loss, and (c) decrease in methanol ν(OC) band areas versus the temperature of methanol desorption on P-MgO measured on the coupled IR–thermogravimetry setup. T1, T2 and T3: characteristic temperature zones of methanol desorption. From [66].

the C−O bond is weakened by the chemisorption process. Therefore, the increase in the amount of back-donation into the $2\pi^*$ orbital leads to a decrease in the C−O stretching frequency. Hence the ν(CO/metal) signal appears at lower wavenumbers than that of the gas phase (2143 cm^{-1}). For spectral interpretation, it is important to take into account the dipolar coupling effects which induce marked wavenumber shifts and intensity transfers. By following frequency shifts for various coverages, bandwidths, and intensities, CO allows one to specify whether the probe molecule forms islands or is well dispersed on the surface. In addition, using IR spectroscopy

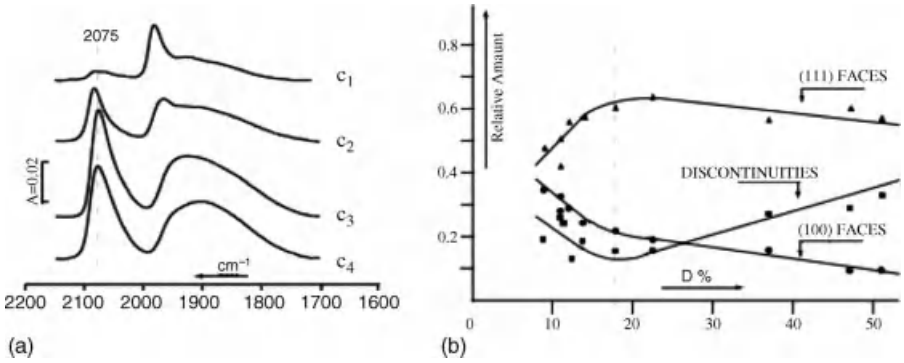


Figure 1.28 (a) Comparison of CO adsorption for saturation dose, on Pd/Al_2O_3 reduced at 373 K presenting various dispersions ($c_1 < c_2 < c_3 \approx c_4$). (b) Relative amount of faces and discontinuities versus the dispersion. From [74]

coupled with volumetric measurements, the amount of CO adsorbed on metal sites can be determined, allowing one to calculate the dispersion of the metal particles. In their earlier work [74], Binet *et al.* showed that on an alumina-supported Pd catalyst, changing the dispersion of metallic particles leads to modification of preferentially exposed metallic phase (Figure 1.28).

1.4.7 Probes for Sulfide Catalysts

Hydrotreatment is a key process in refineries that aims at reducing the heteroatom content (sulfur, nitrogen, and metals) of petroleum feedstock. The active phases of hydrotreating catalysts generally consist of nanosized mixed sulfide particles (Co–Mo–S or Ni–Mo–S or equivalent with W) supported on alumina-based oxides or more acidic oxides.

Sulfided catalysts are extremely sensitive to oxygen contact. Therefore, characterization of their surface sites requires *in situ* sulfidation, generally performed by heating the oxidic catalyst at atmospheric pressure under a flow of H_2–H_2S. Only a few papers have reported IR characterization after sulfidation in conditions close to the industrial ones, such as under a high pressure of H_2S–H_2 [75, 76] or under a liquid phase. Note that sulfided samples show a very high absorbance towards the IR beam, which makes their analysis difficult.

Nitrogen monoxide is the most commonly employed probe molecule for sulfide catalyst characterization since it has the advantage of being strongly adsorbed on the sulfide phase [77]. However, partial oxidation of the sulfide phase may occur, even at very low temperatures, which could explain the many disagreements found in the literature on IR observations of NO adsorbed on sulfide catalysts.

CO is very informative in characterizing sulfide catalysts and no undesired reaction between the sulfide phase and CO occurs if the adsorption is performed at low temperature (~100 K) [78–80]. On unpromoted sulfide Mo catalyst, a ν(CO)

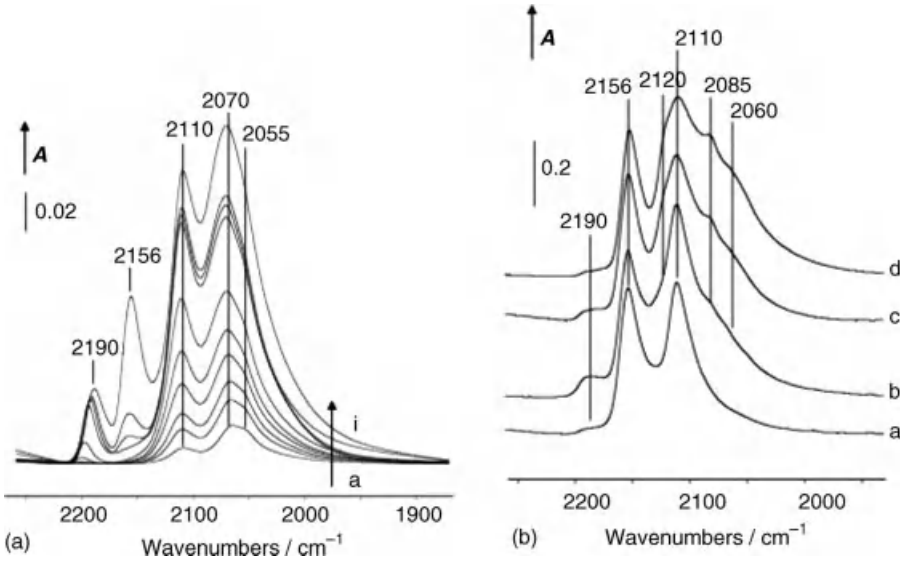


Figure 1.29 IR spectra of CO adsorbed (100 K) on (a) sulfided $CoMo/Al_2O_3$ catalyst (3.2 wt% Co–8.7% Mo). Spectra a–i: increasing CO doses. (b) On sulfided (Ni)Mo/Al_2O_3 catalysts. Spectrum a: Mo/Al_2O_3 (8.7% Mo);. Spectra b, c, and d: $NiMo/Al_2O_3$ containing 0.5, 1.5, and 3.4 wt% Ni, respectively (133 Pa of CO). From [78].

band at 2110 cm^{-1} is detected that characterizes edge sites of MoS_2 slabs. With the CoMo system, as expected, the band at 2110 cm^{-1} is decreased (but generally still present) while a band at 2070 cm^{-1} specific to the promotion by Co appears (Figure 1.29). It is assigned to CO interacting either with a Co atom or with a Mo atom adjacent to a Co atom. With the NiMo system, CO adsorption on Ni centers of the promoted phase leads to high wavenumber band at ~2120 cm^{-1} that strongly overlap the band at 2110 cm^{-1} characteristic of non-promoted Mo sites. For NiMo and CoMo catalysts, broad shoulders at low wavenumbers (below 2060 cm^{-1}) are characteristic of Mo centers adjacent to promoter atoms, indicating partial decoration of the MoS_2 edges by the promoter. Hence CO characterizes the nature [unpromoted Mo, Co, or Ni-promoted Mo (W) sites], the environment, and the amount of sulfide sites. It is a unique tool to account for the degree of promotion of the sulfide slabs. A good correlation could be established between the degree of promotion of a catalyst and its hydrodesulfurization activity (Figure 1.30).

In addition, CO informs on the fraction of support sites not covered by the sulfide phase. Thus, CO characterizes the nature, the strength, and the number (allowing calculation of the degree of coverage) of accessible acidic sites of the support. A relationship between the acidity of the support and electronic properties of the sulfide phase was evidenced, revealing that the turnover frequency of sulfide sites can be modified by acidic properties of the support.

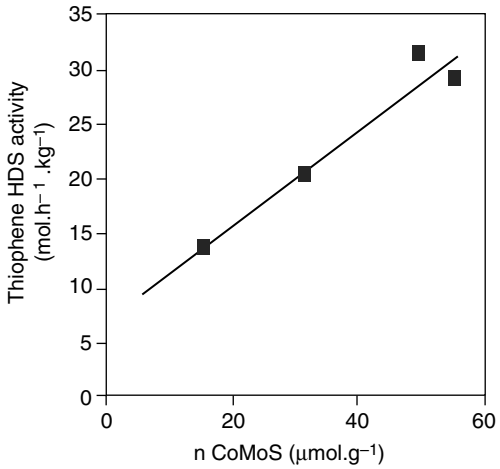


Figure 1.30 Comparison between the concentration of CoMoS sites and detected by CO (100 K) and their thiophene HDS activity on various NTA-CoMo/Al_2O_3 catalysts sulfided at 623 K. From [80].

1.4.8
Quantitative Analysis by Coupling IR Spectroscopy with Gravimetry

Quantification of IR data is a key point that generally requires the determination of molar absorption coefficients. Molar absorption coefficients can be measured by progressively adsorbing measured amounts of the probe molecule, and the reader is directed to publications for such advanced measurements [35, 81]. However, even for classical probe molecules such as pyridine, the discrepancies between the values reported in the literature are worth noting. This is likely mainly due to a lack of precise control of the amount of probe adsorbed on the sample. One way to overcome this problem is to couple IR spectroscopy and gravimetric analysis.

Thermogravimetric analysis (TGA) allows weight changes in the sample to be monitored. It has been combined with IR spectroscopy to give reliable quantitative information. It was used to determine the molar absorption coefficients for IR bands of OH groups on silica and HY zeolites, and also for adsorbed probe molecules [82]. Important information was obtained on the quantity of OH groups located in the different cages of HY zeolite and also on the quantity of inner and surface silanol groups on silica. The number of silanol groups accessible to water molecules was shown to be constant whatever the sample of precipitated silica, and also the ratio of water to silanol groups under room atmosphere. Even in the complex cases where several coadsorbed species are formed simultaneously, the molar absorption coefficients could be determined with good accuracy using this setup. An example was presented for methanol adsorption on MgO in Figure 1.27 [66].

Combined TGA and IR spectroscopy was also applied to operando conditions, and denoted AGIR (analysis by gravimetry and infrared) [83]: a modified microbalance was used to follow mass changes (microgram accuracy) inside a catalytic reactor

equipped with IR windows. The spectroscopic response of water and ammonium ions coadsorbed together on zeolites was shown to vary depending on the conditions. The molar absorption coefficients for $\delta(H_2O)$ and $\delta(NH_4^+)$ at 1640 and 1540 cm^{-1} for water and ammonia on an HY zeolite were studied under a dry gas flow at various temperatures. The results showed the influence of coverage on the IR response of adsorbed species in zeolites. Adsorption sites change with coverage, bands are shifted and their shape and intensity are modified. Other interesting facts were observed: water modifies strongly the aspect of the $\delta(NH_4^+)$ vibration band in ammoniated zeolites, without changing the absorption coefficient. Measuring the sample mass while at the same time recording its IR spectrum showed the key importance of conditions under which the measurements are made. The presence of coadsorbed species (water in particular) strongly modifies the spectrum of surface species. Under reaction conditions, this new technique is especially important for a correct assignment of IR features and catalytic behavior [83].

1.5
Application to Surface Reactivity: *Operando* Spectroscopy

Owing to its ease of use and its efficiency, IR spectroscopy is one of the most commonly used techniques for studying the surface of a catalyst during a chemical reaction. In 2002, a new term (*operando* spectroscopy) was coined to describe the IR monitoring of the surface under real reaction conditions [84]. The term *in situ*, which was commonly used previously, was more ambiguous and described a measurement which was made in the same place where the reaction was performed (which is the exact meaning of the Latin *in situ*), but not necessarily during the surface reaction. In order to be sure that a study deals with a working catalyst, under meaningful conditions, the word *operando* can only be used when the spectroscopic measurement is combined with a measurement of the catalytic activity by on-line analysis of the reaction products. In this way, changes in the nature and concentration of surface species can be related to catalyst activity and selectivity. The surface of the catalyst under working conditions can be very different from the surface of the activated fresh catalyst under vacuum, and observing the working catalyst under real reaction conditions is critical.

Operando IR spectroscopy has progressed considerably since its origin. In 1991, volume 9 of *Catalysis Today* grouped 28 papers after a meeting on "*in situ* methods in catalysis" in the United Kingdom. Of these 28 contributions, 10 dealt with *operando* IR spectroscopy and gave state-of-the-art perspectives. The technique was reaching maturity, but the observed phenomena were complex and conclusions were hardly general. Other review papers appeared over time [4, 84]. Many aspects of heterogeneous catalysis can be treated, from deactivation and coke formation [85–87] to the identification of intermediate species [88, 89] and determination of the mechanism by reaction kinetics (combining the kinetics of surface processes with the usual time change analysis of the reaction products in the gas phase), sometimes with transient isotope labeling [90]. Kinetics have also been studied by imposing periodic variations

of reactant concentrations [91], creating a sort of imposed oscillatory reaction (which has also been studied on its own by *operando* IR spectroscopy [92].

1.5.1 Experimental Setup for *Operando* IR Spectroscopy and Reactions Conditions

The reactor-cell must obey specific constraints for reactivity studies. The residence time must be controlled accurately, and the gas volume was chosen is some designs to be as small as possible in order to increase the time resolution of online analysis and to remove the contribution of the gas phase to the spectrum.

Operando IR spectroscopy is most often applied to gas–solid heterogeneous catalysis. The contribution of the gas phase to the IR spectrum can then be taken into account and removed from the spectrum of the surface of the solid. The typical setup is very similar to the usual setup for catalytic tests. It includes gas mixing devices (mass flow regulators with automatic control), the reactor (here with IR windows), and online gas analysis techniques (mass spectrometry, gas chromatography, chemoluminescence, IR gas analysis, etc.) (Figure 1.31).

The main difference between the *operando* IR setup and any usual catalysis test setup is the limit to the reaction conditions imposed by the use of IR windows. In order to maintain gas tightness between 1 and 10–20 atm, gaskets must be placed between the KBr or CaF_2 windows and the cell walls. Most gasket materials can only be used below 200 °C, and the design of the reactor cell must include a careful design of the heating so that the temperature is homogeneous enough around the catalyst, with cooling of the windows and gaskets (Figure 1.32). This must be combined with a small dead volume around the solid catalyst so that the kinetic behavior of the reactor can be analyzed with the best possible time resolution. With a short residence time for reactants inside the reactor, a fast spectroscopic measurement on the surface combined with fast online analysis techniques can lead to a detailed description of complex kinetics on the surface [93].

1.5.2 Examples of *Operando* IR Measurements

When studied under reaction conditions, the surface of metal oxides is often covered by unreactive species called "spectators," which do not participate in the reaction of interest. This means that only a few of the surface sites are really catalytically active. This was observed, for instance, in the hydrogenation of methyl benzoate to benzaldehyde on various metal oxides: on ZrO_2 under working conditions, IR spectroscopy showed the presence of large amount of benzoate species, mostly inactive towards H_2.

Zeolitic materials are very convenient for active site identification since the Brønsted sites are characterized by well-defined ν(OH) bands. On dealuminated HY samples (at 673 K under flow) it was shown that *n*-hexane cracking was related to OH groups characterized by a ν(OH) at 3600 cm^{-1}, assigned to strongly acidic hydroxyl groups that correspond to framework OH groups perturbed by extra-

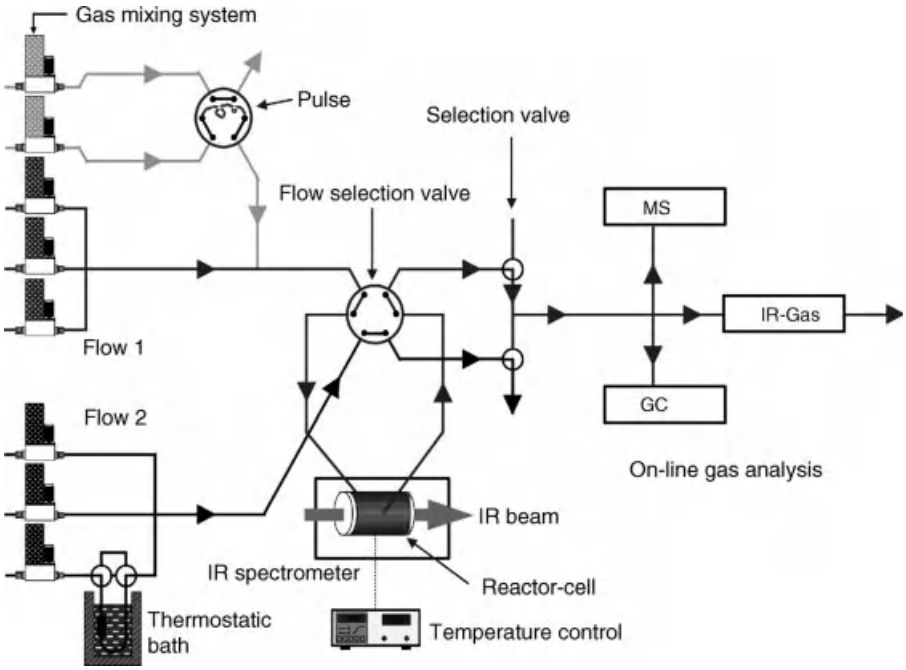


Figure 1.31 Typical *operando* IR setup. Mass flow regulators are used to prepare gas mixtures that are sent in the reactor cell. Several separate flows are often used to allow fast switching between different gas mixtures for time-resolved studies of fast triansients. Six-way valves are used for switching between flows or for sending 10–100 μl pulses without disturbing the main flow in the reactor. A saturator is used for introducing liquids in the flow (by passing the carrier gas in a loop where the liquid is placed, in a thermostatic bath – the flow is then loaded with the vapor pressure of the liquid at the temperature of the bath – the gas lines must then be heated slightly higher than the bath). The flows exiting the reactor are then directed via a selection valve to the chosen online gas analysis technique.

framework species. Moreover, poisoning experiments with DMP confirmed the involvement of these sites [94].

Alumina-based additives are used on an industrial scale to reduce the amount of sulfur in fluid catalytically cracked (FCC) gasoline. Recent *operando* IR studies allowed the elucidation of the mechanism by which gasoline sulfur-reductive additives reduce thiophenic compounds [95]. Recording the surface species during the reaction of tetrahydrothiophene decomposition and measuring the evolution of the conversion versus time-on-stream showed that the accumulation of carboxylate is at the origin of catalyst deactivation (Figure 1.33). The *operando* setup also allows control poisoning of the strongest Lewis acid that clearly shows their implication in catalytic activity. Hence tetrahydrothiophene (THT) cracking requires both Lewis acid and basic sites. The involvement of strong tetrahedral Al^{3+} sites has been directly evidenced by specific poisoning using pyridine under reaction conditions. A strong indication that basic sites are also involved in the reaction mechanism is the

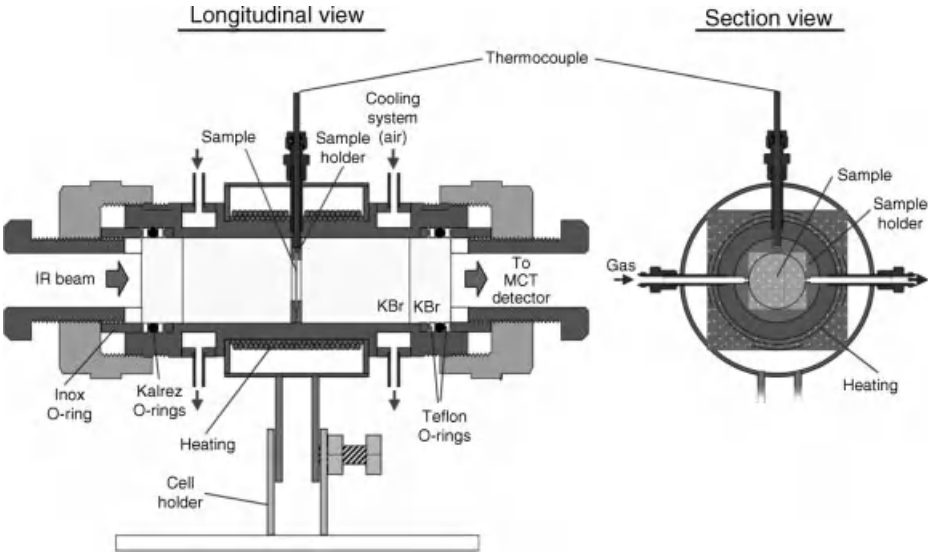


Figure 1.32 Operando reactor cell for experiments in the range 25–450 °C, 1–20 atm, gas velocity up to 70 000 h^{-1}. The dead volume is <0.1 ml. From [93].

fact that deactivation originates from the formation of carboxylate species, leading to blocking of surface oxygen centers. Overall, these results show that a good balance of the acid–base properties of alumina-based additive is required for optimum activity, suggesting that THT cracking occurs on Lewis acid–base pairs through successive *E*2 eliminations.

The *operando* setup is well adapted to transient experiments. As a simple example, in a flow of propane and O_2 at 623 K on a VPO/TiO_2 catalyst, it was observed that introduction of a pulse of pyridine drastically decreased the activity. When the

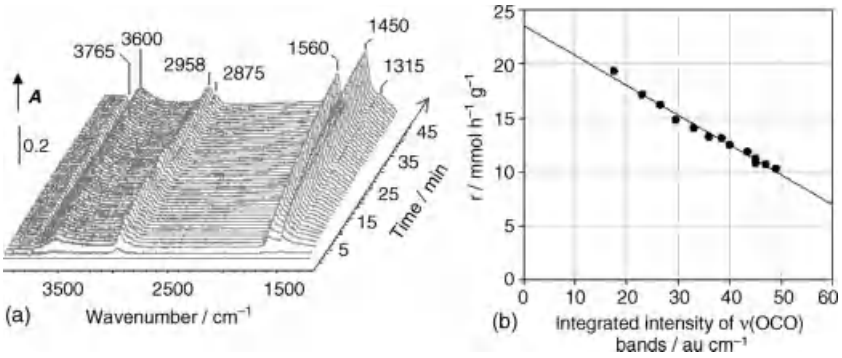


Figure 1.33 (a) IR spectra recorded during THT conversion on alumina at 688 K. (b) THT conversion versus surface of the carboxylate ν(OCO) bands [the units for integrated intensity are absorbance unit (au) cm^{-1}]. From [95].

pyridine flow was stopped, IR spectroscopy showed that Lewis acid sites were preferentially recovered, whereas the CO_2 selectively increased, indicating that CO_2 formation was linked to Lewis sites presence whereas Brønsted sites were linked to propene formation [96].

The state of the adsorbed reactant can sometimes directly be an indication of the state of the active sites under reaction conditions. In the CO conversion reaction on zeolite-supported Pt catalysts at various stages of aging, the reactant is at the same time the probe molecule [97]. When a temperature-programmed reaction is studied by *operando* IR spectroscopy [CO (4000 ppm)–O_2 (12 000 ppm) in 30 ml min^{-1} Ar, gas velocity 60 000 h^{-1}, 298–523 K], oxidized Pt ($Pt^{\delta+}$) is first detected on the aged catalyst, with the formation of dicarbonyls. The frequency of the ν(CO) vibration band is a clear indicator of the state of the Pt atoms (Figure 1.34). The complex feature for the CO bands was analyzed by chemometrics [multivariate curve resolution (MCR)]. Heating in the reactant flow induces the transformation of dicarbonyls into monocarbonyls, and further reduction of the Pt particles. The conversion is monitored at the same time, and the light off is observed when the temperature is high enough on the reduced Pt catalyst.

Very high time resolution (~10 ns) can be achieved by special recording techniques such as step scan interferometry. Step scan interferometry only records one point of the interferogram over time, and the measurement has to be repeated many times so that all the points in the interferogram can be collected. The IR spectra themselves are obtained after Fourier transformation of all the recomposed interferograms. The catalytic experiment therefore needs to be well controlled in time but also highly reproducible. If the start of the reaction is well controlled in time, the various states of the surface can be recorded over time and the observation can be reproduced so that results are co-added to lower the detection limit. Fast valves allow millisecond control over the reaction, which can be coupled with millisecond step

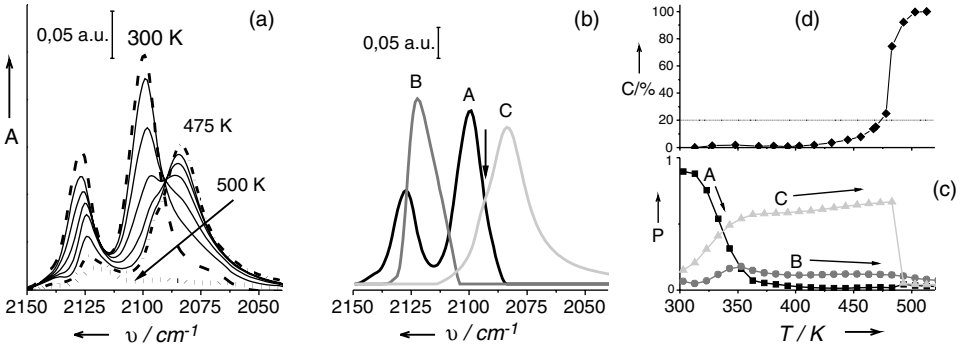


Figure 1.34 (a) IR spectra obtained during the heating ramp after addition of CO–O_2 mixture on an aged catalyst, (b) corresponding MCR decomposition into three reference spectra, where A is the $Pt^{\delta+}$ dicarbonyl, B is the $Pt^{\delta+}$ monocarbonyl, and C is the CO on Pt^0), and (c) concentration profiles. *P* is dimensionless and expressed as the relative contribution of the three reference spectra in (b) to the spectra displayed in (a). (d) The conversion of CO into CO_2 (*C* %). From [97].

scan interferometry [98]. Nanosecond control of a reaction is achieved with laser-triggered reaction, mostly in photochemistry [99]. Thermal reactions can also be observed, and a laser can provide the heat necessary to induce a reaction followed by step scan FTIR spectroscopy at the nanosecond time scale. Measuring the conversion and selectivity is not really possible under such conditions, because online analysis techniques can hardly follow such a small "reaction pulse," but these studies can be combined with slower but real *operando* measurements.

The importance of isocyanate species in the pathway from $C_2H_5OH + NO + O_2$ reaction to N_2 formation on an Ag/Al_2O_3 sample was established with true *operando* measurements (temperature-programmed reaction from 623 to 923 K, NO 500 ppm, EtOH 1000 ppm, O_2 10%; $W/F = 0.048\ g\ s\ cm^{-3}$, conversion measured by online mass spectrometry) [100]. The coordination and transformation sites were determined via the use of isotopically labeled species in IR spectroscopy [101]. In a second study, the reaction of CO and NO on Ag supported on alumina was induced by an ultrafast pulsed laser, after which the state of the adsorbed species was monitored by step scan FTIR spectroscopy with 33 ns time resolution [102] (Figure 1.35). The reaction was studied in a closed reactor, with CO and NO at a partial pressure of 10 mbar. The system was at 473 K, and the laser provided the additional heat to induce the reaction. The transformation of cyanides on silver into isocyanates on alumina is the limiting step of the reaction. This step could be recorded, and a bridged intermediate was detected between the silver particle and the alumina surface. This intermediate only lasts 2 µs, and it leads to the formation of an isocyanide on Al^{VI} (Al^{VI} is statistically the most accessible site), which in turn is quickly oxidized to an isocyanate and transferred to the stronger Lewis acid Al^{IV}. The interface between the

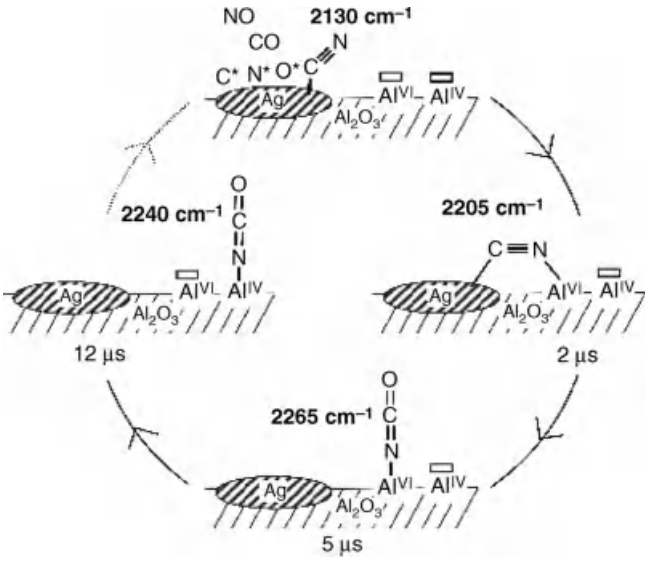


Figure 1.35 Mechanism of the reaction of cyanide species on alumina-supported silver catalysts in a $deNO_x$ reaction as seen by real time IR spectroscopy in the reactor. After [102]

Ag particle and the alumina support plays a key role in the catalytic activity, and this helps in understanding the role of the particle size.

Many other examples can be found in the literature, and a complete description of the procedure for IR characterization of the working catalyst has been extensively described in a recent review on the characterization of catalytically active sites by IR spectroscopy [5].

1.6 Conclusion

IR spectroscopy is widely available in the laboratory. The spectrometer is not expensive, and measurements are easy. This has made IR spectroscopy one of the basic techniques for the characterization of solids, especially for heterogeneous catalysis. The surface properties of the solid can be measured by using a suitable probe molecule, and information can be obtained on the acid–base properties and on the metal sites. New developments have appeared with combined techniques (e.g., IR spectroscopy and gravimetry). IR spectroscopy has been used for more than 20 years to study surface reactivity. Catalytic reactors can be equipped with IR windows, to study the solid under reaction conditions. Elementary steps in heterogeneous catalysis can thus be observed, and IR spectroscopy is now established as one of the main tools in understanding heterogeneous catalysis. Optical and molecular spectroscopies such as infrared might still become more important with the coming of TeraHertz spectroscopy, bridging the gap towards the very far infrared and the microwaves and bringing a whole new domain for understanfing heterogeneous catalysis.

References

1 Herschel, W. (1800) *Philos. Trans. R. Soc. London*, **90**, 284–292.
2 Herschel, W. and Dreyer, J.L.E. (1912) *The Scientific Papers of Sir William Herschel*, Royal Society and Royal Astronomical Society, London.
3 Baddour, R.F., Modell, M., and Goldsmith, R.L. (1970) *J. Phys. Chem.*, **74**, 1787–1796.
4 Thibault-Starzyk, F. and Saussey, J. (2004) in *In Situ Characterization of Catalysts* (ed. B.M. Weckhuysen), American Scientific Publishers, Stevenson Ranch, CA, pp. 15–31.
5 Vimont, A., Thibault-Starzyk, F., and Daturi, M. (2010) *Chem. Soc. Rev.*, **39**, 4928–4950.
6 Morterra, C., Magnacca, G., and Bolis, V. (2001) *Catal. Today*, **70**, 43–58.
7 Flanigen, E.M. (1976) in *Zeolite Chemistry and Catalysis* (ed. J.A. Rabo), American Chemical Society, Washington, DC, pp. 80–117.
8 Sohn, J.R., Decanio, S.J., and Lunsford, J.H. (1986) *Zeolites*, **6**, 225–227.
9 Cairon, O., Khabtou, S., Balanzat, E., Janin, A., Marzin, M., Chambellan, A., Lavalley, J.C., and Chevreau, T. (1994) *Stud. Surf. Sci. Catal.*, **84**, 997–1004.
10 Maache, M., Janin, A., Lavalley, J.C., Joly, J.F., and Benazzi, E. (1993) *Zeolites*, **13**, 419–426.
11 Maache, M., Janin, A., Lavalley, J.C., and Benazzi, E. (1995) *Zeolites*, **15**, 507–516.
12 Thibault-Starzyk, F., Janin, A., and Lavalley, J.C. (1997) *Angew. Chem. Int. Ed. Engl.*, **36**, 989–991.

13 Crépeau, G., Montouillout, V., Vimont, A., Mariey, L., Cseri, T., and Maugé, F. (2006) *J. Phys. Chem. B*, **110**, 15172–15185.

14 Tsyganenko, A.A. and Filimonov, V.N. (1973) *J. Mol. Struct.*, **19**, 579–589.

15 Knözinger, H. and Ratnasamy, P. (1978) *Catal. Rev.*, **17**, 31–70.

16 Digne, M., Sautet, P., Raybaud, P., Euzen, P., and Toulhoat, H. (2002) *J. Catal.*, **211**, 1–5.

17 Knoezinger, H. (1993) in *Elementary Reaction Steps in Heterogeneous Catalysis* (eds R.W. Joyner and R.A. Van Santen), Kluwer, Dordrecht, pp. 267–285.

18 Lercher, J.A., Grundling, C., and Edermirth, G. (1996) *Catal. Today*, **27**, 353–376.

19 Knozinger, H. and Huber, S. (1998) *J. Chem. Soc. Faraday Trans.*, **94**, 2047–2059.

20 Donoso-Tauda, O., Jaque, P., and Santos, J.C. (2011) *Phys. Chem. Chem. Phys.*, **13**, 1552–1559.

21 Lavalley, J.C., Jolly-Feaugas, S., Janin, A., and Saussey, J. (1997) *Mikrochim. Acta (Suppl.)*, **14**, 51–56.

22 Rouxhet, P.G. and Sempels, R.E. (1974) *J. Chem. Soc. Faraday Trans.*, **70**, 2021–2032.

23 Evans, J.C. and Wright, N. (1960) *Spectrochim. Acta, Part A*, **16**, 352–357.

24 Bratos, S. and Ratajczak, H. (1982) *J. Chem. Phys.*, **76**, 77–85.

25 Pelmenschikov, A.G., van Wolput, J.H.M.C., Janchen, J., and van Santen, R.A. (1995) *J. Phys. Chem.*, **99**, 3612–3617.

26 Claydon, M.F. and Sheppard, N. (1969) *J. Chem. Soc., Chem. Commun.*, 1431–1433.

27 Maugé, F., Sahibed-Dine, A., Gaillard, M., and Ziolek, M. (2002) *J. Catal.*, **207**, 353–360.

28 Travert, A., Manoilova, O.V., Tsyganenko, A.A., Maugé, F., and Lavalley, J.C. (2002) *J. Phys. Chem. B*, **106**, 1350–1362.

29 Vimont, A., Leclerc, H., Maugé, F., Daturi, M., Lavalley, J.-C., Surblé, S., Serre, C., and Férey, G. (2007) *J. Phys. Chem. C*, **111**, 383–388.

30 Thibault-Starzyk, F., Payen, R., and Lavalley, J.C. (1996) *Chem. Commun.*, 2667–2668.

31 Thibault-Starzyk, F., Bettahar, M.M., Saussey, J., and Lavalley, J.C. (1997) *Stud. Surf. Sci. Catal.*, **105**, 925–931.

32 Glazunov, V.P. and Odinokov, S.E. (1982) *Spectrochim. Acta*, **38**, 399–408.

33 Odinokov, S.E., Mashkovsky, A.A., Glazunov, V.P., Iogansen, A.V., and Rassadin, B.V. (1976) *Spectrochim. Acta*, **32**, 1355–1363.

34 Janin, A., Maache, M., Lavalley, J.C., Joly, J.F., Raatz, F., and Szydlowski, N. (1991) *Zeolites*, **11**, 391–396.

35 Khabtou, S., Chevreau, T., and Lavalley, J.C. (1994) *Micropor. Mesopor. Mater.*, **3**, 133–148.

36 Travert, A., Vimont, A., Sahibed-Dine, A., Daturi, M., and Lavalley, J.-C. (2006) *Appl. Catal. A: Gen.*, **307**, 98–107.

37 Hunter, E.P.L. and Lias, S.G. (1998) *J. Phys. Chem. Ref. Data*, **27**, 413–657.

38 Jacobs, P.A. and Heylen, C.F. (1974) *J. Catal.*, **34**, 267–274.

39 Morterra, C., Cerrato, G., and Meligrana, G. (2001) *Langmuir*, **17**, 7053–7060.

40 Lahousse, C., Aboulayt, A., Maugé, F., Bachelier, J., and Lavalley, J.C. (1993) *J. Mol. Catal.*, **84**, 283–297.

41 Oliviero, L., Vimont, A., Lavalley, J.-C., Romero Sarria, F., Gaillard, M., and Mauge, F. (2005) *Phys. Chem. Chem. Phys.*, **7**, 1861–1869.

42 Onfroy, T., Clet, G., Bukallah, S.B., Visser, T., and Houalla, M. (2006) *Appl. Catal. A: Gen.*, **298**, 80–87.

43 Thibault-Starzyk, F., Stan, I., Abelló, S., Bonilla, A., Thomas, K., Fernandez, C., Gilson, J.-P., and Pérez-Ramírez, J. (2009) *J. Catal.*, **264**, 11–14.

44 Daniell, W., Topsoe, N.Y., and Knozinger, H. (2001) *Langmuir*, **17**, 6233–6239.

45 Bolis, V., Fubini, B., Garrone, E., and Morterra, C. (1989) *J. Chem. Soc. Faraday Trans. 1*, **85**, 1383–1395.

46 Hadjiivanov, K.I. and Vayssilov, G.N. (2002) *Adv. Catal.*, **47**, 307–511.

47 Cairon, O. and Chevreau, T. (1998) *J. Chem. Soc. Faraday Trans.*, **94**, 323–330.

48 Chevreau, T., Cairon, O., Janin, A., and Lavalley, J.C. (1996) *J. Chim. Phys. Phys. Chim. Biol.*, **93**, 355–372.

49 Marie, O., Massiani, P., and Thibault-Starzyk, F. (2004) *J. Phys. Chem. B*, **108**, 5073–5081.

50 Nesterenko, N.S., Thibault-Starzyk, F., Montouillout, V., Yuschenko, V.V., Fernandez, C., Gilson, J.-P., Fajula, F., and Ivanova, I.I. (2004) *Micropor. Mesopor. Mater.*, **71**, 157–166.

51 Nesterenko, N.S., Thibault-Starzyk, F., Montouillout, V., Yushchenko, V.V., Fernandez, C., Gilson, J.-P., Fajula, F., and Ivanova, I.I. (2006) *Kinet. Catal.*, **47**, 40–48.

52 Soltanov, R.I., Paukshtis, E.A., and Yurchenko, E.N. (1987) *React. Kinet. Catal. Lett.*, **34**, 421–426.

53 Pelmenschikov, A.G., van Santen, R.A., Jänchen, J., and Meijer, E.L. (1993) *J. Phys. Chem.*, **97**, 11071–11074.

54 Jolly, S., Saussey, J., and Lavalley, J.C. (1994) *Catal. Lett.*, **24**, 141–146.

55 Anquetil, R., Saussey, J., and Lavalley, J.C. (1999) *Phys. Chem. Chem. Phys.*, **1**, 555–560.

56 Thibault-Starzyk, F., Travert, A., Saussey, J., and Lavalley, J.C. (1998) *Top. Catal.*, **6**, 111–118.

57 Zecchina, A., Marchese, L., Bordiga, S., Paze, C., and Gianotti, E. (1997) *J. Phys. Chem. B*, **101**, 10128–10135.

58 Lavalley, J.C. (1996) *Catal. Today*, **27**, 377–401.

59 Barthomeuf, D. (1996) *Catal. Rev. Sci. Eng.*, **38**, 521–612.

60 Vimont, A., Thibault-Starzyk, F., and Lavalley, J.C. (2000) *J. Phys. Chem. B*, **104**, 286–291.

61 Bachelier, J., Aboulayt, A., Lavalley, J.C., Legendre, O., and Luck, F. (1993) *Catal. Today*, **17**, 55–62.

62 Bensitel, M., Saur, O., and Lavalley, J.C. (1991) *Mater. Chem. Phys.*, **28**, 309–320.

63 Daturi, M., Binet, C., Lavalley, J.C., and Blanchard, G. (2000) *Surf. Interface Anal.*, **30**, 273–277.

64 Sánchez-Sánchez, M. and Blasco, T. (2009) *Catal. Today*, **143**, 293–301.

65 Kuhn, J.N. and Ozkan, U.S. (2008) *J. Catal.*, **253**, 200–211.

66 Moulin, B., Oliviero, L., Bazin, P., Daturi, M., Costentin, G., and Maugé, F. (2010) *Phys. Chem.*, **13**, 10797–10807.

67 Petitjean, H., Tarasov, K., Delbecq, F., Sautet, P., Krafft, J.M., Bazin, P., Paganini, M.C., Giamello, E., Che, M., Lauron-Pernot, H., and Costentin, G. (2010) *J. Phys. Chem. C*, **114**, 3008–3016.

68 Chizallet, C., Costentin, G., Che, M., Delbecq, F., and Sautet, P. (2006) *J. Phys. Chem. B*, **110**, 15878–15886.

69 Branda, M.M., Ferullo, R.M., Belelli, P.G., and Castellani, N.J. (2003) *Surf. Sci.*, **527**, 89–99.

70 Hadjiivanov, K. (2000) *Catal. Rev. Sci. Eng.*, **42**, 71–144.

71 Maugé, F., Binet, C., and Lavalley, J.C. (1997) in *Catalysis by Metals*, (eds A.-J. Renouprez and H. Jobic), Les Éditions de Physique, Paris, pp. 3–27.

72 Hollins, F. P. (1992) *Surf. Sci. Rep.*, **16**, 51–94.

73 Yates, J.T. Jr (1994) *Surf. Sci.*, **299–300**, 731–741.

74 Binet, C., Jadi, A., and Lavalley, J.-C. (1989) *J. Chim. Phys. Phys. Chim. Biol.*, **86**, 451–470.

75 Oliviero, L., Mariey, L., Lélias, M.A., Aiello, S., Gestel, J., and Maugé, F. (2010) *Catal. Lett.*, **135**, 62–67.

76 Koizumi, N., Yamazaki, M., Hatanaka, S., and Yamada, M. (1997) *Catal. Today*, **39**, 33–44.

77 Topsøe, H., Clausen, B.S., and Massoth, F.E. (1996) *Hydrotreating Catalysis*, Springer, Berlin.

78 Travert, A., Dujardin, C., Maugé, F., Veilly, E., Cristol, S., Paul, J.-F., and Payen, E. (2006) *J. Phys. Chem.*, **110**, 1261–1270.

79 Dujardin, C., Lelias, M.A., van Gestel, J., Travert, A., Duchet, J.C., and Maugé, F. (2007) *Appl. Catal.*, **322**, 46–57.

80 Lelias, M.A., Kooyman, P.J., Mariey, L., Oliviero, L., Travert, A., van Gestel, J., van Veen, J.A.R, and Mauge, F. (2009) *J. Catal.*, **267**, 14–23.

81 Thibault-Starzyk, F., Gil, B., Aiello, S., Chevreau, T., and Gilson, J.-P. (2004) *Micropor. Mesopor. Mater.*, **67**, 107–112.

82 Gallas, J.-P., Goupil, J.-M., Vimont, A., Lavalley, J.-C., Gil, B., Gilson, J.-P., and Miserque, O. (2009) *Langmuir*, **25**, 5825–5834.

83 Bazin, P., Alenda, A., and Thibault-Starzyk, F. (2010) *Dalton Trans.*, **39**, 8432–8436.

84 Weckhuysen, B.M. (2002) *Chem. Commun.*, 97–110.

85 Karge, H.G., Niessen, W., and Bludau, H. (1996) *Appl. Catal. A: Gen.*, **146**, 339–349.

86 Vimont, A., Thibault-Starzyk, F., and Lavalley, J.C. (2000) *Stud. Surf. Sci. Catal.*, **130**, 2963–2969.

87 Vimont, A., Marie, O., Gilson, J.P., Saussey, J., Thibault-Starzyk, F., and Lavalley, J.C. (1999) *Stud. Surf. Sci. Catal.*, **126**, 147–154.

88 Centi, G., Perathoner, S., and Tonini, S. (2000) *Catal. Today*, **61**, 211–221.

89 Amblard, M., Burch, R., and Southward, B.W.L. (2000) *Catal. Today*, **59**, 365–371.

90 Meunier, F.C., Tibiletti, D., Goguet, A., Shekhtman, S., Hardacre, C., and Burch, R. (2007) *Catal. Today*, **126**, 143–147.

91 Ortelli, E.E., Wambach, J., and Wokaun, A. (2000) *Appl. Catal. A: Gen.*, **192**, 137–152.

92 Miners, J.H., Martin, R., Gardner, P., Nalezinski, R., and Bradshaw, A.M. (1997) *Surf. Sci.*, **377**, 791–795.

93 Lesage, T., Verrier, C., Bazin, P., Saussey, J., and Daturi, M. (2003) *Phys. Chem. Chem. Phys.*, **5**, 4435–4440.

94 Jolly, S., Saussey, J., and Lavalley, J.C. (1994) *J. Mol. Catal.*, **86**, 401–421.

95 Can, F., Travert, A., Ruaux, V., Gilson, J.-P., Maugé, F., Hu, R., and Wormsbecher, R.F. (2007) *J. Catal.*, **249**, 79–92.

96 Savary, L., Saussey, J., Costentin, G., Bettahar, M., and Gubelmann Bonneau, M. (1996) *Catal. Today*, **32**, 57–61.

97 Rivallan, M., Thomas, S., Lepage, M., Takagi, N., Hirata, H., and Thibault-Starzyk, F. (2010) *ChemCatChem*, **2**, 1599–1605.

98 Wasylenko, W. and Frei, H. (2007) *Phys. Chem. Chem. Phys.*, **9**, 5497–5502.

99 Frei, H. and Yeom, Y.H. (2004) in *In Situ Spectroscopy of Catalysts* (ed. B. Weckhuysen), American Scientific Publishers, Stevenson Ranch, CA, pp. 20–34.

100 Bion, F N, Saussey, J., Haneda, M., and Daturi, M. (2003) *J. Catal.*, **217**, 47–58.

101 Bion, N., Saussey, J., Hedouin, C., Seguelong, T., and Daturi, M. (2001) *Phys. Chem. Chem. Phys.*, **3**, 4811–4816.

102 Thibault-Starzyk, F., Seguin, E., Thomas, S., Daturi, M., Arnolds, H., and King, D.A. (2009) *Science*, **324**, 1048–1051.

2
Raman and UV-Raman Spectroscopies

Fengtao Fan, Zhaochi Feng, and Can Li

2.1
Introduction

The scattering of monochromatic radiation with change in frequency was predicted theoretically by the Austrian quantum physicist A. Smekal in 1923 [1]. In 1922, Indian physicist C.V. Raman published his work on the "Molecular Diffraction of Light," the first of a series of investigations with his collaborators, and this work ultimately led to his discovery (on 28 February 1928) of the radiation effect which bears his name [2]. In 1930, Raman received the Nobel Prize for his work on the scattering of light. Raman spectroscopy, based on the shift in energy of the excitation line, can be used to study vibrational, rotational, and other low-frequency modes in a system. However, at that time, the excitation source, spectrograph and scanning techniques were primitive and lacked efficiency. Moreover, the intrinsic weak signals of spontaneous Raman scattering and the strong fluorescence interference from impurities in the sample severely restricted the application of Raman spectroscopy. However, since the 1960s, the development of laser technology, holographic gratings, photomultiplier tubes, charge-coupled devices and computer technology has made Raman spectroscopic techniques widely applicable in science and technology. In recent decades, Raman spectroscopy has become a powerful tool for studying the structure of catalysts and identifying their active sites, and also solid materials, along with the development of catalysis, nanotechnology and material science.

2.1.1
Raman Spectroscopy

The origin of Raman effect can be explained by classic and quantum mechanics theories. For the classic theory, the Raman effect can be explained by considering that the incident light of frequency ν is modulated by the vibration of a molecule with frequency ν_1.

Consider a light wave of frequency ν with an electronic field strength E:

$$E = E_0 \cos 2\pi\nu t \tag{2.1}$$

Characterization of Solid Materials and Heterogeneous Catalysts: From Structure to Surface Reactivity, First Edition. Edited by Michel Che and Jacques C. Védrine.
© 2012 Wiley-VCH Verlag GmbH & Co. KGaA. Published 2012 by Wiley-VCH Verlag GmbH & Co. KGaA.

where t is time and E_0 and E are the amplitudes of the incident light at $t=0$ and t, respectively. The dipole moment P for a molecule irradiated by light can be expressed as

$$P = \alpha E = \alpha E_0 \cos 2\pi\nu t \tag{2.2}$$

where α is the polarizability. If the molecule is vibrating with frequency ν_1, the nuclear displacement q is written as

$$q = q_0 \cos 2\pi\nu_1 t \tag{2.3}$$

where q_0 is the equilibrium normal coordinate. If the polarizability changes during the vibration, its value for a small vibration $(\partial\alpha/\partial q)_0$ is the rate of change of α with respect to the change in q, evaluated at the equilibrium position. We then obtain

$$\begin{aligned} P &= \alpha E_0 \cos 2\pi\nu t \\ &= \alpha_0 E_0 \cos 2\pi\nu t + \left(\frac{\partial\alpha}{\partial q}\right)_0 q_0 E_0 \cos 2\pi\nu t \cos 2\pi\nu_1 t \\ &= \alpha_0 E_0 \cos 2\pi\nu t + \left(\frac{\partial\alpha}{\partial q}\right)_0 q_0 E_0 \{\cos[2\pi(\nu+\nu_1)t] + \cos[2\pi(\nu-\nu_1)t]\}/2 \end{aligned} \tag{2.4}$$

The second and third terms give the Raman scattering of frequencies $(\nu+\nu_1)$, anti-Stokes and $(\nu-\nu_1)$, Stokes scatterings. Thus, the incident monochromatic radiation is modulated by the vibrating molecule with frequency ν_1, as shown in Figure 2.1a. In addition, Eq. (2.4) requires

$$\left(\frac{\partial\alpha}{\partial q}\right)_0 \neq 0 \tag{2.5}$$

Hence the polarizability of the molecule must change during the vibration for a Raman-active mode.

The origin of the Raman effect and Rayleigh scattering can also be quantitatively explained by the electron transition from the vibrational energy levels of a molecule in

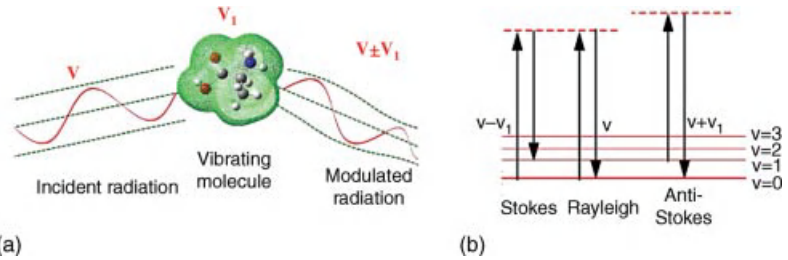


Figure 2.1 Schematic illustration of Rayleigh scattering and Raman scattering by (a) classic and (b) quantum mechanism theory.

quantum theory. The scattering originates from the transition of an electron from an initial vibrational energy level of a molecule to an intermediate virtual state excited by the incident photon and then transition to the final vibrational energy level. For Rayleigh scattering, electron transitions start and finish at the same vibrational energy level. For Raman scattering, transitions start and finish at different vibrational energy levels. In the case of Stokes lines, the molecule at $\nu = 0$ state is excited to the $\nu = 1$ state, giving scattered light at a frequency of $\nu - \nu_1$. Anti-Stokes lines arise when the molecule initially in the $\nu = 1$ state scatters radiation of frequency $\nu + \nu_1$ and reverts to the $\nu = 0$ state, as shown in Figure 2.1b.

Theoretically, the intensities of Raman bands can be expressed as

$$I_{mn} = CI_0(\nu_0 - \nu)^4 \sum_{ij} \left|\left(\alpha_{ij}\right)_{nm}\right|^2 \tag{2.6}$$

where C is a constant. I_0 is the incident intensity, and α_{ij} are the components of the polarizability tensor associated with the transition from state m to n.

The quantum mechanics expression of Raman scattering, through second-order perturbation theory, is given by the Kramers–Heisenberg–Dirac dispersion equation [3]:

$$\left(\alpha_{ij}\right)_{mn} = \frac{1}{h} \sum_{e} \left(\frac{M^i_{me} M_{en}}{\nu_{em} - \nu_0 + i\Gamma_e} + \frac{M_{me} M^i_{en}}{\nu_{en} + \nu_0 + i\Gamma_e} \right) \tag{2.7}$$

where ν_{em} and ν_{en} are the frequencies corresponding to the energy differences between the states indicated, h is Planck's constant, M_{me} and M_{en} are the electric transition moments, and Γ_e is the bandwidth of the eth state.

For the Raman scattering effect, approximately one photon out of 10^8 photons of an incident flux could be Raman scattered. Fluorescence, on the other hand, is a resonant phenomenon, which can be several orders of magnitude stronger than Raman scattering. Therefore, the fluorescence from even trace amounts of fluorescent impurities in samples often totally swamps the Raman signal. The fluorescence spectra of condensed material are usually in the range from 300 to 700 nm, or even longer wavelengths, as illustrated in Figure 2.2a. To avoid fluorescence interference of a Raman spectrum in the visible region, it is necessary to shift the excitation source from the visible to the UV region, or to the IR region. In the 1990s, ultraviolet (UV) Raman spectroscopy and Fourier transform (FT) Raman spectroscopy were developed with an aim of shifting the Raman spectra away from the visible region [5, 6].

2.1.2 FT-Raman Spectroscopy

Using near-infrared (IR) lasers to produce excitation lines, an FT-Raman spectrometer equipped with a Michelson interferometer has the advantage of increase the spectral signal-to-noise ratio while avoiding generating fluorescence, as shown in Figure 2.3 [7, 8], since the photon energy of near-IR lasers is too low to excite the electrons from the ground state to highly excited states. The effectiveness of this

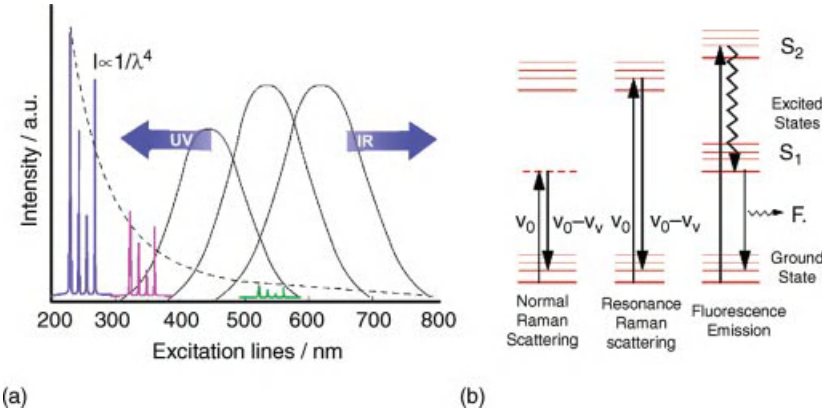


Figure 2.2 (a) Illustration of UV Raman spectroscopy in avoiding fluorescence interference while increasing Raman scattering intensity. (b) Energy level scheme illustrating the normal Raman scattering and resonance Raman scattering processes. The fluorescence band usually has a longer wavelength than the excited laser because the existence of the internal conversion from the high-energy electronic states (e.g., S_2) to the lowest singlet excited electronic state (S_1), where the fluorescence happens. Adapted from [4].

approach can be readily seen in the following examples. Figure 2.3a, trace A, shows a Raman spectrum of a sample of anthracene obtained on a conventional instrument with 514.5 nm excitation and a total measurement time of 1 h. The severe fluorescent background due to impurities or some small amount of sample degradation masks the whole spectrum. Figure 2.3a, trace B, shows an FT-Raman spectrum obtained on the same sample with 1064 nm excitation. Since there is no fluorescence, the signal-to-noise ratio is drastically improved over the conventional spectrum.

As one can see, FT-Raman equipment has benefited tremendously from using IR lasers and Michelson interferometers associated with microcomputers for data processing [8]. However, FT-Raman measurements at elevated temperatures are

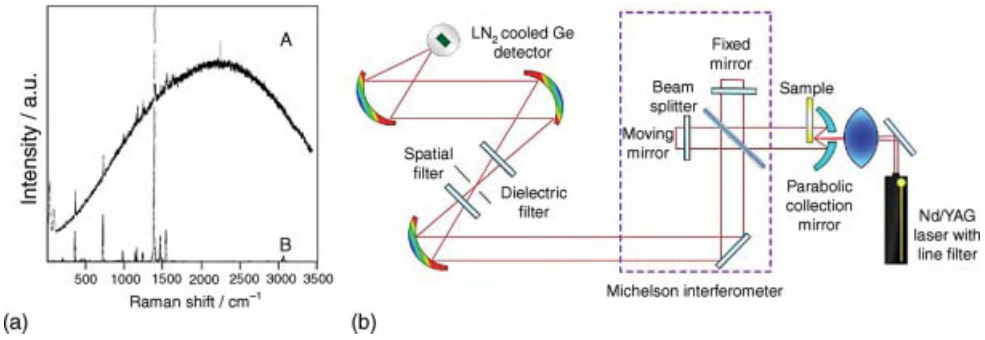


Figure 2.3 (a) Conventional Raman spectrum of anthracene (A) and FT-Raman spectrum of anthracene (B). (b) Optical diagram of FT-Raman spectrometer. Adapted from [7, 8].

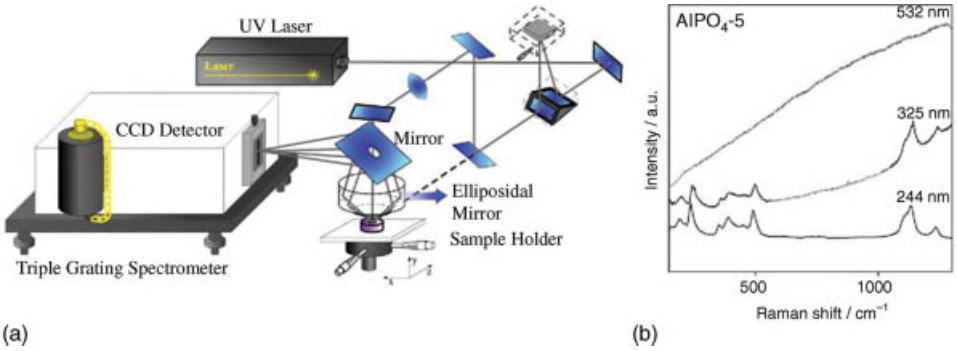


Figure 2.4 (a) Schematic diagram of a UV Raman spectrometer. (b) Raman spectra of $AlPO_4$-5 excited at 244, 325 and 532 nm. Adapted from [10].

problematic because of the strong background arising from sample luminescence and thermal emission [9].

2.1.3
UV Raman Spectroscopy

Fluorescence interference in Raman spectra could be also avoided if the excitation source is shifted from the visible to the UV region, as illustrated in Figure 2.2a. A typical example of a UV Raman spectrometer is shown in Figure 2.4a; an ellipsoidal mirror is used to collect and focus the scattered photons into a triple-grating spectrometer [11, 12]. Figure 2.4b shows the Raman spectra of $AlPO_4$-5 molecular sieve excited at 244, 325 and 532 nm. The spectral features obtained by excitation at 532 nm have been obscured by strong fluorescence. When the excitation line is shifted to 325 nm, Raman signals partly shifted away from the fluorescence region can be obtained. In contrast, a well-resolved spectrum of $AlPO_4$-5, with a high signal-to-noise ratio, can be obtained with 244 nm excitation. In addition, because the Raman scattering intensity is proportional to the fourth power of the scattered light frequency, the sensitivity of UV Raman spectroscopy is much higher than that of visible or near-IR Raman spectroscopy.

2.1.4
Resonance Raman Spectroscopy

Resonance Raman scattering occurs when the sample is irradiated with an exciting line whose energy corresponds to that of the electronic transitions of a chromophoric group in a molecular system.

From Eq. (2.7), when the energy of the laser excitation line approaches that of the electronic transitions, $\nu_{em} - \nu_0$ becomes very small. Thus, the Raman intensity can be increased dramatically, and the process is referred to resonance Raman spectroscopy (RRS).

Resonance Raman scattering is an extensively studied subject. An excellent, qualitative discussion of UV RRS can be found elsewhere [13]. Here, we only consider simple cases so that the essential features can be established. Resonance Raman spectra typically exhibit a pattern of peak intensities that varies with excitation wavelength and differs significantly from the pattern observed in normal Raman spectra. The intensity enhancement depends on (i) the strength of the absorption at the excitation wavelength, (ii) whether the electronic absorption is dipole allowed or vibronically coupled, (iii) the amount of change in equilibrium normal coordinates between the ground and excited electronic states, and (iv) the vibronic coupling between the excited electronic states and between the ground and excited states. Three primary mechanisms for enhanced intensity have been identified as the so-called A, B, and C terms [14, 15]. When the laser frequency is in resonance with a dipole-allowed electronic transition, the A and B terms give rise to enhancement of totally symmetric and non-totally symmetric fundamental vibrations, respectively. When the laser is in resonance with a vibronically coupled electronic transition, the A and B terms are zero, and the resonant intensity is mainly contributed by the C term. This term gives rise to enhancement of totally symmetric vibrations and also overtones and combinations of non-totally symmetric vibrations that are vibronically active [16].

A resonance-enhanced signal can be several orders of magnitude more intense than the normal Raman signal [3]. RRS is particularly useful for detecting an individual species in a sample mixture [14]. Raman bands associated with different components can be selectively enhanced by exciting their electronic transitions. As shown schematically in Figure 2.5b, there are two absorbance bands centered at 250 and 400 nm for A and B, corresponding to two different components. The laser

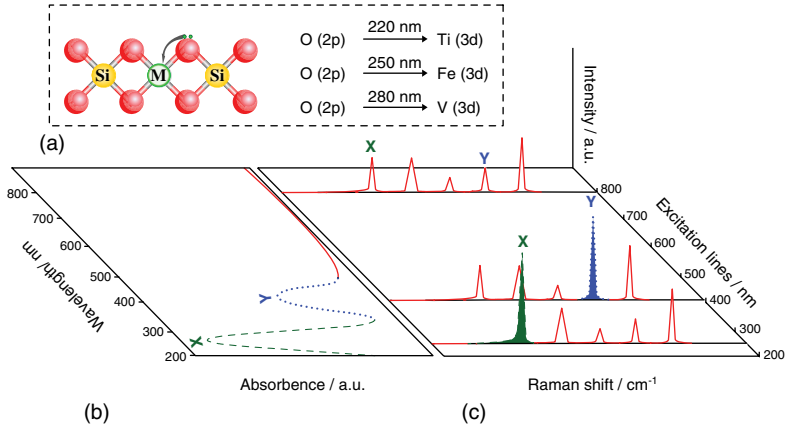


Figure 2.5 (a) Charge transfer transition between oxygen and transition metal ions in the framework of molecular sieves; the schematic shows the relationship between (b) UV–visible spectra and (c) UV resonance Raman spectroscopy. The Raman bands of X and Y components can be selectively enhanced by shifting the excitation laser lines towards their UV–visible absorbance bands. Adapted from [4].

excitations at 250 and 450 nm approach the centers of the two absorbance bands. The Raman bands associated with component A can be enhanced when excited with 250 nm radiation whereas the Raman bands associated with the component B can be enhanced when excited with 450 nm radiation due to the resonance Raman effect (Figure 2.5c).

Transition metal ions substituted into the framework of microporous and mesoporous materials show a charge-transfer transition between transition metal ions and the framework oxygen ions. The charge-transfer transitions usually occur in the UV region, for example, 250 nm for Fe-ZSM-5, 220 nm for TS-1, and 280 nm for V-MCM-41. Accordingly, the characteristic Raman bands directly associated with the framework transition metal ions can be enhanced by exciting these transition metal ion-containing zeolites with UV lasers. Therefore, it is possible to identify isolated framework or semi-framework transition metal ions in microporous and mesoporous materials.

2.2
Characterization of Active Sites and Phase Structure of Metal Oxides

2.2.1
Identification of the Active Species on Metal Oxides

The infinite variety of structural motifs and properties makes metal oxides indispensable in many fields. For example, cerium oxide has been extensively used as a catalyst or promoter in heterogeneous catalysts. Raman spectroscopy was used to characterize the nature of the CeO_2 support and the oxygen species formed on it [17].

Corma and co-workers found that nanocrystalline CeO_2 increases the activity of gold for CO oxidation by two orders of magnitude with respect to a conventionally precipitated CeO_2 support [19]. To explain this phenomenon, Raman spectroscopy was employed to investigate the oxygen species formed upon O_2 adsorption on nanocrystalline CeO_2 [18]. The Raman spectrum in Figure 2.6a of oxygen species upon O_2 adsorption on conventionally prepared CeO_2 shows bands at 1314, 1361, 1408, 1428, 1470, 1527, and 1571 cm^{-1}. The band at 1571 cm^{-1} is assigned to the physically adsorbed molecular O_2, and the bands above 1300 cm^{-1} may be assigned to $O_2^{\delta-}$ oxygen ($0 < \delta < 1$) adspecies [20, 21]. The Raman spectrum of O_2 adsorbed on nanocrystalline CeO_2 shows bands at 1123, 964, 871, and 831 cm^{-1}. The band at 1123 cm^{-1} is assigned to the superoxide species according to early IR evidence [22, 23]. The band at 964 cm^{-1} is assigned to peroxide adspecies at so-called one-electron defect sites [21]. The results clearly demonstrate that the nanocrystalline CeO_2 stabilizes O_2 as superoxide and peroxide species, whereas the precipitated CeO_2 tends to stabilize the molecular O_2.

In order to investigate the reactivity of the oxygen species on a highly active gold catalyst, the sample of gold-supported nanocrystalline CeO_2 is placed in an O_2 flow, followed by CO + O_2 flow under reaction conditions. Figure 2.6b shows the Raman spectra taken on the catalyst sample before and after the CO oxidation. The intensities

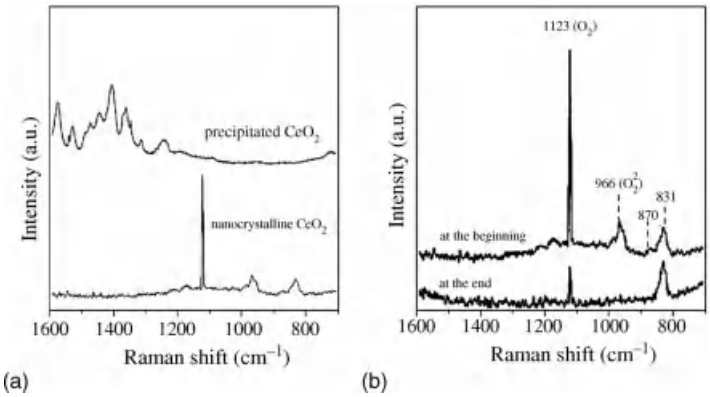


Figure 2.6 (a) Raman spectra of oxygen species upon O_2 adsorption on conventionally precipitated CeO_2 and nanocrystalline CeO_2; (b) Raman spectra of the 1.92 wt% Au/CeO_2 sample before and after CO oxidation reaction. Adapted from [18].

of the Raman bands at 1123 and 966 cm^{-1} are decreased after CO oxidation. The results indicate that the superoxide species and peroxide adspecies at the one-electron defect site in the oxidation of CO are responsible for the oxidation of CO.

2.2.2
Phase Transformation in the Surface Region of Metal Oxides

Catalytic performance depends largely on the surface properties of catalysts. Therefore, the surface phase composition should contribute more directly to the catalytic reaction, and research on surface phase composition may reveal the general essence of the active phase.

Vanadium phosphorus oxide (VPO) is an efficient catalyst for the vapor-phase oxidation of *n*-butane to maleic anhydride. Different phases in the VPO precursors and catalysts can be identified by Raman spectroscopy. Among them, $(VO)_2P_2O_7$ is considered to be the main active component. *In situ* Raman spectroscopy was employed to study the conversion of precursor $[VO(HPO_4)\cdot 5H_2O]$ to the active form $[(VO)_2P_2O_7]$ in real time. It was found that during this process, the crystalline structure of the precursor became totally disordered with increasing selectivity for maleic anhydride. The selective reaction product assists in the creation of the active sites by crystallization of the surface structure of the catalyst as a template [24].

Generally, Raman scattering comes from both the surface and the bulk of a solid sample. However, the signal from the bulk is attenuated when the sample strongly absorbs the excitation light and the scattering light, and the Raman spectra then contain more signals from the surface top region than the bulk of the sample. Therefore, UV Raman spectroscopy is more sensitive to the surface region than to the bulk as these samples strongly absorb UV laser light (Figure 2.7). Visible Raman spectroscopy gives information from both the bulk and the surface of a sample

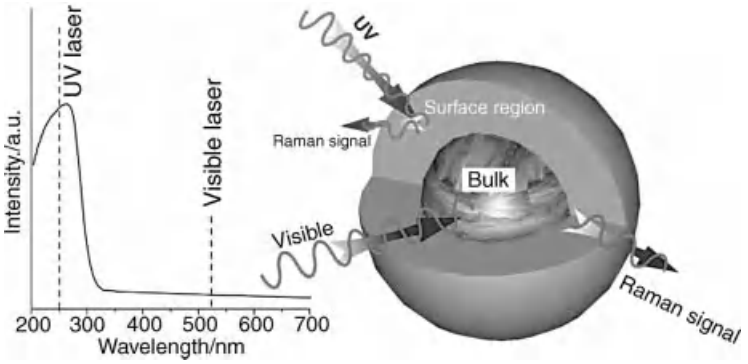


Figure 2.7 Schematic illustration of UV Raman spectroscopy becoming more sensitive to the surface region than to the bulk region when a sample particle absorbs UV laser light.

because there is usually no electronic absorption in the visible region for most metal oxide samples.

Titania (TiO_2) has been widely studied because of its unique optical and chemical properties in catalysis, photocatalysis, and so on [25, 26]. Li and co-workers studied the phase transformation of TiO_2 from anatase to rutile by UV Raman spectroscopy, visible Raman spectroscopy, X-ray diffraction (XRD), and transmission electron microscopy (TEM) [27].

Figure 2.8b displays the visible Raman spectra of TiO_2 calcined at different temperatures. The Raman spectrum of the sample before calcinations gives two broad bands at about 430 and 605 cm^{-1}, indicating that the sample is in the amorphous phase [27]. After calcination at 300 °C, characteristic bands of anatase phase appear at 195, 395, 515, and 638 cm^{-1}. The bands of anatase phase increased in intensity and decreased in linewidth when the sample was calcined at 500 °C. A very weak band appears at 445 cm^{-1} due to rutile phase after calcination at 550 °C. The visible Raman spectroscopic result indicates that the anatase phase starts to change into the rutile phase at 550 °C.

Figure 2.8a displays the UV Raman spectra excited at 325 nm of TiO_2 calcined at different temperatures. All bands assigned to the anatase phase become sharp and strong after calcination at 500 °C. These findings agree well with those of XRD and visible Raman spectra. Notably, the UV Raman spectra of the sample with calcination temperatures from 550 to 680 °C are essentially the same as that of the sample calcined at 500 °C. However, according to the XRD patterns and visible Raman spectra, the anatase phase starts to transform into the rutile phase at only 550 °C, and the anatase phase gradually changes into the rutile phase in the temperature range 550–680 °C. After calcination at 700 °C, a new band appears at 612 cm^{-1} and two weak bands at 235 and 445 cm^{-1} due to the appearance of the rutile phase, while the intensities of the bands of the anatase phase begin to decrease.

The inconsistency in the results from the above three techniques suggests that the anatase phase of TiO_2 at the surface region can remain at relatively higher calcination temperatures than that in the bulk during the phase transformation. The TEM results

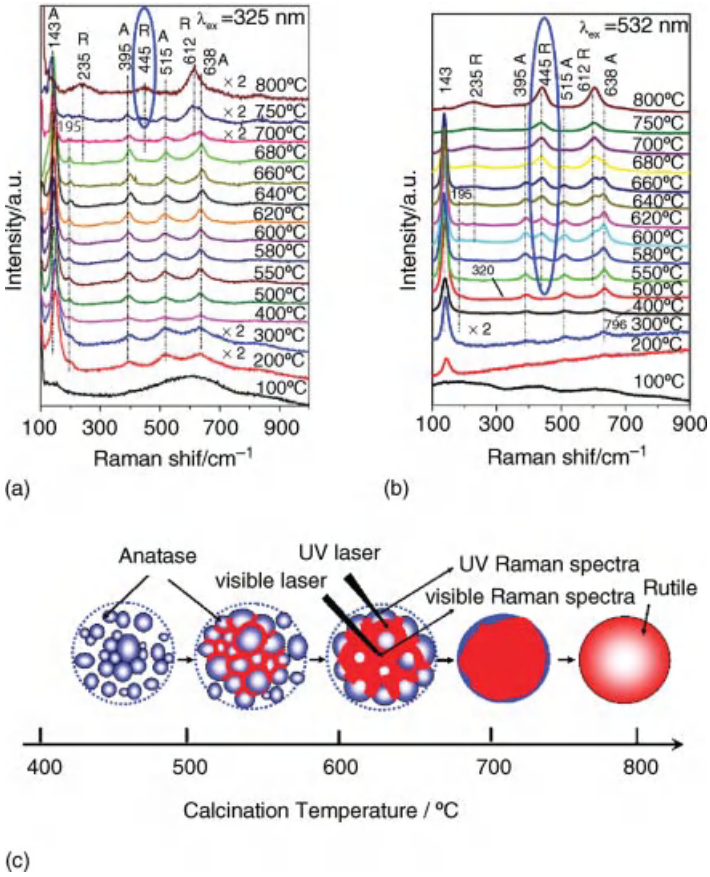


Figure 2.8 (a) UV and (b) visible Raman spectra of TiO_2 calcined at different temperatures with the excitation line at 325 and 532 nm. (c) A proposed scheme for the phase transformation of TiO_2 with increasing calcination temperature. Adapted from [27].

show that small particles agglomerate into large particles when the TiO_2 sample is calcined at elevated temperatures and the agglomeration of the TiO_2 particles occurs along with the phase transformation from anatase to rutile.

A proposed scheme for the phase transformation of TiO_2 with increasing calcination temperature is illustrated in Figure 2.8c: the TiO_2 particles with anatase phase intimately contact each other, revealed by the TEM results. Hence the surface and the bulk region of the TiO_2 sample actually refer to the outer surface region and the inner region of agglomerated TiO_2 particles, respectively. The nucleation of the rutile phase occurs on the interfaces of contacting anatase particles in the inner region of agglomerated particles. At this moment, the rutile phase is first detected by XRD and visible Raman spectroscopy for the sample calcined at 550–680 °C. Once phase transformation takes place, the particle size increases rapidly. The agglomeration of the TiO_2 particles occurs along with the phase transformation from anatase to rutile.

When the calcination temperature is higher than 700 °C, the anatase phase in the outer surface region of agglomerated particles begins to change into the rutile phase. Therefore, mixed phases of anatase and rutile are observed by UV Raman spectroscopy while the inner region of agglomerated particles is nearly in the rutile phase. Both XRD and visible Raman spectra show that the inner region of agglomerated particles is in the rutile phase when the sample is calcined at 750 °C. After calcination at 800 °C, the anatase phase in the outer surface region is completely transformed into the rutile phase; and then the whole agglomerated particles are in the rutile phase.

2.3
Characterization of Surface Metal Oxide Species on Supported Metal Oxides

Supported metal oxide catalysts have attracted much attention owing to their wide application in the selective oxidation of hydrocarbons [28], catalytic reduction of NO_x [29], and so on. It is found that surface metal oxide species tend to form a two-dimensional surface metal oxide overlayer rather than a separate crystalline metal oxide phase or compound. Raman spectroscopy can provide major structural information about these surface metal oxide species, such as the molecular structure of the surface metal oxide species, surface coverage of the metal oxide overlayer, distribution of surface Lewis and Brønsted acid sites, and the structure of the active surface metal oxide species during catalytic reactions [30–33].

The molecular vibrations of different molecular bonds in surface metal oxides can be revealed by Raman spectroscopy. The relationship between the Mo−O bond order and the Mo−O stretching frequency is presented in Figure 2.9b [34]. According to this correlation, the Mo−O vibrations at $\sim$1000 cm^{-1} can be assigned to terminal Mo=O bonds, vibrations at $\sim$600 cm^{-1} can be assigned to single Mo−O bonds. and vibrations at 100–300 cm^{-1} are associated with long bonds. According to this scheme, the M−O bond lengths of surface metal oxide species on oxide supports can be estimated from the M−O stretching frequency in the Raman spectra. These correlations are useful for the estimation of the bond length in high wavenumber

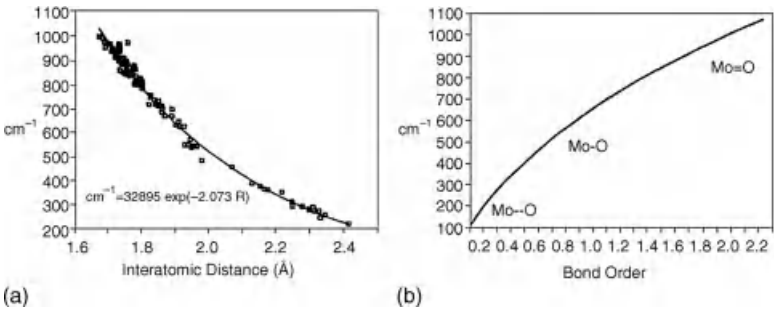


Figure 2.9 The relationship of (a) Mo−O bond length versus Raman stretching frequency, and (b) Mo−O bond strength versus Raman stretching frequency. Adapted from [31].

regions (>800 cm^{-1}). For example, the 10–20 cm^{-1} vibrational shifts observed for the terminal M=O bonds of dehydrated surface metal oxide species are due to the shortening of the terminal M=O bonds by ~0.01 Å [34].

The Raman spectroscopic detection of surface metal oxides began in the 1970s, with a series of studies on supported MoO_3 [35, 36], WO_3 [37], V_2O_5 [38], and Re_2O_7 [39] species, attempting to reveal the structure of the supported metal oxide and the degree of surface coverage. Medema *et al.* reported Raman spectroscopic studies on the structures of molybdenum and cobalt species present in Co–Mo/γ-Al_2O_3 catalyst systems [40]. They found that these catalyst systems contain Mo and Co in different modifications depending on the degree of surface coverage. In the absence of Co, four different Mo species are found: isolated molybdate tetrahedra at low coverages, octahedral polymolybdate phase with increasing surface coverage, "bulk" aluminum molybdate at higher coverage, and MoO_3 crystals at very high coverage. The addition of Co to Mo/γ-Al_2O_3 leads to the conversion of MoO_3 crystals into "$CoMoO_4$", and a decrease in the isolated Mo tetrahedra concentration leads to the formation of the polymeric molybdate.

In some cases, surface metal oxides dispersed on a support may be present as a monolayer. By using various characterization techniques such as XRD, EXAFS (extended X-ray absorption fine structure), and Raman spectroscopy, Xie and Tang first proposed the spontaneous monolayer dispersion of metal oxides on supports with high surface specific area [41]. Monolayer-dispersed oxide usually gives a Raman spectrum different from its crystalline counterpart. By using KNO_3 as an internal reference for the crystalline MoO_3 in the Raman spectra, Xie and Tang studied the content of crystalline MoO_3 as a function of the total content of MoO_3 in MoO_3/TiO_2 [41]. The threshold value corresponds to 0.115 g MoO_3 per 100 m^2 surface of TiO_2. This value agrees well with the XRD value of the monolayer capacity.

Deo and Wachs [42] found that molecular structures of surface vanadium oxide were dependent on the net pH at which the surface possesses zero surface charge [point of zero charge (PZC)]. This arises from the fact that the surface vanadium oxide overlayer is essentially in an aqueous medium under ambient conditions and the surface of the oxide support is hydrated. The net surface pH at the PZC is determined by the properties of the oxide support and the surface coverage of the acidic vanadium oxide overlayer. Oxide supports possessing a basic aqueous pH at the PZC were found to form predominantly tetrahedral surface vanadium oxide species (orthovanadate, pyrovanadate, and metavanadate), and oxide supports possessing an acidic aqueous pH at the PZC could lead to the formation of octahedral surface vanadium oxide species (decavanadate).

The Raman spectra of 3–10% V_2O_5/MgO are presented in Figure 2.10a and exhibit bands due to the vanadium–oxygen stretching vibrations at 820, 890, and 950 cm^{-1}, which are characteristic of orthovanadate (VO_4), pyrovanadate (V_2O_7), and metavanadate [$(VO_3)_n$], respectively. Thus, MgO (pH at PZC = 12) has a high preference for the formation of tetrahedrally coordinated surface vanadium oxide species (VO_4, V_2O_7) [42].

Figure 2.10b shows Raman spectra of V_2O_5/$A1_2O_3$ as a function of V_2O_5 loading (surface coverage). $A1_2O_3$ (pH at PZC = 9) has a preference for the formation of

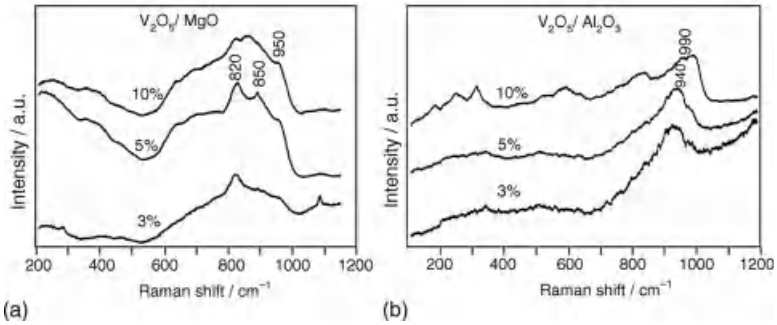


Figure 2.10 Raman spectra of (a) $V_2O_5/A1_2O_3$ as a function of MgO loading (surface coverage); (b) V_2O_5/Al_2O_3 as a function of V_2O_5 loading (surface coverage). Adapted from [42].

tetrahedrally coordinated surface vanadium oxide species $[(VO_3)_n]$ at low surface coverages (3–5%), characterized by the major Raman band at 940 cm^{-1}, and octahedrally coordinated surface vanadium oxide species ($V_{10}O_{28}$) at high surface coverages (10%), characterized by the broad Raman band at 990–1000 cm^{-1}.

Oxide supports such as TiO_2, ZrO_2, and SiO_2 possessing a pH of 6.0–2.0 at the PZC exhibit a high preference for the formation of octahedrally coordinated surface vanadium oxide species ($V_{10}O_{28}$) [42].

According to these studies, the preparation method will not affect the final molecular structures of the surface metal oxide species because it cannot influence the final pH at the PZC of the hydrated oxide surface [42].

Molybdenum oxides are usually in the aggregated/polymerized form or even in the bulk oxide form on the alumina surfaces when the loading of molybdenum oxide is high [43]. One may not only detect isolated transition metal oxides but also understand the coordination and interaction between the metal oxides and the support surfaces when the loading is sufficiently low. For the low-loading catalyst, it is difficult to obtain its Raman spectrum because of the fluorescence and the relatively low sensitivity of conventional Raman spectroscopy. Fortunately, UV RRS has the possibility of being able to detect the surface species with low concentration.

Figure 2.11 shows the UV Raman spectra of supported molybdate on γ-alumina with extremely low loading (0.10 wt% MoO_3). The Raman spectrum is greatly improved when the laser excitation is shifted from 488 to 325 nm, and Raman bands at 325, 837, 910, and 1670 cm^{-1} can be observed despite the fluorescence background (Figure 2.11a, trace B). The fluorescence is completely avoided when the excitation laser is shifted to the UV region, as clearly shown in Figure 2.11a, trace A. The Raman bands traces A and B in Figure 2.11a are clearly observed owing not only to the avoidance of fluorescence but also to the resonance Raman enhancement. As Figure 2.11b shows, there are two absorbance bands centered at 220 and 290 nm for MoO_3/γ-Al_2O_3. The band at 220 nm is mainly associated with the tetrahedral molybdate species and the band at 290 nm is associated with the octahedral molybdate species. The laser excitation at 325 nm is close to the band at 290 nm, which results in enhancement of the Raman bands at 837 and 1670 cm^{-1}

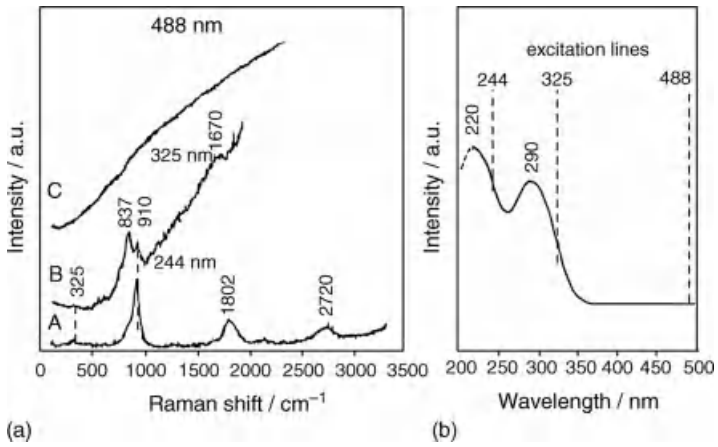


Figure 2.11 (a) Raman spectra of 0.1 wt% MoO_3/γ-Al_2O_3 using (A) 244, (B) 325, and (C) 488 nm lines as the excitation sources. (b) UV–visible diffuse reflectance spectrum [43].

(asymmetric vibration of Mo−O−Mo) in octahedral species due to the resonance Raman effect. The band at 910 cm^{-1} for the stretching vibration of Mo=O in tetrahedral species is observed, which may also be due to the resonance Raman effect since the surface concentration of either octahedral or tetrahedral species is very low.

Utilizing the advantages of UV RRS, Li and co-workers studied the evolution of surface molybdate species on γ-alumina during catalyst preparation with various pH values of the impregnating solution, by an equilibrium adsorption method [43]. When the impregnating solution is at pH 10.0, only tetrahedral molybdate species are formed on γ-alumina in the wet state. At pH 6.0, both tetrahedral and octahedral species are formed on γ-alumina in the wet state. In these two cases, the molybdate species adsorbed on the support for MoO_3/γ-alumina in the wet state are similar to those in the impregnating solution. However, both tetrahedral and octahedral species are formed on γ-alumina at pH 3.0 whereas the molybdate in the impregnation solution is in the octahedral form only. The results indicate that some polymolybdate species decompose when they interact with γ-alumina in the strongly acidic solution.

This study concluded that the structure of the surface molybdate species is controlled by the "surface pH value," which is a function of the pH value of the impregnating solution and the net pH value at the PZC of the support.

Raman spectroscopy is ideally suitable for the investigation of the behavior of surface metal oxide species during catalytic reactions because there is very little scattering from the gas phase [34]. Since the surface metal oxide species are often present as hydrated structures under ambient conditions, it is essential to understand the effect of moisture at elevated temperatures on the nature of the surface metal oxide species.

The effect of water vapor on the molecular structures of V_2O_3 on supports (SiO_2 Al_2O_3, TiO_2, and CeO_2) at elevated temperatures (from 500 to 120 °C) was investigated by *in situ* Raman spectroscopy [44]. Only isolated surface VO_4 species are

present on the dehydrated SiO_2 surface under dry conditions, while isolated VO_4 species and polymeric vanadate species can be found on dehydrated Al_2O_3, TiO_2, and CeO_2 surfaces. On introducing water vapor, the Raman features of the surface vanadium oxide species on the SiO_2 support are not affected owing to the hydrophobic nature of the SiO_2 support. However, the surface vanadium oxide species on the other supports (Al_2O_3, TiO_2, and CeO_2) exhibit pronounced behaviors on introducing water vapor. The Raman band of the terminal V=O bond of the surface vanadia species on these oxide supports becomes broad while shifting to lower wavenumbers by 5–30 cm^{-1} upon exposure to moisture. Above 230 °C, the small Raman shift for the surface vanadium oxide species is due to the formation of the hydrogen bonds with small amounts of moisture. At ~200 °C and below, the surface vanadium oxide species are heavily solvated and not accessible for gas-phase catalytic oxidation reactions. The *in situ* Raman results promoted the understanding of the inhibiting effect of moisture upon oxidation reactions over supported metal oxide catalysts.

2.4
Electron–Phonon Coupling in Nanostructured Materials

Nanostructured materials possess unique electronic, magnetic, optic, catalytic, and thermodynamic properties in comparison with their bulk properties [45]. Phonon scattering in nanostructured materials is one of the most important topics in optoelectronic and thermoelectric research [46], and also in semiconductor-based photocatalysis. Raman spectroscopy has been widely used to investigate the vibrational and structural properties of nanosized materials, such as the confinement effect on optical phonons.

The important issue of the size dependence of electron–phonon coupling has attracted much attention. Several experimental studies including absorption [47], photoluminescence [48], and spectral hole burning [49] indicate that the electron–LO-phonon coupling is larger with decreasing nanocrystals radius. However, there is still confusion when considering this basic point because contradictory results have been published with different characterization methods, particularly for Raman spectroscopy [50]. Surprisingly, several resonance Raman scattering experiments, in which in principle the electron–phonon interaction can be directly probed, suggested size-independent coupling [51] or even a decrease of the electron–phonon interaction strength with decreasing nanocrystal radius [52].

Scamarcio *et al.* reported the size dependence of the ratio between two-phonon and one-phonon Raman cross-sections in a prototype system: CdS_xSe_{1-x} nanocrystals embedded in a glass matrix [50]. In their experiment, the resonance condition was kept constant for each investigated nanocrystal size, which is a monotonic function $R(x)$ of the position x along the glass rod. The sample was scanned along the x direction by five different laser lines, in order to seek the positions x corresponding to the maximum resonant enhancement of the first order. A typical resonance profile, recorded with the excitation wavelength in proximity to the corresponding position x,

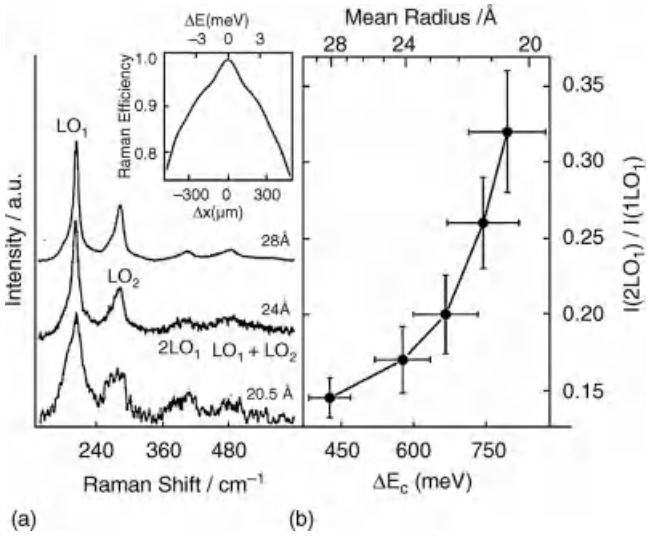


Figure 2.12 (a) Representative set of resonance Raman spectra of $CdS_{0.35}Se_{0.65}$ nanocrystals with different mean radii, recorded with the different exciting laser wavelengths, 457.9 nm (bottom), 488.0 nm (middle), and 514.5 nm (top), each under the same resonance condition corresponding to the maximum enhancement of the first-order bands. The inset shows the resonance profile obtained at 488.0 nm as a function of the distance Δx along the slab from the position of strongest resonance. (b) Ratio between two-phonon and one-phonon Raman bands as a function of the confinement energy and the mean nanocrystal radius. Adapted from [50].

is shown in the inset in Figure 2.12a. Figure 2.12b shows the size dependence of the ratio $I(2LO_1)/I(1LO_1)$. By maintaining a constant resonance condition, the increase in the ratio with decreasing crystal size can be observed, which was ascribed to the corresponding increase in the electron–phonon coupling. This result arises from the fact that the ratio between two-phonon and one-phonon scattering cross-sections is also strongly dependent on the exciting photon energy.

2.5 Characterization of sp^2 Carbon Materials

Among the different types of supports used in heterogeneous catalysis, carbon materials have attracted increasing interest owing to their unique properties. Carbon materials possess unusual properties such as high tensile strength, high resilience and electronic properties ranging from metallic to semiconducting [53]. Hence it is of great interest to characterize these materials, especially from an applications point of view. Raman spectroscopy is a useful tool for characterizing sp^2 carbon materials, such as 3D graphite, 2D graphene, 1D carbon nanotubes, and 0D fullerenes. Raman spectra of sp^2 carbons provide valuable information about defects, stacking of the

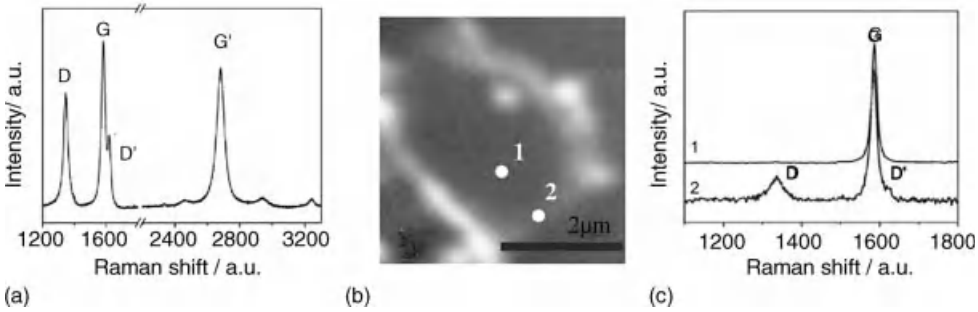


Figure 2.13 (a) Raman spectrum of a nanographite sample, showing the main Raman features, the D, G, D′, and G′ bands taken with a laser excitation energy of 2.41 eV. (b) Raman images of a graphite crystallite deposited on a glass substrate. (c) Raman spectra obtained in regions 1 and 2 (white circles) depicted in (b). Adapted from [54].

graphene layers, and the finite sizes of the crystallites, in particular, information about the properties that are relevant to electrons and phonons [54, 55]. Moreover, the Raman signal from even a single layer of graphene (1-LG), or from an isolated single-walled carbon nanotube (SWNT) can be greatly enhanced due to the resonance Raman effect.

The most prominent features of graphitic materials in the Raman spectra are the so-called G band appearing at 1582 cm^{-1} and the G′ band at about 2700 cm^{-1} using laser excitation at 514.5 nm, as shown in Figure 2.13a [54]. The G band is a doubly degenerate (TO and LO) phonon mode (E_{2g} symmetry) at the Brillouin zone center that is Raman active for sp^2 carbon networks [55]. The appearance of the G band in the Raman spectra indicates that the sample must contain sp^2 carbon networks. In addition to the G and G′ bands, D and D′ bands might also be found in the Raman spectra of graphitic materials. The appearance of D and D′ bands is associated with the defects in graphitic materials, and these bands cannot be seen for a highly crystalline graphite. Figure 2.13b shows the Raman image of a graphite crystallite deposited on a glass substrate. In comparison with the bulk region of the graphite crystallite, one can also see the so-called disorder-induced D-band (Figure 2.13c), at about half of the frequency of the G′ band (around 1350 cm^{-1}), at the edge of the graphite sample. Therefore, the integrated intensity ratio I_D/I_G for the D and G bands is often used for characterizing the defects in graphitic materials.

RRS is useful for the characterization of nanographite crystallites in evaluating the crystallite size L_a. A group of nanographites with different L_a values were prepared by thermal treatment of diamond-like carbon (DLC) films at different temperatures. ($L_a = 20$, 35, 65, 150, 190, 340, and 490 nm for the samples treated at $T_{htt} = 1800$, 2000, 2200, 2000, 2300, 2400, 2600, and 2700 °C, respectively) [56].

Figure 2.14a shows the Raman spectra of the D, G, and D′ bands for the $T_{htt} = 2000$ °C sample for five different lasers excitations at 1.92, 2.18, 2.41, 2.54, and 2.71 eV, respectively. It can be seen that the ratio I_D/I_G is strongly dependent on the energy of the excitation laser. Figure 2.14b shows the Raman spectra using

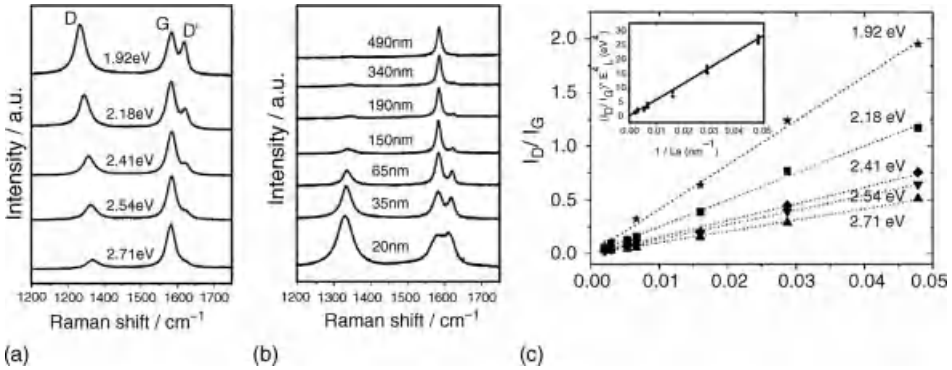


Figure 2.14 First-order Raman spectra of (a) the sample treated at 2000 °C, for five different laser energy values (1.92, 2.18, 2.41, 2.54, and 2.71 eV) and (b) samples with different crystallite sizes using 1.92 eV laser excitation energy. (c) The intensity ratio I_D/I_G versus $1/L_a$ using five different laser excitation energies. Inset: all curves shown in (c) collapse on the same curve in the $(I_D/I_G)E_L^4$ versus $1/L_a$ plot, where $E_L = E_{laser}$. Adapted from [56].

$E_{laser} = 1.92$ eV for samples with different L_a values. The ratio I_D/I_G varies significantly with different L_a values. A plot of I_D/I_G versus $1/L_a$ for all samples and using five different E_{laser} values is shown in Figure 2.14c. A good linear relationship between I_D/I_G and E_{laser} can be found for a given sample. Interestingly, these curves will collapse on to the same curve in the $(I_D/I_G)E_{laser}^4$ versus $1/L_a$ plot, as illustrated in the inset in Figure 2.14c. Thus, for the nanographite sample, the ratio I_D/I_G is inversely proportional to the fourth power of E_{laser}.

Compared with other characterization techniques such as atomic force microscopy (AFM), Raman spectroscopy provides a quick and facile structural and quality characterization of graphene material. The number of layers for graphene samples exfoliated from HOPG (highly ordered pyrolytic graphite) has been successfully determined by analyzing the shape of the 2D band [58].

Raman spectra of monolayer, bilayer, and trilayer graphene obtained from the graphitization of Si-terminated SiC were reported by Lee *et al.* [57], as shown in Figure 2.15a. The 2D band position increases monotonically from 2721 to 2760 cm^{-1} with increasing layer number. Further, the peak width of a monolayer graphene is substantially smaller than that for bi- and trilayer graphene, increasing from 46 to 64 and to 74 cm^{-1}.

Figure 2.15b shows the Raman spectra of monolayer, bilayer, and trilayer graphene flakes transferred from SiC on to SiO_2. It is worth noting that the 2D band becomes more asymmetric after the transfer to the SiO_2 substrate. The 2D band now became similar to that of exfoliated multilayer graphene from HOPG. Therefore, the deviant shape of the 2D band and its blued-shifted behavior in Figure 2.15a cannot be explained only by the stacking sequence, because the stacking should not be changed after being transferred on to SiO_2 [57]. It is proposed that this shift and the single-peak appearance of the 2D feature of epitaxial graphene on SiC are caused by interaction between the SiC substrate and the epitaxial graphene.

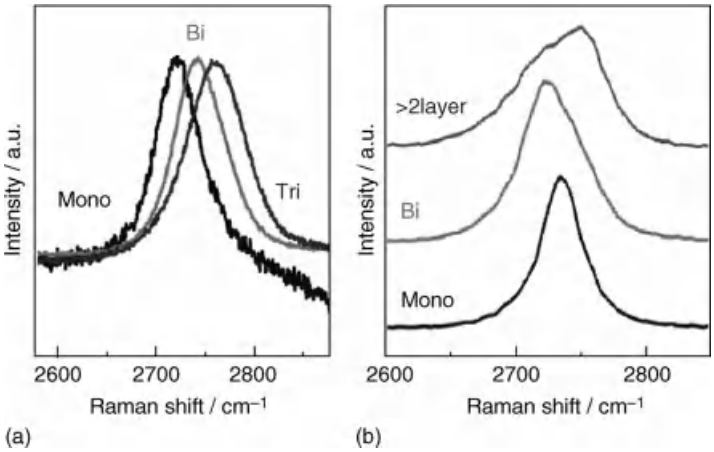


Figure 2.15 (a) Raman spectra of monolayer, bilayer, and trilayer graphene grown epitaxially on SiC. (b) Raman spectra of monolayer, bilayer, and trilayer graphene flakes transferred from SiC on to SiO_2. Adapted from [57].

2.6 Characterization of Transition Metal-Containing Microporous and Mesoporous Materials

Transition metal-containing microporous and mesoporous materials such as Fe-ZSM-5, TS-1, and Ti-MCM-41 have been successfully applied in a number of catalytic processes [59–64], and their catalytic properties depend largely on their composition and structure. A deep understanding of the structure of the metal sites in microporous materials is helpful for developing zeolite-based catalysts with more selective and active performance [65]. Various characterization methods have been used to collect information on the transition metal ion in molecular sieves. However, information on the incorporation of transition metal ions into microporous and mesoporous materials is typically difficult to obtain owing to the extremely low concentration of the substituted transition metal ions. Therefore, complementary techniques are often required to characterize the zeolite samples.

2.6.1 Identification of the Isolated Quadrivalent Transition Metal Sites in Microporous and Mesoporous Materials

The discovery of TS-1 was a milestone in zeolite and heterogeneous catalysis research. TS-1 shows remarkably high catalytic efficiency and selectivity in phenol hydroxylation, olefin epoxidation, and secondary alcohol dehydrogenation using H_2O_2 as oxidant [66]. It has been one of the most extensively studied heterogeneous catalysts in recent decades [67]. The Ti content in TS-1, however, is usually less than 2 wt% [68, 69], hence characterization of the Ti active sites is challenging [70–72].

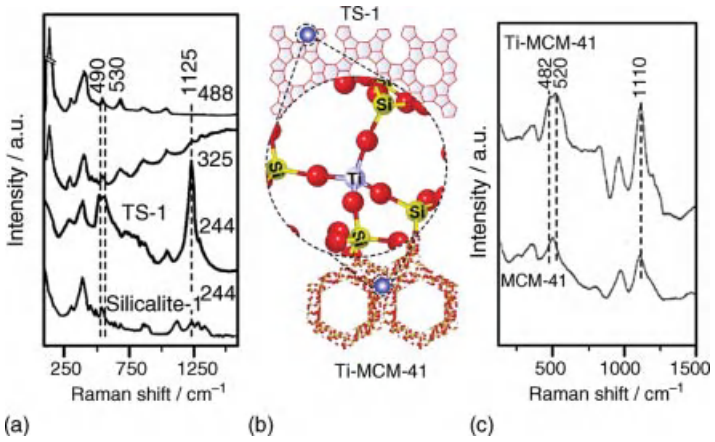


Figure 2.16 (a) Raman spectra excited with different laser lines at 244, 325, and 532 nm of silicalite-1 and TS-1; (b) a schematic description of the titanium sites in the framework of TS-1 and Ti-MCM-41; (c) UV Raman spectra of MCM-41 and Ti-MCM-41 (Si/Ti = 200) excited at 244 nm. Adapted from [73, 76, 77].

The charge transfer of pπ–dπ transitions between oxygen and titanium atoms in the framework of TS-1 is at 220 nm in the UV–visible diffuse reflectance spectrum. The laser line at 244 nm is chosen to excite the electronic transition absorption of the Ti species in TS-1 for the Raman spectrum (Figure 2.16a). Three new bands at 490, 530, and 1125 cm^{-1} are observed in the UV Raman spectrum of TS-1. The appearance of these bands is associated with framework Ti but not with silicalite-1 [73]. The resonance Raman bands at 490, 530, and 1125 cm^{-1} can be attributed to a local unit of $[Ti(OSi)_4]$ of TS-1, denoted by Ti−O−Si. The bands at 490 and 530 cm^{-1} are ascribed to the bending and symmetric stretching modes of the framework Ti−O−Si species, respectively. The band at 1125 cm^{-1} is assigned to the asymmetric stretching vibration of Ti−O−Si [74]. This represents the first UV RRS characterization of framework titanium sites for TS-1 zeolite. Subsequently, theoretical work further validated the Raman results [75].

UV resonance Raman spectra of Ti-MCM-41 are shown in Figure 2.16c. Three additional Raman bands at 482, 520, and 1110 cm^{-1} are observed in the spectrum of Ti-MCM-41 compared with pure siliceous MCM-41. These bands are attributed to tetrahedrally coordinated Ti species in the amorphous wall of Ti-MCM-41. The fact that the frequency of the characteristic band at 1110 cm^{-1} of Ti-MCM-41 is lower than that of TS-1 (1125 cm^{-1}) indicates that the coordination environment of Ti atoms in Ti-MCM-41 and TS-1 is different. The Ti atoms in TS-1 are fixed in the rigid framework sites, and the Ti atoms in Ti-MCM-41 are relatively flexible [76, 77], whereas the highly dispersed titanium species on the SiO_2 surface (prepared by chemical grafting) are flexible and possess a distorted tetrahedral coordination geometry.

The characteristic frequency of Ti−O−Si is sensitive to the coordination environment. The red shift from 1125 to 1085 cm^{-1} for rigid tetrahedral coordination of

the titanium site in TS-1 for very flexible coordination of titanium sites on SiO_2 can be used as a figure of merit in assessing the coordination geometry of Ti^{4+} in microporous and mesoporous materials [78].

2.6.2 Identification of the Isolated Trivalent Transition Metal Sites in Microporous and Mesoporous Materials

The incorporation of trivalent transition metal ions into microporous and mesoporous materials, such as Fe-ZSM-5 and Fe-SBA-15, has been successfully applied in numerous catalytic processes [79–81]. These materials exhibit different spectral features compared with quadrivalent transition metal-containing microporous and mesoporous materials.

Figure 2.17a shows the UV–visible diffuse reflectance spectrum of Fe-ZSM-5. The strong absorption band at 263 nm is assigned to the charge transfer of pπ–dπ transitions between oxygen and iron atoms in the framework of Fe-ZSM-5. The above analysis was validated by projected density of state (PDOS) calculations of the framework Fe tetrahedron in Fe-ZSM-5 using DFT calculations [82].

UV Raman spectroscopy excited at 244 nm was employed to study the coordination environment of iron atoms in the framework of ZSM-5 (Figure 2.17b). The UV Raman spectrum of Fe-ZSM-5 exhibits new bands at 516, 1016, 1115, and 1165 cm^{-1}. The Raman bands at 516, 1115, and 1165 cm^{-1} become considerably weaker when excited at 325 nm, and disappear when excited at 532 nm. The bands at 516 and 1115 cm^{-1} are resonance enhanced and attributed to the symmetric and asymmetric stretching vibrations of the framework Fe−O−Si species in tetrahedral coordination (Figure 2.17c). Notably, the band at 1016 cm^{-1} is observed regardless of the different excitation wavelengths. This band is not due to the resonance

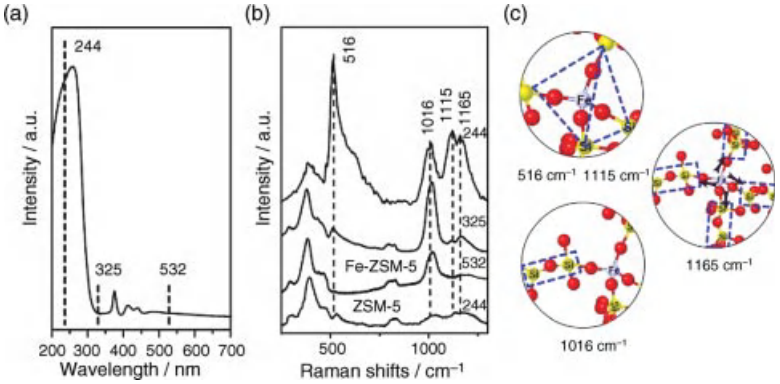


Figure 2.17 (a) UV–visible diffuse reflectance spectrum of Fe-ZSM-5; (b) Raman spectra of Fe-ZSM-5 with excitation lines at 244, 325 and 532 nm and Raman spectra of ZSM-5 excited at 244 nm; and (c) schematic showing the different vibration models of the Raman bands at 516, 1016, 1115, and 1165 cm^{-1}. Adapted from [82, 85].

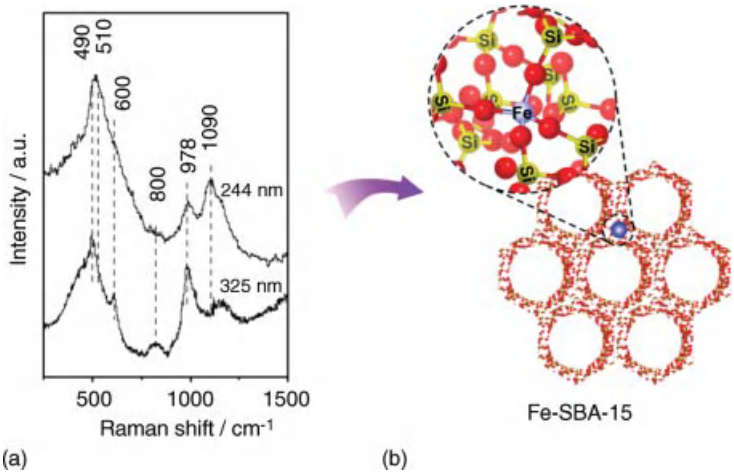


Figure 2.18 (a) UV resonance Raman spectra of Fe-SBA-15 excited at 244 and 325 nm and (b) a schematic description of the iron site in the framework of MCM-41. Adapted from [86].

Raman band and is associated with the Si−O−Si bonds near framework iron as shown in Figure 2.17c [83, 84].

The band at 1165 cm^{-1} is a resonance Raman band and can be excited with laser light of 244 nm. Periodic DFT calculations confirmed that this band is asymmetric stretching vibrations of the framework Fe−O−Si [82]. Compared with the vibration mode of the Raman band at 1115 cm^{-1}, this vibration mode is driven by the stretching of the four neighboring framework Si−O−Si bonds as shown in Figure 2.17c.

To investigate the different coordination environments of the framework Fe species in mesoporous materials, Fe-SBA-15 samples were studied by UV Raman spectroscopy. Figure 2.18 shows the UV Raman spectra of Fe-SBA-15 excited with laser light at 244 and 325 nm. Two strong Raman bands at 510 and 1090 cm^{-1} are detected for Fe-SBA-15 when excited at 244 nm. These bands are assigned to the symmetric and asymmetric Fe−O−Si stretching modes for the amorphous silica framework of Fe-SBA-15 [86]. The Raman spectrum of Fe-SBA-15 excited at 325 nm shows only a strong Raman band at 978 cm^{-1} which can also be seen in the Raman spectra excited at 244 nm. Obviously, this Raman band is a nonresonance Raman band, and is associated with the Si−O−Si bonds near the framework iron species [86].

In summary, there are four characteristic bands at 516, 1016, 1115, and 1165 cm^{-1} for Fe-ZSM-5, whereas only three bands at 510, 978, and 1090 cm^{-1} are observed for Fe-SBA-15, suggesting that coordination environment of the framework iron varies with the matrix materials. The red shift from 1115 cm^{-1} for rigid tetrahedral coordination of iron in Fe-ZSM-5 to 1090 cm^{-1} for flexible coordination of iron sites in Fe-SBA-15 has a similar trend to the titanium sites in TS-1 and Ti-MCM-41. These results are very useful for evaluating the coordination geometry of transition metal ions incorporated in microporous and mesoporous materials.

2.6.3
Identification of Extra-Framework Active Sites in Microporous and Mesoporous Materials

The direct oxidation of benzene to phenol is one of the most challenging reactions in the field of catalytic chemistry [88, 89]. It was found that a special Fe–oxo species, which was formed after high-temperature pretreatment of Fe/ZSM-5 followed by reaction with N_2O, could selectively oxidize methane and benzene even at 243 K, which could mimic the biocatalysis of soluble methane monooxygenase (sMMO) [90].

Figure 2.19a, trace a, shows the UV–visible diffuse reflectance spectrum of the catalyst pretreated at 1173 K [87]. A new band with a maximum around 605 nm is observed after exposing the high-temperature pretreated Fe/ZSM-5 to N_2O at 523 K, indicating the presence of the active oxygen species. (Figure 2.19a, trace b) A band at 340 nm together with a broad band at 500–900 nm centered at 690 nm appears after subsequent exposure of the oxygen-containing sample to benzene at room temperature (Figure 2.19a, trace c).

In order to differentiate the active site, a Raman spectrum excited near 605 nm was collected after exposing the high-temperature-pretreated Fe/ZSM-5 to N_2O at 523 K, as shown in Figure 2.19b, trace b. A new band at 867 cm^{-1} appears after the reaction. Combined with previous characterization of iron–oxo complexes in inorganic chemistry and biological sMMO and the DFT results, the band at 867 cm^{-1} could be assigned to a peroxo species bridged on the binuclear Fe sites [87]. A number of evident Raman bands are observed at 643, 896, 990, 1149, 1228, 1475, 1580, and 1607 cm^{-1}, after a further reaction with benzene (Figure 2.19b, trace c). These Raman

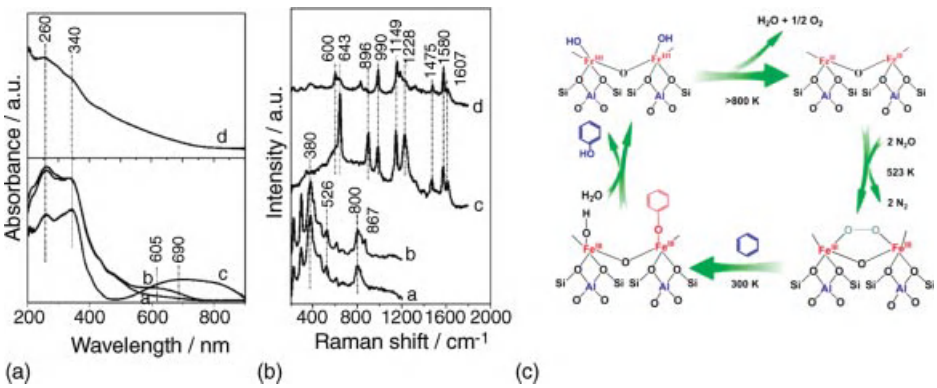


Figure 2.19 (a) UV–visible diffuse reflectance spectra and (b) visible Raman spectra of Fe/ZSM-5 (a) after pretreatment at 1173 K in an He flow, (b) after exposing the high-temperature pretreated Fe/ZSM-5 to N_2O at 523 K, (c) after the reaction of benzene with the Fe/ZSM-5 preloaded with the active oxygen species at room temperature, and (d) after benzene adsorbed on the Fe/ZSM-5 without the preloaded active oxygen species at room temperature. (c) The possible reaction pathways of the active oxygen species reacted with benzene on ZSM-5 at room temperature. Adapted from. [87].

bands are due to the Fe(III)–phenolate complex, an intermediate formed by the reaction of benzene with active oxygen species at room temperature. The possible reaction pathway of the active oxygen species reacted with benzene on Fe/ZSM-5 is proposed as shown in Figure 2.19c. The Raman spectral results clearly demonstrate that the peroxide bridged on the binuclear iron sites is the active center, which reacts directly with benzene to form an Fe(III)–phenolate intermediate at room temperature [87].

O_2-activated zeolite Cu/ZSM-5 has been shown to convert methane to methanol at low temperatures (100 °C) with selectivity up to 98% [91]. However, only a small fraction of the total copper sites in the zeolite is active for this reaction. The elucidation of the structure of the active site with extremely low concentration is difficult.

The resonance enhancement of Raman vibrations associated only with the active sites for methanol synthesis can be successfully achieved by tuning a laser into the characteristic absorption feature of the oxygen-activated Cu-ZSM-5 active site. It is found that a number of these resonance-enhanced vibrations (237, 457, 514, and 870 cm^{-1}) are sensitive to isotope perturbation when the active species is generated with $^{18}O_2$, as shown in Figure 2.20a. The different band shifts of these Raman bands due to the isotope exchange provide the geometric and electronic structure of the oxygen-activated Cu-ZSM-5 active sites. By using normal coordinate analysis (NCA) and DFT calculations in combination with experimentally observed resonance Raman features, a mono-oxygen bridged binuclear Cu active site is proposed as shown in Figure 2.20b. It is found that the constrained lattice of ZSM-5 restricts the coordination environment of the bound Cu atoms and their spatial orientation resulted in the formation of a bent mono-μ-oxo dicupric core.

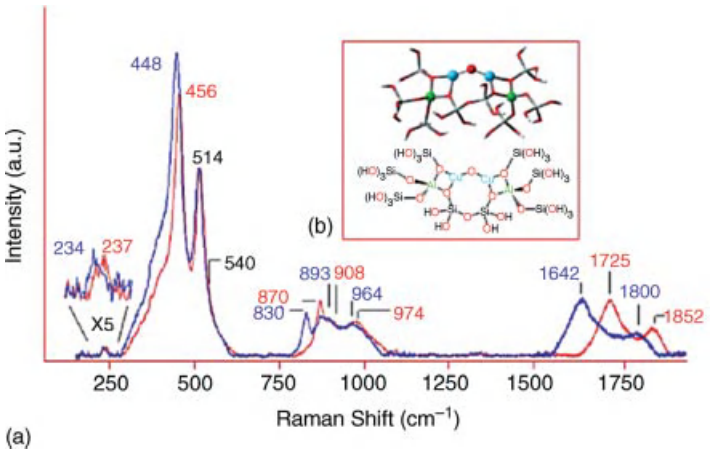


Figure 2.20 (a) Resonance Raman spectra (457.9 nm) of Cu-ZSM-5 $^{16}O_2$ (red) and $^{18}O_2$ (blue). (b) Structural model of the Cu_2O intermediate constructed from part of a 10-membered ring used for DFT calculations. Adapted from [92].

2.7
Synthesis Mechanisms of Molecular Sieves

Their unique porosity endows zeolites with special properties such as catalysis, adsorptive separation, purification, and molecular sensing. Zeolites are among the most sophisticated inorganic solids, with crystallographic unit cells often containing hundreds of atoms [93]. The characterization of molecular sieves aimed at gaining an understanding of the synthesis process was initiated in the 1960s [94]. Numerous studies have addressed the preparation of zeolites, and several assembly mechanisms regarding the nucleation and crystal growth have been proposed, including growth from soluble and prefabricated units [95–98], autocatalytic nucleation [99, 100], and solid–liquid interfacial nucleation [101, 102]. A basic understanding of the crystallization process at a molecular level coupled with the enormous body of existing empirical knowledge will provide opportunities for the synthesis of new zeolites [103].

In addition to the accumulating knowledge of zeolite synthesis mechanisms, a large variety of analytical tools have become available for the identification of the presence of species/fragments during zeolite synthesis. These techniques include X-ray diffraction and scattering, solid-state/liquid-state NMR spectroscopy, mass spectrometry, AFM, and electron microscopy. New insights into the zeolites synthesis mechanism through different analytical tools have been reported [102, 104, 105].

Among these techniques, Raman spectroscopy is a suitable approach for investigating aqueous solutions and solid phases of zeolite synthesis mixtures due to the low Raman scattering cross-section of water. Raman spectroscopy, based on vibrational motions of the framework, can also provide detailed structural information on zeolite synthesis mixtures. Even zeolites with same topology but different Si/Al ratios or ion-exchanged cations can be well differentiated by framework fingerprinting in the low- framework region in Raman spectra [106, 107]. Raman spectroscopic studies on the zeolite synthesis mechanism were initiated from the pioneering work of McNicol *et al.* studying the synthesis of zeolite A and faujasite [108]. The work by Dutta and co-workers [103, 109] and Roozebom *et al.* [110] further promoted the understanding of the synthesis mechanism of zeolites through Raman spectroscopic investigations.

These studies contributed abundant convincing results: solution-mediated mechanism via soluble complex polymeric aluminosilicates during zeolite crystallization, formation of entities interpreted as the first zeolite crystals before crystallinity was evident from diffraction patterns, and the conformational change of the organic template at the earliest stage of the synthesis.

2.7.1
Assembling Zeolites from Prefabricated Units

The transformation of aluminosilicate gel to mordenite was investigated through Raman spectroscopy by Dutta and co-workers [111]. The synthesis mixture in the early stages (4–12 h) is characterized by Raman bands at 495, 800, 900, and

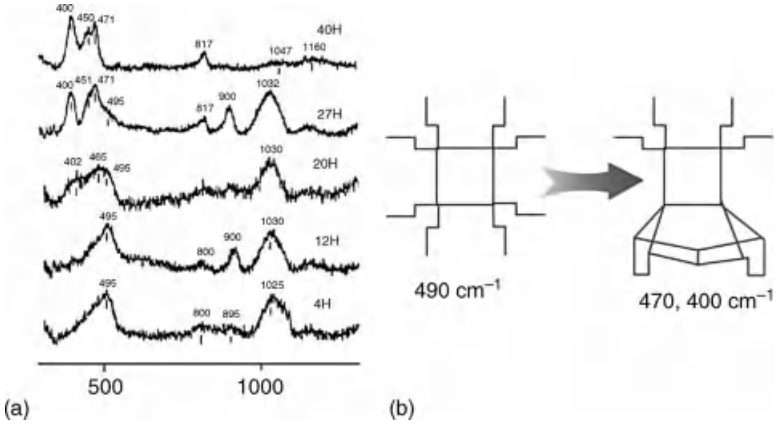


Figure 2.21 (a) Raman spectra of the solid phase during mordenite synthesis at various times. (b) A schematic description of the formation process of "mordenite-like" intermediates from four-membered rings. Adapted from [111].

1030 cm^{-1}. The Raman band at 495 cm^{-1} is characteristic of the breathing vibrations of the four-membered ring. Raman bands at 900 and 1030 cm^{-1} could be assigned to the Si−O stretches of nonbonded oxygen atoms. After synthetic reaction of the synthesis mixture for 20 h, two Raman bands at 402 and 465 cm^{-1} appear. These two Raman bands become sharp and develop into the characteristic bands of the mordenite framework upon further heating (27 h). The species with the Raman bands at 402 and 465 cm^{-1} are assigned to intermediates with "mordenite-like" structures. Raman spectroscopic results indicate that the four-membered rings initially present in the amorphous gel undergo changes in structure as they accommodate five-membered rings around them, as shown in Figure 2.21b.

2.7.2
Assembling Fe-ZSM-5 from Active Centers and Silicate Building Units

UV Raman spectroscopy is a powerful technique for zeolite characterization, particularly for transition metal-containing microporous and mesoporous materials. These advantages together with the UV resonance Raman effect make UV Raman spectroscopy a potentially powerful tool to study the synthesis mechanism of transition metal-substituted zeolites.

The evolution of the ZSM-5 framework and the iron species during the synthesis of Fe-ZSM-5 was studied by UV Raman spectroscopy with excitation at 325 and 244 nm, respectively. The Raman spectrum shown in Figure 2.22a of the initial precursor excited at 325 nm is characterized by two broad Raman bands centered at 460 and 984 cm^{-1}, which are assigned to ν_s (Si−O−Si) of five- and six-membered silicate rings [113], and Si−O−Si bond near framework iron species, respectively [77, 83, 111, 112]. As the synthesis mixture is heated (Figure 2.22b, 6 h), the broad band at 460 cm^{-1} becomes prominent.

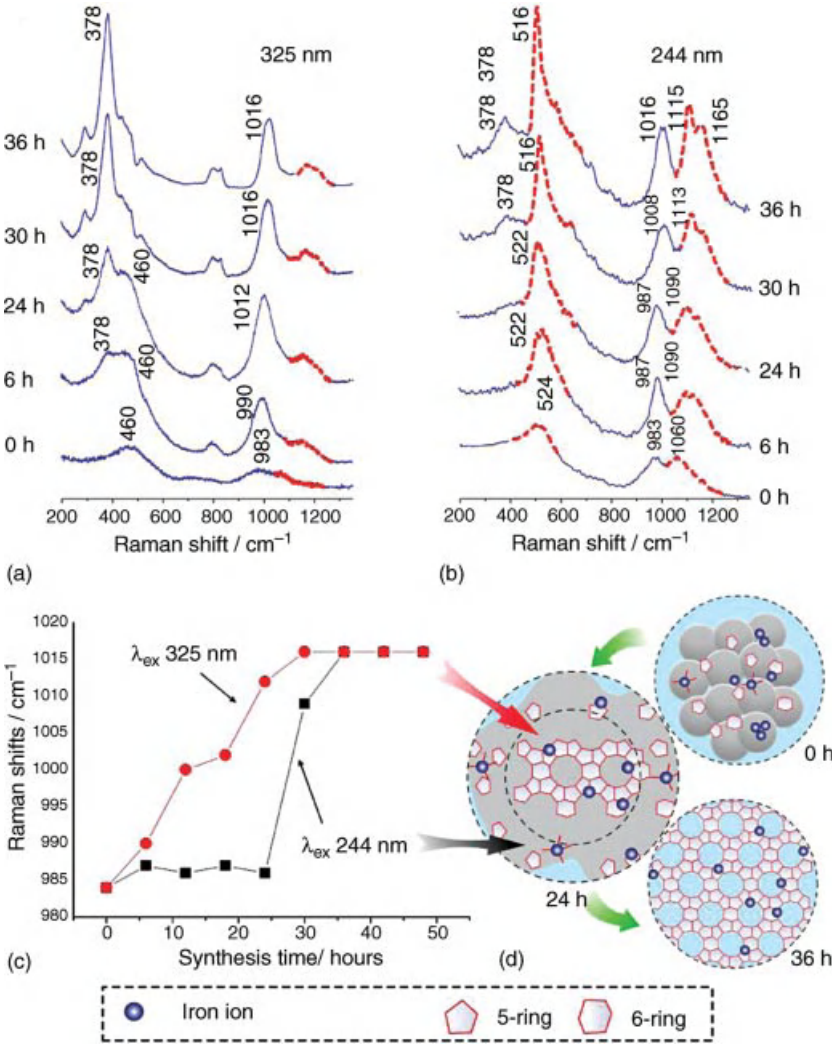


Figure 2.22 (a) UV Raman spectra excited at 325 nm for different crystallization stages at various times of synthesis of Fe-ZSM-5 (Si/Fe = 152). (b) UV resonance Raman spectra excited at 244 nm for different crystallization stages at various times of synthesis of Fe-ZSM-5. (c) Plots of the frequency variation of the Raman band at 984 cm^{-1} of Fe-ZSM-5 (excited at 325 and 244 nm) versus the crystallization time, (d) A proposed scheme for the mechanism of formation of Fe-ZSM-5. Adapted from Ref..

With further increase in the synthesis time (0–30 h), a Raman band at 380 cm^{-1} appears with increasing intensity, indicating the formation of the MFI structures. Meanwhile, the intensity of the Raman band at 460 cm^{-1} decreases. The results reflect that the five- and six-membered silicate rings in the amorphous gel are connected with each other to form the MFI structures.

The entire synthesis process is monitored by UV Raman spectroscopy with excitation at 244 nm (Figure 2.22b). Upon hydrothermal treatment, the broad band at 524 cm^{-1} becomes sharp and strong, and shifts to a lower frequency at 516 cm^{-1}. The bands at 983 and 1060 cm^{-1} shift to higher frequencies at 1016 and 1115 cm^{-1}, respectively. These results indicate the existence of tetrahedrally coordinated [Fe $(OSi)_4$] units in the early stages of Fe-ZSM-5 formation. A Raman band at 1165 cm^{-1} appears as a shoulder of the band at 1080 cm^{-1} after a synthesis time of 6 h, and then becomes narrow and strong with increasing crystallinity. Periodic DFT calculations confirmed that this band corresponds to asymmetric stretching of framework Fe−O−Si driven by the stretching of four neighboring framework Si−O−Si bonds. Thus, the intensity of this band relates to the crystallinity of the zeolite framework [114].

It is interesting to find that the rate of hipsochromic shift of the band at 983 cm^{-1} when $\lambda_{ex} = 244$ nm is slower than when $\lambda_{ex} = 325$ nm (Figure 2.22c). As mentioned in the Section 2.2.2, UV Raman spectroscopy is more sensitive to the surface region than to the bulk for those samples which absorb UV light. All the sample particles at various time intervals during the synthesis of Fe-ZSM-5 have strong absorbance below 300 nm. Thus, the Raman scattering signal excited by 244 nm laser light is mainly from the skin region of the sample particles due to the strong light absorbance of the sample particles, whereas that excited at 325 nm reflect the overall information from the whole particle (Figure 2.22d) [112].

It is proposed that crystalline Fe-ZSM-5 is formed by the aggregation and nucleation of the distorted tetrahedrally coordinated [$Fe(OSi)_4$] species, and five- and six-membered silicate rings which are formed in the early stages of the synthesis process (Figure 2.22d). The nucleation takes place in the core of the amorphous phase, as indicated by the non-parallel evolution of the Raman bands at 984 cm^{-1} excited at 325 and 244 nm, respectively. Crystalline Fe-ZSM-5 develops into larger crystals by consuming the iron species in distorted tetrahedral coordination and silicate species in the amorphous shell, and ultimately becomes a well-crystallized sample.

2.7.3
A Real-Time Probing for the Crystallization Process: *In Situ* Raman Spectroscopy

Zeolites are usually synthesized under hydrothermal conditions, and the need for sample quenching and work-up may cause dramatic structural changes [115]. Moreover, it is very difficult to follow the complex mechanism by which they assemble from precursor species. A powerful but relatively unexplored way of probing this process is to perform *in situ* characterization under working conditions [116, 117]. Raman spectroscopy is a suitable technique to investigate both aqueous solutions and solid phases of zeolite synthesis mixtures.

The power of the *in situ* visible Raman technique has been demonstrated through studies on the synthesis mechanism of aluminophosphate molecular sieves by Weckhuysen and co-workers [116, 117]. Examples of *in situ* Raman spectroscopic studies on zeolite synthesis mechanism are given in Figure 2.23. The plotted region is

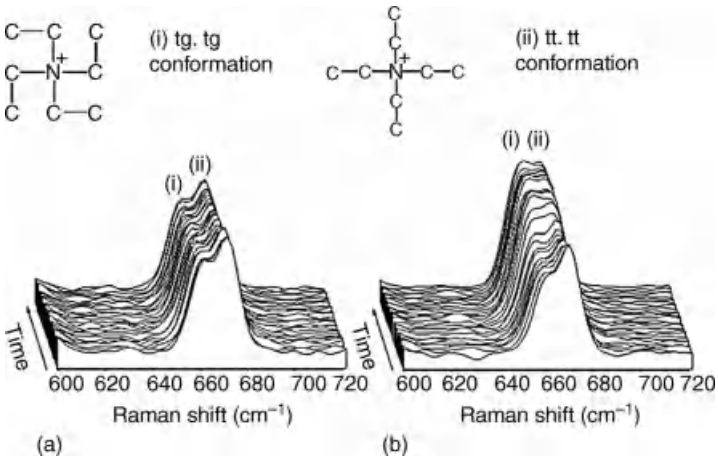


Figure 2.23 Time-resolved *in situ* Raman spectra for synthesis gels with (a) no framework substitution and (b) 30% substituted Zn^{2+}. The structures of the two TEAOH conformations are also indicated. Adapted from [117].

dominated by two bands indicative of two template conformers: tg.tg and tt.tt as shown in Figure 2.23. Obvious changes occur in the relative intensities of these two bands for the 30% Zn^{2+}-substituted gel during crystallization, where there were almost no changes for the unsubstituted systems that did not crystallize. A comparative *ex situ* XRD study on the crystallization of the ZnAPO gel at 80 °C suggested that the change in conformer occurred prior to the onset of Bragg peak formation, indicating that the conformational changes play an important role in the formation of a prephase of microcrystallites. The above results reveal the existence of an intimate relationship between the Zn^{2+} substituted into an Al^{3+} site of the microporous framework. This is considered a necessary step for the formation of the MeAPO-34 framework.

Recently, Li and co-workers developed an *in situ* hydrothermal cell coupled with UV Raman spectroscopy to study zeolite crystallization under hydrothermal conditions [118, 119]. The cell is equipped with a focusing lens instead of a flat window, which realized a significantly stronger Raman signal. By using deep versus shallow sample holders in the cell, the hydrothermal synthesis of zeolite X was studied for investigating both the solid and liquid phases under hydrothermal conditions, *in situ* [118]. The liquid phase during the synthesis process of zeolite X is dominated by monomeric silicate species characterized by the Raman band at 774 cm^{-1}, as shown in Figure 2.24a. The concentration of the monomeric silicate species increases with increase in temperature, indicating that the monomers are formed from the depolymerization of amorphous precursors. As the reaction proceeds, the growing product crystals require more monomers. Finally, all amorphous precursors are consumed and transformed into crystalline zeolite.

Figure 2.24b shows *in situ* UV Raman spectra recorded for the solid phase at 373 K under hydrothermal conditions. The appearance of the sharp band at 500 cm^{-1}

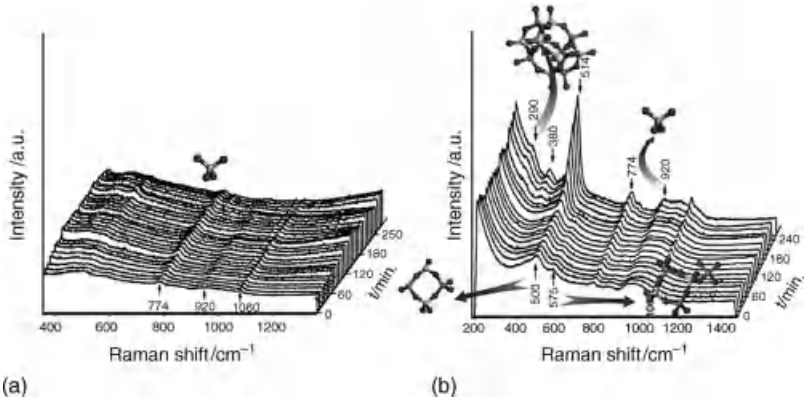


Figure 2.24 *In situ* UV Raman spectra of (a) liquid and (b) solid phase of zeolite X synthesis at 373 K; spectra were collected from 0 to 270 min. Adapted from [118].

indicates that the gel consists predominantly of four-membered rings [120, 121]. The shift of the Raman band at 500 to 514 cm^{-1} indicates the assembly process of zeolite X from four-membered ring fragments in the initial gel. A Raman band at 575 cm^{-1} appears at very beginning of the synthesis. Its intensity decreases with increasing crystallization, accompanied by the appearance of bands at 298 and 380 cm^{-1}. The Raman bands at 298 and 380 cm^{-1} can be assigned to the bending mode of double six-membered ring, reflecting the formation of zeolite X crystals. According to the experiments and theoretical calculations, the Raman band at 575 cm^{-1} arises from the Si−O−Al stretching modes on the branches of the ring structure. It is proposed that the crystalline zeolite X framework is formed via the assembly of these branched units and four-membered rings in the solid phase and monomeric silicate species in the liquid phase [118].

An important aspect of the synthesis mechanism is the role of organic templates in the synthesis process. Several mechanisms for templating have been proposed, involving hydrogen bonding [122], van der Waals shape of the template [123] and favored formation of specific structures [124]. Despite these efforts, a thorough understanding of the template effect, particularly the significance of the role of templating in zeolite channel formation, is still lacking owing to the complexity of the zeolite formation process.

In situ UV Raman spectroscopy provides the opportunity to study the role of the template played in channel formation and also the identification of the building blocks during the framework formation [119]. The whole hydrothermal synthesis process of AlPO-5 from the precursor to the final crystals was monitored *in situ* by UV Raman spectroscopy as shown in Figure 2.25a. The decreasing intensities of the Raman bands at 370 and 899 cm^{-1} indicate the consumption and reaction of the octahedral AlO_6 and phosphate species. Between 100 and 200 min, two Raman bands at 260 and 500 cm^{-1} appear and their intensities increase in parallel. These two bands have been assigned to the channel breathing vibrational modes and deformations involving the four-membered rings, respectively [125].

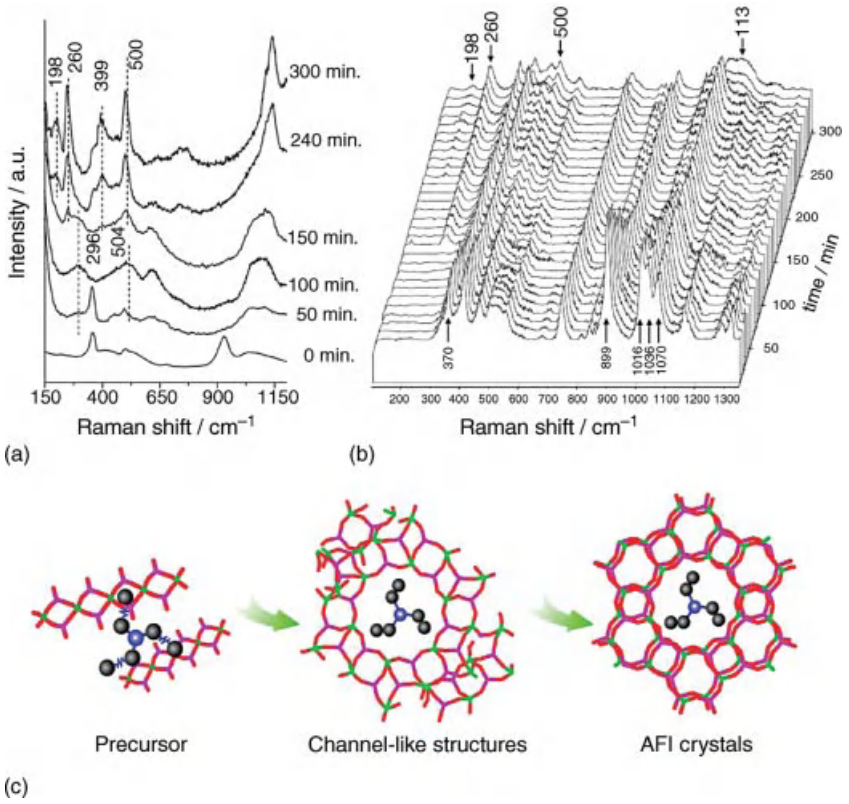


Figure 2.25 (a) UV Raman spectra recorded *in situ* during crystallization of AlPO-5. The synthesis temperature was 453 K, $\lambda_{ex} = 325$ nm. (b) A proposed scheme for the mechanism of formation of AlPO-5. (c) UV Raman spectra excited at 266 nm of AlPO-5 for different crystallization stages at various times of synthesis. Adapted from [119].

It is interesting that the intensities of the Raman bands at 1016 and 1035 cm^{-1} decrease in the early stages before the appearance of the channel breathing vibrational mode at 260 cm^{-1}, and remain nearly constant as the intensities of the bands at 198, 260 and 500 cm^{-1} increase. The results reflect that TEA^+ templates are constrained due to the condensation of amorphous aluminophosphate gel in the early stages, whereas during the formation of the crystalline channel, the templates are less affected by the surrounding environment during the formation of the crystalline channel. Therefore, it was proposed that a channel-like structure has been already formed before the formation of the crystalline channels. An *ex situ* study of the inorganic phase, after removing the TEA template with Fenton's reagent (Fe^{3+}/H_2O_2), supported this interpretation, as shown in Figure 2.25b.

The appearance of the broad Raman band at 504 cm^{-1} in the early stages of synthesis suggests that distorted four-membered rings were formed in the very early stages of synthesis. The growth in the Raman band at 260 cm^{-1}, indicative of

crystalline channel formation, is accompanied by a decrease in the intensity of the broad Raman band at 296 cm^{-1}. This band is attributed to the existence of channel-like structures in amorphous phase [119].

A synthesis mechanism for AlPO-5 is proposed in Figure 2.25c. UV Raman spectroscopy combined with the *in situ* technique and Fenton's reaction provides direct evidence for the existence of the four-membered ring species in the very early stages of the synthesis. The condensation of the four-membered ring species with the steric role of the organic templates resulted in an amorphous pre-state with channel-like structures, which subsequently transform into 3D AFI architectures via the newly-built six-membered rings.

2.8 Conclusions

In recent decades, Raman spectroscopy has become a powerful tool in characterizing solid materials and heterogeneous catalysts. Raman spectroscopy can provide substantial information about transition metal oxides by elucidating the phase structure and phase transformation mechanism. Information including the molecular structure of the surface metal oxide species, distribution of the surface metal oxide species, and the role of active surface metal oxide species in catalytic reactions can be obtained by Raman and *in situ* Raman spectroscopy. RRS of sp^2 carbons provides not only vibrational and crystallographic information, but also unique information about the properties that are relevant to electrons and phonons. Isolated transition metal ions in both the framework and extra-framework of microporous and mesoporous materials can be identified by UV RRS, revealing the coordination and elucidating the reaction mechanism; The understanding of the crystallization mechanism of zeolites has been greatly enhanced through *in situ* Raman spectroscopy, which can sensitively monitor the precursors and intermediates evolved during the synthesis under working conditions.

We anticipate that in the future progress will be made in the following areas.

Raman spectroscopy has been widely used in the characterization of a wide variety of catalytic materials and reactions, such as metal oxides and semiconductors, and in the identification of active oxygen species. Raman spectroscopy is a promising technique in studying photocatalysis, which is a growing area. So Raman and UV Raman spectroscopy will play more important roles in studying the photoelectrical properties of semiconductor materials from bulk to nanostructures, understanding the structural changes in the excited state that are associated with the photocatalytic reactions, and elucidating the mechanism of the oxygen- generating process. In this respect, much can be learned from the interplay between Raman experiments and computer-assisted calculations and modeling. Such efforts will greatly promote the understanding of the nature of active sites and establishing their reaction pathways at the molecular level.

It is not very risky to predict that *in situ* UV Raman will be an upcoming powerful option for studying the mechanisms of nanomaterial formation, particularly in

syntheses at high pressures and temperatures. *In situ* UV Raman spectroscopy will provide information on the important intermediate, key steps and optimized parameters for nanomaterial synthesis.

Raman spectroscopic imaging combined with TEM, AFM, and scanning tunneling microscopy (STM) will probably become a very important technical development in the future, allowing the study of structural features of active sites in a specific region of particles at the molecular, nanometer, or micrometer scale.

References

1 Smekal, A. (1923) The quantum theory of dispersion. *Naturwissenschaften*, **11**, 873.
2 Landsberg, G. and Mandelstam, L. (1928) A novel effect of light scattering in crystals. *Naturwissenschaften*, **16**, 557.
3 Spiro, T.G. (1974) Resonance Raman spectroscopy. New structure probe for biological chromophores. *Acc. Chem. Res.*, **7** (10), 339–344.
4 Fan, F., Feng, Z., and Li, C. (2010) UV Raman spectroscopic study on the synthesis mechanism and assembly of molecular sieves. *Chem. Soc. Rev.*, **39** (12), 4794–4801.
5 Asher, S.A. (1993) UV resonance Raman spectroscopy for analytical, physical, and biophysical chemistry. Part 1. *Anal. Chem.*, **65** (2), 59A–66A.
6 Asher, S.A. and Johnson, C.R. (1984) Raman spectroscopy of a coal liquid shows that fluorescence interference is minimized with ultraviolet excitation. *Science*, **225** (4659), 311–313.
7 Chase, B. (1986) Fourier transform Raman spectroscopy. *J. Am. Chem. Soc.*, **108**, 7485–7488.
8 Chase, B. (1987) Fourier transform Raman spectroscopy. *Anal. Chem.*, **59** (14), 881A–890A.
9 Stair, P.C. (2007) The application of UV Raman spectroscopy for the characterization of catalysts and catalytic reactions. *Adv. Catal.*, **51**, 75–98.
10 Li, C. and Stair, P.C. (1996) Ultraviolet Raman spectroscopy characterization of sulfated zirconia catalysts: fresh, deactivated and regenerated. *Catal. Lett.*, **36** (3–4), 119–123.
11 Chua, Y.T. and Stair, P.C. (2000) A novel fluidized bed technique for measuring UV Raman spectra of catalysts and adsorbates. *J. Catal.*, **196** (1), 66–72.
12 Li, C. (2003) Identifying the isolated transition metal ions/oxides in molecular sieves and on oxide supports by UV resonance Raman spectroscopy. *J. Catal.*, **216** (1–2), 203–212.
13 Hagen, G., Glavaski, B.S., and Yeager, E. (1978) Raman spectrum of an adsorbed species on electrode surface. *J. Electroanal. Chem.*, **88** (2), 269–275.
14 Asher, S.A. (1988) UV-resonance Raman studies of molecular structure and dynamics applications in physical and biophysical chemistry. *Annu. Rev. Phys. Chem.*, **39**, 537.
15 Hudson, B., Kelly, P.B., Ziegler, L.D., Desiderio, R.A., Gerrity, D.P., Hess, W., and Bates, R. (1986) *Advances in Laser Spectroscopy*, John Wiley & Sons, Inc., New York.
16 Ziegler, L.D. and Hudson, B. (1981) Resonance Raman scattering of benzene and benzene-D6 with 212.8-nm excitation. *J. Chem. Phys*, **74** (2), 982–992.
17 Sanchez, M.G. and Gazquez, J.L. (1987) Oxygen vacancy model in strong metal support interaction. *J. Catal.*, **104** (1), 120–135.
18 Guzman, J., Carrettin, S., and Corma, A. (2005) Spectroscopic evidence for the supply of reactive oxygen during CO oxidation catalyzed by gold supported on nanocrystalline CeO_2. *J. Am. Chem. Soc.*, **127** (10), 3286–3287.
19 Carrettin, S., Concepcion, P., Corma, A., Nieto, J.M.L., and Puntes, V.F. (2004) Nanocrystalline CeO_2 increases the activity of an for CO oxidation by two

orders of magnitude. *Angew. Chem. Int. Ed.*, **43** (19), 2538–2540.

20 Long, R.Q., Huang, Y.P., and Wan, H.L. (1997) Surface oxygen species over cerium oxide and their reactivities with methane and ethane by means of *in situ* confocal microprobe Raman spectroscopy. *J. Raman Spectrosc.*, **28** (1), 29–32.

21 Long, R.Q. and Wan, H.L. (1997) *In situ* confocal microprobe Raman spectroscopy study of CeO_2/BaF_2 catalyst for the oxidative coupling of methane. *J. Chem. Soc., Faraday Trans.*, **93** (2), 355–358.

22 Li, C., Domen, K., Maruya, K., and Onishi, T. (1988) IR spectra of dioxygen species formed on CeO_2 at room temperature. *J. Chem. Soc., Chem. Commun.*, (23), 1541–1542.

23 Li, C., Domen, K., Maruya, K., and Onishi, T. (1989) Dioxygen adsorption on well outgassed and partially reduced cerium oxide studied by FT-IR. *J. Am. Chem. Soc.*, **111** (20), 7683–7687.

24 Hutchings, G.J., Desmartin-Chomel, A., Olier, R., and Volta, J.-C. (1994) Role of the product in the transformation of a catalyst to its active state. *Nature*, **368** (6466), 41–45.

25 Hagfeldt, A. and Gratzel, M. (1995) Light redox reactions in nanocrystalline systems. *Chem.Rev.*, **95** (1), 49–68.

26 Hoffmann, M.R., Martin, S.T., Choi, W.Y., and Bahnemann, D.W. (1995) Environmental applications of semiconductor photocatalysis. *Chem. Rev.*, **95** (1), 69–96.

27 Zhang, J., Li, M.J., Feng, Z.C., Chen, J., and Li, C. (2006) UV Raman spectroscopic study on TiO_2. I. Phase transformation at the surface and in the bulk. *J. Phys. Chem. B*, **110** (2), 927–935.

28 Faraldos, M., Banares, M.A., Anderson, J.A., Hu, H.C., Wachs, I.E., and Fierro, J.L.G. (1996) Comparison of silica-supported MoO_3 and V_2O_5 catalysts in the selective partial oxidation of methane. *J. Catal.*, **160** (2), 214–221.

29 Wachs, I.E., Deo, G., Andreini, A., Vuurman, M.A., and deBoer, M. (1996) The selective catalytic reduction of NO_x with NH_3 over titania supported rhenium oxide catalysts. *J. Catal.*, **160** (2), 322–325.

30 Hardcastle, F.D. and Wachs, I.E. (1988) Raman spectroscopy of chromium oxide supported on Al_2O_3, TiO_2 and SiO_2 – a comparative study. *J. Mol. Catal.*, **46** (1–3), 173–186.

31 Hardcastle, F.D. and Wachs, I.E. (1990) Determination of molybdenum oxygen bond distances and bond orders by Raman spectroscopy. *J. Raman Spectrosc.*, **21** (10), 683–691.

32 Hardcastle, F.D. and Wachs, I.E. (1991) Determination of vanadium oxygen bond distances and bond orders by Raman spectroscopy. *J. Phys. Chem.*, **95** (13), 5031–5041.

33 Vuurman, M.A. and Wachs, I.E. (1992) *In situ* Raman spectroscopy of alumina supported metal oxide catalysts. *J. Phys. Chem.*, **96** (12), 5008–5016.

34 Wachs, I.E. (1996) Raman and IR studies of surface metal oxide species on oxide supports: supported metal oxide catalysts. *Catal. Today*, **27** (3–4), 437–455.

35 Brown, F.R., Makovsky, L.E., and Rhee, K.H. (1977) Raman spectra of supported molybdena catalysts. 1. Oxide catalysts. *J. Catal.*, **50** (1), 162–171.

36 Brown, F.R., Makovsky, L.E., and Rhee, K.H. (1977) Raman spectra of supported molybdena catalysts. 2. Sulfided, used, and regenerated catalysts. *J. Catal.*, **50** (3), 385–389.

37 Thomas, R., Moulijn, J.A., and Kerkhof, F. (1977) Raman spectra of metathesis catalysts tungsten oxide on silica and tungsten oxide on gamma alumina. *Recl. Trav. Chim. Pays-Bas*, **96** (11), M134–M135.

38 Roozeboom, F., Medema, J., and Gellings, P.J. (1978) Vanadium oxide monolayer catalysts. 2. Laser Raman spectroscopic study of oxidic vanadium gamma-alumina catalysts. 1. *Z. Phys. Chem.*, **111** (2), 215–224.

39 Kerkhof, F., Moulijn, J.A., and Thomas, R. (1979) Laser Raman spectroscopy of the alumina-supported rhenium oxide metathesis catalyst. *J. Catal.*, **56** (2), 279–283.

40 Medema, J., van Stam, C., de Beer, V.H.J., Konings, A.J.A., and Koningsberger, D.C.

(1978) Raman spectroscopic study of Co–Mo–gamma-Al_2O_3 catalysts. *J. Catal.*, **53** (3), 386–400.

41 Xie, Y.-C. and Tang, Y.-Q. (1990) Spontaneous monolayer dispersion of oxides and salts onto surfaces of supports: applications to heterogeneous catalysis. *Adv. Catal.*, **37**, 1–43.

42 Deo, G. and Wachs, I.E. (1991) Predicting molecular structures of surface metal-oxide species on oxide supports under ambient conditions. *J. Phys. Chem.*, **95** (15), 5889–5895.

43 Xiong, G., Li, C., Feng, Z.C., Ying, P.L., Xin, Q., and Liu, J.K. (1999) Surface coordination structure of molybdate with extremely low loading on gamma-alumina characterized by UV resonance Raman spectroscopy. *J. Catal.*, **186** (1), 234–237.

44 Jehng, J.M., Deo, G., Weckhuysen, B.M., and Wachs, I.E. (1996) Effect of water vapor on the molecular structures of supported vanadium oxide catalysts at elevated temperatures. *J. Mol. Catal. A: Chem.*, **110** (1), 41–54.

45 Gleiter, H. (2000) Nanostructured materials: basic concepts and microstructure. *Acta Mater.*, **48** (1), 1–29.

46 Yang, C.C. and Li, S. (2008) Size-dependent Raman red shifts of semiconductor nanocrystals. *J. Phys. Chem. B*, **112** (45), 14193–14197.

47 Nomura, S. and Kobayashi, T. (1992) Exciton LO-phonon couplings in spherical semiconductor microcrystallites. *Phys. Rev. B*, **45** (3), 1305–1316.

48 Banyai, L., Hu, Y.Z., Lindberg, M., and Koch, S.W. (1988) 3rd-order optical nonlinearities in semiconductor microstructures. *Phys. Rev. B*, **38** (12), 8142–8153.

49 Roussignol, P., Ricard, D., Flytzanis, C., and Neuroth, N. (1989) Phonon broadening and spectral hole burning in very small semiconductor particles. *Phys. Rev. Lett.*, **62** (3), 312–315.

50 Scamarcio, G., Spagnolo, V., Ventruti, G., Lugara, M., and Righini, G.C. (1996) Size dependence of electron–LO-phonon coupling in semiconductor nanocrystals. *Phys. Rev. B*, **53** (16), 10489–10492.

51 Klein, M.C., Hache, F., Ricard, D., and Flytzanis, C. (1990) Size dependence of electron–phonon coupling in semiconductor nanospheres: the case of CdSe. *Phys. Rev. B*, **42** (17), 11123.

52 Shiang, J.J., Goldstein, A.N., and Alivisatos, A.P. (1990) Lattice reorganization in electronically excited semiconductor clusters. *J. Chem. Phys.*, **92** (5), 3232–3233.

53 Niyogi, S., Hamon, M.A., Hu, H., Zhao, B., Bhowmik, P., Sen, R., Itkis, M.E., and Haddon, R.C. (2002) Chemistry of single-walled carbon nanotubes. *Acc. Chem. Res.*, **35** (12), 1105–1113.

54 Dresselhaus, M.S., Dresselhaus, G., and Jorio, A. (2007) Raman spectroscopy of carbon nanotubes in 1997 and 2007. *J. Phys. Chem. C*, **111** (48), 17887–17893.

55 Pimenta, M.A., Dresselhaus, G., Dresselhaus, M.S., Cancado, L.G., Jorio, A., and Saito, R. (2007) Studying disorder in graphite-based systems by Raman spectroscopy. *Phys. Chem. Chem. Phys.*, **9**, 1276–1291.

56 Cancado, L.G., Takai, K., Enoki, T., Endo, M., Kim, Y.A., Mizusaki, H., Jorio, A., Coelho, L.N., Magalhaes-Paniago, R., and Pimenta, M.A. (2006) General equation for the determination of the crystallite size L_a of nanographite by Raman spectroscopy. *Appl. Phys. Lett.*, **88** (16), 163106-1–163106-3.

57 Lee, D.S., Riedl, C., Krauss, B., von Klitzing, K., Starke, U., and Smet, J.H. (2008) Raman spectra of epitaxial graphene on SiC and of epitaxial graphene transferred to SiO_2. *Nano Lett.*, **8** (12), 4320–4325.

58 Malard, L.M., Pimenta, M.A., Dresselhaus, G., and Dresselhaus, M.S. (2009) Raman spectroscopy in graphene. *Phys. Rep.*, **473** (5–6), 51–87.

59 Corma, A. (1997) From microporous to mesoporous molecular sieve materials and their use in catalysis. *Chem. Rev.*, **97** (6), 2373–2420.

60 Kosuge, K. (1999) Titanium containing porous silica prepared by a modified sol–gel method. *J. Phys. Chem. B*, **103** (18), 3563–3569.

61 Long, R.Q. and Yang, R.T. (1999) Superior Fe-ZSM-5 catalyst for selective catalytic reduction of nitric oxide by ammonia. *J. Am. Chem. Soc.*, **121** (23), 5595–5596.

62 Parker, W.O. and Millini, R. (2006) Ti coordination in titanium silicalite-1. *J. Am. Chem. Soc.*, **128** (5), 1450–1451.

63 Sayari, A. (1996) Catalysis by crystalline mesoporous molecular sieves. *Chem. Mater.*, **8** (8), 1840–1852.

64 Taramasso, M., Perego, G., and Notari, B. (1983) Crystalline, porous material with silicalite structure – prepared from silica and titanium oxide compounds. and used e.g. for alkylation, cracking etc. of organic compounds, US Patent 4,410,501.

65 Ricchiardi, G., Damin, A., Bordiga, S., Lamberti, C., Spano, G., Rivetti, F., and Zecchina, A. (2001) Vibrational structure of titanium silicate catalysts. A spectroscopic and theoretical study. *J. Am. Chem. Soc.*, **123** (46), 11409–11419.

66 Tanev, P.T., Chibwe, M., and Pinnavaia, T.J. (1994) Titanium-containing mesoporous molecular sieves for catalytic oxidation of aromatic compounds. *Nature*, **368** (6469), 321–323.

67 Fan, W.B., Duan, R.G., Yokoi, T., Wu, P., Kubota, Y., and Tatsumi, T. (2008) Synthesis, crystallization mechanism, and catalytic properties of titanium rich TS-1 free of extraframework titanium species. *J. Am. Chem. Soc.*, **130** (31), 10150–10164.

68 Bordiga, S., Bonino, F., Damin, A., and Lamberti, C. (2007) Reactivity of Ti(IV) species hosted in TS-1 towards H_2O_2–H_2O solutions investigated by *ab initio* cluster and periodic approaches combined with experimental XANES and EXAFS data: a review and new highlights. *Phys. Chem. Chem. Phys.*, **9**, 4854–4878.

69 Bordiga, S., Damin, A., Bonino, F., Ricchiardi, G., Lamberti, C., and Zecchina, A. (2002) The structure of the peroxo species in the TS-1 catalyst as investigated by resonance Raman spectroscopy. *Angew. Chem. Int. Ed.*, **41** (24), 4734–4737.

70 Lamberti, C., Bordiga, S., Zecchina, A., Carati, A., Fitch, A.N., Artioli, G., Petrini, G., Salvalaggio, M., and Marra, G.L. (1999) Structural characterization of Ti-silicalite-1: a synchrotron radiation X-ray powder diffraction study. *J. Catal.*, **183** (2), 222–231.

71 Scarano, D., Zecchina, A., Bordiga, S., Geobaldo, F., and Spoto, G. (1993) Fourier-transform infrared and Raman spectra of pure and Al-, B-, Ti- and Fe-substituted silicalites: stretching-mode region. *J. Chem. Soc., Faraday Trans.*, **89**, 4123–4130.

72 Tuel, A. (1996) Crystallization of titanium silicalite-1 (TS-1) from gels containing hexanediamine and tetrapropylammonium bromide. *Zeolites*, **16**, 108–117.

73 Li, C., Xiong, G., Xin, Q., Liu, J.K., Ying, P.L., Feng, Z.C., Li, J., Yang, W.B., Wang, Y.Z., Wang, G.R., Liu, X.Y., Lin, M., Wang, X.Q., and Min, E.Z. (1999) UV resonance Raman spectroscopic identification of titanium atoms in the framework of TS-1 zeolite. *Angew. Chem. Int. Ed. Engl.*, **38** (15), 2220–2222.

74 Li, C., Xiong, G., Liu, J.K., Ying, P.L., Xin, Q., and Feng, Z.C. (2001) Identifying framework titanium in TS-1 zeolite by UV resonance Raman spectroscopy. *J. Phys. Chem. B*, **105** (15), 2993–2997.

75 Ricchiardi, G., Damin, A., Bordiga, S., Lamberti, C., Spano, G., Rivetti, F., and Zecchina, A. (2001) Vibrational structure of titanium silicate catalysts. A spectroscopic and theoretical study. *J. Am. Chem. Soc.*, **123** (46), 11409–11419.

76 Yu, J.Q., Feng, Z.C., Xu, L., Li, M.J., Xin, Q., Liu, Z.M., and Li, C. (2001) Ti-MCM-41 synthesized from colloidal silica and titanium trichloride: synthesis, characterization, and catalysis. *Chem. Mater.*, **13**, 994–998.

77 Zhang, W.H., Lu, J.Q., Han, B., Li, M.J., Xiu, J.H., Ying, P.L., and Li, C. (2002) Direct synthesis and characterization of titanium-substituted mesoporous molecular sieve SBA-15. *Chem. Mater.*, **14** (8), 3413–3421.

78 Li, C. (2007) UV Raman spectroscopic studies on transition metal-containing

microporous and mesoporous materials: active sites and synthesis mechanism. *Stud. Surf. Sci. Catal.*, **170**, 561–576.

79 Feng, X. and Keith Hall, W. (1997) FeZSM-5: a durable SCR catalyst for NO_x removal from combustion streams. *J. Catal.*, **166** (2), 368–376.

80 Long, R.Q. and Yang, R.T. (1999) Superior Fe-ZSM-5 catalyst for selective catalytic reduction of nitric oxide by ammonia. *J. Am. Chem. Soc.*, **121** (23), 5595–5596.

81 Yoshizawa, K., Shiota, Y., and Yamabe, T. (1999) Reaction pathway for the direct benzene hydroxylation by iron–oxo species. *J. Am. Chem. Soc.*, **121** (1), 147–153.

82 Sun, K., Fan, F., Xia, H., Feng, Z., Li, W.-X., and Li, C. (2008) Framework Fe ions in Fe-ZSM-5 zeolite studied by UV resonance Raman spectroscopy and density functional theory calculations. *J. Phys. Chem. C*, **112** (41), 16036–16041.

83 Li, Y., Feng, Z.C., Lian, Y.X., Sun, K.Q., Zhang, L., Jia, G.Q., Yang, Q.H., and Li, C. (2005) Direct synthesis of highly ordered Fe-SBA-15 mesoporous materials under weak acidic conditions. *Micropor. Mesopor. Mater.*, **84** (1–3), 41–49.

84 Zhang, W.-H., Lu, J.-Q., Han, B., Li, M.-J., Xiu, J.-H., Ying, P.-L., and Li, C. (2002) Direct synthesis and characterization of titanium-substituted mesoporous molecular sieve SBA-15. *Chem. Mater.*, **14** (8), 3413–3421.

85 Fan, F.T., Feng, Z.C., and Li, C. (2010) UV Raman spectroscopic studies on active sites and synthesis mechanisms of transition metal-containing microporous and mesoporous materials. *Acc. Chem. Res.*, **43** (3), 378–387.

86 Li, Y., Feng, Z.C., Xin, H.C., Fan, F.T., Zhang, J., Magusin, P., Hensen, E.J.M., van Santen, R.A., Yang, Q.H., and Li, C. (2006) Effect of aluminum on the nature of the iron species in Fe-SBA-15. *J. Phys. Chem. B*, **110** (51), 26114–26121.

87 Xia, H.A., Sun, K.Q., Sun, K.J., Feng, Z.C., Li, W.X., and Li, C. (2008) Direct spectroscopic observation of Fe (III)–phenolate complex formed from the reaction of benzene with peroxide species on Fe/ZSM-5 at room temperature. *J. Phys. Chem. C*, **112** (24), 9001–9005.

88 Hensen, E.J.M., Zhu, Q., Janssen, R.A.J., Magusin, P., Kooyman, P.J., and van Santen, R.A. (2005) Selective oxidation of benzene to phenol with nitrous oxide over MFI zeolites. 1. On the role of iron and aluminum. *J. Catal.*, **233** (1), 123–135.

89 Hensen, E.J.M., Zhu, Q., and van Santen, R.A. (2005) Selective oxidation of benzene to phenol with nitrous oxide over MFI zeolites. 2. On the effect of the iron and aluminum content and the preparation route. *J. Catal.*, **233** (1), 136–146.

90 Panov, G.I., Uriarte, A.K., Rodkin, M.A., and Sobolev, V.I. (1998) Generation of active oxygen species on solid surfaces. Opportunity for novel oxidation technologies over zeolites. *Catal. Today*, **41** (4), 365–385.

91 Groothaert, M.H., Smeets, P.J., Sels, B.F., Jacobs, P.A., and Schoonheydt, R.A. (2005) Selective oxidation of methane by the bis(μ-oxo)dicopper core stabilized on ZSM-5 and mordenite zeolites. *J. Am. Chem. Soc.*, **127** (5), 1394–1395.

92 Woertink, J.S., Smeets, P.J., Groothaert, M.H., Vance, M.A., Sels, B.F., Schoonheydt, R.A., and Solomon, E.I. (2009) A $[Cu_2O]^{2+}$ core in Cu-ZSM-5, the active site in the oxidation of methane to methanol. *Proc. Natl. Acad. Sci. U. S. A.*, **106** (45), 18908–18913.

93 Aerts, A., Kirschhock, C.E.A., and Martens, J.A. (2010) Methods for *in situ* spectroscopic probing of the synthesis of a zeolite. *Chem. Soc. Rev.*, **39** (12), 4626–4642.

94 Cundy, C.S. and Cox, P.A. (2005) The hydrothermal synthesis of zeolites: precursors, intermediates and reaction mechanism. *Micropor. Mesopor. Mater.*, **82** (1–2), 1–78.

95 Burkett, S.L. and Davis, M.E. (1994) Mechanism of structure direction in the synthesis of Si-ZSM-5 – an investigation by intermolecular ^{1}H–^{29}Si CP MAS NMR. *J. Phys. Chem.*, **98** (17), 4647–4653.

96 Kirschhock, C.E.A., Buschmann, V., Kremer, S., Ravishankar, R., Houssin, C.J.Y., Mojet, B.L., van Santen, R.A., Grobet, P.J., Jacobs, P.A., and Martens, J.A. (2001) Zeosil nanoslabs: building

blocks in nPr_4N^+-mediated synthesis of MFI zeolite. *Angew. Chem. Int. Ed.*, **40** (14), 2637–2640.

97 Kirschhock, C.E.A., Kremer, S.P.B., Grobet, P.J., Jacobs, P.A., and Martens, J.A. (2002) New evidence for precursor species in the formation of MFI zeolite in the tetrapropylammonium hydroxide–tetraethyl orthosilicate–water system. *J. Phys. Chem. B*, **106** (19), 4897–4900.

98 Kirschhock, C.E.A., Kremer, S.P.B., Vermant, J., Van Tendeloo, G., Jacobs, P.A., and Martens, J.A. (2005) Design and synthesis of hierarchical materials from ordered zeolitic building units. *Chem. Eur. J.*, **11** (15), 4306–4313.

99 Gonthier, S., Gora, L., Guray, I., and Thompson, R.W. (1993) Further comments on the role of autocatalytic nucleation in hydrothermal zeolite syntheses. *Zeolites*, **13** (6), 414–418.

100 Thompson, R.W. (1992) Comments on the autocatalytic nucleation of (Na, TPA)-ZSM-5. *Zeolites*, **12** (7), 837–840.

101 Nikolakis, V., Vlacho, D.G., and Tsapatsis, M. (1998) Modeling of zeolite crystallization: the role of gel microstructure. *Micropor. Mesopor. Mater.*, **21** (4–6), 337–346.

102 Valtchev, V.P. and Bozhilov, K.N. (2005) Evidences for zeolite nucleation at the solid–liquid interface of gel cavities. *J. Am. Chem. Soc.*, **127** (46), 16171–16177.

103 Dutta, P.K., Shieh, D.C., and Puri, M. (1987) Raman spectroscopic study of the synthesis of zeolite-Y. *J. Phys. Chem.*, **91** (9), 2332–2336.

104 Mintova, S., Olson, N.H., and Bein, T. (1999) Electron microscopy reveals the nucleation mechanism of zeolite Y from precursor colloids. *Angew. Chem. Int. Ed.*, **38** (21), 3201–3204.

105 Mintova, S., Olson, N.H., Valtchev, V., and Bein, T. (1999) Mechanism of zeolite A nanocrystal growth from colloids at room temperature. *Science*, **283** (5404), 958–960.

106 Dutta, P.K. and Del Barco, B. (1988) Raman spectroscopy of zeolite A: influence of silicon/aluminum ratio. *J. Phys. Chem.*, **92** (2), 354–357.

107 Dutta, P.K. and Delbarco, B. (1985) Raman spectroscopic studies of zeolite framework – hydrated zeolite A and the influence of cations. *J. Phys. Chem.*, **89** (10), 1861–1865.

108 McNicol, B.D., Loos, K.R., and Pott, G.T. (1972) Spectroscopic studies of zeolite synthesis. *J. Phys. Chem.*, **76** (23), 3388.

109 Dutta, P.K. and Puri, M. (1987) Synthesis and structure of zeolite ZSM-5: a Raman spectroscopic study. *J. Phys. Chem.*, **91** (16), 4329–4333.

110 Roozeboom, F., Robson, H.E., and Chan, S.S. (1983) Laser Raman study on the crystallization of zeolite-A, zeolite-X and zeolite-Y. *Zeolites*, **3** (4), 321–328.

111 Twu, J., Dutta, P.K., and Kresge, C.T. (1991) Vibrational spectroscopic examination of the formation of mordenite crystals. *J. Phys. Chem.*, **95** (13), 5267–5271.

112 Fan, F.T., Sun, K.J., Feng, Z.C., Xia, H.A., Han, B., Lian, Y.X., Ying, P.L., and Li, C. (2009) From molecular fragments to crystals: A UV Raman spectroscopic study on the mechanism of Fe-ZSM-5 synthesis. *Chem. Eur. J.*, **15** (13), 3268–3276.

113 Galeener, F.L. (1982) Planar rings in glasses. *Solid State Commun.*, **44** (7), 1037–1040.

114 Sun, K.J., Fan, F.T., Xia, H.A., Feng, Z.C., Li, W.-X., and Li, C. (2008) Framework Fe ions in Fe-ZSM-5 zeolite studied by UV resonance Raman spectroscopy and density functional theory calculations. *J. Phys. Chem. C*, **112** (41), 16036–16041.

115 Francis, R.J. and O'Hare, D. (1998) The kinetics and mechanisms of the crystallisation of microporous materials. *J. Chem. Soc., Dalton. Trans.*, **19**, 3133–3148.

116 Grandjean, D., Beale, A.M., Petukhov, A.V., and Weckhuysen, B.M. (2005) Unraveling the crystallization mechanism of CoAPO-5 molecular sieves under hydrothermal conditions. *J. Am. Chem. Soc.*, **127** (41), 14454–14465.

117 O'Brien, M.G., Beale, A.M., Catlow, C.R.A., and Weckhuysen, B.M. (2006) Unique organic–inorganic interactions leading to a structure-directed microporous aluminophosphate

crystallization as observed with *in situ* Raman spectroscopy. *J. Am. Chem. Soc.*, **128** (36), 11744–11745.

118 Fan, F.T., Feng, Z.C., Li, G.N., Sun, K.J., Ying, P.L., and Li, C. (2008) *In situ* UV Raman spectroscopic studies on the synthesis mechanism of zeolite X. *Chem. Eur. J.*, **14** (17), 5125–5129.

119 Fan, F.T., Feng, Z.C., Sun, K.J., Guo, M.L., Guo, Q., Song, Y., Li, W.-x., and Li, C. (2009) *In situ* UV Raman spectroscopic study on the synthesis mechanism of AlPO-5. *Angew. Chem., Int. Ed.*, **46**, 8899–8903.

120 Maston, D.W., Sharma, S.K., and Philpotts, J.A. (1986) Raman spectra of some tectosilicates and of glasses along the orthoclase–anorthite and nepheline–anorthite joins. *Am. Mineral.*, **71**, 694–704.

121 McMillan, P. (1984) Structural studies of silicate glasses and melts applications and limitations of Raman spectroscopy. *Am. Mineral.*, **69**, 622–644.

122 Davis, M.E. and Lobo, R.F. (1992) Zeolite and molecular sieve synthesis. *Chem. Mater.*, **4** (4), 756–768.

123 Lewis, D.W., Freeman, C.M., and Catlow, C.R.A. (1995) Predicting the templating ability of organic additives for the synthesis of microporous materials. *J. Phys. Chem.*, **99** (28), 11194–11202.

124 Pelster, S.A., Schrader, W., and Schuth, F. (2006) Monitoring temporal evolution of silicate species during hydrolysis and condensation of silicates using mass spectrometry. *J. Am. Chem. Soc.*, **128** (13), 4310–4317.

125 Holmes, A.J., Kirkby, S.J., Ozin, G.A., and Young, D. (1994) Raman spectra of the unidimensional aluminophosphate molecular sieves $AlPO_4$-11, $A1PO_4$-5, $AlPO_4$-8, and VPI-5. *J. Phys. Chem.*, **98**, 4677–4682.

3
Electronic Spectroscopy: Ultra Violet-visible and Near IR Spectroscopies

Friederike C. Jentoft

3.1
Introduction and Overview

3.1.1
Scope

This chapter focuses on the spectroscopy of electronic transitions in solids and includes treatment of molecular species that are used in the preparation of solids or are adsorbed on their surfaces. These electronic transitions are excited through the absorption of radiation in the ultraviolet (UV), visible (vis) and near-infrared (NIR) ranges. Atomic absorption, which also occurs in the UV–vis range, is excluded as it has no value for the characterization of a material beyond the quantitative analysis of its composition; the method is excellently described in books [1]. Methods that are based on phenomena following the absorption of UV–vis–NIR radiation, such as Raman spectroscopy and photoluminescence, are discussed in Chapters 2 and 4, respectively; absorption of UV radiation leading to ionization is integrated into Chapter 13.

Electronic transitions in the UV–vis–NIR range characterize molecules, metal cations, complexes consisting of metal cations and ligands, highly dispersed metal or metal oxide moieties with properties different from those of the corresponding bulk species, and bulk solids. The UV–vis–NIR spectrum provides information on the electronic structure of molecules, the valence and coordination of metal cations, the particle size and shape (in some cases), the bandgap of solids, and the presence and nature of defects in solids. Qualitative analysis, that is, the identification and characterization of bulk and surface species, is in the foreground; possibilities for quantification, when feasible, are outlined.

3.1.2
History

An excellent chronology and description of the developments leading to modern optical spectroscopy can be found in [2]; they are briefly reiterated here. Three areas that promoted or limited progress can be identified, namely the observation of

Characterization of Solid Materials and Heterogeneous Catalysts: From Structure to Surface Reactivity, First Edition. Edited by Michel Che and Jacques C. Védrine.
© 2012 Wiley-VCH Verlag GmbH & Co. KGaA. Published 2012 by Wiley-VCH Verlag GmbH & Co. KGaA.

physical phenomena, the formulation of theories to describe these phenomena, and the design of instrumentation.

Not very surprisingly, the development of UV–vis–NIR spectroscopy started in the visible range, characterized by radiation detectable by the human eye. In 1666, Newton used a prism to disperse sunlight into visible light of various colors. The "invisible" parts of the spectrum were detected much later, IR radiation in 1800 by Herschel and UV radiation 1801 by Ritter. Already in 1758, the coloration of a flame by light emission from thermally excited atoms was used for the detection of certain chemical substances. The distinction of lithium and strontium by Talbot through the use of a flame and a prism in 1834 can be seen as the actual birth of spectral analysis. In 1885, Balmer discovered what is now called the Balmer series, which is the part of the electronic spectrum of the hydrogen atom that is located in the visible range. Electronic spectroscopy was thus first applied to atoms, and its diagnostic value for molecules or larger structures was recognized later.

Understanding the wavelength dependence of light absorption requires the description and calculation of electronic ground and excited states. The electronic absorption lines of hydrogen were first mathematically captured by the Rydberg equation. Later, analytical solution of the Schrödinger equation allowed exact calculation of the transitions. Although much progress has been made in the methods of theoretical chemistry, the description of electronically excited states of complex structures remains a challenge.

The absorption properties of materials can be gathered from measurements in transmission or in reflection geometry. The phenomenology of light transmission through clear media was analyzed by Bouguer (1729) and Lambert (1760), who recognized that the attenuation of light that passes through a clear medium depends on the incident intensity and specimen thickness. Beer (1852) demonstrated that the attenuation is related to the concentration of absorbing species. These findings led to the formulation of the well-known Bouguer–Lambert–Beer or Lambert–Beer law. Regarding light reflection, two limiting cases need to be distinguished, that of specular or mirror reflection on glossy surfaces and that of diffuse reflection on matt surfaces. The reflection, refraction, and transmission of electromagnetic waves on flat surfaces are described by the Fresnel equations. A phenomenological description of diffuse reflection was formulated by Kubelka and Munk in 1931 [3] using the two-photon flux formalism introduced by Schuster in 1905 [4], and the Kubelka–Munk function has become the most frequently used equation for diffuse reflection analysis.

A path-breaking step in the technical development of UV–vis–NIR spectroscopy was the invention of the grating by Fraunhofer in 1814. However, for many years optical spectroscopy was limited to the wavelength range of 500–700 nm as a result of the lack of suitable light sources, prisms and gratings, and also detectors. The first commercial instrument that included the UV range became available in 1941; it required special quartz for the prism and a new type of source. Another important development was the integrating sphere, which for many years was the main device for measurements in reflection geometry, although it was originally employed for more reliable measurements in transmission in the 1920s [5]. A better description of the theory of spheres [6] and improved designs [7] became available in the 1950s, with alternative devices for reflectance measurement being used to investigate, for

example, biological materials such as leaves [8]. Mirror optics accessories for diffuse reflectance measurements were introduced in the early 1990s [9]; they accommodate reaction chambers that facilitate the investigation of specimens under conditions of controlled atmosphere and temperature. Fiber-optic probes, which have seen rapid development in the past decade, make such investigations even more flexible. They are often combined with spectrometers equipped with array detectors so that unprecedented time resolution can be achieved. The classical types of spectrometer have lately seen improvements in detector technology, specifically in the NIR range (InGaAs detectors).

3.1.3 Overview

Spectroscopy in the UV, vis, and NIR ranges is the basis for numerous analytical procedures, and many quantitative standard analyses described in the protocols of various agencies make use of photometry. Solids are commonly analyzed by UV–vis–NIR spectroscopy, and integrating spheres, mirror optics accessories, and fiber-optic probes are all being used for measurements in diffuse reflection; which device is most suitable depends on the specific problem (see Section 3.3.2).

UV–vis–NIR spectroscopy has a long tradition in the field of adsorption and catalysis. Table 3.1 summarizes review articles relevant to these subjects. Until about the mid-1960s, measurements were carried out in transmission on thin films or self-supporting wafers obtained through compression of polycrystalline materials. However, adsorbents and catalysts are typically fine powders with high surface area, and many of them scatter too strongly for transmission measurements. The diffuse reflection technique experienced a breakthrough, highlighted by Kortüm's book in 1969, and is now the predominantly applied measurement geometry (see Section 3.2.3 and subsequent sections).

In addition to the characterization of the sample as such, measurements after treatments in vacuum or a gas atmosphere at elevated temperatures are of particular interest. Treatments may be performed at a location remote from the sample position in the spectrometer; with the sample sometimes already being inside a cell with a suitable window for spectroscopy, or sometimes in another container. Sample transfer between treatment location and measurement position in the spectrometer typically occurs within the apparatus, and exposure to the ambient is avoided. Measurements at room temperature in vacuum or a gas atmosphere are unproblematic, whereas elevated temperatures are difficult to realize next to an integrating sphere, which for a long time was the only possibility for measurements in diffuse reflection. The investigation of solids at high temperatures and in flows experienced a major step forward when mirror optics and suitable reaction chambers became commercially available. The advent of fiber optics led to a paradigm shift: rather than bringing the reactor to the spectrometer, which unavoidably means adapting it to fit an optical accessory, the fiber-optic probes now "bring the spectrometer to the reactor." Temperature and pressure ranges of reaction chambers for mirror optics accessories and of fiber-optic probes have been extended in recent years. Fibers have

Table 3.1 Review articles on UV–vis–NIR spectroscopy of solids with relevance to adsorption and catalysis.

Authors	Focus	Year	Ref.
De Boer and co-workers	Adsorption of alkali metal atoms, halogens, and aromatics on salt films	1930–1938	Numerous papers
Leftin and Hobson	Principles of the technique, examples addressing physisorption and chemisorption on silica, ionic salts, and cracking catalysts	1963	[10]
Terenin	Adsorption of aromatic compounds on silica and silica–alumina materials	1964	[11]
Klier	Fundamentals and application of the diffuse reflectance technique; examples addressing analysis of the electronic structures of solids and the nature of surface-coordinated species	1968	[12]
Kortüm	Book entitled *Reflectance Spectroscopy*	1969	[13]
Kellermann	Application of Schuster–Kubelka–Munk theory, examples addressing transition metal ions in zeolites, nature and mobility of adsorbed water (NIR spectra), determination of bandgap	1979	[14]
Stone	Description of theory and experiment, examples concerning alkaline earth metal oxides and nickel compounds	1983	[15]
Schoonheydt	Interpretation of spectra of transition metal ions with the aid of ligand field theory and short introduction to NIR spectroscopy; examples concerning bulk and supported oxides	1984	[16]
Garbowski and Praliaud	Condensed version of essentials	1994	[17]
Weckhuysen and Schoonheydt	Brief overview of integrating spheres, mirror optics, and fiber optics; crystal field, ligand field, and molecular orbital theories; examples concerning supported chromium, copper, and cobalt species	2000	[18]
Weckhuysen	Instrumental detail concerning measurements under reaction conditions; case studies involving supported chromium, copper, and cobalt species as catalysts	2004	[19]
Che, Bozon-Verduraz, and Sojka	Types of transitions, examples concerning various stages of catalyst preparation and the interaction of catalysts with reactants	1997 and 2008	[20, 21]
Jentoft	Theory of diffuse reflection and description of optical accessories; comprehensive summary of investigations of catalysts after treatment and under working conditions	2009	[22]
Schoonheydt	Brief overview of transitions and experimental techniques including UV–vis microscopy; examples concerning transition metal oxidation state and coordination analysis and spatial distribution of hydrocarbons in zeolites	2010	[23]

become available for various ranges, and spectrometers with array detectors increase in range, resolution, and speed, described in Section 3.3.2.7.

3.2
UV–vis–NIR Spectra

In this section, the various representations of data are explained, data processing to ensure correct referencing is outlined, and the types of electronic transition that can be observed in the spectra and how they can be identified are discussed.

3.2.1
Spectra Representation

The absorption features in UV–vis–NIR spectra are characterized by an energy and the quantity of radiation that is absorbed at that particular energy (or wavelength). The spectra are considered to be composed of bands (as opposed to lines) because lower energy transitions such as vibrations are typically co-excited and are responsible for the band shape and, if resolved, the fine structure.

3.2.1.1 Spectral Position of Absorption Features

The position, or energy, of a spectral feature, which is determined with the help of a spectrometer, corresponds to the energy difference between the two electronic levels involved in the transition. The independent variable in a spectrum is typically the

- wavelength λ, mostly in nanometers (nm), sometimes in ångstroms (Å) or millimicrometers (mμ, equal to nanometers)
- energy E, in electronvolts (eV)
- wavenumber $\tilde{\nu}$, in inverse centimeters (cm^{-1}).

The scales can be converted as follows:

$$\tilde{\nu} = \frac{1}{\lambda} \tag{3.1}$$

where $\tilde{\nu}$ is the wavenumber in m^{-1} and λ the wavelength in m.

$$E = \frac{hc}{\lambda e} \tag{3.2}$$

where E is the energy in eV, $h = 6.602 \times 10^{-34}$ J s (Planck's constant), $c = 2.998 \times 10^{6}$ m s^{-1} (speed of light in vacuum), λ the wavelength in m, and $e = 1.602 \times 10^{-19}$ C (elementary charge of the electron).

3.2.1.2 Intensity of Absorption Features

The intensity of an absorption band in a UV–vis spectrum depends on material-specific properties, that is, the absorption coefficient and the concentration of

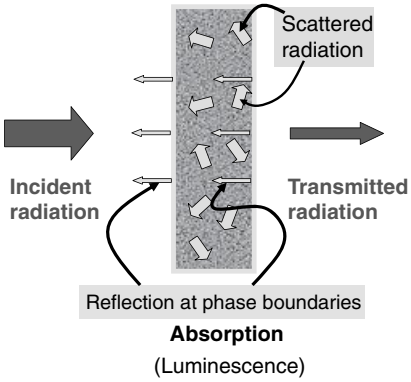


Figure 3.1 Phenomena that occur when radiation interacts with a specimen.

absorbing centers, and on a property that can be controlled by the user in the preparation of the specimen, that is, the optical pathlength. Often, absorption is not the only phenomenon occurring when radiation interacts with a specimen, and the fraction of absorbed light is not easily determined.

Figure 3.1 summarizes the phenomena that can occur when a specimen is irradiated. If luminescence, scattering, and regular reflection are absent, then the absorbed radiation can be determined from the transmitted fraction. The ratio of transmitted light (transmitted radiation) I to the incident light I_0 is called τ, the transmittance or transmission factor. In this simple case, the absorbance A can be calculated using the following equations:

$$A_e = -\ln \tau \tag{3.3}$$

$$A_{10} = -\log \tau \tag{3.4}$$

The term "optical density" (OD) is synonymous with absorbance, but its use is discouraged by IUPAC. When quantitative measurements are to be made, and absorbance or absorption coefficients are compared with literature data, it is necessary to identify whether the spectroscopy software package uses A_{10} (which is mostly the case) or A_e. The absorbance is related to the sample and specimen properties by the Lambert–Beer law:

$$\log \frac{I}{I_0} = \log \tau = -ad = -\varepsilon cd = A_{10} \tag{3.5}$$

$$\ln \frac{I}{I_0} = \ln \tau = -\alpha d = -\kappa cd = A_e \tag{3.6}$$

where a and α are the linear decadic (A_{10}) and Napierian (A_e) absorption coefficients, respectively, in units of cm^{-1}, ε and κ are the molar decadic and Napierian absorption coefficients, respectively, in units of $mol\,cm^{-2}$, c is the amount concentration in $mol\,cm^{-3}$, and d is the pathlength in cm. Note that amount concentrations are commonly specified in $mol\,dm^{-3}$ or $mol\,l^{-1}$, and absorption coefficients may be specified in $mol\,cm\,dm^{-3}$ or $mol\,cm\,l^{-1}$.

It follows that the linear absorption coefficients are obtained by division of the absorbance by the optical pathlength. The molar absorption coefficients are the linear coefficients divided by the amount concentration [24].

The derivation of the Lambert–Beer law can be found in textbooks and other reviews [22]. The Lambert–Beer law is valid only in the limiting case of weak absorption.

Whereas luminescence occurs only in a small fraction of all compounds, regular reflection occurs at each phase boundary. Regular reflection amounts to a few percent of the incident light, depending on the ratio of the refractive indices, and can be eliminated (i) mathematically after measurement of samples of various thicknesses or (ii) experimentally by use of similar phase boundaries in the measurement of the sample and the reference specimen (e.g., a reference cuvette).

Scattering, generally defined as the deflection of electromagnetic or corpuscular radiation from its original direction, is negligible in molecularly dispersed media (solutions) but is significant in colloidal dispersions or in powders. Unless a solid sample is a single crystal or a glass, scattering is expected, particularly in high surface area powders, such as materials typically used in catalysis or adsorption. The scattered intensity strongly depends on the relative dimensions of wavelength and particle size. Scattering can be reduced by embedding a powder in a material of similar refractive index; the fabrication of KBr wafers or immersion in Nujol are frequently applied techniques in specimen preparation for IR spectroscopy.

Absorbance, scattering, and luminescence are all included when using the terms "attenuance" and "attenuation coefficient," which were formerly called extinction and extinction coefficient (terms now discouraged by IUPAC). Note that the term "attenuation" has a more general use and refers to "reduction of a radiation quantity upon passage of radiation through matter resulting from interactions of the radiation with the matter it traverses" [25].

It is also possible to determine the absorption properties of a solid by analyzing radiation reflected from a specimen. Two limiting cases must be considered, that of regular reflection, also termed specular or mirror-type reflection, and that of diffuse reflection. Regular reflection will occur on a mirror-type (polished) surface according to the laws of geometric optics (Figure 3.2a). The reflected radiation is thus most intense in the forward direction, that is, at an azimuth of 180° (Figure 3.2b). The reflecting power in the case of regular reflection is called reflectivity (R_{reg}) and is high in the spectral range where absorption is high, as can be seen from the Fresnel equations for absorbing media in the case of normal incidence [12, 26]:

$$R_{reg} = \frac{(n_1 - n_0)^2 + (n_1\kappa_1)^2}{(n_1 + n_0)^2 + (n_1\kappa_1)^2} \tag{3.7}$$

where n_0 and n_1 are the refractive indices of the surrounding medium and the sample, respectively, and κ_1 is the absorption coefficient of the sample. For spectral regions with high absorbance (κ_1 large), R_{reg} will approach unity.

Diffuse reflection occurs on matt (dull) surfaces and is defined by an angular distribution of the reflected radiation that is independent of the angle of incidence

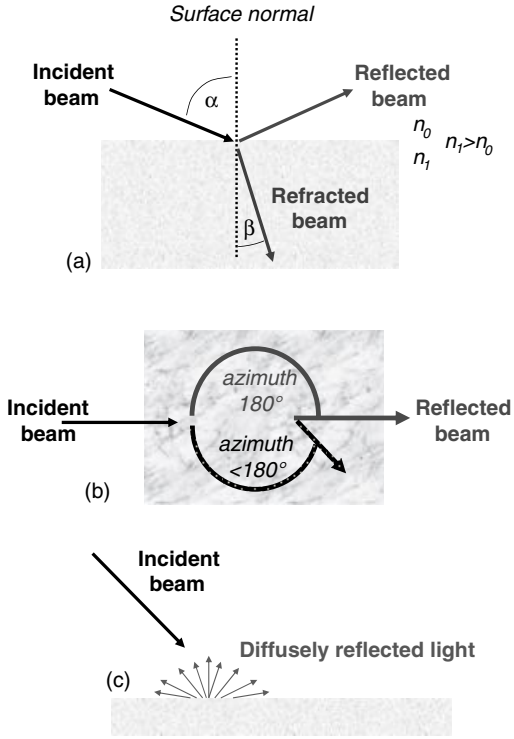


Figure 3.2 (a) Regular reflection and refraction, side view; (b) regular reflection, top view; (c) diffuse reflection, side view.

(Figure 3.2c). A perfectly matt surface will appear equally bright at all observation angles when illuminated from one direction; such a surface is called a Lambertian surface. The distribution of the reflected light is the result of multiple scattering; light is redirected "inside" the sample by regular reflection, refraction, and diffraction. These phenomena, which occur through interaction of the radiation with the specimen, for example with the many small particles of a powder, are not separable under the conditions of ideal diffuse reflection. The reflecting power in the case of diffuse reflection is called reflectance, and it is low in the spectral range where absorption is high.

Specular and diffuse reflection are idealized cases, and no surface fits perfectly into either one or the other scheme. The surfaces of loosely assembled powders can usually be considered as diffusely reflecting provided that the particles are randomly oriented. Flattening of the surface or pressing the material can lead to a parallel orientation of crystals, which will produce "shiny" spots, which specularly reflect light. The absorption properties of polycrystalline powder samples can be determined by diffuse reflectance measurements, where care must be taken to avoid contributions of specularly reflected radiation, which would falsify the result. Optical accessories for diffuse reflectance measurements are designed to optimize the yield

of diffusely reflected radiation and minimize the yield of specularly reflected radiation (see Sections 3.3.2.3, 3.3.2.5, and 3.3.2.7).

The phenomenon of multiple scattering (as opposed to a single event) in a heterogeneous sample escapes rigorous description. A frequently used phenomenological description is the Schuster–Kubelka–Munk theory. Schuster [4] introduced a formalism involving two photon fluxes in opposite directions (representing the incident and the reflected radiation) and a scattering and an absorption coefficient. Kubelka and Munk [3] treated the cases of finite and infinite thickness of a sample, and the cases of mere scattering (no absorption) and mere absorption (no scattering). The reflectance was found to depend solely on the ratio of the absorption and scattering coefficients, both of which are wavelength-dependent material properties. The so-called Kubelka–Munk function is the counterpart in reflection spectroscopy of what the absorbance function is in transmission spectroscopy. Its derivation, which can be achieved similarly to the Lambert–Beer law by assuming the sample to be sliced into infinitesimally thin layers, can be found elsewhere [13, 22]. The Kubelka–Munk function $F(\varrho_\infty)$, sometimes also called the remission function, is dimensionless (as is the absorbance) and is calculated as follows:

$$F(\varrho_\infty) = \frac{(1-\varrho_\infty)^2}{2\varrho_\infty} = \frac{K}{S} \tag{3.8}$$

where ϱ_∞ is the reflectance at infinite sample thickness (no radiation transmitted), unitless, K the absorption coefficient, and S the scattering coefficient, the last two in units of inverse length such as cm^{-1}.

The Kubelka–Munk function correctly describes the limiting cases. A non-absorbing sample ($K \to 0$), will reflect all light, and indeed $F(\varrho_\infty) = 0$ as $\varrho_\infty \to 1$. A non-scattering sample ($S \to 0$) will not reflect any light, and indeed $\varrho_\infty \to 0$. Because the Kubelka–Munk function depends on two quantities, more than one measurement is necessary to obtain values of K or S. A typical strategy is to measure ϱ_∞ and, additionally, a value ϱ_0 at a finite sample thickness with the specimen in front of a non-reflecting background [27].

Like the absorbance, the Kubelka–Munk function becomes proportional to the amount concentration if a number of conditions are fulfilled, specifically, the absorption coefficient K must be small and the scattering coefficient S should not vary with the amount concentration c. The following proportionality becomes valid:

$$F(\varrho_\infty) = \frac{K}{S} \propto \frac{KC}{S} \tag{3.9}$$

If, in addition, the amount concentration is constant and the scattering coefficient does not vary as a function of wavelength, further simplification becomes possible and the logarithm of $F(\varrho_\infty)$ represents the logarithm of the molar absorption coefficient plus a constant:

$$\log[F(\varrho_\infty)] = \log k + C \tag{3.10}$$

Hence the logarithm of the Kubelka–Munk function, $\log[F(\varrho_\infty)]$, can be used to represent the absorption spectrum of a sample [28]. A plot of $\log[F(\varrho_\infty)]$ versus the

wavelength, sometimes called the typical color curve, will give the correct band position, but is shifted along the ordinate.

Reflectance is measured relative to a standard, which should be a "perfectly reflecting diffuser," that is, a material that diffusely reflects radiation over the wavelength range of interest, without absorbing any radiation. For a primer on reflectance standards, see [29]. Traditionally used materials in UV–vis spectroscopy are freshly prepared MgO, which reflects more than 95% of radiation at wavelengths between 400 and 700 nm, and $BaSO_4$ (spectroscopic grade), which reflects more than 95% of radiation at wavelengths between 340 and 1400 nm. In the mid-1970s, polymer materials based on polytetrafluoroethylene were introduced, with excellent reflectance properties over a wavelength range from 190 to 2500 nm. Frequently used materials are Spectralon® (Labsphere) and Fluorilon™ (Avian Technologies). The polymers can be machined into pieces that will fit a particular sample holder or cell, and cleaning the equipment (as is necessary after use of a powder standard) becomes obsolete; however, the pieces can become dirty during handling and will not retain their high reflectance forever.

3.2.2 Spectra Processing

UV–vis–NIR spectra can contain a number of artifacts as a result of switches between sources, gratings, detectors, and filters. These artifacts can have the shape of small peaks or steps. The positions of these switches are documented in the instrument manual, and often the switch can be shifted by some wavenumbers to avoid overlap with important spectral features.

The measured reflectance is relative to that of the employed white standard and has to be corrected for the standard's reflectance. The measured reflectance ϱ'_∞ and the true reflectance of the sample ϱ_∞ are linked through the standard's reflectance ϱ_{std}:

$$\varrho'_\infty = \frac{\varrho_\infty}{\varrho_{\mathrm{std}}} \tag{3.11}$$

Some spectroscopy software packages have the reflectance characteristics of the most important standards stored, and an automatic correction is possible.

In addition, it is necessary to correct for any other optical elements in the beam path, and they need to be included in the reference measurement. If the sample is in a closed environment, then a correction for the windows, which will absorb and reflect some radiation, becomes necessary. In transmission, typically the empty (i.e., evacuated or purged) cell will be used to create a background correction file; in reflection, the evacuated or purged cell with a white standard in the sample position will be used. In a double-beam spectrometer, the second beam path may remain empty during the background correction for a transmission measurement or a measurement with mirror optics; it is advisable, however, to use an attenuator in the reference beam to match the intensities in both beam paths. A white standard has to be placed in the reference position of an integrating sphere.

The absorption and scattering properties of the sample will affect the analyzed depth (or volume), which may vary throughout an experiment depending on how the investigated specimen responds to treatments. Few systematic investigations are available; the influence of materials properties such as particle size and refractive index on the size of the sampled volume has been investigated for mid-infrared (MIR) radiation [30].

3.2.3 Transitions in Molecular Species

3.2.3.1 Selection Rules

For an electronic transition to be observed, the transition moment integral, which includes the wavefunctions of the initial and final states and the dipole moment operator, must be nonzero. This restriction has implications for the nature of the states involved; their relative properties must satisfy several conditions for a transition to occur between them. These conditions are formulated in the selection rules.

Parity (odd versus even) has to change for an electric dipole transition according to Laporte's rule, and many transitions in molecules or complexes with a center of symmetry are Laporte-forbidden; however, symmetry may be broken, for example, through vibration. Moreover, magnetic dipole transitions (induced by the magnetic component of the incident radiation) are possible between states of equal parity whereas they are forbidden between states of different parity. However, magnetic dipole transitions are, in general, orders of magnitude less intense than electric dipole transitions [31].

A second rule is that the total spin quantum number S (and hence the multiplicity $2S + 1$) may not change.

Forbidden transitions may still be observed but will have small absorption coefficients. Absorption coefficients for spin- and Laporte-forbidden transitions are around 10^{-3}–$1\,\mathrm{l\,mol^{-1}\,cm^{-1}}$, for spin-allowed and Laporte-forbidden 1–$10^{3}\,\mathrm{l\,mol^{-1}\,cm^{-1}}$, and for fully allowed transitions 10^{2}–$10^{6}\,\mathrm{l\,mol^{-1}\,cm^{-1}}$ [39].

3.2.3.2 Individual Molecules

The electronic transitions between molecular orbitals in organic and inorganic entities are described in chemistry and spectroscopy textbooks [32–35]. Various notations are in use to describe the electronic states and transitions, including those of Kasha, Platt, and Mulliken, together with enumerative and group theory notations. Bands may also be classified according to Clar (α, β, p bands) or Burawoy (K, B, E, R bands).

Transitions from occupied bonding (in the nomenclature of Kasha: σ, π) orbitals and non-bonding (n) orbitals to unoccupied (π^* and σ^*) orbitals can be excited by incident radiation. Various nomenclatures are in use for these transitions, with classifications according to singlet and triplet states, symmetry, ground and excited states, and so on.

Molecules with closed-shell (noble gas) configurations can be classified according to the types of molecular orbitals and their population with electrons, as detailed in

the following. Molecules with only σ bonds, without any π bonds or free electron pairs, mostly do not show absorptions in the visible range because an excitation $\sigma \rightarrow \sigma^*$ typically requires energies corresponding to wavelengths of less than 200 nm. Molecules with conjugated double bonds will have $\pi \rightarrow \pi^*$ transitions that fall into the UV–vis range. In general, the HOMO–LUMO transitions of more extended, that is, more highly conjugated, π systems are lower in energy than those of smaller systems. Molecules with single bonds and free electron pairs exhibit color only when heavy elements are involved. Molecules containing functional groups with double bonds of nonmetals such as carbonyl, nitroso, or azo groups are characterized through absorptions in the UV–vis range. Molecules and molecular ions with incomplete valence shells frequently show absorptions in the UV–vis range.

Reference works provide lists of band positions for a large number of molecules [36, 37]. Band positions can also be estimated by finding the positions for the chromophore, that is, the part of the molecule responsible for the absorption bands. Then, increment rules can be applied or values can be gleaned from tables which specify the band shifts that are induced by one or more substituents on that chromophore.

High absorption coefficients make UV–vis spectroscopy orders of magnitude more sensitive than, for example, IR and Raman spectroscopy (Table 3.2). UV–vis spectroscopy is extremely sensitive towards unsaturated compounds and an excellent tool in catalysis research to detect coke precursors and coke on surfaces.

The absorption coefficients increase with increasing size of the π system; for example, the lowest energy transition in all-*trans* polyenes increases by a factor of six from a molecule with a single double bond to a molecule with six conjugated double bonds. Absorption coefficients of organic molecules vary by several orders of magnitude; they are typically reported together with the band position. As a result of the large variations, observed intensities can be deceiving with respect to the concentrations of the species present.

Selection rules can be softened through various phenomena; for example, symmetry can be lowered through substituents on the π-system. More importantly, symmetry can be altered through adsorption, and the intensity distribution can differ significantly from that observed for the free molecule. In Figure 3.3 [38], the absorption spectrum of benzene in the liquid phase is compared with the spectrum of benzene adsorbed on a zeolite. The β band is observed at 189 nm with the p band as a shoulder at 200–220 nm, and the α band is hardly discernible. After adsorption, the p band is prominent with a maximum at 207 nm, and the α band with a maximum at

Table 3.2 Ranges of molar absorption coefficients for various processes [2].

Excitation process	Molar absorption coefficient ($mol\,l^{-1}\,cm^{-1}$)
Electronic absorption (atoms)	3×10^8
Electronic absorption (molecules)	3×10^4
Infrared absorption	3×10^1
Raman scattering	3×10^{-9}

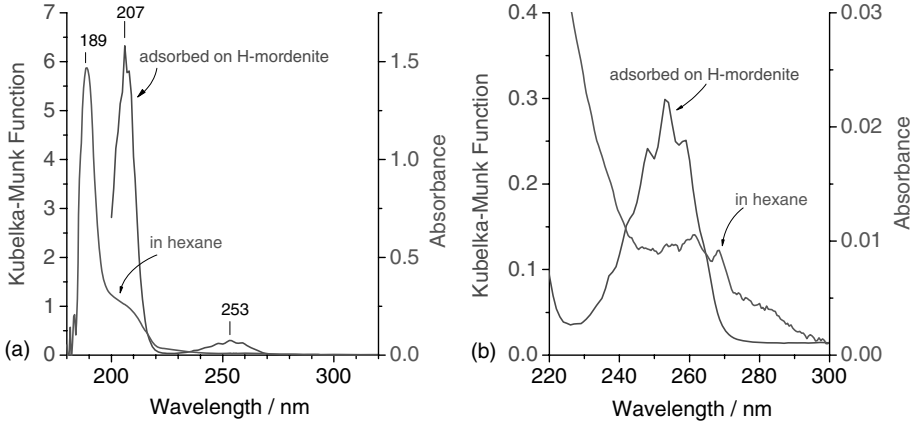


Figure 3.3 UV–vis spectra of benzene dissolved in *n*-hexane (right axes) and adsorbed on H-mordenite (left axes) [38]. (a) Full spectrum; (b) vibrational fine structure of the α band.

253 nm is clearly visible. Band shifts observed upon adsorption can be relatively small, unless secondary reactions occur, such as protonation or oligomerization.

Electronic absorption bands can have a vibrational and a rotational fine structure, which is most pronounced in vapor-phase spectra. In the liquid or solid state, motion can be hindered and the fine structure may be partially subdued or not discernible at all. The band at 253 nm in Figure 3.3 exhibits a weak fine structure. In general, vibrational fine structures sharpen in nonpolar solvents and at low temperature.

Computational software packages with the ability for time-dependent DFT calculations can be used to simulate UV–vis spectra.

3.2.3.3 **Composite Species: Metal Complexes**

Various electronic transitions of free atoms and ions can be excited by UV–vis radiation. These observable transitions include excitations between orbitals of different types but also between nondegenerate states of orbitals of the same type, particularly between various states of d or f orbitals (so-called d–d or f–f transitions). In multielectron systems, these orbitals are nondegenerate because of coupling of the electrons, as described through Russell–Saunders or spin–orbit coupling.

The electric field created by the surrounding ions in a crystal or by the ligands in a metal complex effects a much larger splitting of the orbitals into different levels (than the coupling does). Such d–d or f–f electronic transitions are of high diagnostic value for the oxidation state of the central ion, symmetry of the surroundings, and nature of the neighboring ions or ligands.

The principles of the energetic splitting of the orbitals through the electric field of the surrounding ions or molecular ligands can be found in many inorganic chemistry textbooks or books dedicated to spectroscopy or metal complexes [32, 39]. Several theories were developed, in part in parallel, to describe metal ions in complexes and crystals. Pauling's valence bond theory was used for a while to describe coordination compounds, but has been superseded by other approaches. In 1929, Bethe [40]

formulated the crystal field theory. The surrounding ions or ligands are considered as point charges and undergo electrostatic interactions with the central metal cation. In 1935, Van Vleck [41] combined the crystal field theory with the molecular orbital theory to the ligand field theory, which allows for a partially covalent character of the bonding between the ligands and the central metal cation. The main elements of the ligand field theory will be outlined as far as they are useful for a quick spectral interpretation and for reading research articles; for more detail, the reader is referred to the relevant literature.

In any nonspherical ligand field, d (and f) orbitals will split into multiple levels. If they are already split as a result of the presence of multiple electrons, the situation can become very complex and the sequence of levels will depend on the field strength. The field is considered weak if the field splitting is small in comparison with the original splitting into multiple terms, and strong if the field splitting is large in comparison with the term splitting. In a weak field, the splitting is energy neutral, that is, the sum of the negative and positive deviations from the original level(s) is zero.

In octahedral, tetrahedral, and cubic environments, the five d orbitals of a d^1 system split into two groups separated by an energy splitting designated Δ_{oct}, Δ_{tet}, or Δ_{cub}. This difference is expressed in energy units, with $\Delta = 10Dq$. In the octahedral field, two d orbitals are elevated by $4Dq$ and three are lowered by $6Dq$; in the tetrahedral and the cubic field, three levels are elevated and two lowered (Figure 3.4). Considering equal central ions and ligands, the splitting in the octahedral field is significantly larger than that in the tetrahedral field and slightly larger than that in the cubic field, as the following relations show and Figure 3.4 illustrates:

$$Dq_{oct} = -(9/4)\,Dq_{tet} = -(9/8)\,Dq_{cub} \tag{3.12}$$

The value of Δ thus depends on the number of ligands and their geometry around the central ion.

In addition, the order of magnitude of the splitting depends on the oxidation state of the metal. In octahedral complexes, the splitting increases with the charge of metal ions in d^1 configuration; roughly, $10Dq = 10\,000\ cm^{-1}$ (1.24 eV) are found for many

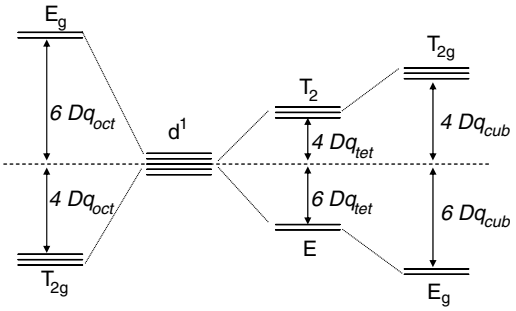


Figure 3.4 Energy splitting of d electron levels in the d^1 system in octahedral, tetrahedral, and cubic crystal or ligand field.

bivalent ions, 20 000 cm^{-1} (2.48 eV) for trivalent metal ions, and, for example 32 500 cm^{-1} for ReF_6. Another factor is the nature of the metal ion. Within one group, Δ increases towards heavier elements (i.e., $\Delta_{5d\,elements} > \Delta_{4d} > \Delta_{3d}$).

However, the field strength depends on the nature of the ligand. The spectrochemical series orders the ligands according to the splitting that they inflict, with, for example, I^- being a weak ligand, water being an intermediate strength ligand, and CN^- and CO being strong ligands.

Fields of lower symmetry will generate more levels than fields of higher symmetry. The term and field splittings are often illustrated in diagrams, which can take various forms. A simple form is the so-called Orgel diagrams, which correlate the energy splitting of ground and excited levels of the same multiplicity with the field strength expressed in *Dq*. Only weak fields are considered. More complex are correlation diagrams, which include excited states of different multiplicity. Another useful form for spectra interpretation are Tanabe–Sugano diagrams [42], which include weak and strong fields. The energy of the levels and the energy of the field are normalized to the Racah parameter *B*, which describes the repulsion between electrons. Note that there are additional Racah parameters *A* and *C* [43].

The shape of an absorption band is influenced by the interaction of the absorption center with its surroundings. An ion embedded in a crystal will be coupled to a vibrating lattice, and electronic absorption bands are broadened by electron–phonon coupling. When including the vibrations in calculations, two simplifications are made in the so-called configurational coordinate model. The first is the adiabatic approximation introduced by Born and Oppenheimer, which, on the basis of their vastly different masses, considers the motion of the electrons relative to the motions of the nuclei as fast. Second, only a single vibrational mode is considered, typically the breathing mode. The shape of the band depends on the difference in electron–lattice coupling between the excited and ground states, typically characterized by the dimensionless Huang–Rhys parameter *S*, which increases with increasing difference. For small values of *S*, absorption bands are narrow and have a Pekarian shape [44], that is, an asymmetric shape with a tail towards higher energies. For large values of *S* ($\sim$20), bands are broad and the shape becomes Gaussian-like [45]. The band width increases with increasing temperature.

Electronic transitions can also occur in the ligands, and are referred to as ligand-centered (LC) transitions. Their energies can be derived through evaluating the changes of the atomic or molecular orbitals of the ligand upon formation of the complex compound.

Electronic transitions become also possible between the central ion and its neighbors and are referred to as ligand-to-metal charge transfer (LMCT) or metal-to-ligand charge transfer (MLCT) transitions. With respect to metal cations, which are often present in solid catalysts, it should be mentioned that LMCT bands shift to lower energies and become more intense as the oxidation state increases and electron transfer become more facile. Electrons can also be transferred to the next-nearest neighbor, typically another metal cation, in a so-called intervalence charge transfer (IVCT), which can occur between like ions or between unlike ions (referred to as homonuclear and heteronuclear IVCT). IVCT bands have been found to undergo a

shift towards lower energies with increasing temperature [46]. Charge transfer bands tend to be intense and broad.

3.2.4
Transitions in Extended Solid Structures

3.2.4.1 Bandgaps

Bulk solids are characterized by energy bands rather than discrete states. Population of these bands can be forbidden or allowed, and the allowed states can be fully or partially occupied with electrons. Metals, metalloids, semiconductors, and insulators are defined by the population of electrons in these bands and the size of the gap between allowed states. From the perspective of UV–vis spectroscopy, semiconductors are most interesting because excitation from occupied to unoccupied levels can be effected by UV–vis radiation.

These transitions produce a feature with the shape of an edge, that is, above a certain threshold continuous absorption is observed. Once the excitation energy suffices to lift electrons across the bandgap, defined by the highest level in the valence band and the lowest level of the conduction band, transitions of electrons from the various levels in one band to the levels in the other band become possible.

Bandgap transitions can be classified as direct and as indirect. If the lowest point (in energy) of the conduction band and the highest point of the valence band are located at the same position in reciprocal space (same wave vector $\boldsymbol{k}$; Figure 3.5a), then a direct transition requires the lowest energy (Figure 3.6a). If the lowest point of the conduction band and the highest point of the valence band are located far away from each other in k space, then the transition with the lowest energy is an indirect transition, which produces a phonon in addition to a free hole and a free electron. The energy of the absorbed photon is larger than that of the bandgap by the energy of

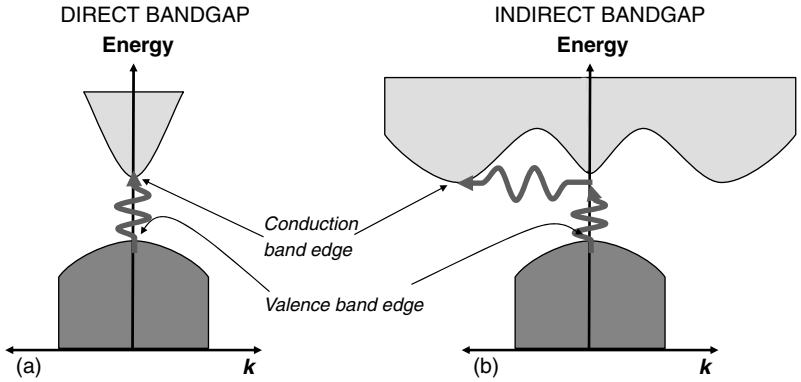


Figure 3.5 (a) Direct bandgap, highest point of valence band, and lowest point of the conduction band coincide at the same value of $\boldsymbol{k}$ (wave vector). (b) Indirect bandgap, highest point of valence band, and lowest point of the conduction band are offset, and electronic transitions occur only with participation of a phonon. After [47].

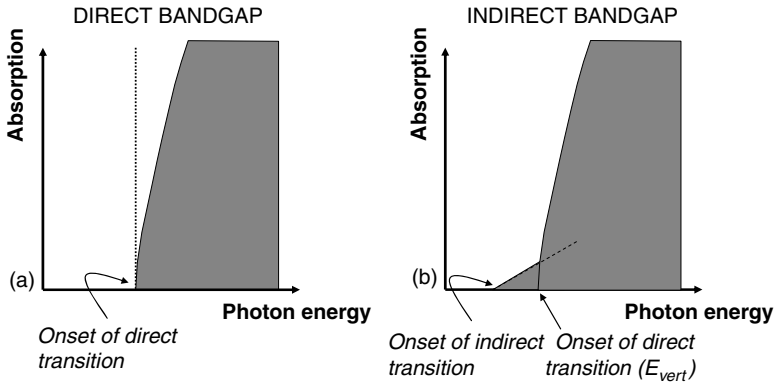


Figure 3.6 Optical absorption in pure insulators at 0 K. (a) Direct bandgap determines optical absorption; (b) indirect transition involves absorption or emission of a phonon. After [47].

the phonon. An indirect transition can also be effected by the absorption of an already existing phonon (at elevated temperatures) and a photon; and the photon energy is then smaller than the bandgap energy by the value of the phonon energy. At the energy that characterizes the smallest gap between valence and conduction band at the same $\boldsymbol{k}$, a so-called vertical transition without involvement of a phonon occurs (Figure 3.6b).

Additional transitions at energies lower than the threshold energy (of direct or indirect bandgap transitions) can be observed when excitons, that is, electron–hole pairs, are generated. In this case, the absorption energy is lower by the binding energy of the electron–hole pair. The binding energy characterizes the attraction between electron and hole and can vary between 1 meV and 1 eV [47]. Weakly bound excitons are called Mott–Wannier excitons (and occur mostly in semiconductors), whereas tightly bound excitons are called Frenkel excitons (and occur, for example, in alkali metal halides). Excitons can move freely through the crystal.

A number of methods of analysis are in use for the determination of the bandgap from optical absorption spectra. Sometimes, simply the absorbance or the Kubelka–Munk function may be plotted against the wavelength, and then various features in the spectrum can be used to determine the bandgap energy. These features include the inflection point of the typically S-shaped absorption edge [48], the energy at the start of the exponential increase of the absorption, and the intercept with the energy axis of an extrapolation of the linear section of the absorption spectrum [49]. More elaborate types of analysis distinguish between direct and indirect bandgaps. The following relation is valid for direct bandgaps [50]:

$$\alpha h\nu = A\left(h\nu - E_g\right)^{\frac{1}{2}} \tag{3.13}$$

where α is the absorption coefficient, A a constant, $h\nu$ the photon energy, and E_g the bandgap energy. Thus, plotting $(\alpha h\nu)^2$ as a function of $h\nu$ will deliver an x-axis intercept representing E_g.

The following relation is valid for indirect bandgaps [51, 52]:

$$\alpha h\nu = A\left(h\nu - E_g\right)^n \tag{3.14}$$

with $n = 2$ or 3, and then $(\alpha h\nu)^{1/n}$ is plotted against $h\nu$ to obtain E_g.

If the scattering coefficient is assumed to be constant across the range of interest, then α can be replaced by $F(\varrho)$, the Kubelka–Munk function.

It has been found that the bandgap of nanosized particles is shifted to higher energies in comparison with the gap of bulk particles of the same material [53]. In addition, the valence and conduction bands in nanoparticles may comprise discrete electronic levels [54]. Hence electronic spectroscopy is a valuable diagnostic tool for the properties of nanoparticles.

Solids can have a variety of defects, some of which are associated with electronic transitions and are thus detectable by UV–vis spectroscopy. Point defects such as anion vacancies can be void, or filled with one or two electrons. These centers produce bands in optical absorption spectra, through excitons that are created in their proximity or through excitation of electrons trapped in the vacancies. Details of these transitions, which are not always understood, can be found in the specialty literature [45]. When the absorption is in the visible range, the defects are called color centers [46]. One variety of such color centers are F centers, which have electrons trapped in anion vacancies and occur, for example, in alkali metal halides.

3.2.4.2 Metallic Colloids: Localized Surface Plasmon Resonance

Small metal particles exhibit the phenomenon of localized surface plasmon resonance. Plasmons are quanta of plasma vibrations, which are collective excitations of electrons. Incident electromagnetic radiation with a wavelength larger than the metal particle dimensions excites collective oscillations of the conduction electrons in the particle. The surface plasmon resonance effect contributes substantially to the optical properties of small metal particles and, in turn, optical spectroscopy can be used to analyze the properties of such particles and even of their surroundings [55, 56].

The first theory to describe the optical properties of small metal particles was developed by Mie [57] and was limited to spherical particles. The theory gives the absorption constant as a function of the wavelength, the particle concentration, the real and imaginary part of the dielectric constant of the particle, and the dielectric constant of the surrounding medium. Gans [58] extended the theory to ellipsoids, which exhibit two resonances. Various numerical methods have been developed to treat particles with arbitrary shape (which prevents analytical solution of the equations), such as the discrete dipole approximation (DDA); for an overview see [59].

The wavelength position of the surface plasmon resonance depends on the nature of the material. The surface plasmon resonance of the coinage metals occurs in the visible range; for example, it produces the well-known red color of gold colloids. Consequently, many papers in the field of surface plasmon resonance concern these elements [60]. Positions of the resonances have been calculated for 52 metallic elements, assuming a particle diameter of 10 nm [61].

The surface plasmon resonance gives indications about the nature of bimetallic particles. The behavior of alloys may be exemplified by silver and gold; a single

resonance and a linear relationship between its position and the Ag molar fraction was reported, ranging from 540 nm (pure Au) to 400 nm (pure Ag) [62]. The shift was ascribed to the gradual change in d band structure in the alloy particles [63]. Core–shell particles can be distinguished from alloy particles; a coating attenuates the resonance of the core metal, and the resonance of the shell metal becomes dominant with the formation of a full shell. Various optical constants can be extracted from spectra of such particles [63].

The influence of the size and shape on the resonance has been extensively investigated. In general, the resonance shifts to longer wavelengths with increasing particle diameter. The resonance position does not vary significantly for particles smaller than about 20 nm [61, 64]. With decreasing particle size, the resonance broadens [64]. Non-spherical shape results in splitting into two bands, an oscillation perpendicular and another parallel to the major axis (transverse and longitudinal resonance). The splitting can increase to several hundred nanometers with increasing aspect ratio [61]. Aggregation of spherical particles into strings has a similar effect to elongation of a particle; a second resonance band is detected at longer wavelengths [65]. With increasing temperature, the plasmon resonance broadens; this effect is more noticeable for larger than for smaller particles [64].

The surface plasmon resonance is sensitive to the surroundings of the metal particle; for example, a change in solvent can change the position of the plasmon resonance [56]. This sensitivity has led to the development of sensors, particularly biosensors [66].

3.2.5
Quantitative Analysis

Quantitative analysis can be conducted in various ways. In the investigation of catalysts, the route to determine the molar absorption coefficient of a species of interest is rarely pursued. Because the Kubelka–Munk function depends on two more quantities, the scattering coefficient would have to be determined to obtain a value for the absorption coefficient (see Section 3.2.1.2). If the scattering coefficient is not a function of composition, a calibration can be performed, with the obtained apparent absorption coefficient deviating from the true coefficient by an unknown factor.

A standard procedure is to prepare a series of calibration samples with varying concentrations of the species of interest, record their spectra, and then establish a calibration curve. For example, $VOSO_4$ and NH_4VO_3 were used to prepare supported catalysts containing known amounts of V^{4+} or V^{5+} [67]. The calibration curves obtained may not be universally valid; the absorption coefficient of the V^{4+} species depended strongly on the nature of support (zeolites USY, Al_2O_3, SiO_2), whereas that of V^{5+} did not. The validity of the V^{4+} measurement was confirmed by comparison with electron paramagnetic resonance measurements. A linear relationship between the Kubelka–Munk function (at wavelengths of the respective transitions) and the content was observed only up to vanadium loadings of 0.2 wt% (V^{4+}) and 0.4 wt% (V^{5+}). It can be speculated that the linearity is limited because the relative fractions of isolated V species and oligomers, most likely characterized by different absorption coefficients, change with the loading.

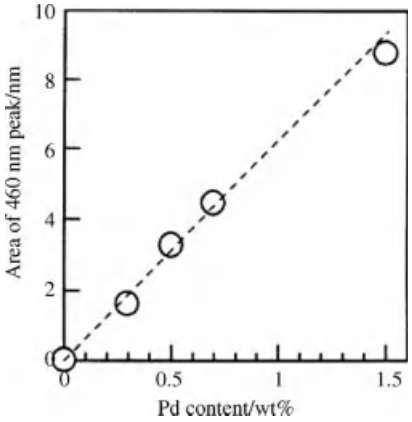


Figure 3.7 Integrated intensity of band around (460–480 nm) of a d–d transition band assigned to $Pd(O_z)_n^{2+}$ species in palladium-doped zeolite H-mordenite as a function of palladium content. Reprinted with permission from [68].

Figure 3.7 shows an excellent linear relation between the intensity of a particular palladium transition and the palladium concentration; the data were obtained for a series of zeolite catalysts containing small amounts of well-dispersed palladium [68]. Such linearity can only be obtained if the scattering coefficient is not a function of composition, which is often the case when the scattering properties are dominated by the morphology of a majority compound, such as a high surface area support. However, particularly in catalysts, the nature of an analyte often changes with the concentration; molecularly dispersed species may be present at low loading and oligomers or even nanoparticles at higher concentrations. Such species will exhibit different absorption properties. Extrapolation of calibration curves is therefore not recommended.

A lower level of quantitative analysis is the extraction of trends in series of spectra representing a family of samples or an evolution with time. UV–vis spectra can be analyzed by the usual means. Overlapping bands can be fitted to identify contributions of individual species. Principal component analysis can be applied to determine the number of changing species in a series of spectra. Examples of application of such methods to spectra of catalysts can be found in the literature [69].

3.3 Experimental Considerations

3.3.1 Instrumentation: Spectrometers, Sources, and Detectors

3.3.1.1 Overview of Essential Instrument Components

The electromagnetic radiation in the wavelength range of 100–3000 nm is classified as follows: the UV range, including the vacuum UV, extends from 100 to 400 nm [70],

the visible range from 400 to 760 nm [71], and the NIR range from about 760 to 3000 nm, thus combining the IR-A and the IR-B bands, which are specified as 760–1400 nm and 1.4–3 μm [72]. Spectrometers are optimized for a particular wavelength range, with the limits not coinciding with these classifications.

UV–vis spectrometers cover a typical wavelength range of 175–900 nm. The NIR range may be combined with the UV–vis range in UV–vis–NIR spectrometers; alternatively, it is, to a certain extent, also accessible with many Fourier transform (FT) IR spectrometers, somewhat dependent on the choice of optical elements and detectors. NIR analyzers or spectrometers are used for a variety of industrial applications and are also available for specialty applications such as feed and forage analysis. Depending on the range that is to be covered, several sources, gratings, and detectors may have to be combined in one instrument. Wavelengths below 185 nm require a spectrometer purge with N_2 because O_2 from air absorbs in this range.

Sources are typically gas discharge lamps; deuterium lamps for the UV range (emission maximum at 220 nm) and tungsten–halogen lamps for the vis–NIR range, with some overlap between these lamps in the wavelength range of 300–350 nm. These lamps have a finite lifetime and replacement should be considered when estimating operating costs. A recent development is pulsed xenon lamps.

Classical UV–vis spectrometers are wavelength dispersive, that is, a grating or prism monochromator is used to disperse the incident light by diffraction or refraction, respectively. To cover the desired wavelength range, the spectrometer may switch between several (sets of) gratings. Scanning spectrometers, with the monochromator placed between source and sample, have moving gratings and analyze the wavelengths consecutively. Scanning spectrometers may have a single- or double-beam configuration, and sample and reference may be measured sequentially or in parallel. Spectrometers with fixed monochromators, placed after the sample, disperse the radiation onto array detectors, thus allowing simultaneous analysis at various wavelengths.

The detector of choice in the UV–vis range is a photomultiplier tube (PMT); in these highly sensitive devices, the incident photons release electrons (external photo effect) and are multiplied through a set of dynodes before being collected at the anode. Most common for the NIR range are photoconductive detectors such as PbS detectors; the incident IR radiation changes the electrical resistance as electrons from the valence band are elevated into the conduction band. These detectors can be Peltier-cooled to extend their range towards lower energies; spectrometers with such cooled detectors typically are specified to a wavelength of 3300 nm. Recently, InGaAs detectors have been introduced to obtain high sensitivity also in the NIR range, to about 1800 nm [73], or, when cooled, also to 2500 nm [74]. This technology is currently only available for high-end spectrometers. These detectors are not wavelength-specific, and therefore fluorescence can contribute to the spectral intensity at the wavelength that excites the transition leading to fluorescence.

Array detectors are also available, allowing parallel analysis at multiple wavelengths and thus much higher recording speeds than can be achieved by scanning spectrometers. Various technologies are in use, including charge-coupled devices (CCD), active pixel sensors (also called CMOS sensors), and diode arrays, resulting in

variations in, for example, wavelength range, signal-to-noise ratio, sensitivity, and speed.

3.3.1.2 Instrument Selection Criteria for Measurements of Solids

When selecting an instrument, a variety of performance parameters need to be considered:

Wavelength range: The wavelength range of interest needs to be determined. The variations in range between UV–vis spectrometers are relatively small. If the entire NIR range is to be included, the choice of instruments will be limited and the cost will be higher.

Diffuse reflection mode: The spectrometer should allow for the installation of an optical accessory for diffuse reflection measurements. Such accessories can be integrating spheres, mirror optics, or the connection of optical fibers; they may be available through the spectrometer company or specialized manufacturers, most of which can adapt their equipment to a variety of spectrometers.

Photometric range: Polycrystalline solids are predominantly measured in reflection mode, with little radiation reaching the detector. Hence not to be underestimated is the photometric range, which gives the maximum value of "extinction" (attenuance) that can be measured with the instrument, typically somewhere between 4 and 8. When investigating strongly absorbing samples in diffuse reflection geometry, that is, when working with low light intensities, a large range is advisable.

Time resolution: When monitoring dynamic changes of a solid, the time resolution can become important. Scanning spectrometers need several minutes to record a spectrum; spectrometers with array detectors need less than 10 ms [75]. However, scanning spectrometers can also be operated in single-wavelength mode and then provide a measurement at a particular wavelength with high time resolution.

There are a number of other instrument specifications, such as wavelength accuracy, spectral resolution, stray light, stability, and so on. Some of them are not crucial, for examples, the bands of solids and adsorbates are typically broad, and resolution is rarely an issue. However, the stability of the spectrometer performance may become important when it is desired to analyze the state of a solid over many hours, perhaps in changing conditions.

3.3.2 Optical Configuration and Cells for Controlled Environments

There are multiple optical configurations for the measurement of electronic absorption spectra. These configurations are characterized by collecting either transmitted or reflected light. Reflection mode requires optical accessories such as integrating spheres, mirror optics, or suitable fiber probe heads. Any type of cell that allows control of specimen temperature and the gas or liquid surrounding a solid sample has to be adapted to the optical accessory, which requires specific designs when using

integrating spheres or mirror optics, whereas fiber optics give more flexibility with the cell design. Cells must have windows that are transparent to UV–vis–NIR radiation; typically, high-purity silica (made by flame hydrolysis) is used, such as Suprasil.

3.3.2.1 Transmission Mode

Many standard analytical procedures rely on photometry in the UV–vis or NIR range, confirming the ease of use, the high sensitivity, and the possibility for quantification with high accuracy and precision. Nonscattering media such as molecularly disperse solutions are measured well in transmission geometry.

Scattering media such as colloidal dispersions or powders usually require a favorable measurement geometry and the preparation of a thin specimen. Scattering leads to a wide angular distribution of the transmitted light, and it is advantageous to place the detector in close proximity to the specimen or to use collecting elements. In commercial spectrometers, the detector position is typically fixed. However, modern integrating spheres provide a sample position where the light enters the sphere. A simple cuvette may be placed in this position; there are no reports of cells that would allow control of temperature or gas atmosphere.

Strongly scattering media will not transmit any radiation unless the thickness of the specimen is minimized. Liquid scattering media can be placed in cuvettes with a short pathlength. Solids in powder form are pressed into so-called self-supporting wafers characterized by a small area weight in the range of 10–20 $mg\,cm^{-2}$, depending on the density of the material.

3.3.2.2 Cells for Use in Transmission Mode

Cells for use in transmission geometry are characterized by parallel optical quartz windows, with the sample sandwiched in between. The sample cells are often made from glass or quartz, and the windows can be integrated without having to use seals, which would normally restrict the temperature range. The cells are connected to a vacuum and gas dosing apparatus, as shown for example in the design published by Leftin [76], who used a second specimen in a second cell as a reference in the second beam. Such cells are heated by placing them in a furnace, and spectra are taken at room temperature after the treatment [77], sometimes after detaching the cell from the dosing apparatus and sealing it [78]. Melsheimer and Ziegler [79] developed a "scattered transmission accessory" and placed the detector (a photomultiplier) only 28 mm behind the sample. A compact quartz cell could be heated to a temperature of 573 K by means of a wire wrapped around its body.

Whereas this type of design is suitable for treatments of solids in vacuum or gas atmospheres and also for equilibrium chemisorption measurements, it has limitations when monitoring dynamic processes such as catalytic reactions. The temperatures that can be reached during measurement are not very high with the reported designs. Many cells are not equipped for flow-through operation, and those that have two ports are characterized by a high volume (e.g., 45 cm^3 in [79]). The small amount of sample may lead to immeasurably low conversions in the catalytic reaction [79]. Further, the reported designs are not commercially available. Heatable transmission

cells are available for IR spectroscopy, and if the windows can be exchanged they could be adapted for UV–vis spectroscopy. One issue is that such cells are designed for the circular beams of FTIR spectrometers and not for the slit-shaped beams of UV–vis spectrometers. Moreover, transmission UV–vis spectroscopy has almost exclusively been applied to zeolites and silica–aluminas [10, 80], that is, with any unknown sample sufficient light transmittance needs to be ensured in a preliminary experiment before investing in a cell for transmission experiments.

3.3.2.3 Diffuse Reflection Mode: Integrating Spheres

Integrating spheres, also called Ulbricht or photometer spheres, are the classical accessory of reflection spectroscopy. The sample is placed such that it becomes virtually part of the sphere (Figure 3.8 [81]), and the radiation reflected by the specimen is collected over almost the entire solid angle. Radiation is diffusely reflected multiple times inside the sphere, which is coated with high-reflectance materials, for example, MgO, $BaSO_4$, or polymers such as Spectralon®. At wavelengths above 800 nm, gold coatings may be used. Spheres may have to be recoated occasionally, which can be costly, depending on the material.

Spheres have ports to admit the incident beam, place the sample, and integrate one or more detectors. Although spheres collect almost all the light, the measurement area (labeled f_m in Figure 3.8) that determines the flux reaching the detector is actually small (for the relevant equations, see [22]). The relative area imaged onto the detector becomes smaller with increasing sphere size, whereas the so-called sphere error becomes smaller because the relative area of the ports becomes smaller. Spheres become more expensive with increasing size.

Spheres can be equipped with additional devices. A baffle (screen) can prevent direct reflection of light from the sample onto the measurement area, which simplifies the equations that need to be applied to describe reflection inside the sphere. To avoid that regularly reflected light reaches the detector, measurements may be performed either at an incident angle of 0° so that regularly reflected light will mostly be reflected towards the input port. Alternatively, as shown in Figure 3.8, an 8° angle and a gloss trap may be used. A gloss trap is a section that can be opened so that

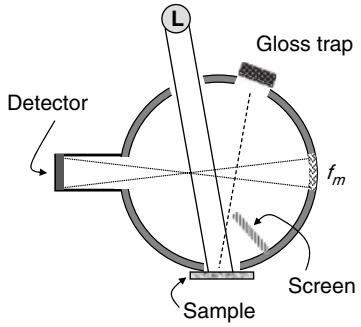


Figure 3.8 Schematic drawing (after [81]) of an integrating sphere with incident light from source (L), screen, and gloss trap. The area imaged on to the detector, f_m, is relatively small.

regularly reflected light escapes from the sphere and will not reach the detector, or closed so that the diffusely and regularly reflected light are collected. With the aid of the gloss trap, the contribution of regularly reflected light can be determined.

In general, integrating spheres are used to measure materials properties with high accuracy and precision.

3.3.2.4 Cells for Use with Integrating Spheres

Because the sample has to become part of the sphere and no interfering parts should extend into the sphere, the sample can only be located at the window of a cell, or additional optical elements must be introduced that guide the light to a reactor with window.

Numerous cell designs for placement of the sample at the sphere have been published ([12, 13, 15, 16, 20, 82]) but not commercialized. The cells are characterized by a window fitting the size of the port in the sphere. Such cells require gram amounts of sample if the entire port opening of the sphere is to be covered with a spectroscopically infinitely (i.e., several millimeters) thick layer of pure material. In principle, the window can be integrated into any type of container, and samples can then be treated under vacuum or in inert or reactive gases, in either flow or batch mode. A reference measurement can be made in sequence using the same reactor cell and window, or in parallel by placing a reference materials behind an equivalent window in the reference position. An alternative is to place the reference material and the sample next to each other, by using the same port of the sphere and thus achieving exact position equivalency [83].

Measurements in various gas atmospheres are easily conducted, in either static atmosphere or flow. The pathlength in the gas phase is limited to the intrastitial space between the particles (and the window), and gas-phase contributions are typically negligible.

Measurement of samples after a heat treatment (through relocation of the cell or the sample within the apparatus) is feasible, whereas it is a problem to record spectra at high temperature because the window is directed towards the "cold" inner part of the sphere. Moreover, the sphere should not be heated to preserve its shape and coating. To conduct measurements at low temperatures, condensation on the window needs to be prevented. A solution to these problems is the use of double windows separated by vacuum, which improves thermal insulation [14, 84]. These types of cell, however, do not permit measurement at elevated temperature at all [84] or are heated by means of a fluid with a maximum possible temperature of 425 K [14]. Measurements of catalytic reactions at high temperatures using an integrating sphere are therefore a challenge and problems with temperature gradients have to be expected. As a consequence of the large sample amount, the sensitivity of conventional analytical methods usually suffices to measure catalytic conversion.

A possible design of a heatable fixed-bed flow-through reactor is shown in Figure 3.9 [85]. The heated zone is at a 12 mm distance from the sphere, and this gap is bridged by a tubular ceramic spacer with high reflection power. The reference port is equipped with an equivalent ceramic piece. The powder bed is held in place next to an optical window by a frit, and the gas enters through an "inner tube" and

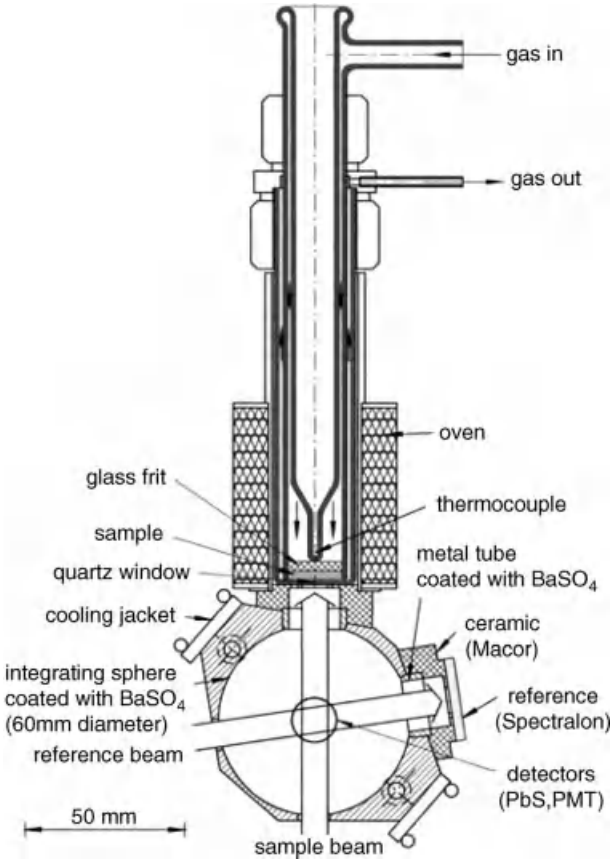


Figure 3.9 Schematic drawing of a heatable flow-through reactor for use with integrating sphere. View from the top. Reprinted with permission from [85].

exits through an "outer tube." Cooling blocks purged with room temperature water prevent overheating of the sphere. This reactor has reportedly been used at temperatures up to 623 K [85]. Difficulties were encountered with keeping the sandwiched powder bed in position between the window and the vertically oriented frit, with a non-ideal flow pattern, and a temperature gradient in the bed [22]. A further development of this arrangement involved a light conduit that allowed placing the cell with the bed in the center of an oven [86]. The temperature range was extended to 723 K, and the bed could be supported on a horizontally oriented frit. However, the inequality of sample and reference beam and the presence of stray light required that various reference measurements were taken and an elaborate background correction was conducted.

Solids in liquid media can also be analyzed by diffuse reflection–UV–vis spectroscopy using an integrating sphere. This experiment can be realized by placing a cell with a quartz window as shown in Figure 3.10 [87] close to the opening at the

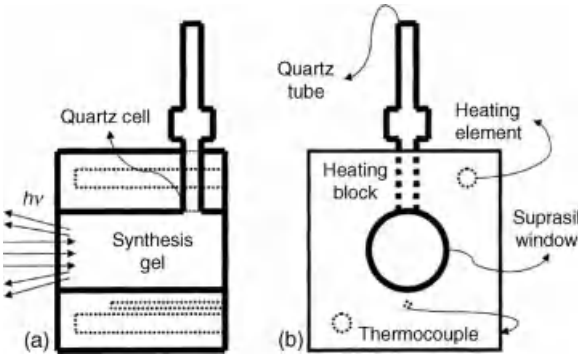


Figure 3.10 Quartz cell used in combination with an integrating sphere to analyze solid formation in the liquid phase by UV–vis spectroscopy. Wall thickness 0.5 cm, Suprasil window. (a) Side view on window; (b) window in the plane of the paper. Reprinted with permission from [87].

sample position of an integrating sphere. Pressure in this cell is limited by the stability of the quartz; data recorded at temperatures up to 448 K have been published [88].

3.3.2.5 **Diffuse Reflection Mode: Mirror Optics**

Diffuse reflectance measurements in the UV–vis–NIR region can be conducted with the help of optical accessories, specifically mirror optics. This type of accessory has already been in use for a while in the MIR range, to conduct diffuse reflectance infrared spectroscopy (DRIFTS). In the MIR range, DRIFTS is the prevailing method for the investigation of solids in comparison with integrating spheres and fiber-optic probes; lately, the attenuated total reflection technique has become more widely used. In the UV–vis range, the application determines which technique is preferable.

Commercially available diffuse reflectance accessories are characterized by a series of flat and curved mirrors, which redirect and focus the incident beam onto the sample and then collect the diffusely reflected light over a substantial solid angle before directing it towards the detector, as indicated in Figure 3.11. A total of seven reflections (including the sample) is used to have the beam exiting the accessory continue exactly the trajectory of the incident beam. This beam path allows the placement of the accessory in any sample compartment of sufficient size, and most manufacturers offer baseplates to fit their accessories into various spectrometers. If the relative positions of source and detector are flexible, fewer mirrors are necessary, which is desirable because of losses at each mirror. Such designs can be found in the open literature [89] but are typically not commercially available.

Mirror optics for diffuse reflectance measurements are designed such that contributions from regularly reflected light are minimized while contributions from diffusely reflected are maximized. The key to this selection is the so-called off-axis arrangement of the two curved mirrors, which focus the beam and collect the diffusely reflected light. Because regularly reflected light is maximal in the forward direction, rotating the mirrors can reduce these contributions. The mirrors of the accessory need to be properly aligned for optimum performance. The measured

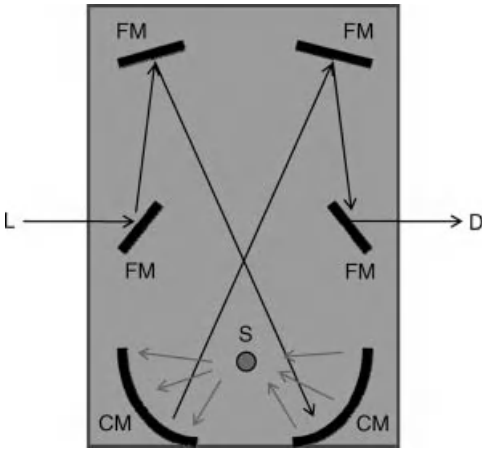


Figure 3.11 Sketch of beam path in diffuse reflectance accessory, top view. L, light source; D, detector; S, sample; FM, flat mirror (4 in total); CM, curved mirror (2).

intensity is very sensitive to the alignment, and the accuracy of the reflectance value is not ensured when in consecutive reference and sample measurements the specimen position cannot be exactly reproduced. A solution to this problem is the use of an integrating sphere to collect the radiation exiting the mirror optical accessory with less position sensitivity.

Mirror optics can be conveniently used with many spectrometers. However, whereas in the MIR range the throughput is largely independent of the wavelength of the incident radiation, severe variations may be observed in the UV–vis–NIR range. The throughput of such an accessory can be easily measured by placing a (tilted) mirror in the sampling position. Published data regarding one commercial accessory [22] show excellent throughput of about 70% at wavelengths longer than 1350 nm, a minimum of 30% around 825 nm, a reasonable value of 50% at 450 nm, and a decline towards the UV region. These variations can translate to variations in data quality such as increased noise in regions of low throughput.

3.3.2.6 **Cells for Use with Mirror Optics Attachment**

Reaction chambers that fit into mirror optics accessories (typically by replacing the standard sample holder) are commercially available. The example shown in Figure 3.12 is made from steel and has optical quartz windows sealed by Teflon® and Viton® rings. The sample stage in the center of the cell is thermally insulated from the outer chamber and heated from the bottom by a cartridge heater. A coolable version includes a liquid nitrogen Dewar.

A wide temperature range can be covered with the same cell, from 120 to 873 K [90]. Cells designed for high-temperature operation are specified for temperatures as high as 1183 K [91]. The extreme temperatures can only be reached when the chamber is evacuated. Some literature reports suggest that the sample temperature must not correspond to the nominal (display) temperature [92, 93]. Attempts to calibrate the

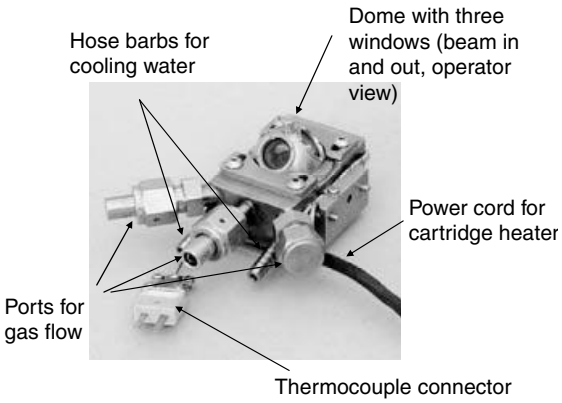


Figure 3.12 Photograph of heatable reaction chamber for diffuse reflectance spectroscopy using mirror optics. Design by Harrick Scientific Products [91].

temperature have been made, which were further complicated by the influence of gas type and flow rate. Recent versions of such reaction chambers are fitted with a second thermocouple that penetrates the sample cup on the side and extends into the bed. Alternatively, specimens were prepared for improved heat transfer [94], or the chamber was modified to minimize heat transfer [92].

The pressure range is high vacuum (133 μPa) to 133 kPa for the standard version, or up to 3.44 MPa (500 psi) with a specially designed high-pressure dome. These cells have various ports, and evacuation or flow-through is possible. One port is underneath the sample well, and by resting the sample on a wire mesh a fixed bed with flow-through operation can be realized. Attempts have been made to suppress gas bypassing by placing the sample on a quartz frit [95]. Pressure fluctuations associated with switching gas flows have been found to upset the powder bed. Gas-phase contributions can be observed in the spectra because the beam path through the gas phase is several centimeters, but the magnitude depends on concentrations and absorption coefficients. The volume of a chamber from Harrick Scientific Products has been found to be roughly 16 ml. The sample volume is typically fixed and one must operate with 100–150 mg depending on the packing density of the material (if in powder form). Catalytic conversions are measurable, for example, by online gas chromatography.

3.3.2.7 **Diffuse Reflection Mode: Fiber-Optic Probes**

Fiber-optic probes guide the radiation by total internal reflection, which becomes possible when the fiber is surrounded by a medium with lower refractive index, and the angle of incidence (relative to the surface normal) is larger than a critical value. As a result of the reflection at the phase boundary when radiation transfers from the optically less dense air into the fiber, there will be some losses at the fiber entrance.

Fibers are typically made from silica. Initially, the lack of fibers with sufficient throughput in the NIR range limited their application, but suitable fibers with low OH group concentrations are now available. To cover a wide spectral range, including UV, vis, and NIR, two different fibers are usually necessary. Fibers can be coupled into

the beam path of a dispersive spectrometer via an adapter. Frequently, however, fibers are sold in combination with spectrometers equipped with array detectors [96–98]. These instruments have excellent time resolution, but the spectral resolution is inferior to that of good scanning spectrometers.

The analyzed spot depends on the fiber diameter and can be as small as 50–100 μm [99]. If the probe and the specimen can be moved with respect to each other, the spot size is an advantage because information can be collected from multiple locations on the sample and spectra are obtained with some spatial resolution, which may be useful to characterize various zones in a reactor or a species distribution in a catalyst pellet. However, if the probe needs to be integrated into a reactor and the position is fixed, then this position needs to be chosen carefully to ensure a representative measurement [100]. The resolution can be improved to the order of several micrometers through combination of the fiber-optic probe with an optical microscope [101].

Typically, a number of fibers are combined in a bundle, with several illumination fibers surrounding a read fiber, or vice versa. Contributions from regular (specular) reflection can be reduced if, at the probe head, the faces of the illumination fibers and the read fiber are not parallel; for example, the illumination fibers may be placed at a 30° angle relative to the read fiber [102]. The fiber bundle can be several meters long and the probe head can be remote from the spectrometer. This flexibility of the beam path is one of the main advantages of fiber-optic probes.

Standard reflectance probe heads are suitable for temperatures of several hundred degrees Celsius and pressures of several tens of bars. Probe heads are available that can withstand temperatures of 1023–1073 K [75, 103] or, for example, a pressure of 50 bar (at 473 K) [103].

3.3.2.8 Cells for Use with Fiber-Optic Probes

Integrating spheres and mirror optics are in predetermined positions in the spectrometer, and any specimen has to be placed in the sample position as defined by the beam path. This restriction limits the size and shape of any reactor cell that is used in combination with the accessory. In contrast, fiber optics are flexible and of sufficient length that the probe can be brought to the sample or reactor. Measurements can be taken through a transparent window, or the probe can be immersed in gas atmospheres and liquids. However, fibers have been reported to degrade over months in a high-temperature environment [104], and the formation of coke [75] or other deposits on the probe head can be a problem.

Because the probes are relatively small, several probes may be used to perform a spatially resolved analysis. Figure 3.13 shows a configuration assembled to obtain an axial profile of the catalyst state in a fixed-bed flow reactor [105].

Reflection probes can also be applied for measurements in turbid media, with the probe immersed or placed outside a suitable window in the container. Suspended particles serve as the reflecting medium, and spectra may contain contributions from dissolved species in addition to the solid. In this way, the crystallization of microporous materials from precursor gels can be monitored [106].

A slightly different application is the analysis of flat surfaces in a liquid medium, as shown in Figure 3.14. Here, a fiber-optic probe is integrated into a cell for *in situ*

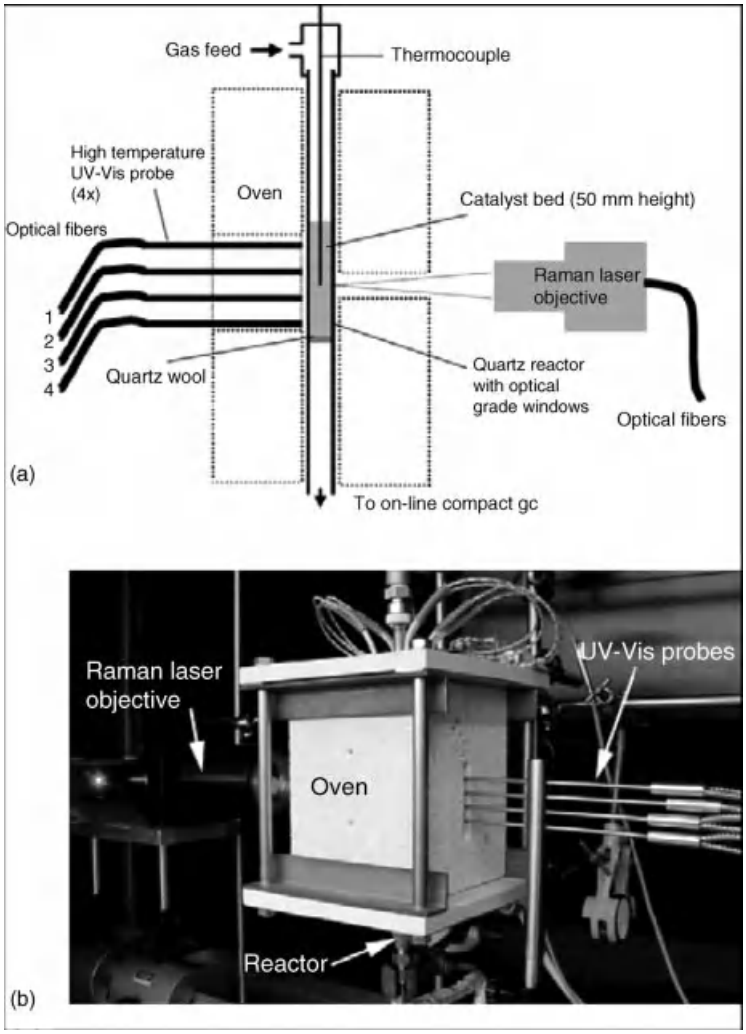


Figure 3.13 Integration of four fiber-optic probes into an oven with catalytic reactor. Optical quartz windows are integrated into the reactor. (a) Sketch; (b) photograph. Reprinted with permission from [105].

attenuated reflection IR spectroscopy [107] and is used to analyze the powder catalyst (a supported metal), which has been deposited as a thin layer on the attenuated total reflection (ATR) crystal [108].

3.3.2.9 **Combination of UV–vis–NIR with Other Techniques**

Combination of UV–vis spectroscopy with other techniques almost always relies on fiber-optics technology because the probes are small and easily integrated into a cell optimized for a different method. UV–vis spectroscopy has been combined with other *in situ* techniques, specifically with Raman spectroscopy [105, 109], X-ray

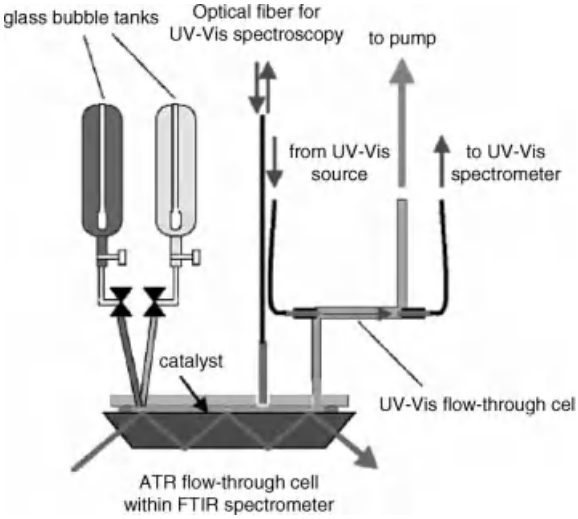


Figure 3.14 Integration of an optical fiber for diffuse reflection–UV–vis spectroscopy into an ATR cell. UV–vis spectroscopy is also used to analyze the effluent stream of the cell. Reprinted with permission from [107].

absorption spectroscopy [110, 111], Raman and X-ray absorption spectroscopy [112], electron paramagnetic resonance [113], electron paramagnetic resonance and Raman spectroscopy [114, 115], NMR spectroscopy [116, 117], transmission IR [118] or attenuated total reflection IR spectroscopy [107], attenuated total reflection IR spectroscopy and Raman spectroscopy [119], and cyclic voltammetry [120]. Chapter 23 provides details.

3.4 Formation and Alteration of Solids

3.4.1 Precursor Analysis

Transmission UV–vis spectroscopy is an excellent tool for investigating liquid precursor media for catalyst preparation such as solutions of metal complexes or metal sols. These data can be used to identify whether a desired complex or metal colloid has formed and whether the medium is homogeneous or contains a variety of species.

Complexes are typically in equilibrium with their metal ions and ligands; in some cases, from the same starting compounds, complexes of various compositions may form. An excellent example is platinum–tin complexes with various metal ratios, which can be employed as precursors for bimetallic reforming catalysts. Multinuclear complexes are formed from hexachloroplatinic acid and tin(II) chloride in hydrochloric acid [121], as illustrated in Figure 3.15. Spectrum (a) does not exhibit the

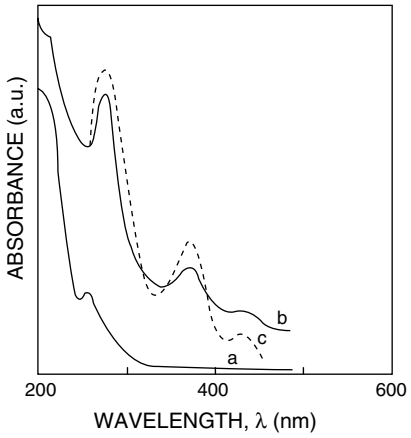


Figure 3.15 UV–vis spectra of solutions of H_2PtCl_6 and $SnC1_2$ in HCl with molar Sn:Pt ratios of (a) 1:l, (b) 1.6:1, and (c) 3:l. Reprinted with permission from [121].

bands characteristic of $[PtCl_2(SnCl_3)_2]^{2-}$, whereas spectra (b) and (c) feature three bands at 278, 376, and 445 nm, which evidence the presence of the complex. Spectra recorded after deposition of the complexes on alumina were reported [121]. UV–vis spectroscopy was also used to investigate the influence of the solvent on the stability of such platinum–tin complexes [122].

Metal colloids of the coinage metals exhibit the phenomenon of surface plasmon resonance (see Section 3.2.4.2), which can be used to extract a number of particle properties. Bianchi *et al.* [123], for example, used UV–vis spectroscopy to follow the reduction of tetrachloroaurate to give a gold sol, characterized by a surface plasmon resonance at 510 nm (Figure 3.16). To the sol, tetrachloropalladate was added and then a reducing agent was added to generate the bimetallic sol. These sols were deposited on activated carbon.

The analysis of precursor solutions is valuable for verifying the formation of a desired species. Moreover, after deposition of the precursor on a support, it is often possible to determine whether a species has remained intact or has undergone reaction with the support surface. In general, spectra of dissolved species may be collected as reference to identify surface species. There are some limitations, for example, if the support itself is strongly absorbing in the region of interest.

3.4.2
Solid Formation

Diffuse reflection–UV–vis spectroscopy can be used to detect the formation of a solid from a solution, for example, the formation of a catalyst precursor by crystallization or precipitation. The contribution of dissolved species, which are in the beam path to or from the solid, and a change in the turbidity as a result of nucleation and growth can interfere with the qualitative and quantitative analysis of spectral contributions

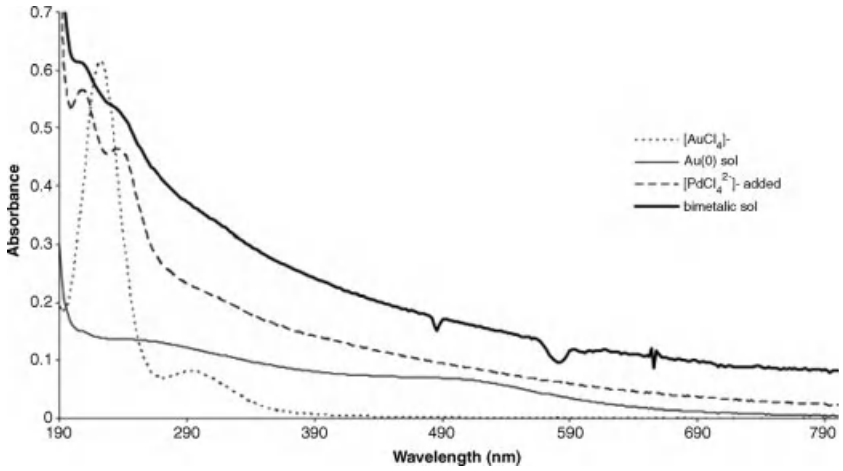


Figure 3.16 UV–vis spectra recorded during preparation of a bimetallic gold–platinum sol. Spectra represent $AuCl_4^-$ solution (dotted line), Au(0) sol (thin solid line), sol after addition of $PdCl_4^{2-}$ (dashed line), and after formation of the bimetallic sol (thick solid line). Reprinted with permission from [123].

from the solid particles. Only a few reports on the applications of UV–vis spectroscopy during synthesis of solids have been published.

Weckhuysen *et al.* [87] used this technique to follow the crystallization of CoAPO-5, an aluminophosphate molecular sieve of AFI framework type, from a synthesis gel during heating (Figure 3.17). The band at 521 nm is assigned to the $^4T_{1g}(F) \rightarrow {}^4T_{1g}(P)$ transition of the starting complex $[Co(H_2O)_6]^{2+}$ and the band at 470 nm to the $^4T_{1g}(F) \rightarrow {}^4A_{2g}(P)$ transition of tetragonally coordinated high-spin Co^{2+} species such as $[CoO_4(H_2O)_2]$, a presumed intermediate that is formed initially. The triplet of bands with maxima at 542, 584, and 625 nm is assigned to a high-spin pseudo-tetrahedral Co^{2+} species, as is encountered in the CoAPO-5 structure.

To obtain interpretable data, the formation of the solid should be accompanied by a change in coordination or valence of a metal cation, with the resulting species absorbing in the UV–vis regime and at a different position from any absorbers in solution. In principle, it should also be possible to observe the evolution of a band edge, if a semiconducting solid is formed.

3.4.3
Characterization of Solids

Depending on the nature of a solid, a variety of questions can be answered using UV–vis spectroscopy. Applications include verification of isomorphous substitution and ion exchange in zeolites, detection of contaminants from synthesis, analysis of defects, estimation of the dispersion of supported species, bandgap determination, and particle size and shape analysis from plasmon resonance. Measurements with spatial resolution are useful for the analysis of specimens with variation in composition or structure.

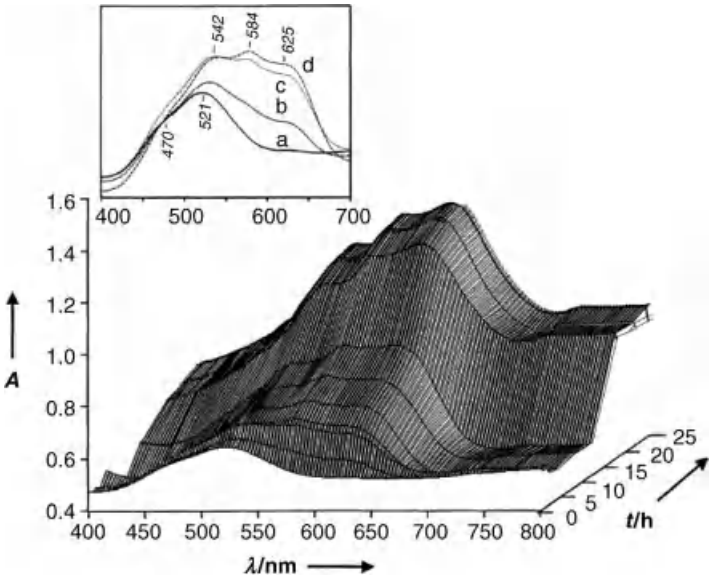


Figure 3.17 Diffuse reflection-UV–vis spectra recorded during the synthesis of CoAPO-5. The cell used is shown in Figure 3.10. Reprinted with permission from [87].

3.4.3.1 Isomorphous Substitution of Framework Cations in Zeolites

UV–vis spectroscopy is one of the primary methods to verify framework substitution of transition metal cations into zeolites. The coordination or valence of the ion must be unique to the framework species and different from extra-framework species. Typically, several methods are used initially to verify the incorporation of the cation in the framework and, once the position of the corresponding charge-transfer absorption band is known, UV–vis spectroscopy is a simple method to ensure successful substitution and also the absence of a large quantity of extra-framework species. UV–vis spectroscopy is particularly advantageous when the ion of interest is EPR silent or the presence of several species complicates the analysis of data from averaging techniques such as EXAFS spectroscopy.

The formation of titanium silicalite (TS-1) can be demonstrated by the presence of absorption bands at 48 000–50 000 cm^{-1} (208–200 nm) and at 960 cm^{-1}, which arise from charge-transfer and vibrational transitions of $[TiO_4]$ and $[O_3TiOH]$ species ([124] and references therein). Figure 3.18 shows TS-1 in vacuum; the intense band at 48 000–50 000 cm^{-1} of tetrahedral Ti(IV) evidences the substitution, and the small band at 32 000–36 000 cm^{-1} (313–278 nm) indicates a small amount of extra-framework Ti(IV). Hydration shifts the charge-transfer band to 43 000 cm^{-1} (233 nm). Immersion in H_2O_2 produces a band at 26 000 cm^{-1} (385 nm), which was ascribed to a charge-transfer transition from a hydroperoxo ligand to Ti(IV). These data demonstrate that UV–vis spectroscopy can be used to identify coordination changes upon hydration or, more generally, adsorption. At the same time, the spectra prove that the Ti(IV) species in the zeolite framework are accessible to fluids.

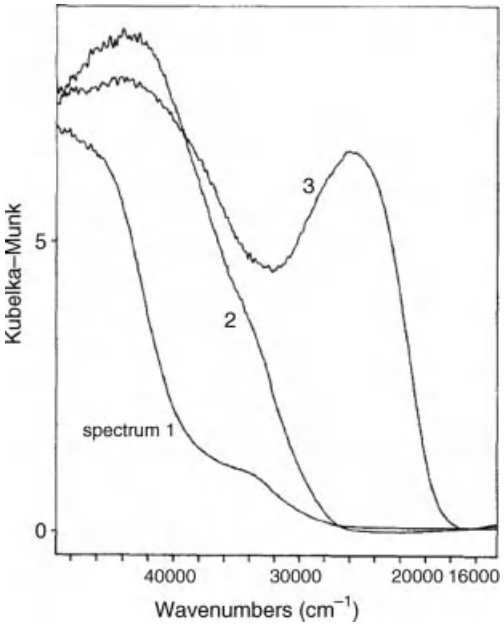


Figure 3.18 Diffuse reflection-UV–vis spectra of TS-1: 1, after outgassing at 393 K in vacuum; 2, after immersion in H_2O; 3, after immersion in H_2O_2. Reprinted with permission from [124].

It is not always possible to distinguish species by UV–vis spectroscopy, and other methods have to be used to obtain complementary information. Analysis of vanadium-substituted zeolite beta by UV–vis spectroscopy [125] reveals vanadium species in tetrahedral coordination in the as-prepared material, without further distinction. Photoluminescence spectra demonstrate the presence of three different kinds of tetrahedral vanadium species.

3.4.3.2 **Ion Exchange in Zeolites**

The valence and coordination of transition metals introduced into zeolites via ion exchange can be garnered from UV–vis spectra. Typically, changes in coordination, for example through hydration and dehydration, can be observed during treatments in humid or dry atmospheres, respectively. Moreover, through the adsorption of suitable molecules, the location and mobility of the ions may be probed.

Such an experiment is depicted in Figure 3.19 [126]. Spectrum (a) characterizes a nickel-exchanged zeolite X after dehydration under mild conditions. Introduction of ammonia produces spectrum (b), which is similar to that of $Ni(NH_3)_6^{2+}$ in spectrum (e).

Dehydration at high temperature leads to migration of nickel cations into the hexagonal prisms (S_I sites), and coordination of ammonia no longer seems possible, as the absence of the characteristic bands of the complex at 395, 610, and 1030 nm shows. NIR bands at 1460 and 1550 nm are attributable to overtones of O−H and N−H stretching bands; the band at 2050 nm represents a combination mode of

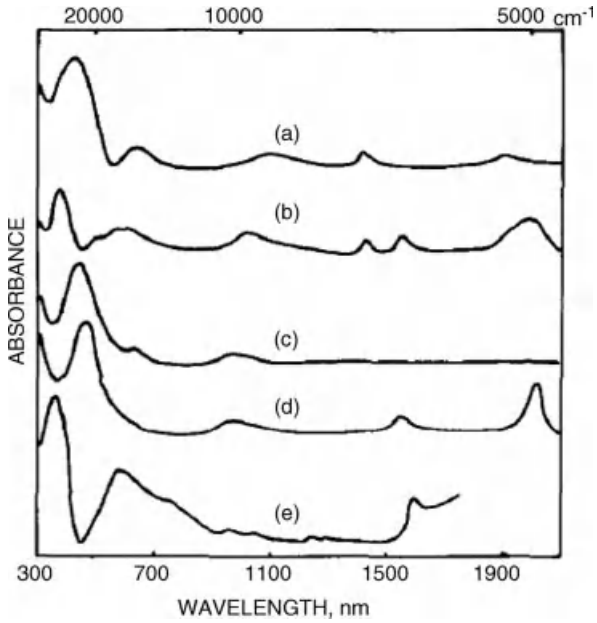


Figure 3.19 Transmission UV–vis spectra of nickel-exchanged zeolite X with 30% exchange degree. (a) After evacuation at 100 °C; (b) adsorption of ammonia on NiX evacuated at 100 °C; (c) after evacuation at 100 °C; (d) adsorption of ammonia on NiX evacuated at 500 °C; (e) $Ni(NH_3)_6^{2+}$ in aqueous solution. Reprinted with permission from [126].

asymmetric N−H deformation and N−H stretching. The NIR data are useful for assessing the degree of hydration and confirm the adsorption of NH_3.

3.4.3.3 Dispersion of Supported Metal Oxide Species

UV–vis spectroscopy is useful to determine the nature and degree of aggregation of supported oxometallate (MO_x) species. The charge-transfer transition from oxygen to metal is sensitive to the coordination and to the cross-linkage of such MO_x units. Through analysis of reference compounds that may contain variously coordinated MO_x units and may be characterized by individual MO_x units, or chains, sheets, or three-dimensional assemblies thereof, the band positions of various mono- and polymeric forms of MO_x can be identified. Often, Raman spectroscopy or X-ray diffraction [127] is used as an additional analytical method. In Figure 3.20, spectra of silica-supported VO_x catalysts with various vanadium loadings are shown [128]. The silica is the mesoporous material SBA-15. The spectra evidence isolated tetrahedral VO_4 units at low loadings (absorbing at 250 and 292 nm), polymerized VO_4 species at intermediate loadings (absorbing between 300 and 400 nm), and V_2O_5 at high loadings (absorbing at >400 nm).

3.4.3.4 Bandgap Determination in Semiconductors

UV–vis spectroscopy can be employed to determine the bandgap energy in semiconductors. The various methods of spectral analysis to obtain the bandgap energy are

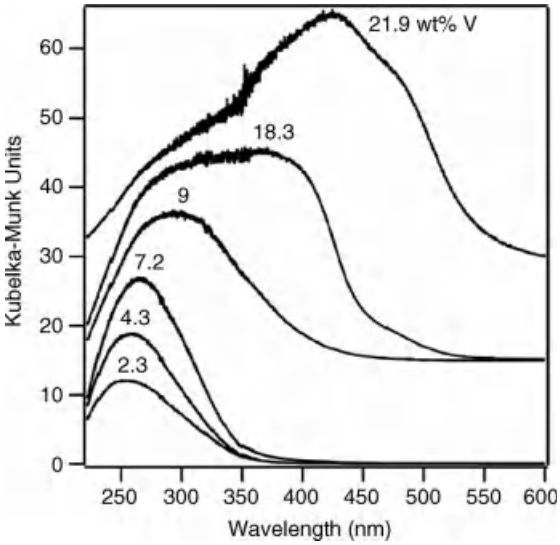


Figure 3.20 Diffuse reflection-UV–vis spectra of dehydrated SBA-15-supported vanadia samples. The three spectra characterizing materials with high vanadium loading have been shifted along the ordinate for clarity. Reprinted with permission from [127].

described in Section 3.2.4.1. This information is particularly important in the development of photocatalysts, which should optimally exploit (absorb) the radiation from the Sun. The spectra of a series of titania catalysts, doped with nitrogen by using various precursors, are shown in Figure 3.21 [129]. In comparison with pure titania, two effects are introduced by the nitrogen: the position of the bandgap varies slightly and an additional transition is observed in the range $397 < \lambda < 550$ nm, which is ascribed to excitation of electrons from local states in the bandgap to unoccupied states.

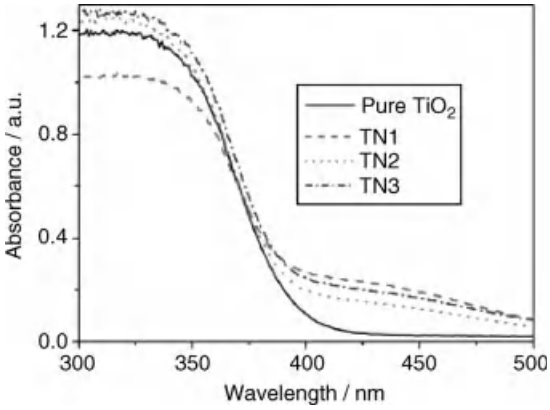


Figure 3.21 Diffuse reflection-UV–vis spectra of pure and nitrogen-doped titania: TN1, ammonia precursor; TN2, hydrazine hydrate precursor; TN3, mixed precursor. Reprinted with permission from [129].

3.4.3.5 Spatially Resolved Spectroscopy of Specimens with Compositional Variation on the Millimeter Scale

The small beam spot of 100 μm or smaller of some fiber-optic probes can be used to obtain spatially resolved UV–vis spectra of specimens with compositional variations on this scale. Various applications can be envisioned; for example, the impregnation of a shaped catalyst support but also reduction or oxidation of shaped catalysts. The probe and specimen have to be moved with respect to each other, which can be achieved with a movable stage [99]. Profiles across a pellet can be mapped out, as illustrated in Figure 3.22 [130]. In this particular case, almost no cobalt was found in the center (core) of the alumina pellet, whereas the spectra indicate $CoAl_2O_4$ in the middle ring and Co_3O_4 in the outer ring. Such spectra can be recorded after various treatments, and may be particularly useful when the profiles are not discernible by visual inspection, that is, when the species of interest absorb in the UV range.

3.4.3.6 Spatially Resolved Spectroscopy of Specimens with Compositional Variation on the Micrometer Scale

Combination of fiber-optic probes with an optical microscope permits UV–vis spectroscopy with a spatial resolution of a few micrometers [101]. This resolution suffices to detect variations even in an individual crystal of larger size. An interesting application is the analysis of microporous materials such as zeolites, which form sizable crystals. Regarding their use in catalysis, the question is often raised of whether only the pore mouth or the entire pore system participates in a reaction.

In the example in Figure 3.23, a ZSM-5 crystal was exposed to methoxystyrene. The spectra indicate that dimers form at the edges of the crystal (cations absorbing at 590 nm), and higher oligomers, probably trimers, form in the center of the crystal (cations absorbing at 635 nm).

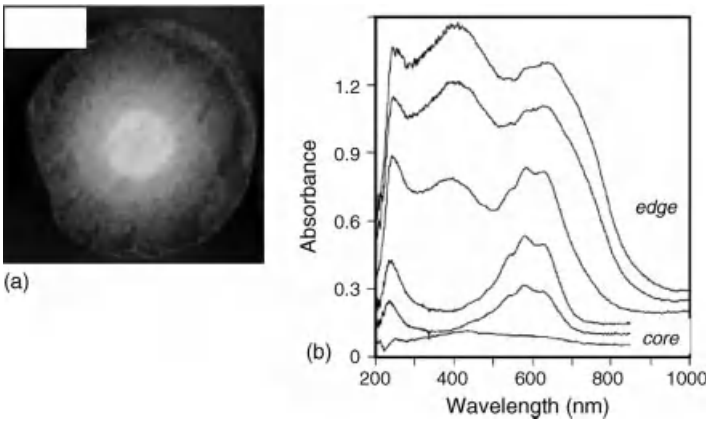


Figure 3.22 (a) Photograph and (b) diffuse reflection–UV – vis spectra of a bisected γ-Al_2O_3 pellet impregnated with $Co(NO_3)_2$, from edge to core, measured after calcination at 550 °C. Pellet diameter, 3 mm; estimated spatial resolution, 100 μm (diameter of individual fiber in probe head, 100 μm). Reprinted with permission from [130].

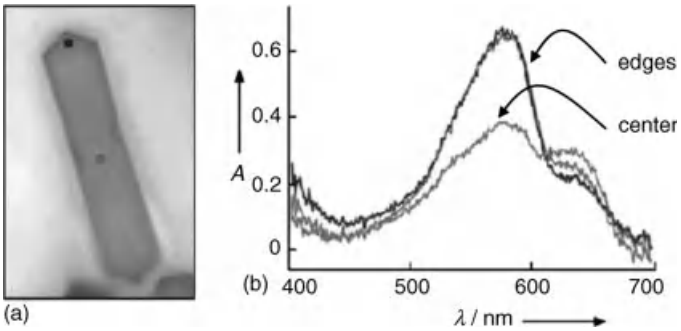


Figure 3.23 (a) Optical microphotograph of a ZSM-5 crystal (length ~100 μm) after addition of 4-methoxystyrene. (b) Spatially resolved optical absorption spectra at the edges (red and blue) and at the center (pink) measured after reaction with 4-methoxystyrene. Reprinted with permission from [101].

3.4.4
Probing of Surface Properties

The acidity of solid acids is frequently measured by adsorption of Hammett indicators [131], where the color change of the indicator can be detected by visual inspection or photometrically. An example of the use of UV–vis spectroscopy to follow the protonation of phenylazonaphthylamine is given in Figure 3.24 [10]. The spectrum of the neutral molecule was obtained in isooctane, the acid (protonated) form was obtained in ethanol–HCl and after adsorption on solid acids.

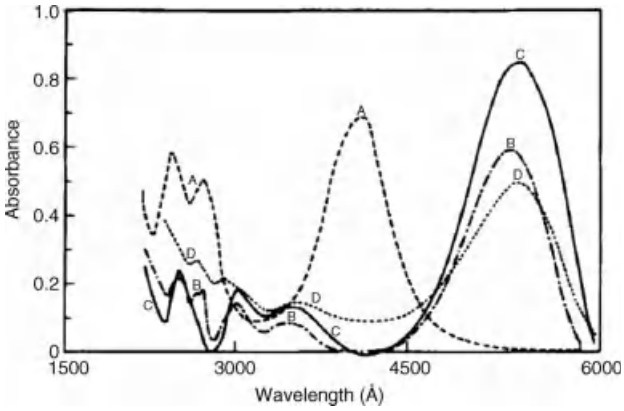


Figure 3.24 UV–vis spectra of phenylazonaphthylamine. A, in isooctane solution; B, in ethanolic HCl; C, adsorbed on DSA-1 (silica–alumina with 12% $A1_2O_3$); D, adsorbed on SA-11 (silica–alumina with 0.1% Al_2O_3). Reprinted with permission from [10].

3.4.5 Dynamic Experiments

Transformations of solids during treatment in a controlled atmosphere and at elevated temperatures can often be successfully monitored using UV–vis spectroscopy. Adsorbents or catalysts need to be cleaned from adsorbates such as water or other contaminants, which is discussed below. Many catalysts need to be chemically activated, for example, through reduction; the analysis of redox processes is extensively illustrated in Section 3.5.

3.4.5.1 Dehydration

To remove adsorbed species, specimens are heated, often in vacuum or an inert gas. *In situ* UV–vis spectroscopy can identify changes in the coordination of transition metal surface species; for example, molecularly adsorbed water may serve as an additional ligand, and the coordination will be reduced after dehydration [132]. Easily reducible species may change oxidation state. In these cases, having the option to record spectra simultaneously far into the NIR range is helpful because overtones and combination modes of water vibrations can be detected, and the state of hydration can be correlated with the electronic state. In the example shown in Figure 3.25, dehydration of the heteropoly acid $H_4PVMo_{11}O_{40}{\cdot}xH_2O$ is evidenced by the disappearance of bands at 1430 nm (overtone of OH stretching vibrations) and 1925 nm (combination mode of OH stretching and OH deformation of molecular water) [46]. Concomitantly with the dehydration, a band at 740–780 nm with a shoulder at 900–1000 nm developed as a result of reduction of the compound. These absorption features are assignable to optical d–d transitions in V^{4+} and Mo^{5+} ions and the intervalence V^{4+}–Mo^{6+} optical transition. The data show nicely that dehydration of the heteropoly acid in inert gas is accompanied by partial reduction.

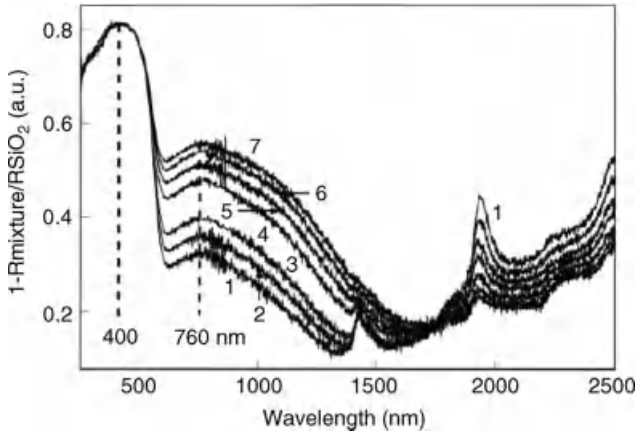


Figure 3.25 Diffuse reflection-UV–vis spectra of $H_4PVMo_{11}O_{40}{\cdot}xH_2O$ during dehydration in a helium flow at 300 K. Trace 1, 1.4 h; **2**, 1.9 h; 3, 2.4 h; 4, 4.1 h; 5, 7.4 h; 6, 9.9 h; 7, 12.2 h. Reprinted with permission from [46].

3.5
Surface Reactivity and Catalysis

3.5.1
Oxidation State and Coordination Changes

3.5.1.1 Oxidation State of Transition Metals in Supported MO_x Moieties or Solid Solutions

The key to the catalytic activity of transition metals is their ability to change their oxidation state in a redox cycle. UV–vis spectroscopy is an excellent tool to determine the individual oxidation states that are present in a sample. However, the molar absorption coefficients of the species, which are often supported and in various degrees of aggregation, are typically not known. *Ex situ* preparation of a set of samples with a defined mixture of oxidation states is often not feasible. Therefore, a calibration needs to be performed *in situ*. A second independent method is necessary to determine the concentration of a species of interest. Spectral intensity in UV–vis spectra can, for example, be compared with the intensity of electron paramagnetic resonance signals (see Section 3.2.5). When the spectra become complex and the identification of individual absorption bands is no longer possible, a solution can be to relate overall intensity at a particular wavelength or in a range to an average valence. The latter can be determined well *in situ*, by starting with a defined state and then counting the reduction or oxidation equivalents consumed in a particular treatment.

A suitable independent measurement of the oxidation state of a sample is temperature-programmed reduction (TPR). This method has been applied, for example, to investigate supported vanadium [133] and chromium [134] catalysts. In the TPR experiment, the sample is first fully oxidized, then reduced under certain conditions, and the amount of H_2 consumed is measured and the average oxidation state of the supported transition metal is determined. Equivalent conditions are then applied in an *in situ* UV–vis experiment, and the area of the shrinkage in LMCT bands of the fully oxidized species is determined and related to the area of the bands before reduction. A relative degree of reduction under catalytic reaction conditions can then be estimated by relating the observed relative shrinkages in band area to the relative shrinkage measured in the calibration. Alternatively, instead of the area, the value of the Kubelka–Munk function at a certain wavelength can be used. This method can be classified as a two-point calibration that is based on the endpoints, that is, the fully oxidized and the fully reduced states.

A more elaborate variant of this method is the collection of multiple calibration points, with the degree of reduction determined *in situ* rather than in a separate measurement. Figure 3.26 shows an example of such a correlation, obtained for a titania-supported vanadium catalyst [135]. The change in intensity at a particular wavelength (800 nm) was related to the average valence, expressed as O/V ratio and determined by TPR in H_2. This relationship is not linear.

Various spectral features may be analyzed, as shown in Figure 3.27 [136]. Supported vanadium catalysts were reduced *in situ* using a H_2 flow while spectra were recorded, then the amount of O_2 to recover the initial spectrum was determined by

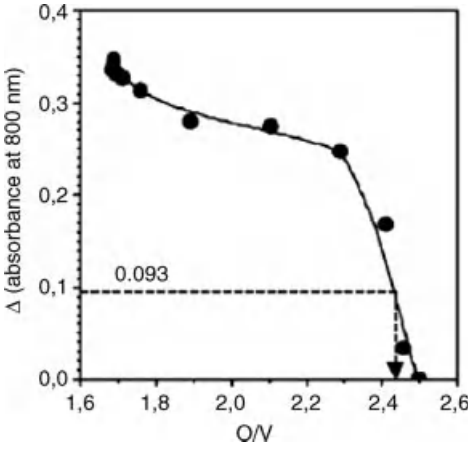


Figure 3.26 Relationship between spectral intensity at 800 nm and average valence, expressed as oxygen to vanadium ratio, in a 6 wt % V/TiO_2 catalyst. Ordinate values represent the difference in the absorption intensity at 800 nm from the intensity measured for an oxidized catalyst. Reprinted with permission from [135].

online mass spectrometry, and the degree of reduction was calculated assuming that each O atom accepts two electrons. A pre-edge feature in the spectra (1.49–1.86 eV, shown in Figure 3.27), was integrated for the calibration curve, shown in Figure 3.28. This linear calibration was used to determine the extent of reduction of such catalysts under the conditions of propane oxidative dehydrogenation.

Figure 3.29 shows the result of such an analysis. The extent of reduction per surface vanadium atom increases with increasing propane to O_2 ratio in the feed and also with increasing vanadium content in the catalysts.

If the transition metal cations are in a defined local environment, for example because they are part of an oxide solid solution, then crystal field theory can be employed to estimate the relative oscillator strength of d–d transitions. If all ions present give rise to d–d bands of significant intensity, then this information can be used to determine the fraction of each species. This method may also be combined with measurements of the average valence, for example, by the methods described above, or by X-ray absorption spectroscopy, which delivers an edge position that can often be correlated with the valence. Zirconia is known to incorporate a large variety of ions into its lattice, manganese being one of them. The fractions of Mn^{2+}, Mn^{3+}, and Mn^{4+} in manganese-promoted sulfated zirconia catalysts were determined from the oscillator strengths of the d–d transitions of Mn^{3+} and Mn^{4+} species located in the zirconia lattice, and information on the average valence from the Mn K edge position [137].

3.5.1.2 **Supported Metals: Oxidation State and Particle Size and Shape**

UV–vis spectroscopy is a powerful technique for investigating supported metal particles: individual ions may be distinguished from small charged clusters and metallic species. For the coinage metals, information on the size and aspect ratio of

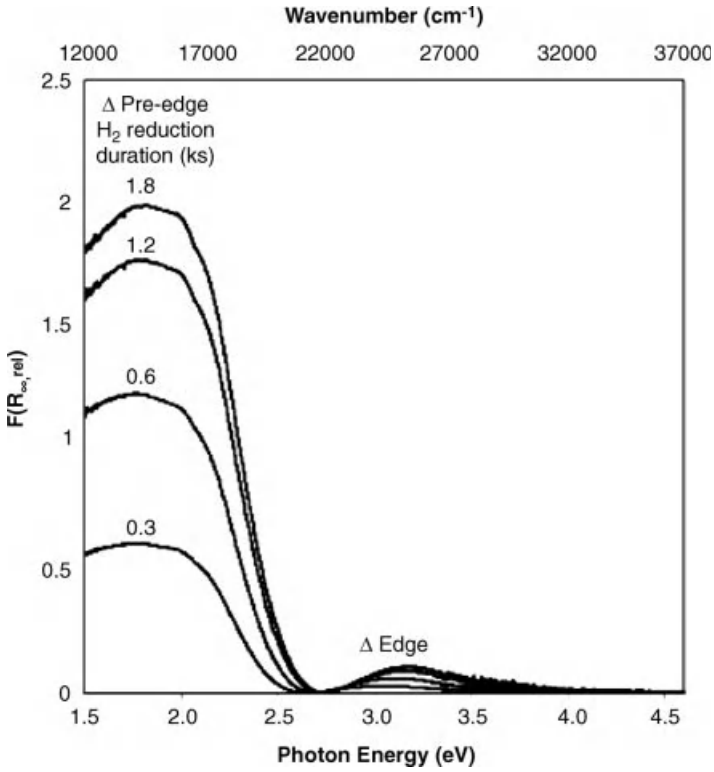


Figure 3.27 Diffuse reflection-UV–vis spectra of a 10 wt% V_2O_5/Al_2O_3 catalyst during reduction in flowing H_2. H_2 pressure, 101 kPa; temperature, 603 K. R_∞ is the reflectance of the fully oxidized catalyst. Reprinted with permission from [136].

small particles can be obtained from surface plasmon resonance. As a result, redox reactions and sintering or reshaping of metal particles under reaction conditions can be detected.

Several of these effects are seen in Figure 3.30, which shows spectra of a supported silver catalyst under ethylene oxidation conditions [138]. The authors interpreted the three main features in the spectra series as follows: silver plasmon resonance (2.4–3.7 eV or 517–335 nm), Ag^0 band transitions (3.8–4.6 eV or 326–270 nm), and Ag^+ band transitions (5.4–6.2 eV or 230–200 nm). The spectra indicate two processes: reduction of the silver with time (band disappearing at high energies) and a restructuring of the silver particles from spherical to oblate (red shift of plasmon resonance), perhaps associated with the formation of an oxygen-containing surface phase. These spectra demonstrate that a laboratory experiment with commercial equipment can provide a wealth of information regarding supported metal catalysts; particularly if well-defined coinage metal particles are investigated.

The coordination of finely dispersed noble metals on surfaces can also be monitored. Figure 3.31 shows spectra of a palladium-doped zeolite H-mordenite [48].

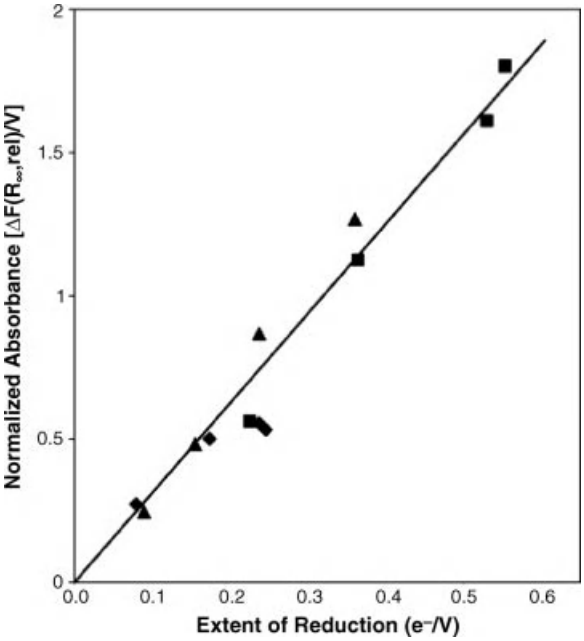


Figure 3.28 Relation between relative changes in the pre-edge spectral feature of V_2O_5/Al_2O_3 catalysts during H_2 reduction and the extent of catalyst reduction quantified by subsequent O_2 temperature-programmed oxidation. Diamonds, triangles, and squares: 3.5, 10, and 30 wt% V_2O_5, respectively. Reprinted with permission from [136].

Before calcination, the palladium is in a hydrated state, described as $Pd(H_2O)_n^{2+}$, which gives rise to a d–d transition at 400 nm. After calcination at 823 K, a $Pd(O_z)_n^{2+}$ complex is formed, which absorbs at about 480 nm (d–d band) and around 250 nm (LMCT band). A slight change occurs when the catalyst is exposed to NO; a more dramatic change is observed under reaction conditions for selective catalytic reduction of NO with CH_4. These data show that UV–vis spectroscopy is suitable for monitoring the coordination and redox chemistry of low concentrations of supported noble metals.

3.5.2 Hydrocarbon Species on Surfaces

3.5.2.1 Reference Spectra

UV–vis spectroscopy is a highly sensitive analytical tool for analyzing organic surface species during catalytic conversion, provided that they absorb in the respective range. In general, the method is promising for reactions that involve unsaturated reactants, intermediates, or products, including side products that deactivate the catalyst by blocking sites. The interpretation of such spectra is not trivial; it is helpful to collect reference spectra or to react the species in question further.

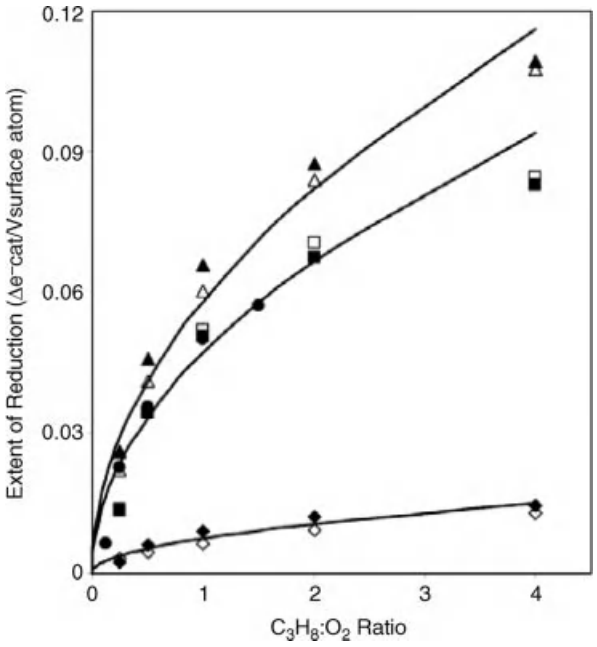


Figure 3.29 Dependence of the extent of catalytically relevant reduction per surface V-atom on the C_3H_8/O_2 ratio for VO_x/Al_2O_3 catalysts during propane oxidative dehydrogenation. Filled and open symbols, C_3H_8 and O_2 dependence, respectively. Diamonds, squares, and triangles: 3.5, 10, and 30 wt% V_2O_5/Al_2O_3, corresponding to 2.3, 8.0, and 34 V nm^{-2}, respectively. Reprinted with permission from [136].

Examples of UV–vis spectra monitoring the adsorption and reaction of organic molecules such as alkenes, alkynes, aromatics, and alcohols on solid surfaces can be found widely in the literature, with the most systematic investigations conducted by Förster and co-workers [80]. The following example demonstrates how analogous reactions in the liquid phase and on the surface and further conversion of surface species can be used for spectral interpretation. The bottom panel of Figure 3.32 shows spectra of hexamethylbenzene adsorbed on zeolite H-beta [139]. The molecule is retained on the surface even after evacuation at elevated temperature. Reference spectra of hexamethylbenzene and its protonated form were obtained by dissolving it in cyclohexane and sulfuric acid. Comparison of the spectra in Figure 3.32 a and b suggests that the molecule is present in neutral form (absorbing at 37 000 cm^{-1} or 270 nm) and protonated (absorbing at 26 000 cm^{-1} or 385 nm) on the surface of zeolite. Further proof for the presence of benzenium ions is the disappearance of the respective band through reaction of the adsorbate with an excess of a strong nucleophile, NH_3. Similarly to the example shown in Figure 3.3, the spectrum of the neutral form does not change much through adsorption. The molar absorption coefficient of the protonated species was estimated to be a factor of 50 higher than that of the neutral species; and only ~15% were believed to be protonated [139].

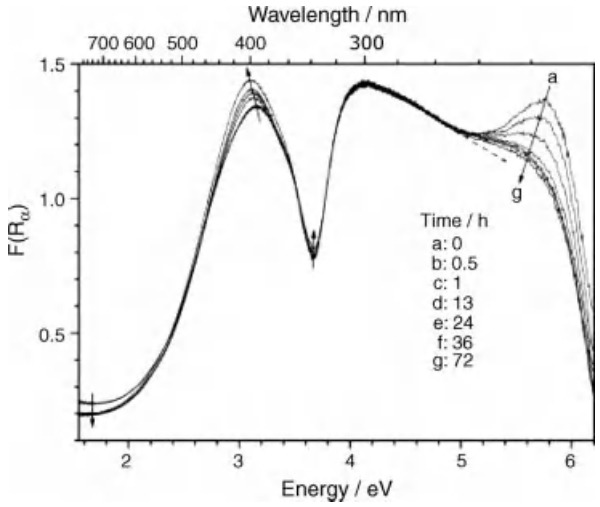


Figure 3.30 Diffuse reflection-UV–vis spectra of $Ag/CaCO_3$ catalyst at different times on-stream at 493 K and 0.3 MPa in C_2H_4–O_2–He. Reprinted with permission from [138].

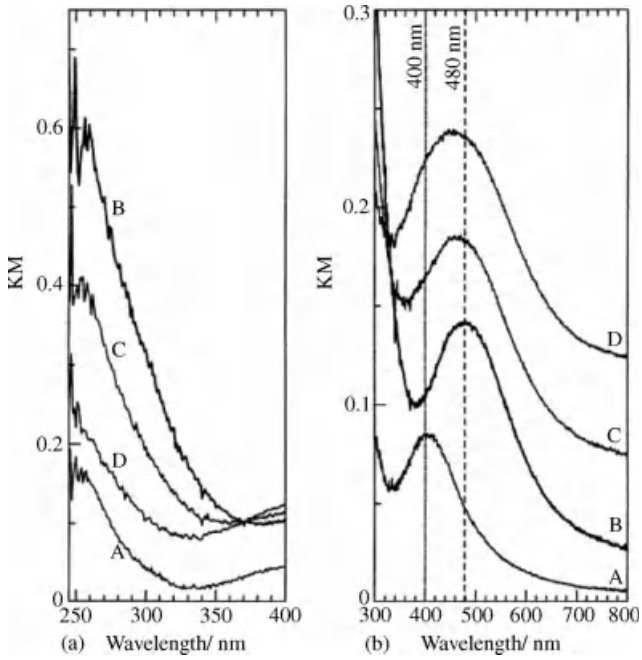


Figure 3.31 (a) The CT band and (b) the d–d band regions in *in situ* diffuse reflection–UV–vis spectra of 1.5 wt% Pd–H-mordenite (A) at 300 K without any pretreatment (*ex situ*), (B) after calcination in 10% O_2 at 823 K for 30 min, followed by purging in He for 30 min at 623 K, (C) in flowing 1000 ppm NO at 623 K for 30 min after (B), and (D) in flowing NO + CH_4 + O_2 at 623 K for 30 min after (B). Reprinted with permission from [67].

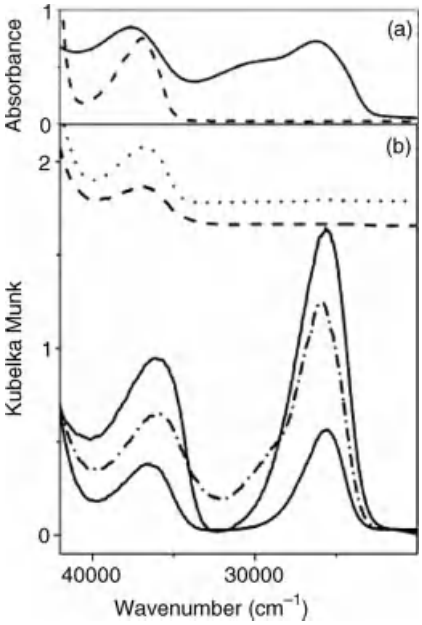


Figure 3.32 Diffuse reflection-UV–vis spectra of hexamethylbenzene. (a) In 96% sulfuric acid (solid line) and cyclohexane (dashed line); (b) increasing coverages on H-beta (Si/Al = 12) (two solid lines) followed by outgassing at 200 °C for 2 h (dashed-dotted line), and exposure to 40 Torr ammonia (dashed plot, upper part), adsorption on dealuminated H-beta (Si/Al = 210). Reprinted with permission from [139].

Highly reactive surface species can also be transformed upon exposure to the ambient, typically through reaction with O_2 or H_2O. If color changes occur upon removal of an active or spent catalyst from a reactor, an *in situ* UV–vis experiment with the catalytic reaction followed by exposure to O_2 or H_2O vapor can yield valuable information. An example of such an observation is presented in Figure 3.33 [140],

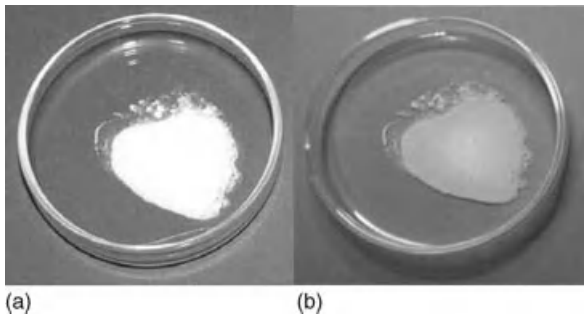


Figure 3.33 Photographs of a spent sulfated zirconia catalyst (after *n*-pentane isomerization) (a) immediately after removal from the reactor and (b) 5 min after exposure to ambient conditions [140].

which shows the color change of a catalyst after exposure to the ambient. This exposure experiment was re-enacted inside an *in situ* UV–vis cell and the catalyst was contacted with O_2, which did not cause a spectral change, and subsequently with H_2O vapor, which resulted in spectral features corresponding to the observed tan color.

3.5.2.2 Surface Hydrocarbon Pool Under Reaction Conditions

The role of surface species in a catalytic reaction can only be discerned through careful correlation with the performance. An example of the simultaneous presence of possible intermediates and deactivating coke species, and of their respective precursors, is the conversion of methanol to alkenes on molecular sieves such as the aluminophosphate H-SAPO-34. This reaction has been inferred to proceed via alkyl-substituted benzenes, that is, spectra obtained during reaction should resemble those shown in Figure 3.32. The reality is more complicated, as shown in Figure 3.34 [141]. Since the positions of the transitions of aromatics change insignificantly upon mere adsorption on zeolites, one would expect a minor role of the adsorbent; however, the bands in Figure 3.34 do not coincide with those reported in Figure 3.32. Many more bands are observed, indicating additional species. The bands were assigned as follows: 245 nm, dienic species; 280 nm, polyalkylaromatics; 300 nm, monoenylic carbenium ions; 345 nm, dienylic carbenium ions; 400 nm, nonprotonated polycyclic aromatics such as polymethylanthracenes; and 430 nm, trienylic carbenium ions. By connecting the catalytic performance and the evolution of the spectra, the carbenium ions could be identified as precursors to a pool of aromatic hydrocarbons, which are presumed to be active intermediates. The polycyclic aromatic compounds were seen as indicators of coke formation, which is considered to be the cause of deactivation.

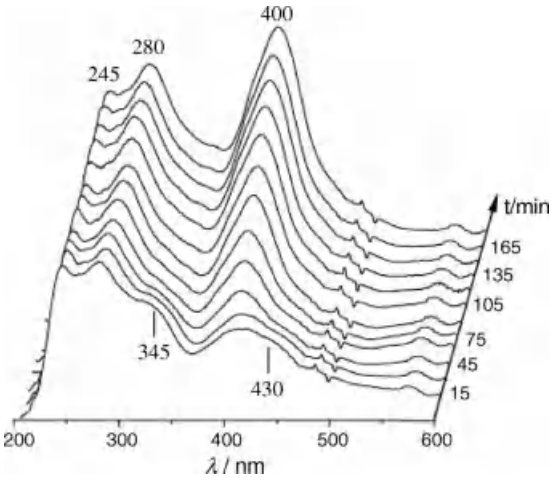


Figure 3.34 Diffuse reflection-UV–vis spectra of H-SAPO-34 during methanol conversion at 673 K. Reprinted with permission from [141].

In many of the examples in the literature, acidic forms of zeolites are used as catalysts. Bare zeolites containing only Si, Al, P, and O, and also several other oxidic supports such as silica and alumina, have no intense absorptions in the UV–vis range, and do not undergo redox reactions that produce absorption bands. These materials present the simplest scenario for the investigation of adsorbed species. However, the examples also illustrate the difficulties that can arise with the interpretation of UV–vis spectra and the occasional lack of specificity of the absorption bands.

UV–vis spectroscopy can also be used as a supporting method to assist with the data evaluation of simultaneously applied techniques such as Raman spectroscopy. The "darkening" (or lightening) of a catalyst through redox reactions or coking (or combustion of coke) at the wavelength position of the Raman band (calculated from the laser wavelength plus the Raman shift) will affect the measured Raman intensity. UV–vis spectra can be used to correct for such changes in absorption at the wavelength in question [142].

3.5.2.3 **Deactivation and Regeneration**

The regeneration of catalysts can also be monitored by UV–vis spectroscopy and may include phenomena such as change in oxidation state, re-dispersion, and removal of carbonaceous deposits. Figure 3.35 [143] shows spectra that were recorded while an H-mordenite catalyst deactivated in *n*-butane isomerization was heated in an O_2-containing atmosphere. Several bands indicate the presence of carbonaceous surface species in the deactivated catalyst. A series of defined bands in the NIR range evolves during heating and indicates that, first, polycondensed aromatic species are formed, probably through oxidative dehydrogenation of surface species. These distinct bands disappear at high temperatures. UV–vis spectroscopy can be used to optimize such regeneration procedures.

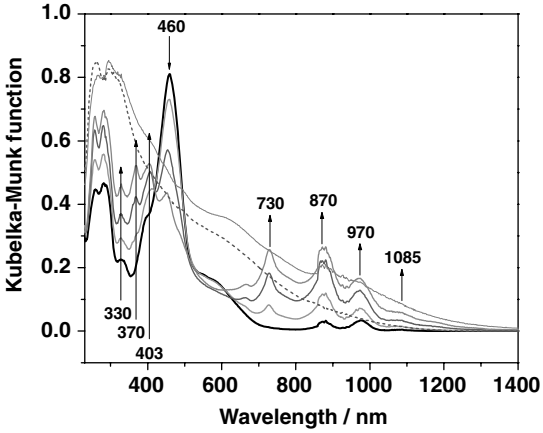


Figure 3.35 Diffuse reflection-UV–vis spectra of zeolite H-mordenite recorded during regeneration in a flow of 20% O_2–He. Black (thick) line, deactivated after use in *n*-butane conversion at 350 °C; red (dashed) line, at 450 °C at the end of oxidizing treatment [143].

3.6 Conclusions

UV–vis–NIR spectroscopy is a versatile technique because it can provide useful information about molecular species, small particles, and extended structures through probing their electronic transitions. Specifically, the nature of chromophores in organic and inorganic molecules can be observed, which provides information on molecular structure. Regarding metal complexes, the valence of the central metal ion, the coordination and information on the nature of the ligands can be obtained. The size and shape of small particles of some metals can be determined on the basis of localized surface plasmon resonance. Bandgap transitions are important to characterize the nature of a solid, for example, as a function of its composition or particle size. Defects in solids may also be detected. However, there are a large number of species (including many saturated organic compounds) that do not absorb in the wavelength range that is easily accessible (i.e., with standard spectrometers).

Spectral interpretation can be a challenge, for various reasons. The observed bands may be unspecific, because many species can have transitions in the same wavelength range. These species may be of the same type; for example, they could all be organic molecules. The species could also be of different type; for example, a complex working catalyst sample may consist of a supported metal with a variety of organic adsorbates. In this case, a large variety of transitions are possible, and several may fall in the same wavelength range. Precise theoretical descriptions are often lacking, for example, for cationic organic adsorbates.

UV–vis–NIR spectroscopy is one of the most important quantitative techniques (cf. photometry, NIR analyzers) and is highly sensitive, much more so than IR, Raman or NMR spectroscopy.

The analyzed species may be present in the gas phase, in a liquid phase, or in a solid. They may constitute the bulk of a material or a minority species that is dissolved or dispersed on a surface. UV–vis spectroscopy can be considered a bulk analysis method; conducted in transmission mode, the entire sample in the beam path is analyzed; in reflection mode, a considerable (yet sample-dependent) depth is analyzed. Acquisition of spatially resolved spectra is possible and is easily achieved with fiber-optic probes with small beam spots (of around 100 μm). Spatial resolution can be further enhanced (reportedly to about 1 μm) through addition of a microscope.

Only small amounts of sample are necessary; in transmission mode, small cuvettes with a short pathlength and thin solid wafers of 10–20 mg can be used; in reflection mode, small sample holders and small beam spots also allow for the analysis of about 1- mg of material. UV–vis–NIR spectroscopy is nondestructive, except for photosensitive materials. The equipment for UV–vis spectroscopy alone is very affordable; adding the NIR range increases the cost. UV–vis–NIR spectroscopy can be conveniently conducted in the laboratory without special infrastructure requirements.

UV–vis–NIR spectroscopy is very suitable for investigating materials under operating conditions, for example, working catalysts. Dynamic experiments with high time resolution are possible operating in single-wavelength mode with conventional spectrometers or using spectrometers with array detectors. Commercial cells for measurements under controlled gas atmosphere and temperature conditions is available. Alternatively, fiber-optic probes can be integrated into reaction chambers. Interference from thermal radiation is limited to the NIR range. Often there is little interference from gas-phase components, and investigation of a solid in a gaseous atmosphere is typically not a problem. Moreover, many solvents are largely transparent for UV–vis radiation, making the technique suitable for the investigation of the solid–liquid interface.

The technology used for UV–vis–NIR spectroscopy is still improving; with various benefits. Better detectors are being introduced, such as the InGaAs detector, providing higher data quality in the NIR range. Fiber optics are a relatively recent development with a strong impact on UV–vis spectroscopy of solids. Measurements under catalytic reaction conditions are facilitated because fibers can be introduced into any kind of vessel. Spatially resolved data can easily be acquired. Because of their small space requirement, fiber optics have also made it easy to combine UV–vis spectroscopy with other techniques.

References

1 Welz, B. and Sperling, M. (1999) *Atomic Absorption Spectroscopy*, 3rd edn., Wiley-VCH Verlag GmbH, Weinheim.

2 Schmidt, W. (2005) *Optical Spectroscopy in Chemistry and Life Sciences – an Introduction*, Wiley-VCH Verlag GmbH, Weinheim.

3 Kubelka, P. and Munk, F. (1931) Ein Beitrag zur Optik der Farbanstriche. *Z. Tech. Phys.*, **12**, 593–601.

4 Schuster, A. (1905) Radiation through a foggy atmosphere. *Astrophys. J.*, **21**, 1–21.

5 Bull, A.J. and Cartwright, H.M. (1923) The measurement of photographic density. *J. Sci. Instrum.*, **1**, 74–81.

6 Jacquez, J.A. and Kuppenheim, H.F. (1955) Theory of the integrating sphere. *J. Opt. Soc. Am.*, **45**, 460–466.

7 Jacquez, J.A., McKeehan, W., Huss, J., Dimitroff, J.M., and Kuppenheim, H.F. (1955) Integrating sphere for the measurement of reflectance with the Beckman model DR recording spectrophotometer. *J. Opt. Soc. Am.*, **45**, 971–975.

8 Shibata, K. (1957) Simple absolute method for measuring diffuse reflectance spectra. *J. Opt. Am. Soc.*, **47**, 172–175.

9 Hogue, R. (1991) 'Praying Mantis' diffuse reflectance accessory for UV−Vis−NIR spectroscopy. *Fresenius' J. Anal. Chem.*, **339**, 68–69.

10 Leftin, H.P. and Hobson, M.C., Jr., (1963) Application of spectrophotometry to the study of catalytic systems. *Adv. Catal.*, **14**, 115–201.

11 Terenin, A. (1964) Electronic spectroscopy of adsorbed gas molecules. *Adv. Catal.*, **15**, 227–284.

12 Klier, K. (1968) Reflectance spectroscopy as a tool for investigating dispersed solids and their surfaces. *Catal. Rev. Sci. Eng.*, **1**, 207–232.

13 Kortüm, G. (1969) *Reflectance Spectroscopy*, Springer, Berlin,.

14 Kellermann, R. (1979) Diffuse reflectance and photoacoustic spectroscopies, in *Spectroscopy in Heterogeneous Catalysis* (eds. W.N. Delgass, G.L. Haller, R.

Kellermann, and J.H. Lunsford), Academic Press, New York, pp. 86–131.
15 Stone, F.S. (1983) UV−visible diffuse reflectance spectroscopy applied to bulk and surface properties of oxides and related solids, in *Surface Properties and Catalysis by Non-Metals* (eds. J.P. Bonnelle, B. Delmon, and E.G. Derouane), Reidel, Boston, pp. 237–272.
16 Schoonheydt, R.A. (1984) Diffuse reflectance spectroscopy, in *Characterization of Heterogeneous Catalysts* (ed. F. Delannay), Marcel Dekker, New York, pp. 125–160.
17 Garbowski, E. and Praliaud, H. (1994) Electronic spectroscopy (for catalyst characterization), in *Catalyst Characterization – Physical Techniques for Solid Materials* (eds. B. Imelik and J.C. Védrine), Plenum Press, New York, pp. 61–90.
18 Weckhuysen, B.M. and Schoonheydt, R.A. (2000) Electronic spectroscopies, in *Spectroscopy of Transition Metal Ions on Surfaces* (eds. B.M. Weckhuysen, P. Van Der Voort, and G. Cantana), Leuven University Press, Leuven, pp. 221–268.
19 Weckhuysen, B.M. (2004) Ultraviolet–visible spectroscopy, in *In Situ Spectroscopy of Catalysts* (ed. B.M. Weckhuysen), American Scientific Publishers, Stevenson Ranch, CA, pp. 255–270.
20 Che, M. and Bozon-Verduraz, F. (1997) UV−vis−NIR and EPR spectroscopies, in *Handbook of Heterogeneous Catalysis*, vol. **2** (eds. G. Ertl, H. Knözinger, and J. Weitkamp), Wiley-VCH Verlag GmbH, Weinheim, pp. 641–671.
21 Sojka, Z., Bozon-Verduraz, F., and Che, M. (2008) UV–Vis–NIR and EPR spectroscopies, in *Handbook of Heterogeneous Catalysis*, vol. **2** (eds G. Ertl, H. Knözinger, F. Schüth, and J. Weitkamp), Wiley-VCH Verlag GmbH, Weinheim, pp. 1039–1065.
22 Jentoft, F.C. (2009) Ultraviolet–visible–near infrared spectroscopy in catalysis: theory, experiment, analysis, and application under reaction conditions. *Adv. Catal.*, **52**, 129–211.
23 Schoonheydt, R.A. (2010) UV−vis−NIR spectroscopy and microscopy of heterogeneous catalysts. *Chem. Soc. Rev.*, **39**, 5051–5066.
24 IUPAC (2010) Gold Book, http://goldbook.iupac.org/A00037.html, last accessed 12 May 2011.
25 IUPAC (2010) Gold Book, http://goldbook.iupac.org/A00515.html, last accessed 12 May 2011.
26 Wendlandt, W.W. and Hecht, H.G. (1966) *Reflectance Spectroscopy*, Interscience, New York, p. 19.
27 Perkampus, H.-H. (1986) *UV–Vis Spektroskopie und ihre Anwendungen*, Springer, Berlin.
28 Kortüm, G. and Schreyer, G. (1955) Über die Gewinnung "typischer Farbkurven" von Pulvern aus Reflexionsmessungen. *Angew. Chem.*, **67**, 694–698.
29 Springsteen, A. (2000) Standards for reflectance measurements, selection and use: a primer (part 1). *Spectroscopy*, **15** (5), 20–27.
30 Moradi, K., Depecker, C., Barbillat, J., and Corset, J. (1999) Diffuse reflectance infrared spectroscopy: an experimental measure and interpretation of the sample volume size involved in the light scattering process. *Spectrochim. Acta Part A*, **55**, 43–64.
31 García Solé, G., Bausá, L.E., and Jaque, D. (2005) *An Introduction to the Optical Spectroscopy of Inorganic Solids*, John Wiley & Sons, Ltd., Chichester.
32 Wiberg, N. (2007) *Anorganische Chemie*, Walter de Gruyter, Berlin.
33 Harris, D.C. and Bertolucci, M.D. (1989) *Symmetry and Spectroscopy – an Introduction to Vibrational and Electronic Spectroscopy*, Dover, New York.
34 Yadav, L.D.S. (2005) *Organic Spectroscopy*, Anamaya Publishers, New Delhi.
35 Lambert, J.B., Gronert, S., Shuvell, H.F., and Lightner, D.A. (2011) *Organic Structural Spectroscopy*, Pearson Prentice Hall, Boston, MA.
36 Hirayama, K. (1967) *Handbook of Ultraviolet and Visible Absorption Spectra of Organic Compounds*, Plenum Press Data Division., New York.

37 Perkampus, H.-H. (1992) *UV–VIS Atlas of Organic Compounds*, 2nd edn., Wiley-VCH Verlag GmbH.

38 Wulfers, M.J. and Jentoft, F.C., unpublished data.

39 Huheey, J., Keiter, E., and Keiter, R. (2003) *Anorganische Chemie*, 3rd edn., Walter de Gruyter, Berlin.

40 Bethe, H. (1929) Termaufspaltung in Kristallen. *Ann. Phys.*, **395**, 133–208.

41 Van Vleck, J.H. (1935) Valence strength and the magnetism of complex salts. *J. Chem. Phy.s*, **3**, 807–813.

42 Tanabe, Y. and Sugano, S. (1954) On the absorption spectra of complex ions. I and II. *J. Phys. Soc. Jpn.*, **9**, 753–769.

43 Racah, G. (1942) Theory of complex spectra II. *Phys. Rev.*, **62**, 438–462.

44 Markham, J.J. (1959) Interaction of normal modes with electron traps. *Rev. Mod. Phys.*, **31**, 956–989.

45 Henderson, B. and Imbusch, G.F. (1989) *Optical Spectroscopy of Inorganic Solids*, Clarendon Press, Oxford.

46 Klokishner, S., Melsheimer, J., Ahmad, R., Jentoft, F.C., Mestl, G., and Schlögl, R. (2002) Influence of dehydration effects on the optical spectra of $H_4PVMo_{11}O_{40}$ in the visible and near infrared range: intra- and intercenter optical transitions in the V–Mo cluster. *Spectrochim. Acta Part A*, **58**, 1–15.

47 Kittel, C. (1986) *Introduction into Solid State Physics*, 6th edn., John Wiley & Sons, Inc., New York.

48 Gilbert, B., Frandsen, C., Maxey, E.R., and Sherman, D.M. (2009) Band-gap measurements of bulk and nanoscale hematite by soft X-ray spectroscopy. *Phys. Rev. B*, **79**, 035108.

49 Tandon, S.P. and Gupta, J.P. (1970) Measurement of forbidden energy gap of semiconductors by diffuse reflectance technique. *Phys. Status Solidi*, **38**, 363–367.

50 Kumar, V., Sharma, S.K., Sharma, T.P., and Singh, V. (1999) Band gap determination in thick films from reflectance measurements. *Opt. Mater.*, **12**, 115–119.

51 MacFarlane, G.G. and Robert, V. (1954) Infrared absorption of germanium near the lattice edge. *Phys. Rev.*, **97**, 1714–1716.

52 Murphy, A.B. (2007) Band-gap determination from diffuse reflectance measurements of semiconductor films, and application to photoelectrochemical water-splitting. *Solar Energy Mater. Solar Cells*, **91**, 1326–1337.

53 Berry, C.V. (1967) Structure and optical absorption of AgI microcrystals. *Phys. Rev.*, **161**, 848–851.

54 Trindade, T., O'Brien, P., and Pickett, N.L. (2001) Nanocrystalline semiconductors: synthesis, properties, and perspectives. *Chem. Mater.*, **13**, 3843–3858.

55 Mulvaney, P. (1996) Surface plasmon spectroscopy of nanosized metal particles. *Langmuir*, **12**, 788–800.

56 Liz-Marzán, L.M. (2006) Tailoring surface plasmons through the morphology and assembly of metal nanoparticles. *Langmuir*, **22**, 32–41.

57 Mie, G. (1908). Beiträge zur Optik trüber Medien, speziell colloidaler Metallösungen. *Ann. Phys.*, **25**, 377–445.

58 Gans, R. (1912) Über die Form ultramikroskopischer Goldteilchen. *Ann. Phys.*, **37**, 881–900.

59 Kelly, K.L., Coronado, E., Zhao, L.L., and Schatz, G.C. (2003) The optical properties of metal nanoparticles: the influence of size, shape, and dielectric environment. *J. Phys. Chem. B*, **107**, 668–677.

60 Pérez-Juste, J., Pastoriza-Santos, I., Liz-Marzán, L.M., and Mulvaney, P. (2005) Gold nanorods: synthesis, characterization and applications. *Coord. Chem. Rev.*, **249**, 1870–1901.

61 Creighton, J.A. and Eadon, D.G. (1991) Ultraviolet−visible absorption spectra of the colloidal metallic elements. *J. Chem. Soc., Faraday Trans.*, **87**, 3881–3891.

62 Papavassiliou, G.C. (1976) Surface plasmons in small Au−Ag alloy particles. *J. Phys. F: Met. Phys.*, **6**, L103–L105.

63 Moskovits, M., Srnová-Sloufová, I., and Vlcková, B. (2002) Bimetallic Ag–Au nanoparticles: extracting meaningful optical constants from the surface-plasmon extinction spectrum. *J. Chem. Phys.*, **116**, 10435–10446.

64 Kreibig, U. (1974) Electronic properties of small silver particles: the optical constants and their temperature dependence. *J. Phys. F: Met. Phys.*, **4**, 999–1014.

65 Blatchford, C.G., Campbell, J.R., and Creighton, J.A. (1982) Plasma resonance – enhanced Raman scattering by absorbates on gold colloids: the effects of aggregation. *Surf. Sci.*, **120**, 435–455.

66 Anker, J.N., Hall, W.P., Lyandres, O., Shah, N.C., Zhao, J., and Van Duyne, R.P. (2008) Biosensing with plasmonic nanosensors. *Nat. Mater.*, **7**, 442–453.

67 Catana, G., Rao, R.R., Weckhuysen, B.M., Van Der Voort, P., Vansant, E., and Schoonheydt, R.A. (1998) Supported vanadium oxide catalysts: quantitative spectroscopy, preferential adsorption of $V^{4+}/^{5+}$, and Al_2O_3 coating of zeolite Y. *J. Phys. Chem. B*, **102**, 8005–8012.

68 Shimizu, K.-i., Okada, F., Nakamura, Y., Satsuma, A., and Hattori, T. (2000) Mechanism of NO reduction by CH_4 in the presence of O_2 over Pd–H-mordenite. *J. Catal.*, **195**, 151–160.

69 Weckhuysen, B.M., Verberckmoes, A.A., De Baets, A.R., and Schoonheydt, R.A. (1997) Diffuse reflectance spectroscopy of supported chromium oxide catalysts: a self-modeling mixture analysis. *J. Catal.*, **166**, 160–171.

70 IUPAC (2010) Gold Book, http://goldbook.iupac.org/UT07492.html, last accessed 23 January 2011.

71 IUPAC (2010) Gold Book, http://goldbook.iupac.org/VT07496.html, last accessed 23 January 2011.

72 IUPAC (2010) Gold Book, http://goldbook.iupac.org/IT07399.html, last accessed 23 January 2011.

73 Agilent (2011) Cary 6000i Specifications, http://www.chem.agilent.com/en-US/Products/instruments/molecularspectroscopy/uv-vis/systems/cary6000i/pages/default.aspx May not work from Europe, last accessed 13 May 2011.

74 PerkinElmer (2011) PerkinElmer Lambda 1050 Specifications, www.perkinelmer.com, last accessed 13 May 2011.

75 Weckhuysen, B.M. (2003) Determining the active site in a catalytic process: *operando* spectroscopy is more than a buzzword. *Phys. Chem. Chem. Phys.*, **5**, 4351–4360.

76 Leftin, H.P. (1960) Electronic spectra of adsorbed molecules: stable carbonium ions on silica–alumina. *J. Phys. Chem.*, **64**, 1714–1717.

77 Förster, H., Franke, S., and Seebode, J. (1983) Transmission ultraviolet–visible–near-infrared spectroscopic investigations of the formation of carbocations in zeolites. *J. Chem. Soc., Faraday Trans. 1*, **79**, 373–382.

78 Pazé, C., Sazak, B., Zecchina, A., and Dwyer, J. (1999) FTIR and UV–vis spectroscopic study of interaction of 1-butene on H-ferrierite zeolite. *J. Phys. Chem. B*, **103**, 9978–9986.

79 Melsheimer, J. and Ziegler, D. (1992) Ethene transformation on HZSM-5 studied by combined UV−vis spectroscopy and on-line gas chromatography. *J. Chem. Soc., Faraday Trans.*, **88**, 2101–2108.

80 Kiricsi, I., Förster, H., Tasi, G., and Nagy, J.B. (1999) Generation, characterization, and transformations of unsaturated carbenium ions in zeolites. *Chem. Rev.*, **99**, 2085–2114. Additions and corrections (1999) in *Chem. Rev.*, 99, 3367–3370. See also references in this article.

81 Georg Thieme (2011) Thieme Römpp Online, www.roempp.com, last accessed 14 May 2011.

82 Klier, K. and Rálek, M. (1968) Spectra of synthetic zeolites containing transition metal ions – II. Ni^{2+} ion in type A Linde molecular sieves. *J. Phys. Chem. Solids*, **29**, 951–957.

83 Zecchina, A., Lofthouse, M.G., and Stone, F.S. (1975) Reflectance spectra of surface states in magnesium oxide and calcium oxide. *J. Chem. Soc., Faraday Trans. 1*, **71**, 1476–1490.

84 Bailes, M., Bordiga, S., Stone, F.S., and Zecchina, A. (1996) UV reflectance and FTIR spectroscopic studies of CO adsorption and reaction on lanthanum oxide. *J. Chem. Soc., Faraday Trans.*, **92**, 4675.

85 Thiede, M. and Melsheimer, J. (2002) *In situ* UV−Vis−near-IR diffuse

reflection measurement of catalysts at temperatures up to 673 K. *Rev. Sci. Instrum.*, **73**, 394–397.

86 Melsheimer, J., Thiede, M., Ahmad, R., Tzolova-Müller, G., and Jentoft, F.C. (2003) Improved experimental setup for *in situ* UV−vis−NIR spectroscopy under catalytic conditions. *Phys. Chem. Chem. Phys.*, **5**, 4366–4370.

87 Weckhuysen, B.M., Baetens, D., and Schoonheydt, R.A. (2000) Spectroscopy of the formation of microporous transition metal containing aluminophosphates under hydrothermal conditions. *Angew. Chem. Int. Ed.*, **39**, 3419–3422.

88 Weckhuysen, B.M. (2002) Snapshots of a working catalyst: possibilities and limitations of *in situ* spectroscopy in the field of heterogeneous catalysis. *Chem. Commun.*, 97–110.

89 Kazansky, V.B., Borovkov, V.Yu., and Karge, H.G. (1997) Diffuse reflectance IR study of molecular hydrogen and deuterium adsorbed at 77 K on NaA zeolite. 1. Fundamentals, combination and vibrational–rotational modes. *J. Chem. Soc., Faraday Trans.*, **93**, 1843–1848.

90 Harrick Scientific Products (2011) Datasheet: Low Temperature Reaction Chamber for the Praying Mantis, www.harricksci.com, last accessed 27 February 2011.

91 Harrick Scientific Products (2011) Datasheet: High Temperature Reaction Chamber for the Praying Mantis, www.harricksci.com, last accessed 27 February 2011.

92 Venter, J.J. and Vannice, M.A. (1988) Modifications of a diffuse reflectance cell to allow the characterization of carbon-supported metals by DRIFTS. *Appl. Spectrosc.*, **42**, 1096–1103.

93 Gao, X., Jehng, J.-M., and Wachs, I.E. (2002) *In situ* UV–vis–NIR diffuse reflectance and Raman spectroscopic studies of propane oxidation over ZrO_2-supported vanadium oxide catalysts. *J. Catal.*, **209**, 43–50.

94 Schulz-Ekloff, G., Lipski, R.J., Jaeger, N.I., Hülstede, P., and Kubelkova, L. (1995) *In situ* FTIR and UV/vis spectroscopic study of the generation of anionic Pt–carbonyl complexes within a faujasite matrix. *Catal. Lett.*, **30**, 65–75.

95 Argyle, M.D., Chen, K., Resini, C., Krebs, C. Bell, A.T., and Iglesia, E. (2004) Extent of reduction of vanadium oxides during catalytic oxidation of alkanes measured by *in-situ* UV−visible spectroscopy. *J. Phys. Chem. B*, **108**, 2345–2353.

96 Ocean Optics (2011) Ocean Optics Homepage, www.oceanoptics.com, last accessed 14 May 2011.

97 Avantes (2011) Solutions in Spectroscopy, www.avantes.com, last accessed 14 May 2011.

98 StellarNet (2011) Developing Intelligence with Light, www.stellarnet-inc.com, last accessed 14 May 2011.

99 van de Water, L.G.A., Bergwerff, J.A., Nijhuis, T.A., de Jong, K.P., and Weckhuysen, B.M. (2005) UV−vis microspectroscopy: probing the initial stages of supported metal oxide catalyst preparation. *J. Am. Chem. Soc.*, **127**, 5024–5025.

100 Groothaert, M.H., Lievens, K., Leeman, H., Weckhuysen, B.M., and Schoonheydt, R.A. (2003) An *operando* optical fiber UV–vis spectroscopic study of the catalytic decomposition of NO and N_2O over Cu-ZSM-5. *J. Catal.*, **220**, 500–512.

101 Kox, M.H.F., Stavitski, E., and Weckhuysen, B.M. (2007) Nonuniform catalytic behavior of zeolite crystals as revealed by *in situ* optical microspectroscopy. *Angew. Chem.*, **119**, 3726–3729.

102 Hellma Analytics (2011) Product Information on Reflection Probes, www.hellma-analytics.com, last accessed 14 May 2011.

103 Scansci (2011) Spectroscopic Solutions, www.scansci.com, last accessed 14 May 2011.

104 Puurunen, R.L., Beheydt, B.G., and Weckhuysen, B.M. (2001) Monitoring chromia/alumina catalysts *in situ* during propane dehydrogenation by optical fiber UV–visible diffuse reflectance spectroscopy. *J. Catal.*, **204**, 253–257.

105 Nijhuis, T.A., Tinnemans, S.J., Visser, T., and Weckhuysen, B.M. (2004) Towards real-time spectroscopic process control for the dehydrogenation of propane over supported chromium oxide catalysts. *Chem. Eng. Sci.*, **59**, 5487–5492.

106 Grandjean, D., Beale, A.M., Petukhov, A.V., and Weckhuysen, B.M. (2005) Unraveling the crystallization mechanism of CoAPO-5 molecular sieves under hydrothermal conditions. *J. Am. Chem. Soc.*, **127**, 14454–14465.

107 Bürgi, T. (2005) Combined *in situ* attenuated total reflection infrared and UV–vis spectroscopic study of alcohol oxidation over Pd/Al_2O_3. *J. Catal.*, **229**, 55–63.

108 Bürgi, T. and Baiker, A. (2006) Attenuated total reflection infrared spectroscopy of solid catalysts functioning in the presence of liquid-phase reactants. *Adv. Catal.*, **50**, 227–283.

109 Nijhuis, T.A., Tinnemans, S.J., Visser, T., and Weckhuysen, B.M. (2003) *Operando* spectroscopic investigation of supported metal oxide catalysts by combined time-resolved UV−VIS/Raman/on-line mass spectrometry. *Phys. Chem. Chem. Phys.*, **5**, 4361–4365.

110 Mesu, J.G., van der Eerden, A.M.J., de Groot, F.M.F., and Weckhuysen, B.M. (2005) Synchrotron radiation effects on catalytic systems as probed with a combined *in-situ* UV−Vis/XAFS spectroscopic setup. *J. Phys. Chem. B*, **109**, 4042–4047.

111 Mesu, J.G., Beale, A.M, de Groot, F.M.F., and Weckhuysen, B.M. (2006) Probing the influence of X-rays on aqueous copper solutions using time-resolved *in situ* combined video/X-ray absorption near-edge/ultraviolet–visible spectroscopy. *J. Phys. Chem. B*, **110**, 17671–17677.

112 Beale, A.M., van der Eerden, A.M.J., Kervinen, K., Newton, M.A., and Weckhuysen, B.M. (2005) Adding a third dimension to *operando* spectroscopy: a combined UV–Vis, Raman and XAFS setup to study heterogeneous catalysts under working conditions. *Chem. Commun.*, 3015–3017.

113 Brückner, A. (2001) Simultaneous combination of *in situ*-EPR/UV–VIS/on line GC: a novel setup for investigating transition metal oxide catalysts under working conditions. *Chem. Commun.*, 2122–2123.

114 Brückner, A. (2005) Killing three birds with one stone – simultaneous *operando* EPR/UV−vis/Raman spectroscopy for monitoring catalytic reactions. *Chem. Commun.*, 1761–1763.

115 Brückner, A. and Kondratenko, E. (2006) Simultaneous *operando* EPR/UV–vis/laser-Raman spectroscopy – a powerful tool for monitoring transition metal oxide catalysts during reaction. *Catal. Today*, **113**, 16–24.

116 Hunger, M. and Wang, W. (2004) Formation of cyclic compounds and carbenium ions by conversion of methanol on weakly dealuminated zeolite H-ZSM-5 investigated via a novel *in situ* CF MAS NMR/UV–Vis technique. *Chem. Commun.*, 584–585.

117 Jiang, Y., Huang, J., Marthala, V.R.R., Ooi, Y.S., Weitkamp, J., and Hunger, M. (2007) *In situ* MAS NMR–UV/Vis investigation of H-SAPO-34 catalysts partially coked in the methanol-to-olefin conversion under continuous-flow conditions and of their regeneration. *Micropor. Mesopor. Mater.*, **105**, 132–139.

118 Sobalik, Z., Jisa, K., Jirglova, H., and Bernauer, B. (2007) Simultaneous FTIR/UV–Vis study of reactions over metallo-zeolites: approach to quantitative *in situ* studies. *Catal. Today*, **126**, 73–80.

119 Bentrup, U., Radnik, J., Armbruster, U., Martin, A., Leiterer, J., Emmerling, F., and Brückner, A. (2009) Linking simultaneous *in situ* WAXS/SAXS/Raman with Raman/ATR/UV–vis spectroscopy: comprehensive insight into the synthesis of molybdate catalyst precursors. *Top. Catal.*, **52**, 1350–1359.

120 Lezna, R.O., Romagnoli, R., de Tacconi, N.R., and Rajeshwar, K. (2003) Spectroelectrochemistry of palladium hexacyanoferrate films on platinum substrates. *J. Electroanal. Chem.*, **544**, 101–106.

121 Baronetti, G.T., de Miguel, S.R., Scelza, O.A., Fritzler, M.A., and Castro, A.A. (1985) $Pt–Sn/A1_2O_3$

catalysts: studies of the impregnation step. *Appl. Catal.*, **19**, 77–85.

122 Carvalho, L.S., Reyes, P., Pecchi, G., Figoli, N., Pieck, C.L., and do Carmo Rangel, M. (2001) Effect of the solvent used during preparation on the properties of Pt/Al_2O_3 and $Pt–Sn/Al_2O_3$ catalysts. *Ind. Eng. Chem. Res.*, **40**, 5557–5563.

123 Bianchi, C.L., Canton, P., Dimitratos, N., Porta, F., and Prati, L. (2005) Selective oxidation of glycerol with oxygen using mono and bimetallic catalysts based on Au, Pd and Pt metals. *Catal. Today*, **102–103**, 203–212.

124 Geobaldo, F., Bordiga, S., Zecchina, A., Giamello, E., Leofanti, G., and Petrini, G. (1992) DRS UV−Vis and EPR spectroscopy of hydroperoxo and superoxo complexes in titanium silicalite. *Catal. Lett.*, **16**, 109–115.

125 Dzwigaj, S., Matsuoka, M., Anpo, M., and Che, M. (2000) Evidence of three kinds of tetrahedral vanadium(V) species in VSi beta zeolite by diffuse reflectance UV–visible and photoluminescence spectroscopies. *J. Phys. Chem. B*, **104**, 6012–6020.

126 Sendoda, Y., Ono, Y., and Keii, T. (1975) Properties of nickel cations in X-zeolite as studied by electronic spectroscopy. *J. Catal.*, **39**, 357–362.

127 Kondratenko, E.V. and Baerns, M. (2001) Catalytic oxidative dehydrogenation of propane in the presence of O_2 and N_2O – the role of vanadia distribution and oxidant activation. *Appl. Catal. A: Gen.*, **222**, 133–143.

128 Hess, C., Hoefelmeyer, J.D., and Tilley, T.D. (2004) Spectroscopic characterization of highly dispersed vanadia supported on SBA-15. *J. Phys. Chem. B*, **108**, 9703–9709.

129 Sun, H., Bai, Y. Liu, H., Jin, W., and Xu, N. (2009) Photocatalytic decomposition of 4-chlorophenol over an efficient N-doped TiO_2 under sunlight irradiation. *J. Photochem. Photobiol. A: Chem.*, **201**, 15–22.

130 van de Water, L.G.A., Bezemer, G.L., Bergwerff, J.A., Versluijs-Helder, M., Weckhuysen, B.M., and de Jong, K.P. (2006) Spatially resolved UV–vis microspectroscopy on the preparation of alumina-supported Co Fischer–Tropsch catalysts: linking activity to Co distribution and speciation. *J. Catal.*, **242**, 287–298.

131 Hammett, L.P. and Deyrup, A.J. (1932) A series of simple basic indicators. I. The acidity functions of mixtures of sulfuric and perchloric acids with water. *J. Am. Chem. Soc.*, **54**, 2721–2739.

132 Hess, C. (2006) Characterization of the synthesis and reactivity behavior of nanostructured vanadia model catalysts using XPS and vibrational spectroscopy. *Surf. Sci.*, **600**, 3695–3701.

133 Gao, X., Bañares, M.A., and Wachs, I.E. (1999) Ethane and *n*-butane oxidation over supported vanadium oxide catalysts: an *in situ* UV–visible diffuse reflectance spectroscopic investigation. *J. Catal.*, **188**, 325–331.

134 Rao, T.V.M., Deo, G., Jehng, J.-M., and Wachs, I.E. (2004) *In situ* UV–Vis–NIR diffuse reflectance and Raman spectroscopy and catalytic activity studies of propane oxidative dehydrogenation over supported CrO_3/ZrO_2 catalysts. *Langmuir*, **20**, 7159–7165.

135 Brückner, A. and Kondratenko, E. (2006) Simultaneous *operando* EPR/UV–vis/laser-Raman spectroscopy – a powerful tool for monitoring transition metal oxide catalysts during reaction. *Catal. Today*, **113**, 16–24.

136 Argyle, M.D., Chen, K., Resini, C., Krebs, C., Bell, A.T., and Iglesia, E. (2004) Extent of reduction of vanadium oxides during catalytic oxidation of alkanes measured by *in-situ* UV–visible spectroscopy. *J. Phys. Chem. B*, **108**, 2345–2353.

137 Klokishner, S.I., Reu, O., Chan Thaw, C., Jentoft, F.C., and Schlögl, R. (2011) Redox properties of manganese-containing zirconia solid solution catalysts analyzed by *in situ* UV−vis spectroscopy and crystal field theory. *J. Phys. Chem. A*, **115**, 8100–8112.

138 Lu, J., Bravo-Suárez, J.J., Takahashi, A., Haruta, M., and Oyama, S.T. (2005) *In situ* UV–vis studies of the effect of particle size on the epoxidation of ethylene and propylene on supported

silver catalysts with molecular oxygen. *J. Catal.*, **232**, 85–95.

139 Bjørgen, M., Bonino, F., Kolboe, S., Lillerud, K.-P., Zecchina, A., and Bordiga, S. (2003) Spectroscopic evidence for a persistent benzenium cation in zeolite H-beta. *J. Am. Chem. Soc.*, **125**, 15863–15868.

140 Tzolova-Müller, G. and Jentoft, F.C., unpublished data.

141 Jiang, Y., Huang, J., Marthala, V.R.R., Ooi, Y.S., Weitkamp, J., and Hunger, M. (2007) *In situ* MAS NMR–UV/Vis investigation of H-SAPO-34 catalysts partially coked in the methanol-to-olefin conversion under continuous-flow conditions and of their regeneration. *Micropor. Mesopor. Mater.*, **105**, 132–139.

142 Tinnemans, S.J., Kox, M.F.H., Nijhuis, T.A., Visser, T., and Weckhuysen, B.M. (2005) Real time quantitative Raman spectroscopy of supported metal oxide catalysts without the need of an internal standard. *Phys. Chem. Chem. Phys.*, **7**, 211–216.

143 Villegas, J.I., Murzin, D.Yu., Tzolova-Müller, G., and Jentoft, F.C., unpublished data.

4
Photoluminescence Spectroscopy

Masaya Matsuoka, Masakazu Saito, and Masakazu Anpo

4.1
Introduction

Photoluminescence spectroscopy is a nondestructive and highly sensitive method with which to investigate the electronic properties of materials, especially in their excited states. Photoluminescence can be defined as the radiation emitted from a molecule or a solid which is excited by absorbing photons (photoexcitation). In the field of solid-state physics, photoluminescence spectroscopy has been widely applied for the determination of the bandgap or impurity levels of semiconducting materials and also their defect sites [1]. Of particular importance are the recent remarkable advances in photoluminescence spectroscopy for applications in biological and medical research. Since the discovery of the green fluorescent protein (GFP) by Osamu Shimomura [2], one of winners of the 2008 Nobel Prize in Chemistry, the GFP gene has been introduced in many mammalian cells to insert GFP into living organisms [3]. Labeled or marked cells can thus be easily monitored by a photoluminescence detection method, which has been widely applied in biological and medical studies involving investigations of cancer metastasis and brain cell interactions [4].

One of the most important advances in photoluminescence spectroscopy has been its application in the field of catalysis. Recent innovations in spectroscopic technologies have allowed photoluminescence acquisition with high resolution and sensitivity on a shorter time scale, leading to a more comprehensive understanding of the chemical nature of catalytically active sites and of the mechanisms driving catalytic reactions. Photoluminescence spectroscopy is thus one of the most powerful and highly sensitive means to investigate coordinatively unsaturated surface sites of solid catalysts and also the local structures of highly dispersed oxide catalysts, both of which exhibit unique photoluminescence under UV irradiation [5–17]. Highly dispersed oxide catalysts with low loadings below 0.1 wt%, for example, exhibit unusual and unique catalytic or photocatalytic properties due to the active phase–support interactions, dispersion effects, and/or quantum size effects, whereas most conventional characterization techniques are not sensitive enough to detect such low

Characterization of Solid Materials and Heterogeneous Catalysts: From Structure to Surface Reactivity, First Edition. Edited by Michel Che and Jacques C. Védrine.
© 2012 Wiley-VCH Verlag GmbH & Co. KGaA. Published 2012 by Wiley-VCH Verlag GmbH & Co. KGaA.

concentrations. In contrast, photoluminescence spectroscopy involving lifetime measurements, photoluminescence intensity and lineshape determination is so sensitive that significant information can be obtained on the structures of the active surface sites, especially for oxide loadings below 0.1 wt%. Moreover, when combined with laser or time-resolved spectroscopy, photoluminescence measurements provide insight not only into the dynamics of catalysis and photocatalysis, including molecular migration and electron transfer processes at surfaces, but also into molecular-level discrimination and identification of the active sites on catalysts. In fact, time-resolved photoluminescence spectroscopy has also been applied to elucidate the dynamics that initiate photocatalytic reactions involving a recombination process of the photo-formed electrons and holes [18–22]. This chapter presents a brief introduction to the basic principles of photoluminescence and time-resolved photoluminescence and their applications in the characterization and reactivity of solid catalysts in relation to the reaction dynamics of photocatalysis.

4.2 Basic Principles of Photoluminescence

Photoluminescence can be defined as the radiation emitted from a molecule or a solid after it has absorbed photon energy from an external source and been transferred into an electronic excited state. The principles of photoluminescence can be understood by assuming some simplifications. Morse potential energy curves (Figure 4.1) can be considered for a certain chemical bond of a molecule excited by light.

The absorption of light close to the fundamental absorption edge of the molecule leads to the excitation of an electron of the molecule. For example, when the $M^{2+}-O^{2-}$ ion pairs at the solid surface of alkaline earth metal oxides are excited by UV light, the excitation is followed by a charge-transfer process from O^{2-} to M^{2+} to create an *exciton*, that is, an electron–hole pair, as follows [23–27]:

$$\left[M^{2+}\text{–}O^{2-}\right](S_0) \xrightarrow{h\nu} [M^{+}\text{–}O^{-}]^{*}(S_1)$$

The horizontal lines in the potential wells shown in Figure 4.1 represent the possible vibrational states of the oscillator, either in the ground electronic singlet state (S_0) or the electronic excited singlet state (S_1). It is readily understood that the potential energy curve of the excited state (S_1) is located at higher energy than that of the ground state (S_0), with its potential located at larger internuclear distances, since, electrostatically, the charge transfer leads to an $M^{+}-O^{-}$ bond, that is, a weakening of the $M^{2+}-O^{2-}$ bond.

The observed spectral transitions, which lead to the absorption spectrum, are related to the energy diagram such as that in Figure 4.1 on the basis of the Franck–Condon principle. This principle is based on the fact that electrons move and rearrange at a much higher rate than that of the vibrational movement of the nuclei of a molecule, that is, an electronic configuration changes within a time so short that the nuclei do not change their positions during absorption. Spectral transitions with the highest

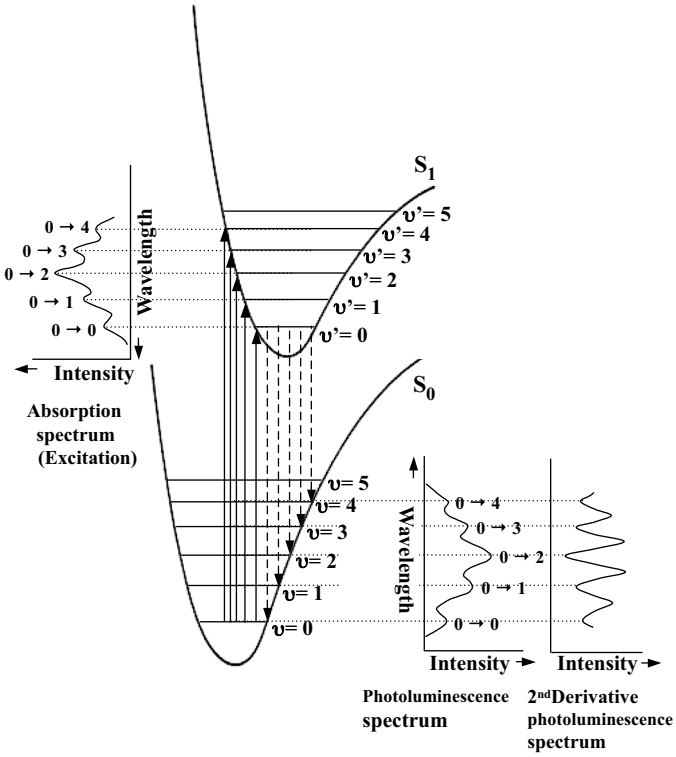


Figure 4.1 Schematic energy diagram showing the origin of absorption, photoluminescence, and the second-derivative photoluminescence spectra.

probability then occur at constant internuclear distance and, therefore, should be drawn vertically and not, as might be expected, from the potential minimum of the lower curve to that of the upper curve. In absorption, an electronic transition may show a series of lines called the vibrational fine structure corresponding to the different vibrational states reached in which the most intense transition refers to the most probable vertical transition.

There are many ways in which the system can return to the lower energy state. The excess energy can be lost to the vibration, rotation, and translation of the surrounding molecules or ions, that is, as heat. Another more interesting possibility is that the excess energy becomes involved in a chemical reaction, resulting in photochemistry. The occurrence of radiative decay is another possibility as opposed to nonradiative or radiationless decay, when the molecule or ion pair loses its excitation energy as a photon.

The sequence of steps involved in the radiative decay process, that is, the photoluminescence process, is also described in Figure 4.1. The initial absorption excites the molecule from the ground electronic singlet state (S_0) to the electronically excited singlet state (S_1). The photoexcited molecule relaxes down the ladder of vibrational levels, releasing its energy into its surroundings as heat, and finally ends

up in the lowest vibrational level of S_1. If the thermal environment cannot accommodate the electronic excitation energy, or transition from S_1 to S_0, the molecule emits this energy as radiation, which can be observed as photoluminescence or fluorescence [28]. When intersystem crossing occurs between S_1 and the triplet state (T_1), phosphorescence can be observed as the radiative deactivation process from the lowest vibrational state of T_1 to S_0 [28]. If the excitation energy is localized on a certain bond of the molecule, the photoluminescence spectrum exhibits a well-resolved vibrational fine structure which reflects the vibrational energy levels of the S_0 state. The second-derivative photoluminescence spectrum can be utilized to determine the energy value between the vibrational energy levels of the S_0 state, since the local minimum of the second-derivative photoluminescence spectrum corresponds exactly to the local maximum of the vibrational fine structure of the photoluminescence spectrum [8].

When the photoexcited molecule loses its excitation energy through only a radiative decay process, the rates of radiative transitions are summarized by the Einstein coefficients of stimulated and spontaneous processes. The rates of stimulated absorption (R_1), stimulated emission (R_2), and spontaneous emission (R_3) between the ground state and excited state with an energy gap of E ($= h\nu$) can be expressed as follows:

$$R_1 = NB\varrho, \quad R_2 = N'B'\varrho, \quad R_3 = N'A$$

where N is the population of the ground state, N' is the population of the excited state, B is an Einstein coefficient of the stimulated absorption, B' is an Einstein coefficient of the stimulated emission, A is an Einstein coefficient of the spontaneous emission, and ϱ is the density of radiation in the blackbody which is given by the Planck distribution as follows:

$$\varrho = \frac{8\pi h\nu^3/c^3}{e^{h\nu/kT}-1}$$

Since the total rates of emission and absorption are equal at thermal equilibrium, the following equation can be obtained:

$$NB\varrho = N'(A + B'\varrho)$$

This expression can be rearranged into the following equation using the Boltzmann expression ($N'/N = e^{-h\nu/kT}$):

$$\varrho = \frac{A/B}{e^{h\nu/kT} - B'/B}$$

By comparing the above equation with the expression for the Planck distribution, the following relationship among the Einstein coefficients can be obtained:

$$A = \left(8\pi h\nu^3/c^3\right)B, \quad B' = B$$

The lifetime (τ) of the photoexcited molecule can be expressed as $\tau = 1/A$, showing that the smaller the Einstein coefficient of the stimulated absorption (B), the longer is

the lifetime of the spontaneous emission. However, except for the spontaneous emission process, excess energy of the photoexcited molecule can be lost through the energy transfer process with the surrounding molecules. In such cases, the rate constant of the energy transfer process can be determined by the photoluminescence quenching measurements, as discussed in Section 4.5.2.3.

4.3
General Aspects of Photoluminescence Measurements

4.3.1
Steady-State Photoluminescence Measurements

The high sensitivity of photoluminescence analysis has allowed the detection and determination of extremely low concentrations of the emitting materials. Lower limits of detection are in the parts per million (ppm) to parts per billion (ppb) range. Selectivity in photoluminescence analysis has become possible using variations in excitation and/or analytical wavelengths, allowing the simultaneous determination of emitting components in many mixtures. Potentially, phosphorescence can be observed with a higher degree of sensitivity and selectivity than fluorescence owing to its longer lifetime, which offers the possibility of investigations with different spectroscopic parameters. Efficient application of photoluminescence spectroscopy can yield insight into the nature of the excited states of the target species and of various photochemical processes. In the excited state, a molecule will have a completely different electron distribution from that of a molecule in the ground state and also a different geometry. It will also usually undergo chemical reactions that are completely different from those of a molecule in the ground state. These photochemical and photophysical processes can be used to explain the basic principles of the photocatalytic reactivity of catalysts [28].

Various commercially available auto-compensating spectrophotofluorimeters (photoluminescence instrumentation) have been employed to measure and analyze the photoluminescence spectra of catalysts. The three principal components of all of the spectrophotofluorimeters are the excitation light source, the chamber to set the sample, and the emitted photon detector (Figure 4.2). The light source is usually either a mercury or xenon arc lamp.

In order to select the excitation radiation to be focused on the sample cell, light passes through a monochromator equipped with a grating or prism. Interference filters can also be used to provide greater selectivity and resolution for analysis of the photoluminescence spectra. The emission leaving the sample cell usually passes directly into the emission monochromator and then into a high-gain photomultiplier tube. The spectrum is recorded with the correct compensation to cover small variations in the excitation light power [8–10, 28]. Although the design of the cell holder may determine the amount of scattered and stray light from the samples, glass filters can be used to minimize scattered light. Also, some kinds of quartz may fluoresce under UV excitation, causing errors in the photoluminescence

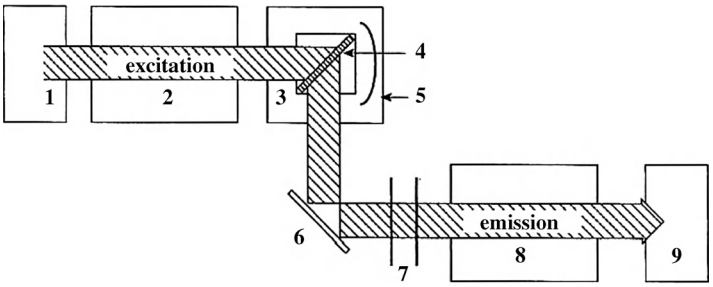


Figure 4.2 Placement of optical components in a conventional spectrophotofluorimeter. 1, Lamp; 2, excitation monochromator; 3, cell; 4, sample; 5, light trap; 6, mirror; 7, filters; 8, emission monochromator; 9, detector.

measurements. Therefore, secondary filters may be used and the sample cell should be made from high-quality nonfluorescent quartz. The presence of oxygen is critical because the interaction of oxygen with the sample can cause serious errors and its ability to quench not only the fluorescence but also phosphorescence makes deaeration necessary. Also, the photoluminescence intensity usually decreases when the temperature of the sample is increased owing to the higher probability of other nonradiative deactivations. Therefore, to minimize such temperature effects, the photoluminescence spectra are often measured at liquid nitrogen temperature and even liquid helium temperature [8–10, 28].

4.3.2
Time-Resolved Photoluminescence Measurements

Normally, the steady-state photoluminescence spectra are measured under continuous irradiation by a light source such as an Xe or high-pressure Hg lamp. In contrast, time-resolved photoluminescence spectra are measured under pulses from light sources such as a nitrogen laser or pulsed Xe lamp. Time-resolved photoluminescence spectra are obtained by collecting the photoluminescence radiation within a certain time interval (sampling time) after a certain time period (delay time) following the pulse excitation, as shown in Figure 4.3.

As an example, three-dimensional plots of time-resolved photoluminescence of Ti-MCM-41 measured at various delay times are shown in Figure 4.4a. A broad photoluminescence due to the surface OH groups (Si−OH) of MCM-41 can be observed at around 400 nm in the spectrum measured at a short delay time (0.5 ms). However, the intensity of the photoluminescence at around 400 nm decreases with an increase in the delay time (~1.0 ms) and another photoluminescence process was observed at around 460 nm. This emission can be attributed to the following charge-transfer processes on the Ti−O moieties of the isolated tetrahedrally coordinated Ti^{4+} oxide species ($Ti^{IV}O_4^{4-}$), involving an electron transfer from the O^{2-} to Ti^{4+} ions and a reverse radiative decay from the charge-transfer excited triplet state [29–38]:

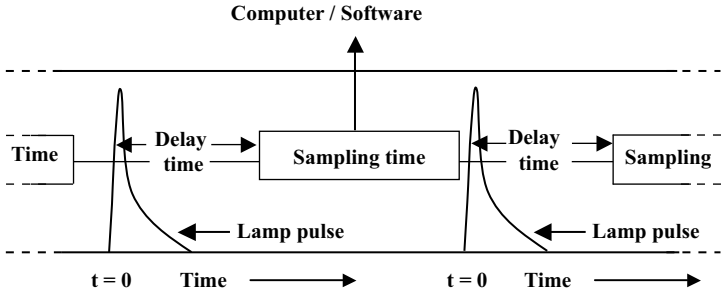


Figure 4.3 Typical sequence of data acquisition for time-resolved photoluminescence measurements.

$$\left[Ti^{4+} - O^{2-}\right] \xrightarrow{h\nu} \left[Ti^{3+} - O^{-}\right]^{*} \xrightarrow{h\nu'} \left[Ti^{4+} - O^{2-}\right]$$

The lifetimes of the excited states of two different photoluminescence moieties can be determined by decay analysis at certain wavelength regions where the overlap of the two photoluminescence moieties is negligible (Si−OH, 0.11 ms at 370 nm; $Ti^{IV}O_4{}^{4-}$, 11.8 ms at 480 nm). It should be noted that under continuous irradiation, the photoluminescence of the Ti^{4+} oxide species can be observed only as a small shoulder for the photoluminescence of MCM-41, as shown in Figure 4.4b. Time-resolved photoluminescence techniques are, therefore, useful in distinguishing different photoluminescence moieties having different photoluminescence

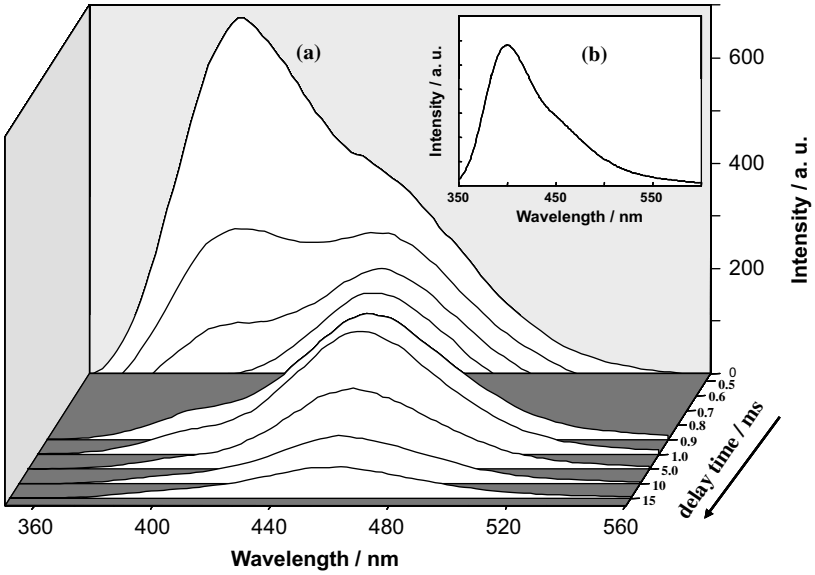


Figure 4.4 Time-resolved photoluminescence spectra (a) and steady-state photoluminescence spectrum (b) of Ti-MCM-41(Si/Ti = 200) measured at 298 K. (a) Sampling time, 0.1 ms; excitation wavelength, 260 nm. (b) Excitation wavelength, 260 nm.

lifetimes. Time-resolved photoluminescence of the tetrahedral Ti^{4+} oxide species at 460 nm revealed them to be efficiently quenched by the addition of NO or propane, accompanied by a decrease in the photoluminescence lifetime. This indicates that the photoexcited Ti^{4+} oxide species interacts dynamically with the added gas-phase molecules. In fact, UV irradiation of Ti-MCM-41 in the presence of NO and propane led to the efficient photocatalytic reduction of NO by propane to produce N_2 and acetone [29–38]. These results clearly demonstrate the advantage of time-resolved photoluminescence measurements for investigations into the reaction dynamics of the photoexcited active site with reactant molecules as compared with steady-state photoluminescence measurements.

4.4
Characterization of Catalysts by Photoluminescence and Time-Resolved Photoluminescence Spectroscopy

It is well known that coordinatively unsaturated sites, which exist on the surface of metal oxides such as bulk MgO, play an important role in various catalytic and photocatalytic reactions. Moreover, the coordinatively unsaturated sites of single-site catalysts such as transition metal oxides or ions highly dispersed on supports also play an important role as catalytically active sites and adsorption sites for the reactant molecules. Photoluminescence spectroscopy is a powerful and sensitive technique to detect and characterize these coordinatively unsaturated sites. The following sections deal with the characterization of catalytically active sites of bulk metal oxides and various single-site catalysts by photoluminescence spectroscopy. Furthermore, the application of time-resolved photoluminescence spectroscopy to elucidate the electronic structure of TiO_2 photocatalysts is also introduced.

4.4.1
In Situ Photoluminescence of Microcrystalline MgO

The normal coordination number of ions in the bulk for octahedrally coordinated alkaline earth metal oxides such as MgO is 6. However, on microcrystalline MgO, in which (100) faces are largely predominant, the coordination number of the surface ions is no longer as high as 6. Generally, as shown in Figure 4.5, they are expressed as $Mg^{2+}{}_{LC}$ or $O^{2-}{}_{LC}$ with such low coordination numbers as 5, 4, or even 3 [23]. Moreover, there have been various reports presenting direct spectroscopic evidence to indicate that such surface ions in low coordination play a significant role in the catalytic and photocatalytic activities of MgO.

Powdered MgO microcrystals with a high surface area degassed at high temperatures have been reported to exhibit photoluminescence when excited by UV light at ~260–400 nm with an energy much lower than the bandgap of MgO single crystals, that is, pure bulk single crystals show no absorption in such near-UV regions [24]. Such photoluminescence is sensitively quenched by the addition of O_2 or air, leading to the conclusion that the photoluminescence of such high surface area MgO

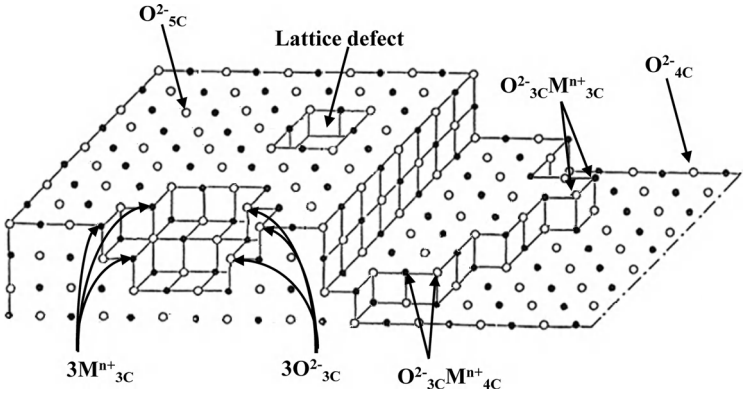


Figure 4.5 Representation of a surface plane (100) of MgO showing surface imperfections such as steps, kinks, and corners which provide sites for ions of low coordination.

powders is associated with a surface phenomenon. It has been shown that the values of the surface bandgap, E_{sg}, for different surface planes of MgO, which were calculated from the expression of Levine and Mark by considering surface Madelung constants, are in good agreement with the excitation energies of the observed photoluminescence spectra of well-degassed MgO powders. Zecchina and Stone [25] found that abnormal absorption bands appear in the UV reflectance spectra of well-degassed powdered MgO at much lower frequencies than those of bulk MgO single crystals. More extensive studies, together with theoretical and electron paramagnetic resonance (EPR) measurements [26], have shown such abnormal absorption bands and the observed short lifetime(10^{-3}–10^{-6} s) of the photoluminescence spectra to be described by the charge-transfer processes involving surface ions in low coordination at the surface of the well-degassed MgO microcrystals:

$$\left(Mg_{LC}{}^{2+} - O_{LC}{}^{2-}\right) \xrightarrow{h\nu} \left(Mg_{LC}{}^{+} - O_{LC}{}^{-}\right)^{*}$$

Anpo *et al.* [27] found that microcrystalline MgO evacuated at high temperatures for a sufficient time (defined as well degassed) exhibits two different types of photoluminescence: an emission with a short lifetime of about 10^{-5} s and another with a long lifetime of about 1–10^{4} s. The former emission is associated with the charge-transfer processes involving surface ions in low coordination and the latter with the presence of surface $F_s{}^{+}$ centers. Consequently, it has been confirmed that both the charge-transfer processes (charge-transfer mechanism) and the radiative process involving the surface $F_s{}^{+}$ center (the defect mechanism) account for the photoluminescence of MgO degassed at temperatures higher than 673 K. It has also been shown that the yields of the photoluminescence with short and long lifetimes vary from sample to sample and depend on the pretreatment temperature. As shown in Figure 4.6, the well-evacuated MgO catalyst exhibits a photoluminescence spectrum at ~340–450 nm when it is excited with UV light at 240–280 nm.

Figure 4.7 shows that increasing the degassing temperature of MgO increases the intensity of the photoluminescence, which passes through a maximum at ~1173 K

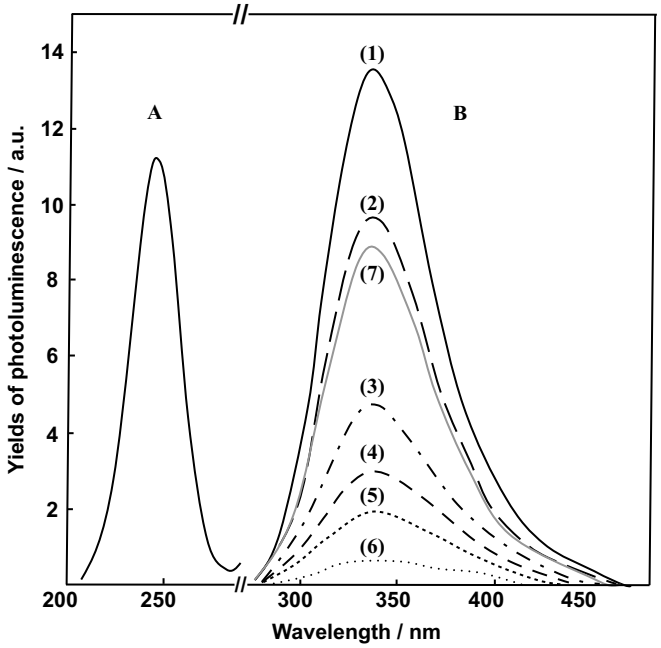


Figure 4.6 Photoluminescence spectrum of powdered MgO degassed at 1273 K for 2 h (1) and the effect of the addition of O_2 on the photoluminescence spectrum at 295 K (2–7). Excitation spectrum (A) and photoluminescence spectra (B). Excitation beams at 240 ± 10 nm, emission monitored at 340 nm, recorded at 298 K, and O_2 added at 298 K. Pressure of O_2 determined: (1) under vacuum, (2) 1.064 Pa, (3) 4.389 Pa, (4) 8.246 Pa, (5) 13.97 Pa, (6) 52.54 Pa, and (7) after evacuation of sample 6.

and then decreases due to sintering of the catalyst. The peak shifts towards shorter wavelength regions, leveling off at around 335 nm at degassing temperatures higher than 1073 K. During degassing treatment, the major desorbed gas was found to be H_2O with minor amounts of CO_2. Moreover, H_2O desorption was observed at temperatures higher than 473 K, mainly at ~673–873 K. It has also been shown that the photoluminescence spectrum of MgO observed at ~330–420 nm appears upon surface dehydroxylation [27]. In other words, the intrinsic surface sites which appear upon removal of the surface OH groups are linked to the photoluminescence observed with the well-degassed powdered MgO catalysts [27]:

$$2OH^- \rightarrow O_{LC}{}^{2-} + H_2O$$

Figure 4.6 also shows that the addition of O_2 at 298 K to MgO degassed at 1273 K leads to efficient quenching of the photoluminescence without any change in the shape of the spectrum. The evacuation of O_2 at the same temperature for about 20 min, after complete quenching, also leads to the recovery of most of the emission. The quenching of the photoluminescence by the addition of O_2 involves two mechanisms: (i) the collisional quenching due to a weak interaction, whereby O_2

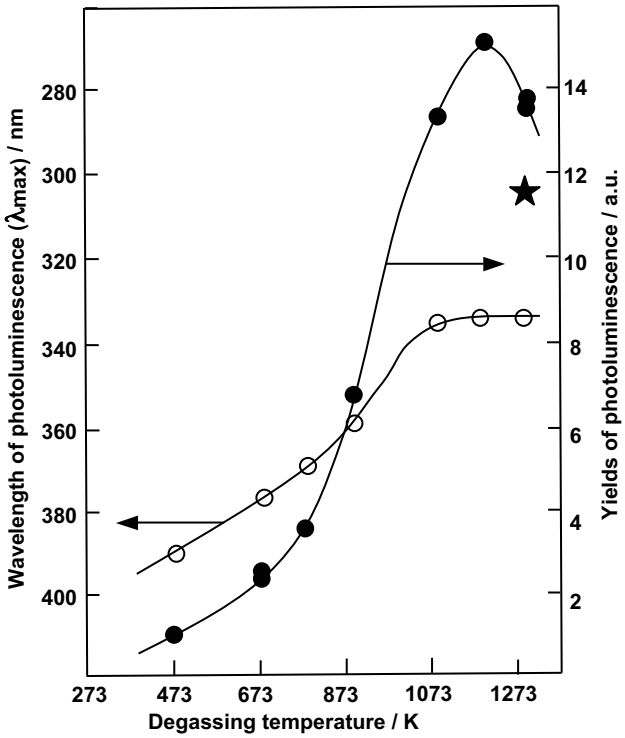


Figure 4.7 Effect of the degassing temperature on the photoluminescence spectrum of powdered MgO. *, MgO degassed for 3 h rather than 2 h.

molecules interact with the active sites in their excited state, and (ii) quenching due to the formation of an adsorbed complex between the adsorbed molecules and the excited active emitting sites even in their ground state. These mechanisms result in the formation of a nonradiative deactivation pathway and/or the destruction of the radiative pathway through the formation of adsorbed complexes such as O_2^- on the emitting sites. For microcrystalline MgO, the former mechanism is predominant since the reversibility suggests that the added molecules interact weakly with the emitting sites.

4.4.2
In Situ Photoluminescence of Bulk TiO_2 Photocatalysts

Anpo investigated the photoluminescence behavior of bulk TiO_2 photocatalysts in the presence of various kinds of reactant molecules and explained the dependence of the photoluminescence intensity on its atmosphere by considering the change in the surface band bending of TiO_2 particles, its extent depending on the electronegativity or electroaffinity of the reactant molecules [39]. The bulk TiO_2 photocatalyst exhibits photoluminescence at about 450–550 nm when excited with light having energies greater than the bandgap of the catalyst, as shown in Figure 4.8.

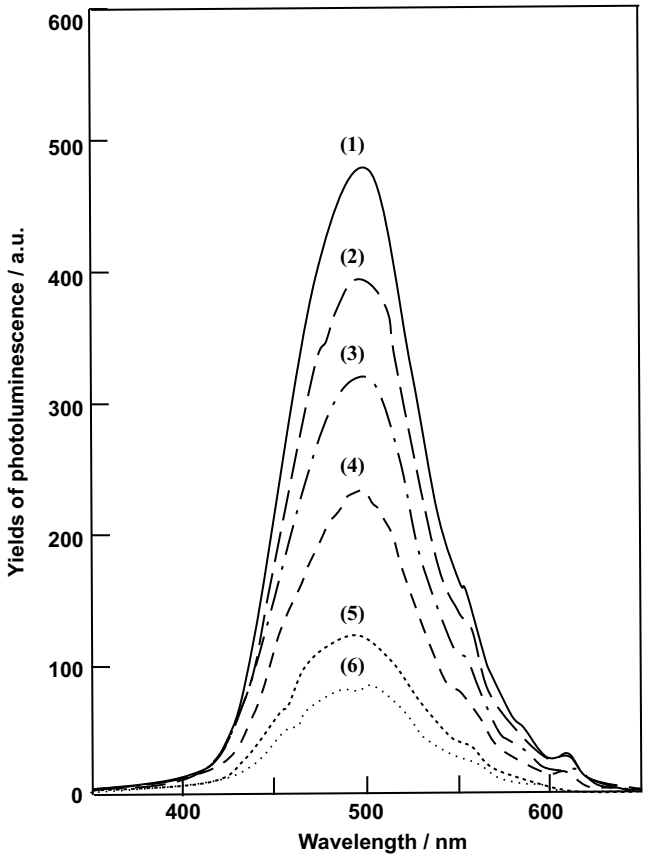


Figure 4.8 Photoluminescence spectra of powdered TiO_2 at 77 K in the absence (1) and presence (2–6) of added O_2. Excitation wavelength, 300 nm; temperature, 77 K. Amount of O_2 added (in 10^{-6} mol g^{-1} catalyst): (1) 0, (2) 1.1, (3) 4.7, (4) 11.8, (5) 38.2, and (6) 72–150.

With increased adsorption of O_2 on the TiO_2, the photoluminescence decreases markedly in intensity. However, the addition of excessive amounts of O_2 does not quench the photoluminescence completely and about 15% of the photoluminescence remains unquenched with the sample under 1 bar of O_2. After sufficient quenching, the intensity recovered only partially upon evacuation of the sample at 298 K. EPR measurements indicated that the addition of O_2 at 298 K to TiO_2, which had been evacuated at 473 K, led to the formation of O_2^- anion radicals adsorbed on Ti^{4+} sites. Therefore, the irreversible quenching of the photoluminescence is attributed to the formation of O_2^- since the superoxide is thermally stable and remains on TiO_2 even after exhaustive evacuation at 298 K. The addition of N_2O also leads to quenching of the photoluminescence but with a much lower efficiency than with O_2. Moreover, it was found that small amounts of N_2O decompose into N_2 and O^- through electron transfer from the TiO_2 to N_2O molecules. Increasing the amounts of added 1-C_4H_8 to the TiO_2 catalyst caused the photoluminescence to increase in intensity [40].

Similarly, the addition of various unsaturated hydrocarbons, such as C_3H_6, $C_2H_5C\equiv CH$, $CH_3C\equiv CH$, C_2H_4, and $CH\equiv CH$, and also H_2O and H_2, enhanced the photoluminescence. The extent of photoluminescence enhancement depends strongly on the ionization potential of the added compounds, that is, the lower the ionization potential of the added compound, the higher is the photoluminescence intensity, as shown in Figure 4.9. The addition of N_2 was responsible for only a negligible change in the photoluminescence intensity. These results suggest that the formation of negatively charged adducts through electron donation by the TiO_2 surface causes the quenching of the photoluminescence, whereas the formation of positive adducts through hole trapping results in enhancement of the photoluminescence. These changes in the observed photoluminescence intensity have been explained by the dead-layer model proposed by Meyer *et al.* [41]. As shown in Figure 4.10, these data suggest that the addition of H_2O and/or $CH_3C\equiv CH$ to TiO_2 causes a decrease in the extent of structural changes in the bending of the surface band, resulting in an increase in the efficiency of the recombination of the photogenerated electrons and holes, and subsequently an enhancement of the photoluminescence. On the other hand, the addition of O_2 to these photocatalysts causes suppression of the recombination efficiency of the photogenerated electrons and holes, that is, a better and more efficient charge separation resulting in quenching of the photoluminescence.

Murabayashi and co-workers subsequently studied the photoluminescence properties of rutile TiO_2 and anatase TiO_2 powders at room temperature in air with and

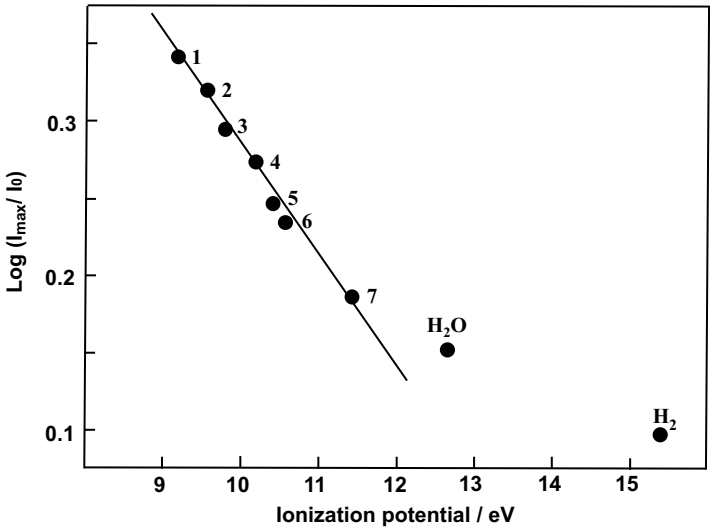


Figure 4.9 Effect of additive ionization potentials on the photoluminescence intensity. I_0 and I_{max} are the maximum photoluminescence intensities, respectively, under vacuum (or in N_2) and in the presence of added compounds: (1) 1,3-butadiene, (2) 1-butene, (3) propene, (4) 1-butyne, (5) 1-propyne, (6) ethylene, and (7) acetylene. Photoluminescence spectra recorded at 77 K.

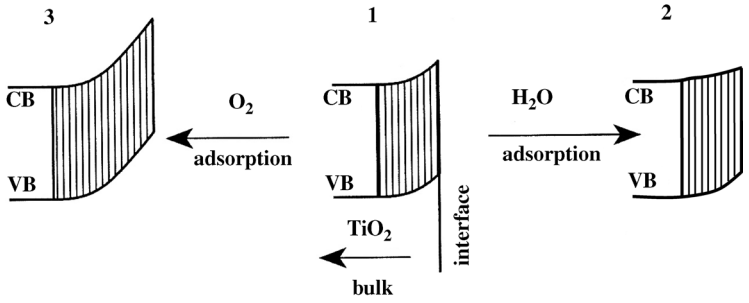


Figure 4.10 Schematic description of the surface band bending of TiO_2: (1) after degassing *in vacuo*, (2) after adsorption of H_2O (decrease in band bending by the formation of positively charged species on the surface), and (3) after adsorption of O_2 (increase in band bending by the formation of negatively charged species on the surface).

without reactant molecules, such as ethanol and methanol, in order to elucidate the reaction mechanisms of the gas-phase photocatalytic reactions [42]. For rutile TiO_2 powders, they observed that the photoluminescence intensities in these atmospheres, except air, increase linearly with the square root of the UV irradiation time, and also found that the time dependence is in good agreement with that of the integrated amount of O_2 photodesorbed from the rutile TiO_2 powder, as can be seen in Figure 4.11. By considering the O_2 photodesorption and its effect on the surface

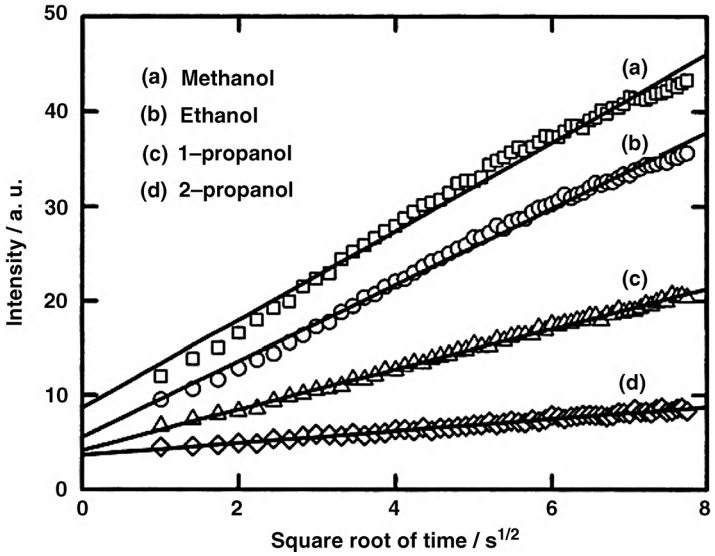


Figure 4.11 Relationship between the photoluminescence (PL) intensities of rutile TiO_2 powder Kanto-R in air with C_1–C_3 alcohols (methanol, ethanol, 1-propanol, and 2-propanol) and the square root of the UV irradiation time from 1 to 60 s [42]. The squares of the regression coefficients are >0.98.

band bending of the powder, the time dependence of the photoluminescence can be explained. However, these photoluminescence behaviors were not observed for anatase TiO_2 powders. Such inconsistencies in photoluminescence behavior between rutile and anatase TiO_2 were explained as being due to the differences in the photocatalytic activities of the alcohols used.

4.4.3
In Situ Photoluminescence of Highly Dispersed Transition Metal Ions and Oxides

4.4.3.1 V-Containing BEA Zeolite Catalysts

Various transition metal ions (Ag^+, Cu^+) and oxides (Ti^{4+}, V^{5+}, Mo^{6+}, Cr^{6+}) highly dispersed on supports such as SiO_2 or zeolites show typical photoluminescence which is fairly sensitive to their local structure or environment. Photoluminescence measurements can, thus, provide effective ways to detect and clarify the precise local structure of metal ions or oxides as the catalytically active center.

The time-resolved photoluminescence spectra of V-containing BEA zeolite catalysts [V/SiBEA (0.05 wt%)] and the corresponding second-derivative spectra are shown in Figure 4.12 [15]. Here, the second-derivative photoluminescence spectra are shown upside-down by multiplying the original spectra by −1 in order to emphasize the good correspondence between the vibrational fine structure and its second-derivative spectrum. The photoluminescence spectrum observed under steady-state irradiation did not show a well-defined vibrational fine structure (Figure 4.12a), whereas its second-derivative spectrum exhibited well-defined peaks (Figure 4.12a′), suggesting that the steady-state photoluminescence spectrum may consist of several overlapping photoluminescence moieties having different vibrational fine structures. In fact, optimizations of the delay and sampling times allow the discrimination of photoluminescence moieties having different lifetimes. Figure 4.12b and c show the time-resolved photoluminescence spectra measured at different delay times and sample windows, the former and latter corresponding to the photoluminescence moieties having short and long lifetimes, respectively. It can be clearly seen that both time-resolved photoluminescence spectra exhibit well-defined vibrational fine structures. Comparisons of the time-resolved spectra with the steady-state spectrum make it possible to conclude that three kinds of isolated tetrahedral vanadium oxide species (α, β, γ) exist within the V/SiBEA catalyst. Moreover, detailed investigations of the second-derivative photoluminescence spectra showed that the energy difference between the (0–0) and (0–1) transitions of the photoluminescence can be determined as follows: $1018\,cm^{-1}$ (α) $< 1036\,cm^{-1}$ (γ) $< 1054\,cm^{-1}$ (β) [15, 16], thus showing characteristic values reported for the stretching vibrational energy of the V=O double bond of the supported vanadium oxide species as determined by Raman or Fourier transform (FT) infrared (IR) measurements ($1035–1050\,cm^{-1}$) [8–10]. These results indicated that the excitation energy of the tetrahedral vanadium oxide species (α, β, γ) is localized in the V=O double bond and that the V=O bond length decreases in the following order: $\alpha < \gamma < \beta$. The distortion of the coordination sphere of the vanadium oxide species from an ideal T_d (tetrahedral) symmetry increases in reverse sequence: $\alpha < \gamma < \beta$ [15,

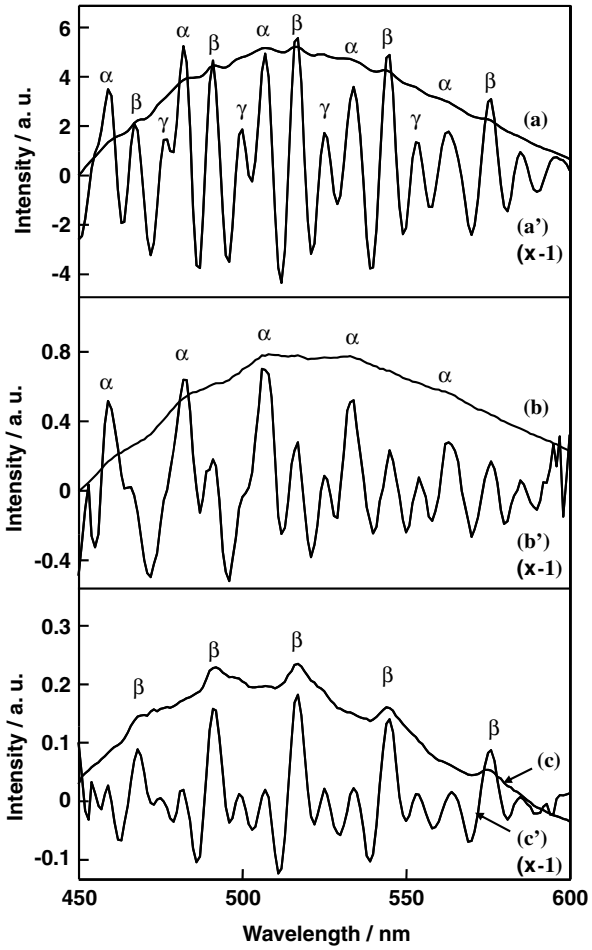
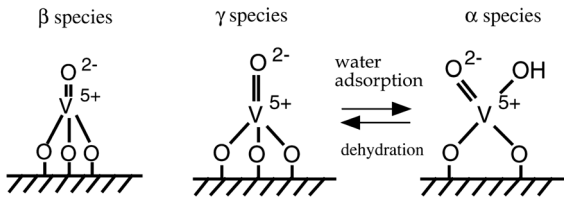


Figure 4.12 Photoluminescence (a, b, c) and their second-derivative (a′, b′, c′)* spectra of V/SiBEA (0.05 wt% as V metal) measured at 77 K. (a, a′) Measured under continuous irradiation at 250 nm. (b, b′) Measured between 0.05 and 3 ms after pulse irradiation at 250 nm. (c, c′) Measured between 50 and 100 ms after pulse irradiation at 250 nm. *Here, the second derivatives are multiplied by −1. V/SiBEA was prepared by a wet process from the dealuminated β-zeolite (Siβ:Si/Al > 1300) and ammonium metavanadate aqueous solution).

16]. It was also found that the photoluminescence lifetime increases with increase in the distortion of the coordination symmetry of the vanadium oxide species, that is, 28 ms (α) < 49 ms (γ) < 88 ms (β), showing good agreement with the previously reported enhancement of the intersystem crossing from the S_1 to T_1 state when the coordination sphere deviates from ideal T_d symmetry [14, 17]. *In situ* photoluminescence investigations revealed that the γ species is converted to an α species in the presence of water vapor whereas the α species is reversibly converted to a γ species by dehydration of the catalyst [15, 16]. Based on these results, the local structure of three kinds of vanadium oxide species have been proposed as follows:



	β species	γ species	α species
V=O vibration energy	1055 cm^{-1}	1035 cm^{-1}	1018 cm^{-1}
lifetime	88 ms	49 ms	28 ms

These results demonstrate that time-resolved photoluminescence spectroscopy can be effectively applied for *in situ* observations of catalytically active surface sites of different coordination symmetry and of changes in the local structure of single-site and bulk catalysts.

4.4.3.2 Ag^+/MFI Catalysts

Photoluminescence investigations of the Ag^+ ion-exchanged MFI (Ag^+/MFI) zeolite revealed that an Ag^+ ion cluster (Ag_m^{n+}) exists in the pore structure of MFI, exhibiting photoluminescence at 380 nm (α) upon excitation at 332 nm. UV irradiation (285 nm) of Ag^+/MFI leads to the transformation of Ag_m^{n+} into a different Ag ion cluster [$Ag_m^{(n-1)+}$], which exhibits photoluminescence at 465 nm (β) upon excitation at 315 nm. Photoluminescence band β can be observed stably at 77 K, except when further UV irradiation is carried out at 285 nm. However, once Ag^+/MFI has been heated to ambient temperature, photoluminescence band β completely disappears and photoluminescence band α is again observed with the same intensity as before UV irradiation at 285 nm. Moreover, these UV-induced changes in the photoluminescence of Ag^+/MFI were found to be completely reversible under vacuum conditions. The time profiles of the changes in the intensities of photoluminescence bands α and β under UV irradiation at 285 nm are shown in Figure 4.13. The intensity of photoluminescence band α decreases with increase in the UV irradiation time, while at the same time, the intensity of photoluminescence band β increases, indicating that the Ag ion cluster species A (Ag_m^{n+}) changes to species B [$Ag_m^{(n-1)+}$] under UV irradiation at 285 nm. These reversible changes in the transformation of the Ag ion clusters indicate that the changes in photoluminescence are not related to the photo-formation of silver clusters of different sizes [$Ag_{(m+n)}^{(n+q)+}$], since such changes in the cluster size could not be easily restored by thermal annealing at temperatures as low as 293 K [43].

4.5 Investigations of the Dynamics of Photocatalysis by Time-Resolved Photoluminescence Spectroscopy

Great advances in laser technology have made possible the application of time-resolved spectroscopy for investigations of reaction dynamics at time resolutions in the order of 100 fs. In various photocatalytic reactions, the recombination of electrons

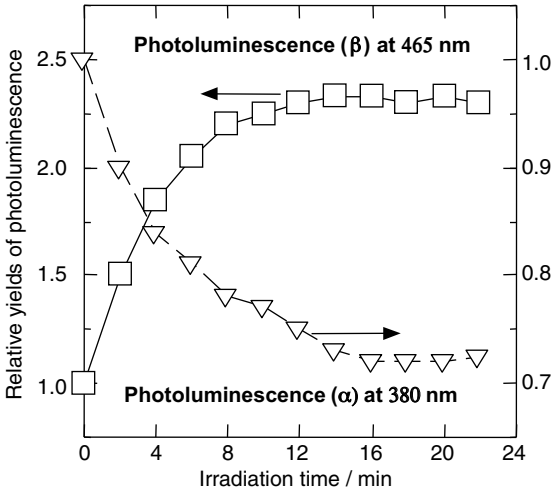


Figure 4.13 Time profiles of the intensities of the photoluminescence spectra of Ag^+/MFI observed at 380 nm ($\lambda_{ex} = 332$ nm) and 465 nm ($\lambda_{ex} = 315$ nm) under UV irradiation at 285 nm at 77 K. Photoluminescence spectra were measured at 77 K.

and holes and also the interaction between reactant molecules and photocatalytically active sites play crucial roles. Time-resolved photoluminescence spectroscopy is a powerful technique for investigating the dynamics involved in various photocatalytic reactions. A detailed elucidation of the dynamics behind photocatalysis on semiconducting TiO_2 photocatalysts and highly dispersed transition metal ion and oxide photocatalysts is presented here.

4.5.1
Dynamics of Photocatalytic Reactions on TiO_2 Photocatalysts

It is known that TiO_2 photocatalysts exhibit various unique properties under UV irradiation, such as the complete oxidation of organic compounds in air or water and also superhydrophilic properties. Such useful characteristics of TiO_2 thin films are currently being widely applied in areas such as self-cleaning glass, tiles, coatings, and anti-fogging mirrors. Moreover, SiO_2/TiO_2 multilayer thin films prepared by an electro-beam vacuum deposition method have been investigated using time-resolved photoluminescence spectroscopy to gain an insight into the recombination dynamics of the photo-formed electrons and holes within the catalyst [18, 19]. A pure, unmodified TiO_2 thin film prepared on a quartz substrate exhibits a broad photoluminescence spectrum centered at 550 nm under femtosecond laser pulse irradiation at 266 nm at 77 K. The photoluminescence is attributed to the emission from the self-trapping excitons (electron–hole pairs) localized on the TiO_2 tetrahedron [20], and/or transition from the charge-transfer excited states $(Ti^{3+}-O^-)^*$ to the Ti–O ground state [8–10]. The intensity of the photoluminescence was found to increase on the introduction of an SiO_2 overlayer of thickness 20 nm for the SiO_2/TiO_2 multilayer

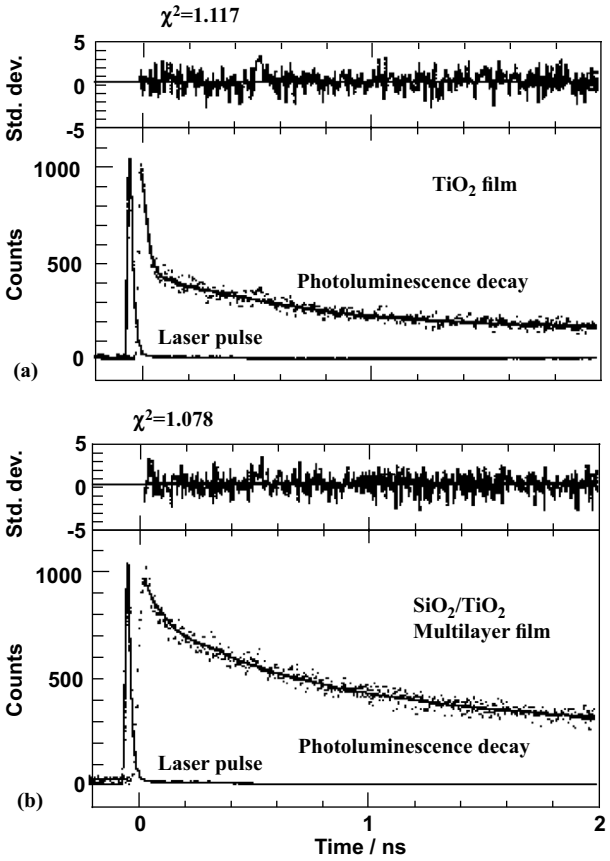


Figure 4.14 Photoluminescence decay profiles of (a) TiO_2 film and (b) SiO_2 (20 nm set-thick)/TiO_2 multilayer film, excited at 266 nm and monitored at 550 nm at 77 K in an N_2-saturated atmosphere [19].

film. The photoluminescence decay profiles of the pure TiO_2 and SiO_2/TiO_2 multilayer thin films are shown in Figure 4.14.

The decay profiles of both films can be fitted by biexponential decay curves (τ_1 and τ_2) and the lifetimes of the fast-decaying components were determined as 19.8 and 82.4 ps for the pure TiO_2 thin film and SiO_2/TiO_2 multilayer thin film, respectively (Table 4.1). These values essentially agree with the recombination rate of the electrons and holes in the TiO_2 nanoparticles, as determined by pump–probe diffuse reflectance spectroscopy [44, 45], showing that the τ_1 component of the photoluminescence decay curve can be ascribed to the electron–hole recombination process. The long lifetime observed for the SiO_2/TiO_2 multilayer thin film (82.4 ps) indicates that the electron–hole recombination is significantly suppressed by the deposition of the SiO_2 overlayer.

The kinetic processes of the photocatalytic degradation of stearic acid and methylene blue were investigated on both pure TiO_2 and SiO_2/TiO_2 multilayer thin

Table 4.1 Lifetimes and relative intensities of the photoluminescence from TiO_2 and SiO_2 (20 nm set-thick)/TiO_2 multilayer films compared with reported photocatalytic activities [19].

Film	Lifetime (ps)	Relative intensity (%)	Photocatalytic activities	
			Apparent rate constant[a)]	
			Stearic acid (10^{-3} min^{-1})[b)]	Methylene blue (10^{-3} h^{-1})[c)]
TiO_2 film	τ_1 19.8	14	16.9	34.6
	τ_2 671	86		
SiO_2/TiO_2 film	τ_1 82.4	24	80.6	78.4
	τ_2 898	76		

a) Irradiation centered at 360 nm from a black light source, 1 mW cm^{-2}.
b) Calculated by elimination of stearic acid from the film surface; absorbance monitored at 2917 cm^{-1} during irradiation.
c) Calculated by decolorization of methylene blue in aqueous solution; absorbance monitored at 663 nm during irradiation.

films. The degradation processes of these compounds followed approximate first-order kinetics, in agreement with the generally observed Langmuir–Hinshelwood mechanism, that is, the reaction rate is proportional to the surface coverage (θ), which becomes proportional to the reactant concentration at low concentrations [46]. The increase in the lifetime of the photoformed electrons and holes and also the dramatic enhancement of the photocatalytic activity observed for the multilayer thin film (Table 4.1) can be attributed to the suppression of the electron–hole recombination process. The effect of the SiO_2 overlayer on the electron–hole recombination rate has yet to be clarified; however, the SiO_2 overlayer may increase the band bending in the space–charge layer of TiO_2 at the SiO_2/TiO_2 interfaces and, thus, enhance the charge separation of the photo-formed electrons and holes [18, 19].

The reaction dynamics between Fe^{3+} ions in aqueous solution and the photo-formed electrons and holes within TiO_2 have also been investigated by time-resolved photoluminescence spectroscopy [21]. Water has been reported to be efficiently oxidized into oxygen on photoirradiated rutile TiO_2 particles in the presence of Fe^{3+} ions; however, the reaction does not proceed on normal anatase TiO_2 even in solutions containing Fe^{3+} ions [22]. The effect of the Fe^{3+} ions on the decay profiles of the photoluminescence for TiO_2 particles suspended in aqueous solution is shown in Figure 4.15.

The addition of Fe^{3+} ions lowers the photoluminescence intensity of rutile TiO_2 (NS51) by 26% over a wide range of pulse intensity. The quantum efficiency of the photocatalytic oxidation of water on rutile TiO_2 was also determined to be around 25%. The good agreement between the quantum efficiency of the reaction and the decrease in the photoluminescence intensity on addition of Fe^{3+} ions indicates that the oxidation of the water and surface recombination of the electrons and holes are competitive processes, as shown in Figure 4.15a [21]. However, in the case of anatase TiO_2 particles (TS-11), the addition of Fe^{3+} ions led to the efficient

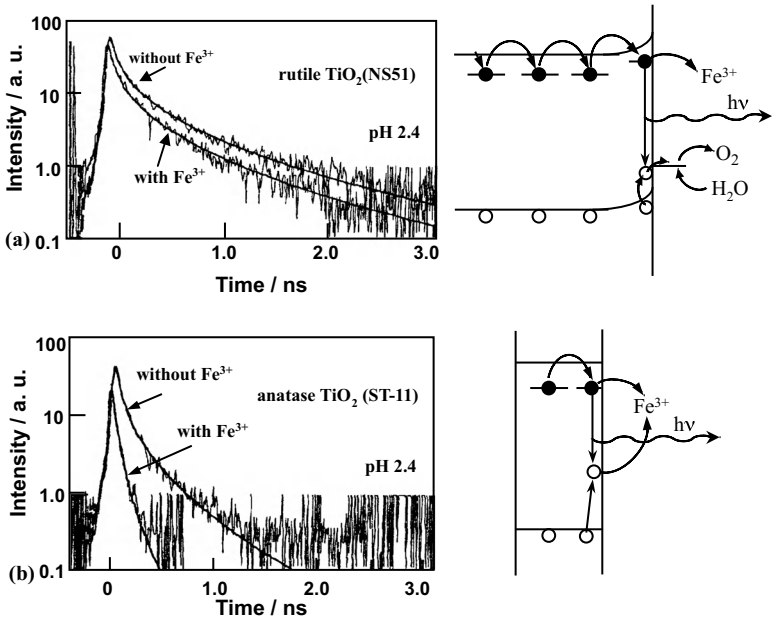


Figure 4.15 Photoluminescence decay profiles of (a) rutile (NS51) and (b) anatase TiO_2 (ST-11) particles dispersed in aqueous solutions (pH 2.4) with and without Fe(III) chloride (5 mM), excited at 355 nm and monitored at 480 nm with the reaction mechanisms on irradiated rutile and anatase TiO_2 particles in an aqueous solution containing Fe^{3+} ions [21].

quenching of the photoluminescence and also a decrease in the photoluminescence lifetime, whereas the photocatalytic oxidation of water did not proceed even in the presence of Fe^{3+} ions [21]. These results suggest that the recombination of the electrons and holes proceeds efficiently at the surface of anatase TiO_2 through the redox cycles between the Fe^{2+} and Fe^{3+} ions, leading to a drastic decrease in the photocatalytic activity. It has also been reported that band bending of about 0.2 V is necessary for the photo-oxidation of water on both rutile and anatase single-crystalline TiO_2 electrodes, which was confirmed by current–voltage investigations [47]. Based on these results, the low efficiency for the oxidation of water on anatase TiO_2 has been ascribed to the small band bending in the space–charge layer of small anatase particles [48].

4.5.2
Dynamics of Photocatalytic Reactions on Highly Dispersed Transition Metal Ion and Oxide Catalysts

4.5.2.1 Cu^+/Zeolite Catalysts

Figure 4.16 shows the Cu K-edge XANES (X-ray absorption near-edge structure) and FT-EXAFS (extended X-ray absorption fine structure) spectra for both the Cu^{2+}/MFI sample (a, a′) and the Cu^+/zeolite catalysts prepared by the evacuation of the original Cu^{2+}/zeolite samples at 973 K (b–c, b′–c′). As shown in Figure 4.16a, the Cu^{2+}/MFI

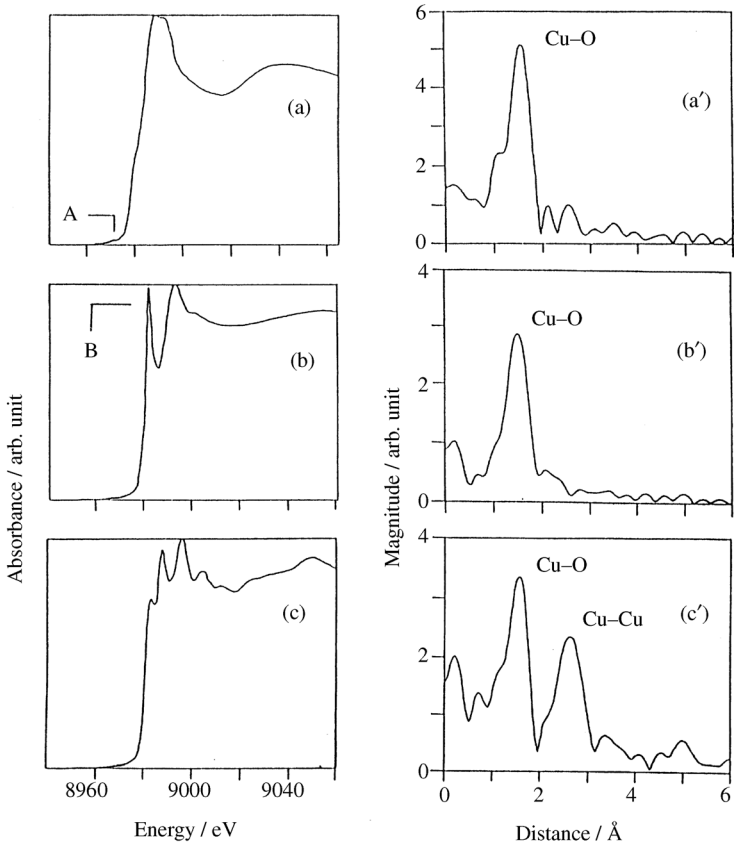


Figure 4.16 XANES (a–c) and FT-EXAFS (a′–c′) spectra of (a, a′) Cu^{2+}/MFI and (b, b′) Cu^{+}/MFI, and (c, c′) Cu^{+}/FAU catalysts. Cu^{+} catalysts were prepared by evacuation of the original Cu^{2+}/zeolite samples at 973 K.

Table 4.2 Results of the curve fitting of Cu K-edge EXAFS data for Cu^{2+}/ZSM-5 sample and Cu^{+}/zeolite catalysts evacuated at various temperatures.

Sample	Edge position (eV)	Shell	*R* (Å)[a]	CN[b]	σ (Å)[c]
Cu^{2+}/ZSM-5	8990.9	Cu–O	2.00	4.2	0.003
Cu^{+}/ZSM-5	8988.7	Cu–O	1.94	2.3	0.003
Cu^{+}/mordenite	8988.8	Cu–O	1.94	2.7	0.004
Cu^{+}/Y-zeolite	8986.3	Cu–O	2.01	3.4	0.005
		Cu–Cu	2.91	6.1	0.021

a) Bond distance.
b) Coordination number.
c) Debye–Waller factor.

sample which was dried at 373 K exhibits a well-separated weak pre-edge band A due to the 1s–3d transition, showing that the sample contains Cu^{2+} ions having slightly distorted symmetries as the major species. These findings coincide with the results obtained by the EPR studies in shape, *g* tensors, and *A* factors, indicating the presence of distorted hydrated Cu^{2+} ions in the Cu^{2+}/zeolite sample [49].

The Cu^{+}/MFI catalyst exhibits band B due to the 1s–4p_z transition, the fingerprint of the Cu^{+} ion, which was intense enough to identify the copper species as Cu^{+} ions with a planar three-coordinate or linear two-coordinate geometry, as shown in Figure 4.16b. The corresponding FT-EXAFS spectra of the copper cation samples and catalysts are also shown in Figure 4.16. Table 4.2 shows the results obtained by curve-fitting analyses of the EXAFS spectra. As shown in Figure 4.16b′, the Cu^{+}/MFI catalysts exhibit only a Cu−O peak due to the neighboring oxygen atoms, indicating the presence of isolated Cu^{+} ions. An increase in the evacuation temperature of the Cu^{2+}/MFI sample also causes the intensity of the Cu−O peak to decrease gradually, resulting in a decrease in the coordination number, as shown in Table 4.2.

A comparison of the Cu−O peak intensity of the reference CuO compound, which contains four-coordinate Cu^{2+} ions, and the intensity of the Cu−O peaks of the Cu^{+}/MFI and Cu^{+}/mordenite catalysts indicates that isolated Cu^{+} ions are present in these Cu^{+}/zeolite catalysts with a two- or three-coordinate geometry. On the other hand, as shown in Figure 4.16c′, the Cu^{+}/FAU exhibits an intense peak attributed to the neighboring copper atoms (Cu−O−Cu), indicating the aggregation of the Cu^{+} ions [50].

The effects of the evacuation temperature of the original Cu^{2+}/MFI samples on the intensity of the EPR signals attributed to the Cu^{2+} ions, the intensities of the UV absorption spectra of the Cu^{2+} and Cu^{+} ions, and the intensity of the XANES band due to the 1s–4p_z transition due to the Cu^{+} ions are shown in Figure 4.17. These results clearly indicate that the Cu^{2+} species are reduced to isolated Cu^{+} ions by evacuation of the Cu^{2+}/MFI samples at temperatures higher than 573 K. In this temperature range, the Cu^{2+} ions are reduced to Cu^{+} by the hydroxide ions formed from the dissociation of the residual water in the zeolite.

Only the sample in which the intensity of the EPR signal due to the Cu^{2+} ions was reduced shows a typical photoluminescence spectrum at around 400–600 nm at 77 K upon excitation at around 300 nm, as shown in Figure 4.18. Previous studies have attributed the absorption (excitation) band at around 280–300 nm and the photoluminescence band at around 400–500 nm to the electronic excitation of the Cu^{+} ion ($3d^{10} \rightarrow 3d^{9}4s^{1}$) and its reverse radiative deactivation ($3d^{9}4s^{1} \rightarrow 3d^{10}$), respectively [51–53]. The absorption band at around 300–320 nm and photoluminescence band at around 500–600 nm are attributed to the presence of the $Cu^{+}-Cu^{+}$ dimer, that is, to the electronic excitation of the dimer ($3d\sigma^{*} \rightarrow 4s\sigma$) and its reverse radiative deactivation ($4s\sigma \rightarrow 3d\sigma^{*}$), respectively [53].

These results show that the relative intensity of the photoluminescence bands at around 450 and 525 nm depends strongly on the type of zeolite used as support. The photoluminescence band at around 430–460 nm is the major component of the total photoluminescence for the Cu^{+}/MFI and Cu^{+}/mordenite catalysts. This clearly indicates that in MFI and mordenite zeolites, most of the copper cations exist as

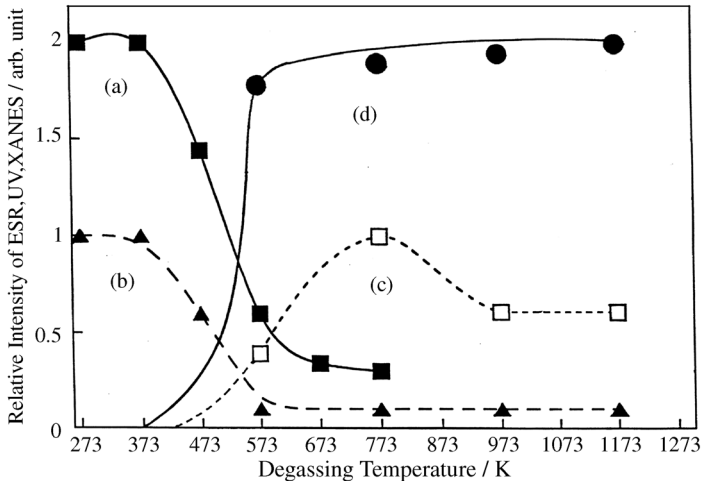


Figure 4.17 Effect of the evacuation temperature of the Cu^{2+}/MFI sample on the relative intensity of the ESR signal due to (a) Cu^{2+}, (b) the relative intensities of the UV absorption at 650 nm due to Cu^{2+}, (c) at 300 nm due to Cu^{+}, and (d) the relative intensity of the XANES band due to the 1s–4p_z transition of Cu^{+}.

isolated Cu^{+} monomer species with planar three-coordinate or linear two-coordinate geometry, in good agreement with the results obtained by XAFS measurements, whereas the Cu^{+}/FAU catalyst exhibits two different intense photoluminescence bands at around 450 and 525 nm. Considering the results obtained by XAFS investigation with the Cu^{+}/FAU, the present findings indicate that in FAU, both

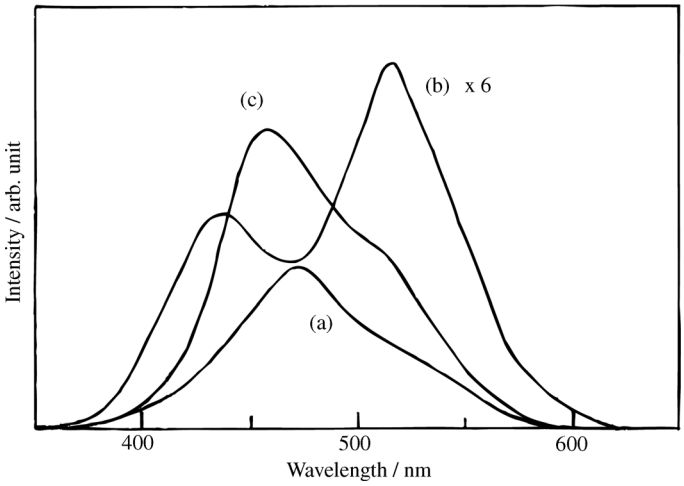


Figure 4.18 Photoluminescence spectra of (a) Cu^{+}/MFI, (b) Cu^{+}/FAU, and (c) Cu^{+}/mordenite catalysts measured at 77 K. The catalysts were prepared by evacuation of the original Cu^{2+}/zeolite samples at 973 K.

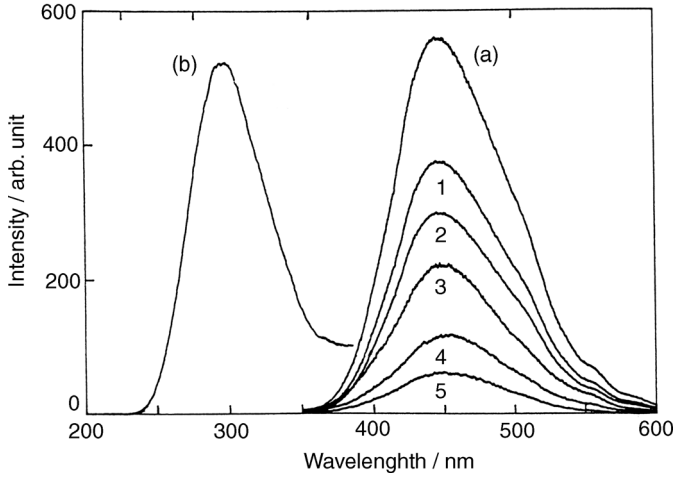


Figure 4.19 Effect of the addition of NO on the photoluminescence spectrum (a) of the Cu^+/MFI catalyst which was prepared by the evacuation of the Cu^{2+}/ MFI sample at 1173 K. (The addition of NO was carried out at 285 K. NO pressure (in Torr): 1, 0.l; 2, 0.3; 3, 0.5; 4, 1; 5, 20.) (The excitation spectrum (b) was monitored at 450 nm emission.)

isolated Cu^+ and aggregated Cu^+-Cu^+ dimer species are present. FAU has a much higher density of ion-exchangeable sites than MFI and mordenite as a result of its higher framework Al/Si atomic ratio. This allows the copper cations to exist in such close proximity to each other that they aggregate easily on treatment at high temperatures. It should be noted that the Cu^+/SiO_2 sample shows a major band at 515 nm due to the Cu^+-Cu^+ dimer species (data not shown) [49].

The addition of NO to the Cu^+/MFI catalyst leads to efficient quenching of the photoluminescence attributed to the Cu^+ species, as shown in Figure 4.19. The lifetime of the photoluminescence was shortened by the addition of NO, becoming even shorter with increase in the NO pressure, while the lifetime changed from 85 μs in vacuum to 50 μs in the presence of NO at a pressure of 133 Pa [49].

Evacuation of the system after quenching of the photoluminescence led to complete recovery of the photoluminescence intensity and lifetime. These findings clearly suggest that the interaction of NO with the catalyst is weak and that the added NO molecules interact readily with the Cu^+ species in both their ground and excited states [49].

UV irradiation of the Cu^+/MFI catalyst, even at 275 K in the presence of NO, led to the formation of N_2 and O_2 with a good linear relationship between the UV irradiation time and NO conversion, as shown in Figure 4.20. The photocatalytic reactivity of the Cu^+ ion species anchored within MFI increases with increase in the evacuation temperature, passing through a maximum at 1173 K, as shown in Figure 4.21. Moreover, Figure 4.21 also shows that the yields of the photoluminescence, that is, the photoluminescence yield attributed to the Cu^+ species, change in a similar manner. Such a good parallel between the yields of the photoluminescence and yields of the photocatalytic decomposition of NO clearly indicates that the excited state of the

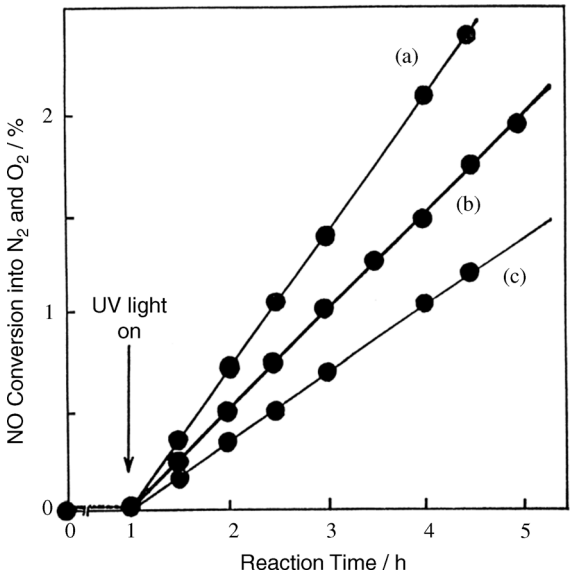


Figure 4.20 Reaction profiles of the photocatalytic decomposition of NO into N_2 and O_2 at 275 K on (a) the Cu^+/MFI catalyst, (b) Cu^+/FAU catalyst, and (c) Cu^+/SiO_2 catalyst, respectively. No reaction was observed at 275 K without UV irradiation.

isolated Cu^+ species plays a decisive role in the decomposition of NO into N_2 and O_2 under UV irradiation of the catalyst at 275 K [49].

Figure 4.20 also shows the reaction time profile of the photocatalytic decomposition of NO at 275 K on Cu^+/SiO_2 (c) and Cu^+/FAU (b). The Cu^+/MFI catalyst exhibits the

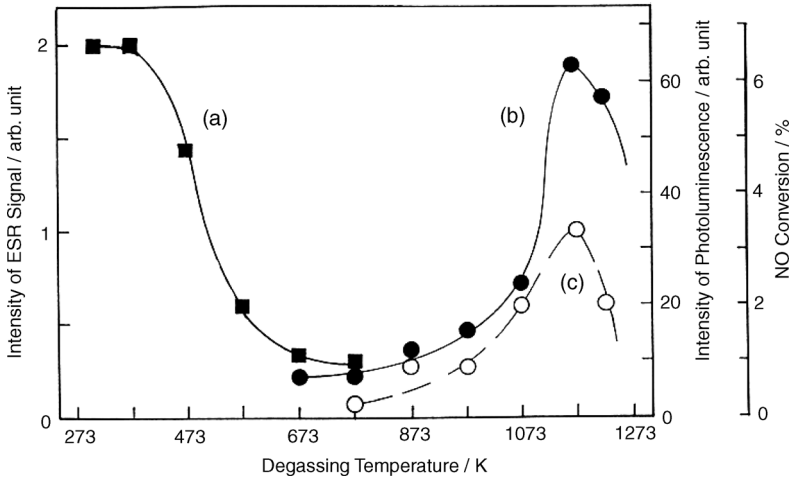


Figure 4.21 Effect of the evacuation temperature of the Cu^{2+}/ZSM-S sample on the relative intensity of the EPR signal due to (a) Cu^{2+}, (b) the relative yields of the photoluminescence due to Cu^+, and (c) the relative conversions (yields) of the photocatalytic decomposition of NO at 275 K.

highest apparent photocatalytic activity for the direct decomposition of NO into N_2 and O_2 at 275 K. With the Cu^+/MFI catalyst, the isolated Cu^+ ion is the predominant species whereas with Cu^+/SiO_2, the Cu^+-Cu^+ species is predominant. The photocatalytic reactivity of the isolated Cu^+ species therefore seems to be much higher than that of the Cu^+-Cu^+ species for the direct decomposition of NO into N_2 and O_2. The direct observation of the $(Cu-NO)^+$ species and its behavior under UV irradiation by means of EPR and IR spectroscopy shows that the local electron transfer from the excited state of the Cu^+ into the anti-π-bonding orbital of NO and the simultaneous electron transfer from the π-bonding orbital of another NO to the vacant orbital of the Cu^+ ion ($3d^9 4s^1$) leads to the direct decomposition of two NO molecules on the Cu^+ site, selectively producing N_2 and O_2, even at 275 K [49].

4.5.2.2 Ti Oxide/Zeolite Catalysts

In situ characterizations of the Ti oxide included within various types of zeolites or anchored on support surfaces were carried out by means of UV–visible, EPR, photoluminescence and XAFS (XANES and FT-EXAFS) investigations. The combination of spectroscopic methods provided important insights into their local structures and photocatalytic reactivity for the decomposition of NO_x into N_2 and O_2 [29–32] and also the reduction of CO_2 with H_2O into CH_3OH and CH_4 [33–38]. The XANES and FT-EXAFS spectra of Ti-containing zeolites such as Ti-MCM-41 and Ti-MCM-48 are shown in Figure 4.22. One of the characteristic features of their XANES spectra was the appearance of a single pre-edge peak with a shape that was similar to that of $Ti(O\text{-}iPr)_4$ having tetrahedral coordination, indicating that the Ti oxides in these catalysts have tetrahedral coordination. The bulk TiO_2 exhibited three peaks with lower intensities, characterizing octahedral coordination as in a rutile or anatase structure. However, the pre-edge peak in the XANES spectra exhibited about 30% of the edge jump, suggesting that these samples include a larger fraction of Ti in square pyramidal or octahedral coordination, which was probably caused by pretreatment problems in the samples, that is, some water may have been adsorbed on the samples before and/or during XAFS measurements. Moreover, in the Fourier transforms of the FT-EXAFS spectra, there is only one peak at around 1.6 Å due to the neighboring oxygen atoms (Ti–O), indicating the presence of isolated Ti oxides in these catalysts. The data obtained by the curve-fitting analysis of the EXAFS spectra for these catalysts are given in Table 4.3 [54].

The photoluminescence spectrum of these Ti oxide-containing zeolite catalysts is shown in Figure 4.23. The observed photoluminescence and its excitation spectrum (absorption spectrum) are in good agreement with those previously observed with highly dispersed tetrahedrally coordinated Ti oxide species, attributed to the following radiative decay process from the charge-transfer excited triplet state to the ground state of the highly dispersed Ti oxides in tetrahedral coordination:

$$\left[Ti^{4+} - O^{2-}\right] \xrightarrow{h\nu} \left[Ti^{3+} - O^{-}\right]^* \xrightarrow{h\nu'} \left[Ti^{4+} - O^{2-}\right]$$

Figure 4.23 also shows that the addition of CO_2 molecules to the catalysts leads to efficient quenching of the photoluminescence and also a shortening of the lifetime

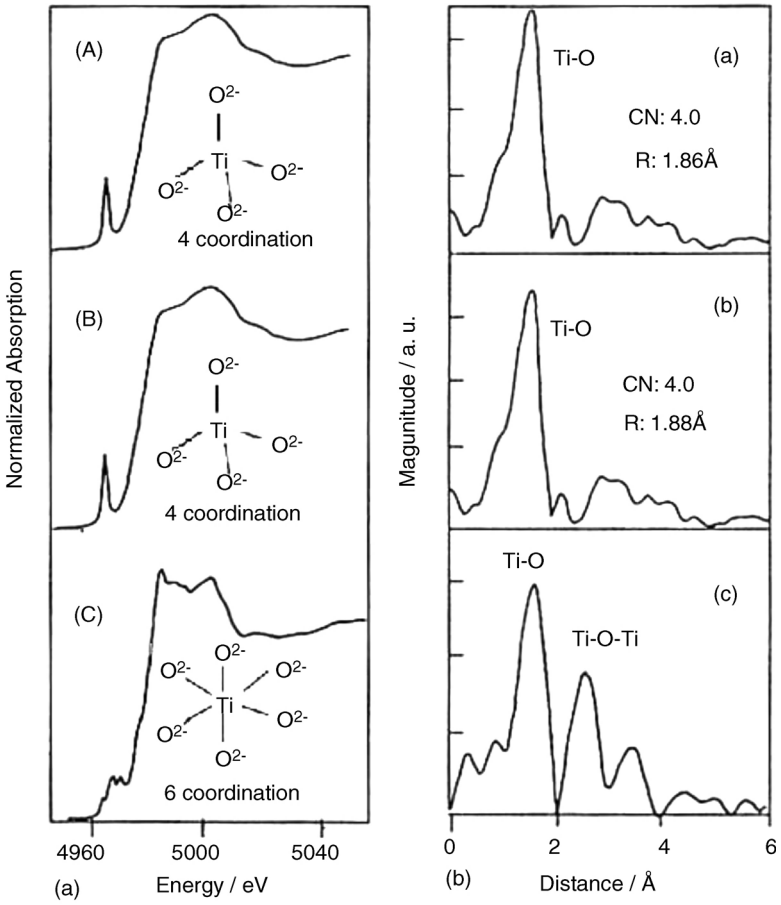


Figure 4.22 XANES (a) and Fourier transforms of EXAFS (b) without phase-shift correction of (A, a) Ti-MCM-41, (B, b) Ti-MCM-48, and (C, c) the bulk powdered TiO_2 as the reference sample.

Table 4.3 Comparison of the various chemical parameters of the Ti oxide species formed within zeolites and on FSM-16 and SiO_2 surfaces and their photocatalytic reactivity.

	TS-1	**TS-2**	**Ti-MCM-41**	**Ti-MCM-48**	**Ti/FSM-16**	**Ti/Vycor glass**	**Bulk TiO_2**
Coordination	Tetra	Tetra	Tetra	Tetra	Tetra	Tetra	Octa
Ti−O bond length (Å)	1.83	1.84	1.86	1.88	–	–	–
Photoluminescence wavelength (nm)	480	480	480	480	465	445	–
Selectivity for CH_3OH formation (%)	20.6	26.5	30.8	28.8	41.2	35.0	Trace
Selectivity for N_2 formation (%)	82.0	80.0	–	89.0	–	88.0	>18

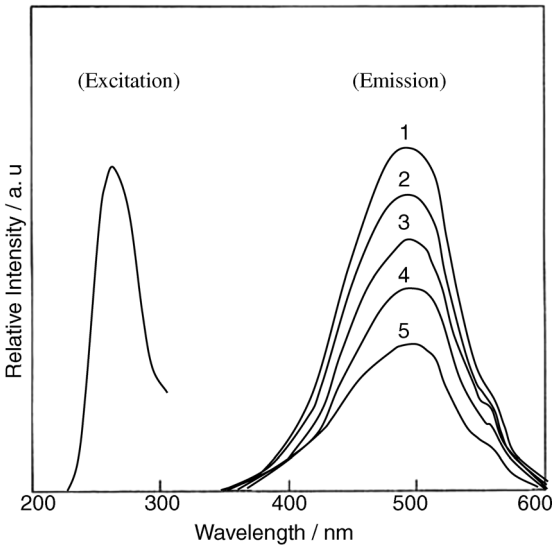


Figure 4.23 Effect of the addition of CO_2 on the photoluminescence spectra of Ti-MCM-48 catalyst measured at 77 K. Pressure of added CO_2: (1) 0, (2) 0.1, (3) 0.5, (4) 2.0, and (5) 10.0 Torr.

for the charge-transfer excited state, its extent depending on the amount of gases added. Such an efficient quenching of the photoluminescence with CO_2, NO, or H_2O molecules (data not shown for NO and H_2O) indicates not only that tetrahedrally coordinated Ti oxides locate at positions accessible to these small molecules but also that they also interact with the Ti oxides in both the ground and excited states [29–38].

The relationship between the coordination number of the Ti oxides and the selectivity for N_2 formation in the photocatalytic decomposition of NO on various Ti oxide photocatalysts is shown in Figure 4.24. The clear dependence of the N_2 selectivity on the coordination number of the Ti oxides can be seen, that is, the lower the coordination number of the Ti oxide, the higher is the N_2 selectivity [38]. Moreover, a clear dependence of the CH_3OH selectivity in the photocatalytic reduction of CO_2 with H_2O on the coordination number of the Ti oxides could also be observed, that is, the lower the coordination number of the Ti oxide, the higher is the CH_3OH selectivity [32]. From these results, it can be proposed that the highly efficient and selective photocatalytic decomposition of NO into N_2 and O_2 and also the reduction of CO_2 with H_2O into CH_3OH can be achieved using Ti-containing zeolites as photocatalysts involving highly dispersed terahedrally coordinated Ti oxides as the active surface species [38].

4.5.2.3 **Mo Oxide/SiO_2 Catalysts**

Transition metal oxides such as Mo and Cr oxide species highly dispersed on SiO_2 have been reported to exhibit typical photoluminescence spectra upon excitation

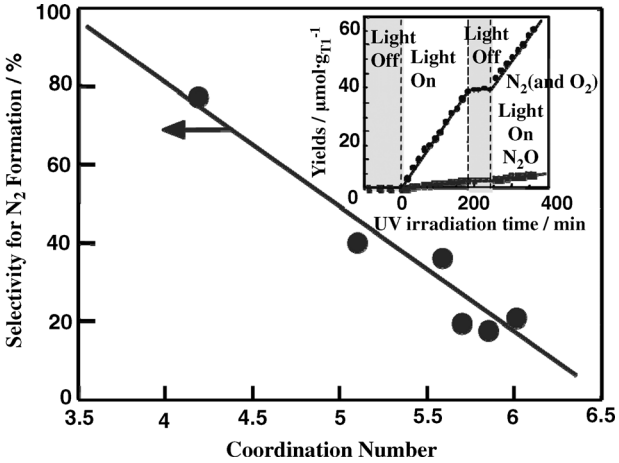


Figure 4.24 Relationship between the coordination numbers and photocatalytic reactivities of the titanium oxides.

with UV light [55–59]. For example, Mo/SiO_2 exhibits a broad photoluminescence spectrum centered at 450 nm under UV irradiation at around 280 nm, as shown in Figure 4.25 [59]. The absorption and emission spectra are attributed to the charge-transfer processes on the Mo=O moieties of the tetrahedral molybdate ions

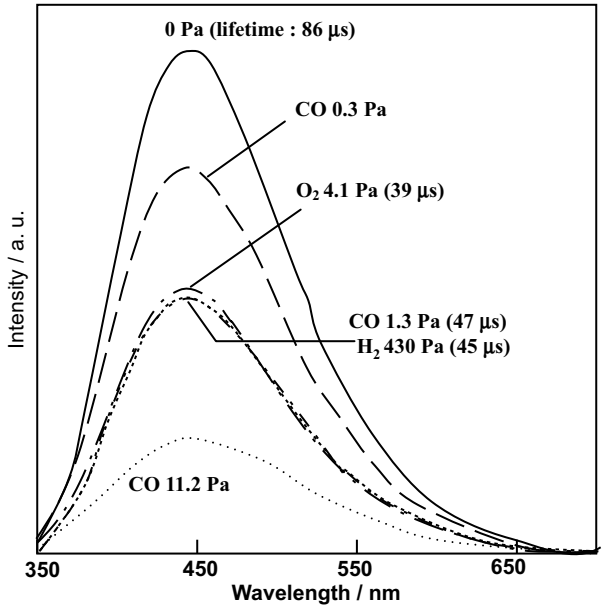
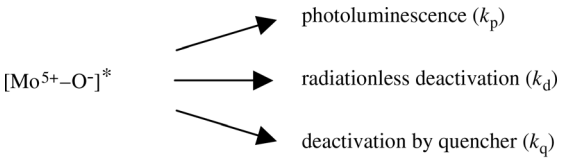


Figure 4.25 Photoluminescence spectrum of Mo/SiO_2 (0.60 wt % as Mo metal) measured at 298 K and effect of the addition of CO, O_2, and H_2 on the spectrum.

(MoO_4^{2-}) involving an electron transfer from the O^{2-} to Mo^{6+} ions and a reverse radiative decay from the charge-transfer excited triplet state, as follows [5–7, 55–59]:

$$\left[Mo^{6+} = O^{2-}\right] \xrightarrow{h\nu} \left[Mo^{5+} - O^{-}\right]^* \xrightarrow{h\nu'} \left[Mo^{6+} = O^{2-}\right]$$

The photoluminescence is quenched in its intensity by the addition of CO, O_2, and H_2, indicating that the Mo oxide species, in its charge-transfer excited triplet state, easily interacts with CO, O_2, and H_2. The photophysical processes on Mo/SiO_2 in the presence of quencher molecules can be described as follows:



The Stern–Volmer equation can be proposed for the quenching of the photoluminescence with the quencher molecules by applying steady-state treatment to the above reaction mechanism, as follows [28]:

$$\Phi_0/\Phi = 1 + \tau_0 k_q [Q]$$

where Φ_0 and Φ are the yields of the photoluminescence in the absence and presence of quencher molecules, respectively, and τ_0, k_q and [Q] are the lifetimes of the charge-transfer excited triplet state of the Mo oxide species in the absence of quencher molecules, the absolute quenching rate constant, and the concentration of the quencher molecules, respectively. The Stern–Volmer plots for the quenching of the photoluminescence yields of Mo/SiO_2 at room temperature, which were obtained by the addition of various quencher molecules at variable pressures, are shown in Figure 4.26. The values of Φ_0/Φ exhibit a good linear relationship with the concentrations of the quencher molecules in low-concentration regions. Moreover, the lifetime of the photoluminescence was seen to decrease on addition of the quencher molecules (Figure 4.25).

These findings clearly show that the quencher molecules interact dynamically with the photoexcited Mo oxide species. The absolute quenching rate constants (k_q) for each gas were determined from the slopes of the Stern–Volmer plots and were found to increase in the order $H_2 \ll O_2 < CO$, indicating that CO interacts most efficiently with the photoexcited Mo oxide species. Evacuation of the added gases after quenching of the photoluminescence led to almost complete recovery of the original photoluminescence yield for H_2 and O_2, whereas only a partial recovery could be observed for CO, indicating that an irreversible reaction between CO and the photoexcited Mo oxide species could proceed under UV irradiation.

The concentration versus time profile of the photocatalytic oxidation of CO with O_2 in the presence of H_2 is shown in Figure 4.27. UV irradiation of Mo/SiO_2 in the presence of CO, O_2, and H_2 led to the efficient oxidation of CO into CO_2, while the

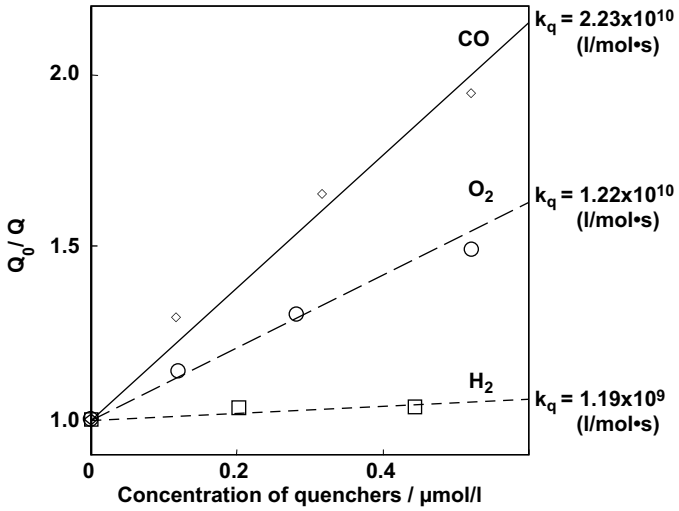


Figure 4.26 Stern–Volmer plots of the Q_0/Q values for the photoluminescence intensity of Mo/SiO_2 (0.60 wt% as Mo metal) versus the concentration of the quencher molecules at 298 K and absolute quenching rate constants (k_q) of the quenchers, as determined by the slope of the corresponding Stern–Volmer plots.

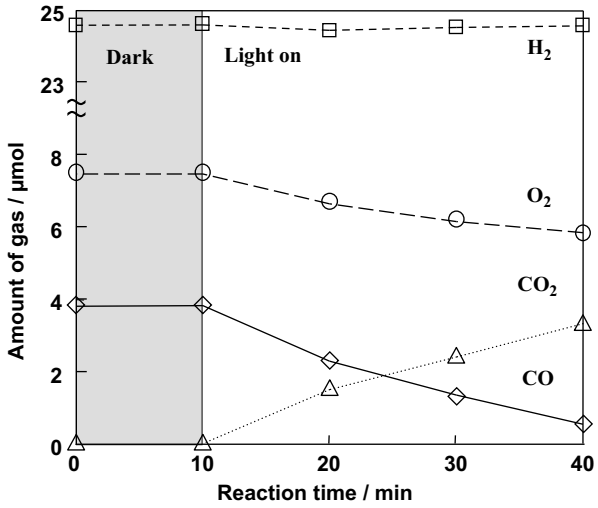
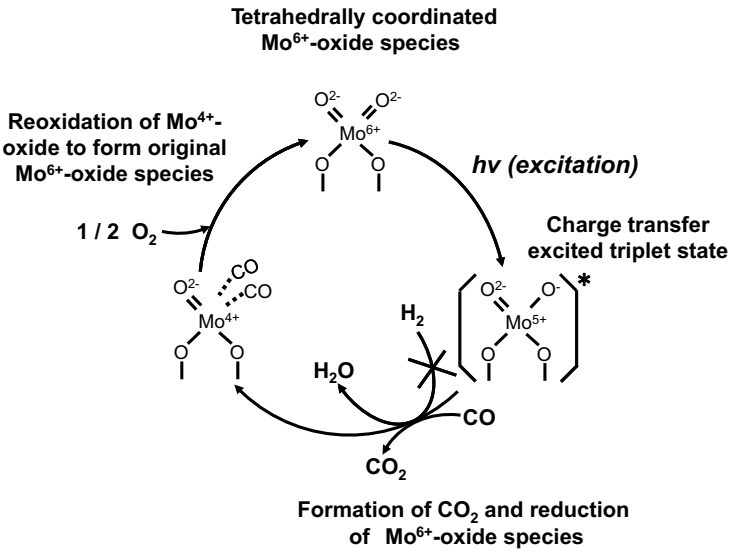


Figure 4.27 Reaction time profiles of the photocatalytic preferential oxidation of CO with O_2 in the presence of H_2 on Mo/SiO_2. Initial amount of gases: CO 3.8, O_2 7.5, and H_2 24.6 µmol. Reaction temperature, 293 K. Photocatalytic reactions were conducted in a closed system using a quartz reaction cell (volume 101 cm^3).

amount of H_2 remained almost constant. CO conversion and CO selectivity after UV irradiation for 180 min were determined as ~100% and 99%, respectively [59].

The quantum yield of the reaction under UV irradiation was also calculated as 12.3%. These findings clearly show that the preferential photocatalytic oxidation of CO with O_2 in the presence of excess amounts of H_2 proceeded on Mo/SiO_2 at temperatures as low as 293 K. It is interesting that this photocatalytic reaction can be applied to the purification of H_2 in fuel cells to remove CO impurities. The proposed reaction mechanism for the preferential photocatalytic oxidation of CO is shown in Scheme 4.1, where the redox cycle of the Mo oxide species plays a significant role [55–59]. The high CO selectivity observed for the Mo/SiO_2 catalyst can be attributed to the high and selective reactivity of the photoexcited Mo oxide species with CO (Scheme 4.1), as indicated by the high quenching efficiency of CO compared with H_2 and O_2 (Figure 4.26).



Scheme 4.1 Complete reaction cycle for the photocatalytic oxidation of CO in the presence of excess amounts of H_2 on Mo/SiO_2.

The preferential photocatalytic oxidation reaction of CO was also performed on standard TiO_2 (P-25) in a comparative reference study. The photocatalytic activity of P-25 was found to be less efficient compared with Mo/SiO_2, although the CO conversion for P-25 was 81% after 6 h of UV irradiation. However, the CO selectivity of about 89% was lower than that measured for Mo/SiO_2 (99%). CO oxidation with O_2 on TiO_2 was seen to proceed by the oxidation of CO(a) or the hole (h^+) trapped CO^+(a) with various oxygen species such as O(a), O^-(a) and O_3^-(a) [60]. The low CO selectivity observed for TiO_2 may be attributed to the strong and nonselective reactivity of these oxygen species. Mo/SiO_2 was therefore seen to be more effective and useful in the selective oxidation of CO into CO_2 in the presence of H_2, in contrast to TiO_2 (P-25) on which H_2 is also oxidized into H_2O.

4.6 Conclusion

In this chapter, the principles of the photoluminescence and detailed methods of photoluminescence acquisition have been summarized for a comprehensive understanding of the catalytic and photocatalytic processes in their working states at the molecular level. It has also been demonstrated that time-resolved photoluminescence measurements can provide a sensitive way to distinguish the catalytically active surface sites with different photoluminescence lifetimes, especially for highly dispersed catalysts with low loadings below 0.1 wt%. Moreover, such techniques are valuable in clarifying the reaction dynamics of the photoexcited active surface sites and also the recombination process of the electrons and holes formed in photoexcited semiconducting catalysts. These advanced photoluminescence investigations of the working states and performances of catalysts and photocatalysts, especially in combination with other spectroscopic investigations, provide detailed information and data for the development of new and clean catalytic sciences and technologies to better our world environment. As a sensitive and nondestructive method, photoluminescence spectroscopy can be widely applied not only in catalysis and photochemistry but also in various fields of medicine, biology, and laser technology to allow shorter time scale investigations of molecular dynamics.

References

1 Lemmer, U. and Göbel, E.O. (1998) in *Primary Photoexcitations in Conjugated Polymers: Molecular Exciton Versus Semiconductor Band Model* (ed. N.S. Sariciftci), World Scientific, Singapore, p. 211.

2 Shimomura, O., Johnson, F.H., and Saiga, Y. (1962) *J. Cell. Comp. Physiol.*, **59**, 223–239.

3 Chalfie, M., Tu, Y., Euskirchen, G., Ward, W.W., and Prasher, D.C. (1994) *Science*, **263**, 802–805.

4 Chishima, T., Miyagi, Y., Wang, X., Yamaoka, H., Shimada, H., Moossa, A.R., and Hoffman, R.M. (1997) *Cancer Res.*, **57**, 2042–2047.

5 Anpo, M. (ed.) (2003) *Curr. Opin. Solid State Mater. Sci.*, **7** (Special Issue on Photoluminescence).

6 Anpo, M., Dzwigaj, S., and Che, M. (2009) *Adv. Catal.*, **52**, 1.

7 Anpo, M. and Che, M. (1999) *Adv. Catal.*, **44**, 119.

8 Matsuoka, M., Kamegawa, T., and Anpo, M. (2008) in *Handbook of Heterogeneous Catalysis* (eds G. Ertl, H. Knözinger, F. Schüth, and J. Weitkamp), Wiley-VCH Verlag GmbH, Weinheim, p. 1065.

9 Takeuchi F M., Kitano, M., Matsuoka, M., and Anpo, M. (2008) in *Handbook of Heterogeneous Catalysis* (eds G. Ertl, H. Knözinger, F. Schüth, and J. Weitkamp), Wiley-VCH Verlag GmbH, Weinheim, p. 1958.

10 Anpo, M. and Matsuoka, M. (2009) in *Turning Points in Solid-State, Materials and Surface Science* (eds K.D.M. Harris and P.P. Edwards), RSC Publishing, Cambridge, p. 496.

11 Anpo F M., Dohshi, S., Kitano, M., Hu, Y., Takeuchi, M., and Matsuoka, M. (2005) *Annu. Rev. Mater. Res.*, **35**, 1.

12 Matsuoka, M. and Anpo, M. (2003) *J. Photochem. Photobiol. C: Photochem. Rev.*, **3**, 225.

13 Anpo, M. and Takeuchi, M. (2003) *J. Catal.*, **216**, 505.

14 Hazenkamp, M.F. and Blasse, G. (1992) *J. Phys. Chem.*, **96**, 3442.

15 Dzwigaj, S., Matsuoka, M., Anpo, M., and Che, M. (2000) *J. Phys. Chem. B*, **104**, 6012.

16 Dzwigaj, S., Matsuoka, M., Anpo, M., and Che, M. (1998) *J. Phys. Chem. B*, **102**, 6309.

17 Hazenkamp, M.F., Vanduijneveldt, F.B., and Blasse, G. (1993) *Chem. Phys.*, **169**, 55.

18 Miyashita, K., Kuroda, S., Ubukata, T., Ozawa, T., and Kubota, H. (2001) *J. Mater. Sci.*, **36**, 3877.

19 Miyashita, K., Kuroda, S., Tajima, S., Takehira, K., Tobita, S., and Kubota, H. (2003) *Chem. Phys. Lett.*, **369**, 225.

20 Tang, H., Berger, H., Schmid, P.E., and Levy, F. (1993) *Solid State Commun.*, **87**, 847.

21 Fujihara, K., Izumi, S., Ohno, T., and Matsumura, M. (2000) *J. Photochem. Photobiol. A: Chem.*, **132**, 99.

22 Ohno, T., Haga, D., Fujihara, K., Kaizaki, K., and Matsumura, M. (1997) *J. Phys. Chem. B*, **101**, 6415.

23 Coluccia, S. (1984) in *Adsorption and Catalysis on Oxide Surfaces* (eds M. Che and G.C. Bond), Elsevier, Amsterdam, p. 59.

24 Tench, A.J. (1971) *Discuss. Faraday Soc.*, **52**, 94.

25 Zecchina, A. and Stone, F.S. (1978) *J. Chem. Soc. Faraday Trans. 1*, **74**, 2278.

26 Che, M. and Tench, A.J. (1983) *Adv. Catal.*, **32**, 1.

27 Anpo, M., Yamada, Y., Kubokawa, Y., Coluccia, S., Zecchina, A., and Che, M. (1988) *J. Chem. Soc. Faraday Trans. 1*, **84**, 751.

28 Turro, N.J. (1978) *Modern Molecular Photochemistry*, Benjamin/Cummings, Menlo Park, CA.

29 Hu F Y., Higashimoto, S., Martra, M., Zhang, J.L., Matsuoka, M., Collucia, S., and Anpo, M. (2003) *Catal. Lett.*, **90**, 161.

30 Hu, Y., Martra, G., Zhang, J.L., Higashimoto, S., Coluccia, S., and Anpo, M. (2006) *J. Phys. Chem. B*, **110**, 1680.

31 Takeuchi, M., Sakai, S., Ebrahimi, A., Matsuoka, M., and Anpo, M. (2009) *Top. Catal.*, **52**, 1651.

32 Yamashita, H., Ichihashi, Y., Anpo, M., Hashimoto, M., Louis, C., and Che, M. (1996) *J. Phys. Chem.*, **100**, 16041.

33 Yamashita, H., Ikeue, K., Takewaki, T., and Anpo, M. (2002) *Top. Catal.*, **18**, 95.

34 Ikeue, K., Nozaki, S., Ogawa, M., and Anpo, M. (2002) *Catal. Today*, **74**, 241.

35 Anpo, M., Takeuchi, M., Ikeue, K., and Dohshi, S. (2002) *Curr. Opin. Solid State Mater. Sci*, **6**, 381.

36 Ikeue, K., Yamashita, H., Anpo, M., and Takewaki, T. (2001) *J. Phys. Chem. B*, **105**, 8350.

37 Yamashita, H. and Anpo, M. (2003) *Curr. Opin. Solid State Mater. Sci.*, **7**, 471.

38 Anpo, M. and Thomas, J.M. (2006) *Chem. Commun.*, **31**, 3273.

39 Anpo, M. (2004) *Bull. Chem. Soc. Jpn.*, **77**, 1427.

40 Anpo, M., Tomonari, M., and Fox, M.A. (1989) *J. Phys. Chem.*, **93**, 7300.

41 Meyer, G.J., Lisensky, G.C., and Ellis, A.B. (1988) *J. Am. Chem. Soc.*, **110**, 4914.

42 Nakajima, H., Itoh, K., and Murabayashi, M. (2002) *Bull. Chem. Soc. Jpn.*, **75**, 601.

43 Matsuoka, M., Ju, W.S., Chen, H.-J., Sakatani, Y., and Anpo, M. (2003) *Res. Chem. Intermed.*, **29**, 477.

44 Ohtani, B., Bowman, R.M., Colombo, D.P., Kominami, H., Noguchi, H., and Uosaki, K. (1998) *Chem. Lett.*, 579.

45 Furube, A., Asahi, T., Masuhara, H., Yamashita, H., and Anpo, M. (1997) *Chem. Lett.*, 735.

46 Hoffman, M.R., Martin, S.T., and Choi, W., and Bahnemann, D.W. (1995) *Chem. Rev.*, **95**, 69.

47 Kevan, L., Gratzel, M., Gilbert, S.E., Klemenz, C., and Scheel, H.J. (1996) *J. Am. Chem. Soc.*, **118**, 6716.

48 Hangfeldt, A. and Gratzel, M. (1995) *Chem. Rev.*, **95**, 49.

49 Anpo, M., Matsuoka, M., Shioya, Y., Yamashita, H., Giamello, E., Morterra, C., Che, M., Patterson, H.H., Webber, S., and Ouellette, S. (1994) *J. Phys. Chem.*, **98**, 5744.

50 Yamashita, H., Matsuoka, M., Tsuji, K., Shioya, Y., Anpo, M., and Che, M. (1996) *J. Phys. Chem.*, **100**, 397.

51 Strome, D.H. and Klier, K. (1980) *J. Phys. Chem.*, **84**, 981.

52 Dedecek, J. and Wichterlova, B. (1994) *J. Phys. Chem.*, **98**, 5721.

53 Shin, K.S., Barrie, J.D., Dunn, B., and Zink, J.I. (1990) *J. Am. Chem. Soc.*, **112**, 5701.

54 Anpo, M., Yamashita, H., Ikeue, K., Fujii, Y., Zhang, S.G., Ichihashi, Y., Park, D.R., Suzuki, Y., Koyano, K., and Tatsumi, T. (1998) *Catal. Today*, **44**, 327.

55 Lisachenko, A.A., Chikhachev, K.S., Zakharov, M.N., Basov, L.L., Shelimov, B.N., Subbotina, I.R., Che, M., and Coluccia, S. (2002) *Top. Catal.*, **20**, 119.

56 Kamegawa, T., Morishima, J., Matsuoka, M., Thomas, J.M., and Anpo, M. (2007) *J. Phys. Chem., C*, **111**, 1076.

57 Tanaka, T., Ito, T., Takenaka, S., Funabiki, T., and Yoshida, S. (1998) *J. Phys. Chem. B*, **102**, 2960.

58 Yamashita, H., Yoshizawa, K., Ariyuki, M., Higashimoto, S., Che, M., and Anpo, M. (2001) *Chem. Commun.*, 435.

59 Kamegawa, T., Takeuchi, R., Matsuoka, M., and Anpo, M. (2006) *Catal. Today*, **111**, 248.

60 Sato, S. and Kadowaki, T. (1987) *J. Catal.*, **106**, 295.

5
Neutron Scattering

Hervé Jobic

5.1
Introduction

Since neutrons are electrically neutral, they penetrate deep into materials. It may seem surprising to use neutrons, which are weakly scattered by matter, to follow surface chemistry. In fact, only catalysts that have a large surface area and scatter neutrons much less than adsorbed species can be studied.

In order to perform neutron scattering measurements, one has to go to a large central facility, and there are just a few in the world. There are some national facilities (e.g., LLB in Saclay, France, and FRM-2 in Munich, Germany), but most of the experiments are carried out using international neutron sources. The so-called "second-generation facilities," Institut Laue–Langevin (ILL) in Grenoble, France, and ISIS near Oxford, United Kingdom, attract the majority of users because they offer a high neutron flux and cutting-edge instrumentation. The ILL is a steady-state reactor whereas ISIS is a pulsed spallation source. The United States and Japan are building third-generation facilities, which will be pulsed. In Europe, scientists are expecting the approval of the construction of the ESS in Lund (Sweden), which should be the world's most powerful neutron source.

The wavelength associated with the neutron ($\sim$1 Å) is comparable to interatomic distances so that the structure of the sample can be studied. Further, the neutron energy covers the range of energies involved in the different molecular motions so that the dynamics of the sample can also be studied. The Nobel Prize in Physics was awarded in 1994 to Brockhouse and Shull for their pioneering contributions to the development of neutron scattering techniques for studies of condensed matter, more specifically to Brockhouse in neutron spectroscopy and to Shull in neutron diffraction techniques. The Nobel press release mentioned that they helped to answer the question of "where the atoms are and how they move." Several types of experiments have been applied to catalytic systems. Structural investigations are performed by neutron diffraction (ND). Textural or clustering studies are followed by small-angle neutron scattering (SANS). The vibrational modes of catalysts and of adsorbed molecules are characterized by inelastic neutron scattering (INS). The term

Characterization of Solid Materials and Heterogeneous Catalysts: From Structure to Surface Reactivity, First Edition. Edited by Michel Che and Jacques C. Védrine.
© 2012 Wiley-VCH Verlag GmbH & Co. KGaA. Published 2012 by Wiley-VCH Verlag GmbH & Co. KGaA.

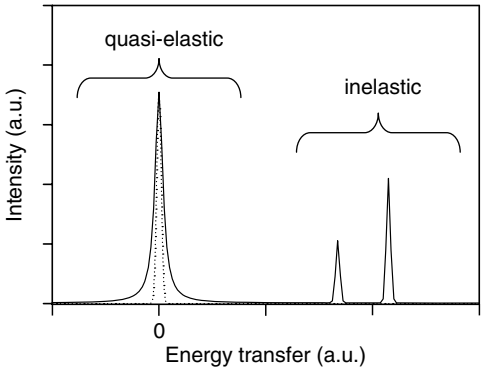


Figure 5.1 Schematic representation of quasi-elastic and inelastic peaks. The dotted line represents the elastic instrumental resolution.

"inelastic" implies that the neutron exchanges energy with the sample and excites transitions between discrete levels such as vibrations (Figure 5.1). The range of very small energy transfers which result from unquantified diffusive motions is called quasi-elastic (Figure 5.1), and the instrumentation which allows one to measure the rotational and translational motions of molecules is called quasi-elastic neutron scattering (QENS). Other neutron techniques, such as reflectometry, have not been used so far for catalytic systems.

5.2
Introduction to the Theory

5.2.1
Properties of Neutrons

A neutron is a particle with a mass m of 1.675×10^{-24} g, it has zero charge, a spin of $^1/_2$, and hence a magnetic moment. Neutrons have both wave-like and particle-like properties:

- The neutron wavelength (λ) is given by de Broglie's relationship, $\lambda = h/mv$, where h is Planck's constant and v the neutron velocity. The associated wave vector $\boldsymbol{k}$ has the magnitude $k = 2\pi/\lambda$. An incident neutron beam is described by a plane wave $\exp(i\boldsymbol{k}\cdot\boldsymbol{r})$, where $\boldsymbol{r}$ is a position vector.
- The neutron momentum is $\boldsymbol{p} = m\boldsymbol{v} = \hbar\boldsymbol{k}$, and the neutron energy corresponds to its kinetic energy, $E = {}^1/_2 mv^2 = \hbar^2 k^2/2m$. A useful conversion relationship between the neutron energy (in meV) and its wavelength (in Å) is $E = 81.807/\lambda^2$.

The two basic quantities in a neutron scattering experiment are the momentum transfer $\hbar\boldsymbol{Q}$ and the energy transfer $\hbar\omega$, given by

$$\hbar\boldsymbol{Q} = \hbar(\boldsymbol{k}_0 - \boldsymbol{k}') \tag{5.1}$$

$$\hbar\omega = E_0 - E' = \left(\hbar^2/2m\right)\left(k_0{}^2 - k'^2\right) \tag{5.2}$$

where $\boldsymbol{k}_0$ and $\boldsymbol{k}'$ are the incident and scattered wave vectors, respectively. Elastic scattering corresponds to $k' = k_0$, so that only momentum is transferred ($\hbar\omega = 0$). The magnitude of $\boldsymbol{Q}$ increases with the scattering angle, 2θ, between the incident and scattered wave vectors. When the neutrons also exchange energy with the sample, $\hbar\omega$ will be positive for $k' < k_0$ (energy loss or creation of an excitation) and the scattering is called inelastic. The scattering vector $\boldsymbol{Q}$ then depends on both the scattering angle and the energy transfer. $\boldsymbol{Q}$ is often referred to as the momentum transfer, although it corresponds strictly to a wave vector transfer.

5.2.2
Scattering Cross-Sections

When a beam of neutrons impinges on a sample, the neutrons can be scattered, absorbed, or transmitted without interaction. Neutrons are scattered by interaction with the atomic nuclei via the strong nuclear force, or the neutron magnetic moment can interact with unpaired electron spins. Since the neutron–nucleus interaction occurs at a much shorter range ($\sim 10^{-4}$ Å) than the neutron wavelength, the interaction potential can be represented by a delta function (Fermi, 1936), which allows the scattered wave to be isotropic:

$$V(\boldsymbol{r}) = \left(2\pi\hbar^2/m\right) b\,\delta(\boldsymbol{r} - \boldsymbol{R}) \tag{5.3}$$

where $\boldsymbol{R}$ gives the nucleus position. The phase is determined by the sign of the nuclear scattering length, b, which can be real or complex. The real part is usually positive and the imaginary part is related to the absorption of neutrons. The amplitude varies irregularly, not only from one element to the next, but also from one isotope to another. This is in contrast to X-ray scattering, where the scattering power increases steadily with the number of electrons in the atom. Further, the amplitude varies from one nucleus to another of the same isotope, if there is a nonzero nuclear spin. The scattering lengths depend on the structure of the nucleus and they are determined by experiment.

In ND or SANS experiments, one measures the number of neutrons scattered per unit time into the element of solid angle $\mathrm{d}\Omega$, which corresponds to

$$N\left(\frac{\mathrm{d}\sigma}{\mathrm{d}\Omega}\right)\mathrm{d}\Omega \tag{5.4}$$

where N is the number of incident neutrons per unit area per unit time and σ the total cross-section. It follows that σ has the dimensions of area; it represents the size of the nucleus during the neutron–nucleus interaction and it is measured in barns ($1\ \text{barn} = 10^{-28}\ \text{m}^2$).

For INS or QENS measurements, one measures the double-differential cross-section, $\mathrm{d}^2\sigma/\mathrm{d}\Omega\mathrm{d}E$, which represents the number of neutrons scattered into $\mathrm{d}\Omega$ with energy in the range $\mathrm{d}E$.

The total cross-section per scatterer is obtained by integrating over energies and solid angles

$$\sigma = \int \mathrm{d}\Omega \frac{\mathrm{d}\sigma}{\mathrm{d}\Omega} = \int \mathrm{d}E \int \mathrm{d}\Omega \frac{\mathrm{d}^2\sigma}{\mathrm{d}\Omega\, \mathrm{d}E} = 4\pi b^2 \tag{5.5}$$

Neutron absorption is small for most nuclei, except for a few notable exceptions such as boron, cadmium (see Table 5.1), ^{3}He, and gadolinium.

5.2.3 Coherent and Incoherent Scattering

The scattering cross-section can be split into coherent and incoherent contributions. The coherent elastic scattering has a phase term in $\exp(i\boldsymbol{Q}\cdot\boldsymbol{R})$ and thus takes into account interference effects between the waves scattered from each nucleus, which

Table 5.1 Coherent, incoherent, and absorption cross-sections σ for various elements[a)].

Element	Atomic number	Mass number (natural abundance, %)	Spin	σ_{coh} (barn)	σ_{inc} (barn)	σ_{abs} (barn)
H	1			1.7586	79.9	0.19
		1 (99.985)	1/2	1.76	79.91	0.19
		2 (0.015)	1	5.59	2.04	0
B	5			3.54	1.7	426.
C	6			5.551	0.001	0
		12 (98.9)	0	5.559	0	0
		13 (1.1)	1/2	4.81	0.034	0
N	7			11.01	0.5	1.1
		14 (99.63)	1	11.03	0.5	1.1
		15 (0.37)	1/2	5.21	0	0
O	8			4.232	0	0
F	9	19 (100)	1/2	4.017	0.0008	0.005
Al	13	27 (100)	5/2	1.495	0.008	0.13
Si	14			2.163	0.004	0.1
P	15	31 (100)	1/2	3.307	0.005	0.1
S	16	32		1.02	.007	0.29
Cl	17			11.531	5.2	18.6
V	23			0.018	5.08	2.82
Ni	28			13.3	5.2	2.5
Ru	44			6.53	0.07	1.42
Cd	48			3.3	2.4	1400
Pt	78			11.65	0.13	5.72

a) The σ values are given in barns (1 barn $= 10^{-28}$ m^2). The absorption cross-section is proportional to the neutron wavelength, here $\lambda = 1$ Å. The nuclear spins are indicated for some isotopes, together with their relative abundances. For the other elements, B, Cl, and so on, the different isotopes are not listed, only the average cross-sections are given.

occurs in diffraction. The mean scattering potential which gives rise to coherent scattering is proportional to the mean scattering length $\langle b \rangle$, where the brackets $\langle\ \rangle$ denote an average value. The coherent scattering cross-section thus corresponds to an average over all isotopes and spin states:

$$\sigma_{\text{coh}} = 4\pi \langle b \rangle^2 \tag{5.6}$$

The incoherent scattering, which has no phase relationship, corresponds to the mean square deviation from the mean potential and is proportional to $(\langle b^2 \rangle - \langle b \rangle^2)^{1/2}$. The incoherent scattering cross-section is thus defined as

$$\sigma_{\text{inc}} = 4\pi \left(\langle b^2 \rangle - \langle b \rangle^2 \right) \tag{5.7}$$

For a sample containing only one type of atom (one isotope) with zero spin, then $\langle b \rangle = b$ and the scattering will be totally coherent (e.g., ^{12}C in Table 5.1).

If we now consider a single isotope of nuclear spin i, it may combine with a neutron of spin $^1/_2$ to give two possible spin states: $i + {}^1/_2$ and $i - {}^1/_2$. There are two scattering lengths associated with the two states: b^+ and b^-. Since for a total spin quantum number t there are $2t + 1$ states, there will be $2(i + {}^1/_2) + 1 = 2(i + 1)$ states for b^+ and $2(i - {}^1/_2) + 1 = 2i$ states for b^-. The total number of states is $2(i + 1) + 2i = 2(2i + 1)$ so that the probability of b^+ occurring is $p^+ = (i + 1)/(2i + 1)$ and of b^- is $p^- = i/(2i + 1)$. This verifies the normalization property

$$p^+ + p^- = 1 \tag{5.8}$$

The average over spin states is

$$\langle b \rangle = p^+ b^+ + p^- b^- \tag{5.9}$$

This gives rise to coherent scattering with a cross-section

$$\sigma_{\text{coh}} = 4\pi \langle b \rangle^2 = 4\pi |p^+ b^+ + p^- b^-|^2 \tag{5.10}$$

while the incoherent scattering cross-section is given by Eq. (5.7) with

$$\langle b^2 \rangle = p^+ |b^+|^2 + p^- |b^-|^2 \tag{5.11}$$

The case of hydrogen ($i = {}^1/_2$) is an important one. The scattering lengths which have been determined experimentally are $b^+ = 1.082 \times 10^{-14}$ m and $b^- = -4.742 \times 10^{-14}$ m, so that

$$\langle b \rangle = {}^3/_4 b^+ + {}^1/_4 b^- = -0.374 \times 10^{-14} \text{ m} \tag{5.12}$$

which gives $\sigma_{\text{coh}} = 1.76$ barn and $\sigma_{\text{inc}} = 79.91$ barn. As can be seen in Table 5.1, the incoherent scattering cross-section for hydrogen is much larger than that for any other element, which is the reason why neutron scattering is a unique tool for the investigation of hydrogenous compounds.

In the case of deuterium, $i = 1$, the scattering lengths are $b^+ = 0.95 \times 10^{-14}$ m and $b^- = 0.1 \times 10^{-14}$ m, which yield $\sigma_{\text{coh}} = 5.59$ barn and $\sigma_{\text{inc}} = 2.04$ barn.

These different cross-sections for H and D have some consequences:

- In diffraction experiments, large incoherent scattering should be avoided since it increases the background below the Bragg peaks. It is therefore better to use deuterated compounds because the incoherent cross-section of D is much weaker than that of H.
- For inelastic studies, where the energy of the scattered neutrons is analyzed, both incoherent and coherent scattering can be probed. For example, coherent scattering allows the determination of the phonon dispersion curves in single crystals. In the case of molecules adsorbed on catalysts, the best signal will be obtained with hydrogenated molecules. However, the scattering from other molecules, such as CO_2, will certainly be studied in the future with high-flux spectrometers. The deuteration technique can be useful to discriminate between different species, as will be shown in the vibrational spectroscopy section.

When the elements are composed of several isotopes, more general expressions are used to calculate the cross-sections, taking into account the concentration c_p of each isotope, p

$$\langle b \rangle = \sum_p \frac{c_p}{2i_p + 1} \left[(i_p + 1) {b_p}^+ + i_p {b_p}^- \right] \tag{5.13a}$$

$$\langle b^2 \rangle = \sum_p \frac{c_p}{2i_p + 1} \left[(i_p + 1) ({b_p}^+)^2 + i_p ({b_p}^-)^2 \right] \tag{5.13b}$$

The coherent and incoherent cross-sections of some elements are given in Table 5.1. Apart from hydrogen, discussed above, it is interesting that light atoms such as nitrogen can scatter more neutrons than heavy atoms such as ruthenium. Vanadium is special in the sense that its coherent cross-section is almost zero so that Bragg peaks are not visible, which is ideal for containing samples for diffraction experiments. This is not the case for aluminum, so this material is used to make thin windows and sample cells in inelastic experiments.

5.3 Experimental

As mentioned in the Introduction, neutrons are produced from steady-state reactors or from pulsed spallation sources. Neutrons issued from the source are slowed in moderators whose temperatures can vary between 25 and 2000 K. This gives neutron wavelengths ranging from 0.2 to 20 Å, or energies ranging between 2.05 eV and 0.2 meV, respectively. The source brightness is several orders of magnitude lower than that from X-ray synchrotrons, the maximum flux at sample position being of the order of 10^8 n cm^{-2} s^{-1}. There are two main classes of instruments: elastic instruments for ND and SANS, and inelastic or quasi-elastic spectrometers for INS or QENS.

A major difference between instruments installed on steady-state or pulsed neutron sources is that time-of-flight (TOF) techniques are used on pulsed sources

to exploit the white neutron beams (large range of wavelengths), whereas one incident wavelength is usually selected on steady-state sources.

The principle of the TOF technique can be understood from de Broglie's relationship, given in Section 5.2.1. Neutrons having different wavelengths travel at different velocities. For example, a wavelength of 1 Å corresponds to neutrons traveling with a speed of $3956\,\mathrm{m\,s^{-1}}$. The neutron TOF t is determined over sufficiently large distances L, and corresponds to L (m)/v ($\mathrm{m\,s^{-1}}$), or $252.77\,\mu\mathrm{s\,m^{-1}}$ for the same wavelength of 1 Å. Therefore, neutron velocities, and hence energies, can be determined by measuring their TOF. Shorter wavelength neutrons travel faster and therefore reach the sample and the detector before the longer wavelength neutrons. There are two classes of TOF instruments:

- Direct geometry, where the incident energy, E_0, is selected using crystal monochromators or choppers, and the final energy, E', is determined by TOF. Spectrometers of this type are obviously found on steady-state sources, such as the multichopper IN5 and the time-focusing IN6, but also on pulsed sources, for example, MARI at ISIS.
- Indirect (or inverted) geometry, where a white beam impinges on the sample, E' is fixed (by a crystal or a filter), and E_0 is determined by TOF. Different designs can be found, such as the crystal analyzer TOSCA at ISIS and the backscattering spectrometer IRIS at ISIS.

Advances in instrumentation and in data treatment are constantly being realized. For example, to obtain information on atomic and molecular motions, scientists performing experiments at the ILL have access to a very wide range of time scales, using different instruments (Figure 5.2). On the high-energy transfer side, inelastic scattering can be observed with TOF and beryllium filter (BeF) spectrometers. TOF instruments are also used to probe quasi-elastic scattering, with elastic energy resolutions ranging from 10 to 100 μeV. Backscattering (BS) spectrometers have a resolution of about 1 μeV and are therefore used to measure quasi-elastic scattering which is too slow for a TOF instrument, or low-frequency inelastic peaks, for example, tunneling. The neutron spin-echo (NSE) technique corresponds to ultra-high resolution machines, about 1 neV, giving access to Fourier times up to hundreds of nanoseconds. Various TOF and BS spectrometers are found in neutron facilities around the world. The NSE method is of more restricted access, since there are only a few instruments. In NSE, one is able to detect very small relative velocity changes (of the order of 10^{-5}), despite a broad wavelength distribution ($\Delta\lambda/\lambda \approx 15\%$). This is made possible by using the Larmor precession angle of the neutron spin in a controlled magnetic field as a measure of the energy transfer associated with the neutron–sample interaction.

The beam size at the sample position is a few square centimeters. The absorption of neutrons by matter is small for small elements so that neutrons are highly penetrating and can be used in complex sample environments, such as a cryostat, furnace, superconducting magnet, high-pressure cell, microwave, and dilution refrigerator. The few elements that absorb neutrons are used for protection (e.g., Cd) or for detection (e.g., B). Sample quantities vary from hundreds of milligrams to

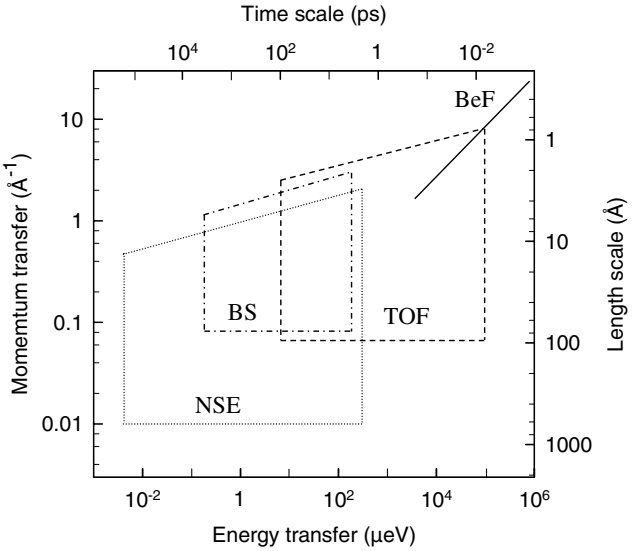


Figure 5.2 Accessible energy and momentum transfer ranges at the ILL, with their corresponding time and length scales. Different techniques are used: neutron spin-echo (NSE), back-scattering (BS), time-of-flight (TOF), and beryllium-filter (BeF). The (Q, E) window on the BeF filter spectrometer is so narrow that it falls on a single line.

tens of grams, depending on the scattering power. For catalytic studies, special care must be taken to avoid contamination of the catalyst by water or hydrocarbons during preparation. Most of the time, the catalyst has to be prepared and transferred into the neutron cell under vacuum, or in a glovebox. The cell can be cylindrical or slab-shaped. Apart from the use of aluminum and vanadium to make neutron cells, already mentioned, stainless steel and quartz have also been used. After a neutron experiment, the sample, or at least the container, becomes activated. The amount of time for it to decay is negligible for silica, less than 1 h for alumina, half a day for Ni, several days for Pd or Pt, and several years for Co.

5.4 Structure

Neutron diffraction, which corresponds to coherent scattering, is analogous to X-ray diffraction, but there are important differences. Neutrons are scattered by the nuclei and X-rays by the electrons. Furthermore, light nuclei are much easier to locate by neutron diffraction in structures that include heavy atoms.

In neutron diffraction, no energy analysis is performed. The observed count rate is proportional to the differential scattering cross-section. Considering a perfect crystal with N unit cells, the volume of the unit cell being v_0, one obtains for the coherent differential scattering cross-section

$$\frac{d\sigma_{coh}}{d\Omega} = N\frac{(2\pi)^3}{v_0}\sum_{\tau}\delta(\boldsymbol{Q}-\tau)|F_{hkl}|^2 \tag{5.14}$$

The delta function ensures that scattering only occurs when $\boldsymbol{Q}$ coincides with the reciprocal lattice vector τ, which corresponds to Bragg scattering. The intensities of the reflections from the lattice planes (*hkl*) of a crystal are governed by the structure factor of the unit cell, F_{hkl}:

$$F_{hkl} = \sum_i \langle b_i \rangle \exp[2\pi i(hx_i + ky_i + lz_i)] \tag{5.15}$$

where the summation is over the atoms of the unit cell, at positions (x_i, y_i, z_i). For a real crystal, the atoms are not located at the sites of a perfect lattice, because of static or dynamic disorder. This implies a higher background and a reduction in intensity of the Bragg peaks which is taken into account by a Debye–Waller factor, $\exp[-2W(\boldsymbol{Q})]$, which is generally calculated in the isotropic approximation.

Most studies performed on surfaces have dealt with small physisorbed molecules; another application of neutron diffraction is the localization of protons and of molecules adsorbed in zeolites [1]. All these studies have been performed using powders, which usually implies overlap between the various reflections. In this case, the appropriate method to deal with the complex diffraction pattern in order to obtain the crystal structure was proposed by Rietveld [2]. As an example, one of the earliest investigations using this method concerned benzene in NaY zeolite (Figure 5.3). Fourier difference maps revealed the presence of two types of adsorbed benzene. The first type sits in a supercage, at an average distance of 2.7 Å from the SII sodium ions, the center of the molecule being on the cube diagonal. There is an interaction between the polarizing sodium ion and the π-electron density of the benzene stabilizing the molecule in this position [3]. At higher coverage, a second adsorption

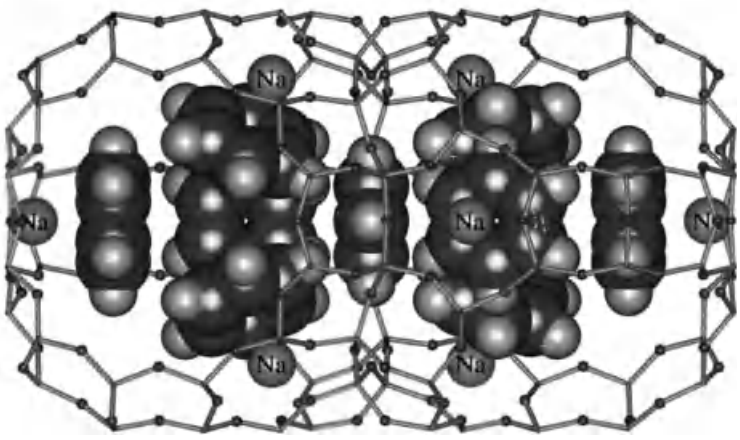


Figure 5.3 Benzene adsorbed in NaY zeolite, showing molecules bonded to Na cations; there are four such molecules per supercage (type 1) and a molecule sitting in the window between two supercages (type 2).

site was found in the 12-ring window between adjacent supercages. The maximum loading is six molecules per supercage (four of type 1 and two of type 2).

Small-angle neutron scattering (SANS) is similar to small-angle X-ray scattering (SAXS). This technique also corresponds to coherent scattering and it gives structural information about inhomogeneities in the sample, with characteristic lengths ranging from 1 nm to 1 μm. Again, an important difference between the two methods is that SAXS is sensitive to inhomogeneities of the electron density whereas SANS detects variations in scattering length densities. For two-phase systems, the scattered intensity is proportional to the square of the difference of the scattering length densities (called the contrast). It is useful to distinguish different regions of the scattering curve. At low Q values, the radius of gyration of the particle R can be obtained in the Guinier range ($QR < 1$). At wider scattering angles, SANS provide information on the shape and dimensions of the heterogeneities. The large Q region, described as the Porod law region, gives information on the specific surface area. Fractal behavior has been observed in some cases.

SANS is of interest in cases of severe absorption of X-rays or lack of scattering contrast. SANS can be used to follow *in situ* the formation of precursor particles and their subsequent aggregation during zeolite crystallization. The advantages of neutrons over X-rays for this special technique have been discussed elsewhere [4].

5.5 Dynamics

To study dynamics, the energy of the scattered neutrons must be analyzed. The measured intensity can be split into coherent and incoherent contributions, as in the case of the scattering cross-sections:

$$\frac{\mathrm{d}^2\sigma}{\mathrm{d}\Omega\,\mathrm{d}E} = \frac{k'}{k_0}\frac{1}{4\pi\hbar}\left[\sigma_{\mathrm{coh}} S_{\mathrm{coh}}(\boldsymbol{Q},\omega) + \sigma_{\mathrm{inc}} S_{\mathrm{inc}}(\boldsymbol{Q},\omega)\right] \tag{5.16}$$

where $S(\boldsymbol{Q}, \omega)$ is called the scattering function or dynamic structure factor. For data fitting, it is easier to work with the scattering function than with the double-differential cross-section, since there are no experimental parameters such as wave vectors.

When studying scattering from a molecular system, the different motions of vibration, rotation, and translation can be treated separately if they are uncoupled. Indeed, they often occur on different time scales such that the total scattering function can then be written as the convolution product of the individual scattering functions for each type of motion:

$$S(\boldsymbol{Q},\omega) = S^{\mathrm{trans}}(\boldsymbol{Q},\omega) \otimes S^{\mathrm{rot}}(\boldsymbol{Q},\omega) \otimes S^{\mathrm{vib}}(\boldsymbol{Q},\omega) \tag{5.17}$$

The two energy ranges illustrated in Figure 5.1 will be discussed separately, vibrational spectroscopy corresponding to inelastic scattering and diffusion to quasi-elastic scattering.

5.5.1 Vibrational Spectroscopy

With current neutron spectrometers, the whole spectral range 1–4000 cm^{-1} can be measured, with a reasonable energy resolution (typically $\Delta E/E \approx 2\%$). The neutron gains or loses energy by interacting with discrete vibrational levels in the sample. The technique is called inelastic neutron scattering (INS) and is analogous to infrared absorption or Raman scattering spectroscopy.

Although the vibrations of non-hydrogenated compounds can be observed with INS [5], in the case of adsorbates the highest intensity will be obtained with hydrogenated molecules. The main term in Eq. (5.16) will then be the incoherent one. The dynamic structure factor can be calculated for a harmonic oscillator and for a polyatomic molecule by resolving molecular vibrations into normal modes. The normal modes are dynamically independent so that the displacement vector for an atom d from its equilibrium position, $\boldsymbol{u}_d$, can be expressed in terms of the normal coordinates $\boldsymbol{q}$:

$$\boldsymbol{u} = \boldsymbol{C}\boldsymbol{q} \tag{5.18}$$

where the $\boldsymbol{C}$ matrix describes the atomic displacements in mass-weighted Cartesian coordinates.

In neutron energy loss, the INS spectrum will consist of delta functions at the frequencies ω_λ corresponding to the normal modes λ. At low temperature, the scattering function corresponding to a fundamental will be given by

$$S(\boldsymbol{Q},\omega) = \sum_d \exp[-2W_d(\boldsymbol{Q})]\frac{\hbar\left|\boldsymbol{Q}\cdot\boldsymbol{C}_d^\lambda\right|^2}{2m_d\omega_\lambda}\delta(\omega-\omega_\lambda) \tag{5.19}$$

The intensity is mainly governed by the product $\left|\boldsymbol{Q}\cdot\boldsymbol{C}_d^\lambda\right|^2$, where the vectors $\boldsymbol{C}_d^\lambda$ describe the displacement of the dth atom during the λth normal mode (a powder average has to be performed to take into account all possible orientations of $\boldsymbol{C}$ relative to $\boldsymbol{Q}$). The Debye–Waller factor, $\exp[-2W_d(\boldsymbol{Q})]$, depends only on dynamic disorder, whereas in diffraction it corresponds to the sum of static and dynamic disorder. It can be written here $\exp(-\boldsymbol{Q}^2\langle\boldsymbol{u}_d{}^2\rangle)$, where $\langle\boldsymbol{u}_d{}^2\rangle$ is the mean-square amplitude for an atom d. Equation (5.19) is useful for highlighting several aspects of the technique:

1) Neutrons are very sensitive to hydrogen because of its large incoherent cross-section, σ_H, and its low mass, m_H. The power of isotopic substitution, for example, D for H, is evident; this will not only shift the vibrational frequencies but also decrease the intensity of the modes involved because deuterium has a smaller cross-section. With new instruments under construction, it will be possible to study non-hydrogenated molecules, for example, CO.
2) There are no considerations on the symmetry of the vibrations so that all modes can be observed. This is in clear contrast with the selection rules operating in infrared and Raman spectroscopy.
3) The modes involving large displacement vectors, $\boldsymbol{C}_d^\lambda$, of light atoms will have high intensities. For crystals, polarization effects can be measured.

4) Information on the vibrational modes can be obtained from the frequencies *and* from the displacement vectors. These two quantities can be calculated in several ways: from a normal coordinate analysis [6], from molecular dynamic simulations [7], from *ab initio* quantum calculations on clusters [8] or on the crystal [9]. A refinement of the force field to give a least-squares fit of the calculated spectrum to the observed profile can also be made.

In general, the fundamentals will be the most intense features of the spectrum, but overtones and combination bands can also be found. Although this complicates the INS spectrum, their intensities can also be calculated. A further complication occurs through the convolution of the high-frequency internal modes by the low-frequency external modes [10, 11]. The scattering function corresponding to the external modes can be expanded in terms of one-phonon, two-phonon, . . . , with another Debye–Waller factor due to the external modes. This factor further decreases the intensity at the frequency ω_λ. The intensity which is taken from the fundamental is redistributed into side bands (or phonon wings) as a function of $\mathbf{Q}$ and temperature. When the effective mass of the molecule is high or when the lattice is stiff, that is, when the Debye–Waller factor is large, phonon wings can be simulated with a limited number of contributions [12]. In the opposite case, one has to consider a larger number of terms in the phonon expansion [13, 14].

For molecular systems, theory and experiment show the necessity to record INS spectra at very low temperature (around 10 K); this will decrease the relative intensity of multiphonon features and sharpen the fundamentals. When the total Debye–Waller factor is larger, for example, for a hydrogen atom bonded to a rigid framework (metal or zeolite), measurements can be performed at room temperature or above.

The applications of INS to surface phenomena have been mainly focused on systems which are difficult or impossible to study by other techniques. In most cases, the catalyst is opaque or completely black, it may have only limited frequency windows, and it may also decompose or fluoresce in a laser beam. On the other hand, it can be almost transparent to neutrons if it includes a small quantity of hydrogen so that the background of the bare catalyst is fairly flat. INS studies include hydrogen chemisorbed on metals, sulfides, and oxides, hydroxyl groups, hydrogen storage [15], hydrogenation reactions [16], hydrocarbons and water on different catalysts and zeolitic systems [17].

As an example, INS spectra of copper chromite as prepared and reduced at various temperatures are shown in Figure 5.4 [18]. The initial catalyst shows bands at low frequencies, due to the mass of the atoms, these bands having a low intensity because no proton motion is involved. Upon reduction, bending modes of OH groups are observed in the energy range displayed in the figure. Increasing the reduction temperature causes a shift of these bending modes to higher frequencies (from 700–800 to 1220 cm^{-1}), while the stretching modes shift to lower energy. This indicates that hydrogen bonding strength with neighboring anions increases with increase in temperature. The band around 400 cm^{-1} was assigned to librations of two geminal protons (i.e., HOH groups).

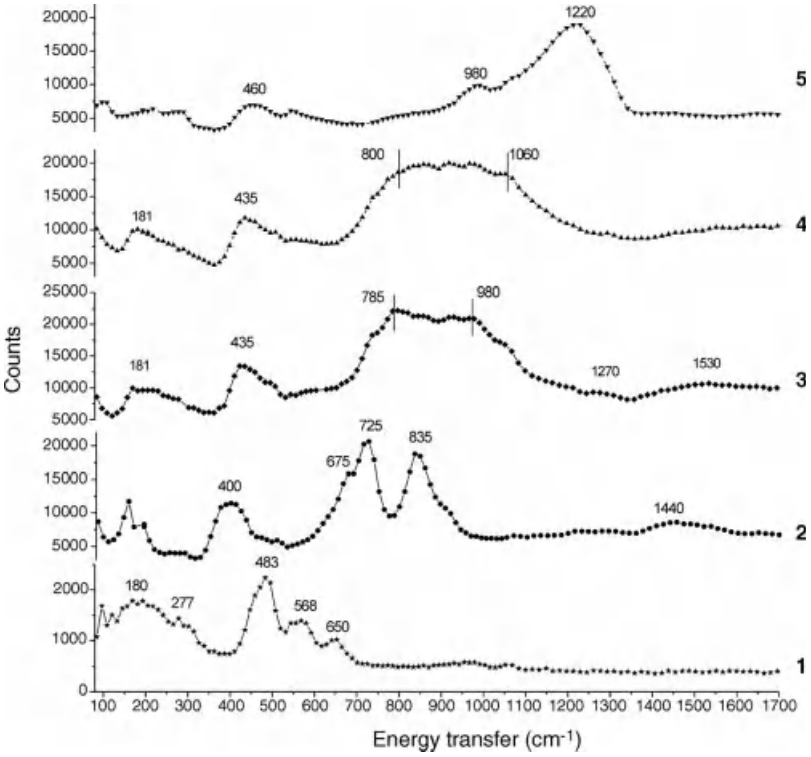


Figure 5.4 INS spectra of initial and reduced samples of copper chromite: (1) initial spectrum; reduced with hydrogen at (2) 250, (3) 290, (4) 320, and (5) 450 °C. Adapted from [18].

5.5.2
Diffusive Motions

In the quasi-elastic domain, that is, at very small energy transfers (Figure 5.1), one can characterize unquantified molecular motions of translation and rotation. Neutrons are Doppler shifted by nuclei moving on a comparable time scale, typically 10^{-8}–10^{-13} s. The faster the motion, the larger is the quasi-elastic linewidth. This is because motions that occur in space and in time are measured in $\boldsymbol{Q}-\omega$ space. The scattering functions, Eq. (5.16), are the four-dimensional Fourier transforms of the van Hove correlation function $G(\boldsymbol{r}, t)$ [19]:

$$S(\boldsymbol{Q},\omega) = \frac{1}{2\pi}\int \mathrm{d}t \exp(-i\omega t)\int \mathrm{d}\boldsymbol{r}\exp(i\boldsymbol{Q}\cdot\boldsymbol{r})G(\boldsymbol{r},t) \tag{5.20}$$

With incoherent scattering, one follows the motions of individual atoms or molecules and it is the self-correlation function, $G_s(\boldsymbol{r}, t)$, which is probed in Eq. (5.20). This function corresponds to the probability of finding an atom at position $\boldsymbol{r}$ at time t if the *same* atom was at the origin at time zero. With coherent scattering, one probes the full correlation function, $G(\boldsymbol{r}, t)$. Here, one considers the relative motions of the atoms

as a function of time. If one atom is at the origin at time zero, $G(\boldsymbol{r}, t)$ gives the probability of finding *any* atom (including the same) at position $\boldsymbol{r}$ at time t.

With neutron spin echo (Section 5.5.2.1), one measures the intermediate scattering function, $I(\boldsymbol{Q}, t)$, defined as

$$I(\boldsymbol{Q}, t) = \int \mathrm{d}\boldsymbol{r} \exp(i\boldsymbol{Q} \cdot \boldsymbol{r}) G(\boldsymbol{r}, t) \tag{5.21}$$

so that the scattering function can also be written:

$$S(\boldsymbol{Q}, \omega) = \frac{1}{2\pi} \int \mathrm{d}t \exp(-i\omega t) I(\boldsymbol{Q}, t) \tag{5.22}$$

Integrating over energy yields the structure factor, $S(\boldsymbol{Q})$:

$$S(\boldsymbol{Q}) = \int_{-\infty}^{+\infty} S(\boldsymbol{Q}, \omega) \mathrm{d}\omega \tag{5.23}$$

For incoherent scattering, $S(\boldsymbol{Q})$ decays smoothly with Q, because of a Debye–Waller factor, but for coherent scattering of adsorbed molecules one has a maximum related to the intermolecular distance and the value at $Q = 0$ governs the coherent intensity (Section 5.5.2.3).

$\boldsymbol{Q}$ and ω are thus the Fourier-transformed variables of $\boldsymbol{r}$ and t. Q has the dimensions of reciprocal distance and ω of angular frequency. Therefore, macroscopic quantities will correspond to small Q, that is, long wavelengths, involving averages over large distances. In analogy, slow diffusivities implying long times in $G(\boldsymbol{r}, t)$ will correspond to small ω. Schematic representations of scattering functions are shown in Figure 5.5, with a typical Gaussian resolution function for a TOF or BS instrument on a steady-state reactor as represented in Figure 5.5b. When the characteristic time, τ, of the dynamic process to be measured is shorter than the inverse of the instrumental resolution, $\Delta\omega$, a broadening of the elastic peak will be observed (Figure 5.5c). In order to derive the true broadening (Figure 5.5d), one has to take into account that the scattering function is convoluted by the energy resolution of the instrument. When τ is larger than $1/\Delta\omega$, the shape is given by the instrumental resolution (Figure 5.5b). In this case, the diffusivity cannot be extracted from the measurements, and a higher energy resolution is required to probe longer times.

5.5.2.1 **Neutron Spin-Echo Technique**

With this method, one is able to detect very small relative velocity changes (of the order of 10^{-5}), despite a broad wavelength distribution ($\Delta\lambda/\lambda \approx 15\%$). The principle of the NSE technique is completely different from the traditional instrumentation. On TOF and BS spectrometers, the incident energy has to be accurately defined, and a higher resolution can only be obtained at the expense of the incident neutron flux. A clear advantage of NSE is that monochromatization is decoupled from energy resolution and therefore a broad wavelength distribution can be used. In NSE, the velocities of polarized neutrons are compared before and after the scattering event,

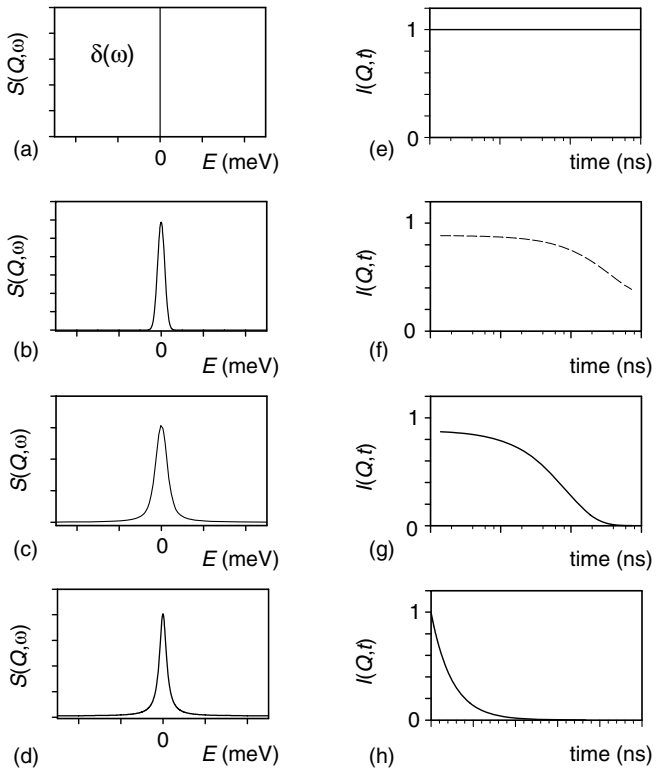


Figure 5.5 Schematic representations, for one Q value, of the scattering function, $S(Q, \omega)$ and of the intermediate scattering function $I(Q, t)$ in the case of purely elastic scattering: (a) and (e). In practice, every instrument has a finite resolution $R(Q, \omega)$ (b) or $R(Q, t)$ (f), so that the signals which are measured in the case of quasi-elastic scattering, (c) and (g), have to be corrected from the resolution effect to yield (d) or (h).

using the Larmor precession of the neutron spin in a B magnetic field region of length ℓ. The precession angle, φ, of the neutron is given by

$$\varphi = \frac{\gamma B \ell}{v} \tag{5.24}$$

where γ is the gyromagnetic ratio of the neutron and v its velocity. A NSE spectrometer is made of two identical precession coils, the sample being located between the two. Close to the sample is placed a π flipper, which inverts the sense of precession: φ becomes $-\varphi$ (the spin is turned by 180°). For elastic scattering, one recovers the original beam polarization and the total precession angle is zero. So far, coherent scatterers or deuterated molecules are preferentially studied since spin-polarized neutrons are used in this method. Spin incoherent scattering (i.e., for hydrogenated molecules) inverts the neutron spin with a probability of 2/3, whereas coherent and isotopic-incoherent scattering involve no spin flip. The polarization of the neutron beam after spin-incoherent scattering is reversed and three times less

intense. However, increases in flux by one or two orders of magnitude are predicted on the new NSE instruments under construction, which will allow the study of hydrogenated molecules also.

In the case of quasi-elastic neutron scattering, the total precession angle can be expressed as a function of the energy transfer ω:

$$\varphi = \omega t \tag{5.25}$$

where the proportionality constant t corresponds to

$$t = \frac{\hbar \gamma B \ell}{m v^3} \tag{5.26}$$

This parameter is called the *spin-echo time* or *Fourier time*. Since v is inversely proportional to λ (de Broglie relation), t is proportional to λ^3, which means that one can use long wavelengths in order to increase rapidly the resolution in Fourier time (up to 20 Å at the ILL).

What is measured experimentally is the beam polarization, which is the average of $\cos \varphi$:

$$\langle \cos \varphi \rangle = \int S(Q, \omega) \cos(\omega t) \mathrm{d}\omega = I(Q, t) \tag{5.27}$$

The time t defined by Eq. (5.26) is a real time; it corresponds in Eq. (5.27) to the Fourier mate of ω. Therefore, NSE directly measures the intermediate scattering function [see Eqs. (5.21) and (5.22)]. Data are not recorded as a function of energy transfer, as is the case on TOF and BS spectrometers, but as a function of time (Figure 5.5).

For example, in the hydrodynamic range where Fick's equations are valid (corresponding to large displacements), the intermediate scattering function has an exponential form when the diffusion is isotropic:

$$I(Q, t) = \exp\left(-DQ^2 t\right) \tag{5.28}$$

One can thus obtain the diffusivity D in a straightforward manner from experimental data similar to Figure 5.5h, by following the decay of $I(Q, t)$ up to several hundred nanoseconds. In zeolites, carbon nanotubes or metal–organic frameworks, the molecular displacements can be confined in one-dimensional channels [20]; in this case the decay no longer has a simple exponential form, as shown in Figure 5.6.

The problem of instrumental resolution, which is determined experimentally using an elastic scatterer, is easier to cope with in NSE than in TOF or BS techniques. Energy spectra are convoluted with the instrumental resolution, $R(Q, \omega)$. In the time domain, the data obtained with the sample (Figure 5.5g) have simply to be divided by the reference scan $R(Q, t)$ obtained with an elastic scatterer (Figure 5.5f) in order to obtain the true intermediate scattering function (Figure 5.5h), which here is the exponential predicted by Eq. (5.28). This comes from the convolution theorem for Fourier transforms: the Fourier transform of the product of two functions is the convolution (symbol $\otimes$) of their Fourier transforms:

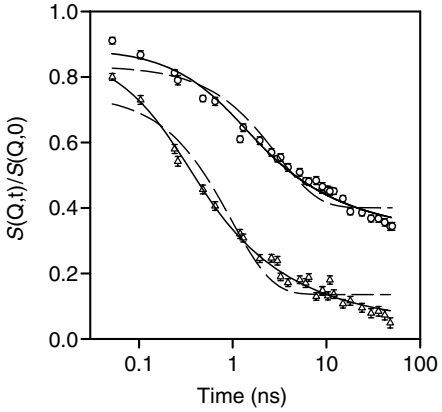


Figure 5.6 Comparison between experimental and calculated normalized intermediate scattering functions for $C_{14}D_{30}$ in silicalite at 300 K; (o) $Q = 0.1\,\text{Å}^{-1}$; (△) $Q = 0.2\,\text{Å}^{-1}$. The dashed lines correspond to three-dimensional diffusion and the solid lines to one-dimensional diffusion (loading: 0.93 molecule per unit cell, on average).

$$S(Q,\omega) \otimes R(Q,\omega) \overset{\text{FT}}{\longleftrightarrow} I(Q,t) \cdot R(Q,t) \tag{5.29}$$

5.5.2.2 **Rotational Motion**

When the time scales of translational and rotational motions are different in magnitude, justifying Eq. (5.17), both motions can be characterized with precision. As a general rule, the incoherent scattering function for a rotational motion can be written as the sum of an elastic term and of a quasi-elastic component:

$$S_{\text{inc}}^{\text{rot}}(\boldsymbol{Q},\omega) = A_0(\boldsymbol{Q})\delta(\omega) + \sum_{\ell} A_\ell(\boldsymbol{Q})\Lambda_\ell \tag{5.30}$$

An elastic component occurs because the self-correlation function has a finite value at long times. This happens, for example, if an atom is rotating around a fixed point. The factor $A_0(\boldsymbol{Q})$, which governs the intensity of the delta function is called the elastic incoherent structure factor (EISF). This factor corresponds to the space Fourier transform of the proton trajectory averaged over the time scale of the experiment [21]. The variation of the EISF with Q gives information on the geometry of rotation. The experimental EISF can be compared with various models, for example, rotational diffusion on a sphere, diffusion within a sphere, uniaxial rotation, and fluctuations around equilibrium positions. Characteristic times of the rotational motions can be obtained from the quasi-elastic component in Eq. (5.30), which consists of a sum of Lorentzians Λ_ℓ.

For methane, the elastic and quasi-elastic incoherent structure factors for an isotropic rotation are shown in Figure 5.7. It appears that only the first three terms of the summation in Eq. (5.30) have to be considered in the Q range that is usually covered.

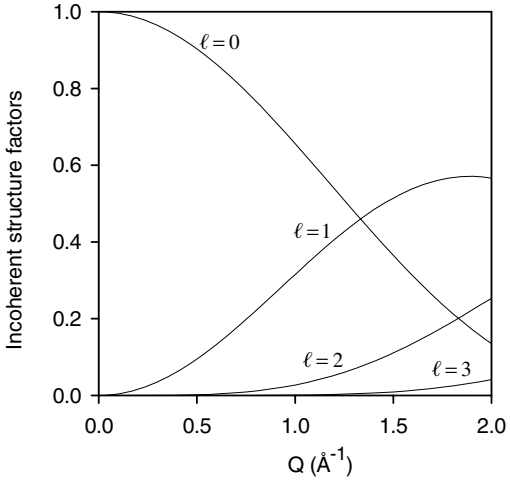


Figure 5.7 Elastic ($\ell = 0$) and quasi-elastic ($\ell = 1, 2, 3$) incoherent structure factors, corresponding to an isotropic rotation of methane, as a function of the wave vector transfer Q.

5.5.2.3 **Translational Motion**

When the translational motion is much slower than the rotations, the QENS spectra measured on BS instruments can be interpreted solely in terms of diffusion [22]. On TOF spectrometers, both molecular motions of translation and rotation may contribute to the scattering. If there are no inelastic features at small energy transfers (Figure 5.1), the vibrational term will only affect the measured intensities through a Debye–Waller factor.

The self-diffusivity, D_s, can be determined from incoherent scattering, whereas the transport diffusivity, D_t, can be obtained from coherent scattering. All experiments are performed at equilibrium. When the scattering is both incoherent and coherent, then both diffusivities can in principle be determined simultaneously [23].

Since hydrogen is an incoherent scatterer and has the largest scattering cross-section, hydrogenated molecules were selected for the first neutron measurements related to diffusion in porous materials. The scattering from these molecules is dominated by incoherent scattering. The motion of a hydrogen atom (or of a single molecule) is described by the diffusion equation (Fick's second law), for long enough times (and distances):

$$\frac{\partial p(\boldsymbol{r}, t)}{\partial t} = D_s \nabla^2 p(\boldsymbol{r}, t) \tag{5.31}$$

The self-correlation function, $G_s(\mathbf{r}, t)$, is an appropriate solution for $p(\mathbf{r}, t)$, the probability of finding the atom (or molecule) at position $\boldsymbol{r}$ at time t. If the atom is at the origin at time zero, $G_s(\boldsymbol{r}, 0) = \delta(\boldsymbol{r})$, the self-correlation function is given by the Gaussian expression

$$G_s(\boldsymbol{r},t) = \frac{1}{(4\pi D_s t)^{\frac{3}{2}}} \exp\left(-\frac{r^2}{4D_s t}\right) \tag{5.32}$$

The spectral profiles can then be calculated. As a first step, the spatial Fourier transform in Eq. (5.20) gives the intermediate self-scattering function:

$$I_s(\boldsymbol{Q},t) = \exp\left(-D_s Q^2 t\right) \tag{5.33}$$

The incoherent scattering function is then obtained from the time Fourier transform of the intermediate self-scattering function

$$S_{inc}(\boldsymbol{Q},\omega) = \frac{1}{\pi} \frac{D_s Q^2}{\omega^2 + \left(D_s Q^2\right)^2} = \Lambda_s \tag{5.34}$$

It corresponds to a Lorentzian profile in energy. Equation (5.34) is obtained for an isotropic diffusion. Other analytical expressions can be derived for anisotropic diffusion (one-dimensional, two-dimensional) or for single-file diffusion [24].

The relative intensities of the elastic and quasi-elastic components in Eq. (5.30) are shown in Figure 5.8 for methane. The narrow peak corresponds to $A_0(Q)\Lambda_s$, that is, the Lorentzian due to translation weighted by the EISF of the rotation. The broader peak (the dashed line in Figure 5.8) corresponds to $\sum_{\ell=1}^{3} A_\ell(Q)\Lambda_\ell^{rot} \otimes \Lambda_s$, and thus to the quasi-elastic components of the rotation convoluted by the translation. The influence of the translation on the profile of the broad component is small. Therefore, the diffusion coefficient of CH_4 will be better determined at small Q values to minimize the contribution of the rotation, and also to reach the hydrodynamic limit. A recent example concerning the increase in mobility of water molecules with water concentration in $CaCl_2$ hydrates dispersed in silica is shown in Figure 5.9 [25]. It can be noted that the larger the radius of gyration, the faster the EISF decays so that smaller wave vector values will be required to characterize the diffusion.

Experimentally, energy spectra are measured at different scattering angles, corresponding to different values of the scattering vector Q. The half-width at half-maximum (HWHM) of Λ_s is

$$\Delta\omega(Q)_{inc} = D_s Q^2 \tag{5.35}$$

It should be noted that this expression is only valid at large distances, corresponding to small wave vector values. Typically, in a molecular liquid, Fickian diffusion is already observed for distances larger than 1 nm. For a molecule diffusing in a zeolite, one has to probe translation over a few unit cells (several nanometers). At smaller distances (larger wave vector values), there is usually a deviation from the linear relation between $\Delta\omega$ and Q^2. This sort of departure is fairly general and is due to the details of the elementary diffusive steps.

The jump models that have been developed in the literature contain as parameters the characteristic lengths and times of the elementary steps. The available models have been discussed elsewhere [24]. If one considers only isotropic systems, the scattering function will always be a Lorentzian function, but the width (HWHM) of

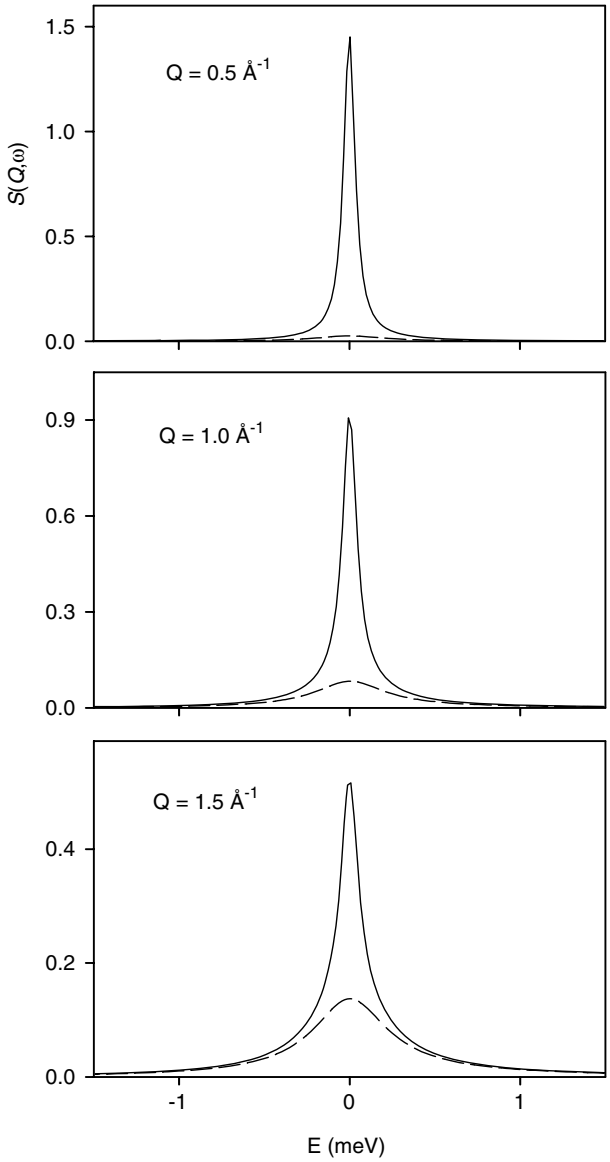


Figure 5.8 Theoretical spectra calculated for a diffusing and rotating CH_4 molecule, at different wave vector values (the effect of instrumental resolution is not taken into account). The translational diffusion coefficient is $6.0 \times 10^{-10}\,m^2\,s^{-1}$ and the rotational diffusion coefficient is $8.0 \times 10^{10}\,s^{-1}$.

the energy spectra will differ from the simple DQ^2 behavior. For each spectrum measured at a given scattering vector, one can extract a diffusion coefficient D. One has to reach small Q values to obtain the Fickian diffusivity, as illustrated in Figure 5.10.

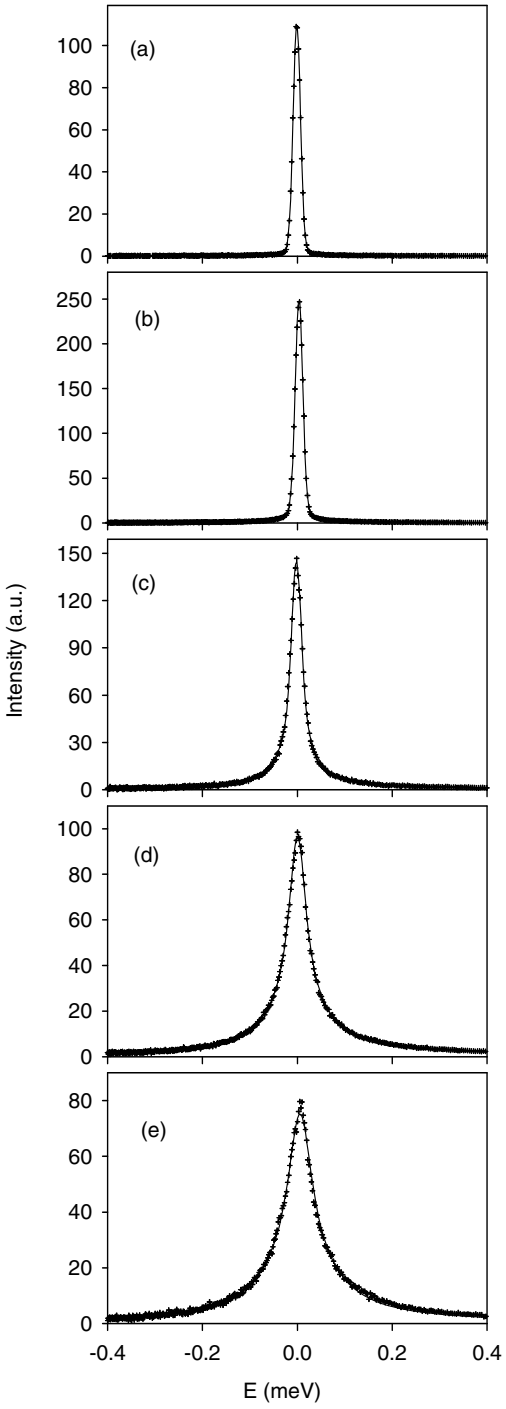


Figure 5.9 QENS spectra obtained for $CaCl_2{\cdot}nH_2O$ hydrates dispersed in silica: (a) $n = 1/3$, (b) $n = 2$, (c) $n = 4$, (d) $n = 6$, and (e) $n = 9$ ($T = 350$ K, $Q = 0.88$ Å^{-1}). The solid lines correspond to fits to the experimental data (+).

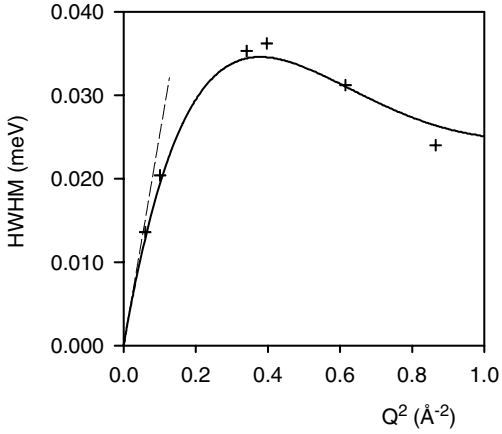


Figure 5.10 Broadenings corresponding to the diffusion of *n*-pentane in NaX zeolite, at 300 K. The crosses are obtained from individual fits of the spectra and the solid line from a simultaneous fit with all spectra using a jump diffusion model. The dashed line corresponds to Fickian diffusion.

For unbounded diffusion, there is no longer pure elastic scattering because the self-correlation function goes to zero for $t \to \infty$. For a rotational motion there is an elastic peak, $\delta(\omega)$, because the self-correlation function has a finite value at long times, so that the intermediate scattering function also has a finite value and the time Fourier transform of this constant yields a purely elastic term $I_s(Q, \infty)\cdot\delta(\omega)$.

For coherent scattering, the scattering function depends on the pair correlation function, $G(\boldsymbol{r}, t)$. This correlation function can be expressed in terms of the microscopic space and time-dependent molecule density (for an adsorbed phase). The transport diffusivity, D_t, can be obtained from QENS experiments because even at equilibrium one has local concentration gradients. However, at saturation, the fluctuations tend to disappear.

At low wave vector values, the coherent scattering function for an isotropic motion has the form

$$S_{\mathrm{coh}}(\boldsymbol{Q}, \omega) = \frac{S(Q)}{\pi} \frac{D_t Q^2}{\omega^2 + (D_t Q^2)^2} = S(Q)\Lambda_t \tag{5.36}$$

The lineshape of the coherent scattering function is still Lorentzian, with an HWHM

$$\Delta\omega(Q)_{\mathrm{coh}} = D_t Q^2 \tag{5.37}$$

An important difference from incoherent scattering is that the intensity varies as $S(Q)$. The extrapolation of $S(Q)$ at zero Q is known to be a measure of the fluctuations of the number of molecules contained in a given volume:

$$S(Q)_{Q\to 0} = \frac{\langle N^2\rangle - \langle N\rangle^2}{\langle N\rangle} \tag{5.38}$$

For molecules adsorbed in zeolites, one therefore expects a larger scattering power per molecule at small loadings than at saturation, where $S(Q)$ goes to zero. In a bulk fluid, particle fluctuations can also be related to the isothermal compressibility. This means that, at small loadings, the sorbate phase is highly compressible, as in a gas, where $S(Q) = 1$, whereas at saturation one has a case similar to a liquid, which is poorly compressible and where $S(Q)$ is almost zero. Comparisons have been made between QENS measurements and molecular simulations [27].

As an illustration of the QENS technique, one can mention the recent elucidation of the large discrepancies that persisted for decades in the determination of diffusivities in zeolites. The diffusion of alkanes in MFI-type zeolites is probably the system that has been the most studied by various experimental and theoretical methods. The macroscopic measurements yielded values orders of magnitude lower than those obtained by the microscopic techniques: pulsed-field gradient (PFG) NMR and QENS. Some of the results are shown in Figure 5.11. The QENS data [28] are in good agreement with the theoretical predictions [29], although the theoretical values are higher, because simulations are made in a perfect crystalline structure for an infinitely diluted sorbed phase. QENS measurements are performed on real crystals at a finite loading, and the self-diffusivity decreases with increasing loading. Both techniques establish that the low-occupancy self-diffusivity is a monotonic function that decreases less than linearly with chain length. The QENS self-diffusivities are more than one order of magnitude higher than PFG-NMR diffusivities [30], for intermediate chain lengths. This shows the strong influence of intracrystalline barriers (defects, twinning, etc.) on molecular diffusion in silicalite. The PFG-NMR

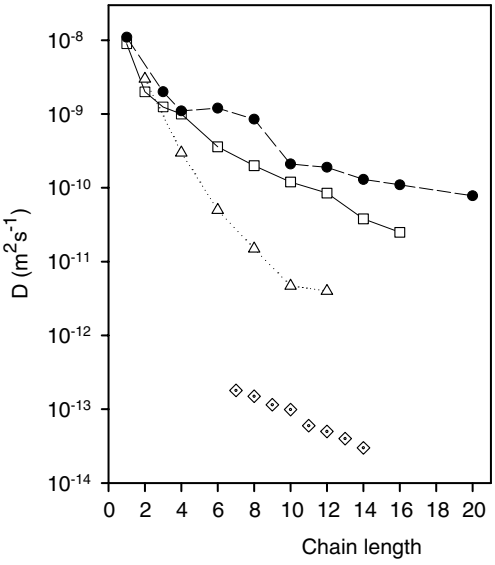


Figure 5.11 Self-diffusion coefficients, obtained at 300 K by different techniques, for *n*-alkanes in MFI-type zeolites, as a function of the number of carbon atoms in the chain: (•) hierarchical simulation, (□) QENS, (△) PFG-NMR, and (◇) ZLC.

method, with its larger length scale of observation (micrometers), is more sensitive than QENS (length scale of several nanometers) to internal barriers in the crystal structure, if the distance between barriers is of hundreds of nanometers. The zero length column (ZLC) diffusivities [31] are orders of magnitude lower than the "microscopic" techniques. The ZLC measurements are performed with a thin bed of zeolite crystals so they are sensitive to all the defects (the influence of surface barriers could be ruled out). The presence of internal transport barriers within zeolite crystals is therefore *the* explanation for the discrepancies that have been reported in the literature for the past 30 years.

5.6 Conclusion

The term "neutron scattering" represents several neutron-based techniques. Apart from its well-known application in structure determination, predicted instrumental developments in inelastic and quasi-elastic scattering will offer unique possibilities to probe molecular motion at the microscopic level. Using various neutron spectrometers, one has the possibility of characterizing the different molecular motions of the adsorbed molecules: vibrations, rotations, and translations.

For studying vibrational modes, the absence of selection rules in INS is in clear contrast with infrared and Raman spectroscopy, where photons interact with electrons. The intensities in INS are simply related to nuclei displacements. Since gains of one to two orders of magnitude in signal-to-noise ratio are expected on the new spectrometers under construction, this will allow the study of catalysts that are available only in small quantities.

In the field of diffusion in nanoporous materials, the time and length scales of the neutron techniques match closely those covered by molecular simulation methods so that combined studies are becoming more and more frequent (e.g., [32, 33]).

References

1 Fitch, A.N. and Jobic, H. (1999) in *Molecular Sieves*, vol. **2** (eds H.G. Karge and J. Weitkamp **)**, Springer, Heidelberg, p. 31.

2 Rietveld, H.M. (1969) *Appl. Crystallogr.*, **2**, 65.

3 Fitch, A.N., Jobic, H., and Renouprez, A. (1986) *J. Phys. Chem.*, **90**, 1311.

4 Walton, R.I., Smith, R.I., and O'Hare, D. (2001) *Micropor. Mesopor. Mater.*, **48**, 79.

5 Coulombeau, C., Jobic, H., Bernier, P., Fabre, C., Schutz, D., and Rassat, A. (1992) *J. Phys. Chem.*, **96**, 22.

6 Wilson, E.B., Decius, J.C., and Cross, P.C. (1955) *Molecular Vibrations*, McGraw-Hill, New York, p. 388.

7 Jobic, H., Smirnov, K.S., and Bougeard, D. (2001) *Chem. Phys. Lett.*, **344**, 147.

8 Jobic, H., Tuel, A., Krossner, M., and Sauer, J. (1996) *J. Phys. Chem.*, **100**, 19545.

9 Plazanet, M., Glaznev, I., Stepanov, A.G., Aristov, Yu.I., and Jobic, H. (2006) *Chem. Phys. Lett.*, **419**, 111.

10 Griffin, A. and Jobic, H. (1981) *J. Chem. Phys.*, **75**, 5940.

11 Warner, M., Lovesy, S.W., and Smith, J. (1983) *Z. Phys. B*, **51**, 109.

12 Jobic, H. and Lauter, H.J. (1988) *J. Chem. Phys.*, **88**, 5450.
13 Tomkinson, J. and Kearley, G.J. (1989) *J. Chem. Phys.*, **91**, 5164.
14 Hochard, F., Jobic, H., Clugnet, G., Renouprez, A., and Tomkinson, J. (1993) *Catal. Lett.*, **21**, 381.
15 Jalowiecki-Duhamel, L., Debeusscher, S., Zarrou, H., D'Huysser, A., Jobic, H., and Payen, E. (2008) *Catal. Today*, **138**, 266.
16 Chojecki, A., Jobic, H., Jentys, A., Müller, T.E., and Lercher, J.A. (2004) *Catal. Lett.*, **97**, 155.
17 Albers, P.W. and Parker, S.F. (2007) *Adv. Catal.*, **51**, 99.
18 Khassin, A.A., Kustova, G.N., Jobic, H., Yurieva, T.M., Chesalov, Y.A., Filonenko, G.A., Plyasova, L.M., and Parmon, V.N. (2009) *Phys. Chem. Chem. Phys.*, **11**, 6090.
19 van Hove, L. (1954) *Phys. Rev.*, **95**, 249.
20 Jobic, H. and Farago, B. (2008) *J. Chem. Phys.*, **129**, 171102.
21 Bée, M. (1988) *Quasielastic Neutron Scattering*, Adam Hilger, Bristol.
22 Jobic, H., Fitch, A.N., and Combet, J. (2000) *J. Phys. Chem. B*, **104**, 8491.
23 Jobic, H., Kärger, J., and Bée, M. (1999) *Phys. Rev. Lett.*, **82**, 4260.
24 Jobic, H. (2000) in *Recent Advances in Gas Separation by Microporous Ceramic Membranes*, Membrane Science and Technology Series 6 (ed. N.K. Kanellopoulos), Elsevier, Amsterdam, pp. 109–137.
25 Kolokolov, D.I., Stepanov, A.G., Glaznev, I., Aristov, Yu.I., Plazanet, M., and Jobic, H. (2009) *Micropor. Mesopor. Mater*, **125**, 46.
26 Jobic, H. (1999) *Phys. Chem. Chem. Phys.*, **1**, 525.
27 Jobic, H., Laloué, N., Laroche, C., van Baten, J.M., and Krishna, R. (2006) *J. Phys. Chem. B*, **110**, 2195.
28 Jobic, H. and Theodorou, D.N. (2006) *J. Phys. Chem.*, **110**, 1964.
29 Maginn, E.J., Bell, A.T., and Theodorou, D.N. (1996) *J. Phys. Chem.*, **100**, 7155.
30 Jobic, H., Schmidt, W., Krause, C.B., and Kärger, J. (2006) *Micropor. Mesopor. Mater.*, **90**, 299.
31 Brandani, S., Caro, J., Jobic, H., Kärger, J., Krause, C., and Staudt, R. (2007) *Stud. Surf. Sci. Catal.*, **170**, 981.
32 Jobic, H., Borah, B.J., and Yashonath, S. (2009) *J. Phys. Chem. B*, **113**, 12635.
33 Nguyen, T.X., Jobic, H., and Bhatia, S.K. (2010) *Phys. Rev. Lett.*, **105**, 085901.

6
Sum Frequency Generation and Infrared Reflection Absorption Spectroscopy

Karin Föttinger, Christian Weilach, and Günther Rupprechter

6.1
Introduction

Solid–gas and solid–liquid interfaces are everywhere: think of phenomena such as corrosion and geochemistry, hard and decorative coatings, electrochemistry, friction and lubrication, biocompatibility and toxicity, and finally chemical reactions of molecules on solid surfaces in heterogeneous catalysis. For all such phenomena, the interaction of molecules with surfaces is most important, including adsorption (bond breaking and bond formation), desorption, surface diffusion and surface-catalyzed reactions. Vibrational spectroscopy provides direct information on the molecular state of surface-adsorbed molecules and thus on the respective surface processes.

The benefits of vibrational spectroscopy for heterogeneous catalysis are innumerable. First, the catalyst itself (in the absence of reactants) can be examined, for example via detection of lattice vibrations or functional groups at the surface (OH, carbonates, sulfates, formates, etc.). Second, and probably more important, vibrational spectroscopy provides access to adsorbed and reacting molecules. It allows the study of the adsorption of reactants and products individually, but can also be applied to examine coadsorption and catalytic reactions. The latter is particularly important because it allows studies to be performed "under catalytic reaction conditions," that is, the characterization of molecules on functioning (working) catalysts, which is the most direct approach for elucidating reaction mechanisms.

Among the vibrational spectroscopic techniques, Fourier transform infrared (FTIR) spectroscopy in transmission mode is certainly the most frequently applied, particularly for industrial-grade (powder) catalysts (see Chapter 1). For materials that do not allow transmission measurements, diffuse reflectance infrared Fourier transform spectroscopy (DRIFTS) or attenuated total reflection (ATR) can be applied. Raman spectroscopy (treated in Chapter 2) is also frequently used but mainly for catalyst characterization, as its sensitivity for adsorbed molecules is rather limited. For surface science model catalysts, such as single crystals and thin

Characterization of Solid Materials and Heterogeneous Catalysts: From Structure to Surface Reactivity, First Edition. Edited by Michel Che and Jacques C. Védrine.
© 2012 Wiley-VCH Verlag GmbH & Co. KGaA. Published 2012 by Wiley-VCH Verlag GmbH & Co. KGaA.

films, infrared reflection adsorption spectroscopy (IRAS, also IRRAS or RAIRS) is mainly employed, operated near grazing incidence [high-resolution electron energy loss spectroscopy (HREELS) [1] will not be treated here]. The application of infrared (IR) spectroscopy to heterogeneous catalysis dates back to the initial experiments of Eischens and Pliskin [2] over 40 years ago, and the subsequent development of the field has been described in a number of reviews (see, e.g., [3–6]). In model catalysis, IRAS allowed researchers to elucidate surface phenomena related to adsorption, coadsorption, and surface reactions, but it still had a major disadvantage. It could only be applied in a vacuum environment because under catalytic reaction conditions, that is, in the presence of a gas phase of millibar pressure, the IR spectra are dominated by the gas-phase signatures which then obscure the relevant surface species information. Eventually there were two solutions to this problem, enabling surface-specific information to be acquired on a functioning catalyst at ambient pressure: (i) sum frequency generation (SFG) spectroscopy and (ii) polarization-modulation infrared reflection adsorption spectroscopy (PM-IRAS).

SFG laser spectroscopy is inherently surface specific because the gas phase does not produce an SFG signal (see Section 6.2). Early applications to model (single-crystal) catalysis were reported by the groups of Somorjai, Shen, Rabinowitz, Hall, and others, and the first study of oxide-supported nanoparticles was performed by Dellwig *et al.* [7]. Apart from its high-pressure capability, SFG also provides access to surface dynamics (pump–probe) and molecular orientation (polarization dependence). More recently, SFG has been applied to technological catalysts, by powder coating of suitable prisms and employing total internal reflection (TIR) geometry.

However, SFG still has the disadvantage of a relatively small frequency range ($\sim$1600–4000 cm^{-1}) and lower resolution and sensitivity, compared with IRAS. This was the incentive to develop the high-pressure variant of IRAS by applying polarization modulation. Although its principle has been known for a long time, its application was only boosted by the eventual availability of photoelastic modulators (PEMs) working at high frequency. Initial model studies were reported in several papers [8–11].

Vibrational spectroscopy alone cannot answer all questions, and its combination with complementary techniques is not only important, but absolutely essential for a deep understanding of catalytic processes. In particular, combination with other *in situ* (high-pressure) methods such as high-pressure X-ray photoelectron spectroscopy (HP-XPS) or extended X-ray absorption fine structure (EXAFS) has proven to be very powerful (Figure 6.1) [11–15] (see Chapters 12 and 13 for details).

In the following, the basics of SFG spectroscopy are explained, followed by a description of the experimental setup and operating modes. IRAS and PM-IRAS are treated in Chapter 7. Then selected case studies are presented for catalysts of increasing complexity: from metal single crystals via bimetallic and oxide surfaces to oxide-supported monometallic and bimetallic nanoparticles. In several cases, a direct comparison is made between corresponding studies on technological and model catalysts. Emphasis is placed, of course, on the quest for the active site and reaction mechanisms.

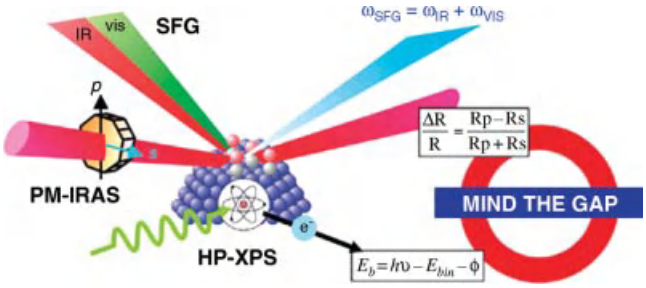


Figure 6.1 Illustration of high-pressure spectroscopic techniques that are capable of monitoring adsorbed and reacting molecules under realistic pressure conditions (kPa to atmospheric pressure and above). Differing results between studies under UHV and ambient pressure indicate the importance to "mind the gap" between low-pressure and high-pressure studies. Reprinted from [87], Copyright (2007), with permission from Elsevier.

6.2
Theoretical Background of SFG

SFG spectroscopy is based on the second-order nonlinear optical process of sum frequency generation. Two light waves at different frequencies interact in a medium characterized by a second-order nonlinear susceptibility tensor $\chi^{(2)}$, generating a wave at the sum of their frequencies ($\omega_{SFG} = \omega_1 + \omega_2$) [16]. However, high incident light intensities, that is, pulsed lasers, are required because the nonlinear process produces only a small signal in most cases. To acquire an SFG vibrational spectrum of adsorbed molecules on a solid (catalyst) surface, two (e.g., picosecond) laser pulses are spatially and temporally overlapped on the sample (Figure 6.2a). One input beam is in the visible range at fixed frequency (ω_{vis}), and the other is tunable in the mid-IR region (ω_{IR}) in order to excite the vibrational modes of the surface species. In a simplified picture, when the IR beam is tuned through a vibrational resonance of the adsorbate, it induces a vibrational transition

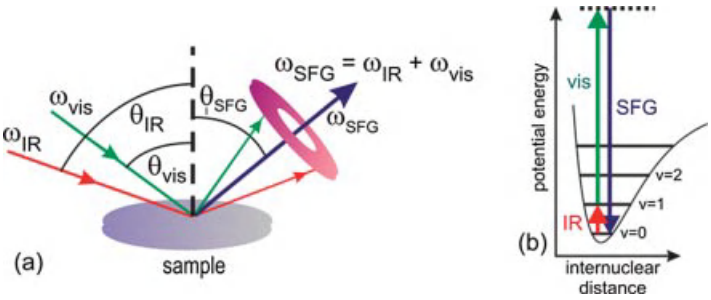


Figure 6.2 (a) Illustration of vibrational IR–visible SFG. In the case of a vibrational resonance of an adsorbed molecule, visible light is generated at a frequency that is the sum of the frequencies of two incident optical fields ($\omega_{SFG} = \omega_{IR} + \omega_{vis}$). (b) Schematic energy level diagram. Adapted from [36, 37]. Reproduced by permission of the PCCP Owner Societies.

from the ground state to an excited state, and simultaneously the visible beam induces a transition to a higher energy virtual state through an anti-Stokes Raman process (see the energy scheme in Figure 6.2b). Once the high-energy virtual state relaxes, light in the visible region is generated at a frequency that is the sum of the frequencies of two incident optical fields ($\omega_{SFG} = \omega_{IR} + \omega_{vis}$). By tuning of the IR wavelength and monitoring of the intensity of the SFG output, plotting of the SFG intensity against the IR wavenumber creates an adsorbate vibrational spectrum. The "uniqueness" of SFG lies in its surface specificity, resulting from the selection rules (see below). Only vibrational modes that simultaneously satisfy both IR *and* Raman selection rules are SFG active. Therefore, SFG is not allowed in media with inversion symmetry (such as in the centrosymmetric bulk of a solid or in an isotropic gas or liquid phase), but has a finite value only at an interface where the inversion symmetry is broken. The underlying physical principles are discussed in the following.

The interaction between light and matter induces a polarization p. In the electric dipole approximation, the microscopic polarization p and the electric field E are related through molecular (hyper)polarizability tensors α, β, and γ [16–18]:

$$p = \alpha E + \beta EE + \gamma EEE + \ldots \tag{6.1}$$

The polarization produced by conventional light sources scales linearly with the electric field E (coefficient α; polarizability), whereas irradiation with intense laser light induces significant *nonlinear* polarization, characterized by the higher order hyperpolarizability tensors β and γ.

However, macroscopic amounts of substances are typically investigated (involving large numbers of molecules). Macroscopic polarizability tensors $\chi^{(n)}$ are obtained by multiplying the ensemble/orientation averages (denoted "$< >$") of the corresponding molecular (hyper)polarizabilities with the number of molecules N:

$$\chi^{(1)} = N\langle\alpha\rangle, \quad \chi^{(2)} = N\langle\beta\rangle, \quad \chi(3) = N\langle\gamma\rangle \tag{6.2}$$

and the macroscopic polarization P can thus be written as

$$P = \chi^{(1)}E + \chi^{(2)}EE + \chi^{(3)}EEE + \ldots \tag{6.3}$$

The magnitude of the local electric field E is described by

$$E(\omega; r, t) = E_0(\omega)\{\exp[i(\omega t - kr)] + \text{c.c.}\} = 2E_0(\omega)\cos(\omega t - kr) \tag{6.4}$$

where r is the position vector, t is the time, $E_0(\omega)$ is the amplitude vector, k is the wave vector, and c.c. stands for the complex conjugate.

For SFG spectroscopy, the second-order polarization is most important because E is (still) too small for the first-order term to become relevant, whereas third- and higher order terms are almost negligible owing to small hyperpolarizabilities. In the following, we will therefore focus on the second-order (nonlinear) polarization $P^{(2)}$:

$$P^{(2)} = \omega^{(2)}EE \tag{6.5}$$

The electric field at a position r irradiated by two light waves with different frequencies ω_1 and ω_2 can be expressed by the vector sum of the two electric fields:

$$E(r,t) = E(\omega_1; r, t) + E(\omega_2; r, t) \tag{6.6}$$

Substituting Eq. (6.6) for E in Eq. (6.5) yields a second-order polarization $P^{(2)}$, comprising polarizations oscillating at $\omega_1 + \omega_2$ (sum frequency generation, SFG) and $\omega_1 - \omega_2$ (difference frequency generation, DFG), in addition to polarizations oscillating at zero frequency (optical rectification), $2\omega_1$ (second harmonic generation, SHG of ω_1), and $2\omega_2$ (SHG of ω_2). For the specific case of sum frequency generation by infrared and visible light (IR–visible SFG), the nonlinear polarization $P^{(2)}$ is

$$P^{(2)}(\omega_{\mathrm{SFG}} = \omega_{\mathrm{IR}} + \omega_{\mathrm{vis}}) = \chi^{(2)} E(\omega_{\mathrm{IR}}) E(\omega_{\mathrm{vis}}) \tag{6.7}$$

As shown below, when the frequency/energy of the IR beam is in resonance with a vibrational transition of a surface/interface species, the SFG intensity is resonantly enhanced, giving rise to a signal. IR–visible SFG has thus become a versatile tool for vibrational spectroscopy of molecules located at surfaces and interfaces, utilizing frequency-tunable or broadband IR and visible lasers [6, 19–24]. As mentioned, not all vibrational modes are SFG active, as discussed below.

6.2.1
SFG Signal Intensity and Selection Rules

The *intensity* of the generated sum frequency output is proportional to the square of $P^{(2)}$, that is, to the absolute square of the effective second-order susceptibility of the surface/interface, denoted $\chi_{\mathrm{s}}^{(2)}$, and to the intensities of the two incident IR and visible beams:

$$I_{\mathrm{SFG}}(\omega_{\mathrm{IR}}) \propto \left|\chi_{\mathrm{s}}^{(2)}(\omega_{\mathrm{IR}})\right|^2 I(\omega_{\mathrm{IR}}) I(\omega_{\mathrm{vis}}) \tag{6.8}$$

Whereas $I(\omega_{\mathrm{IR}})$ and $I(\omega_{\mathrm{vis}})$ "simply" depend on the sources (lasers) of the IR and visible radiation, the surface/interface properties are characterized by $\chi_{\mathrm{s}}^{(2)}$, which has two components. Let us start with the resonant nonlinear susceptibility $\chi_{\mathrm{R}}^{(2)}$ originating from the vibrational resonances:

$$\chi_{\mathrm{R}}^{(2)}(\omega_{\mathrm{IR}}) = \sum_q \frac{A_{\mathrm{R}(q)}}{\omega_{\mathrm{IR}} - \omega_q + i\Gamma_q} \tag{6.9}$$

where $A_{\mathrm{R}(q)}$, ω_q, Γ_q, and ω_{IR} are the resonant amplitude, resonance frequency, and damping constant [homogeneous linewidth $2\Gamma_q$ = full width at half-maximum (FWHM)] of the qth vibrationally resonant mode, and the IR laser frequency, respectively.

The term $\chi_{\mathrm{R}}^{(2)}$ incorporates the resonance condition ($\omega_{\mathrm{IR}} - \omega_q$), and as the IR beam is tuned through vibrational resonances of surface species, $\chi_{\mathrm{R}}^{(2)}$ and hence I_{SFG} reach a maximum. The amplitude of the vibrationally resonant susceptibility $A_{\mathrm{R}(q)}$ is determined by the adsorbate concentration (number density N) and the product of

the IR and Raman transition moments of the vibration (T_q, M_q; $\delta\varrho$ is the population difference between the vibrational ground and excited states):

$$A_{R(q)} \propto NT_qM_q\delta\varrho \tag{6.10}$$

Equation (6.10) represents the selection rule for the SFG process. In order to generate a sum frequency emission, the excited vibrational mode must be *both* IR and Raman active. Therefore, SFG is not allowed in media with inversion symmetry (due to the "rule of mutual exclusion"). SFG, or any other second-order nonlinear optical process, therefore does not occur in (isotropic) gases, liquids, or centrosymmetric solids. The SFG signal is therefore dominated by the vibrational modes of the molecules at the surface/interface *where the inversion symmetry is broken*, making SFG inherently surface/interface specific.

Nevertheless, as most other spectroscopic methods, SFG has to cope with a signal background. In addition to the resonantly enhanced nonlinear susceptibility $\chi_R^{(2)}$ (related to surface vibrations), the *surface/interface itself* generates a vibrational *nonresonant* SFG signal, characterized by $\chi_{NR}^{(2)}$. A nonresonant SFG signal is produced, for example, when a surface electronic state is excited by either the visible or SFG light [25]. However, in many cases the visible or SFG light frequencies are far from resonances of the surface, and the nonresonant response of the surface can therefore be modeled by a frequency-independent nonresonant susceptibility $\chi_{NR}^{(2)}$ [cf., Eq. (6.11); assuming that this also incorporates nonresonant contributions of higher order components].

Consequently, $\chi_s^{(2)}(\omega_{IR})$ can be expressed as

$$\chi_s^{(2)}(\omega_{IR}) = \chi_R^{(2)}(\omega_{IR}) + \chi_{NR}^{(2)} = \sum_q \frac{A_{R(q)}}{\omega_{IR} - \omega_q + i\Gamma_q} + A_{NR}e^{i\phi} \tag{6.11}$$

where A_{NR} is the amplitude of the vibrationally nonresonant susceptibility and ϕ represents its phase relative to the resonant term.

Interference between the resonant and the nonresonant parts governs the SFG lineshape [25]. In the case $\chi_{NR}^{(2)} \ll \chi_R^{(2)}$, nearly symmetric lineshapes are obtained, with an increase of the total SFG intensity at the resonance frequency. However, as is apparent from Eq. (6.11), when $\chi_{NR}^{(2)} \approx \chi_R^{(2)}$, the lineshape of an SFG-resonance is primarily determined by the phase difference ϕ between the resonant and nonresonant signal. The phase difference is a result of the different physical origins of vibrational-resonant and nonresonant SFG fields/signals. Depending on ϕ, the sum $\chi_R^{(2)} + \chi_{NR}^{(2)}$ [Eq. (6.11)] may change sign when ω_{IR} "moves across" ω_q, which may give rise to an asymmetry or even a *signal decrease* at the resonance frequency.

6.2.2
Surface Concentration (Coverage) and SFG Signal Intensity

Experimental SFG spectra are fitted according to Eqs. (6.8) and (6.11), which allows resonance positions, amplitudes, and linewidths to be accurately extracted [25]. Since $A_{R(q)}$ is proportional to the adsorbate concentration (number density N), the molec-

ular density can be estimated, assuming that the IR and Raman transition moments of the vibration do not change. However, these two terms are usually different for different adsorbate species (e.g., bridging versus terminally bonded CO [26]) and may even depend on coverage [25, 27]. Therefore, the SFG signal cannot be easily correlated with a molecular concentration and a direct quantitative analysis is typically difficult. Nevertheless, attempts to place SFG on a quantitative basis are increasing [25, 28–31].

In any case, given that the nonresonant background is small, it may be useful to estimate the molecular concentration N from the SFG intensity. According to Eqs. (6.8)–(6.10), I_{SFG} is proportional to N^2. Vice versa, N is proportional to $\sqrt{I_{SFG}}$ and an estimate can be obtained by multiplying the square-root of the peak intensity with the HWHM, Γ_q:

$$N \propto \sqrt{I_{SFG}}\Gamma_q = \sqrt{I_{SFG}\Gamma_q^2} \tag{6.12}$$

It should be noted that the product of I_{SFG} and the bandwidth $2\Gamma_q$, which approximates the SFG peak area, is not proportional to N.

6.3 Spectrometer Setup

The main components of an SFG spectrometer include (i) a laser system to generate the incident visible and IR beams (pico- or femtosecond pulses), (ii) a sample preparation/manipulation stage (preferentially a spectroscopic cell with controlled environment), and (iii) a detection system for the generated SF signal. Most frequently, neodymium yttrium–aluminum–garnet (Nd:YAG) and titanium sapphire (Ti:Sa) lasers were used [32–37].

Figure 6.3 shows a schematic of a typical laboratory-type "scanning" SFG spectrometer. The output of an Nd:YAG picosecond laser (1064 nm, ~30 mJ per pulse, ~25 ps, 10–50 Hz) is partly converted to 532 nm light by SHG using, for example, a potassium dihydrogenphosphate crystal. About 200 μJ per pulse, 532 nm light is used as a visible (green) beam in the SFG experiment; the 1064 nm and remaining 532 nm beams are mixed in an optical parametric generator/amplifier (OPG/OPA) to generate tunable IR light (3–6 μm, about 200 μJ per pulse, resolution ~3 cm^{-1}) in a DFG stage [32]. A delay line allows optimization of the temporal overlap of IR and visible pulses and there are also devices [half-plates, polarizers (Glan–Taylor prisms)] to adjust the intensity and the polarization of the visible and IR beam. The use of different DFG crystals (such as $AgGaS_2$ or $AgGaSe_2$) or even synchrotron radiation [38] allows spectroscopy to be carried out in the range ~1000–4000 cm^{-1}.

In order to differentiate the (weak) SFG signal from the (strong) reflected visible beam, a dedicated detection system is required, which combines spatial, spectral, and temporal filtering [37]. The IR and visible beams have different incidence angles, ~55° and 50°, respectively, producing an SFG signal that lies in between them and that can be (spatially) separated by an aperture (cf., Figure 6.2; in Figure 6.3 reflected visible and IR beams are not shown for clarity). The SFG signal is then further

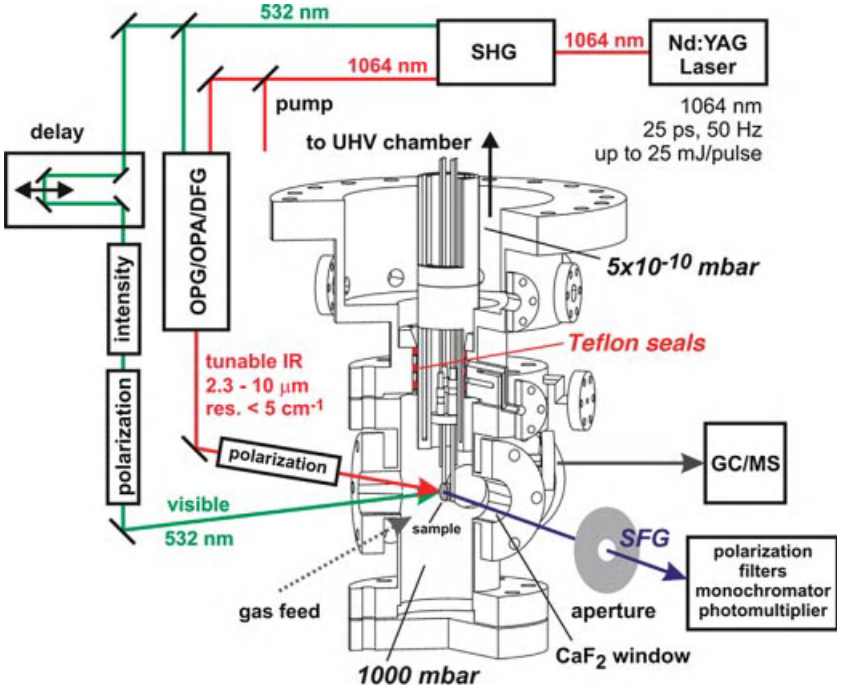


Figure 6.3 Schematic illustration of an SFG spectrometer based on an Nd:YAG picosecond laser system, together with a cross-section of an SFG-compatible UHV–high-pressure reaction cell. The cell is coupled to a UHV sample preparation and analysis system (not shown), allowing SFG spectroscopy to be performed in the pressure range from $\sim 10^{-8}$ to 10^5 Pa. A single crystal is mounted to the sample holder that is inserted into three differentially pumped spring-loaded Teflon seals. Adapted from [36, 37]. Reproduced by permission of the PCCP Owner Societies.

(spectrally) filtered by an edge filter and a monochromator (both remove the remaining 532 nm light and allow only the SFG light to pass) before it reaches a photomultiplier, the signal of which is directed to a gated boxcar integrator (triggered by the laser for temporal filtering) and sent to a PC via an A/D interface.

6.3.1 Modes of Operation

SFG spectroscopic measurements can be carried out in different modes, including scanning SFG, broadband SFG, time-resolved (pump–probe) SFG, and polarization-dependent SFG, as illustrated in Figure 6.4. In the case of scanning SFG (Figure 6.4a), the IR energy is tuned stepwise over the range of interest (which makes this mode rather slow). To reduce spectral acquisition times significantly, broadband SFG takes advantage of ultra-short and thus spectrally broad IR laser pulses (e.g., 150 fs; width $\sim 150\ \mathrm{cm}^{-1}$) (Figure 6.4b), covering an IR region of interest,

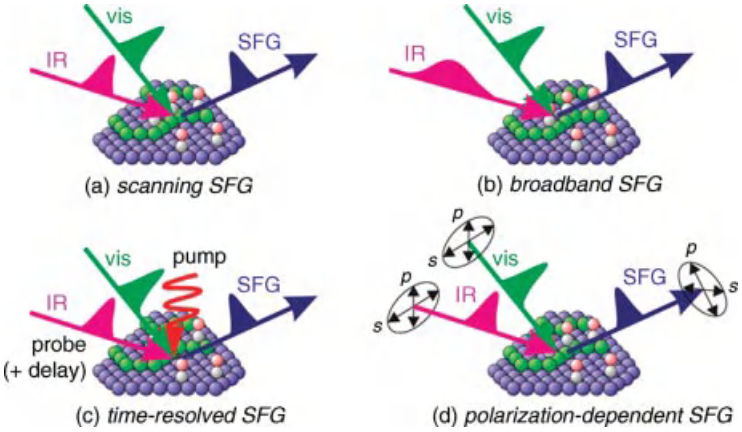


Figure 6.4 Schematics of different modes of operation of SFG: (a) scanning, (b) broadband, (c) pump–probe, and (d) polarization-dependent SFG. Adapted from [139].

for example, centered around C−O or C−H stretching vibrations ([6, 33, 39, 40] and references therein). The broadband IR pulse is overlapped with a narrowband visible pulse (e.g., 7 ps; width 2 cm^{-1}), but only that part of the IR spectrum that is in resonance with a vibrational transition will be upconverted to generate a sum frequency signal. The broadband approach thus allows an entire SFG vibrational spectrum to be captured with a few single laser shots, without tuning of the IR wavelength [the SFG spectrum is dispersed and recorded by a charge-coupled device (CCD) camera].

For time-resolved pump–probe SFG spectroscopy (Figure 6.4c), the surface species are first excited by, for example, an intense near-IR (pico- or femtosecond) laser pulse ("pump," that sets the time to "zero"), followed by a time-delayed weak SFG (IR + visible) "probe," which monitors the changes in the vibrational properties of the adsorbate–substrate complex. By varying the delay time between pump and probe, the effect of the excitation can be examined. For example, excitation (pump) may allow detection of surface reaction intermediates that are too short-lived for steady-state scanning SFG (see Section 6.4.3 for details). By taking "snapshots" of the transient vibrational spectrum at different delay times, the lifetime of transient species can be determined. A prerequisite for such measurements is, of course, that the surface species relax between the pump–probe pulses (e.g., for measurements at 1 kHz, the adsorbate–substrate system must relax within 1 ms).

Using lasers, one can take advantage of the light polarization. SFG is frequently carried out in ppp geometry [i.e., by detecting a p (parallel)-polarized SFG signal produced by a p-polarized visible and a p-polarized IR beam]. This combination is typically used for adsorption/reaction investigations of metal surfaces, because it produces the most intense adsorbate SFG signal [27, 41]. However, other polarization combinations can also be used, for example, ssp (s-polarized SFG, s-polarized visible and p-polarized IR; Figure 6.4d). For metals, the IR beam is always p-polarized because the light field of an s-polarized IR beam is screened by the conduction

electrons of metal surfaces. Comparison of the signal intensities for different polarization combinations (e.g., I_{ppp} versus I_{ssp}) can then be utilized to obtain information about the molecular orientation of surface species [27, 32, 42–44]. The polarization combinations can be selected by adjusting suitable polarizers of the spectrometer. Very briefly (and also somewhat simplified), one can state that an SFG signal is generated only when the electric fields of the visible and IR light have a component parallel to the bond axis. Consequently, ppp detects molecules with molecular axes parallel or inclined to the surface normal, whereas ssp spectra are mainly sensitive for tilted molecules. Consequently, by comparing signal intensities I_{ppp} and I_{ssp} of ppp and ssp spectra, respectively, allows one to deduce the molecular orientation (tilt angles) of molecules (flat-lying molecules with molecular axes parallel to the surface, that is, perpendicular to the surface normal, cannot be detected on metal surfaces, owing to the metal surface selection rule). The analysis of polarization-dependent measurements is complex and not always unambiguous. Details on theory and analysis can be found elsewhere (e.g., [27, 43, 45]).

Up to this point, we have only discussed SFG spectroscopy in reflection mode, which is frequently utilized. However, other geometries can also be used, such as transmission and total internal reflection (TIR) using prisms (cf., Figure 6.5) [23, 46–48]. TIR is especially suitable for performing SFG measurements on powder materials and colloidal nanoparticles. The strong light scattering of powder materials typically prevents SFG spectroscopy but new approaches have recently been demonstrated. Wet-chemically synthesized powders or shape-controlled colloidal nanoparticles were coated on (surface-modified) single-crystal CaF_2, sapphire, or quartz prisms, and by using the TIR geometry much higher signals than by (standard) external reflection could be obtained [47–49]. Examples of measurements in TIR geometry are shown and discussed in the case studies in Section 6.4. Applications of SFG

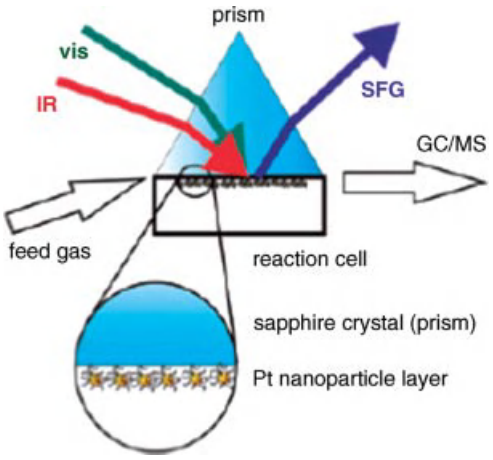


Figure 6.5 Illustration of the setup for SFG spectroscopy on colloidal Pt nanoparticles that were deposited on a single-crystal sapphire prism. The measurement was carried out in TIR geometry. Adapted in part from [49] with permission. Copyright (2006) American Chemical Society.

microscopy have also been reported, imaging the spatial distribution of selected SFG vibrational bands, thus combining the analytical ability of IR spectroscopy with the spatial resolution of visible light microscopy [50–54].

6.4 Case Studies

After explanations of the scope, theory, experimental requirements, and operating modes in the previous sections, the following highlights the possibilities and benefits of SFG and (PM-)IRAS by selected (fairly recent) case studies. The "tour" starts with classical adsorption studies of probe molecules on metal single crystals, covering the pressure range from ultra-high vacuum (UHV) to ambient, continues with more complex systems such as bimetallic and oxide surfaces, and ends with oxide-supported metal nanoparticles. Apart from pure adsorption of probe molecules, special emphasis will be placed on how SFG and PM-IRAS can be applied to investigate catalysts and catalytic reactions under working (functioning) conditions.

As the scope of this book is the characterization of solid materials and heterogeneous catalysts, examples related to biochemistry and life sciences will not be presented here, although the techniques discussed in this chapter definitely have applications in these fields. For further information on applications of SFG and IRAS in bioscience, the reader is referred to recent papers ([55–58] and references therein).

6.4.1 Metal Single-Crystal Surfaces

As mentioned in the Introduction, vibrational spectroscopy was among the first techniques to be applied to study the adsorption of molecules on metal surfaces. Mainly CO was used to "titrate" available adsorption sites and by comparison of different smooth and stepped single-crystal surfaces the different adsorption sites on oxide-supported metal nanoparticles could be identified spectroscopically. CO was considered to be the ideal probe molecule because the mechanism of its bonding to a metal surface was (generally) well explained by the Blyholder model [59, 60]. CO is still of great industrial and environmental importance, for example, its catalytic oxidation is applied in automotive three-way catalysts to clean up exhaust emissions. Preferential oxidation (PROX) of CO in an excess of hydrogen is a key for processing the feed gas of PEM fuel cells. CO has to be removed from the hydrogen feed to a level below 10 ppm, because it acts as a catalyst poison for the Pt-based fuel cell anode catalyst. Of course, this must be achieved selectively without consuming precious hydrogen fuel.

Many IRAS and SFG studies of CO adsorption and oxidation on (noble) metal single-crystal surfaces and metal nanoparticles can be found in literature, covering most transition and noble metal surfaces, dating back to the pioneering reports in the late 1950s (e.g., [61]).

A recent example was reported by Pászti *et al.* [62], who studied CO adsorption on ion-bombarded Au(111) surfaces using SFG. After Ar^+ sputtering (3 keV, 10 min) of

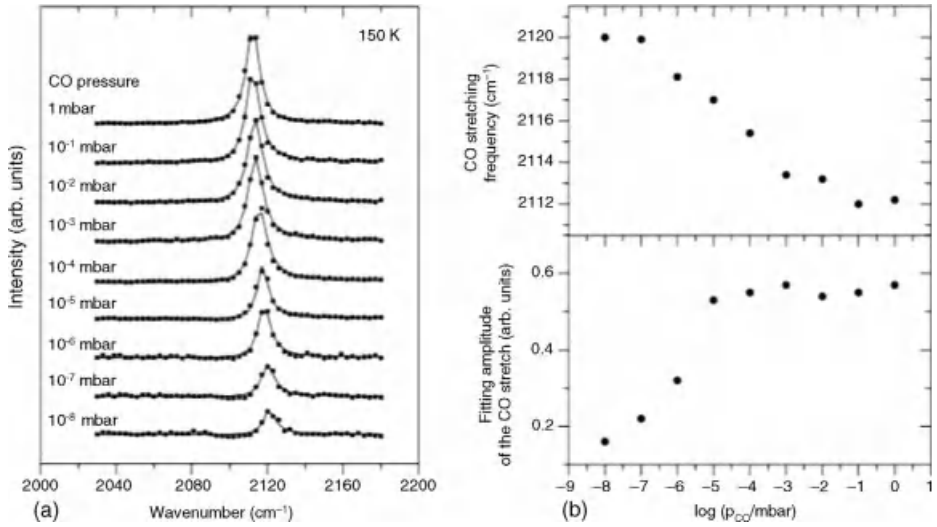


Figure 6.6 (a) Sum frequency spectra of a sputter-modified Au(111) surface exposed to different CO partial pressures. Sputtering took place at room temperature and CO adsorption experiments were carried out at 150 K. All spectra were taken in the ppp polarization combination. (b) Frequency of the CO vibration and amplitude of the resonant peak derived from fitting the spectra in (a), plotted as a function of the CO pressure. Reprinted from [62] with permission. Copyright (2010) American Chemical Society.

an Au(111) single crystal at room temperature, upon CO exposure (10^{-6} Pa) at 150 K a band at 2120 cm^{-1} was observed (lower trace in Figure 6.6a). This band is typical for CO adsorbed on top of single Au atoms (presumably located at defect sites such as steps or kinks). Upon increasing the pressure, the signal amplitude increased while the observed wavenumber decreased to a final value of 2112 cm^{-1} at 100 Pa CO pressure (cf., Figure 6.6a and b), both effects being due to increased coverage. The observed bands and spectral changes agree well with previously published IR data [63, 64]. By connecting the SFG spectroscopic data with X-ray photoelectron spectroscopy (XPS) and scanning tunneling microscopy (STM) measurements, the authors found a very strong correlation between the CO surface density and the number of Au atoms located at step edges. They therefore concluded that step edges are responsible for the high CO adsorption capacity of the ion-bombarded Au(111) surface [no CO adsorption was detected on smooth Au(111)]. This is in line with other model studies on Au surfaces (a comprehensive overview is available [65]) and with recent chemisorption and high-resolution transmission electron microscopy (HRTEM) studies of Au nanoparticles of technological catalysts [66], assigning higher CO binding energies to low-coordinated Au sites (C_4–C_7).

In a follow-up study, it was shown that the CO adsorption capacity of the ion-bombarded Au(111) surface could be further increased by deposition of FeO_x islands [67].

In another recent study, Carrasco *et al.* [68] utilized SFG and PM-IRAS to investigate high coverage structures of CO on a Pt(111) surface. At pressures below 10^{-5} Pa, CO adsorbs in a $c(4 \times 2)$ superstructure with a coverage of 0.5 monolayer (ML). Bands at 2097 and 1853 cm^{-1} were observed in the vibrational spectrum, corresponding to on-top and bridge-bound CO molecules. Upon increasing the pressure, a second on top signal appeared at 2109 cm^{-1} at the expense of the main on top band. Depending on pressure and temperature, the occurrence of the 2109 cm^{-1} band could be attributed to the formation of compressed CO adlayers, resulting in either hexagonal Moiré or coincidence site lattices.

The ability of SFG and (PM-)IRAS to operate at elevated gas pressure is of great importance because some (catalytic) surface processes may only occur under elevated (non-UHV) pressure conditions. For example, Pery *et al.* [69] applied SFG spectroscopy to study CO adsorption on an Rh(111) single crystal surface from UHV up to atmospheric pressure at 300 K. The spectra obtained, together with their analysis, are shown in Figure 6.7. For a CO pressure of 1×10^{-6} Pa, a sharp SFG signal was

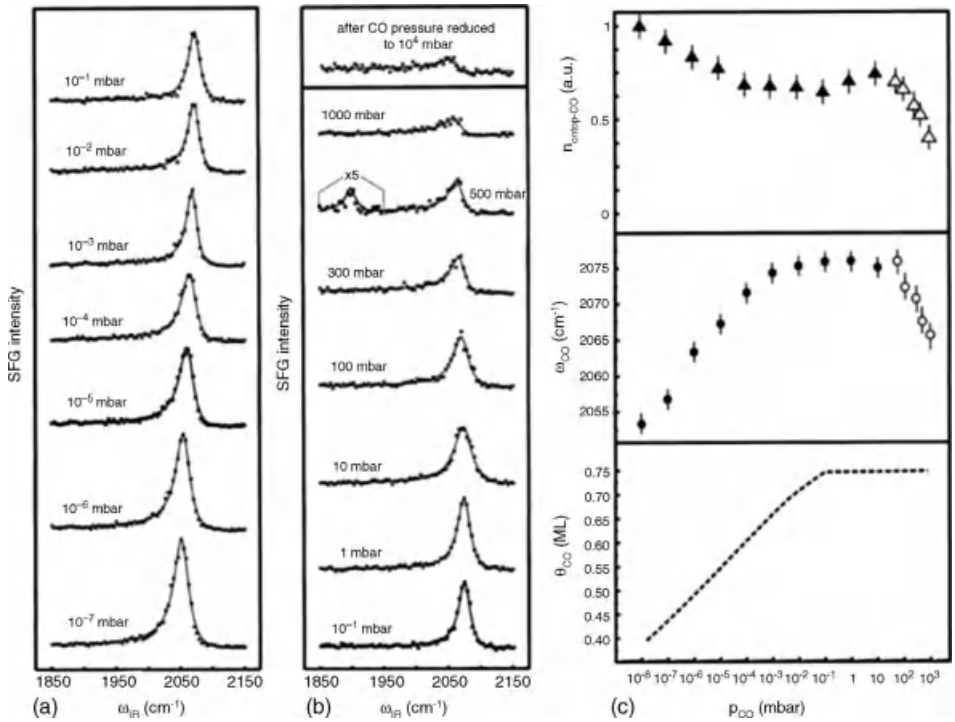


Figure 6.7 (a, b) SFG spectra of CO adsorbed on Rh(111) at 300 K at pressures between 1 and 100 kPa. (c) Analysis of the on-top CO intensity (surface density), resonance position, and CO coverage as a function of the CO pressure. The open symbols indicate the pressure range of irreversible CO adsorption. The equilibrium CO surface coverage in (c) was calculated from adsorption/desorption kinetics. Reprinted from [69], Copyright (2002), with permission from Elsevier.

observed at 2053 cm^{-1}, typical of CO bound linearly to single Rh atoms. Although not visible at first, detailed investigation of the spectra revealed an additional weak band at ~1900 cm^{-1} arising from CO bound to threefold hollow sites (cf., 50 kPa spectrum). Upon increasing the CO pressure up to 100 Pa, a slight intensity decrease of the on top peak was observed, which was attributed to structural rearrangements of the CO adlayer. The observed frequency shift of the on-top signal to 2075 cm^{-1} reflects the coverage increase at higher pressure, resulting from stronger CO dipole–dipole coupling. The saturation coverage of 0.75 ML is reached at 10 Pa. When the CO pressure was increased above 1 kPa (cf., Figure 6.7b), the intensity of on-top CO decreased again, paralleled by a shift to lower wavenumbers. At 100 kPa CO, only a small signal at 2065 cm^{-1} remained, indicating that the number of on-top species was drastically reduced at higher pressure (note that the spectra were corrected for gas-phase absorption). The signal decrease was actually irreversible, that is, upon reducing the CO pressure again to 10^{-4} Pa, the original spectrum could not be restored. Using post-reaction Auger spectroscopy, it was shown that this effect was induced by significant carbon deposition on the surface at kilopascal gas pressures. Accordingly, Pery *et al*. concluded that at elevated gas pressures CO dissociation takes place on Rh(111), apparently to a considerable extent. The topic of CO dissociation on well-defined metal single-crystal surfaces is still rather controversially discussed in the literature. It should also be noted that although strong indications for CO dissociation have been found, deposition of carbonyl impurities [e.g., $Ni(CO)_4$] from the gases used cannot be fully excluded.

A number of excellent reviews on vibrational spectroscopic studies of CO adsorption on metal surface by have been published in the recent years, including many more examples ([3, 6, 70–72] and references therein).

The applications of SFG and IRAS are not limited to the identification of adsorption sites, however. By applying time-resolved SFG spectroscopy, Backus *et al*. [73] were able to follow surface molecular motion in real time, by monitoring laser-induced hopping of CO molecules on a Pt(533) surface from step sites to terrace sites. As illustrated in Figure 6.8a, the Pt(533) surface consists of small (111) terraces (about 7 Å wide) separated by monoatomic (100) steps. CO is able to adsorb on both sites, although due to a small difference in binding energy (BE) adsorption at step edges (BE of ≈2 eV) is preferred to that on terrace sites (BE of ≈1.5 eV). The difference in BE results in a distinct 20 cm^{-1} separation of the two signals in the SFG spectrum. CO adsorbed at step edges produced a narrow band at 2080 cm^{-1}, whereas CO bound to terraces was detected at 2100 cm^{-1} (cf., Figure 6.8b). Similar spectral differences were reported for stepped Pd(111) [6, 26, 74]. The key experiment performed by Backus *et al*. was to prepare a surface with both adsorbate species present (Figure 6.8a). The sample was then subjected to a pump laser pulse and subsequently probed with femtosecond SFG pulses (pump–probe mode at 83 Hz).

In Figure 6.8c, the evolution of the SFG spectra is plotted (red = experimental, black = fitted). In the first spectra at negative delay times, the pump arrived "long before" the IR–visible probe and both adsorbate species were therefore present. The following transient spectra, in which the feature attributed to step sites declined very rapidly, clearly showed the laser-induced hopping of CO molecules from step to

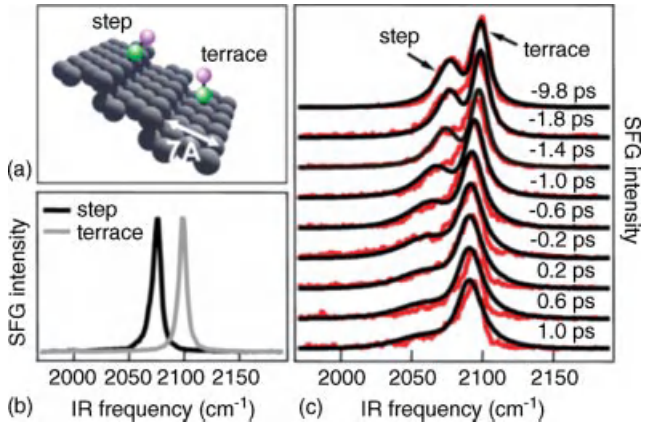


Figure 6.8 (a) Schematic representation of CO molecules on a stepped platinum surface consisting of four atom wide terraces and monatomic steps. (b) SFG spectra for CO molecules at the step edges and on the terraces. The vibrational frequency is 20 cm^{-1} higher for CO molecules on the terraces than CO molecules on steps. (c) Normalized SFG spectra for CO molecules partly on steps and partly on terraces at different times after initiating the hopping process by a femtosecond laser pulse. It is evident that the ratio of the SFG intensities of terrace and step COs changes within a matter of picoseconds. Red lines are data, black lines are the result of a calculation for which 15% of the CO molecules hop from step to terrace sites. That the effect of the pump pulse can already be seen at negative delay times is a result of the perturbed free induction decay. From [73]. Reprinted with permission from AAAS.

terrace sites. The fact that the movement actually started at small negative delay times was explained by a perturbation of the free-induction decay.

The time scale of the diffusion process is on the sub-picosecond scale and could only be resolved by applying ultra-fast (femtosecond) SFG spectroscopy. In combination with DFT calculations, the authors further showed that in this case the molecular movement was governed by the excitation of a frustrated rotational mode rather than just by translational motion [73].

Another characteristic of SFG spectroscopy can be illustrated by the spectra in Figure 6.8c. Detailed analysis of the uppermost spectrum, measured at a delay of −9.8 ps, indicated that only about 20% of the terrace sites but 75% of the step sites were occupied by CO. The relative intensities of the peaks are somewhat misleading because an effective intensity borrowing mechanism via dipole–dipole coupling is active here (from low to high wavenumber). The same effect was also observed in the previous example of CO adsorption on Rh(111) further for CO/Pd(111) [6, 25]. At saturation coverage of 0.75 ML, CO is adsorbed in a $(2 \times 2)3$-CO structure, occupying on-top and threefold hollow sites with a ratio of 1:2. However, at a CO pressure of 10 Pa, when saturation coverage is reached, the signal of CO bound to hollow sites is almost invisible or much weaker in the SFG spectrum.

Therefore, just considering the signal intensities, the number of CO molecules bound to terrace sites would be strongly overestimated. Such intensity transfer via

dipole–dipole coupling occurs fairly frequently and great care should be taken when signal intensities are used to quantify adsorbate species. The same holds for IR intensities, although see, for example, CO adsorption studies on Pd nanoparticles [6, 75, 76].

SFG is also useful for the identification of reaction intermediates of a catalytic process, benefiting from its inherent surface sensitivity even in a high gas pressure environment. For example, during ambient-pressure hydrogenation of ethylene on Pt(111) (4.6 vol.% C_2H_4, 13.2 vol.% H_2, remainder He, total pressure 100 kPa, 295 K), two different adsorbate species were detected by SFG, di-sigma-bonded ethylidyne and pi-bonded ethylene [77]. It was shown that the latter ethylene species is the primary intermediate in ethylene hydrogenation, with ethylidyne being just a spectator species. Although ethylidyne competed with ethylene for adsorption sites, its surface concentration was found not to be correlated with the overall reaction rate. Analogous measurements were performed for Pd(111) and Pd nanoparticles [6, 78, 79].

Somorjai's group also studied benzene hydrogenation on Pt surfaces via SFG [80, 81]. Depending on the surface crystallographic orientation, two different reaction intermediates were detected. Upon heating benzene in an excess atmosphere of hydrogen, pi-allyl *c*-C_6H_9 was identified on Pt(100) but not on Pt(111) (cf., Figure 6.9). This species was characterized by two peaks at 2865 and 2940 cm^{-1}, corresponding to

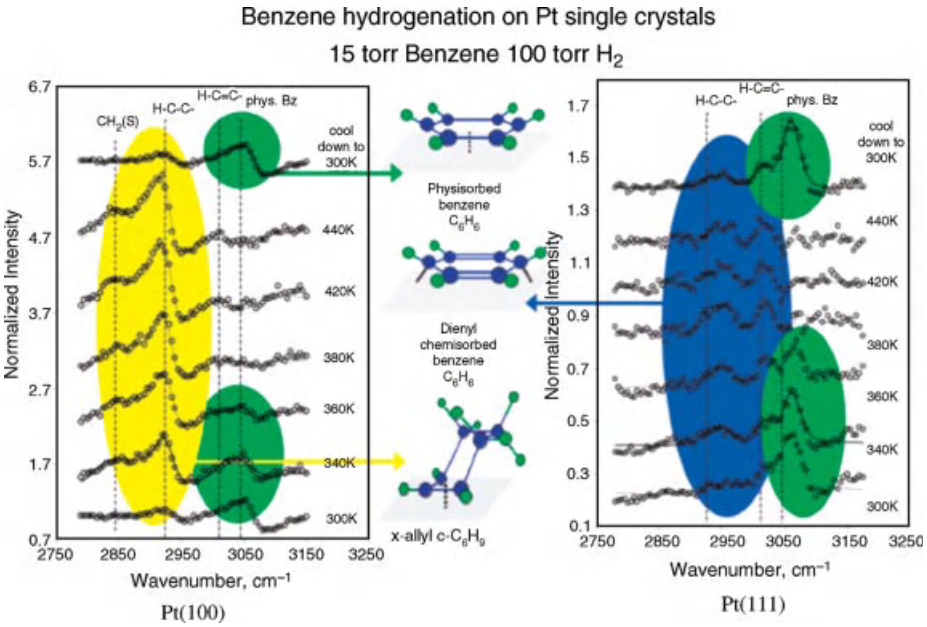


Figure 6.9 Sum frequency generation vibrational spectroscopy spectra of the surface of Pt(100) and (111) during the hydrogenation of benzene, revealing the presence of surface intermediates: π-allyl, physisorbed, and dienyl chemisorbed benzene. Adapted from [80] with permission. Copyright (2006) American Chemical Society.

the symmetric and asymmetric (CH_2) stretching vibrations. In contrast, on Pt(111) chemisorbed dienylbenzene C_6H_6 was detected via features at 3030 and 2945 cm^{-1}, attributed to the vinylic (H−C=C) and (H−C−C) stretching vibrations. In addition to chemisorbed benzene, physisorbed benzene was observed on both surfaces at 300 K, giving rise to an SFG signal at 3060 cm^{-1} (aromatic C−H stretching).

A different behavior of Pt(100) and Pt(111) was also reported by Kliewer and Somorjai [82] in SFG studies of pyridine hydrogenation. It was shown that at 300 K pyridine adsorbed vertically on both surfaces and changed to a flat-lying adsorption geometry on heating to 350 K. However, on Pt(111) only the reaction product piperidine was detected, whereas on Pt(100) spectral features of the reaction intermediate 1,4-dihydropyridine were identified.

The observation of reaction intermediates can, of course, also be addressed by IRAS. An interesting IR study was reported by Chen *et al.* [83]. Instead of looking at the reacting (adsorbed) molecules during the reaction, they examined the surface oxidation state during CO oxidation on Pd(110) and Pd foil by applying *in situ* IRAS. Using KBr windows in a specialized IR setup, they extended the spectral range down to ∼450 cm^{-1}, allowing the observation of Pd−O vibrations. Consequently, they were able to monitor the oxidation state of the Pd surface under reaction conditions. The activity of Pd oxides for CO oxidation has been controversially discussed in the literature [84–89]. Some groups proposed that oxides were the active phase in this reaction [84, 85], whereas others claimed the complete opposite, that is, that the metallic surface was the active phase [86–89].

In Figure 6.10a, the reduction of a preoxidized Pd(110) surface (1.33 kPa O_2, 700 K, 5 min) by CO was examined by IRAS. In the spectra obtained, illustrated in Figure 6.10, two IR bands at 669 and 615 cm^{-1} were observed, and attributed to longitudinal modes of tetrahedral [OPd_4] ensembles, that is, Pd−O vibrations of a Pd oxide. The evolution of the spectra showed that the Pd surface oxide was readily reduced at 450 K in 266 Pa CO [83]. Reduction of the surface oxide was also observed during reaction under stoichiometric conditions ($CO : O_2$ ratio 2 : 1, 450 K). Moreover, starting from clean Pd(110) and Pd foil, at reaction temperatures of 525 and 500 K, respectively, no formation of a surface oxide was detected, even in oxygen-rich conditions ($CO : O_2$ ratio 1 : 2). Therefore, it was concluded that metallic Pd is the active surface. A hyperactive state during CO oxidation, previously correlated with Pd oxides, was found to be metallic Pd instead, and highly occupied with chemisorbed oxygen. The reaction rate in this case is limited by CO transfer to the surface.

A recent *in situ* FTIR, X-ray diffraction (XRD), and HRTEM study by Zorn *et al.* [88] on technological Pd–Al_2O_3 also examined the specific activity of Pd and Pd oxide phases and reported that oxygen-covered metallic Pd represented the active state for CO oxidation. Strong oxidizing conditions were required to obtain (metal-free) oxidic particle surfaces, even in the absence of the reducing agent CO. Therefore, it is very unlikely that a $PdO_{x<1}$ phase constitutes the major active phase (i) when it represents a minor fraction even in pure O_2 and (ii) when it is rapidly reduced in the presence of CO (even around room temperature and at low CO partial pressure; Figure 6.11). In other words, when $PdO_{x<1}$ formation is slower than its reduction (removal), $PdO_{x<1}$ cannot be the active phase. Based on these and molecular beam and XPS model

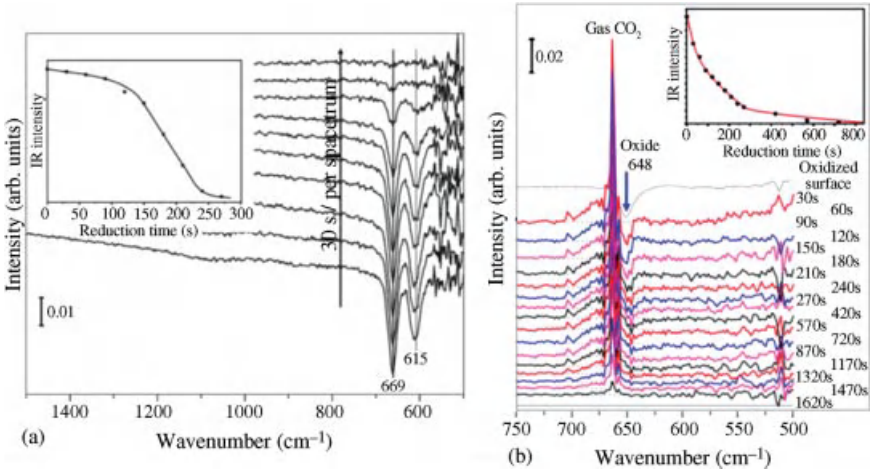


Figure 6.10 (a) *In situ* IRAS spectra for a Pd (100) surface preoxidized in 1.33 kPa of $^{16}O_2$ at 700 K for 5 min, then exposed to 266 Pa of CO at 450 K. From bottom to top, each spectrum was taken over $t = 30$ s. The inset shows the IR intensity of the band at 669 cm^{-1} as a function of CO exposure time at 450 K. (b) *In situ* IRAS spectra for a Pd(100) surface preoxidized in 266 Pa $^{18}O_2$ at 700 K for 5 min, then exposed to 3.6 kPa CO and 2.4 kPa $^{18}O_2$ at 450 K. The spectrum taken at 1620 s was used as a background spectrum to be subtracted for each spectrum above. The inset shows the IR intensity of the band at 648 cm^{-1} as a function of CO exposure time. Reprinted from [83] with permission. Copyright (2010) American Chemical Society.

studies [86, 90], the highest catalytic activity for CO oxidation was assigned to oxygen-covered metallic palladium.

6.4.2
Bimetallic Surfaces

In recent decades, bimetallic systems have attracted great interest in catalysis research. By mixing two (or more) metals, a new catalyst is produced that should ideally combine the advantages of the two metals in one material. Even more so, the bimetallic catalyst may show exciting new catalytic properties, often very different from those of the individual metals. In general, two types of effects are distinguished: (i) the so-called "ensemble effect," indicating that by intermixing two metals A and B new catalytic sites are created on the surface, such as AB bridge sites; and (ii) "electronic effects" based on electron density transfer from one to the other metal, strongly altering the electronic structure (i.e., reactivity) of the resulting catalyst. Both effects are correlated with each other but often the pure geometric "site isolation" (ensemble effect) is sufficient to describe the new catalytic properties.

An illustrative example of how the "ensemble effect" influences catalytic activity is the synthesis reaction of vinyl acetate on bimetallic Pd–Au catalysts. Goodman and co-workers studied this process on Au–Pd surface alloys that had been prepared by

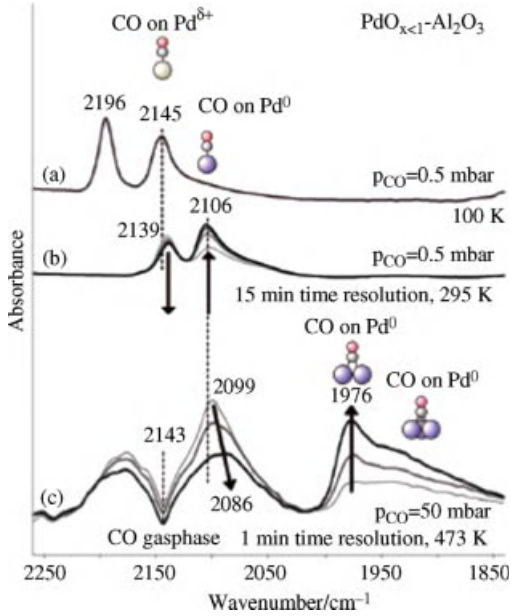


Figure 6.11 FTIR spectra of 50 Pa CO adsorbed on the substoichiometric $PdO_{x<1}$ particles at (a) 100 and (b) 295 K. Reduction at 295 K was followed with a time resolution of 15 min. (c) At 473 K and 5 kPa CO, reduction was complete within 3 min (spectra collected with a time resolution of 1 min). Reprinted from [88] with permission. Copyright (2011) American Chemical Society.

deposition of isolated Pd atoms on Au(111) and Au(100) surfaces [91, 92]. It was found that a pair of Pd atoms ("monomer pair") represents the catalytically active site but the Pd–Pd separation is very critical. Pd deposition on Au(100) resulted in a more active catalyst because the distance between the Pd atoms in the monomer pair was shorter (4.08 Å) than for Pd/Au(111) (4.99 Å), thus being closer to the calculated optimal distance (3.3 Å). For both Au surfaces, Au seems to be required just to dilute and separate the Pd atoms in the surface layer. IRAS played an essential role in these studies, because it was the method of choice to identify and titrate the amount of active surface sites (isolated Pd atoms). Figure 6.12a shows IRAS spectra acquired upon CO adsorption at 90 K after deposition of 4 ML of Pd on Au(111) and Au(100) at 300 K and subsequent annealing at 600 K. After deposition, features for multiply bound CO on Pd in the range 2000–1900 cm^{-1} were clearly visible. The intensity of these features exceeded that observed for on-top CO signals at around 2100 cm^{-1}, attributed to adsorption on the (desired) Pd monomer active sites. However, on both Au surfaces the on-top intensity strongly increased upon annealing, whereas the bands for multiply bound CO vanished. The spectra thus directly reveal the creation of active sites for vinyl acetate synthesis, i.e. Pd monomer pairs. Surface diffusion of Au atoms resulted in the dilution of the deposited Pd films, finally yielding isolated Pd atoms.

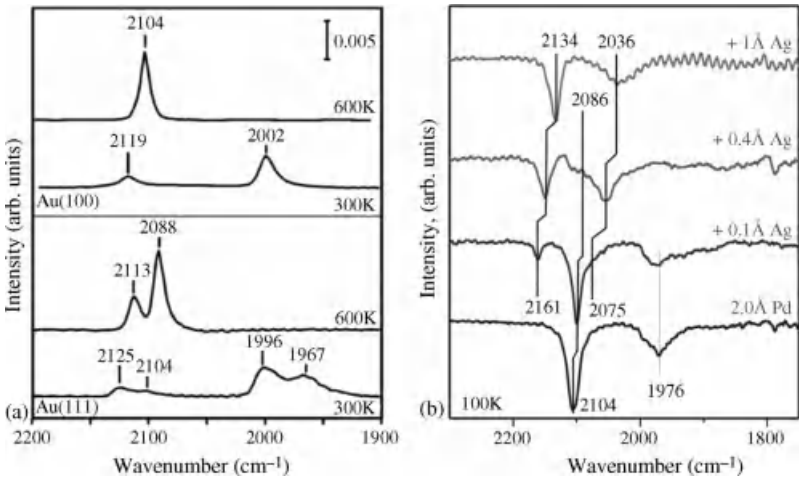


Figure 6.12 (a) IRAS spectra for CO adsorption on Pd/Au(100) and Pd/Au(111) surfaces at 100 K showing the presence (300 K anneal) and absence (600 K anneal) of contiguous Pd sites. The Pd/Au(100) and Pd/Au (111) surfaces were prepared by depositing 4 ML of Pd at 100 K, then annealing to 300 and 600 K, respectively, for 10 min. The annealing temperatures are indicated on each spectrum. From [91]. Reprinted with permission from AAAS. (b) IR spectra of 2 langmuir (L) CO adsorbed on Pd–Ag nanoparticles at 100 K. The amount of Pd and Ag is given as nominal thickness (in ångstroms). Already for very small amounts of Ag, the multiply bonded CO bands decrease (1976 cm^{-1}) whereas linearly bonded CO increases (2075 cm^{-1}) and a new Ag-induced adsorption species appears (2161 cm^{-1}). Adapted from [94], Copyright (2006), with permission from Elsevier.

Another example of the "ensemble effect" was reported by Khan and co-workers, who studied the hydrogenation of acetylene and ethylene over a model catalyst of Pd–Ag nanoparticles supported on a thin alumina film grown on NiAl(110) [93, 94]. Addition (by evaporation) of only small amounts of Ag to Pd nanoparticles resulted in a decrease in the IR band at 1976 cm^{-1}, attributed to CO bridge-bonded to Pd (Figure 6.12b). When additional Ag was added, this feature completely disappeared whereas the band for CO adsorbed linearly on individual Pd atoms remained. This band, observed at 2104 cm^{-1} for the pure Pd particles, decreased upon adding Ag because the number of surface Pd atoms was reduced by Ag dilution. Also, a shift to lower wavenumbers was observed, the final wavenumber being 2036 cm^{-1}. Additionally, a new band evolved in the spectra, which increased in intensity with increasing amount of Ag and shifted from 2161 to 2134 cm^{-1}. The authors attributed this signal to on-top CO bound to electronically modified Ag atoms or Pd–Ag bimetallic sites. Changes in the electronic structure of Ag could be directly monitored by XPS [87, 94]. It should be noted that CO does not adsorb on pure Ag under these conditions. Analogous to the example of Pd–Au, the spectra in Figure 6.12b indicate dilution of the Pd surface by Ag, finally yielding isolated Pd Atoms in an Ag surrounding. Although the overall hydrogenation activity of the catalyst is reduced by this effect, the formation of single Pd atoms is considered crucial for the selective

hydrogenation of acetylene to ethylene [because further hydrogenation of C_2H_4 to ethane is suppressed due to missing multiply bonded (bridge, hollow) Pd sites].

The observation of Ag-related CO adsorption (2161 cm^{-1}) at low temperature in the above example is a good illustration of an "electronic effect" in a bimetallic catalyst, too. A strong "electronic effect" also occurs for bimetallic Pd–Zn catalysts used for hydrogen production via steam reforming of methanol (SRM). Iwasa and co-workers found that Pd supported on ZnO (or In_2O_3 or Ga_2O_3) exhibited very good catalytic activity and stability for SRM [95–97]. Moreover, the CO_2 selectivity of these catalysts was very high, in contrast to monometallic Pd on silica or activated carbon, which produces mainly CO as byproduct. High CO_2 selectivity is a key point when the generated H_2 is to be used for a PEM fuel cell, because CO acts as a poison for the fuel cell catalyst and therefore must be removed from the hydrogen feed. The different behavior of Pd/ZnO and Pd/SiO_2 was attributed to the formation of a Pd–Zn alloy under reaction conditions, which was proved by XRD, EXAFS, and XPS [15, 96]. Density of states calculations and ultraviolet photoemission spectroscopy (UPS) measurements [98, 99] revealed that, owing to transfer of electron density from Zn to Pd, the valence band electronic structure of the Pd–Zn alloy is very similar to that of copper, which is in fact the catalyst used industrially for SRM (Cu has limited thermal stability against sintering, however).

Using IR spectroscopy, Pd–Zn alloy formation could be monitored both on ZnO-supported Pd nanoparticles (technological catalysts) and on model Pd–Zn surface alloys on Pd(111). Figure 6.13 compares the FTIR spectra of CO adsorbed on a Pd/ZnO powder catalyst (a) with IRAS spectra from corresponding Pd–Zn model catalysts (b), before and after alloy formation upon H_2 reduction (a) or upon annealing in UHV (b). First, the spectra very clearly illustrate the relevance of the

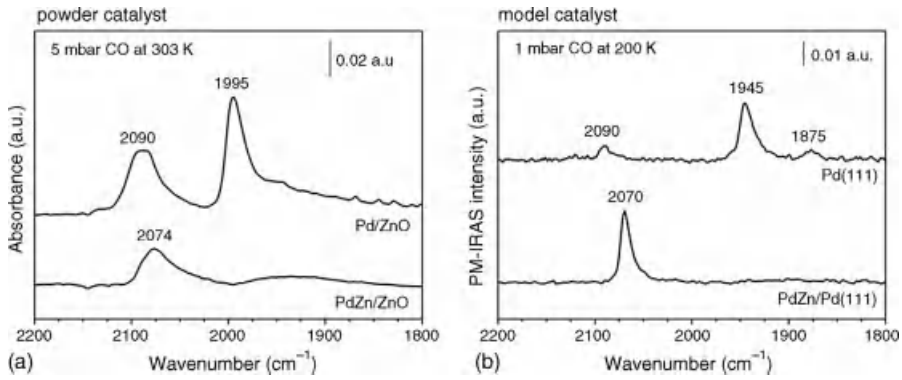


Figure 6.13 (a) FTIR spectra of CO adsorption (303 K, 0.5 kPa CO) on Pd/ZnO after reduction at 303 K (upper trace); after reduction at 623 K (i.e., PdZn, lower trace). Difference spectra are shown, obtained by subtraction of the corresponding spectra before CO exposure. Adapted from [15] with permission. Copyright (2011) American Chemical Society. (b) PM-IRAS spectra of CO adsorption (200 K, 0.1 kPa) on Pd (111), and on 2 ML of Zn/Pd(111) annealed at 550 K. Adapted from [140] with permission. Copyright (2010) American Chemical Society.

model system used. The spectra are almost identical; only the wavenumber detected for bridge bound CO differs, most likely because the band at 1945 cm^{-1} observed on the Pd(111) single crystal originates from bridge sites of extended (111) facets, which are "less abundant" on small and rather disordered Pd nanoparticles of Figure 6.13a. The band at 1995 cm^{-1} is related to bridge sites, for example, at edges or steps of the Pd particles [6]. Furthermore, for Pd nanoparticles, intensity transfer from the ~1950 to the ~1990 cm^{-1} band contributes to the low intensity of the bridge species on the particle facets. Nevertheless, for both the Pd nanoparticles and the model system the "site isolation" upon Pd–Zn alloy formation is clearly evident. The bands of bridge-bound CO disappeared and the only remaining feature was a band at ~2070 cm^{-1}, characteristic of CO molecules linearly bound to Pd atoms in Pd–Zn ensembles. The observed shift of this band from 2090–2070 cm^{-1} on Pd–Zn is direct evidence for the altered electronic structure of the catalyst. As mentioned above, electron density is transferred from Zn to Pd upon alloy formation, resulting in a higher back-bonding from Pd to the CO molecule, thus weakening the internal C−O bond. Therefore, less energy is required to excite the C−O vibration and the band is red shifted.

The described "electronic effect" is responsible for the strong differences in the catalytic performance of Pd and Pd–Zn as reported by Iwasa and co-workers. Furthermore, it was found that for Pd–Zn/Pd(111) surface alloys the strength of the "electronic effect" depends strongly on the thickness of the surface layers. Despite identical surface composition, a Pd–Zn multilayer alloy shows different catalytic activity and selectivity in SRM than a Pd–Zn monolayer (with the former mainly producing CO_2 and the latter mostly CO as byproduct [12]).

Another interesting characteristic of the Pd–Zn/Pd(111) model system was also identified via (PM-)IRAS. It turned out that upon annealing of Zn overlayers deposited on Pd(111), the onset of Pd–Zn alloy formation was strongly dependent on the surrounding gas atmosphere. When the annealing steps were performed at low CO pressure (1×10^{-4} Pa), the on-top CO band characteristic of the Pd–Zn alloy was first detected after annealing to 473 K (Figure 6.14a). The slightly lower wavenumber of 2064 cm^{-1} may indicate that the process of alloy formation was not complete at this temperature. However, upon annealing at 523 K, the characteristic spectrum of CO adsorbed on the Pd–Zn alloy was obtained. After annealing at temperatures of 623 K and above, the surface alloy started gradually to decompose by Zn dissolution in the Pd bulk. Thus, weak features at 1888 cm^{-1} indicative of multiply bound CO appeared in the spectra. Upon increasing the annealing temperature, these features became more intense, whereas the on-top feature declined and shifted to higher wavenumber. In fact, the spectra transformed to those characterizing CO adsorption on pure Pd(111).

When the annealing steps were performed at high CO pressure (0.5 kPa), the overall trend was the same (Figure 6.14b). However, there was a significant difference in the temperature at which the characteristic alloy on-top CO was first observed. Instead of 473 K observed for low CO pressure, an annealing temperature of 548 K was required to induce surface alloy formation. This is somewhat counterintuitive, since owing to the higher heat of adsorption of CO on Pd (compared with CO on Zn), one would expect that CO would pull the Pd atoms to the surface and thus facilitate

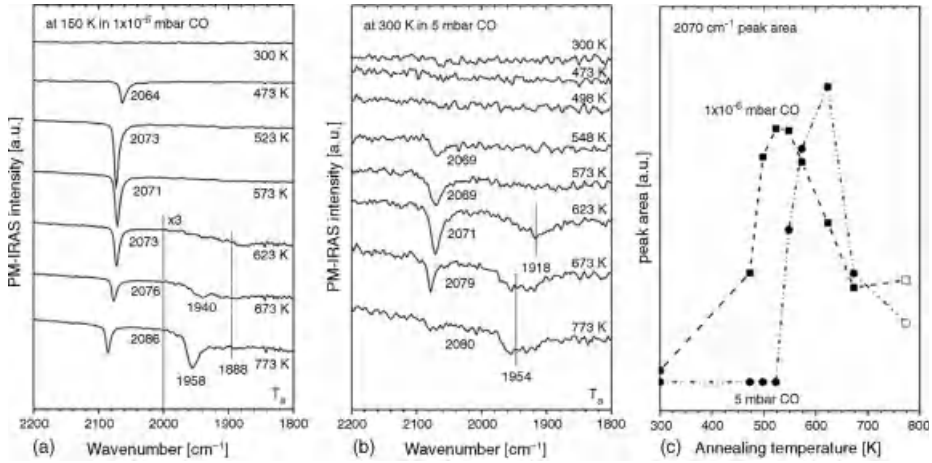


Figure 6.14 (a) PM-IRAS spectroscopy of 3 ML Zn deposited at 300 K on Pd(111). Spectra were acquired at 150 K in 10^{-4} Pa CO (a), and at 300 K in 0.5 kPa CO (b), after successive annealing at the indicated temperatures. The IR intensity in the frequency range of multiply coordinated CO (below 2000 cm^{-1}) was multiplied by three in some spectra. (c) Integrated area of the ~2070 cm^{-1} on-top CO peak as a function of annealing temperature. Reprinted from [141], Copyright (2010), with permission from Elsevier.

alloy formation. It should be noted that this effect can only be observed using *in situ* techniques such as (PM-)IRAS as, for example, electron-based techniques cannot be used at elevated pressure. Currently, the reason for the observed difference (cf., Figure 6.14c) is not yet known. It may be related to surface restructuring at elevated pressures or blocking of diffusion pathways (e.g., through step edges) by CO that makes metal intermixing more difficult.

6.4.3
Oxide Surfaces

Apart from noble and transition metals, oxides represent the most important class of catalysts, exhibiting a rich and complex surface chemistry [71, 100, 101]. We will therefore turn our attention to vibrational spectroscopy on surfaces of selected oxides, considering once again real and model systems.

Alumina is one of the most frequently used oxides in catalysis, often utilized as support for metal nanoparticles. It may contribute indirectly to a reaction by (reverse) spill-over but it may also act as a catalyst [102, 103]. The formation of carbonate species, occurring upon interaction of alumina (and other oxides) with CO and CO_2, was examined in our laboratory by vibrational spectroscopy for both model [104] and real high surface area oxides [105, 106]. For commercial γ-alumina powder catalysts, transmission FTIR spectroscopy was applied. For surface science model studies, a thin alumina film grown on an NiAl(110) single crystal was prepared in UHV and investigated using PM-IRAS. The fundamental difference

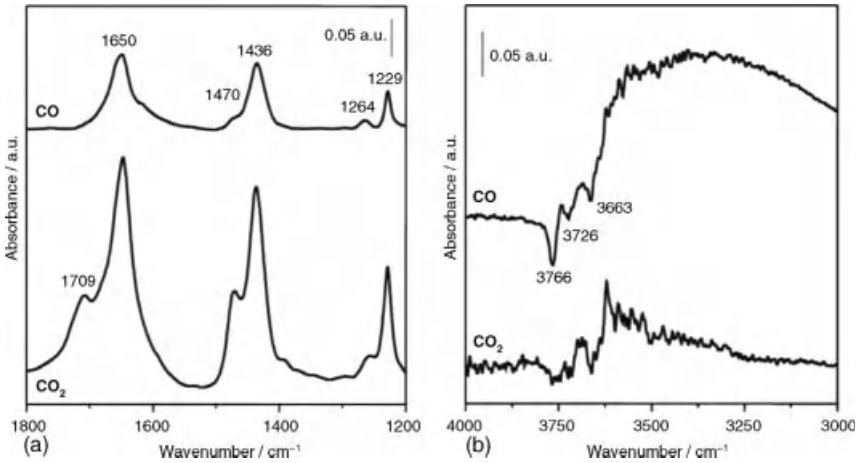


Figure 6.15 Vibrational IR spectra after adsorption of CO and CO_2 (0.5 kPa, 293 K) on Pd–Al_2O_3 and Al_2O_3: (a) carbonate region and (b) OH stretching region. Difference spectra are displayed, obtained by subtracting the corresponding spectra acquired before gas exposure. From [106]. Reproduced by permission of The Royal Society of Chemistry.

between the two materials originates from the presence or absence of hydroxyl groups and of defect sites.

Carbonate and bicarbonate formation readily occurs at room temperature, resulting from the reactive adsorption of CO or CO_2 on the powdered alumina. Carbonate bands were observed at the following positions: the main peaks were located at 1650, 1436, and 1229 cm^{-1}, a shoulder appeared at 1625 and 1470 cm^{-1}, and there was a weak peak at 1264 cm^{-1} (Figure 6.15a). The assignment is not straightforward, but most probably these bands can be assigned to bicarbonate (1625, 1436, 1229 cm^{-1}) and bidentate (1650, 1264 cm^{-1}) carbonate species [107–109]. Upon CO_2 exposure, the same bands/species were observed, but with higher intensity. Changes in the OH stretch region (different for CO and CO_2 exposure) suggest that OH groups were involved in the formation mechanism, but only for CO. Whereas CO led to a strong decrease in the intensity of sharp OH bands at 3766, 3726, and 3663 cm^{-1} (negative peaks in the difference spectra shown in Figure 6.15b) and a broad band appearing at lower frequency (around 3300 cm^{-1}), such changes did not occur upon CO_2 adsorption. This clearly suggests the reaction of CO with surface hydroxyl groups, leading to oxidation of CO to CO_2/carbonate.

The mechanism of carbonate formation was investigated in more detail by adsorbing labeled CO and CO_2 molecules. Exposing γ-alumina to $^{13}C^{18}O$ led to a red shift of the carbonate bands (Figure 6.16). The observed band positions agree well with those obtained upon $^{13}C^{16}O_2$ dosing, but do not match the bands observed on exposure to $^{13}C^{18}O_2$. Based on this observation, a mechanism for carbonate formation with CO was established that involves defect sites in addition to hydroxyls (see the scheme in Figure 6.16). The reaction of $^{13}C^{18}O$ occurs oxygen-down at defect (low-coordinated *cus*) sites with ^{18}O being incorporated in the oxide lattice, and

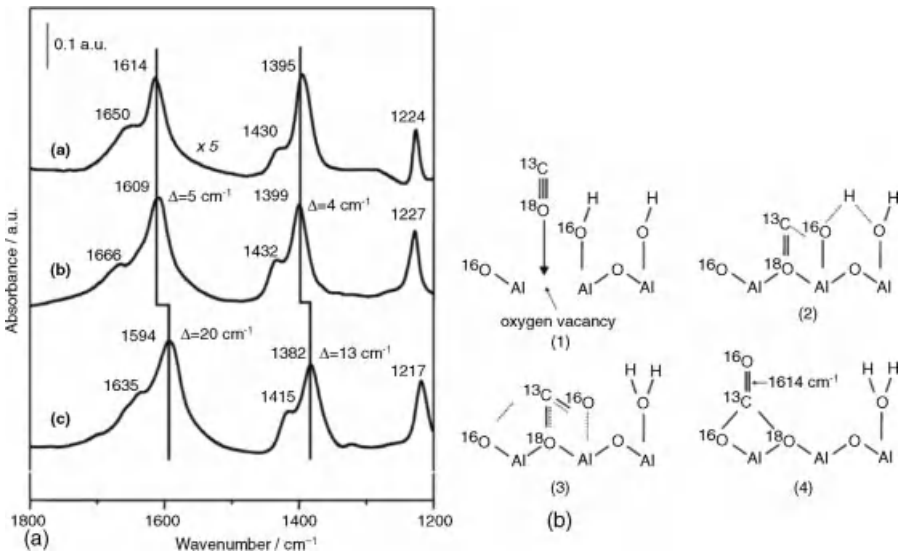


Figure 6.16 (a) Adsorption of (a) $^{13}C^{18}O$, (b) $^{13}C^{16}O_2$, and (c) $^{13}C^{18}O_2$ at 0.5 kPa pressure and 293 K on Pd–Al_2O_3: Difference spectra of the carbonate bands. (b) Scheme of the proposed reaction pathway for carbonate formation with CO on (Pd-)Al_2O_3. Adapted from [106]. Reproduced by permission of The Royal Society of Chemistry.

proceeds in a water-gas shift-like reaction with adjacent OH groups which oxidize CO to carbonates.

In contrast to high surface area (powder) Al_2O_3, no carbonate formation was detected upon CO exposure on model alumina thin films, Al_2O_3/NiAl(110), owing to the absence of the required OH groups [104]. This confirmed the suggested mechanism. Formation of carbonates upon CO_2 dosing occurred at kilopascal pressures, giving rise to a weak vibrational band at 1460 cm^{-1}. This band was assigned to monodentate carbonates [107–109], most probably formed by reaction with *cus* O^{2-}. The model thin films were almost defect free after preparation and annealing, which can explain the low concentration of carbonates and thus the weak absorption band. However, the concentration of the carbonate species could be significantly increased by "softly sputtering" the sample with Ar^+ ions. Figure 6.17 shows PM-IRAS spectra obtained upon exposure of the sputtered defective alumina film to 10 kPa CO and CO_2. Whereas carbonate formation still did not occur with CO owing to the absence of OH groups, the increased concentration of defects after sputtering resulted in more carbonate formation. The presence of carbonates on the alumina film was corroborated by XPS measurements, with a C1s peak at 291.0 eV attributed to carbonate species, in agreement with the literature [110–114].

By combining the information gained from spectroscopic studies of model and real materials, a conclusive reaction mechanism could be established. The carbonate case shows both analogies and differences between real and model systems.

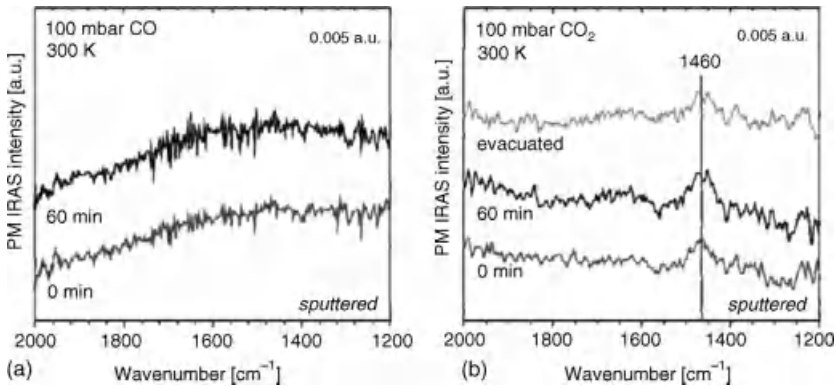


Figure 6.17 PM-IRAS surface spectra of a defective Al_2O_3/NiAl(110) film acquired in 10 kPa CO (a) or 10 kPa CO_2 (b) at 300 K. The spectra in (b) were acquired directly after exposure (bottom), after 60 min in CO_2 (middle) and after removal of the gas (top). Adapted with permission from [104].

Particularly the application of isotopically labeled molecules monitored by vibrational spectroscopy is a suitable tool for mechanistic studies.

The IR spectroscopic investigation of molecule–surface interactions in the liquid phase is a difficult task. For such applications, IR–visible SFG has strong advantages owing to its inherent surface specificity. In the following, this is illustrated for alumina and zirconia.

Strunk and Williams [115] applied SFG in TIR geometry to examine nitrile adsorption on planar Al_2O_3 und ZrO_2 oxide surfaces. Nitrile hydrogenation is applied for production of amines, therefore the interactions with metal/oxide catalysts and with pure support oxides are of interest for understanding this reaction. Since the process is generally carried out in the liquid phase, the benefits of IR–visible SFG are an advantage. Strunk and Williams [115] used internal reflection elements (IREs) made of Al_2O_3 and of ZrO_2 (exhibiting a flat oxide surface) as model supports and then exposed them to liquid nitriles (acetonitrile, butyronitrile). Two different types of adsorbed nitrile species were observed, giving rise to a vibrational band at $\sim$2250 cm^{-1} and a broader resonance $\sim$3 cm^{-1} below the main peak. The weakly interacting species at 2250 cm^{-1}, a frequency similar to that for liquid-phase acetonitrile, was assigned to an end-on adsorption configuration coordinated via the nitrogen of the CN group (see the scheme in Figure 6.18). The broader red-shifted band was attributed to intermolecular polar interactions and adsorbed nitrile cluster species. Less cluster species were formed in the case of butyronitrile than acetonitrile owing to steric constraints. A slightly stronger interaction of the linear end-on species leading to a lower ν_{CN} frequency was observed for the Al_2O_3 surface compared with ZrO_2, probably due to increased hydrogen bonding caused by the larger amount of native OH groups present on the Al_2O_3 surface.

The orientation of the adsorbed molecules was determined by polarization-dependent SFG measurements. This mode represents another benefit of SFG for studying the interaction of solid surfaces with molecules adsorbed from the gas or

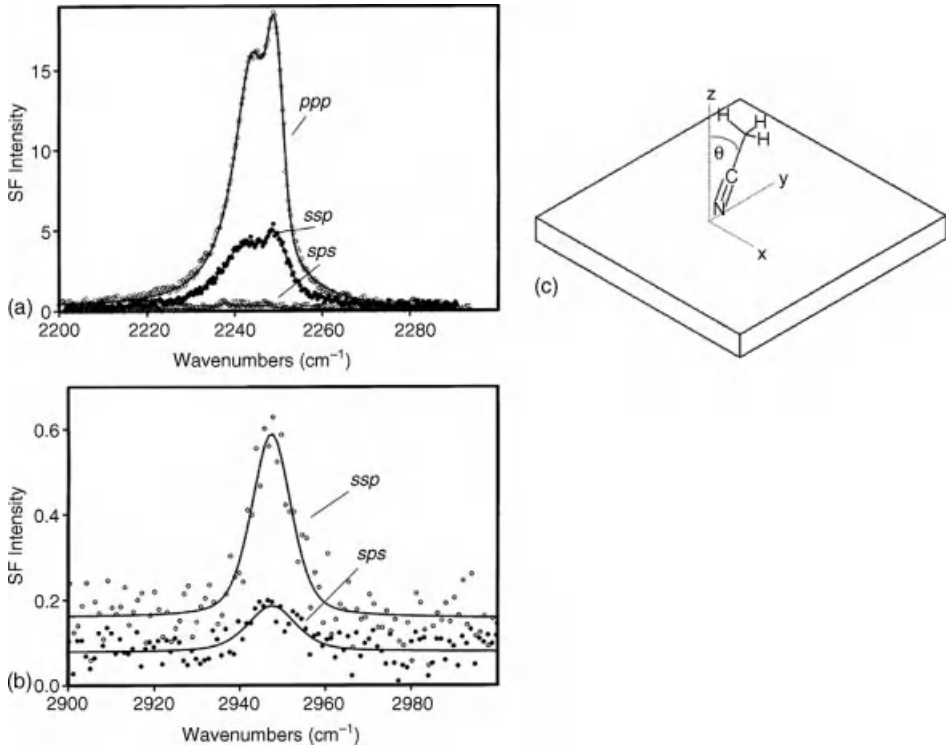


Figure 6.18 Polarized sum frequency spectra of (a) the CN stretching region and (b) the CH stretching region for Al_2O_3 in neat acetonitrile. Solid lines are the fits to the experimental data. Spectra for ZrO_2 are not shown owing to their similarity. (c) Scheme representing the average orientation of acetonitrile on the surfaces of Al_2O_3 and ZrO_2. Adapted from [115] with permission. Copyright (2003) American Chemical Society.

liquid phase. Figure 6.18 compares SFG spectra in the CH stretching region obtained for two different polarization combinations: ssp and sps. These combinations probe orthogonal components of χ and allow information to be extracted on the average orientation of the adsorbed nitrile molecules. Details on the theory and analysis of polarization variation measurements for determination of orientations can be found elsewhere (e.g., [27]). The average orientation of the adsorbed acetonitrile molecules adsorbed on the surface was determined as about 20–25° tilted from the surface normal (see the scheme in Figure 6.18). The low intensity of the sps signal led to relatively large errors of $\pm 6°$.

After addressing the adsorption and interaction of molecules with oxide surfaces, reaction studies will be dealt with in the following. When applying vibrational spectroscopy during reactions, the identification of reaction intermediates and, therefore, of reaction mechanisms are the main interest.

Short-lived reaction intermediates play a key role in many catalytic reactions. However, spectroscopic detection of such short-lived reactive species is typically

difficult, since they exist in low concentrations and (apparently) only for short periods of time. Hence time-resolved techniques able to observe and identify transient species are highly desirable. SFG offers the possibility of studying reactive intermediates by performing pump–probe experiments with laser pulses. An example is the work of Bandara and co-workers [44, 116], who studied formic acid decomposition on an NiO(111) surface. A thin NiO film grown on an Ni single crystal was kept in flowing deuterated formic acid (DCOOD, 3×10^{-5} Pa). Formates are intermediates in a range of catalytic reactions, such as methanol synthesis, SRM, water gas shift, and others.

In Bandara and co-workers' studies, a "picosecond surface temperature jump" was induced by irradiation with a short laser "pump" pulse in order to form and accumulate intermediates, and an SFG "probe" was utilized to monitor the decomposition reaction, providing chemical information on the fast surface process (Figure 6.19). It was found that the decomposition of surface-adsorbed formic acid proceeded via transformation of a stable bidentate formate (C−D vibration at 2160 cm^{-1}) to a monodentate formate (characterized by a transient vibrational C−D band at 2190 cm^{-1}). The latter was unstable and identified as the reactive interme-

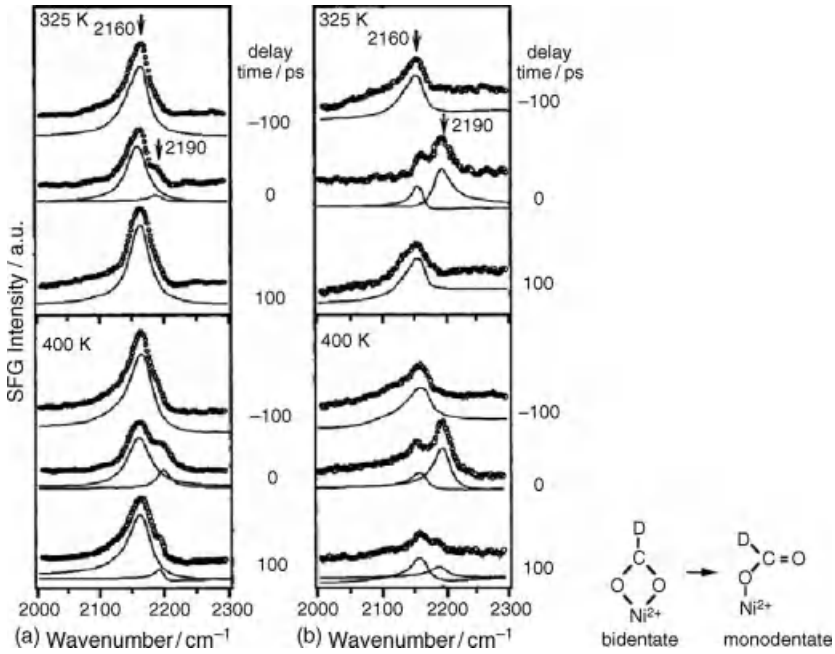


Figure 6.19 SFG spectra of DCOO/NiO(111) under irradiation from 1064 nm pump pulses of 10 mJ per pulse energy and 30 ps width. (a) pp- and (b) sp-polarization. The oxide surface was kept under a continuous flow of DCOOD vapor of 3×10^{-5} Pa pressure, and the measurement was made at substrate temperatures of 325 and 400 K and at 100 ps before, at, and 100 ps after the pump irradiation. Adapted from [44] with permission. Copyright (1998) American Chemical Society.

diate [44]. Molecular orientation was investigated by polarization-dependent SFG. Based on the observation that the C=O stretching band (around 1720 cm^{-1}) was absent for both ppp and ssp conditions, it was concluded that the C=O bond of monodentate formate was oriented parallel to the NiO surface. The C−D bonds of both formate species were oriented at different angles deviating from the surface normal, which confirmed the presence of two different species. The designation of the beam polarizations is explained in Section 6.3 (e.g., ssp-polarized means that SFG light is measured in s-polarization, the visible beam is s- and the IR beam is p-polarized). The temperature jump that was induced by the picosecond laser pulse was ∼300 K, as estimated from the frequency shift of the surface O−D band. The lifetime of the intermediate was ∼100 ps, so that the laser-induced change was restored within the 0.1 s interval between subsequent pulses.

Apart from catalytic reactions, surface processes such as corrosion can also be investigated by surface-sensitive spectroscopy. Corrosion of metal and oxide surfaces is often accelerated by moisture, which is in most cases explained by the effect of surface hydroxyl groups. Applying SFG, Hedberg and co-workers [117, 118] followed the corrosion of Zn/ZnO by formic acid *in situ*. Formic acid is considered one of the most important indoor corrosion accelerators. Under ambient conditions, the surface of Zn metal is covered by a thin layer of ZnO, which is OH terminated. When polycrystalline Zn foil was exposed to humidified N_2 containing a small amount (∼100 ppb) of formic acid [118], the surface hydroxyl groups were gradually replaced by formate species (Figure 6.20a). O−H (3625 and 3675 cm^{-1}) or O−D stretching vibrations (2665 and 2705 cm^{-1}, marked "a" in Figure 6.20b) disappeared while C−H stretching vibrations of formate species appeared at ∼2880 cm^{-1} (marked "b" in Figure 6.20b). Hence ligand exchange at the oxidized metal surface was identified as the initial step of Zn dissolution induced by formic acid. This observation was confirmed by DFT calculations and IRAS measurements [118].

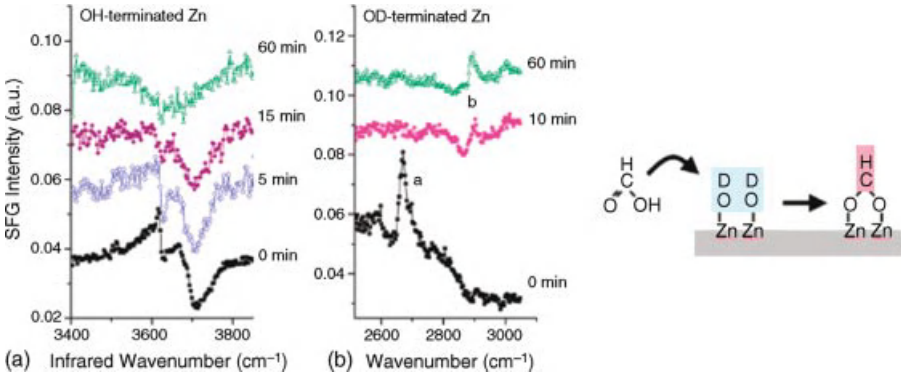


Figure 6.20 SFG spectra of Zn/ZnO exposed to formic acid as a function of time. (a) Spectra from the OH region and (b) spectra from the OD region. All spectra were collected with ppp polarization and are offset for clarity. Reprinted in part from [118] with permission. Copyright (2010) American Chemical Society.

6.4.4
Metal Nanoparticles on Oxide Surfaces

This last section of the case studies deals with oxide-supported nanoparticles, which are the most complex systems. When metal nanoparticles are deposited on reducible oxide supports, for example, TiO_2, an effect known as strong metal support interaction (SMSI) can occur [119]. Also, Nb_2O_5 is an interesting "SMSI material" that has attracted attention as a catalyst and as a support for noble and transition metal or oxide nanoparticles/films. Applications include the Fischer–Tropsch reaction and oxidation reactions. Höbel *et al.* [30] studied Pd particles (~3.5 nm in size) grown in UHV at 90 K on an Nb_2O_5 thin film (film thickness 0.4 nm) that was itself prepared in UHV on a $Cu_3Au(100)$ single-crystal substrate. Details on the film characteristics can be found elsewhere [120, 121]. By combining temperature-programmed desorption (TPD) and vibrational SFG measurements using CO as probe molecule, it was found that thermal treatment above 300 K induced strong structural changes, which led to the formation of mixed Pd–NbO_x sites. TPD measurements revealed a strong loss of CO adsorption capacity by ~50%. IR–visible SFG spectroscopy performed at UHV and kilopascal pressures showed modifications of the nonresonant background which was reflected by a change in the SFG lineshape (Figure 6.21). Alterations of the phase between resonant and nonresonant SFG signals upon annealing revealed a modification in the electronic structure of the surface, thus suggesting the formation of "alloyed" Pd–NbO_x species (sintering or oxide decoration of Pd particles could not explain the spectroscopic changes; see below). As described in the theoretical Section 6.2, the SFG signal consists of two contributions: a resonant part arising

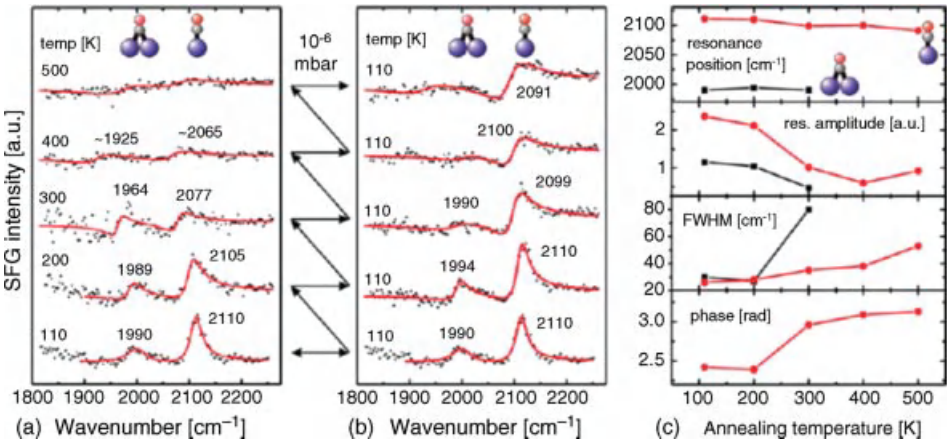


Figure 6.21 (a) SFG spectra of CO (10^{-4} Pa) adsorbed on 3.5 nm Pd particles supported on $Nb_2O_5/Cu_3Au(100)$ at different temperatures. (b) SFG spectra of CO adsorbed on Pd particles measured after cooling the annealed surfaces of (a) in 10^{-4} Pa CO to 110 K. Values obtained for peak position, resonant amplitude, peak width (FWHM), and phase of the spectra in (b) are displayed in (c), for both on-top and bridge-bonded CO. Reprinted from [30], Copyright (2006), with permission from Elsevier.

from the vibrations of adsorbed molecules, and a nonresonant background due to electronic transitions at the surface. The lineshape of the SFG signal depends on the relative magnitudes and on the phase between these contributions. Hence the lineshape can be an indicator for structural, compositional and electronic alterations at the surface. In the SFG spectra shown in Figure 6.21 two CO bands were observed at 110 K at 2110 and 1990 cm^{-1}, typical of on-top and bridge-bonded CO on Pd nanoparticles. In agreement with TPD, CO desorption set in at around 250 K. According to SFG, the on-top CO peak disappeared above 300 K and the band of bridge-bonded CO vanished at 400 K. Upon cooling to 110 K in CO after each annealing step, structural changes were observed above 300 K, as indicated by the modified lineshape (Figure 6.21). The distinct change in the phase between the resonant signals and the nonresonant background upon annealing at 300 K or higher (Figure 6.21c), resulting from a change in the surface susceptibility, indicated that the loss in CO adsorption capacity was not only due to a migration of Nb_2O_5 on to Pd or sintering of the Pd particles, but rather was an effect due to the alteration of the electronic structure of the Pd/Nb_2O_5 system. This change occurred irreversibly and was stable against different treatments (such as H_2 reduction, annealing). Since the same modifications occurred in CO and H_2 (catalytic reaction conditions of CO hydrogenation) and at ambient pressure, it is supposed that this behavior is probably relevant under Fischer–Tropsch reaction conditions.

Such mixed metal–NbO_x compounds have been proposed as key components of Nb_2O_5-supported metal catalysts. In the Fischer–Tropsch reaction, the selectivity is crucial owing to the variety of different products that can be formed. A high selectivity towards long-chain hydrocarbons was observed on Co/Nb_2O_5 [122–126] after reduction at high temperature. A possible explanation is the formation of sites involving the metal and the partially reduced support. In the work of Mendes *et al.* [127] on CO hydrogenation, $Co/Nb_2O_5/Al_2O_3$ catalysts were studied using diffuse reflectance-UV–visible spectroscopy and TPRS (temperature-programmed reaction spectroscopy). They observed the presence of Co^{2+}, Co^0, and Co^0–NbO_x sites, which strongly affect the catalyst's selectivity. It was proposed that the Co^{2+}–Co^0 interface was responsible for the methanation reaction, whereas Co^0–NbO_x sites were responsible for the hydrocarbon chain growth in the Fischer–Tropsch synthesis [127]. Hu *et al.* [128] studied Rh/Nb_2O_5 catalysts and observed partial blocking of the Rh surface by NbO_2 species upon high-temperature reduction. This interaction led to a decrease in H_2 chemisorption capacity and a decrease in activity for ethane hydrogenolysis. IR spectroscopy [129] of adsorbed CO on Pd/Al_2O_3 and $Pd/Nb_2O_5/Al_2O_3$ propane oxidation catalysts showed that the addition of Nb_2O_5 influenced the oxidizability/reducibility of Pd. The amount of Pd^0 and Pd^{2+} was dependent on the Nb_2O_5 loading with partially reduced niobia species preventing Pd oxidation, and the Pd^0/Pd^{2+} ratio affected the catalytic properties.

Another particularly interesting system is Au/TiO_2. Au particles smaller than 5 nm exhibit exceptionally high catalytic activity in several reactions, for example, in low-temperature CO oxidation and PROX. However, basic aspects explaining these extraordinary catalytic properties are still unresolved. Nevertheless, Au particle size is generally considered to be crucial. CO adsorption was studied both on Au/TiO_2

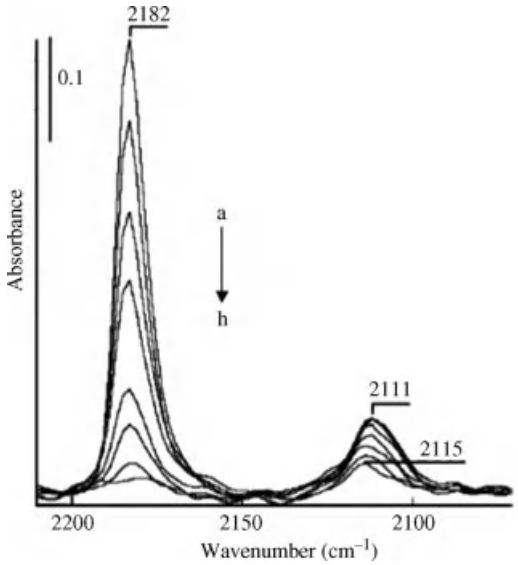


Figure 6.22 Evolution of the FTIR spectra of the adsorbed CO species on 1% Au/TiO_2 at a constant partial pressure $p_{CO} = 10$ kPa with the adsorption temperature, T_a. (a–h) $T_a = 307$, 313, 323, 353, 364, 392, and 407 K, respectively. Reprinted from [135] with permission. Copyright (2004) American Chemical Society.

powder catalysts [130–132] and on model catalysts [133, 134] using vibrational spectroscopy. The observed frequency of $\sim$2100 cm^{-1} is characteristic of CO adsorbed linearly on metallic Au and compares well for powders and model surfaces. The adsorption energy of CO on Au/TiO_2 was determined by vibrational spectroscopy (FTIR, PM-IRAS), for both powders [135] and planar model systems [136], and depended strongly on the Au particle size.

Derrouiche *et al.* [135] determined the heat of adsorption of CO linearly adsorbed on Au^0 particles (2110 cm^{-1}) and on $Ti^{\delta+}$ (2184 cm^{-1}) as a function of coverage, applying temperature-dependent IR spectroscopy at constant CO partial pressure (Figure 6.22). The heat of adsorption varied linearly from 74 to 47 kJ mol^{-1} for CO on Au particles (mean size 3–5 nm) and from 50 to 40 kJ mol^{-1} for CO on $Ti^{\delta+}$.

These data for adsorption energies were in very good agreement with those obtained on Au/TiO_2 model systems [133, 136]. Analogous to the analysis procedure described by Derrouiche *et al.* [135], Diemant *et al.* [136] used PM-IRAS to determine the CO adsorption energy on Au particles on a TiO_2 thin film [grown by Ti deposition in an O_2 atmosphere on an Ru(0001) substrate]. Pronounced Au particle size effects were observed. The initial adsorption energy decreased from 74 kJ mol^{-1} on 2 nm sized Au particles to 62 kJ mol^{-1} on 4 nm Au particles. An illustrative set of spectra is shown in Figure 6.23. The finding is in good agreement with the work of Meier and Goodman [133]. Similarly, Artiglia *et al.* [137] used PM-IRAS to investigate the effect of Au particle size on CO chemisorption, and reported that CO binding depended

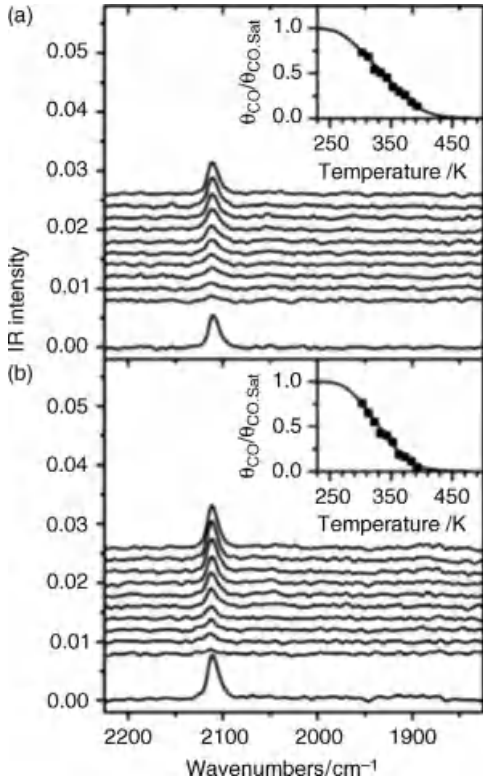


Figure 6.23 IR spectra recorded in 1 kPa CO on Au/TiO_2 model catalysts with different nominal Au coverages at various temperatures: (a) 0.9 ML (corresponds to 3 nm mean particle size) and (b) 1.6 ML (4 nm mean diameter). The insets show the evolution of the relative CO_{ad} coverage on the model catalysts with temperature (squares) and the calculated adsorption isobars (full line). Reprinted from [136], Copyright (2007), with permission from Elsevier.

strongly on the Au particle size and morphology, whereas the Ti oxidation state of the TiO_2 support did not seem to play an important role.

The final example describes the most complex situation, that is, Pd–Au bimetallic nanoparticles supported on MgO [138]. MgO(100) films of about 20 ML thickness were grown on an Ag(100) single crystal, and Pd and Au were loaded by simultaneous co-deposition at 100 K followed by annealing to 600 K. For investigations of the resulting adsorption sites and of surface composition, CO was used as a probe molecule and monitored by SFG (Figure 6.24). On pure Au/MgO no CO signal was observed, probably due to the desorption of weakly bonded CO by laser-induced heating, whereas the typical CO bands at 2105 and 1991 cm^{-1} were found on Pd/MgO. On bimetallic Pd–Au/MgO systems containing small amounts of Au, the 2105 cm^{-1} signal split into two bands at 2117 and 2093 cm^{-1} while the 1991 cm^{-1} band disappeared (Figure 6.24). The peak at 1991 cm^{-1} is attributed to bridge-bonded

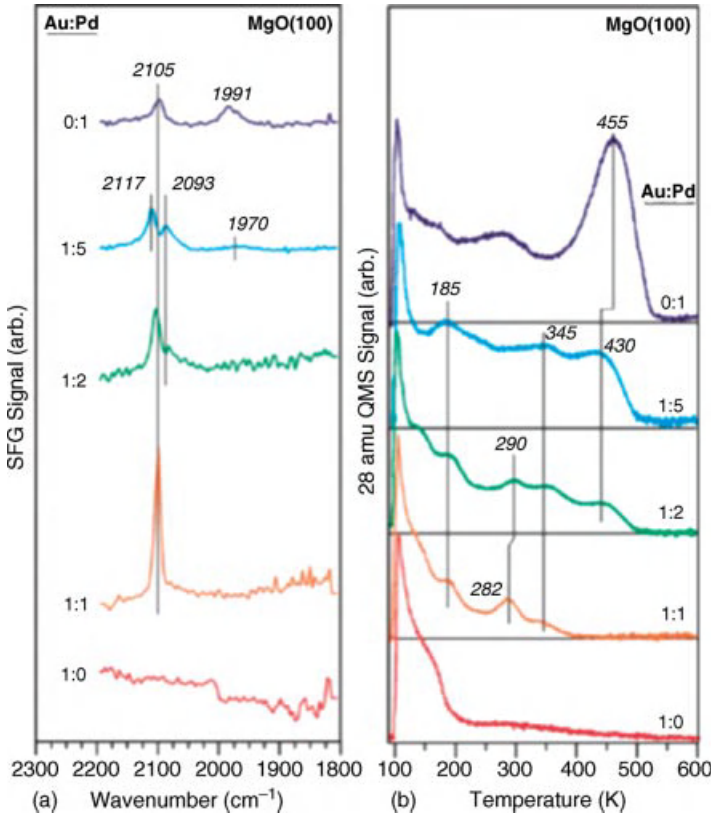


Figure 6.24 (a) SFG and (b) TPD spectra for 10 L CO adsorbed at ~100 K on Pd, Au, and Au–Pd particles supported on MgO(100) thin films. The particle composition was varied as indicated by the relative ratios of Au/Pd, with a nominal Pd thickness of ~2 Å. The SFG spectra were acquired at 100 K. Heating rate in TPD spectra: 1 K s^{-1}. Reprinted from [138] with permission. Copyright (2010) American Chemical Society.

CO on particle steps and edges. Since this band was most strongly affected and vanished at low Au amounts, it was suggested that Au first decorated edge sites. This was confirmed by DFT calculations. An increase in the Au/Pd ratio resulted in the prevalence of the CO band at 2117 cm^{-1} assigned to CO adsorption on Au sites. This evidenced segregation of Au to the surface of the particles. Segregation of Au was corroborated by CO TPD measurements shown in Figure 6.24b. The amount of strongly bonded CO on threefold Pd hollow sites, characterized by a desorption peak at 455 K, was significantly reduced upon Au addition, and Au-induced desorption features at 185, 290, and 345 K evolved.

Analogous studies of CO adsorption on Pd–Au bimetallic particles on CeO_2 and Fe_3O_4 thin films [138] were performed by PM-IRAS and revealed the same observation of Au surface segregation. The nature of the oxide support did not play a role.

6.5 Conclusion

Vibrational spectroscopy is one of the most powerful techniques in catalysis research, providing information solid catalytic surfaces, on adsorbed and reacting molecules, on reaction-induced structural changes, on activation and deactivation processes, and so on. Altogether, these pieces of information allow more or less direct conclusions to be drawn on active sites and reaction mechanisms. Of course, a single technique or operation mode can never answer all questions, but many dedicated strategies are available: SFG for measurements of steady-state and transient kinetics (pump–probe) bridging from UHV to ambient pressure, polarization-dependent SFG for orientation analysis, IRAS and PM-IRAS for extended frequency range, high-resolution/sensitivity and ambient-pressure measurements, and so on. Using isotopically labeled molecules and complementary physical methods for the analysis of atomic structure (HRTEM, EXAFS, STM, LEED, PEEM), composition and electronic structure (XPS, UPS, LEIS, DFT) provides a wealth of information. This allows us to move forward, away from "black magic catalysis," towards a fundamental science-based understanding of catalytic activity and selectivity of complex nanoscale materials.

Acknowledgements

The research was in part funded by the Austrian Science Fund (FWF), the German Research Foundation (DFG), FP7 (Marie Curie program) and the Vienna University of Technology. We are very grateful for the contributions of previous and current coworkers whose names appear in the list of references.

References

1 Ibach, H. and Mills, D.L. (1982) *Electron Energy Loss Spectroscopy and Surface Vibrations*, Academic Press, New York.
2 Eischens, R.P. and Pliskin, W.A. (1958) The infrared spectra of adsorbed molecules. *Adv. Catal.*, **10**, 1–56.
3 Hoffmann, F.M. (1983) Infrared reflection–absorption spectroscopy of adsorbed molecules. *Surf. Sci. Rep.*, **3**, 107–192.
4 Sheppard, N. and de la Cruz, C. (1996) Vibrational spectra of hydrocarbons adsorbed on metals. Part I. Introductory principles, ethylene, and the higher acyclic alkenes. *Adv. Catal.*, **41**, 1–112.
5 Sheppard, N. and de la Cruz, C. (1998) Vibrational spectra of hydrocarbons adsorbed on metals. Part II. Adsorbed acyclic alkynes and alkanes, cyclic hydrocarbons including aromatics, and surface hydrocarbon groups derived from the decomposition of alkyl halides, etc. *Adv. Catal.*, **42**, 181–313.
6 Rupprechter, G. (2007) Sum frequency generation and polarization-modulation infrared reflection absorption spectroscopy of functioning model catalysts from ultrahigh vacuum to ambient pressure. *Adv. Catal.*, **51**, 133–263.

7 Dellwig, T., Rupprechter, G., Unterhalt, H., and Freund, H.J. (2000) Bridging the pressure and materials gaps: high pressure sum frequency generation study on supported Pd nanoparticles. *Phys. Rev. Lett.*, **85** (4), 776–779.

8 Barner, B.J., Green, M.J., Saez, E.I., and Corn, R.M. (1991) Polarization modulation Fourier-transform infrared reflectance measurements of thin-films and monolayers at metal-surfaces utilizing real-time sampling electronics. *Anal. Chem.*, **63** (1), 55–60.

9 Beitel, G.A., Laskov, A., Oosterbeek, H., and Kuipers, E.W.J. (1996) Polarization modulation infrared reflection absorption spectroscopy of CO adsorption on Co(0001) under a high-pressure regime. *J. Phys. Chem.*, **100** (30), 12494–12502.

10 Borasio, M., de la Fuente, O.R., Rupprechter, G., and Freund, H.J. (2005) *In situ* studies of methanol decomposition and oxidation on Pd(111) by PM-IRAS and XPS spectroscopy. *J. Phys. Chem. B*, **109** (38), 17791–17794.

11 Ozensoy, E., Hess, C., and Goodman, D.W.J. (2002) Isocyanate formation in the catalytic reaction of CO + NO on Pd(111): an *in situ* infrared spectroscopic study at elevated pressures. *J. Am. Chem. Soc.*, **124** (29), 8524–8525.

12 Rameshan, C., Stadlmayr, W., Weilach, C., Penner, S., Lorenz, H., Havecker, M., Blume, R., Rocha, T., Teschner, D., Knop-Gericke, A., Schlogl, R., Memmel, N., Zemlyanov, D., Rupprechter, G., and Klotzer, B. (2010) Subsurface-controlled CO_2 selectivity of PdZn near-surface alloys in H_2 generation by methanol steam reforming. *Angew. Chem. Int. Ed.*, **49** (18), 3224–3227.

13 Kaichev, V.V., Prosvirin, I.P., Bukhtiyarov, V.I., Unterhalt, H., Rupprechter, G., and Freund, H.J. (2003) High-pressure studies of CO adsorption on Pd(111) by X-ray photoelectron spectroscopy and sum-frequency generation. *J. Phys. Chem. B*, **107** (15), 3522–3527.

14 Morkel, M., Kaichev, V.V., Rupprechter, G., Freund, H.J., Prosvirin, I.P., and Bukhtiyarov, V.I. (2004) Methanol dehydrogenation and formation of carbonaceous overlayers on Pd(111) studied by high-pressure SFG and XPS spectroscopy. *J. Phys. Chem. B*, **108** (34), 12955–12961.

15 Föttinger, K., van Bokhoven, J.A., Nachtegaal, M., and Rupprechter, G. (2011) Dynamic structure of a working methanol steam reforming catalyst: *in situ* quick-EXAFS on Pd/ZnO nanoparticles. *J. Phys. Chem. Lett.*, **2** (5), 428–433.

16 Shen, Y.R. (1989) Surface-properties probed by 2nd-harmonic and sum-frequency generation. *Nature*, **337** (6207), 519–525.

17 Hirose, C., Akamatsu, N., and Domen, K. (1992) Formulas for the analysis of surface sum-frequency generation spectrum by stretching modes of methyl and methylene groups. *J. Chem. Phys.*, **96** (2), 997–1004.

18 Bain, C.D. (1995) Sum-frequency vibrational spectroscopy of the solid–liquid interface. *J. Chem. Soc., Faraday Trans.*, **91** (9), 1281–1296.

19 Shen, Y.R. (1994) Surfaces probed by nonlinear optics. *Surf. Sci.*, **299** (1–3), 551–562.

20 Richmond, G.L. (2001) Structure and bonding of molecules at aqueous surfaces. *Annu. Rev. Phys. Chem.*, **52**, 357.

21 Somorjai, G.A. and Rupprechter, G.J. (1999) Molecular studies of catalytic reactions on crystal surfaces at high pressures and high temperatures by infrared–visible sum frequency generation (SFG) surface vibrational spectroscopy. *J. Phys. Chem. B*, **103** (10), 1623–1638.

22 Eisenthal, K.B. (1996) Liquid interfaces probed by second-harmonic and sum-frequency spectroscopy. *Chem. Rev.*, **96** (4), 1343–1360.

23 Buck, M. and Himmelhaus, M. (2001) Vibrational spectroscopy of interfaces by infrared–visible sum frequency generation. *J. Vac. Sci. Technol. A*, **19** (6), 2717–2736.

24 Williams, C.T. and Beattie, D.A. (2002) Probing buried interfaces with non-

linear optical spectroscopy. *Surf. Sci.*, **500** (1–3), 545–576.
25 Morkel, M., Unterhalt, H., Kluner, T., Rupprechter, G., and Freund, H.J. (2005) Interpreting intensities in vibrational sum frequency generation (SFG) spectroscopy: CO adsorption on Pd surfaces. *Surf. Sci.*, **586** (1–3), 146–156.
26 Unterhalt, H., Rupprechter, G., and Freund, H.J. (2002) Vibrational sum frequency spectroscopy on Pd(111) and supported Pd nanoparticles: CO adsorption from ultrahigh vacuum to atmospheric pressure. *J. Phys. Chem. B*, **106** (2), 356–367.
27 Galletto, P., Unterhalt, H., and Rupprechter, G. (2003) The molecular orientation of CO on Pd(111): a polarization-dependent SFG study. *Chem. Phys. Lett.*, **367** (5–6), 785–790.
28 Backus, E.H.G. and Bonn, M. (2005) A quantitative comparison between reflection absorption infrared and sum-frequency generation spectroscopy. *Chem. Phys. Lett.*, **412** (1–3), 152–157.
29 Guyot-Sionnest, P. (2005) The mature years of sum-frequency generation are ahead. *Surf. Sci.*, **585** (1–2), 1–2.
30 Höbel, F., Bandara, A., Rupprechter, G., and Freund, H.J. (2006) Deactivation of Pd particles supported on Nb_2O_5/Cu_3Au (100): SFG and TPD studies from UHV to 100 mbar. *Surf. Sci.*, **600** (4), 963–970.
31 Lu, G.Q., Lagutchev, A., Dlott, D.D., and Wieckowski, A. (2005) Quantitative vibrational sum-frequency generation spectroscopy of thin layer electrochemistry: CO on a Pt electrode. *Surf. Sci.*, **585** (1–2), 3–16.
32 Bandara, A., Dobashi, S., Kubota, J., Onda, K., Wada, A., Domen, K., Hirose, C., and Kano, S.S. (1997) Adsorption of CO and NO on NiO(111)/Ni(111) surface studied by infrared–visible sum frequency generation spectroscopy. *Surf. Sci.*, **387** (1–3), 312–319.
33 Richter, L.J., Petralli-Mallow, T.P., and Stephenson, J.C. (1998) Vibrationally resolved sum-frequency generation with broad-bandwidth infrared pulses. *Opt. Lett.*, **23** (20), 1594–1596.
34 Tadjeddine, A. and Peremans, A. (1996) Vibrational spectroscopy of the electrochemical interface by visible infrared sum-frequency generation. *Surf. Sci.*, **368**, 377–383.
35 vanderHam, E.W.M., Vrehen, Q.H.F., and Eliel, E.R. (1996) Self-dispersive sum-frequency generation at interfaces. *Opt. Lett.*, **21** (18), 1448–1450.
36 Rupprechter, G., Dellwig, T., Unterhalt, H., and Freund, H.J. (2001) CO adsorption on Ni(100) and Pt(111) studied by infrared–visible sum frequency generation spectroscopy: design and application of an SFG-compatible UHV–high-pressure reaction cell. *Top. Catal.*, **15**, 19–26.
37 Rupprechter, G. (2001) Surface vibrational spectroscopy from ultrahigh vacuum to atmospheric pressure: adsorption and reactions on single crystals and nanoparticle model catalysts monitored by sum frequency generation spectroscopy. *Phys. Chem. Chem. Phys.*, **3** (21), 4621–4632.
38 Williams, C.T., Yang, Y., and Bain, C.D. (1999) Prospects for detecting metal–adsorbate vibrations by sum-frequency spectroscopy. *Catal. Lett.*, **61** (1–2), 7–13.
39 Roeterdink, W.G., Aarts, J.F.M., Kleyn, A.W., and Bonn, M. (2004) Broadband sum frequency generation spectroscopy to study surface reaction kinetics: a temperature-programmed study of CO oxidation on Pt(111). *J. Phys. Chem. B*, **108** (38), 14491–14496.
40 Bonn, M., Hess, C., Funk, S., Miners, J.H., Persson, B.N.J., Wolf, M., and Ertl, G. (2000) Femtosecond surface vibrational spectroscopy of CO adsorbed on Ru(001) during desorption. *Phys. Rev. Lett.*, **84** (20), 4653–4656.
41 Cremer, P.S., Su, X.C., Somorjai, G.A., and Shen, Y.R. (1998) High pressure catalytic processes studied by infrared–visible sum frequency generation. *J. Mol. Catal. A Chem.*, **131** (1–3), 225–241.
42 Baldelli, S., Markovic, N., Ross, P., Shen, Y.R., and Somorjai, G. (1999) Sum frequency generation of CO on (111) and polycrystalline platinum electrode surfaces: evidence for SFG invisible surface CO. *J. Phys. Chem. B*, **103** (42), 8920–8925.

43 Hunt, J.H., Guyotsionnest, P., and Shen, Y.R. (1987) Observation of C–H stretch vibrations of monolayers of molecules by optical sum-frequency generation. *Chem. Phys. Lett.*, **133** (3), 189–192.

44 Bandara, A., Kubota, J., Onda, K., Wada, A., Kano, S.S., Domen, K., and Hirose, C. (1998) Short-lived reactive intermediate in the decomposition of formate on NiO (111) surface observed by picosecond temperature jump. *J. Phys. Chem. B*, **102**, 5951–5954.

45 Chen, Z., Gracias, D.H., and Somorjai, G.A. (1999) Sum frequency generation (SFG)–surface vibrational spectroscopy studies of buried interfaces: catalytic reaction intermediates on transition metal crystal surfaces at high reactant pressures; polymer surface structures at the solid–gas and solid–liquid interfaces. *Appl. Phys. B*, **68**, 549.

46 Shen, Y.R. (1999) Surface contribution versus bulk contribution in surface nonlinear optical spectroscopy. *Appl. Phys. B Lasers Opt.*, **68** (3), 295–300.

47 Tourillon, G., Dreesen, L., Volcke, C., Sartenaer, Y., Thiry, P.A., and Peremans, A. (2007) Total internal reflection sum-frequency generation spectroscopy and dense gold nanoparticles monolayer: a route for probing adsorbed molecules. *Nanotechnology*, **18** (41), 15301.

48 Yeganeh, M.S., Dougal, S.A., and Silbernagel, B.G. (2006) Sum frequency generation studies of surfaces of high-surface-area powdered materials. *Langmuir*, **22** (2), 637–641.

49 Kweskin, S.J., Rioux, R.M., Habas, S.E., Komvopoulos, K., Yang, P., and Somorjai, G.A. (2006) Carbon monoxide adsorption and oxidation on monolayer films of cubic platinum nanoparticles investigated by infrared–visible sum frequency generation vibrational spectroscopy. *J. Phys. Chem. B*, **110** (32), 15920–15925.

50 Florsheimer, M. (1999) Second-harmonic microscopy – a new tool for the remote sensing of interfaces. *Phys. Status Solidi A*, **173** (1), 15–27.

51 Florsheimer, M., Brillert, C., and Fuchs, H. (1999) Chemical imaging of interfaces by sum-frequency generation. *Mater. Sci. Eng. C Biomim.*, **8–9**, 335–341.

52 Humbert, B., Grausem, J., Burneau, A., Spajer, M., and Tadjeddine, A. (2001) Step towards sum frequency generation spectromicroscopy at a submicronic spatial resolution. *Appl. Phys. Lett.*, **78** (1), 135–137.

53 Schaller, R.D., Johnson, J.C., Wilson, K.R., Lee, L.F., Haber, L.H., and Saykally, R.J. (2002) Nonlinear chemical imaging nanomicroscopy: from second and third harmonic generation to multiplex (broad-bandwidth) sum frequency generation near-field scanning optical microscopy. *J. Phys. Chem. B*, **106** (20), 5143–5154.

54 Kuhnke, K., Hoffmann, D.M.P., Wu, X.C., Bittner, A.M., and Kern, K. (2003) Chemical imaging of interfaces by sum-frequency generation microscopy: application to patterned self-assembled monolayers. *Appl. Phys. Lett.*, **83** (18), 3830–3832.

55 Patel, J.D., Ebert, M., Stokes, K., Ward, R., and Anderson, J.M. (2003) Inhibition of bacterial and leukocyte adhesion under shear stress conditions by material surface chemistry. *J. Biomater. Sci. Polym. Ed.* **14** (3), 279–295.

56 Senaratne, W., Andruzzi, L., and Ober, C.K. (2005) Self-assembled monolayers and polymer brushes in biotechnology: current applications and future perspectives. *Biomacromolecules*, **6** (5), 2427–2448.

57 Somorjai, G.A., Frei, H., and Park, J.Y. (2009) Advancing the frontiers in nanocatalysis, biointerfaces, and renewable energy conversion by innovations of surface techniques. *J. Am. Chem. Soc.*, **131** (46), 16589–16605.

58 Somorjai, G.A. and Aliaga, C. (2010) Molecular studies of model surfaces of metals from single crystals to nanoparticles under catalytic reaction conditions. Evolution from prenatal and postmortem studies of catalysts. *Langmuir*, **26** (21), 16190–16203.

59 Blyholder, G.J. (1964) Molecular orbital view of chemisorbed carbon monoxide. *J. Phys. Chem.*, **68** (10), 2772–2777.

60 Blyholder, G.J. (1975) CNDO model of carbon monoxide chemisorbed on nickel. *J. Phys. Chem.*, **79** (7), 756–761.

61 Eischens, R.P., Pliskin, W.A., and Francis, S.A. (1954) Infrared spectra of chemisorbed carbon monoxide. *J. Chem. Phys.*, **22** (10), 1786–1787.

62 Pászti, Z., Hakkel, O., Keszthelyi, T., Berkó, A., Balázs, N., Bakó, I., and Guczi, L. (2010) Interaction of carbon monoxide with Au(111) modified by ion bombardment: a surface spectroscopy study under elevated pressure. *Langmuir*, **26** (21), 16312–16324.

63 Lemire, C., Meyer, R., Shaikhutdinov, S.K., and Freund, H.J. (2004) CO adsorption on oxide supported gold: from small clusters to monolayer islands and three-dimensional nanoparticles. *Surf. Sci.*, **552** (1–3), 27–34.

64 Yim, W.L., Nowitzki, T., Necke, M., Schnars, H., Nickut, P., Biener, J., Biener, M.M., Zielasek, V., Al-Shamery, K., Kluner, T., and Baumer, M. (2007) Universal phenomena of CO adsorption on gold surfaces with low-coordinated sites. *J. Phys. Chem. C*, **111** (1), 445–451.

65 Meyer, R., Lemire, C., Shaikhutdinov, S.K., and Freund, H. (2004) Surface chemistry of catalysis by gold. *Gold Bull.*, **37** (1–2), 72.

66 Cies, J.M., del Rio, E., Lopez-Haro, M., Delgado, J.J., Blanco, G., Collins, S., Calvino, J.J., and Bernal, S. (2010) Fully reversible metal deactivation effects in gold/ceria–zirconia catalysts: role of the redox state of the support. *Angew. Chem. Int. Ed.*, **49** (50), 9744–9748.

67 Hakkel, O., Paszti, Z., Berko, A., Frey, K., and Guczi, L. (2010) *In situ* sum frequency generation vibrational spectroscopy study of CO adsorption on Au surfaces promoted by Ar^+ sputtering and FeO_x additives. *Catal. Today*, **158** (1–2), 63–68.

68 Carrasco, E., Aumer, A., Brown, M.A., Dowler, R., Palacio, I., Song, S., and Sterrer, M. (2010) Infrared spectra of high coverage CO adsorption structures on Pt(111). *Surf. Sci.*, **604** (15–16), 1320–1325.

69 Pery, T., Schweitzer, M.G., Volpp, H.R., Wolfrum, J., Ciossu, L., Deutschmann, O., and Warnatz, J. (2002) Sum-frequency generation *in situ* study of CO adsorption and catalytic CO oxidation on rhodium at elevated pressures. *Proc. Combust. Inst.*, **29**, 973–980.

70 Suetaka, W. and Yates, J.T. (1995) *Surface Infrared and Raman Spectroscopy*, Plenum Press, New York.

71 Ertl, G., Knoezinger, H., Schueth, F., and Weitkamp, J. (2008) *Handbook of Heterogeneous Catalysis*, Wiley-VCH Verlag GmbH, Weinheim.

72 Wilson, E.L. and Brown, W.A. (2010) Low pressure RAIRS studies of model catalytic systems. *J. Phys. Chem. C*, **114** (15), 6879–6893.

73 Backus, E.H.G., Eichler, A., Kleyn, A.W., and Bonn, M. (2005) Real-time observation of molecular motion on a surface. *Science*, **310** (5755), 1790–1793.

74 Rupprechter, G., Unterhalt, H., Morkel, M., Galletto, P., Hu, L.J., and Freund, H.J.J. (2002) Sum frequency generation vibrational spectroscopy at solid–gas interfaces: CO adsorption on Pd model catalysts at ambient pressure. *Surf. Sci.*, **502**, 109–122.

75 Hollins, P. (1992) The influence of surface-defects on the infrared-spectra of adsorbed molecules. *Surf. Sci. Rep.*, **16** (2), 51–94.

76 Wolter, K., Seiferth, O., Kuhlenbeck, H., Baumer, M., and Freund, H.J. (1998) Infrared spectroscopic investigation of CO adsorbed on Pd aggregates deposited on an alumina model support. *Surf. Sci.*, **399** (2–3), 190–198.

77 Cremer, P.S., Su, X.C., Shen, Y.R., and Somorjai, G.A. (1996) Ethylene hydrogenation on Pt(111) monitored *in situ* at high pressures using sum frequency generation. *J. Am. Chem. Soc.*, **118** (12), 2942–2949.

78 Morkel, M., Rupprechter, G., and Freund, H.J. (2005) Finite size effects on supported Pd nanoparticles: interaction of hydrogen with CO and C_2H_4. *Surf. Sci.*, **588** (1–3), L209–L219.

79 Rupprechter, G., Morkel, M., Freund, H.J., and Hirschl, R.J. (2004) Sum frequency generation and density

functional studies of CO–H interaction and hydrogen bulk dissolution on Pd (111). *Surf. Sci.*, **554** (1), 43–59.

80 Bratlie, K.M., Kliewer, C.J., and Somorjai, G.A. (2006) Structure effects of benzene hydrogenation studied with sum frequency generation vibrational spectroscopy and kinetics on Pt(111) and Pt(100) single-crystal surfaces. *J. Phys. Chem. B*, **110** (36), 17925–17930.

81 Bratlie, K.M., Montano, M.O., Flores, L.D., Paajanen, M., and Somorjai, G.A. (2006) Sum frequency generation vibrational spectroscopic and high-pressure scanning tunneling microscopic studies of benzene hydrogenation on Pt(111). *J. Am. Chem. Soc.*, **128** (39), 12810–12816.

82 Kliewer, C.J. and Somorjai, G.A. (2010) Structure effects on pyridine hydrogenation over Pt(111) and Pt(100) studied with sum frequency generation vibrational spectroscopy. *Catal. Lett.*, **137** (3–4), 118–122.

83 Chen, M.S., Wang, X.V., Zhang, L.H., Tang, Z.Y., and Wan, H.L. (2010) Active surfaces for CO oxidation on palladium in the hyperactive state. *Langmuir*, **26** (23), 18113–18118.

84 Hendriksen, B.L.M., Bobaru, S.C., and Frenken, J.W.M.J. (2005) Bistability and oscillations in CO oxidation studied with scanning tunnelling microscopy inside a reactor. *Catal. Today*, **105** (2), 234–243.

85 van Rijn, R., Ackermann, M.D., Balmes, O., Dufrane, T., Geluk, A., Gonzalez, H., Isern, H., de Kuyper, E., Petit, L., Sole, V.A., Wermeille, D., Felici, R., and Frenken, J.W.M. (2010) Ultrahigh vacuum/high-pressure flow reactor for surface x-ray diffraction and grazing incidence small angle x-ray scattering studies close to conditions for industrial catalysis. *Rev. Sci. Instrum.*, **81** (1), 14101.

86 Gabasch, H., Knop-Gericke, A., Schloegl, R., Borasio, M., Weilach, C., Rupprechter, G., Penner, S., Jenewein, B., Hayek, K., and Kloetzer, B. (2007) Comparison of the reactivity of different Pd–O species in CO oxidation. *Phys. Chem. Chem. Phys.*, **9** (4), 533–540.

87 Rupprechter, G. and Weilach, C. (2007) Mind the gap! Spectroscopy on catalytically active phases. *Nano Today*, **2** (4), 20–29.

88 Zorn, K., Giorgio, S., Halwax, E., Henry, C.R., Gronbeck, H., and Rupprechter, G. (2011) CO oxidation on technological Pd–Al_2O_3 catalysts: oxidation state and activity. *J. Phys. Chem. C*, **115** (4), 1103–1111.

89 Gao, F., McClure, S.M., Cai, Y., Gath, K.K., Wang, Y., Chen, M.S., Guo, Q.L., and Goodman, D.W. (2009) CO oxidation trends on Pt-group metals from ultrahigh vacuum to near atmospheric pressures: a combined *in situ* PM-IRAS and reaction kinetics study. *Surf. Sci.*, **603** (1), 65–70.

90 Schalow, T., Brandt, B., Laurin, M., Schauermann, S., Libuda, J., and Freund, H.J.J. (2006) CO oxidation on partially oxidized Pd nanoparticles. *J. Catal.*, **242** (1), 58–70.

91 Chen, M.S., Kumar, D., Yi, C.W., and Goodman, D.W.J. (2005) The promotional effect of gold in catalysis by palladium–gold. *Science*, **310** (5746), 291–293.

92 Chen, M.S., Luo, K., Wei, T., Yan, Z., Kumar, D., Yi, C.W., and Goodman, D.W.J. (2006) The nature of the active site for vinyl acetate synthesis over Pd–Au. *Catal. Today*, **117** (1–3), 37–45.

93 Khan, N.A., Shaikhutdinov, S., and Freund, H.J. (2006) Acetylene and ethylene hydrogenation on alumina supported Pd–Ag model catalysts. *Catal. Lett.*, **108** (3–4), 159–164.

94 Khan, N.A., Uhl, A., Shaikhutdinov, S., and Freund, H.J. (2006) Alumina supported model Pd–Ag catalysts: a combined STM, XPS, TPD and IRAS study. *Surf. Sci.*, **600** (9), 1849–1853.

95 Iwasa, N., Kudo, S., Takahashi, H., Masuda, S., and Takezawa, N.J. (1993) Highly selective supported Pd catalysts for steam reforming of methanol. *Catal. Lett.*, **19** (2–3), 211–216.

96 Iwasa, N., Masuda, S., Ogawa, N., and Takezawa, N. (1995) Steam reforming of methanol over Pd/ZnO: effect of the formation of PdZn alloys upon reaction. *Appl. Catal. A Gen.*, **125**, 145–157.

97 Iwasa, N., Mayanagi, T., Nomura, W., Arai, M., and Takezawa, N.J. (2003) Effect of Zn addition to supported Pd catalysts in the steam reforming of methanol. *Appl. Catal. A Gen.*, **248** (1–2), 153–160.

98 Bayer, A., Flechtner, K., Denecke, R., Steinrueck, H.P., Neyman, K.M., and Roesch, N.J. (2006) Electronic properties of thin Zn layers on Pd(111) during growth and alloying. *Surf. Sci.*, **600** (1), 78–94.

99 Chen, Z.X., Neyman, K.M., Gordienko, A.B., and Roesch, N.J. (2003) Surface structure and stability of PdZn and PtZn alloys: density-functional slab model studies. *Phys. Rev. B*, **68** (7), 075417.

100 Rupprechter, G. and Penner, S. (2010) Catalysis of thin oxide films and oxide nanoparticles, in *Model Systems in Catalysis – Single Crystals to Supported Enzyme Mimics* (ed. R.M. Rioux), Springer, Berlin, pp. 367–394.

101 Freund, H.-J. and Goodman, D.W. (2008) Ultrathin oxide films, in *Handbook of Heterogeneous Catalysis* (eds G. Ertl, H.K. Knoezinger, F. Schuth, and J. Weitkamp), Wiley-VCH Verlag GmbH, Weinheim, pp. 1309–1338.

102 McInroy, A.R., Lundie, D.T., Winfield, J.M., Dudman, C.C., Jones, P., Parker, S.F., Taylor, J.W., and Lennon, D. (2005) An infrared and inelastic neutron scattering spectroscopic investigation on the interaction of eta-alumina and methanol. *Phys. Chem. Chem. Phys.*, **7** (16), 3093–3101.

103 McInroy, A.R., Lundie, D.T., Winfield, J.M., Dudman, C.C., Jones, P., and Lennon, D. (2007) Improved atom efficiency via an appreciation of the surface activity of alumina catalysts: methyl chloride synthesis. *Appl. Catal. B Environ.*, **70** (1–4), 606–610.

104 Weilach, C., Spiel, C., Foettinger, K., and Rupprechter, G. (2011) Carbonate formation on Al_2O_3 thin film model catalyst supports. *Surf. Sci.*, **605** (15–16), 1503–1509).

105 Bowker, M. (2007) Catalysis resolved using scanning tunnelling microscopy. *Chem. Soc. Rev.*, **36** (10), 1656–1673.

106 Foettinger, K., Schloegl, R., and Rupprechter, G. (2008) The mechanism of carbonate formation on Pd–Al_2O_3 catalysts. *Chem Commun*, (3), 320–322.

107 Davydov, A.A. (1990) *Infrared Spectroscopy of Adsorbed Species on the Surface of Transition Metal Oxides*, John Wiley & Sons, Ltd., Chichester.

108 Hair, L. (1967) *Infrared Spectroscopy in Surface Chemistry*, Marcel Dekker, New York.

109 Hadjiivanov, K.I. and Vayssilov, G.N. (2002) Characterization of oxide surfaces and zeolites by carbon monoxide as an IR probe molecule. *Adv. Catal.*, **47**, 307–511.

110 Illing, G., Heskett, D., Plummer, E.W., Freund, H.J., Somers, J., Lindner, T., Bradshaw, A.M., Buskotte, U., Neumann, M., Starke, U., Heinz, K., Deandres, P.L., Saldin, D., and Pendry, J.B. (1988) Adsorption and reaction of CO_2 on Ni (110) – X-ray photoemission, near-edge X-ray absorption fine structure and diffuse LEED studies. *Surf. Sci.*, **206**, 1–19.

111 Moulder, J.F., Stickle, W.F., Sobol, P.E., and Bomben, K.D. (1995) *Handbook of X-Ray Photoelectron Spectroscopy*, Physical Electronics, Inc., Eden Prairie, MN.

112 Gelius, F., Heden, P.F., Hedman, J., Lindberg, B.J., Manne, R., Nordberg, R., Nording, C., and Siegbahn, K. (1970) Molecular spectroscopy by means of ESCA. *Phys. Scr.*, **2**, 70–80.

113 Kotsis, K., Stodt, D., Staemmler, V., Kovacik, R., Meyer, B., Traeger, F., Langenberg, D., Strunskus, T., Kunat, M., and Wöll, C. (2008) CO_2 adlayers on the mixed terminated ZnO(10-10) surface studied by He atom scattering, photoelectron spectroscopy and *ab initio* electronic structure calculations. *Z. Phys. Chem.*, **222**, 891–915.

114 Verhoeven, J.A.T. and Van Doveren, H. (1982) An XPS investigation of the interaction of CH_4, C_2H_2, C_2H_4 and C_2H_6 with a barium surface. *Surf. Sci.*, **123**, 369–383.

115 Strunk, M.R. and Williams, C.T. (2003) Aliphatic nitrile adsorption on Al_2O_3 and ZrO_2 as studied by total internal reflection sum-frequency spectroscopy. *Langmuir*, **19**, 9210–9215.

116 Bandara, A., Kubota, J., Wada, A., Domen, K., and Hirose, C. (1999) Adsorption and decomposition of formic acid (DCOOD) on NiO(111) and Ni(111) surfaces probed by SFG. *Appl. Phys. B*, **68**, 573–578.

117 Hedberg, J., Henriquez, J., Baldelli, S., Johnson, C.M., and Leygraf, C. (2009) Initial atmospheric corrosion of zinc exposed to formic acid, investigated by *in situ* vibrational sum frequency spectroscopy and density functional theory calculations. *J. Phys. Chem. C*, **113** (6), 2088–2095.

118 Hedberg, J., Baldelli, S., and Leygraf, C. (2010) Evidence for the molecular basis of corrosion of zinc induced by formic acid using sum frequency generation spectroscopy. *J. Phys. Chem. Lett.*, **1** (10), 1679–1682.

119 Hayek, K., Fuchs, M., Kloetzer, B., Reichl, W., and Rupprechter, G.J. (2000) Studies of metal–support interactions with "real" and "inverted" model systems: reactions of CO and small hydrocarbons with hydrogen on noble metals in contact with oxides. *Top. Catal.*, **13** (1–2), 55–66.

120 Starr, D.E., Mendes, F.M.T., Middeke, J., Blum, R.P., Niehus, H., Lahav, D., Guimond, S., Uhl, A., Kluener, T., Schmal, M., Kuhlenbeck, H., Shaikhutdinov, S., and Freund, H.J. (2005) Preparation and characterization of well-ordered, thin niobia films on a metal substrate. *Surf. Sci.*, **599** (1–3), 14–26.

121 Middeke, J., Blum, R.P., Hafemeister, M., and Niehus, H.J. (2005) Controlled preparation of well-ordered transition metal oxide layers on a metallic surface. *Surf. Sci.*, **587** (3), 219–228.

122 Mendes, F., Noronha, F.B., Soares, R.R., Perez, C.A.C., Marcheti, G., and Schmal, M. (2001) The promoting effect of Ru and Re addition to Co/Nb_2O_5 catalyst in the Fischer–Tropsch synthesis. *Stud. Surf. Sci. Catal.*, **136**, 177–183.

123 Frydman, A., Soares, R.R., and Schmal, M. (1993) High selectivity of diesel fraction in Fischer–Tropsch synthesis with CO/Nb_2O_5. *Stud. Surf. Sci. Catal*, **75**, 2797–2800.

124 Mendes, F.T., Noronha, F.B., and Schmal, M. (2001) Effect of Nb_2O_5 addition to Co/Al_2O_3 catalyst on CO hydrogenation reaction. *Stud. Surf. Sci. Catal.*, **130**, 3717–3722.

125 Noronha, F.B., Frydman, A., Aranda, D.A.G., Perez, C., Soares, R.R., Morawek, B., Castner, D., Campbell, C.T., Frety, R., and Schmal, M. (1996) The promoting effect of noble metal addition on niobia-supported cobalt catalysts. *Catal. Today*, **28** (1–2), 147–157.

126 Soares, R.R., Frydman, A., and Schmal, M. (1993) Effect of preparation method on 5-percent CO/Nb_2O_5 in Fischer–Tropsch synthesis (FTS). *Catal. Today*, **16** (3–4), 361–370.

127 Mendes, F.M.T., Perez, C.A.C., Noronha, F.B., and Schmal, M. (2005) TPSR of CO hydrogenation on $Co/Nb_2O_5/Al_2O_3$ catalysts. *Catal. Today*, **101** (1), 45–50.

128 Hu, Z., Kunimori, K., and Uchijima, T. (1991) Interaction of hydrogen and oxygen with niobia-supported and niobia-promoted rhodium catalysts. *Appl. Catal.*, **69**, 253–268.

129 Aranda, D.A.G., Noronha, F.B., Ordine, A.P., and Schmal, M. (1999) Redox properties of $Pd/NbO_x/Al_2O_3$ catalysts. *Phys. Status Solidi A*, **173** (1), 109–116.

130 Bollinger, M.A. and Vannice, M.A.J. (1996) A kinetic and DRIFTS study of low-temperature carbon monoxide oxidation over $Au–TiO_2$ catalysts. *Appl. Catal. B Environ.*, **8** (4), 417–443.

131 Schumacher, B., Denkwitz, Y., Plzak, V., Kinne, M., and Behm, R.J. (2004) Kinetics, mechanism, and the influence of H_2 on the CO oxidation reaction on a Au/TiO_2 catalyst. *J. Catal.*, **224** (2), 449–462.

132 Boccuzzi, F., Chiorino, A., and Manzoli, M. (2000) FTIR study of the electronic effects of CO adsorbed on gold nanoparticles supported on titania. *Surf. Sci.*, **454**, 942–946.

133 Meier, D.C. and Goodman, D.W. (2004) The influence of metal cluster size on adsorption energies: CO adsorbed on Au clusters supported on TiO_2. *J. Am. Chem. Soc.*, **126** (6), 1892–1899.

134 Zhao, Z., Diemant, T., Rosenthal, D., Christmann, K., Bansmann, J., Rauscher, H., and Behm, R.J. (2006) $Au/TiO_2/Ru$ (0001) model catalysts and their interaction with CO. *Surf. Sci.*, **600** (22), 4992–5003.

135 Derrouiche, S., Gravejat, P., and Bianchi, D. (2004) Heats of adsorption of linear CO species adsorbed on the Au-circle and Ti + delta sites of a 1% Au/TiO_2 catalyst using *in situ* FTIR spectroscopy under adsorption equilibrium. *J. Am. Chem. Soc.*, **126** (40), 13010–13015.

136 Diemant, T., Hartmann, H., Bansmann, J., and Behm, R.J. (2007) CO adsorption energy on planar Au/TiO_2 model catalysts under catalytically relevant conditions. *J. Catal.*, **252** (2), 171–177.

137 Artiglia, L., Diemant, T., Hartmann, H., Bansmann, J., Behm, R.J., Gavioli, L., Cavaliere, E., and Granozzi, G. (2010) Stability and chemisorption properties of ultrathin $TiO_x/Pt(111)$ films and $Au/TiO_x/Pt(111)$ model catalysts in reactive atmospheres. *Phys. Chem. Chem. Phys.*, **12** (25), 6864–6874.

138 Abbott, H.L., Aumer, A., Lei, Y., Asokan, C., Meyer, R.J., Sterrer, M., Shaikhutdinov, S., and Freund, H.J. (2010) CO adsorption on monometallic and bimetallic Au–Pd nanoparticles supported on oxide thin films. *J. Phys. Chem. C*, **114** (40), 17099–17104.

139 Rupprechter, G. (2007) Sum frequency laser spectroscopy during chemical reactions on surfaces. *Mater. Res. Soc. Bull.*, **32**, 1031–1037.

140 Stadlmayr, W., Rameshan, C., Weilach, C., Lorenz, H., Havecker, M., Blume, R., Rocha, T., Teschner, D., Knop-Gericke, A., Zemlyanov, D., Penner, S., Schlogl, R., Rupprechter, G., Klotzer, B., and Memmel, N. (2010) Temperature-induced modifications of PdZn layers on Pd(111). *J. Phys. Chem. C*, **114** (24), 10850–10856.

141 Rameshan, C., Weilach, C., Stadlmayr, W., Penner, S., Lorenz, H., Havecker, M., Blume, R., Rocha, T., Teschner, D., Knop-Gericke, A., Schlogl, R., Zemlyanov, D., Memmel, N., Rupprechter, G., and Klotzer, B. (2010) Steam reforming of methanol on PdZn near-surface alloys on Pd(111) and Pd foil studied by *in-situ* XPS, LEIS and PM-IRAS. *J. Catal.*, **276** (1), 101–113.

7
Infra Red Reflection Absorption Spectroscopy and Polarisation Modulation-IRRAS

Christophe Méthivier and Claire-Marie Pradier

7.1
Introduction

Infrared (IR) spectroscopy is one of the most powerful tools for describing and unraveling the adsorption modes of molecules on solid materials. It provides information on chemical groups in the adsorbed layer, their nature, their geometry, and growth mode, and in some favorable cases it is possible to determine the nature of the surface adsorption sites or their acid–base properties, for example. Depending on the kind of material to be characterized, metal or oxide, planar or powder, there are different sampling techniques and ways of applying IR spectroscopy. For powder materials, the most commonly used techniques are transmission, diffusive reflectance, and attenuated total reflection; the last technique is also used on flat surfaces. Since the early theoretical and experimental work of Greenler on the specular reflection of an IR beam on metal surfaces [1, 2], infrared reflection absorption spectroscopy (IRAS, also IRRAS) has been developed to characterize ultra-thin films on solid metal surfaces. Thanks to the electric field enhancement on metal surfaces, this technique has sufficient sensitivity to measure the IR spectra of adsorbed molecules with a surface concentration less than one monolayer. Moreover, the metal surface selection rule induced by the surface electric field anisotropy allows the determination of the orientation of the molecular groups with respect to the surface.

Unlike the classical surface science tools such as X-ray photoelectron spectroscopy (XPS), Auger electron spectroscopy (AES), and electron energy loss spectroscopy (EELS), IRAS spectra can be recorded *in situ* in the presence of a gas phase containing any type of reactive species, which makes this technique particularly interesting for characterizing the transient molecular states and their evolution during a catalytic process. However, obtaining good IRAS spectra under a gas is restricted to pressures of a few hundred pascals for two reasons: first, not to absorb too much of the IR beam and thus not to decrease the light intensity, and second, because slight changes in the gas-phase composition from that corresponding to the background spectrum induce irrelevant spectral features. A differential IR reflectivity technique, polarization modulation infrared reflection absorption spectroscopy (PM-IRAS; see later) was

Characterization of Solid Materials and Heterogeneous Catalysts: From Structure to Surface Reactivity, First Edition. Edited by Michel Che and Jacques C. Védrine.
© 2012 Wiley-VCH Verlag GmbH & Co. KGaA. Published 2012 by Wiley-VCH Verlag GmbH & Co. KGaA.

therefore introduced in order to overcome this problem and allow the characterization of adsorbates at higher pressures, even in the liquid phase.

After recalling the context which gave rise to the development of single-reflection IR spectroscopy, this chapter briefly describes the principle and theory of the IRAS and PM-IRAS techniques, then some examples of applications of these techniques in the fields of catalysis, self-assembled monolayers and biological interfaces are presented.

7.1.1 Some History

IR spectroscopy has been used for more than 50 years to study CO adsorption on various supported metals; in the 1950s, Eischens *et al.* observed several CO absorption bands and frequency shifts, correlated to surface heterogeneities and adsorbate coverage [3]. It was shown, a little later, that band shifts could be ascribed to changes in the catalyst structure during catalytic reaction. Here came the need to work on metal single crystals in order to obtain a reliable CO IR signal for structure correlation. Working on metal surfaces required the use of reflection IR spectroscopy, a method whose principle and optical setups were described by Greenler in the late 1960s [1, 2]. The absolute change in reflectance, resulting from absorption bands, ΔR, was therefore defined to measure the absorption intensity:

$$\Delta R = R^0 - R \text{ and } A = (R^0 - R)/R^0 \tag{7.1}$$

as explained in Figure 7.1.

Greenler also reported the calculated ΔR as a function of the angle of incidence for one or multiple reflections, and described experimental setups for various numbers of reflections on a reflective surface. After the pioneering work by the groups of Ibach [4] and McFeeley [5], who studied, using high-resolution electron loss spectroscopy (HREELS), the vibrational properties of CO on metals, and showed the existence of two configurations for adsorbed CO, Greenler and co-workers characterized the adsorption of CO by IRAS on polycrystalline metals [6, 7].

Hayden and Bradshaw then reported, in 1983, an IRAS study of the adsorption of CO on Pt(111) [8]. By combining IRAS characterization and thermodesorption, they

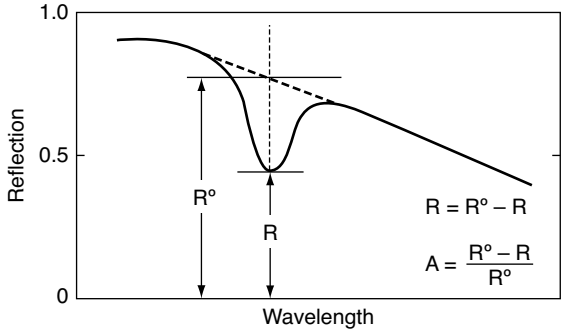


Figure 7.1 Definition of the absorption factor, *A*, and change in reflectance, ΔR, upon light absorption by an adsorbate. Reproduced with permission from [2].

confirmed the existence of linear and bridge adsorption sites for CO; moreover, the high resolution of IRAS, compared with that of HREELS, enabled them to identify two different CO species in bridge positions, which were assigned to CO in twofold bridge and threefold hollow sites (1840–1857 and 1810 cm^{-1}, respectively); the shift of the absorption band observed in the linear region (2094–2110 cm^{-1}) was simply attributed to increased vibrational coupling, when the coverage increases (see Figure 7.2).

Hayden *et al.* then extended their investigation to the adsorption of CO on a stepped Pt surface, Pt(533); they identified two CO binding sites for the linearly bound configuration, one on steps and one on terrace atoms, characterized by different IR frequencies and heats of adsorption [9]. This was a very innovative and relevant result because they were obtained on a Pt surface which exposed the same sites as those of catalytic Pt nanoparticles at their edges, corners, or terraces. Note that, unlike on Pt (111), no bridging CO species was observed on this stepped surface.

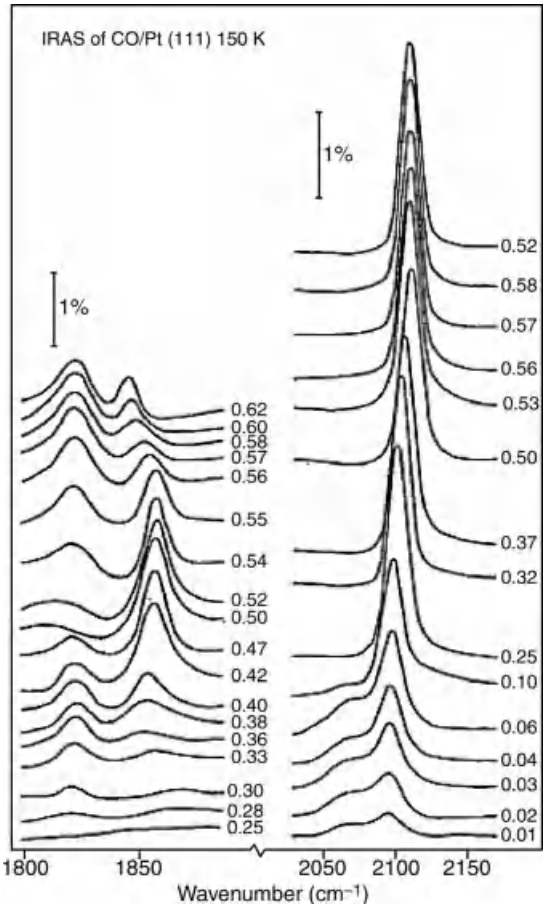


Figure 7.2 IRAS spectra of CO adsorbed on Pt(111) at 150 K. The numbers correspond to the coverage values deduced from temperature-programmed desorption data. Reproduced with permission from [8].

In 1982, Hoffmann rehearsed, in a very comprehensive review, the basic principle of IRAS and its application to the characterization of CO adsorption on metals [10]; he also presented some examples of experimental setups and results dealing with CO on Pd, Ru, and Pt of various orientations. As an example, by citing the studies of Behm *et al.* [11] and Ortega *et al.* [12], the review correlated IRAS and LEED characterization of CO on Pd(100), showing the adsorption of CO in bridge positions, with a CO stretching shifting from 1895 to 1997 cm^{-1} when the coverage increased from almost zero to one monolayer. Also in the review, the pioneering work by Ortega, Bradshaw, Pritchard, and others, all dealing with CO on various metal single crystals, were presented and used to demonstrate the sensitivity of the CO stretching frequency to both the surface structure and coverage [12, 13]. The donation and back-donation phenomenon associated with the CO bonding, similarly to what happens in metal carbonyls, was said to account for the shift of the CO stretching band. This early paper [10] also presented some experimental considerations explaining how to optimize various experimental parameters to achieve the high sensitivity and stability required to detect such small numbers of molecules as fractions of a monolayer on a 1 cm^2 area of surface.

For a diatomic molecule such as CO, the significant frequency shifts induced either by bonding on either on-top or bridging sites, or by increasing surface concentration, have been explained by a combination of dynamic coupling and substrate-mediated interactions; these two contributions to the coverage-dependant shift may be separated by using ^{12}CO–^{13}CO isotopic mixtures [14]. In this way, Hollins and Pritchard showed and explained the exceptional behavior of copper, for which the IR spectra of CO adsorbed on Cu(111) show very little coverage dependence of frequency [15]; they proved the existence of dipole coupling between CO molecules, balanced by an opposing chemical shift; this original behavior was explained by the copper electronic structure which favors π-bonding and thus lowers the extent of σ-donation.

Finally, Hoffmann [10] presented several examples in which the CO absorption band displayed some asymmetry; this was interpreted as CO growth in the form of islands, thus exposing two types of CO environments, at the center and at the edges of the islands, as on Ru(001) or Pt(001) [16, 17]. The IR signature thus became a way to characterize CO growth mode and surface structure.

Theoretical considerations, and more recent experimental considerations for IR spectroscopy in the IRAS configuration, were well explained by Bradshaw and Schweizer in 1988 [18]. They also presented some systems involving molecules other than CO, such as hydrogen on W and Si surfaces, and the first IRAS study of formic acid decomposition on Cu(110) (see below) and ethylidyne formation on Pt(111).

7.2 Principle of IRAS

The vibrational excitation of molecules by IR light is based on the coupling of the electric field of the light with the dipole moment of the molecule. For a vibrational

transition leading to the transition dipole moment, $\partial\vec{\mu}/\partial q$, the intensity I of absorption of IR light by this transition is given by

$$I \propto \left(\frac{\partial\vec{\mu}}{\partial q}\vec{E}\right)^2 = \frac{\partial\mu^2}{\partial q}E^2\cos^2\theta \tag{7.2}$$

where $\vec{E}$ is the electric field of the IR light and $\partial\mu$ the transition moment dipole.

The important consequences of this relation are the following:

1) The transition dipole moment must be non-zero to have a contribution to the IR absorption spectrum.
2) The intensity of absorption is governed by the amplitude of the electric field and its direction with respect to the transition moment dipole.

Let us now consider the specular reflection of an electromagnetic plane wave on a metal surface. The process of reflection can be analyzed by considering the behavior of the electric field for two linear polarizations; an incident wave of any direction can be decomposed into two components:

- an s component whose electric field is parallel to the surface and normal to the wave direction of propagation
- a p component normal to both the s component and the wave direction of propagation (see Figure 7.3).

The process of reflection changes both the magnitude and the directions of the electric fields associated with the s and p components.

The reflection process can be treated theoretically using Fresnel's equation, which gives the reflected intensities R_p and R_s and the phase shift Δ (change of direction) of the two polarizations as a function of the optical properties of the substrates (refractive index n and absorption coefficient k):

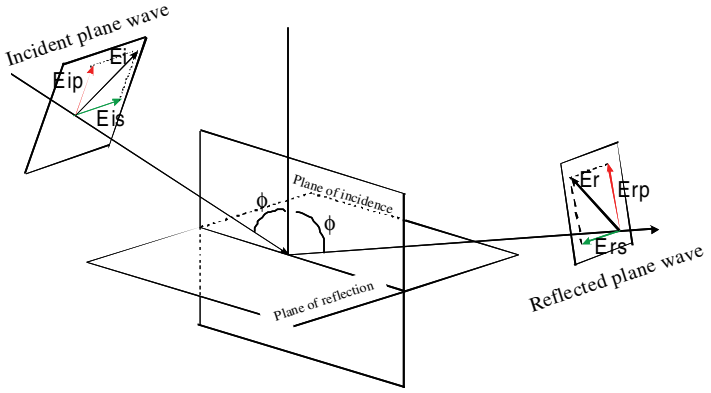


Figure 7.3 Geometry of the electric field vector of s- and p-polarized light incident on a surface at an angle ϕ.

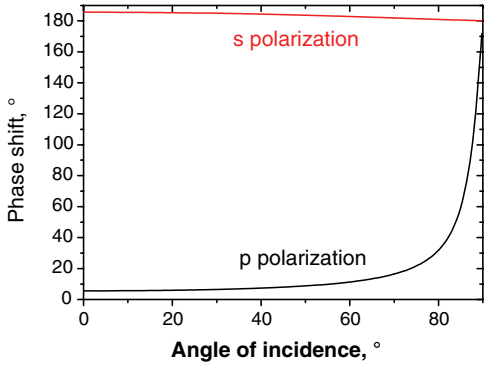


Figure 7.4 Phase shift Δ of the s- and p-polarization of the IR light on reflection from a metal surface as a function of the incidence angle ϕ.

$$R_p = \frac{(n - \sec\phi)^2 + k^2}{(n + \sec\phi)^2 + k^2} \tag{7.3}$$

$$R_s = \frac{(n - \cos\phi)^2 + k^2}{(n + \cos\phi)^2 + k^2} \tag{7.4}$$

$$\tan\Delta = \frac{2k\tan\phi\sin\phi}{\tan^2\phi - (n^2 + k^2)} \tag{7.5}$$

which are Fresnel's equations for $n^2 + k^2 \gg 1$ (case of metal substrate).

Phase shifts of the electric fields upon reflection on a surface with metallic properties, resulting from Fresnel's equation, are given in Figure 7.4. The phase shift of the s component is almost equal to 180° whatever the incident angle, thus giving a vanishing electric field at the surface (destructive interference). On the other hand, the phase shift of the p component depends on the angle of incidence; the combination of the incident, near-grazing incidence, electric field, and the reflected field yields an enhanced resulting electric field in the direction perpendicular to the surface (constructive interference). This is illustrated in Figure 7.5, which shows the resulting light intensity in the vicinity of the surface for s and p polarizations as a function of the angle of incidence.

Keeping in mind Eq. (7.2), and its consequence upon the electric field amplitude and direction, one can understand that specular reflection of IR light on a metallic substrate at grazing incidence is associated with a high sensitivity for molecules in the vicinity of the surface provided that transition dipole moments are not parallel to the surface.

Obtaining an IRAS spectrum thus implies recording the reflectivity of the substrate, modified with adsorbates (sample spectrum), and normalizing it with the reflectivity spectrum that has been recorded on the clean surface (background spectrum), in order to eliminate the contribution of the surrounding gas phase.

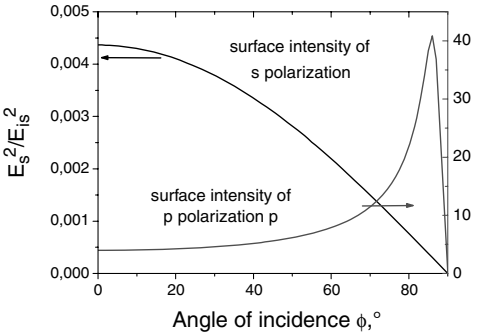


Figure 7.5 Resulting light intensity in the vicinity of the surface for s- and p-polarization as a function of the angle of incidence.

7.3 Principle of PM-IRAS

The main difficulty encountered in IRAS experiments is to achieve accurate control of the composition of the gas phase along the optical path. Unfortunately, drift and instability of the gas-phase composition, occurring between the background and the sample spectra, always exist and strongly affect the sensitivity of the IRAS experiment, especially for *in situ* characterizations.

As indicated earlier, this can be overcome by using a differential technique, for example, polarization modulation. This technique, PM-IRAS, exploits the fact that only p-polarized light yields a vibration signal of adsorbed molecules on metal surfaces.

The principle consists in modulating the polarization of the incident beam very quickly between the two linear polarizations, p and s, to obtain the differential reflectivity ($R_p - R_s$) and the total reflectivity ($R_p + R_s$) simultaneously.

The normalized differential reflectivity is characteristic of the PM-IRAS signal:

$$\frac{R_p - R_s}{R_p + R_s} \tag{7.6}$$

At a certain distance from the surface, molecules are randomly oriented and consequently absorb p- and s-polarized lights similarly, thus yielding no absorption band in the normalized differential reflectivity spectrum. Only molecules in the vicinity of the surface will contribute to the normalized differential reflectivity owing to the strong anisotropy of the electric field.

Figure 7.6 shows the PM-IRAS experimental setup. It is based on a Fourier transform (FT) IR spectrometer, equipped with a two electronic channel facility. The IR beam is first modulated in intensity by a Michelson interferometer (Fourier frequency ω_i). The beam is then focused on the sample after passing through a polarizer (giving p-polarization) and a photoelastic modulator (quick modulation of polarization at a fixed frequency, $\omega_m = 50$ kHz). After reflection on the sample, the IR beam is focused on a HgCdTe photoconductor detector.

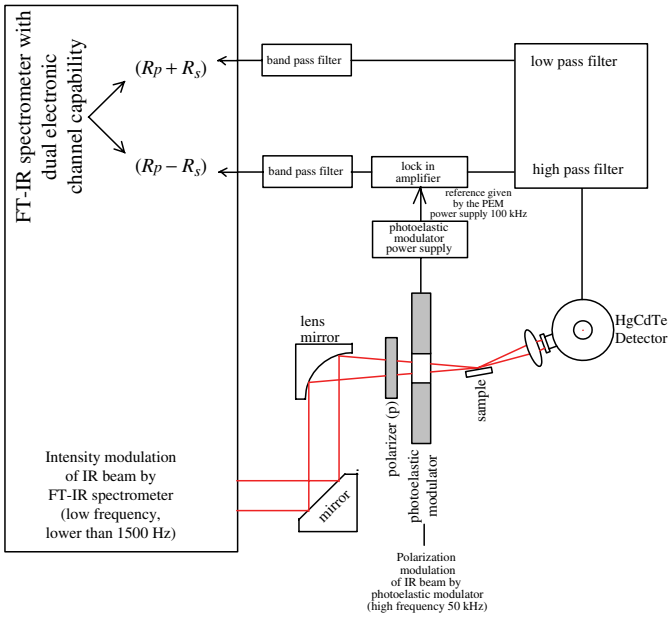


Figure 7.6 PM-IRAS experimental setup.

In this optical configuration, the intensity at the detector is given by

$$I_d = \frac{1}{2} \cdot \underbrace{CI_0(\omega_i)[(R_p + R_s) + (R_p - R_s) \cdot J_0(\phi_0)]}_{\text{A}} + \underbrace{CI_0(\omega_i)[(R_p - R_s)J_2(\phi_0)\cos(2\omega_m t)]}_{\text{B}} \tag{7.6}$$

where C is a constant depending on the transmission function of the optical setup, ϕ_0 is the amplitude of the function of polarization modulation, $\phi(t) = \phi_0 \cos \omega_m t$, $I_0(\omega_i)$ is the intensity of the light before polarization, and $J_n(\phi_0)$ is an n-order Bessel function at the amplitude ϕ_0 (these functions are related to the fact that the photoelastic modulator cannot modulate the polarization with the same efficiency for all light frequencies; experimentally, the modulation yield is adjusted by changing the amplitude of modulation ϕ_0).

Part A of Eq. (7.6) is modulated at the Fourier frequency (lower than 1500 Hz), and part B is modulated twice, at the Fourier frequency, $\omega_{i,}$ and the modulation polarization frequency, $2\omega_m$. There is roughly one order of magnitude difference between the ω_i and ω_m values, thus allowing splitting of parts A and B of the signal at the detector by using electronic filtering.

In the case of a metallic substrate, with optical properties leading to very close values of R_p and R_s, the interferogram is given by part A of Eq. (7.6), quasi-proportional to the sum, $R_p + R_s$. Part B is amplified and demodulated by a lock-in amplifier centered at the frequency $2\omega_m$, and is characteristic of the $J_2(\phi_0)(R_p - R_s)$ interferogram.

Finally, the two interferograms are processed simultaneously and Fourier transformed. The ratio of the two resulting spectra is proportional to the normalized differential reflectivity; it is the so-called PM-IRAS spectrum. Thus, the sensitivity of PM-IRAS on metals results from two physical effects:

- The enhancement of the electric field in the direction perpendicular to the substrate when the metal surface is illuminated with the p-polarized light.
- The R_p and R_s values are almost identical on a metal surface; this enables the IR absorption contributions from the surrounding gas phase to be eliminated in real time.

7.4 Applications of IRAS and PM-IRAS

Owing to its large IR cross-section, CO and its adsorption on metal surfaces gave rise to the first IRAS studies. CO adsorption has been characterized on various metals, such as Pt, Pd, and Cu, of various crystal line orientations, mostly under ultra-high vacuum (UHV) conditions. In this chapter, we will not go into detail into these studies, which really demonstrated the power of the IRAS technique in the 1970s, already mentioned earlier. Our attention will be focused on IRAS and PM-IRAS studies of organic monolayers, in particular of amino acids and of thioalkanes, ands of catalytic processes on metal surfaces, some involving CO, some dealing with other reactants, such as methanol and ammonia. Finally, examples of applications of IRAS and PM-IRAS to biointerface characterizations are given.

7.4.1 Formation of Self-Assembled Monolayers

On metal or thin oxide films, the formation of self-assembled monolayers (SAMs), and their reactivity or stability in various media, have often been studied by using PM-IRAS. SAMs on gold, resulting from the binding of thiols, are well-known examples of organized monolayers which enable one to functionalize surfaces and bind receptors in a controlled manner. The surface density, orientation, and organization of SAMs of alkanethiols on gold have been well characterized in a number of studies, IRAS and PM-IRAS techniques being particularly adapted to assess these parameters [19].

One of the first studies of alkanethiol SAMs on gold by IRAS was realized by Bain *et al.*, who found a correlation between the value of the CH stretching frequency and the layer crystallinity [20]. It was shown in particular that alkanethiols, $HS(CH_2)_nCH_3$, tend to form densely packed layers for $n \geq 10$ [20]. This ν_{CH} organization sensitivity is interesting when studying SAMs composed of a mixture of several alkanethiols of various chain lengths. An example is presented in Figure 7.7, where the ν_{CH} band is seen to increase and shift to lower wavenumbers when the fraction of mercaptoundecanoic acid ($n = 10$) increases in a mixture with mercaptohexanol ($n = 6$) [21].

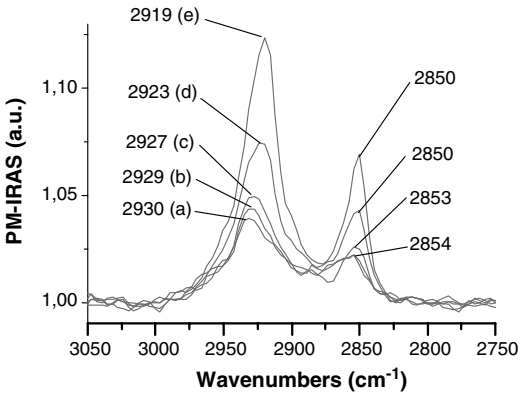


Figure 7.7 ν_{CH} spectral region for a mixture of mercaptoundecanoic acid (10 CH_2 groups) and mercaptohexanol (6 CH_2 groups) adsorbed on gold; the fractions of mercaptoundecanoic acid are equal to 0 (bottom spectrum), 25, 50, 75, and 100 (top spectrum).

Nuzzo *et al.*, by combining IRAS with XPS and ellipsometry, characterized monolayers of a series of $X(CH_2)_{15}SH$ alkanethiols ($X = CH_3$, CH_2OH, COOH, CO_2CH_3); they calculated the IR spectra and showed that the tilt angle of the alkyl chains from the surface can be deduced from the ν_{CH_3}/ν_{CH_2} intensity ratio [22]. Moreover, they concluded that, although the terminal groups adopt specific orientations at the ambient interface, their nature, acid or alcohol or even alkyl, has little effect on the CH chain organization.

There have been numerous papers reporting the adsorption of alkanethiols and thiols terminated by functional groups, and the major results were summarized in a review in 2005 [23].

On an aluminum oxide film, SAMs of an organic acid, octadecylphosphonic acid (ODPA), were characterized by PM-IRAS; in that case, the IR light is reflected at the surface of the underlying metal substrate [24], and, for comparison, monolayers of ODPA on a bulk crystal of aluminum oxide were analyzed by diffuse reflectance infrared Fourier transform (DRIFT) spectroscopy. Figure 7.8 displays the PM-IRAS and DRIFT spectra of ODPA layers on thin aluminum oxide films and on two Al_2O_3 single crystals respectively.

All spectra show that ODPA can indeed be adsorbed on Al_2O_3 surfaces. In the high-wavenumber region, the four bands are easily ascribed to the asymmetric and symmetric stretching bands of CH in CH_2 and CH_3 groups; the intensity ratio, $I(\nu_{CH_3})/I(\nu_{CH_2})$, higher than in bulk ODPA, suggests an organized layer of organic acid with a preferred upright position of the aliphatic chains; moreover, the peak ratio is an indicator of the mean inclination angle from the surface normal. This information could not be deduced from the DRIFT spectra. In the lower wavenumber region, where the phosphonic acid functionalities display IR signals, differences can be seen for ODPA adsorbed on thin oxide films or on bulk oxides. On the two amorphous films, and also on the (0001) crystal, the P = O IR band at $\sim$1200 cm^{-1}, in addition to the broad peak at 1000–1100 cm^{-1}, attributed to the symmetric and

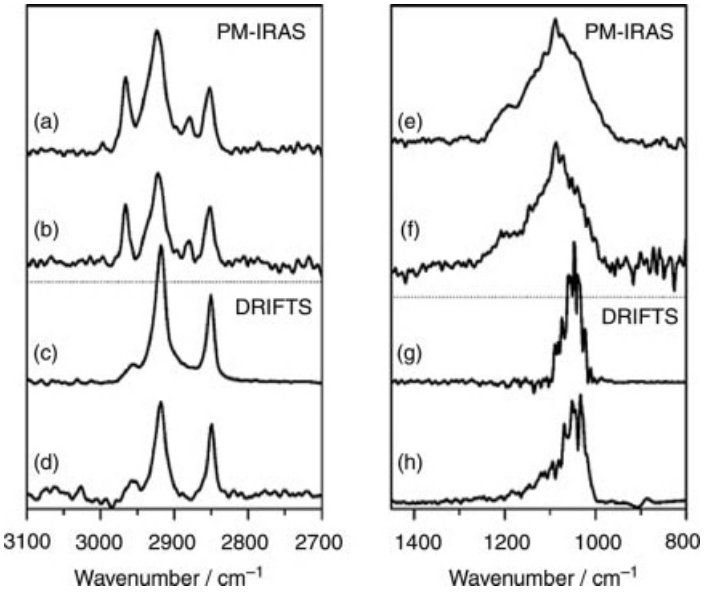


Figure 7.8 Upper spectra: PM-IRAS spectra of ODPA adsorbed on a thin aluminum oxide film (spectrum a, native grown oxide; spectra b, f, vapor-deposited aluminum layer on gold). Lower spectra: DRIFT spectra of ODPA on Al_2O_3(0001) and Al_2O_3(1-102) single crystals (spectra c, g, d, h). Reproduced with permission from [24].

asymmetric PO_3^{2-} stretches, indicate the adsorption of ODPA by two O atoms leaving the P = O bond intact; on the (1-102) single crystals, the disappearance of the P = O IR band suggests an ionic interaction between the PO_3^{2-}groups and the Al ions of the oxide. The two proposed modes of interaction are presented on Figure 7.9.

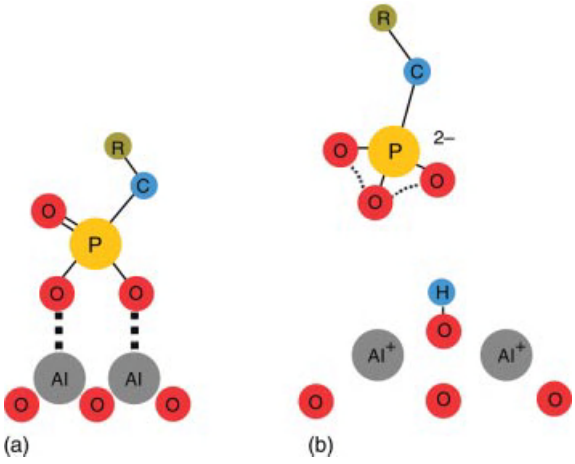


Figure 7.9 Models of interfacial bonding of a phosphonate group on Al_2O_3 surfaces: (a) on amorphous thin film or on the surface; (b) on an Al_2O_3 (0001) surface. Reproduced with permission from [24].

This example, in particular the differences observed in the PM-IRAS and DRIFT spectra on two types of aluminum oxide surfaces, demonstrate the power and respective interest of the two reflection configurations for IR spectroscopy.

7.4.2 Adsorption of Organic Small Molecules and Chirality

Surface science techniques [XPS, atomic force microscopy (AFM), IRAS, etc.] have been successfully applied to the characterization of organic monolayers at metal surfaces, in particular for describing the growth mode, the chemical state, and the geometry of amino acids, widely investigated by the groups of Raval [25], Liedberg [26, 27], and ourselves [28–32]. One of the most typical results concerns the adsorption of chiral amino acids on metal surfaces, which display a polymorphic behavior, and change their binding modes, orientation, and adsorption footprints with surface coverage. Let us take the example of alanine, the simplest chiral amino acid, the adsorption of which on Cu(110), has given rise to a detailed investigation, combining XPS, scanning tunneling microscopy (STM) and IRAS [33]. Figure 7.10 shows the IRAS spectra resulting from the interaction of alanine with Cu(110). Net changes in the absorption bands occur with increase in the coverage, indicating first that the molecule retains an alaninate form (no $\nu_{C=O}$ stretch at $\sim$1720 cm^{-1}), and second that the adsorption mode changes on increasing the coverage; at low coverage, only the symmetric band of carboxylate groups could be observed, and with rather weak intensity, suggesting a molecule adsorbed with the COO^- group symmetric with respect to the surface but tilted towards the surface plane. More information was deduced from the NH_2 wagging (1145 cm^{-1}) and scissoring deformation (1576 cm^{-1}), and from the CH_3 vibration modes, leading to the geometry presented in Figure 7.10g. This geometry corresponds to a chiral triangular footprint on the surface, maintaining the inherent chiral center of the molecule; the surface created by adsorption of (*S*)- or L- alanine in this form will thus lead to a homochiral adlayer. The adsorption phase is modified on increasing the coverage and temperature, as proved by several spectral changes. The main changes are the appearance of a new absorption signal, at 1620 cm^{-1}, attributed to the asymmetric carboxylate stretch, ν_{COO^-}, revealing the emergence of a new alaninate species, with only one oxygen of the carboxylate group bound to the surface (see Figure 7.10h). Warming the sample to 470 K does not change the IR signature of the adsorbed molecules, confirming the stability of the two identified species. Further annealing induces substantial changes, which can be explained by a progressive reorientation of the adsorbed alaninates to a form involving the two O atoms of the carboxylate groups, similar to that appearing at low coverage. The detailed spectral analysis of the system and of its dynamics can be elsewhere [33].

Another example of well-defined adsorption and dynamics of an adsorbed phase, elucidated by IRAS analyses, is that of adsorption of succinic acid on Cu(110) [34]. Figure 7.11 shows the spectra and the proposed geometries of the species resulting from the interaction of succinic acid with the Cu(110) surface.

At low coverage ($\theta \leq 1/6$ monolayer), the spectra (a and b) display one main and broad signal at 1408–1425 cm^{-1}, the symmetric COO^- stretch; the double band is

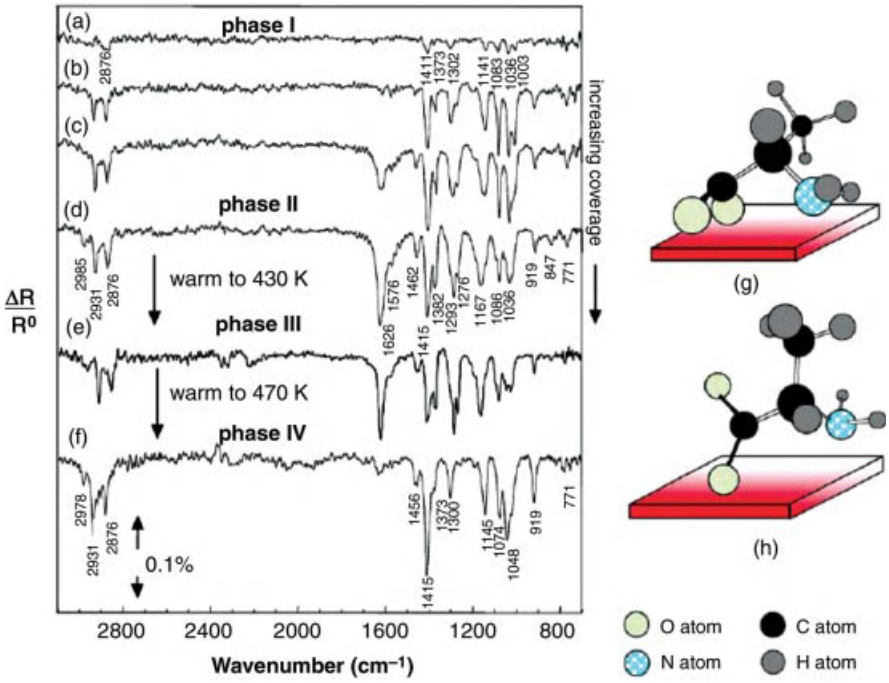


Figure 7.10 IRAS spectra of (*S*)-alaninate species adsorbed on Cu(110), with increasing coverage (a–d) at 300 K, and upon heating the sample (e, f). (g, h) Schematic representations of alanine molecules adsorbed on Cu(110) in the alaninate form. Reproduced with permission from [33].

explained by the coupling between the COO^- groups of two succinate molecules; the molecules adsorb and form bisuccinate species. Moreover, the absence of asymmetric COO^- stretching, expected at $\sim 1600\,cm^{-1}$, indicates symmetrical binding of the two oxygen atoms of the COO^- groups with the surface. Schematic representations of the adsorbed molecules, consistent with the IRAS data, are shown in Figure 7.11.

At higher coverages (spectra c and d), the main change is the appearance of an IR absorption band at $1712\,cm^{-1}$, indicating the presence of a protonated acid species; $1712\,cm^{-1}$ is a low value for an acidic C = O stretch, suggesting the existence of strong H-bondings between acid groups, probably involving two different molecules of succinic acid (Figure 7.11e and f). A detailed description of the IR signatures and their assignments can be found elsewhere [34]. Thus, spectrum c suggests, at elevated coverage, the coexistence of both bisuccinate and monosuccinate adsorbed species. Note that warming the sample obviously leads to conversion of part of the monosuccinate to thermodynamically stable bisuccinate species again (decrease in the band at $1712\,cm^{-1}$). The well-defined bonding of the two chemical forms of the molecule was shown to determine the self-assembly structure, in particular the creation of surface chirality by formation of two organized domains of adsorbed bisuccinates separated by a mirror plane; conversely, no chirality was induced by the monosuccinate adsorbed forms.

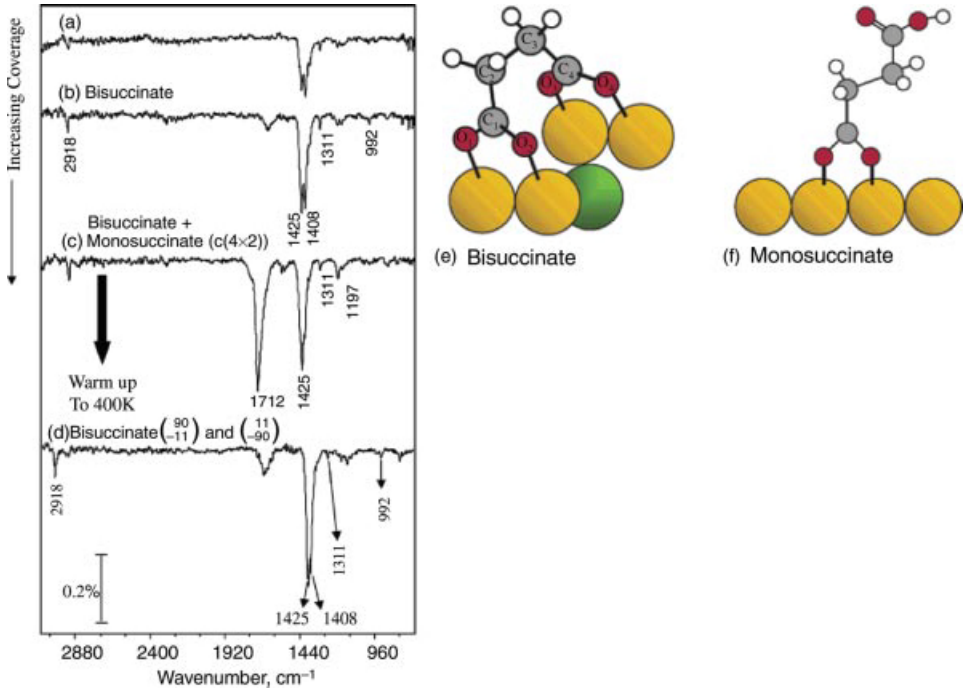


Figure 7.11 IRAS spectra of succinate species adsorbed on Cu(110), with increasing coverage (a, b) at 300 K, and upon heating the sample (c, d). (e, f) Schematic representations of succinic acid molecules adsorbed on Cu(110) in the succinate form. Reproduced with permission from [34].

7.4.3
Monitoring Surface Reactivity and Catalysis

7.4.3.1 Oxidation of CO on Ru

One of the first examples of the catalytic mechanism elucidated by using FT-IRAS was that of CO oxidation on Ru(001), the subject of pioneering work by Peden *et al*. in 1991 [35]. The question addressed by Peden *et al*. was the surprising and anomalous behavior of Ru in the oxidation of CO; in fact, Ru is the only transition metal capable of oxidizing CO on oxygen-rich surfaces. To elucidate the mechanism of CO oxidation, the authors monitored both the formation of CO_2 in the gas phase and the nature of the adsorbed CO species at various CO/O_2 ratios as described below.

An Ru(001) surface was subjected, at 500 K, to 350 Pa of CO and O_2 pressures varying from 700 to 7 Pa. Taking advantage of (i) the wavenumber shift of adsorbed CO stretching in the vicinity of oxygen (see Figure 7.12) and (ii) the adsorption of gas-phase CO_2 at a well-separated wavenumber, the authors correlated the reaction kinetics with the composition of the adsorbed phase. They found that the reactivity was the highest when almost no chemisorbed CO was detected. This was simply accounted for by an Eley–Rideal (ER) mechanism between gas-phase or weakly adsorbed CO and chemisorbed oxygen, the latter suppressing CO adsorption.

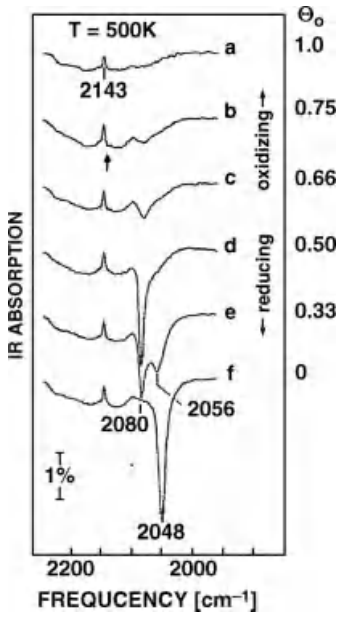


Figure 7.12 IR spectra of the C–O stretching region during the reaction of CO oxidation at 500 K on Ru(001) for a constant partial pressure of CO (350 Pa) and oxygen partial pressures of (a) 700, (b) 350, (c) 130, (d) 13, and (e) 7 Pa O_2; (f) pure CO. Reproduced with permission from [35].

Conversely, under reducing conditions (CO/O_2 ratio >2), both oxygen and CO are chemisorbed, favoring a Langmuir–Hinshelwood (LH) mechanism.

In the reaction corresponding to Figures 7.12 and 7.13, the partial pressure of oxygen was varied, ranging from oxidizing conditions (700 Pa O_2, spectrum a) to a

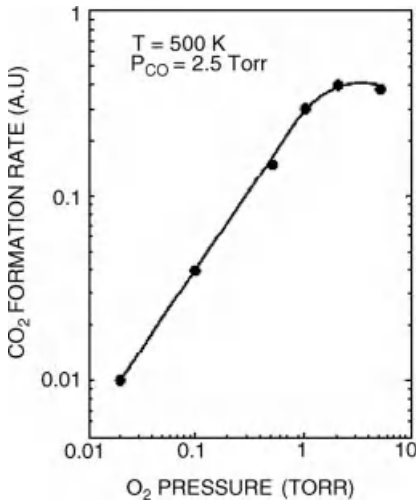


Figure 7.13 Rate of CO_2 formation, from the CO_2 gas-phase IR region; reaction at 500 K in a mixture of 350 Pa CO and various pressures of oxygen. Reproduced with permission from [35].

strongly reducing gas composition (7 Pa O_2, spectrum e). The CO surface coverage could be determined from the C−O stretching frequency (see features on the right side of Figure 7.12). The presence of oxygen in the gas phase induces both a shift and a decrease of the band at ~2050 cm^{-1}, until it totally disappears, being replaced by a new band at 2080 cm^{-1}. Figure 7.13 indicates that the rate of CO_2 formation increases with the pressure of oxygen until it reaches a saturation value, for high, or full, oxygen coverage of the surface. In other words, under strongly oxidizing conditions, the rate of CO_2 formation is the highest and no CO was detected on the surface! This is typical of an ER mechanism, implying the reaction of CO from the gas phase, or weakly adsorbed CO.

Note that the ER mechanism was, until this study, controversial; in particular, some argued that an LH mechanism could still prevail just by occurring on the surface defects. This was rejected by the present study, showing similar activation energies on single crystals and on supported Ru; compelling arguments in favor of an ER mechanism arose from the *in situ* characterization of the surface in the presence of an oxidizing atmosphere (CO/O_2 ratio ~1). Note that these investigations were successful thanks to a combination of surface science studies under UHV conditions with *in situ* IRAS reaction studies at "high" pressures (a few hundred pascals).

7.4.3.2 **CO hydrogenation on Ru**

Another reaction, the hydrogenation of CO to give oxygenates, was elucidated in the same period by Hoffmann and co-workers using FT-IRAS [36, 37]. The water gas shift reaction, catalyzed by copper, is known to be promoted by alkali, and, only in that case, could the formation of a formate intermediate be evidenced. By studying the decomposition of formic acid on clean Ru(001) and potassium-promoted Ru (001), the authors characterized a KOOCH surface species, in the presence of the reacting phase, thanks to the appearance of ν_{CH}, ν_{OCO}, and δ_{OCO} vibrations at 2782, 1363, and 761 cm^{-1} respectively; the CH stretching frequency is characteristic of the interaction of the species with potassium atoms. On clean Ru, the CH frequency is much higher, 2939 cm^{-1} (see Figure 7.14). These data demonstrated that potassium stabilizes the formate intermediate and possibly changes the pathway of its further decomposition, thus explaining the change in selectivity of the $CO + H_2$ reaction [36].

7.4.3.3 **Vinyl Acetate Synthesis Reaction on Pd**

More complex, the mechanism of the vinyl acetate synthesis reaction was recently elucidated by Gao *et al.* using FT-IRAS on a model palladium surface [38]. For this reaction, involving acetic acid, ethylene, and oxygen, two mechanisms have been proposed, either the coupling of ethylene with chemisorbed acetate, leading to an acetoxyethyl–Pd intermediate and then to vinyl acetate, or the formation of a vinyl–Pd intermediate which then reacts with a surface acetate species. First, the reaction was performed by reacting ethylene ($P = 2.6 \times 10^{-5}$ Pa) with adsorbed methyl acetate

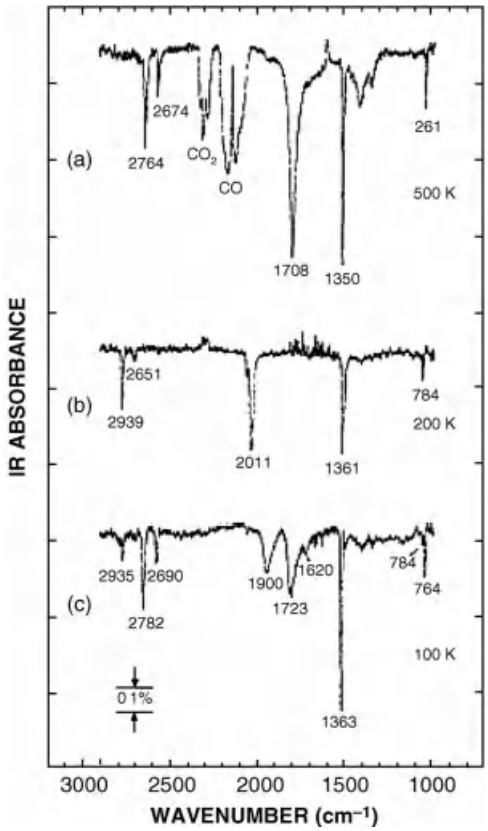


Figure 7.14 FT-IRAS spectra of formate species (a), during the CO + H_2 reaction on a K–Ru(001) surface, (b) upon decomposition of formic acid on clean Ru(001), and (c) from the decomposition of formic acid on a K–Ru(001) surface. Reproduced with permission from [37].

species. The resulting spectra are shown in Figure 7.15 at time 0, 500, and 1250 s. One obviously sees a progressive decrease in the IR signal at 1414 cm^{-1}, an acetate-specific vibration mode. The spectra also show increases in two features, one at 1327 cm^{-1}, ascribed to the formation of ethylidyne, and the other at 1788 cm^{-1}, in the C = O stretch region. Having checked that heating an acetate-covered surface in the absence of ethylene does not yield such a signal, the authors used isotopically labeled reactants, C_2D_4, CH_2CD_2, and CHDCHD, in order to interpret this 1778 cm^{-1} vibration band, and unravel the mechanism. Testing the reaction with deuterated ethylene showed significant variations in the reaction rate, thus proving that hydrogen is involved in the rate-determining step; moreover, the position of the D atoms in the molecule influences the reaction rate; this excludes the second mechanism. Finally, the reaction of ethylene with adsorbed acetate induced the growth of an IR signal at 1718 cm^{-1} that could be attributed to none of the reactants.

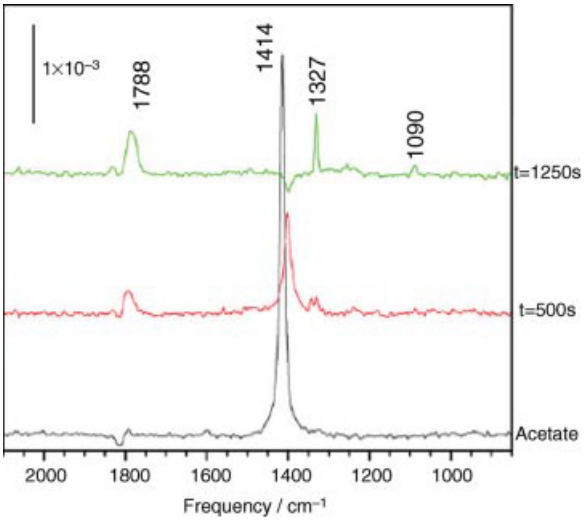


Figure 7.15 IR spectra of acetate species on Pd(111) reacted with ethylene at a pressure of 2.6×10^{-5} Pa at 327 K for various times, collected for 1000 scans to improve the signal-to-noise ratio. Reproduced with permission from [38].

This band was attributed to the C = O stretch of an acetoxyethyl–Pd intermediate, resulting from the insertion of ethylene into the acetate–Pd bond, thus confirming that the former mechanism is the most likely!

7.4.3.4 Oxidation of NH_3 and reduction of N_2O by NH_3 on Cu

Another catalytic study using FT-IRAS was reported by our group, namely the oxidation of NH_3 by oxygen and the closely related reduction of N_2O by ammonia. The ultimate goal was the understanding of the mechanism of N_2O decomposition and catalytic reduction of N_2O by NH_3 on a Cu(110) single-crystal surface [39, 40].

A Cu(110) sample was first subjected to pure ammonia, $P = 1.3 \times 10^{-3}$ Pa, and then to oxygen, $P = 1.3 \times 10^{-3}$ Pa; the PM-IRAS spectra, acquired in the presence of the gas phase to limit the desorption of weakly bound intermediates, are shown in Figure 7.16. The first-appearing band at 1200 cm^{-1} is the symmetric deformation of an ammonia molecule adsorbed in a C_{3v} configuration; the signal growing at 2180 cm^{-1} is attributed to a polarized dinitrogen species resulting from the dehydrogenation of NH_3. Vibration bands, growing at 1430 and 1550 cm^{-1}, were attributed to NH imide and NH_2 imine intermediate species. Another intermediate, H_2NO, identified by an IR signal at ~1800 cm^{-1}, was evidenced when the reaction was run at lower pressure (4×10^{-5} Pa). Interestingly, the involvement of adsorbed oxygen in the formation of these intermediates was demonstrated by probing the reaction of NH_3 with an O-modified Cu(110) surface (see Figure 7.17), whereas such a reaction did not take place on a fully oxidized Cu_2O surface.

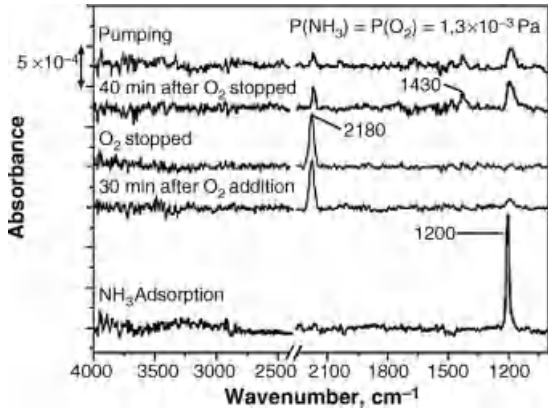


Figure 7.16 IRAS spectra recorded on Cu(110) in the presence of NH_3, $NH_3 + O_2$, and in vacuum. Reproduced with permission from [40].

The reduction of N_2O was then investigated in the presence of NH_3 and oxygen on the same Cu(110) surface [39]. Whereas XPS results enabled us to identify the active surface as being a mixture of metallic Cu and Cu_3N, FT-IRAS showed the formation of NH_2 and NH species (bands at 1550 and 1440 cm^{-1}, respectively), and of two $N_2^{\delta-}$ species (absorption bands at 2170 and 2204 cm^{-1}), which were interpreted by comparing two different experimental cases. When $N_2^{\delta-}$ species are formed by oxydehydrogenation of NH_3, N, NH, and NH_2 surface intermediates were identified, and an N−N stretching close to 2170 cm^{-1} was observed, attributed to negatively charged $N_2^{\delta-}$ species (Figure 7.18, lower spectrum). The N−N stretching frequency is lower for N_2 adsorbed on a transition metal compared with the same N−N stretch

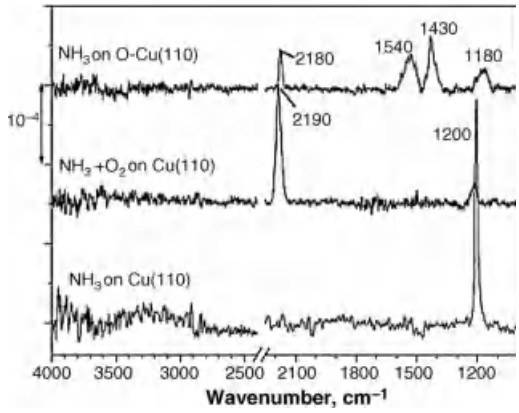


Figure 7.17 IRAS spectra recorded on Cu(110) after 50 min NH_3 ($P_{NH_3} = 10^{-3}$ Pa), $NH_3 + O_2$ ($P_{NH_3} = P_{O_2} = 10^{-3}$ Pa), and on Cu(110)c(6 × 2)-O in the presence of NH_3 ($P_{NH_3} = 10^{-3}$ Pa). Reproduced with permission from [40].

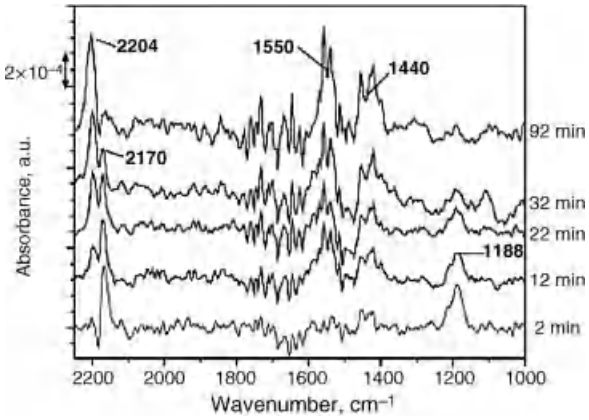


Figure 7.18 IRAS spectra of Cu(110) surface recorded in the presence of N_2O and NH_3 at room temperature ($P_{N_2O} = P_{NH_3} = P_{O_2} = 1.3 \times 10^{-3}$ Pa). Reproduced with permission from [39].

in the N_2O gas-phase species; this is due, as for CO, to the electron back-donation from the metallic d orbitals to the empty π^* orbitals of N_2O. Conversely, when $N_2^{\delta-}$ is formed by decomposition of N_2O, it is adsorbed in the vicinity of electron-accepting O species, which induce a decrease in the back-donation towards the antibonding orbitals of the N−N bond, thus explaining the higher frequency value (see Figure 7.19, upper spectrum). The experiment, corresponding to the intermediate spectrum in Figure 7.19, results in the coexistence on the surface of $N_2^{\delta-}$ species in the vicinity of NH_s species, or of oxygen, whether they result from NH_3 dehydrogenation or N_2O decomposition, respectively. This study demonstrated that N_2O decomposed into N_2 and O species during the selective catalytic reduction (SCR) reaction, leading to several adsorbed surface species, N, NH, NH_2 and $N_2^{\delta-}$, which

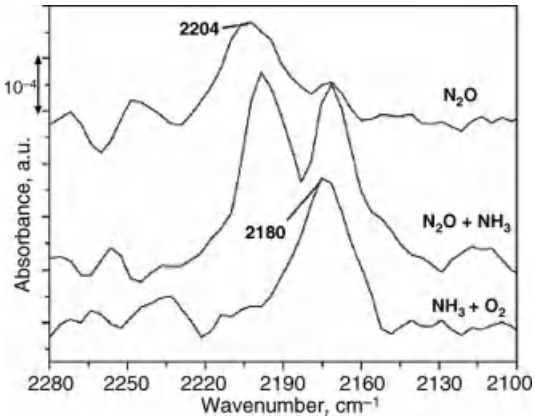


Figure 7.19 IRAS spectra of Cu(110) surface recorded in the presence of N_2O, $N_2O + NH_3$ and $NH_3 + O_2$ ($P_{N_2O} = P_{NH_3} = P_{O_2} = 1.3 \times 10^{-3}$ Pa) after 20 min of exposure at room temperature. Reproduced with permission from [39].

were identified by FT-IRAS in the presence of the reactants at room temperature. The most important result is that N_2 can be considered as a powerful IR probe to characterize the surrounding environment of surface sites that cannot be identified in any other way.

These few examples, although demonstrating the great advances brought by FT-IRAS towards the understanding of various reaction mechanisms, all correspond to reaction processes measured under rather low pressure (usually less than 10^{-3} Pa).

A few years later, the PM-IRAS technique was set-up and applied to the investigation of surface characterization in the presence of higher pressures (up to atmospheric pressure), and with much better sensitivity (see the principle of the technique in Section 7.3).

As described in the experimental part, infrared signals arising from gas-phase absorption are subtracted thanks to the use of s- and p-polarized light beams and a demodulator/multiplexer device. An important advantage of the PM-IRAS technique over the classical IRAS method is that the signal is directly extracted from the $\Delta R/R$ data, thus avoiding the use of a reference spectrum recorded at the beginning of the whole experiment. The following examples describe the application of PM-IRAS to the study of catalytic processes under reasonable pressures (up to atmospheric pressure), or probing biointerfaces either in the liquid phase or in air after immersion in solution.

7.4.3.5 **Decomposition of Methanol on Pd**

One of the first results was described by Rodriguez de la Fuente *et al.* in 2004 and concerns the mechanism of methanol decomposition on Pd(111) [41]. The Pd(111) surface was first characterized by XPS after adsorbing 15 L of CH_3OH (L = langmuir = 1.33×10^{-4} Pa s^{-1}), revealing a carbon signal whose shape and intensity depended very much on the sample temperature. Because CH_3OH, CH_xO, and CO, possibly formed on the surface, could not be differentiated by XPS, further experiments were carried out by PM-IRAS. The Pd(111) sample, subjected to 6 L of methanol, leads to the spectrum in Figure 7.20, with typical absorption bands at 2830, 1455, 1130, and 1045 cm^{-1}, strongly suggesting the presence of CH_3OH on the surface; note that the signal from molecular CO, at ~2040 cm^{-1}, is very weak. Carbonaceous residues would therefore originate from these precursors rather than from CO dissociation. This was confirmed by the PM-IRAS and sum frequency generation (SFG) spectra of the surface recorded in the presence of 1.7×10^4 and 1×10^4 Pa of CO (see inset in Figure 7.20); the two signals are those of hollow (1885 cm^{-1}) and on-top (2099 cm^{-1}) bonded CO, but no decrease in signal intensity was observed with time as would have been expected from CO dissociation. This conclusion, that is, no surface deactivation by CO, is of primary importance for catalytic studies.

7.4.3.6 **Dissociation of NO on Rh**

Soon afterwards, Wallace *et al.* described the mechanism of NO dissociation on Rh (111), paying special attention to the role of adsorbed oxygen and nitrogen on the formation of adsorbed NO surface structures [42]. A significant number of studies have been carried out on model Rh surfaces, both experimental and theoretical, and

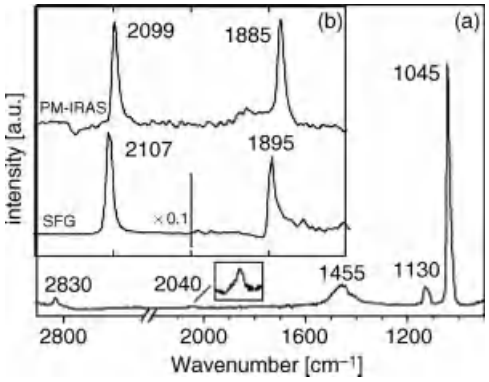


Figure 7.20 (a) PM-IRAS spectrum of 6 L CH_3OH on Pd(111) at 100 K. (b) PM-IRAS and SFG spectra of 1.7×10^4 and 1×10^4 Pa CO on Pd(111) at 190 K. Reproduced with permission from [41].

there remains some disagreement concerning the failure to account for dissociated N and O species in the structural models. PM-IRAS experiments were then used to characterize NO dissociation at elevated pressure (10^{-4} Pa); the spectra, acquired after dosing 300 L of NO on Rh(111), revealed a change in the adsorption site of NO from threefold hollow sites (1650 cm^{-1}) to on-top sites (1850 cm^{-1}) when the temperature increased (see Figure 7.21). In a further experiment, the sample was subjected to a second 20 L of NO, involving the growth of the on-top feature,

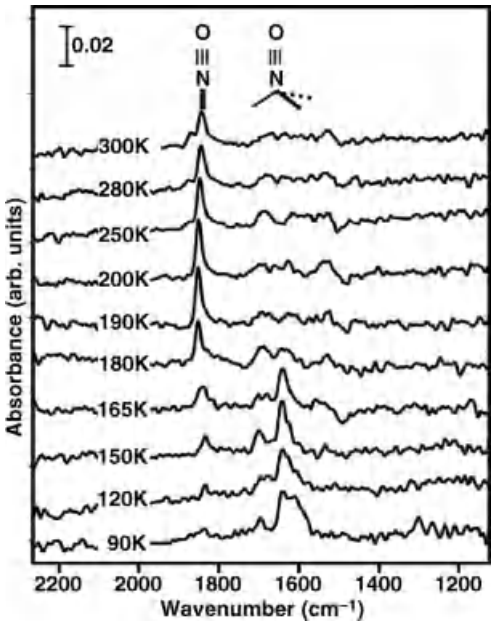


Figure 7.21 PM-IRAS spectra of NO on Rh(111), after dosing 300 L of NO at various temperatures. Reproduced with permission from [42].

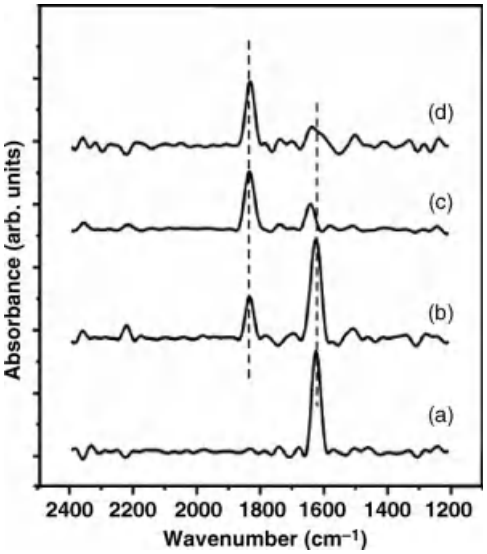


Figure 7.22 PM-IRAS spectra of NO (2 L) on Rh(111) pretreated with various coverages of oxygen: (a) no O_2, (b) 2, (c) 4, and (d) 6 L of O_2. Reproduced with permission from [42].

evidencing that dissociation of NO occurs, thus occupying the threefold sites. With time, the features corresponding to the threefold hollow sites vanish and the only signal that appears is that of molecular NO on on-top sites; this result suggests that dissociation of NO likely takes place on the threefold hollow sites which become filled by O_{ads}, as a product of NO dissociation. One may then wonder how these atomic oxygen species may influence NO dissociation. To address this question, the Rh(111) surface was subjected to various doses of oxygen before NO; in the absence of oxygen, NO adsorbs only on threefold hollow sites (spectrum a in Figure 7.22), whereas pretreatment with oxygen induces the growth of an on-top feature with a simultaneous decrease in the hollow site signal (spectra b–d in Figure 7.22), suggesting that O_{ads} is progressively formed on the threefold sites and coexists with adsorbed NO on the on-top sites. Eventually, PM-IRAS allowed the characterization of the surface in the presence of 133 Pa of NO, showing that the surface was mainly covered with on-top NO (see Figure 7.23). These PM-IRAS studies produced important results regarding the dissociation of NO on Rh(111).

7.4.3.7 **Reactivity/Storage of NO on Metal and Oxide Surfaces**

More recently, our group investigated the reactivity of NO on a thin film of alumina by combining *in situ* PM-IRAS and quartz crystal microbalance (QCM) measurements, using the setup shown in Figure 7.24 [43, 44].

PM-IRAS, performed immediately after exposure, at room temperature, of a hydroxylated alumina thin film to NO diluted in N_2 (900 ppm of NO under 2×10^5 Pa total pressure) revealed the formation of nitrite surface species (absorption bands

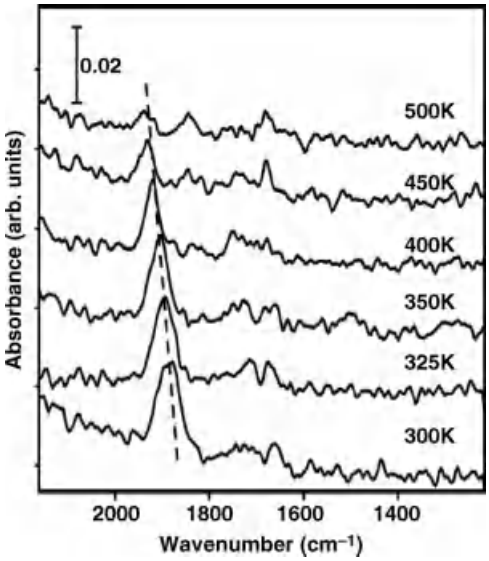


Figure 7.23 PM-IRAS spectra of NO, during exposure of an Rh(111) surface to 1.3×10^2 Pa of NO, at 300 K. Reproduced with permission from [42].

peaking at 1235, 1330, 1470, and 1635 cm^{-1} in Figure 7.25), assigned to $\nu_{asHONO,\ Al–ONO–Al\ and\ Al–ONO}$, $\nu_{sAl–ONO–Al}$, $\nu_{s\ Al–ONO}$, and δ_{OH}, respectively. In the OH stretching region of absorption (not shown), the exposure of the Al sample to the NO–N_2 mixture results in a slight increase in the 3600–2500 cm^{-1} bands and a decrease in the sharp band peaking at 3660 cm^{-1}.

In a further experiment, oxygen was admitted on to the nitrite-modified sample, but oxygen alone hardly reacts with adsorbed nitrites (no spectral changes).

Conversely, the introduction of O_2 and NO in N_2 leads to the rapid transformation of nitrites to nitrates, as evidenced by the major changes observed in the

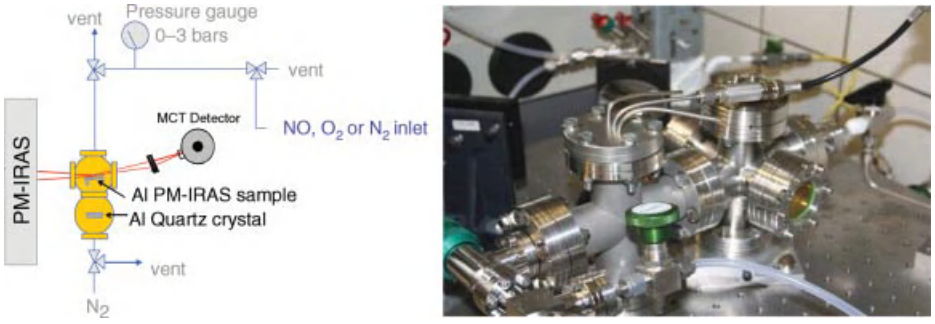


Figure 7.24 Experimental set-up for simultaneous PM-IRAS and QCM analyses under a gas flow: schematic representation and photograph of the set-up.

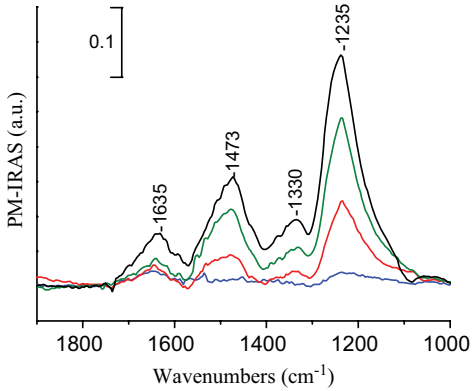


Figure 7.25 PM-IRAS spectra of NO, adsorbed on a hydroxylated Al_2O_3 thin film, from an NO–N_2 mixture (*in situ* measurements) after 1 h, 5 h, 19 h, and 6 days of contact, from the bottom to up.

1900–1100 cm^{-1} absorption region (see Figure 7.26). The band peaking at 1235 cm^{-1} (ν_{NO} in NO_3^- species) decreases, whereas several strong contributions appear at 1320, 1430, 1477, 1531, and 1650 cm^{-1} which grow continuously from 0 to 16 h of exposure to the NO + O_2/N_2 mixture.

Two other contributions peaking at 1595 and 1874 cm^{-1} also appear after 6 h of exposure. An isosbestic point is observed at 1260 cm^{-1} between the decrease in the contribution peaking at 1235 cm^{-1} and the increase in that peaking at 1320 cm^{-1}; the high reactivity of adsorbed nitrites, when subjected to a mixture of NO + O_2, was attributed to the formation of NO_2 in the gas phase, which is reactive. In addition,

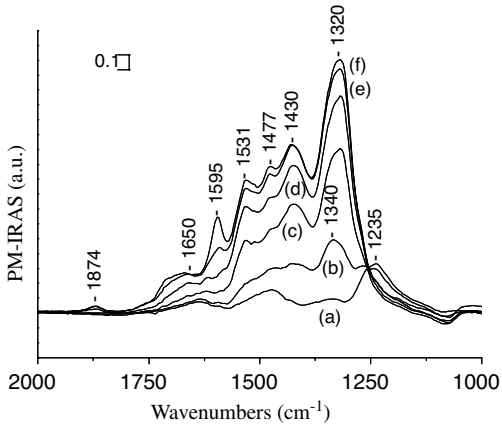


Figure 7.26 PM-IRAS spectra of NO, adsorbed on a hydroxylated Al_2O_3 thin film, from an O_2–NO–N_2 mixture (*in situ* measurements). PM-IRAS spectra of a hydroxylated sample exposed to an NO–N_2 mixture followed by addition of O_2 (7000 ppm) after (a) 6 days of NO exposure, (b) 1 min after exposure to NO + O_2, (c) 6 min, (d) 1 h 20 min, (e) 6 h, and (f) 16 h. Reproduced with permission from [44].

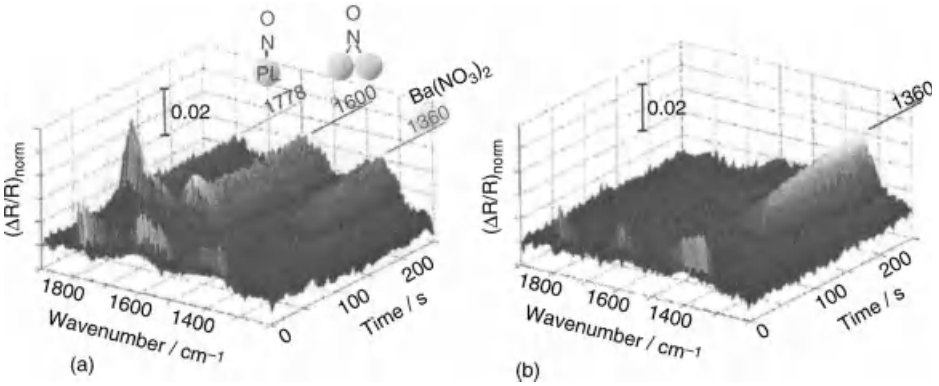


Figure 7.27 Time-resolved PM-IRAS spectra of a Pt (20 nm)/BaO film surface during a cycle of rich (3.3% H_2 in He) to lean (1000 ppm NO + 3.3% O_2 in He) cycles, at 473 K. Reproduced with permission from [45].

water-solvated and oxide-coordinated species were identified on the surface. Changes in the PM-IRAS spectra of the Al surface, with the composition of the gaseous phase, were fully correlated with the mass uptake changes measured with a QCM. A systematic correlation between PM-IRAS and QCM data led, for the first time, to an estimation of the ratio of the IR response coefficient of adsorbed nitrates to that of nitrites. This ratio was estimated to be close to 3 [44].

A recent example shows the possibility of monitoring NO_x storage–reduction cycles on Pt particles deposited on a BaO film by PM-IRAS [45]. The catalyst was a thin film of BaO_3 deposited on a polished Al substrate to make it highly reflective, and both the gas phase and the catalyst surface were characterized simultaneously in the presence of a gas phase, with high time resolution. Ba oxide is known to capture NO_x species as barium nitrites and nitrates; then, under fuel-rich conditions, NO_x is released and reduced, on Pt, to N_2 or NH_3. The detailed surface reactions could be better understood thanks to the experiments reported in this work. Figure 7.27 shows the PM-IRAS spectra recorded under rich (3.3% H_2) to lean (1000 ppm NO + 3.3% O_2) conditions. Three surface species were identified from characteristic vibration bands, NO (on-top and bridged, bonded to Pt) and nitrates [$Ba(NO_3)_2$], the latter increasing under lean conditions whereas the former decreases in intensity; the adsorbed bridge NO species remain at an almost constant surface concentration. The simultaneous recording of the gas phase revealed the rapid depletion of NO_2 and N_2O under rich conditions; in the lean regime, the formation of N_2O and NO_2 is rapid, but the N_2O is rapidly consumed whereas the concentration of NO_2 is stabilized.

The gas-phase evolution can be directly correlated with changes in the surface species: NO is mainly adsorbed on Pt at the beginning of the lean phase; its concentration decreases rapidly in the presence of oxygen, leading to the formation of NO_2 in the gas phase; moreover, the consumption of N_2O correlates with the growth of the bulk NO_3 species. This study makes clear the role of on-top NO, adsorbed on Pt particles, in the oxidation of NO, and its further storage by barium oxide.

7.4.4
Surface Functionalization and Elaboration of Sensors

The successive steps in the elaboration of sensor surfaces can be precisely monitored by PM-IRAS, by a simple analysis of the sample, in the air after rinsing and drying the samples.

First, the formation of SAMs of thiolates on gold or of silanes on silica can be checked, including the order within the adsorbed layer and the presence of some terminal head groups expected to serve as linking sites for proteins or any molecular receptors. As an example, Figure 7.28a shows a series of spectra corresponding to the grafting of a mercaptoundecanoic acid SAM (spectrum a, terminal acid groups, with a $\nu_{C=O}$ band at 1720 cm^{-1}), the activation of the acid into ester groups (spectrum b, $\nu_{C=O}$ bands at 1817, 1788 and 1745 cm^{-1}), and the attachment of a protein (spectrum c) [46]. Such a surface chemistry and also its PM-IRAS characterization were applied to the elaboration of immunosensors, attached proteins being antibodies directed against various types of targets, contaminating toxins or bacteria, for example. In the following example, immunosensors were elaborated by grafting a thiol SAM and antibodies against polycyclic aromatic hydrocarbons (PAHs), a family of carcinogenic environmental pollutants, on a gold substrate [47]. Figure 7.28b shows a series of

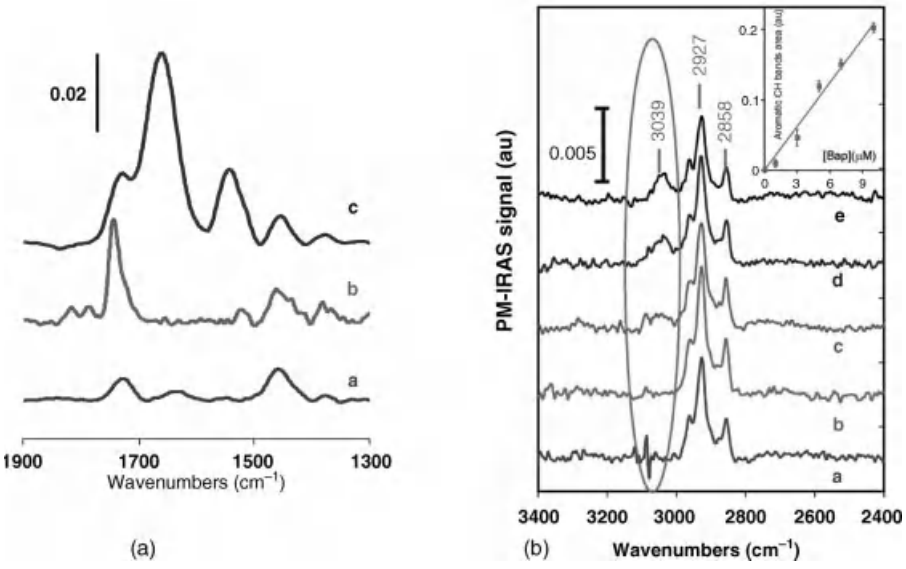


Figure 7.28 (a) PM-IRAS spectra of a gold surface after mercaptoundecanoic acid SAM (spectrum a), activation of the acid terminal groups (spectrum b), and binding of a protein (spectrum c). Reproduced with permission from [46]. (b) PM-IRAS spectra of an immunosensing gold surface functionalized with anti-HAP antibodies (spectrum a), and after immersion in benzo[*a*] pyrene solutions of 1, 3, 5, 7, 10×10^{-6} M (spectra a, b, c, d, and e, respectively). Reproduced with permission from [47].

spectra of the anti-PAH-coated surface after exposure to solutions of benzo[a]pyrène (BAP), one pollutant of the HAP family, of various concentrations (1–10 μM). In the 2400–3400 cm^{-1} region, the spectra are dominated by the CH stretching bands of the thiols and the proteins; interestingly, thanks to the aromatic ring of BAP molecules, the recognition of the pollutant could be monitored from the ν_{CH} band at 3039 cm^{-1}. The PM-IRAS-based sensor was able to detect the target with a limit of detection slightly below 5 μM.

7.4.5
PM-IRAS in the Liquid Phase

PM-IRAS was also utilized to characterize a metal–liquid interface in the presence of a thin water film. The cell, inspired by that developed by Tadjeddine's group for SFG measurements [48], used to run these experiments is shown in Figure 7.29; it enables a sample to be hit with the IR beam passing through a thin (~1 μm) film of water between the window and the sample. A half-cylindrical CaF_2 window is used to eliminate the air–window interface outside the cell. CaF_2 material was chosen owing to its good transmission in the mid-IR frequencies and its good chemical inertness; moreover, its refractive index is close to that of water, which enables the reflection at the window–water interface to be restricted. After many experiments, the optimal angle of incidence was set at 70°. The device enables the sample to be placed far from the window between two spectral acquisitions (a few millimeters) so

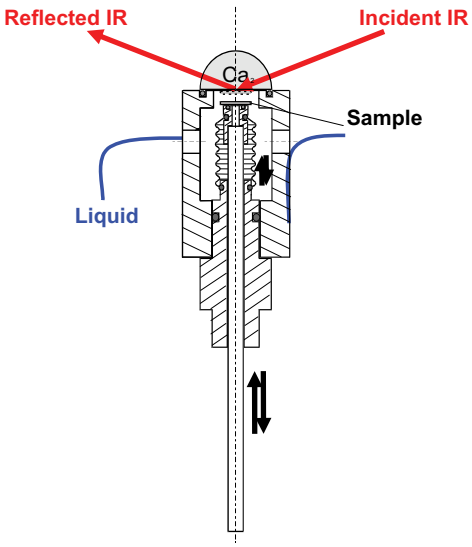


Figure 7.29 Representation of the cell for *in situ* PM-IRAS characterization in liquids.

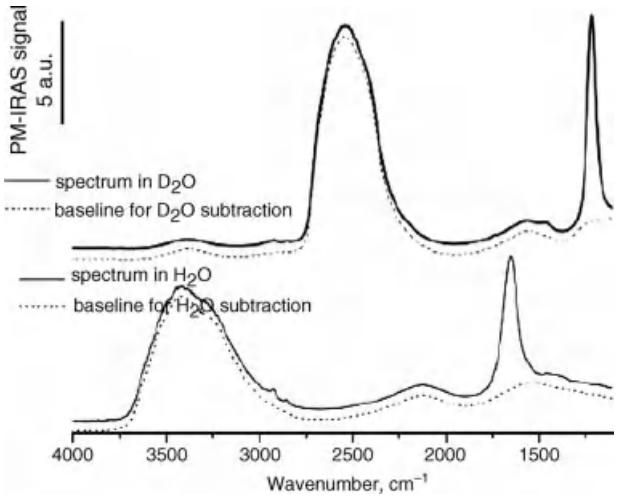


Figure 7.30 PM-IRAS spectra of MUA-functionalized gold surface in water, H_2O and D_2O, and dotted lines used for the baseline correction. Reproduced with permission from [49].

that the adsorption is not limited by the amount of molecules present in the thin layer of liquid.

By acquiring PM-IRAS spectra while the solution was modified, for instance by changing the pH or the ionic strength, adsorption of molecules could be monitored and the effect of the solution concentration investigated. The first example concerns the formation of a SAM of mercaptoundecanoic acid (MUA) on gold and the influence of the pH on the chemical state of the terminal SAM groups [49, 50]. The second example is the characterization of the adsorption of polypeptides on a stainless-steel surface, through a thin layer of water [51]. Note that all *in situ* PM-IRAS spectra in liquids were performed in D_2O because, although the modulated light polarization should avoid all contributions from the environment, strong water bands were observed at $\sim$1650 cm^{-1}, thus preventing an accurate analysis in this relevant region. This phenomenon, very clear in Figure 7.30, was attributed to either some orientation of the water molecule or to some heterogeneity of the electric field in the vicinity of the surface which makes molecules in an isotropic phase detectable even in an isotropic phase [52]. Figure 7.31 shows the PM-IRAS spectra of the MUA-modified gold surface in pure D_2O, in acidic and basic D_2O solutions. The spectra are very sensitive to the pH of the solution; in the 1400–1500 cm^{-1} region, one sees an increase of the symmetric stretch of COO^- groups while in the C = O stretch of COOH groups decreases when the pH increases. Note the evolution of the latter band: the signal at 1740 cm^{-1} is attributed to the $\nu_{C=O}$ vibration of isolated carboxylic groups; it decreases to the benefit of one at 1710 cm^{-1} when the number of protonated groups increases on the surface; this low-wavenumber shift is ascribed to the interactions between adjacent COOH groups [49].

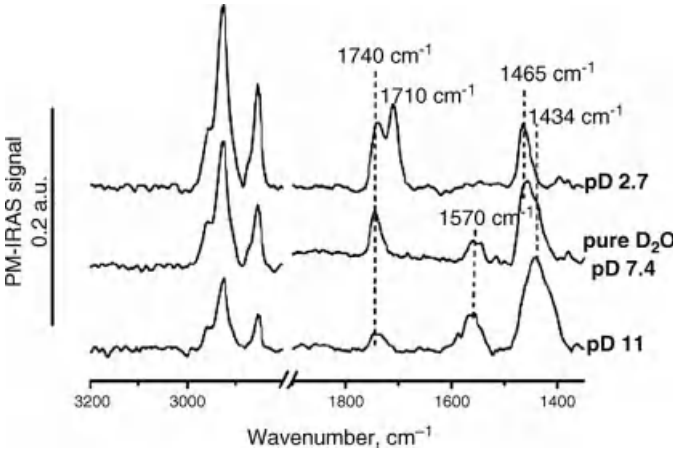


Figure 7.31 PM-IRAS spectra of MUA-coated gold surface, recorded in pure D_2O and in acidic and basic D_2O solutions. Reproduced with permission from [49].

Note finally the decrease in the CH stretching vibration bands, at ~2850 and 2920 cm^{-1}; this is the fingerprint of the loss of order within the layer occurring when the pH increases from 2.7 to 11.

The second example of PM-IRAS run in a liquid concerns experiments performed in deuterated water solutions containing poly-L-glutamic acid (PG). In pure water, a small amount of any of these two polypeptides could be detected on the alumina surface. Interesting differences were noted when PG was adsorbed from solutions containing $CaCl_2$, at various pH values. PM-IRAS, applied in the dedicated "liquid" cell, permitted the observation of the influence of pH and salts on polypeptide adsorption. Figure 7.32 shows the most stable chemical forms of the PG peptide in solution at pH 2 and 11; Figure 7.33 shows a series of spectra of the aluminum substrate recorded in solutions of PG at pH 2 (lower spectra) and pH 11 (upper

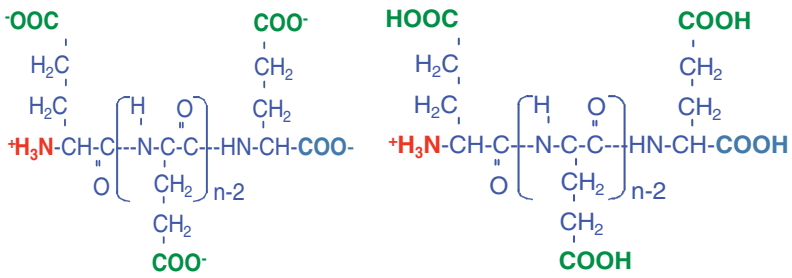


Figure 7.32 Stable chemical forms of polyglutamic acid (PG), in solution at pH 11 (a), or pH 2 (b). Reproduced with permission from [51].

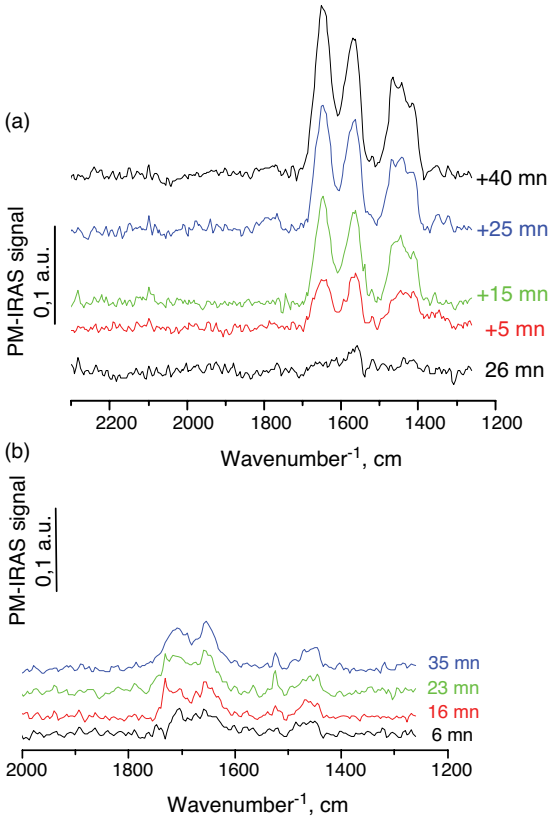


Figure 7.33 PM-IRAS spectra of an aluminum sample immersed in PG solutions, at pH 11 (a) and at pH 2 (b). Reproduced with permission from [51].

spectra). At pH values higher than 5, and in the presence of $CaCl_2$ in solution, a net increase in the amount of PG adsorbed was observed, whereas no such effect could be detected at pH 2, that is, when all carboxylic groups of the molecules were protonated. Specific interactions between the COO^- groups on the side chains and the surface, or between those of two different molecules, were considered to account for the enhanced adsorption of PG. Calcium ions likely play a role by favoring intermolecular linkages.

7.5 Conclusion

In situ IRAS or PM-IRAS experiments benefit from the enhanced electric field intensity in the vicinity of a metallic surface; when performed at grazing angle, the

technique is sensitive to amounts of adsorbates as low as a fraction of a monolayer. Moreover, working with modulation of the polarization allows surface analyses to be achieved in the presence of a gas phase, or even a liquid phase. IRAS and PM-IRAS can thus bring unique information on surfaces involved in reactive phenomena, such as adsorption, dissociation, catalytic reactions, bio-recognition, and so on. These vibrational techniques, often combined with classical surface science tools such as XPS, LEED, and HREELS, enabled some surface species, reaction intermediates, or spectator species to be identified that shed some light on the mechanism of some catalytic reactions. This is the case with the water gas shift reaction and some oxidations (see NH_3 oxidation). Performing surface characterization under moderate pressures of reactants has become a prerequisite to obtain good information before discussing the nature of the elementary steps or the determining steps of a catalytic reaction. IRAS and PM-IRAS are also valuable tools for the intrinsic sensitivity of IR frequency. In the case of adsorbed species, the technique was shown to provide information about the adsorbate growth mode, its environment on a surface, and the protonation state of acid or amine groups, for example.

New PM-IRAS developments, in a dedicated cell allowing measurements under high pressures, or even in a liquid environment, provide *in situ* chemical and quantitative characterization of a reactive surface in even more realistic reactive media. Application to biointerfaces, where molecules display strong and very informative IR signals, opens up new, promising perspectives to this technique.

References

1 Greenler, R.G. (1966) *J. Chem. Phys.*, **44**, 310–315.
2 Greenler, R.G. (1969) *J. Chem. Phys.*, **50**, 1963–1968.
3 Eischens, R.P., Francis, S.A., and Pliskin, W.A. (1956) *J. Phys. Chem.*, **60** (2), pp 194–201.
4 Hopster, H. and Ibach, H. (1978) *Surf. Sci.*, **77**, 109.
5 McClellan, M.R., Gland, J.L., and McFeeley, F.R. (1981) *Surf. Sci.*, **112**, 63.
6 Wells, M.G., Cant, N.W., and Greenler, R.G. (1977) *Surf. Sci.*, **67**, 541–554.
7 Yates, J.T. Jr., Greenler, R.G., Ratajczykowa, I., and King, D.A. (1973) *Surf. Sci.*, **36**, 739–755.
8 Hayden, B.E. and Bradshaw, A.M. (1983) *Surf. Sci.*, **125**, 767.
9 Hayden, B.E., Kretzschmar, K., Bradshaw, A.M., and Greenler, R.G. (1985) *Surf. Sci.*, **149**, 394–406.
10 Hoffmann, F.M. (1982) *Surf. Sci. Rep.*, **3**, 107–192.
11 Behm, R.J., Christmann, K., and Ertl, G. (1980) *J. Chem. Phys.*, **73**, 2984.
12 Ortega, A., Hoffmann, F.M., and Bradshaw, A.M. (1982) *Surf. Sci.*, **119**, 79.
13 Bradshaw, A.M. and Hoffmann, F.M. (1978) *Surf. Sci.*, **72**, 513.
14 Ortega, A. (1980) PhD thesis, Frei Universität, Berlin.
15 Hollins, P. and Pritchard, J. (1979) *Surf. Sci.*, **89**, 486–495.
16 Crossley, A. and King, D. (1980) *Surf. Sci.*, **95**, 131.
17 Pfnür, D.M., Hoffmann, F.M., Ortega, A., and Bradshaw, A.M. (1980) *Surf. Sci.*, **93**, 431.
18 Bradshaw, A.M. and Schweizer, E. (1988) Infrared reflection-absorption spectroscopy of adsorbed molecules, in *Spectroscopy of Surfaces* (eds R.J.H. Clark and R.E. Hester), John Wiley & Sons, Ltd., Chichester. p. 413–483.
19 Love, J.C., Estroff, L.A., Kriebel, J.K., Nuzzo, R.G., and Whitesides, G.M., (2005) *Chem. Rev.*, **105**, 1103–1169.

20 Bain, C.D., Troughton, E.B., Tao, Y.-T., Evall, J., Whitesides, G.M., and Nuzzo, R.G. (1989) *J. Am. Chem. Soc.*, **111**, 321.

21 Briand, E., Salmain, M., Compère, C., and Pradier, C.M. (2006) *Colloids Surf. B: Biointerfaces*, **53**, 222–231.

22 Nuzzo, R.G., Dubois, L.H., and Allara, D.L. (1990) *J. Am. Chem. Soc.*, **112**, 558–569.

23 Love, J.C., Estroff, L.A., Kriebel, J.K., Nuzzo, R.G., and Whitesides, G.M. (2005) *Chem. Rev.*, **105**, 1103.

24 Thissen, P., Valtiner, M., and Grundmeier, G. (2010) *Langmuir*, **26**, 156–164.

25 Barlow, S.M. and Raval, R. (2003) *Surf. Sci. Rep.*, **50**, 201–341.

26 Ihs, A., Liedberg, B., Uvdal, K., Törnkvist, C., Bodö, P., and Lundström, I. (1990) *J. Colloid Interface Sci.*, **140**, 192–206.

27 Liedberg, B., Lundström, I., Wu, C.R., and Salanek, W.R. (1985) *J. Colloid Interface Sci.*, **108**, 123–132.

28 Humblot, V., Methivier, C., and Pradier, C.-M. (2006) *Langmuir*, **22**, 3089–3096.

29 Mateo-Marti, E., Methivier, C., Dubot, P., and Pradier, C.-M. (2003) *J. Phys. Chem. B*, **107**, 10785–10792.

30 Mateo-Marti, E., Methivier, C., and Pradier, C.-M. (2004) *Langmuir*, **20**, 10223–10230.

31 Vallée, A., Humblot, V., Methivier, C., and Pradier, C.-M. (2008) *Surf. Sci.*, **602**, 2256–2263.

32 Vallée, A., Humblot, V., Méthivier, C., and Pradier, C.M. (2009) *J. Phys. Chem. C*, **113**, 9336–9344.

33 Barlow, S.M., Louafi, S., Le Roux, D., Williams, J., Muryn, C., Haq, S., and Raval, R. (2005) *Surf. Sci.*, **501**, 243–263.

34 Humblot, V., Ortega, M., Christopher, L., Baddeley, J., Haq, S., and Raval, R. (2004) *J. Am. Chem. Soc.*, **126**, 6460–6469.

35 Peden, C.H.F., Goodman, D.W., Weisel, M.D., and Hoffmann, F.M. (1991) *Surf. Sci.*, **253**, 44–58.

36 Hoffmann, F.M. and Weisel, M.D. (1992) *Surf. Sci.*, **269–270**, 495–499.

37 Weisel, M.D., Chen, J.G., and Hoffmann, F.M. (1990) *J. Electron Spectrosc. Relat. Phenom.*, **54/55**, 787–794.

38 Gao, F., Wang, Y., Calaza, F., Stacchiola, D., and Tysoe, W.T. (2008) *J. Mol. Catal. A*, **281**, 14–23.

39 Louis-Rose, I., Methivier, C., Védrine, J.C., and Pradier, C.M. (2006) *Appl. Catal. B*, **62**, 1–11.

40 Louis-Rose, I., Méthivier, C., and Pradier, C.M. (2003) *Catal. Today*, **85**, 267–278.

41 Rodriguez de la Fuente, R., Borasio, M., Galletto, P., Rupprechter, G., and Freund, H.-J. (2004) *Surf. Sci.*, **566–568**, 740–745.

42 Wallace, W.T., Cai, Y., Chen, M.S., and Goodman, D.W. (2006) *J. Phys. Chem. B*, **110**, 6245–6249.

43 Delebecque, A., Thomas, C., Pradier, C.M., Méthivier, C., Paoli, H., Carré, M., and Coffre, E. (2008) *J. Phys. Chem. C*, **112**, 2964–2971.

44 Delebecque, A., Thomas, C., Pradier, C.M., Methivier, C., Paoli, H., Coffe, E., and Carré, M. (2008) *Surf. Sci.*, **602**, 283–290.

45 Maeda, N., Urakawa, A., and Baiker, A. (2010) *J. Phys. Chem. Lett.*, **1**, 54–58.

46 Thébault, P., Boujday, S., Sénéchal, H., and Pradier, C.M. (2010) *J. Phys. Chem. B*, **114**, 10612–10619.

47 Boujday, S., Gu, C., Girardot, M., Salmain, M., and Pradier, C.M. (2009) *Talanta*, **78**, 165–170.

48 Vidal, F., Busson, B., Six, C., Pluchery, O., and Tadjeddine, A. (2002) *Surf. Sci.*, **502–503**, 485–489.

49 Methivier, C., Beccard, B., and Pradier, C.M. (2003) *Langmuir*, **19**, 8807–8812.

50 Martins, M.C.L., Ratner, B.D., and Barbosa, M.A. (2003) *J. Biomed. Mater. Res.*, **67** (A1), 158–174.

51 Pradier, C.M., Humblot, V., Stievano, L., Methivier, C., and Lambert, J.F. (2007) *Langmuir*, **23**, 2463–2471.

52 Golden, W.G., Kunimatsu, K., and Seki, H. (1984) *J. Phys. Chem.*, **88**, 1275–1277.

8
Nuclear Magnetic Resonance Spectroscopy

Lynn F. Gladden, Michal Lutecki, and James McGregor

8.1
Introduction and Historical Perspective

Nuclear magnetic resonance (NMR) was first used in the study of liquids and solids in 1946 by Felix Bloch [1] and Edward Mills Purcell [2], an achievement for which they were rewarded with the Nobel Prize in Physics in 1952. Recognition of the potential of magnetic resonance methods in studying surfaces and catalysis was rapid [3], and applications of magnetic resonance in physics, chemistry, and biology still continue to increase. The theoretical and technical advances that were required to provide real insight into the structure of solid-state materials came with the advent of magic angle spinning (MAS) in 1958 [4] and the array of techniques that developed from these ideas. The 1980s saw a surge in the application of MAS techniques for structural and, to some extent, surface characterization of solids. During this period, the application of double-resonance, multiple quantum, and two-dimensional spectroscopy to characterize catalytic materials and the surface-bound intermediates formed during catalytic reactions became increasingly widespread. The implementation of polarization transfer techniques, developed in the early 1970s, for the study of surfaces and of catalysis also came to the fore at this time. The best known of these methods, cross-polarization, transfers magnetization from a highly abundant spin system, typically ^{1}H, to a low-abundance, low-gyromagnetic ratio spin system. This allows for the selective study of, for example, ^{29}Si and ^{13}C atoms which are adjacent to hydrogen atoms. Such advances opened up opportunities to study hydroxyl species on catalyst surfaces and spillover phenomena, among many other applications. Although, of course, excellent work on the characterization of solids and their surfaces using the aforementioned NMR techniques continues to this day; the late 1980s and early 1990s were marked by initial, so-called *in situ*, studies of adsorption and catalytic properties. These studies were performed in batch mode, that is, in small, sealed ampoules which were contained within the NMR MAS rotor. Ever more elegant methods for the study of catalysts under working conditions continue to be reported and will be discussed in this chapter in some detail, along with examples. Since the early 1990s there has also been much interest in overcoming the intrinsic

Characterization of Solid Materials and Heterogeneous Catalysts: From Structure to Surface Reactivity, First Edition. Edited by Michel Che and Jacques C. Védrine.
© 2012 Wiley-VCH Verlag GmbH & Co. KGaA. Published 2012 by Wiley-VCH Verlag GmbH & Co. KGaA.

low sensitivity of NMR. At room temperature in a magnet with a magnetic field strength of 10 tesla (T), 10^{18} spins are the order of magnitude estimate of the detection limit [5]. By far the most popular approach to enhance sensitivity has involved the Xe nucleus; enhanced nuclear spin polarization of Xe nuclei can be achieved via van der Waals collisions with optically pumped Rb vapor [6]. Along with a large chemical shift range, this property of Xe nuclei (^{129}Xe and ^{131}Xe) makes Xe isotopes very sensitive probes of their local environment. As such, a number of studies have been conducted in which Xe adsorbates on materials have been studied directly by Xe NMR, or Xe has been used to enhance the signal of coadsorbed species (e.g., CO_2) via ^{129}Xe–^{13}C cross-polarization [7]. Another type of polarization enhancement technique which has emerged more recently along with its application in catalysis is parahydrogen-induced sensitivity enhancement. In particular, Duckett and co-workers [8] used parahydrogen techniques to probe catalytic reaction mechanisms. To date however, sensitivity enhancement techniques remain more at the development stage and are not routinely used in the characterization of materials under working conditions. The 1990s also saw the emergence of magnetic resonance imaging (MRI) and diffusion measurements as further magnetic resonance probes of the structure and properties of solid-state materials, and catalysts in particular. Early work focused on imaging single-phase liquid hydrodynamics in reactors and this continues to be an area of considerable interest. More recently, these studies have been extended to spatial mapping of chemical composition in heterogeneous catalytic reactors [9, 10].

The structure of this chapter is as follows. Section 8.2 introduces the basic principles of magnetic resonance measurements and illustrates these with examples of what can be done in application to the characterization of the surfaces of materials and in assessing their catalytic function. The principles underlying spectroscopy, imaging, diffusion, and flow measurements are introduced. Section 8.3 summarizes some of the more popular solid-state NMR techniques used in characterizing materials, their surfaces, and the adsorption processes associated with them that determine their catalytic performance, and Section 8.4 gives examples of how these techniques have been used in the characterization of heterogeneous catalysts in terms of both their bulk structure and their surface properties. Section 8.5 continues this theme but considers the physical structure and properties of materials, in particular the characterization of porosity and the molecular adsorption and diffusion processes occurring within the pores of catalytic materials. Section 8.6 presents a summary of what are typically defined as *in situ* NMR experiments, and we describe the sample environments used and distinguish between experiments performed in closed sample (batch) and open, flow environments. Finally, in Section 8.7, we consider the emerging field of so-called *operando* measurements, in which we begin to study the catalyst operating in the reactor environment. Such experiments are in their infancy and in most cases necessarily require the use of substantially scaled-down reactor units. Although there remain many exciting challenges ahead, magnetic resonance techniques are reaching a level of maturity such that we can measure adsorption, diffusion, and reaction phenomena in porous solids, and in particular catalysts, ranging from model systems in powder form through to the characteristics and function of formed catalyst pellets in working reactors.

8.2
Theory

Many excellent texts exist on the fundamentals of NMR (e.g., [11, 12]). This section attempts to give the non-expert an overview of the physical principles upon which magnetic resonance measurements are based. What is often overlooked is the power of NMR not just to yield information on chemical structure but also to probe sorbate–sorbent interactions and molecular diffusion processes within porous materials – all of which play an important role in the performance of these materials as catalysts. At larger length scales, MRI offers the potential to study how the macroscopic flow fields inside the reactor and the resulting reactant–catalyst contacting patterns further influence catalytic performance. Figure 8.1 shows a schematic of a typical NMR setup with the key components indicated [13].

8.2.1
Basic Principles of NMR

A general Hamiltonian, H, describing the interactions experienced by a nucleus of spin I may be expressed as the sum of contributions from the Zeeman (H_Z), dipolar (H_D), quadrupolar (H_Q), chemical shift (H_{CS}), and indirect electron coupled (H_J) interactions:

$$H = H_Z + H_D + H_Q + H_{CS} + H_J \tag{8.1}$$

The precise energy level splitting is therefore sensitive to a number of nuclear spin interactions which are themselves determined by the physical and chemical properties of the nuclear spin system. Thus, by careful design of the NMR experiment,

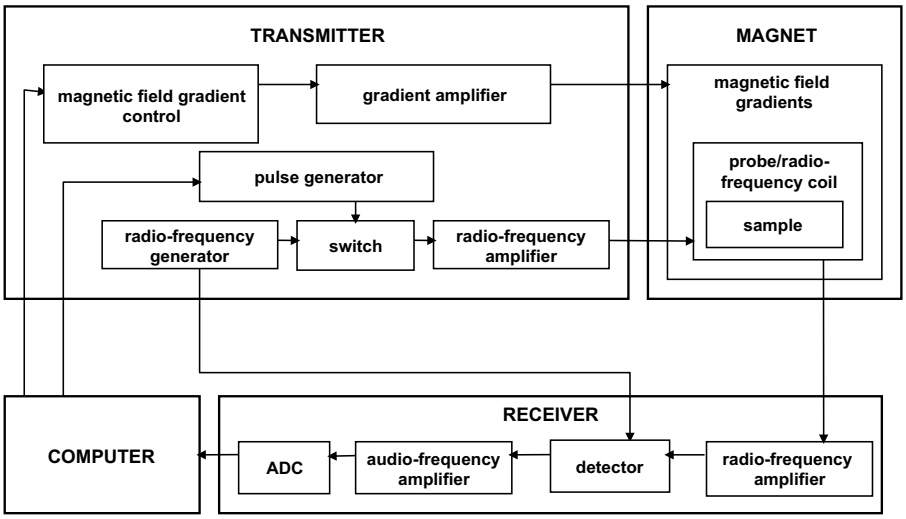


Figure 8.1 Schematic of a modern NMR spectrometer. ADC: analog-to-digital converter [13].

such that we probe a specific contribution to the overall nuclear interaction, much can be learned about the physical and chemical structure and also the dynamics of the sample under study. Only a phenomenological description of the various interactions is given here, in particular the origin of the interactions is noted so as to appreciate the different characteristics of the spin system that can be probed. Each of the interactions will now be considered in turn, and brief examples of how they can be exploited in application to the study of materials are given.

8.2.1.1 Zeeman Interaction

The Zeeman interaction is the dominant interaction and lies at the heart of the magnetic resonance experiment, since it is responsible for the lifting of the degeneracy of the energy states within a nucleus upon application of the magnetic field B_0 (typically a superconducting magnetic field of 2–10 T). As a result of the splitting of the nuclear spin energy levels, there exists, at equilibrium, a net magnetization vector aligned parallel to the direction of the external magnetic field, assumed to be along the z-direction. By exposing the system to electromagnetic energy of appropriate frequency [radiofrequency (r.f.)], a resonant absorption occurs between these nuclear spin energy levels. The specific frequency at which this resonance occurs is called the resonance (or Larmor) frequency and is proportional to the strength of the external magnetic field, B_0, used in the experiment. The precise energy level splitting arising from the Zeeman effect is specific to a given isotope of an element, and the resonance frequency (ω_0) is given by

$$\omega_0 = \gamma B_0 \tag{8.2}$$

where γ is the gyromagnetic ratio. This is an isotope-specific property, thereby explaining the intrinsic isotope specificity of magnetic resonance.

8.2.1.2 Dipolar Interaction

Dipolar interactions arise because each magnetic moment is associated with a nuclear spin dipole which produces a local magnetic field. This induced field will then interact with neighboring dipoles, causing splitting and broadening of the resonance signal. The Hamiltonian for the dipolar interaction between a single spin pair separated by a distance r_{ij} can be shown to be proportional to the term

$$H_{D_{ij}} = \frac{\gamma_i \gamma_j}{r_{ij}^3}\left(3\cos^2\,\theta_{ij} - 1\right) \tag{8.3}$$

where θ_{ij} is the angle between r_{ij} and B_0. Hence we see that the strength of the dipole–dipole interaction depends on both the magnitude of the magnetic moments, as reflected in their gyromagnetic ratios, and the internuclear distance between the two spins. The dipolar interaction is independent of the magnitude of the field B_0. If there is molecular motion, the direction of the internuclear vector will be time dependent and cause an effective reduction in the magnetic dipolar field. In the presence of rapid molecular motion, that is, in solutions or gases when θ covers all angles, only the mean value of the dipolar interaction is effective and since this is zero

(the time-averaged value of $\cos^2\theta = {}^1/_3$), sharp resonance spectra can be acquired. In solids, such averaging does not occur. This results in linewidths of the order of kilohertz as opposed to the hertz linewidths observed for liquids. A classic example of how this interaction can be used to gain insight into a catalytic system is the work of Wang *et al.* [14], who measured dipolar couplings for the system of acetylene adsorbed on Pt/Al_2O_3. $^{13}C-^{13}C$, $^{13}C-^{1}H$, and $^{1}H-^{1}H$ dipolar couplings were measured from which the C−C bond length of the CCH_2 species was found to be 1.44 ± 0.02 Å, mid-way between the lengths of a single and a double bond, suggesting that both C atoms were bonded to the surface.

8.2.1.3 **Chemical Shift Interaction**

The very foundations of much of solid-state NMR in its application to the characterization of materials structure has developed around the interpretation of chemical shift phenomena. In condensed matter, nuclei are surrounded by atomic or molecular electron clouds which interact with the nuclear spin angular momentum, thereby causing a shift in the resonance frequency of the nucleus under study; this shift is directly related to the electronic structure of the molecule. The chemical shift interaction is directly proportional to the strength of the static magnetic field B_0. Given the spatially anisotropic nature of the distribution of electrons in molecules, especially in multiple bonds, it is apparent that this effect will also be anisotropic. In a powdered sample, each molecular group is oriented at all possible directions to the magnetic field, so that a whole range of chemically shifted signals is produced. It follows that the resulting signal will be very broad with the source of this broadening again being dependent on the term $(3\cos^2\theta - 1)$. As with the dipolar interaction, anisotropic chemical shift effects are not present in liquids or gases. In contrast to the dipolar interaction where rapid isotropic motion causes the disappearance of the interaction, in the case of the chemical shift interaction, isotropic rotation leaves a residual interaction which is identified as the "chemical shift" of a species recorded in an NMR spectrum. Thus, not only is NMR a nuclear-specific probe as a result of the Zeeman effect, but also the subtle modifications to the energy splitting resulting from the chemical shift interaction make NMR sensitive to particular chemical groups and it therefore becomes molecule and molecular group specific. In order that chemical shift values can be compared between acquisitions at different field strengths, chemical shift values, δ, are quoted relative to a standard, where δ is defined as

$$\delta = 10^6\left(\frac{\nu_{\text{sample}} - \nu_{\text{reference}}}{\nu_{\text{reference}}}\right) \tag{8.4}$$

at constant B_0, where $\omega = 2\pi\nu$, and has units of parts per million (ppm).

8.2.1.4 **Quadrupolar Interaction**

The quadrupolar interaction arises from the interaction of the nuclear quadrupole moment (associated with spins of $I > {}^1/_2$) with the non-spherically symmetrical field gradient around the nucleus. The magnitude of the interaction is such that

for most nuclei it completely dominates the spectrum; this is even the case for deuterium, ^{2}H, which has the smallest quadrupole moment. The quadrupolar interaction is sensitive to the presence of molecular motion and ^{2}H NMR has been used by a number of workers to investigate the dynamics of molecules at surfaces. Under conditions of molecular reorientation, the precise lineshape depends on the nature of the motion and its correlation time. When the molecular motion is such that the electric field gradient at the nucleus is averaging rapidly and isotropically on the time scale of the experiment, the lineshape collapses to a single resonance line from which the correlation time of the motion can be estimated. NMR studies of the quadrupolar interaction allow us to probe the nature of adsorption sites in porous solids and the molecular mobility of adsorbed species [15–17].

8.2.1.5 **Indirect Electron Coupled Interaction**

Finally, we consider the indirect electron-coupled interaction (or scalar coupling). Indirect coupling is an intramolecular interaction which acts through covalent bonds; magnetic moments within a common electron cloud interact to give a splitting of the resonance signal which is independent of the external magnetic field B_0. The magnitude of this effect is small ($\sim$20 Hz for ^{1}H) and is therefore observed only in liquid-state spectroscopy and high-resolution solid-sate NMR. However, if it can be observed, it is extremely useful in determining molecular structure.

8.2.2
Relaxation Times

At equilibrium, the net magnetization vector, $\boldsymbol{M}$, associated with the nuclear spin system is aligned along the direction of the magnetic field (say the z-direction). The action of the excitation pulse, in this case a pulse of r.f. applied at right-angles to the direction of the superconducting field, is therefore to rotate $\boldsymbol{M}$ about the axis along which the excitation was applied (say the x-axis). Conventionally, we consider the action of the r.f. pulses from within the frame of reference of the spin system – the so-called rotating frame. In this frame, a $\pi/2$ (or 90°) pulse will rotate $\boldsymbol{M}$ through $\pi/2$ radians (rad). The magnetic resonance time domain signal, following r.f. excitation, will then be measured by acquiring the signal (i.e., the magnitude of the magnetization vector) aligned along y as a function of time; this signal will decay with time due to the recovery of the magnetization along z and, at shorter time scales, due to the loss of phase coherence of the spin isochromats comprising the net magnetization vector along the y-axis. These decay processes are termed the spin–lattice (or longitudinal), T_1, and spin–spin (or transverse), T_2, relaxation processes, respectively. Fourier transformation of this time-domain signal, usually referred to as the free induction decay, yields the frequency domain spectral response in which the area under the spectral peak, following appropriate calibration, gives a quantitative measure of the number of nuclear spins associated with that spectral frequency (i.e., a quantitative measure of the number of molecules of a given molecular species that are present). Thus, magnetic resonance is both an intrinsically chemical specific, as follows from Section 8.2.1, and a quantitative measurement. It is important to

remember that the T_1 and T_2 characteristics of a material should always be measured prior to implementing a given pulse sequence if the quantitative nature of the NMR measurement is to be retained.

T_1 and T_2 time constants are of particular use in studying materials because their measurement can be used to characterize the physicochemical environment of the molecules being investigated (see Section 8.5.1.2). T_1, as the name suggests, characterizes the energy exchange between the excited spin and the surrounding physical environment (i.e., the lattice), whereas T_2 characterizes the loss of phase coherence between nuclear spins within the nuclear spin ensemble. Each chemical species will have its own T_1 and T_2 characteristics, and these will vary depending on the physical state in which that species exists. Measurements of T_1 and T_2 are straightforward and both can be spatially resolved by combining the relaxation time measurement pulse sequence with an imaging pulse sequence. When this is done, the signal intensity associated with each image pixel (or voxel) represents a quantitative determination of the relaxation time of interest in that element of the image. Of particular note is the spin-echo pulse sequence which lies at the heart of a T_2 measurement. The principle of such an experiment is that the spin system is given a $\pi/2$ excitation which rotates the magnetization away from the z-axis to lie along, say, the y-axis. The system is allowed to evolve for a time, τ, during which the spins which would all have originally been aligned along y begin to dephase in the x–y plane. At a time τ, a π pulse is applied which acts to rotate the spins by π rad about the y-axis. Hence, after a further time τ, the spins will realign back along y forming an "echo." In this simple echo experiment, the π pulse refocuses all dephasing due to inhomogeneous broadening, chemical shift, and heteronuclear scalar spin–spin interactions. The observed attenuation of the echo is therefore due to spin–spin relaxation alone. "Echoes" have widespread use in magnetic resonance methods, far beyond simple measurement of T_2, and they lie at the heart of many double-resonance experiments and also MRI experiments.

8.2.3
Application of Magnetic Field Gradients

8.2.3.1 Magnetic Resonance Imaging

To understand how magnetic resonance is used as an imaging technique, we return to Eq. (8.2). Spatial resolution in the NMR measurement is obtained by exposing the sample to a spatially varying magnetic field, in addition to the large static field B_0. For example, when a magnetic field gradient is applied along the z-direction, G_z:

$$\omega_z = \gamma(B_0 + G_z z) \tag{8.5}$$

that is, the resonance frequency is now a function of spatial position in the z-direction. By applying magnetic field gradients in a second and third dimension, we obtain two- and three-dimensional images. The fact that spatial position can now be encoded within the magnetic resonance signal also lies at the foundation of using magnetic resonance to measure transport phenomena.

To understand MRI fully, it is useful to introduce the $\boldsymbol{k}$-space formalism, where $\boldsymbol{k} = \gamma \boldsymbol{G}t/2\pi$. For the general case of the variation of resonance frequency with spatial position $\boldsymbol{r}$ we rewrite Eq. (8.5) as

$$\omega(\boldsymbol{r}) = \gamma(B_0 + \boldsymbol{G} \cdot \boldsymbol{r}) \tag{8.6}$$

Introducing the substitution $\boldsymbol{k} = \gamma\ \boldsymbol{G}t/2\pi$, it can be shown that the acquired magnetic resonance signal $S(\boldsymbol{k})$ is given by

$$S(\boldsymbol{k}) = \iiint \varrho(\boldsymbol{r}) \exp(i2\pi \boldsymbol{k} \cdot \boldsymbol{r}) \mathrm{d}\,\boldsymbol{r} \tag{8.7}$$

where $\varrho(\boldsymbol{r})$ is the density of spins at position $\boldsymbol{r}$. It follows that the spatial distribution of spins is then given by the inverse three-dimensional Fourier transform:

$$\varrho(\boldsymbol{r}) = \iiint S(\boldsymbol{k}) \exp(-i2\pi \mathbf{k} \cdot \boldsymbol{r}) \mathrm{d}\,\boldsymbol{k} \tag{8.8}$$

The imaging experiment can therefore be considered as acquisition of data in the time domain, sampling a $\boldsymbol{k}$-space raster, followed by Fourier transformation to the frequency domain, which in turn is directly related to real space. An important area of technique development, which is of particular relevance to studies of catalysts under working conditions, is to decrease data acquisition times. This is done in a number of ways including novel approaches to acquiring the $\boldsymbol{k}$-space data points within the raster and, increasingly, to sample only a sub-set of the $\boldsymbol{k}$-space points [9, 18].

In the context of catalysis, being able to make the signal intensity of each image pixel sensitive to chemical species is one of the major motivations for using magnetic resonance techniques. The most direct way of achieving this goal is to use chemical shift imaging techniques. This method increases the dimensionality of the acquisition process, so that frequency associated with the zero-gradient spectrum becomes the nth dimension in addition to the spatial dimensions of imaging. Using this approach, the magnetic resonance signal is first spatially encoded, and the data are then acquired in the absence of a magnetic field gradient [19]. The second approach is the volume-selective spectroscopy method, which integrates spectroscopy and imaging methods in such a way that volume-localized spectra are recorded within the system [20].

8.2.3.2 Measuring Flow and Diffusion

Since spatial information is encoded in the magnetic resonance measurement by applying a magnetic field gradient [Eq. (8.5)], it follows that diffusion, dispersion, and flow processes can be measured by means of applying pulsed magnetic field gradients to the system, in addition to the normal r.f. pulses. These pulsed field gradient techniques measure molecular displacement as a function of time without the need to introduce tracers into the experiment.

The principle of the pulsed field gradient method is that a magnetic field gradient is applied for a short period of time, which causes a nuclear spin to be given a *phase offset* (say ϕ_1) characteristic of its spatial position when the pulse was applied. In the rotating frame of the spin system, this phase offset, $\phi_{1,}$ is equal to $\gamma g \delta z_1$, where δ is

the duration of the applied magnetic field gradient, z_1 is position of the spin, and g is the magnitude of the magnetic field gradient along the z-direction. Although many variations on this theme exist, the basic concept underpinning most transport measurements is that after an observation time, Δ, an equal but opposite polarity magnetic field gradient pulse is applied which gives the spins a further phase offset, ϕ_2, such that the total phase offset is $\phi_1 + \phi_2 = \gamma g \delta(z_1 - z_2)$. Clearly, if the molecule (i.e., spin) has not moved during the time Δ, it will experience a net phase shift of $\phi_1 + \phi_2 = 0$, that is, the magnetization vector will again be aligned along the same direction that it was aligned along immediately after application of the initial excitation pulse, and therefore signals acquired with and without the application of the pulsed gradient pair will be equal in magnitude and phase. If, however, the molecule has moved during the time Δ (i.e., $z_1 \neq z_2$), then $\phi_1 + \phi_2 \neq 0$ and the signal acquired when the gradient pair has been applied will show a phase shift that is proportional to the distance moved $(z_1 - z_2)$. It follows that since γ, g, and δ are known, the displacement or average velocity over the time scale Δ is obtained. A typical transport measurement proceeds by making several measurements at differing values of δ or g and recording the resulting *phase shift* and *amplitude* of the signal. These two different properties of the acquired magnetic resonance signal provide measurements of *coherent* (flow) and *incoherent* (diffusion, dispersion) transport processes, respectively. Since both the phase and amplitude of the magnetic resonance signal are acquired at the same time, both types of transport process can therefore be measured in the same experiment. When pulsed magnetic field gradients are applied to study diffusive processes, the magnetic resonance technique is often referred to as pulsed field gradient (PFG) or pulsed gradient spin-echo (PGSE) magnetic resonance. Application of these techniques to quantify molecular diffusion was pioneered by Stejskal and Tanner [21, 22], and the techniques typically probe molecular displacements of $10^{-6} - 10^{-5}$ m over time scales of the order 10^{-3}–10^{0} s.

8.3
Popular NMR Techniques for Studying Solids

Before discussing some of the applications of NMR in the characterization of bulk and surface structure, and reactions occurring on these surfaces, it is worth summarizing the different groups of NMR methods that exist in order to provide some insight into how they are implemented. These techniques are discussed in much greater detail, including theoretical analyses, elsewhere (e.g., [11]). An excellent review of the various solid-state NMR techniques and their application to the study of structure and dynamics in solid-state chemistry and materials science has been given by Eckert [5]. A more recent paper be van Wüllen *et al.* [23] brings together many of the techniques mentioned below to perform detailed structural characterization of aluminophosphate glasses; this paper serves as an excellent demonstration of how these techniques can be used in combination to give unprecedented insight into solid-state structures.

8.3.1 General Techniques for Bulk and Surface Characterization

This section briefly outlines the key techniques that have been developed for application to the characterization of the bulk and surface structure of solid materials. Specific examples of the application of these techniques are provided in Section 8.4.

i) **MAS: magic angle spinning [4].** Sample rotation at the "magic angle" (i.e., 54°44′; the value where $3\cos^2\theta - 1$, which is proportional to the dipolar coupling, is equal to zero) reduces the line broadening effect of dipolar, chemical shift anisotropy, and quadrupolar interactions on the spectrum. The dipolar interaction is averaged to zero, the chemical shift anisotropy is averaged to a non-zero value, and the quadrupolar interaction is only partially averaged, leaving a residual secondary quadrupolar interaction. Overall, the effect of MAS is to increase spectral resolution so that spectral features associated with different chemical environments are identified. MAS and MAS-based techniques remain the routine method for characterization of solid-state materials.

ii) **MAH: magic angle hopping [24].** Whereas MAS averages the orientational dependence of the chemical shift through rapid and continuous spinning about the magic angle, MAH achieves the same averaging by using discrete "hops" to three angular orientations at 120° intervals relative to B_0. In general, there are fewer physical constraints associated with implementing MAH than MAS, thereby allowing for a greater variety of experimental setups; hence MAH is frequently employed in so-called *in situ* studies (see Section 8.6).

iii) **CP: cross-polarization [25].** This is usually used to observe low abundance (often referred to as "dilute") spins such as ^{29}Si or ^{13}C. During the CP process, magnetization is transferred from an abundant spin system source (I, usually ^{1}H) to the dilute nucleus, S, for a specified "contact time" when r.f. fields for both I and S are turned on. During this contact time, the ratio of the power levels between I and S must be equal to the ratio of the gyromagnetic ratios between S and I. The enhanced magnetization of the dilute spin is then detected while the abundant spins are decoupled. The maximum gain in sensitivity is equal to the ratio of gyromagnetic ratios between I and S. CP is most often combined with MAS, so that the MAS reduces line broadening to aid spectral assignment. ^{29}Si NMR, using CP-MAS techniques, has been shown to provide valuable information on the types of silicon sites present on a silica surface; here the technique becomes surface sensitive since it is on the surface that there is a high population of ^{1}H (existing in OH groups) from which to transfer polarization to the ^{29}Si nuclei [26, 27]. A less commonly used application of CP-MAS NMR is found in the characterization of metal oxides, where surface oxygen species have been studied by magnetization transfer from metal nuclei [28].

iv) **CRAMPS: combined rotation and multiple pulse spectroscopy [29].** This technique combines multiple pulse decoupling techniques with MAS to reduce linewidths further, and hence improve spectral resolution. A classic

example occurs in the characterization of silica surfaces. In principle, simple ^{1}H MAS NMR spectroscopy alone should be an extremely useful tool in the characterization of surface hydroxyls. Indeed, this is the case if ^{1}H–^{1}H internuclear distances are large and/or there is fast motional averaging, thereby giving rise to small ^{1}H–^{1}H interactions. However, for a system in which the ^{1}H–^{1}H dipolar line broadening effects are significant, say 20 kHz, sample rotation alone is insufficient and must be combined with multiple pulse spectroscopy methods for averaging out dipolar interactions to yield sufficiently narrow linewidths for spectral assignment. A good example is the application of CRAMPS to study the evolution of silanol populations during the dehydration of a silica gel, as reported by Bronnimann *et al.* [30]. CRAMPS is not used exclusively in surface analysis, but the majority of the catalytic applications using this method concentrate on studying adsorbed species and surface structure [31].

8.3.2 Studying Quadrupolar Systems with $I > {}^1/_2$

A range of solid-state NMR techniques exist to study quadrupolar systems. As discussed earlier in Section 8.2.1, NMR spectra of quadrupolar nuclei are dominated by the nuclear quadrupolar spin interaction. For half-integer quadrupolar nuclei, relatively narrow spectral lines are obtained by limiting observation only to the central $^1/_2 \leftrightarrow {}^1/_2$ NMR transition for which the fist-order quadrupolar effect vanishes. The second-order quadrupolar effect contains high-rank anisotropic terms which are not completely averaged by MAS, hence the motivation to develop a range of pulse sequences – including DOR, DAS, MQMAS, and STMAS (SATRAS), which are discussed below.

i) **DOR: double rotation [32].** Second-order quadrupole effects mean that the frequency of the central transition is dependent on molecular orientation, being determined by both second- and fourth-rank rotation matrices. DOR achieves high resolution of the central transitions by spinning the sample simultaneously at two angles. The first is the magic angle, thereby averaging the second-rank rotation matrix terms to zero. The second angle (30.6° or 70.1°) averages the fourth-rank terms to zero. This experiment is challenging to implement since it involves one rotor spinning inside another. Furthermore, the sample volume of the inner rotor is very small in comparison with the volume of the r.f. coil around the large outer rotor, leading to a relatively low signal-to-noise ratio.

ii) **DAS: dynamic-angle spinning.** This is a two-dimensional NMR experiment which achieves isotropic signals in one dimension and quadrupolar-broadened, anisotropic powder patterns in the other [33]. The experiment takes advantage of the fact that the transition frequency depends on the sample spinning angle. Experiments are performed at two spinning angles – but not with simultaneous spinning at the two angles, so the technique is technically simpler to implement than DOR. A disadvantage compared with DOR, however, is that none of the DAS spinning angle pairs include the magic angle. DAS spectra may be

acquired without contributions from dipole–dipole coupling or chemical shift anisotropy by the addition of an extra "hop" to the magic angle, although this results in loss of signal and hence longer acquisition times. A good example of DAS, including a magic angle "hop," is the observation of five oxygen sites in the SiO_2 polymorph coesite obtained from a ^{17}O spectrum [34].

iii) **MQMAS: multiple-quantum magic angle spinning.** MQMAS was first proposed in 1995 [35] for achieving high-resolution spectra for half-integer quadrupolar nuclei while spinning the sample at the magic angle throughout the experiment. It is much easier to implement than DOR or DAS, and it has now become the primary method by which high-resolution spectra of quadrupolar nuclei are obtained.

iv) **SATRAS or STMAS: satellite transition magic angle spinning.** This was first reported by Gan [36], and is very similar to MQMAS. As with MQMAS, SATRAS is performed only at the magic angle. The advantage of SATRAS over MQMAS is that as it involves only single-quantum coherences throughout, it affords potentially much greater signal-to-noise ratio in a given acquisition time. Further, since the excitation of the satellite transition also has a much weaker dependence on the quadrupole coupling constant than does the excitation of multiple-quantum coherence, SATRAS is more likely than MQMAS to result in observation of all the sites in the spectrum; in MQMAS, excitation conditions are necessarily more site selective. SATRAS itself can, however, suffer from resolution problems and is extremely sensitive to the setting of the magic angle.

8.3.3
Techniques for Measuring Heteronuclear Dipolar Couplings

A variety of approaches have been developed for measuring heteronuclear dipolar couplings (see Section 8.2.1). All of these techniques take a similar form in that they are based on some sort of echo experiment, in which the heteronuclear dipolar couplings would normally be refocused. By applying r.f. pulses to one of the two coupled spins (I and S), complete refocusing can be prevented. The approach taken in the experiments described below is therefore to measure the extent to which the perturbing pulses prevent refocusing, since this will be a measure of the dipolar coupling strength, and hence interatomic distances [see Eq. (8.3)].

i) **SEDOR: spin-echo double resonance [37].** SEDOR is performed on static samples and therefore lacks the spectral resolution usually required for material characterization; for this reason, it is relatively little-used nowadays. The principle of the measurement is as follows. After initial excitation of transverse magnetization on one spin, I, a series of π pulses are applied to the I spin system. This results in refocusing of the dephasing due to heteronuclear decoupling at times 2τ, 4τ, 6τ, and so on later. The echo intensities at these times are recorded as a reference data set. The only loss of intensity between echoes will be due to transverse relaxation. A second experiment is then performed in which π pulses are also applied to the second spin system, S, at times τ, 3τ, 5τ,

and so on. These have the effect of inverting the S spins at these points in time and thus changing the sign associated with the strength of the dipolar coupling interaction between I and S. This, in turn, prevents the compete refocusing of the I–S dipolar coupling at the echo points of 2τ, 4τ, 6τ, and so on. The difference in intensity of the echo maxima between the two experiments depends on the dipolar coupling strength, and the dipolar coupling constant is then relatively easily extracted from plots of echo intensity versus $n\tau$, $n = 2$, 4, 6, and so on.

ii) **REDOR: rotational-echo double resonance [38].** This experiment is very similar to SEDOR except that the I spin echoes are provided by MAS. Under MAS, any I spin transverse magnetization dephases under the I–S dipolar coupling during the first half of the rotor period and is then refocused during the second half of the rotor period. If π pulses are applied to the spin S during the rotor period, the I–S dipolar coupling is only partially refocused at the end of the rotor period for the same reason as the π pulses in the SEDOR experiment perturb the I echoes. In practice, the extent to which the I spin is dephased as a result of incomplete refocusing of the rotational echoes is monitored as a function of the number of rotor periods for which the dephasing is allowed to occur. A π pulse is also applied to the I spins in each experiment half way through the dephasing period to refocus any I spin chemical shift offset, which would otherwise contribute to the net I spin dephasing. REDOR is ideal for measuring dipolar coupling constants of a few hundred to a few thousand hertz. The net I-spin dephasing depends on the rotor period and is larger for slower spinning rates, so it is necessary to consider what spinning rate is most suitable for the particular dipolar coupling constants to be measured.

iii) **TEDOR: transferred-echo double resonance [39].** TEDOR is very similar to REDOR but avoids the background signals from uncoupled nuclei – a TEDOR sequence shows only resonances of dipole-coupled nuclei. Fyfe *et al.* [40] used a combination of REDOR and one- and two-dimensional TEDOR to provide information about connectivities and distances between coupled nuclei in the very large-pore aluminophosphate VPI-5.

iv) **TRAPDOR: transfer of population in double resonance [41].** The principle of the TRAPDOR experiment is the same as that of REDOR. As we have seen, in REDOR the perturbation which prevents the complete refocusing of dipolar couplings is a series of rotor-synchronized 180° pulses applied to one of the spins. In TRAPDOR, the perturbation is caused by adiabatic passages among the Zeeman states, brought about by application of a continuous r.f. pulse to the quadrupolar spin for the first half of the required dephasing period. Grey and Vega [42] applied $^{1}H/^{27}Al$ TRAPDOR NMR to study the ^{1}H and ^{27}Al nuclei of Brønsted acid sites in dehydrated zeolite HY. It was demonstrated that Al atoms located at the surfaces of alumina supports and at acid sites, which were invisible to standard MAS NMR (see Section 8.4.1.1), could be observed. The quadrupole coupling constant of ^{27}Al nuclei coupled to ^{1}H was obtained with high accuracy, and other quantities such as the asymmetry parameter and the ^{1}H–^{27}Al distance were also be determined, albeit with less certainty.

v) **REAPDOR: rotational-echo adiabatic-passage double-resonance [43].** This technique couples REDOR with TRAPDOR to detect heteronuclear dipolar couplings from which the internuclear distance can be calculated. In comparison with TRAPDOR, the REAPDOR experiment causes the transfer of populations between the spin states of the quadrupolar nucleus in the second experiment in a different way. It therefore follows that the two approaches are susceptible to different sources of error, which are discussed elsewhere [43]. An early example of REAPDOR being used to study the location of cations in molecular sieves was reported by Ganapathy and Vega [44]. In the context of zeolites, it has been used to characterize Brønsted acid sites, silicon cluster formation, and the location of cations in the zeolite framework. In addition to referring to these previous works, Holland and Alam [45] also demonstrated that REAPDOR can be used to obtain information on the location and orientation of adsorbed molecules in zeolites.

8.4 Characterization of Heterogeneous Catalysts

Solid-state NMR techniques find many applications in the characterization of solid materials: both in characterizing bulk and surface structure and, in the case of catalysts, understanding surface reactivity. The investigation of bulk structure provides information on local coordination environments. For catalysts, the characterization of active centers on the catalyst surface is frequently a key motivation for study. This includes the detection of acidic or basic sites and elucidation of the structure, and sometimes oxidation state, of active surface species. A number of excellent reviews and books exist to which the reader is referred [46–49]. NMR spectroscopy provides additional and complementary information to alternative methods such as X-ray diffraction and high-resolution electron microscopy. A particular advantage of NMR is in probing amorphous or weakly crystalline materials, as it is most sensitive to the short- to medium-range order of the structure. An excellent general review of NMR spectroscopy as a probe of surfaces of supported-metal catalysts was presented by Van der Klink [50]. A more detailed review of aspects of NMR applied to the study of metals, metal particles, and metal cluster compounds was reported by Van der Klink and Brom [51]. Increasingly, NMR studies are undertaken in combination with numerical simulations in order to aid the interpretation of the NMR data in terms of specific structural features or dynamics of the system of interest.

In the following section, we focus on two families of solids which are of particular interest in catalysis: silicon- and aluminum-containing materials, and vanadium-containing materials. In addition to being a nucleus of particular interest in the context of catalysis, vanadium also serves as an example of a quadrupolar nucleus for study by NMR. The full multinuclear capability of NMR is regularly exploited in catalysis and other nuclei studied include ^{95}Mo [52], ^{89}Y [53], ^{71}Ga [54], and ^{43}Ca [55].

8.4.1 Silica- and Alumina-Containing Materials

Silica- and alumina-based materials are among the most widely employed materials in catalysis; they can be used either as a support for the catalytically active component or as the catalyst itself. Although the majority of ^{29}Si and ^{27}Al NMR studies focus on zeolites and related structures, pure silicas and aluminas remain materials of significant interest, particularly with respect to the characterization of their surfaces.

8.4.1.1 Pure Silicas and Aluminas

In noncrystalline silicas, the characterization of bulk structure takes the form of the determination of the Si−O−Si bond- angle distribution, which can be correlated with the ^{29}Si chemical shift [56, 57]. A review of ^{29}Si NMR of inorganic solids was published by Engelhard and Koller [47]. ^{29}Si and ^{1}H NMR methods are widely used to characterize the surface structure of porous silicas. Such methods include ^{1}H MAS, ^{1}H CRAMPS [30], and, of course, ^{29}Si–^{1}H CP-MAS and other multinuclear strategies. These methods are used to characterize the surface in terms of the main two types of silanol species: the silanol Q3 [$(-O)_3SiOH$] and geminal Q2 [$(-O)_2Si(OH)_2$] species. More recent extensions of these studies include the discrimination of internal and external hydroxyl groups in terms of both their chemical nature, local mobility, and proximity to trapped water [58], and also using ^{29}Si–^{1}H CP-MAS, to distinguish hydrogen-bonded silanols from non-hydrogen-bonded silanols [59]. Maciel and co-workers reported a study of the molecular dynamics of deuterated surface silanols using ^{2}H NMR. Modeling of the ^{2}H lineshape allowed the possible motions of the hydroxyl bond to be identified [60].

A complication of NMR studies on aluminas, as compared with silicas, is the presence of what is often referred to as "invisible" Al. There is a wealth of literature on this topic since it is as relevant to studies of zeolites and aluminosilicates as it is to pure aluminas. In 1960, O'Reilly first reported that when using ^{27}Al NMR to study α- and γ-Al_2O_3, the total integrated intensity of the signal from γ-Al_2O_3 was only 25% of that from α-Al_2O_3 [61]. This effect was exacerbated by increasing the surface area of γ-Al_2O_3, which resulted in a further decrease in signal intensity. The origin of this effect was originally assigned to the magnitude of the large electric field gradient experienced by an ^{27}Al nucleus at the surface, in contrast to nuclei in more symmetrical environments. In 1992, Huggins and Ellis suggested that the effect instead derived from dynamic events occurring on the surface associated with the movement of surface protons or hydroxyl groups [62]. More recently, Kraus *et al.* [63] undertook a detailed, systematic study of a number of γ- and η-Al_2O_3 samples, investigating the effect of spinning speed on Al visibility. It was shown that spinning at ∼10 kHz in a 9.4 T field was insufficient to resolve all of the Al sites present; however, the spectrum acquired while spinning at 29 kHz was able to account for all of the Al present. It should be noted that this result would be a manifestation of the hypothesis proposed by O'Reilly [61]. All of the studies in this area have clearly demonstrated that the nature of the surface has a direct influence on the visibility of Al nuclei to the NMR experiment.

^{27}Al NMR studies have, as with the application of ^{29}Si NMR to the study of silicas, been widely used as a probe of the bulk and surface character of aluminas for a variety of applications. An elegant example was reported by Kraus and Prins [64], who utilized ^{27}Al MQMAS and off-resonance nutation experiments to study both γ-Al_2O_3 and γ-Al_2O_3 impregnated with phosphorus and/or molybdenum. This combination of NMR techniques revealed the formation of amorphous $AlPO_4$, which could not be detected by, for example, X-ray diffraction.

8.4.1.2 Zeolites and Aluminosilicates

Zeolites, and aluminosilicates in general, have applications in separations (e.g., water purification), thermal collection, medicine, and catalysis. NMR studies of these materials focus on ^{29}Si (natural abundance 4.6%) and ^{27}Al (natural abundance 100%). ^{17}O may also be studied although isotopic enrichment is required because of its low natural abundance (0.04%) [65]. As such, ^{17}O NMR studies of aluminosilicates are not described here; however, the interested reader can find a good introduction to this area elsewhere [66].

Early NMR studies of zeolites were based on straightforward ^{29}Si MAS NMR [67]. It was demonstrated that ^{29}Si MAS NMR spectra can show up to five peaks, each associated with a different distribution of Si and Al around a central Si nucleus at the center of the SiO_4 tetrahedron; that is, Si[4Al], Si[3Al,1Si], Si[2Al,2Si], Si[Al,3Si], and Si[4Si]. Assuming that Lowenstein's rule applies, which states that Al−O−Al linkages do not exist, it is therefore possible to calculate the framework Si/Al ratio of a zeolite directly from the ^{29}Si NMR spectrum [68]. The framework compositions of zeolitic materials containing other elements such as zinc (zincosilicates) [69], gallium (gallosilicates) [70], or titanium (titanoaluminosilicates) [71] have also been reported. Many more sophisticated techniques are now applied, often with simulations required for their interpretation. Elegant examples include a symmetry-based ^{29}Si dipolar recoupling MAS NMR experiment, which was applied by Brouwer *et al.* [72] to a pure silica zeolite to extract bonding connectivities and long-range distance information between Si sites.

In principle, the ^{27}Al NMR spectra of aluminosilicates should be much simpler than ^{29}Si NMR spectra. Given Loewenstein's rule, only a single line in the NMR spectrum should be observed. However, both six- and five-coordinate Al also exist, in addition to Al in distorted tetrahedral environments [73]. The full range of DOS, DAS, MAS, MQMAS, TRAPDOR, and very high–field NMR (i.e., 14.4 and 18.8 T) have been brought to bear in addressing the challenges of observing and characterizing the different Al environments (e.g., [74, 75]). Connectivities and distances between specific nuclei are now routinely obtained through CP and TEDOR/REDOR experiments. A good example is the series of ^{27}Al–^{29}Si connectivity experiments reported for zeolites A, X, Y, and Ω reported by Fyfe *et al.* [76].

NMR is also now a standard tool for the investigation of extra-framework cations in zeolites. The zeolitic framework is negatively charged due to the presence of tetrahedrally coordinated aluminum atoms. This charge can be compensated either by positively charged protons from hydroxyl bridging groups or exchangeable extra-network cations. These cations are located in well-defined positions within the

zeolitic framework and therefore influence the effective pore diameter. They also act as strong adsorption centers due to their strong electrostatic charge, thus making them catalytically relevant. Solid-state NMR has proven to be a very useful tool for determining both the distribution of such extra-framework cations within the zeolitic framework and their mobility. A good example is the application of very fast ^{23}Na MAS and MQMAS NMR to identify the cations in zeolites NaX and NaY and changes in their distribution upon adsorption of different hydrofluorocarbons [77]. Other cations studied using solid-state NMR include ^{6}Li, ^{7}Li, ^{133}Cs, ^{139}La, and ^{205}Tl. An excellent review is provided by Hunger and Brunner [78].

8.4.2
Vanadium-Containing Materials

A particularly important class of vanadium-containing materials are VPO catalysts, which are employed in maleic anhydride production from *n*-butane. It is believed that the distribution of V^{4+} and V^{5+} is important in determining catalytic activity. The presence of paramagnetic V^{4+}, however, poses a problem in the application of conventional ^{51}V or ^{31}P NMR due to signal broadening. Li *et al.* [79] first proposed the ^{31}P spin-echo mapping NMR technique to overcome this problem, thereby enabling the indirect observation of paramagnetic V^{4+} species in VPO catalysts and their evolution upon treatment with *n*-butane. As a result, it was possible to determine that β-$VOPO_4$ was a precursor to the catalytically $(VO)_2P_2O_7$ phase into which it transformed during reaction. Much of the early work in this area has been comprehensively reviewed by Tuel *et al.* [80], and the technique was discussed in detail by Tong [81]. Other vanadate materials that have been studied by NMR include: K–V–O catalysts [82–86] and vanadium-doped aluminum oxides for applications in the ceramics industry [87].

In addition to the characterization of their bulk structure, the characterization of surface species in vanadium-containing catalysts is also a subject of extensive interest. Supported vanadium oxide catalysts are widely investigated for the oxidative dehydrogenation of alkanes. Vanadium can exist on the surface in various forms: mono-, di-, or polyvanadate species or as bulk-like tetrahedral V_2O_5 crystals (see Figure 8.2). Solid-state NMR is a particularly useful technique to provide insight into the local environment of vanadium nuclei, including the determination of coordination number, geometry, the number of nonequivalent V^{5+} sites, first coordination sphere, and the distortion of this sphere.

Static and MAS ^{51}V NMR techniques have been applied to study the structure of vanadium species on oxide supports with varying loadings of vanadium [89, 90]. At loadings below 1 wt%, isolated VO_4 units in a tetrahedral coordination are present as indicated by a chemical shift of −750 ppm. At higher loadings, the appearance of polymeric vanadates with distorted octahedrally coordinated vanadium nuclei is observed (−350 ppm) followed by the formation of V_2O_5-like structures (−612 ppm). Additionally, in the case of samples with high vanadium loadings, the formation of $AlVO_4$ may be observed after calcination at high temperatures.

It is possible to correlate observations from NMR investigations with catalytic performance. For example, Steinfeldt *et al.* studied the influence of vanadium loading

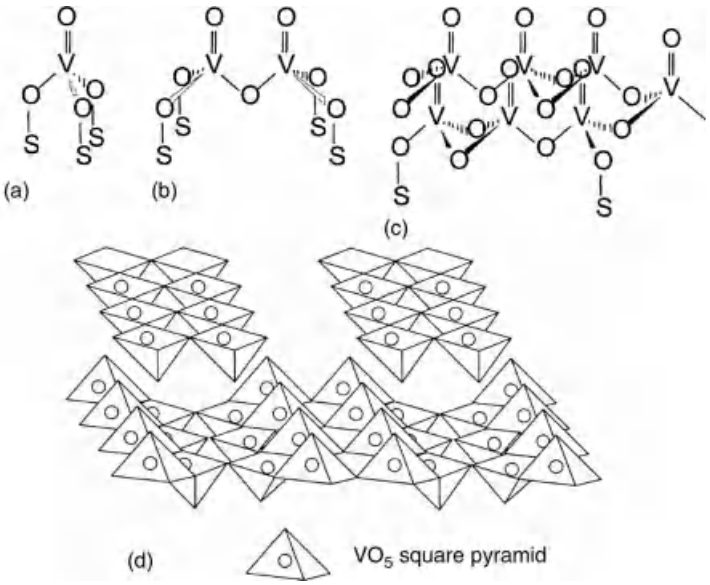


Figure 8.2 Possible molecular configurations for supported vanadium oxides (S represents the support): (a) monomeric vanadate; (b) dimeric vanadate; (c) polymeric vanadate; (d) V_2O_5 crystals. Reproduced from [88] with permission.

and calcination temperature on catalytic activity in the oxidative dehydrogenation of propane [91] over alumina-supported vanadia catalysts. It was concluded that isolated and polymeric tetrahedrally coordinated V^{5+} species are much more active in comparison with $AlVO_4$ and V_2O_5 structures.

8.4.3
Surface Acidity and Basicity

The strength and accessibility of Brønsted sites play an important role in many catalytic processes. Determination of these parameters via NMR typically involves the use of probe molecules which can be studied by ^{1}H, ^{2}H, ^{13}C, ^{15}N, or ^{31}P NMR spectroscopy. In order to distinguish between acidic and nonacidic sites, the ability of the site to protonate a strongly basic molecule such as pyridine or trimethylphosphine is utilized [49]. Quantification of the strength of different Brønsted sites requires the use of weaker base molecules such as acetone, perchloroethylene, or trimethylphosphine oxide. Generally, these molecules do not form complexes, instead interacting via hydrogen bonds with the surface, which then give rise to changes in the chemical shift that reflect the strength of that interaction. Additional information about the accessibility of Brønsted centers can be obtained by using a probe molecule which is bulky enough to have only limited access to hydroxyl groups existing on the catalyst surface. An example of such a molecule used in the identification of the Brønsted sites within H-ZSM-5 and Mo-exchanged ZSM-5

zeolites is perfluorotributylamine [92]. In that work, ^{1}H MAS NMR was used for the quantitative evaluation of external acidity, and also to determine the position of nonacidic silanols and some nonframework Al species.

Investigation of Lewis acidic centers by NMR is also carried out with the use of probe molecules. The most frequently used are pyridine, trimethylphosphine, trimethylphosphine oxide, acetone, and carbon monoxide [49] with ^{31}P, ^{15}N, and ^{13}C NMR employed as required. Haw *et al.* [93] used ^{15}N NMR to study the evolution of acid sites on a sulfated zirconia catalyst at low temperatures; [^{15}N]pyridine was used as a probe molecule. Figure 8.3 shows that two different signals at −180 and −106 ppm were observed, corresponding to Brønsted and Lewis acid sites, respectively. An additional signal at −65 ppm, observed at high pyridine loadings, was assigned to excess pyridine not bonded to any particular site.

Basic centers also exist on the surface of catalysts, for example, as framework basic oxygen atoms within zeolites. The most common method of using NMR to characterize basic sites is, as with acid sites, through the use of probe molecules. In this case, probe molecules include trichloromethane, trifluoromethane, chloroform, methyl iodide, and pyrrole [49, 94]. It is also possible to study basic sites directly using ^{17}O NMR spectroscopy. For example, ^{17}O MQMAS and DOR NMR investigations of a series of alkali metal cation-exchanged zeolites LSX have been performed

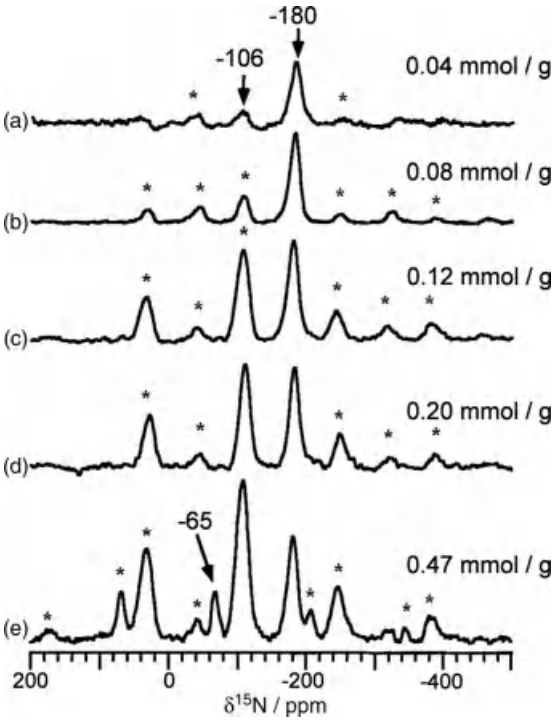


Figure 8.3 ^{15}N CP-MAS spectra of [^{15}N]pyridine titrating sulfated zirconia (4.57 wt% S): (a) 0.04, (b) 0.08, (c) 0.12, (d) 0.20, and (e) 0.47 mmol g^{-1}. Reproduced from [93] with permission.

and a correlation between the chemical shift of ^{17}O nuclei and the radius of the alkali metal cation was found [95]. This work indicated that the framework oxygen atoms in the zeolite structure were influenced by the introduction of alkali metal cations and, as a consequence, the basic properties of the material were altered.

8.5 Porosity, Adsorption, and Transport Processes

8.5.1 Porosity

8.5.1.1 ^{129}Xe NMR

^{129}Xe is a particularly useful species for characterizing porous solids and in particular the nature of surfaces. This is a consequence of the large chemical shift range exhibited by xenon as a result of its large electron cloud. As such, subtle changes to the environment of Xe are reflected in measurable chemical shifts. Ito and Fraissard first showed that the ^{129}Xe NMR chemical shift of adsorbed Xe is given by the following expression [96]:

$$\delta_0 + \delta_S + \delta_E + \delta_{Xe-Xe}\varrho_{Xe} \tag{8.9}$$

where δ_0 is the shift of the gaseous reference, δ_S is the shift due to collisions between Xe and the cage walls, and δ_E is the contribution to the chemical shift due to the electric field created by any cations present. The final term, in which ϱ_{Xe} is the density of Xe adsorbed in the cavities and/or channels, corresponds to the increase in chemical shift caused by Xe–Xe collisions.

^{129}Xe NMR has been used extensively to investigate the pore architecture of microporous structures such as zeolites; and to identify different adsorption environments within such structures, for example, L, Z, and ZSM zeolites [97]. These studies were subsequently extended in order to determine the dimensions of cavities within those materials [98]. ^{129}Xe NMR spectroscopy has also been used to investigate the crystallinity of zeolites [99] and in the investigation of coke formation inside the zeolite cages [100]. In the latter study, it was concluded that, at up to 10 wt% coke laydown, coke was deposited only in the supercages; at higher coke laydowns, coke also accumulated on the external surface of the zeolite.

More recently, hyperpolarized xenon has been used in the characterization of solids. The principal advantage of hyperpolarized xenon is a substantial gain in signal-to-noise ratio, typically 4–6 orders of magnitude greater than that obtained by thermal polarization. Examples of the use of hyperpolarized xenon include characterization of the pore structure of zeolites [101] and mesoporous films [102] and chemical shift imaging of adsorbents [103]. This method has also been combined with MAS NMR (Section 8.3.1) to characterize the pore architecture of ITQ-6 zeolite, a dealuminated form of ferrierite [101]. Ferrierite contains nearly spherical cages, which only a single Xe atom can enter. These connect one-dimensional channels in which Xe can pack in a manner facilitating Xe–Xe interactions. Two resonances are

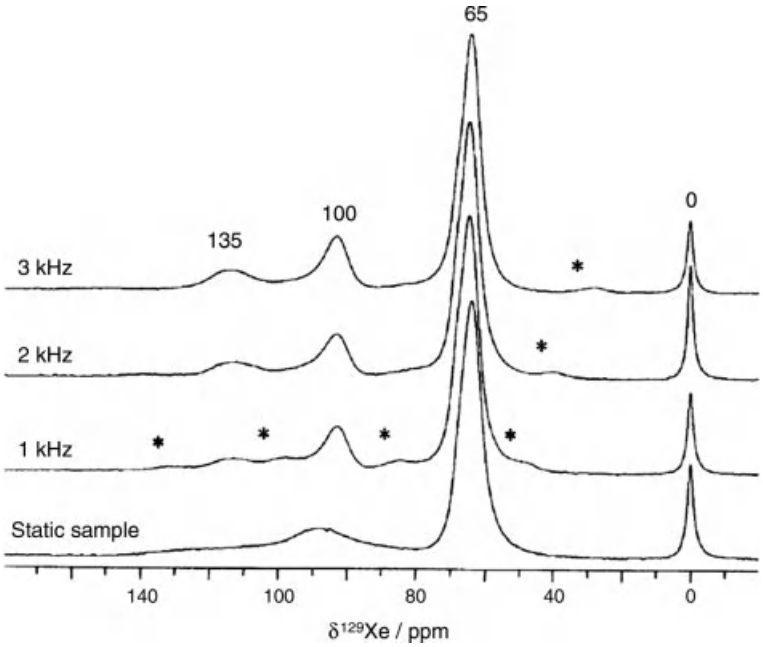


Figure 8.4 Solid-state ^{129}Xe NMR spectra of zeolite ITQ-6 recorded under a flow of 100 ml min^{-1} of 1% hyperpolarized xenon and sample spinning rates of 0 kHz (static sample) to 3 kHz. The experiments were performed in a magnetic field of $B_0 = 7.0$ T, at the resonance frequency of 83.0 MHz, with a repetition time of 1 s, and 1024 scans per spectrum. Reproduced from [101] by permission of the PCCP Owner Societies.

therefore observed, at 135 and 100 ppm, corresponding to Xe adsorbed in the channels and cavities of the zeolite, respectively. Interestingly, when the dealuminated sample, ITQ-6 is studied, an additional signal corresponding to Xe adsorbed in the inter-lamellar space is observed at 65 ppm (Figure 8.4). The dealuminated sample also shows a significant decrease in the signal at 135 ppm relative to that at 100 ppm, consistent with dealumination proceeding along the channels.

8.5.1.2 T_1 and T_2 Relaxometry

T_1 and T_2 relaxation time measurements are well established as a method of characterizing porous materials [104, 105] and provide an *in situ* determination of pore-size distributions [106]. The majority of these techniques were initially developed for characterizing oil-bearing rocks in the oil recovery industry. Throughout the years, there has been extensive debate about the relative merits of selecting either T_1 or T_2 for the characterization of porous media. In summary, it is easiest to differentiate between them on the basis that T_1 and T_2 processes are averaged over different temporal scales. T_1 probes variations occurring over milliseconds to seconds whereas T_2 probes variations occurring on a microsecond time scale. For this reason, T_1 is often considered to be an indicator of the overall pore structure whereas T_2 reflects local pore geometry and surface chemistry.

The assumptions upon which pore size is determined using NMR relaxation time analysis are most commonly referred to as the Brownstein and Tarr model [107]. This assumes two environments for a liquid contained within a pore: the first is a layer of thickness λ at the surface of the pore where the relaxation time is T_{1s}. In the remainder of the pore, the relaxation rate takes on the value T_{1b}, characteristic of the free or "bulk" liquid. The surface relaxation rate is enhanced with respect to the bulk relaxation rate due to short-range dipole–dipole, fluid–solid interactions; hence λ is assumed to be of the order of a few molecular diameters. If the pore size is large compared with λ, then the proportion of the pore volume in the surface-affected phase, p_s, is given by

$$p_s = \lambda \frac{s}{v} \tag{8.10}$$

where s and v are the surface area and volume of the pore, respectively. The remainder of the pore volume, $p_b = 1 - p_s$, experiences bulk relaxation. The observed relaxation time for the liquid in the pore as described by the "two-fraction fast-exchange" limit is therefore

$$\frac{1}{T_1} = \frac{p_s}{T_{1s}} + \frac{p_b}{T_{1b}} \tag{8.11}$$

By assuming a pore shape (typically spherical or cylindrical), the observed relaxation time for that pore can now be expressed as a function of the pore radius. In a real material, there will be a distribution of pore sizes and hence a distribution of T_1 values. An experimental measurement proceeds by recording the T_1 of the sample and then fitting the magnetization recovery curve to a distribution of T_1 values and hence pore sizes, thereby yielding the pore-size distribution. Exactly the same approach can be used based on a measurement of T_2. The relative strengths of T_1 and T_2 measurements in this application are discussed elsewhere [108]. An extension of these relaxometry measurements is to resolve spatially the relaxation time measurement by combining it with an imaging pulse sequence. In this case, each image pixel is associated with its own value of the relaxation time, hence we obtain a spatially resolved measurement of the pore-size distribution. Such measurements are useful in characterizing sub-millimeter scale variations in porosity such as those that are introduced into a porous material, for example, a catalyst pellet, as a result of the manufacturing process [109]. Recently, two-dimensional (2D) relaxation time correlations have become popular for exploring surface interactions and transport at the microscopic scale in liquid-saturated porous materials; these methods will be discussed in Section 8.5.2.

8.5.1.3 **Magnetic Resonance Imaging**

The majority of early MRI studies specific to catalysis addressed the heterogeneity in structure and transport within oxide catalyst pellets. The in-plane spatial resolution achieved in these studies was of the order of 30–50 μm for an image slice thickness of 0.3 mm and the pellets themselves were of typical dimension 1–5 mm. In particular, spatially resolved maps of spin density, T_1, and molecular diffusivity of water within a

porous catalyst support pellet [110] were reported with an in-plane spatial resolution of $45 \times 45\,\mu m$. Estimates of overall pellet voidage obtained from spin density maps agreed to within 5% with that obtained by gravimetric analysis. Even though the coarse resolution T_1 maps provide only an estimate of mean pore size within a given image pixel, these data give us insights additional to those from bulk pore-size distributions as obtained, for example, by mercury porosimetry or nitrogen adsorption. There have been a number of studies exploiting this type of magnetic resonance measurement. For example, water spin density imaging studies have been used to explore the 3D structure of activated alumina spheres – the spheres were observed to exhibit a uniform ball structure, comprising spherically layered substructures and voids [111]. Simple spin-density imaging has also been used to characterize the tortuosity of catalyst pellets manufactured by different processes [109, 112]. This was achieved by initially impregnating the catalyst with deuterated water (invisible to a ^1H MRI experiment) and then immersing it in normal protonated water. The diffusive exchange of ^1H_2O with ^2H_2O within the pellet was then followed by ^1H imaging. The effective water diffusivity and hence catalyst tortuosity were obtained by fitting the time-resolved ^1H_2O concentration profiles to a standard diffusion equation. Measurements of this type are straightforward to perform and give immediate insight into transport anisotropies within the catalyst resulting from the manufacturing process. Later work demonstrated that it is possible to characterize the mesoscale porosity of a given batch of catalyst pellets by a fractal dimension [113]. Numerical modeling strategies employing simulation lattices constructed to have the same fractal dimension as those obtained from the magnetic resonance images have shown some success in predicting mass transfer characteristics in porous catalyst supports [114]. This toolkit of magnetic resonance measurements, namely ^1H spin density imaging with the ability to exploit relaxation contrast, has also been used to study aspects of catalyst preparation, for example, the impregnation of oxide supports with metal ions [115].

Magnetic resonance has also been applied to pellet-scale imaging of the effects of reaction occurring within catalyst pellets. Koptyug *et al.* [116] reported ^1H images of liquid distribution during α-methylstyrene evaporation accompanied by its vapor-phase hydrogenation within a cylindrical $Pt/\gamma\text{-}Al_2O_3$ catalyst pellet (diameter and height 4.7 mm). Imaging and relaxometry methods have also been used to probe how hydrocarbon (coke) residues are deposited within a catalyst, thereby modifying its surface chemistry and pore structure and hence influencing transport and reaction processes. A number of different approaches have been reported for monitoring both the spatial distribution of coke and the qualitative evolution of the carbon-to-hydrogen ratio which characterizes that coke, within porous alumina pellets and zeolites [117–119].

8.5.2
Adsorption

A range of NMR techniques are applied to probe adsorption processes on catalyst surfaces. In addition to ^{129}Xe studies (Section 8.5.1.1) and simple ^1H NMR [120], ^2H

and double resonance methods are utilized, yielding completely different information. The ^2H approach lies in the analysis of the NMR lineshape, which can be modeled to identify the motions being demonstrated by the adsorbed molecule and, if the molecule is undergoing an isotropic motion, the correlation time of that motion can be obtained. Thus, ^2H NMR is a very sensitive probe of sorbate mobility at an adsorption site, and will identify multiple types of adsorption site on the surface. If a site-to-site distance is assumed, surface diffusion coefficients can be estimated using this approach [121, 122]. Another example of using ^2H to probe adsorption is the work of Klug *et al.* [123] on the formation of ethylidene from acetylene and hydrogen coadsorbed on platinum. Double resonance methods came to prominence in the late 1980s when Schlicter and co-workers [124] reported ^{195}Pt–^{13}C distance measurements on CO adsorbed on platinum. More recent examples include the characterization of the adsorption of toluene within zeolite LiNa-Y [125] and the determination of the structure of trimethylphosphine bound to Brønsted acid sites in zeolite HY [126]. A further approach to investigating events occurring at the catalyst surface has been the use of one- and two-dimensional NMR exchange measurements [127].

More recently, novel approaches to using T_1 and T_2 relaxation time measurements for characterizing adsorption have been reported. In particular, T_1–T_2 and T_2–T_2 correlations are finding widespread application. In general, T_1–T_2 correlations are used to characterize sorbate–surface interactions, whereas T_2–T_2 correlations are useful in characterizing transport and exchange processes at the pore scale of microporous and mesoporous materials. The T_1–T_2 correlation [128] is used to determine the ratio T_1/T_2, which yields information on the strength of sorbate–surface interactions [129–131]. As a rule, the stronger the interaction (adsorption) between a liquid molecule and the pore surface, the larger the observed (averaged) T_1/T_2 ratio of the liquid becomes. In practice, the exact value of the T_1/T_2 ratio will be determined by a number of factors, including surface molecular mobility, concentration of pore-surface paramagnetic species, partial saturation of pores, local pore geometry, and bulk liquid properties. However, T_1/T_2 does provide a qualitative comparison between similar samples (e.g., same porous solid, different imbibed liquids), in which case it can be assumed that the reduction in T_1 and T_2 relaxation times due to local pore geometry and bulk liquid properties will be constant and will therefore have a negligible influence on the ratio. This approach may be of particular use in probing which species dominates the catalyst surface in a multicomponent adsorption process. Weber *et al.* [131] reported results of such an investigation in which they studied the relative strengths of interaction of molecular species associated with the liquid-phase hydrogenation of 2-butanone (namely 2-butanone, 2-propanol, and water) over Ru/SiO_2 and Pd/Al_2O_3 catalysts.

8.5.3 Diffusion

PFG or PGSE NMR (Section 8.2.3.2) is widely used to characterize molecular diffusion in porous solids and, in particular, zeolites [132–134]. The PFG NMR technique measures the self-diffusion coefficient, which is defined as the molecular

displacement due to Brownian motion, in the absence of any concentration gradient [135]. Note that this differs from the mutual diffusion coefficient, which is the diffusion due to a concentration gradient; although in some cases mutual and self-diffusivity may coincide.

When conducting NMR measurements of diffusion, care must be taken if quantitative data are to be acquired. In particular, it is important to make sure that the diffusion measurement is not influenced by any convection currents in the sample cell, and more importantly when studying diffusion in catalysts, it is necessary to know the typical root-mean-square displacement expected during a given observation time such that the optimum selection of pulse sequence parameters is made. In the case of diffusion in microporous solids, such as zeolites, this is particularly important as the diffusing molecules may diffuse both within the microporous cavities and between the crystallites in the mesoporous space [136]. While such measurements most frequently employ ^{1}H NMR, ^{2}H NMR has also been used to characterize intra-cage and inter-cage transport of aromatics in Y-zeolites [122].

A wider range of NMR techniques have been applied to study molecular diffusion, particularly of liquids, inside mesoporous oxide catalyst supports and supported-metal catalysts. Weber *et al*. [137] used a PFG-based technique to probe diffusion in liquid-saturated catalyst pellets. For the first time, evidence was seen for the existence of two diffusion regimes, attributed to bulk liquid diffusion in the catalyst pores and restricted diffusion of molecules in the vicinity of the pore surfaces, where adsorption occurs. By fitting a model for two-site exchange to these data, the values obtained for bulk pore and pore-surface diffusion for 1-octene within a 1 wt% Pd/Al_2O_3 catalyst were found to be 1.3×10^{-9} and 1.7×10^{-11} $m^2 s^{-1}$, respectively, with the estimated mean residence time of a molecule on the pore surface being of order 150 ms. In a related study, data were also recorded for pure 2-propanol and pure water within porous alumina pellets, and the results were compared with those of molecular dynamics simulations [138]. Trends in the magnetic resonance and molecular dynamics results were consistent and a direct comparison suggested that the magnetic resonance measurement of surface diffusion probes two molecular layers adjacent to the catalyst surface. This result is consistent with the chemical engineers' "rule-of-thumb" regarding the extent of the surface-influenced layer. This comparison of magnetic resonance measurement with molecular dynamics simulation therefore provided a useful confirmation of this assumption.

8.6 "*In Situ*" NMR

Inevitably there is an inherent limitation to the extrapolation of information acquired under *ex situ* conditions to describe processes occurring under reaction conditions. For that reason, as outlined in other chapters in this volume, there is a drive towards conducting measurements during the process of interest, either under conditions adapted to facilitate measurement or, ideally, under conditions approximating that of

a working reactor. Within the magnetic resonance literature these are referred to as *in situ* and *operando*, respectively. To avoid confusion, the same terminology will therefore be applied herein. The experimental considerations for *in situ* measurements are described in Section 8.6.1, and Section 8.6.2 provides selected examples of areas in which these measurements have been applied; in all cases, the examples derive from studies of heterogeneous catalytic process, although *in situ* NMR studies have also been applied to, for example, lithium ion batteries [139].

8.6.1 Experimental Apparatus

In situ NMR methods can be broadly divided into two main areas: those methods that operate under "batch" conditions in sealed vessels and those that operate under "flow" conditions. These methods will be described in Sections 8.6.1.1 and 8.6.1.2, respectively.

8.6.1.1 Batch Conditions

The initial approach developed for experiments under batch conditions was to load the catalyst and reactants, the latter usually via a vacuum line, into a glass ampoule designed to fit precisely inside an NMR rotor [140]. This ampoule is subsequently sealed and placed inside the rotor within which the sample is then heated in order to effect the desired catalytic transformation. Nowadays, commercial Pyrex inserts designed to fit inside MAS rotors are available. Heating of the sample may be carried out either within the NMR instrument itself, or *ex situ* with the NMR spectra acquired at room temperature afterwards. Of these, however, only the former can be considered as an *in situ* approach. A number of variations on this method have been demonstrated and are the subject of numerous reviews [141–144]. One of the most widely adopted approaches to *in situ* NMR is the use of the CAVERN experimental setup developed by Haw *et al.* [145]. A diagram of a CAVERN device is shown in Figure 8.5a. In this apparatus, the adsorption step is carried out under cryogenic conditions, allowing the study of reactive species at both low and elevated temperature. Pretreatment and adsorption of reactant upon the catalyst take place outwith the MAS rotor prior to transfer into the rotor. A broadly similar setup was also developed by Zhang *et al.* [92] and is shown in Figure 8.5b. This technique also involves sealing of the rotor inside the apparatus after transfer of the catalyst without contact to air. Additionally, the apparatus may be used for *ex situ* studies under flow conditions.

The temperatures that can be achieved in the apparatus described above are necessarily constrained by the operating parameters of the NMR equipment. In order to overcome this limitation, and study reactions at higher temperatures, techniques have been developed employing infrared laser heating [146, 147] or inductive heating via a platinum metal coating on the MAS rotor [147]. These methods, however, have yet to find widespread application. Infrared laser heating is experimentally challenging and results in inhomogeneous temperature across the sample, and the temperature must be calibrated against an external standard. The inductive heating

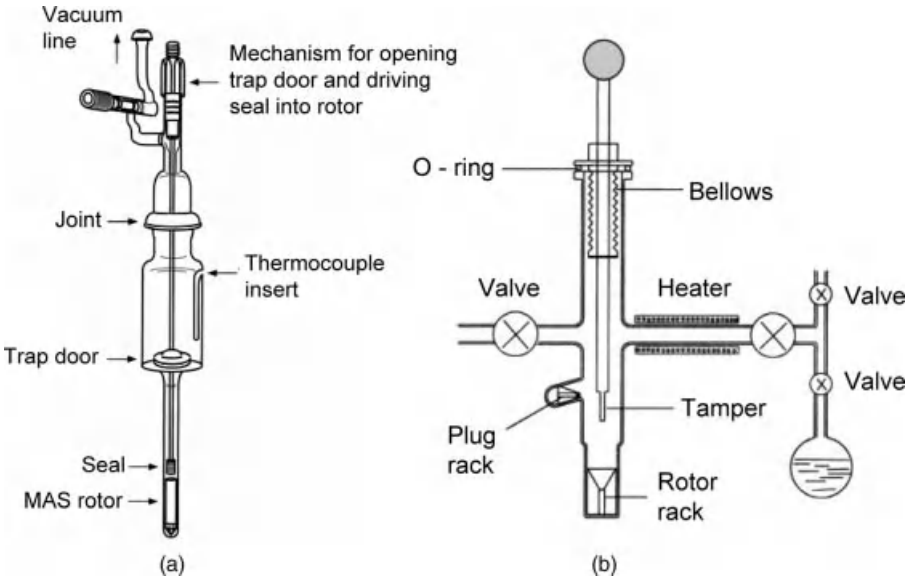


Figure 8.5 Examples of experimental setups developed for *in situ* MAS NMR studies under batch conditions. (a) The CAVERN device developed by Haw *et al.* Adapted from [145] with permission. (b) Apparatus developed by Zhang *et al.* Adapted from [92] by permission of The Royal Society of Chemistry.

approach also suffers from significant temperature gradients and the need to calibrate the temperature against an external standard. Also, the short periods for which heating is carried out may be insufficient to acquire a sufficiently high-resolution NMR spectrum.

In addition to reactions where catalysis is effected through an increase in sample temperature, photocatalytic reactions may also be carried out under *in situ* NMR conditions. This approach, developed by Raftery and co-workers (e.g., [148, 149]) incorporates a light guide into the NMR probe which allows the irradiation of optical microfibers coated with TiO_2 catalyst particles. Both ^{1}H and ^{13}C NMR spectra have been successfully acquired under *in situ* conditions using such a technique.

8.6.1.2 **Flow Conditions**

Experimental techniques for *in situ* NMR measurements of catalytic reactions under flow conditions have recently been reviewed [150]. It is important to distinguish between those methods which are true *in situ* approaches where the catalytic reaction is conducted under flow conditions inside the NMR probe and those in which the reaction is conducted *ex situ*, and then stopped or quenched prior to transfer of the sample to the NMR probe. Although only the former can be considered a true *in situ* method, both techniques can be used to provide valuable mechanistic insights.

The first demonstration of *in situ* NMR of catalytic processes under flow conditions was carried out in 1987 [151, 152]. MAS was not applied in these studies, however, hence the spectra obtained comprised very broad NMR signals and interpretation of

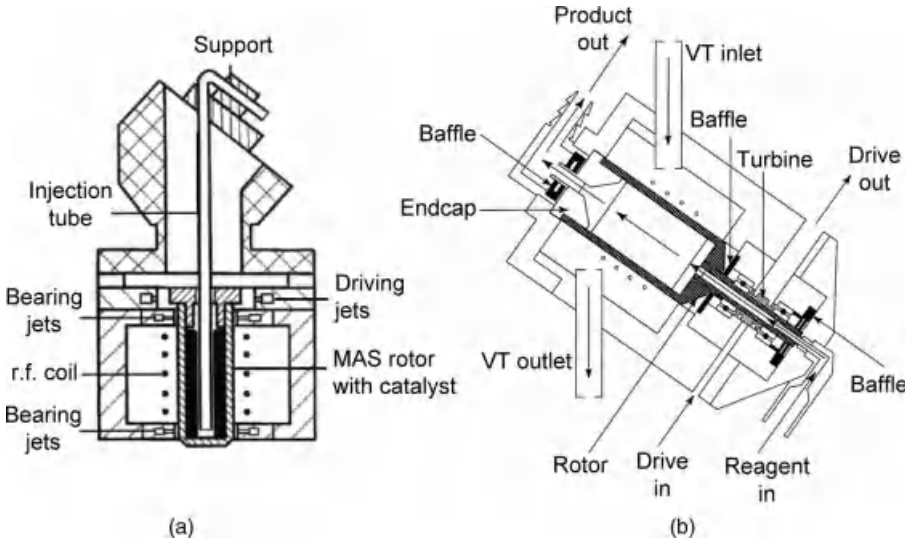


Figure 8.6 Examples of experimental setups developed for *in situ* NMR under flow conditions. (a) A modified MAS cell developed by Hunger and Horvath. Adapted from [153] by permission of The Royal Society of Chemistry. (b) An alternative design developed by Munson and co-workers Adapted from [155] with permission.

the data was limited. The combination of MAS with flow conditions has since been demonstrated by a number of workers [153–155]. In each of these cases, reactions may be carried out at elevated temperatures, with the possibility of reaching up to 973 K in some apparatus. Schematics of the designs developed by Hunger and Horvath [153] and Munson and co-workers [155] are shown in Figure 8.6a and b, respectively. The approaches exemplified therein involve the continuous injection of reactant gases directly into the MAS rotor via an injection tube, while effluent gases leave via a tube in the rotor cap. A detailed description of a modified MAS probe was provided by Buchholz *et al*. [156]. It is worth noting that the significant centripetal forces exerted under spinning pack the catalyst particles against the wall of the rotor and as a result the gas stream may not pass directly through the catalyst itself.

A number of variations on the theme of *in situ* flow measurements have been developed. For example, the stopped-flow method involves changing from reactant flow to an inert gas flow such as N_2 during reaction [157]. This has the advantage that it allows the detection of transient surface species that that may persist on the surface for a time scale that is less than that required to record a sufficiently high-resolution NMR spectrum. Additionally, labile species may be removed from the catalyst surface, facilitating the determination of intermediates. This method requires the same instrumentation as continuous-flow measurements. A variant on the stopped-flow method is the pulse–quench technique. This employs a switch for rapidly changing between the reactant stream ("pulse") and cryogenically cooled nitrogen ("quench") in a microreactor *ex situ* to the NMR instrumentation [158, 159]. The switch is achieved via a pneumatically actuated valve. After quenching, the catalyst is

transferred to a MAS rotor under a controlled atmosphere, allowing for acquisition of spectral data. Although this cannot be considered a true *in situ* NMR method, it allows for analysis of the surface chemistry at intermediate stages of reaction. The time required for acquisition of a high-resolution NMR spectrum is often long in comparison with the time scale of reaction or the persistence of intermediate species on the catalyst surface and therefore their analysis would not be possible under true *in situ* conditions. The most striking application of the pulse–quench technique has been in the elucidation of the reaction mechanism in the methanol-to-hydrocarbon reaction (see Section 8.6.2.2.4).

As mentioned earlier (Section 8.3.1), the use of MAH makes the implementation of *in situ* experiments somewhat easier than when using MAS. Further, because the sample is not spinning, the catalyst particles are not forced against the walls of the rotor. The first MAH setup was developed by Keeler *et al*. and was named the gas reactor and solid sample hopper (GRASSHopper) [160]. MacNamara and Raftery [161] independently described a setup based on the MAH technique called FlowMAH. Both of these setups allow NMR spectroscopic data, including 2D datasets, to be acquired under true *in situ* conditions.

8.6.2 Applications

In situ NMR measurements have been applied to a wide range of catalytic applications, ranging from the characterization of catalyst structure, and in particular of acid sites, to monitoring the conversion of hydrocarbons and the determination of reaction mechanisms. Section 8.6.2.1 describes measurements carried out under batch conditions and Section 8.6.2.2 focuses on flow setups.

8.6.2.1 Batch Conditions

The main focus of *in situ* NMR studies under batch conditions has been on processes of relevance to the processing of fossil fuel and renewable resources into platform and specialty chemicals, namely hydrocarbon activation, alkylation, isomerization, and aromatization. Another area where *in situ* NMR studies have revealed significant insights is in the Beckmann rearrangement reaction, a reaction of industrial importance with regard to the production of nylon-6. Each of these areas is discussed in turn below.

8.6.2.1.1 Hydrocarbon Activation The activation of C−X bonds is essential in any catalytic reaction of a hydrocarbon, and is often probed using H–D exchange experiments [162, 163]. Stepanov and co-workers used the method of loading flame-sealed ampoules into MAS rotors in order to probe H–D exchange between adsorbed propane-d_8 [144, 164] or isobutane-d_{10} [165] and Si−OH−Al groups on the acid zeolite H-ZSM-5 at temperatures of 457–543 K. The adsorbates exhibited different behaviors, with regiospecific H–D exchange observed in the case of isobutane but not in the case of propane. Through measurement of the activation energies ($\sim$110 and $\sim$50 kJ mol^{-1} for propane and isobutane, respectively) in

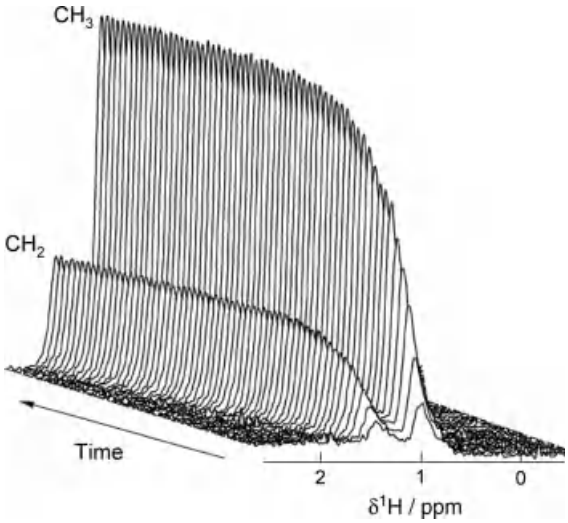


Figure 8.7 Stack plot of ^{1}H MAS NMR spectra acquired upon adsorption of propane-d_8 on H-ZSM-5 under batch conditions at 519 K. The change in intensity of CH_2 (1.45 ppm) and CH_3 (1.0 ppm) resonances with time demonstrates hydrogen transfer from adsorbent to adsorbate. Adapted from [164] with permission.

combination with the spectroscopic results, it was concluded that the nature of the transition state for the two reactants was different. Specifically, a carbenium ion intermediate was proposed in the case of isobutane and a pentacoordinated carbon atom intermediate for propane. Figure 8.7 shows the variation of the ^{1}H MAS NMR spectrum over time upon adsorption of propane-d_8 on H-ZSM-5 at 519 K. These spectra show the evolution of the populations of methyl and methylene groups of propane-d_8, and hence provide evidence of the transfer of protons from the acidic hydroxyl groups to the predeuterated propane molecules. This demonstrates that both CH_3 and CH_2 groups are involved in hydrogen exchange and that no isotope effect can be observed with respect to methyl and methylene groups. Further, the reaction of propane on alumina modified with sulfated zirconia was followed using ^{1}H, ^{2}H, and ^{13}C NMR by Haouas *et al.* [166].

Recently, the sealed ampoule technique has also been employed to elucidate the mechanism of methane, ethane, and propane activation over a Zn^{2+}-exchanged MFI zeolite [167]. The interaction of the adsorbates with the Zn sites was revealed through changes in the chemical shift of the alkanes upon adsorption, arising from the increased shielding of the metal-bound carbon atoms. Furthermore, the results indicated that all three alkanes undergo dissociative adsorption, which in the case of ethane and propane ultimately led to the formation of the corresponding alkenes.

Measurements employing the CAVERN technique (Section 8.6.1.1) were applied to C−H bond activation studies by Truitt and co-workers [168, 169]. ^{1}H MAS NMR spectra of ^{1}H atoms associated with both the reactants and the catalyst (surface OH groups) were monitored. Considering the interaction of isobutane-d_{10} over

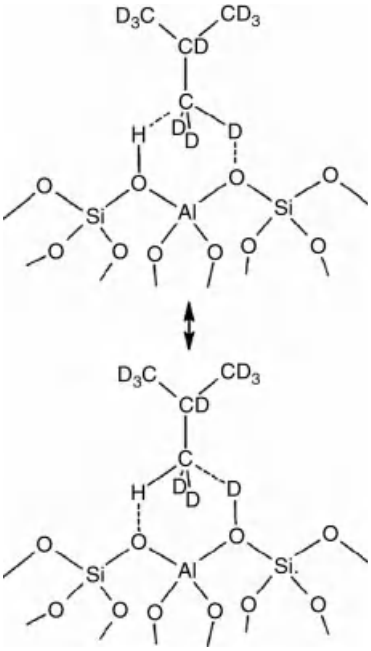


Figure 8.8 Complex postulated to form upon the adsorption of isobutane-d_{10} on H-ZSM-5 as determined through *in situ* CAVERN studies. Adapted from [169] with permission.

H-ZSM-5, it was observed that adsorption took place at surface acid sites, with H–D exchange occurring between the reactant and catalyst. Furthermore, the kinetics of this latter process were identified. NMR data also identified that the adsorbed species was not molecular isobutane but instead was an adsorption complex, and it was through the formation of this complex that C−H bond activation occurred and H–D exchange was facilitated, as shown in Figure 8.8.

8.6.2.1.2 **Alkylation Reactions** The alkylation of alkanes and aromatics is an important step in upgrading petrochemical and renewable feedstocks. The side-chain alkylation of toluene over zeolite catalysts has been studied under batch conditions using *in situ* NMR by a number of workers [170–172]. The study by Hunger *et al.* [172] employed both batch and flow methods to study toluene alkylation with methanol. For the batch experiments, the samples were prepared in sealed glass ampoules, and the reaction was followed by ^{13}C MAS NMR as shown in Figure 8.9. The peak at 166 ppm indicated in Figure 8.9 was assigned to a formate species, and that at 171 ppm was assigned to a carbonate species. These studies indicated that the formate species may act as the alkylating agent. In addition to toluene alkylation, the alkylation of benzene [173] has also been studied by *in situ* NMR in sealed ampoules, and studies under flow conditions have examined the reactions of both toluene and aniline.

8.6.2.1.3 **Isomerization and Aromatization Reactions** Derouane *et al.* followed the isomerization of cumene to *n*-propylbenzene over H-ZSM-11 in the presence of

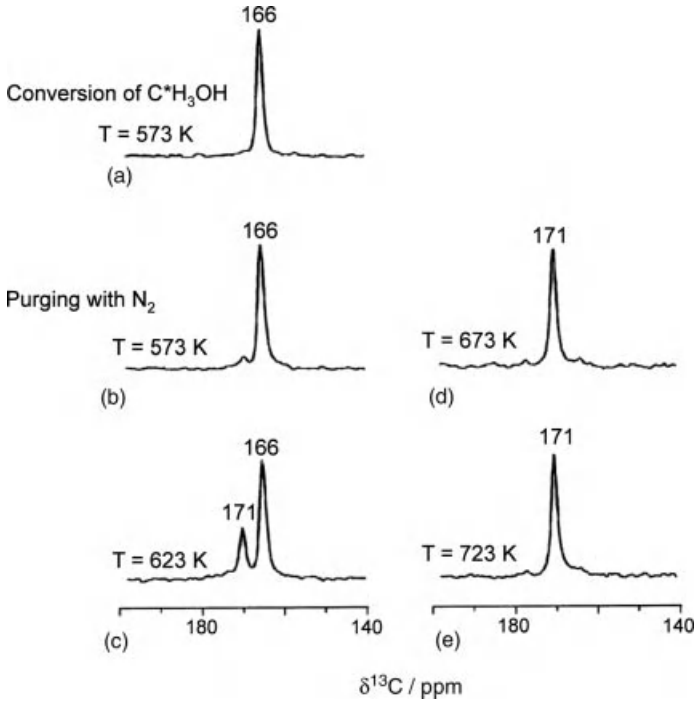


Figure 8.9 ^{13}C MAS NMR spectra recorded during conversion of methanol on zeolite CsNaX/24CsOH under flow conditions. Spectra were obtained after (a) a methanol pulse over the catalyst at 573 K and subsequent purging with nitrogen at (b) 573, (c) 623, (d) 673, and (e) 723 K. The peak at 166 ppm was assigned to a formate species and that at 171 ppm to a carbonate species. Adapted from [172] with permission.

benzene in sealed ampoules at temperatures up to 413 K using *in situ* NMR [173]. Two possible mechanisms exist for this reaction: an intermolecular and an intramolecular mechanism. In order to identify unambiguously that the reaction occurred via an intermolecular pathway, *in situ* ^{13}C NMR was used to monitor this reaction, utilizing isotopically labeled reactants. A further example is provided by the work of Stepanov *et al.* [174]. Using ^{13}C-labeled reactant, the isomerization of *n*-butane to isobutane over sulfated zirconia was investigated. Isobutane is used as an alkylating agent in reactions similar to those described above and is also used as a feed for isobutene production, isobutene being employed as an additive in gasoline. Figure 8.10 shows the evolution of the spectra acquired as a function of time at 313 K. The signal at 27.1 ppm corresponds to the methylene group of *n*-butane. The growth of this peak (0–100 min) indicates carbon scrambling, and the subsequent decrease in peak intensity indicates the consumption of *n*-butane to form isobutane. The kinetics of both the isomerization reaction and the accompanying carbon scrambling can therefore be established. Further studies elucidated further information on the mechanism of this reaction, as reviewed by Stepanov *et al.* [144].

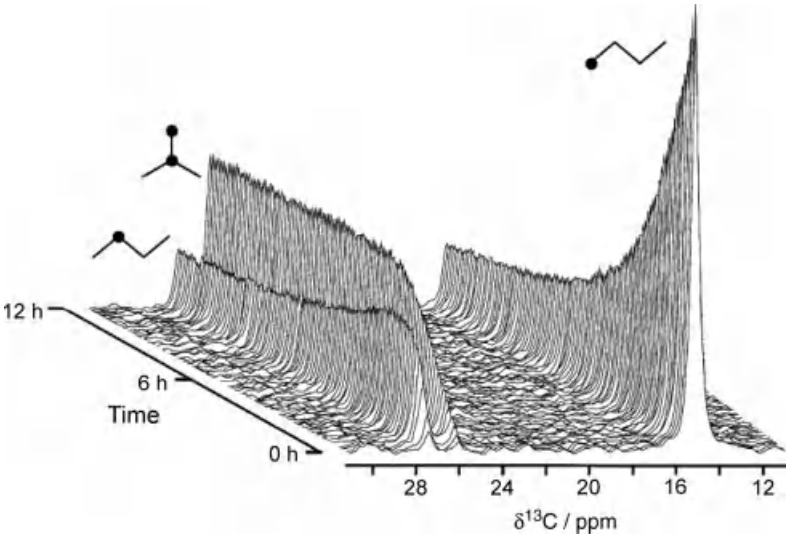


Figure 8.10 Stack plot of ^{13}C MAS NMR spectra acquired upon adsorption of [1-^{13}C]-*n*-butane on sulfated zirconia under batch conditions at 313 K after different heating times. The change in intensity of the resonances corresponding to the *n*-butane CH_3 (14.7 ppm), isobutane CH_3 and CH (26.0 ppm), and *n*-butane CH_2 (27.0 ppm) groups indicates the progress of isomerization and label scrambling reactions. Reproduced from [174] with permission.

In addition to isomerization, Stepanov and co-workers also studied alkane aromatization. For instance, using sealed ampoules, the kinetics of ethane aromatization at 573 K over Zn-modified zeolite BEA were monitored by ^{1}H MAS NMR [175]. Zn–ethyl species were identified as the reaction intermediate and kinetic analysis suggested that the methane byproduct observed was largely produced through ethane hydrogenolysis. Aromatization reactions have also been the subject of studies by Derouane *et al*. [173].

8.6.2.1.4 **Beckmann Rearrangement** The Beckmann rearrangement of oximes to imines is of significant importance in industry as a route to the formation of caprolactam from cyclohexanone. Caprolactam is an intermediate in the manufacture of nylon-6. Industrial attention has recently shifted towards a heterogeneously catalyzed process utilizing high-silica MFI-zeolite as a catalyst as opposed to the traditional, less environmentally friendly process employing sulfuric acid or oleum as a catalyst [176]. Studies employing sealed glass ampoules have compared ^{15}N NMR spectra with the predictions of computational studies to identify that the most selective catalytic sites for caprolactam formation are hydrogen-bonded networks of silanol groups located on the interior pore surface of MFI-zeolite, as compared with isolated functionalities on the external surface of the catalyst [177]. In addition, silicalite-1, H-ZSM-5, and H-[B]ZSM-5 [178] and SBA-15 [179] have also been investigated as catalysts, with ^{13}C NMR applied in addition to ^{15}N NMR in the final case. A detailed review of these studies was provided by Lezcano-Gonzalez *et al*. [176].

8.6.2.2 Flow Conditions

The first *in situ* NMR studies under flow conditions were conducted under static, that is, non-MAS conditions [151, 152]. As discussed earlier, since those initial studies, techniques based on MAS have been developed. Although the range of reactions that has been studied with such MAS techniques is wide and varied, a common theme is the importance of C−X bond activation and in particular C−H and C−O activation. This process is fundamental in alkylation reactions, methyl *tert*-butyl ether (MTBE) synthesis, and the methanol-to-hydrocarbons reaction. All of these reactions have been studied using *in situ* NMR under flow conditions and are discussed in the following sections.

8.6.2.2.1 **Hydrocarbon Activation** The increasing importance of functionalizing light alkanes has resulted in the application of both batch and flow *in situ* NMR analysis to this problem. One area of research has been the activation and subsequent aromatization of methane over Mo-modified H-ZSM-5. Zhang *et al.* [92] conducted stopped-flow measurements, carrying out the reaction steps at temperatures $\leq$873 K and at 973 K. ^{1}H NMR measurements were used to correlate the decrease in Brønsted acid sites, with an increase in surface-bound aromatics thereby implicating Brønsted sites as playing a key role in the reaction mechanism. Hydrocarbon activation also plays a key role in the specific examples described in Sections 8.6.2.2.2–8.6.2.2.4.

8.6.2.2.2 **Alkylation Reactions** Extending the studies on toluene alkylation with methanol described in Section 8.6.2.1.2 to continuous-flow conditions, Hunger's group has studied both the adsorption and reaction of a mixture of methanol and toluene and the individual components over Cs-modified Na-X zeolite at 723 K [172]. Through analysis of the spectroscopic data, these results supported the conclusion that formate species were a key reaction intermediate. Other alkylation reactions which have been studied by *in situ* NMR under flow conditions include the alkylation of aniline with methanol over zeolites. Investigations into this reaction have used both continuous-flow and stopped-flow measurements [180, 181]. ^{13}C MAS NMR spectra acquired under stopped-flow conditions at temperatures from 473 to 523 K (within a single experiment) are shown in Figure 8.11. At 473 K, the only observable resonance (49 ppm) can be assigned to adsorbed methanol. Upon heating to 498 K, additional signals appear corresponding to the desired reaction product *N*-methylaniline (29 ppm) and to *N*-methyleneaniline (157 ppm). At 523 K, formate species (166 ppm) are observed. After ramping through these three temperatures under continuous flow, the reactant flow was stopped and a further spectrum was acquired at 523 K. The resonances corresponding to methanol and *N*-methyleneaniline disappeared from the spectrum, that of *N*-methylaniline increased and the formate signal remained constant, suggesting that *N*-methyleneaniline is an intermediate in the alkylation reaction.

8.6.2.2.3 **MTBE Synthesis** MTBE has traditionally been used as an additive to gasoline fuels in order to raise their octane number. *In situ* natural abundance (i.e., not isotopically enriched) ^{13}C NMR flow experiments have been used to investigate the mechanism of MTBE synthesis from methanol and isobutene over

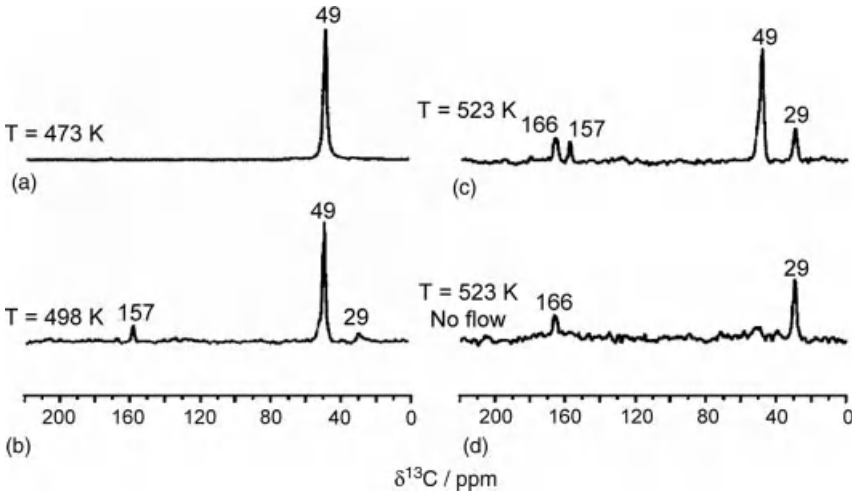


Figure 8.11 ^{13}C MAS NMR spectra recorded during methanol–aniline alkylation over zeolite CsOH/Cs,Na-Y under continuous-flow conditions at reaction temperatures of (a) 473, (b) 498, and (c) 523 K, and (d) after stopping the reactant flow at 523 K (stopped-flow conditions). The identified resonances are assigned to *N*-methylaniline (29 ppm), methanol (49 ppm), *N*-methyleneaniline (157 ppm), and a formate species (166 ppm). The loss of the *N*-methyleneaniline under stopped-flow conditions indicates that this is an intermediate in the alkylation reaction. Adapted from [181] by permission of The Royal Society of Chemistry.

zeolite catalysts [182, 183]. Employing H-Beta as the catalyst, Hunger and co-workers studied this reaction at 333 and 353 K under continuous-flow conditions with an isobutene residence time of 150 g h mol^{-1} and a methanol:isobutene ratio of 2:1. Comparing the spectra acquired at the two reaction temperatures (Figure 8.12), a lower concentration of isobutoxy species, which form over Brønsted acid sites, was observed at 353 K. Through comparison with gas chromatography (GC) data acquired simultaneously, it was seen that the yield of MTBE correlated with the concentration of such alkoxy species, leading to their identification as intermediates in this reaction.

8.6.2.2.4 **Methanol-to-Hydrocarbons Reaction** The methanol-to-hydrocarbons reaction is of particular interest because it provides an attractive route to the synthesis of light olefins, and is also capable of producing higher hydrocarbons and aromatic products. As a result, methanol may be considered as a platform chemical with the potential to replace traditional feedstocks. The conversion of methanol to olefins (MTO), or more generally to higher hydrocarbons (methanol-to-hydrocarbons), represents a specific example of C–H activation. It is in understanding this reaction where *in situ* NMR techniques have perhaps had the most significant impact in catalysis. As a result, the achievements of NMR in this area have been the subject of numerous reviews [142, 143, 184–186]. The review by Wang *et al.* [185] provides a comprehensive description of the mechanistic conclusions reached through *in situ* NMR studies and of the apparatus used to acquire these data. As a result of the wide availability of reviews on this subject, only a selection of the available data will be discussed here.

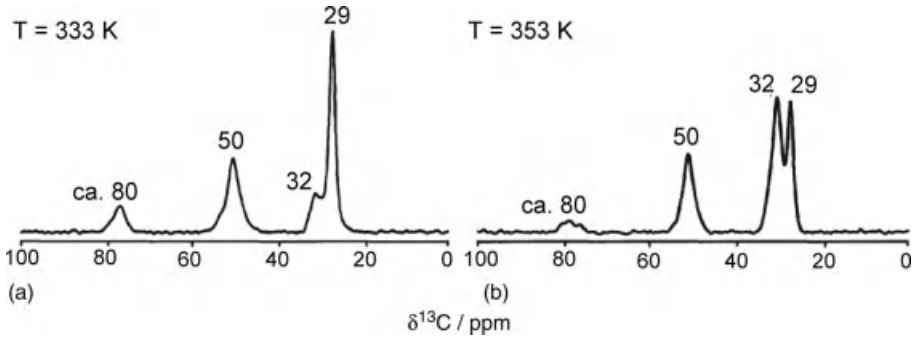


Figure 8.12 ^{13}C MAS NMR spectra acquired under continuous-flow conditions during MTBE synthesis over zeolite H-Beta at (a) 333 and (b) 353 K. The identified resonances correspond to CH_3 groups of isobutene oligomers (32 ppm), CH_3 groups of physisorbed methanol (50 ppm), and isobutoxy species (29 and ~80 ppm). The concentration of isobutoxy species is greater at 333 K. Adapted from [182] with permission.

Whereas the conversion of methanol was commercialized and the subject of considerable research interest over a period in excess of 30 years, the mechanism of the reaction remained unknown at the turn of the twenty-first century. In particular, the induction period prior to the observation of significant concentrations of product species was the subject of speculation. It was not until *in situ* NMR methods were applied to this subject that a definitive answer to this problem was realized. NMR experiments confirmed that the reaction proceeds via a "hydrocarbon pool," that is, methanol is adsorbed on the surface of the catalyst, normally H-ZSM-5 or H-SAPO-34, and converted into a variety of adsorbed hydrocarbonaceous species. These species then play a role in the conversion of further methanol molecules into the observed higher hydrocarbons which desorb from this hydrocarbon pool. This finding, and associated NMR results, were the subject of two patents by ExxonMobil [187, 188].

The earliest experiments in this area were batch experiments using sealed ampoules, and were summarized by Hunger and Wang [143]. Flow experiments were, however, able to provide greater insights. Stopped-flow and pulse–quench [158, 189] experiments were utilized both by researchers at ExxonMobil and by Haw's group. For instance, utilizing an isotopically enriched methanol feed, H-SAPO-34 as the catalyst, and a reaction temperature of 673 K, Song *et al.* [189] used pulse–quench studies to analyze the surface species present at various times on-stream, and hence different levels of conversion. The times on-stream investigated ranged from 2 s to 2 h. Even after 4 s on-stream, methyl-substituted aromatics were observed on the catalyst surface. Conversion data, from GC measurements, indicated that substantial conversion of methanol into higher hydrocarbons occurred only when such methylbenzenes were present. The formation of alkylated aromatics was confirmed through independent *in situ* NMR measurements reported by Wang *et al.* [190]. Continuous-flow experiments have also been carried out. For example, Hunger and co-workers [191, 192] reacted ^{13}C-enriched methanol (25 g h mol^{-1}) over catalysts including H-ZSM-5 and H-SAPO-34 at temperatures from 373 to 673 K. Below 623 K, a mixture of olefinic compounds dominated the NMR spectra, whereas aromatics

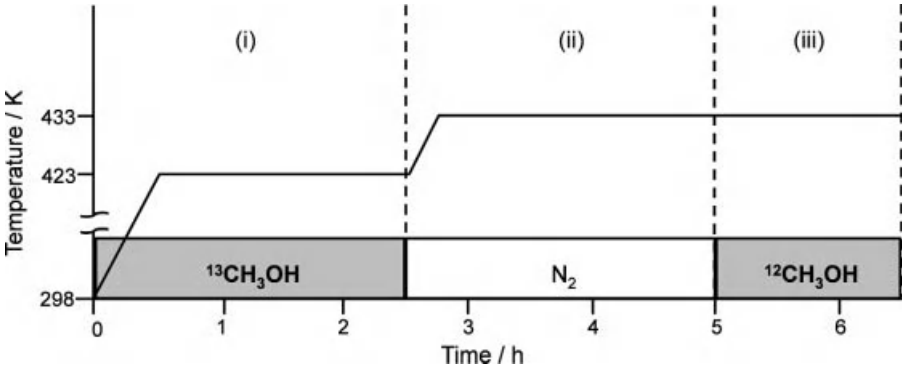


Figure 8.13 Reaction protocol for *in situ* NMR experiments under stopped-flow conditions to study methanol conversion over zeolite catalysts. Three periods are indicated: (i) recording of spectra at during reaction of ^{13}C-enriched methanol at 423 K, (ii) recording of spectra during purging the catalyst with N_2 at 433 K, and (iii) recording of spectra during reaction of methanol with ^{13}C at natural abundance at 433 K. Reproduced with permission from [180].

including methylbenzenes were observed at higher temperatures. Through the above and other studies, the hydrocarbon pool was revealed to contain methylbenzene and methylaromatic structures. Additionally, surface alkoxy groups have been demonstrated to provide high catalytic activity through stopped-flow measurements where the reaction was stopped at specific times on-stream and the reactant flow replaced with a nitrogen flow [180]. The reaction protocol for these experiments is shown in Figure 8.13. Seiler *et al.* [193] employed flow measurements, switching not between a reacting and an inert feed but between a ^{13}C isotopically labeled feed and methanol with ^{13}C at natural abundance. In this case the catalyst was H-ZSM-5, the methanol residence time was 25 g h mol^{-1} and the reaction temperature was 548 or 573 K. As shown in Figure 8.14, for reaction at 573 K, a reduction in intensity of the NMR resonances of ~40% was observed after switching. The indicated resonances correspond to components of the hydrocarbon pool formed on the catalyst surface. That the quantity of labeled ^{13}C atoms decreases after switching indicates that the reaction products (light olefins) are desorbing from the hydrocarbon pool, thereby supporting the role of the hydrocarbon pool in the reaction mechanism. Note that not all of the ^{13}C atoms desorb to be replaced by ^{12}C atoms, and therefore not all of the pool is reactive or accessible.

It is worthy of note that the results of Haw *et al.* also suggested that the initial carbon–carbon bonds were formed not from methanol but from trace impurities in the feed stream [184]. The subsequent conversion of methanol is, however, facilitated through interaction with these newly formed species.

8.6.2.3 **Coupling with a Second Technique**

As demonstrated in the preceding sections, *in situ* NMR techniques are capable of revealing mechanistic insights for a multitude of different catalytic transformations.

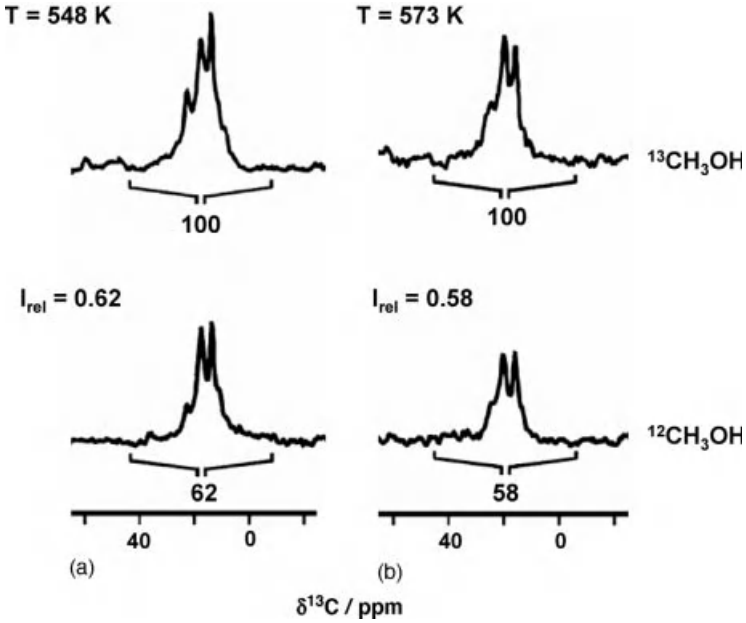


Figure 8.14 ^{13}C MAS NMR spectra acquired under continuous-flow conditions during the MTO reaction over H-ZSM-5 at (a) 548 K and (b) 573 K. In both cases the lower spectra (denoted $^{12}CH_3OH$) were acquired upon switching from ^{13}C-labeled reactants to ^{13}C at natural abundance. The reduction in intensity (I_{rel} is relative intensity) of the indicated resonances upon switching indicates the desorption of reaction products from the surface "hydrocarbon pool." Reproduced with permission from [193].

In some of the examples provided, experimental measurements were complemented by theoretical calculations. The coupling of a second experimental technique with the NMR measurement can, however, significantly increase the value of the information garnered. In the case of experiments conducted under flowing conditions, the most straightforward way to gain added information is to analyze the effluent stream leaving the rotor during reaction. The coupling of GC analysis with flow measurements in the methanol-to-hydrocarbons reaction has been actualized by Hunger *et al*. [192], helping to demonstrate further the role played by the hydrocarbon pool. Similar combined NMR–GC studies have also been applied to MTBE synthesis [182]. In addition to GC analysis, on-line mass spectrometric measurements may be possible, as outlined in the novel flow system described by Isbester *et al*. [155]. A more radical approach is to acquire additional spectroscopic data simultaneously with NMR data. This has been achieved by Hunger and Wang through the combination of *in situ* flow NMR with *in situ* UV–visible spectroscopy [194]. These two techniques provide complementary information, specifically the resolution and identification of adsorbate species by MAS NMR and the high sensitivity for allylic compounds, aromatic species and carbenium ions provided by UV–visible spectroscopy. The experimental setup for this system is based on the MAS flow cell described

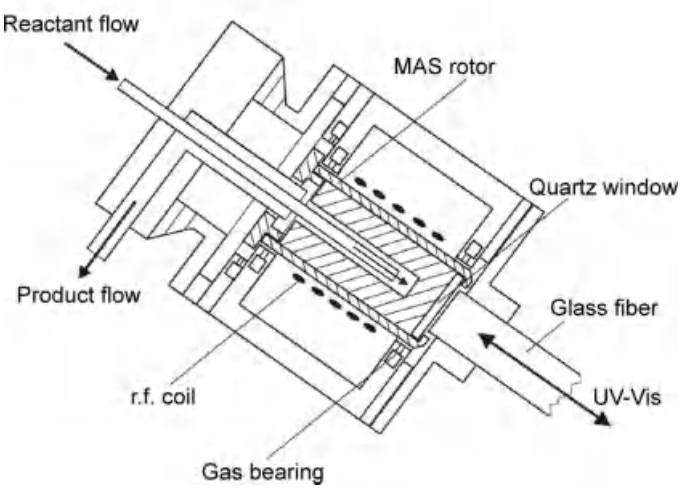
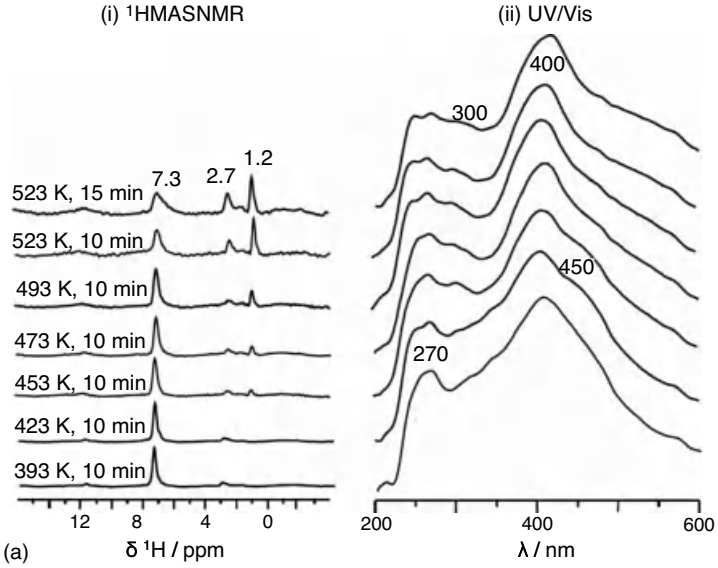


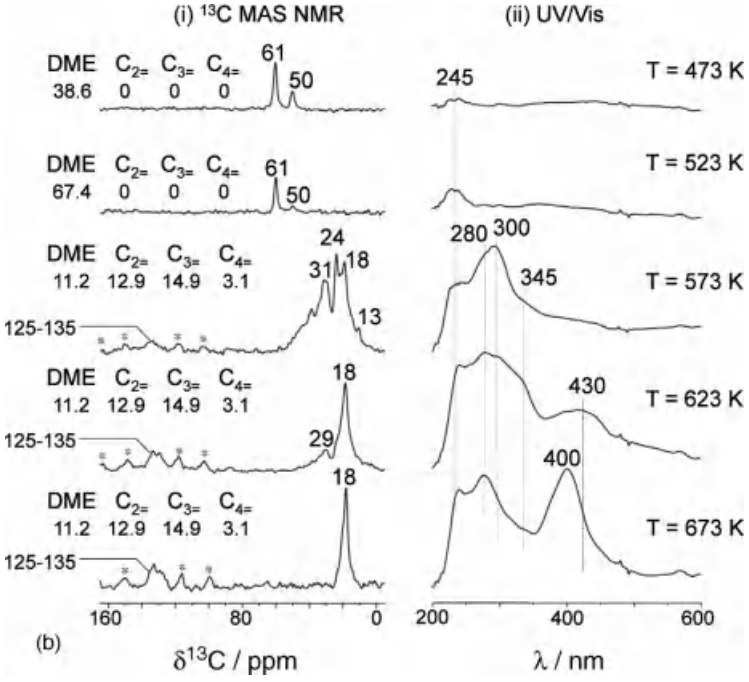
Figure 8.15 Experimental setup for combined MAS NMR and UV–visible spectroscopic studies under continuous flow conditions developed by Hunger and Wang. The probe consists of a MAS NMR turbine equipped with an injection system for solid-state NMR studies and a quartz fiber-optic for simultaneous UV–visible investigations. Reproduced from [194] by permission of The Royal Society of Chemistry.

earlier [153], modified to include a quartz window at the base of the NMR rotor providing access for fiber-optic UV–visible spectroscopy as shown in Figure 8.15.

Combined *in situ* NMR with UV–visible spectroscopy has been applied to the study of H–D exchange at the side chain of ethylbenzene over zeolite H-Y [150]. Figure 8.16a shows ^{1}H NMR and UV–visible spectra recorded *in situ* after pulses of ethylbenzene-d_5 at temperatures from 393 to 523 K. As can be seen, upon raising the temperature, peaks corresponding to CH_3 groups (1.2 ppm) and CH_2 groups (2.7 ppm) are observed, indicating H–D exchange with Brønsted acid sites. Simultaneously with the development of these peaks, a broad band at ~450 nm is observed in the UV–visible spectra, which is assigned to the formation of *sec*-ethylphenylcarbenium ions. This species is identified as an intermediate in the H–D exchange reaction.

This combined technique has also been applied to studies of the methanol-to-hydrocarbons reaction [194, 195]. The advantages of NMR in such studies have been described in detail in Section 8.6.2.2.4. UV–visible spectroscopy is also well suited to such investigations as it has a high sensitivity for aromatics, compounds with conjugated double bonds, and carbenium ions, all of which are believed to be present in the hydrocarbon pool that forms on the catalyst surface during reaction. Figure 8.16b shows ^{13}C NMR and UV–visible spectra recorded during the conversion of ^{13}C-enriched methanol (25 g h mol^{-1}, reaction temperature 473–673 K). In addition to spectroscopic measurements, on-line GC data are also acquired and the reaction yields are indicated in Figure 8.16b. At low temperature, the main reaction product is dimethylether (DME), as shown by GC and NMR data. Only a weak band at


(i) 1HMASNMR
(ii) UV/Vis
523 K, 15 min
523 K, 10 min
493 K, 10 min
473 K, 10 min
453 K, 10 min
423 K, 10 min
393 K, 10 min
7.3
2.7
1.2
12
8
4
0
δ 1H / ppm
400
300
450
270
200
400
600
λ / nm
(a)


(i) 13C MAS NMR
(ii) UV/Vis
DME C2= C3= C4=
38.6 0 0 0
61
50
T = 473 K
245
DME C2= C3= C4=
67.4 0 0 0
61
50
T = 523 K
DME C2= C3= C4=
11.2 12.9 14.9 3.1
24
31
18
13
125-135
280
300
345
T = 573 K
DME C2= C3= C4=
11.2 12.9 14.9 3.1
18
29
125-135
430
T = 623 K
400
DME C2= C3= C4=
11.2 12.9 14.9 3.1
18
125-135
T = 673 K
160
80
0
δ13C / ppm
200
400
600
λ / nm
(b)

245 nm, assigned to diene species, is observed in the UV–visible spectrum. At 523 K, the NMR spectrum is interpreted as consisting of predominately polyaromatic species. This can also be inferred from the UV–visible spectrum, although this is dominated by a band at 300 nm assigned to monoenylenic carbenium ions. The main reaction products this time are light alkenes. The information gained by the combined technique is therefore greater than that from either of the two methods in isolation. The carbenium ion and polyaromatic molecules identified at higher reaction temperatures are coke precursors which lead to catalyst deactivation. Subsequent regeneration of the deactivated catalyst has also been studied by combined *in situ* flow NMR and UV–visible spectroscopy [195].

8.7 Towards "*Operando*" Studies

MRI offers opportunities to study materials operating in their true working environment, for example, observing a catalyst functioning in the reactor environment and under realistic operating conditions of temperature and pressure. Here we focus primarily on the spatial mapping of conversion inside a reactor environment. More detailed reviews of the applications of MRI to study flow fields and reactions in catalytic reaction engineering can be found elsewhere [9]. Reactor designs that have been explored by MRI are fixed beds and gas–solid fluidized beds. In the latter, the flow fields of the solid particles are usually followed [196, 197]. Different approaches may be taken to acquire signals from the solid phase. The most common approach is to use edible solid particles such as poppy seeds, in which the natural oil content provides a strong ^{1}H magnetic resonance signal. Alternatively, a porous solid can be impregnated with a liquid (typically containing ^{1}H species) to provide the magnetic resonance signal. Flow fields in microchannel reactors have also been studied [198]. Here, we focus on fixed-bed catalytic reactors and chemical mapping inside these units.

To illustrate the imaging of flow fields within a reactor, Figure 8.17 shows a single-phase flow map of water through a fixed bed of glass beads [199]. Such measurements are routinely performed with real catalyst packings, but Figure 8.17 clearly illustrates the important message that individual catalyst pellets will see very different flow fields adjacent to them. These flow velocities will, in turn, influence mass transfer of

Figure 8.16 Examples of the information that can be acquired from simultaneous MAS NMR and UV–visible spectroscopy measurements. (a) ^{1}H MAS NMR (i) and UV–visible spectra (ii) recorded during the H–D exchange of ethylbenzene-d_5 on dealuminated zeolite H-Y. Exchange is indicated by the increase in intensity of the resonances corresponding to CH_3 groups (1.2 ppm) and CH_2 groups (2.7 ppm) with increasing temperature. Reproduced with permission from [150]. (b) ^{13}C MAS NMR (i) and UV–visible spectra (ii) recorded during the conversion of ^{13}C-enriched methanol over H-SAPO-34 at 473, 523, 573, 623, and 673 K. Yields as measured by online GC are also indicated in percentages. The distribution of reaction products is strongly dependent upon the reaction temperature. Reproduced with permission from [195].

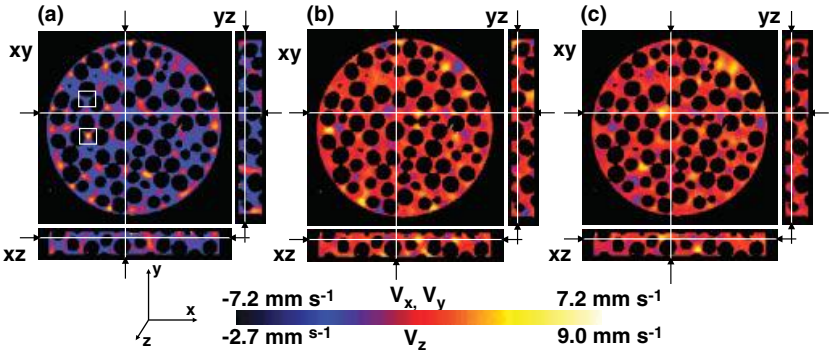


Figure 8.17 Magnetic resonance visualization of water flowing within a fixed bed of spherical glass beads; the beads have no magnetic resonance signal intensity associated with them and are identified as black voxels. Flow velocities in the (a) *z*- (b) *x*-, and (c) *y*-directions are shown with slices taken in the *xy*, *yz* and *xz* planes for each of the velocity components. For each image the positions at which the slices in the other two directions have been taken are identified. Voxel resolution is 195 × 195 × 195 μm. The glass beads are of diameter 5 mm and are packed within a column of internal diameter 46 mm. Typically 40% of the flow is carried by ~20% of the inter-particle space within any 2D slice section through the bed, perpendicular to the direction of superficial flow. Regions of high and low flow velocity in the direction of superficial flow are highlighted in (a). Reproduced from [9] with permission.

feed molecules into the catalyst and the transfer of molecular species back out in the exit stream. It becomes clear that simply optimizing the performance of the catalyst in powder form will not necessarily optimize the process performance: the reactor design has to be optimized simultaneously with the catalyst design. Since these early studies, measurements of hydrodynamics have been extended to imaging both gas and velocity fields in two-phase gas–liquid flows in fixed-bed reactors [200], in addition to providing insight into hydrodynamic transitions in reactors. In particular, the transition from a trickling (steady-state) gas–liquid flow to a pulsing flow has been investigated, and demonstrated to occur via local pulsatile events within the bed which increase with liquid velocity and merge, until the entire bed is associated with a time-varying liquid distribution [201].

Chemical mapping in a fixed-bed reactor was first demonstrated by Yuen *et al.* [202] using the liquid-phase esterification of methanol and acetic acid catalyzed within a fixed bed of H^+ ion-exchange resin (particle size 600–850 μm) using volume-selective spectroscopy [20]. The ability to estimate mass transfer coefficients *in situ* and to explore correlations between local conversion and hydrodynamics has also been demonstrated in application to this esterification reaction [203, 204]. In order to study the hydrocarbon conversions more typical of the chemical industry, ^{13}C observation is needed so as to benefit from the increased chemical shift range such that reactants, intermediates, and products can be identified. As we have already seen, ^{13}C observation is routinely employed in *in situ* studies. However, because of the low natural abundance of ^{13}C, wherever possible samples will be enriched with ^{13}C. In moving to *operando* studies under continuous flow conditions, the cost of

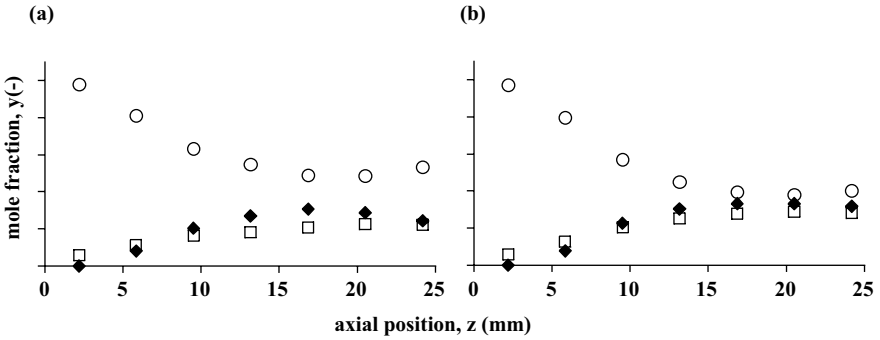


Figure 8.18 Time-resolved axial composition profiles obtained from ^{13}C DEPT MRI measurements during start-up of the hydrogenation of 1-octene over a fixed bed of 1 wt% Pd/Al_2O_3 catalyst, for a 1-octene:hydrogen mole ratio of 2.0. Concentrations of 1-octene (○), 2-octene (□), and *n*-octane (◆) along the length of the bed are shown (a) 22.5 and (b) 180 min after start-up. Each set of axial profiles at a given time takes 15 min to acquire. The time stated is the mid-point of the acquisition. Reproduced from [10] with permission.

using high-volume ^{13}C-enriched feeds is prohibitively expensive and therefore polarization enhancement techniques are implemented. Thus, ^{13}C DEPT MRI has been employed and was demonstrated initially in the study of competing etherification and hydration reactions of 2-methyl-2-butene [205]. Following this work, ^{13}C DEPT MRI was applied to map isomerization and full conversion of 1-octene during hydrogenation over a Pd/Al_2O_3 catalyst [206]. Quantitative interpretation of these data is challenging because of the influences on the spectral lineshape from species existing in both the intra- and inter-particle space and also individual peaks within the spectrum of a given molecular species being attenuated to differing extents due to their different interactions with the catalyst surface. In Figure 8.18, the mole fractions of 1-octene, 2-octene, and *n*-octane along the length of the reactor are shown at two times: 22.5 and 180 min after introduction of hydrogen. The time associated with a given dataset is the time at the half-way point through the total data acquisition time. From these data, the conversion and selectivity to 2-octene and *n*-octane can be obtained as a function of both time and axial position along the bed.

8.8 Conclusion and Outlook

The phenomenon of magnetic resonance provides an array of techniques for probing chemical conversion and adsorption, diffusion, and flow in a chemically selective and noninvasive manner. The versatility of magnetic resonance represents a challenge since great care must be taken to ensure that the magnetic resonance signal that is acquired is sensitive only to the effect that the investigator wishes to probe. However, more and more sophisticated techniques are now becoming "routine" in materials

characterization laboratories. In terms of surfaces and catalysis, the areas of current interest which are likely to have most impact almost certainly lie in advances in signal enhancement, which will decrease data acquisition rates, and being able to resolve information spatially within both the working catalyst itself and at larger length scales within the reactor.

References

1 Bloch, F., Hansen, W.W., and Packard, M. (1946) Nuclear induction. *Phys. Rev.*, **69**, 127.

2 Purcell, E.M., Torrey, H.C., and Pound, R.V. (1946) Resonance absorption by nuclear magnetic moments in a solid. *Phys. Rev.*, **69**, 37–38.

3 Zimmermann, J.R., Holmes, B.G., and Lasater, J.A. (1956) A study of adsorbed wateron silica gel by nuclear resonance techniques. *J. Phys. Chem.*, **60**, 1157–1161.

4 Andrew, E.R., Bradbury, A., and Eades, R.G. (1958) Nuclear magnetic resonance spectra from a crystal rotated at high speed. *Nature*, **182**, 1659.

5 Eckert, H. (1996) Solid state NMR as a tool of structure and dynamics in solid state chemistry and materials science: recent progress and challenges. *Curr. Opin. Solid State Mater Sci.*, **1**, 465–476.

6 Raftery, D. (2006) Xenon NMR spectroscopy. *Annu. Rep. NMR Spectrosc.*, **57**, 205–271.

7 Bowers, C.R., Long, H.W., Pietrass, T., Gaede, H.C., and Pines, A. (1993) Cross polarization from laser-polarized solid xenon to $^{13}CO_2$ by low-field thermal mixing. *Chem. Phys. Lett.*, **205**, 168–170.

8 Adams, R.W., Aguilar, J.A., Atkinson, K.D., Cowley, M.J., Elliott, P.I.P., Duckett, S.B., Green, G.G.R., Khazal, I.G., Lopez-Serrano, J., and Williamson, D.C. (2009) Reversible interactions with para-hydrogen enhance NMR sensitivity by polarization transfer. *Science*, **323**, 1708–1711.

9 Gladden, L.F., Mantle, M.D., and Sederman, A.J. (2006) Magnetic resonance imaging of catalysts and catalytic processes. *Adv. Catal.*, **50**, 1–75.

10 Gladden, L.F., Abegao, F.J.R., Dunckley, C.P., Holland, D.J., Sankey, M.H., and Sederman, A.J. (2010) MRI: *operando* measurements of temperature, hydrodynamics and local reaction rate in a heterogenous reactor. *Catal. Today*, **155**, 157–163.

11 Duer, M.J. (ed.) (2004) *Introduction to Solid-State NMR Spectroscopy*, Blackwell, Oxford.

12 Blümich, B. (ed.) (2005) *Essential NMR for Scientists and Engineers*, Springer, Berlin.

13 Anadon, L.D. (2006) Transient hydrodynamics and reaction in trickle-bed reactors using NMR and MRI. Dissertation, University of Cambridge.

14 Wang, P.-K., Slichter, C.P., and Sinfelt, J.H. (1984) NMR study of the structure of simple molecules adsorbed on metal surfaces: C_2H_2 on Pt. *Phys. Rev. Lett.*, **53**, 82–85.

15 Duncan, T.M. and Dybowski, C. (1981) Chemisorption and surfaces studied by nuclear magnetic resonance spectroscopy. *Surf. Sci. Rep.*, **1**, 157–250.

16 Slichter, C.P. (1986) Probing phenomena at metal surfaces by NMR. *Annu. Rev. Phys. Chem.*, **37**, 25–51.

17 Ansermet, J.P., Slichter, C.P., and Sinfelt, J.H. (1990) Solid state NMR techniques for the study of surface phenomena. *Prog. Nucl. Magn. Reson. Spectrosc.*, **22**, 401–421.

18 Holland, D.J., Malioutov, D.M., Blake, A., Sederman, A.J., and Gladden, L.F. (2010) Reducing data acquisition times in phase-encoded velocity imaging using compressed sensing. *J. Magn. Reson.*, **203**, 236–246.

19 Maudsley, A.A., Hilal, S.K., Perman, W.H., and Simon, H.E. (1983) Spatially resolved high resolution spectroscopy by "four-dimensional" NMR. *J. Magn. Reson.*, **51**, 147–152.

20 Kimmich, R. and Hoepfel, D. (1987) Volume-selective multipulse spin-echo spectroscopy. *J. Magn. Reson.*, **72**, 379–384.

21 Stejskal, E.O. and Tanner, J.E. (1965) Spin diffusion measurements: spin echoes in the presence of a time-dependent field gradient. *J. Chem. Phys.*, **42**, 288–292.

22 Stejskal, E.O. (1965) Use of spin echoes in a pulsed magnetic-field gradient to study anisotropic, restricted diffusion and flow. *J. Chem. Phys.*, **43**, 3597–3603.

23 van Wüllen, L., Tricot, G., and Wegner, S. (2007) An advanced NMR protocol for the structural characterization of aluminophosphate glasses. *Solid State Magn. Reson.*, **32**, 44–52.

24 Bax, A., Szeverenyi, N.M., and Maciel, G.E. (1983) Correlation of isotropic shifts and chemical shift anisotropies by two-dimensional Fourier-transform magic-angle hopping NMR spectroscopy. *J. Magn. Reson.*, **52**, 147–152.

25 Pines, A., Gibby, M.G., and Waugh, J.S. (1973) Proton-enhanccd NMR of dilute spins in solids. *J. Chem. Phys.*, **59**, 569–590.

26 Sindorf, D.W. and Maciel, G.E. (1983) NMR studies of pyridine on silica–alumina. *J. Am. Chem. Soc.*, **105**, 5529–5535.

27 Sindorf, D.W. and Maciel, G.E. (1983) ^{29}Si nuclear magnetic resonance study of hydroxyl sites on dehydrated silica gel surfaces, using silylation as a probe. *J. Phys. Chem.*, **87**, 5516–5521.

28 Haase, J. and Oldfield, E. (1994) Aluminum to oxygen cross-polarization in α-Al_2O_3 (corundum). *Solid State Nucl. Magn. Reson.*, **3**, 171–175.

29 Gerstein, B.C., Pembleton, R.G., Wilson, R.C., and Ryan, L. (1977) High resolution NMR in randomly oriented solids with homonuclear dipolar broadening: combined multiple pulse NMR and magic angle spinning. *J. Chem. Phys.*, **66**, 361–362.

30 Bronnimann, C.E., Zeigler, R.C., and Maciel, G.E. (1988) Proton NMR study of dehydration of the silica gel surface. *J. Am. Chem. Soc.*, **110**, 2023–2026.

31 Fitzgerald, J.J., Piedra, G., Dec, S.F., Seger, M., and Maciel, G.E. (1997) Dehydration studies of a high-surface-area alumina (pseudo-boehmite) using solid-state ^{1}H and ^{27}Al NMR. *J. Am. Chem. Soc.*, **119**, 7832–7842.

32 Samoson, A., Lippmaa, E., and Pines, A. (1988) High-resolution solid-state NMR. Averaging of second-order effects by means of a double-rotor. *Mol. Phys.*, **56**, 1013–1018.

33 Mueller, K.T., Sun, B.Q., Chingas, G.C., Zwanziger, J.W., Terao, T., and Pines, A. (1990) Dynamic-angle spinning of quadrupolar nuclei. *J. Magn. Reson.*, **86**, 470–487.

34 Grandinetti, P.J., Baltisberger, J.H., Farnan, I., Stebbins, J.F., Werner, U., and Pines, A. (1995) Solid-state ^{17}O magic-angle and dynamic-angle spinning NMR study of the SiO_2 polymorph coesite. *J. Phys. Chem.*, **99**, 12341–12348.

35 Frydman, L. and Harwood, J.S. (1995) Isotropic spectra of half-integer quadrupolar spins from bidimensional magic-angle spinning NMR. *J. Am. Chem. Soc.*, **117**, 5367–5368.

36 Gan, Z. (2000) Isotropic NMR spectra of half-integer quadrupolar nuclei using satellite transitions and magic-angle spinning. *J. Am. Chem. Soc.*, **122**, 3242–3243.

37 Shore, S.E., Ansermet, J.P., Slichter, C.P., and Sinfelt, J.H. (1987) Nuclear magnetic resonance study of the bonding and diffusion of CO chemisorbed on Pd. *Phys. Rev. Lett.*, **58**, 953–956.

38 Gullion, T. and Schaefer, J. (1989) Rotational-echo double-resonance NMR. *J. Magn. Reson.*, **81**, 196–200.

39 Hing, A.W., Vega, S., and Schaefer, J. (1992) Transferred-echo double-resonance NMR. *J. Magn. Reson.*, **96**, 205–209.

40 Fyfe, C.A., Mueller, K.T., Grondey, H., and Wong-Moon, K.C. (1992) Dipolar dephasing between quadrupolar and spin-$^{1}/_{2}$ nuclei. REDOR and TEDOR NMR experiments on VPI-5. *Chem. Phys. Lett.*, **199**, 198–204.

41 Grey, C.P. and Veeman, W.S. (1992) The detection of weak heteronuclear coupling between spin 1 and spin $^{1}/_{2}$

nuclei in MAS NMR; $^{14}N/^{13}C/^{1}H$ triple resonance experiments. *Chem. Phys. Lett.*, **192**, 379–385.

42 Grey, C.P. and Vega, A.J. (1995) Determination of the quadrupole coupling constant of the invisible aluminum spins in zeolite HY with $^{1}H/^{27}Al$ TRAPDOR NMR. *J. Am. Chem. Soc.*, **117**, 8232–8242.

43 Gullion, T. (1995) Measurement of dipolar interactions between spin-$^{1}/_{2}$ and quadrupolar nuclei by rotational-echo, adiabatic-passage, double-resonance NMR. *Chem. Phys. Lett.*, **246**, 325–330.

44 Ganapathy, S. and Vega, S. (1998) REAPDOR NMR spectroscopy and location of cations in molecular sieves. *J. Am. Chem. Soc.*, **120**, 1078–1079.

45 Holland, G.P. and Alam, T.M. (2005) Location and orientation of adsorbed molecules in zeolites from solid-state REAPDOR NMR. *Phys. Chem. Chem. Phys.*, **7**, 1739–1742.

46 Bell, A.T. and Pines, A. (eds.) (1994) *NMR Techniques in Catalysis*, Marcel Dekker, New York.

47 Engelhardt, G. and Koller, H. (1994) 29Si NMR of inorganic solids, in *NMR Basic Principles and Progress*, 2nd edn. (ed. B. Blümich), Springer, Berlin, pp. 1–29.

48 Pfiefer, H. (1994) NMR of solid surfaces, in *NMR Basic Principles and Progress*, 2nd edn. (ed. B. Blümich), Springer, Berlin, pp. 31–90.

49 Hunger, M. and Wang, W. (2008) Solid state NMR spectroscopy, in *Handbook of Heterogeneous Catalysis*, 2nd edn. (eds. G. Ertl, H. Knoezinger, F. Schueth, and J. Weitkamp), Wiley-VCH Verlag GmbH, Weinheim, pp. 912–932.

50 van der Klink, J.J. (1999) The surface of supported metal catalysts probed by NMR. *Adv. Catal.*, **44**, 1–117.

51 van der Klink, J.J. and Brom, H.B. (2000) NMR in metals, metal particles and metal cluster compounds. *Prog. Nucl. Magn. Reson. Spectrosc.*, **36**, 89–201.

52 Kraus, H., Prins, R., and Kentgens, A.P.M. (1996) A ^{27}Al MQMAS and off-resonance nutation NMR investigation of Mo–P/γ-Al_2O_3 hydrotreating catalyst precursors. *J. Phys. Chem.*, **100**, 16336–16345.

53 Grey, C.P., Smith, M.E., Cheetham, A.K., Dobson, C.M., and Dupree, R. (1990) Yttrium-89 magic angle spinning NMR study of rare-earth pyrochlores: paramagnetic shifts in the solid state. *J. Am. Chem. Soc.*, **112**, 4670–4675.

54 Massiot, D., Revel, R., Magnenet, C., and Bazin, D. (2000) Characterization of an Al-, Ga-based catalyst by Ga NMR and XAS. *Solid State Nucl. Magn. Reson.*, **16**, 103–108.

55 Trokiner, A., Bessiere, A., Thouvenot, R., Hau, D., Marko, J., Nardello, V., Pierlot, C., and Aubry, J.-M. (2004) Solid state and solution ^{43}Ca NMR of calcium peroxides involved in the disproportionation of hydrogen peroxide by calcium hydroxide. *Solid State Nucl. Magn. Reson.*, **25**, 209–215.

56 Smith, J.V. and Blackwell, C.S. (1983) Nuclear magnetic resonance of silica polymorphs. *Nature*, **303**, 223–225.

57 Gladden, L.F., Carpenter, T.A., and Elliott, S.R. (1986) ^{29}Si MAS NMR studies of the spin–lattice relaxation time and bond-angle distribution in vitreous silica. *Philos. Mag. B*, **53**, L81–L87.

58 Chuang, I.-S., Kinney, D.R., and Maciel, G.E. (1993) Interior hydroxyls of the silica gel system as studied by silicon-29 CP-MAS NMR spectroscopy. *J. Am. Chem. Soc.*, **115**, 8695–8705.

59 Chuang, I.-S. and Maciel, G.E. (1996) Probing hydrogen bonding and the local environment of silanols on silica surfaces via nuclear spin cross polarization dynamics. *J. Am. Chem. Soc.*, **118**, 401–406.

60 Kobayashi, T., DiVerdi, J.A., and Maciel, G.E. (2008) Silica gel surface: molecular dynamics of surface silanols. *J. Phys. Chem. C*, **112**, 4315–4326.

61 O'Reilly, D.E. (1960) Magnetic resonance techniques in catalytic research. *Adv. Catal.*, **12**, 31–116.

62 Huggins, B.A. and Ellis, P.D. (1992) Aluminum-27 nuclear magnetic resonance study of aluminas and their surfaces. *J. Am. Chem. Soc.*, **114**, 2098–2108.

63 Kraus, H., Müller, M., Prins, R., and Kentgens, A.P.M. (1998) Comments on

the ^{27}Al NMR visibility of aluminas. *J. Phys. Chem. B*, **102**, 3862–3865.

64 Kraus, H. and Prins, R. (1996) Composition of impregnation solutions and wet impregnated Mo–P/γ-Al_2O_3 catalysts as investigated by ^{31}P and ^{95}Mo NMR. *J. Catal.*, **164**, 251–259.

65 Pingel, U.-T., Amoureux, J.-P., Anupold, T., Bauer, F., Ernst, H., Fernandez, C., Freude, D., and Samoson, A. (1998) High-field ^{17}O NMR studies of the SiOAl bond in solids. *Chem. Phys. Lett.*, **294**, 345–350.

66 Readman, J.E., Grey, C.P., Ziliox, M., Bull, L.M., and Samoson, A. (2004) Comparison of the ^{17}O NMR spectra of zeolites LTA and LSX. *Solid State Nucl. Magn. Reson.*, **26**, 153–159.

67 Lippmaa, E., Magi, M., Samoson, A., Grimmer, A.R., and Engelhardt, G. (1980) Structural studies of silicates by solid-state high-resolution silicon-29 NMR. *J. Am. Chem. Soc.*, **102**, 4889–4893.

68 Engelhardt, G. and Michel, D. (eds.) (1987) *High-Resolution Solid-State NMR of Silicates and Zeolites*, John Wiley & Sons, Ltd., Chichester.

69 Camblor, M.A. and Davis, M.E. (1994) ^{29}Si MAS NMR spectroscopy of tectozincosilicates. *J. Phys. Chem.*, **98**, 13151–13156.

70 Bradley, S.M. and Howe, R.T. (1995) ^{129}Xe nuclear magnetic resonance studies of H-Ga-MFI zeolites. *Micropor. Mater.*, **4**, 131–139.

71 Rocha, J., Lin, Z., Ferreira, A., and Anderson, M.W. (1995) Ga, Ti avoidance in the microporous titanogallosilicate ETGS-10. *J. Chem. Soc., Chem. Commun.*, 867–868.

72 Brouwer, D.H., Kristiansen, P.E., Fyfe, C.A., and Levitt, M.H. (2005) Symmetry-based ^{29}Si dipolar recoupling magic angle spinning NMR spectroscopy: a new method for investigating three-dimensional structures of zeolite frameworks. *J. Am. Chem. Soc.*, **127**, 542–543.

73 Fyfe, C.A., Bretherton, J.L., and Lam, L.Y. (2000) Detection of the 'invisible aluminium' and characterisation of the multiple aluminium environments in zeolite USY by high-field solid-state NMR. *J. Chem. Soc., Chem. Commun.*, 1575–1576.

74 Fyfe, C.A., Brouwer, D.H., Lewis, A.R., and Chézeau, J.-M. (2001) Location of the fluoride ion in tetrapropylammonium fluoride silicalite-1 determined by ^{1}H/^{19}F/^{29}Si triple resonance CP, REDOR, and TEDOR NMR experiments. *J. Am. Chem. Soc.*, **123**, 6882–6891.

75 Deng, F., Yue, Y., and Ye, C. (1998) ^{1}H/^{27}Al TRAPDOR NMR studies on aluminum species in dealuminated zeolites. *Solid State Nucl. Magn. Reson.*, **10**, 151–160.

76 Fyfe, C.A., Wong-Moon, K.C., Huang, Y., Grondey, H., and Mueller, K.T. (1995) Dipolar-based ^{27}Al and ^{29}Si solid state NMR connectivity experiments in zeolite molecular sieve frameworks. *J. Phys. Chem.*, **99**, 8707–8716.

77 Lim, K.H. and Grey, C.P. (2000) Characterization of extra-framework cation positions in zeolites NaX and NaY with very fast ^{23}Na MAS and multiple quantum MAS NMR spectroscopy. *J. Am. Chem. Soc.*, **122**, 9768–9780.

78 Hunger, M. and Brunner, E. (2004) Characterization I – NMR spectroscopy, in *Molecular Sieves – Science and Technology* (eds. H.G. Karge and J. Weitkamp), Springer, Berlin, pp. 201–293.

79 Li, J., Lashier, M.E., Schrader, G.L., and Gerstein, B.C. (1991) Oxidation states of vanadium in V–P–O oxidation catalysts by ^{31}P NMR spin-echo mapping. *Appl. Catal.*, **73**, 83–95.

80 Tuel, A., Sananes-Schulz, M.T., and Volta, J.C. (1997) ^{31}P nuclear magnetic resonance by spin echo mapping: a new tool to approach the oxidation state in VPO catalysts. *Catal. Today*, **37**, 59–68.

81 Tong, Y.Y. (1996) Nuclear spin-echo Fourier-transform mapping spectroscopy for broad NMR lines in solids. *J. Magn. Reson. A*, **119**, 22–28.

82 Lapina, O.B., Mastikhin, V.M., Shubin, A.A., Krasilnikov, V.N., and Zamaraev, K.I. (1992) ^{51}V solid state NMR studies of vanadia based catalysts. *Prog. Nucl. Mag. Reson. Spectrosc.*, **24**, 457–525.

83 Lapina, O.B., Simakov, A.V., Mastikhin, V.M., Veniaminov, S.A., and Shubin, A.A. (1989) Composition of the active component of supported vanadium–magnesium catalysts according to ^{51}V NMR data. *J. Mol. Catal.*, **50**, 55–65.

84 Hardcastle, F.D., Wachs, I.E., Eckert, H., and Jefferson, D.A. (1991) Vanadium(V) environments in bismuth vanadates: a structural investigation using Raman spectroscopy and solid state ^{51}V NMR. *J. Solid State Chem.*, **90**, 194–210.

85 Nielsen, U.G., Jakobsen, H.J., and Skibsted, J. (2003) Small ^{51}V chemical shift anisotropy for $LaVO_4$ from MQMAS and MAS NMR spectroscopy. *Solid State Nucl. Magn. Reson.*, **23**, 107–115.

86 Ekambaram, S. and Patil, K.C. (1995) Rapid synthesis and properties of $FeVO_4$, $AlVO_4$, YVO_4 and Eu^{3+}-doped YVO_4. *J. Alloys Compd.*, **217**, 104–107.

87 Bye, G.C. and Gavin, D.G. (1974) Crystallization of metastable aluminas in the presence of V_2O_5. *J. Am. Ceram. Soc.*, **57**, 55–57.

88 Weckhuysen, B.M. and Keller, D.E. (2003) Chemistry, spectroscopy and the role of supported vanadium oxides in heterogeneous catalysis. *Catal. Today*, **78**, 25–46.

89 Lapina, O.B., Khabibulin, D.F., Shubin, A.A., and Bondareva, V.M. (2000) ^{51}V and ^{31}P NMR studies of VO_x/TiO_2 catalysts modified by phosphorus. *J. Mol. Catal. A*, **162**, 381–390.

90 McGregor, J., Huang, Z., Shiko, G., Gladden, L.F., Stein, R.S., Duer, M.J., Wu, Z., Stair, P.C., Rugmini, S., and Jackson, S.D. (2009) The role of surface vanadia species in butane dehydrogenation over VO_x/Al_2O_3. *Catal. Today*, **142**, 143–151.

91 Steinfeldt, N., Muller, D., and Berndt, H. (2004) VO_x species on alumina at high vanadia loadings and calcination temperature and their role in the ODP reaction. *Appl. Catal. A*, **272**, 201–214.

92 Zhang, W.P., Ma, D., Liu, X.C., Liu, X.M., and Bao, X.H. (1999) Perfluorotributylamine as a probe for distinguishing internal and external acidic sites in zeolites by high-resolution ^{1}H MAS NMR spectroscopy. *J. Chem. Soc., Chem. Commun.*, 1091–1092.

93 Haw, J.F., Zhang, J.H., Shimizu, K., Venkatraman, T.N., Luigi, D.P., Song, W.G., Barich, D.H., and Nicholas, J.B. (2000) NMR and theoretical study of acidity probes on sulfated zirconia catalysts. *J. Am. Chem. Soc.*, **122**, 12561–12570.

94 Sánchez-Sánchez, M. and Blasco, T. (2000) Pyrrole as an NMR probe molecule to characterise zeolite basicity. *J. Chem. Soc., Chem. Commun.*, 491–492.

95 Freude, D., Loeser, T., Michel, D., Pingel, U., and Prochnow, D. (2001) ^{17}O NMR studies of low silicate zeolites. *Solid State Nucl. Magn. Reson.*, **20**, 46–60.

96 Ito, T. and Fraissard, J. (1982) ^{129}Xe NMR study of xenon adsorbed on Y zeolites. *J. Chem. Phys.*, **76**, 5225–5229.

97 Ito, T., de Menorval, L.C., Guerrier, E., and Fraissard, J.P. (1984) NMR study of ^{129}Xe adsorbed on L, Z and ZSM zeolites. *Chem. Phys. Lett.*, **111**, 271–274.

98 Demarquay, J. and Fraissard, J. (1987) ^{129}Xe NMR of xenon adsorbed on zeolites: relationship between the chemical shift and the void space. *Chem. Phys. Lett.*, **136**, 314–318.

99 Fraissard, J. and Ito, T. (1988) ^{129}Xe NMR study of adsorbed xenon: a new method for studying zeolites and metal–zeolites. *Zeolites*, **8**, 350–361.

100 Barrage, M.C., Bonardet, J.L., and Fraissard, J. (1990) ^{129}Xe-NMR study of coke distribution in dealuminated HY zeolites. *Catal. Lett.*, **5**, 143–154.

101 Nossov, A., Guenneau, F., Springuel-Huet, M.-A., Haddad, E., Montouillout, V., Knott, B., Engelke, F., Fernandez, C., and Gédéon, A. (2003) Continuous flow hyperpolarized ^{129}Xe-MAS NMR studies of microporous materials. *Phys. Chem. Chem. Phys.*, **5**, 4479–4483.

102 Nossov, A., Haddad, E., Guenneau, F., Mignon, C., Gédéon, A., Grosso, D., Babonneau, F., Bonhomme, C., and Sanchez, C. (2002) The first direct probing of porosity on supported mesoporous silica thin films through

hyperpolarised ^{129}Xe NMR. *J. Chem. Soc., Chem. Commun.*, 2476–2477.

103 Moudrakovski, I.L., Lang, S., Ratcliffe, C.I., Simard, B., Santyr, G., and Ripmeester, J.A. (2000) Chemical shift imaging with continuously flowing hyperpolarized xenon for the characterization of materials. *J. Magn. Reson.*, **144**, 372–377.

104 Brownstein, K.R. and Tarr, C.E. (1977) Spin–lattice relaxation in a system governed by diffusion. *J. Magn. Reson.*, **26**, 17–28.

105 Watson, A.T. and Chang, C.T.P. (1997) Characterizing porous media with NMR methods. *Prog. Nucl. Magn. Reson. Spectrosc.*, **31**, 343–386.

106 Davies, S. and Packer, K.J. (1990) Pore-size distributions from nuclear magnetic resonance spin–lattice relaxation measurements of fluid-saturated porous solids. I. Theory and simulation. *J. Appl. Phys.*, **67**, 3163–3170.

107 Brownstein, K.R. and Tarr, C.E. (1979) Importance of classical diffusion in NMR studies of water in biological cells. *Phys. Rev. A*, **19**, 2446–2453.

108 Gladden, L.F. and Mitchell, J. (2011) Measuring adsorption, diffusion and flow in chemical engineering: applications of magnetic resonance to porous media. *New J. Phys.*, **13**, 035001.

109 Rigby, S.P., Cheah, K.-Y., and Gladden, L.F. (1996) NMR imaging studies of transport heterogeneity and anisotropic diffusion in porous alumina pellets. *Appl. Catal. A*, **144**, 377–388.

110 Hollewand, M.P. and Gladden, L.F. (1993) Heterogeneities in structure and diffusion within porous catalyst support pellets observed by NMR imaging. *J. Catal.*, **144**, 254–272.

111 Timonen, J., Alvila, L., Hirva, P., Pakkanen, T.T., Gross, D., and Lehmann, V. (1995) NMR imaging of aluminum oxide catalyst spheres. *Appl. Catal. A*, **129**, 117–123.

112 Hollewand, M.P. and Gladden, L.F. (1995) Transport heterogeneity in porous pellets II. NMR imaging studies under transient and steady-state conditions. *Chem. Eng. Sci.*, **50**, 327–344.

113 Gladden, L.F., Hollewand, M.P., and Alexander, P. (1995) Characterization of structural inhomogeneities in porous media. *AIChE J.*, **41**, 894–906.

114 Rigby, S.P. and Gladden, L.F. (1998) The use of magnetic resonance images in the simulation of diffusion in porous catalyst support pellets. *J. Catal.*, **173**, 484–489.

115 Espinosa-Alonso, L., Lysova, A.A., de Peinder, P., de Jong, K.P., Koptyug, I.V., and Weckhuysen, B.M. (2009) Magnetic resonance imaging studies on catalyst impregnation processes: discriminating metal ion complexes within millimeter-sized γ-Al_2O_3 catalyst bodies. *J. Am. Chem. Soc.*, **131**, 6525–6534.

116 Koptyug, I.V., Kulikov, A.V., Lysova, A.A., Kirillov, V.A., Parmon, V.N., and Sagdeev, R.Z. (2002) NMR imaging of the distribution of the liquid phase in a catalyst pellet during α-methylstyrene evaporation accompanied by its vapor-phase hydrogenation. *J. Am. Chem. Soc.*, **124**, 9684–9685.

117 Cheah, K.Y., Chiaranussati, N., Hollewand, M.P., and Gladden, L.F. (1994) Coke profiles in deactivated alumina pellets studied by NMR imaging. *Appl. Catal. A*, **115**, 147–155.

118 Bonardet, J.-L., Domeniconi, T., N'Gokoli-Kékélé, P., Spinguel-Huet, M.-A., and Fraissard, J. (1999) Hydrocarbon diffusion measurements and coke distribution in zeolite pellets: a study by ^{1}H NMR imaging and ^{129}Xe NMR spectroscopy. *Langmuir*, **15**, 5836–5840.

119 Bar, N.-K., Bauer, F., Ruthven, D.M., and Balcom, B. (2002) Direct and indirect observation of coke deposits on H-ZSM-5 by ^{1}H NMR imaging. *J. Catal.*, **208**, 224–228.

120 Chesters, M.A., Packer, K.J., Viner, H.E., Wright, M.A.P., and Lennon, D. (1996) Variable-temperature, ^{1}H NMR study of hydrogen chemisorption on EuroPt-1. *J. Chem. Soc., Faraday Trans.*, **92**, 4709–4716.

121 Boddenberg, B. and Beerwerth, B. (1989) Proton and deuteron magnetic resonance spectra of benzene adsorbed on alumina

and on a platinum/alumina catalyst. *J. Phys. Chem.*, **93**, 1435–1440.

122 Goncalves, J.A.S., Portsmouth, R.L., Alexander, P., and Gladden, L.F. (1995) Intercage and intracage transport of aromatics in zeolites NaY, HY, and USY studied by ^{2}H NMR. *J. Phys. Chem.*, **99**, 3317–3325.

123 Klug, C.A., Slichter, C.P., and Sinfelt, J.H. (1991) A ^{2}H NMR study of the formation of ethylidyne from acetylene and hydrogen coadsorbed on platinum. *J. Phys. Chem.*, **95**, 2119–2121.

124 Ansermet, J.P., Wang, P.K., Slichter, C.P., and Sinfelt, J.H. (1988) NMR study of electronic properties of the chemisorption of CO on supported Pt catalysts. *Phys. Rev. B*, **37**, 1417–1428.

125 Zhu, J.F., Mosey, N., Woo, T., and Huang, Y.N. (2007) Study of the adsorption of toluene in zeolite LiNa-Y by solid-state NMR spectroscopy. *J. Phys. Chem. C*, **111**, 13427–13436.

126 Kao, H.M., Liu, H.M., Liang, J.C., Lin, S.H., and Grey, C.P. (2000) Determining the structure of trimethylphosphine bound to the Brønsted acid site in zeolite HY: souble-resonance NMR and *ab initio* studies. *J. Phys. Chem. B*, **104**, 4923–4933.

127 Engelke, F., Bhatia, S., King, T.S., and Pruski, M. (1994) Dynamics of hydrogen at the surface of supported ruthenium. *Phys. Rev. B*, **49**, 2730–2738.

128 Song, Y.Q., Venkataramanan, L., Hürlimann, M.D., Flaum, M., Frulla, P., and Straley, C. (2002) T_1–T_2 correlation spectra obtained using a fast two-dimensional Laplace inversion. *J. Magn. Reson.*, **154**, 261–268.

129 McDonald, P.J., Korb, J.P., Mitchell, J., and Monteilhet, L. (2005) Surface relaxation and chemical exchange in hydrating cement pastes: a two-dimensional NMR relaxation study. *Phys. Rev. E*, **72**, 011409.

130 Mitchell, J., Hürlimann, M.D., and Fordham, E.J. (2009) A rapid measurement of T_1/T_2: the DECPMG sequence. *J. Magn. Reson.*, **200**, 198–206.

131 Weber, D., Mitchell, J., McGregor, J., and Gladden, L.F. (2009) Comparing strengths of surface interactions for reactants and solvents in porous catalysts using two-dimensional NMR relaxation correlations. *J. Phys. Chem. C*, **113**, 6610–6615.

132 Caro, J., Bulow, M., Jobic, H., Karger, J., and Zibrowius, B. (1993) Molecular mobility measurement of hydrocarbons in zeolites by NMR techniques. *Adv. Catal.*, **39**, 351–414.

133 Karger, J. and Stallmach, F. (2005) Diffusion, in *Condensed Matter: Methods and Models* (eds. P. Heitjans and J. Karger), Springer, Berlin, pp. 417–460.

134 Feldhoff F A., Caro, J., Jobic, H., Ollivier, J., Krause, C.B., Galvosas, P., and Karger, J. (2009) Intracrystalline transport resistances in nanoporous zeolite X. *ChemPhysChem*, **10**, 2429–2433.

135 Bearman, R.J. (1961) On the molecular basis of some current theories of diffusion. *J. Phys. Chem.*, **65**, 1961–1968.

136 Karger, J. and Caro, J. (1977) Interpretation and correlation of zeolitic diffusivities obtained from nuclear magnetic resonance and sorption experiments. *J. Chem. Soc., Faraday Trans. 1*, **73**, 1363–1376.

137 Weber, D., Sederman, A.J., Mantle, M.D., Mitchell, J., and Gladden, L.F. (2010) Surface diffusion in porous catalysts. *Phys. Chem. Chem. Phys.*, **12**, 2619–2624.

138 Youngs, T.G.A., Weber, D., Gladden, L.F., and Hardacre, C. (2009) Liquid structure and dynamics of aqueous isopropanol over γ-alumina. *J. Phys. Chem. C*, **113**, 21342–21352.

139 Bhattacharyya, R., Key, B., Chen, H., Best, A.S., Hollenkamp, A.F., and Grey, C.P. (2010) *In situ* NMR observation of the formation of metallic lithium microstructures in lithium batteries. *Nat. Mater.*, **9**, 504–510.

140 Anderson, M.W. and Klinowski, J. (1989) Direct observation of shape selectivity in zeolite ZSM-5 by magic-angle-spinning NMR. *Nature*, **339**, 200–203.

141 Han, X., Yan, Z., Zhang, W., and Bao, X. (2001) Applications of *in situ* NMR in catalytic processes of organic reactions. *Curr. Org. Chem.*, **5**, 1017–1037.

142 Haw, J.F. (ed.) (2002) *In Situ Spectroscopy in Heterogeneous Catalysis*, Wiley-VCH Verlag GmbH, Weinheim.

143 Hunger, M. and Wang, W. (2006) Characterization of solid catalysts in the functioning state by nuclear magnetic resonance spectroscopy. *Adv. Catal.*, **50**, 149–225.

144 Stepanov, A.G., Parmon, V., and Freude, D. (2007) *In situ* NMR spectroscopy in heterogeneous catalysis: kinetic study of hydrocarbon conversion mechanisms. *Kinet. Catal.*, **48**, 521–534.

145 Haw, J.F., Nicholas, J.B., Xu, T., Beck, L.W., and Ferguson, D.B. (1996) Physical organic chemistry of solid acids: lessons from *in situ* NMR and theoretical chemistry. *Acc. Chem. Res.*, **29**, 259–267.

146 Ernst, H., Freude, D., and Mildner, T. (1994) Temperature-switched MAS NMR: a new method for time-resolved *in situ* studies of reaction steps in heterogeneous catalysis. *Chem. Phys. Lett.*, **229**, 291–296.

147 Ferguson, D.B. and Haw, J.F. (1995) Transient methods for *in situ* NMR of reactions on solid catalysts using temperature jumps. *Anal. Chem.*, **67**, 3342–3348.

148 Hwang, S.J., Petucci, C., and Raftery, D. (1998) *In situ* solid-state NMR studies of trichloroethylene photocatalysis: formation and characterization of surface-bound intermediates. *J. Am. Chem. Soc.*, **120**, 4388–4397.

149 Raftery, D., Pilkenson, S., Rice, C.V., Pradhan, A., Macnaughtan, M., Klosek, S., and Hou, T. (2000) Investigation of environmental photocatalysis by solid-state NMR spectroscopy. *Stud. Surf. Sci. Catal.*, **130**, 671–676.

150 Hunger, M. (2008) *In situ* flow MAS NMR spectroscopy: state of the art and applications in heterogeneous catalysis. *Prog. Nucl. Magn. Reson. Spectrosc.*, **53**, 105–127.

151 Haddix, G.W., Reimer, J.A., and Bell, A.T. (1987) A nuclear magnetic resonance probe for *in situ* studies of adsorbed species on catalysts. *J. Catal.*, **106**, 111–115.

152 Haddix, G.W., Reimer, J.A., and Bell, A.T. (1987) Characterization of H_2 adsorbed on γ-Mo_2N by NMR spectroscopy. *J. Catal.*, **108**, 50–54.

153 Hunger, M. and Horvath, T. (1995) A new MAS NMR probe for *in situ* investigations of hydrocarbon conversion on solid catalysts under continuous-flow conditions. *J. Chem. Soc., Chem. Commun.*, 1423–1424.

154 Gougen, P.W. and Haw, J.F. (1996) An *in situ* NMR probe with reagent flow and magic angle spinning. *J. Catal.*, **161**, 870–872.

155 Isbester, P.K., Zalusky, A., Lewis, D.H., Douskey, M.C., Pomije, M.J., Mann, K.R., and Munson, E.J. (1999) NMR probe for heterogeneous catalysis with isolated reagent flow and magic-angle spinning. *Catal. Today*, **49**, 363–375.

156 Buchholz, A., Wang, W., Arnold, A., Xu, M., and Hunger, M. (2003) Successive steps of hydration and dehydration of silicoaluminophosphates H-SAPO-34 and H-SAPO-37 investigated by *in situ* CF MAS NMR spectroscopy. *Micropor. Mesopor. Mater.*, **57**, 157–168.

157 Wang, W., Seiler, M., Ivanova, I.I., Ternberg, U., Weitkamp, J., and Hunger, M. (2002) Formation and decomposition of *N,N,N*-trimethylanilinium cations on zeolite H-Y investigated by *in situ* stopped-flow (SF) MAS NMR spectroscopy. *J. Am. Chem. Soc.*, **124**, 7548–7554.

158 Gougen, P.W., Xu, T., Barich, D.H., Skloss, T.W., Song, W., Wang, Z., Nicholas, J.B., and Haw, J.F. (1998) Pulse–quench catalytic reactor studies reveal a carbon-pool mechanism in methanol-to-gasoline chemistry on zeolite H-ZSM-5. *J. Am. Chem. Soc.*, **120**, 2650–2651.

159 Haw, J.F., Nicholas, J.B., Song, W., Deng, F., Wang, F., Xu, T., and Heneghan, C.S. (2000) Roles for cyclopentenyl cations in the synthesis of hydrocarbons from methanol on zeolite catalyst H-ZSM-5. *J. Am. Chem. Soc.*, **122**, 4763–4775.

160 Keeler, C., Xiong, J.C., Lock, H., Dec, S., Tao, T., and Maciel, G.E. (1999) A new *in situ* chemical reactor for studying heterogeneous catalysis by NMR: the GRASSHopper. *Catal. Today*, **49**, 377–383.

161 MacNamara, E. and Raftery, D. (1998) A high-resolution solid-state NMR probe for *in-situ* studies of heterogeneous catalysis under flowing conditions. *J. Catal.*, **175**, 135–137.

162 Smith, G.V. and Notheisz, F. (eds.) (1999) *Heterogeneous Catalysis in Organic Chemistry*, Academic Press, New York.

163 McGregor, J., Canning, A.S., Mitchell, S., Jackson, S.D., and Gladden, L.F. (2010) The influence of carbon laydown on selectivity in the hydrogenation of pentenenitriles over supported-nickel catalysts. *Appl. Catal. A*, **384**, 192–200.

164 Stepanov, A.G., Ernst, H., and Freude, D. (1998) *In situ*^{1}H MAS NMR studies of the H/D exchange of deuterated propane adsorbed on zeolite H-ZSM-5. *Catal. Lett.*, **54**, 1–4.

165 Sommer, J., Habermacher, D., Jost, R., Sassi, A., Stepanov, A.G., Luzgin, M.V., Freude, D., Ersnt, H., and Martens, J. (1999) Activation of small alkanes on solid acids. An H/D exchange study by liquid and solid-state NMR: the activation energy and the inhibiting effect of carbon monoxide. *J. Catal.*, **181**, 265–270.

166 Haouas, M., Walspurger, S., Taulelle, F., and Sommer, J. (2004) The initial stages of solid acid-catalyzed reactions of adsorbed propane. A mechanistic study by *in situ* MAS NMR. *J. Am. Chem. Soc.*, **126**, 599–606.

167 Kolyagin, Y.G., Ivanova, I.I., and Pirogov, Y.A. (2009) ^{1}H and ^{13}C MAS NMR studies of light alkanes activation over MFI zeolite modified by Zn vapour. *Solid State Nucl. Magn. Reson.*, **35**, 104–112.

168 Truitt, M.J., Toporek, S.S., Rovira-Hernandez, R., Hatcher, K., and White, J.L. (2004) Identification of an adsorption complex between an alkane and zeolite active sites. *J. Am. Chem. Soc.*, **126**, 11144–11145.

169 Truitt, M.J., Toporek, S.S., Rovira-Truitt, R., and White, J.L. (2006) Alkane C−H bond activation in zeolites: evidence for direct protium exchange. *J. Am. Chem. Soc.*, **128**, 1847–1852.

170 Philippou, A. and Anderson, M.W. (1994) Solid-state NMR investigation of the alkylation of toluene with methanol over basic zeolite X. *J. Am. Chem. Soc.*, **116**, 5774–5783.

171 Hathaway, P.E. and Davis, M.E. (1989) Base catalysis by alkali-modified zeolites: I. Catalytic activity. *J. Catal.*, **116**, 263–278.

172 Hunger, M., Schenk, U., Seiler, M., and Weitkamp, J. (2000) *In situ* MAS NMR spectroscopy of surface compounds formed from methanol and from a toluene/methanol mixture on basic zeolite X. *J. Mol. Catal. A*, **156**, 153–161.

173 Derouane, E.G., He, H.Y., Derouane Abd-Hamid, S.B., and Ivanova, I.I. (1999) *In situ* MAS NMR investigations of molecular sieves and zeolite-catalyzed reactions. *Catal. Lett.*, **58**, 1–19.

174 Stepanov, A.G., Luzgin, M.V., Arzumanov, S.S., Wang, W., Hunger, M., and Freude, D. (2005) *n*-Butane conversion on sulfated zirconia: *in situ*^{13}C MAS NMR monitoring of the kinetics of the C-13-label scrambling and isomerization. *Catal. Lett.*, **101**, 181–185.

175 Arzumanov, S.S., Gabrienko, A.A., Freude, D., and Stepanov, A.G. (2009) *In situ* high temperature MAS NMR study of the mechanisms of catalysis. Ethane aromatization on Zn-modified zeolite BEA. *Solid State Nucl. Magn. Reson.*, **35**, 113–119.

176 Lezcano-Gonzalez, I., Boronat, M., and Blasco, T. (2009) Investigation on the Beckmann rearrangement reaction catalyzed by porous solids: MAS NMR and theoretical calculations. *Solid State Nucl. Magn. Reson.*, **35**, 120–129.

177 Fernandez, A.B., Lezcano-Gonzalez, I., Boronat, M., Blasco, T., and Corma, A. (2007) NMR spectroscopy and theoretical calculations demonstrate the nature and location of active sites for the Beckmann rearrangement reaction in microporous materials. *J. Catal.*, **249**, 116–119.

178 Reddy Marthala, V.R., Jiang, Y., Huang, J., Wang, W., Glaeser, R., and Hunger, M. (2006) Beckmann rearrangement of ^{15}N-cyclohexanone oxime on zeolites silicalite-1, H-ZSM-5, and H-[B]ZSM-5 studied by solid-state NMR spectroscopy. *J. Am. Chem. Soc.*, **128**, 14812–14813.

179 Reddy Marthala, V.R., Rabl, S., Huang, J., Rezai, S.A.S., Thomas, B., and Hunger, M. (2008) *In situ* solid-state NMR investigations of the vapor-phase Beckmann rearrangement of ^{15}N-cyclohexanone oxime on MFI-type zeolites and mesoporous SBA-15 materials in the absence and presence of the additive ^{13}C-methanol. *J. Catal.*, **257**, 134–141.

180 Wang, W., Seiler, M., and Hunger, M. (2001) The role of surface methoxy species in the conversion of methanol to dimethyl ether on acidic zeolites investigated by *in situ* stopped-flow (SF) MAS NMR spectroscopy. *J. Phys. Chem. B*, **105**, 12553–12558.

181 Wang, W., Seiler, M., Ivanova, I.I., Weitkamp, J., and Hunger, M. (2001) *In situ* stopped-flow (SF) MAS NMR spectroscopy: a novel NMR technique applied for the study of aniline methylation on a solid base catalyst. *J. Chem. Soc., Chem. Commun.*, 1362–1363.

182 Hunger, M., Seiler, M., and Horvath, T. (1999) A technique for simultaneous *in situ* MAS NMR and on-line gas chromatographic studies of hydrocarbon conversions on solid catalysts under flow conditions. *Catal. Lett.*, **57**, 199–204.

183 Horvath, T., Seiler, M., and Hunger, M. (2000) A comparative study of methyl-*tert*-butyl ether synthesis on zeolites H-Y, H-Beta, H-Beta/F and H-ZSM-5 by *in situ* MAS NMR spectroscopy under flow conditions and on-line gas chromatography. *Appl. Catal. A*, **193**, 227–236.

184 Haw, J.F., Song, W.G., Marcus, D.M., and Nicholas, J.B. (2003) The mechanism of methanol to hydrocarbon catalysis. *Acc. Chem. Res.*, **36**, 317–326.

185 Wang, W., Jiang, Y., and Hunger, M. (2006) Mechanistic investigations of the methanol-to-olefin (MTO) process on acidic zeolite catalysts by *in situ* solid-state NMR spectroscopy. *Catal. Today*, **113**, 102–114.

186 White, J.L. and Truitt, M.J. (2007) Heterogeneous catalysis in solid acids. *Prog. Nucl. Magn. Reons. Spectrosc.*, **51**, 139–154.

187 Xu, T. and White, J.L. (2004) Catalyst pretreatment in an oxygenate to olefins reaction system. US Patent 6,734,330, filed 12 July 2000, issued 11 May 2004.

188 Xu, T. and White, J.L. (2004) Catalyst pretreatment in an oxygenate to olefins reaction system. US Patent 6,743,747, filed 24 February 2000, issued 1 June 2004.

189 Song, W.G., Haw, J.F., Nicholas, J.B., and Heneghan, C.S. (2000) Methylbenzenes are the organic reaction centers for methanol-to-olefin catalysis on H-SAPO-34. *J. Am. Chem. Soc.*, **122**, 10726–10727.

190 Wang, W., Buchholz, A., Seiler, M., and Hunger, M. (2003) Evidence for an initiation of the methanol-to-olefin process by reactive surface methoxy groups on acidic zeolite catalysts. *J. Am. Chem. Soc.*, **125**, 15260–15267.

191 Seiler, M., Schenk, U., and Hunger, M. (1999) Conversion of methanol to hydrocarbons on zeolite H-ZSM-5 investigated by *in situ* MAS NMR spectroscopy under flow conditions and on-line gas chromatography. *Catal. Lett.*, **62**, 139–145.

192 Hunger, M., Seiler, M., and Buchholz, A. (2001) *In situ* MAS NMR spectroscopic investigation of the conversion of methanol to olefins on silicoaluminophosphates SAPO-34 and SAPO-18 under continuous flow conditions. *Catal. Lett.*, **74**, 61–68.

193 Seiler, M., Wang, W., Buchholz, A., and Hunger, M. (2003) Direct evidence for the catalytically active role of the hydrocarbon pool formed on zeolite H-ZSM-5 during the methanol to olefin conversion. *Catal. Lett.*, **88**, 187–191.

194 Hunger, M. and Wang, W. (2004) Formation of cyclic compounds and carbenium ions by conversion of methanol on weakly dealuminated zeolite H-ZSM-5 investigated via a novel *in situ*

CF MAS NMR/UV–Vis technique. *J. Chem. Soc., Chem. Commun.*, 584–585.

195 Jiang, Y., Huang, J., Reddy Marthala, V.R., Ooi, Y.S., Weitkamp, J., and Hunger, M. (2007) *In situ* MAS NMR–UV/Vis investigation of H-SAPO-34 catalysts partially coked in the methanol-to-olefin conversion under continuous-flow conditions and of their regeneration. *Micropor. Mesopor. Mater.*, **105**, 132–139.

196 Savelsberg, R., Demco, D.E., Blümich, B., and Stapf, S. (2002) Particle motion in gas-fluidized granular systems by pulsed-field gradient nuclear magnetic resonance. *Phys. Rev. E*, **65** (2 Pt 1), 020301.

197 Müller, C.R., Davidson, J.F., Dennis, J.S., Fennell, P.S., Gladden, L.F., Hayhurst, A.N., Mantle, M.D., Rees, A.C., and Sederman, A.J. (2006) Real-time measurement of bubbling phenomena in a three-dimensional gas-fluidized bed using ultrafast magnetic resonance imaging. *Phys. Rev. Lett.*, **96**, 154504.

198 Akpa, B.S., Matthews, S.M., Sederman, A.J., Yunus, K., Fisher, A.C., Johns, M.L., and Gladden, L.F. (2007) Study of miscible and immiscible flow in a microfluidic device using magnetic resonance imaging. *Anal. Chem.*, **79**, 6128–6134.

199 Sederman, A.J. and Gladden, L.F. (2001) Magnetic resonance visualisation of single- and two-phase flow in porous media. *Magn. Reson. Imaging*, **19**, 339–343.

200 Sankey, M.H., Holland, D.J., Sederman, A.J., and Gladden, L.F. (2009) Magnetic resonance velocity imaging of liquid and gas two-phase flow in packed beds. *J. Magn. Reson.*, **196**, 142–148.

201 Gladden, L.F., Anadon, L.D., Lim, M.H.M., Sederman, A.J., and Stitt, E.H. (2005) Insights into the mechanism of the trickle-to-pulse transition in trickle-bed reactors. *Ind. Eng. Chem. Res.*, **44**, 6320–6331.

202 Yuen, E.H.L., Sederman, A.J., and Gladden, L.F. (2002) *In situ* magnetic resonance visualisation of the spatial variation of catalytic conversion within a fixed-bed reactor. *Appl. Catal. A*, **232**, 29–38.

203 Gladden, L.F., Alexander, P., Britton, M.M., Mantle, M.D., Sederman, A.J., and Yuen, E.H.L. (2003) *In situ* magnetic resonance measurement of conversion, hydrodynamics and mass transfer during single- and two-phase flow in fixed-bed reactors. *Magn. Reson. Imaging*, **21**, 213–219.

204 Yuen, E.H.L., Sederman, A.J., Sani, F., Alexander, P., and Gladden, L.F. (2003) Correlations between local conversion and hydrodynamics in a 3-D fixed-bed esterification process: an MRI and lattice-Boltzmann study. *Chem. Eng. Sci.*, **58**, 613–619.

205 Akpa, B.S., Mantle, M.D., Sederman, A.J., and Gladden, L.F. (2005) *In situ* ^{13}C DEPT-MRI as a tool to spatially resolve chemical conversion and selectivity of a heterogeneous catalytic reaction occurring in a fixed-bed reactor. *J. Chem. Soc., Chem. Commun.*, 2741–2743.

206 Sederman, A.J., Mantle, M.D., Dunckley, C.P., Huang, Z.Y., and Gladden, L.F. (2005) *In situ* MRI study of 1-octene isomerisation and hydrogenation within a trickle-bed reactor. *Catal. Lett.*, **103**, 1–8.

9
Electron Paramagnetic Resonance Spectroscopy

Piotr Pietrzyk, Zbigniew Sojka, and Elio Giamello

9.1
Introduction

The term electron paramagnetic resonance (EPR) encompasses a family of techniques based on the absorption of electromagnetic radiation in the microwave frequency region by a paramagnetic sample placed in a magnetic field. EPR has a broad range of applications in catalysis and related fields as it represents a very powerful tool for investigating paramagnetic entities. The first EPR experiment was performed by E. K. Zavoisky in 1945, observing the resonance of $CuCl_2{\cdot}2H_2O$ with a radiofrequency source operating at 133 MHz and a magnetic field provided by a solenoid. The limitation of EPR is evident from the previous definition in that diamagnetic systems, which represent the majority of the substances, are excluded from EPR investigations. However, this limitation is also an advantage since, for instance, reactive paramagnetic intermediates or paramagnetic centers belonging to a complex chemical system (e.g., a paramagnetic ion in a zeolitic network) can be studied without any interference. The relevant information provided by EPR concerns the nature, symmetry, and electronic structure of the paramagnetic center and of its surrounding. A second advantage of EPR, apart from its specificity, is its high sensitivity, which, in the investigations of solid surfaces, allows the detection of paramagnetic species in concentrations well below monolayer coverage. The first applications of EPR in the field of surface chemistry and heterogeneous catalysis were reported at the beginning of the 1960s. Since then, review articles oriented towards catalytic phenomena have appeared periodically in the literature [1–9].

9.1.1
Interaction of Matter with a Magnetic Field

Before describing the concepts of EPR spectroscopy, it must be recalled that a paramagnetic body, when placed in a magnetic field, increases the magnetic flux density (or magnetic induction, $\boldsymbol{B}$) within its own volume. In contrast, a diamagnetic substance slightly decreases the magnetic flux density. Diamagnetism is present in

Characterization of Solid Materials and Heterogeneous Catalysts: From Structure to Surface Reactivity, First Edition. Edited by Michel Che and Jacques C. Védrine.
© 2012 Wiley-VCH Verlag GmbH & Co. KGaA. Published 2012 by Wiley-VCH Verlag GmbH & Co. KGaA.

all substances and is produced by electron circulation in atoms, ions, and molecules having a closed shell of electrons under the influence of a magnetic field. Paramagnetism is typical of substances having centers with one or more unpaired electrons and, therefore, bearing an intrinsic angular momentum – the spin – and a corresponding magnetic moment.

Whereas in the absence of an external magnetic field the unpaired electrons of each paramagnetic center are aligned randomly, in the presence of such a field ($\boldsymbol{B}$) the magnetic moments of different centers tend to align with the field and hence with each other. In such conditions, the system acquires a magnetization $\boldsymbol{M}$, related to the difference between the number of electrons in the two allowed spin states (i.e., with magnetic moments aligned and counter-aligned with respect to the magnetic field vector, respectively). This aligning effect is contrasted by the randomizing effect of thermal energy. The magnetization or alternatively the magnetic susceptibility χ ($\chi = \boldsymbol{M}/\boldsymbol{H}$, where $\boldsymbol{H}$ is the strength of magnetic field) therefore tends to increase by lowering the temperature according to the Curie law: $\chi = C/T$, C being a constant and T the temperature.

Electron magnetic resonance occurs when an electromagnetic wave of suitable frequency (usually in the microwave region) interacts with the sample immersed in a magnetic field and causes the inversion of the spin (and thus of the magnetic moment) of the unpaired electrons, so that a certain amount of the electromagnetic energy is absorbed by the system. In quantum mechanical terms, the description of the electron spin resonance can be reduced to the description of the behavior of a single unpaired electron undergoing, under the effect of an external magnetic field, an energy splitting between the two allowed spin states. In such conditions, an electron in the lower state is promoted to the upper state by absorption of a photon of suitable energy.

9.1.2
Experimental Approaches in EPR

In most molecular spectroscopy techniques, the electric field component of the radiation interacts with an electric dipole moment in the molecules. In magnetic resonance spectroscopy, in contrast, it is the magnetic component of the radiation that interacts with the magnetic dipoles of paramagnetic centers. There are two approaches to record EPR spectra: in the more common one, low-intensity microwave radiation continuously irradiates the sample (continuous-wave or CW-EPR). In the second approach, pulses of high-power microwave radiation are sent to the sample and the response is recorded in the absence of radiation (pulse-EPR). Since the majority of the EPR applications to surface chemistry and catalysis employ CW-EPR, this technique will be mainly described here. In a CW-EPR experiment with the sample under irradiation with microwaves having fixed frequency, a given range of the magnetic field is swept to reach the condition of magnetic resonance. A CW-EPR spectrum is therefore a diagram where the microwave absorption, or more commonly, its first derivative is reported as a function of the magnetic field swept in the experiment. It usually consists of several

absorption lines and is characterized by (i) the positions of the absorption lines, that is, the magnetic field values at which the absorptions occur, (ii) the number, separation, and relative intensity of the lines, and (iii) the widths and shapes of the lines. A careful analysis of these parameters provides information about the nature and the structure of the species responsible for the spectrum (i, ii), their interaction with the environment (ii), and the dynamic processes that the paramagnetic species undergo (iii).

9.2 Principles of EPR

Elementary particles are characterized by mass, by charge (both scalar quantities), and by the intrinsic angular momentum, a vector quantity also called the spin. In the case of an electron, the spin is denoted by the symbol $\boldsymbol{S}$, its components along the x, y, z axes of a Cartesian frame being S_x, S_y, S_z. Quantum mechanics introduces severe limitations in the knowledge of the spin vector features. In fact, only the square of the intrinsic angular momentum (S^2) and one component in a given direction (conventionally z, hence S_z) can be measured simultaneously with certainty. The intrinsic angular momentum of a given quantum system is defined by the spin quantum number S, which can assume integer or half-integer values only (0, 1/2, 1, ...). The magnitude of $\boldsymbol{S}$ is given by the general equation

$$|\boldsymbol{S}| = \sqrt{S(S+1)}\hbar \tag{9.1}$$

where $\hbar = h/2\pi$ (with h being Planck's constant, equal to 6.626×10^{-34} J·s). For an electron, the spin quantum number is $S = 1/2$, and therefore $|\boldsymbol{S}| = \left(\sqrt{3}/2\right)\hbar$. Since the number of allowed S_z values is, in general, $2S + 1$, in the case of an electron with $S = 1/2$ the spin exists in two states only, usually labeled by the Greek letters α and β. These states have an opposite orientation of the angular momentum in space. In particular, the allowed S_z values are $S_z = 1/2\hbar$ (sometime referred to as the $\uparrow$ or α state, quantum number $M_S = 1/2$) and $S_z = -1/2\hbar$ ($\downarrow$ or β, $M_S = -1/2$). In the absence of an external magnetic field, α and β electron spin states have the same energy and are said to be degenerate (a so-called Kramer's doublet).

The electron spin angular momentum, or briefly the spin, has an associated magnetic moment $\boldsymbol{\mu}_S$ which is antiparallel to the spin itself and given by

$$\boldsymbol{\mu}_S = -g_e \frac{\mu_B}{\hbar} \boldsymbol{S} \tag{9.2}$$

where g_e is the free electron g value ($g_e = 2.002\,319$), μ_B is an atomic unit of the magnetic moment called the Bohr magneton $\mu_B = e\hbar/2m_e$ ($\mu_B = 9.274 \times 10^{-24}$ J·T^{-1}) with e and m_e being the electron charge and mass, respectively.

In the absence of a magnetic field, the spin vectors $\boldsymbol{S}$ (and the corresponding magnetic moments) of an assembly of the free electrons are randomly aligned, but in the presence of an external magnetic field the magnetic moments tend to align and

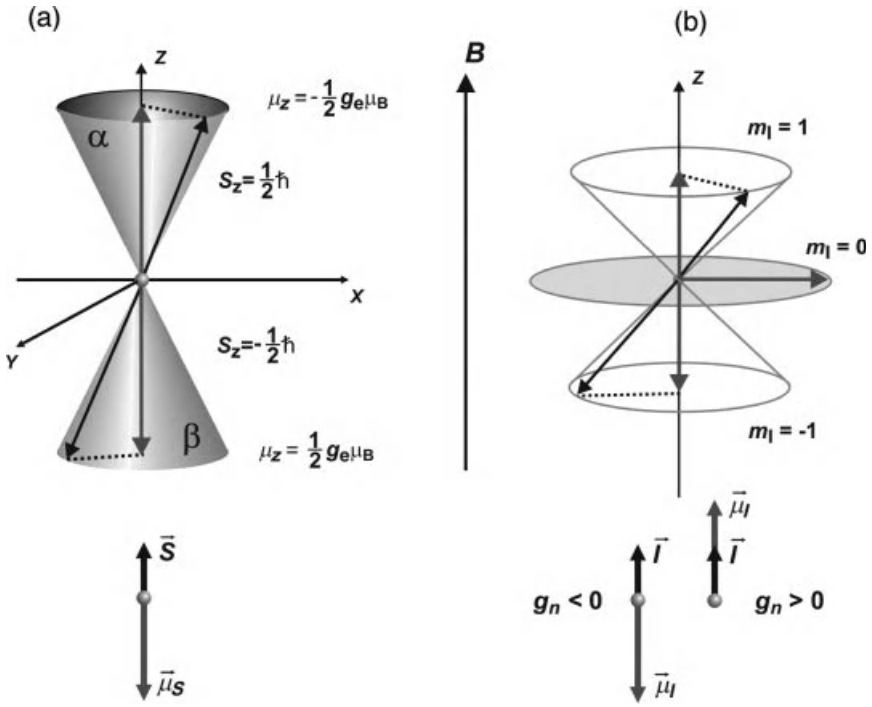


Figure 9.1 Possible orientations of the electron ($S = 1/2$) and nuclear ($I = 1$) spins in an external magnetic field. The magnetic moments corresponding to the α and β electron spin states and also the relative alignment of the spins and their magnetic moments are also indicated.

define the axis of orientation of the S_z component (Figure 9.1). Because of the complete uncertainty of the S_x and S_y components, the vectors representing the spin can lie on the surface of one of the two cones, whose axes coincide with the z-axis. In this way, all electrons assume one of the two permitted S_z values and the populations of the α and β states are equal.

9.2.1
The Zeeman Effect and the Resonance Phenomenon

The magnetic moment $\boldsymbol{\mu}_S$ associated with the electron spin is responsible for the energy separation between the α and β electron spin states, when the electron is immersed in the static magnetic field $\boldsymbol{B}$ whose induction is measured in the units tesla (T) or gauss (G) ($1\,\mathrm{T} = 10^4\,\mathrm{G}$). The energy of such a system is given by the scalar product between $\boldsymbol{\mu}_S$ and $\boldsymbol{B}$, so it will depend on the orientation of $\boldsymbol{\mu}_S$ with respect to $\boldsymbol{B}$:

$$E = -\boldsymbol{\mu}_S \cdot \boldsymbol{B} = g\frac{\mu_B}{\hbar}\boldsymbol{S} \cdot \boldsymbol{B} \tag{9.3}$$

Since the direction of the reference frame is arbitrary, the direction of $\boldsymbol{B}$ can be chosen in such a way as to coincide with the z-axis. In this case, Eq. (9.3) becomes

$$E = g\frac{\mu_B}{\hbar} S_z B \tag{9.4}$$

where $\boldsymbol{B} = B_z$ is the magnetic field induction.

For the two allowed states of the electron spin (α or β) in which the z component of the spin is $1/2\hbar$ and $-1/2\hbar$, respectively, in the presence of a magnetic field the electron spin energy can assume only the two values:

$$E = M_S g\mu_B B = \pm\frac{1}{2} g\mu_B B \tag{9.5}$$

the positive sign referring to the α state and the negative sign to the β state, which is therefore more stable than the α state.

The splitting of the electron spin energy level into two levels in the presence of a magnetic field is called the Zeeman effect (Figure 9.2). The energy splitting of the two

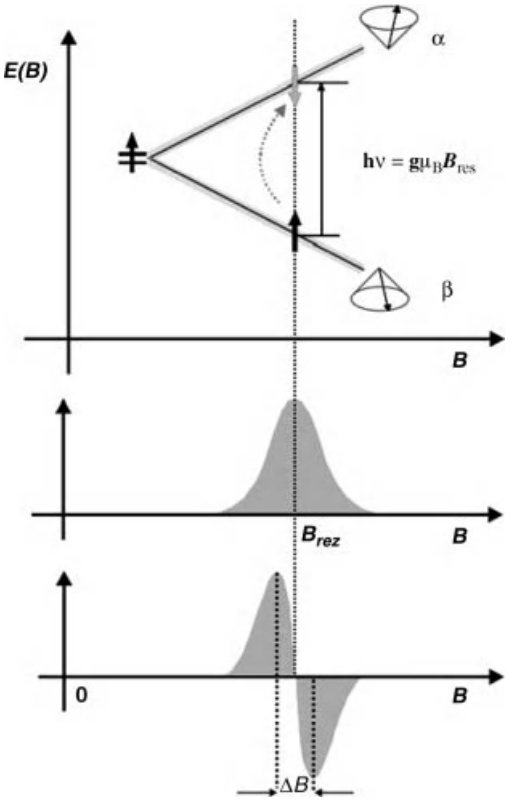


Figure 9.2 Zeeman effect and detection of an EPR signal by sweeping the magnetic field at fixed microwave frequency. The resonance occurs at the field (B_{res}) when the two terms of Eq. (9.9) become equal. The corresponding absorption line and its first derivative are also shown.

allowed spin states is proportional to the induction of the applied magnetic field. In a field of 300 mT, for example, the β state lies $\sim$0.3 cm^{-1} below the α state.

The scalar product between $\boldsymbol{\mu}_S$ and $\boldsymbol{B}$ in Eqs. (9.3) and (9.4) can be written in quantum mechanical terms replacing $\boldsymbol{S}$ with the corresponding operator leading to the following Hamiltonian, that is, the energy operator:

$$\hat{H}_{EZ} = g\mu_B B\hat{\boldsymbol{S}}_z \tag{9.6}$$

Equation (9.6) is the simplest example of a spin Hamiltonian acting on the spin components of the whole electron wavefunction with the $\hat{\boldsymbol{S}}_z$ operator acting on the spin functions α and β in the following way: $\hat{\boldsymbol{S}}_z|\alpha\rangle = +\frac{1}{2}|\alpha\rangle$ and $\hat{\boldsymbol{S}}_z|\beta\rangle = -\frac{1}{2}|\beta\rangle$.

The energy values corresponding to the two allowed orientation of the spin already reported in Eq. (9.5) show up also by applying the spin Hamiltonian in Eq. (9.6) to the α and β wavefunctions. The energy difference between these two states is therefore

$$\Delta E = g\mu_B B \tag{9.7}$$

At thermal equilibrium, under the influence of the applied external magnetic field, the spin population of the two levels is dictated by the Maxwell–Boltzmann law:

$$\frac{n_\alpha}{n_\beta} = \exp\left(-\frac{\Delta E}{kT}\right) \tag{9.8}$$

where k is the Boltzmann constant, T the temperature and n_α and n_β the spin populations of the α and β states, respectively. At room temperature, in a magnetic field of about 300 mT, typical of an X-band spectrometer, there is a very small excess of β spins ($\sim$0.1%) over the α spins.

9.2.2
Spin Resonance and Spin Relaxation

The electron spin resonance experiment is the observation of the energy required to reverse the direction of a magnetic moment associated with electron spin in the presence of an external magnetic field. Electrons in the lower Zeeman state (β) can be promoted to the upper state (α) by absorption of a quantum of the electromagnetic radiation energy, provided that the quantum energy $h\nu$ coincides with the energy difference [Eq. (9.7)] between the α and β states:

$$h\nu = g\mu_B B \tag{9.9}$$

where ν is the radiation frequency. Equation (9.9) is the fundamental equation of EPR spectroscopy.

In a magnetic field of 0.35 T, which is the standard magnetic field induction used in the most common type of EPR instrumentation, for $g = 2.0023$ Eq. (9.9) gives $\nu = 9.5$ GHz. This radiation frequency is in the X-band region of the microwaves, which ranges from 8 to 12 GHz. The EPR instruments operating in this frequency range are denoted as X-band spectrometers. Other regions of higher microwave frequencies used in commercial EPR spectrometers are K-band ($\sim$24 GHz), Q-band

(~35 GHz), and W-band (95 GHz). Less important to the field of surface chemistry and catalysis are the low frequency bands such as L- and S-bands at 1.1 and 3.0 GHz, respectively (see Section 9.12.2).

As mentioned above, an EPR spectrum is not measured by monitoring the absorption of the sample as a function of a progressively varying frequency. The available microwave sources, in fact, are essentially monochromatic and emit radiation in a limited range of frequency. This problem is circumvented taking advantage of Eq. (9.9), which shows how magnetic resonance is related to a pair of external quantities, that is, the microwave frequency and the magnetic field induction. The EPR experiment is, therefore, conducted by irradiating the sample with a fixed frequency and sweeping a suitable range of the magnetic field using an electromagnet. When the magnetic field reaches the value necessary to fulfill the resonance condition of Eq. (9.9), which is also called the resonant field or B_{res}, absorption of the microwave energy is observed which results in appearance of a spectral line. Figure 9.2 illustrates the Zeeman splitting at increasing B and the conditions of the resonance. At the bottom of the figure the microwave absorption and its first derivative are also shown. The first derivative of the absorption is the normal output in CW-EPR spectroscopy experiments (see Section 9.4).

The observation of an EPR signal, however, depends on the delicate balance between the absorption of the microwave energy (excitation) and the efficiency of the mechanism through which the excited system returns to the ground state. This latter phenomenon is called relaxation. By the absorption process, in fact, the populations of the two energy levels n_α and n_β which, prior to irradiation, are already fairly close to each other [Eq. (9.8)], tend to equalize. The excess of energy of the excited system must therefore be dissipated in order to restore the Maxwell–Boltzmann distribution. This occurs by means of two different types of relaxation processes: the spin–lattice and the spin–spin relaxation. None of these processes involve re-emission of the microwave radiation. In the former mechanism, an excited electron in the α state reverses its spin by transferring the excess energy to vibrational degrees of freedom of the lattice. The vibrations of the lattice (phonons), in fact, give rise to the fluctuating magnetic fields at the unpaired electron; if these fluctuations happen to have a component that oscillates at the transition frequency, then the spin transition can be induced.

The spin–lattice interaction tends to restore the excess of spins in the low energy level, allowing continuation of the observation of the EPR absorption signal. The spin–lattice relaxation involves an exponential decay of energy whose rate is usually reported as the inverse of a characteristic time T_1, called the spin–lattice relaxation time. It can easily be shown, in terms of the Heisenberg uncertainty principle, that the linewidth of the resonance line is inversely proportional to T_1. This parameter has been found to be sensitive to the temperature and the presence of nearby electronic excited states. A decrease in temperature decreases the population of phonons, leading to longer relaxation times, and correspondingly narrower EPR lines. For this reason, it is convenient, in most investigations of the solid state, to measure EPR spectra at low temperature. The energy of excited electronic states of the investigated system also affects the relaxation time. When excited electronic states are close

($\sim 100\,cm^{-1}$) to the ground state, the relaxation time will be very short and the linewidths become very large, and such EPR spectra could even be not observable.

A parameter to be considered for a correct detection of the electron magnetic resonance is the power of the incident microwave radiation. When a spin system is irradiated with a microwave power that is too high for the efficiency of the relaxation mechanisms, the populations of the two Zeeman levels tend to equalize and the intensity of the signal decreases, being no longer proportional to the number of spins present in the sample. This effect, known as saturation, can be avoided by exposing the sample to sufficiently low microwave power.

The other relaxation process that can take place is the spin–spin relaxation process. This phenomenon is characterized by a time constant T_2 called the spin–spin relaxation time, and involves an energy exchange between the electron spins without transfer of energy to the lattice. When both the spin–lattice and spin–spin relaxation operate simultaneously, a rough expression of the resonance linewidth is

$$\Delta B \propto \frac{1}{T_1} + \frac{1}{T_2} \tag{9.10}$$

In general, $T_1 > T_2$ and the linewidth depends mainly on the spin–spin interactions. There are two typical lineshapes that are useful to describe the EPR lines. They correspond to the Gaussian (f_G) or Lorentzian (f_L) functions, whose normalized analytical expressions are [10]

$$\begin{aligned} f_G &= \frac{\sqrt{2/\pi}}{\Delta B} \exp\left[-2\left(\frac{B-B_{res}}{\Delta B}\right)^2\right] \\ f_L &= \frac{2\sqrt{3}}{\pi}\left[\frac{\Delta B}{3\Delta B^2 + 4(B-B_{res})^2}\right] \end{aligned} \tag{9.11}$$

where ΔB is the peak-to-peak linewidth.

A detailed description of the lineshape in EPR is beyond the scope of this chapter. It is sufficient to note that the Gaussian lineshape occurs in the magnetic resonance for statistical distribution of similar paramagnetic centers. This is fairly common in the study of catalytic surfaces, which often exhibit an appreciable heterogeneity of the active sites.

9.3 Electron–Nucleus Hyperfine Interaction

Like the electrons, the nuclei are characterized by a spin angular momentum, usually represented by $\boldsymbol{I}$, and by the corresponding quantum numbers. Depending on the type of nucleus, the nuclear spin quantum number I may have values other than 1/2, including zero and integer values. The allowed components of any nuclear spin vector are $I_z = -I, (-I+1), \ldots, (I-1), I$. A few examples of the nuclear spin values for

Table 9.1 Nuclear spin quantum number of various nuclei.

	***I* value**					
	0	**1/2**	**1**	**3/2**	**5/2**	**7/2**
Isotope	^{12}C, ^{16}O	^{1}H, ^{13}C, ^{31}P, ^{15}N	^{2}H, ^{14}N,	^{23}Na, ^{35}Cl, ^{41}K, ^{63}Cu, ^{65}Cu	^{17}O, ^{27}Al, ^{55}Mn, ^{95}Mo, ^{97}Mo	^{51}V, ^{59}Co

atoms of interest in catalysis are reported in Table 9.1. The interaction between the magnetic moments of the unpaired electron and those associated with the magnetic nuclei ($I \neq 0$) present in the system gives rise to an EPR spectrum with a series of lines with well-defined separation, which is called the hyperfine structure. Most of the information which can be deduced from EPR spectra usually arises from the analysis of the hyperfine structure.

The magnetic moment $\boldsymbol{\mu}_N$ associated with a nucleus is given by

$$\boldsymbol{\mu}_N = g_N \frac{\mu_n}{\hbar} \boldsymbol{I} \tag{9.12}$$

where g_N is the nuclear *g*-factor and μ_n is the nuclear magneton (an analog of the Bohr magneton for the proton mass). Depending on the nucleus, the nuclear magnetic moment is collinear or anticollinear to the nuclear spin vector $\boldsymbol{I}$ as shown in Figure 9.1.

For a nucleus with the spin $I = 1/2$, the interaction of the nuclear magnetic moment with an external applied magnetic field lying along the *z*-axis can be described in terms of the following Hamiltonian:

$$\hat{H}_{NZ} = -g_N \mu_n B \hat{\boldsymbol{I}}_z \tag{9.13}$$

and the energy corresponding to the two allowed orientations of the nuclear spin (nuclear Zeeman effect) is equal to

$$E = M_I g_N \mu_n B = \pm \frac{1}{2} g_N \mu_n B \tag{9.14}$$

In the general case of an isotope with the nuclear spin I, the number of sublevels generated by the nuclear Zeeman effect is equal to $2I + 1$.

Considering the simplest possible case of the electron–nucleus interaction (a system such as the hydrogen atom with the unpaired electron interacting with one $I = 1/2$ nucleus), the total spin-Hamiltonian is composed of three terms and can be written as follows:

$$\hat{H} = g \mu_B B \hat{\boldsymbol{S}}_z - g_N \mu_n B \hat{\boldsymbol{I}}_z + a \hat{\boldsymbol{I}} \cdot \hat{\boldsymbol{S}} \tag{9.15}$$

The first and second terms account for the electron–Zeeman [Eq. (9.6)] and nucleus–Zeeman [Eq. (9.13)] interactions, respectively. The third term accounts for the electron spin–nuclear spin interaction (or hyperfine interaction), and a is called the hyperfine splitting constant. This interaction originates from the fact that the electron spin experiences an additional magnetic field generated by the nuclear magnetic moment.

Two different types of electron spin–nuclear spin interactions have to be considered depending on whether the electron interacting with the nucleus is in an s or in any other orbital of higher l (p, d, f orbitals). In the first case, the interaction is called the isotropic hyperfine coupling or Fermi contact interaction, and is related to the finite probability of the unpaired electron being at the nucleus. For an electron located in nonspherical orbitals (having nodes at the nucleus) the classic dipolar interaction between magnetic moments can be used. The interaction is anisotropic in that it depends on the orientation of the orbital with respect to the applied magnetic field.

The interaction energy between two magnetic moments ($\boldsymbol{\mu}_1$ and $\boldsymbol{\mu}_2$) is classically given by

$$E = \frac{\boldsymbol{\mu}_1 \cdot \boldsymbol{\mu}_2}{r^3} - \frac{3(\boldsymbol{\mu}_1 \cdot \boldsymbol{r})(\boldsymbol{\mu}_2 \cdot \boldsymbol{r})}{r^5} \tag{9.16}$$

where $\boldsymbol{r}$ is the vector relating the two moments and r is the distance between them. The quantum mechanical analog of Eq. (9.16) is obtained by replacing the $\boldsymbol{\mu}_1$ and $\boldsymbol{\mu}_2$ by the corresponding operators related to the electronic and nuclear magnetic moments [Eqs. (9.2) and (9.12)]:

$$\hat{H}_{\text{dipol}} = -g\mu_{\text{B}}g_{\text{N}}\mu_{\text{n}}\left[\frac{\boldsymbol{I}\cdot\boldsymbol{S}}{r^3} - \frac{3(\boldsymbol{I}\cdot\boldsymbol{r})(\boldsymbol{S}\cdot\boldsymbol{r})}{r^5}\right] \tag{9.17}$$

The dipolar Hamiltonian can be processed by expanding the scalar products in Eq. (9.17):

$$\begin{aligned}\hat{H}_{\text{dipol}} = -g\mu_{\text{B}}g_{\text{N}}\mu_{\text{n}}\Bigg[&\left\langle\frac{r^2-3x^2}{r^5}\right\rangle\hat{\boldsymbol{S}}_x\hat{\boldsymbol{I}}_x + \left\langle\frac{r^2-3y^2}{r^5}\right\rangle\hat{\boldsymbol{S}}_y\hat{\boldsymbol{I}}_y + \left\langle\frac{r^2-3z^2}{r^5}\right\rangle\hat{\boldsymbol{S}}_z\hat{\boldsymbol{I}}_z \\ &-\left\langle\frac{3xy}{r^5}\right\rangle\left(\hat{\boldsymbol{S}}_x\hat{\boldsymbol{I}}_y + \hat{\boldsymbol{S}}_y\hat{\boldsymbol{I}}_x\right) - \left\langle\frac{3xz}{r^5}\right\rangle\left(\hat{\boldsymbol{S}}_x\hat{\boldsymbol{I}}_z + \hat{\boldsymbol{S}}_z\hat{\boldsymbol{I}}_x\right) \\ &-\left\langle\frac{3yz}{r^5}\right\rangle\left(\hat{\boldsymbol{S}}_y\hat{\boldsymbol{I}}_z + \hat{\boldsymbol{S}}_z\hat{\boldsymbol{I}}_y\right)\Bigg]\end{aligned} \tag{9.18}$$

and rearranging the appropriate terms into the matrix form:

$$\hat{H}_{\text{dipol}} = (-g\mu_{\text{B}}g_{\text{N}}\mu_{\text{n}})\left[\hat{\boldsymbol{S}}_x, \hat{\boldsymbol{S}}_y, \hat{\boldsymbol{S}}_z\right] \cdot \begin{bmatrix} \left\langle\frac{r^2-3x^2}{r^5}\right\rangle & -\left\langle\frac{3xy}{r^5}\right\rangle & -\left\langle\frac{3xz}{r^5}\right\rangle \\ -\left\langle\frac{3xy}{r^5}\right\rangle & \left\langle\frac{r^2-3y^2}{r^5}\right\rangle & -\left\langle\frac{3yz}{r^5}\right\rangle \\ -\left\langle\frac{3xz}{r^5}\right\rangle & -\left\langle\frac{3yz}{r^5}\right\rangle & \left\langle\frac{r^2-3z^2}{r^5}\right\rangle \end{bmatrix} \cdot \begin{bmatrix} \hat{\boldsymbol{I}}_x \\ \hat{\boldsymbol{I}}_y \\ \hat{\boldsymbol{I}}_z \end{bmatrix} = \hat{\boldsymbol{S}}\cdot\tilde{\boldsymbol{T}}\cdot\hat{\boldsymbol{I}} \tag{9.19}$$

The angular brackets imply an average taken over the electronic wavefunction, as the electron is not fixed in space. Equation (9.19) thus defines the anisotropic, dipolar, part $\tilde{\boldsymbol{T}}$ of the hyperfine interaction (see Section 9.5.2).

Since the electron is not localized at one position in the space, Eq. (9.17) must be averaged over the electron probability distribution function. $\hat{H}_{\text{dipol}}$ is averaged out to zero when the electron cloud is spherical (s orbital) but comes to a finite value in the case of other orbitals (p, d, etc.). However, when a paramagnet is rapidly tumbling in a nonviscous liquid system, the dipolar interaction is again averaged out to zero. The measure of the anisotropic hyperfine interaction is therefore limited to solid systems.

9.3.1
The Hydrogen Atom ($S = 1/2$ and $I = 1/2$)

The simplest example of an isotropic hyperfine interaction is that observed for the hydrogen atom. The classical dipolar interaction is averaged to zero for the 1s orbital so that the only interaction between the unpaired electron and the proton is the Fermi contact, which is given by

$$a = a_{\text{iso}} = \frac{2}{3}\mu_0 g\mu_{\text{B}} g_{\text{N}}\mu_{\text{n}}|\Psi(r=0)|^2 \tag{9.20}$$

where $|\Psi(r=0)|^2$ is the square of the wavefunction of the unpaired electron evaluated at the nucleus.

Since the nuclear spin may assume two possible orientations with $M_I = \pm 1/2$, two nuclear sublevels for each electronic spin level arise. The energy of these four electron–nuclear Zeeman levels is determined by the three terms of the Hamiltonian in Eq. (9.15). The last term in this equation modifies the energies of the four levels as shown in Figure 9.3. The EPR selection rules allow for transitions between the β and α electron spin states, with the nuclear spin kept constant. This is expressed as $\Delta M_S = \pm 1$, $\Delta M_I = 0$. In the case of the system described here, there are only two allowed transitions that correspond to the following energy differences:

$$\begin{aligned} \Delta E_1 &= h\nu_1 = g\mu_{\text{B}} B + \frac{1}{2}a \\ \Delta E_2 &= h\nu_2 = g\mu_{\text{B}} B - \frac{1}{2}a \end{aligned} \tag{9.21}$$

from which it can be easily seen that the nuclear Zeeman effect [the second term in Eq. (9.15)] influences the energy of the four spin levels, but not the energy difference of the allowed spin transitions. The scheme in Figure 9.3 and the energy differences obtained with Eq. (9.21) have been conceived for a virtual CW-EPR experiment at constant B and variable microwave frequency. In these terms, the two allowed transitions are separated by the hyperfine splitting constant, expressed in energy units:

$$h\nu_1 - h\nu_2 = a \tag{9.22}$$

In a real CW-EPR experiment, two transitions take place at two different B values (B_1 and B_2) separated by $a' = a/g\mu_{\text{B}}$ (in magnetic field units). As already mentioned,

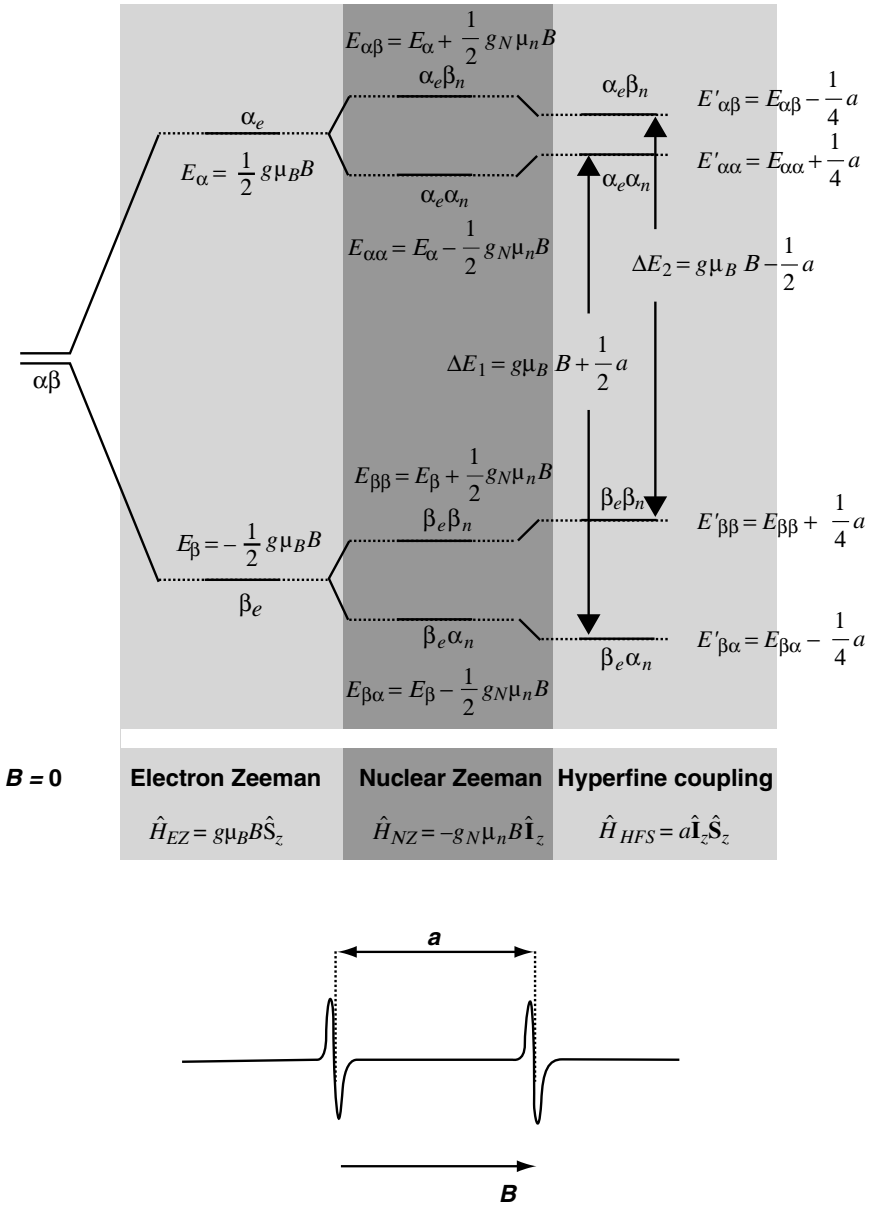


Figure 9.3 Influence of various terms in the spin-Hamiltonian on the energy levels of the hydrogen atom in a magnetic field and a corresponding EPR spectrum.

the EPR spectrum of the hydrogen atom is composed of two lines split by ~50.8 mT (Figure 9.3). This value is the measure of the Fermi contact term at the hydrogen nucleus. In the case of other s-systems interacting with nuclei having $I > 1/2$, the number of lines is higher. This is the case, for instance, with the spectra of alkali

metals such as Na and K. Both nuclei have $I = 3/2$ and their EPR spectrum is composed of four equally spaced lines of the same intensity whose separation measures the Fermi contact a_{iso}. In general, the number of lines for the interaction of the odd electron with a single nucleus is equal to $2I + 1$.

9.3.2
Hyperfine Interaction in Polynuclear Systems

When the unpaired electron interacts with more than one nucleus with $I \neq 0$, the hyperfine structure becomes more complex. The number and the intensity of the lines depend on three factors: (i) the I value of the magnetic nuclei involved, (ii) the number of each type of nuclei interacting with the unpaired electron, and (iii) the equivalence (or the nonequivalence) of these nuclei (i.e., the extent of the interaction of each of them with the unpaired electron).

As an example, Figure 9.4 illustrates the energy levels of three species in which the unpaired electron interacts respectively with two (Figure 9.4a), three (Figure 9.4b), and many (Figure 9.4c) equivalent nuclei with $I = 1/2$. Spectra having these features are usually those of organic radicals in solutions, the nucleus being in this case ^{1}H. The spectra recorded in solution are free from anisotropic effects and are therefore symmetric. Owing to the equivalence of the nuclei, the hyperfine effects produce degenerate levels. The allowed transitions give rise to a triplet of lines with ratio 1 : 2 : 1 in the case of two and a quartet of lines 1 : 3 : 3 : 1 in the case of three equivalent nuclei with $I = 1/2$. The hyperfine constant tends to decrease with increasing number of interacting nuclei in the paramagnetic species since, in parallel, the wavefunction of the unpaired electron (SOMO, singly occupied molecular

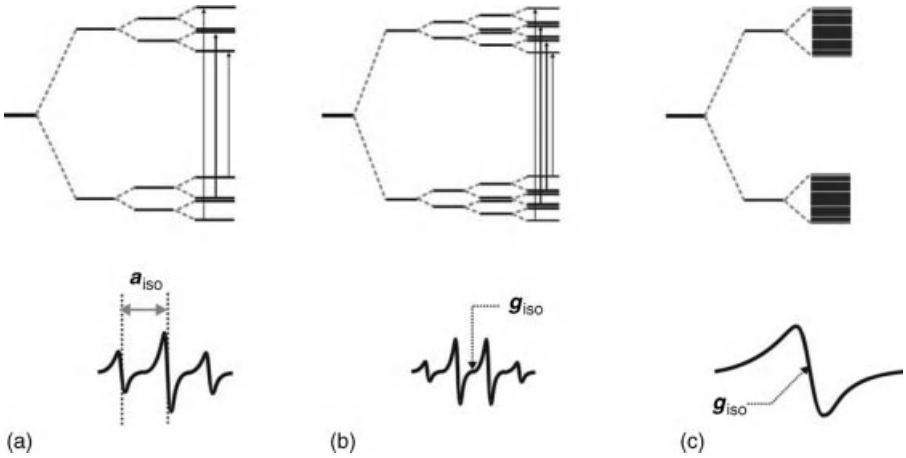


Figure 9.4 Scheme of the energy levels for an $S = 1/2$ species in a magnetic field having the unpaired electron interacting with two (a), three (b), and many (c) nuclei with $I = 1/2$. The corresponding solution spectra are also shown.

orbital) becomes increasingly more spread in space to involve all nuclei. In case of many equivalent nuclei (Figure 9.4c), the number of levels is so high (and their separation so small) that the hyperfine structure remains unresolved, and a single broad line is observed.

The hyperfine constants measured from an experimental spectrum as a separation of the spectral lines in the magnetic field units (i.e., tesla or gauss), should be transformed into the energy units. These units are, however, not widely used and it is much more frequent to find coupling constants expressed in terms of frequency (hertz) or wavenumber (cm^{-1}). Conversion from the units of mT into the frequency or wavenumber units involves the *g*-value:

$$\begin{aligned} a/\mathrm{MHz} &= 28.025(g/g_e)a/\mathrm{mT} \\ a/(10^{-4}\mathrm{cm}^{-1}) &= 9.3480(g/g_e)a/\mathrm{mT} \end{aligned} \tag{9.23}$$

An exhaustive analysis of the various possible structures of spectra related to the polynuclear systems is beyond the purposes of the present account. Some examples of relevance for surface chemistry and catalysis will be given in the subsequent parts of this chapter.

9.4 Experimental Background

A CW-EPR spectrometer is designed to detect with high sensitivity the microwave absorption in a sample as a function of the applied external magnetic field. The basic components of the spectrometer (Figure 9.5) are described below as follows.

The microwave bridge, a complex device made up of various components, provides microwaves at a desired power and directs them to a resonator containing the sample. The main components of the bridge are the oscillator, a source of microwaves in the miliwatt range (Gunn diodes are the most often employed device in EPR), and the attenuator, a device allowing for precise control of the microwave power. The microwaves, once generated, travel through the waveguide towards the resonant cavity. The latter is a metal box with highly reflecting inner walls (whose size is comparable to the microwave wavelength), which stores the microwave energy in the form of a standing wave, and converts the sample response into a microwave signal. When the microwave power is fully stored in the resonator, prior to recording spectra, the resonator is said to be matched to the oscillator.

A high-quality electromagnet is used, connected to a power supply, capable of providing a homogeneous field, which is controlled by a field probe (very often a Hall sensor or, for higher accuracy, an NMR gaussmeter). The rate and range of the magnetic field scanning are adjusted to provide the most suitable conditions for observation of the microwave absorption.

In addition, a detector diode to measure the energy absorbed by the sample at the resonance, a convenient amplifier system, an oscilloscope, and a computer are indispensable components of the EPR system.

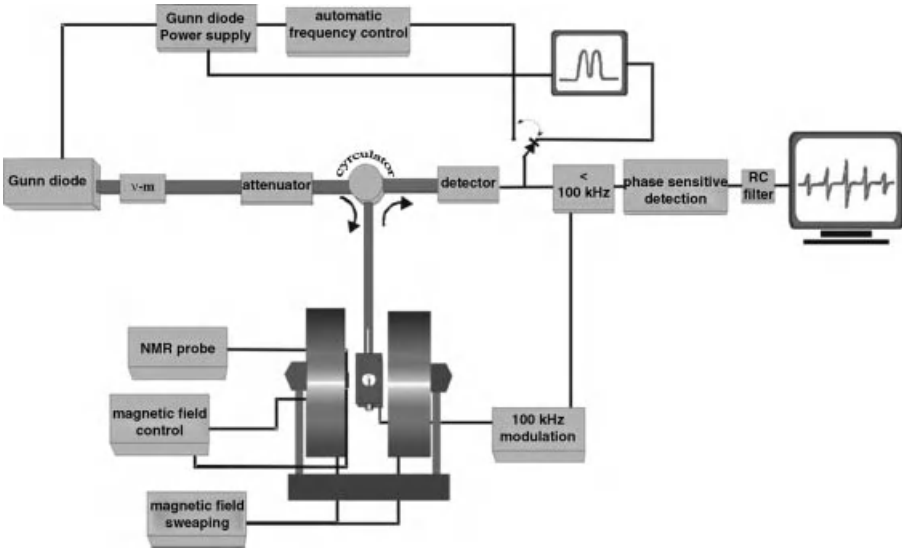


Figure 9.5 Block diagram of a typical continuous wave CW-EPR spectrometer employing 100 kHz phase-sensitive detection.

Superimposed on the main magnetic field, an oscillating high-frequency field is obtained by applying an alternating current (typically 100 kHz) to a pair of coils in the cavity walls. This modulating field converts the resonance into an alternating signal which can be separated from random noise using a phase-sensitive detection system. This method of detection has a very high sensitivity, and its output is the first-derivative curve of the absorption signal (Figure 9.6a and b). The operator selects the amplitude of the modulating field, which should be large enough to obtain a good signal-to-noise ratio but small enough to prevent distortions, which occur if the value of the amplitude exceeds $\sim 1/3$ of the resonance linewidth (Figure 9.6c).

EPR spectra are usually recorded by putting the sample into a highly pure quartz tube (traces of transition metal ions usually present in normal silica glasses have to be avoided as they are often paramagnetic), the size of which depends on the microwave band used. In the case of X-band EPR, the tube usually has an external diameter of about 4 mm. For experiments involving catalytic materials, it is necessary, in most cases, to perform thermo-vacuum treatments on the material and to adsorb gases at the surface. For these reasons, the EPR tube is usually connected to a special cell (sealed under vacuum or having special stopcocks allowing the catalyst to be maintained under vacuum), which is inserted, after the treatment of the sample in a vacuum line, directly to the spectrometer cavity (Figure 9.7a).

Low-temperature EPR spectra are usually beneficial for improving the resolution and the spectral intensity. They can be recorded in liquid nitrogen at 77 K using a special Dewar inserted in the cavity (Figure 9.7b). Variable-temperature EPR spectra

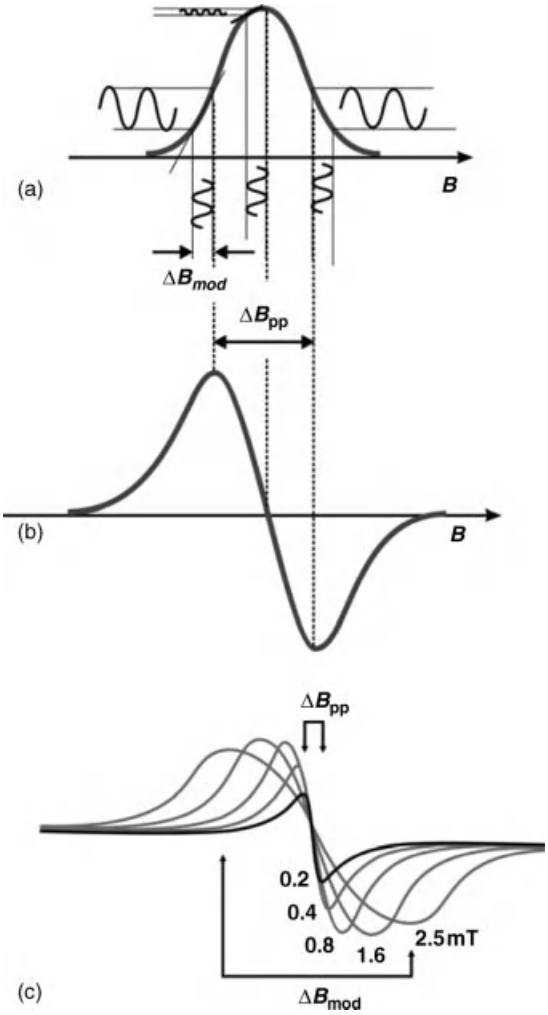


Figure 9.6 Effect of the small-amplitude field modulation on the detector output current (a) and first-derivative EPR signal (b) along with the effect of 100 kHz modulation of increasing amplitude (ΔB_{mod}) on an EPR line (c).

can be measured by using a flow of cooled nitrogen in a liquid nitrogen cryostat for temperatures from about 90 up to 450 K. A liquid helium cryostat allows spectra to be recorded down to ~4 K.

The digital acquisition of spectra allows improvement of the signal-to-noise ratio both by spectra accumulation and by spectral curve smoothing.

The value of g is derived, from an experimental EPR spectrum, by the simultaneous measurements of the resonant field, B_{res}, and of the frequency, ν, according to Eq. (9.9). In practice, the g value can be also determined by comparing the field values

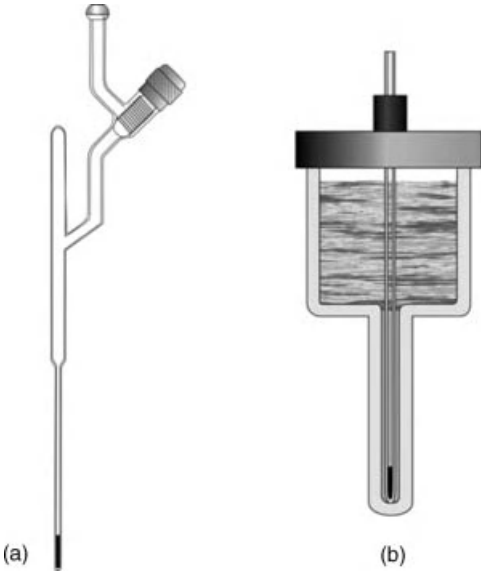


Figure 9.7 Schematic diagrams of a typical cell for EPR measurements under vacuum or in controlled atmosphere (a) and a Dewar fitting employed for recording spectra in liquid nitrogen (b).

at resonance for the investigated sample and that of a reference sample of known g_{ref}. Both samples must be inserted into the resonant cavity during spectrum recording in order to experience the same microwave frequency.

The measure of spin concentration is done by the double integration of the first-derivative EPR signal and comparison of the intensity of the integrated signal (which is proportional to the number of spins present in the system) with that of standard samples with known number of spins.

9.5
Anisotropy of Magnetic Interactions in EPR: the *g*, *A*, and *D* Tensors

EPR spectra are more complex for samples in the solid state than in the liquid phase. The reason for this additional complexity comes from anisotropies of the magnetic interactions, first of all the Zeeman (or electron spin–magnetic field) and the hyperfine (electron spin–nucleus spin) interactions. The term anisotropy is used here with the meaning that the spectral features depend on the orientation of the paramagnetic center with respect to the magnetic field. As an example, we can consider the case of copper(II) ions diluted into a solid single crystal. Cu^{2+} ions ($3d^9$) are $S = 1/2$ systems in which the unpaired electron interacts with the $I = 3/2$ nuclei of both ^{63}Cu and ^{65}Cu isotopes. In this case, at $\theta = 0$, a spectrum composed of four ($2I + 1 = 4$) equally spaced hyperfine lines of similar intensity is expected (Figure 9.8). From the resonant field at the center of the spectrum, the $g = g_{||}$ value is

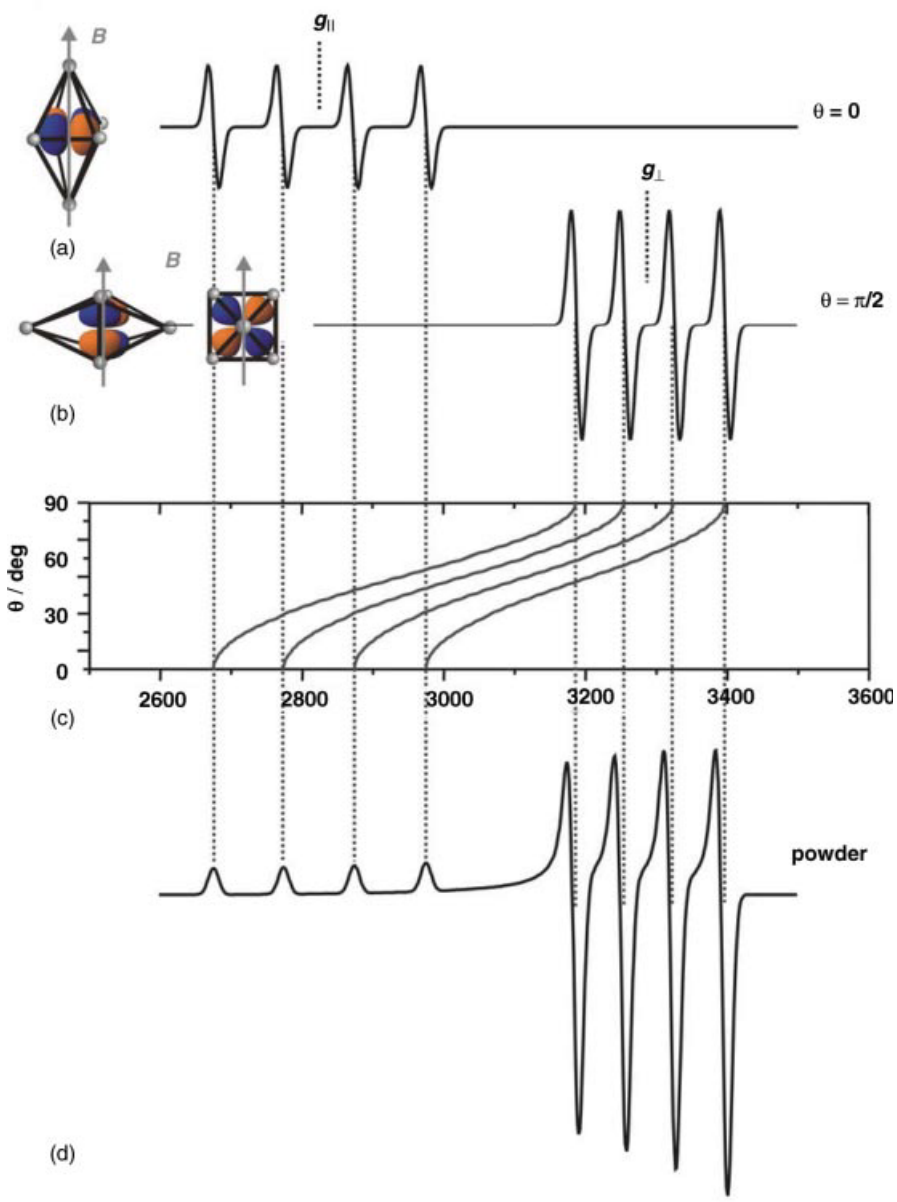


Figure 9.8 Simulated EPR spectra of a hypothetical single-crystal copper species in elongated octahedral surrounding with $3d_{x^2-y^2}$ ground state (a, b), the corresponding angular dependence of the resonant magnetic field (c), and powder EPR spectrum (d).

determined [Eq. (9.9)], and the hyperfine coupling constant ($A_{||}$, in magnetic field units) is directly measured from the separation of the adjacent lines. Upon changing the orientation of the crystal inside the cavity from $\theta = 0$ to $\pi/2$, a second spectrum is recorded which has different resonant field, hence $g = g_\perp$, and different

hyperfine splitting ($A_\perp$) from the former spectrum. In the first two cases in Figure 9.8, the direction of the external magnetic field coincides with the principal axes of the paramagnetic system, two of which (x and y) are equivalent and give rise to the coincident (perpendicular) EPR spectra. The reported system is said to have axial symmetry. The orientation for $\theta = 0$ in Figure 9.8 is called "parallel" and those for $\theta = \pi/2$ (and arbitrary ϕ value) are called "perpendicular." The variation of g with the orientation reflects the anisotropy of the Zeeman interaction, whereas the variation of the hyperfine interaction A, as already mentioned, is due to the dipolar interaction.

9.5.1
The *g* Tensor

Equation (9.9), where g is a simple scalar value, is generally no longer valid in the case of solid materials, and therefore has to be modified to include its angular dependence:

$$h\nu = \mu_B g(\theta, \phi) B \tag{9.24}$$

Therefore, to describe fully the observed changes for all possible orientations, the scalar value of g is substituted in the spin-Hamiltonian by the 3×3 symmetric $\boldsymbol{g}$ matrix. Equation (9.6) therefore becomes

$$\hat{H}_{EZ} = \mu_B \vec{\boldsymbol{B}} \tilde{\boldsymbol{g}} \hat{\boldsymbol{S}} \tag{9.25}$$

In any arbitrary coordinate system, the $\boldsymbol{g}$ tensor has a general form:

$$\tilde{\boldsymbol{g}} = \begin{bmatrix} g'_{xx} & g'_{xy} & g'_{xz} \\ g'_{yx} & g'_{yy} & g'_{yz} \\ g'_{zx} & g'_{zy} & g'_{zz} \end{bmatrix} \tag{9.26}$$

The example shown in Figure 9.8 is an ideal case. In real systems, the orientation of the axes of paramagnetic species is, in principle, unknown. The structure of the $\boldsymbol{g}$ tensor is therefore derived by recording several EPR spectra for various orientations of the investigated single crystal with respect to the magnetic field. The (3×3) $\boldsymbol{g}$ matrix [Eq. (9.26)] obtained from the single-crystal study can next be diagonalized, which allows the principal values of the $\boldsymbol{g}$ tensor to be obtained:

$$\tilde{\boldsymbol{g}} = \begin{bmatrix} g_{xx} & 0 & 0 \\ 0 & g_{yy} & 0 \\ 0 & 0 & g_{zz} \end{bmatrix} \tag{9.27}$$

This operation is equivalent to a rotation of the laboratory axes in which the $\boldsymbol{g}$ tensor was measured, after which the principal axes of the $\boldsymbol{g}$ tensor and the laboratory axes coincide. The three values $g_{zz} = g_{||}$, $g_{xx} = g_{yy} = g_\perp$ corresponding to the principal orientations (Figure 9.8) are the diagonal elements of the $\boldsymbol{g}$ matrix (Eq. (9.27)). In the more general case of rhombic symmetry, the three diagonal elements of the $\boldsymbol{g}$ tensor have distinct values ($g_{xx} \neq g_{yy} \neq g_{zz}$) and the angular dependence of the g value

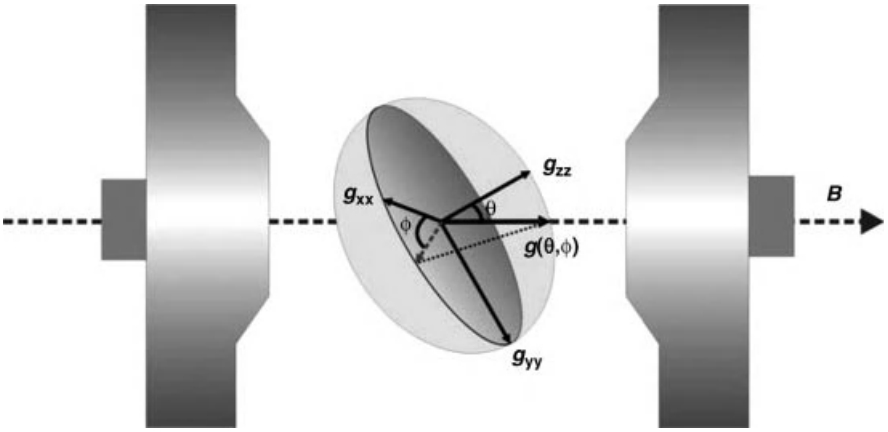


Figure 9.9 Angular dependence of $g(\theta,\phi)$ shown as an orthorhombic $\boldsymbol{g}$ tensor ellipsoid with indicated principal axes.

$g^2(\theta,\phi) = (g_{xx}{}^2\cos^2\phi + g_{yy}{}^2\sin^2\phi)\sin^2\theta + g_{zz}{}^2\cos^2\theta$ may be visualized by an ellipsoid as shown in Figure 9.9.

To explain the origin of the g factor, the interaction between the unpaired electron and its environment has to be considered. In particular, since in a real system the unpaired electron belongs to a SOMO associated with the paramagnetic species, the interaction occurring between the spin $\boldsymbol{S}$ and the angular orbital momentum $\boldsymbol{L}$ must be considered, if the latter is different from zero ($\boldsymbol{S} + \boldsymbol{L} = \boldsymbol{J}$). Actually, owing to electric fields present in molecules and solid systems, the orbital angular momentum $\boldsymbol{L}$ is often quenched and its ground-state contribution to the total angular momentum vanishes. However, $\boldsymbol{L}$ is partially restored by a magnetic interaction that operates via an admixture of excited electronic states to the ground state. This interaction is called the spin–orbit coupling (SOC), and explains the deviation of the g values of real systems from the free electron value (g_e). This point is discussed in Section 9.9.1 in more detail.

9.5.2
The *A* Tensor

The existence of two types of electron–nucleus hyperfine interactions, isotropic and anisotropic, was introduced in Section 9.3. The orientation dependence of the hyperfine interaction, described at the beginning of the present Section (Figure 9.8), takes place in the solid state. In general, since both isotropic and anisotropic interactions usually contribute to an EPR spectrum simultaneously, the whole hyperfine interaction becomes anisotropic and, therefore, must be expressed as a tensor. In analogy with what was previously described for the Zeeman interaction, we can write the hyperfine term in the spin-Hamiltonian as

$$\hat{H}_{\mathrm{HFS}} = \hat{\boldsymbol{I}}\tilde{\boldsymbol{A}}\hat{\boldsymbol{S}} \tag{9.28}$$

The $\boldsymbol{A}$ tensor may be split into the isotropic and anisotropic parts, as follows:

$$\boldsymbol{A} = \begin{bmatrix} A_{xx} & 0 & 0 \\ 0 & A_{yy} & 0 \\ 0 & 0 & A_{zz} \end{bmatrix} = a_{\text{iso}}\mathbf{I} + \begin{bmatrix} T_{xx} & 0 & 0 \\ 0 & T_{yy} & 0 \\ 0 & 0 & T_{zz} \end{bmatrix} \tag{9.29}$$

with $a_{\text{iso}} = (A_{xx} + A_{yy} + A_{zz})/3$. The anisotropic part ($\boldsymbol{T}$) of the $\boldsymbol{A}$ tensor corresponds to the dipolar interaction as expressed by the Hamiltonian in Eq. (9.19). In a number of cases, the second traceless matrix term in Eq. (9.29) has the form $(-T, -T, +2T)$. For this reason, in the case of paramagnetic species undergoing rapid tumbling in a low-viscosity solution, the anisotropic term can be averaged to zero, and the observed hyperfine coupling corresponds to the isotropic part only (a_{iso}). Molecular interpretation of the hyperfine tensor is described in Section 9.9.2.

9.5.3
The Electron–Electron Interactions in $S > 1/2$ Systems: The D Tensor

The previous sections were devoted to discussion of $S = 1/2$ systems, that is, to molecules or ions having one unpaired electron only. However, several paramagnetic systems may have more than one unpaired electron and, consequently, $S > 1/2$. The simplest cases are related to molecules in a triplet ($S = 1$) ground or excited state and to d^2–d^8 transition metal ions. In such cases, a new term must be added to the spin-Hamiltonian to account for the electron–electron dipole interactions. Here we briefly describe the simplest case of two unpaired electrons, referring the reader to specific textbooks for a more involved treatment [11].

The effect of an external magnetic field on the energy of the spin levels for an $S > 1/2$ system, is the splitting into $2S + 1$ Zeeman sublevels characterized by different M_S values. Figure 9.10a illustrates the case of $S = 1$ in an isotropic surrounding with the three $M_S = +1$, $M_S = 0$, $M_S = -1$ levels produced by the magnetic field. The Zeeman splitting increases with increasing B as in the case of $S = 1/2$. The selection rule $\Delta M_S = \pm 1$ is still valid and produces $2S$ coincident transitions (two in Figure 9.10a). In this case, the two allowed transitions occur at the same magnetic field value, resulting in a single resonance line. For axial symmetry, the position of the absorption lines can vary remarkably, however, according to the extent of an interaction called the zero field splitting (ZFS). The latter, similarly to the hyperfine interaction described before, occurs in the absence of external magnetic field. The ZFS term is a measure of the energy difference between the magnetic sublevels ($M_S = \pm 1$ and $M_S = 0$ shown in Figure 9.10b) at $B = 0$.

The interaction between the two electron spins can be expressed by the following spin-Hamiltonian:

$$\hat{H}_{ZFS} = \hat{\boldsymbol{S}}\tilde{\boldsymbol{D}}\hat{\boldsymbol{S}} \tag{9.30}$$

where $\boldsymbol{D}$ is again a 3×3 traceless matrix analogous to the $\boldsymbol{T}$ tensor [Eqs. (9.19) and (9.29)]. Usually, the components of the $\boldsymbol{D}$ tensor are expressed as $D = 3/2D_{zz}$ and

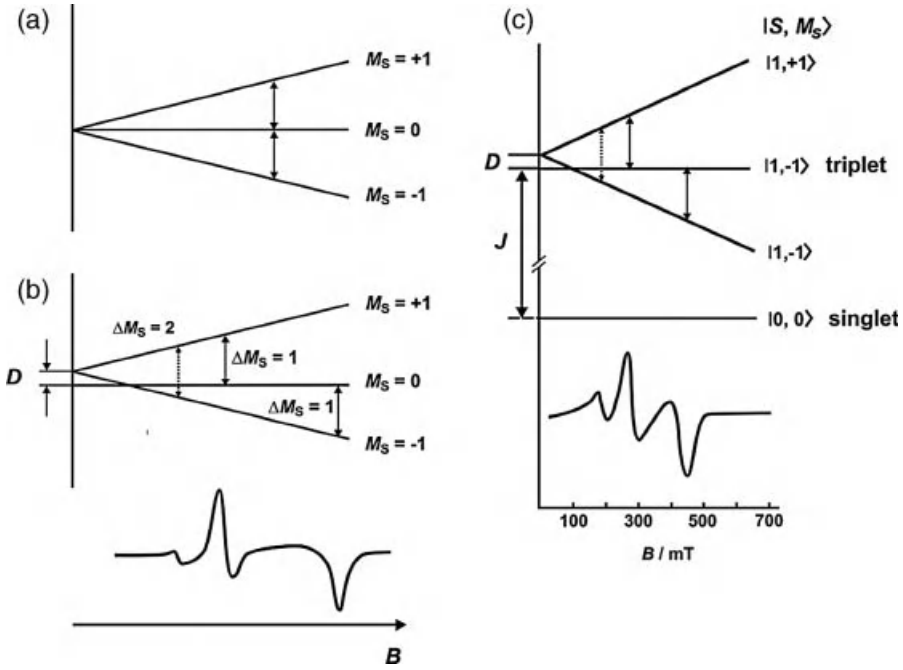


Figure 9.10 Energy levels for $S = 1$ system for isotropic symmetry (a), axial symmetry with the corresponding EPR spectrum (b), and for an exchange-coupled antiferromagnetic pair (c). The EPR signal can only be observed if the magnetic triplet state is thermally populated. Dotted lines indicate forbidden half-field transitions.

$E = 1/2(D_{xx} - D_{yy})$, since only two independent variables are required. In such a case, $\hat{H}_{ZFS}$ can be rewritten in the form

$$\hat{H}_{ZFS} = D\left(\hat{\boldsymbol{S}}_z^{\,2} - \frac{1}{3}\hat{\boldsymbol{S}}^2\right) + E\left(\hat{\boldsymbol{S}}_x^{\,2} - \hat{\boldsymbol{S}}_y^{\,2}\right) \tag{9.31}$$

For axial symmetry $D \neq 0$ and $E = 0$, whereas for rhombic symmetry $D \neq 0$ and $E \neq 0$. Also in the case of the electron–electron interaction (or fine structure interaction), the extent of the coupling varies as a function of the orientation of the paramagnetic centers in the external magnetic field. Owing to some mixing between the magnetic states, the $\Delta M_S = \pm 2$ transitions (in principle forbidden) become partially allowed and appear, usually with weak intensity, at low magnetic fields (Figure 9.10b).

The theoretical EPR profile of a randomly oriented triplet related to a system of axial symmetry with isotropic g (for the sake of simplicity), is shown in Figure 9.11.

An experimental spectrum with the fine structure is reported in Figure 9.12 and is related to a pair of O^- ions at the surface of titanium dioxide generated via interaction with hydrogen peroxide and forming an $S = 1$ system [12]. The spectrum is dominated by the features of an adsorbed superoxide radical ion (O_2^-, $S = 1/2$) while the

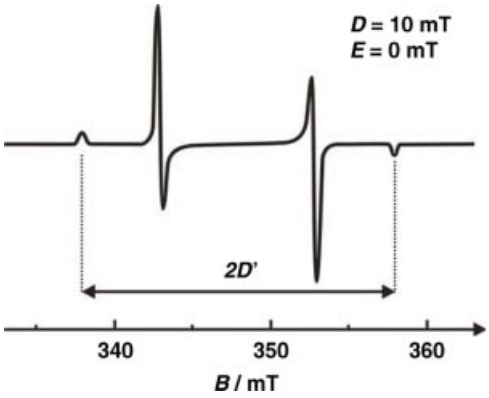


Figure 9.11 Typical EPR spectrum of a randomly oriented triplet species with isotropic *g*.

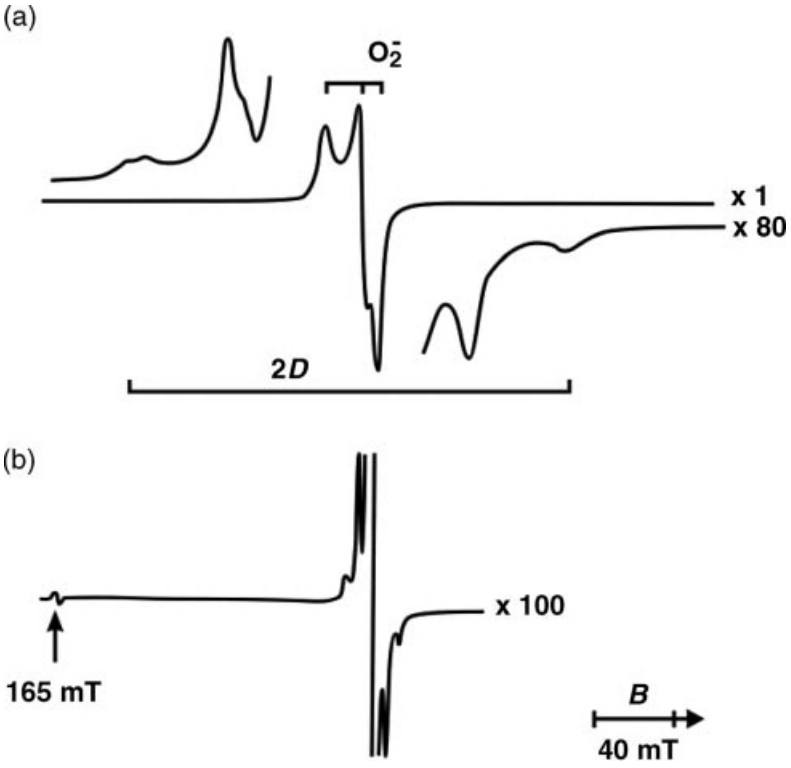


Figure 9.12 EPR spectrum of the $O^- - O^-$ triplet state observed at the surface of titanium dioxide treated with hydrogen peroxide (a) and magnified spectrum showing the forbidden transition at the low field (b). Adapted from [11].

outer wings (Figure 9.12a) are due to the triplet formed by the two interacting O^- ions and characterized by a D value of 13.7 mT. The weak feature visible in Figure 9.12b at low field is due to the "forbidden" $\Delta M_S = \pm 2$ transition. This line is the unambiguous fingerprint of the presence of a triplet state.

In transition-metal ions with $S > 1/2$, the SOC is mainly responsible for ZFS and for the large shift of the apparent g values from g_e. The EPR spectra of these ions, because of the very fast relaxation rates, are generally very broad and in most cases difficult to detect or are detectable at extremely low temperature.

In the case when $S = 1$ comes from pair centers ($\boldsymbol{S}_1$ and $\boldsymbol{S}_2$), in addition to the ZFS also the exchange interactions gauged by the J constant have to be accounted for. By assuming the exchange energy operator $-J\boldsymbol{S}_1 \cdot \boldsymbol{S}_2$, the value of $J < 0$ implies antiferromagnetic interaction, which tends to align spins antiparallel in the ground state, whereas $J > 0$ (ferromagnetic interaction) tends to align spins parallel. The effect of $J < 0$ is a separation of the system into a singlet ground state $|0,0\rangle$ and a triplet excited state $|1,0\rangle$, $|1,-1\rangle$, and $|1,1\rangle$. ZFS splits the triplet state into two levels ($|1,0\rangle$ and $|1,\pm 1\rangle$) separated by the D value (in the case of an axial symmetry) as shown in Figure 9.10c. For $J < 0$, the order of the states should be reversed. For $J < 0$, the population of the triplet state is governed by the Boltzmann distribution $3/T[\exp(-J/kT)]$, hence the EPR signal can only be observed if the magnetic triplet state is thermally populated. Further discussion of the exchange-coupled paramagnets can be found in Section 9.7.

9.5.4
The Spin-Hamiltonian

Summarizing the discussion, the EPR spectrum of a paramagnetic species in a solid can be described by the spin-Hamiltonian. This energy operator is composed of a series of terms:

$$\hat{H} = \hat{H}_{EZ} + \hat{H}_{HFS} + \hat{H}_{ZFS} + \hat{H}_{NZ} + \hat{H}_{Q} \tag{9.32}$$

the most important being those related to the electron–Zeeman interaction, $\hat{H}_{EZ}$, the hyperfine interaction, $\hat{H}_{HFS}$, and the fine interactions, $\hat{H}_{ZFS}$. They are gauged by the $\boldsymbol{g}$ [Eq. (9.25)], $\boldsymbol{A}$ [Eq. (9.28)], and $\boldsymbol{D}$ [Eq. (9.30)] tensors, respectively. The nature of these tensors reflects the magnitude and the anisotropy of the corresponding magnetic interactions. Less important in surface and catalysis studies is the term related to the quadrupolar interaction $\hat{H}_Q$, not discussed here. Practically irrelevant is also the nucleus–Zeeman interaction [$\hat{H}_{NZ}$, second term of Eq. (9.15)], because its energy is too weak to be resolved in powder EPR spectra.

9.6
EPR Spectra and the Solid State: Single Crystal Versus Powders

When dealing with EPR spectra of the solid state, it is necessary to distinguish between the two principal cases of single crystals and powders. In the case of single

crystals, qualitatively illustrated in Figure 9.8, different spectra are obtained at the various orientations. The single-crystal spectra are usually recorded with the paramagnetic crystal mounted so that it can be rotated in the resonant cavity with respect to the applied external magnetic field about three orthogonal reference axes. An EPR spectrum is recorded stepwise during the rotation about each axis. After repeating this procedure in each of the coordinate planes, the curves obtained (resonant field versus angle) must be fitted to the theoretical equations discussed in Section 9.5.1. Most of the EPR spectra recorded in catalytic studies, however, do not come from single crystals but from polycrystalline materials or powders, the spectra of which are usually called powder spectra.

9.6.1
Powder EPR Spectra

A polycrystalline material is constituted by a large number of microcrystals randomly oriented in space so that all possible orientations of one crystal in the external field are equally probable. For this reason, the resultant powder EPR spectrum is the envelope of single-crystal spectra corresponding to all possible orientations of the paramagnetic species with respect to the applied magnetic field and is, therefore, invariant with the rotation of the sample within the magnetic field. Let us consider a simple case of an $S = 1/2$ paramagnetic center with axial symmetry ($g_{zz} = g_{||}$, $g_{xx} = g_{yy} = g_{\perp}$) and no hyperfine splitting. The powder EPR spectrum is spread over the entire resonant field range ($\Delta B = B_{||} - B_{\perp}$) determined by the values of the principal g components. The simultaneous presence of resonance in the whole range of fields does not create, fortunately, a uniform envelope, because the intensity of the resonant absorption is not uniformly distributed over this range. An analytical treatment shows, in fact, that the EPR absorption reported as a function of the magnetic field B exhibits particular features for orientations corresponding only to the principal components of the $\boldsymbol{g}$ tensor (Figure 9.13). In other words, the turning points in a powder spectrum that can be individuated on the $B_{\mathrm{res}}(\theta)$ curve (axial case) appear when $\partial B/\partial\theta = 0$.

Referring to the case in Figure 9.13, two turning points are found at $\theta = 0$ (corresponding to $g_{||}$) and $\theta = \pi/2$ ($g_{\perp}$). Between these two extrema, a continuous absorption is observed, the derivative of which leads to the typical shape of an axial powder spectrum with $g_{\perp} > g_{||}$. In this figure, the angular dependence for the resonant field (B_{res} versus θ) is also shown, which indicates that in a powder spectrum, at a given value of the magnetic field, only certain paramagnets with a proper orientation with respect to the magnetic field "fall in resonance." At the $g_{||}$ position, only a few paramagnets having the symmetry axis aligned along the magnetic field axis ($B_{||}$, $\theta = 0$) contribute to the pattern. Moving progressively to $B_{\perp}$, more spins come into resonance and the absorption intensity increases, reaching a maximum corresponding to $B_{\perp}$ for which all spins oriented in the xy or perpendicular plane are in resonance. Owing to the axial symmetry, in fact, there is no dependence of the resonance on the ϕ angle.

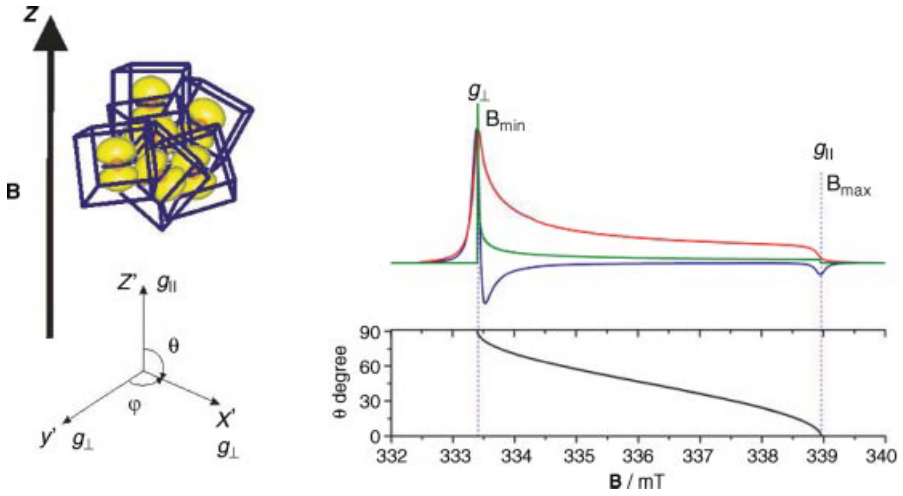


Figure 9.13 EPR powder spectra (absorption and first derivative of absorption) of an $S = 1/2$ species with axial symmetry. The various microcrystals are randomly oriented with respect to the magnetic field. Also, the angular dependence of the resonant field (B_{res} versus θ) is shown with the turning points determining the spectral features.

Similar arguments hold for the more complex case of a rhombic $\boldsymbol{g}$ tensor. In this case, the resonant field depends on both the θ and ϕ angles, and the turning points in a powder spectrum are individuated on the $B_{res}(\theta,\phi)$ surface. This issue is discussed in Section 9.7.1 in more detail. Figure 9.14 summarizes the shapes observed for the powder spectra of $S = 1/2$, $I = 0$ systems having axial and rhombic symmetry. These typical shapes are, of course, modified by the hyperfine interaction when the nuclei with $I \neq 0$ are present in the investigated system.

9.7
Guidelines to Interpretation of EPR Spectra

9.7.1
Classification of EPR Spectra and Determination of Spectral Parameters

As already mentioned, virtually all catalysts suitable for EPR studies exhibit appreciable specific surface areas and are composed of small, randomly oriented crystallites or even amorphous particles, giving rise to complicated and spatially averaged patterns [7, 13–15]. Depending on the extent of magnetic interactions with the surroundings, paramagnetic bulk and surface species appearing in catalytic systems can be classified into (i) magnetically diluted discrete (mononuclear) centers, (ii) clustered (polynuclear) centers, and (iii) magnetically undiluted extended centers. As a result, depending on the relative magnitude of particular interactions, four generic

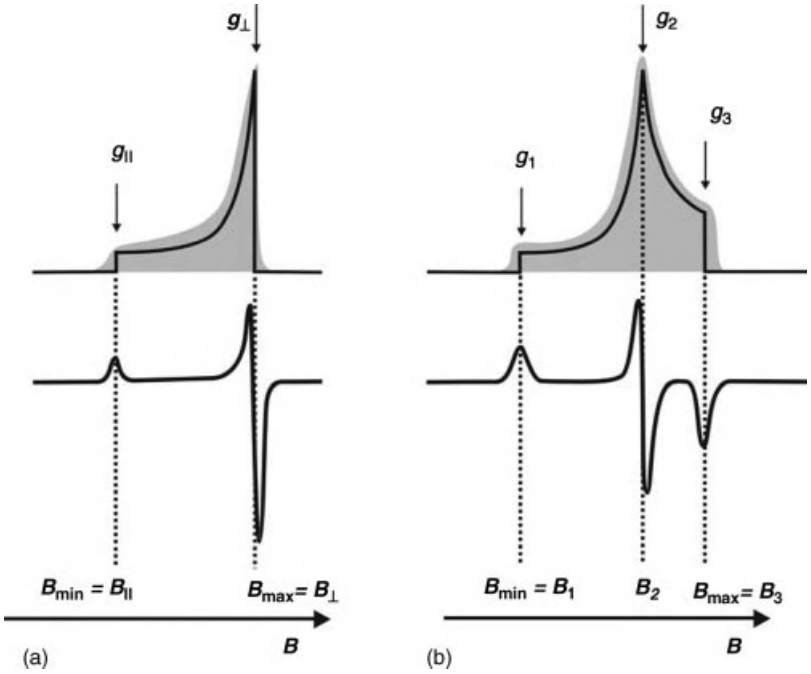


Figure 9.14 Typical profiles of powder EPR spectra with axial (a) and rhombic symmetry (b).

cases with (i) $|D^{dip}| < |A|$ but $J \approx 0$, (ii) $|J| < |A|$, (iii) $|A| < |J| < h\nu$, and (iv) $|J| > h\nu$ [15, 16] can be distinguished.

For the magnetically diluted isolated species, as outlined in Section 9.6.1, diagnostic features in the first derivative powder spectrum arise from the turning points in angular variation of the resonant field when $\partial B/\partial\phi = 0$ and $\partial B/\partial\theta = 0$. The three solutions, where $\theta = 0$ (B_z), $\theta = \pi/2$ and $\phi = 0$ (B_x), $\theta = \pi/2$ and $\phi = \pi/2$ (B_y), correspond to the minimum resonant field, the maximum resonant field, and a saddle point on the $B(\theta,\phi)$ surface, respectively (Figure 9.15a). They give rise to characteristic features in the EPR spectrum, defining the principal components of the $\boldsymbol{g}$ tensor (Figure 9.15b). For paramagnetic centers with $I > 0$, these extrema of the resonant field occur along the common principal directions of both the $\boldsymbol{g}$ and $\boldsymbol{A}$ tensors for all $|M_I|$ values, provided that both axes systems are coincident (Figure 9.15b). Typical shapes of powder EPR spectra for the randomly oriented catalytic systems with $S = 1/2$, $I > 0$ and coincident axes are shown in Figure 9.16a and b. When the high-field first-order approximation is fulfilled ($g\mu_B B \gg A$), the hyperfine lines are evenly spaced in the magnetic field [$B(M_I) = B_0 - \sum_i A^i_{qq} M^i_I$, were $q = x$, y or z], and the g_{qq} values can be easily determined from the centers of the corresponding hyperfine patterns, for each principal x, y (perpendicular), and z (parallel) directions, as indicated in the corresponding stick diagrams (Figure 9.16a and b) and discussed in Section 9.3. Uneven spacing of the hyperfine lines may indicate that the second-order effects become appreciable. The center of the hyperfine pattern is now

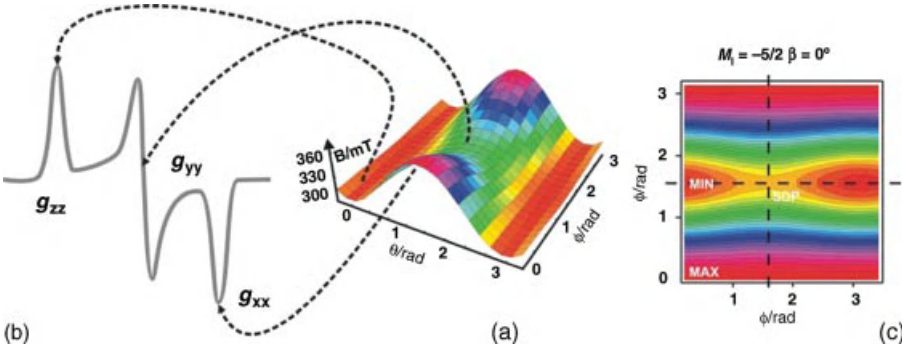


Figure 9.15 Plot of a resonant magnetic field as a function of θ and ϕ angles for $M_I = -5/2$ for orthorhombic paramagnetic species with $g_{xx} = 1.96$, $g_{yy} = 1.94$, $g_{zz} = 1.81$, $A_{xx} = 37 \times 10^{-4}\,cm^{-1}$, $A_{yy} = 34 \times 10^{-4}\,cm^{-1}$, $A_{zz} = 85 \times 10^{-4}\,cm^{-1}$, $\nu = 9.28$ GHz (a), and its relation to the EPR spectrum (b). The characteristic features in the first-derivative powder EPR signal are associated with the magnetic field minimum (MIN), maximum (MAX), and the saddle point (SDP), appearing along the x (0, 0), y ($\pi/2$, $\pi/2$), and z ($\pi/2$, 0) axes (c).

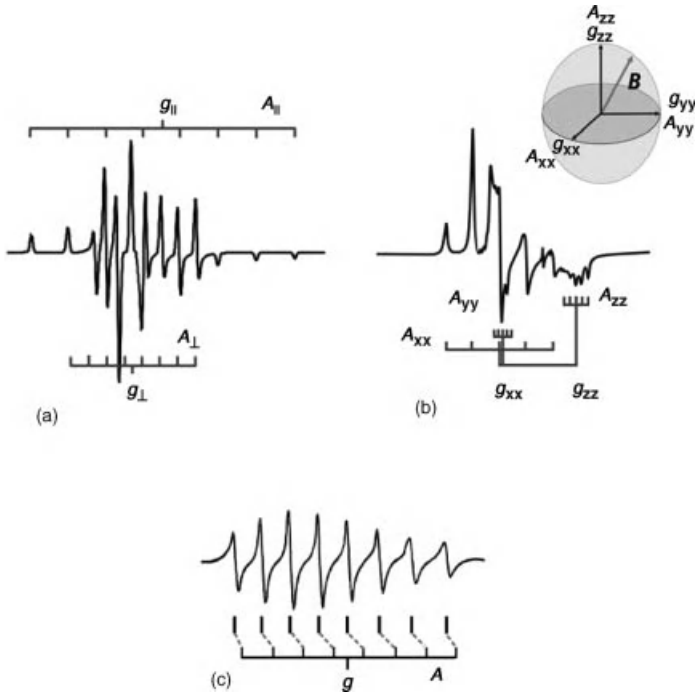


Figure 9.16 EPR spectra of paramagnetic centers with coincident principal ***g*** and ***A*** axes, axial spectrum of vanadyl species entrapped in ZSM-5 zeolite (a), N_2^- radical trapped on MgO surface (b), and vanadyl complex exhibiting a pronounced uneven hyperfine splitting due to the second-order effects (c) (adapted from [38, 71]).

no longer congruent with the magnetic field corresponding to the particular g_{qq} value. In such cases, the positions of the individual hyperfine lines can be determined using the following equation [16]:

$$B(m_I) = B_0 - \sum_i \left\{ A^i_{qq} M^i_I + \frac{\left(A^i_{qq}\right)^2}{2B} \left[I_i(I_i+1) - \left(M^i_I\right)^2 \right] \right\} \tag{9.33}$$

A failure to account for the second-order terms in the analysis of a powder spectrum results in a significant error in calculating g_{qq} values and also the hyperfine coupling constants [17]. An example of an EPR spectrum with uneven hyperfine spacing is shown in Figure 9.16c.

A large number of important catalytic materials [e.g., $(VO)_2P_2O_7$, MoO_3, $Fe_2V_{14}O_{13}$] can be classified as magnetically undiluted systems, exhibiting EPR signals featured by the dipolar and exchange interactions (see Section 9.5.3). Whereas the former tend to broaden the spectral lines, the latter average out the broadening. In the simplest case, a through-space dipolar interaction between the S_1 and S_2 magnetic moments for paired centers can be described as $\mathcal{H}_{\text{dip}} = S_1 D^{\text{dip}}_{12} S_2$. Dipolar interactions give rise to inhomogeneous broadening of the EPR spectra and Gaussian lineshapes. When they are dominant, the D^{dip} tensor provides information on the distance between the individual paramagnetic centers. In the simplest cases, the relation $D^{\text{dip}}/\text{cm}^{-1} = 0.433 \times g^2/r^3$ can be used for converting the measured D^{dip} value into the distance r expressed in a ångstroms, and a more general account can be found elsewhere [16]. An example of an EPR spectrum with dominant $\mathcal{H}_{\text{dip}}$ is shown in Figure 9.17a for NO radicals trapped inside zeolite A [18]. The corresponding model of an interacting pair of the NO adspecies is presented in Figure 9.17b.

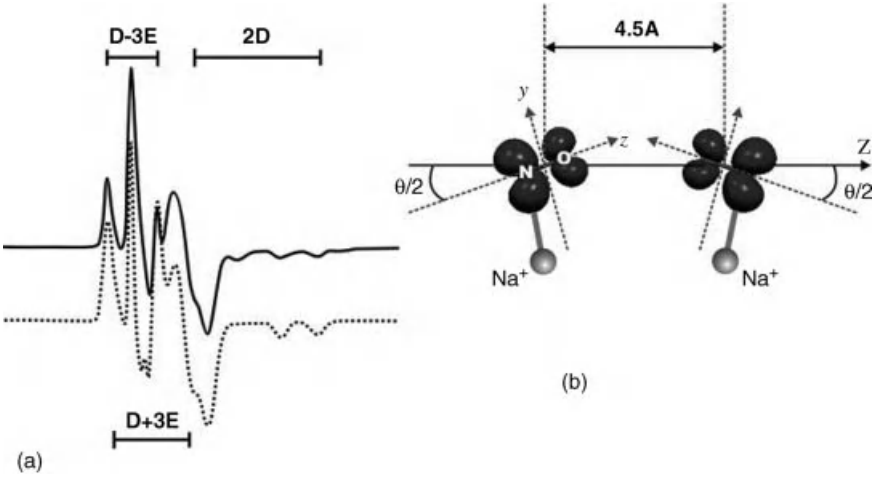


Figure 9.17 EPR spectrum of NO radical pairs with contribution from monomer species (solid line, experimental spectrum; dotted line, simulation) (a), and possible structure of NO–NO entities associated with two sodium cations with the inter-radical distance deduced form the analysis of the dipolar coupling (b). Adapted from [18].

The paramagnetic centers can also interact with each other via the exchange mechanism (see Section 9.5.3). When isotropic term dominates, such an interaction can be described in terms of the Heisenberg–Dirac–van Vleck Hamiltonian $\mathcal{H}_{ex} = -J_{12} S_1 \cdot S_2$. The exchange mechanism allows the unpaired electron to jump between the centers. If the frequency of this jumping is higher than the frequency of the dipolar interactions, it gives rise to averaging of the dipolar term to zero. In such a case, the EPR line is said to be exchange-narrowed and assumes a Lorentzian shape.

The g_{qq}, A_{qq}, and D values in the exchange-coupled systems determined from the EPR spectrum can be related to the individual values of the interacting paramagnetic centers [19, 20]. They may be used, for instance, to rationalize an unusual low-field resonance at $g = 1.965$ observed for $CaNi_8$-Y zeolites, and associated with the nickel(II)–nickel(I) antiferromagnetically coupled pairs with $S = 1/2$. Since the $\boldsymbol{g}$ tensor is an integral property of the dinuclear complex, its value, under the assumption of the overwhelming isotropic exchange [19], can be expressed as $\boldsymbol{g}_{pair} = 4/3\boldsymbol{g}(Ni^{II}) + 1/3\boldsymbol{g}(Ni^{I})$. For $\boldsymbol{g}(Ni^{II})$ larger than $\boldsymbol{g}(Ni^{I})$, a significant downfield shift of $\boldsymbol{g}_{pair}$ is expected [21].

Copper-doped CeO_2 is probably one of the best examples with a clearly resolved EPR spectrum due to a pair of nearly equivalent Cu^{2+} ions with $g_{||} = 2.2079$, $g_{\perp} = 2.0403$, $|A_{||}| = 8.5$ mT, $|A_{\perp}| = 1.35$ mT, $D = 0.066\,cm^{-1}$, $D^{dip} = -0.081\,cm^{-1}$, $D_{ex} = 0.147\,cm^{-1}$, and $J = -52.5\,cm^{-1}$ [22]. Apart from the allowed transitions ($\Delta M_S = 1$) observed in the mid-field, a weaker forbidden line ($\Delta M_S = 2$) has also been observed. From the relative intensities R of the forbidden and allowed lines, the inter-ion separation of 0.34 nm can be evaluated using a simple equation, $R = B/r^6(9.1/\nu)^2$, where ν is the microwave frequency and B is an empirical constant [23].

Another notable example of undiluted oxide systems is provided by V_2O_5–Fe_2O_3 catalysts [24]. On the basis of S-, X-, and Q-band measurements, the low-field signal at $g_{eff} = 18$ was assigned to the antiferromagnetically coupled Fe^{3+}–$V_O(e^-)$ centers with $|D/h|$ in the range 3600–4800 MHz. The $V_O(e^-)$ defect consists of an electron trapped in the surface oxygen vacancy. The value of the exchange integral $J = -157\,cm^{-1}$ indicated that the individual Fe^{3+} and $V_O(e^-)$ centers are coupled via a superexchange mechanism. The signal at $g_{eff} = 2$ was assigned to the coupled Fe^{3+} ions ($|J| = 0.95\,cm^{-1}$) in the $Fe_2V_{14}O_{13}$ phase, produced by filling the vacancies in the Fe^{3+}–$V_O(e^-)$ sites by adsorbed oxygen. Other examples of magnetically undiluted catalytic systems include $(VO)_2P_2O_7$ catalyst for the ammoxidation of butane [25], and reduced MoO_3 [26] and V_2O_5 [27], both used for the selective oxidation of propene.

The electron–electron dipolar and exchange interactions depend primarily on the distance between paramagnetic centers. Although, in principle, the latter can be reduced by magnetic dilution, this cannot be applied for catalytic materials since it may destroy catalytic properties. It has been shown, however, that the lack of the resolution in the X-band due to spin exchange and the local magnetic fields in undiluted solids can be overcome by using high-field EPR [28].

9.7.2
Unusual Spectral Features and Puzzling Lineshapes

Concerted effects of large anisotropy of the $\boldsymbol{g}$ and $\boldsymbol{A}$ tensors and high nuclear spin favor the appearance of the so-called "extra lines" (off-axis extra lines) in the powder

spectra of $S = 1/2$ and $I > 0$ systems, when the following inequalities are satisfied [29]:

$$2A_i^2 - h\nu A_i/M_I < \frac{g_i^2 A_i^2 - g_j^2 A_j^2}{g_i^2 - g_j^2} < 2A_j^2 - h\nu A_j/M_I \tag{9.34}$$

Such extra features correspond to additional solutions for the $\partial B/\partial\theta = 0$ and $\partial B/\partial\phi = 0$ relations, which do not coincide with the principal magnetic axes. As an example, the plot of the angular dependence of the resonant field $B_{res}(\theta,\phi)$ for a selected $M_I = 3/2$ transition of the EPR spectrum due to $^{17}O_2^-$ radicals trapped on an MgO surface [30] is shown in Figure 9.18a. It indicates that apart from the usual field extrema along the principal directions, there is an additional local minimum at $\theta = 28.8°$ in the zx plane which gives rise to an extra absorption line. The appearance of such lines, often more intense that the "normal" ones, may be used for analyzing less-resolved spectral features. For instance, the EPR spectrum of $^{17}O_2^-$ radicals stabilized on a high surface area MgO is complicated by the simultaneous presence of copious regular hyperfine lines, which are dominated by the much more intense off-axis extra peaks (Figure 9.18b). Using the procedure explained elsewhere [30], their positions have provided auxiliary information allowing to determine the complete ^{17}O hyperfine tensor ($^{O}\boldsymbol{A}/\mu_B\boldsymbol{g} = |-7.64, 0.718, 0.824|$ mT).

Apart from the extra lines, another possible complication of the powder EPR spectra stems from noncoincidence of the $\boldsymbol{g}$ and $\boldsymbol{A}$ tensors. Symmetry considerations impose restrictions on the components of the $\boldsymbol{g}$ and $\boldsymbol{A}$ tensors and the relative orientation of their principal axes [16, 31], providing the basis for classification of the EPR spectra for magnetically diluted $S = 1/2$ species (Table 9.2). For the analysis of the hyperfine coupling, only those symmetry elements that the corresponding

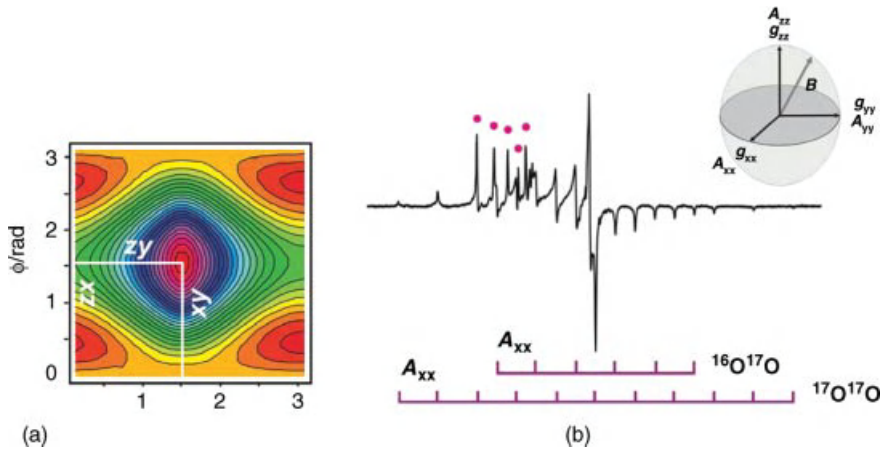


Figure 9.18 Plot of the angular dependence of the resonant field $B_{res}(\theta,\phi)$ for $M_I = 3/2$ transition of an $^{17}O_2^-$ radical trapped on an MgO surface showing a local minimum at $\theta = 28.8°$ (a) and the corresponding powder EPR spectrum with the off-axis extra lines indicated with dots (b). Adapted from [30].

Table 9.2 Relationships between the EPR spectrum symmetry and the components of ***g*** and ***A*** tensors, the coincidence angles (α, β, γ), and the molecular point symmetry including its reduction induced by surface.

EPR symmetry	*g* and *A* tensor constraints	Coincidence of principal axes of *g* and *A* tensors	Point symmetry	Surface point symmetry
Isotropic	$g_{xx} = g_{yy} = g_{zz}$ $A_{xx} = A_{yy} = A_{zz}$	All coincident $\alpha = \beta = \gamma = 0°$	O_h, T_d, O, T_h, T	—
Axial	$g_{xx} = g_{yy} \neq g_{zz}$ $A_{xx} = A_{yy} \neq A_{zz}$	All coincident $\alpha = \beta = \gamma = 0°$	D_{4h}, C_{4v}, D_4, D_{2d}, D_{6h}, C_{6v}, D_6, D_{3h}, D_{3d}, C_{3v}, D_3	C_{4v}, C_{6v}, C_{3v}
Rhombic	$g_{xx} \neq g_{yy} \neq g_{zz}$ $A_{xx} \neq A_{yy} \neq A_{zz}$	All coincident $\alpha = \beta = \gamma = 0°$	D_{2h}, C_{2v}, C_2	C_{2v}
Axial non-collinear	$g_{xx} = g_{yy} \neq g_{zz}$ $A_{xx} = A_{yy} \neq A_{zz}$	Only g_{zz} and A_{zz} coincident, $\alpha \neq 0° \; \beta = \gamma = 0°$	C_3, S_6, C_4, S_4, C_{4h}, C_6, C_{3h}, C_{6h},	C_3, C_4, C_6
Monoclinic	$g_{xx} \neq g_{yy} \neq g_{zz}$ $A_{xx} \neq A_{yy} \neq A_{zz}$	One axis of ***g*** and one axis of ***A*** coincident, $\alpha \neq 0° \; \beta = \gamma = 0°$	C_{2h}, C_s, C_2	C_s, C_2
Triclinic	$g_{xx} \neq g_{yy} \neq g_{zz}$ $A_{xx} \neq A_{yy} \neq A_{zz}$	All noncoincident, $\alpha \neq \beta \neq \gamma \neq 0°$	C_1, C_i	C_1

After [16].

magnetic nucleus shares with the whole complex are decisive [17]. In axial and orthorhombic symmetries, both $\boldsymbol{g}$ and $\boldsymbol{A}$ tensors share the same principal axes, whereas in mono- and triclinic symmetries the orientation of $\boldsymbol{g}$ and $\boldsymbol{A}$ axes may be different. It should be noted that the inherent heterogeneity of the interfacial region decreases permissible symmetry elements of surface species, often leading to low-symmetry spectra [13].

At first glance, it might appear that the relative orientations of the principal axes of the $\boldsymbol{g}$ and $\boldsymbol{A}$ tensors cannot be determined from powder EPR spectra. Although this is probably valid for triclinic symmetry, in the case of monoclinic spectra a noncoincidence of the axes can be revealed provided that $I > 1$ and both tensors exhibit large anisotropies comparable in magnitude at best ($\Delta g \mu_B B \approx \Delta A$) [17]. Then, taking an example of a paramagnet with $I = 5/2$, for small $|M_I|$ values ($\pm 1/2$), the magnetic field extrema ($\partial B/\partial\theta = 0$ and $\partial B/\partial\phi = 0$), associated with characteristic features in the powder spectra occur at the angles close to the principal axes of the $\boldsymbol{g}$ tensor (Figure 9.19a). However, for large $|M_I|$ values ($\pm 5/2$), they appear at angles close

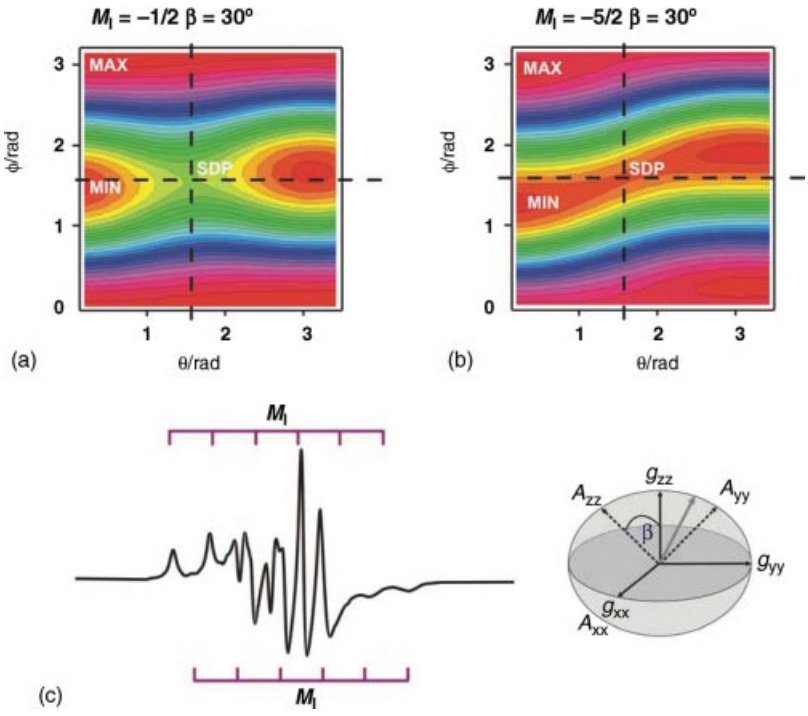


Figure 9.19 Plot of the resonant field ($\nu = 9.28$ GHz, $g_{xx} = 1.96$, $g_{yy} = 1.94$, $g_{zz} = 1.81$, $A_{xx} = 37 \times 10^{-4}$ cm^{-1}, $A_{yy} = 34 \times 10^{-4}$ cm^{-1}, $A_{zz} = 85 \times 10^{-4}$ cm^{-1}) for noncoincident angle $\beta = 30^\circ$ and $M_I = -1/2$ (a) appear at different angles than those for $M_I = -5/2$ (b), in contrast to $\beta = 0^\circ$ (see Figure 9.15). The corresponding monoclinic spectrum of $(CO)^{95}Mo{=}O(OH)/SiO_2$ surface species is shown in (c). Adapted from [15].

to the hyperfine principal axes (Figure 9.19b). The result of such competition is the presence of hyperfine lines with strong variation in spacing with M_I (exceeding the second-order effects) or the appearance of too many features in the spectrum. Another simple criterion of noncoincidence of axes is the presence of lines which are unaccounted for, or a lack of lines at positions expected from simple extrapolation starting from either side of the spectrum (Figure 9.19c). The failure to simulate spectra with correct line positions and intensities provides yet another useful indication of a low symmetry. Since all these effects depend on the M_I value and the magnitude of the anisotropy of the relevant interactions, the relative orientation of principal axes of the hyperfine tensor for nuclei with small hyperfine splitting cannot be determined, even if the relative anisotropies are large [32]. This can be expected in the case of superhyperfine structure coming from magnetic ligands, when the unpaired electron is delocalized predominantly on the metal center, or for magnetic metal centers when the unpaired electron is mainly confined to the ligand [33]. The $I = 1/2$ nuclei give rise to only two hyperfine lines and obviously no M_I variation of the spacing. Therefore, exclusively paramagnetic species having nuclei with $I > 1$ (such as ^{51}V and ^{59}Co with $I = 7/2$, ^{55}Mn, ^{95,97}Mo, and ^{99}Ru with $I = 5/2$, ^{63,65}Cu with $I = 3/2$ for magnetic metal cores, and ^{17}O with $I = 5/2$, ^{33}S and ^{35,37}Cl with $I = 3/2$ for ligands) are relevant in this context.

Although symmetry considerations suggest that low symmetry should often be expected for surface species, there are relatively few well-documented cases. They include (OH)CO–$^{95}Mo^{V}/SiO_2$ [7], ^{13}CO–Ni^{I}/SiO_2 [34], and O^-–Mo^{VI}/SiO_2 surface complex with the O^- ligand bearing most of the spin density [35]. Other examples are provided by bent surface adducts with paramagnetic ligands exhibiting C_s symmetry such as $\eta^1\{CoO_2\}^9$, $\eta^1\{NaNO\}^1$, and $\eta^1\{CuNO\}^{11}$ [33, 36, 37] and N_2^- radical interacting with a nearby proton on the MgO surface [38].

9.7.3
Dynamic Lineshape Effects and Partially Averaged Signals

Any dynamic processes within and around the paramagnetic centers such as hindered rotations, tumbling at the surface, and chemical processes can cause lineshape changes manifesting as line broadening or shifting of the line positions. A theoretical description of these time-dependent effects based on the stochastic Liouville equation is rather involved and can be found in textbooks and original articles [39, 40].

Four main ranges of the time scale for the molecular motion, gauged by the ratio of the correlation time to EPR signal spread ($\tau_c^{-1}/\Delta\omega$, where $\Delta\omega = \Delta A/\hbar$, $\Delta g\beta B/\hbar$), can be distinguished here: (i) rigid limit, (ii) slow-motion limit, (iii) fast-motion limit, and (iv) isotropic limit. In the rigid limit ($\tau_c^{-1}/\Delta\omega < 10^{-2}$–$10^{-3}$) the spectra are powder-like, and their shapes are discussed in Section 9.6.1. The slow-motion regime covers correlation times 10^{-2}–$10^{-3} < (\tau_c^{-1}/\Delta\omega) \approx 1$, and gives rise to more complex EPR spectra that can be analyzed by simulation using the software developed by Freed and co-workers [41] and Stoll and Schweiger [42]. For the fast-motion regime, 10^{3}–$10^{2} > (\tau_c^{-1}/\Delta\omega) \approx 1$, the EPR spectra approach the liquid-like limit, but random

modulation of the energy levels gives rise to M_I-dependent line broadening, $\sigma(M_I) = \alpha + \beta M_I + \gamma M_I^2$, since the $\boldsymbol{g}$ and $\boldsymbol{A}$ tensor anisotropies are not completely averaged. From the temperature dependence of the correlation time τ_c, derived form the analysis of the EPR spectra, the activation energy for the corresponding motional process can be obtained [43] using the Arrhenius plot:

$$\ln[1/\tau_c(T)] = \ln(1/\tau_0) - E_a/RT \tag{9.35}$$

The superoxide radicals are formed on many surfaces via electron-transfer activation of the adsorbed dioxygen (see Section 9.13). Evidence has been obtained for mobility of those adsorbed paramagnetic species in the slow-motion regime using naturally abundant and ^{17}O-enriched oxygen [44, 45]. Rotation around the g_{yy} axis leads to a pronounced temperature dependence of A_{xx} splitting (Figure 9.20b) due to

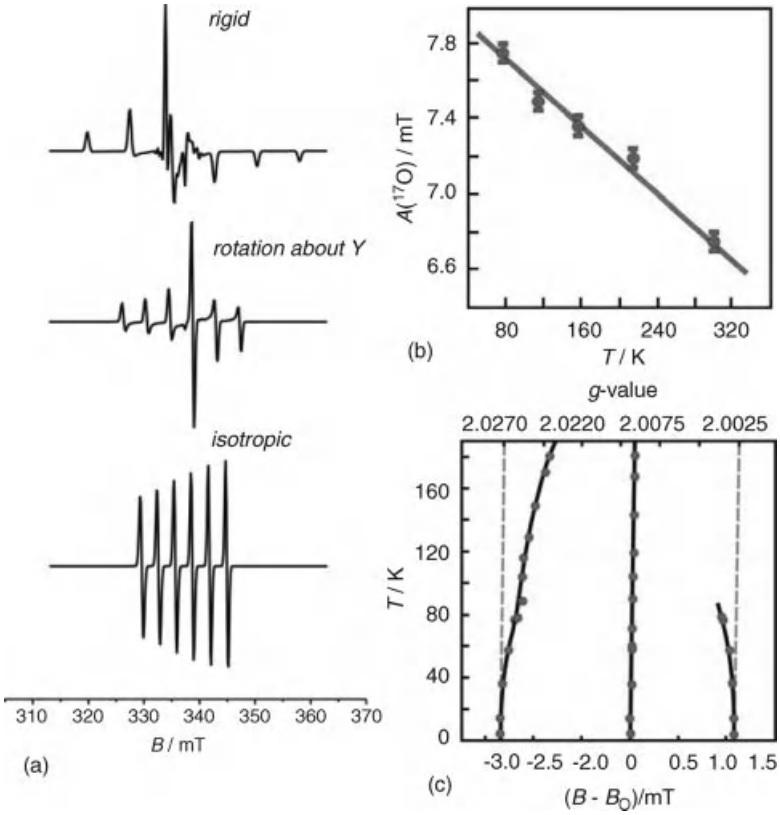


Figure 9.20 Theoretical spectra of $^{17}O_2^-$ radicals illustrating the rigid spectrum, the effect of a fast rotation along the *y*-axis, and rotationally averaged isotropic spectrum (a), change in the $A_{xx}(^{17}O)$ hyperfine splitting (b), and shifts of the g_{zz} and g_{xx} values (c) for partially averaged signals. Adapted from [45, 49].

motional averaging of the A_{xx} and A_{zz} values, resulting in apparent axial symmetry of the observed EPR spectrum with $A_{\perp} = 1/2(A_{xx} + A_{zz})$ and $A_{||} = A_{yy}$, in the fast motion limit. A similar averaging of the g_{zz} and g_{xx} values results in a temperature-induced shift of these components with the g_{yy} value remaining intact (Figure 9.20c) [45]. In Figure 9.20a, the corresponding EPR spectra are shown for the rigid superoxide radical, for the radical with fast rotation about the *y*-axis, and the totally averaged isotropic spectrum.

Dynamic effects in the EPR spectra are also associated with electron spin exchange and interconversion between two chemical forms. As the rate (τ_s) of this process increases, the EPR line broadens and finally coalesces into a single line, appearing at the weighted average of the original positions B_a and B_b (associated with two parent chemical forms). When the lines are broadened but no line shift appears, the increase in the linewidth can be described as $\sigma = \sigma_0 + |2\gamma_e\tau_s|^{-1}$, whereas the point of coalescence is found to occur at $\tau_s = (\sqrt{2}/\gamma_{av})(B_a - B_b)$ (where $\gamma_e = g_e\beta_e/h$ and $\gamma_{av} = g_{av}\beta_e/h$). One of the most common dynamic effects is the uneven line broadening observed for surface-trapped nitrogen-containing radicals experiencing molecular motion. Examples are provided by variable-temperature X-band studies of NO_2 in zeolites [46] and Q-band measurements of TEMPO radicals adsorbed on an alumina surface [47]. More information about mobility effects on the EPR spectra of the adsorbed species can be found in review papers [48–50].

9.8
Computer Simulation of Powder Spectra

By reading out the positions of the characteristic points (Figure 9.16), fairly accurate values of the EPR parameters can be extracted from the experimental spectra only in simple cases, when signals are not too complex, are sufficiently well resolved, and exhibit coincident axes [51]. For more complicated powder EPR spectra, the number of lines may vary considerably depending on the anisotropy, multiplicity of the magnetic nuclei, and the symmetry. Because the line positions generally are not strictly linear in any of the magnetic parameters, the analysis of powder EPR spectra is often a nontrivial task [16]. The problem proliferates when several paramagnetic species occur simultaneously, giving rise to multicomponent EPR spectra with overlapping component signals. In such cases, computer simulation combined with robust fitting is practically the only means of reliable analysis of the experimental data, especially when performed at several frequencies.

To simulate a powder spectrum of a paramagnetic center with given *S* and *I* values, a set of adjustable spin Hamiltonian parameters [$\boldsymbol{g}$, $\boldsymbol{A}$, and $\boldsymbol{D}$ tensors, their mutual orientations, intrinsic linewidths $\sigma_q(B)$, etc.], complemented by associated parametric variables, containing auxiliary information about the resonance frequency (ν), the number of θ and ϕ angle increments used for integration, and the number of simulation points (n), are required. Once the full set of the parameters $\boldsymbol{P}$ is known, the associated spectrum $Y(B,\nu) = f(\boldsymbol{P})$ can readily be obtained in the following way [52]:

$$Y(B,\nu) = C \int_{\theta=0}^{\pi/2} \int_{\phi=0}^{2\pi} \sum_i P_i(\theta,\phi,\nu) f(B - B_o[\nu], \sigma_B) \mathrm{d}\cos\theta \mathrm{d}\phi \tag{9.36}$$

where $P_i(\theta,\phi,\nu)$ is the transition probability, C is a constant that incorporates all instrumental parameters, and $f(B - B_0[\nu], \sigma_B)$ is the lineshape function. As implied by Eq. (9.36), the powder spectrum can be considered as a superposition of single-crystal EPR signals of Gaussian or Lorentzian shapes (see Section 9.2.2) computed for a large number of orientations (θ, ϕ) of the external magnetic field $\boldsymbol{B}$ over the unit sphere weighted in proportion to $\sin\theta \mathrm{d}\theta \mathrm{d}\phi$ [52]. For a rapid simulation of the powder spectra, when the Zeeman term is larger than the fine structure and the hyperfine couplings, the perturbation theory can be used to obtain closed-form expressions for the resonance fields as a function of the spin-Hamiltonian parameters [17]:

$$B = \frac{h\nu}{g(\theta,\phi)\mu_B} - \sum_i \left[\frac{\left(A_{ix}^2 S_{ix}^2 + A_{iy}^2 S_{iy}^2 + A_{iz}^2 S_{iz}^2 \right)^{\frac{1}{2}} m_i}{g(\theta,\phi)\mu_B} \right] + \text{second-order terms} \tag{9.37}$$

where $S_{ik} = (g_x \sin\theta\cos\phi l_{ixk} + g_y \sin\theta\cos\phi l_{iyk} + g_z \cos\theta l_{izk})/g$, and l_{ijk} are direction cosines indicating the orientation of the kth principal axis of the ith hyperfine tensor relative to the principal axis of the jth component of the $\boldsymbol{g}$ tensor. Transition probabilities can be evaluated by applying an approximate powder-averaged expression [53]:

$$\langle g_1^{\,2} \rangle / g \cong \frac{2}{3} \left[\left(g_x^{\,2} + g_y^{\,2} + g_z^{\,2} \right)/3 \right]^{\frac{1}{2}} + \frac{1}{3} \left(g_x + g_y + g_z \right) \tag{9.38}$$

Alternatively, when exact treatment is required (i.e., when the high-field approximation fails), diagonalization of the full energy matrix is performed. The transition probabilities are then calculated explicitly using the eigenvectors derived from the diagonalization steps. Although this approach is much more demanding in terms of computing time than the perturbation treatment, it is rigorous and of general validity. Therefore, diagonalization is recommended in the case of a large hyperfine coupling or zero-field splitting exceeding the Zeeman term. A more detailed discussion of the simulation algorithms can be found in review articles [54] and EPR textbooks [16, 52].

Automated fitting of the EPR spectra is an indispensable component of their quantitative analysis. Extraction of a complete set of the parameters with maximum possible accuracy requires application of robust optimization procedures to be effective. Various optimization algorithms such as the simplex method, stimulated annealing, grid search, and Powell algorithm have been employed, but the best results have been obtained with a hybrid approach combining a global search (e.g., by means of genetic algorithm) with local refinement by the Powell or simplex method [55]. A large number of computer programs of various sophistication levels, such as EPRsim32 [55] and POW [56] for $S = 1/2$, and EasySpin [42] and XSophe [57] for $S \geq 1/2$, have been developed in recent decades for this purpose.

Whatever the complexity of the spectrum, there are some key steps that must be carefully observed for its successful simulation: (i) an experimental spectrum must be recorded with a good signal-to-noise ratio; (ii) baseline drift and spurious signals must be removed by appropriate data processing software; (iii) the spectrum should be simulated within the minimum magnetic field range, and with the smallest possible number of points, assuring, however, correct reproduction of the narrowest lines; (iv) an appropriate spin-Hamiltonian has to be cautiously selected; (v) iterative optimization, where only few sensibly selected parameters are currently optimized in a given run, leads to more efficient convergences; (vi) in the case of multicomponent spectra, the number of the partaking signals should, *a priori*, be minimal; and (vii) verification of the parametric sensitivity of the simulated spectrum is recommended to provide statistically significant uncertainties of the determined values.

9.9 Molecular Interpretation of Parameters

9.9.1 *g*-Tensor

The principal values of the $\boldsymbol{g}$ tensor depend on the symmetry and structure of the electronic levels of a paramagnet. In the case of a nondegenerate ground state $|0\rangle$, well separated from the excited states, the g_{ij} components can be calculated using the second-order perturbation theory equation:

$$g_{ij} = g_e\delta_{ij} + 2\lambda \sum_n \frac{\langle 0|L_i|n\rangle\langle n|L_j|0\rangle}{E_0 - E_n} \tag{9.39}$$

where $g_e = 2.0023$ is free electron value, λ is the SOC constant, $|n\rangle$ are the excited states with energies E_n, $|0\rangle$ is the singly-occupied molecular orbital (SOMO) with the energy E_0, and L_i is the ith component of the orbital angular momentum operator. The integrals $\langle 0|L_i|n\rangle$ and $\langle n|L_j|0\rangle$ can be computed simply if the molecular orbitals (MOs) are written as linear combinations of the atomic orbitals, since the products of L_i operators on the atomic orbital (AO) (s, p, d) involved in the linear combination are tabulated (Table 9.3) [17]. However, according to the symmetry properties, only those matrix elements that contain a totally symmetric representation of the point group to which the paramagnetic center belongs need to be calculated [58]. To decide which pairs of the states are coupled by the spin–orbital interaction, it is just sufficient to evaluate whether the direct product of the irreducible representations $\Gamma_m \times \Gamma_{L_i} \times \Gamma_n$ (L_i transforms according to rotation about the i direction) contains a fully symmetric irreducible representation.

A simple tutorial example is represented by a system defined by O^- paramagnetic defects stabilized within the crystal field of C_{2v} point symmetry, as often encountered in an MgO matrix doped with Li^+. For this p-type radical, the p_z, p_x, and p_y states transform according to the A_1, B_1, and B_2 irreducible representations, respectively,

Table 9.3 Angular momentum operations on the real p and d orbitals [16].

Atomic orbital	L_x	L_y	L_z
$\|x\rangle$	0	$-i\|z\rangle$	$i\|y\rangle$
$\|y\rangle$	$i\|z\rangle$	0	$-i\|x\rangle$
$\|z\rangle$	$-i\|y\rangle$	$i\|x\rangle$	0
$\|x^2-y^2\rangle$	$-i\|yz\rangle$	$-i\|xz\rangle$	$2i\|xy\rangle$
$\|xy\rangle$	$i\|xz\rangle$	$-i\|yz\rangle$	$-2i\|x^2-y^2\rangle$
$\|yz\rangle$	$i\|x^2-y^2\rangle+\sqrt{3}i\|z^2\rangle$	$i\|xy\rangle$	$-i\|xz\rangle$
$\|xz\rangle$	$-i\|xy\rangle$	$i\|x^2-y^2\rangle-\sqrt{3}i\|z^2\rangle$	$i\|yz\rangle$
$\|z^2\rangle$	$-\sqrt{3}i\|yz\rangle$	$\sqrt{3}i\|xz\rangle$	0

whereas the operators of angular momenta L_z, L_x, L_y according to the A_2, B_2, B_1, respectively. Assuming a $2p_x^{\,2}2p_y^{\,2}2p_z^{\,1}$ electron configuration of the O^- ion, to evaluate, for example, the possible SOC contributions to the g_{yy} shift, the following direct products have to be calculated: $A_1(p_z) \times B_1(L_y) \times B_2(p_y) = A_2$ and $A_1(p_z) \times B_1(L_y) \times B_1(p_x) = A_1$. Hence the g_{yy} component deviates from the g_e value ($\Delta g_{yy} > 0$) due to the coupling of the SOMO [p_z (A_1) orbital] with the doubly occupied p_x (B_1) only. From Eq. (9.39), with the help of Table 9.3, the value of this shift can be calculated readily:

$$\Delta g_{yy} = (2\lambda/\Delta)\langle p_z|L_y|p_x\rangle\langle p_x|L_y|p_z\rangle = (2\lambda/\Delta)\langle p_z|-ip_z\rangle\langle p_x|ip_x\rangle = 2\lambda/\Delta \tag{9.40}$$

where Δ is the energy separation between the $2p_z$ and $2p_x$ states.

The physical meaning of Eq. (9.39) is that the SOC gives rise to a deviation of the $\boldsymbol{g}$ tensor components from the spin-only value (g_e). Since this shift is proportional to the SOC constant, anisotropies of the $\boldsymbol{g}$ tensor for paramagnets composed of heavy atoms are larger than those for species containing light elements only. Separation of the excited states from the ground state is another important factor determining the $\boldsymbol{g}$ tensor anisotropy. As implied by Eq. (9.39), the smaller the separation, the larger is the shift of the g_{ij} values. When reliably assigned optical spectra are available, the energy differences $E_n - E_0$ appearing in the denominator can be used for calculating the values of the g components. Generally, the SOC to an empty MO gives rise to negative contributions to g_{ii}, whereas coupling to a filled MO has the opposite effect (Figure 9.21). Thus, for instance, EPR spectra of d^1 species exhibit $g_{ii} < g_e$ due to admixture of empty MOs (Figure 9.21a), whereas d^9 paramagnets have $g_{ii} > g_e$ due to admixture of filled MOs (Figure 9.21b). In the case of tetragonal Cu(II) with a $3d_{x^2-y^2}$ ground state (SOMO) and an orbital separation of the order of 10 000 cm^{-1}, Eq. (9.39) gives $g_{\|} = g_e + 8\lambda_{Cu}/(E_{x^2-y^2} - E_{xy}) \approx 2.3$, $g_{\perp} = g_e + 2\lambda_{Cu}/(E_{x^2-y^2} - E_{xy,yz}) \approx 2.1$, where $\lambda_{Cu} = 830\,cm^{-1}$.

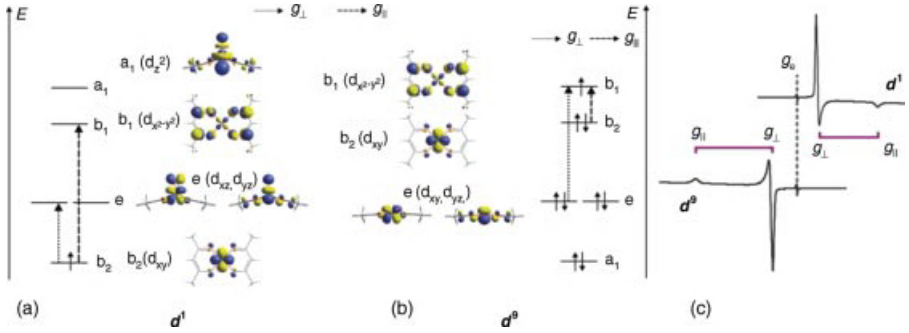


Figure 9.21 Energy level schemes and the magnetic transitions for d^1 (a) and d^9 (b) transition metal ions in a C_{4v} environment together with the corresponding simulated EPR spectra (c). The couplings with empty states give rise to $g_{\|} < g_{\perp}$ whereas for the couplings with occupied states $g_{\|} > g_{\perp}$ is observed.

The same result can be obtained in a more straightforward way by using a simplified equation:

$$g_i = g_e \pm \frac{n\lambda}{\Delta E} \tag{9.41}$$

where the n values can be obtained from the magic pentagon shown in Figure 9.22. The $(x^2 - y^2)$ vertex (due to the ground state) is connected to (xy) with the coefficient 8 and to (xz) and (yz) with the coefficient 2, in accordance with the previously calculated values. More involved working examples of using Eq. (9.39) in practice can be found elsewhere [17].

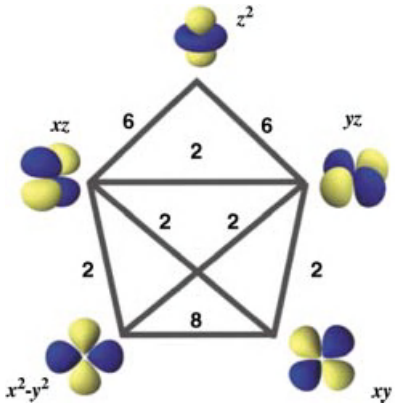


Figure 9.22 Magic pentagon showing magnetic couplings for interpretation of the ***g*** tensor anisotropy of mononuclear paramagnetic centers with transition metal ion cores.

Surface-trapped paramagnetic species with degenerate ground states exhibit highly anisotropic $\boldsymbol{g}$ tensors, with the g_{zz} component being very sensitive to the local environment, as implied by Eq. (9.39). They can, therefore, serve as probe molecules for identification of the oxidation state of the adsorption sites [50]. Classic examples are provided by superoxide O_2^- ($^2\Pi_{3/2}$) and NO ($^2\Pi_{1/2}$) radicals. The local heterogeneity of the surface crystal field can be particularly well revealed using a monoatomic O^- radical as a probe that can easily penetrate confined spaces. An example is provided by high surface-area MgO, where multiplicity of the adsorption sites of various topographic locations has been nicely unraveled by EPR [59]. In contrast, for radicals with a nondegenerate ground state and well-separated energy levels, such as NO_2, CO_2^-, SO_2^-, and O_3^-, the $\boldsymbol{g}$ tensor is only slightly influenced by the interaction with the surface. The measured g_{ii} values can then be used for identification of a given radical on a simple fingerprint basis [13].

9.9.2 Hyperfine Tensor

As discussed in Section 9.5.2, the complete hyperfine tensor $\boldsymbol{A}$ can be decomposed into isotropic and traceless dipolar parts ($\boldsymbol{A} = a_{\mathrm{iso}}\boldsymbol{I} + \boldsymbol{T}$). When performing such a decomposition, the signs of the $\boldsymbol{A}$ tensor components, not available from experiment, should be assigned by judicious analysis of the magnetic interactions involved or by auxiliary density functional theory (DFT) calculations, which is recommended nowadays.

The isotropic hyperfine coupling [$^{\mathrm{n}}a_{\mathrm{iso}} = 2/3\mu_0 g\mu_{\mathrm{B}} g_{\mathrm{n}}\mu_{\mathrm{N}}\varrho^{\alpha-\beta}(\boldsymbol{R}_{\mathrm{n}})$] take place if a nonzero spin density, $\varrho^{\alpha-\beta}(\boldsymbol{r}) = \varrho^{\alpha}(\boldsymbol{r}) - \varrho^{\beta}(\boldsymbol{r})$, is in contact with a given magnetic nucleus n (*i.e.* when $\boldsymbol{r} = \boldsymbol{R}_{\mathrm{n}}$). The Fermi contact interaction may originate from the symmetry-allowed admixture of s orbitals to the SOMO (direct mechanism, already discussed in Section 9.3.1) or from polarization of the inner core s levels by the spin density localized on other orthogonal orbitals (indirect mechanism). The latter term is usually accounted for by a simple expression of the type $Q\varrho^{\alpha-\beta}(\boldsymbol{r})$, where Q is a polarization constant. However, in more complicated cases, when the spin density is delocalized on several nuclei, a more advanced expression should be used [17, 39]. When the spin polarization is negligible, the spin density is equal to the unpaired electron density $\varrho^{\alpha-\beta}(\boldsymbol{r}) = \varrho(\boldsymbol{r}) = |\Psi(\boldsymbol{r})|^2$, providing a direct measure of involvement of the s orbital in the SOMO, expressed as linear combination of atomic orbitals: $|\mathrm{SOMO}\rangle = c_{\mathrm{s}}|\mathrm{s}\rangle + c_{\mathrm{p}}|\mathrm{p}\rangle + c_{\mathrm{d}}|\mathrm{d}\rangle$ (see below).

The SOC perturbs these results by adding a pseudo-contact term of the form of $\kappa P\langle r^{-3}\rangle$. As a result, the a_{iso} value can be partitioned in the following way:

$$a_{\mathrm{iso}} = a_{\mathrm{iso}}^{\mathrm{Fermi}} + Q\varrho^{\alpha-\beta}(\mathbf{r}) + \kappa P\langle r^{-3}\rangle \tag{9.42}$$

The contribution of the SOC is of the order of $P(g_{ii} - g_{\mathrm{e}})$, where $P = g_{\mathrm{e}}\mu_{\mathrm{e}} g_{\mathrm{n}}\mu_{\mathrm{N}}\langle r^{-3}\rangle$. It can be ignored only when the $\boldsymbol{g}$ tensor anisotropy is small, as occurs for most radicals containing light atoms with a nondegenerate ground state. However, if a radical has unquenched orbital momentum or contains heavy atoms with an appreciable spin–orbit interaction, such neglect cannot be so simply performed.

The anisotropic part of the hyperfine coupling is due to the magnetic dipolar interactions. The components of the dipolar tensor T_{ii} are given by the integrals (see Section 9.3)

$$T_{ii} = (g_e \mu_e g_n \mu_N)/r^3 \langle 3\cos^2\theta - 1 \rangle = P\langle 3\cos^2\theta - 1 \rangle \tag{9.43}$$

where $i = x, y, z$, r is the distance between the electron and nucleus of interest, θ is the angle between $\boldsymbol{r}$ and $\boldsymbol{B}$ vectors, and the angular brackets imply an average taken over the electronic wavefunctions, as the electron is not fixed in the space. For s orbitals, T_{ii} averages to zero upon integration, whereas for p and d orbitals they assume the generic form

$$\frac{2}{5}P_p \begin{pmatrix} 2 & & \\ & -1 & \\ & & -1 \end{pmatrix} \quad \text{and} \quad \pm\frac{2}{7}P_d \begin{pmatrix} 2 & & \\ & -1 & \\ & & -1 \end{pmatrix} \tag{9.44}$$

respectively, and depend on the particular angular orientation of these orbitals (Table 9.4).

When the isotropic and anisotropic parts of the hyperfine tensor are determined and corrected for polarization and spin–orbit effects, approximate spin densities on the s, p, and d AOs constituting the SOMO can be calculated. By using the tabulated atomic hyperfine constants of a given nucleus n and assuming that the unpaired electron is entirely localized on a particular type of the atomic orbital (s, p, d), we obtain

$$\begin{aligned} c_s{}^2 &= \varrho_s{}^n = a_{iso}{}^n(\text{experimental})/a_{iso}^n(\text{atomic}) \\ c_{p,d}{}^2 &= \varrho_{p,d}{}^n = T_{ii}{}^n(\text{experimental})/T_{ii}^n(\text{atomic}) \end{aligned} \tag{9.45}$$

The calculated $a_{iso}{}^n$(atomic) and $T_{ii}{}^n$(atomic) values for various nuclei and oxidation states can be found elsewhere [60].

An axial hyperfine tensor can be usually associated with SOMO composed of a single p or d orbital. A departure from axial symmetry that cannot be accounted for by

Table 9.4 Components of dipolar hyperfine tensor for various p and d orbitals [16, 17].

Orbital	T_{zz}	T_{yy}	T_{xx}
p_z	4/5P	−2/5P	−2/5P
p_y	−2/5P	4/5P	−2/5P
p_x	−2/5P	−2/5P	4/5P
d_{z^2}	4/7P	−2/7P	−2/7P
$d_{x^2-y^2}$	−4/7P	2/7P	2/7P
d_{yz}	2/7P	2/7P	−4/7P
d_{xz}	2/7P	−4/7P	2/7P
d_{xy}	−4/7P	2/7P	2/7P

the SOC correction is usually caused by hybridization (simultaneous contribution of several AOs to the SOMO). When p_x, p_y, or p_z orbitals constitute the SOMO

$$|\mathrm{SOMO}\rangle = c_x|p_x\rangle + c_y\left|p_y\right\rangle + c_z|p_z\rangle \tag{9.46}$$

the dipolar matrix elements, neglecting the spin–orbit effects, are given by [17]

$$\begin{aligned} T_{xx} &= \frac{2}{5}P\left(2{c_x}^2 - {c_y}^2 - {c_z}^2\right) \\ T_{yy} &= \frac{2}{5}P\left(-{c_x}^2 + 2{c_y}^2 - {c_z}^2\right) \\ T_{zz} &= \frac{2}{5}P\left(-{c_x}^2 - {c_y}^2 + 2{c_z}^2\right) \\ T_{ij} &= -3c_ic_j,\ (i \neq j) \end{aligned} \tag{9.47}$$

Thus, the SOMO of radicals with a hybrid p-orbital contribution may exhibit a nondiagonal hyperfine tensor (i.e., $T_{ij} \neq 0$), and the corresponding principal hyperfine axes are different from the molecular *xyz* axes defining the p orbitals. Analogous set of equations may be written for a SOMO composed of d orbitals for paramagnetic centers constituted by transition metal ions [17]:

$$|\mathrm{SOMO}\rangle = c_{z^2}\left|z^2\right\rangle + c_{yz}|yz\rangle + c_{xz}|xz\rangle + c_{x^2-y^2}\left|x^2-y^2\right\rangle + c_{xy}|xy\rangle \tag{9.48}$$

and

$$\begin{aligned} T_{xx} &= \frac{2}{7}P\left[-(c_{z^2})^2 - 2\left(c_{yz}\right)^2 + (c_{xz})^2 + \left(c_{x^2-y^2}\right)^2 + \left(c_{xy}\right)^2 - 2\sqrt{3}(c_{z^2})\left(c_{x^2-y^2}\right)\right] \\ T_{yy} &= \frac{2}{7}P\left[-(c_{z^2})^2 - 2\left(c_{yz}\right)^2 + (c_{xz})^2 + \left(c_{x^2-y^2}\right)^2 + \left(c_{xy}\right)^2 + 2\sqrt{3}(c_{z^2})\left(c_{x^2-y^2}\right)\right] \\ T_{zz} &= \frac{2}{7}P\left[2(c_{z^2})^2 + \left(c_{yz}\right)^2 + (c_{xz})^2 - 2\left(c_{x^2-y^2}\right)^2 - 2\left(c_{xy}\right)^2\right] \\ T_{xy} &= \frac{2}{7}P\left[-2\sqrt{3}(c_{z^2})\left(c_{xy}\right) + 3\left(c_{yz}\right)\left(c_{xz}\right)\right] \\ T_{yz} &= \frac{2}{7}P\left[\sqrt{3}(c_{z^2})\left(c_{yz}\right) + 3(c_{xz})\left(c_{xy}\right) - 3\left(c_{yz}\right)\left(c_{x^2-y^2}\right)\right] \\ T_{xz} &= \frac{2}{7}P\left[\sqrt{3}(c_{z^2})(c_{xz}) + 3\left(c_{yz}\right)\left(c_{xy}\right) + 3(c_{xz})\left(c_{x^2-y^2}\right)\right] \end{aligned} \tag{9.49}$$

It should then be noted that for certain combinations of the p and d orbitals involved in SOMO, a nondiagonal hyperfine tensor will be obtained. It must next be diagonalized to be compared with experiment. Furthermore, the SOC perturbs these results by adding terms to the diagonal matrix components of the order of $P(g_{ii} - g_e)$. Therefore, a departure from, say, axial symmetry may be due to the SOC effects if $A_{||} = A_{zz}$ and $A_{xx} - A_{yy} \approx P(g_{xx} - g_{yy})$ or it may arise from d-orbital hybridization when the rhombicity is larger. A straightforward analysis of such cases was proposed

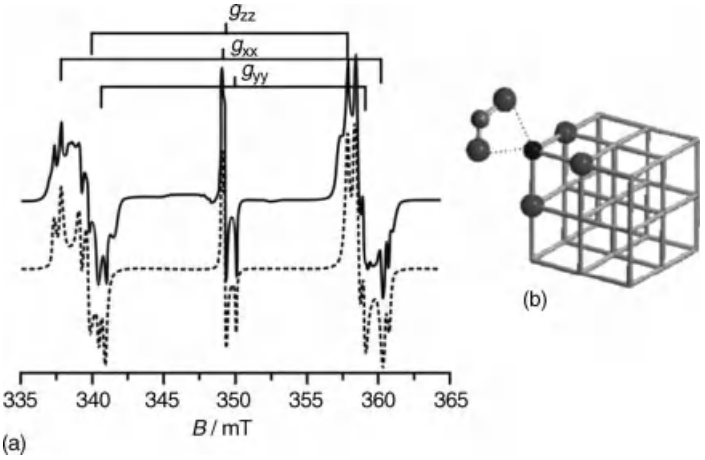


Figure 9.23 Experimental (solid line) and simulated (dotted line) EPR spectra of $^{13}CO_2^-$ adsorbed on an MgO surface (a). Structure and possible localization of CO_2^- radical deduced from the analysis of the hyperfine structure (b). Adapted from [62].

by Rieger [17]. The analysis of the hyperfine tensor of a copper mononitrosyl adduct entrapped in ZSM-5 zeolite may serve here as a good illustration of the use of this procedure in practice [33].

When the SOMO is composed of an sp^n hybrid, the spin density distribution derived from analysis of the hyperfine tensor [Eq. (9.43)] may be used for the determination of the bond angles using the orthogonality condition $\lambda_i\lambda_j\cos\phi_{ij} = 0$, where $\lambda^2 = c_{2p}{}^2/c_{2s}{}^2 = \varrho_p/\varrho_s$ and ϕ is the angle between the bonds i and j [61]. For ABA radicals of C_{2v} symmetry this leads to $\phi = 2\cos^{-1}(\lambda^2 + 2)^{-1/2}$, whereas for a BA_3 species of C_{3v} symmetry $\phi = \cos^{-1}[1.5/(2\lambda^2 + 3)^{-1/2}]$. For instance, from the analysis of hyperfine data obtained for $^{13}CO_2^-$ radicals trapped on an MgO surface (Figure 9.23), the hyperfine tensor of the dominant species attached to the edges of MgO nanocrystals can be decomposed into the isotropic and dipolar components: $|507.5,\ 495.2,\ 629.3|/\mathrm{MHz} = 544.0/\mathrm{MHz} + |-36.5,\ -48.8,\ +85.3|/\mathrm{MHz}$ [62]. Assuming that $\mathrm{SOMO} = c_s|2s_C\rangle + c_x|2p_x\rangle + c_z|2p_z\rangle$, on the basis of Eq. (9.47) the dipolar part can be written as $T_{xx} = {}^2/_5P(2c_x{}^2 - c_z{}^2)$, $T_{yy} = {}^2/_5P(-c_x{}^2 - c_z{}^2)$, $T_{zz} = {}^2/_5P(-c_x{}^2 + 2c_z{}^2)$. By taking $P = 265{,}9\,\mathrm{MHz}$, from the experimental dipolar $\boldsymbol{T}$ tensor $c_z{}^2 = 0.42$ and $c_x{}^2 = 0.038$ are obtained, whereas from the isotropic constant $c^2_{C_{2s}}$ can be calculated by applying Eq. (9.45) and using $a^C_{iso}(\mathrm{atomic}) = 3777\,\mathrm{MHz}$. As a result, the spin density projected onto atomic orbitals have been calculated to be $c^2_{C_{2s}} = 0.144$ and $c^2_{C_{2p}} = 0.458$, and the ensuing bond angle is $\phi = 126^\circ$.

9.10
Quantum Chemical Calculations of Magnetic Parameters

Molecular interpretation of magnetic parameters is not a trivial issue for paramagnetic species of low symmetry exhibiting complex electronic structure. In such

cases, quantum chemical calculations may greatly improve the interpretation of the EPR parameters.

Molecular modeling of heterogeneous systems and computational EPR spectroscopy using DFT is a rapidly developing field [63, 64]. Widely available and easy-to-use quantum chemical packages (Gaussian, ADF, ORCA, Materials Studio, deMon, ReSpect, Turbomol, CP2K, and others) have made such calculations accessible to researchers without a profound theoretical background. However, despite the progress made, quantum mechanical calculations can only be carried out for hundreds of atoms, and judicious selection of an appropriate exchange-correlation functional, use of adequate basis sets, and the level of theory of the relativistic effects treatment are mandatory to obtain sensible results. The calculated parameters must be carefully compared with experiment using representative reference molecular systems of well-known structure bearing the same magnetophore as the investigated surface or bulk catalytic species.

The components of the $\boldsymbol{g}$ and $\boldsymbol{A}$ tensors can be obtained as the formal second derivatives of the total energy E of the system:

$$g_{pq} = \frac{1}{\mu_B} \frac{\partial^2 E}{\partial B_q \partial S_p}\bigg|_{B=S=0} \quad \text{and} \quad A_{pq} = \frac{\partial^2 E}{\partial I_q \partial S_p}\bigg|_{I=S=0} \tag{9.50}$$

However, to calculate the energy response to magnetic field and spin variables, numerous approximations are used in practical applications [64]. Successful reproduction of the $\boldsymbol{g}$ and $\boldsymbol{A}$ tensors provides a quantitative connection between the detailed molecular structure of the examined paramagnet and its spectroscopic fingerprints. This approach is nowadays becoming a well-established technique for advanced analysis of complex EPR spectra, often encountered in heterogeneous systems [65–70]. Its interpretative ability is well illustrated in Figure 9.24, taking the molecular analysis of the $\boldsymbol{g}$ tensor due to copper nitrosyl $(CuNO)^+$ complexes in ZSM-5 zeolite as an example [71].

Using the quasi-relativistic approach based on the Pauli Hamiltonian [72], deviations of the $\boldsymbol{g}$ tensor components from the g_e value can be discussed in terms of couplings induced by the magnetic field between the occupied and virtual magnetic orbitals. For the particular Cu^+–NO complex, such an approach reveals that the coupling α-22a′ (SOMO) ↔ α-23a″ (LUMO) is responsible for the observed g_{zz} value and exhibits a largely intra-ligand character. However, as can be seen, the involvement of the copper $3d_{z^2}$ and $3d_{yz}$ orbitals is significant here (Figure 9.24a). This effect influences the $\boldsymbol{g}$ tensor mainly by decreasing the SOMO–LUMO gap due to the covalent interactions between the Cu core and the NO ligand, and has a tremendous impact on the copper hyperfine tensor [33]. The metal-based β-17a′ and β-20a′ orbitals mix with the β-SOMO to determine a slightly positive shift of the g_{xx} component. The value of g_{yy} is determined by one stronger metal to ligand coupling β-19a′ ↔ β-22a′ and two weaker intra-ligand β-14a′ ↔ β-22a′ and β-16a′ ↔ β-22a′ couplings. The 14a′ and 16a′ orbitals are produced by mixing of the hybridized π^b and σ(2p) MOs of the NO ligand with the in-plane copper 3d orbitals. As a result, the involvement of copper d orbitals leads to a much more complicated electronic nature of the $\boldsymbol{g}$ tensor in comparison with a classic model of the electrostatically bound NO [73] and, in consequence, to a much more complicated EPR spectrum (Figure 9.24b).

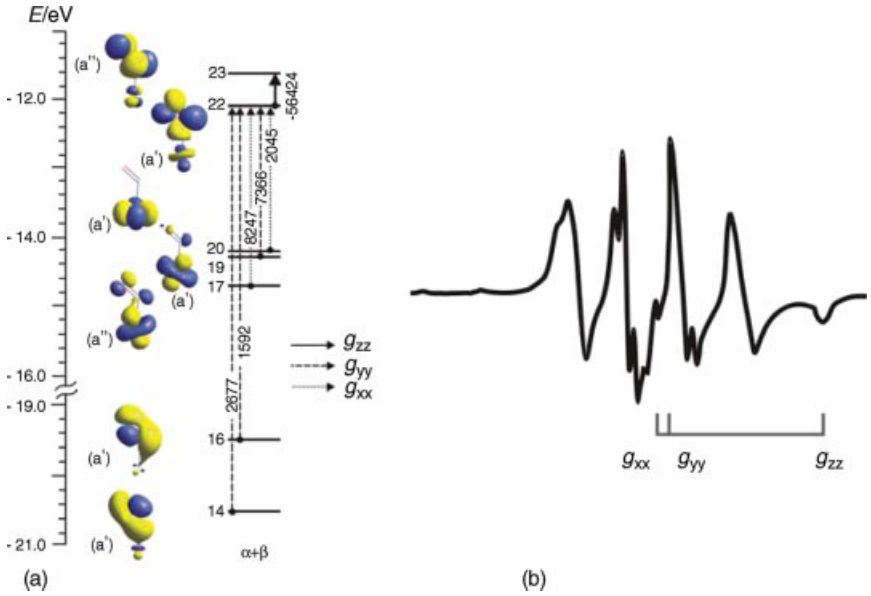


Figure 9.24 Orbital diagram showing the most important paramagnetic contributions to the *g* shifts in spin-restricted DFT calculations using the Pauli Hamiltonian (a) and the corresponding EPR spectrum of $(CuNO)^+$ZSM-5 radical (b). The pronounced g_{zz} shift is accounted for by the intraligand α-22a′ (SOMO) ↔ α-23a″ (LUMO) transition. Adapted from [33, 71].

9.11 Advanced EPR Techniques

9.11.1 Electron Spin Echo-Based Techniques

Although in favorable cases even for surface radicals it is possible to resolve EPR features smaller than 0.1 mT [13], usually the hyperfine splitting of distant atoms remains unresolved, giving rise to inhomogeneous broadening of the lines. An increase in the hyperfine structure resolution and, therefore, of the spatial range around a radical center that can be explored by magnetic resonance techniques may be achieved by multiple resonance techniques [electron nuclear double resonance (ENDOR)] or pulse techniques based on measurements of the electron spin echo [electron spin echo envelope modulation (ESEEM), hyperfine sublevel correlation spectroscopy (HYSCORE)]. In comparison with CW-EPR, these methods are experimentally much more demanding, but they provide a direct measure of the nuclear quadruple ($H_Q = \boldsymbol{I}\cdot\boldsymbol{P}\cdot\boldsymbol{I}$) and nuclear Zeeman ($H_{NZ} = -\mu_N g_n \boldsymbol{I}\cdot\boldsymbol{B}$) effects as well (introduced in Section 9.5.4).

In the ENDOR experiment, the signal arises from the combined use of the microwave and radiofrequency to excite simultaneously the EPR and NMR

transitions (the nuclear transitions are thus monitored indirectly through EPR transitions). If the microwave power is high enough to produce significant saturation of the EPR signal and the system is swept with the radiofrequency, then, when the resonance conditions for the transitions between the energy levels in each M_S manifold are met, there will be an increase in the EPR absorption. By recording this absorption as a function of the radiofrequency, the ENDOR spectrum is obtained.

In contrast, in the time-domain ESEEM experiment, the NMR transitions are observed due to mixing of the frequencies of the semi-forbidden and allowed EPR transitions, which have been coherently excited using short and intense pulses of the microwave radiation [74]. The magnetic field is set at a value corresponding to an EPR transition, and the system is subjected to the sequence of pulses. The subsequent electron echo signal is modulated by superposition of the frequencies corresponding to the transitions between the energy levels in each of the M_S manifolds. The nuclear frequencies associated with the modulations are obtained by Fourier transform of this spectrum into the frequency domain.

The ENDOR, ESEEM, and HYSCORE [75] techniques give complementary information concerning the unresolved (in CW-EPR) hyperfine splittings, and there is a certain hierarchy of their usefulness in relation to the magnitude of the hyperfine interactions. Whereas ENDOR is most appropriate in the range 0.5–0.1 mT, ESEEM and HYSCORE are capable of resolving even smaller splittings from distant nuclei. The principal advantages of the ENDOR technique with respect to CW-EPR are higher resolution of the spectrum (about two orders of magnitude with respect to conventional EPR) and simplification of the complex spectra. In the ENDOR experiment on powders, one given spectral line is selectively saturated to observe the corresponding hyperfine couplings. The most relevant drawback of ENDOR is its distinctly lower sensitivity. Owing to progress in the instrumentation and data processing, there is steadily growing number of ESEEM, HYSCORE, and ENDOR applications in studies of surface chemistry and catalysis [76–82].

Nanoporous calcium aluminate ($12CaO{\cdot}7Al_2O_3$) provides a notable example of the application of HYSCORE for studying catalytic materials [81]. Distribution of the counterbalancing OH^- anions within the positively charged framework seen through their interaction with the isomorphously substituted copper(II) has been achieved based on the measured proton hyperfine dipolar tensor. Deduced locations of the extra-framework hydroxyl species along with the corresponding proton spectral ridge are shown in Figure 9.25.

9.12
Characteristics of EPR Techniques in Application to Catalysis and Surfaces

As a rule, catalytic materials are prepared in a powder form with a high surface area. When a crystalline material is finely divided, additional line broadening effects can appear in the EPR spectrum due to the particle-size dispersion (usually in the range 1–50 nm), and also because of distribution of the dislocation strains, surface-related defects, and local microheterogeneity in the nearest environment of the

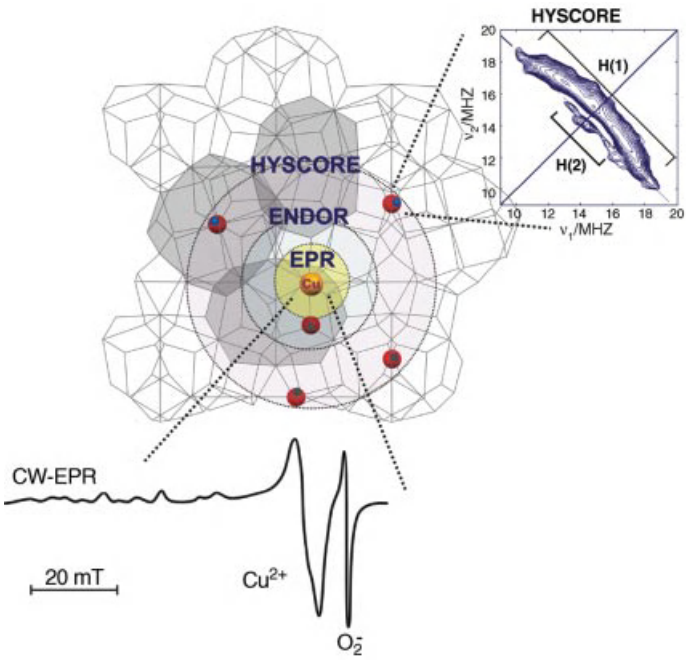


Figure 9.25 Fragment of the mayenite structure containing a Cu^{2+} ion and extra-lattice O_2^- and OH^- species showing the spatial extent of information accessible for EPR, ENDOR, and HYSCORE. Adapted from [81].

paramagnetic centers [15]. Because of the intrinsic heterogeneity of the interfaces and surfaces, several paramagnetic species may be encountered simultaneously (speciation) [83, 84]. As a result, the use of powders often gives rise to numerous difficulties for the analysis of the EPR data, associated with poor resolution, overlapping signals, and low-symmetry phenomena, in addition to frequent extra broadening of the lines produced by *D*-, *g*- and *A*-strains. Vanishing of the strongly angle-dependent fine structure lines may further restrain the amount of information that can be extracted from the experimental spectra.

9.12.1
Distinction Between Surface and Bulk Species

A primary task when dealing with catalytic surfaces is to establish the location of the investigated paramagnetic centers. Experimental techniques to distinguish between the bulk and the surface species employ various physical and chemical approaches, such as registration of the spectra at various temperatures, frequencies or microwave powers, isotopic labeling, and spin trapping, often applied in combination [15, 32]. They are summarized in Table 9.5. Whereas the physical methods exploit

Table 9.5 Distinction between paramagnetic surface and bulk centers using various physical and chemical approaches.

	Approach	Observed effects	
		Surface centers	**Bulk centers**
1	Adsorption of probe molecules at low temperatures:		
	– Paramagnetic probes	– EPR signal broadens reversibly	– No effect
	– Diamagnetic probes with ($I = 0$) acting as ligands	– Change in the coordination	– No effect
	– Diamagnetic probes with ($I \neq 0$) acting as ligands	– Superhyperfine structure appears	– No effect
	– Redox probes	– Fast reaction	– No or very slow reaction
2	Analysis of linewidths	Often broad lines due to micro-heterogeneity of the local environment	Narrower lines, usually better resolved
3	Variable-temperature measurements	Possible mobility of adsorbed species	Essentially rigid
4	Measurements of $\boldsymbol{g}$ and $\boldsymbol{A}$ values	Values different from those of bulk species	Values different from those of surface species
5	Analysis of $\boldsymbol{g}$ and $\boldsymbol{A}$ tensor symmetry	Lower than that of the corresponding bulk species	Determined by the host type and the location site
6	Measurements of D and E values	Fine structure often smeared out	Detected in favorable cases

After [15].

differences in the magnetic parameters for surface and bulk species, the chemical approaches consist of adsorption of the various probe molecules of the specific magnetic and coordinative properties profiting from easy accessibility of the surface species.

9.12.2 Poorly Resolved Spectra – Multifrequency Approach

As already discussed, paramagnetic centers constituted by light atoms, characterized with well-separated energy levels, exhibit small anisotropies of their $\boldsymbol{g}$ tensors. Their EPR spectra usually remain unresolved at the conventional X-band due to the line broadening. Although clear EPR features smaller than 0.1 mT have been observed even for surface species [13, 85], usually the resolution is a serious concern, particularly for high surface area catalytic materials. In such cases, the anisotropy of the $\boldsymbol{g}$ tensor can be resolved using high-frequency electron paramagnetic resonance (HF-EPR). Since the Zeeman interaction increases linearly with the external magnetic field, the field separation (ΔB_{12}) of two slightly different g_1 and g_2 values increases with the frequency according to the equation

$$\Delta B_{12} = h/\mu_B \left(\frac{1}{g_1} - \frac{1}{g_2}\right) \nu \tag{9.51}$$

When unresolved hyperfine structure primarily determines the linewidths, a condition $(\Delta g/g_{iso})B_0 > \Delta B_{hfs}$, that is, the anisotropic Zeeman interaction must exceed the inhomogeneous line broadening, must be satisfied to observe g anisotropy [86]. As an example, radical intermediates appear at $g \approx 2.0$, and their typical Δg shifts are of the order of 10^{-3}–10^{-4}. At the X-band, the corresponding $(\Delta g/g_{iso})B_0$ values are in the range 0.03–0.3 mT, whereas for powder samples linewidths are usually around 1–3 mT.

For the investigation of catalytic materials, a multifrequency approach in the range 0.5–400 GHz has proved its diagnostic capability [87, 88]. It allows for a straightforward discrimination between the $\boldsymbol{g}$ and hyperfine features in the complex EPR spectra, and also the determination of principal components of both tensors. It is nicely illustrated by the enhanced resolution obtained at 374.6 GHz revealing a clear rhombicity of the Cr^V signal even in an undiluted Na_3CrO_8 specimen, whereas in the X-band only a single unstructured line could be observed (Figure 9.26). Another notable example is provided by nitrosyl complexes in Na-A and Na-ZSM-5 zeolites, were application of X-, Q-, and W-band EPR helped to separate the $\boldsymbol{g}$ and $\boldsymbol{A}$ tensors, and to resolve a weak difference in the g_{xx} and g_{yy} values [87]. An additional benefit of high-frequency measurements is simplification of the EPR spectra with the very large hyperfine structure, where recovery of the high-field approximation eliminates forbidden transitions observed in the X-band, helping in assignment of the spectral features [89]. Undoubtedly, a major advantage of using HF-EPR spectroscopy is connected with the studies of high-spin systems with dominant ZFS. Combination of high-spin and large ZFS results in spectra that usually cannot be observed at

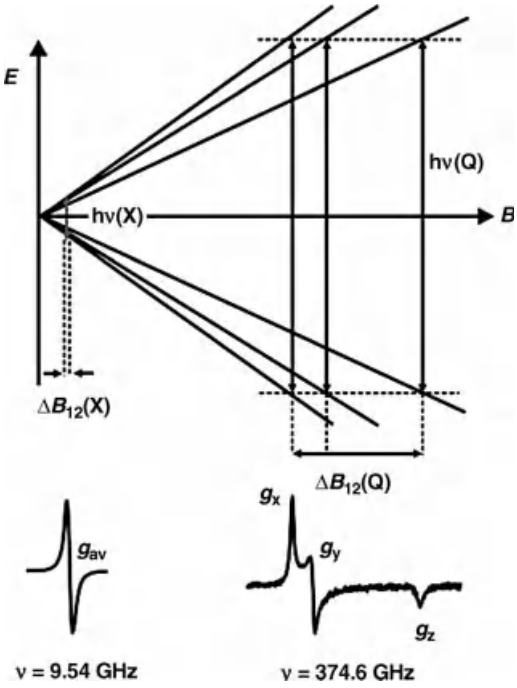


Figure 9.26 Resolution enhancement of Cr^{5+} ($S = 1/2$) ***g*** tensor anisotropy by applying high-field EPR for a magnetically undiluted specimen of Na_3CrO_8. Adapted from [28].

customary X- or even Q-bands. There are many materials of catalytic interest that contain high-spin Fe^{2+}, Mn^{3+}, or Ni^{2+} centers that are apparently "EPR silent" when the probing frequencies are smaller than the ZFS, but can be revealed in HF-EPR.

Low-frequency EPR may also be of practical benefit. At L or S frequencies for systems with small *g* anisotropy, the Zeeman term appears nearly isotropic. As a result, the spectrum is simplified, facilitating the determination of the field-independent features such as hyperfine couplings. Due to the decreased Zeeman interaction, a state mixing with field-invariant terms may become significant if they are of similar magnitude. This may break the usual high-field selection rules ($\Delta M_S = \pm 1$ and $\Delta M_I \neq 0$), leading to the appearance of new features associated with the already mentioned forbidden transitions (see Section 9.5.3), which may provide an extra source of useful spectroscopic information.

The resolution of EPR spectra may also be improved by using higher derivative spectra. Owing to its similarity with the first derivative, the third derivative may be recommended [14, 15]. In the context of systems of catalytic interest, this method has been successfully used for resolving the spectra of ^{13}CO adsorbed on silica-supported Ni^{I} [34], Mo^{V} [90], and V^{IV} ions [91] and to unravel the speciation of cobalt(II) carbonyl complexes in ZSM-5 zeolite [92].

9.12.3
Overlapping Signals

Owing to the inherently heterogeneous nature of catalysts, it is rather unusual to deal with only one type of surface species. The resultant overlapping signals can be disentangled by recording the EPR spectra at different microwave frequencies and power or by studying the thermal behavior and stability of the species involved, including response to various chemical perturbations (such as interactions with probe molecules) [7, 15, 51].

Simple recording of EPR spectra at two frequencies (usually X and Q), pioneered by Bray and Vanngard [93], is often sufficient to discriminate between the overlapping signals due to surface and bulk species. It has been used, for instance, in the case of superimposed EPR signals of vanadium(IV) and molybdenum(V) centers in $H_4PVMo_{11}O_{40}$ heteropolyacids (Figure 9.27) [47], and to distinguish the spectral features of surface V(IV) and bulk Zr(III) in a zirconia-supported vanadia catalyst [88].

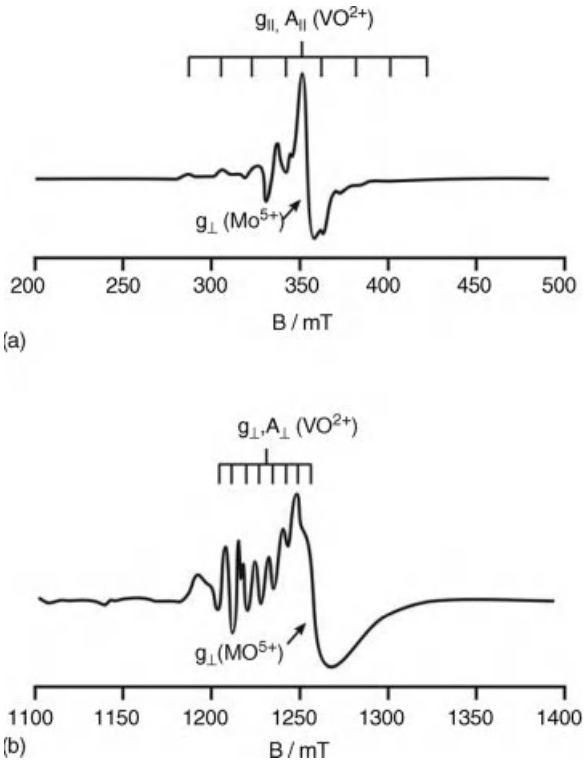


Figure 9.27 Separation of the overlapping signals due to VO^{2+} and Mo^{5+} by means of multifrequency EPR measurements: X-band spectrum (a) and Q-band spectrum (b) (adapted from [47]).

Partial saturation of one signal to reveal the presence of another may be used if they exhibit sufficiently distinct relaxation times. This technique has been used, for example, to distinguish between the paramagnetic F_s^+ centers ($g_{||} = 2.0014$, $g_\perp = 2.0003$), Li_3^{2+} clusters ($g = 2.0011$), and Li metal particles ($g = 2.0013$) formed upon contacting MgO with lithium vapor [94].

A chemical method of dealing with the overlapping signals consists in separate identification of the paramagnetic centers involved, which give rise to the observed complex spectrum in separate model experiments. By finding specific conditions where the centers appear independently or prevail in the spectrum, sorting out the contributing species becomes a question of the appropriate chemical manipulations. As a result, the reliability of computer simulation of multicomponent spectra can be substantially enhanced, because the contributing signals extracted from the best fit can be confronted with their counterparts revealed in the model studies. Such a method has been used to analyze the EPR spectra of various V^{4+} entities present in alkali metal-doped vanadium oxide supported on ZrO_2, where four superimposed components assigned to the isolated ($g_{||} = 1.923$, $g_\perp = 1.976$, $|A_{||}| = 18.5$, $|A_\perp| = 6.4$ mT) and clustered ($g_{||} = 1.947$, $g_\perp = 1.974$) surface VO^{2+} species, bulk V^{4+} ions ($g_1 = 1.889$, $g_2 = 1.977$, $g_3 = 1.942$, $|A_1| = 15.9$, $|A_2| = 6.7$, $|A_3| = 1.5$ mT) and matrix defect Zr^{3+} ($g_{||} = 1.980$, $g_\perp = 1.969$) have been revealed [84].

9.12.4
Strain Broadening and Smearing of Features with High Angular Anisotropy

Resolution enhancement at high frequencies is possible only when the contribution of *g*-strain to the linewidth is small [95]. Paramagnetic centers with considerable **g** tensor anisotropy, which is sensitive to the local environment, are more likely to exhibit pronounced *g*-strain broadening in heterogeneous systems. If such effects are already apparent at lower frequencies (X-band), most probably little or no resolution enhancement can be expected at high frequencies. An example is given by an X- and Q-band study of MoO_x/SiO_2 catalyst, in which upon passing to the higher frequency the resolution of the spectrum was lost completely [96]. Indeed, the appearance of a broad unstructured EPR signal indicates that the enhanced *g*-anisotropy could not overtake the strain effects. Surface complexes formed upon contact of $P(C_2H_5)_3$ with silica-supported Ni^I ions provide another case of the appearance of such a phenomenon. Whereas in the X-band the linewidths are small enough to allow determination of the ^{31}P superhyperfine structure, in the Q-band the ^{31}P splitting remains unresolved due to the increased inhomogeneous broadening caused by the *g*-strain [97]. It should be noted that in the case of marked *g*-strain, the resolution of hyperfine structure can also be enhanced upon decreasing the microwave frequency to the L- or S-band [95]. This line narrowing has been exploited for studying the ligation of copper to polymeric matrices [98].

The *g*-strain is often correlated with *A*-strain, reflecting local microheterogeneity of the sites. Such a situation is typically encountered in the case of hydrated transition metal ions exchanged into zeolites, leading to a pronounced M_I dependence of

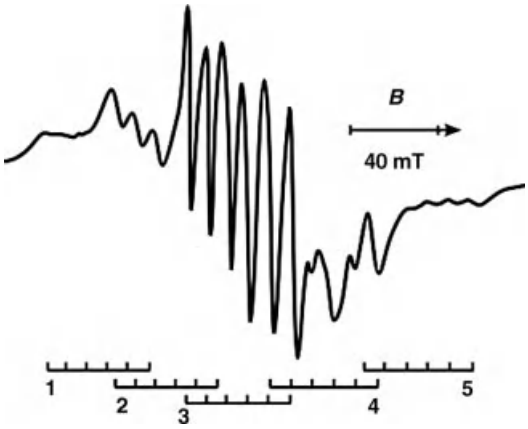


Figure 9.28 X-band EPR spectrum of hydrated MnK-A zeolite (0.1 wt% Mn) showing smearing of the outer lines. The stick diagram corresponds to the following transitions: $M_S = \pm 5/2 \leftrightarrow \pm 3/2$ (1 and 5), $M_S = \pm 3/2 \leftrightarrow \pm 1/2$ (2 and 4), $M_S = +1/2 \leftrightarrow -1/2$ (3). Adapted from [100].

the hyperfine linewidths. Here EPR studies on copper zeolites provide a classic example [99]. The strain values for Cu-mordenite and Cu-Y specimens are significantly larger than those observed for ZSM-5 and BEA zeolites. The analysis of the correlated *g*- and *A*-strains is not only a necessary condition for correct determination of the EPR parameters, but also provides a valuable insight into the heterogeneity of the sites in hydrated and dehydrated states.

In powder environments, for the systems with $S > 1/2$, large and nonuniform distortions together with pronounced angular anisotropy of the resonant fields associated with the fine structure lines result in EPR signals covering several hundreds of mT. Depending on the M_S value, they may often be totally or partially smeared out below the detection limit, in contrast to those species with an effective spin $S = 1/2$ [100]. This phenomenon is illustrated in Figure 9.28 for Mn ions dispersed in A zeolites, where central $M_S = -1/2 \leftrightarrow M_S = 1/2$ transitions exhibiting small angular variations are clearly resolved, whereas the remaining lines ($M_S = \pm 3/2 \leftrightarrow \pm 1/2$, $M_S = \pm 5/2 \leftrightarrow \pm 3/2$) with strong angular dependence are progressively smeared out.

9.12.5
Use of Probe Molecules and Spin Labels

The applicability of EPR for examining catalytic surfaces may be extended considerably by using probe molecules [5, 32]. Following Sojka and Che [15], the probe molecules can be classified as spin probes used for studying diamagnetic centers [101], coordination and space-filling probes used for exploring the local arrangement of surface transition metal ions [6, 15, 32], and spin traps for revealing paramagnetic short-lived intermediates [49, 102]. Most of the probe molecules

interact with the investigated centers via Lewis acid–base interactions; however, in the case of redox probes (discussed in the next section), electron exchange between the active center and the probe molecule take place [13, 103].

When speciation of the surface active centers complicates the analysis of EPR spectra, adsorption of σ-type donor probe molecules with magnetic ($I \neq 0$) and nonmagnetic ($I = 0$) nuclei such as H_2O [90], CH_3OH [104], and ^{13}CO [34] may be recommended. Whereas water and methanol provide information on the coordinative unsaturation of the metal centers via $\boldsymbol{g}$ tensor changes, adsorption of ^{13}CO probe may lead to a diagnostic superhyperfine structure. Counting of vacancies in the coordination sphere with ^{13}CO is particularly efficient for transition metal sites with $I = 0$ and the unpaired electron localized on $3d_\sigma$ orbitals. They allow for sizable interaction with the donor pair of the ^{13}CO probe. The resultant superhyperfine coupling is usually large enough (2.0–5.0 mT) to be resolved, and counting of the ligated CO molecules is usually straightforward. For centers with a $3d_\pi$ ground state, due to the mismatch between the metal d_π and the σ-donor orbitals of the ligand, the superhyperfine splitting is much smaller (0.4–0.75 mT), and often remains unresolved [105]. However, in favorable cases, it can be revealed by using a third-derivative recording [7, 34].

For exploring vacancies in the coordination sphere of surface transition metal ions, alkylphosphine probes with larger atomic hyperfine values of ^{31}P ($A^\circ_{iso} = 364$ mT, $A^\circ_{aniso} = 20.6$ mT) than those of ^{13}C ($A^\circ_{iso} = 113$ mT, $A^\circ_{aniso} = 6.6$ mT) can be used. These probes have been applied to identify tetracoordinated surface molybdenum species grafted on silica, in the presence of dominant hexa- and pentacoordinated Mo (V) [32] and Ni(I) [106] complexes.

Surface Lewis acid–base centers can be monitored by EPR using nitroxide probes. The nitroxide group $>N^\bullet–O:$, acting as a Lewis base, binds to surface electron acceptor sites A through the oxygen lone pair ($>N^\bullet–O: + A \rightarrow >N^\bullet–O:A$). This gives rise to redistribution of the spin density within the N–O moiety and modification of the ^{14}N hyperfine splitting. It is shown that the value of $^{N}A_{||}$ varies monotonically with the strengths of the surface Lewis acid centers, providing a rational basis for the measurements [6, 107]. Lewis acidity can also be characterized with the NO molecule as a probe and an example is given by ZSM-5 zeolite [108].

To identify short-lived intermediates appearing in catalytic reactions, a spin trapping technique can be applied. The method rests on the reaction between the investigated radical $R^\bullet$ and a diamagnetic spin trap T to produce a radical adduct $(R–T)^\bullet$ that is stable enough to be observed by EPR. The purity of the traps is here of crucial importance. Analysis of the spectrum due to the resultant adduct [usually based on hyperfine patterns of nitrogen (a_N) and β- and γ-hydrogen ($a_H^{\beta,\gamma}$)] allows for indirect identification of the elusive radical $R^\bullet$. Using α-phenyl-*N*-*tert*-butylnitrone as a spin trap, radicals formed during propylene oxidation over bismuth molybdate catalyst were detected [49]. The other prominent examples include trapping of the $OH^\bullet$ and $HO_2^\bullet$ intermediates produced in the photocatalytic decomposition of water [109] and the study of the spillover of hydrogen on the surface of $Pd/\gamma\text{-}Al_2O_3$ catalyst during hydrogenation of ethylene [102].

9.13
Interfacial and Surface Charge-Transfer Processes

Catalytic reactions proceeding according to a redox mechanism are intimately associated with the elementary steps involving interfacial charge-transfer events between the active sites and the reactant molecules, and/or surface charge transfer between the intermediates and the intact coadsorbed reactants. The radical transient species stabilized on the surface or escaping into the gas phase that are often produced in such processes can be detected by EPR using the appropriate experimental setups described in Section 9.14. For oxide catalytic systems, the following generic charge-transfer processes can be formulated:

(a) nondissociative surface electron transfer:

$$M^{n+}{}_{surf} + XY \rightarrow M^{(n\pm1)+}{}_{surf} + {}^{\bullet}XY^{\mp}$$

(b) dissociative surface electron transfer:

$$M^{n+}{}_{surf} + XY \rightarrow M^{(n\pm1)+}{}_{surf} + X + {}^{\bullet}Y^{\mp}$$

(c) heterolytic dissociation of adsorbed reactant/probe molecule coupled with surface intermolecular electron transfer (SIET):

$$R{-}H + M^{n+}{-}O^{2-} \rightarrow R^{-}{-}M^{n+} + OH^{-}$$
$$R^{-} + X \rightarrow {}^{\bullet}R + X^{-}$$

(M^{n+} and O^{2-} are the constituent ions of the oxide surface).

Because in such processes paramagnetic species are produced, spin changes monitored with EPR techniques can be regarded as a sensitive tracer of the occuring events. Moreover, by using a series of probe molecules of specified electron donor (D) or electron acceptor (A) properties, the strength and concentration of surface donor/acceptor centers (S) can be assessed by means of the quantitative EPR measurements, provided that the charge-transfer process can be described exclusively by the following reactions: $S + A \rightarrow S^{+} + A^{-}$ and $S + D \rightarrow S^{-} + D^{+}$ (see below). In addition to the most common transition metal sites, surface hydroxyl groups OH^{-} or exposed O^{2-} anions of low coordination are believed to act as electron donor centers also. Some organic molecules of low ionization potential, such as perylene, anthracene, and naphthalene, and of high electron affinity, such as nitrobenzene and tetracyanoethylene, have been the most frequently used as suitable probes in such investigations [110].

Nondissociative electron transfer is most often observed when dioxygen or nitric oxide is contacted with transition metal ions dispersed on oxides. Examples are provided by variable-temperature interaction of dioxygen with the surface of dilute CoO–MgO solid solutions [36] or MoO_x/SiO_2 catalysts [6] and by NO adsorption on Ni/SiO_2 [111]. The dissociative electron transfer between N_2O and Mo^{5+} centers was

investigated in detail by EPR with MoO_x/SiO_2 catalysts [35], leading to the formation of O^- species bound to the molybdenum complex O^-–$Mo_{4c}{}^{6+}$ ($g_\perp = 2.020$, $g_{||} = 2.005$, $^{Mo}A_\perp = 0.67$, $^{Mo}A_{||} = 0.78$ mT) and N_2 release.

The heterolytic dissociation of the adsorbed reactant coupled with SIET is observed when the aromatic or olefinic organic molecules are adsorbed on Lewis acid–base oxide surfaces such as silica–alumina, alumina, and alkaline earth metal oxides [7, 110]. Since upon adsorption the radical products were observed by EPR, their appearance was interpreted in the past in terms of a simple electron transfer between the surface donor/acceptor centers and the intact organic admolecule. However, more detailed spectroscopic investigations using several techniques jointly (EPR, UV–visible, and IR spectroscopy) show that the actual process is more involved and includes heterolytic splitting of the H–R bond on the surface Lewis acid (M^{z+}) – Lewis base (O^{2-}) pairs, followed by electron transfer between the resultant R^- anion and the coadsorbed electrophilic RH molecule (SIET) [112]. Therefore, due to the intermingling of the electron-pair donor/acceptor processes (acid–base reactivity) with the one-electron donor/acceptor processes (redox reactivity), special care is needed in the interpretation of such results in terms of a single surface-electron transfer only. On this basis, it seems that some of the data available in the literature on direct surface charge transfer towards relatively large organic molecules are probably misinterpreted.

9.14
In Situ and *Operando* EPR Techniques

Despite the progress made since the pioneering work of Lunsford and co-workers [113, 114] and some later developments [115–118], investigations of catalytic reaction mechanisms by EPR cannot be performed on a routine basis for an arbitrary catalytic system. This is largely due to the inherent limitations of the EPR techniques, such as exclusive sensitivity to the reaction steps involving paramagnetic species, differences in the optimal temperatures for spectra recording ($T < 300$ K at best) and for performing catalytic reactions (usually $T >$ few hundred K). Further restrictions are imposed by the use of the resonant cavities and space confinement within the electromagnet gap.

Nonetheless, in favorable cases when those constraints can be circumvented, catalytic reactions can be investigated in real or more likely quasi-real conditions provided that the relevant EPR signals are detectable at the reaction temperatures [115, 117]. The EPR catalytic studies may consist of a post mortem analysis of the quenched samples [84, 119], *in situ* measurements including full *operando* conditions (i.e., simultaneous spectroscopic and reactivity measurements) [115, 116], or investigations employing external flow microreactors in tandem with matrix isolation devices for trapping intermediates that escape from the surface [113]. The variety of the experimental devices developed for catalytic measurements include thermally shielded microreactors placed in a normal EPR cavity [120, 121], flow reaction cells inserted into a high-temperature cavity [24, 117, 122], and photocells for

in situ studies of photocatalytic processes [123, 124]. For spin trapping, the MIESR (matrix-isolated electron spin resonance) method developed by Lunsford and co-workers [113, 114] and the KRFM (kinetic radical freezing method) are the most common [125]. In the case of radical reactions occurring at conventional temperatures, commercially available variable-temperature EPR units may also be used successfully. For EPR *operando* investigations combined with UV–visible and Raman spectroscopy, a fixed-bed flow reactor, heated with a bifilar Pt winding and equipped with fiber-optic sensors, has been described [115]. Recently, this multi-technique approach was successfully extended to Q-band measurements [47]. Figure 9.29 shows the design of selected experimental devices and solutions used for the reactivity investigations by EPR in flow conditions, and selected applications are collated in Table 9.6.

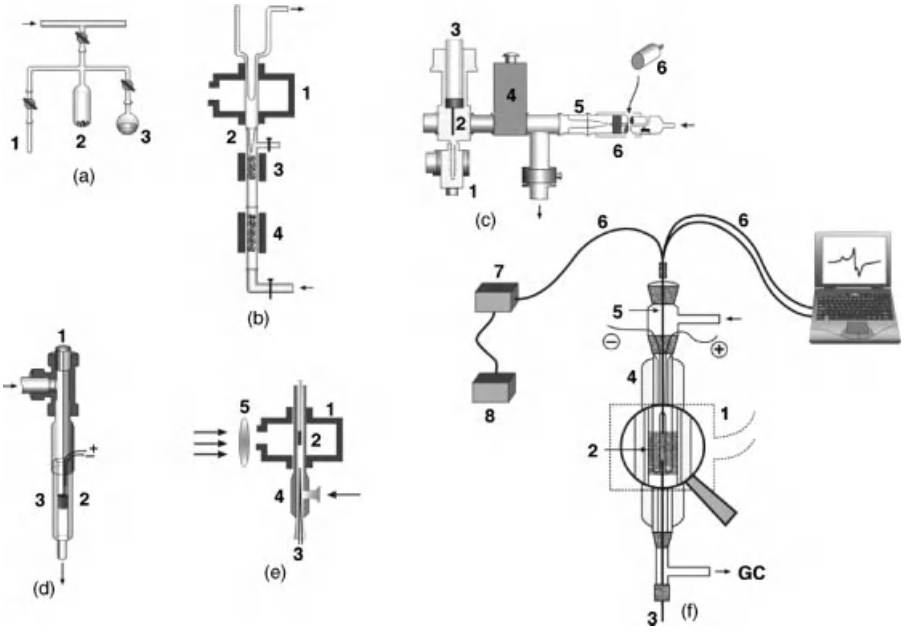


Figure 9.29 Selected experimental setups used for EPR investigations of catalytic reactions. (a) Apparatus used for EPR investigations with the spin trapping method (1, EPR tube; 2, catalyst; 3, spin trap solution). (b) KRFM setup used in the matrix isolation method (1, cavity; 2 capillary leak; 3, reactor; 4, heating unit). Adapted from [125]. (c) MIESR device (1, cavity; 2, sapphire rod; 3, vacuum shroud; 4, gate valve; 5, capillary leak; 6, catalyst). Adapted from [114]. (d) Microreactor for *in situ* studies (1, thermocouple; 2, Pt heating wires; 3, catalyst). Adapted from [117]. (e) Photocatalytic cell (1, cavity; 2, EPR tube; 3, thermocouple; 4, variable-temperature Dewar insert; 5, lens). Adapted from [124]. (f) *Operando* setup (1, cavity; 2, catalyst bed; 3, thermocouple; 4, quartz reactor with Dewar wall; 5, UV probe; 6, fiber optics; 7, UV source; 8, power supply). Adapted from [102] Adapted from [115].

Table 9.6 Selected applications of EPR techniques in catalysis research.

Experiment	Catalyst	Reaction	Results	Ref.
Post mortem	A–V_2O_5/ZrO_2, A = Li, Na, K	C_3H_8 oxidation	Speciation, structure and abundance of surface and bulk V^{4+} species, role of alkali metal promoter	[84]
	WO_3–ZrO_2	1-Butene isomerization	Identification of W^{4+}/W^{5+} active sites and O_2^- intermediates	[126]
Ex situ				
Model studies	MoO_x/SiO_2	CH_3OH oxidation	Determination of O^-–$Mo_{4c}{}^{5+}$ active sites, $^{\bullet}CH_2OH$ intermediates, and evaluation of reaction mechanism	[104]
	MoO_3	Reduction by C_3H_6 and $^{\bullet}C_3H_5$	Anisotropy of surface redox processes, spillover of allyl radical intermediates	[127]
Selective poisoning with H_2S	Al_2O_3	1-Butane isomerization	Identification of Lewis acid Al^{3+} active sites	[128]
Use of spin traps	Pd/Al_2O_3	Hydrogenation of C_2H_4	Reaction mechanism, hydrogen spillover, $^{\bullet}C_2H_5$ intermediates	[102]
KRFM	SiO_2, Al_2O_3	$CH_2O + O_2$	Quantification of radicals in gas phase	[125]
MIESR	Bi_2O_3	$C_3H_6 + O_2$	Determination of kinetic isotope effect k_H/k_D for allyl radicals	[129]
	$Mn/NaWO_4/SiO_2$	$CH_4 + O_2$	Quantification of $^{\bullet}CH_3$ intermediates, determination of active sites	[130]
	Li/MgO	$CH_4 + O_2$	Intermediates, discrimination between hetero- and homogeneous processes	[113]

(*Continued*)

Table 9.6 (*Continued*)

Experiment	Catalyst	Reaction	Results	Ref.
Quasi-*in situ*	Ni/SiO_2		Identification of $Ni^+O_{s2}(PEt_3)_n$ active sites and $(C_2H_4)_2$ Ni^+-$O_{s2}(PEt_3)_n$ intermediates	[97]
	Pd–Na, Ca–X	Dimerization of C_2H_4	Identification of Pd^+–C_2H_4 and Pd^+–C_4H_8 intermediates, reaction mechanism	[131]
In situ				
Using high-temperature cavity	V_2O_5–$M_2S_2O_7$	SO_2 oxidation	Identification of active sites and side processes	[120]
	CuH–ZSM-5	C_2H_6 oxidation	Quantification of square-planar Cu^{2+} sites	[121]
In situ photocell	RuO_2–$A_2TiO_6O_{13}$, A = Na, K, Rb, Cs	H_2O decomposition	Identification of O^- intermediates, evaluation of photoprocess efficiency	[132]
In situ microreactor studies	H-mordenite	Carbonization of C_2H_4	Determination of olefinic (>C = C<) and allylic (>C = C = C<) intermediates	[117]
	VPO, $(VO)_2P_2O_7$	Oxidation of *n*-C_4	Characterization of clustered V sites, evaluation of catalytic redox cycle	[25]
	V_2O_5–Fe_2O_3	Fluorene oxidation	Identification of Fe^{3+}–$V_O(e^-)$ active sites, evidence for reaction mechanism, evaluation of the mechanism from kinetics	[24]
	MoO_3–V_2O_5	Allyl alcohol oxidation	Studies, identification, and quantification of V^{4+}/V^{5+} redox-active sites	[122]
Operando EPR	VO_x/SiO_2, VO_x/Al_2O_3	Oxidative dehydrogenation of propane	Mechanistic studies	[115]

Adapted from [15].

9.15
Conclusions and Prospects

EPR spectroscopy is a nondestructive, powerful, and sensitive technique that can be fruitfully applied to investigations within the field of surface chemistry and catalysis. The method appears most efficient in characterizing active sites and reaction intermediates, and in monitoring the elementary processes occurring within the coordination sphere of surface transition metal ions. Judicious analysis of the spectra provides detailed information about the electronic structure and dynamic behavior of the investigated species. Various physical and chemical treatments can be used in different combinations to arrive at better resolution, information content, understanding, and interpretation of complex EPR spectra. New research perspectives have been opened by HF-EPR and pulse electron spin echo techniques (ESEEM, HYSCORE, ENDOR), and by the use of quantum chemical methods for calculations of spectral parameters and their in-depth molecular interpretation.

References

1 Adrian, F. (1968) *J. Colloid Interface Sci.*, **26**, 317–354.
2 Lunsford, J.H. (1972) *Adv. Catal.*, **22**, 265–344.
3 Che, M. and Giamello, E. (1990) *Stud. Surf. Sci. Catal.*, **12**, B265–B332.
4 Howe, R.F. (1993) *Colloids Surf. A*, **72**, 353–363.
5 Che, M. and Giamello, E. (1994) in *Catalyst Characterization: Physical Techniques for Solid Materials* (eds. B. Imelik and J.C. Vedrine), Plenum Press, New York, pp. 131–179.
6 Sojka, Z. (1995) *Catal. Rev. Sci. Eng.*, **37**, 461–512.
7 Dyrek, K. and Che, M. (1997) *Chem. Rev.*, **97**, 305–332.
8 Murphy, D.M. (2008) in *Metal Oxide Catalysis* (eds. J.S. Hargraves and S.D. Jackson), Wiley-VCH Verlag GmbH, Weinheim, pp. 1–50.
9 Brustolon, M. and Giamello, E. (eds.) (2009) *Electron Paramagnetic Resonance. A Practitioner's Toolkit*, John Wiley and Sons, Inc., Hoboken, NJ.
10 Wertz, J.E. and Bolton, J.R. (1986) *Electron Spin Resonance. Elementary Theory and Practical Applications*, Chapman and Hall, London.
11 Bencini, A. and Gatteschi, D. (1990) *Electron Paramagnetic Resonance of Exchange-Coupled Systems*, Springer, Berlin.
12 Murphy, D.M., Griffiths, E., Rowlands, C.C., Hancock, F.E., and Giamello, E. (1997) *Chem. Commun.*, 2177–2178.
13 Chiesa, M., Giamello, E., and Che, M. (2010) *Chem. Rev.*, **110**, 1320–1347.
14 Sojka, Z. and Che, M. (1999) *Colloids Surf. A*, **158**, 165–178.
15 Sojka, Z. and Che, M. (2001) *Appl. Magn. Reson.*, **20**, 433–456.
16 Mabbs, F.E. and Collison, D. (1992) *Electron Paramagnetic Resonance of d Transition Metal Compounds*, Elsevier, Amsterdam.
17 Rieger, P.H. (2007) *Electron Spin Resonance. Analysis and Interpretation*, RSC Publishing, Cambridge.
18 Yahiro, H., Lund, A., Aasa, R., Benetis, N.P., and Shiotani, M. (2000) *J. Phys. Chem. A*, **104**, 7950–7956.
19 Schäfer, K.O., Bittl, R., Zweygart, W., Lendzian, F., Haselhorst, G., Weyhermüller, T., Wieghardt, K., and Lubitz, W. (1998) *J. Am. Chem. Soc.*, **120**, 13104–13120.
20 Sands, R.H. and Dunham, W.R.Q. (1974) *Rev. Biophys.*, **7**, 443–504.

21 Bencini, A. and Gateschi, D. (1999) in *Inorganic Structure and Spectroscopy*, vol. 1 (eds. E.I. Solomon and B.P. Lever), John Wiley & Sons, Inc., New York, p. 93.

22 Aboukaïs A., Bennani, A., Aissi, C.F., Wrobel, G., Guelton, M., and Vedrine, J.C. (1992) *J. Chem. Soc., Faraday Trans. 1*, **88**, 615–620.

23 Eaton, S.S., More, K.M., Sawant, B.M., and Eaton, G.R. (1983) *J. Am. Chem. Soc.*, **105**, 6560–6567.

24 Brückner, A., Wolf, G.-U., Meisel, M., Stösser, R., and Mehner, H. (1994) *J. Chem. Soc., Faraday Trans.*, **90**, 3159–3165.

25 Brückner, A., Kubias, B., and Lücke, B. (1996) *Catal. Today*, **32**, 215–222.

26 Dyrek, K. and Labanowska, M. (1991) *J. Chem. Soc., Faraday Trans.*, **87**, 1003–1009.

27 Serwicka, E.M. (1990) *Crit. Rev. Surf. Chem.*, **1**, 27–69.

28 Cage, B., Hassan, A.K., Pardi, L., Krzystek, J., Brunel, L.C., and Dalal, N.S. (1997) *J. Magn. Reson.*, **124**, 495–498.

29 Ovchinnikov, V. and Konstantinov, V.N. (1979) *J. Magn. Reson.*, **32**, 179–190.

30 Chiesa, M., Giamello, E., Paganini, M.C., Sojka, Z., and Murphy, D. (2002) *J. Chem. Phys.*, **116**, 4266–4274.

31 Pilbrow, J.R. and Lowerey, M.R. (1980) *Rep. Prog. Phys.*, **43**, 433–495.

32 Sojka, Z., Adamski, A., and Che, M. (1996) *J. Mol. Catal.*, **112**, 469–482.

33 Sojka, Z., Che, M., and Giamello, E. (1997) *J. Phys. Chem. B*, **101**, 4831–4838.

34 Benneviot, L., Olivier, D., and Che, M. (1983) *J. Mol. Catal.*, **21**, 415–430.

35 Sojka, Z. and Che, M. (1996) *J. Phys. Chem.*, **100**, 14776–14785.

36 Sojka, Z., Giamello, E., Che, M., Zecchina, A., and Dyrek, K. (1988) *J. Phys. Chem.*, **92**, 1541–1547.

37 Pöppl, A., Rudolf, T., Manikandan, P., and Goldfarb, D. (2000) *J. Am. Chem. Soc.*, **122**, 10194–10200.

38 Sojka, Z., Chiesa, M., Paganini, M.C., and Giamello, E. (2001) *Stud. Surf. Sci. Catal.*, **140**, 413–420.

39 Atherton, N.M. (1973) *Electron Spin Resonance*, John Wiley & Sons, Inc., New York.

40 Freed, J.H. (1972) *Annu. Rev. Phys. Chem.*, **23**, 265–310.

41 Budil, D.E., Lee, S., Saxena, S., and Freed, J.H. (1996) *J. Magn. Reson. A*, **120**, 155–189.

42 Stoll, S. and Schweiger, A. (2006) *J. Magn. Reson.*, **178**, 42–55.

43 Chamulitrat, W. and Kevan, L. (1985) *J. Phys. Chem.*, **89**, 4989–4993.

44 Kazusaka, A., Yong, L.K., and Howe, R.F. (1978) *Chem. Phys. Lett.*, **57**, 592–595.

45 Shiotani, M., Moro, G., and Freed, J.H. (1981) *J. Chem. Phys.*, **74**, 2616–2640.

46 Biglino, D., Li, H., Erickson, R., Lund, A., Yahiro, H., and Shiotani, M. (1999) *Phys. Chem. Chem. Phys.*, **1**, 2887–2896.

47 Stösser, R., Marx, U., Herrmann, W., Jabor, J.K., and Brückner, A. (2010) *J. Am. Chem. Soc.*, **132**, 9873–9880.

48 Bassetti, V., Burlamacchi, L., and Martini, G. (1979) *J. Am. Chem. Soc.*, **101**, 5471–5477.

49 Howe, R.F. (1982) *Adv. Colloid Interface Sci.*, **18**, 1–55.

50 Dyrek, K., Adamski, A., and Sojka, Z. (1998) *Spectrochim. Acta Part A*, **54**, 2337–2348.

51 Che, M. and Ben Taarit, Y. (1985) *Adv. Colloid Interface Sci.*, **23**, 179–213.

52 Pilbrow, J.R. (1990) *Transition Ion Electron Paramagnetic Resonance*, Clarendon Press, Oxford.

53 Aasa, R. and Vanngard, T. (1975) *J. Magn. Reson.*, **19**, 308–315.

54 Weil, J.A. (1999) *Mol. Phys. Rep.*, **26**, 11–24, and references therein.

55 Spałek, T., Pietrzyk, P., and Sojka, Z. (2005) *J. Chem. Inf. Model.*, **45**, 18–29.

56 Rieger, Ph.H. (1982) *J. Magn. Reson.*, **50**, 485–489.

57 Griffin, M., Muys, A., Noble, C., Wang, D., Eldershaw, C., Gates, K.E., Burrage, K., and Hanson, G.R. (1999) *Mol. Phys. Rep.*, **26**, 60.

58 Goodman, B.A. and Raynor, J.B. (1970) *J. Inorg. Nucl. Chem.*, **32**, 3406–3411.

59 Pinarello, G., Pisani, C., D'Ercole, A., Chiesa, M., Paganini, M.C., Giamello, E., and Diwald, O. (2001) *Surf. Sci.*, **494**, 95–110.

60 Rieger, Ph.H. (1997) *J. Magn. Reson.*, **124**, 140–146.

61 Atkins, P.W. and Symons, M.C.R. (1967) *The Structure of Inorganic Radicals*, Elsevier, Amsterdam.

62 Chiesa, M. and Giamello, E. (2007) *Chem. Eur. J.*, **13**, 1261–1267.

63 Munzarova, M. and Kaupp, M. (1999) *J. Phys. Chem. A*, **103**, 9966–9983.

64 Kaupp, M., Bühl, M., and Malkin, V.G. (eds.) (2004) *Calculation of NMR and EPR Parameters, Theory and Applications*, Wiley-VCH Verlag GmbH, Weinheim.

65 Carl, P.J., Isley, S., and Larsen, S.C. (2001) *J. Phys. Chem. A*, **105**, 4563–4573.

66 Neyman, K.M., Ganyuszin, D.I., Nasluzov, V.A., Roesch, N., Pöppl, A., and Hartman, M. (2003) *Phys. Chem. Chem. Phys.*, **5**, 2429–2434.

67 Chiesa, M., Paganini, M.C., Giamello, E., Di Valentin, C., and Pacchioni, G. (2003) *J. Mol. Catal. A*, **204**, 779–786.

68 Pietrzyk, P., Piskorz, W., Sojka, Z., and Broclawik, E. (2003) *J. Phys. Chem. B*, **107**, 6105–6113.

69 Pierloot, K., Delabie, A., Groothaert, M.H., and Schoonheydt, R.A. (2001) *Phys. Chem. Chem. Phys.*, **3**, 2174–2183.

70 Pietrzyk, P., Sojka, Z., Dzwigaj, S., and Che, M. (2007) *J. Am. Chem. Soc.*, **129**, 14174–14175.

71 Pietrzyk, P. and Sojka, Z. (2005) *Stud. Surf. Sci. Catal.*, **158**, 617–624.

72 Schreckenbach, G. and Ziegler, T. (1997) *J. Phys. Chem. A*, **101**, 3388–3399.

73 McGarvey, B.R., Ferro, A.A., Tfouni, E., Bezerra, C.W.B., Bagatin, I., and Franco, D.W. (2000) *Inorg. Chem.*, **39**, 3577–3581.

74 Dikanov, S.A. and Tsvetkov, Yu.D. (1992) *Electron Spin Echo Envelope Modulation (ESEEM) Specroscopy*, CRC Press, Boca Raton, FL.

75 Höfer, P., Grupp, A., Nebenführ, G., and Mehring, M. (1986) *Chem. Phys. Lett.*, **132**, 279–282.

76 Heming, M. (1987) *Z. Phys. Chem. N.F.*, **151**, 35.

77 Pöppl, A., Manikandan, P., Köhler, K., Maas, P., Strauch, P., Böttcher, R., and Goldfarb, D. (2001) *J. Am. Chem. Soc.*, **123**, 4577–4584.

78 Arieli, D., Vaughan, D.E.W., Strohmaier, K.G., Thomann, H., Bernardo, M., and Goldfarb, D. (1999) *Magn. Reson. Chem.*, **37**, 43–54.

79 Hartmann, M. and Kevan, L. (1999) *Chem. Rev.*, **99**, 635–663.

80 Ruthstein, S., Frydman, V., Kababya, S., Landau, M., and Goldfarb, D. (2003) *J. Phys. Chem. B.*, **107**, 1739–1748.

81 Maurelli, S., Ruszak, M., Witkowski, S., Pietrzyk, P., Chiesa, M., and Sojka, Z. (2010) *Phys. Chem. Chem. Phys.*, **12**, 10933–10941.

82 Chiesa, M., Meynen, V., Van Doorslaer, S., Cool, P., and Vansant, E.F. (2006) *J. Am. Chem. Soc.*, **128**, 8955–8963.

83 Schoonheydt, R.A. (1993) *Catal. Rev. Sci. Eng.*, **35**, 129–168.

84 Adamski, A., Sojka, Z., Dyrek, K., Che, M., Wendt, G., and Albrecht, S. (1999) *Langmuir*, **15**, 5733–5741.

85 Giamello, E., Paganini, M.C., Murphy, D.M., Ferrari, A.M., and Pacchioni, G. (1997) *J. Phys. Chem. B*, **101**, 971–982.

86 Stehlik, D. and Möbius, K. (1997) *Annu. Rev. Chem.*, **48**, 745–784.

87 Rudolf, T., Pöppl, A., Hofbauer, W., and Michel, D. (2001) *Phys. Chem. Chem. Phys.*, **3**, 2167–2173.

88 Adamski, A., Sojka, Z., Dyrek, K., and Che, M. (1999) *Solid State Ionics*, **117**, 113–122.

89 Dablemont, C., Hammaker, C., Thouvenot, R., Sojka, Z., Che, M., Maatta, E.A., and Proust, A. (2006) *Chem. Eur. J.*, **12**, 9150–9160.

90 Louis, C. and Che, M. (1987) *J. Phys. Chem.*, **91**, 2875–2883.

91 Che, M., Canosa, B., and Gonzalez-Elipe, A.R. (1986) *J. Phys. Chem.*, **90**, 618–621.

92 Pietrzyk, P., Sojka, Z., Gil, B., Datka, J., and Broclawik, E. (2002) *Stud. Surf. Sci. Catal.*, **142**, 453–460.

93 Bray, R.C. and Vanngard, T. (1966) *Biochem. J.*, **114**, 725–734.

94 Murphy, D., Giamello, E., and Zecchina, A. (1993) *J. Phys. Chem.*, **97**, 1739–1742.

95 Froncisz, W. and Hyde, J.S. (1980) *J. Chem. Phys.*, **73**, 3123–3131.

96 Che, M., McAteer, J.C., and Tench, A.J. (1978) *J. Chem. Soc., Faraday Trans. 1*, **74**, 2378–2384.

97 Lepetit, C., Kermarec, M., and Olivier, D. (1989) *J. Mol. Catal.*, **51**, 95–113.

98 Schlick, S., Alonso-Amigo, M.G., and Bednarek, J. (1993) *Colloids Surf. A*, **72**, 1–7.

99 Carl, P.J. and Larsen, S.C. (2000) *J. Phys. Chem. B*, **104**, 6568–6575.

100 De Vos, D.E., Weckhuysen, B.M., and Bein, T. (1996) *J. Am. Chem. Soc.*, **118**, 9615–9622.

101 Parenago, O.O., Pushkar, Yu.N., Turakulova, A.O., Muraveva, G.P., and Lunina, E.V. (1998) *Kinet. Catal.*, **39**, 268–273.

102 Carley, A.F., Edwards, H.A., Mile, B., Roberts, M.W., Rowlands, C., Hancock, F.E., and Jackson, S.D. (1994) *J. Chem. Soc., Faraday Trans.*, **90**, 3341–3346.

103 Pietrzyk, P. and Sojka, Z. (2007) *Stud. Surf. Sci. Catal.*, **171**, 27–65.

104 Sojka, Z. and Che, M. (1995) *J. Phys. Chem.*, **99**, 5418–5430.

105 Pietrzyk, P., Podolska, K., and Sojka, Z. (2008) *J. Phys. Chem. A*, **112**, 12208–12219.

106 Cai, F.X., Lepetit, C., Kermarec, M., and Olivier, D. (1987) *J. Mol. Catal.*, **43**, 93–116.

107 Cohen, A.H. and Hoffman, B.M. (1974) *Inorg. Chem.*, **13**, 1484–1491.

108 Gutsze, A., Plato, M., Karge, H.G., and Witzel, F. (1996) *J. Chem. Soc., Faraday Trans.*, **92**, 2495–2498.

109 Jaeger, C.D. and Bard, A.J. (1979) *J. Phys. Chem.*, **83**, 3146–3152.

110 Che, M., Olivier, D., Bonneviot, L., and Meriaudeau, P. (1998), in *Les Techniques Physiques d'Etude des Catalyseurs* (eds. B. Imelik and J.C. Vedrine), Editions Technip, Paris, pp. 231–292 (in French).

111 Sojka F Z., Pietrzyk, P., Martra, G., Kermarec, M., and Che, M. (2006) *Catal Today*, **114**, 154–161.

112 Anpo, M., Che, M., Fubini, B., Garrone, E., Giamello, E., and Paganini, M.C. (1999) *Top. Catal.*, **8**, 189.

113 Lunsford, J.H. (1987) *Catal. Sci. Technol.*, **8**, 227.

114 Driscoll, D.J., Campbell, K.D., and Lunsford, J.H. (1987) *Adv. Catal.*, **35**, 139–186.

115 Brückner, A. (2003) *Phys. Chem. Chem. Phys.*, **5**, 4461–4472.

116 Brückner, A. (2005) *Chem. Commun.*, **13**, 1761–1763.

117 Karge, H.G., Lange, J.P., Gutsze, A., and Łaniecki, M. (1988) *J. Catal.*, **114**, 144–152.

118 Kucherov, A.V., Gerlock, J.L., Jen, H.-W., and Shelef, M. (1995) *J. Catal.*, **152**, 63–69.

119 Pietrzyk, P. and Sojka, Z. (2007) *Chem. Commun.*, 1930–1932.

120 Lapina, O.B., Balzhinimaev, B.S., Boghosian, S., Eriksen, K.M., and Fehrmann, R. (1999) *Catal. Today*, **51**, 469–479.

121 Kucherov, A.V., Hubbard, C.P., Kucherova, T.N., and Shelef, M. (1997) *Kinet. Catal.*, **38**, 556–564.

122 Then Tai, N., Rozentuller, B.V., and Krylov, O.V. (1998) *Kinet. Catal.*, **39**, 392–399.

123 Inoue, Y., Kubokawa, T., and Sato, K. (1991) *J. Phys. Chem.*, **95**, 4059–4063.

124 Volodin, A.M., Sobolev, V.I., and Zhidomirov, G.M. (1998) *Kinet. Catal.*, **39**, 775–787.

125 Garibyan, T.A. and Margolis, Ya.L. (1989) *Catal. Rev. Sci. Eng.*, **31**, 355–384.

126 Yoshinaga, Y., Kudo, M., Hasegawa, S., and Okuhara, T. (1997) *Appl. Surf. Sci.*, **121/122**, 339–342.

127 Haber, J. and Serwicka, E.M. (1986) *Polyhedron*, **5**, 107–109.

128 Lunsford, J.H., Zingery, L.W., and Rosynek, M.P. (1975) *J. Catal.*, **38**, 179–188.

129 Driscoll, D.J. and Lunsford, J.H. (1983) *J. Phys. Chem.*, **87**, 301–303.

130 Pak, S., Qiu, P., and Lunsford, J.H. (1998) *J. Catal.*, **179**, 222–230.

131 Ghosh, A.K. and Kevan, L. (1988) *J. Phys. Chem.*, **92**, 4439–4446.

132 Ogura, S., Kohno, M., Sato, K., and Ionoue, Y. (1997) *Appl. Surf. Sci.*, **121/122**, 521–524.

10
Mössbauer Spectroscopy

Lorenzo Stievano and Friedrich E. Wagner

10.1
Introduction

More than 50 years have passed since the discovery of recoil-free nuclear gamma resonance in 1957 by R.L. Mössbauer, which is better known as the Mössbauer effect (ME). During the first few years after this discovery, one of the most remarkable events in modern physics (a sort of fairytale in science, a story of a young experimentalist serendipitously discovering and explaining a striking, previously unobserved effect, and being awarded a Nobel Prize just 3 years later [1]), research on the ME was mainly focused on understanding the physics behind it. At the same time, however, this phenomenon, at the borderline between nuclear and solid-state physics, was used as the basis to develop a fully autonomous spectroscopic method called Mössbauer spectroscopy (MbS).

MbS, also known as nuclear gamma resonance (NGR) spectroscopy, is a relatively sophisticated and sensitive technique yielding detailed information about the physicochemical state of atoms of selected elements. In particular, MbS provides unique and valuable information on oxidation states, magnetic hyperfine fields, coordination symmetry, and lattice vibrations. The outstanding feature of MbS is the extremely high accuracy in the analysis of the nuclear energy levels. In this way, MbS is able to measure the hyperfine interactions of the nuclei of a specific element with the surrounding environment.

Nowadays, the application of MbS has extended to many fields, from chemistry to metallurgy, from geology to biology, to the study of cultural heritage. One of the most remarkable recent applications of the ME is surely the extraterrestrial study of the soil on the surface of the planet Mars performed by the two rovers Spirit and Opportunity during the NASA Mars Exploration Rover Mission, which provided a great deal of information about the chemistry of Martian soils and also the final proof of the presence of liquid water in the past history of the red planet [2, 3].

In chemistry, the applications of MbS extend to many subjects, from structural studies of organometallic complexes to surface studies of the corrosion of metal surfaces, from solid-state reaction kinetics to spin crossover systems, from simple

Characterization of Solid Materials and Heterogeneous Catalysts: From Structure to Surface Reactivity, First Edition. Edited by Michel Che and Jacques C. Védrine.
© 2012 Wiley-VCH Verlag GmbH & Co. KGaA. Published 2012 by Wiley-VCH Verlag GmbH & Co. KGaA.

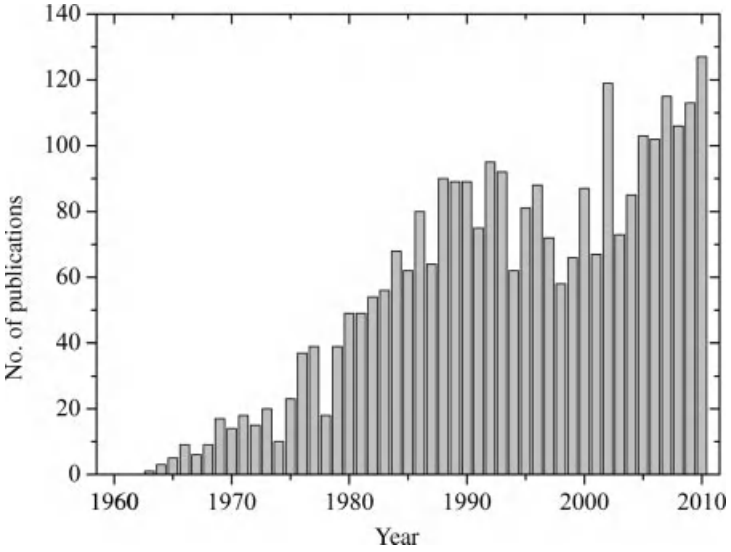


Figure 10.1 Number of indexed publications in the field of catalysis featuring Mössbauer spectroscopy up to 2010. Source: CAS, American Chemical Society.

application as a fingerprint technique to the study of the structure of heterogeneous catalysts. In the field of catalysis, for instance, the introduction of MbS started in the 1960s and, by the end of 2010, about 2900 scientific papers had been published (Figure 10.1), with a steady increase in the number of publications observed throughout the years.

Compared with other techniques, the applications of MbS have been relatively limited, mainly because only a few of the elements relevant in catalysis are suitable for Mössbauer studies. Among them, iron, tin, antimony, iridium, ruthenium, and gold are the most relevant Mössbauer elements in catalysis. However, only for iron and tin has the application of the ME been extensive, and most of the publications on catalysts deal with ^{57}Fe and ^{119}Sn MbS, the other elements mentioned above having been used only sporadically. This is mainly due to the low energies of the nuclear transitions for both ^{57}Fe and ^{119}Sn (and to some extent ^{121}Sb), which allow measurements at ambient temperature, and to the relatively long half-life of the respective ^{57}Co and ^{119m}Sn parent nuclides feeding the nuclear transitions, which allows the use of Mössbauer sources over many months. For elements such as iridium and gold, on the other hand, the high energy of the nuclear transitions allows measurements only at cryogenic temperatures, and the short half-life of the respective sources requires the vicinity of a nuclear reactor for frequent reactivation of the Mössbauer sources.

Most applications of MbS in heterogeneous catalysis concern the identification of phases, the determination of oxidation states, the attainment of structural information, the determination of particle sizes and the study of the kinetics of solid-state reactions. One of great advantages of MbS compared with other techniques is that it uses gamma radiation of high penetrating power such that the technique may be

applied *in situ*, or even under reaction conditions provided that the measurement temperature is not too high. A further advantage is that the technique is relatively inexpensive (more than one order of magnitude cheaper than photoelectron spectroscopy or electron microscopy, for instance). Finally, specific experimental setups of MbS make it also suited to the study of surfaces (with variable probing depths; see Section 10.6.2).

Several excellent books and book chapters devoted to MbS and on its application in these various field are available [4–14]. Such books have been used in this chapter as the source for the following general introduction to the Mössbauer technique. After an explanation of the theoretical background, the available experimental setups are described, and finally a few applications to the characterization of materials and more specifically to the study of heterogeneous catalysts are presented.

10.2
The Mössbauer Effect

The ME, that is, the recoil-free resonance absorption of γ-quanta emitted when a radioactive nuclide decays to a stable daughter nucleus, was discovered experimentally and explained theoretically by Mössbauer in 1957. His discovery is described in two papers published in 1958 [15, 16], and also in his Nobel Lecture presented in 1961 [17]. A radioactive isotope usually decays to the stable ground state of a daughter nuclide by passing through different excited states of the daughter. The transitions between the different excited states and from excited states to the ground state occur by the emission of electromagnetic radiation, that is, of photons which are usually called γ-quanta. Such photons may be reabsorbed by a nucleus of the same isotope by a process called resonance absorption, since the energy of the absorbed photon is just right for the excitation of the energy level in the absorbing nucleus, if the latter is of the same isotope as the emitting nucleus (Figure 10.2). However, this resonance

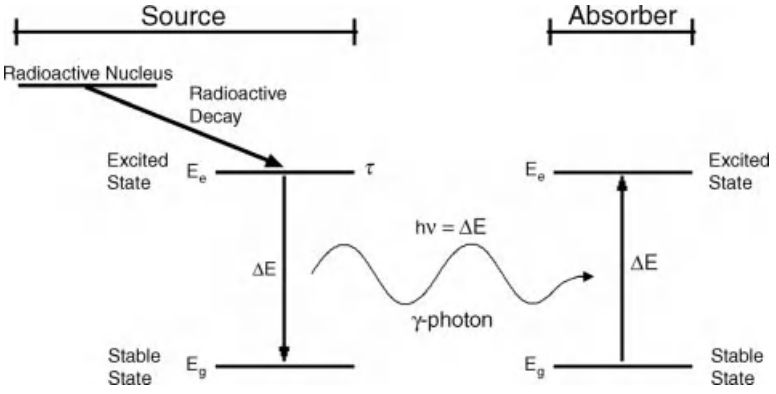


Figure 10.2 Schematic representation of the nuclear resonance transition between the excited and ground states in two nuclei of the same isotope in the source and the absorber.

adsorption phenomenon was very difficult to observe until the discovery of the suppression of recoil energy losses in solids by Mössbauer [15].

The main difficulty in the detection of the resonance absorption is that, due to the momentum carried by the emitted or absorbed photons, the nuclei are usually undergoing a recoil during the emission or the adsorption of γ-quanta. Since in the emission process the kinetic energy of the recoiling nucleus takes up some of the transition energy, the energy of the emitted photon is slightly lower than the energy required for resonance absorption. In fact, to be absorbed resonantly, the photon must even have a slightly higher energy than the resonance energy because some kinetic recoil energy is imparted to the absorbing nucleus. The recoil during emission or adsorption of electromagnetic radiation by atoms or subatomic particles is a general feature of emission and adsorption processes and it is common to all spectroscopic methods, but only for γ-rays is the energy high enough to preclude resonance absorption.

A photon with an energy E_γ has a momentum $P_\gamma = E_\gamma/c$, where c is the speed of light. In the case of a nuclear transition of an isolated nucleus at rest, momentum conservation requires that the decaying nucleus recoils with a momentum $P_n = -P_\gamma$ during the emission of the photon. The total energy of the nuclear transition E_0 must be therefore divided between the emitted photon and the nucleus that recoils with a energy E_R given by

$$E_R = \frac{P_n^2}{2M} = \frac{P_\gamma^2}{2M} = \frac{E_\lambda^2}{2Mc^2}$$

Because of the conservation of energy, the energy of the emitted photon is $E_\gamma = E_0 - E_R$. For the same reasons, for an isolated nucleus to absorb the γ-quantum, the energy of the absorbed photon must be $E_\gamma = E_0 - E_R$. Therefore, it follows that the energies of an emitted photon and a photon that can be absorbed are different by the quantity $2E_R$ (Figure 10.3).

In contrast to optical spectroscopy, where E_R is usually small compared with the linewidth, the recoil energy E_R of γ-rays is usually large compared with the natural widths of the nuclear levels. Therefore, in the common case of ^{57}Fe, the natural linewidth Γ of the emission and absorption line is about 5×10^{-9} eV, whereas the high energy of the 14.4 keV nuclear transition gives rise to a recoil energy of about 2×10^{-3} eV, which is about six orders of magnitude higher than the natural width of

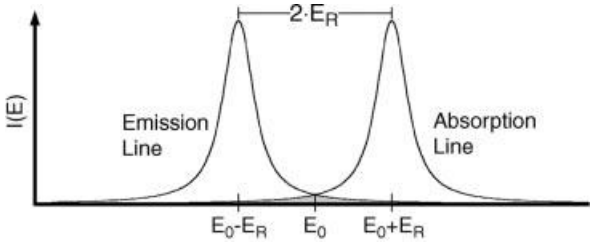


Figure 10.3 Consequences of the recoil effect caused by emission and absorption of photons in isolated nuclei.

the emission and adsorption line. It follows directly that the separation between the adsorption and the emission energies is far too large to allow the resonant adsorption of γ-quanta by free nuclei.

When embedded in a solid lattice, however, an atom cannot recoil as if it were free. The emission and absorption processes may, however, change the vibrational state of the lattice. Like vibrations and rotations of molecules, lattice vibrations are quantized and the quanta of such vibrations are called phonons. Because of the quantum mechanical nature of the lattice vibrations, there is a finite probability that an emission or absorption event takes place without a change in the vibrational state of the lattice and hence without exchange of recoil energy. The recoil momentum imparted to the nucleus, in this case, can be considered as being taken up by the whole crystal, which results in a negligibly small recoil energy E_R, because of the large mass of the crystal. The recoil-free emission and absorption of γ-quanta by nuclei in a solid is known as the ME. The probability of recoil-free emission or adsorption is known as the Lamb–Mössbauer *f*-factor. If a solid is described by the Debye model, it is given by

$$f(T) = \exp\left\{ -\frac{{E_\gamma}^2}{2M_{\text{eff}}c^2}\frac{3}{2k_B\theta_D}\left[1 + 4\left(\frac{T}{\theta_D}\right)\int_0^{\theta_D/T}\frac{x}{\exp x - 1}\,dx\right]\right\}$$

where θ_D is the Debye temperature ($k_B\theta_D$ corresponds to the maximum phonon energy of the crystal). It is worth noting that $f(T)$ decreases rapidly with increasing energy of the γ-photons and also with increasing temperature.

As an example, the dependence of the resonant fractions on the temperature for two relatively common Mössbauer isotopes, ^{57}Fe and ^{121}Sb, having a nuclear transition energy of 14.41 and 37.15 keV, respectively, is shown in Figure 10.4. These graphs indicate that a compound containing equal molar amounts of iron and antimony and characterized by a Debye temperature of 300 K (common values for inorganic compounds) can be easily studied at room temperature with ^{57}Fe (*f*-factor >0.5), whereas cooling to ~100 K is necessary to obtain the same resonance effect with ^{121}Sb.

An even stronger decrease in the *f*-factor is observed at higher transition energies, limiting the observation of the ME to isotopes having excited states at relatively low energies, in practice below ~100 keV. For energies exceeding ~20 keV, cooling below ambient temperature is usually required to obtain sufficiently high *f*-factors.

This effect limits the study of heterogeneous catalysts under reaction conditions by MbS, since most catalyzed reactions occur at temperatures considerably higher than ambient temperature, at which the measured *f*-factors are rather small, except perhaps for ^{57}Fe.

10.3
Radiation Source

The typical radiation source for MbS is a small quantity of a radioactive nuclide which, during its decay, passes through the excited state of the daughter isotope to be

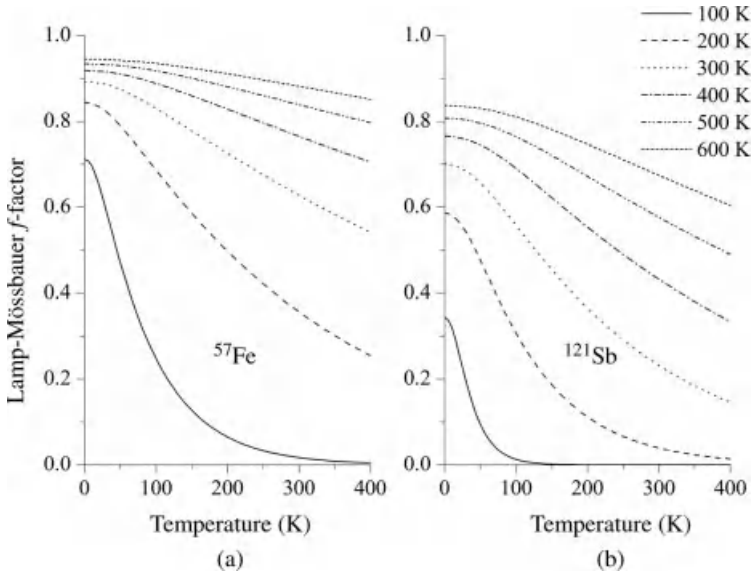


Figure 10.4 Variation of Lamb–Mössbauer *f*-factors (calculated using the Debye model) for (a) ^{57}Fe ($E_\gamma = 14.4$ keV) and (b) ^{121}Sb ($E_\gamma = 37.1$ keV) for increasing values of the Debye temperature (see legend).

studied, producing an intense beam of highly monochromatic recoil-free γ-photons. In the case of ^{57}Fe MbS, for instance, the ^{57}Fe excited state is populated by the electron capture decay of the radioactive isotope ^{57}Co (Figure 10.5). The latter has a half-life of 270 days and is commonly produced by bombarding ^{56}Fe nuclei with 9.5 MeV

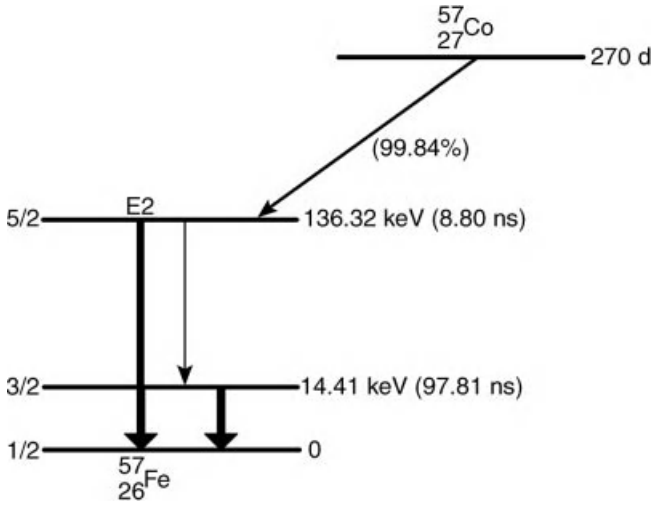


Figure 10.5 ^{57}Fe energy level diagram.

deuterons in a cyclotron following the reaction ^{56}Fe(d,n)^{57}Co. Owing to its relatively long half-life, a ^{57}Co Mössbauer source can often be used for several years.

In the absence of splittings caused by hyperfine interactions, the energy spectrum of the source usually has a Lorentzian lineshape:

$$I(E) \propto \frac{\Gamma^2/4}{\left(E_\gamma - E\right)^2 + \Gamma^2/4}$$

where E_γ is the average energy of the transition. The width at half-height of the emission line Γ depends on the average lifetime of the nuclear excited state τ and it follows from Heisenberg's uncertainty principle:

$$\Gamma = (h/2\pi)\tau^{-1}$$

Typical lifetimes of the excited state in the most common Mössbauer isotopes are in the range 1–100 ns, giving linewidths between roughly 10^{-7} and 10^{-9} eV. For ^{57}Fe, for instance, the excited state has a lifetime of about 140 ns, giving a natural linewidth of 4.7×10^{-9} eV.

In order to detect and measure the energy variations caused by the hyperfine interactions of the absorber nuclei with the surrounding chemical environment, it is necessary to scan a proper range of energies around the resonance energy. This is usually done by moving the source with respect to the absorber, and counting the number of photons passing through the absorber as a function of the relative velocity. When the source is moving with a velocity v relative to the absorber, the energy variation of the emitted γ-rays, E_D, produced by Doppler effect is:

$$E_D = \frac{v}{c} E_\gamma$$

In MbS, the energy scales are therefore conventionally reported in mm s^{-1} rather than in eV or other energy units. For the majority of the Mössbauer isotopes, velocities up to no more than about 30 mm s^{-1} are necessary to observe the effect of the different hyperfine interactions.

The following practical problems may limit the observation or the analytical utility of the ME for many elements:

1) The radioactive isotope used as the source must have a reasonably long half-life, be relatively abundant, and have an acceptable cost.
2) It must be embedded in a matrix of a "stiff" material (high Debye temperature), providing a high recoil-free fraction (Lamb–Mössbauer *f*-factor).
3) The matrix should not be damaged by radiochemical effects of the nuclear decay preceding the emission of the Mössbauer γ-rays.
4) The matrix should be cubic and non-magnetic to produce a single emission line, avoiding hyperfine splittings of the nuclear energy levels that would complicate data analysis.

The source isotopes of the Mössbauer transitions most commonly applied to the characterization of catalytic materials, together with their specific properties and their common preparation methods, are listed in Table 10.1. Nowadays, also due to

Table 10.1 Characteristics of the Mössbauer isotopes mostly used in the field of catalysis and common means of production of their sources.

Isotope	E_γ (keV)	Abundance[a] (%)	Γ[b] (mm s^{-1})	Popular parent	Half-life	Means of production	Host matrix
^{57}Fe	14.4	2.12	0.19	^{57}Co	270 d	^{56}Fe(d,n)^{57}Co	Rh, Pd
^{99}Ru	89.4	12.76	0.15	^{99}Rh	16 d	^{100}Ru(p,2n)^{99}Rh	Ru, Rh
^{119}Sn	23.9	8.58	0.64	^{119m}Sn	250 d	^{118}Sn(n,γ)^{119m}Sn	$CaSnO_3$
^{121}Sb	37.1	57.25	2.11	^{121m}Sn	76 y	^{120}Sn(n,γ)^{121m}Sn	$CaSnO_3$
^{193}Ir	73.0	62.70	0.60	^{193}Os	31 h	^{192}Os(n,γ)^{193}Os	Os
^{197}Au	77.3	100	1.88	^{197}Pt	18 h	^{196}Pt(n,γ)^{197}Pt	Pt

a) Natural isotopic abundance.
b) Natural linewidth of a Mössbauer spectrum, corresponding to twice the natural linewidth of the excited state.

the strict regulations on radiation protection, it is uncommon to produce Mössbauer source materials locally, except for specific isotopes with very short half-lives such as ^{193}Ir and ^{197}Pt. Most commonly, the preparation of Mössbauer sources is done only by specialized radiochemistry laboratories, and the Mössbauer sources are purchased from specialized firms.

10.4 Mössbauer Absorbers

Like the source, the Mössbauer absorber must normally be a solid, although it is sometimes possible to observe the ME also for highly viscous fluids. The absorber can be polycrystalline, a single crystal, or amorphous. In general, it is preferable to cool the absorber in order to increase the recoil-free fraction and minimize the data collection time, which can vary between a few hours and 1 week.

In any Mössbauer measurement it is desirable to work with as close to the ideal absorber thickness as possible in order to obtain the best signal-to-noise ratio in the minimum time. The ideal thickness of the Mössbauer absorber is often a compromise between placing a large amount of the Mössbauer active isotope in the absorber and at the same time keeping the attenuation of the γ-radiation by electronic effects (photoelectric absorption, Compton and Rayleigh scattering) low. Knowing the elemental composition of a sample, the ideal thickness may be estimated at a given Mössbauer γ-ray energy from available tables of mass absorption coefficients [18, 19]. Typical absorption effects are of several percent of the count rate off-resonance.

10.5 Hyperfine Interactions

The high-energy resolution of MbS spectroscopy allows the detection of the interactions between the nuclei and the electrons in a solid, and hence permits one to

obtain information on the chemical environment of the nuclei. These interactions, which are called hyperfine interactions, are as follows:

- the electric monopole interaction, which causes a shift of the resonance lines (*isomer shift*);
- the magnetic dipole interaction, which causes a Zeeman splitting of the Mössbauer line (*magnetic hyperfine splitting*);
- the electric quadrupole interaction, which also causes a splitting of the Mössbauer line (*electric quadrupole splitting*).

10.5.1
Electric Monopole Interaction

The electric monopole interaction causing the isomer shift is part of the Coulomb interaction between the nuclear charge distribution of finite size and the negatively charged s electrons. In the nonrelativistic approximation, the wavefunction of the s electrons, in fact, is the only wavefunction with nonzero amplitude at the nucleus, and therefore with nonzero probability density. The s electrons are therefore the only ones that sense the finite nuclear size. In fact, their binding energies become slightly less because of the finite nuclear size and, consequently, the total energy of an atom becomes slightly higher. Since the size of the nucleus in the excited state is slightly different from that in the ground state, the Coulomb interaction energies are also different (Figure 10.6).

The energy of the nuclear transition is therefore slightly changed because of the different binding energies of the s electrons in the ground and excited states. This energy change is largely the same in the source and the absorber and hence remains

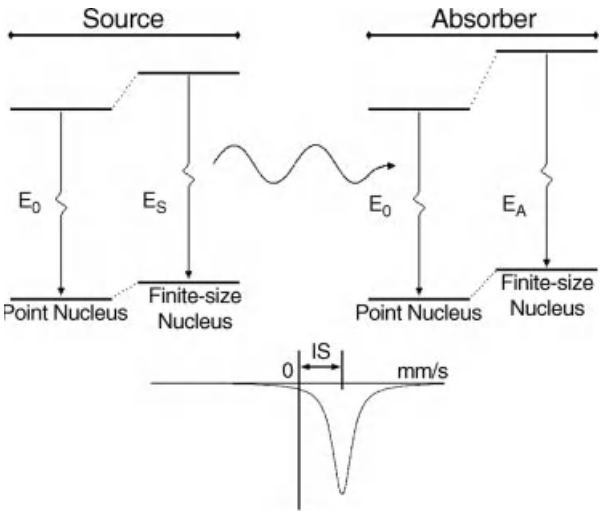


Figure 10.6 Interaction of the nuclear charge distribution with the s electron density in source and absorber.

largely unobserved in MbS. The s electron density at the nucleus is, however, dependent on chemical bonding and therefore usually different in the source and the absorber. Since chemical bonding affects mainly the valence s electrons, whereas the s electrons of the core contribute most to the total electron density at the nucleus, these energy differences are usually only a few parts in 10^4 of the total energy change due to the finite nuclear size. However, owing to the high-energy resolution of MbS, they can be measured fairly easily for many Mössbauer transitions.

Since the different transition energies in the source and the absorber must be made up by the Doppler effect in a Mössbauer experiment, they shift the Mössbauer pattern as a whole. This shift is called the isomer shift and is given by:

$$IS = \left(\frac{c}{E_0}\right)(E_A - E_S)$$

The isomer shift thus measures the variation of the electron density at the nucleus caused by a chemical environment different from that of the atoms in the source, and is expressed as:

$$IS = \left(\frac{c}{E_0}\right)\frac{2\pi Ze^2}{3}\Delta\langle r^2\rangle\left[|\Psi_A(0)|^2 - |\Psi_S(0)|^2\right]$$

where $\Delta\langle r^2\rangle$ is the difference of the average squared nuclear charge radii of the excited and ground states and $|\Psi_A(0)|^2 - |\Psi_S(0)|^2$ is the difference in the electron densities at the nucleus for the absorber and the source.

The isomer shift is then proportional to the product of a nuclear and of an electronic factor:

1) The nuclear $\Delta\langle r^2\rangle$ can be positive or negative because, depending on the nuclide, the nuclear radius of the excited state can be larger or smaller than that of the ground state.
2) The electronic factor $|\Psi_A(0)|^2 - |\Psi_S(0)|^2$ is caused by the s electrons at the nucleus, and as such will be affected not only by the s electron population in the valence shell, but also by the screening effects of p, d, and f electrons. Whatever the details may be in a specific case, the chemical bonding of the Mössbauer atom essentially affects the isomer shift, which therefore can be used to obtain information on chemical bonding.

Since the shift is present in both the source and the absorber, it is a relative quantity and as a consequence it is necessary to establish a reference material for the isomer shift for each Mössbauer isotope. This reference standard should be a common and stable material allowing easily reproducible measurements.

A shift of the Mössbauer line can also be caused by the relativistic Doppler effect, which gives rise to a temperature-dependent contribution due to the thermal motion of the individual atoms in both source and absorber. The frequency of oscillation around the mean position is of the order of $10^{13}\,s^{-1}$, so that the average velocity taken over the decay time of the Mössbauer state is zero. However, there is a relativistic term in the Doppler effect that depends on v^2, and the mean value $\langle v^2\rangle$ is nonzero. It can be

demonstrated [20] that this term causes a shift of the Mössbauer line called the second-order Doppler shift (SOD), given in velocity units as

$$\Delta\delta_{\mathrm{SOD}} = -\frac{\langle v^2 \rangle}{2c}$$

In the Debye model, the term $\langle v^2 \rangle$ depends both on the absolute temperature (T) and on the Debye temperature of the solid (θ_{D}) as follows [7]:

$$\langle v^2 \rangle = \frac{9}{8}\frac{k\theta_{\mathrm{D}}}{M_{\mathrm{eff}}} + 3\frac{kT}{M_{\mathrm{eff}}} f\left(\frac{T}{\theta_{\mathrm{D}}}\right)$$

where M_{eff} is the effective vibrating mass involved in the recoil process and $f(T/\theta_{\mathrm{D}})$ is given by

$$f\left(\frac{T}{\theta_{\mathrm{D}}}\right) = 3\left(\frac{T}{\theta_{\mathrm{D}}}\right)^3 \int_0^{\theta_{\mathrm{D}}/T} \frac{x^3 \mathrm{d}x}{\exp x - 1}$$

In the high-temperature limit ($T > \theta_{\mathrm{D}}$), this term can be approximated by the following expression, given in velocity units:

$$\Delta\delta_{\mathrm{SOD}} \approx -\frac{3k(T_{\mathrm{A}} - T_{\mathrm{S}})}{2M_{\mathrm{eff}}c}$$

where T_{S} and T_{A} are the temperatures of source and absorber, respectively. Therefore, if the source and absorber are kept at the same temperature, their SOD values virtually cancel each other.

If the source and absorber are kept at different temperatures, however, a relevant SOD may arise, and therefore one can derive the value of M_{eff} by analyzing the variation of the isomer shift of the absorber material measured at different temperatures. It is worth noting that the value of M_{eff}, which can be employed for instance to evaluate the Debye temperature of the absorber material from the temperature dependence of the recoil-free fraction (see Section 10.2), represents the effective vibrating mass involved in the recoil process, and may differ significantly from the mass of the studied Mössbauer isotope, especially in the case of covalent compounds [21, 22].

10.5.2
Magnetic Dipole Interaction

If present, a magnetic field $\boldsymbol{B}$ at the nucleus interacts with the nuclear magnetic dipole moment μ. This interaction lifts the degeneracy of the nuclear levels with spin I, producing $2 \cdot I + 1$ sublevels with energy

$$E_{\mathrm{m}} = -\frac{\mu B m_I}{I} = -g_{\mathrm{n}} B m_I$$

where the magnetic quantum number m_I assumes the values $I, I-1, \ldots, -I$, while the nuclear magnetic moment μ, the nuclear magneton μ_n, and the nuclear *g*-factor (g_n) are connected by the following relationship:

$$\mu = g_n \mu_n I$$

The magnetic field $\boldsymbol{B}$, therefore, splits the nuclear levels into equidistant nondegenerate substates, and the energy separation between the nuclear levels (ΔE) is directly proportional to $\boldsymbol{B}$.

The effective magnetic hyperfine field at the nucleus can be extremely high (over 50 T for ^{57}Fe). There are various sources that contribute to the effective hyperfine field, the most important of which are as follows:

1) The Fermi contact field, which arises from the net spin density of the s electrons at the site of the nucleus. This spin density may arise from polarization of the valence or conduction electrons, or indirectly by the polarization of filled s shells by unpaired d or f electrons.
2) A contribution from the orbital motion of valence electrons with a total orbital momentum quantum number *L*.
3) The spin-dipolar field, arising from the dipolar interaction of the nucleus with the total electron spin moment of the atom.

Any externally applied magnetic field adds vectorially to the effective magnetic hyperfine field at the nucleus.

From the previous description of the origin of the magnetic splitting, it might be assumed that all compounds containing unpaired valence electrons would show a hyperfine magnetic splitting effect. However, the observation time scale for magnetic hyperfine interactions of MbS is the Larmor precession time of the nuclear magnetic moment in the hyperfine field, which is usually of the order of nanoseconds. In paramagnetic compounds, the electronic spins that generate the magnetic hyperfine interaction are subject to changes of direction due to spin relaxation, and this spin relaxation is usually much faster than the observation time. The observed value for $\boldsymbol{B}$ is then the time average over the all directions, which is zero. Paramagnets, therefore, usually do not exhibit a magnetic hyperfine splitting, although some exceptions are found, for example, for the rare earths and for magnetically dilute solid solutions, where the spin relaxation may become very slow. On the other hand, static magnetic hyperfine fields usually arise when cooperative phenomena such as ferromagnetism or antiferromagnetism cause a spontaneous coupling of the electronic magnetic moments. There are also intermediate cases in which the paramagnetic spin relaxation occurs on a time scale comparable to the Larmor precession time of the nuclei. In these cases, broadened Mössbauer spectra are observed. In such cases, it is often possible to follow the development of the relaxation by changing the temperature of the measurement.

In ^{57}Fe, the magnetic hyperfine field lifts the degeneracy of both the 3/2 excited state and the 1/2 ground state, producing four and two nuclear energy levels, respectively. The selection rules ($\Delta m_I = 0, \pm 1$) allow only six of the eight possible

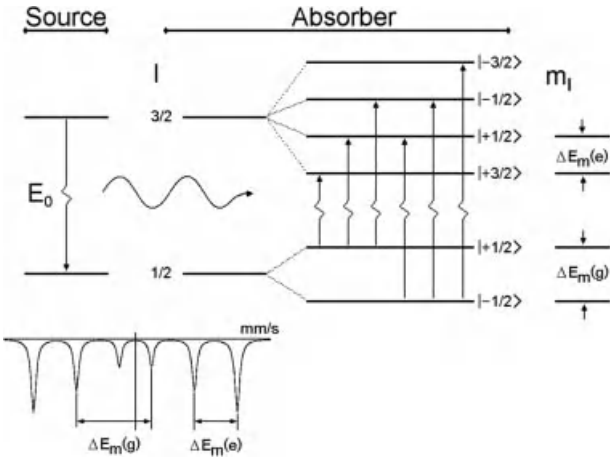


Figure 10.7 Magnetic splitting of the nuclear energy levels in ^{57}Fe.

transitions, determining a six-line pattern, as reported in Figure 10.7. The intensity of the different transitions is dependent on the angle between the direction in which the γ-rays propagate and the magnetic hyperfine field. The relative intensity is usually 3:0:1:1:0:3 if the directions of the photons and the field are parallel, and 3:4:1:1:4:3 if they are perpendicular. For the case of a randomly oriented polycrystalline material, the integration over all possible direction gives an intensity of ratio 3:2:1:1:2:3.

10.5.3
Electric Quadrupole Interaction

The interaction between the nuclear quadrupole moment (Q) and the electric field gradient (EFG) generated by the charge distribution of valence electrons and/or ligands in a chemical compound or, more generally, by the environment of the Mössbauer atom in a solid, produces the electric quadrupole splitting. In fact, any nucleus with a spin quantum number greater than 1/2 has a nonvanishing nuclear quadrupole moment which is caused by the nonspherical nuclear charge distribution. The electric quadrupole interaction removes the degeneracy of states with spin I producing $2I + 1$ levels if I is integer, or $I + 1/2$ sublevels if I is half-integer.

The EFG is a traceless tensor, and therefore in an appropriately chosen coordinate system it can be described by only two independent parameters, the principal component:

$$V_{zz} = \frac{\partial^2 V}{\partial z^2}$$

and the asymmetry parameter:

$$\eta = \frac{V_{xx} - V_{yy}}{V_{zz}}$$

where, by convention, the coordinates are chosen in such a way that $|V_{zz}| > |V_{xx}| > |V_{yy}|$. This choice assures that the asymmetry parameter takes only values between 0 and 1. The resulting Hamiltonian for the quadrupole interaction cannot be diagonalized in closed form except for a few specific cases, which include that nuclear spin $I = 3/2$. When the EFG has axial symmetry, that is, $V_{xx} = V_{yy}$ and $\eta = 0$, the expression for the quadrupole interaction reduces to a simple form for any value of I and the energy levels are given by the relation:

$$E_Q(m_i) = \frac{eQV_{zz}}{4/(2I-1)}\left[3{m_i}^2 - I(I+1)\right]$$

For ^{57}Fe and ^{119}Sn (Figure 10.8), the nuclear ground state has spin 1/2 whereas the nuclear excited state has spin 3/2. Whereas the 1/2 state does not split, the nuclear levels of the 3/2 state can be calculated analytically and also $\eta \neq 0$, and are given by:

$$E_Q = \pm\frac{eQV_{zz}}{4}\sqrt{1 + \frac{1}{3}\eta^2}$$

A similar situation is also observed for other nuclei, such as ^{193}Ir and ^{197}Au, which, in contrast to ^{57}Fe and ^{119}Sn, have an unsplit excited state with spin 1/2 and a split ground state with spin 3/2. In both cases, the resulting spectrum is again a

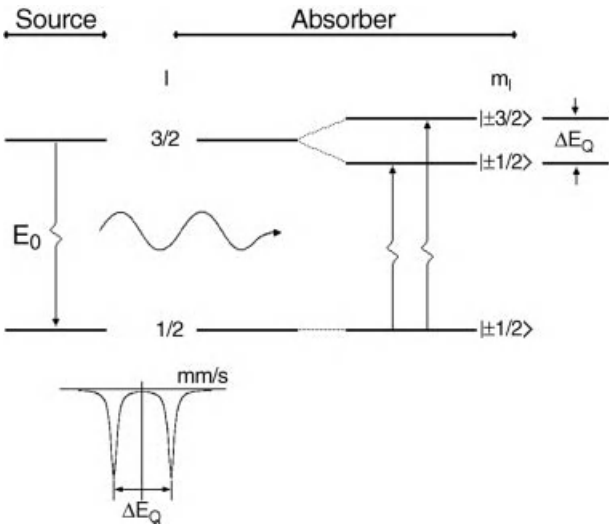


Figure 10.8 Quadrupole splitting of the nuclear energy levels for ^{57}Fe and ^{119}Sn. The scheme assumes that the source exhibits no quadrupole splitting, for example, because it consists of a material with a cubic crystal structure.

quadrupole doublet. The relative intensity of the two lines of the doublet depends on the angle formed by the direction of the principal axis of the electric field gradient and the direction of propagation of the γ-photon. For the common case of polycrystalline randomly oriented materials, the observed intensity is 1:1. For some materials, however, great care must be taken to make unoriented absorbers, that is, to remove any texture that may arise from the special shapes of the individual crystallites.

Sometimes, however, an asymmetry of the quadrupole doublets may be observed even in random polycrystalline materials. The reason for the different intensities of the two components of a quadrupole doublet is the occurrence of the so-called Goldanskii–Karyagin effect. This effect is due to the influence of a directional anisotropy of the Lamb–Mössbauer *f*-factor on the line intensities in the Mössbauer pattern. The Goldanskii–Karyagin effect, for instance, is fairly common in linear complexes of monovalent gold [23] and in divalent tin compounds [4]. The asymmetry due to vibrational anisotropy in polycrystalline materials, however, can sometimes be confused with the effects of a partial orientation of crystallites. These two effects can be distinguished only by measurements at different temperatures; in fact, while the texture effect does not change with the temperature of the measurement, the Goldanskii–Karyagin effect is often strongly temperature dependent.

10.6
Experimental Setups

10.6.1
Transmission Mössbauer Spectroscopy

A Mössbauer spectrum is substantially a plot of the number of photons transmitted through the absorber versus the photon energy given in terms of the instantaneous relative velocity of the source with respect to the absorber. This is obtained by using an electronic multichannel storage system synchronized to the motion of the source. This system, nowadays a simple dedicated computer card, stores the results during the acquisition of the Mössbauer spectrum. A block diagram of a typical Mössbauer apparatus is shown in Figure 10.9.

The function generator produces an electric signal with a specific waveform, which can be sinusoidal, triangular, or half-triangular (sawtooth). The selected waveform serves as a reference for the motion of the source through the desired velocity range with a frequency between 10 and 20 Hz. The movement of the source is obtained by an electromechanical transducer suitably regulated by a feedback system comparing the voltage from the pickup coil with the reference voltage and feeding the difference signal back to the driving coil of the transducer after suitable amplification.

In the simple transmission mode, that is, the common Mössbauer spectrometer, the γ-photons passing through the absorber are collected by a detector, usually a proportional counter, a scintillation counter, or a germanium diode depending on the energy range of the Mössbauer transition under investigation. The detector signals are amplified and discriminated in the region of interest with a single-channel

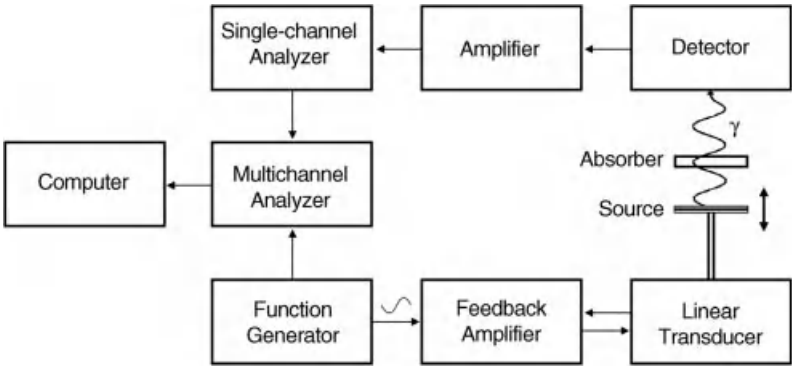


Figure 10.9 Schematic representation of a transmission Mössbauer spectrometer.

analyzer and finally stored in the multichannel acquisition card synchronized to the motion of the source. In order to obtain an acceptable definition, the spectrum is commonly acquired in 512 or 1024 channels.

10.6.2
Surface-Sensitive Mössbauer Spectroscopy

Transmission MbS is a bulk technique and therefore provides average information about the whole material and not about its surface, unless the material is finely divided into nanoparticles and has thus a significant surface atomic fraction. However, MbS can also be performed in alternative surface-sensitive modes. These techniques are based on the collection of the radiation emitted by the absorber after absorption of the γ-photons arriving from the source. In fact, the de-excitation of an excited nucleus can either occur by re-emission of a γ-photon or by internal conversion usually producing a cascade of conversion electrons, X-rays, and Auger electrons of different energies. For ^{57}Fe this is shown in Figure 10.10. The energy and nature of the collected radiation will then determine the probe depth. Three different techniques have been developed depending on which part of the re-emitted radiation detected and selected:

- **Backscattering Mössbauer Spectroscopy** (BSMbS): In BSMbS, the γ-ray and/or X-ray photons emitted by the absorber are collected by an appropriate detector positioned away from the beam direction of the source and discriminated via a single-channel analyzer. The probe depth of this technique depends directly on the energy of the selected radiation and on the composition of the absorber, but, owing to the relatively high energy of the measured radiation (from several to a few tens of keV), an order of magnitude of several tens of micrometers can be estimated for the probe depth. A well-known example of a BSMbS instrument is MIMOS-II, the Mössbauer spectrometer employed to study the composition of the soil on the surface of Mars [2, 3, 24].

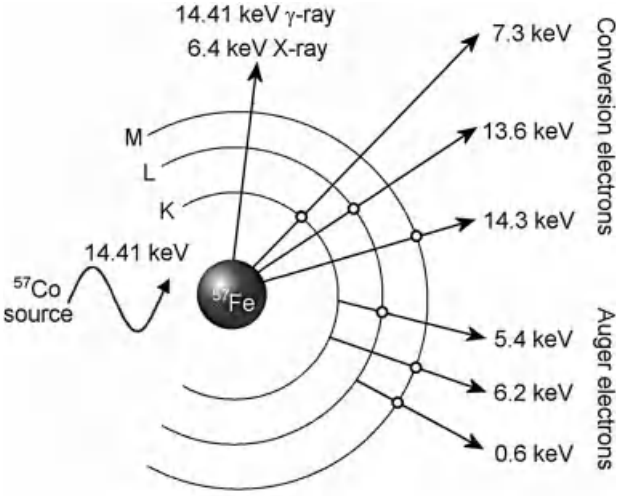


Figure 10.10 Possible decay paths of a ^{57}Fe nucleus after absorption of a 14.4 keV γ-photon.

- **Conversion Electron Mössbauer Spectroscopy (CEMbS):** In this technique, the sample is inserted into a gas-flow proportional counter under a specific gas atmosphere. The γ-rays from the source pass through the counting gas, a mixture of helium and methane, in which they are not noticeably absorbed. The electrons emitted from the sample after resonant absorption of the γ-rays are collected by a cathode filament held at high voltage and positioned over the sample. Alternatively, one can operate in a vacuum and use a channeltron as the electron detector. By energy discrimination of the collected electrons, one can obtain some depth resolution, since the mean free path of an electron in a solid depends on its kinetic energy. The selection of conversion and Auger electrons of different energies allows one to vary the probe depth from ∼100 to ∼10 nm, but this requires reasonably good energy resolution, which is provided only by magnetic or electrostatic electron spectrometers. With gas counters the success is limited.
- **Integral Low-Energy Electron Mössbauer Spectroscopy (ILEEMbS):** ILEEMbS can be considered as a variant of CEMbS, and is performed under vacuum using a channeltron as the detector and collecting only the low-energy electrons ($E_\gamma < 15$ eV). As a consequence of this low energy, the resulting probe depth is of only a few nanometers, very similar to that of photoelectron spectroscopy [25].

10.6.3
Emission Mössbauer Spectroscopy

This method is used to investigate the source element instead of the Mössbauer nuclei. It will work only if the nuclear decay does not induce chemical and structural modifications of the studied material. For instance, Co-containing materials can be

prepared with the radioactive ^{57}Co isotope, and used as Mössbauer sources against reference absorbers producing a single-line spectrum (e.g., stainless steel). Since the measured spectrum is that of a ^{57}Fe species obtained after the decay of ^{57}Co, it is necessary to measure the emission spectra of a large number of reference materials in order to interpret it. An example of the application of this technique is that of Co–Mo–S catalysts given later in Section 10.9.1.

10.7 Evaluation of Experimental Data

The interpretation of a Mössbauer spectrum involves several steps, from the preparation of the data to the least-squares fit of the resonance lines. These steps are summarized in the following paragraphs. For a more complete review of the methods used for data analysis, one can refer to the early publication of Stevens and Bowen [26] or to the already cited general books on MbS.

10.7.1 Spectra Folding

Once the spectrum has been collected using a symmetrical sinusoidal or a triangular source velocity mode, two mirror-symmetrical spectra are obtained. These spectra are commonly folded and added one to another around a folding point F in order to obtain the final Mössbauer spectrum. The folding point F is usually assigned to the point when the source is moving away from the absorber with its maximum velocity. Its true value is calculated using a trial and error method, by folding around different folding points and using the goodness of the match between the two mirror spectra after removal of the geometric effect produced by the variation of the solid angle between the moving source and the detector [7]. This process is usually performed automatically by all common commercial computer programs employed for the further treatment and fitting of the Mössbauer spectra.

10.7.2 Spectra Fitting

The absorption spectrum is generally represented by a superposition of several spectral lines, which can be combined in multiplets (doublets, sextets, etc.). These multiplets are characterized by the parameters typical of the hyperfine interactions producing them, that is, the isomer shift (δ), the quadrupole splitting (Δ), and the magnetic field (B). Each spectral line is characterized by an experimental width at half-height (Γ_{exp}), and, in the approximation of thin absorbers, has a Lorentzian shape. The experimental width, Γ_{exp}, is usually larger than the minimum value of 2Γ, where Γ is the natural linewidth of the source. Increasingly larger linewidths are obtained as the absorber thickness deviates from the thin absorber case. Finally, the total and relative intensities of the resonance lines are also important for identifying

specific multiplet shapes or for estimating the relative concentration of coexisting phases producing different subspectra.

These parameters are obtained by performing a best fit of the experimental data, optimizing appropriate combinations of Lorentzian lines by least-squares fit routines based on specific mathematical methods. These optimizations are commonly performed by commercial computer programs devoted to the treatment of Mössbauer spectra.

For example, in the case of the Marquardt–Levenberg algorithm, one of the most commonly used methods, the best fit is obtained by minimizing the function

$$\Phi(\boldsymbol{b}) = \sum_{i=1}^{N} \left[\frac{y_i - f(x_i; \boldsymbol{b})}{\Delta y_i} \right]^2$$

The components of the vector $\boldsymbol{b}$ are adjustable parameters of the function $f(x;\boldsymbol{b})$, which describes the spectral shape. The experimental data points are represented by the number of counts y_i obtained at velocities x_i. The quantity Δy_i is the standard deviation of the data points and is given by $(y_i)^{1/2}$.

For a fitting performed using Lorentzian lineshapes, the function f(x;$\boldsymbol{b}$) is simply an appropriate sum of Lorentzians. The parameters of $\boldsymbol{b}$ are the total resonance area of the spectrum, the baseline, and the parameters of each Lorentzian (position, width at half maximum and depth) expressed in terms of the Mössbauer hyperfine parameters (quadrupole splitting, isomer shift, linewidth, and magnetic hyperfine field). Corresponding to the minimum of the function $\Phi(\boldsymbol{b})$, a set of parameters $\boldsymbol{b}_{\mathbf{min}}$ exists, which gives the best estimate of the true value of the parameters. Using the usual convention in the propagation of the errors, the computer programs usually also calculate the statistical errors for the Mössbauer parameters.

When the absorbers become thicker, the lineshape slowly deviates from that of a Lorentzian. However, in most cases, the lineshape can still be approximated satisfactorily by a Lorentzian with a larger width or by allowing the Gaussian broadening of the Lorentzian lines into Voigt profiles.

In some cases, however, direct calculation of the transmission integral may be necessary [5]. This is particularly true when one wants to determine precisely the molar fractions of different species from the relative intensity of their respective spectral components. In such cases, some computer programs can calculate the transmission integral spectrum according to the equation [27]

$$I(v) = I_0 \left\{ 1 - f_S \left[1 - \int_{-\infty}^{\infty} \frac{\Gamma_S/2\pi}{(\Gamma_S/2)^2 + (v - v')^2} \exp\left(- \sum_i \frac{d_i(\Gamma_i/2)^2}{(\Gamma_i/2)^2 + (v_i - v')^2} \right) \mathrm{d}v' \right] \right\}$$

where I_0 is the baseline, f_S is ideally the *f*-factor of the source, Γ_S is the width of the source spectrum (in mm s^{-1}), and v_i, Γ_i, and d_i are position, width, and depth of the *i*th Lorentzian in the absorption cross-section of the absorber, respectively.

In reality, f_S is not the true Lamb–Mössbauer factor of the source, but is usually reduced by resonant self-absorption in the source and by the background radiation detected in the single-channel window set on the γ-ray spectrum. Therefore, its value

must be determined separately for a given experimental arrangement by measuring the spectra of a reference material of known thickness, for which the Lamb–Mössbauer factor and the resonant absorption cross-section are known at the temperature of interest [28].

10.8 Theoretical Calculation of Mössbauer Parameters

The physicochemical interpretation of the Mössbauer hyperfine parameters obtained from the best fit of experimental spectra (namely isomer shift, quadrupole splitting, and magnetic hyperfine field) is not always straightforward, especially when they need to be correlated with specific local structure and bonding configurations. Similarly to other spectroscopic methods, an important support for their thorough comprehension has been provided by theoretical semiempirical and *ab initio* calculation methods, which have been increasingly employed over the years to become nowadays one of the main supporting tools for the interpretation of experimental spectra.

The complexity and precision of these calculation methods have been strongly improved in the last 30 years. In fact, whereas simple point-charge crystal field empirical methods were precise enough a few decades ago to study the coordination geometries in closed-shell Sn(IV) complexes [29], for instance, more demanding methods are nowadays necessary for the study of modern materials of complex nature (nanostructures, disordered and nonstoichiometric systems, etc.), in which finely tuned electronic properties must be correlated with small changes in hyperfine parameters. For these systems, improved precision can now be achieved by using quantum mechanics modeling methods such as density functional theory (DFT).

Modern DFT methods are commonly applied using two main approaches: periodic electronic structures and finite-size (cluster) models. The first approach, in which the solid is described by a unit cell that is periodically repeated in all three dimensions, is the method mostly used for the prediction of MbS hyperfine parameters. Although the application of this method is straightforward for crystalline solids, also surfaces, nanostructures, disordered systems, and interfaces can be simulated by creating supercell models, that is, larger unit cells describing the relevant structural features of the material under investigation. Nowadays, on modern computers, such model structures can contain more than 1000 atoms, and hence they commonly allow a sufficiently precise description of the studied system.

The most commonly used DFT approximations are based on the local density approximation (LDA) or the generalized gradient approximation (GGA), where only the local electron density and its gradient enter the equations for the exchange-correlation energy and potential. These methods work well for most solids, but are know to be imprecise when treating correlated electron systems, such as 3d transition metal oxides. In the case of ^{57}Fe-containing material, therefore, more advanced methods such as hybrid-DFT or LDA + U must be used in order to treat the electron–electron interaction appropriately [30].

An important point in calculating the Mössbauer hyperfine parameters, however, is that they depend strongly on the electronic structure at the nuclei, and therefore the wavefunctions must be precisely described in the core region of the investigated atom. The widely used plane wave (PW) pseudopotential methods [31] therefore cannot be used directly for these calculations (even though the wavefunctions can be reconstructed with the projector augmented wave (PAW) method [32]) and also the popular Gaussian basis functions of traditional quantum chemistry (LCAO methods) may not provide a very accurate description at the nucleus, in particular for heavy elements.

A good description, well adapted to the calculation of Mössbauer parameters, is currently obtained by methods employing an adaptive numerical all-electron basis set, such as the augmented plane wave (APW) method, developed by Blaha and coworkers at the University of Vienna, and implemented in the WIEN2k code [33]. This method is the one nowadays employed most often for the determination of Mössbauer hyperfine parameters.

Other DFT methods are available as alternatives to WIEN2k, providing roughly the same precision of calculation; for instance, a successful calculation of the Mössbauer parameters for a large series of Sn compounds was performed by Svane *et al.* using the full-potential linear muffin tin orbitals (FP-LMTO) method implementing the LDA for calculating exchange and correlation effects [34].

10.9
Common Mössbauer-Active Transitions

The set of hyperfine parameters obtained from the least-squares fit of the Mössbauer spectrum of a material are finally interpreted with the aim of understanding its physicochemical properties. The nature of the gathered information is characteristic of the isotope under investigation, as will be briefly reviewed in the following sections for the Mössbauer isotopes that are most commonly used in the field of catalysis and surface science. The individual isotopes will be discussed in order of increasing atomic number.

10.9.1
The 14.4keV Mössbauer Transition of ^{57}Fe

The Mössbauer isotope of iron, ^{57}Fe, has a natural isotopic abundance of 2.19%. The stable ground state has nuclear spin 1/2, whereas the 14.4 keV excited state has nuclear spin 3/2 and a lifetime of 140 ns, which corresponds to a linewidth of 0.097 mm s^{-1}. In a Mössbauer spectrum, therefore, the measured linewidth cannot be smaller than twice this value, that is, 0.19 mm s^{-1} (cf., Table 10.1). The low energy of the ^{57}Fe Mössbauer transition gives rise to high values of the Lamb–Mössbauer *f*-factors, allowing the measurement of Mössbauer spectra well above room temperature. The measurement of spectra at different temperatures often allows one to gain additional information by revealing the presence of temperature-dependent effects, such as paramagnetic relaxation or changes in the magnetic properties.

The common reference used nowadays for the isomer shift scale is metallic α-iron measured at room temperature. However, one must be cautious when considering old literature data, since most of the isomer shifts were once referred to sodium nitroprusside, $Na_2[Fe(CN)_5NO]\cdot 2H_2O$, which is displaced towards lower velocities by $-0.26\,mm\,s^{-1}$ with respect to α-iron.

The change in the mean square nuclear charge radius between the excited and ground states, $\Delta\langle r^2\rangle = -14.3 \times 10^{-3}\,fm^2$, is fairly large, which is important for ^{57}Fe Mössbauer spectroscopy, since it provides good sensitivity in terms of isomer shifts, and indeed the various oxidation states of iron in high-spin compounds are easily discriminated by their isomer shift (δ). For instance, ferrous high-spin ionic species usually have $0.8 < \delta < 1.5\,mm\,s^{-1}$, whereas ferric high-spin ionic compounds are characterized by $0.1 < \delta < 0.5\,mm\,s^{-1}$, relative to metallic iron. However, because of the negative value of $\Delta\langle r^2\rangle$, the higher values of δ in Fe(II) compounds compared with Fe(III) corresponds to a smaller s electron density at the nucleus for Fe(II) than for Fe(III). The main contribution to the increase in the 3s electron density on going from Fe(II) to Fe(III) corresponds to the decrease in the shielding of the s electrons by 3d electrons on going from a $3d^6$ electron configuration in Fe(II) to a $3d^5$ configuration in Fe(III). Similar reasoning can be applied to the other common oxidation states of iron, and in fact the isomer shift decreases regularly on going from Fe(I) ($1.6 < \delta < 1.9\,mm\,s^{-1}$) to Fe(VI) ($\delta \sim -0.9\,mm\,s^{-1}$), as shown in Figure 10.11.

A more complex picture emerges for highly covalent iron compounds or for low-spin complexes, for which the empty 4s and 4p orbitals become more populated by the electrons shared with the ligands through the formation of strongly covalent bonds, while the 3d electrons of the iron center are partially delocalized to the ligands through the π back-donation mechanism. In this case, it is difficult to establish a

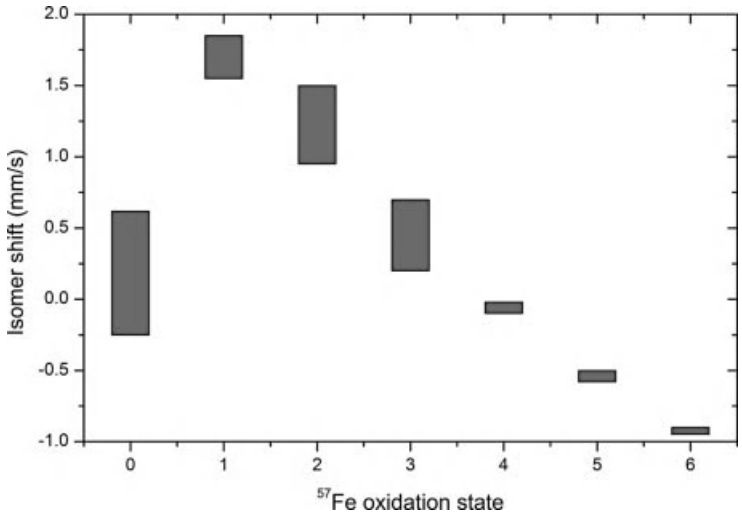


Figure 10.11 Overall view of the ^{57}Fe isomer shifts for ionic compounds of iron in various oxidation states.

trend between isomer shifts and the oxidation state, and compounds such as $Fe(CO)_5$ (formally containing zerovalent iron) and $Na_3Fe(CN)_6$ [formally containing Fe(III)] have virtually identical isomer shifts.

In the case of iron metal and alloys, finally, the partial hybridization of the 4s and of the 3d bands produces a net increase in the electron density at the nucleus and therefore rather small isomer shifts with respect to metallic iron. More positive isomer shifts are observed only when iron is diluted in other metals with largely filled d orbitals, such as Cu, Ag, and Au.

Also the quadrupole splitting is fairly diagnostic for the chemical state of the iron. In the case of high-spin Fe(III) compounds, the $3d^5$ configuration corresponds to a spherical electron density around the iron nuclei, and therefore only the ligand field contributes to the EFG. It is, in fact, amplified by distortions of the half-filled 3d shell. Ideal octahedral coordination should produce no quadrupole splitting, even though small deviations from the octahedral symmetry usually produce small quadrupole splittings of less than 1 mm s^{-1}. Slightly larger quadrupole splitting are commonly observed for tetrahedrally coordinated Fe(III).

In the case of high-spin Fe(II), in contrast, an imbalance of the electron density at the iron nuclei results from the asymmetric occupation of the 3d orbitals, producing a large EFG and therefore rather large quadrupole splittings.

Owing to the large magnetic moment of high-spin Fe(III), trivalent metal centers often undergo magnetic coupling, and many Fe(III) compounds are magnetically ordered, giving rise to local magnetic fields that in some cases become larger than 50 T. Most iron oxides and oxyhydroxides, for instance, are magnetically ordered already at room temperature, and each of them can be identified by its specific set of hyperfine parameters (isomer shift, quadrupole splitting, and magnetic field). Moreover, MbS can also be useful for studying isomorphous substitution, which influences the magnitude of the magnetic field. Finally, the orientation of the hyperfine magnetic field in such compounds is very sensitive to the size and the crystallinity of the oxide particles, and therefore the study of the temperature dependence of the Mössbauer spectra of iron oxides often provides unique information about their morphology and crystalline long-range arrangement (see Section 10.10.2.1) [35].

10.9.2
The 89.4 keV Mössbauer Transition of ^{99}Ru

The Mössbauer active isotope of ruthenium, ^{99}Ru, has a natural abundance of 12.7%. The 89.4 keV transition in ^{99}Ru takes place between the first excited state with spin 3/2 and the 5/2 ground state. The half-life of the excited state of 20.5 ns determines a natural linewidth of 0.075 mm s^{-1}, which corresponds to a minimum experimental width of 0.15 mm s^{-1} (cf., Table 10.1). The ^{99}Rh isotope feeding the 89.4 keV Mössbauer transition is usually prepared in high-energy cyclotrons from enriched ^{99}Ru, and has a half-life of 16 days, so a single source can be used for only a relatively short time (2 months at best). The high transition energy of ^{99}Ru allows the measurement of Mössbauer spectra only at liquid helium temperature.

Similarly to ^{57}Fe, the oxidation states of ruthenium compounds are largely determined by the d electron configuration, and are thus characterized by their isomer shifts. The shift scale is similar to that of ^{57}Fe, but opposite in sign, since $\Delta\langle r^2\rangle = +20.0 \times 10^{-3}$ fm^2 is positive for ^{99}Ru. A more positive isomer shift corresponds to a higher oxidation state of the ruthenium. The reference for the isomer shift scale for ^{99}Ru is ruthenium metal, which is usually also the source matrix. The Mössbauer line of a ruthenium metal absorber is thus observed at zero velocity.

The nuclear spins of 5/2 for the ground state and 3/2 for the excited state cause quadrupole patterns in the Mössbauer spectra to consist of six lines, since the ground state splits into three and the excited state into two sublevels, and all six possible transitions are allowed for the mixed E2/M1 character of the transition. Furthermore, when Ru metal is used as the source matrix, its *hcp* structure gives rise to a small electric quadrupole interaction, corresponding to an unresolved splitting of 0.02 mm s^{-1} for the 3/2 state in the source, resulting in a theoretically complex pattern of 12 lines [36]. However, owing to the very small quadrupole moment of the 5/2 excited state, only the splitting of the 3/2 state (having a quadrupole moment three times larger) is observable and the spectra usually resemble the common quadrupole doublets of ^{57}Fe MbS. Quadrupole splittings in ^{99}Ru MbS anyway are mostly smaller than 1 mm s^{-1} and poorly resolved, except in a few very particular cases [37].

Finally, if the small splitting of the source is taken into account, the experimental linewidth obtained with ruthenium metal sources usually remains close to the natural width of 0.15 mm s^{-1}.

10.9.3
The 23.9 keV Mössbauer Transition of ^{119}Sn

The Mössbauer active isotope of tin, ^{119}Sn, occurs with a natural abundance of 8.58%. As with ^{57}Fe, the nuclear ground state of ^{119}Sn has spin 1/2 and the excited state at 23.9 keV has spin 3/2. The higher energy of the nuclear transition of ^{119}Sn compared with ^{57}Fe allows the measurement of Mössbauer spectra at room temperature only for materials with a sufficiently high Debye temperature. However, good spectra can be measured, in most cases, at liquid nitrogen temperature (77 K). The half-life of the excited state of 17.80 ns corresponds to a linewidth of 0.32 mm s^{-1} and therefore the minimum experimental width is 0.64 mm s^{-1}. Unlike ^{57}Fe, the change in the mean square nuclear charge radius between the excited and ground states is positive, $\Delta\langle r^2\rangle = +3.3 \times 10^{-3}$ fm^2, and hence higher isomer shifts correspond to higher electron densities at the ^{119}Sn nuclei. The reference standard for the isomer shift scale is $CaSnO_3$, which has virtually the same isomer shift as SnO_2 and $BaSnO_3$.

As for ^{57}Fe, in ^{119}Sn MbS the various oxidation states of tin can be discriminated by their isomer shift. Since a filled 4d shell is present in both Sn(IV) and Sn(II), the shielding effect of the 4d electrons does not influence the isomer shift, which depends mainly on the 5s electron population. The higher 5s electron density of divalent tin produces a more positive isomer shift in Sn(II) ($\delta > 2.9$ mm s^{-1}) compounds than in Sn(IV) ($\delta < 2.0$ mm s^{-1}). Tin metal and tin alloys lie in the

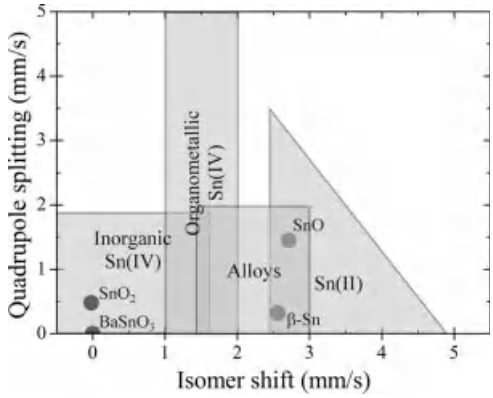


Figure 10.12 Quadrupole splitting versus isomer shift ranges for common tin compounds.

range 1.5–3.0 mm s^{-1}. The observed ranges of isomer shifts and quadrupole splitting for common tin compounds are shown in Figure 10.12.

Ionic Sn(IV) has a $4d^{10}$ closed-shell electron configuration, and the resulting charge distribution due to the electrons is spherical. The only contribution to the quadrupole splitting is thus that produced by the coordination symmetry of the ligands. Therefore, MbS has been largely used for the study of the coordination of tetravalent tin compounds, allowing a rapid check of the coordination symmetry through the quadrupole splitting, and a few simple methods for the study of ligand coordination, such as the partial quadrupole splitting method, have been developed [29]. These methods are nowadays out of date, and *ab initio* calculations give much more precise estimation of the quadrupole splitting in Sn(IV) compounds (see Section 10.8) On the other hand the, isomer shift increases with the population of the 5s orbital, that is, with the covalency of the tin–ligand bonds, and an almost linear correlation between Sn(IV) isomer shift and electronegativity of the ligands is observed.

In stannous compounds, a similar correlation between electronegativity and isomer shift cannot be established. In this case, the correct approach is to start from the ideal free Sn^{2+} ion, which has a $5s^2$ electron configuration corresponding to an isomer shift of 4.84 mm s^{-1}. The existence of an asymmetric ligand field around the stannous nucleus produces a lifting of the degeneracy of the 5p states and a certain degree of 5s–5p hybridization, and consequently a 5s electron population and an isomer shift smaller than those of the free ion. This is also reflected by the inverse correlation existing between isomer shift and quadrupole splitting in Sn(II) compounds: an increase in 5s–5p hybridization corresponds to an increase in the EFG at the tin nucleus (the lattice contribution to the EFG can be neglected), and thus an increase in quadrupole splitting goes along with a decrease in the isomer shift.

In alloys and intermetallic compounds, finally, the isomer shift is strictly related to the population of the tin 5s band. However, the observed range is relatively narrow (about 1.5 mm s^{-1}), indicating that the electronic population of the 5s state does not vary markedly from 1.

10.9.4
The 37.1 keV Mössbauer Transition of ^{121}Sb

The Mössbauer active isotope of antimony, ^{121}Sb, occurs with a natural abundance of 57.25%. The nuclear ground state of ^{121}Sb has spin 5/2 and the excited state at 37.1 keV has spin 7/2, leading to complicated quadrupole splitting spectra consisting of eight resonance lines. The eight lines are, however, almost always unresolved, due to large experimental linewidth of 1.32 mm s^{-1}, deriving from the half-life of the excited state of 3.50 ns. The relatively high energy of the nuclear transition of ^{121}Sb makes it difficult to measure ^{121}Sb Mössbauer spectra at room temperature, and cooling of both source and absorber to at least liquid nitrogen temperature (77 K) is almost always necessary.

Similarly to ^{57}Fe, the relative change in the nuclear radius between the excited and ground states is negative, $\Delta\langle r^2\rangle = -24.6 \times 10^{-3}$ fm^2, hence higher isomer shifts correspond to smaller electron densities at the ^{121}Sb nuclei. The common reference standard for the isomer shift scale is InSb, which has an isomer shift of −8.48 mm s^{-1} referred to a source of Ba^{121m}SnO$_3$. The choice of InSb as the reference of the isomer shift scale is helpful, since it allows one to separate Sb(III) compounds, usually having negative isomer shifts, from Sb(V) species, characterized by positive values of δ. The metal and alloys have isomer shifts around 0 mm s^{-1} or only slightly positive.

10.9.5
The 73.0 keV Mössbauer Transition of ^{193}Ir

Two different stable isotopes of iridium, ^{191}Ir and ^{193}Ir, show a Mössbauer transition suitable for Mössbauer studies. There are several factors, however, that make ^{193}Ir preferable to ^{191}Ir, including its slightly narrower natural linewidth, the weak emission of gamma rays from the ^{191}Pt or ^{191}Os source feeding the ^{191}Ir transition, and the strong K-shell photoabsorption of gamma rays by the iridium in the absorber in the case of ^{191}Ir, the K absorption edge of iridium being at 76.1 keV, whereas the γ-ray energy is 82.3 keV. The latter effect imposes major limitations on the absorber thickness. For these reasons, almost all data in the literature have been acquired with the 73 keV transition of ^{193}Ir.

^{193}Ir occurs with a natural isotopic abundance of 67.3%. The nuclear ground state has spin 3/2, whereas the 73.0 keV excited state has spin 1/2 and a half-life of 6.20 ns, yielding an experimental linewidth of 0.60 mm s^{-1}. The high energy of the nuclear transition of ^{193}Ir allows the measurement of Mössbauer spectra only at liquid helium temperature (4.2 K).

The typical source for ^{193}Ir MbS is ^{193}Os, usually obtained by neutron irradiation of ^{192}Os metal. Since the latter has a hexagonal lattice structure, the emission line of such sources is split into a doublet with a separation of 0.48 mm s^{-1}, which has to be taken into account in the least-squares fits of the spectra. The reference for the isomer shift scale is usually iridium metal, which has an isomer shift of −0.54 mm s^{-1} relative to the source of ^{193}Os in Os metal.

The isomer shift of ^{193}Ir allows the distinction of the oxidation states of iridium. An increase in isomer shift corresponds to an increase in s electron density at the nuclei, since the change in the nuclear charge radius between the excited and ground states, $\Delta\langle r^2\rangle = +5.5 \times 10^{-3}$ fm^2, is positive. The increase in isomer shift with the oxidation state observed for many iridium compounds is attributed to a decrease in the shielding effect of the 5d electron population of the core s electron density at the nucleus. This approach is usually valid for the high oxidation states [Ir(III) through Ir (VI)], whereas a wide range of isomer shifts is obtained for compounds containing iridium in a low oxidation state such as Ir(I). In fact, most of the Ir(I) compounds are stabilized by ligands which are very good π acceptors, such as CO and NO^+. The π back-donation from the iridium to the ligands allows a higher occupation of the 6s orbitals via direct σ-donation to the iridium and hence an increase in the electron population at the nucleus.

10.9.6
The 77.3 keV Mössbauer Transition of ^{197}Au

^{197}Au is the only stable isotope of gold, therefore having a natural abundance of 100%. Like ^{193}Ir, the nuclear ground state of ^{197}Au has spin 3/2, whereas the 77.3 keV excited state has spin 1/2 and a half-life of 1.93 ns, yielding an experimental linewidth that is never below 1.88 mm s^{-1}. Owing to the high energy of the nuclear transition of ^{197}Au, the measurement of Mössbauer spectra must be performed with both source and absorber at liquid helium temperature (4.2 K). The common reference for the isomer shift scale is gold metal, which has an isomer shift of -1.23 mm s^{-1} compared with the source of ^{197}Pt in Pt metal.

As for ^{193}Ir, $\Delta\langle r^2\rangle = +8.6 \times 10^{-3}$ fm^2 is positive also for ^{197}Au. For the identification of the oxidation state of gold, however, one has to use both the quadrupole splitting and the isomer shift. For monovalent gold, which has a closed-shell 5d^{10} configuration, the only contribution to the quadrupole splitting is due to the influence of the ligands. Since Au(I) is usually linearly coordinated to two ligands, the s–p hybridization and the covalent character of the bonds tend to increase in an equal way both the s and the p_z electron population. Therefore, while the increase in the population of the s orbitals increases the isomer shift, the increase in the p_z population increases the magnitude of the EFG due to the increase in the total population imbalance of the three p orbitals, p_x, p_y, and p_z. Thus, for monovalent gold, an increase in the isomer shift is usually correlated with an increase in the quadrupole splitting, which are both correlated to the "softness" of the ligands, from halides to organogold compounds. The higher the electron donation from the ligands, the higher are both quadrupole splitting and isomer shift.

A similar situation is observed for trivalent gold, which has an open-shell d^8 electron configuration. Au(III) is usually four-coordinated with square-planar stereochemistry, which stabilizes the low-spin configuration and yields only diamagnetic compounds. As for Au(I), there is a positive correlation between isomer shift and quadrupole splitting, and both hyperfine parameters increase as the ligands become softer. In fact, the isomer shift increases with increasing donation from the ligands, since the direct

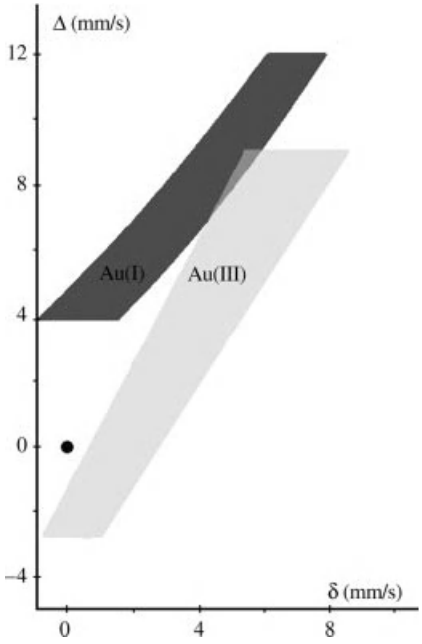


Figure 10.13 Correlation diagram for the isomer shifts and quadrupole splittings of Au(I) and Au (III) compounds with respect to gold metal. The indicated regions are for linear Au(I) and square-planar Au(III) compounds. The dot represents metallic gold.

effect of an increase in the 6s population outweighs the shielding effect of the concurrent increase in the 5d and 6p populations. The isomer shift is usually slightly larger than in Au(I), owing to the incomplete d shell and the greater covalence expected for the higher oxidation state. For the quadrupole splitting, in contrast to Au(I), there are contributions from both the ligands and the unfilled d shell. The principal component of the EFG, V_{zz}, in this case is perpendicular to the plane formed by the ligands. The increase in donation from the ligands will make an increasing positive contribution to the EFG, which in almost all cases (except the halides) outweighs the negative contribution due to the lone pair of electrons in the d_{z^2} orbital. Typical correlation diagrams for Au(I) and Au(III) are shown in Figure 10.13.

It should be noted that the EFG in Au(I) compounds is always negative, although the values represented in Figure 10.13 are positive. In contrast, the EFG is positive in most Au(III) compounds, and it becomes negative in compounds with a highly ionic character. For the sake of clarity, therefore, it must be pointed out that this figure shows the actual values of quadrupole splitting for Au(III), and only the magnitude for Au(I).

10.10
Survey of Applications of the Mössbauer Effect in the Study of Catalytic Materials

The application of MbS in materials science has been significant and widespread. In the case of materials for heterogeneous catalysis, for instance, it has been applied

during almost the whole life of a catalyst, from the identification of phases in the first synthesis steps to the description, in some cases, of the working catalyst under reaction conditions. The information is generally gathered through the interpretation of the observable hyperfine parameters obtained through the analytical fitting of the spectra (see Section 10.7.2). In addition, the dependence of these parameters upon temperature and/or pressure can be studied, in addition to the effect of the application of external magnetic fields.

These data altogether have been used for the following:

- the identification of phases (fingerprint method);
- the identification of specific adsorbed or surface species;
- the study of the electronic properties, including
  - the determination of oxidation states;
  - the identification of coordination structures;
- the study of magnetic properties;
- the determination of particle sizes;
- the kinetics of solid-state reactions.

The following examples will show how this technique can be of help in the study of a material at different stages of its life, from the optimization of the preparation procedure to the description of its active state.

10.10.1
^{197}Au Mössbauer Spectroscopy in the Study of Gold Catalysts

A typical example of the use of MbS in the characterization of a catalytic material is that of ^{197}Au MbS, which, among many different techniques, contributed to the characterization of gold species in supported gold catalysts. Even though the study of the material under catalytic reaction conditions by ^{197}Au MbS is virtually impossible because of the high energy of the Mössbauer transition, allowing the measurement of MbS spectra only at liquid helium temperature, several examples of the characterization of gold-containing catalytic materials during the different synthesis steps to the active catalyst and to the study of the spent catalyst at the end of the catalytic reaction are available [38]. Some of these examples are particularly interesting, from a didactic point of view, to appreciate the potentialities and to be aware of some of the critical points in the application of MbS in this field.

10.10.1.1 Electronic Properties: Au/Al_2O_3 Oxidation Catalysts

Historically, gold was thought to be catalytically almost inactive until the end of the 1980s, and its potential application as a heterogeneous catalyst was seriously considered only after Haruta *et al.* discovered that supported gold nanoparticles are highly active in the oxidation of CO at low temperatures [39]. Since then, the number of scientific studies on supported gold catalysts has increased considerably and extended to other catalyzed reactions, as summarized in several comprehensive reviews [40–42].

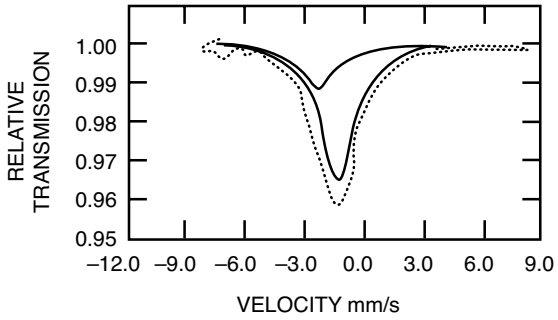


Figure 10.14 ^{197}Au Mössbauer spectrum of an Au/Al_2O_3 catalyst prepared from $HAuCl_4$ and calcined at 370 °C. Reproduced from [43] with permission from the publisher.

However, the utilization of ^{197}Au MbS for the characterization of gold catalysts was introduced in 1968 in a paper by Delgass *et al.* [43], definitely long before the use of gold in catalysis had become of any interest. The innovative point of this early work is the first demonstration of the ability of ^{197}Au MbS to study the chemical interactions of finely divided Au species with a support. In this paper, in fact, Au/Al_2O_3 and Au/MgO catalysts prepared from different precursors are compared, and the products [mainly metallic gold or oxidic Au(III) species] obtained by the transformation of the different monovalent and trivalent gold precursors are identified, although in some cases the attribution of the different spectral components to specific gold species remains problematic. In particular, in the spectrum of one Au/Al_2O_3 sample (Figure 10.14), the authors observed a dominant component representing gold metal together with an additional gold species, which was fitted using a single line with an isomer shift of -1.14 mm s^{-1} versus Au metal, that is, a great deal more negative than that of gold metal. This component was interpreted in terms of a lower s electron density at the gold nucleus than that of Au metal, and was attributed to the electronic interaction of the gold particles with the support producing a strongly electronegative environment. Incidentally, this sample proved to be the most active in the test reaction of oxidation of CO by N_2O, showing how the detection of electronic effects by MbS might be correlated with the catalytic activity.

10.10.1.2 Determination of Chemical Composition: Supported AuPd Alloys

A second interesting example of the use of ^{197}Au MbS in the study of catalytic materials is a study by Lam and Boudart [44], who used ^{197}Au MbS to determine the composition of supported gold/palladium alloy particles. In fact, gold and palladium are miscible over the whole range of compositions, and a linear correlation between isomer shift and the palladium weight fraction is observed. In this case, the measurement of the isomer shift not only provides information about the effective alloying of the two metals, but also gives directly the average composition of the synthesized alloy particles (Figure 10.15). Virtually identical results were obtained in more recent work by Pârvulescu et co-workers [45, 46].

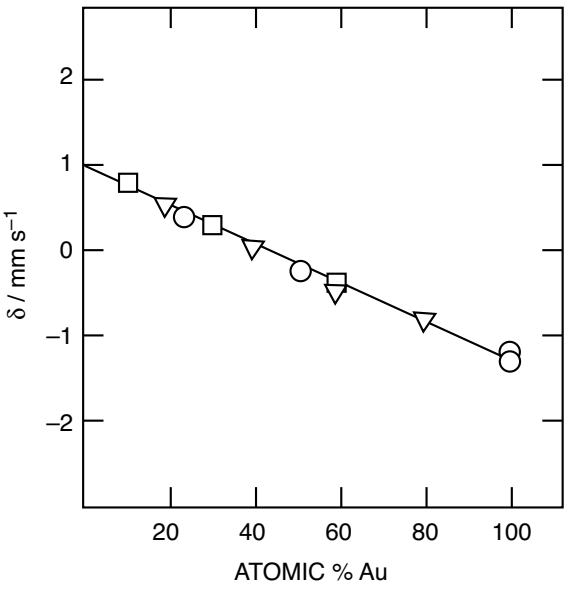


Figure 10.15 Isomer shift dependence on the composition for Au–Pd alloys. Reproduced from [44] with permission from the publisher.

In this case, in fact, a linear correlation between isomer shift and gold concentration in the alloy is observed. Such correlations are fairly common for all Mössbauer active isotopes and, similarly to Vegard's law in X-ray diffraction, usually allow the direct determination of the average alloy composition by the simple measure of the isomer shift.

10.10.1.3 Determination of Lamb–Mössbauer *f*-Factors for Quantitative Analyses: Au/Activated Carbon Catalysts for the Hydrochlorination of Acetylene

^{197}Au MbS was also used to investigate gold catalysts for the hydrochlorination of acetylene prepared by impregnation of activated carbon (AC) with aqueous solutions of $AuCl_4^-$ [47, 48]. In these materials, MbS was found to be very useful for determining the oxidation state of gold, and in particular in clarifying the mechanism of deactivation and reactivation of these materials. For instance, in a typical spectrum of a fresh catalyst (Figure 10.16), two main spectral components can be identified: a single line at $-1.23\,\mathrm{mm\,s^{-1}}$, representing metallic gold, and a quadrupole doublet with parameters in the range of trivalent gold. This doublet was attributed to adsorbed $AuC1_4$ although its hyperfine parameters are slightly different from those of crystalline $HAuC1_4{\cdot}xH_2O$, presumably because the $HAuC1_4$ is not a crystalline species but adsorbed on the AC surface.

If one compares the relative intensity of the two components (both of them around 50%) without taking into account the Lamb–Mössbauer factors of the two species, one might conclude that half of the gold has transformed into metallic gold. However, gold complexes adsorbed on carbon are known to have substantially smaller

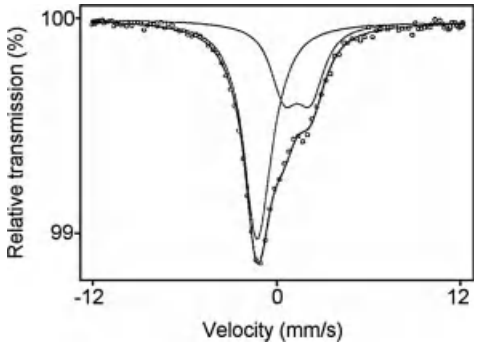


Figure 10.16 ^{197}Au Mössbauer spectrum at 4.2 K of a 2% Au/AC catalyst prepared by impregnation of activated carbon with a solution of aqua regia.

recoilless fractions than metallic gold, and it is therefore necessary to determine the recoilless fraction of the adsorbed gold species before the mass ratio of Au(0) and Au (III) can be given.

This determination was made in a very simple way, by measuring first a spectrum of the sample containing the adsorbed species, and then a second spectrum after the adsorbed species had been completely reduced to metallic gold by heating the absorber to about 600 °C. By comparing the total intensities of the two spectra, the ratio between the *f*-factors of adsorbed and metallic gold was obtained straightforwardly. In order to avoid uncertainties introduced by possible variations in the nonresonant background of the γ-ray spectrum, a standard absorber to which all intensities could be referred and whose spectrum did not overlap with the subspectra of the two gold species (in this case, an alloy of 1% gold in vanadium metal producing a single line with an isomer shift of $+5.63\,\mathrm{mm\,s^{-1}}$) was measured together with the samples in both cases. The result of these experiments gave a ratio of 0.11(1) between the recoilless fractions of $AuCl_4^-$ on carbon and that of metallic gold. Taking this result into account, one concludes that, on the fresh catalyst, about 84% of the gold was present as adsorbed $AuCl_4^-$, and that only 16% of the gold was metallic.

In summary, the accurate determination of the relative amounts of gold in the different forms in as-made, deactivated, and reactivated catalysts showed that trivalent gold is probably the active species in the hydrochlorination, and that this species tends to reduce to metallic gold during the catalytic reaction causing a gradual deactivation of the catalyst. This example is particularly interesting because it shows the importance of the Lamb–Mössbauer factors in the quantitative determination of the relative amounts of different gold species.

10.10.1.4 Identification of Surface Species: Gold Nanoparticles Embedded in Mylar

In a study of isolated gold nanoparticles prepared by evaporating metallic gold on to an inert Mylar matrix, it was demonstrated [49] that, when the sizes are below about 5 nm, MbS becomes able to distinguish between surface and core atoms in gold nanoparticles, and that even nonbonding surface atoms exhibit Mössbauer parameters in the same range as surface gold atoms of ligand-protected clusters [50].

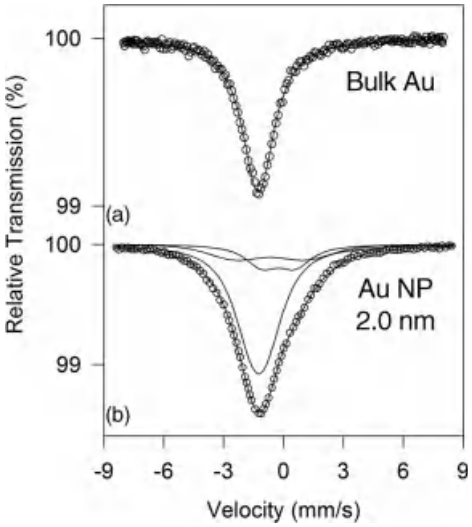


Figure 10.17 ^{197}Au Mössbauer spectra at 4.2 K of bulk gold metal (a) and of gold nanoparticles with an average diameter of 2 nm embedded in Mylar (b).

In the ^{197}Au Mössbauer spectrum of gold nanoparticles with an average diameter of 2 nm (shown in Figure 10.17 together with a reference spectrum of gold metal), in fact, three spectral component are detected. The main component is a single line with an isomer shift only slightly more negative than that of metallic gold. The observed contraction of the lattice in nanoparticles, however, should lead to an increase in the s electron population at the gold nuclei and therefore to a slightly positive value of δ with respect to bulk metallic gold. That this increase is not observed indicates that a net electron flow towards the particle surface compensates the increase in the s electron density and leads to an isomer shift slightly more negative than that of bulk gold.

This electronic transfer mechanism is confirmed by the positive isomer shifts of the two additional quadrupole split components, which are attributed to different positions of the gold atoms on the surface of the nanoparticles. The different quadrupole splittings for the two components probably arise from the different number of gold neighbors to which the different types of surface atoms are coordinated.

The study of the electronic structure of surface atoms is extremely important for the study of electronic effects in catalytic materials, and has been observed not only in recently studied supported gold catalysts [51], but also for similar systems containing other more common Mössbauer isotopes such as ^{57}Fe [52] and ^{119}Sn [53].

10.10.2
^{57}Fe Mössbauer Spectroscopic Study of Iron-Containing Catalysts

^{57}Fe has been the most widely used Mössbauer isotope in the catalysis literature, as the very low energy of the γ-ray transition allows measurements even at relatively

high temperatures (a few hundred degrees Celsius), and therefore at temperatures typical of many catalytic reactions. ^{57}Fe MbS has thus been successfully employed for different catalytic systems during the whole lifespan of catalytic materials, and also for source experiments. In the following, some examples for the information that can be obtained in this way will be presented.

10.10.2.1 Superparamagnetism and the Determination of Particle Sizes: Fe/C Catalysts for CO Hydrogenation

The temperature dependence of Mössbauer spectra can be of great help in the study of catalytic materials, and in some cases it may provide information on particle sizes. This is the case with a study of iron metal nanoparticles supported on carbon black (Fe/C) for CO oxidation [54], providing the series of Mössbauer spectra shown in Figure 10.18.

The spectrum measured at room temperature shows the presence of a badly resolved contribution at zero velocities, whereas, when the temperature is decreased to liquid helium temperature, a magnetic sextet with a hyperfine field of about 34 T, typical of iron metal nanoparticles [55], appears. The appearance of a magnetic hyperfine splitting on decreasing the temperature is due to the blocking of superparamagnetism, an effect occurring at ambient temperature in magnetically ordered nanoparticles with sizes below about 20 nm [56]. Such nanoparticles usually consist of a single magnetic domain, and therefore their magnetization can be considered as

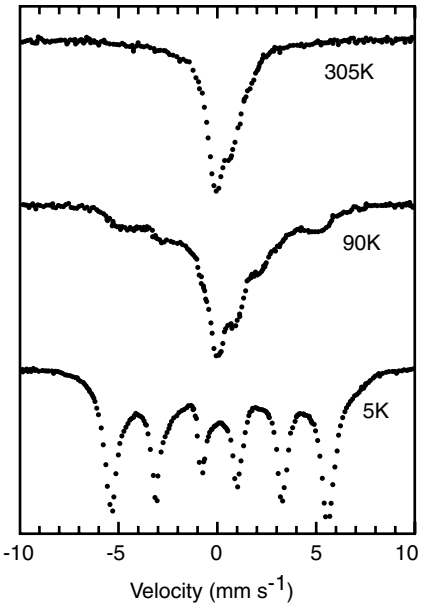


Figure 10.18 Temperature dependence of the ^{57}Fe Mössbauer spectrum of an Fe/C catalyst measured *in situ* after reduction in H_2. Reproduced from [54] with permission from the publisher.

a single giant magnetic moment, the sum of all the individual magnetic moments carried by the atoms of the nanoparticles.

As the lattice interaction with the magnetic field is anisotropic, the magnetic moment often has only two stable antiparallel orientations along the so-called "easy direction" of the magnetization. These two orientations are separated by an energy barrier, and the magnetization therefore has the possibility to flip and reverse its orientation. The average time between two flips, called the Néel relaxation time, is an exponential Boltzmann-type function of the particle volume (which explains why the flipping probability becomes rapidly negligible for large particles) and, for small particles, decreases with increasing temperature [56].

When this time is much shorter than the measuring time (in the case of MbS, the measuring time is essentially the Larmor precession time of the nuclear spin in the hyperfine field, which is of the order of a few nanoseconds for ferric compounds [56]), the nanoparticle magnetization will flip many times during the measuring time, and the observed magnetic hyperfine interaction will average to zero. Only when the Néel relaxation time becomes longer than the measuring time does a magnetic hyperfine splitting appear. In the former case, the nanoparticles are said to be in the superparamagnetic state, that is, they will show a nonmagnetic spectrum, whereas in the latter case they are said to be blocked and a magnetic hyperfine splitting will be measured. The temperature at which the two times are equal is usually called the blocking temperature. In fact, near the blocking temperature the spectra are neither well-split magnetic patterns nor magnetically unsplit, broadened due to superparamagnetic relaxation [56].

When a series of Mössbauer spectra of a superparamagnetic material are measured at decreasing temperature (cf. Figure 10.18), the transition between superparamagnetism and the blocked state is gradual and continuous. The determination of the blocking temperature is not straightforward, the more so since one usually has a distribution of particle volumes and morphologies. Still, a rough estimate of the average particle size can be made.

A relatively accurate method for determining the particle size of a superparamagnetic material is the measurement its Mössbauer spectra with an applied external magnetic field [57]. The spectra of an Fe/C catalyst measured at increasing magnetic fields shown in Figure 10.19 are an example of this technique. The application of a magnetic field splits the single line pattern of the superparamagnetic iron particles spectrum into a magnetic sextet because the magnetization of the particles is polarized in the direction of the applied field. According to the Langevin equation [56], the measured magnetic hyperfine field increases with the applied field. From this increase and the known temperature of the measurement, the magnetic moment of the whole particle can be derived and thus its volume. A distribution of particle sizes will cause a broadening of the observed Mössbauer patterns. Obviously, the technique works only for ferro- or ferrimagnetic materials, and not for antiferromagnetic materials.

The advantage of this technique over other typical characterization methods such as XRD line broadening or line profile analysis, electron microscopy, chemisorption, and magnetic measurements, is the fact that MbS provides simultaneously the

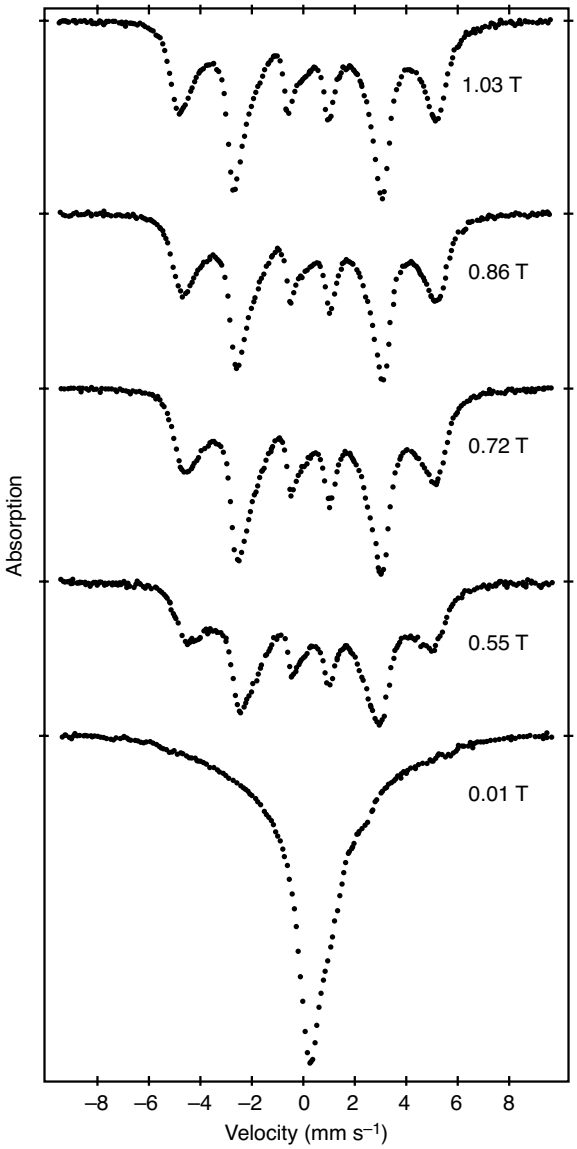


Figure 10.19 ^{57}Fe Mössbauer spectra at 80 K of an Fe/C catalyst containing iron metal particles with a diameter of 2.5 (2) nm measured at increasing external magnetic fields. Reproduced from [57] with permission from the publisher.

characterization of the material and the measurement of the particle size. In the case of supported iron catalysts, for instance, such a measurement made *in situ* just after the activation treatment will provide simultaneously the degree of reduction and the size of the metal particles.

10.10.2.2 *In Situ* Measurements: Iron-Based Fischer–Tropsch Catalysts

One of the main fields of application of MbS in catalysis has concerned the study of the state of iron in iron-containing Fischer–Tropsch catalysts. Most of these studies have been performed using specially developed reactor cells for studying the catalytic material after the activation pretreatments or even under catalytic reaction conditions [58–62].

Bartholomew and co-workers, for instance, performed an MbS study on FePtK/SiO_2 catalysts under industrially relevant conditions of temperature and pressure for Fischer–Tropsch synthesis [63, 64]. In Figure 10.20, the spectra obtained for an FePtK/SiO_2 catalyst sample at different steps of the activation and after 10 h of catalytic reaction are shown. The spectrum of the starting calcined material before activation exhibits a simple Fe^{3+} quadrupole doublet, typical of highly dispersed superparamagnetic iron oxide nanoparticles. After an activation pretreatment under synthesis gas (a mixture of CO and H_2) for 8 h, the Fe_2O_3 nanoparticles are quickly reduced to Fe_3O_4 (magnetite) of different particle sizes (both ferrimagnetic and superparamagnetic), ill-defined divalent iron species, and a mixture of iron carbide phases. A comparison with the spectrum measured after 32 h of pretreatment shows that the amount of carbides and ferrimagnetic magnetite increases with the pretreatment time, whereas the superparamagnetic fraction of Fe_3O_4 decreases strongly, indicating an increase in the size of the magnetite particles. After 10 h under reaction conditions, the magnetite is found to have largely converted back to superparamagnetic hematite, while the carbides persist.

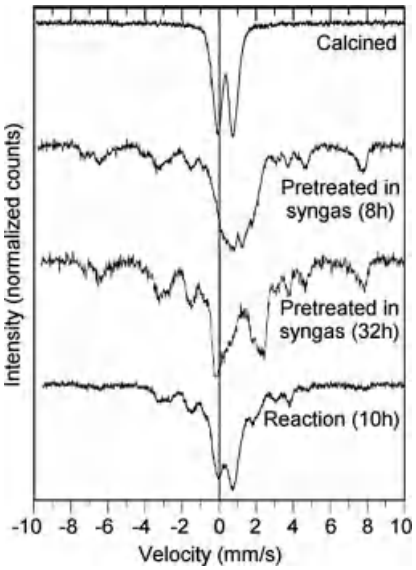


Figure 10.20 ^{57}Fe Mössbauer spectra of FePtK/SiO_2 catalysts after pretreatments and reaction in H_2/CO at 10 atm. Reproduced from [64] with permission from the publisher.

The Mössbauer spectra thus revealed significant changes in phase composition and nanostructure of the catalysts not only during the pretreatment, but also in the course of the catalytic reaction, providing information on different reduced iron nanophases, that is, divalent iron, magnetite, and iron carbides. In particular, it was found that the addition of promoters such as Pt and K favorably influences both the reduction and the dispersion of the initial oxidized iron species. In spite of this influence, platinum appears to be present in separate phases from iron, since no significant amount of PtFe alloys is detected.

By combining these results with those obtained by other characterization methods such as X-ray diffraction and temperature-programmed techniques, a convincing picture of the working catalyst, consisting of relatively large Fe_3O_4 crystallites, the surface of which is covered with highly dispersed nodules of iron carbides, was proposed. The small iron carbide particles are immediately oxidized to Fe(III) oxide species upon exposure of the sample to air, underlining the importance of performing these measurements in the catalytic reactor.

10.10.2.3 Emission Mössbauer Spectroscopy: Cobalt-Based Fischer–Tropsch Catalysts

Cobalt-based catalysts are also widely employed for Fischer–Tropsch syntheses as an alternative to iron-based catalysts. Compared with the latter, cobalt catalysts are particularly suitable for the use of synthesis gas produced via reforming of natural gas, yielding mainly straight-chain hydrocarbons [65]. Since cobalt is much more expensive than iron, the cobalt loading and dispersion on a support must be optimized to help reduce catalyst cost and increase its activity and stability during the catalytic reaction. In particular, the knowledge of their deactivation paths is of great importance to improve their durability, the most important possible contributors to their deactivation being coke formation, oxidation, poisoning, and sintering [60].

In a recent study, Leendert Bezemer *et al.* studied the effect of water on the deactivation mechanism of a Fischer–Tropsch catalyst using cobalt supported on carbon nanofibers [66] by emission MbS (see Section 10.6.3). In fact, even if cobalt is not an active Mössbauer isotope, ^{57}Co is the mother isotope feeding the 14.4 keV transition of ^{57}Fe, hence catalyst samples prepared with radioactive ^{57}Co can be used as Mössbauer sources. In this case, the catalyst samples were kept immobile inside an airtight catalytic cell allowing various activation and reaction treatments, and an absorber of $K_4Fe(CN)_6 \cdot 3H_2O$ enriched in ^{57}Fe, producing a single line at –0.045 mm s^{-1} relative to α-iron metal, was moved at constant acceleration between the catalyst cell and the detector. The resulting spectra are shown in Figure 10.21.

The Mössbauer spectrum of the catalyst after reduction at 350 °C shows a broad singlet representing small superparamagnetic cobalt nanoparticles, and a magnetic sextuplet arising from larger blocked cobalt nanoparticles. By comparison of these results with the particle size distribution for transmission electron spectroscopy, the authors concluded that the magnetic splitting appears at about 5 nm, a value that is similar to the 6 nm observed for α-Fe on carbon [66]. The presence of two spectral contributions in the Mössbauer signal is very helpful in drawing conclusions about the impact of cobalt particle size on catalyst deactivation.

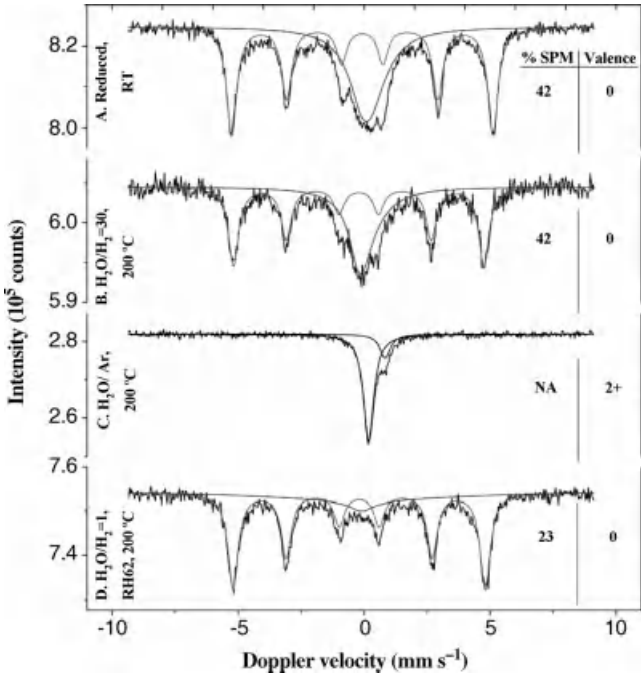


Figure 10.21 ^{57}Fe Mössbauer emission spectra measured at room temperature after reduction of the catalyst and after exposure to gas mixtures containing different amounts of H_2O and H_2 at 220 °C. Reproduced from [66] with permission from the publisher.

After reduction, the catalyst was exposed to a gas stream of mixtures of H_2O, H_2, and Ar, with the H_2O:H_2 ratio varying between 1 and 30, and with varying absolute H_2O content. At a high H_2O:H_2 ratio and low absolute H_2O content, the shape of both cobalt species did not change, clearly showing that oxidation did not occur under these relatively oxidizing conditions. In fact, industrial Fischer–Tropsch synthesis takes place with an H_2O:H_2 ratio around 1, confirming that oxidation is not a likely deactivation mechanism during industrial syntheses. Oxidation of the metal particles occurs, however, when H_2 is exchanged for Ar (cf., Figure 10.21, second spectrum from the bottom). Under these conditions, only the typical spectrum of CoO (a single line with a positive isomer shift associated to a second, less-intense singlet at higher velocities) is observed, showing that oxidation of cobalt by water is possible only in the absence of hydrogen.

Important changes in the Mössbauer spectrum are observed when the absolute H_2O content is increased, even when the H_2O:H_2 ratio is kept around 1 (cf., Figure 10.21, bottom spectrum). Under these conditions, a noticeable decrease in the component attributed to superparamagnetic cobalt nanoparticles and a simultaneous increase in the magnetically split pattern from the larger particles are observed. This effect can undoubtedly be ascribed to sintering of the metal particles, and is in quantitative agreement with the observed decrease in activity of the catalyst.

Based on these observations, the authors concluded that the absolute H_2O content of the gas feed has a very large impact on the sintering behavior of the metal particles, with significant detrimental effects on the Fischer–Tropsch performance of Co supported on carbon nanofiber catalysts.

10.10.3 ^{119}Sn Mössbauer Study of Bimetallic Tin-Containing Catalysts

Tin has often been suggested as a modifier for heterogeneous catalysts based on other supported active metals such as Pt, Rh, Pd, and Ru. For instance, supported bimetallic PtSn catalysts have been used in catalytic reforming processes for gasoline synthesis [67], catalyzing dehydrogenation, isomerization, and aromatization reactions, and thus leading to an increase in the octane number of gasoline. Another important example of tin-containing bimetallic systems concerns the synthesis of fine chemicals, and more precisely the selective hydrogenation of α,β-unsaturated aldehydes to unsaturated alcohols [68]; in this case, the presence of tin strongly improves the selectivity and the durability compared with monometallic systems.

The identification of the exact mechanisms leading to these improvements is still unclear, and two main effects associated with the presence of tin have been proposed:

1) A steric effect, caused by the dilution of adjacent active-metal sites on the surface of the alloy particles.
2) An electronic effect, caused by influencing the electron density on platinum atoms and thereby modifying their bonding properties. In this case, the electronic effect might derive either from the formation of Pt_x–Sn_y alloys, or via the formation of ionic Sn(II) species formed at the interface with the support.

Furthermore, the study of these systems is complicated by the fact that this type of catalyst usually contains Sn(IV), Sn(II), and Sn(0) species in the form of alloys or solid solutions with platinum in variable proportions, depending on the experimental activation conditions, the nature of the support, the pretreatment that the support has undergone (chlorination, substitutions), the preparation method (metals deposited by co-impregnation or two successive impregnation steps, by a sol–gel method, or a controlled surface reaction), and the precursors used (mono- or bimetallic, with or without metal–metal bonds), and so on.

Since the pioneering work of Bussière *et al.* [69, 70], ^{119}Sn MbS have been widely used for the identification and quantification of the various tin species that are formed in supported bimetallic systems [53, 71–82]. Olivier-Fourcade and coworkers [83–86] recently tried to rationalize the large amount of data existing for the Pt–Sn couple in a very precise and accurate study by ^{119}Sn MbS of a large number of samples prepared and pretreated under very different conditions. The authors established a chart of hyperfine parameters (cf., Figure 10.22), which was used to identify a large variety of tin species containing Sn(IV), Sn(II), and Sn(0) that occur on bimetallic tin–platinum catalysts after oxidation or reduction under various conditions.

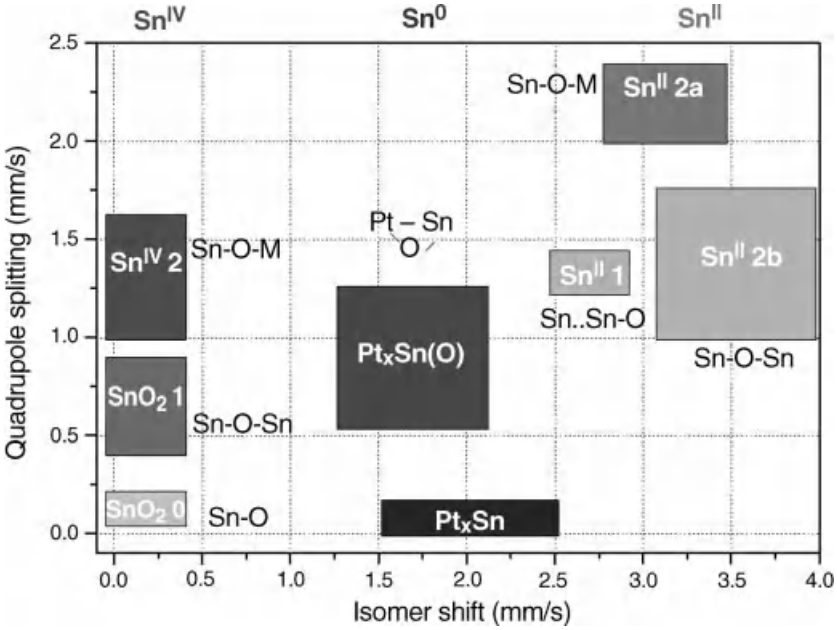


Figure 10.22 Identification diagram of tin species found in $PtSn/Al_2O_3$ catalysts [87].

The use of such classification schemes is very helpful in studies of complex systems such as tin-containing heterogeneous catalysts. Some of the observed species usually vary during activation and/or catalytic reaction. For instance, one of the Sn(IV) species that was identified as tin on the support in direct contact with platinum particles was found to be predominantly reduced to Sn(II) in an H_2 flow at 500 °C.

Depending on the catalytic reaction studied, the possibility of distinguishing the various forms of tin by MbS, to identify those in close contact with platinum, and to follow their evolution during chemical reactions can then be of help in assessing the individual influence of each species on the catalytic properties. A deeper insight into the mechanisms determining the selectivity and stability of the catalysts can thus be obtained.

10.11 Conclusion

The main limitation to the application of MbS in the field of catalysis is the restricted number of elements that can be studied. However, for catalytic systems containing a suitable Mössbauer element, such as iron, cobalt, antimony, ruthenium, iridium, and gold, the technique provides a wealth of useful and often unique information. This is particularly appealing if one considers that some of the Mössbauer elements in

catalysis, such as iron, cobalt, and tin, also have a more complex chemistry than, for instance, the noble metals.

The most important advantages of the application of MbS in heterogeneous catalysis are that it is a highly specific technique with no interference caused by other chemical species, and that in some cases it can be used to study catalysts under catalytic reaction conditions.

The importance of MbS in the field of catalysis can be summarized in a few words by the remark made more than 20 years ago by Hans Niemantsverdriet [88]: "Mössbauer spectroscopy has given highly relevant and often unique information on a relatively small number of, however, extremely important catalyst systems."

Further developments will be made possible by the accessibility of new synchrotron-based MbS techniques, referred to as nuclear resonance scattering (NRS) of synchrotron radiation, and including a wide range of experimental techniques, such as nuclear forward scattering (NFS), nuclear inelastic scattering (NIS), and nuclear Bragg diffraction (NBD) [89]. These techniques profit from the brilliance of synchrotron radiation, up to 10 orders of magnitude more intense than that of the strongest radioactive sources, and therefore producing a count rate within the energy band given by the natural width of the Mössbauer nuclear transition that is comparable to that of conventional transmission MbS experiments. Moreover, they allow the accessibility of Mössbauer isotopes having sources that have very short half-lives or are difficult to prepare, such as ^{193}Ir and ^{197}Au. Finally, techniques such as NFS have the advantage of being time resolved, opening up new areas of research in the investigation of materials under reaction conditions, for example, in the study of adsorption reactions. This wealth of tools is still under development in the field of nuclear physics, but hopefully will become available to materials scientists in the near future [90, 91].

References

1 Adetunji, J. and Dransfield, A.T. (2002) The beginnings of Mössbauer spectroscopy. *Educ. Chem.*, **39** (4), 97–100.

2 Klingelhöfer, G., Morris, R.V., Bernhardt, B., Schröder, C., Rodionov, D.S., de Souza, P.A. Jr., Yen, A., Gellert, R., Evlanov, E.N., Zubkov, B., Foh, J., Bonnes, U., Kankeleit, E., Gütlich, P., Ming, D.W., Renz, F., Wdowiak, T., Squyres, S.W., and Arvidson, R.E. (2004) Jarosite and hematite at Meridiani Planum from Opportunity's Mössbauer spectrometer. *Science*, **306** (5702), 1740–1745.

3 Morris, R.V., Klingelhöfer, G., Bernhardt, B., Schröder, C., Rodionov, D.S., de Souza, P.A. Jr., Yen, A., Gellert, R., Evlanov, E.N., Foh, J., Kankeleit, E., Gütlich, P., Ming, D.W., Renz, F., Wdowiak, T., Squyres, S.W., and Arvidson, R.E. (2004) Mineralogy at Gusev crater from the Mössbauer spectrometer on the Spirit rover. *Science*, **305** (5685), 833–836.

4 Goldanskii, V.I. and Herber, R.H. (eds.) (1968) *Chemical Applications of Mössbauer Spectroscopy*, Academic Press, New York.

5 Greenwood, N.N. and Gibb, T.C. (1971) *Mössbauer Spectroscopy*, Chapman and Hall, London.

6 Gonser, U. (ed.) (1975) *Mössbauer Spectroscopy*, Springer, Berlin.

7 Shenoy, G.K. and Wagner, F.E. (eds.) (1978) *Mössbauer Isomer Shifts*, North-Holland, Amsterdam.

8 Cohen, R.L. (ed.) (1976) *Applications of Mössbauer Spectroscopy*, vol. **1**, Academic Press, New Tork.

9 Cohen, R.L. (ed.) (1980) *Applications of Mössbauer Spectroscopy*, vol. **2**, Academic Press, New York.

10 Long, G.J. (ed.) (1984) *Mössbauer Spectroscopy Applied to Inorganic Chemistry*, vol. 1, Plenum Press, New York.

11 Long, G.J. (ed.) (1987) *Mössbauer Spectroscopy Applied to Inorganic Chemistry*, vol. 2, Plenum Press, New York.

12 Long, G.J. (ed.) (1989) *Mössbauer Spectroscopy Applied to Inorganic Chemistry*, vol. 3, Plenum Press, New York.

13 Niemantsverdriet, J.W.H. (1995) Mössbauer spectroscopy, in *Spectroscopy in Catalysis*, 1st edn, VCH Verlag GmbH, Weinheim, pp. 111–136.

14 Millet, J.-M.M. (2007) Mössbauer spectroscopy in heterogeneous catalysis. *Adv. Catal.*, **51**, 309–350.

15 Mössbauer, R.L. (1958) Kernresonanzabsorption von gammastrahlung in ^{191}Ir. *Naturwissenschaften*, **45** (22), 538–539.

16 Mössbauer, R.L. (1958) Kernresonanzfluoreszenz von gammastrahlung in ^{191}Ir. *Z. Phys.*, **151** (2), 124–143.

17 Mössbauer, R.L. (1961) Recoilless nuclear resonance absorption of gamma radiation *Nobel Prize Lecture*, Stockholm, Sweden (Nobelprize.org) pp. 1–18.

18 Long, G.J., Cranshaw, T.E., and Longworth, G. (1983) The ideal Mössbauer effect absorber thicknesses. *Mössbauer Effect Ref. Data J.*, **6**, 42–49.

19 Rancourt, D.G., McDonald, A.M., Lalonde, A.E., and Ping, J.Y. (1993) Mössbauer absorber thicknesses for accurate site populations in iron-bearing minerals. *Am. Mineral.*, **78** (1–2), 1–7.

20 Hazony, Y. (1966) Effect of zero-point motion on the Mössbauer spectra of $K_4Fe(CN)_6$ and $K_4Fe(CN)_6{\cdot}3H_2O$. *J. Chem. Phys.*, **45** (7), 2664–2668.

21 Herber, R.H. (1983) Mössbauer lattice temperature of tetragonal ($P4/nmm$) SnO. *Phys. Rev. B*, **27** (7), 4013–4017.

22 Herber, R.H., Smelkinson, A.E., Sienko, M.J., and Schneemeyer, L.F. (1978) Lattice dynamics in covalent solids: Sn in $SnS_{2-x}Se_x (0 \leq x \leq 2)$. *J. Chem. Phys.*, **68** (8), 3705–3712.

23 Parish, R.V. (1984) Gold-197 Mössbauer spectroscopy in the characterization of gold compounds, in *Mossbauer Spectroscopy Applied to Inorganic Chemistry* (ed. G.J. Longs), Plenum Press, New York, pp. 577–617.

24 Klingelhöfer, G., Morris, R.V., De Souza, P.A., Rodionov, D.S., and Schröder, C. (2006) Two Earth years of Mössbauer studies of the surface of Mars with MIMOS II. *Hyperfine Interact.*, **170** (1–3), 169–177.

25 De Grave, E., Vandenberghe, R.E., and Dauwe, C. (2005) ILEEMS: methodology and applications to iron oxides. *Hyperfine Interact.*, **161** (1–4), 147–160.

26 Stevens, J.G. and Bowen, L.H. (1978) Mössbauer spectroscopy. *Anal. Chem.*, **50** (5), 176R–188R.

27 Cranshaw, T.E. (1974) The deduction of the best values of the parameters from Mössbauer spectra. *J. Phys. E: Sci. Instrum.*, **7** (2), 122–124.

28 Hohenemser, C. (1965) Measurement of the Mössbauer recoilless fraction in β-Sn for 1.3 to 370 K. *Phys. Rev.*, **139** (1A), A185–A196.

29 Parish, R.V. (1984) Structure and bonding in tin compounds, in *Mossbauer Spectroscopy Applied to Inorganic Chemistry* (ed. G.J. Longs), Plenum Press, New York, pp. 527–576.

30 Blaha, P. (2010) Calculations of Mössbauer parameters in solids by DFT bandstructure calculations. *J. Phys. Conf. Ser.*, **217** (1), 012009.

31 Martin, R.M. (2004) *Electronic Structure: Basic Theory and Practical Methods*, Cambridge University Press, Cambridge.

32 Petrilli, H.M., Blöchl, P.E., Blaha, P., and Schwarz, K. (1998) Electric-field-gradient calculations using the projector augmented wave method. *Phys. Rev. B*, **57** (23), 14690–14697.

33 Blaha, P., Schwarz, K., Madsen, G.K.H., Kvasnicka, D., and Luitz, J. (2010) *WIEN2k - An Augmented PlaneWave + Local Orbitals Program for Calculating Crystal*

Properties Version: 10.1 (Release 16.06.2010) Wien, Austria ISBN: 3-9501031-1-2.

34 Svane, A., Christensen, N.E., Rodriguez, C.O., and Methfessel, M. (1997) Calculations of hyperfine parameters in tin compounds. *Phys. Rev. B*, **55** (18), 12572–12577.

35 Cornell, R.M. and Schwertmann, U. (1996) *The Iron Oxides*, VCH Verlag GmbH, Weinheim.

36 Haas, H. and Shirley, D.A. (1973) Nuclear quadrupole interaction studies by perturbed angular correlations. *J. Chem. Phys.*, **58** (8), 3339–3355.

37 Gibb, T.C., Greatrex, R., Greenwood, N.N., and Meinhold, R.H. (1974) Ruthenium-99 Mössbauer spectra of some nitrido complexes of Ru(VI). *Chem. Phys. Lett.*, **29** (3), 379–382.

38 Stievano, L. and Wagner, F.E. (2005) Investigation of catalytic materials using 197Au Mössbauer spectroscopy. *AIP Conf. Proc.*, **765** (1), 3–12.

39 Haruta, M., Kobayashi, T., Sano, H., and Yamada, N. (1987) Novel gold catalysts for the oxidation of carbon monoxide at a temperature far below 0 °C. *Chem. Lett.*, **4** (2), 405–408.

40 Hutchings, G.J. (2004) New directions in gold catalysis. *Gold Bull.*, **37** (1–2), 3–11.

41 Hashmi, A.S.K. and Hutchings, G.J. (2006) Gold catalysis. *Angew. Chem. Int. Ed.*, **45** (47), 7896–7936.

42 Bond, G.C., Louis, C., and Thompson, D.T. (eds.) (2006) *Catalysis by Gold*, Imperial College Press, London.

43 Delgass, W.N., Boudart, M., and Parravano, G. (1968) Mössbauer spectroscopy of supported gold catalysts. *J. Phys. Chem.*, **72** (10), 3563–3567.

44 Lam, Y.L. and Boudart, M. (1977) Preparation of small Au–Pd particles on silica. *J. Catal.*, **50** (3), 530–540.

45 Bönnemann, H., Endruschat, U., Tesche, B., Rufińska, A., Lehmann, C.W., Wagner, F.E., Filoti, G., Pârvulescu, V., and Pârvulescu, V.I. (2000) An SiO_2-embedded nanoscopic Pd/Au alloy colloid. *Eur. J. Inorg. Chem.*, **2000** (5), 819–822.

46 Pârvulescu, V.I., Pârvulescu, V., Endruschat, U., Filoti, G., Wagner, F.E., Kübel, C., and Richards, R. (2006) Characterization and catalytic-hydrogenation behavior of SiO_2-embedded nanoscopic Pd, Au, and Pd–Au alloy colloids. *Chem. Eur. J.*, **12** (8), 2343–2357.

47 Friedl, J., Wagner, F.E., Nkosi, B., Towert, M., Coville, N.J., Adams, M.D., and Hutchings, G.J. (1991) ^{197}Au Mössbauer study of the deactivation and reactivation of a carbon-supported AuCl. *Hyperfine Interact.*, **69** (1–4), 767–770.

48 Nkosi, B., Coville, N.J., Hutchings, G.J., Adams, M.D., Friedl, J., and Wagner, F.E. (1991) Hydrochlorination of acetylene using gold catalysts: a study of catalyst deactivation. *J. Catal.*, **128** (2), 366–377.

49 Stievano, L., Santucci, S., Lozzi, L., Calogero, S., and Wagner, F.E. (1998) Au-197 Mössbauer study of gold particles obtained by evaporation of metallic gold on Mylar. *J. Non-Cryst. Solids*, **232**, 644–649.

50 Paulus, P.M., Goossens, A., Thiel, R.C., van der Kraan, A.M., Schmid, G., and de Jongh, L.J. (2001) Surface and quantum-size effects in Pt and Au nanoparticles probed by ^{197}Au Mössbauer spectroscopy. *Phys. Rev. B*, **64** (20), 205418.

51 Zwijnenburg, A., Goossens, A., Sloof, W.G., Crajé, M.W.J., van der Kraan, A.M., de Jongh, L.J., Makkee, M., and Moulijn, J.A. (2002) XPS and Mössbauer characterization of Au/TiO_2 propene epoxidation catalysts. *J. Phys. Chem. B*, **106**, 9853–9862.

52 van der Kraan, A.M. (1973) Mössbauer effect studies of surface ions of ultrafine α-Fe_2O_3 particles. *Phys. Status Solidi A*, **18** (1), 215–226.

53 Candy, J.P., Roisin, E., Basset, J.M., Uzio, D., Morin, S., Fischer, L., Olivier-Fourcade, J., and Jumas, J.C. (2005) Evidence for direct observation by Mössbauer spectroscopy of surface tin atoms in platinum–tin particles. *Hyperfine Interact.*, **165** (1–4), 55–60.

54 Bødker, F., Mørup, S., and Niemantsverdriet, J.W.H. (1992) *In situ* Mössbauer spectroscopy of carbon-supported iron catalysts at cryogenic temperatures and in

external magnetic fields. *Catal. Lett.*, **13** (3), 195–202.

55 Niemantsverdriet, J.W.H., van der Kraan, A.M., Delgass, W.N., and Vannice, M.A. (1985) Small-particle effects in Moessbauer spectra of a carbon-supported iron catalyst. *J. Phys. Chem.*, **89** (1), 67–72.

56 Mørup, S., Dumesic, J.A., and Tøpsoe, H. (1980) in *Applications of Mössbauer Spectroscopy* (ed. R.L. Cohens), Academic Press, New York, pp. 1–54.

57 Christensen, P.H., Mørup, S., and Niemantsverdriet, J.W.H. (1985) Particle size determination of superparamagnetic α-iron in carbon-supported catalysts by *in situ* Moessbauer spectroscopy. *J. Phys. Chem.*, **89** (23), 4898–4900.

58 Weckhuysen, B.M. (2002) Snapshots of a working catalyst: possibilities and limitations of *in situ* spectroscopy in the field of heterogeneous catalysis. *Chem. Commun.*, **38** (2), 97–110.

59 Niemantsverdriet, J.W.H. and Delgass, W.N. (1999) *In situ* Mössbauer spectroscopy in catalysis. *Top. Catal.*, **8** (1–2), 133–140.

60 Van der Kraan, A.M. (2000) The role of Mössbauer spectrometry in designing a catalyst. *Hyperfine Interact.*, **126** (1–4), 107–111.

61 Lox, E.S., Marina, G.B., De Grave, E., and Bussière, P. (1988) Characterization of a promoted precipitated iron catalyst for Fischer–Tropsch synthesis. *Appl. Catal.*, **40**, 197–218.

62 Pijolat, M., Perrichon, V., and Bussière, P. (1987) Study of the carburization of an iron catalyst during the Fischer–Tropsch synthesis: influence on its catalytic activity. *J. Catal.*, **107** (1), 82–91.

63 Xu, J., Bartholomew, C.H., Sudweeks, J., and Eggett, D.L. (2003) Design, synthesis, and catalytic properties of silica-supported, Pt-promoted iron Fischer–Tropsch catalysts. *Top. Catal.*, **26** (1–4), 55–71.

64 Xu, J. and Bartholomew, C.H. (2005) Temperature-programmed hydrogenation (TPH) and *in situ* Mössbauer spectroscopy studies of carbonaceous species on silica-supported iron Fischer–Tropsch catalysts. *J. Phys. Chem. B*, **109**, 2392–2403.

65 Moodley, D.J., van de Loosdrecht, J., Saib, A.M., and Niemantsverdriet, J.W.H. (2010) The formation and influence of carbon on cobalt-based Fischer–Tropsch synthesis catalysts: an integrated review, in *Advances in Fischer–Tropsch Synthesis, Catalysts, and Catalysis* (eds. B.H. Davis and M.L. Occellis), CRC Press, Taylor & Francis Group, Boca Raton, FL, pp. 49–81.

66 Leendert Bezemer F G., Remans, T.J., van Bavel, A.P., and Dugulan, A.I. (2010) Direct evidence of water-assisted sintering of cobalt on carbon nanofiber catalysts during simulated Fischer–Tropsch conditions revealed with *in situ* Mössbauer spectroscopy. *J. Am. Chem. Soc.*, **132** (25), 8540–8541.

67 Burch, R. (1981) Platinum–tin reforming catalysts: I. The oxidation state of tin and the interaction between platinum and tin. *J. Catal.*, **71** (2), 348–359.

68 Neri, G., Milone, C., Galvagno, S., Pijpers, A.P.J., and Schwank, J. (2002) Characterization of Pt–Sn/carbon hydrogenation catalysts. *Appl. Catal. A: Gen.*, **227** (1–2), 105–115.

69 Bacaud, R., Bussière, P., and Figueras, F. (1981) Mössbauer spectra investigation of the role of tin in platinum–tin reforming catalysts. *J. Catal.*, **69** (2), 399–409.

70 Bacaud, R., Bussière, P., Figueras, F., and Mathieu, J.-P. (1976) Role of tin in platinum-tin reforming catalysts. *Stud. Surf. Sci. Catal.*, **1**, 509–523.

71 Hobson, M.C., Goresh, S.L., and Khare, G.P. (1993) A Mössbauer spectroscopy study of platinum–tin reforming catalysts. *J. Catal.*, **142** (2), 641–654.

72 Stievano, L., Calogero, S., Wagner, F.E., Galvagno, S., and Milone, C. (1999) Mossbauer characterization of carbon supported ruthenium–tin catalysts. *J. Phys. Chem. B*, **103** (44), 9545–9556.

73 Stievano, L., Wagner, F.E., Calogero, S., Recchia, S., Dossi, C., and Psaro, R. (2000) ^{119}Sn Mössbauer study and catalytic properties of magnesia-supported platinum–tin catalysts prepared by

surface organometallic chemistry. *Stud. Surf. Sci. Catal.*, **130**, 3903–3908.

74 Menzel, M., Mehner, H., Mönnich, I., and Berndt, H. (2000) Investigation of PdSn catalysts for nitrate removal in drinking water processing. *Hyperfine Interact.*, **126** (1–4), 89–93.

75 Sales, E.A., Jove, J., Nectoux, F., Bozon-Verduraz, F., and Mendes, M.J. (1998) Mössbauer study of ^{119}Sn–Pd catalysts for selective hydrogenation of hexa-1,5-diene. *Hyperfine Interact.*, **112** (1–4), 13–18.

76 Lázár, K., Rhodes, W.D., Borbáth, I., Hegedüs, M., and Margitfalvi, J.L. (2002) Reaction-induced transformations in Pt–Sn/SiO_2 catalysts: *in situ*^{119}Sn Mössbauer study. *Hyperfine Interact.*, **139–140** (1–4), 87–96.

77 Berry, F.J. and Zhang, T. (1991) Supported platinum–tin catalysts: the identification by tin-119 Mössbauer spectroscopy of the unusual oxidation of tin during pretreatment under reducing conditions. *Hyperfine Interact.*, **67** (1–4), 543–547.

78 Nava, N., Morales, M.A., Vanoni, W., Toledo, J.A., Baggio-Saitovitch, E., and Viveros, T. (2001) Structural behavior of Pt–Sn supported on MgO. *Hyperfine Interact.*, **134** (1), 81–92.

79 Hassoun, J., Fernicola, A., Navarra, M.A., Panero, S., and Scrosati, B. (2009) An advanced lithium-ion battery based on a nanostructured Sn–C anode and an electrochemically stable LiTFSi-Py24TFSI ionic liquid electrolyte. *J. Power Sources*, **195** (2), 574–579.

80 Margitfalvi, J.L., Borbáth, I., Hegedus, M., Szegedi, Á., Lázár, K., Gobölös, S., and Kristyán, S. (2002) Low temperature oxidation of CO over tin-modified Pt/SiO_2 catalysts. *Catal. Today*, **73** (3–4), 343–353.

81 Cortright, R.D., and Dumesic, J.A. (1994) Microcalorimetric, spectroscopic, and kinetic studies of silica supported Pt and Pt/Sn catalysts for isobutane dehydrogenation. *J. Catal.*, **148** (2), 771–778.

82 Margitfalvi, J.L., Borbáth, I., Hegedüs, M., and Tompos, A. (2002) Preparation of new type of Sn-Pt/SiO_2 catalysts for carbonyl activation. *Appl. Catal. A: Gen.*, **229** (1–2), 35–49.

83 Olivier-Fourcade, J., Womes, M., Jumas, J.C., Le Peltier, F., Morin, S., and Didillon, B. (2004) Investigation of redox properties of different PtSn/Al_2O_3 catalysts. *ChemPhysChem*, **5** (11), 1734–1744.

84 Boualleg, M., Baudouin, D., Basset, J.-M., Bayard, F., Candy, J.-P., Jumas, J.-C., Veyre, L., and Thieuleux, C. (2010) Unexpected, spontaneous and selective formation of colloidal Pt_3Sn nanoparticles using organometallic Pt and Sn complexes. *Chem. Commun.*, **46**, 4722–4724.

85 Jahel, A., Avenier, P., Lacombe, S., Olivier-Fourcade, J., and Jumas, J.-C. (2010) Effect of indium in trimetallic Pt/Al_2O_3SnIn–Cl naphtha-reforming catalysts. *J. Catal.*, **272** (2), 275–286.

86 Jahel, A., Avenier, P., Lacombe, S., Olivier-Fourcade, J., and Jumas, J.-C. (2010) Investigation by Mössbauer spectroscopy of Sn redox transformations during H_2/O_2 titration on Pt/Al_2O_3Sn–Cl and Pt/Al_2O_3SnIn–Cl naphtha reforming catalysts. *J. Phys. Conf. Ser.*, **217** (1), 01204587.

87 Jumas, J.-C. and Olivier-Fourcade, J. (2011) Personal communication.

88 Niemantsverdriet, J.W.H. (1989) How important is Mössbauer spectroscopy in catalysis? *Hyperfine Interact.*, **47**, 219–235.

89 Gerdau, E., van Bürck, U., and Rüffer, R. (1999) Historical overview and introduction. *Hyperfine Interact.*, **123–124** (1–4), 3–10.

90 Hastings, J.B., Siddons, D.P., van, B.U., Hollatz, R., and Bergmann, U. (1991) Mössbauer spectroscopy using synchrotron radiation. *Phys. Rev. Lett.*, **66** (6), 770–776.

91 Seto, M., Masuda, R., Higashitaniguchi, S., Kitao, S., Kobayashi, Y., Inaba, C., Mitsui, T., and Yoda, Y. (2009) Synchrotron-radiation-based Mössbauer spectroscopy. *Phys. Rev. Lett.*, **102** (21), 217602.

11
Low Energy Ion Scattering and Secondary Ion Mass Spectrometry

Norbert Kruse and Sergey Chenakin

11.1
Introduction

When a beam of accelerated ions impinges on the surface of a solid, a number of phenomena occur. Interacting with the solid, the ions experience elastic or inelastic scattering from the surface atoms. Momentum transfer gives rise to the ejection (or sputtering) of atoms and molecules from this solid as charged and neutral species. The dissipation of the incident energy also brings about the emission of electrons and photons. Finally, the primary ions penetrate into the solid, thus producing implantation and radiation defects profiles. All these emission phenomena can be used for the purposes of materials characterization; however, the analysis of the charged components of the scattered and sputtered particles has turned out most promising in the development of powerful spectroscopic techniques known as low-energy ion scattering (LEIS) [or ion scattering spectroscopy (ISS)] and secondary ion mass spectrometry (SIMS). From the viewpoint of detection sensitivity, LEIS and SIMS are undoubtedly the champions in the "surface analysis league": SIMS has an extremely high elemental sensitivity (10^{-2}–10^{-7} at.%) and LEIS demonstrates exclusively first-atomic layer sensitivity (below 10^{-4} monolayer).

Sputtering and scattering appear as a matter of course in present-day materials analyses. However, similarly to other particle–surface interactions, a long history has paved the way to the status quo. In 1910, Thomson suggested a method to identify chemically ions produced in a discharge tube using superimposed electric and magnetic fields for mass separation [1]. He noticed that the accelerated positive ions caused "disintegration" of the metal cathode – a process that has later come to be known as sputtering. The phenomenon of secondary ion emission seems to have been discovered by Campbell, who reported in 1915 [2] on the observation of a charged component in ion-induced "disintegration" of a solid. First experiments which may be regarded as a kind of SIMS precursor were performed in 1938 by Sloane and Press [3], who observed mass spectrometrically the emission of sputtered negative ions and even measured their energy distribution. The history of ion scattering spectroscopy seems to have started with the work of Klein, who reported

Characterization of Solid Materials and Heterogeneous Catalysts: From Structure to Surface Reactivity, First Edition. Edited by Michel Che and Jacques C. Védrine.
© 2012 Wiley-VCH Verlag GmbH & Co. KGaA. Published 2012 by Wiley-VCH Verlag GmbH & Co. KGaA.

in 1925 the results of studying secondary electron and positive ion emission from a nickel surface under positive ion bombardment [4]. Klein revealed two groups of what he considered to be "reflected positive ions": one group had energies between 0 and 2 V (and was, as we know now, related to sputtered secondary ions) and the other had energies of approximately 90% of their primary energy. Soon afterwards, Read [5] and Gurney [6] described general regularities in the intensity, energy, and angular and spatial distributions of positive alkali metal ions scattered from a metal surface.

Nowadays, applications of both SIMS and LEIS extend across all areas of materials research, from the mere determination of the surface elemental composition to studying surface-specific processes such as adsorption, oxidation, corrosion, segregation, thin-film growth, and so on. These processes may be equally important in heterogeneous catalysis and their study may provide clues about the catalyst surface reactivity. As a consequence, a large number of SIMS/LEIS studies have been devoted to demonstrate this reactivity for model catalytic surfaces such as single crystals, thin films and polycrystalline foils. Real catalysts are, however, complex systems in terms of both structure and chemical composition. SIMS and LEIS can be employed to characterize real catalysts and may even provide guidance for the improvement of existing or the development of new highly active catalysts. These features will be of particular concern in this chapter.

Fogel' and co-workers were probably the first to apply SIMS for investigating processes in relation to heterogeneous catalysis. In 1967, a review of their work on the synthesis and decomposition of ammonia over Pt- and Fe-based catalyst surfaces using SIMS as the analytical characterization technique was published [7]. In the same year, LEIS started to impact as a powerful method in surface analysis, as first described by Smith [8].

The wealth of information obtainable by SIMS and LEIS was fast recognized by the community and prompted further studies with model and real catalyst materials. The rising interest in employing SIMS and LEIS in catalysis research was certainly also driven by the routine availability of ultra-high vacuum (UHV) conditions, which must be regarded a prerequisite for such studies. The current steep rise in interest in providing surface chemical and structural information under *in situ* reaction conditions at ambient pressures and temperatures ("*operando*" conditions) using SIMS and LEIS therefore meets the limits of technical feasibility. Earlier studies by the groups of Vickerman, M. and E. Gillet, White, Niemantsverdriet, Kruse, and others have demonstrated the ability of SIMS to provide mechanistic and kinetic information during the ongoing catalytic reaction at overall low pressures. With regard to LEIS, Brongersma's group has developed a differentially pumped continuous-flow pressure cell [9] allowing LEIS measurements in the presence of reactant gases at pressures up to 0.1 Pa and temperatures up to 800 K.

We shall not consider SIMS/LEIS applications in adsorption–desorption, kinetic, and mechanistic research on model catalyst surfaces, as they do not fall within the purpose of this chapter. However, to span the bridge for the interested reader, we shall refer briefly to some of the trendsetting work in that area. Mohri *et al.* [10], for example, used SIMS in combination with temperature-programmed desorption

(TPD) and Auger electron spectroscopy (AES) to elucidate the reaction mechanism governing the catalytic decomposition of deuterium-labeled formic acid (HCOOH, DCOOH, and HCOOD) over Ni. White and co-workers, using static secondary ion mass spectrometry (SSIMS) and TPD, studied the kinetics and mechanism of the formation and decomposition of deuterium-labeled methanol (CH_3OD) on oxygen-covered Pt(111) [11], the decomposition of labeled acetylene and ethylene on Ni (100) [12] and Ni(111) [13], and the polymerization and decomposition of acetaldehyde (CH_3CHO) on Ru(001) [14]. Kruse and co-workers employed SSIMS, TPD, and X-ray photoelectron spectroscopy (XPS) to investigate the mechanisms ruling methanol (CH_3OH, CH_3OD) decomposition on Pd(111) [15, 16] and showed that both O−C and O−H splitting in adsorbing methanol can occur at low temperatures. This finding triggered an interesting controversy with Levis *et al.* [17], who claimed that O−C activation was dominant and thus produced adsorbed methyl radicals. SSIMS, TPD, XPS, and LEIS have also been used for probing the dissociation kinetics of NO on Rh{110} and deriving the kinetic parameters of this reaction [18]. A kinetic compensation effect has been revealed for the same reaction on Rh(111) [19] but has not been explained theoretically in a convincing manner so far. The activities in the field of surface reaction chemistry have been reviewed [20] to show that SIMS offers unique opportunities to trace adsorbed species including reactants and intermediates and also products of catalytic surface reactions in real time at overall low pressures so as to provide information on catalytic reaction mechanisms.

To improve the performance of real catalysts it is essential to understand their proper functioning in terms of their surface chemical, electronic, and structural properties as a function of preparation, activation, and chemical environment. The first combined application of LEIS and SIMS for characterizing catalytic materials in relation to NO_x control was reported in 1975 by Shelef *et al.* [21], who examined spinels $CoAl_2O_4$, $CuAl_2O_4$, $NiAl_2O_4$, $ZnAl_2O_4$, and $CuCr_2O_4$ using LEIS (ISS) and ranked them with respect to their ability to chemisorb nitric oxide. Good qualitative agreement was observed between the presence of certain transition metal ions in the outermost surface layer of these spinels and the chemisorption of nitric oxide. In particular, the complete absence of Co ions in the surface layer of the polycrystalline $CoAl_2O_4$ corresponded to the lowest NO uptake on this spinel surface. Although such materials have not found their way into the market of catalytic converters (because of legislative constraints), this work nicely demonstrated the usefulness of the experimental approach. A similar "early" demonstration was provided by Wheeler and Bettman [22], who employed LEIS and SIMS for characterizing Al_2O_3- and MgO-doped Co_3O_4 samples. They were able to correlate the strong decrease in the ethylene oxidation activity with the presence of these dopants on the surface of the samples.

Since these initial studies, the number of LEIS and SIMS investigations (also in combination with other techniques) for catalyst characterization has increased significantly. This is illustrated in Figure 11.1a, which compiles the evolution of relevant papers for the last 35 years. It seems that the peak activity was in the period between 1996 and 2001. Although it might be argued that the absolute numbers of

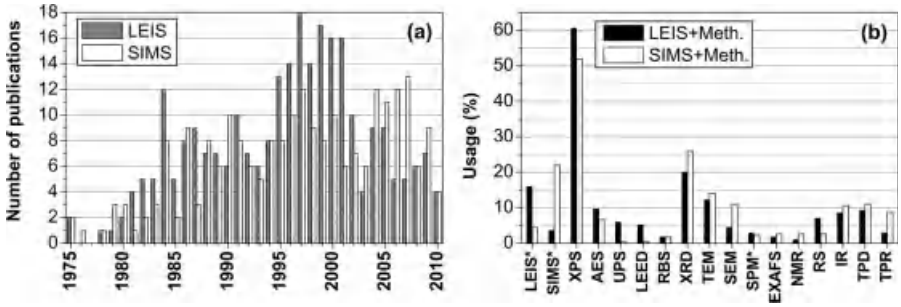


Figure 11.1 (a) The number of studies on LEIS and SIMS characterization of catalytic materials published per year during the last 35 years (the literature search was performed using Google Academy, SCOPUS, and SciFinder engines, and references in the papers found) and (b) frequency of using various analytical methods in combination with LEIS and SIMS. LEIS* and SIMS* refer to studies in which these methods were exclusively used; SPM* = STM + AFM.

SIMS/LEIS catalytic research papers in Figure 11.1 are at the lower limit, we expect the fluctuating trend of employment of both methods to reflect reality fairly well. Overall, the results of joint efforts in providing information on the surface characteristics of catalytic materials by using LEIS and SIMS and relating them to their catalytic performance have been described in more than 500 papers.

Overall, LEIS seems to be employed more frequently than SIMS. To obtain the most complete picture of the physical–chemical state of catalysts, LEIS and SIMS are generally combined with other techniques of surface and bulk analysis, such as XPS, AES, ultraviolet photoelectron spectroscopy (UPS), low-energy electron diffraction (LEED), Rutherford backscattering (RBS), X-ray diffraction (XRD), transmission electron microscopy (TEM), scanning electron microscopy (SEM), scanning tunneling microscopy (STM), atomic force microscopy (AFM), infrared (IR) spectroscopy, extended X-ray absorption fine structure (EXAFS), nuclear magnetic resonance (NMR) spectroscopy, Raman spectroscopy (RS), temperature-programmed desorption (TPD), and temperature-programmed reaction (TPR). Figure 11.1b shows the frequency of using these methods to complement LEIS and SIMS analyses. As can be seen, XPS is the most often used complementary method of surface analysis, being applied in over 60% of LEIS-related and in over 50% of SIMS-related studies.

Various examples of LEIS and SIMS applications [including time-of-flight (TOF) SIMS and surface imaging] for the surface characterization of catalytic materials have been presented in a number of books [20, 23–27] and reviews [28–30]. In this chapter, the main emphasis is on summarizing the efforts made in using both SIMS and LEIS to demonstrate the influence of structure and chemical composition on the performance of catalytic materials. We mainly focus on those studies which provide a clear correlation between parameters of the surface physico-chemical state of solids and catalysts derived from LEIS and SIMS measurements and their surface reactivity/catalytic activity. Some examples are presented in detail. Only a brief account is given

of the achievements of SIMS and LEIS in following the adsorption and reaction kinetics of "simple" molecules on well-behaved single-crystal surfaces. We first briefly consider the basic principles and potential of these techniques.

11.2
Secondary Ion Mass Spectrometry

11.2.1
Basic Principles

Bombarding a solid with a beam of primary ions, typically with energies in the range 1–20 keV, brings about sputtering. A fraction of the sputtered particles leave the surface in a charged state as secondary ions (secondary ion emission phenomenon). The subsequent mass spectrometric analysis of the sputtered secondary ions constitutes the essence of the SIMS technique and delivers information on the chemical composition of the sputtered layer. In general, the mass spectrum of secondary ions contains peaks of various particles: singly or doubly charged atomic ions along with their isotopes of material-specific components and surface- and/or bulk-derived impurities, polyatomic (cluster) ions, and molecular ions. Generally, secondary ions can be emitted in both a positively and negatively charged state.

The formation of secondary ions is the result of a rather complicated multi-step process, which is theoretically far from being completely understood. It involves three main stages: (i) displacement of a surface atom by an impinging energetic primary ion which initiates a collision cascade in the solid; (ii) ejection of an atom (or group of atoms) located in the surface layer into the vacuum as a result of the collision cascade; (iii) intense electronic exchange between the ejected particle and the surface giving rise to the formation of a secondary ion. The depth of origin of sputtered particles depends on several factors; however, it does not exceed ~20 Å. The major part of atoms (and of secondary ions) originates from a depth of 3–6 Å, thus making SIMS a surface-sensitive technique.

The current $I_M{}^{\pm}$ of secondary ions of a given element M emitted from a metal or multicomponent solid is determined by the following parameters:

$$I_M{}^{\pm} \propto I_0 Y C_M \alpha_M{}^{\pm} \eta \tag{11.1}$$

where I_0 is the flux of primary ions, Y the sputtering yield (number of atoms ejected per primary ion), C_M the fractional concentration of the element M in the analyzed volume, $\alpha_M{}^{\pm}$ the ionization probability (number of ions per number of sputtered particles of that element), and η an instrumental factor (transmission and detector efficiency). This dependence is the potential basis for performing a quantitative analysis by SIMS. In reality, however, the determination of C_M is a rather difficult task because the ionization probability $\alpha_M{}^{\pm}$ may vary over 3–4 orders of magnitude depending on the nature of the element, the matrix in which it is present, the chemical state of the surface (availability of oxides, adsorbed species, etc.), and the sort of primary ions used for sputtering (e.g., Ar^+, $O_2{}^+$, or Cs^+). Therefore, in

practice, a "semiquantitative" analysis is most often performed. In this approach, C_M is derived from comparative measurements of the sample and external or internal standards that closely resemble the composition and chemical state of the material and contain a known concentration of M.

Inasmuch as SIMS is based on sputtering, it is a destructive technique. The erosion rate of the surface, which is controlled by the primary ion current density, defines the mode of SIMS analysis. In the dynamic mode, the primary ion current density used to sputter the sample is not limited and typically varies in the range from $\mu A\,cm^{-2}$ to $mA\,cm^{-2}$. In this mode, surface, "bulk," in-depth, and 2D/3D analyses can be performed with unsurpassed sensitivity.

In the static SIMS mode, the primary current density is significantly reduced (to 1–$0.1\,nA\,cm^{-2}$) to ensure extremely small sputter rates of fractions of a monolayer per hour (or less than $0.1\,nm\,h^{-1}$). This allows a very gentle analysis of the surface uppermost chemical structures formed by adsorption. To retain these structures while running static SIMS experiments, it is essential that no primary ion strikes the damaged area twice. This is an area several nanometers in diameter around the point of primary ion impact. Therefore, the total ion dose (the product of the primary ion current density and the total analysis time) must be kept under a given so-called static limit, which is in the range of 10^{12}–10^{13} ions cm^{-2}. Under such conditions only 0.1–1% of the total atomic sites are bombarded during the measurement. This makes static SIMS a truly surface analytical technique, causing overall negligible damage to the surface while ensuring a detection limit as low as 10^{-5} monolayer.

Typically, the SIMS instrument consists of an ion gun generating the beam of primary ions (a Wien filter or a magnetic mass spectrometer can be added to the ion gun to mass separate the primary ion species), a primary ion column for accelerating and focusing the beam on to the sample, a UHV chamber with a sample holder, and the secondary ion extraction lens system along with a mass analyzer separating the ions according to their mass-to-charge ratio.

Depending on the type of ion source and the purpose of the measurement, various primary ions can be used: positive and negative ions, ions of inert gases (Ar^+, Xe^+) or reactive gases (O^-, $O_2{}^+$, $N_2{}^+$), monoatomic ions (Cs^+, Ga^+, In^+), polyatomic ions ($SF_5{}^+$, $Bi_3{}^+$, $C_{60}{}^+$), and so on. To avoid scattering of the primary and secondary ions and to prevent interfering adsorption of gases on the sample surface, the pressure in the vacuum chamber should be below 10^{-5} Pa (10^{-8} Pa for static SIMS). To mass separate the secondary ions, three basic types of mass analyzers are employed: magnetic sector field, quadrupole, and TOF. The sector field mass spectrometer typically uses a combination of an electrostatic analyzer and a magnetic analyzer. The quadrupole mass analyzer separates the masses by resonant electric fields, which allow only selected masses to pass through. To improve the mass resolution, the quadrupole is typically preceded by an energy filter. The TOF mass analyzer separates the ions in a field-free drift tube according to their velocities. It requires a pulsed secondary ion flux which is typically produced by using a pulsed primary ion beam. This type of analyzer is the only one which is able to detect all generated secondary ions simultaneously. Moreover, TOF analyzers provide a high

transmission and can be operated over a wide mass range at high mass resolution ($m/\Delta m > 1000$) to ensure the TOF separation of ionic species of different chemical origins at otherwise the same nominal mass (e.g., $^{54.938}Mn^+$ and $^{55.055}C_4H_7{}^+$). Such analyzers are standard for static SIMS measurements.

It should be noted that despite the high mass resolution of TOF analyzers, the identification and assignment of peaks based on the natural abundance of isotopes can sometimes be cumbersome because of the mass interference of ions with different origins. The interpretation of the spectra and the discrimination of "important" from "less important" ionic species are central to the data analysis.

For the analysis of insulating materials, charge neutralization should be provided. Details can be found in reviews and books devoted to the technical aspects of SIMS analyses.

11.2.2
Potential of SIMS

SIMS is capable of identifying all elements, including hydrogen; in addition, the element's isotope composition can be measured. A quantitative evaluation of the elemental chemical composition is also possible.

Despite the low ionization probability (on average, $\alpha^+ \approx 10^{-3}$), SIMS is one of the most sensitive analytical tools with a detection limit of 10^{-2}–10^{-7} at.%, 10^{-5} monolayer. Its sensitivity is probably only surpassed by atom-probe field evaporation devices, which, however, suffer from a number of limitations as to the sample nature and preparation. The highest sensitivity in measuring positive ion yields is observed for alkali metals and the lowest for noble metals (Pt, Au); halogens and oxygen demonstrate the highest negative ion yields. The positive ion yields can be significantly enhanced by flooding the sample surface with oxygen or using O^- or $O_2{}^+$ primary ions, and for increasing the negative ion yields Cs^+ primary ions are most frequently used.

The direct emission of molecular secondary ions ($M_kX_mY_n{}^+$) is of particular interest for heterogeneous catalysis since it may provide information on the surface phase and molecular composition, the structure of adsorbed layers, the formation of bonds due to interaction between different chemical species, the presence of "surface complexes," and compounds. These secondary ions may be emitted intact or be produced by fragmentation of molecular structures in which relatively strong bonds exist between neighboring atoms. The emission of cluster ions ($M_n{}^+$) formed via recombination processes may reflect the short-range order in a complex or aggregate.

Variations of the secondary ion yield obtained as a function of azimuthal or polar angle of the primary beam incidence or angle of ion emission are indicative of the surface structure and sample crystallography. Energy distributions of secondary ions, being the product of the energy spectrum of sputtered atoms and the energy dependence of their ionization probability, $N^+(E_i) = N(E_a)\alpha^+(E_a)$, where $N(E_a) \propto E_a\,(E_a + E_b)^{-3}$, deliver information on the binding energy, E_b, of surface atoms and the mechanism of secondary ion formation.

One of the attractive features of dynamic SIMS is its capability of depth profiling by the controlled removal of successive sample layers by the ion beam with simultaneous recording of the intensity of secondary ions. In this manner, the in-depth distribution of components, trace elements, and compounds (by monitoring molecular ions) in a solid may be obtained with exceptionally high depth resolution (from several nanometers down to the sub-nanometer level). Profiling may range from a few nanometers to several hundred micrometers into the bulk. The sputtering rate, which defines the depth resolution, can be adjusted in the range from 10^{-1} to 10^{2} nm min^{-1} by changing the primary current density, the ion energy, the type of primary ions, and their angle of incidence. To improve the depth resolution further, the primary ion beam is typically raster-scanned over a well-defined sample area, and secondary ions are collected from the center of the sputter crater using an "electronic aperture."

A further remarkable feature is that SIMS may allow chemical imaging microanalysis of the surface in which the intensities of atomic or molecular secondary ions are monitored as a function of the location on the sample surface. Thus the 2D spatial distribution of elements and compounds is visualized. The image dimensions may vary from 500 μm to less than 10 μm. Two operating modes may be employed to provide images. In ion microscopy, a mass-selected secondary ion beam is transmitted from the sample to the detector without loss of information on the lateral position, to form an image with a lateral resolution of ~0.5 μm. In scanning ion microprobe imaging, a finely focused primary ion beam sweeps the sample in a raster pattern and suitable software registers the secondary ion intensities as a function of beam position. The lateral resolution in imaging SIMS depends on the microprobe diameter and extends down to 20 nm for liquid metal ion sources. Three-dimensional SIMS chemical mapping is also possible and can be obtained by acquiring ion images as a function of the sputtering time (image depth profiles). Since microscope sputtering rates often exceed microprobe rates by several orders of magnitude, microscope 3D imaging produces depth scales which are more compatible with the scale of the lateral images.

Despite a number of very attractive features of the SIMS technique, there are also shortcomings that prevent it from being used as routinely as electron spectroscopy for chemical analysis (ESCA, or XPS). The main drawbacks are certainly the lack of a solid theoretical foundation, the mass interference of "rich" spectra, and the so-called matrix effect, which manifests itself as a dramatic dependence of the secondary ion yield of a particular element on its chemical environment. This sometimes makes quantification rather intricate. To minimize the influence of matrix effects, ion intensity ratios are frequently considered. For example, in adsorbate-covered metal-supported catalysts, such ratios may be formed by relating the secondary ion intensities of metal–adsorbate species to those of the metal. In some cases, such normalized intensities reflect, after proper calibration, the surface coverage of adsorbed species. This will also be demonstrated in this chapter.

The summary of SIMS potentialities given above is not meant to provide a detailed description of the fundamentals, instrumentation, and application of SIMS for materials analysis. The reader is therefore referred to relevant books and reviews [31–37].

11.3
Low-Energy Ion Scattering (Ion Scattering Spectroscopy)

11.3.1
Main Concepts

As has been mentioned, a number of processes may be encountered when bombarding a target surface with primary ions. We shall now inspect those events that result in either reflection (scattering) of ions or recoiling surface atoms and which give rise to LEIS. The primary ion energies usually employed in relevant studies range between 0.5 and 10 keV. Both the scattered primary and recoiled surface particles are atoms that may be in neutral, positive, or negative charge states due to electronic charge exchange processes with the surface. They have discrete kinetic energies that are determined by the nature of the collision. Analyzing energies and angular distributions of the scattered and recoiled particles can provide direct information on the identity of the atoms, their elemental concentration, and structural arrangement in the surface. This analysis is straightforward because the kinematics of atomic collisions may be accurately described by classical mechanics. Accordingly, in an elastic binary collision of a projectile of mass M_1 and primary energy E_0 with a target atom of mass M_2 at rest, the energy transfer to a scattered particle depends only on the scattering angle θ. The kinematic factor, which is defined as the ratio $k = E_f/E_0$, can be derived from the energy and momentum conservation laws as

$$\frac{E_f}{E_0} = \frac{\left[\cos\theta \pm \left(A^2 - \sin^2\theta\right)^{\frac{1}{2}}\right]^2}{(1+A)^2} \tag{11.2}$$

where E_f is the final energy of the scattered particles and $A = M_2/M_1$. Since the E_f for a fixed scattering angle depends only on the mass ratio A, the energy spectra of the scattered ions will directly reflect the elemental composition of the investigated surface. This essentially constitutes the basis of LEIS.

In a similar way, the energy ratio for target recoil atoms can be deduced:

$$\frac{E_t}{E_0} = \frac{4A\cos^2\phi}{(1+A)^2}, \quad \text{for } \phi \leq 90^\circ \tag{11.3}$$

where E_t is the recoil energy of the target atom scattered under the recoil angle ϕ. The recoil atoms may be scattered either into the bulk or into the vacuum depending on the impact point of the primary ions. Direct recoils are thus different from the sputter event analyzed in SIMS, where secondary particles leave the surface after a momentum transfer in a collision cascade and usually have a broad energy distribution with a maximum at about 1–5 eV. The detection of direct recoils can be used for analytical purposes and is the basis of direct recoil spectroscopy (DRS), which is closely related to LEIS.

The yield of ions, S_M, backscattered from a surface atom of element M, is given by

$$S_M \propto I_0 C_M P_M^+ (\mathrm{d}\sigma_M/\mathrm{d}\Omega) R\eta \tag{11.4}$$

where I_0 is the primary ion current, C_M the atomic surface concentration of the element M, $P_M{}^+$ the fraction of ions surviving scattering from element M, $d\sigma_M/d\Omega$ the differential scattering cross-section for scattering from element M (which can be calculated for a given scattering potential), R the "surface geometry" factor, which takes into account the surface roughness and shielding by neighboring atoms, and η the instrumental factor which considers the influence of the detector solid angle, the detector efficiency, and the analyzer transmission. The neutralization of the ions depends on the time of interaction with the target. The ion fraction (or ion survival probability) is, therefore, expressed by the exponential dependence on the reciprocal velocity v of the ion (or its normal component $v_\perp$), considering the incoming (i) and the outgoing (o) trajectories, as

$$P_M^+ = \exp\left[-v_c\left(\frac{1}{v_i} + \frac{1}{v_o}\right)\right] \tag{11.5}$$

where v_c is a characteristic neutralization constant. Since neutralization is a complex process, and the ion fraction is expected to be a fairly complex quantity, the direct quantification of the surface composition using Eq. (11.4) becomes a difficult task.

In contrast to SIMS, in which the ionization probability $\alpha_M{}^+$ of the sputtered particles depends dramatically on the chemical environment of atoms M and thus causes a strong "matrix effect" complicating the quantification (see Section 11.2.1), the survival probability of scattered ions $P_M{}^+$ is rather insensitive to the chemical state of the element M. Brongersma *et al.* [38] have reviewed a great variety of studies in which the authors quantified the surface composition by LEIS and claimed the absence of matrix effects. The examples considered a variety of materials ranging from conductive to insulating, with different surface structures, including highly dispersed catalysts, alloys, and compounds. In the absence of matrix effects, quantification can be achieved by calibrating against well-defined reference materials with known surface concentrations via

$$C_M = C_M^{\text{ref}} \frac{S_M}{S_M^{\text{ref}}} \tag{11.6}$$

For cases where no reliable standards are available, a procedure has been developed [39] allowing the ion fraction for each element to be determined *in situ* by comparing the scattered ion signals for two different isotopes of the primary ions (dual-isotope method).

The composition analysis in LEIS is based on the principle that only ions that have been scattered by a single binary collision contribute to the peaks in the spectrum [Eq. (11.2)]. However, depending on the experimental conditions, scattering from two and more atoms (double and multiple scattering) may become important and even dominate a LEIS spectrum. In general, the energies of ions after double and multiple scattering differ significantly from those after single scattering. Nevertheless, in order to ensure a reliable composition analysis, it is important to recognize the contribution of multiple scattering events and to select conditions where these processes are negligible.

Moreover, surface morphology and topography can affect the measured scattering spectra due to shadowing–blocking effects. Shadowing prevents part of the incident ions from reaching all the target atoms which they could be scattered from, whereas blocking prevents the scattered ions from reaching the analyzer. Generally, a reduction in the scattered ion intensities can be expected not only from this geometric shadowing–blocking but also from the shielding-enhanced neutralization. Due to the first-layer sensitivity, the influence of shielding will be more severe in LEIS than in any other analysis by techniques with a larger sampling depth.

In studies with supported catalysts with widely varying specific surface areas, the influence of surface roughness on the LEIS results deserves particular attention. However, the microtopography developing on an originally "flat" surface under sputtering or chemical etching may also be relevant. For systems with strong variations in roughness, the absolute intensity of the scattering peaks was found to decrease strongly with increasing surface roughness whereas the relative intensities of the surface components remained virtually unchanged [40]. Moreover, there is no effect of surface roughness on the peak position [41]. Alternatively, to obtain reliable and reproducible results, powder catalysts can be compacted by pressing [42]. Just as in SIMS, for insulating powders charge neutralization is of vital importance to guarantee reliable quantification.

Only a brief account of the basic principles governing the LEIS technique could be given here. For more detailed information and applications in the chemical and structural analysis of various materials, the reader is referred to relevant books and reviews [35, 38, 43–45].

11.3.2
Potentialities of LEIS

The experimental setup in LEIS generally includes an ion source (with or without mass selection), ion optics, a UHV chamber with sample manipulator and an energy analyzer along with a detector. Depending on the type of ion source and the research purpose, various primary ions can be produced to form a probing beam. Typically in LEIS experiments, noble gas ions such as He^+, Ne^+, or Ar^+ or alkali metal ions are used. In order to attain good energy resolution, it is necessary for the ion source to ensure the formation of a monoenergetic ion beam with a narrow energy spread ($\Delta E/E < 1\%$). The ions and atoms scattered or recoiled from the sample target can be analyzed either by an electrostatic energy analyzer (ESA), which measures their kinetic energies, or by a TOF analyzer, which measures their velocities. With the ESA only scattered ions are detected, whereas with the TOF analyzer both ions and neutrals are measured. Most commonly used are sector-field ESA, in particular 90° and 127°, and hemispherical energy analyzers, which have an energy resolution of better than 1% but suffer from limited sensitivity. An increase in the analyzer transmission may be obtained by using a cylindrical mirror analyzer (CMA). In an advanced double-toroidal analyzer [46], a large fraction of the energy spectrum is imaged on to a position-sensitive detector and, due to parallel detection, an increase in the sensitivity by about three orders of magnitude can be achieved in comparison

with CMA and hemispherical analyzers. In mass-resolved ion-scattering spectrometry, a combination of a high-transmission electrostatic energy analyzer and a quadrupole mass spectrometer is used, thus permitting measurements of both energy-resolved mass spectra and mass-resolved energy distributions and elimination of the interference between scattered and secondary ions [47].

When using noble gas primary ions and ESA for the detection of the scattered ions, extreme top-atomic layer sensitivity is achieved for all materials. This results from an efficient neutralization of the inert gas ions due to a long sojourn in the vicinity of the surface following either multiple collisions or penetration to the second or deeper layers. Unfortunately, most of the ions scattered even from the topmost layer are also neutralized, which results in a very low signal intensity and complicates the quantification. The problem of low ion fractions can be circumvented by employing a TOF analyzer or by using alkali metal ions (Li^+, Na^+, K^+) for which neutralization is of minor importance. However, in this case the information depth is increased and, as a consequence, the exclusive first-layer sensitivity is lost. In addition, multiple scattering in and out of the plane of incidence can complicate the data and may require computer simulations to be performed.

LEIS is unique in its sensitivity to both the composition and structure of surfaces. In the simplest approach, information on the structure is obtained by determining the elemental composition of the topmost layer of the sample. In such a way, for instance, it has been shown [48] that the tetrahedrally coordinated cations present in the bulk of oxidic spinels are absent on their surfaces. The selective sensitivity of LEIS to the first atomic layer may play a crucial role in many experimental situations. This is certainly the case for highly dispersed systems such as supported catalysts. Whereas SIMS and XPS may encounter problems in the unambiguous identification of surface cluster formation or surface morphology effects for the active phase, LEIS can easily distinguish between a complete monolayer, a layer with pinholes, and a substrate with clusters [46].

By rotating the target under the incident beam, LEIS allows the determination of the surface arrangement of the atoms in the various azimuthal directions of the top layer and information to be obtained on the surface crystallography. The quantitative structural analysis of surfaces by LEIS has become possible in the so-called impact-collision ion scattering spectroscopy (ICISS) mode at scattering angles close to 180°. In coaxial impact-collision ion scattering spectroscopy [49], a pulsed-beam ion source and a TOF energy analyzer detecting all backscattered particles have been reported to be arranged coaxially so as to adjust the scattering angle to 180°. This powerful method allows the determination of the bond direction and the bond length of two neighboring atoms at the same time. Various examples of applications of LEIS and ICISS in surface structure analysis can be found elsewhere [43, 45].

The detection sensitivity in LEIS ranges from a few atom-% for the light elements to less than 10^{-4} of a monolayer ($\sim 1 \times 10^{11}$ atoms cm^{-2}) for the heavy elements. Thus, especially for the heavy elements, the sensitivity is higher than in XPS. However, for the general purpose of elemental analysis of rather unspecified samples, SIMS, XPS, and AES provide advantages because of the poor mass resolution in LEIS. Since E_f/E_0 is not a linear function of M_2 [Eq. (11.2)], the

mass separation of neighboring heavier elements becomes difficult (above ~40 amu with He^+, 60 amu with Ne^+, and 80 amu with Ar^+). For instance, in an LEIS study of Mo–V–Nb–Te–O catalysts [50] with $^4He^+$ primary ions, O and V peaks were clearly resolved whereas Nb, Mo, and Te appeared in a single peak. By switching to $^{20}Ne^+$ primary ions, it was possible to resolve (Nb + Mo) and Te, but not Nb and Mo.

LEIS is one of the few surface-sensitive techniques capable of directly observing hydrogen atoms (in DRS mode). Using accelerated primary ions as a probe inevitably causes sputtering of the surface and therefore it can be used for delicate depth profiling of ultra-thin films and subsurface layers. In-depth information for ultra-thin layers can also be obtained in a nondestructive way by employing neutral impact collision ion scattering spectroscopy (NICISS) with TOF analysis of particles back-scattered at an angle close to 180° [51].

11.4
Single-Crystal and Polycrystalline Metal Surfaces

Decades of experimental research in surface science have contributed substantially to our present-day understanding of adsorption-related phenomena on surfaces and interfaces. Surface-sensitive techniques such as XPS, UPS, AES, LEED, TPD, HREELS (high-resolution electron energy loss spectroscopy), LEIS, and SIMS have played a dominant role in this research and are now routinely available in many laboratories. They are frequently indispensable in elucidating the structure, electronic properties, and chemical composition of solid surfaces that determine surface reactivity to a significant extent. To reduce complexity, studies of model surfaces may be particularly useful since they allow the control of the influence of the crystallinity (single-crystalline versus polycrystalline or amorphous), surface crystallographic orientation (high versus low atomic packing density), surface microtopography (terraces versus steps), morphology (3D shape and size of surface features or nanocrystals), and surface defects. All these structural features may be altered by small amounts of unwanted impurities or when alloys are considered. We start by providing some examples of the use of SIMS and LEIS in revealing those surface properties that influence adsorption and reactions on such model surfaces as they may provide clues when addressing later the fairly complex behavior of real catalyst surfaces.

11.4.1
Surface Defects and Adsorption of Simple Molecules

Static SIMS has been shown to be a valuable tool for studying adsorption processes on catalytic materials and evaluating adsorbate surface coverage. As was first found by Barber *et al.* [52], SSIMS can reliably distinguish between molecular and dissociative CO adsorption on metal surfaces (Ni, Cu, Fe, Pd, W). Detailed studies of CO adsorption on single-crystal and polycrystalline metals (Ni, Pd, Pt, Cu) have

shown [53, 54] that the ratio of molecular ion intensities $\Sigma_n(Me_nCO^+/Me_n^+)$ is proportional to the total surface coverage of CO, whereas the relative intensities of the MCO^+, M_2CO^+, and M_3CO^+ ions are indicative of the adsorption mode, being characteristic of "linear," "bridge," or "threefold" bonded CO, respectively. Despite the fact that SSIMS is not the "classical" method for determining binding modes of adsorbed species – this is clearly a domain of infrared spectroscopy – it is remarkable that such information can be gleaned from these studies.

The formation of surface carbon in the dissociative CO adsorption is accompanied by the appearance of M_nC^+ species in the mass spectra. In a combined SSIMS–TPD study of CO adsorption on supported nanosized (and therefore "single-crystalline" in most instances) Pd particles, Matolin and Gillet found that CO disproportionated to form carbon and that the ion intensity ratio Pd_nC^+/Pd_n^+ was proportional to the surface carbon coverage [55]. This is particularly relevant information for catalytic reaction studies in which CO dissociation or disproportionation must be considered as an essential step in the reaction mechanism. Pd metal has so far been most frequently regarded as incapable of breaking the C−O bond in adsorbing CO. With this background, temperature-programmed (TP) SSIMS studies have been performed in the authors' laboratory [56] along with TPD and XPS to demonstrate that CO can undergo dissociation at defects of a polycrystalline palladium foil. Indeed, whereas on the annealed sample only molecular adsorption was found, on a sputter-treated sample dissociation occurred. To monitor the build-up of surface carbon and oxygen due to dissociation under *in situ* reaction conditions, the intensity ratios Pd_2O^+/Pd_2^+ and Pd_2C^+/Pd_2^+ were measured. The onset temperature for CO_{ad} dissociation was found to be ~410 K. At higher temperatures, a β_1/β_2 CO desorption doublet (~640 and ~725 K) appeared in the TPD spectra, of which the lower temperature feature could be correlated with the associative CO desorption (recombination of carbon and oxygen atoms) from defect sites. Corroborating evidence for CO dissociation on the ion-bombarded Pd surface was provided by measuring the C 1s line with XPS.

Further evidence of the influence of radiation defects on dissociation of CO molecules was obtained under dynamic SIMS conditions. Ivanov and Trukhan [57] studied the adsorption of CO on polycrystalline Ni at room temperature under Ar^+ ion bombardment and reported the emission of CO^+, NiO^+, and C^+ ions resulting from the ion-stimulated dissociation of a weakly bound CO state and NiO formation. The authors suggested that the weakly bound CO state was formed owing to the surface defects produced by ion bombardment. The cross-sections of the ion-induced desorption of the weakly and strongly bound CO states (the latter being associated with the emission of $NiCO^+$ ions) were measured as 1.8×10^{-14} and 0.8×10^{-14} cm^2, respectively.

We now turn to the important question of oxygen chemisorption and consider how surface defects alter its kinetics. Larson and Lauderback [58] applied angle-resolved (AR) SIMS and AES to examine how surface defects affect the oxygen adsorption and oxidation process on Al(100). Two samples were prepared using different surface polishing procedures. Sample 1 was subjected to polishing with small grain size Al_2O_3 whereas sample 2 was polished with larger grain size diamond. After surface

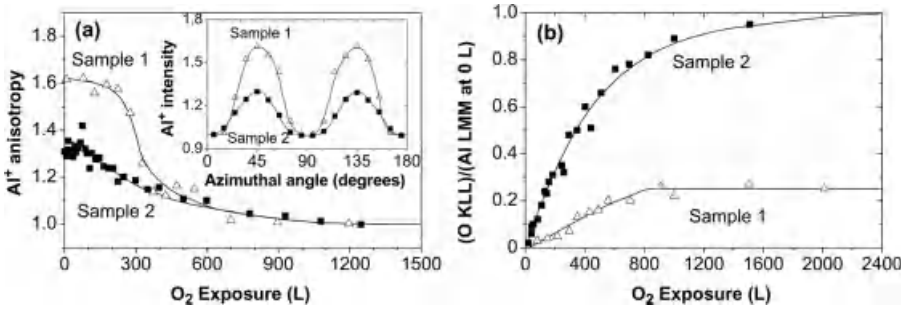


Figure 11.2 Kinetics of oxygen chemisorption on the surface of Al(100) crystals with a low (sample 1) and a high (sample 2) concentration of defects as represented by (a) the angular anisotropy of the Al^+ secondary ion yield and (b) the normalized O KLL Auger peak intensity as a function of oxygen exposure. The inset in (a) shows the Al^+ azimuthal angle distributions for samples 1 and 2 prior to oxygen adsorption. Data from [58].

cleaning by ion bombardment and subsequent annealing, AR-SIMS measurements of the azimuthal angle (φ) distribution of Al^+ secondary ions at a polar angle of 45° from both samples were performed. The angular variations of the Al^+ ion yield shown in the inset of Figure 11.2a exhibit intensity maxima at $\varphi = 45$ and 135° and minima at $\varphi = 0$ and 180°, which are associated with the anisotropy of ejecting atoms in open and closed crystallographic directions and clearly reflect the fourfold symmetry of the Al(100) planes of both samples. The observed Al^+ angle distributions thus serve as a direct probe of the local geometric arrangement of the nearest-neighbor Al atoms in the top atomic layer. A significantly stronger anisotropy of the Al^+ angular distribution for sample 1 compared with sample 2 indicates greater surface disordering and, hence, a higher concentration of surface defects in the latter sample. The much higher concentration of surface defects in crystal 2 was also confirmed by LEED analysis. Since the sputtering–annealing cycles failed to heal the defects in sample 2, it implies that the damaged region probably extended fairly deep into the crystal.

The presence of a large concentration of defects in sample 2 substantially modified the kinetics of oxygen chemisorption. This was demonstrated by monitoring the normalized O KLL AES signal. As shown in Figure 11.2b, the initial rate of oxygen chemisorption and, consequently, of oxide formation was more than four times higher for sample 2 than for sample 1. Furthermore, according to Figure 11.2a, the extent of angular anisotropy of the Al^+ ion yield (defined as the ratio of the maximum to minimum Al^+ ion intensity) during oxygen exposure remained practically constant up to ~250 langmuir ($1\,L = 1.33 \times 10^{-4}$ Pa s) for sample 1 and ~150 L for sample 2. After this initial stage, the angle distributions started to decrease for both samples and became essentially isotropic at ~1200 L. This behavior shows that the presence of surface defects in the crystal reduces the exposure required for the onset of oxide formation, which results in a progressive disordering of the top layer of Al atoms and its complete conversion to an (amorphous) oxide at 1200 L.

As mentioned in Section 11.2.1, the secondary ion yield from the surface of a metal covered with a chemisorbed layer can be significantly larger than that from the atomically clean surface (or from the bulk). The relative enhancement of the secondary ion emission from the metal:

$$R = \frac{I_M{}^+(\text{ads}) - I_M{}^+(\text{clean})}{I_M{}^+(\text{clean})} \tag{11.7}$$

caused by chemisorption or oxidation will be dependent on the sticking coefficient and thus can be taken as a measure of the efficiency of chemisorption or reactivity. With this background, Chenakin and co-workers [59] studied the effect of Ar^+ ion bombardment on the chemisorption properties of 45 metals. It was found that the bombardment with a dose of 5×10^{19} ions cm^{-2} severely modified the oxygen uptake of the metals. The magnitude of R measured after exposing an irradiated metal to 40 L of O_2 turned out to depend on the nature of the element, being a periodical function of the atomic number, and to exhibit a correlation with the density of irradiation defects and implanted argon. Later, in an extensive study [60] of the influence of Ar^+ ion bombardment on the process of metal oxidation, it was shown that the kinetics of oxygen chemisorption depended on the ion dose during bombardment and the ion energy and temperature of the implanted sample, and that it changed at different intervals of O_2 exposure. It was suggested that radiation defects produced by ion bombardment stimulated adsorption, thus increasing the rate of chemisorption, while the implanted argon atoms had a negative effect on sticking and chemisorption at atoms closest to the defect, thereby reducing the maximum attainable surface coverage. From a more general perspective of SIMS applications to materials and catalyst analysis, these data show that care is needed when interpreting the data. All the operational parameters leading to alterations of the sample may influence the secondary ion yields and have to be taken into consideration to arrive at safe (but very useful) conclusions.

The dramatic effect of defect-mediated O_2 chemisorption was also demonstrated by SIMS measurements of the sticking coefficient S on sputter-treated Rh surfaces [61]. An increase from $S = 4 \times 10^{-3}$ for the annealed sample to 0.35 for the irradiated sample along with a significant rise in the rate of oxygen chemisorption was found.

In order to asses the effect of surface damage on the reactivity of polycrystalline beryllium towards oxygen, Zalkind *et al.* [62] performed TOF DRS and AES comparative studies of the oxygen adsorption kinetics for the sputter-treated sample and for the annealed sample. The variation of the normalized intensity of the oxygen direct recoils as a function of oxygen exposure is shown in Figure 11.3a for both surfaces. Obviously, the sputtered Be surface was more reactive, displaying a higher initial adsorption rate and a shorter saturation time than the annealed surface. It was possible to fit the initial adsorption kinetics to a "clustering" model of O atoms on the surface (solid line in Figure 11.3a), which implied nucleation and growth of oxide islands on both surfaces. With this model, the oxygen sticking coefficients were evaluated as 0.1 and 0.05 for the sputtered and annealed surfaces, respectively.

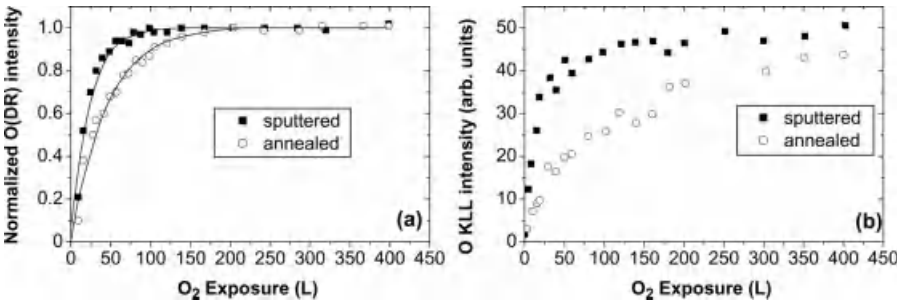


Figure 11.3 Kinetics of oxygen chemisorption on the surface of sputtered and annealed beryllium as represented by (a) the normalized intensity of oxygen direct recoils and (b) O KLL Auger peak intensity as a function of oxygen exposure. The solid line in (a) is the fit to the "clustering" model. Data from [62].

The kinetics of oxygen chemisorption on Be obtained by monitoring the oxygen AES signal (Figure 11.3b) was similar to that measured by DRS. The amount of chemisorbed oxygen measured by AES turned out to be larger for the sputtered surface even at the highest O_2 exposures. By following the Be KLL Auger peak related to BeO, the onset of oxidation of the ion-bombarded surface was found to occur at ~7 L, whereas for the annealed surface it was at ~20 L. Surface and subsurface defects introduced by ion bombardment were also responsible for a permanently larger thickness of the oxide layer growing on the sputtered Be sample.

11.4.2
Adsorption of Organic Molecules

TOF SIMS appears to be especially well suited to follow the time-dependent chemical changes associated with adsorption of complicated organic molecules and self-assembly. Houssiau and Bertrand [63] applied this method to probe the kinetics of octanethiol [OT, $CH_3(CH_2)_7SH$] adsorption on Au and ordering of the OT molecules in a self-assembled monolayer (SAM) by measuring the ion yield of the most relevant fragments as a function of the immersion time in the thiol solution. The yield of small fragment ions of OT molecules such as CH_3^+, CH^-, SH^-, AuS^-, and so on was observed to rise very quickly before reaching saturation after a few minutes, thus indicating surface adsorption. In contrast, the time-dependent emission of large oligomers seemed to indicate monolayer ordering. Accordingly, secondary ion yields of deprotonated thiol molecules $(OT–H)Au_2^-$, $(OT–H)_2Au^-$, $(OT–H)_3Au_2^-$ and $(OT–H)_4Au_3^-$ in which up to four alkanethiol chains are bound to Au atoms were detected and found to develop slowly with time. Saturation of intensities of these oligomers was reached only after a few hours, indicating that the process of ordering is an order of magnitude slower than the adsorption stage.

The adsorption kinetics and self-assembly of octyltrichlorosilane [OS, $CH_3(CH_2)_7SiCl_3$] and octadecyltrichlorosilane [OTS, $CH_3(CH_2)_{17}SiCl_3$] on an

air-oxidized Al substrate were studied by TOF SIMS [64] and found to be dependent on the alkyl chain length. In the mass spectra, characteristic fragments such as $SiH^{\pm}$, $SiOH^{+}$, SiO_2^{-}, AlO^{-}, and, additionally, $C_8H_{17}SiO_2^{-}$ for OS and $C_{18}H_{37}SiO_2^{-}$ for OTS were observed. For OS, the normalized SiH^{+} and AlO^{-} intensities showed a rather peculiar ("oscillatory") behavior as a function of the adsorption time. The alternating adsorption–desorption processes in this case were suggested to be associated with the presence of water molecules at the interface. In contrast to this transient adsorption behavior, OTS adsorption was monotonic, with a coverage slowly increasing with time, which was believed to be related to cross-linking at the interface.

In contrast to the above studies in which the adsorption kinetics was measured *ex situ*, that is, by immersing the substrate in the solution for different times and then transferring the samples into the analysis chamber, Rodríguez *et al.* [65] monitored the kinetics of adsorption of propanethiol on Ag(111) *in situ* by exposing the Ag(111) surface to vapors of $CH_3(CH_2)_2SH$ in a wide exposure range while maintaining UHV conditions and following the scattering and recoiling intensities of H, C, and Ag from the sample by TOF DRS. They showed that the kinetics in the initial stages of adsorption was noticeably influenced by the surface microtopography of the Ag(111) substrate. Accordingly, the sticking probability of organic molecules at defect sites was reported to be higher for a rough than for a smooth surface.

While studying monolayers of hexadecanethiol [HDT, $CH_3(CH_2)_{15}SH$] self-assembled on Au(111) and Ag(111) with LEIS, Chenakin *et al.* [66] found that the character of the sputtering kinetics of these SAMs by low-energy He^{+} ions represented by LEIS signals from the substrates and sulfur atoms depends on the nature of the substrate and is strongly sensitive to the structure of the adsorbed organic monolayer. The difference in structure of the HDT assemblies on gold and silver, which is associated with differences in the metal–sulfur bond strength, resulted in a noticeable modification of the sputtering kinetics. A two-stage process (scission and fragmentation of hydrocarbon chains followed by ion desorption of uncovered sulfur) was revealed on sputtering HDT/Ag, but could not be clearly distinguished for HDT/Au. The estimated values of the initial sputtering yield of large fragments and of the desorption cross-section of sulfur species were several times larger for HDT/Au than for HDT/Ag. Moreover, for two HDT/Au films formed during immersion times of 14 and 92 h, small alterations in the structure of the HDT monolayer could be revealed by detecting changes in the LEIS kinetics.

11.4.3
Oxidation and Corrosion

Although oxidation and corrosion are not the focus here, we present some examples of effective use of SIMS for identifying those surface properties which influence these processes in metallic systems.

The oxidation of many transition metals, such as Ni, usually proceeds via cation transport to the gas–oxide interface followed by reaction with oxygen to form new oxide. For thick scales and suitable temperatures, however, oxygen may be

transported via fissures in the oxide. Czerwinski *et al.* [67] studied the influence of reactive element addition on the mechanism of the early stages of Ni oxidation at 973 and 1073 K by employing SIMS in the depth profiling mode and making use of its isotopic sensitivity. Polycrystalline Ni was implanted with 150 keV Ce^+ ions or coated with CeO_2 thin films by both reactive sputtering and using the sol–gel method. In addition, Ni(100) and Ni(111) single crystals were sol–gel coated by CeO_2. The surface-modified samples were sequentially oxidized first in $^{16}O_2$ and then in $^{18}O_2$, and in-depth distributions of the $Ni^{16}O_2^-$, $Ni^{18}O_2^-$, $Ce^{16}O^+$, and $Ce^{18}O^+$ ion species were measured by SIMS. It was found that the oxide growth mechanism depended on the surface structure of the Ni substrate before modification with reactive Ce–CeO_2. For polycrystalline Ni, the decisive factor was surface finish. CeO_2 sol coatings deposited on mechanically polished surfaces decreased outward Ni^{2+} diffusion, but this mechanism was still predominant for NiO growth. Higher inward oxygen diffusion was observed for chemically polished Ni, both Ce^+ implanted and CeO_2 sputter coated. The oxidation behavior of the CeO_2 sol-coated Ni single crystals depended on the crystallographic orientation (Figure 11.4). For CeO_2-coated Ni(100), the contribution of outward Ni^{2+} diffusion to oxide growth was higher than that for Ni(111), whereas for Ni(111) with the reactive element being present on the outer surface (Figure 11.4d), oxide growth proceeded predominantly by inward oxygen diffusion.

Stainless steels, being frequently used as construction materials in aggressive environments, generally exhibit excellent resistance to corrosion due to the spontaneous formation of a protective film on the surface. This passivation is frequently limited by the susceptibility to pitting or crevice corrosion in the presence of chloride ions, with chemical inhomogeneities, especially nonmetallic inclusions, acting as

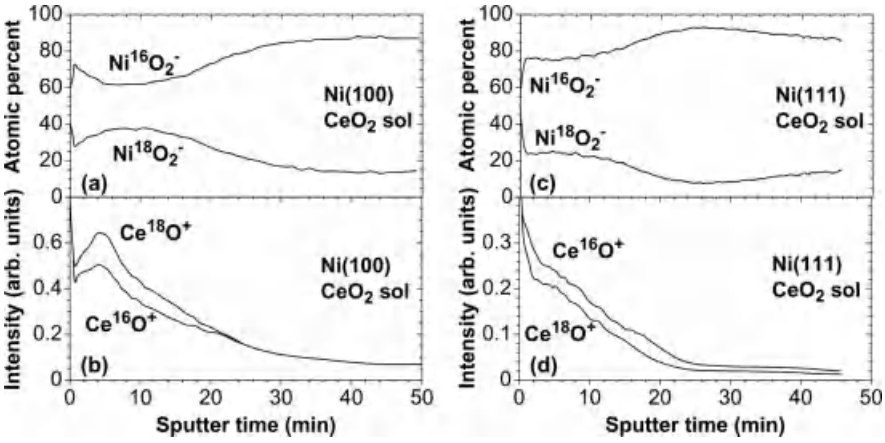


Figure 11.4 SIMS depth profiling of oxide films formed on (a, b) CeO_2 sol-coated Ni(100) and (c, d) CeO_2 sol-coated Ni(111) after oxidation at 1073 K, first in $^{16}O_2$ and then in $^{18}O_2$ for the same time. The oxide/metal interface is at a sputter time of ~30–40 min. Data from [67].

potential nucleation sites for pitting. Rossi *et al.* [68] employed TOF SIMS, XPS, and AES to characterize the chemical composition of the surface films formed on 18Cr8Ni stainless steels with different sulfur contents (0.003 and 0.29% S) following mechanical polishing and immersion in an aggressive 6% $FeCl_3$ solution. Using TOF SIMS imaging at high spatial resolution in various positive and negative secondary ions, it was clearly demonstrated that microinclusions present in the high-sulfur stainless steel are composed of a chromium oxide core flanked by MnS regions that neither contain iron (Fe^+ or FeO^+) nor carry a protective oxyhydroxide film as does CrO_x. The MnS microinclusions, being in contact with chloride-containing solutions, therefore appear to represent the likely nucleation sites for pitting.

11.5
Amorphous Metallic Alloys

Amorphous metallic materials, owing to their specific structure and the absence of long-range order, possess unique bulk and surface properties. In particular, the reactivity of amorphous alloys is determined to a great extent by their surface composition which can be modified alone [69] without being limited by structural constraints such as the crystallographic orientation, grain boundaries, or localized defects present in metal crystals. The commercial interest in amorphous metals has increased considerably in recent years. Applications with the aim of enhancing the corrosion resistance and improving the hardness, wear properties, and solderability have become more advanced. Possibly the most useful property of bulk amorphous alloys is that they are true glasses. This allows easy processing in much the same way as polymers. Applications of amorphous alloys as suitable precursor materials for the preparation of supported catalysts, being another interesting option, have been reviewed by Baiker [70] along with their use in various hydrogenation and oxidation reactions. In fact, catalyst materials usually change their surface structure and chemical composition under reaction conditions, and metastable glassy metals are no exception in this respect.

As-prepared amorphous Ni–P alloys are interesting materials but rather inactive and need to be activated by redox pretreatments in oxygen and hydrogen. Having subjected an amorphous $Ni_{80}P_{20}$ alloy to an oxidation treatment with 0.1 MPa O_2 at temperatures up to 513 K, Muhler and co-workers [71] found no phosphorus-related peaks by LEIS surface analysis. On the other hand, XPS of the same sample indicated the presence of P_2O_5. Consequently, an NiO topmost layer was concluded to be formed with a thin P_2O_5-containing layer beneath. During the subsequent exposure to 0.1 MPa hydrogen at 553 K, the oxide was found to be completely reduced and, due to the outward diffusion of phosphorus, a presumably crystalline Ni_3P compound was formed at the surface (although bulk crystallization was not expected at 553 K). It must be concluded that the initially amorphous catalyst underwent considerable restructuring during the redox pretreatment and that the high catalytic activity for the hydrogenation of vinylbenzene and cyclopentadiene exhibited by the treated amorphous alloy must be associated with the formation of active sites due to this

restructuring. The authors suggested the active sites to be ensembles of surface Ni and P atoms structurally related to Ni_3P.

SIMS depth profiling of oxide films grown on amorphous $Ni_{77}P_{23}$ alloy [72] produced similar results to those obtained for the oxidized $Ni_{80}P_{20}$ alloy [71]. On the basis of analysis of the Ni^-, O^-, P^-, and OH^- secondary ion intensities, NiO was found to form in both air and dry oxygen at 573 K and to be the major component of the oxide film in both of these cases, with hydroxyl groups being present at the surface. Interestingly, underneath the NiO there was a thin layer in which Ni, O, and P were present and which presumably corresponded to $Ni_3(PO_4)_2$.

In order to modify the redox characteristics of amorphous Ni–P alloy and to improve its catalytic performance and long-term stability under reaction conditions, small amounts of tungsten were added to amorphous Ni–P alloy [73]. This resulted in dramatic changes in the surface characteristics of amorphous $Ni_{80.4}W_{1.5}P_{18.1}$ alloy as compared with $Ni_{80}P_{20}$. According to LEIS analysis, the oxidation of this alloy in O_2 at 513 K caused the disappearance of P and W from the surface and significant oxygen-induced segregation of nickel. The subsequent reduction of the oxidized surface with H_2 at 553 K resulted in the reappearance of P and W on the surface. Interestingly, according to the XPS data, a kind of nickel phosphate compound was formed, with only a small portion of Ni and P being reduced to their elemental states. This is clearly different from the $Ni_{80}P_{20}$ case, where the oxidized forms of Ni and P were largely (or even completely) reduced to metallic Ni and elemental P under the same treatment conditions [71]. Thus, the addition of W to the amorphous alloy seemed to decelerate the reduction of the Ni and P oxides and to stimulate the formation of the phosphate structure, which was suggested to be associated with active site formation and distinctly higher activity in the hydrogenation of cyclopentadiene compared with amorphous $Ni_{80}P_{20}$ alloy.

Another example of the correlation between catalytic properties and surface composition can be found in a study of the $Pd_{81}Si_{19}$ amorphous alloy [74]. According to LEIS depth profiling and XPS analyses, the surface of the as-prepared amorphous alloy turned out to be covered by a silicon oxide layer rather than by Pd and Si in their elemental form. Owing to the particular distribution of the Pd on the surface, the alloy in this state was most selective and active in catalytic hydrogenation. Treatments with oxygen at various temperatures up to and above the crystallization temperature altered the surface composition and catalytic activity profoundly.

The few examples outlined above show the importance of correlating catalytic performance with surface structure and composition. The exposure to reactive gases may lead to changes in both features. Phase transformations may occur far below the crystallization temperature and cause changes in the specific surface area (which is welcome as native glassy alloys have inconveniently low BET surface areas). Thus, alterations in structure and composition go hand in hand and cannot be treated separately from each other. Conversely, originally crystalline materials may turn amorphous under reaction conditions. Examples will be presented in the following sections. In any case, the combined use of SIMS and LEIS and electron spectroscopic techniques is useful when it comes to gaining a profound understanding of the near-surface processes underlying such structural/chemical changes.

11.6
From Model to Real Catalysts

11.6.1
Structural Effects

Buhl and Preisinger [75] were probably the first to use (dynamic) SIMS for obtaining direct information on the surface structure of a catalyst. They studied an activated α-Fe + 3% Al_2O_3 ammonia catalyst and observed positive and negative polyatomic and molecular secondary ions such as Fe_n^+, $Fe_xO_y^{\pm}$, $Al_nO_m^{\pm}$, and $Fe_xAl_yO_z^{\pm}$ leaving the surface due to ion bombardment. By analyzing possible structural arrangements corresponding to the ejected ions, the authors concluded that Fe, Al, and O atoms were coordinated so as to form $FeAl_2O_4$ clusters in which one Fe atom is tetrahedrally surrounded by four O atoms and each of the two Al atoms is bonded to two O atoms. This potential of SIMS to provide structural information via emission of molecular ions was successfully used afterwards in studies aimed at elucidating the role of the surface structure in the catalytic activity of materials.

Matolin *et al.* [76] used static SIMS to investigate low-pressure catalytic CO oxidation over well-defined small Pd particles (3 and 10 nm) and films supported on mica. They used the method in an *operando* mode and reported the occurrence of various molecular ionic species of the type Pd_nX^+ (X = C, O, CO; $n = 1, 2$) in the mass spectra. The temperature dependence of the relative ion intensities allowed them to demonstrate that CO oxidation is structure sensitive rather than insensitive as is often believed. Whereas at low temperatures molecular CO chemisorption was dominant, CO dissociation came into play at medium temperatures and was more intense for small Pd particle sizes. This was concluded from the behavior of the temperature-dependent Pd_2CO^+/Pd_2^+ and Pd_2C^+/Pd_2^+ ratios. The build-up of surface carbon was, however, "transient" since the Pd_2C^+/Pd_2^+ ratio was seen to pass through a temperature-dependent maximum. Obviously, a reaction with chemisorbed oxygen was responsible for the decrease in the amount of surface carbon at higher temperatures. This conclusion is compatible with the behavior of the Pd_2O^+/Pd_2^+ ratio, which increased with rising temperature due to thermal desorption of CO_{ad} (Figure 11.5a). Interestingly, the minimum in the Pd_2CO^+/Pd_2^+ ratios corresponds to the maximum of the "carbon" Pd_2C^+/Pd_2^+ curve. This observation suggests that site blocking occurred and persisted as long as the carbon was not removed by steady CO_2 formation at high temperatures. The fact that the Pd_2C^+/Pd_2^+ ratio and, hence, the amount of deposited carbon were strongly dependent on the CO partial pressure (P_{CO}/P_{O_2} ratio) and on the Pd particle size (Figure 11.5b) provided further support for the above conclusions. Similar data for particle size-dependent CO decomposition during CO oxidation were obtained using MgO and Al_2O_3 as support materials [76]. Subsequent work qualified the particle size effect to be essentially caused by defect sites whose number density increases with decreasing particle size.

The recent interest in Au-based catalysts in various catalytic applications prompted Lee *et al.* [77] to study the effect of gold cluster size on room temperature CO

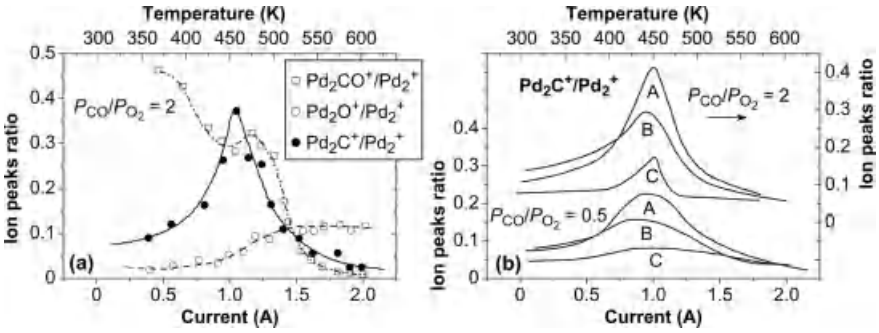


Figure 11.5 (a) Intensity ratios Pd_2CO^+/Pd_2^+ (squares), Pd_2O^+/Pd_2^+ (open circles) and Pd_2C^+/Pd_2^+ (filled circles) as a function of the heating current (substrate temperature) for Pd particles 3 nm in size under catalytic conditions: $P_{O_2} = 2.7 \times 10^{-5}$ Pa, $P_{CO} = 5.4 \times 10^{-5}$ Pa; (b) intensity ratios Pd_2C^+/Pd_2^+ versus heating current for different Pd particle sizes (A, 3 nm; B, 10 nm; C, "continuous" film) and varying gas mixtures: $P_{CO}/P_{O_2} = 2$ (upper curves) and 0.5 (lower curves). Data from [76].

oxidation. They prepared size-selected Au_n ($n = 1$–7) particles and deposited them on rutile TiO_2(110). The measured activities were found to be strongly size dependent, first appearing for Au_3, then declining to Au_5, and finally increasing substantially for Au_6 and Au_7. Most intriguing was the occurrence of an excellent one-to-one correlation between the CO oxidation activity and the O_2-induced attenuation of the Au LEIS signal on a cluster-by-cluster basis. This correlation clearly indicated that the activity was controlled by the ability of the Au clusters to bind oxygen. At the same time, no obvious correlation of activity with the CO binding or cluster morphology was observed.

Another interesting application area for probing the surface structure by SIMS and LEIS is spinel-type materials which may either be employed as such or be formed during the catalytic reaction on metal oxide supported catalysts. Spinels can be represented by the general formula $A^{tet}(II)\,B_2{}^{oct}(III)O_4$, in which the oxide anions are arranged in a cubic closed-packed lattice and the cations A and B with the indicated formal valency occupy some or all of the octahedral and tetrahedral lattice sites. A and B must not be necessarily different elements. Jacobs *et al.* [48] synthesized various spinel-type catalysts starting from Mn_3O_4 and Co_3O_4 and substituting the Mn and Co cations by catalytically inactive Zn in the tetrahedral interstices and Al in the octahedral interstices to produce a series of compounds: α-Mn_3O_4, $ZnMn_2O_4$, $MnAl_2O_4$, Co_3O_4, $ZnCo_2O_4$, $CoAl_2O_4$, and $ZnAl_2O_4$. In addition, a set of $Zn_{1-x}Mn_xAl_2O_4$ catalysts ($x = 0-1$) was prepared to provide a most complete series of samples for a comparative study of the selective reduction of nitrobenzene to nitrosobenzene.

It was found that replacing the cation in the tetrahedral sites of Mn_3O_4 and Co_3O_4 by inactive Zn had practically no effect on the catalytic performance. LEIS detected only a very small Zn signal for these catalysts, while the LEIS signals of the catalytically active Mn (or Co) were about the same for α-Mn_3O_4 and $ZnMn_2O_4$ (or Co_3O_4 and $ZnCo_2O_4$). When the octahedral sites were occupied by inactive Al ions,

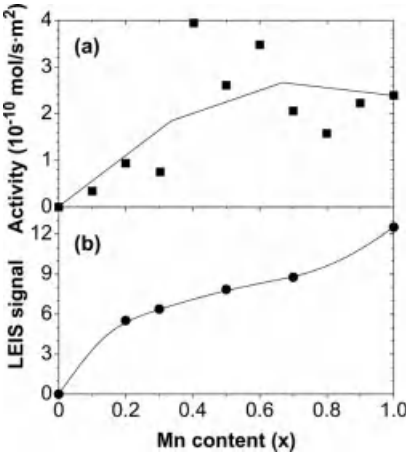


Figure 11.6 (a) Activity in selective reduction of nitrobenzene to nitrosobenzene and (b) LEIS signal from Mn atoms as a function of Mn content in $Zn_{1-x}Mn_xAl_2O_4$ spinels. From [48].

the Mn and Co LEIS signals decreased sharply and so did the catalytic activity. However, whereas for the $CoAl_2O_4$ spinel the surface concentration of Co and also the catalytic activity were negligible, for $MnAl_2O_4$ about half of the Mn content could still be detected on the surface, with the activity being also about half that of α-Mn_3O_4. This difference between the $CoAl_2O_4$ and $MnAl_2O_4$ spinels was attributed to the oxidative transfer of Mn from tetrahedral to octahedral sites.

The dependence of the catalytic activity of the $Zn_{1-x}Mn_xAl_2O_4$ spinels on the Mn content demonstrated a relatively good correlation with the LEIS signal intensity from the catalytically active Mn (cf., Figure 11.6a and b). At the same time, the detected surface concentration of Zn was very small. Since Zn ions do not move to the octahedral sites, it was suggested that oxidative transfer took place in these spinels also, whereby part of the Mn(II) in the tetrahedral sites was oxidized and transferred to Mn^{oct}(III) and thus could be detected by LEIS in the outermost atomic layer.

Hence a clear correlation was found between the surface concentration of Mn or Co and the catalytic activity of the spinels. From these results and the fact that the Zn content on the surface of the Zn-containing spinels and the Co content on the surface of $CoAl_2O_4$ were observed to be negligible, Jacobs *et al.* [48] drew the important conclusion that practically no tetrahedral sites are exposed at the surface. Accordingly, the surface structure of the spinels was almost exclusively represented by octahedral sites and only these sites participated in the reaction. The only two low-index planes of the (cubic) spinel structure which can satisfy this condition were identified as *B*(111) and *D*(110). These findings confirmed and refined previous LEIS studies of spinels [21] which showed the complete absence of tetrahedral Co ions on the surface of polycrystalline $CoAl_2O_4$ and a respective negligible catalytic activity of this spinel. We note once again that such site-specific information cannot be gleaned from XPS since, in contrast to LEIS, the sampling depth of this technique extends to several layers, thus averaging information over both tetrahedral and octahedral sites.

The structural peculiarities of spinels and their influence on the reactivity were also observed in SIMS studies. Analyzing the various secondary molecular ions emitted from the surface of $Mg_{0.9}Cu_{0.1}Al_2O_4$ spinel after oxychlorination of ethylene to 1,2-dichloroethane showed [78] that the three surface cations had to fulfill different tasks. In particular, chlorination was found to occur at the Mg^{2+} and Cu^{2+} sites (as indicated by emission of $MgCl^+$, $MgOH_3Cl^+$, $CuCl^+$, and $CuOCl^+$ ions) but not at Al^{3+}. On the other hand, the chlorohydrocarbons formed during reaction were adsorbed on the Al^{3+} or Al–O sites (emission of $AlCH_2Cl^+$, $AlC_2H_2Cl^+$, and $AlOCH_2C1^+$ ions) but not on Mg^{2+} and Cu^{2+}. Ethylene appeared to adsorb on the Cu^{2+} ion whereas there was little or no evidence of hydrocarbon attachment at the Mg^{2+} site.

There are, of course, many more examples of structural probing by SIMS/LEIS which cannot be developed in detail here. We finish this section by referring to the work of Tanaka *et al.* [79], who investigated superbases in relation to olefin isomerization. Only alkali-treated NaOH/γ-Al_2O_3 exhibited sufficient catalytic activity, and TOF SIMS revealed the emission of $Na_3AlO_2H^+$ secondary ions to be a reliable indicator of the necessary superbasicity in this material.

11.6.2 Dispersion Effects

It has been demonstrated in a number of studies that SIMS and LEIS are highly efficient in monitoring the dispersion of supported metal or metal oxide catalysts. Clearly, "dispersion" may be argued to be a "structure effect," which would have allowed the previous section to be combined with the present one. Since catalyst preparation and activation in most cases aim at producing high surface-to-bulk ratios of the active component, we prefer to develop "dispersion" separately. An interference with structural effects will be clearly encountered for systems where the dispersion increases to produce nano- or subnano-sized clusters. We shall summarize some examples in which SIMS and LEIS have been demonstrated to be a reliable tool to probe the dispersion and to provide quantification of support coverage by active components.

Rodrigo *et al.* [80] employed static SIMS to study changes in the dispersion of SiO_2- and Al_2O_3-supported molybdena catalysts as a function of preparation and treatment conditions. First, the relative Mo^+/SiO^+, MoO^+/SiO^+, and $MoO_2{}^+/SiO^+$ intensities for Mo/SiO_2 catalysts were found to increase with the Mo loading independent of the preparation procedure. These ratios turned out to be the highest for impregnated catalysts and indicated Mo surface segregation which was supported by LEIS–XPS data. Second, again in agreement with LEIS, XPS, UV, and Raman data, the same intensity ratios demonstrated an increase after calcination of the catalysts and a decrease to nearly the original values upon exposure to water vapor. This behavior associated with reversible polymolybdate cluster formation indicated that considerable structural reorganizations accompanied changes in the dispersion. Third, no such behavior was found for Al_2O_3-supported molybdena, that is, the above changes in dispersion and structural reorganization were absent for this type of catalyst. Fourth,

the MoO^+/Mo^+ and $MoO_2{}^+/Mo^+$ intensity ratios in SiO_2-supported molybdena also were sensitive to Mo loading and were reversible in cycles of calcination/hydration. However, no details on the structural changes associated with these processes could be derived from mere inspection of the MoO^+/Mo^+ and $MoO_2{}^+/Mo^+$ ratios.

The structural properties of Nb_2O_5-supported molybdate were investigated by Jin *et al.* [81] using SIMS in combination with other spectroscopic techniques. In contrast to the above studies with SiO_2 as a support, the authors reported the formation of polymeric molybdate species at low and of MoO_3 crystallites at high Mo loadings. SIMS analysis showed that for low Mo loading the catalytically active top layer was much richer in oxygen ions than for MoO_3 crystallites.

Investigating a series of Nb_2O_5/TiO_2 catalysts with TOF SIMS, Bukallah *et al.* [82] not only obtained information on the dispersion but also claimed the molecular structure of the supported species to be accessible. The degree of aggregation of the Nb oxide species (e.g., monomeric versus polymeric) was evaluated by the intensities of distinct oligomeric Nb oxide species (monomeric, dimeric, trimeric, and tetrameric) relative to the sum intensities of all Nb oxide species (i.e., $\Sigma Nb_nO_y{}^-/\Sigma Nb_xO_y{}^-$, $n = 1, 2, 3, 4$) as a function of Nb loading, while the dispersion of these Nb species was derived from intensity ratios of the sum of oligomeric Nb oxide species to the ions of the support (i.e., $\Sigma Nb_nO_y{}^-/TiO_2{}^-$). It was found that tetrameric Nb oxide clusters emerged in the catalysts only above critical Nb loadings.

Although the above examples demonstrate the usefulness of evaluating relative ion intensities in SIMS, we feel that the wealth of information can only be fully exploited once a sound theoretical description of the secondary ion formation process in such multiple oxide systems is available. Complicated fragmentation patterns remain an issue in evaluating the mass spectra.

TOF SIMS imaging has been demonstrated to be exceptionally useful in obtaining information on the dispersion and active phase distribution in catalysts [26]. For example, calcined bimetallic Ni–Pt catalysts supported on TiO_2–SiO_2 [83] not only revealed good and uniform dispersion of platinum on the support surface but also pointed to the preferential location of nickel on titania rather than on silica. Also, fairly complex metal-loaded MCM-41 mesoporous catalysts were imaged to provide information on variations of the Pt dispersion and its effect on catalytic properties [84]. In NbMCM-41, oxygen transfer from Nb–O to Pt species (resulting in PtO^- and $PtO_2{}^-$ ion emission) and Cl location on Pt (causing emission of $PtCl^-$ and $PtClO^-$ ions due to "relics" from the catalyst preparation procedure with H_2PtCl_6) were revealed. For Au/MCM-41 catalysts, TOF SIMS images demonstrated that the size and dispersion of Au particles were dependent on the preparation method [85]. Interestingly, $AuCl^-$ ion emission was only observed to occur in the coprecipitated catalyst, possibly due to the interaction of the $HAuCl_4$ precursor with the cationic surfactant during catalyst synthesis. TOF SIMS imaging was very demonstrative in proving the successful platinum encapsulation in microporous KA-zeolite (Pt/NaA-zeolite ion exchanged with KCl solution) during the preparation of a sulfur-tolerant catalyst for the hydrogenation of naphthalene. No Pt was detected on the external surface of the untreated catalyst; only prolonged sputtering made it visible and demonstrated its homogeneous dispersion [86].

Numerous studies have demonstrated that the extreme top layer sensitivity of LEIS is very useful for evaluating surface coverage (reflecting dispersion) of the supported phase. Similarly to SIMS, intensity ratios of the scattered ions are evaluated in LEIS as a function of the loading. For example, in studies of NiO–WO_3/Al_2O_3 catalysts [87] the changes in the coverage were traced by measuring the Ni/O and W/O LEIS peak ratios as a function of the NiO and WO_3 loadings. In a series of studies by Houalla, Hercules and co-workers, surface coverage was quantitatively evaluated. For alumina-supported catalysts [88–90] it was found that the surface coverage by the active phase, Θ^a, can be derived from the attenuation of the support signal according to

$$\Theta^a = 1 - R^{cat}/R^{supp} \tag{11.8}$$

where R^{cat} and R^{supp} are the (Al/O) peak intensity ratios for the catalyst and the support, respectively. Variations of the absolute coverage determined by LEIS as a function of the active phase loading (V, Mo, Cr, W, Re) and the preparation conditions were compared with XPS and IR data and also with measurements of CO_2 chemisorption (which is seemingly selective for surface hydroxyls on alumina) and low-temperature CO adsorption. Good agreement was found between the LEIS-derived data and those measured by CO adsorption and IR spectroscopy. The CO_2 chemisorption data overestimated the coverage that could be reasonably explained on the basis of the sample chemistry.

For titania-supported catalysts [91], the absolute coverage was evaluated using $R = \mathrm{Ti/O}$ in Eq. (11.8). Further, the coverage for an Mo/TiO_2 catalyst could be consistently described by the peak ratio as $\mathrm{Mo/Ti} = k\Theta^a/(1 - \Theta^a)$. In contrast to the alumina-supported catalysts, the LEIS-derived coverage for the Mo/TiO_2 catalysts was in good agreement with the CO_2 chemisorption data. For WO_3/ZrO_2 catalysts, the surface coverage was determined [92] by using Eq. (11.8) with $R = \mathrm{Zr}$ peak intensity or by using $\mathrm{W/Zr} = k\Theta^a/(1 - \Theta^a)$, and reasonable agreement with CO adsorption data and theoretical predictions was obtained.

In catalysis by metals, the size of the active metal aggregates can become fairly small. Ultimately, cluster sizes with very specific intrinsic activity may be reached. While the size analysis of such systems is usually a domain of electron microscopy, interesting information may be also gleaned from LEIS in combination with XPS, as shown for supported Rh model catalysts. For an $Rh/SiO_2/Mo$ catalyst [93], the cluster size was estimated from the decrease in intensity of the Rh LEIS peak by assuming an initially ideal dispersion of the Rh atoms. It was found that heating a two-monolayer Rh coverage on a thin SiO_2 film in UHV up to 773 K resulted in agglomeration of rhodium, with the final cluster height being increased by a factor of four (up to 0.96 nm). LEIS and XPS employed for studying the growth of Rh nanoparticles on $TiO_2(110)$ support [94] revealed that the size of the Rh clusters produced by evaporation increased as a function of coverage. The substrate temperature during evaporation also influenced the cluster size, causing formation of smaller nanoparticles at low temperatures (160 K). Annealing the $Rh/TiO_2(110)$ sample led to agglomeration of the Rh and finally to encapsulation of the Rh clusters by TiO_x at $\sim$900 K.

The LEIS yield from the surface of a supported catalyst depends not only on the total metal loading and the specific surface area but also on the fraction of atoms in a cluster that are accessible to the probing ions, that is, on the cluster size. With this background, Jansen *et al.* [95] developed a method for determining the average cluster size of highly dispersed metals in supported catalysts using LEIS. The average cluster diameter, d, was suggested to derive from the relationship $d = 2G/(c_\alpha \sigma \varrho \vartheta)$, where G is the metal weight fraction, c_α a geometric factor, σ the BET specific surface area, ϱ the metal volumetric density, and ϑ the coverage in monolayers as measured by LEIS. The average cluster size (1.6 nm) determined by LEIS for $Pt/\gamma\text{-}Al_2O_3$ was in quantitative agreement with that determined by TEM. In the case of three-way catalysts for automotive pollution control, classical methods for determining the cluster size, such as TEM or CO chemisorption, often fail or produce ambiguous results because of the presence of ceria. Using LEIS, an average noble metal cluster size of 2.7 nm for a ceria-supported $Pt/Rh/CeO_2/\gamma\text{-}Al_2O_3$ commercial three-way catalyst was determined.

11.6.3
Preparation and Activation Effects

The influence of preparation and treatment conditions on the activity of solid catalysts was investigated in a number of studies [96–101]. LEIS in combination with other spectroscopic techniques turned out to be useful indicators of the structural and textural characteristics. We mention here some LEIS studies which demonstrate nicely the influence of the calcination temperature on the active phase morphology of transition metal oxides on oxidic support materials. Jeziorowski *et al.* [102] followed the development of the He^+ scattering from $Ni–Mo/Al_2O_3$ catalysts by monitoring the O, Al, Mo, and Ni signals as a function of bombardment time (depth profiling mode). From the behavior of the Mo/Al and Ni/Mo intensity ratios, in conjunction with Raman and diffuse reflection spectroscopy, they arrived at the conclusion that calcination below 770 K produced three-dimensional molybdate features leaving parts of the support uncovered whereas calcination at 870 K led to spreading of the molybdate, thus forming a two-dimensional layer of edge-sharing MoO_6 octahedra. With regard to the Ni^{2+} distribution, the depth profiles indicated it to be increasingly diffused into the support where it formed spinel structures, thereby occupying both tetrahedral and octahedral positions. In LEIS and XPS studies of molybdena [103] and vanadia supported catalysts [104], Briand and co-workers demonstrated the importance of *in situ* calcination and the easy damage of the oxide surface by sputtering in LEIS and by photo-induced reduction in XPS analyses. Extrapolating their LEIS spectra to the zero-sputtering case, the authors reported that in calcined MoO_3/TiO_2, V_2O_5/ZrO_2, V_2O_5/CeO_2, and V_2O_5/Nb_2O_5 catalysts the support was completely covered by an oxide layer, whereas in MoO_3/Al_2O_3 and V_2O_5/Al_2O_3 catalysts some of the Al^{3+} cations remained uncovered under identical coverage conditions. The authors considered this to be a "curvature effect" due to small particles in high surface area alumina. Valenzuela *et al.* [105] studied the effect of preparation conditions on the surface structure and activity of $ZnAl_2O_4$ spinel used

as a support of Pt and Pt–Sn catalysts. $ZnAl_2O_4$ was prepared via sol–gel, coprecipitation, or wet mixing and, according to LEIS, only the first two methods produced samples in which the Zn mainly occupied the tetrahedral positions of the spinel (see also Section 11.6.1), leaving only a very small amount of extra Zn on the surface. Adding Ca during the synthesis led to its deposition on the spinel surface whereas Sn addition caused a surface reconstruction, possibly due to the formation of an inverse spinel, with both dopants poisoning the activity.

We shall now consider a few SIMS–LEIS examples in which the surface structure and composition formed during catalyst preparation with varying aqueous solution pH and chemical compositions of agents and solutions could be successfully correlated with the activity performance. Houalla *et al.* [106] used LEIS in combination with XPS to investigate how the pH in incipient wet impregnation influenced the state and dispersion of Mo species in Mo/Al_2O_3 catalysts. Accordingly, with increasing pH, the LEIS and XPS I_{Mo}/I_{Al} ratios for calcined catalysts first increased slightly (at pH 5.4) and then decreased steadily (Figure 11.7), pointing to deterioration of the Mo dispersion. Calcination was always found to have a positive influence on the Mo dispersion at any pH. Interestingly, the authors reported a clear correlation between the LEIS–XPS data and the thiophene HDS (hydrodesulfurization) activity (Figure 11.7). Obviously, low-pH preparations with subsequent calcinations showed the best Mo dispersion and, consequently, the highest HDS activities. Note also the closer correlation between the activity data and those of LEIS compared with XPS, which may be explained in terms of the higher surface sensitivity of LEIS (the sampling depths of LEIS and XPS are 0.2 and 1.5 nm, respectively).

Chenakin *et al.* employed TOF SIMS and XPS to demonstrate the influence of pH on the coprecipitation of aluminovanadate oxide catalyst precursors (V−Al−O) [107]. Varying the pH was found to be accompanied by pronounced step-like changes in a number of surface characteristics and occurred at pH 7.5–8.5. Interestingly, the catalytic properties of the V−Al−O catalysts in oxidative propane dehydrogenation were observed to change likewise in this range of pH values. More specifically,

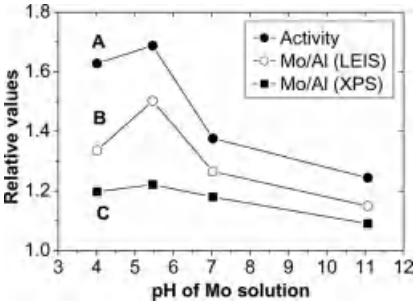


Figure 11.7 Correlation between HDS activity and surface structure of Mo/Al_2O_3 catalysts: (A) relative values of thiophene HDS activity expressed as half-order rate constant at steady state and (B) variations of LEIS and (C) XPS Mo/Al intensity ratios for the calcined catalyst as a function of impregnation pH. From [106].

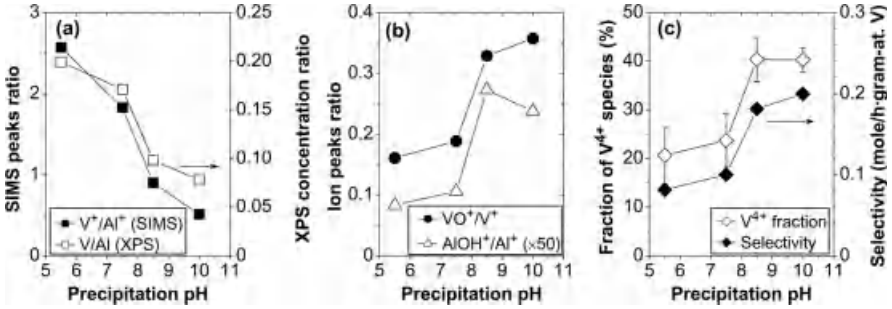


Figure 11.8 Correlation between catalytic activity and surface structure of V–Al–O catalysts: variations of (a) ion peaks ratio V^+/Al^+ from SIMS and surface atomic concentration ratio V/Al from XPS; (b) ion peaks ratios VO^+/V^+ and $AlOH^+/A1^+$; (c) fraction of V^{4+} species from XPS and rate of propylene formation in oxidative propane dehydrogenation as a function of precipitation pH. Data from [107].

increasing the solution pH from 5.5 to 10 resulted in progressive surface depletion of vanadium and enrichment of aluminum, as revealed by both SIMS and XPS (Figure 11.8a). As the pH increased, the VO^+/V^+ ion peak ratios increased, indicating a higher oxygen coordination of vanadium atoms due to structural transformations in the catalyst and preferential formation of O−V−O bonds in the precipitated V−Al−O. Also, the extent of Al hydration ($AlOH^+/Al^+$) and the amount of Al hydroxide increased (Figure 11.8b). Concurrently, the coverage of the Al hydroxide support surface with vanadium oxide decreased continuously, as indicated by the behavior of the $VO^+/AlOH^+$ ratios. Deconvoluting the V $2p_{3/2}$ XP spectra showed that the dispersed vanadium oxide species contained an appreciable fraction of reduced V^{4+} states in addition to V^{5+}, and this fraction was larger in catalysts precipitated at higher pH (Figure 11.8c). Finally, a very good correlation was established between the selectivity of propylene formation and the measured SIMS–XPS surface characteristics (Figure 11.8). Hence the occurrence of lower oxidation states of vanadium and the formation of isolated highly dispersed VO_x species on the surface appeared to play an important role in this process.

We finally turn to gold-supported catalysts, which have been extensively studied in the last few years. Au/TiO_2 has proven to be a benchmark system owing to its high activity in CO oxidation at low temperatures. Since the method of preparation is key to obtaining highly active catalysts, we employed TOF SIMS and XPS along with catalytic tests to reveal the surface composition and electronic structure of various preparations and to correlate them with the catalytic performance [108]. All samples were prepared by deposition–precipitation (DP) using, however, different recipes than usually applied in producing TiO_2 supports. Furthermore, the Au-precipitating agents were varied along with the alkali/alkaline earth metal content of the solutions. The data were then compared with those obtained for a commercial Au/TiO_2 catalyst (same 1.51 wt% Au loading on commercial Degussa TiO_2) supplied by the World Gold Council (WGC). In particular, TiO_2 in its anatase form was produced via the oxalate route, that is, $TiO(C_2O_4)$ was precipitated from $Ti[OC(CH_3)_3]_4$ in an excess of

oxalic acid dihydrate in acetone followed by filtration, drying, and decomposition of the precipitate in O_2–Ar at 833 K. DP of Au on to the TiO_2 occurred from an aqueous solution of $HAuCl_4$ using NaOH (pH 7) as the precipitating agent. The final catalyst (DP1) was obtained after calcination in air at 673 K. To obtain a Na-free catalyst (DP3), the DP on to TiO_2, prepared essentially as described above, was repeated using urea (H_2NCONH_2) as the precipitating agent. To test the possible catalytic influence of Mg, the oxalate route to TiO_2 was modified by adding $MgNO_3{\cdot}6H_2O$ to the solution (at reduced oxalic acid excess) before the DP of Au with urea (sample DP2). The CO oxidation was measured with a 2% CO + 2% O_2 (Ar balance) gas mixture at room temperature for 1 h, always using the same amount of catalyst such that the conversion to CO_2 fell in the range where a comparison between the different catalysts became possible.

Concerning the possible influence of the alkali/alkali earth metals on the catalytic activity, no clear statement can be made at present. Owing to the high sensitivity of SIMS to alkali metals, Na was detected (at much lower levels, however) even in the sodium-free samples DP2 and DP3 (Figure 11.9a). At the same time, the level of contamination by potassium, which was not controlled, was the highest in DP2 and the lowest in WGC. We note, without going into the details, that the amount of Mg in DP2 was about the same as that present in the WGC reference sample. Regarding the Au/Ti atomic ratios, no clear correlation with the catalytic activity was found either (cf., Figure 11.9b and d). Assuming these ratios to be representative for the dispersion of the Au nanoparticles, this result would imply that "dispersion" is not a decisive factor.

On the other hand, the TiO^+/Ti^+ ratios, being dependent on the oxygen coordination of the Ti ions in the support, exhibited a clear correlation with the CO conversion (cf., Figure 11.9c and d). In line with this, the fraction of reduced Ti^{3+} species in the support and the O^{2-}/Ti^{4+} atomic ratio as derived by deconvoluting the Ti 2p and O 1s XP spectra of the catalysts also displayed good correlation with the

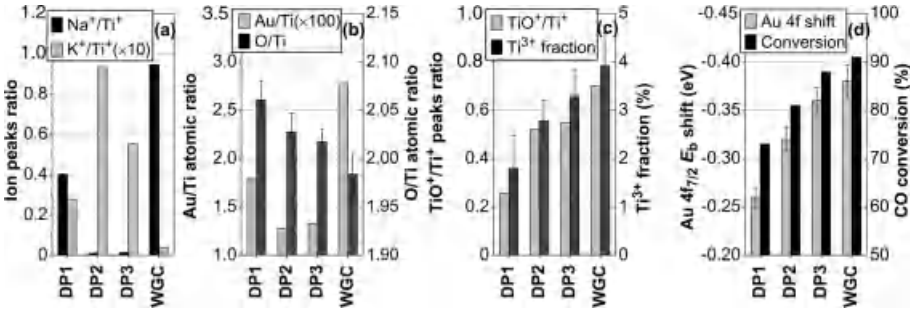


Figure 11.9 Correlation between catalytic activity and surface structure of Au/TiO_2 catalysts: ion peaks ratios (a) Na^+/Ti^+, K^+/Ti^+, and (c) TiO^+/Ti^+ derived from SIMS data; (b) Au/Ti and O^{2-}/Ti^{4+} atomic ratios and (c) fraction of Ti^{3+} species in the Ti 2p spectrum derived from XPS data; (d) shift of the Au $4f_{7/2}$ binding energy and catalytic activity represented by CO-to-CO_2 conversion.

activity (Figure 11.9b–d). For all the catalysts studied, the Au 4f core level was observed to be shifted to lower binding energies compared with bulk Au due to the interaction of the reduced Ti^{3+} species with interfacial Au atoms [109], and the CO conversion exhibited a practically linear correlation with the magnitude of this negative shift of the Au $4f_{7/2}$ line in different catalysts (Figure 11.9d). These correlations imply that the electron transfer from oxygen vacancies in the support (Ti^{3+} species) to Au particles thereby producing $Au^{\delta-}$ state is crucial for the necessary activation of the O_2 molecule in CO oxidation over Au/TiO_2.

That the oxygen vacancies on the support surface may serve as centers for O_2 activation was corroborated by a correlation between the activity and reducibility of supported Au catalysts. According to Dobrosz-Gómez *et al.* [110], who employed TOF SIMS and other techniques, the surface composition, structure and catalytic performance of $Au/Ce_{1-x}Zr_xO_2$ ($x = 0$, 0.25, 0.5, 0.75, 1) catalysts produced by direct anion exchange depended on the support composition x and the washing treatment (no washing, washing with warm water or with ammonia). The presence of ionic Cl and O in the close vicinity of gold atoms at the catalysts surface was revealed by the emission of molecular secondary ions ($AuCl^-$, $AuCl_2^-$, AuO^-, AuO_2^-, etc.). The relative intensity of these chlorine- and oxygen-containing ions was found to be dependent on the support composition and was significantly reduced in the catalysts washed with ammonia, which demonstrated the highest activity.

11.6.4
Compositional Effects in Various Catalytic Reactions

The surface composition of real and model catalysts can be followed straightforwardly by varying the relative amount of components in alloys or mixed metal oxides, or simply by changing the catalyst loading in supported catalysts. The examples presented here are not meant to demonstrate optimal catalytic performance, that is, they are not part of a research strategy aimed at developing highly active catalysts, but rather follow the purpose of understanding changes in the surface composition and in the activity along with segregation phenomena on the basis of SIMS and LEIS studies.

11.6.4.1 CO Hydrogenation

We start by inspecting some data in relation to the formation of methanol. Chen *et al.* [111] employed static SIMS and XPS for *in situ* studies of various Cu/ZnO-based model catalysts before and after adsorption/reaction at pressures below 10^{-4} Pa. The aim was to clarify the role of the ZnO sites and to demonstrate possible synergetic effects between Cu and Zn in such catalysts. Gases of nominal composition (10% CO + 10% CO_2 + 80% H_2) were used for the adsorption/reaction studies at temperatures between 90 and 573 K. The SIMS data were only qualitatively evaluated; no quantification was presented by the authors. Furthermore, no negative ionic species were reported, so some care is advised in assessing the data. Nevertheless, in studies with both $Cu/ZnO/Al_2O_3$ and Cu/ZnO catalysts, after syngas adsorption the positive SIMS spectra contained $CuCO^+$ molecular ions whereas analogous Zn

carbonyls were absent. Methoxy, considered to be an intermediate in the formation of methanol, was found to be bound to Zn (emission of $ZnOCH_3^+$) rather than to Cu sites. It was concluded that the coexistence of ZnO with Cu increased the capability of Cu to adsorb CO, which then migrated to Zn sites where further hydrogenation occurred. These conclusions were supported by the observation that Al_2O_3 showed no synergetic effect with Cu since neither CO nor methoxy was observed in respective Cu/Al_2O_3 catalysts. We consider that it would be interesting to look also for possible changes in the spectral features by performing reaction studies at higher gas pressures.

Turning now to hydrocarbon synthesis, Houalla *et al.* [112] studied the influence of the Ni content in Ni_xSi_y ($NiSi_2$, Ni_3Si_2, Ni_2Si, and Ni_5Si_2) and Ni_xTh_y (Ni_3Th_7, Ni_2Th, NiTh, and Ni_5Th) intermetallics on their methanation activity using LEIS and XPS. Oxygen treatment of the nickel-poor Ni_xTh_y samples at 623 K resulted in surface enrichment with nickel (Figure 11.10a and b). The opposite behavior was found for Ni_xSi_y and ascribed to the preferential oxidation of Si to form a passivating SiO_2 layer. The strongest enrichment effect was observed for Ni_5Th, which also turned out to be the most active catalyst in methanation over oxygen-treated Ni_xTh_y samples (cf., Figure 11.10b and c). It was suggested that the high amounts of Ni in Ni_5Th were accommodated not only in the porosity of ThO_2 but also in the outer part of the catalyst particle.

Ott *et al.* [113] performed SIMS and XPS analyses of Ru, Fe, and unsupported 97Ru3Fe, 75Ru25Fe, and 33Ru67Fe alloys in order to correlate their surface structure and composition with the catalytic behavior in the Fischer–Tropsch synthesis. The surface region of the reduced alloys was enriched in iron, with Ru and Fe being in the metallic state. Owing to the higher surface sensitivity, SIMS indicated a greater Fe enrichment in the first layer of the alloys than XPS. After atmospheric CO hydrogenation under differential conditions at 573 K, the alloys were found to follow the general trend of increasing Fe surface enrichment but also to develop special features in the high and low Fe content regions. Accordingly, the 97Ru3Fe alloy exhibited an unusually high C_2 yield with very high selectivity to ethylene compared with pure Ru.

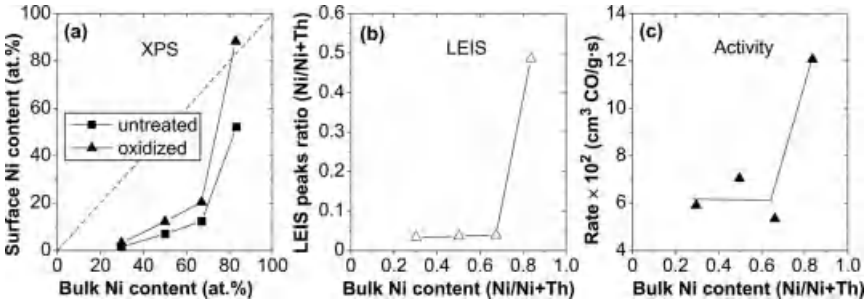


Figure 11.10 (a) Variation of the surface composition of Ni_xTh_y alloys (untreated, squares; oxidized, triangles) measured by XPS and (b) by LEIS (oxidized alloys). (c) Variation of CO conversion rate of oxidized alloys as a function of the bulk nickel content. Data from [112].

This correlated with the sharp changes in the Ru^+ ion yield, suggesting an alteration of the surface electronic properties in this alloy upon addition of a small amount of Fe to Ru. In a subsequent study by the same group [114], the reaction-induced build-up of carbon was analyzed. Surprisingly, none was found for pure Ru and 97Ru3Fe after 24 h of Fischer–Tropsch synthesis at 573 K whereas 75Ru25Fe and 33Ru67Fe rapidly produced surface carbon which entrained changes in the selectivity of the reaction.

In a later study by Sellmer *et al.*, the surface composition of a Co/SiO_2 catalyst was studied by static SIMS before and after catalytic CO hydrogenation [115]. After the catalytic reaction at 458 K, groups of ion species with masses ranging from $C_1H_x^+$ to $C_8H_x^+$ were detected, indicating that individual hydrocarbon species up to at least C_8H_y were adsorbed on the catalyst surface. This was in accordance with the considerable chain growth probability ($\alpha = 0.78$) observed for CO hydrogenation at 0.44 MPa. At the same time, no $Co_xCO_y^+$, CoH_z^+, or $CoC_xH_y^+$ molecular ions were observed in the mass spectra, which prevented the authors from drawing conclusions on the local chemical environment of the hydrocarbon entities. However, a H_2-TPR experiment after the reaction studies also showed individual hydrocarbon desorption up to at least C_5.

The surface structure of Th-modified Ni/SiO_2 catalysts was studied by Ledford *et al.* [116] using LEIS, XPS, and other techniques. They reported a correlation between the surface Th content as measured by Th/Si atomic LEIS ratios as a function of the Th loading and the turnover frequency for CO hydrogenation calculated from the rate data and the Ni surface titrated via H_2 chemisorption. Up to a Th/Si atomic ratio of 0.015 (6.1 wt% ThO_2), the turnover frequency increased; for larger amounts it decreased somewhat. The selectivity to higher hydrocarbons and olefins was also significantly increased by Th promotion. The structural effects related to Th promotion were discussed in the frame of the formation of active sites by Th decoration of the Ni metal particles.

11.6.4.2 Hydrocarbon Oxidation

Yan and Andersson [117] performed SIMS along with catalytic studies of the oxidation of toluene using V_2O_5–WO_3 catalysts of variable composition. The occurrence of various molecular ions in the SIMS spectra including both tungsten and vanadium (WVO_x^+) indicated that vanadium and tungsten ions were at least to some extent intimately mixed in the catalysts. The WO^+/V^+ ion peak ratios showed a linear correlation with the $WO_3/(V_2O_5 + WO_3)$ molar ratio in a wide concentration range. The rate of oxidation of toluene and selectivity for benzaldehyde formation decreased on increasing the V_2O_5 loading and correlated with the increase in the amount of V^{4+} [or $V^{4+}/(V^{5+} + V^{4+} + V^{3+})$ ratio] formed upon reaction, indicating the importance of reduced phases and surface defects for high activity and selectivity.

Debecker *et al.* [118] employed a variety of methods including TOF SIMS and XPS to study the surface chemical composition and structure of nanosized vanadia–titania mixed oxide particles with varying V_2O_5 loadings prepared by a nonhydrolytic sol–gel route and used in benzene total oxidation. TOF SIMS measurements of the outermost surface of the spherically aggregated particles were in good correlation

with the XPS data. The presence of intense peaks of negative $V_2O_5^-$ and $TiVO_5^-$ molecular secondary ions was related to surface species in which V−O−V bridges (vanadium oxide oligomers) and V−O−Ti bridges, respectively, occurred. In the reference vanadia–titania catalyst prepared by a classical wet impregnation, a high proportion of $V_2O_5^-$ ions was found, consistent with the fact that a V_2O_5 phase was formed on the surface of TiO_2. $TiVO_5^-$ ions were also detected, indicating the formation of V−O−Ti chemical bonds during the preparation. In as-prepared xerogels, a high proportion of $TiVO_5^-$ and a low contribution of $V_2O_5^-$ ions were observed, which was argued to be consistent with vanadium atoms being dispersed within the titania matrix. Calcination of the xerogels in air at 773 K caused vanadia species to migrate toward the surface of the TiO_2 nanoparticles. As a result, an increase in the proportion of $V_2O_5^-$ ions was revealed. In the same way, TOF SIMS and XPS indicated that the proportion of oligomeric vanadate species in the sol–gel catalysts increased with the V_2O_5 loading. A clear correlation between the $V_2O_5^-/(TiVO_5^- + V_2O_5^-)$ peak ratios and the V $2p_{3/2}$ binding energy was found, that is, increasing fractions of V−O−V at the expense of V−O−Ti bonds shifted the V $2p_{3/2}$ XPS peak to higher binding energies. Correlating this insight with catalytic activity data in the benzene oxidation led the authors to suggest that oligomeric vanadates formed at high V_2O_5 loadings were catalytically more efficient than isolated VO_x species formed at low V_2O_5 loadings.

$(VO)_2P_2O_7$ catalysts (VPO) are very suitable catalysts for the oxidation of *n*-butane to maleic anhydride. The composition of the outermost atomic layer of these catalysts is one of the crucial issues in understanding their catalytic performance. LEIS and XPS measurements by different groups produced different results for the P/V ratios. Quite generally, owing to the higher surface sensitivity, these values were found to be higher for LEIS than XPS. P/V ratios between 2 and 3, pointing to significant phosphorus surface enrichment, were found by using $^4He^+$ [119] and also $^3He^+/^4He^+$ scattering [120]. Several shortcomings not considered in these studies, including sputtering effects and reference adequacy, prompted Brongersma's group to perform for these types of catalysts strictly static LEIS experiments with at least two orders of magnitude lower $^3He^+$ ion current density than in conventional setups. Accordingly, Jansen *et al.* [121] were able to determine the absolute atomic densities in the topmost layer of a carbon-free VPO catalyst as 1.7×10^{14} P atoms cm^{-2} and 0.86×10^{14} V atoms cm^{-2}, corresponding to a surface P/V ratio of 2.0 ± 0.2. Much of what caused higher P/V ratios in former measurements [119, 120] could be attributed to preferential shielding of V by carbon. It was suggested [121] that their measured P/V ratios are an indication of VPO catalysts being terminated by a distorted vanadyl pyrophosphate structure or containing a significant contribution of a phase such as α_{II}-$VOPO_4$. Vanadium vacancies were therefore discarded as being the major reason for the reported P/V ratios.

As a further example of hydrocarbon oxidation, we consider the partial oxidation of propane to acrylic acid. Bulk mixed Mo–V–Te oxides possess high activity and selectivity for this reaction. Guliants *et al.* [122] employed LEIS and XPS to investigate the elemental compositions, metal oxidation states, and catalytic functions of V, Mo, and Te in the surface region of three model catalysts with synthesis compositions

corresponding to $Mo_{0.6}V_{0.3}Te_{0.1}$, $Mo_{0.5}V_{0.4}Te_{0.1}$, and $Mo_{0.3}V_{0.6}Te_{0.1}$. In order to mass-resolve all the components in the catalysts, the LEIS analysis was performed with both $^4He^+$ and $^{20}Ne^+$ ions. It was found by LEIS that after the catalytic studies at 653 K the outer surface of the Mo–V–Te–O catalysts was enriched in vanadium (~1.4–1.7-fold excess) and tellurium species (~1.5-4-fold excess) and thus depleted in Mo. Removing approximately one surface monolayer by 3 keV Ne^+ sputtering caused the values to approach those measured by XPS for the near-surface region and by ICP for the bulk (the latter being very similar). It was further observed that the subsurface contained ~30% more Mo than the topmost layer, thus confirming that the Mo–V–Te–O outer surface was indeed depleted in Mo. Correlating the surface composition data with the catalytic performance of the oxidation indicated that both the propylene and acrylic acid rates of formation and also the selectivity to acrylic acid were dependent on the topmost surface V concentration. No such dependence was seen for the surface Mo or Te concentrations. The dependence of the average reaction orders for product formation on the topmost surface V concentration implied that multiple surface VO_x sites were more efficient in the propane activation and acrylic acid formation than isolated sites. The likely role of the surface Mo and Te species in propane oxidation was to tune the activity and selectivity of the surface V^{5+} species by forming bridging V−O−M bonds.

We finish this section by mentioning SIMS and XPS analyses in relation to methane oxidative coupling over a series of Na_2MoO_4/SiO_2 supported catalysts with various loadings of Na_2MoO_4 [123]. Highly dispersed Mo-containing species were reported to favor the formation of low-coordination surface sites, and the catalytic activity of the samples exhibited a correlation with the amount of such sites.

Wang *et al.* employed LEIS and XPS to study $Mn/Na_2WO_4/SiO_2$, $Mn/Na_2WO_4/MgO$, and $NaMnO_4/MgO$ supported catalysts with different loadings of Mn and Na_2WO_4 for the $Mn/Na_2WO_4/MgO$ system [124]. The XPS analysis showed that the near-surface region of fresh calcined catalysts was enriched in Na and W (with an Na/W atomic ratio of ~5) but not in Mn. According to the LEIS data, the surface layers of both SiO_2- and MgO-supported catalysts contained some W and only a small amount of Mn, while Na and O were dominant species. A linear relationship was found between the specific activity in oxidative coupling of methane and the surface Mn concentration, implying that Mn played an essential role in achieving high activities and selectivities despite its low concentrations. Since the catalytic behavior was observed to be similar for all three types of catalysts, it was concluded that a common Mn-containing active site, consisting of an Na−O−Mn species, was involved. Na ions dominating the near-surface region of the catalyst were assumed to promote the dispersion of the Mn ions.

Catalysts for the total oxidation of methane are usually Pd based and "simpler" in composition than those used in the above coupling studies. LEIS along with intermittent Ar^+ sputtering was used to obtain depth profiles for 5 wt% Pd/Co_3O_4 catalysts [125]. The Pd/Co ratios in both as-prepared and used catalysts decreased with sputtering. These ratios were observed to be smaller in the used catalyst, and strong C- and O-related spectral features encountered after the reaction, possibly due to an oxyhydroxide, caused shielding effects that were difficult to handle.

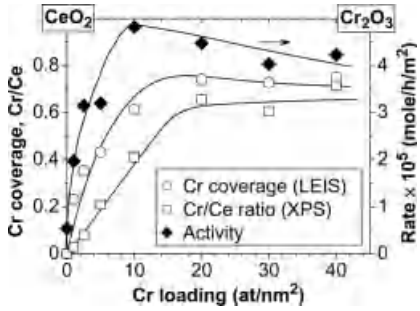


Figure 11.11 Effect of Cr loading of the impregnated Ce–Cr–O catalysts on the Cr coverage determined by LEIS, the Cr/Ce ratios obtained by XPS and the rate of isobutene formation at 543 K. Data from [127].

11.6.4.3 **Hydrogenation and Oxidative Dehydrogenation**

Renouprez *et al.* [126] studied the catalytic activity of a series of silica-supported Pd–Ni catalysts in the hydrogenation of 1,3-butadiene in relation to their surface composition measured by LEIS with depth profiling and XPS. Both methods demonstrated a strong Pd surface segregation and, as expected, the effect was even stronger for LEIS. The initial activities plotted in terms of the turnover frequency values as a function of the Pd surface composition were well represented by a third-degree polynomial which implied that, to a first approximation, the activity should be proportional to small ensembles of ~2–3 Pd atoms, without any synergy effect between the two metals. Variations in the initial activity were explained by invoking particle size effects.

Moriceau *et al.* studied the catalytic performance of Cr–Ce–O catalysts in the oxidative dehydrogenation (ODH) of isobutane to isobutene in relation to their surface composition and structure, which were characterized by LEIS, XPS, XRD, and other techniques [127]. For catalysts prepared via impregnation, the Cr coverage, θ, derived from LEIS data increased with the Cr loading before attaining a practically constant value of ~75% at loadings above 20 Cr atoms nm^{-2}. Interestingly, similar behavior was also observed for the surface Cr/Ce atomic ratio determined by XPS (Figure 11.11). The conclusion was drawn that aggregates of Cr_2O_3 crystals could be formed on the CeO_2 support at high Cr loadings. The variation of the rate of isobutene formation at 543–573 K as a function of the Cr loading exhibited a correlation with the variations of the Cr surface coverage (LEIS) and the surface Cr/Ce atomic ratio (XPS), irrespective of the catalyst preparation method (Figure 11.11). The linear increase in the activity with the Cr content in the range where only $Cr(VI)O_x$ species were present (according to XPS data) was suggested to indicate involvement of the Cr^{6+} species in the active sites for ODH of isobutane.

11.6.5
Promotion and Poisoning Effects

Promoters are added to a solid catalyst in order to improve its performance in catalytic reactions. By itself the promoter has little or no catalytic effect. Some promoters

interact with active components of catalysts and thereby cause stabilization via chemical/structural changes; others intervene directly in the catalytic reaction, thereby improving the catalytic performance in terms of activity and selectivity. On the other hand, poisoning by small amounts of contaminants, either introduced unintentionally during catalyst preparation or surface-accumulated during the catalytic process, is usually undesirable and shortens the catalyst lifetime or deteriorates the kinetic performance. In many cases, promotion and poisoning involve fairly small amounts (disregarding, for example, the frequently encountered strong coking in reforming and other reactions) and render detection by XPS–AES difficult. The high sensitivity of SIMS and LEIS can help in this respect. We provide some examples by considering a few catalytic reactions and, more specifically, Cl-related effects.

11.6.5.1 **CO Hydrogenation to Methanol**

Promoted Pd-based catalysts are of interest in relation to the selectivity of the methanol synthesis and its dependence on the purity of the SiO_2 support. Sellmer *et al*. [128] employed SIMS and XPS to investigate the role of promoters in methanol synthesis over 5–6 wt% Pd/SiO_2 catalysts by using ultra-pure SiO_2 and Li, Ca, and La promoters at a molar concentration of 5000 ppm (which produced saturated promoter action). The CO hydrogenation at $p = 0.9$ MPa and $T = 553$ K in a flow reactor exhibited high selectivity (usually above 99%) for methanol synthesis and activities which were found to increase in the order Li < Ca < La. The subsequent SIMS analysis revealed, besides other things, the presence of surface formate [emission of $COO(H)^+$ secondary ions] and methoxy bound to the silica support ($SiOCH_3^+$ ions). Neither formate nor OCH_x species were found to be bound on the Pd particle surface. Furthermore, neither COO(H) nor $SiOCH_3$ species were observed for pure or promoted SiO_2 samples. Therefore, it was suggested that the reaction mechanism involved a synergistic effect between the support and the Pd metal, in which the main task of the noble metal was to activate hydrogen and to supply it in atomic form to the support for further reaction with formate to form methanol. The XPS data implied that the promoters might have caused local structural changes in the silica matrix that influenced the catalytic activity during CO hydrogenation.

11.6.5.2 **CO Oxidation**

Vepřek *et al*. performed a detailed study of the thermal deactivation of a commercial hopcalite catalyst ($CuMn_2O_4$) using LEIS, XPS, SEM, and other techniques [129]. LEIS in the depth profiling mode showed that the surface of the deactivated catalyst was completely covered by a potassium overlayer, with no Cu or Mn being visible. Thus, the sites for CO and O_2 adsorption appeared to be blocked. In contrast, the active catalyst exhibited a negligible amount of potassium on the surface. On the basis of the LEIS data, it was concluded that the deactivation was due to the segregation of potassium to the surface of the catalyst, with the driving force of the segregation being the amorphous-to-spinel phase transformation at temperatures above 773 K.

Silica-supported Pt/SnO_x catalysts show low-temperature activity in this reaction; however, they also undergo partly reversible self-poisoning via carbonate formation. With this background, Hoflund *et al*. [130] studied the effect of Fe addition in

promoter quantities (≤1%) using LEIS to characterize the catalyst after reduction with CO only. While demonstrating that the low-temperature CO oxidation in the presence of 8 at.% CO_2 resulted in a higher oxidation rate and a lower decay rate compared with the nonpromoted catalyst, the authors, surprisingly, did not report LEIS analysis showing the changes due to reaction. In the LEIS analysis, after reduction with CO, they found no Fe. They concluded that the Fe was present beneath the surface and most likely at the SiO_2/Pt–SnO_x interface so as to prevent "agglomeration" (as seen in the nonpromoted catalyst) and to maintain a large catalytically active surface area enriched in Pt.

As already mentioned in Section 11.6.3, highly dispersed metal oxide-supported gold catalysts such as Au/TiO_2 or Au/MnO_x are currently regarded as benchmark systems for high CO oxidation activity. Moma *et al.* employed SIMS and XPS to study the influence of various anions and cations on the performance of Au/TiO_2 catalysts [131]. Depending on the amounts added, promoter or poisoning effects were observed. Accordingly, 2.5 mol% of anionic PO_4^{3-}, SO_4^{2-}, F^-, and Cl^- and cationic Li^+, Na^+, and K^+ were found to decrease the catalytic activity compared with pure Au/TiO_2, whether they were added to the TiO_2 support prior to Au nanoparticles deposition or to the as-prepared Au/TiO_2 catalyst. On the other hand, addition of 0.4 mol% of the ions to the support, prior to gold deposition, resulted in most cases in some enhancement of the activity whereas similar addition of the ions to as-prepared Au/TiO_2 caused a decrease. It should be noted that the added ions were not detectable by XPS (except for phosphorus) whereas SIMS revealed their presence. Qualitative examination of the SIMS data provided no evidence for any species on the surface that could originate from the direct interaction between Au centers and the added anion or cation. Therefore, the authors considered indirect rather than direct interactions between the gold atoms and the added entities to be responsible for the promoter effect. Alternatively, the improvement of the catalytic action was considered possibly to be brought about by subtle changes in the support surface prior to gold deposition.

In the case of very small sulfate additions (0.05–0.09 mol%, before Au deposition), a dramatic promotional enhancement (nearly fivefold) of the Au/TiO_2 activity was reported [132]. The respective SIMS spectra contained some Au-related peaks which could be associated with emission of AuS_2O^+ and/or $AuSO_3^+$ molecular ions. Hence in this case, a direct Au–sulfate ion interaction was suggested to be responsible for the origin of the promotional effect.

A poisoning effect by Cl was observed in Au/$Ce_{1-x}Zr_xO_2$ catalysts [110]. TOF SIMS of these catalysts revealed the emission of a number of Cl-containing molecular ions such as $AuCl^-$, $AuClO^-$, and $AuCl_2^-$, indicating chloride ions to be associated with the supported Au particles. The occurrence of Cl^- was attributed to incomplete washing after catalyst preparation using $HAuCl_4$. Since the average Au particle size for these catalysts was much higher than expected, Cl-induced sintering of the particles was considered to take place. Indeed, chlorine removal by washing with ammonia seemed to inhibit the sintering and led to catalytic activity several times higher than occurred without washing.

TOF SIMS and XPS in combination with AFM were used in order to elucidate the promoting role of gold in the catalytic activity of sandwich-type FeO_x/Au/SiO_2/

Si(100) samples [133]. Iron oxide layers with a thickness of 5–10 nm were deposited on either nano-sized Au particles or Au films 80 nm thick supported by SiO_2/Si(100). CO oxidation tests at 803 K showed low rates which, however, turned out to be higher than those over FeO_x/SiO_2/Si(100) and Au/SiO_2/Si(100) reference samples. Obviously, the catalytic activity of the iron oxide overlayer was promoted by both bulk-like Au and Au nano-sized particles underneath, with the activity enhancement being significantly larger for the $FeO_x/Au/SiO_2$/Si(100) samples. The iron oxide layer was composed of a mixture of FeO, Fe_2O_3, and FeOOH and proved to be continuous, since neither SIMS nor XPS detected the presence of gold within the limits of their elemental sensitivities and sampling depths. Despite some reaction-induced chemical alterations in the surface composition of the FeO_x layer, no Au segregation at the surface was detected by TOF SIMS after the reaction. The XPS Au 4f spectra, however, indicated that Au atoms were injected and trapped in the FeO_x layer. Therefore, the catalytic activity of the $FeO_x/Au/SiO_2$/Si(100) samples was suggested to be associated with active sites located on the iron oxide overlayer promoted by gold underneath. Since both Au nanoparticles and Au films caused promotion, it was inferred that an electronic effect was in operation due to the occurrence of an FeO_x/Au interface in both cases. A stronger promotion for Au nanoparticles implied also a particle size-dependent electronic effect. For thicker FeO_x layers of about 40–80 nm, this promotion did not reach the surface and was therefore no longer detectable.

11.6.5.3 **Hydrocarbon Partial and Total Oxidation**

We start this section by considering the epoxidation of ethylene to ethylene oxide, which is an important industrial process necessitating high selectivity. Minahan *et al.* [134] performed a comparative study of low-area Ag/α-Al_2O_3 catalysts either unpromoted or Cs promoted using LEIS, SIMS, XPS, AES, and SEM for chemical and structural characterization. The LEIS spectra showed that the surface of the promoted catalyst was covered to a great extent by an Ag film, so that the signal from the Al_2O_3 support was hardly observable. For the unpromoted catalyst, both the LEIS- and AES-derived signals from Ag and O increased relative to those from Al. A structural model was suggested according to which, in the Cs-promoted catalyst, the α-Al_2O_3 support was largely covered with Ag, whereas in the unpromoted catalyst, more small Ag clusters were present, leaving fractions of the support uncovered and therefore favoring the total rather than partial oxidation of the ethylene. A few further observations in this study are noteworthy from the methodological point of view. First, owing to the high surface sensitivity of LEIS, a number of contaminants were observed but not discussed further by the authors in terms of structural implications. Only LEIS and SIMS were capable of detecting Cs and determining its location and XPS was not. Using LEIS and SIMS in the depth profiling mode revealed the fairly complicated 3D distribution of the Cs promoter. Accordingly, although a small amount of Cs was present at the outermost surface, most of it was hidden beneath and most probably at the Ag/α-Al_2O_3 interface, thereby acting as a "binder" and increasing the interfacial metal/oxide area.

In Section 11.6.4.2, we have already mentioned Mo–V–Te oxides as catalysts for the (amm)oxidation of propane to acrylic acid (acrylonitrile). To improve the selectivity

further, mixed-phase multicomponent Mo–V–Te(Sb)–Nb–O catalysts have been developed. Guliants *et al.* [135] used LEIS in combination with ion sputtering (using both $^4He^+$ and $^{20}Ne^+$) to investigate the promoting effect of Nb, Te, and Sb oxide by introducing them at a theoretical monolayer coverage of 7.5 $MO_x\,nm^{-2}$ to the unpromoted Mo–V–O catalyst. Also, double-promoted (Nb + Te), (Nb + Sb) catalysts were synthesized. According to the LEIS results, the surface and several subsurface layers of the original orthorhombic (M1) Mo–V–O catalyst were Mo enriched (by ~25%) and V depleted (by ~50%) compared with the bulk composition, with the maximum enrichment/depletion (i.e., the highest Mo/V molar ratio) occurring in the subsurface layer. This was in contrast to the case of the orthorhombic Mo–V–Te–O catalysts [122], in which Mo depletion and V enrichment were observed in the topmost surface layer. In the promoted Mo–V–O catalysts, the Mo/V molar ratios were found to follow a similar trend: they were always higher at the surface and in the subsurface layers than in the bulk and demonstrated a maximum in the subsurface layer. Furthermore, clear evidence for surface and subsurface enrichment of all the promoters was obtained, although the promoters did not form a complete monolayer in the topmost surface. The degree of enrichment derived from the promoter concentrations, averaged over several surface layers, increased in the series Sb (for Sb + Nb) < Te < Sb = Te (for Te + Nb) < Nb < Nb (for Nb + Sb) < Nb (for Nb + Te) and was in the range 1.5–15.2. It was striking that the Nb enrichment factors in the double-promoter catalysts were significantly higher than in the single-promoter systems [e.g., 15.2 for (Nb + Te) versus 4.9 for Nb], indicating the occurrence of some interaction between these promoter species. The highest selectivity to acrylic acid observed for the (Nb + Te)- and (Nb + Sb)-promoted catalysts therefore appeared to be linked to the high surface enrichment factor of the Nb promoter.

With the above examples we have reviewed some promotion effects in the partial oxidation of hydrocarbons. We now briefly turn to catalyst poisoning due to carbon deposition and coke formation, which frequently accompany the total oxidation of hydrocarbons. For example, Brongersma's group at Eindhoven performed LEIS studies [136] with a commercial $Pt/Rh/CeO_2/\gamma\text{-}Al_2O_3$ three-way catalyst used in automotive pollution control and showed a significant decrease in the detectable Pt surface concentration after use in ethylene or acetylene (total) oxidation under cold-start conditions. The effect was reversible by treating the catalyst in oxygen. This proved the selective deposition of carbonaceous species during hydrocarbon oxidation rather than Pt sintering to be the reason for the decreasing Pt surface concentrations.

By employing SIMS in combination with XPS, Albers *et al.* [137] studied the nature of carbon deposits on Pt/Al_2O_3 and Pd/SiO_2 catalyst surfaces accumulated during various reactions under technical conditions. In addition to Fe and Cl, Na and K were also found inside the coke deposits of a strongly deactivated Pd/SiO_2 catalyst. The CH^-/C_2H^- SIMS fragment ion ratio was suggested to be a rough tool for differentiating carbons of lower, sp^2-character from amorphous carbons and also structured carbons of higher graphiticity. SIMS studies of various fragment ions from activated carbons used as support materials for precious metal catalysts were also

carried out [138], but we feel that the distinction between different carbon hybridization states and their implication in hydrogen bonding will need more quantitative SIMS data than are currently available.

An SIMS imaging analysis of an electrochemical sensor-type material rendered visible the distribution of reacted species (H, C, O) around the metal/oxide interfaces for Ni and Au electrodes on an Y_2O_3-stabilized ZrO_2 substrate after annealing in a mixture of CH_4, $^{18}O_2$, and D_2O at 973 K [139]. These species were produced in the decomposition of CH_4 and the adsorption of reformed gases (H_2, O_2, CO, CO_2, and C). As would be expected, Ni was found to be active in the CH_4 decomposition and reaction with the reformed gases which eventually led to poisoning whereas Au was not. The respective SIMS images and line analyses clearly showed significant carbon deposition and isotope oxygen $^{16}O/^{18}O$ exchange on the Ni surface, whereas almost no C and no exchange at the Au surface occurred.

11.6.5.4 **Cracking**

Vanadium and nickel are recognized as being the major metal contaminants involved in the poisoning of fluid catalytic cracking (FCC) catalysts. In order to mitigate the deactivation of the catalyst due to accumulating amounts of vanadium in the FCC zeolite, various methods are in use and include the scavenging of the V by reaction with metal oxide additions. Chao *et al.* [140] studied the passivation effect of calcium-exchanged clay (montmorillonite) added to commercial FCC catalysts. By applying SIMS in the imaging mode, they investigated the vanadium distribution over these and over vanadium-loaded cracking catalysts mixed with Ca-exchanged clay. The results of a two-dimensional analysis of the surface composition using the Si^+, Al^+, Ca^+, La^+, and V^+ secondary ion images were found to be consistent with the cracking activity data and showed that vanadium was preferentially accumulated on the calcium-exchanged clay in the presence of FCC catalyst.

11.6.5.5 **Beckmann Rearrangement**

The industrially most important application of the acid-catalyzed Beckmann rearrangement is the transformation of cyclohexanone oxime into ε-caprolactam (feedstock for nylon 6 formation). Albers *et al.* employed XPS and SIMS in the depth profiling mode to study deactivation and reactivation phenomena on the surface and in the subsurface layers of weakly acidic borosilicate B-MFI-type catalysts used for vapor-phase transformation [141]. The in-depth variations of the B^+, C^+, CH_x^+, O^+, OH^+, Si^+, SiO^+, $SiOH^+$, Na^+, Mg^+, K^+, and Ca^+ secondary ion intensities were monitored during sputtering of a fresh B-MFI catalyst and compared with those of a catalyst which underwent reaction-induced deactivation and one which was regenerated in air at 773 K. For the fresh catalyst, no significant changes of the Si^+ and B^+ signal intensities occurred as a function of depth, whereas the respective intensities in the surface regions of the deactivated catalyst were much lower owing to the deposition of carbon (causing the emission of C^+, CH^+, CH_2^+, and CH_3^+ ions). However, the enhanced deposition of carbon on the catalyst surface during reaction was not considered to be mainly responsible for the deactivation of the B-MFI catalyst (the overall aliphatic carbon amounts were too small to do so). Also, no

irreversible deboration in the surface regions of the zeolite was observed. Therefore, other reasons for the deactivation had to be considered. Although no final assessment was provided by the authors, it seems that they paid most attention to the SiO^+/$SiOH^+$ ion ratios, which changed significantly in the near-surface region with increasing run time of the catalyst. This was taken as an indication that the silanol groups change in number and distribution in the near-surface region of the zeolite pore system. On the other hand, after regeneration, the $SiO^+/SiOH^+$ ion ratio in the surface region was almost the same as in the fresh catalyst. This finding shows that the silanol group density in the topmost surface regions, being responsible for the catalytic activity, was not changed irreversibly due to the reaction, whereas the silanol group density in the pore system below the surface was tremendously affected. The authors also reported changes in the Ca^+ and K^+ profiles relative to the Si^+ profile in the near-surface regions of the zeolite, whereas the Na^+ profiles remained largely unchanged. This suggested that Na was located on lattice sites, whereas the Ca was able to diffuse inside the pore system.

11.6.5.6 **Aldose Oxidation**

Karski *et al*. [142] used TOF SIMS (including its imaging mode) and XRD to study the influence of thallium on the catalytic performance of a 5 wt% Pd/SiO_2 catalyst. Obviously, during hydrogen activation at 533 K, intermetallic PdTl-type compounds were formed as a result of the Pd–Tl interaction. This was concluded from the emission of $PdTl^+$, $PdTlO^+$, and $PdTlO_2^+$ molecular ions. Although thallium did not have any activity by itself, it acted as a promoter in the oxidation of glucose and lactose. Although the catalytic performance was not observed to change monotonically with the Tl content, Pd–Tl/SiO_2 catalysts demonstrated much higher selectivity in aldonic acid formation than Pd/SiO_2, possibly due to the formation of PdTl intermetallic compounds.

When doping the same type of catalysts with bismuth at similar loadings of up to 8 wt%, a similar positive influence was found [143]. However, depending on the bismuth promoter content, significant differences were also observed in the catalytic performance in glucose and lactose oxidation. It was suggested that this is due to the different structure of the active sites formed during activation of Pd–Bi/SiO_2 compared with Pd–Tl/SiO_2 catalysts. Indeed, both XRD and TOF SIMS suggested the formation of intermetallic BiPd-type compounds in Pd–Bi/SiO_2 catalysts containing small amounts of Bi and of BiPd- and Bi_2Pd-type compounds in those containing larger amounts of Bi.

11.6.5.7 **Nitrite and Nitrate Reduction**

Witońska *et al*. [144] showed bimetallic 5% Pd–In/Al_2O_3 catalysts with indium contents in the range 0.5–5 wt% to exhibit high activity in the reduction of nitrates and nitrites in water, with pure In being completely inactive. However, they also found that large amounts of In (Pd–5% In/Al_2O_3) may cause a deterioration. TOF SIMS spectra of the activated Pd–In/Al_2O_3 catalysts revealed $PdIn^+$ secondary ion emission, and it was concluded that a PdIn-type intermetallic compound was formed in all the samples. Even at the lowest In content of only 0.5%, SIMS was capable of

detecting the formation of PdIn on the surface of the catalyst. XRD, on the other hand, allowed the identification of an $In_{0.52}Pd_{0.48}$ intermetallic phase only in the highest loaded Pd–5% In/Al_2O_3 catalyst. The large amount of this phase along with a high In surface concentration were suggested to be responsible for the low activity of this catalyst composition.

11.6.5.8 Cl-Related Effects in Various Reactions

Cl is most frequently regarded as a poison in heterogeneous catalysis and cannot always be removed from the catalyst when, for example, Cl-containing precursors are used in catalyst preparation or Cl is formed during the reaction. There are literature reports, however, which also indicate promotion effects due to chlorine-induced improvement of certain catalyst properties such as dispersion, chemical phase stabilization, and reducibility.

Liu and Ozkan [145] studied the effect of chlorine addition on the surface compositional and structural characteristics of MoO_x supported on the surface of silica–titania (1:1) mixed oxides (10 wt% MoO_x/Si–Ti) and used a number of spectroscopic tools, including TOF SIMS, to provide a correlation with the catalytic performance for the oxidative dehydrogenation of ethane. All Cl-modified catalysts (the Cl/Mo ratios ranged from 0 to 2) demonstrated a clear promotional effect, exhibiting a significant augmentation of the ethylene formation turnover frequency with increasing Cl loading. XPS data showed that Cl could significantly alter the electronic structure of molybdena species and oxygen environment around the Mo and Si species in the Si–Ti matrix; no molybdenum chloride was formed, however. Actually, XPS failed to detect any Cl in the catalysts. TOF SIMS, on the other hand, revealed the relative concentration of Cl (as represented by the Cl^-/O_2^- ion yields ratio) to increase at higher chlorine loadings. Moreover, the emission of $SiCl^+$ secondary molecular ions was also observed. This provided direct evidence for chlorine being located in the Mo/Si–Ti catalysts and Si—Cl groups forming on the surface. More generally, it was suggested that the chlorine changed the electronegativity of the Si—O ligands so as to provide a preferential reaction of the molybdena species with the silica support, which could be responsible for the improved catalytic performance.

A promoting effect of chlorine was also reported by Sobczak *et al.* [85] for AuMCM-41 mesoporous catalyst containing Au nanoparticles, which was produced by coprecipitation in a one-step synthesis with sodium silicate and $HAuCl_4$ and demonstrated a high selectivity in acetonylacetone cyclization to methylcyclopentenone (MCP). Also, an intense emission of $AuCl^-$ molecular ions was observed by TOF SIMS for this catalyst, indicating the presence of chloride ions in the close surroundings of gold centers, whereas no $AuCl^-$ ion emission was detected for the impregnated Au/MCM-41 catalyst. Since the coprecipitated catalyst was much more selective in MCP formation, it was suggested that the presence of Au—Cl species is responsible for the necessary strong basicity of AuMCM-41. A similar Cl^- promoter mechanism was invoked to explain the electron transfer to oxygen in HC-SCR (selective catalytic reduction) of NO (using propene as "HC"). Propene oxidation was already observed at room temperature and only on the catalyst prepared by coprecipitation.

Bertinchamps *et al.* [146] employed TOF SIMS and XPS to study the resistance to chlorine of transition metal oxides, VO_x, CrO_x and MnO_x, supported on TiO_2. The total oxidation of benzene and chlorobenzene was studied and it was found that the tendency for deactivation in the presence of chlorinated species is dependent on the transition metal. Accordingly, VO_x-based catalysts exhibited very good resistance and did not suffer from any deactivation. Conversely, MnO_x catalysts showed a huge deactivation and CrO_x-based catalysts were intermediate. For as-prepared catalysts, Cl-containing secondary ions Cl_n^-, ClO^-, and $Cl_nTiO_m^-$ were observed in the TOF SIMS spectra. For VO_x- and CrO_x-based catalysts recovered after oxidation of chlorobenzene, the relative emission intensities of these molecular ions were similar to those measured for the fresh samples, and no new chlorine fragments were detected. By contrast, for used MnO_x-based catalysts, a dramatic increase in the summed relative intensity of all chlorinated fragments was observed, indicating true chlorination of the catalyst involving the support. Moreover, chlorinated fragments $ClMnO^-$, Cl_2Mn^-, Cl_2MnO^-, Cl_3Mn^- related to the MnO_x phase were detected. Hence the very good resistance to deactivation of the VO_x catalysts was suggested to be due to the absence of chlorine on their surface after the catalytic reaction, whereas the huge deactivation of the MnO_x catalysts was associated with strong chlorination of the MnO_x during the oxidation of chlorobenzene and the formation of manganese chlorides ($MnCl_x$) and oxychlorides ($MnCl_yO_z$).

11.6.6
Active Sites

The question of the nature of the active sites in heterogeneous catalysis is crucial for the understanding of catalytic activity and selectivity. Despite the fact that neither SIMS nor LEIS can be employed *operando* at ambient reactant pressures, remarkable insight into the nature of the catalytically active sites has recently been obtained in studies with structurally and chemically complex catalysts. There are cases where discrimination between different sites and their accessibility to the reactant has become possible. These cases frequently comprise materials with little "flexibility" in their surface. Spinels certainly belong to these materials, and it has been shown exclusively by LEIS that cations in octahedral positions are catalytically active sites in various spinels [21, 48].

The isotopic discrimination ability of SIMS can be advantageously employed in the identification of active sites for oxygen uptake in mixed metal oxide catalysts and for studying exchange processes in catalytic reactions. Using the SIMS ^{18}O tracer technique, it was shown that surface Sb ions acted as adsorption sites for oxygen on an Fe_2O_3–Sb_2O_4 catalyst [147].

SIMS in combination with XPS and other surface characterization techniques has demonstrated the importance of a reduced V^{4+}-containing phase in V–Al–O [107], V_2O_5–WO_3 [117] and V_2O_5–SnO_2 catalysts [148] as a surface-active site for high activity and selectivity in the partial and total oxidation of hydrocarbons.

Smits *et al.* employed LEIS and XPS to study the effect of vanadium on the surface composition of V–Nb–O oxide catalysts in relation to their catalytic performance in

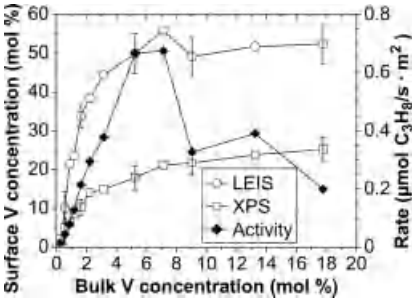


Figure 11.12 Surface concentration of vanadium in V–Nb–O catalysts as determined by LEIS and XPS and the rate of propane consumption as a function of the bulk V concentration. Data from [149].

the oxidative dehydrogenation of propane [149]. It was found that with an increase in vanadium loading (ranging from 0.25 to 20 mol%), the surface concentration of vanadium as determined by XPS and LEIS increased strongly before leveling off (Figure 11.12). The LEIS data also revealed that vanadium replaced niobium atoms at the surface without changing the oxygen structure. Owing to the higher surface sensitivity of LEIS, the V surface content determined by this method was significantly larger than that measured by XPS. From the similarity between the LEIS-derived V surface concentrations and the rate of propane consumption (Figure 11.12), it was concluded that the catalytically active surface sites consisted of vanadium. More precisely, the dependence of the reaction rate on the LEIS-derived V surface concentration could be fitted by a power function with an average exponent of 2.0 ± 0.3, suggesting that the active site on the catalyst surface contained 2.0 ± 0.3 vanadium atoms on average. The spread in the reaction order indicated the existence of several different sites: isolated vanadium atoms, pairs of vanadium atoms, and ensembles of three vanadium atoms. The isolated vanadium sites were inferred to be less active than the clusters of V atoms, and at higher V concentration more V clusters with a higher activity occurred at the surface.

Guliants *et al.* [50] suggested a novel method for studying the chemical nature of active surface sites present in orthorhombic (M1) Mo–V–O and Mo–V–Te–Nb–O metal oxide catalysts by using LEIS with 3 keV $^4He^+$ and 5 keV Ne^+ ions in combination with methanol and allyl alcohol selective chemisorption and reaction. With regard to the catalytic performance of the catalysts, the additional presence of bulk Te and Nb oxides in the M1 phase was highly beneficial for the selective formation of acrylic acid and acrylonitrile by propane (amm)oxidation over Mo–V–Te–Nb–O. According to the LEIS analysis, the outer surface of this catalyst was depleted in V and Mo whereas it was enriched in Nb and Te. After sputtering off one monolayer, the subsurface was still depleted in V, and Nb persisted to have much larger subsurface concentrations than those in the bulk whereas both Mo and Te came closer to the bulk values. Concerning the alcohol adsorption, methanol apparently probed the number of surface-active sites in both catalysts whereas allyl alcohol was more discriminating but also led to more reconstruction than methanol. In both cases, the thermal desorption was not complete and additional chemical or

sputter treatments were necessary before revealing the relevant surface compositions. By monitoring the attenuation of the LEIS signals for all surface metal oxide ions, direct evidence was obtained that the topmost surface VO_x sites in the Mo–V–Te–Nb–O catalyst were preferentially covered by chemisorbed allyloxy species, whereas methanol was significantly less selective and preferentially chemisorbed at the surface VO_x and MoO_x sites. It was finally concluded that the different surface locations for V^{5+} ions in the Mo–V–O and Mo–V–Te–Nb–O catalysts were primarily responsible for the vastly different catalytic behaviors exhibited by these two orthorhombic phases.

A key question in the selective oxidation of hydrocarbons over metal oxides is how the oxygen is inserted into the hydrocarbon molecules. Guerrero-Ruíz *et al*. made use of the isotopic sensitivity and depth profiling capabilities of SIMS to investigate the nature and participation of oxygen species of MoO_3 crystals in the selective oxidation of propylene [150]. The MoO_3 (010)- and MoO_3 [100]-oriented crystals were first conditioned in $^{16}O_2$ at 673 K and then exposed to a reaction mixture of $^{18}O_2$ + propylene (2:1) at room temperature. The SIMS depth profiles of $^{92}Mo^{16}O^+$ and $^{100}Mo^{18}O^+$ secondary ions measured subsequently clearly indicated that ^{18}O species diffused (slowly) into the solid, with a higher $Mo^{18}O^+/Mo^{16}O^+$ ion ratio being attained for the (010)- and a slower decreasing $Mo^{18}O^+$ profile being observed for the [100]-oriented crystal. Therefore, it was inferred that dioxygen was activated on the (010) basal planes and was then incorporated into the allylic species generated in the lateral faces, possessing a step-surface structure with (010) and [100] orientations.

The role of lattice and adsorbed oxygen in the oxidation of *n*-butane to maleic anhydride and CO_x over $(VO)_2P_2O_7$ catalyst was also studied by using gaseous $^{18}O_2$ [151]. Post-reaction LEIS analysis of the used catalyst showed the presence of V, P, and two isotopes, ^{16}O and ^{18}O. The occurrence of ^{18}O on the surface and in the subsurface layers of the catalyst in amounts of nearly 50% provided direct evidence that only lattice oxygens are active and participate in the reaction, which was in good agreement with the occurrence of ^{18}O-labeled products.

The ability of SIMS to provide valuable information about the atomic arrangement on the surface, about the nearest-neighbor environment of a particular atom, and the formation of strong interatomic bonds in this arrangement through emission of molecular secondary ions was employed in a number of studies to unravel the chemical nature of catalytically active sites [85, 152–156]. The salient examples of identifying the catalytic sites on the basis of an established correlation between the emission of specific molecular ions and the electrocatalytic activity for oxygen reduction in fuel cells can be found in a series of papers by Lefèvre and coworkers [157–159]. They used TOF SIMS to analyze various Fe-based catalysts prepared as follows. In procedure I, the Fe precursor, either Fe^{II} acetate (FeAc) or $Cl–Fe^{III}$ tetramethoxyphenylporphyrin (ClFeTMPP), was adsorbed on perylenetetracarboxylic dianhydride (PTCDA) and the composite material was pyrolyzed at 1173 K in $NH_3–H_2–Ar$ (2:2:1). In procedure II, PTCDA was first pyrolyzed under the same conditions in $NH_3–H_2–Ar$ to produce a nitrogen-doped synthetic carbon (p-PTCDA) followed by Fe precursor adsorption on to p-PTCDA, and pyrolyzed again at different temperatures in $H_2–Ar$ (1:1). The catalytic activity of the samples was

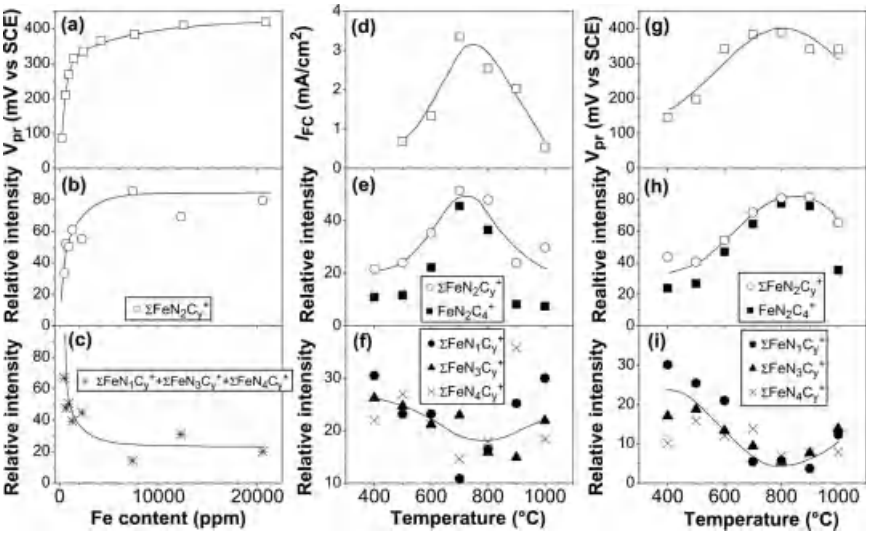


Figure 11.13 Comparison between the catalytic activity for oxygen reduction reaction expressed as (a, g) RDE V_{pr} or (d) fuel cell current I_{FC} and the SIMS relative intensity (b, e, h) of $\Sigma FeN_2C_y^+$ (open circles) or (e, h) of the $FeN_2C_4^+$ ion peak alone (filled squares) and the relative intensity of (c) $\Sigma FeN_1C_y^+ + \Sigma FeN_3C_y^+ + \Sigma FeN_4C_y^+$ (stars) and (f, i) $\Sigma FeN_1C_y^+$ (filled circles), $\Sigma FeN_3C_y^+$ (filled triangles), $\Sigma FeN_4C_y^+$ (crosses) as a function of the Fe content or pyrolysis temperature for (a, b, c) type I Fe TMPP, (d, e, f) type II Fe(0.2) TMPP and (g, h, i) type II Fe(0.2) Ac catalysts. Data from [158, 159].

measured either as a function of the Fe loading in the pyrolyzed material for the procedure I catalyst or as a function of the pyrolysis temperature at a given Fe content for the procedure II catalyst. The catalytic activity for oxygen reduction reaction (ORR) was evaluated electrochemically in half-cells by the rotating disk electrode (RDE) technique (at room temperature) and in full cells using gas diffusion electrodes at 353 K.

It was observed that the catalytic activity of materials prepared according to procedure I with various Fe loadings improved drastically as soon as the Fe content on PTCDA was increased to a few tens of ppm and then saturated (Figure 11.13a), with the behavior being similar for both Fe precursors [156, 157]. The catalytic activity of the samples produced by procedure II with an Fe loading of 2000 ppm (0.2 wt%) and pyrolyzed at different temperatures demonstrated a non-monotonic variation and attained a maximum at pyrolysis temperatures of about 700–800 °C depending on the Fe precursor (Figure 11.13d and g). The analysis of the secondary ion mass spectra of the catalysts revealed a striking correlation between the catalytic activity and emission of particular molecular ions belonging to the $FeN_2C_y^+$ family ($y = 1$–6) represented by the relative intensity either of the most abundant ion peak $FeN_2C_4^+$ in that family or of the sum of the ion peaks $\Sigma FeN_2C_y^+$ (see top and middle panels in Figure 11.13). In view of this correlation, the molecular fragment $FeN_2C_4^+$ was considered the signature of the catalytic site since it was detected in all catalysts, whatever the Fe precursor or the synthesis procedure [157]. The relative intensities of

the sum emission of molecular ions belonging to the families $FeN_1C_y^+$ ($y = 1–3$), $FeN_3C_y^+$ ($y = 1–9$), and $FeN_4C_y^+$ ($y = 1–12$) demonstrated similar variations but they were in an inverse correlation with the catalytic activity (and the emission of $FeN_2C_y^+$) and attained maximum values at the lowest Fe content and pyrolysis temperatures (bottom panels in Figure 11.13). It was therefore concluded [158] that two different catalytic sites existed simultaneously at all pyrolysis temperatures in catalysts synthesized with both Fe precursors. One catalytic site (labeled FeN_4/C) was responsible for the emission of ions of the $FeN_4C_y^+$, $FeN_3C_y^+$, and $FeN_1C_y^+$ families, whereas the other catalytic site (labeled FeN_2/C) favored the emission of the $FeN_2C_y^+$ family, with the $FeN_2C_4^+$ ion being most representative of the site. The abundance of the FeN_2/C catalytic site displays a maximum in the pyrolysis temperature range from 700 to 900 °C (depending on the Fe precursor), and this maximum corresponds to a minimum abundance of the FeN_4/C sites (see middle and bottom panels in Figure 11.13). A commensurable correlation with the catalytic activity implied that the FeN_2/C site was more active than the FeN_4/C site. For catalysts prepared from Fe acetate, FeN_2/C was found to be the main catalytic site, representing up to 80% of the two catalytic sites in these materials. Structurally, the FeN_2/C moiety was suggested to be composed of an Fe ion forming a complex with two nitrogen atoms which themselves were bound to the carbon support.

A direct correlation was also found [159] between the relative abundance of the FeN_2/C catalytic site in the Fe-based catalysts (represented by the relative intensity of the sum ion emission $\Sigma FeN_2C_y^+$), their catalytic activity, and the apparent number of electrons transferred during the oxygen reduction reaction in H_2SO_4 at pH 1, whereas an inverse correlation was observed for the percentage of peroxide H_2O_2 released during ORR.

Analogous TOF SIMS measurements of Co-based electrocatalysts prepared using cobalt acetate and a cobalt porphyrin (CoTMPP) as Co precursors [160] showed the presence of four similar families of $CoN_1C_y^+$, $CoN_2C_y^+$, $CoN_3C_y^+$, and $CoN_4C_y^+$ ions, but there was no dominant $CoN_xC_y^+$ ion signature. The only catalytic site that was certainly present in Co-based catalysts was identified as CoN_4/C. However, no strong support for (or against) the existence of CoN_2/C was obtained on comparing the SIMS data with the electrochemical activity for ORR. In contrast to the Fe-based catalysts, all catalytic sites (if there were any besides CoN_4/C) in the Co-based electrocatalysts were inferred to be roughly equally active.

11.7 Conclusion

In this chapter we have presented, from our point of view, the most demonstrative and trend-setting examples of what has been achieved by SIMS and LEIS during the last 35 years in terms of knowledge of the surface composition and structure of solid materials, especially of catalysts. We focused on those data which were very valuable, sometimes decisive, in the elucidation of the surface reactivity and catalytic performance of materials. When considering a large number of relevant papers, it is

inevitable that some of the interesting work unfortunately does not get a mention, as is the case here.

SIMS and LEIS are powerful, highly informative techniques with unsurpassed surface sensitivity, capable of determining surface elemental and isotopic composition, and the in-depth distribution of elements in subsurface layers. In addition, SIMS allows surface imaging, visualizing lateral and spatial distributions of various ion species, and supplies information about the local atomic arrangement and the formation of interatomic bonds and phases. LEIS and SIMS are often used in combination with other techniques; however, in some cases they turn out to provide important clues when it comes to solving a problem. We have tried to illustrate how these advantageous features of SIMS and LEIS can help us understand adsorption, oxidation, corrosion, and catalytic phenomena by revealing modifications of the surface composition and structure of catalysts associated with the preparation, treatment, and reaction conditions and determining their effect on catalytic performance. The data provided by SIMS and LEIS should help improve the catalytic properties of existing materials and give rise to the development of new and highly efficient ones.

References

1 Thomson, J.J. (1910) Rays of positive electricity. *Philos. Mag., Ser. 6*, **20** (118), 752–767.

2 Campbell, N. (1915) Ionization by positive rays. *Philos. Mag., Ser. 6*, **29** (174), 783–794.

3 Sloane, R.H. and Press, R. (1938) The formation of negative ions by positive-ion impact on surfaces. *Proc. R. Soc. London, Ser. A*, **168** (933), 284–301.

4 Klein, A.L. (1925) The secondary emission from a nickel surface due to slow positive ion bombardment. *Phys. Rev.*, **26** (6), 800–806.

5 Read, G.E. (1928) The reflection of positive rays by a platinum surface. *Phys. Rev.*, **31** (4), 629–633.

6 Gurney, R.W. (1928) The scattering of positive ions from a platinum surface. *Phys. Rev.*, **32** (3), 467–477.

7 Fogel', Ya.M. (1967) Secondary ion emission. *Sov. Phys. Usp.*, **10** (1), 17–39.

8 Smith, D.P. (1967) Scattering of low-energy noble gas ions from metal surfaces. *J. Appl. Phys.*, **38** (1), 340–347.

9 Jansen, W.P.A., Denier van der Gon, A.W., Wijers, G.M., Rikers, Y.G.M., Brongersma, H.H., van den Hoogen, P.W., de Laat, J.A.M., Maas, T.M., Dekkers, E.C.A., and Brinkgreve, P. (2002) A differentially pumped pressure cell for *in situ* low-energy ion scattering analysis of catalysts during reactions. *Rev. Sci. Instrum.*, **73** (2), 354–361.

10 Mohri, M., Kakibayashi, H., Watanabe, K., and Yamashina, T. (1978) Application of SIMS–FDS–AES combined system to surface studies – adsorption and decomposition of formic acid over clean surface of nickel. *Appl. Surf. Sci.*, **1** (2), 170–185.

11 Akhter, S. and White, J.M. (1986) A static SIMS/TPD study of the kinetics of methoxy formation and decomposition on O/Pt(111). *Surf. Sci.*, **167** (1), 101–126.

12 Zhu, X.-Y., Castro, M.E., Akhter, S., White, J.M., and Houston, J.E. (1988) C−H bond cleavage for ethylene and acetylene on Ni(100). *Surf. Sci.*, **207** (1), 1–16.

13 Zhu, X.-Y. and White, J.M. (1988) Evidence for ethylidyne formation on Ni (111). *Catal. Lett.*, **1** (8–9), 247–254.

14 Henderson, M.A., Zhou, Y., and White, J.M. (1989) Polymerization and decomposition of acetaldehyde on

ruthenium(001). *J. Am. Chem. Soc.*, **111** (4), 1185–1193.
15 Kruse, N., Rebholz, M., Matolin, V., Chuah, G.K., and Block, J.H. (1990) Methanol decomposition on Pd(111) single crystal surfaces. *Surf. Sci.*, **238** (1–3), L457–L462.
16 Rebholz, M. and Kruse, N. (1991) Mechanisms of methanol decomposition on Pd {111}. *J. Chem. Phys.*, **95** (10), 7745–7759.
17 Levis, R.J., Zhicheng, J., and Winograd, N. (1989) Thermal decomposition of CH_3OH absorbed on Pd{111}. A new reaction pathway involving CH_3 formation. *J. Am. Chem. Soc.*, **111** (13), 4605–4612.
18 Schmatloch, V., Jirka, I., and Kruse, N. (1994) Surface reaction kinetics of NO on Rh{110}. *J. Chem. Phys.*, **100** (11), 8471–8482.
19 Borg, H.J., Reijerse, J.F.C.-J.M., van Santen, R.A., and Niemantsverdriet, J.W. (1994) The dissociation kinetics of NO on Rh(111) as studied by temperature programmed static secondary ion mass spectrometry and desorption. *J. Chem. Phys.*, **101** (11), 10052–10063.
20 Borg, H.J. and Niemantsverdriet, J.W. (1994) Applications of secondary ion mass spectrometry in catalysis and surface chemistry, in *Catalysis*, vol. 11 (eds. J.J. Spivey and S.K. Agarwal), RSC Publishing, Cambridge, pp. 1–50.
21 Shelef, M., Wheeler, M.A.Z., and Yao, H.C. (1975) Ion scattering spectra from spinel surfaces. *Surf. Sci.*, **47** (2), 697–703.
22 Wheeler, M.A. and Bettman, M. (1975) On the poisoning of Co_3O_4 catalysts by alumina and magnesia. *J. Catal.*, **40** (1), 124–128.
23 Brongersma, H.H. and van Santen, R.A. (eds.). (1991) *Fundamental Aspects of Heterogeneous Catalysis Studied by Particle Beams (NATO Science Series B: Physics)*, Plenum Press, New York.
24 Hopstaken, M.J.P., Linke, R., van Gennip, W.J.H., and Niemantsverdriet, J.W. (2001) Applications in catalysis, in *ToF-SIMS: Surface Analysis by Mass Spectrometry* (eds. J.C. Vickerman and D. Briggs), IM Publications, Chichester, pp. 697–725.
25 Thomas, J.M. and Thomas, W.J. (2005) *Principles and Practice of Heterogeneous Catalysis*, 3rd edn., Wiley-VCH Verlag GmbH, Weinheim, pp. 145–254.
26 Grams, J. and Szynkowska, M.I. (2006) Application of time-of-flight secondary ion mass spectrometry (TOF-SIMS) to the investigations of metal/support catalysts, in *Focus on Surface Science Research* (ed. C.P. Norris), Nova Science Publishers, Hauppauge, NY, pp. 69–97.
27 Niemantsverdriet, J.W. (2007) *Spectroscopy in Catalysis: an Introduction*, 3rd edn., Wiley-VCH Verlag GmbH, Weinheim, pp. 85–119.
28 Horrell, B.A. and Cocke, D.L. (1987) Application of ion-scattering spectroscopy to catalyst characterization. *Catal. Rev. Sci. Eng.*, **29** (4), 447–491.
29 Taglauer, E. and Knözinger, H. (1995) Characterization of supported catalyst systems with surface spectroscopies. *Phys. Status Solidi B*, **192** (2), 465–475.
30 Vickerman, J.C., Oakes, A., and Gamble, H. (2000) Static SIMS studies of catalyst structure and activity. *Surf. Interface Anal.*, **29** (6), 349–361.
31 Benninghoven, A., Rüdenauer, F.G., and Werner, H.W. (1987) *Secondary Ion Mass Spectrometry: Basic Concepts, Instrumental Aspects, Applications, and Trends*, John Wiley & Sons, Inc., New York.
32 Cherepin, V.T. (1987) *Secondary Ion Mass Spectroscopy of Solid Surfaces*, VNU Science Press, Utrecht.
33 Wilson, R.G., Stevie, F.A., and Magee, C.W. (1989) *Secondary Ion Mass Spectrometry: a Practical Handbook for Depth Profiling and Bulk Impurity Analysis*, John Wiley & Sons, Inc., New York.
34 Vickerman, J.C., Brown, A., and Reed, N.M. (1989) *Secondary Ion Mass Spectrometry: Principles and Applications*, Clarendon Press, Oxford.
35 Briggs, D. and Seah, M.P. (eds.) (1992) *Practical Surface Analysis: Ion and Neutral Spectroscopy*, vol. 2, John Wiley & Sons, Ltd., Chichester.
36 Vickerman, J.C. and Briggs, D. (eds.) (2001) *ToF-SIMS: Surface Analysis by Mass*

Spectrometry, IM Publications, Chichester.

37 Van Vaeck, L., Adriaens, A., and Gijbels, R. (1999) Static secondary ion mass spectrometry (S-SIMS). Part 1: methodology and structural interpretation. *Mass Spectrom. Rev.*, **18** (1), 1–47.

38 Brongersma, H.H., Draxler, M., de Ridder, M., and Bauer, P. (2007) Surface composition analysis by low-energy ion scattering. *Surf. Sci. Rep.*, **62** (3), 63–109.

39 Ackermans, P.A.J., Creuwels, M.A.P., Brongersma, H.H., and Scanlon, P.J. (1990) Preferential sputtering of B studied by low-energy ion scattering using the dual-isotope surface composition (DISC) method. *Surf. Sci.*, **227** (3), 361–368.

40 Margraf, R., Knözinger, H., and Taglauer, E. (1989) The influence of surface roughness on ISS analysis of supported catalysts. *Surf. Sci.*, **211–212**, 1083–1090.

41 ter Veen, H.R.J., Kim, T., Wachs, I.E., and Brongersma, H.H. (2009) Applications of high sensitivity–low energy ion scattering (HS-LEIS) in heterogeneous catalysis. *Catal. Today*, **140** (3–4), 197–201.

42 Jansen, W.P.A., Knoester, A., Maas, A.J.H., Schmit, P., Kytökivi, A., Denier van der Gon, A.W., and Brongersma, H.H. (2004) Influence of compaction and surface roughness on low-energy ion scattering signals. *Surf. Interface Anal.*, **36** (11), 1469–1478.

43 Niehus, H., Heiland, W., and Taglauer, E. (1993) Low-energy ion scattering at surfaces. *Surf. Sci. Rep.*, **17** (4–5), 213–303.

44 Mashkova, E.S. and Molchanov, V.A. (1985) *Medium-Energy Ion Reflection from Solids*, North-Holland, Amsterdam.

45 Rabalais, J.W. (2003) *Principles and Applications of Ion Scattering Spectrometry: Surface Chemical and Structural Analysis*, John Wiley & Sons, Lts., Chichester.

46 Brongersma, H.H., Gildenpfennig, A., Denier van der Gon, A.W., van de Grampel, R.D., Jansen, W.P.A., Knoester, A., Laven, J., and Viitanen, M.M. (2002) Insight in the outside: new applications of low-energy ion scattering. *Nucl. Instrum. Methods Phys. Res. B*, **190** (1–4), 11–18.

47 Tolstogouzov, A., Daolio, S., and Pagura, C. (1999) Evaluation of inelastic energy losses for low-energy Ne^+ ions scattered from aluminum and silicon surfaces. *Surf. Sci.*, **441** (1), 213–222.

48 Jacobs, J.P., Maltha, A., Reintjes, J.G.H., Drimal, J., Ponec, V., and Brongersma, H.H. (1994) The surface of catalytically active spinels. *J. Catal.*, **147** (1), 294–300.

49 Aono, M., Katayama, M., Nomura, E., Chassé, T., Choi, D., and Kato, M. (1989) Recent developments in low-energy ion scattering spectroscopy (ISS) for surface structural analysis. *Nucl. Instrum. Methods Phys. Res. B*, **37–38**, 264–269.

50 Guliants, V.V., Bhandari, R., Hughett, A.R., Bhatt, S., Schuler, B.D., Brongersma, H.H., Knoester, A., Gaffney, A.M., and Han, S. (2006) Probe molecule chemisorption–low energy ion scattering study of surface active sites present in the orthorhombic Mo–V–(Te–Nb)–O catalysts for propane (amm) oxidation. *J. Phys. Chem. B*, **110** (12), 6129–6140.

51 Andersson, G. and Morgner, H. (2000) Investigations on solutions of tetrabutylonium salts in formamide with NICISS and ICISS: concentration depth profiles and composition of the outermost layer. *Surf. Sci.*, **445** (1), 89–99.

52 Barber, M., Vickerman, J.C., and Wolstenholme, J. (1977) The application of SIMS to the study of CO adsorption on polycrystalline metal surfaces. *Surf. Sci.*, **68**, 130–137.

53 Bordoli, R.S., Vickerman, J.C., and Wolstenholme, J. (1979) Surface coverage measurements by SIMS for CO adsorption on a number of metals and for CO and H_2S co-adsorption on Ni (110) (100) and (111). *Surf. Sci.*, **85** (2), 244–262.

54 Brown, A. and Vickerman, J.C. (1983) Static SIMS studies of adsorbate structure: II. CO adsorption on Pd(111); adsorbate–adsorbate interactions on Ru (001), Ni(111) and Pd(111). *Surf. Sci.*, **124** (1), 267–278.

55 Matolin, V. and Gillet, E. (1990) CO disproportionation over supported Pd particles: a TPD and static SIMS study. *Surf. Sci.*, **238** (1–3), 75–82.

56 Matolin, V., Rebholz, M., and Kruse, N. (1991) Defect-induced dissociation of CO on palladium. *Surf. Sci.*, **245** (3), 233–243.

57 Ivanov, V.P. and Trukhan, S.N. (1995) Ion-induced CO adsorption on polycrystalline nickel. Secondary ion mass spectrometry study. *React. Kinet. Catal. Lett.*, **55** (1), 111–120.

58 Larson, S.A. and Lauderback, L.L. (1991) The influence of surface defects on the O_2/Al(100) interaction. *Surf. Sci.*, **254** (1–3), 161–168.

59 Vasilyev, M.A., Goncharenko, A.B., Chenakin, S.P., and Cherepin, V.T. (1980) Adsorption ability of the surface of metals after ion bombardment. *Metallofizika*, **2** (5), 113–119 (in Russian).

60 Chenakin, S.P. (1986) The effect of inert gas ion bombardment on the oxidation of metal surfaces. *Vacuum*, **36** (10), 635–641.

61 Rar, A.A. and Ivanov, V.P. (1988) Effect of surface defects on the adsorption rate of oxygen on polycrystalline rhodium. *React. Kinet. Catal. Lett.*, **36** (1), 47–51.

62 Zalkind, S., Polak, M., and Shamir, N. (2002) Oxidation of ion-bombarded vs. annealed beryllium. *Surf. Sci.*, **513** (3), 501–510.

63 Houssiau, L. and Bertrand, P. (2001) TOF-SIMS study of alkanethiol adsorption and ordering on gold. *Appl. Surf. Sci.*, **175–176**, 399–406.

64 Houssiau, L. and Bertrand, P. (2001) ToF-SIMS study of organosilane self-assembly on aluminum surfaces. *Appl. Surf. Sci.*, **175–176**, 351–356.

65 Rodríguez, L.M., Gayone, J.E., Sánchez, E.A., Ascolani, H., Grizzi, O., Sánchez, M., Blum, B., Benitez, G., and Salvarezza, R.C. (2006) Adsorption of short-chain alkanethiols on Ag(111) studied by direct recoiling spectroscopy. *Surf. Sci.*, **600** (11), 2305–2316.

66 Chenakin, S.P., Heinz, B., and Morgner, H. (1999) Substrate effect in sputtering of self-assembled monolayers: hexadecanethiol on Au(111) and Ag(111). *Surf. Sci.*, **421** (3), 337–352.

67 Czerwinski, F., Sproule, G.I., Graham, M.J., and Smeltzer, W.W. (1995) An ^{18}O-SIMS study of oxide growth on nickel modified with Ce implants and CeO_2 coatings. *Corros. Sci.*, **37** (4), 541–556.

68 Rossi, A., Elsener, B., Hähner, G., Textor, M., and Spencer, N.D. (2000) XPS, AES and ToF-SIMS investigation of surface films and the role of inclusions on pitting corrosion in austenitic stainless steels. *Surf. Interface Anal.*, **29** (7), 460–467.

69 Chenakin, S.P., Galstyan, G.G., Tolstogouzov, A.B., and Kruse, N. (2009) XPS and ToF-SIMS characterization of a Finemet surface: effect of heating. *Surf. Interface Anal.*, **41** (3), 231–237.

70 Baiker, A. (1994) Glassy metals in catalysis. *Top. Appl. Phys.*, **72**, 121–162.

71 Deng, J., Chen, H., Bao, X., and Muhler, M. (1994) The effect of cyclic oxidation–reduction pretreatments on an amorphous $Ni_{80}P_{20}$ catalyst: an XPS/UPS/ISS study. *Appl. Surf. Sci*, **81** (3), 341–346.

72 Shimizu, K., Kobayashi, K., Skeldon, P., Thompson, G.E., and Wood, G.C. (1995) Oxidation of an amorphous $Ni_{77}P_{23}$ alloy in air and dry oxygen at 300 °C. *Mater. Sci. Eng. A*, **198** (1–2), 35–41.

73 Song, Z., Bao, X., and Muhler, M. (1999) The effect of tungsten additive on the surface characteristics of amorphous Ni–P alloy. *Appl. Surf. Sci.*, **148** (3–4), 241–247.

74 Noack, K., Rehren, C., Zbinden, H., and Schloegl, R. (1995) Modification of the catalytic hydrogenation activity of glassy $Pd_{81}Si_{19}$. Surface analysis by ISS and XPS. *Langmuir*, **11** (6), 2018–2030.

75 Buhl, R. and Preisinger, A. (1975) Crystal structures and their secondary ion mass spectra. *Surf. Sci.*, **47** (1), 344–357.

76 Matolin, V., Gillet, E., and Kruse, N. (1987) Steady carbon formation during CO oxidation over small Pd particles: a static SIMS study. *Surf. Sci.*, **186** (1–2), L541–L547.

77 Lee, S., Fan, C., Wu, T., and Anderson, S.L. (2005) Cluster size effects on CO oxidation activity, adsorbate affinity, and temporal behavior of model Au_n/TiO_2 catalysts. *J. Chem. Phys.*, **123** (12), 124710.

78 Barber, M., Sharpe, P.K., and Vickerman, J.C. (1976) Studies of the surface behavior of oxide catalysts by secondary ion mass spectrometry (SIMS): 1. The surface composition of copper-containing spinel catalysts and their precursors. *J. Catal.*, **41** (2), 240–248.

79 Tanaka, K., Yanashima, H., Minobe, M., and Suzukamo, G. (1997) Characterization of solid superbases prepared from γ-alumina and their catalytic activity. *Appl. Surf. Sci.*, **121–122**, 461–467.

80 Rodrigo, L., Adnot, A., Roberge, P.C., and Kaliaguine, S. (1987) Characterization of supported molybdena catalysts by SIMS. *J. Catal.*, **105** (1), 175–186.

81 Jin, Y.S., Auroux, A., and Vedrine, J.C. (1989) Spectroscopic studies of molybdate species deposited on a Nb_2O_5 support. *J. Chem. Soc., Faraday Trans. 1*, **85**, 4179–4191.

82 Bukallah, S.B., Houalla, M., and Hercules, D.M. (2000) Characterization of supported Nb catalysts by ToF-SIMS. *Surf. Interface Anal.*, **29** (12), 818–822.

83 Rynkowski, J., Rajski, D., Szyszka, I., and Grzechowiak, J.R. (2004) Effect of platinum on the hydrogenation activity of nickel catalysts. *Catal. Today*, **90** (1–2), 159–166.

84 Sobczak, I., Grams, J., and Ziolek, M. (2007) Surface properties of platinum catalysts based on various nanoporous matrices. *Micropor. Mesopor. Mater.*, **99** (3), 345–354.

85 Sobczak, I., Kusior, A., Grams, J., and Ziolek, M. (2007) The role of chlorine in the generation of catalytic active species located in Au-containing MCM-41 materials. *J. Catal.*, **245** (2), 259–266.

86 Yang, H., Chen, H., Chen, J., Omotoso, O., and Ring, Z. (2006) Shape selective and hydrogen spillover approach in the design of sulfur-tolerant hydrogenation catalysts. *J. Catal.*, **243** (1), 36–42.

87 Ouafi, D., Mauge, F., Lavalley, J.-C., Payen, E., Kasztelan, S., Houari, M., Grimblot, J., and Bonnelle, J.-P. (1988) Nature and structure of tungsten surface species present on NiO–WO_3/Al_2O_3 hydrotreating catalysts. *Catal. Today*, **4** (1), 23–37.

88 Eberhardt, M.A., Houalla, M., and Hercules, D.M. (1993) Ion scattering and electron spectroscopic study of the surface coverage of V/Al_2O_3 catalysts. *Surf. Interface Anal.*, **20** (9), 766–770.

89 Sazo, V., Gonzales, L., Goldwasser, J., Houalla, M., and Hercules, D.M. (1995) Determination of the surface coverage of Mo/Al_2O_3 catalysts. *Surf. Interface Anal.*, **23** (6), 367–373.

90 Cornaglia, L., Houalla, M., Goldwasser, J., and Hercules, D.M. (1999) Determination of the surface coverage of Re/Al_2O_3 catalysts by ion scattering spectroscopy and low-temperature CO adsorption. *Catal. Lett.*, **63** (3–4), 131–133.

91 Rondon, S., Houalla, M., and Hercules, D.M. (1998) Determination of the surface coverage of Mo/TiO_2 catalysts by ISS and CO_2 chemisorption. *Surf. Interface Anal*, **26** (4), 329–334.

92 Vaidyanathan, N., Houalla, M., and Hercules, D.M. (1998) Surface coverage of WO_3/ZrO_2 catalysts measured by ion scattering spectroscopy and low temperature CO adsorption. *Surf. Interface Anal*, **26** (6), 415–419.

93 Kohl, A., Labich, S., Taglauer, E., and Knözinger, H. (2000) Agglomeration of supported rhodium on model catalysts. *Surf. Sci.*, **454–456**, 974–978.

94 Óvári, L. and Kiss, J. (2006) Growth of Rh nanoclusters on TiO_2(110): XPS and LEIS studies. *Appl. Surf. Sci.*, **252** (24), 8624–8629.

95 Jansen, W.P.A., Harmsen, J.M.A., Denier ven der Gon, A.W., Hoebink, J.H.B.J., Schouten, J.C., and Brongersma, H.H. (2001) Noble metal segregation and cluster size of Pt/Rh/CeO_2/γ-Al_2O_3 automotive three-way catalysts studied with low-energy ion scattering. *J. Catal.*, **204** (2), 420–427.

96 Prada Silvy, R., Delannay, F., Grange, P., and Delmon, B. (1986) Effect of the activation conditions on the structure and catalytic activity of a Co–Mo–γ-Al_2O_3 hydrodesulfurization catalyst. *Polyhedron*, **5** (1–2), 195–198.

97 Huang, C., Houalla, M., Hercules, D.M., Kibby, C.L., and Petrakis, L. (1989) Comparison of catalysts derived from oxidation of Ru_3Th_7 with impregnated Ru/ThO_2 catalysts. *J. Phys. Chem.*, **93** (11), 4540–4544.

98 Gardner, S.D., Hoflund, G.B., Schryer, D.R., and Upchurch, B.T. (1991) Characterization study of silica-supported platinized tin oxide catalysts used for low-temperature carbon monoxide oxidation: effect of pretreatment temperature. *J. Phys. Chem.*, **95** (2), 835–838.

99 Skoglundh, M., Löwendahl, L.O., Menon, P.G., Stenbom, B., Jacobs, J.P., van Kessel, O., and Brongersma, H.H. (1992) Characterization of a Pt–Pd combustion catalyst on an alumina washcoat, with and without prior hydrothermal treatment of the washcoat. *Catal. Lett.*, **13** (1–2), 27–37.

100 Xiong, Y.L., Cadus, L.E., Daza, L., Bertrand, P., Ladrière, J., Ruiz, P., and Delmon, B. (2000) Solid-state reactivity of iron molybdate artificially contaminated by antimony ions and its relation with catalytic activity in the selective oxidation of isobutene to methacrolein. *Top. Catal.*, **11–12** (1–4), 167–180.

101 Mestl, G., Linsmeier, Ch., Gottschall, R., Dieterle, M., Find, J., Herein, D., Jäger, J., Uchida, Y., and Schlögl, R. (2000) Molybdenum oxide based partial oxidation catalyst: 1. Thermally induced oxygen deficiency, elemental and structural heterogeneity and the relation to catalytic performance. *J. Mol. Catal. A: Chem.*, **162** (1–2), 463–492.

102 Jeziorowski, H., Knözinger, H., Taglauer, E., and Vogdt, C. (1983) Low energy ion scattering study of Ni–Mo/Al_2O_3 catalysts. *J. Catal.*, **80** (2), 286–295.

103 Briand, L.E., Tkachenko, O.P., Guraya, M., Wachs, I.E., and Grünert, W. (2004) Methodical aspects in the surface analysis of supported molybdena catalysts. *Surf. Interface Anal.*, **36** (3), 238–245.

104 Briand, L.E., Tkachenko, O.P., Guraya, M., Gao, X., Wachs, I.E., and Grünert, W. (2004) Surface-analytical studies of supported vanadium oxide monolayer catalysts. *J. Phys. Chem. B*, **108** (15), 4823–4830.

105 Valenzuela, M.A., Jacobs, J.-P., Bosch, P., Reijne, S., Zapata, B., and Brongersma, H.H. (1997) The influence of the preparation method on the surface structure of $ZnAl_2O_4$. *Appl. Catal. A*, **148** (2), 315–324.

106 Houalla, M., Kibby, C.L., Petrakis, L., and Hercules, D.M. (1983) Effects of impregnation pH on the surface structure and hydrodesulfurization activity of Mo/Al_2O_3 catalysts. *J. Catal.*, **83** (1), 50–60.

107 Chenakin, S.P., Prada Silvy, R., and Kruse, N. (2007) TOF-SIMS characterization of an aluminovanadate oxide catalyst. *Surf. Interface Anal.*, **39** (7), 567–574.

108 Chenakin, S.P., Bongiovanni, A., Vasylyev, M.A., Makeeva, I.N., and Kruse, N. (2009) XPS–SIMS characterization of a gold catalyst supported on TiO_2: effect of preparation conditions. *Metallofiz. Nov. Tekhnol.*, **31** (5), 589–602.

109 Kruse, N. and Chenakin, S. (2011) XPS characterization of Au/TiO_2 catalysts: binding energy assessment and irradiation effects. *Appl. Catal., A*, **391** (1–2), 367–376.

110 Dobrosz-Gómez, I., Kocemba, I., and Rynkowski, J.M. (2009) Factors influencing structure and catalytic activity of $Au/Ce_{1-x}Zr_xO_2$ catalysts in CO oxidation. *Appl. Catal., B*, **88** (1–2), 83–97.

111 Chen, H.Y., Lau, S.P., Chen, L., Lin, J., Huan, C.H.A., Tan, K.L., and Pan, J.S. (1999) Synergism between Cu and Zn sites in Cu/Zn catalysts for methanol synthesis. *Appl. Surf. Sci.*, **152** (3–4), 193–199.

112 Houalla, M., Dang, T.A., Kibby, C.L., Petrakis, L., and Hercules, D.M. (1984) The spectroscopic characterization of intermetallic synthesis gas conversion catalysts and the correlation of their activity with surface structure. *Appl. Surf. Sci.*, **19** (1–4), 414–429.

113 Ott, G.L., Fleisch, T., and Delgass, W.N. (1979) Fischer–Tropsch synthesis over freshly reduced iron–ruthenium alloys. *J. Catal.*, **60** (3), 394–403.

114 Ott, G.L., Fleisch, T., and Delgass, W.N. (1980) Carbon deposition and activity changes over FeRu alloys during Fischer–Tropsch synthesis. *J. Catal.*, **65** (2), 253–262.

115 Sellmer, C., Decker, S., and Kruse, N. (1998) CO hydrogenation over Co/SiO_2: catalytic tests and surface analysis of adsorbed hydrocarbons. *Catal. Lett.*, **52** (3–4), 131–137.

116 Ledford, J.S., Houalla, M., Proctor, A., and Hercules, D.M. (1990) Influence of thorium on the surface structure and CO hydrogenation activity of silica-supported nickel catalysts. *J. Catal*, **125** (2), 554–564.

117 Yan, Z.-G. and Andersson, S.L.T. (1990) Catalytic oxidation of toluene over V_2O_5–WO_3 catalysts. *Appl. Catal.*, **66** (1), 149–165.

118 Debecker, D.P., Bouchmella, K., Delaigle, R., Eloy, P., Poleunis, C., Bertrand, P., Gaigneaux, E.M., and Mutin, P.H. (2010) One-step non-hydrolytic sol–gel preparation of efficient V_2O_5–TiO_2 catalysts for VOC total oxidation. *Appl. Catal. B*, **94** (1–2), 38–45.

119 Richter, F., Papp, H., Wolf, G.U., Götze, Th., and Kubias, B. (1999) Study of the surface composition of vanadyl pyrophosphate catalysts by XPS and ISS – Influence of Cs^+ and water vapor on the surface P/V ratio of $(VO)_2P_2O_7$ catalysts. *Fresenius' J. Anal. Chem.*, **365** (1–3), 150–153.

120 Delichère, P., Béré, K.E., and Abon, M. (1998) Vanadyl pyrophosphate catalysts: surface analysis by XPS and LEIS. *Appl. Catal. A*, **172** (2), 295–309.

121 Jansen, W.P.A., Ruitenbeek, M., Denier van der Gon, A.W., Geus, J.W., and Brongersma, H.H. (2000) New insights into the nature of the active phase of VPO catalysts – a quantitative static LEIS study. *J. Catal.*, **196** (2), 379–387.

122 Guliants, V.V., Bhandari, R., Brongersma, H.H., Knoester, A., Gaffiiey, A.M., and Han, S. (2005) A study of the surface region of the Mo–V–Te–O catalysts for propane oxidation to acrylic acid. *J. Phys. Chem. B*, **109** (20), 10234–10242.

123 Jin, Y.S., Yan, Q.J., Yin, Z.R., and Chen, Y. (1995) Secondary ion mass spectrometry and X-ray photoelectron spectroscopy of Na_2MoO_4/SiO_2 catalysts for methane oxidative coupling. *J. Chem. Soc., Faraday Trans.*, **91** (2), 381–384.

124 Wang, D.J., Rosynek, M.P., and Lunsford, J.H. (1995) Oxidative coupling of methane over oxide-supported sodium–manganese catalysts. *J. Catal.*, **155** (2), 390–402.

125 Hoflund, G.B. and Li, Z. (2006) Surface characterization study of a Pd/Co_3O_4 methane oxidation catalyst. *Appl. Surf. Sci.*, **253** (5), 2830–2834.

126 Renouprez, A., Faudon, J.F., Massardier, J., Rousset, J.L., Delichère, P., and Bergeret, G. (1997) Properties of supported Pd–Ni catalysts prepared by coexchange and organometallic chemistry. 2. Correlation between the reactivity for butadiene hydrogenation and the surface properties studied by XPS and LEIS. *J. Catal.*, **170** (1), 181–190.

127 Moriceau, P., Grzybowska, B., Gengembre, L., and Barbaux, Y. (2000) Oxidative dehydrogenation of isobutane on Cr–Ce–O oxide: II. Physical characterizations and determination of the chromium active species. *Appl. Catal. A*, **199** (1), 73–82.

128 Sellmer, C., Prins, R., and Kruse, N. (1997) XPS/SIMS studies of the promoter action in methanol synthesis over silica-supported Pd catalysts. *Catal. Lett.*, **47** (2), 83–89.

129 Vepřek, S., Cocke, D.L., Kehl, S., and Oswald, H.R. (1986) Mechanism of the deactivation of Hopcalite catalysts studied by XPS, ISS, and other techniques. *J. Catal.*, **100** (1), 250–263.

130 Hoflund, G.B., Upchurch, B.T., Kielin, E.J., and Schryer, D.R. (1995) Influence of an Fe promoter on silica-supported Pt/SnO_x catalysts used for low-temperature CO oxidation. *Catal. Lett.*, **31** (2–3), 133–141.

131 Moma, J.A., Scurrell, M.S., and Jordaan, W.A. (2007) Effects of incorporation of ions into Au/TiO_2 catalysts for carbon monoxide oxidation. *Top. Catal.*, **44** (1–2), 167–172.

132 Mohapatra, P., Moma, J., Parida, K.M., Jordaan, W.A., and Scurrell, M.S. (2007) Dramatic promotion of gold/titania for

CO oxidation by sulfate ions. *Chem. Commun.*, (10), 1044–1046.

133 Guczi, L., Frey, K., Beck, A., Petõ, G., Daróczi, C.S., Kruse, N., and Chenakin, S. (2005) Iron oxide overlayers on Au/SiO_2/Si(100): promoting effect of Au on the catalytic activity of iron oxide in CO oxidation. *Appl. Catal. A*, **291** (1–2), 116–125.

134 Minahan, D.M., Hoflund, G.B., Epling, W.S., and Schoenfeld, D.W. (1997) Study of Cs-promoted, α-alumina-supported silver, ethylene epoxidation catalysts: III. Characterization of Cs-promoted and nonpromoted catalysts. *J. Catal.*, **168** (2), 393–399.

135 Guliants, V.V., Bhandari, R., Swaminathan, B., Vasudevan, V.K., Brongersma, H.H., Knoester, A., Gaffney, A.M., and Han, S. (2005) Roles of surface Te, Nb, and Sb oxides in propane oxidation to acrylic acid over bulk orthorhombic Mo–V–O phase. *J. Phys. Chem. B*, **109** (50), 24046–24055.

136 Harmsen, J.M.A., Jansen, W.P.A., Hoebink, J.H.B.J., Schouten, J.C., and Brongersma, H.H. (2001) Coke deposition on automotive three-way catalysts studied with LEIS. *Catal. Lett.*, **74** (3–4), 133–137.

137 Albers, P., Seibold, K., Prescher, G., and Müller, H. (1999) XPS and SIMS studies of carbon deposits on Pt/Al_2O_3 and Pd/SiO_2 catalysts applied in the synthesis of hydrogen cyanide and selective hydrogenation of acetylene. *Appl. Catal. A*, **176** (1), 135–146.

138 Albers, P., Deller, K., Despeyroux, B.M., Schäfer, A., and Seibold, K. (1992) XPS–SIMS study on the surface chemistry of commercially available activated carbons used as catalyst supports. *J. Catal.*, **133** (2), 467–478.

139 Horita, T., Yamaji, K., Kato, T., Sakai, N., and Yokokawa, H. (2004) Comparison of catalytic activity for CH_4 decomposition at the metal/oxide interfaces by isotope-labeling technique. *Solid State Ionics*, **172** (1–4), 93–99.

140 Chao, K.-J., Lin, L.-H., Ling, Y.-C., Hwang, J.-F., and Hou, L.-Y. (1995) Vanadium passivation of cracking catalysts by imaging secondary ion mass spectrometry. *Appl. Catal. A*, **121** (2), 217–229.

141 Albers, P., Seibold, K., Haas, T., Prescher, G., and Hölderich, W.F. (1998) SIMS/XPS study on the deactivation and reactivation of B-MFI catalysts used in the vapour-phase Beckmann rearrangement. *J. Catal.*, **176** (2), 561–568.

142 Karski, S., Witońska, I., and Goluchowska, J. (2006) Catalytic properties of $Pd–Tl/SiO_2$ systems in the reaction of liquid phase oxidation of aldoses. *J. Mol. Catal. A: Chem.*, **245** (1–2), 225–230.

143 Karski, S. (2006) Activity and selectivity of $Pd–Bi/SiO_2$ catalysts in the light of mutual interaction between Pd and Bi. *J. Mol. Catal. A: Chem.*, **253** (1–2), 147–154.

144 Witońska, I., Karski, S., Rogowski, J., and Krawczyk, N. (2008) The influence of interaction between palladium and indium on the activity of $Pd–In/Al_2O_3$ catalysts in reduction of nitrates and nitrites. *J. Mol. Catal. A: Chem.*, **287** (1–2), 87–94.

145 Liu, C. and Ozkan, U.S. (2005) Spectroscopic and structural characterization of chlorine loading effects on Mo/Si:Ti catalysts in oxidative dehydrogenation of ethane. *J. Phys. Chem. A*, **109** (6), 1260–1268.

146 Bertinchamps, F., Poleunis, C., Grégoire, C., Eloy, P., Bertrand, P., and Gaigneaux, E.M. (2008) Elucidation of deactivation or resistance mechanisms of CrO_x, VO_x and MnO_x supported phases in the total oxidation of chlorobenzene via ToF-SIMS and XPS analyses. *Surf. Interface Anal.*, **40** (3–4), 231–236.

147 Aso, I., Amamoto, T., Yamazoe, N., and Seiyama, T. (1980) Oxygen adsorption sites of $Fe_2O_3–Sb_2O_4$ catalyst determined by secondary ion mass spectrometry-^{18}O tracer method. *Chem. Lett.*, **9** (11), 1435–1438.

148 Okada, F., Satsuma, A., Furuta, A., Miyamoto, A., Hattori, T., and Murakami, Y. (1990) Surface active sites of $V_2O_5–SnO_2$ catalysts. *J. Phys. Chem.*, **94** (15), 5900–5908.

149 Smits, R.H.H., Seshan, K., Ross, J.R.H., Vandenoetelaar, L.C.A., Helwegen,

J.H.J.M., Anantharaman, M.R., and Brongersma, H.H. (1995) A low-energy ion scattering (LEIS) study of the influence of the vanadium concentration on the activity of vanadium–niobium oxide catalysts for the oxidative dehydrogenation of propane. *J. Catal.*, **157** (2), 584–591.

150 Guerrero-Ruíz, A., Blanco, J.M., Aguilar, M., Rodríguez-Ramos, I., and Fierro, J.L.G. (1992) A mechanistic study of the oxygen insertion into MoO_3 crystals as revealed by SIMS and TPSR techniques. *J. Catal.*, **137** (2), 429–436.

151 Abon, M., Béré, K.E., and Delichère, P. (1997) Nature of active oxygen in the *n*-butane selective oxidation over well-defined V–P–O catalysts: an oxygen isotopic labelling study. *Catal. Today*, **33** (1–3), 15–23.

152 Fu, L., Wu, N.Q., Yang, J.H., Qu, F., Johnson, D.L., Kung, M.C., Kung, H.H., and Dravid, V.P. (2005) Direct evidence of oxidized gold on supported gold catalysts. *J. Phys. Chem. B*, **109** (9), 3704–3706.

153 Lalande, G., Côté, R., Tamizhmani, G., Guay, D., Dodelet, J.P., Dignard-Bailey, L., Weng, L.T., and Bertrand, P. (1995) Physical, chemical and electrochemical characterization of heat-treated tetracarboxylic cobalt phthalocyanine adsorbed on carbon black as electrocatalyst for oxygen reduction in polymer electrolyte fuel cells. *Electrochim. Acta*, **40** (16), 2635–2646.

154 Lalande, G., Faubert, G., Côté, R., Guay, D., Dodelet, J.P., Weng, L.T., and Bertrand, P. (1996) Catalytic activity and stability of heat-treated iron phthalocyanines for the electroreduction of oxygen in polymer electrolyte fuel cells. *J. Power Sources*, **61** (1–2), 227–237.

155 Faubert, G., Lalande, G., Côté, R., Guay, D., Dodelet, J.P., Weng, L.T., Bertrand, P., and Dénès, G. (1996) Heat-treated iron and cobalt tetraphenylporphyrins adsorbed on carbon black: physical characterization and catalytic properties of these materials for the reduction of oxygen in polymer electrolyte fuel cells. *Electrochim. Acta*, **41** (10), 1689–1701.

156 Faubert, G., Côté, R., Dodelet, J.P., Lefèvre, M., and Bertrand, P. (1999) Oxygen reduction catalysts for polymer electrolyte fuel cells from the pyrolysis of FeII acetate adsorbed on 3,4,9,10-perylenetetracarboxylic dianhydride. *Electrochim. Acta*, **44** (15), 2589–2603.

157 Lefèvre, M., Dodelet, J.P., and Bertrand, P. (2000) O_2 reduction in PEM fuel cells: activity and active site structural information for catalysts obtained by the pyrolysis at high temperature of Fe precursors. *J. Phys. Chem. B*, **104** (47), 11238–11247.

158 Lefèvre, M., Dodelet, J.P., and Bertrand, P. (2002) Molecular oxygen reduction in PEM fuel cells: evidence for the simultaneous presence of two active sites in Fe-based catalysts. *J. Phys. Chem. B*, **106** (34), 8705–8713.

159 Lefèvre, M. and Dodelet, J.P. (2003) Fe-based catalysts for the reduction of oxygen in polymer electrolyte membrane fuel cell conditions: determination of the amount of peroxide released during electroreduction and its influence on the stability of the catalysts. *Electrochim. Acta*, **48** (19), 2749–2760.

160 Lefèvre, M., Dodelet, J.P., and Bertrand, P. (2005) Molecular oxygen reduction in PEM fuel cell conditions: ToF-SIMS analysis of Co-based electrocatalysts. *J. Phys. Chem. B*, **109** (35), 16718–16724.

12
X-ray Absorption Spectroscopy[1)]

C. Geantet and C. Pichon

12.1
Introduction

Owing to their nanometric size, the characterization of solid materials and especially heterogeneous catalysts always involves a range of techniques supplying complementary information. X-ray diffraction and infrared spectroscopy are the most frequently used techniques.

With heterogeneous catalysts, however, X-ray diffraction provides little information on the catalyst owing to the high dispersion of the active phase, despite mass contents which may be high. Infrared spectroscopy can be used to characterize the active sites via probe molecules but provides no information on their structure.

This information can be obtained with X-ray absorption spectroscopy (XAS), which can be used to investigate both the electronic and atomic structure in the vicinity of a type of atom. The major limitation of XAS, perfectly adapted to studying catalysts [2], is in fact related to accessing the synchrotron sources required to conduct these studies.

After an overview of the history and basic principle of X-ray absorption and its experimental aspects, we illustrate the major advantages offered by this technique for a better understanding of solid materials involved in surface reactions (oxide materials, metal- and sulfide-supported metal catalysts).

12.2
History of X-Ray Absorption Spectroscopy

The history of the beginning of XAS was nicely described by S. van Bordwehr [3] and F.W. Lyttle [4]. In fact, XAS was invented by Maurice and Louis de Broglie in 1913;

1) This chapter is dedicated to the memory of John Lynch (1955–2010), who developed X-ray absorption spectroscopy at IFP Energies Nouvelles and contributed to its expansion by conducting numerous collaborative studies on the subject [1], where his knowledge, teaching and human qualities were valuable assets.

Characterization of Solid Materials and Heterogeneous Catalysts: From Structure to Surface Reactivity, First Edition. Edited by Michel Che and Jacques C. Védrine.
© 2012 Wiley-VCH Verlag GmbH & Co. KGaA. Published 2012 by Wiley-VCH Verlag GmbH & Co. KGaA.

using a rotating single crystal as a source of various X-ray energies, they were able to make the first observation of an absorption edge. First measurements of extended X-ray absorption fine structure (EXAFS) fine structures were obtained in 1920 by Fricke and later by many other groups which made fundamental mistakes in the interpretation of the phenomena involved. The modern interpretation of EXAFS has its foundation in the work published by R. Kroning in 1931. The first application of XAS for the characterization of materials can be attributed to R. van Norstand, who concluded from these studies that "For study of the chemistry of catalysts and other non-crystalline systems this technique may have a role comparable to that of X-ray and electron diffraction in crystalline systems." This visionary conclusion was confirmed with the simultaneous elaboration of the theory of EXAFS by E.A. Stern, D.E. Sayers, and R.W. Lyttle in 1974, and the development of synchrotron radiation sources after the mid-1960s (Tantalus I in 1968).

12.3
Principle of X-Ray Absorption Spectroscopy: XANES, EXAFS

XAS is based on the phenomenon of inelastic scattering, where the intensity of a primary beam of X-ray photons decreases as it passes through a substance depending on the wavelength of the beam (or its energy ***E***).

In terms of energy, it should be remembered that an X-ray photon transfers either all or none of its energy to the atom. The photon cannot be split and if an energy transfer occurs, all the energy $h\nu$ of the photon is transferred during absorption. This X-ray photon of variable energy $E = h\nu$ excites an electron of the internal shells (1s at the K edge, 2s for the L_I edges, 2p for the L_{II} and L_{III} edges) of an absorbing atom A (see Figure 12.1). The energy transfer causes emission of an atomic core electron whose associated wavelength is determined by its kinetic energy E_{kin} and, indirectly, by the energy transferred $\Delta E = E_{kin} + E_l$, where E_l is the binding energy of the core level involved, that is, the energy edge above which transfer is possible.

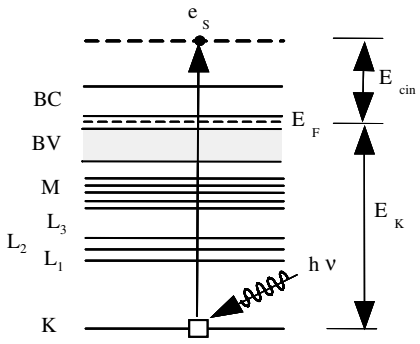


Figure 12.1 Diagrams of electron energies corresponding to the photoelectric effect. VB, valence band; CB, conduction band.

This type of spectroscopy will therefore specifically probe a constituent atom of the sample to be analyzed (e.g., the metal forming the active phase of a heterogeneous catalyst). At low energy, the transition of an electron from the lowest level is not yet possible: at this stage, the absorption coefficient is obtained from the other electron shells or other constitutive elements of the sample. This residual absorption coefficient has no special modulation, it decreases monotonically with the energy.

At the macroscopic scale, when these X-rays cross through the material, their intensity is attenuated according to a Beer–Lambert-type absorption law. The loss of intensity I is therefore proportional to the initial intensity and the thickness x crossed:

$$\Delta I(E) = -\mu(E) I(E) \mathrm{d}x$$

where μ is the linear absorption coefficient. By integration, we obtain the relation

$$I/I_0 = \mathrm{e}^{-\mu x}$$

where I and I_0 are the incident intensity and the intensity transmitted after crossing through the homogeneous sample.

The absorption coefficient varies with the wavelength and changes suddenly at the binding energy of the excited edge (absorption edge). This sudden transition, resulting from the photon–electron interaction creating a dipole, obeys Fermi's golden rule:

$$\mu(E) \propto N(E) < \Psi_{\mathrm{exc}} | O_{\mathrm{dip}} | \Psi_{\mathrm{fund}} >^2 \delta(h\nu - E_{\mathrm{exc}} + E_{\mathrm{fund}})$$

where $N(E)$ is the vacant state density, Ψ_{exc} and Ψ_{fund} are wavefunctions of the excited and fundamental state, and O_{dip} is the electric dipole transition operator (product of the electric-field polarization vector and the electron coordinates).

For the dipole approximation to be valid, the photon wavelength must be much larger than the size of the initial state. This criterion is perfectly satisfied, even for light atoms and poorly bound states. This dipole is expressed as an interaction Hamiltonian. At the edge energy, the effective cross-section of interaction, and therefore the absorption coefficient, increase suddenly. The ejected electron will first be considered as a probe of the vacant levels located above the Fermi level. Above the ionization energy, the photoelectron propagates through the medium with kinetic energy E_{kin} and an associated wave of wavevector $\boldsymbol{k}$. In a range less than 50 eV, the electronic wave has a high mean free path and will probe the electronic structure of the material studied, thereby supplying a projected partial state density in agreement with the selection rules, that is

$$\Delta n \neq 0 \quad \Delta l = +1, -1 \quad \Delta j = +1, 0, -1$$

We can nevertheless deviate from dipolar conditions and observe at pre-edge level characteristic signatures due to quadrupolar interactions or an sp hybridization state, for example. This energy range (between a few eV before the edge and 50 eV after the edge) corresponds to X-ray absorption near-edge spectroscopy (XANES). The signal amplitude is then directly related to the electronic levels of the vacant states. These electronic states are highly dependent on the electronic density, that is, the occupied

states of the material. Since the initial level is located in space, absorption spectroscopy is a probe, located around the absorbing atom, of the occupied and unoccupied electronic states of the material. The electronic states are closely related to the geometric structure of the material (position of atoms, local symmetry). Since the early 2000s, it has been easy to simulate these edges via the "multiple scattering" and "band structure" approaches [5, 6]. Without calculations, however, we can easily establish a correlation between the position of the absorption edge and the degree of oxidation of the atom or ion probed. The hole due to absorption of the photon creates a Coulomb interaction with all the other electrons of the excited atom. The shift between the positions of the absorption edges of two species with different valences reflects the energy gain due to the Coulomb interaction of the hole with the additional electronic charge of the least oxidized ion. It is therefore possible to monitor the charge transfers, and therefore the change in degree of oxidation, between the atoms during a chemical conversion.

Above 50 eV after the edge, the mean free path of the photoelectron becomes low and enters a simple scattering context where the spherical wave emitted by the absorbing atom is backscattered by the neighboring atoms. We are now in the context of extended X-ray absorption fine structure (EXAFS), which will supply local structural information. The amplitude of the wave produced towards a neighbor j located at a distance r_j from the absorbing atom A can be expressed as ψ_0/r_j. After backscattering, at the emitter, it has an amplitude $f(E)$ (value at angle 180°) characteristic of the neighboring atom j and divided again by r_j. This wave is modulated by a phase term characteristic of the distance and the potentials of the two atoms involved. The result of this intensity modulation is oscillatory behavior of the absorption rate, measured by the coefficient μ. To normalize the signals, the EXAFS signal is expressed by an interference function $\chi(E)$ given by

$$\sum \chi(E) = \frac{\mu(E) - \mu_0(E)}{\mu_0(E)}$$

which is an interference function consisting of the sum of all interactions

$$\chi(E) = \sum_j N_j \chi_j(E)$$

with each neighboring atom N_j. We are in fact interested in the function $\chi(k)$, which expresses the impact of the photoelectron on the absorption coefficient. E must therefore be converted into k using the equation

$$k = \sqrt{\frac{2m}{h^2}(E - E_0)^{\frac{1}{2}}}$$

where m is the electron mass and h is the reduced Planck's constant. Hence $k = (0.2624 E_{\text{kin}})^{1}/_{2}$.

To simplify the analysis of this function, we use a Fourier transform (FT) of $\chi(k)$ [or $k^n\chi(k)$] in the moment space k bounded by $k_{\min}$ and $k_{\max}$ to obtain a pseudo-function of the radial distribution $\varrho_n(r)$ in the real space. We then use a weighting window in

order to perform an FT on a bounded function. Hence

$$FT(r) = \frac{1}{\sqrt{2\pi}} \int_{k_{min}}^{k_{max}} k^n \chi(k)\, e^{-2ikr} dk$$

The peaks are generally displaced towards lower values of r due to the influence of dephasing. Note the weighting term k^n, which increases the contributions at high k values due mainly to the presence of heavy atoms in the coordination sphere.

Simulation of EXAFS spectra with dedicated programs is generally carried out when making a Gaussian approximation of the radial distribution of the atoms around their equilibrium positions, resulting in the following EXAFS equation:

$$\chi(k) = {S_0}^2 \sum_j N_j A_j(k)(k) \left(\frac{1}{k} {R_j}^2\right) \exp\left(-2R_j/\lambda\right) \exp\left(-2k^2{\sigma_j}^2\right) \sin\left[2kR_j + \phi_{i,j}(k)\right]$$

where S_0 is a scaling factor (amplitude reduction factor) created when a valence electron fills the hole created by absorption. This expression must also take into account two damping factors: that of the electron mean free path and that related to the disorder on the distribution of neighbors j. The photoelectron lifetime is limited using a factor $\exp(-2R_j/\lambda)$; the atoms are distributed around position R with standard deviation σ_j: these terms imply that the structural information contained in the interference function is limited to a maximum of 10 Å around the absorbing atom.

This equation contains *structural parameters* which are those to be determined during a study, that is, the number of neighbors $\boldsymbol{N_j}$, their respective distance $\boldsymbol{R_j}$ and the Debye–Waller factor $\boldsymbol{\sigma}_j$, which contains information on thermal disorder and static disorder. It also contains *electronic parameters* calculated using dedicated programs (such as FEFF) or obtained from reference samples. These parameters are the backscattering amplitude $\boldsymbol{A_j(k)}$, the dephasing $\boldsymbol{\phi}_{i,j}(\boldsymbol{k})$ including the contribution of the absorbing atom and the backscattering atom, and the mean free path $\boldsymbol{\lambda}$. These three parameters vary with the photoelectron energy.

One limitation with EXAFS is that, in the coordination sphere, it is impossible to distinguish between two neighboring atoms in the periodic table since their backscattering amplitudes and dephasings are virtually identical. As a structural determination method, the accuracy of EXAFS is determined by the relation $k_{max} \geq \pi/(2\Delta R)$, that is, for $k_{max} \approx 20$ Å^{-1} an accuracy of 0.08 Å^{-1}. The accuracy of the coordination is highly dependent on the correlation between the number of neighbors and the Debye–Waller factor. In addition to a thermal agitation term, this factor also contains the static disorder term $\sigma^2 = {\sigma_{stat}}^2 + {\sigma_{ther}}^2$, which may be high in the case of small metal particles of light atoms (Cu, Ni, Co, etc.) or lamellar compounds such as MoS_2.

12.4 Experimentation and Data Processing

Compared with other characterization techniques, X-ray absorption is highly special. In the laboratory, dull rotating anodes require long counting times and are therefore

rarely used; dedicated synchrotron sources are preferred. Their development in the 1970s, together with the theoretical understanding of EXAFS, led to the advent of this type of spectroscopy. Compared with other techniques and apart from the difficulty of the availability of these sources (for example, machine time allocated by program committees), XAS can be used to conduct studies on all states of matter, under practically all experimental conditions (temperature, pressure, etc.), and with no concentration limits (up to ppb). Although absorption of a sample may be very high, preventing the use of transmission techniques, it is always possible to use detection of photons or electrons resulting from de-excitation phenomena (fluorescence photon, Auger electron, etc.) and to measure the ratio between the intensity of the transmitted radiation (I_1) and that of the incident radiation (I_0), which will also supply an absorption spectrum. Electron detection is generally reserved for the study of light element edges (soft X-rays from a few hundred eV to 6–7 keV) and require the use of high-vacuum equipment. In the range of hard X-rays (6–100 keV), studies will be conducted in a traditional transmission or fluorescence mode where energy selection is carried out using a double-mirror monochromator by measuring the photon flow before and after the sample (see Figure 12.2).

To give priority to time resolution (acquisition in a few hundred milliseconds or less), studies will be conducted:

- either in dispersive mode in which a curved mirror focuses all wavelengths on the sample simultaneously (see Figure 12.3)
- or in traditional mode using quick-scanning monochromators (Quick-EXAFS).

The only equipment required is X-ray-transparent windows (made from beryllium, carbon, or boron nitride) integrated in a cell containing the sample to be analyzed. Work is generally carried out with a pellet more or less diluted in a poorly absorbing inert compound (cellulose, boron nitride, etc.) containing a quantity of the element to be analyzed. This quantity, optimized to obtain an absorption edge of 1, is calculated using mass absorption coefficients μ/ϱ (μ is expressed in cm^{-1} and the density ϱ in $g\,cm^{-3}$). μ/ϱ is virtually independent of the physical state of the material and is

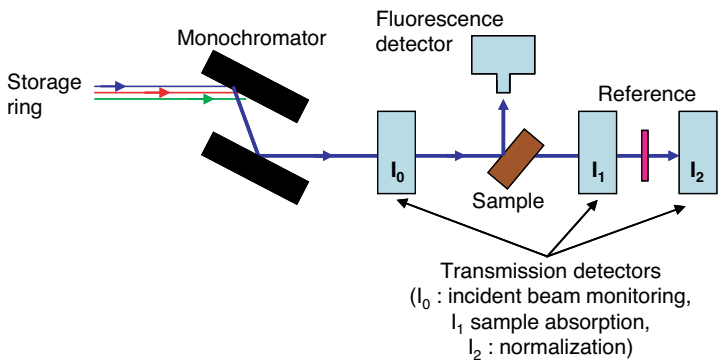


Figure 12.2 Diagrammatic representation of an XAS line operating in traditional mode (with detection in transmission and fluorescence).

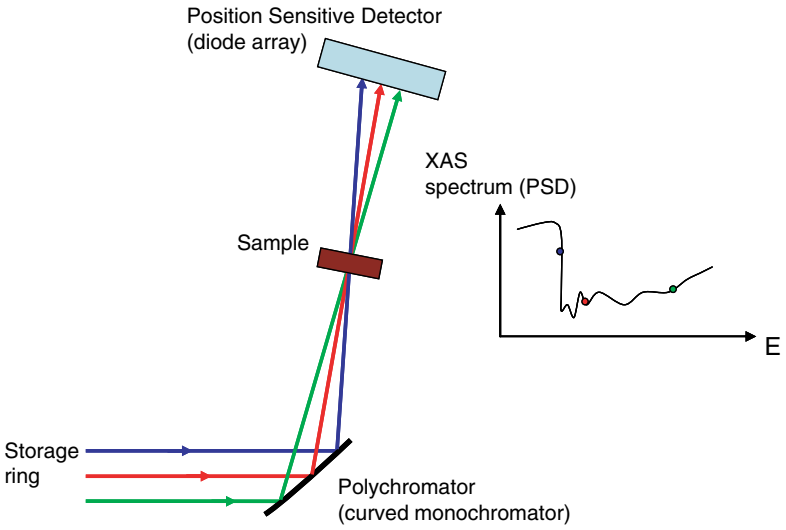


Figure 12.3 Diagrammatic representation of an XAS line operating in energy-dispersive mode.

therefore additive:

$$\mu/\varrho = \Sigma_j g_j (\mu/\varrho)_j$$

where g_j represents the mass fraction of element j of mass absorption coefficient $(\mu/\varrho)_j$.

The linear absorption coefficient μ of the sample is then given by

$$\mu = \sum_j n_j (\mu_a)_j / V$$

where μ_a is the atomic absorption coefficient and n_j the number of atoms of element j in volume V. Values of μ/ϱ and μ_a have been tabulated (International Tables for Crystallography, XAS data processing programs).

To a first approximation, μ is proportional to $\varrho Z^4/ME^3$, where Z is the atomic number, M the atomic mass and E the X-ray energy. The sample absorption will therefore be determined before and after the edge. For *ex situ* characterization of the sample, it is often better to take measurements at low temperature to reduce the contribution of the Debye–Waller factor. Liquid nitrogen (or liquid helium if necessary) is therefore frequently used with a dedicated cryostat. Above 7 keV, absorption by air (or another gas or low-density liquid) is negligible. The sample can therefore be studied in a liquid or gaseous environment, allowing the samples to be characterized *in situ* or *operando*, that is, under their actual use or operating conditions (in particular under activation or reaction conditions).

Suitable sample-holder cells are required to conduct *in situ* XAS experiments. Numerous variants adapted to this type of study and described elsewhere [7–9] are available.

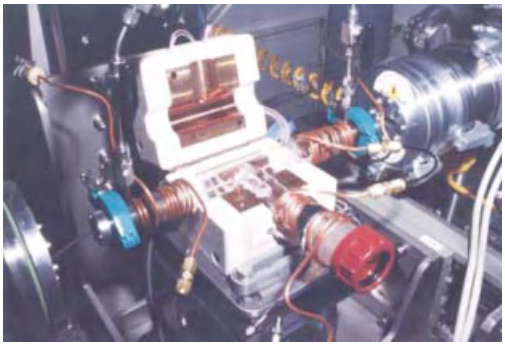


Figure 12.4 *In situ* reactor developed at IRCELYON.

Figures 12.4 and 12.5 show examples of *in situ* cells developed by IRCELYON (Figure 12.4) and IFP Energies Nouvelles (Figure 12.5).

The IRCELYON cell consists of two quartz tubes connected together in a T-shape and an electric oven surrounding the tubes. The sample, which consists of a self-supporting pellet, can be subjected to gas flows at temperatures of up to 600 °C and pressures of a few bar. This cell can be used to work in transmission and fluorescence modes and therefore to study low concentrations of promoters, for example, PtNiW/Al_2O_3 (0.3 wt% Pt) [10].

With the IFP Energies Nouvelles cell initially developed for studies on diffraction (and anomalous diffraction) of X-rays by powders, work can be carried out under a gas flow (neutral gas, pure hydrocarbons or hydrocarbons diluted in a vector gas), at temperatures up to 250 °C and pressures up to a dozen bar. In this cell, the sample to be analyzed consists of a fine powder in a crossed fixed-bed configuration placed in a 1 mm diameter quartz or glass capillary tube. This cell owes its originality to the way in which the sample is heated, that is, by a tubular electric micro-oven perforated by

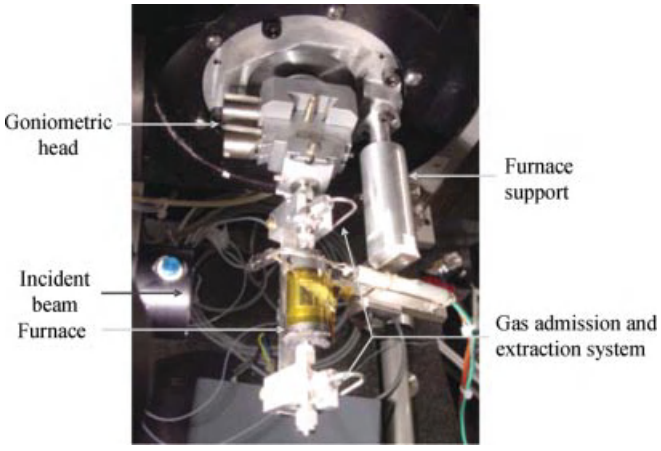


Figure 12.5 *In situ* cell developed at IFP Energies Nouvelles.

Table 12.1 Typical recording conditions of an XAS spectrum[a)]

Region	Initial energy (eV)	Final energy (eV)	Increment (eV)
Pre-edge	−200	−20	5.0
XANES	−20	+ 30	0.5
EXAFS	+ 30	+ 800	0.05 $Å^{-1}$

a) The energies are given with respect to the energy of the X-ray absorption edge considered.

X-ray-transparent windows (Capton windows), which guarantees a perfectly homogeneous temperature everywhere (temperature variation less than 1 °C over a sample area 6 mm long) [11, 12].

In conventional XAS, the recording conditions can typically be used to obtain an XAS spectrum (XANES and EXAFS) in about 30 min. To improve the quality of the information, the experiment should be repeated several times (generally three). The typical recording conditions of an XAS spectrum are indicated in Table 12.1.

It is generally essential to calibrate the monochromator with a reference element before recording in order to avoid excessive energy shifts. After recording, all glitches caused by spurious reflections must be removed. Once the spectrum has been acquired, data processing software (Athéna, etc.) is first used to extract the interference function. This operation is carried out in several steps.

First, the continuous absorption background before the edge is subtracted. The second step, which is more difficult, consists in determining the atomic absorption after the edge. Before the edge, the absorption variation is generally modeled by a linear function or a Victoreen-type empirical function in $C\lambda^3 - D\lambda^4$, where λ is the photoelectron wavelength. The contribution after the edge is generally modeled by a polynomial of variable degree. The degree of the polynomial (generally 4 or 5) and the value of the first point (anchor point) must be chosen carefully. The points are generally chosen in the first EXAFS half-oscillation. The polynomial extraction removes the low frequencies (which produce high noise at short distances).

The set forms the absorption function of the isolated atom $\mu_0(E)$ and therefore the extraction of $\chi(E)$ then of $\chi(k)$ using the relation

$$k = \sqrt{\frac{2m}{h^2}}(E - E_0)^{\frac{1}{2}}$$

A pseudo-radial distribution function representative of the local environment around the absorbing atom can then be obtained with the Fourier transform.

In a second step, the experimental spectra are simulated using dedicated programs (Artémis, etc.). The electronic parameters (backscattering amplitude, dephasings, etc.) are generally calculated with the program FEFF. The number of parameters that can be refined simultaneously (N_{free}) depending on the type of experimental data is given by the following relation:

$$N_{free} \leq \frac{2}{\pi \Delta r (k_{max} - k_{min})}$$

where Δr corresponds to the width of the inverse Fourier window from which the EXAFS spectrum was obtained; Δk is the width of the EXAFS spectrum.

The structural parameters R, N and σ (or inversely the amplitudes and phases) are obtained from data for $\phi_{i,j}(k)$, ${S_0}^2$, $\exp(-2R_j/\lambda)$, and $A_j(k)$ with a filter method applied to the various neighboring shells, then adjusting the curve obtained to the theoretical expression for the EXAFS function using minimization algorithms [13]. We assume that the amplitudes and phases obtained from a calculation or a reference compound can be transferred to the compound studied (as well as a scaling factor ${S_0}^2$ and the term $\exp(-2R_j/\lambda)$.This refinement can either be carried out on the interference function, the Fourier transform module, or the imaginary (or real) part of the Fourier transform. The refinement results are typically shown in tables containing for each shell the number of neighbors, the distance to the neighbors, the Debye–Waller factor, and ΔE_0.

The approach described here is one of the most common, but there are other types of processing that involve an asymmetric radial distribution function $g(r)$ or analysis using cumulants [14]. The wavelet method, a new data processing method replacing the Fourier transform, has recently been proposed [15].

EXAFS data processing is relatively complex and the analysis parameters must be kept strictly identical. The EXAFS signal is in fact sensitive to numerous parameters. The EXAFS signal frequency is affected by

- the distance R (dephasing over the entire spectrum);
- the position of edge E_0 (main dephasing at start of spectrum);
- the type of atoms.

There is little correlation between these parameters and they can be separated during the refinement.

The EXAFS signal amplitude is affected by

- the nature of the backscattering atom;
- the number of neighbors N (affects the entire spectrum);
- the Debye–Waller factor (mainly affects the end of the spectrum);
- the mean free path (mainly affects the start of the spectrum); there is a very high correlation between N and the pair σ, $\lambda(k)$;
- the scaling factor ${S_0}^2$ (theoretically, this is not a refinement variable, it lies between 0.7 and 1).

As we have seen previously, in the spectral range close to the edge (XANES region), the mean free path of the photoelectron becomes high and the simple scattering approximation is no longer applicable. Numerous effects (multiple scattering, polarization, n bodies, etc.) make the signal more complex and its simulation requires sophisticated calculation methods.

Various approaches can in fact be used to simulate the absorption spectra in the XANES region (a few eV before the edge and about 50 eV after). The approach developed from the local density approximation to calculate the final states is the one most frequently used. It is based on a band structure calculation using periodic calculation methods (VASP, etc.) or on the multiple scattering theory. Another approach is based on the multiplet theory for an atom in a crystal field [16]. The

most accessible programs developed by the synchrotron community are those based on the multiple scattering theory and implementing a "muffin-tin" approximation [6] or the finite differences method [5]. Since the 2000s, good simulations of XANES spectra have been obtained using these methods, with inexpensive calculation means.

12.5 Application to Oxide Materials

Oxide materials and especially oxide catalysts are widely used in industry and can be divided into two groups: selective oxidation, ammoxidation, and oxychlorination on the one hand, and total oxidation on the other. In most cases, these solids are also the precursor states of the metal or supported sulfide catalysts. In selective oxidation catalysis, unsupported metal oxides with highly complex compositions associating numerous metals are generally used. In total oxidation catalysis, supported catalysts based on transition metals, dispersed as monomers or polymers, are more frequently encountered. XAS represents a unique way of monitoring *in situ* the structural changes to these catalysts during their preparation or under reaction conditions and, when the species are dispersed, XAS is similar to a surface characterization technique. This technique can be used in particular to monitor the changes in the degree of oxidation or in the coordination of atoms forming the active phase of the catalyst during the catalytic process.

By studying the grafting of an Ni complex [Ni(II) bisglycinate] on alumina, we can demonstrate that after impregnation and drying, there is an interaction with the support with identification of an Ni−O−Al (Ni−Al = 3.05 Å) bond even if the structure of the complex remains stable (see Figure 12.6) [17].

Condensed oxides such as polyoxometalates can also be studied to determine whether the structure is preserved during an interaction with the support and its thermal stabilization during pretreatment or during catalysis. For instance, Ressler *et al.* [18] studied heteropolymolybdates $PVMo_{11}O_{40}$ supported on silica SBA-15. This Keggin ion can be supported without modification on the mesoporous silica but, during selective oxidation of propene, the heteropolyanion becomes unstable, as illustrated in Figure 12.7, unlike the unsupported Keggin complex.

The compositions of unsupported selective oxidation catalysts are often highly complex. The system MoVTe(Sb)NbO, for example, is extremely efficient for the controlled oxidation of light alkanes or ammoxidation of propane. The active phase of this system, known as the M1 phase, has the formula $(AO)_{2-2x}(A_2O)_xM_{20}O_{56}$, where A = Sb or Te, M = Mo, V, Nb, and $0 < x < 1$ and the V:Mo and Nb:Mo ratios can vary only slightly; at ambient temperature, we consider that the formula of the catalyst is $[Sb^{5+}O]_{1.0}[Sb^{3+}O_{0.5}]_{0.8}V^{4+}{}_{3.4}V^{5+}Mo^{6+}Mo^{5+}{}_{14.5}Nb_{2.2}O_{56}$. An XAS study conducted at the V and Mo K edge and the Sb L_1 edge determined the oxidation states of several metals under catalysis conditions [19] and by coupling this reaction with electric conductivity measurements. With Sb, for example, we can record the XANES at equilibrium under various atmospheres and temperatures (pure He, pure O_2, and various O_2/C_3H_8/He compositions) and deduce the Sb^{III} and Sb^{V} fraction in the

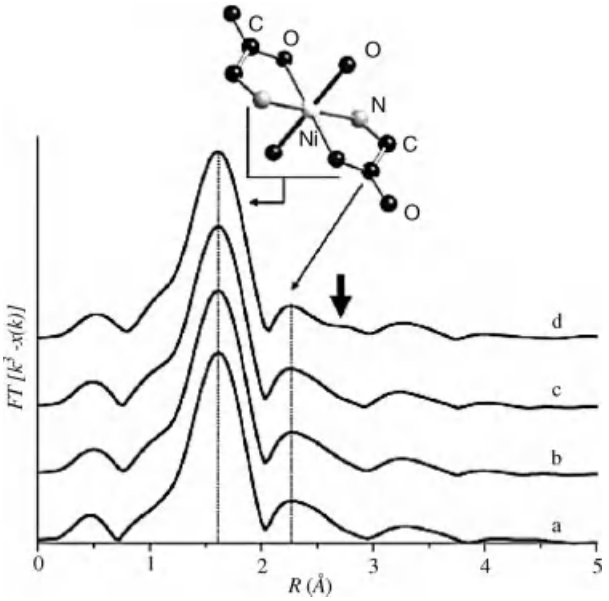


Figure 12.6 Fourier transform ($k = 2.2$–$11.8\,Å^{-1}$) of k^3-weighted EXAFS spectra of (a) nickel bisglycinate in aqueous solution ($0.08\,mol\,l^{-1}$), (b) crystals of nickel bisglycinate, (c) impregnated solution of Ni(II) complex on alumina prepared at ambient temperature, and (d) at 333 K [15].

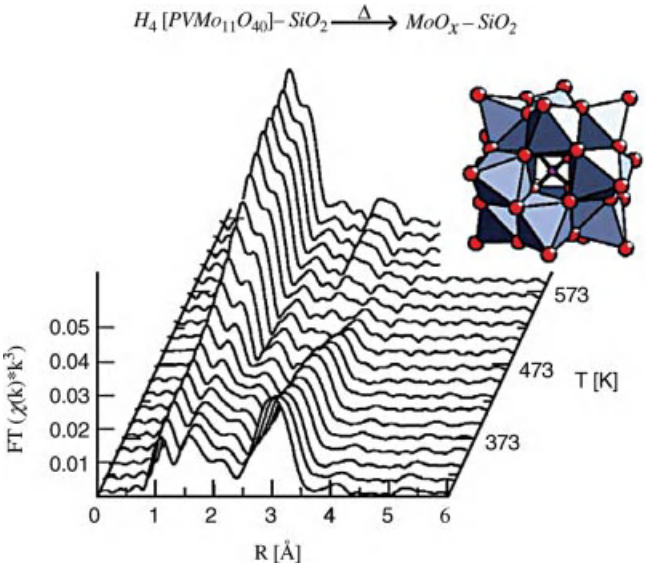


Figure 12.7 Evolution of Mo K edge FT[$\chi(k)k^3$] of as-prepared PVMo11-SBA-15 during temperature-programmed treatment in propene and oxygen ($4\,K\,min^{-1}$, 5% propene and 5% oxygen in He). From [16].

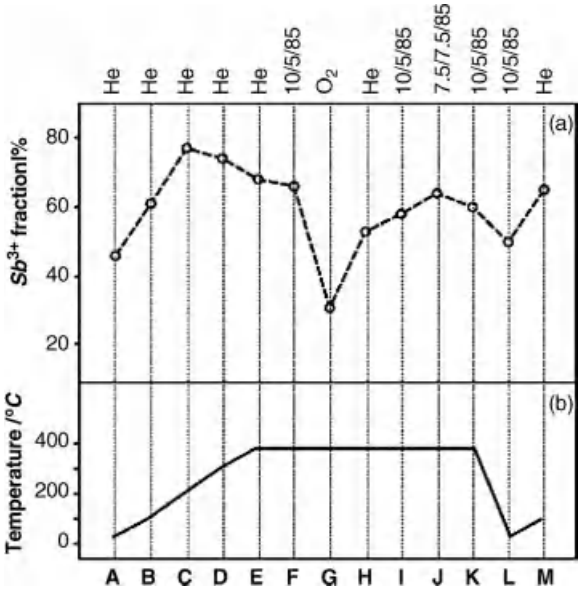


Figure 12.8 (a) Fraction of Sb^{3+} cations in the structure of the M1 phase under different redox conditions. (b) Temperature plot [17]. The numbers *X*/*Y*/*Z* at the top refer to the molar ratio between O_2 (*X*), C_3H_8 (*Y*) and He (*Z*).

sample, or monitor this modification dynamically during the reaction (see Figures 12.8 and 12.9). At the V K edge, these variations are less sensitive but simultaneous with those of V; only 10% of the V would appear to be involved in the redox process.

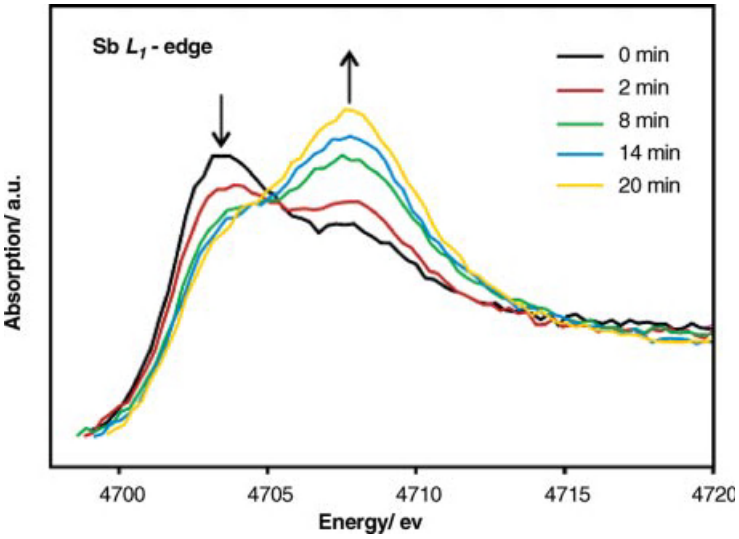


Figure 12.9 Time variation of Sb L_1 XANES spectra of the M1 phase in O_2 at 380 °C [17].

12.6
Applications to the Study of Sulfide Catalysts

With catalytic cracking, hydrotreatments using sulfide catalysts represent the major oil refining processes. For more than 50 years, these catalysts deposited on alumina have consisted of Co- or Ni-doped Mo or W disulfide nanoparticles, the active phase causing the synergy effect, the CoMoS phase, being composed of doping agents substituting the Mo edge atoms of the disulfide layers [20].

Among the techniques used to detect a CoMoS-type mixed phase [Mössbauer, infrared (IR) of CO, and more recently X-ray photoelectron spectroscopy), EXAFS is the only technique capable of supplying structural information, under *in situ* conditions, on the mixed phase and its conversion, during activation, of the oxide phase into sulfide phase. It is therefore a valuable tool in understanding this type of catalyst; XAS was even the first technique to identify the presence of MoS_2 particles. A first review on the application of XAS to sulfide catalysts was published in 1988 [21] and a second in 1996 [22]. Since then, XAS has continued to supply exceptional information on the synthesis and structure of hydrotreatment catalysts.

12.6.1
Structure of the Active Phase

The other important result of applying XAS to hydrotreating (HDT) catalysis is that it confirmed the CoMoS model proposed using Mössbauer spectroscopy. After determining the lamellar structure, Clausen *et al.* [23] observed in the Co coordination sphere, apart from sulfur, the presence of a Co–Mo contribution located at 2.75–2.85 Å characteristic of the structure decorating the layers. These results will serve as a basis for the theoretical models and calculations and the advent of methods to optimize these calculations will confirm this structural description (see Figure 12.10). Note that in this case, if performed at the edge of the promoter (Co or Ni), XAS becomes a surface technique probing edge atoms only. XAS very rapidly became an essential technique for the characterization of HDT catalysts and is applied to all states of these catalysts, whether oxide or sulfide, during activation or reaction. X-AS can therefore be used to monitor *in situ*:

- the evolution of a precursor element of the oxide phase;
- its activation to convert it into a sulfide active phase;
- the sulfide state under an H_2/H_2S atmosphere or during reaction;,
- the structural modifications induced by the deactivation phenomena.

In view of the lamellar structure of MoS_2, EXAFS analysis of this compound exhibits the characteristic of probing only the metal layer between two sulfide layers and not the layers located beyond. This characteristic allowed us to identify the formation of solid solutions such as $Mo_xW_{(1-x)}S_2$ in reference unsupported solids [24] or in 20–30 Å nanoparticles supported on alumina [25]. During the formation of this solid solution, simulations and analyses at the Mo and W K edges (Figure 12.11) show that the phase interference between Mo and W reduces the

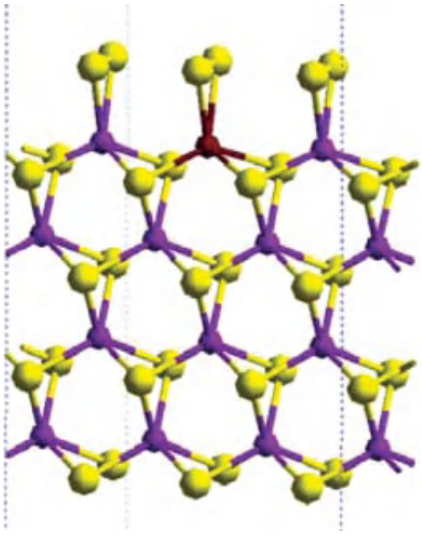


Figure 12.10 Modeling of the CoMoS phase (Co atom in red, S in yellow and Mo in purple).

amplitude of the characteristic peak of the second coordination sphere but refinement indicates the relative presence of the two elements in the layer with the required stoichiometry. EXAFS is therefore the only technique capable of demonstrating the presence of the two metal cations within a given layer, thereby forming a nanometric solid solution (see Table 12.2).

12.6.2
Activation of Sulfide Catalysts

Activation of HDT catalysts is a determining factor with respect to the final activity of the catalyst. It can be carried out *in situ* in a hydrotreatment unit – in this case, a sulfurization agent (e.g., dimethyl disulfide) is added to the feedstock to be treated – or *ex situ* (in the gaseous phase), the passivated catalyst being reactivated by the sulfur

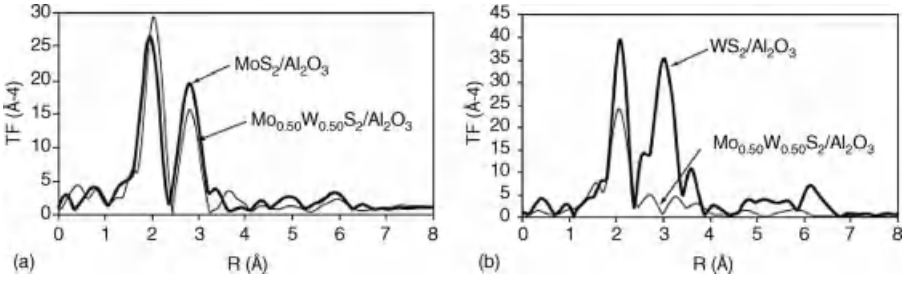


Figure 12.11 Fourier transforms obtained at the Mo K edge for MoS_2/Al_2O_3 and $W_{0.50}Mo_{0.50}S_2/Al_2O_3$; (b) Fourier transforms obtained at the W L_{III} edge for WS_2/Al_2O_3 and $W_{0.50}Mo_{0.50}S_2/Al_2O_3$ [22, 23].

Table 12.2 EXAFS refinement results (W L_{III} edge): characteristics of the cationic in-plane environment of molybdenum in alumina-supported WS_2 and $W_{0.50}Mo_{0.50}S_2$ [22].

	Mo shell[a)]				W shell[a)]			
	***R*(Mo) (Å)**	***N*(Mo)**	$\sigma^2 \times 10^3$ **(Å^2)**	ΔE_0 **(eV)**	***R*(W) (Å)**	***N*(W)**	$\sigma^2 \times 10^3$ **(Å^2)**	ΔE_0 **(eV)**
MoS_2	3.14	5.9	4.24	−1.6	/	/	/	/
$W_{0.50}Mo_{0.50}S_2$	3.16	3.3	4.45	2.4	3.17	2.1	4.7	6.9

a) $\Delta R = \pm 0.01$ Å, $\Delta N = \pm 0.7$, $\Delta(\Delta E_0) = \pm 0.6$ eV, $\Delta(\sigma^2) = \pm 0.5 \times 10^{-3}$ Å^2.

in the feedstock. This is a critical step since it allows the formation of the active phase (CoMoS or NiMoS).

Even though industrial hydrotreatment catalysts have similar elementary compositions, their activation procedure introducing various temperature stages (maximum 350–400 °C) is highly dependent on their preparation history, the use of doping agents, and other molecules present on the surface of the catalyst.

Consequently, organic additives can be used to modify the oxide precursor but also to control the sulfurization kinetics of the elements forming the active phase such as Co and Mo. For example, Mazoyer *et al.* [26] studied activation by H_2/H_2S (15%) of a $CoMoP/Al_2O_3$ catalyst at the Co and Mo K edges. Use of a non-chelating additive such as diethylene glycol monobutyl ether (DEGBE) impregnated on the oxide catalyst increases the quantity of promoted phase on the catalyst and consequently its activity. This additive modifies the surface state of the precursors in the oxide state but also affects the sulfurization kinetics of the two elements in the active phase. *In situ* study at the Mo and Co K edges (Figures 12.12 and 12.13) indicates a decrease in the sulfurization rate of the two elements. With Co, elongation of the Co–first neighbor bond from 2.0 Å for Co−O to 2.2 Å for Co−S is delayed and appears at 200 °C instead

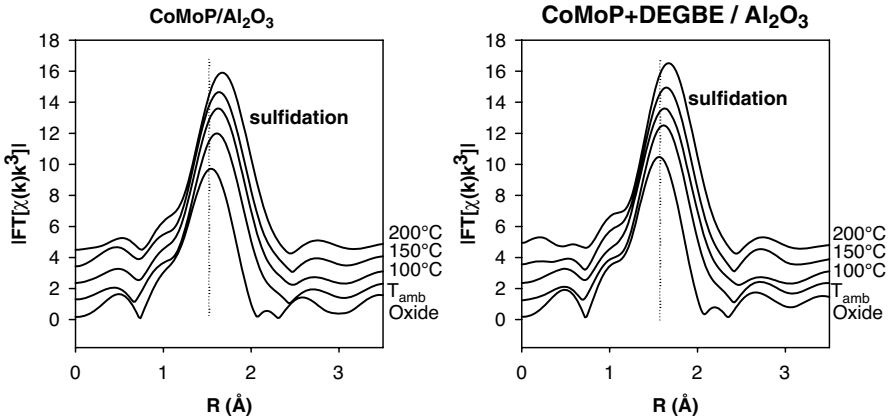


Figure 12.12 Magnitude of the Fourier transformed k^3- weighted data at the Co K edge of CoMoP on alumina reference catalyst and DEGBE modified catalyst in the oxidic state and after sulfidation from room temperature up to 200 °C [24].

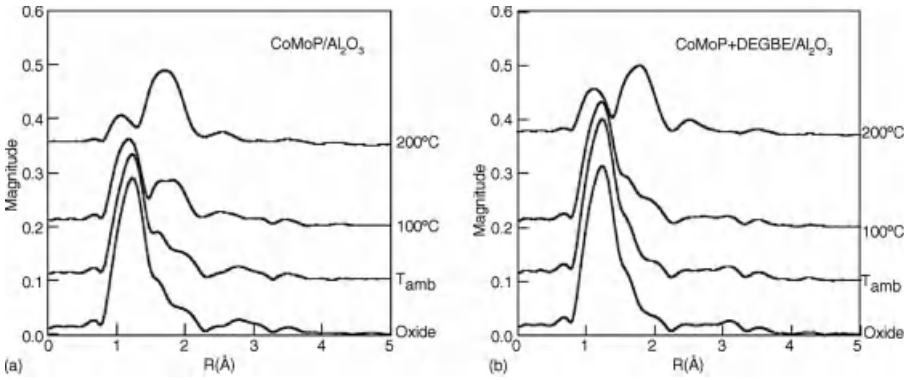


Figure 12.13 Magnitude of the Fourier transformed k^3-weighted data at the Mo K edge of CoMoP on alumina reference catalyst and DEGBE modified catalyst in the oxidic state and after sulfidation at room temperature, at 100 and at 200 °C [24].

of 150 °C. Similarly, elongation of the Mo–first neighbor bond (Mo−O to 1.7 Å and Mo−S to 2.4 Å) only occurs at 200 °C in the presence of DEGBE whereas it starts at 100 °C without additive. The additive therefore plays a determining role during sulfurization, favoring the formation of the mixed phase.

12.7 Application to Metal Catalysts

Supported metal catalysts are used in numerous industrial processes in the field of refining and petrochemistry: catalytic reforming for the production of high-octane fuels, hydrogenation of aromatic or polyaromatic compounds for the production of diesel cuts respecting present or future environmental standards, selective hydrogenation of unsaturated hydrocarbons, and dehydrogenation of alkanes.

For these materials, the catalytic properties (activity, selectivity, stability, regenerability, etc.) depend largely on the structure of the catalyst and in particular their active phase (mono- or bimetallic particles), which itself depends on the activation (reduction) or reaction conditions to which the material is subjected.

For supported metal catalysts, XAS provides a wide range of information: type of atoms in the vicinity of a metal atom (oxidized or reduced particles, presence of a second metal in the particle, etc.), number of neighbors of each type for the absorbing metal atom (structure of bimetallic particles, size of particles depending on their morphology, etc.), metal–metal distances in the particle (identification of stress effects, etc.), and electronic properties (XANES study).

The contribution of XAS in the characterization of supported metal catalysts is illustrated below through examples taken from exploratory research studies or studies conducted on industrial catalysts. These examples demonstrate the benefit of the technique in characterizing the structure and size of metallic (possibly bimetallic) particles or obtain information on the changes to these characteristics

when the catalyst is under reaction conditions or subjected to an inhibitor or even a poison.

12.7.1 Structure and Size of (Bi-)Metallic Particles

EXAFS analysis is one of the rare techniques allowing the direct characterization of the structure of metallic nanoparticles deposited on a support and may allow the study of subnanometric particles that are impossible to detect using transmission electron microscopy.

This is the case, for example, with catalysts for the selective hydrogenation of unsaturated hydrocarbons composed of palladium (0.3 wt%) supported on alumina. For these catalysts, poorly loaded with noble metals, the metal is so finely dispersed that the metallic particles obtained after reducing the active phase do not appear in transmission electron microscopy, which cannot detect particles smaller than 8 Å on this type of material.

Analysis of EXAFS spectra (at the palladium K edge) obtained for the reduced catalysts revealed that each palladium atom in the material has on average 5–6 neighboring palladium atoms (Figure 12.14). This result is compatible with an evaluation of about 7–8 Å for the size of the metallic particles (Figure 12.15). For this type of material where the metallic particles are highly sensitive to air – in contact with air they reoxidize very quickly – the possibility of conducting the analysis *in situ* (at high temperature and under a hydrogen flow) is a significant advantage [27].

When several metals are involved in the composition of the active phase of supported metal catalysts, this active phase may consist of bimetallic particles (or, otherwise, by the juxtaposition of monometallic particles). The atomic arrangement in bimetallic particles may vary considerably from an alloy structure to a structure exhibiting phase segregation such as the core–shell structure. This highly special structure is generally obtained by reaction of an organometallic compound (whose metal will form the shell of the final bimetallic particle) on the surface of a monometallic particle (consisting of the core metal).

These catalysts may exhibit special properties, different from those of the monometallic catalysts. This is the case with selective hydrogenation catalysts whose active

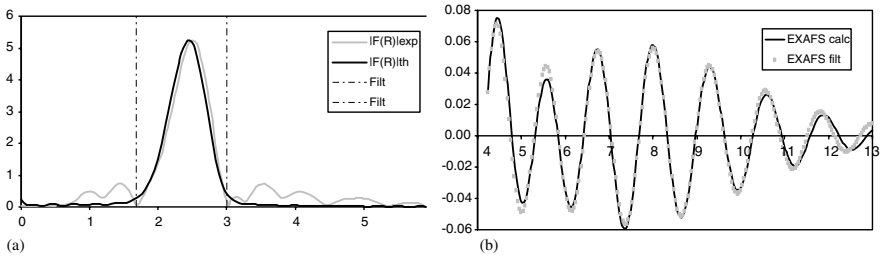


Figure 12.14 Fourier transform and adjustment of the filtered area (a) and filtered (EXAFS filt) and adjusted (EXAFS calc) experimental interference functions (b) for a Pd/Al_2O_3 sample [25].

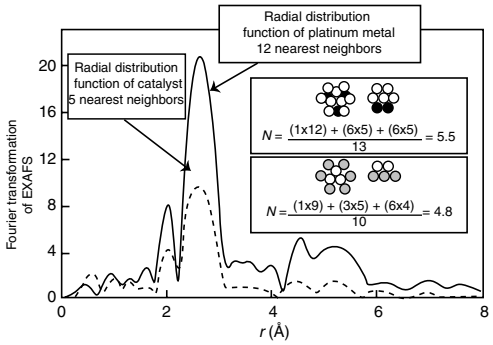


Figure 12.15 Relation between number of neighbors and particle size [28].

phase consists of palladium particles (in the shell) and platinum particles (in the core) and which exhibit special thioresistant properties.

By conducting crossed experiments at the X-ray absorption edge of each of the two elements, Pt (Figure 12.16) and Pd (Figure 12.17) forming the bimetallic particle, additional information can be obtained on the average local structure of these two elements before determining the complete (average) structure of the core–shell particles.

By adjusting the Fourier transforms of the EXAFS spectra obtained at the palladium K edge and the platinum L_{III} edge by elementary contributions modeling a local environment composed, for these two elements, of palladium and platinum, the average local environment of these two atoms in the metallic particles can be determined (see Table 12.3).

Comparing these values with those obtained theoretically for bimetallic particles exhibiting a core–shell structure whose shell consists of a palladium monolayer and whose core is a spherical platinum particle of variable size (Figure 12.18), it appears

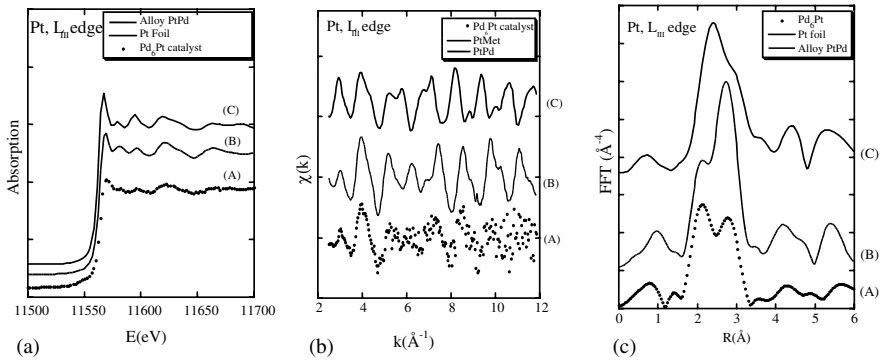


Figure 12.16 XANES spectra (a), EXAFS spectra (b), and Fourier transform modules (c) at the platinum L_{III}-edge of the Pd_6Pt catalyst (A) compared with that of a metallic sheet of PtPd alloy (B) and that of a metallic sheet of platinum (C) [26].

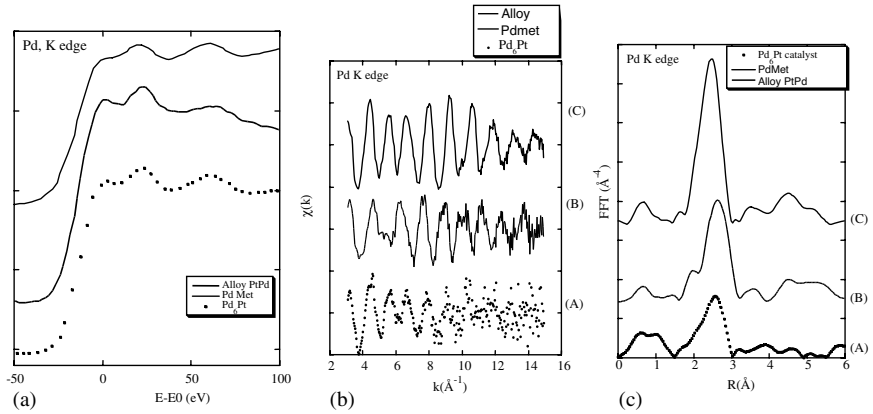


Figure 12.17 XANES spectra (a), EXAFS spectra (b) and Fourier transform modules (c) at the palladium K edge of the Pd_6Pt catalyst (A) compared with that of a metallic sheet of PtPd alloy (B) and that of a metallic sheet of platinum (C) [26].

that the Pd_6Pt catalyst consists of a platinum core with slightly less than 13 atoms, covered by an (incomplete) palladium monolayer [28].

12.7.2
Evolution of the Bimetallic Structure Under Reaction or Poisoning Conditions

The compatibility of high-energy X-rays with the operating conditions of heterogeneous catalysts (temperature, pressure, flow of gaseous hydrocarbons) gives this technique a further advantage: it can characterize these materials *in situ*. This type of analysis allows a more realistic approach to the characterization of this type of solid for the activation (reduction at high temperature and under a hydrogen flow) or reaction steps.

Table 12.3 Parameters of the digital simulations of EXAFS data obtained at the palladium K edge and the platinum L_{III} edge [25].

Edge	Palladium K edge	Platinum L_{III} edge
Scale factor	1.00	1.00
Number of shells	2	2
Type of neighbor	Pd	Pt
Number of neighbors	6.9 (±0.5)	3.4 (±0.5)
Distance to neighbor (Å)	2.73 (±0.05)	2.67 (±0.05)
Debye–Waller factor (Å)	0.02	0.01
Energy shift (eV)	2.5	−3.2
Type of neighbor	Pt	Pd
Number of neighbors	0.9 (±0.5)	6.7 (±0.5)
Distance to neighbor (Å)	2.77 (±0.05)	2.82 (±0.05)
Debye–Waller factor (Å)	0.03	0.01
Energy shift (eV)	2.1	0.0

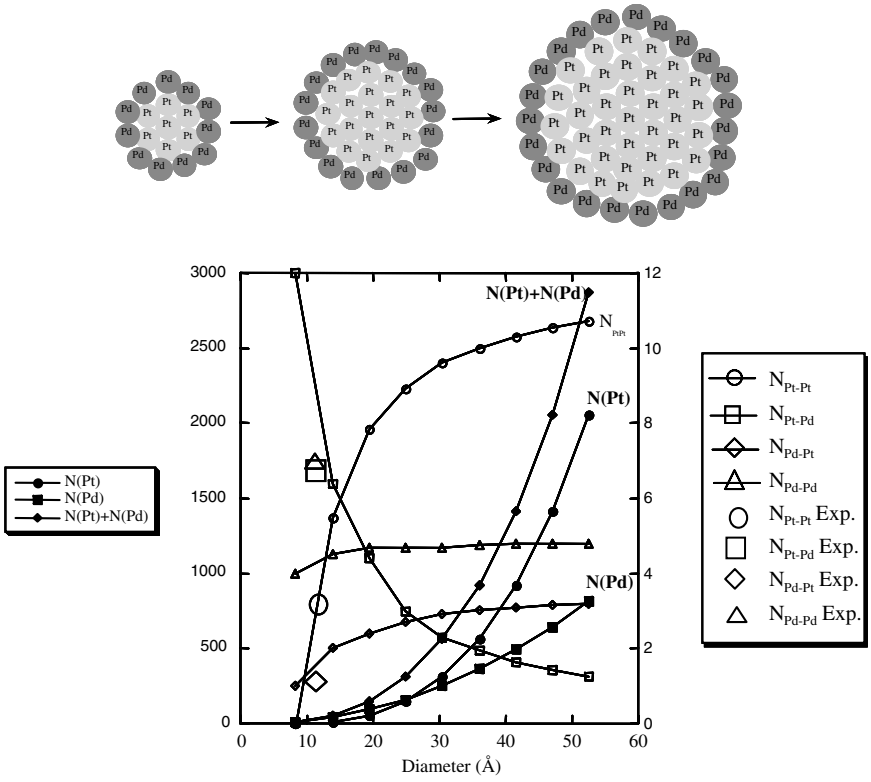


Figure 12.18 Coordination numbers N_{PtPt}, N_{PtPd}, N_{PtPd}, N_{PdPd} [the particle core consists of N(Pt) Pt atoms and the surface consists of N(Pd) Pd atoms; the size of the platinum core is considered as a parameter] compared with the experimental values [26].

With catalytic reforming catalysts, used to convert naphthas into high-octane aromatics which are then incorporated into the gasoline pool, EXAFS was first used to characterize *in situ* the effect of the presence of hydrocarbons (*n*-heptane), at high temperature (623 K) and under pressure (3 bar), on the structure of the active phase composed of metallic platinum nanoparticles. The Fourier transforms of the EXAFS spectra shown in Figure 12.19 demonstrate that the metallic structure is preserved throughout the reaction and that the presence of *n*-heptane (*n*-C7) leads to the appearance of a Pt–C bond characteristic of the presence of a carbonated deposit on the surface of the metallic particles. When the catalyst is no longer under hydrocarbon flow and is returned under hydrogen flow, this deposit progressively disappears, as shown by the reduction over time of the Fourier transform peak attributed to the Pt–C bond [29, 30].

Whereas the first industrial reforming catalysts were composed of a single metal (platinum), the next generations of materials adopted a bimetallic formulation (based on platinum and rhenium, for example) to improve the resistance of this catalyst with respect to the low quantities of sulfur present in the naphthas to be treated with this

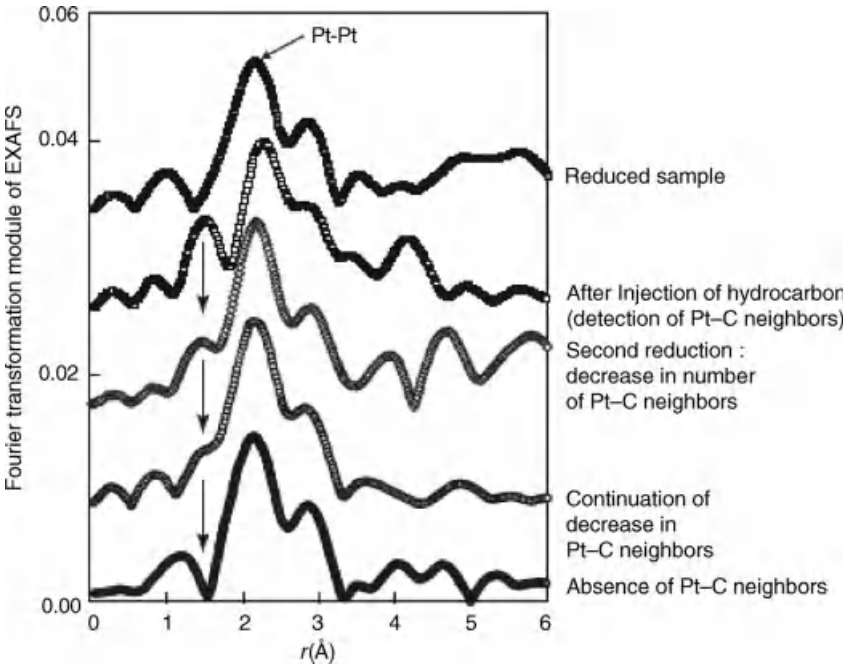


Figure 12.19 Evolution of the Fourier transform of the EXAFS spectra obtained for a reforming catalyst in the presence of hydrogen and possibly a hydrocarbon (*n*-heptane) [28].

process. Whereas the (platinum-based) monometallic catalyst deactivated rapidly and irreversibly in the presence of sulfur, the activity of bimetallic catalysts was more resistant and, above all, could be quickly restored when the catalyst was no longer subjected to feedstocks containing sulfur (e.g., after regeneration under pure hydrogen). This phenomenon was explained thanks to EXAFS by implementing *in situ* characterization.

It has therefore been demonstrated that during reduction under hydrogen, platinum oxide (where each platinum atom is surrounded by six oxygen atoms) and rhenium oxide (where each rhenium atom is surrounded by four oxygen atoms) are converted into metallic particles (bimetallic alloy for the Pt–Re/alumina catalyst). EXAFS analysis shows that, at this stage, the presence of a second metal results in the formation of smaller metallic particles. Addition of sulfur which is adsorbed on the metallic atoms leads to total and rapid disappearance of the Fourier transform peak of the EXAFS spectrum obtained at the platinum L_{III} edge for the monometallic sample, whereas this peak remains unchanged with the bimetallic catalyst; in both cases, a peak attributed to a Pt−S bond appears on the Fourier transforms. This information shows that, whereas the metallic structure of platinum particles does not withstand the presence of sulfur (which then acts as a poison since the formation of highly dispersed platinum sulfide is irreversible), that of bimetallic particles is retained in the presence of sulfur (which then acts as an inhibitor since adsorption of sulfur is reversible). A diagram, compatible with the information resulting from analysis of

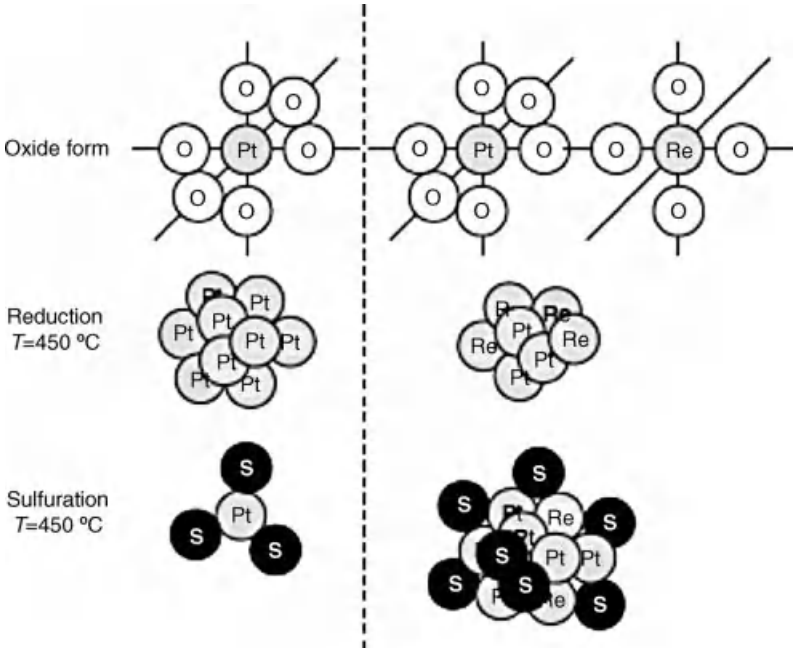


Figure 12.20 Diagrammatic representation of the evolution in the environment of the metals in monometallic Pt/Al_2O_3 and bimetallic $Pt–Sn/Al_2O_3$ catalysts during reduction and sulfurization [28].

the EXAFS spectra, showing a change in the environment of the metals in these catalysts is proposed in Figure 12.20 [30, 31].

12.8 Conclusion and Perspectives

Solid materials (especially heterogeneous catalysts) and the use of synchrotron radiation are two inseparable research fields. Materials science creates objects that are often nanometric and increasingly complex, for which synchrotron radiation represents a unique method of characterizing these materials, especially under reaction conditions. As we have seen through the few examples described above, XAS is, in principle, a volume technique. However, when exploring the properties of atoms located on the surface (segregation in bimetallic particles, decoration for sulfides) or of isolated atoms (supported monomers), this type of spectroscopy truly becomes a technique for the characterization of the surface and active sites of solid materials. We must also mention the SEXAFS (surface extended X-ray absorption fine structure) technique which detects Auger or secondary electrons and therefore requires equipment under high vacuum. It is more suitable for light atom edges and uses soft X-rays. This technique can be used in particular to describe an adsorbate on a monocrystalline model surface.

In the field of hard X-rays, recent technological progress made with light lines provides new opportunities in terms of spatial, energy, temporal, and sensitivity resolution. In 2009, two special journal volumes entitled Catalysis With Hard X-Rays [32, 33], dedicated mainly to studies related to heterogeneous catalysis, illustrated the numerous developments under way in this field. In terms of temporal resolution, dispersive mode and QEXAFS (quick scanning extended X-ray absorption fine structure) can be used to acquire absorption spectra in a few hundred milliseconds; we have also seen the description of the first results concerning heterogeneous catalysis with acquisition in a few microseconds. The detectors are now sufficiently sensitive to analyze a few parts per million or even parts per billion of an element in a matrix. Spatial resolution is also improved by microfocusing the incident beam [Kirkpatrick–Baez (K–B) mirrors] to reach a beam size of the order of μm^2 or by using high spatial resolution detectors of charge-coupled device camera type. A large number of other combinations such as XAS–Raman, XAS–differential scanning calorimetry, XAS–IR or UV spectroscopy, and so on, can be added to the historic XAS–X-ray diffraction coupling (and associated techniques WAXS, SAXS, AWAXS, ASAXS). All these couplings are generally carried out under *in situ* conditions. The energy resolution of the XANES spectra is considerably improved with the introduction of analyzer crystals, which also allow X-ray spectrometry or resonant inelastic X-ray scattering to be developed. These spectroscopic techniques provide new information, in particular on the spin states or the electronic structure of light elements. Interpretation of these XANES spectra is simplified with the emergence of more powerful computation means and constantly improving dedicated programs.

As with all the other techniques, XAS has made outstanding progress which will be of benefit to catalysis and material sciences, for the study of both the reactivity of model surfaces and industrial solid materials and catalysts.

References

1 Pichon, C. and Lynch, J. (eds.) (2005) Synchrotron and neutron solutions to oil industry problems. *Oil Gas Sci. Technol. Rev. IFP*, **60** (5), 673–805.

2 Geantet, C. and Millet, J.M.M. (2009) Use of *in situ* XAS techniques for catalysts characterization and design, in *Design of Heterogeneous Catalysts* (ed. U. Ozkan), Wiley-VCH Verlag GmbH, Weinheim, pp. 259–293.

3 van Bordwher, S. (1989) A history of the X-ray absorption fine structure. *Ann. Phys. Fr.*, **14**, 377–466.

4 Lyttle, F.W. (1999) The EXAFS family tree: a personal history of the development of extended X-ray absorption fine structure. *J. Synchrotron Radiat.*, **6**, 123–134.

5 Joly, Y. (2001) X-ray absorption near edge structure calculations beyond the muffin-tin approximation. *Phys. Rev. B*, **63**, 125120–125129.

6 Rehr, J.J. and Ankudinov, A.L. (2005) Progress in the theory and interpretation of XANES. *Coord. Chem. Rev.*, **249**, 131–140.

7 Lytle, F.W., Wei, P.S.P., Gregor, R.B., Via, G.H., and Sinfelt, J.F. (1979) Effect of chemical environment on magnitude of X-ray absorption resonance at L_{III} edges – studies on metallic elements, compounds,

and catalysts. *J. Chem. Phys.*, **70**, 4849–4855.

8 Jentoft, R.E., Deutsch, S.E., and Gates, B.C. (1996) Low-cost, heated, and/or cooled flow-through cell for transmission X-ray absorption spectroscopy. *Rev. Sci. Instrum.*, **67**, 2111–2112.

9 Clausen, B.S., Steffensen, G., Fabius, B., Villadsen, J., Feidenhans'l, R., and Topsøe, H. (1991) *In situ* cell for combined XRD and online catalysis tests – studies of Cu-based water gas shift and methanol catalysts. *J. Catal.*, **132**, 524–535.

10 Breysse, M., Djega-Mariadassou, G., Pessayre, S., Geantet, C., Vrinat, M., Perot, G., and Lemaire, M. (2003) Deep desulfurization reaction catalysts and technological challenges. *Catal. Today*, **84**, 129–138.

11 Palancher, H. (2004) Caractérisation *in situ* par diffraction anomale de la distribution cationique de zéolithes X bicationiques dans des conditions proches de leur utilisation industrielle, Thèse de l'Université Joseph Fourier–Grenoble I.

12 Palancher, H., Pichon, C., Rebours, B., Hodeau, J.L., Lynch, J., Bérar, J.F., Prévot, S., Conan, G., and Bouchard, C. (2005) A cell for *in situ* dynamic X-ray diffraction studies: application to the dehydration of zeolite SrX. *J. Appl. Crystallogr.*, **38**, 370–373.

13 Marquardt, D. (1963) An algorithm for least-squares estimation of nonlinear parameters. *SIAM J. Appl. Math.*, **11**, 431–441.

14 Dalba, G., Fornasini, P., and Rocca, F. (1993) Cumulant analysis of the extended X-ray fine structure of β-AgI. *Phys. Rev. B*, **47**, 8502–8514.

15 Shao, X., Shao, L., and Zhao, G. (1998) Extraction of extended X-ray absorption fine structure information from the experimental data using the wavelet transform. *Anal. Commun.*, **35**, 135–137.

16 de Groot, F. (2005) Multiplet effects in X-ray spectroscopy. *Coord. Chem. Rev.*, **249**, 31–64.

17 Carrier, X., Marceau, E., Carabineiro, H., Rodrıguez-Gonzalez, V., and Che, M. (2009) EXAFS spectroscopy as a tool to probe metal–support interaction and surface molecular structures in oxide-supported catalysts: application to Al_2O_3-supported Ni(II) complexes and ZrO_2-supported tungstates. *Phys. Chem. Chem. Phys.*, **11**, 7527–7539.

18 Ressler, T., Dorn, U., Walter, A., Schwarz, S., and Hahn, A.H.P. (2010) Structure and properties of $PVMo_{11}O_{40}$ heteropolyoxomolybdate supported on silica SBA-15 as selective oxidation catalyst. *J. Catal.*, **275**, 1–10.

19 Safonova, O., Deniau, B., and Millet, J.M.M. (2006) Mechanism of the oxidation–reduction of the MoVSbNbO catalyst: in operando X-ray absorption spectroscopy and electrical conductivity measurements. *J. Phys. Chem. B*, **110**, 23962–23967.

20 Topsøe, H., Clausen, B.S., and Massoth, F.E. (1996) Catalysts characterization, in *Catalysis Sciences and Technology* (eds. R. Anderson and M. Boudart,), Springer, Berlin, pp. 31–33.

21 Koningsberger, D.C. and Prins, R. (eds.) (1988) *X-Ray Absorption – Principles, Applications, Techniques of EXAFS, SEXAFS and XANES*, John Wiley and Sons, Ltd., Chichester.

22 Clausen, B.S. and Topsøe, H. (1996) Sulfide catalysts, in *X-Ray Absorption Fine Structure for Catalysts and Surfaces* (ed. Y. Iwasawa), World Scientific, Singapore, pp. 235–256.

23 Clausen, B.S., Lengeler, B., Candia, R., Als Nielsen, J., and Topsøe, H. (1981) EXAFS studies of calcined and sulfided Co–Mo HDS catalysts. *Bull. Soc. Chim. Belg.*, **90**, 1249–1259.

24 Thomazeau, C., Geantet, C., Lacroix, M., Harlé, V., Benazeth, S., Marhic, C., and Danot, M. (2001) Two cation disulfide layers in the $W_xMo_{(1-x)}S_2$ lamellar solid solution. *J. Solid State Chem.*, **160**, 147–155.

25 Thomazeau, C., Geantet, C., Lacroix, M., Danot, M., and Harle, V. (2005) EXAFS characterization of new active phases for catalytic hydrotreatment: two cations disulfide layers in the $Mo_xMo_{(1-x)}S_2$ lamellar solid solution. *Oil Gas Sci. Technol. Rev. IFP*, **60**, 781–790.

26 Mazoyer, P., Geantet, C., Diehl, F., Pichon, C., Nguyen, T.S., and Lacroix, M. (2005) *In situ* EXAFS study of the sulfidation of a

hydrotreating catalyst doped with a non chelating organic additive. *Oil Gas Sci. Technol. Rev. IFP*, **60**, 791–799.

27 Benkhaled, M., Morin, S., Pichon, C., Thomazeau, C., Verdon, C., and Uzio, D. (2006) Synthesis of highly dispersed palladium alumina supported particles: inflence of the particle surface density on physico-chemical properties. *Appl. Catal. A: Gen.*, **312**, 1–11.

28 Bazin, D., Guillaume, D., Pichon, C., Uzio, D., and Lopez, S. (2005) Structure and size of bimetallic palladium–platinum clusters in an hydrotreatment catalyst. *Oil Gas Sci. Technol. Rev. IFP*, **60**, 801–813.

29 Somorjai Guyot-Sionnest, N. (1991) Structural evolution of $PtAl_2O_3$ catalysts during reduction and hydrocarbon reaction: a high temperature, high pressure EXAFS study. Thèse Université Paris-Sud.

30 Lynch, J. (2001) EXAFS, in *Analyse Physico-Chimique des Catalyseurs Industriels* (ed. J. Lynch), Editions Technip, Paris, pp. 225–242.

31 Bensaddik F A., Dexpert, H., Bazin, D., Caballero, A., Villain, F., Didillion, B., and Lynch, J. (1995) *In situ* study by XAS of the sulfidation of the Pt and $PtRe/Al_2O_3$ systems. *Physica B*, **208/209**, 677–678.

32 Special issue (2009) Catalysis With Hard X-Rays, Part I. *Synchrotron Radiat. News*, **22** (1), 1–38.

33 Special issue (2009) Catalysis With Hard X-Rays, Part II. *Synchrotron Radiat. News*, **22** (2) 1–35.

13
Auger Electron, X ray and UV Photoelectron Spectroscopies

Wolfgang Grünert

13.1
Introduction

13.1.1
The Relation Between XPS, UPS, and AES

X-ray photoelectron spectroscopy (XPS), ultraviolet photoelectron spectroscopy (UPS) and Auger electron spectroscopy (AES) are surface-sensitive analytical techniques. They use diagnostic information encoded in the kinetic energy (KE) (E_{kin}) of low-energy electrons, which are emitted in the samples by different excitation processes. The surface sensitivity of these methods is due to the strong interactions of low-energy electrons with matter, which allow only electrons emitted in near-surface layers to escape from the sample without suffering inelastic collisions. Therefore, their average sampling depth roughly coincides with the inelastic mean free path of the electrons in the material under investigation.

In XPS and UPS, the absorption of an X-ray or ultraviolet (UV) photon drives the emission of a (photo)electron. As long as the emitting atom is in the gas phase, the KE of the photoelectron is the difference between the photon energy absorbed ($h\nu$) and the binding energy (E_B), which is characteristic for the atomic or molecular orbital from which the electron was ejected and is related to the (joint) vacuum level (Figure 13.1a). For solids exemplified by a metal, contact between the sample and the spectrometer causes their Fermi levels to equalize and their vacuum levels to disagree (contact potential difference). The energy balance (Figure 13.1b) now includes the work function of the spectrometer ($e\phi_{spec}$), which can be easily calibrated, and the binding energy is related to the Fermi level [complications arising with non-conducting samples are discussed later (Section 13.2.1.3)]. The driving force of the Auger emission is the energy released when an electron of a higher level (binding energy $E_{B,2}$, see Figure 13.2) fills a hole previously created in a lower level (binding energy $E_{B,1}$). The energy balance of the Auger transition follows from that of XPS (Figure 13.1b) by replacing the driving force $h\nu$ by $E_{B,1} - E_{B,2}$ and the binding energy of the emitted electron by $E_{B,3}$. It should be noted that the KE of Auger transitions

Characterization of Solid Materials and Heterogeneous Catalysts: From Structure to Surface Reactivity, First Edition. Edited by Michel Che and Jacques C. Védrine.
© 2012 Wiley-VCH Verlag GmbH & Co. KGaA. Published 2012 by Wiley-VCH Verlag GmbH & Co. KGaA.

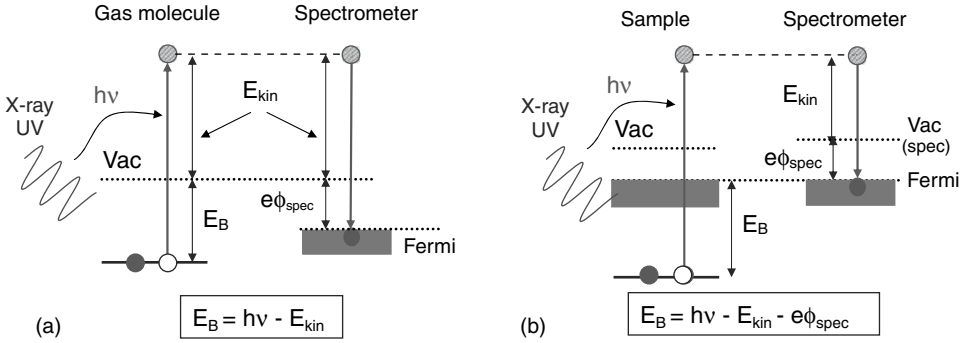


Figure 13.1 Energy levels in photoemission and analysis of photoelectrons. (a) Gas molecules; (b) solid (metal).

does not depend on an external excitation energy because the driving force is an intra-atomic transition. The primary core-hole can be created by electron bombardment, which is the basis of Auger electron spectroscopy and microscopy, or by previous emission of a photoelectron. In the latter version, the Auger transition is a decay process of the highly excited final state created by photoemission (see Figure 13.1b), that is, it is a secondary process accompanying XPS. Auger emission competes with X-ray fluorescence where the energy $E_{B,1} - E_{B,2}$ is released as a photon. Concerning AES, this chapter is largely confined to X-ray-induced Auger electron spectroscopy (XAES) and the relation of the latter to XPS.

Several texts can be recommended for further reading to those interested in more detailed coverage of these methods. *Surface Analysis by Auger and X-ray Photoelectron Spectroscopy*, edited by Briggs and Grant [1], is a standard book that should be present on the desks of all practitioners. It provides valuable information on many important aspects of the methods and data useful for practical work with them. Databases on XPS binding energies and AES KE, which were included in earlier editions (edited by Briggs and Seah [2]), are nowadays available on the Internet (e.g., [3]), and are cited

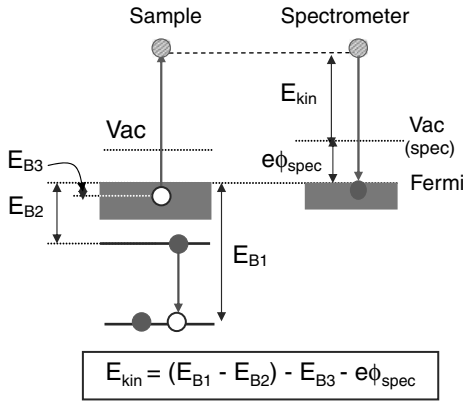


Figure 13.2 Energy levels in Auger emission and analysis of Auger electrons.

in [1] together with other important practical handbooks for XPS and AES. A comprehensive treatment of photoelectron spectroscopy was published by Hüfner [4], and UPS and its tremendous contributions to the study of band structures of metals and alloys was well described by Ertl and Küppers [5]. A good overview over the older literature was presented by Védrine [6].

13.1.2 A Glimpse at History [1]

XPS and UPS are applications of the photoelectric effect discovered by Hertz in 1887. Experiments in which photoelectrons obtained by X-irradiation of metals were velocity selected in a magnetic field were reported as early as 1907 [7]. At that time, early XPS took advantage of β-ray spectroscopy which required energetic differentiation of electrons as well. The spectra measured in the first two decades of the last century, which were obtained primarily to elucidate the electronic structure of matter, consisted only of asymmetric bands led by sharp edges because the XPS lines on top of the edges could not be resolved by the equipment available. Later, the competition of X-ray spectroscopy in electron structure studies discouraged the early activities in XPS.

After the Second World War, the potential of photoelectron spectroscopy for surface studies was recognized by Steinhardt and Serfass [8], although they used the rather high-energy Mo Kα line (17.5 keV) for excitation. The credit for developing XPS to a surface analysis tool routinely available to the scientific community belongs to Kai Siegbahn, who was awarded the Nobel Prize in 1981. The breakthrough was initiated by the development of improved (still magnetic) electron analyzers, which permitted the detection of lines on the (background) bands registered so far. Chemical shifts were observed and related to the differences in chemical states. As Siegbahn's group published exclusively in the journal of their Uppsala institute, this progress became widely appreciated only after publication of his book [9], which appeared in 1967 and also popularized Siegbahn's name for the method: ESCA (electron spectroscopy for chemical analysis). Shortly after, in 1969, the first commercial instruments appeared, now with electrostatic analyzers, the development of which had also been advanced by the Uppsala group. The potential of XPS and its application to various types of materials was explored all over the world from this time on – only in the (nowadays) Lawrence Berkeley National Laboratory had the method already been available following the purchase of one of Siegbahn's instruments in 1960. However, only in the early 1970s was attention focused on the surface sensitivity of XPS, inspired, for example, by the interest of the (petro)chemical industry in the surface properties of their catalysts.

The Auger effect was discovered by Pierre Auger in 1923 during cloud chamber experiments designed to visualize atomic excitations and consecutive processes with Ar gas. Instead of observing the traces of the primary photoelectrons and of consecutive photoemissions caused by secondary fluorescence photons starting at different points, primary and secondary traces started at the same points as if the fluorescence photon was reabsorbed in the same atom. Taking advantage of a prediction by Rosseland [10], Auger finally interpreted his observation as being due

to a nonradiative transition [11] which now bears his name. Not until nearly 30 years later were Auger transitions detected in the secondary electron background of solids by Lander [12], who also observed chemical shifts of Auger lines and predicted a surface analytical potential of the Auger effect. Given the frequent interference of the often broad Auger lines with uneven backgrounds, the practice of recording the spectra in the first derivative (started by Harris in 1964) was an important move. There was some priority conflict on this point as papers by Harris were delayed by referees while a colleague to whom he had communicated his approach realized that he could do the same with his low-energy electron diffraction (LEED) grids and preceded Harris with his report ([13, 14]). Still, measuring Auger electron spectra with LEED optics was an achievement on its own. It has since enabled many surface scientists to judge the purity of their substrates up to present times, and triggered the determination of realistic inelastic electron mean free path data earlier than in the field of XPS. While the LEED–AES combination was also offered in commercial instruments, the introduction of the cylindrical mirror analyzer (CMA) in the 1970s offered a strongly improved signal-to-noise ratio (for more information on instrumentation, e.g., the analyzer types, see Section 13.3.1). This has remained the standard configuration in dedicated Auger electron spectrometers.

13.2
Sources of Analytical Information

13.2.1
XPS Binding Energies

13.2.1.1 Parameters Affecting XPS Binding Energies

From Figure 13.1b, it is obvious that the binding energy (E_B) of a photoelectron is related to the energy of the ionized electron level, that is, it indicates the emitting element, the ionized orbital, and, in a finer energy resolution, also the oxidation state of the atom. With the excitation energies usually employed in laboratory XPS (Mg Kα, 1253.6 eV; Al Kα, 1486.6 eV), the most intense lines arise from atomic core levels. Valence states or molecular orbitals, which carry the binding information, can also be measured although with low intensity and poor energy resolution due to the intrinsic linewidth of the excitation radiation (cf., Section 13.3.1). Valence-band spectroscopy is therefore a domain of UPS, whereas XPS provides primarily atomic information. XPS would easily differentiate several cations and anions present in the surface region of a sample, but would often be unable to elucidate which cation is coordinated by which anion. However, although XPS is largely a surface-sensitive technique for the analysis of elements and their oxidation states, it also offers features that unveil structural information in favorable cases. These are often related to final state effects (see below).

In the photoemission process, the energy of the initial atom (ion) with full configuration of n electrons plus the energy of the incident photon are balanced with the energy of the same atom (ion) after ionization of the ith shell plus the KE of

the photoelectron:

$$E_{\mathrm{ini}}(n) + h\nu = E_{\mathrm{fin}}(n{-}1, i) + E_{\mathrm{kin}} \tag{13.1}$$

Together with the energy balance of the measurement (cf. Figure 13.1b)

$$E_{\mathrm{B}} = h\nu - E_{\mathrm{kin}} - e\phi_{\mathrm{spec}} \tag{13.2a}$$

this yields

$$E_{\mathrm{B}}(i) = E_{\mathrm{fin}}(n{-}1, i) - E_{\mathrm{ini}}(n) - e\phi_{\mathrm{spec}} \tag{13.2b}$$

Binding energies are therefore the differences between the total energy of the final ionized state of the emitting atom/ion and its state prior to photoionization. The work function term $e\phi_{\mathrm{spec}}$ reflects the reference of the binding energy scale to the Fermi level instead of the vacuum level (cf., Figure 13.1a and b). Frequently, chemical shifts are discussed which are binding-energy differences between the element in an unknown sample and in a reference state, often the elemental (or metallic) state. In this case, the work function term is canceled anyway.

Binding energy data are often discussed in terms of the major quantities determining them. These are properties of the atom/ion before photoionization (largely the orbital energies ε_i of the states to be ionized) and of the final (additionally) ionized state, which reflect the immediate response of the electron system to the emerging core hole ("relaxation"). Initial and final state energies in Eqs. (13.1) and (13.2b) are often understood with the tacit assumption that there is no electric field at the location of the emitting atom, which would affect both the KE of the photoelectron and the energy of the charged final state. In reality, this is not usually the case, and as such the influence of the electric field (the Madelung field in ionic compounds) is a third significant term in the discussion of binding energies. For chemical shifts ΔE_{B}, this is

$$\Delta E_{\mathrm{B}} = \Delta\varepsilon_k + \Delta E_{\mathrm{rel}} + \Delta V_{\mathrm{M}} \tag{13.3}$$

where the first term on the right-hand side represents initial-state effects, the second represents final state effects and the third is the Madelung term.

As the orbital energies usually scale with the formal charge on the emitting atom, the initial-state contribution is the origin of the well-known rule that XPS binding energies tend to increase by an increment of 0.8–1 eV per unit increase in the formal oxidation state. Final-state effects and the Madelung term cause the numerous deviations from this rule. The final state effects cover electronic effects by which the system attempts to screen the emerging positive charge in the core level: contraction of external shells, polarization of electron density from neighboring atoms (in nonconducting materials), and conduction (in metals). As the intra-atomic effects do not depend on the chemical state of the emitting atom, only extra-atomic contributions to relaxation are of interest for chemical shifts.

Figure 13.3 shows that the linear relation between binding energy and oxidation state is indeed a useful rule of thumb, but it is by no means more than that. Some deviations from this rule are also presented. They might be discussed in terms of a ligand effect: the fluoride "ligand" would increase the charge on sulfur relative to the

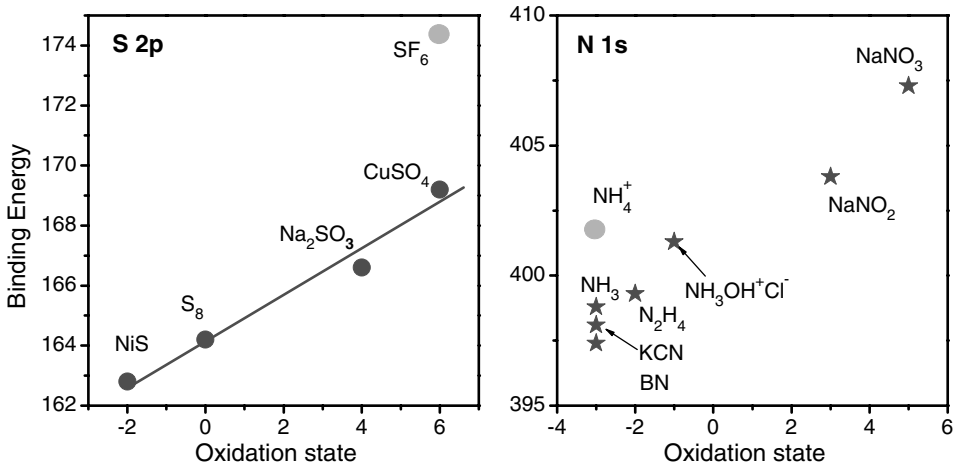


Figure 13.3 Examples for the dependence of binding energies on formal oxidation states.

oxygen "ligand" due to its higher electronegativity. Indeed, linear correlations between binding energies and estimated charges on the central atom have been reported to hold for a variety of counter ions, for example, in Ni compounds [15]. The ligand effect does not rely on the initial state alone as the chemical change will also affect the final state, for example, via the polarizability. It is one of the features that sometimes offers the chance to identify cation–anion relations in the XPS sampling region, and therefore provides an element of structural sensitivity

Deviations of binding energies from the linearity rule can be expected when an ionic compound exhibits metallic conductivity. Thus, a chemical shift of 3.4 eV relative to Ru metal (280.2 eV) was found for the Ru $3d_{5/2}$ signal of Ru(IV) supported on γ-Al_2O_3 [16], which would agree well with the linearity rule. RuO_2, however, exhibits a chemical shift of just 0.7 eV, which is most likely due to its metallic conductivity.

Among the Mo and W oxides, the chemical shift between Mo 3d and W 4f in the M (VI) oxides MoO_3 and WO_3 and the M(IV) oxides MoO_2 and WO_2 is as large as 3.2 eV, which was the basis of strongly nonlinear relations between binding energy and oxidation state proposed by several groups [17–21]. However, MoO_2 and WO_2 exhibit metallic conductivity caused by structural features: rows of M−M triple bonds with high electron mobility along shear planes, in which two-thirds of the M^{4+} cations are engaged. For these cations, an extra contribution of final state effects is very likely. Binding energies of Mo(IV) or W(IV) oxo species *in the absence* of this structural feature, for example, in interaction with an oxide support, might well be different, as was indicated by Haber *et al.* [22] and supported by other studies [23, 24]. Notably, for tungsten chlorides, a binding energy shift of just 1.7 eV was found between WCl_6 and WCl_4 [25]. Evidence offered to support the alternative concept of a linear relation between Mo or W binding energies and oxidation states in an oxide environment [22] has not resolved the controversy because the spectra of partially reduced oxides are

difficult to analyze owing to the coexistence of a multitude of oxidation states. A plausible assignment of the oxidation state in the active site precursors for olefin metathesis [M(IV) – instead of what would have been identified as M(III) or M(II)] [26, 27], which was within the mainstream of the literature on analogous homogeneous metathesis catalysts, provided only indirect support for the spectroscopic approach applied. Apparently the nonlinear relation between binding energy and oxidation states as outlined, for example, in [18] is still very much in use today, but it should be kept in mind that MoO_2 and WO_2 are highly problematic references for Mo (IV)/W(IV) in an oxide environment as long as the presence of the related structural motif (short M−M bonds) is not safe.

Relaxation effects are also thought to provide a major contribution to positive chemical shifts observed with extremely disperse metal particles relative to the bulk metal, which range up to 1 eV. It is assumed that the limited number of conduction electrons available at very small size or the loss of metallic properties decreases the screening effects. These shifts should not be mixed up with the surface core level shifts observed mostly with d metals, although the latter will certainly contribute to the former. Surface core level shifts are caused by band compression at the surface due to a decreased number of neighbors and the resulting shifts of the band centers. They originate only from the outermost surface atoms and their signs and magnitudes depend on the position in the d rows.

Changes in the Madelung term in Eq. (13.3) were suggested to explain the trends of the binding energies measured for the components of zeolites [28]. It had been found that these binding energies exhibit pronounced variations with the Si/Al ratio (see Figure 13.4a), but also between H-form and cationic forms, which could be explained with electron transfer only by involving unphysical assumptions. Assessments of the electric field at the various framework and cation positions using simple electrostatic

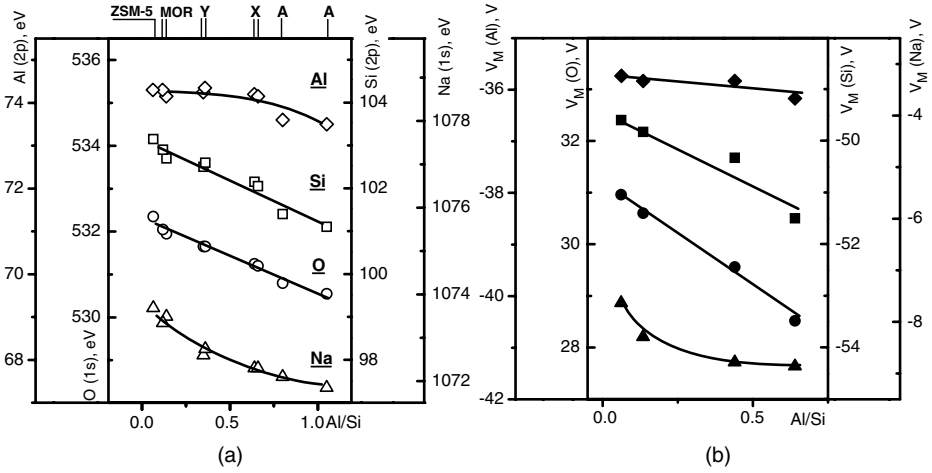


Figure 13.4 Dependence of binding energies and averaged Madelung potentials in zeolites on the Al content: (a) binding energies (eV); (b) averaged Madelung potentials. Based on data from [28].

models showed that the experimental trends of the binding energies correlated well with the averages of the calculated Madelung potentials (Figure 13.4).

The examples provided above illustrate the problem of correct XPS signal assignment merely on the basis of binding energies. In unknown samples with elements in coexisting oxidation states, sometimes only the signals with the highest and the lowest binding energy can be unanimously identified on the basis of plausibility arguments; beyond that, assignments often have to remain tentative. Even the metallic state does not offer a reliable benchmark because binding energies may vary for very small particles. Apart from the positive shifts mentioned above, negative shifts have often been observed and not yet conclusively explained.

Figure 13.5 shows spectra of supported Ru catalysts (0.5 wt% Ru) reduced under identical conditions [29]. On TiO_2, the metal appears at a Ru $3d_{5/2}$ binding energy identical with that of bulk Ru (curves a–c, linewidth varying due to differential

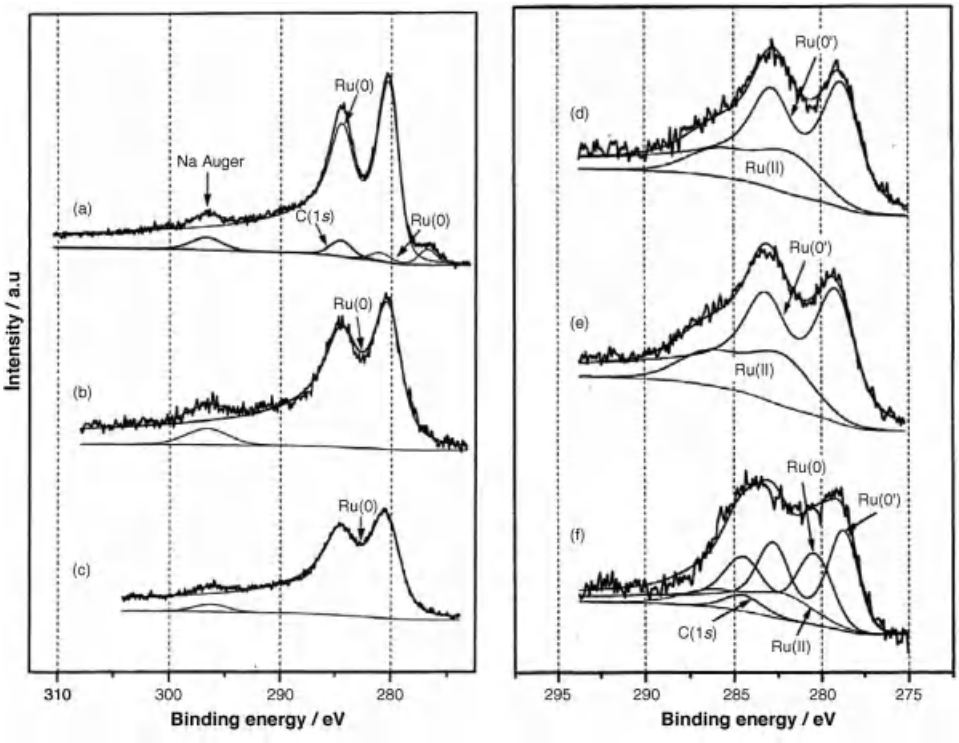


Figure 13.5 Negative chemical shifts of Ru $3d_{5/2}$ of metallic Ru particles in supported Ru catalysts. Curves (a–c) 0.5 wt% Ru/TiO_2; curves (d–f) 0.5 wt% Ru/Al_2O_3. Reduction conditions: (a) and (d) 20% H_2/N_2, 823 K, 2 h; (b) and (e) as (a) and (d), followed by 10% methane, 2% O_2 in N_2, 30 min, 773 K; (c) and (f) as (b) and (e), treatment in methane–O_2 mixture at 973 K. Reproduced from [29], C. Elmasides *et al.*, XPS and FTIR study of Ru/Al_2O_3 and Ru/TiO_2 catalysts: reduction characteristics and interaction with a methane–oxygen mixture, *J. Phys. Chem. B*, 1999, **102**, 5227, with permission from the American Chemical Society.

charging, see Section 13.2.1.3), and the same was observed on Al_2O_3 at a higher Ru content [29]. In 0.5% Ru/Al_2O_3, the Ru metal particles exhibited, however, a clear decrease in binding energy [Ru(0)′]. Under more drastic reduction conditions, the analysis of the complex spectra strongly suggested the coexistence of both forms (curve f). It was therefore concluded that the negative shift was associated with a higher dispersion and a stronger, but unknown, influence of the support on the particles [29]. Negative binding energy shifts have been reported for many systems prepared by reduction of oxide precursors or by vacuum deposition [30–32], among them Ag and Au on TiO_2 [33–36]. These shifts have been ascribed to several effects, as discussed in some detail elsewhere [33], but there does not seem to be a conclusive interpretation for the experimental data so far. Thus, electron transfer from reduced support sites to the metal as discussed recently with respect to the negative shift of Au on TiO_2 [36] could hardly explain the data shown in Figure 13.5.

The cautious attitude towards using XPS binding energies as a key tool for the identification of oxidation states does not mitigate against the analytical potential of the method, it should rather encourage its appropriate use. Obviously, the information on oxidation states is strongly superimposed by structural influences. Assignments of remarkable reliability are possible in situations where broad experimental data sets can be correlated with data from different techniques or are to be rationalized by chemical arguments. An example of the first approach is assignments of surface and subsurface oxygen species on and in different metals via their O 1s binding energy, which have been substantiated by reference to related X-ray absorption measurements [37, 38], to simultaneous catalytic measurements [39], and to depth-sensitive analysis (variation of excitation energy) [40]. The assignment of polymer surface groups via their C 1s binding energies ([1], Appendix E; [2], Chapter 9) or of nitrogen in organic and biomolecules (including active pharmaceutical ingredients) via its N 1s line [41] illustrates the latter. Even here, the number of species appearing in relatively narrow binding-energy regions may cause some ambiguity. As long as such support is not available, it is highly recommended to take advantage also of other spectral features as highlighted in Sections 13.2.2 and 13.2.4.

13.2.1.2 **Theoretical Prediction of XPS Binding Energies**

A theoretical prediction of the binding energy $E_B(i)$ of a level i will require the calculation of the total energies of both the ground state and the ionized state of the emitting atom/ion [see Eq. (13.2b); in the following the term $-e\phi_{spec}$ is dropped for convenience]. This is a considerable challenge for the final state, which is a highly excited state due to the hole in a core level. The simplest approach is to represent the states involved by single configuration wavefunctions and to calculate their orbitals ϕ_i and orbital energies ε_i by quantum chemical methods. If one can assume that the orbitals occupied in the initial and final states are identical, the binding energy $E_B(i)$ is simply given by the negative energy ε_i of the orbital from which the electron was ionized [Koopmans theorem (KT) [42]]:

$$E_B(i) = -\varepsilon_i \tag{13.4}$$

The appealing simplicity of the KT approach lies in the fact that the treatment of the ionized state is avoided and only the orbital energies for the ground state of the neutral system are calculated. This can be done both by DFT (density functional theory) or wavefunction-based methods [Hartree–Fock or self-consistent field (SCF)] yielding either Kohn–Sham or Hartree–Fock orbitals. The KT approach can be employed for (embedded) cluster calculations and also for periodic, that is, band structure, calculations. However, since this approach uses only the properties of the neutral system prior to ionization, it can only cover the initial state effects.

Unfortunately, the absolute values of core-level binding energies obtained with the KT approach have serious errors. For the 1s core levels of the first-row atoms, they are too high by 10–20 eV if Hartree–Fock orbitals are used. The errors for Kohn–Sham orbitals in DFT calculations are generally smaller, but depend strongly on the functional employed in the calculation [43, 44]. Relative energies (binding-energy shifts), for instance for C 1s core levels of C atoms in different chemical environments, are mostly fairly reliable, with an accuracy of 0.5–1.0 eV. Therefore, many authors refrain from calculating absolute values of core-level binding energies, but use a uniform shift to align the calculated spectrum with experimental data [45].

The main source of error in the KT approach is that the relaxation of the electronic wavefunction after ionization (final state effects) is completely ignored. The error is particularly large for ionizations from localized core orbitals, but considerably less for delocalized valence orbitals, for example, for UPS. There are also smaller additional errors due to electron correlation and relativistic effects, which will not be considered here. The easiest way to account for relaxation effects is Slater's "transition-state concept" [46, 47]. In this approach, the orbitals are determined for an artificial state, in which the occupation of the orbital ϕ_i to be ionized is reduced by $^1/_2$ instead of 1. The binding energy $E_B(i)$ is again given by the orbital energy:

$$E_B(i) = -\varepsilon_i\left(n_i - \frac{1}{2}\right) \tag{13.5}$$

and it can be shown that this is correct to second order in the occupation numbers [46, 48].

Whereas wavefunction-based methods have problems with a noninteger number of electrons, this approach is frequently used with surprisingly good results in DFT calculations, and can be employed both in periodic [49] and in cluster calculations, as implemented, for instance, in the StoBe code [50, 51]. The disadvantage is, of course, that initial and final state effects cannot be determined separately.

The most rigorous way to treat relaxation effects is to perform separate calculations for the (core-level) ionized state in addition to the neutral ground state and to evaluate the binding energy through Eq. (13.2b). This can be done in the Hartree–Fock (SCF) approximation, ("ΔSCF"), or by DFT ("ΔKS", ΔKohn–Sham). Since core-level ionized states are highly excited states of the respective ion, care has to be taken to avoid convergence to a lower state or even the ground state of the ion. Several schemes have been proposed for this purpose, for instance, the "frozen core hole" (FCH) approach [52, 53]. The ΔSCF and ΔKS approaches are most frequently used for isolated molecules and for cluster models of extended systems. They yield both

Table 13.1 Calculated Zn 2p core level shifts in Zn metal and ZnO (relative to the free Zn atom, in eV [53]).

	Initial state	Final state	Total	Experimental [4, 58]
Zn metal	+2.4	−5.1	−2.7	−2.9
Bulk ZnO	−2.1	−1.0	−3.1	−2.9

absolute core-level binding energies and binding energy shifts with errors in the order of 1.0 eV or less [54, 55]. The numerical costs are, of course, higher than for the KT and transition-state methods since the final state also has to be calculated. The difficulty for periodic calculations is that the local positive charge due to the core ionization is repeated periodically and has to be neutralized. This is generally done in the spirit of the $z + 1$ approximation by removing one core electron and adding one valence electron in each cell [56, 57].

It should be noted that in all these approaches, the Madelung energy, or more precisely the change in the Madelung energy between the initial and final states, need not be added separately as in Eq. (13.3), since it is implicitly included in the orbital energies in the KT approach or in the total energies in the ΔSCF and ΔKS approaches. The interpretation of the terms "initial state effect" and "final state effect" therefore differs slightly between the communities of theoreticians and spectroscopists.

A nice example of the interplay of initial and final state effects and the performance of cluster calculations was presented by Staemmler and co-workers in their study of Zn XPS [52, 53]. In contrast to most other metals, the binding energies of the 2p (and 2s) core level of Zn are the same for Zn^0 in metallic Zn and for Zn^{2+} in ZnO. The explanation obtained by embedded cluster calculations with the ΔSCF method is presented in Table 13.1. The metallic behavior of Zn is caused by the promotion of the 4s electrons to 4p orbitals. This moves electronic charge from the Zn atom into the interstitial region, makes the Zn atom slightly positive and leads to an increased 2p binding energy and thus to a positive initial state effect. In the oxide, on the other hand, the four O^{2-} anions surrounding the Zn^{2+} cation create a negative Madelung field and cause a negative initial state effect which is larger than the positive initial effect due to the charge of the Zn^{2+} cation. The final state effects are both negative, but much larger in the metal than in the ion due to more effective screening in the former. Thus, initial and final state effects add up to nearly the same value. This example also shows that it might be seriously misleading to account only for the initial state effects by using the KT approach.

13.2.1.3 **Practical Aspects**

The determination of the XPS binding energy from a single line is straightforward. Upon compliance with good experimental practice (analyzer calibration, ground contact of sample, etc.), the data are well reproduced provided that there is electrical contact between the sample and spectrometer pinning the binding-energy scale to the joint Fermi level and allowing replacement of the ejected electrons in the sample by a sample current from the spectrometer. For non-metals, the measured binding energies are not referenced to the Fermi level for two reasons: the Fermi level is

ill-defined in most cases, and the ejected electrons cannot be sufficiently replenished by a sample current. As a consequence, the sample surface becomes positively charged to an extent that depends on the instrumental configuration. Usually, a steady state of the surface charge evolves or can be achieved by injecting low-energy electrons (flood-gun), except for UPS which is impossible with charged surfaces. In XPS/XAES, the scale of the KE (binding energy) is shifted by the surface charging and can be corrected by an internal standard (the binding-energy reference).

The C 1s line of adventitious carbon, which is a common contamination in instruments dedicated to the surface analysis of real-world samples, is often employed for this purpose. Its binding energy is set to a value typically observed on metal surfaces (284.5–285.0 eV used by different groups), thus providing an indirect reference of the binding-energy scale to the Fermi level of the instrument. The use of alternative references (e.g., the Au 4f line of Au particles evaporated on to the sample) seems to be in strong decline.

The binding energy reference introduces some problems due to which binding energies measured with nonconducting samples are less reproducible than those from conducting samples. The tacit assumption that all parts of the sample surface are equally charged is not necessarily fulfilled. Such "differential charging" may, for instance, occur in metal-supported systems with insufficient contact between metal and the support (e.g., metal particles segregated on to the external zeolite surface [59]). Another type of differential charging may occur with semiconductors, where sample reduction may cause a conductivity gradient perpendicular to the surface. This will primarily cause a line broadening (cf. Figure 13.5, curves a–c), but the line center may also shift relative to the signal of the reference carbon adsorbed on the external surface.

Other problems may originate from the unknown actual identity of the adsorbed carbon species, which are assumed to be hydrocarbons. If the predominant carbon is of different nature, a calibration error can result. In practical work, there are sometimes situations where it is clear that a referencing problem has occurred (all binding energies off the expected values to the same extent) without a conclusive explanation being available. Therefore, secondary binding-energy references are employed wherever possible: the measured binding energies are related to that of a component assumed to be invariable (often the cation signal of a catalyst support). As long as the secondary standard remains invariable to all chemical changes between samples or treatments applied, this approach can abolish some of the inconsistencies encountered in the practical use of the C 1s reference.

When several oxidation states of an element coexist, the individual binding energies may be assessed by fitting the experimental signal with contributions expected from the species. This topic will be discussed in some detail in Section 13.2.3.3.

13.2.2
The Analytical Potential of XPS Lineshapes

13.2.2.1 Spin–Orbit Splitting

Photoemission lines are generally doublets, except for those originating from s levels. The reason for this is the coupling between spin and angular momentum, which

results in different energies in parallel or antiparallel coupling. The binding-energy difference between the doublet components is an atomic constant and is therefore not influenced by the chemical state of the atom. Likewise, the intensity ratio between them is fixed: it is the multiplicity of the corresponding states, for example, 2:4 for $p_{1/2}$:$p_{3/2}$, 4:6 for $d_{3/2}$:$d_{5/2}$, and so on. However, superposition by multiplet splitting effects (see Section 13.2.2.4) can sometimes affect the measured splitting between spin-orbit components, and their intensity ratio can be affected by superimposed satellites (see Sections 13.2.2.2 and 13.2.2.4). If such a reason is unlikely, an untypical intensity ratio between spin–orbit components may indicate an incorrect choice of baseline (cf., Section 13.2.3.3).

13.2.2.2 **Charge Transfer Satellites**

In photoemission from a metal cation, the positive effective charge of the emerging core-hole attracts and stabilizes the external electron states ("intra-atomic relaxation"), among them the unfilled ones. Such empty cation states may downshift to energies just a few eV above the edge of the valence band, which gives rise to a new energy state originating from a hybridization of the valence band with the stabilized cation state. It may be populated by an electron from the valence band with a probability depending on the energy separation between valence band and the stabilized cation state and the degree of hybridization between them. The existence of this second (sometimes, e.g., Ce^{4+}, even a third) final state gives rise to two (or three) signals, the satellite(s) originating from the filled stabilized cation state(s), the main line with the usual cation electron configuration. These "shake-up satellites" appear at higher binding energies than the main line due to the energy required to access the stabilized cation state. They are highly useful features as their properties depend on the oxidation state of the emitting atom and also on the nature of the coordination sphere. The latter constitutes another element of structural sensitivity in XPS.

Satellites are observed with most first-row transition elements (charge transfer into d states) and with lanthanides (charge transfer into f states). Typical applications are the differentiation between Cu(II) and Cu(I) [61] (the latter is without a satellite due to its d_{10} configuration), between Co(II) and Co(III) [62], and between Ce(IV) and Ce (III) [63]. Likewise, Fe(III) and Fe(II) can be differentiated by their typical satellites [64]. The satellite structure of Ce(IV) and Ce(III) in an oxide environment is depicted schematically in Figure 13.6, where the typical labeling of the signal components is also given. The fitting of such signals is troublesome. Fortunately, the u‴ satellite, which originates from Ce(IV) alone, is not superimposed by any other line. Therefore, the conversion in reductions starting from Ce(IV) can be assessed via the ratio of this satellite to the whole signal [63].

The structural sensitivity of the satellites is illustrated in Figure 13.7, which compares the satellites of Fe(II) compounds on an energy scale related to the center of gravity of the signal. The intensity of the satellites depends significantly on the counter ion, which can be utilized to identify compounds having been formed in a sample. In favorable cases, the satellite structure can depend on the geometry of the coordination sphere even without change of the anion. One example is the ratio

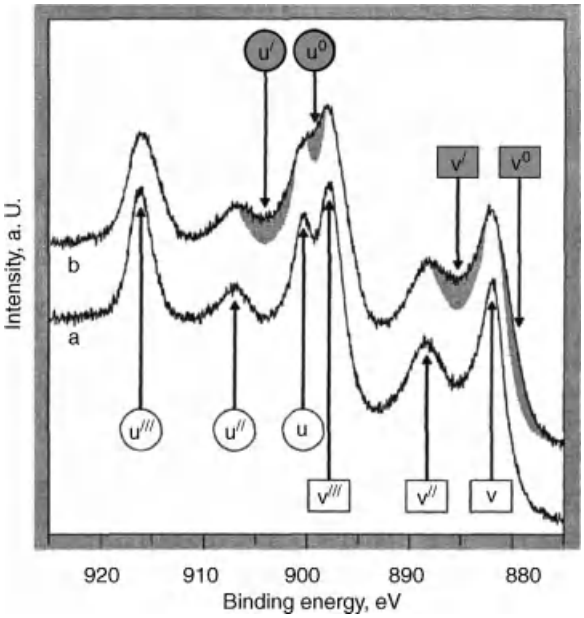


Figure 13.6 Ce 3d spectra of a 10% Ca/CeO_2 mixed oxide in different states: (a) as prepared; (b) after thermoevacuation at 550 °C. Ce^{4+}: components v, v″, and v‴ (Ce $3d_{5/2}$) and components u, u″, and u‴ (Ce $3d_{3/2}$). Ce^{3+} components v^0, v′ (Ce $3d_{5/2}$) and components u^0, u′ (Ce $3d_{3/2}$). From [60].

between satellite and main line of La $3d_{5/2}$ in LaY zeolites [67]. Variations of this ratio observed upon calcination of La^{3+}-exchanged NaY samples were ascribed to the well-known transition of the hydrated La^{3+} ion from the supercage into the β-cage, where it is coordinated largely by zeolite oxygen [68]. Figure 13.8, in which the satellite main line ratio of La $3d_{5/2}$ is compared between $LaCoO_3$ and a sample which was intended to contain $LaCoO_3$ hosted in MCM-41, reports a more recent application of this effect [66]. The spectra show clearly that the perovskite had not been formed in the mesopores, which was supported by the Co 2p spectra and X-ray absorption fine structure (XAFS) at the Co K edge. The favorable catalytic properties of the material were therefore assigned to a highly defective CoO_x phase.

13.2.2.3 **Other Shake-Up Type Satellites**

Similar shake-up processes can also occur in nonionic compounds, for example, organic matter or metals. They occur with atoms in conjugated unsaturated or in particular aromatic systems, where the excitation causing the satellite arises from a $\pi \rightarrow \pi^*$ transition [1]. These satellites are often observed in polymers and can also be used for diagnostic purposes [69].

In metals, a continuum of empty states is available above the Fermi level to form additional final state orbitals. Therefore, the shake-up processes result in line asymmetries instead of discrete satellites. The extent of line asymmetry is related

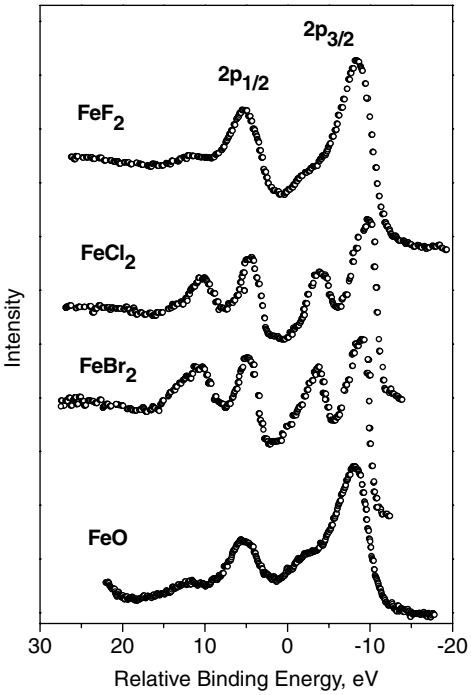


Figure 13.7 Fe 2p spectra of Fe(II) compounds. Based on data from [65].

to the density of states above the Fermi level and is large in the d metals and much smaller for metals with the Fermi level in the sp band. In the analysis of coexisting states the line asymmetry must be taken into account by appropriate line profiles. Significant differences in the line asymmetry of a metal on different supports (Ru/Al_2O_3, Ru/TiO_2 [29]) or on a support modified by a pretreatment (Pt/TiO_2 after reduction at different severity [70]) have been sometimes observed, which may suggest electronic effects in the metal–support interaction. This topic certainly deserves more attention.

Plasmon excitations are additional channels to which energy can be transferred during photoemission. Such plasmon-loss features are, however, observed only with clean metal surfaces.

Shake-off satellites originate from transitions during which an electron to which energy is transferred during photoemission, is also ejected. Consequently, they are asymmetric features with an onset and a smooth decay, which are normally difficult to observe in the spectra.

13.2.2.4 **Multiplet Splitting**

Photoemission leaves behind an unpaired core electron, the magnetic moment of which can interact with that of unpaired valence electrons. This creates a number of final states with different energies and multiplicities. In the upper core levels, the effects can be strong enough to cause splitting of lines. With the lower core levels

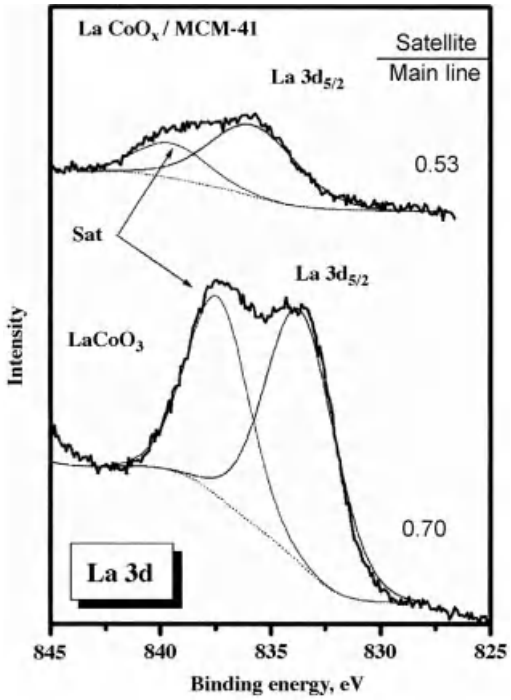


Figure 13.8 Analysis of a catalyst intended to be $LaCoO_3$ in MCM-41 via the La $3d_{5/2}$ satellite structure. Reproduced from [66], E. V. Makshina *et al.*, Characterization and catalytic properties of nanosized cobaltate particles prepared by *in situ* synthesis inside mesoporous molecular sieves, *Appl. Catal. A*, 2005, **312**, 59, with permission from Elsevier.

usually studied due to their more favorable interaction cross-sections, multiplet splitting still causes line broadening, asymmetries, and shifts in signal position. This is exemplified in Figure 13.9, where calculated 2p, 3p, and 3s spectra of Cr_2O_3 are depicted, which agree very well with the experimental spectra [71].

Multiplet splitting has both favorable and unfavorable consequences for practical work with XPS. The broad and asymmetric lineshapes often caused by it affect detection limits and complicate identification of useful charge-transfer satellites and analysis of signals from coexisting states. On the other hand, as the multiplet components depend on the magnetic moment created in the core level, the effect is different for the two spin–orbit components. Therefore, the binding-energy difference between these components can be modulated depending on the electron configuration of the emitting ion, which has considerable diagnostic potential. Thus, the experimental spin–orbit splitting varies between 16.0 eV in high-spin Co^{2+} ions and 15.0 eV in diamagnetic Co compounds [Co(III)] [72, 73], in Cr compounds the splitting varies between 9.1 eV [Cr(VI) and Cr(0)] and 9.8 eV [Cr(III)], and for Ni between 18.4 eV [Ni^{2+} in NiO; in $Ni(OH)_2$, 17.9 eV!] and 17.2 eV [Ni(0)] [72, 74]. Anomalous values for spin–orbit splitting have sometimes been found, for example,

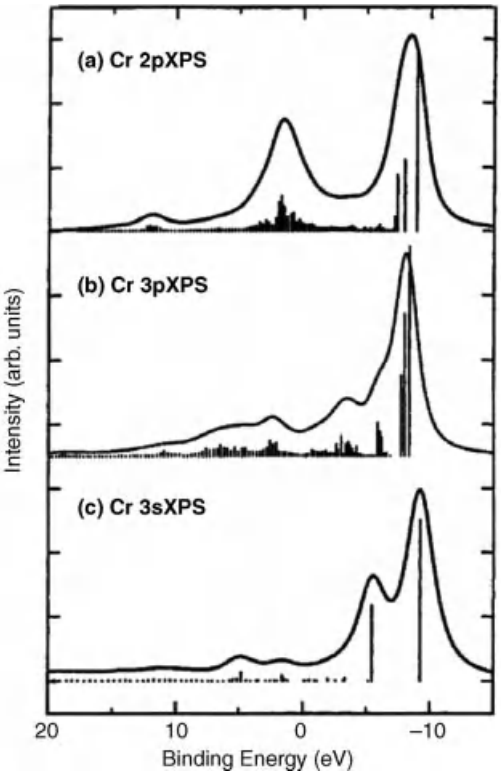


Figure 13.9 Influence of multiplet splitting on the lineshape of Cr XPS lines (calculated spectra with 10 Dq = 1.2 eV). Reproduced from [71], T. Uozumi *et al.*, Theoretical and experimental studies on the electronic structure of M_2O_3 (M = Ti, V, Cr, Mn, Fe) compounds by systematic analysis of high-energy spectroscopy, *J. Electron Spectrosc. Relat. Phenom.*, 1997, **83**, 9, with permission from Elsevier.

down to 9.2 eV for Cr(III) in probably very high dispersion [75, 76], up to 9.6 eV for Cr (0) in phases coreduced with Pt (probably alloyed) [75], and not yet explained conclusively. Therefore, more attention to this useful tool of structural differentiation is certainly desirable.

13.2.3
Surface Sensitivity: Working with XPS Intensities

13.2.3.1 Homogeneous and Inhomogeneous Sampling Region

The intensity of an XPS line is given by

$$I = FTDA\Delta\Omega\sigma \int_0^\infty \varrho(z)\phi(z,\Theta)\mathrm{d}z \tag{13.6}$$

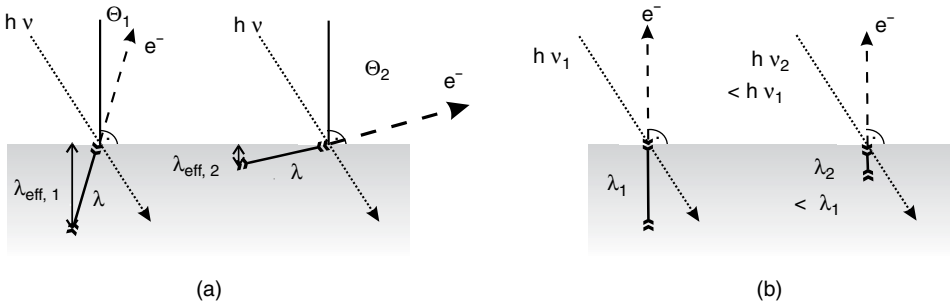


Figure 13.10 Measurement geometries for angular resolved and excitation-energy resolved XPS. Θ = photoemission angle.

where F = incident flux, T = analyzer transmission, D = detector sensitivity, A = analyzed area, $\Delta\Omega$ = solid angle of analysis, and σ = interaction cross-section for electron emission. Under the integral, $\varrho(z)$ describes the variation of the atomic concentration ϱ (atoms nm^{-3}) along the depth coordinate z, and ϕ is the probability that an electron emitted at a depth z will reach the surface along a trajectory inclined to the surface normal by an angle Θ without losing its KE (Figure 13.10). A similar equation is valid for AES. Often one compares intensity ratios I_A/I_B to obtain elemental ratios ϱ_A/ϱ_B, then factors not depending on the signals involved (F, A, $\Delta\Omega$) will cancel.

The elemental concentration in the near-surface region, which is the target of the analysis, is under the integral in Eq. (13.6). As it may vary along the depth coordinate z, the signal intensity will be an average over contributions from all depths z, from which photoelectrons can still escape from the solid without losing their analytical information encoded in the KE. The integral describes the average where the concentrations are weighted with the photoelectron escape probability. Traditionally, for this "escape function" the exponential form of the Lambert–Beer law was assumed, where the characteristic length λ was interpreted as the inelastic mean free path (IMFP) The intensity contribution from z is then related to that created by the outermost surface layer by

$$\phi = \frac{I(z)}{I(z=0)} = \exp\left(-\frac{z}{\lambda\cos\Theta}\right) \tag{13.7}$$

which becomes $\phi = \exp(-z/\lambda)$ for analysis along the surface normal (see Figure 13.10). Therefore, the intensity is a Laplace transformation of the concentration profile (analyzer transmission and detector sensitivity combined to an instrumental sensitivity S):

$$I \propto S\sigma \int_0^\infty \varrho(z)\exp\left(-\frac{z}{\lambda\cos\Theta}\right)\mathrm{d}z \tag{13.8}$$

The intensity decay along the straight photoelectron trajectory is, however, caused not only by inelastic collisions but also by elastic scattering which deflects electron intensity without loss of energy. This and other effects (multiple and nonisotropic scattering) violate the exponential decay law in Eq. (13.7). It can, however, still be used to approximate the real situation when λ is taken as an (effective) attenuation length, which is typically 20–30% shorter than the IMFP (for more details, see [77, 78]).

In the kinetic energy (KE) range most relevant for XPS with laboratory sources (200–1500 eV), the effective attenuation length λ_{AL} scales with $(KE)^n$, where $0.5 < n < 1$. The depth λ_{AL}, from which an intensity decays to $100/e \approx 36.8\%$, is the average sampling depth. It ranges from 1 to 3 nm depending on the KE. Obviously, the experimental signal will also contain information from layers below; therefore, the depth of $3\lambda_{AL}$, from which 95% of the signal originates, is sometimes referred to as the "sampling depth". In porous solids, the (average) sampling depths are increased in proportion to the void fraction.

Inelastic mean free paths were determined for many materials from optical measurements and correlated with KE by different approaches. From this work, equations emerged that allow the prediction of the IMFP of electrons in any solid, the best known being the TPP-2M equation of Tanuma, Powell, and Penn [79]:

$$\lambda(\text{Å}) = \frac{E_k}{E_p{}^2\left[\beta \ln(\gamma E_k) - C E_k{}^{-1} + D E_k{}^{-2}\right]} \tag{13.9}$$

where the number of valence electrons, the density of the solid, and its atomic (molecular) weight are required to calculate the free-electron plasmon energy E_p and correlations of the parameters β, γ, C, and D with the same properties and (for nonconductors) the bandgap energy E_g are available [78, 79]. Examples of the predictive power of Eq. (13.9) are given in Figure 13.11. Apparently, the TPP-2M equation is a useful tool for the estimation of IMFP data for a wide range of solids.

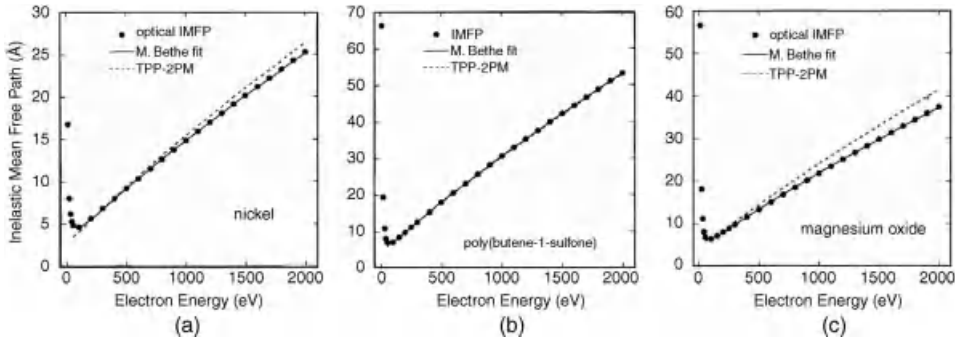


Figure 13.11 Comparison of experimental and predicted (TPP-2M) inelastic mean free path data Reproduced from [78], S. Tanuma, Electron attenuation lengths, in *Surface Analysis by Auger and X-Ray Photoelectron Spectroscopy* (Eds. D. Briggs and J.T. Grant), IM Publications, Chichester and Surface Spectra Ltd., Manchester, 2003, p. 235, with permission from IM publications Ltd.

More details and a discussion and calculation of (effective) attenuation lengths can be found elsewhere [78].

Unfortunately, the satisfactory description of the escape function ϕ in Eq. (13.6) does not help with the problem of the unknown concentration depth profile $\varrho(z)$. Its representation will usually require more than one parameter, and its determination would therefore require measurements with (significantly) different escape depths λ or at different photoemission angles Θ (see Section 13.2.3.2). In standard analysis, with a measurement using Al Kα or Mg Kα irradiation at a single photoemission angle (usually $\Theta = 0$), there is no real alternative to neglecting the concentration gradient in the sampling region, that is, $\varrho_i(z) = \varrho_{i,\mathrm{av}}$. Integrating Eq. (13.8) for constant $\varrho_{i,\mathrm{av}}$ we obtain the following equation for the intensity ratio between elements A and B:

$$\frac{I_\mathrm{A}}{I_\mathrm{B}} = \frac{\sigma_\mathrm{A}(h\nu)S\left(E_{\mathrm{kin,A}}\right)\lambda_\mathrm{A}\left(E_{\mathrm{kin,A}}\right)\varrho_\mathrm{A}}{\sigma_\mathrm{B}(h\nu)S\left(E_{\mathrm{kin,B}}\right)\lambda_\mathrm{B}\left(E_{\mathrm{kin,B}}\right)\varrho_\mathrm{B}} = \frac{N_\mathrm{A}\varrho_\mathrm{A}}{N_\mathrm{B}\varrho_\mathrm{B}} \tag{13.10}$$

which is the basis of the ubiquitous concentration analysis via sensitivity factors. Obviously, these sensitivity factors, which are provided in handbooks and in XPS data handling software, contain different kinds of information: interaction cross-sections σ_i of the ionized orbitals at the incident energy $h\nu$, tabulated, for example, in [80, 81], escape depths λ_i ($E_{\mathrm{kin},i}$), which might be approximated by results from the TPP-2M equation [78], but also instrumental properties [$S(E_{\mathrm{kin,i}})$]. For the latter, properties encountered in the most widespread instrumental configurations are usually assumed. It may therefore be useful to check their validity for one's own instrument.

As the assumption of a homogeneous sampling region is difficult to avoid in routine XPS analysis, it is important to qualify the results as averages over the depth coordinate. Homogeneity of this region cannot, of course, be at all taken for granted and is rather unlikely just for catalysts, and therefore no conclusions can be drawn from the data about the properties (elemental composition, oxidation states) of the outermost surface layer, which is of course of most interest in heterogeneous catalysis. This limitation does not really affect the importance of the method: quantitative analysis of species present in the near-surface layer remains highly relevant for catalyst research. It raises, however, the need to improve the surface sensitivity of XPS (see Section 13.2.3.2).

In fully segregated systems, Eq. (13.8) can be integrated with suitable assumptions about the structure of the system. If a component B is covered by a layer of A, it is straightforward to determine the thickness of the A layer by a single measurement of the intensity ratio. Likewise, one can determine the average size of segregated particles with an appropriate assumption about their shape [82]. A more refined model takes into account that in highly porous solids, photons originating from near-surface pores can travel through pore walls without losing their analytical information [83]. A method derived on this basis allows the assessment of the average particle dispersions in porous catalysts, which is important not so much for metals where powerful chemisorption techniques are available, but for nonmetallic materials.

13.2.3.2 Increasing the Surface Sensitivity of XPS

According to Eq. (13.8), the opportunities for enhancing the surface sensitivity are to increase the photoemission angle or to decrease the excitation energy. These methods, which at the same time offer some depth differentiation of the analytical information, are widely used, but their scope of application is different.

In angular resolved XPS (ARXPS [84, 85]), intensities are measured under different photoemission angles. The method was first developed for layered systems (oxide layers on Si, Al, lubricant layers, etc.), and most of the data analysis algorithms rely on the assumption of such morphology. However, there are also approaches to extract concentration depth profiles causing the experimental intensity trends with Θ [86–88]. Among the layer-oriented algorithms, those utilizing intensities of both substrate (s) and overlayer (o) should certainly be preferred over equations employing overlayer intensities alone. When lines of similar KE can be used, the layer thickness t can be derived from the Hill equation:

$$t = \lambda_o \cos\Theta \ln\left(1 + \frac{I_o}{s_o}\frac{s_s}{I_s}\right) \tag{13.11}$$

where $s_i = \varrho_i \sigma_i \lambda_i$, ϱ_i being the atomic density in the pure layers, which can easily be derived from approaches given in [89]. For lines with different KE, a graphic method for thickness assessment ("thickogram") is provided in [85].

Attempts to resolve the depth coordinate from (AR)XPS data have been discouraged by the observation that the reversal of the Laplace transformation in Eq. (13.8) is an "ill-posed" problem, suffering from a dramatic impact of any experimental noise and from poor stability of solutions [85, 88]. It has been found that ARXPS data could be equally well reproduced by depth profiles, which differed significantly in deeper layers but were similar near the surface [86], which offers promise at least if only the external surface layer is of interest.

A lot of effort has been made to explore the influence of surface roughness on ARXPS, which causes a distribution of real photoemission angles Θ and shadowing effects. In earlier studies with regular profiles of the scale of the XPS sampling depth, a magic photoemission angle of about 45° was identified at which roughness-induced errors in the Hill equation vanish [90]. Later it was found that such a magic angle indeed exists for various types of roughness profiles, but it is not universal [91–93]. Apparently, a reliable correction of the data is in principle possible, but it requires *a priori* knowledge on the type of roughness profile exposed.

Improving surface sensitivity by decreasing the excitation energy is one of the incentives of synchrotron XPS. However, owing to the minimum in the λ–E relation at λ values above monolayer thickness (Figure 13.11), the results will remain averaged over some (although fewer) layers. For this reason, it has also been attempted to derive depth profiles from intensity data measured at various excitation energies [excitation-energy resolved X-ray photoelectron spectroscopy (ERXPS)] [40, 94–96]. In such a method, experimental intensity ratios I_A/I_B are fitted by model ratios obtained on the basis of Eq. (13.8) ($\Theta = 0$), varying the mathematical functionality and the parameters of assumed concentration depth profiles $\varrho_A(z)$, $\varrho_B(z)$ and relying on stoichiometric relations wherever possible.

This method has been validated and compared with ARXPS using well-characterized reference samples of different surface roughness [96]. The sample morphology was created by self-assembled octadecanethiol monolayers on gold, which are known to produce an ~2.2 nm thick carbon layer on Au (S layer neglected in a first approximation). The roughness of the Au substrates ranged from an atomically flat surface [Au(111)/mica] via a profile with root mean square deviation of about 2 nm (Au evaporated on to a silicon wafer) to profiles with average surface roughness (R_a) of 0.25–0.4 and 1.5–3 μm (1 or 4 μm Au/Au, according to the particle size of Au powders sintered to flat Au foil during preparation).

From the results (Figures 13.12 and 13.13), it is obvious that both methods are able to analyze the situation on the atomically flat surface correctly. In ERXPS (Figure 13.12a), only the step function gave a satisfactory fit of the intensity data, hence it is a result of the analysis rather than a preassumption. In ARXPS (Figure 13.13a), the layer-oriented approach (black curves) performed better than the free model, but this may be due to some experimental scatter in the measurements with a non-dedicated instrument (manual angle setting).

The effect of surface roughness on ERXPS is mainly an overestimation of the depth extensions (Figure 13.12b–d). This is in line with expectations because with inclined

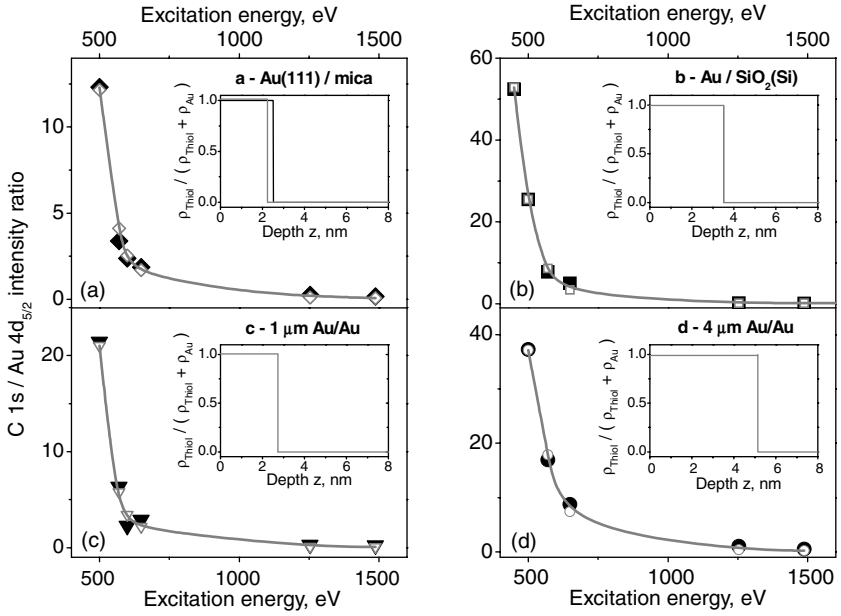


Figure 13.12 ERXPS analysis of *n*-octadecanethiol/Au self-assembled monolayers on gold substrates of different roughness (see text). Experimental data (black) and model results (gray). Insets:, concentration depth function: gray, free models; black, thiol percentage in overlayer constrained (≤100%), only panel (a). Reproduced from ref. [96], S. V. Merzlikin *et al.*, Resolving the depth coordinate in photoelectron spectroscopy – comparison of excitation energy variation vs. angular-resolved XPS for the analysis of a self-assembled monolayer model system, *Surf. Sci.*, 2008, **602**, 755, with permission from Elsevier.

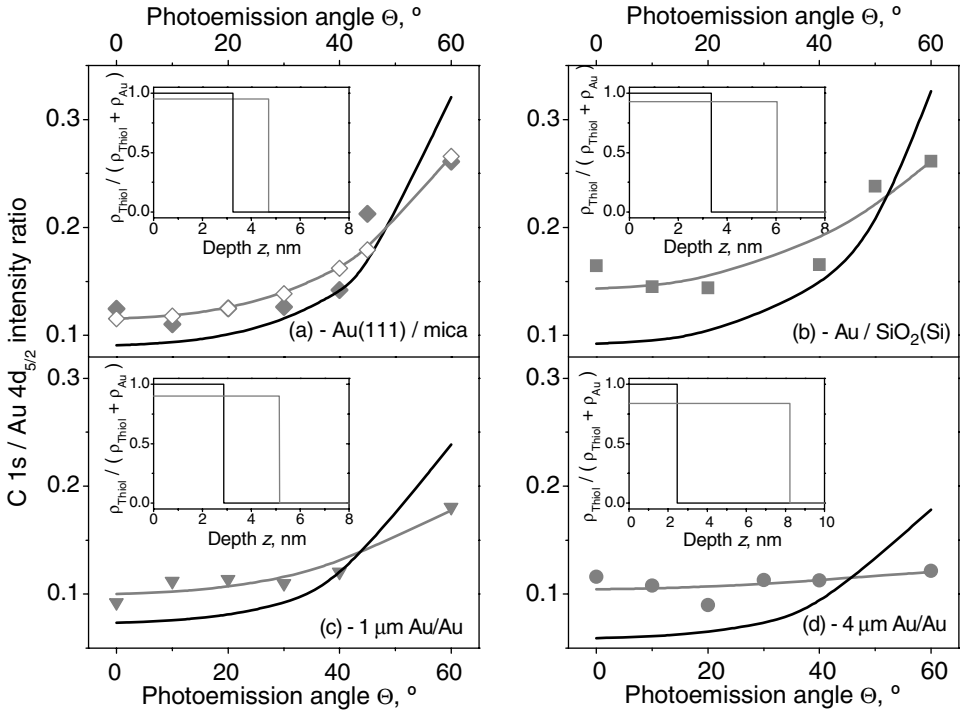


Figure 13.13 ARXPS analysis of *n*-octadecanethiol/Au self-assembled monolayers on gold substrates of different roughness (see text). Concentration depth functions given in insets. Gray, free models; black, thiol percentage in overlayer set to 100%. Reproduced from [96], S. V. Merzlikin *et al.*, Resolving the depth coordinate in photoelectron spectroscopy – comparison of excitation energy variation vs. angular-resolved XPS for the analysis of a self-assembled monolayer model system, *Surf. Sci.* 2008, **602**, 755, with permission from Elsevier.

surfaces, the photoelectron path per unit depth coordinate is longer than at the nominal photoemission angle of 0° (cf., Figure 13.10a). Notably, the ERXPS models reproduced the correct concentrations in the overlayer even at the greatest roughness (Figure 13.12d), where the profile was characterized by canyon-like channels [96]. In ARXPS, the dynamic range of the C 1s/Au 4d intensity ratio decreased with increasing roughness (Figure 13.13b–d). At the greatest roughness, this ratio did not respond to the photoemission angle any longer, that is, ARXPS identified this sample as a homogeneous mixture of C and Au. Correspondingly, the fits were also unsatisfactory: with a preset layer concentration (black curves), acceptable layer thicknesses were still obtained, but the deviations between experiment and model were large. With free layer concentration, the result falsely fitted in with a significant admixture of gold to the carbon layer.

Together with the model calculations of Zemek and co-workers [91–93], these results suggest that ERXPS should be preferred with materials where a rough surface has to be expected. This may be ascribed to the minimization of shadowing effects at

normal emission and to the smaller effect of surface roughness on the effective pathlengths: At a deviation of $\Delta\Theta$ of the photoemission angle, the pathlength changes with $(\cos\Delta\Theta)^{-1}$, which is smallest at $\Theta = 0$.

13.2.3.3 Determining XPS Intensities – Lineshapes and Signal Backgrounds

Intensity determination for a single line requires especially the definition of the background above which the signal is to be integrated. When several signals have to be differentiated by peak fitting, considerations on lineshape and component line identification become important.

Owing to the energy losses by inelastic scattering, the background increases with decreasing KE, and its course below a signal will not be linear: the higher the signal intensity at a particular KE, the more electrons decelerated by inelastic events are created at the same time. This is the idea behind the Shirley background [97], which is used most frequently in quantitative analysis. As the actual intensity has to be determined over an *a priori* unknown background, the Shirley background is calculated in an iterative procedure.

There are situations where a linear background may be suitable. If the increase in background intensity by a peak is minor, the error by a linear background will also be minor. If a peak sits on a strongly inclined background feature, the underlying gradient would have to be superimposed on the Shirley function. If the data handling package employed does not offer this option, a linear background may be preferable.

Actually, the shape of the background at the lower KE side of a peak contains significant information on the morphology of the near-surface region. It depends on the abundance of inelastic events, which will be larger when the element studied is deeper below the surface. Figure 13.14a shows distributions of Cu and Au, which would all give the same Cu 2p/Au 4f intensity ratio but provide very different backgrounds: the deeper the Cu is located in the heavy Au matrix, the higher is the background step. In some of these spectra, a Shirley background would intersect with the experimental background, which is unphysical.

The underlying phenomena were studied by Tougaard (reviewed in [98]), and strategies for extraction of information about the morphology of the near-surface layer were derived. Information can be obtained about concentration depth distributions, but also on lateral distribution (cf., Figure 13.14a), which is rare in XPS (see Section 13.3.2). On a less sophisticated level, a procedure for realistic background description was also developed by Tougaard [98]. In Figure 13.14c, its performance is compared with that of the Shirley method.

Experimental XPS lines have shapes exhibiting both Lorentzian (L) and Gaussian (G) contributions, the latter being mostly from instrumental influences. They are represented by Voigt functions obtained by convolution of a G with an L component. Often the convolution function is replaced, however, by an approximated Voigt-function, which can be based on a product or a linear combination. Experimental lineshapes are then fitted by varying the binding energy, the height, the linewidth (FWHM – full width at half-maximum) and a Voigt mixing parameter. There are also functions that can account for minor asymmetries arising from several effects [99] (e.g., shape of excitation line, see Section 13.3.1). The pronounced tailings of metal

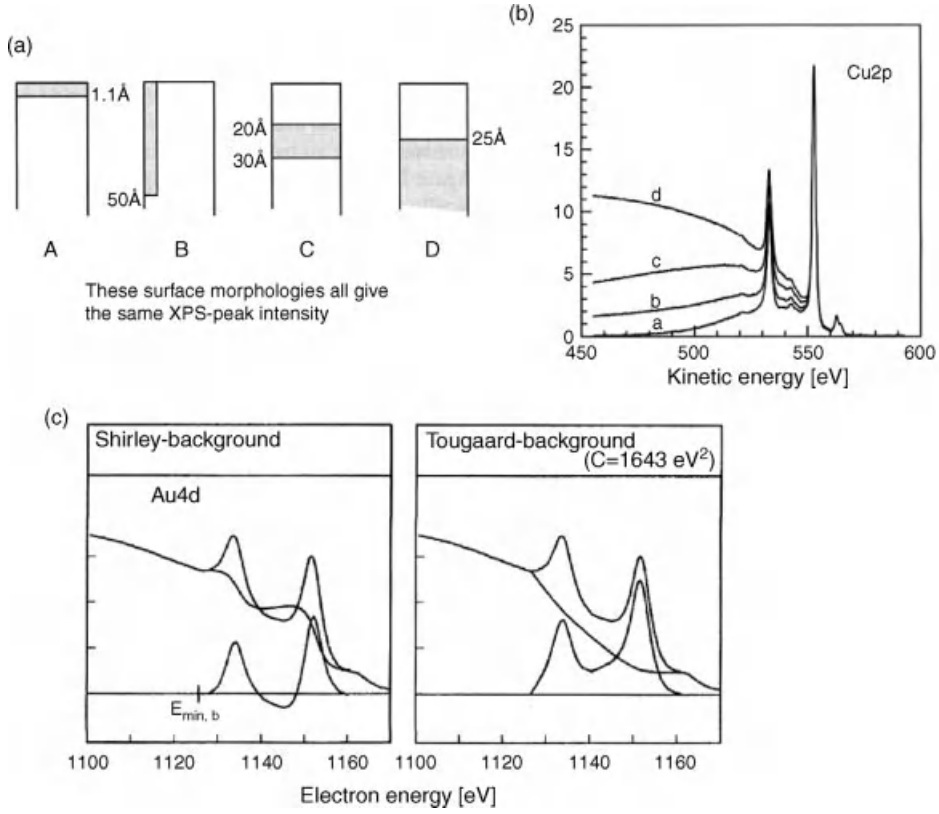


Figure 13.14 Surface morphology and XPS background. (a) Surface morphologies of Cu/Au systems providing identical Cu/Au intensity ratios with Al Kα; (b) resulting backgrounds of Cu 2p signal; (c) comparison of background subtraction below an Au 4d doublet according to methods by Shirley and Tougaard. From [98], S. Tougaard, Quantification of nano-structures by electron spectroscopy, in *Surface Analysis by Auger and X-Ray Photoelectron Spectroscopy* (Eds. D. Briggs and J.T. Grant), IM Publications, Chichester and Surface Spectra Ltd., Manchester, 2003, p. 295, with permission from IM publications Ltd.

lines are usually fitted using the Doniach–Sunjic function (DS) [100], where an asymmetry parameter gauges the extent of skewing. As the DS shape tails out to infinity, integrated areas for intensity determination will depend on the energy cutoff selected. Such intensity data are difficult to be compared or combined with results obtained with other line shapes.

When several signals are superimposed, they can often be isolated by a peak-fitting approach. Results of such analyses are sometimes suspicious, for example, when a rather unspecific signal form is fitted by a large number of component peaks. However, there are rules that allow the arbitrariness to be confined fairly effectively.

The binding energies, widths, and shapes of most individual component peaks are often unknown. The reliability of the results will depend on the shape of the

experimental signal, where peaks, leading edges, or pronounced shoulders may pin individual lines, leaving less ambiguity for the remaining lines. In such an analysis, it is crucial to have a set of spectra with the expected species present in different ratios. They have to be fitted with a consistent parameter set allowing only minor deviations between spectral parameters of individual species obtained from the different spectra. It is favorable if a spectrum is available where the element of interest can be expected to be in a single oxidation state (fully oxidized or reduced). A simple approach is to keep lineshape parameters constant for all species except for components with metallic conductivity. Results from preliminary studies, for example, on the reduction of the unsupported oxide if reduction of the supported oxide has to be analyzed, may give additional hints (e.g., on binding energy differences between states). It goes without saying that for spin-orbit doublets (Section 13.2.2.1), distance and relations between the components have to be kept constant, except for signals affected by multiplet splitting (Section 13.2.2.4). The existence of intense charge-transfer satellites (Section 13.2.2.2) may complicate the task considerably.

When experimental signal shapes suggest that the element of interest is present in several oxidation states, it may be useful to apply methods of multivariate statistics [e.g., principal component analysis (PCA)] as has been exemplified for a number of systems by Hercules and his group [101–104]. PCA reveals the number of species to be unanimously identified on the basis of the data set. Other methods (target testing) are available to explore their contributions. It should be kept in mind, however, that PCA deals with the information value of data and not with the number of species actually present. If the same signal shapes can be produced by more than the minimum of species derived by PCA, a complete spectroscopic characterization of the samples will not be possible on the basis of the given data [27]. More details about the use of chemometric methods in XPS and AES can be found in [105].

13.2.4
XAES and XPS – Structural Sensitivity via the Auger Parameter

AES is a surface analysis method on its own, where an electron beam is used to create the core hole required to initiate the Auger transition (Figure 13.2). Large incident electron beam intensities and the use of electron analyzers optimized for transmittance rather than for energy resolution (cylindrical mirror analyzer; cf., Section 13.3.1) allow for high speeds of data acquisition. As electron beams can be easily focused, AES by far outperforms XPS with respect to lateral resolution (cf., Section 13.3.2). It can be used in scanning microscopy mode providing, for instance, patterns of the spatial distribution of elements. AES has a similar potential to differentiate oxidation states of elements as XPS, because the electron states involved (Figure 13.2) are subject to similar influences to those participating in photoemission (see Eq. (13.3)). The lines are broader and the chemical shifts larger than in XPS. Actually, just the final state effetcs are much stronger because the final state of the Auger transition is doubly charged (Figure 13.2). However, electron beam induced AES has not gained popularity in the catalysis community because the high energies introduced by the electron beam

are prohibitive and are expected to cause sample damage, in particular regarding adsorbates and unstable oxidation states

The more intense final state effects in the Auger transitions are, however, of high interest also for the surface analysis of catalysts because extra-atomic relaxation gives access to properties of compounds. Therefore, the X-ray-induced Auger lines that appear in every XPS spectrum are a valuable tool to explore chemical identities in the near-surface region.

To avoid interference by surface charging, the analytical potential of XPS and XAES is usually utilized in the form of the Auger parameter α, which is the sum of the binding energy and the KE of the most prominent XPS line and Auger transition, respectively:

$$\alpha = E_B(i) + E_{kin}(jkl) \tag{13.12}$$

The benefits of this combination are best visualized by plotting the Auger KE of identified species against their XPS binding energies [106] (chemical state plot or Wagner plot).

The following considerations show that differences in α between samples are largely caused by extra-atomic relaxation, which is primarily related to polarizability, that is, a property of compounds. Neglecting differences in intra-atomic relaxation, the binding-energy shift is [cf., Eq. (13.3)]

$$\Delta E_B = \Delta\varepsilon + \Delta E_{rel,ext}(1) + \Delta V_M(XPS) \tag{13.13a}$$

where $\Delta E_{rel,ext}(1)$ designates the relaxation energy of the singly charged final state. Assuming that all ground-state orbitals experience the same shift between the samples, the difference in the kinetic Auger energies can be written as

$$\Delta E_{kin} = -\Delta\varepsilon - \Delta E_{rel,ext}(2) + \Delta E_{rel,ext}(1) - \Delta V_M(AES) \tag{13.13b}$$

As the energy associated with the polarization of a dielectric medium by a point charge q is proportional to q^2, we have $\Delta E_{rel,ext}(2) \approx 4\Delta E_{rel,ext}(1)$, and

$$\Delta E_{kin} = -\Delta\varepsilon - 3\Delta E_{rel,ext}(1) - \Delta V_M(AES)$$

which results in

$$\Delta\alpha \approx -2\Delta E_{rel,ext}(1) \tag{13.14}$$

In Eq. (13.14), it was assumed that the Madelung contribution is small as both XPS and Auger emission increase the charge on the emitting atom by formally 1 unit. Indeed, in zeolites where Madelung influences on XPS binding energies are prominent, the Auger parameters of Si, O, and Na were constant over a wide range of Si:Al ratios [28]. Some variation in the Al Auger parameter could be ascribed to the presence of different species.

The discussion of Auger parameter shifts in terms of changes in polarizability [107, 108, 110–112] allows plausible explanations of earlier observations. Figure 13.15a shows Auger lines measured with Cu-ZSM-5 catalysts of different Cu content and preparation [109]. XPS showed the copper in all but the catalyst denoted by D in the

+1 state, which was due to rapid photoreduction under the X-ray beam and was probably true also for the intra-zeolite species in sample d. It can be seen that with increasing Cu content, two Auger lines are obtained although there were no significant changes in the XPS lines (not shown). One of the species had a Cu LVV KE and Auger parameter close to Cu_2O; the other one exhibited values far below. Based on similar observations in earlier studies [61, 113, 114], this signal was assigned to intra-zeolite isolated or oligomeric Cu oxo species. In one study [61], intermediate values for Cu LVV and α_{Cu} were noted for (uncalcined) Cu oxide species precipitated on to the external zeolite surface.

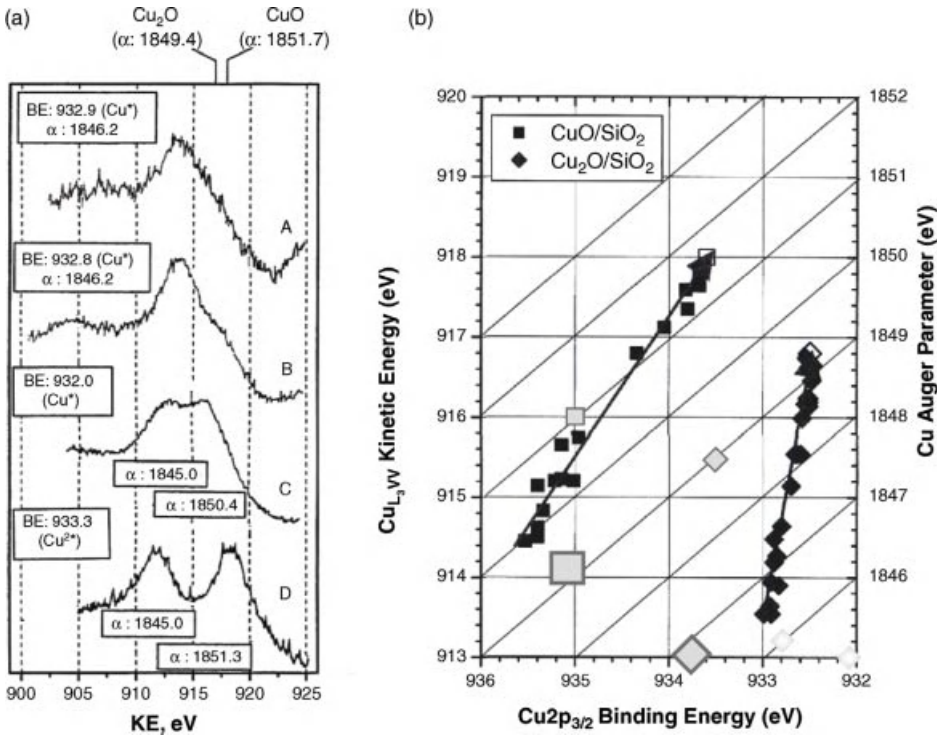


Figure 13.15 (a) Auger spectra of Cu-ZSM-5 samples prepared by ion exchange (A–C) and impregnation (D). Cu contents [exchange degree]: (A) 1.6 wt% [45%], (B) 2.8 w-% [80%], (C) 7.7 wt% [220 %], (D) 2.1 wt%. (b) Wagner plot showing data from Cu oxide particles of varying dispersion prepared by evaporation and oxidation of Cu on to SiO_2 (black symbols [107, 108]) and from Cu in and on zeolites (gray symbols, dark rim– data from [61], white center– data from [109]). Panel (a) reproduced from [109], T. Liese and W. Grünert, Cu–Na-ZSM-5 catalysts prepared by chemical transport: investigations on the role of Brønsted acidity and of excess copper in the Selective catalytic reduction of NO by propene, *J. Catal.*, 1997, **172**, 34, with permission from Elsevier. Basic Wagner plot in panel (b) reproduced from [108], J. Morales *et al.*, XPS study of interface and ligand effects in supported Cu_2O and CuO nanometric particles, *J. Phys. Chem. B*, 2005, **109**, 7758, with permission from the American Chemical Society.

Such phenomena have been interpreted by Gonzalez-Elipe's group on the basis of measurements with Cu oxide particles of different dispersion on flat SiO_2 and ZrO_2 substrates [107, 108]. In Figure 13.15b, their chemical state plot is complemented by data from Cu-ZSM-5 (gray symbols), which are in general in good accordance with the data for the model systems, despite some inconsistencies between other results [61, 109] regarding Cu^+. According to Gonzalez-Elipe and co-workers [108], there are three components of the shifts: a minor component arises from beyond the first coordination sphere where the copper oxide environment is replaced by the less polarizable SiO_2 or the gas phase. The major effects are the replacement of Cu−O−Cu bonds by Cu−O−Si bonds and changes in the coordination number.

13.2.5
Ultraviolet Photoelectron Spectroscopy

UPS was in the past one of the most powerful methods of surface science. When applied to ordered surfaces in its angle-resolved version, UPS has the potential to elucidate the spatial band structure in the solids. With excitation by polarized light, adsorbate orientation relative to the surface can be elucidated [5].

The opportunities for UPS in the analysis of real-world materials are quite different, but one has always to handle the problem that spectra cannot be obtained in the presence of surface charging. Nevertheless, a considerable range of oxide layers, real oxides, sulfides, and zeolites have been studied by UPS [59, 115–123]. Sometimes, the surface charge was removed by measurement at elevated sample temperature [59, 118–123], which bears the risk, however, of sample damage and of contamination of the vacuum system. Reference spectra for the identification of surface compounds are available from studies with thin-film samples (e.g., [115, 116, 124–126]).

UPS, which is typically excited by He I or He II irradiation (21.2 and 40.8 eV, respectively), offers the highest possible surface sensitivity with exceptional energy resolution, which is determined by instrumental limitations rather than by the width of the excitation lines, together with high signal intensities. It provides structural sensitivity and is a simple tool for the determination of work functions. The latter is based on the fact that the KE of the photoelectron above the sample (Figure 13.1b, left part) can be measured by taking the cutoff of the spectrum (decay of secondary electron peak) as the origin of the KE scale. On such a scale, the Fermi level will appear at the energy $h\nu - e\phi_{\mathrm{sample}}$. The surface sensitivity is due to the photoelectrons emitted with KE near the minimum in the relation between escape depth and KE (Figure 13.11). Structural sensitivity is provided because UPS gives access to the properties of the valence region which contains the information on chemical bonding. This means at the same time that interpretation of UPS spectra beyond a fingerprint level requires theoretical models for the electron structure of solids and adsorbates. Unfortunately, this information is compressed in a rather narrow binding-energy range, which raises problems with signal superposition in complex samples. Therefore, UPS studies have so far been confined to simple systems where the spectra can often be well interpreted on the basis of quantum chemical model calculations, for example, in the case of vanadium oxides [119, 127, 128].

The surface sensitivity of UPS was utilized in early ERXPS-type work on depth profiles of the reduction degree during reduction of V_2O_5. In this work, the average V^{4+} content was determined for different sampling depths by UPS, V 2p XPS and valence-band XPS measurements [119]. The structural sensitivity of UPS was explored with Ca/CeO_2 mixed oxides and bismuth molybdates. It was demonstrated that the surfaces of mixed phases ($Bi_2Mo_3O_{12}$, $BiMoO_6$) were not made up from surface-segregated Bi_2O_3 and MoO_3 because the spectra of the former were not linear combinations of the binary oxide spectra [118]. In Ca/CeO_2 mixed oxides with different Ca contents, thermal decomposition of initially present surface $CaCO_3$ species was shown to result in different situations – a clean mixed oxide surface or a surface carrying segregated CaO [120]. Here, UPS showed promise as a complementary method to infrared (IR) spectroscopy for materials with small external surface areas.

In the study of adsorbed species, a problem arises because unlike in IR spectroscopy, one cannot be sure that the spectrum of the substrate, which has to be subtracted to isolate the adsorbate spectrum, remains unchanged during adsorption. Thus, in the interaction of NH_3 with polycrystalline V_2O_5, surface reduction was noted by the appearance of intensity in the bandgap. The intense adsorbate bands suggested the presence of two adsorbates, one of them most likely to be molecular NH_3. The assignment of the second one (=NH?) remained tentative because of changes in the V_2O_5 background expected in this energy region [118].

Measuring work functions by UPS has a long tradition in surface science. Recently, it has been applied to determine the effect of surface modifications in carbon nanotubes [129, 130].

13.2.6
XPS and Other Methods

Owing to the problems with the identification of oxidation states via XPS binding energies, there have been many attempts to combine evidence by XPS with results of other methods in the identification of species and discussion of surface properties. Although such combinations are useful (cf., Section 13.2.1.1 on the identification of oxygen species), some aspects should be considered to avoid misinterpretation.

The method most suitable for combination with XPS is certainly low-energy ion scattering (LEIS) (or ISS – ion scattering spectroscopy) (see Chapter 11). LEIS offers ideal surface sensitivity. Although its use as a quantitative method [131] is not yet very common, it can be conveniently applied to draw conclusions on surface enrichment or depletion of components, as has been exemplified, for instance, with vanadium phosphate catalysts [132–134], Ca/CeO_2 mixed oxides [135], and $Rh–VO_x/SiO_2$ model catalysts [136]. Such conclusions are most reliable when they are based on the observation of intensity trends in LEIS sputter series [33, 137, 138] (cf., Sections 13.4.1 and 13.4.2). Owing to its surface sensitivity, its combination with ERXPS has also been found very fruitful [139].

In the past, assignments of XPS lines were discussed with reference to other techniques such as electron paramagnetic resonance (EPR), UV–visible spectroscopy, XAFS, Mössbauer spectroscopy, IR spectroscopy with probe molecules, and

volumetric reduction studies. With most of them, differences in the sampling depth have to be taken into account. With EPR, the comparison is further complicated by a limited overlap in the concentration ranges analyzed. EPR can detect paramagnetic states at extremely low concentrations, whereas XPS may be unable to identify such species in the presence of other oxidation states unless their concentration is in the region of 10%, which would probably cause interaction broadening and disappearance of the corresponding EPR signal.

With supported high surface area catalysts, combinations even with bulk techniques may be adequate as XPS will see the supported component completely, although only in the external layers of the porous grains. Direct coupling of XPS with IR spectroscopy is most appealing. It is well known that probe molecules such as CO or NO permit differentiation of oxidation states by IR spectroscopy in a perfectly surface-sensitive manner, but the assignments are not always well supported and quantification is difficult. The technical problems encountered in such a coupling appear surmountable and the benefit for further development of the diagnostic potential of both techniques should be considerable.

13.3 Instrumentation

13.3.1 Conventional XPS

In Figure 13.16, a spectrometer for XPS is depicted schematically, with the vacuum system, sample handling facilities, and some other details omitted. When fitted additionally with a UV source and an ion source, the spectrometer can also be used for UPS and LEIS.

Dual X-ray sources employed in laboratory spectrometers offer the choice between Al Kα and Mg Kα irradiation (1486.6 and 1253.6 eV, respectively), which allows shifting of Auger lines on the binding energy scale to help identify unknown signals and avoid interference between Auger and XPS lines. Owing to their doublet structure, the excitation lines are slightly asymmetric and rather broad (Al Kα ∼0.85 eV, Mg Kα ∼0.7 eV), which limits the energy resolution in the spectra. The excitation radiation is emitted on a bremsstrahlung background and contains a set of satellites. These produce their own photoemission lines (X-ray satellites, the first visible features 8–10 eV off the main line), which have to be removed by standard algorithms. The bremsstrahlung would cause sample damage and a high spectral background and is therefore suppressed by an Al foil between the source and sample (omitted in Figure 13.16). Secondary electrons from this "window" which neutralize some of the surface charge on nonconducting samples help to handle the charging problem.

Modern high-resolution instruments are fitted with a monochromated X-ray source (always Al Kα). It includes a focusing monochromator producing a radiation line of width typically 0.25 eV, which can be focused into 10–50 μm spots. Owing to

the absence of an Al window near the sample, surface charging cannot be neutralized by stray electrons. Therefore, measurements with nonconducting samples require charge neutralization with a flood gun.

In XPS with synchrotron radiation, the excitation energy can be tuned in a range limited by the monochromators of the station only. The spot size can be regulated with slits, which also influences the excitation line width. The latter is on the order of 0.1 eV, but due to large intensity reserves, <0.05 eV can be easily achieved. Charging problems with nonconducting samples are serious and not well managed in conventional synchrotron XPS. They are somewhat alleviated in *in situ* XPS (see Sections 13.3.3 and 13.4.3), probably due to collision of gas molecules with the surface and stray electrons from the gas phase. Owing to the high X-ray intensities, sample damage is a problem with reducible oxides.

The width of UV excitation lines (He I 21.2 eV, He II 40.8 eV) is only some meV. UPS is impossible in presence of surface charging. Attempts to remove the charge with slow electrons have so far been unsuccessful even with He II.

The photoelectrons emitted from the sample are focused on the entrance slit of an electrostatic analyzer (cf., Figure 13.16), which differentiates them according to their KE. Those transmitted through the analyzer are counted by a detector, nowadays mostly a position-sensitive channel plate allowing multichannel detection. Before entering the analyzer, the photoelectrons are decelerated by a retarding field grid (omitted in Figure 13.16). In XPS, it usually retards the electrons to a constant pass energy (CPE) because the analyzer potentials are set to focus incoming electrons of that pass energy on to the detector exit. In this mode [alternative term: FAT (fixed analyzer transmission) mode], the energy scan is accomplished by scanning the retarding potential. In an alternative mode, the electrons are retarded by a constant retardation ratio (CRR, FRR mode). As the relative resolution $\Delta E/E$ depends only on instrumental properties or settings, the absolute resolution ΔE will deteriorate at

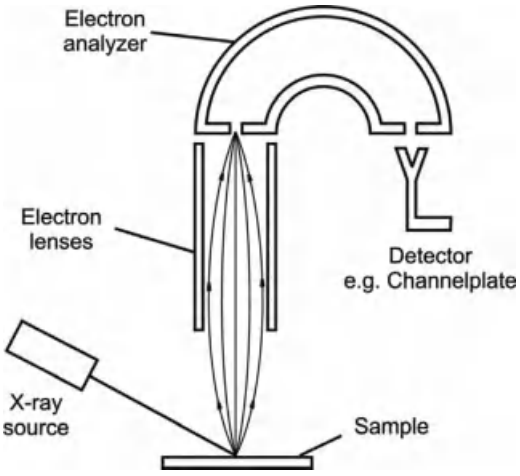


Figure 13.16 Components of photoelectron spectrometer (without UHV system and sample handling facilities).

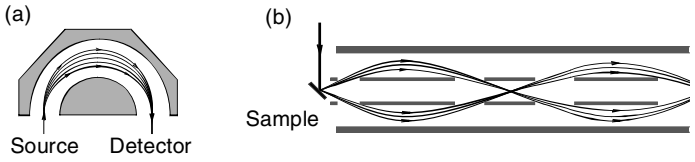


Figure 13.17 Schematic showing the hemispherical analyzer (HSA) (a) and the cylindrical mirror analyzer (CMA) (b).

higher KE, but the increasing analyzer transmission is favorable for rapid measurements. CRR is therefore used for survey spectra in which the elemental composition of a sample is checked qualitatively before regions for detailed analysis (in CPE mode) are defined. It is also the preferred mode in AES.

In XPS, the electrons are differentiated with hemispherical analyzers (HSAs) (Figure 13.17a; there are constructions not utilizing the full hemisphere). Their relative energy resolution is

$$\frac{\Delta E}{E} = \frac{w_1 + w_2}{r_0}(\delta\alpha)^2$$

where r_0 is the mean radius of the hemisphere, w_1 and w_2 are input and output slit widths, and $\delta\alpha$ is the angular spread of the incoming electrons. Therefore, the resolution is better for analyzers with large radius. The alternative CMA (Figure 13.17b) was used in the early days of XPS. Its advantage is a very high transmission due to a large acceptance angle, although the spectra can be affected by misalignment of the sample position S. Its energy resolution is inferior to that of the HSA, therefore the CMA is applied in dedicated Auger electron spectrometers because of less stringent resolution requirements with the broader Auger signals. Together with high fluxes of excitation electrons, the high analyzer transmission allows high speed of AES analysis.

The polarity of electron analyzers can be switched, which enables them to analyze positively charged particles. With an ion source available, LEIS can be measured in such a configuration.

13.3.2
Lateral Resolution, Imaging

Although XPS can resolve the depth coordinate into a solid on the nanometer scale, it is much less suitable for achieving lateral resolution. In conventional XPS, which provides only intensity data, there is little chance of differentiating between situations as shown in Figure 13.14a and b. With respect to lateral resolution, XPS is inferior to AES with electron excitation because electrons can be easily focused into nanometer-sized spots which are scanned across the surface.

In XPS, spatial resolution can be obtained by limiting the X-ray beam size (focusing monochromator, Section 13.3.1) or the spot from which photoelectrons are selected by the electron optics. A micro-X-ray beam can be scanned across the

surface, yielding a full spectrum at any point. The procedure is similar with imaging optics selecting individual sample points. Other systems image one line (direction x) on the two-dimensional channel plate while the spectrum at the individual points of x appears in the second detector dimension. The second sample direction (y) is accessed when the x-line is moved stepwise along y by the electron optics.

With modern imaging systems, spatial resolutions of 2–3 μm can be achieved. This is far too coarse to resolve atomic details of a surface, whereas differences between catalyst grains might be well explored. In catalysis research, XPS has been used so far for analyzing averaged properties from random samples thought to be representative of the whole material rather than to study deviations from such an average. Therefore, XPS imaging on the scale offered by present instrumentation has not attracted much interest in the catalysis community.

13.3.3
Ambient-Pressure Photoelectron Spectroscopy (APPES)

There are two reasons for the ultra-high vacuum (UHV) requirement in XPS – the protection of reactive surfaces from contamination or unwanted adsorption and the loss of analytical information by inelastic collisions of photoelectrons with gas molecules. The latter would allow the sample to be kept at elevated pressures if the pressure was effectively reduced along the photoelectron trajectory, for example, by differential pumping. The required dimensions may be understood by appreciating that the mean free path of 1000 eV photoelectrons in 1 mbar oxygen is on the order of 10 mm.

On this basis, gases and even liquids have been studied by photoemission and XPS from the early days of these techniques [140, 141], and studies of surface interactions with the gas phase were pioneered by Joyner and co-workers with work on oxygen adsorption on silver [142, 143]. Commercial instruments on this basis available in the early 1980s have been modernized and are still in use in some laboratories (e.g., Cardiff, Novosibirsk). Despite substantial improvements to the equipment, excluding for instance sources of contamination and using advanced analyzers, work with such instruments remained tedious owing to the low intensities recovered from the samples. This changed less than a decade ago when the differential pumping stages inherent in ambient-pressure XPS were combined with the electron optics [144] and instruments were installed at end stations of synchrotrons (more details can be found elsewhere [145, 146]). This initiated the age of ambent-pressure photoelectron spectroscopy (APPES).

In Figure 13.18, the conceptual designs of the differential pumping stages in traditional instruments and in combination with the electron optics are compared. The apertures between the pumping stages are located at the focal or crossover points of electron lenses, which minimizes intensity losses and allows the use of higher pressures in the sample chamber (typically some millibars). The X-ray beam enters the sample chamber through an X-ray window to protect the storage ring from pressurization. Two instruments of this type are currently in use, at the Advanced Light Source (&) (Berkeley, CA, USA) and at BESSY II (Berlin, Germany).

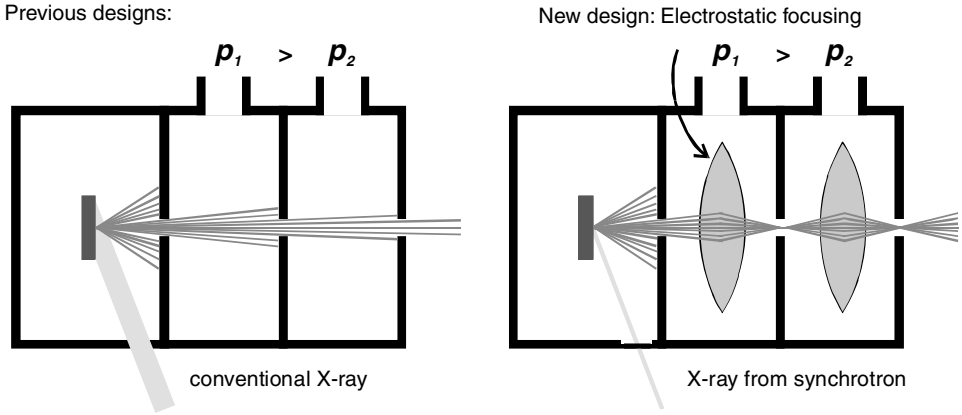


Figure 13.18 Differential pumping without and with combination with electron optics.

Meanwhile, the combination of electron optics and differential pumping has also been implemented in some modern laboratory instruments [147–149] and is commercially available.

13.4
Case Studies

13.4.1
Combination of Methods: Strong Metal–Support Interaction in a Ag/TiO_2 Catalyst

The study to be reported [33] deals with a 7 wt% Ag/TiO_2 catalyst for selective hydrogenation of acrolein, in which reduction at different temperatures had resulted in surprising particle dispersions: in a transmission electron microscopy (TEM) study, smaller particles ($d_{Ag} = 1.4 \pm 0.5$ nm) were observed after high-temperature reduction (HTR) (773 K) than after low-temperature reduction (LTR) (473 K, $d_{Ag} = 2.8 \pm 1.9$ nm) [150]. Surface analysis of these samples was performed with techniques all available at the same instrument. For comparison, a sample subjected to HTR and subsequently stored under ambient conditions for months ("HTR′/air") was also studied.

The XPS contribution to this analysis is summarized in Table 13.2. The binding energies alone are not more than a piece of a mosaic. They are lower than that of silver metal (368.3 eV) and fairly close to Ag_2O (367.8 eV), but owing to a number of possible influences (support effects, problems with C 1s referencing) this is not conclusive. Indeed, the Auger parameter allows a fairly unambiguous conclusion that the silver is metallic after reduction because α_{Ag} is 726.1 eV for silver metal but 724.5 eV for Ag_2O. After prolonged storage in air (HTR′/air), the slightly decreased Auger parameter might indicate the presence of some Ag^+.

Table 13.2 XPS and XAES analysis of Ag(7 wt-%)/TiO_2 in different states.

State	E_B (Ag $3d_{5/2}$), ev	E_k (Ag M_5VV) (eV)	α_{Ag}[a)] (eV)	Ag/Ti atomic ratio
LTR[b)]	367.5	358.5	726.0	0.058
HTR[c)]	367.5	358.4	725.9	0.046
HTR′/air[d)]	367.8	357.7	725.5	0.17

a) $\alpha_{Ag} = E_B$ (Ag $3d_{5/2}$) + E_k (Ag M_5VV); cf., Eq. (13.12).
b) H_2, 473 K.
c) H_2, 773 K.
d) HTR, stored in air for months.

The Ag/Ti atomic ratios are smaller after reduction, and smallest after HTR. The tempting conclusion that the silver is more aggregated after HTR is, however, not consistent with the fact that storage in air leads to a huge increase in the visibility of Ag. If the silver was always accessible from the gas phase (or vacuum), one would have to resort to extensive oxidative corrosion of the Ag particles to explain such trends, but this is at variance with the Auger parameters. Therefore, the Ag particles seem to be covered by an overlayer after HTR.

This is nicely confirmed by the LEIS results shown in Figure 13.19a, where intensity trends of the sputter series are reported (first scans on the samples are compared in the inset). The difference in visibility of Ag is dramatic: after HTR, the silver is almost completely covered. Upon sputtering, the Ag/Ti intensity ratio recovers so slowly that very large ion doses will be required to reach the ratios of HTR′/air or even of LTR.

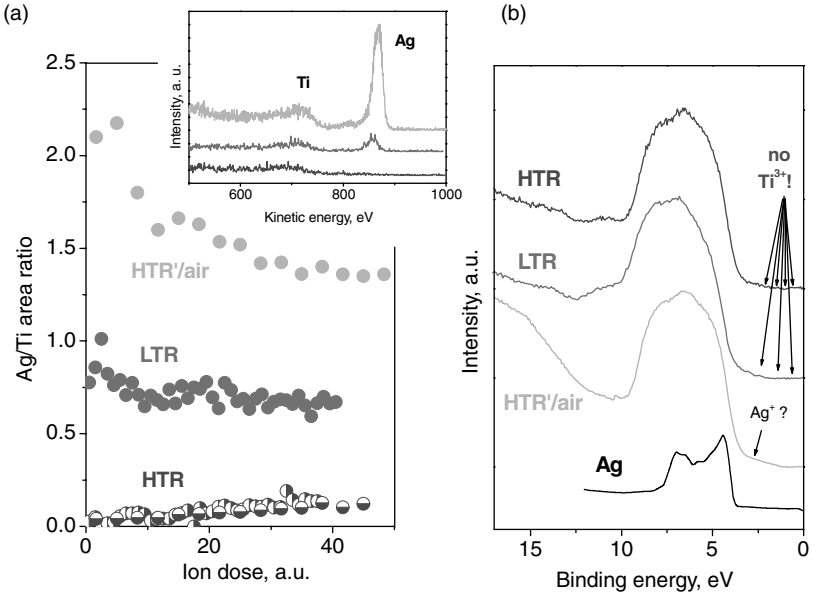


Figure 13.19 Analysis of Ag/TiO_2 catalysts by LEIS and UPS. (a) Intensity trends in LEIS sputter series (first spectrum shown in inset); (b) UPS spectra. Based on data in [33].

Although the sputter rate could only be estimated roughly, it is apparent that the TiO_x overlayer is several atomic layers thick. After long air contact, the decreasing Ag/Ti ratio upon sputtering shows that the cover was completely removed.

Particle dimensions were estimated with the help of the Kerkhof–Moulijn model for porous supports [83] (cf., Section 13.2.3.1). In the reoxidized HTR sample, a particle size of 1.5 nm was obtained, in good agreement with the TEM data. The result for LTR (4.5 nm) somewhat exceeds the particle size from TEM, which may suggest that the encapsulation process was already under way: indeed, further studies indicated that encapsulation of Ag particles starts under surprisingly mild conditions. Assuming that 1.5 nm was the Ag particle size in the HTR sample also prior to reoxidation, the thickness of the overlayer was estimated to be on the order of 1.5 nm. This is well consistent with the LEIS results and was also supported by high-resolution TEM images [33]. However, unlike TEM, surface analysis gives results of a representative sample, and it allowed the identification of the nature of the overlayer, which was also seen in TEM.

From these results, a tentative explanation for the smaller particle size after HTR was offered: the crucial point is a kinetic competition between particle growth and encapsulation. If the catalyst is kept at 473 K where encapsulation appears to be slow, the result is determined by sintering. If the temperature is ramped beyond 473 K at an appreciable rate, encapsulation becomes rapid and locks the particles while being still small.

Figure 13.19b shows UPS spectra of the Ag/TiO_2 surface after the different treatments. From comparison of the spectra with that of silver metal, it is clear that any signal of the Ag nanoparticles is superimposed by the intense TiO_2 valence band signal except for a weak low-energy shoulder of HTR′/air, which may arise from some Ag^+ present. More significant is that there was no indication of Ti^{3+} in the bandgap after reduction, although this state was clearly identified by the bulk technique EPR [33]. This suggests that Ti^{3+} was not present in the first few atomic layers and, therefore, not exposed to the gas phase to any appreciable extent. Most likely, the Ti^{3+} defects remained near the metal surface, that is, they were buried together with the silver nanoparticles by the TiO_2 overlayer.

13.4.2
Depth Resolution: the Surface Composition of Stoichiometric Bulk Mixed Vanadates and Molybdates

Knowledge of the surface composition of mixed oxides is of prime importance for heterogeneous catalysis because such materials are widely used as catalysts in selective oxidation reactions. Until recently, discussion of reaction mechanisms and active sites was often based on the assumption that the structures of exposed surfaces may be derived by truncation of the bulk structure (reviewed in, e.g., [151]). There have, however, been reports on surface enrichment and depletion in solid oxide solutions (e.g., $Co_xNi_{1-x}O$) [152] or on TiO_2-rich overlayers on $SrTiO_3(001)$ model surfaces [153]. Evidence for the formation of amorphous overlayers on catalyst surfaces with compositions deviating from the bulk were obtained under selective

oxidation reaction conditions by APPES and near-edge X-ray absorption fine structure (NEXAFS) [154].

In an alternative approach, stoichiometric bulk mixed metal vanadates and molybdates were studied by chemical probes – methanol adsorption, which allows the discrimination of CH_3O^* and intact CH_3OH^* adsorbates on different cations by IR spectroscopy, combined with kinetic studies of methanol oxidation, which gives access to turnover frequency (TOF). From the comparison of TOFs obtained from bulk mixed vanadates and molybdates and from related supported oxide catalysts, it was suggested that the external surfaces of the bulk phases are covered by monolayers of surface V (Mo) oxide species – like a supported catalyst, the support being the mixed phase [155, 156].

LEIS spectra of a set of samples from this study indeed confirmed a strong surface enrichment in V (Mo) oxide for many (although not all) of them already in the initial, calcined state, that is, without any contact to a reaction atmosphere [139]. This is exemplified in Figure 13.20 by the comparison of Zr/V intensity trends in sputter series from bulk ZrV_2O_7 and a supported V_2O_5/ZrO_2 catalyst with vanadium content near the theoretical monolayer limit. Back-extrapolation of the trends to zero sputtering time shows that no Zr was exposed on the supported catalyst while Zr exposure was near zero on the bulk phase. With ongoing sputtering, the Zr/V ratio continued to increase in the supported catalyst (Figure 13.20b) because the underlying phase was pure ZrO_2. The bulk phase exhibited an asymptotic trend (Figure 13.20a), obviously tending towards the value characteristic for bulk ZrV_2O_7.

An ERXPS study was performed with selected materials in order to support these results by an independent technique and to assess the dimensions of the enrichment layers. Figure 13.21 presents results obtained with ZrV_2O_7 [139]. From the intensity trends (Figure 13.21b) modeled by various types of concentration depth profiles (Figure 13.21c), it is obvious that a homogeneous sampling region cannot describe the experimental results. These are reproduced by a number functions, most of which can be discarded, however, for physical reasons (>100% V in the surface region or 0% V in the bulk). A realistic model was obtained only with a step function starting at 100% V and decreasing to the bulk value (66.7%) with an intermediate step. The latter may indicate that the transition is less sharp than suggested by the step function.

According to this model, the external surface V oxide layer is ~0.6 nm thick. It has been shown, however, that ERXPS overestimates depth dimensions below rough surfaces [96]. As the extent of overestimation is normally in the range of 20–60%, the actual thickness of the oxide layer is probably 0.3–0.4 nm, that is, well in accord with previous suggestions that the bulk vanadate is covered by a surface vanadium oxide monolayer.

13.4.3
APPES: on the Doorstep of a New Age of XPS

Owing to the immense progress in instrumentation (cf., Section 13.3.3), XPS in its version APPES is nowadays also a tool for *in situ* studies of catalytic surfaces. It offers the advantage of adsorbates, substrate, and gas-phase species being monitored

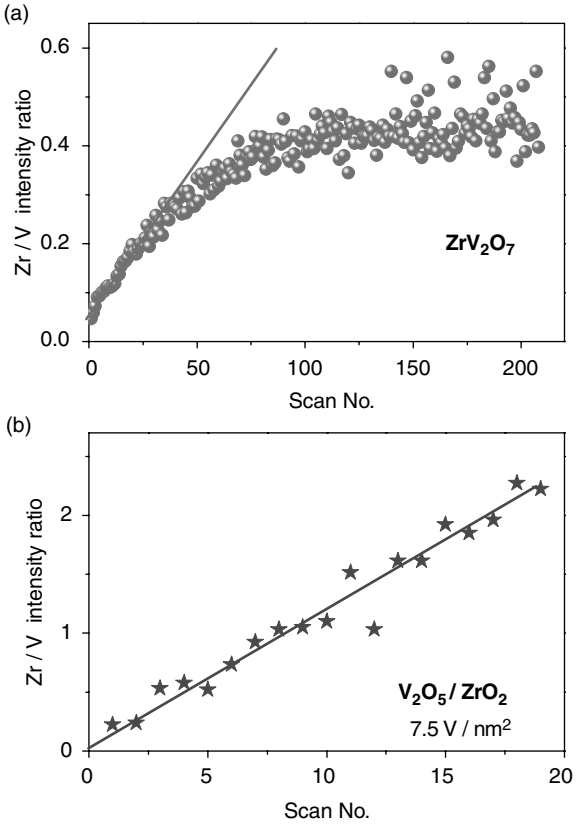


Figure 13.20 Development of Zr/V intensity ratio in LEIS sputter series with Zr–V–O oxide systems. (a) Stoichiometric bulk mixed oxide; (b) V_2O_5/ZrO_2 supported catalyst. Reproduced from. [139], S. V. Merzlikin *et al.*, Anomalous surface compositions of stoichiometric mixed oxide compounds, *Angew. Chem. Int. Ed.*, 2010, **49**, 8037, with permission from Wiley-VCH Verlag GmbH.

simultaneously, with the opportunity for quantitative analysis for adsorbate and substrate. Although such investigations can also be performed in laboratory instruments, dedicated instruments at synchrotron beamlines (cf., Section 13.3.3) certainly provide the most productive environment.

In catalysis, work has been so far been concentrated on reactions over metal surfaces because these allow the use of the full range of the O 1s region for the identification of O-containing species involved. In supported catalysts, this region would be dominated by lines from the support, and the differentiation between species interacting with the support or the active component would add a new dimension of complexity. Numerous examples of successful work have been presented in recent reviews [145, 146], among them investigations on the oxidation of Pd (111) [145], dehydrogenation and oxidation of methanol over Pd(111) [146], ethene epoxidation over Ag [146], methanol oxidation and steam reforming over Cu [145,

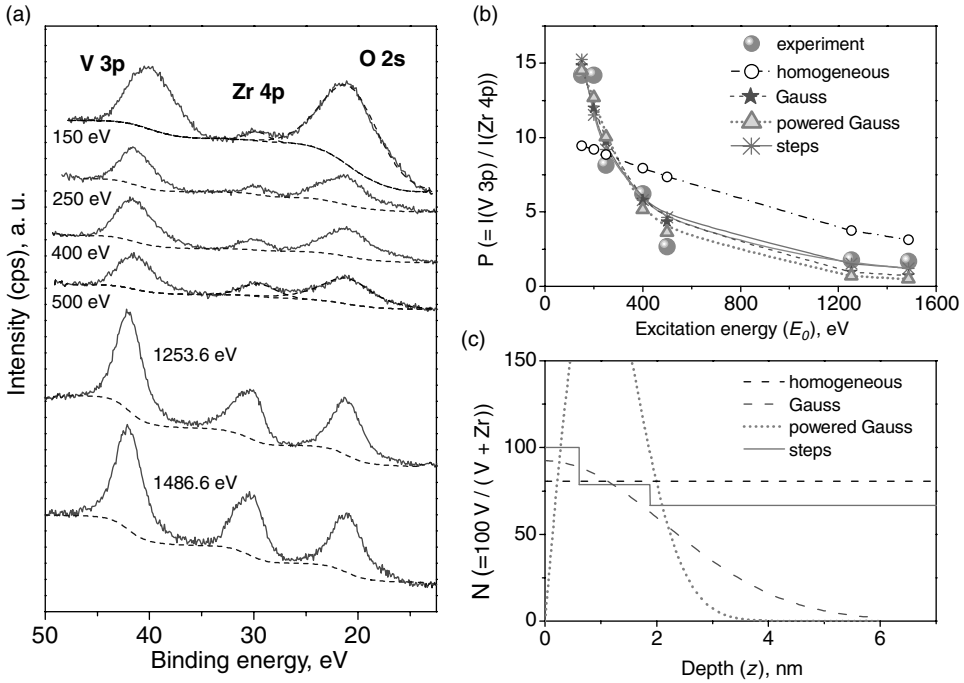


Figure 13.21 ERXPS analysis of the ZrV_2O_7 surface. (a) Spectra taken at different excitation energies (intensities rescaled for presentation in a single figure); (b) dependence of experimental intensity ratios on excitation energies and results of optimized models on the basis of different mathematical concentration depth profile types [see (c)]; (c) Optimized depth profile functions. Reproduced from [139], S. V. Merzlikin *et al.*, Anomalous surface compositions of stoichiometric mixed oxide compounds, *Angew. Chem. Int. Ed.*, 2010, **49**, 8037, with permission from Wiley-VCH Verlag GmbH.

146], and CO oxidation over Ru(0001) [145, 146]. Beyond catalysis, studies on melting of ice, cation surface enrichment in aqueous solutions, and water films on oxide surfaces have been reported [145]. For this chapter, we focus on studies with Pd – the oxidation of its (111) facet [145] and the relation of metastable subsurface carbide phases to its selective hydrogenation capabilities [40].

In Figure 13.22, Pd $3d_{5/2}$ and O 1s signals (adjacent to the Pd $3p_{3/2}$ peak) of a Pd (111) surface under different conditions are shown. The well-known $O(2 \times 2)$/Pd (111) chemisorption phase gave rise to only one O 1s peak, the Pd surface state shifted due to the interaction with oxygen (spectrum b). With increasing temperature and O_2 pressure, two intermediate phases were observed before the bulk oxide (spectrum e) was formed: a monolayer surface oxide and a bilayer "subsurface oxide." They both exhibited two different O-related Pd states (Pd coordinated by two or four O atoms, signals II and III in spectra c and d coexisting with the line of Pd metal) and two O 1s signals (O coordinated by three or four Pd atoms). The different structure of the layers follows from the increased quantity of Pd coordinated by four O atoms while the

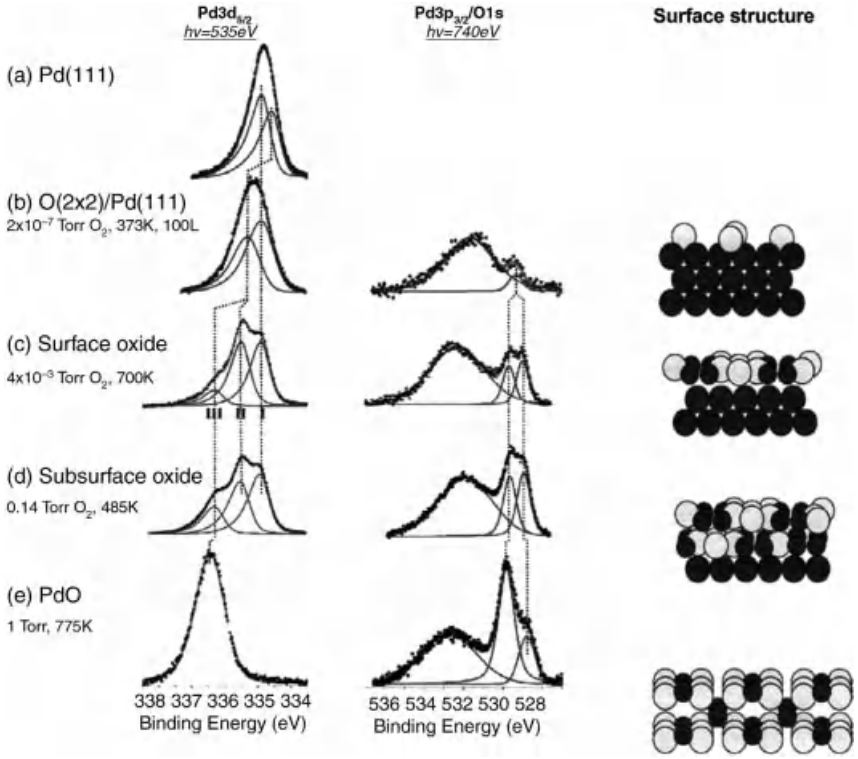


Figure 13.22 Surface phases formed between Pd(111) and oxygen, characterized by their Pd $3d_{5/2}$ and O 1s spectra. Reproduced from [145], M. Salmeron and R. Schlögl, Ambient pressure photoelectron spectroscopy: a new tool for surface science and nanotechnology, *Surf. Sci. Rep.*, 2008, **63**, 169, with permission from Elsevier.

unchanged ratio between the O 1s signals suggests the limited thickness of the layers (cf., O 1s spectrum of bulk PdO). The subsurface oxide existed only in the presence of oxygen in the millibar pressure range; it decomposed to the surface oxide when the oxygen supply was switched off. The conditions under which these phases can be formed are detailed elsewhere [145].

Pd is a highly selective catalyst for the hydrogenation of alkynes and alkadienes to monoalkenes. Such selectivity is, however, not obtained under all conditions: at high H_2 pressures, and also at too low temperatures, the reaction may proceed directly to the corresponding alkanes. The selectivity observed was therefore attributed to a cooperation between Pd and carbonaceous deposits, for which different models were proposed [157, 158]. A fairly recent APPES investigation of *n*-pentyne hydrogenation provided significant new experimental evidence and a plausible new model of the selective surface phase [40].

Figure 13.23a and b shows Pd $3d_{5/2}$ spectra of a clean Pd foil and of the same foil during hydrogenation of *t*-2-pentene (a) and of 1-pentyne (b) at 358 K (selective conditions for 1-pentyne). In both cases, the Pd surface state shifts to a higher binding

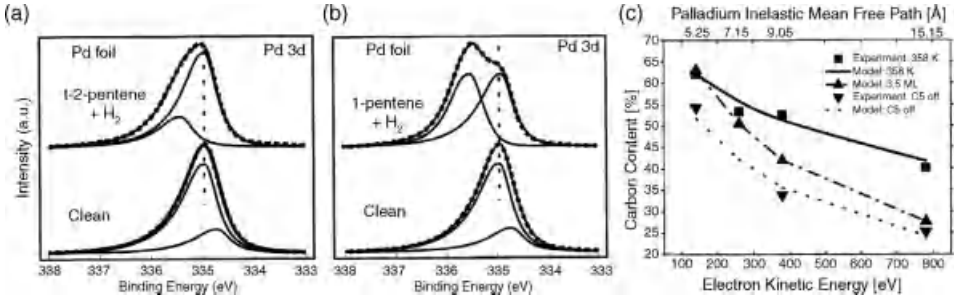


Figure 13.23 *In situ* XPS study with a Pd foil during hydrogenation. (a) *t*-2-Pentene–H_2 mixture at 358 K, compared with clean foil; (b) 1-pentyne–H_2 mixture compared with clean foil; (c) depth profile analysis of C/Pd intensity ratios, experimental data taken during 1-pentyne hydrogenation and after removal of hydrocarbon from gas phase, compared with model results (for details, see text). Reproduced from [40], D. Teschner *et al.*, Alkyne hydrogenation over Pd catalysts: a new paradigm, *J. Catal.*, 2006, **242**, 26, with permission from Elsevier.

energy due to interaction with the hydrocarbon, but the intensity of the C-related Pd state is much higher in the case of 1-pentyne. Qualitative depth profiling by variation of the photoelectron KE suggested that the additional Pd–C interaction species are largely located near the surface and not in deeper layers. C/Pd intensity ratios from these experiments were modeled in an ERXPS-type approach, and some relevant results are shown in Figure 13.23c. The experimental data ("Experiment: 358 K") could obviously not be reproduced by just a simple carbon multilayer on the Pd surface ("Model: 3.5 ML"). Instead, the authors assumed that the surface region consists of three layers above the bulk pure Pd. The successful "Model: 358 K" consists of a 0.3 nm carbon overlayer (adsorbate phase) above an ~1.4 nm Pd–C surface phase of nearly 1:1 stoichiometry (Pd–$C_{0.82}$), followed by a rather thick (14 nm) Pd layer with C dissolved in it (Pd–$C_{0.15}$). The stability of this Pd-C surface phase consisting of 3 layers is related to the presence of the pentyne in the gas phase: upon switching off the pentyne, carbon was released, and the resulting layer model ("Model: C5 off") showed the Pd–$C_{0.82}$ layer below the adsorbate phase shrunk to 0.7 nm and followed by a considerably depleted C-in-Pd solution (Pd–$C_{0.03}$) of only 4 nm thickness.

Combining spectroscopic with reactivity data, the authors assigned the selectivity of Pd in pentyne hydrogenation to the Pd–C surface phase. In this phase, hydrogen absorption seems to be suppressed, which prevents the highly active but unselective subsurface hydrogen [159, 160] from interfering with the more selective hydrogenation by surface hydrogen.

13.5 Outlook

XPS was a major surface analysis technique for catalysts and other materials over many years owing to its unique promise of surface sensitivity combined with

quantitative analysis of elemental compositions and distribution of oxidation states. Its popularity was on the decline after some of its limitations had been realized: its output being averaged over a finite sampling depth, the often nontrivial assignment of signals detected, and the UHV requirement, which is a serious setback in the age of *in situ* and *operando* studies.

This chapter has shown, however, that even traditional XPS offers an analytical potential highly relevant for material synthesis and application. The utilization of this potential will often require going beyond binding energy-based assignments and making use of the wealth of final state-related features such as satellites and multiplet splitting, and of Auger lines (chemical state plots), applying UPS where possible, and combining XPS with other techniques, in particular LEIS. Recent developments in instrumentation have effectively alleviated the UHV requirement, allowing XPS to be performed under some millibarbar reactant pressures. Although this is still below the pressures usually encountered in real catalysis, this approach has already provided exciting insight into catalyst dynamics involving not just the outermost surface layer but also the adjacent region. In its APPES version, XPS is therefore at the doorstep of its *in situ* age. Apart from increasing accessible pressure ranges, future developments will also have to deal with the minimization of sample damage with sensitive oxidation states by the very intense synchrotron radiation. Quantitative depth profiling by ERXPS, having considerable promise also for rough surfaces, might be further developed, for example, for distributions of oxidation states, and become a valuable aid in synchrotron XPS work.

Acknowledgments

I would like to express my gratitude to Professor Volker Staemmler, Bochum, for contributing Section 13.2.2.2 and for critical reading of the manuscript. Thanks are due also to many colleagues who helped me with details of their methods and hints on the literature, among them Professor G. Witte (Marburg) and Drs. A. Knop-Gericke (Berlin), M. Gottfried (Erlangen), and T. Strunskus (Kiel).

References

1 Briggs, D. and Grant, J.T. (eds.) (2003) *Surface Analysis by Auger and X-Ray Photoelectron Spectroscopy*, IM Publications, Chichester and Surface Spectra Ltd., Manchester.

2 Briggs, D. and Seah, M.P. (eds.) (1990) *Practical Surface Analysis*, 2nd edn., John Wiley & Sons, Ltd., Chichester.

3 Wagner, C.D., Naumkin, A.V., Raut-Vass, A., Allison, J.W., Powell, C.J., and Rumble, J.R. Jr. (2003) NIST X-Ray Photoelectron Spectroscopy Database, National Institute of Standards and Technology, http://srdata.nist.gov/xps/Default.aspx (last accessed 4 July 2011).

4 Hüfner, S. (2003) *Photoelectron Spectroscopy: Principles and Applications*, Springer, Berlin.

5 Ertl, G. and Küppers, J. (1985) *Low Energy Electrons and Surface Chemistry*, 2nd edn., VCH Verlag GmbH, Weinheim.

6 Védrine, J.C. (1994) in *Catalysts Characterisation. Physical Techniques for Solid Materials* (eds. B. Imelik and J.C. Védrine), Plenum Press, New York, p. 467.
7 Innes, P.D. (1907) *Proc. R. Soc. Lond., Ser. A*, **79**, 442.
8 Steinhardt, R.G. and Serfass, E.J. (1951) *Anal. Chem.*, **23**, 1585.
9 Siegbahn, K., Nording, C., Fahlmarn, A., Nordberg, R., Hamrin, K., Hedman, J., Johansson, G., Bergmark, T., Karlsson, S., Lindgren, I., and Lindberg, B. (1967) *ESCA: Atomic, Molecular and Solid State Structure by Means of Electron Spectroscopy*, Almqvist and Wiksells, Uppsala.
10 Rosseland, S. (1923) *Z. Phys.*, **14**, 173.
11 Auger, P. (1926) *Ann. Phys. (Paris)*, **6**, 183.
12 Lander, J.J. (1953) *Phys. Rev.*, **91**, 1382.
13 Weber, R.E. and Peria, W.T. (1967) *J. Appl. Phys.*, **38**, 4355.
14 Harris, L.A. (1968) *J. Appl. Phys.*, **39**, 1419.
15 Matienzo, L.J., Yin, L.I., Grim, S.O., and Swartz, W.E. (1973) *Inorg. Chem.*, **12**, 2762.
16 Tsisun, E.L., Nefedov, B.K., Shpiro, E.S., Antoshin, G.V., and Minachev, K.M. (1984) *React. Kinet. Catal. Lett.*, **24**, 37.
17 Cimino, A. and de Angelis, B.A. (1975) *J. Catal.*, **36**, 11.
18 Yamada, M., Yasumaru, J., Houalla, M., and Hercules, D.M. (1991) *J. Phys. Chem.*, **95**, 7037.
19 Biloen, P. and Pott, G.T. (1973) *J. Catal.*, **30**, 169.
20 Patterson, T.A., Carver, J.C., Leyden, D.E., and Hercules, D.M. (1976) *J. Phys. Chem.*, **80**, 1700.
21 Goldwasser, J., Fang, S.M., Houalla, M., and Hall, W.K. (1989) *J. Catal.*, **115**, 34.
22 Haber, J., Marczewski, W., Stoch, J., and Ungier, L. (1975) *Ber. Bunsenges. Phys. Chem.*, **79**, 970.
23 Brox, B. and Olefjord, I. (1988) *Surf. Interface Anal.*, **13**, 3.
24 Grünert, W., Stakheev, A.Y., Feldhaus, R., Anders, K., Shpiro, E.S., and Minachev, K.M. (1991) *J. Phys. Chem.*, **95**, 1323.
25 Gassman, P.G., Macomber, D.W., and Willging, S.M. (1985) *J. Am. Chem. Soc.*, **107**, 2380.
26 Grünert, W., Stakheev, A.Y., Mörke, W., Feldhaus, R., Anders, K., Shpiro, E.S., and Minachev, K.M. (1992) *J. Catal.*, **135**, 287.
27 Grünert, W., Stakheev, A.Y., Mörke, W., Feldhaus, R., Anders, K., Shpiro, E.S., and Minachev, K.M. (1992) *J. Catal.*, **135**, 269.
28 Grünert, W., Muhler, M., Schroeder, K.-P., Sauer, J., and Schlögl, R. (1994) *J. Phys. Chem.*, **98**, 10920.
29 Elmasides, C., Kontarides, D.I., Grünert, W., and Verykios, X.E. (1999) *J. Phys. Chem. B*, **103**, 5227.
30 Grünert, W., Saffert, W., Feldhaus, R., and Anders, K. (1986) *J. Catal.*, **99**, 149.
31 Grünert, W., Shpiro, E.S., Feldhaus, R., Anders, K., Antoshin, G.V., and Minachev, K.M. (1987) *J. Catal.*, **107**, 522.
32 Bastl, Z. (1989) *Izv. Khim.*, **22**, 173.
33 Grünert, W., Brückner, A., Hofmeister, H., and Claus, P. (2004) *J. Phys. Chem. B*, **108**, 5709.
34 Radnik, J., Mohr, C., and Claus, P. (2003) *Phys. Chem. Chem. Phys.*, **5**, 172.
35 Zwijnenburg, A., Goossens, A., Sloof, W.G., Crajé, M.W.J., van der Kraan, A.M., de Jongh, L.J., Makkee, M., and Moulijn, J.A. (2002) *J. Phys. Chem. B*, **106**, 9853.
36 Kruse, N. and Chenakin, S. (2011) *Appl. Catal. A*, **391**, 367.
37 Bukhtiyarov, V.I., Hävecker, M., Kaichev, V.V., Knop-Gericke, A., Mayer, R.W., and Schlögl, R. (2001) *Catal. Lett.*, **74**, 121.
38 Knop-Gericke, A., Hävecker, M., Schedel-Niedrig, T., and Schlögl, R. (2001) *Top. Catal.*, **15**, 27.
39 Bluhm, H., Hävecker, M., Knop-Gericke, A., Kleimenov, E., Schlögl, R., Teschner, D., Bukhtiyarov, V.I., Ogletree, D.F., and Salmeron, M. (2004) *J. Phys. Chem. B*, **38**, 14340.
40 Teschner, D., Vass, E., Hävecker, M., Zafeiratos, S., Schnörch, P., Sauer, H., Knop-Gericke, A., Schlögl, R., Chamam, M., Wootsch, A., Canning, A.S., Gamman, J.J., Jackson, S.D., McGregor, J., and Gladden, L.F. (2006) *J. Catal.*, **242** 26.
41 Stevens, J.S., Byard, S.J., Muryn, C.A., and Schroeder, S.L.M. (2010) *J. Phys. Chem. B*, **114**, 13961.
42 Koopmans, T. (1933) *Physica*, **1**, 104.
43 Irrera, S. and Costa, D. (2008) *J. Chem. Phys.*, **128**, 114709.
44 Tu, G., Carravetta, V., Vahtras, O., and Agren, H. (2007) *J. Chem. Phys.*, **127**, 174110.
45 Oji, H., Mitsumoto, R., Ito, E., Ishii, H., Ouchi, Y., Seki, K., Yokoyama, T., Ohta, T.,

and Kosugi, N. (1998) *J. Chem. Phys.*, **109**, 10409.
46 Slater, J.C. (1972) *Adv. Quantum Chem.*, **6**, 1.
47 Janak, J.F. (1978) *Phys. Rev. B*, **18**, 7165.
48 Slater, J.C. and Johnson, K.H. (1972) *Phys. Rev. B*, **5**, 844.
49 Ganduglia-Pirovano, M.V., Scheffler, M., Baraldi, A., Lizzit, S., Comelli, G., Paolucci, G., and Rosei, R. (2001) *Phys. Rev. B*, **63**, 205415.
50 Hermann, K., Petterson, L.G.M., Casida, M.E., Daul, C., Goursot, A., Koester, A., Prognov, E., St-Amant, A., and Salahub, D.R. (2009) StoBe-deMon version 3.0.
51 Cavalleri, M., Hermann, K., Knop-Gericke, A., Haevecker, M., Herbert, R., Hess, C., Oestereich, A., Döbler, J., and Schlögl, R. (2009) *J. Catal.*, **262**, 215.
52 Rössler, N. and Staemmler, V. (2003) *Phys. Chem. Chem. Phys.*, **5**, 3580.
53 Rössler, N., Kotsis, K., and Staemmler, V. (2006) *Phys. Chem. Chem. Phys.*, **8**, 697.
54 Alagia, M., Baldacchini, C., Grazia Betti, M., Bussolotti, F., Carravetta, V., Ekström, U., Mariani, C., and Stranges, S. (2005) *J. Chem. Phys.*, **122**, 124305.
55 Kotsis, K. and Staemmler, V. (2006) *Phys. Chem. Chem. Phys.*, **9**, 1490.
56 Takahashi, M., Igarashi, J., and Hamada, N. (2008) *Phys. Rev. B*, **78**, 155108.
57 Torelli, P., Giordano, L., Benedetti, S., Luches, P., Annese, E., Valeri, S., and Pacchioni, G. (2009) *J. Phys. Chem. C*, **113**, 19957.
58 Banna, M.S., Frost, D.C., McDowell, C.A., and Wallbank, B. (1978) *J. Chem. Phys.*, **68**, 696.
59 Grünert, W., Schlögl, R., and Karge, H.G. (1993) *J. Phys. Chem.*, **97**, 8638.
60 Heber, M. (1999) PhD thesis, Ruhr-Universität (Bochum).
61 Grünert, W., Hayes, N.W., Joyner, R.W., Shpiro, E.S., Siddiqui, M.R.H., and Baeva, G.N. (1994) *J. Phys. Chem.*, **98**, 10832.
62 Omata, K., Takada, T., Kasahara, S., and Yamada, M. (2006) *Appl. Catal. B*, **24**, 255.
63 Shyu, J.Z., Weber, W.H., and Gandhi, H.S. (1989) *J. Phys. Chem.*, **92**, 4964.
64 Muhler, M., Schlögl, R., and Ertl, G. (1992) *J. Catal.*, **138**, 413.
65 Okada, K. and Kotani, A. (1992) *Bull. Phys. Soc. Jpn.*, **61**, 4619.
66 Makshina, E.V., Sirotin, S.V., van den Berg, M.W.E., Klementiev, K.V., Yushchenko, V.V., Mazo, G.N., Grünert, W., and Romanovsky, B.V. (2006) *Appl. Catal. A*, **312**, 59.
67 Grünert, W., Sauerlandt, U., Schlögl, R., and Karge, H.G. (1993) *J. Phys. Chem.*, **97**, 1413.
68 Lee, E.F.T. and Rees, L.V.C. (1987) *Zeolites*, **7**, 143.
69 Gardella, J.A., Ferguson, S.A., and Chin, R.L. (1986) *Appl. Spectrosc.*, **40**, 224.
70 Stakheev, Yu.A., Shulga, Yu.M., Gaidai, N.A., Telegina, N.S., Tkachenko, O.P., Kustov, L.M., and Minachev, K.M. (2001) *Mendeleev Commun.*, 186.
71 Uozumi, T., Okada, K., Kotani, A., Zimmermann, R., Steiner, P., Hüfner, S., Tezuka, Y., and Shin, S. (1997) *J. Electron Spectrosc. Relat. Phenom.*, **83**, 9.
72 Okamoto, Y., Masaki, M., Imanaka, T., and Teranishi, S. (1976) *Bull. Chem. Soc. Jpn.*, **49**, 859.
73 Frost, D.C., McDowell, C.A., and Woolsey, I.S. (1972) *Chem. Phys. Lett.*, **17**, 320.
74 Vedrine, J.C., Holliger, G., and Duc, T.M. (1978) *J. Phys. Chem.*, **82**, 1515.
75 Grünert, W., Shpiro, E.S., Feldhaus, R., Anders, K., Antoshin, G.V., and Minachev, K.M. (1986) *J. Catal.*, **100**, 138.
76 Wichterlova, B., Krajcikova, L., Tvaruzková, Z., and Beran, S. (1984) *J. Chem. Soc., Faraday Trans. 1*, **80**, 2639.
77 Werner, W.S.M. (2003) in *Surface Analysis by Auger and X-Ray Photoelectron Spectroscopy* (eds. D. Briggs and J.T. Grant), IM Publications, Chichester and Surface Spectra Ltd., Manchester, p. 235.
78 Tanuma, S. (2003) in *Surface Analysis by Auger and X-Ray Photoelectron Spectroscopy* (eds. D. Briggs and J.T. Grant), IM Publications, Chichester and Surface Spectra Ltd., Manchester, p. 259.
79 Tanuma, S., Powell, C.J., and Penn, D.R. (1994) *Surf. Interface Anal.*, **21**, 165.
80 Scofield, J.H. (1976) *J. Electron Spectrosc. Relat. Phenom.*, **8**, 129.
81 Yeh, J.J. and Lindau, I. (1985) *At. Data Nucl. Data*, **32**, 2.
82 Angevine, P.J., Delgass, W.N., and Vartulli, J.C. (1976) in *6th International Congress on Catalysis*, vol. 2 (eds. G.C. Boln, P.B. Wells, and F.C. Tompkins), Chemical Society, London, p. 611.
83 Kerkhof, F.P.J.M. and Moulijn, J.A. (1979) *J. Phys. Chem.*, **83**, 1612.

84 Cumpson, P.J. (1995) *J. Electron Spectrosc. Relat. Phenom.*, **73**, 25.

85 Cumpson, P.J. (2003) in *Surface Analysis by Auger and X-Ray Photoelectron Spectroscopy* (eds. D. Briggs and J.T. Grant), IM Publications, Chichester and Surface Spectra Ltd., Manchester, p. 651.

86 Pijolat, M. and Hollinger, G. (1981) *Surf. Sci.*, **105**, 114.

87 Tyler, B.J., Castner, D.G., and Ratner, B.D. (1989) *Surf. Interface Anal.*, **14**, 443.

88 Smith, G.C. and Livesey, A.K. (1992) *Surf. Interface Anal.*, **19**, 175.

89 Fadley, C.S., Baird, R.J., Siekhaus, W., Novakov, T., and Bergström, S.A.L. (1974) *J. Electron Spectrosc. Relat. Phenom.*, **4**, 93.

90 Gunter, P.L.J., Gijzeman, O.L.J., and Niemantsverdriet, J.W. (1997) *Appl. Surf. Sci.*, **115**, 342.

91 Olejnik, K., Zemek, J., and Werner, W.S.M. (2005) *Surf. Sci.*, **595**, 212.

92 Zemek, J., Olejnik, K., and Klapetek, P. (2008) *Surf. Sci.*, **602**, 1440.

93 Zemek, J. and Olejnik, K. (2008) *Surf. Sci.*, **602**, 2581.

94 Esaka, F., Furuya, K., Shimada, H., Imamura, M., Matsubayashi, N., Sato, T., Nishijima, A., Kikuchi, T., Kawana, A., and Ichimura, H. (1997) *Surf. Sci.*, **377**, 197.

95 Zier, M., Oswald, S., Reiche, R., and Wetzig, K. (2007) *Microchim. Acta*, **156**, 99.

96 Merzlikin, S.V., Tolkachev, N.N., Strunskus, T., Witte, G., Glogowski, T., Wöll, C., and Grünert, W. (2008) *Surf. Sci.*, **602**, 755.

97 Shirley, D.A. (1972) *Phys. Rev. B*, **5**, 4709.

98 Tougaard, S. (2003) in *Surface Analysis by Auger and X-Ray Photoelectron Spectroscopy* (eds. D. Briggs and J.T. Grant), IM Publications, Chichester and Surface Spectra Ltd., Manchester, p. 295.

99 Fairley, N. (2003) in *Surface Analysis by Auger and X-Ray Photoelectron Spectroscopy* (eds. D. Briggs and J.T. Grant), IM Publications, Chichester and Surface Spectra Ltd., Manchester, p. 397.

100 Doniach, S. and Sunjic, M. (1970) *J. Phys. C*, **3**, 285.

101 Fiedor, J.N., Proctor, A., Houalla, M., and Hercules, D.M. (1993) *Surf. Interface Anal.*, **20**, 1.

102 Scierka, S.J., Proctor, A., Houalla, M., Fiedor, J.N., and Hercules, D.M. (1993) *Surf. Interface Anal.*, **20**, 901.

103 Fiedor, J.N., Proctor, A., Houalla, M., and Hercules, D.M. (1995) *Surf. Interface Anal.*, **23**, 204.

104 Eberhardt, M.A., Proctor, A., Houalla, M., and Hercules, D.M. (1996) *J. Catal.*, **160**, 27.

105 Stickle, W.F. (2003) in *Surface Analysis by Auger and X-Ray Photoelectron Spectroscopy* (eds D. Briggs and J.T. Grant), IM Publications, Chichester and Surface Spectra Ltd., Manchester, p. 377.

106 Wagner, C.D., Gale, L.H., and Raymond, R.H. (1979) *Anal. Chem.*, **51**, 466.

107 Espinos, J.P., Morales, J., Barranco, A., Caballero, A., Holgado, J.P., and Gonzalez-Elipe, A.R. (2002) *J. Phys. Chem. B*, **106**, 6921.

108 Morales, J., Espinos, J.P., Caballero, A., Gonzalez-Elipe, A.R., and Mejias, J.A. (2005) *J. Phys. Chem. B*, **109**, 7758.

109 Liese, T. and Grünert, W. (1997) *J. Catal.*, **172**, 34.

110 Moretti, G. (1997) in *Handbook of Heterogeneous Catalysis*, 1st edn., vol. 2 (eds. G. Ertl, H. Knözinger, and J. Weitkamp), VCH Verlag GmbH, Weinheim, p. 632.

111 Moretti, G. (1994) *Zeolites*, **14**, 469.

112 Satta, M. and Moretti, G. (2010) *J. Electron Spectrosc. Relat. Phenom.*, **178**, 123.

113 Sexton, B.A., Smith, T.D., and Sanders, J.V. (1985) *J. Electron Spectrosc. Relat. Phenom.*, **35**, 27.

114 Jirka, I., Wichterlova, B., and Maryska, M. (1991) *Stud. Surf. Sci. Catal.*, **69**, 269.

115 Wandelt, K. (1982) *Surf. Sci. Rep.*, **2**, 1.

116 Henrich, V.E. and Cox, P.A. (1994) *The Surface Science of Metal Oxides*, Cambridge University Press, Cambridge.

117 Liang, K.S., Hughes, G.J., and Chianelli, R.R. (1984) *J. Vac. Sci. Technol. A*, **2**, 991.

118 Heber, M. and Grünert, W. (2001) *Top. Catal.*, **15**, 3.

119 Heber, M. and Grünert, W. (2000) *J. Phys. Chem. B*, **104**, 5288.

120 Heber, M. and Grünert, W. (2000) *Stud. Surf. Sci. Catal.*, **130**, 3279.

121 Heber, M. and Grünert, W. (2000) *Mat.-Wiss. Werkstofftech.*, **31**, 864.

122 Grünert, W., Schlögl, R., and Karge, H.G. (1993) *Surf. Interface Anal.*, **20**, 603.

123 Grünert, W., Muhler, M., and Karge, H.-G. (1996) *J. Chem. Soc., Faraday Trans.*, **92**, 701.

124 Kurtz, R.L., Stockbauer, R., Madey, T.E., Mueller, D., Shih, A., and Toth, L. (1988) *Phys. Rev. B*, **37**, 7936.

125 Connor, J.A., Considine, M., Hiller, H., and Briggs, D. (1977) *J. Electron Spectrosc. Relat. Phenom.*, **12**, 143.

126 Liu, P., Kendelewicz, T., Brown, G.E. Jr., Parks, G.A., and Pianetta, P. (1998) *Surf. Sci.*, **416**, 326.

127 Hermann, K., Witko, M., Druzinic, R., Chakrabarti, A., Tepper, B., Elsner, M., Gorschlüter, A., Kuhlenbeck, H., and Freund, H.-J. (1999) *J. Electron Spectrosc. Relat. Phenom.*, **98–99**, 245.

128 Guimond, S., Abu Haija, M., Kaya, S., Lu, J., Weissenrieder, J., Shaikhutdinov, S., Kuhlenbeck, H., Freund, H.J., Döbler, J., and Sauer, J. (2006) *Top. Catal.*, **38**, 117.

129 Chen, P., Wu, X.D., Lin, J., Li, H.X., and Tan, K.L. (2000) *Carbon*, **38**, 139.

130 Wiggins-Camacho, J.D. and Stevenson, K.J. (2009) *J. Phys. Chem. C*, **113**, 19082.

131 Brongersma, H.H., Draxler, M., de Ridder, M., and Bauer, P. (2007) *Surf. Sci. Rep.*, **62**, 63.

132 Jansen, W.P.A., Ruitenbeck, M., van der Gron, A.W.D., Geus, J.W., and Brongersma, H.H. (2000) *J. Catal.*, **196**, 379.

133 Delichere, P., Bere, K., and Abon, M. (1998) *Appl. Catal. A*, **172**, 295.

134 Richter, F., Papp, H., Götze, T., Wolf, G.U., and Kubias, B. (1998) *Surf. Interface Anal.*, **26**, 736.

135 Wolf, D., Heber, M., Grünert, W., and Muhler, M. (2002) *J. Catal.*, **199**, 92.

136 Kohl, A., Taglauer, E., and Knözinger, H. (1999) *Phys. Status Solidi A*, **173**, 85.

137 Briand, L.E., Tkachenko, O.P., Guraya, M., Wachs, I.E., and Grünert, W. (2004) *Surf. Interface Anal.*, **36**, 238.

138 Briand, L.E., Tkachenko, O.P., Guraya, M., Gao, X., Wachs, I.E., and Grünert, W. (2004) *J. Phys. Chem. B*, **108**, 4823.

139 Merzlikin, S.V., Tolkachev, N.N., Briand, L.E., Strunskus, T., Wöll, C., Wachs, I.E., and Grünert, W. (2010) *Angew. Chem. Int. Ed.*, **49**, 8037.

140 Siegbahn, H. and Siegbahn, K. (1973) *J. Electron Spectrosc. Relat. Phenom.*, **2**, 319.

141 Thompson, M., Hewitt, P.A., and Woollscroft, D.S. (1976) *Anal. Chem.*, **48**, 1336.

142 Joyner, R.W. and Roberts, M.W. (1979) *Chem. Phys. Lett.*, **60**, 459.

143 Joyner, R.W., Roberts, M.W., and Yates, K. (1979) *Surf. Sci.*, **87**, 501.

144 Ogletree, D.F., Bluhm, H., Lebedev, G., Fadley, C.S., Hussain, Z., and Salmeron, M. (2002) *Rev. Sci. Instrum.*, **73**, 3872.

145 Salmeron, M. and Schlögl, R. (2008) *Surf. Sci. Rep.*, **63**, 169.

146 Knop-Gericke, A., Kleimenov, E., Hävecker, M., Blume, R., Teschner, D., Zafeiratos, S., Schlögl, R., Bukhtiyarov, V.I., Kaichev, V.V., Prosvirin, I.P., Nizovskii, A.I., Bluhm, H., Barinov, A., Dudin, P., and Kisinova, M. (2009) *Adv. Catal.*, **52** 213.

147 Denecke, R., Kinne, M., Whelan, C.M., and Steinrück, H.P. (2002) *Surf. Rev. Lett.*, **9**, 797.

148 Pantförder, J., Pollmann, S., Zhu, J.F., Borgmann, D., Denecke, R., and Steinrück, H.P. (2005) *Rev. Sci. Instrum.*, **76**, 014102.

149 Kelly, M.A., Shek, M.L., Pianetta, A., Gür, T.M., and Beasley, M.R. (2001) *J. Vac. Sci. Technol. A*, **19**, 2127.

150 Claus, P. and Hofmeister, H. (1999) *J. Phys. Chem. B*, **103**, 2766.

151 Grasselli, R.K. (2005) *Catal. Today*, **99**, 23.

152 Pawelec, B. (2006) in *Metal Oxides – Chemistry and Applications* (ed. J.L.G. Fierro), CRC Press, Francis & Taylor, Boca Raton, FL, p. 111.

153 Erdman N., Poeppelmeier, K.R., Asta, M., Warschkow, O., Ellis, D.E., and Marks, L.D. (2002) *Nature*, **419**, 55.

154 Bluhm, H., Hävecker, M., Kleimenov, E., Knop-Gericke, A., Liskowski, A., Schlögl, R., and Su, D.S. (2003) *Top. Catal.*, **23**, 99.

155 Briand, L.E., Hirt, A.H., and Wachs, I.E. (2001) *J. Catal.*, **202**, 268.

156 Briand, L.E., Jehng, J.-M., Cornaglia, L., Hirt, A.H., and Wachs, I.E. (2003) *Catal. Today*, **78**, 257.

157 Al-Ammar, A.S. and Webb, G. (1978) *J. Chem. Soc., Faraday Trans. 1*, **74**, 657.

158 Den Hartog, A.J., Deng, M., Jongerius, F., and Ponec, V. (1990) *J. Mol. Catal.*, **60**, 99.

159 Haug, K.L., Bürgi, T., Trautmann, T.R., and Ceyer, S.T. (1998) *J. Am. Chem. Soc.*, **120**, 8885.

160 Doyle, A.M., Shaikhutdinov, S.K., Jackson, S.D., and Freund, H.J. (2005) *Angew. Chem. Int. Ed.*, **42**, 5240.

14
Single Molecule Spectroscopy

Timo Lebold, Jens Michaelis, Thomas Bein, and Christoph Bräuchle

14.1
Introduction

The idea of magnifying and visualizing objects that are too small to be seen by the naked eye has a long history dating back to the early seventeenth century, when Janssen and Galilei independently developed the first working light microscopes. Since those early days, optical microscopy has undergone a tremendous evolution, leading to a variety of different techniques that nowadays constitute key analysis and characterization methods in many scientific disciplines.

This chapter describes the utilization of optical microscopy to observe the fluorescence of individual molecules. The single-molecule spectroscopy (SMS) technique was pioneered by Moerner and Kador [1] and Orrit and Bernard [2], who, in 1989–1990, for the first time reported the optical detection of individual fluorophores in a solid matrix at liquid helium temperature [3]. Already in those early days it became clear that a single molecule is an ultrasensitive reporter for changes in its local environment, which result in abrupt changes of its excitation [4] and emission spectra. Moreover, owing to its transition dipole moment, the single-molecule orientation is also detectable [5] and, as will be shown later in this chapter, this has great potential for characterizing local interactions, which are likely to change during catalytic reactions.

About 5 years later, it was also shown that individual fluorescent molecules could be detected at room temperature, thus opening the route to many interesting applications in materials and life sciences. With that, the field of single-molecule microscopy (SMM) quickly emerged: Funatsu *et al.* [6] imaged single fluorescently labeled myosin molecules and thereby detected individual ATP turnover reactions. Around the same time, Schmidt *et al.* [7, 8] utilized sensitive fluorescence microscopy to analyze the diffusion of single fluorescently labeled lipids in a phospholipid membrane at room temperature. In these studies, maps were also shown that depict the diffusion pathways of the individual molecules, their so-called trajectories. These trajectories were obtained by fitting the single-molecule fluorescence signal to a two-dimensional Gaussian function and tracking the molecular position throughout the

Characterization of Solid Materials and Heterogeneous Catalysts: From Structure to Surface Reactivity, First Edition. Edited by Michel Che and Jacques C. Védrine.
© 2012 Wiley-VCH Verlag GmbH & Co. KGaA. Published 2012 by Wiley-VCH Verlag GmbH & Co. KGaA.

recorded frame sequence [single-particle tracking (SPT)]. Thus, the potential of SPT methods to analyze membrane dynamics and characterize different modes of motion, that is, anomalous, normal, confined, and directed diffusion, was already recognized at that time [9]. Later, SPT studies of biomolecules *in vitro* and *in vivo* followed [10–12]. Subsequently, SMS and SMM in combination with SPT were applied also in materials science to analyze the diffusion of individual molecules inside porous hosts [13–18]. As will be shown in this chapter, a combination of SMS and SMM techniques allows for a detailed mechanistic investigation of the interactions of the molecules with the surrounding host matrix, and these interactions also yield much information about the properties of the host. The molecular probes can be accurately mapped along their diffusion pathway in real time, even in the case of highly dynamic processes. This can make the SMM techniques an interesting tool for studying catalytic processes, such as the diffusion of reactants inside a catalyst substrate. Moreover, with SMS the spectral and orientational dynamics of the observed molecules can be analyzed in great detail. This also offers insights into the mechanisms of guest–host interactions. Therefore, SMS/SMM approaches are an important complement to electron microscopy techniques [19, 20] that can characterize the structural properties of a host, but cannot easily yield dynamic information about the guest molecules and their interactions with the host.

Conventional fluorescence microscopy techniques usually apply ensemble concentrations of the fluorescent molecules. This leads to an inevitable averaging of all observed parameters over the entire ensemble. In contrast, single-molecule techniques visualize each individual molecular event and therefore can reveal subpopulations of differently behaving molecules. Only then can heterogeneities in the behavior of the individual fluorophores and also in the structure of the host matrix be detected. This is of particular importance for catalysis, since the functionality of the catalyst is highly dependent on its exact structural and morphological constitution. Moreover, owing to the ultra-low concentrations (10^{-10}–10^{-11} mol l^{-1}), using individual molecules as probes to characterize a host substrate is a noninvasive technique that does not alter the studied substrate. Single-molecule techniques therefore often prevail over ensemble fluorescence approaches and have impacted on many different scientific disciplines, such as biology [10, 11, 21–25] and materials science [18, 26]. There are several comprehensive reviews in the literature about single-molecule techniques and their applications, which provide an excellent overview of this rapidly developing field [20, 27–29].

14.2 Description of the Method

Detecting the weak fluorescence of single molecules by optical methods is very challenging. The fluorophores can be excited by a laser, yet only a tiny fraction of the incident laser photons are actually absorbed by the molecule. The absorption cross-section σ of a molecule, a measure of the area with which the molecule can "harvest" the photons, is in the range of nm^2 and therefore small compared with the

illuminated region. Additionally, fluorescent impurities in the sample and also resonant or nonresonant scattering further complicate single-molecule detection. Hence, as a prerequisite for single-molecule detection, one needs to reduce the excitation volume in order to maximize the signal-to-background ratio. One way to minimize the background and reach single-molecule sensitivity is to use a confocal microscope. Figure 14.1a depicts a schematic view of a laser scanning confocal microscope (LSCM). The sample can be excited by a laser through a high numerical aperture (NA) oil-immersion objective, and the fluorescent light is collected through the same objective (epi-fluorescence setup). With such a setup, single-molecule sensitivity can be achieved using a small detection volume created by a pinhole in front of the detector. A prominent choice for detecting single-molecule fluorescence is a single-photon counting avalanche photodiode (SPAPD). Although the time response of an SPAPD is extremely fast and therefore dynamic processes can also be recorded, imaging with an SPAPD is rather slow, since the excitation light has to be scanned over the entire region of interest (ROI). Moreover, in order to investigate the movement of molecules, the same ROI has to be scanned repeatedly. Therefore, a widefield fluorescence microscope (Figure 14.1b), where a large area of the sample (e.g., $30 \times 30\,\mu m$) can be illuminated homogeneously, thereby exciting all molecules in the illuminated region simultaneously, is often preferred for imaging applications. The individual fluorescence signals can be recorded by a cooled charge-coupled device (CCD) camera, which allows recording of images with an integration time down to a few milliseconds per image and a high frame rate. By using on-chip electron multiplying gain, the electronic noise of the camera can be greatly reduced and counting of single photons is possible. Hence, highly dynamic processes can be monitored. The data acquisition is then only limited by the photostability of the utilized fluorophore. In contrast to LSCM, out-of-focus fluorescence can be a bigger problem for widefield microscopy, owing to the low resolution in the axial direction ($\sim 1\,\mu m$). However, this can be overcome by the use of a total internal reflection (TIRF) geometry for excitation or the utilization of thin samples such as thin films. However, TIRF requires a significant change in the refractive index between the glass substrate and the sample. A similar reduction of the background can be achieved by imaging thin ($\sim 100\,nm$) sample films as discussed in this chapter. Confocal and widefield fluorescence microscopy methods complement each other very well and thus provide valuable tools for single-molecule investigations.

Further important parameters that characterize the single molecule and yield important information about the interaction of the individual molecule with its local environment are the molecule's orientation and its fluorescence emission spectrum. Figure 14.2 depicts schematically a setup for the simultaneous measurement of these parameters.

In order to determine the molecular orientation, a technique called fluorescence polarization modulation microscopy (FPM) can be applied [5]. The polarization of the excitation light can be modulated using a rotating $\lambda/2$ retardation plate. If the transition dipole moment of the molecule is oriented parallel to the excitation polarization, the excitation is maximized whereas the molecule does not become excited at all in case of a perpendicular orientation. Thus, by rotating the polarization

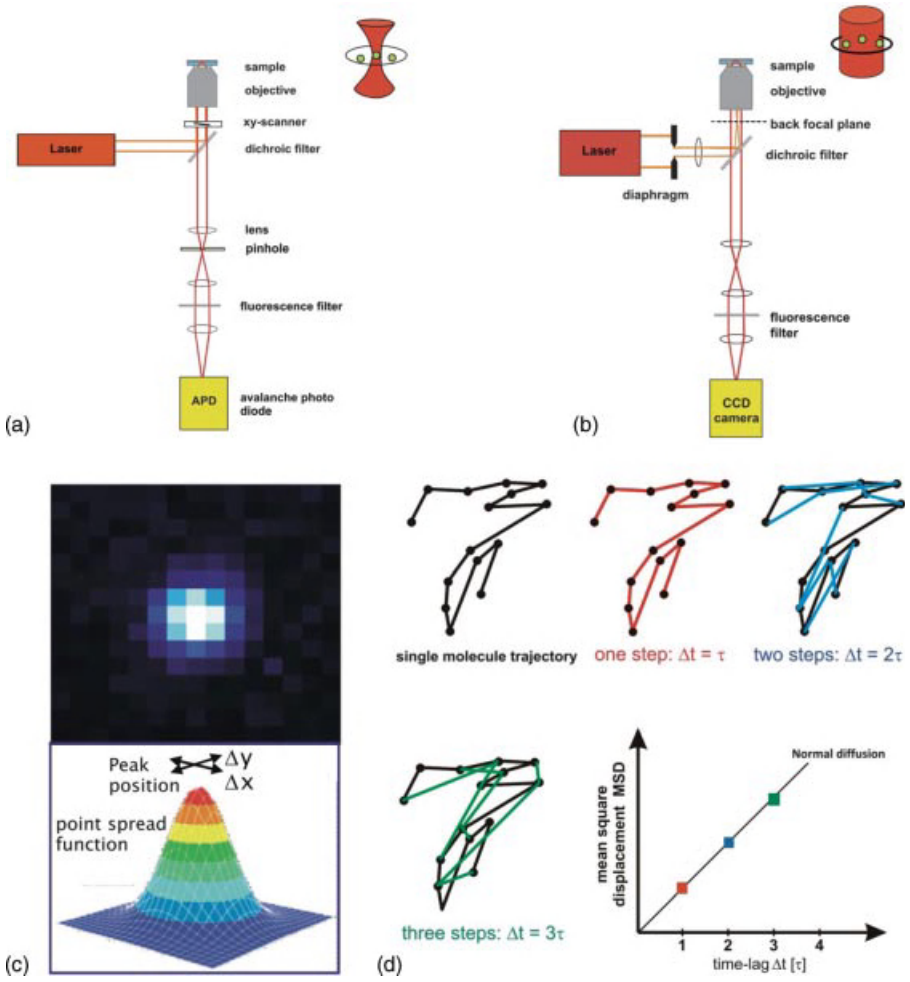


Figure 14.1 Typical SMM setups and SPT. (a) LSCM with an avalanche photodiode (APD) for single-molecule detection. The laser light is focused on to the sample using a high numerical aperture oil-immersion objective. The same objective is used to collect the single molecule fluorescence efficiently (epi-fluorescence setup). The confocal volume (see schematic inset) needs to be scanned over the entire ROI for recording an image. (b) Widefield microscope for homogeneous illumination of an ROI, resulting in simultaneous excitation of all fluorophores (see inset). Highly efficient dielectric bandpass filters are important for detecting the weak fluorescence of a single molecule in order to remove stray light due to scattering. The attached CCD camera provides single-molecule sensitivity and allows recording of images with a high frame rate and a low integration time per image. (c) The recorded diffraction-limited spot of a single molecule is fitted by a two-dimensional Gaussian function [Eq. (14.1)]. This yields the x and y coordinates of the molecule at a certain time, with a positioning accuracy far below the optical resolution limit determined by the Rayleigh criterion. (d) Schematic representation of the analysis of a single-molecule trajectory in order to extract the time dependence of the MSD. The individual step lengths are evaluated for various time-lags $\Delta t = n\tau$, where τ is the integration time per frame (for clarity, only some steps that comply with the selected time lag are marked in each trajectory). The average of all steps for a certain time lag is represented by a point in the MSD plot.

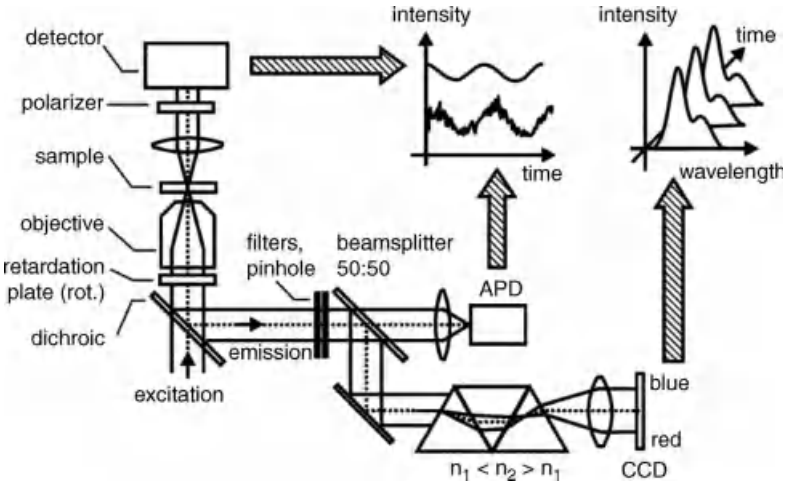


Figure 14.2 Simultaneous observation of single-molecule fluorescence polarization and emission spectra. This setup, based on an LSCM, allows one to measure the molecular orientation and spectrum at the same time. For measuring the orientation of the transition dipole moment of the single molecule in the focal plane (in-plane orientation), the confocal setup is modified by introducing polarization optics: with a rotating $\lambda/2$ retardation plate, the polarization of the excitation light can be modulated. It is placed in the excitation beam directly below the objective. The polarization plane of the excitation light is monitored by a detector in transmission placed behind a polarizer (thereby defining the reference for the orientation measurements). An attached sensitive APD records the modulation of the fluorescence signal as a response to the polarization modulation of the excitation light. If the transition dipole moment of the molecule in the sample is oriented parallel to the excitation polarization, the excitation is maximized whereas the molecule does not become excited at all in case of a perpendicular orientation. From the detected modulation, the in-plane orientation of the molecule can be computed. Simultaneously, the spectrum of a single molecule can be measured by a prism-CCD spectrometer implemented in the detection pathway via a 50 : 50 beamsplitter. This allows the characterization of the spectral characteristics of the molecule and temporal variations in its fluorescence emission spectrum (spectral diffusion).

of the excitation light the fluorescence of the single molecule is modulated. The modulation of the excitation and fluorescence obeys a cosine-square law. The molecular orientation in the focal plane of the microscope (in-plane orientation) then results from the phase shift between the reference modulation and the detected molecular fluorescence modulation (for an application of the method, see Section 14.5.3) [5, 30, 31].

The second detection pathway depicted in Figure 14.2, consisting of the prism-CCD spectrometer, allows recording of single-molecule fluorescence emission spectra as a function of time. The spectrum of an individual molecule is highly sensitive to changes in the molecule's environment and is therefore a valuable source of information about the molecule's immediate surroundings. Additional to the characterization of the host–guest interaction, the molecular spectra can also reveal

aggregation phenomena. In combination with fluorophores that act as labeling dyes on biomolecules, the dye spectra can be used to monitor Förster resonance-energy transfer (FRET). Since FRET acts on a distance range of 2–10 nm, it is often used as a molecular ruler, that is, to measure distances between donor and acceptor and their variations in time [32].

In order to resolve single molecules as individual objects, they have to be no closer from each other than the resolution limit determined by the Rayleigh criterion (about half of the wavelength of the utilized laser light). However, the position of the fluorescent molecules in an image can be determined with much higher accuracy by fitting the recorded fluorescence signal to a two-dimensional Gaussian function [9]:

$$I_0 = A_0 \exp\left[\frac{-(x-x_0)^2}{2\sigma^2}\right] \exp\left[\frac{-(y-y_0)^2}{2\sigma^2}\right] \tag{14.1}$$

where I_0 is the recorded fluorescence intensity, A_0 the amplitude of the signal, σ the full width at half-maximum of the Gaussian curve (Figure 14.1c), and x_0 and y_0 denote the coordinates of the position of the molecule. The positioning accuracy is only limited by the signal-to-noise ratio (SNR), given a sufficient number of photons in the spot [33, 34]. As a rule of thumb, the accuracy Δx scales as $\Delta x \approx \Delta x_0/\mathrm{SNR}$. Since the SNR scales with the square root of the intensity, doubling the accuracy requires a four-times higher signal intensity. Repeating this fitting procedure throughout the entire recorded image sequence, a technique called single-molecule/particle tracking yields the trajectory as a detailed map of the molecular movement. In order to characterize the diffusion of the particle, the mean square displacement (MSD) $\langle r^2(t)\rangle$ is a very useful parameter. It describes the average of the squared distances between a molecule's start and end positions for all time lags of certain length $\Delta t = n\tau$ within one trajectory. Figure 14.1d depicts a schematic trajectory and the resulting step lengths (red, blue, green) for individual time lags. The MSD curve then results by plotting the average of the evaluated step lengths for a certain time lag. This plot offers detailed information about the mode of motion of the individual molecule. For an undisturbed normal Brownian diffusion of the particle, a so-called random walk, Einstein developed the following model [35]:

$$\left\langle r^2(t)\right\rangle = 2nD\Delta t \tag{14.2}$$

with the spatial dimension n ($n = 1, 2, 3$), in which the diffusion takes place. The MSD is thus linearly dependent on t (graph in Figure 14.1d). In addition to normal diffusion, other diffusion modes such as diffusion with drift (quadratic dependence), anomalous diffusion (obeying a power law), and confined/corralled diffusion (asymptotic convergence of the MSD) can be distinguished by their typical MSD [36].

In order to analyze the diffusion of a single molecule one typically computes the distribution $p(u,t)$ of the observed squared displacements u (with $u = r^2$) during a certain time interval t [37, 38]:

$$p(u,t) = \frac{1}{\sqrt{2\pi[\langle r^2(t)\rangle + \sigma^2]u}} \exp\left\{\frac{-u}{2[\langle r^2(t)\rangle + \sigma^2]}\right\} \tag{14.3}$$

with the positioning accuracy σ of the SPT analysis. If the molecular motion follows a one-dimensional diffusion process inside a pore, the so-called cumulative probability distribution $P(U,t)$ is thus

$$P(U,t) = \int_0^U p(u,t)\,\mathrm{d}u = \mathrm{erf}\left\{\sqrt{\frac{U}{2[\langle r^2(t)\rangle + \sigma^2]}}\right\} \tag{14.4}$$

where erf is the error function and $P(U,t)$ is the probability that the squared displacements u do not exceed a value U. For each time lag, $P(U,t)$ can be obtained by counting the number of squared displacements that are $\leq U$, normalized by the total number of data points N. Often, single-molecule diffusion is not a homogeneous process, but periods of diffusion are interrupted by periods of adsorption to specific sites. For such a situation, the cumulative probability distribution is given by

$$P(U,t) = (1-\alpha)\mathrm{erf}\left\{\sqrt{\frac{U}{2[\langle r^2(t)\rangle + \sigma^2]}}\right\} + \alpha\mathrm{erf}\left(\sqrt{\frac{U}{2\sigma^2}}\right) \tag{14.5}$$

where α is the fraction of time the molecule is adsorbed during the trajectory. The analysis of diffusion and adsorption is of particular importance for catalytic applications since single-molecule observations can reveal heterogeneities of catalytic materials. An example of the application of this analysis method is displayed later in Figure 14.4d–g.

14.3
Experimental Considerations and Constraints

There are several considerations that make chromophores well suited for SMM/SMS experiments. Important characteristics include a high fluorescence quantum yield Φ, that is, a high ratio of the number of emitted photons to the number of absorbed photons, and a high extinction coefficient ε. Moreover, the fluorophores should show a minimum amount of photoblinking (reversible deactivation due to nonradiative states) and a low rate of photobleaching (irreversible degradation processes).

For single-molecule microscopy, the fluorophores then need to be highly diluted to about 10^{-10}–10^{-11} mol l^{-1} such that the recorded fluorescence signals are spatially well separated, since otherwise the single-particle tracking algorithms are not able to fit the signals properly and the individual molecules cannot be distinguished.

If the single molecules are embedded inside a host matrix, this matrix also needs to meet requirements. Especially, it must be optically transparent such that the fluorophores can be excited and their fluorescence can be collected efficiently. Moreover, the host materials need to be extremely clean since a large variety of organic and inorganic impurities can lead to a substantial fluorescent background. Samples that meet these criteria are good candidates for SMM/SMS studies.

Furthermore, it has to be emphasized that the measurement of a single molecule is not sufficient to characterize a sample. In order to obtain good statistics and to sample all the various behaviors of single molecules in a sample, a large number of molecules have to be measured. Therefore, measurement techniques in which several single molecules can be observed in parallel are preferred.

14.4 Mesoporous Silica Materials

Mesoporous silica structures constitute a class of materials with a high potential for catalytic applications owing to their high surface-to-volume ratio and the possibility of tailoring their structure, morphology, and physical and chemical nature to specific applications [39–42]. These materials date back to 1992, when scientists at Mobil discovered a new type of silica–aluminosilicate hybrid system, which they called M41S material [39, 40]. In 1998, the portfolio of mesoporous silica materials was extended by the so-called Santa Barbara Amorphous (SBA)-type materials [41, 42]. Mesoporous materials can be synthesized through the cooperative self-assembly of surfactants and silica (or other) framework building blocks, forming a channel network that offers pore sizes ranging from about 2 to 30 nm. Consequently, the porous network is accessible to a wide range of differently sized and charged guest molecules (such as chemical reactants, drugs, biomolecules, and dye molecules). Moreover, the morphology of mesoporous materials can be altered from powders [43] via thin films [44] to filaments with an ordered channel structure [45, 46]. Additionally, the internal and external surfaces can be modified with a variety of organic functional groups [47–52], in order to control the interaction of the host with the guest species. Also, different pore topologies (e.g., hexagonal, cubic, or lamellar phases) can be synthesized [53–55]. This high degree of versatility makes these materials ideal platforms for various applications, which in addition to catalysis [56] includes molecular sieves [57], chromatography [58], stabilization of conducting nanoscale wires [59–61], and novel drug-delivery systems [62–67], to mention only a few.

We will show in this chapter that porous silica systems are ideally suited for single-molecule studies since the materials are optically transparent. We will focus on experiments where the mesoporous materials are used in the form of thin films coated on a glass substrate. This yields the best conditions for single-molecule characterization since this minimizes the background scattering due to non-matching refractive indices. As discussed above, especially for widefield microscopy, thin films with a thickness of a few hundred nanometers, prepared through a process

called evaporation induced self assembly (EISA) via dip- or spin-coating [68, 69], prove very useful since no out-of-focus fluorescence occurs.

14.5
Selected Studies

14.5.1
Correlating Dynamic and Structural Information by Combining Single-Molecule Microscopy and High-Resolution Transmission Electron Microscopy

In order to make mesoporous silica accessible for applications, it is essential to characterize the host structure in detail and to understand how the incorporated guest molecules interact with the host matrix. These important insights can be gained by a combination of single-molecule microscopy, which yields detailed dynamic information about the guest diffusion, with high-resolution transmission electron microscopy (HRTEM), which is an excellent method for the visualization of the host structure [70]. SMM and HRTEM complement each other well and overlaying the individual data sets allows one to correlate the motion of the guest molecules with structural features (dead ends, defects, etc.) of the host [71].

To this end, first mesoporous silica samples with a well-ordered channel network have to be synthesized. In the study considered [71], mesoporous poly(ethylene glycol) hexadecyl ether (Brij-56)-templated mesoporous silica with a hexagonal pore topology was chosen. These samples then have to be prepared in a way that allows for a simultaneous SMM and HRTEM characterization. This requires extremely thin optically transparent mesoporous films on electron-transparent substrates. Next, the individual SMM and HRTEM experiments have to be conducted. For SMM, highly photostable and quantum-efficient terrylene diimide dyes [72, 73] can be used as probe molecules to gain detailed trajectories of the molecular motion inside the porous network of the silica host. Since the sample was coated on an electron-transparent substrate, HRTEM images of the thin silica film can be recorded directly. In order to cover the dimensions of a single-molecule trajectory in these materials (up to several micrometers), a large map consisting of many individual HRTEM images has to be acquired. Finally, it is essential to guarantee an accurate overlay of both SMM and HRTEM data sets. Consequently, markers are necessary that are visible by both techniques. A good candidate is polystyrene beads with a diameter of 280 nm, since they yield a low fluorescent background and do not interfere significantly with the thin-film synthesis. By correlating the bead positions an overlay accuracy of typically 4–30 nm was achieved [71].

An exemplary overlay of a single-molecule trajectory with an HRTEM map is shown in Figure 14.3a. Within each HRTEM image, locally a fast Fourier transformation (FFT) can be used to determine an "FFT director" that depicts the average orientation of the pores in that area. To guide the eye, black bars display these FFT directors, where the degree of structural order, which is obtained in the FFT, is encoded in the thickness of the bars. By looking at the orientation of the directors, a

direct overview of the sizes of the domains of parallel aligned pores can be gained. As an overlay to the HRTEM map, Figure 14.3a displays the trajectory of a single dye molecule moving in that region of the mesoporous thin film. It is evident that the trajectory follows the direction of the channels indicated by the FFT directors accurately. For clarity, selected regions of the trajectory (orange boxes in Figure 14.3a) are enlarged in Figure 14.3b and c.

In Figure 14.3b, the molecule first diffuses along linearly aligned pores. During that time it accesses different adjacent channels. For these experiments, the positioning accuracy indicated by light blue boxes lies typically in the range 15–30 nm. Consequently, the molecule's positions cannot be assigned to a single channel, but rather to an ensemble of about three to six parallel channels.

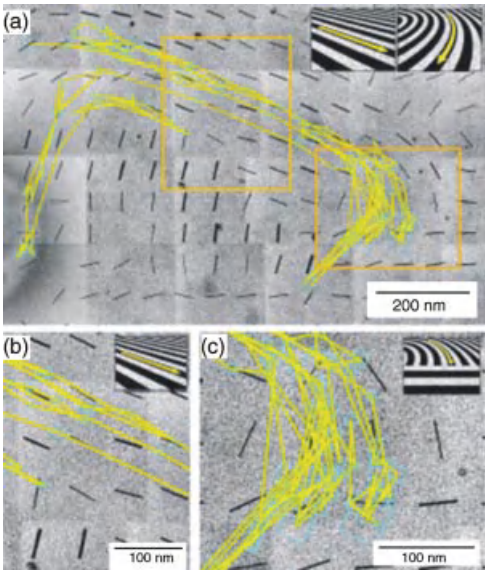


Figure 14.3 Correlative SPT and HRTEM reveal structural features of thin mesoporous films [71]. (a) Single-molecule exploring regions of parallel linear channels and strongly curved channel networks and domain boundaries. The parts of the trajectory marked with orange boxes are enlarged in (b) and (c). The insets in (a) – (c) depict schematically the structure of the channel network. The black bars are directors resulting from an FFT analysis that visualize the orientation of the channels, and the light blue boxes indicate the positioning accuracy for the individual molecular positions in the trajectory (typically in the range 15–30 nm). (b) Magnified part of the trajectory that shows parallel-aligned linear channels in which the molecule can diffuse without any obstructions. In the lower part of the trajectory, a domain boundary blocks the diffusing molecule such that it bounces back from the boundary and reverses its diffusion direction. (c) Strongly curved section of the trajectory with numerous parallel channels. Moreover, a domain boundary to a domain with horizontally aligned channels is observed. The data indicate that this boundary is silicalized such that the molecule cannot penetrate the adjacent domain. However, in the left part of the trajectory the molecule can access a domain with vertically aligned channels by crossing a domain boundary. Obviously, this boundary contains openings such that the molecule can traverse into the adjacent domain.

Nevertheless, important structural features of the film are evidenced by the molecular trajectory: in the lower part of the trajectory the channel is blocked and the molecule needs to reverse its diffusion direction due to the obstruction. It is therefore important that the molecules can penetrate into adjacent channels in order to circumvent such obstructions.

In contrast, Figure 14.3c shows a highly curved region of the same trajectory. The FFT directors show that in the right part of the trajectory the molecule hits a domain boundary that is blocked by other silica structures. The schematic inset depicts that situation, which can be described as a dead end. The channels of the inaccessible domain are oriented horizontally. However, in the left part of Figure 14.3c, at a boundary towards vertically aligned channels, the molecule can continue to diffuse without encountering any obstructions. By examining several single-molecule trajectories in detail, many more structural elements can be identified that are characteristic of mesoporous silica materials, such as openings in the channel walls or unstructured defect regions [71].

Through a combination of HRTEM and single-molecule optical techniques, this study provides the first direct proof that the molecular diffusion pathway through the pore system correlates with the pore orientation of the hexagonal structure. With this approach, it is possible to determine, in unprecedented detail, how a single fluorophore travels through linear or strongly curved sections of the hexagonal system, why it changes its apparent diffusion constant, and how it reverses its diffusion direction at dead ends due to domain boundaries. Additionally, this technique helps to detect less-ordered defect regions that minimize the functionality and applicability of the material. Also, leaky channels within the otherwise well-ordered periodic structure can be identified that allow a molecule to traverse into adjacent channels and that may be important for the functionality of the material. Such correlative studies also highlight the structural heterogeneity of these mesoporous materials. The above-described experiments therefore permit a thorough understanding of such complicated materials, which is essential for future applications, including catalysis, nanomedicine [74–76], and materials science [71].

14.5.2
Analyzing the Diffusion Dynamics Within a Silica Mesopore with One-Channel Accuracy Using Single-Molecule Microscopy and Single-Particle Tracking

A maximum amount of information about the interconnectivity of the channels in the mesoporous material can only be gained if the fluorescent molecule can be localized with one-channel-accuracy. In the following example [77], this high positioning accuracy allows us to visualize molecular diffusion between adjacent channels, which proves the existence of openings in the channel walls.

To realize such a high positioning accuracy, cetyltrimethylammonium bromide (CTAB)-templated mesoporous thin films with hexagonal pore topology were chosen in combination with a highly photostable terrylene diimide derivative. The small pore diameter of about 2–3 nm in this material and also the ionic template slow the diffusion of the dye, which is only poorly water soluble. These slow dynamics are

favorable for achieving high positioning accuracy since they allow for a long integration time per image. Additionally, the measurements were made using a high laser intensity since this maximizes the SNR.

Figure 14.4a shows the $x(t)$ and $y(t)$ graphs resulting from a single-molecule trajectory of TDI inside linear domains of a CTAB-templated thin film. The $y(t)$ graph clearly reveals the existence of two distinct parts within the trajectory, before (black) and after (green) 103 s. In Figure 14.4b, the histograms of the $y(t)$ graph from Figure 14.4a are plotted for these individual parts. Fitting the data with Gaussian functions reveals that the maxima of these functions are separated by 5–6 nm. This can be attributed to a molecule switching between at least two pores. Moreover, the $x(t)$ graph displayed in Figure 14.4a illustrates another interesting motional behavior. First, the molecule diffuses back and forth, yet confined between $x = 0$ and $x =$ 40 nm. Only after the molecule has traversed into a different pore (after ~103 s, Figure 14.4c) does it find an unobstructed pore such that it can diffuse further (see also the corresponding original movie [77]). In order to circumvent the obstructions, it is necessary that the molecule can switch between adjacent pores. The presence of "leaky" channel walls therefore adds to the functionality of the materials. These nanodefects are typical for mesoporous silica films.

Although much information about the host–guest system can be obtained by looking at exemplary trajectories, in order to understand the complete behavior of the guest within the host and to decipher material specifics that are also relevant for concentrations above the single-molecule level, it is important to analyze statistically the diffusion behavior of the single molecule. Figure 14.4d shows the cumulative probability distribution $P(U,t)$ plotted versus the squared displacements u for a time lag of 1 s (see Section 14.2) for one single-molecule trajectory out of 80. Assuming a one-dimensional random walk, the experimental data can be fitted by an error function according to Eq. (14.4) (red dashed line in Figure 14.4d). However, this model is not sufficient to describe the observed data. It is clear that the model also needs to account for adsorption sites [Eq. (14.5)] to describe the data (blue dashed line in Figure 14.4d). For this particular sample, the molecules are localized at adsorption sites for about 13% of the time ($\alpha = 13\%$). In Figure 14.4e, the individual MSD curves for 80 analyzed single molecules are plotted. For ~10 s the MSD curves are nearly linear such that according to Eq. (14.2) a diffusion coefficient for each molecule can be computed assuming a one-dimensional random walk. For long time scales, some of the investigated molecules show an asymptotic convergence of the MSD curve (lower red line in Figure 14.4e). This is due to a confinement resulting from obstructions in the pores that form "dead ends" for the molecule. The distribution of individual diffusion coefficients is displayed in Figure 14.4f. A Gaussian fit (red line) yields a mean diffusion coefficient $\langle D \rangle = 390\,\mathrm{nm^2\,s^{-1}}$. The computed distribution of adsorption times for all analyzed molecules can be seen in Figure 14.4g. The Gaussian fit (red line) yields a mean adsorption percentage of 18%, thus confirming the data in Figure 14.4d. These histograms are a good illustration of the observed structural heterogeneities of the investigated thin films. The width of the distributions is thus another important structural parameter, which becomes apparent through the single-molecule analysis.

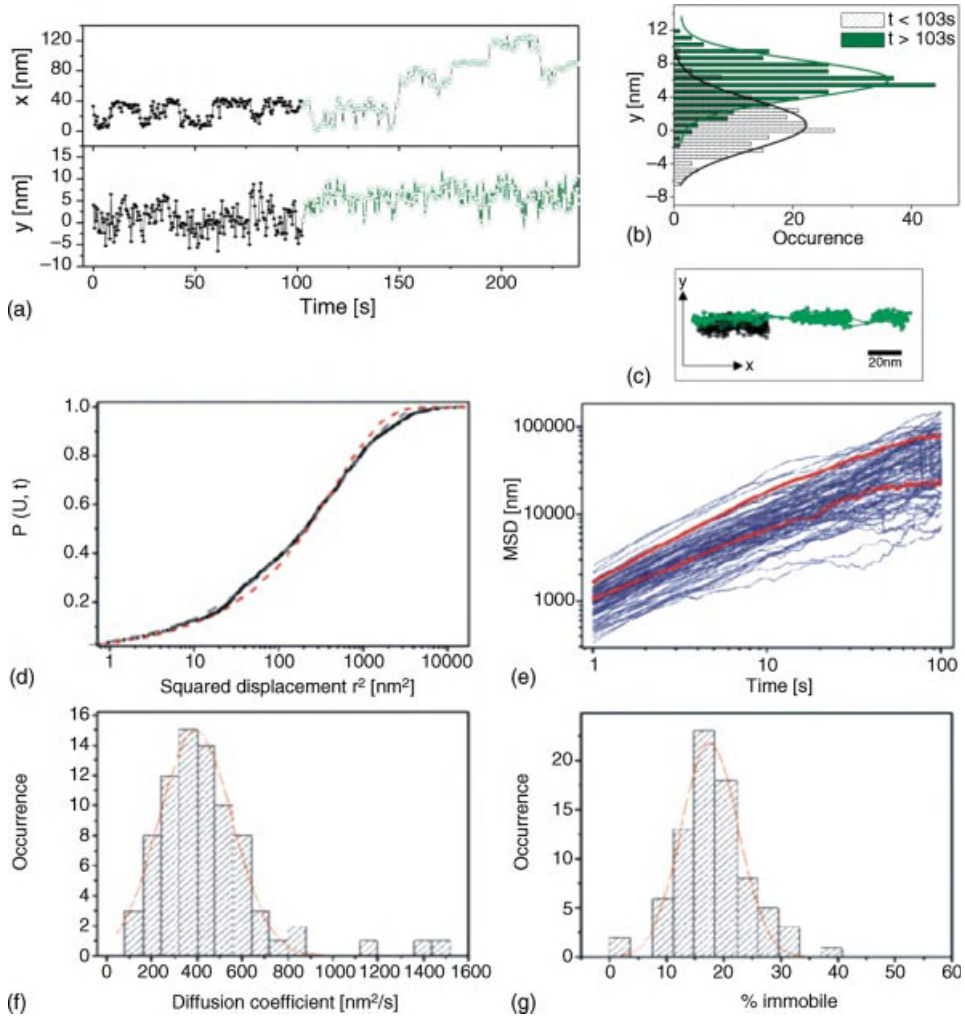


Figure 14.4 Analyzing the diffusion dynamics within a silica mesopore with one-channel accuracy using SMM and SPT [77]. (a) Projected *x* and *y* coordinates for a single TDI molecule diffusing in at least two distinct neighboring pores of a CTAB-templated mesoporous thin silica film. In the first 103 s the molecule diffuses back and forth in one pore (black squares), then it switches to another pore, where it continues its lateral diffusion (green circles). (b) Histograms extracted from the *y* coordinate before (black striped bars) and after (green full bars) time $t = 103$ s. The respective Gaussian fits are overlaid (black and green line). (c) Color-coded two-dimensional trajectory of the molecule displayed in (a) and (b). (d) Cumulative probability distribution $P(u, 1s)$ for a time lag $t_{lag} = 1$ s for a typical TDI trajectory. The analysis [see Eq. (14.5)] reveals the coexistence of one-dimensional diffusion and adsorbed states. (e) Time dependence of the MSD. The upper red line displays the MSD curve for the trajectory in (c). The lower red line shows the MSD curve for a diffusion which is confined, resulting from an obstruction in the pore creating a "dead end". (f) Histogram of the diffusion coefficients *D* extracted from the MSD curves in (e). A Gaussian fit (red) leads to a mean diffusion coefficient $\langle D \rangle = 390\,\mathrm{nm^2\,s^{-1}}$. (g) Histogram of the percentage of adsorbed states in a typical trajectory for a time lag $t_{lag} = 1$ s. The Gaussian fit (red) yields a mean adsorption time per trajectory of 18%.

The above examples demonstrate that mesoporous CTAB-templated thin films possess linearly arranged pores in which the molecules can diffuse back and forth well until they occasionally reach "dead ends." These "dead ends" can be circumvented by the molecule diffusing laterally through openings in the channel walls. The openings thus allow the molecules to diffuse over macroscopic distances in the film despite the existence of obstructions inside the pores. "Leaky" channel walls are therefore necessary for the functionality of the material. The detection of these openings was only possible through single-molecule microscopy with a one-channel positioning accuracy. Moreover, the sophisticated analysis methods reveal the presence of adsorption sites that partially immobilize the molecule during its motion inside the structure. Such adsorption sites are of particular importance for applications of these materials in the field of catalysis and therefore the nature of these sites will be examined in more detail in the next example.

14.5.3
Analyzing Orientational and Spectral Dynamics at Adsorption Sites Inside a CTAB Templated Thin Mesoporous Silica Film

Besides the translational diffusion of a single molecule, its orientational and spectral dynamics contain a vast amount of information about the molecule and its interactions with the host matrix. In Section 14.2, we introduced a setup for the simultaneous measurement of single-molecule spectra and orientations using a prism-based spectrometer in combination with polarization modulated excitation of the individual fluorophores. A setup of that type is used in the following study [5] to unravel the complicated host–guest interplay in mesoporous silica structures on a single-molecule level. Understanding this interplay is essential for nearly all applications ranging from catalysis to biomedicine and materials science.

In order to investigate the orientational diffusion of the guest molecules at adsorption sites, FPM was used (see Section 14.2).

Figure 14.5a displays an FPM image of single TDI molecules inside a CTAB-templated thin film [30]. If a molecule shows a distinct orientation, the fluorescence signal occurs as a striped pattern (see, e.g., molecule A). In contrast, a freely rotating molecule shows a homogeneous pattern without characteristic stripes (molecule B). In order to determine the molecular orientation and to track the position of the molecule at the same time, the recorded fluorescence signal can be fitted by a cosine-squared modulated two-dimensional Gaussian function derived from Eq. (14.1):

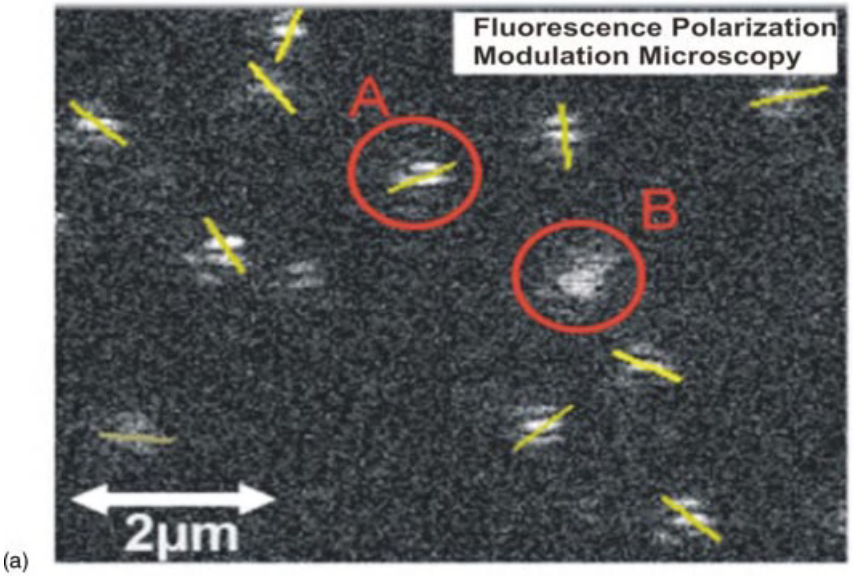
$$I_0 = A_0 \exp\left[\frac{-(x-x_0)^2}{2\sigma^2}\right] \exp\left[\frac{-(y-y_0)^2}{2\sigma^2}\right] \cos^2(\omega t - \Phi_0) \tag{14.6}$$

with the angular speed ω of the rotating $\lambda/2$ plate and the phase of the signal Φ_0. The in-plane orientation of the molecule in the focal plane then results from the phase shift between the fitted signal and the reference modulation (for details, see Section 14.2). For each molecule, the orientation of the transition dipole moment is determined in this way (displayed as the yellow line in Figure 14.5a).

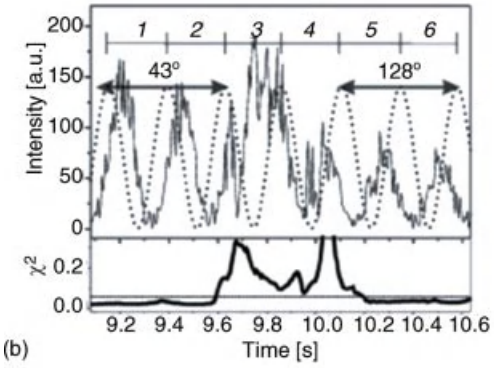
Figure 14.5b presents an exemplary time trajectory of the orientation of a single TDI dye molecule incorporated in the pores of CTAB-templated silica films determined by FPM. The observed molecule shows pronounced orientational dynamics: first, the molecular orientation remains stable at $43 \pm 2^\circ$ for about 0.6 s, then in the time interval between 9.6 and 10.1 s a molecular orientation cannot be determined. This is a sign of rapid rotation of the molecule below the temporal resolution of the setup (300 ms). After 10.1 s, the molecule finds another stable orientation of $128 \pm 3^\circ$ for the rest of the observation period (500 ms). The lower part of Figure 14.5b displays the χ_2, determined from the orientation analysis, which is used as a threshold for the assignment of a stable orientation. The observed orientational dynamics are characteristic of this host–guest system. It is interpreted as a movement of the TDI dye between two adsorption sites inside the mesoporous material. The nature of these adsorption sites remains unclear for that specific case; possible explanations include direct electrostatic interaction with the silica walls and/or the template or trapping at defect sites. The adsorption time at a particular site can be considered as a measure of the strength of the interaction.

In parallel with the determination of the molecular orientation, the spectrum of the same single -molecule was observed (Figure 14.5c; see Section 14.2 for a general description of the method). The data reveal pronounced spectral dynamics, which are called spectral jumps. These jumps are isolated events, usually large in magnitude (here they span a range of 27 nm), and occur less frequently than spectral fluctuations, which can be observed continuously and occur on a fast time scale, leading to broadening of the emission spectrum. The numbered spectra correspond to the segments in the orientation trace in Figure 14.5b. This correlation of spectra and orientation allows more information to be gained about the nature of the adsorption sites. In segments 1 and 2, the orientation remains stable at 43° and the emission maximum of the spectrum also remains nearly stable at about 685 nm. During the molecular rotation (segments 3 and 4), the emission maximum shifts until in segments 5 and 6 a stable orientation is found. This new stable orientation of 128° also is correlated with a bathochromically shifted spectrum with an emission maximum of 688 nm. Interestingly, the width of the spectrum also changes (segments 1–5). This width is a measure of the spectral fluctuations that occur during that integrated time. It is therefore not surprising that the width of the fluorescence emission spectrum of the molecule during its rotation is substantially broadened (segment 4).

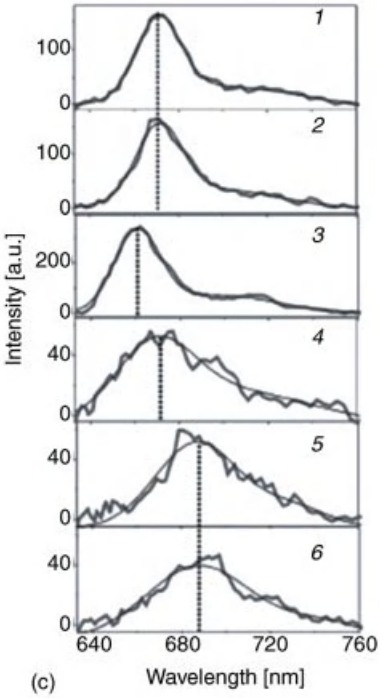
Figure 14.5d shows another illustrative example of the correlation of spectral and orientational dynamics. One can clearly see that both the spectrum and the orientation show pronounced dynamics during the observation time. For the first 16 s, the dye molecule undergoes a process of rapid reorientations accompanied by high spectral dynamics. A similar behavior can be found for the time interval between 36 and 47 s. In contrast, between second 16 and 20 s a stable orientation and a steady spectrum are observed, as evidenced by the characteristic plateaus in the graph. This is a good example of an adsorption site. Even stronger adsorption can be found in the time interval between 22 and 36 s, where the molecule remains attached to the same site, just interrupted by a short time of fluorescence quenching around 28 s.


Fluorescence Polarization
Modulation Microscopy
A
B
2µm

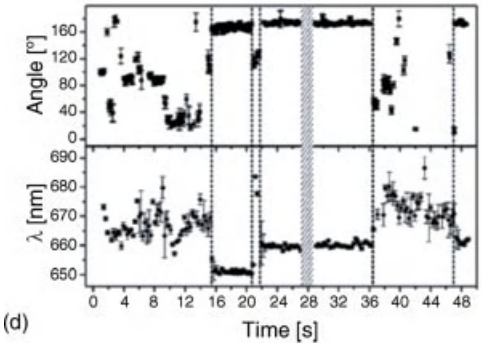
(a)


1
2
3
4
5
6
43°
128°
Intensity [a.u.]
χ²
Time [s]

(b)


1
2
3
4
5
6
Intensity [a.u.]
Wavelength [nm]

(c)


Angle [°]
λ [nm]
Time [s]

(d)

Moreover, this long time trace reveals another interesting feature. After 47 s, the molecule shows an orientational angle and fluorescence emission maximum that are identical with those between 22 and 36 s. This can be considered as a case where the molecule, during its diffusion inside the mesoporous material, returns to the same adsorption site.

The correlation of spectra and orientations of single molecules embedded in mesoporous silica provides detailed information about the host–guest interactions. Gaining knowledge about this subtle host–guest interplay is essential for many applications. In particular, it is important to assess the strength of the adsorptive interactions and also the frequency with which such adsorption occurs. In catalysis, it is very valuable to know for how long and how strongly reactant molecules are bound to reactive centers in the catalyst. Moreover, the structural and chemical heterogeneity of the host substrate can be analyzed. It must be emphasized that these details would be obscured by ensemble fluorescence methods. Consequently, this noninvasive single-molecule approach is highly useful not only for the characterization of porous silica but also for maximizing the application potential.

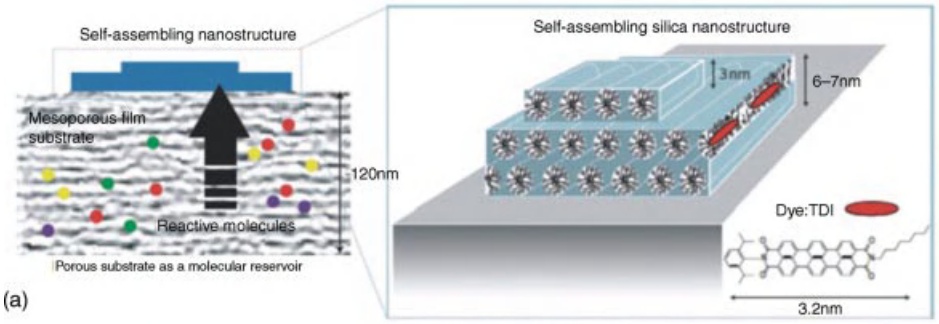
14.5.4
Visualization of the Mechanisms Governing the Structure Formation of Mesoporous Silica Nanochannels

Applications of mesoporous silica materials require not only a thorough characterization after synthesis but also a knowledge about aging and transformation processes that structurally alter the materials over time, as this can potentially influence the material properties. One characteristic parameter of porous silica materials that can change with time is the size of the domains of parallel-aligned channels. The study described in this section shows how the growth of these domains can be observed using fluorescence microscopy [78]. Understanding the parameters that govern this growth can also open up the possibility of controlling the growth and create large domains with a well-ordered channel alignment, which is a desirable feature for many applications.

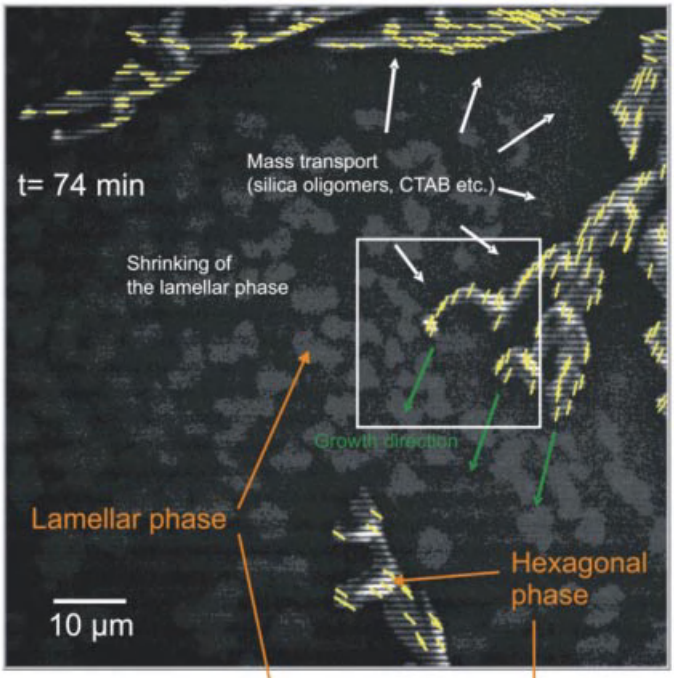
Figure 14.5 Analyzing orientational and spectral dynamics at adsorption sites inside a CTAB-templated thin mesoporous silica film [5, 30]. (a) FPM image of single TDI molecules diffusing in the pores of the CTAB-templated film. The computed orientations of the molecules' transition dipole moment are overlaid (yellow bars). Typically, the molecules appear with a striped pattern (see molecule A). Occasionally, molecules are detected that rotate freely during the typical scanning time of 0.8 s and thus do not show a distinct orientation (see molecule B). (b) Polarization-dependent fluorescence intensity trace (full line) and transmitted excitation light trace (dotted line) depicting orientational dynamics of a single TDI molecule in the thin film. The lower graph shows the normalized χ^2, the magnitude of which is a used as a criterion to assign an orientation to the molecule. The dotted line shows the threshold value below which a stable orientation was ascribed to the molecule. (c) Sequence of spectra corresponding to the segments indicated in (c). The dashed line indicates the fitted center position of the spectrum. (d) Angular and spectral trajectories of a single TDI molecule inside the pores of the thin film displaying the dynamic behavior. The error bars denote the standard deviations of the fits.

The system investigated in this example consists of a CTAB-templated thin-film substrate (Figure 14.6a, left) loaded with TDI. In contrast to all other studies described in this chapter, here the substrate acts as a reservoir that provides all necessary precursor chemicals (indicated schematically by red, green, yellow and violet points) for the formation of a new porous silica nanostructure on top of the substrate (blue). The growth of this new structure and the control of its growth dynamics are the focus of interest here. This nanostructure self-assembles due to the transport of the precursor molecules to the top of the film through openings in the channel walls and on the surface (see Sections 14.5.1 and 14.5.3). The right part of Figure 14.6a shows a magnified scheme of the self-assembling nanostructure. It consists of several layers of channels filled with template molecules and loaded with individual TDI dyes. Evidence for this large structure comes from atomic force microscopy (AFM) measurements. They reveal that the self-assembled structure always shows a base of two layers of porous silica 6–7 nm in height on top of which several individual layers (each about 3 nm in height) can form. Interestingly, while the domain sizes in the substrate (gray) are typically on the order of hundreds of nanometers, the assembling nanostructures on top of the substrate (blue) can have domain sizes up to the millimeter range. The formation kinetics and domain sizes of these domains can be controlled by adjusting the temperature and the relative humidity (RH) [79].

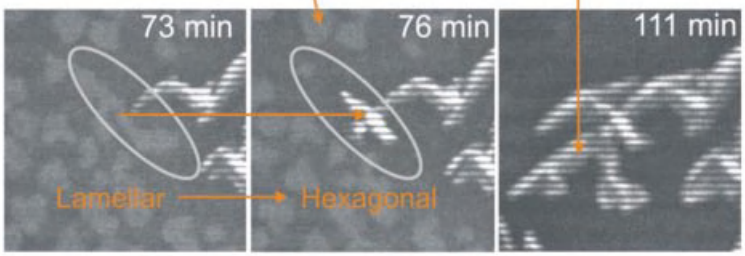
The orientation of these ultra-large domains can be obtained by FPM, since the channels are so narrow that the incorporated dye molecules cannot rotate freely. In these experiments, the dye concentration can be increased to ensemble concentration, which has the advantage that a single FPM image is sufficient to determine the channel orientation over the entire image. Figure 14.6b shows such an FPM image, revealing the coexistence of lamellar phases (unstructured gray spots) and also hexagonal phases of porous silica (gray striped patterns). In the lamellar phases, the dyes do not show a preferential orientation, while the determined orientation of the transition dipole moment of the dye molecules incorporated inside hexagonal channels is displayed as yellow bars, thus also indicating the channel orientation. These *in-situ* observations could reveal two mechanisms for the growth of the hexagonal layers. Growth occurs by a rapid conversion of lamellar to hexagonal structures through a "seeding" process. Figure 14.6c shows magnified images (white box) of Figure 14.6b that display such a transition of a lamellar phase (left, 73 min) to a hexagonal phase (middle, 76 min) (see also the original supporting movie [78]). This process is typically observed when a lamellar area is reached by a growing hexagonal domain. The shape of the freshly formed hexagonal structure follows roughly the shape of the former lamellar area (right, 111 min). A second proposed growth mechanism is deduced from the observation that lamellar structures in the vicinity of growing hexagonal domains successively vanish as the hexagonal domains expand (see the top part of Figure 14.6b for an example). This process is comparable to Ostwald ripening, yet in the samples discussed here the growth of the hexagonal domains proceeds at the cost of the smaller lamellar structures, which provide precursor chemicals that diffuse to the site of the self-assembling hexagonal layer. For both mechanisms, the growth of the hexagonal domains is anisotropic (green arrows in Figure 14.6b) and the orientation of the channels follows the growth direction.


Self-assembling nanostructure
Mesoporous film substrate
120nm
Reactive molecules
Porous substrate as a molecular reservoir
Self-assembling silica nanostructure
3nm
6–7nm
Dye:TDI
3.2nm

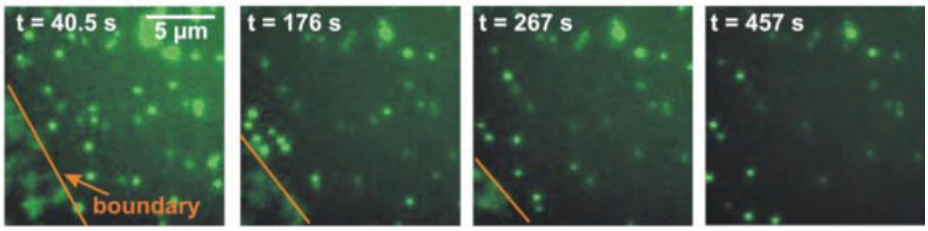
(a)


t= 74 min
Mass transport
(silica oligomers, CTAB etc.)
Shrinking of
the lamellar phase
Growth direction
Lamellar phase
Hexagonal
phase
10 µm

(b)


73 min
76 min
111 min
Lamellar
Hexagonal

(c)


t = 40.5 s
5 µm
boundary
t = 176 s
t = 267 s
t = 457 s

(d)

A similar situation can be observed in Figure 14.6d, which displays a time series of single-molecule images ($t = 40.5$, 176, 267, and 457 s) acquired on a widefield fluorescence microscope (see also the corresponding original movie [78]). The images show a large hexagonal phase (top right in all panels) and the corresponding phase boundary (indicated by an orange line). The single TDI molecules inside the hexagonal domain appear with a diffraction-limited fluorescence pattern, whereas beyond the phase boundary the detected fluorescence is diffuse owing to the fast motion of several individual molecules on a time scale faster than the integration time of the image. These molecules diffuse inside a lamellar phase, or simply on the surface of the porous substrate that acts as a reservoir. During the recorded time series, the same region of interest is observed in all images. One can see that the hexagonal phase grows, new hexagonal channels are created, and individual molecules become incorporated into these new channels. Consequently, the region showing unstructured diffusion become smaller until it totally disappears ($t = 457$ s). The entire process takes about 400 s. Interestingly, the direction of the mesoporous channels depicted by an orange arrow for $t = 40.5$ s is again perpendicular to the growth direction of the domain, similar to the observations in Figure 14.6b. The single-molecule data illustrate in detail how individual fluorescent molecules are "caught" and incorporated by the freshly formed domain.

In summary, the visualization of the domain growth of mesoporous silica layers (i) offers important insights into the mechanistic details of the self-assembly process, (ii) allows domain growth to be controlled, and (iii) leads to ultra-large domains inaccessible so far. The study also outlines the heterogeneity of the porous silica materials. Moreover, FPM allows one to determine the orientations of the pores using dye molecules as sensitive probes. Hence, this section provides an example of how the described technology can be used to investigate the kinetics of chemical reactions in nanostructured environments.

Figure 14.6 Visualizing the self-assembly of mesoporous silica nanochannels [78]. (a) Left: sketch of a CTAB-templated mesoporous film substrate (gray) that acts as a reservoir providing the precursors (red, yellow, green, blue dots) for the self-assembly of a silica nanostructure (blue) on top of the substrate. Right: magnification of the templated self-assembling silica channels. The dye (red) is incorporated into the pores during the self-assembly. (b) Fluorescence microscopy image showing a snapshot of the growth of the self-assembling silica nanostructures. Hexagonal and lamellar pore topologies can be distinguished by their FPM appearance. Whereas in the hexagonal channels the dye molecules cannot rotate freely and therefore their orientation and also the channel orientation can be determined (stripes), the orientation is not defined in the lamellar phase (gray uniform patterns). (c) Magnified part (white box) of the region displayed in (b). The phase transition from a lamellar to a hexagonal topology can be observed during the growth of the hexagonal domain by comparing different time points. (d) Time series of images acquired on a widefield fluorescence microscopy setup showing single TDI molecules inside the pores of a CTAB-templated film. The orange line marks a phase boundary between a large hexagonal domain (top right part in all panels) and a lamellar phase or the substrate surface (bottom left part). In the hexagonal domains, the single molecules appear with a diffraction-limited fluorescence pattern (some aggregates can also be seen), whereas the molecules beyond the phase boundary diffuse fast and unstructured, resulting in a diffuse pattern. The time series shows the growth of the hexagonal domain.

14.6 Conclusion

Single-molecule microscopy and spectroscopy techniques are highly valuable tools for the characterization of mesoporous silica nanomaterials. They are noninvasive and yield information even about highly dynamic processes of the fluorescent guest molecules (e.g., spectral, translational, and orientational diffusion), including subpopulations. Moreover, the techniques offer means for the thorough structural characterization of the silica host since the subtle host–guest interactions influence the properties of the guest molecules that act as probes. This reveals structural, spatial, and temporal heterogeneities of the host matrix. The detail of information that can be gained with SMM/SMS is unprecedented and exceeds that of many other characterization techniques. The techniques introduced here are transferable to other solid samples provided that they are optically transparent and a suitable fluorophore is chosen. Single-molecule techniques thus contribute to a profound understanding of complex nanomaterials, which is an essential prerequisite for optimizing their structure towards potential applications ranging from catalysis to nanomedicine and materials science.

References

1 Moerner, W.E. and Kador, L. (1989) *Phys. Rev. Lett.*, **62** (21), 2535–2538.
2 Orrit, M. and Bernard, J. (1990) *Phys. Rev. Lett.*, **65** (21), 2716–2719.
3 Basché, T., Moerner, H.W., Orrit, M., and Wild, U.P. (1996) *Single Molecule Optical Detection, Imaging and Spectroscopy*, VCH Verlag GmbH, Weinheim.
4 Basche, T., Kummer, S., and Brauchle, C. (1995) *Nature*, **373** (6510), 132–134.
5 Jung, C., Hellriegel, C., Platschek, B., Wohrle, D., Bein, T., Michaelis, J., and Bräuchle, C. (2007) *J. Am. Chem. Soc.*, **129** (17), 5570–5579.
6 Funatsu, T., Harada, Y., Tokunaga, M., Saito, K., and Yanagida, T. (1995) *Nature*, **374** (6522), 555–559.
7 Schmidt, T., Schütz, G.J., Baumgartner, W., Gruber, H.J., and Schindler, H. (1995) *J. Phys. Chem.*, **99** (49), 17662–17668.
8 Schmidt, T., Schütz, G.J., Baumgartner, W., Gruber, H.J., and Schindler, H. (1996) *Proc. Natl. Acad. Sci. U. S. A.*, **93** (7), 2926–2929.
9 Saxton, M.J. and Jacobsen, K. (1997) *Annu. Rev. Biophys. Biomol. Struct.*, **26**, 373–399.
10 Yildiz, A., Forkey, J.N., McKinney, S.A., Ha, T., Goldman, Y.E., and Selvin, P.R. (2003) *Science*, **300** (5628), 2061–2065.
11 Seisenberger, G., Ried, M.U., Endreß, T., Büning, H., Hallek, M., and Bräuchle, C. (2001) *Science*, **294** (5548), 1929–1932.
12 Tardin, C., Cognet, L., Bats, C., Lounis, B., and Choquet, D. (2003) *EMBO J.*, **22** (18), 4656–4665.
13 Seebacher, C., Hellriegel, C., Deeg, F.-W., Bräuchle, C., Altmaier, S., Behrens, P., and Müllen, K. (2002) *J. Phys. Chem. B*, **106**, 5591–5595.
14 Seebacher, C., Hellriegel, C., Brauchle, C., Ganschow, M., and Wohrle, D. (2003) *J. Phys. Chem. B*, **107** (23), 5445–5452.
15 McCain, K.S., Hanley, D.C., and Harris, J.M. (2003) *Anal. Chem.*, **75**, 4351–4359.
16 Hellriegel, C., Kirstein, J., Bräuchle, C., Latour, V., Pigot, T., Olivier, R., Lacombe, S., Brown, R., Guieu, V., Payrastre, C., Izquierdo, A., and Mocho, P. (2004) *J. Phys. Chem. B*, **108** (38), 14699–14709.
17 Hellriegel, C., Kirstein, J., and Bräuchle, C. (2005) *New J. Phys.*, **7**, 23–36.

18 Werley, C.A. and Moerner, W.E. (2006) *J. Phys. Chem. B*, **110** (38), 18939–18944.
19 Tamarat, P., Maali, A., Lounis, B., and Orrit, M. (2000) *J. Phys. Chem. A*, **104** (1), 1–16.
20 Kulzer, F. and Orrit, M. (2004) *Annu. Rev. Phys. Chem.*, **55**, 585–611.
21 Weiss, S. (1999) *Science*, **283** (5408), 1676–1683.
22 Shiroguchi, K. and Kinosita, K. (2007) *Science*, **316** (5828), 1208–1212.
23 Kitamura, K., Tokunaga, M., Iwane, A.H., and Yanagida, T. (1999) *Nature*, **397** (6715), 129–134.
24 Bacia, K., Kim, S.A., and Schwille, P. (2006) *Nat. Methods*, **3** (2), 83–89.
25 Woermke, S., Mackowski, S., Brotosudarmo, T.H.P., Jung, C., Zumbusch, A., Ehrl, M., Scheer, H., HofMann, E., Hiller, R.G., and Brauchle, C. (2007) *Biochim. Biophys. Acta*, **1767** (7), 956–964.
26 Schindler, F., Lupton, J.M., Muller, J., Feldmann, J., and Scherf, U. (2006) *Nat. Mater.*, **5** (2), 141–146.
27 Moerner, W.E. (2002) *J. Phys. Chem. B*, **106**, 910–927.
28 Moerner, W.E. and Orrit, M. (1999) *Science*, **283**, 1670–1676.
29 Moerner, W.E. and Fromm, D.P. (2003) *Rev. Sci. Instrum.*, **74** (8), 3597–3619.
30 Jung, C. (2007) Single Molecule Traffic in Mesoporous Materials and New Photostable Water-Soluble Terrylenediimide Derivatives. PhD thesis, Ludwig-Maximilians-Universität, Munich.
31 Ha, T., Laurence, T.A., Chemla, D.S., and Weiss, S. (1999) *J. Phys. Chem. B*, **103** (33), 6839–6850.
32 Ha, T., Enderle, T., Ogletree, D.F., Chemla, D.S., Selvin, P.R., and Weiss, S. (1996) *Proc. Natl. Acad. Sci. U. S. A.*, **93** (13), 6264–6268.
33 Bobroff, N. (1986) *Rev. Sci. Instrum.*, **57** (6), 1152–1157.
34 Lampton, M., Margon, B., and Bowyer, S. (1976) *Astrophys. J.*, **208** (1), 177–190.
35 Einstein, A. (1905) *Ann. Phys. (Leipzig)*, **17** (8), 549–560.
36 Berg, H.C. (1993) *Random Walks in Biology*, Princeton University Press, Princeton, NJ.
37 Anderson, C.M., Georgiou, G.N., Morrison, I.E.G., Stevenson, G.V.W., and Cherry, R.J. (1992) *J. Cell Sci.*, **101**, 415–425.
38 Schütz, G.J., Schindler, H., and Schmidt, T. (1997) *Biophys. J.*, **73** (2), 1073–1080.
39 Beck, J.S., Vartuli, J.C., Roth, W.J., Leonowicz, M.E., Kresge, C.T., Schmitt, K.D., Chu, C.T.W., Olson, D.H., Sheppard, E.W., McCullen, S.B., Higgins, J.B., and Schlenker, J.L. (1992) *J. Am. Chem. Soc.*, **114** (27), 10834–10843.
40 Kresge, C.T., Leonowicz, M.E., Roth, W.J., Vartuli, C.E., and Beck, J.S. (1992) *Nature*, **359**, 710–712.
41 Zhao, D.Y., Feng, J.L., Huo, Q.S., Melosh, N., Fredrickson, G.H., Chmelka, B.F., and Stucky, G.D. (1998) *Science*, **279** (5350), 548–552.
42 Zhao, D.Y., Huo, Q.S., Feng, J.L., Chmelka, B.F., and Stucky, G.D. (1998) *J. Am. Chem. Soc.*, **120** (24), 6024–6036.
43 Katiyar, A., Yadav, S., Smirniotis, P.G., and Pinto, N.G. (2006) *J. Chromatogr. A*, **1122** (1–2), 13–20.
44 Brinker, C.J., Lu, Y.F., Sellinger, A., and Fan, H.Y. (1999) *Adv. Mater.*, **11** (7), 579–585.
45 Platschek, B., Petkov, N., and Bein, T. (2006) *Angew. Chem. Int. Ed.*, **45** (7), 1134–1138.
46 Cauda, V., Muhlstein, L., Onida, B., and Bein, T. (2009) *Micropor. Mesopor. Mater.*, **118** (1–3), 435–442.
47 Maschmeyer, T., Rey, F., Sankar, G., and Thomas, J.M. (1995) *Nature*, **378** (6553), 159–162.
48 Yokoi, T., Yoshitake, H., and Tatsumi, T. (2004) *J. Mater. Chem.*, **14** (6), 951–957.
49 Yamamoto, K. and Tatsumi, T. (2000) *Chem. Lett.* (6), 624–625.
50 Angloher, S. and Bein, T. (2006) *J. Mater. Chem.*, **16** (36), 3629–3634.
51 Fowler, C.E., Burkett, S.L., and Mann, S. (1997) *Chem. Commun.*, 1769–1770.
52 Lebold, T., Mühlstein, L.A., Blechinger, J., Riederer, M., Amenitsch, H., Köhn, R., Peneva, K., Müllen, K., Michaelis, J., Bräuchle, C., and Bein, T. (2009) *Chem. Eur. J.*, **15** (7), 1661–1672.
53 Alberius, P.C.A., Frindell, K.L., Hayward, R.C., Kramer, E.J., Stucky, G.D., and Chmelka, B.F. (2002) *Chem. Mater.*, **14** (8), 3284–3294.

54 Besson, S., Gacoin, T., Ricolleau, C., Jacquiod, C., and Boilot, J.P. (2003) *J. Mater. Chem.*, **13** (2), 404–409.

55 Cagnol, F., Grosso, D., Soler-Illia, G.J.deA.A., Crepaldi, E.L., Babonneau, F., Amenitsch, H., and Sanchez, C. (2003) *J. Mater. Chem.*, **13** (1), 61–66.

56 De Vos, D.E., Dams, M., Sels, B.F., and Jacobs, P.A. (2002) *Chem. Rev.*, **102** (10), 3615–3640.

57 Billinge, S.J.L., McKimmy, E.J., Shatnawi, M., Kim, H., Petkov, V., Wermeille, D., and Pinnavaia, T.J. (2005) *J. Am. Chem. Soc.*, **127** (23), 8492–8498.

58 Rebbin, V., Schmidt, R., and Fröba, M. (2006) *Angew. Chem. Int. Ed.*, **45** (31), 5210–5214.

59 Petkov, N., Stock, N., and Bein, T. (2005) *J. Phys. Chem. B*, **109** (21), 10737–10743.

60 Ye, B., Trudeau, M.L., and Antonelli, D.M. (2001) *Adv. Mater.*, **13** (8), 561.

61 Cott, D.J., Petkov, N., Morris, M.A., Platschek, B., Bein, T., and Holmes, J.D. (2006) *J. Am. Chem. Soc.*, **128** (12), 3920–3921.

62 Lai, C.-Y., Trewyn, B.G., Jeftinija, D.M., Jeftinija, K., Xu, S., Jeftinija, S., and Lin, V.S.Y. (2003) *J. Am. Chem. Soc.*, **125**, 4451–4459.

63 Roy, I., Ohulchanskyy, T.Y., Bharali, D.J., Pudavar, H.E., Mistretta, R.A., Kaur, N., and Prasad, P.N. (2005) *Proc. Natl. Acad. Sci. U. S. A.*, **102** (2), 279–284.

64 Giri, S., Trewyn, B.G., and Lin, V.S.Y. (2007) *Nanomedicine*, **2** (1), 99–111.

65 Giri, S., Trewyn, B.G., Stellmaker, M.P., and Lin, V.S.Y. (2005) *Angew. Chem. Int. Ed.*, **44** (32), 5038–5044.

66 Torney, F., Trewyn, B.G., Lin, V.S.Y., and Wang, K. (2007) *Nat. Nanotechnol.*, **2** (5), 295–300.

67 Lebold, T., Jung, C., Michaelis, J., and Brauchle, C. (2009) *Nano Lett.*, **9** (8), 2877–2883.

68 Ying, J.Y., Mehnert, C.P., and Wong, M.S. (1999) *Angew. Chem. Int. Ed.*, **38** (1–2), 56–77.

69 Oye, G., Sjoeblom, J., and Stoecker, M. (2001) *Adv. Colloid Interface Sci.*, **89**, 439–466.

70 Sakamoto, Y., Kaneda, M., Terasaki, O., Zhao, D.Y., Kim, J.M., Stucky, G., Shim, H.J., and Ryoo, R. (2000) *Nature*, **408** (6811), 449–453.

71 Zürner, A., Kirstein, J., Doblinger, M., Bräuchle, C., and Bein, T. (2007) *Nature*, **450** (7170), 705–709.

72 Holtrup, F.O., Muller, G.R.J., Quante, H., Defeyter, S., DeSchryver, F.C., and Mullen, K. (1997) *Chem. Eur. J.*, **3** (2), 219–225.

73 Jung, C., Muller, B.K., Lamb, D.C., Nolde, F., Mullen, K., and Bräuchle, C. (2006) *J. Am. Chem. Soc.*, **128** (15), 5283–5291.

74 Silva, G.A. (2004) *Surg. Neurol.*, **61** (3), 216–220.

75 Kubik, T., Bogunia-Kubik, K., and Sugisaka, M. (2005) *Curr. Pharm. Biotechnol.*, **6** (1), 17–33.

76 Ferrari, M. (2005) *Nat. Rev. Cancer*, **5** (3), 161–171.

77 Jung, C., Kirstein, J., Platschek, B., Bein, T., Budde, M., Frank, I., Müllen, K., Michaelis, J., and Bräuchle, C. (2008) *J. Am. Chem. Soc.*, **130** (5), 1638–1648.

78 Jung, C., Schwaderer, P., Dethlefsen, M., Kohn, R., Michaelis, J., and Brauchle, C. (2011) *Nat. Nanotechnol.*, **6** (2), 86–91.

79 Riehemann, K., Schneider, S.W., Luger, T.A., Godin, B., Ferrari, M., and Fuchs, H. (2009) *Angew. Chem. Int. Ed.*, **48** (5), 872–897.

Part Two
Macroscopic Techniques

Characterization of Solid Materials and Heterogeneous Catalysts: From Structure to Surface Reactivity, First Edition.
Edited by Michel Che and Jacques C. Védrine.
© 2012 Wiley-VCH Verlag GmbH & Co. KGaA. Published 2012 by Wiley-VCH Verlag GmbH & Co. KGaA.

15
X-Ray Diffraction and Small Angle X-Ray Scattering

Malte Behrens and Robert Schlögl

15.1
Introduction

X-ray scattering techniques are among of the most widely applied methods used for the characterization of solids. After the discovery of X-rays by W.C. Röntgen in 1895, the pioneering experiments by W. Friedrich, P. Knipping, M. von Laue, and W.H. and W.L. Bragg in 1912–1913 and their full interpretation by P.P. Ewald in 1921 laid the basis for their application in studies of condensed crystalline matter. X-ray diffraction (XRD) became a standard laboratory technique in the second half of the last century with a mature theoretical background and powerful analytical tools such as the structure refinement method for crystalline powders developed by H.M. Rietveld in 1967 [1, 2]. New technical opportunities for XRD experiments arose in the late twentieth century with the easy access to synchrotron radiation for structural studies. Current trends in the field of catalyst characterization are the application of XRD under reactive conditions using laboratory equipment and synchrotron sources [3, 4], the combination with other complementary techniques [5, 6], and the development of evaluation methods for detailed defect analysis using peak-fitting procedures [7, 8].

From an XRD experiment, one can learn if the sample is (at least partially) crystalline and how many and which crystalline phases are present. By further evaluation, the relative amounts of the crystalline components can be determined and the crystal structures can be refined. In addition, some microstructural parameters such as crystallite size and lattice strain will affect the diffraction pattern and can be derived by line profile analysis.

Small-angle X-ray scattering (SAXS) is a complementary technique discovered in 1939 by A. Guinier [9], which gives information about the surface area and particle or pore size distribution in a material. Its application to the characterization of heterogeneous catalysts [10–13] is not as widespread as that of powder XRD, which is used as a standard laboratory method for monitoring all steps of catalyst synthesis and a sophisticated tool for the *in situ* characterization of working catalysts. It essentially gives integrated information on the crystalline bulk of a sample. As catalysis is a surface phenomenon and catalytic materials in addition are often only weakly diffracting, the scope of applying diffraction methods in catalysis, is often

Characterization of Solid Materials and Heterogeneous Catalysts: From Structure to Surface Reactivity, First Edition. Edited by Michel Che and Jacques C. Védrine.
© 2012 Wiley-VCH Verlag GmbH & Co. KGaA. Published 2012 by Wiley-VCH Verlag GmbH & Co. KGaA.

different from, for example, that in classical solid-state chemistry, where XRD is one of the workhorse methods to elucidate inter-atomic bond distances and angles. Attempts to prepare a sample in a well-crystalline form (or even as macroscopic crystals) in order to extract the maximum information from a diffraction experiment are usually not useful for investigations of powder catalysts as they hardly lead to high catalytic activity. The targeted establishment of structure–performance relationships is, therefore, not possible for such materials owing to a lack of performance.

Researchers have to face the challenge that structural studies and phase identification of catalysts relying on ideal Bragg diffraction are often hindered by the special properties of high-performance catalysts, which are typically nanosized composite materials. Thus, in catalysis it is the not obvious information, which is indirectly contained in a diffraction pattern, which is of particular interest. In almost all cases, the ideal (and often inactive) structures of catalytic materials are well known and single-crystal structure analyses are not at the focus of the work with catalysts. Instead, one major question is that of the deviation from the ideal structure. Thus, in addition to phase identification and quantitative phase analysis, insights into the effects of small crystallite sizes, lattice imperfections, and formation and degradation of solid solutions on the diffraction pattern are desired. X-ray scattering methods are a powerful tool to answer these questions. A number of review articles and book chapters addressing the use of XRD methods in heterogeneous catalysis are available and can be recommended for further reading [3, 4, 14–18].

In this chapter, after introducing some fundamentals of diffraction, the above-mentioned aspects of phase identification and quantification, characterization of the ideal and real structure, determination of crystallite size and strain, by powder diffraction methods are covered, with special emphasis on the characterization of composite and nanostructured materials and *in situ* experimentation. Examples of catalytically relevant materials are included to illustrate the wealth of information extractable from an XRD experiment but also the limitations of the method. In addition, the use of SAXS to determine the particle size, porosity, and size distribution in catalyst samples is considered.

15.2
Theoretical Background of X-Ray Diffraction

This section serves as an introduction to the fundamentals of diffraction and their relation to practical applications, and the basic background and the nomenclature of this method are presented. For an in-depth treatment of the kinematic theory of diffraction the reader is referred to one of the many general textbooks on XRD [19–24]. The beginning of this section follows the treatment by Schwarz and Cohen [24].

15.2.1
Fundamentals of X-Ray Diffraction

Transverse plane waves from different sources may interfere when their paths overlap. This interference may be constructive, destructive, or partially destructive.

The simplest diffraction experiment consists of two adjacent slits, which are hit by an incoming wave front and spaced at a distance similar to the wavelength. Each slit acts as a source of waves and together they allow interference, which is amplified if a periodic arrangement of slits, a diffraction grating, is used rather than only two.

These simple considerations are the basis of an XRD experiment, in which layers of periodically spaced atoms in a crystalline solid act like a diffraction grating. The physical scattering process may be considered as the incoming wave exciting the electrons of an atom that emits radiation of the same wavelength but in a direction different from that of the incoming wave. In order to generate interference patterns, the wavelength has to be of the same order of magnitude as the interatomic distances, which is the case for X-rays ($\lambda \approx 1$ Å). The conditions for constructive interference, that is, the relation of the wavelength λ, the interatomic distance d, and the incident angle of the X-ray θ, are given by the fundamental equation of XRD, Bragg's law:

$$n\lambda = 2d \sin\theta$$

where n is the diffraction order. Bragg's law can be envisaged with the help of the reflection analog of a scattering event shown in Figure 15.1a.

If the path difference of the two rays scattered at the first and second layers of atoms (the red path in Figure 15.1a) is an integral multiple n of λ, the interference of the scattered rays will be constructive and a diffraction peak will be produced for an incident angle θ. Recording the amplitude of the diffracted beam as a function of $2\lambda^{-1}\sin\theta$ or n/d would result in the idealized pattern shown schematically in Figure 15.1c.

It is noted that in the representation in Figure 15.1a, only two layers of atoms are sufficient to explain the constructive interference if the Bragg equation is fulfilled.

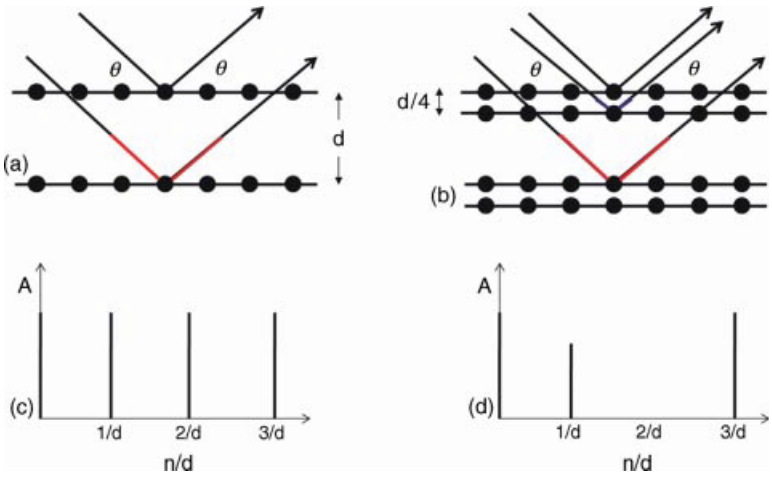


Figure 15.1 Geometric derivation of the Bragg equation for two layers of atoms with an interlayer spacing d (a) and idealized amplitude of the scattered waves (c). Effect of an additional layer of atoms at $d/4$ (b, d). Adapted from [24].

However, to understand that interference is destructive for all conditions not fulfilling the Bragg equation, it is necessary to consider more or ideally an infinite number of atom layers. Otherwise, no sharp reflections over a flat background as shown in Figure 15.1c are produced, but a gradual decay and rise of the scattered intensity in between two orders of reflections n and $n + 1$ would be present. This is the origin of the size broadening effect which is discussed in Section 15.2.1 in detail and which is often used for the estimation of the crystallite size of a sample.

If now an extra atom layer is introduced at $d/4$ below the topmost layer (Figure 15.1b), the intensity distribution of the diffracted beams changes. For the first-order diffraction ($n = 1$, path difference λ), the scattered beam from the newly introduced layers will have a path difference of $\lambda/4$ (the blue path in Figure 15.1b), which leads to partial destructive interference and attenuation of the diffracted beam (Figure 15.1d). For $n = 2$, the path difference will be $\lambda/2$ and the waves scattered at the original and the new layers will be anti-phase. Hence there will be completely destructive interference and the diffraction peak for $n = 2$ will be absent (Figure 15.1d). This simple schematic consideration shows how the symmetry of a crystal determines its diffraction pattern. It is noted that if the atoms at $d/4$ were different from the original ones, the interference for $n = 2$ would not be completely destructive, leading to an attenuated peak, showing that the positions of the atoms in the unit cell and also their kinds are reflected in the intensity distribution in an XRD pattern.

15.2.2 Crystallography

Crystals can be described as three-dimensional lattices. A lattice point at the origin of the unit cell is reproduced by three translations, a, b, and c, and three angles, α, β, and γ, called the lattice or unit cell parameters. An infinite number of lattice planes run through the lattice points and their orientation with respect to the unit cell is given by the fractional parts of the cell axes at which they intercept. Sets of equally spaced and parallel lattice planes are defined by Miller indices, hkl, representing the reciprocals of these intercepts in the directions of a, b, and c. The spacing of adjacent planes is termed d_{hkl} and, for example, in a cubic lattice $d_{100} = d_{010} = d_{001} = a$ and $d_{200} = d_{020} = d_{002} = a/2$.

Cubic lattices, $a = b = c$ and $\alpha = \beta = \gamma = 90°$, are the simplest and highest symmetrical case. Other lattice symmetries are hexagonal, trigonal, tetragonal, orthorhombic, monoclinic, and triclinic. These seven crystal systems may contain translational symmetry within the unit cell, giving rise to 14 Bravais lattices, which may be primitive or differently centered. In analogy with the simplified example shown in Figure 15.1, centered cells and also certain symmetry elements will lead to systematic absences of certain classes of reflections, because the arrangement of certain atoms occurs exactly anti-phase. For example, in a face-centered (*F*-) cell, only reflections with h, k, and l all odd or all even are observed.

A crystal structure is completely described by the lattice parameters defining the geometry of the unit cell, the kinds and coordinates x, y, and z as fractions of a, b and c

of crystallographically independent atoms in the unit cell forming the asymmetric unit, and the space group containing the symmetry operations needed to reproduce the asymmetric unit to fill the unit cell completely.

A simple example is NaCl. The lattice symmetry is cubic and one lattice parameter a is sufficient to describe the geometry of the unit cell; a is 5.6402 Å for NaCl. A sodium atom is located at the origin of the unit cell has the atomic coordinates $x = 0$, $y = 0$, and $z = 0$. A chlorine atom is located at the center of the cell at $x = {}^1/_2$, $y = {}^1/_2$ and $z = {}^1/_2$ and completes the asymmetric unit. This pair of atoms is reproduced three times according to the space group $Fm\bar{3}m$, leading to a unit cell content of Na_4Cl_4 (Figure 15.2), in fact with ${}^1/_8$ of an Na atom at each of the eight corners and ${}^1/_2$ of an Na atom in the middle of each of the six faces of the cube. A full Cl atom is located in the middle of the cell and ${}^1/_4$ of a Cl atom in the middle of each of the 12 edges. The structure can be understood as a cubic close-packing (ccp, or fcc, face-centered cubic) of Cl^- anions with Na^+ cations residing in each octahedral void, alternatively as two interwoven fcc lattices of Na and Cl. Two sets of lattice planes are depicted in Figure 15.2. The (111) planes are shown in purple. They contain the hexagonally packed layers of the atoms and are spaced by $d_{111} = 3.620$ Å. The (200) planes are shown in orange and are oriented normal to the a-axis and spaced by $d_{200} = 2.821$ Å.

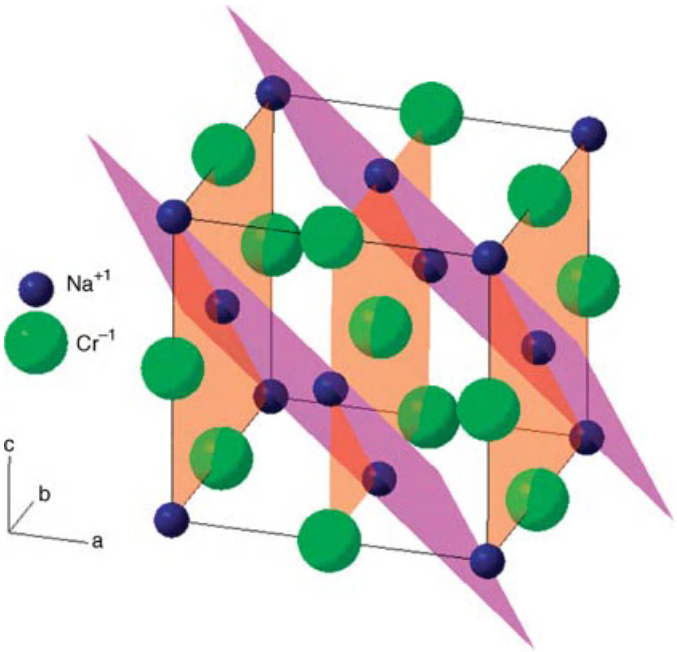


Figure 15.2 One unit cell of NaCl with two sets of lattice planes, (111) (purple) and (200) (orange). The spacing of the former (d_{111}) is larger and the corresponding Bragg peak is observed at a lower diffraction angle.

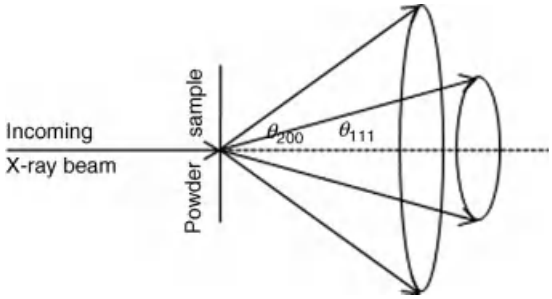


Figure 15.3 Production of diffraction cones from a powder sample illuminated by an incoming X-ray beam.

15.2.3
Powder X-Ray Diffraction

If a fine powder, say of NaCl, instead of a single crystal is used as a sample in a diffraction experiment, statistically all possible orientations of the unit cell are present in the volume probed by the incoming X-ray beam. Thus, for each lattice plane *hkl*, a certain part of the sample will fulfill the Bragg equation at the respective angle corresponding to d_{hkl}. This gives rise to diffraction cones as shown in Figure 15.3. Scanning the incident angle at a section of these cones and recording the positions of constructive interference will result in a powder diffraction pattern containing characteristic Bragg peaks at a position related to the unit cell geometry by d_{hkl}. As λ and θ are known from the experiment, d can be determined from the peak position. Assignment (indexing) of the peaks to the corresponding set of lattice planes *hkl* is relatively simple in cubic symmetry, but may be much more difficult for more complex crystal structures. In many cases involving catalytic materials, the ideal crystal structures are known and the indices can be readily taken from literature databases.

The integral intensity of a given diffraction peak *hkl* is proportional to the structure factor F_{hkl}, which is defined as

$$F_{hkl} = \sum_n f_n \cos 2\pi(hx_n + ky_n + lz_n)$$

where x_n, y_n, and z_n are the fractional coordinates of the nth atom. In addition to the structure factor, also the multiplicity, an experimental scaling factor, and the Lorentz polarization contribute to the total scattering amplitude of a Bragg peak. f_n is the atomic scattering factor, which describes the scattering power of a single atom. This factor is proportional to the atomic number, which leads to two important limitations of the XRD method: the scattering power of light elements such as H or Li is too low detect them accurately by conventional XRD, and the difference in scattering power of neighboring atoms in the periodic table is only small, which makes them difficult to discriminate.

In Figure 15.4, a real XRD pattern of NaCl is shown, which carries background and noise in addition to the desired signals. Due to the *F*-centered cell, only selected Bragg

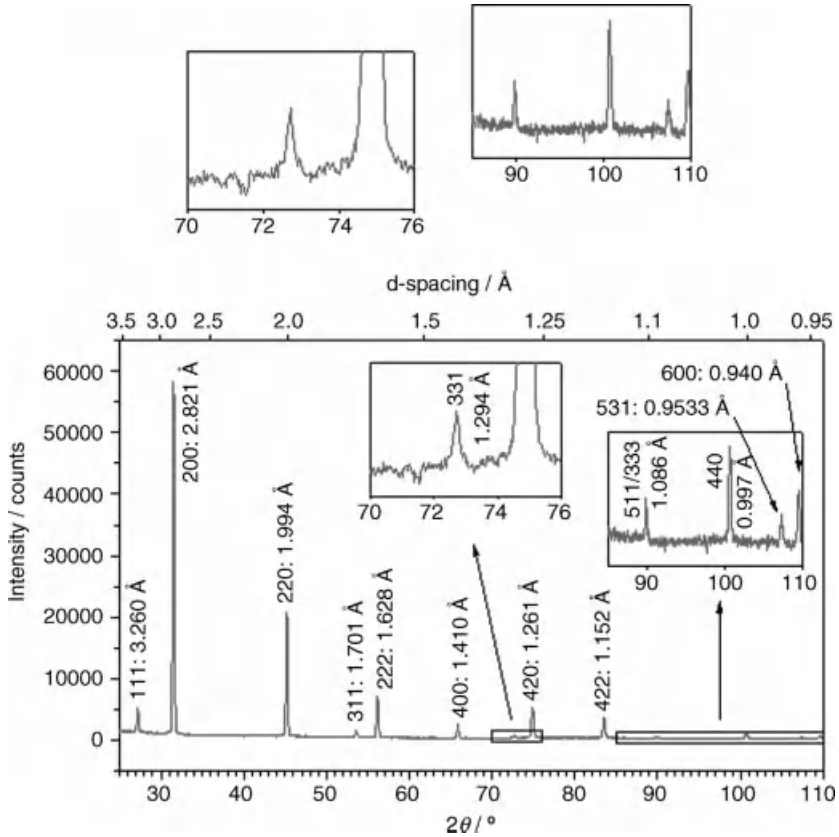


Figure 15.4 Powder diffraction pattern of NaCl.

peaks appear. For instance, the 001 with h and k even and l odd is absent. The positions of the peaks on the angular scale correspond via the Bragg equation to the d-spacing of the respective lattice planes; for example, the 111 peak at 27.335° 2θ corresponds to 3.620 Å for the wavelength used of 1.542 Å.

Some general features of a powder XRD pattern can be seen in Figure 15.4. The density of Bragg reflections increases with decreasing d-spacing (see the upper axis in Figure 15.4). Owing to the spreading of the d-scale with higher diffraction angles, this effect is partially compensated on the 2θ-scale for simple highly symmetric structures, but for more complex crystal structures, which exhibit more Bragg peaks over the whole angular range, the peaks at higher angles tend to overlap and are often difficult to resolve. Another general trend is that the average intensities decrease with the angle of diffraction. Scattering of X-rays takes place at the electrons of the atoms, which exhibit a certain spatial distribution. Thus, X-rays can be scattered at slightly different positions at the same atom. These slightly different sources of the scattered beam lead to a partially destructive interference, which increases with the angle of

diffraction. As a consequence, the atomic form factor f decays with 2θ and Bragg peaks at higher angles tend to be weaker than those at lower angles.

15.2.4
Information Content of a Powder X-Ray Diffraction Pattern

Above we have seen that the positions of the Bragg peaks in a powder XRD pattern are determined by the geometry of the unit cell, that is, a, b, c, α, β, and γ, while the arrangement and kinds of atoms within the unit cell are reflected in the relative intensities of the diffraction peaks. This is emphasized in Figure 15.5a, showing a simulated powder pattern of a hypothetical ccp of Na^+ cations. The relative peak positions and intensities are the same for any fcc metal and, owing to the similar lattice parameter, the pattern almost coincides with that of elemental Ca (except for the total diffracted intensity, which owing to the difference in scattering power of Ca and Na would be different). If now the octahedral positions are filled with Cl^- anions forming the lattice of NaCl, only the relative intensities are affected, and not the peak positions or the peak indexing (Figure 15.5b). In particular, the addition of the anionic

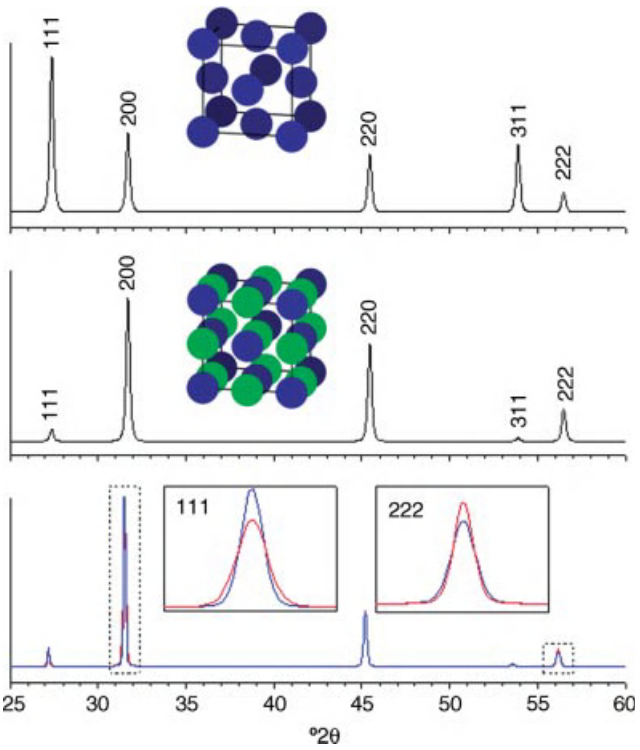


Figure 15.5 Simulated powder diffraction patterns (Cu Kα radiation, $\lambda = 1.542$ Å) of a hypothetical fcc packing of Na atoms (a) and of NaCl (b). Superposition of two NaCl patterns (c) simulated with 12% lattice strain (blue) and a finite crystallite size of 40 nm (red), respectively.

Cl^- sub-lattice is not associated with the production of new Bragg peaks, but, for instance, the first-order reflection at the hexagonally packed layers, the 111 peak, is attenuated by partially destructive interference due to scattering at the Cl atoms located in the middle between the Na layers.

Generally, the unit cell dimensions and the atomic positions of the asymmetric unit can be refined by powder XRD pattern fitting, if a suitable model containing the space group and appropriate starting values is available. Note that in the case of NaCl, the refinement of atomic coordinates is not necessary as the atoms are located on sites of defined symmetry. The refinement procedure will be described in more detail in Section 15.5. In addition to the ideal crystal structure, manifested in the peak positions and relative intensities, more information is contained in the shapes of the peaks. Finite crystallite sizes and also lattice strain lead to peak broadening. Both effects have a slightly different broadening effect on the line profiles, which is shown in Figure 15.5c, where the peak widths in the simulated patterns of NaCl are due to strain ($\varepsilon = 12\%$, blue curve) and small crystallize size ($D = 40\,\text{nm}$, red curve). The simulation was done in such a way that the profile widths of the 220 peaks match. Note that the peaks of the strained NaCl are broader for the 222 at higher 2θ, whereas they are narrower for the 111 at lower 2θ. The simulation illustrates that information on size and strain can be obtained from the peak widths and the two effects can be separated by their different 2θ dependences. Such line profile analysis is described in detail in Section 15.6.

Finally, it should be mentioned that some more structural information, which is not related to translational symmetry, is contained in the diffuse and modulated background, which is due to incoherent scattering of X-rays by the sample [25]. Methods of extracting this type of information and elastic Bragg scattering, which is dealt with in this chapter, are summarized as wide-angle X-ray scattering (WAXS) techniques. SAXS is described in Section 15.8.

15.3 Experimental Aspects

Commercially available diffractometers are nowadays standard laboratory equipment. The basic components are an X-ray source, a monochromator, a goniometer for varying the angle, a sample holder system, optionally a dedicated chamber to realize special sample environments, and a detector. In addition, slits and collimators may be present to guide the X-ray beam. Some modern diffractometers are equipped with large and curved position-sensitive detectors and do not need a goniometer. Typically, X-ray tubes, in which electrons are emitted from a tungsten filament and accelerated by high voltage towards a water-cooled metal target, are used for the generation of X-rays. The energy of the incoming electrons is absorbed by exciting core electrons of the metal atoms. The generated core holes are refilled with electrons from outer shells, leading to characteristic X-ray emission lines. A special type of X-ray tube is the rotating anode, providing higher intensities but causing higher costs and greater maintenance requirements. The most widely used target material is copper metal

and the overwhelming number of XRD patterns are recorded using Cu Kα radiation of $\lambda = 1.542$ Å for the Kα doublet, which is selectively reflected by a monochromator crystal positioned at a fixed Bragg angle. Graphite or germanium crystals can be used for this purpose. Alternatively, to filter one characteristic X-ray line from the bremsstrahlung background, and the other emission lines, such as Kβ, metal filters with suitable absorption edges can be placed in the beam. Cu Kα radiation, for instance, can be filtered by a Ni foil.

The sample is placed in the middle of the goniometer circle and the incident angle of the X-rays is varied. This can be achieved by arranging the components in different geometries (Figure 15.6).

In the classic reflection geometry (Bragg–Brentano geometry, Figure 15.6a), the divergent primary beam illuminates a relatively large sample area, which decreases with increasing diffraction angle (unless variable slits are used). This is the preferred arrangement for strongly absorbing samples and, in addition to powders, for bulky specimens with a flat surface such as wafers, thin films on a substrate, and pellets. In reflection diffractometers, the monochromator is usually not placed between the X-ray source and sample, but between the sample and detector. These secondary monchromators help to remove fluorescence from the sample, but usually do not separate $K\alpha_1$ and $K\alpha_2$ radiation. In the classic transmission geometry (Figure 15.6b),

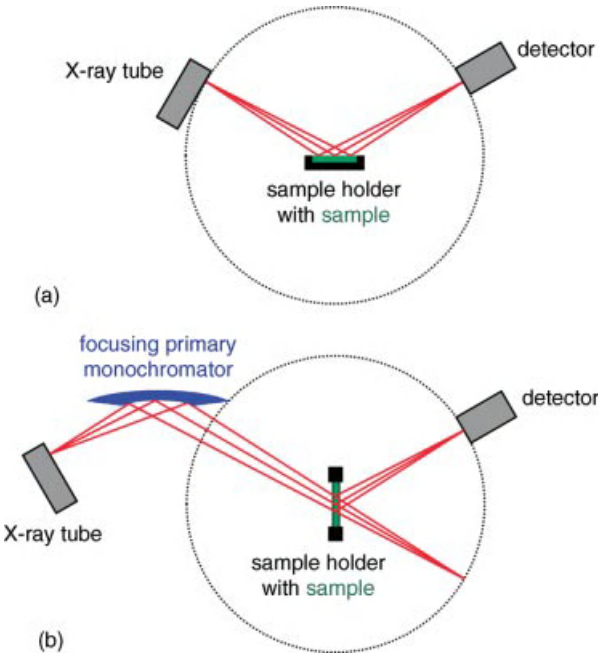


Figure 15.6 Simplified representations of the Bragg–Brentano (a) and transmission geometries (b). In (a) either the sample can be rotated by θ and the detector moved simultaneously by 2θ (θ–2θ geometry) or the X-ray source and the detector each by θ (θ–θ geometry) without movement of the sample.

a bent primary monochromator yields pure $K\alpha_1$ radiation and focuses the primary beam through the sample into the detector slit. Only a relatively small sample area is illuminated, which increases with increasing diffraction angle.

Transmission XRD requires special sample holders. Thin layers of powders have to be prepared and kept in place during the experiment. This is typically achieved by filling the powder sample into glass capillaries or fixing it between two layers of a polymer film. The films or capillary walls are located in the X-ray beam path and will contribute to the background of the XRD pattern. This effect is often detected as a broad modulation in XRD patterns, which is visible especially in patterns of poorly diffracting samples. For the sake of better statistics, the sample should be rotated around the scattering vector if possible.

For experiments under reactive conditions [3], dedicated temperature and pressure chambers have to be used. For investigation of working catalysts, the reaction cell must serve the conflicting goals of providing a suitable geometry for diffraction experiments and being a good catalytic reactor. Conventional high-temperature chambers equipped with a strip heater and mounted on a θ–2θ Bragg–Brentano diffractometer can be used, but suffer from large dead volumes, ill-defined solid–gas contact and possible movement of the sample as the chamber is rotated during recording a pattern. The last two drawbacks are minimized with dedicated catalysis chambers mounted on θ–θ diffractometers [26–28]. The sample is not moving during the measurement and the gas can be forced through the bed of the catalyst sample lying on a frit. Such a cell is shown in Figure 15.7. Alternatively, packed capillaries may be used in transmission geometry to simulate a tubular catalytic reactor for *in situ* studies of catalysts under reactive conditions [29–32]. The dead volume is not a problem in such experiments, but it has to be kept in mind that the X-ray usually probes only a very small fraction of the catalyst bed, which has to be representative to allow relation of the structural information with the integrated catalytic measurements. In addition to a suitable reaction cell, instrumentation for an *in situ* diffraction

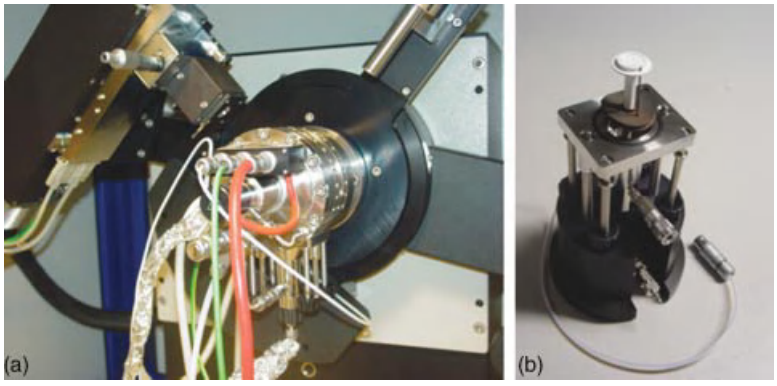


Figure 15.7 A Paar XRK 900 cell mounted on a STOE $\theta - \theta$ goniometer. Note the heated piping for the gas supply (a). The sample holder with a ceramic frit and the gas tubing forcing the feed through the catalyst bed (b).

experiment includes auxiliary equipment for reactant dosing and product analytics, which has to be robust enough to run under continuous operation for long periods on-stream.

Synchrotron radiation should be mentioned here as a very powerful alternative for laboratory XRD. Such experiments offer further possibilities for very high-quality patterns and time-resolved investigation of solid materials. The advantages are the high flux, the options of energy-dispersive detection [33–35], and tuning the wavelength near the absorption edges of selected elements in the sample (anomalous scattering for discrimination of neighboring elements in the periodic table) [36]. Furthermore, the possible combination with complementary extended X-ray absorption fine structure (EXAFS) experiments can lead to valuable results [4, 6].

15.3.1 Practical Aspects

The wavelength for a powder XRD experiment is typically chosen according to the X-ray tubes mounted on the available diffractometer. In most laboratory work this will be Cu Kα radiation. This is convenient as is favors easy comparison of the results between different laboratories, but is not necessarily the best choice. Harder X-rays of shorter wavelength, for example, from Mo or Ag targets, exhibit less interference and absorption from the measurement environment and help penetration of the X-rays. However, they suffer from lower intrinsic resolution resulting from the contraction of the d-scale per $^{\circ}2\theta$ with decreasing wavelength. Limitation in resolution may become a problem especially for wide diffraction angles. Cu Kα radiation is a good compromise between the loss of intensity by absorption and the precision of the XRD experiment. Another aspect that might play an important role is fluorescence from the sample. Radiation from a given target material in the X-ray tube will excite fluorescence of the elements located on the left in the periodic table. Fluorescence will lead to higher background intensities and lower signal-to-noise ratios. Patterns suffering from a fluorescence background need much longer counting times to achieve a reasonable quality. In the case of Cu Kα radiation, fluorescence may a problem for samples containing large amounts of Co, Fe, Mn, and Cr. The fluorescence contribution to the pattern can be filtered by secondary monochromators, but still the loss of intensity due to fluorescence will be reflected in longer counting times.

The measurement time needed for an XRD pattern depends heavily on the exact conditions of the experiment, especially on the X-ray source and detector, and ranges from several minutes up to days for laboratory machines and down to <1 s if synchrotron radiation is used. No general limit for the signal-to-noise ratio can be given. The counting time has to be adjusted to the scientific questions that should be addressed and to the method that should be applied for evaluation. For a simple phase identification of components with significantly different crystal structure and lattice parameters, a relatively high noise level may be tolerable. For quantitative analysis, lattice constant determination, structural refinement, or line profile analysis, a progressively higher quality of the XRD pattern is required. As a crude rule of thumb, most problems due to high noise levels can be circumvented and standard

evaluation should be possible in most cases if the maximum intensity of the strongest peak is at least 10 000 counts above the background.

Generally, no special sample preparation is necessary for a powder XRD experiment. If the sample is not obtained in the form of a fine powder, grinding may be required. This is obviously necessary for transmission experiments, but also generally required for coarse-grained samples to guarantee sufficient statistics concerning the orientations of the grains. Furthermore, surface roughness due to coarse grains may affect the relative intensities in XRD patterns. Mechanochemical changes to the samples have to be avoided during grinding. In special cases of layered structures, grinding may easily induce disorder, which will be reflected in the XRD patterns. Careful sample preparation helps to avoid the effects of coarse grains and preferred orientation (see Section 15.4.3), induced, for example, by pressing anisotropic crystals into pellets. Both effects lead to intensity fluctuations within the diffraction cones and affect the intensity distribution of the XRD pattern.

15.4
Application to Phase Identification

Typically, the first step in the evaluation of a powder XRD pattern is the qualitative analysis of the crystalline phase(s) present in the sample. In the simplest case, this can be done by comparison of the positions and intensities of the Bragg peaks with respect to the patterns of reference compounds. If one reference compound is not sufficient to explain the experimental pattern, a phase mixture may be present. In such a case, information on the quantitative phase composition is also desirable. In this section, methods for phase identification and quantification by XRD are introduced.

15.4.1
Identification Using Reference Compounds and Structure Databases

Phase identification can be done by a "fingerprint" comparison using the raw pattern and available reference patterns from databases. The most commonly used database is the Powder Diffraction File (PDF) of the International Center for Diffraction Data (ICDD) [37]. Other databases of crystal structure data, which can be used to calculate reference powder patterns, are the Inorganic Crystal Structure Database (ICSD) for inorganic solids, the Cambridge Structural Database (CSD) for organic and organometallic solids, and the American Mineralogist Crystal Structure Database for minerals. An entry in the PDF database contains a list of d-spacings and corresponding relative intensities of the diffraction lines for a pure phase. In addition, information on the source of the measurement or calculation of the reference pattern and further crystallographic and experimental details, if available, can be found. Modern software packages, usually obtained with the purchase of a diffractometer from the supplier, allow fast and easy comparison of measured and literature data using a graphical interface. A typical procedure to check for the success of a synthesis step would be to preselect all PDF cards containing the elements involved in

the preparation including counter ions and solvents and to compare this selection of possible crystalline phases with the experimental pattern. Some programs also offer automatic search–match options, for which some additional data treatment such as background subtraction may be required.

An example of straightforward phase identification is shown in Figure 15.8a. The crystalline component in a VPO catalyst precursor can be identified as $VOHPO_4 \cdot {}^1/_2 H_2O$ by comparison of the raw data with the PDF card 38–291. Note that the bars reflect the integrated peak intensities for a hypothetical sharp line profile. Thus, deviations between the bars and the measured peak heights may occur if the measured profiles significantly change for different peaks. In general, all peaks listed in the PDF card in the measured angular range must be present in the experimental pattern to identify a compound unambiguously. However, the presence of poorly crystalline or nanostructured materials, as often encountered during catalyst preparation, may complicate the phase identification. If no perfect match of the experimental pattern with reference pattern can be obtained, the best match should be considered and the deviation should be closely examined. What might happen, especially if the sample is not macrocrystalline, is that "missing" peaks of low intensity may be covered in the noise or modulations of the background. Missing peaks may also result from effects of preferred orientation and anisotropy, which affects the relative intensities in an XRD pattern (see below). In extreme cases certain peaks can be weakened or broadened below the detection limit. In these cases, a systematic *hkl* dependence of these missing peaks should be present. Such effects may contain valuable information about the sample and, in order to allow for a critical evaluation, it is desirable to report XRD patterns together with the literature data in the form of an indexed bar diagram as shown in Figure 15.8, instead of just marking selected peaks with symbols assigned to certain phases.

If additional peaks are detected, which are not explained by an otherwise suitable reference pattern, the most obvious explanation is the presence of a phase mixture and two or more PDF cards have to be considered to account for the experimental pattern. The pattern in Figure 15.8b shows the XRD pattern of a sulfated stabilized zirconia catalyst for isomerization reactions and is an example of a more complex phase identification. At first glance, the present phase can be satisfactorily assigned to cubic ZrO_2 by comparison with PFD card 49–1642 (red lines). A very small unassigned peak near 43° 2θ, however, and the asymmetric peak profiles of the 200 and 311 indicated the presence of an impurity phase. In fact, the "impurity" is not a different compound, but another polymorph of ZrO_2. In tetragonal ZrO_2, the distortion of the cubic structure leads to a lower symmetry and splitting of the XRD peaks. This effect is relatively small and, furthermore, the split peaks usually overlap with those of cubic ZrO_2. Hence the splitting is hard to resolve and is detected as a slight asymmetry of the peak shapes at the positions of the cubic phase. The extra peak corresponds to the 012 diffraction line of the tetragonal phase, which is systematically absent in the cubic phase due to symmetry reasons and is a clear indicator of the presence of tetragonal ZrO_2. In this case of very similar crystal structures, it is impossible to tell, without pattern fitting, if the sample contains pure tetragonal zirconia or a mixture of the tetragonal and cubic phases. In this special

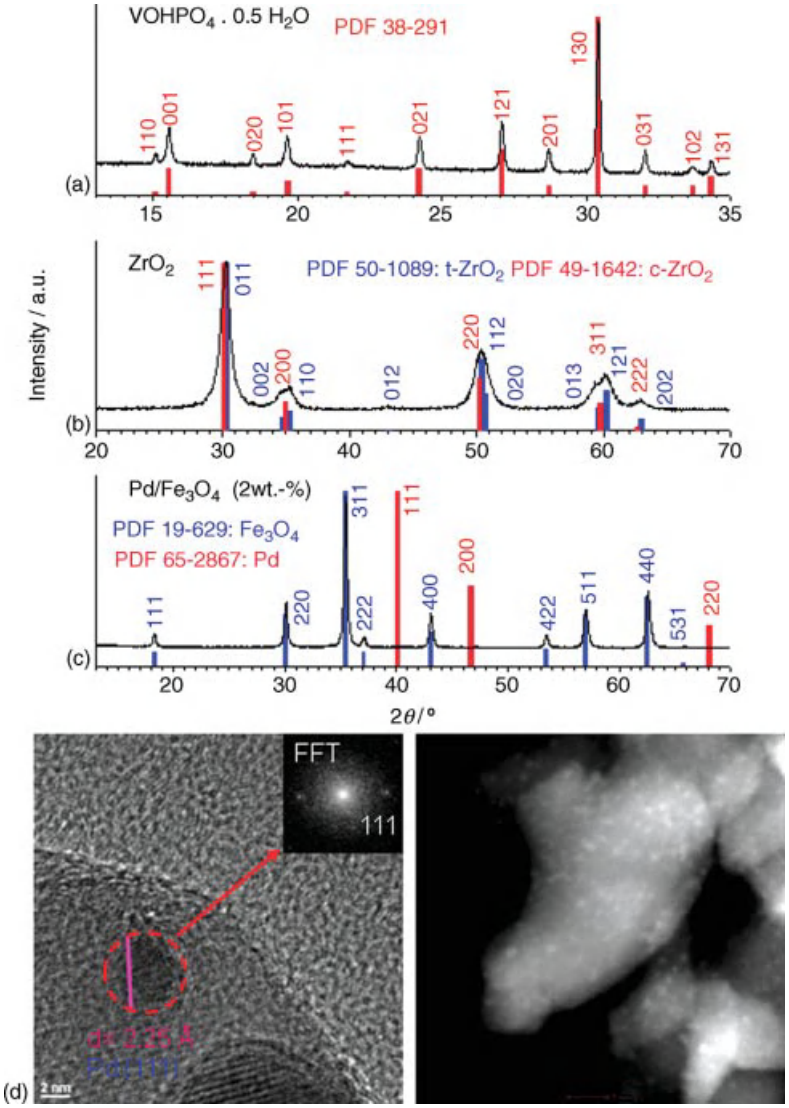


Figure 15.8 Examples for phase identification of catalytic materials by XRD pattern comparison. Straightforward identification of a VPO catalyst precursor (a), more complex case of tetragonal versus cubic ZrO_2 (b), and XRD pattern of a highly dispersed metal phase on an oxide support (c); only the latter can be seen by XRD despite the phase ordering of the highly dispersed metal evidenced by HRTEM (d).

case, qualitative analysis by Rietveld refinement (see below) revealed that only tetragonal ZrO_2 is present.

Sometimes a situation is encountered in which all peaks of the experimental pattern do not perfectly match but are close to those of a reference phase and no better

agreement can be found in the structure database. In such a case, the deviations have to be analyzed in more detail, especially with respect to their *hkl* dependence. Systematic deviations in the relative intensities indicate the presence of preferred orientation in the sample, while a systematic deviation of the peak position is due to differences in the chemical composition (if thermal expansion can be excluded; note that some PDF cards report XRD patterns recorded at elevated temperatures). A proper treatment of these effects requires the application of pattern fitting procedures, which are described in Section 15.5.1.

A significant problem in phase analysis arises when several phases are present in widely different crystallite sizes and states of ordering. XRD will then indicate only the phase which is well ordered and occurs as large crystallites. It should always be kept in mind that successful assignment of all peaks in an XRD pattern to a targeted reference phase still does not exclude the presence of impurities. They may be amorphous or present in small amounts below the detection limit of XRD (less than roughly 5%). Also, crystalline but nanosized phases may be present with crystallite sizes below ~3 nm (see Section 15.6.1). In catalysis, such a situation is often encountered not for undesired impurities, but for the active phase in supported catalysts. Here, the absence of strong and sharp XRD peaks of the active phase is a desired indicator of successful preparation of a highly dispersed and homogeneous supported phase. An example is presented in Figure 15.8c [38], showing the XRD pattern of a catalyst containing 2 wt% Pd supported on iron oxide. Only the reflections of the support phase can be observed and assigned to PDF 19–629 (Fe_3O_4, magnetite). The Pd fraction of the sample is highly dispersed, but in fact crystalline, and exhibits perfect phase ordering, as can be shown by complementary transmission electron microscopy (TEM) investigations (Figure 15.8d). However, the total amount and in particular the average crystallite size of ~1–3 nm are too small to be detected by XRD. It is obvious that it is inadequate to call such a nanomaterial, which is one example of many in catalysis, "amorphous." It may be termed "X-ray amorphous," but truly amorphous, that is, glassy, solids are only rarely encountered in catalytic samples, with the exception of some silica materials. The absence of a sharp diffraction pattern is usually an indication of nanocrystalline rather than amorphous structures.

15.4.2
Quantification of Phase Mixtures

For proper quantification of the phases in a mixture, fitting procedures and/or internal standards can be used. The relative amount of a phase is to a first approximation proportional to the scattered intensity. It is important to note that this correlation refers to the integral intensity of the Bragg peaks. Simple comparison of peak heights may easily lead to false estimations of the phase fractions, especially underestimation of a phase showing severely broadened peaks. Moreover, differences in the scattering strengths of the two phases lead to different proportionality factors in the above-mentioned correlation and have to be considered.

For exact determination the phase fractions in a mixture, the full pattern has to be taken into account or standards should be used. Standardless comparison of only

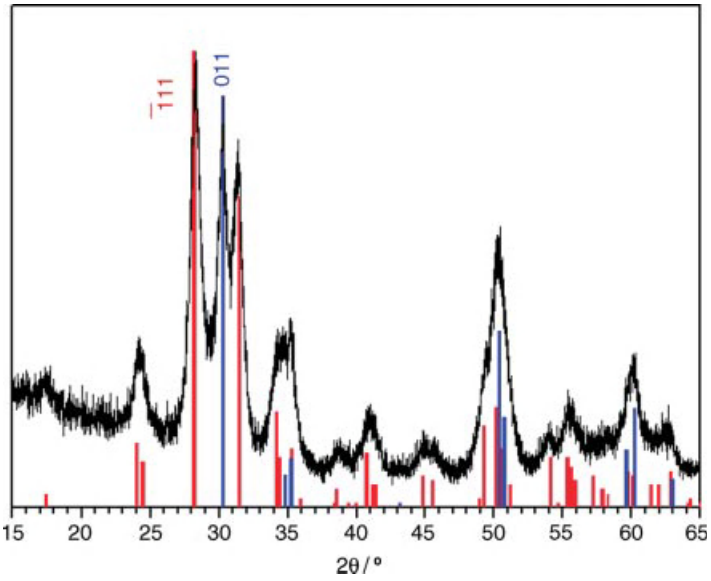


Figure 15.9 XRD pattern of a sulfated Mn-promoted zirconia catalyst comprising a phase mixture of tetragonal (blue) and monoclinic ZrO_2 (red).

selected peaks (typically the strongest line of each phase is chosen) may lead to wrong results, even if the integral intensity instead of the peak height is considered and the scattering powers of the two phases are similar. The polymorphism of ZrO_2 is again a nice example to demonstrate this pitfall. In Figure 15.9, the powder pattern of a mixture of tetragonal and monoclinic ZrO_2 is shown. According to the PDF files 37–1484 (m-ZrO_2) and 50–1089 (t-ZrO_2), the strong neighboring peaks at 28 and 30° 2θ can be assigned to the $\bar{1}11$ of the monoclinic and the 011 peak of the tetragonal phase, respectively. The heights and integral intensities of both peaks are similar. However, for the monoclinic phase, which owing to its lower symmetry is richer in peaks, the scattered intensity is more evenly distributed over the angular range. Therefore, taking only the strongest reflections into account, one is tempted to estimate roughly that both samples are present in similar amounts, but refinement shows that the monoclinic polymorph clearly is the majority phase by 2 : 1.

A more reliable quantitative estimation of the phase composition can be obtained if standards are used. The relative intensities of selected individual reflections of the phases in a mixture are determined and related to the intensity of a reference peak of the standard material. Standards should be well-crystalline and inert materials with few and non-overlapping peaks such as Si, MgO, α-Al_2O_3, or SiO_2. The ratio of the peak intensities in the unknown mixture can be scaled according to the known ratio of the individual peaks to the reference peak in a mixture of known composition of each single phase with the standard material. Such intensity ratios are listed for some phases in the PDF database as I/I_{cor} values [39]. This is the ratio of the integral peak intensities of the strongest peak of the sample divided by that of the strongest peak of

α-Al_2O_3 (corundum) in a 1 : 1 (w/w) phase mixture. In the case of ZrO_2, for example, I/I_{cor} for monoclinic zirconia is roughly half of that of the tetragonal phase.

The most reliable and accurate method of quantitative phase analysis is full pattern refinement, which is treated in more detail in Section 15.5.1. In such a fitting procedure, the full pattern of the phase mixture is modeled using the crystal structure data of each component and some experimental parameters. Among these parameters there is a scaling factor which is refined for each phase. The fitting program can calculate the relative phase fractions from the ratio of these scaling factors taking into account all the aspects mentioned above such as differences in scattering power and crystal symmetry or preferred orientation. The combination of refinement and the use of standards can be used to obtain information also on the amorphous fraction in a sample. The precision of this method can be around 1%, but depends critically on the question of whether the starting model chosen for refinement is indeed a good representation of the sample under investigation.

15.4.3
Effects of Anisotropy and Preferred Orientation

Prerequisites for recording a full powder pattern are not only that all possible orientations of the individual crystallites in a powder are present, but also that these orientations occur in a homogeneous, that is, statistical, distribution. What might happen if the particles in the powder have an anisotropic shape, such as needles or platelets, is that certain orientations will be under-represented in the sample simply by the fact that not many needles will stand on their tips, or platelets on their edges. This effect is shown in Figure 15.10a for the extreme case of an oriented thin film.

Assuming that the crystallites in the film have grown with their *c*-axis perpendicular to the substrate, only the (00*l*) reflections would appear in a powder pattern recorded in reflection geometry, and spinning the sample around an axis normal to the film surface would not help. The situation for a powder of platelet-like crystals

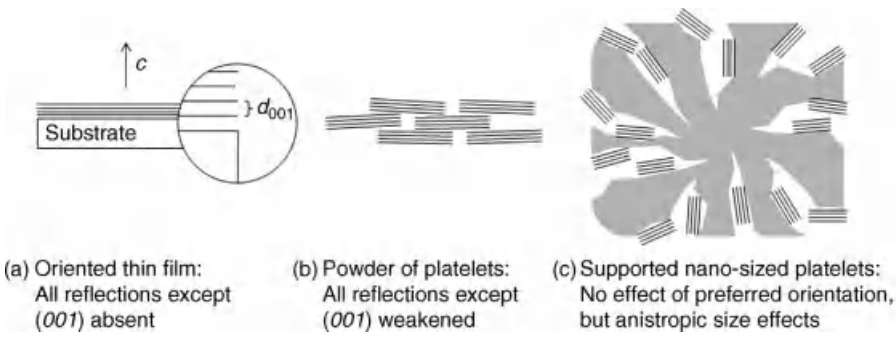


Figure 15.10 Schematic representation of samples exhibiting preferred orientation due to oriented growth (a) or anisotropic particle shape (b). Anisotropic nanoparticles on an isotropic support should not show preferred orientation (c).

(Figure 15.10b) would be less drastic, but still all reflections other than (00*l*) would be weakened due the preferred orientation of the sample. For polycrystalline samples, this effect may become stronger if mechanical force was used to prepare such a sample, such as pressing of a pellet or cold working of a metal foil.

Preferred orientation should not play a significant role if the platelets are supported on a material with an isotropic pore structure, such as shown in Figure 15.10c. In this case, all orientations should be present and a relation of preferred orientation and exposed surface facets, which may be relevant in the situations shown in Figure 15.10a and b, will not apply; rather, an anisotropic size effect (see Section 15.6.1) will be detectable.

15.5
Application to Phase Characterization: Ideal Structure

As we have seen in Section 15.2, for a known crystal structure the positions and intensities of Bragg peaks can be calculated on the basis of the Bragg equation and the structure factor. Thus, idealized powder patterns can be simulated and it is possible to apply least-squares methods to fit such a calculated pattern to an experimental pattern if a suitable starting model is available. In principle, all of the information contained in a powder pattern can be extracted from such a fitted model. Various methods of pattern refinement have been developed and, for practical reasons, it is useful to choose a suitable method according to the scientific question addressed rather than trying to obtain all results in a single evaluation process. In this section, the Rietveld method for determination of the unit cell parameters and refinement of the atomic coordinates will be introduced. Line profile analysis for determination of microstructural parameters and defects will be covered in the next section.

15.5.1
Structure Refinement

The most powerful method of structure refinement of powder patterns is the Rietveld method [40]. This is a whole pattern-fitting procedure, which uses least-squares refinement to reach the best agreement of a calculated and the entire experimental pattern as a whole. Crystal structure(s), diffraction optics, instrumental factors, and specimen characteristics are refined simultaneously, meaning that pattern decomposition and parameter variation are not separate steps. Hence the Rietveld method can cope with complex structures and phase mixtures even if some reflections heavily overlap.

The intensities for each calculated data point $y_{c,i}$, i being the increment in 2θ of the measurement, is fitted simultaneously to minimize the difference from the corresponding experimentally measured data point y_i:

$$S_y = \Sigma_i {y_y}^{-1} \left(y_i - y_{c,i}\right)^2$$

The expression for $y_{c,i}$ is

$$y_{c,i} = s\Sigma_{hkl} L_{hkl} |F_{hkl}|^2 \Phi(2\theta_i - 2\theta_{hkl}) P_{hkl} A + y_{b,i}$$

where s is a scaling factor, L_{hkl} contains the Lorentz polarization and multiplicity factors, Φ is the profile function of the Bragg peaks, P_{hkl} is the preferred orientation function, A the absorption factor, F_{hkl} is the structure factor, and $y_{b,i}$ is the intensity of the background. The structural parameters are contained in the structure factor and the relative phase fractions can be derived from the scaling factors. As in all nonlinear least-squares refinements, false (local) minima may occur and good (near the global minimum) starting models are required. Those are usually obtained after qualitative phase analysis (Section 15.4) from the single-crystal structure of the phase(s) giving the best match.

After suitable starting models have been assigned, approximately 10–100 independent parameters are refined and it is advisable to allow the parameters subsequently to vary in order always to obtain a stable fit. One has to keep an eye on the total number of free parameters and its ratio to the observed reflections to avoid overfitting. The total number of parameters to be refined depends strongly on the complexity of the structure and the on the question to be answered. Among these parameters, some have to be refined for each phase, whereas others are global. The latter are the variables of the background polynomial, the zero shift of the 2θ scale, and instrumental and specimen characteristics such as sample displacement and transparency. For each phase, the lattice parameters, scale factor, and profile breadth parameters have to be refined. The latter describe the 2θ dependence of the peak half-widths, often according to the Cagliotti function [40, 41]:

$$\mathrm{FWHM}^2 = U\tan^2\theta + V\tan\theta + W$$

where FWHM is the full width at half-maximum of the Bragg peaks, which limits the problem to three variables for each phase. For each crystallographically independent position in the unit cell, the atomic coordinates x, y, and z, if not predetermined by symmetry, and the corresponding occupancy factors can be refined. Disorder parameters or temperature factors can be refined either for the whole phase or individually for each site. The quality of a fit can be judged by different fit criteria, the most commonly used ones being the R-Bragg and the R-wp factors (wp = weighted pattern). The former resembles the R-value used in single-crystal structure refinement and is insensitive to misfits in the pattern that do not involve the Bragg intensities of the refined phase(s). In general, the R-values should reflect the progress during the refinement process and ideally fall well below 10% at the end. A discussion of the fit criteria in Rietveld refinement can be found elsewhere [40, 42].

To evaluate the success of a Rietveld refinement, not only the criteria of fit should be reported. A graphical representation is just as important and a typical example is shown in Figure 15.11. It consists of the experimental pattern represented as individual data points and the calculated pattern shown as a line. The latter can be further decomposed into the contributions of the individual phase and the background. Sometimes the positions of the Bragg peaks of the constituent phases are

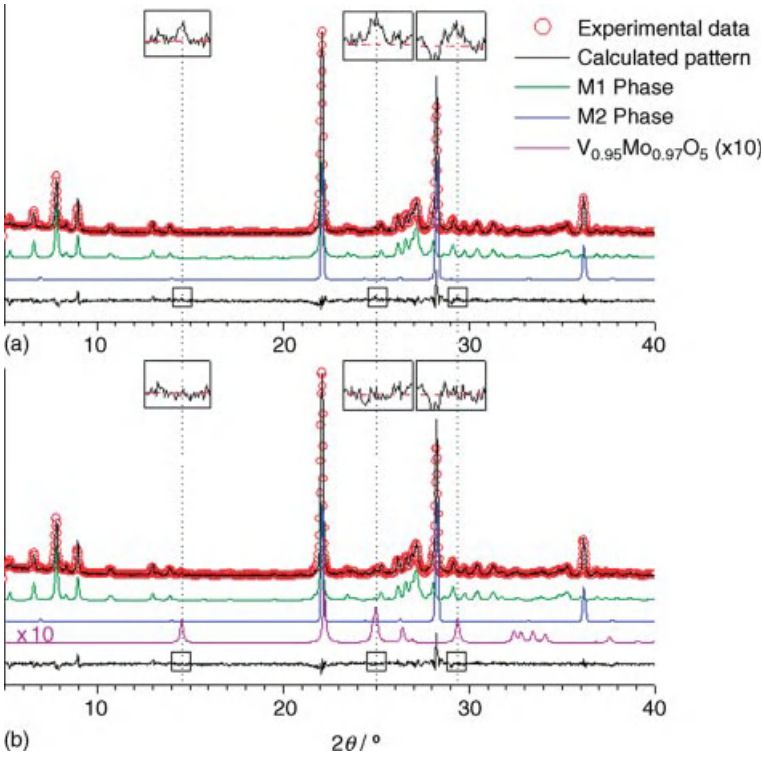


Figure 15.11 Graphical representation of a Rietveld fit of $MoVTeNbO_x$ mixed metal oxide catalyst for hydrocarbon oxidation containing two major phases M1 and M2, refined without (a) and with (b) an additional impurity phase.

given at the bottom. Interesting is the difference plot of measured and calculated data, which ideally should only contain the noise of the measurement, although stronger oscillations of this curve at the positions of the Bragg peaks are usually difficult to avoid. The difference curve is very useful in identifying minor phases in a mixture, which can be more easily recognized if the deviations take the form of Bragg peaks. Figure 15.11 shows a phase mixture of two phases, denoted M1 and M2, in a mixed metal oxide $MoVTeNbO_x$ catalyst for the selective oxidation of propane [43]. The Rietveld fitting in Figure 15.11a is satisfactory at first sight and the difference curve is relatively smooth. The ratio of the two phases could be determined as M1: M2 = 60:40.

Close inspection of the difference curve, however, revealed deviations at angles where the M1 or M2 phases do not exhibit reflections (insets). Adding a third phase, $V_{0.95}Mo_{0.97}O_5$ (PFD 77–649, purple line), removes these deviations and proves the presence of this impurity phase, which would have been difficult to discover without refinement. The amount of the impurity phase is approximately 5 wt% and the M1: M2 ratio is hardly changed.

It should be mentioned that these mixed metal oxides are also a nice example of the limitations of laboratory XRD. Owing to the large unit cell, the complex metal distribution, and the variety of structural motifs, not all details of the M1 crystal structure are reflected in the conventional powder XRD pattern. Finding the structural model of M1 [44, 45] used for the Rietveld refinement shown in Figure 15.11 required the combined application of complementary techniques such as synchrotron XRD, neutron diffraction, and electron microscopy, and can be seen as a prototype example of the solution and refinement of a complex crystal structure of a catalytic material using complementary diffraction and imaging methods.

Solid solutions can be well characterized by structural refinement. For this purpose, it is often sufficient of determine the unit cell parameters without knowledge of the full set of atomic coordinates, the site occupancy factors, or the contribution of preferred orientation. In such cases, whole pattern decomposition methods can be applied for fitting. The intensities of the reflections are not calculated using the structure factor, but are individually fitted. As the intensity information is not used, such methods, like the Pawley [46] or LeBail refinement methods [47], gives results only on the peak shapes and the geometry of the unit cell, not on its content. Also, quantitative analysis is not possible. Using a refinement procedure for the determination of cell parameters is strongly recommended even for simple structures as its precision is clearly superior compared with the evaluation of single peak positions, because the information of the full pattern is used and the refinement accounts for errors due to a zero shift of the 2θ-scale and sample displacement effects.

XRD pattern fitting can be used conveniently to determine the composition of a solid solution. In the simple case of fcc metals showing a miscibility of the full range of composition, the lattice parameters of the alloys fall on a straight line between those of the pure elements. This empirically found correlation can be understood as the averaged size effect of substitution and is known as Vegard's law. It can be seen in Figure 15.12 for the combinations Pd–Ag, Pd–Pt, and Pd–Ni that the refined lattice parameters of Pd75X25 alloys (X = Ag, Pt, Ni) fall on a line connecting the lattice parameters of pure Pd and pure X. Vegard-type behavior is not limited to simple alloys

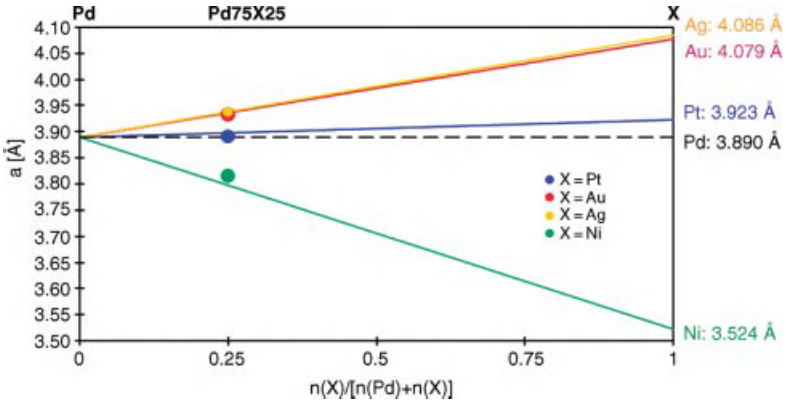


Figure 15.12 Vergard lines for PdX alloys (X = Ag, Au, Pt, Ni) connecting the lattice parameters of pure Pd and pure X. The experimentally determined lattice parameters for Pd75X25 alloys fall on the Vegard line.

but is found for most kinds of solid solutions. If a series of reference samples with different known compositions is used for recording a calibration curve of lattice parameters versus composition, the measured lattice parameter of an unknown sample can be assigned to a composition by linear interpolation within the homogeneity range of the solid solution. Deviations from linear behavior can be used to determine solubility limits accurately. Above that limit, often a new storage phase for the substituent crystallizes in addition to the fully substituted material showing no further variation in its lattice parameters. For catalytic materials, such a situation holds the risk of being misinterpreted as a "phase cooperation" phenomenon.

A more complex example relevant for catalyst synthesis is shown in Figure 15.13. During the preparation of Cu/ZnO catalysts for the synthesis of methanol, $(Cu,Zn)_2(OH)_2CO_3$, a phase named zincian malachite after the pure Cu mineral malachite, $Cu_2(OH)_2CO_3$, is obtained as the product of coprecipitation of mixed Cu,Zn solutions and aging [48]. Owing to their similar scattering power, the neighboring elements Cu and Zn cannot be discriminated by XRD. Also, their ionic radii are very similar, limiting the expansion or contraction effects on the unit cell usually observed upon cation substitution. Hence determination of the composition of this solid solution catalyst precursor phase by XRD is difficult and further complicated by the fact that often other by-phases are obtained, which may also form solid solutions of Cu and Zn in their cationic sublattice [49]. Therefore, knowledge of the average chemical composition is of little help for determining the composition of the individual phases. The positions of most Bragg reflections hardly change as the nominal composition is changed from Cu:Zn = 100:0, pure malachite, towards 70:30, which is the composition of the industrial methanol synthesis catalyst. Four XRD patterns of Cu,Zn coprecipitates with decreasing Cu content are shown in Figure 15.13a. The catalyst precursors are single-phase (zincian) malachite except for the Cu:Zn = 70:30 sample. In addition to changes in peak widths and the background modulation, careful inspection revealed that two reflections indexed $20\bar{1}$ and $21\bar{1}$ can be identified, which show a pronounced shift to higher diffraction angles apparently independent of the other peaks (Figure 15.13b) [50]. This is a remarkable result because the positions of the Bragg peaks should be inter-related by the geometry of the unit cell. Rietveld refinement revealed that the monoclinic lattice parameters of the malachite phase indeed exhibit an anisotropic Vegard-type behavior for the three single-phase samples, as expected for a solid solution (Figure 15.13c). This trend is hardly reflected in the XRD peaks because in a nonrectangular monoclinic structure the relation between lattice parameters and d_{hkl} is often indirect. For instance, the effect of the c-axis contraction on d_{002} is compensated by the decrease in the monoclinic angle β. The strong effect on the characteristic $20\bar{1}$ and $21\bar{1}$ reflections can be explained by a special geometric effect due to substitution of Cu^{2+} cations preferring a Jahn–Teller elongated environment by Zn^{2+} not showing this effect. This comprehensive XRD characterization has been shown to be very useful for the directed synthesis of Cu/ZnO catalysts as a relation between the precursor structure and the Cu surface area in the final catalyst could be found (Figure 15.13d) [51]. The fully substituted zincian malachite precursor phase with a composition near 72:28 shows the largest con-

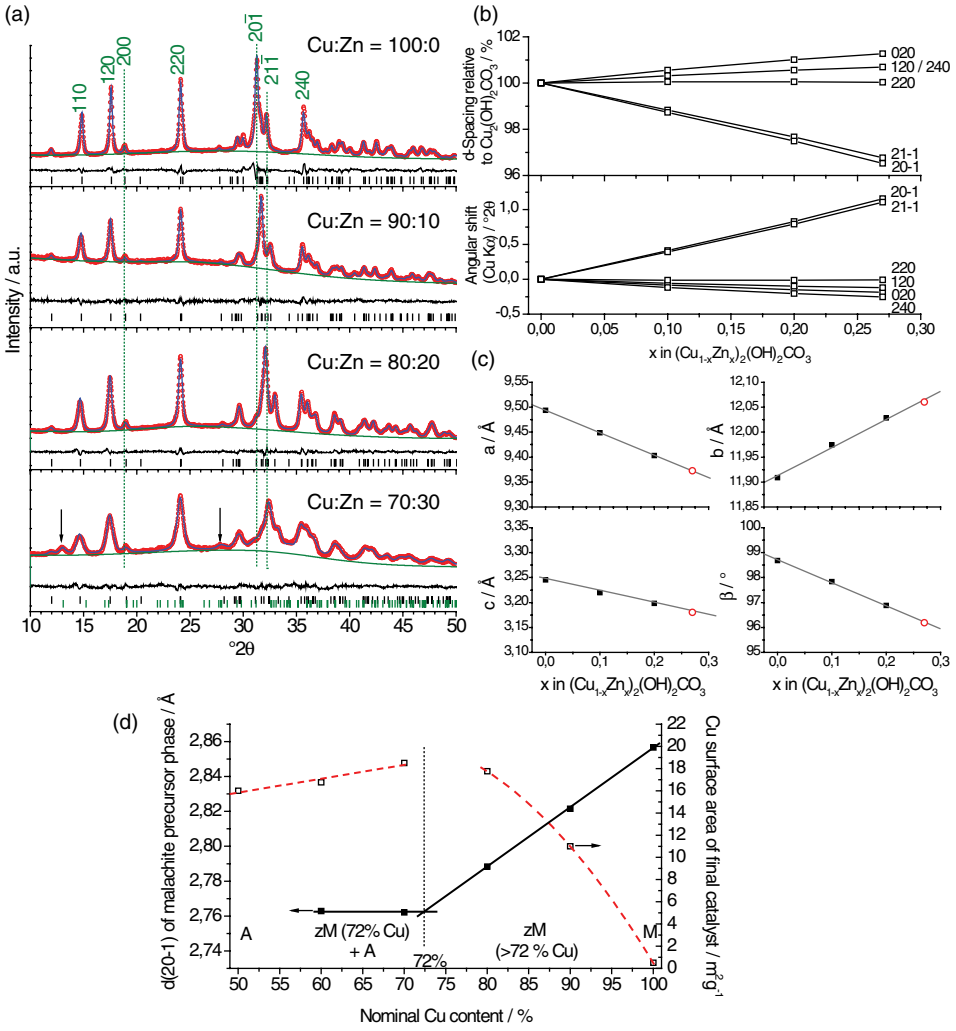


Figure 15.13 Rietveld refinements of zincian malachite precursors for Cu/ZnO catalysts with different Cu:Zn ratios (a), anisotropic peak shift of certain characteristic reflection (b), Vegard-type behavior of the lattice parameters upon Cu, Zn substitution (c), and relationship of substitution in zincian malachite and accessible Cu surface area in the final catalyst (d). M = malachite; zM = zincian malachite; A = aurichalcite.

traction of the $d_{20\text{-}1}$ lattice planes and yields Cu/ZnO catalysis with the largest Cu surface area. Beyond ~28% Zn, a precursor by-phase, aurichalcite $[(Cu,Zn)_5(OH)_6(CO_3)_2]$, crystallizes (arrows in Figure 15.13a), which does not decompose to an as efficient catalyst. This critical limit of the Cu:Zn composition has been determined by locating the refined lattice parameters of the phase mixture sample (Cu:Zn = 70:30) as a fourth point on the Vegard lines in Figure 15.13c.

15.6
Application for Phase Characterization: Real Structure

Information on the real structure of a solid, which includes the deviation from the ideal lattice structure, can be extracted from XRD patterns by line profile analysis, also called pattern decomposition [7, 22, 52, 53]. In such an analysis, individual well-resolved Bragg peaks are fitted with a background and profile function, typically Gaussian, Lorentzian, or a mixture of both (for example, Voigt function), without constraints like the Cagliotti function (see Section 15.5.1). The resulting profile parameters, especially the peak widths, are evaluated and converted to microstructural parameters. Peak fitting can be done relatively easily for non-overlapping peaks using computer programs. Care has to be taken in the case of extremely broad reflections when defining the background. The parameters obtained by peak fitting are the position of the peak maximum on the 2θ scale, the integrated area under the peak, the height of the peak maximum and the FWHM. For some profile functions, additional parameters are also fitted, for instance, in the case of Voigt profiles the mixing parameter of Gaussian and Lorentzian contributions. Peak widths can be obtained either directly as FWHM or as integral breadth, often denoted $\beta_{1/2}$ and β_i, respectively. The integral breadth β_i is defined as the area under the peak divided by the peak height at the maximum intensity. Lattice imperfections leading to peak broadening are in particular the finite size of coherently scattering domains, fluctuations in the geometry of the lattice, and strain.

If the peak width is to be used for the determination of the domain size or estimation of strain, it has to be corrected for instrumental contributions to β [54–56]. A macrocrystalline unstrained standard, for which size broadening should be negligible, will never show ideally sharp lines, but a narrow profile. The reasons may be blurred wavelength of the incoming beam, slits widths, transparency of the sample, or misalignment of the specimen. Correction for these instrumental contributions to the peak width can be neglected to a first approximation for very small ($<$10 nm) or heavily strained crystallites, but may significantly change the result for samples with larger crystallites or if small amounts of strain should be detected. Domain sizes beyond $\sim$100 nm usually cannot be determined accurately by XRD line broadening. In the case of Gaussian profiles, the corrections can be made according to [22]

$$\beta^2 = \beta_{\text{observed}}{}^2 - \beta_{\text{standard}}{}^2$$

Algorithms for correcting peak widths using a measurement of an ideally crystalline standard material are often included in XRD evaluation software.

15.6.1
Crystalline Domain Size and Shape

The term size has to be carefully defined when used when describing a crystalline solid. This is shown schematically in Figure 15.14. Particle size determined by means

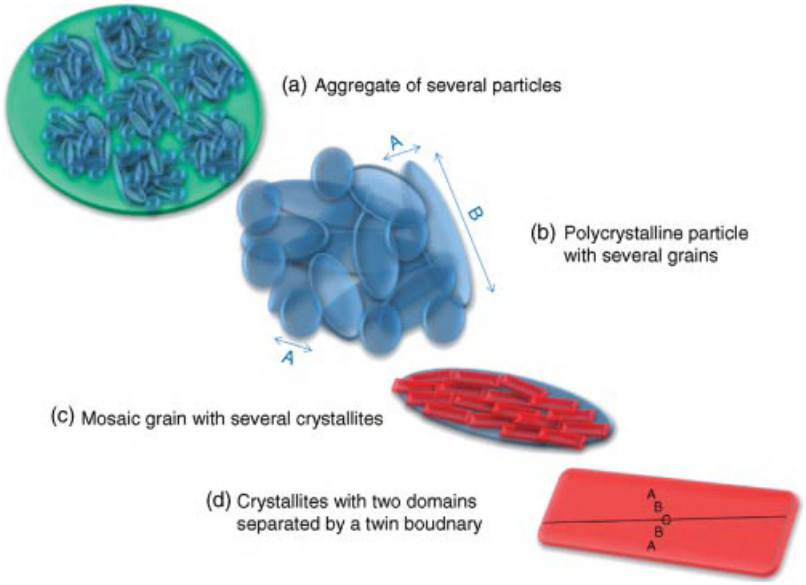


Figure 15.14 Schematic representations of the term "size" in a crystalline solid.

of light microscopes, scanning electron microscopy, or sieving are often aggregate sizes as shown in Figure 15.14a by the green area. Such aggregates may contain different phases. Primary polycrystalline particles of a single phase typically consist of smaller grains, which show different orientation and are separated by grain boundaries. This is shown in Figure 15.14b for anisotropically elongated grains of dimensions A × B. These single grains show mosaicity, that is, they consist of crystallites or mosaic blocks, which typically deviate only slightly in their relative orientation (Figure 15.14c). Individual crystallites may furthermore be separated into several coherently diffracting domains, such as those shown in Figure 15.14d, where a distinct relation of the orientations of the two domains is given by the presence of a twin boundary. Primary particle sizes can be evaluated by TEM, crystallite sizes, and sometimes also domain sizes by high-resolution (HR) TEM. It is important to note that line broadening analysis of XRD peaks in a strict sense only probes the domain size (Figure 15.14d), which for samples with small amounts of extended lattice faults can be very similar to the size of crystallites (Figure 15.14c).

Hence the relation of crystallite or domain sizes measured by XRD and particle sizes measured by other techniques has to be carefully evaluated, which is even more critical if the results are used for the calculation of derived properties such as the dispersion of the active phase in a supported catalyst. This can only be done properly on the basis of XRD data, if the particle size roughly equals the crystallite (and domain) size. Such a fortunate situation is indeed frequently encountered for small supported metal particles, but this is by no means necessarily the case for all systems, in particular oxides or sulfides, as will be shown below. If a primary particle, however, is small enough and maybe even approaches the dimensions of a few unit cells, that

is, if the situations in Figure 15.14a–c are absent due to skillful preparation of a highly disperse phase, such a particle cannot contain many individual crystallites or domains for geometric reasons and the size determined by XRD analysis can be an accurate estimate of the particle size, which is of interest in a solid material. However, one has to keep in mind that for macrocrystalline solids, the more complex situation shown in Figure 15.14 cannot be neglected, usually leading to an underestimation of the particle size by XRD. Therefore, it is also obvious that an accurate estimation of the particle size of inhomogeneous solids containing macrocrystalline and highly dispersed species of the same phase cannot be done on the basis of simple XRD evaluation as no homogeneous profile will be found. The average value resulting from the evaluation of a single breadth parameter cannot reflect a multi-modal situation.

Two examples of the relevance of these considerations for catalytic materials are shown in Figure 15.15. Careful analysis of the primary particle size distribution was performed by TEM analysis for an oxide, sulfated tetragonal zirconia, and a metal, copper in a methanol synthesis catalyst. To achieve statistically meaningful values, several thousand particles have been evaluated. Interestingly, the average size determined by this method is significantly larger in both cases than the average size determined by line profile analysis of XRD patterns. The reason can be seen in

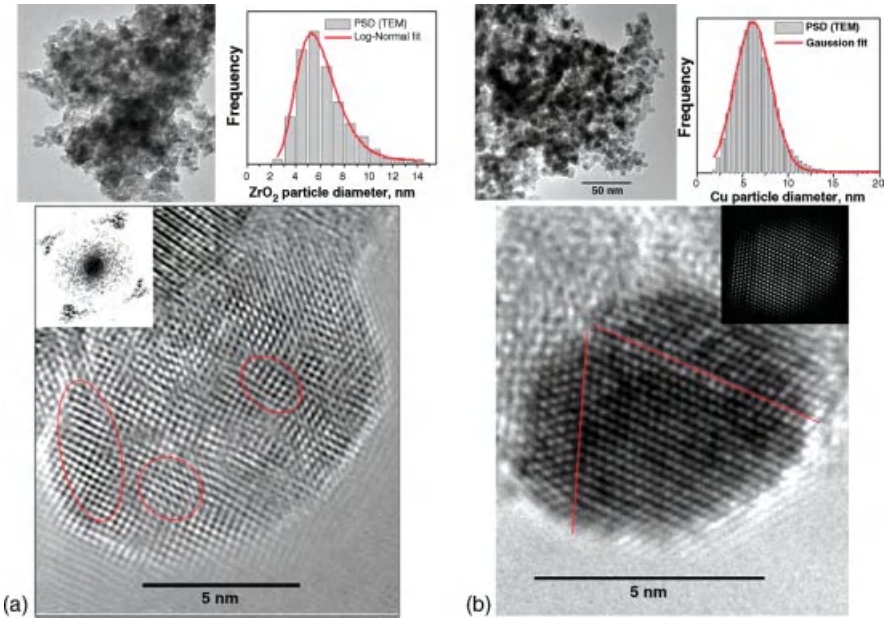


Figure 15.15 TEM, particle size distributions, and HRTEM images of a sulfated zirconia catalyst (a) and a Cu/ZnO catalyst (b). In the former, mosaicity (circles) is present and leads blurred diffraction spots in the power spectrum (inset); in the latter the Cu particles contain planar defects such as twin boundaries and stacking faults (lines). In both cases, the XRD-determined size is significantly smaller than the TEM-determined size.

HRTEM images showing a nanostructure within the primary particles. In the case of the zirconia catalyst [57], domains of high contrast (red circles) are separated by blurred contrast. These domains measure ~1–2 nm, which agrees well with the domain size determined by XRD analysis. The primary particles, on the other hand, have a diameter of 5–6 nm on average. A similar situation is observed for the Cu catalyst. Here, the HRTEM images show that smaller domains within one Cu particle are separated by stacking faults and twin boundaries (red lines). As a consequence, the XRD size of 3–4 nm is again significantly smaller than the TEM particle size of 7–8 nm. This discrepancy has been quantitatively interpreted as a measure for the planar defect density in nanostructured Cu [58] and sulfated zirconia [57].

Bragg peaks are broadened by a size effect, which is used for estimation of the crystallite size, because for a limited number of lattice planes the selection of constructive and destructive interference becomes blurred near the Bragg angle. Therefore, if the size of a diffracting domain is small in relation to the wavelength, the Bragg peak will be recorded at a range of diffraction angles $\theta \pm \delta\theta$ and appear broad. The crudest approximation of the crystallite size can be obtained from the Scherrer equation [59]:

$$D = \frac{k\lambda \times 57.3}{\beta \cos\theta}$$

where D is the crystallite size, λ the wavelength, β the peak width in $^\circ 2\theta$, k a correction factor and θ the Bragg angle. For a given reflection *hkl*, D is the volume-weighted average size obtained as $D = Nd_{hkl}$, where N is the absolute number of lattice planes normal to the direction *hkl*. Therefore, in fact, an average column length in a specific dimension of a crystallite is obtained. In the case of anisotropic shapes, such as platelets or needles, the broadening of the Bragg peaks will systematically differ for different *hkl*, resulting in different column lengths. The column lengths in a given direction are averaged over the whole particle. Even for spherical particles, the column length has to be corrected for a shape effect. For a sphere of a given diameter, a lower value will be obtained than for a cube of the same edge length, because the columns in a sphere become shorter away from the center. This effect is accounted for by the correction factor k, also called the shape factor. In practice, k is often taken as unity (or 0.9 if $\beta_{1/2}$ is used instead of β_i). If a very accurate estimation of the crystallite size is desired, k should be adjusted according to the crystallite shape and the orientation *hkl*. Such advanced Scherrer analysis is described elsewhere [3, 19]. The simple form of the Scherrer equation works best for $D < 5$ nm and can only be used in the absence of strain. An indication of the absence of strain is if the crystallite size determined for higher order reflections, for example, D_{111} and D_{222}, are similar (see below).

It is generally recommended to use the integral breadth β_i rather than the FWHM $\beta_{1/2}$. Both values can be easily obtained by peak fitting and the former is independent of the line profile and the more fundamental description for peak broadening. It is noted that more sophisticated methods of size analysis from XRD data such as the Warren–Averbach method [53, 60, 61] are available. These methods require high-

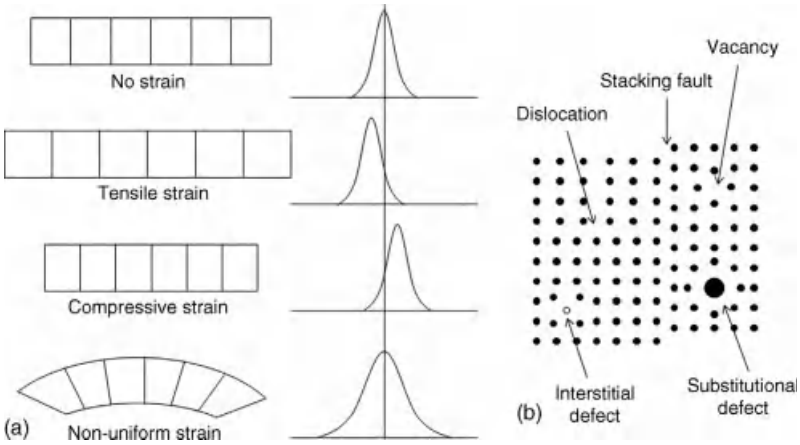


Figure 15.16 Schematic representation of different kinds of lattice strain as a result of external stress and their effects on Bragg diffraction peaks (a), and different kinds of defects that contribute to nonuniform lattice strain (b).

quality data and use the full profile information, width, and shape of more than one reflection and yield not only a single size parameter, but also a distribution of sizes.

15.6.2
Lattice Strain and Separation of Size and Strain Effects

Lattice strain or microstrain ε is defined as a variation in d-spacing $\delta d/d$ and is usually given as a percentage. The variation may be uniform, that is, compressive or tensile, which leads to a shift of a Bragg peak, but not necessarily to broadening (Figure 15.16a). This type of strain may result from external stress or lattice mismatch at epitaxial phase boundaries. The shift of Bragg peaks reflects a significant change in the lattice parameter and the interatomic distances. This may have a significant impact on the electronic structure, for example, in the form of a d-band shift in the case of transition metals [62], and affect the adsorptive and catalytic properties of a material. Nonuniform strain includes undirected fluctuations in the crystal lattice and is a general description of different local deviations of the lattice planes from their ideal d-spacing (Figure 15.16a). Nonuniform strain may be due to defects such as vacancies or interstitials. Dislocations and planar faults also induce a strain field in their surroundings. It is not easy to identify or quantify the different contributions to lattice strain and to a first approximation it can be regarded as a general measure of static structural disorder in a phase. A schematic representation of how different kinds of lattice defects may locally change the interatomic distances without affecting the average d-spacing is given in Figure 15.16b.

The origin of strain broadening of XRD peaks is easily understood from the Bragg equation. Domains with an enlarged d-spacing will give rise to shoulders of the ideal Bragg peak at the lower angle, whereas those domains showing lattice contraction lead to shoulders at the high angle side of the reflection. Microstrain in a

sample can be quantified directly from the peak width according to the Wilson equation [63]:

$$\beta = 4\varepsilon \tan\theta$$

Similarly to the Scherrer equation, which does not give reliable results for strained samples, the Wilson equation should only be applied if the presence of size broadening can be excluded.

A major challenge in the microstructural analysis of XRD data is, therefore, to separate the broadening effects of size and strain. In general, the peak broadening contains contributions from both size and strain (and instrumental broadening):

$$\beta_{\text{obs}} = \beta_{\text{instr}} + \beta_{\text{sample}} = \beta_{\text{instr}} + \beta_{\text{size}} + \beta_{\text{strain}}$$

Several methods to separate size and strain broadening are available. The Williamson–Hall method [64, 65] makes use of the different 2θ dependences of the two effects. Strain broadening depends on δd and obviously increases with the diffraction angle together with the spreading of the d-scale on the angular scale. This is not the case for size broadening, which originates from an incomplete destructive interference at $\delta\theta$ around the Bragg angle. In a Williamson–Hall analysis, the 2θ dependence of β is evaluated in the form of a plot of the reciprocal integral breadths β_i^* versus the reciprocal d-spacing d^*, which can be obtained from

$$\beta^* = \beta\cos\theta/\lambda \quad \text{and} \quad d^* = 2\sin\beta/\lambda$$

In the simple case of isotropic broadening, this plot will give a straight line and the crystallite size can be calculated from the intercept with the y-axis and the strain from the slope. A nanosized but unstrained sample will give a horizontal line in the Williamson–Hall plot. Conversely, a strained but macrocrystalline material leads to a line with a positive slope intercepting the y-axis at zero. In the case of an anisotropic crystallite shape or preferred direction of strain, no straight line will be obtained. Evaluation will be more complex and involves the hkl dependence of the data points [66].

An alternative method is based on fitting of a single peak [56, 67]. This method is based on the assumption that size broadening contributes as a Lorentzian profile, whereas strain broadening contributes as a Gaussian profile. The single well-resolved Bragg peak of interest is fitted with a profile function allowing deconvolution of the observed profile into a Gaussian and a Lorentzian part, for example, a Voigt function. The two resulting values for the peak width β_{Lorentz} and β_{Gauss} can then be used in the Scherrer and Wilson equations, respectively, to determine size and strain.

An example of microstructural effects such as sintering on the XRD pattern of a catalytic material is shown in Figure 15.17. A powder of the unsupported intermetallic compound PdGa, a catalyst material for selective hydrogenation [68], was ball-milled to increase its surface area by decreasing the particle size [69]. The highly strained material was then heated from 50 to 400 °C in an inert atmosphere in a temperature chamber mounted on the diffractometer. The isotropic peak shift observed in the XRD patterns recorded at different temperatures is due to thermal

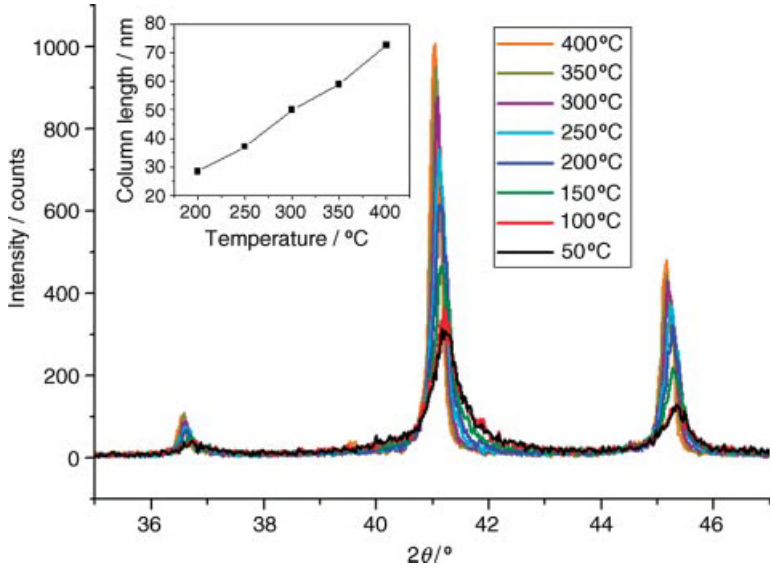


Figure 15.17 Section of *in situ* XRD patterns recorded during annealing of a ball-milled sample of the intermetallic compound PdGa. The increase in crystallite size with temperature (inset) was determined from peak sharpening by Williamson–Hall analysis.

expansion of the lattice. In addition to the shift, a pronounced sharpening of all reflections is also observed. For temperatures below 200 °C, no homogeneous peak profiles could be fitted and the patterns were not considered for the evaluation of broadening effects. The decrease of integral peak breadths above 200 °C could be identified by a Williamson–Hall analysis as being due to a size effect. This seems reasonable as the intermetallic compound PdGa has significant covalent bonding, making it a brittle compound, which is expected to be less prone to accumulate strain in the crystal lattice compared with ductile alloys. The average column length increases from 28 nm at 200 °C to 72 nm at 400 °C.

However, in general one has to be careful with the physical interpretation of such sharpening effects as size, strain, and segregation effects may be involved. In catalysis research, owing to the often weakly diffracting samples, the data quality of time-resolved studies is in many cases not sufficient to conclude unambiguously if the sharpening is due to crystallite growth, strain relaxation, defect annealing, or recrystallization or to quantify the contribution of these effects. In such cases, it may be helpful not to select arbitrarily one of the models for peak width evaluation, but rather to interpret the sharpening as a general development of the catalyst towards its equilibrium form.

To answer conclusively the interesting question of whether the catalytic properties vary with the intrinsic properties of the surface, for example, with the defect concentration at the surface, or rather with the amount of available active surface area, that is, in a "structure-insensitive" manner, complementary techniques, such as chemisorption methods, should be applied to support the XRD data. Careful line

profile analysis can, however, give valuable, although indirect, information as it permits access to measure the disorder in the bulk of nanomaterials. For a detailed microstructural analysis of a catalyst, it is important to collect XRD data of high quality in terms of signal-to-noise ratio, background, and peak definition, comparable to the standards common for macrocrystalline samples in materials science. The price to pay is often the enormous increase in the data accumulation time. Literature examples of the determination of the real structure using XRD can be found, for example, for silver nanoparticles [70] and nano-diamond [71].

15.7
X-Ray Diffraction of Catalysts in a Reactive Atmosphere

XRD is an indispensable tool for monitoring catalyst preparation and is routinely applied for this task in almost any literature report on the synthesis of solid catalysts. Looking at certain synthesis steps such as calcinations or reductions [72, 73] by means of *in situ* XRD in a reactive atmosphere may give valuable information on solid-state transformations and guide the development of synthesis protocols [27, 74–77]. A practical reason for conducting such investigations is the instability of the active forms of many catalysts. For example, in air many catalysts do not even exist in their activated form. In the case of highly dispersed metals on supports, one is interested in the phase [78–80] (e.g., metal or alloy) and the morphology [29, 81–85] of the active material (e.g., size, shape, and dispersion). These characteristics may change dramatically with changes in the gas atmosphere [3].

The formation of the activated form is only the start of a catalyst's lifetime and much important information is missing if only the fresh catalyst is considered, as has been done in many catalytic investigations with XRD. The deactivated state after a long time on-stream in a catalytic experiment should also be characterized and the ample evidence of structural modifications provides overwhelming justification for applying XRD to functioning catalysts under reactive conditions. Some of the changes are irreversible, such as structural deactivation either by sintering or segregation and crystallization, and can be detected by pre- and post-operation analysis of catalysts, but many are reversible and will not be evident in such experiments. As solid catalysts are dynamic systems, their ideal and real structure may well change as a result of changes in the chemical potential of a constituent in a reactive environment. Such defect-driven structural transformations are effectively investigated by powder XRD analysis of samples kept in reactive atmospheres. It is a key challenge of XRD to assign the various phases present in a catalyst to functions. It is particularly important to identify the nature of the active phase, which can only be done if a systematic relationship between some measure of the catalyst performance (such as activity) and the abundance of the phase can be found. The active phase is, according to the paradigm of the dynamic catalyst [28, 32, 86], not present from the beginning of its life but forms under operating conditions. A suitable method for identification of the active phase is the addition of a catalyst poison to the gas phase flowing over the catalyst that removes the active phase [87, 88].

A common hesitancy regarding the application of XRD for this purpose stems from the inherent bulk sensitivity of XRD. XRD cannot deliver direct information on catalytically active surfaces. It seems clear, however, that the bulk below the surface will determine the surface properties as surfaces are terminations of bulk solids. The importance of surface defects such as surface steps and kinks is accepted for many catalytic reactions and diffraction methods, capable of characterizing defects and disorder in the bulk of nanomaterials, may very well contribute to the understanding of catalytic activity. This should not lead to the still widely accepted but incorrect view that knowledge of the bulk structure of a solid allows one, by inference, to determine the structure of the surface exposed by cuts through the lattice. Rather, restructuring and relaxation effects [89–93] lead to sometimes massive deviations from idealized cuts through bulk solid structures [94].

It is not just effects of temperature that are important in determining the phases present in a catalyst, but also those of the reactive atmosphere. At elevated temperatures and operating pressures, both reactants and products can form compounds with the initial catalyst phases. Hence the initial form of the catalyst would merely represent a precatalyst and not the active phases. The formation of structures including (sub-)oxides, nitrides, or carbides or solid solutions of hydrogen, nitrogen, carbon, or oxygen with metals may occur.

The investigation of ammonia synthesis catalysts is a prominent example of this problem [95–98]. The technological iron catalyst used for ammonia synthesis has recently been shown to be a subnitride under catalytic reaction conditions. Insufficient pressures of the product ammonia prevent the formation of the relevant nitride phase. At ambient pressure, the chemical potential of ammonia is only sufficient to form the phase $Fe_{18}N$, being a subnitride of Fe_3N. This structure, which is distinctly different from the α-iron in the precatalyst, is only barely detectable by XRD. The subnitride formation was found in diffraction experiments and later in investigations with single crystals at elevated pressure. It resolved a long-standing issue of the nature of the active phase [99–101] of so-called "ammonia iron" [102].

Hence the characterization of working catalysts by XRD is very useful and an overview of recent literature reports with many case studies has been compiled [3]. The experiment is demanding for the determination of phases and even more so if the other structural parameters are also to be determined. Analysis of size and strain by integrated XRD measurements is limited with regard to the information it provides about the average catalyst particle (Section 15.6). The data may well fail to provide information about the distribution of crystallite sizes and strain fields, which can change during the experiment. As the structural dynamics of working catalysts can occur on multiple time scales, ranging from seconds to weeks, it is essential to ascertain the steady state of a catalyst under working conditions [103]. The catalytic performance is often analyzed in terms of a model of the kinetics and the results may be used to make the connection with the conditions of the XRD experiments [104].

The relevant details of the structure depend critically on the exact chemical nature of the reacting environment. It is generally not useful to approximate the reaction environment by convenient mixtures, for example, replacement of hydrocarbons by

hydrogen or CO is not appropriate, nor is it appropriate to omit steam as either a feed or a product component. Steam strongly affects the chemical potential of reductants or oxidants. Furthermore, steam tends to modify the kinetics of solid-state conversions strongly by enhancing structural transformations through hydroxylation of outer or interior surfaces of solids.

Other experimental pitfalls, that are not common to normal XRD, may occur and affect the results. The samples are not spun, so that for coarse-grained materials the statistical averaging over the grains may no longer be valid. This may be initiated by sintering and occur during the experiment. Some materials may move during the measurement due to reaction with the gas phase or thermal expansion, which leads to modifications of the line profiles, which have no basis in structure.

It should be noted that the relevance of the results of such XRD experiments for the structure determination of the active site in high-performance catalysts should not be overestimated. Such attempts may be guided by the single-crystal approach, in which it is implicitly assumed that all sites in a given surface contribute to the catalytic function. It has become clear in recent years that often only a small fraction of sites are catalytically active. Hence it is very speculative to use the averaging information obtained from XRD data to draw uncritical conclusions about the structure of the active sites. Diffraction analysis of active sites is only applicable when a large number of active sites are present on termination of a catalyst and when all these sites are characterized by sufficient long-range ordering. Bulk diffraction is a poorly sensitive method for identifying high-energy nonequilibrium sites at the surface of a material. It is better used to determine the average metastability of a sample by its real structure and to try to correlate this parameter with catalytic function.

15.8
Small-Angle X-Ray Scattering (SAXS)

15.8.1
Fundamentals

Small-angle scattering is a term used in the catalysis community synonymously for two completely different physical phenomena. With the advent of catalytic materials exhibiting large dimensions of unit cells (more than 2 nm), it became customary to designate conventional Bragg diffraction patterns with reflections at angles below 5° as “small-angle XRD”. A prominent example is investigations into the integrity of mesoporous systems such as MCM-41 and SBA-15, where for the hexagonal phase diffraction peaks can occur at angles of about 1°. Even if for technical reasons it is preferred to measure such regions of the diffraction pattern with a nonstandard alignment and with a special recording technique, the physics and also the instrumentation are identical with those of conventional wide-angle X-ray scattering (WAXS).

The situation for genuine small-angle scattering is completely different. The intensity distribution around the primary X-ray beam occurs from photon scattering at the electron density of the material. The distribution thus follows without contributions from interference the atomic form factors of the constituent species. The interesting information is generated by the sensitivity of this scattering towards "inhomogeneities." The atomic form factor curve is modulated by a correlation function [1, 105] describing the distances of inhomogeneities in a homogeneous solid. The formalism is similar to the scattering theory on lattice points but with two important exceptions. First, the condition of periodicity is lifted as no interference is considered. Small-angle scattering occurs from any material object irrespective of its atomic structure. Hence the method is insensitive to crystalline ordering. The other exception considers the dimension of the scattering vector. At small angles in reciprocal space, the length of this vector reaches many tens of nanometers in real space.

Scattering data therefore require a precise intensity measurement at small angular displacements when mesoscopic objects such as pores in a solid or nanoparticles in a liquid or on a support are to be studied. It is customary to scale the x-axis of such measurements not in angles but in a quantity

$$h = (4\pi/\lambda)\sin\theta$$

that must not be mistaken for the non-integer values of the Miller index h relevant for the description of scattering rods. This scaling relates the x-axis of the measurement directly to the scattering vector and thus to the correlation function. As the usual relation between reciprocal space (scattering vector) and real space (correlation function of density fluctuations or object shapes) also holds here, it is possible to obtain the correlation function by Fourier transforming the accurate intensity profile measured as a function of the scattering vector.

As in reality there are many types of density inhomogeneities and the shapes of objects defined by regions of homogeneous electron density (particles) are often heterogeneous and anisotropic (not just spheres [106]), we obtain not one correlation function but a superposition of correlation functions for each type of shape and material present in the sample. Methods have been devised [106, 107] to separate individual contributions and to model the correlation function by distributions of objects (pores, particles).

A particular property of small-angle information is that it can be used to determine the surface area of particles of random shape in any medium providing sufficient contrast for the radiation used. This can be done in particular for objects in fluid water, where the application of neutrons and the use of deuterium oxide give the possibility for highly accurate shape analysis. As this also works for polymers, the technique can be used to elucidate the inner structure of polymers [108], even during condensation.

An elegant derivation [10, 51] of the relation between the intensity of the scattering profile and the surface area of a sample was given by Debye, who also showed in a pioneering study back in 1957 the practical use of surface area determination being in good agreement with gas adsorption data for catalytic solids.

15.8.2 Experimental Aspects

Small-angle scattering is a very versatile technique for studying the texture and morphology of catalytic solids. Because it does not, unlike wide-angle XRD, require periodicity of its objects, it can deal with complex objects such as pore systems and nonspherical nanoparticles in size distributions. As it works with the primary beam of an X-ray source, it is possible to study easily systems *in situ*, being either in solution or in pressurized gas-phase conditions and at elevated temperature.

The reason why the technique is infrequently used despite its many advantages lies in the difficulty of the data analysis. All that is measured is the profile of the decay of the primary beam as a function of the scattering angle. For macroscopic objects, this angle is low (less than a few $^\circ 2\theta$) and for surface area determination it approaches the tangent of the profile at zero scattering angle. Any deviation from the theoretical power law decay is of great relevance as it contains the modulation information for the correlation function. Noise-free high-resolution data are therefore needed.

As the scattering profile is symmetric with respect to the primary beam, special small-angle scattering cameras are used that allow the scattered intensity to be recorded symmetrically around the primary beam. In order to reach the desired high resolution, it is necessary to extend the distance between the sample and the detector. Whereas traditional instruments use distances of about 0.5 m, modern high-resolution instruments extend the distance to several meters and on central facilities 10 m instruments are in use. Long distances of scattered intensity require evacuation of the beam path, as otherwise air scattering will contribute strongly to the profile function. Modern instruments therefore use a high-intensity source such as a rotating anode generator, a long evacuated camera and a sensitive X-ray camera as detector.

In order to maintain constant illumination of the sample when using standard diffraction geometries, special moving slit systems need to be applied. Such data recorded on conventional laboratory instruments or on small-angle cameras are of limited use for complex materials but are sufficient for some gross evaluations of porous systems.

The most critical step in the analysis is the data reduction and interpretation. As the intensity profile needs Fourier transformation, one is confronted with multiple termination errors at the primary beam end and at the experimental end of the profile that need special treatment. In addition, special "de-smearing" routines are applied to sharpen the measured profile and remove strong artifacts from slit systems.

Then two different strategies are possible: one can try to unfold the correlation functions from the data or one can construct a model correlation function and fit its size parameters to the experimental profile. It is very instructive to see the relative similarity [107, 108] of model functions for very different real-space objects. Whereas in cases of multiple forms of objects and superposition of pores and shape functions the analysis is relatively ambiguous, good results can be obtained for homogeneous crystalline or amorphous objects with pores. Other useful sample systems are nanoparticles dispersed in a weak contrasting solid (metal on carbon, polymer, silica, alumina supports) or in a fluid (catalyst particles in suspension) medium.

It is the fairly convoluted form of data encoded in a single observable that strongly reduced the popularity of small-angle scattering in catalysis. However, the extensive success of the method in soft condensed matter physics and the availability of commercial instrumentation may eventually enhance the use of this undervalued technique in catalysis.

15.8.3 Application in Catalysis

Here some typical applications are briefly mentioned. An exhaustive analysis is hampered by the unfortunate dual use of the term "small-angle scattering" both for Bragg diffraction and for diffuse scattering.

Of course, in practice both scattering mechanisms occur in any X-ray diffraction experiment. Due to the much higher intensity of Bragg diffraction, the "Debye scattering" contribution is usually discarded. The simultaneous action of both mechanisms probing the translational symmetric part of a system and the Debye scattering examining the disordered part of a system has been used to study [109] the filling of a mesoporous system (SBA-15) with a solvent. Substantial dynamic effects were observed and a generalized method for the investigation of such phenomena is given.

An example of the creative use of following the evolution of metal nanoparticles in a poorly ordered matrix was reported by Kiraly *et al.* [110]. Valuable information on the formation and distribution of Pd nanoparticles in swollen organic clay matrices was obtained from an only semiquantitative analysis of small-angle scattering information that was described well in the paper. The paper compares the information from SAXS with that of TEM and fluid phase adsorption data and serves as an example of the ambiguity of the description of complex morphologies with one structural characterization technique only. This theme was impressively followed by a multi-method study [111] of Ti/Zr silica systems obtained via sol–gel techniques. Reaction pathways, morphologies, and the evolution of mixed metal oxide domains were followed in great detail.

A classical example of SAXS is the study of the formation and texture of support materials. Carbon supports were studied in a pioneering set of X-ray experiments [112] both for their similarity with small graphite particles and for their mesoscopic globular structure. This example was chosen not only because it marks the beginning of many studies concerning the secondary structure of graphenes but also because it indicates what kind of information can be obtained with relatively modest experimental effort far below dedicated large-distance detection systems. The agglomeration of silicate platelets in relation to catalyst support structures [113] was studied with SAXS, making use of the fact that the technique is equally sensitive to crystalline and amorphous structures.

The pore structure and ordering of some mesoporous systems was investigated [114] by a combination of small-angle scattering of the Bragg type and of electron microscopy. In this work, the useful combination of real-space imaging and reciprocal space lattice information was applied to elucidate the complex pore

structure of mesoporous systems. The ability of small-angle scattering to work in fluids and with noncrystalline objects was used in a combined X-ray and neutron study [115] on the crystallization of SBA-15. Using *in situ* time-resolved experiments, it was possible to discriminate three stages of formation, namely the formation of micelles, the creation of organic–inorganic hybrid building blocks, and their aggregation to form "crystals."

In all these examples, a common feature is the use of small-angle scattering in combination with various other techniques for obtaining a qualitative or semiquantitative picture of chemical processes relevant for catalysis. The full potential of the method with *in situ* cells and a deep quantitative analysis as developed in soft condensed matter science and in materials science is not frequently used in catalysis. Here a potential exists for studying dynamics phenomena of catalyst particles *in situ* and with high spatial precision not available with other methods.

15.9 Conclusion

XRD is a basic characterization technique for solid-state analysis. It provides basic material information on amorphous versus crystalline states, on phases and their mixtures, and on particle sizes. Deeper analysis reveals particle anisotropy, concentrations of line defects, and information on stress and strain. Precision analysis finally allows the determination of the accurate structure of the phase and gives information on the degree of internal ordering and on compositional details in the case of solid solution systems. All this wealth of information can be derived from static laboratory experiments when carried out so as to obtain high-quality data suitable for a full profile analysis.

In catalysis science, this is mostly still infrequently done, because the materials represent limiting cases for XRD with respect to particles sizes, phase mixtures, and defect concentrations. This chapter has shown, however, that also for not so well-behaved solids such information can be derived with sufficient quality. Great concern about the results obtained exists in the community when using them for explanations of catalytic function. This function is a surface phenomenon and often considered to be unaffected by the bulk structure. As XRD is almost exclusively bulk sensitive, it may occur that extended efforts in XRD analysis are wasteful as irrelevant for the function. This is obviously incorrect for the families of solids with internal surface area such as zeolites and mesoporous materials. Here XRD delivers immediately relevant information and progress in zeolite chemistry would be impossible without advanced XRD techniques. Less commonly known but equally important is the concept that the surface structure and reactivity are uniquely determined by the real structure of the underlying bulk. It is the bulk chemical potential that determines the surface free energy and hence the tendency to segregate or to accept atomic species from the environment. The bulk structure thus decides the integrity and stability of a catalyst under reactive conditions. As the bulk–surface equilibration is strongly transport limited under conditions of catalytic applications, it is not only the

translational phase part of the structure but also the defect disposition often referred to as "defect engineering" or "nanostructuring" that controls the effectiveness of the response of the solid to the chemical potential of its environment. XRD is therefore at the center stage when it comes to the evaluation of structure–function correlations. This should not be misunderstood in the sense that XRD information gives direct mechanistic insight in catalytic processes as is often seen in the literature. In particular, the construction of hypothetical active sites from cuts through the crystal structures identified by XRD is in most cases inappropriate. XRD cannot analyze the surface structure being almost inevitably due to thermodynamic restraints (maximum stability under reactive conditions, see above) different from the bulk structure. The information from XRD is, however, a prerequisite for designing and analyzing surface analytical experiments addressing the catalytic function more directly.

XRD can, from the nature of its basic physics, fall short of describing the structure of a catalyst at all length scales. It misses out on variations of the local structure that are better addressed by EXAFS spectroscopy. Furthermore, XRD is insensitive to texture and microstructure with dimensions larger than about 10 nm, which are better investigated by small-angle scattering techniques [SAXS, small-angle neutron scattering (SANS)], by electron microscopy, or by gas adsorption techniques. Examples in the literature clearly illustrate that it is highly desirable to apply several structural tools simultaneously to the same sample. Only then can a full picture of the real structure of a nanostructured solid including its phases and textures be obtained. As it is often not clear what aspects of the complex property "structure" are relevant for the reactivity under study, it can be misleading to limit the structural investigation to a routine XRD pattern followed by phase analysis as is so frequently found in literature.

Being more rigorous in the evaluation of the application of XRD in catalysis, it is not enough to investigate the structure of a catalyst under static conditions. Following the observations that catalysts are dynamic functional materials, it is of course essential to include the dynamics in the description of the catalyst. In cases where precursor systems are used in the catalyst synthesis, it may be sufficient to study all stages of the solid-state transformations rather than the isolated materials. The final catalyst itself must, however, be studied even for phase composition under *in situ* conditions. Reaction conditions tend to render catalysts unstable, although they are stable under ambient conditions. This simple fact is opposed by the high technical hurdles [3] to study a catalyst by XRD under operating conditions. This study must include the observation of its catalytic operation undisturbed by background reactions in the camera and by detection artifacts. Such studies yield data amenable to exactly the same extent of analysis as shown in this chapter. The resulting structural information can be directly related to catalytic productivity and thus yield immediate and not inferred structure–function correlations. Such studies are rare in the literature [3, 88, 96, 116–120] but yield deep insights into the material properties of working catalysts that in most cases cannot be predicted from knowing the bulk structure under ambient conditions.

In summary, despite the frequent use of XRD as one of the most common analytical techniques for the characterization of solid materials, there is much more

information available from in-depth analysis of XRD patterns than is commonly reported. This chapter may provide motivation and support in planning more complete data evaluation or even in considering *in situ* XRD as a source of multiple information on structural dynamics.

Acknowledgments

The members of the Inorganic Chemistry Department at the Fritz-Haber-Institut are acknowledged for support, fruitful discussions, and providing the materials used as examples in this chapter. Special thanks are due to Frank Girgsdies for his very valuable contributions to this chapter.

References

1 Rietveld, H.M. (1967) *Acta Cystallogr.*, **22**, 151–152.
2 Rietveld, H.M. (1969) *J. Appl. Crystallogr.*, **2**, 65–71.
3 Schlögl, R. (2009) *Adv. Catal.*, **52**, 273–338.
4 Canton, P., Meneghini, C., Riello, P., and Benedetti, A. (2004) in *In Situ Spectroscopy of Catalysts: X-Ray Diffraction and Scattering* (ed. B.M. Weckhuysen), American Scientific Publishers, Valencia, CA, pp. 293–322.
5 Brückner F A. (2003) *Catal. Rev. Sci. Eng.*, **45**, 97.
6 Grunwaldt, J.-D. and Clausen, B.S. (2002) *Top. Catal.*, **18**, 37.
7 Cherepanova, S.V. and Tsybulya, S.V. (2004) *Mater. Sci. Forum*, **443–444**, 87–90.
8 Mittemeijer, E.J. and Welzel, U. (2008) *Z. Kristallogr.*, **223**, 532–560.
9 Guinier, A. (1939) *Ann. Phys.*, **12**, 161.
10 Renouprez, A.J. (1994) in *Catalyst Characterization – Physical Techniques for Solid Materials* (eds. B. Imelik and J.C. Védrine), Plenum Press, New York, pp. 445–465.
11 Gallezot, P. (1984) in *Catalysis: Science and Technology* (eds. J.R. Anderson and M. Boudart), Springer, Berlin, pp. 221–273.
12 Bergeret, G. and Gallezot, P. (2008) in *Handbook of Heterogeneous Catalysis* (eds. G. Ertl, H. Knözinger, F. Schüth, and J. Weitkamp), Wiley-VCH Verlag GmbH, Weinheim, pp. 738–765.
13 Matyi, R.J., Schwartz, L.R., and Butt, J.B. (1987) *Catal. Rev. Sci. Eng.*, **29**, 41–99.
14 Herein, D. (2008) in *Handbook of Heterogeneous Catalysis* (eds. G. Ertl, H. Knözinger, F. Schüth, and J. Weitkamp), Wiley-VCH Verlag GmbH, Weinheim, pp. 765–774.
15 Bergeret, G. (2008) in *Handbook of Heterogeneous Catalysis* (eds. G. Ertl, H. Knözinger, F. Schüth, and J. Weitkamp), Wiley-VCH Verlag GmbH, Weinheim, pp. 765–774.
16 Anderson, J.R. and Pratt, K.C. (1985) *Introduction to Characterization and Testing of Catalysts*, Academic Press, New York.
17 Gallezot, P. (1984) in *Catalysis, Science and Technology*, vol. **5** (eds. J.R. Anderson and M. Boudart), Springer, Berlin, pp. 221–273.
18 Hargreaves, J.S.J. (2005) *Crystallogr. Rev.*, **11**, 21–34.
19 Klug, H.P. and Alexander, L.E. (1974) *X-Ray Diffraction Procedures for Polycrystalline and Amorphous Materials*, 2nd edn, John Wiley & Sons, Inc., New York.
20 Stout, G.H. and Jensen, L.H. (1968) *X-Ray Structure Determination*, Macmillan, New York.

21 Hammond, C. (1997) *The Basics of Crystallography and Diffraction*, Oxford University Press, Oxford.
22 Warren, B.F. (1969) *X-Ray Diffraction*, Addison-Wesley, Reading, MA.
23 McKie, D. and McKie, C. (1986) *Essentials of Crystallography*, Blackwell, Oxford.
24 Schwarz, L.H. and Cohen, J.B. (1977) *Diffraction from Materials*, Academic Press, New York.
25 Vogel, W., Duff, D.G., and Baiker, A. (1995) *Langmuir*, **11**, 401.
26 Conte, M., Budroni, G., Bartley, J.K., Taylor, S.H., Carley, A.F., Schmidt, A., Murphy, D.M., Girgsdies, F., Ressler, T., Schlögl, R., and Hutchings, G. (2006) *Science*, **313**, 1270.
27 Kirilenko, O., Girgsdies, F., Jentoft, R.E., and Ressler, T. (2005) *Eur. J. Inorg. Chem.*, 2124.
28 Ressler, T., Timpe., O., and Girgsdies, F. (2005) *Z. Kristallogr.*, **220**, 295.
29 Clausen, B.S., Grabaek, L., Steffensen, G., Hansen, P.L., and Topsøe., H. (1993) *Catal. Lett.*, **20**, 23.
30 Martorana, A., Deganello, G., Longo, A., Deganello, F., Liotta, L., Macaluso, A., Pantaleo, G., Balerna, A., Meneghini, C., and Mobilio, S. (2003) *J. Synchroton Radiat.*, **10**, 177.
31 Palancher, H., Pichon, C., Rebours, B., Hodeau, J.L., Lynch, J., Berar, F., Prevot, S., Conan, G., and Bouchard, C. (2005) *J. Appl. Crystallogr.*, **38**, 370.
32 Zunic, T.B., Steffensen, G., and Villadsen, J. (1998) in *European Powder Diffraction. Proceedings of PDIC 5, Parts 1 and 2 (Materials Science Forum, vol. 278–281)* (eds. R. Delhez and E.J. Mittemeijer), Trans Tech Publications, Zürich, p. 270.
33 Michailovski A., Grunwaldt, J.-D., Baiker, A., Kiebach, R., Bensch, W., and Patzke, G.R. (2005) *Angew. Chem.*, **117**, 5787–5792.
34 Engelke, L., Schaefer, M., Schur, M., and Bensch, W. (2001) *Chem. Mater.*, **13**, 1383.
35 Walton, R.I. and O'Hare, D. (2000) *Chem. Commun.*, 2283.
36 Waseda, Y. (2002) *Anomalous X-Ray Scattering for Materials Characterization*, Springer, Berlin.
37 International Centre for Diffraction Data, http://www.icdd.com (last accessed 6 July 2011).
38 Naumann d'Alnoncourt, R., Kunkes, E., Rosenthal, D., Girgsdies, F., Zhang, B., Shao, L., Schuster, M., Behrens, M., and Schlögl, R. (2011) Submitted to *J. Catal.*
39 Johnson, Q. and Zhou, R.S. (2000) *Adv. X-ray Anal.*, **42**, 287–296.
40 Young, R.A. (1993) in *The Rietveld Method* (ed. R.A. Young), Oxford University, Press, Oxford, pp. 1–38.
41 Cagliotti, G., Paoletti, A., and Ricci, F.P. (1958) *Nucl. Instrum. Methods*, **35**, 223–228.
42 Toby, B.H. (2006) *Powder Diffract.*, **21**, 67.
43 Zhang, W., Trunschke, A., Schlögl, R., and Su, D. (2010) *Angew. Chem.*, **122**, 6220–6225.
44 DeSanto, P., Buttrey, D.J., Grasselli, R.K., Lugmair, C.G., Volpe, A.F., Toby, B.H., and Vogt, T. (2004) *Z. Kristallogr.*, **219**, 152–165.
45 Pyrz, W.D., Blom, D.A., Vogt, T.J., and Buttrey, D.J. (2008) *Angew. Chem. Int. Ed.*, **47**, 2788–2791.
46 Pawley, G.S. (1981) *J. Appl. Crystallogr.*, **14**, 357–361.
47 Le Bail, A., Duroy, H., and Fourquet, J.L. (1988) *Mater. Res. Bull.*, **23**, 447–452.
48 Spencer, M.S. (1999) *Top. Catal.*, **8**, 259.
49 Behrens, M., Girgsdies, F., Trunschke, A., and Schlögl, R. (2009) *Eur. J. Inorg. Chem.*, **7**, 1347–1357.
50 Behrens, M. and Girgsdies, F. (2010) *Z. Anorg. Allg. Chem.*, **636**, 919–927.
51 Behrens, M. (2009) *J. Catal.*, **267**, 24–29.
52 Louër, D. (1999) in *Defect and Microstructure Analysis by Diffraction* (eds. R.L. Snyder, J. Fiala, and H.J. Bunge), Oxford University Press, Oxford, pp. 673–697.
53 Langford, J.I. (2000) in *Industrial Applications of X-Ray Diffraction* (eds. F.H. Chung and D.K. Smith), Marcel Dekker, New York, pp. 751–776.
54 Stokes, A.R. (1948) *Proc. Phys. Soc.*, **61**, 382–391.
55 Delhez, R., de Kejser, Th.H., and Mittemeijer, E.J. (1982) *Fresenius' Z. Anal. Chem.*, **312**, 1–16.
56 Scardi, P., Leoni, M., and Delhez, R. (2004) *J. Appl. Crystallogr.*, **37**, 381–390.

57 Giliard, N. (2011) PhD thesis, Technical Universtiy Berlin.

58 Kasatkin, I., Kurr, P., Kniep, B., Trunschke, A., and Schlögl, R. (2007) *Angew. Chem.*, **119**, 7465.

59 Scherrer, P. (1918) *Goettingen. Nachr.*, **2**, 98.

60 Warren, B.E. and Averbach, B.L. (1950) *J. Appl. Phys.*, **21**, 595–599.

61 Warren, B.E. and Averbach, B.L. (1952) *J. Appl. Phys.*, **23**, 497.

62 Hammer, B. and Nørskov, J.K. (1995) *Surf. Sci.*, **343**, 211.

63 Stokes, A.R. and Wilson, A.J.C. (1944) *Proc. Phys. Soc.*, **56**, 174.

64 Williamson, G.K. and Hall, W.H. (1953) *Acta Metall.*, **1**, 22–31.

65 Hall, W.H. (1949) *Proc. Phys. Soc. London*, **62**, 741–743.

66 Langford, J.I., Boultif, A., Auffrédic, J.P., and Louër, D. (1993) *J. Appl. Crystallogr.*, **26**, 22.

67 de Keijser, T.H., Langford, J.I., Mittemeijer, E.J., and Vogels, A.B.P. (1982) *J. Appl. Crystallogr.*, **15**, 308–314.

68 Armbürster, M., Kovnir, K., Behrens, M., Teschner, D., Grin, Y., and Schlögl, R. (2010) *J. Am. Chem. Soc.*, **132**, 14145.

69 Osswald, J., Giedigkeit, R., Jentoft, R.E., Armbrüster, M., Girgsdies, F., Kovnir, K., Ressler, T., Grin, Y., and Schlögl, R. (2008) *J. Catal.*, **258**, 210–218.

70 Savaloni, H., Gholipour-Shahraki, M., and Player, M.A. (2006) *J. Phys. D*, **39**, 2231.

71 Palosz, B., Grzanka, E., Gierlotka, S., Stel'makh, S., Pielaszek, R., Bismayer, U., Neuefeind, J., Weber, H.P., Proffen, T., von Dreele, R., and Palosz, W. (2002) *Z. Kristallogr.*, **217**, 497.

72 Thomas, J.M. and Sankar, G. (2001) *J. Synchroton Radiat.*, **8**, 55.

73 Sankar, G., Rao, C.N.R., and Rayment, T. (1991) *J. Mater. Chem.*, **1**, 299.

74 Günter, M.M., Ressler, T., Jentoft, R.E., and Bems, B. (2001) *J. Catal.*, **203**, 133.

75 Ressler, T., Wienold, J., and Jentoft, R.E. (2001) *Solid State Ionics*, **141**, 243.

76 Ressler, T., Wienold, J., Jentoft, R.E., and Neisius, T. (2002) *J. Catal.*, **210**, 67.

77 Wienold, J., Timpe, O., and Ressler, T. (2003) *Chem. Eur. J.*, **9**, 6007–6017.

78 Hills, C.W., Nashner, M.S., Frenkel, A.I., Shapley, J.R., and Nuzzo, R.G. (1999) *Langmuir*, **15**, 690.

79 Fu, W.Y., Yang, H.B., Chang, L.X., Li, M.H., Bala, H., Yu, Q.J., and Zou, G.T. (2005) *Colloids Surf. A*, **263**, 71.

80 Frenkel, A.I., Hills, C.W., and Nuzzo, R.G. (2001) *J. Phys. Chem. B*, **105**, 12689.

81 Canton, P., Fagherazzi, F.B., Battagliarin, M., Menegazzo, F., Pinna, F., and Pernicone, N. (2002) *Langmuir*, **18**, 6530.

82 Clausen, B.S., Steffensen, G., Villadsen, J., Feidenhansl, R., and Topsøe, H. (1991) *J. Catal.*, **132**, 524.

83 Fagherazzi, G., Canton, P., Riello, P., Pernicone, N., Pinna, F., and Battagliarin, A. (2000) *Langmuir*, **16**, 4539.

84 Grunwaldt, J.D. and Clausen, B.S. (2002) *Top. Catal.*, **18**, 37.

85 Riello, P., Polizzi, S., Fagherazzi, G., Finotto, T., and Ceresara, S. (2001) *Phys. Chem. Chem. Phys.*, **3**, 3213.

86 Topsøe, H., Ovesen, C.V., Clausen, B.S., and Topsøe, N.Y. (1997) *Stud. Surf. Sci. Catal.*, **109**, 121.

87 Busca, G., Cavani, F., Centi, G., and Trifiro, F. (1986) *J. Catal.*, **99**, 400.

88 Muhler, M., Schütze, J., Wesemann, M., Rayment, T., Dent, A., Schlögl, R., and Ertl., G. (1990) *J. Catal.*, **126**, 339.

89 Ammer, C., Meinel, K., Wolter, H., and Neddermeyer, H. (1997) *Surf. Sci.*, **377–379**, 81.

90 Diebold, U. (2003) *Surf. Sci. Rep.*, **48**, 53.

91 Jansen, R., Brabers, V.A.M., and van Kempen, H. (1995) *Surf. Sci.*, **328**, 237.

92 Saint-Lager, M.C., Jugnet, Y., Dolle, P., Piccolo, L., Baudoing-Savois, R., Bertolini, J.C., Bailly, A., Robach, O., Walker, C., and Ferrer, S. (2005) *Surf. Sci.*, **587**, 229.

93 Wang, Z.H., Choi, C.J., Kim, J.C., Kim, B.K., and Zhang, Z.D. (2003) *Mater. Lett.*, **57**, 3560.

94 Lemire, C., Meyer, R., Henrich, V.E., Shaikhutdinov, S., and Freund, H.J. (2004) *Surf. Sci.*, **572**, 103.

95 Greeley, J. and Mavrikakis, M. (2005) *J. Phys. Chem. B*, **109**, 3460.

96 Herzog, B., Herein, D., and Schlögl, R. (1996) *Appl. Catal. A*, **141**, 71.

97 Walker, A.P., Rayment, T., and Lambert, R.M. (1989) *J. Catal.*, **117**, 102.

98 Schlögl, R. (1991) in *Ammonia Synthesis* (ed. J.R. Jennings), Plenum Press, New York, p. 19.

99 Rayment, T., Schlögl, R., Thomas, J.M., and Ertl, G. (1985) *Nature*, **315**, 311.

100 Topsøe, H., Dumesic, J.A., and Boudart, M. (1973) *J. Catal.*, **28**, 477.

101 Wyckoff, R.W.G. and Crittenden, E.D. (1925) *J. Am. Chem. Soc.*, **47**, 2866.

102 Alstrup, I., Chorkendorff, I., and Ullmann, S. (1997) *J. Catal.*, **168**, 217.

103 Epple, M. (1994) *J. Thermal Anal.*, **42**, 559.

104 Schlögl, R. and Baerns, M. (2004) in *Basic Principles of Applied Catalysis* (eds. A.W. Castleman, J.P. Toennies, F.P. Schüfer, and W Zinth), Springer, Berlin, pp. 321–360.

105 Debye, P., Anderson, H.R. and Brumberger, H. (1957) *J. Appl. Phys.*, **28**, 679–683.

106 Glatter, O. (1977) *J. Appl. Crystallogr.*, **10**, 415–421.

107 Glatter, O. (1979) *J. Appl. Crystallogr.*, **12**, 166–175.

108 Pedersen, J.S. (1997) *Adv. Colloid Interface Sci.*, **70**, 171–210.

109 Findenegg, G.H., Jähnert, S., Müter, D., Prass, J., and Paris, O. (2010) *Phys. Chem. Chem. Phys.*, **12**, 7211–7220.

110 Kiraly, Z., Dékány, I., Mastalir, A., and Bartók, M. (1996) *J. Catal.*, **161**, 401–408.

111 Mountjoy, G., Holland, M.A., Wallidge, G.W., Gunawidjaja, P., Smith, M.E., Pickup, D.M., and Newport, R.J. (2003) *J. Phys. Chem. B*, **107**, 7557–7566.

112 Biscoe, J. and Warren, B.E. (1942) *J. Appl. Phys.*, **13**, 364–371.

113 Brinker, C.J., Keefer, K.D., Schaefer, D.W., and Ashley, C.S. (1982) *J. Non-Cryst. Solids*, **48**, 47–64.

114 Sakamoto, Y., Kaneda, M., Terasaki, O., Zhao, D.Y., Kim, J.M., Stucky, G., Shin, H.J., and Ryoo, R. (2000) *Nature*, **408**, 449–453.

115 Zholobenko, V.L., Khodakov, A.Y., Impéror-Clerc, M., Durand, D., and Grillo, I. (2008) *Adv. Colloid Interface Sci.*, **142**, 67–74.

116 Dieterle, M., Mestl, G., Jäger, J., Uchida, Y., Hibst, H., and Schlögl, R. (2001) *J. Mol. Catal. A*, **174**, 169–185.

117 Paál, Z., Wild, U., Wootsch, A., Find, J., and Schlögl, R. (2001) *Phys. Chem. Chem. Phys.*, **3**, 2148–2155.

118 Ovsitser, O., Uchida, Y., Mestl, G., Weinberg, G., Blume, A., Jäger, J., Dieterle, M., Hibst, H., and Schlögl, R. (2002) *J. Mol. Catal. A*, **185**, 291–303.

119 Jentoft, F., Klokishner, S., Kröhnert, J., Melsheimer, J., Ressler, T., Timpe, O., Wienold, J., and Schlögl., R. (2003) *Appl. Catal. A*, **256**, 291–317.

120 Rosenthal, D., Girgsdies, F., Timpe, O., Blume, R., Weinberg, G., Teschner, D., and Schlögl, R. (2009) *Z. Phys. Chem.*, **233**, 183–208.

16
Transmission Electron Microscopy

John Meurig Thomas and Caterina Ducati

16.1
History and Overview

When equipped with the necessary attachments and detectors, the modern transmission electron microscope is capable of yielding a unique combination of structural and electronic information that entails microscopic, diffractive, spectroscopic, and tomographic measurements, and sometimes a combination of these. Electron microscopy (EM) yields information in four distinct ways: in real space, in reciprocal (Fourier) space, in energy space, and in the time domain. Few other instruments can rival it in determining all of the following:

- elemental composition;
- oxidation states of constituent elements;
- bond distances – and under favorable conditions nature of bonding and coordination fingerprints;
- symmetry and space groups (both local and global);
- morphology;
- nanoporosity and topological parameters of a material.

Moreover, most of these properties can be retrieved when the quantity of material under investigation may be as little as 1 attogram (1 ag $= 10^{-18}$ g) and up to 1 μg or so.

The first electron microscope was built in 1932 by Knoll and Ruska [1], and within a few years they showed that resolutions surpassing those attained by the best optical microscopes could be achieved. Five or so years later, electron microscopes began to be produced commercially, the first by Metropolitan Vickers in the UK, the second by Siemens in Germany. Gradually, numerous other manufacturers were involved in assembling microscopes of progressively increasing quality: RCA, JEOL, Hitachi, Philips, and others. The advantage in operating at high accelerating voltages was soon realized because the wavelength λ of the electrons of mass m_0 is related inversely to the accelerating voltage V:

$$\lambda = \frac{h}{(2m_0eV)^{\frac{1}{2}}} \tag{16.1}$$

Characterization of Solid Materials and Heterogeneous Catalysts: From Structure to Surface Reactivity, First Edition. Edited by Michel Che and Jacques C. Védrine.
© 2012 Wiley-VCH Verlag GmbH & Co. KGaA. Published 2012 by Wiley-VCH Verlag GmbH & Co. KGaA.

and, from the Rayleigh criterion, $\delta \approx 0.6\lambda$, where δ is the smallest distance that can be resolved. At a voltage of 200 kV the relativistic wavelength of electrons is 0.00251 nm, and at 400 kV it is 0.00164 nm. However, unlike optical lenses, which can be made to a high degree of perfection, electron optical lenses are far from ideal. The attainable resolution even in the best electron microscopes (see later) is far below what one would expect from a knowledge of the wavelength of the accelerated electrons. Nevertheless, pioneers of EM deemed it prudent to build instruments that could operate at 750 kV or higher; further details can be found elsewhere [2]. Recent advances in the technical design of electron microscopes (in particular that of aberration correction) has meant that high-resolution electron microscopy (HREM) can now comfortably separate atoms down to 0.5 Å (see Figure 16.1).

Concise accounts of the emergence of high-quality electron microscopes in which key landmarks in technical advances (such as the introduction of the field emission gun (FEG) and its use in scanning transmission electron microscopy by Crewe) are given are available [3–5], but it is instructive to acquaint ourselves at the outset with the improvements in resolution that have occurred in recent years (see Figure 16.1).

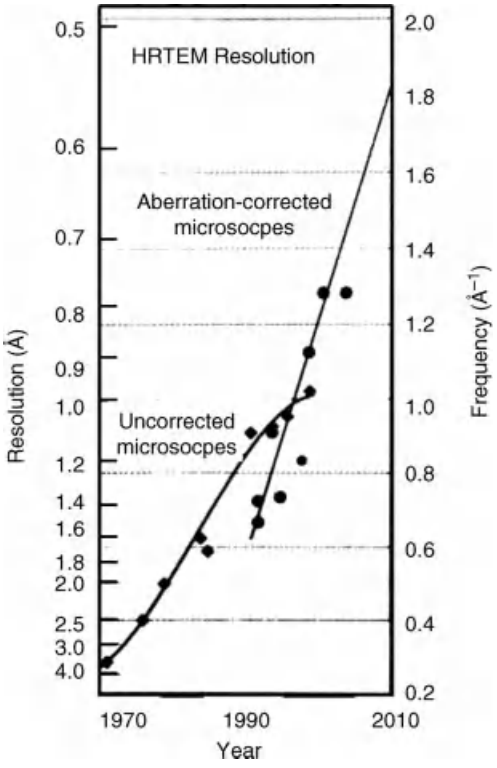


Figure 16.1 Progress in high-resolution transmission electron microscopy (HRTEM), from 1970 to the present. Adapted from [6].

The reader is recommended to consult an early authoritative short review by Howie [7]. Apart from recalling that electrons interact with matter much more strongly than neutrons, X-rays, and most regions of the electromagnetic spectrum, Howie gives a synoptic account of the kind of instrumentation used in EM and, crucially, he adumbrates the kind of errors of image interpretation which "threaten the cause of most electron microscopic investigations."

At their best, conventional transmission electron microscopy (TEM) and scanning transmission electron microscopy (STEM) yield their optimum information on materials, for example, catalysts, that are examined either *post mortem* or *pre natal*, but substantial progress has been made over the years in evolving *in situ* methods of characterization, whereby the material in question may be heated in a given atmosphere up to 800 °C or higher, but seldom at pressures higher than 0.5 bar, and often at much lower pressures, such as 1–1000 mbar. This is due to electron mean-free path limitations (see below), and depends on the gas used in the experiment. Most *in situ* studies have entailed TV video rates of recording, which means that individual frames are taken every 60 ms or so.

Two-dimensional (2D) and three-dimensional (3D) techniques are now almost routine, thanks to recent developments in electron tomography (ET). In the past 5 years, four-dimensional (4D) EM, which entails the addition of the time domain to the three spatial dimensions in such a manner as to combine sub-nanometer spatial resolution with femtosecond time resolution, has opened up exciting new vistas in the general field of EM. As yet, however, only a few catalytic systems can be probed using the various 4D techniques pioneered by Zewail and co-workers (see below).

The main drawback with EM as a general characterization tool is that it inflicts radiation damage on the material under investigation. Fortunately, metals, alloys, homometallic and bimetallic clusters, and numerous types of inorganic ceramic materials are largely invulnerable to radiation damage. However, there are several kinds of solid catalysts, for example, those derived from open-structure aluminophosphates (ALPOs) and metal–organic open structures (MOFs) which are very sensitive to high doses of electron irradiation [8, 9]. Certain organic molecular crystals, which may exhibit photoactive behavior, can, however, withstand the modest electron doses that yield electron diffraction.

Here we have adopted the following approach in order to acquaint the novice electron microscopist or the interested onlooker who wants to appreciate the scope and limitations of EM with its unique power to characterize reactive solids in general and solid catalysts in particular: first, in Section 16.2, we summarize the salient principles involved in the main techniques of EM. Section 16.3 describes general experimental considerations valid for characterization by EM. Section 16.4 is subdivided to give examples of general characterization using HREM, electron energy-loss spectroscopy (EELS), energy-filtered transmission electron microscopy (EFTEM), and ET. Section 16.5 gives examples of the use of *in situ* EM in reactivity and catalysis studies, and of the revolutionary developments that have emerged in 4D EM, where the time domain is added to steady-state (static) EM. Necessarily, our illustrative examples in this section display personal predilections.

16.2 Introduction

16.2.1 Why Electrons?

Electrons are elementary particles that possess a mass, a quantum of negative charge, and a constant angular momentum (spin). Electron beams can easily be generated by thermionic emission, field emission, and photoemission, and can be accelerated using electromagnetic fields. Electrons display wave–particle duality, and their wavelength can be calculated using the de Broglie equation. For fast-moving electrons, the relativistic correction is used, so the wavelength is expressed as

$$\lambda = \frac{h}{m_0 v\sqrt{1-\frac{v^2}{c^2}}} = \frac{h}{\sqrt{2m_0 eV\left(1+\frac{eV}{2m_0c^2}\right)}} \tag{16.2}$$

where h is Planck's constant, m_0 the rest mass, v the velocity of the electron, and c the speed of light. By varying the beam acceleration voltage V, the electron wavelength can be continuously tuned. An acceleration voltage of 1 kV corresponds to a wavelength of about 40 pm, whereas 1 MV corresponds to 0.9 pm. Electrons interact strongly with matter (100–1000 times more than X-rays and neutrons), and generate a variety of signals, which makes them also easy to detect. The main types of signals generated and used in TEM/STEM are shown in Figure 16.2.

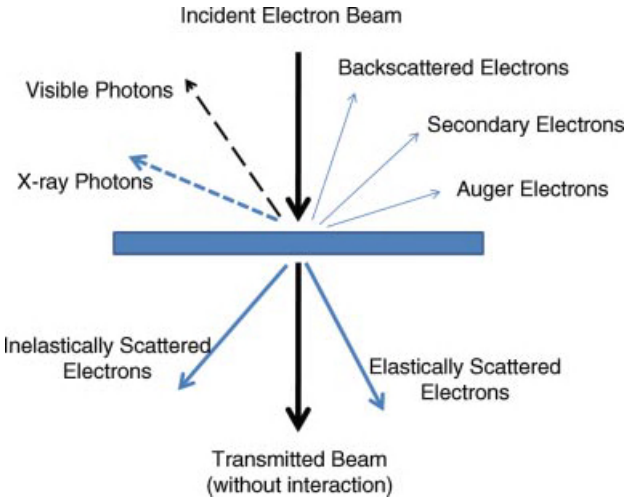


Figure 16.2 The main types of signal generated in the electron beam–specimen interaction in TEM/STEM.

Table 16.1 Commonly used acronyms in transmission electron microscopy.

TEM	Transmission electron microscopy
CTEM	Conventional transmission electron microscopy
STEM	Scanning transmission electron microscopy
AC-EM	Aberration-corrected electron microscopy
ETEM	Environmental transmission electron microscopy
EDS	Energy-dispersive spectroscopy
EELS	Electron energy-loss spectroscopy
EFTEM	Energy-filtered transmission electron microscopy
ADF	Annular dark field
HAADF	High-angle annular dark field
HRTEM	High-resolution transmission electron microscopy
HRSTEM	High-resolution scanning transmission electron microscopy

16.2.2 Electron Microscopy in Transmission

It is instructive to recite at the outset the various acronyms that the technique of EM has acquired (see Table 16.1).

Transmission electron microscopes and scanning transmission electron microscopes are complex optical systems that produce high-magnification images of thin specimens. These microscopes use a high-energy electron beam to probe the specimen and collect electrons that have been scattered in the forward direction, that is, they operate in transmission. The magnification in electron microscopes can be tuned between $\times 10^3$ and $\times 10^6$, to resolve distances down to 1.5–1.8 Å.

Electron microscopes are used to obtain accurate data on the morphology, size, and spatial distribution of small particles on supports. They are essential in the study of crystallography, defects, surfaces, and interfaces in a wide variety of solids. In particular, EM plays an essential role in the characterization of nanoscale materials for catalytic, electronic, optical, and photovoltaic applications, but also in biology and the life sciences. TEM and STEM instruments appear in many models, and perform to widely different specifications, depending mostly on the applications they are designed to address. The field of EM is in continuous evolution, as shown by the resolution curve in Figure 16.1. Advances in the design of the electron optical components, usually aiming at improving the spatial and energy resolution of the microscope, are accompanied by the development of detectors, analytical techniques, and computer interfaces, which transform the microscope into a flexible tool for the study of the physical and chemical properties of materials.

TEM and STEM instruments generally consist of the following: (a) electron gun, (b) probe-forming lenses and apertures, (c) specimen holder, (d) image-forming lenses and apertures, (e) electron detectors, (f) vacuum system. Thorough descriptions of the electron optical components and functions can be found elsewhere [3, 10, 11]. Interactive TEM and diffraction learning resources are available through the portal http://www.mater.org.uk/. The main difference between TEM and STEM

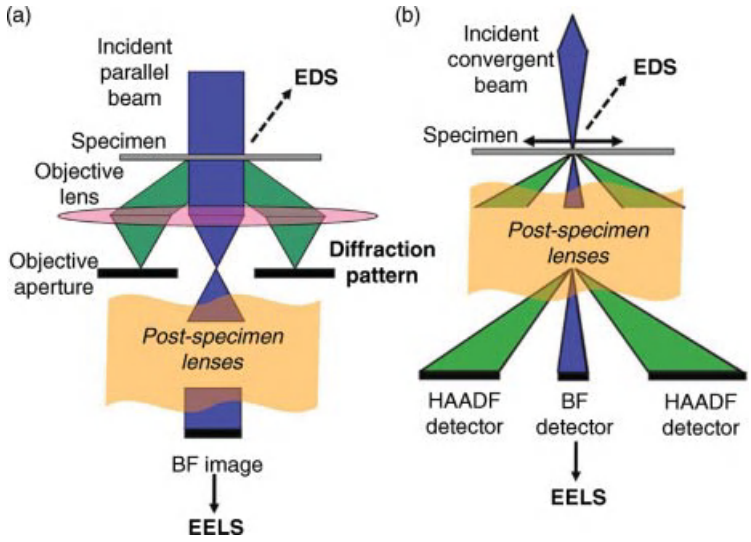


Figure 16.3 Schematic diagram illustrating the illumination and image formation in (a) TEM and (b) STEM. Adapted from [12].

is in the specimen illumination strategy, parallel beam and convergent beam, and in the detection approach, parallel and serial (or point-by-point), respectively (Figure 16.3). Here we will only briefly describe the basics of instrumentation and EM techniques, just to introduce the relevant terminology, focusing on the advanced application to materials in the following sections.

16.2.3 Basic TEM Techniques

In conventional transmission electron microscopy (CTEM), the two basic operating modes are referred to as diffraction and imaging. Here we recall the role of the objective lens in the formation of diffraction patterns and images of the specimen. Electrons traveling along parallel trajectories when they emerge from the specimen, such as those scattered from a set of crystalline planes at Bragg condition with the beam, are brought to a focus – a spot, or disc – in the (back) focal plane of the objective lens. This plane therefore contains diffraction patterns representing the spatial frequencies in the specimen. This plane is called reciprocal space or Fourier space. As the electrons propagate towards the image plane of the objective lens, their trajectories recombine to give a real-space, weakly magnified (and inverted) image of the specimen. This is a 2D projection of the specimen in the direction of the electron beam. Projector lenses are then used to select and magnify on the viewing screen either the diffraction pattern or the image of the specimen.

Electron diffraction can be performed with parallel beam illumination by selecting the appropriate region of the specimen with an aperture – the selected area aperture –

placed in the image plane of the objective lens (conjugate to the specimen plane). Selected area electron diffraction (SAED) is generally used to characterize the crystallographic phase of extended regions of the specimen. SAED patterns contain arrays of spots (for single crystals), fine nested rings (for nano- or polycrystalline materials), and diffuse nested rings (for amorphous materials). Kikuchi bands can be observed in thicker single-crystal specimens. The spatial distribution of these diffraction features, or reflections, contain information about crystal structure and lattice parameters. By converging the electron beam into a fine probe, it is possible to obtain diffraction patterns from nanometer-scale regions. In convergent beam electron diffraction (CBED), the diffraction spots become discs, and from the analysis of their fine structure it is possible to obtain information about specimen thickness, and also crystal structure and lattice parameters.

The most common imaging technique is bright-field (BF) imaging, whereby the central unscattered beam is selected using the objective aperture (in the back focal plane of the objective lens) while excluding all diffracted beams. In dark-field (DF) imaging, the objective aperture is used to select a specific reflection so that only regions in that crystallographic orientation appear bright in the image over a dark background. Image contrast in BF and DF is based on mass thickness and diffraction effects. These effects are often combined in real images, making data interpretation less immediate.

16.2.4
High-Resolution Transmission Electron Microscopy (HRTEM)

Phase contrast is at the heart of high-resolution transmission electron microscopy (HRTEM) imaging. Many authoritative accounts have been given on this topic, notably the book by Spence [13]. In very simple terms, if an array of reflections centered on the direct unscattered beam is included in the objective aperture, the image is a cross-grating of sine fringes generated by the interference between all the beams included in the aperture. These "lattice fringes" are not necessarily direct images of the crystal structure, because the phase relationship between the beams is distorted by the aberrations of the lenses. However, an image produced by HRTEM corresponds to a map of the projected electrostatic potential for electrons, along the direction of incidence of the beam.

Mathematically, if the object (specimen) is represented by the function $g(\boldsymbol{r})$, and the image is $f(\boldsymbol{r})$, then

$$f(\boldsymbol{r}) = g(\boldsymbol{r}) \otimes h(\boldsymbol{r}) \tag{16.3}$$

that is, the image is a *convolution* of the object function with a suitable function $h(\boldsymbol{r})$ describing the way in which the microscope processes the information present in the object.

In Fourier space (i.e., reciprocal space, with $\boldsymbol{u}$ as a reciprocal-lattice vector), Eq. (16.3) becomes

$$F(\boldsymbol{u}) = G(\boldsymbol{u})H(\boldsymbol{u}) \tag{16.4}$$

where $H(\boldsymbol{u})$ is the so-called *contrast transfer function* of the imaging system, dependent mainly on the aberrations of the objective lens. The contrast transfer function can be written as the product of three terms:

- The aperture function $A(\boldsymbol{u})$, which describes the fact that information transfer can only occur within the objective aperture.
- The envelope function $E(\boldsymbol{u})$, which attenuates high-frequency (small d spacing) information, since it does not contribute as strongly to the contrast transfer.
- The aberration, or phase-transfer function $B(\boldsymbol{u})$, which describes the effect of microscope aberrations on the phase of the electron wave in the object-to-image information transfer.

Hence

$$H(\boldsymbol{u}) = A(\boldsymbol{u})E(\boldsymbol{u})B(\boldsymbol{u}) \tag{16.5}$$

The phase-transfer function is written as

$$B(\boldsymbol{u}) = \mathrm{e}^{-i\chi(\boldsymbol{u})} \tag{16.6}$$

where $\chi(\boldsymbol{u})$, the phase shift (or phase "distortion") induced on the electron beam, is

$$\chi(\boldsymbol{u}) = \pi\Delta f\lambda u^2 + \frac{1}{2}\pi C_S\lambda^3 u^4 \tag{16.7}$$

in which Δf is the defocus and C_S is the spherical aberration coefficient, a constant of the microscope (or a variable, in the latest generation of TEM instruments fitted with spherical aberration correctors).

The function $\sin\chi(\boldsymbol{u})$ is a complicated oscillating curve which depends strongly on Δf and C_S.

An important quantity used when describing the phase contrast in HRTEM instruments is the *objective lens transfer function*:

$$T(\boldsymbol{u}) = A(\boldsymbol{u})E(\boldsymbol{u})2\sin\chi\,(\boldsymbol{u}) \tag{16.8}$$

which is related to $H(\boldsymbol{u})$ (and coincides with it for incoherent illumination, that is, non-FEG microscopes). A detailed derivation of these equations is given is available [3]. An example of a plot of $T(\boldsymbol{u})$ versus $\boldsymbol{u}$ is shown in Figure 16.4 for a 200 kV microscope.

The contrast transfer function can be optimized by balancing the effect of spherical aberration against a particular negative value of defocus, the so-called Scherzer defocus:

$$\Delta f_{\mathrm{Sch}} = -\left(\frac{4}{3}C_S\lambda\right)^{\frac{1}{2}} \tag{16.9}$$

At this value of defocus, all the beams will have nearly constant phase out to the "first crossover" of the zero axis. This crossover is defines as the instrumental resolution limit, given by

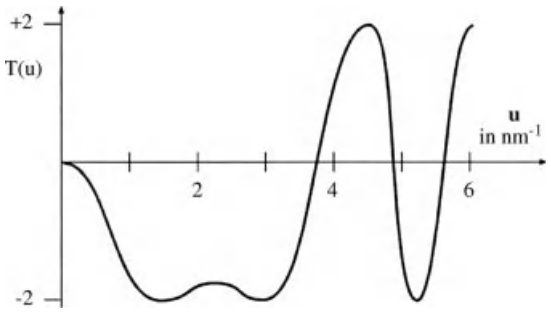


Figure 16.4 A plot of $T(\boldsymbol{u})$ versus $\boldsymbol{u}$ for a 200 kV TEM with $C_S = 1$ mm and $\Delta f = -58$ nm. Reproduced from [3].

$$\delta_{\mathrm{Sch}} = 0.66\left(C_S\lambda^3\right)^{\frac{1}{4}} \tag{16.10}$$

Hence for a given C_S, the resolution of the microscope improves with acceleration voltage (smaller λ). The example of a high resolution image of a Si nanowire is shown in Figure 16.5.

There are both fundamental and practical difficulties that demand great caution in the interpretation of HRTEM images. The strong interaction between electrons and atoms leads to multiple scattering (i.e., dynamic phenomena), which are complex, although computable. In addition to the effect of spherical aberration, image information is limited by the chromatic aberration created by energy losses in the sample.

By using computational methods, it is possible to simulate (and therefore reduce) the effect of lens aberrations. In practice, this involves recording a series of images at different objective defocus or beam-tilt settings. By comparing an observed image with that computed through the well-proven multislice procedure [15, 16], the

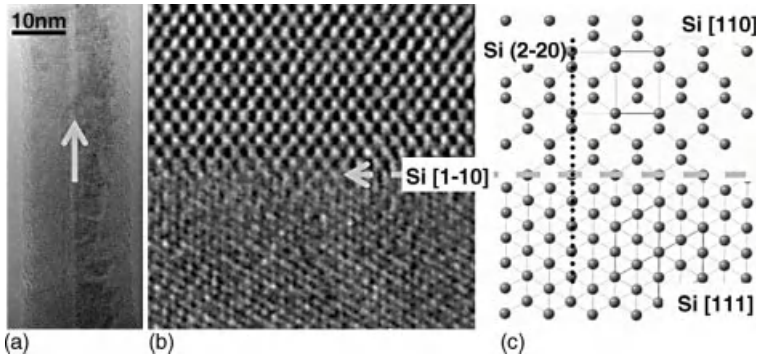


Figure 16.5 (a) HRTEM image of an Si nanowire with a grain boundary running parallel to the wire growth axis, namely Si [1–10]. (b) A magnified image of the grain boundary running through the center of the wire. (c) Ball-and-stick computer model showing the relative orientation of the two crystalline regions. Reproduced from [14].

resolution and interpretability of HRTEM images is greatly improved. A classic book on computing in EM is that by E.J. Kirkland [17]. A.I. Kirkland and R. Meyer reviewed the theory behind exit plane wavefunction reconstruction and described methods for the accurate and automated determination of the required coefficients of the wave aberration function [18]. Interestingly they described the applications of indirect reconstruction in the structural analysis of complex oxides.

A second method of retrieving structures from EM is that pioneered by Klug [19] for determining the structures of viruses and other materials in molecular biology. This entails using the amplitudes from the intensities of the electron diffraction spots and the extraction of the phases of the corresponding reflections from the high-resolution image. As is well known, phases are more important for solving the structure, whereas amplitudes are more important for refining it. Provided that the phases are correct, errors in the amplitudes do not materially change the atomic positions. This procedure has not been applied routinely to inorganic structures (with a few notable exceptions) on complex oxides and chalcogenides [20] and on zeolites [21]. It has the great advantage of yielding a structure from about 10^4 unit cells.

16.2.5
High-Resolution Scanning Transmission Electron Microscopy (HRSTEM)

High-resolution scanning transmission electron microscopy (HRSTEM) images are formed by scanning a finely focused probe (~0.8 nm) over a thin specimen in a raster pattern, and collecting the signal generated pixel by pixel. The HRSTEM approach has at least two important advantages over HRTEM: first, it can have ultra-high-resolution microanalytical capabilities of X-ray (and visible light) emission and Auger spectroscopy and EELS, and second, all these signals may be collected simultaneously, together with forward-scattered electrons. HRTEM yields both BF images, formed from the transmitted electrons, and ordinary DF images, formed from Bragg scattered beams, in addition to high-angle annular dark field (HAADF) images, and is therefore an excellent tool for the imaging and analysis of nanoparticles composed of as little as two- or three-atom clusters [22, 23]. Recently, Findlay *et al.* [24] explored the dynamics of image formation in the so-called annular bright field mode in STEM, whereby an annular detector is used with the detector collection range lying within the cone of illumination, that is, the BF region. They showed that this imaging mode allows reliable imaging of both light and heavy columns over a range of thickness and defocus values.

An important aspect of HRSTEM is *Z*-contrast imaging (or atomic number imaging), which exploits the fact that the high-angle scattering intensity of electrons from thin specimens follows the Z^2 dependence of Rutherford's law, where Z is the atomic number. Thus one Pt atom scatters as strongly as about 100 oxygen atoms or 32 silicon atoms. The technique is highly successful in detecting clusters of catalytically active metals or bimetals such as Pt, Pd, or Ru, or clusters thereof, on light supports such as zeolites, MAPOs, or mesoporous silica and alumina [25].

16.2.6
High-Precision Composition Analysis in the Electron Microscope

Composition analysis in the electron microscope by the various processes of inelastic scattering of electrons during the beam–sample interactions is particularly effective in studies of micro- and mesoporous catalysts and molecular sieves. Chemical analyses using electron probe sizes of a few nanometers or less are now possible in modern HRTEM/STEM, and they yield chemical composition at high spatial resolution, including stoichiometric and valence variations from areas of the order of 1 nm or less. Energy-dispersive X-ray spectroscopy (EDX), where X-ray intensities are measured as a function of the X-ray energy, is the most convenient method to use. EELS is another method for chemical analysis, especially of light elements, the ratios of which may be determined to about 5% [26]. EELS is discussed in more detail in the following section.

Prior to the arrival of aberration-corrected (AC) high-resolution microscopes, it was extremely difficult, if not impossible, to detect and identify individual atoms or small clusters of supported metal atom catalysts. Nowadays, however, it has become almost routine to image individual, in addition to small clusters of, metal atoms on supports such as carbon, Al_2O_3, SiO_2, and TiO_2. The consequences of improved resolution are manifold. First, it is now increasingly argued that it is not the nanostructures (nanoparticles of 3–10 nm diameter) in systems such as supported Au or Pt (on CeO_2 and other oxides) that are the loci of catalytic activity, but, instead, catalytic activity is thought to be located at much smaller entities, possibly consisting of one or a few individual metal atoms [27–29], in which the single atoms of Pt are anchored directly to Al ions at the surface of the Al_2O_3 support). Aberration correction has the effect of not only improving the resolution of the image, but also, through the near elimination of delocalization, the interpretability of image contrast.

16.2.7
Electron Energy-Loss Spectroscopy (EELS) and Energy-Filtered TEM (EFTEM)

EELS is an important analytical technique for the quantitative study of catalysts and solids by EM. By adding an electron spectrometer to either a STEM or a TEM instrument, the energy lost by primary beam electrons through inelastic interactions with the specimen can be recorded to reveal structural and electronic information. Comprehensive reference texts on the subject include [30, 31].

The range of energies over which EELS signals may be obtained extends to about 2000 eV below the incident energy. Proceeding from the zero-loss peak, the first feature of interest is the plasmon peak, which usually occurs between about 5 and 25 eV. Since plasmons are collective excitations of the electron gas, their energies are governed by the density of the electrons in the sample and the extent to which they are free or bound (obviously electrons in different orbitals have different energies). It is often possible to distinguish between a surface and a bulk plasmon. Plasmon resonance is triggered by interaction with the electromagnetic field associated with

primary beam electrons or with photons. Structural information, such as local thickness, can be extracted from the strength of the plasmon peaks relative to the strength of the zero loss peak [32].

At higher energy loss, the electron intensity is much weaker and the features are analogous to the absorption edges found in X-ray absorption spectra, and they arise from scattering of the transmitted electrons by inner-shell (core) electrons of each element present in the specimen.

In TEM, if a slit is used in conjunction with a spectrometer to select the electrons that have lost energy within a set range (e.g., at the onset of a core loss peak), the resulting image contains spatially resolved compositional information. Background subtraction is very important when computing compositional maps, so multiple acquisitions are required. This technique is called energy-filtered TEM (EFTEM) [33]. The great merit of EELS and electron-loss imaging in STEM and EFTEM is the information pertaining to composition and structure that it yields: valence states, bond distances, and composition may all, under ideal conditions, be retrieved from EEL spectra.

An overview of the methodology commonly adopted in EELS and EFTEM quantification was given by Thomas and Midgley [34]. Interesting examples of EELS and EFTEM studies of solid catalysts were reported by Egerton [32].

The number of d electrons in a transition metal or platinum group metal ion, coordination fingerprints, bond mapping, and bond distances may also, under favorable circumstances, be deduced from EEL spectra [4, 35].

Owing to the recent availability of high-intensity, sharply focused (~1 Å diameter) electron beams operating within AC-STEM instruments, truly atomic-scale chemical imaging is now possible, as demonstrated by Muller *et al.* [36], who examined perovskite layers (Figure 16.6). Such a development augurs well for the future of EM studies of a wide variety of oxide catalysts, especially those based on novel perovskites now used increasingly in photocatalysis [37]. Because of the availability of AC-STEM instruments, an increase of ~100-fold in the signal becomes possible compared with what was achievable prior to their advent. New possibilities in EELS studies are discussed in subsequent sections.

Multiple least-squares fitting has been employed for a long time in elemental EELS analysis, in particular in biology, but with the hypothesis of a rather stable shape for the used core-loss signals. In the present case, we explore its use for identifying the variations in the edges' fine structures in complex boron nitride samples and in particular for mapping the bonding types of boron in such samples. Details about this improved procedure applied to data acquired in the spectrum-imaging mode are reported here.

16.2.8
Electron Crystallography

The approach of electron crystallography entails solving the structure of small, 3D crystals using the diffraction pattern and the image formed in an electron microscope. One of the great advantages of solving 3D structures by electron

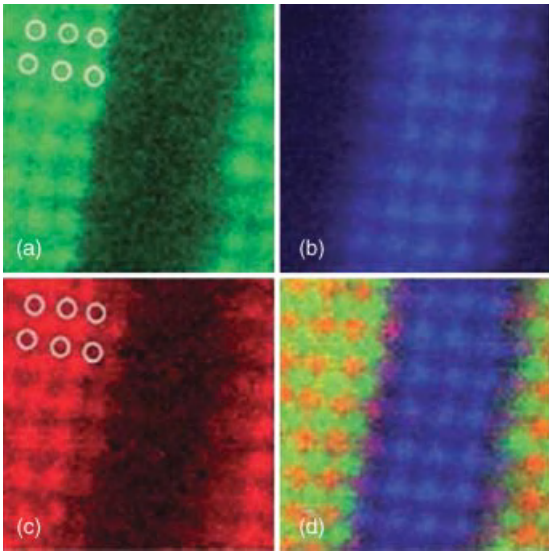


Figure 16.6 Spectroscopic imaging of an $La_{0.7}Sr_{0.3}MnO_3/SrTiO_3$ multilayer, showing the different chemical sublattices in a spectrum. Image extracted from 650 eV, wide electron energy loss spectra: (a) La M edge; (b) Ti L edge; (c) Mn L edge; (d) RGB false color composite image. White circles indicate the position of the La columns. Field of view is 3.1 nm [36]. Reprinted from; [36] with permission from AAAS.

crystallography is that the electron beams that form the diffraction pattern may be recombined to form an image (the electron micrograph). This electron micrograph is, in essence, a hologram constructed from the diffracted beams and contains all the information about the phase shifts of the scattered waves, that is, the micrograph is a result of both the reconstructed amplitude and relative phases of the diffracted beam. The process is depicted in Figure 16.7. Because the crystallography is carried out in the electron microscope, the 3D structural determination can be focused on minute regions of the crystal of differing chemical composition, a feature that is becoming increasingly important in the study of new solid catalysts of complicated stoichiometry that is sometimes spatially variable.

The method operates by using suitable regions of the electron micrograph rather than the electron diffraction pattern itself [35, 38, 39] [this is also known as a selected-area Fourier diffractogram (SAFD)]. In practice, very thin regions of the specimens are selected (to avoid multiple scattering) and micrographs are recorded along several suitable zone axes. This technique is particularly useful in solving the structures of mesoporous solids, typified by MCM-48 [39], in which, because their unit cell dimensions are so large and the walls of the "vacancy lattice" (composed of large channels and cages) are amorphous, the structures are nearly impossible to solve by X-ray crystallography. Structure solutions algorithms developed for X-ray crystallography (e.g., direct methods or charge flipping) can also be used with electron

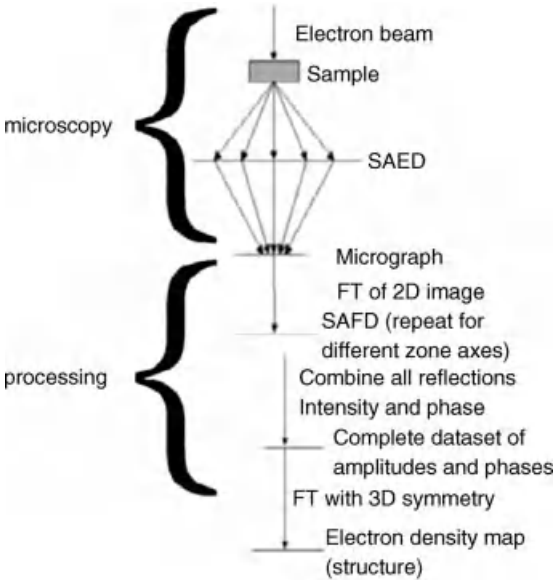


Figure 16.7 Schematic of the electron crystallography method. Reprinted from [38] with permission from the Royal Society of Chemistry.

intensities but care must be taken to avoid dynamic effects if conventional SAED patterns are used. For zeolites, such effects tend to be weak [40].

Electron crystallography alone has been used to determine the structure of a wide range of polycrystalline compounds, especially nano- and micro-sized intermetallic compounds and metal clusters [41, 42].

16.2.9
Electron Tomography

Many complex devices and materials are 3D in nature at many different length scales. A large fraction of catalysts used are highly porous structures with complex 3D structural networks and particle distributions. These are often challenging structures to investigate by EM, and electron tomography has proven to be a very powerful tool in unraveling the 3D structure at the nanoscale. Electron tomography [43] is a method by which a series of images (projections) are acquired, normally about a single tilt axis, so that the 3D structure is viewed from many directions. The ensemble of images within the tilt series is then "back-projected" into a 3D space and the object is reconstructed. The reconstruction (or tomogram) can then be visualized in many ways, including an isosurface render to pick out a particular phase, a volume projection to visualize the 3D mass thickness of the object, and, by taking slices, to reveal clearly internal structures, such as second phases and pore distributions.

Early electron tomography experiments used a tilt series of BF images but very quickly it became apparent that HAADF-STEM imaging was the image mode of

choice for the study of catalysts [44]. The great advantages of HAADF-STEM imaging are twofold. First, the HAADF-STEM images are incoherent in nature, meaning that such images are far less prone to contrast reversals with changes in thickness and defocus, compared with BF (coherent) imaging. Second, the HAADF-STEM images have higher sensitivity to atomic contrast. As discussed above, this varies approximately as the square of the atomic number, approaching Rutherford-type scattering. This is, of course, extremely useful in seeing ultra-small metallic nanoparticles in light element supports, as is often needed in the study of heterogeneous catalysts [45].

16.3
Specimen Preparation and Experimental Considerations

TEM/STEM analysis can only be performed on relatively electron-transparent specimens which transmit sufficient intensity to form an image with minimum energy loss through inelastic scattering. This generally is the case for particles, films, and sections below 50 nm in thickness. The maximum thickness obviously depends on the density of the material and the scattering probability for the incident electrons in the solid. It is therefore necessary to consider the issue of specimen preparation with great care, not only for bulk materials but also for nanoscale particles, and aim at obtaining a thin enough region that is sufficiently electron transparent and yet is representative of the material/properties to be examined. Ideally, the TEM specimen should not show spurious effects introduced by the preparation procedure, for example, mechanical deformation or contamination. For nanoparticles in solution, for example, it is important to be aware of the density of the solute, and evaluate the possibility that surfactants, nonvolatile solvents, and unwanted reagents may be transferred to the microscope. Other important factors to consider are the stability of the specimen in vacuum and under the electron beam, and its long-term response to the storage environment. Indeed, for some materials it may be advisable to store specimens in high vacuum or under an inert atmosphere. Another strict requirement is the cleanliness of the specimen. Contamination with hydrocarbons, solvents, and even water vapor can be deleterious for the specimen and problematic for the microscope.

Nanostructured specimens, or materials in powder form, are usually deposited on to 3 mm diameter copper grids (50–400 mesh), in some cases covered with a thin, holey or lacey amorphous carbon film (the name depends on the size distribution and average morphology of the holes in the film). These grids are available commercially, but can also be prepared in-house by sputtering carbon on a collodion-covered grid and then dissolving the collodion with isoamyl acetate [5].

Thin films can be lifted off their original substrates by chemical attack and deposited directly on to TEM support grids. Often this involves dissolution of a crystalline salt substrate, or hydrofluoric acid attack of the native SiO_2 layer on crystalline Si substrates.

Increasingly, electron-transparent membranes of amorphous SiO_2 or SiN are used to grow and support specimens for advanced applications. For example, ZnO

nanowires can be grown directly on perforated SiO_2 membranes, using temperatures and precursors that would not be compatible with holey carbon grids. If possible, to achieve the best contrast, TEM observations should be carried out on solid particles spanning across holes. This in general is relatively straightforward for conducting and semiconducting solids, provided that the material is in good contact with the supporting TEM grid or membrane. Nonconductive materials can suffer from charging effects, which may result in vaporization (for polymers), or excessive movement under the electron beam.

Strategies for the preparation of self-supporting TEM specimens from bulk materials include forming a thin slice from the sample, cutting and prethinning a 3 mm disk, and finally thinning the disk to the desired thickness. Different types of materials must be treated differently to avoid introducing damage and artifacts, for example, ductile metals can be pre-cut using a string saw, mechanically punched, and electropolished, whereas a brittle ceramic could be cleaved or microtomed, spark eroded to a 3 mm disk, pre-thinned by tripod polishing, and ion milled to the final thickness.

In the study of interfaces, it is essential to obtain cross-sections of the region of interest. Cross-sectional specimens can be prepared by cutting the specimen into thin slices normal to the interface to be studied, then gluing these together between spacers (e.g., Si or glass) and on to a slot grid, and finally ion milling the stack to perforation. The focused ion beam (FIB) is becoming increasingly popular as a method for preparation of thin sections of semiconducting and conductive materials.

A useful overview of sample preparation techniques, their application to specific materials, and the possible artifacts and problems that may arise is available [3].

Beam damage is an important concern in EM characterization in the cases both of radiolysis and of knock-on damage induced by the high-energy incident electrons on the specimen. Strategies adopted to tackle this issue aim at reducing the electron dose (by short exposures or dim illumination), or at reducing the acceleration voltage below the threshold value for atomic displacement damage. It is essential to be aware of the possible beam-induced effects on the specimen: atomic or cluster migration in metallic specimens, ripening, preferential desorption of a species from a compound (e.g., oxygen from metal oxides), localized heating, creation of vacancies and extended defects (holes!), and so on. This is particularly relevant for longer/multiple acquisitions and more laborious EM techniques, such as electron tomography, EELS, or EDX mapping, and focal series acquisitions, for which it is often assumed that the specimen remains unchanged during the experiment.

Lastly, sampling a nonuniform sample morphology, as for nanotube or nanowire specimens grown in small reactors, may be problematic in TEM.

16.4
Examples of General Characterization Studies

In the mid-1960s and for a decade or so thereafter, electron microscopes of moderate performance were able to shed considerable light on both the defect concentration

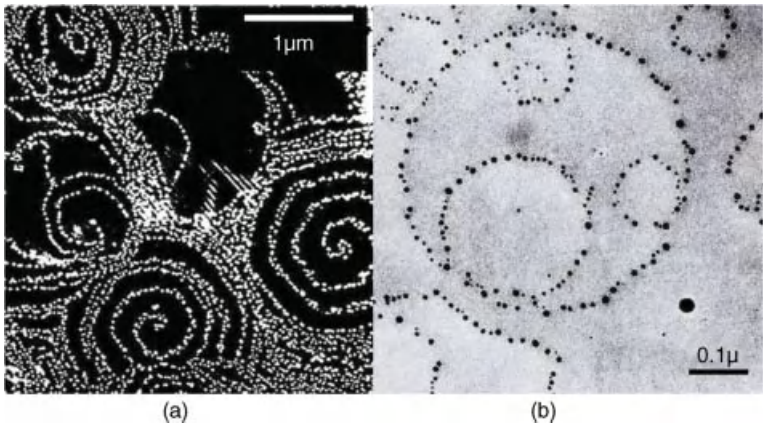


Figure 16.8 (a) The occurrence of emergent screw dislocations (of opposite chirality) at the cleaved basal surface of graphite, rendered visible by the gold-decoration technique of Bethge *et al.* [46, 56]. The Burgers vector of these delineated screw dislocations is 3.35 Å, the interlayer separation in graphite. Reproduced from [48]. (b) Mass contrast image obtained from a low-power microscope (EM100C), revealing vacancy (point) defects in successive graphene layers in natural graphite decorated by gold nanoparticles [35].

and catalytic oxidation of graphite and other layered structures such as MoS_2 [46]. In Figure 16.8, vacancy (point) defects in graphite are rendered "visible" by first oxidizing the solid in O_2, followed by evaporation of Au on to the greatly heated solid after oxidation. The Au atoms migrate and nucleate at monoatomic depressions in the graphene layer. The Au-decoration technique, apart from its power in charting topographical irregularities (down to monolayer thicknesses) on graphite and MoS_2 surfaces, enables the concentrations of vacancies and emergent screw dislocations at the $\{000l\}$ surfaces of these solids to be determined in quantitative detail. Screw dislocations, which are loci of enhanced reactivity [47], are present in naturally occurring (Ticonderoga) graphite at a concentration of $\sim 10^7$ cm^{-2}, and vacancies are also present at a concentration of one in 10^8 carbon atoms.

EM has been at the heart of the discovery of nanomaterials, from the first studies of the catalytic decomposition of CO and a number of hydrocarbons leading to the growth of filamentous carbon structures [48, 49], to the identification of helical graphitic tubules in arc discharge-evaporated carbon soot [50]. With the advent of nanotechnology, numerous studies have been published on the growth and properties of nanotubes and nanowires characterized by TEM [51]. These are divided into static *post-growth* studies, and dynamic *in situ growth* studies (for the latter, see Section 16.5). Apart from the morphological and crystallographic characterization of nanoscale materials, post-growth TEM studies are essential in determining the role of transition metal catalysts in the formation of high aspect ratio nanostructures. HRTEM analysis of carbon nanotube catalyst particles, for example, reveals the formation of metastable carbides during growth by chemical vapor deposition (CVD). The case of Ni_3C is shown in Figure 16.9 [52]. Using HRTEM, it has been possible to

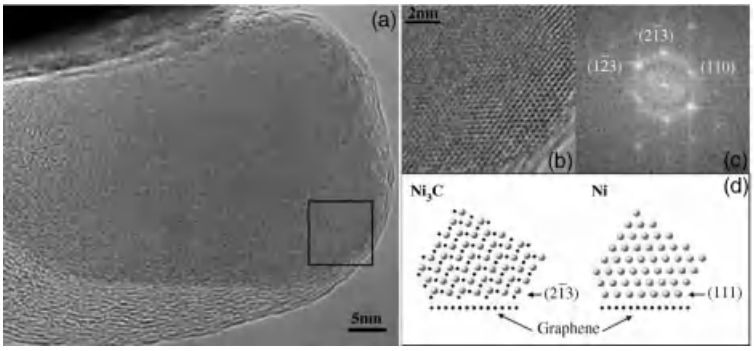


Figure 16.9 (a) High-resolution TEM image of a particle at the tip of a tube grown by plasma-enhanced CVD at 700 °C; (b) an enlarged image of the region indicated in (a); (c) the Fourier diffractogram of the lattice in (b). The particle was identified as Ni_3C, seen along the [−111] zone axis. In (d) the ball-and-stick computer models of Ni_3C and Ni are shown to emphasize the analogy between Ni_3C (2–13) planes and Ni(111) planes as interfaces between catalyst particle and graphene sheets. Reproduced from [52].

determine the crystallographic relationship between the catalyst particle and the nanostructure of interest [52–55], thus providing valuable insight into the growth mechanism and also useful data for comparison with first-principle calculations.

In the traditional approach to HRTEM, 2D images are recorded down two or more high-symmetry axes. A sequence of such images is readily converted to that of a 3D image. This is how the structure of the well-known zeolite ZSM-5 (which is isostructural with silicalite and now designated by the International Zeolite Association as MFI) was determined [58–60]. (Interestingly, this structure determination was done even before it was determined by X-ray single-crystal diffraction [12].)

Insofar as zeolitic solids are concerned, HREM has proved invaluable in identifying coexisting (intergrowth) structures of similar materials, and thereby greatly clarified the prior confusion that had existed concerning phase purity. The arrival of the JEOL 200 CX commercial microscope led to a rapid burgeoning of HREM studies of zeolites, starting with the work of Bursill *et al.* on zeolite A in 1980 [57]. Some of the key discoveries made by HREM that are of great interest in the catalytic performance of zeolites are listed below:

- The coexistence of rotational twist boundaries (typified by $\sqrt{13} \cdot \sqrt{13}R32.2°$) in zeolite L, an important catalyst (when used with nanoparticle Pt) in the aromatization of alkanes. Such boundaries greatly diminish the diffusivity of reactant alkanes into, and aromatic products from, the interior of the catalyst [61].
- The "discovery" of the so-called Breck Structure Six (now designated EMT) within crystallites of fanjasitic (FAU) cracking catalysts [62], and of minute intergrowths of (i) sodalite, (ii) gmelinite and (iii) erionite within chabazite (that are effective in facilitating dehydration of alcohols) [63] (see Figure 16.10).
- The demonstration that so-called "new" zeolitic catalysts are recurrent, often twin-related or coherent intergrowths of two separate structures. Thus the dehydroi-

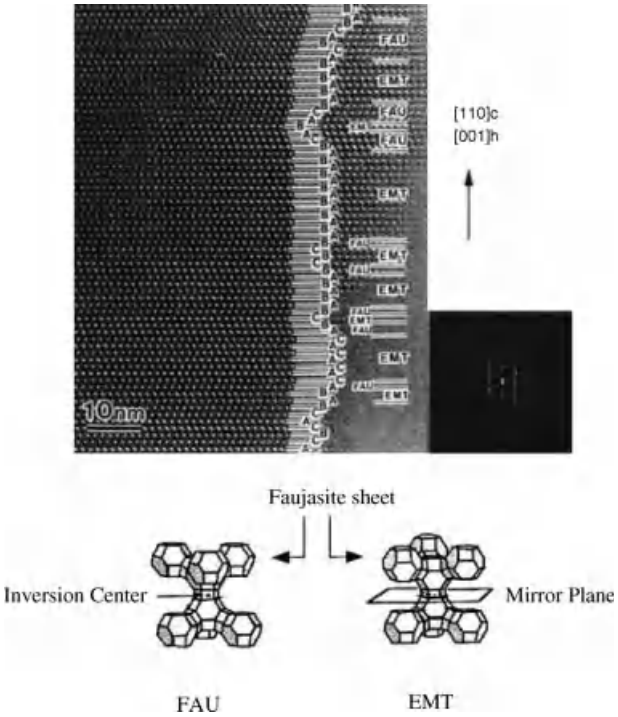


Figure 16.10 HRTEM of FAU/EMT intergrowths along [110]. The stackings ABC... and AB... correspond to the FAU and EMT structures, respectively [60].

somerization catalysts ZSM-23 and Theta-one (TON) are related in that the former is the recurrently twinned version of TON [60] (see Figure 16.11).

- The visualization of abnormal structural defects within the important catalyst zeolite-beta [64] (see Figure 16.12).

The earliest proof, provided by HREM, that intergrowths on a unit cell or sub-unit cell scale were seemingly a universal feature of zeolitic structures came in studies of ZSM-5 and ZSM-11 [59, 65]. It is clear from the lower part of Figure 16.13 that an almost infinite series of intergrowth structures may be formed between the end-members ZSM-5 and ZSM-11 (designated i and σ, respectively). The key difference between ZSM-5 and ZSM-11 is that, in the latter, at the intersections of the channels running into the structure there is about a 60% larger volume than in the former. This fact has important consequences in the catalytic conversion of methanol to gasoline by these solid Brønsted acid catalysts, as a larger fraction of bulkier aromatic molecules are formed in ZSM-11 than ZSM-5.

It was mentioned earlier that ALPO molecular sieve catalysts, which are important in their metal ion (M)-substituted variants for selective oxidations of alkanes [67], tend to be unstable under examination by EM. With great care, however, significant progress may be made in solving the structure of important members of MALPO family by combining HREM, high-resolution X-ray diffractometry (XRD), solid-state

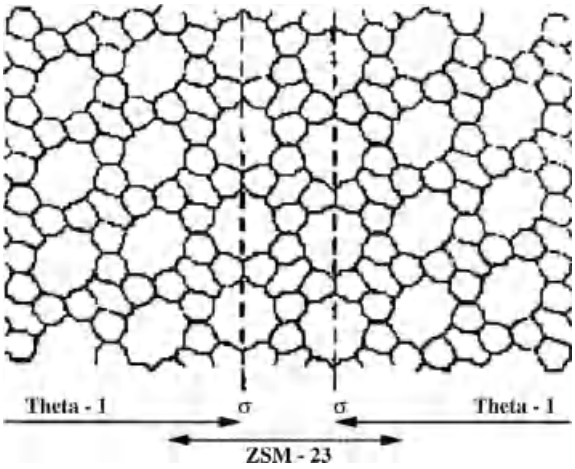


Figure 16.11 The structure of ZSM-23 is revealed by HRTEM to be a recurrently-twinned version of zeolite TON [60].

high-resolution NMR and atomistic calculations. Such an approach proved fruitful in the case of CoALPO-36, which is a particularly good selective oxidation catalyst for the oxidation of alkanes [60] (see Figure 16.14).

A recent *tour de force* in the determination of the structure of a complex zeolitic solid, the catalyst IM-5, which is used in the thermal cracking of hydrocarbons and in

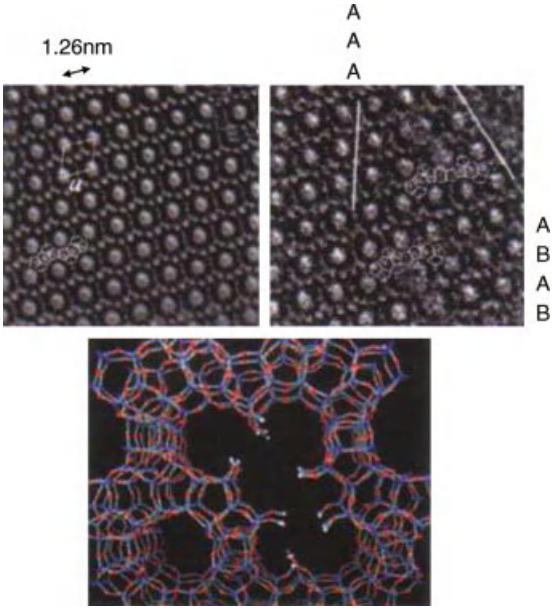


Figure 16.12 Local abnormal structure and the coexistence of distinct crystallographic phases in zeolite beta [66].

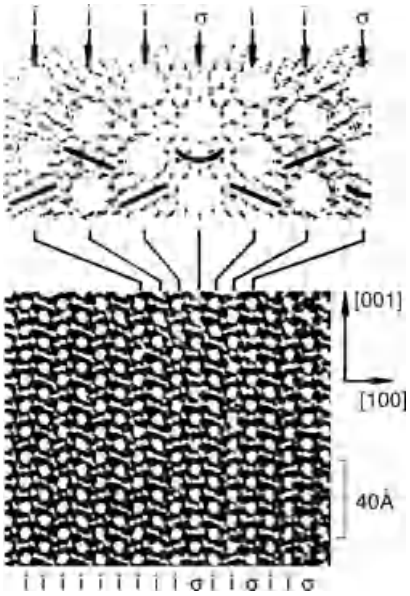


Figure 16.13 HRTEM image of a specimen of ZSM-5 in which the regular inversion symmetry (i) of successive sub-unit cell sheets are interspersed with some sheets that are in mirror relation (σ); see Thomas *et al.* [60].

the reduction of NO, was reported by Sun *et al.* [69]. They solved the structure of the crystalline siliceous zeolite IM-5 ($Si_{288-m}O_{576-2m}Al_m$), which is an open-structure catalyst that exhibits strong Brønsted acidity and has 24 distinct tetrahedral sites in the asymmetric unit. The unit cell dimensions are $a = 14.334$, $b = 56.92$, $c = 20.327$ Å, space group *Cmcm*. To arrive at the 3D structure, they combined SAED patterns, the images down three axes, [100], [010], and [001], and a distance least-squares (DLS) refinement procedure [70]. Using the structure factor amplitudes and phases of 144 independent reflections obtained from the three sets of HRTEM (2D) images, a 3D

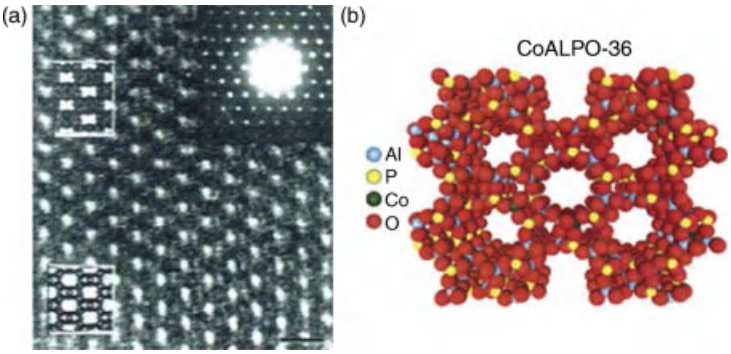


Figure 16.14 (a) HREM image, computed images, and corresponding diffraction pattern (insets) from CoAlPO-36; (b) the atomic arrangement showing the ordered channels [68].

electrostatic potential map was calculated by inverse Fourier transformations, and from this 3D potential map all 24 unique Si positions could be determined. Oxygen atoms were added between each Si–Si pair and further refined together with the Si positions by DLS refinement. The final structure deviates on average by 0.16 Å for Si and 0.31 Å for O atoms from the structure refined by XRD.

As indicated elsewhere [71], when bimetallic or trimetallic nanoclusters need to be prepared for catalytic testing, a reliable procedure is to use a precursor organometallic molecule (or ion) in which the two (or three) metals are an integral part of the structure of that precursor. The organic component of the precursor molecule is readily removed (by gentle thermolysis or oxidation at low temperature, for example) so as to yield the desired monodispersed catalyst. This method is used for systems such as $Ru_{10}Pt_2C_2$, Ru_5PtC, and Pd_6Ru_6 [71, 72]. The same strategy was used by Turner *et al.* [73] in a study of nanocluster gold catalysts, where they took an Au_{55} cluster compound as a precursor. The whole question of catalytic activity and cluster size in gold catalysis is still a deeply enigmatic issue. Thus the recent work of Tsukuda and co-workers [74] on the dependence of catalytic activity on size (in the range 1.0–9.5 nm), which straddles the cluster–particle divide, is shown in Figure 16.15. It can be seen that the normalized rate constant falls dramatically with increase in size of the Au cluster nanoparticle. In the Au preparations of Tsukuda and co-workers, and also in many other reports in this field (e.g., [75]), the Au clusters are partially covered with weakly bound poly(*N*-vinyl-2-pyrrolidine) (PVP), which still allows sufficient access of reactants to bare regions of the Au surface. Tsunoyama and Tsukuda recently studied a series of Au preparations in which "magic numbers" of atoms were stabilized by PVP, and studied them using matrix-assisted laser desorption/ionization mass spectrometry (MALDI-MS) [76]. They concluded that the reactivity of magic numbers smaller than 70 atoms is broadly in line with those of free clusters (in the gas phase). An altogether different approach to the preparation of nanosized metals has recently been described by Zheng *et al.* [77]. They employed an *in situ* TEM approach, in which the growth trajectories of Pt nanoparticle colloids (stabilized by a surfactant) were

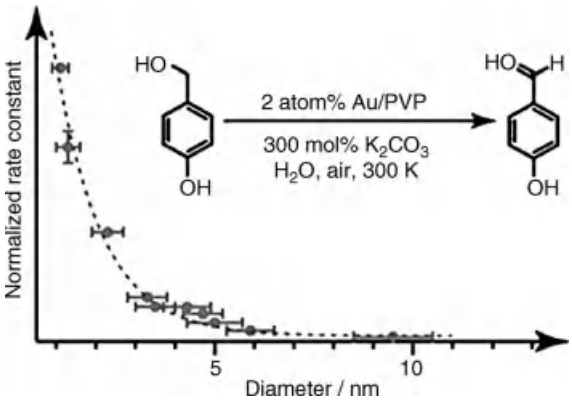


Figure 16.15 Dependence of catalytic activity on the size of Au/PVP for the oxidation of *p*-HBA [74]. Reprinted from [74] with permission from the American Chemical Society.

investigated, using a liquid cell that operates inside a TEM instrument [78, 79]. It was shown that nanocrystals of Pt can grow either by monomer attachment from solution or by particle coalescence. Through the combination of these two processes, an initially broad size distribution can spontaneously narrow into a nearly monodisperse distribution. With these two distinct modes of preparation, the role of advanced HREM studies will take further significance in pinning down precisely the roles of the enhanced catalytic performance of nanocluster metallic or bimetallic entities.

Wang *et al.* [80] examined the effects of the thickness of the Pt shell, lattice mismatch, and particle size on specific and mass activities from the changes in effective surface area and activity for oxygen reduction induced by stepwise Pt monolayer depositions on Pd and Pd_3Co nanoparticles. The core–shell structure was characterized at the atomic level using *Z*-contrast in HAADF-STEM imaging coupled with EELS. The enhanced specific activity of these catalysts is attributed to the compressive strain effect based due to nanosize-induced surface contraction on facet-dependent oxygen binding energy. The results suggest that moderately compressed (111) facets are most conducive to oxygen reduction reaction on small nanoparticles [80].

Nowadays, many catalysts are designed such that they have a ferromagnetic core (of Fe or Co) covered with a coating of either carbon or silica, to which are attached the active centers that impart the activity to the entire composite. The merit in doing this devolved upon the ease of separation (magnetically) of the catalyst itself (for further use) from the mixture of products and unconverted reactant species. A striking example of the implementation of this concept is contained in the work of Lu *et al.* [81, 82] (Figure 16.16), who nanoengineered a magnetically separable hydrogenation catalyst. They used carbon (as a coating for the ferromagnetic cobalt particles) and also as a support for metallic palladium, which constitutes the hydrogenating center. Electron holography assists in characterizing such catalysts [83].

A recent spectacular illustration of the power of EM in elucidating the structure of complex oxide catalysts was reported by Pyrz *et al.* [84], who examined the "MoVTeNbO" M1 phase (for converting propane in O_2 and NH_3 directly to acrylonitrile) using HAADF imaging in AC-STEM.

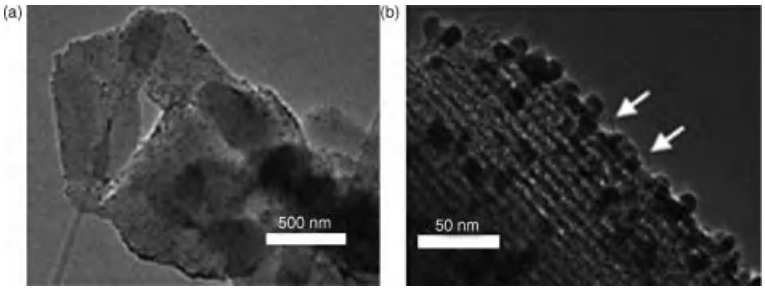


Figure 16.16 BF TEM images of Co particles on ordered mesoporous carbon: (a) low magnification; (b) high magnification. Arrows indicate hollow carbon shells following leaching. Reprinted from [81].

Selective oxidation catalysts, capable of converting propane (by ammoxidation) to acrylonitrile [85], are extremely complicated structurally (see below). Before proceeding to outline how such insights have been gained, we first recall some relevant background facts. First, for the selective oxidation and ammoxidation of propane, several families of vanadium-containing oxides, such as the Mo–V–W–O, Mo–V–Nb–Sb–O, and Mo–V–Nb–Te–O systems [84, 86–89], have been identified as particularly promising catalysts for acrylic acid and acrylonitrile production. Second, one of the most promising of these catalysts is the two-phase Mo–V–Nb–Te–O system, commonly referred to as the M1/M2 system [84, 90]. A detailed model of the (more important) M1 structure, which has the composition $TeO_{0.94}(Mo_{7.8}V_{12}Nb)O_{28}$, based on a simultaneous Rietveld refinement of high-resolution X-ray and neutron powder diffraction data, has been reported [90]. The TeO entities are accommodated in the channels formed by rings of corner-shared transition metal octahedra. The third point to emphasize is that the difficulty plaguing the structure refinements of such complex materials is that the model may have up to ~200 adjustable parameters, requiring very high-quality diffraction data and a suitable starting model with imposed constraints to ensure an acceptable and converging refinement. Lastly, a representation of the structure (projected along [001]) of the M1 phase of this complex oxide is shown in Figure 16.17a. It is a fortunate fact that the unit cell repeat distance along the *c*-axis is 4.02 Å (effectively the thickness of one octahedron). This is a most favorable situation for HAADF images to be recorded along the [001] direction. Figure 16.17 compares the projected images (by HREM) of the M1 phase taken with a conventional microscope (with and without aberration correction). A quantitative comparison of the *x*,*y* coordinates derived from the HAADF image with the Rietveld method is depicted in Figure 16.18. Because there is only a single layer of octahedra in the repeat distance, there are no overlapping crystallographically distinct metal sites. This allows for the direct extraction of *x* and *y* atomic coordinates from the HAADF images. The comparison between the HAADF-based *x*,*y* coordinates and those from the Rietveld-refined model reveals good agreement, with discrepancies in atomic

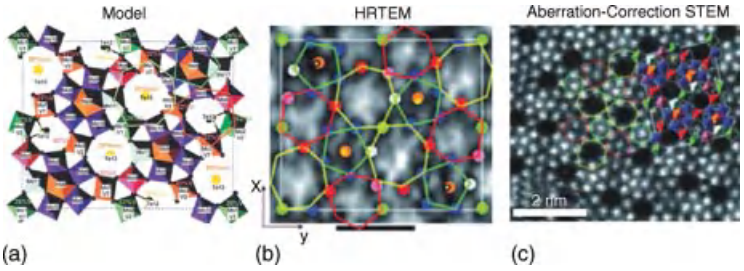


Figure 16.17 (a) Representation of the structure (projected along [001]) of the M1 complex oxide (see text) composed of Mo, V, Nb, Te, and oxygen. Green, Mo^{5+}/V^{4+}; red, Mo^{6+}/V^{5+}; yellow, Te^{4+}; pink, Mo^{6+}/Mo^{5+}; teal, Mo^{5+}; orange, Nb^{5+}; purple, Mo^{6+}. Comparison of the projected EM image of a thin section of the M1 phase along [001] taken using conventional high-resolution STEM (b) and AC-STEM (c). Note the occurrence of empty heptagonal and hexagonal channels. Reprinted from [84].

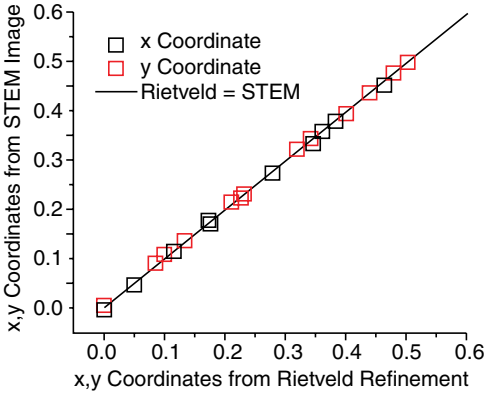


Figure 16.18 Fractional coordinates of the Rietveld model plotted against the experimentally determined coordinates measured directly from raw high-resolution (HAADF-STEM) images. Note how small the error lines are. Reprinted from [84].

positions that are less than 0.3 Å (Figure 16.18). With samples such as the M1 phase, there is a major advantage in using high-resolution HAADF imaging because, to a first approximation, the image contrast scales with the square of Z, the atomic number. A comparison of the expected contrast ratios from the (Rietveld) refined M1 model and HAADF images is shown in Figure 16.19, and it can be seen that most of

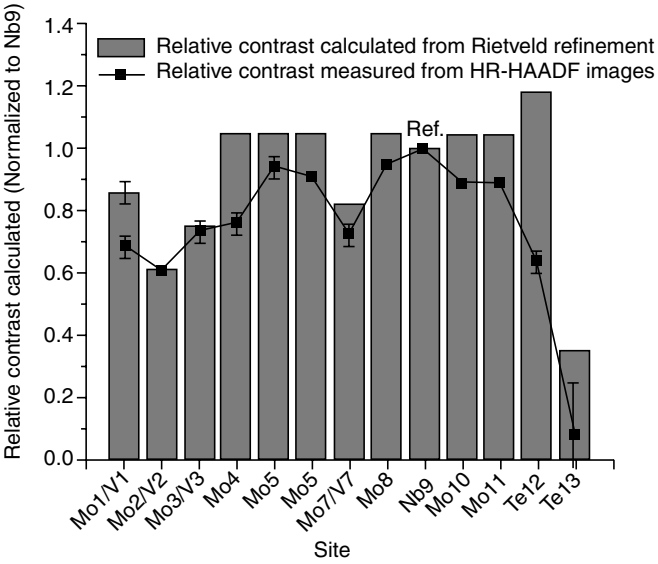


Figure 16.19 Comparison of occupancies derived from HAADF-STEM with those obtained by Rietveld refinement. Normalization was achieved with reference to complete occupancy of Nb in the Nb 9 site. Discrepancies for the occupancies of the Te sites are expected, owing to sublimation of this element under electron irradiation . Reprinted from [84].

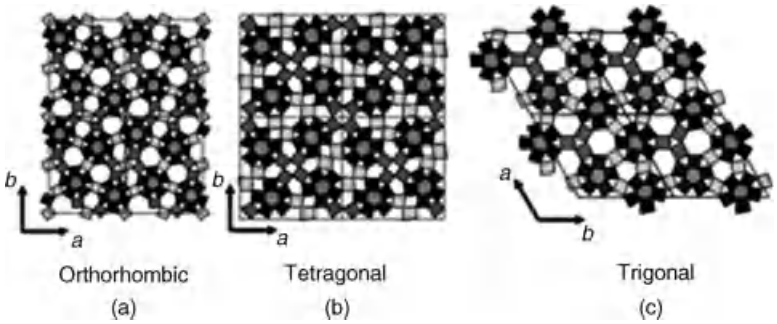


Figure 16.20 Ideal two-dimensional 2×2 unit cells for three MoVO structures: M1 type (a), Mo_5O_{14} type (b), and the trigonal form (c). Reprinted from [91].

the measured intensities follow the trends in the site occupancies predicted by the Rietveld model.

Buttrey and co-workers have recently reported that, in an investigation of the structural subtleties exhibited by M1 phases in which Ta replaced Nb, there were definite indications of there being miscibility gaps in the solid state [91]. To what extent such gaps may have catalytic significance remains to be discovered. They also uncovered three distinct Mo–V–O motifs in the complex (selective oxidation) catalysts, which are depicted in Figure 16.20 [91]. There is no known *in situ* technique for probing the individual and collective roles of the various redox systems (e.g., Mo^{VI}/Mo^{V} and V^{V}/V^{IV}) during the actual course of the cascade of catalytic processes from $CH_3CH_2CH_3$ to CH_3CH_2CHO and to $CH_2 = CH–COOH$.

Another vitally important application of HREM in the elucidation of the structures of catalysts is contained in the extensive work of Terasaki and co-workers [60, 92, 93], who determined the structures of many mesoporous silicas, typified by MCM-48 and SBA-15, using electron crystallography (as outlined in Section 16.2).

The direct imaging of extremely minute clusters (some of which looked like individual atoms) within a zeolite support was first reported in 1981 by Treacy and Gibson [94] using a high-angle annular detector in STEM. Of late with AC-STEM instruments, the direct imaging of single metal atoms and clusters in the pores of zeolites is much more readily accomplished. This is well exemplified in the recent work of Ortalan *et al.* [95], who imaged iridium atoms and Ir_4 clusters inside dealuminated zeolite-HY.

There are many other noteworthy advances that HREM has contributed to our knowledge of catalytically significant microporous and mesoporous solids, especially by Zou and co-workers in Stockholm. Not only have novel germanosilicates (some of which are chiral) been elucidated by Zou and co-workers [69] in this group, they have also developed novel multiply pronged structural approaches to solve structures synthesized elsewhere (such as ITQ-37 [96]). Such work entails the development of a combination of techniques; for example, Kwak *et al.* [29] showed by joint ^{27}Al high-resolution solid-state NMR and AC-HR(S)TEM studies that Pt on γ-Al_2O_3 catalysts (at low loadings of Pt) consists of isolated Pt atoms anchored to coordinatively unsaturated Al^{3+} ions in the alumina support.

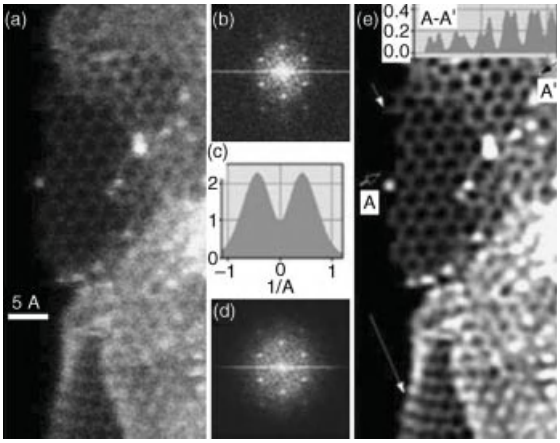


Figure 16.21 ADF images of single- and multiple-layer graphene. (a) As recorded; (b) fast Fourier transform (FFT) of the image; (c) profile of a smoothing plus defogging filter; (d) the adjusted FFT; (e) the filtered image. The inset in (e) shows line profile A–A′. Reprinted from [97] with permission from Elsevier.

There are several other aspects of HREM that are likely to have an impact on the study of reactive solids. One of these is low-voltage STEM, sometimes designated "gentle STEM", a term coined by Krivanek *et al.* [97] Gentle STEM refers to the practice of recording annular dark-field images (and EELS) at low energies of the primary electron beam. It is possible, for example, to operate at 60 keV electron beam energy (with a probe size of 1 Å), that is, under conditions that avoid direct knock-on damage in materials consisting of light elements (such as layers of graphene or BN). Krivanek *et al.* showed that this approach permits a direct, atom-by-atom chemical identification of both heavy and light atoms (see Figure 16.21). The main concern in low-voltage STEM is radiolytic damage, and also contamination of the specimen (a good vacuum is essential).

16.5
Examples of Reactivity and Catalysis Studies

Our appreciation of the properties of mono-, bi-, and trimetallic catalysts mounted on various supports has been greatly improved by the use of HREM (see Figure 16.22) [98–104]. By combining HREM data with XAFS results and molecular mechanics plus molecular dynamics, detailed insights into the morphology and binding energy of solids can be gained, for example, to determine the precise atomic separation distances of nanoclusters composed of $Cu_4Ru_{12}C_2$ supported on mesoporous silica, these being highly efficient selective hydrogenation catalysts (Figure 16.23).

With the arrival of AC-HRTEM and AC-HRSTEM, it is now readily possible to identify individual (high Z) atoms of catalysts such as Au or Pt supported on TiO_2 or

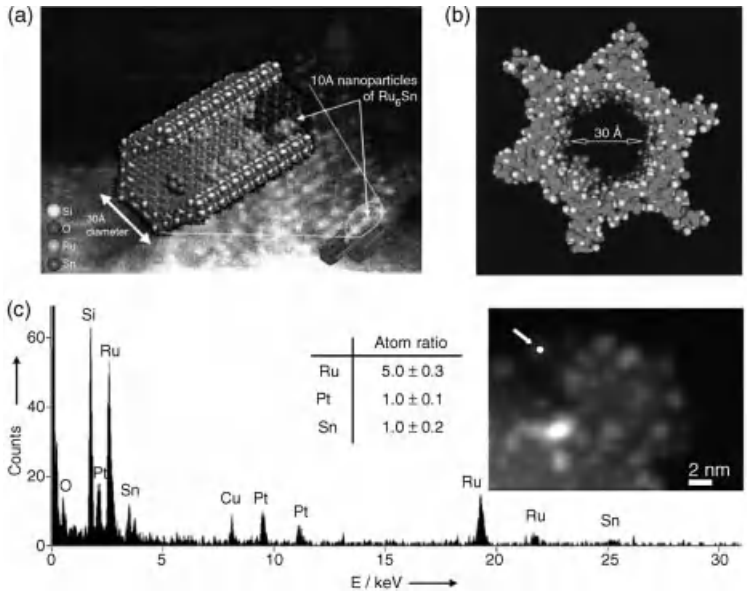


Figure 16.22 (a) A model of Ru_6Sn clusters (for selective hydrogenation) anchored at the inner surface of mesoporous silica is superimposed on a HAADF-STEM image (bright aligned features in the image in background correspond to the metallic particles of about 1 nm diameter) [103]. (b) An example of trimetallic clusters anchored in mesoporous silica. (c) EDX spectrum of nanoparticles of Ru_5PtSn nanoclusters on Davison 38 Å silica. The arrow in the inset HAADF-STEM image points to the particle for which this emission spectrum was recorded. The peak for Cu in this spectrum originates from the sample holder. Reproduced from [104].

FeOOH on carbon. Such goals have been reached by Gai [102], Kiely [105], and others. Herzing *et al.* [106] came to the conclusion that in the Au/FeO_x system for the low-temperature oxidation of CO in O_2 to CO_2, it was a bilayer of eight Au atoms that was the catalytically active entity. The question of how small the clusters of Au must be to effect this particular catalytic reaction has recently been examined by Liu *et al.* [27] Their approach was to prepare Au nanoclusters by the colloidal deposition method. They ensured that, in testing the performance of their Au/FeOOH catalysts, all the organic species shrouding the colloidal nanoparticles were burned away during preliminary oxidation (Figure 16.24). They then investigated the resulting Au nanoparticles using AC-HREM, during the course of which they identified individual atoms of Au, which then enabled them to calibrate the intensity of a single Au atom. By examining minute nanoclusters systematically, and recording the integrated intensity of each atom column, they concluded that their nanoparticles (of approximate diameter 2.1 ± 0.5 nm) were roughly spherical in shape, and of heights up to about four atoms. Their further conclusion was that, contrary to the statement of Herzing *et al.* [106], bilayer gold clusters are not mandatory to obtain high activity. So significant is this work of Liu *et al.* [27], in the light of the continuing debate pertaining to the root cause of exception, that it now seems desirable that carefully

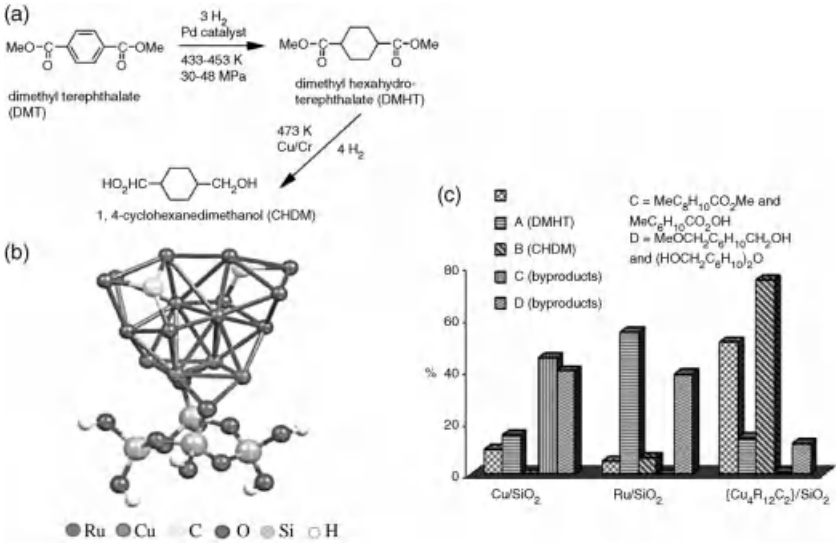


Figure 16.23 (a) Present industrial method for production of 1,4-cyclohexanedimethanol (CHDM) involving two distinct catalytic processes; (b) molecular structure of the anchored $Cu_4Ru_{12}C_2$ nanocluster, which catalyzes CHDM production in a cascade reaction; (c) comparison of the catalytic performance of the anchored $Cu_4Ru_{12}C_2$ nanocluster (conversion and selectivity) with those of the supported Cu and Ru nanoparticles in CHDM production at 353 K and 20 bar H_2 [102].

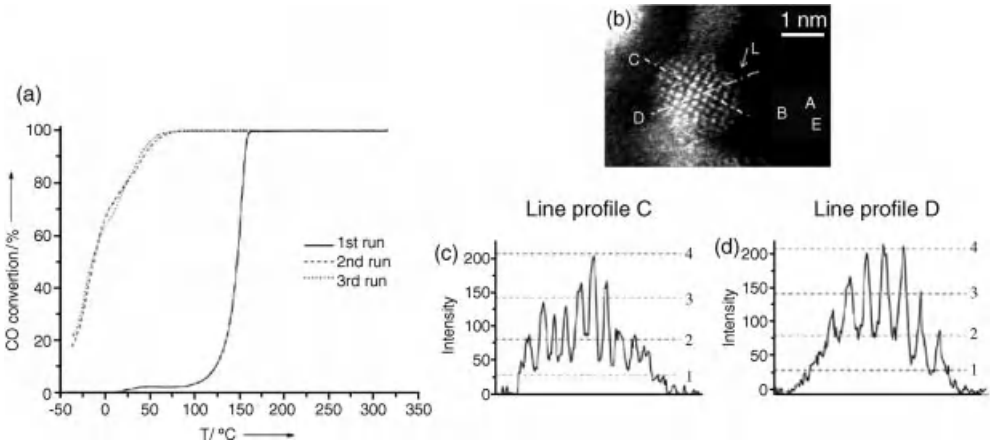


Figure 16.24 (a) CO oxidation curves of the Au/FeO_x catalyst studied by Liu *et al.* [27], in which the nanoclusters of Au were prepared by a colloidal method. The first curve shows a much slower rate of oxidation because the Au nanoclusters are still covered by an organic stabilizer. Once that has been removed by oxidation, the catalyst exhibits remarkably high activity, with 50% CO oxidation occurring at about 10 °C (second and third curves). (b) HAADF-STEM image of the Au/FeO_x catalyst, showing the location of some single atoms (A, B, E, L). The plots in (c) and (d) show the intensity profiles along the dashed lines C and D. Adapted from [27].

designed experiments, using mass-selected minute clusters of Au are prepared (in the manner of Bernhardt and co-workers [107], Li *et al.* [108], or Tsunoyama and Tsukuda [76], so that such monodisperse preparations of Au_n ($n = 1, 2, \ldots$, up to 10 or so) could then be systematically tested for various catalytic reactions.

16.5.1
Clarifying the Nature and Designing Superior Supported Oxide-on-Oxide, Solid-Acid Catalysts. The Case of WO_x on ZrO_2

It has long been known that tungsten oxide supported on zirconia is a good catalyst for isomerizing light alkanes (C_4–C_8) through the intermediacy of surface protons. Much, however, remains to be learnt about this kind of catalyst. In particular, what is the precise nature and optimum size of the clusters of WO_3 (generally designated WO_x) when bound to a ZrO_2 support? Is the most active catalyst one that has monotungstate or polytungstate moieties at the surface? By ingenious application of HAADF-STEM investigations, Kiely and co-workers [109] identified the key active site, and were thereby led to design a superior catalyst. Their work is, in essence, summarized in Figure 16.25, in which both mono- and polytungstate entities

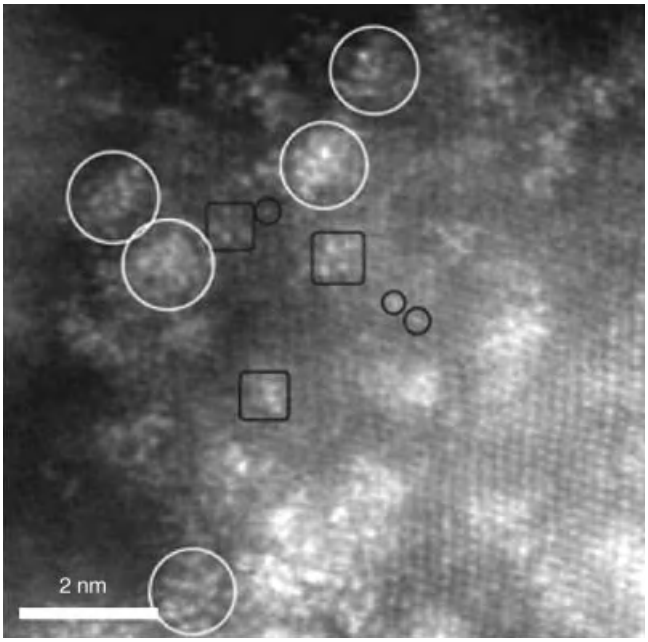


Figure 16.25 HAADF image of a high-activity WZrOH catalyst particle. Black circles indicate the presence of single tungsten atoms corresponding to surface monotungstate species. Black squares indicate surface polytungstate species with several tungsten atoms linked by oxygen bridging bonds. White circles indicate WO_x clusters with diameters of ~0.8–1.0 nm. These clusters were found only in samples with a surface density above monolayer coverage, which show higher catalytic performance [109].

supported on ZrO_2 are clearly visible (through the utilization of a 200 kV JEOL 2200FS (STEM) microscope equipped with a CEOS probe Cs-corrector). Images such as that in Figure 16.25 clearly reveal [from the intensities of the octahedrally arranged M (where M is either W or Zr) centers] that small Zr–WO_x clusters exist at the surface of high-activity samples. By deliberately altering the support of the introduced WO_3 units [from ZrO_2 to $ZrO_x(OH)_{4-2x}$], Kiely and co-workers could boost the quantity of Zr–WO_x entities at the surface, thereby greatly improving the performance of the resulting solid as an acidic catalyst in, for example, the dehydration of methanol to yield dimethyl ether. As was subsequently been pointed out by Weckhuysen [110], the exact role of the minute amounts of Zr incorporated into the subnanometer Zr–WO_3 cluster awaits clarification (by spectroscopic, computational, and kinetic means). It has also been pointed out that metal oxide catalysts consisting of ZrO_2 and TiO_2 as supports frequently outperform those composed of SiO_2 or Al_2O_3 supports. In part, this may well be due to electronic factors: silica and alumina are insulators and are less readily oxidized or reduced in comparison with TiO_2 or ZrO_2. However, it now seems prudent to probe afresh (by HAADF-STEM) subnanometer entities of V–Ti, V–Zr, and Cr–Zr clusters in cases in which hydrated oxide supports are used.

16.5.2
Oxygen Storage and Automobile Exhaust Catalysts

The excellent oxygen storage capacity found in cerium-based solid solutions has made them an essential component of the three-way catalyst (TWC) used in the automotive industry [111, 112]. Ceria-based solid solutions are also being considered for other important catalytic processes such as the water-gas shift reaction [113, 114] and solid oxide fuel cell anodes [115]. High redox activity (low-temperature reducibility and a high percentage of Ce with an easily reversible oxidation state) is one of the most attractive properties of $Ce_xZr_{1-x}O_2$ solid solutions.

An example of the application of EM to the study of nanoscale ceria zirconia is the work of Wang *et al.* [116]. A series of solid solution samples were prepared under different conditions to optimize the low-temperature redox properties. X-ray diffraction and thermogravimetric analysis were used to characterize the average structures and redox properties of the materials. By performing atomic-resolution phase-contrast imaging, *Z*-contrast imaging, and EELS, the authors found that most active materials exhibit significant compositional and structural heterogeneity at the nanometer level [116]. By using environmental TEM and monitoring the fine structure of the Ce $M_{4,5}$ edge as a function of temperature (1.5 Torr H_2), Wang *et al.* [117] were able to follow the dynamic redox process taking place in individual ceria and zirconia nanoparticles.

The work of Calvino and co-workers [118] on the oxygen storage capacity of CeO_2-based solids that are used in TWC benefited enormously from investigations involving HREM (STEM) and electron tomography. Typically, a composition such as $Ce_{0.68}Zr_{0.32}O_2$ releases its oxygen (from within the bulk) when heated in H_2 up to 900 °C, and it does so initially at temperatures in the vicinity of 700 °C. However, when about 0.3% of Rh is distributed over the surface of this (Ce–Zr)O_2 support, it is

seen that on heating again, the oxygen from the bulk is released at ~450 °C. A spillover process occurs on the Rh and the dissociated hydrogen combine with the oxygen from the bulk, thereby creating vacancies. HREM proved invaluable in the hands of Calvino and co-workers in elucidating the nature of this kind of phenomenon. In particular, an in-depth structural and analytical investigation of two 25 wt% $Ce_{0.8}Pr_{0.2}O_2$ (supported on δ-Al_2O_3) catalysts (with 3.5 wt% SiO_2 and 4 wt% La_2O_3) was performed [118], in which they aimed at clarifying the origin of the difference in evolution of their oxygen storage capacity with temperature. Using a combination of TEM and STEM, the details of the structural and compositional changes of the two catalysts with reduction temperature established the role of SiO_2 as a stabilizer of the oxygen handling properties of the Ce–Pr mixed oxide phase in high-temperature reducing environments. Pr does not fully mix with Ce during the synthesis of the two catalysts and the SiO_2 doping provides a barrier against incorporation of lanthanide elements in the alumina support. This hinders the formation of $LnAlO_3$ (Ln = Ce, Pr) perovskite, thought to be responsible for the loss of oxygen storage capacity during hydrogen treatment at temperatures above 800 °C.

EM has proved indispensable in the study of complex (mixed-metal) reducible oxides. Many of these oxides (notably those possessing the perovskite structure) function as efficient selective oxidation catalysts through the mechanism proposed by Mars and van Krevelen [119] who showed that a sacrificial process occurs. Thus, the hydrocarbon that is to be partially or fully oxidized is converted by the oxygen lost from the structure, not directly from the gas-phase oxygen. Lattice oxygen is extracted by the hydrocarbon reactant, and it is made good by incorporation of oxygen from the gas-phase. In the conversion of propane to benzene by oxidative dehydrogenation, for example, the oxygen in the solid catalyst, $CaMnO_3$, is what selectively converts the $CH_3CH_2CH_3$ (two molecules) to benzene [120]. Simple investigation of the superlattice reflections in electron diffraction led to the discovery of six new catalytically active oxide phases. The very important bismuth molybdate phases pioneered by Grasselli and co-workers [90] for the selective oxidation of propane (and propene) to acrylic acid were found by Buttrey *et al.* [121] to exhibit a number of superlattice structures, all of which were derived from the so-called defect fluorite structure of Bi_2O_3 (the latter is more appropriately described as Bi_2O_3 Ω, where Ω refers to an oxygen vacancy in the structure). Figure 16.26 summarizes the situation.

16.5.3
Pt–Al_2O_3 Hydrogenation Catalysts

Kwak *et al.* [29] recently examined catalysts composed of various loadings of metallic platinum on alumina supports. Whereas the AC-STEM studies reveal atomically dispersed Pt at low loadings (~1 wt%), at higher loadings 2D rafts of Pt are present. By combining their EM studies with ^{27}Al high-resolution solid-state NMR measurements, it was concluded that the active site for catalytic hydrogenation (at low coverages) is a Pt atom bound to a single five-coordinated (to oxygen) Al^{3+} ion (which is coordinatively unsaturated) present on the 100 facets of the γ-Al_2O_3 surface.

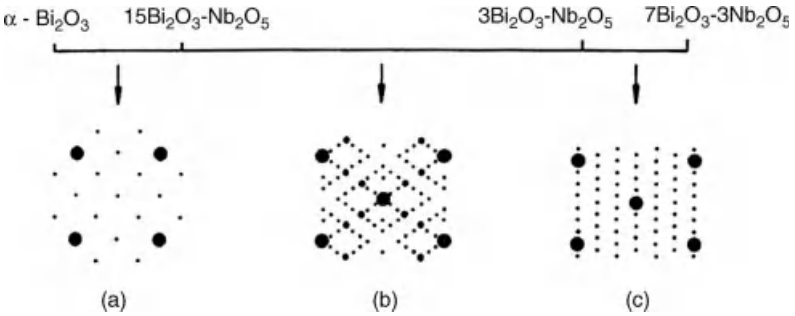


Figure 16.26 SAED reveals that, in the solid solutions formed within the compositional extremes of Bi_2O_3 and $7Bi_2O_3 3Nb_2O_5$ three distinct ordered phases (designated Types I, II and III) exist. Schematic SAED (reciprocal lattice) patterns of these three fluorite-derived phases are shown: (a) Type I, down the [100] zone axis; (b) Type II, down [110]; and (c) Type III down [110]. In each case the reciprocal lattice points of the fluorite structure are shown as large filled circles. Reprinted with permission from [122]. Copyright 1987 American Chemical Society.

16.5.4
Time-Resolved *In Situ* Studies of Catalysts by Electron Microscopy

It is no mean task to operate TEM and STEM instruments in such a manner as to allow routine gas–solid or solid–liquid interactions under reaction conditions, simply because the mean free path of the electron is infinitesimal under severe (catalytic) conditions. Nevertheless, very encouraging progress has been made by various groups in designing environmental transmission electron microscopy (ETEM) systems that permit high-resolution EM images of catalysts and related materials to be recorded under modest (reduced) pressures and even in contact with liquids. An extended introduction to techniques and methodologies in the study of heterogeneous catalysts by TEM and ETEM can be found elsewhere [123].

Work done several decades ago on the catalytic oxidation of single crystals of graphite by nanoparticles of a range of metals involved an electron microscope fitted with a hot stage that "tolerated" an ambient pressure of O_2 up to 3 mbar [124]. The stage in which the specimen was mounted and the dynamics of the catalyst investigated involved a differential pumping system, which was a primitive form of the methods pioneered by Gai and co-workers [125–129]. They perfected *in situ* environmental TEM in such a manner as to achieve atomic resolution in the imaging of nanoparticles (specifically Pt on TiO_2) participating in catalytic turnover [127, 128]. The set-up devised by them and adapted by others is schematized in Figure 16.27. A typical result, illustrating how time- and temperature-resolved heterogeneously catalyzed reactions may be followed by EM imaging, is shown in Figure 16.28 [130]. The highest degree of time resolution so far attained by Gai and co-workers falls in the range of milliseconds [129]. However, their instrument can routinely be employed to cope with gas pressures of up to 50 000 Pa of H_2.

An especially important aspect of heterogeneous catalysts, concerned with *nanoparticle shape dynamics*, is of considerable interest. The size, shape, and detailed

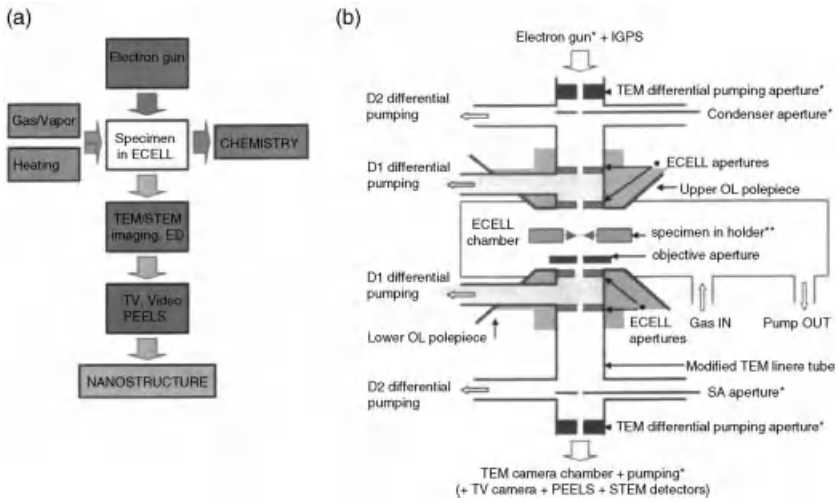


Figure 16.27 Environmental TEM. (a) Block diagram illustrating the setup of Gai and co-workers used for environmental TEM (ETEM). (b) Details of the ETEM pioneered by Gai and co-workers. PEELS stands for parallel recording of electron energy-loss spectra [129].

surface structure of supported metal nanoparticles play a key role in their catalytic performance. Although nanoparticles with predefined shapes can be readily synthesized, there is no guarantee that such materials remain stable when exposed to reaction conditions. The gas constituents may induce changes in surface and interface energies and hence drive restructuring of the nanoparticles. Inspection of the ETEM images provides direct insight into the nature of gas-induced shape changes and helps to elucidate the driving forces for such transformations.

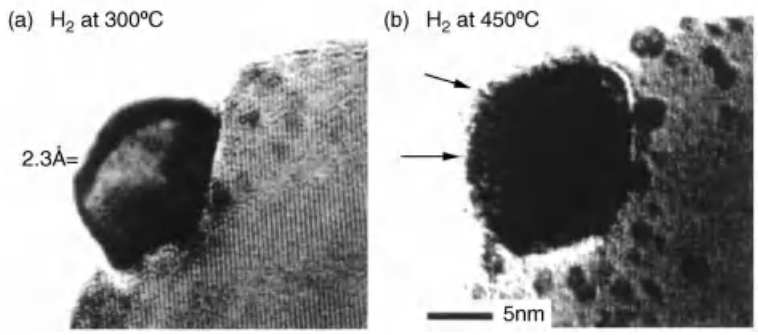


Figure 16.28 The first atomically resolved *in situ* images of a Pt nanoparticle catalyst supported on TiO_2 in an atmosphere (3 mbar) of H_2 at high temperatures: (a) 300 and (b) 450 °C. The horizontal arrows show the passivation of TiO_x coating on the same Pt particle (P). Direct evidence of strong metal–support interactions (SMSI) and particle shape changes was obtained. Reproduced from [130].

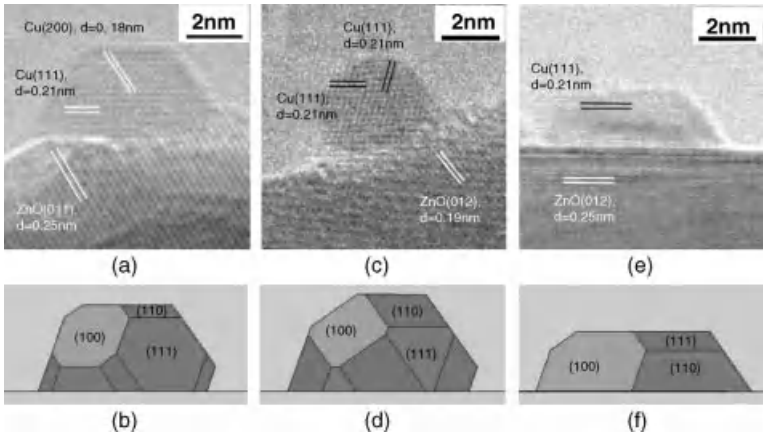


Figure 16.29 High-resolution imaging of exposed catalysts. (a–c) High-resolution ETEM images of a Cu/ZnO catalyst in various gas environments. (d–f) The corresponding Wulff constructions of the Cu nanocrystals. (a) Image recorded at a pressure of 1.5 mbar H_2 at 220 °C. (b) Image obtained with the nanocrystals exposed to a gas mixture of H_2 and H_2O (H_2: $H_2O = 3:1$), at a total pressure of 1.5 mbar at 220 °C. (c) Image obtained with the Cu nanocrystal exposed to a gas mixture of H_2 (95%) and CO (5%) at a total pressure of 5 mbar at 220 °C [132].

A model system for studying complex gas-induced structural dynamics consists of copper nanoparticles dispersed on zinc oxide crystallites representing industrial methanol synthesis catalysts. It has been shown that the Cu particles undergo shape changes in response to changes in the gas environment and that the shape changes in turn affect the catalytic activities of the Cu nanoparticles [131, 132]. Figure 16.29 shows atomically resolved ETEM images reflecting the equilibrated shapes of Cu nanocrystals on ZnO during exposure to different gas environments. In hydrogen gas, faceted metallic copper nanocrystals are observed (Figure 16.29a). Upon addition of water vapor to the hydrogen gas (Figure 16.29b), the Cu nanocrystals transform into a more spherical shape, and this reshaping is attributed to adsorption of water on the exposed Cu facets, driving surface reconstruction. Upon addition of carbon monoxide (Figure 16.29c), the Cu nanocrystals transform into more disc-like structures (Figure 16.29f). It was proposed that this wetting effect is due to a CO-induced change in the oxygen content of the ZnO surface and, thereby, the Cu/ZnO interface energy [131, 132].

Insight into gas-dependent metal–support interactions and confirmation of this interpretation can be obtained by combining the ETEM images with *in situ* EELS experiments [133]. A sufficient increase in the reduction potential of the gas, caused by CO, induces changes in the electron-loss near-edge structure (ELNES) of the Cu L_3 ionization edge, which can be attributed to Cu–Zn alloy formation either at the Cu/Zn interface or on the Cu surface [133]. Furthermore, on the basis of the lattice-resolved ETEM images, the crystallographic identity of the exposed facets on the projected Cu nanocrystals and the epitaxial relationship between Cu and ZnO are

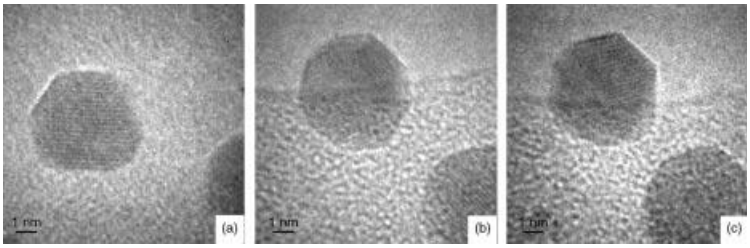


Figure 16.30 High-resolution imaging of exposed clusters. Lattice-resolved ETEM images of an Au cluster during exposure to a cycle of (a) H_2, (b) O_2, and (c) H_2 at room temperature [134].

revealed. Information on the Wulff constructions of the Cu nanoparticles can be obtained from the atomic resolution images (Figure 16.29d–f), thus providing a quantitative determination of the relative surface and interface free energies in different gas environments. The determination of surface and interface properties *in situ* represents an important perspective as it provides information about the concentrations of the different types of surface sites (facets, corners, steps, etc.) under the various environmental conditions. The finding that the nanoclusters can undergo dynamic shape changes has the general implication that the distribution of catalytic active sites, and hence the catalytic activity, can be self-regulated by the reaction conditions.

Another aspect of structure–activity relationships in Au nanoparticle catalysts was presented by Giorgio *et al.* [134] (Figure 16.30) in a study of the reversible change in the shape of Au nanoparticles depending on the gas to which they are exposed. Atomically resolved images were produced of Au nanoparticles deposited at room temperature on carbon in 2 mbar of H_2 (Figure 16.30a), then 2 mbar of O_2 (Figure 16.30b), and again 2 mbar of H_2 (Figure 16.30c). These images show a reversible change from a faceted shape in H_2 to a more spherical shape during O_2 exposure. Because this behavior of Au particles was observed on both TiO_2 and amorphous carbon substrates, this indicated that the shape changes are driven by the process of gas adsorption on the metal surface.

ETEM has been used successfully to study the nucleation of growth of semiconducting nanowires from metal catalyst particles, allowing a much deeper understanding of the nanoscale processes involved in the synthesis by vapor–liquid–solid (VLS) or vapor–solid–solid (VSS) methods. For example, contrary to the common beliefs that the catalyst droplet does not change during growth, and that the nanowire sidewalls consist of clean facets, Hannon *et al.* [135] were able to demonstrate by *in situ* TEM that the diffusion of gold during growth determines the length, shape, and sidewall properties of the nanowires [135] in epitaxial VLS growth. For the case of VSS, Hofmann *et al.* [136], showed through video-rate ETEM acquisitions that Si nanowires grow from a (Pd) solid catalyst by lateral propagation of ledges from the coherent Pd silicide/Si growth interface, driven by catalytic dissociation of disilane and coupled Pd and Si diffusion, as shown in Figure 16.31.

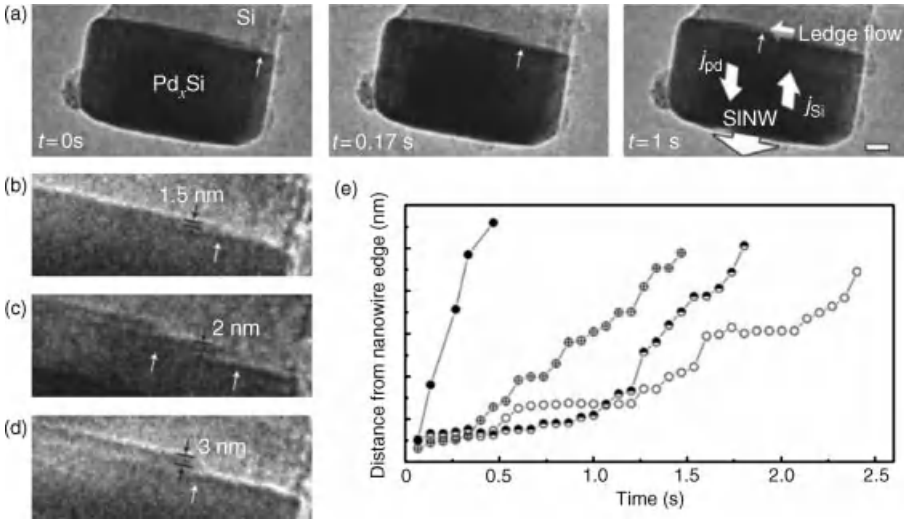


Figure 16.31 Ledge flow-controlled catalyst interface dynamics. (a) ETEM image sequence of growing SiNW at about 560 °C in 1.2×10^{-2} mbar Si_2H_6 (scale bar = 10 nm); *t* indicates elapsed time with respect to the first image. The ledge flow, growth direction, and diffusion fluxes are shown schematically. (b–d) Various ledge configurations at the Pd silicide/SiNW interface during disilane exposure. (e) Measured step edge position versus time for four independent ledges roughly equal to 1.7 nm height in projection. Reproduced from [136].

A significant advance in environmental *in situ* TEM has been made recently in a joint Dutch–Danish collaboration reported by Creemer *et al.* [137]. The strategy used by this group (in order to limit the number of gas atoms in the specimen stage of the microscope) was to build a novel nanoreactor that is functionalized with micrometer-sized gas-flow channels, electron-transparent windows (made of amorphous SiN_x), and a special heating device shown in Figure 16.32. This microelectromechanical system (MEMS) approach allows the integration of a heater and a thermal sensor for variable-temperature experiments on a subsecond time scale. In a proof-of-principle experiment, Creemer *et al.* [137] investigated the Cu/ZnO system, the catalyst of choice in methanol synthesis from CO and H_2 mixtures. Figure 16.33 illustrates the results obtained.

This work is well suited for the *in situ* study of a variety of other academically and commercially important problems at very high spatial resolution and good temporal resolution. The concept of the nanoreactor devised by Creemer *et al.* [137] and extended by Allard *et al.* [138] seems versatile enough to be extended to other environments, including high pressures, heavier constituents, and possibly even liquids. Moreover, parallel measurements may be made with the nanoreactor by utilizing mass spectrometric, optical, and X-ray techniques. However, in practical terms, the vulnerability to failure of these fragile SiN_x membranes may limit the application of this approach.

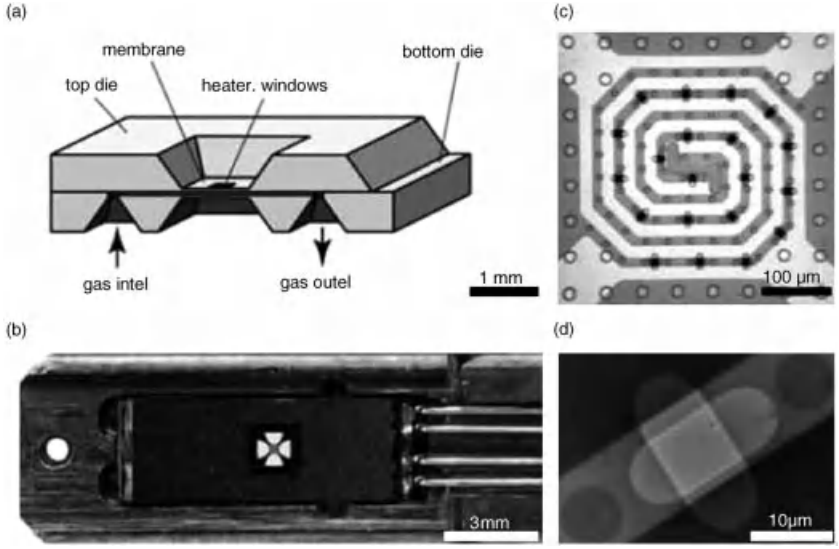


Figure 16.32 Illustration of the nanoreactor device. (a) Schematic cross-section of the nanoreactor; (b) Optical image of the TEM holder with the integrated nanoreactor and the four probe contacts. (c) Optical close-up of the nanoreactor membrane. The bright spiral is the Pt heater. The small oval features are the electron-transparent windows. The circles are the SiO_2 spacers that define the minimum height of the gas channel. (d) A low-magnification TEM image of a pair of superimposed 10 nm thick windows. Their alignment creates a highly electron-transparent (bright) square through which high-resolution TEM imaging can be performed [137].

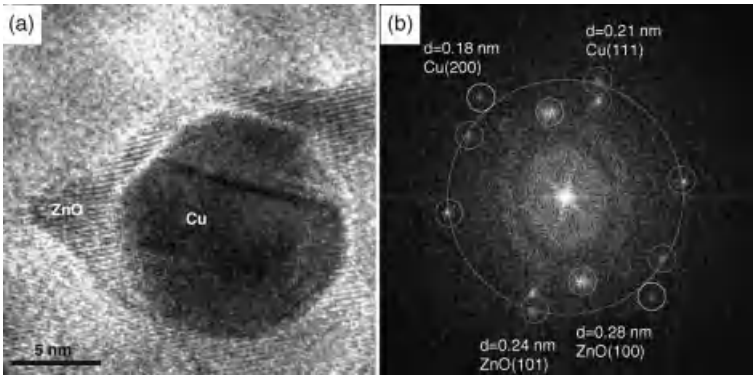


Figure 16.33 A representative HRTEM image of the Cu/ZnO catalyst during exposure to 1.2 mbar hydrogen at 500 °C. (a) The image displays lattice fringes of a twinned Cu nanocrystal and of the ZnO support. (b) A Fourier transform of (a), with overlaid color-coded circles indicating the positions of various Cu and ZnO reflections (the corresponding lattice spacings are also reported). The large red circle corresponds to a spacing of 0.21 nm. The smallest resolved lattice spacing is 0.18 nm [137].

16.6
Recent Developments and Future Prospects

Zewail and co-workers [139, 140] examined graphite by 4D EM and observed nonequilibrium compression and subsequent expansion of the graphene layers, correlated with the direction of change from sp^2 to sp^3 (i.e., to a 3D diamond-like structure) electronic hybridization. With the reality of achieving even shorter optical pulses [141], Zewail's group provided the methodology to generate attosecond (10^{-18} s) electron pulses for imaging and for EELS, that is, on the time scale at which electrons move. With such spatial and temporal resolutions, one has reached the ultimate scale of discrimination in bond lengths and angles and also in the movement of bonding electrons. In principle, therefore, unprecedented degrees of insight into the processes that occur at the surface of catalysts after the transfer of electrons to or from the reactant species and the solid catalyst become possible.

There are many growth points in EM that will lead to further advances in the elucidation of the nature and properties of novel catalysts. On the purely instrumental side, the so-called SMART project centered in Berlin is concerned with, among other aims, producing a spectro-microscope with lateral resolution of 2 nm with an energy resolution of 100 meV; both spherical and chromatic aberration being corrected, it is energy filtered and combines low-energy electron microscopy (LEEM) and photoemission electron microscopy (PEEM), using an X-ray synchrotron as the source of radiation. Another significant development in this area is that pioneered by Asakura and co-workers [142] involving an aberration-corrected multipole Wien filter for energy-filtered X-ray PEEM. PEEM, using UV light as a source, proved immensely valuable in the hands of Ertl [143] in investigating the dynamics of surface reactions on model catalysts, in which the various "chaotic" and well-behaved features of reactants at surfaces could be followed from the local changes in work function during reactions.

With the availability of monochromated electron sources, there is increasing interest in using energy loss spectroscopy to study ultra-low-energy excitations. Howie first discussed the possibility of photon-assisted EELS to investigate excitations generated by a tuned photon beam or pulse train [144]. Energy gain spectroscopy is then possible, discussed further theoretically by Garcia de Abajo and Kociak [145] and realized experimentally by Zewail's group [146].

Au and Ag nanoparticles exhibit a fascinating array of low-energy modes that can be probed with monochromated EELS. The low energy of the excitations, however, means that the signal collected is delocalized, possibly over several tens of nanometers. One way to improve the localization of such a signal is to acquire only those electrons that have scattered to relatively high angles. Such energy-filtered low-loss STEM (EF-STEM) HAADF imaging is possible in some instruments and one of the first examples of this is shown in Figure 16.34 from the Stuttgart group [147] using their SESAM instrument.

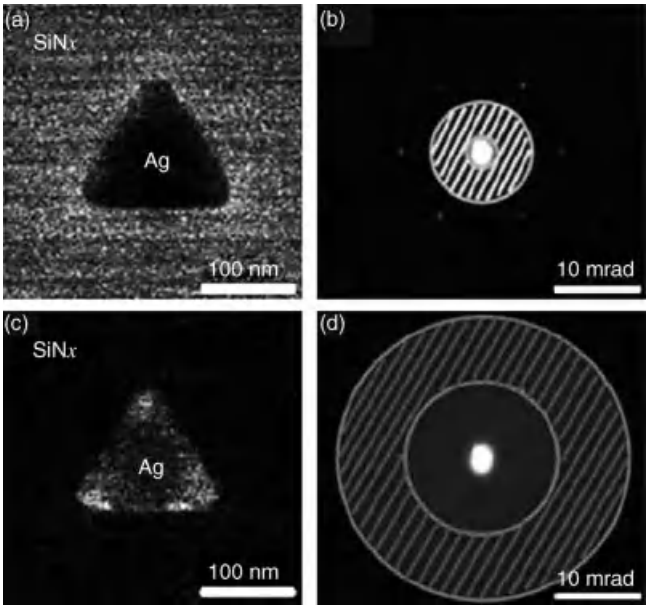


Figure 16.34 (a) EF-STEM images of an Ag nanoparticle acquired at 1 eV with collection angles less than 6 mrad as shown in (b). (c) EF-STEM images of the Ag nanoparticle acquired at 1 eV with collection angles between 12 and 24 mrad, as shown in (d) [147]. Reprinted from [147] with permission from Elsevier.

16.6.1 4D Electron Microscopy

The technique of 4D ultrafast (stroboscopic) EM became feasible about 6 years ago, thanks to the efforts of Zewail and co-workers [148]. It is an approach that has brought and continues to bring revolutionary advances in the study of inorganic and biological materials [4, 149]. It adds the dimension of time to the three spatial dimensions that are retrievable by HREM; and it has opened up new vistas and applications by using timed, single-electron (or just a few electron) packets. Full details of this approach are contained in the monograph by Zewail and Thomas [4], and also in a recent short review [150]. Real-space imaging, Fourier-space (diffraction pattern) recording and EELS studies may all be carried out at femtosecond scale resolution. All this is achieved through coherent electron packets, which are liberated from a photocathode with femtosecond laser pulses, accelerated at 120 or 200 keV and contain as little as one electron per pulse (Figure 16.35).

The monograph by Zewail and Thomas [4] deals in depth with the principles and applications (up to late 2009) of 4D EM. It also shows how ultrafast convergent beam (CB) recording and electron energy gain by photon-induced near-field electron microscopy (PINEM) [151] is carried out.

To understand how it becomes possible to effect the new technique of PINEM using 4D EM, it is necessary to recall the prescient paper of Kapitza and Dirac [152]

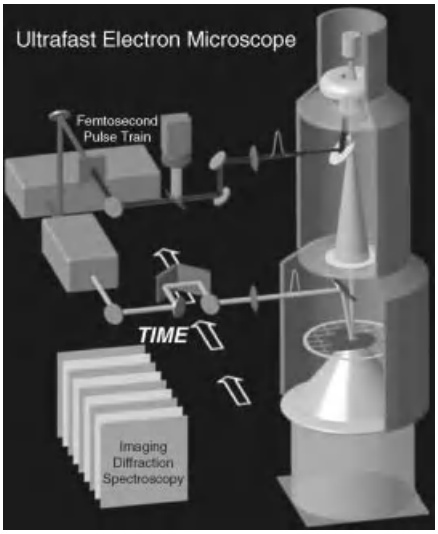


Figure 16.35 Schematic diagram of the "ultrafast" electron microscope introduced by Zewail and Thomas [4].

published in 1933, shortly after it had been shown that electrons possessed wave properties. The Kapitza–Dirac effect is analogous to the diffraction of light by a grating: what Kapitza and Dirac showed was that electrons should be diffracted by a standing light wave [152]. In free space, an electron cannot absorb a quantum of electromagnetic energy because of the lack of conservation of energy momentum. However, Kapitza and Dirac suggested that absorption followed by simulated emission can occur when two (counter-propagating) photons are used. This prediction was demonstrated experimentally in 2001 by Freimund *et al.* [153] and the phenomenon was capitalized upon by Barwick *et al.* [151] at the California Institute of Technology in their proof-of principle investigation of individual carbon nanotubes and silver nanowires. By energy filtering only those electrons resulting from the strong absorption of (integer multiples) of photon quanta by the relativistic electrons accelerated to 200 keV, Barwick *et al.* [151] were able to image directly in space the near-field electronic field distribution, obtain the temporal behavior of the field on the femtosecond time scale, and map its spatial polarization dependence. This advance in ultrafast (4D) EM promises to contribute significantly to the direct space–time imaging of localized fields at interfaces and the visualization of phenomena associated with the plasmonics and photonics of nanostructures. A schematic summary is shown in Figure 16.36.

In a recent development, Kwon and Zewail [154] extended even further the power of 4D EM by introducing 4D (temporal) electron tomography. They integrated a fourth dimension (time resolution) with the 3D spatial resolution obtained from a complete tilt series of 3D projections of an object. The different time frames of tomograms constitute a movie of the object in motion, thus allowing studies on nonequilibrium structures and transient processes. They demonstrated the feasi-

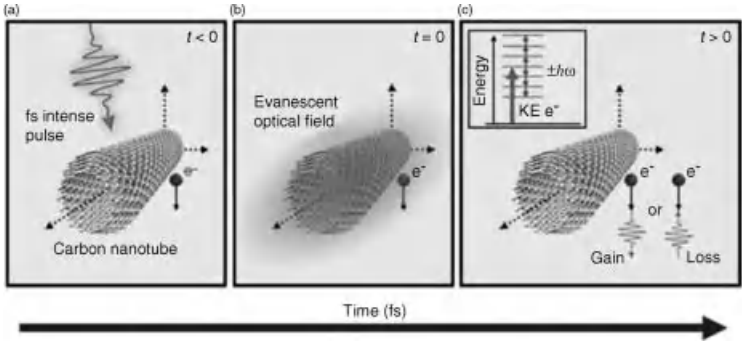


Figure 16.36 Physical depiction of the interaction between the electron, photon, and the evanescent field. (a) A frame when the electron packet arrives at the nanotube before the femtosecond laser pulse ($t < 0$); no spatiotemporal overlap has yet occurred. (b) The precise moment at $t = 0$ when the electron packet, femtosecond laser pulse, and evanescent field are at maximum overlap at the carbon nanotube. (c) Illustration of the process during and immediately after the interaction ($t > 0$) when the electron gains or loses energy equal to integer multiples of femtosecond laser photons. Inset: the possible final energies in the continuum due to the free–free transitions between the imaging electron and the photon in the femtosecond laser pulse. KE, kinetic energy [151].

bility of 4D electron tomography using carbon nanotubes with a bracelet-like ring structure for which 4D tomograms display different modes of motion (with resonant frequencies up to 30 MHz). Effectively, this technique builds up each frame of the movie from thousands of individual shots taken at precisely defined times. There are prospects that the "atomic turmoil" that occurs in the environment of single-site catalysts may be rendered "visible." One system under investigation involves the Ti (IV)-centered site (anchored to mesoporous silica), which is an efficient catalyst for the epoxidation of alkenes [155]. It is planned to use 4D tomography in real time to monitor the atomic displacements immediately after the active site is stimulated by either a thermal or photochemical pulse [156]. Another system of great relevance in biological catalysis is the direct 4D filming of folding and unfolding of protein chains,

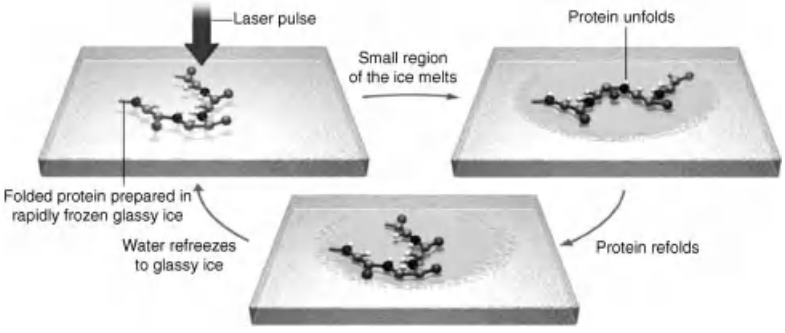


Figure 16.37 Watching biology's clockwork. After Zewail [158].

embedded originally in vitreous ice and held at cryogenic temperatures (using cryoelectron tomography of the type pioneered by Baumeister and co-workers [157]) prior to being subjected to a thermal (clocking) pulse, as illustrated in Figure 16.37 [158].

References

1 Knoll, M. and Ruska, E. (1932) *Z. Phys.*, **78**, 318.
2 Cosslett, V. (1979) *J. Microsc.*, **117**, 1.
3 Williams, D. and Carter, C. (2009) *Transmission Electron Microscopy*, 2nd edn., Springer, New York.
4 Zewail, A. and Thomas, J. (2010) *4D Electron Microscopy*, Imperial College Press, London.
5 Datye, A., Hansen, P., and Helveg, S. (2008) in *Handbook of Heterogeneous Catalysis*, vol. 2 (eds. G. Ertl, H. Hnözinger, F. Shüth, and J. Weitkamp), Wiley-VCH Verlag GmbH, Weinheim, pp. 803 *et seq*.
6 O'Keefe, M. (2008) *Ultramicroscopy*, **108**, 196.
7 Howie, A. (1980) The study of supported catalysts by transmission electron microscopy, in *Characterization of Catalysts* (eds. J. Thomas and R. Lambert), John Wiley & Sons, Ltd., Chichester, pp. 89–104.
8 Thomas, J. (1999) *Angew. Chem. Int. Ed.*, **38** (24), 3589–3628.
9 Thomas, J., Hernandez-Garrido, J.C., Raja, R., and Bell, R. (2009) *Phys. Chem. Chem. Phys.*, **11** (16), 2799–2825.
10 Goodhew, P., Humphreys, J., and Beanland, R. (2001) *Electron Microscopy and Analysis*, Taylor & Francis, London.
11 Graef, M.D. (2003) *Introduction to Conventional Transmission Electron Microscopy*, Cambridge University Press, Cambridge.
12 Thomas, J. (2008) in *Revolutionary Developments from Atomic to Extended Structural Imaging in Physical Biology: from Atoms to Medicine* (ed. A. Zewail), Imperial College Press, London, pp. 51–114.
13 Spence, J.C.H. (2003) *High-Resolution Electron Microscopy*, 3rd edn., Oxford University Press, Oxford.
14 Ducati, C. (2007) in *Advances in Nanoengineering* (eds. A. Davies and J. Thompson), Imperial College Press, London, p. 39.
15 Cowley, J. and Moodie, A. (1957) *Acta Crystallogr.*, **10**, 609–619.
16 Lynch, D. and O'Keefe, M. (1972) *Acta Crystallogr.*, **A28**, 536–548.
17 Kirkland, E.J. (1998) *Advanced Computing in Electron Microscopy*, Plenum Prss, New York.
18 Kirkland, A.I and Meyer, R. (2004) *Microsc. Microanal.*, **10**, 401–413.
19 Klug, A. (1982) From Macromolecules to Biological Assemblies. Nobel Lecture, Nobel Foundation, Stockholm, pp. 77–109.
20 Hovmoeller, S. (1992) *Ultramicroscopy*, **41**, 121–135.
21 Nicolopoulos, S., Gonzales-Calbet, J., Vallet-Regi, M., Corma, A., Conell, C., Guil, J., and Perez-Paniente, J. (1995) *J. Am. Chem. Soc.*, **117**, 8947–8956.
22 Ozkaya, D., Zhou, W., Thomas, J., Midgley, P., Keast, V., and Hermans, S. (1999) *Catal. Lett.*, **60**, 113–120.
23 Vaughan, D., Treacy, M., and Newsam, J. (1990) in *Guidelines for Mastering the Properties of Molecular Sieves* (eds. D. Barthomeuf, E. Derouane, and W. Hoelderic), Plenum Press, New York, pp. 99–120.
24 Findlay, S., Shibata, N., Sawada, H., Okunishi, E., Kondo, Y., and Ikuhara, Y. (2010) *Ultramicroscopy*, **110**, 903–923
25 Ozkaya, D., Thomas, J., Shephard, D., Maschmeyer, T., Johnson, B., and Sankar, G. (1997) *Proc. Inst. Phys. Electron Microsc. Anal. Group Conf.*, 403–406.
26 Thomas, J., Williams, B., and Uppal, M. (1984) *Philos. Trans. R. Soc. London*, **311**, 271–285.
27 Liu, Y., Jia, C., Yamasaki, J., Terasaki, O., and Schuth, F. (2010) *Angew. Chem. Int. Ed.*, **49**, 5771–5775.

28 Zhai, Y., Pierre, D., Si, R., Deng, W., Ferrin, P., Nilekar, A., Peng, G., Herron, J., Bell, D., Saltsburg, H., Mavrikakis, M., and Flytzani-Stephanopoulos, M. (2010) *Science*, **329**, 1633.

29 Kwak, J.H., Hu, J., Mei, D., Yi, C.-M., Kim, D.H., Peden, C.H.F., Allard, L.F., and Szanyi, J. (2009) *Science*, **325** (5948), 1670–1673.

30 Egerton, R. (1996) *Electron Energy-Loss Spectroscopy in the Electron Microscope*, Plenum Press, New York.

31 Brydson, R. (2001) *Electron Energy Loss Spectroscopy*, BIOS Scientific Publishers, Oxford.

32 Egerton, R. (2002) *Top. Catal.*, **21**, 185–190.

33 Reimer, L. (1995) *Energy-Filtering Transmission Electron Microscopy*, Springer, New York.

34 Thomas, P. and Midgley, P. (2002) *Top. Catal.*, **21**, 109.

35 Thomas, J. and Midgley, P. (2004) *Chem. Commun.*, (11), 1253–1267.

36 Muller, D.A., Kourkoutis, L., Murfitt, M., Song, J.H., Hwang, H.Y., Silcox, J., Dellby, N., and Krivanek, O.L. (2008) *Science*, **319** (5866), 1073–1076.

37 Maeda, K. and Domen, K. (2007) *J. Phys. Chem. C*, **111**, 7851.

38 Anderson, M., Ohsuna, T., Sakamoto, Y., Liu, Z., Carlsson, A., and Terasaki, O. (2004) *Chem. Commun.*, (8), 907–916.

39 Kaneda, M., Tsubakiyama, T., Carlsson, A., Sakamoto, Y., Ohsuna, T., Terasaki, O., Joo, S., and Ryoo, R. (2002) *J. Phys. Chem. B*, **106** (6), 1256–1266.

40 Wagner, P., Terasaki, O., Ritsch, S., Nery, J., Zones, S., Davis, M., and Hiraga, K. (1999) *J. Phys. Chem. B*, **103** (39), 8245–8250.

41 Weirich, T., Ramlau, R., Simon, A., Hovmoller, S., and Zou, X. (1996) *Nature*, **382** (6587), 144–146.

42 Zandbergen, H., Andersen, S., and Jansen, J. (1997) *Science*, **277** (5330), 1221–1225.

43 Midgley, P., Ward, E., Hungria, A., and Thomas, J. (2007) *Chem. Soc. Rev.*, **36**, 1477.

44 Midgley, P., Weyland, M., Thomas, J., and Johnson, B. (2001) *Chem. Commun.*, 907.

45 Thomas, J. and Midgley, P. (2010) *ChemCatChem*, (2), 783–798.

46 Thomas, J., Evans, E., and Williams, J. (1972) *Proc. R. Soc. London, Ser. A*, **331**, 417.

47 Thomas, J. (1969) *Adv. Catal.*, **19**, 293.

48 Evans, E., Thomas, J., Thrower, P., and Walker, P. (1973) *Carbon*, **11** (5), 441–445.

49 Thomas, J. (1982) *Ultramicroscopy*, **8** (1–2), 13–25.

50 Iijima, S. (1991) *Nature*, **354**, 56–58.

51 Wang, Z. and Hui, C. (eds.) (2003) *Electron Microscopy of Nanotubes*, Kluwer, Dordrecht.

52 Ducati, C., Alexandrou, I., Chhowalla, M., Robertson, J., and Amaratunga, G. (2004) *J. Appl. Phys.*, **95** (11, Part 1), 6387–6391.

53 Koziol, K., Ducati, C., and Windle, A. (2010) *Chem. Mater.*, **22** (17), 4904–4911.

54 Zhu, H., Suenaga, K., Wei, J., Wang, K., and Wu, D. (2008) *J. Cryst. Growth*, **310** (24), 5473–5476.

55 Homma, Y., Kobayashi, Y., Ogino, T., Takagi, D., Ito, R., Jung, Y., and Ajayan, P. (2003) *J. Phys. Chem. B*, **107** (44), 12161–12164.

56 Bethge, H., Keller, K.W., and Ziegler, E. (1968) *J. Cryst. Growth*, **3–4**, 184.

57 Bursill, L., Lodge, E., and Thomas, J. (1980) *Nature*, **289**, 111–113.

58 Thomas, J., Millward, G., and Bursill, L. (1981) *Philos. Trans. R. Soc. London, Ser. A*, **300** (1453), 43.

59 Terasaki, O., Thomas, J., Watanabe, D., and Millward, G. (1989) *Chem. Mater.*, **1**, 158.

60 Thomas, J., Terasaki, O., Gai, P., Zhou, W., and Gonzalez-Calbet, J. (2001) *Acc. Chem. Res.*, **34** (7), 583–594.

61 Terasaki, O., Thomas, J., and Ramdas, S. (1984) *J. Chem. Soc., Chem. Commun.*, (4), 216–217.

62 Audler, M., Thomas, J., Klinowski, J., Jefferson, D., and Bursill, L. (1982) *J. Phys. Chem.*, **86** (4), 581–584.

63 Millward, G., Ramdas, S., and Thomas, J. (1985) *Proc. R. Soc. London, Ser. A*, **399** (1816), 57.

64 Wright, P., Zhou, W., Perez-Pariente, J., and Arranz, M. (2005) *J. Am. Chem. Soc.*, **127** (2), 494–495.

65 Thomas, J. and Millward, G. (1982) *J. Chem. Soc., Chem. Commun.*, (24), 1380–1383.

66 Wright, P. (2007) *Microporous Framework Solids*, Royal Society of Chemistry, Cambridge.

67 Thomas, J., Raja, R., Sankar, G., and Bell, R. (1999) *Nature*, **398** (6724), 227–230.

68 Thomas, J. and Gai, P. (2006) *Adv. Catal.*, **48**, 174.

69 Sun, J., Zhanbing, H., Høvmoller, S., Zou, X., Gramm, F., Baerlocher, G., and McCusker, L.B. (2010) *Z. Kristallogr.*, **225**, 77.

70 Baerlochen, C., Hepp, A., and Meier, W. (1976) DLS Refinement Program, ETH, Zurich.

71 Thomas, J., Adams, R.D., Bowell, E.M., Captain, B., Gronbeck, H., and Raja, R. (2008) *Faraday Discuss.*, **138**, 301.

72 Schmid, G. and Fenske, D. (2010) *Philos. Trans. R. Soc. London, Ser. A*, **368**, 1207.

73 Turner, M., Golovko, V.B., Vaughan, O.P.H., Abdulkin, P., Berenguer-Murcia, A., Tikhov, M.S., Johnson, B.F.G., and Lambert, R.M. (2008) *Nature*, **454** (7207), 981–983.

74 Tsunoyama, H., Ichikuni, N., Sakurai, H., and Tsukuda, T. (2009) *J. Am. Chem. Soc.*, **131** (20), 7086–7093.

75 Narayanan, R. and El-Sayed, M. (2005) *J. Phys. Chem. B*, **109** (26), 12663–12676.

76 Tsunoyama, H. and Tsukuda, T. (2009) *J. Am. Chem. Soc.*, **131** (51), 18216–18217.

77 Zheng, H., Smith, R.K., Jun, Y.-W., Kisielowski, C., Dahmen, U., and Alivisatos, A.P. (2009) *Science*, **324** (5932), 1309–1312.

78 Gai, P. (2002) *Microsc. Microanal.*, **8**, 21.

79 Williamson, M., Tromp, R., Vereecken, P., Hull, R., and Ross, F. (2003) *Nat. Mater.*, **2** (8), 532–536.

80 Wang, J., Inada, H., Wu, L., Zhu, Y., Choi, Y., Liu, P., Zhou, W.P., and Adzic, R. (2009) *J. Am. Chem. Soc.*, **131**, 17298–17302.

81 Lu, A.H., Schmidt, W., Matoussevitch, N., Bonnemann, H., Spliethoff, B., Tesche, B., Bile, E., Kiefer, W., and Schüth, F. (2004) *Angew. Chem.* **116**, 4403.

82 Lu, A.H., Schmidt, W., Matoussevitch, N., Bonnemann, H., Spliethoff, B., Tesche, B., Bile, E., Kiefer, W., and Schüth, F. (2004) *Angew. Chem. Int. Ed.* **43**, 4303.

83 Thomas, J., Simpson, E., Kasama, T., and Dunin-Borkowski, R. (2008) *Acc. Chem. Res.*, **41**, 665–674.

84 Pyrz, W., Blom, D., Vogt, T., and Buttrey, D. (2008) *Angew. Chem. Int. Ed.*, **47** (15), 2788–2791.

85 Grasselli, R., Buttrey, D., Burrington, J., Andersson, A., Holmberg, J., Ueda, W., Kubo, J., Lugmair, C., and Volpe, J. (2006) *Top. Catal.*, **38** (1–3), 7–16.

86 Thomas, J. (2008) *ChemPhysChem*, **9** (10), 1363–1365.

87 Aouine, M., Dubois, J., and Millet, J. (2001) *Chem. Commun.*, (13), 1180–1181.

88 Shiju, N.R. and Guliants, V.V. (2007) *ChemPhysChem*, **8** (11), 1615–1617.

89 Lopez Nieto, J., Botella, P., Solsona, B., and Oliver, J. (2003) *Catal. Today*, **81** (2), 87–94.

90 DeSanto, P., Buttrey, D., Grasselli, R., Lugmair, C., Volpe, A., Toby, B., and Vogt, T. (2004) *Z. Kristallogr.*, **219** (3), 152–165.

91 Pyrz, W., Blom, D., Sadakane, M., Kodato, K., Ueda, W., Vogt, T., and Buttrey, D. (2010) *Chem. Mater.*, **22** (6), 2033–2040.

92 Terasaki, O. and Ohsuna, T. (2003) *Top. Catal.*, **24** (1–4), 13–18.

93 Anderson, M., Ohsuna, T., Sakamoto, Y., Liu, Z., Carlsson, A., and Terasaki, O. (2004) *Chem. Commun.*, (8), 907–916.

94 Treacy, M. and Gibson, J. (1981) *Ultramicroscopy*, **7**, 109.

95 Ortalan, V., Uzun, A., Gates, B., and Browning, N. (2010) *Nat. Nanotechnol.*, **5**, 506–510.

96 Sun, J., Bonneau, C., Cantin, A., Corma, A., Diaz-Cabanas, M., Moliner, M., Zhang, D., Li, M., and Zou, X. (2009) *Nature*, **458**, 1154.

97 Krivanek, O.L., Chisholm, M.F., Nicolosi, V., Pennycook, T.J., Corbin, G.J., Dellby, N., Murfitt, M.F., Own, C.S., Szilagyi, Z.S., Oxley, M.P., Pantelides, S.T., and Pennycook, S.J. (2010) *Nature*, **464**, 571–574.

98 Rodriguez-Luque, M., Hernandez, J., Yeste, M., Bernal, S., Cauqui, M., Pintado, J., Perez-Omil, J., Stephan, O., Calvino, J., and Trasobares, S. (2008) *J. Phys. Chem. C*, **112**, 5900–5910.

99 Thomas, J., Johnson, B., Raja, R., Sankar, G., and Midgley, P. (2003) *Acc. Chem. Res.*, **36** (1), 20–30.

100 Bromley, S., Sankar, G., Catlow, C., Maschmeyer, T., Johnson, B., and Thomas, J. (2001) *Chem. Phys. Lett.*, **340** (5–6), 524–530.

101 Zhou, W., Thomas, J., Shephard, D., Johnson, B., Ozkaya, D., Maschmeyer, T., Bell, R., and Ge, Q. (1998) *Science*, **280** (5364), 705–708.

102 Thomas, J., Raja, R., Gai, P., Gronbeck, H., and Hernandez-Garrido, J. (2010) *ChemCatChem*, **2** (4), 402–406.

103 Hermans, S., Raja, R., Thomas, J., Johnson, B., Sankar, G., and Gleeson, D. (2001) *Angew. Chem. Int. Ed.*, **40**, 1211–1215.

104 Hungria, A., Raja, R., Adams, R., Captain, B., Thomas, J., Midgley, P., Golovko, V., and Johnson, B. (2006) *Angew. Chem. Int. Ed.*, **45**, 4782–4785.

105 Kiely, C. (2010) *Nat. Mater.*, **9**, 296–297.

106 Herzing, A., Kiely, C., Carley, A., Landon, P., and Hutchings, G. (2008) *Science*, **321**, 1331–1335.

107 Hagen, J., Socaciu, L., Elijazyfer, M., Heiz, U., Bernhardt, T., and Woste, L. (2002) *Phys. Chem. Chem. Phys.*, **4** (10), 1707–1709.

108 Li, Z.Y., Young, N.P., Di Vece, M., Palomba, S., Palmer, R.E., Bleloch, A.L., Curley, B.C., Johnston, R.L., Jiang, J., and Yuan, J. (2008) *Nature*, **451** (7174), 46–48.

109 Zhou, W., Ross-Medgaanden, E., Knowles, W., Wong, M., Wacks, I., and Kiely, C.J. (2009) *Nat. Chem.*, **1**, 722–728.

110 Weckhuysen, B. (2009) *Nat. Chem.*, **1**, 690.

111 Marecot, P., Pirault, L., Mabilon, G., Prigent, M., and Barbier, J. (1994) *Appl. Catal. B*, **5**, 57.

112 Trovarelli, A., Zamar, F., Liorca, J., Deleitenburg, C., Dolcetti, G., and Kiss, J. (1997) *J. Catal.*, **169**, 490.

113 Bunluesin, T. (1998) *Appl. Catal. B*, **15**, 107.

114 Wang, X., Rodriguez, J., Hanson, J., Gamarra, D., Martinez-Arias, A., and Fernandez-Garcia, M. (2006) *J. Phys. Chem. B*, **110**, 428.

115 Park, S., Vohs, J., and Gorte, R. (2000) *Nature*, **404**, 265.

116 Wang, R., Croizer, P., Sharma, R., and Adams, J. (2006) *J. Phys. Chem. B*, **110**, 18278–18285.

117 Wang, R., Croizer, P., Sharma, R., and Adams, J. (2008) *Nano Lett.*, **8**, 962–967.

118 Lopez-Haro, M., Aboussaid, K., Gonzalez, J., Hernandez, J., Pintado, J., Blanco, G., Calvino, J., Midgley, P., Bayle-Guillemaud, P., and Trasobares, S. (2009) *Chem. Mater.*, **21**, 1035.

119 Mars, P. and Krevelen, D. W. van. (1954) *Spec. Suppl. to Chem. Eng. Sci.*, **3**, 41.

120 Reller, A., Thomas, J., Jefferson, D., and Uppal, M. (1984) *Proc. R. Soc. London, Ser. A*, **394** (1807), 223.

121 Buttrey, D., Jefferson, D., and Thomas, J. (1986) *Philos. Mag. A*, **53** (6), 897–906.

122 Zhou, W., Jefferson, D., Alario-Franco, M., and Thomas, J. (1987) *J. Phys. Chem C*, **91**, 512–514.

123 Gai, P. and Boyes, E. (2003) *Electron Microscopy in Heterogeneous Catalysis*, Institute of Physics Publishing, Bristol.

124 Thomas, J. (1965) in *Chemistry and Physics of Carbon* (ed. P. Walker), Marcel Dekker, New York, p. 122.

125 Gai-Boyes, P. (1992) *Catal. Rev.*, **34**, 1.

126 Gai, P. and Kourtakis, K. (1995) *Science*, **267**, 661.

127 Thomas, J. and Gai, P. (2004) in *Advances in Catalysis* (eds. H. Knözinger and B. Gates), Academic Press, London, p. 171.

128 Gai, P. (2007) in *Nanocharacterization* (eds. A. Kirkland and J. Hutchinson), Royal Society of Chemistry, Cambridge, p. 268.

129 Gai, P., Boyes, E., Helveg, S., Hansen, P., Giorgio, S., and Henry, C. (2007) *MRS Bull.*, **32** (12), 1044–1050.

130 Boyes, E. and Gai, P. (1997) *Ultramicroscopy*, **67**, 219–232.

131 Grunwaldt, J., Molenbroek, A., Topsoe, N., Topsoe, H., and Clausen, B. (2000) *J. Catal.*, **194** (2), 452–460.

132 Hansen, P., Wagner, J., Helveg, S., Rostrup-Nielsen, J., Clausen, B., and

Topsoe, H. (2002) *Science*, **295** (5562), 2053–2055.
133 Wagner, J., Hansen, P., Molenbroek, A., Topsoe, H., Clausen, B., and Helveg, S. (2003) *J. Phys. Chem. B*, **107** (31), 7753–7758.
134 Giorgio, S., Joao, S., Nitsche, S., Chaudanson, D., Sitja, G., and Henry, C. (2006) *Ultramicroscopy*, **106** (6), 503–507.
135 Hannon, J., Kodambaka, S., Ross, F., and Tromp, R. (2006) *Nature*, **440** (7080), 69–71.
136 Hofmann, S., Sharma, R., Wirth, C., Cervantes-Sodi, F., Ducati, C., Kasama, T., Dunin-Borkowski, R., Drucker, J., Bennett, P., and Robertson, J. (2008) *Nat. Mater.*, **7** (5), 372–375.
137 Creemer, J.F., Helveg, S., Hoveling, G.H., Ullmann, S., Molenbroek, A.M., Sarro, P.M., and Zandbergen, H.W. (2008) *Ultramicroscopy*, **108** (9), 993–998.
138 Allard, L., Bigelow, W., Jose-Yacaman, M., Nackashi, D., Damiano, J., and Mick, S. (2009) *Microsc. Res. Technol.*, **72** (3), 208–215.
139 Carbone, F., Barwick, B., Kwon, O.H., Park, H., Baskin, J., and Zewail, A. (2009) *Chem. Phys. Lett.*, **468** (4–6), 107–111.
140 Carbone, F., Kwon, O.H., and Zewail, A. (2009) *Science*, **325** (5937), 181–184.
141 Krausz, F. and Ivanov, M. (2009) *Rev. Mod. Phys.*, **81** (1), 163–234.
142 Niimi, H., Chun, W.J., Suzuki, S., Asakura, K., and Kato, M. (2007) *Rev. Sci. Instrum.*, **78** (6)
143 Ertl, G. (2008) *Angew. Chem.*, **120**, 3578–3590.
144 Howie, A. (2004) *Microsc. Microanal.*, **10** (6), 685–690.
145 Garcia de Abajo, F.J. and Kociak, M. (2008) *New J. Phys.*, **10**, 073035.
146 Yurtsever, A. and Zewail, A. (2009) *Science*, **326** (5953), 708–712.
147 Gu, L., Sigle, W., Koch, C.T., Nelayah, J., Srot, V., and van Aken, P.A. (2009) *Ultramicroscopy*, **109**, 1164.
148 Lobastov, V., Srinivasan, R., and Zewail, A. (2005) *Proc. Natl. Acad. Sci. U. S. A.*, **102**, 7069.
149 Thomas, J. (2005) *Angew. Chem. Int. Ed.*, **44**, 5563–5566.
150 Zewail, A. (2010) *Science*, **328**, 187–191.
151 Barwick, B., Flannigan, D., and Zewail, A. (2009) *Nature*, **462**, 902–906.
152 Kapitza, P. and Dirac, P. (1933) *Proc. Camb. Philos. Soc.*, **29**, 297–300.
153 Freimund, D., Aflatooni, K., and Batelaan, H. (2001) *Nature*, **413**, 142–143.
154 Kwon, O.H. and Zewail, A. (2010) *Science*, **328**, 1668–1673.
155 Maschmeyer, T., Rey, F., Sankar, G., and Thomas, J. (1995) *Nature*, **378**, 159.
156 Zewail, A., Thomas, J., *et al.*, work in progress.
157 Plitzko, J., Frangakis, A., Nicholl, S., Foster, F., Gross, A., and Baumeister, W. (2002) *Trends Biol.*, **20**, S40–S44
158 Zewail, A. (2010) *Sci. Am.*, **16**, 112–118.

17
Scanning Probe Microscopy and Spectroscopy

Tomoaki Nishino

17.1
Introduction

Scanning probe microscopy (SPM) is a powerful technique to image solid surfaces directly on the atomic scale. The SPM instrument differs from conventional microscopes, such as optical or electron microscopes, in that it has no lens to magnify a specimen's image. Instead, SPM utilizes an atomically sharp probe tip to measure a local topography or chemical/physical property of a sample surface (Figure 17.1). The first SPM technique was scanning tunneling microscopy (STM), reported in the early 1980s by Binnig, Rohrer, and their colleagues [1–3]. Soon after its invention, STM successfully revealed the atomic arrangement on the reconstructed surface of silicon crystals (Figure 17.2), which could not be strictly defined for a couple of decades. Since then, STM has been accepted as a useful tool in surface science because of the extremely high spatial resolution, the ability for observations in real space, and wide applicability in a variety of environments.

When two metal surfaces face each other very closely with bias voltage applied, electrons flow between them. STM relies on this phenomenon, which is called electron tunneling, as an operating principle. In STM observations, one of these two surfaces is that of an atomically sharp metal tip and the other is the sample surface. The tip is in close proximity to the sample surface, of the order of 1 nm or less, and a certain voltage of the order of 1–2 V is applied in between. This results in a tunneling current flow of the order of 1–2 nA between them. The current, I, can be roughly approximated by

$$I \approx \exp\left(-\frac{2z}{\lambda}\right) \tag{17.1}$$

where $\lambda = \hbar/\sqrt{2m\phi}$, $\hbar$ is Plank's constant, m the electron rest mass, and ϕ the work function of the sample [4]. The tunneling current thus depends on the distance z between the two surfaces. The exponential dependence of the current on the distance between tip and sample surface provides the high resolution achieved by STM. The tip scans over the sample surface keeping either the distance (constant height mode)

Characterization of Solid Materials and Heterogeneous Catalysts: From Structure to Surface Reactivity, First Edition. Edited by Michel Che and Jacques C. Védrine.
© 2012 Wiley-VCH Verlag GmbH & Co. KGaA. Published 2012 by Wiley-VCH Verlag GmbH & Co. KGaA.

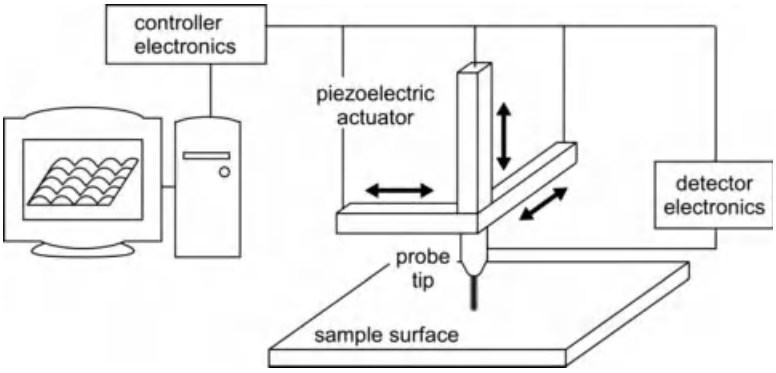


Figure 17.1 Schematic illustration of the SPM instrument.

or the tunneling current (constant current mode) between the tip and sample constant. The modulation of the tunneling current and the distance between the tip and the surface is mapped in constant height and current mode, respectively. Both of the two modulations reflect the topography of the sample surface as indicated by Eq. (17.1). The tunneling current primarily reflects the separation between the tip and sample surface. In addition, it depends on the electronic structure, and STM can be used for mapping the local electronic property of the sample [scanning tunneling spectroscopy (STS)]. Furthermore, STM also permits visualization of surface magnetic properties [spin-polarized scanning tunneling microscopy (SP-STM)].

After the invention of STM, atomic force microscopy (AFM) was reported in 1986 by Binnig *et al.* [5]. In AFM, a cantilever spring having a sharp tip at its free end is

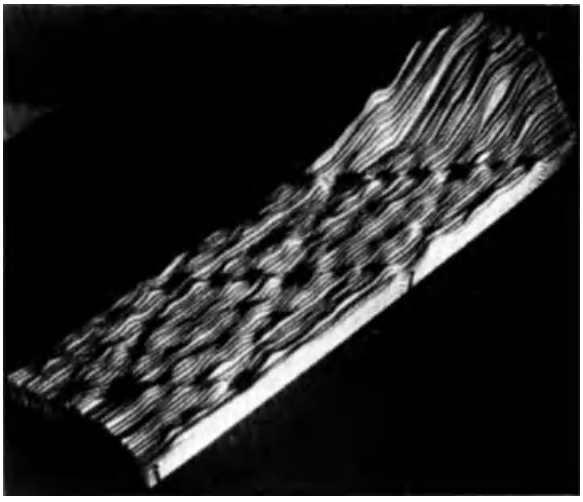


Figure 17.2 The first STM image of an Si(111)-7 × 7 surface. Reprinted with permission from [3]. Copyright 1983 the American Physical Society.

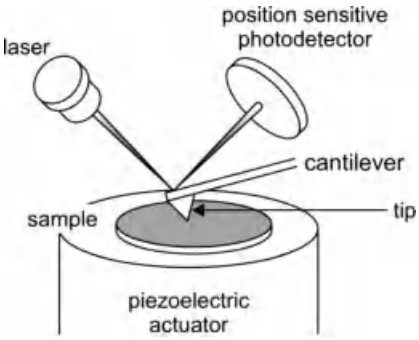


Figure 17.3 Schematic illustration of the AFM instrument.

brought into contact with, or in close proximity to, a sample surface (Figure 17.3). AFM utilizes the resulting atomic force exerted between the tip and the sample to map out the sample topography based on the fact that the atomic force depends strongly on the tip–sample separation. The sample stage is scanned horizontally while keeping the atomic force between the tip and the sample constant. The movement of the sample stage duplicates the structure of the sample surface, and therefore the topography of the sample surface is constructed. Precise measurement of the atomic force is crucial in AFM and is achieved by the detection of a cantilever's deflection. The most popular way to sense such a deflection is optical beam deflection sensing. A laser beam is focused on the rear side of the cantilever and reflected into a position-sensitive photodetector, which measures the cantilever deflection as depicted in Figure 17.3. STM is only applicable to conducting and semiconducting surfaces because STM probes tunneling electrons to measure surface topography. In contrast, AFM can be useful for characterizing not only conducting and semiconducting surfaces but also insulators, including polymers and biological samples, since the atomic force arises for all materials regardless of their conductivity.

17.2
Scanning Tunneling Microscopy

17.2.1
Principle

STM relies on electron tunneling as the operating principle, and atomic resolution is achieved because of the exponential dependence of the tunneling current on the separation between the tip and the sample. The wavefunctions extending from the tip and sample surfaces decay exponentially within the gap between these two surfaces. If the gap is thin enough, the decaying wavefunctions overlap with each other, and electron tunneling takes place. In STM experiments, a bias voltage is applied between the tip and sample to shift their Fermi levels. The direction of electron tunneling is

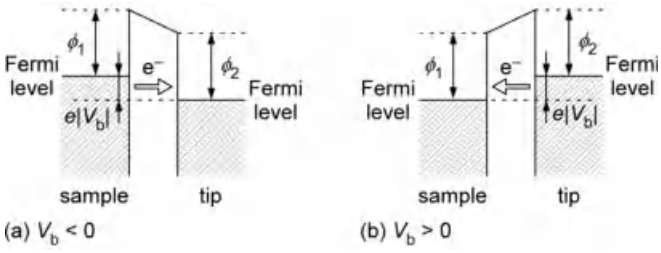


Figure 17.4 Energy diagrams for electron tunneling with (a) sample-negative and (b) sample-positive biases. ϕ_1 and ϕ_2 are work functions of the sample and tip, respectively, and V_b is the bias voltage.

dependent on the polarity of the bias voltage. With sample-negative bias (Figure 17.4a), electrons tunnel from the filled density of states (DOS) of the sample surface to the empty DOS of the tip. The resultant STM image is, therefore, dominated by filled states of the sample. In contrast, with sample-positive bias (Figure 17.4b), the tunneling current flows from the empty DOS of the sample surface to the filled DOS of the tip. Accordingly, empty states of the sample primarily contribute to the STM image. This polarity dependence is well exemplified in STM images of the GaAs(110) surface (Figure 17.5). The filled state density is concentrated around the As atoms of this surface and the empty state density around the Ga atoms. Consequently, the As and Ga atoms were selectively observed with sample-negative

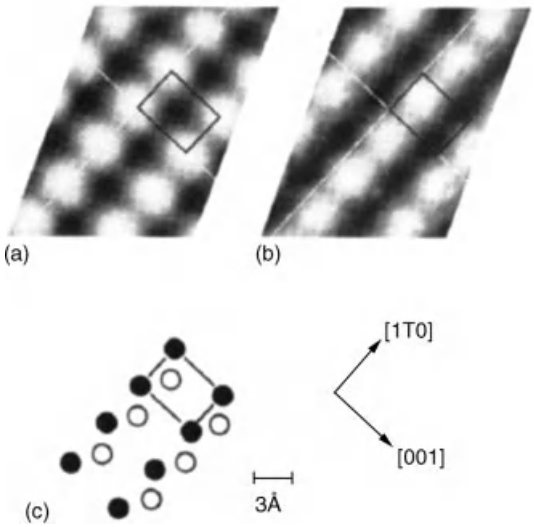


Figure 17.5 STM images of GaAs(110) obtained at sample voltages of $+1.9$ and -1.9 V. (c) Schematic of the atomic arrangement of the GaAs(110) surface. The open and closed circles represent As and Ga atoms, respectively. The rectangle indicates a unit cell, whose position is the same in all three panels. Reprinted with permission from [6]. Copyright 1987 the American Physical Society.

(Figure 17.5b) and -positive (Figure 17.5a) biases, respectively [6]. The different atoms on the sample surface were differentiated from each other in this case due to the spatially separated filled and empty surface states. However, STM generally lacks chemical selectivity, and it is often difficult to discriminate different atoms or molecules in STM.

The tunneling current was first described theoretically based on perturbation theory by Tersoff and Hamann [7, 8]. According to their approach, Bardeen's equation for the tunneling current I is expressed as [9]

$$I = \frac{2\pi e}{\hbar}\sum_{\mu,\nu}\left[f\left(E_\mu\right) - f\left(E_\nu + eV\right)\right]\left|M_{\mu\nu}\right|^2\delta\left(E_\mu - E_\nu\right) \tag{17.2}$$

where the tunneling matrix element, $M_{\mu\nu}$, is given by

$$M_{\mu\nu} = \frac{\hbar^2}{2m}\int_{S_0} \mathrm{d}S\left(\psi_\mu^*\nabla\psi_\nu - \psi_\nu\nabla\psi_\mu^*\right) \tag{17.3}$$

ψ_μ, and E_μ (ψ_ν, E_ν) are the eigenfunction and its corresponding eigenenergy of the surface (tip) system, respectively, $f(E)$ is the Fermi distribution function, and V is the bias voltage between the tip and sample. If we assume that the wavefunction of the tip can be approximated by an s-type wavefunction, the tunneling current for the weak bias case is expressed as [7]

$$I = V\varrho(\boldsymbol{R}, E_\mathrm{F}) \tag{17.4}$$

where $\varrho(\boldsymbol{R}, E_\mathrm{F})$ is the local density of states (LDOS) of the surface at the center position $\boldsymbol{R}$ of the spherical tip and at the Fermi level E_F. Because

$$\varrho(\boldsymbol{r}, E) \equiv \sum_\nu |\psi_\nu(\boldsymbol{r})|^2\delta(E_\nu - E) \tag{17.5}$$

and

$$|\psi_\nu(\boldsymbol{r})|^2 \propto \mathrm{e}^{2k(\boldsymbol{R}+d)} \tag{17.6}$$

we can see the exponential dependence of the tunneling current on the distance between the tip and sample surface. In Eq. (17.6), $k = \hbar^{-1}(2m\varphi)^{1/2}$ is the inverse decay length of the wavefunction, φ, in vacuum.

The equations derived by Tersoff and Hamann have frequently been adopted for the analysis of experimental results. However, it should be noted that their validity depends strongly on the electronic states of the STM tip due to the spherical tip approximation. In contrast, a first-principle theory of STM was developed to include the realistic atomic structure of the tip [10]. Such theory demonstrates that the spherical tip approximation is valid when a tiny protrusion exists on the surface of the tip extremity. Furthermore, the first-principle theory has been utilized for the theoretical simulation of STM imaging [11], which clarified that the microscopic structure of the tip apex significantly affects the STM image.

Precise interpretation of STM images has not been simple and straightforward because the tunneling current reflects not the geometric topography of the sample

surface but the electronic structure at the Fermi level. The tunneling currents were theoretically calculated for Na, S, and He adsorbed on a substrate represented by jellium model [12]. It was found that the Na and S atoms were imaged as protrusions. In contrast, the calculation predicted that the He atom would be imaged as a depression. This counterintuitive result stems from decreased density of states near the Fermi level. Similarly, it has been found both theoretically and experimentally that O atoms on metal surfaces appeared as depressions in the STM images [13].

17.2.2 Catalytic Model Systems

In heterogeneous catalysis, the catalytic reaction takes place between reactants in gas or solution phases and a solid surface. The catalyzed reaction consists of a series of elementary steps, each of which may influence the reaction rate and catalytic efficiency. The elementary steps include adsorption, diffusion, chemical reaction, and desorption. STM possesses an outstanding ability to monitor some of these steps at the atomic scale, such as the atomic structure of the catalyst surface, surface reconstruction induced by adsorption, and adsorbate molecular structure. As a result, STM has become a widely used tool in catalytically relevant surface analysis. In addition to STM, a wide range of surface-sensitive techniques have been employed in research on catalytic systems. The local imaging capability of STM confers a distinct advantage over spectroscopic and diffraction techniques, which provide averaged information over a large surface area. Catalytically active sites on a sample surface are often heterogeneously located at the surface. Hence imaging local atomic structures in real space by STM can provide an invaluable insight into catalysis. The applicability of STM in different environments is another advantage. STM can operate not only in ultra-high vacuum (UHV) but also in more realistic or reactive environments, which is in sharp contrast to most surface analysis techniques.

17.2.2.1 Adsorption

Numerous studies have been devoted to the adsorption of oxygen on metal surfaces because oxygen adsorption is closely related to a wide range of technical applications, including heterogeneous catalysis. The early STM studies on oxygen chemisorption on Cu(110) provide an important insight into the formation of the chemisorbed layer [14, 15]. The STM observations were performed at room temperature in UHV, and a Cu(110) single-crystal surface was exposed to oxygen by backfilling the UHV chamber. The resulting STM images revealed that a $p(2 \times 1)$ phase along the [001] direction appeared on the Cu(110)–(1×1) surface (Figure 17.6), consistent with the results obtained with low-energy electron diffraction (LEED). The $p(2 \times 1)$ phase was ascribed to the formation of $-$Cu$-$O$-$ chains on the surface. It was found by consecutive STM imaging during additional oxygen exposure that the terrace size of the substrate decreased as these phases grew. On the basis of these observations, the mechanism of the formation of the $p(2 \times 1)$ phase was established. The oxygen first adsorbs dissociatively on the Cu(110) surface at room temperature. Mobile copper adatoms exist on the surface at this temperature, and a strongly attractive interaction

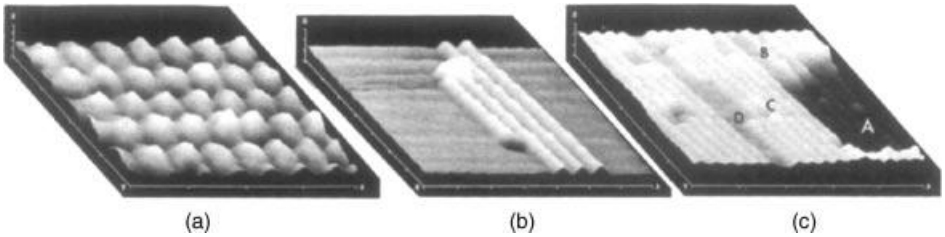


Figure 17.6 (a) STM image of a clean Cu(110) surface. Image size, $2.0 \times 2.0\,nm^2$; bias voltage, 0.53 V; set-point current, 2.5 nA. (b) STM image showing the formation of the $-Cu-O-$ chains after an O_2 exposure of $\sim$1 l. Image size, $7.0 \times 7.0\,nm^2$. (c) STM image of the $p(2 \times 1)$ phase at an O_2 exposure of 10 l. Image size, $10 \times 10\,nm^2$; bias voltage, 0.8 V; set-point current, 0.8 nA. Reprinted with permission from [15]. Copyright 1990 the American Physical Society.

between the two chemical species leads to the formation of $-Cu-O-Cu$ chains. The anisotropy of these chains results from the fact that the attractive interaction is strongest in the [001] direction. Coalescence of the chains results in the $p(2 \times 1)$ phase. It should be noted that STM cannot detect mobile species. Therefore, the adsorbed oxygens, Cu adatoms, and extremely short $-Cu-O-$ chains did not appear in the STM images. These studies clearly illustrate that the structure of a metal surface is not static but changes dynamically by chemisorption of an adsorbate.

17.2.2.2 **Diffusion**

Diffusion of a molecular adsorbate on a solid surface comprises an important elementary step in heterogeneous catalysis. It has been demonstrated that STM is capable of providing atomic-scale data on the surface diffusion. An Ru(0001) surface exposed to NO was observed by STM at room temperature [16, 17]. The NO molecules adsorb dissociatively on the surface at this temperature. More importantly, steps on the surface were found to be the active sites of the adsorption, and adsorbed species were present exclusively at these sites soon after the NO exposure. The N and O atoms were easily discriminated from each other on the basis of their different appearances in STM images. Although both atoms were imaged as depressions, the oxygen atoms appeared with streaky lines, which reflected their high mobility on the surface compared with the nitrogen atoms. Figure 17.7a and b show the STM images of the Ru(0001) surface taken after 6 min and 2 h after the NO exposure, respectively. One can clearly see that the N atoms localized sharply around the step running in the top right area of the image under the initial conditions (Figure 17.7a) and diffused away from the step (Figure 17.7b). This time-lapse imaging was successfully applied to the determination of the diffusion constant of the adsorbate, and temperature-dependent measurements allowed the estimation of the activation energy for the diffusion. Diffusion experiments have sometimes suffered from unwanted effects of impurities, defects, which are common even on a well-prepared single-crystal surfaces, and adsorbate–adsorbate interactions. This study avoided these difficulties by the use of well-defined terraces confirmed by STM and the low surface concentration of N atoms.

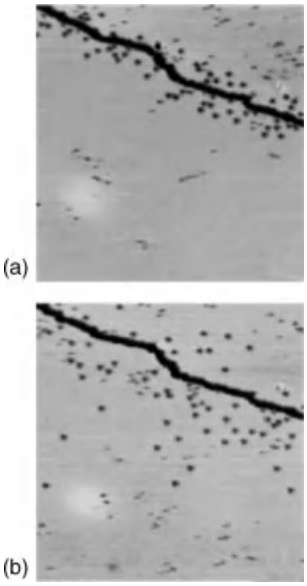


Figure 17.7 (a) STM image of Ru(0001) recorded 6 min after adsorption of 0.1 l of NO at 300 K. Image size, $18 \times 20\,nm^2$; bias voltage, -0.6 V; set-point current, 1 nA. (b) Same area after 2 h. Reprinted with permission from [17]. Copyright 1996 the American Physical Society.

Adsorption of carbon monoxide is a key issue in catalysis and has been thoroughly studied by a variety of experimental techniques. A CO overlayer structure on Ni(110) was elucidated by STM [18]. Observation of adsorbed CO molecules was impossible when the adlayer was below saturation coverage. This "transparency" of CO is attributed to its high mobility on the surface at room temperature, such as hindered translation and rotation. A saturated adlayer of CO on the surface was therefore employed for the STM study. Under this experimental condition, the CO molecules were firmly immobilized on the surface, allowing direct imaging of each adsorbate. However, the atomic structure of the underlying substrate was unknown in the presence of the saturated overlayer because only the outermost surface is generally observed in STM. This result hampers the direct determination of the surface bonding geometry of the CO molecules. However, the bonding site of CO can be assigned by means of a coadsorbed reference overlayer. The Ni(110) surface was pre-exposed to a small amount of sulfur, which is known to adsorb in twofold hollow sites on Ni(110) [19], followed by subsequent CO exposure. Simultaneous STM observation of the CO and S overlayers that coexist on the same substrate revealed that the CO bonded in short bridge sites on the basis of the known S bonding site. Consistent results were obtained with the use of an oxygen reference adlayer.

STM operating at low temperatures allows detailed analysis of diffusion behavior because of the reduced mobility of the adsorbate. The diffusion of CO on the Cu(110) surface was investigated by STM in the temperature range 42–53 K [20]. At these temperatures, each CO molecule was clearly resolved in the STM images even at low

surface coverages. It was revealed that the CO molecule was adsorbed on the atop site on the basis of the concurrent observation of the isolated molecule and atomic structure of the substrate. In addition to the isolated species, CO dimers and longer chains were found on the surface. The chain formation was attributed to an attractive interaction between the CO molecules. The mobility of these adsorbed species was evaluated by consecutive STM imaging at constant temperature. The diffusion of the molecular chain took place by successive jumps of its constituent CO molecules. Nevertheless, it was found by the STM measurements that the chains diffuse substantially faster than the isolated single molecule. Arrhenius plot analysis of the CO hopping observed by STM revealed comparable activation energies for the isolated molecule and molecular chain. The pre-exponential factor in the Arrhenius law was significantly higher for the chain than for the single molecule, which is responsible for the faster diffusion. As indicated by these results, STM at low temperatures can be used to probe surface diffusion of an adsorbate weakly bound to a metal surface. However, care must be taken in extrapolating the data obtained under these conditions to higher temperatures.

It should be noted that the STM tip can influence the surface diffusion of adsorbates. Therefore, in diffusion experiments by STM, the interaction between the tip and adsorbate should be minimized by carefully choosing the tunneling parameters, such as set-point currents and bias voltages. Also, the tunneling electrons in STM can induce surface diffusion. When a bias voltage larger than a certain threshold value is applied between the STM tip and the adsorbate, the tunneling electrons cause excitation of adsorbate–substrate vibration modes (inelastic tunneling) [21]. The lateral hopping of a CO molecule induced by the inelastic process was investigated, and it was demonstrated that such hopping is useful in fundamental studies of the surface diffusion [22]. STM observations were carried out for CO adsorbed on a Pd(110) surface at 4.8 K. The thermal diffusion of CO on the surface was negligible at this temperature, and no lateral motion was observed by STM imaging using common tunneling parameters (bias voltage 100 mV and tunneling current 1 nA). CO lateral motion was induced when a higher bias voltage (350 mV) and set-point current (7 nA) were employed (Figure 17.8a and b). The hopping probability was measured as a function of the bias voltage, and a threshold energy of 240 meV was found. The excitation energy of the C−O stretching mode agrees well with the threshold energy, and this result suggests that the excitation of this vibration mode accounted for the CO hopping. The CO molecules diffused only along the $[1\bar{1}0]$direction of the Pd(110) surface. The CO motion was visualized by scanning the STM tip only in this direction, as shown in Figure 17.8c and d. The x- and y-axes of these images correspond to the position along the $[1\bar{1}0]$ direction and passage of time, respectively. One can clearly see the negligible (Figure 17.8c) and frequent (Figure 17.8d) hopping of the CO molecule with the bias voltages below and above the threshold voltage, respectively.

17.2.2.3 **Surface Reactions**

A chemical reaction on a solid surface is clearly the most important step among the elementary steps in heterogeneous catalysis. A wide range of analytical techniques

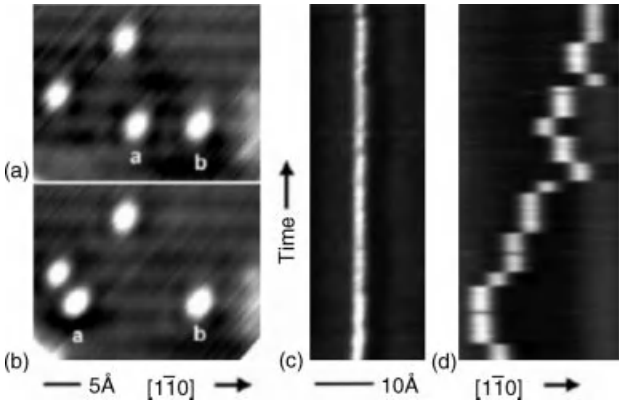


Figure 17.8 (a), (b) STM images of four CO molecules on Pd(110). One of the CO molecule labeled "a" moved by hopping induced by tunneling electrons between (a) and (b). Image size, $3.1 \times 2.5\,nm^2$; bias voltage, 50 mV; set-point current, 1 nA. (c), (d) Time lapse STM images of an isolated CO molecule on Pd(110). The scanning was restricted to a single Pd row along the [1$\bar{1}$0] direction. Bias voltage: (c) 200 and (d) 300 mV. Reprinted from [22].

are available to investigate the kinetics of surface reactions, which provide averaged information about the reactions. By contrast, STM allows direct visualization of surface reactions in real space at the single atom level, and such observations have revealed detailed mechanistic effects of surface reactions, such as formation/consumption of reactant domains and site-specific reactivities.

The catalytic oxidation of CO to CO_2 over oxygen-covered Cu(110) was studied by STM at 400 K [23]. As described above, oxygen forms a well-ordered $p(2 \times 1)$ phase on the Cu(110) surface. The oxygen rows grow along the [001] direction and organize into islands 7–9 rows thick. The reaction of the adsorbed oxygen with CO was examined. The CO oxidation is known to proceed via a Langmuir–Hinshelwood process, where a reaction takes place between adsorbed reactants. The CO molecule, therefore, should first adsorb on the surface and diffuse to react with the adsorbed oxygens. The CO molecules cannot be imaged by STM because of the short lifetime and significantly low equilibrium concentration of CO on the surface. However, the time evolution of the oxygen islands during the reaction gave a invaluable insight into the reaction. Sequential STM images revealed that the oxygen rows at the perimeter of the $p(2 \times 1)$ phase first reacted with CO and disappeared, as can be seen in Figure 17.9. It was found that the CO oxidation occurred predominantly at defects in the oxygen overlayer, such as the end of the −Cu−O− chain or kink. Comparison of the STM results with Monte Carlo simulation suggested that the defect sites were 500–1000 times more reactive than non-defect sites. The higher reactivity was attributed to the decreased stability of the oxygen atoms at the defects. A detailed knowledge of the reaction was gained by a variable-temperature STM study [24]. The CO oxidation on the oxygen-covered Cu(110) surface was examined at 150 K. At this temperature, oxygen exposure resulted in the formation of short −Cu−O− chains, which is different from the $p(2 \times 1)$ overlayer observed at 400 K. In addition, CO

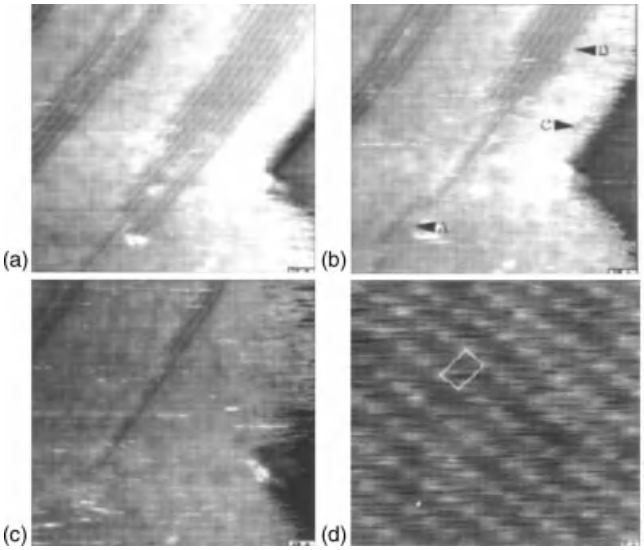


Figure 17.9 (a)–(c) Sequential STM images of $p(2 \times 1)$-O reduced by CO. The time between each frame is 150 s. The Co exposures for (a), (b), and (c) are 1.31×10^5, 1.47×10^5, and 1.63×10^5 l, respectively. Image size, $22 \times 20\,nm^2$; bias voltage, -25 mV; set-point current, 1 nA. (d) STM image of the clean Cu (110) surface after the complete consumption of the adsorbed oxygen. Image size, $3.5 \times 3.0\,nm^2$; bias voltage, -17 mV; set-point current, 1.7 nA. Reprinted with permission from [23]. Copyright 1996 Elsevier.

molecules formed long molecular chains that can be imaged by STM due to the reduced thermal diffusion at the low temperature. The CO molecular chains were oriented along the $[1\bar{1}0]$ direction, perpendicular to the $-$Cu$-$O$-$ chains. The neighboring CO and $-$Cu$-$O$-$ chains were found to exist stably, indicating that the CO oxidation did not proceed at this temperature. However, the CO chains disappeared and CO_2 was formed when the CO-covered surface was exposed to oxygen. This result was attributed to higher reactivity of intermediate atomic oxygen that adsorbed weakly and had not yet formed the $-$Cu$-$O$-$ chain.

CO oxidation on a Pt(111) surface was visualized by STM [25]. The experiment was performed at a low temperature (274 K), reducing the reaction rate in order to monitor the reaction process easily by STM. The Pt(111) surface was first covered with a submonolayer of oxygen. The adsorbed oxygens, observed as dark depressions in the STM images, exhibit a (2×2) structure, consistent with previous observations. Series of STM images were recorded while the sample surface was exposed to constant CO pressures. During the exposure, the area of the (2×2) islands decreased, which indicated the progress of the reaction. At the same time, CO islands having $c(4 \times 2)$ structures emerged. No CO_2 molecules that should be produced by the reaction appeared in the STM images since they desorb immediately after their formation (Figure 17.10). These observations demonstrated that the CO oxidation takes place only at the boundary between oxygen and CO islands. This conclusion is corrborated by the reaction rate determined from the time-lapse STM

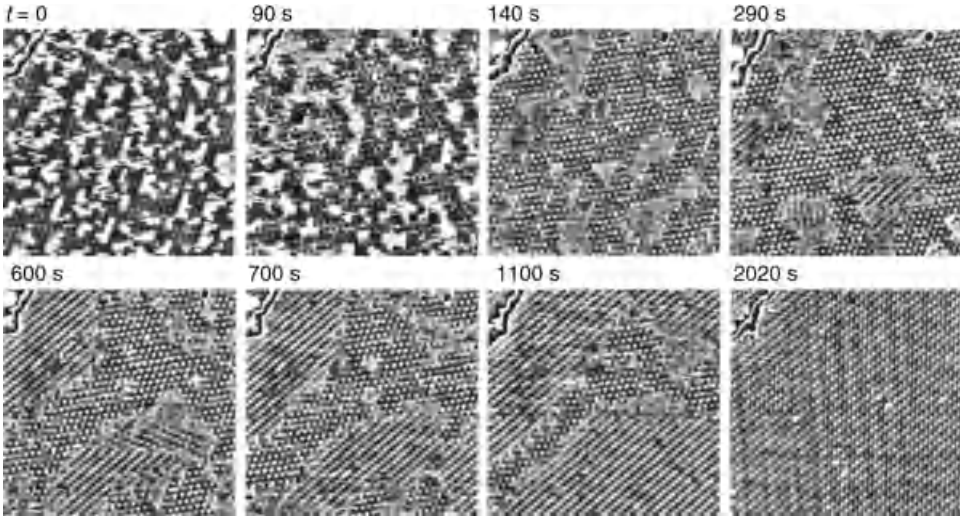


Figure 17.10 Series of STM images recorded during the reaction of adsorbed oxygen atoms with co-adsorbed CO molecules at 247 K. All images were recorded at the same area of the Pt(111) surface. Image size, $18 \times 17\,nm^2$; bias voltage, 0.5 V; set-point current, 0.8 nA. Reprinted from [25].

imaging. As expected, the reaction rate was proportional to the length of the boundaries between the O and CO islands.

Catalytic oxidation of ammonia has been the subject of extensive research. X-ray photoelectron spectroscopy (XPS) and high-resolution electron energy loss spectroscopy (HREELS) studies revealed that ammonia oxidation took place by coadsorption of ammonia and oxygen on the Cu(110) surface [26, 27]. The oxidation reactions afford various nitrogen-containing species on the surface, that is, amide (NH_2), imide (NH), and atomic nitrogen (N), depending on the reaction temperature. STM investigations were performed to observe directly the ammonia oxidation by exposing the Cu(110) precovered with oxygen to ammonia [28]. As described previously, oxygen forms −Cu−O− chains along the [001] direction on the Cu(110) surface, and these chains organized into a well-ordered $p(2 \times 1)$ overlayer at increased coverages. It was observed by STM that the −Cu−O− chains were shortened and finally disappeared upon exposure to NH_3 at 300 K. Simultaneously, new chain structures along the $[1\bar{1}0]$ direction, perpendicular to the −Cu−O− chain, appeared, and this structure was attributed to the surface NH species on the basis of the XPS and HREELS results [26, 27]. Similar results were obtained for NH_3 oxidation by preadsorbed $p(2 \times 1)$ oxygen islands (Figure 17.11). The $p(2 \times 1)$ island and adsorbed NH chains were resolved in the lower-left and middle parts of the STM images in Figure 17.11, respectively. The time-lapse images clearly revealed that oxygen atoms at the edge of the $p(2 \times 1)$ island were consumed at a rate of 2–5 atoms min^{-1}. These results led to the conclusion that the NH_3 oxidation proceeds by consuming the oxygen atoms in the −Cu−O− chains to produce NH adsorbates. The reaction was similarly monitored at the elevated temperature, 400 K, where a fraction of the

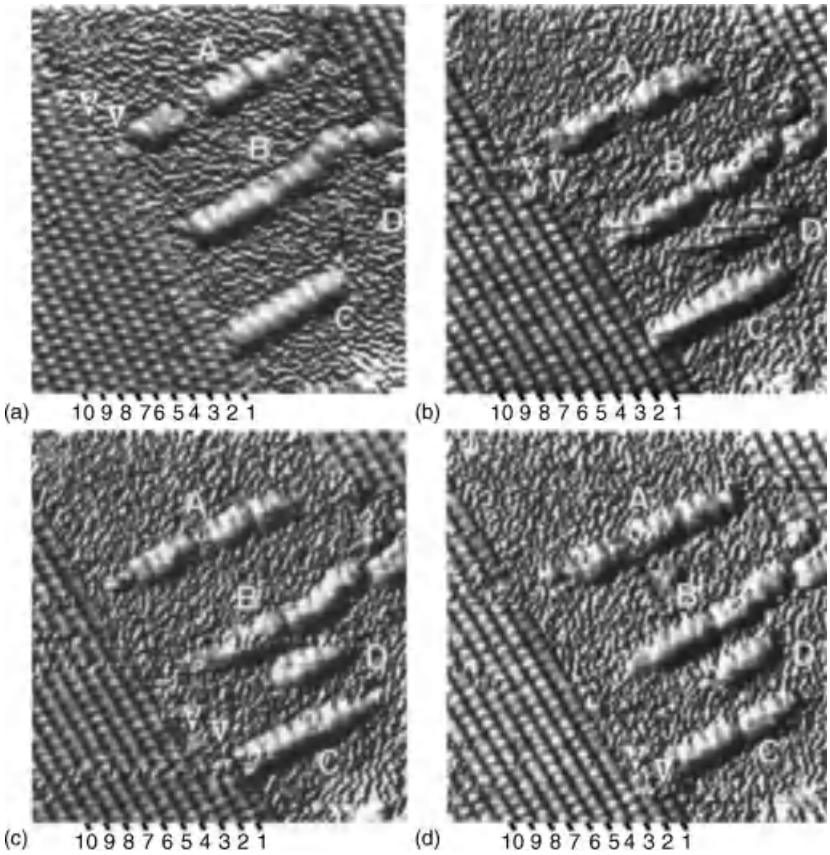


Figure 17.11 Sequential STM images of an oxygen-preadsorbed Cu(110) surface under an ammonia pressure of 2×10^{-9} Torr at 300 K. The time between each frame is 205 s. Bias voltage, −84.9 mV; set-point current, 1.24 nA. Reprinted with permission from [28]. Copyright 1996 the Royal Society of Chemistry.

adsorbed NH was further oxidized to atomic nitrogen by surface reaction. In addition to the $p(2 \times 1)$-O overlayers, randomly distributed bright spots were observed in the STM images. These features were interpreted as NH and N species, which were proved to be stable on the surface at this temperature by XPS and HREELS [26, 27]. Some −Cu−O− chains adjoining the bright spots were found to persist stably, indicating that the oxygen atoms in these chains were unreactive towards the oxidation reaction. It was proposed that the atomic nitrogen, observed as bright spots, inhibited the surface reaction by blocking the −Cu−O− chains.

NH_3 oxidation on Ni(110) preadsorbed with oxygen was investigated by STM at room temperature [29]. The clean Ni(110) surface was exposed to oxygen at 420 K, which resulted in the formation of −Ni−O− rows along the [001] direction. New rows parallel to the −Ni−O− row appeared upon exposing the sample to NH_3, and these rows were ascribed to OH species. The formation of the OH species

resulted from reaction between NH_3 and the terminal oxygen atom of the $-Ni-O-$ row as

$$-Ni-O-Ni-O + NH_3 \rightarrow -Ni-O-Ni + OH(a) + NH_2(a)$$

The other product of the reaction, NH_2, was confirmed by formation of the well-known $c(2 \times 2)$ structure of NH_2 after prolonged exposure to NH_3.

NH_3 oxidation was examined also by coadsorption of ammonia and oxygen on a clean Cu(110) surface [30]. The STM image of the surface exposed to an NH_3–O_2 (30:1) mixture revealed that chains of chemisorbed NH aligned in the $[1\bar{1}0]$ direction closely covered the surface. The inter-chain spacing was uniform and found to be 7.2 Å. The separation between the NH species along the chain could not be inferred from STM because of the limited spatial resolution of the image. However, the $NH-NH$ spacing was estimated on the basis of the inter-chain separation determined by STM and the N 1s spectrum of *in situ* XPS. This study demonstrates that the combination of STM with *in situ* XPS is powerful technique in research on chemically heterogeneous surfaces.

17.2.2.4 **High-Pressure Environment**

STM studies as described above have advanced the atomistic understanding of catalytically relevant phenomena on a well-defined single-crystal surface, such as adsorption, diffusion, and reaction of adsorbates, in UHV. However, it is not necessarily clear whether the knowledge gained under well-controlled UHV conditions can apply to a real catalyst, because catalytic reactions are usually performed at high pressures. STM can operate not only in UHV but also at ambient and even high pressures, and thereby bridge the gap between the model systems extensively studied in UHV and catalytically active surfaces at high pressures. High-pressure STM (HP-STM) was developed for *in situ* investigations of such surface structures. The first HP-STM instrument was installed in a reaction chamber connected to the UHV system through a transfer cell. The surface structure of Pt(111) under atmospheric pressure of hydrogen, oxygen, or carbon monoxide was visualized by HP-STM [31]. The Pt(111) surface in H_2 was found to consist of parallel rows along the $[\bar{1}10]$ direction, resulting from missing-row reconstructions. In CO, flat terraces separated by steps were seen on the surface, and this observation agreed with the result that the surface reconstruction was lifted by CO in UHV. Large hill and valley structures merged on the surface in O_2 owing to the formation of enlarged (111) microfacets. This reconstruction was ascribed to occupation of the threefold hollow sites by O_2.

The adsorption of CO on the Pt(111) surface was investigated in atomic detail at room temperature over the pressure range 10^{-6}–760 Torr [32]. STM images of the sample surface exhibited Moiré structures, as shown in Figure 17.12. The Moiré patterns arose due to periodic modulation of the tunneling current by superposition of the hexagonally arranged CO adsorbate and underlying Pt(111) surface atoms. Because the atomic arrangement of Pt(111) is well known, the lattice constants of the CO overlayer could be deduced from the periodicities of the Moiré patterns, which were measured by fast Fourier transforms of the STM images. In addition, the CO coverage was calculated from the lattice constants of the adsorbate molecules and

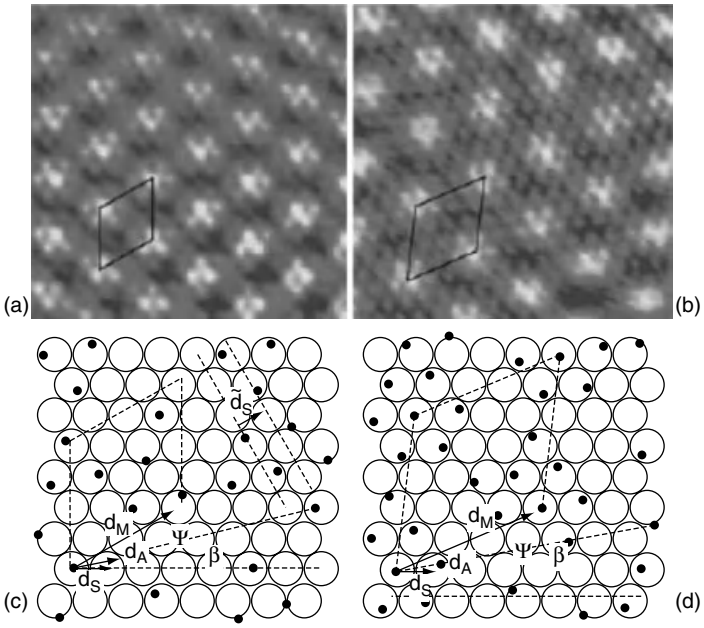


Figure 17.12 STM images of the Moiré superstructures of CO on Pt(111) at room temperature. (a) Observed at a CO pressure of 10^{-2} Torr. Image size, $5.5 \times 5.5\,nm^2$; bias voltage, 8.2 mV; set-point current, 1.06 nA. (b) Observed at a CO pressure of 720 Torr. Bias voltage, 4.9 mV; set-point current, 1.27 nA. (c), (d) Ball models of the Moiré superstructures of (a) and (b), respectively. Reprinted with permission from [32]. Copyright 2004 the American Chemical Society.

substrate atoms. It was found that the CO coverage increased continuously as the CO gas pressure increased. However, the coverage saturated before the gas pressure reached atmospheric pressure because of repulsive CO−CO interactions. The adlayer structure of CO at saturated coverage was in agreement with those observed at low temperature in UHV [33], indicating that there was no noticeable effect of the high-pressure environment on the CO adsorption in this system. In contrast, a new overlayer structure was found for nitrogen monoxide on Rh(111) [34]. In addition to a (2×2) structure of NO, which is known at low pressure, HP-STM observations revealed the formation of a new (3×3) structure in equilibrium with the gas phase at high pressure.

Poisoning of ethylene hydrogenation by CO was studied with HP-STM [35]. A Pt (111) surface was exposed to 20 mTorr of ethylene and hydrogen. Whereas the formation of hydrogenated product, ethane, was confirmed by mass spectrometry (MS), no ordered structure was found by STM. The results indicated the fast surface diffusion of the reactants and product of the hydrogenation reaction. Upon addition of CO to the gas mixture, the STM images revealed the formation of an ordered structure. At the same time, no ethane production was detected by MS. The ordered adlayer was found to be a $(\sqrt{19} \times \sqrt{19})R23.4^\circ$ structure, which is similar to the

structure observed at the same pressure of CO. The presence of the stable CO adlayer suppresses the catalytic reaction by reducing the mobility of the adsorbed and intermediate species by blocking their adsorption. This study demonstrated that the diffusion of the surface species is very important for catalytic reactions.

Destruction of a bimetallic catalyst by high-pressure CO was revealed by STM [36]. When Au/Ni(111) catalysts were exposed to CO at room temperature, numerous clusters appeared on the surface, which was atomically smooth before the exposure. The height and coverage of these clusters were consistent with the Au monatomic step height and initial Au coverage in the Au/Ni alloy, respectively. Therefore, it was concluded that the clusters were composed of Au and formed by selective evaporation of Ni from the alloy surface. The removal of Ni was monitored *in situ* by HP-STM at a CO pressure of 10 Torr (Figure 17.13). One can clearly see in the time-lapse STM images that Ni atoms evaporated from the step edges of the surface. It was found that the rate of Ni removal was linearly dependent on the CO pressure. The formation of nickel carbonyl complexes and their subsequent desorption were ascribed to the Ni removal, and this model was supported by calculations using density functional theory.

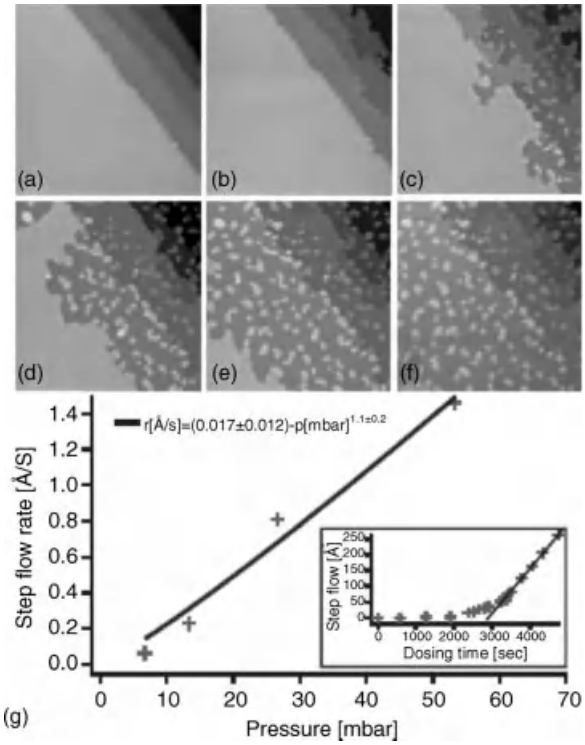


Figure 17.13 (a)–(f) Sequential STM images of an Au/Ni(111) surface recorded in 10 Torr CO. Time of CO exposure: (a) 0, (b) 25, (c) 50, (d) 75, (e) 100, and (f) 125 min. Image size, 100 × 100 nm. (g) Plot of the reaction rate of Ni removal as a function of the CO pressure. Reprinted with permission from [36]. Copyright 2005 the American Physical Society.

17.2.3
Solid–Liquid Interfaces

The solid–liquid interface plays a fundamental role in a wide range of chemical processes, including heterogeneous catalysis. One of the prominent advantages of STM is its wide applicability in a variety of environments, in contrast to other techniques for surface analysis operated typically only in UHV. The first study of STM in solution was reported for the surface of highly oriented pyrolytic graphite (HOPG) submerged in water [37]. After this pioneering work, extensive research was conducted to provide an atomistic understanding of the electrochemical interfaces and processes.

When the STM tip is immersed in an electrolyte solution, the bias voltage between the tip and sample causes a faradaic current, associated with electrochemical processes, in addition to the tunneling current. The faradaic current is independent of the tip–sample distance and can be much larger than the tunneling current. STM observations cannot be properly carried out under this circumstance. Therefore, tips must be insulated except for their apices. The faradaic current is suppressed by the insulation while the tunneling current is detected at the exposed apices. Various methods have been reported for producing these insulated tips, and coating metal STM tips with Apiezon wax is a convenient and popular choice [38]. Alternatively, electrophoretic painting has been applied to insulate STM tips [39]. In addition to the tip insulation, an electrochemical bipotentiostat is required for STM observation in solutions. The bipotentiostat allows independent control of the two working electrodes, that is, the STM tip and substrate, with respect to a reference electrode (Figure 17.14). Pt wires are frequently employed as the (quasi-)reference electrode because of their simplicity and because they are less likely to contaminate the solution, unlike an Ag/AgCl reference electrode. Under this potential control, the sample potential can be chosen so as to investigate the effects of the potential on the properties of solid–liquid interfaces.

The preparation of a well-defined single-crystal surface is essential in order to elucidate the surface structure and reactivity of solid–liquid interfaces. Fortunately, a convenient and reliable method [40, 41] is available to prepare such single-crystal electrodes of noble metals (Au, Pt, etc.). This method, called flame annealing, consists in mechanical and/or electrochemical polishing of the electrode surface,

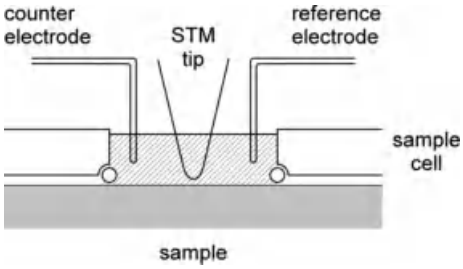


Figure 17.14 Schematic illustration of STM observation in aqueous solutions.

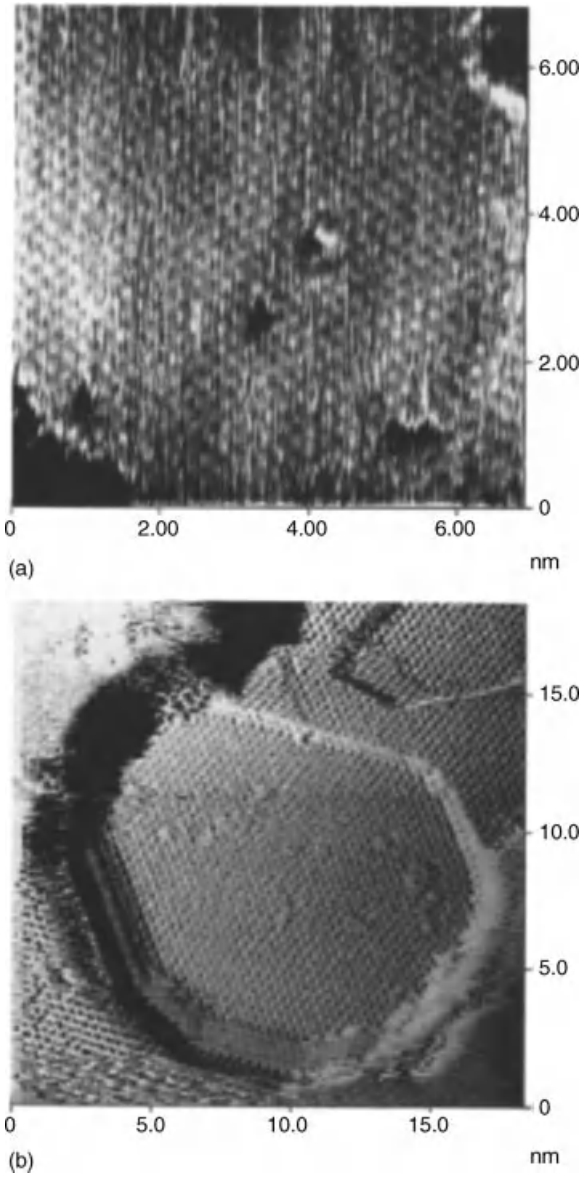


Figure 17.15 STM images of a Pt(111) surface. Reprinted with permission from [42]. Copyright 1995 Elsevier.

annealing in a flame, and cooling in air or in pure water. Figure 17.15 shows an STM image of a Pt(111) surface prepared by the flame-annealing method observed in a solution of 10 mM $KClO_4$ (pH 4) and 3 mM KBr [42]. The image exhibited the unreconstructed Pt(111) structure, and individual Pt atoms were clearly seen on the

flat terraces. The Br atoms could not be observed in the image because of their rapid diffusion on the surface.

17.2.3.1 Surface Reconstruction

Surface atoms rearrange their position by lateral displacement relative to the positions expected for the ideal bulk structure because of the highly asymmetric environment on a surface compared with that in bulk. This phenomenon, surface reconstruction, has been a major topic in surface science, and understanding the reconstruction provides a critical insight into surface topological effects in catalysis. Surface reconstruction has been extensively studied in UHV primarily by LEED. It was demonstrated that STM yields detailed *in situ* information on the reconstruction at the atomic level. Furthermore, STM offers a unique opportunity to explore the effect of surface electronic states on the reconstruction by precise control of the surface potential. For example, atomically resolved STM imaging was reported for surface structures of an Au(100) surface as a function of electrode potential [43]. The sample surface was prepared by the flame annealing method and transferred to the STM cell containing 0.1 M $HClO_4$ solution as an electrolyte. The STM image acquired at 0.2 V versus a saturated calomel electrode (SCE) showed large flat terraces, where individual Au atoms in an unconstructed arrangement were observed. *In situ* STM imaging revealed a dramatic structural change on the surface induced by a decrease in the electrode potential from 0.2 to −0.4 V vs. SCE. The flat terraces progressively transformed into corrugated domains during the potential excursion. The separation between the corrugations was 14.5 ± 0.5 Å, which is equal to five interatomic separations of Au. The structural change resulted in a quasi-hexagonal close-packed arrangement of the surface Au atoms, as clearly observed by STM, agreeing with the previous results obtained in UHV. On the basis of these observations, the potential-induced structural change was assigned as a (1×5) reconstruction. It was suggested that the corrugation, or height differences among the surface atoms, arose from the commensurability between the atom positions of the first and second surface atomic layers. Returning the electrode potential to 0.2 V vs. SCE caused the reconstruction to disappear, demonstrating reversibility of the potential-induced reconstruction of the surface. It was shown that the reconstruction took place at a potential where specific adsorption of anions was negligible. This result indicates that the reconstruction was driven not by such adsorption but by the charge density of the electrode surface.

Surface reconstructions at other low- and high-index surfaces of Au and other materials have been investigated by STM in electrochemical environments [44, 45]. In almost all cases, the results obtained by STM in solution are in agreement with those obtained in UHV by *ex situ* experimental techniques. It is shown that STM provided a detailed *in situ* structural insight into solid–liquid interfaces at the atomic level.

17.2.3.2 Specifically Adsorbed Anions

Adsorption of anions on an electrode surface has been extensively studied by electrochemistry. In addition to its fundamental importance in describing an

electrical double layer at the solid–liquid interface, anion adsorption is known to affect a variety of chemical processes on electrodes. Adsorption of halides on an electrode surface, such as Pt and Au, has been widely investigated owing to the strong interactions between these anions and metal surfaces. *Ex situ* surface characterization techniques in UHV, including LEED, can provide structural information on the halide adlayers on the electrodes. In addition, their local structure and structural transformations at the atomic level can be directly visualized *in situ* by STM. The first STM imaging of an iodine adlayer was carried out for a Pt(111) surface prepared by flame annealing and subsequently exposed to gaseous iodine [46]. The resultant STM images of this surface obtained in air exhibited two kinds of adlattice unit cell. The first is a $(\sqrt{7} \times \sqrt{7})R19.1^\circ$ unit cell with an interatomic distance of 0.424 nm, and the other a (3×3) unit cell with an interatomic distance of 0.417 nm. Later, the (3×3) overlayer structure of the iodine adlayer was confirmed on a Pt(111) surface in aqueous solution [46]. The iodine adlayers on different crystal faces, such as Pt(110) and Pt(100), were also investigated and different overlayer structures were found thereon. Iodine exhibits weaker adsorption to Au surfaces than to the Pt surfaces, and consequently potential-dependent rearrangements of the adlayer were found on Au surfaces. At low electrode potential, a $(\sqrt{3} \times \sqrt{3})R30^\circ$ adlayer of iodine was observed on an Au(111) surface [47–50], and this structure was consistent with an *ex situ* LEED experiment. It was reported that the $(\sqrt{3} \times \sqrt{3})R30^\circ$ structure changed to a (3×3) close-packed structure at increased electrode potential [47]. In addition, continuous compression of the iodine adlayer was observed [49, 50]. With increase in electrode potential, the $(\sqrt{3} \times \sqrt{3})R30^\circ$ adlattice was compressed along the <110> direction of the Au(111) substrate. This adlayer structure was described as a $c(p \times \sqrt{3}R{-}30^\circ)$ phase, where p decreased from 3 to ~2.5 with increasing electrode potential. At higher potential, the STM observations revealed a hexagonally symmetric structure different from $c(p \times \sqrt{3}R{-}30^\circ)$. The STM image exhibited Moiré patterns in the adlayer structure, which resulted from different adsorption sites of the neighboring iodine atoms on the Au substrate. The periodicity of the Moiré pattern also decreased with increasing potential, reflecting the decrease in the interatomic distance between the iodine atoms in the adlayer.

In addition to halides, specific adsorption of sulfate (SO_4^{2-}) and bisulfate (HSO_4^-) on metal surfaces has been widely studied by STM in solution because of its relevance to earlier electrochemical studies. The first STM observation [51] indicated that a $(\sqrt{3} \times \sqrt{7})$ bisulfate adlayer was formed on Au(111) in aqueous sulfuric acid solutions at high potentials (Figure 17.16). The calculated surface coverage of the anion of the $(\sqrt{3} \times \sqrt{7})$ structure was 0.4. Later, this adlayer was further investigated by a combined analysis of infrared reflection–absorption spectroscopy (IRAS) and STM [52]. The IRAS measurements indicated the presence of sulfate anions in the adlayer and a surface coverage of 0.2. On the basis of this observation, it was suggested that hydronium cations coadsorbed with sulfate anions on the Au(111) surface. This interpretation agreed with the sulfate surface coverage of 0.2 revealed by the IRAS study. This study highlights the importance of combining STM with other spectroscopic techniques. In addition, it should be noted that the discrimination of different ions or chemical species in STM images is often difficult.

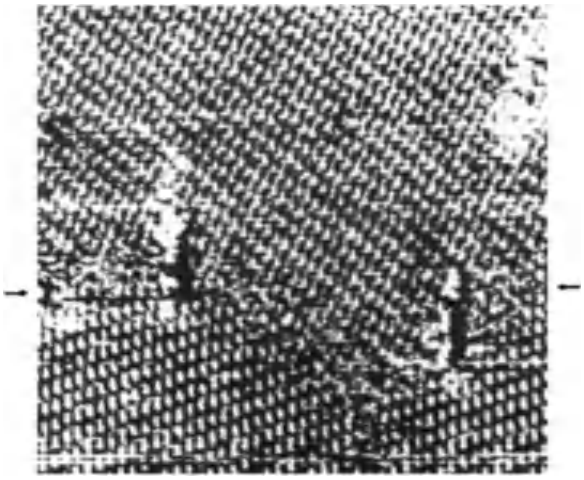


Figure 17.16 STM image of a bisulfate adlayer on Au(111) observed in 0.5 M H_2SO_4. Image size, $21 \times 24\,nm^2$; set-point current, 10 nA. Reprinted with permission from [51]. Copyright 1992 the Royal Society of Chemistry.

A similar adlayer was found on Rh(111) in H_2SO_4. STM observation of the Rh(111) surface in 0.1 M $HClO_4$ revealed an unreconstructed (1×1) structure of the metal surface, indicating that chemical species such as water molecules were invisible under these experimental conditions due to their rapid diffusion on the surface [53]. The sulfate overlayers defined by the $(\sqrt{3} \times \sqrt{7})$ structure on Rh(111) in 0.5 M H_2SO_4 was visualized by STM (Figure 17.17). In this case, bright and dark spots were observed in the $(\sqrt{3} \times \sqrt{7})$ adlayer. The bright spots were ascribed to sulfate or bisulfate anions, whereas the dark spots were interpreted as water molecules that form hydrogen-bonded chains between them on the basis of geometric consideration of the interatomic spacings of the $(\sqrt{3} \times \sqrt{7})$ structure.

17.2.3.3 **Molecular Adsorbates**

Organic molecules are promising building blocks of functional interfaces, including catalysis, photovoltaic devices, and miniaturized electronic devices. Because of their chemical diversity, organic molecules often display complex and interesting adsorption geometries and phenomena on solid surfaces. A variety of techniques, such as infrared and Raman spectroscopy and LEED, have been applied to investigate the adsorbed structures and molecular orientations of molecular adsorbates. Among them, STM offers a unique opportunity to visualize directly the adsorbed structures on a single-molecule basis.

Adsorption of benzene, a simple aromatic molecule, on an Rh(111) surface was investigated by STM in HF solution [54]. After confirming the (1×1) structure of the Rh(111) electrode by STM in the solution, a small amount of a benzene solution was injected into an STM cell. The subsequent STM imaging showed the appearance of a well-ordered benzene adlayer of a $c(2\sqrt{3} \times \sqrt{3})$*rect* structure at an electrode potential of 0.45 V versus a reversible hydrogen electrode (RHE). It was found that application

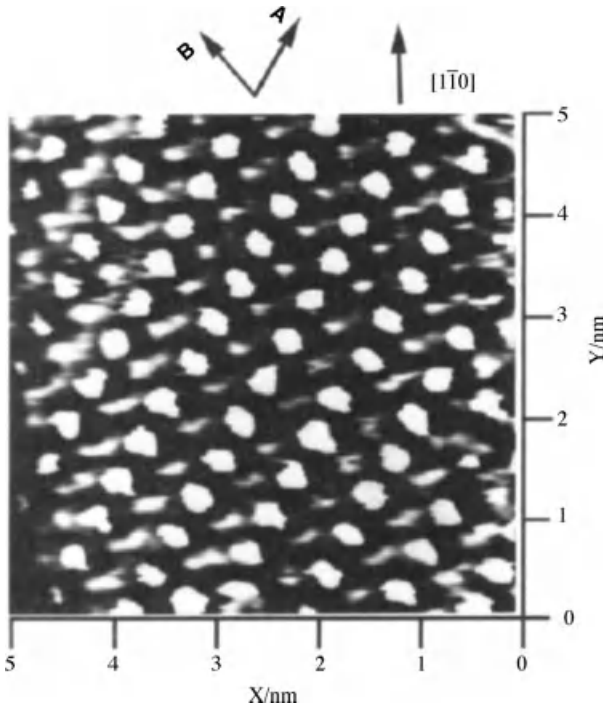


Figure 17.17 STM image of a sulfate adlayer on Rh(111) observed in 0.5 M H_2SO_4. Image size, $5 \times 5\,nm^2$; set-point current 20 nA. Reprinted with permission from [53]. Copyright 1995 the American Chemical Society.

of a negative potential step to 0.35 V vs. RHE resulted in transformation of the overlayer structure from a $c(2\sqrt{3} \times \sqrt{3})rect$ to a (3×3) structure (Figure 17.18). The transformation resulted from partial desorption of benzene molecules from the metal surface by the potential step. Each benzene molecule appeared as a triangular-shaped protrusion in the image in Figure 17.18. In addition to the adlayer structure, an internal structure of a single benzene molecule can be clearly seen; the triangular protrusion consisted of three small spots with similar intensity. Moreover, it is noteworthy that this adlayer structure observed in the solution is nearly identical with that observed in UHV for benzene molecules coadsorbed with carbon monoxide on Rh(111), except for the absence of carbon monoxide [55]. It was envisaged that water molecules or hydronium cations, instead of carbon monoxide, coadsorbed with benzene to stabilize the (3×3) overlayer.

Organic molecules at solid–liquid interfaces constitute excellent model systems to explore a broad range of surface phenomena. Adsorption of 2,2′-bipyridine (22BPY) on Au(111) was studied in 0.1 M $NaClO_4$ by STM under electrode potential control to investigate the order–disorder transition of the molecular adlayer as a function of the electrode potential [56]. Each sample molecule was observed as an elongated ellipse in the STM image, which reflects the molecular geometry. It was found that the 2BBPY molecules were adsorbed on Au(111) with their molecular planes perpendicular to

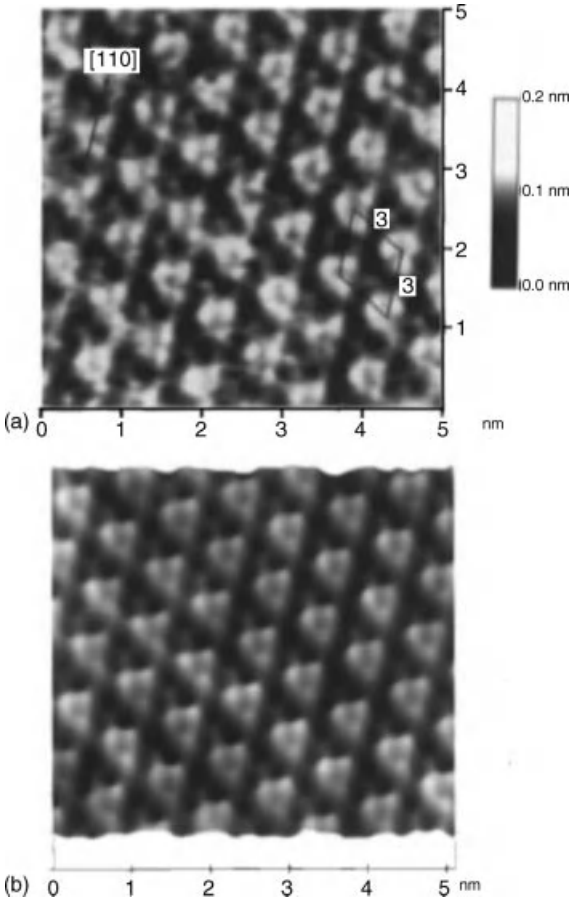


Figure 17.18 STM images of a benzene (3 × 3) adlayer on Rh(111) observed in 0.01 M HF. Bias voltage, 30 mV; set-point current 20 nA. Reprinted with permission from [54]. Copyright 1996 the American Chemical Society.

the surface. These standing molecules assembled themselves into a chain-like structure (Figure 17.19). At a low electrode potential of −0.1 V vs. SCE, the molecular chains are randomly oriented on the surface. Rearrangement of the chains induced by the electrode potential was visualized in real time by STM. The chains started to align themselves with one another, and a partially ordered domain emerged at 0.14 V vs. SCE. Further increase in the potential caused increase in the number of these domains. Finally, the ordered domains entirely covered the electrode surface at about 0.25 V vs. SCE. It was found that this potential-induced phase transition was reversible. The ordered domain transformed to disordered on decreasing the potential.

The supramolecular structures of molecular adsorbates on surfaces are controlled by rational design of chemical structures of the molecules. Controlled molecular architectures can be realized by utilizing intermolecular noncovalent interactions,

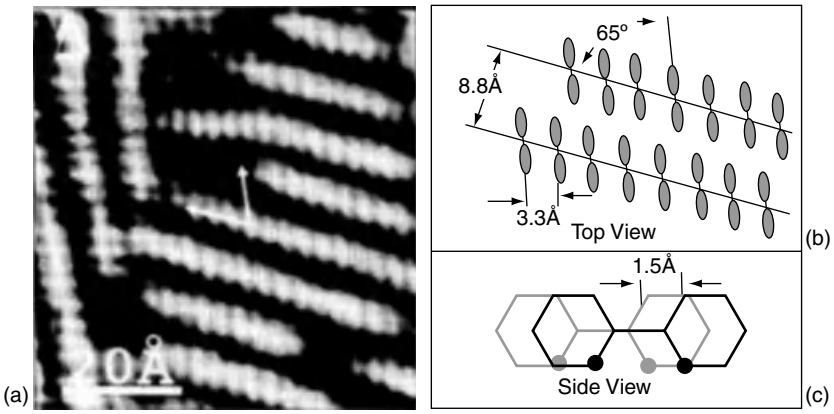


Figure 17.19 (a) STM image of a 22BPY monolayer on Au(111) in 0.1 M $NaClO_4$. (b), (c) A model for the packing structure of 22BPY. The filled circles in (c) represent nitrogen atoms of 22BPY. Reprinted with permission from [56]. Copyright 1995 the American Physical Society.

including hydrogen bonding, metal-coordination bonding, and dipole–dipole interaction. STM is a powerful tool to visualize the self-assembly process on the surface on a single-molecule basis [57, 58]. Supramolecular organization by self-assembly is nicely exemplified by successful control of supramolecular aggregates by careful placement of functional groups in molecular adsorbates in UHV [59]. Four kinds of porphyrin derivative were employed as sample molecules, and STM observations were carried out to investigate their adsorbed structure. The porphyrin bearing no cyanophenyl substituent formed a closely packed monolayer on an Au(111) surface. In contrast, replacing the dibutylphenyl group of the porphyrin with a cyanophenyl group resulted in the formation of supramolecular trimers on the surface. The porphyrins substituted with two cyanophenyl groups at *cis* and *trans* positions produced tetramers and extended wire structures, respectively. Each supramolecular structure was rationally explained on the basis of noncovalent dipole–dipole interactions between the cyano groups introduced in the porphyrins in a controlled manner.

Molecular adlayers are useful for functionalizing the solid surface. In addition, these adlayers can serve as scaffolds to immobilize other molecular species on the surface. Such host–guest complexation on a surface allows for construction of complicated multicomponent interfaces, which can offer sophisticated functionality. STM investigations were carried out to demonstrate the inclusion of fullerene into a surface-tethered calix[8]arene derivative, 5,11,17,23,29,35,41,47-octa-*tert*-butyl-49,50,51,52,53,54,55,56-octakis(carboxymethoxy)calix[8]arene (OBOCMC8) [60]. The structural details of the OBOCMC8 adlayer on Au(111) in 0.1 M $HClO_4$ was revealed by STM. In the absence of fullerene, closely packed arrays of calix-shaped structures having central cavities were observed, and naturally each calix was assigned to the OBOCMC8 molecule. In the presence of fullerene, these cavities were not observed, and bright spots surrounded by circular protrusions were observed instead. The spots and circles were attributed to fullerene and OBOCMC8,

respectively, demonstrating the successful construction and immobilization of the inclusion complexes on the surface. Similarly, fullerene–porphyrin complexation has been extensively studied by STM because of the potential application of these complexes in photovoltaic devices [61].

17.2.4 Chemical Selectivity

STM allows the direct visualization of surface topography and adsorbate structures at the atomic level as described above. However, STM does have disadvantages, one being its lack of chemical selectivity. It is often difficult to discriminate different atoms or molecules in STM images. The lack of chemical selectivity hampers the applicability of STM especially in characterizing catalyst surfaces, where a variety of chemical species, such as reactants, intermediates, and products, coexist. Consequently, STM has frequently been utilized in combination with spectroscopy for chemical identification. Recently, several techniques have been developed to permit chemically selective STM imaging.

17.2.4.1 Molecular Tip

The molecular tips are prepared by chemical modification of underlying metal tips typically with a self-assembled monolayer (SAM) of thiols, and the outermost single adsorbate probes electron tunneling to or from a sample molecule. Importantly, the tunneling current increases when sample and tip molecules undergo chemical interactions that provide overlap of their electronic wavefunctions, that is, hydrogen bonding, metal-coordination bonding, and charge-transfer interactions. The current increase is ascribed to the facilitated tunneling through the overlapped wavefunctions. It was demonstrated that this phenomenon can be utilized for the selective observation of chemical species to overcome the poor chemical selectivity in conventional STM [62, 63].

A fullerene molecular tip was used to observe porphyrin molecules adsorbed on the surface of HOPG [64]. Porphyrin and fullerene have been known to undergo a charge-transfer interaction. Therefore, this system is suitable for investigating the effect of charge-transfer interaction on the electron tunneling between electron-donating and -accepting molecules. Figure 17.20a shows an STM image of a cobalt(II) porphyrin (CoPor) monolayer observed with a gold tip, in which ordered arrays of porphyrin rings were observed. The porphyrin rings were found to have central protrusions when gold tips were used, as indicated by arrows in the STM image (Figure 17.20a). The protrusions are assigned to the central cobalt(II) ions. The large tunneling probability at the cobalt(II) ions has been suggested to result from d orbital-mediated electron tunneling in a resonant way, where the unoccupied orbitals of the half-filled d_{z^2} orbitals coherently couple to the states of the substrate. When the fullerene tips were used and electron tunneling between the single fullerene and individual porphyrin was measured, significantly different images were observed (Figure 17.20b). In strong contrast to Figure 17.20a, the cobalt(II) ions (arrows) were observed as depressions, and the pyrrole groups around the cobalt ions appeared as

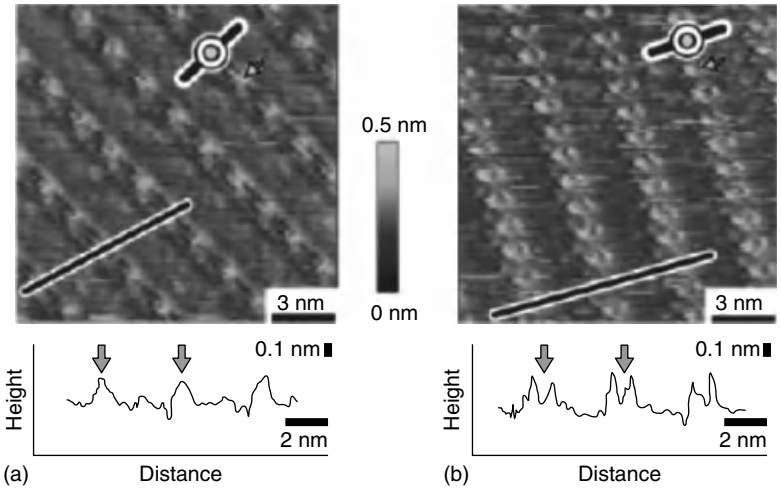


Figure 17.20 STM images of a CoPor adlayer on HOPG. (a) Observed with an unmodified gold tip. Bias voltage, −1.30 V; set-point current, 0.30 nA. (b) Observed with a fullerene tip. Bias voltage, −1.25 V; set-point current 0.30 nA. Arrows indicate the positions of the Co (II) ions. The cross-sectional profiles measured along with the lines in the STM images are presented under the images.

protrusions, which reveals that the tunnel electrons are localized at the pyrrole moieties. The change in image contrast observed with the fullerene tips was ascribed to the charge-transfer interaction concomitant with the overlapped π orbitals between a fullerene moiety of the molecular tip and a pyrrole moiety of the CoPor. The charge-transfer interaction facilitates electron tunneling locally at the pyrrole moiety. These results demonstrate that the localized electron tunneling through charge-transfer interactions can be applied to visualize spatially frontier orbitals involved in the interaction.

Chiral surfaces are attracting increasing interest owing to their vital role in a variety of fields, such as in chiral separations and heterogeneous enantioselective catalysis. The most urgent issue in research on such two-dimensional chirality is a lack of methodologies that recognize molecular chirality on a surface. Recently, it was shown that chiral molecular tips (Figure 17.21a) permit for the first time discrimination of enantiomers on a single-molecule basis [65]. With the *S*-chiral molecular tips (Figure 17.21b, bottom), STM images as shown in Figure 17.22 were observed. The images exhibit closely packed arrays of cysteine molecules adsorbed on the surface. This result demonstrates that the chiral molecular tips probe the electron tunneling from individual sample molecules and reveal their adsorbed structures at the molecular level. The SAM structures of the D- and L-cysteine enantiomers are identical, and as a result the D- and L-cysteine molecules are indistinguishable from their molecular packing in the STM images. However, the most important observation is the extent of intermolecular electron tunneling between the chiral molecular tips and cysteine enantiomers. Figure 17.22c shows cross-sectional profiles of the STM images of the cysteine enantiomers taken with the *S*-chiral molecular tips.

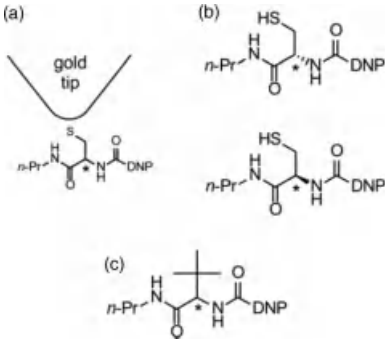


Figure 17.21 Structures of molecules capable of chiral recognition. (a) Schematic of the chiral molecular tips. (b) Precursor molecules of *R*- and *S*-chiral molecular tips (top and bottom, respectively). (c) Chiral selector from which a chiral stationary phase is derived. DNP = 3,5-dinitrophenyl and *n*-Pr = *n*-propyl.

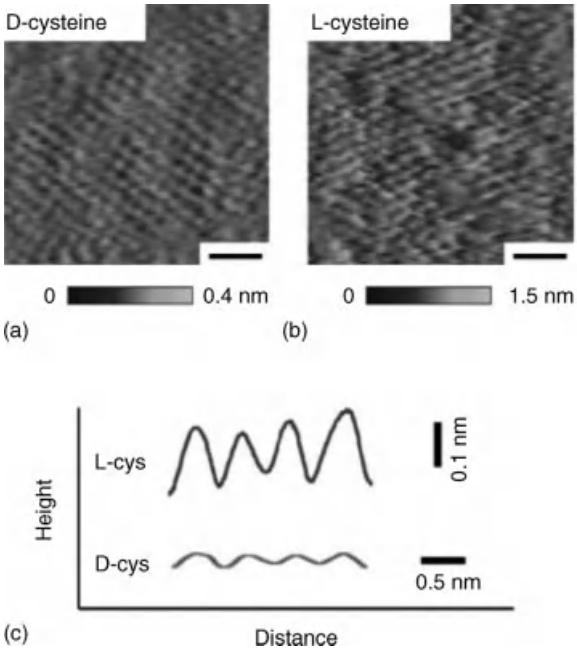


Figure 17.22 STM observation of cysteine SAMs with the *S*-chiral molecular tip. STM images of (a) D-cysteine and (b) L-cysteine. Bias voltages, −200 mV; tunneling currents, 0.75 nA; scale bars, 2.0 nm. (c) Cross-sectional profiles of the cysteine enantiomers taken with the *S*-chiral molecular tips. Reprinted with permission from [65]. Copyright 2008 the American Chemical Society.

With molecular tips, the profiles are a quantitative measure of intermolecular electron tunneling between the sample and tip molecules. As the chemical interaction between the sample and tip facilitates electron tunneling in between, the sample molecules are observed as higher (brighter) protrusions in the images in the constant-current mode. It can be seen from Figure 17.22c that the *S*-chiral molecular tip enhanced electron tunneling from L-cysteine molecules to a much larger extent than from D-cysteine molecules. Interestingly, the oppositely handed molecular tip, the *R*-chiral molecular tip, caused the reverse situation, that is, a larger tunneling current from D-cysteine than from L-cysteine. In contrast, metal tips exhibited the same tunneling current from both the D- and L-cysteine molecules, showing that the conventional metal tips are completely silent on the chirality. It is concluded that the chiral molecular tips discriminate the stereochemistry of the cysteine molecules by the differing extents of the intermolecular electron tunneling. The chiral molecular tips (Figure 17.21a) were designed according to a chiral stationary phase (CSP) derived from the molecule shown in Figure 17.21c in high-performance liquid chromatography (HPLC) [66]. The CSP tethered to a solid support is able to separate enantiomers of numerous kinds of chiral molecules as a result of a set of stereoselective interactions occurring preferentially between the CSP and one of enantiomers. Because of the structural similarity, the chiral molecular tips achieve stereoselective observation analogously to the CSP. The chiral molecular tip forms favorable hydrogen bond interactions preferentially with one of the sample cysteine enantiomers. The enantioselective formation of the chemical interactions facilitates the intermolecular electron tunneling from one enantiomer to a greater extent than the opposite enantiomer, whereas these interactions result in longer retention times for a particular enantiomer in HPLC with the CSP. The reversal of the stereoselectivity by replacing the *S*-chiral molecular tip with the *R*-isomer is a clear evidence for the enantioselective formation of the hydrogen bond interactions.

It was shown that a nucleobase molecular tip is capable of electrically pinpointing each complementary nucleobase [67]. Nucleobase molecular tips were prepared by chemical modification of the underlying metal tips with thiol derivatives of adenine, guanine, cytosine, and uracil. Figure 17.23a, b, and c show typical STM images of guanine SAMs observed with complementary cytosine, noncomplementary adenine, and unmodified tips, respectively. Cross-sectional profiles of the images are shown in Figure 17.23d, which represents the extent of electron tunneling between the tip and nucleobase. The complementary cytosine tip exhibited the most facilitated electron tunneling and therefore the brightest guanine images among the three tips. Similarly, for adenine, cytosine, and uracil, their complementary nucleobase tips gave the brightest images of their counterparts. It was concluded that the complementary combinations of the tip and sample base pairs facilitated the largest electron tunneling through hydrogen bonds between complementary base pairs, and particular nucleobases were thus discriminated from other nucleobases in STM images by using the complementary nucleobase tips. It should be noted that the formation of specific hydrogen bonds between complementary bases requires coplanar configurations, in which the molecular planes of the sample and tip nucleobases coincide with each other. The selective large facilitation observed with complementary base

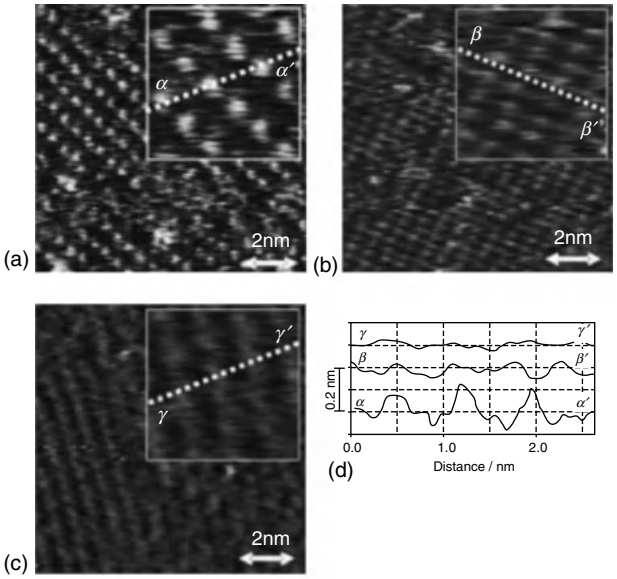


Figure 17.23 Changes in the image contrast for guanines; comparison with unmodified, noncomplementary, and complementary nucleobase tips. STM image of guanines observed (a) with a complementary cytosine tip, (b) with a noncomplementary adenine tip, and (c) with an unmodified tip. Magnified images ($2.5 \times 2.5\ nm^2$) are shown in the insets. (d) Cross-sectional profiles along the dashed lines (α–α′, β–β′, and γ–γ′) in the insets in (a), (b), and (c), respectively. Reprinted with permission from [63]. Copyright 2010 the Japan Society for Analytical Chemistry.

pairs on a tip and substrate indicates that the base–base coplanar orientation was in fact achieved. The base–base coplanarity is probably attained by the rotation of a carbon–sulfur bond in the thiolated nucleobase on a tip, which is well known even in the close-packed structure of alkanethiolate SAMs. An example of the detection of particular nucleobases was demonstrated here with the present method in an 18-mer strand of a peptide nucleic acid (PNA), an analog of DNA [68]. A typical STM image with an unmodified tip of a PNA strand is shown in Figure 17.24a, showing that bases in the strand were observed as rows of bright spots and the components of the strand, guanines and thymines, were not discriminated. In contrast, cytosine tips pinpointed the complementary guanines among the noncomplementary thymines in the strands (Figure 17.24b–d and insets). The extent of electron tunneling along the strands shows that a single- and double-base substitution in the strands was distinguished with the cytosine tip. These results demonstrate that the complementary nucleobase tip is capable of electrically pinpointing each DNA base.

17.2.4.2 **Inelastic Tunneling Spectroscopy**

Inelastic tunneling spectroscopy with STM (IETS-STM) is a spectroscopic technique that allows the determination of the chemical identity of a single molecule on a solid

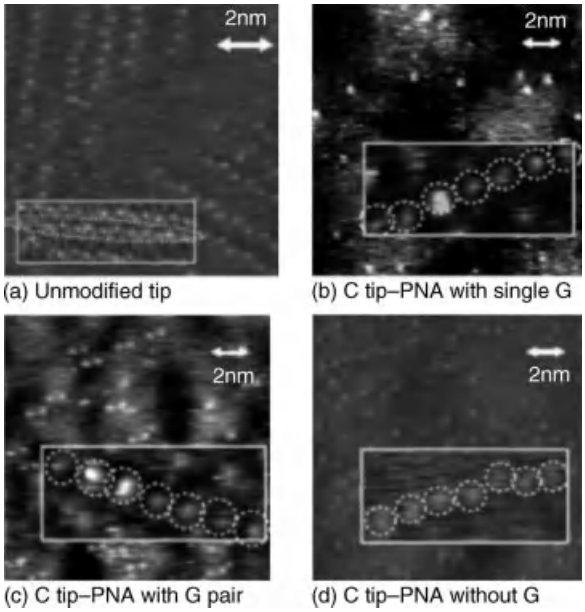


Figure 17.24 (a) An STM image ($10 \times 10\,nm^2$) with an unmodified tip of single-stranded 18-mer PNAs, the sequence of which is TTTTTTTGGTTTTTTTTT. STM images ($15 \times 15\,nm^2$) with cytosine tips of three kinds of PNA strands: (b) TTTTTTTGTTTTTTTTT, (c) TTTTTTTGGTTTTTTTTT, and (d) TTTTTTTTTTTTTTTTT. The magnified images ($2.0 \times 5.0\,nm^2$) are shown in the insets. Reprinted with permission from [63]. Copyright 2010 the Japan Society for Analytical Chemistry.

surfaced [69]. Tunneling electrons of STM can be used to excite the vibration of chemical bonds in single molecules. Because the energies required for the excitation are characteristic of the chemical bonds, chemical selectivity is attained by measuring the vibration properties with the tunneling electrons. Specifically, excitation of a vibration mode of a single adsorbate is induced by tunneling electrons having sufficiently high energy. The electron loses its energy by the excitation, and this process is called inelastic tunneling. The conductance of the adsorbate increases upon the vibration excitation, since inelastic electron tunneling occurs in addition to elastic tunneling. Although this increase in the conductance (dI/dV) is small, the conductance change can be detected by the differential change in the conductance with respect to the bias voltage (d^2I/dV^2).

IETS-STM was first used to investigate acetylene on Cu(100) at 8 K in UHV [70]. STM imaging indicated that the C_2H_2 molecule adsorbed on the hollow site of the substrate with its C−C bond parallel to the surface. The STM tip was stopped over the center of the molecule, and the d^2I/dV^2 signal was recorded by ramping the bias voltage (Figure 17.25). The d^2I/dV^2 spectrum exhibited a distinct peak at a bias voltage of 385 mV for C_2H_2, which is attributed to the C−H stretch mode. This vibration assignment was confirmed by isotopic substitution of the sample molecule. The peak at 358 mV for the C−H stretch shifted to 266 mV for the C−D stretch of C_2D_2, as

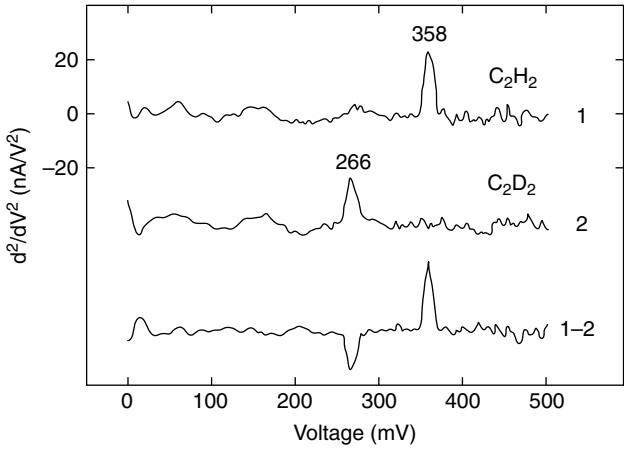


Figure 17.25 d^2I/dV^2 spectra for C_2H_2 (1) and C_2D_2 (2) adsorbed on Cu(100) taken at 8 K. Reprinted from [70].

expected. Moreover, the d^2I/dV^2 signals were utilized for chemically selective imaging. The two molecules, C_2H_2 and C_2D_2, appeared similarly in the STM images (Figure 17.26a), and, as a result, they cannot be distinguished from each other. In contrast, the C_2H_2 and C_2D_2 molecules were selectively observed in the image constructed by two-dimensional mapping of the d^2I/dV^2 signal at the 358 and 226 mV, respectively.

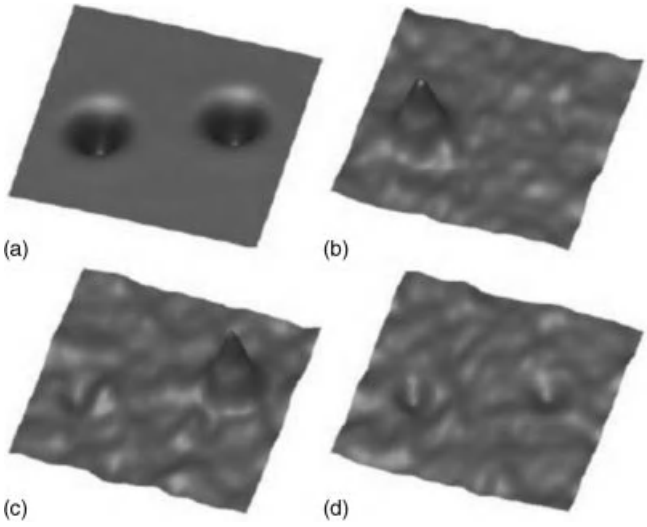


Figure 17.26 (a) STM image of a C_2H_2 molecule (left) and a C_2D_2 molecule (right). (b)–(d) d^2I/dV^2 signal of the same area as (a) recorded at the DC bias voltage of (b) 358, (c) 266, and (d) 311 mV. Reprinted from [70].

17.3
Atomic Force Microscopy

17.3.1
Principle and Operation Modes

Whereas STM utilizes the tunneling current to measure surface topography, forces acting between the tip and sample surface are used as the imaging signal in AFM. Interactions between two uncharged atoms can be described by the Lennard–Jones potential:

$$V = 4\varepsilon\left\{\left(\frac{\sigma}{r}\right)^{12} - \left(\frac{\sigma}{r}\right)^{6}\right\} \tag{17.7}$$

where ε and σ are the specific parameters and r is the separation between the two atoms. The interaction force derived from Eq. (17.7) is depicted in Figure 17.27. As illustrated, the atoms show the attractive interaction resulting from the induced dipole–dipole moment interaction at larger distances. In contrast, there exists a repulsive interaction due to the Pauli repulsion. The tip–sample force in AFM likewise consists of long- and short-range forces. For example, there are short-range chemical forces and van der Waals electrostatic forces with long ranges.

AFM operates in either a static or dynamic mode. In the static mode, the AFM tip is always in contact with the sample surface during scanning. The repulsive force exerted on the tip from the sample is measured by the deflection of the cantilever (Figure 17.3) and recorded to map out the topography of the sample surface. In the dynamic mode, the AFM cantilever is periodically oscillated near the sample surface. The tip–sample interaction modulates the amplitude, phase, and resonant frequency

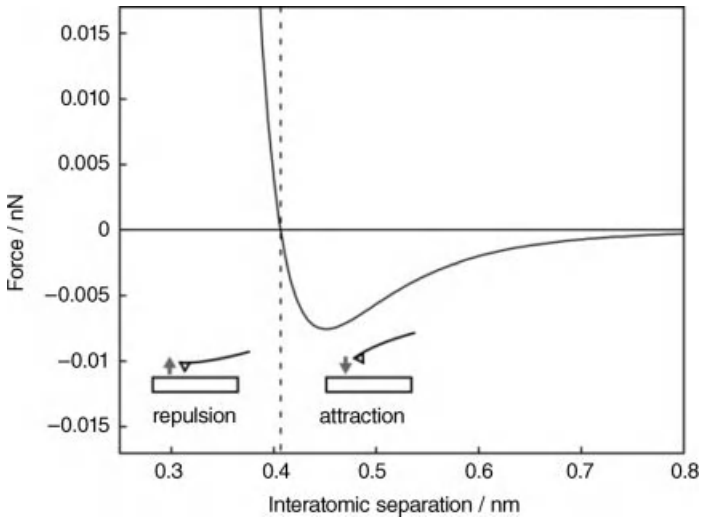


Figure 17.27 Forces acting between two uncharged atoms.

of the cantilever oscillation. Hence the force can be measured from the changes in these oscillation parameters. There are two modes in dynamic AFM, namely amplitude-modulation atomic force microscopy (AM-AFM) and frequency-modulation atomic force microscopy (FM-AFM) [71]. In AM-AFM, the cantilever is oscillated at a fixed frequency, and the changes in the oscillation amplitude provide information about the tip–sample interaction. The tip intermittently contacts the sample surface in AM-AFM, and amplitude changes arise from repulsive forces. The AM mode is suitable for high-resolution imaging of soft materials, such as biomolecules and polymers, in ambient or liquid environments. In FM-AFM, the oscillation amplitude is fixed, and the changes in the resonant frequency of the oscillation are employed as imaging signals. FM-AFM significantly improved the spatial resolution of AFM, and atomic resolution was achieved in UHV for the Si(111)-(7×7) surface [72].

17.3.1.1 Imaging Solid Surfaces and Single Adsorbates

FM-AFM achieves atomic resolution is UHV. This capability was demonstrated by, for example, the observation of the atomic arrangement of the Si(111)-(7×7) surface [72]. Furthermore, discrimination of different surface atoms is in some cases possible. An Sn/Si(111) surface prepared by deposition of a small amount of Sn on the Si(111) surface was observed with FM-AFM in UHV [73]. Each atom was clearly observed, and it was found that a (7×7) structure having Sn-substituted adatoms coexisted with the 1/6 monolayer Sn/Si(111)-$(\sqrt{3} \times \sqrt{3})R30^\circ$ structure. Importantly, two kinds of image contrast for the surface atoms were observed, as shown in Figure 17.28. By considering the surface stoichiometry of the sample, the brighter (higher) adatoms were attributed to the Sn atoms. A first-principles calculation revealed that the Sn atoms protruded 0.5 Å from the Si atom, being qualitatively consistent with the higher appearance of Sn in the FM-AFM image. However, the observed height difference between the Sn and Si atoms (0.23 Å) was smaller than the theoretically predicted value. This result was explained on the basis of the interaction strengths of the two adatoms with the AFM tip. A stronger interaction between the surface Si atom and the tip apex compared with the interaction between the surface Sn atom and the tip apex could reduce the apparent height difference between the two adatoms in the AFM image. Later, it was further demonstrated that precise measurements of the short-range force by FM-AFM in UHV allowed the identification of Sn, Pb, and Si atoms on the sample surface [74].

Biomolecules, such as DNA, proteins, and membranes, have been extensively investigated by AFM. AFM is particularly suitable for these biological samples because the observations can be carried out in physiological conditions. Firm immobilization of a sample molecule is required for reliable imaging by static-mode AFM. Weakly adsorbed molecules can be swept away by the AFM tip during raster scanning. In addition, the sample molecule should be rigid enough to avoid damage by the forced exerted by the AFM tip. These restrictions are less relevant for AM-AFM because the forces that act on the sample by the intermittent contact with the tip are fairly small.

Figure 17.29 illustrates an example of high-resolution imaging of proteins by AFM [75]. A crystal of membrane proteins (aquaporin Z) was imaged with AFM, and each sample molecule was clearly observed with submolecular resolution

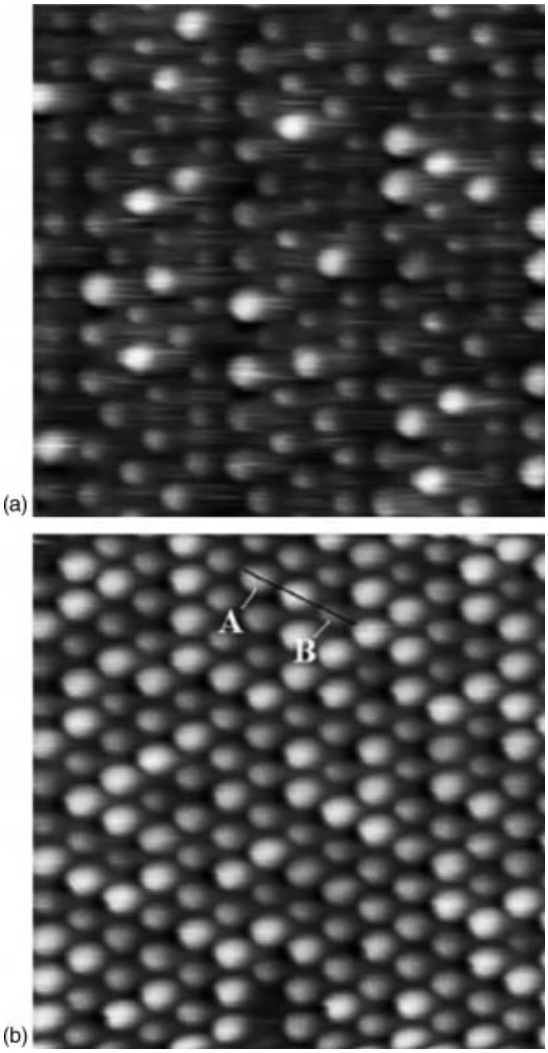


Figure 17.28 AFM images of (a) Si(111)-(7 × 7) with Sn substitutional adatoms and (b) Si(111)-($\sqrt{3} \times \sqrt{3}$) phase. Reprinted with permission from [73]. Copyright 2005 Elsevier.

(Figure 17.29a). Data processing techniques commonly used in transmission electron microscopy were applied to the raw AFM image. Thereby, the averaged topography of the protein (Figure 17.29b) and the standard deviation from this averaged structure (Figure 17.29c) were obtained. The analysis of these images provided detailed information about the structure of the adsorbed protein, that is, the probability distribution of topographic peaks under thermal motion (Figure 17.29d) and free energy landscape (Figure 17.29e).

Membrane protein assemblies are also a class of biological molecules that have been thoroughly examined with AFM. For example, photosynthetic membranes

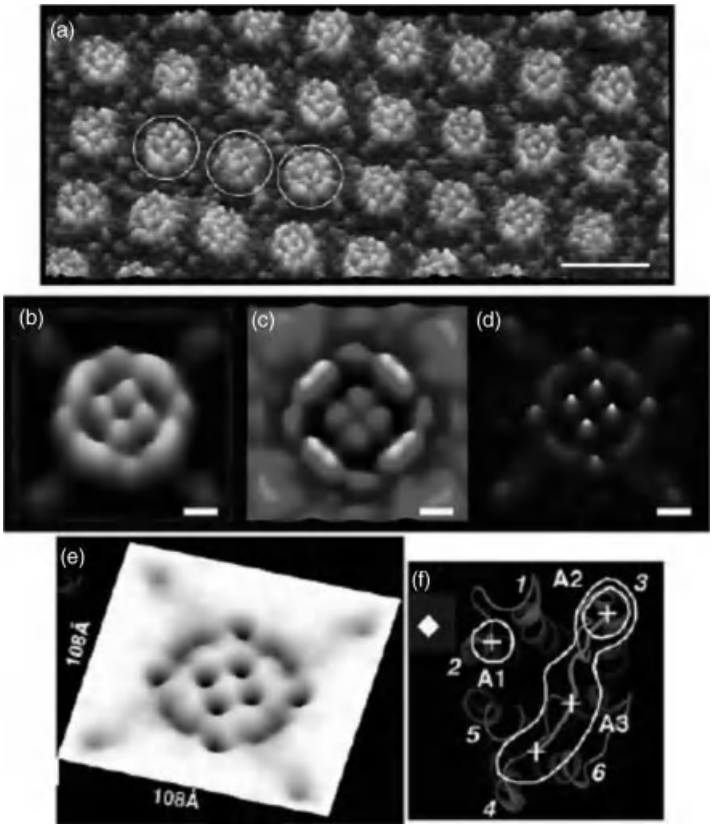


Figure 17.29 (a) AFM image of aquaporin Z. Scale bar, 10 nm. (b) Averaged topography of a single protein. Scale bar, 1 nm. (c) Standard deviation map. (d) Probability position map. (e) Free energy landscape calculated from (d). (f) Correlation between the free energy landscape and atomic structure of the protein. Reprinted from [75].

from the bacterium *Rhodospirillum photometricum* were investigated [76, 77]. The sample membrane contained all the components of the photosynthetic unit (PSU), that is, the light-harvesting complexes (LH1 and LH2) and the reaction center (RC). AFM imaging was performed in static mode for the membranes immobilized on a mica surface by drop casting. High-resolution imaging was hindered in the sample area where the lipids formed a bilayer because of large corrugation and loose immobilization of the top layer of the bilayer. Therefore, the top layers were removed with the AFM tip by intentionally applying higher loading forces. The imaging of the bottom layer left on the mica surface achieved molecular resolution, allowing the observation of the precise organization of the photosynthetic apparatus. The AFM images revealed molecular assemblies of the light-harvesting complexes and RC (Figure 17.30). The LH1 and RC formed elliptical complexes, with long and short axes of 95 and 85 Å, respectively. The AFM images showed that the single RC was located at the center of the complex and 16 LH1 subunits surrounded the RC to form the

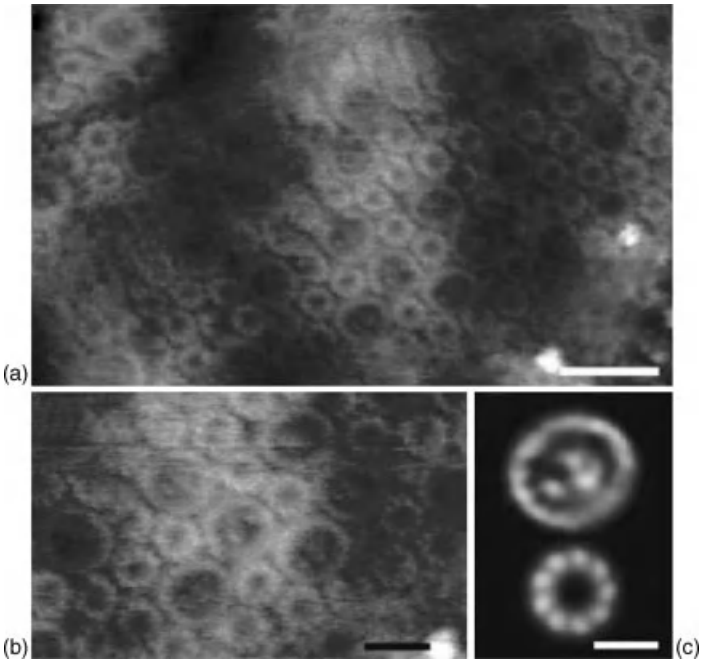


Figure 17.30 (a) AFM image of a native photosynthetic membrane on a mica substrate. Scale bar, 20 nm. (b) Close-up view of an assembly of multiple core complexes and LH2s. Scale bar, 10 nm. (c) Averaged images of the core complexes (top) and the LH2 (bottom). Reprinted from [76].

circumference of the ellipse (Figure 17.30c, top). The LH2 assembled as circular complexes without the RC (Figure 17.30c, bottom). It was found that the diameters of the complexes were not uniform. The geometric considerations together with the symmetry of the complexes indicated that ~70% of the complexes were a nonameric assembly of the LH2. The remaining complexes were assigned to either smaller octamers or larger decamers. The RC–LH1 core complexes exhibited no such heterogeneity. The AFM images revealed also the molecular organization of the LH2 and RC–LH1 core complexes within the membrane (Figure 17.30a and b). Almost all of the core complexes were surrounded by four to seven LH2 complexes. It was found that 73% of the core complexes were in touch with other core complexes. The remaining cores were completely surrounded by the LH2 complexes. As described above, the AFM imaging provided important insight into the organization of the proteins that holds close relevance to the light-harvesting and electron transfer processes in photosynthesis.

17.3.2 High-Speed Imaging

Low time resolution is a drawback of SPM. The acquisition rate for a single image is typically on the order of tens of seconds to minutes. The low imaging rate primarily

results from mechanical scanning of the probe tip to measure the surface topography at each data point. However, the fast electronics with large bandwidth in the modern controllers of SPM have enhanced the imaging rate. In STM, imaging rates as high as 20 images per second were achieved in the constant-height mode [78]. In this mode of operation, the tip height is kept constant during scanning, so that the scanning speed is not limited by the cut-off frequency of the feedback circuit. Technological progress has resulted in the improvement in the imaging rate of AFM [79–81]. This high-speed AFM utilizes small cantilevers having a resonance frequency orders of magnitude higher than conventional cantilevers, and a specially designed tip scanner, and is able to acquire a single image in 30–60 ms. Furthermore, the tip–sample interaction was greatly reduced by further development of the electric devices. The high time resolution and weak tip–sample interaction permit *in situ* imaging of dynamic processes on a fragile sample or adsorbates weakly bound on a solid surface. Time-resolved imaging has been performed with high-speed AFM for biomolecules performing their intrinsic functions without disturbing delicate biomolecular interactions. For example, mechanical motion of a motor protein, myosin V, was captured [82]. The myosin V molecules were closely immobilized on a mica surface, and subsequent imaging with high-speed AFM revealed unidirectional displacements of actin filaments propelled by the mechanical motion of myosin V. The velocity of the actin filament agreed well with that observed by fluorescence microscopy.

17.3.3
Kelvin Probe Force Microscopy

Kelvin probe force microscopy (KFM) allows mapping of the work function or surface potential of a variety of sample surfaces with high spatial resolution [83]. KFM measurements are performed on the instrumentation of an AFM system with the use of conducting AFM probes. Heavily doped Si cantilevers or metal-coated cantilevers can serve as the conducting probes. When the AFM tip is placed in proximity to a sample surface, a contact potential difference arises between the tip and sample, which causes an electrostatic force in between. This force can be nullified by applying an external bias that has the same magnitude as the contact potential difference with the opposite direction. Because this external bias that nullifies the electrostatic force is equal to the work function difference between the tip and sample, the work function of the sample can be determined on the basis of a predetermined work function of the tip. KFM is suitable for the investigation of working devices, such as thin-film transistors and solar cells, since KFM injects no electrons from the tip to the sample, unlike STM.

It is known that the work function depends on the crystal orientation of the surface. KFM was used to measure the work function of p-type $CuGaSe_2$ thin films, which is relevant to thin-film solar cells, grown on ZnSe(110) surfaces [84]. The KFM measurement was performed in UHV and achieved high energy ($\sim$5 meV) and spatial ($\sim$25 nm) resolutions. Figure 17.31 shows images of the topography and simultaneously measured work functions of the sample surface. The topography

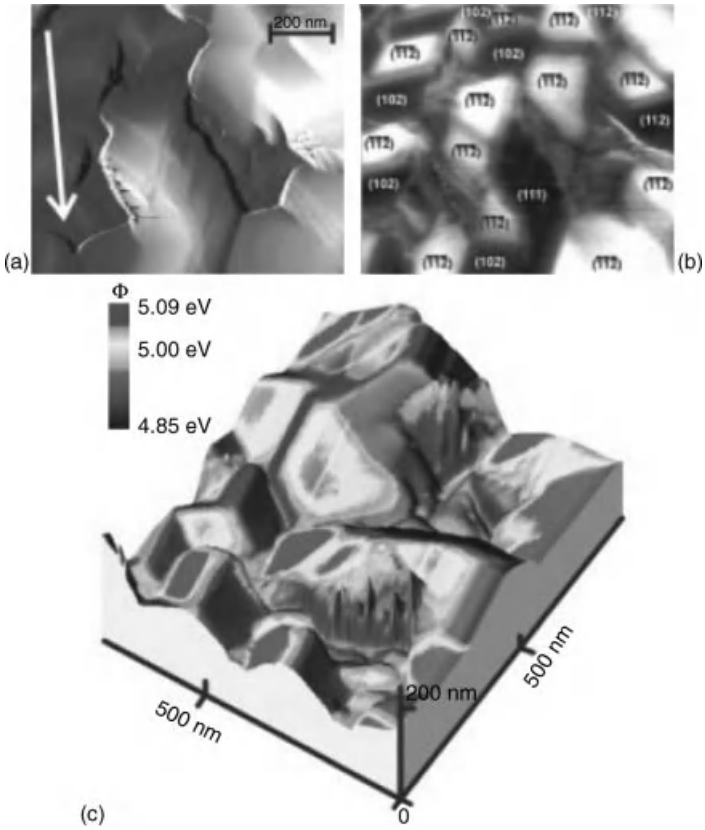


Figure 17.31 KFM measurement of a $CuGaSe_2$ thin film on a ZnSe(110) substrate. (a) Topography and (b) simultaneously measured work function of the sample surface. (c) Three-dimensional image merging the topography and work function. The origin corresponds to the lower left corner of (a) and (b). Reprinted with permission from [84]. Copyright 2002 the American Institute of Physics.

image (Figure 17.31a) allows the determination of the crystallographic orientation of each facet by comparison between the angles of the facets and the $CuGeSe_2$ crystal structure. This analysis allowed the determination of the work function of each crystallographic orientation of the sample surface.

17.4 Conclusion

This chapter has demonstrated that SPM techniques reveal surface structures and chemical processes at the atomic level in real space. Catalytically relevant model systems have been extensively investigated *in situ* with STM. These studies provide a detailed insight into the structures of metal surfaces and molecular overlayers.

A basic understanding of the catalytic processes has been gained with a well-defined single-crystal surface under UHV conditions. There have been considerable advances towards catalyst characterization by STM under more realistic conditions. For example, atomically resolved STM imaging was achieved in high-pressure environments. It can be envisaged that STM will allows the imaging of catalyst surfaces under working conditions in the near future. STM operated in aqueous solutions allows direct visualization of electrified solid–liquid interfaces. Investigations of the electrode surface and specifically adsorbed species thereon will lead to a complete understanding of the electric double layer. Systematic studies have been carried out on the adsorption and self-assembly of organic molecules at solid–liquid interfaces, and knowledge of factors that govern the assembled structure of the molecules has been obtained. Lack of chemical selectivity is a major drawback of STM, but several techniques, such as molecular tips and IETS, have been developed to overcome this disadvantage. AFM has also been used as a powerful tool in surface science. Unlike STM, this methodology can be applied not only to metals and semiconductors but also to insulators. Recent advances in dynamic AFM have significantly enhanced the spatial resolution. Furthermore, high-speed AFM opens up a new way to monitor biomolecular processes in real time. AFM has great potential for observing surface phenomena and their dynamics in a wide range of scientific disciplines. KFM allows the simultaneous observation of surface morphology and work functions. KFM offers a unique means to characterize the electrical properties of working devices, including thin-film organic transistors and solar cells.

References

1 Binnig, G. and Rohrer, H. (1982) Scanning tunneling microscopy. *Helv. Phys. Acta*, **55**, 726–735.

2 Binnig, G., Rohrer, H., Gerber, C., and Weibel, E. (1982) Tunneling through a controllable vacuum gap. *Appl. Phys. Lett.*, **40**, 178–180.

3 Binnig, G., Rohrer, H., Gerber, C., and Weibel, E. (1983) 7×7 reconstruction on Si(111) resolved in real space. *Phys. Rev. Lett.*, **50**, 120–123.

4 Ikai, A. (1996) STM and AFM of bio/organic molecules and structures. *Surf. Sci. Rep.*, **26**, 261–332.

5 Binnig, G., Quate, C.F., and Gerber, C. (1986) Atomic force microscope. *Phys. Rev. Lett.*, **56**, 930–933.

6 Feenstra, R.M., Stroscio, J.A., Tersoff, J., and Fein, A.P. (1987) Atom-selective imaging of the GaAs(110) surface. *Phys. Rev. Lett.*, **58**, 1192–1195.

7 Tersoff, J. and Hamann, D.R. (1983) Theory and application for the scanning tunneling microscope. *Phys. Rev. Lett.*, **50**, 1998–2001.

8 Tersoff, J. and Hamann, D.R. (1985) Theory of the scanning tunneling microscope. *Phys. Rev. B*, **31**, 805–813.

9 Bardeen, J. (1961) Tunnelling from a many-particle point of view. *Phys. Rev. Lett.*, **6**, 57.

10 Tsukada, M., Kobayashi, K., Isshiki, N., and Kageshima, H. (1991) First-principles theory of scanning tunneling microscopy. *Surf. Sci. Rep.*, **13**, 267–304.

11 Tsukada, M., Kobayashi, K., and Ohnishi, S. (1990) First-principles theory of the scanning tunneling microscopy simulation. *J. Vac. Sci. Technol. A*, **8**, 160–165.

12 Lang, N.D. (1986) Theory of single-atom imaging in the scanning tunneling

microscope. *Phys. Rev. Lett.*, **56**, 1164–1167.
13 Sautet, P. (1997) Images of adsorbates with the scanning tunneling microscope: theoretical approaches to the contrast mechanism. *Chem. Rev*, **97**, 1097–1116.
14 Coulman, D.J., Wintterlin, J., Behm, R.J., and Ertl, G. (1990) Novel mechanism for the formation of chemisorption phases; the (2 × 1)O-Cu(110) "added row" reconstruction. *Phys. Rev. Lett.*, **64**, 1761–1764.
15 Jensen, F., Besenbacher, F., Laegsgaard, E., and Stensgaard, I. (1990) Surface reconstruction of Cu(110) induced by oxygen-chemisorption. *Phys. Rev. B*, **41**, 10233–10236.
16 Zambelli, T., Wintterlin, J., Trost, J., and Ertl, G. (1996) Identification of the "active sites" of a surface-catalyzed reaction. *Science*, **273**, 1688–1690.
17 Zambelli, T., Trost, J., Wintterlin, J., and Ertl, G. (1996) Diffusion and atomic hopping of N atoms on Ru(0001) studied by scanning tunneling microscopy. *Phys. Rev. Lett.*, **76**, 795–798.
18 Sprunger, P., Besenbacher, F., and Stensgaard, I. (1995) STM study of the Ni (110)-(2 × 1)-2CO system: structure and bonding-site determination. *Surf. Sci.*, **324**, L321–L327.
19 Besenbacher, F., Stensgaard, I., Ruan, L., Norskov, J.K., and Jacobsen, K.W. (1992) Chemisorption of H, O, and S on Ni(110): general trends. *Surf. Sci.*, **272**, 334–341.
20 Briner, B.G., Doering, M., Rust, H.P., and Bradshaw, A.M. (1997) Microscopic molecular diffusion enhanced by adsorbate interactions. *Science*, **278**, 257–260.
21 Shen, T.C., Wang, C., Abeln, G.C., Tucker, J.R., Lyding, J.W., Avouris, P., and Walkup, R.E. (1995) Atomic-scale desorption through electronic and vibrational-excitation mechanisms. *Science*, **268**, 1590–1592.
22 Komeda, T., Kim, Y., Kawai, M., Persson, B.N.J., and Ueba, H. (2002) Lateral hopping of molecules induced by excitation of internal vibration mode. *Science*, **295**, 2055–2058.
23 Crew, W.W. and Madix, R.J. (1996) A scanning tunneling microscopy study of the oxidation of CO on Cu(110) at 400 K: site specificity and reaction kinetics. *Surf. Sci.*, **349**, 275–293.
24 Crew, W.W. and Madix, R.J. (1996) CO adsorption and oxidation on oxygen precovered Cu(110) at 150 K: reactivity of two types of adsorbed atomic oxygen determined by scanning tunneling microscopy. *Surf. Sci.*, **356**, 1–18.
25 Wintterlin, J., Volkening, S., Janssens, T.V.W., Zambelli, T., and Ertl, G. (1997) Atomic and macroscopic reaction rates of a surface-catalyzed reaction. *Science*, **278**, 1931–1934.
26 Afsin, B., Davies, P.R., Pashusky, A., Roberts, M.W., and Vincent, D. (1993) Reaction pathways in the oxydehydrogenation of ammonia at Cu (110) surfaces. *Surf. Sci.*, **284**, 109–120.
27 Afsin, B., Davies, P.R., Pashuski, A., and Roberts, M.W. (1991) The role of a dioxygen precursor in the selective formation of imide NH(a) species at a Cu(110) surface. *Surf. Sci.*, **259**, L724–L728.
28 Guo, X.C. and Madix, R.J. (1996) Atom-resolved investigation of surface reactions: ammonia and oxygen on Cu(110) at 300 and 400 K. *Faraday Discuss.*, **105**, 139–149.
29 Ruan, L., Stensgaard, I., Laegsgaard, E., and Besenbacher, F. (1994) The decomposition of ammonia on an oxygen-precovered Ni(110) surface studied by scanning tunneling microscopy. *Surf. Sci.*, **314**, L873–L878.
30 Carley, A.F., Davies, P.R., and Roberts, M.W. (1998) An STM–XPS study of ammonia oxidation: the molecular architecture of chemisorbed imide 'strings' at Cu(110) surfaces. *Chem. Commun.*, 1793–1794.
31 McIntyre, B.J., Salmeron, M., and Somorjai, G.A. (1993) *In situ* scanning tunneling microscopy study of platinum (110) in a reactor cell at high pressures and temperatures. *J. Vac. Sci. Technol. A*, **11**, 1964–1968.
32 Longwitz, S.R., Schnadt, J., Vestergaard, E.K., Vang, R.T., Laegsgaard, E., Stensgaard, I., Brune, H., and Besenbacher, F. (2004) High-coverage structures of carbon monoxide adsorbed on Pt(111) studied by high-pressure

scanning tunneling microscopy. *J. Phys. Chem. B*, **108**, 14497–14502.

33 Vestergaard, E.K., Thostrup, P., An, T., Laegsgaard, E., Stensgaard, I., Hammer, B., and Besenbacher, F. (2002) Comment on "High pressure adsorbate structures studied by scanning tunneling microscopy: CO on Pt(111) in equilibrium with the gas phase". *Phys. Rev. Lett.*, **88**, 259601.

34 Rider, K.B., Hwang, K.S., Salmeron, M., and Somorjai, G.A. (2001) Structure and dynamics of dense monolayers of NO adsorbed on Rh(111) in equilibrium with the gas phase in the Torr pressure range. *Phys. Rev. Lett.*, **86**, 4330–4333.

35 Tang, D.C., Hwang, K.S., Salmeron, M., and Somorjai, G.A. (2004) High pressure scanning tunneling microscopy study of CO poisoning of ethylene hydrogenation on Pt(111) and Rh(111) single crystals. *J. Phys. Chem. B*, **108**, 13300–13306.

36 Vestergaard, E.K., Vang, R.T., Knudsen, J., Pedersen, T.M., An, T., Laegsgaard, E., Stensgaard, I., Hammer, B., and Besenbacher, F. (2005) Adsorbate-induced alloy phase separation: a direct view by high-pressure scanning tunneling microscopy. *Phys. Rev. Lett.*, 95.

37 Sonnenfeld, R. and Hansma, P.K. (1986) Atomic-resolution microscopy in water. *Science*, **232**, 211–213.

38 Robinson, R.S. and Widrig, C.A. (1992) Differential conductance tunneling spectroscopy in electrolytic solution. *Langmuir*, **8**, 2311–2316.

39 Bach, C.E., Nichols, R.J., Meyer, H., and Besenhard, J.O. (1994) An electropainting method for coating STM tips for electrochemical measurements. *Surf. Coat. Technol.*, **67**, 139–144.

40 Clavilier, J., Faure, R., Guinet, G., and Durand, R. (1980) Preparation of monocrystalline Pt microelectrodes and electrochemical study of the plane surfaces cut in the direction of the (111) and (110) planes. *J. Electroanal. Chem.*, **107**, 205–209.

41 Clavilier, J. (1980) Role of anion on the electrochemical behavior of a (111) platinum surface; an unusual splitting of the voltammogram in the hydrogen region. *J. Electroanal. Chem.*, **107**, 211–216.

42 Tanaka, S., Yau, S.L., and Itaya, K. (1995) *In-situ* scanning tunneling microscopy of bromine adlayers on Pt(111). *J. Electroanal. Chem.*, **396**, 125–130.

43 Gao, X.P., Hamelin, A., and Weaver, M.J. (1991) Potential-dependent reconstruction at ordered Au(100)–aqueous interfaces as probed by atomic-resolution scanning tunneling microscopy. *Phys. Rev. Lett.*, **67**, 618–621.

44 Kolb, D.M. (1996) Reconstruction phenomena at metal–electrolyte interfaces. *Prog. Surf. Sci.*, **51**, 109–173.

45 Gewirth, A.A. and Niece, B.K. (1997) Electrochemical applications of *in situ* scanning probe microscopy. *Chem. Rev*, **97**, 1129–1162.

46 Schardt, B.C., Yau, S.L., and Rinaldi, F. (1989) Atomic resolution imaging of adsorbates on metal surfaces in air: iodine adsorption on Pt(111). *Science*, **243**, 1050–1053.

47 Tao, N.J. and Lindsay, S.M. (1992) *In situ* scanning tunneling microscopy study of iodine and bromine adsorption on Au (111) under potential control. *J. Phys. Chem.*, **96**, 5213–5217

48 Gao, X.P. and Weaver, M.J. (1992) Probing redox-induced molecular transformations by atomic-resolution scanning tunneling microscopy: iodide adsorption and electrooxidation on Au(111) in aqueous solution. *J. Am. Chem. Soc.*, **114**, 8544–8551.

49 Batina, N., Yamada, T., and Itaya, K. (1995) Atomic level characterization of the iodine-modified Au(111) electrode surface in perchloric acid solution by *in situ* STM and *ex situ* LEED. *Langmuir*, **11**, 4568–4576.

50 Yamada, T., Batina, N., and Itaya, K. (1995) Structure of electrochemically deposited iodine adlayer on Au(111) studied by ultrahigh-vacuum instrumentation and *in situ* STM. *J. Phys. Chem.*, **99**, 8817–8823.

51 Magnussen, O.M., Hagebock, J., Hotlos, J., and Behm, R.J. (1992) *In-situ* scanning-tunneling-microscopy observations of a disorder–order phase-transition in hydrogensulfate adlayers on Au(111). *Faraday Discuss.*, **94**, 329–338.

52 Edens, G.J., Gao, X.P., and Weaver, M.J. (1994) The adsorption of sulfate on gold (111) in acidic aqueous media: adlayer structural inferences from infrared spectroscopy and scanning tunneling microscopy. *J. Electroanal. Chem.*, **375**, 357–366.

53 Wan, L.J., Yau, S.L., and Itaya, K. (1995) Atomic structure of adsorbed sulfate on Rh(111) in sulfuric acid solution. *J. Phys. Chem.*, **99**, 9507–9513.

54 Yau, S.L., Kim, Y.G., and Itaya, K. (1996) *In situ* scanning tunneling microscopy of benzene adsorbed on Rh(111) and Pt(111) in HF solution. *J. Am. Chem. Soc.*, **118**, 7795–7803.

55 Ohtani, H., Wilson, R.J., Chiang, S., and Mate, C.M. (1988) Scanning tunneling microscopy observations of benzene molecules on the Rh(111)-(3 × 3) ($C_6H_6 + 2CO$) surface. *Phys. Rev. Lett.*, **60**, 2398–2401.

56 Cunha, F. and Tao, N.J. (1995) Surface-charge induced order–disorder transition in an organic monolayer. *Phys. Rev. Lett.*, **75**, 2376–2379.

57 De Feyter, S. and De Schryver, F.C. (2003) Two-dimensional supramolecular self-assembly probed by scanning tunneling microscopy. *Chem. Soc. Rev.*, **32**, 139–150.

58 Liang, H., He, Y., Ye, Y.C., Xu, X.G., Cheng, F., Sun, W., Shao, X., Wang, Y.F., Li, J.L., and Wu, K. (2009) Two-dimensional molecular porous networks constructed by surface assembling. *Coord. Chem. Rev.*, **253**, 2959–2979.

59 Yokoyama, T., Yokoyama, S., Kamikado, T., Okuno, Y., and Mashiko, S. (2001) Selective assembly on a surface of supramolecular aggregates with controlled size and shape. *Nature*, **413**, 619–621.

60 Pan, G.B., Liu, J.M., Zhang, H.M., Wan, L.J., Zheng, Q.Y., and Bai, C.L. (2003) Configurations of a calix[8]arene and a C_{60}/calix[8]arene complex on a Au(111) surface. *Angew. Chem. Int. Ed.*, **42**, 2747–2751.

61 Wang, D. and Wan, L.J. (2007) Electrochemical scanning tunneling microscopy: adlayer structure and reaction at solid/liquid interface. *J. Phys. Chem. C*, **111**, 16109–16130.

62 Nishino, T., Ohshiro, T., and Umezawa, Y. (2007) Molecular tips for "intermolecular tunneling microscopy". *Jpn. J. Appl. Phys.*, **46**, 5519–5527.

63 Nishino, T. and Umezawa, Y. (2010) Recognition of chemical identity of organic adsorbates on solid surfaces at the nanoscale by molecular STM tips. *Anal. Sci.*, **26**, 1023–1032.

64 Nishino, T., Ito, T., and Umezawa, Y. (2005) A fullerene molecular tip can detect localized and rectified electron tunneling within a single fullerene–porphyrin pair. *Proc. Natl. Acad. Sci. U. S. A.*, **102**, 5659–5662.

65 Nishino, T. and Umezawa, Y. (2008) Single-molecule chiral recognition on a surface by chiral molecular tips. *Anal. Chem.*, **80**, 6968–6973.

66 Pirkle, W.H. and Pochapsky, T.C. (1989) Consideration of chiral recognition relevant to the liquid chromatographic separation of enantiomers. *Chem. Rev.*, **89**, 347–362.

67 Ohshiro, T. and Umezawa, Y. (2006) Complementary base-pair-facilitated electron tunneling for electrically pinpointing complementary nucleobases. *Proc. Natl. Acad. Sci. U. S. A.*, **103**, 10–14.

68 Nielsen, P.E., Egholm, M., Berg, R.H., and Buchardt, O. (1991) Sequence-selective recognition of DNA by strand displacement with a thymine-substituted polyamide. *Science*, **254**, 1497–1500.

69 Ho, W. (2002) Single-molecule chemistry. *J. Chem. Phys.*, **117**, 11033–11061.

70 Stipe, B.C., Rezaei, M.A., and Ho, W. (1998) Single-molecule vibrational spectroscopy and microscopy. *Science*, **280**, 1732–1735.

71 Garcia, R. and Perez, R. (2002) Dynamic atomic force microscopy methods. *Surf. Sci. Rep.*, **47**, 197–301.

72 Giessibl, F.J. (1995) Atomic-resolution of the silicon (111)-(7 × 7) surface by atomic-force microscopy. *Science*, **267**, 68–71.

73 Sugimoto, Y., Abe, M., Yoshimoto, K., Custance, O., Yi, I., and Morita, S. (2005) Non-contact atomic force microscopy study of the Sn/Si(111) mosaic phase. *Appl. Surf. Sci.*, **241**, 23–27.

74 Sugimoto, Y., Pou, P., Abe, M., Jelinek, P., Perez, R., Morita, S., and Custance, O.

(2007) Chemical identification of individual surface atoms by atomic force microscopy. *Nature*, **446**, 64–67.

75 Horber, J.K.H. and Miles, M.J. (2003) Scanning probe evolution in biology. *Science*, **302**, 1002–1005.

76 Scheuring, S., Rigaud, J.L., and Sturgis, J.N. (2004) Variable LH2 stoichiometry and core clustering in native membranes of *Rhodospirillum photometricum*. *EMBO J.*, **23**, 4127–4133.

77 Scheuring, S., Sturgis, J.N., Prima, V., Bernadac, A., Levy, D., and Rigaud, J.L. (2004) Watching the photosynthetic apparatus in native membranes. *Proc. Natl. Acad. Sci. U. S. A.*, **101**, 11293–11297.

78 Wintterlin, J., Trost, J., Renisch, S., Schuster, R., Zambelli, T., and Ertl, G. (1997) Real-time STM observations of atomic equilibrium fluctuations in an adsorbate system: O/Ru(0001). *Surf. Sci.*, **394**, 159–169.

79 Viani, M.B., Schaffer, T.E., Chand, A., Rief, M., Gaub, H.E., and Hansma, P.K. (1999) Small cantilevers for force spectroscopy of single molecules. *J. Appl. Phys.*, **86**, 2258–2262.

80 Manalis, S.R., Minne, S.C., and Quate, C.F. (1996) Atomic force microscopy for high speed imaging using cantilevers with an integrated actuator and sensor. *Appl. Phys. Lett.*, **68**, 871–873.

81 Ando, T., Kodera, N., Takai, E., Maruyama, D., Saito, K., and Toda, A. (2001) A high-speed atomic force microscope for studying biological macromolecules. *Proc. Natl. Acad. Sci. U. S. A.*, **98**, 12468–12472.

82 Ando, T., Uchihashi, T., and Fukuma, T. (2008) High-speed atomic force microscopy for nano-visualization of dynamic biomolecular processes. *Prog. Surf. Sci.*, **83**, 337–437.

83 Palermo, V., Palma, M., and Samori, P. (2006) Electronic characterization of organic thin films by Kelvin probe force microscopy. *Adv. Mater.*, **18**, 145–164.

84 Sadewasser, S., Glatzel, T., Rusu, M., Jager-Waldau, A., and Lux-Steiner, M.C. (2002) High-resolution work function imaging of single grains of semiconductor surfaces. *Appl. Phys. Lett.*, **80**, 2979–2981.

18
Thermal Methods

Adrien Mekki-Berrada and Aline Auroux

Present-day thermal analysis instruments represent the culmination of a long period of development, including temperature programming and control, controlled furnace and sample environment, and data manipulation (differentiation, integration, etc.). These techniques are applicable to a broad range of materials and in particular to the study of catalysts, supports and adsorbents. Efforts are made to establish relationship of such techniques with other more accepted or developed methods or to combine them with other analytical techniques in order to handle and evaluate more completely the complex results often provided by thermal analysis.

These methods allow us to evaluate the heat involved in thermal transformations, adsorptions or reactions, to measure thermal effects as a function of time, to establish the thermodynamic parameters of unstable states, and to follow the kinetics of changes over a certain range of rates. Most of these techniques are dynamic in nature and flexible in capacity, but produce data that are highly dependent upon the procedure.

This chapter provides a detailed description of the most common thermal analysis techniques such as DTA, TGA, calorimetry, TPR, TPO, TPD, and TPSR (see Table 18.1) together with some examples of applications.

As catalysts are involved by their acid–base sites in many reactions, an overview of the different ways to determine accurately the number, strength and strength distribution of these sites with thermal techniques is given. Further, the redox character of supported metals and metal oxides can also be determined by such techniques, which is illustrated by the case study of DeNOx reactions.

18.1
Main Thermal Methods

18.1.1
Short History of Thermal Measurement

Based on Joseph Black's work on latent and specific heats, the first calorimetric study was performed with an ice calorimeter in 1782–1783 by Lavoisier and Laplace,

Characterization of Solid Materials and Heterogeneous Catalysts: From Structure to Surface Reactivity, First Edition. Edited by Michel Che and Jacques C. Védrine.
© 2012 Wiley-VCH Verlag GmbH & Co. KGaA. Published 2012 by Wiley-VCH Verlag GmbH & Co. KGaA.

Table 18.1 Various thermal techniques and their application.

Abbreviation	Technique	Application
–	Calorimetry, microcalorimetry	Heat-flow variation
DTA	Differential thermal analysis	Temperature variation
TG	Thermogravimetry	Mass variation
DTG	Differential thermogravimetry	Mass variation
TGA	Thermogravimetric analysis	Mass variation
DSC	Differential scanning calorimetry	Heat-flow variation while a temperature program is run
TPD	Temperature-programmed desorption	Any variation while a temperature program is run
TPR	Temperature-programmed reduction	Reductant consumption while a temperature program is run
TPO	Temperature-programmed oxidation	Oxidant consumption while a temperature program is run
TPSR	Temperature-programmed surface reaction	Any variation while a temperature program is run

focusing on the heat evolved with chemical reactions and the relation of combustion phenomena with the production of carbon dioxide (experimenting on a guinea pig inside the ice calorimeter). Later developed by Berthelot in 1879, the bomb calorimeter was used for determining the combustion enthalpies at constant volume [1].

The first studies on the application of calorimetry to surface sciences appeared in 1932 with Beebe, then Garner *et al.* in 1935, 1947 and 1949, Beeck in 1949, and Morrison *et al.* in 1950 and 1951 [2]. In the 1930s, the apparatus, consisting of thermocouples measuring the evolution of a sample's temperature inside a controlled environment and being mainly of the isoperibolic type, provided data on the adsorption of oxygen or hydrogen on charcoal and zinc–chromium catalysts; subsequently Morrison provided data on the adsorption of argon on titanium dioxide [2].

At the same time, Roberts was experimenting on the adsorption of gases on a tungsten filament that was introduced into a Wheatstone bridge scheme, the heat evolved being correlated with variations of the resistance of the filament [2].

Heat-flow calorimeters were developed by Calvet and Prat in the 1950s, based on the earlier work of Tian in 1924, and overcame most limitations of previously developed calorimeters for surface adsorption. Gravelle discussed the theory of heat-flow calorimetry and the advantages and limitations of various applications of adsorption calorimetry [2, 3].

Heats of adsorption of ammonia were measured in 1963 by Hshieh, Kevorkian, and Steiner on alumina-derived and silica–alumina catalysts in order to correlate their acidity with their catalytic activity in cracking, and in 1967 by Stone and Whalley on various acidic catalysts (silica–alumina, zeolites, etc.) [2]. Since then, technological evolution has allowed access to new coupled methods and enhanced accuracy.

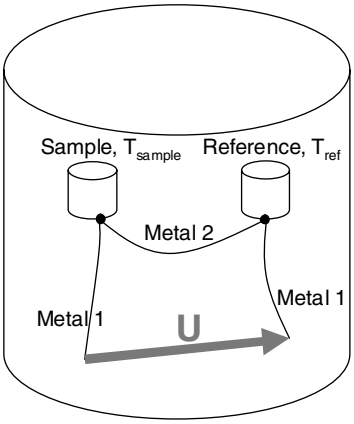
Several reviews have appeared on the application of calorimetry to heterogeneous catalysis, such as those by Cardona-Martinez and Dumesic [4], Farneth and Gorte [5], Andersen and Kung [6], Auroux [7–10] and Bennici [9].

18.1.2
Differential Thermal Analysis (DTA)

According to ICTAC (International Confederation for Thermal Analysis and Calorimetry), DTA is defined as a technique in which the difference in temperature between a sample and a reference material is measured versus time or temperature, while the temperature is programmed in a controlled atmosphere. The energies related to the physicochemical changes (structural transformation, reaction with the surroundings, etc.) of the tested substance can be then observed and quantified.

A DTA apparatus consists of a pair of crucibles containing the sample and the reference, both encaged in a heating vessel, with control over the atmosphere (Figure 18.1).

- Crucibles are chosen if possible among good heat conductors which do not react with the sample (e.g. Al_2O_3, graphite, Pt); they usually contain 20–100 μl and are shaped to enhance the contact with the thermocouples.
- The DTA detector is a combination of thermocouples, with the wires of the first metal connecting each crucible to the voltmeter and the wires of the second metal connecting the two crucibles together. The nature of the thermocouple depends on the temperature range of the analysis (e.g. [−150; 800 °C] for chromel–constantan and [20; 2400 °C] for W–Re(3%)/W–Re(26%)). The recorded signal is in microvolts and is converted to temperature through a quasi-linear law. Usually, calibration is performed with the melting of standard metallic or mineral substances.



$$U = f(T_{sample} - T_{ref}) \rightarrow T_{sample} = T_{ref} + f^{-1}(U)$$

Figure 18.1 Scheme of a DTA setup.

- Different furnaces and heating elements are available, depending on the temperature range:
  - **Furnaces:** ceramic or graphite (for high temperatures); a high thermal conductivity conveys better homogeneity of the heating; weak thermal resistance allows a faster scanning rate.
  - **Heating elements:** [−150; 500 °C] for nickel–chromium, silver ($T_{melting}$ = 962 °C).
- Control of the atmosphere is essential to the accuracy of the experiment. Reactive or inert atmospheres and also vacuum can be used with DTA.

18.1.2.1 Principle

The system is heated following a programmed rise in temperature. In the absence of reaction, the difference in temperature with the heating vessel is low and constant; this signal is called the baseline. Any change related to a heat transfer will be observed as a step (glass transition, . . .) or a peak, either endothermic (melting, dehydration, . . .) or exothermic (oxidation, crystallization, . . .).

18.1.2.2 Data Processing

The integral of this signal deviating from the baseline is proportional to the amount of heat exchanged, via the calibration. The *specific heat* can therefore be derived according to

$$\int_{t_1}^{t_2}\left(\frac{\mathrm{d}H}{\mathrm{d}t}\right)_P \mathrm{d}t = \int_{t_1}^{t_2} C_P[T(t)]\left(\frac{\mathrm{d}T}{\mathrm{d}t}\right)_P \mathrm{d}t \cong \overline{C_P}\int_{t_1}^{t_2}\left(\frac{\mathrm{d}T}{\mathrm{d}t}\right)_P \mathrm{d}t \tag{18.1}$$

where $\mathrm{d}H$ is the heat evolved during $\mathrm{d}t$ while the temperature increases as $\mathrm{d}T$ and the specific heat C_P is a function of the temperature, and $\overline{C_P}$ its mean value during $[t_1, t_2]$.

Kinetic values can also be derived for an Arrhenius dependence of the rate constant on temperature, and the "reaction order model" of the conversion function with *Kissinger's* equation [11]:

$$\frac{\ln\beta}{T_{\mathrm{m}}{}^2} = \ln\frac{AR}{E_a} + \ln\left[n(1-\alpha_{\mathrm{m}})^{n-1}\right] - \frac{E_{\mathrm{a}}}{RT_m} \tag{18.2}$$

where E_{a} is the activation energy, A is the pre-exponential factor, β is the heating rate, n is the reaction order, α is the conversion degree, T is the temperature, R is the gas constant, and subscript m represents the maximum of the reaction rate.

Kissinger also proposed a kinetic interpretation of the shape of the thermogram as a function of the order of reaction by defining the shape index S as the ratio of the slopes of tangents to the curve at the inflection points before (1) and after (2) the peak [11]. This can be pragmatically determined by the ratio of the base lengths of the triangles constructed from the intersection of both inflection tangents with the baseline. Then the reaction order n is found to be related simply to the square root of S (Figure 18.2).

In addition, two characteristic features are often recorded: the maximum temperature T_{max} and the temperature of onset T_{onset}, defined by the intersection of the

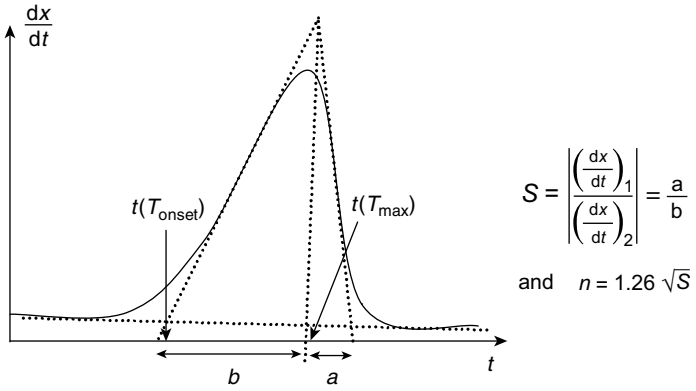


Figure 18.2 Thermogram and the relative definition of the shape *S* and the reaction order *n*.

tangent at the first inflection point with the baseline. However, DTA is more a qualitative than a quantitative method. Furthermore, it is limited by the small amount of substrate that can be loaded and the difficulty of closing or tightening the container.

18.1.2.3 **Examples**

DTA is widely used to determine the stability of catalysts as a function of temperature and the decomposition temperature of precursors. Narayanan and Krishna studied hydrotalcites and hydrotalcite-like compounds as supports to disperse palladium for performing the selective hydrogenation of phenol to cyclohexanone [12, 13]. The nature of the support and the method of preparation affect the morphology and the particle size and dispersion of the active metal (supported), and therefore the catalytic properties. Then the synthesized precursors ("HT*x*") obtained by coprecipitation of $Mg(NO_3)_2{\cdot}6H_2O$ and $Al(NO_3)_3{\cdot}9H_2O$ at pH > 13 and with a tuned molar ratio (*x*) of aluminum were characterized by DTA at $10\,K\,min^{-1}$ in air (Figure 18.3). The differential thermograms of HT*x* samples show two main transitions which depend qualitatively and quantitatively on the values of *x*. With an increase in this value, the relative intensity of the lower temperature endothermic peak at 433 K, corresponding to the loss of interlayer water, increases and shifts towards higher temperatures (for HT0.15 $T_{max} \approx 433$ K and for HT0.35 $T_{max} \approx 523$ K). This indicates that the quantity of interlayer water and the strength with which it is bound to the carbonate anions and the hydroxyl sheet increase with increasing *x*, that is, the aluminum content of the sample.

The high-temperature endothermic peak, which is due to the loss of hydroxyls from brucite-like sheet and carbonate ion, is shifted towards lower temperatures only for HT0.15 ($T_{max} \approx 678$ K). This could be due to the loosely bound carbonate anion in the interlayer region. This peak is found to occur in two steps in HT0.30 and HT0.35, explaining the appearance of a shoulder. The first step corresponds to the loss of the hydroxyl groups bound to Al^{3+} and the second step to the decomposition of $Mg(OH)_2$ and carbonate anions. Since the samples HT0.30 and HT0.35 have high aluminum contents, the shoulder appearing towards the lower temperature side can be attributed to the loss of hydroxyl groups associated with Al^{3+}.

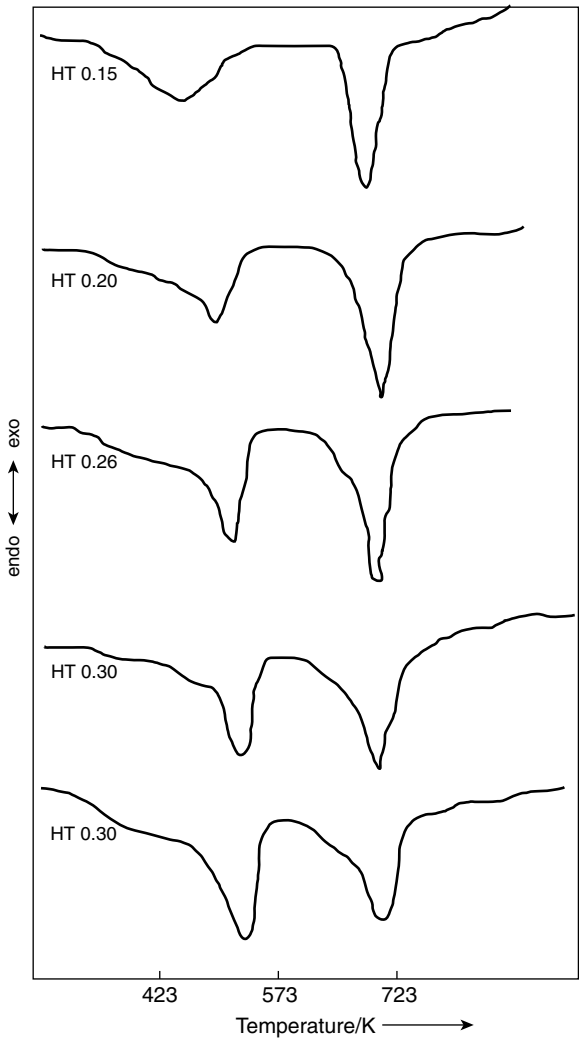


Figure 18.3 Differential thermograms of uncalcined hydrotalcites (HTx).

18.1.3
Differential Scanning Calorimetry (DSC)

Similarly to DTA, DSC is a temperature-programmed method. However, for DSC, the difference in the heat flow (or thermal power) and not the temperature is measured between a sample and a reference, versus time or temperature, in a controlled atmosphere. According to the definition, only setups providing heat detectors between the containers and the heat sink correspond to DSC; however, some higher accuracy DTA setups are still sometimes called DSC. Nowadays three

types of DSC exist: power-compensated DSC and flowmatic DSCs with a plate detector or with a surrounding detector. Because of its improved accuracy (relative to DTA), and the possibility of having closed containers, it is widely used [14, 15].

A DSC apparatus consists of a pair of crucibles containing the sample and the reference, both encaged in a heating vessel, with control over the atmosphere.

- **Crucibles**: crucibles for DSC are either similar to DTA crucibles (open) or can be closed or even tight to perform experiments under high pressure [up to 100 bar with stainless steel and 500 bar with Incoloy (nickel–iron–chromium alloy)]. The volume may vary from few microliters to several tens of microliters.
- **Heat detectors**:

  For power-compensated and flowmatic DSC, both crucibles are supported on a heat-conducting plate, which is the first half of the thermocouple, the second part being the wires connecting the plate to the recorder (Figure 18.4).

  For surrounding detector DSC, two thermopiles (series of several thermocouples) are shaped in cylinders and installed around each of the crucibles and as much as possible in contact with them (Figure 18.4).

  The efficiency of plate-type DSCs decreases with the temperature and thickness of the plate, ranging from 20 to 50%. Calvet heat-flow type DSC techniques (surrounding sensor) can achieve $94 \pm 1\%$ efficiency over their full temperature range. The DSC instrument can be calibrated by the Joule effect (only for Calvet-type DSC), melting of a standard metal (indium, tin, zinc), or heat capacity of sapphire (Table 18.2).
- According to the tightness and composition of the experimental chamber and of the crucible, all kinds of gaseous *environments* can be used: inert, oxidative, reductive, water vapor, corrosive, or vacuum.

18.1.3.1 Principle

While the system is heated following a temperature program, a signal proportional to the heat flow between the furnace and each container is recorded. Enthalpy changes can be recorded, and also reaction rates. The thermogram can present steps (glass transition, etc.) or peaks, either endothermic or exothermic. The specific heats can also be easily derived. In the case of power-compensated DSC, as soon as a deviation from the temperature program is detected, heat is brought to or taken from the sample. This is similar to the concept of an adiabatic calorimeter; the analysis is effected on the compensation signal. For heat-flux DSC, the heat flow signal from both thermopiles is measured through a differential setup.

18.1.3.2 Data Processing

18.1.3.2.1 Thermogram Equation Let us consider the reference (r) and the sample (s) crucibles – the expression for the heat flows is as follows:

$$\frac{\mathrm{d}q_r}{\mathrm{d}t} = C_\mathrm{r}\frac{\mathrm{d}T_\mathrm{r}}{\mathrm{d}t} \quad \text{and} \quad \frac{\mathrm{d}q_\mathrm{s}}{\mathrm{d}t} = C_\mathrm{s}\frac{\mathrm{d}T_\mathrm{s}}{\mathrm{d}t} + \frac{\mathrm{d}h}{\mathrm{d}t} \tag{18.3}$$

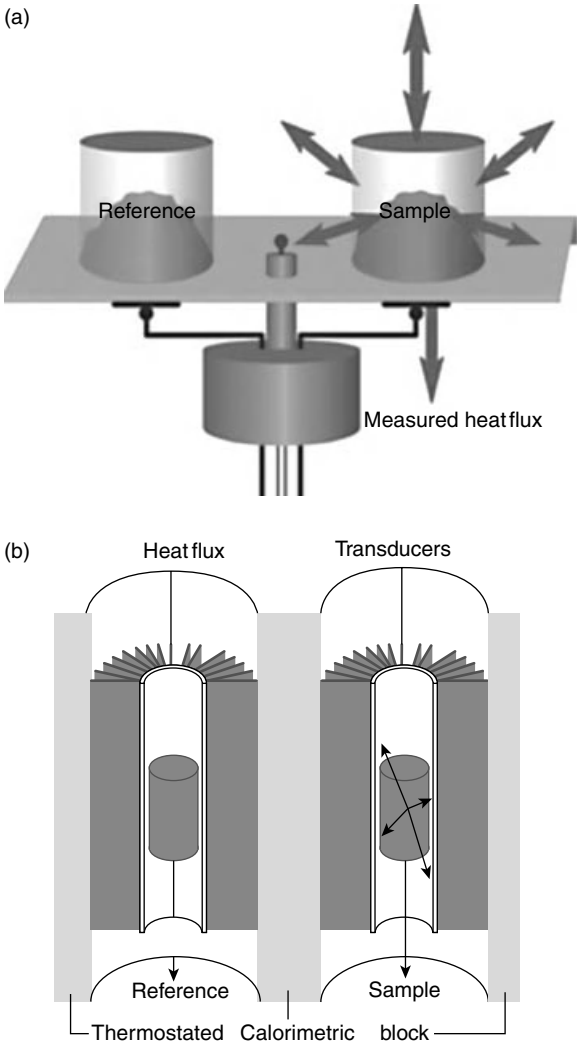


Figure 18.4 Schematic diagrams of a plate-type DSC (a) and a Calvet-type DSC (b).

where C_r and C_s are the heat capacities of the reference and sample-filled crucibles at constant pressure, respectively, and dh/dt, the absorbed thermal power resulting from the change in the sample.

The heat flow is also related to the difference in temperature via the thermal resistance of the thermocouple:

$$\frac{dq}{dt} = \frac{dq_s}{dt} - \frac{dq_r}{dt} = -\frac{T_s - T_r}{R} \quad \text{or} \quad R\frac{d^2q}{dt^2} = -\frac{dT_s}{dt} + \frac{dT_r}{dt} \tag{18.4}$$

Since the reference crucible is inert, its temperature T_r and the furnace temperature T are very close to each other and their derivative also. Therefore, $dT_r/dt \cong dT/dt$.

Table 18.2 Standard elements for calibration by melting [16].

Substance	Melting point (°C)	Melting enthalpy (J g^{-1})
Naphthalene	80.3	149
Benzoic acid	122.4	148
Indium	156.6	28.5
Tin	231.9	60.7
Lead	327.4	22.6
Zinc	419.5	113
Aluminum	660.4	396
Silver	960.8	105
Gold	1 063.0	62.8

Finally the equation of a DSC thermogram consists of a heat capacity factor, a kinetic factor and a thermal lag:

$$\frac{dq}{dt} = (C_s - C_r)\frac{dT}{dt} + \frac{dh}{dt} - C_s R\frac{d^2q}{dt^2} \tag{18.5}$$

18.1.3.2.2 **Kinetic Measurements** Let us consider a reaction peak. The advancement α of this reaction at a certain point of the thermogram is proportional to the heat h exchanged from the beginning of the peak to that specified moment, that is, the integral of the thermogram. Therefore, the time derivative of the reaction rate is proportional to the direct measurement of the heat flow:

$$\frac{dh}{dt} \propto \frac{d\alpha}{dt} = k(1-\alpha)^n \quad \text{with} \quad k[T(t)] = A\exp\left(-\frac{E_a}{RT(t)}\right) \tag{18.6}$$

A being the Arrhenius constant and E_a the activation energy. At the maximum of the peak $T = T_{max}$ and $(d^2\alpha/dt^2)T_{max} \cong 0$, then kinetic values can be derived:

$$\frac{d\alpha}{dt}(T_{max}) = -\frac{E_a}{nRT_{max}^2}\frac{dT}{dt}[1-\alpha(T_{max})] \tag{18.7}$$

which gives information on E_a and n. The order of reaction n can also be determined via the Kissinger equation (see equation 18.2 (see page 750)).

18.1.3.2.3 **Heat Capacity Determination** Two methods can be used for the determination of heat capacity [17]. For both, either two or three tests can be made:

1) a *first one* with a mass m_s of the sample (s) in the sample crucible (sc) (of mass m_{sc}),
2) a *second one* ("blank") with an empty sample crucible (rc) (of mass m_{rc}),
3) a *third one* with a reference sample (sapphire) with known C_p,

the reference crucible remaining empty for the three tests.

The option of running only the first two tests is quicker and less expensive but less precise than the other option, and a sensitivity function of the temperature $S(T)$

has to be considered, whereas this function cancels out in the three-tests method (by division).

The Continuous Method A sample is heated at a constant rate, while no reaction occurs. Its specific heat at constant pressure (C_p) can be determined. The equations for the heat flow $HF_{(i)}$ as a function of temperature T are as follows:

$$HF_{(1)}(T) = HF_{(s)} - HF_{(r)} = S(T)\left[m_s c_{p(s)} + m_{sc} c_{p(sc)} - m_{rc} c_{p(rc)}\right]\frac{dT}{dt} \tag{18.8}$$

$$HF_{(2)}(T) = S(T)\left[m_{sc} c_{p(sc)} - m_{rc} c_{p(rc)}\right]\frac{dT}{dt} \tag{18.9}$$

$$HF_{(3)}(T) = S(T)\left[m_{sapphire} c_{p(sapphire)} - m_{rc} c_{p(rc)} - m_{rc} c_{p(rc)}\right]\frac{dT}{dt} \tag{18.10}$$

Then we obtain

$$c_{p(s)}(T) = \frac{HF_{(1)} - HF_{(2)}}{S(T) m_s \dfrac{dT}{dt}} \tag{18.11}$$

with two tests and

$$c_{p(s)}(T) = c_{p(sapphire)}(T)\frac{m_{sapphire}}{m_s}\left[\frac{HF_{(1)} - HF_{(2)}}{HF_{(3)} - HF_{(2)}}\right] \tag{18.12}$$

with three tests.

The Step Method The temperature program consists of alternate steps of constant heating and isotherm, the latter letting the signal come back to the baseline. Instead of picking a value of evolved heat, it integrates it over the temperature range of the step. The heat capacity is obtained with better accuracy and a temperature profile can even be derived. The same three steps as in the previous method are observed but with a step temperature program. Then we obtain for each step

$$c_{p(s)}(T_i \to T_{i+1}) = \frac{\int_{T_i}^{T_{i+1}} HF_{(1)} dT - \int_{T_i}^{T_{i+1}} HF_{(2)} dT}{S\left(\dfrac{T_i + T_{i+1}}{2}\right) m_s (T_i - T_{i+1})} \tag{18.13}$$

with two tests and

$$c_{p(s)}(T_i \to T_{i+1}) = c_{p(sapphire)}(T_i \to T_{i+1})\frac{m_{sapphire}}{m_s}\left[\frac{\int_{T_i}^{T_{i+1}} HF_{(1)} dT - \int_{T_i}^{T_{i+1}} HF_{(2)} dT}{\int_{Ti}^{T_{i+1}} HF_{(3)} dT - \int_{T_i}^{T_{i+1}} HF_{(2)} dT}\right] \tag{18.14}$$

with three tests.

18.1.3.3 Example

DSC is used in a vast range of domains, from the pharmaceutical and polymer industries to safety screening and purity analysis. The performance of DSC can be

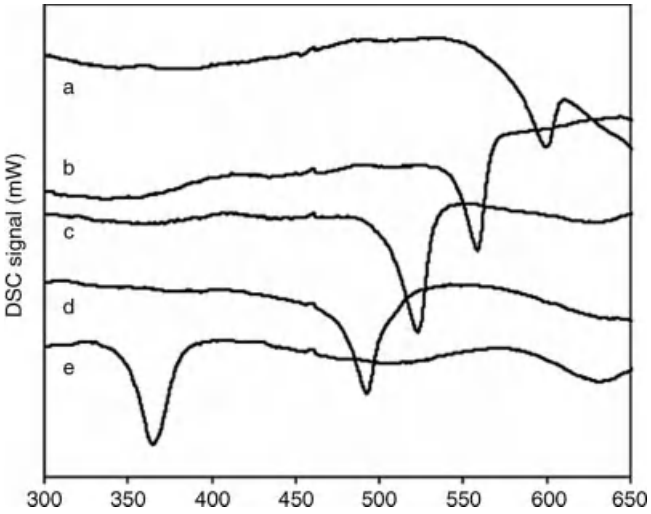


Figure 18.5 DSC analysis of calcined samples: (a) Li–MD; (b) Li–Na–MD; (c) Li–Ba–MD; (d) Li–Sr–MD; (e) Li–K–MD (MD = Dy_2O_3/MgO).

enhanced by coupling with other techniques to obtain better characterization: modulated DSC, TG–DSC–mass spectrometry (MS), TPD & DSC-gas chromatography (GC), DSC–MS, DSC–TCD, etc.

Tope *et al.* reported the use of DSC in the study of the phase transformation of their catalyst for the oxidative dehydrogenation of ethane [18]. Alkali or akaline earth metal chloride mixtures with LiCl on Dy_2O_3/MgO (∼15 mg) were heated linearly from 100 to 700 °C at 10 °C min^{-1}. The decrease in the melting point relative to LiCl was attributed to the formation of eutectic mixtures, and thermodynamic predictions of the metal chloride mixtures gave conclusive results for this assumption (Figure 18.5).

18.1.4
Thermogravimetry or Thermogravimetric Analysis (TGA)

TGA is the analysis of the mass variations of a sample versus time or temperature in a controlled atmosphere, while a temperature program is run. It is a very useful technique for any reaction related to a mass loss (drying, desorption, reduction, degradation in an active atmosphere, ...) or a mass gain (wetting, oxidation, adsorption, ...), and therefore especially in solid–gas systems. Even if it is blind to mass conservative phenomena, this can become valuable information when coupled to other techniques, to reveal mass conservative changes, for example a phase transition.

A thermogravimetric analyzer consists of a crucible connected to a balance and inserted into a furnace with control over the atmosphere.

- *Crucibles* can be made of various materials depending on the temperature range, of different shapes depending on the type of analysis (cylindrical is the standard,

latticed platinum is devoted to gas–solid interactions, . . .) and of volume ranging from a few to several hundred microliters.

- The quality of the *furnace* is also of prime necessity. Many aspects are expected: a high maximum temperature, a large homogeneity zone, high mobility and rate of rise and decrease in temperature, the possibility of working under a controlled atmosphere (tightness of the system), a high reject of the magnetic field born from the heat current, and a weak influence of convection or radiation on the sample's heating.
- *Control of the atmosphere* allows numerous possibilities for reactions. Corrosive gases or a vacuum atmosphere will need appropriate materials and it may then be easier to use a magnetic suspension balance, in order to protect the balance.
- The key element of the thermogravimeter is the *balance*. Nowadays it mostly works on the "zero method": the mobile part is kept stable by exerting a compensating force, most often thanks to an electromagnetic device, and therefore the obtained signal is this compensation. Three main types can be distinguished:
  –**Asymmetric balance:** only one container is weighted. Then the container and the environment's influence have to be taken into account.
  –**Symmetric balance:** two containers are symmetrically set up, one receiving the sample and the other a reference or remaining empty. If well adjusted, this can minimize many errors, such as thermal dilatation or aerostatic buoyancy (Figure 18.6) [19].
  –**Magnetic suspension balance:** in order to work with corrosive atmospheres or variable pressure without affecting the integrity or the sensitivity of the balance. The balance and the container can be separated providing a magnetic suspension setup (Figure 18.7) [20].

18.1.4.1 Principle

The sample is heated following a temperature program and control over the atmosphere; the weight is recorded versus time and temperature. Many parameters affect the signal: increasing the mass of the sample raises the reaction temperature, and increasing the scanning rate also raises the temperature. Therefore, the mass and scanning rate ought to be kept equal in order to compare results. The derivative of the thermogravimetric signal (differential thermogravimetry: DTG) allows one to define more accurately the mass variations (temperature and mass variation in wt% min^{-1} at the peak's maximum) and gives information on the kinetics of the phenomenon.

18.1.4.2 Data Processing

The record of the mass variations relative to time can be related to the reaction rate when the reaction is already known, allowing the calculation of kinetic values.

Depending on the gas (acidic, basic, oxidative, . . .), all sorts of physicochemical properties of the surface or the bulk of a solid can be tested. For example, with a "pulse-TG," successive doses of a gas probe can be injected while the effective amount of adsorbed gas is measured by the balance, leading to an adsorption isotherm.

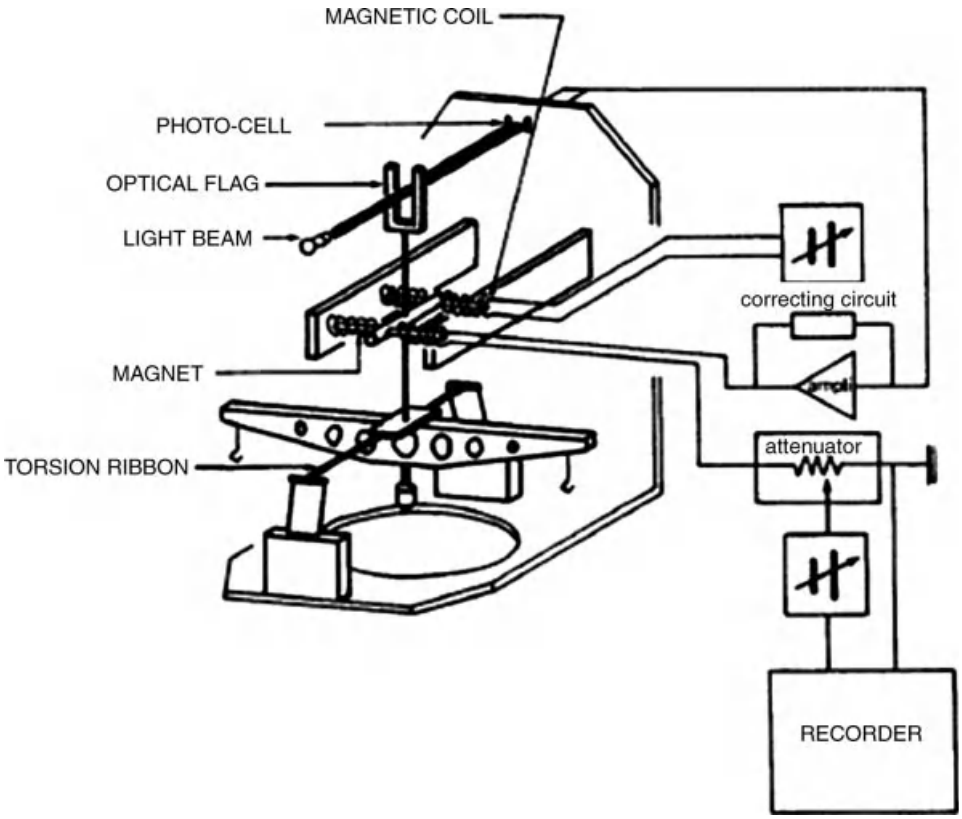


Figure 18.6 Schematic diagram of a common symmetric thermobalance working with the "zero method."

18.1.4.3 **Examples**

18.1.4.3.1 **Example 1** The range of applications of TGA is very broad, from catalysis for the preparation and characterization (adsorption isotherms, etc.) of catalysts, to polymers and metals/metal alloys, via pharmaceuticals (degradation, polymorphs, crystallization, . . .), or explosives/propellants (risk assessment, etc.).

The acidic properties of several sol–gel-prepared catalysts were determined by thermal desorption of 2-phenylethylamine (PEA), chosen as a base probe molecule, by Gervasini *et al.* [21]. The experiments were carried out with a thermogravimetric analyzer. The PEA thermodesorption curves, collected at different heating rates, were treated numerically in order to interpret them kinetically (Kissinger method) and derive the kinetic and activation parameters for each type of acidic site of the surface in addition to the number of sites of each type. This allowed the acid sites to be connected to the activation energies for PEA desorption.

Prior to the adsorption/desorption analysis, the powders were activated in vacuum for 16 h at 400 °C. PEA (purity >99%) was then introduced, up to complete coverage of

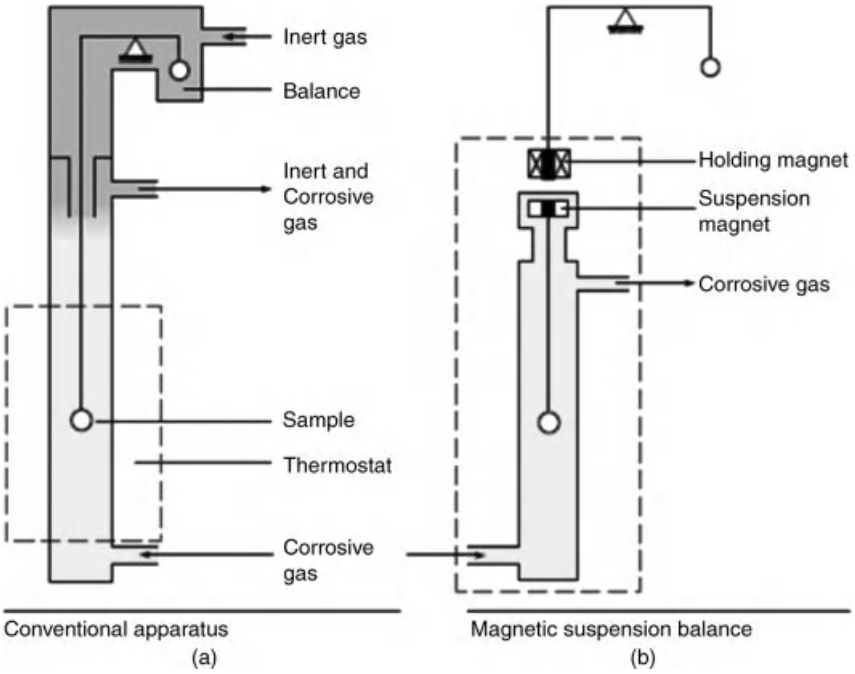


Figure 18.7 Schematic diagrams comparing a conventional setup (a) and a magnetic suspension setup (b).

the powder. The saturated powder obtained was loaded in the pan of the TGA apparatus (10–15 mg) and then subjected to a two-step analysis performed under a nitrogen flow (30 ml min^{-1}). The first isothermal step, carried out at 50 °C, removed all the excess PEA from the surface, while the second step was non-isothermal, with a temperature increase from 50 to 800 °C at a constant heating rate ($\beta = 5, 10, 15, 20, 30$ °C min^{-1}) in order to remove PEA completely from the surface. The total and intermediate PEA mass losses were determined by subtracting the final mass at 800 °C from the mass measured at the end of the first isothermal step or from the masses at definite times/temperatures of analysis corresponding to well-defined steps of the thermogram.

Figure 18.8 reports the thermogram obtained for silica–alumina. The total amount of acid sites can be calculated from the height of the plateau at 50 °C (Figure 18.8a), that is, 2.75 meq g^{-1}. The DTG of the second step gives two distinct peaks at $T_{max,1} \approx 200$ °C and $T_{max,2} \approx 400$ °C. The peak at $T_{max,1}$ can be clearly individuated at any β, whereas the other peak at higher temperature $T_{max,2}$ is better detected at higher β. In this case, it is difficult to detect a clear shift of $T_{max,2}$ with β. As a general trend, E_a values similar to the enthalpy of PEA vaporization ($\Delta H = 42$ kJ mol^{-1}) were obtained for the acidic sites associated with $T_{max,1}$; a value of 108 kJ mol^{-1} was associated with $T_{max,2}$.

18.1.4.3.2 **Example 2** Navarro Lopez *et al.* used an isothermal pulsed-TGA technique combined with transmission electron microscopy (TEM) observations to determine the mechanisms of growth of multiwalled carbon nanotubes (CNTs) on an iron-based catalyst [22]. After purge and heating of the substrate under helium

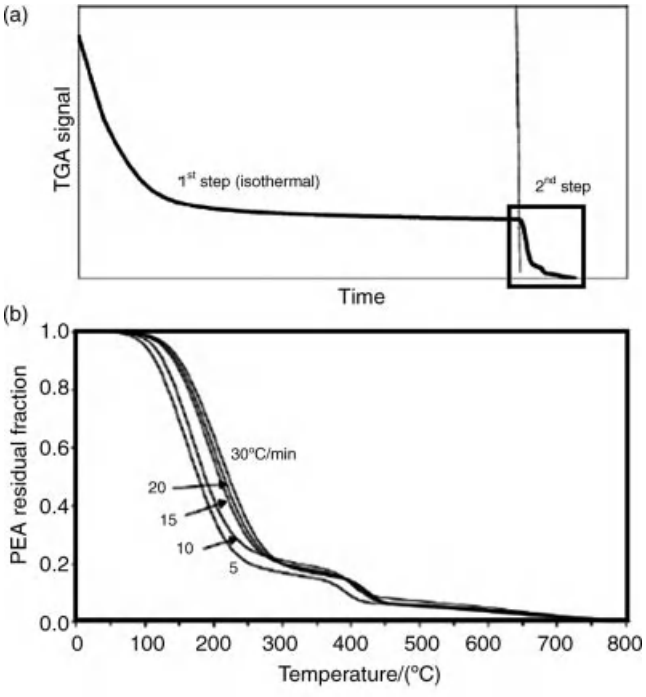


Figure 18.8 (a) Two-step TGA performed to study the surface acidity of the sample surfaces: the first step is carried out at 50 °C. (b) Second step at increasing temperature from 50 to 800 °C [enlarged from the boxed area in (a)].

until the desired temperature, pulses of 0.2 mmol of ethylene were injected every 10 min into a stream of helium. Features on the first mass variation steps could be ascribed to nucleation and lengthening/thickening of the nanotubes, thanks to the TEM observations. Evidence of the catalytic behavior of iron in the CNT growth process is presented in Figure 18.9.

The main fact to observe is that the total weight gain in the experiment and weight in each pulse depend on the amount of iron in the sample; the more iron is exposed, the more carbon is deposited. It is also important to consider the different shapes of the thermographs. The thermograph for 5% Fe/SiO_2 catalyst shows four sharp increases in weight whereas for the 2% Fe/SiO_2 catalyst just one sharp increase is observed. This suggests that the weight gain due to carbon deposition on the catalyst is a function of the number of exposed metal atoms acting as catalytic centers and the amount of acetylene pulsed.

18.1.5
Thermogravimetric Analysis Coupled with Calorimetry (TGA–DTA, TGA–DSC)

The TGA–DSC coupled technique was developed to provide complementary information on the nature of the catalysts. The simultaneous accurate measurement of heat

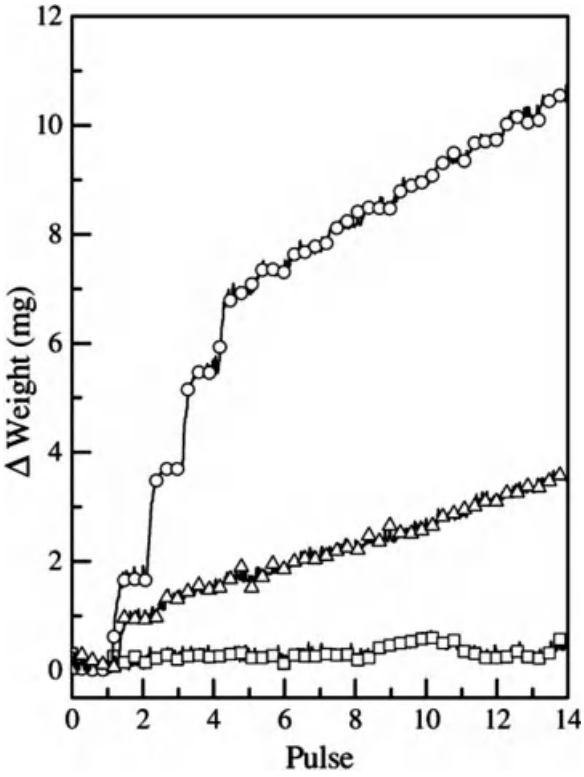


Figure 18.9 Weight gain for the SiO_2-supported catalysts (○) 5% Fe/SiO_2 and (Δ) 2% Fe/SiO_2 and for the silica (□) SiO_2. Reaction temperature, 973 K, sample weight, 40 mg.

and weight of a sample can be achieved via a dedicated setup, where none of the measurements affects another. Nowadays such devices are in common use and various technological setups are available on the market (Calvet type, plate-DSC, . . .) [19].

TGA–DSC and TGA–DTA systems integrate both measurement devices. Many setups exist for both DTA/DSC and TGA, so that a wide range of apparatus is available providing various degrees of precision which we are not comparing here. Subchapters on TGA and DSC can be consulted for further insights. Although the technology exists, so far the magnetic suspension devices are mostly asymmetric (one container) and only couplings with density or viscosity measurements are provided. Thus mainly two setups can be distinguished:

- **TGA–DTA or TGA–plate-DSC:** the temperature or heat measuring device is disposed along the suspension rod connecting the crucibles to the thermobalance. Usual DTA thermocouples, tripod or plate setup can be used (Figure 18.10).
- **Calvet-type TGA–DSC:** the crucibles are suspended symmetrically to the thermobalance into the surrounding thermopiles of the Calvet-type DSC (Figure 18.10).

18.1.5.1 **Principle**

The sample is heated following a temperature program and control of the atmosphere. The weight and the heat or temperature difference are recorded versus time and temperature.

18.1.5.2 **Examples**

TGA–DTA/DSC is a common way of studying the behavior of synthesized catalysts at high temperature. Thus the dehydration and degradation temperatures can be obtained, and eventually phase changes (corresponding to heat exchanges due to variation of heat capacity, while no mass is lost).

18.1.5.2.1 **Example 1** The thermal decomposition of $Sr(OAc)_2{\cdot}0.5H_2O$ in N_2 at 600 °C was investigated by TGA–DTA/DSC–FTIR (Fourier transform infrared) spectrometry by Duan *et al.* [23]. Two main mass loss steps were observed: dehydration and decomposition of anhydrous $Sr(OAc)_2$ to $SrCO_3$. Two phase changes were observed between dehydration and decomposition thanks to DSC (two endotherms around 350 °C in Figure 18.11). The coupling with FTIR provided valuable information on the online gaseous products during the thermal events (not plotted here).

18.1.5.2.2 **Example 2** Malecka *et al.* studied the thermal decomposition of $NiC_2O_4{\cdot}2H_2O$ with TG, DTA, MS, and FTIR analyses [24]. TGA–DTA–MS experiments on 6–20 mg samples consisted of linear heating in a standard platinum sample pan, from room temperature to 420 °C at 5 °C min^{-1}, in a dynamic flow of helium or synthetic air at 0.1 l min^{-1}. The decomposition proceeded generally in two steps,

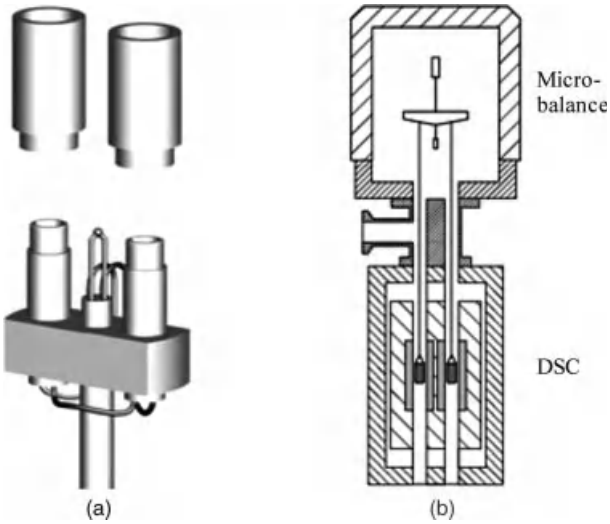


Figure 18.10 (a) TGA–plate DSC; the DTA detector is connected along the rod of the thermobalance. (b) Calvet-type TGA–DSC [19].

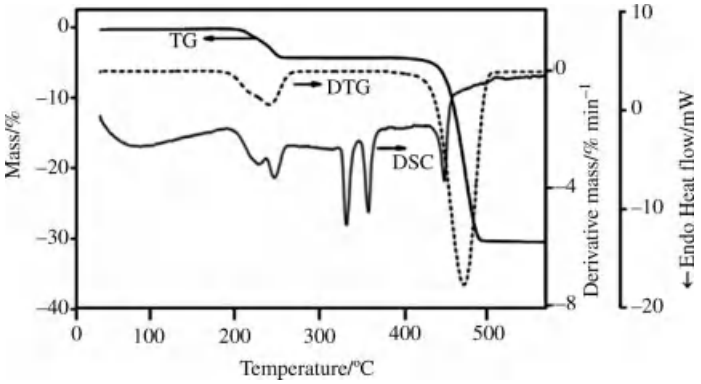


Figure 18.11 TGA–DTG–DSC curves for the decomposition of $Sr(OAc)_2 \cdot 0.5H_2O$ at 10 K min^{-1}; N_2 flow rate, 50 ml min^{-1}.

dehydration [endotherm below 250 °C, correlated to the mass signal at $m/z = 18$ (H_2O)] and decomposition of the anhydrous oxalate [mass signals at $m/z = 44$ (CO_2) and $m/z = 28$ (CO_2 and CO)] correlated to an exotherm above 300 °C in air (Figure 18.12). Further FTIR experiments led to the establishment of the main

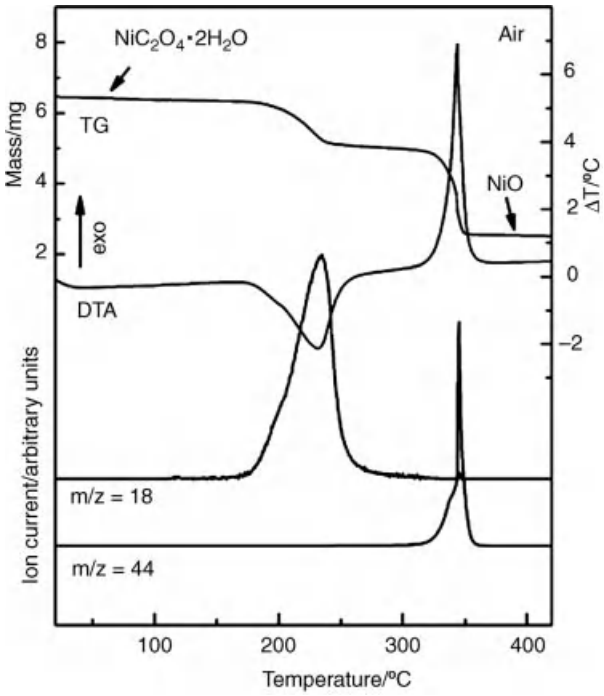


Figure 18.12 Thermogravimetric and mass spectrometric results for decomposition of $NiC_2O_4 \cdot 2H_2O$ in air (heating rate $\beta = 5$ °C min^{-1}).

reaction as

$$NiC_2O_4 \rightarrow Ni + 2CO_2 \xrightarrow{\text{air, fast}} NiO \qquad (18.15)$$

18.1.6 Calorimetry

Calorimetry is the science of measuring heats related to chemical or physical phenomena. The concepts of *heat* and *temperature* are distinct. According to the first law of thermodynamics, heat and work are the only media of energy transfer, and heat corresponds to various phenomena that cannot be described as work (radiation, conduction, convection). Heat is only related to temperature by the entropy (second law of thermodynamics).

Temperature is measured at thermal equilibrium, that is, when no heat flows between a system and its surroundings. Then a thermocouple will be able to measure either a heat flow or a temperature [25].

Three kinds of calorimetric devices can be distinguished (Figure 18.13):

- **Adiabatic calorimeters**: the temperature of the surroundings is constantly fitted to the temperature of the sample in order to minimize the heat flow, then the evolved heat can be calculated from the measured temperature. These are devices such as accelerating rate calorimeters (ARCs), Berthelot bomb calorimeters and *reaction calorimeters* in adiabatic mode. Power-compensated DSC is a *quasi-adiabatic* method.
- **Heat-exchanging calorimeters**: the thermal detector binds the surroundings to the sample container, and the amount of heat flowing from one to the other is measured via the Seebeck/Peltier effect, proportional to the difference in temperature. The *Calvet microcalorimeters*, some of the DSCs, and the reaction calorimeters in isothermal mode correspond to this category. If the heat flow is fast enough compared with the phenomenon occurring, the system is in a *quasi-isothermal* situation.
- **Isoperibolic calorimeters**: the temperature of the surroundings (in Greek *peri-bolos*) is kept constant while the temperature of the sample is measured. Reaction calorimeters belong to this category.

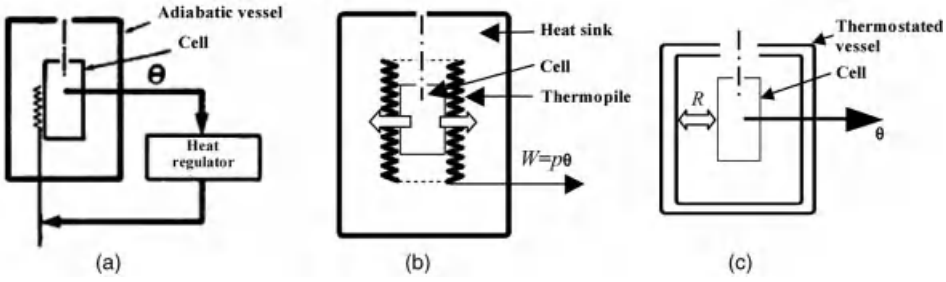


Figure 18.13 Schematic diagrams of (a) an adiabatic, (b) a heat-exchanging, and (c) an isoperibolic calorimeter. θ, Measured temperature; W, heat flow; R, thermal coupling between the vessel and the cell.

Prefixes such as micro or nano can be used for calorimetric devices, corresponding to the sensitivity of the voltage measurement at the thermal detector. Microcalorimeters usually achieve a sensitivity in the milliwatts range in heat flow. High sensitivity is obtained with devices performing very accurate thermostating of the calorimetric block, efficient collection of the heat signal, and enhanced thermal detectors such as semiconductors.

18.1.6.1 The Tian–Calvet microcalorimeter

The microcalorimeter developed by Tian and Calvet in 1948 is a heat-flow calorimeter based on a differential setup, that is, the measure is a comparison of the heat flows occurring on one part between the sample and the thermostated jacket and on the other part between a reference and the same jacket [3, 26].

The apparatus consists of a thermostated jacket in which two symmetrical calorimetric cells are placed (sample and reference). Two twin (same thermal resistance) thermopiles, consisting of hundreds of thermocouples linked in a series circuit, in the shape of a cylinder, collect the heat flow between the cells and the jacket (Figure 18.14).

- *Calorimetric cells*, or "*inner vessel*," must be inert and good thermal conductors (e.g., metal alloys, very thin quartz . . .). Their shape must adjust to the thermopiles in order to enhance the thermal contact. The volume is usually of the order of 10 ml and they are located symmetrically inside the thermostated jacket. Any kind of cell can then be designed to perform an experiment; however, a large range of cells is already commercially available (e.g., "*batch*" *closed vessel*, up to 1000 bar; *ampoule vessel*, for dissolution experiments: a rod is pushed to break the ampoule inside the cell; *fluid circulation vessel*, in order to flush a gas or a liquid to interact with the sample)
- *The thermostated jacket*, or "*external vessel*," usually achieves a stability of 10^{-2} K but thicker calorimeters (used for risk assessment) display higher stability. The higher the inertia, the better is the stability, but also the longer is the time for the experimental temperature to be changed.
- *Thermal detectors* are cylindrical thermopiles of the same resistance covering more than the height of the cells and ensuring good efficiency of heat collection. The calibration is performed via the Joule effect (a resistance is heated at a known voltage and current for a precise time and the corresponding generated energy $E = UIt$ is calculated and compared with the recorded thermogram in the output of the calorimeter).

18.1.6.1.1 **Principle** While the jacket is kept at a constant temperature, the phenomena occurring in the calorimetric cell generate a heat flow through the thermal detector that is recorded as a function of time and is called a thermogram [3, 26].

The first part of the evolved heat affects the temperature of the sample while the other part is flowing through the thermal detector. Let us denote the calorimetric capacity of the inner vessel μ, then the resulting power for a temperature evolution $d\theta$ during a time dt is equal to $\mu(d\theta/dt)$.

The second part is partly collected by the thermopile as an emf, via the Seebeck effect in the thermopile. Every thermocouple has one junction in contact with the cell and the other with the thermostat; therefore, for each one an emf e_j is developed, proportional to the thermoelectric power ε and the temperature difference $\Delta\theta_j$. As the

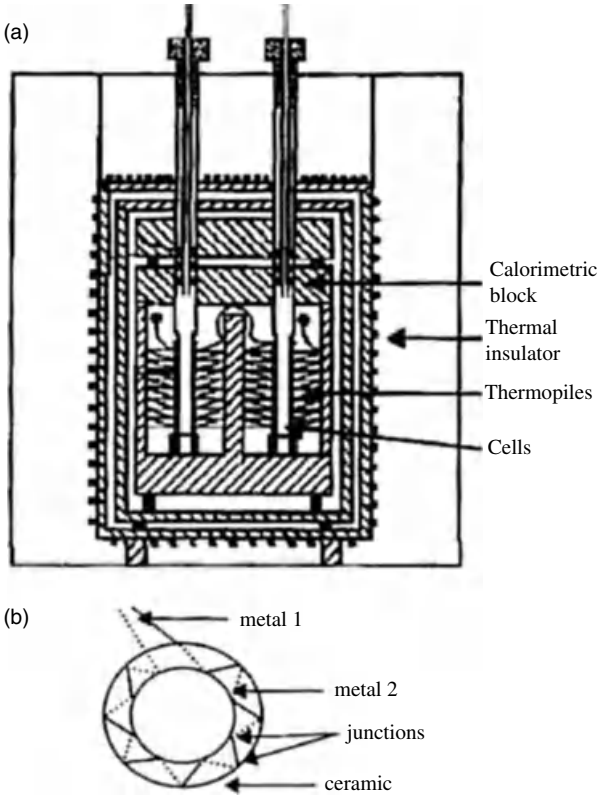


Figure 18.14 Schematic diagrams of a differential heat-flow calorimeter (a) and of a thermopile element (b) [14].

thermopile is a series circuit, the emfs are summed and the total emf E is proportional to the difference between a conceptual mean temperature of the sample θ_i and the temperature of the jacket θ_e:

$$E = \sum_{j=1}^{n} e_j = \varepsilon \sum_{j=1}^{n} \left(\theta_j - \theta_e\right) \approx n\varepsilon\theta \tag{8.16}$$

where $\theta \equiv (\theta_i - \theta_e)$. The thermal power can be calculated, knowing the thermal conductance γ of the thermocouples, and assuming that the ratio of heat collected λ is constant:

$$\phi = \sum_{j=1}^{n} \phi_j = \frac{1}{\lambda} \sum_{j=1}^{n} \varphi_j = \frac{1}{\lambda} \sum_{j=1}^{n} \gamma\left(\theta_j - \theta_e\right) = \frac{\gamma}{\lambda\varepsilon} E \approx p\theta \tag{18.17}$$

where $p \equiv n\gamma/\lambda$ and p is called the heat transfer coefficient.

Finally, we obtain an expression for the thermal power, known as the Tian equation:

$$w = p\theta + \mu \frac{\mathrm{d}\theta}{\mathrm{d}t} \tag{18.18}$$

The registered emf E is proportional to θ and the thermal power can be determined:

$$w(t) = \frac{p}{\varepsilon} E(t) + \frac{\mu}{\varepsilon} \frac{\mathrm{d}E(t)}{\mathrm{d}t} \tag{18.19}$$

Let us consider a simple calibration experiment, also called the Joule effect. A known constant thermal power W is brought inside the sample cell as a step function of time during $[t_0, t_1]$ (Figure 18.15).

$$for\ t < t_0, \qquad w(t) = 0, \quad E(t) = 0, \tag{18.20}$$

$$for\ t \in [t_0, t_1], \quad w(t) = W, \quad E(t) = \frac{W\varepsilon}{p}\left(1 - e^{-\frac{p}{\mu}(t-t_0)}\right), \tag{18.21}$$

$$for\ t > t_1 \gg \frac{\mu}{p} + t_0, \quad w(t) = 0, \quad E(t) \approx \frac{W\varepsilon}{p} e^{-\frac{p}{\mu}(t-t_1)}, \tag{18.22}$$

Then the integration of the recorded signal can provide an evaluation of the evolved thermal power:

$$\int_{t_0}^{t_2} E(t)\mathrm{d}t \approx \frac{W\varepsilon}{p}(t_1 - t_0) = \frac{\varepsilon}{p}[W(t_1 - t_0)] = \frac{\varepsilon}{p}\int_{t_0}^{t_1} w(t)\mathrm{d}t = \frac{\varepsilon}{p}\int_{t_0}^{t_2} w(t)\mathrm{d}t \tag{18.23}$$

As the output signal $\Delta(t)$ is proportional to the emf E, $\Delta(t) \equiv g\theta = (g/n\varepsilon)E(t)$, we obtain

$$w(t) = \frac{p}{g}\left[\Delta(t) + \tau \frac{d\Delta(t)}{dt}\right] \tag{18.24}$$

where $\tau \equiv \mu/p$ is the cell time constant.

Also, the quantity of heat Q developed by the process under investigation recorded during $[t, t']$ is given by

$$Q([t, t']) = \frac{p}{g}\int_t^{t'} \Delta(t)\mathrm{d}t + \frac{\mu}{g}\int_t^{t'} \mathrm{d}\Delta(t) \tag{18.25}$$

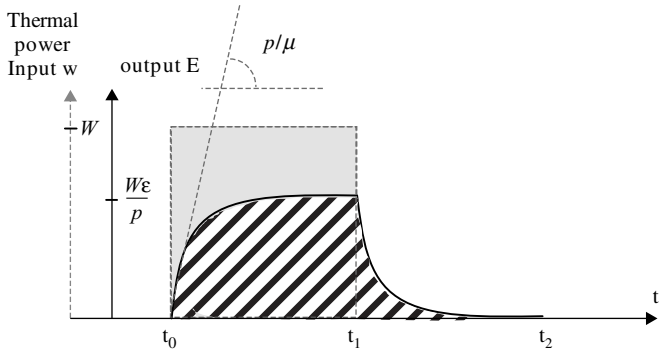


Figure 18.15 Joule effect calibration and the related Eqs. (18.20)–(18.22).

However, the thermal inertia of the apparatus can create artifacts for non-isothermal methods; therefore, differential setups have been developed, replacing $\theta \equiv (\theta_{\text{int. vessel}} - \theta_{\text{ext.}})$ by $\theta \equiv (\theta_{\text{sample cell}} - \theta_{\text{reference cell}})$, but eventually bringing thermal couplings between both cells ($p \rightarrow p + p_{\text{sample} \leftrightarrow \text{ref. thermic exchange}}$).

If the symmetry and the separation of the cells are well taken care of, then the accuracy and the stability of the signal are enhanced.

18.1.6.2 **Calorimetry–Volumetry**

In order to determine heats of adsorption (in kJ mol^{-1}), calorimetric measurements need to be correlated with adsorbed amounts in order to be valuable. Then the reactant (gas or liquid) can be delivered into the calorimetric cell either in a continuous flow (capillary setup) or in a fragmented manner (doses via a volumetric setup). The fragmented method is more often used when it comes to gas–solid interactions, providing the acquisition of adsorption isotherms and correlated energies.

A volumetric line consists of two parts, the measuring section [between valves R_0 and R_1 (Figure 18.16)] and the calorimetric cell section (between R_0 and R_2), both of known volume and connected to a vacuum pump allowing a residual pressure of about 0.1 mPa. The experiment consists in sending successive amounts ("doses") of gas on to the catalyst and waiting for thermal equilibrium before each new dose.

For every dose, pressure and heat evolution are recorded continuously, hence the equilibrium pressure (at the end of the peak of adsorption), the amount adsorbed (calculated from the pressure variation), and the heat involved for each dose (integration of the thermogram) can be obtained. By theoretically minimizing the amount of each dose, we would obtain a precise correlation of the adsorbed amount with its adsorption energy; however, this is limited by the resolution of the recorded thermogram, which needs a minimal exchanged heat to be well integrated. The mass of the investigated catalyst is usually adapted in order to obtain good resolution (heat is extensive) while avoiding diffusion phenomena.

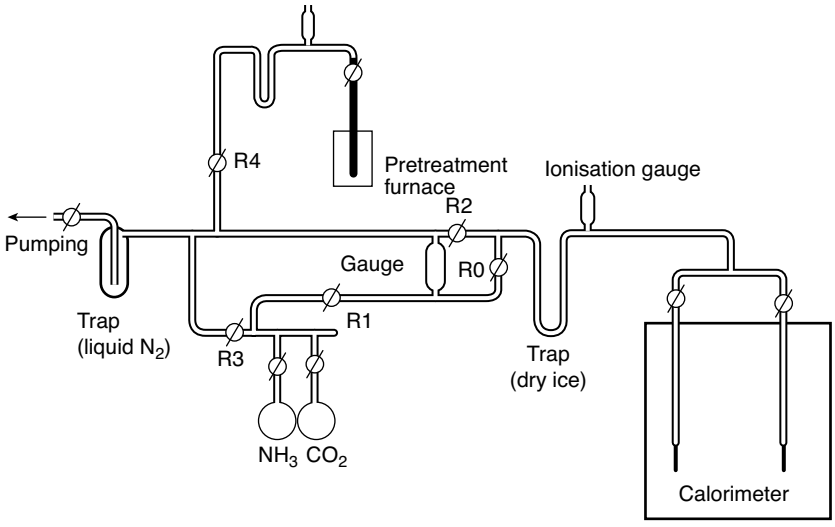


Figure 18.16 Schematic diagram of a coupled volumetry–calorimetry apparatus [7].

The data can be expressed in different ways (Figure 18.17) [26]:

a) The *time constant* of the thermogram can be evaluated. However, a thermogram can consist of many phenomena with many time constants superposed.
b) The *volumetric isotherms* (the amount adsorbed as a function of the equilibrium pressure), usually by plotting a cycle of adsorption/desorption/readsorption in order to calculate the chemisorbed and physisorbed amounts at given pressures.
c) The *differential heat*, $q_{diff}(n_\alpha) = \partial Q_{int}/\partial n_\alpha$, as a function of the amount adsorbed, by plotting the integrated heat of each recorded thermogram as a step function of the successive doses of adsorbed amounts. However, the histogram steps are often replaced by a curve connecting the centers of each step. When the adsorption temperature is well adjusted, this plot conveys information about the surface heterogeneity, with chemisorption in the first steps and physisorption in the last.
d) The *integral heats* as a function of the amount adsorbed.

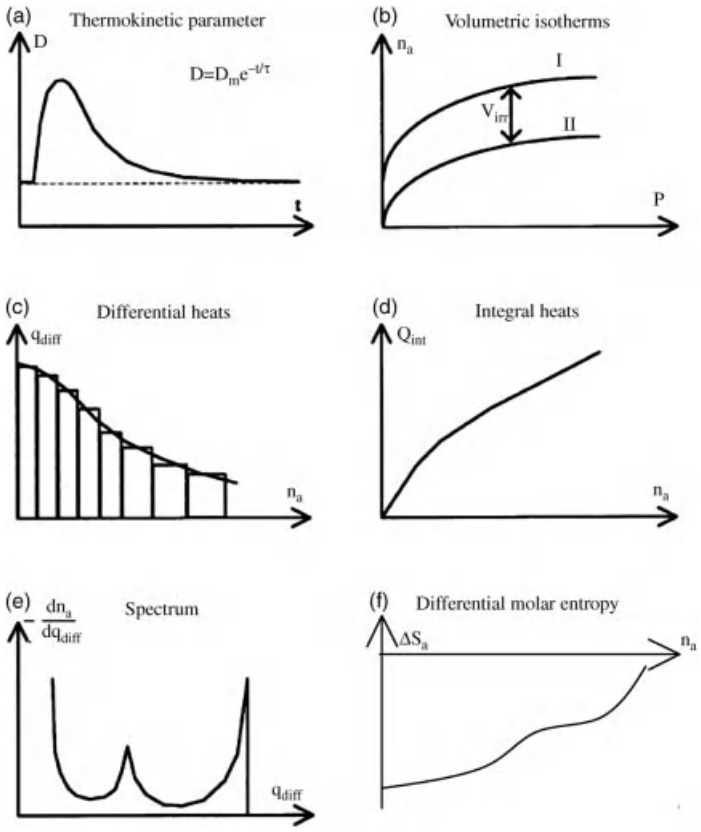


Figure 18.17 Schematic diagrams from data processing with volumetry–calorimetry [26].

e) The *energy spectrum*, $-(\partial n_\alpha/\partial q_{\text{diff}}) = f(q_{\text{diff}})$, plotting the differential heat derivative of the adsorbed amounts as a function of the differential heat (corresponding to the distribution of the n_α molecules among the energy range). In order for this representation to be relevant, very small steps have to be performed in order to maintain good resolution in differential heat, which may be incompatible with the minimal evolved heat for a thermogram to be well integrated. Therefore, differential heat plots are most often used to determine surface heterogeneity. A qualitative and false compromise can consist in using the approximation of the differential heat (curve) instead of the histogram version.

f) The *differential molar entropy of adsorption* can be estimated by combination of the adsorption isotherm and the differential heats, provided that the heat exchange is reversible:

$$\Delta_\alpha S = \overline{S_\alpha}(n_\alpha) - \overline{S_g}(n_\alpha) = \frac{Q_{\text{int}}(n_\alpha)}{n_\alpha T} + \frac{R}{n_\alpha}\int_0^{n_\alpha} n_\alpha \mathrm{d}\ln\left(\frac{p}{p^\circ}\right) \tag{18.26}$$

where $\overline{S_\alpha}$ is the molar entropy of the adsorbed phase, $\overline{S_g}$ the molar entropy of the same quantity of adsorbate but in the gas phase, and p° the standard pressure at temperature T. The molar entropy becomes especially relevant when studying the more reversible part of adsorption: physisorption.

Many examples of the application of this technique will be given in the acidity/basicity section, as it is the most common way to determine the acid–base properties of catalysts.

18.1.6.3 Isoperibolic Calorimeter, Liquid Flow Calorimeter, Titration Calorimeter, and Solid–Liquid Calorimetry

Calorimetry can also be used to measure the energies evolved at the solid–liquid interface. Isoperibolic calorimetry is a simple method mainly used for the determination of dissolution, immersion, or reaction heats in the liquid phase. Titration microcalorimeters have been developed to provide a precise measurement of heat flow, while the liquid or solid–liquid sample inside the calorimetric cell is being stirred, without perturbing the signal, and precise amounts of liquid can be introduced via precision syringes. Wetting measurements can also be achieved with an immersion calorimeter: a sealed ampoule inside the calorimetric cell is broken at the beginning of the experiment, bringing a solid in contact with a solvent.

Half way between a flowmetric and an adiabatic calorimeter, the isoperibolic calorimeter consists of a calorimetric bath at constant temperature in which an adiabatic jacket is immersed. Inside this jacket is brought a calorimetric cell (10–100 ml) with thin glass walls, in which a thermometer, a calibration resistor, and a stirring device are set. The experiment consists of two steps: a calibration, then the reaction [14].

Another type of isoperibolic calorimeter is the differential reaction calorimeter (DRC) (Figure 18.18). The DRC apparatus consists of two symmetric thermostated glass vessels into which the same quantity of liquid is poured and a thermometer inserted [27]. The introduction of sample in the flask via a dropping funnel induces a

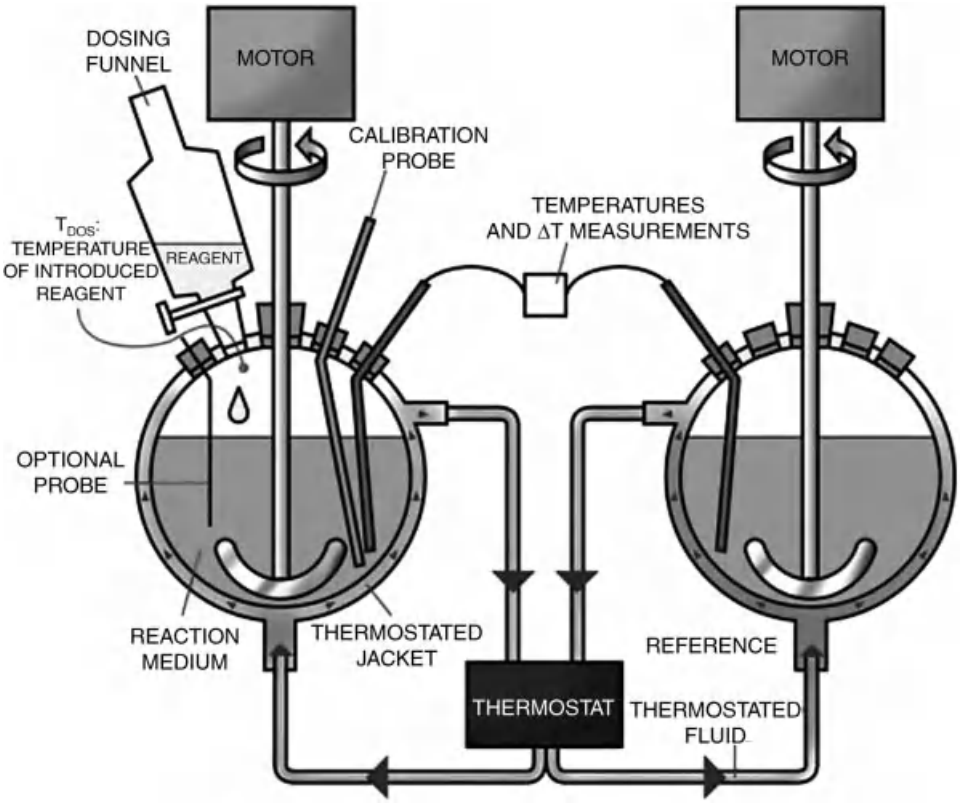


Figure 18.18 Schematic diagram of a DRC apparatus [27].

temperature change that is recorded relative to time. The experiment needs a calibration via the Joule effect for the calculation of reaction energies by integration of the obtained thermograms.

Calibration has to be redone any time the mixture is changed, because of the drift in heat capacity. Then, for a multi-injection experiment, alternate steps of reaction/calibration will be run.

Solid–liquid calorimetry is intrinsically competitive and thus more complex than solid–gas experiments. The presence of a solvent has to be considered in order to derive the appropriate energies of adsorption, and several parameters interfere with the actual phenomena occurring at the interface, such as the ionic species (surfactant, buffer, etc.) or the effective interface seen by the probes. Basically, the interaction between the catalyst and the probe is disturbed by the interactions between the catalyst and the solvent and between the solvent and the probe, which can be illustrated schematically as a triangle of basic interactions always to be considered in solid–liquid experiments (Figure 18.19). Moreover, the measurement of adsorbed amounts (by spectrofluorimetry, ellipsometry, etc.) has to be performed on dense and

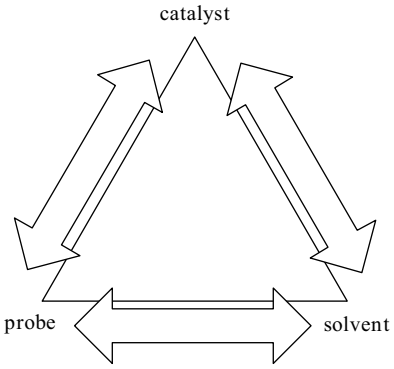


Figure 18.19 Catalyst–probe–solvent triangle.

sometime turbid media, which makes the correlation between energies and quantities even more difficult to establish.

Let us distinguish flow calorimetry from titration calorimetry experiments. A *liquid flow calorimetry* experiment proceeds in four steps:

1) **Initiation**: the flow cell is filled with a known mass of solid, then evacuated and filled with the solvent.
2) **Adsorption**: the flow of solvent is replaced by a flow of the probe solution.
3) **Desorption**: the flow of probe solution is replaced by a flow of solvent.
4) **Calibration**: the nature of the medium has changed, and therefore its thermal capacity; a Joule heating step recalibrates the signal.

Then several adsorption–desorption cycles are performed with increasing amounts of adsorbent (Figure 18.20). An online detector (UV, refractometer, etc.) at the output of the cell monitors the remaining adsorbent concentration, so that the energies are related to the amounts adsorbed.

A *titration calorimetry* experiment proceeds by several small injection steps ($\sim$0.1 ml min^{-1}) of the stock solution (probe) into the calorimetric cell, which is stirred, thus giving a calorimetric signal of adsorption (or dilution). Then, in order to correlate these signals with adsorbed amounts, either a similar experiment is run in parallel to determine an adsorption isotherm or, by an optic guide brought into the calorimetric cell, the concentration may be derived by UV–visible spectrophotometry or spectrofluorimetry (Figure 18.21).

18.1.6.3.1 **Examples** Investigations by liquid-phase calorimetry of the mechanism of hydrogen generation by hydrolysis of sodium borohydride catalyzed using Co_2B nanoparticles generated *in situ* from a $CoCl_2$ solution were made by Garron *et al.* using a DRC coupled with volumetry, allowing a simultaneous thermodynamic and kinetic study of the reaction [28]. In Figure 18.22a, the plot of the differential temperature as a function of time, measured in the DRC, shows two peaks corresponding to an initial Joule effect calibration (1200 J during 900 s) and to the

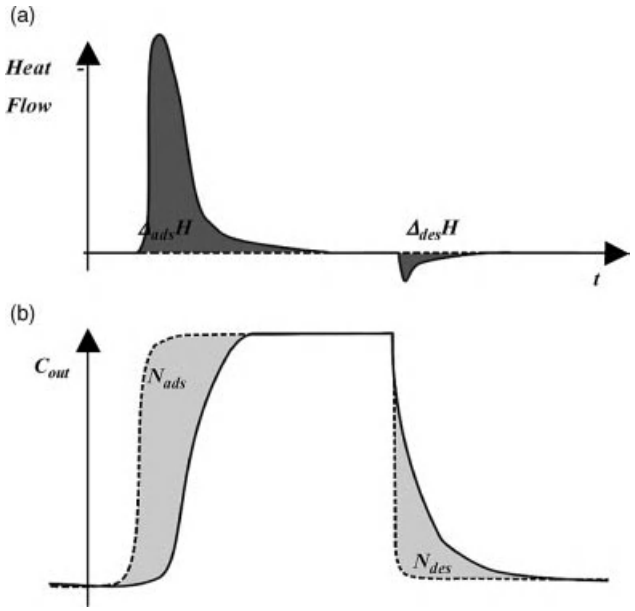


Figure 18.20 Adsorption–desorption cycle monitored by the heat flow (a) and simultaneously by the adsorbent concentration in the outflow C_{out} (b), with (solid line) and without adsorbent (dashed line). The integration of both signals with time provides the relative energy (dark grey, in $J\,g^{-1}$) and adsorbed/desorbed amount (light grey, in $mol\,g^{-1}$).

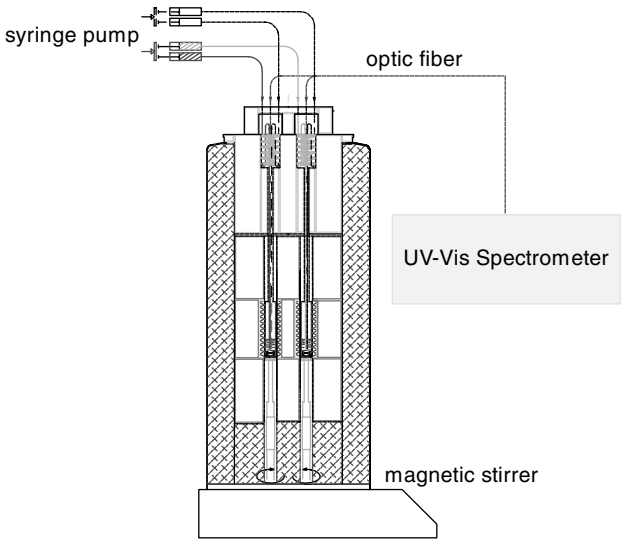


Figure 18.21 Titration calorimeter setup coupled with a UV–visible spectrometer.

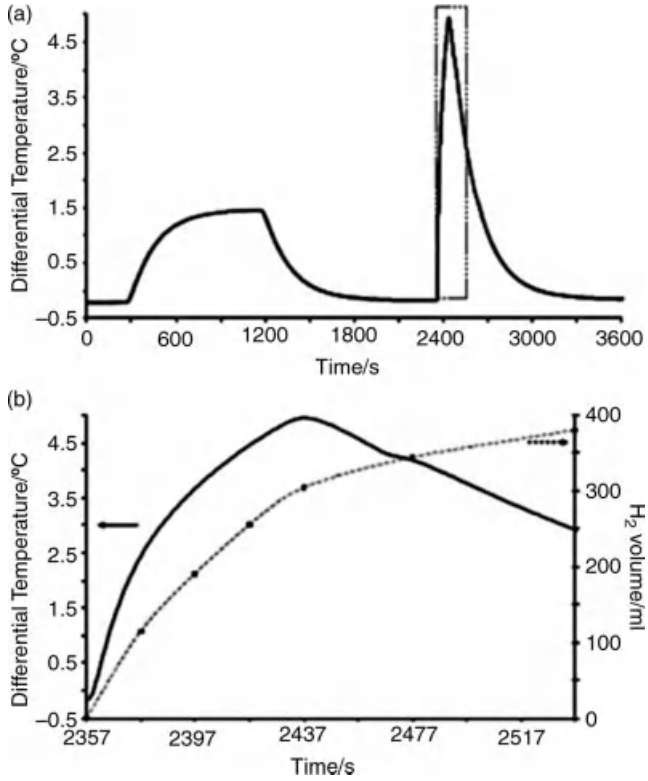


Figure 18.22 (a) Differential temperature signal versus time. First peak, Joule effect; second peak, *in situ* generation of nanoparticles (in CoB). (b) Details of the calorimetric peak and hydrogen generation.

catalyst generation, respectively. The generation of the active phase corresponding to the second peak is highly energetic and much faster than the well-equilibrated Joule-effect peak. Figure 18.22b shows a close-up of the second peak and the corresponding volume of hydrogen generated; this peak is the result of different thermal phenomena that occur in a short time, and at least two contributions to the measured enthalpy can be deduced from the peak shape. Two different kinetic rates could also be observed on the hydrogen generation curve (Figure 18.22b): in the first part, the rate was about 3.75 ml s^{-1}, whereas for the final part it was about 0.8 ml s^{-1}. In fact, two parallel reactions occur when solutions of $CoCl_2$ and $NaBH_4$ come into contact at acidic or neutral pH. The first is the direct reaction of borohydride with the protons (the solution is at pH 6.3) provided by chloride present in the salt leading to the formation of boric acid:

$$H^+{}_{(aq)} + 3H_2O_{(l)} + BH_4^-{}_{(aq)} \rightarrow 4H_{2(g)} + H_3BO_{3(aq)} \tag{18.27}$$

$\Delta H^\circ = -285.1\ \text{kJ mol}_{NaBH_4}{}^{-1}$.

The other reaction is the formation of Co_2B, the active phase of the catalyst:

$$2Co^{2+}{}_{(aq)} + 4BH_4{}^{-}{}_{(aq)} + 3OH^{-}{}_{(aq)} + 9H_2O_{(l)} \rightarrow Co_2B_{(s)} + 12.5H_{2(g)} + 3B(OH)_4{}^{-}{}_{(aq)} \quad (18.28)$$

$\Delta H^{\circ} = -227.2\ \text{kJ mol}_{NaBH_4}{}^{-1}$.

Lantenois *et al.* investigated the adsorption of two heavy metal ions [Cd(II) and Pb (II)] on macroporous silica (Spherosil) by flow calorimetry [29]. The samples (about 60 mg of Spherosil) were evacuated for 1 h, then wetted and equilibrated with a flow of $NaNO_3$ solution (10^{-1} M) at a suitable pH (3.3 ml h^{-1} for 3 h). The flow fluid was then switched to a solution containing the metal ion at a fixed concentration in 10^{-1} M $NaNO_3$ at the same pH. This adsorption step was followed by a desorption step which consisted in reintroduction of the initial $NaNO_3$ solution (Figure 18.23). The heats related to the adsorption, as measured with the calorimeter, were normalized to the unit surface area of solid in order to obtain the differential enthalpy of adsorption of the cations. The values of $\Delta_{ads}H$ presented in Figure 18.24 show that unlike lead adsorption, cadmium requires heat to be adsorbed. It demonstrates also that the adsorption of the first Cd(II) cations (below 3 mM) is more expensive in energy ($\sim$20 kJ mol^{-1}) than the following ones ($\sim$10 kJ mol^{-1}). The variations of the adsorption free energy ($\Delta_{ads}G$) per m^2 were estimated from the integration of the adsorption isotherms and according to Gibbs law. The entropic data corresponding to the adsorption process can be calculated from $\Delta_{ads}G$ and $\Delta_{ads}H$. The variation of entropy is positive during the adsorption process and at 298 K is almost equivalent to the free energy variation. The introduction of heavy metal ions in the surface phase can be viewed as the transition from a situation where the heavy metal ion is surrounded by a "complete" hydration shell (i.e., that corresponding to the bulk situation) to a situation where it is surrounded by a smaller number of water molecules. The observed decrease in adsorption entropy versus concentration can

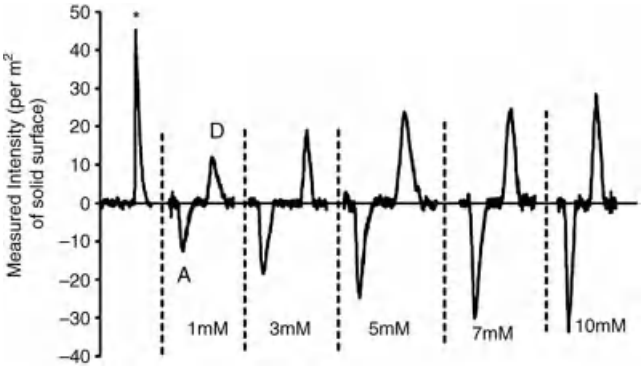


Figure 18.23 Calorimetric effect related to the adsorption of Cd(II) [Pb(II) gives no signal] in a 0.1 M $NaNO_3$ flow on Spherosil silica. The first peak (marked with an asterisk, *) is the thermal calibration (7 mJ). For each concentration, the adsorption (A)–desorption (D) cycle is performed.

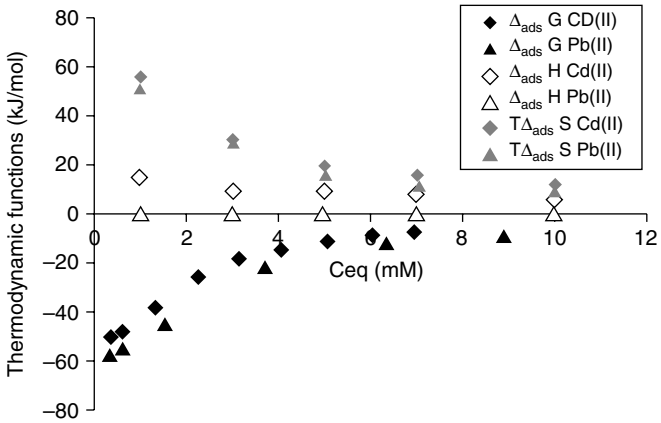


Figure 18.24 Evolution of thermodynamic functions (open symbol, $\Delta_{ads}H$; black symbol, $\Delta_{ads}G$; gray symbol, $T\Delta_{ads}S$) for Pb(II) (triangle) and Cd(II) (diamond).

then be interpreted as a decrease in the number of water molecules released from the bulk hydration shell during introduction into the surface phase.

18.1.6.4 **Power-Compensated Calorimeter**

The power-compensated method is a differential method that consists in minimizing the temperature difference between the sample and the reference pans by continuously adjusting the heat flow via a feedback mechanism. Either the isothermal mode or the temperature scanning mode (power-compensated DSC) can be chosen. The recorded signal is the compensation power dH/dt relative to time or temperature. The sensitivity is usually of the order of 0.1 mW and the temperature range from -175 to $+725\,^{\circ}C$ (Figures 18.25 and 18.26).

The two pans are loaded onto separate symmetrical heating devices, the mean temperature of the sample and the reference are measured, and an automatic continuous feedback circuit adjusts the heat to be administered to the sample, either by heating with a resistor or by cooling with a cooling gas–liquid circuit or a Peltier cooler [30, 31].

18.1.7
Temperature-Programmed Desorption (TPD)

Temperature-programmed techniques, usually denoted TPX, X standing for the process studied (Desorption, Reduction, Oxidation, Sulfidation, . . .), are in common use in the field of catalysis. While a temperature program $T(t)$ is run (often a linear increase), the evolution of the sample is monitored via either a calorimetric, a gravimetric, or a spectroscopic apparatus. Therefore, a wide range of such techniques exists.

The TPD techniques allow the study of the nature and/or the amount of desorbed species from an initially impregnated substrate while a temperature program is run.

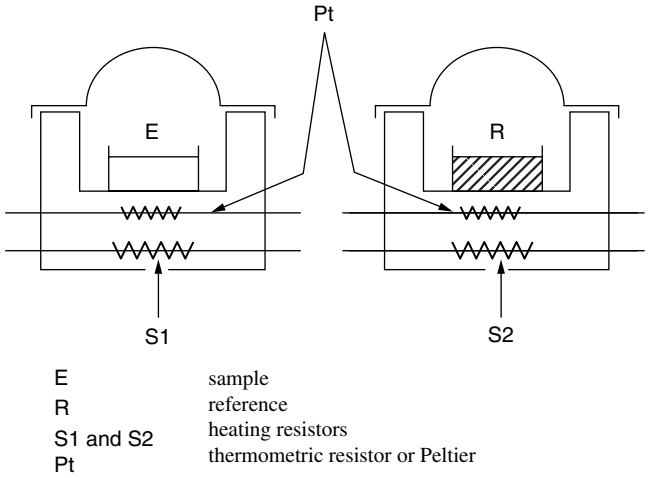


Figure 18.25 Schematic diagram of a power-compensated DSC apparatus [16].

TPD is most often used to characterize the acidic or basic properties of surfaces and the decomposition phenomena of adsorbed species at given temperatures. The TPD apparatus consists of a furnace, a sample holder adapted to one or many calorimetric (DSC, TGA, ...), gravimetric (TG, DTG), or spectroscopic (MS, FTIR, UV, X-ray

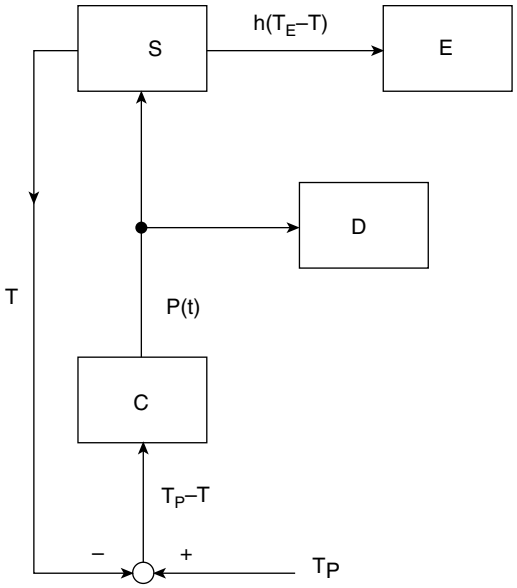


Figure 18.26 Block diagram of power-compensated system: S, sample holder; C, temperature controller; D, display; E, environment; T, temperature of the sample holder; T_P, programmed temperature; T_E, temperature of the environment; h, heat transfer coefficient; P(t), electric power fed to the sample holder [30].

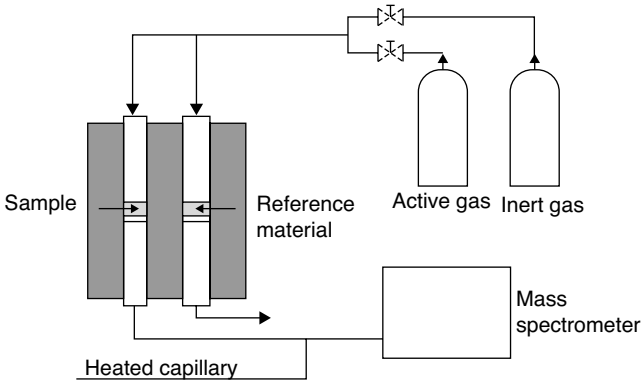


Figure 18.27 An example of a TPD setup: TPD–MS [10].

photoelectron spectroscopy (XPS), Raman, . . .) devices and a system for the admission of gases (possibly a mixture) (Figure 18.27).

18.1.7.1.1 **Principle** A *TPD experiment* consists of three phases:

- **Pretreatment**: the sample is brought to a low pressure or inert gas flow and a temperature high enough to clean the surface, without degrading the sample's structure.
- **Adsorption**: one or many species are then adsorbed on the sample surface at low temperature (frequently room temperature but sometimes subambient), up to some specific surface coverage or until saturation.
- **Desorption**: the sample is heated in a controlled manner (often linearly) while either a flow of inert gas carries the desorbed molecules into a detector, or an ultrahigh vacuum pump prevents the desorbed molecules from being readsorbed. The desorption can be performed in two steps in order to distinguish *physisorbed* from *chemisorbed* species. Also, it is common to observe products of decomposition of the originally adsorbed molecules at high temperatures.

In pioneering work in 1967, Amenomiya *et al*. [32] proposed a setup derived from the flash-desorption method consisting of a temperature controller, a furnace, and a catharometer (thermal conductivity detector) to measure the rate of desorption of ethylene from the surface of a catalyst. Therefore the "TPD" appellation often refers to TPD–TCD.

18.1.7.1.2 **Data Processing** Depending on the analytical technique, various data can be obtained from a TPD experiment:

Surface coverage: the area under a peak is proportional to the amount of desorbed particles. Then a value of the surface coverage can be determined if a quantitative setup is applied: a flow system with TCD or any other quantitative analytical device.
Thermokinetics: the temperature T_m of the maximum of a peak is related to the *energy* of desorption, which can be assumed under conditions to relate to the adsorption enthalpy.

Adsorption and desorption phenomena usually obey a first-order kinetic law:

$$-\frac{d\theta}{dt} = A(\theta)\theta^x \exp\left(-\frac{E_a}{RT}\right) \tag{18.29}$$

where $x = 1$.

Under steady-state conditions and neglecting any diffusion phenomenon (inside porous substrates), the mass balance can be established and the concentration C_g of the desorbed molecules in the gas phase can be estimated as a function of the variations of the surface coverage θ:

$$C_g(T) = -\left(\frac{V_s \nu_m \beta}{F}\right)\frac{d\theta}{dT} = \frac{V_s \nu_m k_d \theta}{F + V_s k_a (1-\theta)} \tag{18.30}$$

where V_s is the volume of the catalytic bed, ν_m the amount of adsorbed molecules per unit volume of the solid phase at total coverage ($\theta = 1$), F the flow rate of the inert gas carrier, k_d and k_a the rate constants of desorption and adsorption, and β the slope of the linear temperature program.

Let us first consider a system with no readsorption [$F \ll V_s k_a(1 - \theta)$]. Then the rate constant of desorption can be written as follows:

$$k_d = A_d \exp\left(-\frac{E_a^{des}}{RT}\right) \tag{18.31}$$

where A_d is the pre-exponential factor, R the gas constant and E_a^{des} the desorption activation energy. Then, at the maximum of a desorption peak, $T = T_m$ and $(dC/dT)(T_m) = (d^2\theta/dT^2)(T_m) = 0$, then

$$E_a^{des} = RT_m \ln\left(\frac{\nu R {T_m}^2}{\beta E_a^{des}}\right) \;\leftrightarrow\; \ln\left(\frac{{T_m}^2}{\beta}\right) = E_a^{des}\frac{1}{RT_m} + \ln\left(\frac{R\nu}{E_a^{des}}\right) \tag{18.32}$$

Then E_a^{des} can be obtained from the slope of the following function:

$$\ln\left(\frac{{T_m}^2}{\beta}\right) = f\left(\frac{1}{RT_m}\right) \tag{18.33}$$

This requires a series of experiments, varying the scanning rate β.

In the case of reactions of order other than one, the expression of the energy is as follows:

$$E_d = RT_m \ln\left[\frac{\nu R {T_m}^2 x \theta^{x-1}(T_m)}{\beta E_d}\right] \tag{18.34}$$

and can be determined iteratively, assuming a value for ν (usually in the range 10^{13}–$10^{16}\,s^{-1}$ for desorption), and a calculation of $\theta(T_m)$.

Let us now consider a free readsorption scenario [$F \ll V_s k_a(1 - \theta)$], then we obtain

$$\ln\left(\frac{{T_m}^2}{\beta}\right) = \Delta H_{ads\leftrightarrow des}\left(\frac{1}{RT_m}\right) + \ln\left\{\frac{[1-\theta(T_m)]^2 V_s \Delta H_{ads\leftrightarrow des}}{RF\exp(\Delta S_{ads\leftrightarrow des}/R)}\right\} \tag{18.35}$$

where $\Delta H_{ads\leftrightarrow des}$ and $\Delta S_{ads\leftrightarrow des}$ are the reaction enthalpy and entropy, respectively, of the adsorption–desorption equilibrium.

Kinetics: kinetic values of the desorption process can also be obtained from the peak shape S ($n = 1.26\sqrt{S}$; see Section 18.1.2) and from the coverage dependence of the process (isoconversional methods [33]).

18.1.7.1.3 **Examples** TPD is mainly used for the characterization of the acidic/basic sites in gas–solid interactions, providing the amount and the energy of sites. Different gas probes of various pK_a can be used; however, mainly four probes are used: NH_3 [$pK_{a(liq)} = 9.2$] and pyridine [$pK_{a(liq)} = 5.2$] (or various amines) for testing acid sites, and SO_2 [$pK_{a(liq)} \approx 1.9$] and CO_2 [$pK_{a(liq)} \approx 6.4$] for testing basic sites [10]. Other probes are used for special measurements, such as CO for testing the SMSI (strong metal–support interaction) effect.

Palladium oxide (1 wt%) supported on high surface area (184 $m^2\,g^{-1}$) hexagonal boron nitride (PdO/BN) was synthesized and characterized by Postole *et al.* for the catalysis of hydrocarbon oxidation [34].

NH_3-TPD thermograms were obtained by flushing (10 $cm^3\,min^{-1}$) with He (for BN and PdO/BN) or air (for BN) about 10 mg of sample previously saturated with NH_3, in the range 25–650 °C. The desorbed gases were analyzed by mass spectrometry at $m/z = 15$ in order to observe the ammonia desorption while avoiding the interference of m/z peaks of water fragmentation (Figure 18.28). TPD was here used to cross-check the more precise calorimetric adsorption measurements.

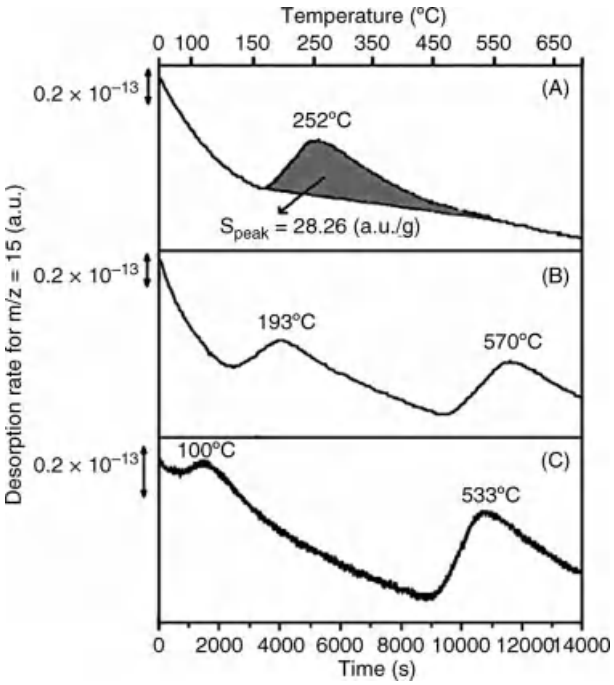


Figure 18.28 TPD after NH_3 adsorption on (a) BN support under He, (b) BN support under air, and (c) PdO/BN catalyst under He.

The TPD–MS trace of BN under helium shows one broad and asymmetric peak centered at 252 °C (Figure 18.28a), whereas under air two peaks can be observed, one centered at 193 °C corresponding to more labile NH_3 and the other at 570 °C of more strongly bound NH_3 (Figure 18.28b). The trace for PdO/BN consists of two peaks centered at 100 and 533 °C (Figure 18.28c).

18.1.8
Temperature-Programmed Reduction and Oxidation (TPR and TPO)

The TPR and TPO methods allow the investigation of the redox properties of a catalyst. They are destructive methods and often characterize not only the surface but also, at least partially, the bulk. The method can be used as a titration of the active sites for redox catalysts or as a preparation method (for example, when zerovalent metals are needed). These methods become surface methods for the generation of supported catalysts, assuming that the support is redox resistant.

The apparatus is the same as for TPD: a temperature controller, a gas delivery system, and a characterization device. A quantitative setup (flow system and reproducible collection of the gases) will provide data for the calculation of the reducing/oxidizing properties, the dispersion, and the average oxidation state of the active particles and allow useful redox cycling (TPR + TPO).

18.1.8.1 Principle

A *TPR/TPO experiment* consists of two phases:

- **Pretreatment**: the sample is brought to a sufficiently low pressure and high temperature to clean the surface, without degrading the sample's structure.
- **Adsorption/desorption**: the sample is heated in a controlled manner (often linearly) while a flow of inert gas carries either oxidizing (O_2, N_2O, ...) or reducing (H_2, CO, ...) molecules on to the sample. The amount of gas absorbed or reacted can be deduced from the amount flowing out of the furnace by a quantitative technique (TCD, MS, IR, etc.).

A series of TPR/TPO experiments are often run as follows: a first TPR tests the reducible amount of sample, then a TPO reoxidizes it, then a second TPR is run to test the reversibility. The same applies with TPO/TPR/TPO. Cycling studies can also be performed.

The diffusion processes of the oxidation/reduction inside the particles play an important role in the analysis of the signal, being dominated by either the nucleation model or the contracting-sphere (coarse-grain) model. Phenomena of passivation may also occur. The reaction is not always total:

- Reduction with H_2 (complete if $n = y$):

$$M_xO_{y(\text{solid})} + nH_2 \rightarrow \frac{y-n}{y} M_xO_{y(\text{solid})} + \frac{nx}{y} M_{(\text{solid})} + nH_2O \qquad (18.36)$$

- Oxidation with O_2 (complete if $n = \gamma/2$):

$$M_{(solid)} + nO_2 \rightarrow \left(1 - \frac{2nx}{\gamma}\right) M_{(solid)} + \frac{2n}{\gamma} M_x O_{\gamma(solid)} \tag{18.37}$$

  For other gas probes (CO, NO, N_2O, etc.), the reaction equation becomes less obvious, many reactions can occur, and the nature of the gas flowing out has to be determined.

However, we should also point out a surface-dedicated method, temperature-programmed reduction of oxidized surfaces (s-TPR) [35], where a weak oxidant probe, N_2O, is used to interact at low temperature (20–50 °C) on the surface particles only, in which case H_2-TPR is used to titrate and characterize them.

18.1.8.2 Data Processing

The amount of reduced/oxidized species can be calculated from the amount of gas consumed. Kinetic analysis however, needs assumptions about the surface mechanisms, especially on the diffusion model: *none* (if the reaction only occurs on the surface), *nucleation* (increase of the reaction interface at an early stage), or *contracting sphere* (decrease of the reaction interface throughout the reaction).

Many parameters affect the acquisition, such as the active gas concentration C_0, the rate of temperature increase β, the total flow rate F, the sample weight, and the contact time. Therefore, two parameters, K (sensitivity) and P (resolution), have been set to standardize the data and establish the best setup to use for enhanced sensitivity/resolution [36, 37]:

$$K = \frac{S_0}{FC_0} \in [55, 150\ \text{s}] \tag{18.38}$$

$$P = K\beta \in [20, 50\ ^\circ\text{C}] \tag{18.39}$$

where S_0 is the presumed amount of initial reactive species on the sample (μmol) and FC_0 is the molar flow rate of the reactive gas (μmol s^{-1}).

18.1.8.3 Example

Rombi *et al.* investigated the catalytic properties of K-containing and standard chromia/alumina for the nitroxidation of 1-methylnaphthalene to 1-naphthonitrile [38]. The TPR results for the K-containing chromia/alumina catalysts (ACr10K*x*: 10 wt% of chromium on γ-alumina and about *x* wt% of potassium) are shown in Figure 18.29, where the reduction profile for ACr10 is also reported. Remarkable differences in the reduction behavior of the samples are evident from both the shape and maximum temperature, T_{max}, of the peaks. The latter are listed in Table 18.3, together with the calculated extent of reduction of Cr(VI).

From compared X-ray diffraction (XRD) measurements between ACr10K1N and ACr10K1, it could be suggested that the second peak in ACr10K1 ($T_{max} = 722$ K) originates from Cr(VI) present as bichromate. Also, the peaks at 761, 771, and 804 K in ACr10K2, ACr10K4, and ACr10K8, respectively, would be related to the reduction

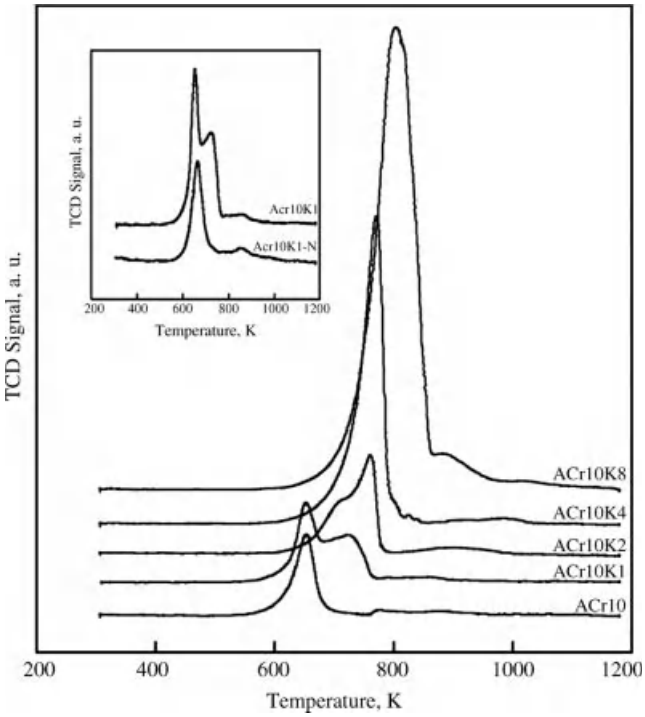


Figure 18.29 TPR of K-containing chromia/alumina catalysts. Chromia/alumina (ACr10) is also shown. ACr10K1N, obtained by calcining in nitrogen instead of air, is compared with ACr10K1 in the inset.

of bichromate Cr(VI) species, the amount of which increases with the K loading. The shoulder in ACr10K2 and the heading in ACr10K4 profiles would stem from residual Cr(VI) present as chromium oxide, which progressively declines along the series ACr10 > ACr10K1 > ACr10K2 > ACr10K4.

By suitably dosing the amount of potassium, new Cr(VI) species can be generated, and the extent of catalyst reduction can be enhanced, although higher reduction temperatures are needed.

Table 18.3 Measured maximum temperatures and reduction extents: TPR results for chromia/alumina and K-containing chromia/alumina catalysts.

Catalyst	T_{max} [a] (K)	α [b] (mol%)
ACr10	380	45
ACr10K1	379; 449	55
ACr10K2	488	42
ACr10K4	498	55
ACr10K8	531	69

[a] Maximum temperature of H_2 consumption.
[b] Reduction extent.

18.1.9 Temperature-Programmed Surface Reaction (TPSR)

TPSR is part of the family of temperature-programmed methods, but this particular technique focuses on the study of the evolution (adsorption, desorption, reaction, etc.) of species flushed on a sample when a temperature program is run. Unlike the usual temperature-programmed methods, in which the physicochemical properties of the catalyst are directly investigated, TPSR measures the properties of the reaction catalyzed by the studied sample. Accurate conditions can be set up to reproduce the catalyst's environment and observe the thermal properties of the catalysis.

The apparatus is the same as for TPD experiments, but the gas admission setup has to allow precise mixtures in order to reproduce the desired conditions accurately.

18.1.9.1 Principle

A *TPSR experiment* consists mainly of two phases:

Desorption: the sample is inserted in the furnace and heated under a flow of inert gas at a sufficiently high temperature to ensure a desorbed and active surface, then the sample is cooled to room temperature.
Surface reaction: the flow is now a mixture of the carrier inert gas and an active gas that reacts with the surface of the sample, while a temperature program is run (usually linearly). The active gas can be administered through pulses.

Due to the first step of "desorption," it is often natural to couple TPD and TPSR experiments. However, a desorption experiment brings the sample to a high temperature, so special care has to be taken in order to prevent its degradation, if it is needed for further analysis.

Mainly three types of methods are performed:

- The *bare surface method*, in which a mixture of reactive gases carried by an inert gas is flushed on the bare surface of the catalyst throughout the experiment. Then the principle is almost the same as for TPD, but more complex, either because of the presence of a mixture of gases or the interpretation of adsorption and readsorption phenomena [39].
- The *preadsorbed surface* method, in which an intermediate phase of adsorption is introduced in order to chemisorb one of the reactants on the surface of the catalyst. The pretreated catalyst is flushed with the reactant gas, then with an inert gas in order to remove the physisorbed molecules. This method is similar to an *indirect TPD* experiment, in which the chemisorbed molecules are dosed instead of the active sites [40].
- The *pulse method*, in which pulses of the gas mixture are injected at different temperatures in a temperature step program, in order to investigate the temperature dependence of the kinetics. The surface of the catalyst is assumed to desorb before each new pulse, which is a difficult condition to guarantee [41].

18.1.9.2 Data Processing

The processing of the data is similar to that in TPD, but it is often more complex. The kinetics are the focus of this method, where the Kissinger and also the various isoconversional methods (Kissinger–Ozawa, Friedmann, Vyazovkin, Freeman–Caroll, Malek, etc.) [33], helped by an accurate peak deconvolution method, are useful.

18.1.9.3 Example

The methane assisted DeNOx activity of catalysts of palladium (1 wt%) supported on ceria–zirconia "CZ28" (Pd species on $Ce_{0.2}Zr_{0.8}O_2$) compared with the support alone was measured by TPSR scanning from 25 to 700 °C at 10 °C min^{-1} under a flow of CH_4–NO_2 mixture ($C_0/C_0 = 1000/1000$ ppm He) by Zenboury *et al.* [39]. For the sake of clarity, only the TPSR profiles obtained for CH_4 and the sum of NO and NO_2 (total NO_x) are presented in Figure 18.30. Below 280 °C, the TPSR profiles are dominated by the strong adsorption of NO_2 on the ceria–zirconia support, which explains why the total NO_x is below C_0 (1000 ppm). For the Pd/CZ28 catalyst, the measurement of NO_x concentrations well above C_0 between 350 and 480 °C indicates that desorption of surface nitrates is preponderant within this temperature range. Noteworthily, the occurrence of the desorption peak is delayed by about 40 °C for the CZ28 support. For both samples, methane consumption starts simultaneously with the onset of the NO_x desorption peak.

On the support alone, methane conversion starts at 390 °C and always remains below 85% over the whole temperature range. By contrast, the CH_4-TPSR profile obtained for the Pd-supported catalyst displays some conversion already at 280 °C and nearly 100% conversion above 520 °C. For both the support and the catalyst, CO_2 was the major product obtained following methane consumption (not shown here).

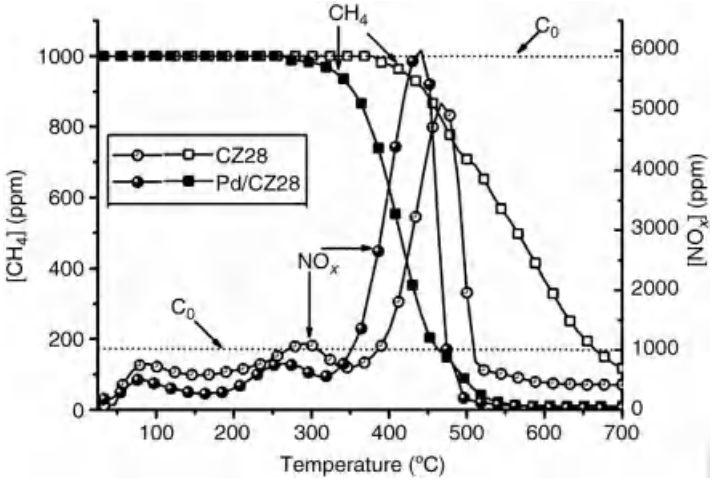


Figure 18.30 TPSR profiles corresponding to the reaction of CZ28 and Pd/CZ28 in $CH_4 + NO_2$ (1000/1000 ppm/He) from 25 to 700 °C in the absence of O_2 added ($\nu = 10$ °C min^{-1}) following 2 h adsorption at room temperature.

Meanwhile, measurable DeNOx activity is observed from 508 °C for CZ28 and 475 °C for Pd/CZ28. Here, the term DeNOx is used because N_2O was never observed during the TPSR reaction. Therefore, the obtaining of total NO_x concentrations below C_0 probably means that conversion to N_2 has occurred. Above 495 °C, DeNOx is almost total in presence of Pd whereas the best performance of the support alone is limited to 57% DeNOx in the range 600–700 °C. TPSR profiles obtained under a $CH_4 + NO_2$ atmosphere in absence of added oxygen clearly demonstrated the beneficial role of Pd in the activation of methane by NO_x. For the $Pd/Ce_{0.2}Zr_{0.8}O_2$ catalyst, the onset of methane consumption started at 280 °C (410 °C for the support alone) and almost 100% NO_2 conversion to N_2 was reached above 500 °C.

18.2 Acidity/Basicity

Many of the properties of a solid catalyst can be related to its acidity. For example, the performance of fluid cracking catalysts is controlled in part by the Si/Al ratio in the faujasite framework and hence by the acidity [42]. Therefore, methods that can give information on the nature, number, strength, and strength distribution of the surface acid sites are continuously sought.

Although such methods as TPD, Hammett titrations, chemisorption of bases, XPS analyses, solid-state NMR spectroscopy, infrared spectroscopy, and reactivity studies can provide information regarding the strength of acid/base sites, the most accurate and meaningful results are still those obtained from the heats of adsorption of basic/acidic probes as a function of coverage. Desorption and adsorption methods require different couplings in order to determine the amount of probe molecule desorbed or adsorbed (while the thermal technique provides the associated heat), then one or another technique can be more suitable, depending on the investigated results or parameters. Here are presented some of these coupled techniques.

18.2.1 Acid–Base Properties of Solids

The existence of a heterogeneous distribution of active sites at a catalyst surface is an old concept in heterogeneous catalysis, more often assumed than actually verified. It can be appraised by plotting the heat derivative of the amount of probe adsorbed as a function of the interaction heat, also called "acidity spectrum" in the case of basic probes (Figure 18.31). Direct and indirect measurements can provide heats of adsorption. An example of an indirect measurement is the recording of adsorption isotherms at various temperatures and the calculation of the isosteric heats for reversible adsorption [from the Clausius–Clapeyron equation and considering the gas is perfect (Figure 18.32)] or with the Kissinger equation derived from the outflow signal (see Section 18.1.7). However, a direct measurement at an equilibrium state provides more accurate data, for example, with heat-flow microcalorimetry coupled with volumetry (see Section 18.1.6).

Various models describe gas–solid and liquid–solid interactions [3, 26].

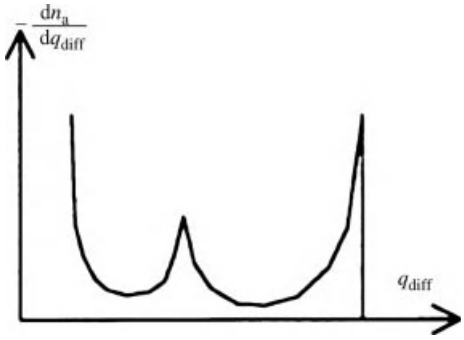
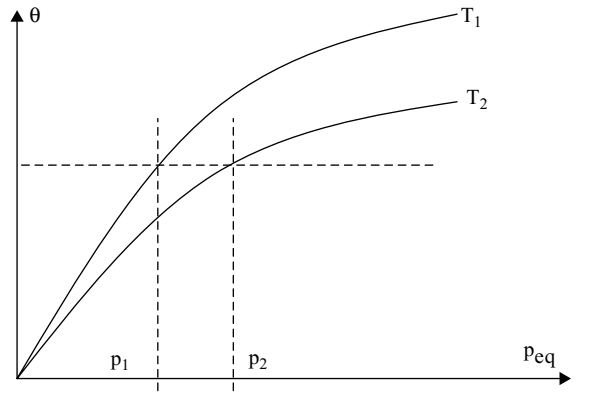


Figure 18.31 "Acidity spectrum" corresponding to the ratio of an increment dn_a of adsorbed molecules to the corresponding heat evolved dq_{diff} as a function of given heat (see Section 18.1.6.2) [26].

The gas–solid interaction discriminates mainly two adsorption processes:

- **Chemisorption**: irreversible adsorption, high binding energy (>100–120 kJ mol^{-1}).
- **Physisorption**: reversible adsorption, low binding energy (of the order of the liquefaction heat) relevant to van der Waals interactions.

Chemisorption acidity and basicity can occur in two forms: Lewis sites (accepting or donating a pair of electrons) or Brønsted sites (donating or accepting a proton). Thermal methods alone cannot distinguish these sites because their binding energies are very close and not ordered, hence couplings or comparative studies with spectroscopic methods have to be undertaken.



$$Q_{st}(\theta, \tilde{T}) = -R \left(\frac{\delta ln p}{\delta\, 1/T} \right)_{\theta} \approx -R \frac{\ln(p_1/p_2)}{(T_1^{-1} - T_2^{-1})} \tag{18.40}$$

Figure 18.32 Determination of the isosteric heat (Q_{st}) for a reversible process (physisorption), perfect gas conditions, tight range around the mean temperature ($\tilde{T}$) and a given coverage θ [Eq. (18.40)].

Further, the heat of interaction between an adsorbate and the surface of a catalyst (adsorbent) depends on many parameters, such as the nature of both the adsorbate and adsorbent and the adsorption temperature:

- **The nature of the adsorbent**: porosity, crystallite size or crystalline phases, hydroxyl groups, cationic centers, and so on.
- **The nature of the adsorbate**: polar or nonpolar (interaction with the surface polarity or adsorbate–adsorbate interaction), "size" (steric interactions, surface diffusion, penetration into the pores of the catalyst), redox behavior.

  The acid–base character of the probe can be evaluated by the corresponding pK_a in solution or preferentially by the proton affinity in the gas phase (*PA*) and the effect of the size can be evaluated from the kinetic diameter, that is, the diameter of a pore needed to let that molecule pass.
- **The adsorption temperature**: an appropriate temperature has to be set. At too low temperatures the molecules do not have sufficient energy to move freely on the surface to find the strongest sites (assumed to be the more stable), and at too high temperatures the probe molecules are decomposed. In the appropriate temperature range, the shapes are similar and the energies mainly vary with the evolution of the adsorbate heat capacity.

Ammonia and amines are commonly used as basic probe molecules: ammonia (NH_3, $pK_a = 9.24$, $PA = 857.7\,kJ\,mol^{-1}$, kinetic diameter $= 0.375\,nm$) is among the smallest basic molecules and is often used to characterize the acidity of porous materials, whereas pyridine ($pK_a = 5.19$, $PA = 922.2\,kJ\,mol^{-1}$, kinetic diameter $= 0.533\,nm$), which is larger, is often used to characterize the "surface acidity." However, both ammonia and pyridine are strongly basic and therefore their interaction with the surface sites is relatively unspecified. Then other probe molecules are used to characterize the location of specific active sites, for example, substituted pyridines (lutidines) as probes for Brønsted sites in HY zeolites [43], or acetonitrile as a probe of Lewis acidic sites in dealuminated Y-zeolites [44].

The mostly commonly used acidic probes are CO_2 ($pK_a = 6.37$, $PA = 540.5\,kJ\,mol^{-1}$) and SO_2 ($pK_a = 1.89$, $PA = 672.3\,kJ\,mol^{-1}$). Both are able to characterize the surface basicity by forming carbonate- or sulfate-like species on oxide catalysts; however, they can also coordinate linearly on surface Lewis acidic metal systems. SO_2 is assumed to probe the total basicity of a surface, whereas CO_2, which is less acidic, only probes the strongest basic sites. The number of available acidic probes is rather small, and also the range of acidic strengths and the range of kinetic diameters. Table 18.4 summarizes the properties of some acid–base probes [45].

18.2.2 Adsorption Techniques

18.2.2.1 Volumetry–Microcalorimetry

The volumetry–calorimetry method is based on the assumption that, by small successive doses (pressure increments) of adsorbate followed by equilibration of the system (quasi-static process), the adsorption heat can be measured accurately

Table 18.4 Dissociation constants in water (pK_a) and proton affinity in the gas phase (*PA*) of the probe molecules' acidic and basic species [45].

Probe molecule	pK_a		PA (kJ mol^{-1})	Acid species	Basic species
	Basic	Acidic			
Basic					
Piperidine	11.12		954	$C_5H_{10}NH_3^+$	$C_5H_{10}NH_2$
Diethylamine	11.00		952.4	$(C_2H_5)_2NH_2^+$	$(C_2H_5)_2NH$
n-Butylamine	10.77		921.5	$C_4H_9NH_3^+$	$C_4H_9NH_2$
Ammonia	9.24		853.6	NH_4^+	NH_3
Pyridine	5.19		930	$C_5H_5NH_2^+$	C_5H_5NH
Aniline	4.63		882.5	$C_6H_5NH_3^+$	$C_6H_5NH_2$
Amphoteric					
Pyrrole	0.40	16.50	875.4	$C_4H_4NH_2^+$	$C_4H_4N^-$
Water	−1.74	15.75	691	H_3O^+	HO^-
Methanol	−2.00	16.00	754.3	$CH_3OH_2^+$	CH_3O^-
tert-Butyl alcohol	−5.00	19.00	802.6	$(CH_3)_3COH_2^+$	$(CH_3)_3CO^-$
Acetonitrile	−10.00	25.00	779.2	CH_3CNH^+	CH_2CN^-
Acidic					
m-Cresol		10.01	ø	$(CH_3)C_6H_{10}OH$	$(CH_3)C_6H_{10}O^-$
Carbon dioxide		6.37	540.5	CO_2	HCO_3^-
Acetic acid		4.75	783.7	CH_3COOH	CH_3COO^-
Sulfur dioxide		1.89	672.3	SO_2	HSO_3^-

as a function of coverage at quasi constant temperature. The volumetric apparatus, generally equipped with a precise capacitance manometer, can give the equilibrium pressure, from which the adsorbed amount is calculated, then the simultaneously recorded thermogram gives the average heat relative to the amount adsorbed.

Impregnated zirconia-supported tungsta species were investigated by Kourieh *et al.* by adsorption calorimetry [46]. The SO_2 adsorption experiments on catalysts with various tungsta loadings (Figure 18.33) revealed a direct correlation between the basic strength and the tungsta coverage. Tungsta being a strong acid, it hardly adsorbs SO_2, hence the acidic probe reveals the basic sites (surface O^{2-} and hydroxyls) of the uncovered amphoteric zirconia.

Quaternary ("QN") series of hydrotalcites derived with different Mg/Ni/Cu/Al molar ratios (keeping the amount of divalent cations almost equal to twice the amount of trivalent cations) were prepared by Meloni *et al.* [47] and Leon *et al.* [48] by pH-controlled coprecipitation and then thermally decomposed at 723 K for 2 h (still carbonated; see Section 18.2.2.2) and characterized by NH_3 and CO_2 adsorption microcalorimetry.

Figure 18.34 shows the differential heats of adsorption of NH_3 and CO_2 at 353 K for three differently loaded compounds, QN-0, QN-09, and QN-1, with Ni:Cu loadings of 0:0.91, 0.8:0.1, and 0.96:0, respectively (expressed as molar ratio to Al). It was deduced that the acidity, the total basicity, and the amount of strongly basic sites follow the total

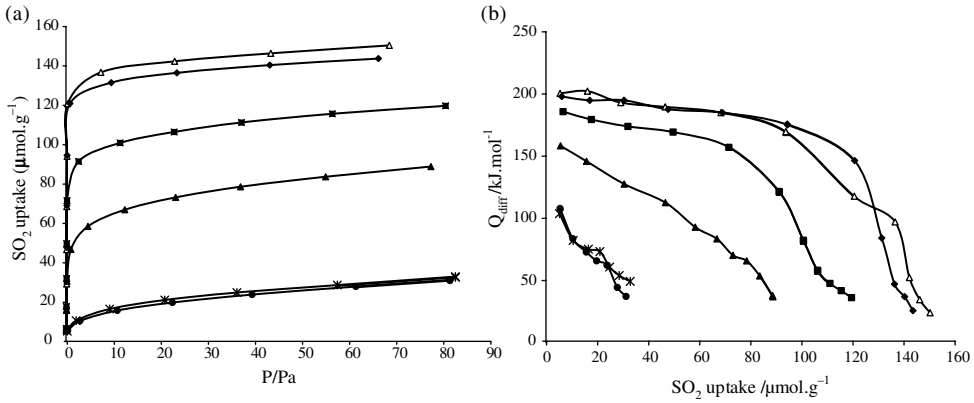


Figure 18.33 SO_2 adsorption isotherms (a) and differential heat (b) curves of tungsta-impregnated zirconia catalysts with various tungsta loadings: pure ZrO_2 (Δ), 1.2-WO_3/ZrO_2 (◆), 5-WO_3/ZrO_2 (■), 9.7-WO_3/ZrO_2 (▲), 16.7-WO_3/ZrO_2 (•), and 20.9-WO_3/ZrO_2 (*).

nickel content. Further, the coexistence of both magnesium and nickel cations improves the basicity of materials.

The catalytic behavior of the catalysts was related to their acid–base properties, which govern the competition between the dehydration over acid sites (giving olefins: 4-methyl-1-pentene, 4-methyl-2-pentene, and skeletal isomers of C_6 alkenes) and the dehydrogenation over basic sites (giving 4-methyl-2-pentanone and higher ketones) of the reactant 4-methyl-2-pentanol (MPO). Moreover, the role of copper was taken into account. It was found that in the absence of copper only dehydration reactions take place at 423 K; the dehydrogenation of MPO can be catalyzed by basic centers, but the reaction occurs only at 523 K (and above). The addition of 10% copper increases the dehydrogenation properties of the catalyst just enough to obtain a significant conversion (58%) of MPO with a large selectivity to ketones (81%) at temperatures as low as 473 K. The increase in the conversion and selectivity to dehydrogenation products with the copper content is mainly due to the dehydrogenating properties of the copper even if the contribution of very strong basic sites to this reaction also has to be taken into account.

18.2.2.2 **Adsorption Thermogravimetry–Calorimetry (TG–DSC)**

By coupling the information on the mass variations and the heat evolved, the same data as in volumetry–microcalorimetry can be obtained, provided that there is an isothermal setup and control over the nature of the adsorbate. The TG–DSC coupled method is mostly used for desorption studies (see Section 18.2.3.3); however, this setup can also achieve adsorption studies of high accuracy, depending on the stability of the temperature.

Zelenak *et al.* [49] studied the CO_2 capture properties of amine-modified SBA-12 mesoporous silica with a TGA–DTA setup. Figure 18.35 shows sorption/desorption cycles of CO_2 sorption over an SBA-12/AP (aminopropylsilyl) sample. By grafting amines on SBA-12, the basicity increased, providing more adsorption sites for CO_2

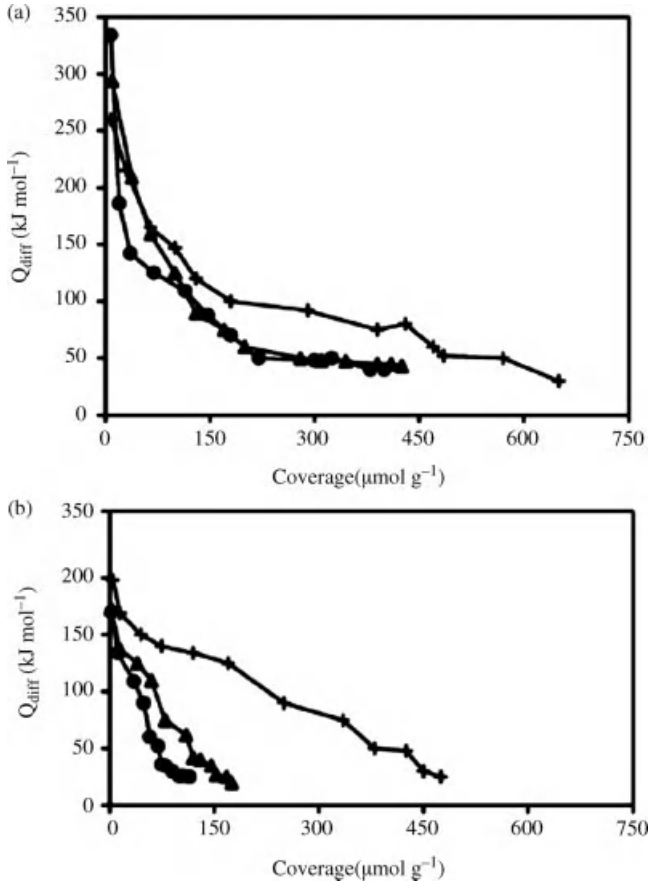


Figure 18.34 (a) Differential heat of NH_3 adsorption at 353 K for hydrotalcites QN-0 (•), QN-09 (▲), and QN-1 (+) samples as a function of NH_3 uptake. (b) Differential heat of CO_2 adsorption at 353 K as a function of CO_2 uptake.

(acidic probe). The degree of capture increases with basicity; however, the regeneration becomes poorer, so a compromise of basicity was aimed at.

Schärringer *et al.* [50] characterized the surface of a Raney nickel-supported cobalt catalyst with an adsorption TGA–DSC setup for the study of the reaction intermediates during hydrogenation of CD_3CN. The data on differential heats of adsorption of CD_3CN distinguish strong (208 ± 8 kJ mol^{-1}) chemisorption sites from weak (61 ± 4 kJ mol^{-1}) physisorption sites (Figure 18.36). The full hydrogenation of CD_3CN involving 120 kJ mol^{-1} (a surface reaction phenomenon) was hypothesized, then confirmed by incoherent neutron scattering (INS) measurements.

18.2.2.3 Adsorption Calorimetry–Mass Spectrometry

Mass spectrometry can be coupled to flow calorimetry in order to quantify the amount adsorbed. The comparison between the outflow concentration in active molecules

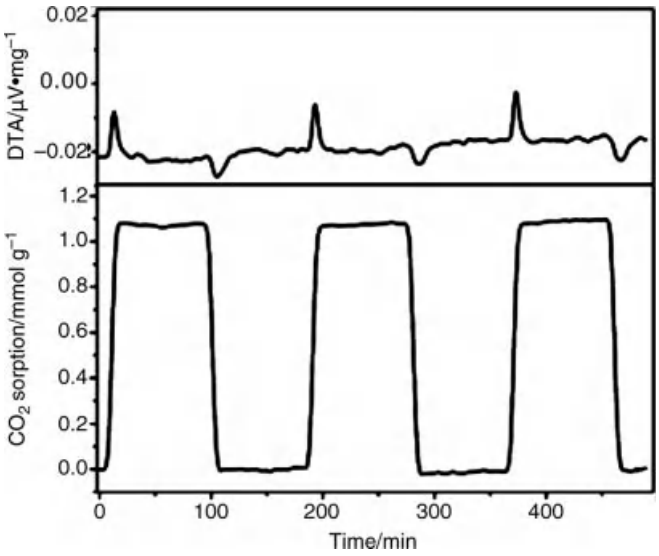


Figure 18.35 Cycles of CO_2 sorption–desorption studied by TG/DTA at 25 °C over an SBA-12/AP sample.

calculated with MS and the input concentration controlled by a precise flowmeter or TCD gives the adsorbed quantities, while the calorimetric part gives the corresponding heats. As in every adsorption technique, the temperature has to be stable in order to guarantee accurate results. As a difference from TGA and volumetry coupled adsorption calorimetry techniques, the MS coupling provides a qualification of the outflow that can detect eventual surface reactions. This coupled technique can be considered similar to adsorption microcalorimetry only when the flow is weak enough to let readsorption processes occur and a thermodynamic equilibrium exist.

Brown and co-workers [51–54] characterized sulfonic acid supported catalysts by NH_3 adsorption using DSC–MS with a Calvet-type DSC instrument. Amberlysts

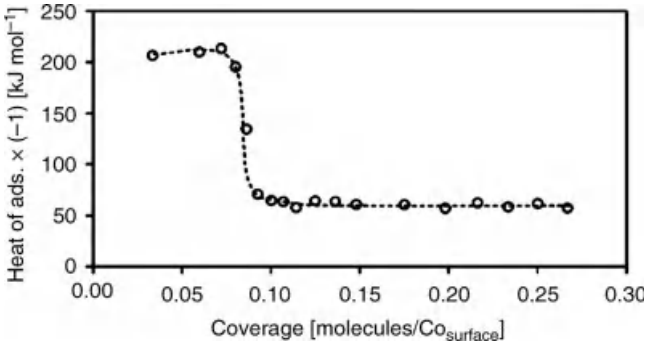


Figure 18.36 Differential heat of adsorption of CD_3CN on Raney-Co from calorimetry at 308 K.

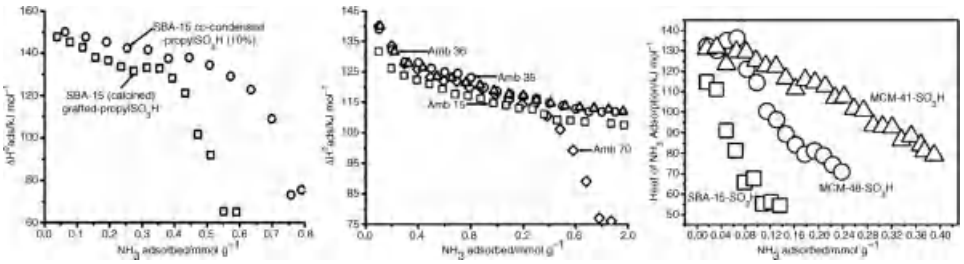


Figure 18.37 Differential heats of ammonia adsorption for sulfate-grafted SBA-15 (a), Amberlyst catalysts (b), and mesoporous silica (c).

(sulfonated resins) and supported SBA-15, MCM-41, and MCM-48 (ordered mesoporous silica) were tested (Figure 18.37). The supported silica displayed increasing catalytic activity (benzyl alcohol conversion) with increasing acidity, and the functionalization process (grafting or co-condensation) yielded similar catalytic activity but higher sulfonic acid loading with co-condensation. The resins displayed similar acidity strengths for various sulfonic acid loadings but different catalytic activities (α-pinene conversion) and thermal stabilities. The porosity of the catalyst and the swelling properties of the solvent/reactant were investigated. α-Pinene being a "non-swelling" and benzyl alcohol a "swelling" solvent, the catalytic tests achieved non-comparable results, and this has to be considered in industrial applications. Further, it was observed that the experiments were sensitive to the sample mass.

18.2.2.4 Other Coupled Methods for Adsorption Calorimetry

TCD detectors can also be used to provide information on the nature of the outflow when surface reactions might occur. However, in this case spectroscopic techniques such as FTIR and Raman spectroscopy will achieve better qualitative analysis. Adsorption methods are usually performed under appropriate conditions in order not to degrade either the adsorbate or the adsorbent; therefore, such techniques will be considered here to quantify the nonadsorbed molecules in pulse-programmed methods such as seen earlier.

18.2.3 Desorption Techniques

Whereas adsorption techniques are isothermal and provide thermodynamic data at given temperatures, desorption techniques are usually temperature programmed, most often linearly, and will give average thermodynamic values over a temperature range or kinetic data.

In order to desorb molecules, either the pressure can be decreased or the temperature can be increased, or both. As seen for adsorption techniques, usually physisorption and chemisorption are distinguished. In any desorption method, the sample will be first desorbed of its weakly bonded molecules (physisorption) then, with more power, of its chemisorbed molecules. "Temperature-programmed deso-

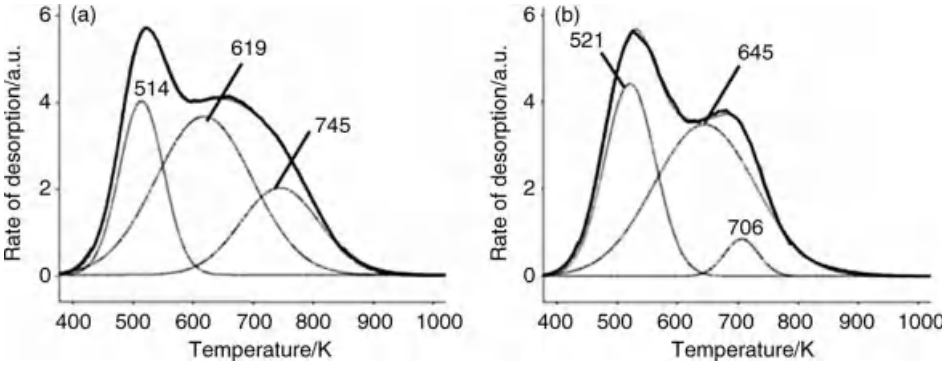


Figure 18.38 TPD of ammonia from LaX (a) and LaY (b): experimental curves (black) and fits (grey).

rption" is the generic name for any desorption setup with a temperature-controlled increase, hence the following methods will often be abbreviated as TPD. Tools for calculating the heats and heat capacities can be found in Section 18.1.7.

18.2.3.1 Temperature-Programmed Desorption followed by Mass Spectrometry (TPD–MS)

Since the pioneering article of Amenomiya *et al.* in 1967 [32], using a TCD detector for ethylene detection, TPD has been generalized to all kinds of desorption. Then other detectors were used to monitor the desorbed or reacting gases, the most frequent being a mass spectrometer. MS can achieve quantitative and qualitative analysis of the outflow gases, more specifically than TCD. From the sensitivity of the signal derives the accuracy of the calculated values (see Section 18.1.7).

From the TPD–MS data, acidity or basicity can be characterized by desorption of basic or acidic probes, respectively. For example, Sievers *et al.* [55] investigated the catalytic activity of LaX and LaY zeolites in isobutane/2-butene alkylation by relating it to surface acidity. NH_3-TPD–MS experiments followed the desorption signal of both NH_3-loaded zeolites at m/z 16 during a linear heating at 10 K min^{-1} up to 1000 K under a helium flow (Figure 18.38). In both cases, three contributions were identified and deconvoluted as Gaussian peaks. The first two peaks were centered at slightly higher temperatures for LaY, and hardly any strongly acidic sites were observed in LaY. The differences in the catalytic performance were attributed to a higher concentration of strong Brønsted acid sites in LaX (Figure 18.39).

18.2.3.2 Thermogravimetry–Mass Spectrometry (TG–MS)

Thermogravimetry in itself is already a TPD method and some thermodynamic values can be calculated from its signal (see Section 18.1.4). Coupling it with MS permits cross-calculations or working with less stable gases or mixtures. The amount desorbed is followed by TG and the nature of desorbed species is monitored on the MS signal.

Gorte and co-workers [56] investigated the adsorption of typical acylating agents (acetic acid, acetic anhydride, and acetyl chloride) on the Brønsted acid sites of an H-

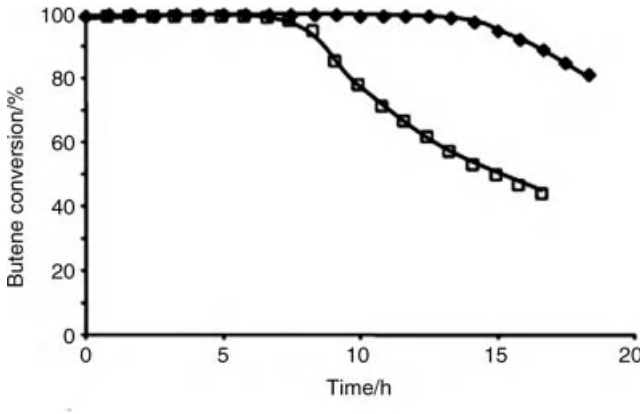


Figure 18.39 Conversion of 2-butene over LaX (◆) and LaY (□) at $T = 348$ K, $p = 20$ bar, P:O ratio = 10, OSV (olefin space velocity) = 0.2 h^{-1}.

ZSM-5 (Si/Al = 60) using TPD–TGA–MS. In these experiments, the exposure was controlled to obtain an initial coverage of about one molecule per site to minimize secondary chemistry. They observed the early formation of an acetyl-zeolite intermediate at temperatures below 450 K, which is likely the important intermediate in the Friedel–Crafts acylation reactions carried out over zeolite catalysts. Figure 18.40 shows the TGA–MS curves for the acetyl chloride TPD of H-ZSM-5, with HCl (m/z 36) degassing below 400 K and various decomposition products above. However, this zeolite is often not an effective catalyst, probably because of the decomposition of the acetyl-zeolite into other intermediates such as ketones or olefins above 450 K, leading to the formation of coke on the zeolites and thus poisoning it.

Leon *et al.* [48] studied the acid–base properties of mixed oxides obtained from layered double hydroxides (LDHs), that is, hydrotalcite-like compounds. TGA–DSC–MS was used to follow the thermal decomposition of the LDHs (Figure 18.41) and showed four decomposition stages (dehydration, losses of hydroxyls until 723 K, then decarbonation completed around 963 K). From this study, two series of catalysts were synthesized, either degraded at 973 K for 7 h leading to decarbonated oxides or degraded at 723 K for 7 h leading to carbonated oxides.

18.2.3.3 Thermogravimetry–Calorimetry–Mass Spectrometry (TG–DSC–MS, TG–DTA–MS)

The coupling of TG with calorimetry in desorption methods is in common use nowadays and necessitates a special setup so that the collections of the two signal types do not interfere with each other. Most commercial systems provide such devices. However, the thermobalance gives an unspecific signal that can lead to misunderstandings if any surface reaction occurs during the heating of the catalyst, especially when the molecules adsorbed prior to the desorption process are reactive or large. A solution consists in analyzing the outflow [evolved gas analysis (EGA)] and the most commonly used device is a mass spectrometer.

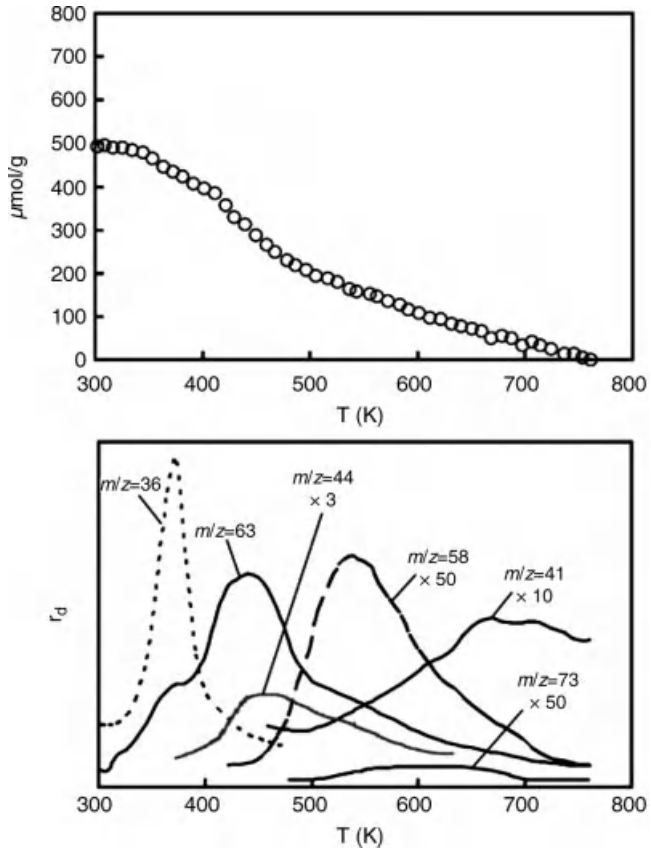


Figure 18.40 TPD–TGA results for acetyl chloride on H-ZSM-5 following controlled exposure at 298 K. The TPD peaks correspond to HCl (m/z 36), unreacted acetyl chloride (m/z 63), CO_2 (m/z 44), acetone (m/z 58), propylene (m/z 41), and C_6 hydrocarbons (m/z 73).

Although TGA can be used for determining isosteric heats, the calorimetric device provides better accuracy, and although MS can be used for determining absolute amounts, the accuracy of a thermobalance will be preferred. TGA–DSC–MS provides data on the heats, amounts, and nature of the evolved molecules at the surface of the catalyst via a synergic setup that adopts the best of each technique.

This setup can be used for the desorption of many types of molecules. For the purpose of acidity or basicity characterization, basic or acidic gas probes will be chosen. See Section 18.2.2.1 for a discussion on these molecules.

Figueras *et al.* [57] investigated the isomerization of β-isophorone to α-isophorone as a model reaction characteristic of basic sites. For this purpose, they screened various known basic catalysts [hydrotalcite (HT), mixed oxides of magnesium–lanthanum (MgLa), barium–aluminum (BaAlO), and doped alumina (KF1α)] with both TPD of CO_2 (Figure 18.42), which is an acidic probe, and their catalytic test. A TGA–DTA–MS setup was used for the TPD of CO_2 and the integration of the MS signal (m/z 44 for

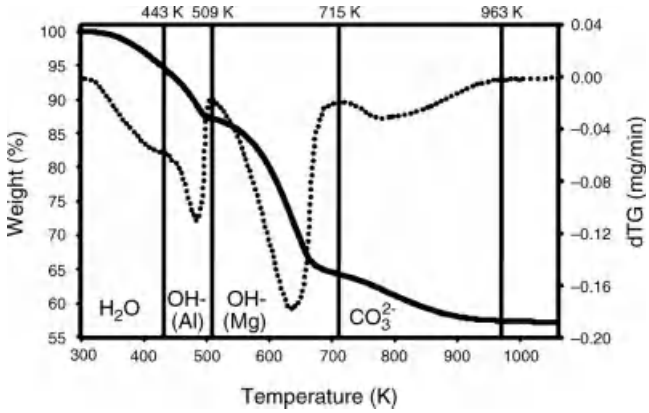


Figure 18.41 Thermogram for the formation of the mixed oxide from the 1K (1: low supersaturation of K potassium) hydrotalcite precursor.

CO_2) was normalized to 1 g of sample, then related to the rate of isomerization (Figure 18.43). The isomerization process was found to be strongly related to the total amount of basic sites (even though CO_2 is less acidic than SO_2, for example, weaker sites may have not been dosed), and poorly related to the strength of basicity, which can be qualitatively evaluated by the shifts of the temperatures at the MS peak maxima.

18.2.3.4 **Other Coupled Methods (TPD–TCD, TPD–IR–MS, etc.)**

For the characterization of acidic/basic sites on catalysts, many analytical devices can be used to monitor the desorption of the gas probes, provided that the technique is

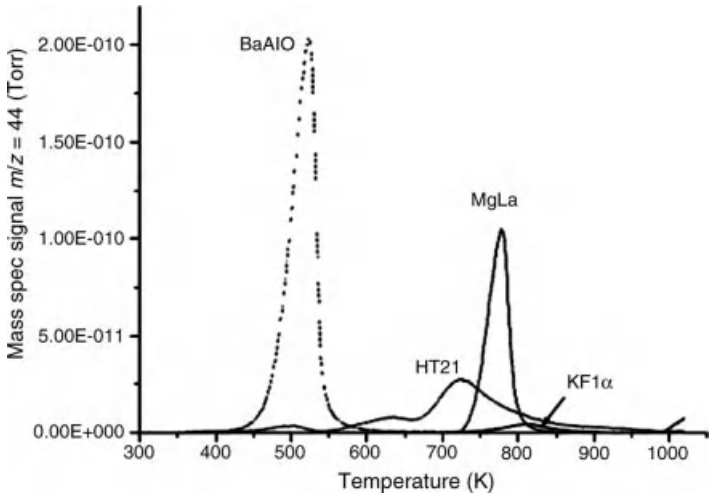


Figure 18.42 Desorption of CO_2 followed by mass spectrometry during the thermal analysis of hydrotalcite HT-21, KF1α (KF/alumina), LaMg mixed oxide, and barium hexaaluminate.

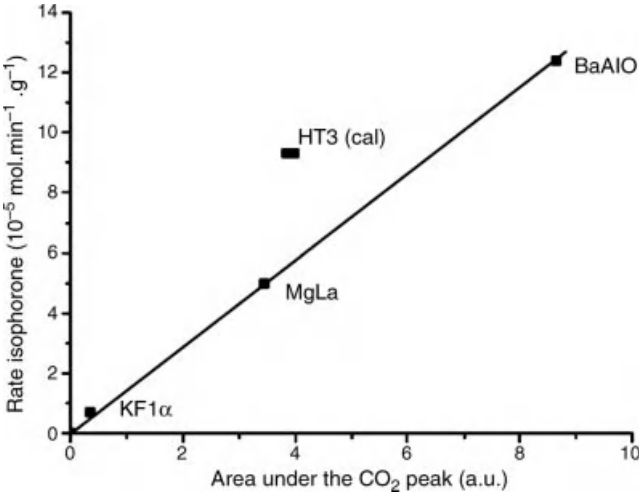


Figure 18.43 Rate constant for isophorone isomerization at 308 K as a function of the number of sites determined by CO_2 adsorption for a series of basic samples.

appropriate for the accurate detection of the desorbed species. For example, TCD detectors are often used for the detection of hydrocarbons and hydrogen, whereas FTIR detectors are more often used for the detection of organic probes, and GC or high-performance liquid chromatography (HPLC) can also be coupled to a temperature programmer and a furnace.

Provided that a non-destructive detector is used, the coupling of techniques can be set for the analysis of the outflow. For example, a TPD–IR–MS setup was developed for the study of the reaction of acetic acid on NaHY zeolites by Kukulska-Zajac *et al.* [58] The zeolite was reacted for 30 min at 470 K with acetic acid in an IR cell, then cooled to 250 K and the cell was connected to a mass spectrometer before starting the TPD at 5 K min^{-1} until 800 K. The zeolite's Si–OH–Al groups were found to act as acceptors of protons originating from organic acids.

18.2.4
Acid–Base Properties of Common Catalysts

Most often, both acidic and basic sites can be observed on solid surfaces and their respective dispersion can eventually allow concerted catalytic mechanisms (i.e., bifunctional reaction pathways). The acid–base properties of numerous amorphous metal oxides and molecular sieves investigated by microcalorimetry were summarized in an extensive review by Cardona-Martinez and Dumesic [4] and in book chapters by Auroux and co-workers [7–10, 59–60].

18.2.4.1 Zeolites and Molecular Sieves

18.2.4.1.1 **Zeolites** Zeolites are crystalline aluminosilicates in which all aluminum and silicon atoms form tetrahedra which are linked by shared oxygen atoms. These

tetrahedra join to form secondary building units, which can be interconnected to give numerous distinctive zeolite structures. Each has a regular and well-defined pore structure together with inner cavities. The precise control of pore size is one of the greatest distinctions between zeolites and amorphous silica–aluminas. The morphology, free volume, pore geometry, and electric field gradients determine their acidity and selectivity. Zeolites have been the focus of numerous studies of their adsorption capacities and acid–base properties [4, 8, 59–61]. Here are presented only some case studies highlighting the thermal techniques developed for their characterization.

The acidity of high-silica zeolites produced either by direct synthesis or by chemical dealumination of parent zeolites either by steaming and acid leaching or by $SiCl_4$ vapor treatment (keeping the structure intact) was extensively studied in the 1990s. ZSM-5 and dealuminated Y faujasites (called ultra-stable "USY") have also been widely investigated for petrochemistry applications [fluid cracking catalysts (FCCs)] [42]. The active centers were found to be Brønsted acid sites carried by the zeolite framework.

The chemical treatment generating USY from Y faujasites partially removes Al atoms from the crystal framework, thus decreasing the number of Brønsted sites but also generating extra-framework aluminum (EFAL) species and framework defects, which are generally associated with Lewis acidity. The Lewis sites may have their own catalytic activity and also may interact with Brønsted sites, increasing their strength.

The effect of dealumination on Y faujasites and mordenites was studied for various Si/Al ratios by Stach *et al.* [62, 63]. From many experimental and theoretical investigations, it had been concluded that the number of bridging hydroxyl groups increases with increase in the number of Al atoms in the lattice; however, the dependence of the acid strength on the aluminum content is more complicated. The number of strong acid sites presents a distinct maximum, corresponding to an Al content of 4.6/u.c. (Si/Al = 9.5) for dealuminated mordenites, and an Al content of about 29/u.c. (Si/Al = 5.5) for dealuminated Y zeolites (Figure 18.44).

A similar study performed on Y faujasites with Si/Al ratios of 2.6, 5.8, 12.8, and 24 agreed with these observations and attributed the higher number of very strong acid sites on the two most dealuminated zeolites to the presence of EFAL species [8].

Flow adsorption microcalorimetry was used to measure the heats of adsorption of ammonia on HY and NaY zeolites by Brown and Groszek [64]. Ammonia pulses carried by nitrogen at atmospheric pressure were flushed on the sample and the effluent was quantified by TCD. It was observed that, as the surface coverage increased, the sites covered first were not necessarily those with the highest molar heats of adsorption, due to considerations of mobility of the probe (related to temperature) and of accessibility of the sites.

Calorimetric investigations of the adsorption of H_2O, NH_3, methanol, and other small polar molecules on the Na forms of synthetic zeolites A, X, and Y demonstrated the heterogeneous nature of the acid strength, which can be explained by the successive interactions of the exchange cations at the various crystallographic positions [60]. Others studies on the influence of cations on acidity were performed on X and Y faujasites exchanged with Ca^{2+}, La^{+}, and Li^{+} by ammonia and amine

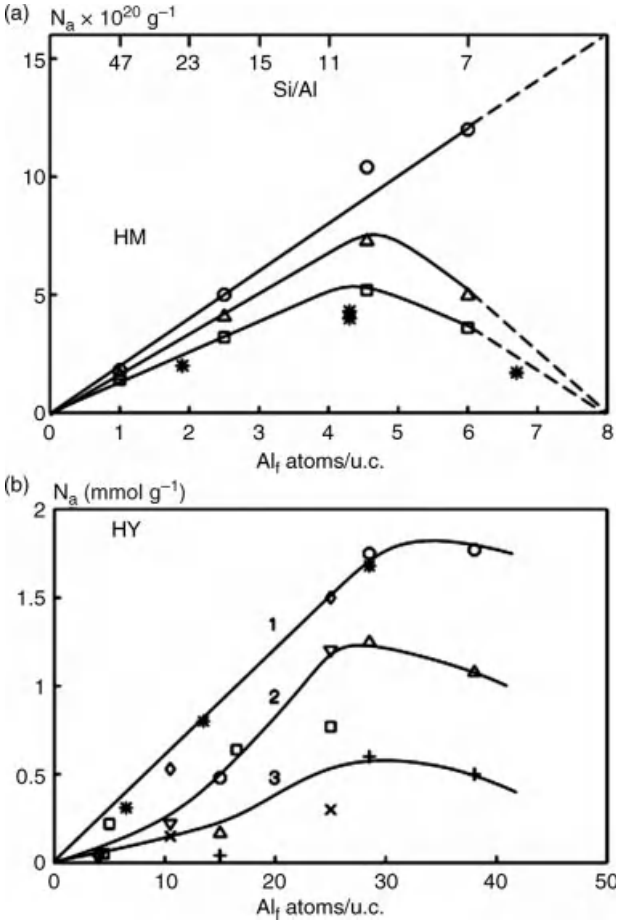


Figure 18.44 Dependence of acid strength distribution (ammonia probe at 423 K) on Al(IV) content per unit cell of dealuminated (a) mordenite: N_a, number of acid sites in molecules g^{-1} with $Q > 80$ kJ mol^{-1} (○), with $Q > 100$ kJ mol^{-1} (Δ), and with $Q > 120$ kJ mol^{-1} (□, ∗); and (b) Y zeolites: total number of acid sites with (1) $Q > 80$ kJ mol^{-1}, (2) $Q > 100$ kJ mol^{-1}, and (3) $Q > 120$ kJ mol^{-1}.

adsorption calorimetry [65–67]. The shapes and initial heats were found to vary substantially with the nature of the cation, due to many parameters such as the effective charge and the position in the crystal lattice.

A systematic study on cation-exchanged X and Y faujasites was performed by SO_2 and NH_3 adsorption calorimetry [68] and revealed different binding energies of the cations to the zeolite framework. The activity in catalytic MPO conversion increased from Cs to Li for both X and Y zeolites, which correlated with an increase in acidity. Linear correlations were found between the heat of NH_3 adsorption evolved per site and the intermediate electronegativity and between the irreversibly adsorbed volume of SO_2 and the partial oxygen charge (Figure 18.45).

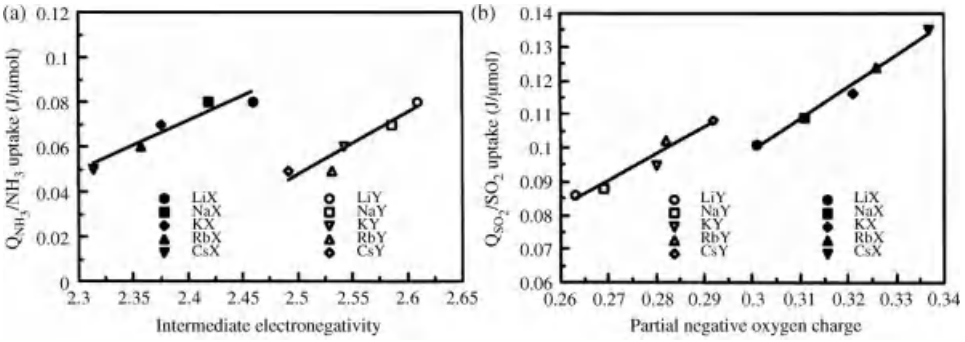


Figure 18.45 Heats of adsorption of NH_3 (a) evolved per site versus the intermediate electronegativity and heats of adsorption of SO_2 (b) evolved per site versus the partial negative charge, for alkali metal-exchanged X and Y zeolites.

The influence of cation exchange was also evaluated by Shimizu *et al.* [69] on K-10 montmorillonites (Mont) for cations of various charge to ionic radius ratios (0.9–4.7) and cation electronegativities (2.7–12.6). Fe^{3+}- and Yb^{3+}-exchanged zeolites achieved better catalytic activity of acetylation of cyclohexanol with acetic anhydride and their acidity was investigated by acetone adsorption calorimetry at 323 K. Acetone ($pK_a \approx 20$, $PA = 812\,kJ\,mol^{-1}$) adsorbs irreversibly on Lewis acid coordinatively unsaturated (cus) metal sites. The order of Lewis acid strength, Fe^{3+}-Mont > Yb^{3+}-Mont > $FeCl_3/SiO_2$, was consistent with the order of catalytic activity, indicating that Lewis acid strength is an important factor affecting the activity, and confirming the better suitability of Lewis acid catalysts for acetylation than typical Brønsted acid catalysts (H-ZSM-5).

Other amine probes are widely used to characterize the acidity of solids, the most often used being pyridine, and the range of evolved heats differs from one to another, influenced by the respective proton affinities. Further, such large molecules are often unable to enter the pores of zeolites, hence they will not dose the same amount of sites, but more probably the surface acid sites.

The adsorption of pyridine and aniline has also been used in order to predict the adsorption properties of various zeolites in the frame of the depollution of aromatics [dissolved volatile organic compounds (VOCs)] and alkaloids in water. Adsorption calorimetry of pyridine ($pK_a = 5.2$, $PA = 930\,kJ\,mol^{-1}$) in the gas phase and aniline ($pK_a = 4.62$, $PA = 882.5\,kJ\,mol^{-1}$, molecular diameter = 0.562 nm) in *n*-decane was performed on four molecular sieves [H-ZSM-5, H-Beta, H-MCM-22, and clinoptilolite (Clino)] with different pore sizes and acid properties (Figure 18.46a), revealing heterogeneity of acid strength [70]. According to the initial heats of adsorption, a different order between the gas phase (Clino > H-ZSM-5 > H-MCM-22 > H-Beta) and liquid phase (H-MCM-22 > H-ZSM-5 > H-Beta > Clino) could be observed, explained by the occurrence in the liquid phase of the endothermic enthalpy of solvent displacement and by a particular effect due to the framework. Titration calorimetry of nicotine ($pK_a = 8.01$) in water was then performed (Figure 18.46b) and displayed an unexpected high heat for H-Beta zeolite until full adsorption, whereas

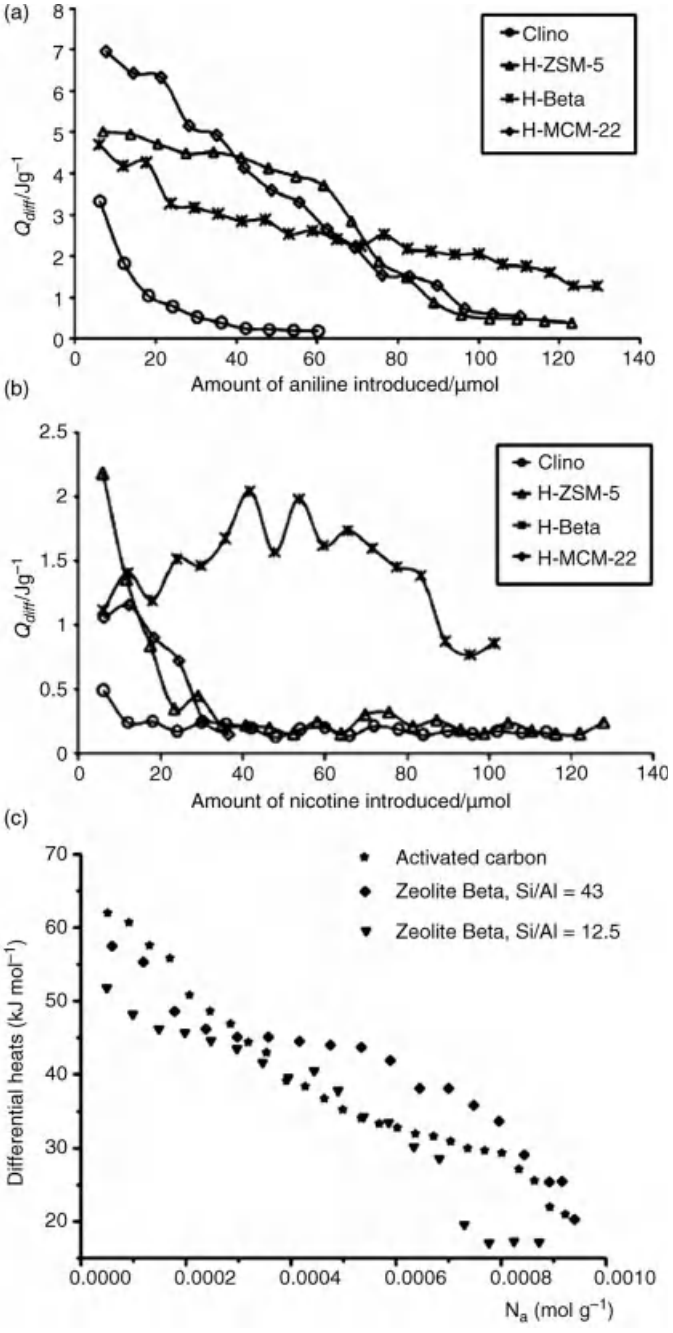


Figure 18.46 Differential heats of adsorption of aniline (a) and nicotine (b) for four types of molecular sieves versus the amount introduced, and of nicotine (c) for activated carbon and two Beta zeolites, versus the amount adsorbed.

other samples displayed the usual decrease. Initial acid strength sorted zeolites in the order H-ZSM-5 > H-Beta > H-MCM-22 > Clino. The correlation of these heats with the amount adsorbed instead of the amount injected needed a parallel isotherm experiment (using UV–visible spectrophotometry), that confirmed the unusual high interaction of Beta zeolites with nicotine and good adsorption properties [~1 mmol of nicotine per gram of zeolite (Figure 18.46c)]. Finally, it was demonstrated that high nicotine adsorption correlates with high acidity and hydrophilicity, but also an appropriate (large enough) pore size [71].

Various interactions can actually occur in the zeolite's cavities; thus adsorption calorimetry of N_2, CO, CH_3CN, and NH_3 was performed on H-BEA and H-MFI zeolites at 303 K in order to assess the energetic features of the specific adsorption on Lewis and Brønsted acid sites, the H-bonding interaction with hydroxyl nests, and the confinement effects [72]. N_2 and CO were found to single out mainly Lewis sites and also to be sensitive to confinement effects due to dispersive forces which are governed by the size of the micropores. Polar molecules such as CH_3CN and NH_3 were not preferentially adsorbed on Lewis acid with respect to the Brønsted sites, by virtue of their ability to generate either protonated species or strongly H-bonded adducts.

The heats of adsorption of quadrupolar (N_2 and CO_2) and nonpolar (Ar, O_2, CH_4, C_2H_6, and SF_6) gases were determined on a silicalite in order to study the effect of adsorbate size and polarity on the energetics of adsorption in molecular sieves [73]. The heats of adsorption were found to be almost constant or to increase slightly with coverage and increased roughly in proportion to the polarizability of the adsorbate molecules, indicating the predominance of dispersion compared with electrostatic interactions. Silicalite was classified as a relatively homogeneous adsorbent compared with X-type zeolite. The calculated isosteric heats of adsorption were in good agreement with heats measured by adsorption calorimetry and their accuracy was estimated to be $\pm 2\%$ for heats larger than 30 kJ mol^{-1} and $\pm 5\%$ for heats smaller than 30 kJ mol^{-1}.

A fairly large number of papers have been published on the use of calorimetry to study the acidity of mesoporous materials [8, 60]. Mesoporous molecular sieves are close to microporous zeolites in their methods of preparation and principal regions of application. These materials are usually synthesized by using supermolecular templates and, in particular, the micelles of cationic surfactants. Li *et al.* [74] fabricated via a template method three-dimensionally ordered macroporous (3DOM) oxides (MgO, Al_2O_3) and mixed oxides ($Ce_{0.6}Zr_{0.4}O_2$, $Ce_{0.7}Zr_{0.3}O_2$) displaying single-phase polycrystalline structures. The alumina compound exhibited 3DOM walls whereas the others exhibited wormhole-like mesoporous walls. 3DOM alumina and magnesia displayed high CO_2 chemisorption uptake, measured by CO_2 TPD, whereas the 3DOM $Ce_{0.6}Zr_{0.4}O_2$ sample showed excellent low-temperature reducibility.

The MCM-41 mesoporous molecular sieve (pure silica) was investigated by NH_3 adsorption calorimetry and was found to possess specific although weak acidity. The introduction of titanium or zirconium, and particularly aluminum, ions into the structure of this sieve substantially increased the acid strength of the sorbent. The investigated samples were ordered by acid strength for ammonia adsorption as

follows: silica gel < Si-MCM-41 < Si,Zr-MCM-41 < Si,Ti-MCM-41 < Si,Al-MCM-41. Experiments on the adsorption of acetonitrile on Si,Al-MCM-41 demonstrated the presence of strong Lewis acidity and poorly defined Brønsted acidity, whereas flow calorimetry of 1-butanol adsorption in *n*-hexane determined the correlation between the aluminum content and the amount of strong Lewis sites, found to vary between 43 and 70% of the total acidity [75–77].

18.2.4.1.2 **Pillared Clays and Layered Silicates** Natural clays such as montmorillonite, hectorite, and smectite have been extensively investigated and modified by intercalation of metal oxides or hydroxides, leading to a new type of compound, pillared clays (PILCs), which were reported to show catalytic properties comparable to those of zeolites in several reactions, and therefore to have comparable acidities. Further, the intercalation of hydroxysilicoaluminum compounds was found to increase the acidity of the PILCs and also their thermal stability, necessary for industrial applications.

The distributions of acid strengths of various PILCs obtained by NH_3 adsorption calorimetry showed that Al-PILC displays high acidity (160 kJ mol^{-1} in pillared beidelite), with a small number of sites as strong as those measured on zeolites [78], that a natural clay pillared with mixed solutions containing both Al and Fe, Ti, or Cr displayed a distribution of acid strengths comparable to that of zeolites, and that the inclusion of SiO_2–TiO_2 clusters drastically increased the Brønsted and Lewis acidity of a mesoporous expanded clay, in terms of both strength and density of acid sites [79].

The acidity of PILCs has been characterized by both microcalorimetric measurements of the adsorption of aromatic molecules and pyridine and the catalytic ethylbenzene test reaction [80, 81]. The aromatic probe molecules used were a reactant and a product of the catalytic reaction: ethylbenzene and *m*-diethylbenzene, respectively. In this way, only the strongest of the accessible acid sites were titrated. The heats of adsorption of these molecules indicated that a zirconium oxide PILC had stronger acidity than an aluminum oxide PILC, whereas the pyridine adsorption results were the same for both samples.

18.2.4.2 Metal Oxide Catalysts

18.2.4.2.1 **Bulk Oxide** The sample pretreatment for a coupled volumetry–calorimetry experiment is effected under vacuum in order to remove surface water, hence the temperature of this pretreatment strongly affects the surface properties of both Brønsted (protons) and Lewis (cus metals) types.

An NH_3 adsorption microcalorimetry study on γ-alumina with pretreatment temperatures between 573 and 1073 K provides a pertinent example of such an influence. The number and strength of the strongly acidic sites, which should be mainly Lewis acid sites, have been found to increase with the pretreatment temperature (dehydroxylation) which was also affecting not only the initial heat but the whole spectrum of adsorption.

A practical way of evaluating the relative acidic and basic characteristics of a catalyst is to display together the differential heats of adsorption of a basic and an acidic probe

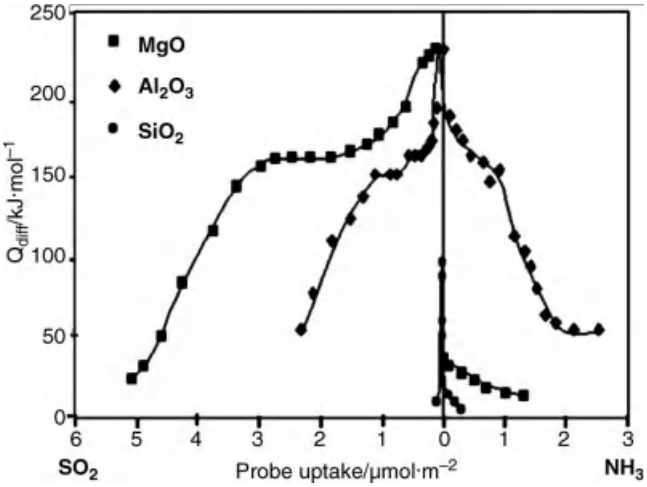


Figure 18.47 Differential heat curves of SO_2 and NH_3 adsorption for magnesia, alumina, and silica [59].

as a function of the amounts adsorbed. Figure 18.47 shows the differential heats of adsorption of NH_3 and SO_2 as a function of probe uptake for silica, magnesia, and γ-alumina samples [59]. Silica's basic and acidic sites are few and weak and correspond to hydrogen bonding and van der Waals interactions. Alumina presents both strongly acidic and basic sites and equilibrated amounts of adsorbed probes and is thus considered relatively amphoteric. Magnesium oxide's acidic sites are few and bond weakly with ammonia ($<35\,kJ\,mol^{-1}$) whereas its basic sites are four times more prevalent and interact strongly with sulfur dioxide with a plateau at 160 kJ mol^{-1}. indicating that it is a strongly basic solid.

A large number of bulk oxides have now been investigated for their acid–base properties. Auroux and Gervasini [82, 83] determined the differential heats of adsorption of NH_3 and CO_2 over 18 bulk oxides and distinguished acidic oxides Cr_2O_3, WO_3, Nb_2O_5, V_2O_5, and MoO_3 from amphoteric oxides BeO, TiO_2, Al_2O_3, ZrO_2, and ZnO and basic oxides ThO_2, Nd_2O_3, MgO, CaO, and La_2O_3 (Figure 18.48). The "amphoteric" character corresponds to an equilibrated amount of basic and acidic sites; several amphoteric oxides can display higher acidity or basicity than so-called "acidic" or "basic" oxides. It is worth noting that, on alkaline earth metal oxides, the heats of adsorption of CO_2 were only 120–160 kJ mol^{-1}, perhaps because of bidentate adsorption of CO_2. A fair correlation was found between the average heats of adsorption and the percentage of ionic character of the oxides.

The differential heats of adsorption of NH_3 and CO_2 show a wide range of variability, displaying either a plateau of constant heat or a continuous decrease indicative of adsorption heterogeneity. The ratio between the number of basic and acidic sites, n_B/n_A, was calculated for ceria, zirconia, and lanthana catalysts from the microcalorimetry results, by dividing the amount of adsorbed CO_2 by the amount of adsorbed NH_3 [84]. These catalysts were used to produce 1-alkenes from 4-methyl-

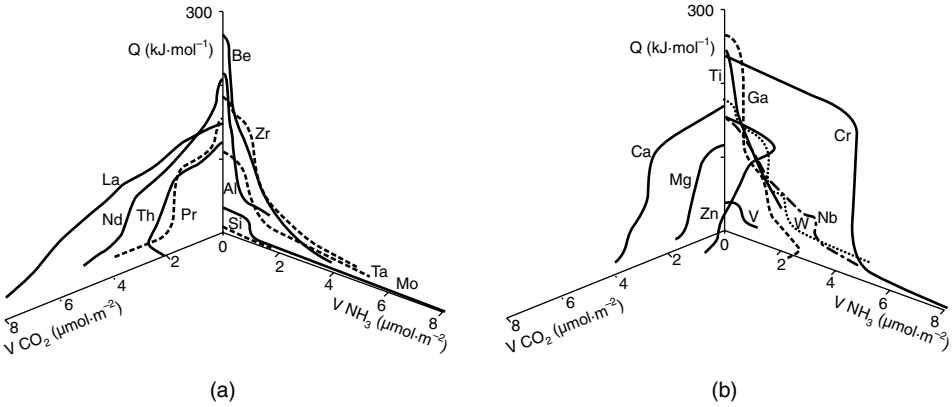


Figure 18.48 Amounts of adsorbed CO_2 at 296 K and NH_3 at 423 K for a given differential heat for various metal oxides, displayed on two separate graphs (a) and (b) for the sake of clarity.

2-pentanol (MPO). The 1-alkene selectivity was found first to increase with the n_B/n_A ratio, reach a maximum, and then decrease, whereas ketone formation increased continuously, being negligible for low n_B/n_A values (Figures 18.49 and 18.50).

18.2.4.2.2 **Doped and Modified Oxides** Doped metal oxide catalysts are widely used in various catalytic processes. The doping affects the overall surface electronic properties and can often be correlated with acidic or basic variations relative to the undoped material. Gervasini *et al.* [85] investigated the doping by various ions (Li^+, Ca^{2+}, Nd^{3+}, Ni^{2+}, Zr^{4+}, and SO_4^{2-}) of bulk γ-alumina, silica, and magnesia by adsorption microcalorimetry of NH_3 and SO_2 and the catalytic reaction of 2-propanol conversion. Alumina (amphoteric oxide, high adsorption) was almost unaffected, whereas medium and weakly basic sites appeared on magnesia (basic oxide) and the overall acidity and basicity spectra of doped silica (poorly adsorbing) was modified. The acidity of the catalysts was correlated with the charge/radius ratio and with the electronegativity of the doping ions. The basicity was correlated with the partial oxygen charge of the corresponding oxides. Medium acid strength sites were correlated with the catalytic conversion of 2-propanol to propene. Ca doping of alumina-supported chromia was found to suppress the medium and strongly acidic sites. The sulfation of zirconia-, titania-, ceria-, and alumina-supported vanadia was investigated by NH_3 adsorption calorimetry and an overall change of the spectrum could be observed. Some of the sulfated materials displayed a strange phenomenon of low initial heat of adsorption at low ammonia coverage, but only for samples possessing enough weak sulfate species, such as bisulfate and low-polymerized sulfate species. This very low initial enthalpy of adsorption observed by calorimetry on sulfated titanias suggests the occurrence of an endothermic process (dissociation of NH_3) counterbalancing the exothermic process of adsorption.

18.2.4.2.3 **Supported Metal Oxide or Metal Catalysts** Supported active materials (metal or metal oxide) on less expensive or high surface area materials have been

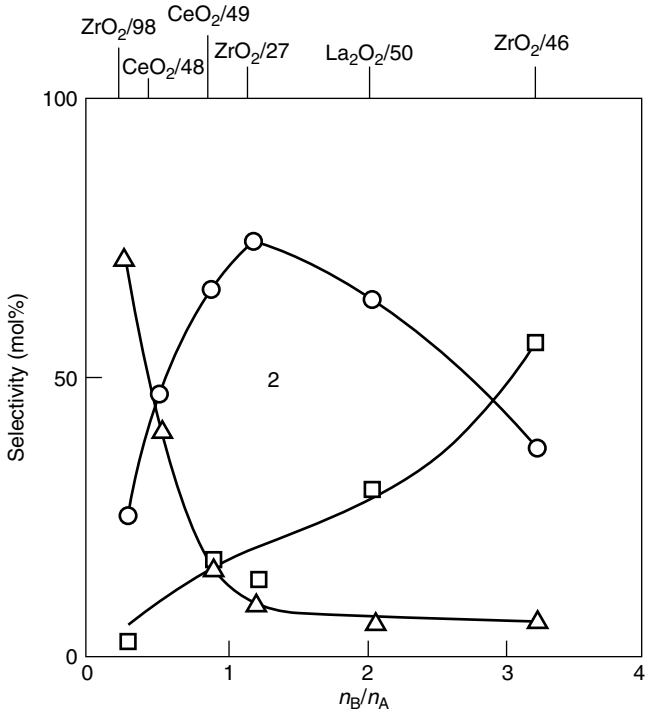


Figure 18.49 Selectivity to 4-methyl-1-pentene (○), 2-alkenes (Δ), and 4-methyl-2-pentanone (□) versus n_B/n_A for lanthanum, cerium, and zirconium oxides.

widely investigated. The support can also often play a major role in the catalytic mechanism. In the case of molecular sieves, the key question will often be the characterization of the location of such active materials inside the porous structure; in the case of metal oxides as support, depending on the coverage, different types of species are deposited, for instance, monomeric, polymeric, or bulk-type species, these three main types of species often exhibiting different catalytic and acidic properties.

Supported Metal Oxides Gervasini *et al.* [86] demonstrated by NH_3 and SO_2 adsorption microcalorimetry that the addition of lithium, nickel, or sulfate ions

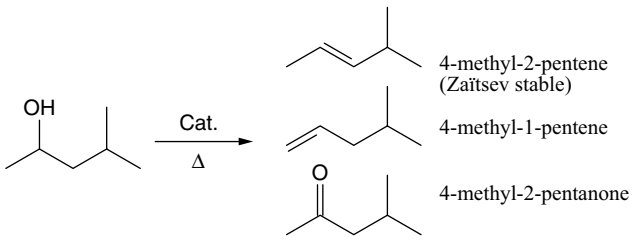


Figure 18.50 Dehydration and dehydrogenation products of 4-methyl-2-pentanol.

from 1 to 50% coverage of γ-Al_2O_3, SiO_2, or MgO resulted in nonlinear changes in the number and character of acid–base sites, displaying almost no change at low loading (1–10%) and a drastic change when half of the support is covered.

Supported boria catalysts have been prepared by an impregnation method and chemical vapor deposition on porous and nonporous γ-aluminas with loadings from 0 to 30 wt%, and studied using NH_3 and SO_2 adsorption microcalorimetry [87]. SO_2 adsorption with increasing boria loading showed a progressive decrease of basicity and thus a good dispersion of B_2O_3 at high coverage. Monolayer coverage was attained for 21 wt% on porous alumina and 7 wt% for nonporous alumina, and a large number of weakly acidic sites were created on the catalyst surface when the amount of boria was greater than the theoretical monolayer. Ammonia was shown to cover all types of sites from strongly to weakly acidic sites, whereas pyridine only titrated the stronger sites of the samples, probably because of steric hindrance. Moreover, the catalytic activity for partial oxidation of ethane increased with increase in acidity and reached a maximum constant value for the monolayer.

Highly dispersed silica-supported titania surfaces were obtained by atomic layer deposition (ALD) at a growth rate of 1 atom $nm_{support}^{-2}$ per ALD cycle, reaching monolayer coverage at 4 Ti atom $nm_{support}^{-2}$ (i.e., four cycles), and were characterized by NH_3 adsorption calorimetry [88]. The highly dispersed titania species on silica contributed to the creation of strongly surface acidic sites (differential heat values from 120 to 150 kJ mol^{-1}) by the formation of strong Ti−O−Si bonds. The 7 TiSi sample (7.2 Ti atom $nm_{support}^{-2}$), however, mainly displayed additional weak and medium-strength acidic sites (60–120 kJ mol^{-1}) and few strong sites relative to approximately monolayer samples.

Alumina-supported tin and gallium oxides with varying amounts of tin and gallium were prepared by wet impregnation and characterized by NH_3, SO_2, NO_2, and NO adsorption microcalorimetry [89]. Ga_2O_3 was deduced to be more bonded to the acidic sites of alumina or to create new basic sites whereas SnO_2 would be more bonded to alumina's basic sites or create new acidic sites. NO showed only physisorption properties whatever the amount of tin or gallium oxide loaded, and NO_2 appeared to behave as an acidic probe, showing the same behavior as SO_2 on the tin dioxide samples.

Several other supports have been tested for supporting tin oxide by ammonia adsorption calorimetry [90, 91]. The properties of the resulting samples were strongly determined by the support. Supporting SnO_2 on TiO_2 or ZrO_2 did not result in an appreciable change in acidity, whereas remarkable increases were observed for SiO_2 and MgO. Al_2O_3 was mainly modified in the medium acid strength domain (decrease of strong sites, increase of medium and weak sites). The amount of deposited tin dioxide had little influence.

Two series of In_2O_3-containing catalysts with low (∼3 wt%) and theoretical geometric monolayer (from 20 to 40 wt%) In_2O_3 content were prepared on γ-Al_2O_3 and their surface properties were compared with those of bulk In_2O_3 material by NH_3 and SO_2 adsorption microcalorimetry [92]. Stronger basic sites on the india-loaded samples and an overall decrease in acidity and increase in basicity were observed. These results are compatible with the general basic character of indium oxide.

Petre *et al.* [93] prepared a series of oxides of group III metals (Al_2O_3, Ga_2O_3, In_2O_3) supported on niobia, prepared by incipient wetness impregnation and with a loading close to the theoretical monolayer, and characterized them by NH_3 and SO_2 adsorption microcalorimetry. Acidity followed the order Ga/Nb < In/Nb < Al/Nb and basicity the order Ga/Nb ≈ In/Nb ≪ Al/Nb. In that case, the poor basicity observed for the indium oxide-supported sample was attributed to very poor dispersion.

Jin *et al.* [94] studied the deposition of molybdenum oxide species on niobium oxide for optimizing catalysts for the oxidative dehydrogenation of alkanes or oxygenated compounds. They determined the acid–base properties by NH_3 adsorption calorimetry and FTIR spectroscopy and obtained samples displaying more strong Lewis acid sites and fewer Brønsted acid sites, which showed poor catalytic activity.

Supported Metals Transition metals can act as active centers in redox catalysis and the acidity of the support is often of major importance, for example, for enhancing the selectivity of redox phenomena [95–98]. Metal cations themselves are Lewis-type acid sites. CO adsorption calorimetry then gives valuable information on the dispersion and the surface state of supported or incorporated metal cations, whereas other probes (acidic, basic) will characterize the cation's environment.

Auroux and co-workers [95] determined the adsorption properties towards NH_3 and NO, at 353 and 313 K, respectively, by coupled calorimetric–volumetric measurements on supported catalysts consisting of cobalt, copper, or nickel metal ions deposited by ion exchange or impregnation on an amorphous silica–alumina and a ZSM-5 zeolite. The support usually adsorbs NO poorly, hence NO is used for dosing the metal cations. The average acid strength of the catalysts supported on silica–alumina was stronger than that of the parent support, whereas the zeolite-based catalysts had (with the exception of the nickel sample) weaker acid sites than its parent. In the case of zeolites and more generally molecular sieves, the transition metals are incorporated into the structure more than for supported homologs. Complementary information can be found in the section on zeolites (Section 18.2.4.1), in the DeNOx case study (Section 18.3.2), and in the dedicated literature [60].

In the case of bifunctional supported metal-heteropolyacid (HPA) for the catalytic isomerization of *n*-hexane, the acid strength, influenced by the HPA–support interactions, was found to play a critical role in controlling the selectivity. Supported palladium-HPA on silica, zirconia, and carbon was characterized by 2,4,6-trimethylpyridine TPD [96]. The Brønsted acidity of the bifunctional catalysts and of the corresponding supported HPA was linearly correlated with the catalytic activity. Supported ruthenium-HPA was characterized for various supports using ammonia adsorption calorimetry. The best catalytic activity was attributed to the silica-supported catalyst with a higher overall acidity, but no direct correlation was determined.

A series of Pd catalysts supported on zeolites (BEA, Y), metal oxides (SiO_2, SiO_2–Al_2O_3), and tungstated metal oxides (Pd/W–MO_x) were prepared by Lin *et al.* [98] and tested for pyrene hydrogenation. The acidity of the supports was investigated by

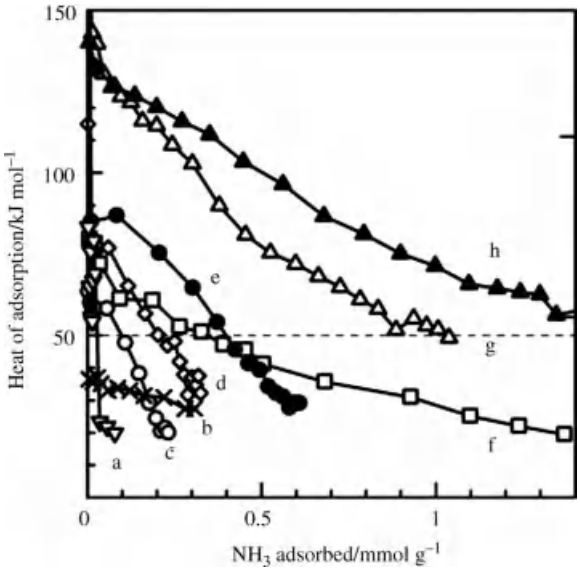


Figure 18.51 Differential heat of adsorption of NH_3 on (a) WMg, (b) SiO_2, (c) WTi, (d) 25WZr, (e) WAl, (f) SiO_2–Al_2O_3, (g) BEA zeolite, and (h) Y zeolite.

ammonia adsorption calorimetry. The differential heats are displayed in Figure 18.51 and are characteristic of heterogeneous acidity (no real plateau) with various initial heats: in the range 130–150 kJ mol^{-1} for the zeolites, 60–90 kJ mol^{-1} for the metal oxides with and without tungsta, and 37 kJ mol^{-1} for silica. The 0.02 wt% Pd-loaded catalysts were tested, and a correlation was found between the catalytic hydrogenation results and the acidity of the zeolite and metal oxide supports but not for tungstated supports. The hydrogenation activity of Pd/W–MOx was well correlated with the equilibrium constant of the reversible reduction–oxidation of the surface W species, which represents the on-site formation of protonic acid from gaseous H_2. It was concluded that the promoted hydrogenation activities of Pd/W–MOx can be attributed to the on-site formation of protonic acids involving the reduction of surface tungstate.

18.2.4.2.4 **Mixed Metal Oxides** The acid–base properties of mixed metal oxides have been found to change with the nature and the relative amounts of the constituents but also with the preparation and pretreatment procedures. By tuning these parameters, desired acid–base properties could be designed. Several processes can be used, such as grafting of metal alkoxides on surface hydroxyl groups, coprecipitation of metal salts by base addition, and a sol–gel procedure, providing structures of the core–shell (supported oxides), solid solution, or multi-layered type.

Qualitative models have been developed concerning the generation of new acidic features, derived from the small perturbation that a guest metal can cause in a host oxide matrix (based on charge and coordination concepts). The most cited models are from Tanabe *et al.* [99] and Seiyama *et al.* [100] and describe systems where guest

metals are far from each other. So far, no general rule has been proposed to predict quantitatively the acid–base properties of mixed oxides.

While tuning the redox properties of ceria–zirconia solid solutions and ceria–lanthana coprecipitated mixed oxides, Cutrufello *et al.* [101] observed variations in the acid–base properties by calorimetry. The inclusion of increasingly high contents of zirconium in the ceria lattice exerted a complex influence on both the acidity and basicity of the pure parent oxide (Figure 18.52). The coprecipitated ceria–lanthana presented a low ammonia uptake and a complex basicity, consisting of a heteroge-

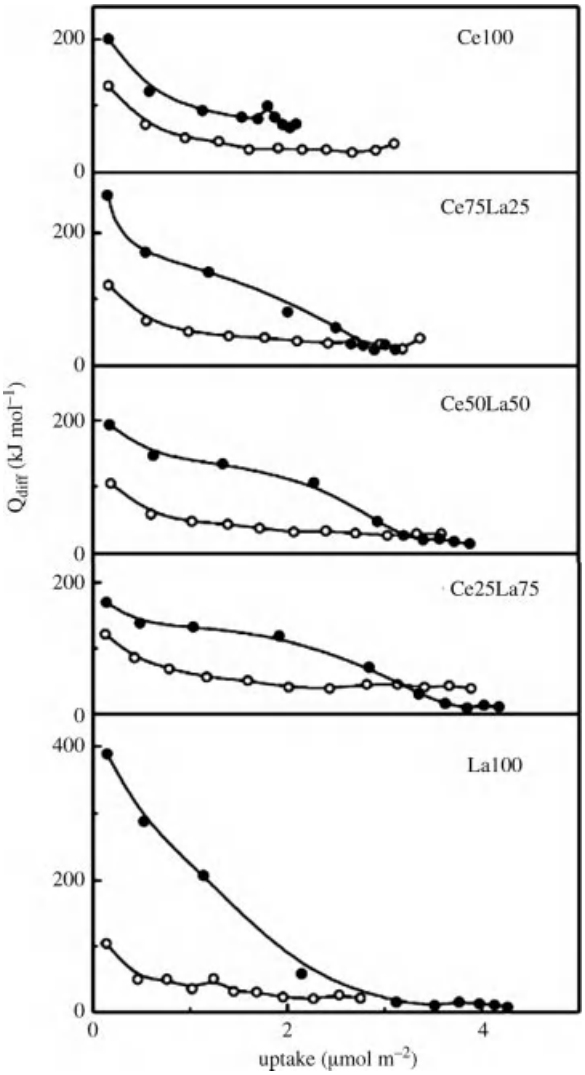


Figure 18.52 Differential heat of adsorption, $Q_{diff.}$, versus NH_3 uptake (○) and CO_2 uptake (•) for CeO_2–La_2O_3 samples [101].

neous distribution of cus O^{2-}. Some very high and very low heats of adsorption of CO_2 were ascribed to the formation of bicarbonates held either very strongly or very weakly.

Other redox processes, such as the partial oxidation of propane to acrylic acid and the oxidation of propene to acrolein and of acrolein to acrylic acid, using molybdenum- and vanadium-based catalysts, are influenced by the acidic features of the catalyst.

Mo–V–Te and Mo–V–Te–Nb mixed oxide catalysts have been characterized by propane-TPR and ammonia adsorption calorimetry [102]. With increasing content of niobium, the initial heat of NH_3 adsorption decreased from 100–80 to 60 kJ mol^{-1} and the amount of weak acid ($<$30 kJ mol^{-1}) increased considerably.

A combined influence of the redox and acid–base properties of the surface was also observed in the oxidative dehydrogenation (ODH) of lower alkanes (vanadia-, molybdena- and, tungsta-based catalysts). Intermediate reducibility, weak Lewis acid centers, and oxygen mobility were found to optimize selectivity in ODH.

Ceria-based catalysts are also widely used for their redox properties (easy cycling of Ce^{3+}/Ce^{4+}) and because of their high chemical and physical stability. The combination of ceria with another metal oxide from group III (boria, alumina, gallia, and india) using either a coprecipitation or a sol–gel method was investigated by Auroux and co-workers [103] with the aim of tuning the acid–base and redox features for possible applications as promoters in fluid cracking catalysts, active components of three-way catalysts, and several groups of emerging catalytic processes.

Only the content of boria was found to enhance significantly the acidity of ceria, whereas the basicity was found to depend on the nature and amount of all group III metals. All catalysts synthesized displayed a slightly amphoteric behavior, differing from the parent CeO_2 with a trend corresponding to the guest oxide: alumina and india more basic than acidic, boria more acidic and more pronounced with increasing content. In addition, the sol–gel-produced catalysts displayed a poor distribution of the guest oxide, resulting in reduced tuning.

Some systematic studies were performed in order to determine the acid–base variation related to mixed oxides by adsorption calorimetry and TPD [104, 105]. Depending on the preparation method, on the SiO_2/Al_2O_3 ratio, and on the micro- or mesoporous structure, very different acidic properties have been observed for silica–alumina catalysts. Some samples contain both Brønsted and Lewis sites, whereas for others only acidity of the Lewis type was observed.

Similar studies on acid–base properties of mixed silica–titania, silica–zirconia, and silica–alumina were performed on the one hand by TPD of 2-phenylethylamine and on the other hand by ammonia adsorption calorimetry [106]. TPD–TGA were performed at different heating rates ($\beta = 5$–30 K min^{-1}) in an inert atmosphere on sol–gel-prepared samples, with about 87 wt% silica, and the calorimetric experiments were also performed on sol–gel-prepared silica–alumina, silica–titania, and silica–zirconia but with ratios of 31, 26, and 26, respectively (94–95 wt% silica). In both cases, both the energies and amounts determined an order of acidity between the catalysts; however, this order differed between both techniques and sample series: SiO_2–TiO_2 < SiO_2–ZrO_2 < SiO_2–Al_2O_3 for 87 wt% SiO_2, and SiO_2–ZrO_2 < SiO_2–TiO_2 < SiO_2–Al_2O_3 for 96–97 wt% SiO_2.

Silica–alumina (SA) has been used as a support for dispersing CuO–Ga_2O_3 and CuO–SnO_2 binary systems, and tested for NO_x reduction and methane combustion reactions [107, 108]. Microcalorimetry was used to monitor the tuning of the acid strength of metal oxide surfaces by suitable dispersion of the two oxides on the SA surface. The CuO species were found to increase the capacity to adsorb NH_3 (in particular on medium and weakly acidic sites, $100 < Q_{diff} < 150\,kJ\,mol^{-1}$), while the fraction of strongest acidic sites ($Q_{diff} > 150\,kJ\,mol^{-1}$) was enhanced by the addition of Ga_2O_3 and SnO_2. Figure 18.53 shows the decreasing medium and weak acidity related to a decreasing amount of copper oxide.

Tungsten/zirconia catalysts prepared by different techniques were investigated by ammonia adsorption calorimetry [109]. Coprecipitation-prepared catalysts displayed a greater number of acidic sites than impregnated samples. Further, the addition of small amounts of iron to the tungsten/zirconia catalyst increased the acid site strength.

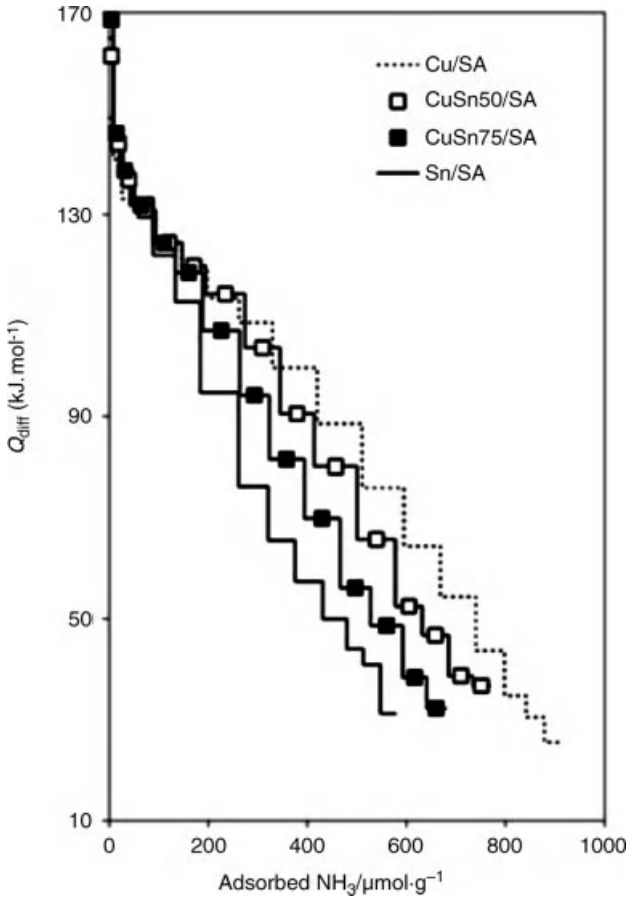


Figure 18.53 Differential heats of ammonia adsorption versus coverage [107].

18.2.4.2.5 **Hydrotalcite-Derived Oxides** Hydrotalcites are layered double hydroxides with general formula $[M_{1-x}^{2+}M_x^{3+}(OH)_2]^{x+}(Al_{x/m}^{m-})\cdot nH_2O$, where the divalent ion may be Mg^{2+}, Ca^{2+}, Zn^{2+}, or Ni^{2+}, the trivalent ion Al^{3+}, Fe^{3+}, Cr^{3+}, and so on, and the charge-compensating anions OH^-, Cl^-, NO_3^-, CO_3^{2-}, or SO_4^{2-}, with values of x between 0.25 and 0.33.

Thermal treatments of hydrotalcites induce dehydration, dehydroxylation, and loss of the charge-compensating anions, resulting in mixed oxides with the MgO-type structure. Hydrotalcites are therefore a class of precursors useful for the preparation of catalytically active oxides showing basic properties.

In various studies on Mg–Al mixed oxides obtained from calcination of a hydrotalcite, the Mg:Al ratio was found to greatly influence the acid–base properties [110], Al-rich compounds showing Lewis acid sites similar to Al_2O_3, and Mg-rich compounds showing rather basic features (MgO is a basic bulk oxide) [111].

The acid–base properties of CuMgAl and NiCuMgAl mixed oxides with hydrotalcite-like structures containing different proportions of Ni^{2+}, Cu^{2+}, Mg^{2+}, and Al^{3+} cations have been investigated using adsorption microcalorimetry and XPS with SO_2 (for basicity) and NH_3 (for acidity) as probe molecules [112, 113]. The optimum acidity for CuMgAl mixed oxides corresponded to a ratio Cu:Mg:Al = 1:1:1; moreover, Mg-rich compounds still displayed more basicity. The basicity of the NiCuMgAl materials was found to principally depend on the Ni/Cu ratio and to increase with the proportion of Ni. The basic sites are strong and particularly homogeneous (plateau around 150–170 kJ mol^{-1} depending on the samples), and XPS confirmed the presence of Brønsted and Lewis basic sites. The acidity was found of Lewis type only (XPS), weak and related to the Ni:Cu ratio. Both the acidity and the basicity increased with the Ni/Cu ratio, as shown in Figure 18.54, whereas the basicity decreased with increasing Mg:Al ratio.

Mixed oxides obtained from modified and calcined hydrotalcites were studied by Leon *et al.* [48]. The effects of various preparation parameters, such as the incorporated cation (K^+ or Na^+), the mode of addition of magnesium and aluminum precursors, the presence of sonication, and the calcination temperature, on the adsorption capacity under mild conditions were studied using TG and calorimetry (CO_2 probe). Sonication and high-supersaturation conditions in the preparation of

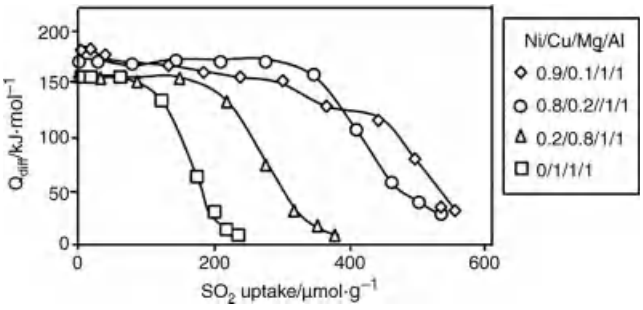


Figure 18.54 Differential heats of sulfur dioxide adsorption versus coverage on NiCuMgAl mixed oxides.

the mixed oxides were found to lead to materials with the strongest basic sites, relative to the formation of unidentate CO_2–adsorbent species. The weaker basic sites, where bidentate and surface bicarbonates formed, were found to lead to highly reversible CO_2 adsorption.

18.2.4.3 Heteropolyacids

Keggin-type heteropoly compounds consist of heteropolyanions and counter-cations (H^+, Cs^+, $NH_4{}^+$, etc.). Heteropolyacids (HPAs) correspond to those with protons and thus present very strong Brønsted acid sites; however, they are known to depend strongly on temperature and humidity. HPAs are used industrially as acid catalysts (hydration of alkanes) and redox catalysts (synthesis of methacrolein and isobutyric acid), in which case they often need to be supported on high surface area material. They have attracted considerable attention because the large amounts of available polyanions and cations provide tools for tuning specific redox and acid properties appropriate to a specific application.

The Brønsted acidity of various proton-countered Keggin heteropolyanions, characterized by NH_3 adsorption calorimetry, was found to decrease in strength with the number of protons (initial heats: $H_3PW_{12}O_{40} > H_4SiW_{12}O_{40} > H_6P_2W_{21}O_{71} > H_6P_2W_{18}O_{62}$) [114].

Carbon-supported and unsupported HPA catalysts were also characterized by ammonia adsorption calorimetry at 423 K and resulted in an increase in heterogeneity among carbon-supported catalysts and a decrease in acidity except for $H_{21}B_3W_{39}O_{132}$ [115].

The alkaline earth metal salts of 12-tungstophosphoric acid, as a result of the substitution of two protons with one alkaline earth metal cation, displayed a decrease in both the total number of acid sites and the number of the strongest acid sites probed by ammonia ($>150\,kJ\,mol^{-1}$) [116]. In the case of Sr salts, some steric effects were observed, and every catalyst showed a strong energetic heterogeneity of acidic sites. Ammonia adsorption calorimetry showed that the water treatment of $Cs_{2.5}H_{0.5}PW_{12}O_{40}$ reduced the acid site number, whereas the acid strength was little changed, indicating that the decrease observed in catalytic activity was due to the number of acidic sites. In the study of $Cs_xH_{3-x}PW_{12}O_{40}$, the incorporation of Cs was observed to lower the number of titratable acidic sites (Figure 18.55), in quantitative agreement with the theoretical degree of proton exchange. The decrease in acid strength with increase in x was slow until $x = 2.3$ but then decreased dramatically.

A family of Cs-doped $H_4SiW_{12}O_{40}$, in contrast to the phosphotungstic analogs which only formed a well-defined doped phase upon complete Cs exchange, displayed a recrystallization of $H_4SiW_{12}O_{40}$ occurring via an intermediate phase of approximate composition $Cs_2H_2SiW_{12}O_{40}$. Additional substitution promoted recrystallization as the Cs_4 salt. The catalyst morphology evolved with Cs incorporation, resulting in the formation of mesoporous voids (~3.4–4 nm) over the range $Cs_{1.9}$–$Cs_{3.4}$. All Cs-exchanged silicotungstates showed weaker acidity than their $H_3PW_{12}O_{40}$ counterparts (Figure 18.55) [117]. The catalytic activity was correlated with the number of accessible H^+ sites residing within mesopores.

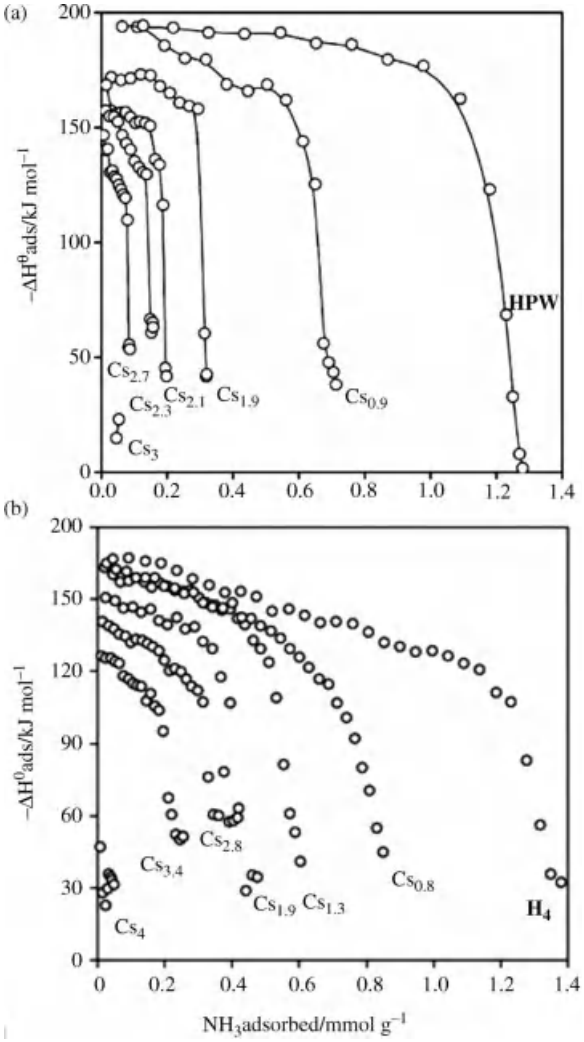


Figure 18.55 NH_3 calorimetry on Cs-exchanged HPW (a) and HSiW (b) samples.

Damjanovic and Auroux proposed a thermodynamic scale of acidity and basicity from the volumetric–calorimetric data for NH_3, CO_2, and SO_2 adsorptions (Figure 18.56) [59]. The scales are based on average heats of adsorption rather than on initial heats, because the latter determination is not always reliable. Initial heats are also of interest for catalysis, but their value is strongly dependent on the experimental conditions. These scales do not inform on the heterogeneity of the active sites and only propose a concise overview of the various types of catalysts.

It is worth noting a recent study by Dryzun *et al.* [118] on the chirality of zeolites using comparative isothermal titration calorimetry (ITC) of the D- and L-enantiomers of histidine ($pK_a = 1.7$, 6.04, and 9.09, $PA = 988$ kJ mol^{-1}). The thermograms of both

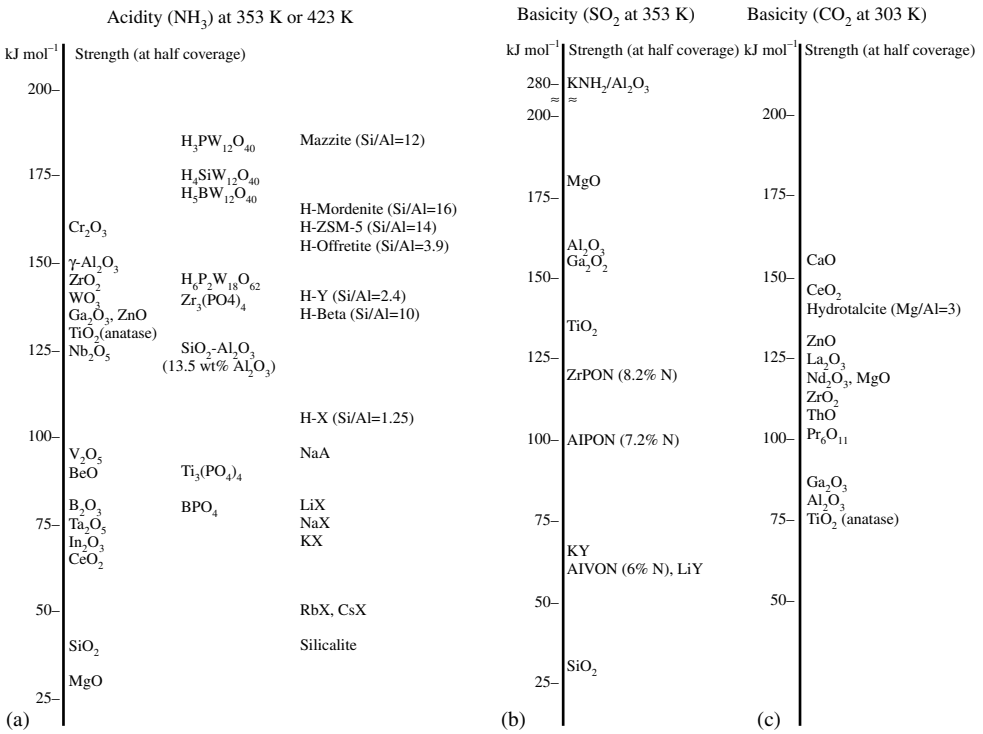


Figure 18.56 Strength at half coverage for the adsorption of ammonia (a), a basic probe, and sulfur dioxide (b) and carbon dioxide (c), two acidic probes, measured by adsorption calorimetry at 353 and 303 K, on various oxides and zeolites.

enantiomers of the amino acid with nabesite are shown in Figure 18.57. They differed in intensity, revealing the asymmetric interaction with the zeolite. A total of 20 zeolites displaying such behavior were listed. The smaller usual acid–base probes are not chiral; however, some more complex probes could display some chirality, depending on the temperature, then it would become an important parameter. Moreover, with this study, several new leads in zeolite chemistry and in their characterization are worthy of investigation.

18.3
Redox Properties of Solids

Heterogeneous catalysts have long been developed for the selective oxidation of hydrocarbons for industrial applications, and nowadays the redox properties of solids are widely investigated for environmental needs (DeNOx, depollution, etc.).

The redox properties of metal oxides were studied by Mars and Van Krevelen in 1954 [119] for hydrocarbon cracking and were found to consist of two phases: oxidation by the catalyst and regeneration of the catalyst. Then the lability of the

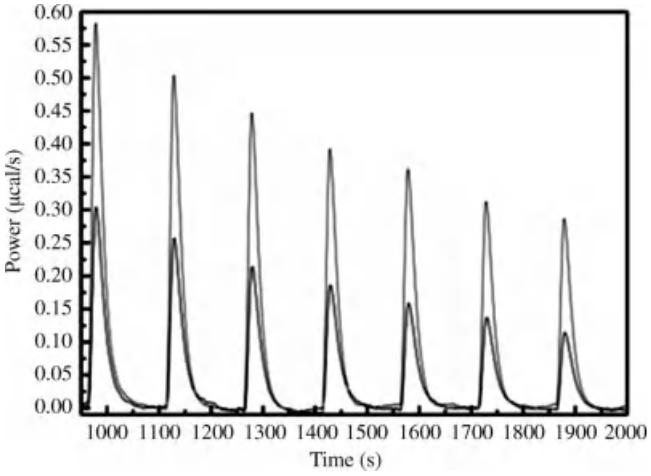


Figure 18.57 ITC experiment on D-histidine and L-histidine on Nabesite (L-histidine, top curve).

oxygen atoms was the key point: the ability to donate its structural oxygen determines the activity of a catalyst; however, if the reduction of the catalyst is too easy, the process is less selective.

Whereas for heterogeneous catalysis the reaction is assumed to occur on the surface, the redox properties of catalysts are often determined via the adsorption of small molecules such as hydrogen or oxygen, which are able to diffuse easily inside the catalyst. Therefore, special care has to be taken in the analysis of the data.

The methods for determining the amounts and energies of redox sites include adsorption, desorption, and reaction thermal analysis techniques; however, the nature of the probe or reactive gas, the experimental protocol, and the data processing will be the key points in achieving ways of understanding the catalytic phenomena. The main techniques are described below.

18.3.1 Characterization Techniques

18.3.1.1 Characterization by TPR/TPO

TPR and TPO are the main types of redox methods. They can simply consist of a temperature controller and an evolved gas analyzer (EGA). Depending on the nature of the analyzer (MS, thermal conductivity, infrared or Raman spectroscopy, etc.) different equipment will be used in order to record as accurately as possible data for better integration and calculation of energies and amounts. Pioneering TPR/TPO experiments were monitored by TCD. As the thermal conductivity of hydrogen is high, the signal was accurate; however, for oxygen, especially at low concentrations inside the carrier, a noisy signal may be obtained. MS can overcome the problems of noise for the detection of low thermal conductivity molecules (O_2, CO, NO, N_2O, etc.). In order to obtain good resolution and better reproducibility of the TPR/TPO

acquisitions, two parameters, *K* (sensitivity) and *P* (resolution), have to be considered (see Section 18.1.8.2).

In addition, TPR and TPO are often run in a sequence of reduction–oxidation–re-reduction in order to test the reversibility of the reduction or oxidation process. The oxygen storage capacity (OSC) experiment is an example of such reversibility studies, where an isothermal sequential process of alternate hydrogen or oxygen pulses is flushed on to a catalyst.

From the TPR and TPO acquisitions can be derived the amounts reacted and then the degree of reduction or oxidation of the active particles; however, it often corresponds to partial or complete bulk reduction or oxidation of the catalyst, so this has to be carefully handled. Further, some of the subsurface properties can also affect the catalysis. Kinetic analysis of such acquisition can also be done, providing *a priori* knowledge of the surface mechanisms. Mainly two kinetic models of reaction can be observed: nucleation and contracting sphere scenario. The former corresponds to a multitude of growing surface nuclei that appear increasingly until the whole surface has reacted and the bulk diffusion replaces it (acceleration–deceleration); the latter corresponds to a first step of rapid nucleation covering the catalyst's surface by a thin layer, then diffusion phenomena lead the whole process (continuous deceleration due to decrease of the interface) [120].

Most recent redox studies involving thermal methods have been carried out on precious metals and metal alloys loaded on high surface area supports for various catalytic reactions: platinum [121–123] (*hydrogenating–dehydrogenating function*), palladium [34], ruthenium [96], copper [124, 125], or nickel [126] catalysts, in the fields of DeNOx, hydrogen production from biomass, evaluation of organic compounds (fine chemistry), and several catalytic reactions involving cooperative acid and redox properties.

Various metal oxides also often possess many oxidation states, making them potentially interesting redox catalysts (iron, cupper, tin, indium, chromium, vanadium oxides, etc.), whereas other metal oxides are known to be very difficult to reduce (e.g., Al_2O_3, SiO_2, Ga_2O_3, Nb_2O_5), making them good supports for the previous category [93, 127].

Zhao *et al*. investigated sulfated vanadia–titania (VTiS) catalysts for the partial oxidation of methanol to dimethoxymethane by TPR/TPO and NH_3 adsorption calorimetry [128]. Catalysts were obtained by wetness impregnation of titania by ammonium vanadate followed after calcination by sulfate impregnation. Ammonia adsorption studies revealed the increasingly strong acidity with sulfate loading, whereas the TPR/TPO studies revealed the presence of isolated monomeric vanadia species ($T_{m1} \leq 770$ K) and polymeric vanadia species ($T_{m2} = 774$–813 K) on the support surface, the monomeric species being more easily reduced but more difficult to oxidize than the polymeric and crystalline species (Figure 18.58). The supported vanadia catalysts were also observed to be easier to reduce and oxidize than bulk vanadia, indicating an effect of promotion by the support (titania). The second reduction experiment following the oxidation program showed a change in the position and shape of the peaks, suggesting a mobility of vanadia species leading to a more aggregated phase, a source of higher crystallinity. The best catalytic behavior

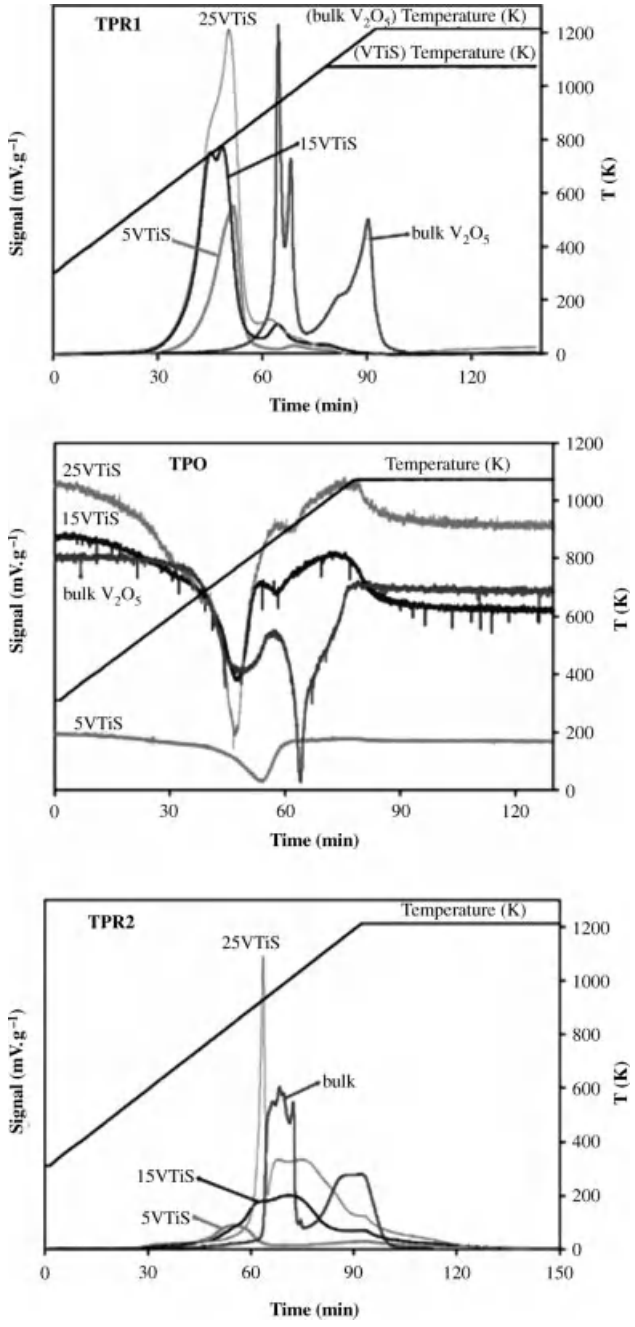


Figure 18.58 Redox cycles of VTiS catalysts and bulk V_2O_5. Profiles of reduction (TPR1, TPR2) and oxidation (TPO) as a function of temperature and time (10 K min^{-1}).

was found for the catalyst with ~15 wt% surface vanadia loading and ~5.4 wt% surface SO_4^{2-} loading (25VTiS), corresponding to an enhanced sulfate–carrier–vanadia interaction.

18.3.1.2 **TPD of Redox Probes**

TPD of redox probes such as NO, N_2O, CO, and O_2 can provide information on the redox sites. However, NO and CO can act also as weak Lewis bases and both of them are prone to react or be degraded at too high temperatures. In contrast to TPR and TPO, TPD is assumed to be a surface method and the identification of the desorption peaks has to be carefully effected. For example, O_2-TPD is especially delicate: the sample has to be originally sufficiently oxygenated so as to not react with the previously adsorbed oxygen (otherwise it is half way between TPD and TPR); in addition, during the desorption program, the first desorption of "mobile" surface oxygen will often be followed by desorption of lattice oxygen (thus degrading the catalyst), which will then not be integrated as a "desorption" signal [129]. The investigation using this setup will focus more on the adsorption properties of soft redox probes, and especially NO_x and CO_x species in the field of depollution.

Dumesic and co-workers studied the effect of Pt and Pd promoters on catalysts based on Ni supported on alumina nanofibers (Ni/Alnf) for the production of hydrogen from biomass [130]. TPR was carried out on mono- and bimetallic catalysts of Ni, Pt, and Pd, suggesting that the addition of Pt and Pd to a Ni catalyst increases the reducibility of the catalyst and therefore the number of active sites. Figure 18.59 shows the parallel CO desorption and CO_2 emission during CO-TPD, the latter resulting from water-gas shift (WGS) and Boudouard reactions of CO with the mobile hydroxyls. The peaks were categorized in three broad regions in the rate of CO desorption (α, β_1, β_2) and also in the corresponding rate of CO_2 emission (α', β_1', β_2') for all the catalysts, and then deconvoluted. The α and β_1 regions displayed an increase in peak heights for bimetallic catalysts, from which it was hypothesized that

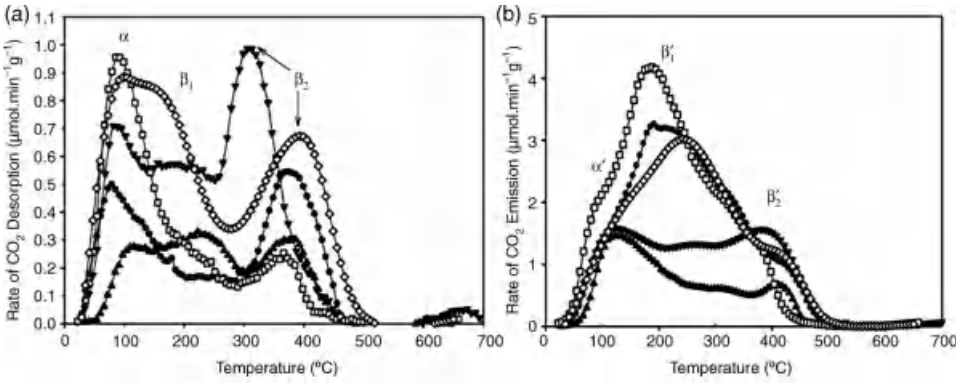


Figure 18.59 Results from CO–TPD of monometallic and bimetallic catalysts over an alumina nanofiber support: (a) rate of CO desorption and (b) rate of CO_2 emission, produced during CO desorption. Pt/Alnf (▼); Ni/Alnf (•); Pd/Alnf (▲); Ni–Pt/Alnf (□); Ni–Pd/Alnf (◇).

the addition of Pt and Pd to Ni may form surface alloys and create heterogeneity or different lattice spacings leading to a decrease in bridge-site chemisorption. Results from CO-TPD also suggested that in the case of bimetallic catalysts there was a reduction in the number of strong CO adsorption sites, the alloying effect of these systems leading to the lowering of the CO heat of adsorption (as confirmed by CO adsorption microcalorimetry). The reaction study conducted on a fixed-bed reactor provided evidence that the bimetallic catalysts exhibit substantially greater activity than the corresponding pure metal catalysts.

18.3.1.3 **Adsorption Calorimetry of Redox Probes**

The redox properties of catalysts can also be investigated under isothermal conditions, thus providing better insights into the kinetics. O_2 and H_2 adsorption calorimetry investigations have been run; however, the structural changes that occur (absorption, reaction) have to be modeled (see above). The main use of adsorption calorimetry in redox investigations is in the titration of active metal sites on the surface of catalysts by adsorption of carbon monoxide; because of its ability to act as a weak σ-donor and as a π-acceptor, CO is sensitive to the strong electrostatic fields surrounding transition metal cations. Hence the dispersion of metals such as platinum [130, 131], ruthenium [132], nickel [126, 133], and copper [134–137] have been investigated by CO adsorption calorimetry on supports such as heteropolyacids, carbon nanoparticles, and zeolites.

Bennici and co-workers studied binary oxide catalysts of CuO coupled with Ga_2O_3 and SnO_2 supported on high surface area SA for the decomposition and reduction of N_2O and NO and also CH_4 combustion [108]. Figure 18.60 shows the differential heats and isotherms of CO adsorption on selected samples: Cu/SA, CuGa50/SA (76 at% Cu), and CuSn50/SA (67 at% Cu). Only the copper phase could adsorb CO, hence the uptakes and energies were correlated with its dispersion and interaction with the coupled metal (Ga or Sn). The irreversible uptake at 0.27 mbar was correlated with the total copper loading and also the surface copper loading (evaluated by XPS). The rather high initial heats of adsorption also confirmed the abundant presence of Cu(I) species, strongly interacting with CO. More generally, the calorimetric experiment evidenced the formation of well-dispersed partially reduced Cu centers. The

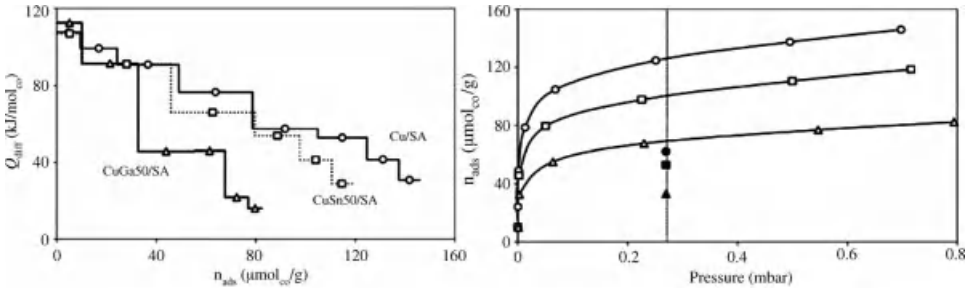


Figure 18.60 Differential heats (q_{diff}) and equilibrium isotherms of CO adsorption versus coverage (n_{ads}) for the Cu/SA (•), CuGa50/SA (Δ), and CuSn50/SA (□) oxide samples collected at 303 K. Filled symbols represent the amount of CO irreversibly retained by each.

affinity of Ga for the primary deposited copper phase was high and gave rise to active metal–support interactions. In contrast, Sn was deposited preferentially on the bare support, without any interaction with the copper phase. These differences in the surface properties of the two series of catalysts, imparted to the CuO phase, enhanced the reducing (Cu/Ga) or oxidizing (Cu/Sn) catalytic properties, and was evidenced in NO_x reduction and CH_4 oxidation reactions.

Guerrero-Ruiz and co-workers studied various supported metal (Ru, Rh, Co, Cu, Ni, Pd) catalysts and characterized the heterogeneous distribution of active metal sites by CO adsorption calorimetry [132, 138–146]. In the case of alumina-, zirconia-, zirconia–silica- and zirconia–lanthana-supported palladium, three types of active sites corresponding to different differential heats of adsorption lying in high (210–170 kJ mol^{-1}), medium (140–120 kJ mol^{-1}) and low (95–60 kJ mol^{-1}) value ranges, were observed (Figure 18.61). The support material, the reduction temperature, and the treatment conditions were found to affect the surface morphology of the Pd catalysts, thus influencing the fraction of sites adsorbing CO in a specific mode. As most of the adsorbed CO molecules were in a bridged state, a correction factor was introduced in order to calculate the Pd dispersion using the total amount of CO adsorption.

Silver-based catalysts have been investigated in order to confirm a possible correlation between the catalysts' affinity towards oxygen and their activity in ethene epoxidation. At 473 K, adsorption of oxygen at the surface of silver is a fast process; incorporation of oxygen into deeper metal layers, although present, is a slow process. Pulses of oxygen were applied to silica-supported silver catalysts set inside a heat-flow calorimeter linked to a gas chromatograph. The differential heats of interaction were found to decrease with the amount of oxygen consumed but always exceeded the heat of formation of bulk silver oxides (30.5 kJ mol^{-1} for Ag_2O and 26.4 kJ mol^{-1} for

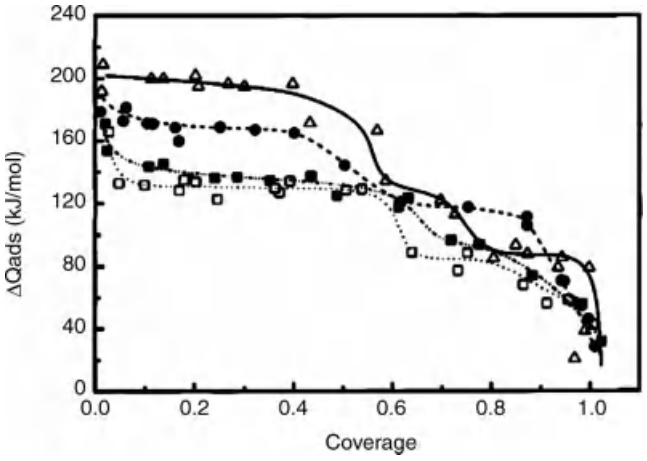


Figure 18.61 Differential heats of CO adsorption at 330 K as a function of surface coverage for Pd catalysts supported on (Δ) Al_2O_3, (•) ZrO_2, (□) ZrO_2–SiO_2, and (■) ZrO_2–La_2O_3 reduced at 673 K [146].

Ag_2O_2). The average heat of formation of an oxygen monolayer correlated linearly with the intrinsic activity of the catalysts for ethene oxidation. Surface oxygen species appeared more catalytically active when they were less energetically bonded to the silver surface [147].

18.3.1.4 "Surface" Techniques (RFC, s-TPR) in Redox Studies

A special case of TPR consists in controlling the diffusion of the oxidation, limiting it to the formation of a surface layer, thanks to soft redox probes, essentially N_2O which is decomposed into surface oxygen and nitrogen outflow. The purpose is to titrate and characterize the dispersion of active metal particles on a support.

Many setups have been developed to monitor the adsorption on copper-based catalysts and to ensure that it stops after the establishment of a monolayer: reactive frontal chromatography (RFC) [148], where the outflow of N_2O and N_2 is monitored, and TPR of oxidized surfaces (s-TPR) [35], where the prior controlled N_2O oxidation of the surface is titrated by H_2 reaction. The relevance of the method depends on the temperature of N_2O treatment (low enough to prevent bulk diffusion, ~20–50 °C for Cu_2O supported on silica).

Figure 18.62 shows the reduction profiles of three supported copper catalysts prepared by Gervasini and Bennici [35]: on silica–alumina (Cu/SA), on silica–zirconia (Cu/SZ), and on silica–titania (Cu/ST). After a prereducing treatment, the samples were preoxidized in an N_2O atmosphere for 1 h at a fixed temperature in the range 30–120 °C. From a comparative analysis of the TPR with and without surface oxidation, it was decided to consider only the first peak, the second being more relevant to lattice oxygen reduction. Different amounts of adsorbed hydrogen were calculated from the integration of the TPR peaks and led to an "S-shaped" curve featuring a leap above 50 °C for Cu/ST and Cu/SZ and above 70 °C for Cu/SA, corresponding to the reduction of sublattice oxygen. It was therefore concluded that the N_2O preoxidation treatment provided an accurate dosing of surface copper active sites when performed in the range 30–50 °C, and an inaccurate dosing at higher temperatures.

18.3.2
Case Study of DeNOx Investigations with Thermal Methods

Becoming more and more concerned by environmental externalities through increasing regulations, industries have been developing processes to minimize their gas pollution. "NO_x" represents the family of nitrogen oxides (NO, NO_2, N_2O, ...) and is a common gas emission from factories, especially those burning biomass, and also a common pollutant from vehicles. NO_x species are partly responsible for acid rain, smog, and low-altitude ozone. In order to reduce this pollution, heterogeneous catalysts have been investigated at various temperatures and in different environments.

Two cases with different histories can be distinguished, the stationary case and the mobile case. Factories have been developing processes based on the selective catalytic

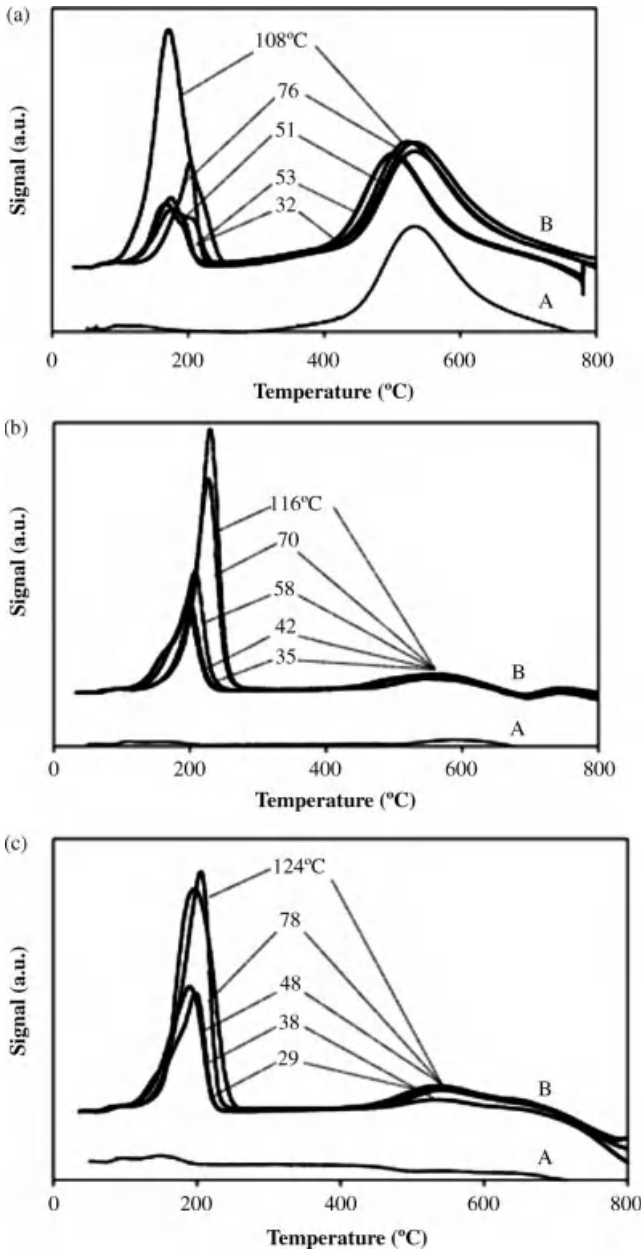


Figure 18.62 Reduction profiles of Cu/SA (a), Cu/ST (b), and Cu/SZ (c): (A) TPR after prereducing treatment (step 0 analysis); (B) s-TPR of freshly oxidized Cu_2O phase (step 2 analysis) after N_2O oxidation at various temperatures (step 1 analysis).

reduction (SCR) of NO_x by ammonia (NH_3-SCR), while the automobile sector has been following multiple leads, such as exhaust gas recirculation (EGR), NO_x trapping, and also SCR but with various reducing agents (hydrocarbons, hydrogen, etc.).

The first investigations using catalytic tests to screen over good and bad catalysts led to a further understanding of the mechanisms (bifunctional: acid and redox) and thus led to other ways of screening and elucidation, especially thermal methods that focus on characterizing the strength and dispersion of such sites on the surface of catalysts.

18.3.2.1 Selective Catalytic Reduction (SCR) of NOx by Various Reductants

18.3.2.1.1 NH_3- and Urea-SCR The reduction of NO_x species needs a reducing agent, and investigations on heterogeneous catalysts then focused on adsorbing both of these species (NO_x and reductant) and leading them to a controlled reaction. Many types of reactions can occur: partial reduction (N_2O species are liberated), parasitic reactions (oxidation, degradation, poisoning, ...), or complete reduction. "Standard SCR" corresponds to the sought controlled reaction when using ammonia or a precursor of it as reducing agent, whereas "fast SCR" corresponds to a coupled method involving a partial preoxidation of exhaust gases, thus producing NO_2 in a consequent amount and enhancing the total reduction:

$$4NH_3 + 4NO + O_2 \rightarrow 4N_2 + 6H_2O \quad (\textit{standard SCR}) \tag{18.41}$$

$$4NH_3 + 2NO + 2NO_2 \rightarrow 4N_2 + 6H_2O \quad (\textit{fast SCR}) \tag{18.42}$$

The NH_3-SCR process has been widely studied, mainly with Fe [149–151] and Cu [124, 152, 153] catalysts supported on zeolites (ZSM-5 [154], HBEA [155], montmorillonites, Y, ...) in recent years. However, ammonia cannot be easily stored for mobile applications (corrosive, toxic), hence urea was considered as a precursor for "*in situ ammonia*," being non-toxic, non-corrosive, and odor free. Its degradation to ammonia was investigated by Fang and Da Costa [154] with the aim of preventing undesirable reactions from occurring (melamine complexes or polymers), consuming the reducing agent and obstructing the pores (where the active sites are located).

DSC spectra of urea (with a scan rate of $20\,^{\circ}C\,min^{-1}$ fast enough not to let partially decomposed urea deposits form a passivating layer on the catalyst surface) with or without catalyst (commercial Siemens vanadia–tungsta–titania) and after decomposition at 350 °C ("T_5") led to the characterization of two stages of decomposition of urea to ammonia (mainly at 240 °C, and also around 350 °C) followed by an undesirable degradation to ammelide and ammeline from 360 to 430 °C that can be minimized by using an appropriate catalyst (Figure 18.63).

Porous clays are resistant and active at various temperatures and are a common microporous support for heterogeneous catalysts. Iron-supported zeolites, Fe-ZSM-5, were modified by ion exchange with ammonia (or sodium) for testing in urea-SCR by Sullivan and Keane [156]. These good catalysts for NH_3-SCR partially lost their activity with urea, probably because of the enhanced production of isocyanic acid

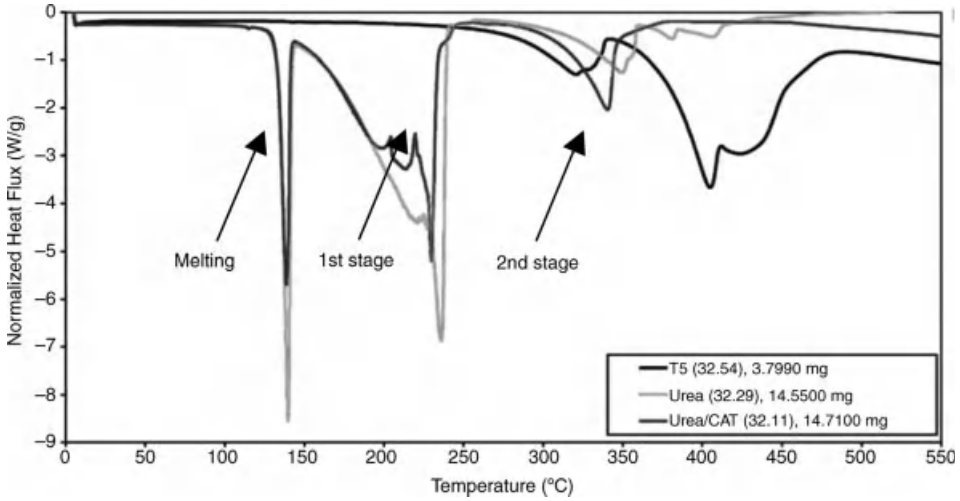


Figure 18.63 DSC spectra of neat urea, urea–catalyst mixture, and the decomposed product of urea after the second decomposition stage (T5).

(HNCO, precursor of melamine) on the Brønsted acid sites. TPSR performed on exchanged-NH_4^+–Fe-ZSM-5, however, displayed a consumption of isocyanic acid (Figure 18.64b) at the optimal NO reduction temperature (~375 °C, Figure 18.64a). It was concluded that the transient conditions of the TPSR did not mimic the real conditions.

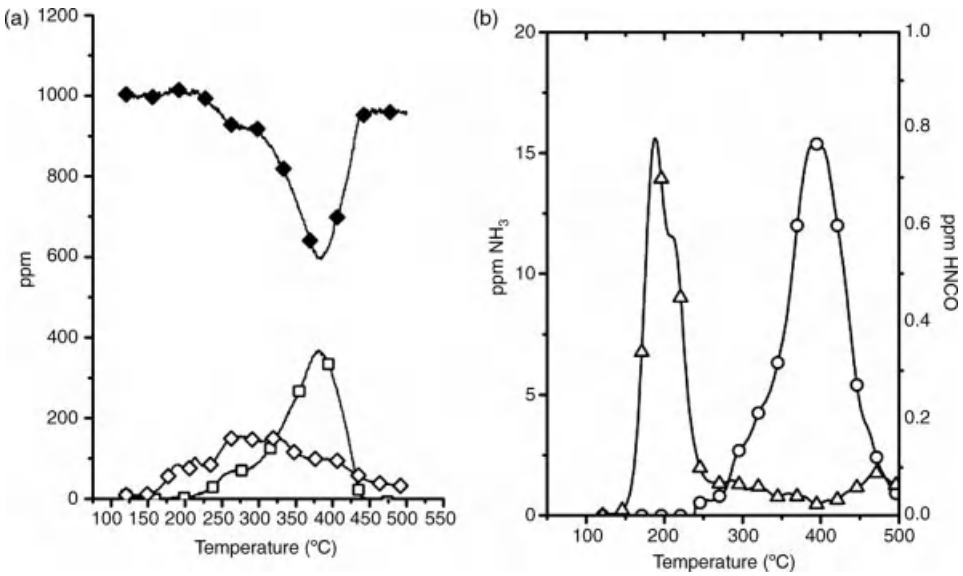


Figure 18.64 Main peaks of interest following TPSR of urea(ads) + NO/O_2(g) over exch.-NH_4^+ FeZSM-5 (0.6% Fe): (a) N_2 (□), CO_2(◇), and NO (◆); (b) NH_3 (•) and HNCO (Δ) (estimate).

18.3.2.1.2 **Hydrocarbons- and Alcohol-SCR** NH_3-SCR is the most popular industrial method for neutralization of NO_x, but it is connected with high investment costs, non-mobility and secondary pollutants (ammonia, cyanates, isocyanates). Therefore, other reducing agents have been investigated, especially those already present in the gas mixture outflow. In the case of automobile catalytic converters, several residues are not burnt during the combustion process, mainly hydrocarbons and alcohols [157, 158]. These molecules are able to reduce NO_x if both are adsorbed on the surface of an appropriate catalyst.

A DeNOx catalyst consisting of Cu-ZSM-5 with an external coating of cerium oxide was investigated by Komvokis *et al.* [159] for application in the catalytic converters of diesel engines. The characterization of the redox properties by H_2-TPR coupled with *in situ*XANES (X-ray adsorption near edge structure) (Figure 18.65) of the copper–zeolite-supported ceria and the copper–zeolite displays a shift of 50 K in the reduction process of copper ($Cu^{2+} \rightarrow Cu^{+} \rightarrow Cu^{0}$), confirming a Ce–Cu interaction leading

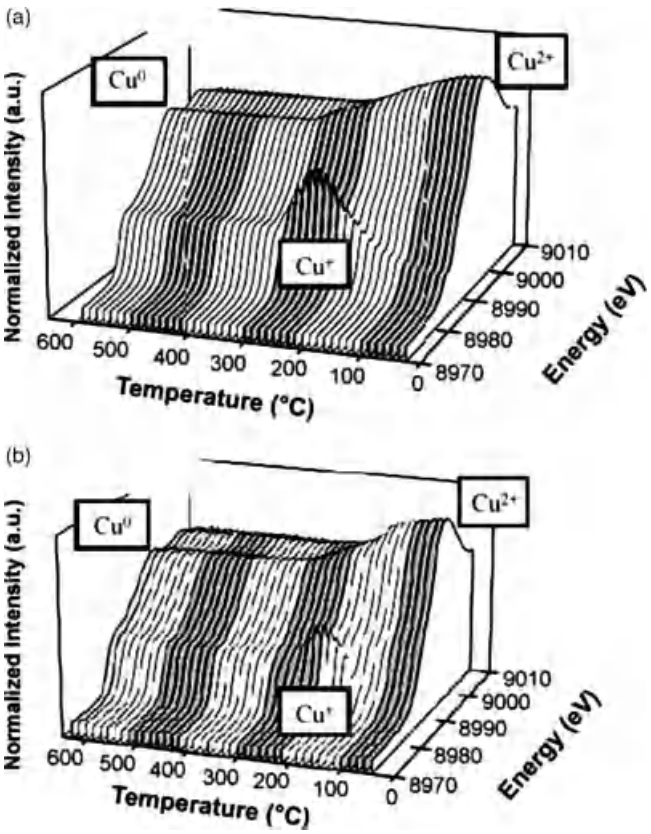


Figure 18.65 TPR of (a) Cu-ZSM-5 and (b) CeO_2/Cu-ZSM-5 as detected by the Cu K edge in XANES. The peak at 8983 eV corresponds to Cu^{+}.

to enhanced reducibility of both Cu and Ce, thus shifting the whole SCR activity to lower temperatures.

Currently propene (C_3H_6), methane (CH_4), isobutane (C_4H_{10}), and ethanol (C_2H_5OH) [160] are often used as reducing agents for SCR studies, corresponding to probable short-chain exhaust gases.

The mechanism was studied for alumina-supported indium oxide and tin oxide and consists of a "bifunctional mechanism": a first phase of oxidation of the hydrocarbon on the supported sites, then after migration on the surface of the catalyst a second phase of reduction of the NO_x occurring on the alumina with the help of the oxygenated hydrocarbon [90, 161–164]. The investigations on supported metal oxides led to the finding that balanced redox and acidic properties are indispensable for efficient conversion of NO_x in hydrocarbon-SCR. Thus thermal methods are valuable tools for monitoring such catalysts.

Turek *et al*. investigated spinels for their "unique" redox properties, their low cost, and their stability towards usual poisoning (SO_2, H_2O), and compared SCR processes for ethanol and propene on $CoFe_2O_4$ and Co_3O_4 [165]. NO-TPD and NO-TPSR experiments discriminated Co_3O_4 and ethanol as better catalysts and reducing agents, in relation to their redox properties.

The other class of catalysts for DeNOx, supported zeolites, also showed evidence of bifunctional behavior of acidic sites (zeolite) and redox sites (mostly platinum, copper, and iron). In the case of HC-SCR, CO is suggested to facilitate the reduction of NO *in situ*. Further, the platinum particles dispersed on the zeolite were found to undergo sintering under HC-SCR conditions, thus eventually improving the NO_x conversion.

18.3.2.1.3 **H_2-SCR** Recently, with the aim of obtaining DeNOx processes that are efficient at lower temperatures, metal oxide-supported platinum catalysts were studied in H_2-SCR. H_2 can be stored or even generated by the WGSR and/or reforming/recirculation of the exhaust gas. Platinum acts as a redox center while the metal oxide (alumina, tungsta, zirconia) acts as an acidic center [166, 167]. Such catalysts have been reported to display very high conversion of NO_x at low temperature; however, huge amounts of N_2O were produced. Costa *et al*. [168], however, achieved 93% conversion to N_2 at 140 °C, as can be seen in the TPSR study of a 0.1 wt % Pt supported on $La_{0.7}Sr_{0.2}Ce_{0.1}FeO_3$ in an $NO/H_2/O_2$ lean DeNOx process with 5% water (Figure 18.66). The mechanism is postulated to imply the production of nitro and nitrato surface species from the chemisorption of NO_x, these then reacting with the free hydrogen dissociatively adsorbed on Pt.

18.3.2.1.4 **Temperature Range of Catalysts** Currently, a broad range of engine development strategies are followed, resulting in either low exhaust gas temperatures, for engines using excessive EGR and because of environmental regulations (in the driving cycle of the European Union the exhaust temperature is below 150 °C for about 60% of the cycle time), or very high exhaust gas temperatures, for engines without EGR but hot diesel particulate filter (DPF) regeneration [166]. Further, the whole industry sector still needs improvement over the DeNOx catalysts devoted to stationary

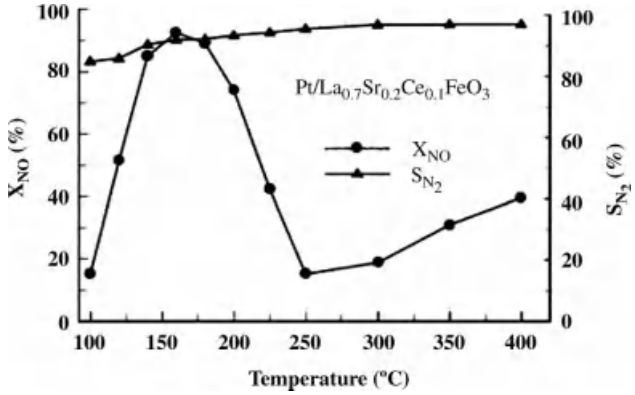


Figure 18.66 NO-TPSR of 0.1 wt% $Pt/La_{0.7}Sr_{0.2}Ce_{0.1}FeO_3$: effect of 5% H_2O in the feed stream on NO conversion (•) and N_2 selectivity (▲) as a function of reaction temperature. Reaction conditions: NO = 0.25%, H_2 = 1.0%, O_2 = 5%, H_2O = 5%, W = 0.15 g, GHSV = 80 000 h^{-1}.

units. The conventional stationary DeNOx catalyst from Siemens (vanadia–tungsta–titania) only covers the 300–400 °C range, higher temperatures leading to parasitic ammonia oxidation to N_2O or even to exhaust of toxic volatile vanadia (T_{melt} = 690 °C). Therefore, the stability, activity, and selectivity of the catalysts should be checked from 150 to 700 °C (by techniques such as TGA–DSC or TPSR). [164, 169, 170]

For the removal of NO_x from oxygen-rich exhaust, SCR using an NH_3 and NO_x storage reduction (NSR) catalyst is currently the most favored technology. However, a serious constraint of such techniques is the minor DeNOx performance below 200 °C. In contrast, the catalytic reduction of NO_x by H_2 (H_2-DeNOx) reveals an interesting potential for the low-temperature NO_x abatement that is particularly crucial for diesel cars.

Further, most investigated catalysts are really efficient for NO_x conversion over a tight range (50–100 K temperature interval). Looking for a more stable catalyst, Kröcher *et al.* studied Fe-ZSM-5 catalysts for NH_3- and urea-SCR and reported high activity and selectivity towards N_2 in the temperature range 250–650 °C, achieving 90% conversion efficiency above 400 °C [151].

18.3.2.2 **Tuning the Surface Properties with Thermal Methods for DeNOx**

For SCR processes involving redox and acid catalysis, bifunctional catalysts were investigated and characterized, no longer only by catalytic tests but also by thermal methods, in order to achieve a better understanding of the kinetics. Several strategies were developed to control the acid and redox sites on high surface area supports.

18.3.2.2.1 **Metal Oxide-Supported Catalysts** Metal oxides can display acidic, basic, or redox properties and are usually stable over a wide range of temperatures. Bifunctional catalysts consisting of acid sites deposited on a redox support are scarce because of the lack of high surface area redox supports and the difficulty of keeping intact both the acidity and redox properties during the synthesis or under real catalysis conditions.

However, let us consider the studies of Li *et al.* [171] on ceria–zirconia-supported tungsta for NH_3-SCR, achieving 80% NO_x conversion in the range 230–500 °C, and also Casapu *et al.* [172], achieving 80% NO_x conversion (NH_3-SCR) with niobia-doped MnO_x–CeO_2 (molar ratio Mn:Nb:Ce = 23:23:54) in the range 200–350 °C. However, in the latter case, significant degradation of the properties occurred in the presence of sulfur oxides. Studies on doped ceria (Pd, Pt, or Rh doped) focusing on CO + NO reactants (no mention of sulfur oxides) also achieved a high yield and selectivity, mainly relative to the oxide ion vacancies of the catalyst [173].

The main metal oxide-supported catalysts consist of either an acidic support (γ-alumina) on which are deposited redox centers (transition metals or metal oxides: Pt, Ag, In_2O_3, ...) [164, 167, 174] or high surface area supports on which are deposited both acidic and redox centers [175], for example, the commercial vanadia–tungsta–titania, where titania is the support for tungsta (very acidic) and vanadia (redox) centers.

18.3.2.2.2 **Influence of the Supported Material** By correlating the screening experiments with thermal methods, a better insight into the mechanism can be obtained, therefore leading to a more efficient search. Microcalorimetric adsorption studies were performed by Shimizu *et al.* [176] on alumina-supported silver catalysts with variable silver loadings. H_2 and O_2 adsorption experiments were carried out with a microcalorimetry–volumetry isothermal setup at 573 K, with pretreatment under vacuum for 2 h at 573 K.

H_2 adsorption microcalorimetric experiments led to quantitative information on the reduction of Ag^+ ions on Ag/Al_2O_3 catalysts. Figure 18.67a compares the curves of the differential heat of H_2 adsorption on Ag/Al_2O_3 with various Ag loadings (the indicated number corresponds to the loading in weight-%). It was reported that H_2 adsorption on the alumina surface produced heats below 30 kJ mol^{-1} (dashed line). Sazama *et al.* [177] reported an H_2-TPR experiment on Ag/Al_2O_3 and found a single H_2 consumption peak at 540 K (below 573 K), at which 50% of the Ag^+ was reduced to Ag^0 (Figure 18.68). Shimizu *et al.* [176] also showed that Ag^+ species are reduced by hydrogen to generate acidic protons on the alumina support and silver clusters. From these facts, it was concluded that H_2 adsorption with heats above 30 kJ mol^{-1} is due to the reduction of Ag^+ with H_2.

Ag/Al_2O_3-2 showed an initial heat of adsorption above 200 kJ mol^{-1} and a gradual drop in the heat. Gradual change in the heat may be associated either with surface non-uniformity or lateral interactions. The amount of H_2 consumption with differential heat above 30 kJ mol^{-1} was 0.036 mmol g^{-1}, corresponding to an H_2:Ag ratio of 0.2. The H_2:Ag ratio increased with Ag loading, indicating that the thermodynamic reducibility of Ag^+ increases with Ag loading. The amount of H_2 reacted on Ag/Al_2O_3-0.5 was significantly small (consistent with EXAFS and UV–visible spectroscopic results), which indicates that reductive agglomeration of Ag^+ to Ag cluster ($Ag_n^{\delta+}$) does not occur in this sample. After the H_2 adsorption microcalorimetric experiment at 573 K, followed by evacuation at 573 K for 1 h, the reoxidation heat in an O_2 adsorption microcalorimetric experiment at 573 K was performed (Figure 18.67b). There are sharp drops in the heat in the range 100–200 kJ mol^{-1}, hence it was

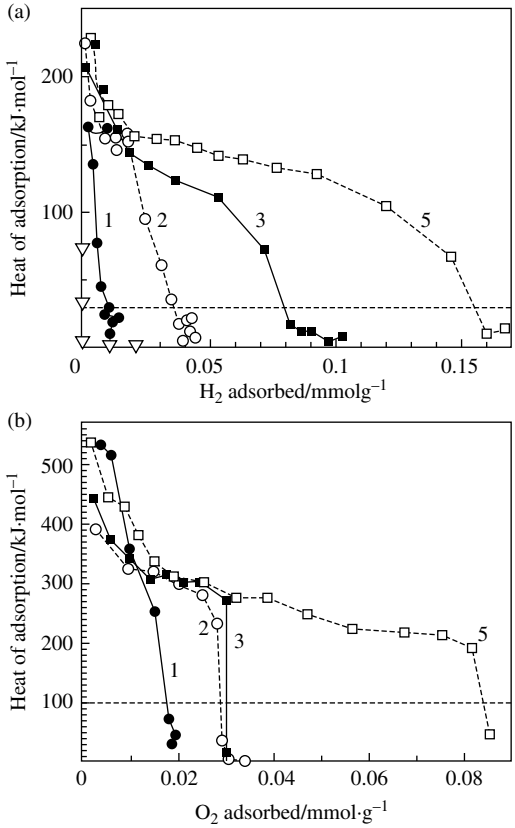


Figure 18.67 Differential heat of adsorption at 573 K of (a) H_2 and (b) O_2 after H_2 saturation followed by evacuation for 1 h on Ag/Al_2O_3 with various Ag loadings (wt%).

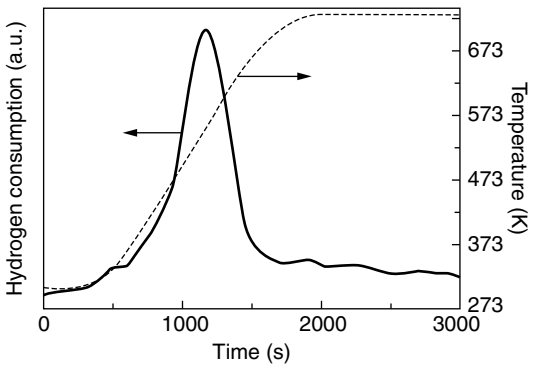


Figure 18.68 H_2-TPR of Ag/Al_2O_3 catalyst.

concluded that O_2 adsorption with heats above 100 kJ mol^{-1} is due to the reoxidation of the Ag_n clusters that are redispersed to Ag^+ ions. The O_2:Ag ratio was 0.15–0.16 for the medium-loaded catalysts (2–3 wt%).

During the $H_2 + O_2$ and H_2-assisted C_3H_8-SCR reactions, Ag^+ ions and the $Ag_n^{\delta+}$ cluster coexist, and superoxide ions are generated *in situ* in these reactions. The steady-state NO reduction rate (<0.1 without H_2, 68 nmol g^{-1} s^{-1} with H_2) correlated fairly well with the relative amount of the $Ag_n^{\delta+}$ cluster during the SCR reaction, indicating that $Ag_n^{\delta+}$ acts as the active species in H_2-assisted C_3H_8-SCR.

The Ag^+ ions in the lowest loaded catalyst (0.5 wt %), having very low kinetic and thermodynamic reducibility, are not converted to clusters during H_2-C_3H_8-SCR, and consequently the reductive O_2 activation does not occur. Over the medium-loading catalyst (1–3 wt%), having Ag^+ ions with moderate reducibility, $Ag_n^{\delta+}$ and cooperating protons formed by H_2 reduction react with O_2 to yield O_2^-. On the high-loaded catalysts (5–10 wt%), the reduced Ag species with larger particle size are less reactive in reoxidation and, hence, less reactive in the O_2 reduction to O_2^-, which results in a relatively low catalytic activity of these catalysts. It was concluded that a balance between the rate of reduction and reoxidation is an important factor that controls the nature of the active sites and consequently the catalytic activity of Ag/Al_2O_3.

Sazama *et al.* [177] reported that the acceleration of the H_2-SCR originates mainly from the increased rate of oxidation of hydrocarbons and the −CN to −NCO reaction step, but not from the increased rate of the NO–NO_2 reaction (preoxidation). It is considered that hydrogen itself participates in the SCR-NO_x reaction by dissociating with the formation of silver hydride, proton sites, and then hydroperoxy and hydroxy radical species. These radical species might dramatically enhance the propagation of the SCR-NO_x reaction.

Alumina-supported silver catalysts were also tested by Wang *et al.* [178] for DeNOx properties with propane as a reducing agent, while varying the amounts of loaded silver. An increase in the total amount of basic sites was globally observed with increasing Ag loading. This enhanced basicity was correlated with inhibition of the DeNOx activity.

18.3.2.2.3 **Influence of the Support** Supported particles often play the role of "active" redox sites and are often chosen among transition metals; however, their properties may be changed when dispersed on a metal oxide support, through metal–oxygen–metal interactions. Further, the acid–base properties of the support were reported to play a major role in the catalytic mechanism. Calorimetric investigations on the influence of the support were made by Auroux, Gervasini and co-workers on supported tin oxide and on supported indium oxide [90, 161–163].

Series of SnAl-*x*- and SnTi-*x*-supported oxides were synthesized by Guimon and co-workers [163] by the impregnation method in order to achieve an Sn loading of *x* in weight-%. The SnO_2/TiO_2 series of samples investigated is more acidic than the SnO_2/Al_2O_3 series, judging from the differential heats of adsorption (Q in kJ mol^{-1}) compared for acidic (SO_2) and basic (NH_3) probes. It should be noted that in this study the SO_2 adsorption experiments were aimed both at the characterization of

Table 18.5 Calorimetric data for NH_3 and SO_2 adsorption (the differential heat Q is expressed in kJ mol^{-1} and the number of sites in μmol g^{-1}).

Sample	NH_3				SO_2			
	Number of sites				Number of sites			
	$Q > 150$	$150 > Q > 120$	$120 > Q > 100$	$100 > Q > 80$	$Q > 150$	$150 > Q > 120$	$120 > Q > 100$	$100 > Q > 80$
γ-Al_2O_3	27	54	73	33	104	45	16	11
SnAl-0.2	0	36	110	44	50	45	18	12
SnAl-2	0	145	23	42	35	43	14	12
SnAl-8	11.5	150	23	76	9.5	49	20	17.5
SnAl-12	19	92	67	34	0	43	38	10
SnAl-24	40	76	33	32	6	66	7.5	7.5
SnO_2	114	18	9	9	65	13	7	3.5
TiO_2	32	156	59	39	0	61	44	41
SnTi-5	30	119	60	39	0	19	19	25
SnTi-12	37	114	51	39	0	20	18	20
SnTi-21	0	114	50	21	7	19	14	17
SnO_2	114	18	9	9	65	13	7	3.5

basic properties and gaining an insight into the behavior in a poisoning environment (SO_x in exhaust gases).

On varying the concentration of tin dioxide deposited on γ-Al_2O_3, a coverage of about 8 wt% of Sn gives rise to the highest acidity in terms of number and strength of sites. The addition of tin dioxide on titanium dioxide leads to a slight decrease in the initial heats of NH_3 adsorption and in the number and strength of acid sites with increasing loading, which can be attributed mainly to the decrease in the surface area of the samples (Table 18.5). In fact, the calorimetric data recalculated per square meter (instead per gram) show that the number and strength of acid sites remain nearly constant and these results can be attributed to poor dispersion of SnO_2 on the titania surface with increasing loading.

The addition of SnO_2 on γ-Al_2O_3 decreased the initial heat of SO_2 adsorption, and also the amounts of SO_2 irreversibly adsorbed were found to decrease from about 190 to less than 90 μmol g^{-1} (Table 18.2). The minimum uptake is reached for the sample close to a monolayer (8 wt% Sn), which is certainly the loaded sample with the best dispersion, as confirmed by XRD. Tin dioxide supported on titania also leads to a drastic decrease in the number of basic sites compared with the bare support, but the loading has little influence. The poor dispersion of tin dioxide at the surface of titania may explain these results.

The acidic sites created by the addition of tin are of Lewis type (confirmed by XPS measurements). The number of acidic sites seems to increase with increase in the Sn content when SnO_2 is well dispersed on the support. This is the case when alumina is used as the support, up to 12% Sn content. Moreover, the newly generated sites are

stronger than those of alumina. In the case of TiO_2-supported catalysts, the Sn loading affected neither the number nor the strength of the adsorption sites, because of the poor dispersion of the active phase. Despite the decrease in the number of Brønsted acid sites observed by XPS after deposition of SnO_2 over TiO_2, the global acidity of these solids is not affected. It has been shown that sulfur dioxide adsorption leads to the formation of three types of species: SO_2, sulfites, and sulfates. These species reflect the presence of Lewis basic sites, and also of Lewis acidic sites in the case of Al_2O_3 ($SO_2\cdots M^{n+}$). Over SnO_2 and TiO_2, desorption at high temperature favors the formation of sulfate species. However, the basicity of the SnAl series of samples is weaker than that of the alumina support and seems to pass through a minimum (around SnAl12). In contrast, the basicity of the SnTi series appears to be independent of the Sn concentration, just like the acidity. This can be correlated with the poor dispersion of SnO_2 on TiO_2, as evidenced by the XPS data.

The comparison among tin dioxide catalysts with different Sn contents and on different supports, active in NO reduction by C_2H_4, suggested that the turnover frequency depends mainly on the Sn dispersion, but the structures of the Sn crystallites and the support are also important variables. The acidity is more related to the uncovered support than to the amount of tin dioxide. The support is responsible for the quality of the dispersion, and Sn centers are very active even at low amounts.

Auroux *et al.* [90] compared highly loaded (~20 wt%) supported SnO_2 over alumina, titania, zirconia, silica, and magnesia and found a correlation between the reducibility, evaluated from the temperature of the peak maxima in TPR experiments, and the competitiveness factor, an indicator of the efficiency of NO_x reduction in NO–C_2H_4–O_2 flow conditions (Figure 18.69). It was also concluded that the acidity of the support plays a major role in stabilizing the active phase, whereas the catalytic activity is mostly determined by the redox character of the catalyst.

The selective reduction of NO_x by hydrocarbons (HC-SCR) was studied using calorimetry by Gervasini *et al.* [161] over four different catalytic systems prepared by dispersing various amounts (either 3 wt%, "3," or a high loading enough to cover a

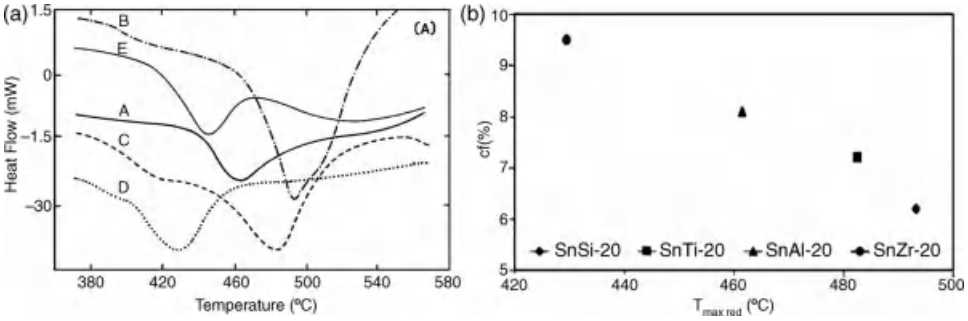


Figure 18.69 (a) TPR profiles (heat flow signal versus temperature) of highly loaded supported tin dioxide samples: SnAl-20 (A), SnSi-20 (B), SnTi-20 (C), SnZr-20 (D), and SnMg-20 (E). (b) Competitiveness factor, cf (%), as a function of the temperature of the reduction peak maxima (°C) for highly loaded tin dioxide samples [90].

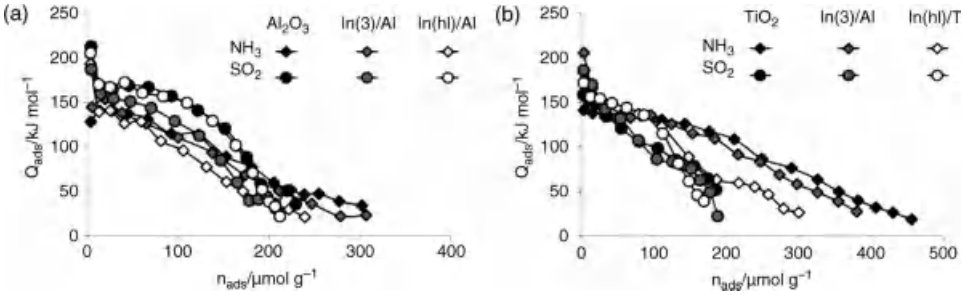


Figure 18.70 Adsorption heats at 353 K of NH_3 and SO_2 on indium oxide supported on alumina (a) and titania (b) compared with bare support.

complete monolayer, "hl") of In_2O_3 over different supports. Indium oxide can be considered as an amphoteric solid (slightly more basic than acidic) that can be reversibly oxidized or reduced.

As a general rule (on silica, alumina, titania, and niobia), the global acidity decreased and the basicity increased upon deposition of indium oxide on the support. In the case of alumina, however, the results for the characterization of basic sites showed unexpectedly an identical curve for the bare support and the highly loaded (hl) sample, whereas that for the less loaded one was significantly shifted down. Also, contrary to expectations, the deposition of indium oxide increased neither the heat nor the adsorption capacity of the bare alumina support, whereas for the less basic titania support the acidity was lowered and the basicity increased by indium oxide deposition (Figure 18.70).

As shown by TGA–DSC, indium oxide was effectively reversibly reduced by H_2 and oxidized by O_2; the temperature of reduction was mostly related to the particle size, whereas oxidation was found more influenced by the support. The oxidation of indium oxide takes place at a lower temperature than the reduction. The In(hl)/Ti sample presented the highest oxidation temperature, indicating that titania stabilizes metallic indium. Alumina and titania were found to be the best supports in order to prepare active and selective DeNOx catalysts, judging by the yield of NO_x conversion to nitrogen and the comparison with concurrent ethene conversion to carbon oxides.

The better stabilization of In_2O_3 by titania, detected by XRD and TPR/TPO profiles, could explain the higher activity in the reaction of NO_x reduction by hydrocarbons observed for the low-loading sample In(3)/Ti. More generally, supports that are able to disperse the In_2O_3 aggregates with high In stabilization were predicted to give rise to active catalytic systems.

18.3.2.2.4 **Noble-Metal-Exchanged Zeolites** Zeolites were extensively investigated and *a fortiori* in the case of DeNOx catalysis [155, 179, 180]. These large-pore systems with high specific surface area and tunable acidity are perfect supports, and various methods have been developed to control the dispersion of redox sites upon them.

Various zeolites (MCM-36, ZSM-5, beta, ferrierite, etc.) [155, 157, 158, 180] and other molecular sieves (mesoporous silica SBA-15, titanosilicate ETS-10, etc.) were

tested as supports for redox-active particles such as iron, silver, copper, and cobalt. Most of the molecular sieves had already been tested for their acidic properties [60], then only establishing the appropriate amount of redox partner particles and their dispersion remained.

Ion- exchange remains the most appropriate and commonly used technique for tuning the active centers of molecular sieves; however, the control of their dispersion on to the sieve has still not been completely mastered. Further, the relationship between the acidic sites and the redox sites is of major interest in the case of DeNOx processes, as they need to interact constructively in order to enhance selectivity and durability.

Copper-exchanged pentasils (ZSM-5) have been studied by several groups during the last decade. Kuroda and co-workers [135, 152, 181] investigated the DeNOx-active sites on CuZSM-5 by combined calorimetric and spectroscopic methods and demonstrated the existence of two different copper active sites (redox) and the necessary presence of both for NO decomposition. Starting from a study by Itoh *et al.* [167] on enhancing DeNOx, they used two different catalysts differing in their Si:Al ratio, 11.9 and 36.7, and therefore also with different ion-exchange levels (and natures). CuZSM-5-11.9 displayed two types of active Cu^+ species (two- and three-coordinated structures involving lattice oxygens) whereas CuZSM-5-36.7 showed only one (the three-coordinated structure), as demonstrated by photoluminescence spectrometry. Monovalent copper ions (Cu^+) had already been determined as active centers in previous work and by other groups but not characterized further. The strategy was built on the combined advantages of calorimetry and IR spectroscopy in four steps:

1) determination of an acidity spectrum of CO adsorption in order to assign amounts and energy to both sites
2) observation of the reduction of NO to N_2 by FTIR spectroscopy to determine the characteristic bands on which to focus
3) occultation of the stronger sites to see if NO reduction can occur on the weaker sites alone
4) occultation of the weaker sites to see if NO reduction can occur on the stronger sites alone.

Adsorption calorimetry of CO on CuZSM-5-11.9 highlights two plateaus at 122 and 110 kJ mol^{-1}, corresponding to the two- and three-coordinated copper species, respectively, and relative to 0.23 and 0.47 surface coverage (Figure 18.71).

The same samples (CuZSM-5-11.9) were evacuated at 873 K and then CO adsorption was carried out at a definite CO pressure before exposure to 25 Pa NO at 300 K; IR spectra were recorded for CO coverage from 0.08 to 0.53 (Figure 18.72). Several absorbance bands were detected: 1811 and 1911 cm^{-1} ascribed to NO species on Cu^{2+} and Cu^+ species. respectively, 2159 cm^{-1} corresponding to CO adsorbed on Cu^+, and a band at 2295 cm^{-1} assigned to N_2 produced from NO reaction on the catalyst (confirmed by MS). The *a posteriori* adsorbed NO molecules could not reach the sites already covered by CO and it was demonstrated that DeNOx activity could occur when both Cu^+ sites were available and not when the stronger were

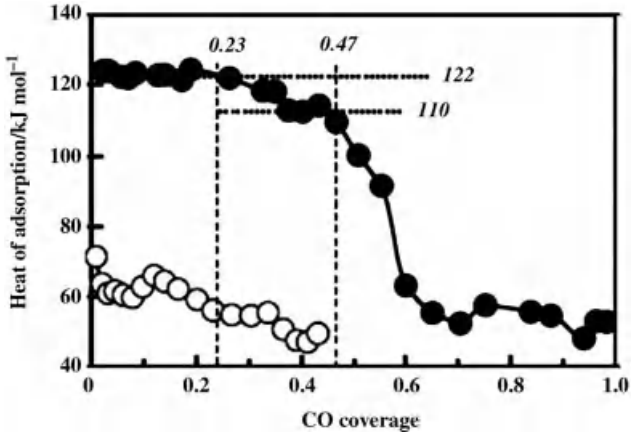


Figure 18.71 Differential heats of adsorption of CO at 301 K for the CuZSM-5-11.9 sample: (•) first adsorption and (○) second adsorption.

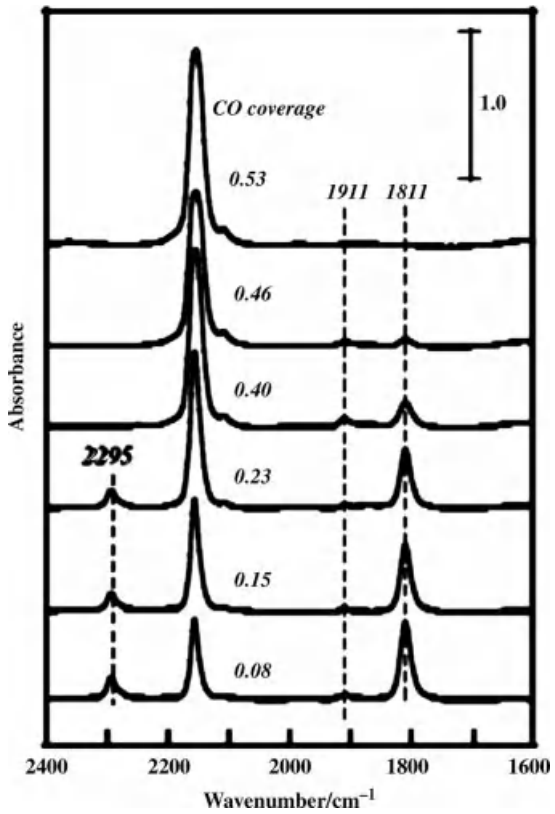


Figure 18.72 IR spectra for the CuZSM-5-11.9 sample that was exposed to NO gas of about 25 Pa at 300 K after CO adsorption. The sample was first evacuated at 873 K and then CO adsorption was carried out at a definite CO pressure.

unavailable (CO coverage below 0.23). A series of tests on CuZSM-5-36.7 (only the weaker three-coordinated Cu^+) confirmed these results, then a last series was performed on modified CuZSM-5(C)-11.9 with almost only two-coordinated Cu^+ sites, confirming the necessity to have the presence of both Cu^+ sites for the DeNOx activity to be displayed.

A range of zeolite topologies available with a range of local structures accommodating various metal ion species offers the possibility to tune their adsorption and redox properties over a wide range, then different reducing agents and environments lead to different most appropriate catalysts.

Carniti *et al.* [182] investigated the copper site energy distribution of ETS-10-based DeNOx catalysts by calorimetry and parameterized computational methods (fed with calorimetric–volumetric data). The two Cu-ETS-10 catalysts analyzed were obtained by ion exchange with high, "H" (11.4 wt%), and low, "L" (5.8 wt%), copper loadings.

The copper site energy distributions calculated for the two copper catalysts on ETS-10 matrix were in agreement with the experimental microcalorimetric data, from which heterogeneity of the Cu sites could be observed, with a large predominance of low-enthalpy Cu–NO interactions (Figure 18.73). Only rather small CuO-like aggregates were present on Cu-ETS-L, whereas larger aggregates were also present on Cu-ETS-H. The former are those mainly involved in the NO reduction activity, whereas large Cu aggregates favor the combustion of the hydrocarbon which can no longer react with NO to give N_2 (in the NO–C_2H_4–O_2 SCR reaction over Cu-ETS-10).

Over both catalysts, the profile of N_2 formed as a function of reaction temperature attained a maximum value and then decreased. This behavior was expected, as both NO and O_2 compete for the oxidation of C_2H_4 species. At low temperature, the active sites are able to activate NO to react with the hydrocarbon rather than to promote the hydrocarbon combustion, whereas at high temperature combustion of C_2H_4 by O_2 prevails (Table 18.6). The conversion of NO to N_2 at any temperature did not differ greatly between the two catalysts, despite their different copper contents. This

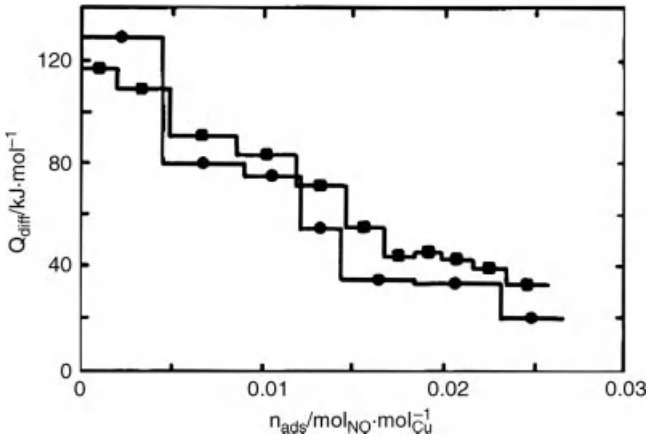


Figure 18.73 Differential heat (q_{diff}) of NO desorption versus coverage (mol$_{NO}$ mol$_{Cu}^{-1}$) for Cu-ETS-L (•) and Cu-ETS-H (■) samples.

Table 18.6 Catalytic results for the NO–C_2H_4–O_2 reaction[a].

Sample	T_R[b] (°C)	N_2 yield (%)	CO_2 yield (%)	10^5TOF[c] (s^{-1})
Cu–ETS-L	250	12.8	22.1	6.04
	300	21.3	57.1	10.1
	325	23.4	69.1	11.1
	350	21.7	79.1	10.4
Cu–ETS-H	250	19.3	50.1	3.42
	300	23.4	94.6	3.98
	325	19.8	100	3.99
	350	20.8	100	3.70

[a] Feed composition: 0.4% of NO and C_2H_4, 4% of O_2 with balance He; GHSV = 7500 h^{-1}.
[b] Reaction temperature.
[c] Expressed as $mol_{N_2} mol_{Cu}^{-1} s^{-1}$.

suggests that on both catalysts the same number of active sites might be present, hence Cu dispersion should be involved. Accordingly, Coq *et al.* [183] showed that the activity for the NO reduction by hydrocarbons is proportional to the number of Cu^{2+} ions up to 53% exchange and then no increase in activity was observed.

The redox properties of catalysts are nowadays attracting the interest of the depollution field community. Not only NO_x but also carbon and sulfur oxides and several large molecules require the action of redox catalysts to be degraded. As seen above, the acid–base properties often orientate the selectivity, whereas the redox strength influences the overall degradation efficiency. Therefore, it was often observed that specific acid–base and redox features were to be aimed for to degrade a targeted pollutant. Albonetti *et al.* [184], however, investigated the polyfunctionality of vanadia–titania-based DeNOx catalysts in the degradation of other pollutants (dioxins, furans, and chlorinated organics). The acid–base properties of the catalysts were also found to determine the partial versus complete oxidation of the intermediate products of degradation, whereas the efficiency was related to the vanadia (redox) sites. Good efficiency was achieved for the destruction of *o*-dichlorobenzene with these catalysts; thus with a similar nature of the catalyst but different redox and acid–base features the authors obtained catalysts either dedicated to DeNOx or chlorinated organics. We could then consider that tuning these features is more relevant than screening different natures of catalysts, with the aim of optimizing a redox catalyst for a specific task. For that purpose, thermal analysis techniques have been developed to bring greater insight.

18.4 Conclusion

This chapter has combined the reporting of new applications and recent developments in thermal analysis instrumentation as well as methodology. These techniques were shown to be of great help for elucidating the fundamental behavior and

structure of materials such as catalysts. To accompany any DTA, TGA, or calorimetry record, information such as the history, pretreatment, and chemical purity of the sample should be reported. Further, the sample's atmosphere should be clearly identified by pressure, composition, whether the atmosphere is static or dynamic, and through or over the sample.

The investigations reported here have shown that it is possible to determine by thermal analysis methods the heat evolved or absorbed in a process or reaction under study. Moreover, such techniques demonstrated how powerful they are for assessing the redox character of metals and some metal oxides, and for determining the acid–base properties of solid catalysts. When coupled with other techniques, additional data can be obtained, such as the quality of the active sites, thus providing interesting correlations between the number, strength, nature, and catalytic activity of the sites.

References

1 Willson, R.J. (2002) Calorimetry, in *Principles of Thermal Analysis and Calorimetry* (ed. P.J. Haines), Royal Society of Chemistry, Cambridge, p. 130.

2 Le, Q.T. and Auroux, A. (1996) La calorimétrie en catalyse hétérogène. *Bull. AFCAT*, **60**, 15–18.

3 Gravelle, P.C. (1972) Heat-flow microcalorimetry and its application to heterogeneous catalysis, in *Advances in Catalysis*, vol. 22 (eds. D.D. Eley, H. Pines, and P.B. Weisz), Academic Press, New York, pp. 191–263.

4 Cardona-Martinez, N. and Dumesic, J.A. (1992) Applications of adsorption microcalorimetry to the study of heterogeneous catalysis. *Adv. Catal.*, **38**, 149–244.

5 Farneth, W.E. and Gorte, R.J. (1995) Methods for characterizing zeolite acidity. *Chem. Rev.*, **95**, 615–635.

6 Andersen, P.J. and Kung, H.H. (1995) Characterization of catalysts with microcalorimetry. *Catalysis*, **11**, 441.

7 Auroux, A. (1994) Thermal methods: calorimetry, differential thermal analysis and thermogravimetry, in *Thermal Methods in Catalysts Characterization* (eds. B. Imelik and J.C. Vedrine), Plenum Press, New York, pp. 611–650.

8 Auroux A. (2008) Acidity and basicity: determination by adsorption microcalorimetry, in *Molecular Sieves – Science and Technology*, vol. 6 (eds. H.G. Karge and J. Weitkamp), Springer, Berlin, pp. 45–152.

9 Bennici, S. and Auroux, A. (2009) Thermal analysis and calorimetric methods, in *Metal Oxide Catalysis*, vol. 1 (eds. S.D. Jackson and S.J. Hargreaves), Wiley-VCH Verlag GmbH, Weinheim, pp. 391–441.

10 Damjanovic, L. and Auroux, A. (2010) Chapter 3: Determination of Acid/Base Properties by Temperature Programmed Desorption (TPD) and Adsorption Calorimetry in *Zeolite Characterization and Catalysis – a Tutorial*, (eds A.W. Chester and E.G. Derouane), Springer-verlag, pp. 107–167.

11 Kissinger, H.E. (1957) Reaction kinetics in differential thermal analysis. *Anal. Chem.*, **29** (11), 1702–1706.

12 Narayanan, S. and Krishna, K. (2000) Hydrotalcite-supported palladium catalysts: Part II. Preparation, characterization of hydrotalcites and palladium hydrotalcites for CO chemisorption and phenol hydrogenation. *Appl. Catal. A: Gen.*, **198**, 13–21.

13 Narayanan, S. and Krishna, K. (1998) Hydrotalcite-supported palladium catalysts: Part I. Preparation, characterization of hydrotalcites and palladium on uncalcined hydrotalcites for CO chemisorption and phenol

hydrogenation. *Appl. Catal. A: Gen.*, **174**, 221–229.
14 Claudy, P. (2005) *Analyse Calorimétrique Différentielle – Théorie et Applications de la D.S.C.*, Editions Tec & Doc.
15 McNaughton, J.L. and Mortimer, C.T. (1975) Differential scanning calorimetry, in *Thermochemistry and Thermodynamics, IRS, Physical Chemistry Series 2* (ed. H.A. Skinner), Butterworths, London, pp. 24–29.
16 Rouquerol, J. and Elégant, L. (1996) Application des Microcalorimètres aux Mesures Thermiques, Ref. R3010, Editions Techniques de l'Ingénieur, Paris, pp. 1–11.
17 Diot, M. (1993) Capacités Thermiques, Ref. R2970, Editions Techniques de l'Ingénieur, Paris, pp. 1–12.
18 Tope, B., Zhu, Y., and Lercher, J.A. (2007) Oxidative dehydrogenation of ethane over Dy_2O_3/MgO supported LiCl containing eutectic chloride catalysts. *Catal. Today*, **123**, 113–121.
19 Daudon, J.-L. (2001) Thermogravimétrie, Ref. P1260, Editions Techniques de l'Ingénieur, Paris, pp. 1–21.
20 Rubotherm Präzisionmesstechnik (2010) Magnetic Suspension Balance Brochure, Rubotherm Präzisionsmesstechnik, Bochum
21 Gervasini, A., Carniti, P., and Auroux, A. (2005) Surface acidity of catalytic solids studied by base desorption: experimental and modelling approaches. *Thermochim. Acta*, **434**, 42–49.
22 Navarro Lopez, P., Rodríguez Ramos, I., and Guerrero Ruiz, A. (2003) A study of carbon nanotube formation by C_2H_2 decomposition on an iron based catalyst using a pulsed method. *Carbon*, **41**, 2509–2517.
23 Duan, Y., Li, J., Yang, X., Cao, X.M., Hu, L., Wang, Z.Y., Liu, Y.W., and Wang, C.X. (2008) Thermal investigation of strontium acetate hemihydrate in nitrogen gas. *J. Thermal Anal. Calorim.*, **94**, 169–174.
24 Małecka, B., Małecki, A., Drozdz-Ciesla, E., Tortet, L., Llewellyn, P., and Rouquerol, F. (2007) Some aspects of thermal decomposition of $NiC_2O_4{\cdot}2H_2O$. *Thermochim. Acta*, **466**, 57–62.
25 Zielenkiewicz, W. and Margas, E. (2002) *Theory of Calorimetry*, Kluwer, Dordrecht.
26 Auroux, A. (1997) Acidity characterization by microcalorimetry and relationship with reactivity. *Top. Catal.*, **4**, 71–89.
27 André, R., Giordano, M., Mathonat, C., and Naumann, R. (2003) A new reaction calorimeter and calorimetric tools for safety testing at laboratory scale. *Thermochim. Acta*, **405**, 43–50.
28 Garron, A., Swierczynski, D., Bennici, S., and Auroux, A. (2009) New insights into the mechanism of H_2 generation through $NaBH_4$ hydrolysis on Co-based nanocatalysts studied by differential reaction calorimetry. *Int. J. Hydrogen Energy*, **34**, 1185–1199.
29 Lantenois, S., Prélot, B., Douillard, J.M., Szczodrowski, K., and Charbonnel, M.C. (2007) Flow microcalorimetry: experimental development and application to adsorption of heavy metal cations on silica. *Appl. Surf. Sci.*, **253**, 5807–5813.
30 Tanaka, S. (1992) Theory of power-compensated DSC. *Thermochim. Acta*, **210**, 67–76.
31 Saito, Y., Saito, K., and Atake, T. (1986) Theoretical analysis of peak height in classical DTA, power-compensated DSC and heat-flux DSC. *Thermochim. Acta*, **107**, 277–282; Saito, Y., Saito, K., and Atake, T. (1986) Base line drawing for the determination of the enthalpy of transition in classical DTA, power-compensated DSC and heat-flux DSC. *Thermochim. Acta*, **104**, 275–283.
32 Amenomiya, Y., Chenier, J.H.B., and Cvetanovic, R.J. (1967) Hydrogenation of olefins on alumina: I. Active sites for hydrogenation of ethylene. *J. Catal.*, **9**, 28–37.
33 Šimon, P. (2004) Isoconversional methods: fundamentals, meaning and application. *J. Thermal Anal. Calorim.*, **76**, 123–132.
34 Postole, G., Bonnetot, B., Gervasini, A., Guimon, C., Auroux, A., Ionescu, N.I., and Caldararu, M. (2007) Characterization of BN-supported palladium oxide catalyst used for hydrocarbon oxidation. *Appl. Catal. A: Gen.l*, **316**, 250–258.

35 Gervasini, A. and Bennici, S. (2005) Dispersion and surface states of copper catalysts by temperature-programmed-reduction of oxidized surfaces (s-TPR). *Appl. Catal. A: Gen.*, **281**, 199–205.

36 Malet, P. and Caballero, A. (1988) The selection of experimental conditions in temperature-programmed reduction experiments. *J. Chem. Soc., Faraday Trans. 1*, **84** (7), 2369–2375.

37 Monti, D.A.M. and Baiker, A. (1983) Temperature-programmed reduction. Parametric sensitivity and estimation of kinetic parameters. *J. Catal.*, **83**, 323–335.

38 Rombi, E., Cutrufello, M.G., De Rossi, S., Sini, M.F., and Ferino, I. (2006) Catalytic nitroxidation of 1-methylnaphthalene: I. Preparation, characterization and NO–surface interactions of chromia/alumina-based catalysts. *J. Mol. Catal. A: Chem.*, **247**, 171–181.

39 Zenboury, L., Azambre, B., and Weber, J.V. (2008) Transient TPSR, DRIFT-MS and TGA studies of a Pd/ceria–zirconia catalyst in CH_4 and NO_2 atmospheres. *Catal. Today*, **137**, 167–173.

40 Sakakini, B.H. and Verbrugge, A.S. (1997) Temperature-programmed surface reaction as a means of characterizing supported-metal catalysts and probing their surface reactivity. *J. Chem. Soc., Faraday Trans.*, **93** (8), 1637–1640.

41 Ji, S., Yang, J., Xu, C., Wang, J., and Xue, J. (2006) Temperature-programmed desorption/pulse surface reaction (TPD/TPSR) studies of CH_4, C_2H_6, C_2H_4 and CO over a cobalt/MWNTS catalyst. *React. Kinet. Catal. Lett.*, **89** (2), 209–217.

42 Shen, J. and Auroux, A. (2004) in *Fluid Catalytic Cracking IV: Preparation and Characterization of Catalysts, Studies in Surface Science and Catalysis*, vol. 149 (ed. M.L. Occelli), Elsevier, Amsterdam, pp. 35–70.

43 Boréave, A., Auroux, A., and Guimon, C. (1997) Nature and strength of acid sites in HY zeolites: a multitechnical approach. *Micropor. Mater.*, **11**, 275–291.

44 Auroux, A., Shi, Z.C., Echoufi, N., and Ben Taarit, Y. (1989) Calorimetric investigation of the acidity of dealuminated Y-type zeolites using various basic probes. *Stud. Surf. Sci. Catal.*, **46**, 377–387.

45 Gervasini, A. and Auroux, A. (1993) Thermodynamics of adsorbed molecules for a new acid–base topochemistry of alumina. *J. Phys. Chem.*, **97**, 2628–2639.

46 Kourieh, R., Bennici, S., and Auroux, A. (2010) Study of acidic commercial WO_x/ZrO_2 catalysts by adsorption microcalorimetry and thermal analysis techniques. *J. Thermal Anal. Calorim.*, **99**, 849–853.

47 Meloni, D., Monaci, R., Solinas, V., Auroux, A., and Dumitriu, E. (2008) Characterisation of the active sites in mixed oxides derived from LDH precursors by physico-chemical and catalytic techniques. *Appl. Catal. A: Gen.*, **350**, 86–95.

48 Leon, M., Díaz, E., Bennici, S., Vega, A., Ordonez, S., and Auroux, A. (2010) Adsorption of CO_2 on hydrotalcite-derived mixed oxides: sorption mechanisms and consequences for adsorption irreversibility. *Ind. Eng. Chem. Res.*, **49**, 3663–3671.

49 Zelenak, V., Halamova, D., Gaberova, L., Bloch, E., and Llewellyn, P. (2008) Amine-modified SB1-12 mesoporous silica for carbon dioxide capture: effect of amine basicity on sorption properties. *Micropor. Mesopor. Mater.*, **116**, 358–364.

50 Schärringer, P., Müller, T.E., Jentys, A., and Lercher, J.A. (2009) Identification of reaction intermediates during hydrogenation of CD_3CN on Raney-Co. *J. Catal.*, **263**, 34–41.

51 Siril, P.F., Cross, H.E., and Brown, D.R. (2008) New polystyrene sulfonic acid resin catalyst with enhanced acidic and catalytic properties. *J. Mol. Catal. A: Chem.*, **279**, 63–68.

52 Siril, P.F., Shiju, N.R., Brown, D.R., and Wilson, K. (2009) Optimising catalytic properties of supported sulfonic acid catalysts. *Appl. Catal. A: Gen.*, **364**, 95–100.

53 Bandyopadhyay, M., Shiju, N.R., and Brown, D.R. (2010) MCM-48 as a support for sulfonic acid catalysts. *Catal. Commun.*, **11**, 660–664.

54 Siril, P.F., Davison, A.D., Randhawa, J.K., and Brown, D.R. (2007) Acid strength and catalytic activities of sulfonic acid on polymeric and silica supports. *J. Mol. Catal. A: Chem.*, **267**, 72–78.

55 Sievers, C., Liebert, J.S., Stratmann, M.M., Olindo, R., and Lercher, J.A. (2008) Comparison of zeolites LaX and LaY as catalysts for isobutane/2-butene alkylation. *Appl. Catal. A: Gen.*, **336**, 89–100.

56 Kresnawahjuesa, O., Gorte, R.J., and White, D. (2004) Characterisation of acylating intermediates formed on H-ZSM-5. *J. Mol. Catal. A: Chem.*, **208**, 175–185.

57 Figueras, F., Lopez, J., Sanchez-Valente, J., Vu, T.T.H., Clacens, J.-M., and Palomeque, J. (2002) Isophorone isomerization as model reaction for the characterization of solid bases: application to the determination of the number of sites. *J. Catal.*, **211**, 144–149.

58 Kukulska-Zajac, E., Gora-Marek, K., and Datka, J. (2006) IR and TPD studies of the reaction of acetic acid in zeolites NaHY. *Micropor. Mesopor. Mater.*, **96**, 216–221.

59 Damjanovic, L. and Auroux, A. (2008) Heterogeneous catalysis on solids, in *Handbook of Thermal Analysis and Calorimetry. Vol. 5, Recent Advances and Applications* (eds. M.E. Brown and P.K. Gallagher), Elsevier, Amsterdam.

60 Auroux A. (2004) La microcalorimétrie appliquée à l'étude des zéolithes, in *Matériaux Micro et Mésoporeux - Caractérisation* (ed. F. Thibaut-Starzyk), EDP Sciences, Les Ulis.

61 Cardona-Martinez, N. and Dumesic, J.A. (1991) Microcalorimetric measurements of basic molecule adsorption on silica and silica-alumina. *J. Catal.*, **128**, 23–33.

62 Stach, H, and Jänchen, J. (1992) Relationship between acid-strength and framework aluminum content in dealuminated mordenites. *Zeolites*, **12**, 152–154.

63 Stach, H., Jänchen, J., and Lohse, U. (1992) Relationship between acid strength and framework aluminum content in dealuminated faujasites. *Catal. Lett.*, **13**, 389–393.

64 Brown, D.R. and Groszek, A.J. (2000) Heats of adsorption of ammonia on a zeolite catalyst and an activated clay catalyst determined by flow adsorption microcalorimetry. *Langmuir*, **16**, 4207–4212.

65 Khvoshchev, S.S. and Vasileva, E.A. (1982) Heats of adsorption of carbon dioxide and ammonia on synthetic zeolites of various structures. Part 1. Ammonia on sodium and lithium zeolites. *Izvest. Akad. Nauk SSSR Ser. Khim.*, **5**, 973–978.

66 Karge, H.G. and Jozefowicz, L.C. (1994) Zeolites and related microporous materials: state of the art, 1994, *Stud. Surf. Sci. Catal.*, **84**, 685.

67 Stone, F.S. and Whalley, L. (1967) Heats of adsorption of ammonia on acidic catalysts. *J. Catal.*, **8**, 173–182.

68 Auroux, A., Artizzu, P., Ferino, I., Monaci, R., Rombi, E., and Solinas, V. (1997) Conversion of 4-methylpentan-2-ol over alkali-metal ion-exchanged X and Y zeolites: a microcalorimetric and catalytic investigation. *Micropor. Mater.*, **11**, 117–126.

69 Shimizu, K., Higuchi, T., Takasugi, E., Hatamachi, T., Kodama, T., and Satsuma, A. (2008) Characterization of Lewis acidity of cation-exchanged montmorillonite K-10 clay as effective heterogeneous catalyst for acetylation of alcohol. *J. Mol. Catal. A: Chem.*, **284**, 89–96.

70 Dragoi, B., Rakic, V., Dumitriu, E., and Auroux, A. (2010) Adsorption of organic pollutants over microporous solids investigated by microcalorimetry techniques. *J. Thermal Anal. Calorim.*, **99**, 733–740.

71 Rakic, V., Damjanovic, L., Rac, V., Stosic, D., Dondur, V., and Auroux, A. (2010) The adsorption of nicotine from aqueous solutions on different zeolite structures. *Water Res.*, **44**, 2047–2057.

72 Busco, C., Barbaglia, A., Broyer, M., Bolis, V., Foddanu, G.M., and Ugliengo, P. (2004) Characterization of Lewis and Brønsted acidic sites in H-MFI and H-BEA zeolites: a thermodynamic and ab initio study. *Thermochim. Acta*, **418**, 3–9.

73 Sircar, S. (2005) Heat of adsorption on heterogeneous adsorbents. *Appl. Surf. Sci.*, **252**, 647–653.

74 Li, H., Zhang, L., Dai, H., and He, H. (2009) Facile synthesis and unique physicochemical properties of three-dimensionally ordered macroporous magnesium oxide, gamma-alumina and ceria–zirconia solid solutions with crystalline mesoporous walls. *Inorg. Chem.*, **48** (10), 4421–4434.

75 Occelli, M.L., Biz, S., and Auroux, A. (1999) Effects of isomorphous substitution of Si with Ti and Zr in mesoporous silicates with the MCM-41 structure. *Appl. Catal. A: Gen.*, **183**, 231–239.

76 Occelli, M.L., Biz, S., Auroux, A., and Ray, G.J. (1998) Effects of the nature of the aluminum source on the acidic properties of some mesostructured materials. *Micropor. Mesopor. Mater.*, **26**, 193–213.

77 Janchen, J., Stach, H., Busio, M., and Van Wolput, J.H. (1998) Microcalorimetric and spectroscopic studies of the acidic- and physisorption characterisctics of MCM-41 and zeolites. *Thermochim. Acta*, **312**, 33–45.

78 Figueras, F., Klapyta, Z., Massiani, P., Mountassir, Z., Tichit, D., Fajula, F., Guegen, C., Bousquet, J., and Auroux, A. (1990) Use of competitive ion exchange for intercalation of montmorillonite with hydroxyl-aluminum species. *Clay Clay Miner.*, **38**, 257–264.

79 Belkhadem, F., Clacens, J.M., Bengueddoch, A., and Figueras, F. (2006) Acidity and catalytic properties for the alkylation of aromatics of PILCs with mixed oxide pillars prepared from two different bentonites. *Appl. Catal. A: Gen.*, **298**, 188–193.

80 Occelli, M.L., Olivier, J.P., Perdigon, J.A., and Auroux, A. (2002) Surface area, pore volume distribution and acidity in mesoporous expanded clay catalysts from hybrid density functional theory (DFT) and adsorption microcalorimetry methods. *Langmuir*, **18**, 9816–9823.

81 Jeronimo, D., Guil, J.M., Corbella, B.M., Vasques, H., Miranda, A., Silva, J.M., Lobato, A., Pires, J., and Corvalho, A.P. (2007) Acidity characterization of pillared clays through microcalorimetric measurements and catalytic ethylbenzene test reaction. *Appl. Catal. A: Gen.*, **330**, 89–95.

82 Auroux, A. and Gervasini, A. (1990) Microcalorimetric study of the acidity and basicity of metal oxide surfaces. *J. Phys. Chem.*, **94**, 6371–6379.

83 Gervasini, A. and Auroux, A. (1991) Microcalorimetric investigation of the acidity and basicity of metal oxides. *J. Thermal Anal.*, **37**, 1737–1744.

84 Auroux, A., Artizzu, P., Ferino, I., Monad, R., Rombi, E., Solinas, V., and Petrini, G. (1996) Dehydration of 4-methylpentan-2-ol over lanthanum and cerium oxides. *J. Chem. Soc., Faraday Trans.*, **92** (14), 2619–2624.

85 Gervasini, A., Bellussi, G., Fenyvesi, J., and Auroux, A. (1995) Microcalorimetric and catalytic studies of the acidic character of modified metal oxide surfaces. 1. Doping ions on alumina, magnesia and silica. *J. Phys. Chem.*, **99**, 5117–5125.

86 Gervasini, A., Fenyvesi, J., and Auroux, A. (1996) Microcalorimetric study of the acidic character of modified oxide surfaces. Influence of the loading amount on alumina, magnesia and silica. *Langmuir*, **12**, 5356–5364.

87 Colorio, G., Védrine, J.C., Auroux, A., and Bonnetot, B. (1996) Partial oxidation of ethane over alumina–boria catalysts. *Appl. Catal. A: Gen.*, **137**, 55–68.

88 Keranen, J., Guimon, C., Iiskola, E., Auroux, A., and Niinisto, L. (2003) Gas-phase synthesis, structure and surface acid–base properties of highly dispersed vanadia/titania/silica catalysts. *Phys. Chem. Chem. Phys.*, **5**, 5333–5342.

89 Gergely, B. and Auroux, A. (1999) Calorimetric study of the adsorption of air pollutants on alumina-supported tin and gallium oxides. *Res. Chem. Intermed.*, **25**, 13–24.

90 Auroux, A., Sprinceana, D., and Gervasini, A. (2000) Support effects on de-NO_x catalytic properties of supported tin oxides. *J. Catal.*, **195**, 140–150.

91 Sprinceana, D., Caldararu, M., Ionescu, N.I., and Auroux, A. (1999) Calorimetric study of the acidity and interface effects of tin dioxide layers deposited on another

metal oxide. *J. Thermal Anal. Calorim.*, **56**, 109–115.

92 Perdigon-Melon, J.A., Gervasini, A., and Auroux, A. (2005) Study of the influence of the In_2O_3 loading on γ-alumina for the development of de-NO_x catalysts. *J. Catal.*, **234** (2005), 421–430.

93 Petre, A.L., Perdigón-Melón, J.A., Gervasini, A., and Auroux, A. (2003) Characterization and reactivity of group III oxides supported on niobium oxide. *Catal. Today*, **78**, 377–386.

94 Jin, Y.S., Ouqour, A., Auroux, A., and Védrine, J.C. (1989) Molybdena on niobium oxide catalysts: preparation and characterization. *Stud. Surf. Sci. Catal.*, **48**, 525–534.

95 Gervasini, A., Ragaini, V., and Auroux, A. (1995) Characterization and activity of new solid acid catalysts for NO decomposition, in *Environmental Catalysis for a Better World and Life* (eds. G. Centi, C. Cristiani, P. Forzatti, and S. Perathoner), Società Chimica Italiana, Rome, pp. 279–282.

96 Bachiller-Baeza, B., Alvarez-Rodríguez, J., Guerrero-Ruiz, A., and Rodríguez-Ramos, I. (2007) Support effects on Ru-HPA bifunctional catalysts: surface characterization and catalytic performance. *Appl. Catal. A: Gen.*, **333**, 281–289.

97 Yori, J.C., Grau, J.M., Benítez, V.M., and Sepulveda, J. (2005) Hydroisomerization-cracking of *n*-octane on heteropolyacid $H_3PW_{12}O_{40}$ supported ZrO_2, SiO_2 and carbon. Effect of Pt incorporation on catalyst performance. *Appl. Catal. A: Gen.*, **286**, 71–78.

98 Lin, Q., Shimizu, K., and Satsuma, A. (2010) Hydrogenation of pyrene using Pd catalysts supported on tungstated metal oxides. *Appl. Catal. A: Gen.*, **387**, 166–172.

99 Tanabe, K., Sumiyoshi, T., Shibata, K., Kiyoura, T., and Kitagawa, J. (1974) A new hypothesis regarding the surface acidity of binary metal oxides. *Bull. Chem. Soc. Jpn.*, **47**, 1064–1066.

100 Seiyama, T., Tanabe, K., and Fueki, K. (eds.) (1978) *Metal oxides and their catalytic actions (Kinzoku Sankabutsu to Fukugo Sankabutsu)*, Kodansha, Tokyo.

101 Cutrufello, M.G., Ferino, I., Monaci, R., Rombi, E., and Solinas, V. (2002) Acid–base properties of zirconium, cerium and lanthanum oxides by calorimetric and catalytic investigation. *Top. Catal.*, **19** (3–4), 225–240.

102 Feng, R.M., Yang, X.J., Ji, W.J., Zhu, H.Y., Gu, X.D., Chen, Y., Han, S., and Hibst, H. (2007) The study on the source of Te and the dispersion of TeO_2 in fabricating Mo–V–Te and Mo–V–Te–Nb mixed metal oxide catalysts for propane partial oxidation. *J. Mol. Catal. A: Chem.*, **267**, 245–254.

103 Bonnetot, B., Rakic, V., Yuzhakova, T., Guimon, C., and Auroux, A. (2008) Preparation and characterization of Me_2O_3–CeO_2 (Me=B, Al, Ga, In) mixed oxide catalysts. 2. Preparation by sol–gel method. *Chem. Mater.*, **20**, 1585–1596.

104 Occelli, M.L., Biz, S., Auroux, A., and Iyer, P.S. (1999) Physicochemical properties of some metal supports for hydrotreating catalysts preparation. *Appl. Catal. A: Gen.*, **179**, 117–129.

105 Dragoi, B., Gervasini, A., Dumitriu, E., and Auroux, A. (2004) Calorimetric determination of the acidic character of amorphous and crystalline aluminosilicates. *Thermochim. Acta*, **420**, 127–134.

106 Gervasini, A., Carniti, P., and Auroux, A. (2005) Surface acidity of catalytic solids studied by base desorption: experimental and modeling approaches. *Thermochim. Acta*, **434**, 42–49.

107 Bennici, S., Auroux, A., Guimon, C., and Gervasini, A. (2006) Supported binary oxide catalysts containing CuO coupled with Ga_2O_3 and SnO_2. *Chem. Mater.*, **18**, 3641–3650.

108 Gervasini, A., Bennici, S., Auroux, A., and Guimon, C. (2007) Surface acidic properties of supported binary oxides containing CuO coupled with Ga_2O_3 and SnO_2 studied by complementary techniques. *Appl. Catal. A: Gen.*, **331**, 129–137.

109 Vartuli, J.C., Santiesteban, J.G., Traverso, P., Cardona-Martinez, N., Chang, C.D., and Stevenson, S.A. (1999) Characterization of the acid properties of tungsten/zirconia catalysts using adsorption microcalorimetry and *n*-pentane isomerization activity. *J. Catal.*, **187**, 131–138.

110 Tichit, D., Lhouty, M.H., Guida, A., Chiche, B.H., Figueras, F., Auroux, A., Bartolani, D., and Garrone, E. (1995) Textural properties and catalytic activity of hydrotalcites. *J. Catal.*, **151**, 50–59.

111 Prescott, H.A., Li, Z.J., Kemnitz, E., Trunschke, A., Deutsch, J., Lieske, H., and Auroux, A. (2005) Application of calcined Mg–Al hydrotalcites for Michael additions: an investigation of catalytic activity and acid–base properties. *J. Catal.*, **234**, 119–130.

112 Dussault, L., Dupin, J.C., Dumitriu, E., Auroux, A., and Guimon, C. (2005) Microcalorimetry, TPR and XPS studies of acid–base properties of NiCuMgAl mixed oxides using LDHs as precursors. *Thermochim. Acta*, **434**, 93–99.

113 Dussault, L., Dupin, J.C., Martinez, H., Dumitriu, E., Auroux, A., and Guimon, C. (2006) Influence of the metal nature (Ni, Cu, Mg) on the surface acid–base properties of mixed oxides elaborated from LDH. *Surf. Interface Anal.*, **38**, 234–237.

114 Lefebvre, F., Liu-Cai, F.X., and Auroux, A. (1994) Microcalorimetric study of the acidity of tungstic heteropolyanions. *J. Mater. Chem.*, **4**, 125–131.

115 Liu-Cai, F.X., Sahut, B., Faydi, E., Auroux, A., and Hervé, G. (1999) Study of the acidity of carbon supported and unsupported heteropolyacid catalysts by ammonia sorption microcalorimetry. *Appl. Catal. A: Gen.*, **185**, 75–83.

116 Narasimharao, K., Brown, D.R., Lee, A.F., Newman, A.D., Siril, P.F., Tavener, S.J., and Wilson, K. (2007) Structure–activity relations in Cs-doped heteropolyacid catalysts for biodiesel production. *J. Catal.*, **248**, 226–234.

117 Pesaresi, L., Brown, D.R., Lee, A.F., Montero, J.M., Williams, H., and Wilson, K. (2009) Cs-doped $H_4SiW_{12}O_{40}$ catalysts for biodiesel applications. *Appl. Catal. A: Gen.*, **360**, 50–58.

118 Dryzun, C., Mastai, Y., Shvalb, A., and Avnir, D. (2009) Chiral silicate zeolites. *J. Mater. Chem.*, **19**, 2062–2069.

119 Mars, P. and Van Krevelen, D.W. (1954) *Chem. Eng. Sci.*, **3** (Spec. Suppl.), 41.

120 Jones, A. and McNicol, B.D. (1986) *Temperature-Programmed Reduction for Solid Materials Characterization, Chemical Industries*, vol. 24, Marcel. Dekker, New York.

121 Zhou, G., Luo, T., and Gorte, R.J. (2006) An investigation of NO_x storage on Pt–BaO–Al_2O_3. *Appl. Catal. B: Environ.*, **64**, 88–95.

122 Shen, S.-C. and Kawi, S. (2003) Mechanism of selective catalytic reduction of NO in the presence of excess O_2 over Pt/Si-MCM-41 catalyst. *J. Catal.*, **213**, 241–250.

123 Postole, G., Gervasini, A., Guimon, C., Auroux, A., and Bonnetot, B. (2006) Influence of the preparation method on the surface characteristics and activity of boron nitride-supported noble metal catalysts. *J. Phys. Chem. B*, **110**, 12572–12580.

124 Chmielarz, L., Kustrowski, P., Zbroja, M., Gil-Knap, B., Datka, J., and Dziembaj, R. (2004) SCR of NO by NH_3 on alumina or titania pillared montmorillonite modified with Cu or Co: Part II. Temperature programmed studies. *Appl. Catal. B: Environ.*, **53**, 47–61.

125 Arous, W., Tounsi, H., Djemel, S., Ghorbel, A., and Delahay, G. (2005) Selective catalytic reduction of nitric oxide with ammonia on copper(II) ion-exchanged offretite. *Catal. Commun.*, **6**, 281–285.

126 Halliche, D., Cherifi, O., and Auroux, A. (2005) Microcalorimetric studies and methane reforming by CO_2 on Ni-based zeolite catalysts. *Thermochim. Acta*, **434**, 125–131.

127 Wachs, I.E., Jehng, J.M., Deo, G., Hu, H., and Arora, N. (1996) Redox properties of niobium oxide catalysts. *Catal. Today*, **28**, 199–205.

128 Zhao, H., Bennici, S., Cai, J., Shen, J., and Auroux, A. (2010) Effect of vanadia loading on the acidic, redox and catalytic properties of V_2O_5–TiO_2 and V_2O_5–TiO_2/SO_4^{2-} catalysts for partial oxidation of methanol. *Catal. Today*, **152**, 70–77.

129 Gurbani, A., Ayastuy, J.L., Gonzalez-Marcos, M.P., Herrero, J.E., Guil, J.M., and Gutierrez-Ortiz, M.A. (2009) Comparative study of CuO–CeO_2 catalysts prepared by wet impregnation

and deposition–precipitation. *Int. J. Hydrogen Energy*, **34**, 547–553.

130 Tanksale, A., Beltramini, J.N., Dumesic, J.A., and Lu, G.Q. (2008) Effect of Pt and Pd promoter on Ni supported catalysts – a TPR/TPO/TPD and microcalorimetry study. *J. Catal.*, **258**, 366–377.

131 Kunkes, E.L., Simonetti, D.A., Dumesic, J.A., Pyrz, W.D., Murillo, L.E., Chen, J.G., and Buttrey, D.J. (2008) The role of rhenium in the conversion of glycerol to synthesis gas over carbon supported platinum–rhenium catalysts. *J. Catal.*, **260**, 164–177.

132 Cerro-Alarcon, M., Maroto-Valiente, A., Rodríguez-Ramos, I., and Guerrero-Ruiz, A. (2005) Further insights into the Ru nanoparticles–carbon interactions and their role in the catalytic properties. *Carbon*, **43**, 2711–2722.

133 Shabaker, J.W., Simonetti, D.A., Cortright, R.D., and Dumesic, J.A. (2005) Sn-modified Ni catalysts for aqueous-phase reforming: characterization and deactivation studies. *J. Catal.*, **231**, 67–76.

134 Itadani, A., Kumashiro, R., Kuroda, Y., and Nagao, M. (2004) Calorimetric study of N_2 adsorption on copper-ion-exchanged ZSM-5 zeolite. *Thermochim. Acta*, **416**, 99–104.

135 Itadani, A., Kuroda, Y., Tanaka, M., and Nagao, M. (2005) Unambiguous evidence supporting the decomposition reaction of NO on two types of monovalent copper-ion in CuZSM-5 zeolite. *Micropor. Mesopor. Mater.*, **86**, 159–165.

136 Naumann d'Alnoncourt, R., Bergmann, M., Strunk, J., Löffler, E., Hinrichsen, O., and Muhler, M. (2005) The coverage-dependent adsorption of carbon monoxide on hydrogen-reduced copper catalyst: the combined application of microcalorimetry, temperature-programmed desorption and FTIR spectroscopy. *Thermochim. Acta*, **434**, 132–139.

137 Naumann d'Alnoncourt, R., Kurtz, M., Wilmer, H., Löffler, E., Hagen, V., Shen, J., and Muhler, M. (2003) The influence of ZnO on the differential heat of adsorption of CO on Cu catalysts: a microcalorimetric study. *J. Catal.*, **220**, 249–253.

138 Maroto-Valiente, A., Rodríguez-Ramos, I., and Guerrero-Ruiz, A. (2004) Surface study of rhodium nanoparticles supported on alumina. *Catal. Today*, **93-95**, 567–574.

139 Asedegbega-Nieto, E., Guerrero-Ruíz, A., and Rodríguez-Ramos, I. (2005) Study of CO chemisorptions on graphite-supported Ru–Cu and Ni–Cu bimetallic catalysts. *Thermochim. Acta*, **434**, 113–118.

140 Cerro-Alarcon, M., Maroto-Valiente, A., Rodríguez-Ramos, I., and Guerrero-Ruíz, A. (2005) Surface sites on carbon-supported Ru, Co and Ni nanoparticles as determined by microcalorimetry of CO adsorption. *Thermochim. Acta*, **434**, 100–106.

141 Cerro-Alarcon, M., Maroto-Valiente, A., Rodríguez-Ramos, I., and Guerrero-Ruiz, A. (2004) Surface study of graphite-supported Ru–Co and Ru–Ni bimetallic catalysts. *Appl. Catal. A: Gen.*, **275**, 257–269.

142 Maroto-Valiente, A., Cerro-Alarcon, M., Guerrero-Ruiz, A., and Rodríguez-Ramos, I. (2003) Effect of the metal precursor on the surface site distribution of Al_2O_3-supported Ru catalysts: catalytic effects of the *n*-butane/H_2 test. *Appl. Catal. A: Gen.*, **283**, 23–32.

143 Bachiller-Baeza, B., Alvarez-Rodríguez, J., Guerrero-Ruiz, A., and Rodríguez-Ramos, I. (2007) Support effects on Ru-HPA bifunctional catalysts: surface characterization and catalytic performance. *Appl. Catal. A: Gen.*, **333**, 281–289.

144 Cerro-Alarcon, M., Bachiller-Baeza, B., Guerrero-Ruiz, A., and Rodríguez-Ramos, I. (2006) Effect of the reduction–preparation method on the surface states and catalytic properties of supported-nickel particles. *J. Mol. Catal. A: Chem.*, **258**, 221–230.

145 Zhang, Y.J., Maroto-Valiente, A., Rodríguez-Ramos, I., Xin, Q., and Guerrero-Ruiz, A. (2004) Synthesis and characterization of carbon black supported Pt–Ru alloy as a model catalyst for fuel cells. *Catal. Today*, **93–95**, 619–626.

146 Guerrero-Ruiz, A., Yang, S., Xin, Q., Maroto-Valiente, A., Benito-Gonzalez, M., and Rodríguez-Ramos, I. (2000) Comparative study by infrared spectroscopy and microcalorimetry of the CO adsorption over supported palladium catalysts. *Langmuir*, **16**, 8100–8106.

147 Auroux, A., and Gravelle, P.C. (1981) Comparative study of the bond energy of oxygen at the surface of supported silver catalysts and of the activity of these catalysts for ethylene epoxidation. *Thermochim. Acta*, **47**, 333–341.

148 Hinrichsen, O., Genger, T., and Muhler, M. (2000) Modeling of temperature-programmed surface reactions. *Chem. Eng. Technol.*, **23**, 11.

149 Iwasaki, M., Yamazaki, K., Banno, K., and Shinjoh, H. (2008) Characterization of Fe/ZSM-5 DeNOx catalysts prepared by different methods: relationship between active Fe sites and NH_3-SCR performance. *J. Catal.*, **260**, 205–216.

150 Iwasaki, M. and Shinjoh, H. (2008) Analysis of the adsorption state and desorption kinetics of NO_2 over Fe-zeolite catalyst by FT-IR and temperature-programmed desorption. *Phys. Chem. Chem. Phys.*, **12**, 2365–2372.

151 Kröcher, O., Devadas, M., Elsener, M., Wokaun, A., Söger, N., Pfeifer, M., Demel, Y., and Mussmann, L. (2006) Investigation of the selective catalytic reduction of NO by NH_3 on Fe-ZSM5 monolith catalysts. *Appl. Catal. B: Environ.*, **66**, 208–216.

152 Kuroda, Y., Mori, T., Yoshikawa, Y., Kittaka, S., Kumashiro, R., and Nagao, M. (1999) What are the important factors determining the state of copper ion on various supports? Analysis using spectroscopic methods and adsorption calorimetry. *Phys. Chem. Chem. Phys.*, **1**, 3807–3816.

153 Figueras, F., Coq, B., Ensuque, E., Tachon, D., and Delahay, G. (1998) Catalytic properties of Cu on sulphated zirconias for DeNOx in excess of oxygen using *n*-decane as reductant. *Catal. Today*, **42**, 117–125.

154 Fang, H.L. and Da Costa, H.F.M. (2003) Urea thermolysis and NO_x reduction with and without SCR catalysts. *Appl. Catal. B: Environ.*, **46**, 17–34.

155 Klukowski, D., Balle, P., Geiger, B., Wagloehner, S., Kureti, S., Kimmerle, B., Baiker, A., and Grunwaldt, J.-D. (2009) On the mechanism of the SCR reaction on Fe/HBEA zeolite. *Appl. Catal. B: Environ.*, **93**, 185–193.

156 Sullivan, J.A. and Keane, O. (2005) The role of Brønsted acidity in poisoning the SCR–urea reaction over FeZSM-5 catalysts. *Appl. Catal. B: Environ.*, **61**, 244–252.

157 Ferreira, A.P., Capela, S., Da Costa, P., Henriques, C., Ribeiro, M.F., and Ramôa Ribeiro, F. (2007) CH_4-SCR of NO over Co and Pd ferrierite catalysts: effect of preparation on catalytic performance. *Catal. Today*, **119**, 156–165.

158 García-Cortés, J.M., Pérez-Ramírez, J., Rouzaud, J.N., Vaccaro, A.R., Illán-Gómez, M.J., and Salinas-Martínez de Lecea, C. (2003) On the structure sensitivity of deNOx HC-SCR over Pt-beta catalysts. *J. Catal.*, **218**, 111–122.

159 Komvokis, V.G., Iliopoulou, E.F., Vasalos, I.A., Triantafyllidis, K.S., and Marshall, C.L. (2007) Development of optimized Cu-ZSM-5 deNOx catalytic materials both for HC-SCR applications and as FCC catalytic additives. *Appl. Catal. A: Gen.*, **325**, 345–352.

160 Boutros, M., Trichard, J.M., and Da Costa, P. (2009) Silver supported mesoporous SBA-15 as potential catalysts for SCR NOx by ethanol. *Appl. Catal. B: Environ.*, **91**, 640–648.

161 Gervasini, A., Perdigon-Melon, J.A., Guimon, C., and Auroux, A. (2006) An in-depth study of supported In_2O_3 catalysts for the selective catalytic reduction of NO_x: the influence of the oxide support. *J. Phys. Chem. B*, **110**, 240–249.

162 Perdigon-Melon, J.A., Gervasini, A., and Auroux, A. (2005) Study of the influence of the In_2O_3 loading on γ-alumina for the development of de-NO_x catalysts. *J. Catal.*, **234**, 421–430.

163 Guimon, C., Gervasini, A., and Auroux, A. (2001) XPS study of the adsorption of SO_2 and NH_3 over supported tin dioxide catalysts used in de-NO_x catalytic reaction. *J. Phys. Chem. B*, **105**, 10316–10325.

164 Park, P.W., Ragle, C.S., Boyer, C.L., Lou Balmer, M., Engelhard, M., and McCready, D. (2002) In_2O_3/Al_2O_3 catalysts for NO_x reduction in lean conditions. *J. Catal.*, **210**, 97–105.

165 Turek, W., Plis, A., Da Costa, P., and Krzton, A. (2010) Investigation of oxide catalysts activity in the NO_x neutralisation with organic reductants. *Appl. Surf. Sci.*, **256**, 5572–5575.

166 Schott, F.J.P., Balle, P., Adler, J., and Kureti, S. (2009) Reduction of NO_x by H_2 on $Pt/WO_3/ZrO_2$ catalysts in oxygen-rich exhaust. *Appl. Catal. B: Environ.*, **87**, 18–29.

167 Itoh, M., Iwamoto, J., Tajima, N., and Machida, K. (2010) DeNOx catalytic activity over Pt/Al_2O_3 prepared by solvothermal method. *Mater. Chem. Phys.*, **124**, 587–591.

168 Costa, C.N., Savva, P.G., Andronikou, C., Lambrou, P.S., Polychronopoulou, K., Belessi, V.C., Stathopoulos, V.N., Pomonis, P.J., and Efstathiou, A.M. (2002) An investigation of the $NO/H_2/O_2$ (lean De-NOx) reaction on a highly active and selective $Pt/La_{0.7}Sr_{0.2}Ce_{0.1}FeO_3$ catalyst at low temperatures. *J. Catal.*, **209**, 456–471.

169 Sobalík, Z., Vondrová, A., Tvaružková, Z., and Wichterlová, B. (2002) Analysis of the structural parameters controlling the temperature window of the process of SCR-NOx by low paraffins over metal-exchanged zeolites. *Catal. Today*, **75**, 347–351.

170 Moura de Oliveira, M.L., Monteiro Silva, C., Moreno-Tost, R., Lopes Farias, T., Jimenez-Lopez, A., and Rodríguez-Castellon, E. (2009) A study of copper-exchanged mordenite natural and ZSM-5 zeolites as SCR-NOx catalysts for diesel road vehicles: simulation by neural networks approach. *Appl. Catal. B: Environ.*, **88**, 420–429.

171 Li, Y., Cheng, H., Lin, D., Qin, Y., Xie, Y., and Wang, S. (2008) WO_3/CeO_2-ZrO_2, a promising catalyst for selective catalytic reduction (SCR) of NO_x with NH_3 in diesel exhaust, *Chem. Commun.*, **12**, 1470–1472.

172 Casapu, M., Kröcher, O., and Elsener, M. (2009) Screening of doped MnO_x–CeO_2 catalysts for low-temperature NO-SCR. *Appl.Catal. B: Environ.*, **88**, 413–419.

173 Roy, S. and Hegde, M.S. (2008) Pd ion substituted CeO_2: a superior de-NOx catalyst to Pt or Rh metal ion doped ceria. *Catal. Commun.*, **9**, 811–815.

174 Zhang, R. and Kaliaguine, S. (2008) Lean reduction of NO by C_3H_6 over Ag/alumina derived from Al_2O_3,AlOOH and $Al(OH)_3$. *Appl. Catal. B: Environ.*, **78**, 275–287.

175 Wachs, I.E., Deo, G., Weckhuysen, B.M., Andreini, A., Vuurman, M.A., de Boer, M., and Amiridis, M.D. (1996) Selective catalytic reduction of NO with NH_3 over supported vanadia catalysts. *J. Catal.*, **161**, 211–221.

176 Shimizu, K., Tsuzuki, M., Kato, K., Yokota, S., Okumura, K., and Satsuma, A. (2007) Reductive activation of O_2 with H_2-reduced silver clusters as a key step in the H_2-promoted selective catalytic reduction of NO with C_3H_8 over Ag/Al_2O_3. *J. Phys. Chem. C*, **111**, 950–959.

177 Sazama, P., Capek, L., Drobná, H., Sobalík, Z., Dedecek, J., Arve, K., and Wichterlová, B. (2005) Enhancement of decane-SCR-NOx over Ag/alumina by hydrogen. Reaction kinetics and *in situ* FTIR and UV–vis study. *J. Catal.*, **232**, 302–317.

178 Wang, Z.-M., Yamaguchi, M., Goto, I., and Kumagai, M. (2000) Characterization of Ag/Al_2O_3 de-NOx catalysts by probing surface acidity and basicity of the supporting substrate. *Phys. Chem. Chem. Phys.*, **2**, 3007–3015.

179 Chmielarz, L., Kowalczyk, A., Michalik, M., Dudek, B., Piwowarska, Z., and Matusiewicz, A. (2010) Acid-activated vermiculites and phlogophites as catalysts for the DeNOx process. *Appl. Clay Sci.*, **49**, 156–162.

180 Santhosh Kumar, M., Schwidder, M., Grünert, W., and Brückner, A. (2004) On the nature of different iron sites and their catalytic role in Fe-ZSM-5 DeNOx catalysts: new insights by a combined EPR and UV/VIS spectroscopic approach. *J. Catal.*, **227**, 384–397.

181 Kumashiro, R., Fujie, K., Kondo, A., Mori, T., Nagao, M., Kobayashi, H., and Kuroda, Y. (2009) Development of a new analysis

method evaluating adsorption energies for the respective ion-exchanged sites on alkali-metal ion-exchanged ZSM-5 utilizing CO as a probe molecule: IR-spectroscopic and calorimetric studies combined with a DFT method. *Phys. Chem. Chem. Phys.*, **11**, 5041–5051.

182 Carniti, P., Gervasini, A., and Auroux, A. (2001) Copper site energy distribution of de-NOx catalysts based on titanosilicate (ETS-10). *Langmuir*, **17**, 6938–6945.

183 Coq, B., Tachon, D., Figukas, F., Mabilon, G., and Prigent, M. (1995) Selective catalytic reduction of nitrogen monoxide by decane on copper-exchanged mordenites. *Appl. Catal. B: Environ.*, **6**, 271–289.

184 Albonetti, S., Epoupa Mengou, J., and Trifiro, F. (2007) Polyfunctionality of DeNOx catalysts in other pollutant abatement. *Catal. Today*, **119**, 295–300.

19
Surface Area/Porosity, Adsorption, Diffusion

Philip L. Llewellyn, Emily Bloch, and Sandrine Bourrelly

19.1
Introduction

Nanoporous materials are widely used in adsorption-related applications and so can be found in many domains, including catalysis, pollution control, gas separation, and storage, as well as in the fields of agriculture, pharmacy, and medicine. Adsorbents can be found in the household as water filters, stain removers, extractor hoods, alcohol tests, stoppers in medicine tubes, and even in certain capsules themselves.

This use of adsorption phenomena is not new. Indeed, the adsorption properties of porous materials have been known since Egyptian times, where carbons and clays have been applied in the purification of oils and water. Specific adsorption measurements can be dated back to the late 1700s when Fontana [1] noted that charcoal could take up several times its own volume of different gases on cooling and Scheele [2] showed that air expelled from charcoal on heating could be recovered on cooling. The concept that the amount of gas adsorbed is related to the exposed surface area can be attributed to de Saussure in 1814 [3], whereas the role of porosity was suggested by Mitscherlich in 1843 [4]. The term "*adsorption*" seems to have been introduced by Kayser in 1881 [5], whereas the wider term "sorption" (which encompasses both adsorption and absorption) was first proposed by McBain in 1909 [6]. Interesting from an experimental standpoint is that the "McBain adsorption balance" can still be found in some laboratories today.

For many, the wider interest in adsorption research dates from the First World War and the use of active carbons in gas masks. Freundlich [7] was one of the first to describe the adsorption isotherm mathematically, but it was not until the work of Zsigmondy (1911) [8], Polanyi (1914) [9] and Langmuir (1915) [10] that thermodynamically consistent theoretical models were developed. A further step in the characterization of solids was made with the introduction of the Brunauer–Emmett–Teller (BET) method in 1938 [11] (see later). Currently, the use of computer-generated models and isotherm reconstruction methods provide an excellent means to characterize solids.

However, it is the current extensive use of adsorption in industrial processes which explains why so much research effort is devoted to both experimental and theoretical

Characterization of Solid Materials and Heterogeneous Catalysts: From Structure to Surface Reactivity, First Edition. Edited by Michel Che and Jacques C. Védrine.
© 2012 Wiley-VCH Verlag GmbH & Co. KGaA. Published 2012 by Wiley-VCH Verlag GmbH & Co. KGaA.

aspects of the phenomena in play. Indeed, with respect to any adsorption-based processes, it is of importance to gain a deeper understanding of the adsorption phenomena under conditions close to those of applications. In the case of pressure swing adsorption (PSA) applications, for example, experiments can be carried out at pressures of up to around 3 MPa at 323 K, whereas for some hydrogen storage applications, experiments can be performed at pressures up to 20 MPa.

However, prior to this "process evaluation" of these nanoporous materials, it is convenient to characterize such solids simply in terms of their surface area, pore volume, and pore size. Such a characterization permits an initial screening of products or can be used to establish trends when a series of materials are under investigation. These experiments are most often carried out with gases such as nitrogen and argon at liquid nitrogen temperature (77.4 K) with instruments that are readily available commercially. Such instruments are fairly simple to use and often provide data of high quality. Nevertheless, the theoretical exploitation of these raw data is also more or less automatic and as such a "black box" which can lead to poor exploitation and misinterpreted results. The first part of this chapter therefore aims to give the reader a "practical guide" to the interpretation of adsorption data using three examples of nanoporous materials: a, NaX zeolite, an ordered mesoporous silica, SBA-15, and a metal–organic framework (MOF), MIL100Fe.

The various points that are taken on an adsorption isotherm are at thermodynamic equilibrium, which often leads one to forget that adsorption is a dynamic process. As such, it is also of interest to characterize the gas–solid system with respect to the diffusion of the gas within the pores. However, unlike adsorption, the techniques used to characterize diffusion in nanoporous materials are less readily available commercially. The second part of this chapter therefore gives some basic theory and an overview of the various different techniques to access diffusion data.

19.2
Gas Adsorption for the Characterization of Surface Area and Porosity

As mentioned above, gas adsorption can be used for the characterization of surface area and porosity in nanoporous materials. The majority of such experiments are performed with simple gases such as nitrogen, argon, and krypton at 77 K in a liquid nitrogen cryostat. Other gases (such as CO_2) and conditions (273 K for CO_2) have been proposed for porous solid characterization [12], but they are less widely used and the next few pages are therefore devoted to the use of nitrogen at 77 K for the characterization of nanoporous solids.

More detailed descriptions and complementary information concerning this section can be found elsewhere [13–18].

19.2.1
What is Adsorption, Why and How Do Gases Adsorb?

Adsorption is a general phenomenon which occurs every time that a gas or liquid (fluid) comes in contact with a solid. This fluid is retained by the superficial atoms of

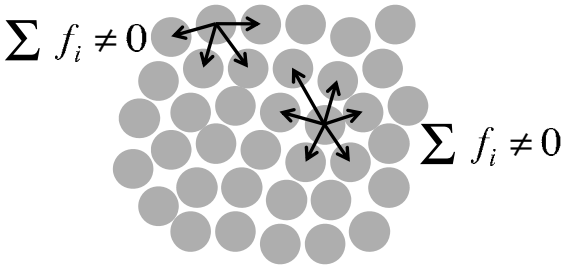


Figure 19.1 Scheme showing why surfaces will adsorb molecules. The resultant forces of a solid in the bulk will be zero, whereas a molecule on a solid surface will be stabilized by a resultant force pointing towards the bulk. This leads to a solid surface tension which can be reduced on adsorption of a gas molecule.

the solid and is concentrated at the solid surface. The term *ad*sorption indicates that this is a surface phenomenon. This should not be confused with the term *ab*sorption, which means that the fluid penetrates the solid mass.

Adsorption can be defined as the enrichment of a solid surface by an interface of liquid or gas. The fluid (gas or liquid) which is available for adsorption is named the adsorptive and the adsorbed phase is named the adsorbate. The solid on which adsorption occurs is known as the adsorbent. The word desorption indicates the liberation of fluid retained by adsorption on the solid surface.

From a conceptual point of view, surfaces will adsorb in order to reduce their surface tension. This is shown schematically in Figure 19.1. For a molecule in the bulk of a solid, the resultant forces are zero. However, for a molecule on the surface of a solid, the resultant forces point towards the bulk and as such a surface tension is created. Therefore, to reduce this resultant force, the surface of a solid will readily accept a molecule on its surface (adsorption). A more thorough treatment of the thermodynamics of adsorption can be found in the literature [13, 17, 19].

The interaction of a fluid with a solid can involve van der Waals-type forces and in this case one refers to physical adsorption or physisorption. Such forces are analogous to vapor condensation and do not change the properties of the solid or fluid. In the case where electron transfer occurs and the properties of the solid are changed, then one refers to chemical adsorption or chemisorption.

The forces involved in physisorption are such that, at the equilibrium of charge distribution, there is no transfer or sharing of electrons among the participating atoms. What is more, the individuality of each species during physisorption is maintained. In principle, it is possible to calculate these forces of interaction by determining the quantum mechanical state of the system, although in practice many approximations have to be used. For ease of conception and computation, the interactions involved in adsorption are split up, even though it is artificial to do so. The most commonly held view of the total adsorption interaction ϕ was that first proposed by Barrer [20, 21]:

$$\phi = \phi_{\mathrm{D}} + \phi_{\mathrm{R}} + \phi_{\mathrm{P}} + \phi_{\mathrm{F}\mu} + \phi_{\bar{\mathrm{F}}Q} + \phi_{\mathrm{SP}} \tag{19.1}$$

The first three terms of this expression, ϕ_D the dispersion, ϕ_R the repulsion and ϕ_P the polarization interactions, occur for every adsorbate–adsorbent system and can consequently be considered as "nonspecific" interactions. The last three terms, $\phi_{F\mu}$ the dipole, ϕ_{FQ} the quadrupole and ϕ_{SP} the self-potential interactions, are unique to the nature of the particular adsorbate–adsorbent system in question. They are therefore known as "specific" interactions. Indeed, molecules such as carbon monoxide possess a permanent dipole, carbon dioxide and nitrogen possess a quadrupole, and these polar molecules will induce specific interactions with a surface. Furthermore, any surface heterogeneities such as hydroxyls, cations, or other functionalization may also induce "specific" interactions with an adsorbing molecule.

In a general sense, the Lennard-Jones potential function can be used to obtain a global picture of physisorption [22]:

$$\phi(r) = Br^{-12} - A_{(6-12)}r^{-6} \tag{19.2}$$

which is more often written in the form

$$\phi(r) = 4\varepsilon\left[\left(\frac{\sigma}{r}\right)^{12} - \left(\frac{\sigma}{r}\right)^{6}\right] \tag{19.3}$$

where ε is the depth of the potential well, σ is the finite distance at which the inter-particle potential is zero, and r is the distance between the particles. Although this is an approximate potential, it has the features needed to describe the interactions between two closed-shell atoms, namely a strong repulsive short-range interaction, a long-range van der Waals attraction, and a potential well. The first term, r^{-12}, describes Pauli repulsion at short ranges due to overlapping electron orbitals. The second term, r^{-6}, describes van der Waals or dispersion force attraction at long ranges. Tables are available for these values [23] for different species. This function can be drawn as a plot of ϕ_i against r, as shown in Figure 19.2a.

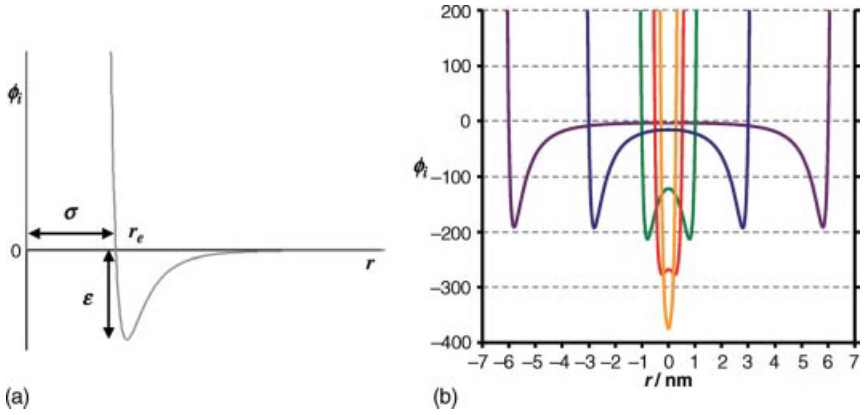


Figure 19.2 Plots of the Lennard-Jones potential function: (a) between two molecules; (b) for a molecule in a slit-shaped pore of different sizes.

The depth of the potential well describes the maximum interaction and it can be seen that as the two molecules approach each other, the attraction will increase. The 12–6 exponents used for the interaction between two atoms can be modified to 10–4 exponents can be used for the interaction of a molecule and a flat surface or to 9–3 exponents for the interaction between a molecule and a slit-shaped pore. This latter expression was used to construct Figure 19.2b. The different curves are plotted as the distance between two plates as they move closer together. It can be seen that at some point, the potentials overlap, leading to enhanced interactions within the pores. This illustrates why there are fairly strong interactions in these narrow pores, less than 2 nm in width, often termed micropores.

19.2.2
How Do We Measure and Represent Adsorption Isotherms

19.2.2.1 Different Adsorption Devices

Equilibrium adsorption measurements can be carried out using different methodologies. The most common methods employed are the manometric or volumetric method and the gravimetric method.

With *gravimetry*, it is possible to measure directly the change in weight of a solid after equilibration at various gas pressures using an adsorption balance. This method is highly accurate and well adapted to follow adsorption at ambient temperature and above provided that the buoyancy effect is well estimated or measured. However, for experiments at 77 K, this gravimetric method has some drawbacks in terms of accurate sample temperature control and measurement. This can be understood because whereas the sample should be at 77 K, the balance mechanism itself is at room temperature, which leads to significant temperature gradients. Furthermore, the sample holder is inside a tube and not in direct contact with the cryogenic bath, which again leads to variations in temperature between the sample and bath, especially for the first adsorption points which are essentially under various states of vacuum.

The *volumetric* or *manometric* method, although slightly less accurate than the gravimetric method, involves a simpler (and cheaper) experimental setup which allows, among other things, direct contact between the sample and cryostat, permitting better control of the sample temperature. The fact that adsorption is favored at lower temperatures often means that the extra accuracy obtained with gravimetry is superficial for experiments at 77 K.

The term volumetry is still widely used instead of manometry to describe modern experiments, even though there is no measurement of a change in volume. This misuse dates back to earlier experiments in which mercury was used to measure differences in the volume of the gas phase. All modern equipment uses sensitive pressure gauges. A schematic representation of a manometric device is described below and given later in Figure 19.4. Commercial devices are almost all variations on this scheme, with various means of gas introduction or removal and several pressure gauges to allow for accurate measurement of low pressures.

There exist a number of other devices which can be used to measure adsorption isotherms. A quartz microbalance can be used as an interesting method to follow

adsorption. Here, the sample is attached to an oscillating quartz crystal. The frequency of the oscillation is a function of the weight. This leads to a very sensitive measurement of the amount adsorbed. However, this method is most often used in the liquid phase. It is also possible to follow the uptake in flat thin films using ellipsometry. Here a polarized, elliptical light beam is shone on to the surface and the reflected beam is measured. This method allows the direct measurement of film thickness on a flat surface. However, this method has recently been used to follow the uptake on porous solids. Again, this method has been limited to liquid- and vapor-phase adsorption, although currently trials are being carried out to adapt this method to gas adsorption at 77 K. Further techniques such as chromatography can also give details of adsorption phenomena, although these are outside the scope of this chapter.

19.2.2.2 Experimental Protocol

The general experimental protocol is relatively simple. After weighing the sample into the measuring cell, there are essentially four steps:

- activation
- dead space volume calibration
- adsorption
- desorption.

The ideal amount of sample used for adsorption experiments depends on the approach used. For a manometric experiment, around 40 m^2 of surface is ideal. Thus, for a sample with a surface area around 500 m^2-g^{-1}, this translates to 80 mg of sample in the cell. However, for low surface area samples, this can translate to a large amount of powder in the cell, which can lead to diffusion problems in the sample bed, and for very high surface area samples, one should ensure a minimum of sample to avoid problems with sampling.

The activation, or outgassing, should ensure a defined and reproducible state of the sample prior to the experiment. Often one aims to remove any physisorbed species (contaminants, humidity, etc.) without degrading the structure. In some cases, however, one may wish to study the effect of different activation temperatures of the sample, for example, to observe the effect of sample dehydroxylation. It is recommended that a thermogravimetric analysis experiment be carried out on a small amount of sample prior to the adsorption analysis. One would therefore aim to outgas up to a temperature region where the curve is horizontal. The example in Figure 19.3, for an NaX zeolite, shows a quasi-horizontal region between 623 K (400 °C) and 1073 K (800 °C). One should also take into account that one often outgases the sample under vacuum and that the thermogravimetric analysis curve is obtained in a dry atmosphere. As a general rule, therefore, one should choose a temperature towards the start of the temperature plateau, which corresponds to 473 K (200 °C) for the NaY sample in Figure 19.3. Other samples may be less stable, as is the case for the MIL100Fe sample (Figure 19.3b). Here, the weight loss above 473 K (200 °C) corresponds to the degradation of the structure and thus, outgassing in the region between 373 K (100 °C) and 473 K (200 °C) would be recommended. As just

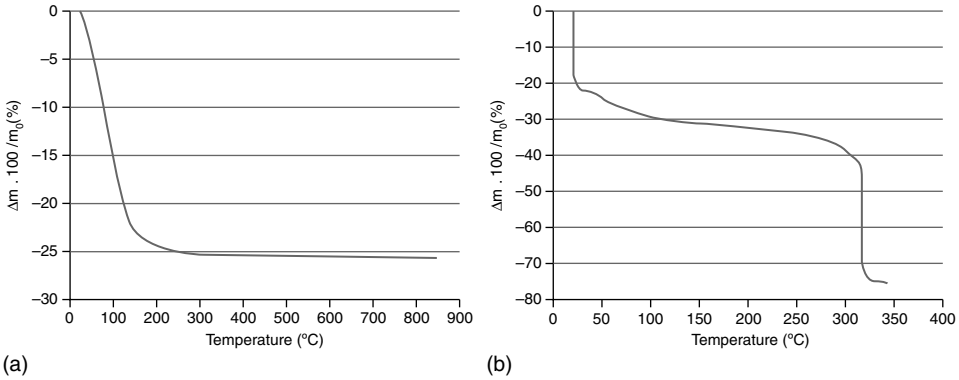


Figure 19.3 Example of a thermogravimetric analysis obtained with a 13X zeolite sample (a) and a MIL100Fe sample (b).

mentioned, the sample outgassing often occurs under vacuum, and this vacuum should be applied slowly so as not to suck up any powder into the vacuum pump. This option is now implemented in all commercial equipment. Once under vacuum, an outgassing temperature can be fixed. Again, one can look at the thermogravimetric analysis curve to see if any intermediate temperatures could be used. This can be the case when one has a significant amount of weakly adsorbed species, and leaving the sample at around 353 K (80 °C) for a while can prevent sample degradation due to the overly rapid loss of these weakly bound species. A far more elegant solution is to use a sample-controlled thermal analysis (SCTA) approach [24]. In its most appropriate form for outgassing, the heating of the sample to its final temperature is adjusted so that the vacuum pressure above the sample is maintained constant. This therefore ensures that the heating rate decelerates when physisorbed species evolve from the sample and accelerates when there is no evolution of such species. This is not often employed, although an intermediate solution can be found on some adsorption equipment in which the sample is only heated if the vacuum pressure is below a fixed limit.

After outgassing, the sample is reweighed and then placed on the adsorption manifold. A simplified schematic diagram of such a manifold is given in Figure 19.4. The experimental protocol varies more or less around the same steps. An initial evaluation of the dead space is made using helium. The dead space includes the sample cell and part of the manifold. As the different sample cells are not exactly identical and the sample volume is different for each experiment, the dead space should be determined prior to each experiment. Helium is used for this as it is considered that this gas does not adsorb. The actual measurement of the dead space using helium is similar to that for the isotherm with the adsorptive gas.

The adsorption measurement itself consists of dosing a known amount of adsorptive gas into the reference volume, V_{ref}. The reference volume is then opened to the sample volume V_{sample} and the system is followed until equilibrium between the sample and the gas is attained. Various criteria can be used to evaluate this equilibrium. One can follow the pressure above the sample and consider equilibrium

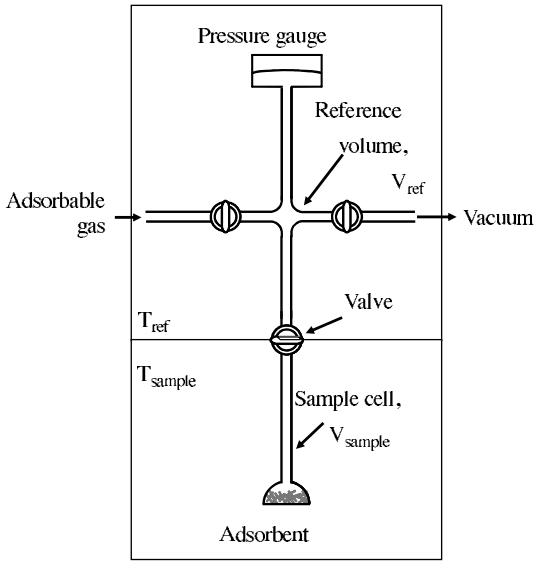


Figure 19.4 Schematic representation of a manometric device to measure adsorption isotherms. Adapted from [2].

when the pressure change is below a certain limit for a given time. In other cases, a simple time limit can be set. This equilibrium is an important part of the experiment as it is easy to misinterpret results just as a result of points taken after poor equilibrium.

For each adsorption dose, the amount of gas in the reference volume and sample volume is calculated. This amount can be calculated using the simple ideal gas law relationship or by a more complicated expression if gas nonideality has to be taken into account. Nevertheless, the departure from nonideality is small for gases at 77 K. Using the ideal gas relationship, the initial amount of gas in the system n^{i}, before the adsorption dose, is therefore

$$n^{\mathrm{i}} = n^{\mathrm{i}}_{V_{\mathrm{ref}}} + n^{\mathrm{i}}_{V_{\mathrm{sample}}} = \frac{p^{\mathrm{i}}_{\mathrm{ref}} V_{\mathrm{ref}}}{RT_{\mathrm{ref}}} + \frac{p^{\mathrm{i}}_{\mathrm{sample}} V_{\mathrm{sample}}}{RT_{\mathrm{sample}}} \tag{19.4}$$

where $n^{\mathrm{i}}_{V_{\mathrm{ref}}}$ and $n^{\mathrm{i}}_{V_{\mathrm{sample}}}$ are the initial amounts of gas in the reference and sample volumes, respectively, and $p^{\mathrm{i}}_{\mathrm{ref}}$ and $p^{\mathrm{i}}_{\mathrm{sample}}$ are the pressures in the reference and sample volumes, respectively. Note that for the initial dose, $p^{\mathrm{i}}_{\mathrm{sample}}$ is zero if the sample is outgassed under vacuum. The temperatures of the sample volume, T_{sample}, and reference volume, T_{ref}, should be taken into account in addition to the gradient in temperature between these sample and reference volumes.

A similar expression is used to calculate the final amount of gas phase, n^{f}, after adsorption equilibrium:

$$n^{\mathrm{f}} = n^{\mathrm{f}}_{V_{\mathrm{ref}}} + n^{\mathrm{f}}_{V_{\mathrm{sample}}} = \frac{p^{\mathrm{f}} V_{\mathrm{ref}}}{RT_{\mathrm{ref}}} + \frac{p^{\mathrm{f}} V_{\mathrm{sample}}}{RT_{\mathrm{sample}}} \tag{19.5}$$

Note that as the reference volume and sample volume are in communication, the measured final pressure p^{f} is the same in each term. Furthermore, for following doses

$$\frac{p^{f} V_{sample}}{RT_{sample}} = \frac{p^{i+1}_{sample} V_{sample}}{RT_{sample}} \tag{19.6}$$

Hence to calculate the amount adsorbed per dose:

$$n^{ads} = n^{i} - n^{f} \tag{19.7}$$

The amount adsorbed is then given per gram of sample for the equilibrium pressure. This pressure can be given in relation to the saturation vapor pressure p°, which is measured separately. One therefore represents the adsorption isotherm as n^{a} (in $\mathrm{mmol\,g^{-1}}$) as a function of p or p/p°. Note that most commercial equipment still represents the amount adsorbed in terms of gas volume v^{a} (in $\mathrm{cm_{STP}^{3}\,g^{-1}}$) which is not advisable as it leads to difficulties when comparing with isotherms measured using other methods (gravimetric, chromatographic, etc.). Nevertheless, it is possible to relate the amount adsorbed n^{a} (in $\mathrm{mmol\,g^{-1}}$) to the gas volume adsorbed v^{a} (in $\mathrm{m_{STP}^{3}\,g^{-1}}$) via the expression

$$n^{a}\left(\mathrm{mmol\,g^{-1}}\right) = v^{a}\left(\mathrm{cm_{STP}^{3}\,g^{-1}}\right)/22.414\left(\mathrm{cm^{3}\,mmol^{-1}}\right) \tag{19.8}$$

It can be appreciated that adsorption manometry is a fairly straightforward method. However, systematic errors can be incurred due to small errors in the reference and sample volumes. One can appreciate this as the calculation of the amount adsorbed is represented by the difference in the terms n^{i} and n^{f}, so if this difference is small, that is, n^{f} is relatively large, then the error in n^{a} can be significant. This is even more critical when the sample volume is estimated prior to the adsorption experiment via helium calibration. One assumes that helium does not adsorb on the sample, but this assumption rarely holds in the case of microporous samples. One therefore has an overestimation of the sample cell volume and an underestimation of the amount adsorbed. As with other techniques, a blank experiment with a cell without sample gives an excellent means to estimate the errors on a given apparatus.

The experiments thus give the amount of fluid retained on the surface of an adsorbent. This amount of fluid is known as the amount adsorbed and depends on the following parameters:

- the extent of the interface
- the fluid concentration (gas pressure, liquid concentration)
- the temperature.

In the case of the adsorption of nitrogen at its normal temperature of liquefaction (77.4 K), the *adsorption isotherm* (Figure 19.5) thus represents the totality of equilibrium states for pressures from zero to the saturation vapor pressure of the adsorptive. Nevertheless, it is worth bearing in mind that each isotherm is characteristic of the adsorbate–adsorbent pair under study and, as mentioned above, one should consider specificities such as gas polarity or solid surface chemistry (hydroxyls, cations, free

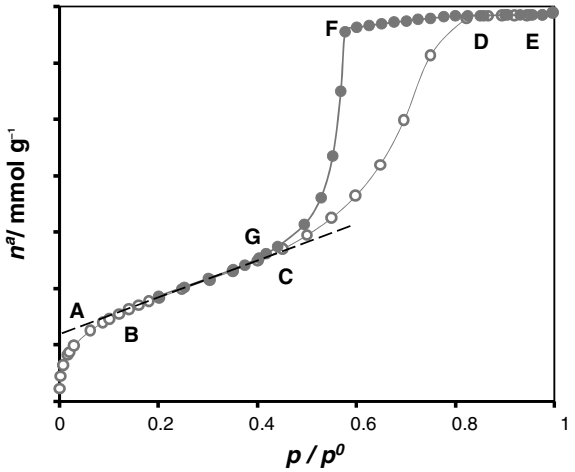


Figure 19.5 Adsorption (open circles)–desorption (closed circles) isotherm obtained with nitrogen on a porous glass at 77 K. The various points A–G are discussed in the text.

metal sites, etc.). The main points to consider, however, are the pore size and pore volume. Concerning the pore size, the terms *micropore* and *mesopore* are normally used for solids with pore openings from 0.4 to 2 nm and from 2 to 50 nm, respectively. In both cases, one often now uses the term *nanoporous* to describe these materials with pores of nanometer dimensions.

IUPAC recommends that the isotherm is shown graphically as the amount adsorbed per gram of adsorbent as a function of the equilibrium pressure [25]. If the experiment occurs below the triple point, then the amount adsorbed is plotted as a function of the relative equilibrium pressure, denoted p/p°, where p° is the saturation vapor pressure of the adsorptive. An example of an isotherm is given in Figure 19.5 with an adsorption branch and a desorption branch. There are several significant points on this isotherm which can be used to get some initial ideas about the adsorption. Point A is the back-extrapolation to $p/p^\circ = 0$ of the quasi-linear region B–C. The amount adsorbed at this point A can, in some cases, be related to the volume of micropores. Point B is the start of a quasi-linear region of the isotherm to point C. This point B is interpreted as the region where a monolayer of gas forms on the surface of the solid. In a first instance, therefore, one can take the amount adsorbed at this point to calculate an approximate surface area (see below). The quasi-linear region B–C corresponds to the formation of a multilayer. The region C–D corresponds to an upswing in the isotherm due to pore filling via capillary condensation, which is typical of mesoporous solids. The region D–E corresponds to the end of pore filling and the value of the amount adsorbed can be related to the total pore volume. Point F on the desorption branch of the isotherm corresponds to the start of pore emptying and the relative pressure at which this occurs can be related to the pore size. Point G is where the desorption isotherm rejoins the adsorption branch. There is a minimal value of this point for a given gas at a given temperature which corresponds to the point of meniscus instability. That is to say, for a given gas at a given

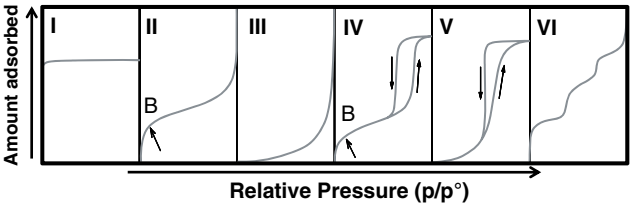


Figure 19.6 Representation of the six isotherms classified by IUPAC [25].

temperature, there is a minimal pore size where the liquid meniscus will spontaneously break, allowing complete desorption from any mesopores. For nitrogen at 77 K, this corresponds to $p/p^{\circ} = 0.42$ and for argon at the same temperature this meniscus instability occurs at $p/p^{\circ} = 0.28$.

IUPAC classifies six types of isotherm (Figure 19.6) [25], which correspond to limiting cases for nonporous solids (Type II), nonporous and non-wetting solids (Type III), mesoporous solids (Type IV), mesoporous non-wetting solids (Type V), and extremely well ordered nonporous systems such as graphite systems where adsorption occurs layer by layer (Type VI). Once again, the hysteresis loops observed for the Type IV and Type V isotherms correspond to a capillary condensation phenomena associated with the mesporosity.

Microporous solids such as zeolites usually give rise to Type I isotherms characterized by an increase in amount adsorbed at low pressure followed by a distinct plateau. The low-pressure adsorption corresponds to filling of the micropore volume.

IUPAC also considers four limiting cases for hysteresis (Figure 19.7) [25]. The H1 hysteresis loop is characterized by parallel adsorption and desorption branches and can be considered to be due to adsorption in unconnected mesopores with a relatively narrow pore size distribution. This type of hysteresis can typically be observed for MCM-41 and SBA-15 materials, for example. The H2 type of hysteresis is almost of triangular shape and is typically due to pores which are interconnected, often with smaller entrances than bodies. In such cases, one often refers to ink bottle-shaped pores. Hysteresis types H3 and H4 are due to non-rigid pore structures which can be between particle grains (H3) or flat plates (H4). The non-rigidity in each of these latter two cases is characterized by a lack of a defined flat plateau region near $p/p^{\circ} = 1$ without any overlapping adsorption and desorption branches.

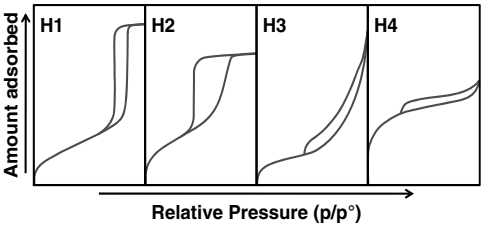


Figure 19.7 Representation of the different hysteresis loops described by IUPAC [25].

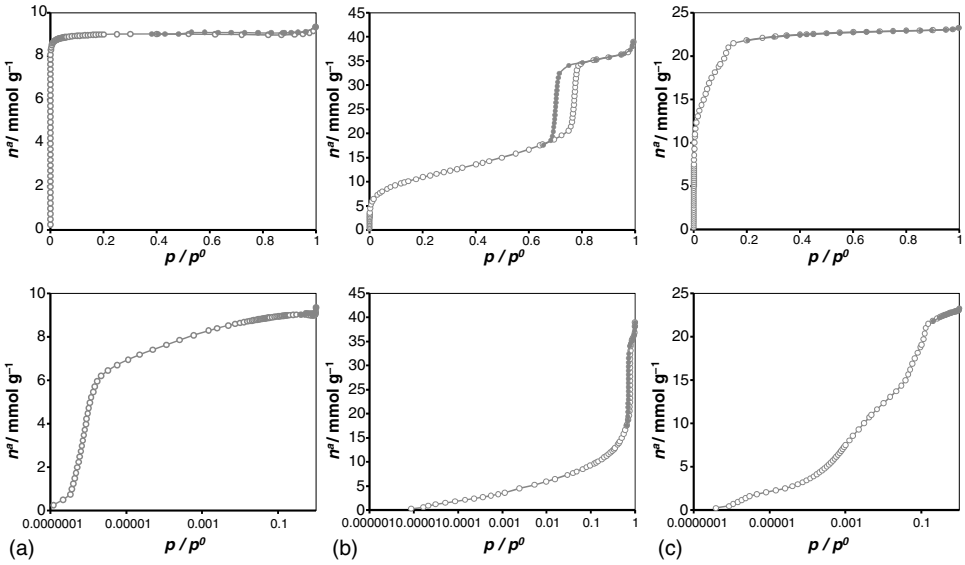


Figure 19.8 Adsorption of nitrogen at 77.4 K on NaX (a), SBA-15 (b), and MIL100Fe (c); the upper figures show the normal plots and the semi-logarithmic plots are given below. The adsorption branches are represented by the open symbols and the desorption branches by the closed symbols.

19.2.3 How Do We Interpret These Isotherms to Estimate Various Porous Solid Characteristics

19.2.3.1 Evaluation of the Isotherm Type and Shape

Examples of nitrogen adsorption–desorption isotherms at 77 K obtained with a zeolite, mesoporous silica, and MOF are given in Figure 19.8. The NaX zeolite leads to a Type I isotherm which is characteristic of a microporous sample with a sharp intake at low relative pressure followed by a "plateau" region. This can simply be interpreted by an initial pore filling followed by adsorption on the external surface of the sample. To highlight the pore filling process, one can plot the same data in semi-logarithmic form (Figure 19.8, lower curves).

SBA-15 mesoporous silica leads to an isotherm which can be classified as Type IV, which is characteristic of a gradual uptake up to $p/p^\circ = 0.7$. This gradual uptake is more visible in the semi-logarithmic plot, which, as no upswing is visible, indicates the absence of any microporosity. A sharp upswing in the isotherm is visible at around $p/p^\circ = 0.75$, followed by a final plateau region which corresponds to the filling of all the available porosity. The sharp upswing in the adsorption branch is accompanied by a hysteresis loop on desorption. This hysteresis is typical of rigid mesoporosity and can be classified as H1.

The isotherm obtained with MIL100Fe is not easily identified using the IUPAC classification. Indeed, the long plateau at p/p° above 0.2 resembles that of a Type I isotherm, although there seem to be several features at lower loadings. These features

are more readily visible in the semi-logarithmic plot and seem to correspond to adsorption in different regions. The interpretation of this isotherm is aided by a knowledge of the structure and chemistry of this solid. Indeed, this solid can contain specific adsorption sites at the iron metal center and there exist two cages of internal diameter around 2.6 and 2.8 nm. There therefore seems to an initial adsorption at $p/p^\circ = 10^{-6}$ which could be due to the interaction of nitrogen at the iron sites. There then seems to be a gradual coverage of the pore walls, followed by the completion of the filling of the pores at $p/p^\circ \approx 0.05$ and 0.12, respectively. This pore filling should not be confused with capillary condensation as both pores are too small and the isotherm is reversible in this region. Nevertheless, this isotherm highlights the fact that many isotherms are not always so readily identified using the IUPAC classification.

In each of these cases, even though the pore filling can be attributed to different phenomena (primary and secondary micropore filling, capillary condensation), the pressure at which pore filling occurs can be related to the pore size.

As mentioned above, IUPAC [25] recommends the use of nitrogen at its liquefaction temperature (77.4 K) for the characterization of porous and powder materials by adsorption. However, it can be argued that the quadrupole moment of nitrogen can interact with specific surface groups such as hydroxyls or extra-framework charge-compensating cations. Therefore, other probes such as argon and krypton are also used either at 77.4 K or at slightly higher temperatures such as 87 K, which is the liquefaction temperature of argon. Krypton is often used for the evaluation of low surface areas; however, some discrepancies occur regarding the cross-sectional area of the adsorbed molecule due to uncertainties about the adsorbed state and wetting capacity of this adsorbate at 77 K. Argon can be used as a compromise as it is a nonpolar molecule which has no specific interaction with a surface. Hence ideally it would be of interest to characterize solids with this adsorbate at 87 K. However, this is not often done owing to the expense of liquid argon. Using argon at 77 K can be of interest for probing microporosity, surface area, and small mesoporosity. However, it is not possible to characterize large mesoporosity due to the solidification of argon. Where possible, however, it is of great interest to compare the adsorption of both nitrogen and argon at 77 K due to the complementary information that can be obtained.

This can be seen in Figure 19.9 for the adsorption of argon and nitrogen in MCM-41. Two points can be noted with this comparison. First, more nitrogen is adsorbed at pressures below $p/p^\circ = 0.1$ due to the interaction of the nitrogen with the surface silanol groups in the MCM-41. A comparison of the BET surface areas of the two samples suggests a surface area of 614 $m^2\,g^{-1}$ in the case of nitrogen and 522 $m^2\,g^{-1}$ in the case of argon. Owing to the specific interaction induced by the nitrogen quadrupole, the result given by argon adsorption would seem to be more significant. This is because the diatomic nitrogen does not always sit flat on the surface but can orient itself at various angles depending on the surface chemistry. Hence it is possible to recalculate the cross-sectional area occupied by the nitrogen molecule on the mesoporous silica and a value of 0.140 nm^2 is found [26]. This value is close to that found on other silica surfaces [27–29]. The second point to note is that no hysteresis is

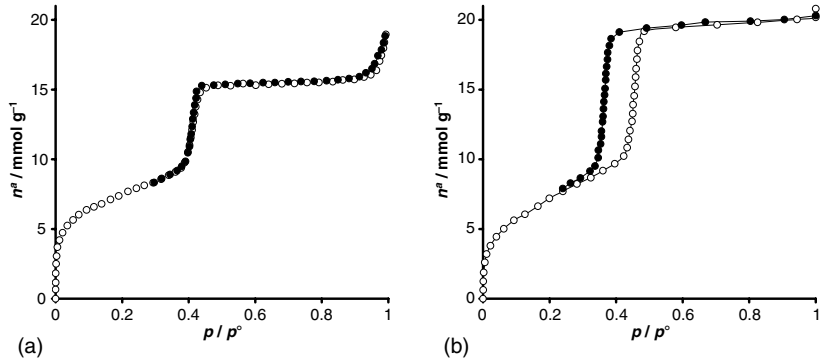


Figure 19.9 Adsorption of nitrogen (a) and argon (a) on MCM-41 at 77.4 K.

visible for the adsorption of nitrogen whereas a significant hysteresis loop is observed in the case of argon. This loop closes above the limiting pressure for argon ($p/p^\circ = 0.28$) and therefore can be used for the estimation of the pore size distribution.

19.2.3.2 Evaluation of Specific Surface Area Using the BET Model

The BET equation is commonly used for the evaluation of specific surface area. Proposed by Brunauer, Emmett, and Teller in 1938 [11, 30], the BET model is based on the assumption of multilayer adsorption on a flat surface, and it does not strictly apply to porous solids. In reality, the BET equation can correctly be used for adsorption on mesoporous solids, that is, before the onset of capillary condensation. However, for microporous solids, the BET theory does not hold. However, as the BET method for the evaluation of surface area is accepted as the standard, it is possible to apply it to microporous solids and the term "*equivalent* surface area" is used to imply that the value given is one if the adsorption process in micropores occurs in the same manner as on a planar surface.

The BET model is based on that which Langmuir proposed in 1915–1917 [10, 31]. The Langmuir model considers the limiting case of the adsorption of one monolayer of strongly adsorbed species on a flat surface. Although this model can be used to estimate surface areas, it should be not used in the case of physisorption as the model does not correspond to the phenomena in play, even though the numbers obtained are higher than those obtained with the BET model. Brunauer, Emmett, and Teller hypothesized that after the formation of a statistical monolayer, there is the possibility of forming supplementary layers. The molecules adsorbed in one layer are considered adsorption sites for the next layer, which thus allows for the adsorption of a large number of layers. The assumptions that there is only one type of adsorption site and that there are no lateral interactions between adsorbed layers are the same as those of Langmuir. Further to this, Brunauer, Emmett, and Teller added the assumption that the second and following layers are considered to have the same characteristics as the bulk fluid phase. Thus, for example, the energy of adsorption of the first layer, E_1, is considered to be different from that of further layers which are considered to adsorb with the enthalpy of liquefaction, E_L.

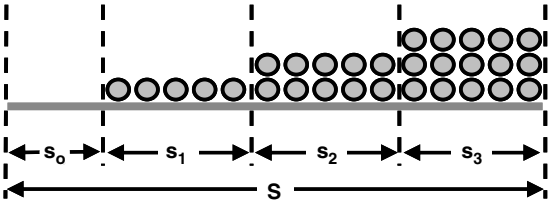


Figure 19.10 Schematic representation of an adsorbed film on an adsorbent surface.

From this, at a given point in pressure, the surface can be covered with 0, 1, 2, or more layers. The surface can thus be represented by the sum of surfaces, s_0, s_1, s_2, s_3, ... with 0, 1, 2, 3, ... layers of molecules, respectively (Figure 19.10). At each equilibrium pressure p, Langmuir theory applies between the fraction of uncovered solid s_0/S and the fraction of solid with one layer s_1/S, between the fraction of solid covered with one layer s_1/S and the fraction of solid covered with two layers s_2/S, and so on. Hence with this schema and the above hypotheses, we obtain the following expression relating the amount adsorbed n^a and the relative equilibrium pressure $x = p/p^\circ$:

$$\frac{n^a}{n_m^a} = \left(\frac{Cx}{1-x}\right)\left[\frac{1-(N+1)x^N + Nx^{N+1}}{1+(C-1)x-Cx^{N+1}}\right] \tag{19.9}$$

where n_m^a is the amount adsorbed at the statistical monolayer, N is the number of layers, and C is a constant related to the energy of adsorption, given by

$$C \approx \exp\left(\frac{E_1 - E_L}{RT}\right) \tag{19.10}$$

Most often, one considers that N tends towards infinity, which then gives the simplified expression

$$\frac{n^a}{n_m^a} = \frac{Cx}{(1-x)(1-x+Cx)} \tag{19.11}$$

It can be shown that Eq. (19.11) is valid for $N > 4$ and for $p/p^\circ < 0.35$. This equation is more often used in a the linear form:

$$\frac{p/p^\circ}{n^a(1-p/p^\circ)} = \frac{1}{n_m^a C} + \left(\frac{C-1}{n_m^a C}\right)\left(\frac{p}{p^\circ}\right) \tag{19.12}$$

The BET plot is thus a plot of $(p/p^\circ)/[n^a(1-p/p^\circ)]$ versus p/p° and one looks for a linear region below $p/p^\circ = 0.35$. The slope $[(C-1)/n_m^a C)]$ and intercept $[1/(n_m^a C)]$ can then be used to obtain the values of C and n_m^a.

The value of the monolayer capacity, n_m^a, can then be used for the calculation of the specific surface area by taking into account the equivalent area, σ_m, that the probe molecule takes up when in the monolayer. Thus the BET specific surface area of a solid is given by

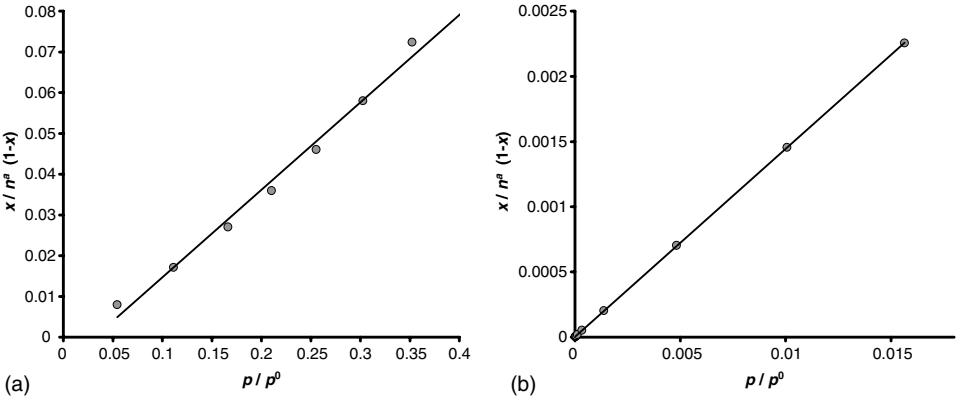


Figure 19.11 BET transformations obtained for the nitrogen isotherm on an NaX sample in the accepted region $0.05 < p/p^\circ < 0.35$ (a) and linear region $1.4 \times 10^{-5} < p/p^\circ < 0.016$ selected via the criteria noted in the text (b).

$$a_{\mathrm{BET}} = \frac{A}{m^{\mathrm{s}}} = \left(\frac{n_{\mathrm{m}}^{\mathrm{a}}}{m^{\mathrm{s}}}\right) N_{\mathrm{A}} \sigma_{\mathrm{m}} \tag{19.13}$$

As stated above, in the case of nonporous and mesoporous solids, the BET equation is valid. One often will look for a linear region in the BET plot between $p/p^\circ = 0.05$ and 0.35. In the case of microporous solids, this linear region will be found at a much lower region of p/p°, often below 0.05.

The example given in Figure 19.11 shows the adsorption of nitrogen at 77 K on the NaX sample whose isotherm is shown in Figure 19.8. Figure 19.11a shows the BET transformation in the accepted domain of validity, $0.05 < p/p^\circ < 0.35$, where it can be seen that there is no linearity in this region. Furthermore, the intercept at $p/p^\circ = 0$ is negative, which has no physical sense. To aid the identification of a linear region, a number of criteria can be used. The first, initially proposed by Rouquerol and co-workers [13, 32], is that the term $n^a(p^\circ - p)$ should increase with increasing p/p°. The BET treatment can then be validated by ensuring that the relative pressure at which the $n_{\mathrm{m}}^{\mathrm{a}}$ term is found should be within the region considered and that this relative pressure should be close to that calculated via the term $1/(\sqrt{C}+1)$. A linear region in the BET transformation can be found at lower relative pressures in the region $1.4 \times 10^{-5} < p/p^\circ < 0.016$ in which the above criteria hold (Figure 19.11b). An *equivalent* BET surface area of 685 $\mathrm{m^2\,g^{-1}}$ is thus obtained for an $n_{\mathrm{m}}^{\mathrm{a}}$ term at $p/p^\circ = 0.0048$ and $C = 42\,649$. The very high value of C is due to the strong attraction of nitrogen in this microporous solid, although this high number should not be over-interpreted.

19.2.3.3 Evaluation of the External Surface Area and Pore Volume Using the t and α_{S} Methods

The t and α_{S} methods can be used to estimate the external surface area and micropore volumes of microporous solids. In some cases, the α_{S} method can additionally be used to calculate the total surface area of microporous solids.

The *t* method of Lippens and de Boer [33] consists of a comparison of the amount adsorbed of given isotherm with the thickness of the adsorbed layer of known reference isotherm at the same relative pressure. The reference isotherm is obtained with a nonporous solid.

In this method, the thickness, *t*, of the adsorbed multimolecular layer is calculated as the sum of the number of layers, *N*, and the thickness of each layer, *l*:

$$t = Nl \tag{19.14}$$

The following hypotheses are then made:

- the adsorbed layer is assumed to be a liquid of molecular mass *M*, density ϱ^{ℓ}, and volume v^{ℓ}:

$$v^{\ell} = n^{\mathrm{a}}\left(M/\varrho^{\ell}\right) \tag{19.15}$$

- the surface $a(t)$ per gram of solid is covered by an adsorbed layer is thus given by

$$a(t) = v^{\ell}/t \tag{19.16}$$

- each molecular layer has the same thickness, *l*:

$$l = \left(M/\varrho^{\ell}\right)/N_{\mathrm{A}}\sigma \tag{19.17}$$

  where N_{A} is Avogadro's number and σ is the cross-sectional area of a single molecule of adsorptive. Thus, for liquid nitrogen at 77 K where $M = 28\,\mathrm{g\,mol^{-1}}$, $\varrho^{\ell} = 0809\,\mathrm{g\,cm^{-3}}$, and $\sigma = 0162\,\mathrm{nm^2}$, the thickness of a monomolecular layer $l = 0354\,\mathrm{nm}$.
- the number of monomolecular layers *N* in an adsorbed film can be calculated using $N = n^{\mathrm{a}}/n_m^a$, where n^{a} is measured for each relative pressure and the monolayer capacity $n_{\mathrm{m}}^{\mathrm{a}}$ is calculated using the BET method. For nitrogen at 77 K, $t/\mathrm{nm} = 0.354(n^{\mathrm{a}}/n_{\mathrm{m}}^{\mathrm{a}})$.

Hence the isotherm obtained with a nonporous adsorbent can be plotted with *t* as a function of p/p°. Lippens and de Boer [34] showed for the adsorption of nitrogen at 77 K on a number of nonporous oxides that the plots of *t* as a function of p/p° are almost identical, thus leading to a "universal" plot. A number of expressions attempt to fit this universal plot. It can be shown that of the most widely proposed, that by Harkins and Jura [34] fits the original data the closest:

$$t/\mathrm{nm} = \left[\frac{0.1399}{0.034 - \log(p/p^0)}\right]^{0.5} \tag{19.18}$$

The construction of the *t* plot is obtained by plotting n^{a} for the unknown solid as a function of *t*, as shown schematically in Figure 19.12.

Microporous and mesoporous solids lead to *t* plots similar to that shown in Figure 19.13 for NaX (a) and SBA-15 (b). It can be seen that these plots show distinct linear regions whose slope, S_t, is related to the surface area via

$$\begin{aligned} a(t) &= v^{\ell} S_t \quad \text{or} \\ a(t) &= 34.6 \times (S_t/\mathrm{mmol\,g^{-1}\,nm^{-1}}) \end{aligned} \tag{19.19}$$

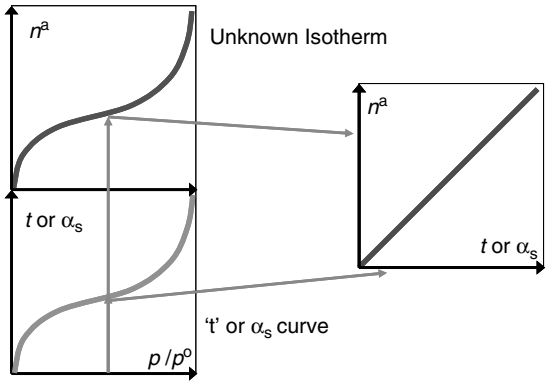


Figure 19.12 Schematic representation of the construction of the t and α_S plots.

In the case of the zeolite sample, a single linear region with a positive intercept can be observed. This can be related to an external surface area, not taking into account any microporosity. The intercept at the origin can be used to calculate the micropore volume.

In the case of the mesoporous silica, two linear regions can be distinguished. The first, denoted t_1, can be related to the total surface area although a small positive intercept could be related to a small amount of microporosity. The second linear region, t_2, occurs after the mesopore filling and so can be related to the external surface area. The difference in the values of the intercepts of t_1 and t_2 can be related to the mesopore volume.

In both of these examples an initial linear region at low t can be observed. However, any linear region that crosses the y-axis at negative n^a cannot be exploited as unphysical. To remedy this, one can use the α_S plot of Sing [35].

Sing noted a number of inconveniences in the t plot method [35]. The first is that the BET method for the calculation of the surface area is not always applicable. This is especially the case for nitrogen, which does not always take up the cross-section of 0.164 nm^2 normally assumed. The second is that the "universal" curve is not so

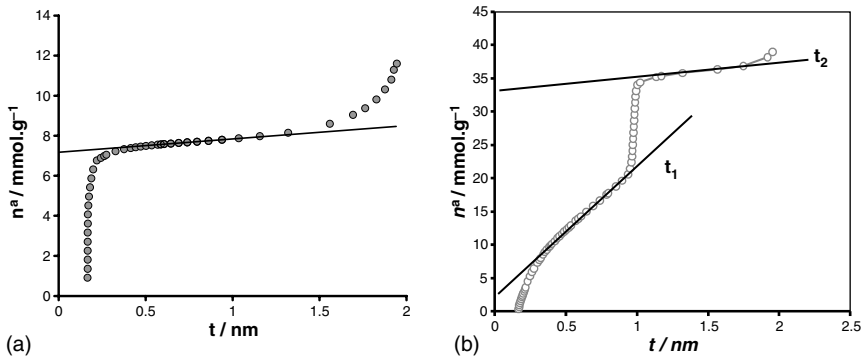


Figure 19.13 A t plot obtained from the nitrogen isotherm on NaX zeolite (a) and SBA-15 (b).

universal and one should therefore ideally compare a given adsorbent with a nonporous material of the *same chemical nature*. To overcome these points, Sing [35] proposed to modify the t method by replacing the monolayer capacity n_m^a with the value n_S^a, which is amount adsorbed on the nonporous reference at a given p/p°. To simplify the comparison, one most often takes the value at $p/p^\circ = 0.4$ as this is a region well after any micropore filling and before capillary condensation. The ratio $n^a/n_{0.4}^a$ is known as α_S. The curve of α_S versus p/p° for the nonporous reference solid is taken as the reference α_S curve. It is evident that such a curve is obtained without any hypothesis and directly relates to the chemical nature of the adsorbate–adsorbent pair under investigation. The α_S plot is thus a plot of n^a versus α_S for each value of p/p° in analogy with the t plot.

Any linear region, s_S, in the α_S plot can be related to an unknown surface, a_x, via the expression

$$a_x = \left[a_{ref}/n_{0.4(ref)}^a\right] s_S \tag{19.20}$$

where a_{ref} is the area of the reference material and $n_{0.4(ref)}^a$ is the amount adsorbed on the reference materials at $p/p^\circ = 0.4$. a_{ref} can be estimated via the BET equation and also by other suitable methods such as immersion calorimetry.

19.2.3.4 Evaluation of the Micropore Size: Horwath–Kawazoe

An estimate of micropore size can be obtained using the methodology proposed by Horwath and Kawazoe [36]. This approach was originally put forward to estimate the pore sizes of microporous carbon and further extensions are proposed for other microporous solids. However, one can question the relevance of such methodology in the case of ordered materials such as zeolites or MOFs. Nevertheless, it may be of some interest to use such methods to follow any pore size modification due to post-synthesis methods such as dealumination.

The basic methodology rests on a simple representation of the pore geometry (slit-shaped, cylindrical, etc.) as in Figure 19.14. The width of the pore, W, is given as the distance between atom centers. The interaction of a molecule inside the pore can be given, in the case of a simple slit-shaped pore, as the sum of interactions between each pore wall.

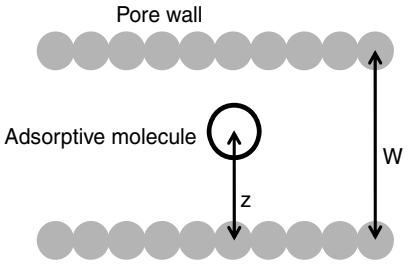


Figure 19.14 Schematic of slit-shaped micropores used as the basic assumption for the original Horwath–Kawazoe method.

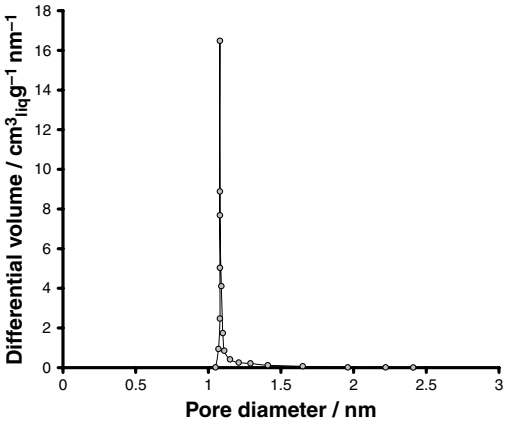


Figure 19.15 Horwath–Kawazoe method exploited for the nitrogen isotherm on NaX.

A Lennard-Jones-type expression is then used for the interaction potential ϕ of a molecule in a pore:

$$\varphi(z)_{\text{pore}} = k\left[\left(\frac{\sigma}{z}\right)^{a} - \left(\frac{\sigma}{z}\right)^{b} + \left(\frac{\sigma}{W-z}\right)^{a} - \left(\frac{\sigma}{W-z}\right)^{b}\right] \tag{19.21}$$

where k is a constant for each adsorbate–adsorbent system, σ is the interaction strength, z the distance between the adsorbed species and the first pore wall, and a and b are constants which vary with respect to the pore geometry. A simple relationship between this interaction potential and the adsorption potential, $-RT\ln(p/p^{\circ})_{\text{pore}}$, is then used to relate the relative pressure at which pore filling occurs to the pore size.

It has been shown that such an expression can be used to estimate mesopore sizes; however, in general this methodology is limited to pores smaller that 2 nm.

In the case of NaX zeolite, this methodology does not give the expected pore size (Figure 19.15). Nevertheless, as mentioned above, Horwath–Kawazoe analysis is of interest to follow pore size variations in similar solids.

19.2.3.5 Evaluation of Both Micropore and Mesopore Size Using DFT/GCMC Treatment and Isotherm Reconstruction

In recent years, the possibility of using isotherm reconstruction methods has become available in most commercial adsorption instrument software. These methods give information on pore size distribution or energy distribution. The basic methodology starts with the construction of reference isotherms obtained by mathematical modeling.

This library of reference isotherms is built taking into account variations in pore geometry (cylinder, slit, etc.) and chemical nature (silica, aluminosilicate, carbon, etc.).

The mathematical modeling most often used at the present time adopts a non-local density functional theory (DFT) approach [37–39]. More recently, other more

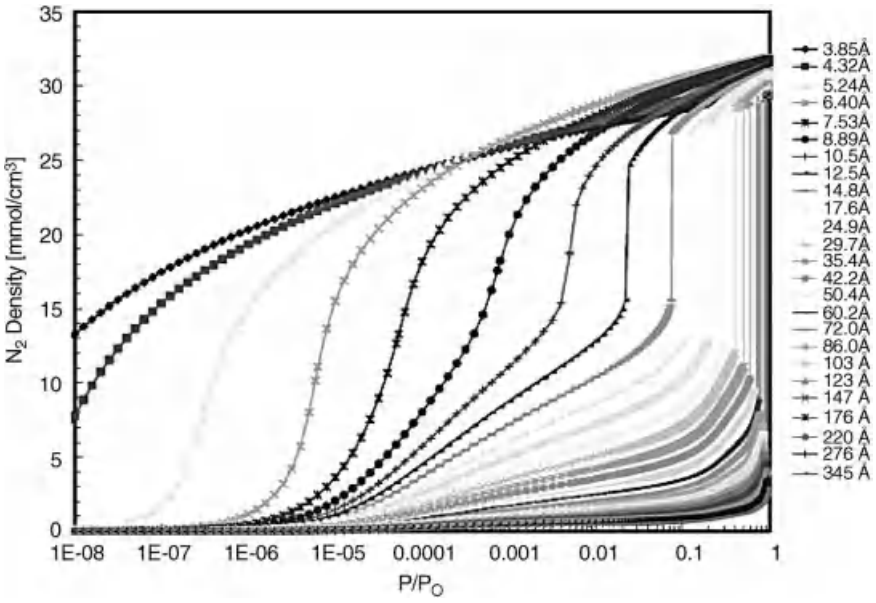


Figure 19.16 An example of a kernel of selected equilibrium adsorption isotherms of nitrogen at 77.4 K in slit-shaped pores with molecularly rough walls obtained using the quenched solid DFT [39]. The pore widths are given on the right.

elaborate simulation methods such as grand canonical Monte Carlo (GCMC) have been used to construct these reference isotherms. An example of such reference isotherms is given in Figure 19.16.

It is then possible to reconstruct the unknown "measured" isotherm from the reference isotherms using various weighting factors assuming a given pore geometry and chemical nature. One advantage of such an approach is that it is the only one that can provide a single method to analyze both microporosity and mesoporosity. The main disadvantage is that kernels of reference data are required for each type of pore structure and chemical nature. These kernels can be found in the programs provided by the instrument manufacturers. However, for novel materials such as MOFs and some disordered materials, these kernels do not yet exist, so an "exact" estimation of pore size or pore size distribution is difficult.

19.3 Diffusion in Porous Solids

The phenomenon of adsorption is often considered as being "immediate." However, in reality the adsorptive molecules need to diffuse at different levels or length scales in order to reach the adsorption site. This point is illustrated in Figure 19.17. In an adsorption process in which the solid is in the form of pellets in a column, the gas has to travel between the pellets in the column (a). The pellets themselves are often made

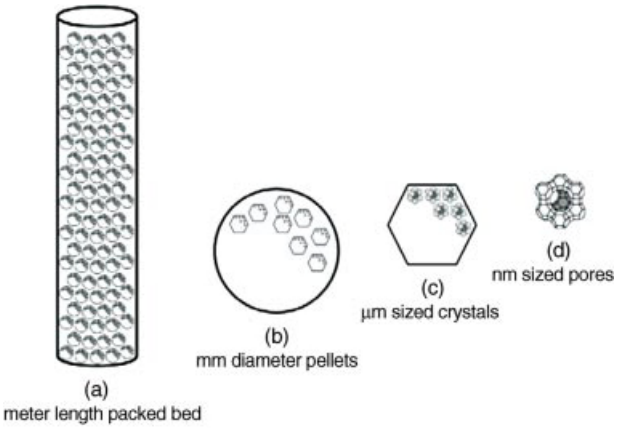


Figure 19.17 Different length scales that can be encountered in an adsorption process.

up of the active material (zeolite, MOF, etc.) and are held together by a binder (clay, alumina, resin, etc.), so the gas has to diffuse inside the pellets to reach the crystals (b). The crystals themselves may present an external diffusion barrier (c) before the gas is able to enter the pores and access any active sites (d). With these different length scales in mind, one can appreciate that the measured adsorption rate is strongly related to the diffusion of the gas molecules to the sorption sites.

This section therefore aims to give the reader the first notions of the different types of diffusion, some basic equations, and the authors' suggestions for the most significant methods for following diffusion. Further reading can be found in a number of specialized articles and books, notably [40].

19.3.1
Some Notions of Diffusion

Diffusion itself can be considered as the movement of molecules through random motion (of Brownian motion) from regions of high concentration to those of lower concentration. To be more exact, one should consider this movement in terms of a gradient in chemical potential rather than concentration. The diffusion coefficient can thus be defined with Fick's first law:

$$J = -\frac{D(q)\partial q}{\partial z} \quad \text{or} \quad J = -B(q)q\frac{\partial \mu}{\partial z} \tag{19.22}$$

where J is the diffusion flux, q the concentration, z the distance, and μ the chemical potential. The *transport diffusivity, D*, can be related to the mobility, B, via the Darken equation:

$$D(q) = B(q)RT\frac{\mathrm{dln}p}{\mathrm{dln}q} = \frac{D_0(q)(\mathrm{dln}p)}{\mathrm{dln}q} \tag{19.23}$$

where D_0 is the corrected transport diffusivity.

One can also consider the case of *self-diffusivity*, where there is no concentration gradient. It is possible to follow self-diffusion with a tracer molecule and as such define a tracer diffusivity which describes the migration of gas molecules in a uniform concentration. Tracer diffusivity (***D***) can be defined by an equation analogous to Fick's first law, although it is also possible to use the Einstein equation:

$$D = \frac{1}{2n}\frac{\left(\overline{z^2}\right)}{t} \tag{19.24}$$

where n is the dimensionality considered and $\overline{z^2}$ is the mean square displacement over time t.

Such notions become less evident when considering the case of diffusion inside highly confined systems such as in microporous structures. One can use the term of single-file diffusion in the case of zeolites where one assumes a mechanism of steps of equal spacing between adjacent sites. The main difference between this type of diffusion mechanism and that of diffusion in the bulk is that the mean square displacement increases in proportion to the square root of the observation time in the case of single-file diffusion rather than to the observation time itself in the case of bulk diffusion.

19.3.2
Experiments Allowing the Measurement of Diffusion Constants

There are a large variety of experiments that can be used to follow the diffusion inside porous systems [40]. Simple approaches such as following the gravimetric uptake with a stepped change in pressure can give an idea of the diffusion parameters but cannot be used to give absolute values, notably due to the problems of heat effects associated with the adsorption itself.

However, there seems to be a certain consensus in the literature that the following methods can give meaningful information about the diffusion of molecular species. Note that single-molecule spectroscopy is treated separately in Chapter 14.

19.3.2.1 Pulsed Field Gradient Nuclear Magnetic Resonance (PFG NMR)

It is possible to use nuclear magnetic resonance (NMR) to gain information about the diffusion of molecules. Here, one uses relaxation analysis from the magnetic resonance times. To do this, field gradient pulses are made over short periods of time. Pulsed field gradient (PFG) NMR analysis has benefited greatly from the relatively recent improvement in the sensitivity of signal detection, which has enabled users to observe nuclei other than the standard proton. Indeed, reports have demonstrated the use of such methods to follow multicomponent adsorption.

PFG NMR is a nonintrusive technique and it is possible to obtain information about molecular migration on several different levels, between crystallites, inside pores, and transport resistances due to surface barriers. It is also possible to work under equilibrium and nonequilibrium conditions. More information on this method can be found elsewhere [40].

19.3.2.2 Quasi-Elastic Neutron Scattering

Large neutron scattering facilities can be used for diffusion studies. In these facilities, it is often possible to find time of flight (TOF) and backscattering (BS) spectrometers. In some cases, it is also possible to find neutron spin echo (NSE) facilities. An advantage of the NSE technique is the decoupling of the monochromator from the energy resolution, which ensures that a broad wavelength distribution can be used. This in turn allows a very large range of characteristic times to be studied, from femtoseconds to microseconds.

In terms of distances, it is possible to explore from the ångstrom level to around 100 Å, which allows elementary jumps in single-file diffusion to be explored and also Fickian motion. Furthermore, it is possible to compare results directly with PFG NMR and also with molecular dynamics simulation.

Incoherent neutron scattering is used to obtain self-diffusivities (D_s), which can be compared with PFG NMR. Coherent scattering, however, can be used to follow transport diffusivity (D_t). These experiments are most often performed at equilibrium, eliminating any heat effects related to adsorption. In some cases, the scattering is both coherent and incoherent, where it can be possible to estimate both D_s and D_t.

19.3.2.3 Zero Length Column (ZLC)

The zero length column (ZLC) method is one of a series of macroscopic methods that can be used to obtain information about molecular diffusion. These other methods include uptake rate measurements, chromatographic measurements, TAP (temporal analysis of products), and frequency response. All of these measurements are dynamic or nonequilibrium and as such heat effects generated during adsorption of the probe species have to be taken into account. The interest in the ZLC method is that very small amounts of sample are used, hence these heat effects can be controlled.

The ZLC method can be considered as a chromatographic desorption method from an infinitesimally small column. A small amount of sample is placed as a single layer between two disks in order to minimize heat and mass transfer. The sample is pre-equilibrated with the sorbent and it is the desorption into a neutral carrier stream which is followed. Transport diffusivities are thus obtained. It is possible to estimate self-diffusivities using the tracer ZLC method, in which a mixture of deuterated and protonated molecules is used.

In many cases, the system can be considered isothermal, avoiding the heat effects observed with many other macroscopic methods, although this has to be checked in the case of strongly adsorbed species. A number of parameters can be varied, including flow rate, vector gas, and partial loading. Therefore, via an astute variation of these parameters, meaningful experiments can be produced which can lead to information about intra-crystalline diffusion and surface barriers, for example.

19.3.2.4 Optical Impedance Spectroscopy

It is possible to use spectroscopic techniques such as infrared (IR) spectroscopy or IR microscopy to follow molecule uptake inside crystals of minimum size around $40 \times 40\,\mu m$. Here, uptake and desorption curves can be attained. The interest in such

methods with respect to gravimetric uptake curves, for example, is that it is possible to follow different species and so follow coadsorption or counter-diffusion.

Optical impedence spectroscopy has been developed relatively recently. This method relies on the use of fairly large single crystals and, again, uptake or desorption curves can be obtained. In this method, a light beam is split with one part focused through the crystal and the other, reference beam passing through the atmosphere. The optical density changes depend on the concentration of gas molecules and difference curves can thus be obtained. As for the IR methods, crystals of minimum size of around 40×40 μm are required and a spatial resolution of 0.5×0.5 μm can be obtained. It is therefore possible to follow the relative uptakes across the crystals in different sections to further understand molecular loading at different points with time. It is thus possible to follow one-dimensional uptake in rectilinear channels but also the differences in uptake rate of molecules through different channel type in three-dimensional pore structures. Studies have highlighted surface barriers and also the effect of internal dislocations or other channel defects.

These methods are of great interest for understanding the diffusion mechanisms inside these crystals, but are still limited to slowly diffusing species such as hydrocarbons.

19.4 Conclusion

This chapter has aimed to give the reader the basic ideas of how adsorption can be used to characterize porous solids. Related to the mechanisms of adsorption is the transport of molecules to the adsorption sites, and some initial pointers have been given related to diffusion.

Although this chapter relates well to most nanoporous solids, in many areas of research there are specific cases in which it is essential to combine the above-mentioned methods with complementary characterization techniques. This has historically been the case for the adsorption of simple molecules on well-defined graphite, where two-dimensional epitaxial phases are formed to give rise to Type VI isotherms [41, 42]. Similar, well-ordered phases have equally been observed with the pure silica zeolite silicalite-1. Here, gases such as nitrogen and carbon monoxide show two successive well-ordered phases [43], and other gases (argon, oxygen, krypton) equally show one well-ordered phase [44]. In these cases, one often uses the term *commensurate phases* when the adsorbed species seem to be strongly influenced by the pore structure. The phase transitions associated with this adsorption are extremely well highlighted with direct measurements of the energies of adsorption using calorimetry. The structures have been determined using diffraction methods, often on large-scale facilities such as synchrotron X-ray diffraction and neutron scattering.

The family of metal–organic frameworks (MOFs, COFs, ZIFs. etc.) provide a huge challenge to those interested in their characterization and evaluation with respect to gas separation and storage. This is for several reasons, including the fact that the

surface energy of the organic parts of these materials is not taken into account in the DFT or GCMC models (Section 19.2.3.5). Furthermore, an interesting feature of some MOFs is their very large flexibility during gas adsorption [45–48]. This again poses some interesting problems for their characterization, requiring, again, the use of complementary techniques such as calorimetry and X-ray or neutron diffraction. Other techniques have also been used successfully to characterize the host–guest interactions in this fascinating family of materials. Indeed, spectroscopic methods (IR, UV, etc.) have been used to explore adsorption on specific sites, Mössbauer spectroscopy has been used to follow the variation in valence of the metal center, and all of these experimental methods are complemented by various modeling approaches (*ab initio*, DFT, Monte Carlo, molecular dynamics, etc.).

In conclusion, the majority of materials can be characterized in terms of available surface area with the BET method, external surface area and pore volume with the *t* method, and pore size distribution with the DFT/GCMC isotherm reconstruction approaches. Each of these methods comes with a series of assumptions and it is therefore impossible to consider the values obtained as absolute. In some cases, it is of interest to combine adsorption measurements with various *in situ* complementary techniques.

References

1 Fontana, F. (1777) *Mem. Mat. Fis. Soc. Ital. Sci.*, **1**, 679.
2 Scheele, C.W. (1780) *Chemical Observations and Experiments on Air and Fire*, translated by J. R. Forster, with additions by R. Kirwan and J. Priestley, printed for J. Johnson, London.
3 de Saussure, N.T. (1814) *Gilbert's Ann. Phys.*, **47**, 113.
4 Mitscherlich, E. (1843) *Pogg. Ann.*, **59**, 94.
5 Kayser, H. (1881) *Wied. Ann.*, **14**, 451.
6 McBain, J.W. (1909) *Philos. Mag.*, **18**, 916.
7 Freundlich, H. (1906) *Z. Phys. Chem., Stoech. Verwandt.*, **57**, 385.
8 Zsigmondy, R. (1911) *Z. Anorg. Chem.*, **71**, 356.
9 Polyani, M. (1914) *Ver. Dtsch. Phys. Ges.*, **16**, 333.
10 Langmuir, I. (1915) *Phys. Rev.*, **6**, 79.
11 Brunauer, S., Emmett, P.H., and Teller, E. (1938) *J. Am. Chem. Soc.*, **60**, 309.
12 Rodriguez-Reinoso, F. and Molina-Sabio, M. (1998) *Adv. Colloid Interface Sci.*, **76**, 271.
13 Rouquerol, F., Rouquerol, J., and Sing, K.S.W. (1999) *Adsorption by Powders and Porous Solids: Principles, Methodology and Applications*, Academic Press, London.
14 Gregg, S.J. and Sing, K.S.W. (1982) *Adsorption, Surface Area and Porosity*, 2nd edn., Academic Press, London.
15 Breck, D.W. (1974) *Zeolite Molecular Sieves*, John Wiley & Sons, Inc., New York.
16 Yang, R.T. (2003) *Adsorbents: Fundamentals and Applications*, John Wiley & Sons, Inc., Hoboken, NJ.
17 Ruthven, D.M. (1984) *Principals of Adsorption and Adsorption Processes*, John Wiley & Sons, Inc., New York.
18 van Bekkum, H., Flannigen, E.M., Jacobs, P.A., and Jansen, J.C. (eds.) (2001) *Introduction to Zeolite Science and Practice*, 2nd edn., Elsevier, Amsterdam.
19 Gibbs, J.W. (1877) *Collected Works*, Longmans Green, New York.
20 Barrer, R.M. (1966) *J. Colloid Interface Sci.*, **21**, 415.
21 Barrer, R.M. (1978) *Zeolites and Clay Minerals as Sorbents and Molecular Sieves*, Academic Press, London.
22 Lennard-Jones, J.E. (1937) *Physica (Eindhoven)*, **4**, 941.

23 Hirschfelder, J.O. and Crowell, A.D. (1962) *Physical Adsorption of Gases*, Butterworths, London.

24 Rouquerol, J. (1989) *Thermochim. Acta*, **144**, 209.

25 Toft Sorensen, O. and Rouquerol, J. (2003) *Sample Controlled Thermal Analysis*, Kluwer, Dordrecht.

26 Sing, K.S.W., Everett, D.H., Haul, R.A.W., Moscou, L., Pierotti, R.A., Rouquerol, J., and Siemieniewska, T. (1985) *Pure Appl. Chem.*, **57**, 603.

27 Llewellyn, P.L., Sauerland, C., Martin, C., Grillet, Y., Coulomb, J.-P., Rouquerol, F., and Rouquerol, J. (1997) *Characterisation of Porous Solids IV, Special Publication 213*, Royal Society of Chemistry, Cambridge, p. 111.

28 Rouquerol, J., Rouquerol, F., Peres, C., Grillet, Y., and Boudellal, M. (1979) in *Characterisation of Porous Solids* (eds. S.J. Gregg, K.S.W. Sing, and H.F. Stoeckli), Society for Chemical Industry, London, p. 107.

29 Ismail, M.K. (1992) *Langmuir*, **8** (2), 360.

30 Jelinek, J.L. and Kovats, E. (1994) *Langmuir*, **10** (11), 4225.

31 Brunauer, S. (1945) *The Adsorption of Gases and Vapors*, Princeton University Press, Princeton, NJ.

32 Langmuir, I. (1917) *Proc. Natl. Acad. Sci. U. S. A.*, **3**, 141.

33 Rouquerol, J., Llewellyn, P., and Rouquerol, F. (2006) in *Characterization of Porous Solids VII* (eds. P.L. Llewellyn, J. Rouquerol, F. Rodriguez-Reinoso, and N.A. Seaton), Studies in Surface Science and Catalysis, vol. **160**, Elsevier, Amsterdam, p. 49.

34 Lippens, B.C. and de Boer, J.H. (1965) *J. Catal.*, **4**, 319.

35 Harkins, W.D. and Jura, G. (1944) *J. Am. Chem. Soc.*, **66**, 1362.

36 Sing, K.S.W. (1968) *Chem. Ind. (London)*, 1520.

37 Horwath, G. and Kawazoe, K. (1983) *J. Chem. Eng. Jpn.*, **16**, 470.

38 Lastoskie, C., Gubbins, K.E., and Quirke, N. (1993) *J. Phys. Chem.*, **97**, 4786.

39 Jagiello, J.Z. and Tolles, E.D. (1998) in *Fundamentals of Adsorption 6* (ed. F. Meunier), Elsevier, Amsterdam, p. 629.

40 Neimark, A.V., Lin, Y., Ravikovitch, P.I., and Thommes, M. (2009) *Carbon*, **47**, 1617.

41 Karge, H.G. and Weitkamp, J. (eds.) (2008) *Adsorption and Diffusion*, Springer, Berlin.

42 Thomy, A. and Duval, X. (1970) *J. Chim. Phys.*, **67**, 110.

43 Rouquerol, J., Partyka, S., and Roquerol, F. (1977) *J. Chem. Soc., Faraday Trans. 1*, **73**, 306.

44 Llewellyn, P.L., Coulomb, J.-P., Grillet, Y., Patarin, J., Lauter, H., Reichert, H., and Rouquerol, J. (1993) *Langmuir*, **9**, 1846.

45 Llewellyn, P.L., Coulomb, J.-P., Grillet, Y., Patarin, J., André, G., and Rouquerol, J. (1993) *Langmuir*, **9**, 1852.

46 Bourrelly, S., Llewellyn, P.L., Serre, C., Millange, F., Loiseau, T., and Férey, G. (2005) *J. Am. Chem. Soc.*, **127**, 13519.

47 Llewellyn, P.L., Maurin, G., Devic, T., Loera-Serna, S., Rosenbach, N., Serre, C., Bourrelly, S., Horcajada, P., Filinchuk, Y., and Ferey, G. (2008) *J. Am. Chem. Soc.*, **130**, 12808.

48 Bourrelly, S., Moulin, B., Rivera, A., Maurin, G., Devautour-Vino, S., Serre, C., Devic, T., Horcajada, P., Vimont, A., Clet, G., Daturi, M., Lavalley, J.C., Loera-Serna, S., Denoyel, R., Llewellyn, P.L., and Ferey, G. (2010) *J. Am. Chem. Soc.*, **132** 9488.

49 Salles, F., Maurin, G., Serre, C., Llewellyn, P.L., Knofel, C., Choi, H.J., Filinchuk, Y., Oliviero, L., Vimont, A., Long, J.R., and Ferey, G. (2010) *J. Am. Chem. Soc.*, **132**, 13782.

Part Three
Characterization of the Fluid Phase (Gas and/or Liquid)

Characterization of Solid Materials and Heterogeneous Catalysts: From Structure to Surface Reactivity, First Edition.
Edited by Michel Che and Jacques C. Védrine.
© 2012 Wiley-VCH Verlag GmbH & Co. KGaA. Published 2012 by Wiley-VCH Verlag GmbH & Co. KGaA.

20
Mass Spectrometry

Sandra Alves and Jean-Claude Tabet

20.1
Linked Atom Theory and the Mass Spectrometry Stories: the Premises of Modern Mass Spectrometry Technology

Mass spectrometry (MS) is a spectroscopic method that allows the molecular mass determination mass of representative parts of a sample, through gas-phase ion formation. Today, MS is a well-suited method in various fields of physics, organic and inorganic chemistry, analytical chemistry, the materials industry, environmental and forensic areas, pharmaceutics, and life sciences. The analytical power of today's MS can be traced to its historical instrumental development, with the first experiments dating from the late nineteenth century. Initial studies in MS were motivated by the need to answer fundamental concepts in physics, for example, the resolution of an adequate model for describing atoms.

The first studies to elucidate the constitution of atoms were carried out in 1886 by E. Goldstein, who studied the stream formed in a discharge lamp with reduced pressure of gas. He called these cathode rays "canal rays." Eleven years later, J.J. Thomson (awarded the Nobel Prize in Physics in 1906), who worked at the Cavendish Laboratory, Cambridge University, demonstrated that these rays are constituted by negatively charged "corpuscules," as he called these particles. He proved that the canal ray deviated when it was subjected to a magnetic field and later to an electric field. Next, the combination of electric (E) and magnetic (B) coaxial fields, first developed by W. Wien (awarded the Nobel Prize in Physics in 1911), was further improved by J.J. Thomson, who measured the e/m ratio of these cathode rays [note that the elementary charge is no longer considered in mass spectrometry and only an integer, the z value, characterizes the number of charge(s) on ions characterized by the m/z ratio]. He found a corpuscule mass 2000 times smaller than that of the hydrogen ion (considered, at that time, to be the smallest particle). This was the first experimental evidence of electrons and Thomson described the atom theory with a *plum pudding* model in which the electrons are assumed to be in an environment of positive charges. Later, this model was ruled out since the positive charges are concentrated in the nucleus whereas the electrons orbit around the nucleus. Nevertheless, these preliminary experiments initiated the evolution of MS technol-

Characterization of Solid Materials and Heterogeneous Catalysts: From Structure to Surface Reactivity, First Edition. Edited by Michel Che and Jacques C. Védrine.
© 2012 Wiley-VCH Verlag GmbH & Co. KGaA. Published 2012 by Wiley-VCH Verlag GmbH & Co. KGaA.

ogy at the end of the nineteenth century, which was intimately linked to the discovery of the characteristics and properties of atoms.

Subsequently, superimposed E and B coaxial fields were used to measure the e/m ratio of positively charged atomic ions. Thomson demonstrated that the stream of ionized gas impacting on a photographic plate displays a parabolic flight path. Most important, he showed that the parabola picture recorded on a photographic plate is specific to the gas under study. The parabolic trace profile is defined by the relation $x^2/y = ke/m$ (where k is a constant, e/m is the charge to mass ratio of the corpuscule, and x and y are coordinates that define the orthogonal plane to the incident ion beam). This first mass "spectrograph" was applied in 1907 to measure the e/m value of neon ions with a resolving power of 130 [defined as $m/\Delta m$, where m is the ion mass and Δm is the full width at half-maximum height of the mass spectral peak (except for sector instruments, where Δm is measured at 10% height)] [1]. Later, his assistant, F.W. Aston (awarded the Nobel Prize in Chemistry in 1922), proved the existence of ^{20}Ne and ^{22}Ne isotopes by detection of two parabola traces and clarified the isotope notion (introduced by F. Soddy) with the study of other atoms. Aston developed a higher performance vacuum pumping system and, in 1919, a new mass spectrometer concept in which the electric and magnetic fields are arranged in a consecutive fashion, separated by a field-free region, leading to an improved resolution power of 1300. With this instrument, he measured more accurately the atomic mass of the element hydrogen (1922) and both the masses and relative abundances of 53 stable elements associated with their own isotopes [2].

New mass spectrographs were designed, by A.J. Dempster [3], who developed a magnetic sector instrument with 180° angle deflection associated with several slits and a new spark source technique (1918), and by A.O. Nier, who improved ion detection by creating an electrometer based upon ion bombardment at the surface, and also a new 60° magnet sector analyzer. These instrumental developments allowed the mass and relative abundance determinations of heavier atomic isotopes with a high resolving power. For example, in 1939, Nier published measurements of the relative abundance of the isotopes of uranium (e.g., ^{238}U/^{234}U with a 17 000:1 ratio) [4]. It must be emphasized that the strong development of MS was pushed in the 1930s and, above all, during the Second World War, by the Manhattan project, which was a political effort, led by the United States, that resulted in the development of the first atomic bomb. E. O. Lawrence built a new MS instrument based upon "electromagnetic isotope separation," called the Calutron, that is especially suited to collect large quantities of separated uranium isotopes. Additional war efforts in the petroleum industry concerning, for example, fuel and rubber production, also motivated innovations in MS technology, particularly with respect to mass analyzers.

First, different types of E–B sector arrangements were proposed with different angle sector analyzer configurations for the ion beam pathway, such as (i) Mattauch–Herzog and (ii) Nier–Johnson instruments, allowing improved resolution. Interestingly, using these "double" instruments, the presence of metastable peaks was evidenced, that is broad peaks (which may have a composite structure) detected in the mass spectrum at non-integer mass values. They result from unimolecular ion dissociation with lower kinetic energy, which took place in the second field-free

region (between the *E* and *B* fields) [5]. These experimental observations constitute the premises of tandem mass spectrometry (MS/MS) and of collision-induced dissociation (CID) (see below) processes as the activation method [6, 7] for gas-phase ion fragmentations. This drove extensive fundamental work [8, 9] on ion unimolecular dissociations. The theoretical description of these reactions was based on the quasi-equilibrium theory of Rosenstock *et al.* [10] (1952), which describes the rate constant by the use of transition-state properties and the activation energy E_0 (similar to RRKM theory). A decisive experimental study was carried out by Haddon and McLafferty which demonstrated the role of the E_{int} factor in the rearrangement processes [11]. This paper provided a systematic electron ionization (EI) mass spectral interpretation based on both thermochemistry and kinetic aspects and also on the rules of organic chemistry. Subsequently a major thrust was made into the structural elucidation of organic molecules by MS/MS and consequently into new combined *E* and *B* field scanning modes [12–14] (called linked scans), allowing such MS/MS experiments by (a) product ions of a selected parent ion, (b) precursor ions of one selected fragment ion, and (c) parent ions able to release the same neutral species, all processes occurring into the first field-free region of a double sector *E*/*B* instrument. Alternative keV kinetic energy ranges of collisions during CID were further developed for structural elucidation [15].

Finally, efforts were made to build new instruments with easier maintenance and lower cost and size. Mass analyzers based upon electric fields such as quadrupolar (Q) filters (and triple quadrupole, QqQ [16, 17]) and ion traps [16] (IT) considered as bench-top instruments were proposed. In parallel, mass analyzers based upon field-free scanning modes, that is, time-of-flight (TOF) instruments, were developed as stand-alone instruments [18, 19] or in double instruments [20].

In fact, an ion's mass-to-charge ratio in a TOF-MS instrument is determined via a time measurement of the ion's flight path into a field-free region. For that purpose, ions are accelerated by a fixed electric field. The accelerated ions have the same kinetic energy, meaning a velocity dependent on the mass-to-charge ratio. However, actual high-resolution TOF instruments largely evolved from the earlier versions described by Stephens in 1946 [18] and by Cameron and Eggers [21] in 1948. Instrumental developments began in 1955, with the work of Katzenstein and Friedland [22], who introduced (a) pulsed axial electron beam injection into the source and (b) integration of the resolved ion current from several consecutive cycles thanks to a gated ion detector. Important instrumental improvement was offered around the same time by Wiley and McLaren [23], who proposed a new time-lag focusing technique source allowing a two-step ion acceleration, which strongly diminishes (a) the initial ion spatial dispersion and (b) the kinetic energy spread of the ions (responsible for peak broadening and low resolving power). A final and decisive innovative system for TOF performance was proposed by Mamyrin *et al.* [24]. They corrected the lack of resolution of TOF-MS by using a reflectron, that is, an electrostatic mirror (ReTOF/MS), which reflects the ion beam towards the "reflectron" detector, and concomitantly corrects the kinetic energy distribution due to the initial velocity spread and to the kinetic energy release of metastable fragmentations into the flight tube. Additionally, the neutral species are separated, which

also improves the peak resolution. By this means, a resolving power of 3500 is available for an m/z 1300 ion. Finally, this high-resolution mass analyzer was coupled, at the end of the 1970s, with various desorption/ionization techniques based upon pulsed ion beam formation such as plasma desorption mass spectrometry (PDMS), secondary ion mass spectrometry (SIMS) and LD techniques [25, 26]. Today, all commercial TOF instruments possess a reflectron (or double, triple reflectron) systems. This modified pulsed ion injection system was implemented 30 years later in the infrared (IR) laser desorption (LD) ionization method [27], where the desorbed ions under laser irradiation are stored for a few microseconds in the source prior to being accelerated with a high voltage of several kilovolts. In 1995, Vestal [28] applied a similar system in an ultraviolet (UV) matrix-assisted laser desorption/ionization (MALDI)-TOF instrument for the analysis of high-mass molecules (up to 2000) and a resolving power of 4000 was achieved for peptide ions.

Fundamental work aimed at understanding ion–molecule reactions also promoted the development of ion trapping devices. Historically, based on the cyclotron principle as previously introduced, Hipple and co-workers [29] built a new MS system called an omegatron to obtain higher resolution and mass accuracy. They measured the ion cyclotron resonance (ICR) frequency of the proton from its spin precessional frequency in the B field. They calculated the proton mass to the electron mass ratio as $M_p/m_e = 1836.12 \pm 0.05$ (compared with the earlier result of 2000 obtained by J.J. Thomson. The ICR concept was particularly studied by Beauchamp [30], who explained how a charged particle remains in orbital motion around of a B field axis. This orbital ion motion is characterized by a particular angular frequency called the cyclotron frequency. If an alternative electric field is applied at the same frequency to that of the ions, it results in an increase in velocity and orbit radius [31]. The absorption can be detected by using a marginal oscillator receptor and, thus, the frequency can be accurately determined, allowing the calculation of the m/z value. This system was mainly applied for the study of ion–molecule reactions [32, 33]. McIver reported a resolving power of 5000 for ions formed in EI and stored in an ICR cell for 0.10 seconds, before mass analysis [34]. More revolutionary, by analogy with NMR spectroscopy, Comisarow and Marshall [35] demonstrated the advantage of analyzing ion cyclotron frequencies by Fourier transform treatment. Today, this type of mass analyzer provides the highest available resolution of up to 20 million for reserpine ions at m/z 609 with the use of a 7 T magnet with an infinite cell (see below) [36].

Alternatively, instead of using magnetic and electric field combination just an electric field can be applied, providing either quadrupolar or linear fields, in which a stable ion motion, is obtained characterized by a pseudo-potential well of harmonic shape. Two analytical solutions appear when the ion is in resonance in a quadrupole field: either it can emerge from the field (quadrupole filter principle) or it is stored in the field (3D ion trap). This double concept was introduced by Paul and Steinwedel in 1953 [16]. It took a long time to develop both the quadrupole filter and ion trap instruments into suitable mass analyzers because many technical limitations. However, since the 1970s, the quadrupole filter has become a very popular instrument, in contrast to the ion trap, due to ion–molecule reactions in the *in situ* ionization mode. It took several years and the introduction of an external ion source for ion trap instruments to become a popular MS technique.

Parallel instrumental studies of ionization methods have been performed. The first mass spectrometers were based upon solid-state sample introduction as it was easiest way to introduce a sample into the high vacuum of the mass spectrometer. The ionization principle, carried out with spark sources, for example, involves the production of gas phase ions after sample evaporation. If this approach is suitable for organic molecules, electron-induced processes in vacuum conditions were strongly limited in terms of available mass range, without real control of energy transfer to gas-phase ions. In fact, a large internal energy, $E_{int,}$ with a tail up to 15 eV, is carried by the molecular ions ($M^{+\bullet}$), resulting in substantial $M^{+\bullet}$ fragmentation. Therefore, "softer" ionization techniques were developed by implementing gas-phase ion–molecule reactions in the vacuum source, resulting in less extensive fragmentation. A first in-vacuum ionization alternative was proposed in 1966 by Munson and Field [37], who introduced positive chemical ionization and, several years later, the negative chemical ionization. The latter method enjoyed great success for the detection of industrial pollutants in the 1970s (after the Seveso disaster), pesticides and insecticides, chemical warfare agents, and the detection of various drugs in doping control.

At that time, one of the major limitations of MS concerned the analysis of nonvolatile inorganic salts and also polar, low- or nonvolatile and thermally labile biomolecules. To solve this problem, desorption processes in vacuum from the condensed-phase samples (solid or liquid deposits) were explored from the mid-1960s until 1985 [38]. The first approach was field desorption (FD), introduced by Beckey [39] in 1969. Then appeared methods involving bombardment of solid samples by fast (several MeV kinetic energy) particles as developed by McFarlane and Torgerson [25] and LeBeyec *et al.* [40] with radioactive decay of nuclides such as ^{252}Cf (PDMS). Such particles led to desorption of biomolecules of several thousand daltons. At the same time, bombardment by ionic particles of several keV kinetic energy [41] (SIMS) provided desorbed charged and excited molecules. Later, biomolecules dispersed in a liquid matrix subjected to bombardment with a fast atom beam [42] [fast atom bombardment (FAB)] or fast ion beam [liquid secondary ion mass spectrometry (LSIMS)] yield charged molecular species with very low internal energy and, thus, limited fragmentations. The desorption/ionizaton techniques approach became popular and initiated the systematic MS analysis of peptides and small proteins on the nanomole scale. Use of laser pulse irradiation for molecular desorption was developed by Hillenkamp and Tabet and Cotter [27].

Likely, the use of a matrix in the former FAB and LSIMS modes initiated the further introduction of a matrix crystals to embed the sample for the laser desorption technique. Indeed, laser irradiation on an analyte embedded into matrix crystals results into Eint relaxation (at least partially). Two closely related approaches appeared in 1988: (a) soft laser desorption (SLD) by the group of Tanaka [43] (awarded the Nobel Prize in Chemistry in 2002) with a 330 nm nitrogen laser, which permits the analysis of large intact proteins (e.g., cytochrome *c* and carboxypeptidase A) thanks to the analyte dispersion into colloids in glycerol, and (b) matrix-assisted laser desorption/ionization (MALDI) by Karas and Hillenkamp [44] using a 266 nm laser bombarding crystals constituted of protein embedded in aromatic matrices such as nicotinic acid.

Later the MALDI method was extensively developed and is now the most widely used analytical high-throughput approach for the "-omics" fields such as proteomics. Since the 1990s, various instrumental developments in the MALDI field have emerged. The most promising recent application is MALDI imaging mass spectrometry (IMS), which allows the study of lipids, peptides, proteins, and nucleic acids directly on sections of biopsies or tissue, and thus provides real molecular maps useful for disease diagnostics.

Alternatively, instead of using bulk/target systems, a solution can be directly analyzed by spraying it under ambient conditions. Indeed, small-sized molecules (M_w <2000 Da) can be ionized under atmospheric conditions, by subsequent gas-phase ionization processes [45]. Typically, atmospheric pressure chemical ionization (APCI), atmospheric pressure photoionization (APPI) and direct analysis in real time (DART) are based on ion–molecule reactions initiated by corona discharge, photo-ionization and Penning ionization involving solvent/dopant and/or air. However, these stepwise ionization methods imply in all cases, charge (proton or electron) exchange reactions leading to singly charged analyte species. For larger sized labile molecules (polymers and biomolecules, e.g., lipids, oligosaccharides, peptides, proteins, DNA, and noncovalent systems), desorption processes are required. This was reached with the electrospray ionization (ESI) technique, introduced by the group of J.B. Fenn [46] (awarded the Nobel Prize in Chemistry in 2002) based on preliminary studies conducted by Dole *et al.* [47] nearly 20 years earlier. ESI mode was the result of extensive studies of charged mists and aerosols generated under a local intense electric field conditions. The above Nobel Prize in 2002 rewarded both ESI and SLD desorption/ionization techniques (with NMR spectroscopy) able to ionize high-mass, labile, polar biomolecules [48].

The first objective of this chapter is to give a detailed description of the basis of mass spectrometry. As already pointed out, there have been major instrumental developments and major impacts of the ionization principles involved. Here we discuss the most recently MS applications based upon surface analysis. The first promising MS technology concerns the application of some ionization techniques to spatially resolved sample analysis, hence its capacity has been developed to give a chemical two-dimensional image of the condensed-phase sample. We describe the growing interest in Imaging Mass Spectrometry (IMS) in the last decade in the biological field. The second application area is again more recent and concerns the "soft landing" (SL) approach. This is based on an old research subject, that is, ion–surface collision phenomena that open up a new field of preparative MS. In fact, MS instrumentation offers *in situ* control of each step of the ion–surface collision process, that is, the formation of ions, and the ion collision conditions, and finally allows control of the results by subsequent mass analysis. For these reasons, preparative MS appears is now a very promising approach for obtaining controlled surface modifications and/or molecule handling. Finally, a different MS application that is described concerns petroleum, a natural organic matter that is a highly complex mixture. It has been extensively studied in the last decade using ultra-high resolution mass spectrometry (HRMS) coupled with the powerful desorption/ionization ESI technique.

20.2
Basics of Mass Spectrometry

20.2.1
Experimental Parameters for a High-Quality Mass Spectrum

In a typical MS experiment, the sample is introduced into the ionization source of the instrument, where the sample molecules are ionized and subsequently extracted into the in-vacuum *mass analyzer* region of the mass spectrometer. The ions are separated according to their mass-to-charge ratios (m/z). The separated ions are finally detected and the signals are collected by a data processing system in which the m/z values of the different ions are stored together with their relative abundance in order to present the data as a graph of the absolute or relative intensity versus m/z (the *mass spectrum*).

The characteristics of a mass spectrum are dependent on the configuration of the mass spectrometer. The most important is the ionization source, which is responsible for the type of ionic species produced (atomic versus molecular ions or fragment ions, singly versus multiply charged species, even versus odd-electron species), which also directs the characteristics of the ion beam. The performance of the mass analyzer in terms of resolution and mass accuracy measurements is important for the accurate determination of element/isotopic compositions and also to eliminate isobaric interferences. A high resolving power of the mass analyzer is a prerequisite for accurate mass determination, but it depends also on well-defined calibration standards and calibration procedures. Reproducibility and sensitivity are two critical factors (as in any spectroscopic technique) that determine the absolute but also relative detection limits. In fact, the sensitivity is limited by a number of factors, the most important of which are (a) ionization efficiency of the sample material, (b) efficiency of the ion beam extraction from the source region, (c) the transmission to the mass analyzer, and (d) the detection efficiency. The *dynamic range* of instruments, which is the available ratio of the highest-to-lowest magnitude peaks, will impact the sensitivity directly, and also the observed mass measurement accuracy for the lowest intensity peaks [49].

Numerous types of laboratory-built and commercial *MS* instruments exist today. For bulk sample analysis, former mass spectrometers combined glow discharge (GD) and/or spark source (SS) ionization techniques to a dynamic single-stage sector analyzer (see the schematic representation in Figure 20.1). Today, most commercially available instruments for elemental detection of solid samples are based upon single- or double-focusing sector field mass spectrometers (B–E or E–B geometry) and Q and/or TOF based-instruments (see Figure 20.1). Mainly "in-space" mass analyzers (with pulsed or continuous ion beam injections) are proposed to give an optimal quantification capacity. In recent times, for organic and biomolecular analysis, larger panels of mass spectrometers have become available and applications are increasingly performed with ultra-high resolution Fourier transform (FT) ICR instruments. ICR cells with FT treatment offer the best performances in terms of mass resolving power (typically $>200\,000$), mass accuracy of less than 1 ppm, and also the most

powerful dynamic range (>10 000). For that purpose, the ion cyclotron frequency arising from the motion of a trapped ion in a spatially uniform static magnetic field (with simultaneous axial trapping by the application of quadrupolar DC electric field) is accurately measured.

An FTICR experiment consists in a series of temporally separated events [50–52]. After the ion trapping operation, ion cyclotron frequency detection is performed, preceded by an excitation step to form a spatially coherent ion packet motion at a detectable orbital radius. Then, an ICR (time-domain) signal, termed transient, results from the detection of an oscillating charge "image" on two conductive opposed parallel electrodes (see Figure 20.1). A frequency-domain spectrum is then obtained by Fourier transformation of the digitized time-domain ICR signal. Note that the transient duration impacts directly on the resolving power and therefore on the mass accuracy measurements. Ion–neutral collisions in the ICR cell induce time-domain ICR signal damping, and thus ultra-high vacuum conditions ($\sim 10^{-10}$ mbar) are a prerequisite for FTMS instruments. Finally, a proportional relationship between the ion cyclotron frequency and the m/z value results in an ultra-high resolved mass spectrum, using a simple mass scale calibration rule after FT treatment.

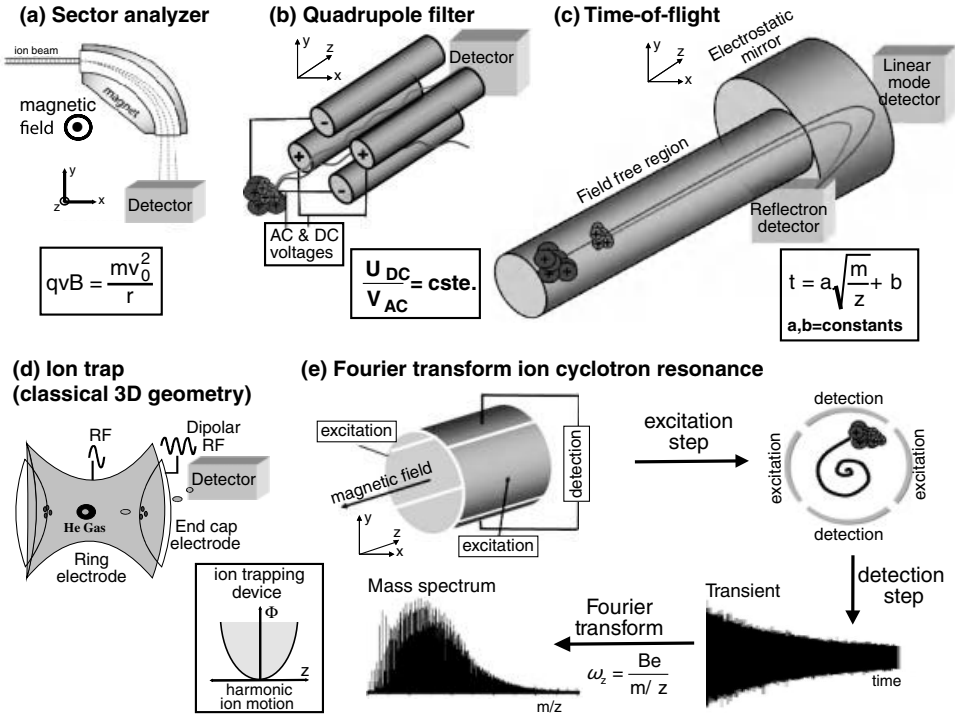


Figure 20.1 Schematic representation of (a) single magnet sector, (b) quadrupole filter and (c) time-of-flight dynamic mass analyzers, of (d) 3D ion trap, and (e) cylindrical ICR cells with the principle of operation of the FTICR instrument.

As an alternative to direct mass analysis of the ion beam produced in the source (MS), tandem mass spectrometry [53] (MS/MS) is an essential technique for the structural analysis of a wide range of organic and biologically relevant compounds. MS/MS involves the activation of an isolated precursor ion formed in the ion source and the subsequent mass analysis of its fragmentation products. The ion activation step is crucial to the experiment quality and ultimately defines what types of product ion result. A less common activation mode, particularly discussed here, is surface-induced dissociation (SID), where the precursor ion excitation step occurs through ion collisions with a surface.

20.2.2
Spectacular Developments of Sources for Nonvolatile Materials

The basic principle of all ionization sources is to deposit (a) sufficient energy into the evaporated (or ablated) molecule from the solid or liquid samples to be ionized and/or (b) sufficient energy into the bulk sample to desorb and ionize a representative part of it, as atomic or molecular species. Diverse vaporization and ionization processes exist and, consequently, different ions sources are well suited for a wide range of applications [36–48]. In fact, the internal energy (E_{int}) that characterizes the ion species is dependent on the operating conditions of the ionization source: (a) in vacuum, the ionized molecules are like-isolated systems (not sufficiently relaxed), and their E_{int} distribution can be broad and high; in contrast (b) under atmospheric pressure conditions, the molecular ionic species produced (as solvated-aggregate intermediate species) are relaxed by collisions and, consequently, the internal energy distribution is like-thermal and narrow, and can be well controlled in the source low-pressure interface (see discussion below).

20.2.2.1 In-Vacuum Ionization Techniques

For bulk solid analysis, earlier GD and SS techniques, SIMS, sputtered neutral mass spectrometry (SNMS), and laser ablation/desorption (LA/LD) MS have been successfully used, and also inductively coupled plasma (ICP) MS [54–57]. Ionization techniques can be classified, for example, according to the protocol used for sample introduction, either by dissolving the solid sample (e.g., ICP) or by using a solid sampling method (e.g., SIMS). Another type of classification is to consider the type of desorption and ionization processes involved between plasma-based methods and particle (or photon)-beam based methods; see Table 20.1 and Figure 20.2.

Available plasma-based methods are distinguished by the way in which the energy is deposited in the sample and the amount of this energy. Today, trace element determinations in high-purity solid materials are less frequently performed by the older techniques such as SS [54, 55, 57], GD [56, 58], SIMS, and thermal ionization mass spectrometry (TIMS) [54]. These approaches have been increasingly replaced by powerful and more sensitive atmospheric pressure ICP-MS [55, 56, 59]. A typical ICP instrument consists of a solution sample introduction system (a nebulizer and spray chamber), an ICP source, a differentially pumped interface, and ion optics for ion beam transmission to the mass analyzer (see Figure 20.2). The solution sample is

introduced into the source as an aerosol, which is completely desolvated, and the elements in the aerosol are then ionized through ICP plasma processes, involving argon ions and metastable argon neutrals. However, the ICP source is based on solution sample introduction and implies a complex sample preparation treatment for bulk materials [59].

Other Class of ionization methods includes techniques based on surface bombardment by either ^{252}Cf radiation (PDMS) [38] or a neutral atom beam (FAB) [38] or ion beam (SIMS, SNMS) [56], and also using pulsed laser irradiation [60, 61] (LA/LD, MALDI and other laser-assisted modes. In such approaches, sufficient energy for sample "evaporation" and ionization is deposited through the bias of kinetic energy of the impacting particle/photon, allowing direct solid analysis. Hence their ability for elemental/chemical detection can be combined with analyte micro-localization with depth and/or lateral resolution capacities [62].

The SIMS procedure [41, 63] is based on the production of secondary ions, created when a primary ion beam impacts the surface of solids. However, the physical principles behind the formation of secondary ions are not yet fully understood and certainly imply a large diversity of mechanisms. Nevertheless, when a surface is exposed to an ion beam, energy is transferred to the sample surface region by a collisional cascade (see Figure 20.3) [64]. Some of the energy will return to the surface and stimulate the ejection of atoms, ions, and multi-atomic clusters as a secondary ion beam. Conventional SIMS has been widely employed to characterize inorganic materials by detecting elements and small-sized fragment ions. The use of SIMS for the analysis of organic and biologically related systems as intact species has historically been limited by low secondary ion yields and ion beam-induced structural damage that results from the use of atomic primary atomic ion beams (Ar^+, Cs^+, or Ga^+). With the advent of new molecular sources such as $C_{60}{}^+$, $Au_3{}^+$, $SF_5{}^+$, and $Bi_3{}^+$, considerable increases in secondary ion signal have been observed, allowing larger application areas at the molecular level. When a cluster ion impacts a surface, the cluster breaks apart and each atom in the cluster retains a fraction of the initial kinetic energy, thus resulting in a significant reduction in penetration depth of the primary ion beam [64] (since penetration depth is proportional to impact energy; see dynamic simulations in Figure 20.3). This causes surface-localized damage and, consequently, preserves the chemical structure in the subsurface region. Hence cluster SIMS [65] has played a critical role in the characterization of polymeric materials and organic and bioorganic compounds present directly on the surface (as material or contamination on the surface) [62].

LA/LD and derivative laser-assisted techniques (such as MALDI and matrix-free approaches) have been extensively applied to various solid material analyses through elemental and/or chemical detection [60, 61]. Typically, gas-phase ions are generated by laser irradiation of the sample surface and LA/LD or other laser-assisted approaches depending on the operating and/or sample conditions. LA and LD experiments are conducted on the same instrument [66], but within different laser energy regimes. LA takes place at high irradiance, whereas LD is performed at low irradiance ($<5 \times 10^6\,W\,cm^{-2}$), resulting in greater amounts of expelled matter with visible surface alterations under LA conditions, and thus in different type of produced

Table 20.1 Typical features of the sources.

Method	Source	Introduction	Sample transfer to GP	Sample ionization	Advantages	Limits
Plasma based	TI	Solid	Simultaneous electron-induced sputtering and ionization (or consecutive with two filaments)		Elemental detection	
	SS	Solid	Thermal vaporization	Electron-induced GP process	Elemental detection	Inhomogeneities Nonconducting samples
	GD	Solid	Sputtering by ion gas impact	Penning and electron-induced GP processes	Elemental detection	Nonconducting samples
	ICP	Solution, P_{atm}	Aerosol heating	Plasma torch-induced processes	Elemental detection Best detection limit for trace analysis	Solution samples Sample preparation
	DART	Solid, solution, P_{atm}	Vaporization	Penning processes and ion–molecule reactions	Chemical and biomedical detection	Few ku mass range
	APCI	Solution, P_{atm}	Heating, electron-induced, and ion–molecule reactions			Few ku mass range
	APPI	Solution, P_{atm}	Heating, photoionization and ion–molecule reactions			Few ku mass range
Particle beam	SIMS	Solid	Ion sputtering by primary ion bombardment		Elemental and chemical detection, with depth and/or lateral resolution	Inhomogeneities Matrix effects

(*Continued*)

Table 20.1 (*Continued*)

Method	Source	Introduction	Sample transfer to GP	Sample ionization	Advantages	Limits
	LA	Solid	Laser-induced evaporation		Elemental and chemical detection of insulating materials, MS imaging	Few ku mass range
	LD MALDI matrix-free	Solid	Laser-induced vaporization	Desorption/ionization processes	organic, biological molecule detection MS imaging	In MALDI matrix addition
ESI based	ESI	Solution, P_{atm}	Droplet evaporation/explosion and desorption/ionization processes and aggregate desolvation		Organic, biomolecular detection for polar in-solution compounds	Ionization discrimination
	DESI	Solid, P_{atm}	Prior pick-up mechanism from surfaces, droplet evaporation/explosion and desorption/ionization processes		As above, ESI mode, with imaging MS ability	
Combined method	SNMS	solid	Primary ion bombardment sputtering	Post-ionization by electron-induced CI or laser-induced GP processes	As above, SIMS, with better sensitivity and lower matrix effects	Inhomogeneities
	LAICP	solid	Laser ablation	Plasma torch-induced post-ionization processes	Elemental detection	
	LAESI–ELDI	solid	Laser ablation	Desorption/ionization from charged droplets	Chemical/biological detection, imaging MS	

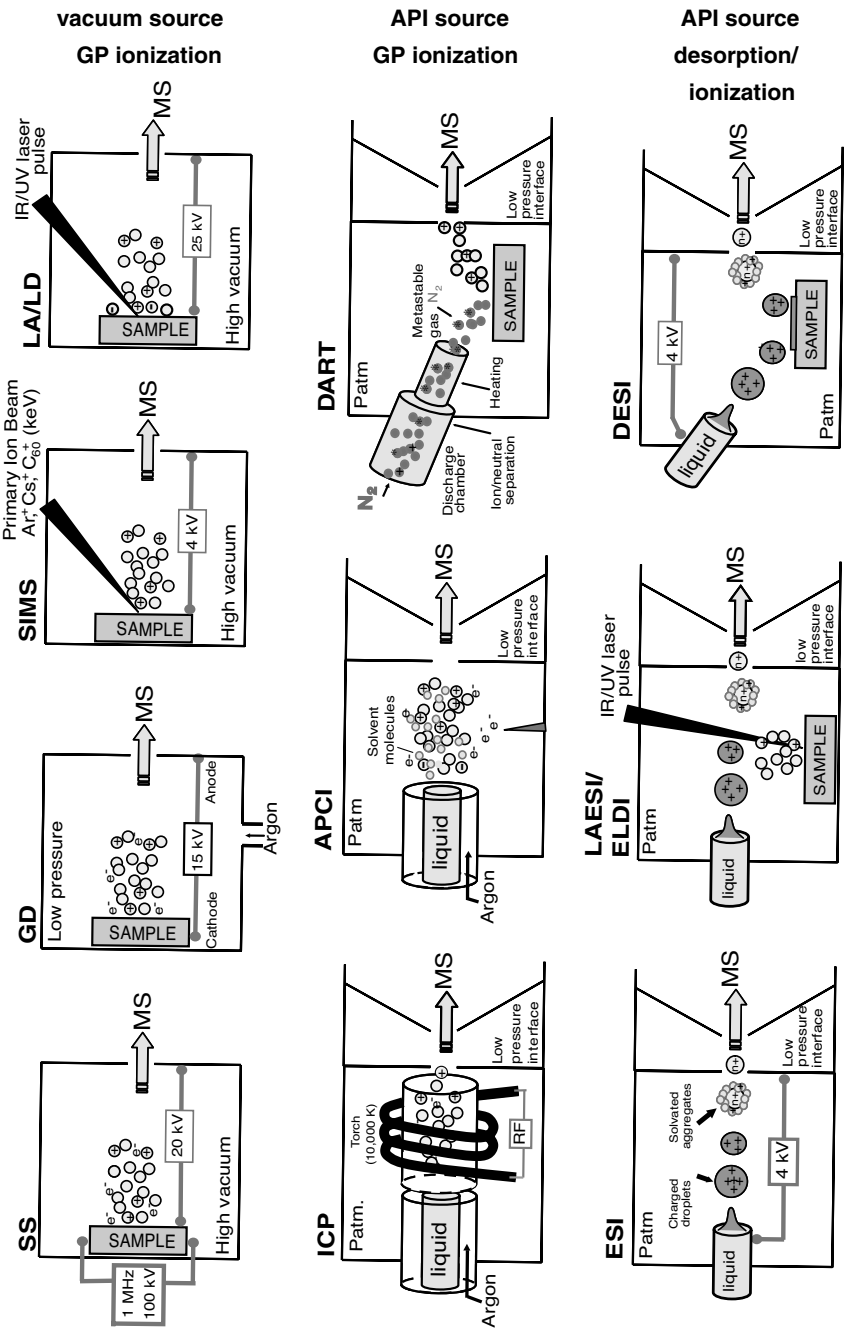


Figure 20.2 Typical ionization sources with their operating processes. SS, spark source; GD, glow discharge; ICP, inductively coupled plasma; SIMS, secondary ion mass spectrometry; LA, laser ablation; LD, laser desorption; APCI, atmospheric pressure chemical ionization; ESI, electrospray; DART, direct analysis in real time; ELDI, electrospray laser desorption/ionization; LAESI, laser ablation electrospray ionization; DESI, desorption electrospray ionization.

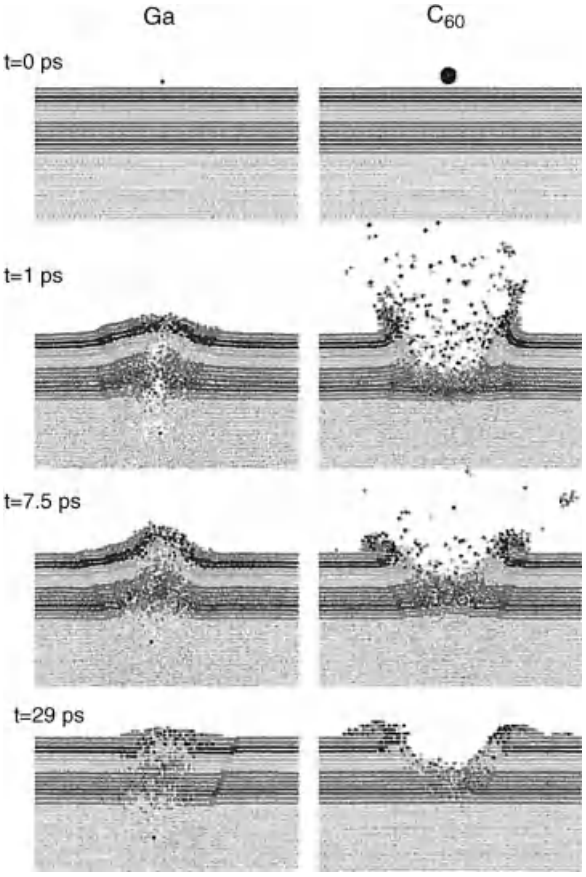


Figure 20.3 Cross-sectional view obtained by dynamic simulations of a typical SIMS collision by 15 keV Ga and C_{60} primary ions on to an Ag {111} surface at normal incidence. The temporal evolution is described, leading to ejection of atoms/clusters. Reprinted from [64].

species. The LA technique is then an analytical method for the simultaneous determination of concentrations of trace elements in solid samples [60, 61, 63]. In contrast, the LD approach [24], using either IR or UV pulsed lasers, has been extensively developed for organic and biologically relevant compounds, but with a limited mass range of a few kilodaltons. The LD ionization mechanism involves different steps: (a) after the laser energy absorption [one or a few photon(s)] by the sample, (b) an energy conversion associated with relaxation processes, (c) followed by the ejection of particles (excited atoms, molecules, and ion species), and (d) plume expansion (high-density matter), leading to the formation of molecular species. Note that if a lot of neutral species are generated under laser irradiation, only a minority of ions are produced from the solid (ion/neutral ratios in the range 10^{-3}–10^{-6}).

Alternatively, a laser-induced acoustic desorption (LIAD) source has been developed, in which the sample deposited on a thin metal foil is irradiated from the back side. The metal ablation induced by the laser pulse results into wave propagation through the foil, producing a large-amplitude acoustic shockwave and sample sputtering [67].

LA/LD and LIAD techniques are well suited for surface analysis, but they display low ionization efficiency, for a limited analyte mass range. Therefore, different target supports and/or sample preparations have been further developed in order to assist desorption/ionization processes. The MALDI technique introduced by Hillenkamp and Karas [44] has a wide biological application field. Another "matrix-free" approach proposed tailoring of the surface plate in order to allow better laser energy transfer and consequently enhancement of the desorption/ionization yields without matrix addition.

Matrix-free laser-assisted modes were initially developed for a limited analyte mass range as alternative to MALDI MS, thanks to the absence of matrix ions in the low mass range. These techniques correlate the preliminary work, termed soft laser desorption, of Tanaka *et al.* [43]. Various matrix-free techniques have been proposed, for example by Sunner *et al.* [68], who introduced graphite targets [graphite plate laser desorption/ionization (GPLDI) mode]. A successful matrix-free preparation was reported by Wei *et al.* [69] based on a modified porous silica surface. This method, called desorption/ionization on porous silicon (DIOS) is characterized by a high area surface and efficient UV absorption for the analysis of small-sized compounds (masses lower than 2000 u) [70]. Other studies demonstrated the utility of nanostructured materials for performing matrix-free LD experiments, such as carbon nanotubes [71], which act as an efficient matrix as they can trap analytes on their surface and efficiently transfer energy to the analyte. Finally, an article in 2007 reviewed matrix-free techniques that have been successfully applied to the analysis of low molecular weight compounds [72] such as drugs, pharmaceutical compounds, and small peptide and lipid molecules.

Nevertheless, MALDI is a soft desorption/ionization method that has become a pre-eminent technique for the analysis of a wide variety of high-mass compounds (from 600 to more than 10^6 u), including polymers and macromolecular proteins [73]. MALDI was introduced in the late 1980s [43, 44], and involves the co-crystallization of the analyte with a matrix, which is generally a low molecular weight aromatic compound that can absorb the energy of a laser light pulse. A large number of operating parameters may affect the MALDI processes, including the irradiation parameters (laser wavelength, pulse duration, irradiation and focusing, etc.), the spot preparation (nature of the matrix, analyte–matrix interactions, sample morphology), and the plume dynamics (initial velocity, gas-phase dynamics, internal energies). Above all, the matrix plays a critical role in MALDI processes by (a) absorbing strongly and resonantly the laser wavelength, (b) forcing the separation of analyte molecules from each other (matrix isolation), and (c) helping or initiating analyte ionization. Extensive reviews on MALDI desorption/ionization processes were published in 2003 in *Chemical Reviews* [74–76]. Typically, absorption of the laser energy causes the matrix to undergo a phase transition

leading to material ablation. After the absorption maximum of the matrix has been reached, extensive material ablation and plume production occur [74], because most of the energy is absorbed by the matrix. The subsequent gas-phase analyte ionization processes in the plume have still not been resolved, but an increasingly accepted model of the MALDI ionization event takes into account the existence of large matrix–analyte aggregates, undergoing intramolecular reactions and desolvation steps [75, 77].

20.2.2.2 **Atmospheric Pressure Ionization Techniques**

Atmospheric pressure ionization methods [through gas-phase ionization processes such as APCI, APPI, and DART or desorption/ionization processes such as ESI and desorption electrospray ionization (DESI)] have been extensively developed since the 1980s for chemical analysis of solution-phase samples. The most widely used ionization technique today is ESI, wherein ions are created from solutions at low concentrations (from a few hundred nanomolar to a few micromolar), by electrically charging a flowing stream of sample, resulting in the emission of singly or multiply charged molecular species from the charged droplets in the subsequent spray [78]. The process of droplet generation involves the formation of a Taylor cone, under the high electric field, that emits charged droplets from the apex where the field is high enough to overcome the liquid surface tension forces. The droplets initially produced can be readily evaporated with gentle heating over short distances at atmospheric pressure. Two types of desorption mechanism have been proposed to describe the subsequent formation of gas-phase solvated multiply protonated ions from the ultimate nanometer-sized droplets [79]. The aggregate intermediate ions are transferred to the high vacuum of the mass spectrometer. Most important, concomitant control of aggregate desolvation occurs in the source interface, through low-energy collisions with the residual gas at the interface, resulting in the final production of solvent-free singly or multiply-charged molecular species. The desolvation pathways can be controlled by the electric potential values applied along the ion optics setup, which is very useful for limiting or enhancing in-source fragmentations. Gentle ESI desorption/ionization processes allow the transfer of the very large biomolecules to the gas phase as intact multiply charged species, giving successful applications in biomolecule large "-omics" scale fields such as genomics and proteomics [80]. In fact, these application areas were systematically developed with both the desorption/ionization MALDI and ESI techniques [48].

A myriad of atmospheric pressure ionization (API) sources [45] have been developed over the past decade. Some of them are based on sample solution introduction systems and are multiplexed ESI versions [e.g., electrosonic spray ionization (ESSI)], whereas others have moved back to the earlier concept of solid sample introduction, such as ambient ionization techniques [81, 82]. Chen *et al.* [83] reviewed ambient ionization techniques involving direct sampling and ionization under ambient conditions, with no or minimal effort for sample preparation. However, they underlined the misuse of various acronyms for closely related ionization techniques. Rapid, high-throughput, direct solid surface analysis is possible with laser-assisted techniques at atmospheric pressure (AP) (such as AP

LD, and/or other AP MALDI, AP matrix-free LD modes) but also with new ambient techniques such as DART and DESI [84]. While the in-vacuum MALDI mode has been widely applied for many years, to analyze large biomolecules, ionization techniques such as AP LD or AP MALDI have been less frequently used. Only singly protonated/cationized species are produced in the above-mentioned API sources, this prevents their coupling with analyzers that have a limited m/z range (e.g., <6000 Th) [85].

The DART technique [86] was developed primarily as a surface ionization source where primary ions are created with a discharge in a flowing stream of hot noble gas such as argon or helium, forming metastable excited-state atoms. As the gas enters the ion source, an electric potential in the range of $+5$ kV is applied. This generates a glow discharge containing ionized gas, electrons, and excited metastable-state atoms. The DC potential removes charged particles from the gas stream and only metastable species flow to the third chamber, where the gas stream is heated, resulting in the partial evaporation of analyte molecules from the surface. Then, the ionization processes, under ambient conditions, involve gas-phase Penning processes and ion–molecule reaction cascades (close to APCI processes), producing mainly singly protonated/deprotonated species (see Figure 20.2).

Another concept proposed by Cooks and co-workers [87–89] was desorption electrospray ionization that operates by impacting the surface to be analyzed with charged droplets. The microdroplets act as projectiles and desorb secondary/progeny droplets and/or gas-phase ions from the surface as a result of electrostatic and pneumatic forces. Costa and Cooks [90] used computational fluid dynamics to model secondary droplet formation and transport processes (see Figure 20.4). They concluded that first primary droplets impact on the surface, resulting in a thin solvent film, and stochastic momentum transfer events occurring between primary droplets and the liquid layer are responsible for the production of analyte-containing droplets. Subsequently, evaporation/Coulombic explosion processes similar to the ESI mode [78], generate singly and/or multiply charged molecular species. In this case, the desorption/ionization mechanisms emphasize the importance of (a) the chosen surface/target to deposit the sample [91] and (b) the selected ESI solvent [92]. Indeed,

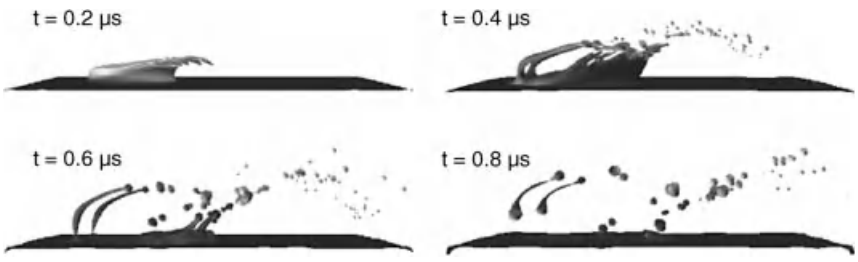


Figure 20.4 Modeling of progeny droplet formation and transport in DESI technique at different time steps. Reproduced with permission from [90].

the sensitivity is primarily dictated by the extraction efficiency that occurs during the impact event. In conclusion, DESI is a recent ambient method that allows MS analysis of condensed-phase samples; it has been successfully applied to detect organic compounds [93] such as traces of explosives present on different surfaces [94] and pharmaceutical samples [88, 95] (solid counterfeit drug pills). This ionization method allows the detection of biologically relevant compounds, such as lipids [96], carbohydrates [97], and proteins [98], and to direct biological sample examination, particularly blood [99], tissues [89, 96], and even entire bacteria [100].

20.2.2.3 **Combined Ionization Techniques**

Combined ionization techniques were also proposed in order to combine the advantages of different sources techniques. For example, SNMS [101] is an intermediate method between SIMS and GDMS, in which the neutral particles sputtered from the sample are post-ionized, for example, by EI, before their mass is analyzed. The decoupling of the sputtering and the ionization processes minimizes the matrix effects compared with SIMS [62–63]. Although it was initially developed for solution samples, an attractive approach for solid analysis is the use of a pulsed laser (such as LA ICP MS [102]) to ablate the sample directly from the solid into the injector gas of the ICP ion source. The sensitivity achieved for trace elements appears to be similar or superior to that of laser ionization methods, but is lower than that of the classical ICP mode.

In the last decade, API techniques were developed in which the LA/LD of the condensed-phase sample is followed by post-ionization of ablated neutral particles, resulting in enhanced analyte ionization. For example, electrospray-assisted laser desorption/ionization (ELDI) MS [103] utilizes a nitrogen laser to desorb directly large amount of neutral species, which are then post-ionized through interactions with charged droplets provided from the ESI source. A closely related approach is the laser ablation electrospray ionization (LAESI) technique developed by Nemes and Vertes [104], which combines laser ablation by a mid-IR (2.94 μm) laser with secondary ESI processes. Note that under matrix-assisted laser desorption/electrospray ionization (MALDESI) conditions, the sample is indirectly desorbed via a transfer of energy through the matrix which embedded the sample. Because the ESI charged droplets are used for post-ionization, the LAESI mass spectra are similar to traditional ESI spectra, exhibiting multiply charged analyte peaks, allowing an extended effective mass range detection of biomolecules up to 100 000 u. Other combined techniques are based on the laser ablation of solid samples at atmospheric pressure and post-ionization by APCI processes as in the case of Laser Diode Thermal Desorption (LDTD) and atmospheric pressure laser desorption/chemical ionization (APLD/CI) [105]. Similarly, LIAD desorption followed by gas-phase post-ionization either in vacuum [106] using EI or Chemical Ionization (CI) or at atmospheric pressure by APCI processes [107] have been developed (see examples of applications for petroleum analysis below).

20.3
Direct Surface Analysis: Imaging Mass Spectrometry for Biologists

Imaging mass spectrometry [108] (IMS) has become an increasingly powerful and unique method compared with other analytical and spectroscopic imaging methods thanks to its sensitivity and the specific chemical information it provides. A first crucial question must be addressed: "How is an MS image constructed?" In fact, mass spectra are recorded in a systematic fashion over the surface by moving the sample stage. Each individual spot correlated with a discrete (x,y) coordinate location on the entire tissue has an associated mass spectrum (see a typical procedure for MALDI-IMS in Figure 20.5) that is analogous to a pixel in a digital image. To generate an MS image, the intensity of one m/z value is expressed over the array of pixels as a 2D ion density map. Here, we describe only the microprobe approach. Microscope mode imaging uses ion-optical microscope elements to project the spatial origin of the ions generated at the sample. In contrast, microprobe imaging capacities and limitations are directly related to the mass spectrometer performance.

In fact, there are different types of resolution in an IMS experiment: in addition to the mass resolution, a characteristic of the mass analyzer, resolution of the reconstructed MS image is described by the dimensional parameter, that is, the lateral resolution, and eventually depth resolution [108]. If the mass resolving power is an important parameter of the mass analyzer, leading to the preferential use of a high-resolution mass spectrometer, an additional limiting parameter is the image acquisition time. Therefore, the majority of imaging experiments are performed using a TOF mass analyzer, which displays a fast scan acquisition, rendering feasible image construction from an organ tissue section (millimeters long) (see Figure 20.1). Another advantage of a TOF instrument is that the mass range is virtually unlimited in the linear mode, with detected analyte masses above 200 kDa. In addition, high-resolution mass measurements are available for a small mass range (up to a few kDa) using the reflectron mode, and a typical mass resolving power of up to 10 000 is obtained for peptides in the range of about 3000 u. Nevertheless, a recent IMS approach is based on the use of high-field FTICR systems (see the discussion below). Concerning the image "pixel" resolution, spatial and eventually depth resolution abilities [62] (3D image) directly correlate the ionization principles. So, the following discussion is mainly about source technology advantages and limitations for IMS purposes.

However, for the success of IMS experiments, there are crucial questions such as "What is the studied sample?" and "How do we obtain its image by mass spectrometry?" For the first question, IMS created new fundamental research opportunities in many fields because of its unique ability to acquire molecule- (and/or element-) specific pictures in a micron spatial region. Here, we discuss more about the use of IMS in biological applications. However, the potential of IMS has long been recognized for industrial applications in materials science and engineering [57, 62]. The first elemental imaging experiments using SIMS were described in the 1960s [109]. Both SIMS and LA/LD techniques provided excellent spatially resolved elemental and small-molecule analysis capabilities, helping to fabricate nanometer-

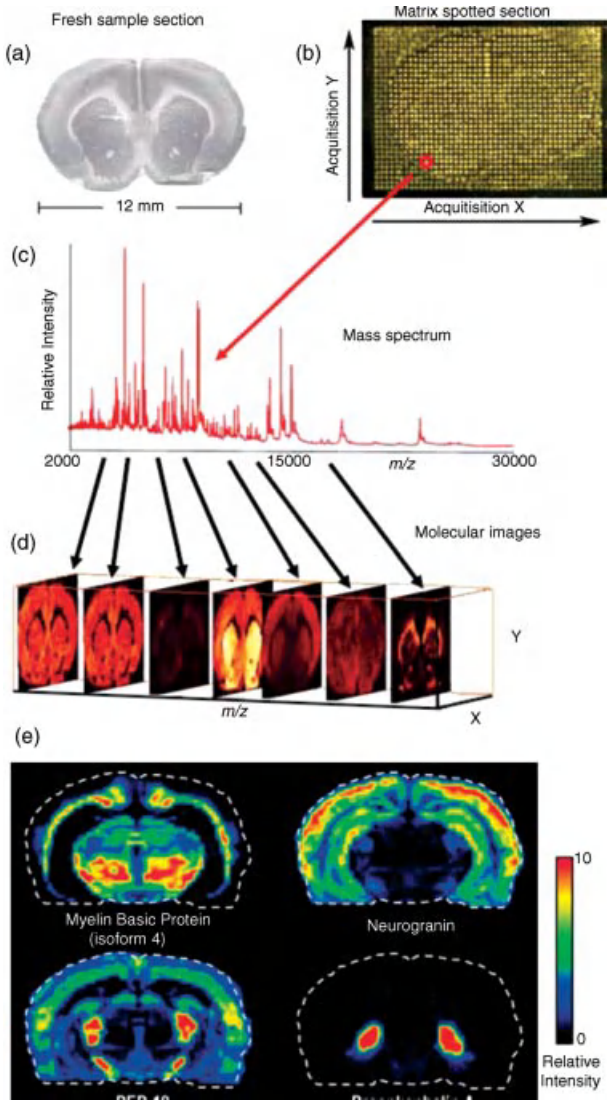


Figure 20.5 Description of typical MALDI-IMS procedure. It involves (a) the collection of a thick tissue section on a conductive MALDI plate after microdissection, followed by (b) a matrix deposition step, by robotic spotter. (c) A typical MALDI-TOF mass spectrum, which is used to generate hundreds of protein IMS images (color-coded ion density), and (d) molecular images. (e) Experimental coronal rat brain IMS images obtained by detection of four different proteins; these images show very different distributions throughout the brain, with pixel values (i.e., matrix spots) of about 180 μm in diameter. Adapted from [129].

scale devices and to miniaturize many aspects of scientific research [110]. They have been applied in industrial applications to assess material compositions, controlled impurity doping, segregation effects at the interface, grain boundary migration, and recrystallization effects, for diverse inorganic and organic materials [109–111]. Of

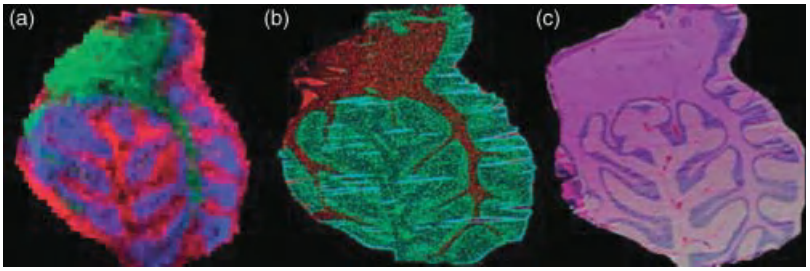


Figure 20.6 Human cerebellum: (a) imaged with MALDI-TOF-TOF after washing of the tissue in several organic solvents and matrix deposition α-Cyano-4-hydroxycinnamic acid (CHCA) (reported protein peaks are in green, *m/z* 18 598, blue, *m/z* 13 975, and red, *m/z* 8495); (b) unwashed tissue image measured with SIMS (by detection of small-sized lipids such as in red, cholesterol, *m/z* 386; green, phosphocholine headgroup, *m/z* 184); and (c) tissue stained with H&E showing gray matter (light pink), white matter (pink), and granular layer (purple). Theses images illustrate the complementary of the two techniques with well-resolved spatial ion location of the SIMS image but with low chemical specificity whereas MALDI allows specific protein profiling, with limited spatial resolution (due to the washing and matrix deposition steps), Note that, nevertheless, both IMS images are consistent with the classical biological approach. Reproduced from [138].

course, these industrial applications and their needs have driven the MS community to improve the sensitivity and the ultimate spatial resolution of imaging techniques, which is now successfully applied in biomedical research.

20.3.1 State-of-the-Art of Imaging Mass Spectrometry Technology for Biological Applications: In-Vacuum Desorption Techniques

The most promising potential of IMS today is for biological applications, generated by chemical detection of biologically relevant compounds. Dominant techniques in the last decade are SIMS [108, 110, 112] and the complementary MALDI mode [108, 112]. SIMS is best suited for the study of small-sized molecules such as carcinogens and phospholipids [65], whereas the MALDI-TOF approach has a unique ability to measure high molecular weight compounds such as proteins [73]. However, MALDI and matrix-free approaches have also been used to image drug, metabolite, and lipid distributions on a tissue (see the SIMS and MALDI images of the same tissue section displayed in the Figure 20.6). A major advantage of IMS for biological purposes over immunoassay-based methods is that IMS is a label-free approach, with multiple compound detection. Immunohistochemical approaches allow preservation of spatial information with excellent sensitivity, but have limitations as the targeted protein must be known in advance in order to use the correct antibody for staining, and generally only one or two antibodies can be studied simultaneously [113]. In contrast, direct tissue MS analysis can be carried out by global profiling of the molecular composition within the tissue section. IMS has been successfully applied to cell populations and various tissue sections, and organs from plants, animals, and humans [108]. Note that the ability of SIMS to extend the analysis to depth profiling allows the constitution of

three-dimensional images [114]; in MALDI-IMS experiments, a 3D image can eventually be reconstituted by study of serial tissue sections.

20.3.1.1 Highly Resolved SIMS Images

The SIMS approach offers the most useful capacity of ion microcopy for industrial applications by element (or small fragment) detection, with micrometer lateral resolution and eventually depth profiling resolution and eventually depth profiling [110, 114]. Until recently, the m/z range of the ions that could be imaged was limited to 20–200 u [110]. Today, IMS experiments with SIMS [114, 115] involve the use of primary cluster ion beam such as C_{60}^{+}, Au_3^{+}, SF_5^{+} and Bi_3^{+}. Cluster SIMS technique is characterized by the production of larger intact molecular ion species and then, allows molecular profiling of biological sample surface using this mode [108]. Nevertheless, a few examples of elemental detection using an atomic ion beam have been reported in the biological field [116, 117]. For example, SIMS images of the entire karyotype for all 46 human chromosomes have been constructed by Mg^{2+} and Ca^{2+} species detection [117]. Nowadays, most of the applications already published relate to lipid composition in various tissues [118, 119]. Fewer examples exist on other biologically relevant molecules, such as the detection of surfactants in single-cell analysis [120]. Finally, the SIMS technique is able to localize atoms, small fragments, or molecules (mainly lipids) up to m/z 1000–1500 with a routine spatial lateral resolution from a few hundred nanometers up to 1–2 μm, allowing the acquisition of the highest spatially resolved IMS images. Indeed, the attainable lateral resolution is directly correlated with the experimental setup of the SIMS technique (primary atomic ion versus cluster ion beams, nature of cluster ions, and change of sample preparation). Classical SIMS offers a unique lateral resolution of few nanometers, but displays a lack of detection specificity [110, 116, 117]. In contrast, using cluster primary ions, lower spatial resolution in the micrometer range is available, but remains better than MALDI image resolution. In addition, in contrast to MALDI, no special tissue section preparation is needed. For example, using bismuth clusters as primary ions on a rat brain tissue section, IMS images with an ultimate spatial resolution of about 400 nm was reported by Touboul *et al.* [121].

Alternative approaches with a change of target preparation have been also tested to improve the precision and sensitivity of molecular profiling in biological samples IMS. Usually, SIMS images (atomic or cluster primary ions) are obtained with a minimum of handling or sample preparation, but alternative protocols have been proposed to increase significantly the secondary ion yield and thus the analysis sensitivity, in addition to allowing the ionization of larger lipids and eventually peptides. Two alternative methods are matrix-enhanced secondary ion mass spectrometry (ME-SIMS) [122, 123] and metal-assisted secondary ion mass spectrometry (Meta-SIMS) [123–125]. The first approach showed, by application of an organic acid compound (typical MALDI matrix), a greater secondary ion signal intensity for larger analytes up to several kilodaltons, but with a drastic loss of spatial resolution. In Meta-SIMS experiments, coating the sample with a thin layer of a metal such as silver or gold results in a large increase in the secondary ion

yield of molecular ions. Application of a metal on the target plate was first reported by Bouneau *et al.* [126], who produced gold clusters as primary ion source using a liquid metal ion source; these clusters penetrate deeply into several surface layers. Such an instrumental set up does not impact on the image pixel resolution but complex mass spectra are obtained due to the formation of metal adduct species [125]. Finally, both of these approaches aimed to offer the same application fields as the MALDI technique, detrimental to the spatial resolution; nevertheless, MALDI still remains the better IMS technique for large protein tissue profiling.

20.3.1.2 **MALDI for Highly Selective Peptide/Protein Profiles**

MALDI-MS of intact tissue has had a major impact on molecular biology and biochemistry by permitting sensitive, rapid, and, above all, molecularly specific analyses of peptide and protein distributions on a surface. The first MALDI imaging experiments through peptide profiling on a rat pancreas section were reported by Caprioli *et al.* [127], who further extensively developed the use of MALDI for biological IMS. Today, MALDI-IMS, which is the most popular molecular imaging method, aims to localize peptides and proteins with a spatial resolution of a few tens of microns (10–100 μm) at the surface of the tissue section, (see extensive reviews [108, 127–134]). The reasons for this success rely on the ability of this desorption/ionization technique (with ESI) for the analytical study of high-throughput proteome (set of proteins expressed by a genome, cell, tissue, or organism) [135] with the additional information of spatial localization (not available in the ESI mode). Thus, although the pixel resolution of a MALDI image is lower than that of a SIMS image, MALDI offers better chemical specificity from access to a high mass range and limited fragmentations (lower ion internal energy). MALDI is able to determine the spatial distribution of large intact biomolecule species (e.g.; protein biomarkers) and their relative expression levels without the need for molecularly specific exogenous compounds such as antibody-based reagents. The MALDI approach allows the direct correlation of MS protein profiling with anatomic or pathological features of tissue sections; this can be achieved by comparison with established histological tissue sections (see Figure 20.6). It offers the possibility of *in situ* study of the mid- to low-molecular mass proteome and eventually subsequent biomarker identification. Indeed, biomarker identification is provided by analyzing protein expression patterns of the same tissue or organism but from varying disease conditions, allowing one to designate a potential biomarker of interest. It can be identified in a second run, either by using a classical proteomic approach [135] or, alternatively, by *in situ* tryptic digestion on a tissue followed by peptide sequencing using MALDI-MS/MS experiments.

Maps or images obtained using the MALDI technique provide a powerful tool for investigating a broad array of pathologies, chemotherapeutics, and discovery of disease biomarkers [127–134]. The feasibility of protein profiling by MALDI-IMS has been tested for various breast, lung, colon, brain, and gastric cancers, and also other diseases, such as Parkinson's and Alzheimer's disease. Most important for biomed-

ical research, differential IMS studies can be carried out to study therapeutic treatments. For example, MALDI-IMS experiments on a mouse model of Parkinson's disease revealed a significant decrease in PEP-19 (neuronal calmodulin-binding protein) expression levels in the striatum after administration of the drug MPTP (1-methyl-4-phenyl-1,2,3,6-tetrahydropyridine), giving new insights into the studied therapeutic treatment [136].

So, why is MALDI not the unique IMS approach used in biological fields? [137]. It is because MALDI-IMS is hampered by its available spatial resolution (in routine analysis, several hundred microns), which is mainly limited by the size of the matrix crystals deposited on the tissue and the laser spot size of the instrument [138]. During the tissue sectioning procedure, the section thickness, temperature, but also the use of any fixation protocol, of embedding media (e.g., protein fixation by formalin fixing, paraffin embedding), of washing steps or optionally the use of *in situ* enzymatic digestion (see target preparation description in Figure 20.5) are important parameters in subsequent MALDI analysis quality [139]. However, the main limiting parameter is the target spot preparation. Indeed, the ability of MALDI to ionize high-mass compounds as intact molecular species is due to the physicochemical properties of the matrix. Unfortunately, matrix deposition will have a direct impact on the image pixel resolution. Indeed, inhomogeneous co-crystallization of the analyte with matrices such as SA (3,5-dimethoxy-4-hydroxycinnamic acid) shows the existence of "sweet spots" on the sample, which cause quantitative errors. To obtain smaller target spots, optimized target preparation protocols have been proposed such as the application of matrix along the entire tissue section using robotic spotting [127], nebulization [140], sublimation protocols [141, 142], or the use of ionic solid and ionic liquid matrices [143]. Alternatively, the use of an IR laser can be promising, as matrices for IR-MALDI technique are water and glycerol, but in-vacuum conditions preclude this target preparation. Naito *et al*. [144] tested IR-MALDI with a MALDI target plate at very low temperature (within a cryostage), allowing a liquid matrix to be crystallized and introduced into a vacuum system. Alternatively, atmospheric pressure conditions with IR-MALDI was successfully applied to frozen tissue sections [145].

MALDI-IMS has been successfully applied to the study of drugs and other small molecules in tissues [146, 147], although the limited the ability of MALDI to detect low-mass molecules due to matrix ion interferences. Interesting results were reported by Colsch *et al*. [147], who demonstrated that better chemical selectivity is obtained for ganglioside species profiling in rat brain tissue sections using MALDI conditions. In contrast, SIMS spectra (even with cluster primary ions) generally display abundant molecular ion fragments.

Nevertheless, alternative MS experiments such as the use of the MS/MS mode or HRMS detection can be performed for better chemical characterization. The use of alternative laser-assisted ionization techniques without matrix addition (matrix-free approach), and even new ambient modes, have also been performed to increase the IMS performances.

20.3.2 New Perspectives for Imaging Mass Spectrometry Technology

20.3.2.1 Mass Spectrometry Technology Development

Instrumental and methodological improvements have been performed for the critical IMS area. The first bias concerns the ion peak assignment with only a single TOF mass analyzer. With extraction delay and electrostatic mirror devices, a maximum resolving power above 15 000 is available for peptides in the mass range $<$3000 Th. For larger systems, linear mode detection is characterized by only average molecular mass measurements. To gain specificity in chemical detection, one can replaced TOF-MS analysis by MS/MS experiments [53, 146]. Alternatively, FTICR instruments are capable of achieving a resolving power in excess of 300 000 for peptides $<$2000 Th, which allows enhanced image quality by higher ion detection specificity [137, 141, 148, 149]. However, MALDI FTICR experiments present some limitations. The first limiting parameter is the mass range (a few ku) that allows only low-mass peptide detection as singly charged ions (typical from MALDI ionization). Nevertheless, MALDI FTICR images of drugs in hair [148] and images of cell populations [141] have been successfully obtained, with excellent sensitivity. The powerful dynamic range of FTICR allows broader compound detection in a single mass spectrum. Second, IMS experiments are hampered by the IMS image acquisition time, using FTICR instruments (seconds). A compromise must be found in the total transient duration and the mass resolving power; an alternative is the use of higher strength of the magnet (in Tesla) [49–52].

Matrix-free approaches have also been applied for biomolecule IMS [149–152]. LD or its derivatives DIOS and graphite-assisted techniques gave an enhanced image pixel resolution, by eliminating the matrix application step, but only through limited mass range detection of organic and biologically relevant molecules. An interesting approach was proposed by Thiery *et al.* [150], who used multiplex immunostaining of proteins, with mass-tagged antibodies. Subsequent, IMS experiments were performed by detection of photocleaved tags by the LD technique. This method, termed TAMSIM (targeted multiplex mass spectrometry imaging) allows, indirectly, protein profiling in tissue sections.

Recently, an additional "conformational resolution" has been proposed for IMS images [137] by providing a direct insight into the shape, structure, and position of biomolecules in tissue sections. For this purpose, a combination of ion mobility mass spectrometry (IM-MS) [153] with IMS [154, 155] was proposed, where the post-ionization separation occurs on the basis of the gas-phase ion mobility through a high-pressure collision cell filled with an inert gas. IM-MS generates extra analytical information used for protein conformer and isobaric structural identifications.

However, SIMS and laser irradiation modes (e.g., MALDI, LD, and other matrix-free derivatives) require vacuum experimental conditions, implying limited sample manipulation, problematic tissue sample storage, and complex target preparation, which is a time-consuming step. Another important limiting feature of these

in-vacuum ionization techniques is the absence of the ion internal energy control; which results in in-source fragmentation and thus loss of chemical specificity for the constitution of the IMS image. Of course, this effect is much more pronounced in a SIMS approach (even with cluster SIMS), but has been also observed in the MALDI approach for labile biomolecules [147]. Hence a novel research thrust appears, based on MS experiments under atmospheric pressure conditions, for example, using ambient DESI and LAESI techniques.

20.3.2.2 **Imaging Mass Spectrometry Under Ambient Conditions**

Ambient methods permit the direct, high-throughput analysis of samples in open air conditions, which implies minimal target preparation (no matrix addition), without chemical labeling or additional tissue section treatment. The first IMS experiments were conducted using laser-assisted sources at atmospheric pressure (AP), such as AP-MALDI (or AP-LD [156] without matrix addition), by recording IMS images from fruit skin, plants, cell populations, and tissues [157, 158]. Guenther *et al*. [159] recently proposed AP-MALDI imaging of mammalian tissue by detection of selected neuropeptides with a spatial resolution down to 10 μm. The advantage of a matrix-free approach is the improved spatial resolution at the micron level, limited only by the laser diffraction limit. However, as already pointed out earlier, laser-based approaches are limited by the ionization yield; further combination with a post-ionization mode resolves at least partially such limitations, as demonstrated for the LAESI approach (see discussion below) [145].

Alternatively, the ability of an ambient DESI method, to localize the compounds on a surface has been applied in IMS applications. The recent development of IMS based on DESI for two-dimensional chemical mapping of condensed-phase samples was initiated by Cooks' group [160, 161]. The first DESI experiments were carried out in special applications of organic chemistry and forensic samples. Cooks and coworkers [162] tested DESI-MS for the direct chemical analysis of inks from different pens to investigate the potential of imaging DESI in forensic analysis. DESI-MS was also used to detect and identify the peptides from two-dimensional separations of cytochrome *c* and myoglobin tryptic digests on ProteoChrom HPTLC cellulose sheets [163]. Further biological applications of DESI imaging were reported, for example, to determine the spatial abundance distributions of the antipsychotic drug clozapine and its desmethyl metabolite directly in untreated, histological sections of brain, lung, kidney, and testis [161]. A lung tissue section taken from an animal after dose administration was imaged with a pixel size of 230×230 μm. These results indicated the use ability of DESI-MS imaging in pharmacology, toxicology, and oncology [160, 164, 165] as a means of seeking information about the distribution of drugs and their metabolites, lipids [166], or endogenous compounds in tissue without any type of chemical treatment. The DESI mode has been also applied to image the distribution of antifungal natural products across the surface of marine algae [167]. However, to date, the principal limitation of DESI-IMS is the image pixel size of about 250 μm. Some instrumental efforts have been made to improve that situation; for example, Kertesz and Van Berkel [168] reported a practical application of

DESI imaging of rhodamine dyes with a pixel resolution of 40 μm by careful control of the operating parameters such as the spray tip-to-surface distance, solvent flow rate, and spacing of lane scans. In fact, pixel sizes of the order of 10–40 μm are representative of the minimum area of tissue resolved that can be reached with the DESI approach. The thin-film layer of solvent on the local area of bombarded tissue leads to blurred images due to the recovery of some border areas. Nevertheless, a promising nanoDESI setup was proposed by Roach *et al.* [169], who used nanospray capillaries to transport and ionize the analyte, desorbed from the surface, allowing sampling spots smaller than 10 μm. Finally, DESI has been proposed as an ambient IMS technique for the rapid diagnostics of tissues. For example, Cooks and co-workers [170] demonstrated that improved IMS images of atheroma state can be obtained by using the charge labeling reagent betaine aldehyde directly in the DESI solvent spray (reactive DESI-MS), resulting in *in situ* chemical derivatization of cholesterol, which is selectively detected via adduct ion formation with ammonium. An additional example is displayed in Figure 20.7, where DESI-IMS imaging was

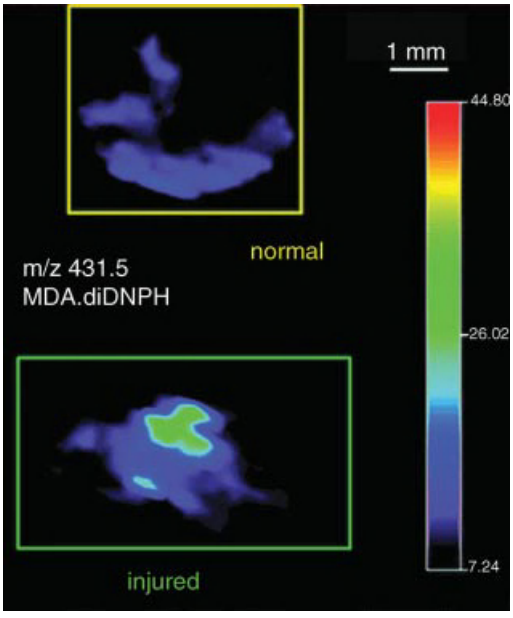


Figure 20.7 DESI-IMS images obtained from rat spinal cord cross-sections including normal and injured tissue. Images were obtained by detection of molecular $[M - H]^-$ species of the MDA·diDNPH compound, by the reactive DESI technique in the negative-ion mode. Selective detection of malondialdehyde (MDA) is used for rapid diagnostics as MDA is a marker of peroxidation processes of the tissue; the selectivity is obtained by *in situ* chemical derivatization of MDA on the tissue by using a solvent spray with dinitrophenylhydrazine (DNPH) reagent (reactive DESI conditions). Adapted from [171].

performed to interrogate the tissue cross-sections of injured rat spinal cord and normal healthy tissue. A clear distinction was obtained between the two spinal cord sections by detection of *in situ* chemically derivatized malondialdehyde (which assesses the peroxidation processes of the tissue) using dinitrophenylhydrazine reagent [171]. In this study, the combination of the DESI experiment and implementation of chemical reactions (reactive DESI mode) with MS/MS acquisition significantly improves the sensitivity and selectivity of the detection of target molecules.

The ambient LAESI technique was proposed by Vertes and co-workers [104, 145] as a method for the MS analysis of many different classes of compounds, ranging from small molecules such as pharmaceuticals, saccharides, lipids, and metabolites to larger biomolecules such as peptides and proteins. The interest in LAESI in comparison with AP-IR-MALDI is higher ionization yields (one to two orders of magnitude higher) [145]. Subsequently, a LAESI ionization source was used for IMS of plants [104], tissues [172], and cell populations [173]. Single cells were obtained as pixels of the IMS image of small cell populations by LAESI imaging experiments. Thus very promising IMS results are expected with the use of etched optical fibers, able to produce laser spot sizes of $<50\,\mu m$.

20.4
From Collision Activation to Ion–Surface Chemical Reactions for New Preparative Mass Spectrometry

Interactions of gas-phase ions with surfaces are an area of growing interest for both practical and fundamental reasons [174]. Practical interest in ion–surface interactions often involves their use in obtaining analytical information regarding either the ions or the surface. Depending on the operating conditions (nature of the surface and/or that of polyatomic ions [175], but also the kinetic energy regime, etc.), different phenomena occur: simple elastic collisions (resulting in reflection), inelastic collisions, which can eventually lead to surface-induced dissociation (SID), chemical sputtering, and also reactive collisions and finally soft landing (SL) of impacting ions at the surface (see Figure 20.8). At present, two main ion-collision processes display interesting MS applications, namely SID and its utility for structural analysis of biomolecules as an efficient activation mode for MS/MS experiments, and the SL of ions at the surface, which offers a preparative MS approach for modified surfaces.

20.4.1
Surface-Induced Dissociation

20.4.1.1 Tandem Mass Spectrometry and Collisional Activation

Among the various advances in MS, the development of MS/MS experiments have benefited major progress, leading to improved analytical performance (e.g., structural elucidation) [53]. Various activation modes exist, for example, specific activation

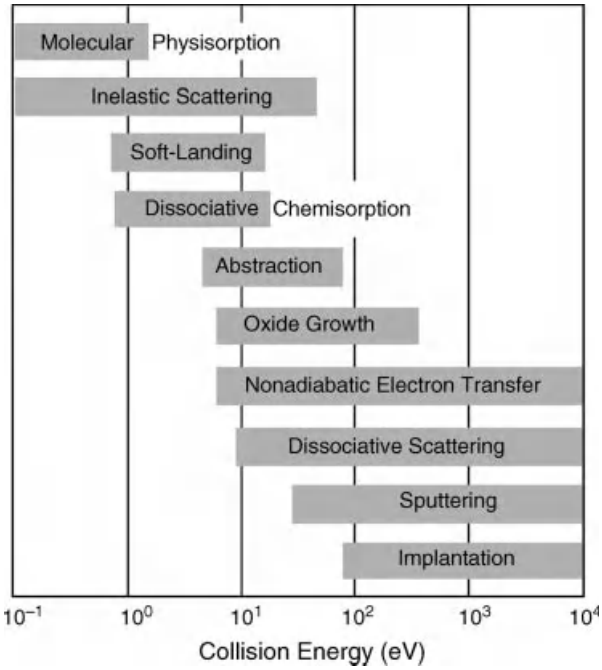


Figure 20.8 Fundamental processes associated with molecule–surface collisions. The shaded regions indicate the approximate kinetic energy ranges over which the processes occur or are typically studied. Reproduced from [175].

techniques have been designed for the ICR cell [52] such as electron capture dissociation (ECD), along with its specific uses for biomolecule analysis [176], and infrared excitation techniques such as infrared multiphoton dissociation (IRMPD) [177] and blackbody infrared radiative dissociation (BIRD) [50–52]. However, collision-induced dissociation (CID) is actually the most popular activation mode, implemented in most mass spectrometers [53]. CID has technology evolved along with the MS history. At the beginning of the 1980s, double-sector focusing instruments allowed the selection of the precursor ion by a magnetic field analyzer, its subsequent activation in a collision cell, and analysis of the final product ions by electrical sector scanning. The reverse geometry (i.e., *B*–*E*) instrument was characterized by high kinetic energy (KE) (several keV) collisions with the target gas (generally helium). Subsequently, the tandem triple quadrupole instrument was developed, allowing low collision energy processes (typically 10–100 eV).

The resulting CID spectra display strong differences in fragmentation channels. In fact, the former high KE regime mode yields both electronic and vibrational excitations. This results in fragmentation routes almost independent of the high KE conditions (i.e., target gas, pressure, collision energy of the selected ions, ion preparation, ion transfer, and dissociation time windows) in contrast to the low KE regime. Today, the low collision energy range is mostly applied in structural

determination [53]. Under these collisional conditions, the maximum internal energy transferred could be approximately determined from the "center of mass" energy (E_{cm}) according to the equation

$$E_{cm} = E_{lab} * \left[\frac{m_t}{m_t + m_i}\right]$$

where E_{lab} is the KE value and m_t and m_i are the mass of the target and selected ion, respectively). In contrast, in the high *KE* regime, the internal energy represents a very small fraction of E_{cm}, which explains why the product ion spectrum is almost independent of the collision conditions.

Nevertheless, it appears from the above relationship that, in the low KE regime with infinite m_t (target) values, the available E_{cm} will equal to the experimental E_{lab}. Thus, the maximum KE could be converted into vibrational energy for precursor ion activation. Consequently, the idea of collisionally activating the precursor ions on a surface was naturally introduced, to enhance the efficiency of the collisional activation process [178]. This activation method, called surface-induced dissociation SID), was pioneered by Cooks and co-workers [179, 180], who implemented SID technology in MS/MS (and later sequential MS^n) experiments in various combinations of spatial analyzers (called "hybrid" instruments) [181, 182], and also in various ion trapping devices [183].

20.4.1.2 Mass Spectrometers for SID Experiments

Many combinations of dynamic analyzers ("hybrid" instruments) developed for MS/MS applications have subsequently been modified to implement SID. For example, quadrupole-based hybrid instruments were altered from commercial versions, in which after precursor ion selection and ion-beam transmission to the surface under controlled KE, the second Q mass analyzer is placed at right-angles to allow subsequent SID product ion detection. Alternatively, combined sector instruments can be used, generally with a 45° (or lower) angle between the selected ion beam and the collision surface. Thus, various laboratory-built multisector [182, 184], QQ [185], and QQQQ [181, 186, 187] hybrid instruments have been proposed to conduct SID experiments. Cooks' group [182] developed a laboratory-built BEEQ hybrid instrument that allows the study of SID experiments in high and low KE regimes and also fundamental studies of other reactive ion–surface processes that occur at low KE. The incident and emerging beam angles, and also the KE of the incoming and emerging ion beams, can be controlled in such instrumentation. A pulsed ion beam without field scanning, such as a TOF analyzer, can be used for SID experiments. Actually, TOF analyzers can also be combined with sector, quadrupole dynamic analyzers, and even with ion trapping devices [188, 189]. More recently, SID was also combined with ion mobility instrumentation [190].

Alternative instrumental setups involving ion trapping devices have been proposed as one would expect more effective dissociation with multiple stages of SID activation (sequential MS^n experiments). Unfortunately, most of these instruments

suffer from poor transmission of the emerging ion beams. Nevertheless, the SID mode was introduced in an ion trap mass spectrometer [183] and also in an FTICR cell [178, 191] by first trapping the ions and subsequently accelerating them into either the walls of the trap or to a probe placed at one end of the trapping cell. Note that SID is especially advantageous for FTICR-MS instruments, given that CID in this ultra-high vacuum mass analyzer requires the introduction of gas, which has a negative effect on the peak resolving power.

20.4.1.3 From Surface-Induced Dissociations to Competing Ion–Surface Reactions

MS/MS experiments using the collisional activation were mainly dedicated to ion structure elucidation and fundamental studies of ion dissociation mechanisms. However, the detected fragmentation channels of SID fragments are mostly dependent on the KE conditions. In the high-energy collision regime, collisions with the surface lead to extended chemical ion sputtering, a process in which surface molecules are ejected into the gas phase after being ionized by chemical reactions with the projectile ions. Such a phenomenon is strongly assumed in SIMS ionization. In contrast, surface impact in the low KE range may produce both nonelastic (and thus ion fragmentation) and reactive collisions. Hence the most promising phenomena are then observed in the hyperthermal regime (KE between 1 and 100 eV), and have been extensively studied by the groups of Cooks [179–183, 185, 188] and Laskin [178, 191, 192].

The SID activation method remains a very promising technique, especially for high-mass ions, such as peptides and proteins, with relatively high dissociation thresholds, even though commercial instruments are rarely available [186, 190, 193]. SID spectra have been shown to be reproducible, with good signal-to-noise ratios, and gave comparable results to the CID mode. SID spectra display broader fragmentation patterns, allowing in a proteomic approach [135] better protein sequencing [178, 193]. Interestingly, charge-remote processes typical of high-KE CID experiments are also observed in SID experiments for KE of about 100 eV, whereas they are never detected in low-KE CID experiments. However, it is difficult to explain such contrasting observations by taking into account only electronic excitation during SID. Obviously, peptide fragmentations are initiated by both electronic and vibrational excitation steps. However, in the case of fatty acids [194], the SID spectra are characterized by extended charge-remote product ions, which suggest major mostly electronic excitations. In addition, it is also possible to determine the activation energies of fragmentation channels of polyatomic ions [195]. Different operating conditions have been also extensively studied [174, 179–189]. It has been shown that experimental factors such as surface composition, projectile structure, and incidence angle influence the amount of energy transferred into the internal energy of the ion and thus the precursor ion fragmentation patterns [175, 180]. An interesting feature of SID experiments is its reproducibility under controlled experimental ion–surface collision conditions, as shown in the Figure 20.9, where similar SID spectra of pyrene ions are obtained using two different BEQQ and QQ hybrid instruments.

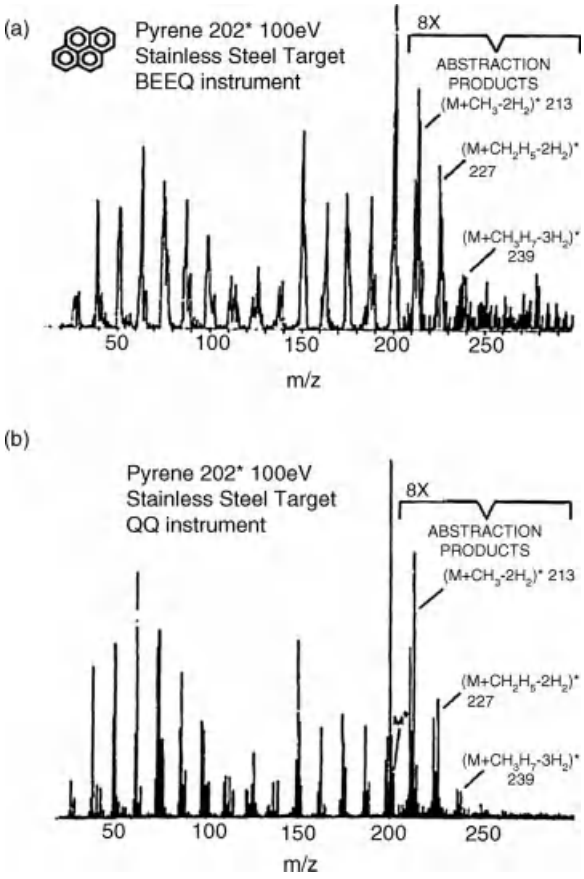


Figure 20.9 SID spectra of the pyrene molecular ion colliding with stainless-steel plates at 100 eV KE, obtained in (a) BEEQ and (b) QQ instruments. These SID experiments illustrate the reproducibility, independent of the instrument. Reproduced from [182].

However, the advantages of SID over CID activation modes are often diluted for metal surfaces owing to the presence of several competing processes, namely neutralization, chemical sputtering, and ion–surface complex formation reactions. In fact, the collided surface under vacuum conditions is generally recovered by an adsorbed pumping oil monolayer, which was considered to be at the origin of these particular product ions (see typically the abstraction product ions displayed in Figure 20.9).Hence different ion–surface reactions have been extensively studied to gain an improved understanding of the fundamentals of the related processes. However, no real applications involving these ion–surface reactions exist at present. Ion–surface reactions, such as abstraction of a hydrogen atom or a methyl group, are common when surfaces bear adsorbates and compete with the SID product ions. Hayward *et al*. [196] studied the low-energy collisions (30 eV) of benzene molecular ions with surfaces covered with a hydrocarbon overlayer. They showed in the SID spectra, the unexpected presence of $C_7H_7^+$ ions. They proposed that the formation of

the $C_7H_7^+$ product ions occurs from odd-electron molecular $C_6H_6^{+\cdot}$ by a charge-exchange reaction with the surface according to the following equation:

$$C_6H_6^{+\bullet} + CH_2\text{-Surface} \rightarrow [C_6H_6 + CH_2\text{-Surface}]^{+\bullet} \rightarrow C_7H_7^+ + {}^{\bullet}H\text{-Surface}$$

These preliminary observations led several authors to scrutinize the nature of the surface able to react with the impacting polyatomic ions. Early SID experiments displayed many ion–surface processes using a self-assembled monolayer (SAM) [197] as a well-known defined surface. These surfaces consist of alkanethiol monolayers adsorbed on gold mirrors evaporated on to silicon wafers, with terminal groups able to be held at the outer surface of the monolayer. Consequently, by appropriate choice of the terminal functional group, it is possible to obtain targets with different characteristics. These SAMs and other surfaces [198] have been tested with the aim of optimizing the efficiency of SID spectra and resolving the fundamentals of different ion–surface processes. Cooks and co-workers [199] compared low 20 eV collision product ions of impacting molecular $Si(C_2H_5)_4^{+\cdot}$ ions on different SAM surfaces, namely common, H-SAM, a hydroxyl-terminated SAM (HO-SAM) and a fluorocarbon SAM (F-SAM), as shown in Figure 20.10. They demonstrated that the SAM surface strongly influences the extent of fragmentation, that is, internal energy transfer variation during the collision (related to the effective mass of terminal groups), according to the relative order $CF_3 > CH_2OH > CH_3$. Finally, various systems (polyatomic ions versus surface nature) [198–201] have been studied. All systems display SID processes, resulting in precursor ion covalent bond fragmentations and additional competing ion–surface reactions, for example, neutralization by electron transfer, atom/group abstractions, and chemical sputtering.

Alternatively, a very promising ion–surface process observed at hyperthermal KE energy is SL. It is possible to collect a mass-selected gas-phase polyatomic ion on a surface as intact species (see Figure 20.11). This type of experiment opens up a new preparative mass spectrometry area [202].

20.4.2
Soft Landing and Preparative Mass Spectrometry

20.4.2.1 Soft Landing Instrumental Devices

Historically, the initial instrumental devices for SL experiments were those described for SID studies (see above) [202]. Subsequent analysis of the modified surfaces should be done in a second run. Post-analysis of the modified surfaces can be performed by either *in situ* or *ex situ* MS approaches (e.g., SIMS MS surface analysis) and/or by using spectroscopic methods (e.g., IR spectroscopy). It is impossible to circumvent this second analytical step (i.e., post-analysis of SL target analysis) to study the structural and chemical properties of "parked" charged molecular species. Various combinations of modified multiple sector, hybrid EB[SL]qQ [203], and quadrupole–TOF hybrid instruments [204, 205] were modified to implement *in situ* post-analysis of soft-landed products. However, such a MS approach still awaits incorporation into a commercial instrument [206]. For example, a QqTOF [205] (Q, quadrupole; q, RF-only quadruple;

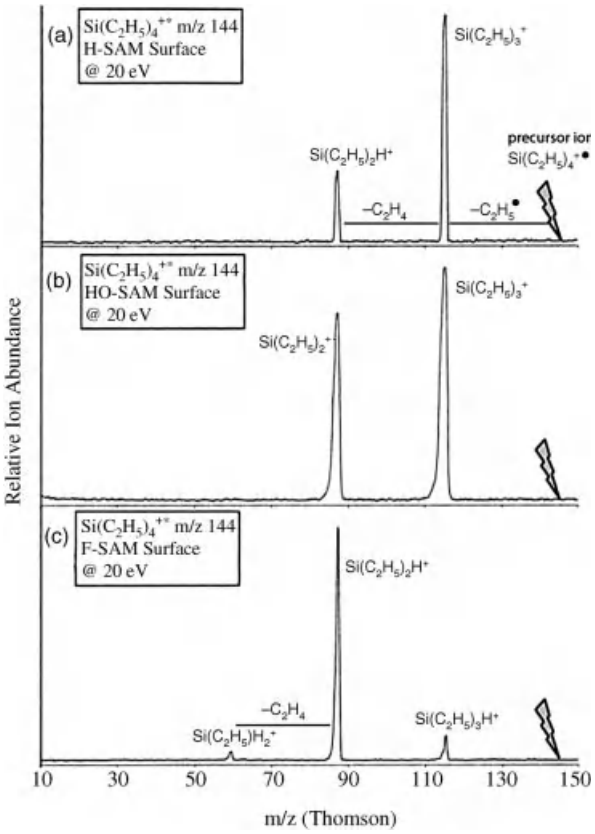


Figure 20.10 SID spectra of molecular $Si(C_2H_5)_4^{+\cdot}$ ions impacting (a) hydrocarbon SAM (as SAM), (b) end-hydroxyl SAM (HO-SAM), and (c) end-fluorocarbon SAM (F-SAM) surfaces at a collision energy of 20 eV. Reproduced from [199].

TOF, time-of-flight mass analyzers) has been modified from a commercial version by implementation of a retractable microscopic probe and ion beam imaging system (see the experimental setup described in Figure 20.12). This device allows direct visualization of soft-landed large macromolecular GroEL multimers ions (multiply charged species from 72+ to 64+ in an ESI source) deposited on a surface, using transmission electron microscope (TEM) imaging. A similar QqTOF hybrid instrument was reported by Rauschenbach *et al.* [207], in which the "landed" ions can be *in situ* analyzed using an in-vacuum SIMS ionization technique.

Another instrumental setup based upon ion storage has been proposed by Cooks' group, involving linear two-dimensional [208] or rectilinear [209] geometry ion traps. Such systems allow sequential ion trapping steps (of a large range of different m/z values) and the transmission (by axial ejection) of the mass-selected ions into an in-axis collection plate (see the temporal sequences of SL experiments in the linear ion trap in Figure 20.13). Note that the modified rectilinear ion trap instrument [209] is constituted of ion funnel interface and a bent square quadrupole for ion beam

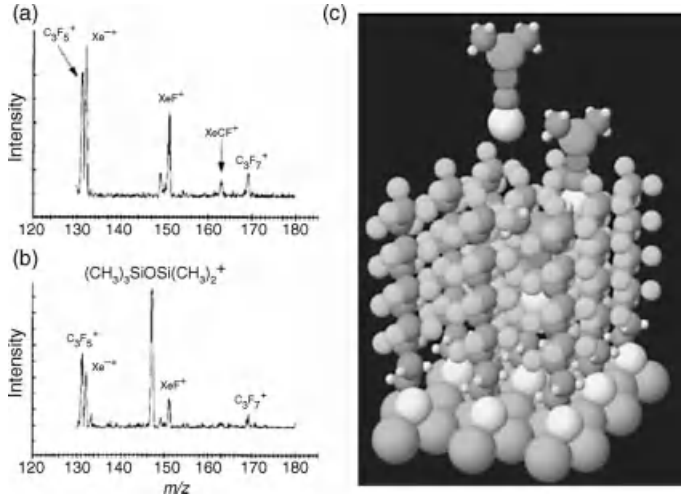


Figure 20.11 Mass spectrum recorded by TOF-SIMS after (a) 60 eV $Xe^{+\cdot}$ ion sputtering of an F-SAM surface and (b) subsequent impact on the same surface of $(CH_3)_3SiOSi(CH_3)_2^+$ ions (m/z 147) during 1 h at 5 eV collision energy. We observed in both SID spectra product ions formed by chemical sputtering (e.g., m/z 85) at the surface, and in spectrum (b) the presence of intact $(CH_3)_3SiOSi(CH_3)_2^+$ ions at m/z 147, which have been soft landed. (c) A three-dimensional molecular modeling representation of the soft-landing process for $(CH_3)_2SiNCS^+$ projectile ions on to an F-SAM monolayer surface. Adapted from [202].

transmission, which allows the elimination of neutral species for reliable SL experiments. In addition, this ion trap device has been adapted for post-landing analysis using an *in situ* SIMS technique [210]. SL devices have also been implemented in ultra-high resolution FTICR [211] instruments, with which *in situ* post-analysis of modified surfaces can also be performed.

A typical ion SL experiment implies first, the production of polyatomic ions from a suitable external source (i.e., multiply protonated proteins formed by ESI), before being gas-phase mass selected (into the mass spectrometer) to collide with the reactive surface at controlled collision energies. Subsequently, different offline MS analysis, using typically surface analysis SIMS or LD techniques [203, 204, 207] or alternatively ambient ESI [208] and DESI [209] modes or other spectroscopic methods [204, 207], were used to scrutinize the modified surfaces after the SL event. Today, as already pointed out, innovative instrument features allow *in situ* analysis [205, 210, 211], for example, using infrared reflection absorption spectroscopy (IRAS) [212]. Direct modified (inert or reactive SAMs) surface analysis (see Figure 20.14), is performed after gentle deposition of doubly protonated gramicidin S peptide, by monitoring the temporal evolution of peptide physisorption on the surface. For that purpose, the authors plotted specific soft-landed peptide absorbance bands, recorded with the IRAS technique. Alternatively, Cooks and co-workers [213] proposed an instrumental setup with two complementary characterization tools, *in situ* SIMS and *ex situ* surface-enhanced Raman spectroscopy (SERS).

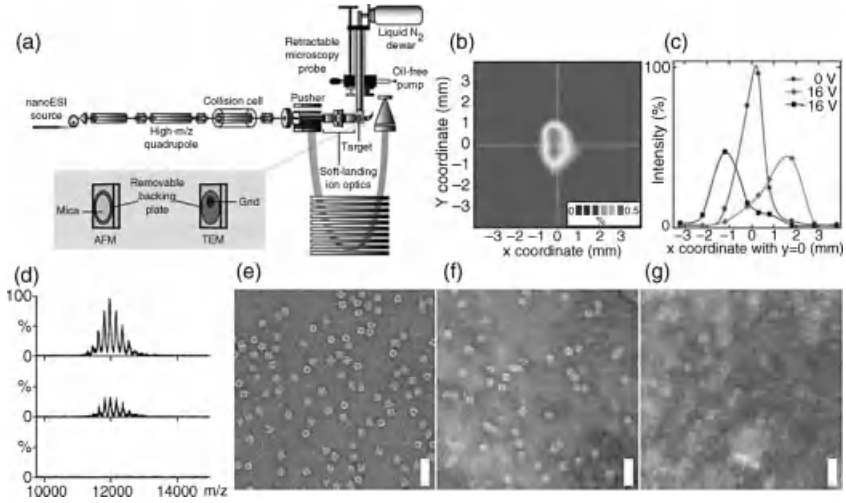


Figure 20.12 (a) Schematic diagram of the Q-TOF instrumentation modified for preparative MS. The modifications include a lens stack following the TOF orthogonal extraction source (SL ion optics), an interlock system for direct insertion of the SL target into the vacuum system (retractable microscopy probe) and a miniature line-of-sight detector for ion beam imaging. (b) Image of the ion beam at the SL target position recorded by intercepting the ion beam with a disc. In this way, an approximate cross-section profile of the ion beam is obtained. (c) Intensity of the ion beam versus the *x*-coordinate of the disc (with the *y* coordinate fixed at 0). This demonstrates the control of the ion beam lateral direction using deflection plates. After such control experiments, GroEL multimers are soft landed, and are visualized by using either AFM or TEM. (d) NanoESI spectra of GroEL multimers (with an average 70 + charge state centered at m/z 11 500, i.e., for a mass of about 803.2 kDa) acquired from the SL target containing no grid (top), grid with holes (middle), and a carbon-coated grid (bottom). These control experiments evidenced that the ion beam is aligned with the landing stage. TEM images showing (e) GroEL tetradecamer directly deposited from solution, (f) by nanoelectrospray deposition outside the mass spectrometer, and (g) after passing through the vacuum system. Scale bars are 50 nm. GroEL tetradecamers are clearly visible in (g), demonstrating their successful SL on to the surface. Adapted from [205].

20.4.2.2 **Applications of Preparative Mass Spectrometry**

Preliminary SL experiments demonstrated that silyl ether molecular ions can be gently landed on SAM films (see Figure 20.11). This ability to deposit polyatomic ions on a reactive surface opens a new preparative MS field. Various studies have shown promising applications for the purification and storage of biomolecules as intact molecular species [205, 214]. Most important, they demonstrated that soft-landed biomolecule ions can be recovered (post-analysis) with retention of the charges (at least partially) [215], of their native conformations [216], and of their biological activity [217]. For example, SL experiments display the unique ability to store, for long periods, multi-protonated proteins, which can subsequently be mass analyzed after surface washing (purification step) and readily characterized by an *in situ* proteomic approach [135] (enzymatic digestion and subsequent MS/MS experiments) [215, 217].

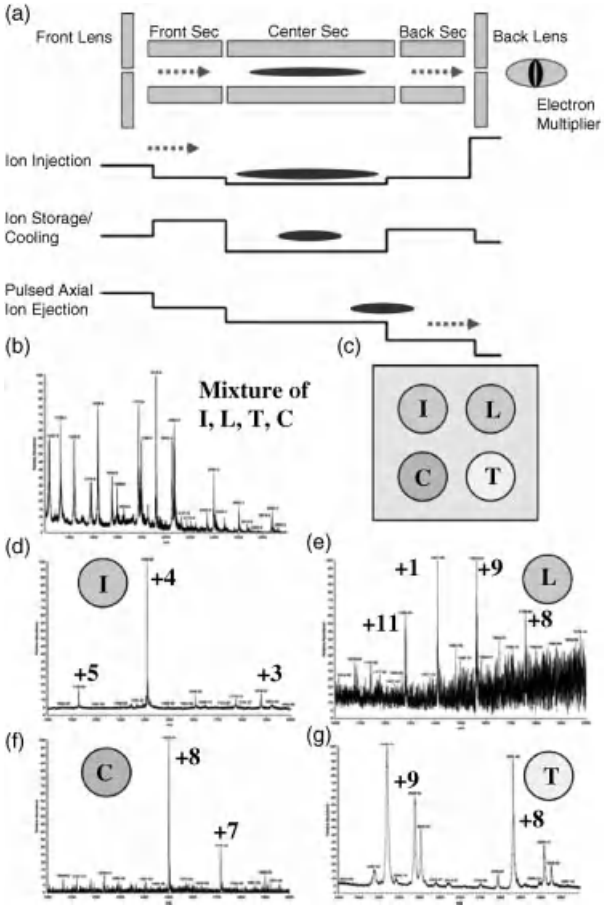


Figure 20.13 (a) Temporal sequences of DC voltages applied to the lenses and sections of the linear ion trap to achieve (i) ion injection, ion accumulation and mass-selective isolation (by radial ejection of unwanted ions) and (ii) axial ejection of trapped ions to the SL OH-SAM surface. The preparation of a protein microarray is exemplified in (b)–(g). First, the ESI spectrum (b) of the four protein mixture solution [composed of insulin (I), lysozyme (L), trypsin (T), and cytochrome *c* (C)]. (c) Depiction of the arrangement of spots in the prepared array; spots are spaced 5 mm apart. Finally, *ex situ* nanoESI analyses were performed after rinsing individually each protein spot, that is, nanoESI mass spectra of soft-landed (d) insulin, (e) lysozyme, (f) cytochrome *c*, and (g) trypsin peaks (note the presence of autolysis peaks for trypsin at m/z 2520 and 2831). Adapted from [208].

A typical example of protein microarray preparation is displayed in Figure 20.13, in which different mass spectra were obtained by direct ESI analysis of a protein mixture solution and by *ex situ* ESI post-analysis of purified SL proteins at different spots. In this study, Blake *et al.* [208] used a modified linear ion trap instrument (see above) equipped with an ESI source, where after ionization of the protein mixture solution (with a total concentration of 0.1 mg ml^{-1} of insulin, lysozyme, cytochrome *c*, and trypsin (I, L, C, and T, respectively in Figure 20.13), one multiply protonated protein

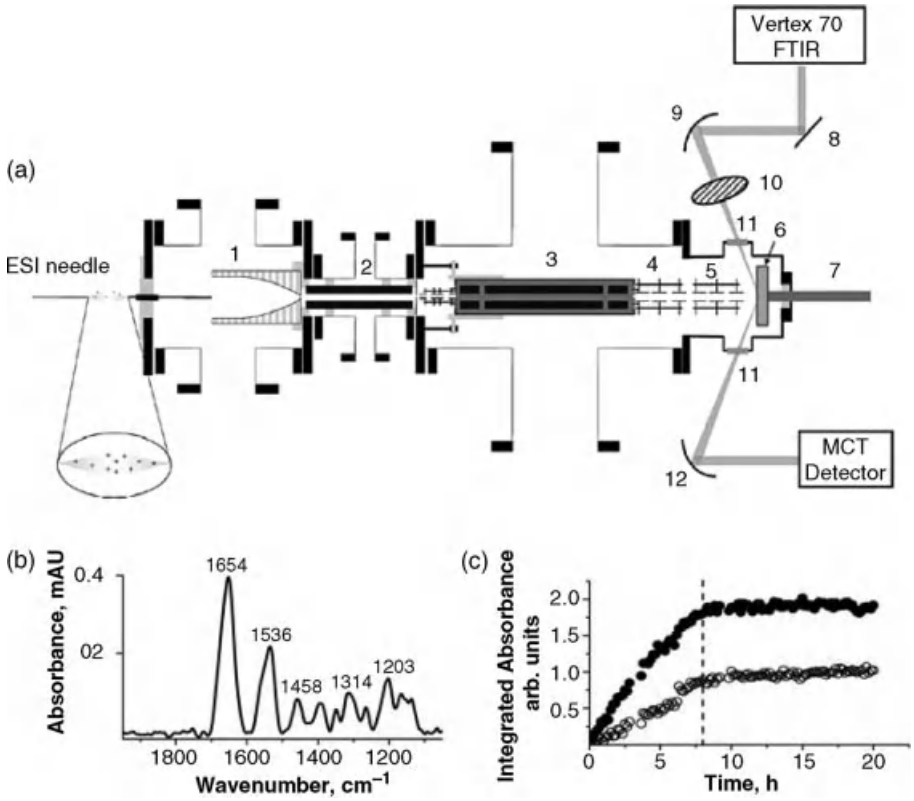


Figure 20.14 (a) Schematic view of the modified multiple quadrupole instrument: (1) ion funnel; (2) collisional quadrupole (CQ); (3) RF/DC quadrupole mass filter (RQ); (4) and (5) two Einzel lenses; (6) surface; (7) linear motion feedthrough for positioning of the surface; (8) flat mirror; (9) and (12) parabolic mirrors; (10) MIR wire grid polarizer; (11) ZnSe vacuum viewports. (b) The recorded *in situ* IRAS spectrum obtained from SL of doubly protonated gramicidin S, $[GS + 2H]^{2+}$, on to the F-SAM surface, with (c) the integrated absorbance of the amide I (closed symbols) and amide II (open symbols) bands as a function of time, obtained for 8 h of ion deposition and an additional 12 h after the end of SL (the dashed vertical line shows the end of SL). This example of *in situ* analysis of SL experiments evidences the ability for gas-phase biomolecule storage. Adapted from [212].

ion (e.g., $[I + 4H]^{4+}$ lysozyme ions at m/z 1438 in Figure 20.13e) is isolated into the ion trap analyzer and accelerated to impact the OH-SAM surface. The resulting spots (for each mass-selected protein as displayed in Figure 20.13d) are then *ex situ* analyzed with the same ESI-MS instrument from the recovered solution sample (a few nanograms of protein) after rinsing each spot. Note that the ESI spectra of soft-landed purified proteins in Figure 20.13 display partial charge neutralization [i.e., observation of a narrow charge state distribution in ESI spectra (d)–(g)] and, in the particular case of trypsin enzyme, additional peaks due to autoproteolysis, which demonstrated the retention of its biological activity. A similar biomolecule purification procedure was published, about 12 years ago, by Feng *et al.* [214], concerning the SL

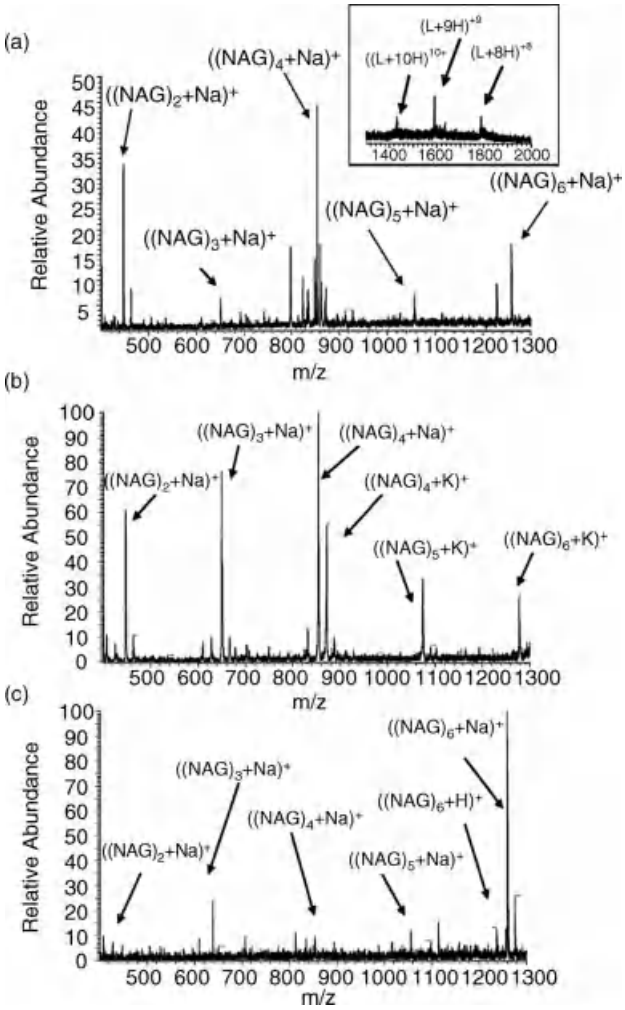


Figure 20.15 (a) ESI mass spectrum obtained after SL of $[M + 8H]^{8+}$ lysozyme ions on to a glycerol–fructose–hexa-*N*-acetylchitohexose liquid surface. The landed material and the supporting liquid substrate were recovered in a buffered solution, incubated, diluted with methanol, and finally analyzed by ESI-MS. The ESI mass spectrum displays the sodiated *N*-acetylglucosamine hexamer $(NAG)_6$ and also the sodiated *N*-acetylglucosamine multimers $(NAG)_5$, $(NAG)_4$, $(NAG)_3$, and $(NAG)_2$ resulting from lysozyme hydrolysis. Soft-landed lysozyme (L) is also observed (see inset at high *m/z* values). (b) ESI mass spectrum corresponding to hydrolysis of NAG_6 by solution-phase lysozyme. (c) ESI mass spectrum corresponding to NAG_6 stored overnight at the same temperature and pH and in the same reaction medium as in cases (a) and (b) without lysozyme. Reproduced from [217].

of a low-concentration DNA strand mixture. They used polymerase chain reaction (PCR) amplification treatment (strong amplification of DNA) to demonstrate that few traces of the ejected DNA strands (low signal-to-noise ratio) are present on the surface.

A preparative MS approach was applied for protein purification, separation, and identification by SL of the proteins on to liquid surfaces, namely a glycerol–fructose mixture [217]. Such a particular surface allows the retention of protein biological activity after protein collection and gas-phase separation [217]. This feature is exemplified in Figure 20.15, where lysozyme, an antibacterial enzyme, which degrades the polysaccharide component of the cell walls of many bacteria, was soft landed on to the liquid (glycerol–fructose) surface containing *N*-hexa-*N*-acetylchitohexaose, an oligosaccharide. The ESI mass spectrum (a) displays an efficient enzymatic action for the oligosaccharide (cleaved products) of lysozyme after being soft landed, by comparison with two control experiments, an in-solution enzymatic digestion, directly analyzed by ESI MS [mass spectrum (b)], and a control *N*-hexa-*N*-acetylchitohexaose SL experiments without lysozyme addition [mass spectrum (c)]. A similar capacity to retain biological activity has been evidenced for trypsin enzyme soft landed on a metallic surface [218] using atomic force microscopy and fluorescence post-analysis.

Alternative studies demonstrated the possibility of fabricating molecular coatings or nanostructures [219] from deposition of (nonvolatile) organic and/or biomolecular ions (e.g., peptide/protein) on the uppermost layers of films. Indeed, preparatory MS using SL of gas-phase mass-selected ions on surfaces permits highly specific modification of surfaces [217–220]. Note that recently SL experiments were conducted under ambient conditions by combining a commercial atmospheric ion source with a heated tube and a special ion switch system (for mass selection) [221].

20.5
Petroleomics: Role of Ultra-High Resolution and Data Treatment

As in other "-omics" areas of science such as genomics, proteomics, and metabolomics, high-throughput MS analysis of petroleum samples, termed "petroleomics," requires the acquisition of chemical fingerprints. However, Petroleum crude oil is a very compositionally complex organic mixture, with a large number of chemically distinct constituents, within an abundance range above 10 000. It is composed of saturated and unsaturated hydrocarbons, heteroatom (such as N, S, and O)-containing compounds, and a small percentage of metals, particularly Va, Ni, Fe, and Cu. The hydrocarbon fraction can be as high as 90 wt% in the lighter oils, compared with about 70 wt% in heavy crude oil.

For such complex mixtures, chemists have traditionally performed multiple wet chemical separations (extraction, precipitation, distillation, chromatography, etc...) to reduce the number of components and thus simplify the determination of molecular elemental compositions [222, 223]. A typical fractionation procedure of crude oils into SARA (saturates, aromatics, resins, and asphaltenes) fractions is based on the solubility of different compound families in various solvents. After removal of asphaltenes, the SAR mixture can be treated with increasingly polar solvents as the mobile phase. The aromatic and resin fractions are partially composed of polar N-, S-, and O-containing species. Apart from the traditional

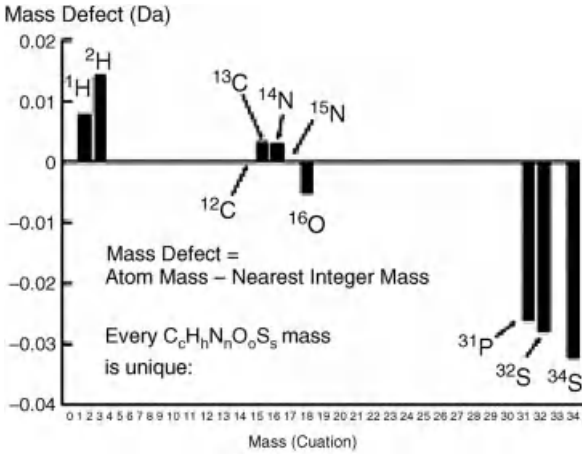


Figure 20.16 Isotopic mass defects of some common chemical elements. Reproduced from [227].

methods for the study of global physicochemical properties of petroleum, spectroscopic methods allow insights into petroleum composition [223]. To give a detailed picture of the composition of petroleum and/or that of its fractions at the molecular level, MS has become a well-suited method. MS yields a chemical fingerprint of a crude oil and also of its fractions, distillates. Interest in such a global MS approach relies on the fact that the physical properties and chemical composition of crude oil vary according to its origin [224–228].

20.5.1
Ultra-High Resolution Mass Spectrometry for Complex Petroleum Samples

However, a MS global approach suffers from limitations arising from the diversity of petroleum chemical composition and physicochemical properties. This results in strong discrimination of ionization yields, even though the ESI technique is well suited for a wide polar analyte mass range. In addition, thousands of peaks corresponding to molecular species (and potentially fragment ions from in-source dissociations) of oil components are detected in a small mass range in a single MS acquisition. The molecular masses of petroleum constituents are <1000 u; higher molecular masses have been attributed to noncovalent aggregates formed during petroleum processes or during gas-phase ionization processes [228]. Fortunately, each isotope of each atom is characterized by a unique mass defect [i.e., the difference between its exact mass and the nearest integer mass as nominal mass (see Figure 20.16)]. Thus, with sufficiently high mass resolving power, $m/\Delta m$, it is possible in principle, to resolve and identify the elemental composition of any molecule, even in a complex mixture. Finally, Ultra-High Resolution Mass Spectrometry (HRMS) has recently created a new "-omics" field, "petroleomics," namely the relationship between the chemical composition of a fossil fuel and its properties and reactivity.

Marshall's group [224–228] has extensively developed HRMS approaches for studies of petroleum products and refining processes.

20.5.1.1 Accurate Mass Measurement

Ultra-high resolution FTICR mass analysis [50–52] allows resolving species with very close elemental compositions and thus the structural characterization of all (in fact, of a major part) of the chemical constituents of petroleum. Actually, a mass resolving power $m/\Delta m$ from 400 000 to 1 000 000 is accessible with an 9.4 T FTICR instrument then, it is possible to resolve close isotopic peaks up to 900 u [224]. For example, the simultaneous detection of a sulfur–nitrogen-containing compound ($C_{36}H_{43}NS$) and a sulfur–oxygen-containing compound ($C_{28}H_{53}O_3S_2$) implies to be able of distinguishing peaks separated by 720 μu, hence it requires resolution of 1 000 000. An accurate mass measurement below 0.0001 u allows the assignment of a unique elemental composition, $C_cH_hN_nO_oS_s$, to singly charged ions in the 300–400 u mass range. At higher mass, an assignment based on the only mass measurement accuracy within a ppm experimental mass measurement error, is not able to provide a unique elemental composition [229].

Resolution of isobaric ions allows the speciation of chemical classes that are not observed with other MS techniques. However, ultra-high mass resolution is not sufficient for determining the tens of thousands of petroleum compounds with very different relative intensities. The dynamic range in FTICR-MS, even though the most powerful, is limited to up to 10 000 from a single acquisition. In addition, the mass measurement accuracy will be poorest for ions of low relative abundance. The most direct (and expensive) way to improve the performance of FTICR is to increase the magnetic field strength [230], B, as the mass resolution and mass resolving power increase linearly with B [50–52]. Alternatively, Marshall and coworkers proposed a phase correction procedure for the measured FTICR signal, which allows data display in the absorption mode, resulting in an increased resolving power and improved mass accuracy measurements [50–52, 228]. Today, the routine broadband ultra-high resolution FTICR-MS [223] is able to resolve up to thousands of different elemental compositions in the original sample from a single mass spectrum (see the example of a global negative ESI mass spectrum and a zoom into a narrow mass range of crude oils in Figure 20.17) [224–228, 230].

However, among thousands of detected petroleum components, their chemical compositions are related to each other, forming compound families, as displayed in Figure 20.17. Considering that each component possesses an elemental composition $C_cH_hN_nO_oS_sP_p$, a compound "class" is defined for compounds that possess elemental compositions with the same heteroatom content. For a given compound class, each additional ring or double bond decreases the number of hydrogen atoms by 2 u, hence it is possible to determine the compound "type" (i.e., the number of insaturations) from the number of hydrogens relative to carbons. Note that in industry, it is common to use the Z values in the elemental composition, expressed as $C_cH_{(2c+Z)}N_nO_oS_sP_p$, where Z is termed the hydrogen deficiency and characterizes the aromatic character of the compound. In addition, the repeating mass (CH_2) for a

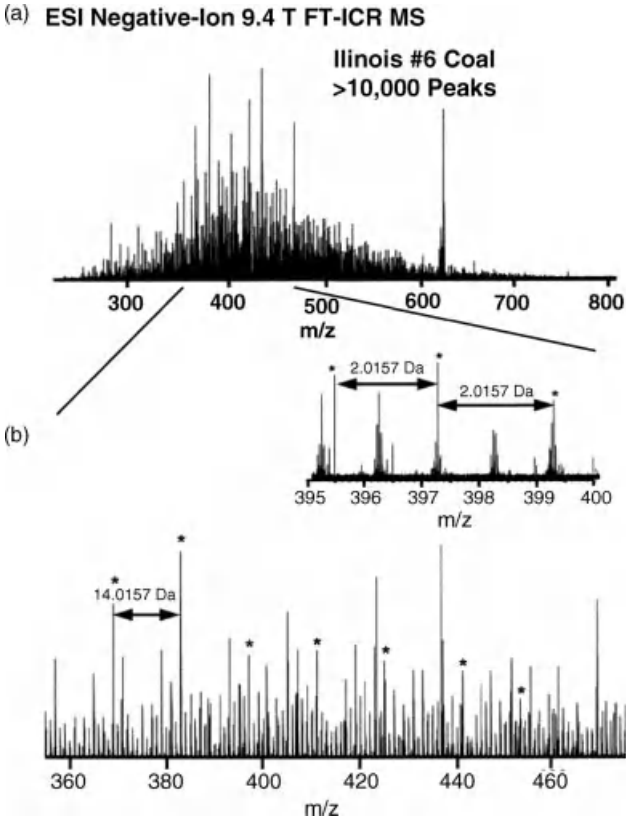


Figure 20.17 (a) Negative-ion ESI mass spectrum of Illinois No. 6 coal obtained in a 9.4 T FTICR instrument and (b) expanded mass spectra, $360 < m/z < 460$ and $395 < m/z < 400$, from the same ESI mass spectrum. Typical petroleum analysis displays compound families. Asterisks denote members of the same alkylation series, separated by 14.0157 Da (CH_2) (bottom). Peaks separated by 2.0157 Da (upper right) correspond to addition of a ring or double bond (DBE value increase). Adapted from [225].

hydrocarbon family is 14.01565 u. Finally, species of the same "class" (i.e., the same numbers of heteroatoms) and the same "type" (i.e., the same number of rings plus double bonds) display different numbers of CH_2 groups (i.e., a "carbon number distribution").

20.5.1.2 **Data Graphical Representations**

Finally, a routine broadband FTICR mass spectrum of petroleum displays thousands of peaks, differing by few mDa along 200–1000 Th mass range, which need additional data treatment or at least, simpler data representation. A variety of graphical methods were used to visually display *HRMS* data and characterize crude oil samples. However, reducing and visualizing the complex ultrahigh-resolution mass spectra is not trivial.

First, mass spectra were rescaled from the IUPAC mass scale (based on the ^{12}C atomic mass as exactly 12 u) to the Kendrick mass scale [231]. Kendrick mass is obtained from the IUPAC mass according to the following equation:

$$\text{Kendrick mass} = \text{IUPAC mass} \times (14/14.01565)$$

Homologous series (compounds with the same constitution of heteroatoms and number of rings plus double bonds, but different numbers of CH_2 groups) will have identical Kendrick mass defect, defined by:

$$\text{Kendrick mass defect(KMD)} = \text{nominal Kendrick mass(NKM)} - \text{exact Kendrick mass}$$

Useful graphical methods can also categorize petroleum constituents according to their aromatic characters; molecular formulae could be abbreviated according to their *type*, double bond equivalents (DBE), and *class*, heteroatomic components, that is

$$\text{DBE}\left(C_cH_hN_nO_oS_sP_p\right) = c - h/2 + n/2 + 1$$

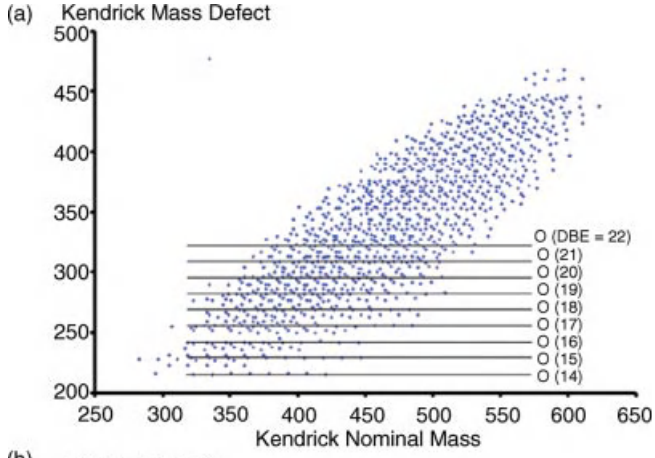
Note that with the index "hydrogen deficiency," Z, defined from the elemental composition, a relationship exists between Z and DBE:

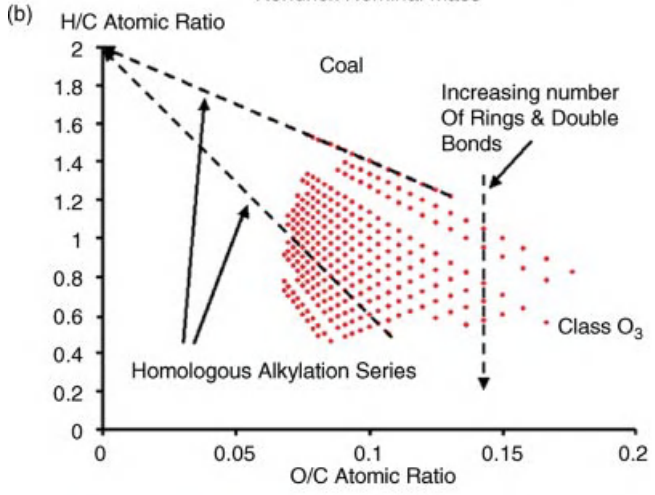
$$Z = 2(\text{DBE}) + n + 2$$

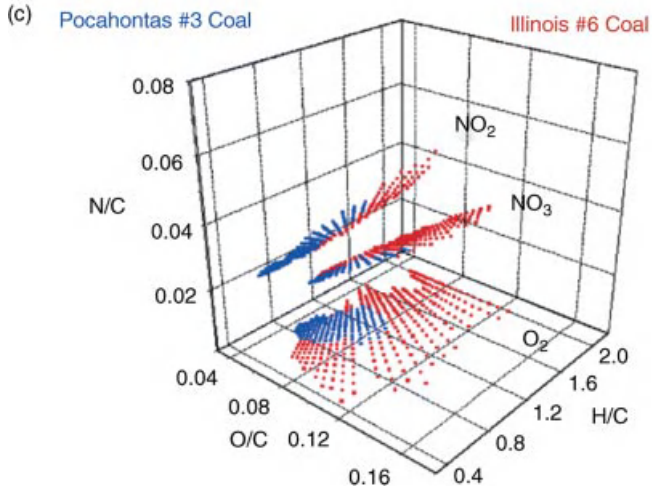
Within these rescaled data, different graphical modes have been proposed to display HRMS data from a petroleum sample.

Kendrick mass defect (KMD) and nominal Kendrick mass (NKM) values are plotted to produce Kendrick plots [230]. This compact mass spectral display allows visual resolution of up to thousands of peaks and the assignment of the species (see Figure 20.18). Typical two-dimensional Kendrick plot sorts compounds into homologous series according to their carbon skeleton size, classes, and types. Compounds of the same class and type but different alkyl chain lengths are separated by 14 u in nominal Kendrick mass, but display zero difference in Kendrick mass defect, and therefore fall on a single horizontal line. Compounds of different classes are readily identified, because their Kendrick mass defects are displaced vertically from each to other classes. In addition, every additional ring or double bond lowers the nominal Kendrick mass by 2 u, but also increases the Kendrick mass defect. Hence clear vertical separation is also visualized between carbon number distributions (see the different DBE values displayed for the O-compound family in Figure 20.18).

van Krevelen diagrams were introduced in the 1950s as a means to analyze bulk elemental data of coal samples. The diagram consists of a plot of the ratio of hydrogen to carbon as the ordinate and oxygen to carbon as the abscissa [232, 233]. Three- or two-dimensional plots of H/C versus O/C, with (or without) additional their relative abundances or N/O ratio scales, can be obtained (see Figure 20.18). This attractive procedure allows one to separate graphically all the compound classes for a given sample, and to provide a pattern of unsaturations and skeleton size for each class; heteroatom classes may be separated on one axis (e.g., S/C ratio to distinguish classes differing in the number of S atoms), and DBE differences spread out along the other


(a)
Kendrick Mass Defect
500
450
400
350
300
250
200
250
300
350
400
450
500
550
600
650
Kendrick Nominal Mass
O (DBE = 22)
O (21)
O (20)
O (19)
O (18)
O (17)
O (16)
O (15)
O (14)


(b)
H/C Atomic Ratio
2
1.8
1.6
1.4
1.2
1
0.8
0.6
0.4
0.2
0
0
0.05
0.1
0.15
0.2
O/C Atomic Ratio
Coal
Increasing number
Of Rings & Double
Bonds
Class O3
Homologous Alkylation Series


(c)
Pocahontas #3 Coal
Illinois #6 Coal
N/C
0.08
0.06
0.04
0.02
NO2
NO3
O2
0.04
0.08
O/C
0.12
0.16
2.0
1.6
1.2
0.8
0.4
H/C

axis (H/C ratio). A homologous series of compounds that contain the same number of rings plus double bonds and the same heteroatom composition, but different numbers of CH_2 groups, are displayed as diagonals.

Alternatively, other visualization methods have been devised to characterize petroleum samples, for example, by sorting compositions according to heteroatom class, as displayed in Figure 20.19. For a given heteroatom class, plots of the DBE distributions, that of the DBE versus carbon number, or also that of the carbon versus mass (CvM) diagram can be selected for data presentation. Such visualization methods are reported in Figure 20.19 for the comparison of aromatic fraction with crude oil compositions obtained from positive ion ESI-FTICR experiments [234]. In this study, similar graphics between the two distributions were observed, demonstrating that the efficiency of ESI for polar species is relatively unaffected by the presence of other species in the crude oil.

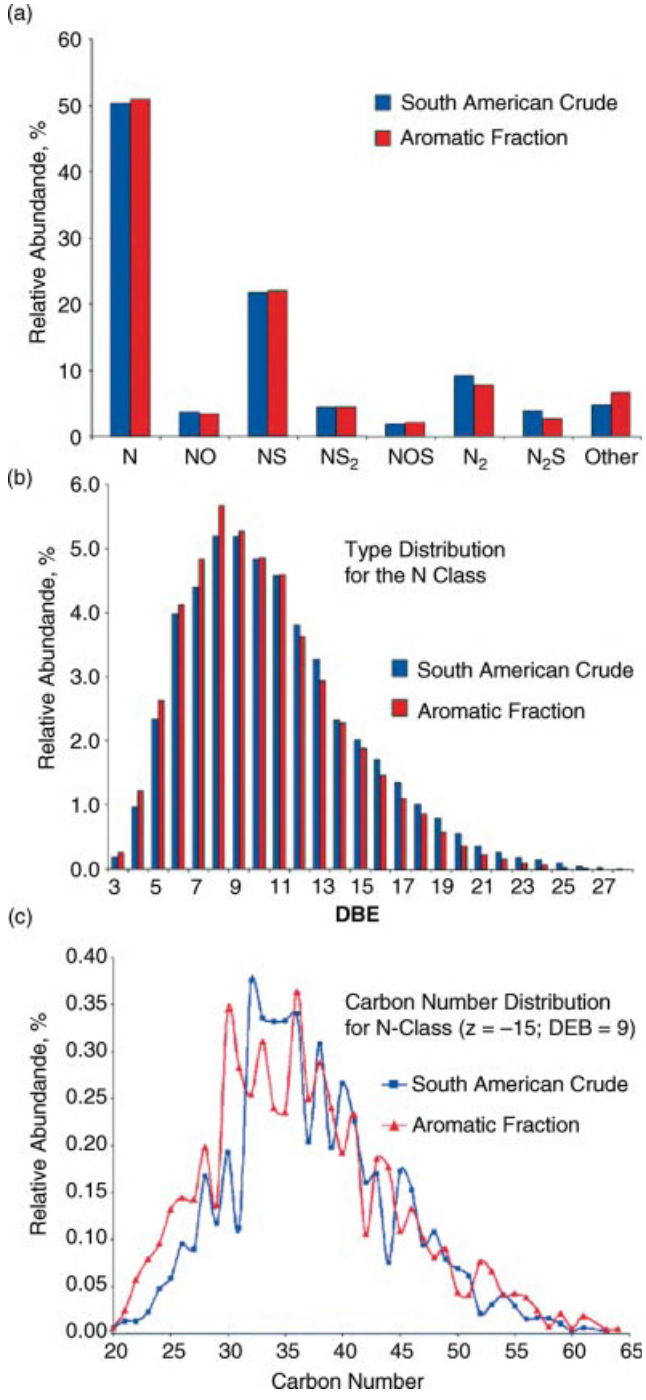
These graphical modes can be rendered more informative by color coding the relative abundances of each identified species, thereby converting the mass spectrum to an image (see Figure 20.20). The preferred graphical image is generally a plot of DBE versus carbon number for a given heteroatom class with a color coding of relative ion abundances [228]. These graphical images were used to characterize in Figure 20.20, distillation cuts obtained at different boiling points [235, 236].

Note that statistical methods such as principal component analysis have been applied to the treatment of HRMS data for petroleum [237]. In all cases, graphical representations provide easy data visualization from different petroleum samples and thus facilitate sample comparison. It also allows the assignment of unique elemental compositions to be extended from accurate mass measurement up to 900 u or higher by extrapolation from the graphics.

20.5.2
Improvements to Mass Spectrometry Methodology

Petroleomics benefits from the development of MS technology, above all upon improvements in desorption/ionization techniques. Previous illustrative examples related to recent ESI-FTICR instruments [224–228], but petroleum analysis has been extensively performed since the beginning of the history of MS. Today, the chemical composition of petroleum samples can be determined using a combination of various ionization technologies with a FTICR mass spectrometer to gain complementary data, with the advantages and disadvantages associated with each ionization method. Molecular ions ($M^{+\bullet}$) from low-voltage electron ionization (EI) [238], field ionization/field desorption (FI/FD [238–240], or protonated/deprotonated molecules

Figure 20.18 (a) Kendrick mass defect versus Kendrick nominal mass (DBE denotes double bond equivalence, that is, number of rings plus double bonds), (b) two-dimensional van Krevelen diagram from pyridine-extracted Pocahontas No. 3 coal, and (c) three-dimensional van Krevelen diagram for members of the classes, N, NO, and NO_2, from the same pyridine-extracted Pocahontas No. 3 coal (red) and from Illinois No. 6 coal (blue). Note that 3D van Krevelen diagrams allow the clear distinction of the two different coals. Adapted from [233].


(a)
Relative Abundande, %
South American Crude
Aromatic Fraction
N
NO
NS
NS2
NOS
N2
N2S
Other
(b)
Relative Abundande, %
Type Distribution
for the N Class
South American Crude
Aromatic Fraction
DBE
(c)
Relative Abundande, %
Carbon Number Distribution
for N-Class (z = –15; DEB = 9)
South American Crude
Aromatic Fraction
Carbon Number

by CI [241], laser-assisted ionization techniques, ESI [224], and other API sources [230] without significant fragmentation have been produced from crude oils.

Historically, the principal ionization method was bombardment with high-energy electrons [238] (EI typically at 10–18 eV acceleration energy). This gas-phase technique is typically limited to volatile, low-mass and nonpolar hydrocarbons and is characterized by extensive in-source fragmentation of molecular radical cations ($M^{+\bullet}$). Additionally, the presence of closely related components precludes the use of characteristic fragments ions for precursor identification. This problem can be partially resolved by coupling gas chromatography (GC) with MS (GC and/or two-dimensional GC–GC) by adding retention time information. Moreover, to acquire chemical information on higher molecular weight compounds and higher boiling fractions, GC–FTICR has also been coupled with pyrolysis systems [242]. Nevertheless, GC–MS methods were, and still are, restricted by the maximum temperature of the GC ramp (thermal integrity column). Moreover, extensive fragmentation of molecular ions (weak ion dipoles) into common fragment ions of the same family of compounds [e.g., typical $C_nH_{(2n+1)}^{+}$ fragment ions of alkanes] makes the determination of exact isomer structures difficult. This gas-phase approach has very limited performance, providing a limited insight into the chemical composition of petroleum.

"Softer" gas-phase ionization modes have been tested, such as Penning ionization [243], field ionization (FI) [239] and field desorption (FD) [238, 240] techniques, which provided an interpretable molecular profile of the petroleum samples. The principles of FI and FD are based on electric field-assisted gas-phase ionization, resulting in limited fragmentation of molecular ions, compared with the EI mode. FD is an offspring of FI; both are accessible in the same instrumentation setup. However, whereas FI is based on tunneling effects from the strong local electric field (by supplying the sample close to the electrical emitter), in FD, the sample is desorbed on a reactive surface (an activated emitter such as dendrites or carbonaceous/polymer materials), resulting in desorption processes induced by multiple field-enhanced microneedles of dendrites [244]. Under FD conditions, cationization and proton transfer processes occur. For petroleum samples, FD-FTICR experiments yield abundant ions from several species of petroleum not observed by ESI, including benzo- and dibenzothiophenes, furans, cycloalkanes, and polycyclic aromatic hydrocarbons (PAHs) and appears as a complementary technique to the usual ESI-FTICR experiments. A Penning ionization [243] coupled FTICR analyzer could be an alternative for producing intact molecular ions. Indeed, this gas-phase ionization mode allows control of the internal energy transfer to $M^{+\bullet}$ ions with the choice of excited gas (i.e., He, Ar, Xe, Kr, or N_2).

Nevertheless, today, ESI-FTICR is the preferred MS approach for petroleum, extensively developed by Marshall's group. Zhan and Fenn [245] first demonstrated that ESI technique could generate abundant molecular ions from the most polar N-,

Figure 20.19 Visualization methods applied to crude oil and its aromatic fractions from positive ion ESI FTICR mass spectra. The compound relative abundances are plotted according to (a) the compound class, (b) the relative abundances to the DBE values for the basic N compounds (DBE indicates the number of rings plus double bonds), and (c) the carbon number distributions for N_1-class compound. The carbon number range indicates the carbon skeleton size. Reproduced from [234].

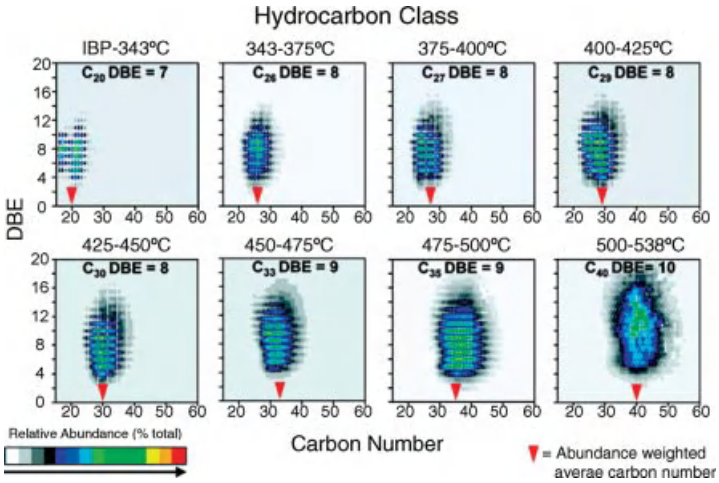


Figure 20.20 Color-coded isoabundance contour plots of DBE versus carbon number for the hydrocarbon class of Athabasca bitumen distillate. The carbon number abundance distribution maximum (red arrow) shifts from C_{20} at 343 °C to C_{40} at 500–538 °C boiling points. The DBE values also show a gradual increase in aromaticity from DBE ≈ 7 to DBE ≈ 10 with increasing boiling point. Reproduced from [235].

S-, and O-containing compounds in petroleum distillates. Although such species represent a small fraction (<15%) of most crude oils, they are important for petroleum exploration, production, and refining [246].

However, the ionization efficiency of ESI for one species can be greatly affected by the presence of other species. To elucidate a chemical composition that is as detailed as possible, one solution is to perform both positive and negative ESI experiments to acquire complementary MS data. Positive-ion ESI favors the most basic compounds and thus preferentially ionizes nitrogen-containing compounds [224–228, 246], whereas the negative-ion mode allows successful analysis of neutral and acidic compounds [238, 247] such as naphthenic acids [248]. Note that coupling of liquid chromatography (LC) to API-MS techniques has been tested [249, 250]. However, most LC–MS experiments display insufficient chromatographic resolution, which limits composition determination. This explains the current preferential use of the ultra-high resolving power and mass accuracy of FTICR instruments, without prior chromatographic separation.

ESI selectively desorbs and ionizes the relatively minor polar constituents of crude oil, so it can be interesting to gain access to less polar species (e.g., paraffins, cycloparaffins, aromatics, thiophenes, etc.) and possibly in the same instrumentation interfaced with API sources, by using APCI [251] and APPI [230, 252] techniques, which are characterized by gas-phase ionization of less polar compounds.

Ionization methods such as in-vacuum FD [238] and APPI [45] are used to observe less polar components, such as S-containing components (largely discriminated in the ESI mode, compared with N-containing compounds). The APPI technique [253], based on photoionization processes, displays efficient ionization towards low-polarity

compounds, almost excluded from APCI and ESI sources [230, 252]. However, in APPI of petroleum samples, a broader range of compound classes [230], not only N-, S-, and O-containing compounds, as displayed with ESI, are produced, nonpolar aromatic compounds can also be ionized by direct photoionization. In addition, the same analyte (e.g., N-containing compounds) may produce both $M^{+\bullet}$ by direct photoionization and $[M + H]^+$ ions by subsequent ion–molecule reactions. APPI applications typically use a dopant (typically toluene or acetone) to promote proton transfer reactions, resulting in major $[M + H]^+$ ions. Thus, an APPI-based mass spectrum is considerably more complex, with protonated and radical ions, leading to an increased need for high performance from the coupled mass analyzer.

Other ionization techniques have been tested, for the analysis of different petroleum fractions particularly laser samples-assisted techniques such as laser desorption [254], MALDI [255], and also two-step laser MS [256], the latter was presented as an alternative to MALDI for measuring molecular weight distributions of aggregates without the need for matrix addition.

Additionally, ambient techniques have also been applied to test the complementary capacities of these modes, compared to the current use of ESI. Schrader *et al.* [257] proposed AP-LD technique coupled to FTICR as a novel tool for analyzing nonpolar aromatic heterocyclic compounds including the S-containing compounds, in crude oils. LIAD coupled with subsequent gas-phase ion–molecule reactions was also tested for analysis of Athabasca bitumen distillates [106]. This source decouples sample evaporation from the ionization step by reagent ions. Preliminary results showed efficient ionization under ambient conditions of saturated hydrocarbons (without extensive in-source fragmentation) over a wide molecular mass range [258]. An interesting and innovative approach was also proposed by Wu *et al.* [259], which used the ambient DESI ionization mode under particular conditions for the successful analysis of saturated hydrocarbons. Reactive DESI-MS takes advantage of discharge-induced oxidation in conjunction with *in situ* alcohol derivation using betaine aldehyde as the reactive DESI reagent (see Figure 20.21). The major advantages over gas-phase modes with heating and/or vacuum conditions is the absence of hydrocarbon ion fragmentations. Note also that an Atmospheric Solids Analysis Probe (ASAP) introduction technique [260] [combined with ion mobility mass spectrometry (IM-MS)] was used to fractionate compounds according to their boiling points, by using a ramp of source temperature.

Alternatively, IM-MS was combined with an FTICR instruments to achieve rapid sample post-ionization separation without wet chemical prefractionation [261]. The ion mobility approach is used to determine the chemical structures of compounds found in crude oils on the basis of their relative gas-phase ion mobility through a high-pressure collision cell filled with an inert gas. The ions were separated according to their cross-section values (i.e., related to their shape, size, and conformation); thus IM-MS helps to distinguish isomeric compounds of petroleum samples. Molecules sharing a similar core structure (e.g., a homologous $–CH_2–$ series) are aligned in the plot and molecules differing in the number of hydrogen atoms display significant changes in the core structure and thus different cross-sections [262]. Additional

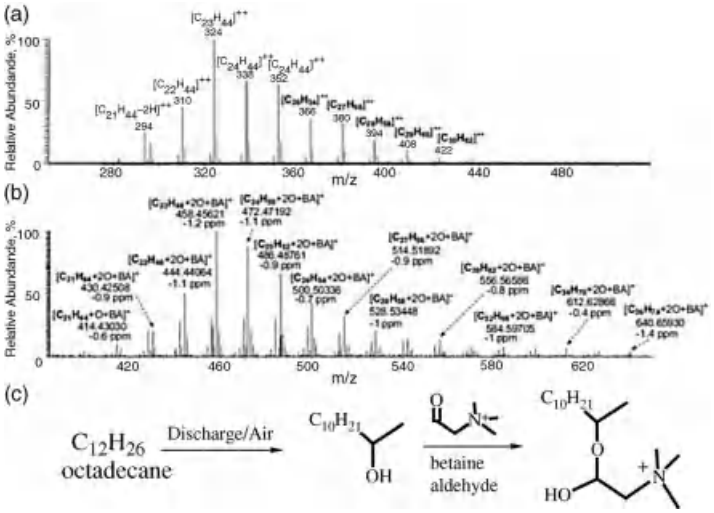


Figure 20.21 (a) Field ionization TOF mass spectrum and (b) reactive DESI-Orbitrap mass spectrum of vacuum gas oil saturates. In the latter case, reactive DESI experiments were conducted by spraying on to the deposited petroleum an acetonitrile–chloroform solvent mixture (1:2 v/v) containing 50 ppm of betaine aldehyde (BA). (c) Mechanism of oxidation of hydrocarbons under ambient conditions and *in situ* reaction between the oxidation produced alcohol and betaine aldehyde. Adapted from [259].

structural information obtained from IM-MS experiments concerns high mass aggregates. Their reduced ion mobility values suggested that higher mass components of petroleum crude oils result from noncovalent aggregation rather than planar structures obtained from additional fused rings [261].

20.5.3 HRMS Analysis of Oil

20.5.3.1 Chemical Composition of Crude Oils and Fractions

Extensive MS studies have been performed to determine the simpler chemical composition of SARA fractions of crude oil. Nonvolatile hydrocarbons found in saturate and aromatic fractions of petroleum have been successfully characterized by GC–MS (sometimes with prior chemical derivatization) [239]. In contrast, the resin and asphaltene fractions are composed of most polar, nonvolatile, and high-boiling materials, so GC–MS analysis is not suitable. Recently, ESI coupled with FTICR-MS has been successfully applied to characterize SARA fractions [234, 263] of crude oils and bitumens. Of course, in this approach, a detailed picture of the fractions is obtained by polar molecule detection. Nevertheless, Klein *et al.* [234] reported that positive-ion ESI mass spectra of crude oil and the aromatic fraction are highly similar,

as revealed by the plots of relative abundances according to the compound class in Figure 20.19, demonstrating that it is not necessary to isolate the polar aromatic fraction to characterize its chemical composition in a petroleum crude oil.

Additional insights into fraction chemical compositions have been gained by scrutinizing the specific sulfur content. Sulfur species are removed during refining operations as they are known to promote corrosion in refinery materials and petroleum handling. Determination of their detailed composition in crude oil and in SARA fractions is then very important. In light distillate fractions, S-containing compounds can be readily analyzed using gas chromaography approach with sulfur-selective detection or MS [264]. However, under positive-ion ESI conditions, sulfur compounds are discriminated against most basic N-containing compounds. Finally, a detailed composition of sulfur species was obtained within prior methylation derivatization, followed by HRMS analysis of the synthesized methylsulfonium salts [265]. Variable sulfur compound compositions were detected in SARA fractions, demonstrating, that the saturate fraction contains the least amount of sulfur species and most S_1 class species, whereas the resin and asphaltene fractions contain higher amounts of multi-heteroatom (N_1S_y, O_xS_y, $N_1O_yS_z$) class species [266]. Alternatively, the APPI technique revealed a better ionization efficiency for nonpolar S-containing petroleum compounds, given a successful molecular characterization of crude oil and that of its SARA fractions [267].

The ESI-FTICR approach has already proved capable of distinguishing crude oils and/or its distillates according to their geochemical origin and maturity [233, 250, 266, 268]. Understanding the physical characteristics of different oils and relating them to their chemical compositions are important industrial concerns, in developing new refining technologies and processing methods, better suited for heavier feedstocks and residues. The availability of "light" crudes is diminishing; the petroleum industry is therefore shifting towards "heavier" oils rich in heteroatoms. Ultra-high resolution FTICR-MS was, for example, applied to the Athabasca oil sands in Canada, a crude bitumen [269], and Venezuela extra heavy oil [266]. Further, shale oil [230], composed of fine-grained sedimentary rock, which contains significant amounts of kerogen, was characterized by HRMS. In fact, highly abundant shale oil is expected to be a very important fuel resource in the future. Van Krevelen diagram comparisons of shale and light oils display abundant O-containing compounds with DBE = 1 for shale oil, see Figure 20.22 (i.e., saturated carboxylic acids), led the authors to conclude that shale oil can be considered as a less biodegraded oil. The development and study of biofuels is a relatively new area and, with growing concerns about the future of crude oil, it is easy to explain why petroleum companies have begun to invest in this area.

20.5.3.2 **Consequences for Oil Refinery Processes**

In the petroleum refinery, where crude oil is processed into more useful petroleum products, such as gasoline, diesel fuel, and kerosene, many different processes are applied. The major process is crude oil distillation, where their different boiling points allow the separation of the hydrocarbons. Additionally, catalytic cracking protocols are performed to convert long-chain heavy oils into smaller molecules in

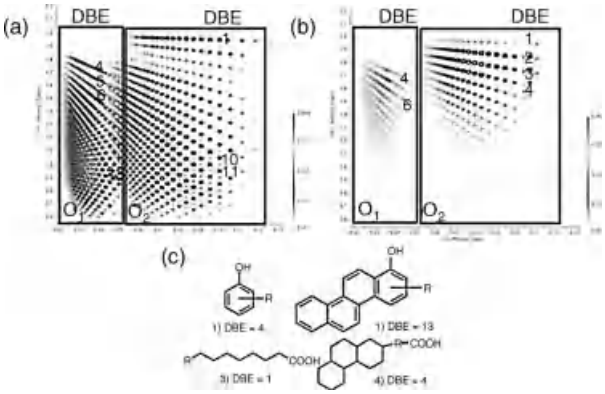


Figure 20.22 van Krevelen diagram of the O_1 and O_2 class compounds detected in negative-mode APPI spectra of (a) shale oil and (b) conventional oil. (c) Suggested structures of O_1 and O_2 compounds based on their DBE distributions. Reproduced from [230].

the naphtha and distillate boiling range, to increase gasoline and diesel production. Note that the different operating units are specific to the origin of the petroleum sample. Hence compositional knowledge of a petroleum sample has important economic issues.

The crude oil and its distillate compositions are compared by HRMS in order to give new insights into the distillation protocols by elucidating the compositions of atmospheric distillate fractions [235, 236, 252] versus vacuum distillate fractions [265, 270]. McKenna and co-workers [235, 236] studied the molecular composition of distillation series at different boiling points. They observed changes in molecular weight, heteroatom content, and aromaticity as a function of the boiling point. Plots of DBE versus carbon number for the hydrocarbon class, displayed in Figure 20.20, showed an increasing molecular weight of hydrocarbons for higher boiling point fractions, concomitant with an increase in compound aromaticity. For the first time, the authors experimentally validated the accuracy of the Boduszynski model, which describes the evolution of petroleum composition (effect of molecular weights and structures) as a function of atmospheric equivalent boiling point.

Similarly, other refinery processes such as extraction [263] and catalytic processing have been studied by ESI-HRMS. For example, hydrotreatment is the preferred process for removing the N-, S-, and O-containing species from crude oil [238, 246, 265], but is expensive. Compounds that contain oxygen and sulfur are known to cause corrosion, ultimately requiring replacement of production equipment. Nitrogen-containing species in finished fuels also form gums and solid precipitates during storage. Fu *et al.* [238] tested treated and untreated samples using three different ionization methods (10 eV EI, FD, and ESI modes) and found similar DBE distributions for both samples for all members of the N-containing class, demonstrating that N_1 class compounds are highly resistant to removal by hydrotreatment, whereas compounds containing multiple heteroatoms, such as NS, NOS, OS, and NO and also O-containing

species are successfully eliminated. By such an approach, rational basis for optimizing operating parameters of hydrotreatment [238, 265] were obtained.

Finally, the ESI-FTICR approach gave new insights into industrial issues, but these HRMS approach has been also applied as an analytical tool for environmental studies [271]. For example, the presence of naphthenic acids in crude oils is one of the greatest concerns in the oil refining industry as they [248] are toxic towards aquatic organisms. Successful characterizations of naphthenic acids within crude oils and aquatic environments were performed using various MS approaches, as the use of negative-ion ESI coupled with FTICR-MS [272]. Similarly, crude oil sludge obtained from an electric dehydrator was characterized as a stable emulsion consisting of oil, water, solids, and polyethers, which are chemical additives commonly used in oilfield and refinery operations [273].

20.6 Conclusion

In this chapter, we have tried to demonstrate the power of the MS technology, in the characterization of condensed-phase materials, and also, for solutions, gas phase samples. Today, the most important feature is the identification of the most appropriate MS technique(s) to solve a specific analytical problem. This is not a simple task, because although such a spectroscopic approach provides detailed chemical information, one must remember that the obtained data do not represent the mass of the molecule in the bulk sample, but the m/z ratio of gas-phase ions. These m/z ratios are representative of the sample but not necessary identical. The capacity of the ionization source to produce mono atomic ions (constituting the material), or charged molecular species, and fragment ions, must be taken into account. For this reason, an almost exhaustive picture of source technology is given in this chapter. Nevertheless, the performances of a mass analyzer (and above all its resolving power) will also direct the quality of the mass spectral data.

The presented variety of MS solutions has resulted from the constant technological development of mass spectrometers since J.J. Thomson's first experiments. Above all, in the last 20 years, advances in analytical chemistry and MS area, occurred with the development of desorption/ionization sources, which has opened up the ability to study intact labile high-mass biomolecule ions with high sensitivity and reproducibility. This still continues, with the advent of ambient sources but also with the recent concept of an ultra-high resolution mass analyzer using an electrostatic ion trap, called the Orbitrap. The new mass spectrometric strategies have been driven by the analysis of biomolecules such as proteins in supramolecular chemistry. Once developed, they have affected the analysis of other classes of compounds, including metabolites, lipids, and carbohydrates.

In this chapter, we discussed about the most recent MS methods such as imaging mass spectrometry (IMS) and soft landing (SL) of biomolecular ions experiments, where common MS data information (e.g., m/z ratio of molecular species, structural

elucidation using MS/MS experiments) is provided, but these MS approaches possess additional capacities. Spatial resolution with chemical MS information opens up the IMS area, which nowadays complements classical biochemical approaches. The most important characteristics of IMS in a discovery setting are its multiplexicity (multiple compound detection). MS may discover biomarker structures for which specific antibodies cannot easily be developed. For the first time, mass spectrometers entered in clinical research as they can aid the diagnosis and prognosis of several different cancers and diseases. This application area is still being developed with the rehabilitation of the SIMS technique, the application of recent DESI-IMS technique for IMS approach, and thus the IMS ability to answer life science concerns. The ambient nature of DESI makes it extremely useful for high-throughput sample analysis and *in vitro* analysis.

From another point of view, some fundamental concepts such as the collisions in the vacuum of polyatomic ions on a surface open up the possibility for biochemists to handle low-concentrated biomolecules, with the capabilities of MS (such as MS/MS for structural determination). The SL technique is promising for the formation of biofilms, for the study of surface reactivity. Most important are the specific chemical modifications of these surfaces using the common features of MS (mass selection of polyatomic ions, well defined KE regime, etc...). Of course, SL can be considered as an "accidental experimental observation" during the SID activation processes. However, SID activation has found only limited applications so far, in FTICR and triple quadrupole instruments. It represents potentially a method of choice for the structural characterization of large molecules, or that of PAHs using a high KE regime. It can therefore be predicted that the use of MS in the life sciences will become more prevalent and diversified.

Finally, we described the suitability of MS for the analysis of a natural, complex organic material, namely the petroleum. We exemplified this application area because it is a typical concern of MS technology in the 20 years, with high-throughput analysis of complex samples as encountered in the biological fields of genomics, proteomics, and metabolomics. For all "-omics" sciences, analytical difficulties and limitations arose from the polar nature of the sample compounds and the large number of sample components, and they led to strong instrumental developments. Here, we considered that the recent developments in routine FTMS and the incorporation of soft desorption/ionization techniques that enable us to probe the detailed chemical composition of petroleum high-end heavy oils, residua, asphaltenes, and so on. This was provided by the high mass measurement accuracy for the determination of the elemental composition of individual molecular species, by its powerful dynamic range, which allows the detection of more than 50 000 ionic species in a single scan, and of course thanks to the coupling with atmospheric pressure ionization methods and their ability to ionize a large diversity of species.

Finally, various perspectives of MS exist in to numerous application areas. As already pointed out, this concerns not only improvements in instrument performances, but also the implications in new fields such as surface reactivity and catalyst studies as well as the clinical area.

References

1 Thomson, J.J. (1913) Rays of positive electricity. *Proc. R. Soc. Lond. A*, **89**, 1–20.

2 Aston, F.W. (1933) *Mass Spectra and Isotopes*, 1st and 2nd edns., Longmans, London, p. 1941.

3 Dempster, A.J. (1918) A new method of positive ray analysis. *Phys. Rev.*, **11** (4), 316–325.

4 Nier, A.O. (1939) The isotopic constitution of uranium and the half-lives of the uranium isotopes. I. *Phys. Rev.*, **55**, 150–153.

5 Hipple, J.A. and Condon, E.U. (1945) Detection of metastable ions with the mass spectrometer. *Phys. Rev.*, **68**, 54–55.

6 Jennings, K. (1968) Collision-induced decompositions of aromatic molecular ions. *Int. J. Mass Spectrom. Ion Phys.*, **1**, 227–235.

7 Beynon, J.H., Caprioli, R.M., Baitinger, W.E., and Amy, J.W. (1970) Ion kinetic energy spectra of some aromatic hydrocarbons. *Org. Mass Spectrom.*, **3**, 455–477.

8 Houver, J.C., Baudon, J., Abignoli, M., Barat, M., Fournier, P., and Durup, J. (1970) Unimolecular and collision-induced dissociations of HeH^+ ions. *Int. J. Mass Spectrom. Ion Phys.*, **4**, 137–144.

9 Beynon, J.H., Cooks, R.G., and Caprioli, R.M. (1972) Mass and ion kinetic energy spectra of molecular hydrogen, hydrogen deuteride, and molecular deuterium. *Proc. R. Soc. Lond. A*, **327** (1568), 1–11.

10 Rosenstock, H.M., Wallstein, M.B., Wahrhaftig, M.B., and Eyring, H. (1952) Absolute rate theory for isolated systems and the mass spectra of polyatomic molecules. *Proc. Natl. Acad. Sci. USA*, **38** (8), 667–678.

11 Haddon, W.F. and McLafferty, F.W. (1968) Metastable ion characteristics. VII. Collision-induced metastables. *J. Am. Chem. Soc.*, **90**, 4745–4746.

12 Beynon, J.H., Caprioli, R.M., and Ast, T. (1971) Simple modification of a mass spectrometer for the study of collision-induced fragments. *Int. J. Mass Spectrom. Ion Phys.*, **7**, 88–92.

13 Cooks, R.G. and Beynon, J.H. (1974) Metastable ions and ion kinetic energy spectrometry: the development of a new research area. *J. Chem. Educ.*, **51** (7), 437.

14 Bruins, A.P., Jennings, K., and Evans, R.S. (1978) The observation of metastable transitions in a double-focussing mass spectrometer using a linked scan of the electric sector and magnetic sector fields. *Int. J. Mass Spectrom. Ion Phys.*, **26** (4), 395–404.

15 McLafferty, F.W. (1980) Tandem mass spectrometry (MS/MS): a promising new analytical technique for specific component determination in complex mixtures. *Acc. Chem. Res.*, **13** (2), 3–9.

16 Paul, W., and Steinwedel, H. (1953) A new mass spectrometer without magnetic field. *Z. Naturforsch.*, **8a**, 448–450.

17 Yost, R.A. and Enke, C.G. (1978) Selected ion fragmentation with a tandem quadrupole mass spectrometer. *J. Am. Chem. Soc.*, **100**, 2274–2275.

18 Stephens, W.E. (1946) A pulsed mass spectrometer with time dispersion. *Phys. Rev.*, **69**, 691–693.

19 Hipple, J.A. and Thomas, H.A. (1949) A time-of-flight mass spectrometer with varying field. *Phys. Rev.*, **75**, 1616.

20 Goudsmit, S.A. (1948) Time-of-flight mass spectrometer. *Phys. Rev.*, **74**, 622–623.

21 Cameron, A.E. and Eggers, D.F. (1948) Ion velocitron. *Rev. Sci. Instrum.*, **19**, 605–607.

22 Katzenstein, H.S. and Friedland, S.S. (1955) New time-of-flight mass spectrometer, *Rev. Sci. Instrum.*, **26**, 324–327.

23 Wiley, W.C. and McLaren, I.H. (1955) Time-of-flight mass spectrometer with improved resolution. *Rev. Sci. Instrum.*, **26**, 1150–1157.

24 Mamyrin, B.A., Karataev, V.I., Shmikk, D.V., and Zagulin, V.A. (1973) Mass reflectron. New nonmagnetic time-of-flight high-resolution mass spectrometer. *Sov. Phys. JETP*, **37**, 45–48.

25 Macfarlane, R.D. and Torgerson, D.F. (1976) Californium-252 plasma desorption mass spectroscopy. *Science*, **191**, 920–925.

26 Della-Negra, S. and Le Beyec, Y. (1985) New method for metastable ion studies with a time of flight mass spectrometer. Future application to molecular structure determinations. *Anal. Chem.*, **57**, 2035–2040.

27 Tabet, J.-C. and Cotter, R.J. (1984) Laser desorption time-of-flight mass spectrometry of high mass molecules. *Anal. Chem.*, **56** (9), 1662–1667.

28 Vestal, M.L., Juhasz, P., and Martin S.A. (1995) Delayed Extraction Matrix-assisted Laser Desorption Time-of-flight Mass Spectrometry, *Rapid Comm. Mass Spectrom.*, **9**, 1044–1050.

29 Sommer, H., Thomas, H.A., and Hipple, J.A. (1951) Measurement of e/M by cyclotron resonance. *Phys. Rev.*, **82**, 697–702.

30 Beauchamp, J.L. (1967) Theory of collision-broadened ion cyclotron resonance spectra. *J. Chem. Phys.*, **46**, 1231–1243.

31 Anders, L.R., Beauchamp, J.L., Dunbar, R.C., and Baldeschwieler, J.D. (1966) Ion-cyclotron double resonance. *J. Chem. Phys.*, **45**, 1062–1063.

32 Beauchamp, J.L., Anders, L.R., and Baldeschwieler, J.D. (1967) Ion–molecule reactions in chloroethylene by ion cyclotron resonance spectroscopy. *J. Am. Chem. Soc.*, **89**, 4569–4577.

33 Clow, R.P. and Futrell, J.H. (2011) Ion-cyclotron resonance study of the kinetic energy dependence of ion–molecule reaction rates: I. Methane, hydrogen and rare gas–hydrogen systems. *Int. J. Mass Spectrom.*, **4** (2), 165–179.

34 McIver, R.T. Jr. (1970) Trapped ion analyzer cell for ion cyclotron resonance spectroscopy. *Rev. Sci. Instrum.*, **41**, 555–558.

35 Comisarow, M.B. and Marshall, A.G. (1974) Fourier transform ion cyclotron resonance spectroscopy. *Chem. Phys. Lett.*, **25**, 282–283.

36 Nikolaev, E.N., Boldin, I.A., Jertz, R., and Baykut, G. (2011) Initial experimental characterization of a new ultra-high resolution FTICR cell with dynamic harmonization. *J. Am. Soc. Mass Spectrom.*, **22** (7), 1125–1133.

37 Munson, M.S.B. and Field, F.H. (1966) Chemical ionization mass spectrometry. I. General introduction. *J. Am. Chem. Soc.*, **88** (12), 2621–2630.

38 Busch, K.L. (1995) Desorption ionization mass spectrometry. *J. Mass Spectrom.*, **30**, 233–240.

39 Beckey, H.D. (1969) Field ionization mass spectrometry. *Research/ Development*, **20** (11), 26.

40 Le Beyec, Y., Della Negra, S., Deprun, C., Vigny, P., and Ginot, Y.M. (1980) Mass determination of molecules of biological interest by fast heavy ions induced desorption mass spectrometry. *Rev. Phys. Appl.*, **15**, 1631–1637.

41 Benninghoven, A., Rüdenauer, F.G., and Werner, H.W. (1987) *Secondary Ion Mass Spectrometry: Basic Concepts, Instrumental Aspects, Applications, and Trends*, John Wiley & Sons, Inc., New York, p. 1227.

42 Barber, M., Bordoli, R.S., Sedgwick, R.D., and Tyler, A. (1981) Fast atom bombardment of solids (F.A.B.): a new ion source for mass spectrometry. *J. Chem. Soc., Chem. Commun.*, 325–327.

43 Tanaka, K., Hiroaki, W., Yutaka, I., Satoshi, A., Yoshikazu, Y., Tamio, Y., and Matsuo, T. (1988) Protein and polymer analyses up to m/z 100 000 by laser ionization time-of-flight mass spectrometry. *Rapid Commun. Mass Spectrom.*, **2** (8), 151–153.

44 Karas, M. and Hillenkamp, F. (1988) Laser desorption ionization of proteins with molecular masses exceeding 10 000 daltons. *Anal. Chem.*, **60** (20), 2299–2301.

45 Covey, T.R., Thomson, B.A., and Schneider, B.B. (2009) Atmospheric pressure ion sources. *Mass Spectrom. Rev.*, **28**, 870–897.

46 Whitehouse, C.M., Dreyer, R.N., Yamashita, M., and Fenn, J.B. (1985) Electrospray interface for liquid chromatographs and mass spectrometers. *Anal. Chem.*, **57**, 675–679.

47 Dole, M., Mack, L.L., Hines, R.L., Mobley, R.C., Ferguson, L.D., and Alice, M.B. (1968) Molecular beams of macroions. *J. Chem. Phys.*, **49**, 2240–2249.

48 Tabet, J.-C. and Rebuffat, S. (2003) Nobel Prize 2002 for Chemistry: mass spectrometry and nuclear magnetic

resonance. *Med. Sci. (Paris)*, **19** (8–9), 865–872 (in French).

49 de Hoffmann, E. and Stroobant, V. (2002) *Mass Spectrometry: Principles and Applications*, 2nd edn., John Wiley & Sons, Ltd., Chichester.

50 Marshall, A.G., Hendrickson, C.L., and Jackson, G.S. (1998) Fourier transform ion cyclotron mass spectrometry: a primer. *Mass Spectrom. Rev.*, **17**, 1–35.

51 Marshall, A.G. and Hendrickson, C.L. (2002) Fourier transform ion cyclotron resonance detection: principles and experimental configurations. *Int. J. Mass Spectrom.*, **215**, 59–75.

52 Barrow, M.P., Burkitt, W.I., and Derrick, P.J. (2005) Principles of Fourier transform ion cyclotron resonance mass spectrometry and its application in structural biology. *Analyst*, **130**, 18–28.

53 Slezo, L. and Volmer, D.A. (2004) Ion activation methods for tandem mass spectrometry. *J. Mass Spectrom.*, **39**, 1091–1112.

54 Wilson, H.W. and Daly, N.R. (1963) Mass spectrometry of solids. *J. Sci. Instrum.*, **40**, 273–285.

55 Adams, F. and Vertes, A. (1990) Inorganic mass spectrometry of solid samples. *Fresenius' J. Anal. Chem.*, **337**, 638–647.

56 Gijbels, R. and Bogaerts, A. (1997) Recent trends in solid mass spectrometry: GDMS and other methods. *Fresenius' J. Anal. Chem.*, **359**, 326–330.

57 Becker, J.S. and Dietze, H.-J. (2003) State-of-the-art in inorganic mass spectrometry for analysis of high-purity materials. *Int. J. Mass Spectrom.*, **228**, 127–150.

58 Steiner, R.E., Barshick, C.M., and Bogaerts, A. (2009) Glow discharge optical spectroscopy and mass spectrometry, in *Encyclopedia of Analytical Chemistry* (ed. R.A. Meyers), John Wiley & Sons Ltd., Chichester.

59 Ammann, A.A. (2007) Inductively coupled plasma mass spectrometry (ICP MS): a versatile tool. *J. Mass Spectrom.*, **42**, 419–427.

60 Bingham, R.A. and Salter, P.L. (1976) Analysis of solid materials by laser probe mass spectrometry. *Anal. Chem.*, **48** (12), 1735–1740.

61 Opauszky, I. (1982) Lasers in solid state mass spectrometry. *Pure Appl. Chem.*, **54** (4), 879–887.

62 Fernández, B. and Costa, J.M. (2010) Inorganic mass spectrometry as a tool for characterization at the nanoscale. *Anal. Bioanal. Chem.*, **396**, 15–29.

63 Grasserbauer, M. (1992) Solid state mass spectrometry for materials science. *Pure Appl. Chem.*, **64** (4), 485–495.

64 Postawa, Z., Czerwinski, B., Szewczyk, M., Smiley, E.J., Winograd, N., and Garrison, B.J. (2004) Microscopic insights into the sputtering of Ag{111} induced by C60 and Ga bombardment. *J. Phys. Chem. B*, **108**, 7831–7838.

65 Seah, M.P. and Gilmore, I.S. (2011) Cluster primary ion sputtering: correlations in secondary ion intensities in TOF SIMS. *Surf. Interface Anal.*, **43**, 228–235.

66 Carré, V., Aubriet, F., Scheepers, P.T., Krier, G., and Muller, J.-F. (2005) Potential of laser ablation and laser desorption mass spectrometry to characterize organic and inorganic environmental pollutants on dust particles. *Rapid Commun. Mass Spectrom.*, **19**, 871–880.

67 Golovlev, V.V., Allman, S.L., Garrett, W.R., and Chen, C.H. (1997) Laser-induced acoustic desorption of electrons and ions. *Appl. Phys. Lett.*, **71** (6), 852–854.

68 Sunner, J., Dratz, E., and Chen, Y.-C. (1995) Graphite surface-assisted laser desorption/ionization time-of-flight mass spectrometry of peptides and proteins from liquid solutions. *Anal. Chem.*, **67** (23), 4335–4342.

69 Wei, J., Buriak, J.M., and Siuzdak, G. (1999) Desorption/ionization mass spectrometry on porous silicon. *Nature*, **399**, 243–246.

70 Go, E.P., Apon, J.V., Luo, G., Saghatelian, A., Daniels, R.H., Sahi, V., Dubrow, R., Cravatt, B.F., Vertes, A., and Siuzdak, G. (2005) Desorption/ionization on silicon nanowires. *Anal. Chem.*, **77**, 1641–1646.

71 Xu, S., Li, Y., Zou, H., Qiu, J., Guo, Z., and Guo, B. (2003) Carbon nanotubes as assisted matrix for laser desorption/

ionization time-of-flight mass spectrometry. *Anal. Chem.*, **75**, 6191–6195.
72 Peterson, D.S. (2007) Matrix free methods for laser desorption/ionization mass spectrometry. *Mass Spectrom. Rev.*, **26**, 19–34.
73 Domon, B. and Aebersold, R. (2006) Mass spectrometry and protein analysis. *Science*, **312**, 212–217.
74 Dreisewerd, K. (2003) The desorption process in MALDI. *Chem. Rev.*, **103**, 395–425.
75 Karas, M. and Krüger, R. (2003) Ion formation in MALDI: the cluster ionization mechanism. *Chem. Rev.*, **103**, 427–439.
76 Knochenmuss, R. and Zenobi, R. (2003) MALDI ionization: the role of in-plume processes. *Chem. Rev.*, **103**, 441–452.
77 Alves, S., Fournier, F., Afonso, C., Wind, F., and Tabet, J.-C. (2006) Gas-phase ionization/desolvation processes and their effect on protein charge state distribution under matrix-assisted laser desorption/ionization conditions. *Eur. J. Mass Spectrom.*, **12** (6), 369–383.
78 Kebarle, P. and Verkerk, U.H. (2009) Electrospray: from ions in solution to ions in the gas phase, what we know now. *J. Mass Spectrom.*, **28** (6), 898–917.
79 Iribarne, J.V. and Thomson, B.A. (1976) On the evaporation of small ions from charged droplets. *J. Chem. Phys.*, **64**, 2287–2294.
80 Fenn, J.B., Mann, M., Meng, C.K., Wong, S.F., and Whitehouse, C.M. (1989) Electrospray ionization for mass spectrometry of large biomolecules. *Science*, **246** (4926), 64–71.
81 Venter, A., Nefliu, M., and Cooks, R.G. (2008) Ambient desorption ionization mass spectrometry. *Trends Anal. Chem.*, **27** (4), 284–290.
82 Weston, D.J. (2010) Ambient ionization mass spectrometry: current understanding of mechanistic theory; analytical performance and application areas. *Analyst*, **135**, 661–668.
83 Chen, H., Gamez, G., and Zenobi, R. (2009) What can we learn from ambient ionization techniques? *J. Am. Soc. Mass Spectrom.*, **20**, 1947–1963.
84 Fernandez, F.M., Cody, R.B., Green, M.D., Hampton, C.Y., McGready, R., Sengaloundeth, S., White, N.J., and Newton, P.N. (2006) Characterization of solid counterfeit drug samples by desorption electrospray ionization and direct analysis-in-real-time coupled to time-of-flight mass spectrometry. *ChemMedChem*, **1**, 702–705.
85 Moyer, S.C. and Cotter, R.J. (2002) Atmospheric pressure MALDI. *Anal. Chem.*, **74** (17), 468A–476A.
86 Cody, R.B., Laramée, J.A., Nilles, J.M., and Dupont Durst, H. (2005) Direct analysis in real time (DART™) mass spectrometry. *JEOL News*, **40**, 8–12.
87 Takats, Z., Wiseman, J.M., Gologan, B., and Cooks, R.G. (2004) Mass spectrometry sampling under ambient conditions with desorption electrospray ionization. *Science*, **306**, 471–473.
88 Takats, Z., Wiseman, J.M., and Cooks, R.G. (2005) Ambient mass spectrometry using desorption electrospray ionization (DESI): instrumentation, mechanisms and applications in forensics, chemistry, and biology. *J. Mass Spectrom.*, **40**, 261–1275.
89 Ifa, D.R., Wu, C., Ouyang, Z., and Cooks, R.G. (2010) Desorption electrospray ionization and other ambient ionization methods: current progress and preview. *Analyst*, **135**, 669–681.
90 Costa, A.B. and Cooks, R.G. (2008) Simulated splashes: elucidating the mechanism of desorption electrospray ionization mass spectrometry. *Chem. Phys. Lett.*, **464**, 1–8.
91 Sen, A.K., Nayak, R., Darabi, J., and Knapp, D.R. (2008) Use of nanoporous alumina surface for desorption electrospray ionization mass spectrometry in proteomic analysis. *Biomed. Microdevices*, **10**, 531–538.
92 Badu-Tawiah, A., Bland, C., Campbell, D.I., and Cooks, R.G. (2010) Non-aqueous spray solvents and solubility effects in desorption electrospray ionization. *J. Am. Soc. Mass Spectrom.*, **21**, 572–579.

93 Hagan, N.A., Cornish, T.J., Pilato, R.S., Van Houten, K.A., Antoine, M.D., Lippa, T.P., Becknell, A.F., and Demirev, P.A. (2008) Detection and identification of immobilized low-volatility organophosphates by desorption ionization mass spectrometry. *Int. J. Mass Spectrom.*, **278**, 158–165.

94 Takats, Z., Cotte-Rodriguez, I., Talaty, N., Chen, H., and Cooks, R.G. (2005) Direct, trace level detection of explosives on ambient surfaces by desorption electrospray ionization mass spectrometry. *Chem. Commun.*, 1950–1952.

95 Chen, H., Talaty, N.N., Takats, Z., and Cooks, R.G. (2005) Desorption electrospray ionization mass spectrometry for high-throughput analysis of pharmaceutical samples in the ambient environment. *Anal. Chem.*, **77**, 6915–6927.

96 Basile, F., Sibray, T., Belisle, J.T., and Bowen, R.A. (2011) Analysis of lipids from crude lung tissue extracts by desorption electrospray ionization mass spectrometry and pattern recognition. *Anal. Biochem.*, **408**, 289–296.

97 Bereman, M.S., Williams, T.I., and Muddiman, D.C. (2007) Carbohydrate analysis by desorption electrospray ionization Fourier transform ion cyclotron resonance mass spectrometry. *Anal. Chem.*, **79**, 8812–8815.

98 Shin, Y.-S., Drolet, B., Mayer, R., Dolence, K., and Basile, F. (2007) Desorption electrospray ionization-mass spectrometry of proteins. *Anal. Chem.*, **79**, 3514–3518.

99 Wiseman, J.M., Evans, C.A., Bowen, C.L., and Kennedy, J.H. (2010) Direct analysis of dried blood spots utilizing desorption electrospray ionization (DESI) mass spectrometry. *Analyst*, **135**, 720–725.

100 Zhang, J.I., Talaty, N., Costa, A.B., Xia, Y., Tao, W.A., Bell, R., Callahan, J.H., and Cooks, R.G. (2011) Rapid direct lipid profiling of bacteria using desorption electrospray ionization mass spectrometry. *Int. J. Mass Spectrom.*, **301**, 37–44.

101 Oechsner, H. (1995) Secondary neutral mass spectrometry (SNMS) – recent methodical progress and applications to fundamental studies in particle/surface interaction. *Int. J. Mass Spectrom. Ion Processes*, **143**, 271–282.

102 Gray, A.L. (1985) Solid sample introduction by laser ablation for inductively coupled plasma source mass spectrometry. *Analyst*, **110**, 551–556.

103 Shiea, J., Huang, M.-Z., H.S.u, H.-J., Lee, C.-Y., Yuan, C.-H., Beech, I., and Sunner, J. (2005) Electrospray-assisted laser desorption/ionization mass spectrometry for direct ambient analysis of solids. *Rapid Commun. Mass Spectrom.*, **19**, 3701–3704.

104 Nemes, P. and Vertes, A. (2007) Laser ablation electrospray ionization for atmospheric pressure, *in vivo*, and imaging mass spectrometry. *Anal. Chem.*, **79**, 8098–8106.

105 Coon, J.J., McHale, K.J., and Harrison, W.W. (2002) Atmospheric pressure laser desorption/chemical ionization mass spectrometry: a new ionization method based on existing themes. *Rapid Commun. Mass Spectrom.*, **16**, 681–685.

106 Crawford, K.E., Campbell, J.L., Fiddler, M.N., Duan, P., Qian, K., Gorbaty, M.L., and Kenttamaa, H.I. (2005) Laser-induced acoustic desorption/ Fourier transform ion cyclotron resonance mass spectrometry for petroleum distillate analysis. *Anal. Chem.*, **77**, 7916–7923.

107 Gao, J., Borton, D. II, Owen, B.C., Jin, Z., Hurt, M., Amundson, L.M., Madden, J.T., Qian, K., and Kenttämaa, H.I. (2011) Laser-induced acoustic desorption/ atmospheric pressure chemical ionization mass spectrometry. *J. Am. Soc. Mass Spectrom.*, **22** (3), 531–538.

108 McDonnell, L.A. and Heeren, R.M.A. (2007) Imaging mass spectrometry. *Mass Spectrom. Rev.*, **26**, 606–643.

109 Castaing, R. and Slodzian, G. (1962) Microanalyse par émission ionique secondaire. *J. Microsc.*, **1**, 395–410.

110 Pacholski, M.L. and Winograd, N. (1999) Imaging with mass spectrometry. *Chem. Rev.*, **99**, 2977–3005.

111 Mahoney, C.M. (2010) Cluster secondary ion mass spectrometry of polymers and related materials. *Mass Spectrom. Rev.*, **29** (2), 247–293.

112 Heeren, R.M.A., McDonnell, L.A., Amstalden, E., Luxembourg, S.L., Altelaar, A.F.M., and Piersma, S.R. (2006) Why don't biologists use SIMS? A critical evaluation of imaging MS. *Appl. Surf. Sci.*, **252**, 6827–6835.

113 Burnett, R., Guichard, Y., and Barale, E. (1997) Immunohistochemistry for light microscopy in safety evaluation of therapeutic agents: an overview. *Toxicology*, **119**, 83–93.

114 Fletcher, J.S., Lockyer, N.P., and Vickerman, J.C. (2011) Developments in molecular SIMS depth profiling and 3D imaging of biological systems using polyatomic primary ions. *Mass Spectrom. Rev.*, **30**, 142–174.

115 Guerquin-Kern, J.-L., Wu, T.-D., Quintana, C., and Croisy, A. (2005) Progress in analytical imaging of the cell by dynamic secondary ion mass spectrometry (SIMS microscopy). *Biochim. Biophys. Acta*, **1724**, 228–238.

116 Becker, J.S., Zoriy, M.V., Pickhardt, C., Palomero-Gallagher, N., and Zilles, K. (2005) Imaging of copper, zinc, and other elements in thin sections of human brain samples (hippocampus) by laser ablation inductively coupled plasma mass spectrometry. *Anal. Chem.*, **77**, 3208–3216.

117 Strissel, P.L., Strick, R., Gavrilov, K.L., and Levi-Setti, R. (2005) Specific Mg^{2+} binding at human and Indian muntjac chromosomal Giemsa bands. *Appl. Surf. Sci.*, **231–232**, 485–489.

118 Brunelle, A., Touboul, D. and Laprévote, O. (2005) Biological tissue imaging with time-of-flight secondary ion mass spectrometry and cluster ion sources. *J. Mass Spectrom.*, **40** (8), 985–999.

119 Brunelle, A. and Laprévote, O. (2009) Lipid imaging with cluster time-of-flight secondary ion mass spectrometry. *Anal. Bioanal. Chem.*, **393**, 31–35.

120 Debois, D., Hamze, K., Guérineau, V., Le Caër, J.P., Holland, I.B., Lopes, P., Ouazzani, J., Séror, S.J., Brunelle, A., and Laprévote, O. (2008) *In situ* localisation and quantification of surfactins in a *Bacillus subtilis* swarming community by imaging mass spectrometry. *Proteomics*, **8** (18), 3682–3691.

121 Touboul, D., Kollmer, F., Niehuis, E., Brunelle, A., and Laprévote, O. (2005) Improvement of biological time-of-flight-secondary ion mass spectrometry imaging with a bismuth cluster ion source. *J. Am. Soc. Mass Spectrom.*, **16**, 1608–1618.

122 Heeren, R.M.A., Kükrer-Kaletaş, B., Taban, I.M., MacAleese, L., and McDonnell, L.A. (2008) Quality of surface: the influence of sample preparation on MS-based biomolecular tissue imaging with MALDI-MS and (ME-)SIMS. *Appl. Surf. Sci.*, **255**, 1289–1297.

123 Altelaar, A.F. and Piersma, S.R. (2010) Cellular imaging using matrix-enhanced and metal-assisted SIMS. *Methods Mol. Biol.*, **656**, 197–208.

124 Altelaar, A.F.M., Klinkert, I., Jalink, K., de Lange, R.P., Adan, R.A., Heeren, R.M.A., and Piersma, S.R. (2006) Gold-enhanced biomolecular surface imaging of cells and tissue by SIMS and MALDI mass spectrometry. *Anal. Chem.*, **78** (3), 734–742.

125 Altelaar, A.F.M., van Minnen, J., Heeren, R.M.A., and Piersma, S.R. (2006) The influence of the cholesterol microenvironment in tissue sections on molecular ionization efficiencies and distributions in ToF-SIMS. *Appl. Surf. Sci.*, **252**, 6702–6705.

126 Bouneau, S., Della-Negra, S., Depauw, J., Jacquet, D., Le Beyec, Y., Mouffron, J.-P., Novikov, A., and Pautrat, M. (2004) Heavy gold cluster beams production and identification. *Nucl. Instrum. Methods Phys. Res. B*, **225**, 579–589.

127 Caprioli, R.M., Farmer, T.B., and Gile, J. (1997) Molecular imaging of biological samples: localization of peptides and proteins using MALDI-TOF MS. *Anal. Chem.*, **69**, 4751–4760.

128 Chaurand, P., Schwartz, S.A., Reyzer, M.L., and Caprioli, R.M. (2005) Imaging mass spectrometry: principles and potentials. *Toxicol. Pathol.*, **33**, 92–101.

129 Seeley, E.H. and Caprioli, R.M. (2008) Molecular imaging of proteins in tissues by mass spectrometry. *Proc. Natl. Acad. Sci. USA*, **105** (47), 18126–18131.

130 Seeley, E.H. and Caprioli, R.M. (2008) Imaging mass spectrometry: towards clinical diagnostics. *Proteomics Clin. Appl.*, **2**, 1435–1443.

131 Hardesty, W.M. and Caprioli, R.M. (2008) *In situ* molecular imaging of proteins in tissues using mass spectrometry. *Anal. Bioanal. Chem.*, **391**, 899–903.

132 Schwamborn, K. and Caprioli, R.M. (2010) Molecular imaging by mass spectrometry – looking beyond classical histology. *Nat. Rev.*, **10**, 639–649.

133 Cazares, L.H., Troyer, D.A., Wang, B., Drake, R.R., and Semmes, O.J. (2011) MALDI tissue imaging: from biomarker discovery to clinical applications. *Anal. Bioanal. Chem.*, **401**, 17–27.

134 Seeley, E.H. and Caprioli, R.M. (2011) MALDI imaging mass spectrometry of human tissue: method challenges and clinical perspectives. *Trends Biotechnol.*, **29** (3), 139–143.

135 Aebersold, R. and Mann, M. (2003) Mass spectrometry-based proteomics. *Nature*, **422**, 198–207.

136 Skold, K., Svensson, M., Nilsson, A., Zhang, X., Nydahl, K., Caprioli, R.M., Svenningsson, P., and Andren, P.E. (2006) Decreased striatal levels of PEP-19 following MPTP lesion in the mouse. *J. Proteome Res.*, **5**, 262–269.

137 Heeren, R.M.A., Smith, D.F., Stauber, J., Kükrer-Kaletas, B., and MacAleese, L. (2009) Imaging mass spectrometry: hype or hope? *J. Am. Soc. Mass Spectrom.*, **20**, 1006–1014.

138 Kukrer Kaletas, B., van der Wiel, I.M., Stauber, J., Dekker, L.J., Güzel, C., Kros, J.M., Luider, T.M., and Heeren, R.M.A. (2009) Sample preparation issues for tissue imaging by imaging MS. *Proteomics*, **9**, 2622–2633.

139 Lemaire, R., Desmons, A., Tabet, J.-C., Day, R., Salzet, M., and Fournier, I. (2007) Direct analysis and MALDI imaging of formalin-fixed, paraffin-embedded tissue sections. *J. Proteome Res.*, **6**, 1295–1305.

140 Axelsson, J., Hoberg, A., Waterson, C., Myatt, P., Shield, G.L., Varney, J., Haddleton, D.M., and Derrick, P.J. (1997) Improved reproducibility and increased signal intensity in matrix-assisted laser desorption/ionization as a result of electrospray sample preparation. *Rapid Commun. Mass Spectrom.*, **11**, 209–213.

141 Dekker, L.J.M., van Kampen, J.J.A., Reedijk, M.L., Burgers, P.C., Gruters, R.A., Osterhaus, A.D.M.E., and Luider, T.M. (2009) A mass spectrometry based imaging method developed for the intracellular detection of HIV protease inhibitors. *Rapid Commun. Mass Spectrom.*, **23**, 1183–1188.

142 Yang, J. and Caprioli, R.M. (2011) Matrix sublimation/recrystallization for imaging proteins by mass spectrometry at high spatial resolution. *Anal. Chem.*, **83** (14), 5728–5734.

143 Lemaire, R., Tabet, J.-C., Ducoroy, P., Hendra, J.B., Salzet, M., and Fournier, I. (2006) Solid ionic matrixes for direct tissue analysis and MALDI imaging. *Anal. Chem.*, **78** (3), 809–819.

144 Naito, Y., Miyabayashi, K., and Tsujimoto, K. (2002) Development of cryostage for matrix-assisted laser desorption/ionization Fourier transform ion cyclotron resonance mass spectrometry. *Int. J. Mass Spectrom.*, **221**, 83–92.

145 Vertes, A., Nemes, P., Shrestha, B., Barton, A.A., Chen, ·Z., and Li, Y. (2008) Molecular imaging by mid-IR laser ablation mass spectrometry. *Appl. Phys. A*, **93**, 885–891.

146 Reyzer, M.L., Hsieh, Y., Ng, K., Korfmacher, W.A., and Caprioli, R.M. (2003) Direct analysis of drug candidates in tissue by matrix-assisted laser desorption/ionization mass spectrometry. *J. Mass Spectrom.*, **38**, 1081–1092.

147 Colsch, B., Jackson, S.N., Dutta, S., and Woods, A.S. (2011) Molecular microscopy of brain gangliosides: illustrating their distribution in hippocampal cell layers. *ACS Chem. Neurosci.*, **2** (4), 213–222.

148 Miki, A., Katagi, M., Kamata, T., Zaitsu, K., Tatsuno, M., Nakanishi, T., Tsuchihashi, H., Takubo, T., and Suzuki, K. (2011) MALDI-TOF and MALDI-FTICR imaging mass

spectrometry of methamphetamine incorporated into hair. *J. Mass Spectrom.*, **46**, 411–416.

149 Goodwin, R.J.A., Pitt, A.R., Harrison, D., Weidt, S.K., Langridge-Smith, P.R.R., Barrett, M.P., and Mackay, C.L. (2011) Matrix-free mass spectrometric imaging using laser desorption ionisation Fourier transform ion cyclotron resonance mass spectrometry. *Rapid Commun. Mass Spectrom.*, **25**, 969–972.

150 Thiery, G., Shchepinov, M.S., Southern, E.M., Audebourg, A., Audard, V., Terris, B., and Gut, I.G. (2007) Multiplex target protein imaging in tissue sections by mass spectrometry – TAMSIM. *Rapid Commun. Mass Spectrom.*, **21**, 823–829.

151 Liu, Q., Guo, Z., and He, L. (2007) Mass spectrometry imaging of small molecules using desorption/ionization on silicon. *Anal. Chem.*, **79**, 3535–3541.

152 Cha, S., Zhang, H., Ilarslan, H.I., Wurtele, E.S., Brachova, L., Nikolau, B.J., and Yeung, E.S. (2008) Direct profiling and imaging of plant metabolites in intact tissues by using colloidal graphite-assisted laser desorption ionization mass spectrometry. *Plant J.*, **55**, 348–360.

153 McLean, J.A., Schultz, J.A., and Woods, A.S. (2010) Ion mobility and mass spectrometry, in *Electrospray and MALDI Mass Spectrometry*, 2nd edn. (ed. R.B. Cole), John Wiley & Sons, Inc., New York, pp. 411–439.

154 Stauber J., MacAleese, L., Franck, J., Claude, E., Snel, M., Kükrer Kaletas, B., Wiel, I.M.V.D., Wisztorski, M., Fournier, I., and Heeren, R.M.A. (2010) On-tissue protein identification and imaging by MALDI-ion mobility mass spectrometry. *J. Am. Soc. Mass Spectrom.*, **21**, 338–347.

155 Kiss, A. and Heeren, R.M.A. (2011) Size, weight and position: ion mobility spectrometry and imaging MS combined. *Anal. Bioanal. Chem.*, **399**, 2623–2634.

156 Coello, Y., Jones, A.D., Gunaratne, T.C., and Dantus, M. (2010) Atmospheric pressure femtosecond laser imaging mass spectrometry. *Anal. Chem.*, **82** (7), 2753–2758.

157 Li, Y., Shrestha, B., and Vertes, A. (2007) Atmospheric pressure molecular imaging by infrared MALDI mass spectrometry. *Anal. Chem.*, **79**, 523–532.

158 Li, Y., Shrestha, B., and Vertes, A. (2008) Atmospheric pressure infrared MALDI imaging mass spectrometry for plant metabolomics. *Anal. Chem.*, **80**, 407–420.

159 Guenther, S., Römpp, A., Kummer, W., and Spengler, B. (2011) AP-MALDI imaging of neuropeptides in mouse pituitary gland with 5 µm spatial resolution and high mass accuracy. *Int. J. Mass Spectrom.*, **305** (2–3), 228–237.

160 Wiseman, J.M., Ifa, D.R., Song, Q., and Cooks, R.G. (2006) Tissue imaging at atmospheric pressure using desorption electrospray ionization (DESI) mass spectrometry. *Angew. Chem. Int. Ed.*, **45**, 7188–7192.

161 Wiseman, J.M., Ifa, D.R., Zhu, Y., Kissinger, C.B., Manicke, N.E., Kissinger, P.T., and Cooks, R.G. (2008) Desorption electrospray ionization mass spectrometry: imaging drugs and metabolites in tissues. *Proc. Natl. Acad. Sci. USA*, **105** (47), 18120–18125.

162 Ifa, D.R., Wiseman, J.M., Song, Q., and Cooks, R.G. (2007) Development of capabilities for imaging mass spectrometry under ambient conditions with desorption electrospray ionization (DESI) Int. *J. Mass Spectrom.*, **259**, 8–15.

163 Pasilis, S.P., Kertesz, V., Van Berkel, G.J., Schulz, M., and Schorcht, S. (2008) HPTLC/DESI-MS imaging of tryptic protein digests separated in two dimensions. *J. Mass Spectrom.*, **43**, 1627–1635.

164 Wu, C., Ifa, D.R., Manicke, N.E., and Cooks, R.G. (2010) Molecular imaging of adrenal gland by desorption electrospray ionization mass spectrometry. *Analyst*, **135**, 28–32.

165 Eberlin, L.S., Dill, A.L., Costa, A.B., Ifa, D.R., Cheng, L., Masterson, T., Koch, M., Ratliff, T.L., and Cooks, R.G. (2010) Cholesterol sulfate imaging in human prostate cancer tissue by desorption electrospray ionization mass spectrometry. *Anal. Chem.*, **82**, 3430–3434.

166 Dill, A.L., Ifa, D.R., Manicke, N.E., Ouyang, Z., and Cooks, R.G. (2009) Mass

spectrometric imaging of lipids using desorption electrospray ionization. *J. Chromatogr. B*, **877** (26), 2883–2889.

167 Esquenazi, E., Dorrestein, P.C., and Gerwick, W.H. (2009) Probing marine natural product defenses with DESI-imaging mass spectrometry. *Proc. Natl. Acad. Sci. USA*, **106** (18), 7269–7270.

168 Kertesz, V. and Van Berkel, G.J. (2008) Improved imaging resolution in desorption electrospray ionization mass spectrometry. *Rapid Commun. Mass Spectrom.*, **22**, 2639–2644.

169 Roach, P.J., Laskin, J., and Laskin, A. (2010) Nanospray desorption electrospray ionization: an ambient method for liquid-extraction surface sampling in mass spectrometry. *Analyst*, **135**, 2233–2236.

170 Manicke, N.E., Nefliu, M., Wu, C., Woods, J.W., Reiser, V., Hendrickson, R.C., and Cooks, R.G. (2009) Imaging of lipids in atheroma by desorption electrospray ionization mass spectrometry. *Anal. Chem.*, **81** (21), 8702–8707.

171 Girod, M., Shi, Y., Cheng, J.-X., and Cooks, R.G. (2011) Mapping lipid alterations in traumatically injured rat spinal cord by desorption electrospray ionization imaging mass spectrometry. *Anal. Chem.*, **83**, 207–215.

172 Nemes, P. and Vertes, A. (2010) Atmospheric-pressure molecular imaging of biological tissues and biofilms by LAESI mass spectrometry. *J. Vis. Exp.*, **43**, 1–4.

173 Shrestha, B., Patt, J., and Vertes, A. (2011) *In situ* cell-by-cell imaging and analysis of small cell populations by mass spectrometry. *Anal. Chem.*, **83**, 2947–2955.

174 Kubišta, J., Dolejšek, Z., and Herman, Z. (1998) Energy partioning in collisions of slow polyatomic ions with surfaces: ethanol molecular ions on stainless steel surfaces. *Eur. Mass Spectrom.*, **4**, 311–319.

175 Jacobs, D.C. (2002) Reactive collisions of hyperthermal energy molecular ions with solid surfaces. *Annu. Rev. Phys. Chem.*, **53**, 379–407.

176 Cooper, H.J., Hakansson, K., and Marshall, A.G. (2005) The role of electron capture dissociation in biolmolecular analysis. *Mass Spectrom. Rev.*, **24**, 201–222.

177 Eyler, J.R. (2009) Infrared multiple dissociation spectroscopy of ions in Penning traps. *Mass Spectrom. Rev.*, **28**, 448–467.

178 Laskin, J. and Futrell, J.H. (2005) Activation of large ions in FT-ICR mass spectrometry. *Mass Spectrom. Rev.*, **24**, 135–167.

179 Mabud, M.A., Dekrey, M.J., and Cooks, R.G. (1985) Surface-induced dissociation of molecular ions. *Int. J. Mass Spectrom. Ion Process.*, **67** (3), 285–294.

180 Cooks, R.G., Ast, T., and Mabud, M.A. (1990) Collisions of polyatomic ions with surfaces. *Int. J. Mass Spectrom. Ion Process.*, **31**, 209–265.

181 Ouyang, Z., Grill, V., Alvarez, J., Doerge, C.H., Gianelli, L., Thomas, P., Rohrs, H.W., and Cooks, R.G. (2002) A multiquadrupole tandem mass spectrometer for the study of ion–surface collision processes. *Rev. Sci. Instrum.*, **73** (6), 2375–2391.

182 Winger, B.E., Laue, H.-J., Horning, S.R., Julian, R.K., Lammert, S.A., Riederer, D.E., and Cooks, R.G. (1992) Hybrid BEEQ tandem mass spectrometer for the study of ion/surface collision processes. *Rev. Sci. Instrum.*, **63** (12), 5613–5625.

183 Lammert, S.A. and Cooks, R.G. (1991) Surface-induced dissociation of molecular ions in a quadrupole ion trap mass spectrometer. *J. Am. Soc. Mass Spectrom.*, **2** (6), 487–491.

184 Despeyroux, D., Wright, A.D., and Jennings, K.R. (1993) Comparison of collision-induced dissociation and surface-induced dissociation mass spectra of peptides obtained using a four-sector mass spectrometer. *Int. J. Mass Spectrom. Ion Process.*, **126**, 95–99.

185 Bier, M.E., Amy, J.W., Cooks, R.G., Syka, J.E.P., Ceja, P., and Stafford, G. (1987) A tandem quadrupole mass spectrometer for the study of surface-

induced dissociation. *Int. J. Mass Spectrom. Ion Process.*, **77**, 31–47.

186 Cole, R.B., LeMeillour, S., and Tabet, J.-C. (1992) Surface-induced dissociation of protonated peptides: implications of initial kinetic energy spread. *Anal. Chem.*, **64** (4), 365–371.

187 Gaskell, S.J., Mohammed, S., Chalmers, M.J., and Gielbert, J. (2001) A novel tandem quadrupole mass spectrometer allowing gaseous collisional activation and surface induced dissociation. *J. Mass Spectrom.*, **36** (12), 1260–1268.

188 Schey, K., Cooks, R.G., Grix, R., and Wöllnik, H. (1987) A tandem time-of-flight mass spectrometer for surface-induced dissociation. *Int. J. Mass Spectrom. Ion Process.*, **77** (1), 49–61.

189 Nikolaev, E.N., Somogyi, A., Smith, D.L., Gu, C., Wysocki, V.H., Martin, C.D., and Samuelson, G.L. (2001) Implementation of low-energy surface-induced dissociation (eV SID) and high-energy collision-induced dissociation (keV CID) in a linear sector–TOF hybrid tandem mass spectrometer. *Int. J. Mass Spectrom.*, **212**, 535–551.

190 Stone, E., Gillig, K.J., Ruotolo, B., Fuhrer, K., Gonin, M., Schultz, A., and Russell, D.H. (2001) Surface-induced dissociation on a MALDI–ion mobility–orthogonal time-of-flight mass spectrometer: sequencing peptides from an "in-solution" protein digest. *Anal. Chem.*, **73**, 2233–2238.

191 Laskin, J., Denisov, E.V., Shukla, A.K., Barlow, S.E., and Futrell, J.H. (2002) Surface-induced dissociation in a Fourier transform ion cyclotron resonance mass spectrometer: instrument design and evaluation. *Anal. Chem.*, **74**, 3255–3261.

192 Laskin, J. (2004) Energetics and dynamics of peptide fragmentation from multiple-collision activation and surface-induced dissociation studies. *Eur. Mass Spectrom.*, **10**, 259–267.

193 Fernandez, F.M., Wysocki, V.H., Futrell, J.H., and Laskin, J. (2006) Protein identification via surface-induced dissociation in an FT-ICR mass spectrometer and a patchwork sequencing approach. *J. Am. Soc. Mass Spectrom.*, **17** (5), 700–709.

194 Wysocki, V.H., Bier, M.E., and Cooks, R.G. (1988) Internal energy requirements for remote site fragmentation. *Org. Mass Spectrom.*, **23** (9), 627–633.

195 Lim, H., Schultz, D.G., Gislason, E.A., and Hanley, L. (1998) Activation energies for the fragmentation of thiophene ions by surface-induced dissociation. *J. Phys. Chem. B*, **102**, 4573–4580.

196 Hayward, M.J., Park, F.D.S., Phelan, L.M., Bernasek, S.L., Somogyi, A., and Wysocki, V.H. (1996) Examination of sputtered ion mechanisms leading to the formation of $C_7H_7^+$ during surface induced dissociation (SID) tandem mass spectrometry (MS/MS) of benzene molecular cations. *J. Am. Chem. Soc.*, **118**, 8375–8380.

197 Morris, M.R., Riederer, D.E., Winger, B.E., Cooks, R.G., Ast, T., and Chidsey, C.E.D. (1992) Ion/surface collisions at functionalized self-assembled monolayer surfaces. *Int. J. Mass Spectrom. Ion Process.*, **122**, 181–217.

198 Gu, C. and Wysocki, V.H. (1997) Ion–surface reactions involving isotopically labeled Langmuir–Blodgett films. *J. Am. Chem. Soc.*, **119** (49), 12010–12011.

199 Wade, N., Evans, C., Pepi, F., and Cooks, R.G. (2000) Collisions of silylium cations with hydroxyl-terminated and other self-assembled monolayer surfaces: reactions, dissociation, and surface characterization. *J. Phys. Chem. B*, **104** (47), 11230–11237.

200 Mabud, M.D.A., Dekrey, M.J., Cooks, R.G., and Ast, T. (1986) Charge exchange of doubly charged organic ions at metal surfaces. *Int. J. Mass Spectrom. Ion Process.*, **69** (3), 277–284.

201 Smith, D.L., Selvan, R., and Wysocki, V.H. (2003) Reactive ion scattering spectrometry of mixed methyland hydroxy-terminated alkanethiolate self-assembled monolayers. *Langmuir*, **19**, 7302–7306.

202 Miller, S.A., Luo, H., Pachuta, S.J., and Cooks, R.G. (1997) Soft-landing of polyatomic ions at fluorinated

self-assembled monolayer surfaces. *Science*, **275**, 1447–1450.

203 Geiger, R.J., Melnyk, M.C., Busch, K.L., and Bartlett, M.G. (1999) Modifications to an analytical mass spectrometer for the soft-landing experiment. *Int. J. Mass Spectrom.*, **182/183**, 415–422.

204 Hadjar, O., Wang, P., Futrell, J.H., Dessiaterik, Y., Zhu, Z., Cowin, J.P., Iedema, M.J., and Laskin, J. (2007) Design and performance of an instrument for soft landing of biomolecular ions on surfaces. *Anal. Chem.*, **79** (17), 6566–6574.

205 Benesch, J.L.P., Ruotolo, B.T., Simmons, D.A., Barrera, N.P., Morgner, N., Luchun, W., Saibil, H.R., and Robinson, C.V. (2010) Separating and visualising protein assemblies by means of preparative mass spectrometry and microscopy. *J. Struct. Biol.*, **172**, 161–168.

206 Gologan, B., Green, J.R., Alvarez, J., Laskin, J., and Cooks, R.G. (2005) Ion/surface reactions and ion soft-landing. *Phys. Chem. Chem. Phys.*, **7**, 1490–1500.

207 Rauschenbach, S., Vogelgesang, R., Malinowski, N., Gerlach, J.W., Benyoucef, M., Costantini, G., Deng, Z., Thontasen, N., and Kern, K. (2009) Electrospray ion beam deposition: soft-landing and fragmentation of functional molecules at solid surfaces. *ACS Nano,* **310**, 2901–2910.

208 Blake, T.A., Ouyang, Z., Wiseman, J.M., Takats, Z., Guymon, A.J., Kothari, S., and Cooks, R.G. (2004) Preparative linear ion trap mass spectrometer for separation and collection of purified proteins and peptides in arrays using ion soft landing. *Anal. Chem.*, **76**, 6293–6305.

209 Peng, W.-P., Goodwin, M.P., Nie, Z., Volný, M., Ouyang, Z., and Cooks, R.G. (2008) Ion soft landing using a rectilinear ion trap mass spectrometer. *Anal. Chem.*, **80**, 6640–6649.

210 Nie, Z., Li, G., Goodwin, M.P., Gao, L., Cyriac, J., and Cooks, R.G. (2009) *In situ* SIMS analysis and reactions of surfaces prepared by soft landing of mass-selected cations and anions using an ion trap mass spectrometer. *J. Am. Soc. Mass Spectrom.*, **20**, 949–956.

211 Alvarez, J., Cooks, R.G., Barlow, S.E., Gaspar, D.J., Futrell, J.H., and Laskin, J. (2005) Preparation and *in situ* characterization of surfaces using soft landing in a Fourier transform ion cyclotron resonance mass spectrometer. *Anal. Chem.*, **77**, 3452–3460.

212 Hu, Q., Wang, P., Gassman, P.L., and Laskin, J. (2009) *In situ* studies of soft- and reactive landing of mass-selected ions using infrared reflection absorption spectroscopy. *Anal. Chem.*, **81**, 7302–7308.

213 Cyriac, J., Li, G., and Cooks, R.G. (2011) Vibrational spectroscopy and mass spectrometry for characterization of soft landed polyatomic molecules. *Anal. Chem.*, **83** (13), 5114–5121.

214 Feng, B., Wunschel, D.S., Masselon, C.D., Pasa-Tolic, L., and Smith, R.D. (1999) Retrieval of DNA using soft-landing after mass analysis by ESI-FTICR for enzymatic manipulation. *J. Am. Chem. Soc.*, **121**, 8961–8962.

215 Hadjar, O., Wang, P., Futrell, J.H., and Laskin, J. (2009) Effect of the surface on charge reduction and desorption kinetics of soft landed peptide ions. *J. Am. Soc. Mass Spectrom.*, **20**, 901–906.

216 Wang, P. and Laskin, J. (2008) Helical peptide arrays on self-assembled monolayer surfaces through soft and reactive landing of mass-selected ions. *Angew. Chem. Int. Ed.*, **47**, 6678–6680.

217 Gologan, B., Takáts, Z., Alvarez, J., Wiseman, J.M., Talaty, N., Ouyang, Z., and Cooks, R.G. (2004) Ion soft-landing into liquids: protein identification, separation, and purification with retention of biological activity. *J. Am. Soc. Mass Spectrom.*, **15**, 1874–1884.

218 Volný, M., Elam, W.T., Branca, A., Ratner, B.D., and Turecek, F. (2005) Preparative soft and reactive landing of multiply charged protein ions on a plasma-treated metal surface. *Anal. Chem.*, **77**, 4890–4896.

219 Räder, H.J., Rouhanipour, A., Talarico, A.M., Palermo, V., Samori, P., and Müllen, K. (2006) Processing of giant graphene molecules by soft-landing mass spectrometry. *Nat. Mater.*, **5**, 276–280.

220 Li, G., Cyriac, J., Gao, L., and Cooks, G. (2011) Molecular ion yield enhancement in static secondary ion mass spectrometry by soft landing of protonated water clusters. *Surf. Interface Anal.*, **43**, 498–501.

221 Badu-Tawiah, A.K., Wu, C., and Cooks, R.G. (2011) Ambient ion soft landing. *Anal. Chem.*, **83**, 2648–2654.

222 Hodgson, G.W. (1971) Origin of petroleum: chemical constraints, in *Origin and Refining of Petroleum, Advances in Chemistry*, vol. 103, American Chemical Society, Washington, DC, pp. 1–29, Chapter 1.

223 Caumette, G., Lienemann, C.-P., Merdrignac, I., Bouyssierea, B., and Lobinski, R. (2009) Element speciation analysis of petroleum and related materials. *J. Anal. At. Spectrom.*, **24**, 263–276.

224 Hughey, C.A., Rodgers, R.P., and Marshall, A.G. (2002) Resolution of 11 000 compositionally distinct components in a single electrospray ionization Fourier transform ion cyclotron resonance mass spectrum of crude oil. *Anal. Chem.*, **74**, 4145–4149.

225 Wu, Z., Jernström, S., Hughey, C.A., Rodgers, R.P., and Marshall, A.G. (2003) Resolution of 10 000 compositionally distinct components in polar coal extracts by negative-ion electrospray ionization Fourier transform ion cyclotron resonance mass spectrometry. *Energy Fuels*, **17**, 946–953.

226 Marshall, A.G. and Rodgers, R.P. (2004) Petroleomics: the next grand challenge for chemical analysis. *Acc. Chem. Res.*, **37**, 53–59.

227 Marshall, A.G. and Rodgers, R.P. (2008) Petroleomics: chemistry of the underworld. *Proc. Natl. Acad. Sci. USA*, **10** (47), 18090–18095.

228 Hsu, C.S., Hendrickson, C.L., Rodgers, R.P., McKenna, A.M., and Marshall, A.G. (2011) Petroleomics: advanced molecular probe for petroleum heavy ends. *J. Mass. Spectrom.*, **46**, 337–343.

229 Kim, S., Rodgers, R.P., and Marshall, A.G. (2006) Truly "exact" mass: elemental composition can be determined uniquely from molecular mass measurement at 0.1 mDa accuracy for molecules up to 500 Da. *Int. J. Mass Spectrom.*, **251**, 260–265.

230 Bae, E.J., Na, J.-G., Chung, S.H., Kim, H.S., and Kim, S. (2010) Identification of about 30 000 chemical components in shale oils by electrospray ionization (ESI) and atmospheric pressure photoionization (APPI) coupled with 15 T Fourier transform ion cyclotron resonance mass spectrometry (FT-ICR MS) and a comparison to conventional oil. *Energy Fuels*, **24**, 2563–2569.

231 Hughey, C.A., Hendrickson, C.L., Rodgers, R.P., and Marshall, A.G. (2001) Kendrick mass defect spectrum: a compact visual analysis for ultrahigh-resolution broadband mass spectra. *Anal. Chem.*, **73**, 4676–4681.

232 Kim, S., Kramer, R.W., and Hatcher, P.G. (2003) Graphical method for analysis of ultrahigh-resolution broadband mass spectra of natural organic matter, the van Krevelen diagram. *Anal. Chem.*, **75**, 5336–5344.

233 Wu, Z., Rodgers, R.P., and Marshall, A.G. (2004) Two- and three-dimensional van Krevelen diagrams: a graphical analysis complementary to the Kendrick mass plot for sorting elemental compositions of complex organic mixtures based on ultrahigh-resolution broadband Fourier transform ion cyclotron resonance mass measurements. *Anal. Chem.*, **76**, 2511–2516.

234 Klein, G.C., Angström, A., Rodgers, R.P., and Marshall, A.G. (2006) Use of saturates/aromatics/resins/asphaltenes (SARA) fractionation to determine matrix effects in crude oil analysis by electrospray ionization Fourier transform ion cyclotron resonance mass spectrometry. *Energy Fuels*, **20**, 668–672.

235 McKenna, A.M., Purcell, J.M., Rodgers, R.P., and Marshall, A.G. (2010) Heavy petroleum composition. 1. Exhaustive compositional analysis of Athabasca bitumen HVGO distillates by Fourier transform ion cyclotron resonance mass spectrometry: a definitive test of the Boduszynski model. *Energy Fuels*, **24**, 2929–2938.

236 McKenna, A.M., Blakney, G.T., Xian, F., Glaser, P.B., Rodgers, R.P., and Marshall, A.G. (2010) Heavy petroleum composition. 2. Progression of the Boduszynski model to the limit of distillation by ultrahigh-resolution FT-ICR mass spectrometry. *Energy Fuels*, **24**, 2939–2946.

237 Ventura, G.T., Hall, G.J., Nelson, R.K., Frysinger, G.S., Raghuraman, B., Pomerantz, A.E., Mullins, O.C., and Reddy, C.M. (2011) Analysis of petroleum compositional similarity using multiway principal components analysis (MPCA) with comprehensive two-dimensional gas chromatographic data. *J. Chromatogr. A*, **1218**, 2584–2592.

238 Fu, J., Klein, G.C., Smith, D.F., Kim, S., Rodgers, R.P., Hendrickson, C.L., and Marshall, A.G. (2006) Comprehensive compositional analysis of hydrotreated and untreated nitrogen-concentrated fractions from syncrude oil by electron ionization, field desorption ionization, and electrospray ionization ultrahigh-resolution FT-ICR mass spectrometry. *Energy Fuels*, **20** 1235–1241.

239 Kuras, M., Ryska, M., and Mostecky, J. (1976) Analysis of saturated hydrocarbons by field ionization mass spectrometry. *Anal. Chem.*, **48** (1), 196–198.

240 Schaub, T.M., Hendrickson, C.L., Qian, K., Quinn, J.P., and Marshall, A.G. (2003) High-resolution field desorption/ionization Fourier transform ion cyclotron resonance mass analysis of nonpolar molecules. *Anal. Chem.*, **75**, 2172–2176.

241 Veloski, G.A., Lynn, R.J., and Sprecher, R.F. (1997) Characterization of nitrogen-containing species in coal- and petroleum-derived products by ammonia chemical ionization high-resolution mass spectrometry. *Energy Fuels*, **11** (1), 137–143.

242 Skjevrak, I., Larter, S., Graas, G.V., Jones, M., and Berge, E. (1994) A practical approach to quantitative group type analysis of kerogens using non-dedicated pyrolysis–mass spectrometry equipment: applications and comparison with other methods. *Org. Geochem.*, **22** (3–5), 873–883.

243 Le Vot, C., Afonso, C., Beaugrand, C., and Tabet, J.-C. (2011) Implementation of a Penning ionization source on a FTICR instrument with ion funnel optics. *Int. J. Mass Spectrom.*, **396** (2–3), 150–158.

244 Prókai, L. (1990) *Field desorption Mass Spectrometry*. New York: M. Dekker (I refer to the book, which emphasizes all the FD and FI techniques concepts.

245 Zhan, D. and Fenn, J.B. (2000) Electrospray mass spectrometry of fossil fuels. *Int. J. Mass Spectrom.*, **194** (2–3), 197–208.

246 Hughey, C.A., Hendrickson, C.L., Rodgers, R.P., and Marshall, A.G. (2001) Elemental composition analysis of processed and unprocessed diesel fuel by electrospray ionization Fourier transform ion cyclotron resonance mass spectrometry. *Energy Fuels*, **15** (5), 1186–1193.

247 Shi, Q., Zhao, S., Xu, Z., Chung, K.H., Zhang, Y., and Xu, C. (2010) Distribution of acids and neutral nitrogen compounds in a Chinese crude oil and its fractions: characterized by negative-ion electrospray ionization Fourier transform ion cyclotron resonance mass spectrometry. *Energy Fuels*, **24**, 4005–4011.

248 Headley, J.V., Peru, K.M., and Barrow, M.P. (2009) Mass spectrometric characterization of naphthenic acids in environmental samples, a review. *Mass Spectrom Rev.*, **28**, 121–134.

249 Zhang, Y., Xu, C., Shi, Q., Zhao, S., Chung, K.H., and Hou, D. (2010) Tracking neutral nitrogen compounds in subfractions of crude oil obtained by liquid chromatography separation using negative-ion electrospray ionization Fourier transform ion cyclotron resonance mass spectrometry. *Energy Fuels*, **24**, 6321–6326.

250 Panda, S.K., Schrader, W., Al-Hajji, A., and Andersson, J.T. (2007) Distribution of polycyclic aromatic sulfur heterocycles in three Saudi Arabian crude oils as determined by Fourier transform ion cyclotron resonance mass spectrometry. *Energy Fuels*, **21**, 1071–1077.

251 Kim, Y.H. and Kim, S. (2010) Improved abundance sensitivity of molecular ions in positive-ion APCI MS analysis of petroleum in toluene. *J. Am. Soc. Mass Spectrom.*, **21**, 386–392.

252 Purcell, J.M., Hendrickson, C.L., Rodgers, R.P., and Marshall, A.G. (2007) Atmospheric pressure photoionization proton transfer for complex organic mixtures investigated by Fourier transform ion cyclotron resonance mass spectrometry. *J. Am. Soc. Mass Spectrom.*, **18**, 1682–1689.

253 Marchi, I., Rudaz, S., and Veuthey, J.-L. (2009) Atmospheric pressure photoionization for coupling liquid-chromatography to mass spectrometry: a review. *Talanta*, **78**, 1–18.

254 Hortal, A.R., Hurtado, P., Martinex-Haya, B., and Mullins, O.C. (2007) Molecular weight distributions of coal and petroleum asphaltenes from laser desorption/ionization experiments. *Energy Fuels*, **21**, 2863–2868.

255 Hurtado, P., Hortal, A.R., and Martınez-Haya, B. (2007) Matrix-assisted laser desorption/ionization detection of carbonaceous compounds in ionic liquid matrices. *Rapid. Commun. Mass Spectrom.*, **21**, 3161–3164.

256 Pomerantz, A.E., Hammond, M.R., Morrow, A.L., Mullins, O.C., and Zare, R.N. (2008) Two-step laser mass spectrometry of asphaltenes. *J. Am. Chem. Soc.*, **130**, 7216–7217.

257 Schrader, W., Panda, S.K., Brockmann, K.J., and Benter, T. (2008) Characterization of non-polar aromatic hydrocarbons in crude oil using atmospheric pressure laser ionization and Fourier transform ion cyclotron resonance mass spectrometry (APLI FT-ICR MS). *Analyst*, **133**, 867–869.

258 Nyadong, L., McKenna, A.M., Hendrickson, C.L., Rodgers, R.P., and Marshall, A.G. (2011) Atmospheric pressure laser-induced acoustic desorption chemical ionization Fourier transform ion cyclotron resonance mass spectrometry for the analysis of complex mixtures. *Anal. Chem.*, **83**, 1616–1623.

259 Wu, C., Qian, K., Nefliu, M., and Cooks, R.G. (2010) Ambient analysis of saturated hydrocarbons using discharge-induced oxidation in desorption electrospray ionization. *J. Am. Soc. Mass Spectrom.*, **21**, 261–267.

260 Ahmed, A., Cho, Y.J., No, M.-H., Koh, J., Tomczyk, N., Giles, K., Yoo, J.S., and Kim, S. (2011) Application of the Mason–Schamp equation and ion mobility mass spectrometry to identify structurally related compounds in crude oil. *Anal. Chem.*, **83**, 77–83.

261 Fernandez-Lima, F.A., Becker, C., McKenna, A.M., Rodgers, R.P., Marshall, A.G., and Russell, D.H. (2009) Petroleum crude oil characterization by IMS-MS and FTICR MS. *Anal. Chem.*, **81**, 9941–9947.

262 Ahmed, A., Cho, Y.J., No, M.-H., Koh, J., Tomczyk, N., Giles, K., Yoo, J.S., and Kim, S. (2011) Application of the Mason–Schamp equation and ion mobility mass spectrometry to identify structurally related compounds in crude oil. *Anal. Chem.*, **83**, 77–83.

263 Klein, G.C., Kim, S., Rodgers, R.P., Marshall, A.G., Yen, A., and Asomaning, S. (2006) Mass spectral analysis of asphaltenes. I. compositional differences between pressure-drop and solvent-drop asphaltenes determined by electrospray ionization Fourier transform ion cyclotron resonance mass spectrometry. *Energy Fuels*, **20**, 1965–1972.

264 Schade, T. and Andersson, J.T. (2006) Speciation of alkylated dibenzothiophenes in a deeply desulfurized diesel fuel. *Energy Fuels*, **20** (4), 1614–1620.

265 Ller, H.M. and Andersson, J.T. (2005) Characterization of high-molecular-weight sulfur-containing aromatics in vacuum residues using Fourier transform ion cyclotron resonance mass spectrometry. *Anal. Chem.*, **77**, 2536–2543.

266 Liu, P., Shi, Q., Chung, K.H., Zhang, Y., Pan, N., Zhao, S., and Xu, C. (2010) Molecular characterization of sulfur compounds in venezuela crude oil and its SARA fractions by electrospray ionization Fourier transform ion cyclotron

resonance mass spectrometry. *Energy Fuels*, **24**, 5089–5096.

267 Purcell, J.M., Juyal, P., Kim, D.-G., Rodgers, R.P., Hendrickson, C.L., and Marshall, A.G. (2007) Sulfur speciation in petroleum: atmospheric pressure photoionization or chemical derivatization and electrospray ionization Fourier transform ion cyclotron resonance mass spectrometry. *Energy Fuels*, **21**, 2869–2874.

268 Hughey, C.A., Rodgers, R.P., Marshall, A.G., Qian, K., and Robbins, W.R. (2002) Identification of acidic NSO compounds in crude oils of different geochemical origins by negative ion electrospray Fourier transform ion cyclotron resonance mass spectrometry. *Org. Geochem.*, **33**, 43–759.

269 Smith, D.F., Rodgers, R.P., Rahimi, P., Teclemariam, A., and Marshall, A.G. (2009) Effect of thermal treatment on acidic organic species from athabasca bitumen heavy vacuum gas oil, analyzed by negative-ion electrospray Fourier transform ion cyclotron resonance (FT-ICR) mass spectrometry. *Energy Fuels*, **23**, 314–319.

270 Shi, Q., Xu, C., Zhao, S., Chung, K.H., Zhang, Y., and Gao, W. (2010) Characterization of basic nitrogen species in coker gas oils by positive-ion electrospray ionization Fourier transform ion cyclotron resonance mass spectrometry. *Energy Fuels*, **24**, 563–569.

271 Lu, M., Zhang, Z., Qiao, W., Guan, Y., Xiao, M., and Peng, C. (2010) Removal of residual contaminants in petroleum-contaminated soil by Fenton-like oxidation. *J. Hazard. Mater.*, **179**, 604–611.

272 Barrow, M.P., Headley, J.V., Peru, K.M., and Derrick, P.J. (2004) Fourier transform ion cyclotron resonance mass spectrometry of principal components in oilsands naphthenic acids. *J. Chromatogr. A*, **1058**, 51–59.

273 Zhang, Y., Zhao, H., Shi, Q., Chung, K.H., Zhao, S., and Xu, C. (2011) Molecular investigation of crude oil sludge from electric dehydrator. *Energy Fuels*, **25** (7), 3116–3124.

21
Chromatographic Methods

Fabrice Bertoncini, Didier Thiebaut, Marion Courtiade, and Thomas Dutriez

21.1
Introduction

The development of analytical methods capable of improving the detailed molecular characterization of complex samples represents a key challenge of benefit to all the petroleum sciences, from geochemistry to refining, from petrochemical conversion of a hydrocarbon to its energy recovery and up to its decay (biodegradation).

Indeed, knowledge the detailed composition of petroleum and related products is essential in order:

- to understand the mechanisms leading to their formation (e.g., geochemistry)
- to understand the catalytic mechanisms governing their transformation,
- to design thermodynamic and kinetic models of refining and petrochemistry processes,
- to predict their physical properties when they can be related to the molecular composition,
- to define their specifications and the means to check them.

In addition, taking into account the environmental impact of the refinery's processes and the implementation of strict regulations make molecular information essential.

To meet these requirements, separative sciences offer a crucial advantage over global analysis techniques, such as physical analyses (the so-called petroleum analyses such as density, distillation, etc.) and structural analyses [e.g., elemental analysis, mass spectrometry (MS), nuclear magnetic resonance (NMR) spectrometry]. Separative sciences can be used to establish the matter and structural balances and thereby to determine the transformation pathway for each species.

Among these separative sciences, gas chromatography (GC) has been the preferred molecular analysis technique for applications related to the entire refining industry since the end of the 1980s, as shown in the first part of this chapter (Section 21.2). This part discusses the state of the art of analytical techniques from the general point of view of achieving the molecular characterization of complex

Characterization of Solid Materials and Heterogeneous Catalysts: From Structure to Surface Reactivity, First Edition. Edited by Michel Che and Jacques C. Védrine.
© 2012 Wiley-VCH Verlag GmbH & Co. KGaA. Published 2012 by Wiley-VCH Verlag GmbH & Co. KGaA.

matrices. It provides examples of applications, emphasizing the increasing amount of information that can be obtained depending on the analytical methods compared with the equally increasing complexity of the analytical strategies.

The first part also underlines the advantages and disadvantages of high-resolution (HR) GC to access sufficient information for the heaviest or most complex cuts (i.e., containing molecules of more than 12 carbon atoms) due to its limited separation power. Consequently, no detailed molecular information is available for petroleum cuts such as the middle distillates (kerosene, gas oil) or heavier cuts [vacuum gas oils (VGOs), residues]. Owing to the complexity of petroleum products in terms of number of compounds, volatility range, chemical class, and concentration, we can easily understand that the analysis of these hydrocarbon mixtures requires higher resolution than that offered by HR-GC.

The need for improved information favored the emergence of multi-dimensional chromatographic methods designed to increase the resolution of chromatographic systems. In 1987, the studies conducted by Giddings [1] led to the definition of two-dimensional systems:

- The analytes must undergo at least two independent separations based on different principles (dimensions).
- The system obtained is such that if two compounds are separated in one dimension, they will remain resolved throughout the process (conservation of information from one dimension to another).

The objective of these highly resolving systems is not, however, to identify all the compounds individually, which is sometimes unrealistic and often pointless due to the similarity of the physicochemical properties of isomeric compounds, but to obtain a better characterization of complex cuts.

The second part (Section 21.3) therefore describes a revolutionary technique which, although dating back to the start of the 1990s, has seen growing success since the mid-2000s: comprehensive two-dimensional gas chromatography (GC × GC), whose emergence represents a major innovation in the field of separative sciences. Based on the coupling of two chromatographic columns with different selectivities using a modulator, its main advantage lies in the complete and continuous analysis of the sample in the two separation dimensions. Initiated by Phillips and Xu in the mid-1990s [2], it produced extremely promising results for the analysis of petroleum products, thanks to its high resolution. Since then, it has been described in numerous reviews. GC × GC is therefore potentially interesting for the high-resolution molecular analysis of complex cuts not elucidated by conventional analysis techniques such as conventional HR-GC. The second part describes its principles, instrumentation and performance using several application examples based on various problems taken from the field of refining and petrochemistry.

The advantage of GC × GC is considered in terms of the complementarity of the information obtained in the two separation dimensions. Finally, the limitations of these systems are discussed.

The third part (Section 21.4) describes how the multi-dimensional methods built around GC × GC supply considerably improved molecular information for the

middle distillates (8–30 carbon atoms) and vacuum distillates (30–60 carbon atoms). This part demonstrates how the recent progress of multi-dimensional analysis systems based on GC × GC succeeded in obtaining improved molecular information for extremely complex samples. Recent results obtained by the coupling of an additional dimension to the GC × GC system are discussed in terms of the nature of the chromatographic system (gas, liquid or supercritical mobile phase). Three-dimensional separation spaces can then be obtained for partitioning classes of compounds leading to an enhanced view at the molecular scale for very complex samples.

21.2
Analysis at Different Scales

In recent decades, chromatographic methods, particularly GC, have played a very important role in the analysis of complex samples, allowing the identification of complex mixtures up to the molecular scale.

In this part, the early history of chromatography is briefly reviewed, then various scales of analysis of samples from the oil industry (from global to detailed analyses) are discussed.

Finally, the advantages of HR-GC, the use of selective detection techniques and the drawbacks of GC are highlighted. The additional power of coupled-column techniques to overcome the limitations of GC are also discussed.

21.2.1
Brief History of Chromatography

The history of chromatography begins at the end of the nineteenth century. Chromatography, literally "color writing" from the Greek *khrôma*, was introduced and named in the first decade of the twentieth century, primarily for the separation of plant pigments such as chlorophyll by the Russian botanist Mikhail Tswett in 1903. New types of chromatography developed during the 1930s and 1940s made the technique useful for many types of separation process.

However, chromatography became developed more substantially as a result of the work of Martin and Synge during the 1940s and 1950s [3, 4]. They established the principles and basic techniques of partition chromatography, which means that that two chemical compounds were separated by partitioning them between two (liquid) phases [3, 4]. They were awarded the Nobel Prize in Chemistry in 1952 and their work encouraged the rapid development of several types of chromatographic methods based on varying the nature of mobile phase and the stationary phase to optimize the partitioning phenomena [4]. This period was called latter the "*golden decade for chromatography*" by Ettre [5]. The possibility of using gaseous phase chromatography was already discussed in the 1950s [6].

Since then, the technology has advanced rapidly. Several teams, such as Dutch research teams from the Koninklijke/Shell Laboratorium in Amsterdam, early

demonstrated the potential of GC for the analysis of hydrocarbons mixtures [7]. From its early stages, GC was then associated with the analytical challenges in the oil industry. GC applications grew rapidly between 1955 and 1960 thanks to the introduction of the capillary column by Golay (1957), leading to the introduction of high-temperature in GC. These capillary columns were rapidly compatible with temperatures up to 300 °C, allowing the elution of paraffinic hydrocarbons up to C_{40} [8]. The flame ionization detector (FID) was developed by McWilliam and Dewar around the same time (1958) [9]. The advantages of using this universal detector were immediately picked up by the oil industry. Several concepts, such as plate number and efficiency, were also transposed from oil chemistry. From the 1960s, further advances continually improved the instrumentation of chromatography. In the 1980s and 1990s, huge research efforts were made to allow the analysis of many types of compounds, thanks to the development of HR-GC.

Older "metal made" capillary columns were limited in terms of the nature of the stationary phase coated in the column. Fused-silica columns were introduced by Dandeneau and Zerenener in 1979 [10] and cross-linking polymeric films *in situ* or chemically bonding the stationary phase to the silica capillary became possible soon afterwards [11]. Thus, a new generation of polymeric stationary phases was born, leading to HR-GC. These narrow-bore capillary columns (50 or 100 m in length) nowadays allow the analysis of very complex matrices such as the detailed hydrocarbon analysis (DHA) of light petroleum fractions thanks to the very large number of plates. For readers interested in the history of GC for the oil industry, a detailed review was published by Blomberg *et al.* in 2002 [12].

21.2.2
From Global Analysis to Detailed Analysis of Petroleum Products

The analysis of complex petroleum products is essential to measure the physicochemical properties of the finished products related to their specifications, and also to establish the composition of the feedstocks and the intermediate products to gain a better understanding of the conversion processes involved. We can identify the global characterization methods that apply to all petroleum products, given a certain degree of flexibility of the implementation conditions, and the detailed characterization methods intended to supply molecular information through identification of the individual constituents [13, 14]. This second strategy results from the need to know the detailed composition of the hydrocarbons in order to determine the input data for process modeling. In addition, the macroscopic properties can be deduced by molecular characterization, using blending laws.

Detailed analysis involves identifying and quantifying all constituents present in a petroleum or similar product. However, their number increases intrinsically depending on the number of carbon atoms in the hydrocarbons contained in the product, since the possibilities of associating carbon and hydrogen atoms to form isomeric compounds multiply. Obviously, not all combinations are necessarily present, but this nevertheless gives an idea of the diversity of the structures. For example, the possible number of isomers for a five carbon atom (C_5) paraffin is three, but it

increases to 75 for 10 carbon atoms and to over 4 billion for 30 carbon atoms [15]. For the family of olefins, the number of isomers expected is even greater owing to those related to the position and to the *cis–trans* configuration of the double bond. Faced with this impressive number of constituents, it is obvious that detailed analysis will be increasingly difficult, even unrealistic, as the hydrocarbons become heavier (greater numbers of carbon atoms and isomers).

After giving an overview of the global, elemental and structural characterization methods, this part describes the state of the art of these molecular analysis techniques by family or class of compounds and by compound ("detailed" analysis), specifying their fields of application. Lastly, their limitations are examined.

21.2.3
Global Characterization

A certain number of test methods have been standardized by the American Society for Testing and Materials (ASTM) and are frequently used to monitor pilot units. They concern, for example, the viscosity index (ASTM D2270), density (ASTM D1298 or D4052), and volatility. The volatility of a petroleum product is one of the most critical characteristic: it is determined by its distillation curve, which defines the boiling point as a function of the percentage of material distilled by volume (or mass). Test method ASTM D86 applies to the distillation of most commercial products, while method ASTM D1160, distillation of petroleum products at reduced pressure, is intended for low-volatility or thermolabile products. Products with a wide range of boiling points, in particular crude oils, are characterized by ASTM D2892, the so-called true boiling point method.

21.2.4
Elemental and Structural Analysis

The elemental and structural analysis methods are based on the interaction of matter and electromagnetic radiation. More complete information about the interest of these techniques for petroleum sample analysis can be found elsewhere [16]. Elemental analysis by atomic absorption or X-ray fluorescence methods consists in measuring energy level differences between the electron orbitals of an atom. Based on electron transitions between energy levels of the bonds, ultraviolet (UV) spectrometry can be used to determine mono-, di-, and polyaromatic compounds (ASTM D2269). In infrared (IR) absorption spectrometry, the energy differences associated with the characteristic vibration frequencies of functional groups can be used to deduce the structural patterns and determine, for example, the distribution by type of aromatic and paraffinic carbons. Lastly, NMR concerns the transitions between the spin energy states; the structure of the hydrocarbons can be determined by spectrum analysis according to the position, number, and intensity of the peaks. Although it offers the most complete structural characterization, NMR spectroscopy remains difficult to implement for everyday monitoring of pilot units, expensive, and relatively insensitive.

The various elemental and structural characterization techniques can therefore be used to determine a product's identity card and provide "average" molecular information based on the hydrogen, carbon and, heteroatom contents and the types of chemical bonds. These data can then be correlated with physicochemical properties such as the density and cetane number.

In view of the need for detailed characterization of petroleum products, however, other techniques giving the distribution by hydrocarbon chemical family and, if possible, by number of carbon atoms, must also be implemented.

21.2.5 Hydrocarbon Family Analysis

21.2.5.1 Mass Spectrometry

Mass spectrometry (MS) has become the preferred technique for obtaining the distribution by hydrocarbon family in most petroleum products [17]. The molecules introduced into the mass spectrometer are volatilized, ionized, and detected according to their mass/charge ratio (m/z).

High-energy electron ionization (70 eV), which is widely used, leads to fragmentation of the molecules characteristic of their chemical structure. While fragmentation may facilitate qualitative analysis by family through their specific mass spectral fingerprint, quantitative analysis remains more complex since molecules of different mass may form identical fragments. The less volatile the cut and the greater the diversity of the molecules and the number of isotopes, the more critical it becomes. The intensity of an ion is then proportional to a sensitivity constant and the partial pressure of the molecule in the source, that is, to the concentration of this molecule in the mixture. Since the mass spectrum of a petroleum product is the sum of the mass spectra of all the molecules, we require the same number of independent equations as there are different families, which will be solved using a coefficient matrix. This matrix is simplified to a diagonal matrix if the spectrometer resolution increases. Although high-resolution mass spectrometers facilitate deconvolution of mass spectra and avoid fractionation by liquid-phase chromatography, which is long and can generate errors, they remain very expensive and difficult to use, that is, incompatible with routine analysis [18]. Current developments are converging towards analysis of low-volatility, heavy products requiring soft ionization sources. The time-of-flight analyzer seems in fact to meet best the requirements for sensitive and resolving instruments.

Analysis of middle distillates (cut interval 204–343 °C) using Fitzgerald's method (ASTM D2425), leading to a distribution into 12 hydrocarbon families, including two families of sulfur compounds, requires a resolution of 3000 and prior fractionation between saturated and unsaturated molecules carried out by liquid-phase chromatography (ASTM D2549). Heavier cuts are processed by the Fisher–Hood (ASTM D2786) or Robinson (ASTM D3239) method. Fisher's method [19] is used specifically for heavier cuts such as vacuum distillates or VGOs (350–550 °C) with a resolution of 10 000. It includes a prior separation step by preparative adsorption chromatography, essential to eliminate the resin fractions which will not be taken into account in the

method. Quantification alone of the saturated and aromatic fractions nevertheless represents the first limitation. The quantitative distribution of 32 chemical families of hydrocarbons [20] (paraffins, naphthenes, aromatics) and sulfur compounds (benzothiophenes, dibenzothiophenes, naphthalenobenzothiophenes and disulfurates) is possible.

Mass spectrometry cannot differentiate between the isomers of each chemical type. In view of the resolution used, it is also impossible to determine the exact mass of the compounds. The method will therefore be sensitive to interference between fragments, which will bias the quantitative data obtained. For example, there is interference [19] between the paraffins, alkylnaphthenes, alkyldibenzothiophenes and alkyl disulfides. Differences of 0.0034 Da (fragment C_3 versus SH_4) [21] being encountered between aromatic and thiophenic hydrocarbons with the same aromatic rings, a resolution of at least 100 000 with an m/z of 340 would be required to differentiate between them.

High-resolution MS techniques are required to avoid attribution ambiguities and thereby determine the exact masses of the analytes. For the last few years, Fourier transform ion cyclotron resonance mass spectrometry (FT-ICR-MS) has played an increasingly important role in the characterization of complex petroleum cuts. This technique allows the molecular characterization of more than 20 000 petroleum organic constituents of the type $C_cH_hN_nO_oS_s$, this ultimate identification already being known as "petroleomics" [22]. Three types of characterization can therefore be obtained: by elemental composition "by class," by number of unsaturations [double bond equivalent (DBE)], and "by type" and by degree of alkylation (CH_2).

21.2.5.2 **Liquid-Phase Chromatography**

Liquid-phase chromatography is implemented to obtain the distribution of molecules according to their polarity, either for analytical [high-performance liquid chromatography (HPLC)] or preparative [liquid chromatography (LC)] purposes. In adsorption chromatography (silica or alumina stationary phase), the retention of hydrocarbons increases with their degree of unsaturation. The solvent polarity, characterized by the Hildebrand solubility parameter, takes into account the solute–solvent interactions by hydrogen bonds or van der Waals bonds (dispersion, polarizability), to which may be added electrostatic interactions occurring in the case of ionic or ionizable solutes. LC can be applied to all petroleum products, gasolines and crude oils [23, 24]. Owing to its limited resolution, however, it is used to separate low-volatility products or those which would be decomposed by GC analysis, or to effect fractionation between saturated and aromatic compounds, which is required for MS analysis (ASTM D2549). Chromatograms show blocks for each class of saturated, mono-, di-, and polyaromatic compounds, but there is no intraclass resolution and the lack of sensitive and universal detectors limits the scope of this technique. LC–MS coupling is less widespread in the petroleum industry for routine analysis owing to interfacing difficulties (incompatibility between the mobile phase and the vacuum required in the spectrometer source) and problem of ionizing molecules which are often poorly volatile [25].

Two standardized methods are used for the HPLC separation of the different types of aromatic compounds in kerosenes (ASTM D6379) and gas oils (ASTM D6591). We generally speak of SARA [saturates, aromatics, resins, asphaltenes (resins and asphaltenes are poorly defined chemical structures composed of condensed polyaromatic hydrocarbons of molecular mass 500–1000 for resins and 1000–100 000 for asphaltenes; these compounds are concentrated in the heavy cuts] type analysis to designate fractionation by family applicable to all petroleum products (in particular, vacuum distillates and residues). The compounds are fractionated according to their solubility and interactions with a silica/alumina stationary phase. By increasing the eluting force (mixture of heptane, toluene, dichloromethane, and methanol), the solutes can be separated according to their increasing polarity. SARA fractionation is therefore relatively long (about 6–10 h), and requires large quantities of solvents. Finally, a weight distribution of each family is obtained. In addition, this technique can be used to obtain preseparation, prior to other analyses such as MS or NMR (ASTM D2549 or ASTM D4124). Although it is relatively easy to distinguish between saturated and aromatic compounds, it remains difficult to differentiate between aromatics and resins, owing to their similar chemical properties (high aromaticity and heteroatoms). For SARA fractionation, a deasphalting step is carried out beforehand by flocculation (precipitation of asphaltenes) in a paraffinic solvent (e.g., heptane) (ASTM D2007). For heavy products, size-exclusion chromatography (SEC) [also known as gel permeation chromatography (GPC)] is based on the selective permeation of analytes according to their size after penetrating the pores in the stationary phase, the molecules of highest molecular weight exhibiting the lowest retention. This technique is best suited for the analysis of polyaromatic hydrocarbons [26].

Lastly, other methods are also available to obtain more detailed separation by aromatic family. For example, a stationary phase of aminopropyl-grafted silica can be implemented in LC for the separation of gas oils by mono-, di-, tri-, or polyaromatic hydrocarbon families (ASTM D6591). To isolate sulfur compounds in petroleum matrices, ligand-exchange chromatography can be implemented via a stationary phase containing palladium. Separation is based on the interactions between ligands (solutes) and palladium by formation of coordination complexes. Use of aminocyclopentene-1-dithiocarboxylic acid bonded to silica [27] allows *in situ* complexation and therefore results in better performance. This type of separation has already been implemented for vacuum distillate cuts [28].

21.2.5.3 **Supercritical Fluid Chromatography**

The mobile phase in supercritical fluid chromatography (SFC) is a fluid whose pressure and temperature are greater than its critical parameters. The density characteristics of the supercritical fluid (generally carbon dioxide) are similar to those of a liquid, producing a high solvating power; its diffusion properties are between those of a gas and a liquid, and its viscosity is comparable to that of a gas, and therefore with fast transfer kinetics [29, 30]. One of the advantages lies in the possibility of modulating the solvating power during analysis, by applying a pressure gradient which modifies the fluid density. SFC, which uses a hybrid technology between GC and LC, therefore offers a wide range of columns (filled or capillary) and detectors.

Two main applications are targeted for petroleum products, implementing different retention mechanisms [31]: simulated distillation (elution by volatility), the principle of which is described below and which is used to extend the analysis to hydrocarbons up to the paraffin n-C_{140} and even potentially n-C_{200} [32], and analysis by family of saturated, mono-, di-, and polyaromatic compounds (elution by polarity) [33]. The resolution decreases as the volatility of the cut being analyzed decreases.

The main advantage compared with LC is the shorter analysis time and the use of an FID, which detects all carbon atoms for the quantitative analysis. In particular, SFC is used to determine the total olefin content in gasolines after coupling a silver/silica column for selective retention of olefins (ASTM D6550) via charge-transfer interaction with the empty orbital of the silver atom; strong interactions with the π electrons are therefore developed. SFC is also used to quantify aromatic compound concentrations in diesel fuels and aviation turbine fuels (ASTM D5186).

21.2.6 Molecular Analysis by Gas Chromatography

GC is widely used in the petroleum industry. Depending on its experimental implementation, two types of characterization are targeted:

- simulated distillation
- detailed analysis.

In the first case, analysis is based on separation of hydrocarbons by increasing boiling point in order to reproduce physical analysis. In the second case, the best possible chromatographic resolution is chosen to allow individual identification of the compounds. It is generally utilized with an FID to perform quantitative analyses due to the linear response of this detector over several orders of magnitude (10^7), its sensitivity ($2\ \mathrm{pg\,s^{-1}}$) and its almost total independence with respect to the chemical nature of the hydrocarbons and the chromatographic conditions used.

21.2.6.1 Simulated Distillation

The distillation profile of a petroleum cut can be simulated by GC. Introduced in 1960 [34], simulated distillation (SimDist) by GC is described in a standard test method applicable to petroleum products up to a final boiling point of 540 °C (ASTM D2887). In this case, the aim is to obtain fast rather than resolutive separation. The SimDist principle assumes that the hydrocarbons are eluted from a nonpolar GC column by increasing boiling point for a temperature-programmed analysis. An empirical relationship expressing the retention time as a function of the boiling point is obtained using a mixture of n-paraffins covering the distillation interval of the product to be analyzed. It has been demonstrated that this relation is not strictly valid for the other types of hydrocarbon, in particular for polyaromatic compounds which are eluted before n-paraffins with the same boiling point, being less soluble in the stationary phase. The approximation remains valid, however, since the low resolution of the column smoothes the retention differences. For samples with high aromatic compound content, there may be larger deviations. The response of the FID is

substantially identical for all hydrocarbons and proportional to the sample mass flow. The area under the chromatogram curve represents the mass of matter eluted equivalent to the volume of product recovered during a physical distillation. The chromatogram is integrated by time slots corresponding to 1% of eluted matter. Based on the area–retention time relation, one can deduce the distillation curve representing the boiling point as a function of the total weight percentage of product distilled. This method is fast (maximum 70 min), reproducible, requires a small quantity of sample (1 µl) and is easily automated. Figure 21.1 shows an example of a distillation curve for a gas oil.

This method offers considerable latitude in the choice of operating conditions (column geometry, type of stationary phase, carrier gas, temperature program), provided that the resolution criteria are respected. Short capillary columns are used in order to elute less volatile compounds, extrapolated to 100 carbon atoms by imple-

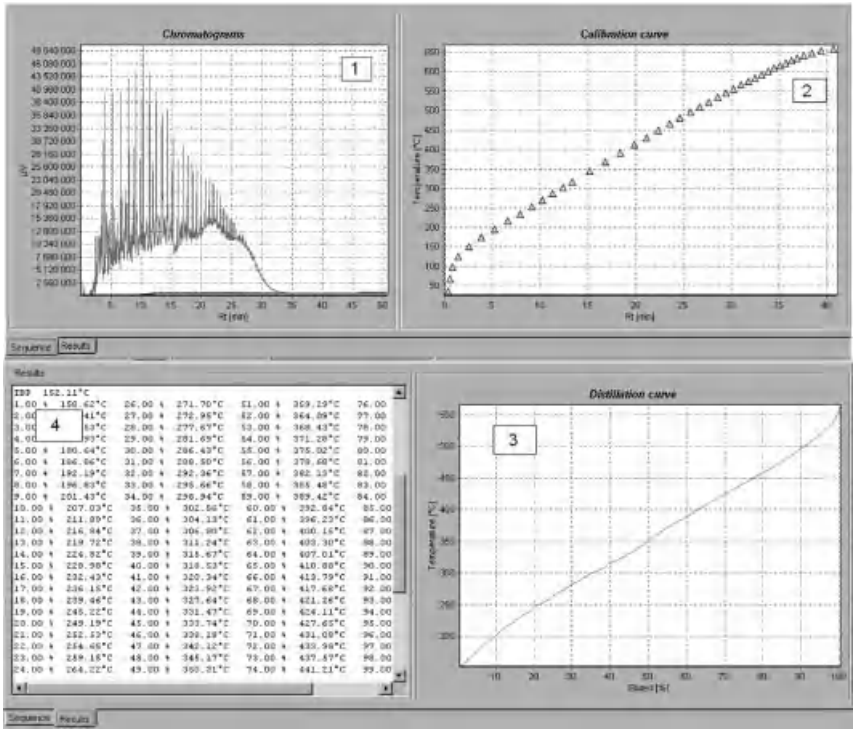


Figure 21.1 Example of a SimDist curve for a gas oil (extract from Chromdis software, Gecil Process). (1) Chromatogram obtained after GC separation on a nonpolar column (intensity of the signal detected as a function of the retention time). (2) Experimental calibration curve obtained after injecting a mixture of *n*-paraffins, expressing the boiling point as a function of the retention time. (3) SimDist curve representing the boiling point as a function of the total percentage of distilled matter, reconstructed by integrating chromatogram (1) in intervals equivalent to 1% of eluted matter and using the calibration law (2). (4) Table of data calculated to reconstruct the SimDist curve (3).

menting deactivated metal columns capable of withstanding temperatures of 420 °C, with low thermal degradation of the stationary phase (high-temperature SimDist) [35]. It is widely used to monitor pilot units.

The current trend is moving towards ultra-fast SimDist, based on resistive heating of capillary columns, in order to obtain temperature increases of up to 20 °C s^{-1} [36]. SimDist of gas oils can therefore be achieved in less than 3 min [37]. In addition, a development of method ASTM D2887, to analyze VGOs up to *n*-C_{60} by ultra-fast GC, is being considered [38]. SimDist profiles by heteroatoms can also be obtained, using specific detectors. For VGOs, for example, simulated distillation profiles by neutral and basic nitrogenated compounds have been produced by associating a nitrogen-specific detector, such as the nitrogen chemiluminescence detector (NCD) [39], whereas sulfur profiles are obtained with a sulfur-specific detector such as the sulfur chemiluminescence detector (SCD). A multi-element detector such as the atomic emission detector (AED) can be used to perform multi-element SimDist, in particular for VGOs.

Note also that SFC, the eluting power of which is greater than that of GC, without the need for high temperatures, can be used to extend SimDist to heavier petroleum products (see Section 21.2.5.3).

21.2.6.2 Detailed Analysis of Hydrocarbons

21.2.6.2.1 Gaseous Phase Until about 10 years ago, analysis of gaseous hydrocarbons was carried out by partition chromatography using very long packed columns. This method has now been replaced by a technique implementing capillary columns coated with an adsorbent film. These much more efficient columns are now highly stable and used in routine laboratories. Alumina and adsorbent polymers are the most widely used adsorbents. The most difficult separation encountered by petrochemistry laboratories, that of isobutene and 1-butene, was achieved using an alumina capillary column. The permanent gases (O_2, N_2, H_2, CO, etc.) are separated on molecular sieves. The use of multi-column chromatographs with switching valves became more widespread [40] to analyze hydrocarbons and permanent gases with a single injection. Natural gas, gases derived from crude oils, and refinery gases are the main applications for which methods have been developed and standardized [41, 42]. Gas analysis has become a key economic challenge, whether for natural gas to determine its calorific value by chromatographic analysis [43] or for petrochemical bases produced by steam cracking (ethylene, propylene, and butadiene) in view of the large volumes sold.

21.2.6.2.2 Liquid Phase To obtain a detailed analysis of liquid-phase hydrocarbon mixtures, a greater resolution of the separative system is required. For that purpose, the introduction of very long (50–100 m) fused-silica capillary columns [10] of small inner diameter (<0.53 μm) has led to considerable progress in this field, owing to the much better efficiency obtained (see also Section 21.2.1). These high-resolution capillary columns are used in HR-GC. Between 200 and 1000 theoretical plates are generated each second for a capillary column, compared with only 10 for a packed

column. To analyze a mixture of hydrocarbons with a wide range of boiling points (e.g., 200 °C), a temperature gradient is required in the chromatographic oven to adapt the elution conditions to the volatility of the compounds with a reasonable analysis time. Hydrocarbon mixtures containing up to eight carbon atoms can then be separated individually. This approach by HR-GC is called the PIONA (paraffins, isoparaffins, olefins, naphthenes, and aromatics) type analysis of naphtha samples (see standard methods ASTM D6729, D6730, D6733). Increasing the resolution by choosing a long column and a low rate of temperature increase, however, leads to long analysis durations (3–4 h), non-negligible for routine analyses. The retention indices in linear temperature programming [44] are frequently used to identify the compounds automatically according to their retention times and those of reference compounds (*n*-paraffins), thereby avoiding possible flow rate or temperature fluctuations (ASTM D6733). These retention indices are generally tabulated, but they can also be determined by prior GC–MS analysis, especially if no standard compounds are available. Quantification is carried out by integrating the chromatogram, the area being directly proportional to the mass flow through the detector.

Figure 21.2 shows an example of a chromatogram for a fluid catalytic cracking (FCC) naphtha cut containing over 180 hydrocarbons.

Thanks to the use of retention indices, all the elution peaks can be identified, leading to the identification of more than 180 compounds. For instance, an enhanced view of the C_8-aromatic elution zone is given with the identification of the main elution peaks: ethylbenzene is separated from *o*-, *m*-, and *p*-xylene. The main isoparaffins and *n*-nonane elution peaks are also reported. In that case, the retention time of nonane is used for calculating the retention indices of all the other compounds. The names of others peaks are not reported but they can also be identified; they are mainly C_9-olefins. Thus, a complete identification of FCC naphtha can be obtained.

The operating conditions for FCC or reforming naphtha cuts samples are given in Table 21.1. Over 200 000 plates can be obtained with these operating conditions (ASTM D6733)

Some of the physicochemical properties of a sample can be calculated by this detailed analysis: density, vapor pressure, research octane number (RON), motor octane number (MON), density, elemental analysis, and so on. These properties can be deduced by applying the simple mixture law (intensive properties) based on the composition by weight of pure compounds, determination of the quantity therefore corresponding to the weighting of the quantity of each constituent according to its concentration according to the relation (21.1)

$$P_{\text{naphtha}} = \sum_{i=1}^{n} (P_i) C_i \tag{21.1}$$

where P_{naphtha} is the property of naphtha being determined, P_i is the property of constituent i, and C_i is the concentration of constituent i expressed in % w/w.

This type of calculation is applied for

- elemental analysis: % C, % H, % O;
- structural analysis: C_p, C_n, C_a, C_o;

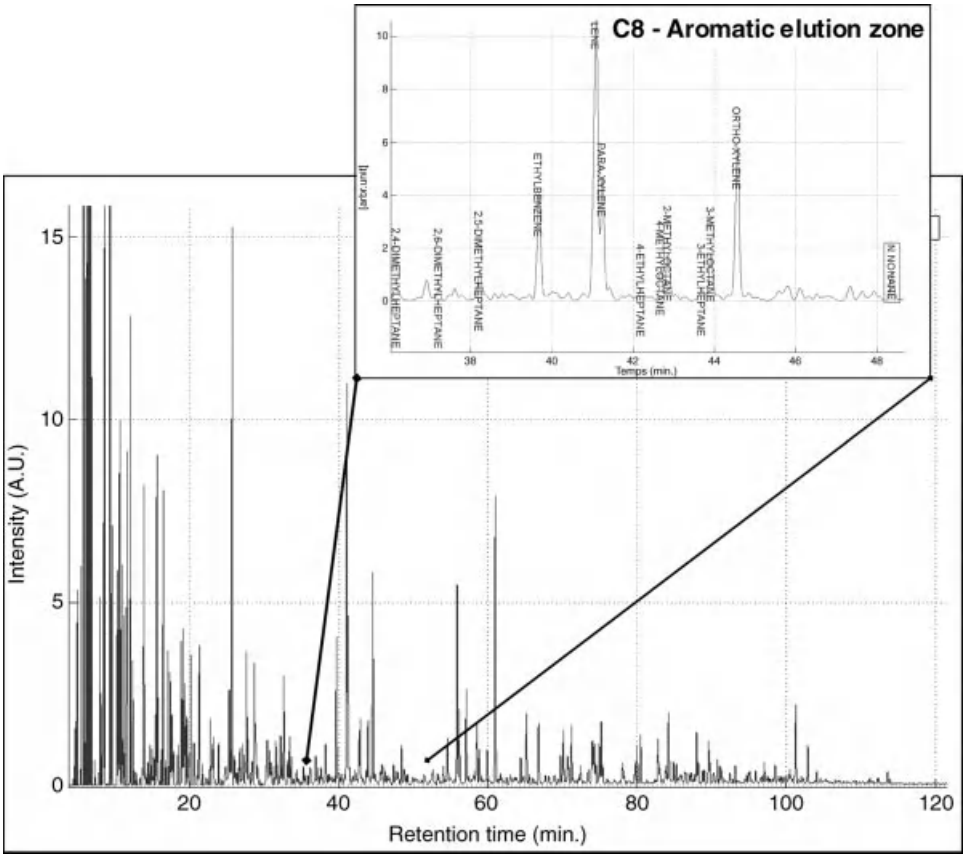


Figure 21.2 Chromatogram of an FCC gasoline sample obtained by high-resolution GC (ASTM D6733; operating condition, see Table 21.1). An enhanced view of the C_8-aromatic elution zone is given with the identification of the main elution peaks.

- molecular weight;
- gross calorific value.

Correlation for the mixture of complex properties such as the RON and MON is also applied. Models with linear correction factors are found in the literature. In this case, the approach chosen consists in determining a correction factor (K_i) for the property of the pure product (P_i) for each solute i in order to assess the mixture property of this constituent ($P_i + K_i$):

$$P_{\text{naphtha}} = \sum_{i=1}^{n} (K_i + P_i) C_i \tag{21.2}$$

where P_{naphtha} is the property of naphtha being determined, P_i is the property of constituent i, K_i is a factor representing the variation in octane number of

Table 21.1 Typical operating conditions for high-resolution chromatographic analysis of naphtha cuts.

		FCC	Reforming
Oven temperature programs	*1st temperature program*		
	Initial temperature (°C)	35	40
	Plateau (min)	10	0
	Final temperature (°C)	114	280
	2nd temperature program		
	Rate (°C min^{-1})	1.1	2
	Final temperature (°C)	280	
	Plateau (min)	10	
	Rate (°C min^{-1})	1.7	
Stationary phase	OV-1 (polymethylsiloxane, J & W Scientific), 50 m × 0.2 mm i.d. × 0.52 μm		
Temperature	Injector (°C)	280	280
	Detector (°C)	300	300
Carrier gas	Helium		
	Flow rate (ml min^{-1})	0.9	0.9
	Pressure (kPa)	200	200
Injection	Volume (μl)	0.5	0.5
	Split ratio	200	200

constituent i when it is in a mixture, and C_i is the concentration of constituent i expressed in % w/w.

Other more complex models involve correlations modeling the property P_i of each pure compound in a mixture. These correlations are not available in the open literature.

As an example of the use of chromatographic data obtained from HR-GC (PIONA type analysis), we may mention two main refining topics: reforming and FCC processes. These processes are frequently monitored by HR-GC.

The detailed data resulting from analysis of the feedstock and the effluents (naphtha cuts) of the reforming units are used to monitor the conversion (% of aromatics, etc.), to model it (RON values, etc.) and to optimize the operation of the units.

The GC methods developed for FCC units can be used to simulate the detailed PIONA analysis of the gasoline with respect to carbon number and to determine the octane numbers of the gasoline cut (0–180/220 °C) directly from the complete effluent (final boiling point at 580 °C). The quality of the products formed can be predicted from these data (density, RON, MON, % olefins, % aromatics, % benzene, etc.). Commercial gasolines can be formulated using HR-GC data which allow the prediction of blending a dozen naphtha cuts.

Recent environmental constraints have led to greater optimization of the mixtures. Whether for constraints on benzene, other aromatics, and olefins or the demands for high octane number due to the progressive elimination of lead, there is a growing

need for detailed characterization of the bases and mixtures and analyses are now conducted in routine laboratories.

Finally, HR-GC on modern polymer-coated narrow-bore capillary columns (with about 200 000 theoretical plates) is well suited for the analysis of samples such as gasolines and other moderately complex mixtures. Nevertheless, the resolution obtained using HR-GC remains insufficient for highly complex mixture. This is the case for heavier cuts (see Section 21.4) or for the analysis of trace compounds containing S or N atoms (i.e., with concentrations lower than 50 ppm). In fact, due to their very low concentrations, these compounds are not separated from other hydrocarbons using HR-GC.

This problem can be overcome by using detectors offering a specific response to a class of compounds ("selective" detectors; see Section 21.2.6.3) or by using chromatographic systems offering superior resolution (see Section 21.4).

21.2.6.3 **Heteroelement Analysis**

To make up for the lack of resolution of chromatographic systems towards trace compounds, coupling to more informative detectors is often considered. Use of heteroelement-selective detectors is highly suitable for detailed analysis of sulfur, nitrogen, or oxygen compounds, since they eliminate the interference with the hydrocarbons, while coupling to a mass spectrometer helps not only to elucidate the chemical structure by consulting a spectrum library but also to increase the resolution by deconvoluting the mass spectra of coeluted compounds. Since GC separation potentially distributes the quantity of matter into several hundred peaks, detector sensitivity represents a key performance criterion.

Section 21.3.3.2 provides a more exhaustive comparison of the various detectors coupled to chromatographic methods, in particular GC × GC.

21.2.6.3.1 Sulfur The efforts made to reduce the sulfur content in petroleum products have led to the development of analytical tools capable of determining the composition of sulfur molecules before and after processing, and therefore in highly different concentration ranges. The concentration ranges are generally very low (from tens to a few hundred ppm of sulfur). To improve the desulfurization processes, speciation of the sulfur compounds is an essential step; it consists in determining the distribution by class of sulfur compounds [benzothiophenes (BT s), dibenzothiophenes (DBTs), non-thiophenic derivatives] according to their degree of alkylation and the positions of the substituents. The flame photometric detector (FPD) [45] has been widely used for this purpose. The detection principle is based on the emission of chemiluminescence generated by sulfur compounds when they are burned in a rich hydrogen–air flame. Despite its straightforward implementation, there are some disadvantages: the response is non-linear, must be corrected by different response factors depending on the compounds, is attenuated by the presence of hydrocarbons coeluted with the sulfur species (quenching), and the selectivity with respect to carbon is only three orders of magnitude. With the introduction of the pulsed flame photometric detector (PFPD) [46], it became possible to increase either the sensitivity or selectivity depending on the adjustment. The sulfur chemiluminescence detector (SCD) is based on the chemilu-

minescent reaction between ozone and sulfur monoxide which is formed by the combustion (oxidation then reduction) of sulfur species. The radiation is detected in the ultraviolet region by a photomultiplier tube (maximum intensity at about 360 nm) [47]. Owing to the low sulfur concentrations and the complexity of the matrices to be analyzed, the SCD turns out to be an extremely useful tool since it offers excellent performance in terms of selectivity (10^8), sensitivity (1 pg s^{-1} sulfur), equimolarity, and linearity [48, 49]. A flameless SCD version has proved more reliable and easier to implement. This detector has been coupled with GC for detailed analysis of sulfur compounds in gasoline [50] described in a standard test method (ASTM D5623) or to obtain the specific simulated distillation curves of sulfur compounds in a gas oil [51].

Figure 21.3 shows an example of a chromatographic profile obtained by GC–SCD for the separation of sulfur species contained in a light cycle oil (LCO). Only S-containing compounds are detected, leading to the elution of numerous peaks. Table 21.2 gives the operating conditions.

We can observe that the sulfur compounds are eluted from the column according to their degree of alkylation and the positions of the substituents. BT and alkyl-BTs are eluted first, then DBT and alkyl-DBTs. The identification of each compound can be achieved via kinetic studies, but databases are not available in the open literature.

The chromatogram is then integrated and the quantification of sulfur compounds is performed by external calibration using the S content of the sample obtained by

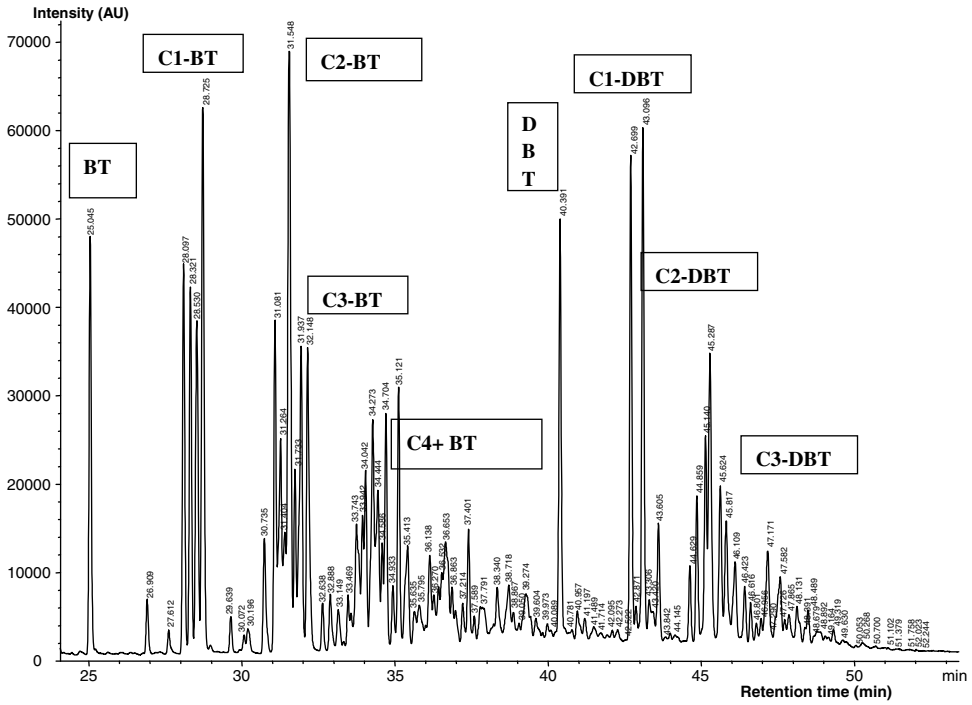


Figure 21.3 Elution profile of sulfur compounds in LCO. The elution areas of BT and DBT sulfur derivatives are indicated.

Table 21.2 Operating conditions for GC–SCD analyses.

Column(s)	SPB-1 (polymethylsiloxane, Supelco), 30 m × 0.32 mm i.d. × 4 μm
Column oven	60–280 °C (40 min); 5 °C min^{-1}
Carrier gas	He; constant flow, 2 ml min^{-1}
Injection	0.5 μl, on-column; 90–270 °C; 200 °C min^{-1}
Detector	SCD, 950 °C
Acquisition rate	5 Hz

other analyses such as elemental analysis. A comparison between the sample chromatogram and a reference chromatogram obtained using standard compounds can also be performed. Usually, accurate results are obtained (2–5% relative standard deviation).

These analyses are usually carried out to compare feedstock and products from hydrodesulfurization (HDS) products in order to monitor the transformation of sulfur compounds. Thus, classes of reactivity of sulfur compounds can be determined. Refractory compounds are also identified.

For various types of diesel, such as straight-run diesel and conversion diesel, strong overlaps between the majority species (eluted as elution peaks) and the minority species are observed, leading to a block of poorly resolved compounds. In this case, the technique is unable to provide a quantitative analysis of the sulfur species. A more complex approach to overcome this limitation is described in Section 21.4.

21.2.6.3.2 Nitrogen Owing to the low nitrogen contents in petroleum products (100–1000 ppm) distributed over a large number of different compounds, a nitrogen-selective detector requires high sensitivity and selectivity towards carbon. The nitrogen–phosphorus thermionic detector (NPD), based on the use of an FID system modified by a rubidium salt in order to ionize the nitrogen present in the matrix, remains limited by poor carbon–nitrogen selectivity and requires precise optimization of the gas flow rates to achieve good performance. The only detector meeting these criteria is the nitrogen chemiluminescent detector (NCD). The operating principle is based on the oxidation of nitrogenated compounds to form nitrogen monoxide, which, by reacting with ozone, produces a chemiluminescence reaction whose radiation is detected in the near-infrared region. GC–NCD coupling has been carried out to determine nitrogenated compounds in gasoline and gas oils [52]. Operating conditions are given in Table 21.3.

Figure 21.4 shows examples of chromatographic profiles obtained by GC–NCD for the resolution of nitrogenated species contained in an LCO. The elution areas of indole, aniline, carbazole, and acridine derivatives are indicated. We observe that detailed information on nitrogenated species can be obtained for an LCO whose profile shows resolved elution peaks. Again, detailed identification databases are not available in the open literature.

For other types of diesel, such as straight-run diesel and conversion diesel, strong overlaps between the majority species and the minority species are also observed. In this case, GC–NCS is unable to provide a quantitative analysis of the nitrogen

Table 21.3 Operating conditions for GC–NCD analyses.

Column(s)	DB1 (J & W Scientific), 60 m × 0.25 mm i.d.; 0.25 μm
Column oven	65–120 °C; 10 °C min^{-1}
	120–240 °C; 1 °C min^{-1}
	240–280 °C (10 min); 10 °C min^{-1}
Carrier gas	He; constant flow, 2 ml min^{-1}
Injection	0.5 μl, split ratio 1:50; 270 °C
Detector	NCD, 800 °C
Acquisition rate	5 Hz
Modulation period	8s

species. Again, a more complex approach to overcome this limitation is described in Section 21.4.

21.2.6.3.3 Oxygen Detection Alcohols, ethers, and other oxygenates are frequently added to gasoline to increase the octane number. Their contents must therefore be determined individually to meet regulatory limitations. The oxygen FID detector [53] consists of a combination of two micro-reactors and an FID to convert any oxygenated compound into carbon monoxide, which is hydrogenated into methane and then detected. The sensitivity and linearity are not as good as for the FID but the selectivity with respect to oxygenated compounds is high. This detector is used in a standard test method for the determination of oxygenates in gasoline (ASTM D5599).

21.2.6.3.4 Multi-Element Detection The AED is a multi-element detector, the principle of which is based on the spectral emission generated by the compounds when they are introduced into a plasma, each atom producing a set of characteristic peaks.

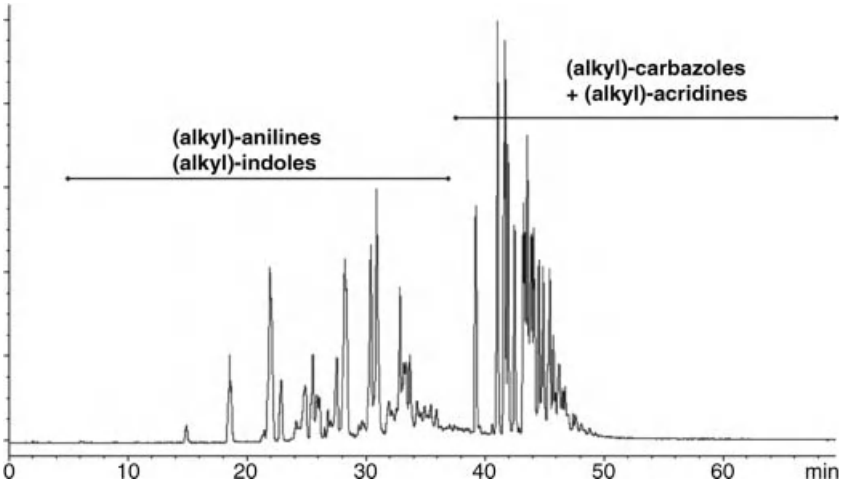


Figure 21.4 Elution profile of nitrogen compounds in an LCO. The elution areas of nitrogen derivatives are indicated.

GC–AED coupling has been used in particular for the determination of sulfur and oxygen compounds in gasoline [54] and to determine simulated distillation profiles for each element (C, H, S, N) in middle distillates [55]. The main disadvantages of this detector are its limited robustness, difficult maintenance, and high cost.

21.2.6.4 **Mass Detection**

GC–MS coupling combines the resolution of chromatographic separation with detection selectivity and sensitivity. The mass spectrometer gives information on the molecular structure and provides an additional separation dimension if the mass spectra of coeluted compounds can be deconvoluted. When the types of expected structures are known, single ion monitoring, by ionization at a targeted m/z value or by extraction of the total ion current (TIC) chromatogram, is an interesting solution to simplify the chromatogram. However, this detector is unable to distinguish between molecules of identical mass, such as olefins and naphthenes. Another limitation of this coupling is the tedious calibration work required for quantitative analysis, since the linearity is not as good as that offered by the FID.

This coupling has been used for the detailed analysis of hydrocarbons in gasoline [56], but HR-GC using retention indices for identification is a serious challenger owing to its straightforward implementation and the reliability of the quantitative analysis. GC–MS therefore remains a powerful tool for the analysis of targeted compounds such as biomarkers in geochemistry and marine pollution analyses [57], since the peaks of these compounds, relatively concentrated in crude oil, stand out clearly from the unresolved chromatographic background and they have characteristic mass spectra.

21.2.7
Conclusion

As mentioned in this part, the insufficient resolution of the most powerful chromatographic conventional approach, HR-GC, limits the quantity of information available for highly complex samples. This is the case for complex petroleum cuts such as middle distillates (12–25 carbon atoms per molecule) or heavier cuts, or those cuts containing traces of various types of sulfur or nitrogen derivatives.

Association of a selective detector described in Section 21.2.6.3 is particularly interesting for the specific monitoring of heteroelement compounds or for more detailed identification of hydrocarbons. In this case, the detection step is considered as an additional separation dimension which provides a simply binary response in the case of specific detectors or in mass spectrometry with single ion monitoring.

The chromatographic resolution can also be increased with systems coupling several chromatographic columns based on independent separation dimensions adapted to the physicochemical nature of the hydrocarbons. Owing to the complexity of petroleum products in terms of number of compounds, volatility range, chemical class, and concentration, we can easily understand that the analysis of these hydrocarbon mixtures requires higher resolution. This context favored the

emergence of multi-dimensional chromatographic methods designed to increase the resolution of chromatographic systems. These systems are described in Sections 21.3 and 21.4.

21.3
GC × GC: a Revolutionary Analytical Technique for Detailed Molecular Analysis

21.3.1
Historical Trends for Improving the Separation Capacity

As discussed in Section 21.2, the detailed characterization of complex hydrocarbon samples aims to provide the separation, identification, and quantification of the different constituents and therefore it requires the highest peak capacities possible.

In the case of a chromatographic column having N theoretical plates, the peak capacity n – which is the number of "peaks or compounds" that can be separated individually and which describes the separation capacity – is given by

$$n_{\text{peak capacity}} = \frac{\sqrt{N}}{4R_s}\ln\left(\frac{t_{\max}}{t_{\min}}\right) + 1 \tag{21.3}$$

where n is the peak capacity, N the number of theoretical plates, R_s the resolution, and $t_{\max}$ and $t_{\min}$ the retention times of the less and the most retained compounds, respectively.

Owing to statistical peak overlap, the peak capacity of the separation system should be much higher than the actual number of components of a given mixture. For instance, a high-resolution 50 m length capillary GC column reaches a theoretical peak capacity of 250 under temperature-programmed condition (e.g., 250 000 plates). Since the number of hydrocarbon isomers increases exponentially with the number of carbon atoms and easily surpasses 250, GC becomes limited when dealing with samples containing more than nine carbon atoms and the detailed analysis of kerosene samples (i.e., C_8–C_{15}) or middle distillate samples (C_{15}–C_{30}), for instance, is not possible.

Multi-dimensional gas chromatography (MDGC) was introduced in the 1980s and 1990s to overcome these limitations and to increase the peak capacities. According to the classical terminology in chromatography, separations are commonly called two- or multi-dimensional when the separation of all or some selected groups of sample components are repeated in two or more analytical chromatographic columns of different selectivity [58]. Therefore, each dimension of separation is associated with a specific type of stationary phase and with a specific molecular interaction developed between this stationary phase and the solute. As stated by Giddings [1], a multi-dimensional separation requires that

- Solutes are separated in two (or more) independent, or orthogonal, dimensions
- The resolution achieved in one dimension is preserved throughout the whole separation.

Various multi-dimensional systems have been developed by "hyphenating" (coupling) dimensions whose natures can be different, such as liquid, gas, or supercritical chromatography [59]. Better efficiency and easier implementation were achieved using two GC dimensions, which was obtained coupling in series additional columns to the primary column in which the first separation is performed. In that case, the continuous transfer of the effluent or the transfer of selected fractions, or cuts, from the first to another column is achieved by the carrier gas flow, which can be diverted to exit ("venting") or reversed for backflushing by flow rate switching between the columns. By the transfer of selected cuts from one column to another (different polarity and selectivity of the separation) [20], the resolution between elution peak groups which are contained in such cuts is improved. This particular way of operation in MDGC is called the heart-cutting technique [12, 59–61].

The increase in peak capacity of MDGC compared with conventional GC can usually be estimated by saying that the heart-cutting technique provides $n_1 + n_2$ results, where n_1 and n_2 are the peak capacities of the first and second columns, respectively. However, the information gained by the first separation (the chromatographic resolution) is partly lost when the cut is reinjected on to the second dimension, due to trapping or focusing processes [59, 61]. Although clever separations can be performed using this so-called heart-cutting technique, drawbacks include the partial analysis of the sample in the two different dimensions and the increased analysis time.

Introduced in the early 1990s by Liu and Phillips [62], comprehensive two-dimensional GC (GC × GC) was designed to overcome these limitations by producing a high-frequency heart-cutting separation of the entire sample (see Section 21.3.2). Ever since, GC × GC has evolved towards a strategic analytical tool sustained by improved instrumentation and has attracted considerable interest from the GC community involving an increasing number of users working in a wide range of application areas [59–64]. The first two sessions of a dedicated symposium were held in Volendam, The Netherlands (2003) and Atlanta (2004).

21.3.2
Principle of GC × GC

As discussed previously, a further distinction can be made between MDGC (or heart-cut system) and comprehensive systems. In the former system, only a limited part of the effluent from the first separation column will be directed towards the second. The principle of GC × GC (Figure 21.5) is based on the hyphenation of two capillary GC columns of different selectivity – that is, two different dimensions of separation connected through a modulation device (see Section 21.3.3) in order to achieve full hyphenation between these two dimensions [59–64].

The interface between the two dimensions allows the sampling of the effluent coming from the first dimension by focusing by trapping successive fractions in narrow bands on to the end of the first column (zone 1, Figure 21.5). Then, it allows

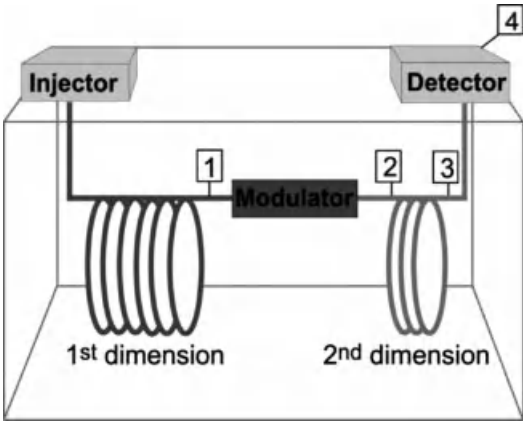


Figure 21.5 GC × GC instrumentation. See text for further explanation.

the reinjection in a continuous way of sharp fractions – also called chemical pulses – of the first column effluent into the second column (zone 2, Figure 21.5). In that case, the entire sample is subjected to the two separation procedures (zone 3, Figure 21.5) and then reaches the detector (zone 4, Figure 21.5), which has to be fast enough for monitoring the elution of compounds from the second column (see Section 21.3.3). Hence this approach is truly comprehensive because the whole sample is separated on two different columns and the information gained during the first separation is not lost during the second separation.

Thus, two solutes coeluting in the first separation – having the same retention time – may be separated in the second dimension provided that their interactions with the second stationary phase are different. The second separation must be very rapid to allow each new injected fraction to be separated during a separation time shorter than the sampling time. Sampling time is usually called modulation period. As the two columns are usually placed in the same oven, a series of very fast separations in the second dimension should be achieved simultaneously with the first dimension separation. As example, Figure 21.6 shows the separation of three compounds which are hardly separated on the first column.

The raw modulated signal recorded by the detector is then processed:

- At the outlet of the first column (Figure 21.6a), elution peaks of these three compounds are overlapped, leading to a broad elution peak.
- After modulation and injection on to the second column, each species presents a different retention time: the raw modulated signal recorded at the detector is then composed of a succession of narrow peaks, which correspond to successive separation of each fraction injected on to the second column (Figure 21.6a).
- This raw signal is then sliced according to the modulation time, and each slide is stacked side-by-side to generate a retention plane (Figure 21.6b).

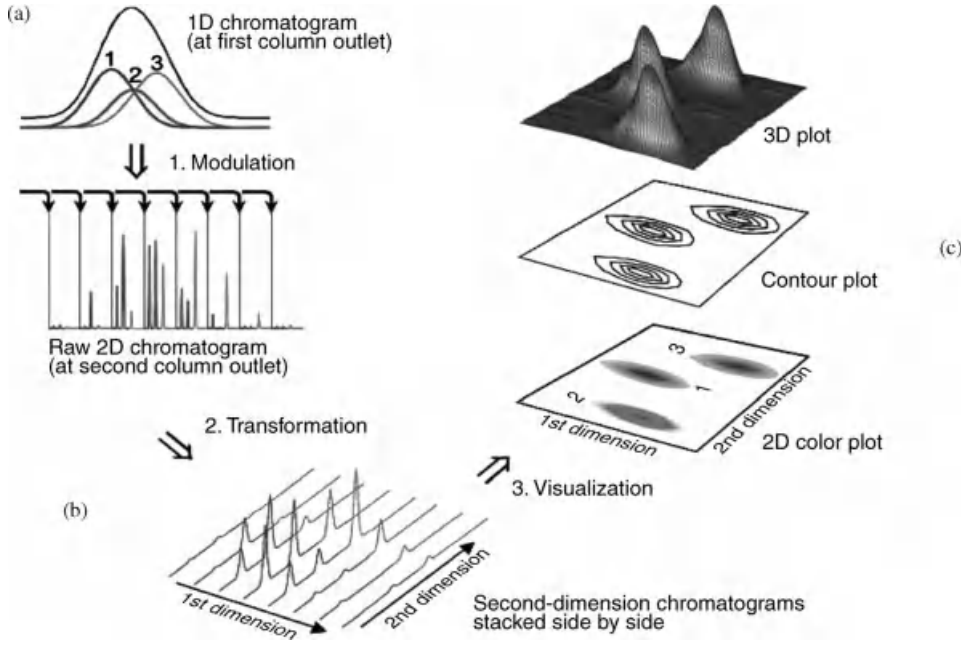


Figure 21.6 GC × GC principle for the separation of three compounds coeluted from the first column: (a) 1D chromatogram before and after modulation; (b) 2D chromatogram obtained from sliced of raw data; (c) visualization after data processing in 2D contour plot or 3D plot. Adapted from [64].

- The resulting chromatogram can be represented as a two-dimensional plane from which elution peaks emerge (Figure 21.6c):
  - –The first dimension of this plane represents the retention time on the first column, which usually is expressed in minutes.
  - –The second dimension represents the retention time on the second dimension, which usually is expressed in seconds.
  - –The third dimension represents the signal intensity, although the usual way to represent a GC × GC chromatogram is a two-dimensional contour plot.

21.3.2.1 Peak Capacity of GC × GC

The entire sample is subjected to both separation procedures and reaches the detector. Hence this approach is truly comprehensive because, rather than a few selected fractions, the whole sample is separated on two different columns and no information gained during the first separation is lost during the second. The increase in peak capacity in comprehensive GC × GC is also estimated by saying that this technique provides $n_1 \times n_2$ results, where n_1 and n_2 are the peak capacities of the first and second columns, respectively. For instance, if the first dimension has a peak capacity of 500 and the second dimension 5, the GC × GC system offers a peak capacity of 2500 (MDGC would be able to offer only 505; see Section 21.3.1), which

would require 10 million theoretical plates in a one-dimensional separation system, that is, 50 times higher than the number available in GC.

21.3.3 Instrumentation for GC × GC

21.3.3.1 Modulation

21.3.3.1.1 Modulation Technology The modulator is considered as the core of a GC × GC system. It must enable one to trap, to focus, to sample, and to transfer online the effluent from the first to the second column without loss of material or of information. For that purpose, various modulators, either valve based or thermal/cryogenic systems, have been developed to ensure complete and online transfer with a focusing effect generating sharp peaks having widths at half-height as low as 100–300 ms. Figure 21.7 shows the basic principles of the main family of different modulators and the modulation processes inside the modulator: (a) thermal heating modulator, (b) cryogenic modulation with a longitudinal cryogenic system, (c) cryogenic jets modulator and (d) valve-based modulator. The principles and advantages or drawbacks of these modulator are briefly discussed below.

- *Thermal heating modulation* (Figure 21.7a) is based on a succession of trapping–desorption cycles obtained by positive temperature differences applied at the"interface" of the two columns. For heated modulators, trapping is achieved in a tube having a thick film of stationary phase and desorption occurs by applying locally a higher temperature of about 100 °C by the Joule effect compared with the oven temperature. The first system, the thermal desorption modulator (TMD), designed by Liu and Phillips, consisted of a resistively heated modulator: solutes were trapped in the modulation tube coated with metallic paint and desorption was achieved by generating periodic hot pulses from current pulses by the Joule effect [62]. Because of a lack of robustness, this system was replaced by a rotating heated assembly (sweeper) moving around the modulator tube, the speed of revolution defining the modulation period [2] (Figure 21.7b). The main drawback of the heated modulator is the temperature limit preventing the analysis of compounds heavier than C_{25}.
- *Cryogenic modulation* (Figure 21.7b and c) is achieved by a succession of trapping–desorption cycles obtained by the decrease in temperature (about −100 °C) generated by the endothermic expansion of a cryogen such as carbon dioxide or liquid nitrogen; desorption occurs when solutes are exposed again to the oven temperature or via a heating system. The LMCS (longitudinal modulation cryogenic system) generates modulation by moving back and forth a cryogenic CO_2 spray along the head of the second column [65, 66]. The dual-jet CO_2 modulator permits modulation by turning on and off two sprays of CO_2 applied on the column [67]. The cryogenic approach is devoted to a wider boiling point range of volatile compounds but liquid nitrogen is to be preferred to CO_2 for trapping of very volatile solutes. The static strategy of jet modulation is obviously more robust and of easier implementation than the mobile strategy (sweeper and LMCS). Two commercial systems

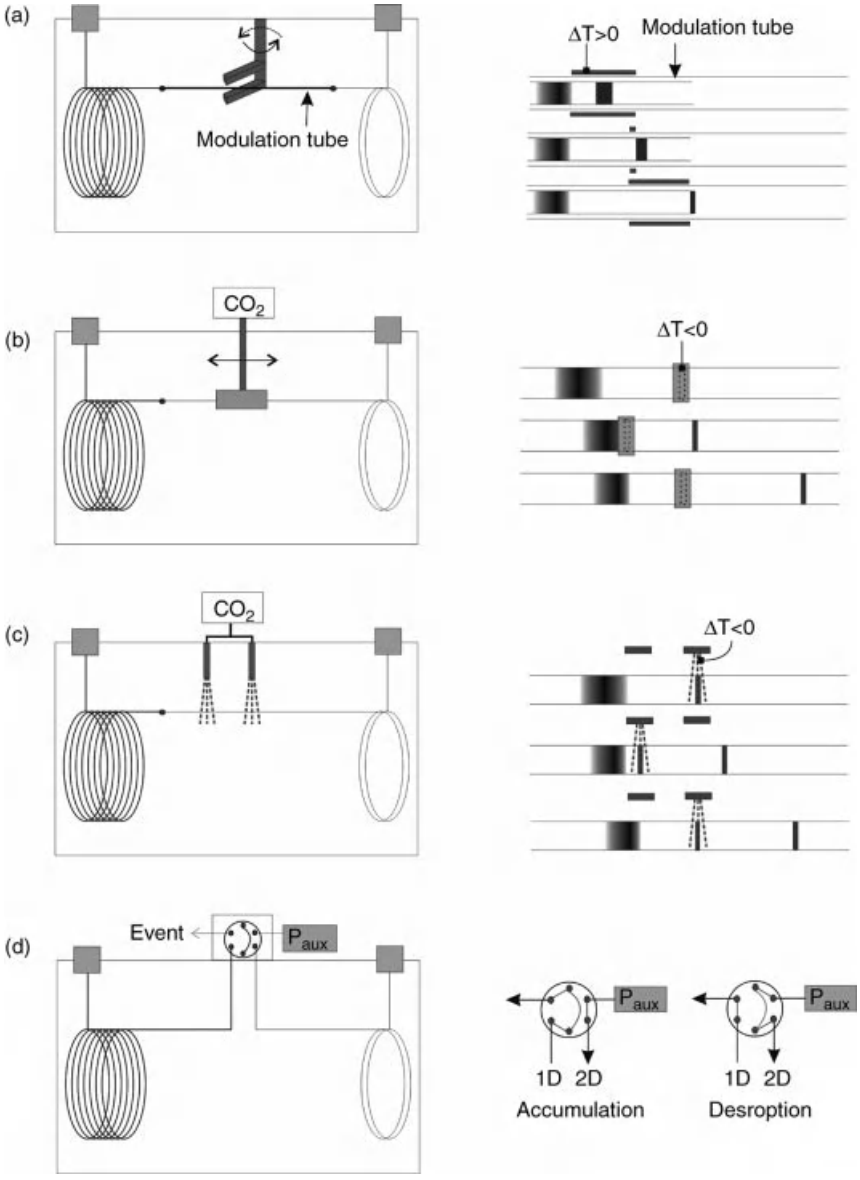


Figure 21.7 The different modulation systems and the processes of modulation. (a) Sweeper modulator; (b) longitudinal modulation system (LMCS); (c) dual-jet CO_2 modulator; (d) valve-based modulator.

using the jet technology supplied by Thermo Fisher Scientific and Leco under Zoex licensing are available.

The efficiency of the modulator is governed by the difference in temperature generated at the interface. Thus, a CO_2 jet-based system allows a local temperature

of −60 to −30 °C to be reached with a jet flow. Consequently, trapping of the most volatile compounds (<C_7) is not achieved. A liquid N_2 jet-based system overcomes these limitations by allowing a local temperature of −160 °C, which allows C_3 compound modulation [68].

The modulation of heavy compounds (>C_{26}) can be also difficult, leading to distortion of the elution peaks [69], which is prevented by continuous adaptation of the N_2 flow rate or use of a heating device [70]. Recent developments have been made to limit the cryogenic fluid consumption, using a single-loop system from Zoex or replacing the cryogenic fluid by cooled air (via a vortex or precooling device) [71, 72]. In this last case, the modulation range is reduced.

- With *valve-based modulators* (Figure 21.7d), sampling of the effluent is achieved via valve switching at a high frequency; focusing is achieved using a secondary circuit of carrier gas at a higher flow rate. This type of modulator has recently attracted interest due to its lower cost and higher compatibility over a wide volatility range. The main drawback of this type of modulator based on flow division is the low sampling rate of effluent from the first column, limiting the separation power of the system [73–76].

In conclusion, the best choice of modulator depends on the target application. For light compounds, it would be preferred to chose N_2 liquid jets as modulator, allowing the best performance in term of focusing. For heavy compounds, CO_2 jets or valve-based modulators would be the best option. Valve-based modulators could be the best choice for control laboratories due to the lower cost of use even if this option is more complicated in the case of development of various methods

21.3.3.1.2 Focusing Phenomena The process of solute focusing/reinjection must be reproducible and nondiscriminatory with regard to analyte properties. The advantage of solute focusing by trapping and desorption with high heating and cooling time constants relies on the possibility of reversing the peak dispersion that occurs in any chromatographic process [77]. The modulation of the primary peak results in a series of sharp peaks with widths below 100 ms. Because of the law of mass conservation, the narrow peaks have a high amplitude. The signal intensity enhancement is typically 10–70-fold higher in GC × GC than in GC. However, regarding the analyte's detectability, the signal-to-noise ratio (S/N) has to be evaluated. As GC × GC requires high acquisition frequencies of detectors (minimum 100 Hz) to define very narrow peaks properly, the expected signal intensity enhancement is reduced. However, a sensitivity enhancement by a factor of 5 is generally achieved [78], which is a great advantage for performing trace analysis.

21.3.3.1.3 Optimization of Modulation Period The modulation period (P_{mod}) is a key parameter to tune GC × GC separations properly, that should be chosen according to the duration of each second separation ($^2t_{r,max}$) and to the width of peaks eluting from the first dimension (^1t_r):

$$^2t_{r,max} < P_{mod} < {}^1t_r/3 \tag{21.4}$$

The first condition ensures that GC × GC chromatograms will be properly structured by avoiding so-called wrapping around. This phenomenon occurs when

more retained compounds in the second dimension are eluted during the following modulation cycle, which involves overlap between compounds having different boiling points. The second condition is required to obtain a sufficient sampling of primary peaks and to avoid a loss of resolution in the first dimension (3–4 samples per peak are recommended [79]).

21.3.3.2 **Detection**

During the trapping/desorption cycles, the modulator focuses the analytes, leading to modulated peaks having narrow bandwidth (100–600 ns) and high amplitude. Thus, taking into account that 10 points are necessary to obtain a complete reconstruction of an elution peak, only detectors having very low time constants (<10 ms) should be coupled with GC × GC. Moreover, detectors should be equipped with a high-speed acquisition rate electronic card. The FID is widely used for universal detection without any modification for GC × GC [80], presenting a negligible void volume combined with a high acquisition rate (50–300 Hz).

The coupling of GC × GC with a specific detector provides a supplementary dimension but electronic upgrades are usually necessary to reach a 50 Hz acquisition frequency in order to be compatible with GC × GC. This is the case for the detection of halogens [micro- electron-capture detector (ECD)] [81], sulfur (SCD [82, 83] or PFPD [84]), and nitrogen (NCD) [85, 86]. Multi-element detection could be performed with NPD (for nitrogen- or phosphorus-selective detection [87, 88] or with AED, but these system suffer from a low acquisition frequency (<10–15 Hz) due to physical limitations and/or an unadapted electronic card. Thus, two-dimensional (2D) chromatograms are limited by tailing peaks. Table 21.4 gives an overview of the specific detectors available for GC × GC.

21.3.3.3 **Data Processing**

In view of the GC × GC resolution, the data are extremely complex to manage. Processing software is designed to display multi-dimensional data, detect peaks, and quantify the analytes [92]. To obtain a reliable quantitative analysis, the GC × GC data

Table 21.4 Overview of specific detectors used in GC × GC.

Detector	Element	Frequency (Hz)	Sensitivity ($g\,s^{-1}$)	Linearity	Ref.
ECD	Halides	50–100	5×10^{-14}	10^3	Pesticides [81, 90]
SCD	S	50–100	5×10^{-13}	10^5	Crude oil [78, 82, 83]
FPD	P, S	50–200	(P) 4.5×10^{-14} (S) 6.2×10^{-13}	10^4	Naphtha, middle distillates [84]
NPD	N, P	50–100	4×10^{-13}	10^5	Middle distillates [88–90]
NCD	N	100	3×10^{-12}	10^5	Middle distillates [85, 86]
AED	Multi-elements	10	Depends upon element	Depends upon element	Middle distillates [91]

must first be processed efficiently. In view of the difficulty in managing the signal processing, most software applications dedicated to GC × GC were first developed to perform qualitative analyses. The quantitative information to be determined will vary depending on the application. The first possibility is analysis of targeted compounds, which corresponds to one or more eluted resolved peaks on the 2D chromatogram. The second possibility is the determination of a group of compounds, therefore involving a 2D elution area of several peaks. The last possibility is the quantitative comparison of two or more 2D chromatograms to determine the differences in composition between several samples. Several software approaches have been considered [93]. The first to be developed is based on evaluating the area of the 2D peaks. This approach is far less obvious than with conventional one-dimensional (1D) GC, since a single compound is divided into several fractions, depending on the number of modulations. Each individual fraction is therefore summed to obtain the total area using an integration algorithm. Commercial systems include 2DChrom (Thermo Fisher Scientific), which can be used to define the elution areas (blobs) manually on the 2D chromatogram. A matching algorithm automatically detects the start and end of the peak to adjust the blob. An integration mask can be defined for other samples and 2D chromatograms can be compared.

According to another approach [94], the concentration of a solute is determined by the volume defined by the modulated peaks. This is similar to a graphical method which processes the 2D chromatogram as an image. Commercial systems include GC image software (Zoex, Agilent, and Shimadzu). The baseline is initially deleted, then the peaks are located using a watershed-type algorithm. As previously, an integration mask can be created. On comparison, the two approaches produce similar results [92]. ChromaTOF (Leco) is one of the most sophisticated commercially available software systems, capable of processing data obtained from both a time-of-flight (TOF) mass spectrometer and an FID. Little information is available on the signal processing algorithm, but it seems to be similar to an area approach.

Chemometric methods have undergone considerable development over the last few years. Examples include principal component analysis (PCA), used to find similarities between two 2D chromatograms, and principal component discriminated analysis (PCDA), to determine their differences.

The generalized rank annihilation method (GRAM), based on a noniterative approach, is used to deconvolute and quantify 2D coeluted peaks. Determination of S/N is therefore more accurate compared with the conventional methods. For analyses with even more complex data, such as GC × GC–TOF-MS [93] or three-dimensional (3D) GC [95], parallel factor analysis (PARAFAC) is preferred. This iterative method can be used in particular to process third-order data. Although they have already given good quantitative results for petroleum products [96], chemometric techniques are still under development.

21.3.3.4 **Chromatographic Aspects**

21.3.3.4.1 Nature of Stationary Phase Considering the nature of the stationary phase, it is necessary to use chromatographic columns that provide independent

separation mechanisms in the first and second dimensions in order to create orthogonal separation conditions. Every separation in GC is based on volatility and on interactions depending on the chemistry of the stationary phase such as dispersive interactions, hydrogen bonding, π−π interactions, or steric effects, which are represented by the activity coefficient in the stationary phase at infinite dilution γ^{∞}. The retention factor k of a compound in GC is related to its vapor pressure p_s and its activity coefficient in the stationary phase at infinite dilution γ^{∞} according to the following equation [97]:

$$k \propto \frac{1}{p_s \gamma^{\infty}} \tag{21.6}$$

In temperature-programmed separations, the different retention factor is expressed according to the same parameters in relation to the elution temperature (T_e):

$$k \propto \frac{1}{\gamma^{\infty}(T_e) p_s(T_e)} \tag{21.7}$$

The main association type is the normal-phase association (nonpolar/polar). In this case, a nonpolar column is chosen for the first dimension and a (semi-)polar column for the second dimension. This configuration leads to an alleged independent separation mechanisms for a temperature-programmed separation [63]. In the first dimension, activity coefficients are close to unity owing to the lack of specific interactions; the retention depends only on the vapor pressure and solutes are therefore separated according to the order of their boiling points, using a temperature gradient. The second dimension can be considered as isothermal at the elution temperature T_e since it takes only a few seconds and the ramp of the temperature achieved for the first dimension separation is relatively low (typically 1–2 °C min^{-1}) [98]. Thus, for one modulation cycle, the second separation is performed at constant temperature corresponding to the temperature T_e at which solutes are reinjected into the second column; owing to the temperature gradient, it increases from cycle to cycle. Under these conditions, volatility effects are nondiscriminative in the second dimension and only specific interactions govern the retention. According to the criteria of Giddings [1], the two dimensions are fully independent, which means that the separation system is orthogonal. By extension, orthogonality refers to the association of columns of different selectivities.

The major advantage of GC × GC separations is that the chromatograms are well organized. The separations in the first and second dimensions are a function of the interactions within each stationary phase, which makes the identification of species easier. Thus, in GC × GC the chromatograms are usually structured upon bands of homologous groups of isomers having similar boiling points and polarities. Hence the different chemical groups of petroleum products (e.g., saturates and mono-, di-, and triaromatics) are then localized in specific areas of the chromatogram, which facilitates identification.

For instance, Figure 21.8 shows the GC × GC separation of a hydrogenated solvent: the typical bands observed for isomer groups, known as the roof-tile effect, are observed and can also contribute to confirm peak assignment [99].

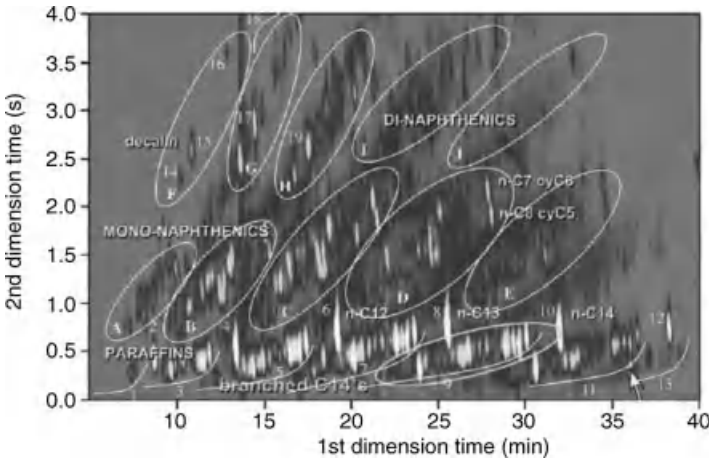


Figure 21.8 GC × GC separation of a hydrogenated solvent containing only saturated hydrocarbons [99].

The roof-tile effect can be explained by the retention of alkanes in each dimension. the boiling point decreases with increase in ramification for homologs: the more ramified the alkane is, the lower is its retention time in the first apolar dimension. On the other hand, the more ramified the alkane is, the lower is the polarity owing to the decrease in molecular volume. Hence the retention time on the second column also decreases, leading to the typical roof-tile effect which allows several isomers to be identified in complex mixture of hydrocarbons.

A reverse-type configuration (first polar column and second nonpolar column) was also shown to be orthogonal [100].

21.3.3.4.2 Dimension Since the GC × GC system relies upon rapid analysis of accumulated bands, it is usual to run the first dimension to obtain a conventional GC elution and the second dimension under fast GC conditions [101]. The features of the first dimension are not crucial compared with those of the second: the second dimension must enable the complete separation of pulsed bands to be achieved within the modulation period of the system. This is most effectively achieved by using a short, narrow-bore, thin-film column. A typical column set might comprise a 25 m × 0.32 mm × 0.25 μm column in the first dimension followed by a 1 m × 0.1 mm × 0.1 μm column in the second dimension.

21.3.3.5 Conclusion

Clearly, trace analysis in the oil and petrochemical industry stands to benefit from the development of a new and extremely powerful separation technique such as comprehensive GC × GC. Compared with conventional MDGC, the main advantages of comprehensive GC × GC are as follows [59–64]:

- A much higher peak capacity, which leads to an improved separation of trace components from other overlapping components. It provides optimal separation

of complex mixtures into very individual peaks (peak capacities of 30 000 and integration of more than 5000 peaks are currently achieved).
- A better sensitivity due to the refocusing process in the thermal modulator [102]. This allows the accurate determination of low concentrations of specified components in a complex mixture.
- If proper orthogonal conditions are used, chemically related compounds show up as ordered structures, which greatly facilitates group-type analysis and the provisional classification of unknowns [59, 61, 63]. It may provide the boiling-point range distribution and polarity distribution and thus increase the amount of information generated per unit time.

21.3.4
Applications of GC × GC to Various Challenges

Selected applications of GC × GC to various analytical challenges encountered in the petroleum industry for which conventional techniques show limitations are presented:

- group-type analysis of middle distillates
- nitrogen and sulfur speciation
- detailed analysis of effluents from linear alkylbenzenes (LABs) or Fischer–Tropsch processes.

21.3.4.1 Group–Type Analysis of Middle Distillates

Conventional techniques used for the characterization of middle distillates are directed towards either the determination of a group-type classification or the boiling point range distribution. The former is usually performed by LC for the saturate/aromatic balance (ASTM D2549) or by MS, providing the repartitioning of hydrocarbons into up to 11 families (ASTM D2425) (see Sections 21.2.4.1 and 21.2.4.2). The latter is obtained by GC simulated distillation (ASTM D2887).

Owing to its huge peak capacity, GC × GC succeeds in providing both types of information with a better insight into the petroleum cut [99–101, 103]. Figure 21.9a, c, and c represent GC × GC chromatograms of a straight-run diesel sample obtained by the distillation of Safaniya oil (boiling point range 213–347 °C) in 1D, 2D, and 3D views, respectively. The operating condition are given in Table 21.5.

As can be seen from the raw chromatogram (a), an impressive number of peaks can be observed (more than 30 000 individual peaks have been integrated from raw data), preventing a simple interpretation of the chromatogram. However, Figure 21.9b shows the second-dimension separation, obtained for one modulation cycle, of about 10 peaks eluted from the polar column (BPX-50) according to the number of aromatic rings as the BPX-50 stationary phase contains a significant amount of phenyl groups that preferentially interact with aromatic compounds through $\pi-\pi$ interactions. Thus, on this column, saturates elute first, then monoaromatics, diaromatics, and triaromatics, whereas all these compounds are potentially coeluted in the first dimension. This is a demonstration of the higher resolving power of GC × GC.

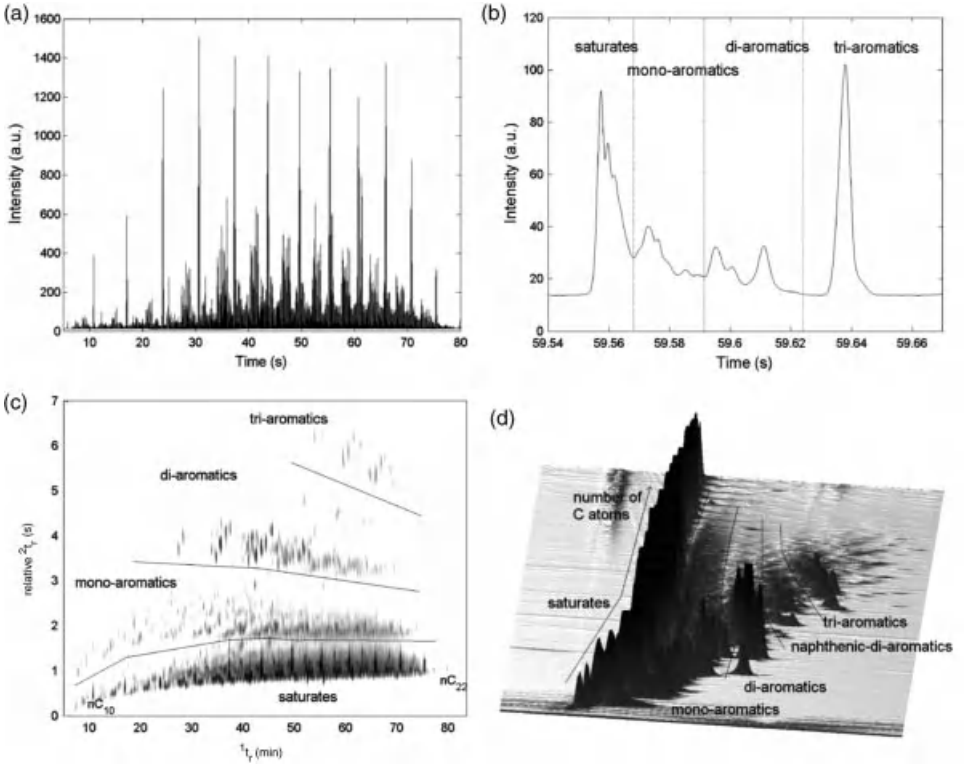


Figure 21.9 Chromatograms of a straight-run diesel sample obtained in one dimension – raw data (a), two dimensions (c), and three dimensions (d). An enhanced view of raw data along a modulation period is shown in (b). From [103].

After data processing, the structure of the GC × GC chromatogram is evidenced (Figure 21.9c). This group-breaking technique offers a polarity versus volatility separation of the sample, leading to a 2D chromatogram:

- In the first dimension, hydrocarbons are eluted according to their increasing boiling point, or number of carbon atoms.

Table 21.5 Operating conditions for GC × GC separation of diesel fuels.

Columns	PONA[a)], 10 m × 0.2 mm i.d.; 0.5 µm
	BPX-50[b)], 0.8 m × 0.1 mm i.d.; 0.1 µm
Column oven	50–280 °C; 2 °C min^{-1}
Carrier gas	He; constant pressure, 200 kPa
Injection	0.2 µl, split ratio 1:100, 280 °C
Detector	FID, 300 °C
Acquisition rate	100 Hz
Modulation period	7 s

a) Dimethylpolysiloxane; Agilent (Massy, France).
b) (50% Phenyl)polysilphenylene-siloxane; SGE (Courtaboeuf, France).

Table 21.6 Composition (% w/w) of the diesel obtained by LC, MS, and GC × GC.

	LC ($n = 4$)	MS ($n = 10$)	[a]GC × GC ($n = 3$)
Saturates	70.4 ± 0.3	71.7 ± 0.9	70.6 ± 0.6
Monoaromatics		18.8 ± 0.4	18.0 ± 0.3
Diaromatics		8.7 ± 0.2	10.3 ± 0.3
Triaromatics		0.8 ± 0.1	1.1 ± 0.1

a) *n*-Paraffins.

- The selectivity of the second dimension allows the separation of hydrocarbons from the less to the most polar, mainly according to the number of aromatic rings in that case.

Group-type bands are then easily distinguished and the contour of each group is adjusted using a specific function of the program indicating peak valleys, the density of which is more abundant at the border between two groups. Finally, the 3D chromatogram (Figure 21.9d) conveniently indicates the relative concentrations of hydrocarbons, but this representation is not suitable for quantitative purposes. Integration of group-type bands, that is, saturates and mono-, di-, and triaromatic hydrocarbons, determined in the GC × GC chromatograms was achieved using the software.

A comparison with results obtained by LC and MS is given in Table 21.6, and demonstrates that the results are in line with ASTM methods and the validity of GC × GC [100].

In contrast to standard methods, a more detailed characterization of diesel products can be obtained from the structure of GC × GC chromatograms. Isomers are grouped in the same location of the chromatogram and can be recognized owing to the roof-tile effect. Clearly, the resolution is still insufficient to allow individual peak identification except for the first (unalkylated) members of a chemical family (naphthalene, anthracene, and phenanthrene). However, elution zones of isomers can be defined into, at least, 60 clusters (Figure 21.10).

Once integration is completed, this novel type of analysis offers the possibility of assigning to each cluster of isomers a macroscopic property, such as mass, viscosity, or cetane number, which can be known for each isomer group, resulting in more accurate information on the physicochemical properties of the diesel cut. In a single analysis, the complete characterization of the sample could be obtained and then directly compared with product specifications; more precise and reliable kinetic and thermodynamic models that can be applied to the operation of hydrodesulfurization (HDS) units are also expected. There is no doubt that GC × GC will rapidly become the industrial benchmark.

However, the clusterization of a petroleum cut has limitations related to the partial overlapping, in the first dimension, of two adjacent series of aromatic isomers resulting from the higher volatility of highly alkylated aromatics than linear alkyl aromatics having one carbon atom less. Instead of performing the discrete characterization as described above, continuous information can be extracted from GC ×

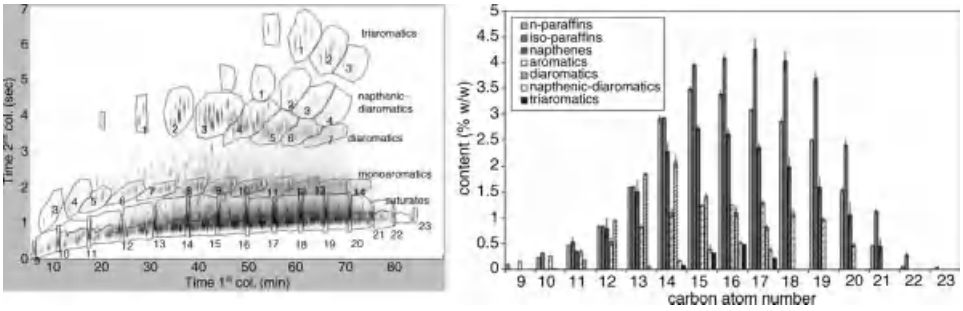


Figure 21.10 Group type of a 2D chromatogram according to the family and the number of carbon atoms of the alkyl group or alkyl chain. Operating conditions: first dimension, PONA (10 m × 0.2 mm, 0.5 μm); second dimension, BPX-50 (0.8 m × 0.1 mm, 0.1 μm); pressure (He), 200 kPa; temperature, 50 °C increased at 2 °C min^{-1} to 280 °C [100].

GC chromatograms using SimDist curves that can be obtained in a similar manner as in GC-SimDist. The decisive advantage of GC × GC relies on the possibility of drawing a specific SimDist curve for each chemical group. Once a group-type band has been selected, it is sliced according to the modulation period. Typical software for GC × GC automatically allows the construction of SimDist curves from the boiling point and the cumulated weight percentage: the first dimension retention time of each slice is converted into a boiling point using a relationship established with *n*-paraffins; the area of each slice determines a weight percentage using specific response factors. The global SimDist curve obtained by summing group-type SimDist curves fits perfectly with the ASTM D2887 SimDist curve, the discrepancies being less than 1 °C over the range 10–90% and less than 2.5 °C over the range 5–95%.

Characterization tools developed from GC × GC were applied to study the effectiveness of a conversion process. The conversion of polyaromatics into naphthenomonoaromatics during the hydrodearomatization (HDA) process can be followed at the molecular level and the activity of catalysts for HDA can be better understood and quantified. The results obtained are used to optimize kinetic models and process operations. Thus, GC × GC SimDist curves of the feed and the product were plotted for saturated and mono-, di-, and triaromatic hydrocarbons (Figure 21.11).

The shift of the SimDist curves demonstrates partial removal of di- and triaromatics to form monoaromatics and saturates, mainly consisting of naphthenic species. Thus, GC × GC is a powerful tool to evaluate qualitatively and quantitatively the performance of an HDS or HDA process as slight modifications in composition can be evidenced by differences in the retention map and by the shift of group-type SimDist curves.

21.3.4.2 **Sulfur and Nitrogen Speciation**

More stringent specifications on sulfur content in gasoline or diesel fuels and the production of unconventional oils with high sulfur contents have strengthened the need for deeper HDS of petroleum feedstocks. Thus, sulfur speciation, which consists in the determination of the repartition of different chemical classes of

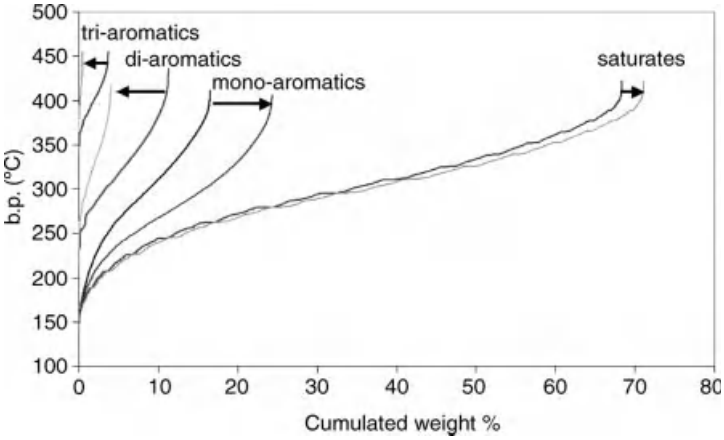


Figure 21.11 Group-type SimDist curves for the feed and the product of hydrotreatment of a straight-run diesel sample [100].

sulfur compounds [sulfides, thiophenes, benzothiophenes (BTs), dibenzothiophenes (DBTs), etc.] according to the number of carbon atoms, is of major interest for refiners, in order to improve kinetic modeling based on molecular composition. Usually, sulfur speciation is achieved using GC-SCD or MS (see Section 21.2.5.3), but these techniques become rather limited when complex samples need to be analyzed. GC × GC was coupled with an SCD to increase the resolution of the chromatographic separation [79, 99] (operating conditions are given in Table 21.7).

GC-SCD and GC × GC-SCD chromatograms are compared in Figure 21.12 for two different straight-run samples, obtained from the distillation of (a) Middle Eastern (SR1) and (b) South American (SR2) crude oils. The GC-SCD chromatograms show

Table 21.7 Operating conditions for GC × GC–SCD and GC–SCD analyses.

	GC × GC–SCD	**GC–SCD**
Column(s)	PONA[a], 10 m × 0.2 mm i.d.; 0.5 μm BPX-50[b], 0.8 m × 0.1 mm i.d.; 0.1 μm	DB1[c], 60 m × 0.25 mm i.d.; 0.25 μm
Column oven	50–280 °C; 2 °C min^{-1}	65–120 °C; 10 °C min^{-1} 120–240 °C; 1 °C min^{-1} 240–280 °C (10 min); 10 °C min^{-1}
Carrier gas	He; constant pressure, 200 kPa	He; constant flow, 2 ml min^{-1}
Injection	1 μl, split ratio 1:50; 280 °C	0.5 μl, split ratio 1:50; 270 °C
Detector	SCD, 800 °C	SCD, 800 °C
Acquisition rate	50 Hz	5 Hz
Modulation period	8 s	—

a) Dimethylpolysiloxane, Agilent (Massy, France).
b) (50%phenyl)polysilphenylene-siloxane, SGE (Courtaboeuf, France).
c) J & W Scientific.

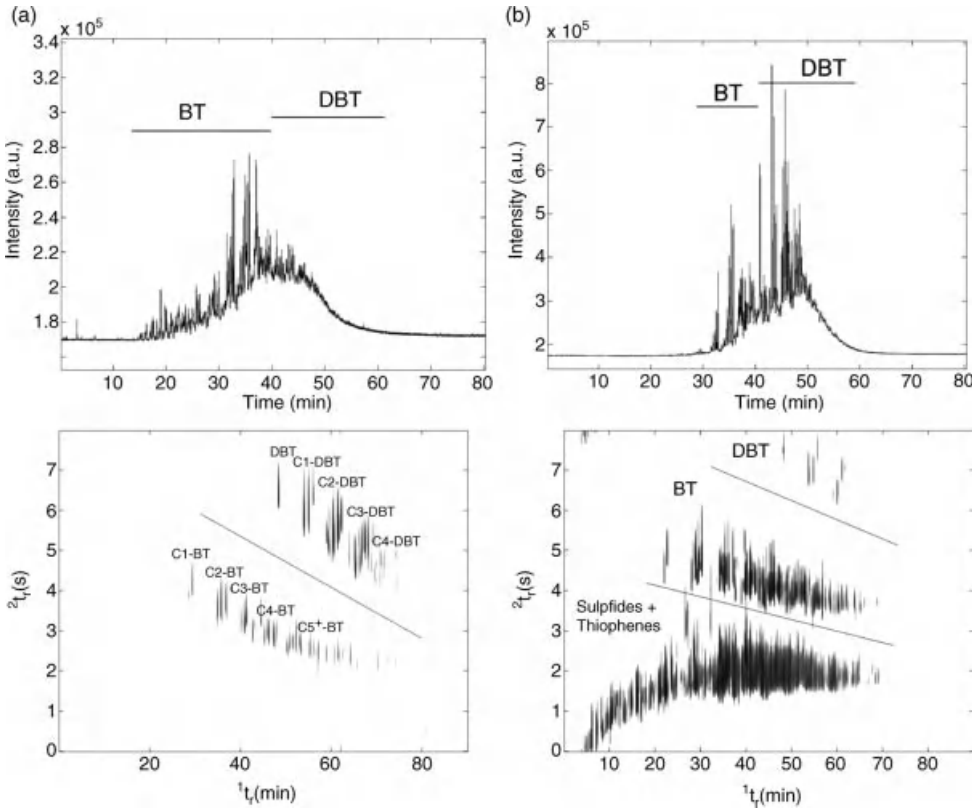


Figure 21.12 GC–SCD and GC × GC–SCD chromatograms of (a) SR1 and (b) SR2 straight-run samples [100].

an important baseline drift due to the coelution of several sulfur compounds. Further, it is generally assumed that all alkyl-BTs are eluted before DBT whereas partial coelution is evident when looking at the GC × GC chromatograms.

Owing to the selectivity of the second dimension, GC × GC-SCD allows alkyl-BTs to be separated from alkyl-DBTs, the latter being more retained on the polar column due to the presence of an additional aromatic ring. Hence, two well-resolved bands of alkyl-BTs and alkyl-DBTs are obtained for the SR1 sample, and a carbon atom breakdown inside each band allows the quantification of alkyl-BTs up to C_9 and of alkyl-DBTs up to C_5 (Table 21.8). A similar distribution is obtained for the SR2 sample, except for the relative concentration of a third group constituted of sulfides and thiophenes, which can also be identified and separated from alkyl-BTs and alkyl-DBTs owing to the lower polarity of these compounds. This third group is not taken into account in GC-SCD analysis, whereas it represents 60% of the sample of SR2. For the SR1 sample, only traces of these compounds have been quantified (<8%) and are not represented in Figure 21.12 owing to the level of the baseline. Hence GC × GC allows the discrimination of straight-run samples from different origins

Table 21.8 Detailed group-type distribution using GC–SCD and GC × GC–SCD for SR1 and SR2.

	SR1			SR2		
	GC	GC × GC	RSD[a)]	GC	GC × GC	RSD[a)]
Alkylthiophenes + sulfides	—[b)]	8.3	0.5	6.6	50.9	0.9
BT	—	0.1	0.0	0.3	0.0	0.0
C_1-BT	0.2	0.8	0.0	3.2	0.6	0.0
C_2-BT	2.0	1.9	0.1	5.7	2.5	0.0
C_3-BT	4.6	2.9	0.4	5.4	5.1	0.3
C_4-BT	8.5	4.6	1.1	6.1	8.5	0.2
C_5-BT	—	7.4	0.4	—	7.6	0.2
C_6-BT	—	9.2	0.5	—	5.2	0.2
C_7-BT	—	6.1	0.1	—	5.3	0.5
C_8-BT	—	7.9	0.2	—	4.6	0.1
C_9-BT	—	4.4	0.4	—	3.5	0.3
DBT	1.4	0.8	0.0	0.5	0.1	0.0
C_1-DBT	8.9	4.6	0.0	2.9	0.6	0.0
C_2-DBT	8.9	7.4	0.1	1.2	0.9	0.1
C_3-DBT	11.9	7.9	0.4	2.6	1.6	0.2
C_4-DBT	—	8.3	0.0	—	2.9	0.4
C_5-DBT	—	4.8	0.1	—	—	
Others	53.5	12.6	0.7	65.7	0.0	0.0

a) RSD is the relative standard deviation in GC × GC.
b) —, Not present.

and provides the quantitative repartition of alkyl-BT and alkyl-DBT groups according to the number of carbon atoms. No other analytical technique currently reaches this level of resolution.

This added knowledge is of significant value in the determination of the operating conditions required to attain product specifications with given feedstocks, and can be used to advantage for optimization of the HDS process in plant operations (space velocity, H_2 partial pressure, and reaction temperature).

As with sulfur compounds, speciation of nitrogen compounds is a major task in the petroleum industry. It is essential to differentiate between basic and neutral compounds in view of their reactivity difference for hydrodenitrification (HDN). The first studies focused in particular on the coupling of a nitrogen-specific detector with GC × GC for gasoil cuts. Despite the first qualitative results, the use of the NPD is limited by precise optimization of the operating conditions and lack of equimolar response [89]. In contrast, the NCD is perfectly suited owing to its detection performance. Although the first operating conditions did not provide sufficient resolution [104], Adam *et al.* [86] optimized the stationary phase combinations. They use a first 5% phenylsiloxane–95% dimethylpolysiloxane column with a second poly(ethylene glycol) column to differentiate between the basic (anilines, quinolines, acridines) and neutral (indoles, carbazoles) families.

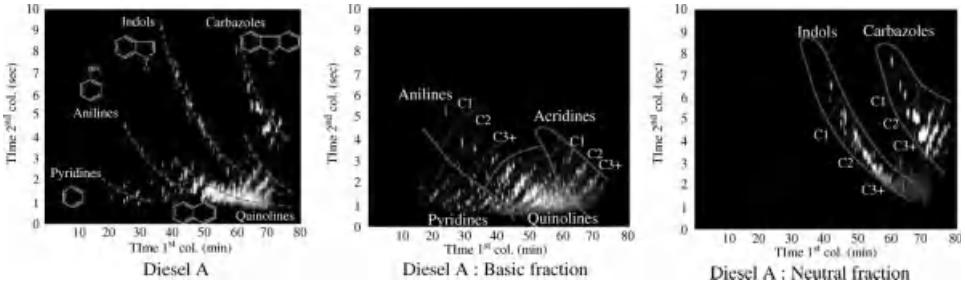


Figure 21.13 GC × GC–NCD chromatogram of a gas oil, of its basic and neutral fraction. Operating conditions: first dimension, SPB-5 (30 m × 0.25 mm, 1 μm); second dimension, Solgel Wax (1.6 m × 0.1 mm, 0.1 μm); constant flow rate (He), 1.4 ml min^{-1}; temperature, 60 °C increased at 3 °C min^{-1} to 290 °C [86].

Identification of the nitrogen compound distributions was simplified by fractionating the neutral from the basic nitrogen compounds, using an ion-exchange LC. Better resolution between the families (Figure 21.13) led to an extended and much more accurate quantification than with the GC–NCD methods [105].

21.3.4.3 **Petrochemical Applications**

21.3.4.3.1 Fischer–Tropsch Process Fischer–Tropsch synthesis, developed in the 1920s, has recently attracted renewed interest since petroleum reserves are known to be limited to some decades. In the present context of higher energy demands with greater environmental concern, alternatives to petroleum are being developed. Fischer–Tropsch technology converts coal, natural gas, and low-value refinery products into high-value clean products. *n*-Paraffins are the main products formed from hydrogen and carbon monoxide. They can be used for wax production but can be readily upgraded to fuels. Hydrocracking/hydroisomerization processes improve their thermal properties at low temperatures to allow their blending in a diesel pool. Actually, these resulting "green" fuels containing no sulfur and no aromatics present good combustion characteristics (with a high cetane number). During this reaction, other products are formed: isoparaffins, olefins, and alcohols, and their correct determination is of importance for the process.

In conventional GC, alcohols are coeluted with isoparaffins. This obviously leads to a conflicting integration. For the analysis of oxygenates by means of GC × GC, a nonpolar–polar combination of stationary phases usually increases the occupation of the 2D chromatographic plane and make the interpretation of the separation plane easy, especially when the distribution according to the number of carbon atoms within each chemically related class of hydrocarbon has to be determined. Column combination consisted of a first nonpolar column (polydimethylsiloxane), which allows a first separation according to the volatility or boiling point. A second polar column consisting of polysilphenylenesiloxane, including 50% phenyl groups (BPX-50), was used for separating compounds according to their polarity.

The GC × GC chromatogram was obtained using a TOF-MS detector recording among selective m/z values [106]. It clearly shows that the optimized chromatographic conditions involve oxygenates being organized into a distinct band of compounds from *n*-paraffins, isoparaffins, and olefins. They have increased polarity and thus increased retention in the second dimension due to strong interactions with the stationary phase. Further, the intensity of elution peaks is fairly weak compared with hydrocarbon elution peaks. Finally, the *n*-paraffin elution peaks are tailed owing to very poor solvation and they are overloaded in the secondary stationary phase.

Figure 21.14 shows chromatograms obtained by GC × GC–TOF-MS. It reveals that various oxygenated compounds are present in the same retention area:

- Figure 21.14a and b show two selected ion chromatograms of the C_{30} fraction of an Fischer–Tropsch sample using specific masses 74 and 60, for alkylmethyl esters and for alkylcarboxylic acids, respectively. The isomers of esters and carboxylic acids were eluted in two different elution bands. Note that the elution peaks of alkanes were removed. Similar identification was performed to evidence the elution zone for alcohol and ketone derivatives.
- Figure 21.14c was obtained by the acquisition of the total ion current (TIC: all the mass spectra were recorded. It reveals the different elution zones for the different classes of oxygenated compounds for a given carbon number. To simplify the comparison, the band corresponding to carboxylic acids has been drawn on the GC × GC chromatogram. Figure 21.4c shows that the different oxygenated compounds are organized within the retention plane upon increasing polarity (methyl ester < ketone < alcohol < carboxylic acid). The carboxylic function has the highest polarity and it results in the most polar molecules which are likely to interact through stronger induced dipole–permanent dipole with the stationary phase of the BPX-50 column used in the second dimension.

Comparing quantitative results, GC and GC × GC give comparable contents of *n*-paraffins (relative difference between 1.5 and 4%), while a higher content of alcohols is found when GC is used (10–30% relative difference for alcohol contents in the range 200–5000 ppm depending on the number of carbon atoms). Once again, this overestimation is related to the coelution of alcohols with olefins in GC.

21.3.4.3.2 LAB Process LABs are high-value products in petrochemistry, especially for their use as surfactants. They can be obtained from the addition of linear olefins to aromatic rings, and linear olefins are produced by the dehydrogenation of *n*-paraffins. Both reactions lead to the formation of secondary products, which are often undesirable. Hence it is crucial to determine precisely the nature and the content of these species in order to evaluate the best operating conditions of the units that avoid their formation. Owing to the limitations encountered with GC, GC × GC was investigated for the detailed characterization of the products of these two reactions.

The feed and the product with 20% conversion in the dehydrogenation of *n*-paraffins were analyzed using GC × GC (Figure 21.15). The structure of the chromatograms allows for the identification of the nature of compounds formed during the reaction. The feed mainly contains *n*-paraffins and no aromatics. The selectivity of the

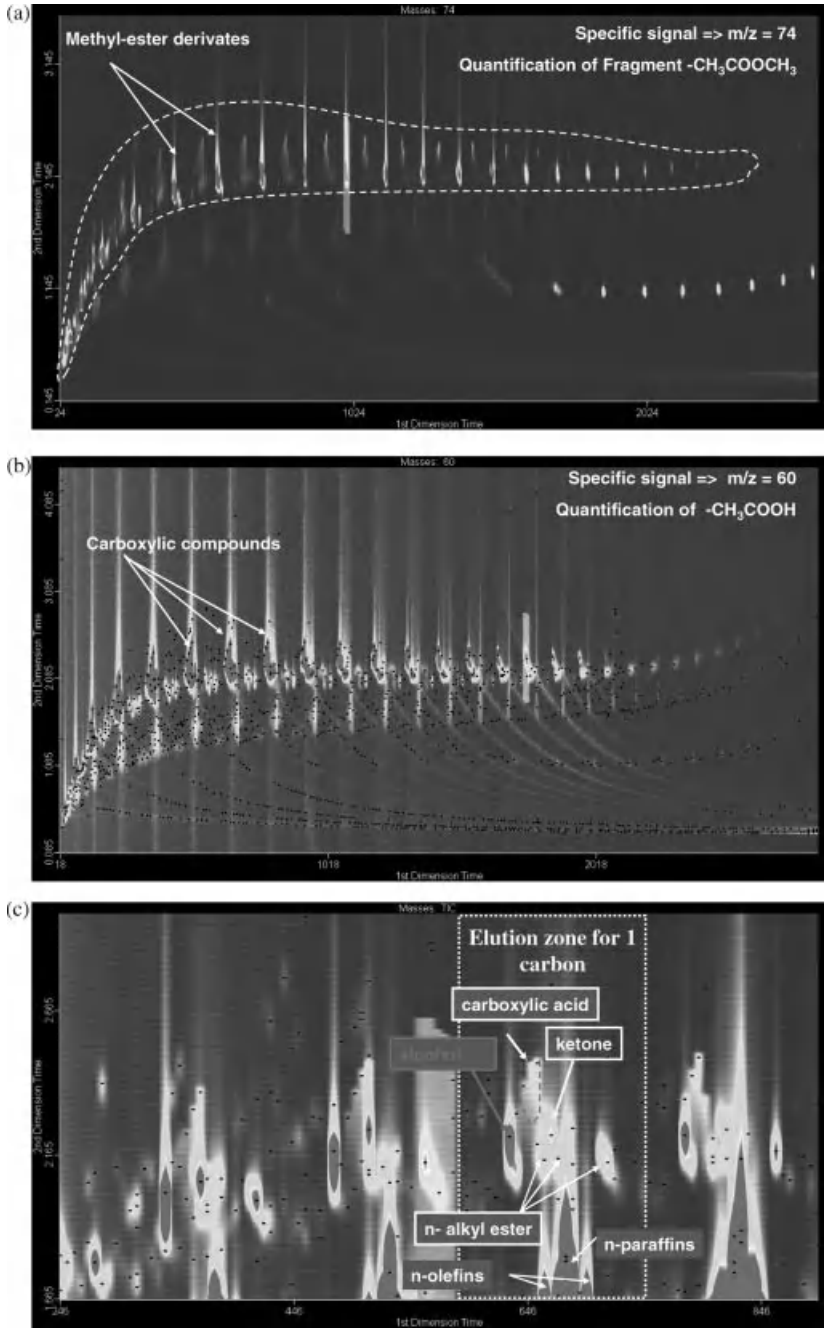


Figure 21.14 2D chromatograms of the C_{30}^{-} fraction of an FT product sample obtained by GC × GC–TOF-MS using the specific signal for $m/z = 74$ (a) and $m/z = 60$ (b). An enhanced view of chromatogram from the total ion current in the range of one carbon is shown in (c) [106].

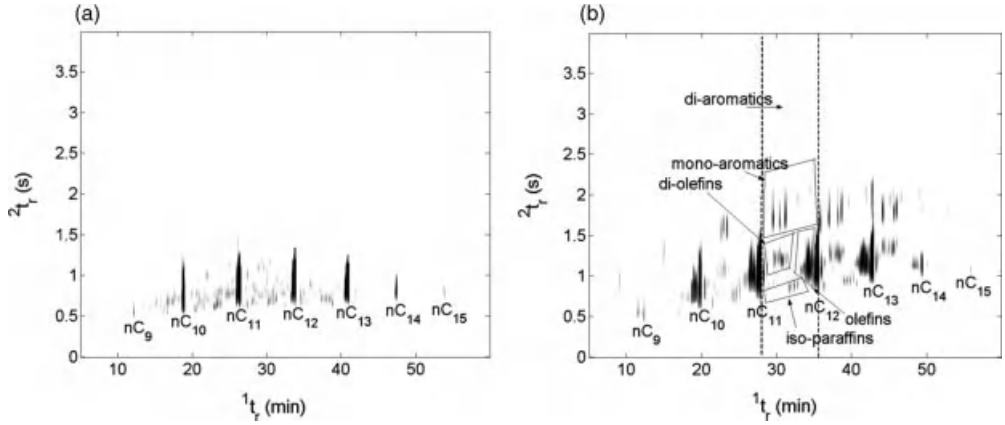


Figure 21.15 GC × GC chromatograms of the feed and the product from the dehydrogenation of *n*-paraffins [103].

second dimension allows the monitoring of products formed after reaction. Olefins are the major products of reaction and diolefins, aromatics, and also diaromatics are also produced at low levels. The formation of these secondary species should be avoided because they are responsible for catalyst coking or polymerization. The advantage of GC × GC relies on the possibility of monitoring precisely the formation of reaction products the polarity of which is different from that of the matrix.

The GC × GC chromatogram of the product from synthesis of LABs is shown in Figure 21.16. This product is principally a mixture of decyl-, dodecyl-, and tetradecylbenzenes. A roof-tile effect results from the arrangement of isomers in the retention plane. Branched-chain isomers are also present [dialkylbenzenes (DABs)].

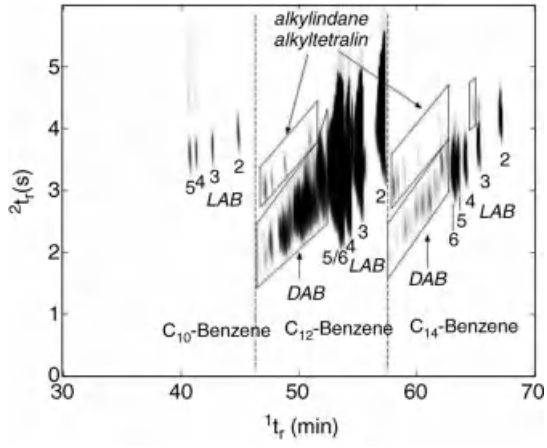


Figure 21.16 GC × GC chromatograms of the product from LAB synthesis [103].

In contrast to a conventional GC analysis, alkylbenzenes substituted by a naphthenic group were also evidenced owing to their slightly higher polarity and the resulting longer retention times in the second dimension. This resolution was achieved using a longer second column to increase the selectivity in that dimension.

21.3.4.4 Other Applications for GC × GC

Table 21.9 summarizes various applications of GC × GC in the petroleum industry.

21.3.5 Conclusion

Multi-dimensional chromatographic techniques were introduced to overcome the separation limitations of conventional high-resolution chromatography. Developments in this sector have progressively positioned GC × GC as a highly resolutive technique. Series coupling of two chromatographic columns increases the peak capacity, in order to separate as many compounds as possible. The modulation

Table 21.9 Examples of application of GC × GC in the oil industry.

Application	Column association	Modulator type	Detector	Ref.
Middle distillates				
Hydrocarbons	PONA × BPX-50 BPX-50 × DB1	Double jet (CO_2)	FID	[80, 100]
Hydrocarbons	BP21 × BPX-35	Double jet (CO_2)	FID or TOF-MS	[107]
Nitrogen compounds	SPB-5 × Solgel Wax BPX-5 × BPX-50	Double jet (CO_2) LMCS	NCD, TOF-MS NPD	[85, 86] [89]
Sulfur compounds	PONA × BPX-50	Double jet (CO_2)	SCD	[82, 83]
Semi-volatile matrices				
Light VGOs	Rtx-1 × BPX-50	Four jets (N_2)	FID, TOF-MS	[70]
Crude oil	Rtx-1 × BPX-50	Four jets (N_2)	FID	[69]
Sulfur compounds	VB5 × BPX-50	Double jets (N_2)	SCD	[108]
Oil spills	Quadrex 007-1 × BPX-50	Thermal	FID	[109]
Sediment hydrocarbons	DB5 × BPX-50	Four jets (N_2)	TOF-MS	[110]
Nonconventional oil products				
Coal liquefiate hydrocracking	HP-5 × DB17	Double jet (N_2)	TOF-MS	[111]
Pyrolysis oil	VF-5MS × BPX-50 or Rtx 1701	Four jets (N_2)	TOF-MS	[112]
Biodiesel	HP-5 × DB-Wax	Flow	FID	[113]
Biodiesel	Solgel Wax × DB1	Double jet (CO_2)	FID or TOF-MS	[114]

interface is the key factor in GC × GC, as underlined in 2000 by Marriott in his guest editorial in the commemorative issue of the *Journal of High Resolution Chromatography*: "*In perhaps the most stimulating technical advance in capillary GC for many years, a new approach has indeed been laid in front of us, thanks largely to the persistence and belief John Phillips had in the concept of modulation in GC*" [12]. The choice of modulation operating parameters (modulation period, transfer rate, or technology) will have a major influence on the separation quality (reinjection bands, wrap-around, S/N, or peak capacity). GC × GC separation can be implemented by adapting a gas chromatograph, but preferably with off-the-shelf instruments. The 2D chromatograms processed by dedicated software applications will allow both qualitative (peak retention time in the two dimensions) and quantitative analysis of complex samples. Optimization of a GC × GC separation is also difficult owing to the number of factors involved (separation kinetics, stationary phases, and dimensions of the two columns). The 2D separation criteria, comparisons of stationary phases, and predictive models can provide powerful tools to guide the development of breakthrough analytical approaches in various fields (the oil industry, as largely described in this part, but also food applications, environmental applications, forensics, etc.).

GC × GC has led to significant progress in the characterization of very complex mixtures such as petroleum products. For middle distillates such as gas oils, GC × GC outclasses all other analytical techniques for quasi-molecular quantification of the compounds. Column (orthogonal or nonorthogonal) combinations allow separations by number of carbon atoms and by chemical family. Unprecedented results, for example, distinction between basic and neutral structures, have been obtained for hydrocarbons such as isoparaffins, sulfur compounds, and nitrogen compounds. GC × GC is therefore becoming a preferred technique for the analysis of processes and products characterization, in research, and even in quality control laboratories.

Despite the high separation potential offered by GC × GC, some chemical families, for example, olefins or specific isomers, are not resolved in the gas oil range. This is even more striking for heavier cuts such as VGOs. The selectivity generated with polar stationary phases in GC × GC is in fact unable to separate a large quantity of solutes. Despite the development of new stationary phases such as ionic liquids, the high-temperature resistance of GC capillary columns seems to limit GC × GC to extension towards high molecular weight matrices. Association of an additional separation dimension could represent one way of increasing selectivity in an attempt to separate a many analytes as possible. This is discussed in Section 21.4.

21.4
Towards Molecular Analysis Systems Highly Coupled Around GC × GC

21.4.1
Position of the Problem

During the development of multi-dimensional separation techniques, GC × GC quickly emerged as the preferred analytical technique. Owing to its instrumental

performance (modulation interfaces between the two columns), high resolution can be achieved.

Although the technique has already led to substantial progress in numerous sectors, in particular the petroleum industry, a certain number of limitations must be pointed out. The thermal stability of the polar stationary phases limits its field of application. Few chemical grafts are in fact capable of withstanding temperatures of over 250–300 °C, resulting in a limited choice of stationary phases for matrices with higher boiling points. Even for the most resistant phases of average to low polarity, their selectivity is somewhat compromised at high temperatures. The limited choice of GC polar phases combined with their poor selectivity at high temperature leads to difficulties in separating a maximum number of compounds on a second very short dimension of a few seconds (apolar configuration in GC × GC). The limitation of GC × GC therefore lies in its ability to separate clearly groups of chemical families, especially for highly complex samples.

Hence the importance of adding a dense phase (LC or SFC), which provides access to a wider range of stationary phases and therefore of different selectivities, can be appreciated. Couplings between dense-phase chromatography and gas-phase chromatography have therefore been developed for applications where GC × GC offers poor performance. To meet the analytical requirements of some more complex matrices, coupling of an additional separation dimension with GC × GC may even be considered. This solution would meet the need for peak capacity with highly complex samples, for example, heavy oil fractions, and would lead to the best possible association between the sample dimensionalities and those of the multi-dimensional systems. In view of the complex optimization or development of a GC × GC analysis, one can easily imagine the experimental difficulties inherent in an instrument with 3D separation capabilities.

This part introduces recent studies conducted on an additional separation dimension and GC × GC. Association of an additional separation dimension proves essential to access comprehensive quantitative information. Since GC × GC methods have been developed relatively recently, only a few examples of 3D instruments are currently available in the literature. Most applications focus on a specific chemical family with the implementation of heart-cutting couplings with GC × GC (GC, LC, and SFC). Although 3D comprehensive couplings can lead to a global increase in resolution over the entire sample, this concerns only very few examples. The duration of GC × GC analysis imposes time constraints for dimension interfacing, which makes the development of 3D separation instruments with total coupling much more complicated.

21.4.2
Couplings Between 1D-GC and GC × GC

21.4.2.1 Simple GC–GC × GC Coupling

Very few examples are available concerning coupling between 1D GC and GC × GC, especially due to the limited choice of GC stationary phases likely to be complementary. However, Vendeuvre *et al.* [115] proposed the first GC–GC × GC coupling

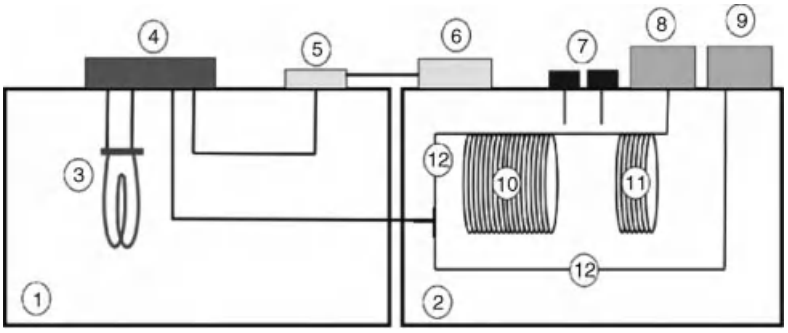


Figure 21.17 Representation of a GC–GC × GC–FID instrument with (1) and (2) two ovens, (3) packed column, (4) heater block of two valves, (5) injector, (6) pressure regulator, (7) modulator with two jets of CO_2, (8) and (9) two FIDs, (10) first GC × GC column, (11) second GC × GC column, and (12) deactivated silica tube [115].

for an application specific to the analysis of olefins in light petroleum cuts. They developed an instrument based on prefractionation of samples using a column packed with silver ion-impregnated silica (Figure 21.17). The specific interactions developed by this phase (charge-transfer mechanism) allow the highly selective separation of saturated and unsaturated compounds by backflushing. The effluents resulting from this separation are sent to the GC × GC dimension by a set of two valves. Reconcentration is carried out by condensing the solutes on a retention gap placed in front of the GC × GC capillary columns in a second chromatographic oven. GC × GC analysis is then carried out independently with injection of first-dimension effluents in two steps: saturates at the start of analysis and unsaturates during GC × GC analysis (with a second temperature increase).

Vendeuvre *et al.* demonstrated higher resolution compared with conventional GC × GC analysis for olefinic compounds contained in FCC heavy gasoline (Figure 21.18).

The olefins are co-eluted in GC × GC with the hydrocarbon matrix (Figure 21.18a), and no longer coeluted in GC–GC × GC, thereby allowing their quantification. The authors nevertheless reported isomerization problems with olefins with more than 15 carbon atoms in the first GC packed column. Their identification and quantification are therefore impossible due to thermal cracking taking place there. Group-type analysis can nevertheless be conducted on FCC heavy naphtha by using a β-cyclodextrin stationary phase [116] in the second GC × GC column, while increasing the resolution on the naphthenic structures at the same time. Similarly, the authors indicated the limitations of the system for the most alkylated olefinic structures with more than 15 carbon atoms.

21.4.2.2 GC × GC × GC Total Coupling

The principle of total coupling between one GC dimension and another GC × GC dimension was reported in 1999 by Phillips *et al.* [117]. They proposed an instru-

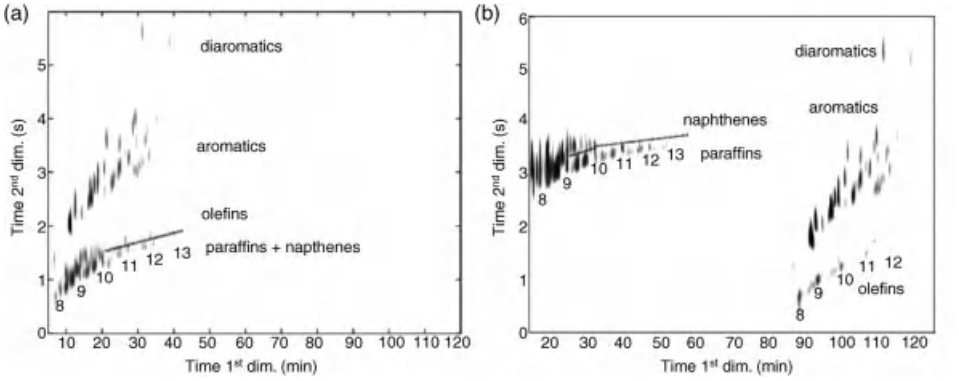


Figure 21.18 GC × GC (a) and GC–GC × GC (b) chromatograms of FCC heavy gasoline. [1]GC: silver-modified silica (30 cm × 3.2 mm); temperature, 180 °C (held for 76 min), increased at 30 °C min^{-1} to 240 °C (held for 20 min). [2]GC: PONA (10 m × 0.2 mm, 0.1 μm). [3]GC: BPX-50 (0.8 m × 0.1 mm, 0.1 μm); temperature, 30 °C increased at 2 °C min^{-1} to 170 °C, then at 30 °C min^{-1} to 30 °C (held for 3.33 min) and at 2 °C min^{-1} to 170 °C [115].

mental design with a thermal modulator and discussed the modulation, resolution, and peak capacity considerations. According to their estimations, a loss of 30% peak capacity can be expected (compared with GC × GC) due to the need for wide peaks in the first dimension. They also mentioned the difficulties of managing two sampling interfaces in real time and the processing of 3D data. The first example applying GC × GC × GC was reported by Watson *et al.* [118] in 2007. The instrument developed is based on a design similar to GC × GC, with two six-way diaphragm valve modulators. Three columns are assembled in series, the first is 25 m long ($1 \times 2P_{Mod} = 5$ s), the second 5 m long ($2 \times 3P_{Mod} = 200$ ms), and the third 55 or 100 cm long. A peak capacity of 3500 is obtained. PARAFAC chemometric methods are used to process the 3D signal by volume and conduct a quantitative analysis of 26 model compounds. Thanks to the recent development of ionic liquid stationary phases, it has been possible to implement three dimensions developing radically different selectivities for GC × GC × GC. Siegler *et al.* [119], for example, proposed the same modulation design as previously to separate a gas oil doped with phosphonate compounds (Figure 21.19). Instrumental modifications increased the production of peak capacity to 180 peaks per minute, which is comparable to GC × GC–FID. However, the additional selectivities offered by GC × GC × GC potentially represent a considerable advantage. New developments can be expected with the emergence of new stationary phases.

21.4.3
Coupling Between 1D LC and GC × GC

21.4.3.1 Simple LC–GC × GC Coupling

For coupling between 1D LC and GC × GC, a problem is related to evaporation of the mobile liquid phase. To avoid managing an online interface, most authors recom-

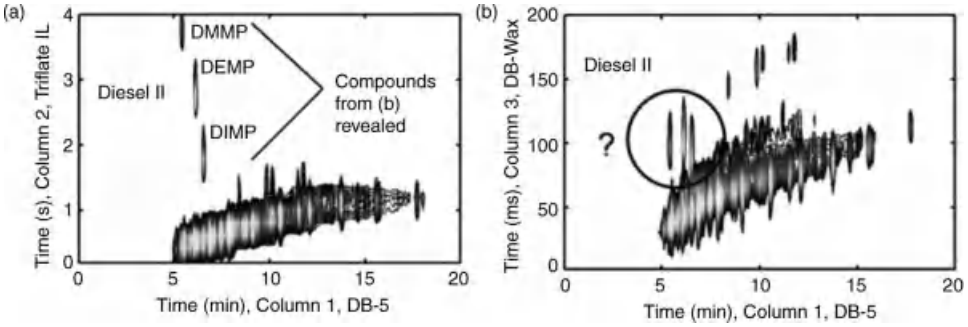


Figure 21.19 2D representations of GC × GC × GC separation of a gas oil doped with phosphonate compounds: (a) ^{1}GC × ^{2}GC and (b) ^{2}GC × ^{3}GC. ^{1}GC: DB5 (30 m × 0.25 mm, 0.5 μm). ^{2}GC: triflate ionic liquid (4 m × 0.1 mm, 0.08 μm). ^{3}GC: DB-Wax (1.0 m × 0.1 mm, 0.1 μm). Temperature, 150 °C increased at 7 °C min^{-1} to 275 °C (held for 7.14 min) [119].

mend an off-line approach. Edam *et al.* [120] proposed LC separation with an aminopropylsilica phase of a petroleum matrix to offer selectivity by number of aromatic rings. Each fraction (saturates and mono- and diaromatics) is then injected manually into the GC × GC system to increase the resolution for each "aromatic" class by accessing the better separation of naphtheno-aromatic compounds. Sciarrone *et al.* [121] applied the same procedure with a gas oil, but with MS detection. To obtain better quality mass spectra, they chose a high-volume interface to inject the LC fractions. Based on the same type of stationary phase as used by Vendeuvre *et al.* (silver-modified silica: GC–GC × GC), some authors [122, 123] also proposed preseparations of hydrocarbon matrices by LC, thereby extending the range of olefins that can be analyzed. Concerning heavier oil samples (e.g., VGOs or Vacuum residue), Dutriez and co-workers [123, 124] recently demonstrated that an offline LC preseparation step was essential to simplify the matrices and thereby obtain a more precise description by chemical group (saturated and unsaturated structures) (Figure 21.20).

Despite the progress in characterization offered by offline approaches, the analysis and handling times are restricting for a reproducible and routine quantitative approach. However, the quantities of liquid effluents limit the application of an online mode, unless high-volume interfaces are considered [121].

21.4.3.2 LC × GC × GC Total Coupling

The first example of total LC × GC × GC coupling was demonstrated by de Koning *et al.* [125] in 2004. Using an offline approach, they proposed LC separation on silver-modified silica of triglycerides of an edible oil by number of double bonds. After recovery of 36 fractions and formation of methylated derivatives, the LC effluents are injected sequentially into the GC × GC system. This 3D analysis lasts a total of 3 days, with 2 h for each GC × GC analysis. The authors compared the characterization potential of their 3D method with the 1D (LC and GC) and 2D (LC × GC and GC × GC) methods. They concluded that the best characterization in terms of

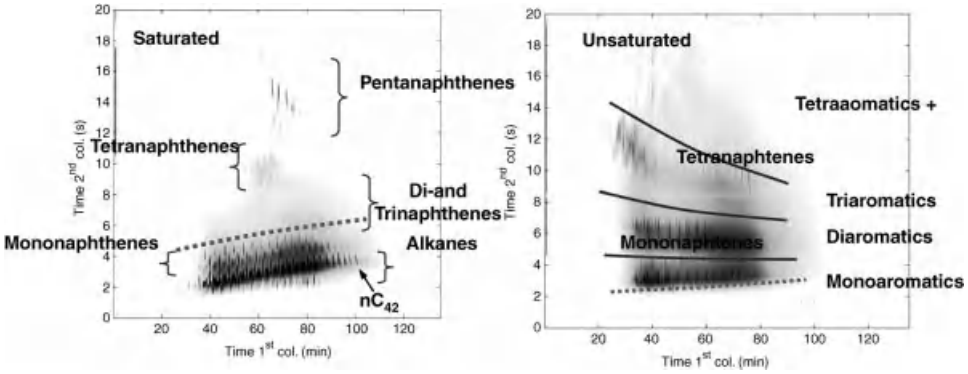


Figure 21.20 High-temperature LC–GC × GC chromatogram of a VGO [124].

dimensionality is obtained with the LC × GC × GC setup, with information by molecular chain length, number of double bonds, position of double bonds, *cis–trans* orientation, and also stereospecific data.

In an earlier study adopting the same type of approach, Blomberg *et al.* [126] reported an LC × GC × GC–TOF-MS analysis for a gas oil sample. The handling time of the LC fractions and/or the derivatization time nevertheless represent serious obstacles in the search for a reproducible quantitative analysis. An online mode is therefore preferable. The very long LC × GC × GC analysis times are also a real handicap. Consequently, instead of strictly implementing an LC × GC × GC analysis, it is better to consider it as a multiple LC–GC × GC analysis of the total sample, to obtain greater consistency with achievable analysis times [127] Although no example of on-line LC × GC × GC analysis has yet been demonstrated, Janssen *et al.* [127] proposed suitable technical solutions. Concerning the interfaces, the real-time approach cannot be reasonably implemented without drastically reducing the LC first-dimension separation flow rate. However, this would have a dramatic effect on separation, due to increases in longitudinal diffusion. In their opinion, the stopped-flow mode must be preferred with an interface similar to that used in LC × GC (valve or syringe mode).

21.4.4
Coupling Between 1D SFC and GC × GC

Coupling between a supercritical fluid separation dimension and another GC × GC dimension has only been recently demonstrated by Adam *et al.* [128]. They developed new instrumentation (Figure 21.21) in partial coupling mode (SFC–twin GC × GC) to overcome the problems encountered when characterizing petroleum matrices. A first SFC separation is therefore carried out with two silica and silver-modified silica columns to separate the saturated compounds and the unsaturated compounds in the middle distillate range (350 °C) into two fractions. In view of the differences in composition and polarity of the compounds contained in the two SFC fractions, two different sets of GC × GC columns are placed in the same

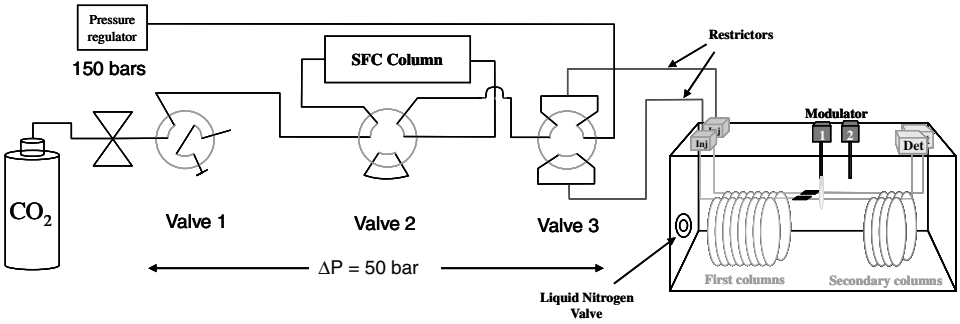


Figure 21.21 SFC–twin GC × GC system for quantitative analysis of middle distillates [128].

chromatographic oven. During the SFC separation, the two fractions will therefore be sent towards the adapted GC × GC setup via a branch and a restrictor inserted in the GC × GC injector.

The interface proposed by Levy *et al.* [129] is therefore used with cold trapping of the solutes at the column head during expansion of the supercritical fluid. The same rate of temperature increase and modulation period (two jets of CO_2) are then applied for the two setups, to obtain simultaneous detection of the two fractions.

For middle distillates, much better resolution is obtained over all chemical family ranges (Figure 21.22). A true group-type analysis by number of carbon atoms is therefore conducted on the heavy cracked oil distillates (HCO) with unprecedented

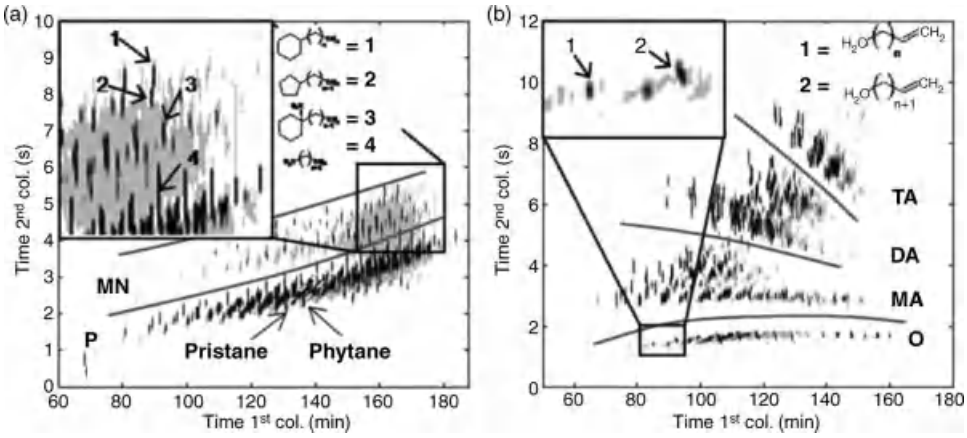


Figure 21.22 GC × GC–FID chromatograms of the saturated (a) and unsaturated (b) fractions of a coker gas oil sample separated by SFC. P, paraffins; MN, mononaphthenes; O, olefins; MA, monoaromatics; DA, diaromatics; TA, triaromatics. [1]SFC: Si (25 cm × 4.6 mm, 5 μm) and Chromsphere lipids (10 cm × 4.6 mm). [2]GC: PONA (15 m × 0.20 mm, 0.5 μm). [3]GC: BPX-50 (4.0 m × 0.1 mm, 0.1 μm) and (2.6 m × 0.1 mm, 0.1 μm). Temperature, −50 °C (held for 50 min), increased at 20 °C min^{-1} to 40 °C, then at 2 °C min^{-1} to 300 °C [128].

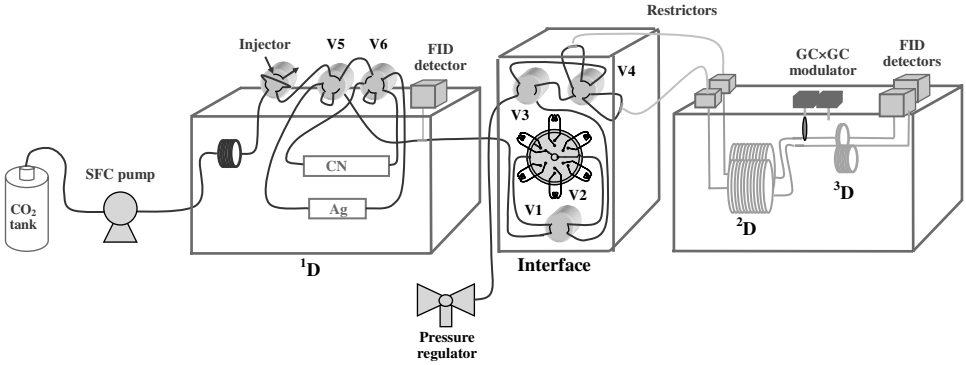


Figure 21.23 Representation of the SFC × twin GC × GC system for detailed quantitative analysis of VGO [130].

access to the entire olefin alkylation range. The level of detail obtained is such that the olefinic and naphthenic isomers can be identified, raising hopes for an extended group-type analysis. The system has been validated by quantitative comparison with reference methods (GC × GC and MS). It exceeds the current techniques, while avoiding the risks of incorrectly identifying chemical structures. The real advantage of this method is obviously the quantitative aspect and the data accessible/analysis duration (about 3 h).

However, the setup developed by Adam *et al.* can only manage a single SFC fraction per set of GC × GC columns. Consequently, in order to perform a multiple SFC–GC × GC analysis or even a total SFC × GC × GC 3D separation, Dutriez *et al.* [130] recently introduced an interface for sampling several supercritical fractions online (Figure 21.23). In view of the operational approach, they selected an innovative interface by temporary storage in a supercritical state in sampling loops rather than real-time or stopped-flow approaches. This overcomes the constraints related to the duration of different analyses between the SFC dimension and GC × GC, but also the dispersions generated when the flow is stopped. Apart from a number of supercritical fractions depending on the number of sampling loops, this approach allows flexible use of the instrument.

The same group [131] therefore adapted their instrumentation for VGOs with a choice of high-temperature conditions in GC × GC and a combination of cyanopropyl-grafted silica and silver-modified silica stationary phases for the SFC dimensions. In a heart-cutting approach, an automated and highly detailed analysis will allow quantitative characterization of saturated, unsaturated, and polar compounds for more than 300 structural groups. By combining SFC and GC × GC separations by chemical groups, it is even possible to obtain 3D representations of saturated and unsaturated compounds (Figure 21.24). These results clearly open the door to new applications for totally orthogonal 3D separations, which will increase the analytical detail of highly complex matrices even further.

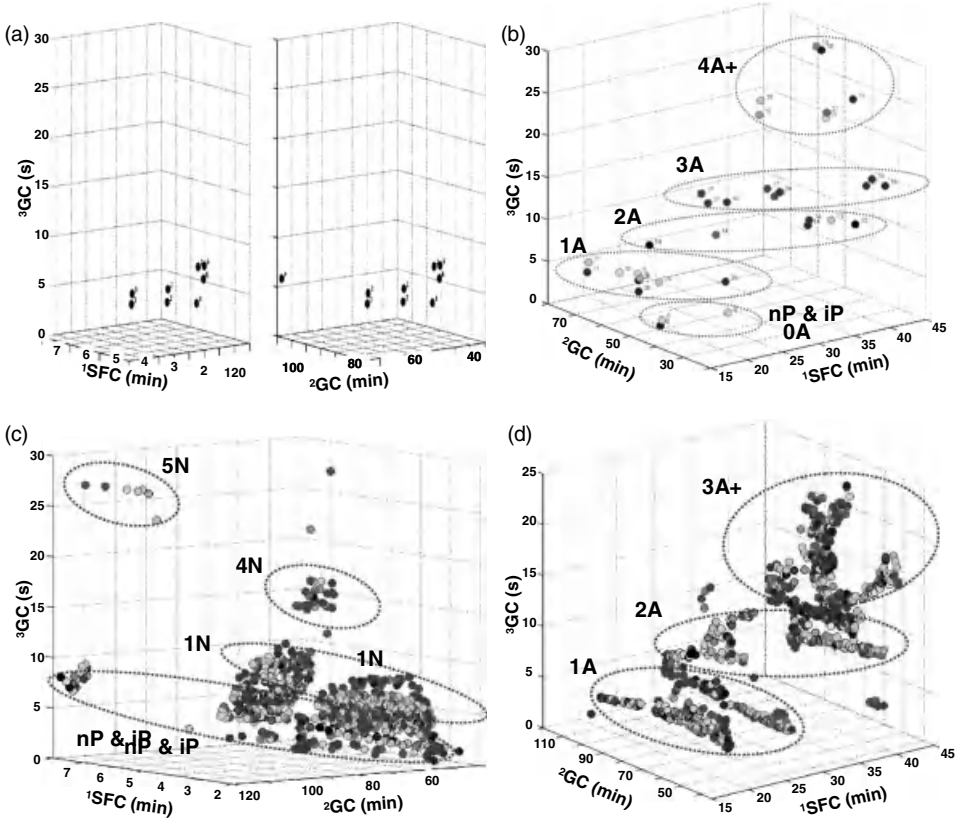


Figure 21.24 Quantitative 3D contour plots of apexes. Results of the SFC × twin GC × GC analysis of VGO [(a) saturates and (b) unsaturates]. nP and iP, *n*- and isoparaffins; 1N, mononaphthenes; 4N, tetranaphthenes; 5N, pentanaphthenes; 1A, monoaromatics; 2A, diaromatics; 3A, triaromatics; 4A + , tetraaromatics and higher [131].

21.5 Conclusion

The limited oil resources, encouraging better use of the barrel and therefore optimization of the production, refining, and petrochemical processes, the increasingly strict manufacturing standards demanding better product quality, and the increase in stringent environmental regulations have accentuated the need for more in-depth knowledge of the molecular composition of hydrocarbon mixtures from the entire oil life cycle. In particular, access to the mass distribution by number of carbon atoms and by type of hydrocarbon for a wide range of samples is vital. To meet this objective, the development of sophisticated analytical tools is a major challenge for the separative sciences. This is obviously critical for all sciences requiring more detailed analytical data at the molecular level.

In this perspective, GC × GC represents a revolutionary approach compared with the highest resolution conventional analytical methods (such as HR-GC), due to its improved resolution. Breakthrough data have been obtained on the characterization of complex mixtures such as hydrocarbon cuts with 12–30 carbon atoms with quantitative results matching the conventional techniques within the limit of their field of applicability. The use of 2D/3D chromatograms can be based on the analysis of targeted compounds, on fractionation of the sample into chemical families or by group of isomer compounds, or on analysis by global sample fingerprint. A 2D chromatogram can be broken down into groups of isomeric compounds to obtain the macroscopic properties from these elemental constituents.

While GC × GC has become the preferred tool for the detailed analysis of complex samples from various fields (e.g., the oil industry, as largely discussed in this chapter, but also forensics, food applications, fragrances, etc.) this revolutionary chromatographic technique is still unable, despite unprecedented peak capacity, to discriminate more complex samples. Hence not all hydrocarbon families are characterized satisfactorily in the range of middle distillates, either because they have very similar chemical structures and are too numerous (hydrocarbons), or because they are present in trace quantities (N- and S-containing compounds) and are coeluted with the majority compounds (hydrocarbons).

Consequently, associating an additional detection or separation dimension with GC × GC is a strategic move.

For derivatives with a heteroelement, the use of a detector specific to GC × GC represents a solution to this challenge.

To separate as many analytes as possible, association of a dense phase (LC or SFC) with multi-dimensional systems has recently led to significant progress, especially regarding separation by hydrocarbon chemical families (saturates, monoaromatics, etc.). Although these highly coupled systems are technically difficult to implement (in terms of time and operating conditions), they produce highly selective separations with high peak capacity. We can expect to see numerous developments in this field, although they remain reserved more for highly complex matrices with large intrinsic dimensionalities.

References

1 Giddings, JC. (1987) Concepts and comparisons in multidimensional separation. *J. High Resolut. Chromatogr.*, **10** (5), 319–323.

2 Phillips, J.B. and Xu, J. (1995) Comprehensive multi-dimensionnal gas chromatography. *J. Chromatogr. A*, **703**, 327–334.

3 Martin, A.J.P. and Synge, R.L.M. (1941) A new form of chromatogram employing two liquid phases. *J. Biochem.*, **35**, 1358–1368.

4 James, A.T. and Martin, A.J.P. (1954) Gas–liquid chromatography: a technique for the analysis and identification of volatile materials. *Br. Med. Bull.*, **10** (3), 170–176.

5 Ettre, L.S. (1991) 1941–1951: the golden decade of chromatography. *Analyst*, **116**, 1231–1235.

6 Martin, A.J.P. (1958) in *Gas Chromatography 1958* (ed. D.H. Desty), Butterworths, London.
7 Keulemans, A.I.M. (1957) in *Gas Chromatography* (ed. C.G. Verver), Reinhold, New York.
8 Adlard, I.E.R. and Whitham, B.T. (1958) in *Gas Chromatography 1958* (ed. D.H. Desty), Butterworths, London, p. 351.
9 McWilliam, I.G. and Dewar, R.A. (1958) in *Gas Chromatography 1958* (ed. D.H. Desty), Butterworths, London, p. 142.
10 Dandeneau, R.D. and Zerenener, E.H. (1979) An investigation of glasses for capillary chromatography. *J. High Resolut. Chromatogr. Chromatogr. Commun.*, **6**, 351–356.
11 Blomberg, L., Buijten, J., Markides, K., and Waenman, T. (1981) Evaluation of bonded methylsilicone rubber as a stationary phase for glass capillary columns. *J. Chromatogr. A*, **208**, 231–238.
12 Blomberg, J., Schoenmakers, P.J., and Brinkman, U.A.Th. (2002) Gas chromatographic methods for oil analysis. *J. Chromatogr. A*, **972**, 137–173.
13 Wauquier, J.P. (ed.) (1994) *Pétrole Brut, Produits Pétroliers, Schémas de Fabrication*, Editions Technip, Paris.
14 Hsu, C.S. (ed.) (2003) *Analytical Advances for Hydrocarbon Research*, Kluwer Academic/Plenum Publishers, New York.
15 Lefebvre, G. (ed.) (1978) *Chimie des Hydrocarbures*, Editions Technip, Paris.
16 Colthup, N.B., Daly, L.H. and Wiberley, S.E. (eds.) (1990) *Introduction to Infrared and Raman Spectroscopy*, Harcourt Brace Jovanovich, Academic Press, Boston.
17 Mendez, A. and Bruzual, J. (2003) Molecular characterization of petroleum and its fractions by mass spectrometry, in *Analytical Advances for Hydrocarbon Research* (ed. C.S. Hsu), Kluwer Academic/Plenum Publishers, New York, pp. 73–93.
18 Gallegos, E.J., Green, J.W., Lindeman, L.P., LeTourneau, R.L., and Teeter, R.M. (1967) Petroleum group-type analysis by high resolution mass spectrometry. *Anal. Chem.*, **39** (14), 1833–1838.
19 Fisher, I.P. and Johnson, A. (1975) Application of mass spectrometry to commercial fluid catalytic cracking studies 867. *Anal. Chem.*, **47** (1), 59–62.
20 Fafet, A., Bonnard, J., and Prigent, F. (1999) New developments in mass spectrometry for group-type analysis of petroleum cuts. Second part: Development and validation of a new inlet system for heavy cuts. *Oil Gas Sci. Technol.*, **54** (4), 453–462.
21 Fu, J.M., Kim, S., Rodgers, R.P., Hendrickson, C.L., Marshall, A.G., and Qian, K.N. (2006) Nonpolar compositional analysis of vacuum gas oil distillation fractions by electron ionization Fourier transform ion cyclotron resonance mass spectrometry. *Energy Fuels*, **20** (2), 661–667.
22 Marshall, A.G. and Rodgers, R.P. (2004) Petroleomics: the next grand challenge for chemical analysis. *Acc. Chem. Res.*, **37** (1), 53–59.
23 Suatoni, J.C. (1979) Hydrocarbon group-type analysis by high performance liquid chromatography, in *Chromatography in Petroleum Analysis* (eds. K.H. Altgelt and T.H. Gouw), Marcel Dekker, New York, pp. 121–136.
24 Neal, A.C. (1995) HPLC and column liquid chromatography, in *Chromatography in the Petroleum Industry* (ed. E.R. Adlar), Elsevier, Amsterdam, pp. 347–374.
25 Hsu, C.S., McLean, M.A., Qian, K., Aczel, T., Blum, S.C., Olmstead, W.N., Kaplan, L.H., Robbins, W.K., and Schulz, W.W. (1991) On line liquid chromatography mass–spectrometry for heavy hydrocarbon characterization. *Energy Fuels*, **5** (3), 395–398.
26 Altgelt, K.H. (1979) Gel permeation chromatography, in *Chromatography in Petroleum Analysis* (eds. K.H. Altgelt and T.H. Gouw), Marcel Dekker, New York, pp. 136–152.
27 Schade, T., Roberz, B., and Andersson, J.T. (2002) Polycyclic aromatic sulfur heterocycles in desulfurized diesel fuels and their separation on a novel palladium(II)-complex stationary phase. *Polycyclic Aromat. Compd.*, **22** (3–4), 311–320.

28 Panda, S.K., Schrader, W., al-Hajji, A., and Andersson, J.T. (2007) Distribution of polycyclic aromatic sulfur heterocycles in three Saudi Arabian crude oils as determined by Fourier transform ion cyclotron resonance mass spectrometry. *Energy Fuels*, **21** (2), 1071–1077.

29 Rosset, R., Caude, M., and Jardy, A. (eds.) (1991) *Chromatographies en Phase Liquide et Supercritique*, Masson, Paris.

30 Caude, M. and Thiebaut, D. (2008) Chromatographie en phase supercritique. *Techn. Ing.*, 1460–1462.

31 Thiebaut, D.R.P. and Robert, E.C. (1999) Group-type separation and simulated distillation: a niche for SFC. *Analusis*, **27** (8), 681–690.

32 Dulaurent, A., Dahan, L., Thiebaut, D., Bertoncini, F., and Espinat, D. (2007) Extended simulated distillation by capillary supercritical fluid chromatography. *Oil Gas. Sci. Technol.*, **62** (1), 33–42.

33 Di Sanzo, F.P., Lane, J.L., and Yoder, R.E. (1988) Application of the state-of-the-art multidimensional high resolution gas chromatography for individual component analysis. *J. Chromatogr. Sci.*, **26**, 206–209.

34 Eggertsen, F.T., Groennings, S., and Holst, J.J. (1960) Analytical distillation by gas chromatography. Programmed temperature operation. *Anal. Chem.*, **32** (8), 904–909.

35 Durand, J.P., Bré, A., Béboulène, J.J., Ducrozet, A., and Carbonneaux, S. (1999) Improvement of simulated distillation methods by gas chromatography in routine analysis. *Oil Gas Sci. Technol.*, **54** (4), 431–438.

36 Luong, J., Gras, R., Mustacich, R., and Cortes, H. (2006) Low thermal mass gas chromatography: principles and applications. *J. Chromatogr. Sci.*, **44** (5), 253–261.

37 Lubkowitz, J.A. and Meneghini, R.I. (2002) Determination of the boiling-point distribution by simulated distillation from *n*-pentane through *n*-tetratetracontane in 70 to 80 seconds? *J. Chromatogr. Sci.*, **40** (5), 269–275.

38 DiSanzo, F., Nicholas, M., Cadoppi, A., and Munari, F. (2008) Optimization and results of an ultrafast (<5 minutes) gas chromatographic technique (UFGC) and instrumentation for simulated distillation of petroleum fractions. Presented at the 32nd ISCC, Riva Del Garda, Italy.

39 Revellin, N., Dulot, H., Lopez-Garcia, C., Baco, F., and Jose, J. (2005) Specific nitrogen boiling point profiles of vacuum gasoils. *Energy Fuels*, **19** (6), 2438–2444.

40 Speight, J.G. (2004) Petroleum asphaltenes – Part 1 – Asphaltenes, resins and the structure of petroleum. *Oil Gas. Sci. Technol.*, **59** (5), 467–477.

41 Merdrignac, I. and Espinat, D. (2007) Physicochemical characterization of petroleum fractions: the state of the art. *Oil Gas. Sci. Technol.*, **62** (1), 7–32.

42 Peters, K.E., Walters, C.C., and Moldowan, J.M. (2005) *The Biomarker Guide. Volume 2: Biomarkers and Isotopes in Petroleum Exploration and Earth History*, Cambridge University Press, Cambridge.

43 Andersen, S.I. and Speight, J.G. (2001) Petroleum resins: separation, character, and role in petroleum. *Pet. Sci. Technol.*, **19** (1–2), 1–34.

44 Van den Dool, H. and Kratz, P.D. (1963) A generalization of the retention index system including linear temperature programmed gas–liquid partition chromatography. *J. Chromatogr. A*, **11**, 463–471.

45 Brody, S.S. and Chaney, J.E. (1966) Flame photometric detector. *J. Gas Chromatogr.*, **4** (2), 42–46.

46 Cheskis, S., Atar, E., and Amirav, A. (1993) Pulsed-flame photometer: a novel gas chromatography detector. *Anal. Chem.*, **65** (5), 539–555.

47 Toby, S. (1984) Chemiluminescence in the reactions of ozone. *Chem. Rev.*, **84** (3), 277–285.

48 Shearer, R.L., O'Neal, D.L., Rios, R., and Baker, M.D. (1990) Analysis of sulphur compounds by capillary column gas chromatography with sulfur chemiluminescence detection. *J. Chromatogr. Sci.*, **28**, 24–28.

49 Yan, X. (2002) Sulfur and nitrogen chemiluminescence detection in gas

chromatographic analysis. *J. Chromatogr. A*, **976** (1–2), 3–10.
50 Shearer, R.L., Poole, E.B., and Nowalk, J.B. (1993) Application of gas chromatography and flameless sulfur chemiluminescence detection to the analysis of petroleum products. *J. Chromatogr. Sci.*, **31**, 82–87.
51 Shearer, R.L. and Meyer, L.M. (1999) Simultaneous measurement of hydrocarbons and sulfur compounds using flame ionization and sulfur chemiluminescence detection for sulfur simulated distillation. *J. High Resolut. Chromatogr.*, **7**, 386–390.
52 Chawla, B. (1997) Speciation of nitrogen compounds in gasoline and diesel range process streams by capillary column gas chromatography with chemiluminescence detection. *J. Chromatogr. Sci.*, **35** (3), 97–104.
53 Sironi, A. and Verga, G.R. (1995) The O-FID and its applications in petroleum product analysis, in *Chromatography in the Petroleum Industry* (ed. E.R. Adlar), Elsevier, Amsterdam, pp. 143–158.
54 Quimby, B.D., Giarrocco, V., Sullivan, J.J., and McCleary, K.A. (1992) Fast analysis of oxygen and sulfur compounds in gasoline by GC–AED. *J. High Resolut. Chromatogr.*, **15** (11), 705–709.
55 Baco, F., Quignard, A., and Szymanski, R. (1999) Elementary analysis of petroleum distillates by GC–AED: validation and application to the calculation of distillation profile properties. *Oil Gas Sci. Technol.*, **54** (4), 473–485.
56 Teng, S.T., Williams, A.D., and Urdal, K. (1994) Detailed hydrocarbon analysis of gasoline by GC–MS (SI-PIONA). *J. High Resolut. Chromatogr.*, **17** (6), 469–475.
57 Wang, Z.D., Fingas, M., and Page, D.S. (1999) Oil spill identification. *J. Chromatogr. A*, **843** (1–2), 369–411.
58 Giddings, J.C. (1995) Sample dimensionality: a predictor of order–disorder in component peak distribution in multidimensional separation. *J. Chromatogr. A*, **703**, 3–15.
59 Bertsch, W. (1999) Two-dimensional gas chromatography. Concepts, instrumentation, and applications. *J. High Resolut. Chromatogr.*, **22**, 647–655.
60 Mondello, L., Lewis, A., and Bartle, K. (eds.) (2002) *Multidimensional Gas Chromatography*, John Wiley & Sons, Ltd., Chichester.
61 Schomburg, G. (1995) Two-dimensional gas chromatography. principe, instrumentation, and methods. *J. Chromatogr. A*, **703**, 309–325.
62 Liu, Z. and Phillips, J.B. (1991) Comprehensive two-dimensional gas chromatography using an on-column thermal modulator interface. *J. Chromatogr. Sci.*, **29**, 227–231.
63 Ong, R. and Marriott, P. (2002) A review of basic concepts in comprehensive two-dimensional gas chromatography. *J. Chromatogr. Sci.*, **40**, 276–291.
64 Adahchour, M., Beens, J., Vreuls, R.J.J., and Brinkman, U.A.Th. (2006) Recent developments in comprehensive two-dimensional gas chromatography (GC×GC). II. Modulation and detection. *Trends Anal. Chem.*, **25** (6), 540–553.
65 Marriott, P.J. and Kinghorn, R.M. (1997) Longitudinally modulated cryogenic system. *Anal. Chem.*, **69**, 2582–2588.
66 Kinghorn, R.M. and Marriott, P.J. (1999) High speed cryogenic modulation – a technology enabling comprehensive multidimensional gas chromatography. *J. High Resolut. Chromatogr.*, **22** (4), 235–238.
67 Beens, J., Adahchour, M., Vreuls, R.J.J., van Altena, K., and Brinkman, U.A.Th. (2001) Simple, non-moving modulation interface for comprehensive two-dimensional gas chromatography. *J. Chromatogr. A*, **919** (1), 127–132.
68 Pursch, M., Eckerle, P., Biel, J., Streck, R., Cortes, H., Sun, K., and Winniford, B. (2003) Comprehensive two-dimensional gas chromatography using liquid nitrogen modulation: set-up and applications. *J. Chromatogr. A*, **1019** (1–2), 43–51.
69 Gaines, R.B. and Frysinger, G.S. (2004) Temperature requirements for thermal modulation in comprehensive

two-dimensional gas chromatography. *J. Sep. Sci.*, **27** (5–6), 380–388.

70 Rathbun, W. (2007) Programmed automation of modulator cold jet flow for comprehensive two-dimensional gas chromatographic analysis of vacuum gas oils. *J. Chromatogr. Sci.*, **45**, 636–642.

71 Gorecki, T., Panic, O., and Oldridge, N. (2008) Cryogen-free thermal modulation: development and applications. Presented at the 5th Symposium on GC × GC, Riva del Garda, Italy.

72 Pizzutti, I.R., Vreuls, R.J.J., de Kok, A., Roehrs, R., Martel, S., Friggi, C.A., and Zanella, R. (2009) Design of a compressed air modulator to be used in comprehensive multidimensional gas chromatography and its application in the determination of pesticide residues in grapes. *J. Chromatogr. A*, **1216** (15), 3305–3311.

73 Bruckner, C.A., Prazen, B.J., and Synovec, R.E. (1998) Comprehensive two-dimensional high-speed gas chromatography with chemometric analysis. *Anal. Chem.*, **70** (14), 2796–2804.

74 Seeley, J.V., Kramp, F., and Hicks, C.J. (2000) Comprehensive two-dimensional gas chromatography via differential flow modulation. *Anal. Chem.*, **72** (18), 4346–4352; Bueno, P.A. and Seeley, J.V. (2004) Flow-switching device for comprehensive two-dimensional gas chromatography. *J. Chromatogr. A*, **1027** (1–2), 3–10; Seeley, J.V., Micyus, N.J., McCurry, J.D., and Seeley, S.K. (2006) Comprehensive two-dimensional gas chromatography with a simple fluidic modulator. *Am. Lab.*, **38** (9), 24–26.

75 Poliak, M., Kochman, M., and Amirav, A. (2008) Pulsed flow modulation comprehensive two-dimensional gas chromatography. *J. Chromatogr. A*, **1186** (1–2), 189–195.

76 Harvey, P.M., Shellie, R.A., and Haddad, P.R. (2010) Design considerations for pulsed-flow comprehensive two-dimensional GC: dynamic flow model approach. *J. Chromatogr. Sci.*, **48** (4), 245.

77 De Geus, H.-J., De Boer, J., Brinkman, U.A.Th., Ledford J, E.B. Jr., and Phillips, J.B. (1998) Increased signal amplitude due to mass conservation in a thermal desorption modulator. *J. High Resolut. Chromatogr.*, **21**, 411–413.

78 Kinghorn, R.M. and Marriott, P.J. (1998) Enhancement of signal-to-noise ratios in capillary gas chromatography by using a longitudinally modulated cryogenic system. *J. High Resolut. Chromatogr.*, **21**, 32–38.

79 Murphy, R.E., Schure, M.R., and Foley, J.P. (1998) Effect of sampling rate on resolution in comprehensive two-dimensional liquid chromatography. *Anal. Chem.*, **70**, 1585–1594.

80 Cavagnino, D., Magni, P., Zilioli, G., and Trestianu, S. (2003) Comprehensive two-dimensional gas chromatography using large sample volume injection for the determination of polynuclear aromatic hydrocarbons in complex matrices. *J. Chromatogr. A*, **1019** (1–2), 211–220.

81 Kristenson, E.M., Korytar, P., Danielsson, C., Kallio, M., Brandt, M., and Makela, J. (2003) Evaluation of modulators and electron-capture detectors for comprehensive two-dimensional GC of halogenated organic compounds. *J. Chromatogr. A*, **1019** (1–2), 65–77.

82 Hua, R., Wang, J., Kong, H., Liu, J., Lu, X., and Xu, G. (2004) Analysis of sulfur-containing compounds in crude oils by comprehensive two-dimensional gas chromatography with sulfur chemiluminescence detection. *J. Sep. Sci.*, **27** (9), 691–698.

83 Ruiz-Guerrero, R., Vendeuvre, C., Thiebaut, D., Bertoncini, F., and Espinat, D. (2006) Comparison of comprehensive two-dimensional gas chromatography coupled with sulfur-chemiluminescence detector to standard methods for speciation of sulfur-containing compounds in middle distillates. *J. Chromatogr. Sci.*, **44** (9), 566–573.

84 Chin, S.T., Wu, Z.Y., Morrison, P.D., and Marriott, P.J. (2010) Observations on comprehensive two dimensional gas chromatography coupled

with flame photometric detection for sulfur- and phosphorus-containing compounds. *Anal. Met.*, **2** (3), 243–253.

85 Wang, F.C.-Y., Robbins, W.K., and Greaney, M.A. (2004) Speciation of nitrogen-containing compounds in diesel fuel by comprehensive two-dimensional gas chromatography. *J. Sep. Sci.*, **27** (5–6), 468–472.

86 Adam, F., Bertoncini, F., Brodusch, N., Durand, E., Thiebaut, D., Espinat, D., and Hennion, M.C. (2007) New benchmark for basic and neutral nitrogen compounds speciation in middle distillates using comprehensive two-dimensional gas chromatography. *J. Chromatogr. A*, **1148** (1), 55–64.

87 Zellner, B.D., Casilli, A., Dugo, P., Dugo, G., and Mondello, L. (2007) Odour fingerprint acquisition by means of comprehensive two-dimensional gas chromatography–olfactometry and comprehensive two-dimensional gas chromatography/mass spectrometry. *J. Chromatogr. A*, **1141** (2), 279–286.

88 Ryan, D. and Marriott, P. (2006) Studies on thermionic ionisation detection in comprehensive two-dimensional gas chromatography. *J. Sep. Sci.*, **29** (15), 2375–2382.

89 Von Muehlen, C., de Oliveira, E.C., Morrison, P.D., Zini, C.A., Caramao, E.B., and Marriott, P.J. (2007) Qualitative and quantitative study of nitrogen-containing compounds in heavy gas oil using comprehensive two-dimensional gas chromatography with nitrogen–phosphorus detection. *J. Sep. Sci.*, **30** (18), 3223–3232.

90 Khummueng, W., Morrison, P., and Marriott, P.J. (2008) Dual NPD/ECD detection in comprehensive two-dimensional gas chromatography for multiclass pesticide analysis. *J. Sep. Sci.*, **31** (19), 3404–3415.

91 Van Stee, L.L.R., Beens, J., Vreuls, R.J.J., and Brinkman, U.A.Th. (2003) Comprehensive two-dimensional gas chromatography with atomic emission detection and correlation with mass spectrometric detection: principles and application in petrochemical analysis. *J. Chromatogr. A*, **1019** (1–2), 89–99.

92 Amador-Munoz, O. and Marriott, P.J. (2008) Quantification in comprehensive two-dimensional gas chromatography and a model of quantification based on selected summed modulated peaks. *J. Chromatogr. A*, **1184** (1–2), 323–340.

93 Hoggard, J.C., Siegler, W.C., and Synovec, R.E. (2009) Toward automated peak resolution in complete GC×GC–TOFMS chromatograms by PARAFAC. *J. Chemom.*, **23** (7–8), 421–431.

94 Adahchour, M., Beens, J., and Brinkman, U.A.Th. (2008) Recent developments in the application of comprehensive two-dimensional gas chromatography. *J. Chromatogr. A*, **1186** (1–2), 67–108.

95 Watson, N.E., Siegler, W.C., Hoggard, J.C., and Synovec, R.E. (2007) Comprehensive three-dimensional gas chromatography with parallel factor analysis. *Anal. Chem.*, **79** (21), 8270–8280.

96 de Godoy, L.A.F., Ferreira, E.C., Pedroso, M.P., Fidelis, C.H.deV., Augusto, F., and Poppi, R.J. (2008) Quantification of kerosene in gasoline by comprehensive two-dimensional gas chromatography and *N*-way multivariate analysis. *Anal. Lett.*, **41** (9), 1603–1614.

97 Khummueng, W. and Marriott, P.J. (2009) The nomenclature of comprehensive two-dimensional gas chromatography: defining the modulation ratio (M-R). *LC·GC Eur.*, **22** (1), 38.

98 Kinghorn, R.M. and Marriott, P.J. (1999) High speed cryogenic modulation – a technology enabling comprehensive multidimensional gas chromatography. *J. High Resolut. Chromatogr.*, **22** (4), 235–238.

99 Schoenmakers, P.J., Oomen, J.L., Blomberg, J., Genuit, W., and van Velzen, G. (2000) Comparison of comprehensive two-dimensional gas chromatography and gas chromatography–mass spectrometry for the characterization of complex hydrocarbon mixtures. *J. Chromatogr. A*, **892** (1–2), 29–46.

100 Vendeuvre, C., Ruiz-Guerrero, R., Bertoncini, F., Duval, L., Thiebaut, D., and Hennion, M.C. (2005) Characterisation of middle-distillates by comprehensive two-dimensional gas chromatography (GC×GC): a powerful alternative for performing various standard analysis of middle-distillates. *J. Chromatogr. A*, **1086** (1–2), 21–28.

101 Beens, J., Blomberg, J., and Schoenmakers, P.J. (2000) Proper tuning of comprehensive two-dimensional gas chromatography to optimize the separation of complex oil fractions. *J. High Resolut. Chromatogr.*, **23**, 182–188.

102 Lee, A.L., Bartle, K.B., and Lewis, A.C. (2001) A model of peak amplitude enhancement in orthogonal two-dimensional gas chromatography. *Anal. Chem.*, **73**, 1330–1335.

103 Bertoncini, F., Vendeuvre, C., and Thiebaut, D. (2005) Interest and applications of multidimensional gas chromatography for trace analysis in the petroleum industry. *Oil Gas. Sci. Technol.*, **60** (6), 937–950.

104 Wang, F.C.-Y., Robbins, W.K., and Greaney, M.A. (2004) Speciation of nitrogen-containing compounds in diesel fuel by comprehensive two-dimensional gas chromatography. *J. Sep. Sci.*, **27** (5–6), 468–472.

105 Adam, F., Bertoncini, F., Dartiguelongue, C., Marchand, K., Thiebaut, D., and Hennion, M.C. (2009) Comprehensive two-dimensional gas chromatography for basic and neutral nitrogen speciation in middle distillates. *Fuel*, **88**, 938–946.

106 Bertoncini, F., Marion, M.C., Brodusch, N., and Esnault, S. (2009) Unravelling molecular composition of products from cobalt catalysed Fischer–Tropsch reaction by comprehensive gas chromatography: methodology and application. *Oil Gas. Sci. Technol.*, **64**, 79–90.

107 Adahchour, M., Beens, J., and Vreuls, R.J., Batenburg, A.M., and Brinkman, U.A.Th. (2004) Comprehensive two-dimensional gas chromatography of complex samples by using a 'reversed-type' column combination: application to food analysis. *J. Chromatogr. A*, **1054** (1–2), 47–55.

108 Hua, R., Wan, J., Kong, H., Liu, J., Lu, X., and Xu, G. (2004) Analysis of sulfur-containing compounds in crude oils by comprehensive two-dimensional gas chromatography with sulfur chemiluminescence detection. *J. Sep. Sci.*, **27** (9), 691–698.

109 Gaines, R.B., Frysinger, G.S., Hendrick-Smith, M.S., and Stuart, J.D. (1999) Oil spill identification by comprehensive two-dimensional gas chromatography (GC×GC). *Environ. Sci. Technol.*, **33**, 2106–2112.

110 Ventura, G.T., Kenig, F., Reddy, C.M., Frysinger, G.S., Nelson, R.K., Mooy, B.V., and Gaines, R.B. (2008) Analysis of unresolved complex mixtures of hydrocarbons extracted from Late Archean sediments by comprehensive two-dimensional gas chromatography (GC×GC). *Org. Geochem.*, **39** (7), 846–867.

111 Hamilton, J.F., Lewis, A.C., Millan, M., Bartle, K.D., Herod, A.A., and Kandiyoti, R. (2007) Comprehensive two-dimensional gas chromatography coupled to time-of-flight mass spectrometry of coal liquids produced during a coal liquefaction process. *Energy Fuels*, **21** (1), 286–294.

112 Marsman, J.H., Wildschut, J., Mahfud, F., and Heeres, H.J. (2007) Identification of components in fast pyrolysis oil and upgraded products by comprehensive two-dimensional gas chromatography and flame ionisation detection. *J. Chromatogr. A*, **1150** (1–2), 21–27.

113 Seeley, J.V., Seeley, S.K., Libby, E.K., and McCurry, J.D. (2007) Analysis of biodiesel/petroleum diesel blends with comprehensive two-dimensional gas chromatography. *J. Chromatogr. Sci.*, **45** (10), 650–656.

114 Adam, F., Bertoncini, F., Coupard, V., Charon, N., Thiebaut, D., Espinat, D., and Hennion, M.C. (2008) Using comprehensive two-dimensional gas chromatography for the analysis of oxygenates in middle distillates – I. Determination of the nature of biodiesels

blend in diesel fuel. *J. Chromatogr. A*, **1186** (1–2), 236–244.

115 Vendeuvre, C., Bertoncini, F., Espinat, D., Thiebaut, D., and Hennion, M.C. (2005) Multidimensional gas chromatography for the detailed PIONA analysis of heavy naphtha: hyphenation of an olefin trap to comprehensive two-dimensional gas chromatography. *J. Chromatogr. A*, **1090** (1–2), 116–125.

116 Adam, F., Vendeuvre, C., Bertoncini, F., Thiebaut, D., Espinat, D., and Hennion, M.C. (2008) Comprehensive two-dimensional gas chromatography for enhanced analysis of naphthas: new column combination involving permethylated cyclodextrin in the second dimension. *J. Chromatogr. A*, **1178**, 171–177.

117 Phillips, J.B., Gaines, R.B., Blomberg, J., van der Wielen, F.W.M., Dimandja, J.M., Green, V., Granger, J., Patterson, D., Racovalis, L., de Geus, H.J., de Boer, J., Haglund, P., Lipsky, J., Sinha, V., and Ledford, E.B. (1999) A robust thermal modulator for comprehensive two-dimensional gas chromatography. *J. High Resolut. Chromatogr.*, **22** (1), 3–10.

118 Watson, N.E., Siegler, W.C., Hoggard, J.C., and Synovec, R.E. (2007) Comprehensive three-dimensional gas chromatography with parallel factor analysis. *Anal. Chem.*, **79** (21), 8270–8280.

119 Siegler, W.C., Crank, J.A., Armstrong, D.W., and Synovec, R.E. (2010) Increasing selectivity in comprehensive three-dimensional gas chromatography via an ionic liquid stationary phase column in one dimension. *J. Chromatogr. A*, **1217** (18), 3144–3149.

120 Edam, R., Blomberg, J., Janssen, H.G., and Schoenmakers, P.J. (2005) Comprehensive multi-dimensional chromatographic studies on the separation of saturated hydrocarbon ring structures in petrochemical samples. *J. Chromatogr. A*, **1086** (1–2), 12–20.

121 Sciarrone, D., Tranchida, P.Q., Costa, R., Donato, P., Ragonese, C., Dugo, P., Dugo, G., and Mondello, L. (2008) Offline LC–GC×GC in combination with rapid-scanning quadrupole mass spectrometry. *J. Sep. Sci.*, **31** (19), 3329–3336.

122 Reddy, C.M., Nelson, R.K., Sylva, S.P., Xu, L., Peacock, E.A., Raghuraman, B., and Mullins, O.C. (2007) Identification and quantification of alkene-based drilling fluids in crude oils by comprehensive two-dimensional gas chromatography with flame ionization detection. *J. Chromatogr. A*, **1148** (1), 100–107.

123 Dutriez, T., Courtiade, M., Thiebaut, D., Dulot, H., Bertoncini, F., and Hennion, M.C. (2010) Extended characterization of a vacuum gas oil by offline LC–high-temperature comprehensive two-dimensional gas chromatography. *J. Sep. Sci.*, **33**, 1787–1796.

124 Dutriez, T., Courtiade, M., Thiebaut, D., Dulot, H., Borras, J., Bertoncini, F., and Hennion, M.C. (2010) Advances in quantitative analysis of heavy petroleum fractions by liquid chromatography–high-temperature comprehensive two-dimensional gas chromatography: breakthrough for conversion processes. *Energy Fuels*, **24**, 4430–4438.

125 de Koning, S., Janssen, H.G., and Brinkman, U.A.Th. (2004) Group-type characterisation of mineral oil samples by two-dimensional comprehensive normal-phase liquid chromatography–gas chromatography with time-of-flight mass spectrometric detection. *J. Chromatogr. A*, **1058** (1–2), 217–221.

126 Blomberg, J., Mes, E.P.C., Schoenmakers, P.J., and van der Does, J.J.B. (1997) Characterization of complex hydrocarbon mixtures using on-line coupling of size-exclusion chromatography and normal-phase liquid chromatography to high-resolution gas chromatography. *J. High Resolut. Chromatogr.*, **20** (3), 125–130.

127 Janssen, H.G., Boers, W., Steenbergen, H., Horsten, R., and Floter, E. (2003) Comprehensive two-dimensional liquid

chromatography×gas chromatography: evaluation of the applicability for the analysis of edible oils and fats. *J. Chromatogr. A*, **1000** (1–2), 385–400.

128 Adam, F., Thiebaut, D., Bertoncini, F., Courtiade, M., and Hennion, M.C. (2010) Supercritical fluid chromatography hyphenated with twin comprehensive two-dimensional gas chromatography for ultimate analysis of middle distillates. *J. Chromatogr. A*, **1217** (8), 1386–1394.

129 Levy, J.M., Guzowski, J.P., and Huhak, W.E. (1987) On-line multidimensional supercritical fluid chromatography/capillary gas chromatography. *J. High Resolut. Chromatogr.*, **10** (6), 337–341.

130 Dutriez, T., Courtiade, M., Dulot, H., Thiebaut, D., Bertoncini, F., and Hennion, M.C. (2011) Switchable online SFC–GC×GC and SFC×GC×GC. I. Design of the instrumentation. *J. Chromatogr. A*, submitted.

131 Dutriez, T., Courtiade, M., Dulot, H., Thiebaut, D., Bertoncini, F., and Hennion, M.C. (2011) Switchable online SFC–GC×GC and SFC×GC×GC. II. Application to heavy petroleum fractions analysis. *J. Chromatogr. A*, submitted.

22
Transient Techniques: Temporal Analysis of Products and Steady State Isotopic Transient Kinetics Analysis

Angelos M. Efstathiou, John T. Gleaves, and Gregory S. Yablonsky

22.1
Scope

Experiments in the transient regime are now widely used in mechanistic and microkinetic studies of heterogeneous catalysis. They permit the quantitative determination of the composition of the adsorbed phase during catalysis and also give important information on the sequence of elementary steps that govern the observed global reaction kinetic rate, information that cannot be obtained by steady-state reaction measurements. Also, they can provide a systematic non-steady-state kinetic characterization of a catalyst surface relating to its intrinsic site reactivity. *Operando* experimental methodologies coupled with the use of stable isotopes and conducted in the transient regime have now become very powerful tools since adsorbed reaction intermediates and surface catalytic sites can be characterized in terms of their structure and concentration under reaction conditions. Thus, a better understanding of the structure–catalytic performance (e.g., rate, selectivity, and stability with time on-stream) relationship can be obtained in the search for better catalyst design.

In this chapter, two important experimental techniques are considered, temporal analysis of products (TAP) and steady-state isotopic transient kinetic analysis (SSITKA), both of which use the transient method with respect to a step or pulse change in the feed gas composition made at the inlet of a catalytic microreactor. In both cases, an attempt is made to describe the essential theoretical and experimental features of the techniques by considering first their general principles followed by a variety of results based on several interesting recent experimental studies.

Characterization of Solid Materials and Heterogeneous Catalysts: From Structure to Surface Reactivity, First Edition.
Edited by Michel Che and Jacques C. Védrine.
© 2012 Wiley-VCH Verlag GmbH & Co. KGaA. Published 2012 by Wiley-VCH Verlag GmbH & Co. KGaA.

22.2
Temporal Analysis of Products (TAP)

22.2.1
Introduction

The TAP experiment was conceived in the late 1970s to study catalytic reaction mechanisms using industrial catalysts [1–6]. A patent for the TAP reactor system was issued to Monsanto in 1986 [7]. Two years later, Gleaves *et al*. [1] described how the TAP experiment was used to elucidate the mechanisms for several heterogeneous catalytic reactions having commercial significance. Reactions included oxidation of *n*-butane to maleic anhydride over vanadium–phosphorus–oxide (VPO) catalysts, oxidation of propylene to acrolein over bismuth molybdates, ammoxidation of methanol to HCN over $MnPO_x$ and $FeMoO_x$, and ethylene epoxidation over silver metal. The TAP-2 reactor system with the capability of operating under vacuum and at atmospheric pressure was developed and patented by Gleaves in 1994 [8].

The initial idea, which evolved into the TAP reactor system, was to build a simplified "molecular beam" experiment for multicomponent technical catalysts, for example, mixed metal oxides and supported metals, which have high surface areas and complex pore structures. Molecular beam scattering (MBS) experiments [7–16] can provide fundamental information on surface structure, reaction dynamics, the elementary steps of a reaction, and the kinetic parameters of individual steps. The goal of early TAP designs was to retain the time-dependent features of a molecular beam experiment, minimize gas-phase interactions, and provide a way to extract intrinsic kinetic information from reactions on bulk catalysts. The TAP experiment can be viewed as a bridge between MBS experiments and conventional microreactor experiments.

Figure 22.1a shows the key components of an MBS apparatus. In a typical experiment, a well-collimated beam of molecules having a known translational energy is directed towards a target surface, and the velocity and angle distributions of the scattered molecules are measured. Molecular beam experiments are performed under single collision conditions so that reactant molecules collide once with the target surface but not with each other. The observed distributions contain dynamic information, which describes the process of energy exchange between gas and surface atoms, and also kinetic and mechanistic information. Scattered molecules from a collimated beam may also exhibit diffraction effects, which provide information on surface structure and bond lengths [9–18].

A basic TAP setup as shown in Figure 22.1b has characteristics common to an MBS experiment, and others common to conventional microreactor experiments. The key components are a "reaction zone" or microreactor, a fast-pulse gas feed system, a mass spectrometer detector, and a high-throughput ultra-high vacuum (UHV) system. The reaction zone, typical dimensions of which are indicated in Figure 22.2, is a temperature-controlled cylindrical tube usually made of stainless steel, Inconel, or quartz. One end of the tube receives input from the feed system and the opposite end is open to vacuum. During an experiment, the reaction zone and catalyst sample

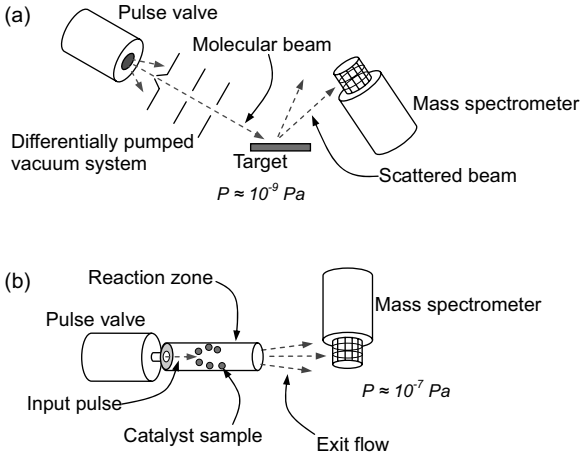


Figure 22.1 Conceptional comparison of key components of (a) molecular beam scattering experiment and (b) TAP experiment.

are continuously evacuated. The reaction zone can hold practical catalysts, which are commonly studied in conventional microreactor experiments, and also single particles, single crystals, or model catalysts, which are studied in MBS experiments. Injecting a narrow pulse of reactant molecules into the reaction zone and monitoring the gas exiting the microreactor with a mass spectrometer performs a TAP experiment.

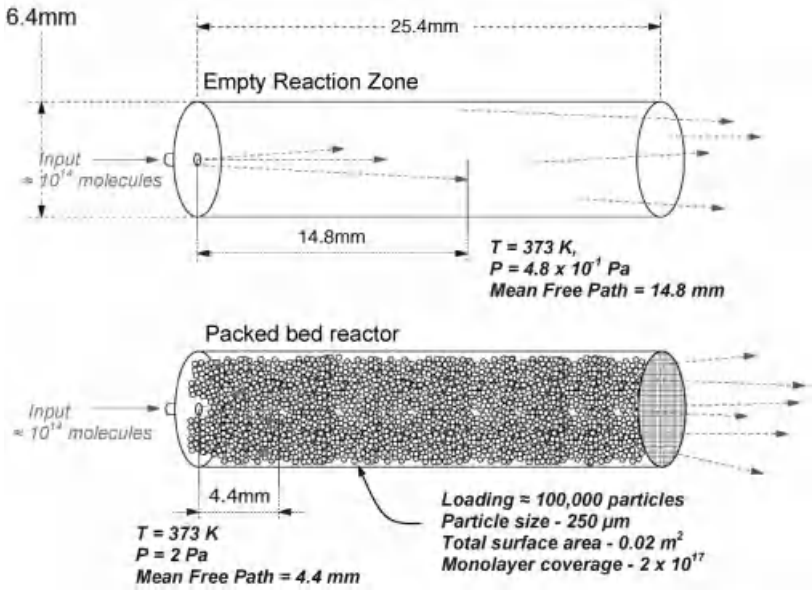


Figure 22.2 Scale drawing of a TAP "reaction zone" and packed-bed microreactor containing a loading of nonporous spherical particles ~250 μm in diameter.

The input pulse in a TAP experiment typically contains $\sim 10^{14}$ molecules, and the local pressure in an empty reaction zone may reach $\sim 10^{-1}$ Pa during a pulse. If unimpeded, an oxygen molecule can traverse the reaction zone in less than 100 μs. If the reaction zone is filled with particles, the pressure may reach ~1.33 Pa in the void spaces if no adsorption occurs. The mean free path in an empty reaction zone is about half the length of the reactor. In an empty reactor, molecules move independently and suffer relatively few collisions. In a packed reactor, the mean free path is ~4000 μm, which is significantly larger than the space between particles. As a result, in a packed-bed reactant molecules collide with particles, but seldom with one another.

MBS experiments obtain essential kinetic and mechanistic information by modulating the reactant flux and measuring the shift in arrival times at the detector between scattered reactant and product molecules. TAP pulse-response experiments [1–7] extract kinetic information in a similar manner. After an input pulse, gas molecules travel through the reaction zone where they encounter the catalyst and can react to form product molecules. The ionizer of the mass spectrometer is positioned perpendicular to the gas flow so that it intercepts molecules exiting the reaction zone.

TAP reactor systems are specially constructed to perform TAP experiments, but the design of the system makes it ideal for performing other types of kinetic experiments, including steady-state and transient experiments at atmospheric pressure. Figure 22.3 shows a commercial TAP-3 reactor system with key parts labeled.

The system is comprised of (a) a pulse-valve manifold assembly that supplies gas reactants for pulsed and flow experiments at user-defined temperatures and pressures, (b) a microreactor assembly that can be operated isothermally or in a temperature-programmed mode, (c) a mass spectrometer contained in a high-throughput UHV system, (d) a gas/liquid feed system for preparing reactant gas blends, and (e) a computer-based control and data acquisition system.

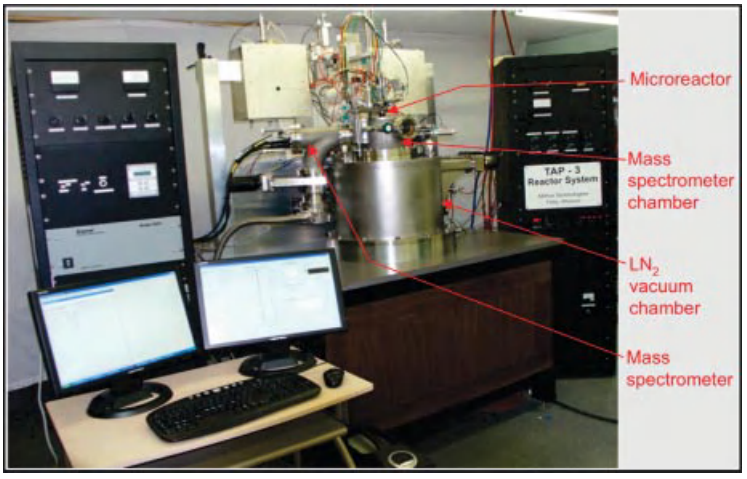


Figure 22.3 TAP-3 reactor system (Courtesy Mithra Technologies).

A simplified schematic of the TAP-3 system showing key features of the design is shown in Figure 22.4. The pulse-valve manifold contains one continuous-flow valve and four high-speed pulse valves (only two are visible) that are arranged to minimize the dead volume between the valves and the microreactor. The four pulse valves can

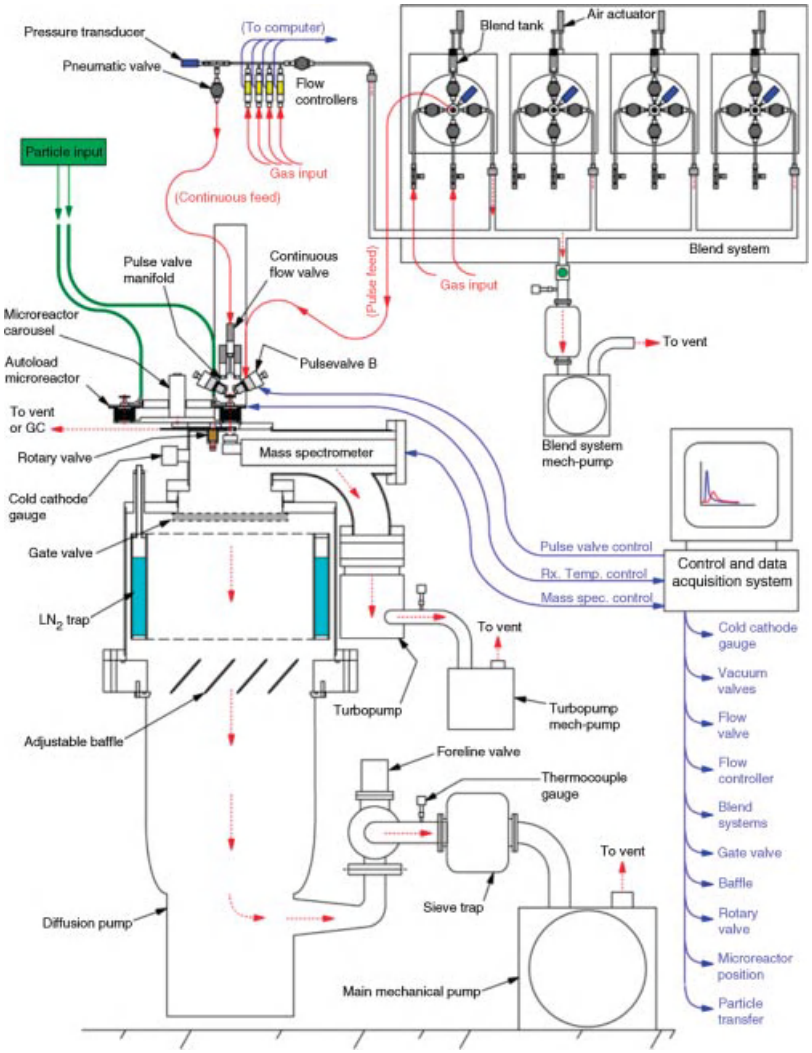


Figure 22.4 Schematic of TAP-3 apparatus showing two-chamber vacuum system (base pressure = 10^{-7} Pa) with gate valve, adjustable baffle, liquid nitrogen trap, rotary valve for switching between vacuum and pressure experiments, and quadrupole mass spectrometer; microreactor carousel with autoload microreactors and catalyst sample input lines; reactant feed manifold with high-speed pulse valves and continuous-flow valve; gas feed system with heatable mass flow controllers, heated blend tanks for preparing gas mixtures, and vacuum pump; computer control and data acquisition system indicating main control lines.

be operated individually or in a programmed alternating sequence. Pulse intervals can be varied from microseconds to minutes. The continuous-flow valve is connected to four flow controllers. The flow controllers and pulse valves can be operated simultaneously. The flow controllers and pulse valves can deliver step responses in addition to continuous flows and pulses.

The TAP-3 vacuum system has two chambers separated by a pneumatically operated gate valve, which is closed when the system is not performing experiments. The lower chamber is evacuated by a 40 cm diameter diffusion pump and associated mechanical pump. The chamber contains a cylindrical liquid nitrogen trap and adjustable baffle that closes when data are not being acquired. The upper chamber holds the mass spectrometer and is pumped by a turbomolecular pump. The background pressure in the mass spectrometer chamber during pulse response experiments is typically $\sim 10^{-7}$ Pa.

The microreactor is positioned directly above the ionizer of the mass spectrometer, and is attached to a movable stainless-steel bellows. A rotary-valve assembly is located between the ionizer and the microreactor. It permits the microreactor to be operated at vacuum conditions or atmospheric pressures, and allows the reactor to be removed from the system without venting the vacuum chambers. The reactor can be easily and rapidly switched from one kinetic regime to another without exposing the catalyst sample to the atmosphere.

TAP experiments are performed with the rotary valve in the open position, so that the reactor effluent vents directly into the vacuum chamber. The movable bellows allows the reactor outlet to be positioned within 2 mm of the ionizer so that most of the effluent passes through the ionizer. As a result, very small inputs of gas can be detected, with a very high signal-to-noise (S/N) ratio. The high S/N ratio allows accurate calculation of the zeroth, first, and second moments of the response curves, and direct determination of many important kinetic characteristics.

When the rotary valve is closed, the TAP microreactor can be operated as a continuous plug-flow type reactor at atmospheric or higher pressures. In the "high-pressure" mode, the bulk of the reactor effluent exits through an external vent. A small amount can be leaked into the vacuum chamber through a variable leak valve and monitored with the mass spectrometer. In high-pressure experiments, the mass signal usually changes relatively slowly, and a complete mass spectrum can be acquired about once every 0.25 s. After performing an experiment at atmospheric pressure, the microreactor can be switched to vacuum conditions by opening the rotary valve.

The TAP-3 system can accommodate microreactors of different lengths (up to 25 cm) and diameters (up to 2 cm), which are useful for handling a variety of catalyst forms (Figure 22.5). A standard TAP microreactor is constructed of 316 stainless steel and can be operated at atmospheric pressure or under vacuum conditions. Reactors are heated electrically and the reactor temperature controller provides an array of control options, which include constant-temperature operation, programmed heating or cooling at a user-defined rate, and the ability to perform multistep ramp–soak programs. The standard microreactor can be heated to 600 °C. Microreactors have also been fabricated from Inconel and quartz that allow operation up to temperatures as high as 1000 °C.

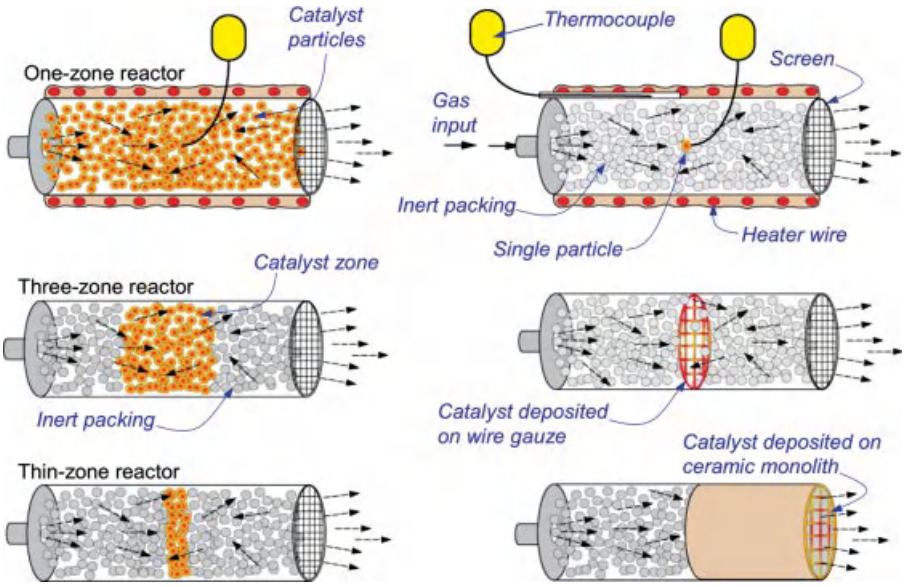


Figure 22.5 Examples of TAP packed-bed microreactor configurations and catalyst forms. See Figure 22.4 for schematic of TAP system with pulse valves, slide valve, and mass spectrometer.

The TAP-3 menu of experiments includes, but is not limited to, high-speed vacuum pulse response experiments (TAP Knudsen pulse response experiments, TAP pump–probe experiments, and TAP multipulse experiments, pulse experiments with a change of time within a pulse and between pulses), atmospheric pressure steady-state, step-transient and SSITKA experiments, temperature-programmed desorption (TPD), and temperature-programmed reaction (TPR). When operated in the high-pressure mode, the TAP-3 system can automatically perform a sequence of atmospheric pressure experiments, including temperature-programmed (TPD, TPR, temperature-programmed oxidation (TPO)) experiments, step response experiments, and SSITKA experiments.

22.2.2
The Goal of TAP Experiments and Theoretical Background

In general, kinetic experiments measure rates of chemical transformation and determine the rate dependence (or other kinetic characteristics of a reaction) on different reaction parameters, such as temperature, gas-phase composition, and pressure. In heterogeneous catalysis, kinetic experiments measure rates of adsorption, desorption, and surface reaction on different solids to determine their catalytic activity. From a fundamental perspective, the key problem is relating the rates of these processes to the composition and structure of a solid. The primary goal of a TAP experiment is to obtain rates of gas–solid interactions on technical catalysts that can be directly related to the catalyst's surface structure and composition, that is, a catalyst's intrinsic activity.

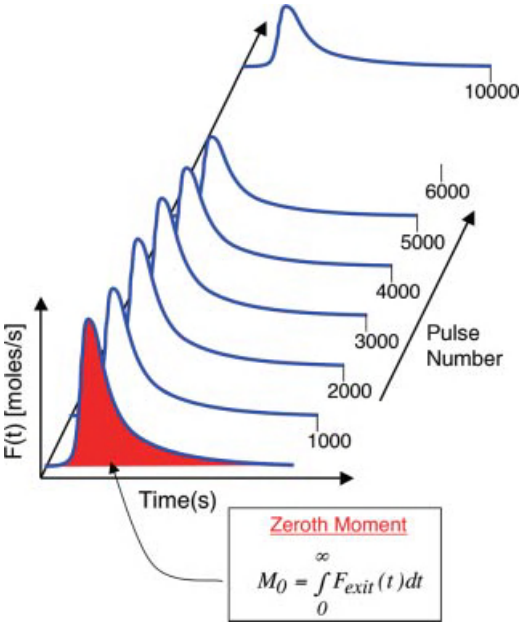


Figure 22.6 Pulse response sequence.

Kinetic characterization involves the collection of reaction-transport data and their interpretation using mathematical models. TAP data are comprised of sets of transient response curves – one set for each reactant, product, or inert gas that is being monitored. Figure 22.6 illustrates a typical data set, which may contain as many as 10 000 responses. An individual reactant or product response is the combined result of kinetic and transport processes. A set of curves includes an additional kinetic dependence on pulse number. An inert gas response is the result of transport without any kinetic dependence. TAP data analysis is concerned with the extraction of reaction rates and other kinetic characteristics from response curves.

The observable in a TAP experiment is the time-dependent gas flow, $F(t)$ (mol s^{-1} or molecules s^{-1}) which exits the microreactor and is detected by the mass spectrometer. In contrast to atmospheric pressure kinetic experiments, gas transport in a TAP experiment involves no convective flow. Transport is solely Knudsen diffusion, which is independent of the gas-phase composition. The effective gas diffusivity, D_{eff} ($m^2\,s^{-1}$) is defined by

$$D_{eff} = \frac{\varepsilon_b}{\tau_c}\frac{d_c}{3}\sqrt{\frac{8R_gT}{\pi M}}; \quad d_c = \frac{2\varepsilon_b}{3(1-\varepsilon_b)}d_p \tag{22.1}$$

where d_c is the diameter of the void space in the bed (m), d_p is the diameter of the catalyst particle (m), R_g is the universal gas constant (J $mol^{-1}\,K^{-1}$), T is the temperature (K), M is the molar mass of the gas (kg mol^{-1}), ε_b is the bed voidage, and τ_c is the tortuosity of the bed. Transport is described by Fick's second law, and is well

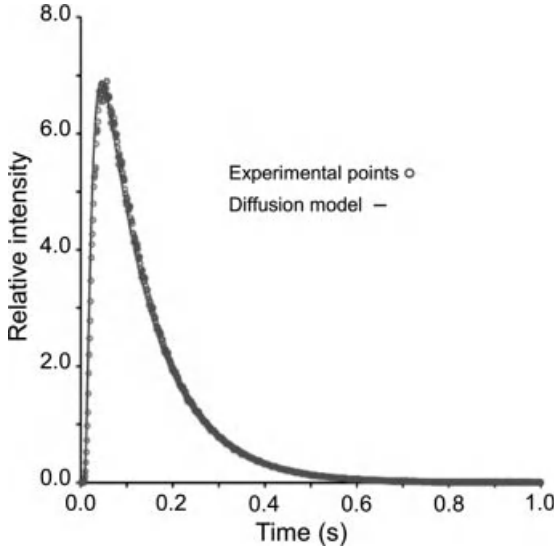


Figure 22.7 Ar standard diffusion curve.

defined. The experimental response curve for an inert gas takes the form of a standard diffusion curve (Figure 22.7) from which the effective diffusivity of the inert gas can be determined. After determining the diffusivity of an inert gas, the diffusivity for any other gas can be calculated, and its standard diffusion curve can be constructed.

In general, a standard diffusion curve is the transient response that a gas exhibits when it only experiences transport. Conversely, if a gas adsorbs on a solid, or reacts to form a product, its response curve will deviate from the standard curve. Mathematical models used to interpret TAP experiments provide the tools to analyze the difference between a standard curve and an experimental curve containing both transport and kinetic information. Thus, an inert gas response provides a standard reference curve, which allows kinetics and transport to be decoupled so that rates of chemical transformation and other kinetic parameters can be extracted from the response curves of reactant and product molecules.

In addition to the problem of decoupling kinetic and transport processes, there are additional issues associated with determining the intrinsic catalytic properties of a solid. Intrinsic properties, commonly discussed in terms of "active centers" or "active sites," are typically generated under kinetically controlled conditions and emerge during catalyst synthesis and pretreatment. Active sites often involve surface defects and unique structural arrangements, which are thermodynamically unstable. During a kinetic experiment, the gas–solid interaction can alter the surface composition and structure of the catalyst. As a result, the absolute number of active sites can change as a result of a change in the catalyst surface area, a change in the crystal morphology, or a change in surface oxidation state. In addition, the specific reactivity of sites can change. Moreover, active sites may occupy only a fraction of the solid surface. As a result, coverage arising from interactions between the solid surface and

the gas phase can limit access to the catalytic surface and mask direct gas–solid interactions.

The TAP experiment is uniquely suited to measuring the intrinsic properties of complex catalysts, especially catalysts composed of mixed metal oxides, supported metals, or structured solids. A characteristic Knudsen pulse contains $\sim 10^{13}$–10^{14} molecules or 10^{-10} mol. Assuming that a catalyst sample has a surface area of $10\,m^2\,g^{-1}$, a single Knudsen pulse would be equivalent to 1/500 000 of the total surface area of a 0.05 g sample (a typical sample size). If the active surface area of the catalyst comprises a reasonable fraction (e.g., $\geq$0.1%) of the total surface area of the catalyst, then a single pulse will have a negligible effect on the active surface. In this case, the transient input causes a very small perturbation to the catalytic system, and the system remains substantially in the same state (e.g., retains the same structure and composition) after the measurement as it was before the measurement. Consequently, the measured kinetic characteristics correspond to a constant kinetic state of the catalyst. Whenever the number of reactant molecules in a pulse is significantly smaller than the number of active species, a TAP pulse response experiment can be termed a "state-defining" experiment. An experiment that perturbs the catalyst and changes its composition or structure in some predetermined fashion can be termed a "state-altering" experiment.

A TAP experiment is considered state defining if (i) the pulse response of a reactant or product changes insignificantly during a series of pulses and (ii) the pulse shape is independent of the pulse intensity. The first criterion indicates that the reactivity of the catalyst surface does not change significantly from pulse to pulse. This criterion can be applied to an irreversible process such as the reduction of a metal oxide catalyst by a hydrocarbon. The second indicates that the number of input molecules is sufficiently small that a decrease in the number does not influence the shape of the exit flow response. State-defining experiments provide kinetic parameters corresponding to a specific catalyst state (e.g., a specific composition and structure). For example, in the irreversible transformation of a hydrocarbon on a metal oxide catalyst, the intrinsic kinetic coefficient depends on the composition and structure of the metal oxide surface, the catalyst oxidation state, and the catalyst bulk structure.

When combined with spectroscopic data, which can be related to the surface composition and/or surface structure, intrinsic kinetic information can be used to develop structure–function relationships. These relationships provide the scientific basis for the development of new or improved catalysts.

22.2.3
Comparison of TAP Experiments with Other Kinetic Methods

Experiments used to obtain kinetic data on technical catalysts are usually based on a steady-state approach. This approach can be readily applied under process reaction conditions, and the techniques to analyze steady-state data are well established. However, steady-state kinetic data are related to the slow steps of a complex kinetic process, and do not provide detailed information on individual steps of a reaction. Transient experiments can supply more detailed information, including information

on individual steps in a reaction sequence. However, transient experiments are usually more difficult to analyze, and as a result have not been used as extensively as those based on a steady-state approach. TAP experiments, on the other hand, do not suffer from the same analysis problem as other non-steady-state techniques. The key features that distinguish TAP pulse response experiments are the following: (i) uniformity of the active zone, (ii) domain of conditions, (iii) relevance of kinetic information, (iv) applicability to developing structure–properties relationships, and (v) model-free interpretation of kinetic data (rate of reaction, yield, selectivity, etc.).

22.2.3.1 Uniformity of the Active Zone

In atmospheric pressure steady-state and non-steady-state kinetic experiments, transport includes both convective and diffusive flow. Convection can be eliminated at sufficiently low pressures, but diffusion is always present in experiments involving mass transport. In CSTR (continuously stirred tank reactor) and PFR (plug flow reactor) systems, the conditions (flow rates, particle size, etc.) are adjusted to minimize effects of diffusion on the observed characteristics, but diffusion is not eliminated. In TAP experiments, convection is eliminated, and diffusion is well defined.

Until recently, it was assumed that concentration gradients within a reactor could be minimized using a CSTR configuration. However, recent results using computational fluid dynamics (CFD) indicate that when more than one phase is involved, the system is not always well mixed. In a PFR, it is generally assumed that the concentration gradients in the radial direction can be neglected. However, it is common to have a concentration gradient in the axial direction, and a corresponding axial nonuniformity of the catalyst composition. A TAP three-zone reactor configuration is similar to a PFR, and at high conversions the catalyst zone will be nonuniform. However, in TAP thin-zone [19] and single-particle configurations [20], the gas and catalyst compositions remain uniform even at high conversions.

22.2.3.2 Domain of Conditions

CSTR and PFR systems typically operate at temperatures and pressures (atmospheric or above) that are close to industrial conditions. For highly exothermic reactions, a CSTR is often run at low conversions to maintain an isothermal regime. The TAP reactor system (e.g., the TAP-2 and TAP-3 systems) can perform experiments over a wide range of conditions from vacuum to atmospheric pressures. The Knudsen regime (where TAP pulse response experiments are carried out) is located within the pressure range $10^{-2} - 10^{-1}$ Pa, which is the upper boundary of the "surface science" domain. A TAP-3 reactor system can also perform TPD experiments at 1.3×10^{-6} Pa, and step-transient and steady-flow experiments at atmospheric pressure. A single catalyst sample can be cycled between the different pressure regimes so that the observed characteristics can be directly compared.

22.2.3.3 Relevance of Kinetic Information

Steady-state kinetic experiments provide essential information for operating a catalytic process under steady-state conditions. However, steady-state kinetic

dependences are usually related to the rate-determining step(s) of a complex catalytic process, and do not provide detailed information on individual steps. In addition, they are complex functions of coverage, catalyst composition, pressure, and temperature. As a result, steady-state dependences are not generally intrinsic characteristics and cannot be used to establish structure–activity relationships. Moreover, switching from one steady state to another can alter the catalyst composition and change its intrinsic properties.

As previously discussed, characteristics obtained in TAP pulse response experiments using a thin-zone configuration are intrinsic and can be directly related to the catalyst composition. In addition, detailed information concerning reaction intermediates, the sequence of steps in a complex mechanism, and the kinetic parameters for adsorption, desorption, and surface reaction can be determined. Using a TAP reactor system, dependences can also be obtained at atmospheric pressure under steady-state conditions. By cycling a sample back and forth between TAP conditions and steady-state conditions (e.g., atmospheric pressure and steady-state gas concentrations), it is possible to determine how the reaction conditions of a specific state change the intrinsic properties of a catalyst. Thus, experiments performed on a TAP reactor system can provide fundamental kinetic parameters and detailed mechanistic information on complex catalysts, and also give insights into the nature of the steady state that controls a catalytic process operating at normal pressures. Extensive information related to TAP studies of many catalytic reactions was presented in a special TAP issue of *Catalysis Today* [6].

22.2.3.4 **Applicability to Developing Structure–Properties Relationships**

The core issue in catalyst development is the relationship between catalyst structure–composition and catalyst performance properties (e.g., selectivity, stability, and activity). The combination of structure–composition and properties defines a material's "catalytic state," which can change with the experimental conditions. Information pertaining to structure (arrangement of atoms on the surface and in the bulk) and composition (type and concentration of atoms on the surface and in the bulk) is obtained using spectroscopic techniques, which generally do not significantly alter the structure–composition of a material. Information concerning the properties of a catalyst is obtained in kinetic experiments that can change the composition and structure of a material, which in turn can change the properties of the material. In addition, if the spectroscopic and kinetic experiments are performed under different conditions (e.g., vacuum conditions for surface analysis and atmospheric pressure for kinetic experiments), the catalytic state of a material can change on going from one experiment to another. Hence the challenge in developing structure–property relationships is to develop an experimental strategy that utilizes or compensates for the tendency of a kinetic experiment to alter a material's catalytic state.

A common strategy employed in surface science studies is to use a model catalyst, such as a metal single crystal, and maintain it under UHV conditions, while characterizing its composition, structure, and properties. This approach provides a clear procedure for obtaining kinetic information on a surface whose structure and composition are precisely known. The key to this strategy is to have a sample that

remains essentially unchanged throughout the experimental sequence. Although the surface science approach can provide activity–structure relationships on model catalysts, it is not well suited for investigating kinetics on technical catalysts. The large difference in pressures (often greater than 9–10 orders of magnitude) and especially the difference in structural complexity between model and technical catalysts give rise to a "pressure–materials gap" that makes it very difficult to apply results from model studies to technical catalysts.

Operando experiments combine direct spectroscopic observation of a catalytic surface and simultaneous measurement of kinetics. Transient experiments combined with infrared (IR) or Raman spectroscopy can provide information on reaction kinetics, the nature of surface intermediates, and structural characteristics under reaction conditions. For example, the SSITKA approach presented in detail in Section 22.3 is based on the determination of isotopic labels in the reactor effluent following a step change in the isotopic label of one of the reactants. SSITKA data can provide information on the concentration ($\mathrm{mol\,g^{-1}}$ or $\mathrm{mol\,m^{-2}}$) of surface-active reaction intermediate species and also rates of formation for a given steady state. SSITKA experiments are typically performed in a PFR to obtain the highest time resolution, but are subject to the same catalyst nonuniformity as a conventional steady-state PFR experiment. Again, the experimental strategy is to maintain the catalyst in a specific steady state so that the kinetics and structural measurements are performed on the same material.

TAP experiments have been combined with *ex situ* spectroscopic Raman analysis using an approach called interrogative kinetics. In contrast to traditional steady-state kinetics, which attempts to obtain kinetic parameters for a specific steady state, interrogative kinetics systematically probes a variety of different states to understand how one state evolves into another. Interrogative kinetics involves "state-defining" experiments that provide kinetic information, which characterize the state, and a "state-altering" experiment, which perturbs the catalyst and changes its composition or structure in some predetermined fashion. To complete the sequence, another "state-defining" experiment is performed to characterize the new state of the catalyst. "State-defining" experiments involve reactions of probe molecules with a catalyst and provide kinetic parameters such as rate parameters of adsorption and desorption to characterize the reactions. One example of a probe reaction is the irreversible chemisorption of a hydrocarbon on a metal oxide catalyst. In this case, the state-defining kinetic parameter of the reaction is the rate parameter of irreversible chemisorption, or the rate of irreversible chemisorption at unit gas concentration. This parameter is "state-defining" because it depends on the kinetic state of the metal oxide surface. In particular, it depends on the concentration and reactivity of the surface species on which the hydrocarbon chemisorbs.

The kinetic parameters obtained in each "state-defining" experiment can be compared with structural characterization data taken for the same state. A change in catalyst state implies a change in properties or a change in the number and/or structure of the active sites, which can give rise to a simultaneous change in structure characteristics. By systematically altering the composition of a catalyst and collecting state-defining kinetic and structure data after each incremental

change, the evolution of kinetic and structural characteristics can be compared to determine if there is a relationship between the two. In this case, the experimental strategy utilizes the tendency of a kinetic experiment to alter a material's catalytic state, and thus to develop a structure–activity relationship. The advantage of this strategy is that it can be used to study very complex systems, since it specifically targets the active site.

22.2.3.5 Theoretical Models

TAP theoretical models, which are described in detail in a series of papers [1, 3–5, 19–22], are systems of "reaction–diffusion" equations in which diffusion is a well-defined process, and boundary and initial conditions are also well defined. An obvious advantage of the TAP method is that the standard diffusion curve (i.e., the diffusion curve for only diffusion process) being presented in the dimensionless form is the same dependence for any TAP response diffusion experiment regardless of the type of gas, reactor length, pellet diameter, or reactor temperature. This curve has simple analytical properties which can be used for verifying the Knudsen domain and extracting the diffusion coefficients.

The theoretical TAP models have been formulated and analyzed at different levels using many modifications. In particular, the following theoretical tools can be described:

a) Analysis of fingerprints. Comparing the "reaction–diffusion" curves with the standard diffusion curve, one can conclude immediately what kind adsorption, irreversible or reversible, has occurred [3, 5]
b) Moment-based analysis, in which analysis of some integral characteristics – moments – of the exit flow rated is performed. These moments reflect the important primary features of the observations in a robust manner [1, 3–5, 21]
c) Analysis of exit flows based on the global transfer-matrix technique [22–25]
d) Traditional computational analysis of "reaction–diffusion" models aiming at the determination of the model parameters [1, 3].

The process of irreversible adsorption – or reaction – combined with Knudsen diffusion is the simplest process studied using TAP pulse-response experiments. If the adsorption or reaction is characterized by a first-order dependence on the gas concentration and the change in surface coverage can be neglected due to a low pulse intensity, the material balance for the gas-phase component A in an isothermal TAP reactor uniformly packed with nonporous catalyst can be written as

$$\varepsilon_b \frac{\partial c_A}{\partial t} = D_{eff,A} \frac{\partial^2 c_A}{\partial z^2} - \Gamma_t S_V (1-\varepsilon_b) k_a c_A \tag{22.2}$$

where Γ_t is the concentration of active sites per unit surface area of catalyst ($\mathrm{mol\,m_{cat}^{-2}}$), S_V is the catalyst surface area per unit volume ($\mathrm{cm^{-1}}$) and k_a is the adsorption coefficient ($\mathrm{m^3\,mol^{-1}\,s^{-1}}$). The dimensionless form of Eq. (22.2) is

$$\frac{\partial \bar{c}_A}{\partial \tau} = \frac{\partial^2 \bar{c}_A}{\partial \varsigma^2} - \bar{k}_a \bar{c}_A \tag{22.3}$$

where

$$\bar{k}_a = \frac{\Gamma_t S_V (1-\varepsilon_b) k_a {L_r}^2}{D_{eff,A}} \tag{22.4}$$

The initial and boundary conditions for Eq. (22.3) are the same as those presented for the case of diffusion only [3–5]. The dimensionless exit flow rate can be expressed as

$$\bar{F}_A = \pi \exp\left(-\bar{k}_a \tau\right) \sum_{n=0}^{\infty} (-1)^n (2n+1) \exp\left[-(n+0.5)^2 \pi^2 \tau\right] \tag{22.5}$$

Equation (22.5) can also be written in normalized dimensional form as

$$\frac{F_A}{N_{p,A}} = \frac{D_{eff,A}\pi}{\varepsilon_b {L_r}^2} \exp(-k'_a t) \sum_{n=0}^{\infty} (-1)^n (2n+1) \exp\left[-(n+0.5)^2 \pi^2 \frac{t D_{eff,A}}{\varepsilon_b {L_r}^2}\right] \tag{22.6}$$

where

$$k'_a = \frac{\Gamma_t S_V (1-\varepsilon_b) k_a}{\varepsilon_b} \tag{22.7}$$

Comparison of the exit flow for the "reaction–diffusion" case and for the diffusion only case [the standard diffusion curve (SDC)] shows the values of the normalized exit-flow curve for the case of combined diffusion and irreversible adsorption/reaction are smaller than the SDC values by a factor of $\exp(-k'_a t)$. Therefore, the normalized exit-flow curve for irreversible adsorption/reaction versus time is always placed "inside" the SDC. Such a feature can be considered as a "fingerprint" for irreversible adsorption/reaction.

22.2.3.6 **Model-Free Interpretation of Kinetic Data**

A specific advantage of the TAP approach established recently is its possibility of extracting the model-free non-steady-state reaction rates and operating with them [26, 27]. Let us consider this advantage in more detail, comparing the TAP approach with other kinetic methods. Heterogeneous kinetic data are obtained by measuring the change in gas concentration, flow rate, or flux that results from the interaction of a gas with a solid. In addition to reaction conditions (e.g., temperature, gas-phase composition, pressure) and catalyst properties, the data are also a function of the reactor configuration, which determines how the gas contacts the catalyst. The data are model-free if the rate of conversion or formation can be expressed in terms of the measured quantities (concentration, flow rate, catalyst weight, etc.) without involving a specific kinetic model. In this case, no bias is introduced by assumptions about the form of the kinetic dependences, detailed mechanisms, reactor models, and so on.

An ideal CSTR operating under steady-state reaction conditions provides model-free kinetic data because the consumption rate of a reactant A, $-R_{W,A}$ ($\mathrm{mol\,kg_{cat}^{-1}\,s^{-1}}$) can be expressed as

$$-R_{W,A} = \frac{q_{V0}(c_{A0} - c_A)}{W} = \frac{F_{A0} - F_A}{W} \tag{22.8}$$

where q_{V0} and F_{A0} are inlet flow rates of the chemical mixture, in $m^{-3}\,s^{-1}$ and $mol\,s^{-1}$, respectively, F_A is the outlet flow rate, c_{AO} and c_A are the inlet and outlet gas concentrations ($mol\,m^{-3}$), and W is the catalyst weight (kg).

Operating under non-steady-state conditions, the consumption rate for a CSTR can be expressed as

$$-R_{W,A} = \frac{F_{A0} - F_A}{W} - \frac{V_g}{W}\frac{dc_A}{dt} \tag{22.9}$$

where V_g is the volume of the gas space within the reactor. The data are model-free provided that the derivative dc_A/dt can be determined experimentally. In practice, the determination of dc_A/dt is not straightforward and gives rise to errors.

For a steady-state PFR, a model-free reaction rate can be determined by taking the derivatives of the experimental "conversion versus space time" dependences. This is known as the differential method of PFR data analysis. For a non-steady-state PFR, the extraction of reaction parameters requires solving a model consisting of a set of partial differential equations, assumptions about the kinetic model, and the detailed mechanism of the reaction. In this case, the kinetic data are not model-free.

Non-steady-state model-free kinetic data can be extracted from TAP pulse response experiments provided that a thin-zone or single-particle reactor configuration is employed. In both cases, the catalyst composition is uniform even under non-steady-state conditions. A theoretical method, called the Y-procedure [26, 27], provides non-steady-state concentrations and reaction rates directly from exit flow data without any assumptions regarding a detailed kinetic model. The main idea of the Y-procedure is that diffusive flow in the inert zones can be used as a "measuring stick" to determine the concentration and reaction rate in the catalyst zone. The approach partly involves the solution of the inverse diffusion problem. The mathematical basis of the Y-procedure is a Laplace-domain analysis of transient behavior in the inert zones; transposition to the Fourier domain, combined with time discretization and filtering of higher frequency noise. The procedure provides a practical method for reconstructing the transient concentration and reaction rate in the catalyst zone. Using the Y-procedure, the concentration and reaction rate for a non-steady-state catalytic process can be determined without any *a priori* assumption about the kinetic dependence. The transformation rate is determined as the difference between diffusive flows on either side of the active zone, and the procedure is model-free. The Y-procedure offers the unique possibility of relating the temporal evolution of reaction rates and kinetic parameters to the surface composition of a catalyst, and is the first such procedure for non-steady-state catalyst characterization.

22.2.4 Experimental Results

22.2.4.1 Bridging the Pressure Gap

With the TAP reactor system, a catalyst sample can be rapidly cycled between vacuum and atmospheric pressure without exposing it to the atmosphere. The process is illustrated in Figure 22.8, which shows the slide valve in the high-pressure (a) and

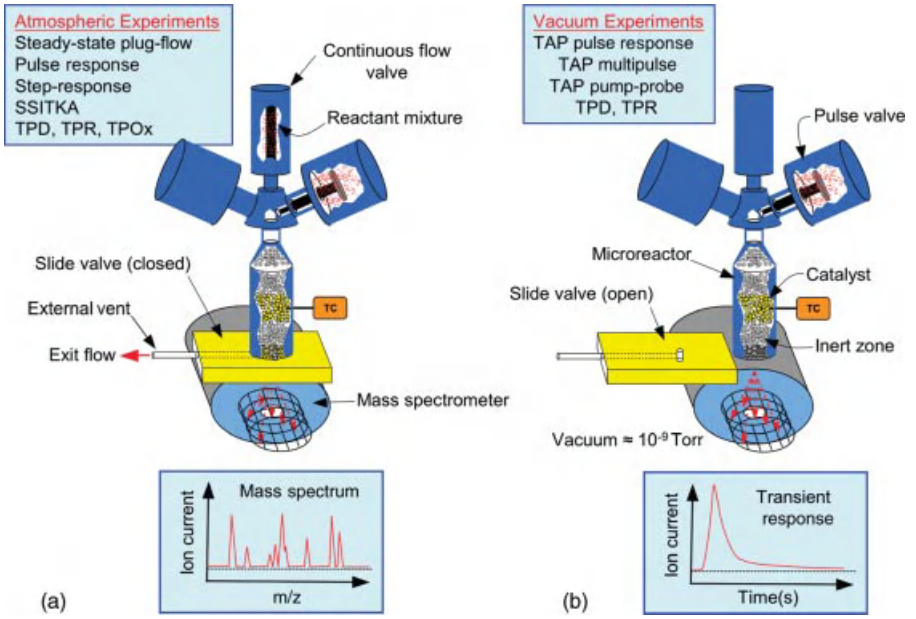


Figure 22.8 Illustration of high-pressure (a) and vacuum (b) configurations of TAP reactor system. The microreactor can be shifted from high-pressure operation to vacuum in minutes by opening the slide valve.

vacuum positions (b). In the high-pressure position, the reactor effluent flows through the slide valve and out an external vent, where it can be analyzed by gas chromatography (GC). A small portion of the effluent can be diverted to the mass spectrometer chamber through an adjustable needle valve. The mass spectrum of the reaction products is collected in real time. After running atmospheric pressure experiments, the reactor can be evacuated and the slide valve moved to the vacuum position. During the switch from high pressure to vacuum, the reactor effluent can be monitored and desorbing adspecies left on the surface during pressure experiments can be measured. TAP pulse response experiments are performed after the reactor reaches vacuum and desorption of adspecies has stopped. Switching back and forth between high-pressure and vacuum operation typically takes less than 30 s.

The ability to relate data in the atmospheric domain to data obtained in vacuum pulse response experiments provides a means of bridging the pressure gap and understanding the key features that distinguish different kinetic regimes. Results from studies of CO oxidation over polycrystalline platinum demonstrate that TAP data are comparable to steady-state data obtained at atmospheric pressure when the catalyst composition remains constant. Experiments were performed using a single 400 μm diameter polycrystalline Pt particle positioned in the center of a packed bed containing ~100 000 inert quartz particles with diameters between 210 and 250 μm. Figure 22.9 presents a scale drawing of the reactor configuration. The particle occupies less than 0.3% of the cross-sectional area of the bed, so the

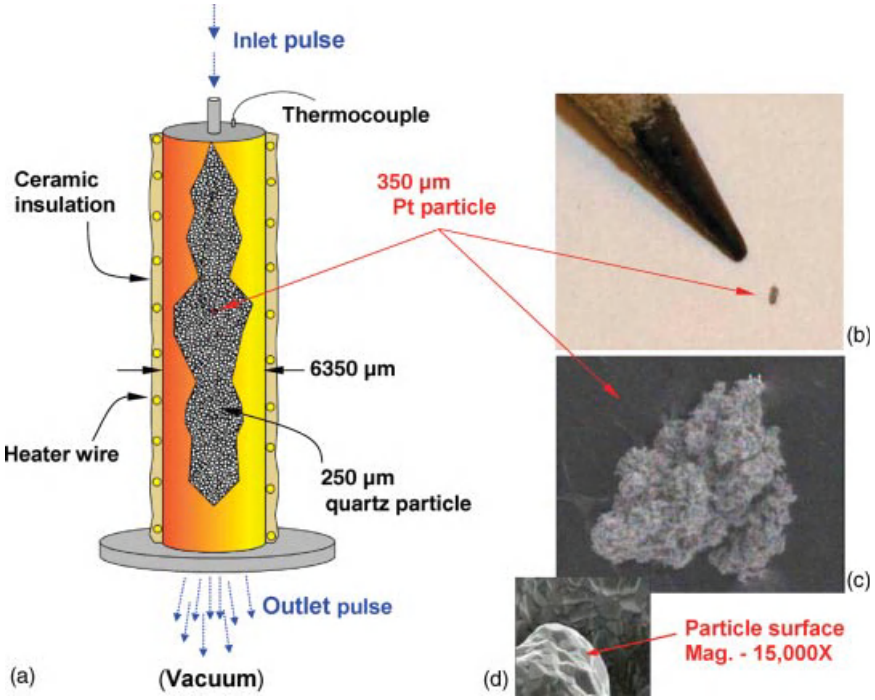


Figure 22.9 (a) Schematic of TAP single-particle microreactor configuration. The 400 µm diameter Pt particle is packed within a sea of inert quartz particles with diameters between 210 and 250 µm. (b) Image comparing a 400 µm Pt particle with a pencil point. (c) SEM image showing the complex surface structure of a polycrystalline Pt particle. (d) Higher magnification (×15 000) of the particle shown in (c), which shows that the surface is nonporous.

reaction zone can be considered a point source. Gas concentration and temperature gradients across the catalyst zone can be assumed to be negligible since the zone is a single particle.

Vacuum pulse response experiments were performed using a "pump–probe" format illustrated in Figure 22.10. O_2–Ar and CO–Ar mixtures are injected from different pulse valves in an alternating sequence, and the CO_2 response is measured during each pulse. Ar is used as an internal standard. CO_2 does not appear on the first O_2 pulse since no CO is present in the reactor. CO_2 appears on the first CO and all subsequent O_2 pulses.

At 170 °C, the yield for the individual O_2 and CO pulses reaches a maximum, making the total yield 95% during one pump–probe cycle, indicating that at least 95% of CO molecules pulsed into the reactor must strike the particle. Above 170 °C, the CO_2 yield decreases, more rapidly for the O_2 pulse than for the CO pulse.

Atmospheric flow experiments were performed after closing the slide valve. The particle bed was first exposed to a hydrogen flow (20 ml min^{-1} diluted in Ar, H_2: Ar = 1) at 350 °C for 1 h. Hydrogen was used to remove any memory of the previous

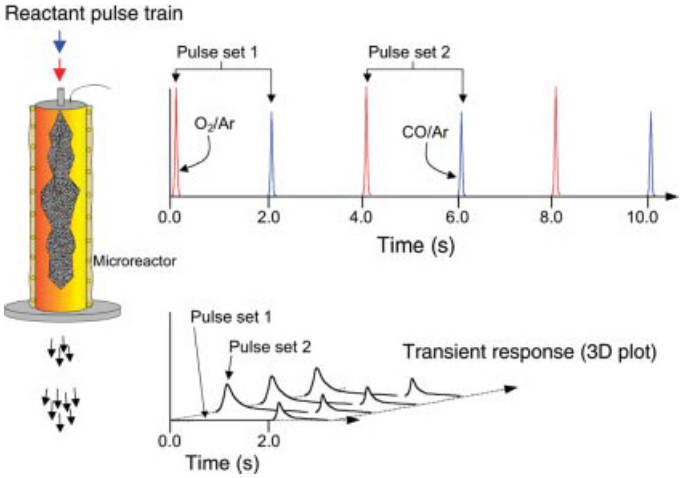


Figure 22.10 Illustration of a TAP pump–probe experiment in which O_2–Ar and CO_2–Ar are pulsed in an alternating sequence and the CO_2 transient response is measured during each pulse.

pump–probe experiments. A total flow of 50 ml min^{-1} of O_2, CO, and Ar (O_2:CO:Ar = 1:1:1) was introduced through the continuous valve, giving a gas residence time in the reactor of 1.8 s.

The temperature dependence of CO_2 production (Figure 22.11a) was obtained by heating or cooling the reactor at a constant rate while maintaining an input flow of 50 ml min^{-1}. The internal reactor temperature was ramped from 40 to 430 °C over a 40 min interval. Upon reaching 430 °C, the reactor temperature was held constant for 5 min and then decreased at the same ramp rate to room temperature. A small amount of the reactor effluent was diverted into the mass spectrometer, and its mass spectrum was continuously monitored.

Both TAP vacuum and atmospheric flow data exhibit a turning point in CO_2 production, indicating a transition from reaction controlled by one adsorbed species to one controlled by a different adsorbed species at 170 °C (Figure 22.11b). The upper branch in the CO_2 curve of the atmospheric flow experiment corresponds to an O_2-covered surface, whereas the lower branch corresponds to a CO-covered Pt surface (Figure 22.11b). From the pulse response data, in the region of the CO_2 maximum, the areas under the CO_2 response curves (CO_2 yield) corresponding to the O_2 and CO pulses are approximately the same, indicating nearly equal coverages of O_2 and CO on the Pt particle (Figure 22.11c). The correspondence in "turning points" indicates that the coverage in vacuum and atmospheric pressure experiments is approximately the same and intrinsic kinetic data obtained in vacuum experiments can be used to describe kinetic behavior in the atmospheric pressure domain.

Taking the conversion of CO or the CO_2 yield at the "turning point" from vacuum pulse response and atmospheric flow data, the apparent kinetic rate constant can be calculated. In atmospheric flow experiments, the CO conversion was $\leq$20% to insure catalyst and gas-phase uniformity. The apparent kinetic rate constant, determined

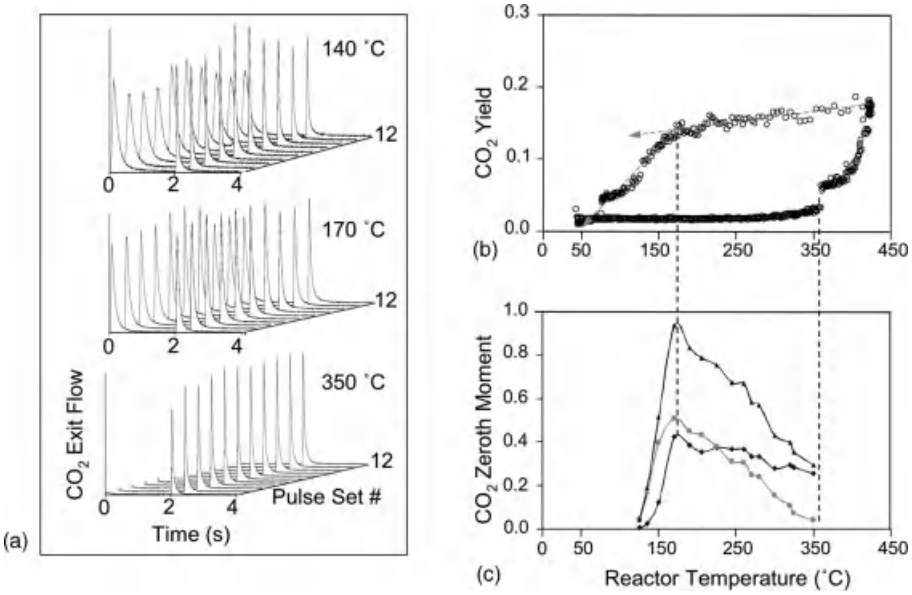


Figure 22.11 Comparison of CO_2 produced during TAP vacuum pump–probe experiments and atmospheric flow experiments for CO oxidation over a single Pt particle with the same composition of reactants. (a) A typical set of pump–probe CO_2 responses ($m/z = 44$) for reaction at 140, 170, and 350 °C. There is a shift in the amount of CO_2 produced during both CO and oxygen pulses as the temperature increases. (b) CO_2 production observed from atmospheric flow experiment. The CO_2 produced with increasing reactor temperature is less than the CO_2 produced during a reactor temperature decrease, as shown by the counter-clockwise hysteresis loop. (c) CO_2 production observed from vacuum pump–probe experiment. The black line represents the total CO_2 yield. The red and blue lines represent the CO_2 yield on the oxygen pulse and CO pulse, respectively.

from the measured conversion and the residence time (τ) in the catalyst zone is given by the following expression:

$$k_{app} = \frac{X}{(1-X)\tau} \tag{22.10}$$

where k_{app} is an apparent kinetic rate constant and X is the conversion of CO. Using an approximate conversion of 90%, the value of k_{app} determined from TAP pulse response data is calculated to be 9000 s^{-1}. In the atmospheric flow experiment, using a conversion of 20%, the value of k_{app} is calculated to be 9280 s^{-1}. The small difference (~3%) between the constants, which can be attributed to error in the determination of the steady-state value, indicates that the kinetic parameters are comparable even though the experimental regimes are different.

22.2.4.2 Tracking the Evolution of Catalytic Properties

Catalysts based on transition metal oxides comprise a major proportion of catalysts used in the chemical industry, and development of metal oxide-based partial

oxidation catalysts is an ongoing research area. A principle focus is to develop catalysts that can perform multistep processes with high selectivity. A key issue, especially with metal oxide catalysts, is that selectivity can change appreciably under reaction conditions. Consequently, understanding how kinetic characteristics evolve during reaction, and how the characteristics can be related to changes in a metal oxide composition and/or structure, is essential from a fundamental and practical perspective.

An example of how the TAP reactor system can provide unique information regarding the evolution of catalytic properties is provided by studies of the oxidation of *n*-butane to maleic anhydride (MA) over $(VO)_2P_2O_7$ [vanadyl pyrophosphate or VPO (vanadium–phosphorus–oxide)]-based catalysts [28]. A combination of atmospheric pressure and TAP pulse response experiments examined how exposure of VPO to oxygen affected its catalytic properties. Industrial VPO samples were "reactor-equilibrated" by heating at 420 °C in an oxygen–*n*-butane (1.4 vol.%) flow at 1 atm until the MA yield remained constant. The reactor-equilibrated samples were then exposed to different oxygen treatments and subsequently reacted with *n*-butane, and other C_4 compounds in TAP pulse-response experiments (Figure 22.12). All the experimental data displayed below were obtained using a TAP-2 reactor system.

Figure 22.13 shows oxygen uptake curves collected on three different reactor-equilibrated samples heat treated at 430, 450, and 460 °C in an oxygen atmosphere at a constant pressure of 10^5 Pa. The vanadium oxidation states were determined by chemical analysis. Figure 22.14 shows the oxygen desorption spectrum when an oxygen-18-treated VPO sample is evacuated and heated to 470 °C. The heated-treated sample emits $^{16}O_2$, $^{16}O^{18}O$, and $^{18}O_2$, whereas reactor-equilibrated samples do not. Analysis of the O^{16}:O^{18} ratio indicates that the adsorbed $^{18}O_2$ does not mix with the entire VPO lattice but is consumed in the first few monolayers of the VPO surface. The oxygen uptake measured on the TAP system matched the measured change in the vanadium oxidation state.

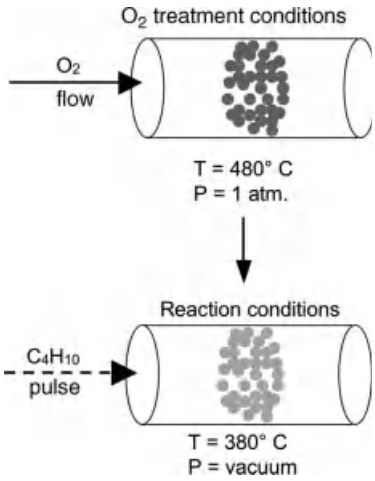


Figure 22.12 Oxygen treatment and TAP experiments.

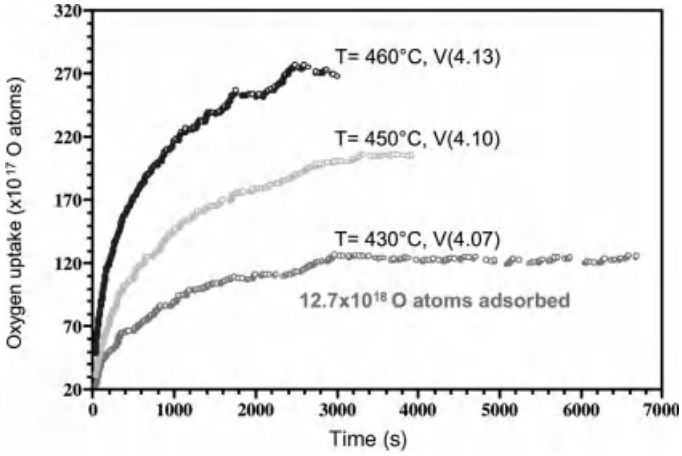


Figure 22.13 Oxygen uptake behavior at different temperatures on reactor-equilibrated VPO (1.066×10^5 Pa O_2).

Figure 22.15 displays a series of steady-state reaction spectra collected at different temperatures for an oxygen–*n*-butane(1.4 vol.%) mixture fed over a reactor-equilibrated VPO catalyst at atmospheric pressure and low conversion. Figure 22.16 shows a set of TAP spectra and model fits obtained by pulsing an *n*-butane–Ar mixture over an oxygen-treated VPO sample at different temperatures. The *n*-butane responses were measured at each temperature under state-defining conditions so that the catalyst composition was changed insignificantly. The area under the response curves provides the *n*-butane conversion in the absence of gas-phase oxygen. The butane response curves, when compared with the argon response, confirm that *n*-butane adsorbs irreversibly. Arrhenius plots for *n*-butane conversion over

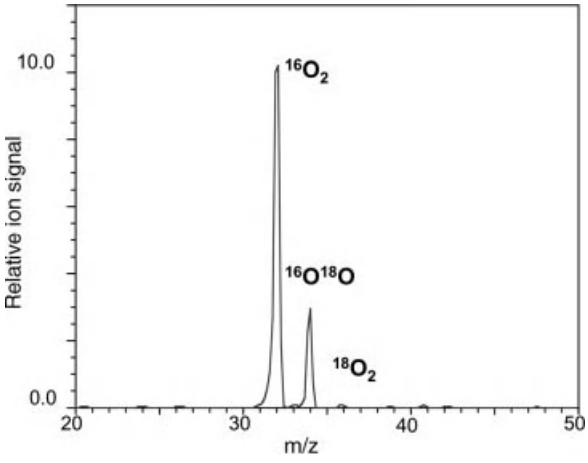


Figure 22.14 Oxygen desorption spectrum from $^{18}O_2$-treated VPO.

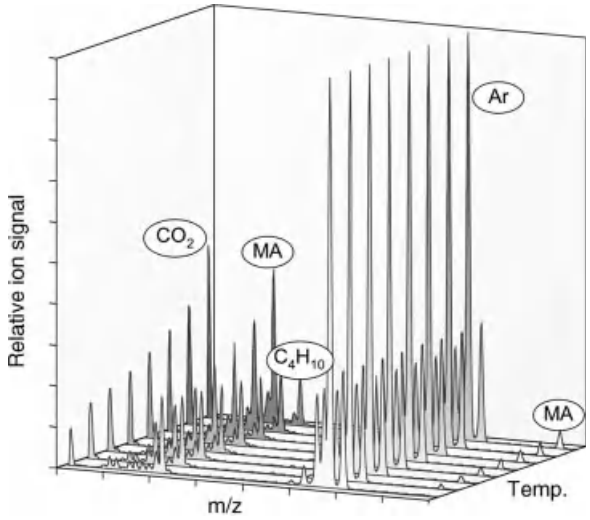


Figure 22.15 Steady-state reaction spectra obtained by flowing an oxygen–butane (1.4 vol.%) mixture over reactor-equilibrated VPO.

reactor-equilibrated and oxygen-treated VPO are displayed in Figure 22.17. Figure 22.18 displays a series of Arrhenius plots obtained on a single VPO sample, which was reduced in a long series of *n*-butane pulses. At different points in the reduction process, state-defining TAP pulse-response experiments were performed at a series of temperatures. The resulting plots indicate how the global and local kinetic characteristics of VPO change with oxidation state. The downward shift in the Arrhenius plots indicates a decrease in the amount of active oxygen or number of active sites over the entire VPO sample. The change in slope, indicative of a change in the activation energy for *n*-butane adsorption, indicates a change in the character of the active sites.

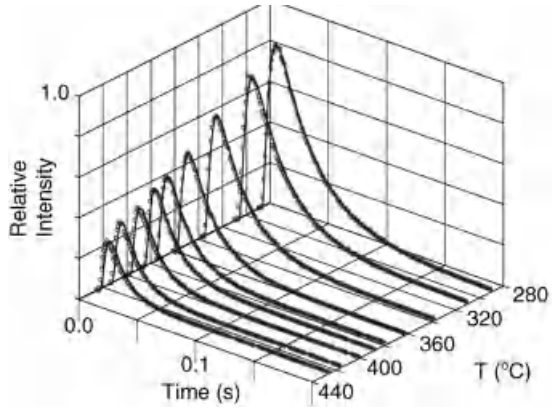


Figure 22.16 TAP spectra obtained by pulsing an argon–butane mixture over an oxygen-treated VPO sample.

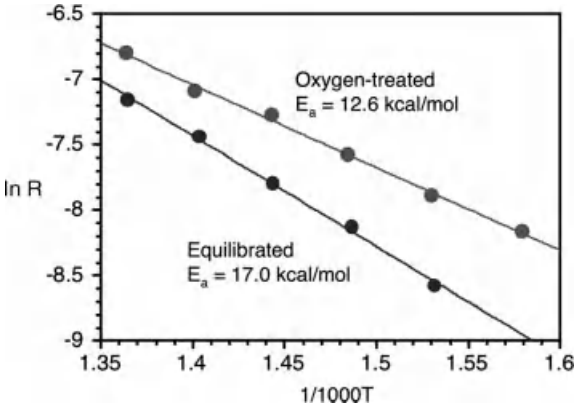


Figure 22.17 Arrhenius plots for butane conversion over reactor-equilibrated and oxygen-treated VPO.

VPO oxygen treatments were also performed at different temperatures and lengths of time. Figure 22.19a shows the MA response for a set of reactor-equilibrated VPO samples that were all oxygen-treated at the same temperature but for different periods. Figure 22.19b indicates the *n*-butane conversion and MA selectivity as a function of the oxygen treatment time. The oxygen exposure time influences both the activity and selectivity of the VPO sample. The data indicate that there is an optimum oxygen treatment time for both activity and selectivity.

In addition to measurements of activity and selectivity, individual response curves can be analyzed to obtain kinetic parameters as a function of another catalyst characteristic. For example, the absolute number of active sites can change as a result of a change in the catalyst surface area, crystal morphology, or surface oxidation

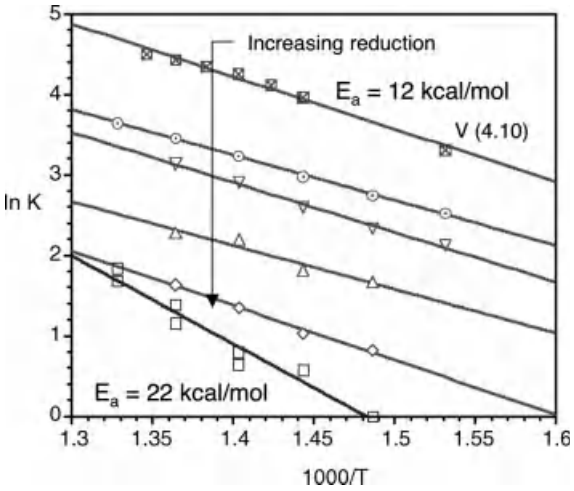


Figure 22.18 Arrhenius plots for butane conversion versus VPO oxidation state.

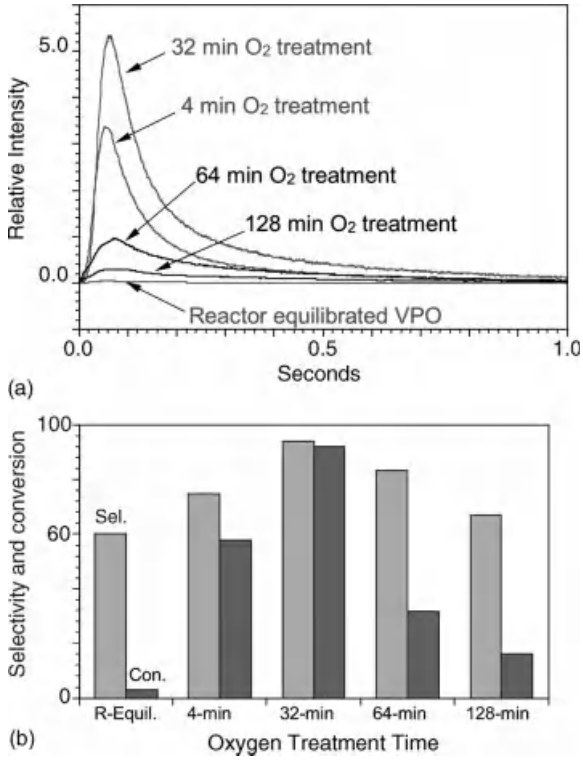


Figure 22.19 (a) MA pulse response curves collected at the same temperature (420 °C) on a set of reactor-equilibrated samples heated in an atmosphere of oxygen at 450 °C for different lengths of time. (b) Comparison of the conversions and selectivities for the different oxygen-treated samples.

state. During reaction, the available number of active sites can change as a result of adsorption. The specific reactivity of sites can change because the composition or structure of the sites changes. A process that causes a change in the number of active sites may also cause a change in structure of the active sites. In this case, the changes may compensate one another. Figure 22.20 displays the apparent kinetic rate constant for a series of reactants as a function of the degree of oxidation of the catalyst. Each point is determined from a response curve. The kinetic rate constant reflects both global and local characteristics and indicates how the VPO catalytic properties evolve as it is reduced.

The TAP reactor system has evolved since its initial conception in the late 1970s into a powerful tool for characterizing complex industrial catalysts. The experimental results obtained in the VPO studies described above indicate the range of experiments that can be performed using a TAP reactor system. Data obtained under steady-state conditions at atmospheric pressure can be directly compared with transient data obtained under vacuum conditions using the same catalyst sample in the same microreactor.

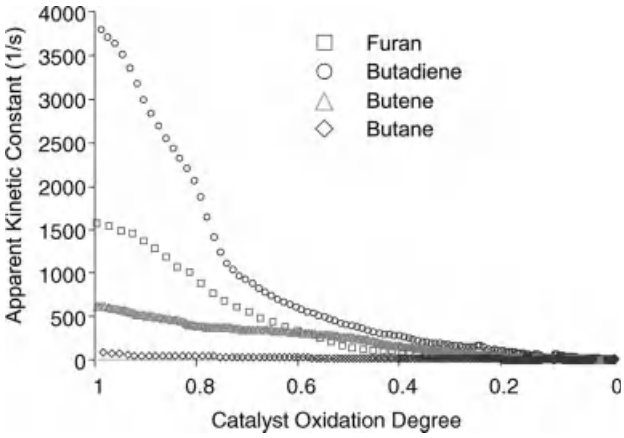


Figure 22.20 Apparent kinetic rate constant for different C_4 reactants as a function of catalyst oxidation degree.

A primary concern in the development of industrial catalytic materials is to establish direct, reproducible correlations between changes in surface composition and changes in activity and selectivity under reaction conditions. The nanoscale features on surfaces that give rise to catalytic properties are generally formed kinetically under non-steady-state reaction conditions, and continue to evolve over the life of a catalyst. The TAP experiment provides non-steady-state reaction data from which quantitative kinetic parameters can be directly extracted using well-established mathematical models. A unique and significant aspect of the kinetic data obtained in TAP vacuum pulse-response experiments is that it can be obtained at zero coverage and reflects the intrinsic kinetic characteristics of a catalytic material. Then, as illustrated with the VPO system, changes in the kinetic characteristics obtained in a series of TAP experiments can be directly related to changes in the surface composition (e.g., surface oxygen concentration) and/or structure of a complex catalyst. Thus, the TAP technique is an essential tool for developing structure–activity relationships on complex, ill-defined catalytic systems.

22.3
Steady-State Isotopic Transient Kinetic Analysis (SSITKA)

22.3.1
Introduction

The catalytic properties (e.g., reaction rate, selectivity, and stability with time on-stream) of a solid surface are determined by its chemical composition and structure *on the atomic scale*. Therefore, the design and improvements of a catalyst's properties require a deep understanding of the *microkinetics* (detailed kinetics of each elementary reaction step) and *mechanism* occurring on the catalyst surface. This requirement

includes the use of *in situ* techniques for obtaining site reactivity and characterization data of the chemical composition and structure of both the active surface catalytic sites and the accommodated adsorbed reaction intermediate species (catalytic adsorbed phase).

The SSITKA technique was initially developed by Happel [29], Bennett [30], and Biloen [31] who were inspired by the earlier seminal work of Tamaru [32] aimed at the use of stable isotopes in homogeneous or heterogeneous catalytic reactions that would permit in a direct way the *in situ* evaluation of forward and reverse reaction rates of individual elementary reaction steps and the surface concentrations of truly *active* reaction intermediates. These measurements are impossible using an overall kinetic rate determination. In the SSITKA technique, once the steady state of the overall reaction rate has been reached, an abrupt switch (step change) of the isotopic composition of the reaction mixture is made, when one of the reactants is suddenly replaced by the same chemical species but with one of its atoms replaced by one of its stable isotopes, while at the same time monitoring (use of gas detectors, usually a mass spectrometer) the relaxation and evolution of both unlabeled and labeled reactants and reaction products, respectively, experimental details of which are given below. In this gas isotopic switch, the ongoing surface catalytic reaction is not disturbed since the partial pressures of reactant components, temperature, and space velocity are kept constant [33–36]. Therefore, the overall reaction remains at the steady state but a transfer of the isotope element from the reactant molecular species through the various active reaction intermediates which contain the equivalent nonisotope element to the various reaction products occurs. This process is properly termed "tracing of the reaction path," during which both gas and surface adsorbed phase dynamics are developed. Based on the gas-phase transient isotopic response curves recorded, usually by online mass spectrometry (MS) with a fast response ($\sim$50 ms) inlet system (SSITKA–mass spectrometry), various intrinsic kinetic parameters can be determined as described in the following section, while the use of a suitable spectroscopic technique [e.g., transmission Fourier transform infrared (FTIR), diffuse reflectance infrared Fourier transform spectroscopy (DRIFTS), or Raman] would also allow the identification of the chemical composition and structure of both the truly active reaction intermediate and inactive (spectator) species [37–44] (e.g., SSITKA–DRIFTS methodology).

The SSITKA technique was first employed successfully in the heterogeneous CO catalytic hydrogenation reaction, for which excellent reviews [33–35] and recent work [45–47] on the subject have appeared. These studies permit the estimation of the abundance, N_p [concentration (mol g^{-1}) or surface coverage (θ) based on the exposed metal surface], and overall mean residence time, τ_p (s), of the true surface reaction intermediate species that are found in the reaction path from the CO reactant to the given final hydrocarbon product, P. These kinetic parameters can also be determined on practical heterogeneous catalytic surfaces without the need to know the prevailing microkinetics and mechanism, as will be illustrated in the following section. Modeling of the gas-phase transient isotopic response curves recorded and based on certain mechanistic assumptions, activity distribution, $f(k)$, surface

concentrations or coverage (θ) of individual adsorbed reaction intermediates, and discrimination among rival mechanisms are obtained [33–35].

During the last 20 years, rigorous application of the SSITKA technique to several gas–solid heterogeneous catalytic reactions and using MS or special GC–MS arrangements has significantly enhanced our understanding of associated fundamental kinetic and mechanistic issues. For example, ammonia, methanol, and vinyl acetate syntheses, ammonia oxidation, ethane hydrogenolysis, methane oxidative coupling, methane partial oxidation, CO oxidation, selective reduction of NO by CO or H_2, propylene partial oxidation, propane dehydrogenation, and isobutene hydrogenation and dehydrogenation are the reactions mostly investigated by the SSITKA technique, as reported by Hammache *et al.* [48].

Recently, important kinetic and mechanistic information regarding the water-gas shift reaction [39, 40, 49–61] and the H_2 selective catalytic reduction (SCR) of NO [62–67] was obtained after applying the SSITKA–MS–DRIFTS methodology. These two specific reactions are selected as key examples for a detailed illustration of the SSITKA technique in the following section.

The above historical background of the SSITKA technique strictly relates to applications in gas–solid heterogeneous catalytic reactions. However, recent and interesting other applications of SSITKA have appeared. Bajusz and Goodwin [68, 69] studied the adsorption behavior of N_2 in zeolites, demonstrating the ability of SSITKA to measure heats of adsorption for N_2–O_2 mixtures in NaCaX zeolite. A mathematical analysis of the application of SSITKA in studying adsorption and desorption processes under equilibrium conditions has also appeared [70]. This analysis provides (a) the exchange rate between the gas and surface phases at the steady state, (b) the intrinsic desorption rate as a function of time under SSITKA, free of readsorption effects, and (c) the intrinsic dependence of the desorption rate constant as a function of surface coverage, $k_d(\theta)$, free of induced heterogeneity effects.

Recently, Davies *et al.* [71] performed SSITKA measurements on the adsorption–desorption of CO over Pt and PtRu surfaces used in proton exchange membrane (PEM) fuel cells at CO concentrations in the 100–1400 ppm range in hydrogen carrier. It was found that at the level of 100 ppm CO in the feed, the exchange rate of CO on PtRu was considerably lower than that on Pt, probing the improved CO tolerance of the PEM fuel cell of PtRu compared with Pt. The important phenomenon of hydrogen spillover in supported metal catalysts was recently investigated by Mihet *et al.* [72] over a series of supported Ni catalysts. A modified SSITKA chemisorption experiment: 2 vol.% D_2–Ar (T) $\rightarrow$ Ar (T) $\rightarrow$ 2 vol.% H_2–Ar (T,t) was performed, where the transient isotopic responses of D_2, HD, and H_2 were modeled [73]. It was shown that this methodology was sensitive enough to probe the effect of temperature and chemical composition of the support on the surface mobility (Ni to support) of adsorbed H species.

The kinetics and mechanism of oxygen exchange over metal oxides and oxygen transport from the metal to the metal oxide support over supported metal catalysts was best investigated using SSITKA (2 vol.% $^{16}O_2$–98 vol.% Ar $\rightarrow$ 2 vol.% $^{18}O_2$–96 vol.% Ar–2 vol.% Ne) in a flow microreactor coupled with mathematical modeling

of the obtained transient oxygen isotopic responses, according to Sadovskaya *et al.* [74]. Rates of oxygen adsorption and desorption on Pt and support (CeO_2–ZrO_2–La_2O_3) surface sites, rates of oxygen transfer (spillover) from Pt to the support, oxygen diffusion coefficient (D, $m^2\,s^{-1}$) in the bulk of metal oxide support, and the amount of mobile oxygen present in the support in the range 650–850 °C were estimated.

SSITKA ^{16}O–^{18}O exchange experiments were recently performed on commercial oxygen storage ceria-based materials for the evaluation of the effect of calcination temperature on the surface and bulk oxygen mobility of these materials [75]. The reader can also obtain a deep understanding of oxygen and hydrogen surface mobility measurements using SSITKA in a recycled closed reactor system in a book chapter by Duprez [76].

22.3.2 SSITKA Theory

22.3.2.1 Kinetic Parameter Estimation

A schematic of the important experimental components needed for the application of the SSITKA technique is shown in Figure 22.21, where the microreactor used could be either a DRIFTS cell (Figure 22.21) or a typical PFR or CSTR system [34, 36]. Figure 22.22 presents an illustrative scheme of the application of SSITKA in studying a reversible gas–solid heterogeneous catalytic reaction:

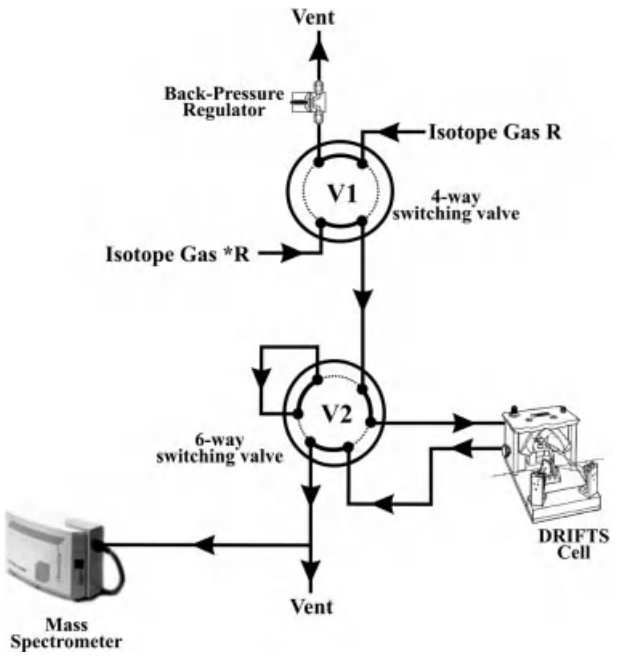


Figure 22.21 Important experimental components for performing *operando* SSITKA studies.

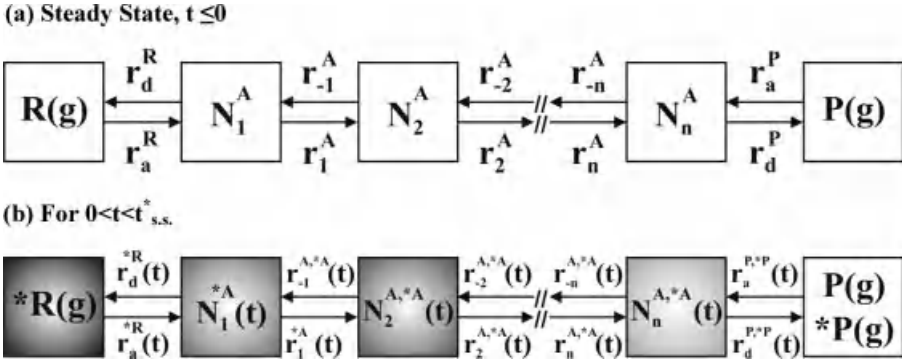


Figure 22.22 Catalyst surface compartmental model showing the isotopic distribution between *n* pools in series (*n* different active reaction intermediates) during SSITKA (R → *R).

$$\mathrm{R(g)} + \text{other reactants(g)} \leftrightarrow \text{A intermediates(ads)} \leftrightarrow \mathrm{P(g)} + \text{other products(g)} \tag{22.11}$$

This scheme was largely adopted from a review by Shannon and Goodwin [33], and depicts the "compartmental model" that best describes the SSITKA experiment. In this model, the catalyst surface is considered to be composed of a system of interconnected "pools" or "compartments" [35], where each pool represents a homogeneous subsystem within the reaction pathway, which reflects a unique adsorbed *active reaction intermediate* species having the same site reactivity, k_n. It is also considered that there is no mixing time associated with each pool except for the mean residence time of the given reaction intermediate, τ_n (s).

After a steady state has been achieved (Figure 22.22a), it is expected that the rate of reaction, r_R (mol R s^{-1} or mol R g_{cat}^{-1} s^{-1}) is the result of the net rate of transfer (sum of rates of input – sum of rates of output) of the nonisotopic species of interest in reactant R from each pool. Furthermore, a constant abundance, N_i (mol) ($i = 1, 2, \ldots, n$), surface concentration (mol m^{-2} or mol g_{cat}^{-1}) or surface coverage (θ) of intermediate species A in the ith pool (the chemical nature of A is different in each ith pool) is established. At time $t = 0$, an instantaneous fast switch of the reaction feed gas stream containing the reactant R to an equivalent one having the same chemical composition and flow rate, and which contains the isotopically labeled species in R*, is made via a four-way chromatographic valve of "zero" dead volume (Figure 22.21) [36].

At $t \geq 0$, a nonideal "step change" [36] in the isotopic composition of R* is made at the inlet of the catalyst bed, and as a result of this the new isotope element is distributed only between the various active adsorbed reaction intermediates which are found in the "reaction path" to form eventually product P. Therefore, as the reactant R* passes through the catalyst bed volume and reacts on the catalyst surface, the new isotope element in R* is transferred via all the reaction intermediates A found in the reaction path from R to P to form eventually the new isotopic labeled P* (Figure 22.22b). Ultimately, the entire old isotope element is displaced by the new

isotope element. The distribution of the isotope element in each reaction intermediate (*i*th pool) is strictly dependent on the intrinsic kinetic rates r_i between the pools and the intrinsic reactivity k_i associated with each adsorbed reaction intermediate A. The transient isotopic rate of product P and P* is decreasing and increasing, respectively during the SSITKA experiment, where after some time a new steady state is achieved ($r_P = r_{P^*}$). In the absence of any mass isotopic effects during SSITKA, the following relationship holds:

$$r_P^{s.s.} = r_P(t) + r_{P^*}(t) \tag{22.12}$$

where $r_P^{s.s.}$ is the overall steady-state reaction rate (mol s^{-1}) determined under the nonisotopic feed gas composition reaction conditions, $r_P(t)$ is the transient rate of product P at a given time *t*, and $r_{P^*}(t)$ is the transient rate of product P* (containing the isotope element) at the same time. Based on a material balance applied at steady-state reaction conditions for an open flow reactor, the following relationship applies:

$$r_P^{s.s.} = F_T y_P^{s.s.} \tag{22.13}$$

where F_T (mol s^{-1}) and $y_P^{s.s.}$ are the total molar flow rate of reaction gas stream and the mole fraction of product P, respectively, measured at the exit of the reactor. A normalized transient response, $Z_P(t)$, can be defined as

$$Z_P(t) = \frac{y_P(t)}{y_P^{s.s.}} \tag{22.14}$$

where, at $t = 0$ (isotopic switch), $Z_P(t) = 1.0$, and at $t \to t_{s.s.}^*$ (new steady state under the isotopic feed gas stream), $Z_P\left(t \to t_{s.s.}^*\right) = 0.0$. The following relationship applies:

$$Z_P(t) + Z_{P^*}(t) = 1.0 \quad \left(0 \le t \le t_{s.s.}^*\right) \tag{22.15}$$

In the absence of any perturbation in the reaction system (e.g., flow rate, pressure, or *T*) and of any mass isotope effects, the functions $Z_P(t)$ and $Z_{P^*}(t)$ are mirror image of each other and they should cross each other at $Z = 0.5$, as illustrated in Figure 22.23. The $Z_I(t)$ function reflects the gas-phase holdup from the switching valve through the reactor to the detector (e.g., mass spectrometer) when the SSITKA gas switch R–other reactants–Ar–He $\rightarrow$ R*–other reactants–He is made; more details on the $Z_I(t)$ function were reported previously [36].

22.3.2.1.1 **Mean Surface Residence Time** One of the kinetic parameters measured in SSITKA is the mean surface residence time, τ_P (s), of all of the surface adsorbed *active* reaction intermediates (Figure 22.22) which lead exclusively to a given reaction product P. This quantity is equivalent to the area between the Z_I and Z_P transient response curves (Figure 22.23) and is given by the following relationship:

$$\tau_P(s) = \int_0^{t_{S.S}^*} [Z_P(t) - Z_{Ar}(t)]dt \tag{22.16}$$

It is clear that this quantity can be estimated regardless of the underlying microkinetic model or reaction path. Its value is strictly determined by the measured $Z_P(t)$

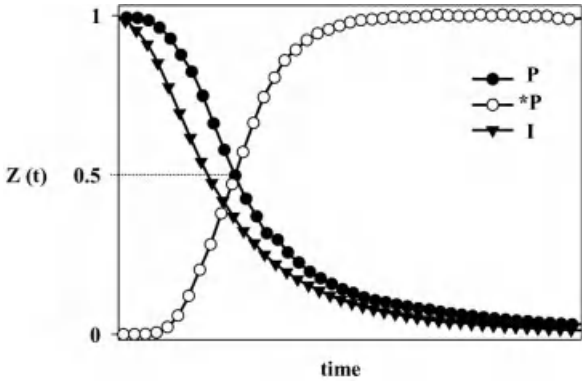


Figure 22.23 Typical SSITKA experiment [R (reactant) ⇌ A (adsorbed reaction intermediates) ⇌ P (product)]. I = inert tracer (e.g., Ar, Kr, or He).

versus time response curve, which reflects the prevailing microkinetics and mechanism of the reaction under investigation.

In the case of Figure 22.22, where reactant R and product P are considered to interact with the catalyst surface by a reversible chemisorption step, it is implied that adsorbed R and P in a molecular form (no dissociation takes place) are considered as reaction intermediates. For example, chemisorption of product P is considered as an important elementary step in the mechanism of reaction:

$$P + s \rightleftharpoons P{-}s \tag{22.17}$$

where this step may turn out to be rate determining. An example is the case of CO hydrogenation on Rh/Al_2O_3 [77, 78], where SSITKA experiments revealed that molecularly adsorbed CO was the abundant chemisorbed species, leading to the conclusion that CO dissociation is the rate-determining step.

In the case where readsorption and desorption processes of product species P on *active reaction sites* are such (heat of adsorption, *T*, partial pressure of P) that the surface coverage of product P is practically zero, but readsorption/desorption could occur on other *inactive catalytic sites*, this result would then lead to a measurable surface concentration for adsorbed P. The latter would overestimate the concentration of active intermediates (see Section 22.3.2.1.2). However, this problem in estimating the true kinetic mean residence time, τ_p, was first addressed by Shannon and Goodwin [33], who proposed an experimental methodology to overcome the problem, in which SSITKA experiments with different catalyst bed volumes but the same space velocity are performed. In this case, the shape of the $Z_P(t)$ transient response curve is different but the estimated τ_P [Eq. (22.16)] might be independent of catalyst bed volume, suggesting that readsorption/desorption of product species P is kinetically insignificant. Extrapolation of the linear part of τ_p^{meas} (s) versus V_{bed} (cm^3) curve as the latter quantity approaches zero allows the estimation of the true kinetic τ_p free of readsorption effects [33].

22.3.2.1.2 **Concentration of Active Reaction Intermediates** Based on the experimental response curves of $Z_I(t)$ and $Z_P(t)$ recorded, and a material balance, the concentration

(mol g_{cat}^{-1}) of all the *active* adsorbed reaction intermediates, $N_p = N_1 + N_2 + \ldots + N_n$ (Figure 22.22) leading to the formation of product P can be estimated according to the following relationship:

$$N_P(\text{mol } g_{cat}^{-1}) = (F_T/W)y_{s.s.}^{P}\int_0^{t^*_{s.s.}}[Z_P(t) - Z_{Ar}(t)]dt \tag{22.18}$$

where $y_P^{s.s.}$ is the steady-state concentration (mole fraction) of product species P measured experimentally under the nonisotopic reaction feed stream, and W is the amount of catalyst used. Equation (22.18) is applicable without the need to know the true microkinetics and mechanism operated for the catalytic reaction system under investigation. This is the power of SSITKA technique, which permits the accurate *in situ* determination of the concentration of only the *active* reaction intermediates and not of any inactive (spectator) species.

It is pointed out for the first time that the fact that the term $(F_T/W)y_P^{s.s.}$ appearing in Eq. (22.18) represents the measurable steady-state intrinsic kinetic rate of reaction (mol g_{cat}^{-1} s^{-1}), which is usually measured at low conversions, X_R (%) (e.g., $2.0 < X_R < 10.0$), means that extrapolation of the τ_p [Eq. (22.16)] versus X_R curve to $X_R \rightarrow 0$ (a series of SSITKA experiments in this range of X_R) would provide the value of τ_P associated with an individual *catalyst particle*, thus strictly accounting for any axial concentration gradients in the catalytic bed even at these low conversions.

Modeling of the $Z_P(t)$ or $Z_{P^*}(t)$ transient response curve allows the determination of the concentration of individual adsorbed active reaction intermediates, N_i, as demonstrated to a great extent in the case of CO hydrogenation (methanation, higher hydrocarbon and alcohol formation) [33, 35, 77, 78]. In particular, in the case of the CO–H_2 reaction towards CH_4 formation ($S_{CH_4} > 90\%$) over Rh/γ-Al_2O_3, the concentrations of the two important carbon-containing reaction intermediates, CO-s and CH_x-s, were estimated after modeling (no kinetics assumed) the $^{13}CO(g)$ and $^{13}CH_4(g)$ transient response curves measured experimentally in a CSTR microreactor [77, 78].

22.3.2.1.3 **Turnover Frequency (TOF_{ITK})** The turnover frequency (TOF, s^{-1}), first proposed in 1968 by Boudart and Djèga-Mariadassou [79], represents the number of product molecules produced per catalytic site per unit time for a given temperature, pressure, reaction feed composition, and extent of reaction. The key importance of evaluating correctly the TOF (site reactivity) in developing better or improving catalyst formulations is now widely accepted. In the special class of supported metal catalysts, where the support does not offer true catalytic sites, the measurement of metal dispersion by H_2 chemisorption allows the determination of TOF_{chem} [79, 80]. The latter parameter, however, is rather a measure of specific rate than a true site activity [79] simply because the catalytically active surface sites and the surface sites accommodating H species may not be the same. In excellent articles written by Goodwin *et al.* [80], and by Che and Bennett [81], the true TOF and TOF_{chem} are discussed further.

As previously outlined, SSITKA allows the determination of the kinetic parameters N_P (mol) and τ_P (s) under reaction conditions. Then, the steady-state rate of reaction, R_P (mol s^{-1}) is given by the following relationship:

$$R_P = \frac{N_P}{\tau_P} \tag{22.19}$$

Based on the definition of TOF and Eq. (22.19):

$$\mathrm{TOF}_{\mathrm{ITK}} = \frac{R_P}{N_P} \tag{22.20}$$

where $\mathrm{TOF}_{\mathrm{ITK}}$ (s^{-1}) represents the true TOF based on the number of active sites determined by SSITKA [33, 80]. Here, it is important to mention the assumption made that for every adsorbed reaction intermediate found in the catalytic cycle it corresponds one "active site." No discrimination among the types of active sites is made (e.g., number of surface metal atoms comprising the active site).

In an elegant book chapter entitled "Turnover frequencies in metal catalysis: meanings, functionalities and relationships" by Goodwin *et al.* [80], the following relationship is demonstrated to hold:

$$\mathrm{TOF}_{\mathrm{chem}} \leq \mathrm{TOF}_{\mathrm{site}} \leq \mathrm{TOF}_{\mathrm{ITK}} \tag{22.21}$$

where $\mathrm{TOF}_{\mathrm{site}}$ is measured based on the number of *active sites* as opposed to $\mathrm{TOF}_{\mathrm{ITK}}$ measured based on the number of *active reaction intermediates*. Therefore, $\mathrm{TOF}_{\mathrm{ITK}}$ (use of SSITKA) can be employed as a guide to how much $\mathrm{TOF}_{\mathrm{chem}}$ may differ from $\mathrm{TOF}_{\mathrm{site}}$, and it is definitely a much more accurate and reliable turnover frequency than $\mathrm{TOF}_{\mathrm{chem}}$ in describing $\mathrm{TOF}_{\mathrm{site}}$ [80].

22.3.2.1.4 **Reactivity Distribution, *f*(*k*)** Bell and co-workers [82] were the first to describe an advanced mathematical analysis of SSITKA response data for the CO to methane hydrogenation reaction in order to provide convincing evidence that the formation of methane proceeds via the dissociation of adsorbed CO and subsequent hydrogenation of adsorbed surface carbon, the latter being of various kinds of structures and reactivity, thus revealing the heterogeneous nature of active sites. These different carbon forms could react independently to produce methane as shown in Figure 22.24, and the activity of each form is characterized by a reactivity distribution function, $f(k)$. Thus, the total rate of $^{13}CD_4$ production during the switch $^{13}CO–D_2 \rightarrow {}^{12}CO–D_2$ can be described by the following equation:

$$r^{13}\mathrm{CD}_4(t) = \theta_0^* \int_0^\infty k f(k) \mathrm{e}^{-kt} \mathrm{d}k \tag{22.22}$$

where θ_0^* is the initial coverage of ^{13}C-labeled carbon and k is the first-order rate coefficient in the case where only one form of carbon with a uniquely defined reactivity exists. For the latter case, it is considered that $r^{13}\mathrm{CD}_4(t) = \theta_0^* k \mathrm{e}^{-kt}$ based on kinetic studies of carbon hydrogenation to methane. It is important to note that no assumption about the form of $f(k)$ is required. Later, Hoost and Goodwin [83]

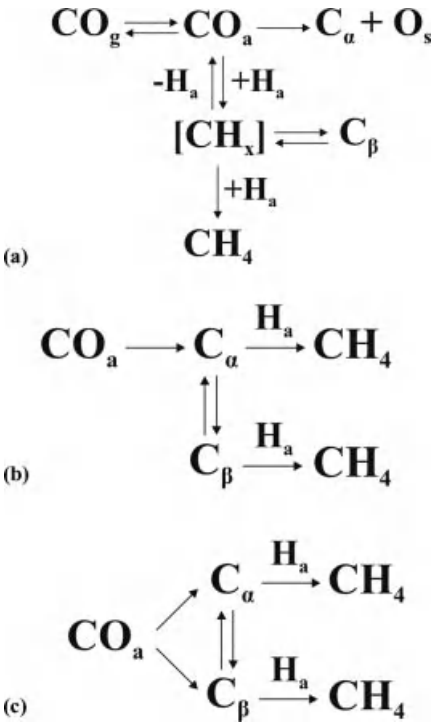


Figure 22.24 Different reaction paths of methane formation through different forms of adsorbed carbon reaction intermediate species (C_α, C_β, CH_x) [82].

proposed a different numerical method for the determination of $f(k)$ first applied to CO hydrogenation over an Ru/SiO_2 catalyst.

Figure 22.25 shows a bimodal distribution of the rate constant k obtained after applying Eq. (22.22) and the numerical analysis proposed, and using the experimental response curve $Z(t) = r^{13}CD_4(t)/r^{13}CD_4{}^{s.s.}$ measured over a Ru/SiO_2 catalyst (D_2:CO = 3:1, $T = 463$ K, $P = 1$ atm) [82]. The right peak was assigned to the hydrogenation of an active carbon species, C_α, and the left peak (smaller k values) to the hydrogenation of a second type of carbon species, C_β, less active than C_α. Average rate constants $k_{C_\beta} = 3.3 \times 10^{-2}\,s^{-1}$ and $k_{C_\alpha} = 1.8 \times 10^{-1}\,s^{-1}$ were estimated. Furthermore, the average surface composition (mole fraction) of C_β was found to be twice that of C_α [82]. Other examples of the application of the above advanced mathematical analysis of SSITKA experiments can be found elsewhere [84].

22.3.2.2 Mechanistic Implications

The simplification of treatment provided by the SSITKA technique in avoiding problems of reaction kinetics in discriminating mechanistic models of a given heterogeneous catalytic reaction was first set forth by Happel [35]. By modeling the transient isotopic responses measured, and after introducing the compartmental scheme (Figure 22.22) and a set of elementary reaction steps (mechanistic model),

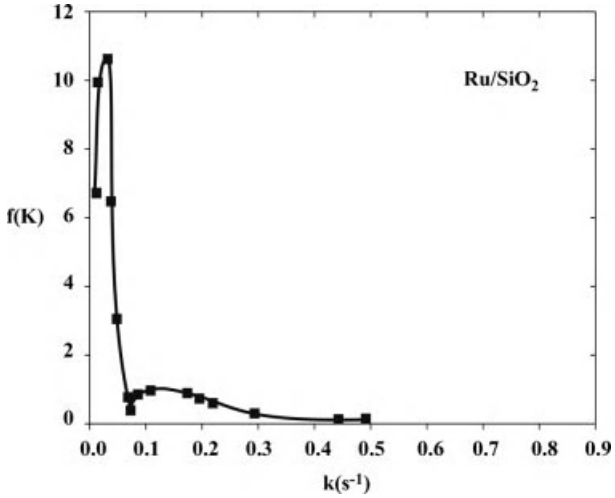


Figure 22.25 Plot of $f(k)$ versus k (s^{-1}) for the methanation reaction over Ru/SiO_2 catalyst [82].

but without assuming the kinetics of any elementary reaction step, it is possible to discriminate rival mechanistic schemes that are not possible, or in many cases questionable, when the familiar Langmuir–Hinshelwood–Hougen–Watson (LHHW) development is followed instead. Happel's approach was used in several catalytic reaction systems [33, 47, 85, 86].

An elegant approach that makes use only of the basic kinetic parameters (τ_i, N_i) determined by SSITKA experiments (see Section 22.3.2.1) for disproving or substantiating a proposed reaction mechanism was reported recently [87]. This example relates to the controversial issue of whether CH_4 and CH_3OH formed by the CO hydrogenation reaction share or not a common intermediate or even the same kind of catalytic site. Let us consider the case where two different reaction products (P_1 and P_2) share a common reaction intermediate, and $\tau_1 > \tau_2$. Here, τ_i (residence time associated with the given product i) is equal to the sum of all the reaction residence times for the intermediates leading to that particular product i. Since the residence time of each reaction intermediate preceding the common intermediate is the same for both reaction routes, then at least one intermediate following the common intermediate leading to product 2 must be more active (smaller τ_i). Under steady-state reaction conditions, it is expected that the number of common intermediate species which participate in the reaction route of product 2 must be larger than that for product 1. This number then comprises the sum of all the subsequent intermediates which eventually form the reaction product. Hence the overall concentration of reaction intermediates N_1 leading to product 1 must be lower than N_2 leading to product 2 ($N_1 < N_2$). Based on the above, and the definition of reaction selectivity, S_P (%) $= r_P/\Sigma r_i \times 100$, where r_P is the rate of reaction leading to product p, and r_i is the rate of reaction leading to a given product i, then $S_1 < S_2$.

Figure 22.26 shows the mechanistic paths for methanol and methane formation following CO hydrogenation over Rh(111) as proposed in the literature [88, 89].

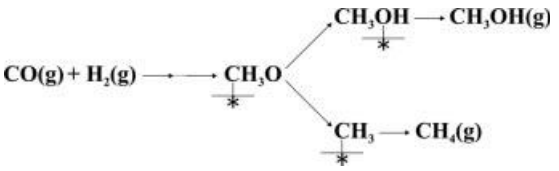


Figure 22.26 Proposed reaction pathways of CH_3OH and CH_4 formation during CO hydrogenation [87].

According to this mechanism, if the surface residence time of all reaction intermediates leading to CH_4 (τ_{CH_4}) is larger than that of CH_3OH, τ_{CH_3OH}, then according to the analysis mentioned in the previous paragraph [87] the selectivity to methanol should be larger than that to methane since they are formed on the same type of site and share common intermediates in their formation. However, the SSITKA experimental results obtained on Rh/SiO_2 [87] revealed that S_{CH_4} was nearly 120 times larger than S_{CH_3OH}, whereas the surface reaction residence times for CH_4 and CH_3OH were found to be 2.7 and 2.3 s, respectively. This important result strongly suggests that the reaction paths leading to CH_3OH and CH_4 on Rh/SiO_2 do not share a common intermediate and are not associated with the same kind of catalytic site. It was suggested [87] that the assumption of a single type of site would appear to be the fundamental cause of the failure of the mechanism shown in Figure 22.26 for CO hydrogenation on supported Rh.

22.3.3 Case Studies

22.3.3.1 The Water-Gas Shift Reaction ($CO + H_2O \leftrightarrow CO_2 + H_2$)

"Water-gas" is a mixture of water (H_2O) and carbon monoxide (CO) and it is used extensively in industry for the manufacture of ammonia, methanol, hydrogen (e.g., used in hydrotreating and hydrocracking of petroleum fractions, hydrogenation reactions in the petroleum refining and petrochemical industry), hydrocarbons (e.g., Fischer–Tropsch process), and metals (e.g., reduction of oxide ore) [90]. Developments in water-gas shift (WGS) catalysis, especially during the last decade, and a critical review of the mechanisms of the WGS reaction over several classes of catalysts have recently been reviewed [90, 91]. With the advent of the PEM fuel cell, local hydrogen production via fuel processors for auxiliary power generation is nowadays receiving considerable attention. Based on the current hydrogen production technologies [90], additional process purification steps are essential to obtain residual CO levels typically below 10 ppm for PEM fuel cell applications. In the light of the equilibrium-limited nature of the WGS reaction and the temperature dependence of the equilibrium constant (K_{WGS}) [90], catalysts with high activity at reaction temperatures close to 150 °C would be the foreseen solution. It has been stated [60] that control of the low-temperature WGS reaction rate can be achieved by designing catalysts that rapidly produce and dehydrogenate formate (–COOH) reaction intermediate species.

The industrial and economic importance of the WGS reaction as briefly mentioned above recently led to great scientific effort towards the understanding of its mechanism and kinetics with the goal of designing new and novel WGS catalytic systems. In this section, the effectiveness of SSITKA applied in the *operando* mode [92] by using DRIFTS and MS (SSITKA–DRIFTS–MS) to measure simultaneously the transient responses of isotopically labeled and unlabeled gas-phase products (use of MS) derived from the active adsorbed reaction intermediates (use of DRIFTS) upon the isotopic switch (see Section 22.2.2) is demonstrated for the WGS reaction performed over a 0.5 wt% $Pt/\gamma\text{-}Al_2O_3$ catalyst [58], where important mechanistic and kinetic information is provided.

Meunier [40, 93] recently presented in a very effective way the points one has to be aware of for the correct use of a DRIFTS cell in an *operando* study. Figure 22.27a illustrates that DRIFTS data are collected at the front part of the catalytic bed (~0.2 mm), whereas MS data are collected at the exit of the cell after the catalytic bed (~2 mm). In Figure 22.27b, the $^{13}CO_2$(g) signal associated with DRIFTS arises from the reaction occurring at the front part of the catalytic bed, whereas the $^{13}CO_2$(g) signal associated with MS arises from the whole catalyst bed and is influenced by the free gas-phase volume in the DRIFTS cell. The fact that the two normalized $^{13}CO_2$(g) response curves are practically identical proves that almost homogeneous surface coverage for the various active WGS reaction intermediates was established, the latter being largely a consequence of the differential reaction conditions applied (X_{CO} <10%). The experimental results to be presented next over a $Pt/\gamma\text{-}Al_2O_3$ catalyst [58] were obtained in a similar apparatus (Figure 22.28) using a commercial DRIFTS cell (Harrick, Praying Mantis/Perkin-Elmer FTIR, Spectrum GXI) and a quadrupole mass spectrometer (Balzers, Omnistar, 1–300 amu). A time constant $\tau = 5$ s was estimated for the DRIFTS cell, the analysis system (MS), and the flow-system used based on the Ar response (200 ml min^{-1}, $T = 200\,^{\circ}C$), which is similar to the Kr response ($\tau = 7$ s) [40].

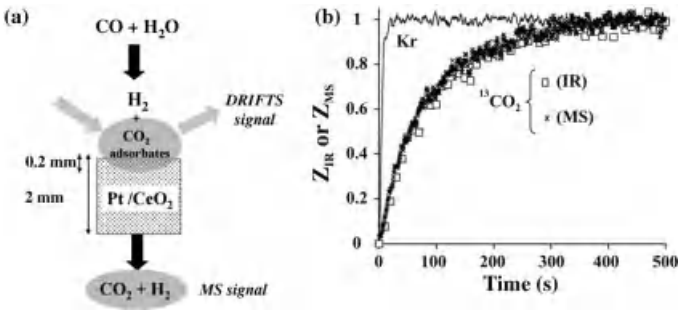


Figure 22.27 (a) Schematic representation of the catalyst bed and the zone probed by DRIFTS. Dimensionless concentration, $Z(t)$ of the Kr tracer (solid line), $^{13}CO_2$(g) measured by MS (×) at the exit of the DRIFTS cell, and $^{13}CO_2$(g) measured by DRIFTS at the inlet of catalyst bed (□) following the isotopic switch ^{12}CO–H_2O–Ar → ^{13}CO–H_2O–Ar/Kr(t) at 200 °C over a 2 wt% Pt/CeO_2 catalyst [40].



Figure 22.28 *Operando* (DRIFTS–MS) experimental setup at the Heterogeneous Catalysis Laboratory of the University of Cyprus.

22.3.3.1.1 ***Operando* SSITKA–DRIFTS–MS on Pt/γ-Al_2O_3: Chemical Structure of Active and Inactive Reaction Intermediates of the "Carbon Path"** Figure 22.29a shows IR bands (2996, 2940, 2903 cm^{-1}) characteristic of the νCH and $\delta CH + \nu OCO_a$ vibrational modes recorded during *operando* SSITKA–DRIFTS–MS on a 0.5 wt% Pt/γ-Al_2O_3 catalyst [58], and which correspond to formate (COOH) species formed on γ-Al_2O_3. The IR bands recorded in the 1650–1300 cm^{-1} range (Figure 22.29b) correspond to the O−C−O stretching vibrational mode of *formate, carbonate,* and/or *carboxylate* species [58]. The important characteristic of these spectra is that more than two IR bands were recorded under ^{12}CO–H_2O, whereas two IR bands provided the red isotopic shift (2996 to 2989 and 2903 to 2892 cm^{-1}; Figure 22.29a), whereas a third IR band (2940 cm^{-1}) did not. It is noted that an adsorbed COOH structure provides two vibrational modes in this range. According to the experimental results in Figure 22.29a, there must be at least *one likely active* formate species that provides the red ^{13}C isotopic shift, and another one that must be considered as an *inactive* (spectator) species; it does not provide the red isotopic shift.

The most intense IR bands recorded at 1594 (band 1) and 1391 cm^{-1} (band 5) for the ^{12}CO–H_2O reaction mixture (Figure 22.29b, top graph) and after deconvolution of the spectrum was made could potentially be assigned to either OCO_{as} and OCO_s vibrational modes of formate or carbonate species. Since the intensity of these bands is about 10 times stronger than those reported in Figure 22.29a (νCH, exclusively to formate), and the ^{13}C red isotopic shift corresponding to the OCO vibrational modes is larger than that of νCH (see Figure 22.29a and b, bottom graph), it would be more accurate to analyze the transient behavior of formate species based on the latter vibrational mode if we know that on the present catalyst and for the experimental conditions used it is possible to differentiate between formate and carbonate adsorbed species. This point was resolved based on *in situ* $^{12}CO_2$ and $^{13}CO_2$ chemisorption/DRIFTS studies [58].

After the new steady-state (under the isotopic ^{13}CO–H_2O gas mixture) had been reached (Figure 22.29b, bottom graph), it is clearly seen that in the region

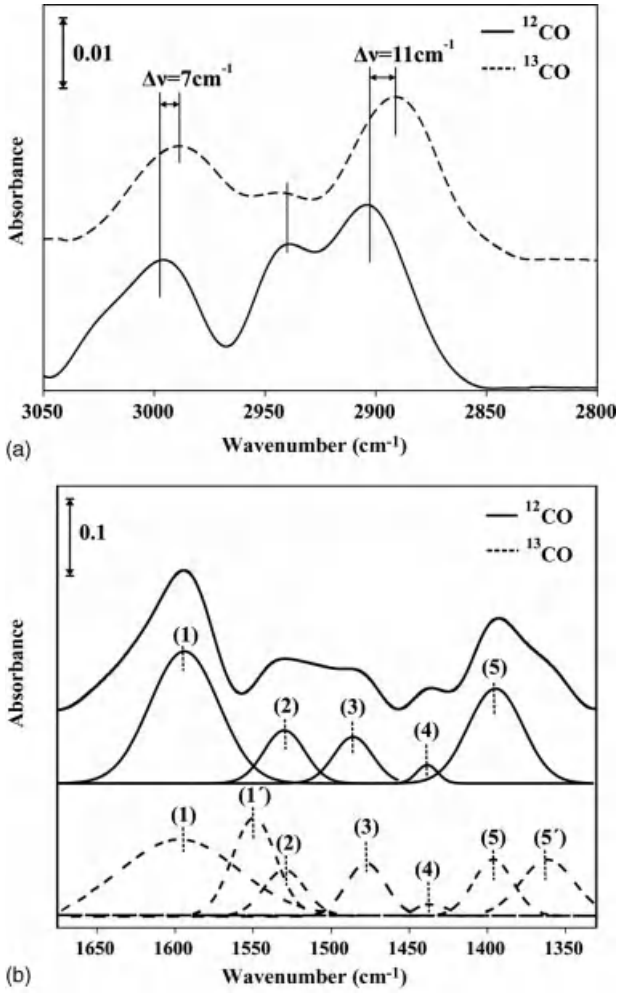


Figure 22.29 DRIFTS spectra recorded in the ranges 3050–2800 cm^{-1} (a) and 1670–1320 cm^{-1} (b) after *operando* SSITKA–DRIFTS–MS of the WGS reaction (3% ^{12}CO–10% H_2O–Ar–He → ^{13}CO–10% H_2O–Ar) over 0.5 wt% Pt/γ-Al_2O_3 at 350 °C. Deconvolution of recorded IR spectra in (b) is also shown [58].

1650–1500 cm^{-1} there exists one IR band that provided the red isotopic shift (band 1′), and a second band that did not show this isotopic shift (band 1). The infrared band at 1529 cm^{-1} (band 2, Figure 22.29b) corresponds to $O-C-O_{as}$ of carboxylate species, which is considered to be an *inactive* adsorbed species (no isotopic shift is observed). The IR bands at 1485 (band 3) and 1439 cm^{-1} (band 4) correspond to unidentate carbonates. It is seen that both kinds of carbonates do not give the red isotopic shift. Therefore, these carbonate species are also considered as *inactive* (spectator) species of the reaction. This is an important mechanistic result that indicates that gaseous CO_2 produced in a steady-state WGS reaction at 350 °C

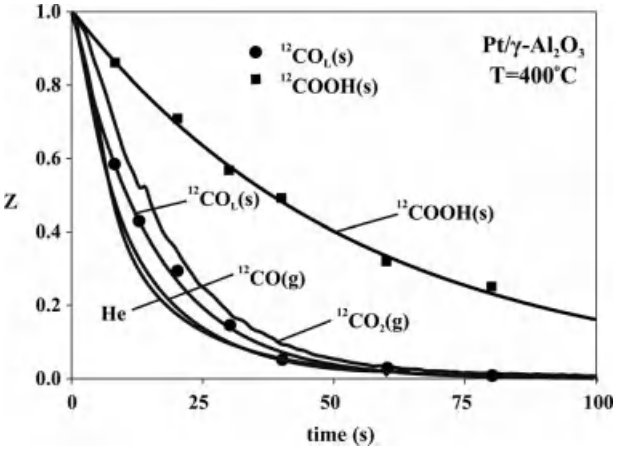


Figure 22.30 Normalized concentration (Z) versus time transient response curves of ^{12}C-labeled gaseous CO and CO_2, and adsorbed CO_L and –COOH species found in the "carbon path" of the WGS reaction over 0.5 wt% Pt/γ-Al_2O_3 catalyst at 400 °C recorded during *operando* SSITKA–DRIFTS–MS studies.

interacts *irreversibly* with surface lattice oxygen of the alumina support to form carbonates.

22.3.3.1.2 ***Operando* SSITKA–DRIFTS–MS on Pt/γ-Al_2O_3: Surface Concentration of Active Reaction Intermediates Found in the "Carbon Path"** Figure 22.30 shows transient response curves in terms of a normalized concentration, Z, for the $^{12}CO(g)$ and $^{12}CO_2(g)$ "carbon-containing" species recorded under the isotopic switch 3% ^{12}CO–10% H_2O–Ar–He (400 °C, 30 min) → 3% ^{13}CO–10% H_2O–Ar (400 °C, t) by MS (*operando* studies). The Z–$^{12}CO_L(s)$ and Z–$^{12}COOH(s)$ response curves were estimated from the DRIFTS spectra recorded every 8 s (use of MCT detector) based on the 2033 (linear adsorbed CO) and 1594 cm^{-1} (O−^{12}C−O ex. COOH) maximum band intensity, respectively, under the ^{13}CO–H_2O–Ar gas mixture according to the following relationship:

$$Z = \frac{I_{abs}(t) - I_{abs}(\infty)}{I_{abs}(0) - I_{abs}(\infty)} \tag{22.23}$$

where $I_{abs}(0)$ and $I_{abs}(\infty)$ refer to the absorbance recorded for $^{12}CO_L$ and $^{12}COOH(s)$ at steady state under the ^{12}CO–H_2O and ^{13}CO–H_2O gas mixtures, respectively. It is important to state here that in the case of the IR band at 1594 cm^{-1} which arises from both formate and carbonate species (Figure 22.29), the use of Eq. (22.23) for quantifying the formate species is valid. This is true because the Z function considers the net absorbance signal after subtracting $I_{abs}(\infty)$, which is the residual absorbance at any given time under the ^{13}CO–H_2O gas mixture, due to carbonates and formates that *do not participate* in the reaction path of the WGS reaction. In other words, the decrease in $I_{abs}(t)$ at 1594 cm^{-1} with time in the ^{13}CO–H_2O gas mixture is due only to formate species which interact with ^{13}CO, as will be further discussed below.

It is clearly seen (Figure 22.30) that the $^{12}CO(g)$ transient response curve lags slightly behind that of He, which is partly associated with the fact that a small concentration of adsorbed ^{12}CO on the catalyst surface under steady-state WGS reaction conditions exchanges with gaseous ^{13}CO, whereas $^{12}CO(g)$ still continues to react during the first 75 s of the transient ($Z_{He} = 0$ at $t \approx 75$ s) to give $^{12}CO_2(g)$. Also, the $^{12}CO_L(s)$ response curve lags behind that of $^{12}CO(g)$ (Figure 22.30) since except for the simple exchange of $^{12}CO_L(s)$ with gaseous ^{13}CO, the former must also be considered as a *precursor intermediate* that forms −COOH, where the latter species in turn decomposes to form $CO_2(g)$ and H(s) according to the following elementary reaction steps:

$$CO(g) + s \rightleftharpoons CO(s) \tag{22.24}$$

$$CO(s) + OH(s)^{I} \rightleftharpoons COOH(s)^{I} + s \tag{22.25}$$

$$CO(s) + OH(s)^{II} \rightarrow COOH(s)^{II} + s \tag{22.26}$$

$$COOH(s)^{II} \rightarrow CO_2(g) + H(s) \tag{22.27}$$

$$2\,H(s) \rightarrow H_2(g) + 2s \tag{22.28}$$

In Figure 22.30 it is shown that the $^{12}COOH(s)$ transient response curve lags behind that of $^{12}CO_2(g)$. If $CO_2(g)$ is assumed to be formed via formate decomposition, then the opposite behavior would have been expected, with the $^{12}CO_2(g)$ response curve lagging behind that of $^{12}COOH(s)$. The relative position of the $^{12}COOH(s)$ transient response curve to that of $^{12}CO_2(g)$ can be explained based on the mechanistic scheme comprising Eqs. (22.24)–(22.28). Elementary reaction steps (22.25) and (22.26) indicate that adsorbed CO on the catalyst surface interacts with two different kinds of hydroxyl groups on the alumina support surface [54]. The CO(s) interaction with hydroxyl group, $OH(s)^{I}$ [Eq. (22.25)] is considered *reversible*, whereas CO(s) can also interact *irreversibly* with another kind of hydroxyl group, $OH(s)^{II}$ [Eq. (22.26)]. The latter interaction leads in turn to an irreversible decomposition of formate towards $CO_2(g)$ and $H_2(g)$ [Eqs. (22.27) and (22.28)]. The elementary step depicted in Eq. (22.27) was proposed to be the rate-determining step for the Pt/CeO_2 catalyst based on D-isotopic kinetic studies [60, 94].

On the other hand, the first kind of formate species, $COOH(s)^{I}$ [Eq. (22.25)] cannot be decomposed to form $CO_2(g)$ and H(s) [Eq. (22.27)]. If formate decomposition requires the presence of a noble metal, then $COOH(s)^{II}$ species must reside in the proximity of the Pt–alumina interface. When the $^{13}CO–H_2O$ mixture is switched over the catalyst, the $^{12}COOH(s)^{I}$ species formed under $^{12}CO–H_2O$ treatment is expected to be replaced by $^{13}COOH(s)^{I}$ according to reaction steps depicted in Eqs. (22.24) and (22.25). This process will contribute to the reduction in the IR band recorded at 1594 cm^{-1} (band 1, Figure 22.29b) and also to the red isotopic shift (band 1′, Figure 22.29b). Similarly, the active $^{12}COOH(s)^{II}$ species will be replaced by the equivalent $^{13}COOH(s)^{II}$ [Eq. (22.26)], which in turn will produce $^{13}CO_2(g)$ [Eq. (22.27)], and this process will contribute to the diminution of the IR band at 1594 cm^{-1}, but it will also provide the red isotopic shift (band 1′, Figure 22.29b). Each

of the two processes described above and which involve $COOH(s)^{I}$ and $COOH(s)^{II}$ should be governed by different kinetics. The IR band 1 (Figure 22.29b) observed under the $^{13}CO–H_2O$ treatment could partly correspond to *inactive formate* irreversibly formed after interaction of CO and/or CO_2 with −OH groups.

Based on the above discussion, the $^{12}COOH(s)$ transient response curve shown in Figure 22.30 can be seen as the result of the sum of two transient rates of $^{12}COOH(s)$ disappearance due to the presence of two kinds of formate species, both of which gave the observed red isotopic shift (Figure 22.29b). Only the second species $COOH(s)^{II}$ that leads to the formation of $CO_2(g)$ and H(s) is considered to be a true *active* reaction intermediate, the first one, $COOH(s)^{I}$, being simply a *spectator*. The latter can exchange with $^{13}CO(g)$ [Eqs. (22.24) and (22.25)]. Therefore, the transient response curve of $^{12}COOH(s)^{II}$ would normally be expected to lie before the $^{12}CO_2(g)$ response.

An accurate quantification of the concentration of *active* reaction intermediates found in the "carbon path" and "hydrogen path" of the WGS reaction was conducted using SSITKA–MS in a quartz microreactor operated differentially as described previously [58]. Figure 22.31a presents dimensionless transient gas concentration response curves (Z) for H_2, HD, D_2, and Kr obtained after the isotopic switch 3% CO–10% H_2O–Ar–Kr (350 °C, 30 min) → 3% CO–10% D_2O–Ar (350 °C, t) was made. The decay of Kr gas concentration was used to monitor the gas-phase hold-up of the system [36]. Kr gas was used instead of He in order to avoid the overlap in the signal of $m/z = 4$ due to He^+ and $D_2{}^+$ ions in the MS analysis. At a given time, t, the sum of Z_is for the three dihydrogen isotopic species should be equal to one if a D-isotopic kinetic effect were absent. However, this was not the case since a normal D-isotopic kinetic effect is observed ($R_{H_2}/R_{D_2} \approx 2.0$). Figure 22.31b presents similar dimensionless transient gas concentration response curves for $^{12}CO_2$, $^{13}CO_2$, and He obtained after the isotopic switch 3% ^{12}CO–10% H_2O–Ar–He (350 °C, 30 min) → 3% ^{13}CO–10% H_2O–Ar (350 °C, t) was made over the same catalyst sample. No ^{13}C isotopic kinetic effect was observed since the steady-state rates for $^{12}CO_2$ and $^{13}CO_2$ under the two reaction mixtures were equal.

The concentration of active "H-containing" intermediate species, termed "H-pool," which is found in the "hydrogen path" of the WGS reaction was estimated based on the transient response curves of H_2, HD, and Kr (Figure 22.31a), details of which were reported [54]. The size of the surface "H-pool" was found to be 335 μmol H g^{-1} or 27.2 equivalent monolayers of surface Pt [$\theta_H = 27.2$, $Pt_s = 12.3$ μmol g^{-1})]. The concentration of active "C-containing" intermediate species ("C-pool") found in the "carbon path" of the WGS reaction was estimated based on the $^{12}CO_2$ and He response curves (Figure 22.31b) [54]. The size of the "C-pool" was found to be 1.1 μmol C g^{-1} or equivalently $\theta_C = 0.085$. Also, the mean residence time, τ_{CO_2} [Eq. (22.19)] was found to be about 2.0 s. Given the steady-state rate of CO_2 formation (0.5 μmol g^{-1} s^{-1}), and considering an upper value for the concentration of active formate species (1.1 μmol g^{-1}), then a lower bound for the rate constant, k, associated with the elementary step of CO_2 formation [Eq. (22.27)] can be estimated. The latter was found to be 0.45 s^{-1} (rate $= k \times C_{COOH}$). It is noted that the accuracy of the "H-pool" and "C-pool" estimation is within 5–8%.

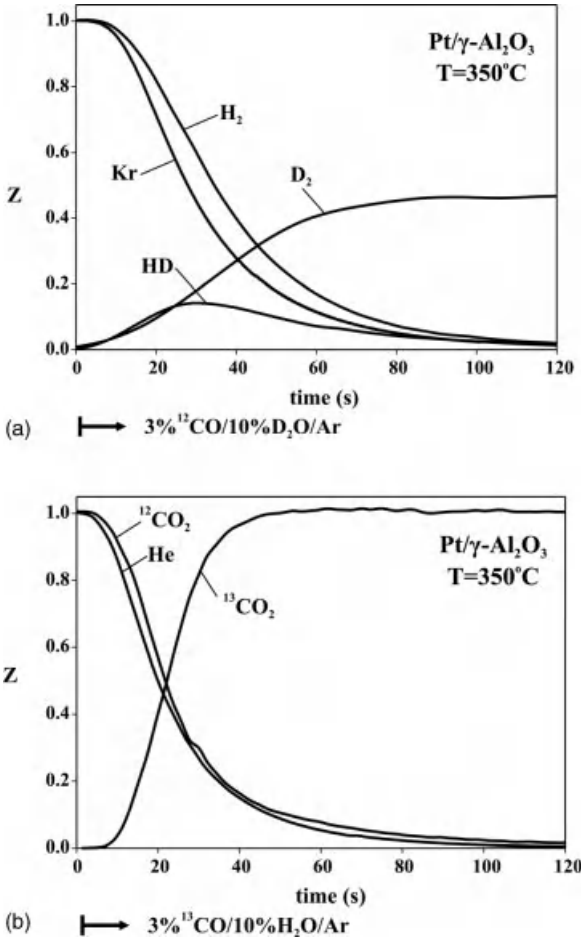


Figure 22.31 SSITKA–MS experiments performed to measure the surface concentration of active reaction intermediates found in the "hydrogen path" (a) and "carbon path" (b) of the WGS reaction at 350 °C over 0.5 wt% Pt/γ-Al_2O_3 catalyst [58].

The chemical nature of active "H-containing" intermediate species is considered to be that of labile hydroxyl groups (–OH), H (attached on surface O of the alumina support, and/or adsorbed on Pt), and formate (–COOH) species. The latter species was clearly identified by the SSITKA–DRIFTS experiments (Figure 22.29). The fact that the size of the "H-pool" measured was very large ($\theta_H = 27.2$) strongly suggests that OH/H species residing on the alumina support must participate in the reaction path forming CO_2 and H_2. It was reported [54] that the size of this "H-pool" is less than 35% of the monolayer value of –OH/H present on the alumina surface. Hence not all –OH/H species present on the alumina surface are energetically able to participate in the hydrogen reaction path of the WGS reaction. It was estimated [54] that this concentration of –OH/H species cannot be justified as being all

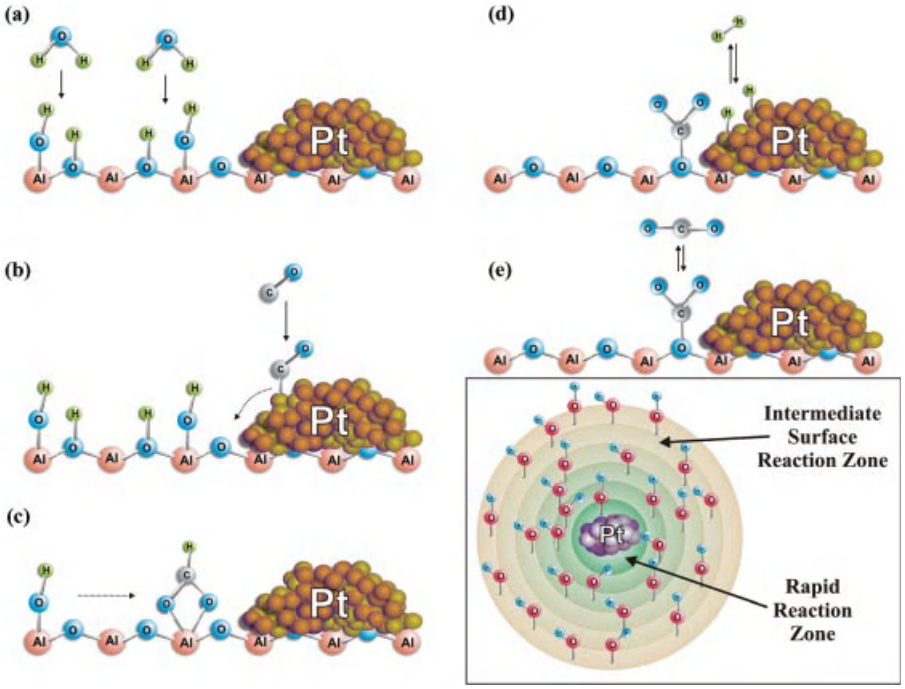


Figure 22.32 Catalytic cycle of WGS reaction on Pt/γ-Al_2O_3 according to *operando* SSITKA–DRIFTS–MS studies.

accommodated along the periphery of the Pt–alumina interface. There must be a region in the vicinity of Pt nanoparticles within which –OH/H participate in the "hydrogen path" of the WGS reaction.

Based on the above elementary reaction steps (22.24)–(22.28) and the estimated surface concentrations of *active* reaction intermediates participating in the "carbon path" and "hydrogen path" of the WGS reaction over the Pt/γ-Al_2O_3 catalyst, a pictorial view of the mechanism of the WGS reaction is illustrated in Figure 22.32.

The effect of Pt particle size (1.3–8.0 nm) on the surface concentration of active intermediates formed in the "carbon path" and "hydrogen path" of the WGS reaction and their chemical structure for the Pt/CeO_2 catalytic system was recently reported [95] using SSITKA–DRIFTS and SSITKA–MS methodologies. In this work, for the first time a transient isotopic experiment was presented that allows the quantification of the "redox" versus the "associative formate with –OH group regeneration" mechanism, the latter two being considered as the most prevailing mechanisms of the WGS reaction over supported metal catalysts.

22.3.3.2 The H_2-SCR of NO

Nitrogen oxides (NO, NO_2, and N_2O) released from both mobile and stationary sources are considered major air pollutants that contribute considerably to the formation of photochemical smog, acid rain, ozone depletion, ground-level ozone,

and greenhouse effects [96]. SCR has proven to be the most effective way for NO_x abatement in gasoline-powered cars by the use of three-way catalysts (TWCs) [97], whereas NH_3-SCR is the most widely implemented industrial NO_x control technology for stationary applications (e.g., power stations, gas boilers, incinerators, nitric acid plants) [98]. Low-temperature ($T < 200\,^{\circ}C$) effective and selective conversion of NO_x into N_2 present in automobile emissions is still a fatal shortcoming of TWC technology. On the other hand, industrial NH_3-SCR encounters several problems, namely catalyst deterioration, NH_3 slip, ash odor, air heaters fouling, and high investment and running costs [99]. Low-temperature industrial NO_x control also offers the advantage of placing the SCR unit at the end-of-the-pipe in existing installations, where NH_3-SCR cannot be used owing to space limitations in several industrial units.

The long-term prospects of using hydrogen as a fuel in internal combustion engines and of on-board autothermal reforming of diesel and gasoline fuel to produce hydrogen [100] make hydrogen the most environmentally benign reductant in the selective catalytic reduction of NO_x in an excess of oxygen environment (H_2-SCR). In addition, *low-temperature* ($T < 200\,^{\circ}C$) industrial H_2-SCR is more attractive than NH_3-SCR in the case where hydrogen is present on the industrial site (e.g., olefin plants, hydrogen production plants, etc.), given the drawbacks of the latter NO_x control technology [99]. The use of hydrogen as a reducing agent to eliminate NO_x from oxygen-rich exhausts at low temperatures ($T < 200\,^{\circ}C$) is relatively new, most of the information related to H_2-SCR having been published in the last 15 years [62–67, 100–104]. Supported Pt and Pd catalysts have been the most intensively studied, and the noble metal particle size and support chemical composition were found to influence strongly the activity and N_2 selectivity of these catalytic systems.

Given the importance of low-temperature H_2-SCR as a novel and green NO_x control technology for industrial applications, the design of optimum catalyst formulations requires extensive research to understand the kinetics and mechanism of this NO_x H_2-SCR process. Very few studies have been devoted so far to the use of the SSITKA technique to unravel important mechanistic aspects of the H_2-SCR of NO [62–67, 104], which is described by the following main reaction network:

$$2\,NO + 4\,H_2 + O_2 \rightarrow N_2 + 4H_2O \tag{22.29}$$

$$2\,NO + H_2 \rightarrow N_2O + H_2O \tag{22.30}$$

$$2\,NO + 5\,H_2 \rightarrow 2\,NH_3 + 2\,H_2O \tag{22.31}$$

$$2\,H_2 + O_2 \rightarrow 2\,H_2O \tag{22.32}$$

In this section, the use of *operando* SSITKA studies over a very promising catalytic system, $Pt/MgO–CeO_2$ for H_2-SCR of NO is presented which highlights (a) the bifunctional catalysis occurring, (b) the role of gaseous oxygen on the N_2 selectivity of the reaction, and (c) the structure of *active* NO_x intermediates as a function of reaction temperature.

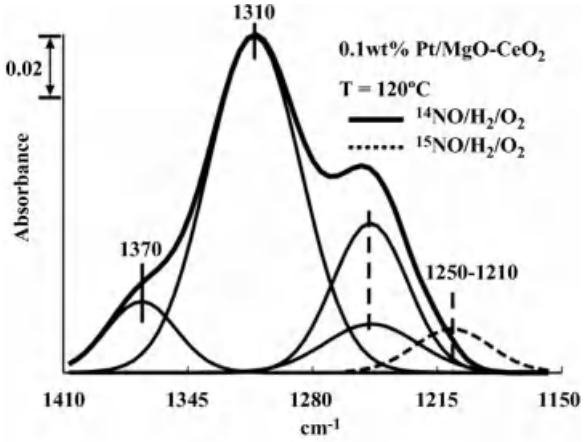


Figure 22.33 Deconvoluted SSITKA–DRIFTS spectra recorded at 120 °C in H_2-SCR of NO over 0.1 wt% Pt/MgO–CeO_2 catalyst in the range 1410–1150 cm^{-1} [67].

22.3.3.2.1 **SSITKA–DRIFTS on Pt/MgO–CeO_2: Chemical Structure of Active NO_x Intermediates and Inactive Species Formed in the "Nitrogen Path"** Figure 22.33 presents the DRIFTS spectrum (solid line) recorded in the 1410–1150 cm^{-1} range after a steady state was achieved with a 2500 ppm ^{14}NO–1.0 vol.% H_2–5 vol.% O_2–He feed gas mixture at 120 °C, and also its deconvolution into various IR bands reported earlier [67]. The IR bands at 1370 and 1310 cm^{-1} are due to adsorbed NO_2^+ and chelating nitrite (NO_2^-) species formed on the MgO and CeO_2 support, whereas the IR band at 1250 cm^{-1} is due to bridged or monodentate nitrate (NO_3^-) also formed on the MgO and CeO_2 supports [67]. After the isotopic switch (2500 ppm ^{15}NO–1.0 vol.% H_2–5 vol.% O_2–He) had been made, and the new steady state had been obtained, the DRIFTS spectrum recorded was deconvoluted. From the latter procedure, it was found that only certain IR bands gave the expected isotopic shift towards lower wavenumbers, as illustrated in Figure 22.33 for the IR band at 1250 cm^{-1} (bridged or monodentate NO_3^- species). This result suggests first that the latter species is an *active* reaction intermediate. A similar isotopic shift would only be expected if the same species were able to exchange with gaseous ^{15}NO during the isotopic switch. After impregnating the same catalyst with NO_3^- species and passing ^{15}NO–He over the catalyst at 120 °C, no shift in the IR bands due to a nitrate species was observed. Therefore, this nitrate species is considered to be a *true active* reaction intermediate.

Table 22.1 describes the chemical structure of *active* "*nitrogen-containing*" reaction intermediates participating in the reaction path from gaseous NO to N_2 and N_2O reaction product formation during H_2-SCR in the range 100–400 °C based on SSITKA–DRIFTS studies [67]. It is shown that the *chemical structure* of the *active* NO_x intermediates depends on the reaction temperature. Table 22.1 also provides the chemical structure of other adsorbed NO_x species formed under H_2-SCR which did not result in any isotopic shift (see Figure 22.33), thus considered an *inactive*

Table 22.1 Chemical structures of *active* NO_x reaction intermediates and *inactive* species formed in H_2-SCR (2500 ppm NO–1 vol.% H_2–5 vol.% O_2–He) over 0.1 wt% Pt/MgO–CeO_2 catalyst as a function of reaction temperature (M = Ce^{4+}, Mg^{2+}).

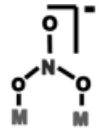
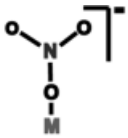
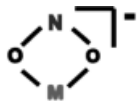
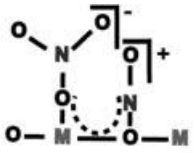
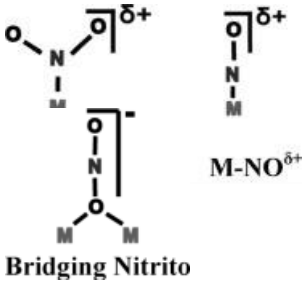
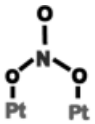
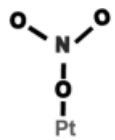
NO_x structure	T (°C)	Active	Inactive
 Bidentate Nitrate	120–200	+	
	200 < T < 400		+
 Monodentate Nitrate	120–200	+	
	200 < T < 400		+
 Chelating Nitrite	120–200		+
	200 < T < 400	+	
 Nitrosyl co-adsorbed with Nitrate	120–200	+	
	200 < T < 400	+	
 Bridging Nitrito	120–400		+
	120–400		+

Table 22.1 (*Continued*)

NO_x structure	T (°C)	Active	Inactive
 **Bidentate Nitrate**	120–400		+
 **Monodentate Nitrate**	120–400		+

(spectator) species of reaction. Figure 22.33 shows that the IR band at 1250 cm^{-1} after deconvolution comprises of two bands with different areas, and thus with different surface concentrations for the same species. This was the result of other DRIFTS experiments which showed that only part of these nitrate species participate in the H_2-SCR of NO [67]. In the following section the concentration of these *active* NO_x species and the magnitude of the reactive zone around the Pt nanoparticles will be illustrated.

22.3.3.2.2 **SSITKA–MS on Pt/MgO-CeO_2: Quantification of Active Reaction Intermediates Present in the "Nitrogen Path"** The surface concentration (μmol g^{-1}) and surface coverage, θ (based on the surface Pt atoms, μmol g^{-1}), of the *active* NO_x intermediates formed during steady-state H_2-SCR in the range 120–300 °C was measured by SSITKA–MS [39, 67]. Figure 22.34 shows transient response curves of the dinitrogen $^{14}N_2$ and $^{14}N^{15}N$ isotopic species obtained after the switch 2500 ppm ^{14}NO–1% H_2–5% O_2–Ar–He (T, 30 min) → 2500 ppm ^{15}NO–1%H_2–5% O_2–He (T, t) at $T = 120$ and 200 °C, respectively, had been made.

The $^{14}N^{15}N$ species is the main one since less $^{14}N_2$ was observed; compare the area difference between the Ar and $^{14}N_2$ transient response curves and that under the $^{14}N^{15}N$ curve. At 120 °C, the transient rate of $^{14}N^{15}N$ formation shows only one peak at $t_M = 35$ s with a shoulder and tail at longer reaction times. As the reaction temperature increases from 120 to 200 °C, a second peak in the $^{14}N^{15}N$ transient production rate is developed ($t_{M1} = 23$ and $t_{M2} = 54$ s, Figure 22.34b); these peaks shifted to lower reaction times at $T = 300$ °C ($t_{M1} = 19$ s and $t_{M2} = 45$ s) [67]. This

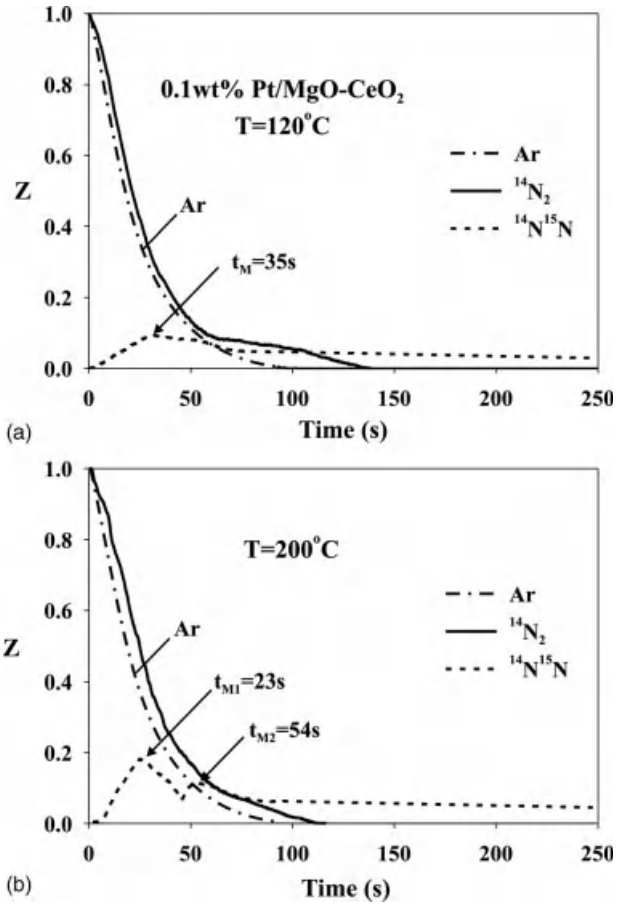


Figure 22.34 Dimensionless transient response curves of $^{14}N_2$, $^{14}N^{15}N$, and Ar obtained during SSITKA–MS experiments on H_2-SCR of NO (^{14}NO–H_2–O_2–Ar–He $\rightarrow$ ^{15}NO–H_2–O_2–He) at 120 °C (a) and 200 °C (b) [67].

result reflects the different reduction kinetics of the *two active* NO_x species formed, the structure of which as identified by SSITKA–DRIFTS experiments (see Table 22.1) was found to depend on the reaction temperature.

The concentration of *active* NO_x that truly participates in the "nitrogen path" of H_2-SCR to form N_2(g) was estimated by integrating the transient response curves of $^{14}N^{15}N$ and of $^{14}N_2$ with respect to the Ar curve (Figure 22.34), and the results are reported in Table 22.2 as a function of reaction temperature. Values of $\theta > 1$ indicate that at least part of the estimated active NO_x cannot reside on Pt. For the present catalytic system, according to SSITKA–DRIFTS and other studies [66, 67], Pt does not accommodate *active* NO_x intermediates. Also, it was found [66] that at 140 °C about 87% of the active NO_x lead to N_2 formation, and only 13% to N_2O formation, in harmony with the N_2 selectivity behavior of this Pt/MgO–CeO_2 catalytic system.

Table 22.2 Concentration ($\mu mol\, g^{-1}$) and surface coverage (θ) of *active* NO_x intermediates formed in H_2-SCR of NO and leading to N_2 and N_2O gas products as determined by SSITKA–MS experiments according to the following gas delivery sequence: 2500 ppm ^{14}NO–1.0 vol.% H_2–5 vol.% O_2–He (30 min, T) $\rightarrow$ 2500 ppm ^{15}NO–1.0 vol.% H_2–5 vol.% O_2–He (T, t).

T (°C)	Total active NO_x ($\mu mol\, g^{-1}$)	θ (surface monolayers of Pt_s)
120	14.3	3.1
150	14.4	3.1
200	13.8	3.0
300	13.2	2.8
400	12.5	2.7

Table 22.2 shows that θ takes values significantly larger than unity, between 2.7 and 3.1 in the 120–400 °C range ($\theta_{max} = 3.1$ at 150 °C). On the other hand, it should be noted that these differences are small. Therefore, the concentration of *active* NO_x remains practically constant in the range 120–400 °C. Based on this result, it was reported [67] that the volcano-type kinetic rate versus temperature profile cannot be explained based on differences in surface concentrations of active NO_x intermediates with reaction temperature but is rather due to (i) differences in the NO_x intrinsic reduction kinetics of the two different active NO_x, (ii) the combustion rate of hydrogen (affecting θ_H), (iii) the surface diffusion of atomic H from Pt to the metal–support interface, and (iv) the oxidation state of Pt. The mean residence time, τ_{N_2}, of active NO_x precursors leading to N_2 was found to be 19.5 and 26.5 s for 120 and 200 °C, respectively, based on the results in Figure 22.34.

22.3.3.2.3 **SSITKA–MS on Pt/MgO-CeO_2: Probing the Role of Gaseous Oxygen in the "Nitrogen Path"** To gather information on the role of gaseous oxygen present in the reaction feed (NO–H_2–O_2) on the mechanism of H_2-SCR, SSITKA–MS experiments with the use of $^{18}O_2$ were conducted. Figure 22.35 presents transient response curves of $N_2{}^{16}O$ and Ar obtained on Pt/MgO–CeO_2 after the switch NO–H_2–$^{16}O_2$–Ar–He $\rightarrow$ NO–H_2–$^{18}O_2$–He was made at 120 °C. As can be clearly seen, the concentration of $N_2{}^{16}O$ produced does not change after the isotopic switch, and at the same time no evolution of $N_2{}^{18}O$ was observed. A completely different result was obtained in the case of Pt/SiO_2 [65], where the concentration of $N_2{}^{16}O$ was reduced after the isotopic switch, and continuous production of $N_2{}^{18}O$ was observed. The latter results strongly indicate that gaseous O_2 participates in N_2O formation in the H_2-SCR of NO in the case of Pt/SiO_2 but not Pt/MgO–CeO_2 catalyst [e.g., see Eq. (22.30)]. These results reveal a *strong support effect* on the "oxygen path" of H_2-SCR towards N_2O formation, and thus on the N_2 selectivity of reaction. It is suggested that oxidation of NO on Pt to form NO_2 leads to its nonselective reduction by hydrogen on Pt/SiO_2, whereas the opposite is true in the case of Pt/MgO–CeO_2.

22.3.3.2.4 **Essential Mechanistic Aspects of the "Nitrogen Path" of H_2-SCR of NO** According to the SSITKA–DRIFTS and SSITKA–MS experiments presented in

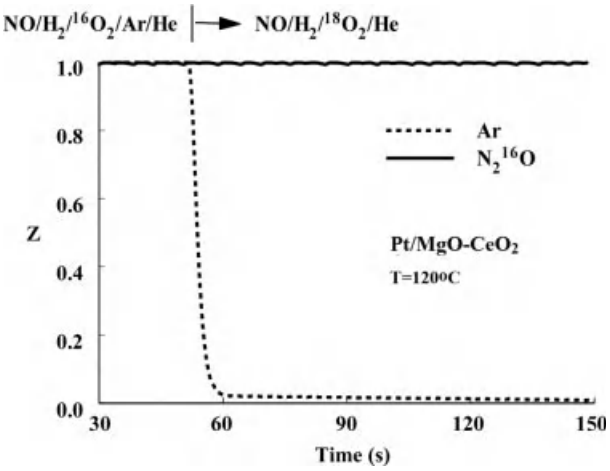


Figure 22.35 Dimensionless transient response curves of $N_2{}^{16}O$ and Ar gases obtained during SSITKA–MS experiments on H_2-SCR of NO (^{14}NO–H_2–O_2–Ar–He → ^{15}NO–H_2–O_2–He) at 120 °C over 0.1 wt% Pt/MgO–CeO_2 catalyst.

Figures 22.33–22.35 and Tables 22.1 and 22.2, essential elements of the mechanism of H_2-SCR of NO are presented in Figure 22.36 and can be summarized as follows:

a) *Two active* adsorbed NO_x intermediates, different in structure, were identified in the "nitrogen path" of H_2-SCR of NO towards N_2 and N_2O formation. The first is located in the vicinity of the Pt–CeO_2 support interface; *nitrosyl* (NO^+) *co-adsorbed with nitrate* (NO_3^-) on an adjacent Ce^{4+}–oxygen anion site pair, whereas the second is located in the vicinity of the Pt–MgO interface [66, 67]. The chemical structure of the latter species was found to depend on reaction temperature. At T <200 °C, the structure of active NO_x is that of *bidentate and/or monodentate nitrate* (NO_3^-), whereas above 200 °C it is *chelating nitrite*, NO_2^- (see Table 22.1). The concentration (μmol g^{-1}) of active NO_x intermediates leading to N_2 formation was found to be practically independent of the reaction

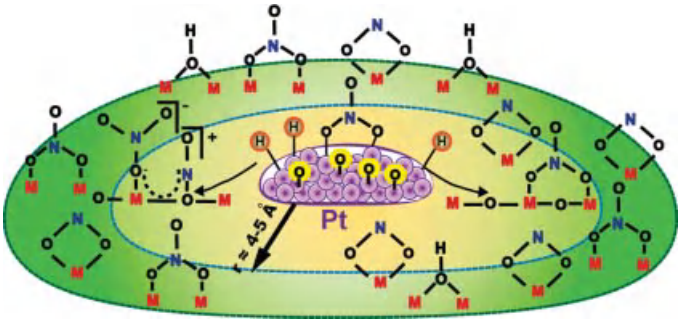


Figure 22.36 Active NO_x reaction intermediates of the H_2-SCR of NO over 0.1 wt% Pt/MgO–CeO_2 catalyst are located within the marked region of about 4–5 Å radius around the Pt nanoparticles [67].

temperature (120–300 °C) and significantly larger than one equivalent monolayer of surface Pt ($\theta_{NO_x} = 2.4$–2.6) [67]. This result cannot explain the volcano-type behavior observed in the profile of catalytic activity (kinetic rate and NO conversion) versus reaction temperature [101–103].

b) Hydrogen is dissociatively adsorbed on Pt sites yielding adsorbed H atoms which can spill over the support. Surface diffusion of H species on the MgO and CeO_2 support surfaces is suggested to be limited to within a region of about 4–5 Å around the Pt nanoparticles [67]. This is the main reason why *not all* NO_x formed on the MgO and CeO_2 support surfaces under H_2-SCR conditions become *active* reaction intermediates (Figure 22.36).

c) Hydrogen atoms spilt over the support are accommodated on support oxygen sites adjacent to adsorbed NO_x species, which eventually are reduced to N_2, N_2O, and H_2O gas products.

d) Gaseous O_2 present in the H_2-SCR of the NO feed stream does not participate in the reaction path towards N_2O formation. Instead, it can oxidize NO on Pt sites to form NO_2, the latter forming active NO_x on the support, which in turn is selectively reduced by hydrogen to N_2 gas.

e) Oxygen adsorbs dissociatively on Pt forming adsorbed atomic O, which mainly reacts with H on Pt to form eventually water. Most of the hydrogen consumed under H_2-SCR reaction conditions is due to this combustion reaction.

22.4 Conclusion

To study heterogeneous catalytic reactions using complex catalytic materials, including industrial catalysts, the TAP and SSITKA methods for kinetic and mechanistic studies were developed at approximately the same time (1970s–1980s). Their usefulness in unraveling complex catalytic reaction mechanisms has been proven during more than 30 years of research on a large variety of catalytic reactions, ranging from selective oxidation and hydrogenation reactions to studies of diffusion in zeolites and of lattice oxygen in mixed metal oxides.

TAP methodology is focused on determining the sequence of steps in a complex reaction mechanism, detection of reaction intermediates, determining the influence of coverage on kinetic parameters and the reaction mechanism, and the precise and systematic non-steady-state kinetic characterization of a catalyst, relating to its intrinsic reactivity. The SSITKA method, based on isotope transfer dynamics associated with the *active* reaction intermediates, provides *in situ* information about lifetimes and surface concentrations of *active* surface reaction intermediates and rate constants of elementary steps under complex steady-state catalytic reaction conditions. These two techniques provide complementary information.

Merging TAP and SSITKA methods into a unified approach combined with other physical characterization methods, including *operando* methodologies (e.g., SSITKA–DRIFTS and SSITKA–Raman spectroscopy) can become an extremely powerful tool for understanding complex catalytic reactions on real solid surfaces.

Notation

a_s	surface concentration of active sites (mol cm^{-2} of catalyst)
A	cross-sectional area of the microreactor (cm^2)
α	ratio of total number of active centers to number of molecules of gas A in the pulse
C_A	concentration of gas A (mol cm^{-3})
$\bar{C}_A$	dimensionless concentration of gas A
D_e	effective Knudsen diffusivity ($cm^2\,s^{-1}$)
D_{eA}	effective Knudsen diffusivity of gas A ($cm^2\,s^{-1}$)
δ_z	delta function with respect to axial coordinate z
δ_ς	delta function with respect to dimensionless axial coordinate ς
ε_b	fractional voidage of the packed bed in the microreactor
f(k)	reactivity distribution function
F_A	flow of gas A at microreactor outlet (mol s^{-1})
$\bar{F}_A$	dimensionless flow of gas A at microreactor outlet
F_T	total molar flow rate of reaction feed stream under steady-state reaction conditions (mol s^{-1})
H_p	peak height of the normalized gas exit flow
k_a	adsorption rate constant ($cm^3\,mol^{-1}\,s^{-1}$)
k'_a	adsorption rate constant (s^{-1})
$\bar{k}_a$	dimensionless adsorption rate constant
k_{ads}	apparent adsorption rate constant (s^{-1})
k_d	desorption rate constant (s^{-1})
$\bar{k}_d$	dimensionless desorption rate constant
k_n	site reactivity (s^{-1})
K_a	dimensionless modified kinetic constant of adsorption
L	length of the microreactor (cm)
L_{II}	length of diffusion zone II (cm)
ΔL	thickness of the catalytic zone (cm)
M	molecular mass
N_n^A	surface abundance (mol), concentration (mol m^{-2}, mol g_{cat}^{-1}) or coverage (θ) of intermediate species A in the nth pool
$N_n^{A,*A}$	surface abundance (mol), concentration (mol m^{-2}, mol g_{cat}^{-1}) or coverage (θ) of both nonisotopic A and isotopic *A intermediates in the nth pool
N_p	concentration of all active adsorbed reaction intermediates leading to the formation of product P (mol g_{cat}^{-1})
N_{pA}	number of moles or molecules of gas A in the input pulse
R	universal gas constant (cal $mol^{-1}\,K^{-1}$)
r_n^A	rate of transfer of nonisotopic species present in the intermediate A from the nth to the $(n+1)^{th}$ pool (mol s^{-1})
$r_n^{A,*A}$	rate of transfer of isotopic species present in the intermediate *A from the nth to the $(n+1)^{th}$ pool (mol s^{-1})
r_{-n}^A	rate of transfer of nonisotopic species present in the intermediate A from the $(n+1)^{th}$ to the nth pool (mol s^{-1})

$r_{-n}^{A,*A}$	rate of transfer of isotopic species present in the intermediate *A from the $(n+1)^{th}$ to the nth pool (mol s^{-1})
r_a^R	rate of adsorption of nonisotopic reactant R species (mol s^{-1})
r_a^{*R}	rate of adsorption of isotopic reactant *R species (mol s^{-1})
r_d^R	rate of desorption of nonisotopic reactant R species (mol s^{-1})
r_d^{*R}	rate of desorption of isotopic reactant *R species (mol s^{-1})
r_a^P	rate of adsorption of nonisotopic product P species (mol s^{-1})
$r_a^{P,*P}$	rate of adsorption of isotopic product *P species (mol s^{-1})
r_d^P	rate of desorption of nonisotopic product P species (mol s^{-1})
$r_d^{P,*P}$	rate of desorption of isotopic product *P species (mol s^{-1})
$r_p(t)$	reaction rate of product P species during SSITKA (mol s^{-1})
$r_p^*(t)$	reaction rate of isotopic product *P species during SSITKA (mol s^{-1})
$r_p^{s.s.}$	steady-state reaction rate of product P species (mol s^{-1})
S_v	surface area of catalyst per unit volume of catalyst (cm^{-1})
t	time (s)
t_p	time at which the gas exit flow is at a maximum
TOF	reaction rate in terms of turn over frequency (s^{-1})
τ	dimensionless time
τ_n	mean residence time of a given reaction intermediate n (s)
τ_p	dimensionless time at which gas exit flow is at a maximum
τp	mean surface residence time of all active reaction intermediates leading to the product P (s)
τ_{res}^{conv}	residence time for convective flow in CSTR (s)
$\tau_{res,cat}^{dif}$	residence time for diffusion through the catalytic zone in a thin-zone TAP microreactor (s)
T	temperature (K)
θ_A	fractional surface coverage
$\bar{\theta}_A$	pulse normalized surface concentration
V_{void}	void volume inside microreactor (cm^3)
W	amount of catalyst sample used (g)
X	conversion
$y_p(t)$	mole fraction of product P in the reaction product stream at the exit of the microreactor during SSITKA
$y_p^{s.s.}$	mole fraction of product P in the reaction product stream at the exit of the microreactor under steady-state reaction conditions
$Z_p(t)$	dimensionless concentration function for product P
$Z_{p^*}(t)$	dimensionless concentration function for the isotopic product *P
$Z_{Ar}(t)$	dimensionless concentration function for Ar gas
z	axial coordinate (cm)
ζ	dimensionless axial coordinate

References

1 Gleaves, J.T., Ebner, J.R., and Kuechler, T.C. (1988) Temporal analysis of products (TAP) – a unique catalyst evaluation system with submillisecond time resolution. *Catal. Rev. Sci. Eng.*, **30** (1), 49–116.

2 Gleaves, J.T., Ebner, J.R., and Mills, P.L. (1988) A novel catalyst evaluation system for temporal analysis of reaction products with submillisecond time resolution. *Stud. Surf. Sci. Catal.*, **38**, 633–644.

3 Gleaves, J.T., Yablonskii, G.S., Phanawadee, P., and Schuurman, Y. (1997) TAP-2. Interrogative kinetics approach. *Appl. Catal. A: Gen.*, **160** (1), 55–88.

4 Gleaves, J.T., Yablonsky, G.S., Zheng, X., Fushimi, R., and Mills, P.L. (2010) Temporal analysis of products (TAP) – recent advances in technology for kinetic analysis of multicomponent catalysts. *J. Mol. Catal. A: Chem.*, **315** (2), 108–134.

5 Yablonsky, G.S., Olea, M., and Marin, G.B. (2003) Temporal analysis of products: basic principles, applications, and theory. *J. Catal.*, **216** (1–2), 120–134.

6 Pérez-Ramírez, J. and Kondratenko, E.V. (eds.) (2007) The TAP reactor in catalysis: recent advances in theory and practice. *Catal. Today*, **121** (3–4), 159–282.

7 Gleaves, J.T. and Ebner, J.R. (1986) Method and apparatus for carrying out catalyzed chemical reactions and for studying catalysts. US Patent 4,626,412, assigned to Monsanto.

8 Gleaves, J.T. (1994) Apparatus for study and analysis of products of catalytic reaction. US Patent 5,376,335.

9 Libuda, J. and Freund, H.-J. (2005) Molecular beam experiments on model catalysts. *Surf. Sci. Rep.*, **57** (7–8), 157–298.

10 D'Evelyn, M.P. and Madix, R.J. (1984) Reactive scattering from solid surfaces. *Surf. Sci. Rep.*, **3** (8), 413–497.

11 Barker, J.A. and Auerbach, D.J. (1984) Gas–surface interactions and dynamics; thermal energy atomic and molecular beam studies. *Surf. Sci. Rep.*, **4** (1–2), 1–99.

12 Asscher, M. and Somorjai, G.A. (1992) Reactive scattering, in *Atomic and Molecular Beam Methods*, vol. **2** (ed. G. Scoles), Oxford University Press, Oxford, pp. 488–517.

13 Yu, M.L. and Delouise, L.A. (1994) Surface science reactions on semiconductors studied by molecular beam reactive scattering. *Surf. Sci. Rep.*, **19** (7–8), 285–380.

14 Rettner, C.T., Auerbach, D.J., Tully, J.C., and Kleyn, A.W. (1996) Chemical dynamics at the gas–surface interface. *J. Phys. Chem.*, **100** (31), 13021–13033.

15 Kleyn, A.W. (2003) Molecular beams and chemical dynamics at surfaces. *Chem. Soc. Rev.*, **32** (2), 87–96.

16 Woodruff, D.P. (2003) *The Chemical Physics of Solid Surfaces, Surface Dynamics*, vol. **11**, Elsevier, Amsterdam, p. 378.

17 Libuda, J. and Freund, H.-J. (2002) Reaction kinetics on complex model catalysts undet single scattering conditions. *J. Phys. Chem. B*, **106** (19), 4901–4915.

18 Libuda, J. (2004) Molecular beams and model catalysts: activity and selectivity of specific reaction centers on supported nanoparticles. *ChemPhysChem.*, **5** (5), 625–631.

19 Shekhtman, S.O., Yablonsky, G.S., Chen, S., and Gleaves, J.T. (1999) Thin-zone TAP-reactor – theory and application. *Chem. Eng. Sci.*, **54** (20), 4371–4378.

20 Zheng, X., Gleaves, J.T., Yablonsky, G.S., Brownscombe, T., Gaffney, A., Clark, M., and Han, S. (2008) A needle in a haystack catalysis. *Appl. Catal. A: Gen.*, **341** (1–2), 86–92.

21 Yablonsky, G.S., Shekhtman, S.O., Chen, S., and Gleaves, J.T. (1998) Moment-based analysis of transient response catalytic studies (TAP-experiment). *Ind. Eng. Chem. Res.*, **37** (6), 2193–2202.

22 Constales, D., Yablonsky, G.S., Marin, G.B., and Gleaves, J.T. (2001) Multi-zone TAP-reactors: theory and

application. I. The global transfer matrix expression. *Chem. Eng. Sci.*, **56** (1), 133–149.
23 Constales, D., Yablonsky, G.S., Marin, G.B., and Gleaves, J.T. (2001) Multi-zone TAP-reactors: theory and application. II. The three dimensional theory. *Chem. Eng. Sci.*, **56** (5), 1913–1923.
24 Constales, D., Yablonsky, G.S., Marin, G.B., and Gleaves, J.T. (2004) Multi-zone TAP-reactors, theory and application. III. Multi-response theory and criteria of instantaneousness. *Chem. Eng. Sci.*, **59** (17), 3725–3736.
25 Constales, D., Shekhtman, S.O., Yablonsky, G.S., Marin, G.B., and Gleaves, J.T. (2006) Multi-zone TAP-reactors, theory and application. IV. The ideal and non-ideal boundary conditions. *Chem. Eng. Sci.*, **61** (6), 878–891.
26 Yablonsky, G.S., Constales, D., and Gleaves, J.T. (2002) Multi-scale problems in the quantitative characterization of complex catalytic materials. *J. Syst. Anal. Model. Simul.*, **42** (8), 1143–1166.
27 Yablonsky, G.S., Constales, D., Shekhtman, S.O., and Gleaves, J.T. (2007) Y-procedure: how to extract the chemical transformation rate from reaction-diffusion data with no assumption on the kinetic model. *Chem. Eng. Sci.*, **62** (23), 6754–6767.
28 (a) Schuurman, Y. and Gleaves, J.T. (1997) A comparison of steady-state and unsteady-state reaction kinetics of *n*-butane oxidation over VPO catalysts using a TAP-2 reactor system. *Catal. Today*, **33** (1–3), 25–37; (b) Schuurman, Y., Gleaves, J.T., Ebner, J.R., and Mummey, M.J. (1994) Activation of vanadium phosphorus oxide catalysts for alkane oxidation: oxygen storage and catalyst performance, in *New Developments in Selective Oxidation II* (eds. C. Corberan and S. Vic Bellon), Elsevier, Amsterdam, pp. 335–342; (c) Schuurman, Y. and Gleaves, J.T. (1994) Activation of vanadium phosphorus oxide catalysts for alkane oxidation – the influence of the oxidation state on catalyst selectivity. *Ind. Eng. Chem. Res.*, **33** (12), 2935–2941.
29 Happel, J. (1978) Transient tracing. *Chem. Eng. Sci.*, **33**, 1567–1572.
30 Bennett, C.O. (1982) Understanding heterogeneous catalysis through the transient method, *ACS Symp. Ser.*, **178**, 1–32.
31 Biloen, P. (1983) Transient kinetic methods. *J. Mol. Catal.*, **21**, 17–24.
32 Tamaru, K. (1964) Adsorption measurements during surface catalysis. *Adv. Catal.*, **15**, 65–90.
33 Shannon, S.L. and Goodwin, J.G. Jr. (1995) Characterization of catalytic surfaces by isotopic-transient kinetics during steady-state reaction. *Chem. Rev.*, **95** (3), 677–695.
34 Bennett, C.O. (1999) Experiments and processes in the transient regime for heterogeneous catalysis. *Adv. Catal.*, **44**, 329–416.
35 Happel, J. (1986) *Isotopic Assessment of Heterogeneous Catalysis*, Academic Press, New York.
36 Efstathiou, A.M. and Verykios, X.E. (1997) Transient methods in heterogeneous catalysis: experimental features and application to study mechanistic aspects of the CH_4/O_2 (OCM), NH_3/O_2 and NO/He reactions. *Appl. Catal. A: Gen.*, **151** (1), 109–166.
37 Balakos, M.W., Chuang, S.S.C., and Srinivas, G. (1993) Transient infrared study of methanation and ethylene hydroformylation over Rh/SiO_2 catalysts. *J. Catal.*, **140** (1), 281–285.
38 Srinivas, G., Chuang, S.S.C., and Balakos, M.W. (1993) An *in situ* IR study coupled with transient kinetic analysis of hydroformylation. *AIChE J.*, **39** (3), 530–532.
39 Kalamaras, C.M., Panagiotopoulou, P., Kondarides, D.I., and Efstathiou, A.M. (2009) Kinetic and mechanistic studies of the water-gas shift reaction on Pt/TiO_2 catalyst. *J. Catal.*, **264** (2), 117–129.
40 Meunier, F.C. (2010) The power of quantitative kinetic studies of adsorbate reactivity by *operando* FTIR spectroscopy carried out at chemical potential steady-state. *Catal. Today*, **155**, 164–171.

41 Chuang, S.S.C. and Guzman, F. (2009) Mechanistic investigation of heterogeneous catalysis by transient infrared methods. *Top. Catal.*, **52** (10), 1448–1458.

42 Schuurman, Y., Van Veen, A.C., and Mirodatos, C. (2007) Characterization and reactivity of working catalysts. *Chim. Ind. (Milan)*, **10**, 125–130.

43 Kuba, S. and Knözinger, H. (2002) Time-resolved *in situ* Raman spectroscopy of working catalysts: sulfated and tungstated zirconia. *J. Raman Spectrosc.*, **33**, 325–332.

44 Bañares, M.A. and Wachs, I.E. (2002) Molecular structures of supported metal oxide catalysts under different environments. *J. Raman Spectrosc.*, **33**, 359–380.

45 Lohitharn, N. and Goodwin, J.G. Jr. (2008) Impact of Cr, Mn and Zr addition on Fe Fischer–Tropsch synthesis catalysis: investigation of the active site level using SSITKA. *J. Catal.*, **257**, 142–151.

46 Govender, N.S., Botes, F.G., de Croon, M.H.J.M., and Schouten, J.C. (2008) Mechanistic pathway for methane formation over an iron-based catalyst. *J. Catal.*, **260**, 254–261.

47 den Breejen, J.P., Radstake, P.B., Bezemer, G.L., Bitter, J.H., Frøseth, V., Holmen, A., and de Jong, K.P. (2009) On the origin of the cobalt particle size effects in Fischer–Tropsch catalysis. *J. Am. Chem. Soc.*, **131**, 7197–7203.

48 Hammache, S., Goodwin, J.G. Jr., Shannon, S.L., and Kim, S.Y. (2002) *Encyclopedia of Surface and Colloid Science*, Marcel Dekker, New York.

49 Goguet, A., Meunier, F.C., Tibiletti, D., Breen, J.P., and Burch, R. (2004) Spectrokinetic investigation of reverse water-gas-shift reaction intermediates over a Pt/CeO_2 catalyst. *J. Phys. Chem. B*, **108** (52), 20240–20246.

50 Jacobs, G. and Davis, B.H. (2005) Reverse water-gas shift reaction: steady state isotope switching study of the reverse water-gas shift reaction using *in situ* DRIFTS and a Pt/ceria catalyst. *Appl. Catal. A: Gen.*, **284**, 31–38.

51 Meunier, F.C., Tibiletti, D., Goguet, A., Reid, D., and Burch, R. (2005) On the reactivity of carbonate species on a Pt/CeO_2 catalyst under various reaction atmospheres: application of the isotopic exchange technique. *Appl. Catal. A: Gen.*, **289**, 104–112.

52 Tibiletti, D., Goguet, A., Reid, D., Meunier, F.C., and Burch, R. (2006) On the need to use steady-state or *operando* techniques to investigate reaction mechanisms: an *in situ* DRIFTS and SSITKA-based study example. *Catal. Today*, **113**, 94–101.

53 Tibiletti, D., Meunier, F.C., Goguet, A., Reid, D., Burch, R., Boaro, M., Vicario, M., and Trovarelli, A. (2006) An investigation of possible mechanisms for the water–gas shift reaction over a ZrO_2-supported Pt catalyst. *J. Catal.*, **244** (2), 183–191.

54 Olympiou, G.G., Kalamaras, C.M., Zeinalipour-Yazdi, C.D., and Efstathiou, A.M. (2007) Mechanistic aspects of the water-gas shift reaction on alumina-supported noble metal catalysts: *in situ* DRIFTS and SSITKA–mass spectrometry studies. *Catal. Today*, **127**, 304–318.

55 Meunier, F.C., Tibiletti, D., Goguet, A., Shekhtman, S., Hardacre, C., and Burch, R. (2007) On the complexity of the water-gas shift reaction mechanism over a Pt/CeO_2 catalyst: effect of the temperature on the reactivity of formate surface species studied by *operando* DRIFT during isotopic transient at chemical steady-state. *Catal. Today*, **126**, 143–147.

56 Jacobs, G. and Davis, B.H. (2007) Low temperature water-gas shift: applications of a modified SSITKA–DRIFTS method under conditions of H_2 co-feeding over metal/ceria and related oxides. *Appl. Catal. A: Gen.*, **333** (2), 192–201.

57 Meunier, F.C., Reid, D., Goguet, A., Shekhtman, S., Hardacre, C., Burch, R., Deng, W., and Flytzani-Stephanopoulos, M. (2007) Quantitative analysis of the reactivity of formate species seen by DRIFTS over a $Au/Ce(La)O_2$ water-gas shift catalyst: first unambiguous evidence of the minority role of formates as

reaction intermediates. *J. Catal.*, **247** (2), 277–288.

58 Kalamaras, C.M., Olympiou, G.G., and Efstathiou, A.M. (2008) The water-gas shift reaction on Pt/γ-Al_2O_3 catalyst: *operando* SSITKA–DRIFTS–mass spectroscopy studies. *Catal. Today*, **138**, 228–234.

59 Daly, H., Ni, J., Thompsett, D., and Meunier, F.C. (2008) On the usefulness of carbon isotopic exchange for the *operando* analysis of metal–carbonyl bands by IR over ceria-containing catalysts. *J. Catal.*, **254** (2), 238–243.

60 Jacobs, G. and Davis, B.H. (2010) Surface interfaces in low temperature water-gas shift: the metal oxide synergy, the assistance of co-adsorbed water, and alkali doping. *Int. J. Hydrogen Energy*, **35** (8), 3522–3536.

61 Jacobs, G., Davis, B.H., Pigos, J.M., and Brooks, C.J. (2009) Low-temperature WGS: assessing formates as potential intermediates over Pt/ZrO_2 and Na-doped Pt/ZrO_2 catalysts employing the SSITKA–DRIFTS technique, in *Advances in Fischer–Tropsch Synthesis, Catalysts and Catalysis* (eds. B.H. Davis and M.L. Occelli), CRC Press, Boca Raton, FL, 365–394.

62 Burch, R., Shestov, A.A., and Sullivan, J.A. (1999) A transient kinetic study of the mechanism of the NO + H_2 reaction over Pt/SiO_2 catalysts: 1. Isotopic transient kinetics and temperature programmed analysis. *J. Catal.*, **186** (2), 353–361.

63 Burch, R., Shestov, A.A., and Sullivan, J.A. (1999) A steady-state isotopic transient kinetic analysis of the NO/O_2/H_2 reaction over Pt/SiO_2 catalysts. *J. Catal.*, **188** (1), 69–82.

64 Burch, R. and Coleman, M.D. (2002) An investigation of promoter effects in the reduction of NO by H_2 under lean-burn conditions. *J. Catal.*, **208** (2), 435–447.

65 Costa, C.N. and Efstathiou, A.M. (2004) Transient isotopic kinetic study of the NO/H_2/O_2 (lean de-NO_x) reaction on Pt/SiO_2 and Pt/La–Ce–Mn–O catalysts. *J. Phys. Chem. B*, **108** (8), 2620–2630.

66 Costa, C.N. and Efstathiou, A.M. (2007) Mechanistic aspects of the H_2-SCR of NO on a novel Pt/MgO–CeO_2 catalyst. *J. Phys. Chem. C*, **111** (7), 3010–3020.

67 Savva, P.G. and Efstathiou, A.M. (2008) The influence of reaction temperature on the chemical structure and surface concentration of active NO_x in H_2-SCR over Pt/MgO–CeO_2: SSITKA–DRIFTS and transient mass spectrometry studies. *J. Catal.*, **257** (2), 324–333.

68 Bajusz, I.G. and Goodwin, J.G. Jr. (1997) N_2 adsorption in LiX zeolite: isotopic transient analysis. *Langmuir*, **13** (24), 6550–6554.

69 Bajusz, I.G. and Goodwin, J.G. Jr. (1998) Effect of Ca^{2+} exchange on adsorption of N_2–O_2 mixtures by NaCaX zeolite. *Langmuir*, **14** (10), 2876–2883.

70 Szedlacsek, P., Efstathiou, A.M., and Verykios, X.E. (1997) A novel analysis of equilibrium adsorption and desorption using transient tracing methods. *Appl. Catal. A: Gen.*, **151** (1), 59–96.

71 Davies, J.C., Tsotridis, G., Varlam, M., Valkiers, S., Berglund, M., and Taylor, P. (2010) SSITKA investigation of CO and H_2 competitive adsorption at PEM fuel cell anode catalysts. *Int. J. Mass Spectrom.*, **291** (3), 152–158.

72 Mihet, M., Lazăr, M., and Almăş an, V. (2009) Mobility of hydrogen species on Ni supported catalysts. *J. Phys. Conf. Ser.*, **182**, 1.

73 Almăşan, V., Hodor, I., and Mărginean, P. (1997) A dynamic method for the study of H/D exchange on Ni catalysts. *Appl. Surf. Sci.*, **120**, 335–339.

74 Sadovskaya, E.M., Ivanova, Y.A., Pinaeva, L.G., Grasso, G., Kuznetsova, T.G., van Veen, A., Sadykov, V.A., and Mirodatos, C. (2007) Kinetics of oxygen exchange over CeO_2–ZrO_2 fluorite-based catalysts. *J. Phys. Chem. A*, **111** (20), 4498–4505.

75 Christou, S.Y., Bradshaw, H., Butler, C., Darab, J., and Efstathiou, A.M. (2009) Effect of thermal aging on the transient kinetics of oxygen storage and release of commercial $Ce_xZr_{1-x}O_2$-based solids. *Top. Catal.*, **52**, 2013–2018.

76 Duprez, D. (2006) in *Isotopes in Heterogeneous Catalysis* (eds. J.S.J. Hargreaves, S.D. Jackson, and G. Webb), Catalytic Science Series, vol. **4**, Imperial College Press, London, pp. 133–182.

77 Efstathiou, A.M. and Bennett, C.O. (1989) Surface species on Rh/Al_2O_3 during CO/H_2 reaction by transient techniques. *Chem. Eng. Commun.*, **83**, 129–146.

78 Efstathiou, A.M. and Bennett, C.O. (1989) The CO/H_2 reaction on Rh/Al_2O_3: II. Kinetic study by transient isotopic methods. *J. Catal.*, **120** (1), 137–156.

79 Boudart, M. and Djèga-Mariadassou, G. (eds.) (1984) *Kinetics of Heterogeneous Catalytic Reactions*, Princeton University Press, Princeton, NJ.

80 Goodwin, J.G. Jr., Kim, S., and Rhodes, W.D. (2004) Turnover frequencies in metal catalysis: meanings, functionalities and relationships, in *Catalysis* (eds. J.J. Spivey and G.W. Roberts), Royal Society of Chemistry, Cambridge, pp. 320–347.

81 Che, M. and Bennett, C.O. (1989) The influence of particle size on the catalytic properties of supported metals. *Adv. Catal.*, **36**, 55–172.

82 De Pontes, M., Yokomizo, G.H., and Bell, A.T. (1987) A novel method for analyzing transient response data obtained in isotopic tracer studies of CO hydrogenation. *J. Catal.*, **104** (1), 147–155.

83 Hoost, T.E. and Goodwin, J.G. Jr. (1992) Non-parametric determination of reactivity distributions from isotopic transient kinetic data. *J. Catal.*, **134** (2), 678–690.

84 Pansare, S., Sirijaruphan, A., and Goodwin, J.G. Jr. (2006) Investigation of reaction at the site level using SSITKA, in *Isotopes in Heterogeneous Catalysis* (eds. J.S.J. Hargreaves, S.D. Jackson, and G. Webb), Catalytic Science Series, vol. **4**, Imperial College Press, London, pp. 183–211.

85 Balakos, M.W. and Chuang, S.C. (1995) Transient response of propionaldehyde formation during $CO/H_2/C_2H_4$ reaction on Rh/SiO_2. *J. Catal.*, **151**, 253–265.

86 Bal'zhinimaev, B.S., Sadovskaya, E.M., and Suknev, A.P. (2009) Transient isotopic kinetics study to investigate reaction mechanisms. *Chem. Eng. J.*, **154**, 2–8.

87 Gao, J., Mo, X., and Goodwin, J.G. Jr. (2010) Relationships between oxygenate and hydrocarbon formation during CO hydrogenation on Rh/SiO_2: use of multiproduct SSITKA. *J. Catal.*, **275**, 211–217.

88 Storsaeter, S., Chen, D., and Holmen, A. (2006) Microkinetic modelling of the formation of C_1 and C_2 products in the Fischer–Tropsch synthesis over cobalt catalysts. *Surf. Sci*, **600** (10), 2051–2063.

89 Choi, Y. and Liu, P. (2009) Mechanism of ethanol synthesis from syngas on Rh(111). *J. Am. Chem. Soc*, **131** (36), 13054–13061.

90 Ratnasamy, C. and Wagner, J.P. (2009) Water gas shift catalysis. *Catal. Rev.*, **51** (3), 325–440.

91 Burch, R. (2006) Gold catalysts for pure hydrogen production in the water-gas shift reaction: activity, structure and reaction mechanism. *Phys. Chem. Chem. Phys.*, **8**, 5483–5500.

92 Guerrero-Pérez, M.O. and Bañares, M.A. (2002) *Operando* Raman study of alumina-supported Sb–V–O catalyst during propane ammoxidation to acrylonitrile with on-line activity measurement. *Chem. Comm.*, **12**, 1292–1293.

93 Meunier, F.C. (2010) The design and testing of kinetically-appropriate *operando* spectroscopic cells for investigating heterogeneous catalytic reactions. *Chem. Soc. Rev.*, **39**, 4602–4614.

94 Jacobs, G., Khalid, S., Patterson, P.M., Williams, L., Sparks, D., and Davis, B.H. (2004) Water-gas shift catalysis: kinetic isotope effect identifies surface formates in rate limiting step for Pt/ceria catalysts. *Appl. Catal. A: Gen.*, **268**, 255–266.

95 Kalamaras, C.M., Americanou, S., and Efstathiou, A.M. (2011) "Redox" vs. "associative formate with –OH group regeneration" WGS reaction mechanism

on Pt/CeO_2: effect of platinum particle size. *J. Catal.*, **279** (2), 287–300.
96 Seinfeld, J.H. (1989) Urban air pollution: state of the science. *Science*, **243**, 745–752.
97 Taylor, K.C. (1986) Automobile catalytic converters, in *Catalysis Science and Technology*, vol. **5** (eds J.R. Anderson and M. Boudart), Springer, Berlin, pp. 1–54.
98 Janssen, F.J. (1999) Environmental catalysis – stationary sources, in *Environmental Catalysis* (eds. G. Ertl, H. Knözinger, and J. Weitkamp), Wiley-VCH Verlag GmbH, Weinheim, pp. 119–174.
99 Nakajima, F. and Hamada, I. (1996) The state-of-the-art technology of NO_x control. *Catal. Today*, **29**, 109–115.
100 Bensaid, S., Borla, E.M., Russo, N., Fino, D., and Specchia, V. (2010) Appraisal of a de-NO_x system based on H_2 for light-duty diesel engine vehicles. *Ind. Eng. Chem. Res.*, **49**, 10323–10333.
101 Costa, C.N. and Efstathiou, A.M. (2004) $Pt/Mg–Ce–O$ catalyst for $NO/H_2/O_2$ lean de-NO_x reaction. *Environ. Chem. Lett.*, **2** (2), 55–58.
102 Costa, C.N. and Efstathiou, A.M. (2007) Low-temperature H_2-SCR of NO on a novel $Pt/MgO–CeO_2$ catalyst. *Appl. Catal. B: Environ.*, **72**, 240–252.
103 Costa, C.N., Savva, P.G., Fierro, J.L.G., and Efstathiou, A.M. (2007) Industrial H_2-SCR of NO on a novel $Pt/MgO–CeO_2$ catalyst. *Appl. Catal. B: Environ.*, **75**, 147–156.
104 Olympiou, G.G. and Efstathiou, A.M. (2011) Industrial NO_x control via H_2-SCR on a novel supported-Pt nanocatalyst. *Chem. Eng. J.*, **170** (2–3), 424–432.

Part Four
Advanced Characterization

Characterization of Solid Materials and Heterogeneous Catalysts: From Structure to Surface Reactivity, First Edition.
Edited by Michel Che and Jacques C. Védrine.
© 2012 Wiley-VCH Verlag GmbH & Co. KGaA. Published 2012 by Wiley-VCH Verlag GmbH & Co. KGaA.

23
Techniques Coupling for Catalyst Characterization

Andrew M. Beale, Matthew G. O'Brien, and Bert M. Weckhuysen

23.1
Introduction

It is often thus, that when a subject matter becomes generally accepted, it becomes *passé*. Such a description could be reasonably levied at the notion of studying catalytic reactions *in situ* or more ideally *operando* is necessary in order to understand the key "life" stages of a catalyst and/or a catalytic process. That *in situ* or *operando* reaction monitoring *could* be labeled in such a way should not, however, be seen as a degenerative step, since in this case it represents a reaching of a general consensus and the inevitable maturing of an active field, as earlier chapters in this book testify. The field has, however, some way to go before reaching full maturity, since for many types of catalytic experiments the necessary spatiotemporal and chemical resolution is not yet sufficient always to provide answers to key questions regarding a catalyst synthesis or reaction process [1, 2]. In many cases, technological developments in modern source/detector/analytical processing technology for various measuring devices will lead to further improvements in the spatiotemporal resolution and with this also the chemical information that can be obtained. Yet ultimately, due to inherent limitations, a ceiling with regard to what can be achieved will be reached with one technique alone. This problem can, of course, be overcome in part by the intelligent combination of *in situ* spectroscopic and/or scattering techniques to study both steady-state and dynamic processes, the resultant multifaceted approach often yielding more relevant information on a catalytic system than the simple summation of the information provided by each technique when considered on an individual basis [3, 4]. A central tenet in technique combining is that the multiple technique data are obtained under precisely the same experimental conditions, thereby avoiding the problems associated with marrying up data from two or more separate experiments that will never be identical and often vary as a function of a number of parameters, such as cell operation, sample response, and data quality. To appreciate where the field lies today, we need to understand the initial motivations for technique combining from the early studies and to trace how factors such as technological

Characterization of Solid Materials and Heterogeneous Catalysts: From Structure to Surface Reactivity, First Edition. Edited by Michel Che and Jacques C. Védrine.
© 2012 Wiley-VCH Verlag GmbH & Co. KGaA. Published 2012 by Wiley-VCH Verlag GmbH & Co. KGaA.

development, scientific innovation, and scientific curiosity have shaped the field since. Where possible, we have used near "true-to-life" examples to illustrate the field, hopefully demonstrating its vibrancy.

Standing center stage in the application of combined techniques has been the utilization of synchrotron radiation (SR) sources. SR has been used heavily in catalysis characterization since the advent of the second-generation source in the late 1970s/early 1980s. It is principally utilized as an X-ray source, but it is in fact brighter than conventional laboratory spectroscopic sources across a large part of the electromagnetic spectrum [5]. In addition, the resultant beams possess higher collimation, higher temporal coherence, and better stability, polarizability and tunability; third- (early 1990s) and fourth- (present day) generation sources naturally offer improved performance metrics. In addition, such facilities are, for a number of reasons, highly amenable to performing challenging experiments. As such, the first reported technique combination utilized a core-based synchrotron technique, X-ray absorption spectroscopy (XAFS), in conjunction with transmission infrared (IR) spectroscopy to study methylene bromide in an argon matrix [6]. Although not tackling a catalysis problem, the study was successful in obtaining good-quality data from both techniques, good enough even to see the interaction of Br species with the Ar matrix. However, shortly after this, Couves *et al*. reported the utilization of two "core" SR-based X-ray characterization methods of XAFS and X-ray diffraction (XRD) to look at the first "catalyst oriented" problem [7]. These techniques are highly relevant for characterizing heterogeneous catalysts since the former is sensitive to structural change at the atomic level whereas the latter is sensitive to changes on a more global scale. The combination was used to study the two-stage activation of the mineral aurichalite [$Cu_{5-x}Zn_x(OH)_6(CO_3)_2$] to form, via a mixed CuO–ZnO oxide, an active Cu–ZnO water-gas shift catalyst. XRD in this case was recorded with a narrow bandpass (30 eV) and a position-sensitive detector to enable correlations to be made between the long-range crystalline phase information of the ZnO and Cu phases ($>\sim$2–3 nm). The XRD measurements were alternated with the acquisition of energy-dispersive extended X-ray absorption fine structure (EDE) (250 eV bandpass) data and a photodiode-array detector for studying the nature of local environment (i.e., oxidation state, near-neighbor distance, and coordination environment) of the Cu species. The aurichalite precursor was revealed to break down to form a mixed CuO–ZnO oxide phase on reaching 310 °C, the local Cu environment thus remaining octahedral Cu^{2+}. The same "lack of variation" was observed at the Zn K-edge when the bandpass was increased. On activation in an H_2–N_2 mixture, both XRD and XAS revealed the reduction of CuO to face-centered cubic (fcc) Cu species at 270 °C, which went on to sinter as the temperature reached 510 °C. While this study essentially focused on demonstrating the power of such a setup and its suitability in tackling the important issue of correlating local and long-range order effects, it also served as a sort of template to future studies of technique combining. For example, an environmental cell was employed that was designed so as to allow for data acquisition from two techniques. Furthermore, although not mentioned, it is highly likely that the X-ray beam was focused at the same point in the sample, thus allowing a direct correlation between the observations made using the two techniques. Perhaps

the greatest problem with the approach used was the quality of the data obtained (or lack of). Notwithstanding the obvious technical limitations associated with the instrumentation available at that time, there are intrinsic problems associated with collecting data in a dispersive mode – hence the subsequent development of the scanning monochromator for quick extended X-ray absorption fine structure (EXAFS) acquisition by Frahm in 1989 [8] that formed the basis of a Mark II X-ray absorption fine structure (XAFS)–XRD setup. Data from such a setup were presented for the first time in 1993 and delivered better quality XAFS data all round. Although the XAFS spectrum was acquired more slowly (minutes versus seconds), the setup was both more straightforward and was also developed with the flexibility to switch between transmission and fluorescence modes. XRD data could now also be collected at a fixed wavelength [9]. This new setup, developed simultaneously at two different synchrotrons [SLS (Daresbury) and HASYLAB] was used to study the evolution of the mineral phase cordierite via amorphization of the ZnO-contaminated disordered zeolite B structure and to study water-gas shift-type (Cu–ZnO) catalysts in what was at the time a "second first" in that it represents the first reported use of a plug-flow reactor for such studies [10, 11]. Importantly, although data acquisition was sequential, the quality obtained with both techniques was now sufficient to be able to identify multiple phases in the XRD pattern, and at the same time obtain detailed information on the local coordination state of the absorber. As a testament to both its robustness and its value, combined XAFS–XRD remains a common technique combination available on many synchrotron beamlines and therefore still plays a central role in the characterization of materials under reaction conditions.

Around the same time came a report detailing the first successful integration of simultaneous time-resolved *in situ* small-angle X-ray scattering (SAXS)–wide-angle X-ray scattering (WAXS) data acquisition (WAXS is also commonly referred to as XRD.) [12]. The technique is normally applied in a time-resolved manner to examine changes in a sample's structural characteristics (e.g., as a function of temperature/time, physical force, etc.). Although the pioneering work with this technique focused on the study of polymer melting, the setup was quickly put to use in studies of the hydrothermal crystallization of the zeolite silicalite-1 from a reaction gel [13]. Impressively, the operational temperature used in this study was 190 °C – the autogenous hydrostatic pressure within the reaction chamber being compensated by virtue of an external pressurized gas atmosphere surrounding a sub-chamber. Whereas WAXS data (incidentally using the same INEL detector as was used for XAFS–WAXS studies) demonstrated the direct evolution of crystalline silicalite-1 from the precursor gel, the SAXS data were characterized by a lack of fine structure, and this was interpreted in terms of the amorphous precursor system exhibiting surface fractal behavior. This was, however, somewhat inferred from the data rather than actually extracted since information on the precrystalline species was obscured by the highly interacting nature of the sample; the lack of real "information" extractable from the SAXS data on this system led to an important switch in methodology from the study of gels to clear solutions where the particles are "less interacting" [14, 15]. The SAXS–WAXS setup proved highly flexible with regard to

the coupling of additional techniques and witnessed the first combinations of synchrotron/non-synchrotron techniques with the creation of a differential scanning calorimetry (DSC)–SAXS–WAXS setup for polymer melt studies and the common laboratory-based attenuated total reflection (ATR)–Fourier transform infrared (FTIR) and Raman spectroscopy for following polymer processing [16]. Given the demonstrable promise that these technique combinations showed, it was surprising that their application was never extended beyond the polymer processing environment, although later we expound on possible reasons why.

Technique combing for the purpose of *in situ* catalytic reaction studies then appeared to hit a hiatus until 2001, when from beyond the walls of the synchrotron, the first coupling of ultraviolet–visible (UV–Vis) spectroscopy with X-band electron paramagnetic resonance (EPR) measurements were reported by Brückner [17]. The setup utilized a flow cell for the study of propane dehydrogenation over supported Cr catalysts under realistic conditions. The UV–Vis data were acquired on an Avantes spectrometer in diffuse reflectance mode from *inside* the reactor, making use of recent developments in optical fiber technology; indeed, one could argue that the introduction of the fiber-optic brought about a "revolution" in the ease of the application of spectroscopic techniques and has, with respect to UV–Vis diffuse reflectance spectroscopy (DRS) data, made it so facile and noninvasive that arguably good reasons need to be made *not* to utilize it if available. The data from this study nicely illustrated the corroborative benefit of such combined studies, that is, that whereas UV–Vis data provide insight into the behavior of Cr^{6+} species (by virtue of a strong charge-transfer (CT) band), EPR is more sensitive to the presence of species such as Cr^{5+}, while both techniques "see" Cr^{3+} and thus the observations made by one technique can be verified against those of the other. Importantly, the presence of a detector (i.e., a gas chromatograph) to determine the gas composition eluting from the reactor also enabled some understanding to be gained of the relation between structure and function.

The above development by Brückner in 2001 seemed to act as a something of a catalyst at the time, inspiring researchers to develop a number of two-technique combination setups, a few of which were first revealed at the inaugural *Operando* Spectroscopy Conference held in Lunteren in 2003 [18]. During this conference, setups with combined FTIR–Raman and Raman–UV–Vis were reported. The former apparatus was in fact a commercial enterprise (by Jobin-Yvon) with the added option of performing infrared (IR) measurements in confocal mode, whereas the latter again made use of the Avantes fiber-optic-based apparatus, although in order to avoid possible catalysis by the stainless-steel sheath that protects the optical fiber the probe was placed outside the reactor [19, 20]. Also in 2003 came the first report of a combined technique setup used for the study of a homogeneous catalytic process [21]. The setup, used for revealing the deactivation behavior of Pd catalysts, utilized a liquid stop-flow cell which allowed the acquisition of both transmission UV–Vis and, perpendicular to this, transmission energy dispersive X-ray data to reveal the stepwise formation of Pd nanoparticles from a Pd complex during allylic amination. Despite the obvious advantages demonstrated by this study, the application of X-rays (particularly EDE) for the study of homogeneous systems and, in particular, in

combination with stopped-flow techniques did not catch on as one might have been expected. This is most likely due to the difficulty in avoiding beam "influence" on the sample, although the advent of the continuous-flow reactor went some way towards reducing the problem of radiation dose [22, 23].

In 2004, a nuclear magnetic resonance (NMR)–UV–Vis setup for studying the methanol to olefin (MTO) process was reported and, shortly after, an FTIR–EDE setup designed principally for the study of automotive catalysts with the capacity for rapid switching between simulated lean and rich conditions [24, 25]. Here both techniques were capable of acquiring spectra with sub-second time resolution and the reactor setup was designed in such a way as to minimize the internal volume so that it was possible to correlate reliably fast spectral changes with gas switching. Interestingly, the setup, at least in its latter manifestation, shows a high degree of transferability, having also been successfully used on both scanning XAFS and high-energy XRD lines [26, 27].

Setups utilizing two techniques were anything but *de rigeur* at the time when combinations involving three techniques were first being reported in the literature in 2005. The driving force for the combination of three techniques was an obvious need to obtain more unique and/or corroborative data on the sample under investigation. Considering the feasibility of three-technique setups purely on a spatial perspective, there was plenty of scope, especially considering the ease with which fiber-optic-based technology for UV–Vis–Raman could be integrated into a reactor setup. Hence the three reported setups that combined three analytical techniques that year for performing simultaneous combined *in situ/operando* measurements all utilized UV–Vis and Raman spectroscopy and one other technique, which was either XAFS (two examples) or EPR, and were used for studying both homogeneous and heterogeneous catalytic processes [28–30]. Although technically more challenging, all studies demonstrated clearly that obtaining congruent data with such multiple technique setups leads to a more definitive understanding of what is happening in a dynamic process. For example, in the work by us [28], both UV–Vis and Raman data pointed towards a darkening of the catalyst, suggesting an initial coke build-up on the catalyst surface leading to an initial deactivation for both types of supported Mo catalyst, whereas changes in the Raman and Mo K-edge X-ray absorption near-edge structure (XANES) spectra suggested a more permanent deactivation associated with a change in the make-up of the active site. Indeed this "corroborative" benefit was observed again a few years later when this reactor setup was transferred to a hard X-ray diffraction line (albeit using now a point-source heater) in order to study the anaerobic oxidation of methanol over MoO_3 where simultaneous changes in the Raman and XRD data suggested that one oxygen of the MoO_3 lattice was more labile than the others [31, 32]. We also exploited the high-energy, intense X-ray source to collect, along with the diffracted beam, the parasitic signals of the inelastic scatter and the Mo Kα fluorescence so as to obtain three different signals from the same incident beam – thus in principle data from five separate techniques were recorded on the sample at the same time. The measuring of multiple signals from the same incident beam is probably the best way to obtain multiple technique spatiotemporal data since all signals originate from the same

position in space which is *defined* by the incident beam. As such, a number of recent reports have appeared in which combined technique data were presented as a function of time resolved in one or two spatial dimensions [5, 33].

The combination of three techniques represents something of a threshold, most probably since the associated technical challenges in combining more than this number of techniques do not as yet appear to outweigh the perceived benefits. However, there are a number of reported three-technique combinations, some of which are very recent, for studying both catalytic reactions and catalyst self-assembly, including SAXS–WAXS–XAFS [34], XAFS–XRD–Raman [35], XAFS–XRD–UV–Vis [36], ATR–UV–Vis–Raman [37] (liquid phase catalysis) and more recently pair distribution function (PDF)–SAXS–WAXS [38], representing an example of a technique combination which utilizes one beam from which three different measurements can be made. Both Table 23.1 and Figure 23.1 contain a more detailed summary of the various techniques that have been used regularly for combined *in situ* studies to date and also illustrate some of the associated strengths and weaknesses of the individual techniques. We then consider the practical implications of combining techniques before assigning a large part of the content to illustrating pertinent studies that have been performed in the field to give the reader a real idea of what is now possible. We end the chapter with a view on current and future perspectives.

23.2
Basic Tenets Behind Technique Combining

Let us first outline how one might expect to benefit from combining multiple techniques. The central tenet behind technique combining is that by recording data simultaneously, one expects to obtain more information on the state/behavior of the catalyst/catalytic process under investigation. For example, by obtaining information on the state of the catalyst while observing the behavior of the reactants and products of the reaction, such information could potentially lead to the revealing of a reaction mechanism that could ultimately lead to the development of better catalytic processes. Ideally, intelligent technique combining should result in information on a catalytic system which amounts to more than the sum of the individual parts. In this regard, certain conditions need to be taken into consideration when developing/designing a combined technique experiment. Below we outline what we consider to be the five most pertinent conditions and we discuss them accordingly:

1) Measurements give complementary chemical information.
2) Probing the same "part" of the catalyst.
3) The cell design/experiment should not impinge greatly on the quality and relevance of the data to be acquired.
4) Sample stability.
5) Data acquisition and analysis.

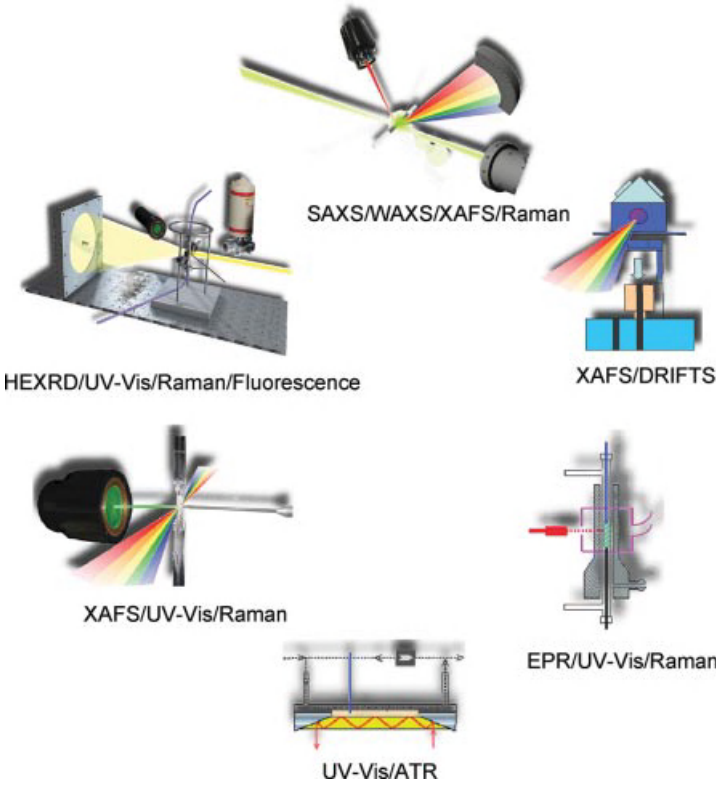


Figure 23.1 Insight from light! An assortment of selected combined technique setups from Table 23.1. Clockwise from bottom to top: combined ATR–UV–Vis, XAFS–UV–Vis–Raman, HEXRD–UV–Vis–Raman, SAXS–WAXS–XAFS–Raman, XAFS–IR, and EPR–UV–Vis–Raman.

23.2.1
Complementary Chemical Information

The primary aim of technique combining is essentially to obtain "congruent" data to unravel a chemical process. These data can provide information in one of two forms – either providing *more unique* information or else *more confirmatory* insight. Important here is the use of the word *more*, since it is not possible to pigeon-hole techniques as providing one particular "type" of insight which is going to be dependent on the subject under study. Almost every technique will provide a degree of unique or complementary information on the subject of interest. An example of the former case could be the combination of a technique sensitive to the reactant species at the catalyst surface (such as IR spectroscopy) with a technique able to probe the structure of the catalyst itself [such as X-ray absorption spectroscopy (XAS)]; the two techniques, when considered separately, are quite parochial [27]. In contrast, more

Table 23.1 Summary of techniques that have been used in technique combinations.

Ab.	SAXS	WAXS*	XAS	EDXRD	PDF	HEXRD	Raman	UV-Vis	IR+	EPR	NMR	
Technique	Small angle X-ray scattering	Wide angle X-ray scattering	X-ray absorption spectroscopy	Energy dispersive X-ray diffraction	Pair Distribution function / correlation function	High energy X-ray diffraction	Raman	Ultra violet-Visible	Infra-red			
Information obtainable	Information on and non-crystalline particle sizes and shapes	Identity of amorphous regions and changes in the intermediate and final crystalline state of the material.	Element specific local (bulk) information on bonding (EXAFS) and coordination and oxidation state (XANES)	Identity of amorphous regions and changes in the intermediate and final crystalline state of the material.	Non-element specific local (bulk) order information	In principle can incorporate SAXS/ WAXS and PDF information	Observation of organics and their interaction with inorganics, changes in organic conformer states, observation of coke	Changes in the electronic state and local environment of the material	Observation of bond formation and the interaction of species with catalyst surface			
Notes and limitations	More correlated systems are difficult to interpret	Monochromatic source (*usually* less penetrating, higher quality)	Element specific, mostly used with heavy heteroatom insertion	polychromatic source (*usually* more penetrating, lower quality)	Requires high energy X-rays, problems with solvent signal obscuring data	Highly penetrating. Not widely available	Can cause interference with UV-Vis signal in combined setups					
Size regime	Å - μ	Å - μ	Å	Å - μ	Å - nm	Å - μ	Å	Å	Å			**Refs.**

2 techs.	**SAXS**	**WAXS**										12,13,14,15,39,48,49,51
		WAXS	**XAS**									7,8,9,10,11,45,58
			XAS						**IR**			6,27,25,47,60,61
			XAS					**UV-Vis**				22,23
				EDXRD				**UV-Vis**				21
						HEXRD			**IR**			26
							Raman	**UV-Vis**				20
							Raman		**IR**			19,65
								UV-Vis		**EPR**		17
								UV-Vis	**IR**			63
								UV-Vis			**NMR**	24,25
3 techs.	**SAXS**	**WAXS**	**XAS**									34,54
	SAXS	**WAXS**			**PDF**							38
		WAXS	**XAS**				**Raman**					35
		WAXS	**XAS**					**UV-Vis**				36
			XAS				**Raman**	**UV-Vis**				28,29
						HEXRD	**Raman**	**UV-Vis**				31,32,42
							Raman	**UV-Vis**	**IR**			37
							Raman	**UV-Vis**		**EPR**		30?
5 techs.	**SAXS**	**WAXS**						**Raman**	**UV-Vis**	**IR**		57

Remember to add WAXS* is often also referred to as XRD. **AND** IR^{+} includes the ATR and FTIR variations. And note in the description that the top part of the graph describes the techniques whilst the bottom highlights the example combinations given in this chapter.

confirmatory insight is obtained by a technique combination such as XAFS–XRD, which together can be used to follow a solid-state change, for example, the oxidation of a metal nanoparticle where changes occur in both the long- and short-range order [39]. However, the extra information here from an XAFS point of view could come from probing the behavior of a particular dopant (e.g., oxidation/coordination state) within the crystalline matrix [40]. Either way, there are advantages for both approaches, the unique approach generating on average more overall information about the system while the confirmatory technique circumvents the need to perform additional experimentation. In both cases, however, there is normally sufficient scope to obtain more information on the sample than a simple sum of the individual measurements.

23.2.2
Probing the Same Part of the Catalyst

Central to obtaining complementary data is that the techniques employed should probe at least the same *area* of the sample, but preferably the same *volume*. For some technique combinations, that is, those involving combinations of transmission X-ray methods which utilize the same incoming source but where different sample characteristics are probed, such as SAXS–WAXS and XAFS–WAXS, this is implicit. However, with other techniques combinations this is more difficult to achieve, particularly the combination of techniques that rely on diffuse reflectance/emission for a signal with those that are bulk sensitive [27]. That the combined techniques probe the same part of the sample is important since many catalysts are by their very nature heterogeneous, comprising a number of species at the surface that could act as spectator, poison, or active sites. Therefore, even if a "sweet spot" is not being probed by one technique, it is important at least that the other technique(s) is(are) focused in the same area so as to maintain complementarity. In reality, the notion of "spot size" for some of the techniques employed (e.g., magnetic resonance techniques) simply does not exist since they sample the entire catalyst, hence it can be more difficult to relate the differences in any observations made. Techniques that generally utilize focused or small beams are normally employed for imaging purposes and it is becoming increasingly obvious that it is not always sufficient to perform simple single-point (0D) measurements of catalyst samples/reactors (due to axial and radial variations) to obtain insight into a catalytic process; the smaller the beam, the greater is the chance of probing an inhomogeneity in the sample and the greater the chance of obtaining less relevant data [1].

23.2.3
Setup Design

In many cases, the *in situ* cell will represent a compromise from the laboratory or plant reactor system, normally because of the need to modify the cell for measurement/data acquisition purposes. Often the parameters of data quality and relevancy are diametrically opposed; both the quality and/or the amount of the data are often

"sacrificed" as the degree of "relevancy" increases, although this will depend to some extent both on the sample under study and on the measurement technique being utilized. It is a moot point as to the best strategy, but many setups try to strike a balance between these two extremes [41]. For technical reasons, very few studies approach the conditions under which the measurements could be classified as real *operando*. In practice, the more techniques that are combined, the more challenging it is to remain close to the *operando* ideal [42]. Combining techniques also affects the quality of the data – sacrifices or compromises in the data quality that can be obtained from a technique are inevitable. This might be because a technique is employed in a suboptimal manner, that is, the signal is acquired through a window material that is highly transparent for one technique (e.g., ZnSe as an IR window) but not another (e.g., Raman) [19]. Alternatively, a parasitic signal from one technique (e.g., Raman) can interfere with the recording of another (e.g., UV–Vis) [20].

The sample under investigation for general *in situ* catalytic studies tends to take one of two forms. Either it is a pressed disc/wafer of controlled thickness or else a packed-bed reactor working as close to plug-flow reactor conditions as possible. The advantage of the former approach is that the data are invariably of better quality since the sample can be "adapted" to an optimal thickness. However, there are often issues with reactant/product diffusion limitations for such samples making it less "relevant" [43]. Alternatively, the packed-bed reactors are more relevant, yet problems such as "pinhole" effects and specular reflection abound which adversely affect data quality [44]. Most combined technique studies are performed on the more realistic packed-bed reactors, termed (capillary) microreactors. Liquid-phase catalysis also uses industrial-like batch reactors, although in comparison with the microcapillary setup, studying such catalytic processes is often technically more straightforward. Likewise for the hydrothermal synthesis of zeolites, where both microreactors and specially designed hydrothermal cells have been constructed, yet here the major requirement is that the reactor maintains an autogenous pressure [13, 45].

23.2.4
Sample Stability

Although by definition a measurement performed on a sample perturbs it, it is desirable to minimize the influence that this has on the sample. In extreme cases, this can lead to beam-induced sample damage. Generally, beam damage can be divided into primary and secondary effects. Primary beam damage is caused by the direct interaction of ionizing radiation with the electrons in the object via photoelectric, Auger, or Compton effects, which can cause direct damage to the chemical bonds within the specimen. This interaction also leads to the generation of heat and in particular energetic electrons, which are capable of generating additional reactive species such as free radicals, which can also react with and alter the chemical state of the specimen. This is known as secondary beam damage. For crystalline samples, a third type of radiation damage may also occur when the initial primary or secondary beam damage can cause a destabilization of the lattice, leading it to collapse, a process often referred to as tertiary beam damage. The primary beam damage depends only

on the energy of the incident radiation and the photons absorbed, whereas secondary and tertiary beam damage depend on the properties of the specimen. This problem could potentially be exacerbated by multiple technique studies where often increased light "loads" on the sample can be expected. This is not unavoidable, however, and simply requires that the radiation dose at the sample be managed, that is, the load at the sample can be estimated and managed accordingly by, for example, minimizing the exposure to the beam by shuttering, moving the sample, or (possibly for some techniques) a judicious choice of wavelength or edge energy (e.g., harder K edge versus the softer L_3) [42, 46, 47]. In the latter case, a shift in energy will result in the suppression of specific electronic processes and thus specific modes of sample degradation. An advantage of technique combining is that beam-induced effects are often easier to detect [22].

23.2.5 Data Analysis

23.2.5.1 Acquisition

In many cases, and for good reasons, the analysis of data is considered only after its acquisition. The problem with such a *post hoc* approach is that it can often be difficult to marry up the data acquisition from the two separate techniques. The extent to which this becomes a problem depends on the speed at which the data are acquired, the problem becoming greater with increased acquisition speed, which in turn is determined by the nature of the problem being tackled – for example, a time resolution of a few minutes for a solid-state change to milliseconds for the detection of chemical intermediates. Normally this is achieved via clock synchronization from the computers that control the acquisition of data from the multiple techniques so that it is possible to relate datasets via the time stamp (the time at which a file is created). However, the problem here can be that some programs create files at the beginning of an acquisition whereas others do so at the end – thus unduly complicating the marrying-up process. For extremely rapid data acquisition (milliseconds), this is simply not an option. Here acquisition synchronicity is crucial and can only be achieved by removing the autonomy of the individual technique acquisition process and using an external program to act as a master that controls the data acquisition from the individual techniques (slaves). This it does by 5 V high electrical triggering, known as a transistor–transistor logic (ttl) pulse, of the primed slave computers and which ensures that true simultaneous data acquisition can be achieved. This pulse can also be used not only to control data acquisition but also to effect an atmosphere modulation within the cell and to synchronize the effluent analysis. An example of this is demonstrated in Figure 23.2 for the acquisition of combined IR–EDE data where the fast-readout, low-noise (FReLoN) EDE detector camera was used to initiate the sequence of valve-switching events which was controlled by the IR software. From then on, the modulation experiment is determined by the IR spectrometer, so that when the gases were switched a subsequent trigger signal for EXAFS data collection was provided [48].

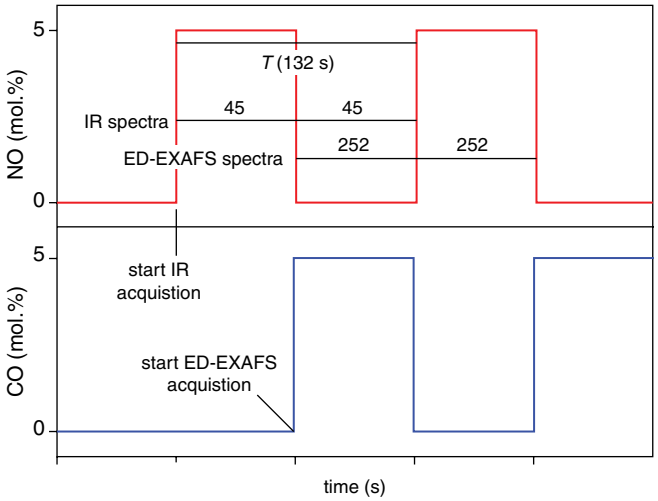


Figure 23.2 Description of a concentration modulation experiment. The experiment is started with the admittance of 5 vol.% NO–He to the cell and the acquisition of DRIFTS. At the first and at all following NO → CO switches (5 vol.% CO–He) the ED-EXAFS detector is triggered to measure 504 consecutive spectra. A total of 90 DRIFT spectra (45 + 45) are measured in a single modulation period ($T = 132$ s). Adapted with permission from [48], copyright 2010 Royal Society of Chemistry.

23.2.5.2 **Analysis**

A major problem associated with time-resolved data acquisition is the large volume of data generated. The more techniques employed, the greater a problem this becomes – the increase in the amount of data is at least linear, whereas the processing time almost certainly is not. Two approaches are then typically employed in order to extract some chemical metrics from the data. Data sets are selected at determined points in the experiment and analyzed/fitted in detail or else a small region of the data is chosen and fitting is performed on a diagnostic signal for a particular contribution over the entire data set. In many cases when handling *in situ* data, both approaches are used since this allows some of the more detailed changes to be put into context with the global changes in the sample. Ideally, all data sets would be treated and analyzed so that a detailed insight into a catalytic system could be obtained across the whole experiment for every technique and that this information could be combined and evaluated against each other to allow a truly integrated multi-technique experiment. This is yet to be achieved but might be possible in the not too distant future.

23.3 Illustrations of Setups Combining Multiple *In Situ* Techniques

In situ combined techniques have been employed to study the entire catalyst life cycle, that is, from catalyst genesis up to deciphering modes of deactivation. In what follows

we delineate the various stages of this cycle and provide examples that demonstrate how combined techniques have been utilized to provide insight into these stages. We begin in chronological order with studies into catalyst synthesis.

23.3.1
Formation of Microporous Materials

Unraveling the mechanisms by which microporous materials self-assemble has been a long-standing challenge. For this purpose, the SAXS–WAXS combination has been regularly used, delivering information on the sample with a time resolution in minutes, which is normally sufficient to measure solid-state transformation processes. The measured signals arise due to in-phase scattering of X-rays by electrons according to Bragg's law ($n\lambda = 2d\sin\theta$); the angle at which X-rays are coherently scattered is proportional to $1/d$ and thus provides a powerful tool for the examination of both inter- and intra-particle scattering. Thus the techniques provide insight into both the structure of small particles (2–200 nm) which scatter at low angles (SAXS) and the long-range order of crystalline entities, where strong scattering occurs primarily from the very small lattice d-spacings between atomic planes (WAXS) and therefore scatters at higher angles ($>10^\circ$ 2θ), are thus well suited for the study of material self-assembly processes.

Far and away the most commonly studied zeolite is silicalite-1. Some of the first work in this area was published by de Moor and co-workers, who revealed that the process was both complex and multi-step [49, 50]. Typical SAXS data recorded from such studies are given in Figure 23.3 and consists of broad contributions at ~2.8 nm

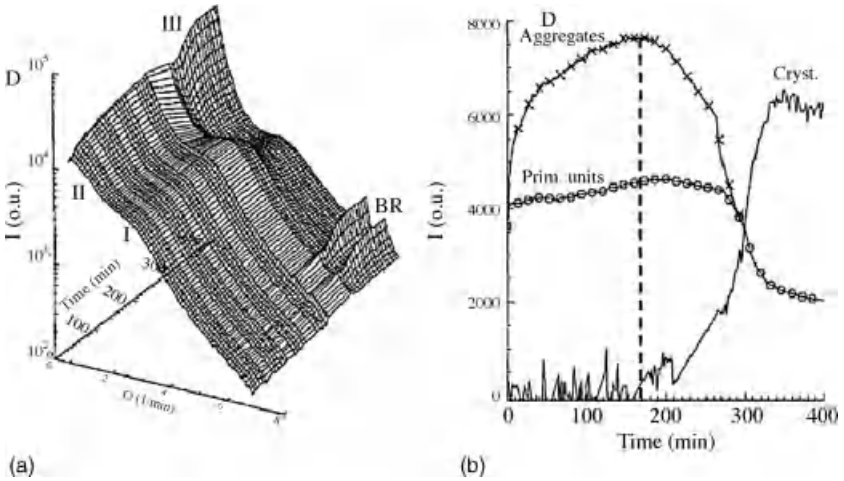


Figure 23.3 Example of the SAXS data obtained by de Moor *et al.* [49] during the synthesis of clear solution silicalite-1, where I = primary units, II = secondary units, III = SAXS crystallites, and BR = Bragg reflections (a) and the measurement of the intensity of some of these features as a function of time (b). Adapted with permission from [48], copyright 2000 American Chemical Society.

d-spacing ($q = 2\pi/d$), which were assigned to primary units, before larger aggregates with a mean size distribution around 10–15 nm (secondary units) and eventually crystallites (inferred from the appearance of Bragg peaks in the WAXS signal) are also observed. The breadth of these contributions suggests that the particle size distribution is fairly large and therefore it is not possible to perform a more detailed size determination via the Guinier radius at low q or the particle size and shape determination from single-particle "form factor" scattering in the mid q region [51]. It has recently been shown that the size estimation of such particles from SAXS measurements should, where possible, be confirmed by other techniques [52]. Although the observation of such particles was at that time not new, these studies allowed for the first time the observation of the formation process occurring "dynamically" over a very large size range (0.17–6000 nm) under truly *in situ* conditions. The experiments therefore not only confirmed the previous "pseudo" *in situ* observations but also provided essential information on how these nanometer particles evolved into crystalline material. From these data, it was proposed that primary units grow to form aggregates (secondary particles), which then continue to evolve and undergo internal re-ordering into crystalline material, with further crystal growth occurring via addition of primary units. The data also focused for the first time on the importance of larger colloidal species in the formation process, as indicated by previous theoretical Derjaguin–Landau–Verwey–Overbeek (DLVO) interaction calculations, and are therefore often accredited with "the emergence of the colloid" in zeolite synthesis [53].

SAXS–WAXS has, since these pioneering studies, been used to study many zeolite formation processes, particularly the industrially relevant zeolites A, β and Y [14, 15]. In comparison, aluminophosphates (AlPOs), a zeotype where it is easier to functionalize the porous framework with other ionic species, have rarely been studied with this technique combination. This is due in no small part to the industrial importance of the zeolite with respect to the AlPO subclass, but at the same time is also due to the difficulty in crystallizing AlPOs from clear solutions. However, this facile substitution behavior of the AlPO has been exploited by utilizing a substituent with a strong spectroscopic signal as a "local structure probe" for *in situ* studies [54]. Thus a technique combination in which atomic, short-range, and long-range order information could be obtained during porous material formation would be a potentially very powerful technique for revealing insight into porous material formation. For AlPO synthesis, several groups had already employed combined XAFS–XRD for such purposes, the XAFS data revealing, for example, changes in the local coordination of the Co^{2+} substituent prior to crystallization of CoAPO-5 [45]. This was subsequently expanded upon by us, when we developed a setup that provided this atomic-to-nano-to-crystalline phase evolution information. They did this by essentially adapting an existing XAFS–XRD setup by adding a SAXS camera (~1.8 m) to study the formation of the microporous AlPO ZnAPO-34 (Figure 23.4) [34]. Although only small changes in the XANES (feature at 7.666 eV) were observed during the self-assembly process, the changes were consistent with the gradual incorporation of tetrahedral Zn^{2+} species into a crystalline material, an observation borne out from analysis of the EXAFS data, where a decrease in the Debye–Waller factor was

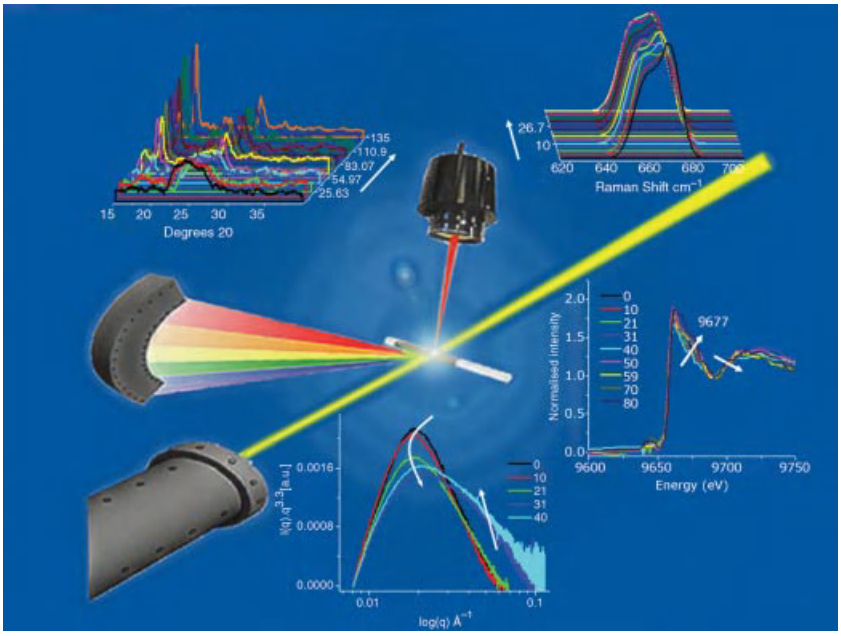


Figure 23.4 Schematic of setup complete with an illustration of the data recorded during ZnAPO-34 crystallization. Moving from top right and then clockwise: two peaks from the Raman data, sensitive to the presence of the conformer states of the TEAOH template, followed by Zn K-edge XANES spectra, in which two features are highlighted that confirm the formation of ZnAPO-34, SAXS data detailing the presence and evolution of two types of particle present in the pre-crystalline gel, and (top left) WAXS data detailing the formation of crystalline ZnAPO-34.

observed for the Zn^{2+} ions. Since AlPO gels are typically thick, no clear shoulder or maxima could be seen in the recorded SAXS data (recorded at 1 Å); however, on subtracting the power law decay dependencies (observed to be –3 over the data), diffraction amorphous broad maxima were revealed [13]. These "nanoparticles" increased only fractionally during the initial stages of reaction from ~11 to 12 nm before disappearing from the camera as crystallization of the ZnAPO-34 phase began. Interestingly, the values obtained for the nanoparticles closely matched the initially formed crystalline particles size (~12 nm estimated from a Scherrer analysis), indicating size retention during crystallization and a similar (but this time two-stage) crystallization mechanism, as seen for zeolite samples, was proposed. This conclusion was further supported by an invariant analysis where no change in the total scattering of the sample during the amorphous-to-crystalline transition was observed [55]. Interestingly, this work revealed the role of the Zn^{2+} ions to act as both a nucleating *and* structure-directing agent [56]. Since then, the setup has been utilized successfully for the study of catalytic systems and in particular the stability of iron molybdate catalysts under anaerobic methanol oxidation [44]. A major drawback, however, of the coupled XAFS technique is that it is not possible to study the "soft"

elements that comprise the majority of the porous material framework structure, that is, Al^{3+} and Si^{4+}. This is mainly due to their possessing an absorption edge energy which is strongly attenuated by air and therefore this requires that such edges are measured in vacuum. Hence in the main, XAFS studies have been restricted to examining "probe" elements (e.g., Zn or Co) substituted in relatively small quantities into the framework. The assumption here is that the substituent accurately mimics the major components and to an extent this is true, although it has also been shown that Co^{2+} ions in CoAPO-5 retard the crystallization process in comparison with unsubstituted AlPO-5 [57].

23.3.2
Online Catalyst Preparation

Microporous catalytic materials are not the only catalytic subjects that have been studied using *in situ* combined techniques. Bentrup *et al.* recently reported the synthesis of a phosphate-containing ammonium iron molybdate catalyst precursor using no less than five complementary methods coupled together (WAXS–SAXS–Raman–ATR–UV–Vis) [58]. Since the simultaneous combination of so many techniques is spatially demanding, they were split into two groups: ATR and UV–Vis measurements were performed immediately downfield of the sample preparation vessel, whereas Raman and X-ray scattering were performed even further down; the overall "outlet distance" was relatively short and since the pumping rate was high, the slurry phase reached the capillary within ~5 s (see Figure 23.5). The study illustrated principally the benefits of combining complementary techniques to yield a more thorough characterization of the sample. For example, initial mixing of ammonium heptamolybdate (AHM) and iron nitrate solution at 20 °C with stirring for 60 min yielded (from the WAXS data) a polymorphic Anderson-type A phase isostructural to

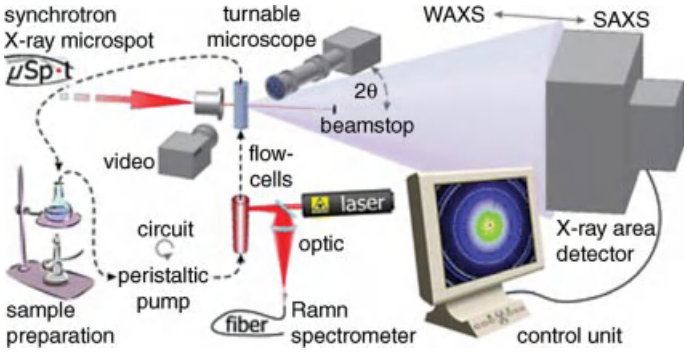


Figure 23.5 Scheme of the experimental setup with fiber-optic probes for ATR and UV–Vis immersed in the reaction solution and the flow cell implemented at the micro focus beamline for SAXS–WAXS and Raman. The reaction slurry was continuously pumped within a closed circuit. The flow cell was permanently observed via a turnable microscope. Adapted with permission from [58], copyright 2009 Springer.

the phase $(NH_4)_3H_6RhMo_6O_{24}{\cdot}6H_2O$ and a second "unknown" phase. Raman data not only confirmed the presence of the Anderson-type A polyion but also suggested, by virtue of the presence of a 967 cm^{-1} band, that the unknown phase comprised $[Mo_8O_{26}]^{4-}$ and probably also contained Fe. UV–Vis data appeared to confirm this Fe incorporation into one of the structures since a coincident shift of the absorption edge of the Mo(VI)–O CT band with the corresponding decrease in the Fe(III)–O CT band intensity was observed. A second stage in the process involved the addition of diammonium hydrogenphosphate (DAHP) solution followed by further stirring for 30 min which saw the disappearance of the unknown phase, whereas the third and final stage involved heating and stirring of the slurry for 60 min at 50 °C. During this last stage, bands in the Raman spectra for the Anderson-type A phase increased, which was proposed to be consistent with the incorporation of phosphate. In addition, a third crystalline phase was observed to form, which, by virtue of a growing band at 1013 cm^{-1} observed in the ATR data, suggested that this crystalline phase might be a molybdatophosphate coexisting with the Anderson-type phase A. In principle, such a setup offers a real means to explore and parameterize catalyst preparation fully. The fact that the techniques are not focused at exactly the same spot is unlikely to be a problem since high pumping speeds are employed and the reaction rate of the self-assembly process is likely to be in the order of minutes. Perhaps the greatest issue here is therefore the challenge in evaluating all the data so as to be able to pinpoint a synthesis mechanism(s).

23.3.3
Probing the Active Cu Species Under Methanol Synthesis Conditions

Copper-based methanol synthesis catalysts were perhaps the first to be studied in a plug-flow capillary microreactor and since that time they have been subject to numerous *in situ* investigations in an attempt to find the active species [59]. Particularly for the industrially relevant Cu–ZnO-based catalysts, where various copper species such as Cu^+, Cu^-, Cu–Zn alloys, and even ZnO on the surface of metallic Cu have been proposed to be the active phase. Either way, the Cu–Zn loadings are such that bulk phases present themselves and are thus clearly important for the activity. However, it took until the turn of the century for Grunwaldt *et al.* to perform an *in situ* XAFS–XRD study in order to shed more light on the possible active phases under reaction conditions [59]. They used a "low-loaded" (4.5 wt% Cu–ZnO) catalyst packed into capillary microreactors, since they offer ideal conditions for catalysis (e.g., plug flow, rapid temperature change, small temperature and concentration gradients) while allowing for the acquisition of data on the same part of the sample. Coupling the outlet of the reactor to a device for measuring the content of the effluent also allowed the determination of realistic structure–performance–activity relationships. In this work, it was demonstrated that after H_2 "activation" at 220 °C, both XAFS and XRD showed that the catalyst comprises metallic face-centered cubic (fcc) Cu particles. These species remain stable under reducing gas conditions (0.5% CO, 5% CO_2, and 4% H_2 in Ar) and start to produce CH_3OH and H_2O ($m/z = 31$ and 18) on a change to synthesis gas conditions (5% CO, 5% CO_2, balance H_2) at 220 °C.

This gas switchover witnessed a change in the Cu environment – the intensity of the peaks in the Cu K-edge Fourier transform decreased, suggesting that morphological changes accompanied an increase in activity. It was observed that the changes were reversible and could be explained in terms of "wetting" of the ZnO by Cu upon changes in the reaction conditions. Such dynamic changes in Cu morphology resulted in a better interaction with the ZnO support. Evidence for alloying in this system is not easy to detect, due in part due to the low Cu loading, but mainly because the major components possess similar X-ray scattering capacity. Additional experiments performed at extreme temperatures (600 °C) resulted in evidence for Zn–Cu alloy formation; however, since this temperature was so vastly in excess of those used in methanol synthesis, it was concluded that this alloying effect is not the critical step in the formation of an active species. Although pioneering, essentially the study used a model catalyst formulation at atmospheric pressure whereas industrially at least, the catalysts contain higher Cu loadings and the reaction is typically carried out at pressures in excess of 20 atm; hence it is some way from being *operando*. Recently, a number of high-pressure gas rigs have been commissioned on XAFS beamlines, hence it would be interesting to see how results obtained under more *operando*-like conditions compare with the above study [60].

23.3.4
Three-Way Catalyst (TWC) Components

23.3.4.1 Examining Local Structure Effects as a Function of the Gas Atmosphere

The synchronous combination of IR spectroscopy with an X-ray probe for the study of catalysts and catalytic processes appeared for the first time in 2004 [25]. The experiment utilized EDE with that of diffuse reflectance infrared Fourier transform spectroscopy (DRIFTS) and comprised a flow cell arrangement through which X-ray attenuation could be measured [boron nitride (BN) being used as both the window material, ensuring a gas-tight sample environment, and the sample holder] while IR spectra were collected perpendicular to this at the top of the sample [61]. Gases were then reacted over the sample (providing more of an atmosphere rather than a real flow environment) and the reactor outlet was coupled to a mass spectrometer for online product analysis. In order to ensure an acceptable compromise in sampling depths, X-rays were focused ~100–300 μm from the top of the sample bed. This setup has since been upgraded (modifications were made to a commercial Spectratech HT/HV DRIFTS chamber) so as to permit plug-flow conditions [62]. In addition, circular, vitreous carbon is now used in place of BN as a window material, thus removing some anomalous "effects" observed at lower X-ray energies (<~10 keV). Characteristic of this setup are the rapid data acquisition rates employed. Essentially this is defined by the detector readout; initially limited to 300 ms, but with improved detector performance (using a FReLoN detector) it can achieve as fast as 1.6 ms. Thus synchronous acquisition of DRIFTS and XAFS data at close to 20 Hz is possible and has been used to follow the behavior of supported precious metal catalysts under oscillatory gas compositions approaching cycling conditions (1–2 Hz) typically experienced by three-way catalysts.

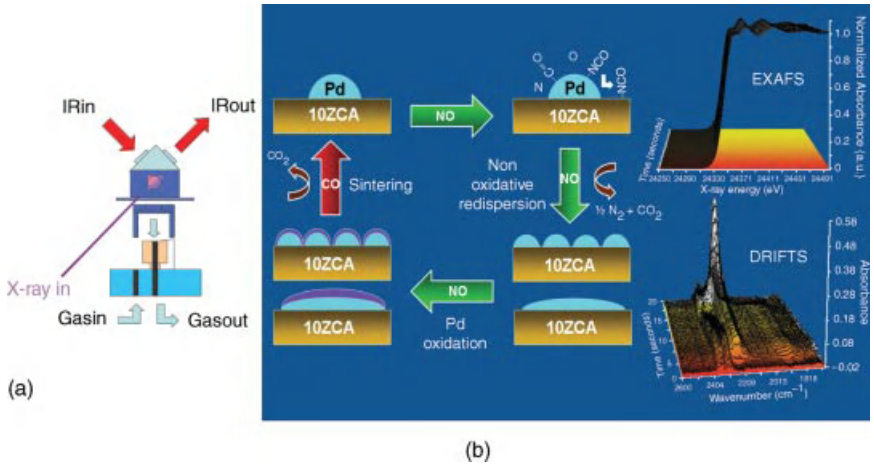


Figure 23.6 (a) Schematic diagram of the experimental cell used at the ESRF for making synchronous DRIFTS–EXAFS–MS. Vitreous carbon windows are used to permit a high level of X-ray transmission through the cell while at the same time minimizing potential interference to the XAFS measurement from glitches due to Bragg diffraction from more ordered windowing materials. (b) Scheme representing the fundamental steps underlying the reversible, nonoxidative, size (redispersion and sintering) and/or shape changes of Pd nanoparticles during CO–NO cycling. On the right, EXAFS and DRIFTS spectra (top and bottom, respectively) during CO–NO cycling to follow Pd structural changes and temporal variations of IR-active adsorbates and CO_2 evolution.

In Figure 23.6 are presented data in which the temporal response of a 1% Pd–CZA (ceria–zirconia on γ-Al_2O_3) catalyst to the gas inlet mixture composition was examined. Previously it has been observed that metal nanoparticles show a tendency to coalesce ("sinter") into larger aggregates under specific process conditions, leading to deactivation of the catalyst, predominantly since the chemistry exhibited by these systems is highly sensitive to the domain size of the active metal itself. It is known that such sintering processes can be reversed, at least in part, through the application of high-temperature oxidation methods and subsequent re-reduction. With this approach, Newton *et al.* studied 1 wt% supported Pd catalyst systems during CO–NO cycling at 673 K [63]. XAFS data revealed that the pre-reduced Pd nanoparticles remain in the metallic state, irrespective of the environment (5% NO–He or 5% CO–He), with little evidence for a PdO-type phase. However, under a CO environment, it can be seen that the Pd–Pd coordination is larger (~8) compared with the situation found under NO (~5). The authors reasoned that this could not be due to partial oxidation of the Pd species since the XANES data showed little evidence (<10%) of Pd^{2+} species being present. Instead, it was proposed that such changes were due to a constant-volume morphological change (that is, a flattening and unflattening of the Pd particles). DRIFTS data showed that a number of species adsorbed at the support surface were various Pd–CO-type species (threefold/bridged at 1864 cm^{-1} and linear, atop at 2048 cm^{-1}), which also showed the same temporal behavior. Hence it was proposed that at the start of the reducing (CO) cycle the Pd exists as dispersed or

flattened particles with partially oxidized surfaces. This surface oxygen is rapidly removed as CO_2 and the particles "sinter" before flattening again under an NO atmosphere. Hence it was concluded that reversible metal sintering and nonoxidative re-dispersion phenomena take place.

23.3.4.2 Rationalizing Short-Range Behavior with the Observations Made at Long Range

Very high-energy XRD beamlines permit Q space compression into smaller and smaller angles (by virtue of Bragg's law) and hence the signal can be squeezed into/out of increasingly smaller reactor volumes. When used in conjunction with the flat-panel Si detectors that have arisen from medical imaging research (fast acquisition, rapid readout, low noise), it is possible to perform XRD with a high time resolution, which complements that of both the DRIFTS and XAFS experiments. Recently, Newton *et al*. reported a successful transplantation of the EDE–DRIFTS setup to a hard energy XRD line in order to study a supported (3 wt% Pd–Al_2O_3) sample, but this time using time-resolved hard energy XRD (HXRD) with DRIFTS and mass spectrometry (MS), with the example of CO–NO cycling over supported Pd nanoparticles [26]. Importantly, and although on a slightly different sample, this technique combination allowed the authors to look again at the cause of the oscillatory behavior of the coordination number seen in the previous XAFS–DRIFTS study [63]. In these experiments, they observed an isotropic expansion of the Pd unit cell with time on-stream in a CO atmosphere, leading them to conclude that dissociation and subsequent storage of atomic carbon within the Pd nanoparticles occurred, leading to the formation of PdC_x. This phase disappears under NO conditions, suggesting that the Pd nanoparticles (3 nm diameter) actively participate in the de-NO_x chemistry. Furthermore, it was shown that the formation of PdC_x promotes the formation of linear CO species on the surface of the changing nanoparticles and that this has a drastic effect on the linear-to-bridge ratio observed in the IR spectra. This, the authors commented, has important implications for the analytical method of using the bridging-to-linear ratio to estimate the Pd particle size under reaction conditions.

23.3.5 Propane Dehydrogenation

Beyond the X-ray world, the first reported novel two-technique setup was described in 2001 and was constructed via embedding a home-made quartz plug-flow reactor within the rectangular cavity of a continuous-wave X-band electron spin resonance (ESR) spectrometer [17]. The cells are thick-walled (1.5 mm) and have an internal diameter of 2.5 mm with a pressure controller/reducer on the inlet and outlet, and have been used to monitor the dimerization of butenes up to a total pressure of 20 bar under flow conditions [64]. UV–Vis diffuse reflectance spectra are recorded using a probe inserted through the top of the reactor into the reactor bed, which is connected via fiber-optics (length 2 m) to a dispersive spectrometer, the outlet of the reactor being connected to a gas chromatograph. The setup has been used to demonstrate the

congruent information that can be obtained when comparing the behavior of two catalysts used for the industrially important dehydrogenation of propane to propene – a reaction resulting in the production of close to 10 million metric tons of olefins per annum.

The catalysts, $Cr/La,Al_2O_3$ and $Cr/La,ZrO_2$, were prepared by two different methods and contained mainly Cr^{6+} (a CT band at 370 nm is seen in the UV–Vis spectrum) although traces of Cr^{5+} species (narrow singlet at $g' \approx 1.97$ in the EPR spectra) and some evidence for Cr^{3+} (*d–d* transition band around 630 nm) could also be seen. Upon heating under propane, the bands due to Cr^{6+} disappear while the *d–d* band for Cr^{3+} increases; confirmation of the presence of Cr^{3+} species is also found in the EPR spectra, where a broad singlet at $g' \approx 2$ arises. Since this occurs at temperatures below the onset of catalytic activity, it was concluded that Cr sites in oxidation states higher than $+3$ do not exist under the reaction conditions. On heating to 810 K and with increasing time on-stream, the EPR singlet of Cr^{3+} loses intensity and a gradual increase in absorbance in the visible range of the spectrum, with a maximum around 470 nm, is seen. This coincides with a decrease in propane conversion for the $Cr/La,ZrO_2$ catalyst – all observations being consistent with partial coverage of active Cr^{3+} sites by coke deposits. For the $Cr/La,Al_2O_3$ sample, similar observations were made, although in this case from the UV–Vis data it was possible to infer that the nature of the carbonaceous deposits were different.

23.3.5.1 Catalyst Activation, Deactivation, and Regeneration

Catalyst deactivation is a major problem for Cr/Al_2O_3 alkane dehydrogenation catalysts and hence an air treatment step is employed to regenerate the catalyst every 20–30 min. An examination of the activation/regeneration behavior of these catalysts was studied using a novel combination of Raman and UV–Vis spectroscopy [20]. The setup developed for such a reaction system consists of a 6 mm diameter quartz reactor tube with a special square section for minimizing specular reflectance, in which the tube wall is made of optical-grade quartz windows. Typically, 300 mg of catalyst is placed in the reactor as a packed bed (15 mm high) supported on a sintered-glass frit just below the optical windows. The reactor is then placed vertically in the center of a 10 cm long tubular oven block. The metal oven block has on opposite sides two horizontal 8 mm holes directed at the catalyst bed, through one side of which a UV–Vis reflection probe is placed and through the other side a Raman laser (532 nm) is focused. The reactor outlet is connected to a quadrupole mass spectrometer–gas chromatograph. After heating to the reaction temperature of 550 °C, the reactor was operated isothermally in cycles of alternating dehydrogenation for ~50 min with 2 ml of propane in 20 ml min^{-1} of He and regeneration for ~50 min with 3 ml min^{-1} of O_2 in 12 ml min^{-1} of He. The catalytic activity was tested over three dehydrogenation–regeneration cycles (see Figure 23.7). Whereas the catalyst performance did not change from one cycle to the next, it changed significantly within one dehydrogenation cycle, with propene conversion increasing with time on-stream, reaching a maximum of 55% after 28 min, after which it began to decrease. Changes occurred in the UV–Vis spectra in the first 6 s of the dehydrogenation reaction, yielding an isosbestic point at 565 nm, indicative of a mixture of Cr^{6+} and Cr^{3+}; thus the Cr^{6+}

was reduced. After 28 min of reaction, the overall absorbance of the sample increased and the Cr^{3+} *d–d* transition band at 630 nm became less pronounced. At the same time, bands appeared in the region 1200–1650 cm^{-1} due to the formation of carbonaceous/coke-like deposits and the same time the baseline at high wavenumbers decreased, due to fluorescence suppression. Hence it was concluded that coke formation is the most likely cause of the decrease in catalyst activity over time. Oxidation regenerates the catalyst by burning off the coke deposits (as witnessed by the evolution of CO_2 at the beginning of the regeneration cycle), yielding UV–Vis and Raman spectra identical with those at the beginning of the dehydrogenation cycle.

Unsurprisingly, deactivation by coke deposition is a common problem for alkane dehydrogenation catalysts, although this can be somewhat ameliorated for Pt/Al_2O_3 by alloying with Sn. However, even this effect is limited to a small number of reaction–regeneration cycles since the Sn does not prevent the age-old problem of Pt sintering [65].

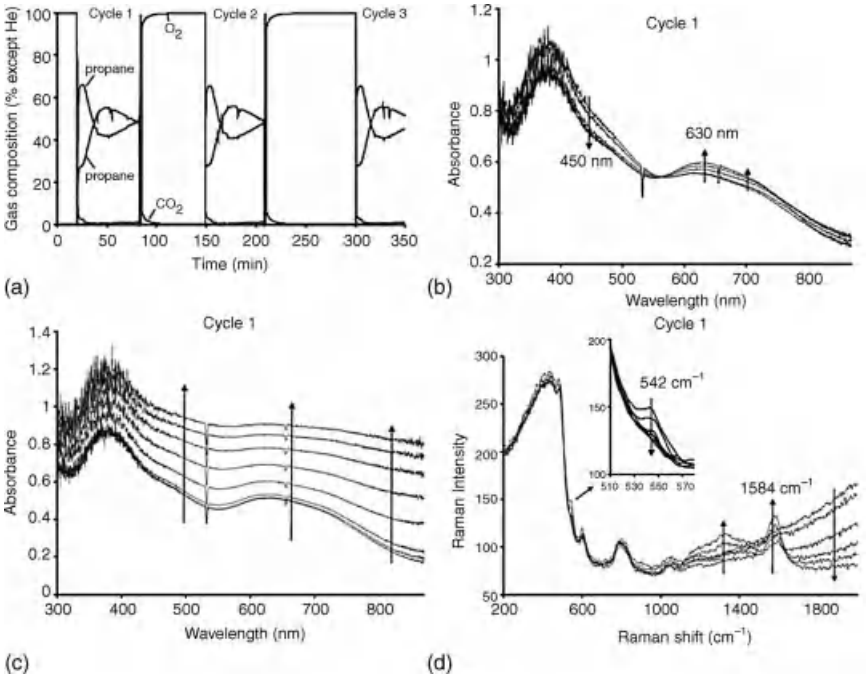


Figure 23.7 Propane dehydrogenation using a 13 wt.% Cr/Al_2O_3 catalyst (1 bar, 823 K). (a) Catalytic activity measurements for three dehydrogenation–regeneration cycles; (b) *operando* UV–Vis spectra showing the rapid changes during the first 6 s of the first dehydrogenation cycle; (c) *operando* UV–Vis spectra of the first dehydrogenation cycle as a function of time-on-stream after the first 6 s; (d) *operando* Raman spectra of the first dehydrogenation cycle as a function of time-on-stream. Adapted with permission from [20], copyright 2003 Royal Society of Chemistry.

23.3.6
Understanding the Key Stages in Methanol to Olefin Conversion

Such is the versatility of the fiber-optic UV–Vis probe that it has also been employed in conjunction with another magnetic resonance technique, NMR [24]. A commercial, variable-temperature 7 mm magic angle spinning (MAS) NMR probe from Bruker BioSpin was first modified with an injection system to allow for continuous-flow measurements, whereas for combined measurements it was further adapted by equipping it with a quartz glass window at the bottom through which UV–Vis data could be collected via a fiber-optic. This combined setup was then used to study the formation of hydrocarbons by the conversion of methanol on a weakly dealuminated zeolite H-ZSM-5 at low reaction temperatures. Here the rationale behind the technique combination was to make use of the better chemical resolution of NMR while retaining the better overall sensitivity of UV–Vis spectroscopy.

The weakly dealuminated zeolite H-ZSM-5 was dehydrated at 673 K under vacuum for 12 h before it was filled into the MAS NMR rotor under dry nitrogen inside a glove box. The methanol ($^{13}CH_3OH$) flow ($W/F = 25\ g\ h\ mol^{-1}$) was started after reaching a temperature of 413 K. The ^{13}C MAS NMR spectrum recorded (Figure 23.8) at this temperature during methanol conversion contained signals at 51, 61, and ~23 ppm, due to methanol, dimethyl ether, and probably alkanes or alkylated cyclic compounds, respectively, indicative of the reaction having already begun. These observations were broadly supported by those in the UV–Vis spectrum, where bands at ~275, 315, and 375 nm were present which were ascribed to the presence of neutral aromatic compounds and possibly mono- and dienylic carbenium ions. It is important to

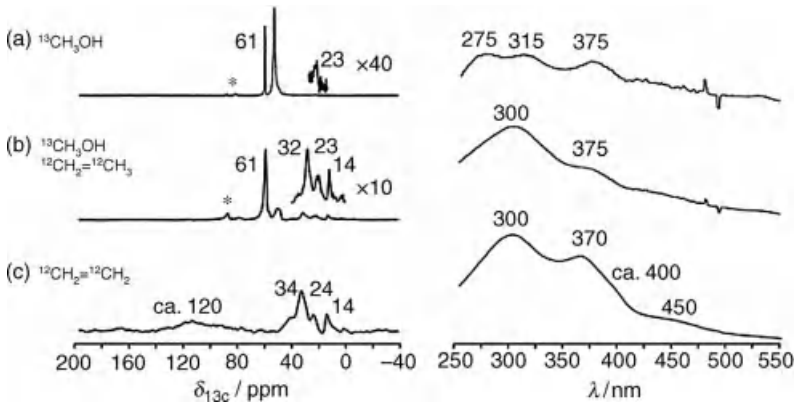


Figure 23.8 ^{13}C continuous-flow MAS NMR (a) and UV–Vis (b) spectra of a dealuminated zeolite H-ZSM-5 recorded (a) during conversion of $^{13}CH_3OH$ under continuous-flow conditions ($W/F = 25\ g\ h\ mol^{-1}$) at 413 K for 2 h, (b) during a subsequent conversion of $^{12}CH_2 = {}^{12}CH_2$ ($W/F = 10\ g\ h\ mol^{-1}$) at 413 K for 1 h, and (c) during conversion of $^{12}CH_2 = {}^{12}CH_2$ ($W/F = 10\ g\ h\ mol^{-1}$) at 413 K on an unused catalyst for 2 h. Asterisks denote the presence of spinning sidebands. Adapted with permission from [24], copyright 2004 Royal Society of Chemistry.

note that the UV–Vis spectrum of the parent zeolite (H-ZSM-5), recorded under the same reaction conditions (not shown), consists only of a very weak band at ~300 nm, hence it was concluded that extra-framework Al^{3+} species acting as Lewis acid sites promote the reaction. In order to eliminate the origin of these products being due to ethylene (the first nonoxygenated product seen in the reaction), the same experiment was performed at 413 K for 1 h. These experiments yielded signals at 14, 23, and 32 ppm, ascribable to alkyl groups of small amounts of alkylated cyclic compounds, such as cyclopentene, cyclohexene, cyclohexadiene, and benzene. The simultaneously recorded UV–Vis spectrum exhibited bands at 300 and 375 nm, which again gave a hint at the formation of neutral cyclic compounds and dienylic carbenium ions, respectively. In addition, similar results were obtained with untreated zeolites but at lower temperatures – hinting at an important role for extra-framework Al^{3+} in methanol activation at low reaction temperatures.

23.3.7
De-NO*x* Over Pd/Al_2O_3

Although at first glance the combination of the two vibrational techniques IR and Raman spectroscopy seems an exercise in complementarity, the different properties of the incident radiation used results in Raman spectroscopy being more sensitive to low wavenumbers where many metal oxides have characteristic lines, whereas FTIR spectroscopy is more sensitive to the presence of adsorbates. A setup designated the LabRAM IR spectrometer, designed and constructed by Jobin-Yvon, comprises a combined dispersive Raman and FTIR microscope with a dedicated cell directly fitted to the microscope stage which uses the SameSpot (laser and IR beams are coincident at the sample) technology to allow a quasi-simultaneous examination of one sample area by both techniques [19]. The apparatus can handle measuring in ATR, transmission, or diffuse reflection–absorption mode, the last utilizing an all-reflecting objective (Cassegrain/Schwarzschild type). The window of the cell was made of 1 mm thick ZnSe, due to the high transmission in the mid-IR region and its inertness. The sample compartment of the cell is divided into two parts, one of which is filled with KBr used as an internal reference and which can be used to correct the DRIFT spectra using the Kubelka–Munk treatment.

The setup was used to study Pd/Al_2O_3 under reaction conditions. The initial Raman spectra exhibited a major line at 639 cm^{-1}, assigned to the Raman B_{1g} active mode of PdO, due to surface "passivation" of Pd after contact with air. The corresponding IR spectrum reveals the presence of adsorbed water (1649 cm^{-1}) and carbonate species (1509 and 1401 cm^{-1}) on alumina. After H_2 reduction at 573 K for 2 h, the IR data showed that the aforementioned species were desorbed while the Raman feature of PdO was no longer observed. During NO exposure, bands at 1461, 1561, 1556, 1614, 1305, and 1556 cm^{-1} could be observed in the IR data, which can be assigned to the two distinct NO stretching modes of chelating bidentate nitrito ($-O_2N$) compounds and nitrato species, bridged nitrate species, and bidentate nitrato species, respectively. The Raman data, in contrast, exhibited intense lines at 828 and 1308 cm^{-1} and a broader one at 332 cm^{-1}, which can be assigned to the

ONO deformation and NO_2 symmetric stretching modes of a nitro compound and the presence of a Pd−N bond vibrational mode of NO species adsorbed on metallic Pd. Cooling in an atmosphere of NO to 298 K led to broadening of an additional band at 1328 cm^{-1} and the appearance of a new broad band at 1428 cm^{-1} assigned to nitro compounds ($-NO_2$) coordinated by the N atom. In contrast, the Raman spectroscopic data revealed that lines previously assigned to nitro species were no longer observed, although free nitrate ions could be seen. The authors proposed that oxygen at the metallic Pd surface reacts quickly with NO, in a first step, to form nitrito compounds, followed by the subsequent formation of nitrato compounds as a result of further reaction of NO and surface O. The rapidity of such a reaction explains the absence of a signal for PdO during NO exposure and suggests that metallic Pd is the active phase.

23.3.8
Killing Three Birds with One Stone

For performing simultaneous *operando* experiments in triplicate, the previously reported EPR–UV–Vis setup was adapted to allow for the collection of a Raman signal through a front hole in the EPR cavity [30]. Furthermore, in contrast to the previous setup, heat was transferred to the reactor by a stream of N_2 which was preheated by passing over an electrical heater. The setup was used to study the oxidative dehydrogenation of propane over 6 wt% V_2O_5/TiO_2 catalyst. *Operando* experiments were performed by the gradual heating of a mixture of 8.3% C_3H_8 and 8.3% O_2–N_2 (total flow 24 ml min^{-1}) to specific temperatures with a 10 min isothermal hold at each temperature for recording the spectra and gas chromatography (GC) analyses. Analysis of the sample was not a simple task since, as could be typically expected for a supported catalyst, the initial material contained a number of vanadium species on the catalyst surface, including: pentavalent V_2O_5 (Raman bands at 1034 and 945 cm^{-1} and a broad band around 470 nm (VO^{3+}) arising from a CT transition in the UV–Vis region) and EPR-sensitive tetravalent VO^{2+} species [possessing a hyperfine structure (hfs) ($g_{||} = 1.940$, $A_{||} = 176.3$ G, derived by spectra simulation) bonded directly to the TiO_2 surface (Figure 23.9). Initial exposure to the feed at 20 °C saw the Raman band at 1034 cm^{-1} disappear and a new high-field signal appear in the EPR spectrum (characterized by ($g_{||} = 1.925$, $A_{||} = 199.2$ G) caused by the reduction of isolated V^{5+} species on TiO_2 to V^{4+}. The disappearance of the 1034 cm^{-1} band revealed the presence of an obscured band at 1024 cm^{-1} due to polymeric surface V_xO_y – although it was proposed that this was probably present before the initial reduction. With a stepwise increase of temperature, this Raman band decreased gradually whereas those for V_2O_5 dropped to a constant low level above 200 °C. The Raman bands of the TiO_2 support also lost intensity although more slowly and at higher temperature compared with V_2O_5, hinting at a possible redox role of the support in the catalytic process. Under these conditions, a broad singlet in the EPR spectra of polymeric $V^{4+}O_x$ species grew from the V^{5+} sources which increased until it reached a constant value at 220 °C. Above 250 °C, further reduction in the EPR signal was observed, probably due to the reduction of isolated VO^{2+} sites to EPR-silent V^{3+} which might be inactive. The color changes in the UV–Vis spectra simply

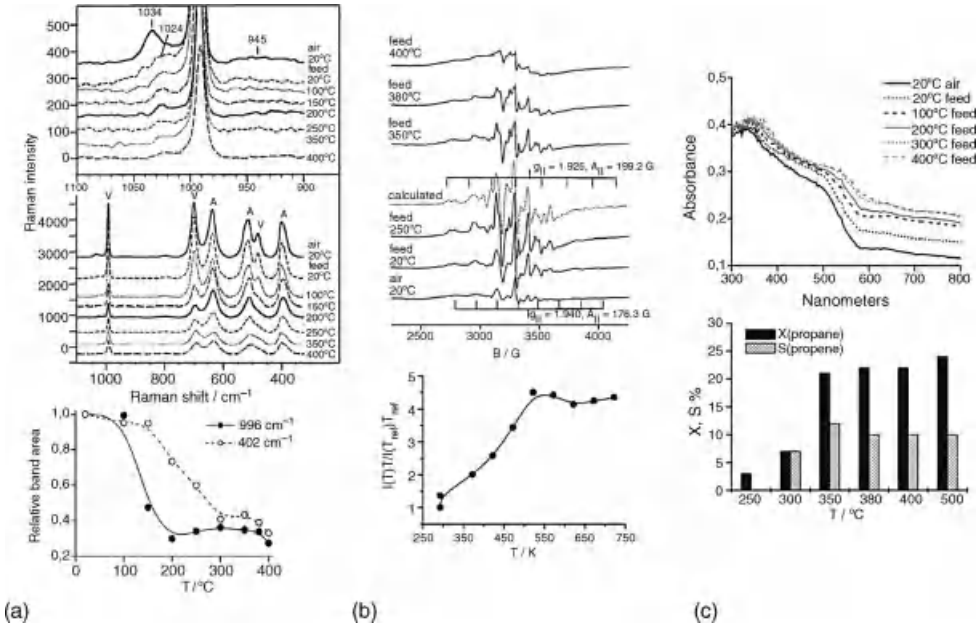


Figure 23.9 (a) Raman spectra before and during oxidative dehydrogenation of propane. Note the Raman bands marked with V = V_2O_5 and A = TiO_2. (b) Simultaneously collected EPR spectra and normalized spectral intensity. (c) Corresponding UV–Vis and catalytic data. Adapted with permission from [30], copyright 2005 Royal Society of Chemistry.

reflect the reduction of the V sites with negligible coke deposition. However, all of this occurred even before propane conversion began at 250 °C. At 350 °C, virtually all monomeric and polymeric $V^{5+}O_x$ surface species and a considerable part of the V_2O_5 crystals were reduced; with an increasing extent of V^{5+} reduction, propene selectivity increased. Thus V^{4+} species (including isolated and polymeric VO^{2+} on TiO_2 and also on the surface of V_2O_5 microcrystals) dominated under the reaction conditions and represent the likely active sites for the reaction. The low temperature (250 °C) for propane conversion clearly indicates the importance of the properties of the TiO_2.

23.3.9
Propane Dehydrogenation Studied Using Three Techniques Simultaneously

Much as with the previous three-technique setup, the setup for obtaining XAFS–UV–Vis–Raman data originated from the two-technique combination of UV–Vis and Raman spectroscopy, albeit this time adapted with a third entrance–exit window for X-ray transmission measurements [28]. The focal point of the setup is a specially adapted quartz reactor tube (6 mm o.d. and 1 mm i.d.), which has been ground down on three sides to ~200 μm to ensure sufficient X-ray transmission. The windows in the furnace, despite being only 1 mm, are sufficiently wide to allow measurements to

be made on the sample. Posing the least problem here is the X-ray source, which in this case is a highly focused Laue EDE beam, hence the spot size at the sample is of the order of 100 μm with little divergence around the sample. Hence the setup comprised a plug-flow reactor in which the same part of the sample is probed simultaneously by the three techniques and was used to study supported metal oxide catalysts (Mo/SiO_2 and Mo/Al_2O_3) under propane dehydrogenation conditions. Again, the strength of the combination is to be found in the complementarity of the techniques employed in that all provide information on the extent of oxidation/coordination states of Mo during dehydrogenation and regeneration. Contrasting catalyst behavior was observed under the cycling conditions. For example, Mo/SiO_2, after an initial flourish of propene production, underwent a gradual deactivation due to coke formation. This was characterized by the disappearance of Raman bands due to clustered MoO_3 at 992 (νMo = O), 820 and 664 (νMo–O–Mo), 335 (δMo–O–Mo), and 281 cm^{-1} (δMo = O) as the overall diffuse reflectance from the sample decreased. Changes in the ED-XANES data suggested that the shift in the white line ~20 min later is consistent with Mo^{6+} reduction to (most probably) Mo^{4+}, this also contributing to catalyst darkening and the decrease in the signal for MoO_3. Switching to oxygen-rich conditions (for catalyst regeneration) revealed the reappearance of MoO_3, although the greater peak intensity in the Raman spectrum suggested that significant clustering had occurred, leading to lower propene yields. Further reaction–regeneration cycles led to continued deactivation through coke formation and also repeatedly lower yields of propene as a result of further sintering of the catalyst. Similar short- and longer-term deactivation behavior was also observed for the Mo/Al_2O_3 sample, although this time, due to a strong affinity of Al_2O_3 for Mo, clustering was not observed as a mode for deactivation, hence a reaction of with the support was proposed to be responsible.

23.3.10
Profiling a Reactor Bed with Multiple Techniques

XRD has proved a popular technique for profiling crystalline structural changes for a number of years. Many of these studies were focused on catalytic materials (from both synthetic and catalytic viewpoints) housed in capillary microreactors on bending magnet lines whose maximum X-ray flux is limited and optimized at comparatively long wavelengths (ca. >0.5 Å, <30 keV). However, there are distinct advantages to be realized when using high-flux/high-energy (e.g., 0.14 Å, 89 keV) insertion device beamlines for performing such measurements, including (a) improved X-ray penetration allowing a larger sampling volume to be probed and thus better sampling statistics, (b) the possibility of obtaining and measuring secondary "parasitic" X-ray signals (e.g., inelastic scatter and fluorescence), and (c) reduced beam influence. Using high-energy XRD as the X-ray-based technique in a setup that combined XRD, UV–Vis, and Raman (along with MS), O'Brien and co-workers looked at the problem of volatilization of Mo from MoO_3 in a large packed bed (5.5 mm i.d. and 15 mm depth) under both methanol and water vapor conditions for up to 15 h [31, 32, 42]. For these experiments, an "open-cell architectural design" was

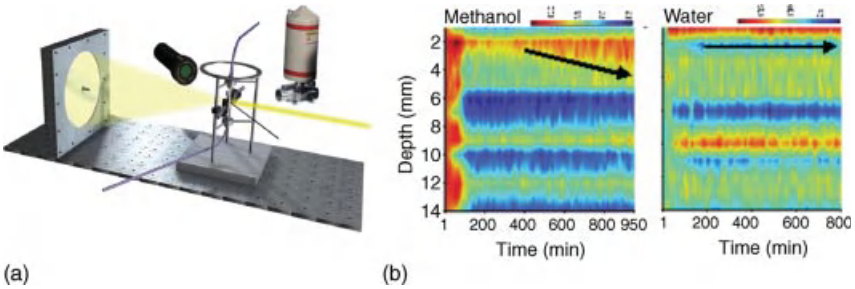


Figure 23.10 (a) Schematic of a multi-technique high-energy setup for spatiotemporal characterization studies on catalytic solids. The SR techniques WAXS, fluorescence and Compton scattering were utilized, and in this experiment complementary Raman–UV–Vis–online MS was also used. The reactor consists of a large (5.5 mm i.d., 0.55 g) quartz reactor heated by air guns in an "open" architecture. (b) One-dimensional spatiotemporal Compton scattering maps of MoO_3 under a reducing methanol vapor and a water vapor. From ~400 min, density reduction (decreased absorption and increased signal intensity) is observed in the top of the reactor but only under methanol conditions. Adapted with permission from [32], copyright 2009, Wiley-VCH Verlag GmbH.

employed (see Figure 23.10) in which heat is supplied by a jet of air from two heat guns directed at the catalyst, allowing for more "room" around the reactor for technique coupling. Helium was used as the carrier gas and was supplied using a heated inlet and mass flow controllers (50 ml min^{-1}). Both water and methanol vapor were mixed using a large dead volume bubbler (for good mixing) maintained at the desired temperature for the correct vapor saturation (15%). Measurements were performed in one dimension along the length of the reactor by moving and then recording during an 8 s stationary "window" at 1 mm intervals along the length of the reactor (12–15 points lasting ~7 min). Spatiotemporal XRD plots from the first 240 min of reduction in methanol revealed significant changes as a function of both space and time during the first 150 min; MoO_3 was reduced (~50 min) evenly down the bed, although the products, $Mo_xO_yC_z$, MoO_xH_y, and MoO_2, were not evenly distributed, the last 2 mm of the bed being richer in MoO_2. These observations were broadly supported by the simultaneous Raman and UV–Vis data, although since the product phases were dark, it was only possible to track the disappearance of MoO_3. A possible cause of this product inhomogeneity was ascribed to the gas-flow regime within the reactor being laminar rather than true plug flow, although interestingly, in comparison with "standard" capillary reactor experiments, this larger reactor system is an order of magnitude more plug flow-like. The reduction of MoO_3 was not unexpected, of course, but interestingly, analysis of the Compton (inelastic) data revealed a gradual reduction in sample density towards the top of the reactor (inlet) with time. This occurred despite the sample undergoing a compositional change to $Mo_xO_yC_z/MoO_xH_y$ and the structurally more dense MoO_2 and is thus strongly suggestive of leaching of the $Mo_xO_yC_z$ and/or MoO_xH_y phase under methanol conditions. No evidence for Mo leaching was observed when the same experiment was repeated with water.

23.3.11 Reactions at the Solid–Liquid Interface

23.3.11.1 Alcohol Oxidation

Comparatively few studies have been performed that probed the catalytic solid–liquid interface, despite their importance for a variety of relevant processes. This is in part due to their relatively lower industrial importance with respect to gas–solid reactions and also to the difficulty in measuring a catalyst from within a liquid phase.

Selective oxidation of alcohols remains a difficult catalytic challenge. Key to understanding these reactions is the identification of reaction intermediates; however, the short-lived nature of such species in a catalytic reaction means that they are often difficult to observe. One way to "catch" such intermediates is the sudden change of a reaction parameter. This approach has been used successfully to identify key intermediates under transient and steady-state conditions in the oxidation of 2-propanol over Pd/Al_2O_3. The approach makes use of a flow-through *in situ* ATR–IR cell combined with online UV–Vis spectroscopy [66]. The setup comprises a dedicated Teflon flow-through cell with a volume of 0.077 ml and a gap between the probe and the surface of the cell of 250 μm. The cell has two inlets allowing for fast exchange between two different fluids and is mounted on an attachment for ATR measurements within the sample compartment of a Bruker Equinox-55 FTIR spectrometer. The ATR cell itself is equipped with a fused-silica window (5 mm diameter and 3 mm thickness), which allows simultaneous recording of UV–Vis spectra using a fiber-optic probe placed 4 mm above and 10 mm from the cell outlet and ATR–IR spectra (36 mm from inlet to outlet) of the catalyst layer. The catalyst was deposited at the ZnSe interface via slurrying of the catalyst powder, with the reactant typically depositing 1–1.5 mg. Reactions were carried out at 30 °C with the catalyst system modulated by the periodic admission of 2-propanol saturated with hydrogen or oxygen; in one modulation period (flow of hydrogen-saturated 2-propanol followed by an equally long flow of oxygen-saturated 2-propanol), 60 IR spectra were recorded at a sampling rate of 40 kHz. For each spectrum, several scans were averaged and repeated for five periods. UV–Vis and ATR spectra were recorded simultaneously via IR triggering of the UV–Vis acquisition. A home-built UV–Vis flow-through transmission cell was also attached to the outlet in order to characterize the effluent.

Experiments performed using Pd/Al_2O_3 with a mixture of ethanol and 2-propanol (50 vol.%) showed the appearance of several bands. Two, between 1700 and 1750 cm^{-1}, were ascribed to acetaldehyde (1724 cm^{-1}) and an ethyl acetate (1742 cm^{-1} and also a band at 1242 cm^{-1}), whilst bands at 1800–1900 cm^{-1} were assigned to the adsorption of CO at the Pd surface. In addition, bands due to acetates on the Al_2O_3 support at 1402 and 1560 cm^{-1} were also observed. Interestingly, the behavior of the signals at 1724 and 1742 cm^{-1} differed under gas modulation, the latter being significantly stronger for a change from hydrogen to oxygen, whereas the acetaldehyde signal increased for a switch to oxygen, decreasing rapidly to a steady-state value. The band at 1860 cm^{-1} associated with Pd−CO bonds increased on switching to oxygen due to acetaldehyde decarbonylation before deceasing on

oxidation to CO_2, whereas under the same conditions the acetates on the support were further oxidized to acetic acid. The modulatory behavior of the acetaldehyde signal in the ATR spectrum was confirmed by the UV–Vis data, where the signal intensity at 300 nm due to acetaldehyde was observed to mimic closely the changes in the ATR spectrum. The UV–Vis data varied with the modulation environment – in particular, the adsorption at 400 nm showed a small but significant increase in the presence of O_2. This adsorption variation also mimicked closely the gas environment switching and was proposed to be related to a change in reflectivity as the catalyst surface became oxidized in the presence of O_2; these changes are however, not reversible and are thought to reflect a change in particle structure initiated by dissolution of Pd.

23.3.11.2 Three Techniques Simultaneously Employed in a Batch Reactor

Bentrup and co-workers recently reported a modified autoclave reactor with the capacity to perform three simultaneous "probe" experiments to study liquid-phase catalysis [37]. Fiber-optic Raman immersion, ATR–IR diamond, and UV–Vis probes protrude through the top cover for simultaneous spectroscopic measurements up to 20 bar pressure and the setup was used for elucidating the reaction mechanism and kinetics of the technically challenging subject of room temperature heterogeneously catalyzed asymmetric imine hydrogenation. Using Pt/Al_2O_3 as the catalyst, modified with a chiral phosphoric acid ester for hydrogen activation, this combined technique enables imine conversion to be traced by Raman spectroscopy and product formation by ATR spectroscopy, while the solid catalyst could (in principle) be probed by UV–Vis spectroscopy, although in this case, owing to the low concentration of the catalyst in the reaction mixture and the difficulty in measuring such samples through a liquid medium (CH_2Cl_2 or ethanol), this was not possible. Initially, the setup was tested by profiling the hydrogenation reactions without the chiral modifier. Raman spectra revealed an intensity loss of typical diagnostic imine bands that was also accompanied by a pressure drop from 20 to 16 bar, indicating the consumption of hydrogen with reaction progress. ATR was used to profile both reactant and product and, in addition to the typical imine IR bands at 1620, 1591, 1573, 1486, and 1458 cm^{-1}, bands of the hydrogenation product appeared at 1603 and 1500 cm^{-1}. The intensity of these bands increased with time, although the authors suspected that this extreme sensitivity to the product might be attributable only to preferential adsorption of the product on the probe head.

23.3.12
Dynamic Imaging Studies

Catalytic solids possess a 3D structure which is rarely uniform. These imperfections result in a heterogeneous surface containing various "chemical sites," some of which possess some sort of catalytic activity and others which do not. Therefore, in order to evaluate effectively and characterize fully the components in the catalytic solids, it is not always sufficient simply to perform single-point measurements. A complete characterization requires that information be obtained at the atomic, nanometer, micrometer, and millimeter scales over the entire 3D structure. The performance of

modern-day detectors coupled to various analytical techniques, together with the improved brilliance of the sources used, allows for the acquisition of data across a number of techniques in the millisecond time regime. For many solid-state processes, this time resolution is excessive; however, this fast acquisition rate can be utilized instead to obtain multiple data sets on a sample as a function of space – that is, spatiotemporal data.

23.3.12.1 Imaging of Catalyst Bodies During Catalyst Preparation

The catalyst body, which can be considered as the workhorse in industrial catalysis, consists of a preshaped porous material such as γ-Al_2O_3 which supports a metal/metal oxide active phase. The bodies typically have dimensions in the millimeter range, and are loaded in their thousands to form large-scale industrial catalytic beds. Since the functioning of the entire catalyst bed (and hence the efficiency of the industrial process) is directly dependent on the properties (e.g., metal/metal oxide–support interactions) and the distribution of the active phase (which is often nonuniform) within the millimeter-sized catalyst body, it becomes extremely important to understand how and where this active phase forms. In recent times, both spectroscopic and scattering techniques have been developed to obtain spatial information on the distribution of chemical species within catalyst bodies. These tools provide "noninvasive", spatially resolved insight into the influence that the preparation procedure and reaction conditions have on the active phase distribution. This information can be used to understand better the preparation and deactivation steps in order to develop more efficient catalyst materials. We highlight here the potential of combined X-ray imaging based on the technique of tomographic energy-dispersive diffraction imaging (TEDDI) for following the active component distribution in a catalyst body (the signal contains both diffraction and fluorescence information from defined volume elements). Through the development of an environmental cell located on a movable (x, y, z) stage with temperature and gas control, it is now possible to provide time-resolved 2D concentration maps during calcination/activation [67]. The setup was used to study the evolution of two Ni/γ-Al_2O_3 hydrogenation catalyst bodies prepared from two different precursor complexes, $[Ni(en)_3](NO_3)_2$ and $[Ni(en)(H_2O)_4]Cl_2$, during calcination. The study revealed that both samples yielded an fcc Ni/γ-Al_2O_3 catalyst, yet the decomposition pathways for the two complexes were different. As Figure 23.11 reveals, for the $[Ni(en)_3](NO_3)_2$ sample the initial crystalline phase $Ni(en)_3(NO_3)$ directly decomposes to yield an even distribution of crystalline fcc Ni nanoparticles (Debye–Scherrer analysis of the 220 reflection, suggesting an average size of the order of 5 nm). In contrast, the $[Ni(en)(H_2O)_4]Cl_2$/γ-Al_2O_3 sample underwent a number of changes in order to form the final fcc Ni phase. Although this sample contained no Ni-containing crystalline phase, Ni fluorescence maps revealed the Ni to be evenly distributed in the form of the complex $[Ni(en)(H_2O)_4]Cl_2$/γ-Al_2O_3. The precursor then decomposes stepwise, forming a variety of crystalline phases including first an unknown phase, followed by Ni_3C, and finally crystalline fcc Ni. 2D y, z mapping revealed significant differences in the phase composition across the sample, with 40% of the Ni_3C species in the core of the pellet, whereas at the edge it amounts to less than 20%, the remainder comprising

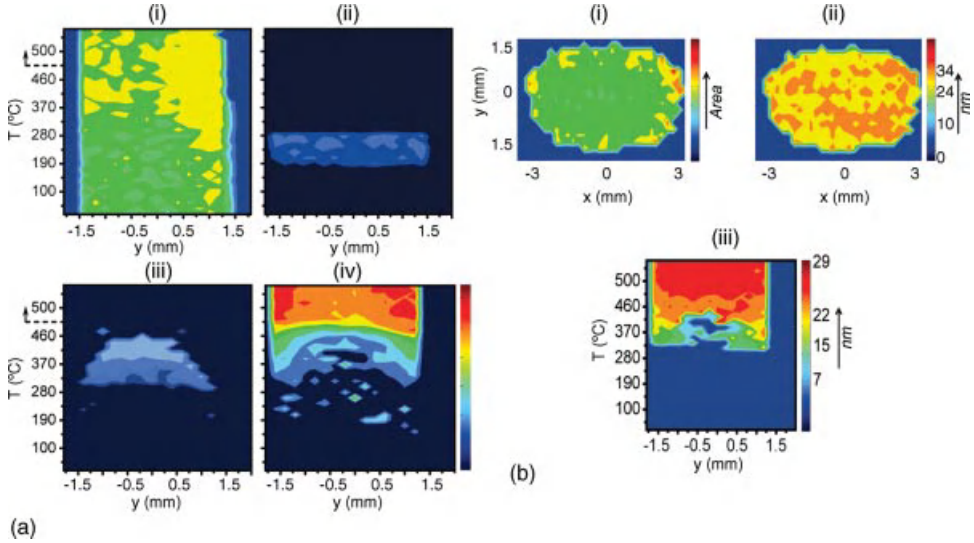


Figure 23.11 (a) *y* scan data as a function of *T* for (i) Ni fluorescence at 7.5 keV (Ni Kα), (ii) the diffraction peak at 36.9 keV (unknown Ni-containing crystalline phase), (iii) the 50.2 keV (101) reflection of Ni_3C, and (iv) the 57.6 keV (200) reflection of metallic fcc Ni, all in the [Ni(en)$(H_2O)_4$]Cl_2/γ-Al_2O_3 pellet. (b) *x*, *y* maps detailing (i) metallic Ni distribution in the [Ni(en)$(H_2O)_4$]Cl_2/γ-Al_2O_3 pellet after calcination at 500 °C, (ii) particle size distribution of metallic Ni in the same slice of the pellet after calcination at 500 °C, and (iii) evolution of metallic Ni crystallites as a function of the *y* direction of the catalyst body. Adapted with permission from [67], copyright 2009 American Chemical Society.

fcc Ni. At 460 °C only fcc Ni is observed with the average particle size being much larger (24–34 nm). The mechanism by which these large metallic Ni particles are formed is not clear and, while this study could not provide mechanistic insight into the phase evolution process, it was able to reveal that the formation of the active component is a multi-step evolution process and that this process shows significant spatial variation. Improving the acquisition time and data quality may well be necessary in order to obtain such mechanistic insight. In this regard, TEDDI experiments utilizing energy-dispersive 2D pixelated array detectors or high-energy monochromatic diffraction imaging Tomographic Angle Dispersive Diffraction Imaging (TADDI) hold much promise.

23.3.12.2 Time- and Space-Resolved NO_x Storage/Release

DRIFTS and Raman spectroscopy have also been used to study the NO_x storage reduction (NSR) process during periodic switching between fuel-lean and fuel-rich conditions. The plug-flow cell design by Urakawa *et al.* allows for the fast exchange of the gaseous atmosphere between lean and rich periods, whereas detection perpendicular to the axial direction of the catalyst bed allows gradient profiling and identification of chemical species along the bed [68]. The Pt–Ba/CeO_2 catalyst (100 mg, 1 wt% Pt, and 20 wt% Ba, 6 mm in length) was placed in a cell.

Measurements were performed at three places in the catalyst bed: front, middle, and back positions (0.5, 3.0, and 5.5 mm from the beginning of the bed at the gas-inlet side, respectively). The atmosphere was cycled between lean ($NO + O_2$) and rich (H_2) at 623 K. Under lean conditions (NO_x storage), a mixture of nitrites and nitrates was observed using DRIFTS at the catalyst surface (bands at 1028, 1204, 1260, 1570, and 1770 cm^{-1}), although Raman data confirmed that the nitrates were present also in the bulk. Under lean conditions, all of the above contributions disappeared, leaving a single band in the Raman spectrum at 985 cm^{-1}, which was assigned to bulk Ba $(OH)_2$, in part due to the use of H_2 as the reducing agent. However, the temporal evolution of the DRIFT and Raman spectra for nitrite species shown in Figure 23.12 demonstrates that there is a delay in their appearance, moving from the front to the back position. Thus, after appearing at the front they appeared at the middle and back positions some 70 and 120 s later, respectively. Conversely, nitrates were formed at the beginning of lean periods, independent of the bed position. Interestingly, the band for bulk ionic nitrate formation shifted from 1750 to 1770 cm^{-1} during lean periods and was attributed to bulk changes in the crystallinity of the solid during nitrate penetration. During rich periods, nitrites were observed first to reduce or desorb from the surface and this was then followed by the reduction of nitrates. This information was derived from comparing the corresponding signals at the middle and back positions. Nitrites, it was concluded, are the most likely source of NO observed on the switch to lean conditions. The Raman spectra indicated a difference

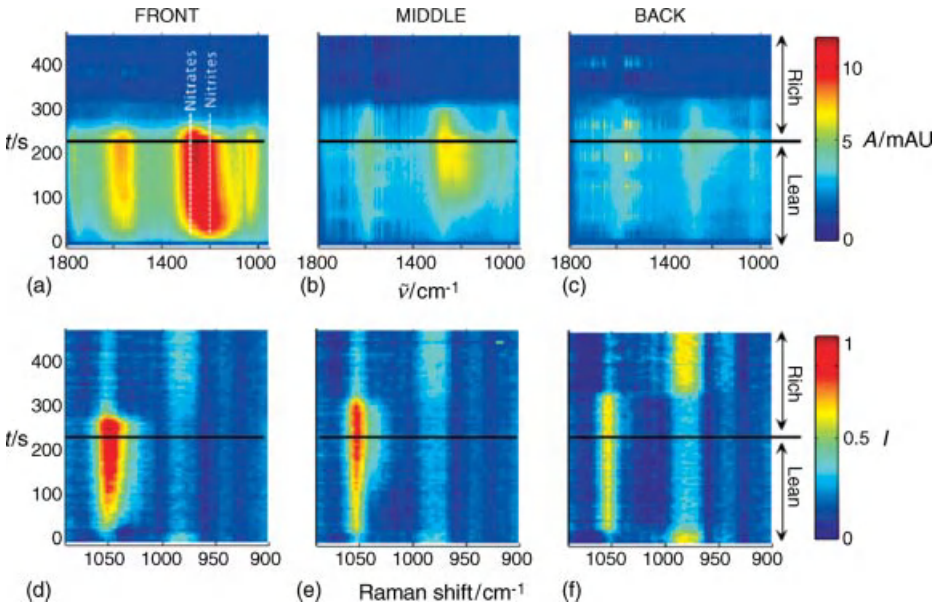


Figure 23.12 Time-resolved DRIFT (a–c) and Raman (d–f) spectra during NSR at the front, middle, and back positions of the catalyst bed. Adapted with permission from [68], copyright 2008 Wiley-VCH Verlag GmbH.

in the amount of bulk $Ba(NO_3)_2$ formed, the front position possessing the most. The DRIFTS spectra also showed much less intense surface nitrite and nitrate bands towards the back position. Thus, although 90% of the NO_x remains stored at the end of lean periods, the majority is located at the front of the catalyst bed, utilizing the bulk Ba component.

23.4 Conclusion

So what is the future for combining *in situ* techniques and what are the exciting possibilities awaiting the intrepid researcher wishing to obtain more information on the state of a catalyst material under reaction conditions? First, a comment on the status quo as we find it today. Many of the publications cited in this chapter are less than 3 years old and this suggests that technique coupling is a thriving field. Further testimony to this fact can be found beyond just the academic literature; for example, a number of commercial instrument manufacturers (e.g., Jobin-Yvon, INEL) now sell combined setups, and a large number of stations in the recently built fourth-generation synchrotron sources possess the capacity to perform combined X-ray–non-X-ray based characterization studies. The breadth of available equipment and/or methodologies suggests that combined technique experiments are more feasible than ever.

In many respects, there is barely any scope left to demonstrate a "first" in a particular technique combination or in the design of a particular reactor setup – a happy medium has seemingly been reached between obtaining acceptable data quality while keeping the conditions as real as possible with respect to a catalytic/synthetic process. The technique combinations are there, ready to use, and have been well demonstrated for a number of chemical and physical problems. We should at this stage remind ourselves of the mantra behind technique combining – no one technique can provide all the understanding of a catalytic process and multiple characterization of a sample *needs* to be carried out anyway in order to generate those all-important structure–activity relationships. However, one should fairly evaluate the possibilities in this regard by stating that there are also limitations with adopting such an approach. For instance, undertaking a combined experiment is more complicated than performing separate independent experiments. In addition, and as remarked on earlier, the more techniques that are combined, the less *operando* the experiment can become, particularly since when one combines techniques, for at least one of the experimental data sets obtained the data will be of sub-optimal quality. This depends very much on which techniques are combined and the experiment being performed, but it is important to realize that the benefits that a combined data set can bring has to be weighed up against the more optimal quality of independent data sets obtained from the individual techniques. However, these problems are not insurmountable and in many ways can be circumvented or at least minimized by a combination of good experimental setup design and appropriate technique combination. These factors, when considered alongside the improvements in the performance of the individual techniques, means

that there should be no good reason as to why good-quality, usable data cannot be obtained from all the techniques combined in one experiment.

Another question that we find ourselves asking is, what are the possibilities for correlating structure with activity from combined technique data? The answer depends upon how quickly a high degree of chemical information can be obtained from the sample as a function of time. For studying solid-state transformation processes/catalyst synthesis, we are already there. This is mainly because these occur more slowly, with a time resolution in minutes, so that it is possible to collect good statistics. For example, a recent study by Kongmark *et al.* [35] produced data from the same spot on the sample using three techniques acquired in a simultaneous fashion with a time resolution in minutes, and all the data collected were of sufficient quality to be further analyzable. The data then confirmed not only a two-step mechanism by which the product phase γ-Bi_2MoO_6 forms, but also provided insight into the evolution of the polycrystallite structure. Thus, for synthetic purposes, combined techniques are in a good position to tackle questions regarding formation mechanisms; the only thing missing is a compliant sample. What about the study of catalytic reactions? Here the main problem is the detection and identification of possible short-lived transients and transition-state intermediates. Currently the detection of such species is often beyond the scope of the combined technique approach since their lifetime is much shorter than the optimum speed (microseconds) at which some techniques (e.g., EDE and IR spectroscopy) can acquire analyzable spectra. Therefore, until either sufficiently improved detectors or more intense sources become available, it seems as though, unless the intermediate is long-lived, that there is little chance of observing transients. This may change, however, when the impending revolution in the availability of free electron laser (FEL) sources begins. Indeed, should the samples survive the increased power load, this "brute force" approach represents the best opportunity to obtain sufficiently quick time-resolved data to be able to identify transient species.

Perhaps the main problem with combining techniques is the volume of data generated. As discussed earlier, the data are rarely treated in their entirety, yet there is likely to be if not missed data/information on intermediate species, at least more detail on the catalyst that is not being extracted from the data generated. This is entirely understandable since the extraction of such information is a labor-intensive process requiring initial data treatment and least-squares fitting/nonlinear least-squares fitting to proposed models of the raw data. Unfortunately, data treatment varies with technique and can be highly specialized. However, of late a number of approaches have been developed to deal with large volumes of data sets that work either on the basis of reducing the number of variables that need to be refined over a large data set by grouping them together as a constant (parametric refinement) [69] or else by automatic identification of unique contributions within multicomponent data [some examples include band target entropy (BTE) methods and cluster analysis] [70–72]. Impressively, such methods treat the entire spectrum and are thus less subjective or correlated. Indeed, some of the methodology (cluster analysis) possesses the capability of identifying patterns from two datasets when considered together.

Comparatively little work has been done at high pressures (>2 bar), despite the number of catalytic processes that operate under such conditions, for example, Fischer–Tropsch reaction, methanol synthesis, and hydrodesulfurization. However, this is beginning to change as a result of both the increasing importance of such reactions in industry and the investment in the required infrastructure for such experiments made at synchrotron radiation facilities (e.g., combining SAXS–WAXS–XAFS–Raman . . .). Interestingly, the major stumbling block to the acquisition of such data was the provision of a gas rig integrated with the data acquisition since the standard capillary microreactor used in such setups has been around for many years and is perfectly capable of withstanding pressures up to 20 bar [39, 60, 73]. Clearly, there is an important message here, namely that both the setting up and undertaking of such studies is a team effort, requiring the work of experts at all four corners of the problem (the corners being the catalyst, the reaction, the recording of data, and the analysis of the data) in order to obtain a successful outcome. Important here is the long-term objectivity of such projects, since results are rarely obtained at first attempt.

Little work has also been carried out at the solid–liquid interface and this will also represent an important challenge for the near future, especially considering the increasing importance of liquid-phase biomass conversion. The challenge here is the development of methodologies and setups for such purposes. There is also an increased risk of "beam influence" since the solvent is a potential source of easy to liberate electrons.

As discussed in Section 23.3.10, using very hard X-rays (e.g., 89 keV) offers a number of advantages, not least because it allows for data to be obtained under more *operando* conditions. In fact, the penetration is sufficiently high to allow data acquisition through millimeters of stainless steel at very high pressures (200 bar), as demonstrated by Middelkoop *et al.* to follow nano oxide crystallization using supercritical water [74]. A further possibility that X-rays of these energies now present us with is that of a "total scattering" approach (PDF) analysis. This method profiles both short- (<5 Å) and mid-range (~5–20 Å) order information and has recently been demonstrated in a combined technique setup (with SAXS–WAXS) for a time-resolved measurement [38]. The technique requires that a very large $2\theta/Q$ ($Å^{-1}$) range is obtained and therefore hard X-rays are clearly favored owing to the flattening of the Ewald sphere. It is currently available at a number of synchrotrons and suitable software is available for performing data analysis, although currently it is a somewhat specialist field.

Continuing along the line of future measurement possibilities, it is worth considering two recent developments in source technology and the impact these could have on future combined technique studies: FELs and table-top synchrotrons. Although FELs are not new, they have not been readily available, being the preserve of the high-energy physicist, although recent developments such as the soft X-ray FLASH facility in Germany and the recently commissioned Linac Coherent Light Source at SLAC have been designed with the end-user in mind [75, 76]. With some further expected developments, FELs are now poised to take center stage as the premier source of tunable, intense, coherent photons of either ultra-short time

resolution or ultra-fine spectral resolution, from the far-IR to the hard X-ray regime (a wavelength of 0.1 nm is currently being targeted for the European XFEL project) [75]. FELs can provide an unprecedented enhancement anywhere from 10^6 to 10^9-fold in the peak brightness compared with a synchrotron storage ring. This is expected to herald a new age of discovery since the ultra-short pulses will yield both femtosecond time resolution and millielectronvolt spectral resolution, which can be used to explore the temporal evolution of phenomena such as atomic motion and chemical reactivity at the single-particle level in real time. However, access to such facilities is limited and in the meantime the development of new laboratory X-ray sources continues. Recent developments have concentrated on making light sources which are small enough to fit into a laboratory yet possess fluxes that are comparable to those of third-generation synchrotron sources. For example, the commercially available MIRROCLE system possesses demonstrable capacity for performing dispersive XAFS and IR absorption spectroscopy [77, 78]. The system possesses an ultra-short duration pulse allowing dynamic measurements which, when combined with the expected developments in both source spectral brightness (improvements in the vacuum quality) and detector sensitivity may eventually allow for synchrotron-based experiments to be performed in the home research laboratory.

Finally, we would like to end this sojourn through the field of combining techniques with a précis of what we have discussed, namely that technique combining is an integral part of studying catalysts but, as with any study, it cannot always come up with definitive answers. For that, as in any other scientific discipline, an integrated multidiscipline approach is needed.

References

1 Weckhuysen, B.M. (2009) *Angew. Chem. Int. Ed.*, **48**, 4910–4943.
2 Urakawa, A. and Baiker, A. (2009) *Top. Catal.*, **52**, 1312–1322.
3 Brückner, A. (2003) *Catal. Rev. Sci. Eng.*, **45**, 97–150.
4 Weckhuysen, B.M. (2003) *Phys. Chem. Chem. Phys.*, **5**, 4351–4360.
5 Beale, A.M., Jacques, S.D.M., and Weckhuysen, B.M. (2010) *Chem. Soc. Rev.*, **39**, 4656–4672.
6 Young, N.A. and Spicer, M.D. (1990) *J. Mol. Struct.*, **222**, 77–86.
7 Couves, J.W., Thomas, J.M., Waller, D., Jones, R.H., Dent, A.J., Derbyshire, G.E., and Greaves, G.N. (1991) *Nature*, **354**, 465–468.
8 Frahm, R. (1989) *Rev. Sci. Instrum.*, **60**, 2515–2518.
9 Sankar, G. and Thomas, J.M. (1999) *Top. Catal.*, **8**, 1–21.
10 Clausen, B.S., Grabaek, L., Steffensen, G., Hansen, P.L., and Topsoe, H. (1993) *Catal. Lett.*, **20**, 23–36.
11 Sankar, G., Wright, P.A., Natarajan, S., Thomas, J.M., Greaves, G.N., Dent, A.J., Dobson, B.R., Ramsdale, C.A., and Jones, R.H. (1993) *J. Phys. Chem.*, **97**, 9550–9554.
12 Bras, W., Derbyshire, G.E., Ryan, A.J., Mant, G.R., Felton, A., Lewis, R.A., Hall, C.J., and Greaves, G.N. (1993) *Nucl. Instrum. Methods Phys. Res. A*, **326**, 587–591.
13 Dokter, W.H., Beelen, T.P.M., Vangarderen, H.F., Vansanten, R.A., Bras, W., Derbyshire, G.E., and Mant, G.R. (1994) *J. Appl. Crystallogr.*, **27**, 901–906.
14 O'Brien, M.G., Beale, A.M., and Weckhuysen, B.M. (2010) *Chem. Soc. Rev.*, **39**, 4767–4782.

15 Aerts, A., Kirschhock, C.E.A., and Martens, J.A. (2010) *Chem. Soc. Rev.*, **39**, 4626–4642.

16 Bras, W., Derbyshire, G.E., Bogg, D., Cooke, J., Elwell, M.J., Komanschek, B.U., Naylor, S., and Ryan, A.J. (1995) *Science*, **267**, 996–999.

17 Brückner, A. (2001) *Chem. Commun.*, 2122–2123.

18 Weckhuysen, B.M. (Ed.) (2004) *In-Situ Spectroscopy of Catalysts*, American Scientific Publishers, Stevenson. Ranch, CA.

19 Le Bourdon, G., Adar, F., Moreau, M., Morel, S., Reffner, J., Mamede, A.S., Dujardin, C., and Payen, E. (2003) *Phys. Chem. Chem. Phys.*, **5**, 4441–4444.

20 Nijhuis, T.A., Tinnemans, S.J., Visser, T., and Weckhuysen, B.M. (2003) *Phys. Chem. Chem. Phys.*, **5**, 4361–4365.

21 Tromp, M., Sietsma, J.R.A., van Bokhoven, J.A., van Strijdonck, G.P.F., van Haaren, R.J., van der Eerden, A.M.J., van Leeuwen, P., and Koningsberger, D.C. (2003) *Chem. Commun.*, 128–129.

22 Mesu, J.G., Beale, A.M., de Groot, F.M.F., and Weckhuysen, B.M. (2006) *J. Phys. Chem. B*, **110**, 17671–17677.

23 Bauer, M., Heusel, G., Mangold, S., and Bertagnolli, H. (2010) *J. Synchrotron Radiat.*, **17**, 273–279.

24 Hunger, M. and Wang, W. (2004) *Chem. Commun.*, 584–585.

25 Newton, M.A., Jyoti, B., Dent, A.J., Fiddy, S.G., and Evans, J. (2004) *Chem. Commun.*, 2382–2383.

26 Newton, M.A., Di Michiel, M., Kubacka, A., and Fernandez-Garcia, M. (2010) *J. Am. Chem. Soc.*, **132**, 4540–4541.

27 Newton, M.A. and van Beek, W. (2010) *Chem. Soc. Rev.*, **39**, 4845–4863.

28 Beale, A.M., van der Eerden, A.M.J., Kervinen, K., Newton, M.A., and Weckhuysen, B.M. (2005) *Chem. Commun.*, 3015–3017.

29 Briois, V., Lutzenkirchen-Hecht, D., Villain, F., Fonda, E., Belin, S., Griesebock, B., and Frahm, R. (2005) *J. Phys. Chem. A*, **109**, 320–329.

30 Brückner, A. (2005) *Chem. Commun.*, 1761–1763.

31 O'Brien, M.G., Beale, A.M., Jacques, S.D.M., Buslaps, T., Honkimaki, V., and Weckhuysen, B.M. (2009) *J. Phys. Chem. C*, **113**, 4890–4897.

32 O'Brien, M.G., Beale, A.M., Jacques, S.D.M., Di Michiel, M., and Weckhuysen, B.M. (2009) *ChemCatChem*, **1**, 99–102.

33 Grunwaldt, J.D. and Schroer, C.G. (2010) *Chem. Soc. Rev.*, **39**, 4741–4753.

34 Beale, A.M., van der Eerden, A.M.J., Jacques, S.D.M., Leynaud, O., O'Brien, M.G., Meneau, F., Nikitenko, S., Bras, W., and Weckhuysen, B.M. (2006) *J. Am. Chem. Soc.*, **128**, 12386–12387.

35 Kongmark, C., Martis, V., Rubbens, A., Pirovano, C., Lofberg, A., Sankar, G., Bordes-Richard, E., Vannier, R.N., and Van Beek, W. (2009) *Chem. Commun.*, 4850–4852.

36 Sankar, G., Fiddy, S., Beale, A.M., Harvey, I., Hayama, S., and Bushnell-Wye, G. (2007) in *13th International Conference on X-Ray Absorption Fine Structure: XAFS13. AIP Conference Proceedings*, vol **882** (eds B. Hedman and P. Painetta), American Institute of Physics, Melville, NY, pp. 585–587.

37 Knopke, L.R., Nemati, N., Kockritz, A., Brückner, A., and Bentrup, U. (2010) *ChemCatChem*, **2**, 273–280.

38 Becker, J., Bremholm, M., Tyrsted, C., Pauw, B., Jensen, K.M.O., Eltzholt, J., Christensen, M., and Iversen, B.B. (2010) *J. Appl. Crystallogr.*, **43**, 729–736.

39 Ronning, M., Tsakoumis, N.E., Voronov, A., Johnsen, R.E., Norby, P., van Beek, W., Borg, O., Rytter, E., and Holmen, A. (2010) *Catal. Today*, **155**, 289–295.

40 Beale, A.M., Paul, M., Sankar, G., Oldman, R.J., Catlow, C.R.A., French, S., and Fowles, M. (2009) *J. Mater. Chem.*, **19**, 4391–4400.

41 Bentrup, U. (2010) *Chem. Soc. Rev.*, **39**, 4718–4730.

42 O'Brien, M.G., Beale, A.M., Jacques, S.D.M., Di Michiel, M., and Weckhuysen, B.M. (2011) *Appl. Catal. A: Gen.*, **391**, 468–476

43 Grunwaldt, J.D., Caravati, M., Hannemann, S., and Baiker, A. (2004) *Phys. Chem. Chem. Phys.*, **6**, 3037–3047.

44 Jacques, S.D.M., Leynaud, O., Strusevich, D., Stukas, P., Barnes, P., Sankar, G., Sheehy, M., O'Brien, M.G., Iglesias-Juez, A., and Beale, A.M. (2009) *Catal. Today*, **145**, 204–212.

45 Sankar, G., Thomas, J.M., Rey, F., and Greaves, G.N. (1995) *J. Chem. Soc., Chem. Commun.*, 2549–2550.

46 Owen, R.L., Holton, J.M., Schulze-Briese, C., and Garman, E.F. (2009) *J. Synchrotron Radiat.*, **16**, 143–151.

47 Chua, Y.T. and Stair, P.C. (2000) *J. Catal.*, **196**, 66–72.

48 Ferri, D., Kumar, M.S., Wirz, R., Eyssler, A., Korsak, O., Hug, P., Weidenkaff, A., and Newton, M.A. (2010) *Phys. Chem. Chem. Phys.*, **12**, 5634–5646.

49 de Moor, P., Beelen, T.P.M., van Santen, R.A., Beck, L.W., and Davis, M.E. (2000) *J. Phys. Chem. B*, **104**, 7600–7611.

50 de Moor, P., Beelen, T.P.M., van Santen, R.A., Tsuji, K., and Davis, M.E. (1999) *Chem. Mater.*, **11**, 36–43.

51 Svergun, D.I. and Koch, M.H.J. (2002) *Curr. Opin. Struct. Biol.*, **12**, 654–660.

52 Aerts, A., Follens, L.R.A., Haouas, M., Caremans, T.P., Delsuc, M.A., Loppinet, B., Vermant, J., Goderis, B., Taulelle, F., Martens, J.A., and Kirschhock, C.E.A. (2007) *Chem. Mater.*, **19**, 3448–3454.

53 Wright, P.A. (2008) *Microporous Framework Solids*, Royal Society of Chemistry, Cambridge.

54 Weckhuysen, B.M., Baetens, D., and Schoonheydt, R.A. (2000) *Angew. Chem. Int. Ed.*, **39**, 3419–3421.

55 Nikitenko, S., Beale, A.M., van der Eerden, A.M.J., Jacques, S.D.M., Leynaud, O., O'Brien, M.G., Detollenaere, D., Kaptein, R., Weckhuysen, B.M., and Bras, W. (2008) *J. Synchrotron Radiat.*, **15**, 632–640.

56 O'Brien, M.G., Beale, A.M., Catlow, C.R.A., and Weckhuysen, B.M. (2006) *J. Am. Chem. Soc.*, **128**, 11744–11745.

57 Beale, A.M., van der Eerden, A.M.J., Grandjean, D., Petukhov, A.V., Smith, A.D., and Weckhuysen, B.M. (2006) *Chem. Commun.*, 4410–4412.

58 Bentrup, U., Radnik, J., Armbruster, U., Martin, A., Leiterer, J., Emmerling, F., and Brückner, A. (2009) *Top. Catal.*, **52**, 1350–1359.

59 Grunwaldt, J.D., Molenbroek, A.M., Topsoe, N.Y., Topsoe, H., and Clausen, B.S. (2000) *J. Catal.*, **194**, 452–460.

60 de Smit, E., Cinquini, F., Beale, A.M., Safonova, O.V., van Beek, W., Sautet, P., and Weckhuysen, B.M. (2010) *J. Am. Chem. Soc.*, **132**, 14928–14941.

61 Newton, M. (2009) *Top. Catal.*, **52**, 1410–1424.

62 Meunier, F.C. (2010) *Chem. Soc. Rev.*, **39**, 4602–4614.

63 Newton, M.A., Belver-Coldeira, C., Martinez-Arias, A., and Fernandez-Garcia, M. (2007) *Nat. Mater.*, **6**, 528–532.

64 Brückner, A. (2010) *Chem. Soc. Rev.*, **39**, 4673–4684.

65 Iglesias-Juez, A., Beale, A.M., Maaijen, K., Weng, T.C., Glatzel, P., and Weckhuysen, B.M. (2010) *J. Catal.*, **276**, 268–279.

66 Burgi, T. (2005) *J. Catal.*, **229**, 55–63.

67 Espinosa-Alonso, L., O'Brien, M.G., Jacques, S.D.M., Beale, A.M., de Jong, K.P., Barnes, P., and Weckhuysen, B.M. (2009) *J. Am. Chem. Soc.*, **131**, 16932–16938.

68 Urakawa, A., Maeda, N., and Baiker, A. (2008) *Angew. Chem. Int. Ed.*, **47**, 9256–9259.

69 Stinton, G.W. and Evans, J.S.O. (2007) *J. Appl. Crystallogr.*, **40**, 87–95.

70 Chew, W., Widjaja, E., and Garland, M. (2002) *Organometallics*, **21**, 1982–1990.

71 Barr, G., Dong, W., and Gilmore, C.J. (2004) *J. Appl. Crystallogr.*, **37**, 658–664.

72 Barr, G., Dong, W., and Gilmore, C.J. (2004) *J. Appl. Crystallogr.*, **37**, 243–252.

73 Karaca, H., Hong, J.P., Fongarland, P., Roussel, P., Griboval-Constant, A., Lacroix, M., Hortmann, K., Safonova, O.V., and Khodakov, A.Y. (2010) *Chem. Commun.*, **46**, 788–790.

74 Middelkoop, V., Boldrin, P., Peel, M., Buslaps, T., Barnes, P., Darr, J.A., and Jacques, S.D.M. (2009) *Chem. Mater.*, **21**, 2430–2435.

75 Tiedtke, K., Azima, A., von Bargen, N., Bittner, L., Bonfigt, S., Dusterer, S., Faatz, B., Fruhling, U., Gensch, M., Gerth, C., Guerassimova, N., Hahn, U., Hans, T., Hesse, M., Honkavaar, K., Jastrow, U., Juranic, P., Kapitzki, S., Keitel, B., Kracht, T., Kuhlmann, M., Li, W.B., Martins, M., Nunez, T., Plonjes, E., Redlin, H., Saldin, E.L., Schneidmiller, E.A., Schneider, J.R., Schreiber, S., Stojanovic, N., Tavella, F., Toleikis, S., Treusch, R., Weigelt, H., Wellhofer, M., Wabnitz, H., Yurkov, M.V., and Feldhaus, J. (2009). *New J. Phys*, **11**, 023029.

76 Barletta, W.A., Bisognano, J., Corlett, J.N., Emma, P., Huang, Z., Kim, K.J., Lindberg, R., Murphy, J.B., Neil, G.R., Nguyen, D.C., Pellegrini, C., Rimmer, R.A., Sannibale, F., Stupakov, G., Walker, R.P., and Zholents, A.A. (2010) *Nucl. Instrum. Methods Phys. Res. A*, **618**, 69–96.

77 Haque, M.M., Yamada, H., Moon, A., and Yamada, M. (2009) *J. Synchrotron Radiat.*, **16**, 299–306.

78 Yamada, H., Hiraia, T., Morita, M., Hasegawa, D., and Hanashima, M. (2008). *Proc. SPIE*, **7078**, 7078P.

24
Quantum Chemistry Methods

Philippe Sautet

24.1
Introduction and Historical Perspective

With the combined developments in algorithms and methods and the advances in computer power, computational chemistry has evolved in an impressive way in the last two decades. Systems with thousands of atoms are now accessible with reasonable accuracy. In consequence, the application domains have expanded dramatically. Initially the field was focused on organic chemistry, then organometallic chemistry, and this early but insightful time can be illustrated by the Nobel Prize in Chemistry awarded in 1981 to Kenichi Fukui and Roald Hoffmann for their theoretical developments in molecular reactivity. It was then extended to solid-state and surface chemistry and now concerns all aspects of chemistry and material sciences. In the field of heterogeneous catalysis, atomistic modeling has started with qualitative molecular orbital methods and semiempirical approaches, mainly in relation to the chemisorption of simple molecules, but also with an analysis of catalytic reactions from a molecular orbital approach. Among the pioneers one can cite R. Hoffmann [1], A.B. Anderson [2], E.M. Shustorovich and R.C. Baetzold [3], and R.A. van Santen [4]. The advent of first principles methods [such as density functional theory (DFT)] was, however, determinant in promoting computational chemistry as an accurate and predictive tool. In 1998, the Nobel Prize in Chemistry was awarded jointly to Walter Kohn for the development of DFT< and to John A. Pople for method development in *ab initio* quantum chemistry. DFT has developed into a key method for the simulation of metallic or oxide surfaces and to study molecular chemisorption [5–9]. *Ab initio* quantum chemical techniques have also been used mainly on small metallic clusters [10] and on simple periodic models [11]. Description of a surface reaction on extended solid surfaces started with a simple dissociation of H_2 [12, 13], while the exploration of more complex reaction pathways from polyatomic molecules came around 2000 [14–17]. This initiated an active field of research on the determination of mechanisms, linked with reaction kinetics.

Characterization of Solid Materials and Heterogeneous Catalysts: From Structure to Surface Reactivity, First Edition. Edited by Michel Che and Jacques C. Védrine.
© 2012 Wiley-VCH Verlag GmbH & Co. KGaA. Published 2012 by Wiley-VCH Verlag GmbH & Co. KGaA.

Computational chemistry can bring different types of insights into the field of heterogeneous catalysis [5]. First, it can estimate total energies of chemical systems. This can be applied to the determination of the structure of the catalytic sites on the solid surface, with maximum realism, taking into account if possible the conditions of the catalytic reaction. It can also model defects on these surfaces such as steps or kinks. Molecule–surface interaction is a wide field of application, with the identification of the adsorption site and the evaluation of the adsorption energy, or of the diffusion barriers for the adsorbates on the surface, related to their mobility.

The exploration of catalytic reactivity is another central avenue, with the determination of the structure and stability of potential intermediate species in the catalytic cycles, and the calculation of the activation barrier for the elementary reaction steps, with potential coupling with microkinetic calculations. The reactivity of simple molecules at surfaces can also be directly addressed with reaction dynamics simulations.

These insights from total energy calculations are already strong, but they can be nicely complemented with electronic properties extracted from the wavefunction or the electronic density. This allows a simulation of the spectroscopic and electronic properties of the catalytic system, in relation to experiment. This includes infrared and other vibrational spectra [17, 18] (with the calculation of the band intensities), photoelectron spectroscopy (for either valence or core electrons), nuclear magnetic resonance [19], scanning tunneling microscopy images [5, 20, 21], X-ray absorption spectroscopy [5, 22], and magnetism. This allows a strong interaction between theory and experiment and validation of the models from their simulated spectra.

Finally, a key objective of computational chemistry is to obtain qualitative trends for molecular adsorption and reaction on surfaces, in order to propose concepts and models that can have a predictive power for the design of improved catalysts [9].

In this chapter, after a short presentation of the various types of models for solid catalysts, an introduction to electronic structure theory is given with the main focus on DFT. Applications are centered on the important and timely question of the identification of the structure of catalytic surfaces under working conditions. A few years ago, calculations were only performed at the solid–vacuum interface, that is, with only a single molecule interacting with the surface. This type of model, in relation to surface science experiments, has brought considerable insights into the structures of metal, oxide, sulfide, and other surfaces, explaining relaxation, reconstruction, segregation processes, in elementary chemisorption phenomena, and in establishing fundamental structure–reactivity relationships. In some cases, however, the environment (gas phase with a given pressure and temperature, liquid phase, solvent, electric field, . . .) plays a key role and cannot be omitted from the model. We illustrate how coupling between electronic structure calculations and atomistic thermodynamics allows the study of the nature and stability of surfaces under a pressure of gas.

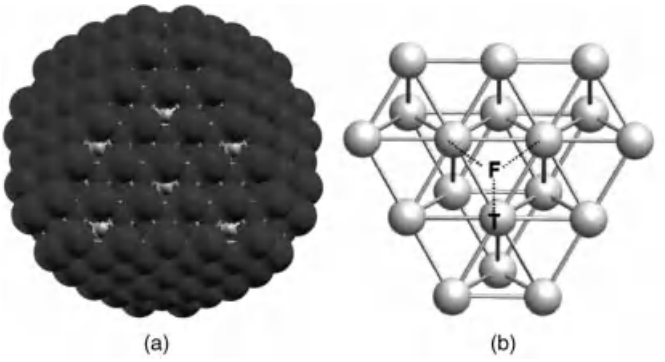


Figure 24.1 (a) Model of a catalyst nanoparticle containing 225 Pd atoms and 32 C atoms. (b) 18-atom cluster modeling a portion of an extended (111) face of an fcc metal. Adapted with permission from [24].

24.2
Building Models of Heterogeneous Catalysts

One of the crucial aspects of a pertinent simulation is the construction of a model, which is a simplified representation of the experimental system. The model results from a subtle balance between simplicity and realism. In order to bring qualitative insights, the model should be simple, with a limited number of structural parameters. Simplicity is also required in order to be able to perform accurate electronic structure calculations, which are limited to a reasonable number of atoms. On the other hand, the model should be realistic enough to grasp the key aspects of the experimental system.

Heterogeneous catalysts are usually particles a few nanometers in size, with from a few tens to several thousands of atoms, or more. Two types of approaches are used in the simulations of heterogeneous catalysts. The first model consists in a molecular cluster of finite size (Figure 24.1). If the catalytic particle is small enough, the cluster can model the whole particle [23], but in the more widespread case of large particles, it is only a fragment representing the local surrounding of a given site of the nanoparticle [6, 10, 24]. The key advantages are that any type of site can be modeled and that all quantum chemistry codes for molecules can be used for the calculation (e.g., Gaussian [25], Turbomole [26], ADF [27]). The main drawbacks are the limited size of the cluster and the error introduced by cutting the cluster. The convergence of the total energy with the size of the considered cluster can be very difficult to reach, for example, for metal particles. Since atoms at the frontier of the cut part have a metal coordination much lower than that in the whole particle, their electronic properties are altered, hence the optimization of their coordinates is not possible. Then adsorption-induced surface relaxation effects are difficult to reproduce with cluster models, unless the cluster describes the whole particle.

The second approach consists in modeling a given facet of the nanoparticle by a periodic slab (Figure 24.2) [1, 9, 28]. Once the orientation of the surface plane is fixed,

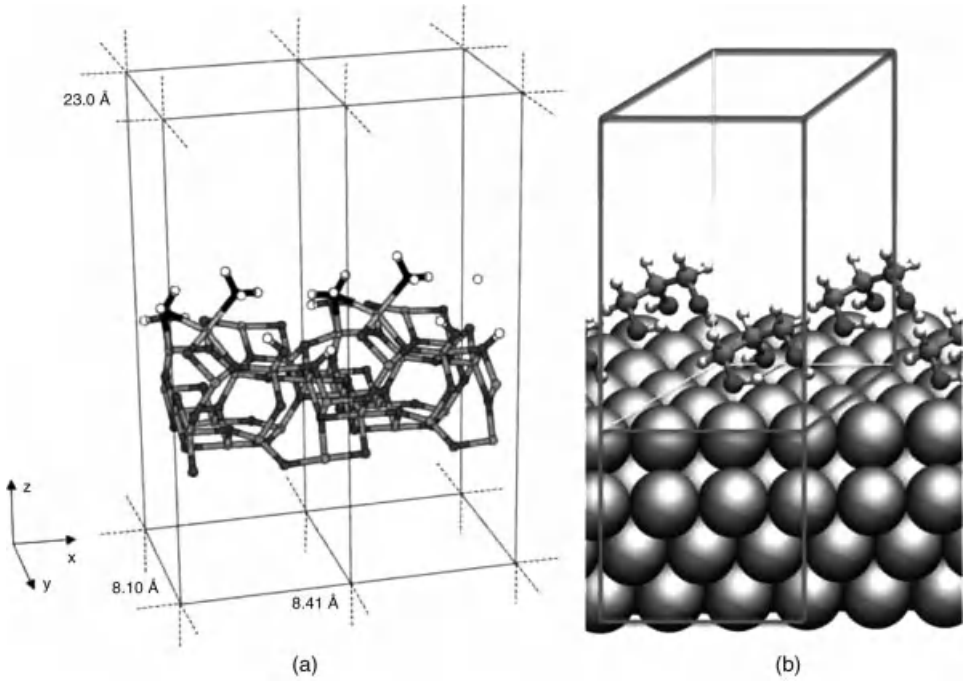


Figure 24.2 (a) Example of a two-dimensional periodic slab model for a surface organometallic system, a Zr complex grafted on a periodic model of γ-alumina. Two boxes of the periodic system are shown. (b) Slab model for glycerol adsorption on an Rh(111) surface, using a four-layer slab and a (3×3) surface supercell. Reprinted with permission from [28].

two main parameters have to be defined: the thickness of the slab and the size of the surface supercell. These parameters clearly control the number of atoms in the slab, and hence the complexity of the calculation. The periodic system can then be calculated using a periodic code, such as CASTEP [29], VASP [30], CP2K [31], SIESTA [32], or CRYSTAL [33]. The advantages of the slab approach are that the surface atoms are represented in their correct coordination (except, of course, the lowest layer) and that the accuracy of the model is controlled only by the slab thickness. In particular, surface relaxation effects can be accurately described [8]. Limitations are that only the atoms at the "center" of the facets are modeled, and that low-coordination atoms at the edge or at defects are not taken into account. It is possible in this approach, however, to define a supercell in order to describe defects such as steps or kinks, within the slab model.

A key issue is the interaction between the surface and adsorbates. If a cluster model is used, generally a single adsorbate is considered and made to interact with the cluster. This refers to the low coverage limit (or single-molecule adsorption). Some attempts have been made to model finite coverage on cluster surfaces [34], but this is delicate since some molecules will interact with the edge of the cluster, that is, with atoms that are represented far from their correct coordination number. In contrast to

the slab model, finite coverage is considered by using a surface supercell. The size of the lateral supervectors defines the minimum accessible coverage, when a single molecule is placed on the cell. Higher coverage can be obtained by decreasing the unit cell size, or better by increasing the number of molecules. This latter possibility offers greater flexibility in the nature of the high-coverage overlayer, but is constrained in any case by the choice of the supercell.

24.3
Electronic Structure Calculations

The purpose of this section is to introduce the methods of quantum chemistry to nonexperts. The reader is directed to the literature [5, 35–37] for further details.

Let us consider a molecule constituted by P nuclei (of charge Z_I and coordinate R_I) and N electrons of coordinate r_i and spin s_i (α or β).

All the information about this molecular system is contained in the wavefunction, solution of the time-independent equation, established by Schrödinger in 1925. The electrons have a much smaller mass than the nuclei, hence they move much faster. We will therefore assume that the Born–Oppenheimer approximation is valid: the nuclei will be frozen in space, and the variables will be restricted to the electron degrees of freedom.

$$\hat{H}_{\mathrm{el}}\Psi = E\Psi$$

with

$$\Psi(r_1, s_1, r_2, s_2, \ldots, r_N, s_N)$$

The wavefunction is a mathematically complicated function, since it explicitly depends on $4N$ variables (three space and one spin coordinate per electron). The electronic hamiltonian $\hat{H}_{\mathrm{el}}$ can be decomposed into three terms, describing the kinetic energy of the electrons $\hat{T}_{\mathrm{e}}$, the attractive electrostatic interaction between nuclei and electrons $\hat{V}_{\mathrm{ne}}$, and the repulsive electron–electron electrostatic interaction $\hat{V}_{\mathrm{ee}}$:

$$\hat{H}_{\mathrm{el}} = \hat{T}_{\mathrm{e}} + \hat{V}_{\mathrm{ne}} + \hat{V}_{\mathrm{ee}}$$

where

$$\hat{T}_{\mathrm{e}} = \sum_{i=1}^{N}\left(-\frac{1}{2}\nabla_i^2\right) \qquad \hat{V}_{\mathrm{ne}} = \sum_{i=1}^{N} v(r_i)$$

$$v(r_i) = -\sum_{I=1}^{P}\frac{Z_I}{|R_I - r_i|} \qquad \hat{V}_{\mathrm{ee}} = \sum_{i<j}^{N}\frac{1}{|r_i - r_j|}$$

Atomic units employed here allow a very compact formulation of these operators.

The kinetic energy $\hat{T}_e$ and nuclei–electron $\hat{V}_{ne}$ interaction parts depend only on the coordinate of a single electron *i*. In contrast, each term of the electron–electron interaction $\hat{V}_{ee}$ depends explicitly on the instantaneous coordinates of two electrons *i* and *j*. This is the key difficulty in the resolution of the Schrödinger equation. The motion of electrons is strongly coupled since the potential felt by electron *i* depends on the coordinates of all other electrons of the system.

Methods in quantum chemistry aim at solving this equation by making approximations and simplifications on the form of the wavefunction Ψ.

24.3.1 The Hartree Approximation

The historical approach of Hartree considered that the wavefunction is a simple product of a set of single electron wavefunctions (spin coordinates are not considered):

$$\Psi(r_1, r_2, \ldots, r_N) = \psi_1(r_1) \times \psi_2(r_2) \times \cdots \times \psi_N(r_N)$$

It follows that each electron wavefunction $\psi_i(r_i)$ verifies a one-particle Schrödinger equation, where the potential energy $V_H(r)$ of the electron is no longer coupled to the individual motions of the other electrons of the molecular system but feels the average electron density generated by all other electrons. This approach is also called the "mean field" approximation.

$$V_H(r) = \int \frac{\sum_{j\neq i}^{N} \varrho_j(r')}{|r-r'|} \mathrm{d}r' \qquad \varrho_j(r) = \left|\psi_j(r)\right|^2$$

The Schrödinger equation, initially depending on the coordinates of *N* electrons, splits into a set of *N* equations depending only on the coordinate of a single electron:

$$\left(\hat{T}_e + \hat{V}_{ne} + \hat{V}_H\right)\psi_i = \varepsilon_i \psi_i$$

These equations are nevertheless coupled since for the electron *i* the Hartree potential V_H depends on the density, and hence on the wavefunctions, of all other electrons. This system of equation is generally solved by an iterative method, called self-consistent field (SCF). An initial wavefunction $\psi_i^0(r)$ is chosen for all electrons, then the Hartree potential V_H is calculated, which allows the resolution of the set of equations, yielding a new set of wavefunctions $\psi_i^1(r)$. The procedure is iterated until convergence of the total energy E_H is reached:

$$E_H = \sum \varepsilon_n - \left[\frac{1}{2}\iint \frac{\varrho(r)\varrho(r')}{|r-r'|}\mathrm{d}r\mathrm{d}r'\right]$$

The second term in this equation corrects for double counting of interactions, since the effective potential V_H makes the electron–electron interactions be counted twice.

However, the replacement of the wavefunction by a simple product of single-electron wavefunctions is a drastic approximation. It especially totally ignores the

Pauli exclusion principle and creates an incorrect bosonic ground state. Its interest is thus only historical and educational.

24.3.2 Pauli Principle and Hartree–Fock Approximation

The Pauli principle expresses the fact that electrons are fermions, and hence cannot be present at the same point of space with the same quantum state. This is translated mathematically into the fact that the wavefunction must be antisymmetric with respect to the interchange of the spatial and spin coordinates of any two electrons:

$$\Psi(r_1, s_1, r_2, s_2, \ldots, r_N, s_N) = -\Psi(r_2, s_2, r_1, s_1, \ldots, r_N, s_N)$$

The Pauli repulsion acts as an effective repulsion between electrons of the same spin.

The Hartree–Fock (HF) approximation is the simplest theory that incorporates the Pauli principle and the permutation antisymmetric character of the wavefunction. This approach is still the cornerstone of modern wavefunction-based quantum chemical methods. It rests on the original idea of Hartree, but it approximates the N-electron wavefunction not by a simple product, but by an antisymmetrized product of N one-electron functions. This product is generally called a Slater determinant:

$$\Psi(x_1, x_2, \ldots, x_N) = \frac{1}{\sqrt{N!}} \begin{vmatrix} \chi_1(x_1) & \cdots & \chi_N(x_1) \\ \vdots & \ddots & \vdots \\ \chi_1(x_N) & \cdots & \chi_N(x_N) \end{vmatrix}$$

The one-electron functions χ_i are called spin orbitals, since they are composed of the product of a spatial orbital ψ and a spin function σ (either spin α or spin β):

$$\chi(x) = \psi(r)\sigma(s), \quad \sigma = \alpha, \beta$$

Again, one can show that the N-electron Schrödinger equation can be decomposed into a system of N coupled one-electron equations:

$$\left(\hat{T}_e + \hat{V}_{ne} + \hat{V}_{HF}\right)\chi_i = \varepsilon_i \chi_i$$

Instead of the individual electron–electron interaction, each electron feels the HF potential, that is, the average repulsive potential due to the remaining $N-1$ electrons:

$$V_{HF}(x) = \sum_j^N \left[J_j(x) - K_j(x)\right]$$

Hence the electron–electron potential $1/|r_i - r_j|$, which depends on the coordinates of two electrons, is replaced by the simpler V_{HF} potential, which depends only on the coordinate of one electron.

J is the coulomb operator, defined as

$$J_j(x) = \int \frac{\varrho_j(x')}{|r - r'|} \mathrm{d}x'$$

It represents the average potential that the electron i at position x feels from the average distribution of a second electron in orbital χ_j.

$$\sum_j^N J_j(x)$$

is hence similar to the Hartree potential V_H, but the sum runs over all the electrons including the electron i.

K is the exchange operator, which has a pure quantum origin and no classical equivalent. It can only be defined by its action on a spin-orbital:

$$K_j(x)\chi_i(x) = \int \frac{\chi_j^*(x')\chi_i(x')}{|r-r'|} \mathrm{d}x' \chi_j(x)$$

It can be seen that the exchange term $K_i(x)\chi_i(x)$ exactly cancels the spurious Coulomb term $J_i(x)$. As a result, the electron i feels the electronic density of all the electrons, excluding itself, as in the case of the Hartree formulation. The HF approach is hence free of self-interaction.

The self-consistent resolution of the coupled equations leads to the Slater determinant which is the closest to the exact solution (i.e., the one with the lowest energy). However, the assumption that the true N-electron wavefunction has the form of a Slater determinant is a drastic one, which induces an error in the total energy. By definition, this error, which is always negative, that is, stabilizing, is called the correlation energy:

$$E^{\text{correlation}} = E^{\text{exact}} - E^{\text{HF}}$$

The correlation energy is generally important, and as a result the HF energy is far from the desired chemical accuracy. For example for an N_2 molecule, the correlation energy represents only 0.5% of the total energy, but 50% of the bond energy. Neglecting correlation is hence an unacceptable approximation for chemical purposes.

24.3.3 Introduction to Post-Hartree–Fock Methods

In the wavefunction-based methods, a natural and systematic way of including the electronic correlation is to increase the flexibility of the form of the wavefunction, so that it can better approach the real N-electron solution [38]. This is done in practice by representing the wavefunction not as a single but as a linear combination of several determinants. Although the approach is systematic, and gives the exact energy in the limit of a large number of determinants, its practical implementation is far from easy since in many cases a very large number (millions!) of determinants (also called configurations), and hence a huge computational cost, is needed for an accurate description of the correlation energy. A large part of the effort in the domain is to design methods that would approach the exact energy at a reduced cost. The first

approaches start for the HF SCF solution and improve it by mixing with other determinants. This mixing is variational (i.e., explicit) in the configuration interaction (CI) methods, while the influence of the other determinants is treated as a perturbation in other approaches (Møller–Plesset MP2, MP4). Mixed variational–perturbative approaches have also been constructed. A second branch consists of the multi-configurational methods, where the SCF solution is searched not for a single determinant, but directly for a linear combination of determinants [multi-configurational self-consistent field (MC-SCF), complete-active-space self-consistent field (CAS-SCF)] [39]. The possible number of determinants here is limited, however, and generally such methods need to be associated with an extensive variational or perturbative correlation approach. The detailed description of these post-HF methods goes beyond the scope of this chapter.

In summary, however, the post-HF methods are very accurate, but the computational cost is very high, hence limiting the accessible systems to the cases with a small number of atoms. These methods are therefore, at present, not adequate for the realistic description of models of heterogeneous catalysts.

24.3.4
Density Functional Theory

Another type of method has been proposed to face the problem of the evaluation of the correlation energy. The wavefunction contains all the information about the electronic structure but shows a complex dependence on the three spatial coordinates and spin coordinate of each electron, hence a total of $4N$ variables. The branch of method related to DFT makes a radical move by changing the fundamental variable, and replacing the wavefunction by the electronic density. The electronic density is derived from the squared modulus of the wavefunction (the probability of finding an electron at a given point of space and spin) by integrating (i.e., averaging) on all coordinates except the spatial coordinate of one electron r_1:

$$\varrho(r_1) = N \int \cdots \int |\Psi(r_1, s_1, r_2, s_2, \ldots, r_N, s_N)|^2 \mathrm{d}r_2 \cdots \mathrm{d}r_N \mathrm{d}s_2 \cdots \mathrm{d}s_N$$

Hence the electronic density depends solely on three space coordinates. The complete integration over the three remaining variable yields the total number of electrons N:

$$\int \varrho(r) \mathrm{d}r = N$$

The key question is therefore: can we use the electronic density? Does it carry the necessary information about the electronic structure of the system?

At first sight, the integration over $4N - 3$ variables reduces the information in the density compared with the initial wavefunction. However, an outstanding theorem firmly sets the mathematical basis of modern DFT, and in simple words demonstrates that the density is a proper variable to characterize the energy of a chemical system.

First, let us define the external potential V_{ext} that acts on a system of electrons. In the definition of the electronic hamiltonian H_{el}, T_e and V_{ee} depend only on the coordinates of the electrons and hence are intrinsic. In contrast, V_{ne} describes the influence on the electrons of the nuclei, external species with respect to the electrons. It is hence called the external potential, V_{ext}. Other terms can contribute to the external potential, such as an imposed electric field.

Established in 1964, the Hohenberg and Kohn theorem states that "the external potential V_{ext} is (to within a constant) a unique functional of the electronic density $\varrho(r)$; since, in turn, $V_{ext}(r)$ fully determines the hamiltonian H, we see that the full many particle ground state is a unique functional of $\varrho(r)$" [40].

Hence the electronic density of a chemical system determines completely the nature of the "molecule," that is, the position and charge of nuclei, and the number of electrons. Two different molecules cannot be associated with the same electronic density. The electronic density hence determines the full hamiltonian and the Schrödinger equation can "formally" be resolved, providing the total energy and the full wavefunction of the system. Therefore, the electronic density contains the necessary information to determine all the ground-state electronic properties of the molecule. In particular, the ground-state energy is a functional of the density (a functional is a function of a function, the electronic density being not a scalar but already a function of r).

The mathematical demonstration of this theorem is performed by a reasoning by absurd. We wish to provide instead a qualitative chemical demonstration. If we know the wavefunction, its integration over space gives the total number of electrons of the system. $\varrho(r)$ shows cusps at the position of the nuclei, hence defining their coordinates. In order to define the type of molecule, the only missing information is the type of nuclei, that is, its atomic charge. It can easily be shown that the values of the density at the nuclei, and of its derivative, are directly related to the atomic charge. Hence the density contains all the necessary information to obtain the nature of the molecule, to set its full hamiltonian.

Although the Hohenberg and Kohn theorem states that the ground-state energy, in addition to all other ground-state properties, are formally a functional of the density, it gives no clue, however, about the practical way to construct this functional. Modern research in DFT aims at proposing approximate but acceptable forms of this functional.

Up to this point, we have considered that we know the exact ground-state density. In practice, this is not the case, and we need to search for the density. How do we know that a given electronic density is adequate? The second theorem by Hohenberg and Kohn provides a guide for this search, with a similar spirit to the variational principle in traditional quantum chemistry. This theorem states that among possible trial densities, the true ground-state density is the one which minimizes the total energy [41]:

$$E_0 \leq E[\varrho_{trial}]$$

This principle, however, is limited to the ground-state energy (or more precisely to the lowest energy state for a given symmetry) and cannot be used for the general search for excited states.

As was previously done for the electronic hamiltonian, the ground-state energy functional can be decomposed into its individual components, kinetic energy, electron–electron interaction, and nuclei–electron external potential:

$$E_0[\varrho_0] = T_e[\varrho_0] + E_{ne}[\varrho_0] + E_{ee}[\varrho_0]$$

where ϱ_0 is the ground-state density At this point, it is pertinent to separate the terms into those which are system dependent (E_{ne}) and those which are universal and are assembled in the so called Hohenberg–Kohn functional F_{HK}:

$$E_0[\varrho_0] = F_{HK}[\varrho_0] + E_{ne}[\varrho_0]$$

where

$$F_{HK}[\varrho_0] = T_e[\varrho_0] + E_{ee}[\varrho_0]$$

The nuclei–electron term is again easy to evaluate:

$$E_{ne}[\varrho_0] = \int \varrho_0(r) V_{ext}(r) \mathrm{d}r$$

This is far from being the case for the universal F_{HK} functional. One practical solution is to determine the terms that can be calculated, and to position all the others in a specific functional that needs to be approximated. For the electron–electron interaction:

$$E_{ee}[\varrho] = \frac{1}{2}\int\int \frac{1}{r_{12}} \varrho(r_1)\varrho(r_2)\mathrm{d}r_1\mathrm{d}r_2 + E_{ee-nc}[\varrho]$$

The classical interaction between the average electronic distribution ϱ of the two electrons can be evaluated from the left part of the above equation. This does not describe the instantaneous correlation energy between these electrons, or the consequences of the Pauli principle and the difference between the true interaction and the classical term, that is, the non-classical term, is called the exchange correlation energy $E_{XC}[\varrho]$. Hence

$$E_0[\varrho_0] = T_e[\varrho_0] + E_{ne}[\varrho_0] + E_{ee-cl}[\varrho_0] + E_{XC}[\varrho_0]$$

Even if one assumes that $E_{XC}[\varrho]$ is known, which is not the case, one still needs to find the optimal density ϱ_0, by following the variational principle. Kohn and Sham introduced a mapping of the real electronic system on a set of "fictitious" noninteracting one-electron wavefunctions [41]. The key constraint is that the density associated with this set of noninteracting orbitals $\varrho_s(r)$is exactly equal to that on the real system $\varrho_0(r)$:

$$\varrho_s(r) = \sum_i^N \sum_s \varphi(r,s)^2 = \varrho_0(r)$$

The exact kinetic energy of the noninteracting system can easily be calculated:

$$T_s = -\frac{1}{2}\sum_i^N \varphi_i \nabla^2 \varphi_i$$

This is not the true kinetic energy of the real interacting system but again the difference is placed in the unknown exchange-correlation energy term. The minimization of the energy using the noninteracting Kohn–Sham orbitals yields a set of coupled one-electron equations, similar to that obtained from the Hartree or Hartree–Fock approaches:

$$\left[-\frac{1}{2}\nabla^2 + V_{\text{ne}} + \int \frac{1}{r_{12}}\varrho(r_2)\mathrm{d}r_2 + V_{\text{XC}}\right]\varphi_i(r) = \varepsilon_i\varphi_i(r) \quad i = 1, \ldots, N$$

where

$$V_{\text{XC}} \equiv \frac{\delta E_{\text{XC}}}{\delta_\varrho}$$

This set can be solved by an SCF approach, as explained above, yielding a set of optimal orbitals, and hence the optimal density. The method would be exact at this point, if the E_{XC} and V_{XC} functionals were known. Unfortunately, this is not the case, and the development of approximate functionals is a very active topic of research.

24.3.5
Exchange-Correlation Functionals

Only a brief introduction will be given here. The most popular, simple, and intuitive approach is the local density approximation (LDA). There is one system for which the exchange-correlation energy can be accurately calculated: the uniform electron gas. The exchange-correlation energy of that model system, $\varepsilon_{\text{XC}}(\varrho_0)$, can be analytically interpolated for any chosen value for the uniform density ϱ_0 [42–44]. The LDA consists in dividing the space into small volumes and at each point of density $\varrho(r)$ associating locally the exchange-correlation contribution of the uniform electron gas of the same density $\varepsilon_{XC}[\varrho(r)]$:

$$E_{\text{XC}}^{\text{LDA}}[\varrho] = \int \varrho(r)\varepsilon_{\text{XC}}[\varrho(r)]\mathrm{d}r$$

The approximation hence consists in associating each point of space with a small piece of uniform electron gas, and integrating over the total volume of the molecule. The LDA approximation is then exact in the limit of a system with an electronic density slowly varying in space. It was the first "efficient" approximation to be proposed and it has been extremely popular (and still is in the domain of solid-state physics). It obviously gives very good results on systems with quasi-uniform density such as metal systems from main group elements. LDA generally gives accurate geometries (typically within 0.03 Å). For the description of energies, trends are

usually correct, but LDA suffers from an important overestimation of bond energies (up to 10%) [35, 45]. Weak bonds such as hydrogen bonds are also not well described. Both aspects have strongly limited the applications of LDA in chemistry.

The general gradient approximation (GGA) aims at improving the description of LDA by taking into account not only the density at a given point in space but also its gradient $\nabla\varrho(r)$. The key idea here is to include information on the spatial variation of the density. A simple gradient expansion is not appropriate, however, and various constraints have to be imposed for the exchange-correlation functional to fulfill fundamental properties. These constraints are embedded in the F_{XC} function:

$$E_{XC}^{GGA}[\varrho] = \int \varrho(r)\varepsilon_{XC}[\varrho(r)]\mathrm{d}r + \int F_{XC}[\varrho(r), \nabla\varrho(r)]\mathrm{d}r$$

Multiple choices of F functions, and hence of GGA functionals, have been proposed. Popular ones are PW91 [46], PBE [47], and BLYP [48, 49], among others. They high popularity is based on the fact that they markedly improve the binding energies in molecules (accuracy of $\sim$20 versus $\sim$180 kJ mol^{-1} with LDA for the atomization energy [35]), hence opening a wide field of applications in chemistry and particularly in catalysis. Geometries are usually slightly improved with respect to LDA and are in very good agreement with experimental data. For the interaction between molecules or atoms and surfaces, the calculated geometries match very well those proposed by surface techniques such as LEED or EXAFS (by $\sim$0.03 Å) [50–52]. The reproduction of adsorption energies is more problematic. GGA adsorption energies for O and CO on transition metal surfaces are significantly overestimated (by $\sim$50 kJ mol^{-1}) [53], whereas that for benzene on Pt(111) is underestimated by $\sim$50 kJ mol^{-1} [54, 55]. Weak hydrogen-bond interactions are well described, both for their structures and energies, opening up the study of liquid water and ice. However, GGA functionals all give a very poor description of dispersion interactions (from induced dipole–induced dipole interactions) and systems such as alkanes in zeolites, where van der Waals contributions are important, are not correctly described [56]. Developments have been made for this treatment of dispersion interaction, by adding semiempirical terms to the DFT energy [57], by improved functionals [58], or by developing new methods beyond DFT [56].

The exchange energy is a large part of the exchange-correlation energy functionals. One popular way to improve GGA functionals is to introduce the exchange energy, calculated in the HF scheme for a Slater determinant. The optimal approach is to mix the exact exchange with the DFT exchange-correlation functional and to fit the mixing coefficient on energetic properties of a large set of molecules. The best functional in this family of hybrid functionals is B3LYP (with an average error of 12 kJ mol^{-1} on atomization energies of main group molecules) [59]:

$$E_{XC}^{GGA} = (1-a)E_X^{LDA} + aE_X^{HF} + bE_X^{GGA} + cE_C^{LYP} + (1-c)E_C^{LDA}$$

with $a = 0.2$, $b = 0.72$, and $c = 0.81$.

24.4
Application of Total Energy Calculations to the Structure of Catalytic Surfaces Under the Conditions of Catalysis

In the previous section, we have seen how to calculate the total energy of a chemical system with DFT. There remain many technical aspects to obtain the energy of systems such as those in Figure 24.2. Periodic boundary conditions need to be applied to the surface unit cell, following the Bloch theorem and describing the Brillouin zone with a finite set of K points. One-electron Kohn–Sham orbitals are usually developed on a basis set of atomic orbitals or alternatively on a set of plane waves. Finally, atomic cores are usually represented by a pseudo-potential. This is especially required in order to supplement a plane-wave basis set for the description of the cusp at the atomic core, allowing the use of a reasonable number of plane waves in the calculation. A detailed description of all these aspects can be found in the literature [5].

In this section, we present applications of total energy calculations to the structure and stability of a catalytic surface under a pressure of gas. The determination of the surface structure of the solid catalyst is a key aspect in fundamental catalysis. In many cases, the surface can have a structure different from that of the bulk of the material: reconstruction can occur, or segregation in the case of a compound. Defects such as steps can play a central role for some reactions. When subjected to the pressure of the reactants, there are several cases where the surface can be transformed by the formation of a few atomic layers of a compound. For example, metal surfaces under a pressure of oxygen might form a surface oxide. In the experiment, this is evidenced by an induction time until the catalytic system is stable, and active or selective. Since the catalytic properties are determined by the external layers of the catalytic solid, it is of great importance to be able to understand and predict the nature and structure of a catalyst under a pressure of gas. In the field of heterogeneous catalysis, the methods presented below were initially applied to the termination of aluminum oxide surfaces under a pressure of O_2 [60, 61] and of molybdenum sulfide surfaces under a pressure of H_2 and H_2S [62, 63].

From a theoretical viewpoint, the most stable surface composition and geometry for a compound $A^1_{N_1} A^2_{N_2} \ldots A^p_{N_p}$ (elements A^i, stoichiometry N_i) minimize the surface free energy $\gamma(T, p)$:

$$\gamma(T,p) = \frac{1}{A}\left[G(T,p,N_1,\ldots,N_p) - \sum N_i \mu_i(T,p)\right]$$

where $G(T, p, N_1, \ldots, N_p)$ is the free energy, A the area of the surface unit cell, $\mu_i(T, p)$ the chemical potential of element i, T the temperature, and p the pressure. Since the compound is a solid, the only contribution to the entropy is associated with the vibrational degrees of freedom, and it is usually negligible ($<10\,\mathrm{meV\,\AA^{-2}}$). Hence the total energy E from the DFT calculation will be used instead of G.

The bulk of the compound acts as a thermodynamic reservoir, and fixes one chemical potential or a relation between them. For a metallic palladium system, for example, μ_{Pd} is just the energy of the Pd atom in the bulk, E^{bulk}_{Pd}.

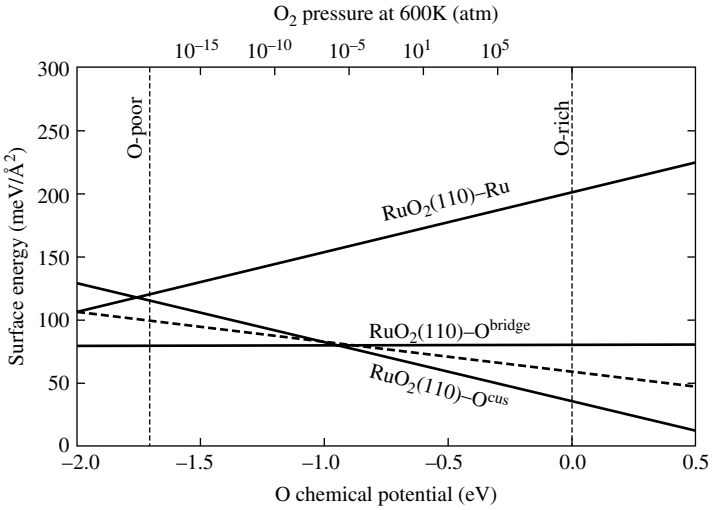


Figure 24.3 Surface energy as a function of oxygen chemical potential for three possible terminations of a RuO_2(110) surface. The origin of oxygen chemical potential is $^1/_2E^{gas}_{O_2}$. Reprinted with permission from [64].

24.4.1
Termination of the (110) Surface of RuO_2

Let us consider as a first example the (110) surface of ruthenium dioxide, RuO_2, submitted to a pressure of oxygen [64]. The bulk fixes the relation between the chemical potentials of oxygen and ruthenium:

$$\mu_{Ru}(T,p) + 2\mu_O(T,p) = E^{bulk}_{RuO_2}$$

Hence there is only one independent chemical potential. If μ_O is chosen, the surface energy of an RuO_2 slab is

$$\gamma(T,p) = \frac{1}{A}\left[E^{slab}(N_{Ru},N_O) - N_{Ru}E^{bulk}_{RuO_2}(T,p) + (2N_{Ru} - N_O)\mu_O(T,p)\right]$$

where $\gamma(T, p)$ is an affine function of μ_O, and the slope depends on the surface composition.

The surface energy is plotted in Figure 24.3 for three possible terminations of RuO_2(110), depending at which plane the crystal structure is truncated. The RuO_2(110)–Ru structure is terminated by the Ru layer of the oxide crystal. It exposes two types of Ru atoms, four- or fivefold coordinated. For the stoichiometric RuO_2(110)–O^{bridge} termination, bridging oxygen atoms between the fourfold coordinated Ru are added, leaving only the fivefold Ru as coordinatively unsaturated sites (cus). Finally, in the O-rich RuO_2(110)–O^{cus} structure, O atoms are added on top of these cus Ru, leading to fully saturated Ru atoms.

The slope of $\gamma(T, p)$ is positive for the Ru termination which is oxygen deficient ($2N_{Ru} - N_O > 0$), zero for the stoichiometric termination O^{bridge} ($2N_{Ru} - N_O = 0$), and negative for the oxygen-rich termination O^{cus} ($2N_{Ru} - N_O < 0$). The total energies were calculated here with DFT and a GGA functional. The most stable surface is that with the smallest surface energy. The graph underlines two zones in the domain of possible values for μ_O. The stoichiometric termination is the most stable one until $\mu_O = -0.9$ eV, and for higher oxygen chemical potentials the oxygen-rich termination becomes the most stable.

In order to relate to the experimental conditions, it is important to link the oxygen chemical potential to the temperature and to the pressure of oxygen in the gas phase. This can be done from thermodynamics tables [65], or by application of statistical thermodynamics of the ideal gas:

$$\mu(T, P) = E + kT \ln\left(\frac{1}{Z_{gas}^{trans} Z_{gas}^{rot}}\right)$$

where Z_{gas}^{trans} and Z_{gas}^{rot} are the translational and rotational partition functions, respectively. The oxygen pressure associated with a given oxygen chemical potential is indicated on the top axis of Figure 24.3 for a temperature of 600 K. The transition from the stoichiometric to the oxygen-rich termination of $RuO_2(110)$ hence occurs at $p \approx 10^{-5}$ bar at this temperature. The accuracy of the calculated surface energies can be estimated to be 10 meV Å^{-2}, not including systematic errors in the DFT exchange correlation functional.

24.4.2
Pd Catalysts Under the Conditions of Partial Hydrogenation of Alkynes

Palladium is a well-known heterogeneous catalyst for hydrogenation reactions. It is especially selective for the partial hydrogenation of alkynes to alkenes [66]. Several models have been proposed in order to explain the hydrogenation of alkynes to alkenes, without the formation of alkanes, on Pd [67]. Recent *in situ* X-ray photoelectron spectroscopy (XPS) studies have, however, given novel insights into the state of the Pd surface during hydrogenation [68, 69]. The Pd $3d_{5/2}$ core state is the chosen descriptor in these experiments. Under a pressure of 1 mbar of C_2H_2 (or other alkynes), a new peak appears in the spectrum, shifted to higher binding energy by 0.6 eV compared with normal metallic Pd. This peak has been assigned to the formation of a PdC phase at the surface of the Pd catalyst [68–70]. Interestingly, this new peak is not present if Pd is subjected to a pressure of ethene, and the spectrum is similar to that of pure Pd metal, implying that the surface carbide would not form in this case.

The interpretation of XPS results being not straightforward, DFT calculations have been undertaken to check this hypothesis of surface carbide formation [70, 71]. A Pd(111) surface was chosen as the model, and the stability of carbon atom adsorption was first studied. Carbon adsorbs on the surface of Pd with a strong binding energy (~7 eV) and an optimal coverage of one-third of a monolayer (ML). Above this

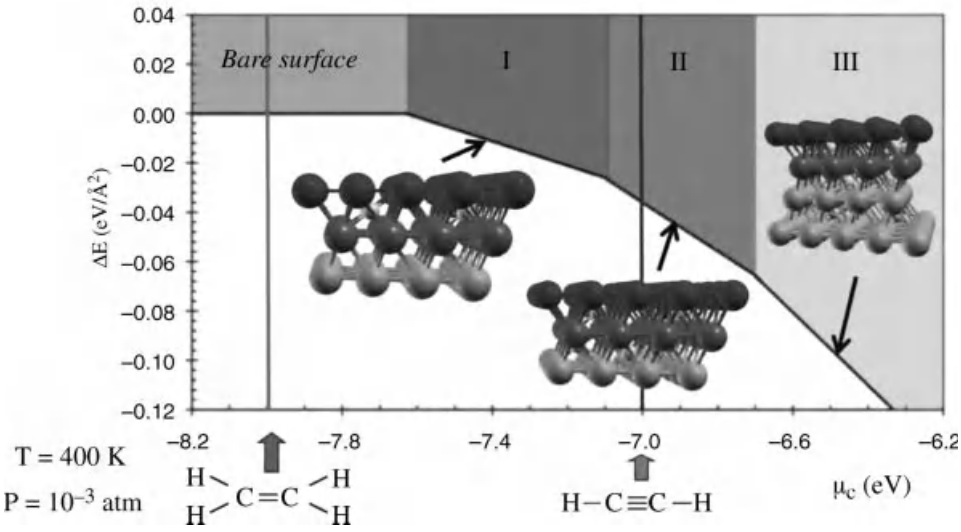


Figure 24.4 Surface energy as a function of carbon chemical potential μ_C for surface carbides of Pd of increasing thickness (I = one layer occupied at 1/3 ML, II = two layers at 1/3 ML per layer, III = three layers at 1/3 ML per layer). The value of the chemical potential imposed by the gas-phase reservoir is indicated for acetylene and ethene at $T = 400$ K and $P = 10^{-3}$ atm. Adapted with permission from [70].

coverage, strong lateral repulsions occur between C adsorbates. Carbon can also penetrate in the subsurface, occupying octahedral sites in the fcc palladium lattice. Carbon is even more stable by 0.6 eV in the first interlayer compared with the surface site, with the same optimal coverage of 1/3 ML. Occupation of the second or deeper interlayer yields a similar but slightly weaker stability. The surface energy of terminations with one, two, or three interlayers occupied with a content of 1/3 ML per layer is shown in Figure 24.4 as a function of the carbon chemical potential μ_C. These systems cannot be compared directly since they do not contain the same number of carbon atoms per unit cell.

If the carbon chemical potential is low, meaning that carbon is stable in the gas-phase compound, the most stable termination is metallic palladium. However, above a threshold value of $\mu_C = -7.6$ eV, the one-layer surface carbide becomes more stable, and for even higher values a thickness of two or three layers can be formed. Hence the value of the carbon chemical potential controls the presence and thickness of the surface carbide phase.

During catalysis, under operating conditions, the carbon chemical potential is controlled by the gas phase, which acts as a reservoir of carbon. During hydrogenation, the Pd surface is subjected to a pressure of acetylene and H_2. Acetylene molecules are decomposed into adsorbed atomic carbon and hydrogen (which is assumed here to desorb as H_2 in the gas phase):

$$C_2H_2{}^{gas} \rightarrow 2C_{ads} + H_2{}^{gas}$$

The carbon chemical potential can be calculated from the two gas-phase species:

$$\mu_C = \frac{1}{2}[\mu(C_2H_2{}^{gas}) - \mu(H_2{}^{gas})]$$

which are themselves evaluated from the statistical thermodynamics of the ideal gas. The carbon chemical potential (−7 eV) obtained for $P_{C_2H_2} = P_{H_2} = 10^{-3}$ atm and $T = 400$ K (conditions for the *in situ* XPS measurements) is shown in Figure 24.4. Under these conditions, the thin surface carbide is more stable than the bare Pd surface, hence confirming the interpretation of the XPS data. The stoichiometry of this surface carbide, $Pd_{75}C_{25}$, agrees reasonably well with the local carbon concentration obtained from XPS analysis (∼35 at%). This result is remarkable since there is no defined carbide compound of palladium. Carbon can be dissolved in Pd bulk up to a content of about 10%. Hence the carbide is specifically a surface compound occurring under the conditions of acetylene hydrogenation. The calculated Pd core level shifts for the surface carbide (+0.6 eV) match the measured value [72].

If the reactant hydrocarbon is ethene, the carbon chemical potential can be calculated as

$$\mu_C = \frac{1}{2}[\mu(C_2H_4{}^{gas}) - 2\mu(H_2{}^{gas})]$$

For similar pressure conditions, μ_C is ∼1 eV lower and falls in the region where the most stable termination is metallic Pd, fully consistent with the XPS data. The type of reactant hence has a key influence on the nature of the surface of the Pd catalyst, with the formation of surface carbide only in the presence of acetylene.

This surface carbide has a strong influence on the catalytic activity. DFT calculations show that the chemisorption of acetylene and ethene is decreased on the surface carbide compared with bare palladium. The decrease in the chemisorption energy of ethene from −0.9 eV on Pd to −0.75 eV on the surface carbide (three layers) is key for the selectivity allowing desorption of ethene at the reaction temperature, instead of its further hydrogenation to ethane. In the experiment, the destruction of the surface carbide by an increase in the hydrogen pressure switches the product from ethene to ethane. The theoretical description of surface carbide formation has been extended to other transition metals [71].

24.4.3
The (110) Surface of Gold Under a Pressure of CO

Gold has unexpectedly become a key element in heterogeneous catalysis for its ability to perform oxidation reactions at low temperature [73]. However, it interacts weakly with molecules and represents a case where the consideration of pressure and temperature is important. We will consider here the (110) surface of gold, which is a simple model of a stepped surface, with low-coordination gold atoms [coordination of 7 versus 9 on the compact (111) surface].

The ideal fcc (110) surface shows compact rows of atoms (Figure 24.5, right). In vacuum, the Au(110) surface shows a (1 × 2) reconstruction with a doubling of the

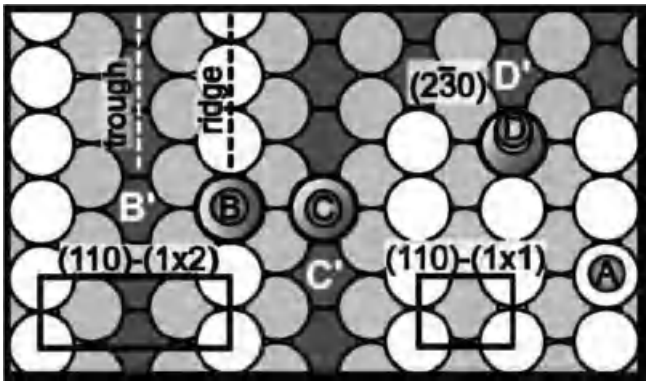


Figure 24.5 Geometric features of the Au(110) surface. Reprinted with permission from [75].

spacing between rows, by removal of a row and formation of a trough (Figure 24.5, left). The Au(110) surface was subjected to a pressure of CO at room temperature and studied with polarization modulation infrared reflection absorption spectroscopy (PM-IRAS) [74]. Initial adsorption occurs at $P = 10^{-4}$ bar, and at higher pressure (2×10^{-2} bar) the reconstruction is lost and an ideal (1×1) termination is again formed.

A surface stability diagram, where the CO pressure is varied at room temperature, is shown in Figure 24.6 [75].

Among the bare surfaces [shown by horizontal segments in (a) and independent of P_{CO}], the 1×2 (blue line) is the most stable, in agreement with experiment. A

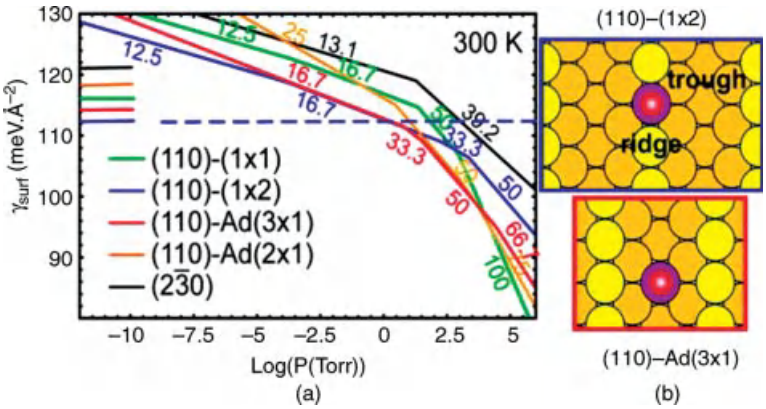


Figure 24.6 Surface energy as a function of CO pressure at 300 K for various structures of Au (110) with adsorbed CO molecules. The surface energies of the bare surfaces are indicated by the horizontal segments in (a). The CO coverage (%) is shown by a label. The label Ad indicates the presence of adatoms on Au(110). The (2–30) surface, corresponding to a stepped surface perpendicular to the rows, is also shown in black. 1 Torr $\approx 10^{-3}$ bar. Adapted with permission from [75].

structure where one gold adatom has been added in the trough is slightly less stable (structure in the red rectangle in Figure 24.6b). The cost of forming the Au adatom (coordination 5) from the ridge (coordination 7) is 0.2 eV. The (1×1) termination in green is less stable. If we first consider the low-pressure regime, the surface energies of the structures with CO adsorbed are above that of the bare surface, meaning that CO adsorption is unstable. This contrasts with the calculated DFT adsorption energy (varying between -0.6 and -0.9 eV upon site, hence stabilizing) and shows the importance of taking into account the loss of entropy for the molecule upon chemisorption. The best chemisorption structures correspond to the adsorption on the ridge of Au(110) (blue line), and to the adsorption on top of an adatom in the trough (red line). The energies of the two structures coincide at a similar coverage of 16.7%. The adsorption energy of CO on the adatom is 0.2 eV higher than that on the ridge, hence compensating the cost to generate the adatom. These adsorption structures become stable for a pressure above 1 Torr. From this point, CO promotes the formation of CO-covered gold adatoms that populate the troughs at increasing concentration. Additional CO molecules can also adsorb on the ridge to stabilize the surface further. Finally, the filling of the trough by CO-covered adatoms forms the ideal (1×1) structure (green line) with a full coverage of CO of 1. In addition to these total energy calculations, calculations of CO stretch frequencies show a very good match with experimental values [76].

Hence the calculations give a clear insight into the pressure threshold and into the origin of the reconstruction. The stability of the (1×2) reconstruction arises from the formation of (111) facets, maximizing the coordination of surface atoms and stabilizing the bare surface. This stabilized surface is not favorable, however, for CO chemisorption. The 1×1 surface provides a double number of ridge sites, which leads to a larger CO adsorption compared with the (111) facets. CO adsorption is hence an alternative mechanism, with respect to the reconstruction, in order to stabilize the ideal (110) gold surface.

24.4.4
Alumina Surface at Realistic Water Pressure

Metal oxides have great importance as catalysts or catalyst supports. γ-Alumina (γ-Al_2O_3) is a key example, with a very large role as support for hydrotreatment or reforming processes and as an adsorbent for dehydration [77, 78]. γ-Al_2O_3 is a metastable phase, however, with high surface area and low crystallinity [79]. The determination of a surface model is therefore an important point. Under a (inevitable) pressure of water, the oxide surface will be covered by hydroxyl groups, hence modifying its surface acid–base properties. The nature, structure, and chemical properties of the surface sites can be studied from quantum simulation.

Let us consider the (110) surface of γ-Al_2O_3, which is the dominant one on nanocrystals [80]. In vacuum, this surface exposes three- and four-coordinated Al atoms. Its structure is strongly affected, however, by the chemisorption of water, which is mainly dissociative, forming two OH groups per water molecule adsorbed.

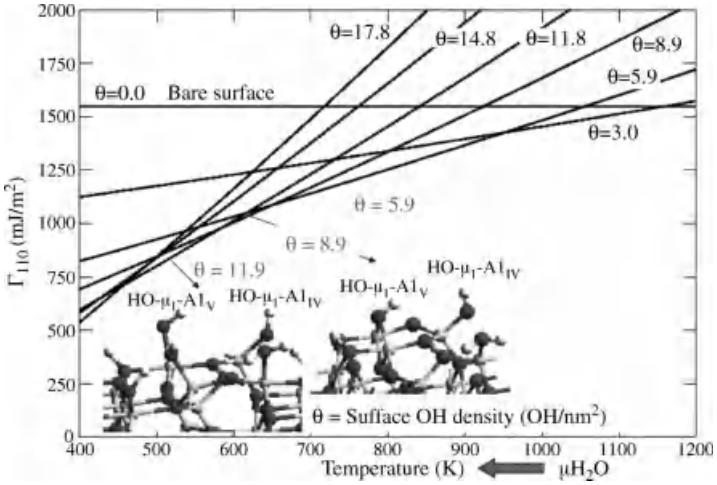


Figure 24.7 Stability diagram for the (110) surface of γ-Al_2O_3 as a function of temperature for a pressure of water of 1 bar. Terminations with various surface OH densities θ (in OH nm^{-2}) are considered. Adapted with permission from [81].

Figure 24.7 shows the surface energy of terminations with various concentrations of OH groups as a function of temperature for a water pressure of 1 bar [81, 82]. The temperature controls the chemical potential of water, which decreases with increase in temperature. The stability of the bare surface does not depend on the water chemical potential, but this bare termination is only stable at high temperature where the entropy gain in the gas phase is high. Water interacts strongly with the low-coordination Al centers, and below 1200 K the surface starts to be populated by OH groups with increasing density at low temperature. Usual pretreatment temperatures are between 500 and 800 K, corresponding to surface OH densities between 12 and 6 nm^{-2}. OH groups can occupy various sites (apical μ^1 on Al_{IV} or Al_V, bridging μ^2, etc.), each corresponding to a distinct OH stretch frequency. The structures hence allow a full understanding of the infrared spectra of alumina as a function of pretreatment temperature.

24.4.5
High Coverage and Reconstruction of Supported Pt Cluster Under a Pressure of Hydrogen

In the previous sections, we have only considered the behavior of extended surfaces under a pressure of gas. Here we describe the reactivity of a small Pt particle supported on alumina subjected to a pressure of hydrogen. Platinum is a versatile catalyst in the petrochemical and fine chemical industries [83, 84]. Hydrogen is a very common reactant in many reactions, for hydrogenation, hydrogenolysis, reforming, and fuel cell technologies. Today there are specific methods allowing the preparation of highly dispersed Pt nanoparticles on a support such as γ-Al_2O_3 [85, 86]. The nature

and structure of these small particles under a pressure of hydrogen are fundamental questions.

These small particles have been modeled by particles of 13 atoms, which can adopt various shapes in the gas phase, including the highly symmetric cuboctahedron (CUB) [87]. However, this symmetric CUB is not at all the most stable structure, because it is 3.3 eV less stable than the optimal low-symmetry 3D shape, and 2 eV less stable that a biplanar (BP) geometry.

The support is the (100) surface of γ-Al_2O_3, which, under the usual pretreatment conditions, is free of OH groups [in contrast to the previously discussed (110) termination] [81, 82]. The interaction with the support modifies the relative stabilities of the gas-phase shapes for Pt_{13}: the BP benefits from a stronger adhesion with the support and becomes the most stable structure (it is shown in Figure 24.8c) [88]. Hydrogen interacts strongly with the particle, more strongly than on the dense (111) surface, and the optimal adsorption positions for 1–36 H atoms have been determined, from an exploration with *ab initio* molecular dynamics [89]. The cluster strongly deforms upon hydrogen adsorption and the cluster–support interaction is weakened by competition with the adsorbates. Remarkably, above a hydrogen coverage of 18 atoms, the cluster reconstructs and switches from the BP shape to the CUB. This quasi-symmetric shape is shown in Figure 24.8a. Each surface Pt atom shows a C_4 symmetric environment, bonding with four external Pt atoms and the central one and with four bridging H atoms. Additional H atoms can further be added

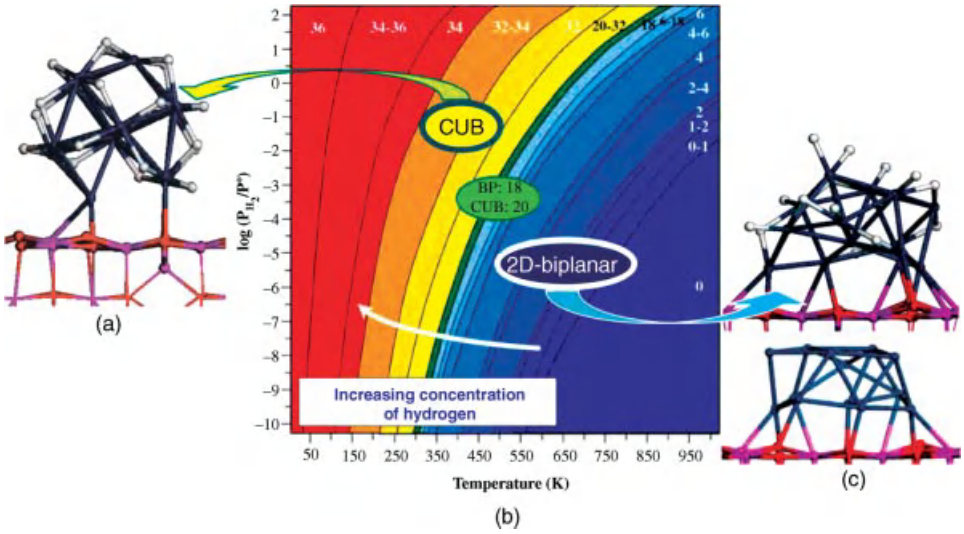


Figure 24.8 Surface stability diagram (b) showing the most stable hydrogen coverage for a Pt_{13} cluster on γ-Al_2O_3 as a function of temperature and H_2 pressure. Structures with zero and 12 hydrogen atoms with a deformed biplanar geometry are shown in (c), and the case with 20 H atoms, with a cuboctahedron shape, is shown in (a). Adapted with permission from [89].

on top of the Pt atoms. Hence a surface hydride is formed with a local formula PtH_2 to PtH_3 for $n_H = 24$ to $n_H = 36$, respectively.

The surface phase diagram (Figure 24.8b) indicates the optimum hydrogen coverage as a function of temperature and H_2 pressure. Keeping a bare particle requires a high temperature or low pressure (more than 800 K at 10^{-5} bar) and the number of hydrogen atoms increases with a decrease in temperature, with a quick rise near the transition from the BP to the CUB shape (in an interval of 100 K, the number of H atoms jumps from six to 32). The cluster reconstruction allows the optimization of the H–cluster interactions and an increase in the H content. If we now refer to catalytic conditions, we see that at room temperature and standard H_2 pressure, the Pt cluster is fully saturated by the surface hydride ($n_H = 34$, ~3 H per surface Pt). This might explain why small clusters are not active in hydrogenation. A much higher temperature of ~800 K is required for a reasonable coverage of six hydrogen (0.5 H per surface Pt), and this is the typical condition where such small Pt clusters are used for catalytic reforming in refining processes. The particle retains a metallic behavior in this case and is able to activate the alkane for dehydrocyclization. Hydrogen is needed here to prevent the formation of coke on the particle.

The surface of the particle is hence strongly affected, in both nature and structure, by the presence of the gas-phase reactant, with an important restructuring and dewetting from the support under the conditions for the formation of a surface hydride. Calculations give a clear insight in all these aspects.

24.5 Conclusions and Outlook

Quantum chemical calculations have made tremendous progress in the last two decades, from a combined advancement of methods and computers. Large systems, including heavy elements, can be calculated with reasonable accuracy. General-purpose and user-friendly software is widely available. In the field of solid materials and heterogeneous catalysts, the structure and reactivity of systems with large unit cell can be simulated. As shown above, this enables us, for example, to understand the surface structure of catalysts in a realistic pressure environment. The detailed calculations possible today allow the study of particles of ~200 metal atoms on an oxide support, hence providing realistic models of a catalyst. Calculations are, in addition, of great assistance to spectroscopic characterization [90].

Several challenges still remain. The first concerns the methods where improved accuracy is needed at a still reasonable cost. There is certainly room for improved DFT exchange and correlation functionals. Important activity is currently focused on the development of adiabatic connection fluctuation–dissipation theory [91], which allows in principle an exact calculation of the exchange-correlation energy within DFT, and especially with one version of this theory, the random phase approximation [92, 93]. Alternative quantum chemical techniques, such as periodic MP2, have been proposed for the treatment of solids beyond DFT [94, 95]. These methods exist today, but making them usable for large systems is difficult. One direction, for

example, is the development of the linear scaling MP2 or linear scaling random phase approximation method. An alternative direction explicitly models the electronic energy as a functional not of the electron density, obtained by integration of the wavefunction on the coordinates of $N-1$ electrons (see Section 24.3.4), but of the two-electron density matrix, where the integration is only performed on $N-2$ electrons [96].

The second challenge lies in the modeling of complex systems, such as the interface between a solid surface and a liquid [97–99], or the synthesis process of a solid, such as a zeolite, by condensation of monomers in solution [100]. The calculation of the free energy from *ab initio* molecular dynamics simulation in such cases is especially CPU demanding, and improved algorithms are required. Finally, coupling with other simulation scales is a timely issue. Multi-scale approaches bridging molecular-scale and continuum models would enable us to bring together chemical, mechanical, and thermal aspects for catalytic materials [101].

Acknowledgments

The author thanks Carine Michel and Fabrizio Cinquini for help with the preparation of Figures 24.1 and 24.2.

References

1 Hoffmann, R. (1988) *Rev. Mod. Phys.*, **60**, 601, and references therein.
2 Anderson, A.B. (1977) *J. Am. Chem. Soc.*, **99**, 696.
3 Shustorovich, E. and Baetzold, R.C. (1985) *Science*, **227**, 876.
4 van Santen, R. (1991) *Theoretical Heterogeneous Catalysis, World Scientific and Course Notes in Chemistry*, vol. **5**, World Scientific, London.
5 van Santen, R. and Sautet, P. (2009) *Computational Methods in Catalysis and Materials Science*, Wiley-VCH Verlag GmbH, Weinheim.
6 Rochefort, A., Andzelm, J., Russo, N., and Salahub, D.R. (1990) *J. Am. Chem. Soc.*, **112**, 8239.
7 Norskov, J.K. (1991) *Prog. Surf. Sci.*, **38**, 103.
8 Norskov, J.K. (1994) *Surf. Sci.*, **299**, 690.
9 Hammer, B. and Norskov, J.K. (2000) *Adv. Catal.*, **45**, 71.
10 Siegbahn, P.E.M. and Panas, I. (1990) *Surf. Sci.*, **240**, 37.
11 Orlando, R., Pisani, C., Ruiz, E., and Sautet, P. (1992) *Surf. Sci.*, **275**, 482.
12 Feibelman, P.J. (1991) *Phys. Rev. Lett.*, **67**, 461.
13 Hammer, B., Jacobsen, K.W., and Norskov, J.K. (1992) *Phys. Rev. Lett.*, **69**, 1971.
14 Ledentu, V., Dong, W., and Sautet, P. (2000) *J. Am. Chem. Soc.*, **122**, 1796.
15 Ciobica, I.M., Frechard, F., van Santen, R.A., Kleyn, A.W., and Hafner, J. (2000) *J. Hafner, J. Phys. Chem.*, **104**, 3364.
16 Pallassana, V. and Neurock, M. (2000) *J. Phys. Chem. B*, **104**, 9449.
17 Loffreda, D., Simon, D., and Sautet, P. (1999) *Surf. Sci.*, **425**, 68.
18 Morin, C., Simon, D., and Sautet, P. (2004) *J. Phys. Chem. B*, **108**, 5653.
19 Buhl, M., Kaupp, M., Malkina, O.L., and Malkin, V.G. (1999) *J. Comput. Chem.*, **20**, 91.
20 Sautet, P. and Joachim, C. (1991) *Chem. Phys. Lett.*, **185**, 23.

21 Cerda, J., Van Hove, M.A., Sautet, P., and Salmeron, M. (1997) *Phys. Rev. B*, **56**, 15885.
22 Takahashi, O. and Pettersson, L.G.M. (2004) *J. Chem. Phys.*, **121**, 10339.
23 Vines, F., Illas, F., and Neyman, K.M. (2008) *J. Phys. Chem. A*, **112**, 8911.
24 Gil, A., Clotet, A., Ricart, J.M., Kresse, G., Garcia-Hernandez, M., Rösch, N., and Sautet, P. (2003) *Surf. Sci.*, **530**, 7187.
25 Frisch, M.J., Trucks, G.W., Schlegel, H.B., Scuseria, G.E., Robb, M.A., Cheeseman, J.R., Scalmani, G., Barone, V., Mennucci, B., Petersson, G.A., Nakatsuji, H., Caricato, M., Li, X., Hratchian, H.P., Izmaylov, A.F., Bloino, J., Zheng, G., Sonnenberg, J.L., Hada, M., Ehara, M., Toyota, K., Fukuda, R., Hasegawa, J., Ishida, M., Nakajima, T., Honda, Y., Kitao, O., Nakai, H., Vreven, T., Montgomery, J.A.Jr., Peralta, J.E., Ogliaro, F., Bearpark, M., Heyd, J.J., Brothers, E., Kudin, K.N., Staroverov, V.N., Kobayashi, R., Normand, J., Raghavachari, K., Rendell, A., Burant, J.C., Iyengar, S.S., Tomasi, J., Cossi, M., Rega, N., Millam, J.M., Klene, M., Knox, J.E., Cross, J.B., Bakken, V., Adamo, C., Jaramillo, J., Gomperts, R., Stratmann, R.E., Yazyev, O., Austin, A.J., Cammi, R., Pomelli, C., Ochterski, J.W., Martin, R.L., Morokuma, K., Zakrzewski, V.G., Voth, G.A., Salvador, P., Dannenberg, J.J., Dapprich, S., Daniels, A.D., Farkas, Ö., Foresman, J.B., Ortiz, J.V., Cioslowski, J., and Fox, D.J. (2009) Gaussian 09, Gaussian, Wallingford, CT.
26 TURBOMOLE GmbH (2009), Turbomole V6.0, http://www.turbomole.com.
27 te Velde, G., Bickelhaupt, F.M., van Gisbergen, S.J.A., Fonseca Guerra, C., Baerends, E.J., Snijders, J.G., and Ziegler, T. (2001) *J. Comput. Chem.*, **22**, 931.
28 Delbecq, F. and Sautet, P. (2010) *Chem. Rev.*, **110**, 1788.
29 Clark, S.J., Segall, M.D., Pickard, C.J., Hasnip, P.J., Probert, M.J., Refson, K., and Payne, M.C. (2005) *Z. Kristallogr.*, **220**, 567.
30 Kresse, G. and Furthmüller, J. (1996) *Phys. Rev. B*, **54**, 11169.
31 http://cp2k.berlios.de, 2.1.208 (2010).
32 Ordejón, P., Artacho, E., and Soler, J.M. (1996) *Phys. Rev. B (Rapid Commun.)*, **53**, R10441.
33 Dovesi, R., Saunders, V.R., Roetti, C., Orlando, R., Zicovich-Wilson, C.M., Pascale, F., Civalleri, B., Doll, K., Harrison, N.M., Bush, I.J., D'Arco, P., and Llunell, M. (2009) CRYSTAL09 User's Manual, University of Turin.
34 Curulla, D., Clotet, A., and Ricart, J.M. (2000) *Surf. Sci.*, **460**, 101.
35 Koch, W. and Holthausen, M.C. (2001) *A Chemist's Guide to Density Functional Theory*, Wiley-VCH Verlag GmbH, Weinheim.
36 Parr, R.G. and Yang, W. (1989) *Density-Functional Theory of Atoms and Molecules*, Oxford University Press, New York.
37 Szabo, A. and Ostlund, N.S. (1982) *Modern Quantum Chemistry: Introduction to Advanced Electronic Structure Theory*, Macmillan, New York.
38 Barlett, R.J. and Stanton, J.F. (1995) *Rev. Comput. Chem.*, **5**, 65.
39 Cramer, C.J. (2002) *Essentials of Computational Chemistry*, John Wiley & Sons, Ltd., Chichester, p. 191.
40 Hohenberg, P. and Kohn, W. (1964) *Phys. Rev. B*, **136**, 864.
41 Kohn, W. and Sham, L.J. (1965) *Phys. Rev. A*, **140**, 1133.
42 Ceperley, D.M. and Alder, B.J. (1980) *Phys. Rev. Lett.*, **45**, 566.
43 Vosko, S.J., Wilk, L., and Nusair, M. (1980) *Can. J. Phys.*, **58**, 1200.
44 Perdew, J.P. and Wang, Y. (1992) *Phys. Rev. B*, **45**, 13244.
45 Johnson, B.G., Gill, P.M.W., and Pople, J.A. (1993) *J. Chem. Phys.*, **98**, 5612.
46 Perdew, J.P. (1991) in *Electronic Structure of Solids* (eds. P. Ziesche and H. Eschrig), Akademie Verlag, Berlin.
47 Perdew, J.P., Burke, K., and Ernzerhof, M. (1996) *Phys. Rev. Lett.*, **77**, 3865.
48 Becke, A.D. (1988) *Phys. Rev. A*, **38**, 3098.
49 Lee, C., Yang, W., and Parr, R.G. (1988) *Phys. Rev. B*, **37**, 785.
50 Loffreda, D., Simon, D., and Sautet, P. (1999) *Surf. Sci.*, **425**, 68.
51 Michaelides, A., Hu, P., Lee, M.H., Alavi, A., and King, D.A. (2003) *Phys. Rev. Lett.*, **90**, 246103.

52 Joubert, J., Delbecq, F., Sautet, P., Le roux, E., Taoufik, M., Thieuleux, C., Blanc, F., Coperet, C., Thivole-Cazat, C., and Basset, J.M. (2006) *J. Am. Chem. Soc.*, **128**, 9157.

53 Hammer, B., Hanse, L.B., and Norskov, J.K. (1999) *Phys. Rev. B*, **59**, 7413.

54 Lytken, O., Lew, W., and Campbell, C. (2008) *Chem. Soc. Rev.*, **37**, 2172.

55 Morin, C., Simon, D., and Sautet, P. (2004) *J. Phys. Chem. B*, **108**, 12084.

56 Goltl, F. and Hafner, J. (2011) *J. Chem. Phys.*, **134**, 064102.

57 Grimme, S. (2004) *J. Comput. Chem.*, **24**, 1463.

58 Dion, M., Rydberg, H., Schröder, E., Langreth, D.C., and Lundqvist, B.I. (2004) *Phys. Rev. Lett*, **92**, 246401.

59 Stephens, P.J., Devlin, F.J., Chabalowski, C.F., and Frisch, M.J. (1994) *J. Phys. Chem.*, **98**, 11623.

60 Wang, X.-G., Weiss, W., Shaikhutdinov, Sh.K., Ritter, M., Petersen, M., Wagner, F., Schlögl, R., and Scheffler, M. (1998) *Phys. Rev. Lett.*, **81**, 1038.

61 Wang, X.-G., Chaka, A., and Scheffler, M. (2000) *Phys. Rev. Lett.*, **84**, 3650.

62 Cristol, S., Paul, J.F., Payen, E., Bougeard, D., Clémendot, S., and Hutschka, F. (2000) *J. Phys. Chem. B*, **104**, 11220.

63 Raybaud, P., Hafner, J., Kresse, G., Kasztelan, S., and Toulhoat, H. (2000) *J. Catal.*, **189**, 129.

64 Reuter, K. and Scheffler, M. (2001) *Phys. Rev. B*, **65**, 035406.

65 Stull, D.R. and Prophet, H. (1971) *JANAF Thermochemical Tables*, 2nd edn, National Bureau of Standards, Washington, DC.

66 Borodziński, A. and Bond, G.C. (2006) *Catal. Rev.*, **48**, 91. (and references therein).

67 Mittendorfer, F., Thomazeau, C., Raybaud, P., and Toulhoat, H. (2003) *J. Phys. Chem. B*, **107**, 12287.

68 Teschner, D., Borsodi, J., Wootsch, A., Révay, Z., Hävecker, M., Knop-Gericke, A., David Jackson, S., and Schlögl, R. (2008) *Science*, **320**, 86.

69 Teschner, D., Vass, E.M., Hävecker, M., Zafeiratos, S., Schnörch, P., Sauer, H., Knop-Gericke, A., Schlögl, R., Chamam, M., Wootsch, A., Canning, A.S., Gamman, J.J., Jackson, S.D., McGregor, J., and Gladden, L.F. (2006) *J. Catal.*, **242**, 16.

70 Teschner, D., Révay, Z., Borsodi, J., Hävecker, M., Knop-Gericke, A., Schlögl, R., Milroy, D., David Jackson, S., Torres, D., and Sautet, P. (2008) *Angew. Chem. Int. Ed.*, **47**, 9274.

71 Sautet, P. and Cinquini, F. (2010) *ChemCatChem*, **2**, 636.

72 Seriani, N., Mittendorfer, F., and Kresse, G. (2010) *J. Chem. Phys.*, **132**, 024711.

73 Haruta, M. and Date, M. (2001) *Appl. Catal. A*, **222**, 427.

74 Jugnet, Y., Cadete Santos Aires, F.J., Deranlot, C., Piccolo, L., and Bertolini, J.C. (2002) *Surf. Sci.*, **521**, L639.

75 Loffreda, D., Piccolo, L., and Sautet, P. (2005) *Phys. Rev. B*, **71**, 113414.

76 Loffreda, D. and Sautet, P. (2005) *J. Phys. Chem. B*, **109**, 959.

77 Ertl, G., Knözinger, H., and Weitkamp, J. (eds.) (1997) *The Handbook of Heterogeneous Catalysis*, Wiley-VCH Verlag GmbH, Weinheim.

78 Euzen, P., Raybaud, P., Krokidis, X., Toulhoat, H., Le Loarer, J.-L., Jolivet, J.-P., and Froidefond, C. (2002) in *Handbook of Porous Materials* (eds. F. Schüth, K. Sing, and J. Weitkamp), Wiley-VCH Verlag GmbH, Weinheim.

79 Krokidis, X., Raybaud, P., Gobichon, A.-E., Rebours, B., Euzen, P., and Toulhoat, H. (2001) *J. Phys. Chem. B*, **105**, 5121.

80 Raybaud, P., Digne, M., Iftimie, R., Wellens, W., Euzen, P., and Toulhoat, H. (2001) *J. Catal.*, **201**, 236.

81 Digne, M., Sautet, P., Raybaud, P., Euzen, P., and Toulhoat, H. (2002) *J. Catal.*, **211**, 1.

82 Digne, M., Sautet, P., Raybaud, P., Euzen, P., and Toulhoat, H. (2004) *J. Catal.*, **226**, 54.

83 Sinfelt, J.H. (1997) in *Handbook of Heterogeneous Catalysis* (eds. G. Ertl, E. Knözinger, and J. Weitkamp), Wiley-VCH Verlag GmbH, Weinheim, p. 1939.

84 Chen, A. and Holt-Hindle, P. (2010) *Chem. Rev.*, **110**, 3767.

85 Kang, J.H., Menard, L.D., Nuzzo, R.G., and Frenkel, A.I. (2006) *J. Am. Chem. Soc.*, **128**, 12068.

86 Singh, J., Nelson, R.C., Vicente, B.C., Scott, S.L., and van Bokhoven, J.A. (2010) *Phys. Chem. Chem. Phys.*, **12**, 5668.

87 Hu, C.-H., Chizallet, C., Toulhoat, H., and Raybaud, P. (2009) *Phys. Rev. B*, **79**, 195416.

88 Hu, C.-H., Chizallet, C., Mager-Maury, C., Corral-Valero, M., Sautet, P., Toulhoat, H., and Raybaud, P. (2010) *J. Catal.*, **274**, 99.

89 Mager-Maury, C., Bonnard, G., Chizallet, C., Sautet, P., and Raybaud, P. (2011) *ChemCatChem*, **3**, 200.

90 de Smit, E., Cinquini, F., Beale, A.M., Safonova, O.V., van Beek, W., Sautet, P., and Weckhuysen, B.M. (2010) *J. Am. Chem. Soc.*, **132**, 14928.

91 Langreth, D.C. and Perdew, J.P. (1975) *Solid State Commun.*, **17**, 1425.

92 Harl, J., Schimka, L., and Kresse, G. (2010) *Phys. Rev. B*, **81**, 115126.

93 Schimka, L., Harl, J., Stroppa, A., Grüneis, A., Marsman, M., Mittendorfer, F., and Kresse, G. (2010) *Nat. Mater.*, **9**, 741.

94 Casassa, S., Halo, M., Maschio, L., Roetti, C., and Pisani, C. (2007) *Theor. Chem. Acc.*, **117**, 781.

95 Marsman, M., Grüneis, A., Paier, J., and Kresse, G. (2009) *J. Chem. Phys.*, **130**, 184103.

96 Buijse, M.A. and Baerends, E.J. (2002) *Mol. Phys.*, **100**, 401.

97 Laref, S., Li, Y., Bocquet, M.-L., Delbecq, F., Sautet, P., and Loffreda, D. (2011) *Phys. Chem. Chem. Phys.*, **13**, 11827.

98 Desai, S.K. and Neurock, M. (2003) *Phys. Rev. B*, **68**, 075420.

99 Calzolari, A., Cicero, G., Cavazzoni, C., Felice, R.D., Catellini, A., and Corni, S. (2010) *J. Am. Chem. Soc.*, **132**, 4790.

100 Trinh, T.T., Jansen, A.P.J., van Santen, R.A., VandeVondele, J., and Meijer, E.J. (2009) *ChemPhysChem*, **10**, 1775.

101 Matera, S. and Reuter, K. (2009) *Catal. Lett.*, **133**, 156.

Conclusions

Michel Che and Jacques C. Védrine

The objective of this book was to survey the latest development of the physical techniques most used or those more recent, to characterize solid materials and to investigate their surface reactivity. Thus particular attention has been paid to techniques such as X-ray, neutron, and electron diffractions, TEM, EXAFS, NMR, IR, Raman and UV-vis for unravelling the structure, particle size and size disribution, and porosity of solid materials, and LEED, EELS, XPS, AES, LEIS and SIMS for determining the structure and chemical composition of their surfaces. The properties of solid materials and the nature of adsorbates and intermediates have been identified by techniques including thermal methods, Mössbauer, XANES, molecular spectroscopies of probe molecules, EPR, MAS-NMR, SFG, PM-IRRAS, photoluminescence, single molecule spectroscopy, SSITKA and TAP.

Each technique described in this book provides specific information on solid materials, derived from basic principles and theoretical calculations. Thus, although X-ray and neutron diffraction techniques both lead to the structure of materials, it is nevertheless important to realize that X-ray diffraction (XRD) occurs via the electron cloud in contrast to neutron diffraction which involves the nuclei. In other words, the structure determined from XRD data is indirect in contrast to neutron diffraction which provides the structure from the location of the nuclei themselves.

Since the publication of earlier books in 1988 [1] and 1994 [2], only a very few physical techniques have been discovered such as single molecule spectroscopy (Chapter 14) and terahertz spectroscopy while the already existing ones have been largely improved. The major improvements concern:

- coupling of several techniques to investigate the same sample in the same setup as described in the majority of chapters and particularly in chapter 23,
- increased dimensionality in several techniques, including 2D, 3D or 4D in HR-TEM, IR, Raman and NMR,
- improved resolution in space (<0.1 nm) and time (time of flight: TOF) to characterize solid materials at the molecular level and to get access to reaction intermediates of very short lifetime (nano or even pico-second),

Characterization of Solid Materials and Heterogeneous Catalysts: From Structure to Surface Reactivity, First Edition. Edited by Michel Che and Jacques C. Védrine.
© 2012 Wiley-VCH Verlag GmbH & Co. KGaA. Published 2012 by Wiley-VCH Verlag GmbH & Co. KGaA.

- characterization of solid materials in real reaction conditions with simultaneous on-line analysis of reactants and products, which has been a major effort in the last two decades with design of the corresponding cells,
- development of theoretical methods of modelling (e.g. DFT), allowing to simulate solid materials such as zeolites and to determine the most probable reaction intermediates and mechanisms,
- high throughput experiments for the establishment of important libraries of solid materials and related reactivity, with particular emphasis on rapid micro-analyses on small samples, on micro-reactors and corresponding chemical engineering reaction kinetic modelling and on characterization techniques adapted to very small particles.

The main questions, which arise to any scientist upon characterizing a solid material and investigating its surface reactivity, can be summarised as follows:

- what are the solid material characteristics (structure, porosity, particle size and atom chemical composition)?,
- what activation is necessary to obtain a highly performing solid within its properties domain and how does activation modify the material surface structure and properties?,
- what are the surface active sites, their structure and concentration?,
- what happens to the solid surface during a physical process or a chemical reaction?,
- can a solid material lose its specific properties during reaction and for which reasons do poisoning, deactivation, phase transformation occur? can it be rejuvenated?,
- what are the conditions to be met for industrial application of a solid material?
- how to characterize gas-solid, liquid-solid, and solid-solid interfaces?

The aim of this book was to try to help the reader answer those questions and choose the most appropriate techniques, while keeping in mind their drawbacks. Because any technique only provides partial information, the simultaneous use of several techniques to investigate the same sample in the same setup (thus avoiding any difference in thermal or activation treatments and preventing any contact with air and humidity upon sample transfer) appeared to be essential to better characterize solid materials and investigate their surface reactivity. Particularly important also is the on-line analysis of reactants and products during reaction with simultaneous characterization of the solid surface as well as adsorbates and reaction intermediates.

It is therefore likely that our vision of surface reactivity will radically change in the future, as a consequence of those efforts. In particular, great attention has been brought to the characterization of the top surface layers at the different stages of the life of a solid material (preparation, functionalisation, activation, application/reaction). Because of the environment experienced by the surface, the outmost layers often exhibit a chemical composition different from that of the bulk. This holds true particularly for bimetallic catalysts as shown in the 1980's for PtNi single crystals investigated by LEED and AES, as well as for mixed oxides [3, 4]. Such changes in

chemical composition have been observed to occur during reaction and in some cases to be reversible. For mixed oxides, the first top layers have also been shown to be disorganised with respect to the bulk, which can thus be considered as a support. This was demonstrated for V_2O_5-WO_3-TiO_2 catalyst [5] for the selective catalytic reduction (SCR) of NOx by high resolution TEM and AFM, which showed that the first outmost layers are amorphous, while deeper layers are well crystallised with the TiO_2 anatase structure.

In order to illustrate the importance of simultaneously using several techniques to characterize the surface and reactivity of solid materials, let us take the example of the MoVTeNb-O mixed oxide described in detail in several chapters of this book (chapters 11,12,15,16). This catalyst is active for the (amm)oxidation of propane to (acrylonitrile) acrylic acid [6–9]. The use of XRD, HR-TEM, EXAFS/XANES allowed to identify the so-called M1 and M2 phases, present with some minor phases such as Mo_5O_{14}. The M1 phase, isomorphous of $Sb_{0.4}MoO_{3.1}$, of formula $(AO)_{2-2x}(A_2O)_xM_{20}O_{56}$ (where A = Sb, Te and M = Mo, Nb, V and $0 < x < 1$) was identified by Rietveld refinement of neutron diffraction and high resolution X-ray diffraction patterns obtained with a synchrotron radiation source, with TeO entities present within the hexagonal channels formed by corner-sharing MO_6 octahedra [10–12]. This was supported by high resolution HAADF analysis of HR-STEM pictures [13].

The oxidation state of the cations in MoVTeNb-O catalysts was determined by XPS, XANES and Mössbauer in the case of ^{125}Te [14, 15]. It was shown by Mössbauer that bulk Te is in the +4 oxidation state. XPS data showed surface Te to be in the +6 oxidation state while the oxidation state of Sb varies from +5 to +3 and that of Mo is +5 or +6 depending on the ambient atmosphere. The nature of the active sites for propane to acrylic acid reaction was identified by XRD, XPS, Raman, IR, NH_3-TPD and oxygen isotopic exchange for MoVTe-O and MoVTeNb-O catalysts, which allowed [16] to suggest that Nb stabilises the M1 phase, by replacing Te in the channels, has a strong acidic character and lowers the lability of surface oxygen, because too mobile oxygens would be detrimental for the selectivity.

Analysis of the MoVTeNb-O catalyst by LEIS [17] showed the outer surface to be depleted in V and Mo and enriched in Te and Nb, while, after sputtering off one monolayer, the subsurface was observed to be enriched in V and Nb, whereas Mo and Te reached the bulk concentrations. Comparing MoV-O and MoVTeNb-O and the adsorption of methanol and allyl alcohol, the authors concluded that the different surface locations of V^{5+} ions are primarily responsible for their very different catalytic behaviour. The determination of the V concentration of topmost layers lead the authors to suggest that surface VO_x oligomers are more efficient and selective than isolated ones with pentagonal bipyramidal structure and that the role of Mo and Te is to tune activity and selectivity by forming bridging MOV bonds, with M=Mo, Te.

This example, together with the previous comments, lead to the following conclusions:

1) Only the simultaneous use of several techniques to investigate the same sample, ideally in the same setup and in conditions typical of its application, allows one to draw a satisfactory picture of a solid material and of its surface reactivity.

2) Fifty years ago, the main techniques available concerned the bulk of solids such as XRD and correlations with reactivity suffered from the absence of surface characterization which has become a major and difficult issue. As a matter of fact, most surface techniques require ultra high vacuum, far removed from reaction conditions. Great efforts have thus been made, over the last decades, to characterise the surface structure and properties of solid materials in conditions close to those of their utilisation and should be pursued in the future (see the latest development of environmental XPS or HR-TEM techniques).
3) In contrast to the gas-solid interface, privileged because of its importance for industrial applications, particularly in heterogeneous catalysis, the liquid-solid interface has been rather neglected [18]. Several chapters of this book cover this aspect and provide examples that this interface can now be satisfactorily investigated. New developments are expected in the future, because of the importance of water-related issues, be they in connection with environmental or biological challenges [19].
4) Improving spatial as well as time resolutions are two important aspects of solid material characterization which still have to be continued in the future as in the case of TOF-SIMS.
5) Theoretical methods (chapter 24) have made very important progress in the last two decades in describing solid materials, surface sites and surface reactivity. It is clear that the contribution of theoretical methods will help modelling and understanding solid material structure and their reactivity.
6) Finally, this book also has some pedagogical implications. It is important to prepare students and young scientists to become familiar with physical techniques. Because of the increasing number of the latter (Table 1 of General Introduction), the question of which physical techniques to teach in the academic curriculum has been repeatedly addressed [20]. To help answer this question, this lead us to i) ask the authors to tell in their introduction how each physical technique had been discovered and on which principle it was based, and ii) to ask two outstanding scholars, G. Ertl and Sir J.M. Thomas, to write overviews on the physical techniques they selected/adapted to characterise solid materials (single crystals and porous solids, corresponding to external and internal surfaces respectively) and investigate their surface reactivity.

In summary, it is very likely that the description of active sites and surface reactivity of solid materials will be considered with new eyes in the future. Presumably new concepts of chemical reactivity, not only in the context of catalysis, but also of surface-related domains, will appear with the help of theoretical calculations and the improvement of techniques and particularly of surface ones.

References

1 Imelik, B. and Védrine, J.C. (Eds.) (1988) *Les techniques physiques d'étude des catalyseurs*, Technip, Paris.
2 Imelik, B. and Védrine, J.C. (Eds.) (1994) *Catalyst Characterization: Physical Techniques for Solid Materials*, Plenum Press, New York.
3 Routray, K., Zhou, W., Kiely, C.J., Grünert, W., and Wachs, I.E. (2010) *J. Catal.*, **275**, 84–98.
4 Merzlikin, S.V., Tolkachev, N.N., Briand, L. E., Strunskus, T., Wöll, C., Wachs, I.E., and Grünert, W. (2010) *Angew. Chem. Int. Ed.*, **49**, 8037–8041.
5 Coudurier, G. and Védrine, J.C. (2000) *Catal. Today*, **56**, 415–430.
6 Ushikubo, T., Oshima, K., Ihara, T., and Amatsu, H. (1996) US patent, 5,534,650 Assigned to Mitsubishi Chemical Co.
7 Ushikubo, T., Oshima, K., Kayou, A., and Hatano, M. (1997) *Stud. Surf. Sci. Catal.*, **112**, 473–480.
8 Ushikubo, T., Oshima, K., Kayou, A., Vaarkamp, M., and Hatano, M. (1997) *J. Catal.*, **169**, 394–396.
9 Védrine, J.C. and Novakova, E.K., (2005) *Metal Oxides: Chemistry and Applications*, (J.F.G. Fierro, Ed.) Marcel Dekker, New York, pp. 413–461.
10 Aouine, M., Dubois, J.L., and Millet, J.M. M. (2001) *Chem. Commun.*, 1180–1181.
11 De Santo, P., Jr., Buttrey, D.J., Grasselli, R. K., Lugmair, C.G., Volpe, A.F., Toby, B.H., and Vogt, T. (2003) *Topics Catal.*, **23**, 23–28.
12 De Santo, P., Buttrey, D.J., Grasselli, R.K., Lugmair, C.G., Volpe, A.F., Toby, B.H., and Vogt, T. (2004) *Z. Kristallogr.-New Cryst. Struct.* **219**, 152–165.
13 Pyrz, W.D., Blom, D.A., Vogt, T., and Buttrey, D.J. (2008) *Angew. Chem. Int. Ed.* **47**, 2788–2791.
14 Millet J.M.M., Roussel, H., Pigamo, A., Dubois, J.L., and Dumas, J.C. (2002) *Appl. Catal. A*, **232**, 77–92.
15 Murayama, H., Vitry, D., Ueda, W., Fuchs, G., Anne, M., and Dubois, J.L. (2007) *Appl. Catal. A*, **318**, 137–142.
16 Concepción, P., Hernández S., and López Nieto, J.M. (2011) *Appl. Catal. A*, **391**, 92–101.
17 Guliants, V.V., Bhandari, R., Hughett, A. R., Bhatt, S., Schuler, B.D., Brongersma, H.H., Knoester, A., Gaffney, A.M., and Han, S. (2006) *J. Phys. Chem. B*, **110**, 6129–6140.
18 Zaera, F. (2011) *Surf. Sci.*, **605**, 1141–1145.
19 Pradier, C-M. and Chabal, Y.J. (Eds.)(2011) *Biointerface Characterization by Advanced IR spectroscopy*, Elsevier Science & Technology, Amsterdam.
20 Sojka, Z. and Che, M. (2008) *J. Chem. Educ.*, **85**, 934–940.

Index

a
AA. *See* Atomic absorption
aberration 661–665, 693
absorption
– coefficients 26, 93, 94, 97, 99, 100, 105, 513
– factor 256
– intensity 256
– schematic energy diagram 151
accessibility index (ACI) 27
acetate species, IR spectra 272
acetonitrile, frequencies 30
acid–base properties
– of common catalysts 799
– of CuMgAl and NiCuMgAl mixed oxides 815
– of mixed metal oxides 811
– of solids 787–789
acid catalysts, BHW curve on 22
acidic probe molecules 32
acidity spectrum 788
activation energy 885
active pixel sensors 109
active sites 497–501
adsorbate–adsorbate interactions 709
adsorbate–adsorbent system 855, 856
adsorbents 853
adsorbent surface, adsorbed film, schematic representation of 867
adsorbed molecules 855
adsorption calorimetry 748
– of CO on CuZSM-5-11.9 838
adsorption–desorption isotherm 862
adsorption heats 837
adsorption isotherms 857, 861
– adsorption devices 857, 858
– BET model, evaluation of 866–868
– evaluation of external surface area/pore volume 864–866, 868–871
– experimental protocol 858–864
– measurement of micropore size 857
–– Horwath–Kawazoe 871, 872
–– volumetric/manometric method 857
adsorption processes 290, 311, 312, 747, 855
– of anions 721
– of argon and nitrogen 865
– of benzene 723
– on catalyst surfaces 311
– chemisorption 788
– definition of 854, 855
– heat of interaction, depends on 788
– nitrogen 861, 864
– NMR techniques for 311, 312
– physisorption 788
– thermodynamics of 855
– use of 853
adsorption-related applications 853
adsorption techniques 789
– adsorption calorimetry–mass spectrometry 792–794
– adsorption thermogravimetry–calorimetry (TG–DSC) 791, 792
– FTIR 794
– Raman spectroscopy 794
– volumetry–microcalorimetry 789–791
AES. *See* Auger electron spectroscopy (AES)
AFM. *See* atomic force microscopy (AFM)
Ag/AgCl reference electrode 719
$Ag/CaCO_3$ catalyst, diffuse reflection-UV–vis spectra 135
Ag^+ ions 834
AGIR. *See* analysis by gravimetry and infrared
(S)-alaninate species, IRAS spectra 267
alcohol oxidation 1106, 1107
aldose oxidation 495
alkali metal cation-exchanged zeolites 307
alkylation reactions 319, 322
– of alkanes and aromatics 319
AlPO-5
– hydrothermal synthesis process 78

Characterization of Solid Materials and Heterogeneous Catalysts: From Structure to Surface Reactivity, First Edition.
Edited by Michel Che and Jacques C. Védrine.
© 2012 Wiley-VCH Verlag GmbH. Published 2012 by Wiley-VCH Verlag GmbH.

– Raman spectra recorded *in situ* during crystallization 79
– synthesis mechanism 80
$AlPO_4$-5 spectrum 53
alumina 963
alumina nanofibers 822
alumina-supported silver catalysts 834
alumina-supported tin and gallium oxides 809
aluminophosphate molecular sieves, synthesis mechanism 76
aluminophosphates (ALPOs) 657, 1091
aluminosilicate gel, transformation 73
aluminosilicates 304, 305
– ^{27}Al NMR spectra of 304
ambient-pressure photoelectron spectroscopy (APPES) 570, 571, 574–578
ambient LAESI technique 910
American Society for Testing and Materials (ASTM) 957
ammonia 30–32
– frequencies 32
– vibrations in 31
ammonia adsorption calorimetry 816
ammonia synthesis catalysts, investigation of 643
ammoxidation 1014
amorphous aluminophosphate gel 79
amplitude-modulation atomic force microscopy (AM-AFM) 735
analog-to-digital converter (ADC) 7, 291
analysis by gravimetry and infrared (AGIR) 38
analytical methods, development of 953
anchored $Cu_4Ru_{12}C_2$ nanocluster 683
angular momentum
– electron spin 345
– intrinsic 344, 345
– operations on real p and d orbitals 381
anisotropic nanoparticles, on isotropic support 628
anisotropy 261, 300, 366
– angular 396, 467
– electron–electron interactions in 363–366
– g tensor 361, 362
– of magnetic interactions in EPR 359–361
– particle 648
– and preferred orientation 628, 629
– a tensor 361, 362
– vibrational 421
anthracene, conventional Raman spectrum 52
apexes 3D representations 1003
Apiezon wax 719
AP-MALDI imaging 908
apodization method, drawback 6
APPES investigation of *n*-pentyne hydrogenation 577
aquaporin Z, AFM image of 737
argon 865
aromatization reactions 317, 319–322
atmospheric pressure chemical ionization (APCI) 888, 900
atmospheric pressure ionization techniques 898–900
atmospheric pressure laser desorption (APLD) 900
atmospheric pressure photoionization (APPI) 888
atmospheric solids analysis probe (ASAP) 932
atomic absorption methods 957
atomic emission detector (AED) 963
atomic force microscopy (AFM) 66, 456, 602, 704
– high-speed imaging 738, 739
– instrumentation of 739
– instrument, schematic illustration of 705
– Kelvin probe force microscopy (KFM) 739, 740
– principle, and operation modes 734, 735
–– imaging solid surfaces 735–738
–– single adsorbates 735–738
Atomic absorption 89, 517, 519, 957
atomic layer deposition (ALD) 809
attenuated reflection IR spectroscopy 119
attenuated total reflection (ATR) 211
– crystal 119
attenuation coefficient 95
Au/Al_2O_3 oxidation catalysts, electronic properties 435, 436
Au-decoration technique 671
Au, geometric features of 1137
Auger electron spectroscopy (AES) 255, 455, 537, 538
Auger emission 537, 538, 563
– competes with X-ray fluorescence 538
– driving force of 537
– energy levels in 538
Auger transitions 537, 538, 563
– core hole required to initiate 562
– detected in secondary electron background of solids 540
^{197}Au Mössbauer spectroscopy, in study of gold catalysts 435–439
^{197}Au Mössbauer spectrum
– of Au/Al_2O_3 catalyst 436

– at 4.2 K of a 2%Au/AC catalyst 438
– at 4.2 K of bulk gold metal 439
Au/Ni alloy 718
Au(111) surface, sulfate anions on 722
Au/TiO_2 model catalysts 242, 243
automobile exhaust catalysts 685, 686
aviation turbine fuels 961
Avogadro number 869

b

back-donation phenomenon 258
background spectrum 6
backscattering Mössbauer spectroscopy (BSMbS) 422
backscattering (BS) spectrometers 191, 876
Balmer series 90
bandgap transitions 104, 139
Bardeen's equation 707
Beckmann rearrangement 317, 321, 494, 495
Beer–Lambert law 9
Beer–Lambert-type absorption law 513
Bellamy– Hallam–Williams (BHW) method 21
benzene
– molecule 724
– UV–vis spectra 101
benzo[a]pyrene (BAP) 282
benzothiophenes (BTs) 967, 987
beryllium filter (BeF) spectrometers 191
BF TEM images of Co particles, on ordered mesoporous carbon 677
bimetallic catalyst, destruction of 718
(bi-)metallic particles 528–530
– EXAFS analysis 528–530
bimetallic Pd–Au/MgO systems 243
bimetallic structure, under reaction/poisoning conditions 530–533
bimetallic tin–platinum catalysts 446
binary oxide catalysts 823
binding energy 105, 224, 483, 513, 541, 542, 546, 548, 549, 565, 572, 579
bismuth molybdates 1014
blackbody infrared radiative dissociation (BIRD) 911
black box 854
Bloch theorem 1132
Bohr magneton 345, 351
Boltzmann distribution 366
Boltzmann expression 152
Born–Oppenheimer approximation 1123
Boudouard reactions, of CO with 822
Bouguer–Lambert–Beer law. *See* Lambert-Beer law
Bragg–Brentano geometry 620
Bragg diffraction 612, 647
– peaks, schematic representation of 639
Bragg equation 613, 616, 639
– geometric derivation of 613
Bragg peaks 193, 615, 616, 618, 630, 631, 638
– formation 77
– full width at half-maximum (FWHM) 630
Bragg reflections 633
– density of 617
Bragg's law 613
Branched-chain isomers 993
Bravais lattices 614
Brillouin zone center 65
Brønsted acid 673, 675, 816
Brønsted acid sites (BASs) 21, 24, 306, 307, 322, 327
Brownian motion 313
Brunauer-Emmett-Teller (BET) method 853
– transformations 867, 868
bulk and surface characterization, techniques 298
– combined rotation and multiple pulse spectroscopy 298, 299
– cross-polarization 298
– magic angle hopping 298
– magic angle spinning 298
bulk diffraction 644
n-butane isomerization 138
2-butanone, liquid-phase hydrogenation 312

c

Caglioti function 630, 635
calorimetry 748, 765, 766
– adiabatic calorimeters 765
– adsorption–desorption cycle, monitored by heat flow 774
– calorimetric effect related to adsorption of Cd(II) 776
– calorimetric peak, and hydrogen generation 775
– calorimetry–volumetry 769
– catalyst–probe–solvent triangle 773
– data processing, with volumetry–calorimetry 770
– devices, kinds of 765
– differential molar entropy of adsorption 771
– differential reaction calorimeter (DRC) 771, 772
– differential temperature signal *vs.* time 775
– energy spectrum 771
– evolution of thermodynamic functions 777
– heat-exchanging calorimeters 765
– to heterogeneous catalysis 749

– isoperibolic calorimeters 765, 766, 771
– liquid flow calorimeter 771, 773
– power-compensated calorimeter 777
– principle 766–769
– solid–liquid calorimetry 771, 772
– Tian–Calvet microcalorimeter 766
– titration calorimeter 771, 773
–– setup coupled with a UV–visible spectrometer 774
Calutron 884
Cambridge Structural Database (CSD) 623
cantilever deflection 705
caprolactam 321
carbenium ion 329
carbonate formation mechanism 234
carbon chemical potential 1135, 1136
carbon monoxide 27, 28
– adsorbed, IR spectra 37
– advantage 34
– analogous studies 244
– characterization 258
– comparison, of adsorption 36
– frequencies 28
– FTIR spectra 231
– hydrogenation 270
– IRAS spectra 230, 257
– linear and bridge adsorption sites 257
– photocatalytic oxidation, complete reaction cycle 181
– preferential oxidation (PROX) 221
– schematic representation 225
– SFG spectra 223, 244
– TPD spectra 244
carbon scrambling 320
carboxypeptidase A 887
case studies
– *active* NO_x reaction intermediates and inactive species 1060, 1061
– ambient-pressure photoelectron spectroscopy (APPES) 570, 571, 574–578
– bimetallic surfaces 228–233
– combination of methods, interaction in Ag/TiO_2 catalyst 571–573
– DeNOx investigations, with thermal methods 825–827
– depth resolution, surface composition of mixed vanadates and 573, 574
– mechanistic aspects, of nitrogen path of H_2-SCR of NO 1063–1065
– metal nanoparticles on oxide surfaces 240–244
– metal single-crystal surfaces 221–228
– *operando* SSITKA–DRIFTS–MS on Pt/γ-Al_2O_3 1051–1057
– oxide surfaces 233–239
– SCR of NOx by various reductants 827–831
– SSITKA–DRIFTS on Pt/MgO–CeO_2 1059, 1061
– SSITKA–MS on Pt/MgO-CeO_2 1061–1063
– tuning surface properties, with thermal methods for DeNOx 831–841
– water-gas shift reaction 1049, 1050
catalyst nanoparticle model 1121
catalytic experiment 43
catalytic mechanism 268, 315
catalytic oxidation 712
– of ammonia 714
catalytic reactions 239
– surface species role 137
catalytic reactors 45
catalytic system 293
– electronic properties of 1120
CAVERN technique, to C–H bond activation 314, 318
CCD camera 109, 219, 587, 588
$CdS_{0.35}Se_{0.65}$ nanocrystals, resonance Raman spectra 64
Ce–Cr–O catalysts 489
cell for EPR measurements 359
CeO_2 sol-coated Ni single crystals, oxidation behavior of 471
ceria-based catalysts 813
cetyltrimethylammonium bromide (CTAB)
– templated mesoporous 597
– templated mesoporous thin films 595
– templated silica films 599
– templated thin mesoporous silica film 598
C_2H_2
– d^2I/dV^2 spectra for 733
– STM image of 733
charge-transfer processes 154, 157, 178, 398
– dissociative surface electron transfer 398
– heterolytic dissociation of adsorbed reactant/probe molecule 398, 399
– nondissociative surface electron transfer 398
charge transfer satellites 549, 550
charge transfer transition 54
C–H bond activation 319
chemical composition determination, of supported AuPd alloys 436, 437
chemical ionization (CI) 900
chemical mapping, in fixed-bed reactor 330
chemical shift imaging techniques 296
chemical shift interaction 293
chemical vapor deposition (CVD) 671
chemisorption 788
– acidity and basicity 788

chiral recognition, structures of molecules 729
chiral stationary phase (CSP) 730
chiral surfaces 728
chlorination 446, 477, 497
chromatograms 959
chromatographic methods, history of 955, 956
chromatographic systems 967
Cl-related effects, in various reactions 496, 497
^{13}C MAS NMR spectra acquired under continuous-flow conditions 326
CoAPO-36 catalyst 674
– HREM image 675
cobalt(II) porphyrin monolayer
– STM images of 727
CO-CO interactions 717
CO_2 emission 822
CO_2 formation rate 268, 269
coherent elastic scattering 188
CO hydrogenation 484–486
– to methanol 490
collision energy 911
collision-induced dissociation (CID) 885
color centers 106
combined rotation and multiple pulse spectroscopy (CRAMPS) 298, 299
combined techniques
– application of 1078
– basic tenets behind technique combining 1082
– complementary chemical information 1083, 1086
– data analysis 1088, 1089
– probing same part of catalyst 1086
– sample stability 1087, 1088
– selected combined technique setups 1083
– setup design 1086, 1087
CoMo catalysts 37
Co–Mo/ $\gamma-Al_2O_3$ catalyst systems 60
Co–Mo–S catalysts 424
CoMoS phase, modeling of 525
CoMo system 37
– concentration 38
competitive processes 168
complete-active-space self-consistent field (CAS-SCF) 1127
conductivity gradient 548
configurational coordinate model 103
configuration interaction (CI) methods 1127
conformational resolution 907
constant current mode. *See* tunneling current
continuous-flow experiments 324
continuous-wave
– CW-EPR spectrometer 356
– CW-EPR spectrum 344
–– characterization 345
conventional spectrophotofluorimeter, placement of optical components 154
conventional transmission electron microscopy (CTEM) 660
conventional XPS 567–569
convergent beam electron diffraction (CBED) 661
conversion electron Mössbauer spectroscopy (CEMbS) 423
CO oxidation 490–492
– curves of Au/FeO_x catalyst 683
copper chromite, initial and reduced samples, INS spectra 197
copper-exchanged pentasils (ZSM-5) 838
CO pressure, surface energy 1137
corrosion 470
cosine functions 6
CO–TPD of monometallic, and bimetallic catalysts over an alumina nanofiber support 822
Coulomb interaction 514
cracking 494
Cr loading 489
cross-polarization (CP) 298
crystal field theory 102
crystalline solid, schematic representations of 636
crystallinity 820
crystallites 628
crystallographic phases, in zeolite beta 674
crystallography 614–616
Cs-exchanged silicotungstates 816
Cu/Al_2O_3 catalysts 485
cuboctahedron (CUB) 1140
Cu K-edge EXAFS, curve fitting results 170
Cu^+/MFI catalyst 171
– evacuation temperature effect 172
Cu nanocrystals 689
Curie law 344
Cu(110) surface
– CO, diffusion of 710
– IRAS spectra 273, 274
– STM image of 709
Cu–Zn alloy 689
Cu:Zn composition, critical limit of 634
Cu/ZnO catalysts 691
– preparation of 633
– synthesis of 633
– zincian malachite precursors for 634
CW. *See* continuous wave

1,4-cyclohexanedimethanol (CHDM) involving catalytic processes, industrial method for 683
D-cysteine 730
L-cysteine 730
cysteine SAMs, STM observation of 729
cytochrome c 887

d

data processing techniques 736
data scattering 645
dead-layer model 161
de Broglie equation 200, 658
Debye scattering 647
Debye–Waller factor 195, 196, 198, 202, 515, 520, 1091
degradation processes 168
dehydration products, of 4-methyl-2-pentanol 808
dehydrocyclization 1141
dehydrogenation products, of 4-methyl-2-pentanol 808
dehydroxylation 858
4D electron microscopy 694–697
– further development in technology 695, 696
– Kapitza–Dirac effect 695
– thermal (clocking) pulse, relevance in 696, 697
deNOx catalysts 829, 830, 837
deNO$_x$ reactions 747
– alumina-supported silver catalysts, cyanide species, reaction mechanism 44
dense-phase chromatography, gas-phase chromatography, couplings 996
density functional theory (DFT) calculations 18, 34, 69, 70, 72, 383, 426, 872, 1119
– adsorption energy 1138
– errors for Kohn–Sham orbitals 546
– exchange-correlation functional 1131
– Hartree–Fock (SCF) approximation 546
– improved precision achieved by 426
– and IRAS measurements 239
depollution 818
desorption electrospray ionization (DESI) imaging 898
– biological applications of 908
–– IMS images from rat spinal cord 909
desorption techniques 795
– FTIR detectors 799
– GC 799
– high-performance liquid chromatography 799
– ionizaton techniques 887
– TCD detectors 799
– temperature-programmed desorption followed by mass spectrometry 795
– thermogravimetry–calorimetry–mass spectrometry 797, 798
– thermogravimetry–mass spectrometry 795–797
– TPD–IR–MS setup 799
desulfurization processes 967
detailed hydrocarbon analysis (DHA) 956
deuterated formic acid 238
deuteration technique 190
deuterium oxide, use of 645
dialkylbenzenes (DABs) 993
diamagnetism 343
diamond-like carbon (DLC) films, thermal treatment 65
diatomic probes, advantages 32
dibenzothiophenes (DBTs) 967, 987
diesel fuels 961
– GC×GC separation of 984
diesel fuels, GC×GC separation 984
diesel, types of 969
m-diethylbenzene 805
diethylene glycol monobutyl ether (DEGBE) 526
difference frequency generation (DFG) 215
differential charging 548
differential heat of adsorption 812, 833
– of CO 824, 839
– of NH_3 on 811
differential scanning calorimetry (DSC) 752, 753
– analysis of calcined samples 757
– apparatus 753
– applications 756, 757
– continuous method 756
– crucibles for 753
– data processing 753
– heat capacity determination 755, 756
– heat detectors 753
– kinetic measurements 755
– principle 753
– SAXS–WAXS setup 1080
– step method 756
– thermogram equation 753–755
differential thermal analysis (DTA) 749, 750
– apparatus 749
– applications 751
– data processing 750, 751
– detector 749
– furnaces 750
– heating elements 750
– principle 750

diffraction experiments 190
diffractometers 619
diffuse eflection technique 91
diffuse reflectance infrared Fourier transform (DRIFT) spectroscopy 115, 211, 264
diffuse reflectance measurements 115
– beam path sketch 116
diffuse reflectance spectroscopy, heatable reaction chamber 117
diffuse reflection, band intensities in 10
diffuse reflection experiment 9, 10
diffuse reflection–UV–vis spectroscopy 114, 123
– optical fiber, integration 120
diffusion 225
– coefficient 203
– constant 595
– diffusion constants, measurement of
–– different length scales 874
–– optical impedance spectroscopy 876, 877
–– pulsed field gradient nuclear magnetic resonance (PFG NMR) 875
–– quasi-elastic neutron scattering 876
–– zero length column (ZLC) method 876
– equation 202
– of molecular adsorbate 709
– in porous solids 873–877
–– notions of 874, 875
dimethylether (DME) 327
2,6-dimethylpyridine (DMP)
– frequencies 26
– spectra in 27
dipolar Hamiltonian 352
dipolar interactions 292, 293, 299, 353, 361, 371, 372, 384, 418
dipole approximation 106, 214, 513
dipole–induced dipole interactions 1131
dipole moment 4, 50
direct analysis in real time (DART) 888
direct bandgap 104
dispersion effects 477–480
distillates, quantitative analysis SFC-twin GC×GC system for 1001
di-*tert*-butylpyridine 29
Doniach–Sunjic function (DS) 561
double-beam spectrometer 98
double bond equivalent (DBE) 959
double resonance methods 312
double rotation (DOR) 299
DRIFTS and Raman spectroscopy to study the NO_x storage reduction (NSR) process 1109, 1110
DTA. *See* differential thermal analysis (DTA)
dynamic-angle spinning (DAS) 299
dynamic range, of instruments 889

e

easy direction, of magnetization 441
echoes 295
EF-STEM images, of Ag nanoparticle 694
EFTEM. *See* energy-filtered transmission electron microscopy (EFTEM)
Einstein coefficients 152
elastic incoherent structure factor (EISF) 201
electric field vector, geometry 259
electromagnetic energy 344
electromagnetic spectrum 3
electromagnetic waves, transmission 90
electron-capture detector (ECD) 979
electron crystallography 666–668
– advantages of 666, 667
– SAED patterns 668
– SAFD operation 667
electron diffraction 660
electron–electron interactions 1124, 1129
electron energy-loss spectroscopy (EELS) 255, 657, 665
electronic absorption bands 101
electronic effects 228, 231, 232, 446
electronic spectroscopy 586
– characterization of solids 122, 123
– controlled environments, optical configuration and cells 110–120
–– diffuse reflection mode, fiber-optic probes 117, 118
–– diffuse reflection mode, integrating spheres 112, 113
–– diffuse reflection mode, mirror optics 115, 116
–– fiber-optic probes, cells for use 118, 119
–– integrating spheres, cells for use 113–115
–– mirror optics attachment, cells for use 116, 117
–– transmission mode, cells for use 111, 112
–– UV–vis–NIR combination, with other techniques 119, 120
– dynamic experiments 129
–– dehydration 129
– experimental considerations 108–120
–– essential instrument components overview 108, 109
–– measurements of solids, instrument selection criteria 109, 110
– high-precision composition analysis in 665
– history 89–91

– overview 91–93
– precursor analysis 120, 121
– scope 89
– semiconductors bandgap determination 125, 126
– small-angle scattering of 647
– solids formation 121, 122
–– and alteration 120–129
– spatially resolved spectroscopy of specimens
–– with compositional variation on micrometer scale 127, 128
–– with compositional variation on millimeter scale 127
– supported metal oxide species dispersion 125
– surface properties probing 128
– surface reactivity, and catalysis 130–138
––hydrocarbon species, on surfaces 133–138
–– oxidation state, and coordination changes 130–133
– in transmission 659, 660
– UV–vis–NIR spectra 93–108
– zeolites
–– ion exchange in 124, 125
–– isomorphous substitution, of framework cations 123, 124
electron-loss near-edge structure (ELNES) 689
electron magnetic resonance 344
electron nuclear double resonance (ENDOR) 388–390, 403
electron–nucleus hyperfine interaction 350–353
– dipolar Hamiltonian 352
– hydrogen atom 353–355
– hyperfine interaction, in polynuclear systems 355, 356
– interaction energy between two magnetic moments 352
– isotropic hyperfine coupling 352
– magnetic moment 351
– nuclear spin values 350, 351
– nuclear Zeeman effect 351
– total spin-Hamiltonian 351
electron paramagnetic resonance (EPR) spectrum 343
– applications of 343, 401, 402
– classification of 368–372
– computer simulation of powder spectra 378–380
– and determination of spectral parameters 368–372
– dynamic lineshape effects 376–378
– experimental approaches 344, 345
– experimental approaches in 344–345
– limitation of 343, 344
– magnetic field
–– matter, interaction of 345
– measurements 157
– of NO radical pairs, with contribution from monomer species 371
– of O^-–O^- triplet state 365
– of $^{17}O_2-$ radicals stabilized on high surface area MgO 373
– of paramagnetic centers with coincident principal g and A axes 370
– partially averaged signals 376–378
– powder EPR spectra 367, 368
– principles of 345, 346
– setup for EPR investigations of catalytic reactions 400
– *in situ* and *operando* 399, 400
– and solid state 366, 367
– spectral features, and puzzling lineshapes 372, 373, 375, 376
– symmetry and components, of g and A tensors, relationships between 374
– with uneven hyperfine spacing 371
electron paramagnetic resonance (EPR) techniques, advanced 388
– in application to catalysis and surfaces, characteristics 388, 389
– multifrequency approach 392, 393
– overlapping signals 394, 395
– probe molecules, and spin labels, use of 396, 397
– strain broadening, and smearing 395, 396
– surface and bulk species, distinction between 390–392
electron–phonon coupling, size dependence 63
electron–phonon interaction 63
electron spectroscopy, for chemical analysis 539
electron spin resonance 344
electron tomography (ET) 657, 668, 669
electron tunneling 703
– density of states (DOS) 706
– energy diagrams for 706
electron wavefunction 1124
electron–Zeeman interaction 366
electrospray ionization (ESI) technique 888
Eley–Rideal (ER) mechanism 268, 270
emission monochromator 153
emission Mössbauer spectroscopy 423, 424, 444–446

e/m ratio 883–885
ENDOR. *See* electron nuclear double resonance (ENDOR)
energetic splitting, principles 101
energy-dispersive X-ray spectroscopy (EDX) 665
energy-filtered transmission electron microscopy (EFTEM) 657, 665, 666
energy transfer process 153
ensemble effect 228, 230
enthalpy 807
environmental transmission electron microscopy (ETEM) 687, 688
– high-resolution imaging of exposed clusters 690
– images of Cu/ZnO catalyst in gas environments 689
– ledge flow-controlled catalyst interface dynamics 691
– to study nucleation of growth of semiconducting nanowires 690
EPR. *See* electron paramagnetic resonance (EPR)
equilibrium adsorption method 62
esterification reaction 330
ETEM. *See* environmental transmission electron microscopy (ETEM)
ethane hydrogenolysis 321
ethene, chemisorption energy of 1136
ethylbenzene 327, 805
ethylene hydrogenation, poisoning of 717
ETS-10-based DeNOx catalysts 840
Evans' windows 23, 24
evaporation induced self assembly (EISA) 593
evolved gas analyzer (EGA) 819
EXAFS. *See* extended X-ray absorption fine structure (EXAFS)
EXAFS Fourier transforms 176
EXAFS spectroscopy 123
excitation-energy resolvedX-ray photoelectron spectroscopy analysis
– of ZrV_2O_7 surface 576
exhaust gas recirculation (EGR) 827
ex situ surface-enhanced Raman spectroscopy (SERS) 917
extended X-ray absorption fine structure (EXAFS) 60, 123, 169, 212, 456, 512, 528, 529, 532, 533, 622, 649
– digital simulations of EXAFS data, parameters of 530
– spectra, evolution of fourier transform 532
extinction coefficient 95

f
fast atom bombardment (FAB) 887
fast Fourier transformation (FFT) 593
fast-pulse gas feed system 1014
faujasite (FAU) structure 12
FCC gasoline, chromatogram of 41, 964, 965, 998
fcc (110) surface 1136
^{57}Fe Mössbauer spectroscopic study, of iron-containing catalysts 439, 440
– temperature dependence of 440
Fenton's reagent 79
$FePtK/SiO_2$ catalyst, ^{57}Fe Mössbauer spectra 443
Fermi contact 353
– interaction 352
Fermi distribution function 707
Fermi level 708
Fermi resonances 23
Fermi's golden rule 513
Fe-SBA-15
– UV resonance Raman spectra 70
Fe-ZSM-5
– catalysts 76, 831
– UV–visible diffuse reflectance spectrum 69
fiber-optic probes 91, 117, 118, 140
– combination 128
– integration 119
fickian diffusion 203, 204
Fick's equations 200
Fick's first law 874
Fick's second law 202
field desorption (FD) 887
field emission gun (FEG) 656
Fischer–Tropsch reaction 240, 241, 983, 990
Fitzgerald's method 958
fixed-bed flow-through reactor 113
fixed-bed reactors 330
– chemical mapping in 330
flame ionization detector (FID) 956
flame photometric detector (FPD) 967
flow adsorption microcalorimetry 800
flow fields in microchannel reactors 329
FlowMAH technique 317
fluid cracking catalysts (FCCs) 800
fluorescence 622
– intensity 590
– microscopy techniques 586
fluorescence polarization modulation microscopy (FPM) 587
fluorocarbon SAM (F-SAM) 915
fluorophores 591
formate species, FT-IRAS spectra 271
Förster resonance-energy transfer (FRET) 590

Fourier frequency 262
Fourier time 200
Fourier transform (FT) 5, 203, 296, 645, 646
– instruments 3
– IR spectrometers 109, 261
– limitations and problems with 6, 7
– Raman spectroscopy 51–53
– technical aspects 7, 8
Fourier transform infrared (FTIR) spectroscopy 3, 44, 112, 211, 810
Fourier transform ion cyclotron resonance mass spectrometry (FT-ICR-MS) 959
Fourier transforms, convolution theorem for 200
Franck–Condon principle 150
Frenkel excitons 105
frequency-modulation atomic force microscopy (FM-AFM) 735
frequency shifts 256, 258
Fresnel equations 90, 259, 260
frozen core hole (FCH) approach 546

g

GaAs(110) STM images of 706
gallium oxides 809
gas adsorption 854
gas analysis 963
gas chromatography (GC) 953, 954
– advantage of 954
– analysis of 323
–– hydrocarbons mixtures 956
– coupling 326
– elemental and structural analysis methods 957, 958
– global characterization 957
– heteroelement analysis
–– multi-element detection 970, 971
–– nitrogen 969, 970
–– oxygen detection 970
–– sulfur 967–969
– high-resolution (HR) 954
– hydrocarbon family analysis 958
–– liquid-phase chromatography 959, 960
–– mass spectrometry (MS) 958, 959
–– supercritical fluid chromatography (SFC) 960, 961
– image software 980
– mass detection 971
– molecular analysis 961
–– hydrocarbons, analysis of 963
–– simulated distillation 961–963
– petroleum products, analysis of 956, 957
– two-dimensional 954
gas emission, from factories 825
gas oil 954
– GC×GC-NCD chromatogram of 990
– SimDist curve for 962
gasoline 961, 986
– hydrocarbons, analysis of 971
– PIONA analysis of 966
gas-phase photocatalytic reactions 162
gas pollution 825
gas–solid interactions 787, 788
gas–solid system 854
Gaussian approximation 515
Gaussian curve 590
Gaussian expression 202
Gaussian fit 596, 597
Gaussian function 585, 590, 598
Gaussian resolution function 198
GC. *See* gas chromatography (GC)
GC chromatograms, SimDist curves 986
GC–GC×GC–FID instrument 997
GC–MS coupling 971
GC–NCD analyses 970
GC–SCD analyses 969
GC×GC 972
– advantage of 954
– applications of 983
–– middle distillates, group-type analysis of 983–986
–– oil industry 994
–– sulfur and nitrogen speciation 986–990
– chromatographic aspects 980
–– dimension 982
–– stationary phase, nature of 980–982
– data processing 979, 980
– detection 979
– 1D-GC, couplings between
–– GC–GC×GC coupling 996, 997
–– GC×GC×GC total coupling 997, 998
– instrumentation for 976
–– focusing phenomena 978
–– modulation period, optimization of 978, 979
–– modulation technology 976–978
– molecular analysis systems 995
– multi-dimensional methods 954, 955
– petrochemical applications
–– Fischer–Tropsch synthesis 990, 991
–– LAB process 991–994
– position of problem 995, 996
– principle of 973
–– peak capacity of 975, 976
– separation capacity 972, 973
GC×GC chromatograms 985, 993
– synthesis of LABs 993
GC×GC data, overview of 979

GC × GC–FID chromatograms 1001
GC × GC instrumentation 974
GC × GC–SCD
– operating conditions for 987
– for SR1/SR2, 988, 989
GC × GC separations, advantage of 981
GC × GC–TOF-MS FT product sample 992
gel permeation chromatography (GPC) 960
generalized gradient approximation (GGA) 426, 1131
generalized rank annihilation method (GRAM) 980
glow discharge (GD) 889
Goldanskii–Karyagin effect 421
gold nanoparticles, embedded in Mylar 438
gold surface, PM-IRAS spectra 281
goniometer 619
grand canonical Monte Carlo (GCMC) 872, 873
graphene, Raman spectra 67
graphite/germanium crystals 620
graphite plate laser desorption/ionization (GPLDI) mode 897
gravimetry 857
green fluorescent protein (GFP) 149
guanines, image contrast, changes in 731
Guinier range 194

h

HAADF image
– in AC-STEM 677
– of Au/FeO_x catalyst 683
– of high-activity WZrOH catalyst particle 684
– with Rietveld method 678
– STEM imaging 668, 669
Harrick scientific products 117
Hartree approximation 1124, 1125
Hartree–Fock approaches 1130
Hartree–Fock approximation 546, 1125, 1126
Hartree formulation 1126
H–cluster interactions 1141
heatable flow-through reactor, schematic drawing 114
heat of adsorption 805, 832
heavy cracked oil distillates (HCO) 1001
hectorite 805
Heisenberg uncertainty principle 349
helium 859
heterogeneous catalysts, characterization of 302–308
– aluminosilicates 304, 305
– pure silicas and aluminas 303, 304
– silica/alumina-containing materials 303–305
– silica- and alumina-containing materials 303
– surface acidity and basicity 306–308
– vanadium-containing materials 305, 306
– zeolites 304, 305
–– and aluminosilicates 304, 305
heterogeneous catalytic process 314
heteronuclear dipolar couplings, techniques for measurements 300
– rotational-echo adiabatic-passage double-resonance 302
– rotational-echo double resonance 301
– spin-echo double resonance 300, 301
– transfer of population in double resonance 301
– transferred-echo double resonance 301
heteropolyacids 816–818
hexamethylbenzene 134
– diffuse reflection-UV-vis spectra 136
high-energy electron ionization 958
high-flux spectrometers 190
high-frequency electron paramagnetic resonance (HF-EPR) 392, 403
highly dispersed oxide catalysts 149
highly ordered pyrolytic graphite (HOPG) 66, 719
– cobalt(II) porphyrin (CoPor) monolayer STM images of 728
high-performance liquid chromatography (HPLC) 730
high-pressure spectroscopic techniques, illustration 213
high-pressure STM (HP-STM) 716
high-pressure X-ray photoelectron spectroscopy (HP-XPS) 212
high-resolution electron energy loss spectroscopy (HREELS) 212, 256
high-resolution electron microscopy 302
high resolution mass spectrometry (HRMS)
– analysis, of oil 933
– chemical composition, of crude oils and fractions 934, 935
– oil refinery processes, consequences for 934–936
high-resolution scanning transmission electron microscopy (HRSTEM) 664
– Z-contrast imaging 664
high-resolution transmission electron microscopy (HRTEM) 222, 593, 638, 656, 661–664
– analysis of carbon nanotube catalyst particles 671

– in catalytic performance of zeolites 672, 673
– contrast transfer function 662
– determining crystallographic relationship 672
– Fourier space 661
– image of Cu/ZnO catalyst during exposure to 692
– image of specimen of ZSM-5, 675
– method of retrieving structures from 664
– multiple scattering 663
– resolution and interpretability of image 664
– resolution limit 662, 663
– Scherzer defocus 662
– structure of ZSM-23 is revealed by 674
– thin mesoporous films, structural features of 594
^{1}H MAS NMR spectroscopy 299
Hohenberg–Kohn functional 1129
Hohenberg theorem 1128
HOMO–LUMO transitions 100
Horwath–Kawazoe analysis 872
host–guest interactions 601
– characterization of 589
host–guest system 596
HRSTEM. *See* high-resolution scanning transmission electron microscopy (HRSTEM)
HRTEM. *See* high-resolution transmission electron microscopy (HRTEM)
H-SAPO-34, diffuse reflection-UV-vis spectra 137
H_2-TPR of Ag/Al_2O_3 catalyst 833
hybrid instruments 912
hydrocarbons
– activation 317–319, 322
– analysis of
–– gaseous phase 963
–– liquid phase 963–967
– cracking 818
– mixtures 964
– oxidation 486–489
– partial, and total oxidation 492–494
– pool 324, 325, 327
– species 133–138
–– deactivation, and regeneration 138
–– reference spectra 133–137
–– surface hydrocarbon pool, under reaction conditions 137, 138
hydrochlorination 437, 438
hydrocracking processes 990
hydrodearomatization (HDA) process 986
hydrodenitrification (HDN) 989
hydrodesulfurization (HDS) 985
– products 969
hydrogenated solvent, GC × GC separation of 981, 982
hydrogenation 472, 473, 489
– of acetylene and ethylene over 230
– benzene 226
– of 2-butanone 312
– CO hydrogenation on Ru 270
– of cyclopentadiene compared with 473
– ethylene 226, 397
– of methyl benzoate 40
– of naphthalene 478
– Pd as highly selective catalyst for 577, 578
– *in situ* XPS study with a Pd foil during 578
– of *t*-2-pentene 577
– of vinylbenzene and cyclopentadiene 472
hydrogenation activity of Pd/W–MOx 811
hydrogen storage applications 854
hydroisomerization processes 990
hydrotalcite-derived oxides 815, 816
hydrothermal crystallization, of zeolite silicalite-1 1079
hydrotreating (HDT) catalysis 524
– activation 525
– CoMoS model 524
hydrotreatment process 36
hydroxyl-terminated SAM (HO-SAM) 915
hyperfine interactions 414, 415
– electric monopole interaction 415–417
– electric quadrupole interaction 419–421
– magnetic dipole interaction 417–419
hyperfine sublevel correlation spectroscopy (HYSCORE) 388–390, 403
hyperpolarized xenon, advantage 308
hysteresis loops, representation of 863
HY zeolite 38
H-ZSM5, spectrum of 28, 31

i

imaging mass spectrometry (IMS) 888
– under ambient conditions 908–910
– for biologists 900–903
– highly resolved SIMS images 904, 905
– in-vacuum desorption techniques 903, 904
– new perspectives for 907
IM-5 catalyst 674
impactcollision ion scattering spectroscopy (ICISS) mode 464
incoherent scattering 189
indirect electron-coupled interaction 294
indium oxide 809
inelastic neutron scattering (INS) 185, 195
– applications 196

inelastic tunneling spectroscopy with STM (IETS-STM) 731
INEL detector 1079
infinite interferogram 6
infrared (IR) absorption spectrometry 956
infrared multiphoton dissociation (IRMPD) 911
infrared reflection absorption spectroscopy (IRAS) 211–213, 212, 255, 256–258, 722, 917
– applications 263–266
– monitoring surface reactivity, and catalysis 268–281
– organic small molecules, and chirality, adsorption 266–268
– principle 258–261
– surface functionalization, and elaboration of sensors 281, 282
infrared (IR) spectroscopy 255, 456, 876
– diffuse reflection 9, 10
– experimental considerations 7–10, 258
– Fourier transform
–– limitationsand problems with 6, 7
–– technical aspects 7, 8
– IR light 3, 4
– matter–radiation interaction 4
– *operando* IR spectroscopy
–– experimental setup 40
–– measurements, examples 40–45
–– reactions conditions 40
–– surface reactivity, applications 39–45
– practical implementation 8–10
– principles and use 3–7
– solids characterization, use 11–39
– spectrometry, interferometry 4–6
– transmission experiments, quantitative aspects 8, 9
In_2O_3-containing catalysts 809
inorganic crystal structure database (ICSD) 623
– powder diffraction file (PDF) 623
in situ calcination 16
in situ hydrothermal cell 77
in situ NMR methods 313–329
– alkylation reactions 319, 322
– applications 317–329
– aromatization reactions 319–321
– batch conditions 314, 315, 317
–– alkylation reactions 319
–– hydrocarbon activation 317–319
–– isomerization, and aromatization reactions 319–321
– Beckmann rearrangement 321
– ^{13}C MAS NMR spectra, Stack plot 321
– coupling with a second technique 325–329
– experimental apparatus for 314
– experimental setups 315, 316
– flow conditions 315–317, 322
–– alkylation reactions 322
–– hydrocarbon activation 322
–– methanol-to-hydrocarbons reaction 323–325
–– MTBE synthesis 322, 323
–– second technique, coupling with 325–329
– ^{1}H MAS NMR spectra, Stack plot 318
– hydrocarbon activation 317–319, 322
– isomerization reactions 319–321
– methanol-to-hydrocarbons reaction 323–325
– MTBE synthesis 322, 323
– reaction protocol for 325
– for studying lithium ion batteries 314
in situ Raman spectroscopy 56
in situ small-angle X-ray scattering (SAXS)–wide-angle X-ray scattering (WAXS) data acquisition 1079
in situ TEM approach 676
in situ UV–visible spectroscopy 326
– experimental setup for 327
in situ visible Raman technique 76
integral low-energy electron Mössbauer spectroscopy (ILEEMbS) 423
intensity borrowing mechanism 225
interfacial bonding models 265
interferometer 4–6
internal reflection elements (IREs) 236
intervalence charge transfer (IVCT) 103
in-vacuum ionization techniques 891, 892, 896–898
– operating processes 895
– typical features of sources 893, 894
inverse Fourier transformations 676
iodine adlayer 722
iodine exhibits 722
ion cyclotron resonance (ICR) frequency 886
ionization efficiency 889
ionization methods 931
ionization sources, basic principle 891
ion mobility mass spectrometry (IM-MS) 907
ion scattering spectroscopy (ISS) 453, 461
– main concept 461–463
IRAS. *See* infrared reflection absorption spectroscopy (IRAS)
IR–gravimetric experiment 26
iron-based Fischer–Tropsch catalysts 443, 444
IR spectra, for CuZSM-5-11.9 sample 839
isomerization 319–321, 798
– and aromatization reactions 319–321
isomer shift scale for ^{99}Ru 430

isothermal titration calorimetry (ITC) 817
– on D-histidine and L-histidine on Nabesite 819
isotherm, types of 863
isotropic hyperfine interaction 353

k

KBr beamsplitters 8
KBr matrix method 11
Keggin-type heteropoly compounds 816
Kelvin probe force microscopy (KFM) 739
Kendrick mass defect (KMD) value 926
kerosene 954
– aromatic compounds in 960
kinetic energy (KE) 537, 555, 911
kinetic radical freezing method 400
Kirchhoff's law 8
Kohn theorem 1128
Kramers–Heisenberg–Dirac dispersion equation 51
krypton 854, 865
KT approach, for cluster calculations 546
Kubelka–Munk function 10, 90, 97, 106, 107, 130
K–V–O catalysts 305

l

LAB synthesis 993
Lambert–Beer law 90, 94, 95, 554
Lambertian surface 96
Lamb–Mössbauer f-factor 421, 438
– determination for quantitative analyses 437, 438
Lamellar phases 602, 603
Langmuir-Hinshelwood (LH) mechanism 269, 712
Langmuir theory 867
Laporte's rule 99
Larmor frequency 292
Larmor precession 199
– angle 191
Larmor precession time of nuclear spin 441
laser desorption (LD) ionization mechanism 896
laser diode thermal desorption (LDTD) 900
laser-induced acoustic desorption (LIAD) source 897
laser irradiation 887
laser scanning confocal microscope (LSCM) 587
laser triggered reaction 44
lateral resolution 569, 570
layered silicates 805
LC-GC × GC coupling 998–1000, 999
– VGO, chromatogram of 1000
LeBail refinement methods 632
LEIS depth profiling 473
Lennard–Jones potential 734, 856
Lennard-Jones-type expression 872
Lewis acid 399
Lewis acidic centers, investigation by NMR 307
Lewis acidity 24
Lewis acid sites (LASs) 24
ligand-centered (LC) transitions 103
ligand-to-metal charge transfer (LMCT) 103
light cycle oil (LCO) 968
– nitrogen compounds, elution profile of 970
light diffusion coefficient 10
light-harvesting complexes (LH1/LH2) 737
– LH1 core complexes 738
light scattering 616
linear absorption coefficients 95
linear alkylbenzenes (LABs) 983
linear polarizations 259
liquid chromatography (LC) 959
liquid nitrogen-cooled MCTdetectors 13
liquid-phase chromatography 958, 959
liquid-phase hydrocarbon mixtures 963
liquid secondary ion mass spectrometry (LSIMS) 887
liquid–solid interactions 787
local density approximation (LDA) 426, 1130
local density of states (LDOS) 707
localized surface plasmon resonance phenomenon 106
Lorentzian function 203
Lorentzian profile 203
Lorentz polarization 616, 630
low-energy electron diffraction (LEED) 258, 286, 456, 465, 467, 708
– grids 540
low-energy electron microscopy (LEEM) 693
low-energy ion scattering (LEIS) 453, 454, 457, 461
– active sites 497–501
– compositional effects, in catalytic reactions 484–489
– dispersion effects 477–480
– main concepts 461–463
– potentialities of 463–465
– promotion, and poisoning effects 489–497
Lowenstein's rule 304
low-temperature EPR spectra 357

m

macrocrystalline solids 637
macroscopic crystals 612

macroscopic polarizability tensors 214
Madelung energy 547
magic angle hopping (MAH) 298
– use 317
magic angle spinning (MAS) 289, 298
magnetic field gradients 295, 296
– application of 295–297
–– diffusion 296, 297
–– magnetic resonance imaging 295, 296
–– measuring flow 296, 297
– magnetic resonance imaging 295, 296
– measuring flow and diffusion 296, 297
magnetic field, interaction of matter with 343, 344
magnetic flux density 343
magnetic moment 351
magnetic parameters, quantum chemical calculations of 386–388
magnetic resonance experiment 292
magnetic resonance imaging (MRI) 290, 295, 296, 310, 311
– applications 329
– *k*-space formalism 296
magnetic resonance measurements 311
– principles of 290
magnetic resonance signal 296
– properties of 297
magnetic resonance visualization 330
magnetization 294, 344
magnetization vector 297
manometric device, schematic representation of 857, 860
Mark II X-ray absorption fine structure (XAFS)-XRD setup 1079
Marquardt–Levenberg algorithm 425
MAS probe 316
mass measurement accuracy 889
mass spectrometry (MS) 883, 953, 958, 959
– atmospheric pressure ionization techniques 898–900
– collisional activation 910–912
– combined ionization techniques 900
– high-quality mass spectrum, experimental parameters for 889–891
– high-resolution 959
– in-vacuum ionization techniques 891, 892, 896–898
– mass spectrum, characteristics of 889
– modified multiple quadrupole instrument 920
– preparative mass spectrometry 918–922
– QTOF instrumentation 918
– for SID experiments 912, 913
– soft landing instrumental devices 915–918
– sources for nonvolatile materials 891
– tandem mass spectrometry 910–912
– technology development 907, 908
– *vs.* immunoassay-based methods 903
matrix-assisted laser desorption/ionization (MALDI) 887, 888
– for highly selective peptide/protein profiles 905, 906
– MALDI-TOF instrument 886
–– image, human cerebellum 903
matrix-assisted laser desorption/ionization mass spectrometry (MALDI-MS) 676
matrix-enhanced secondary ion mass spectrometry (ME-SIMS) 904
matrix-isolated electron spin resonance 400
Maxwell–Boltzmann distribution 349
MCM-41, photoluminescence 155
mean square displacement (MSD) 590
membrane protein 736
mercapto undecanoic acid (MUA) 264, 283
mercury porosimetry 311
mesoporosity 873
mesoporous silica 593, 869
– layers, domain growth of 604
mesoporous silica nanochannels
– self-assembly of 603, 604
– structure formation of 601
metal-assisted secondary ion mass spectrometry (Meta-SIMS) 904
metal organic frameworks (MOFs) 200
metal organic open structures (MOFs) 657, 854
metal oxide catalysts 805
– bulk oxide 805–807
– doped and modified oxides 807
– supported metal oxide/metal catalysts 807, 808
metal oxides 747
– active sites and phase structure, characterization 55–59
– active species identification 55, 56
– surface region, phase transformation in 56–59
metal oxide-supported catalysts 831, 832
metal–support interactions 824
metal-to-ligand charge transfer (MLCT) transitions 103
methanation reaction 241
methane formation, reaction paths of 1047
methanol 33, 34
– IR spectra 34
– synthesis of 633
methanol conversion, ^{13}C MAS NMR spectra 320

methanol-to-hydrocarbons reaction 323–325
methanol to olefins (MTO) conversion 323
N-methylaniline 322
2-methyl-2-butene hydration reactions 331
methyl *tert*-butyl ether (MTBE) synthesis 322
N-methyleneaniline 322
1-methyl-4-phenyl-1,2,3,6-tetrahydropyridine 906
MFI-type zeolites
– ν(OH) bands 16
– spectrum 15
– types of sites 18
Mg–Al mixed oxides 815
Mg:Al ratio 815
mica substrate, native photosynthetic membrane, AFM image of 738
Michelson interferometer 261
microcalorimetry 814
microelectromechanical system (MEMS) approach 691
micropore filling 871
microporosity 873
microporous/mesoporous solids 869
microreactor 1018
mid-infrared (MIR) radiation 99
mixed metal oxides 811–814
mixed oxides 798
– catalysts 813
M1/M2 system 678
modern software packages 623
modulation processes 976
– cryogenic modulation 976–978
– thermal heating modulation 976
– valve-based modulators 978
Moiré structures 716
molar absorption coefficients 9, 26, 34, 38, 39
– ranges 100
molecular beam experiments 1014
– key components 1015
molecular beam scattering (MBS) 1014
molecular diffusion in porous solids, techniques for characterization 312, 313
molecular diffusion processes 291
molecular interpretation, of parameters 380
– g tensor 380–383
– hyperfine tensor 383–386
molecular sieves 799–805
– characterization 73
molecular sieves synthesis mechanisms 73–80
– active centers and silicate building units, assembling Fe-ZSM-5 74–76
– assembling zeolites, from prefabricated units 73, 74
– crystallization process, real-time probing for 76–80
molecule–surface interaction 1120
molybdenum oxides 61
monochromatic light, interferogram 5
monolayer capacity 867
monolayer (ML), optimal coverage of 1134
Monte Carlo simulation 712
montmorillonite 805
Mo–O stretching frequency 59
– *vs.* Raman stretching frequency 59
mordenite synthesis solid phase, Raman spectra 74
Morse curve 21
Mo/SiO_2 photoluminescence spectrum 178
Mössbauer absorber 414
Mössbauer-active transitions 427
– of ^{197}Au 433, 434
– of ^{57}Fe 427–429
– of ^{193}Ir 432, 433
– of ^{99}Ru 429, 430
– of ^{121}Sb 432
– of ^{119}Sn 430, 431
Mössbauer effect 407, 409–411
– consequences of recoil effect 410
– conservation of energy 410
– kinetic recoil energy 410
– Lamb–Mössbauer f-factor 411
– limitations 411, 413
– γ-quanta 409, 410, 411
– recoil momentum 411
– resonance adsorption phenomenon 409, 410
– survey of applications, in study of catalytic materials 434–447
– total energy of nuclear transition 410
Mössbauer parameters, theoretical calculation of 426, 427
– augmented plane wave (APW) method 427
– complexity and precision 426
– DFT approximations 426
– DFTmethods, approaches 426, 427
– full-potential linear muffin tin orbitals (FP-LMTO) method 427
– projector augmented wave (PAW) method 427
– WIEN2k code 427
Mössbauer spectroscopy (MbS) 407
– advantages 407, 408
– applications in heterogeneous catalysis 408
– experimental data, evaluation of 424–426
– limitations 408
– radiation source for 411–414
motor octane number (MON) 964

Mott–Wannier excitons 105
Mo–V–Nb–Te–O system 678
$MoVTeNbO_x$ mixed metal oxide catalyst
– for hydrocarbon oxidation 631
Mo–V–Te–O catalysts 488
MS. *See* mass spectrometry (MS)
MTBE synthesis 322, 323
MUA-coated gold surface, PM-IRAS spectra 284
MUA-functionalized gold surface, PM-IRAS spectra 283
multi-configurational self-consistent field (MC-SCF) 1127
multi-dimensional gas chromatography (MDGC) 972
– peak capacity of 973
multiple-quantum magic angle spinning (MQMAS) 300
multiple scattering 97, 514
multiplet splitting 552
– influence on lineshape of Cr XPS lines 553
multi-technique high-energy setup 1105
multivariate curve resolution (MCR) 43
m/z ratio 883, 886, 936

n

Na atoms, hypothetical fcc packing of 618
NaCl
– powder diffraction pattern of 617
– XRD pattern of 616
nanocluster gold catalysts, study of 676
nanographite sample, Raman spectrum 65
nanoporous materials 853, 854
– process evaluation of 854
nanostructured materials, electron–phonon coupling in 63, 64
nanotechnology 671
nanotube 670
naphtha cuts, high-resolution chromatographic analysis of 966
natural clays 805
natural gas 963
NaX zeolite 858, 872
– nitrogen isotherm 870
– *n*-pentane in 206
NaY zeolite
– benzene adsorbed in 193
near-edge X-ray absorption fine structure (NEXAFS) 574
near-infrared (IR) lasers 51
Néel relaxation time 441
neodymium yttrium–aluminum–garnet (Nd:YAG) 217
neutral impact collision ion scattering spectroscopy (NICISS) 465
neutron diffraction (ND) 185, 192, 632
– application 193
neutron momentum 186
neutron–nucleus interaction 187
neutron scattering
– coherent and incoherent scattering 188–190
– diffusive motions 197–208
– dynamics 194–208
– experimental 190–192
– neutron spin-echo technique 198–201
– neutrons properties 186, 187
– rotational motion 201
– scattering cross-sections 187, 188
– structure 192–194
– translational motion 202–208
– vibrational spectroscopy 195–197
neutron spin echo (NSE) 191, 198–201, 876
– advantage 198
NH_3 adsorption microcalorimetry, study on γ-alumina 805
NH_3 calorimetry, on Cs-exchanged HPW 817
NH_3 oxidation 715, 716
nickel-exchanged zeolite X
– transmission UV–vis spectra 125
nicotinic acid 887
Ni/Cu ratio 815
Ni–P alloys 472
Ni(110) surface 710
nitrite, and nitrate reduction 495, 496
nitrogen
– adsorption of 311, 861, 864, 866
– equilibrium adsorption isotherms of 873
nitrogen chemiluminescence detector (NCD) 963, 969
nitrogen isotherm, Horwath–Kawazoe method 872
nitrogen oxides 825
nitrogen–phosphorus thermionic detector (NPD) 969
NMR. *See* nuclear magnetic resonance
NO dissociation mechanism 275–277
N_2O gas-phase species 274
noise-free high-resolution data 646
nominal Kendrick mass (NKM) value 926
noninteracting system
– kinetic energy of 1130
nonlinear susceptibility tensor 213
$NO–NO_2$ reaction 834
nonporous oxides 869
nonradiative deactivation pathway 159
nonscattering media 111
NO PM-IRAS spectra 276, 277, 278, 279

normal coordinate analysis (NCA) 72
normalized differential reflectivity 261
NO_x storage–reduction cycles 280
[^{15}N]pyridine titrating sulfated zirconia ^{15}N CP-MAS spectra 307
nuclear Bragg diffraction (NBD) 448
nuclear forward scattering (NFS) 448
nuclear gamma resonance (NGR) spectroscopy 407
nuclear inelastic scattering (NIS) 448
NMR spectrometer, schematic presentation 291
nuclear magnetic resonance (NMR) spectroscopy 289, 290, 456, 953
– adsorption process 311, 312
– advantages 327
– basic principles 291–294
– bulk and surface characterization techniques 298, 299
– chemical shift interaction 293
– complication 303
– diffusion process 312, 313
– dipolar interaction 292, 293
– full multinuclear capability 302
– heterogeneous catalysts characterization 302–308
– historical perspective 289, 290
– indirect electron coupled interaction 294
– magnetic field gradients application 295–297
– measuring heteronuclear dipolar couplings techniques 300–302
– modern spectrometer 291
– *operando* studies 329–331
– porosity processes 308–311
– quadrupolar interaction 293, 294
– relaxation time analysis 310
– relaxation times 294, 295
– ^{29}Si MAS 304
– *in situ* 313–329
– solid-state techniques 302
– studying quadrupolar systems with I>1/2, 299, 300
– for studying solids 297–302
–– popular techniques 297
– theory 291–298
– Zeeman interaction 292
nuclear magnetic resonance (NMR)–UV–Vis setup
– for studying methanol to olefin (MTO) process 1081
nuclear resonance scattering (NRS) 448
nuclear spin angular momentum 293
nuclear spin quantum number, of various nuclei 351
nuclear spin system 291
nuclei–electron external potential 1129
nucleus–Zeeman interaction 366
numerical aperture (NA) 587
nylon-6, 317

o

5,11,17,23,29,35,41,47-octa-*tert*-butyl-49,50,51,52,53,54,55,56-octakis (carboxymethoxy)calix[8]arene (OBOCMC8) 726
n-octadecanethiol/Au self-assembled monolayers on gold substrates
– ARXPS analysis of 559
– ERXPS analysis of 558
octadecylphosphonic acid (ODPA) 264
– adsorption 265
– PM-IRAS spectra 265
n-octane 331
2-octene 331
off-resonance nutation experiments 304
oil refinery processes, consequences for 934–936
olefin 961
operando (DRIFTS–MS) experimental setup, at heterogeneous catalysis 1051
operando IR spectroscopy 40
– experimental setup 40
– measurements, examples 40–45
– reactions conditions 40
– setup 41
operando measurements 290
operando reactor cell 42
optical density (OD) 94
optical impedence spectroscopy 877
optical microscopy, utilization of 585
optical parametric generator/amplifier (OPG/OPA) 217
Orgel diagrams 103
oriented thin film
– crystallites 628
– schematic representation of 628
oscillator receptor 886
oxidation
– catalysts, selective 678
– of propylene to acrolein 1014
– of transition metals 470
oxidative dehydrogenation (ODH) 489, 813
oxometallate (MO_x) species 125
oxygen species, Raman spectra 56
oxygen storage capacity (OSC) 685, 686, 820
– of CeO_2-based solids 685, 686
oxygen treatment, and TAP experiments 1033

p
Paar XRK 900 cell mounted on STOE ψ−ψ goniometer 621
palladium 1134
paraffinic solvent 960
n-paraffins, dehydrogenation of 993
paraffins, isoparaffins, olefins, naphthenes, and aromatics (PIONA) 964
parallel factor analysis (PARAFAC) 980
paramagnetism 344
partial oxidation of propane 813
particle dimensions estimation 573
Pauli principle 1125, 1126, 1129
Pauli repulsion 856, 1125
Pd/Al_2O_3 catalyst 331
Pd fraction 626
Pd surface, *in situ* IRAS spectra 228
PdX alloys, Vergard lines for 632
Pd–Zn alloy formation 232
Pd–Zn model 231
peptide nucleic acid (PNA) 731
periodic DFT calculations 70, 76
perturbation theory, second-order 51
petroleomics 922, 923
– accurate mass measurement 924, 925
– for complex petroleum samples, mass spectrometry for 923, 924
– data graphical representations 925–928
– mass spectrometry methodology, improvements to 928–933
– ultra-high resolution and data treatment, role of 922, 923
petroleum product, mass spectrum of 958
PFG-based technique, to probe diffusion 313
phase characterization, application 629
phase contrast 661
phase shift 297
phase transformations 80, 473
phenylazonaphthylamine, UV–vis spectra 128
2-phenylethylamine 759, 813
phonon dispersion curves 190
photobleaching 591
photocatalytic decomposition, reaction profiles 174
photodiode-array detector 1078
photoelastic modulators 212, 261
photoelectron spectroscopy 1120
photoemission 538, 540, 551
photoemission electron microscopy (PEEM) 693
photo-formed electrons 150
photoionization 931
photoluminescence 151
– bands, intensities 165
– degassing temperature effect 159
– intensity 154
–– additive ionization potentials effect 161
–– time profiles 166
– lifetimes and relative intensities 168
– quenching 158, 160
– schematic energy diagram 151
– types 157
photoluminescence spectroscopy
– advances in 149
– Ag^+/MFI catalysts 165
– basic principles 150–153
– bulk TiO_2 photocatalysts, *in situ* photoluminescence 159–163
– highly dispersed transition metal ions and oxides, *in situ* photoluminescence 163–165
– measurements, general aspects 153–156
– microcrystalline MgO, *in situ* photoluminescence 156–159
– steady-state measurements 153, 154
– time-resolved measurements 154–156
– time-resolved photoluminescence spectroscopy
–– characterization of catalysts 156–165
–– dynamics investigations of photocatalysis 165–181
– V-containing BEA zeolite catalysts 163–165
photomultiplier tube (PMT) 109
photon–electron interaction 512, 513
photon-induced near-field electron microscopy (PINEM) 694
physisorption 788, 855
picosecond surface temperature jump 238
pillared clays, acidity of 805
Plank's constant 186, 703
plasma desorption mass spectrometry (PDMS) 886
PM-IRAS. *See* polarization modulation infrared reflection absorption spectroscopy (PM-IRAS)
point defects 106
point of zero charge (PZC) 60, 61
polarizability 50, 1078
– tensor 51
polarization enhancement techniques 290, 331
polarization modulation infrared reflection absorption spectroscopy (PM-IRAS) 233, 255, 275
– advantages 275
– applications 263–266

– cell for *in situ* characterization in liquids 282
– experimental setup 262
– experimental set-up for 278
– in liquid phase 282–285
– monitoring surface reactivity and catalysis 268–281
– organic small molecules and chirality, adsorption 266–268
– principle 261–263
– sensitivity 263
– surface functionalization and elaboration of sensors 281, 282
– surface spectra 236
polarization-modulation infrared reflection adsorption spectroscopy 212
polarization transfer techniques 289
– implementation of 289
polarized sum frequency spectra 237
pollution 825
polycrystalline metal surface 465
– adsorption of organic molecules 469, 470
– adsorption of simple molecules 465–469
– surface defects 465–469
polycrystalline particles 636
polycyclic aromatic hydrocarbons (PAHs) 281
polyglutamic acid (PG)
– aluminum sample, PM-IRAS spectra 285
– stable chemical forms 284
poly-L-glutamic acid (PG) 284
polymerization 455
poly(*N*-vinyl-2-pyrrolidine) (PVP) 676
polysilphenylenesiloxane, polar column consisting of 990
porosity characterization 308, 854
– magnetic resonance imaging 310, 311
– role of 853
– T_1 and T_2 relaxometry 309, 310
– ^{129}Xe NMR 308, 309
porosity processes 308–311
– magnetic resonance imaging 310, 311
– T_1 and T_2 relaxometry 309, 310
– ^{129}Xe NMR 308, 309
porous clays 827
porous solids 308
– diffusion in 873–877
position vector 214
post-Hartree–Fock methods 1126, 1127
post-reaction Auger spectroscopy 224
powder EPR spectra 367, 368, 369
power-compensated DSC apparatus 778
power-compensated system, block diagram 778
pπ–dπ transitions 68, 69
pressure swing adsorption (PSA) applications 854
principal component analysis (PCA) 108, 562, 980
prism-CCD spectrometer 589
probe adsorption processes 311
probe molecule adsorption 14, 20
projected density of state (PDOS) calculations 69
proportionality constant 200
proteomics 888
protic molecules 33
$_{31}$P spin-echomapping NMR technique 305
Pt_{13}
– gas-phase shapes for 1140
– surface stability diagram 1140
Pt–Al_2O_3 hydrogenation catalysts 686, 687
Pt/BaO film time-resolved PM-IRAS spectra 280
Pt nanoparticles 257, 1139
Pt(111) surface
– CO, adsorption of 716
– CO oxidation on 713
– in H_2 716
– STM image of 720
pulsed field gradient (PFG) 297
– NMR 207
–– analysis 875
– principle 296
pulsed flame photometric detector (PFPD) 967
pulsed gradient spin-echo (PGSE) magnetic resonance 297
pulse electron spin echo techniques 403
pulse–quench technique 316, 317, 324
pulse sequences. *See* quadrupolar systems
pump–probe pulses 219
pure insulators, optical absorption in 105
pyridines 24–26
– frequencies for adsorption 25
– spectra for 25

q

quadrupolar interaction 293, 294
quadrupolar systems, studying with 299
– double rotation 299
– dynamic-angle spinning 299, 300
– multiple-quantum magic angle spinning 300
– satellite transition magic angle spinning 300
quadrupole splitting *vs.* isomer shift 431
quantum chemistry methods 1119

– computational chemistry, objective of 1120
– electronic structure calculations 1123
–– density functional theory 1127–1130
–– exchange-correlation functionals 1130, 1131
–– Hartree approximation 1124, 1125
–– Hartree–Fock approximation 1125, 1126
–– Pauli principle 1125, 1126
–– post-Hartree–Fock methods 1126, 1127
– heterogeneous catalysts, models of 1121–1123
– historical perspective 1119–1121
– total energy calculations application
–– alumina surface, at realistic water pressure 1138, 1139
–– Pd catalysts 1134–1136
–– Pt cluster under pressure of hydrogen 1139–1141
–– (110) surface of gold 1136–1138
–– (110) surface of ruthenium dioxide, termination of 1133, 1134
quantum detectors, mercury–cadmium–tellurium (MCT) 7
quartz cell 111, 115
quartz crystal microbalance (QCM) measurements 277
quasi-elastic/inelastic peaks
– schematic representation 186
quasi-elastic neutron scattering (QENS) 186, 187, 200
– spectra 205
– technique 206, 207
quencher molecules 179
quenching 316

r

radiation
– interaction phenomena 94
– in X-ray tube 622
radiative deactivation process 152
radiative decay process 151
radioactive decay of nuclides 887
Raman bands 54, 61, 75
– intensities 51
Raman effect, origin 49
Raman scattering, schematic illustration 50
Raman spectra
– fluorescence interference in 53
– before and during oxidative dehydrogenation of propane 1103
Raman spectroscopy (RS) 49–51, 64, 456, 723
Raman vibrations, resonance enhancement 72
rapid molecular motion 292
Rayleigh criterion 588, 590, 656
Rayleigh scattering 50
reaction center (RC) 737
reactive frontal chromatography (RFC) 825
reciprocal lattice vector 193
redox cycles, of VTiS catalysts and bulk V_2O_5 821
redox properties, of solids 818, 819, 841
– adsorption calorimetry of redox probes 823–825
– characterization by TPR/TPO 819–822
– surface techniques in redox studies 825
– TPD of redox probes 822, 823
reduction profiles of Cu/SA 826
reflectance 95, 96, 98
reflection process 259
region of interest (ROI)
– illumination of 588
relative humidity (RH) 602
relaxation 349
relaxation time 295
– two-dimensional (2D) 310
relaxation times 294, 295
relaxometry measurements 309, 310
relaxometry methods 311
research octane number (RON) 964
resonance
– of $CuCl_2{\cdot}2H_2O$ 343
– frequency 295, 296
– phenomenon 346–348
resonance Raman spectroscopy (RRS) 53–55, 63
resonant intensity 54
resonant magnetic field plot, as a function of ψ and ζ angles 370
reversible hydrogen electrode (RHE) 723
Rhodospirillum photometricum 737
Rh(111) surface
– benzene (3×3) adlayer
–– STM images of 725
– STM observation of 723
root-mean-square displacement 313
rotational-echo adiabatic-passage double-resonance (REAPDOR) 302
rotational-echo double resonance (REDOR) 301
rotation energy 4
RS. *See* Raman spectroscopy (RS)
RuO_2(110) surface
– oxygen chemical potential for 1133
– oxygen-rich termination of 1134
Ru(0001) surface 709
– STM image of 709, 710

Rutherford backscattering (RBS) 456
Rutherford-type scattering 669

S
sample-controlled thermal analysis (SCTA) approach 859
SAMs formation 281
satellite transition magic angle spinning (SATRAS/STMAS) 300
saturated calomel electrode (SCE) 721
SAXS data 1079
SAXS–WAXS setup 1079, 1080
SBA-15 crystallization of 648
SBA-15-supported vanadia samples, diffuse reflection-UV–vis spectra of 126
scanning electron microscopy (SEM) 456
scanning monochromator, for quick extended X-ray absorption fine structure 1079
scanning probe microscopy (SPM) 703
– schematic illustration of 704
scanning transmission electron microscopy (STEM) 657
– experimental considerations 669, 670
– illumination and image formation in 660
– instrument consist of 659
– signal generated in electron beam–specimen interaction 658
– specimen preparation 669, 670
scanning tunneling microscopy (STM) 81, 266, 456, 703, 705
– catalytic model systems 708
–– adsorption 708, 709
–– diffusion 709–711
–– high-pressure environment 716–718
–– surface reactions 711–716
– chemical selectivity 727
–– inelastic tunneling spectroscopy with STM (IETS-STM) 731–733
–– molecular tips 727–731
– electron tunneling 705
– measurements 222
– principles 705–708
– solid–liquid interface 719–721
–– anions, adsorption of 721–723
–– molecular adsorbates 723–727
–– surface reconstruction 721
scanning tunneling spectroscopy (STS) 704
– electronic property of 704
scattering function 194
scattering media 111
scattering vector 187
Schrödinger equation 90, 1124, 1125
Schuster–Kubelka–Munk theory 97
sealed ampoule technique 318
secondary ion mass spectrometry (SIMS) 453–455, 457, 471, 886
– active sites 497–501
– basic principles 457–459
– compositional effects, in catalytic reactions 484–489
– depth profiling of oxide films 473
– dispersion effects 477–480
– dynamic simulations of a typical SIMS collision 896
– for industrial applications 904
– potential of 459, 460
– preparation, and activation effects 480–484
– promotion, and poisoning effects 489–497
secondary ion mass spectrometry (SSIMS) 455
selected area electron diffraction (SAED) 661
– reveal distinct ordered phases in 687
selected combined technique setups 1083
selective catalytic reduction (SCR) 274, 825, 827
self-assembled monolayer (SAM) 263, 915
– of thiols 727
self-consistent field (SCF) 1124
self-diffusion coefficient 207, 312
self-diffusivity 874
self-supporting wafers 111
self-trapping excitons 166, 167
SESAM instrument 693
setups combining multiple *in situ* techniques, illustrations of 1089, 1090
– data recorded during ZnAPO-34 crystallization 1092
– De-NOx Over Pd/Al_2O_3 1101, 1102
– dynamic imaging studies 1107–1111
– key stages in methanol to olefin conversion 1100, 1101
– microporous materials, formation of 1090–1093
– online catalyst preparation 1093, 1094
– probing active Cu species, under methanol synthesis conditions 1094, 1095
– profiling reactor bed, with multiple techniques 1104, 1105
– propane dehydrogenation 1097–1099, 1103, 1104
– reactions at solid–liquid interface 1106, 1107
– to study oxidative dehydrogenation of propane V_2O_5/TiO_2 catalyst 1102, 1103
– three techniques simultaneously employed, in a batch reactor 1107
– three-way catalyst (TWC) components 1095–1097

Si/Al ratios 800
SID spectra
– of molecular $Si(C_2H_5)_4+$ ions impacting 916
– of pyrene molecular ion colliding with 914
signal-to-noise ratio 357, 358, 540, 622, 642, 1018
silica–alumina (SA) 814
– catalysts 748
silica mesopore, diffusion dynamics 597
silica-supported titania surfaces, highly dispersed 809
silver-based catalysts 824
silver nanoparticles 642
silver plasmon resonance 132
SimDist curves 986
SimDist principle 961
single- and multiple-layer graphene, ADF images of 681
single-crystal approach 644
single-crystal surface 465
– adsorption of of simple molecules 465–469
– adsorption of organic molecules 469–470
– surface defects 465–469
single-molecule adsorption 1122
single-molecule fluorescence polarization 589
single-molecule microscopy (SMM) 585, 591, 593
single-molecule spectroscopy (SMS) 585
– setups 588
single-particle tracking (SPT) 586
– membrane dynamics 586
– setups 588
single-photon counting avalanche photodiode (SPAPD) 587
– region of interest (ROI) 587
single-walled carbon nanotube (SWNT) 65
Si(111)-(7×7), AFM images of 736
Si(111)-7×7 surface, STM image of 704
size-exclusion chromatography (SEC) 960
Slater determinant 1126
slit-shaped micropores, schematic of 871
small-angle neutron scattering (SANS) 185, 194
small-angle scattering 647
small-angle X-ray scattering (SAXS) 194, 611, 644
– application in catalysis 647–648
– experimental aspects 646–647
– fundamentals 644–645
SMART project smectite 805
Sn atoms 735
^{119}Sn Mössbauer study, of bimetallic Tin-containing catalysts 446, 447
softer ionization techniques 887
soft landing (SL) approach 888
soft laser desorption (SLD) 887
sol–gel catalyst 487
sol–gel techniques 647
solid acids, acidity 128
solid catalysts 40
– transmission studies, IR cell for 14
solid–liquid interfaces, organic molecules 724
solid powders, surface properties 13
solid sample hopper 317
solids characterization
– accessibility of sites 27
– acetonitrile 30
– acidity characterization, with probe molecules 20–32
– acidity common probe molecules 24–32
– acid sites, probe molecules for 32
– pyridine–CO coadsorption 28, 29
– pyridines 24–26
– activation 13–17
– ammonia 30–32
– basicity characterization, with probe molecules 32–34
– Brønsted sites 21
– carbonates 16, 17
– carbon monoxide 27, 28
– CO_2 as probe 32, 33
– coupling IR spectroscopy with gravimetry, quantitative analysis by 38, 39
– Evans' windows 23, 24
– experimental aspects 13
– infrared cell for *in situ* studies 13, 14
– IR spectroscopy, use 11–39
– IR spectrum and structure of solid 11–13
– Lewis acidity molecular probes 24
– methanol 33, 34
– nitrates 17
– ν(OH) distortion 21–23
– ν(OH) shift quantification 21
– OH groups spectrum 17–20
–– on alumina 18
–– in zeolites 18–20
– protic molecules 33
– residual impurities 15–17
– substituted pyridines 26, 27
– sulfates 17
– sulfide catalysts probes 36–38
– supported metal catalysts probes 34–36
– zeolites example 11, 12, 14, 15
– zeolites structure, substitution of metals 13

solid-state NMR techniques 302
soluble methane monooxygenase (sMMO)
– biocatalysis 71
spark source (SS) ionization techniques 889
sp^2 carbon materials characterization 64–67
Spectralon® polymers 112
spent sulfated zirconia catalyst
– photographs 136
spin-density imaging 311
spin-echo double resonance (SEDOR) 300, 301
spin-echo pulse sequence 295
spin-echo time 200
spin-Hamiltonian 363, 366
spin incoherent scattering 199
spin–lattice interaction 349
spin–lattice relaxation 349, 350
spin orbitals 1125
spin–orbit splitting 548, 549, 552
spin-polarized scanning tunneling microscopy (SP-STM) 704
spin quantum number 189
spin relaxation 348–350
spin resonance 348–350
spin–spin relaxation 295, 349
spin transition 349
s/p-polarization
– light intensity 261
– phase shift 260
SPT thin mesoporous films, structural features of 594
steady-state isotopic transient kinetic analysis (SSITKA) 1038–1041
– active reaction intermediates, concentration of 1044, 1045
– kinetic parameter estimation 1041–1043
– mean surface residence time 1043, 1044
– mechanistic implications 1047–1049
– reactivity distribution 1046, 1047
– turnover frequency (TOF_{ITK}) 1045, 1046
steady-state reactor 198
steamed Y zeolite, spectrum 11
steric effect 446
Stern–Volmer equation 179
Stern–Volmer plots 180
STM. *See* scanning tunneling microscopy (STM)
STM probes tunneling electrons 705
stopped-flow experiments 316, 324
straight-run diesel sample, chromatograms of 984
strong metal support interaction (SMSI) 240
structural effects 474–477
structure–activity relationships, in Au nanoparticle catalysts 690
succinate species, IRAS spectra 268
succinic acid interaction 266
sulfate–carrier–vanadia interaction 822
sulfated Mn-promoted zirconia catalyst, XRD pattern of 627
sulfated zirconia catalyst 307
– HRTEM images of 637
sulfide catalysts, activation of 525–527
sulfur chemiluminescence detector (SCD) 963, 967
– chromatographic profile 968
sum frequency generation (SFG) 211–213
– case studies 221–244
–– bimetallic surfaces 228–233
–– metal nanoparticles on oxide surfaces 240–244
–– metal single-crystal surfaces 221–228
–– oxide surfaces 233–239
– characteristic 225
– schematic illustration 218
– setup illustration 220
– signal intensity 216, 217
– signal intensity and selection rules 215, 216
– spectra 275
– spectrometer setup 217–221
–– modes of operation 218–221
– surface concentration (coverage) 216, 217
– theoretical background 213–215
sum frequency generation vibrational spectroscopy 226
supercritical fluid chromatography (SFC) 960
– coupling mode 1000–1003
– 3D representations 1003
– representation of 1002
– SFC × twin GC × GC system 1000
superparamagnetism, and determination of particle sizes 440–442
supported boria catalysts 809
supported copper catalysts 825
supported metal oxides 808–810
– catalysts 59
supported metals 810, 811
supported vanadium oxides
– molecular configurations 306
surface-adsorbed formic acid, decomposition 238
surface area, characterization of 854
surface bandgap 157
surface chirality 267
surface diffusion probes 313
surface metal oxide species, on supported metal oxides, characterization 59–63

(110) surface of γ-Al_2O_3, stability diagram for 1139
surface phases, formed between Pd(111) and oxygen 577
surface plasmon resonance (SPR) 106, 121
surface reactivity, and catalysis
– monitoring 268–281
–– CO hydrogenation on Ru 270
–– CO on Ru oxidation 268–270
–– methanol decomposition on Pd 275
–– NH_3 oxidation and N_2O reduction by NH_3 on Cu 272–275
–– NO dissociation on Rh 275–277
–– NO reactivity/storage on metal and oxide surfaces 277–280
–– vinyl acetate synthesis reaction on Pd 270–272
surface relaxation effects 1122
surface science techniques
– AES 465, 466, 468, 562
– atomic force microscopy (AFM) 266
– IRAS 266
– ISS 465
– LEIS 465, 492
– SIMS 465, 466
– XPS 266
surface-sensitive Mössbauer spectroscopy 422, 423
surface sensitivity 226, 481, 485, 487, 492, 498, 502, 537, 539, 566
– homogeneous and inhomogeneous sampling region 553–556
– working with XPS intensities 553
– of XPS 557–560
surface species, identification of 438, 439
synchrotron radiation 622
– sources 1078
synthesis gels, time-resolved *in situ* Raman spectra 77

t

Tanabe–Sugano diagrams 103
tandem mass spectrometry 885, 910
TAP. *See* temporal analysis of products
TAP packed-bed microreactor configurations 1019
TAP pulse response experiments, key features 1023
– domain of conditions 1023
– model-free interpretation of kinetic data 1027, 1028
– relevance of kinetic information 1023, 1024
– structure–properties relationships 1024–1026
– theoretical models 1026, 1027
– uniformity of active zone 1023
TAP-2 reactor system 1014
TAP-3 reactor system 1016, 1018
– key features 1017
TAP reactor systems 1016
– bridging pressure gap 1028–1032
– catalytic properties, tracking evolution of 1032–1038
– goal of 1019–1022
– theoretical background 1019–1022
TAP-3 vacuum system 1018
targeted multiplex mass spectrometry imaging (TAMSIM) 907
temperature-programmed desorption (TPD) 240, 454, 455, 456, 777
– after NH_3 adsorption on 781
– apparatus 778, 779
– applications 781
– data processing 779–781
– principle 779
– TPD setup 779
temperature-programmed oxidation (TPO) 782
– applications 783, 784
– data processing 783
– principle 782, 783
temperature-programmed reaction (TPR) 456
temperature-programmed reduction 130, 782
– applications 783, 784
– data processing 783
– of K-containing chromia/alumina catalysts 784
– measured maximum temperatures and reduction extents 784
– principle 782, 783
temperature-programmed surface reaction (TPSR) 785
– applications 786, 787
– data processing 786
– principle 785
– types of methods 785
temporal analysis of products (TAP) 1014–1019
Tera-Hertz spectroscopy 45
tetrahydrofuran (THF) 24
tetrahydrothiophene (THT) cracking 41
– conversion 42
thermal analysis instruments 747
thermal analysis techniques 747
– and their application 748
thermal conductivity 819
thermal/cryogenic systems 976

thermal detectors
– deuterated triglycine sulfate (DTGS) 7
thermal effects 747
thermal measurement, short history of 747–749
thermal methods 747
thermal transformations 747
thermal treatments, of hydrotalcites 815
thermocouples 749
thermodynamic scale, of acidity and basicity 817, 818
thermogravimetric analysis 858
– 13X zeolite sample 859
thermogravimetric analysis (TGA) 38, 757
– applications 759–761
– data processing 758
– principle 758
– thermogravimetric analyzer 757, 758
thermogravimetric analysis, coupled with calorimetry 761, 762
– applications 763–765
– Calvet-type TGA–DSC 762
– principle 763
– TGA–DSC and TGA–DTA systems 761, 762
– TGA–plate-DSC 762
thermogravimetric analyzer 757
– asymmetric balance 758
– control of atmosphere 758
– crucibles 757, 758
– furnace 758
– magnetic suspension balance 758
– symmetric balance 758
thermogravimetry 757
thiols, self-assembled monolayer (SAM) 727
Th-modified Ni/SiO_2 catalysts, surface structure of 486
three-technique combinations, for studying both catalytic reactions and 1082
three-way catalyst (TWC) 685
threshold energy 105
Tian–Calvet microcalorimeter 766
Ti-MCM-48 catalyst
– photoluminescence spectra 177
Ti-MCM-41, UV resonance Raman spectra 68
time-of-flight (TOF) techniques 190, 191, 876
– classes 191
– SIMS 456
time resolution 110
time-resolved axial composition 331
time-resolved photoluminescence measurements
– sequence of data acquisition 155
time-resolved photoluminescence spectroscopy
– characterization of catalysts 156–165
time-resolved pump–probe SFG spectroscopy 219
tin–platinum catalysts 446
tin species in $PtSn/Al_2O_3$ catalysts 447
TiO_2 particles
– photoluminescence spectra 160
– surface band bending 159
TiO_2 photocatalysts 156
TiO_2-supported catalysts 836
Ti oxide-containing zeolite catalysts 175
Ti oxide photocatalysts 177
Ti oxide species, chemical parameters 176
titania (TiO_2)
– anatase phase 57
– phase transformation 58
– photoluminescence (PL) intensities 162
– surface band bending 162
– UV Raman spectra 58
– visible Raman spectra 58
titania catalysts 126
titania pure/nitrogen-doped, diffuse reflection-UV–vis spectra 126
titanium oxides, photocatalytic reactivities 178
titanium silicalite (TS-1)
– diffuse reflection-UV–vis spectra 124
– formation 123
Ti/Zr silica systems 647
TOF-MS detector 991
toluene alkylation 322
tomographic energydispersive diffraction imaging (TEDDI) 1108
total internal reflection (TIR) geometry 212, 220
– use of 587
total ion current (TIC) 991
– chromatogram 971
t plot, schematic representation of 870
transfer of population in double resonance (TRAPDOR) 301
transferred-echo double resonance (TEDOR) 301
transition dipole moment 259
– important consequences 259
transition metal 273
transition metal-containing microporous/mesoporous materials, characterization 67–72
– extra-framework active sites, identification 71, 72

– isolated quadrivalent transition metal sites, identification 67–69
– isolated trivalent transition metal sites, identification 69, 70
transition metal ions 55, 366
transition metal oxides 156, 177
transition metals 810
– catalytic activity 130
transition-state properties 885
transmission electron microscopy (TEM) 57, 456, 571, 626, 657
– basic techniques 660, 661
– common acronyms 659
– experimental considerations 669, 670
– illumination and image formation in 660
– illustration of nanoreactor device 692
– instrument consist of 659
– nanotubes and nanowires characterized by 671
– signal generated in electron beam–specimen interaction 658
– specimen preparation 669, 670
transmission experiment 8
transmission FTIR spectroscopy 233
transmission Mössbauer spectroscopy 421, 422
transmission UV–vis spectroscopy 120
transport diffusivity 874
TS-1
– discovery 67
– framework 68
tungsten/zirconia catalysts 814
12-tungstophosphoric acid 816
tunnel electrons 728
tunneling current, modulation of 704
turnover frequency (TOF) 574

u

Ulbricht/photometer spheres 112
ultrafast electron microscope 695
ultra-high resolution Fourier transform (FT) ICR instruments 889
ultra-high resolution mass spectrometry 888
ultra-high vacuum (UHV) 221, 263, 708
ultraviolet photoelectron spectroscopy (UPS) 231, 456, 537, 565, 566
ultraviolet (UV) Raman spectroscopy 51
uncharged atoms, forces acting 734
unsaturated hydrocarbons 161
UV laser light 56
UV Raman spectrometer, schematic diagram 53
UV Raman spectroscopies 49, 53
– illustration 52
– schematic illustration 57
UV RRS, advantages 62
UV–vis–NIR spectra 93–108
– absorption features intensity 93–98
– absorption features spectral position 93
– extended solid structures transitions 104–108
–– bandgaps 104–106
–– metallic colloids, localized surface plasmon resonance 106, 107
– molecular species transitions 99–104
–– composite species, metal complexes 101–104
–– individual molecules 99–101
–– selection rules 99
– quantitative analysis 107, 108
– representation 93–98
– spectra processing 98, 99
UV–vis–NIR spectroscopy
– absorption features in 93
– development 90
– review articles 92
UV–vis spectrometers 109
UV-vis spectroscopy
– applications 122
– fiber-optic 327
– measurements 329
– with X-band electron paramagnetic resonance (EPR) measurements 1080
–– study of propane dehydrogenation over 1080

v

vacancy (point) defects in graphite 671
vacuum gas oils (VGOs) 954
valence-band spectroscopy 540
vanadia–titania (VTiS) catalysts 820
vanadium 190
– catalysts 130
vanadium-containing materials 305, 306
vanadium-containing oxides 678
vanadium-doped aluminum oxides 305
vanadium oxide species 63, 164
van der Waals attraction 734, 855, 856
van derWaals collisions 290
van Hove correlation function 197
V-containing BEA zeolite catalysts, time-resolved photoluminescence spectra 163
Vegard's law 437, 632
vibrationally resonant susceptibility 215
vibrational spectroscopy 245
– benefits of 211
vinyl acetate synthesis 270–272
Voigt profiles 635

volume-selective spectroscopy method 296
volumetric/manometric method 857
$(VO)_2P_2O_7$ catalysts (VPO) 56, 305, 487, 1014
V_2O_5–WO_3 catalysts 486

w

Warren–Averbach method 638
water-gas shift (WGS) 822
– catalysis 1049
wavefunction 353, 1123
– Hartree approach 1124
wavefunction-based methods 1126
Wheatstone bridge 748
wide-angle X-ray scattering (WAXS) techniques 619, 644
Williamson–Hall analysis 640, 641
Wilson equation 640
Wulff constructions, of Cu nanoparticles 690

x

XAFS. *See* X-ray absorption spectroscopy (XAFS)
XAFS–XRD setup by adding a SAXS camera 1091
XANES. *See* X-ray absorption near-edge spectroscopy (XANES)
Xe isotopes 290
Xe nuclei
– nuclear spin polarization 290
– nuclear spin polarization of 290
Xe–Xe interactions 308
XPS binding energies 540
– parameters affecting 540–545
– practical aspects 547, 548
– theoretical prediction 545–547
XPS intensities 553
– determining, lineshapes, and signal backgrounds 560–562
– surface morphology, and XPS background 561
XPS lineshapes, analytical potential of 548
– charge transfer satellites 549–550
– multiplet splitting 551–553
– shake-up type satellites 550, 551
– spin–orbit splitting 548, 549
X-ray absorption fine structure (EXAFS) 512, 514
– limitation with 515
X-ray absorption near-edge spectroscopy (XANES) 169, 512, 513
– spectra 529, 530
X-ray absorption spectroscopy (XAFS) 131, 511, 512, 1078, 1120
– in conjunction with transmission infrared (IR) spectroscopy 1078
– coupled XAFS technique, major drawback 1092, 1093
– experimentation and data processing 515–521
– history of 511, 512
– line operating in traditional mode 516
– metal catalysts, application to 527–533
– oxide materials, application to 521–523
– principle of 512–515
– *In situ* cell developed at IFP energies nouvelles 518–521
– *in situ* cells developed by IRCELYON 518
– study of sulfide catalysts, applications to 524–527
– XAS line operating in energy-dispersive mode 517
– and X-ray diffraction (XRD) 1078
X-ray amorphous 626
X-ray beam, diffraction cones, production of 616
X-ray diffraction (XRD) 57, 227, 302, 456
– anisotropy, effects of 628, 629
– catalytic materials, phase identification of 625
– crystallography 614–616
– experimental aspects 619
–– practical aspects 622, 623
– fundamentals of 612–614
– international center for diffraction data, powder diffraction file (PDF) 623–626
– microstructural analysis of 640
– NaCl 616
– PDF cards report 626
– phase characterization, applications
–– crystalline domain size and shape 635–639
–– lattice strain 639–642
–– real structure 635
–– structure refinement 629–634
– phase identification, applications 623
– phase mixtures, quantification of 626–628
– powder 616–618
–– information content of 618, 619
– reactive atmosphere
–– of catalysts 642–644
– theoretical background of 612
X-ray fluorescence 538
– methods 957
X-ray-induced Auger electron spectroscopy (XAES) 538
– analysis of Ag(7 wt-%)/TiO_2 in different states 572

– structural sensitivity, via Auger parameter 562–565
X-ray photoelectron spectroscopy (XPS) 222, 255, 455, 537, 714, 1134
– analysis of Ag(7 wt-%)/TiO_2 in different states 572
– direct coupling with IR spectroscopy 567
– structural sensitivity, via Auger parameter 562–565
– *vs.* lateral resolution 569
X-ray scattering 187
– methods 611, 612
X-ray source 1078
XRD. *See* X-ray diffraction (XRD)
13X zeolite sample, thermogravimetric analysis 859

z
Zeeman effect 292, 293, 346
Zeeman interaction 292
Zeeman splitting 349
zeolite-based catalysts 67
zeolite H-mordenite, diffuse reflection-UV–vis spectra 138
zeolites 73, 304, 305, 799–805, 837
– acidity 800
– acid strength 801, 804
– adsorption of pyridine and aniline 802
– amine probes, use of 802
– calculated isosteric heats of adsorption 804
– calorimetric investigations of 800, 801
– differential heats of adsorption of aniline 803
– heats of adsorption 804
– influence of cation exchange 802
– interactions in cavities 804
– ion exchange in 124, 125
– MCM-41 mesoporous molecular sieve, investigation of 804, 805
– mesoporous molecular sieves, close to 804
– structure 799, 800
– supported Pt catalysts 43
– synthesis mechanism 73
zeolite solid-state ^{129}Xe NMR spectra 309
zeolite X synthesis process 77
– *in situ* UV Raman spectra 78
zeolitic materials 40
zero field splitting (ZFS) 363
zero filling 7
zero-gradient spectrum 296
zero length column (ZLC) method 876
– diffusivities 208
zero path difference (ZPD) 7
zirconia 131
ZnSe(110) substrate, $CuGaSe_2$ thin film, KFM measurement of 740
ZrO_2 polymorphism of 627
Zr/V intensity ratio in LEIS sputter series, with Zr–V–O oxide systems 575
ZrV_2O_7 surface, excitation-energy resolved X-ray photoelectron spectroscopy analysis 576
ZSM-5 crystal, optical microphotograph 128
ZSM-5 framework, evolution 74